

Collection of published papers 1995-2022

RICCARDO FANTONI

December 3, 2023

Preface

Short biography of the author: Born in Livorno on the 30 August 1970 lived in Pisa until 1995 where graduated with the highest grade (110/110 cum laude) from the department of Physics of the University under the supervision of Prof. Mario Pio Tosi. Then moved to the University of Illinois at Urbana/Champaign until 2000 and in 1997 got a Master in Physics under the supervision of Prof. David Ceperley. Moved to Trieste and in 2004 got a Ph.D. in Physics under the supervision of Prof. Giorgio Pastore. From 2005 to 2008 worked at the Chemical Physics department of the University of Venice as a postdoctoral fellow in the research group of Prof. Domenico Gazzillo and Prof. Achille Giacometti. From 2009 to 2011 worked at the National Institute for Theoretical Physics of the University of Stellenbosch as a postdoctoral fellow.

Description of the Collection: This book is a collection of the 75 research articles published by Dr. Riccardo Fantoni during the period 1995-2022. It covers various aspects of the statistical physics of classical (non-quantum) and quantum fluids. The application of the results is mainly in the fields of biophysics and condensed matter physics. Various fluid models are taken under exam like the Jellium fluid, the one and two component plasma, the hard sphere fluid, the non additive hard sphere mixture, the Widom-Rowlinson fluid, the sticky hard sphere fluid in his isotropic and patchy version, one component and multicomponent or even polydispersed versions, the Kern-Frenkel fluid, the Janus fluid, and various fluid and polymer mixtures. The results are mainly concerned with the vapor-liquid-solid phase transition, percolation transition, and clustering properties. The quantities being calculated are mainly the correlation functions for the structure with particular attention to the pair distribution function and the structure factor, and the thermodynamic properties, like the reconstruction of the phase diagram through the use of integral equations approximate techniques and (Path Integral) Monte Carlo experiments.

Aim of the research is to develop analytical and computational methods for condensed and soft matter starting from the fundamental many-body equations. Apart from the few analytically exactly solvable models our principal instruments, guided by the various sum-rules, are Integral Equation Theory, Density Functional Theory, Thermodynamic Perturbation Theory, Association Theory, and Monte Carlo simulations which can find exact properties of many-body systems. We are combining these approaches to create new methods and to test the accuracy of calculations on materials. Current studied materials include colloidal suspensions, ionic liquids, polymer mixtures, the electron fluid, the polaron, and boson fluids (like ^4He , $^4\text{He-H}_2$ mixtures, ...). We investigate the structure and thermodynamic properties of the materials including their phase transitions like the gas-liquid-(glass)-solid first order ones and the superfluid-superconducting second order ones, the percolation threshold, the clustering, the localization, the demixing, the polydispersity, and surface properties.

In the latest years we started working on relativistic quantum field theories through Path integral Monte Carlo of lattice field theory subject to different kinds of quantization procedures

The publications cover the following topics:

Non-Equilibrium Statistical Mechanics: From the Liouvillian dynamics to the Fokker-Planck equation. From the Fokker-Planck equation to the Smoluchowski equation. The Langevin equation. Monte Carlo solution of the Smoluchowski equation.

Statistical Mechanics: Sum rules in many body systems, many body models soluble exactly analytically, integral equation theories for fluids (Percus-Yevick, hypernetted chain, mean spherical approximation, rational function approximation, . . .), thermodynamic perturbation theories, Monte Carlo methods, stochastic processes.

Condensed and Soft Matter Physics: Coulomb liquids, the polaron, Bosons fluids, colloidal suspensions, polymers.

Quantum fluid models: The Jellium in one, two, and three spatial dimensions and the polaron problem. The Jellium on parallel planes and on a sphere. Square-well Bosons as a model of cold atoms. The ^4He in three and two dimensions. $^4\text{He-H}_2$ mixtures.

Classical fluid models: The one-dimensional nearest-neighbor fluids, the one- and two-component plasma living in one-, two-, and three-dimensions, the one- and two-component plasma living on curved surfaces, the hard-sphere fluid, the penetrable square-well fluid in one-, two-, and three-dimensions, the non-additive hard-sphere mixture, the Widom-Rowlinson model, the sticky-hard-sphere one- and two-component fluid, the restricted primitive model for charged hard spheres, patchy spheres fluids (the Janus fluid, etc . . .).

Quantum field theory: Path integral Monte Carlo of lattice field theory subject to different kinds of quantization procedures.

Numerical methods (NM) of interest: The solution of integral equation theories and the Monte Carlo methods to perform computer experiments.

NM for the solution of integral equation theories: The Newton Raphson algorithm (with conjugated gradient method) and the Picard algorithm.

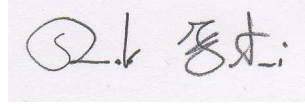
NM for Monte Carlo simulations: Ground state Monte Carlo simulations (variational and diffusion), path integral Monte Carlo simulations (conventional and worm algorithm), classical Monte Carlo simulations (NVT, NPT, grand canonical, Gibbs ensemble).

I would like to thank all my collaborators with whom it has been a pleasure to work in team: Prof. Mario Pio Tosi, Prof. Bernard Jancovici, Prof. Angel Alastuey, Prof. Gabriel Téllez, Prof. Giorgio Pastore, Prof. Domenico Gazzillo, Prof. Achille Giacometti, Dr. Peter Sollich, Dr. Mark Miller, Prof. Andrés Santos, Dr. Alexandr Malijevský, Dr. Miguel Angel Maestre, Prof. Francesco Sciortino, Prof. Kristian K. Müller-Nedebock, Prof. Bert Klumperman, Dr. Johannes W. O. Salari, Prof. Saverio Moroni, Prof. John R. Klauder.

This is the second edition of the Collection. The author took care of the editorial process preparing the book in \LaTeX .

Trieste, April 2023, Dr. Riccardo Fantoni

©Riccardo Fantoni

A handwritten signature in black ink on a light-colored background. The signature consists of a stylized 'R' followed by a vertical line and a dot, and the Chinese characters '李达' (Li Da) followed by a colon.

Contents

Preface	iii
I 1995	1
1 Decay of correlations and related sum rules in a layered classical plasma	3
2 Coordinate space form of interacting reference response function of d -dimensional jellium	17
II 1996	33
3 Some properties of short-range correlations for electrons in quantum wires	35
III 2003	43
4 Pressures for a One-Component Plasma on a Pseudosphere	45
5 Generating functionals, consistency, and uniqueness in the integral equation theory of liquids	77
6 Stability of the iterative solutions of integral equations as one phase freezing criterion	89
IV 2004	95
7 Direct correlation functions of the Widom-Rowlinson model	97
8 Computer simulation study of the closure relations in hard sphere fluids	109
V 2005	121
9 Stability boundaries, percolation threshold, and two phase coexistence for polydisperse fluids of adhesive colloidal particles	123
10 The thermodynamic instabilities of a binary mixture of sticky hard spheres	139

VI	2006	155
11	Multicomponent adhesive hard sphere models and short-ranged attractive interactions in colloidal or micellar solutions	157
12	Phase behavior of polydisperse sticky hard spheres	173
13	Phase behavior of weakly polydisperse sticky hard spheres	183
VII	2007	201
14	Patchy sticky hard spheres: analytical study and Monte Carlo simulations	203
VIII	2008	221
15	Fluids of spherical molecules with dipolarlike nonuniform adhesion	223
16	Penetrable Square-Well fluids: exact results in one dimension	245
17	Two dimensional one-component plasma on a Flamm's paraboloid	261
IX	2009	303
18	Penetrable-Square-Well fluids: Analytical study and Monte Carlo simulations	305
19	Local orientational ordering in fluids of spherical molecules with dipolarlike anisotropic adhesion	321
20	Thermodynamic consistency of energy and virial routes	329
X	2010	333
21	A Numerical Test of a High-Penetrability Approximation for the One-Dimensional Penetrable-Square-Well Model	335
22	Non existence of a phase transition for the Penetrable Square Well model in one dimension	351
XI	2011	367
23	Cluster theory of Janus particles	369
24	Phase diagram of the penetrable square well-model	379

25	Field theoretical approach to a dense polymer with an ideal binary mixture of clustering centers	385
26	The penetrable square-well model: extensive versus non-extensive phases	401
27	Nonadditive hard-sphere fluid mixtures. A simple analytical theory	417
XII	2012	435
28	A cluster theory for a Janus fluid	437
29	Two Component Plasma in a Flamm's Paraboloid	451
30	The structure of colloidosomes with tunable particle density: simulation vs experiment	467
31	Localization of acoustic polarons at low temperatures: A path integral Monte Carlo approach	479
32	The density of a fluid on a curved surface	485
XIII	2013	497
33	Low temperature acoustic polaron localization	499
34	Hellmann and Feynman theorem versus diffusion Monte Carlo experiment	507
35	The restricted primitive model of ionic fluids with nonadditive diameters	513
36	Janus fluid with fixed patch orientations: theory and simulations	521
37	Multicomponent fluid of nonadditive hard spheres near a wall	541
38	Monte Carlo simulation of the nonadditive restricted primitive model of ionic fluids: Phase diagram and clustering	551
39	Radial distribution function in a diffusion Monte Carlo simulation of a Fermion fluid between the ideal gas and the Jellium model	567
40	Phase diagrams of Janus fluids with up-down constrained orientations	587
XIV	2014	597
41	Depletion force in the infinite-dilution limit in a solvent of nonadditive hard spheres	599
42	Wertheim and Bjerrum-Tani-Henderson theories for associating fluids: a critical assessment	609

43 Gas-liquid coexistence for the bosons square-well fluid and the ^4He binodal anomaly	621
44 Quantum Gibbs ensemble Monte Carlo	627
XV 2015	635
45 Wertheim perturbation theory: thermodynamics and structure of patchy colloids	637
46 Bridging and depletion mechanisms in colloid-colloid effective interactions: A reentrant phase diagram?	653
47 Two phase coexistence for the hydrogen-helium mixture	669
XVI 2016	677
48 Supercooled superfluids in Monte Carlo simulations	679
49 Fourth moment sum rule for the charge correlations of a two-component classical plasma	685
50 The Square-Shoulder-Asakura-Oosawa model	713
51 Exact results for one dimensional fluids through functional integration	721
XVII 2017	743
52 One-dimensional fluids with positive potentials	745
53 The moment sum-rules for ionic liquids at criticality	755
54 Andersen-Weeks-Chandler perturbation theory and one-component sticky-hard-sphere	765
55 One-Dimensional Fluids with Second Nearest-Neighbor Interactions	781
56 White-dwarf equation of state and structure: the effect of temperature	813
XVIII 2018	831
57 Effect of quantum dispersion on the radial distribution function of a one-component sticky-hard-sphere fluid	833
58 Two component boson-fermion plasma at finite temperature	843
59 One-component fermion plasma on a sphere at finite temperature	855

60 From the Liouville to the Smoluchowski equation for a colloidal solute particle in a solvent	871
XIX 2019	883
61 Plasma living in a curved surface at some special temperature	885
XX 2021	931
62 Form invariance of the moment sum-rules for jellium with the addition of short-range terms in the pair-potential	933
63 How should we choose the boundary conditions in a simulation which could detect anyons in one and two dimensions?	941
64 Jellium at finite temperature using the restricted worm algorithm	959
65 Affine quantization of $(\varphi^4)_4$ succeeds while canonical quantization fails	971
66 Monte Carlo evaluation of the continuum limit of $(\phi^{12})_3$	977
67 Monte Carlo evaluation of the continuum limit of the two-point function of the Euclidean free real scalar field subject to affine quantization	989
68 Monte Carlo evaluation of the continuum limit of the two-point function of two Euclidean Higgs real scalar fields subject to affine quantization	1001
69 Finite-size effects and thermodynamic limit in one-dimensional Janus fluids	1011
70 Jellium at finite temperature	1037
XXI 2022	1053
71 Eliminating Nonrenormalizability Helps Prove Scaled Affine Quantization of φ_4^4 is Nontrivial	1055
72 Kinetic Factors in Affine Quantization and Their Role in Field Theory Monte Carlo	1063
73 Scaled Affine Quantization of φ_4^4 in the Low Temperature Limit	1075
74 Scaled Affine Quantization of Ultralocal φ_2^4 a comparative Path Integral Monte Carlo study with scaled Canonical Quantization	1081
75 Scaled Affine Quantization of φ_3^{12} is Nontrivial	1087

76 Glossary

1089



Part I
1995

Chapter 1

Decay of correlations and related sum rules in a layered classical plasma

Fantoni R. and Tosi M.P., Nuovo Cimento, **17D**, 155 (1995)

Title: “Decay of correlations and related sum rules in a layered classical plasma”

Abstract: The asymptotic behaviours of particle correlation functions and the related sum rules are discussed for a layered classical plasma with e^2/r interactions in the fluid state, in dependence on the number of layers. These properties derive from consistency conditions imposed by screening on the hierarchical equations, as already treated by A. Alastuey and Ph.A. Martin (J. Stat. Phys., **39**, 405 (1985)) for various Coulomb fluids. The main results concern i) the type of clustering of correlations needed for the validity of multipolar sum rules at various orders, ii) the proof that the pair correlation function in a finite multilayer may carry an electric dipole moment and the calculation of its partitioning among the layers, and iii) the dimensionality crossover in an infinitely extended or periodically repeated multilayer with varying interlayer spacing and wave vector.

Decay of Correlations and Related Sum Rules in a Layered Classical Plasma.

R. FANTONI and M. P. TOSI

Scuola Normale Superiore - Piazza dei Cavalieri 7, I-56126 Pisa, Italy

(ricevuto il 22 Novembre 1994; approvato il 30 Gennaio 1995)

Summary. — The asymptotic behaviours of particle correlation functions and the related sum rules are discussed for a layered classical plasma with e^2/r interactions in the fluid state, in dependence on the number of layers. These properties derive from consistency conditions imposed by screening on the hierarchical equations, as already treated by A. Alastuey and P. A. Martin (*J. Stat. Phys.*, **39**, 405 (1985)) for various Coulomb fluids. The main results concern i) the type of clustering of correlations needed for the validity of multipolar sum rules at various orders, ii) the proof that the pair correlation function in a finite multilayer may carry an electric dipole moment and the calculation of its partitioning among the layers, and iii) the dimensionality crossover in an infinitely extended or periodically repeated multilayer with varying interlayer spacing and wave vector.

PACS 61.20.Gy - Statistical theories of liquid structure.

1. - Introduction.

Systems of electrons with two-dimensional dynamics have long been useful as models for a variety of physical systems such as inversion layers in semiconductors and semiconductor heterostructures[1,2], surface electrons on liquid He[3], intercalated graphite[4] and transition-metal dichalcogenides[5]. The thermodynamic states of physical interest may range from extreme degeneracy to quasi-classical, and the electronic system may be confined to a single layer or form a multiplicity of layers up to a periodic stacking. While most of the theoretical treatments in the literature have taken account of intralayer correlations, specific attention has recently been brought to the role of the interlayer correlations in two-layer structures in relation to Wigner crystallization[6] and collective excitations[7].

Correlations in both homogeneous and inhomogeneous Coulomb fluids have a number of exactly determinable asymptotic properties, which may be conveniently expressed in the form of sum rules arising as consistency relations imposed by the long-range Coulomb interactions[8]. In particular, Alastuey and Martin[9] have shown that correlations in a two-dimensional classical plasma with e^2/r interactions have an algebraic r^{-3} decay as an exact lower bound. In the present work we extend

their treatment to a system consisting of an arbitrary number N_p of equispaced layers confining a classical one-component plasma with e^2/r interactions. In view of the known differences in the asymptotic behaviours of correlations in the classical and quantal three-dimensional plasma [10,11] we do not expect that our results should be generally applicable without further analysis to layered systems of electrons in the quantal regime.

2. – Equilibrium equations and multipolar sum rules.

The model consists of a stack of N_p layers with interlayer spacing d , each layer having area S and containing a classical fluid of N point-like charges embedded in a uniform neutralizing background. The normal to the stack is taken along the z -direction and the z -coordinate of each layer is denoted by md with m an integer. All vectors are decomposed into their in-plane and z components, with the notation $R = (r, z)$ and $K = (k, k_z)$. The medium has a uniform dielectric constant equal to unity, so that image forces are absent and the particles interact via the potential $e^2\phi(|R|) = e^2(r^2 + z^2)^{-1/2}$, with Fourier transform $\tilde{\phi}(k, z) = (2\pi/k)\exp[-k|z|]$.

The usual assumption is made that in the thermodynamic limit ($N \rightarrow \infty$ and $S \rightarrow \infty$ at fixed average density $\rho = N/S$) the instantaneous density correlation functions exist and continue to obey the equilibrium equations of the Born-Green-Yvon (BGY) hierarchy. Starting from the n -body density distribution functions,

$$(2.1) \quad \rho(R_1, \dots, R_n) = \langle [N(R_1) \dots N(R_n)]_{\text{SL}} \rangle,$$

where $N(R)$ is the particle density operator and the suffix SL indicates that the self-terms are omitted, we introduce [8] the density of excess particles at R when n particles are fixed at R_1, \dots, R_n as

$$(2.2) \quad \rho_e(R|R_1, \dots, R_n) = \rho(R, R_1, \dots, R_n) - \rho(R)\rho(R_1, \dots, R_n) + \sum_{i=1}^n \delta(R - R_i)\rho(R_1, \dots, R_n).$$

Furthermore, denoting by $Q = (R_2, \dots, R_n)$ the positions of a set of $(n-1)$ particles we define the truncated n -body and $(n+1)$ -body correlation functions by

$$(2.3) \quad \rho_T(R_1, Q) = \rho(R_1, Q) - \rho(R_1)\rho(Q)$$

and

$$(2.4) \quad \rho_T(R, R_1, Q) = \rho(R, R_1, Q) - \rho(R)\rho_T(R_1, Q) - \rho(R_1)\rho_T(R, Q) - \rho(Q)\rho(R, R_1).$$

The equilibrium equations of the BGY hierarchy can then be written as

$$(2.5) \quad (\beta e^2)^{-1} \nabla_{r_1} \rho_T(R_1, Q) = \rho(R_1) \mathbf{E}_{\parallel}(R_1|Q) + \sum_{i=2}^n \mathbf{F}_{\parallel}(R_1 - R_i) \rho_T(R_1, Q) + \sum_m \int d\mathbf{r}_m \mathbf{F}_{\parallel}(R_1 - R_m) \rho_T(R_m, R_1, Q),$$

where $\beta = (k_B T)^{-1}$ and R_m denotes the position of a particle in the m -th layer. In eq. (2.5) we have defined $\mathbf{F}_{\parallel}(R) = -\nabla_r \phi(|R|)$ and introduced the electric field $\mathbf{E}_{\parallel}(R_1|Q)$

generated at R_1 when $(n - 1)$ particles are at positions Q ,

$$(2.6) \quad \mathbf{E}_{\parallel}(R_1 | Q) = \sum_m \int d\mathbf{r}_m \mathbf{F}_{\parallel}(R_1 - R_m) \rho_e(R_m | Q).$$

The absolute convergence of the integral in eq. (2.6) and of the last integral on the right-hand side of eq. (2.5) requires that the correlations between a particle and any set of other particles should vanish as the particle is moved to infinite distance. The appropriate clustering condition is

$$(2.7) \quad |\rho(R_m, R_1, Q) - \rho(R_m)\rho(R_1, Q)| \leq M |r_m|^{-\eta}$$

with M finite and $\eta > 0$. We also note that

$$(2.8) \quad \int d\mathbf{r}_m \rho_e(R_m | R_1, \dots, R_n) = 0,$$

from the normalization condition relating the integral of the $(n + 1)$ -body distribution function to the n -body one. Both these properties will be taken to be valid to all orders in what follows.

Additional sum rules, relating to multipolar moments of correlations, can be shown to be valid [12, 13] if the decay of correlations is sufficiently rapid. Specifically, assume that the clustering conditions

$$(2.9) \quad |D^{\eta} \rho_T(R_1, \dots, R_n)| \leq M < \infty, \quad D = \sup_{i,j} (|R_i - R_j|)$$

hold for $n = 2, \dots, n_0 + 1$ and $\eta > 2 + l_0$ (for N_p finite) or $\eta > 3 + l_0$ (for $N_p \rightarrow \infty$). Then the (l, n) multipolar sum rules,

$$(2.10) \quad \sum_m \int d\mathbf{r}_m \rho_e(R_m | Q) \left[(R_m \cdot \nabla)^l \frac{R \cdot \hat{u}}{R^3} \right]_{R=\hat{u}} = 0,$$

where \hat{u} is a unit vector in the plane of the layers, hold for $0 \leq l \leq l_0$ and $1 \leq n \leq n_0$. Equation (2.8) ensures that the charge sum rules (eq. (2.10) for $l = 0$) are always valid. If $l_0 = 1$ the dipole sum rules

$$(2.11) \quad \sum_m \int d\mathbf{r}_m \mathbf{r}_m \rho_e(R_m | Q) = 0$$

also hold for the correlation functions up to the n_0 -body one.

Proposition (2.9), (2.10) follows from studying the asymptotic behaviour of the BGY equations for $R_1 = (\lambda \hat{u}, 0)$ with $\lambda \rightarrow \infty$. An integration over the area A of a circle $C(\lambda \hat{u}, r_0)$ centred in R_1 and of given radius r_0 is first carried out to handle the gradient terms, yielding in particular

$$(2.12) \quad \int_A d\mathbf{r}_1 \nabla_{r_1} \rho_T(R_1, Q) = \int_C d\mathbf{y} \rho_T(\lambda \hat{u} + \mathbf{y}, Q) = O(\lambda^{-\eta})$$

for the term on the left-hand side of eq. (2.5). It is easily seen that the second term on the right-hand side decays faster than $\lambda^{-\eta}$, while it shown in appendix A that the third term decays faster than $\lambda^{-(l_0+2)}$ irrespectively of the number of layers. Hence, the electric potential $\Phi(R_1 | Q)$ associated with the field $\mathbf{E}_{\parallel}(R_1 | Q)$

must also decay faster than $\lambda^{-(l_0+2)}$. Comparison with a multipolar expansion yields eq. (2.10) for all $l \leq l_0$.

We shall focus in the following sections on the two-body correlation function. It is therefore useful to show at this point the form taken by the above general formalism in this case. We have

$$(2.13) \quad \rho_T(R_m, R_{m'}) = \rho(R_m) \rho(R_{m'}) [g(R_m, R_{m'}) - 1]$$

and

$$(2.14) \quad \rho_e(R_m | R_{m'}) = \rho_T(R_m, R_{m'}) + \rho(R_m) \delta(R_m - R_{m'}),$$

the first particle being in the m -th layer and the second in the m' -th layer, and $g(R, R')$ being the usual pair distribution function. Equation (2.8) yields

$$(2.15) \quad \int d\mathbf{r}_m \rho_T(R_m, R_{m'}) = -\rho \delta_{m, m'},$$

which may be viewed as a set of charge sum rules holding layer by layer. Finally, the appropriate BGY equilibrium equation involves the three-body correlation function,

$$(2.16) \quad (\beta e^2)^{-1} \nabla_{\mathbf{r}_m} \rho_T(R_m, R_{m'}) = \rho(R_m) \mathbf{E}_{\parallel}(R_m | R_{m'}) + \mathbf{F}_{\parallel}(R_m - R_{m'}) \rho_T(R_m, R_{m'}) + \\ + \sum_{m''} \int d\mathbf{r}_{m''} \mathbf{F}_{\parallel}(R_m - R_{m''}) \rho_T(R_{m''}, R_m, R_{m'}).$$

The electric field \mathbf{E}_{\parallel} entering eq. (2.16) is to be determined from the Poisson equation. It should also be remarked that in the limit $N_p \rightarrow \infty$, according to the proof of proposition (2.9), (2.10) given above and in appendix A, an algebraic decay of two-body correlations implies a slower algebraic decay of the electric field. Therefore, an algebraic decay would not be compatible with eq. (2.16) if the three-body correlations were to decay more rapidly than the two-body ones.

For a homogeneous fluid confined to a single layer Alastuey and Martin[9] have shown that under appropriate clustering conditions on the two, three- and four-body correlation functions the structure factor $S(k)$ at long wavelengths is related to the interaction potential by

$$(2.17) \quad \lim_{k \rightarrow 0} S(k) = [\rho \beta e^2 \tilde{\phi}(k, 0)]^{-1} = k/k_D$$

with $k_D = 2\pi\rho\beta e^2$. However, such a behaviour of $S(k)$ implies that the asymptotic form of the pair correlations contains a term behaving like r^{-3} , which contradicts the assumed validity of the clustering conditions. While the charge sum rule suffices to ensure that $S(k)$ vanishes for $k \rightarrow 0$, a dipole moment arising from the three-body correlation function must supplement the k_D^{-1} term in determining the value of $S(k)/k$ for $k \rightarrow 0$.

Taking $S(k)/k$ as a finite constant for $k \rightarrow 0$ and bearing in mind the possibility of other singularities arising at finite k , the conclusion is that the pair correlations cannot decay asymptotically faster than r^{-3} . According to the BGY equation for the pair correlation function, the excess potential $\Phi(r, z)$ associated with the field $\mathbf{E}(r, z)$

then cannot decay faster than r^{-3} for $z = 0$. In fact, from the Poisson equation

$$(2.18) \quad \frac{1}{r} \frac{\partial}{\partial r} [r E_{\parallel}(\mathbf{r}, z)] + \frac{\partial}{\partial z} E_z(\mathbf{r}, z) = 4\pi \delta(z) \rho_e(r|0)$$

and assuming only the charge sum rule, the first two terms of a multipolar expansion for $\Phi(r, z)$ have the form $P_l(|\cos \theta|)/|R|^{(l+1)}$ where $l = 1$ or 2 , $\cos \theta = z/|R|$ and $P_l(x)$ are the Legendre polynomials. Using $P_1(0) = 0$ and $P_1(1) = 1$ one sees that $\Phi(r, 0)$ decays like r^{-3} and $\Phi(0, z)$ decays like $|z|^{-2}$. These behaviours were derived in early work by Fetter [14] within a hydrodynamic approach, which reduces in the static case to the Debye-Hückel approximation and thus assumes that the relation in eq. (2.17) is valid. The magnitude of the dipole moment associated with the pair correlation function is given in this approximation by the Debye screening length $1/k_D$.

The important point to be stressed is that for a monolayer, at variance from the case of the three-dimensional classical plasma, an algebraic decay of correlations and an algebraic decay of the potential are mutually consistent. We carry out below the same analysis for a multilayered system.

3. - Asymptotic behaviour of correlations in a multilayered plasma: the case of finite N_p .

We have seen in sect. 2 that the type of clustering which ensures the validity of multipolar sum rules up to order (l_0, n_0) is independent of the number N_p of layers provided that N_p is finite. We examine in this section the asymptotic behaviour of the pair correlations in this case. The limit $N_p \rightarrow \infty$ will be discussed in the next section.

As a first step we rewrite the BGY eq. (2.16) as

$$(3.1) \quad (\beta e^2)^{-1} \nabla_r \rho_T(R_m, 0) = \rho E_{\parallel}(R_m | 0) + W_m(\mathbf{r}),$$

where one of the particles has been taken at the origin and we have defined

$$(3.2) \quad W_m(\mathbf{r}) = \sum_{m'} \int d\mathbf{r}' F_{\parallel}(R_{m'}) H(R_m, R_{m'})$$

with

$$(3.3) \quad H(R_m, R_{m'}) = \rho_T(R_m, R_{m'}, 0) + \delta(\mathbf{r} - \mathbf{r}') \delta_{mm'} \rho_T(R_m, 0).$$

Use has been made of the symmetry properties of the three-body correlation function.

We introduce the structure factor $S(K)$ as

$$(3.4) \quad S(K) = \sum_m S_m(k) \exp[-ik_z md],$$

where

$$(3.5) \quad S_m(k) = \delta_{m0} + \rho^{-1} \int d\mathbf{r} \exp[-i\mathbf{k} \cdot \mathbf{r}] \rho_T(R_m, 0)$$

are the partial structure factors describing intralayer ($m = 0$) and interlayer ($m \neq 0$) correlations. Using eq. (2.6) for the excess electric field, the Fourier transform of

160

R. FANTONI and M. P. TOSI

eq. (3.1) then is

$$(3.6) \quad S_m(k) - \delta_{m0} = -(k_D/k) \sum_{m'} \exp[-|m - m'|kd] S_{m'}(k) + k_D \Delta_m(k),$$

where

$$(3.7) \quad \Delta_m(k) = -i(2\pi\phi^2 k^2)^{-1} \sum_m \int d\mathbf{r} \exp[-i\mathbf{k} \cdot \mathbf{r}] \int d\mathbf{r}' \mathbf{k} \cdot \mathbf{F}_{\parallel}(R'_m) H(R_m, R'_m).$$

Hence,

$$(3.8) \quad S_m(k)/k = \sum_{m'} A_{mm'}^{-1}(k) \left[\frac{\delta_{m'0}}{k_D} + \Delta_{m'}(k) \right],$$

where $A_{mm'}^{-1}(k)$ is the inverse of a matrix $A_{mm'}(k)$ which is defined by

$$(3.9) \quad A_{mm'}(k) = (k/k_D) \delta_{mm'} + \exp[-|m - m'|kd].$$

The charge sum rule (2.15) yields

$$(3.10) \quad \lim_{k \rightarrow 0} S_m(k) = 0$$

for all values of m . Using it in eq. (3.6) we find

$$(3.11) \quad \lim_{k \rightarrow 0} \sum_{m'} \frac{S_{m'}(k)}{k} = \frac{\delta_{m0}}{k_D} + \lim_{k \rightarrow 0} \Delta_m(k).$$

Clearly, the quantity on the right-hand side of this equation must be independent of the index m . We denote it thereafter by the symbol Λ . Namely,

$$(3.12) \quad \Lambda \equiv \lim_{k \rightarrow 0} \sum_m \frac{S_m(k)}{k} = \frac{1}{k_D} + \lim_{k \rightarrow 0} \Delta_0(k) = \lim_{k \rightarrow 0} \Delta_{m \neq 0}(k).$$

It is evident from eqs. (3.12) and (3.5) that Λ gives the length of the electric dipole moment associated with the total pair correlation function $\sum_m \rho_e(R_m | 0)/\rho$. Equation (3.12) implies very strong correlations: we can obtain the dipole moment of the whole stack from a three-body correlation function involving a particle in *anyone* of the layers and the particle at the origin, provided that we add the quantity k_D^{-1} when the first particle lies in the same layer as the particle at the origin.

We can now examine the solution of eq. (3.6) in the long-wavelength limit. Using eq. (3.12) in eq. (3.8) we have

$$(3.13) \quad \lim_{k \rightarrow 0} \frac{S_m(k)}{k} = \alpha_m \Lambda,$$

where the coefficients α_m are given by

$$(3.14) \quad \alpha_m = \lim_{k \rightarrow 0} \sum_{m'} A_{mm'}^{-1}(k)$$

and satisfy the sum rule $\sum_m \alpha_m = 1$. For instance, for a bilayer $\alpha_m = 1/2$, while for a

trilayer we find

$$(3.15) \quad \alpha_1 = \alpha_{-1} = \frac{1 + 3 dk_D + 2(dk_D)^2}{3 + 8 dk_D + 4(dk_D)^2}$$

and

$$(3.16) \quad \alpha_0 = \frac{1 + 2 dk_D}{3 + 8 dk_D + 4(dk_D)^2}.$$

We see that the partitioning of the total dipole moment Λ among the various layers is exactly known from eq. (3.13) and (3.14). The coefficients α_m are functions of dk_D which depend only on the number of layers.

The values taken by the quantities $\Delta_m(k)$ at long wavelengths remain to be discussed. It is evident from eq. (3.12) that they cannot be all equal to zero. A more formal argument, relating the behaviour of $\sum_m \Delta_m(k \rightarrow 0)$ to the clustering of correlation functions, is given in appendix B. The result is that, if $\Lambda \neq 0$, the intralayer and interlayer pair correlation functions cannot decay asymptotically faster than r^{-3} .

The discussion given in appendix B does not exclude the possibility $\Lambda = 0$. This would imply $\Delta_m(k \rightarrow 0) = 0$ for all $m \neq 0$ and $\Delta_0(k \rightarrow 0) = -k_D^{-1}$. Evidently, the linear term in the low- k expansion of the intralayer and interlayer structure factors would then be absent and the leading term would presumably have a regular k^2 behaviour, completely invalidating a Debye-Hückel approximation. As is shown in appendix B, in such a case a slow asymptotic decay would still be present in the three-body and/or four-body correlation functions.

4. - Asymptotic behaviour of correlations in the limit $N_p \rightarrow \infty$.

We return to eqs. (3.6) and (3.7), in which we have to take the limit $N_p \rightarrow \infty$ in the sums over the layer index m' . We first take Fourier transforms with respect to the z -coordinate, by multiplying both sides of eq. (3.6) by $\exp[-ik_z md]$ and summing over the layer index m . In the limit $N_p \rightarrow \infty$ we find

$$(4.1) \quad S(K) - 1 = -(k_D/k) \sum_{m=-\infty}^{\infty} \Gamma_m(K) S_m(K) + k_D \Delta(K),$$

where

$$(4.2) \quad \Gamma_m(K) = \exp[-ik_z md] \sum_{m'=-\infty}^{\infty} \exp[-ik_z m' d - k|m'|d] = \\ = \exp[-ik_z md] \frac{\sinh(kd)}{\cosh(kd) - \cos(k_z d)}$$

and

$$(4.3) \quad \Delta(K) = -i(2\pi\rho^2 k^2)^{-1} \sum_{m'=-\infty}^{\infty} \int d\mathbf{r}' \mathbf{k} \cdot \mathbf{F}_{\parallel}(R_{m'}) \cdot \\ \cdot \sum_{m=-\infty}^{\infty} \exp[-ik_z md] \int d\mathbf{r} \exp[-i\mathbf{k} \cdot \mathbf{r}] H(R_m, R_{m'}).$$

We have assumed that the two integrals in eq. (3.7) can be interchanged (see

appendix B). The sum over m in eq. (4.1) can now be carried out, with the result

$$(4.4) \quad S(K) - 1 = -\rho\beta v(K) S(K) + k_D \Delta(K),$$

where [15]

$$(4.5) \quad v(K) = \frac{2\pi e^2}{k} \frac{\sinh(kd)}{\cosh(kd) - \cos(k_z d)}.$$

We may remark that the same result (4.4) is obtained when, instead of taking the limit $N_p \rightarrow \infty$, one imposes periodic boundary conditions along the z -direction on a stack of N_p layers. In this case $S(K)$ and $\Delta(K)$ are the sums of $S_m(\mathbf{k}, k_z)$ and of $\Delta_m(\mathbf{k}, k_z)$ over the layers included in the Born-von Karman periodicity cell.

The effective potential $v(K)$ in eq. (4.5) shows dimensional crossover with varying d , tending to $2\pi e^2/k$ in the limit $d \rightarrow \infty$ (an infinite stack of independent monolayers) and to $4\pi e^2/(K^2 d)$ in the limit $d \rightarrow 0$ (a three-dimensional plasma with mean particle density ρ/d and two-dimensional dynamics). In the latter limit the Poisson equation becomes a local differential equation and one can apply the argument developed by Martin [8] to analyse the clustering of correlations in a fully three-dimensional plasma. In brief, if one assumes an algebraic decay of the total charge density, the Poisson equation yields a slower algebraic decay of the total electric field. This result is not compatible with the asymptotic behaviour of the BGY equation for the pair correlation function, leading to the conclusion that correlations must asymptotically decay more rapidly than any finite inverse power of the distance.

Expression (4.5) for $v(K)$ yields $v(K) \rightarrow 4\pi e^2/(k^2 d)$ in the limit $k \rightarrow 0$ at $k_z = 0$, for any finite value of the layer spacing d . Equation (4.4) yields

$$(4.6) \quad \lim_{k \rightarrow 0} \frac{2}{d} \frac{S(k, 0)}{k^2} = \frac{1}{k_D} + \lim_{k \rightarrow 0} \Delta(k, 0).$$

This relation should be contrasted with the analogous relation which can easily be obtained for the case of a finite number of layers from the results in sect. 3,

$$(4.7) \quad \lim_{k \rightarrow 0} N_p \frac{S(k, 0)}{k} = \frac{1}{k_D} + \lim_{k \rightarrow 0} \Delta(k, 0).$$

The charge sum rules suffice to ensure that the last term on the right-hand side of eq. (4.6) is at most a finite constant, so that $S(k, 0)$ is proportional to k^2 in the limit $kd \ll 1$. Such an analytic behaviour of $S(k, 0)$ at the origin precludes the possibility of drawing conclusions on the existence of algebraic terms in the asymptotic behaviour of the pair correlations. If in addition the dipole sum rule holds for the three-body correlation function $\sum_m H(R_m, R'_m)$ in eq. (4.3), then $\Delta(k \rightarrow 0, 0)$ vanishes and the further sum rule

$$(4.8) \quad \lim_{k \rightarrow 0} \frac{S(k, 0)}{k^2} = L_D^2$$

holds. Here,

$$(4.9) \quad L_D = (4\pi\rho\beta e^2/d)^{-1/2}$$

is the three-dimensional Debye screening length. Equation (4.8), which may also be written as the integral relation

$$(4.10) \quad \sum_{m=-\infty}^{\infty} \rho \int d\mathbf{r} r^2 [g(r, md) - 1] = -4L_D^2$$

on the total pair correlation function, is the form presently taken by the Stillinger-Lovett sum rule [16, 17]. It ensures that the plasma is capable of screening completely any static distribution of external charges having spatial dependence of the form $\rho_{\text{ext}}(\mathbf{r})$.

The partial structure factors $S_m(k)$ are related to the total structure factor $S(K)$ by

$$(4.11) \quad S_m(k) = \frac{2\pi}{d} \int_{-\pi/d}^{\pi/d} dk_z \exp[ik_z md] S(K),$$

thus requiring full knowledge of the k_z dependence of $S(K)$ even in the limit $k \rightarrow 0$. The multipolar sum rules provide no information on the behaviour of $\Delta(0, k_z)$. On the assumption that $\Delta(K)$ can be neglected, Fetter [15] has solved eqs. (4.4) and (4.11) in conjunction with the Poisson equation. Within this approximation he has shown that the partial pair correlation function $\rho_T(r, z)$ decays exponentially both as a function of r at fixed z and as a function of z at fixed r , such a decay being anisotropic except in the limit $dk_D \ll 1$.

4.1. Dynamical implications. – We next wish to point out how the foregoing discussion may be related to the dynamics of the classical layered plasma at long wavelengths. The effective potential $v(K)$ determines a characteristic frequency $\omega_0(K)$ given by

$$(4.12) \quad \omega_0^2(K) = \frac{\rho k^2}{M} v(K),$$

where M is the mass of the particles. In the limit $k \rightarrow 0$ the dispersion relation (4.12) describes an optic mode at $k_z = 0$ and an acoustic one at $k_z \neq 0$. The hydrodynamic treatment given by Fetter [15] leads to a collective mode with a dispersion relation given by (4.12) supplemented by a k^2 term with a coefficient determined by the adiabatic free-gas speed of sound. Olego *et al.* [18] have found that the dispersion relation (4.12) is in good agreement with the results of their inelastic light scattering experiments from GaAs-(AlGa)As heterostructures.

A simple connection between structure and dynamics can be made on the assumption that the f -sum rule on the dynamic structure factor $S(K; \omega)$,

$$(4.13) \quad \int_{-\infty}^{\infty} \frac{d\omega}{2\pi} \omega^2 S(K; \omega) = \frac{k^2}{\beta M},$$

is exhausted by a single collective mode. Since $S(K)$ is the integral of $S(K; \omega)$ over frequency, this would lead one to express $S(K)$ in terms of the collective-mode

frequency as

$$(4.14) \quad S(K) = \frac{k^2}{M\beta\omega_0^2(K)}.$$

Comparison of eq. (4.14) with eq. (4.4) shows that such a single-mode representation of the spectrum is allowed in the limit $k \rightarrow 0$ only if $k_z = 0$, where $\Delta(k \rightarrow 0, 0)$ vanishes. In fact, the work of Totsuji[19] on the dynamics of a classical two-dimensional plasma shows that excitational electron-electron collisions give a relevant spectral contribution at long wavelengths (a Landau-type contribution associated with single-particle excitations is exponentially small in this limit). The collisional damping of the collective mode as calculated by Totsuji is linear in k for $k \rightarrow 0$, *i.e.* of the same order as the frequency of the acoustic mode. It thus appears that a single-mode representation of the spectrum at $k_z \neq 0$ is invalid for a layered classical plasma.

5. – Summary and concluding remarks.

In this work we have applied to a layered classical plasma methods of analysis previously developed to examine the asymptotic behaviours of the correlation functions in Coulomb fluids and the sum rules that are consistent with these behaviours. Our main results concern the conditions for the validity of multipolar sum rules, the dipolar structure of a finite multilayer and the dimensionality crossover in an infinitely extended (or periodically repeated) multilayer with varying interlayer spacing and wave vector.

The theoretical possibility of crystalline order is notoriously related to poor clustering of particle correlations and has drawn considerable attention for Coulomb systems in low dimensionalities. In particular, from an analysis of the BGY hierarchy for a monolayer Gruber and Martin[20] have shown that the pair or three-body correlation functions should decay asymptotically more rapidly than r^{-3} in order to exclude crystallinity. Their analysis is easily extended to a finite multilayer, leading to the same conclusion. However, Requardt and Wagner[21] have recently been able to obtain more stringent conditions through the use of the Mermin inequality for a variety of Coulomb systems including the monolayer with r^{-1} interactions.

* * *

Sponsorship and support by the Istituto Nazionale di Fisica della Materia is gratefully acknowledged.

APPENDIX A

Asymptotic behaviour of the $(n + 1)$ -body term in the BGY equations for layered plasmas.

We prove in this appendix that the $(n + 1)$ -body term in eq. (2.5), under the clustering condition (2.9), decays faster than $\lambda^{-(l_0 + 2)}$ when $R_1 = (\lambda\tilde{u}, 0)$ with $\lambda \rightarrow \infty$, irrespectively of the number N_p of layers. Since the group of particles at Q is kept

fixed in taking the limit, it is sufficient to examine the behaviour of the three-body term.

In the indicated limit we can write the following inequality:

$$\left| \sum_m \int d\mathbf{r}_m F_{\parallel}(R_m) \rho_T(\lambda \hat{u}, R_m, 0) \right| \leq \sum_{m \neq 0} \int d\mathbf{r}_m \frac{r_m}{|R_m|^3} \frac{M}{[\sup(\lambda, |R_m|)]^\eta} + \int d\mathbf{r}_m r_m^{-2} |\rho_T(\lambda \hat{u}, \mathbf{r}_m, 0)|,$$

where, from the results of Gruber *et al.* [12], the second term on the right-hand side decays like $\lambda^{-\eta}$. Hence,

$$(A.1) \quad \left| \sum_m \int d\mathbf{r}_m F_{\parallel}(R_m) \rho_T(\lambda \hat{u}, R_m, 0) \right| \leq \sum_{\substack{m \neq 0 \\ r \geq |m|d}} \int d\mathbf{r} r^{-2} \frac{M}{[\sup(\lambda, r)]^\eta} + O(\lambda^{-\eta}).$$

In the case where N_p is finite, it is evident that the first term on the right-hand side of eq. (A.1) also decays like $\lambda^{-\eta}$, *i.e.* faster than $\lambda^{-(l_0+2)}$ if $\eta > l_0 + 2$.

In the case $N_p \rightarrow \infty$, on the other hand, the above term can be rewritten as

$$2 \sum_{m=1}^{\infty} \int_{r \geq md} d\mathbf{r} r^{-2} \frac{M}{[\sup(\lambda, r)]^\eta} = 4\pi \left\{ \sum_{m=1}^{[\lambda/d]} \left[\lambda^{-\eta} \int_{md}^{\lambda} r^{-1} dr + \int_{\lambda}^{\infty} r^{-(1+\eta)} dr \right] + \sum_{m=[\lambda/d]+1}^{\infty} \int_{md}^{\infty} r^{-(1+\eta)} dr \right\}.$$

For $\lambda \rightarrow \infty$ we have

$$\sum_m f(md/\lambda) = \frac{\lambda}{d} \sum_n f(n) \Delta n \rightarrow \frac{\lambda}{d} \int f(x) dx$$

with $n = md/\lambda$ and $\Delta n = d/\lambda \rightarrow 0$, if $f(x)$ does not change appreciably with x in the range Δn . Hence, in the case $N_p \rightarrow \infty$ the $(n+1)$ -body term decays faster than $\lambda^{-(l_0+2)}$ if $\eta > l_0 + 3$.

APPENDIX B

Clustering of correlations and behaviour of $\Delta_m(k)$ at long wavelengths.

Starting from the definition of $\Delta_m(k)$ in eq. (3.7), we first prove that $\sum_m \Delta_m(k \rightarrow 0) = 0$ if i) the clustering condition (2.9) holds for $\eta > 3$ and $n = 2, 3$ and 4; and ii) for sufficiently large $|x|$ we have $|x|^\eta \int dy \rho_T(xy0) \leq M < \infty$, x and y being any two position coordinates in the layers.

Following the line of argument given by Alastuey and Martin [9] for a similar proposition regarding a monolayer, we use the condition ii) above to interchange the

order of the two integrals in eq. (3.7). We can then write

$$(B.1) \quad \Delta_m(k) = -i(2\pi\rho^2k^2)^{-1} \sum_{m'} \int d\mathbf{r}' \mathbf{k} \cdot \mathbf{F}_{\parallel}(\mathbf{R}'_{m'}) \int d\mathbf{r} \exp[-i\mathbf{k} \cdot \mathbf{r}] H'(\mathbf{R}_m, \mathbf{R}'_{m'}),$$

where

$$(B.2) \quad H'(\mathbf{R}_m, \mathbf{R}'_{m'}) = H(\mathbf{R}_m, \mathbf{R}'_{m'}) + \delta_{m0} \delta(\mathbf{r}) \rho_{\text{T}}(\mathbf{R}'_{m'}, 0) = \\ = \rho_e(\mathbf{R}_m | \mathbf{R}'_{m'}, 0) - \rho \rho_e(\mathbf{R}_m | \mathbf{R}'_{m'}) - \rho \rho_e(\mathbf{R}_m | 0).$$

The difference between H' and H in eq. (B.2) does not contribute to the integral in eq. (B.1) and has been included so that we may make use of the multipolar sum rules given in eq. (2.10). After expanding the factor $\exp[-i\mathbf{k} \cdot \mathbf{r}]$ in eq. (B.1) and using the charge sum rules, we find

$$(B.3) \quad \sum_m \Delta_m(k \rightarrow 0) = -i(2\pi\rho^2)^{-1} \sum_{m'} \int d\mathbf{r}' \hat{\mathbf{k}} \cdot \mathbf{F}_{\parallel}(\mathbf{R}'_{m'}) \sum_m \int d\mathbf{r} \hat{\mathbf{k}} \cdot \mathbf{r} H'(\mathbf{R}_m, \mathbf{R}'_{m'}) + o(1).$$

However, under the condition i) the dipolar sum rule holds for both two-body and three-body correlation functions, so that the first term on the right-hand side of eq. (B.3) vanishes.

By summing eq. (3.11) over all layers we then find that

$$(B.4) \quad \Lambda \equiv \lim_{k \rightarrow 0} \frac{\sum_m S_m(k)}{k} = (N_p k_D)^{-1} + o(1)$$

under the same conditions i) and ii) stated above. It would be natural to assume this result in a Debye-Hückel treatment, its implication being that the dipole moment as read from the large- z behaviour of the electric potential created by a stack of N_p layers is that of a monolayer with particle density $N_p \rho$. However, it follows from eq. (B.4) that the asymptotic form of the total pair correlation function $\sum_m \rho_{\text{T}}(\mathbf{R}_m, 0)$ would contain a term behaving like r^{-3} . We have thus reached a contradiction: the clustering condition i) must hold for the validity of eq. (B.4), but eq. (B.4) refutes the validity of condition i).

We therefore conclude that

$$(B.5) \quad \lim_{k \rightarrow 0} \sum_m \Delta_m(k) = O(1)$$

and that the clustering cannot be faster than r^{-3} for at least one among the two-, three- and four-body correlation functions. It would seem reasonable to expect that the higher-body correlations should not decay more slowly than the two-body ones, leading to the conclusion that the asymptotic decay of the total pair correlation function should not be faster than r^{-3} . In such a case, $\Lambda \neq 0$ and the discussion given in the main text shows that each one of the partial pair correlations cannot decay faster than r^{-3} . However, it seems to us that the possibility $\Lambda = 0$, implying slow decay of correlations at higher order, cannot be excluded.

REFERENCES

- [1] STERN F., *Phys. Rev. Lett.*, **18** (1967) 546; **30** (1973) 278.
 - [2] See, for instance, BUTCHER P., MARCH N. H. and TOSI M. P. (Editors), *Physics of Low-Dimensional Semiconductor Structures* (Plenum, New York, N.Y.) 1993.
 - [3] BROWN T. R. and GRIMES C. C., *Phys. Rev. Lett.*, **29** (1972) 1233.
 - [4] VISSCHER P. B. and FALICOV L. M., *Phys. Rev. B*, **3** (1971) 2541.
 - [5] GAMBLE F. R., DISALVO F. L., KLEMM R. A. and GEBALLE T. H., *Science*, **168** (1970) 568.
 - [6] SWIERKOWSKI L., NEILSON D. and SZYMANSKI J., *Phys. Rev. Lett.*, **67** (1991) 241.
 - [7] NEILSON D., SWIERKOWSKI L., SZYMANSKI J. and LIU L., *Phys. Rev. Lett.*, **71** (1993) 4035.
 - [8] MARTIN P. A., *Rev. Mod. Phys.*, **60** (1988) 1075.
 - [9] ALASTUEY A. and MARTIN P. A., *J. Stat. Phys.*, **39** (1985) 405.
 - [10] ALASTUEY A. and MARTIN P. A., *Europhys. Lett.*, **6** (1988) 385.
 - [11] CORNU F. and MARTIN P. A., *Phys. Rev. A*, **44** (1991) 4893.
 - [12] GRUBER C., LEBOWITZ J. L. and MARTIN P. A., *J. Chem. Phys.*, **75** (1981) 944.
 - [13] BLUM L., GRUBER C., LEBOWITZ J. L. and MARTIN P. A., *Phys. Rev. Lett.*, **48** (1982) 1769.
 - [14] FETTER A. L., *Ann. Phys. (N.Y.)*, **88** (1974) 1.
 - [15] FETTER A. L., *Ann. Phys. (N.Y.)*, **81** (1973) 367.
 - [16] STILLINGER F. H. and LOVETT R., *J. Chem. Phys.*, **48** (1968) 385; **49** (1968) 1991.
 - [17] CARNIE S. L. and CHAN D. Y. C., *Chem. Phys. Lett.*, **77** (1981) 437; CARNIE S. L., *J. Chem. Phys.*, **78** (1983) 2742.
 - [18] OLEGO D., PINCZUK A., GOSSARD A. C. and WIEGMANN W., *Phys. Rev. B*, **25** (1982) 7867.
 - [19] TOTSUJI H., *J. Phys. Soc. Jpn.*, **40** (1976) 857.
 - [20] GRUBER C. and MARTIN P. A., *Ann. Phys. (N.Y.)*, **131** (1981) 56.
 - [21] REQUARDT M. and WAGNER H. J., *J. Stat. Phys.*, **58** (1990) 1165.
-

Chapter 2

Coordinate space form of interacting reference response function of d -dimensional jellium

Fantoni R. and Tosi M.P., Nuovo Cimento, **17D**, 1165 (1995)

Title: “Coordinate space form of interacting reference response function of d -dimensional jellium.”

Abstract: The interacting reference response function $\chi_I^3(k)$ of three-dimensional jellium in k space was defined by Niklasson (1974) in terms of the momentum distribution of the interacting electron assembly. Here the Fourier transform $F_I^d(r)$ of $\chi_I^d(k)$ is studied for the jellium model with e^2/r interactions in dimensionality $d = 1, 2$ and 3 , in an extension of recent work by Holas, March and Tosi for the case $d = 3$. The small- r and large- r forms of $F_I^d(r)$ are explicitly evaluated from the analytic behaviour of the momentum distribution $n_d(p)$. In the appendix, a model of $n_d(p)$ is constructed which interpolates between these limits.

Coordinate Space Form of Interacting Reference Response Function of d -Dimensional Jellium.

R. FANTONI and M. P. TOSI

*Istituto Nazionale di Fisica della Materia and Classe di Scienze, Scuola Normale Superiore
Piazza dei Cavalieri 7, I-56126 Pisa, Italy*

(ricevuto il 4 Luglio 1995; approvato il 31 Luglio 1995)

Summary. — The interacting reference response function $\chi_1^{[3]}(k)$ of three-dimensional jellium in k space was defined by Niklasson in terms of the momentum distribution of the interacting electron assembly. Here the Fourier transform $F_1^{[d]}(r)$ of $\chi_1^{[d]}(k)$ is studied for the jellium model with e^2/r interactions in dimensionality $d = 1, 2$ and 3 , in an extension of recent work by Holas, March and Tosi for the case $d = 3$. The small- r and large- r forms of $F_1^{[d]}(r)$ are explicitly evaluated from the analytic behaviour of the momentum distribution $n_d(p)$. In the appendix, a model of $n_d(p)$ is constructed which interpolates between these limits.

PACS 71.45 – Collective effects.

1. – Introduction.

The linear density response function $\chi^{[d]}(k, \omega)$ of the jellium model in dimensionality d is customarily written in the form of an RPA-like expression involving a single-particle reference susceptibility and a local field factor[1]. While the reference susceptibility is usually taken as the Lindhard function for the ideal Fermi gas, Niklasson[2] introduced for $d = 3$ an interacting reference susceptibility which is defined in a similar way as the Lindhard function but with the ideal Fermi momentum distribution replaced by the true momentum distribution of the interacting electron assembly. This involves, of course, a redefinition of the local field factor, which acquires the appealing feature of tending to a constant at large wave number k instead of being asymptotically proportional to k^2 [3,4].

In recent work Holas, March and Tosi[5], hereafter referred to as HMT, have evaluated the r -dependence of the Fourier transform of Niklasson's interacting reference susceptibility in the static case for $d = 3$, using known analytic properties of the true momentum distribution. The present work extends their approach to lower dimensionalities ($d = 2$ and 1) and contrasts the results with those obtained for $d = 3$.

2. – Interacting reference susceptibility and local field factor.

2.1. Definition of interacting reference susceptibility in \mathbf{k} space. – The interacting reference susceptibility in the static case ($\omega = 0$) is defined in \mathbf{k} or reciprocal space as

$$(2.1) \quad \chi_I^{[d]}(k) = -\frac{2^{(3-d)}m}{\pi^d} P \int d^d p \frac{n_d(p)}{k^2 + 2\mathbf{k} \cdot \mathbf{p}},$$

where m is the electronic mass and $n_d(p)$ is the momentum distribution function of the interacting electron fluid. Owing to the isotropy of the homogeneous phase of jellium, the angular integration in eq. (2.1) can be carried out to yield

$$(2.2) \quad \chi_I^{[3]}(k) = -\frac{m}{\pi^2 k} \int_0^\infty dp p n_3(p) \ln \left| \frac{k+2p}{k-2p} \right|,$$

$$(2.3) \quad \chi_I^{[2]}(k) = -\frac{4m}{\pi k} \int_0^\infty dp p n_2(p) \frac{\theta(k-2p)}{\sqrt{k^2-4p^2}}$$

and

$$(2.4) \quad \chi_I^{[1]}(k) = -\frac{8m}{\pi} \int_0^\infty dp n_1(p) \frac{1}{k^2-4p^2}.$$

When the true momentum distribution in eqs. (2.2)-(2.4) is replaced by the ideal Fermi distribution, one recovers the well-known Lindhard results:

$$(2.5) \quad \chi_0^{[3]}(k) = -\frac{m k_F}{2\pi^2} \left[1 + \frac{(2k_F)^2 - k^2}{4k_F k} \ln \left| \frac{k+2k_F}{k-2k_F} \right| \right],$$

$$(2.6) \quad \chi_0^{[2]}(k) = -\frac{m}{\pi} \left[1 - \theta(k-2k_F) \sqrt{1 - \left(\frac{2k_F}{k} \right)^2} \right]$$

and

$$(2.7) \quad \chi_0^{[1]}(k) = -\frac{4m}{\pi k} \ln \left| \frac{k+2k_F}{k-2k_F} \right|.$$

The Fermi momentum k_F is related to the particle number density ϱ_d by

$$(2.8) \quad k_F = 2\pi^{1/2} \left[\frac{1}{4} d \Gamma\left(\frac{d}{2}\right) \varrho_d \right]^{1/d}.$$

2.2. Local field factor. – The density response function $\chi^{[d]}(k, \omega)$ is written in terms of the interacting reference susceptibility $\chi_I^{[d]}(k, \omega)$ and of a local field factor

$\tilde{G}_d(k, \omega)$ as

$$(2.9) \quad \chi^{[d]}(k, \omega) = \frac{\chi_1^{[d]}(k, \omega)}{1 - v_d(k)[1 - \tilde{G}_d(k, \omega)]\chi_1^{[d]}(k, \omega)}.$$

Here, $v_d(k)$ is the d -dimensional Fourier transform of the e^2/r Coulomb repulsive interaction, given by $4\pi e^2/k^2$ for $d = 3$ and by $2\pi e^2/k$ for $d = 2$. In the jellium model for electrons in a quantum wire the Coulomb matrix element can be taken as

$$(2.10) \quad v_1(k) = e^2 h(kR_0),$$

where R_0 is the effective radius of the wire and the function $h(x)$ can be of various forms depending on the type of transverse confinement. We shall take it to have the asymptotic behaviours

$$(2.11) \quad h(x \rightarrow 0) = C_-(R_0) \ln(x)$$

and

$$(2.12) \quad h(x \rightarrow \infty) = C_+(R_0) \frac{4\pi e^2}{x^2},$$

the latter being valid when both transverse confinement lengths are finite [6]. $C_-(R_0)$ and $C_+(R_0)$ in eqs. (2.11) and (2.12) are confinement-dependent functions.

It was first shown by Niklasson [2] from the equations of motion for the single-particle and two-particle density matrices that, in regions of the (k, ω) -plane well outside the particle-hole continuum, the local field factor introduced in eq. (2.9) satisfies two exact relations in particular limits (see also [7]). These relations are easily expressed in terms of the following function:

$$(2.13) \quad G_d^{\text{PV}}(k) = \frac{1}{N} \sum_{\mathbf{k}'} \left\{ \left(\frac{\mathbf{k} \cdot \mathbf{k}'}{k^2} \right)^2 \frac{v_d(k')}{v_d(k)} - \left(\frac{\mathbf{k} \cdot (\mathbf{k} + \mathbf{k}')}{k^2} \right)^2 \frac{v_d(|\mathbf{k} + \mathbf{k}'|)}{v_d(k)} \right\} (S_d(k') - 1).$$

Here, $S_d(k)$ is the static structure factor of d -dimensional jellium, related to the pair distribution function $g_d(r)$ by

$$(2.14) \quad 1 - g_d(r) = \frac{1}{N} \sum_{\mathbf{k}} [1 - S_d(k)] \exp[i\mathbf{k} \cdot \mathbf{r}].$$

$G_d^{\text{PV}}(k)$ in eq. (2.13) is the form taken in d -dimensional jellium by the static local field factor first introduced by Pathak and Vashishta [8]. Precisely, for $|\omega \pm k^2/2m| \gg \gg k_F/2m$ one has

$$(2.15) \quad \lim_{k \rightarrow \infty} \tilde{G}_d(k, \omega) = G_d^{\text{PV}}(\infty)$$

at finite ω and

$$(2.16) \quad \lim_{\omega \rightarrow \infty} \tilde{G}_d(k, \omega) = G_d^{\text{PV}}(k)$$

at finite k .

2.3. Asymptotic behaviour of local field factors for large k . – Equations (2.13) and (2.15) yield the following exact asymptotic values of the local field factor for large

1168

R. FANTONI and M. P. TOSI

wave number and finite frequency:

$$(2.17) \quad \tilde{G}_d(k \rightarrow \infty, \omega) = \begin{cases} \frac{2}{3}[1 - g_3(0)] & \text{for } d = 3, \\ 1 - g_2(0) & \text{for } d = 2, \\ 1 - g_1(0) + (R_0^2/4\pi Q_1 C_+) \int d\mathbf{q} q^2 h(qR_0)[S_1(q) - 1] & \text{for } d = 1. \end{cases}$$

An alternative form of the local field factor needs to be introduced when one replaces $\chi_1^{[d]}(k, \omega)$ in eq. (2.9) with the Lindhard function $\chi_0^{[d]}(k, \omega)$, namely

$$(2.18) \quad G_d(k, \omega) = 1 + [v_d(k)\chi^{[d]}(k, \omega)]^{-1} - [v_d(k)\chi_0^{[d]}(k, \omega)]^{-1} = \\ = \tilde{G}_d(k, \omega) + [v_d(k)\chi_1^{[d]}(k, \omega)]^{-1} - [v_d(k)\chi_0^{[d]}(k, \omega)]^{-1}.$$

Following the analysis given by Holas[3], the static Lindhard function has the large- k expansion

$$(2.19) \quad \chi_0^{[d]}(k) = -4mQ_d k^{-2} [1 + 4C_1^{[d]} \langle p^2 \rangle_0^{[d]} k^{-2} + 16C_2^{[d]} \langle p^4 \rangle_0^{[d]} k^{-4} + \dots],$$

where

$$(2.20) \quad C_n^{[d]} = \begin{cases} (2n + 1)^{-1} & \text{for } d = 3, \\ (2n - 1)!!/(2n)!! & \text{for } d = 2, \\ 1 & \text{for } d = 1 \end{cases}$$

and the notation

$$(2.21) \quad \langle f(\mathbf{p}) \rangle_0^{[d]} = \frac{2}{N} \sum_{\mathbf{p}} n_d^0(\mathbf{p}) f(\mathbf{p})$$

has been used, $n_d^0(\mathbf{p})$ being the ideal Fermi-momentum distribution. In particular,

$$(2.22) \quad \langle p^{2n} \rangle_0^{[d]} = \frac{d}{2n + d} k_F^{2n}.$$

With the notation $\langle \dots \rangle_I^{[d]}$ for the average in eq. (2.21) when $n_d^0(\mathbf{p})$ is replaced by $n_d(\mathbf{p})$, and using the normalization condition $\sum_{\mathbf{p}} n_d^0(\mathbf{p}) = \sum_{\mathbf{p}} n_d(\mathbf{p}) = N/2$, we reach the result

$$(2.23) \quad G_d(k, 0) = \tilde{G}_d(k, 0) + \frac{1}{mQ_d v_d(k)} \{ (\langle p^2 \rangle_I^{[d]} - \langle p^2 \rangle_0^{[d]}) C_1^{[d]} + \\ + \frac{4}{k^2} [(\langle p^4 \rangle_I^{[d]} - \langle p^4 \rangle_0^{[d]}) C_2^{[d]} - ((\langle p^2 \rangle_I^{[d]})^2 - (\langle p^2 \rangle_0^{[d]})^2) (C_1^{[d]})^2] + O(k^{-4}) \}.$$

Taking into account eq. (2.17), we conclude that the leading term in the high- k

expansion of $G_d(k, 0)$ is given by

$$(2.24) \quad G_d(k, 0) \xrightarrow{k \rightarrow \infty} \begin{cases} \Delta_T^{[3]} k^2 / (6\pi \rho_3 e^2) & \text{for } d = 3, \\ \Delta_T^{[2]} k / (2\pi \rho_2 e^2) & \text{for } d = 2, \\ \Delta_T^{[1]} (R_0 k)^2 / (2\pi \rho_1 e^2 C_+) & \text{for } d = 1, \end{cases}$$

where $\Delta_T^{[d]} = \langle T \rangle_I^{[d]} - \langle T \rangle_0^{[d]}$ and $T = p^2/2m$ is the kinetic energy operator.

2.4. *Asymptotic behaviour of $G_d(k, \omega)$ for large ω .* – Following Iwamoto [9], the asymptotic form of the Lindhard function at high frequency can be given in terms of the frequency-moment sum rules, namely

$$(2.25) \quad \lim_{\omega \rightarrow \infty} \chi_0^{[d]}(k, \omega) = \sum_{j=1}^{\infty} \frac{L_{2j+1}^{[d]}(k)}{\omega^{2j}}.$$

The first two moments in eq. (2.25) are

$$(2.26) \quad L_1^{[d]}(k) = \frac{\rho_d k^2}{m}$$

and

$$(2.27) \quad L_3^{[d]}(k) = \frac{\rho_d k^2}{m} \left[\left(\frac{k^2}{2m} \right)^2 + \frac{12}{d} \langle T \rangle_0^{[d]} \frac{k^2}{2m} \right].$$

The analogous expansion for $\chi_1^{[d]}(k, \omega)$ is obtained by replacing $\langle \dots \rangle_I^{[d]}$ with $\langle \dots \rangle_0^{[d]}$ in the frequency moments. By substituting these expansions into eq. (2.18) we find

$$(2.28) \quad G_d(k, \omega = \infty) = G_d^{\text{PV}}(k) - \frac{12}{d} \frac{\Delta_T^{[d]}}{2\rho_d v_d(k)}.$$

Comparison of eqs. (2.23) and (2.28) shows that their leading terms differ only by a numerical factor.

3. – Coordinate space response function $F_I^{[d]}(r)$.

The response function $F_I^{[d]}(r)$ in coordinate space is defined as the d -dimensional Fourier transform of $\chi_I^{[d]}(k)$. Angular integration yields

$$(3.1) \quad F_I^{[3]}(r) = \frac{1}{2\pi^2 r} \int_0^\infty dk k \chi_I^{[3]}(k) \sin(kr),$$

$$(3.2) \quad F_I^{[2]}(r) = \frac{1}{2\pi} \int_0^\infty dk k \chi_I^{[2]}(k) J_0(kr)$$

1170

R. FANTONI and M. P. TOSI

and

$$(3.3) \quad F_I^{[1]}(r) = \frac{1}{\pi} \int_0^\infty dk k \chi_I^{[1]}(k) \cos(kr).$$

Using eqs. (2.2)-(2.4) in eqs. (3.1)-(3.3) and two definite integrals given by Gradshteyn and Ryzhik[10] we find

$$(3.4) \quad F_I^{[3]}(r) = -\frac{m}{2\pi^3 r^2} \int_0^\infty dp p n_3(p) \sin(2pr),$$

$$(3.5) \quad F_I^{[2]}(r) = \frac{m}{\pi^2 r} \int_0^\infty dp n_2(p) [\pi p r J_0(pr) Y_0(pr)]$$

and

$$(3.6) \quad F_I^{[1]}(r) = -\frac{2m}{\pi} \int_0^\infty dp \frac{n_1(p)}{p} \sin(2pr).$$

Upon inserting the ideal Fermi distribution in place of the true momentum distribution in eqs. (3.1)-(3.3), we recover results for the Lindhard function in r -space[11]:

$$(3.7) \quad F_0^{[3]}(r) = -\frac{m k_F^2}{2\pi^3} \frac{j_1(2k_F r)}{r^2},$$

$$(3.8) \quad F_0^{[2]}(r) = -\frac{m k_F^2}{2\pi} [J_0(k_F r) Y_0(k_F r) + J_1(k_F r) Y_1(k_F r)]$$

and

$$(3.9) \quad F_0^{[1]}(r) = -\frac{2m}{\pi} \text{Si}(2k_F r).$$

In these equations $j_1(x)$ is the spherical Bessel function $[\sin(x) - x \cos(x)]/x^2$, $J_n(x)$ and $Y_n(x)$ are the n -th-order Bessel functions of the first and the second kind and $\text{Si}(x)$ is the sine integral.

Of course, $n_d(p)$ tends to the ideal Fermi distribution in the limit of coupling strength tending to zero. However, at finite coupling strength the momentum distribution acquires a high-momentum tail and its discontinuous jump across the Fermi surface is reduced below unity. Numerical determinations of $n_d(p)$ by quantal simulation methods are available both for $d = 2$ [12] and $d = 3$ [13]. In the following sections we shall use the above-mentioned properties of $n_d(p)$ to determine the behaviours of $F_I^{[d]}(r)$ at small and large r .

4. – Small- r expansion of interacting susceptibility.

The small- r properties of $F_I^{[d]}(r)$ are determined by the behaviour of $n_d(p)$ at large momenta. This is known to be

$$(4.1) \quad n_3(p) = \left(\frac{4\pi Q_3}{a_0} \right)^2 g_3(0) p^{-8} + \dots$$

for $d = 3$, from the work of Kimball[14,15] and

$$(4.2) \quad n_2(p) = \left(\frac{2\pi Q_2}{a_0} \right)^2 g_2(0) p^{-6} + \dots$$

for $d = 2$, from the work of Rajagopal and Kimball[16]. In these equations a_0 is the Bohr radius and $g_d(0)$ is the value of the pair distribution function $g_d(r)$ evaluated at separation $r = 0$. This value is related to the asymptotic behaviour of the structure factor $S_d(k)$ according to

$$(4.3) \quad g_3(0) = \frac{3\pi a_0}{8k_F^3} \lim_{k \rightarrow \infty} k^4 (1 - S_3(k))$$

and

$$(4.4) \quad g_2(0) = \frac{a_0}{2k_F^2} \lim_{k \rightarrow \infty} k^3 (1 - S_2(k)).$$

The asymptotic behaviour of the momentum distribution for the case $d = 1$ has been evaluated in[6]. The result is

$$(4.5) \quad n_1(p) = \left(\frac{4\pi Q_1 C_+}{a_0 R_0^2} \right)^2 g_1(0) p^{-8} + \dots,$$

where

$$(4.6) \quad g_1(0) = \frac{a_0 R_0^2}{4\pi k_F C_+} \lim_{k \rightarrow \infty} k^4 (1 - S_1(k)).$$

Using eq. (4.1) in eq. (3.4) HTM find

$$(4.7) \quad F_I^{[3]}(r) = -\frac{mQ_3}{\pi r} \left\{ 1 - \frac{4}{3} \langle T \rangle_I^{[3]} m r^2 + \frac{8}{15} \langle T^2 \rangle_I^{[3]} m^2 r^4 - \frac{a_8}{45\pi Q_3} r^5 + \dots \right\},$$

where a_8 is the coefficient of p^{-8} in eq. (4.1) and $\langle T^n \rangle_I^{[d]}$ is the n -th moment of the kinetic energy T .

For the other dimensionalities we obtain the following expressions by the same

1172

R. FANTONI and M. P. TOSI

method. For $d = 2$ we get

$$(4.8) \quad F_I^{[2]}(r) = \frac{2mQ_2}{\pi} \left\{ [(\gamma - \ln(2)) + \langle \ln(p) \rangle_I^{[2]}] + \right. \\ \left. + \ln(r) + \left[\left(\frac{1}{2} - \gamma + \ln(2) \right) m \langle T \rangle_I^{[2]} - \langle T \ln(p) \rangle_I^{[2]} \right] r^2 + m \langle T \rangle_I^{[2]} r^2 \ln(r) + \dots \right\},$$

where $\gamma = 0.57721 \dots$ is Euler's constant. For $d = 1$ we find

$$(4.9) \quad F_I^{[1]}(r) = -2mQ_1 r \left\{ \sum_{n=0}^3 \frac{(-8m)^n}{(2n+1)!} \langle T^n \rangle_I^{[1]} r^{2n} + \frac{a_w}{8! Q_1} (2r)^7 + \dots \right\},$$

where a_w is the coefficient of p^{-8} in eq. (4.5).

It should be noticed that higher-order terms in the expansions given in eqs. (4.7)-(4.9) cannot be evaluated without knowledge of the high-momentum behaviour of $n_d(p)$ going beyond that explicitly shown in eqs. (4.1), (4.2) and (4.5). The coefficients of such higher-order terms may diverge for some forms of $n_d(p)$.

5. - Long-range behaviour of $F_I^{[d]}(r)$.

In order to determine the behaviour of $F_I^{[3]}(r)$ at large r , HMT rewrite the right-hand side of eq. (3.4) in the form of the one-dimensional Fourier transform of the function $\vartheta(p) p n_3(p)$ and apply the Lighthill technique for the asymptotic estimation of such Fourier transforms [17].

The momentum distribution in the homogeneous phase of d -dimensional jellium is known to have a discontinuity (reduction by a jump) of magnitude Z_F at $p = k_F$ and most probably discontinuities in its derivatives there. One can thus express $n_d(p)$ as

$$(5.1) \quad n_d(p) = \text{sgn}(p - k_F) \sum_{n=0}^{\infty} \frac{b_n^{[d]}}{n!} (p - k_F)^n + \text{analytical terms},$$

with $b_0^{[d]} = -Z_F/2$. Moreover, we assume that the expansion

$$(5.2) \quad n_d(p) = \sum_{n=0}^{\infty} \frac{c_n^{[d]}}{n!} p^n + \text{analytical terms}$$

holds for $n_d(p)$ near $p = 0$.

HMT conclude from such behaviours of $n_3(p)$ that the asymptotic large- r expansion for $F_I^{[3]}(r)$ has an oscillatory part

$$(5.3) \quad [F_I^{[3]}(r)]^{\text{osc}} = -\frac{m}{\pi^3 r^2} \text{Im} \left\{ \exp[2ik_F r] \sum_{n=0}^{\infty} (k_F b_n^{[3]} + n b_{n-1}^{[3]})^{n+1} \right\}$$

with leading term $-[mk_F b_0^{[3]}/2\pi^3] \cos(2k_F r)/r^3$, as well as a non-oscillatory contribution

$$(5.4) \quad [F_I^{[3]}(r)]^{\text{non-osc}} = -\frac{m}{2\pi^3 r^2} \sum_{n=1}^{\infty} (-1)^n \frac{2nc_{2n-1}^{[3]}}{(2r)^{2n+1}},$$

where only the odd terms in the power series expansion (5.2) contribute, with leading term $[mc_1^{[3]}/(2\pi)^3]/r^3$.

In the following two subsections we shall apply these arguments to determine the long-range behaviour of $F_1^{[2]}(r)$ and $F_1^{[1]}(r)$.

5.1. *Two-dimensional jellium.* – The analysis of the large- r behaviour of $F_1^{[2]}(r)$ on the basis of the behaviours of $n_2(p)$ in eqs. (5.1) and (5.2) is quite complex. There does not seem to be an asymptotic expansion for the product $J_0(x)Y_0(x)$ in eq. (3.5) having a simple expression for its coefficients.

We start by defining the function $f_0(x) = \pi x[J_0(x)Y_0(x)]$ for $x \geq 0$ and its successive integrals

$$(5.5) \quad f_1(x) = \int_0^x f_0(t) dt = \frac{\pi}{2} x^2 [J_0(x)Y_0(x) + J_1(x)Y_1(x)] = \int_0^x f_0(t) dt$$

and

$$(5.6) \quad f_n(x) = \int_0^x f_{n-1}(t) dt.$$

These functions possess an upper bound ($|f_n(x)| \leq \text{constant}$) and have the following asymptotic expansions:

i) the large- x expansion

$$(5.7) \quad f_0(x) = \cos(2x) \left[-1 + \frac{20}{128x^2} + O(x^{-4}) \right] + \sin(2x) \left[-\frac{1}{4x} - \frac{42}{256x^3} + O(x^{-5}) \right]$$

and for any $n > 0$

$$(5.8) \quad f_n(x) \xrightarrow{x \rightarrow \infty} \begin{cases} \frac{(-)^{n/2+1}}{2^n} \cos(2x) + \dots & \text{for even } n, \\ \frac{(-)^{(n-1)/2}}{2^n} \sin(2x) + \dots & \text{for odd } n; \end{cases}$$

ii) the small- x expansion

$$(5.9) \quad f_0(x) = 2x \ln(2x) + O(x)$$

and for any $n > 0$

$$(5.10) \quad f_n(x) \xrightarrow{x \rightarrow 0} \frac{2}{(n+1)!} x^{n+1} \ln(x) + \sum_{i=1}^n \frac{d_i}{(n-i)!} x^{n-i}.$$

Here, the coefficients d_i are the integration constants needed to connect with the large- x behaviour in eq. (5.8). For example, we have $d_1 = 0$ (see eq. (5.5)) and $d_2 \approx$

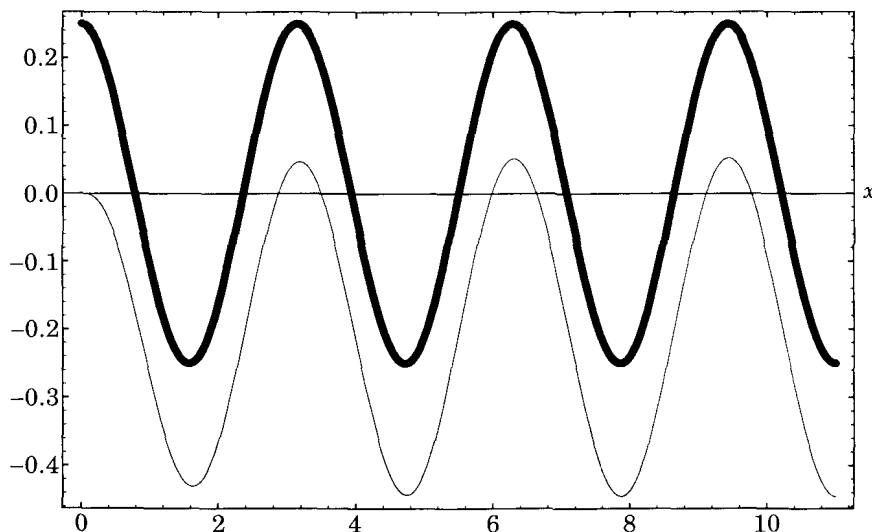


Fig. 1. - Plot of the function $(\pi/2)x^2 \int_0^x [J_0(t)Y_0(t) + J_1(t)Y_1(t)] dt$ (lower curve) compared with $\cos(2x)/4$ (upper curve).

$\approx -0.196344\dots$ (see fig. 1). In general d_n can be obtained by a limiting process,

$$(5.11) \quad d_n = \lim_{j \rightarrow \infty} \begin{cases} \int_0^{(2j+1)(\pi/4)} f_{n-1}(t) dt & \text{for even } n, \\ \int_0^{j(\pi/2)} f_{n-1}(t) dt & \text{for odd } n. \end{cases}$$

Given these definitions, the long-range behaviour of $F_1^{[2]}(r)$ can be obtained by successive integration by parts on eq. (3.5). A first integration by parts yields

$$(5.12) \quad F_1^{[2]}(r) = -\frac{m}{(\pi r)^2} \int_0^\infty (2b_0^{[2]} \delta(p - k_F) + [D_F^1 n_2](p)) f_1(pr) dp =$$

$$= -\frac{m}{\pi^2 r} \left(\frac{2b_0^{[2]} f_1(k_F r)}{r} + \frac{1}{r} \int_0^\infty [D_F^1 n_2](p) f_1(pr) dp \right),$$

where we have introduced the notation $[D_F n_2](p)$ for the derivative of $n_2(p)$ at $p > k_F$ and $p < k_F$ and have made use of the fact that $n_2(p) f_1(pr)$ vanishes both at infinity and in the origin. From eqs. (5.8) and (5.12) we thus find

$$(5.13) \quad F_1^{[2]}(r) = \frac{mb_0^{[2]} \sin(2k_F r)}{(\pi r)^2} + O\left(\frac{1}{r^2}\right).$$

After N integrations by parts, we obtain

$$(5.14) \quad F_I^{[2]}(r) = -\frac{m}{\pi^2 r} \left[\sum_{n=1}^N (-)^n \frac{2b_{n-1}^{[2]} f_n(k_F r)}{r^n} - \sum_{n=1}^N (-)^n \frac{d_n c_{n-1}^{[2]}}{r^n} + \dots \right].$$

Evidently, in analogy with the case $d = 3$ the large- r asymptotic expansion of $F_I^{[2]}(r)$ can be divided into the sum of an oscillatory part and a non-oscillatory part. The former is given by the first term on the right-hand side of eq. (5.14) and its leading term is

$$(5.15) \quad [F_I^{[2]}(r)]^{\text{osc}} \approx \frac{mb_0^{[2]} \sin(2k_F r)}{(\pi r)^2}.$$

The non-oscillatory part is given by the second term on the right-hand side of eq. (5.14) and its leading term is

$$(5.16) \quad [F_I^{[2]}(r)]^{\text{non-osc}} \approx \frac{md_2 c_1^{[2]}}{\pi^2 r^3}.$$

5.2. *One-dimensional jellium.* – In order to apply the Lighthill technique to determine the long-range behaviour of $F_I^{[1]}(r)$, we first rewrite eq. (3.6) in the form of a one-dimensional Fourier transform,

$$(5.17) \quad F_I^{[1]}(r) = -\frac{2m}{\pi} \text{Im} \int_{-\infty}^{\infty} dp \theta(p) \frac{n_1(p)}{p} \exp[2ipr].$$

Because of the θ function the integrand in eq. (5.17) is non-analytic at $p = 0$. This may lead to a non-oscillatory contribution to the large- r expansion. From expansion (5.2) we obtain

$$(5.18) \quad [F_I^{[1]}(r)]^{\text{non-osc}} = -\frac{2m}{\pi} \left[\frac{c_0^{[1]} \pi}{2} + \sum_{n=0}^{\infty} \frac{c_{2n+1}^{[1]}}{(2n+1)!} \left(\frac{-1}{2r} \right)^{2n+1} \right].$$

The singularity of $n_1(p)$ at $p = k_F$ is instead responsible for an oscillatory contribution, following from eq. (5.1) as

$$(5.19) \quad [F_I^{[1]}(r)]^{\text{osc}} = -\frac{2m}{\pi} \text{Im} \sum_{n=0}^{\infty} \left\{ \frac{b_n^{[1]}}{n!} \int_{-\infty}^{\infty} dp \text{sgn}(p) \frac{p^n}{p+k_F} \exp[2ipr] \right\} \exp[-2ik_F r].$$

To leading order the result is

$$(5.20) \quad [F_I^{[1]}(r)]^{\text{osc}} = \frac{2mb_0^{[1]} \cos(2k_F r)}{\pi k_F r} + O\left(\frac{1}{r^2}\right).$$

5.3. *Comparison of results in various dimensionalities.* – In summary, table I compares the leading terms of the large- r asymptotic expansion of $F_I^{[d]}(r)$ in the various dimensionalities. Evidently, the leading term in the asymptotic expansion

1176

R. FANTONI and M. P. TOSI

TABLE I. – Leading terms of the large- r asymptotic expansion for the oscillating and non-oscillating parts of $F_1^{[d]}(r)$.

$F_1^{[d]}(r \rightarrow \infty)$	Oscillating term	Non-oscillating term
$d = 3$	$-\frac{mk_F b_0^{[3]} \cos(2k_F r)}{2(\pi r)^3}$	$\frac{m c_1^{[3]}}{(2\pi)^3 r^5}$
$d = 2$	$\frac{m b_0^{[2]} \sin(2k_F r)}{(\pi r)^2}$	$\frac{m d_2 c_1^{[2]}}{\pi^2 r^3}$
$d = 1$	$\frac{2m b_0^{[1]} \cos(2k_F r)}{\pi k_F r}$	$-m c_0^{[1]}$

is the oscillating one for $d = 3$ and $d = 2$, while in the quantum wire the non-oscillating term is dominant.

6. – Conclusions.

The main results of the present work concern i) the asymptotic behaviours of the local field factors $\tilde{G}_d(k, \omega)$ and $G_d(k, \omega)$ in eqs. (2.17), (2.24) and (2.28); ii) expressions (3.4)-(3.6) for the interacting reference susceptibility $F_1^{[d]}(r)$ in the form of a single integral and iii) the small- r and large- r expansions of $F_1^{[d]}(r)$ in eqs. (4.7)-(4.9), (5.3), (5.4), (5.14) and (5.18)-(5.20). These results were already known in the literature [3-5] for $d = 3$, but are mostly new for $d = 2$ and $d = 1$.

In the Appendix we have evaluated a model for the momentum distribution $n_d(r)$, which leads to a model for $F_1^{[d]}(r)$ allowing an interpolation between the limiting behaviours discussed in sect. 4 and 5.

APPENDIX

Evaluation of $F_1^{[d]}(r)$ using a model $n_d(r)$.

Following HMT we consider a model momentum distribution given for $d = 2$ and $d = 3$ by

$$(A.1) \quad n_d(p) = n_d^A(p) + n_d^B(p) = \vartheta(k_F - p)(\alpha_d + \beta_d p^2) + \frac{a_{2(d+1)}}{(\xi_d^2 + p^2)^{d+1}},$$

and for $d = 1$ by

$$(A.2) \quad n_1(p) = \vartheta(k_F - p)(\alpha_1 + \beta_1 p^2) + \frac{a_w}{(\xi_1^2 + p^2)^4};$$

eqs. (A.1) and (A.2) satisfy properties (4.1), (4.2) and (4.5). Of their five parameters,

k_F and a_8 , a_6 and a_w have an obvious meaning, while α_d , β_d and ζ_d can be determined from three requirements on the momentum distribution:

i) it satisfies the normalization condition $2 \sum_p n_d(p) = N$, leading to

$$(A.3) \quad 1 = \begin{cases} \alpha_3 + \frac{3}{5} \beta_3 k_F^2 + \frac{3\pi}{32} \frac{a_8}{k_F^3 \zeta_3^5} & \text{for } d = 3, \\ \alpha_2 + \frac{1}{2} \beta_2 k_F^2 + \frac{1}{2} \frac{a_6}{k_F^2 \zeta_2^4} & \text{for } d = 2, \\ \alpha_1 + \frac{1}{3} \beta_1 k_F^2 + \frac{5\pi}{32} \frac{a_w}{k_F \zeta_1^7} & \text{for } d = 1; \end{cases}$$

ii) it reproduces the value of the mean kinetic energy $\langle T \rangle_1^{[d]}$, leading to

$$(A.4) \quad \frac{\langle T \rangle_1^{[d]}}{\langle T \rangle_0^{[d]}} = \begin{cases} \alpha_3 + \frac{5}{7} \beta_3 k_F^2 + \frac{5\pi}{32} \frac{a_8}{k_F^5 \zeta_3^3} & \text{for } d = 3, \\ \alpha_2 + \frac{2}{3} \beta_2 k_F^2 + \frac{a_6}{k_F^4 \zeta_2^2} & \text{for } d = 2, \\ \alpha_1 + \frac{3}{5} \beta_1 k_F^2 + \frac{3\pi}{32} \frac{a_w}{k_F^3 \zeta_1^5} & \text{for } d = 1; \end{cases}$$

iii) it reproduces the discontinuity Z_F at $p = k_F$, leading to

$$(A.5) \quad \alpha_d + k_F^2 \beta_d = Z_F.$$

After inserting the model $n_d(p)$ of eqs. (A.1) and (A.2) into eqs. (3.4)-(3.6), all integrations can be performed analytically. The results are reported in the following subsections.

A.1. Three-dimensional jellium. - HMT find for $d = 3$

$$(A.6) \quad F_I^{[3]^A}(r) = -\frac{m k_F}{4(\pi r)^3} \left\{ \left[-(\alpha_3 + k_F^2 \beta_3) + \frac{3\beta_3}{2r^2} \right] \cos(2k_F r) + \left[\frac{\alpha_3 + 3k_F^2 \beta_3}{2k_F r} - \frac{3\beta_3}{4k_F r^3} \right] \sin(2k_F r) \right\}$$

and (assuming $\zeta_3 > 0$)

$$(A.7) \quad F_I^{[3]^B}(r) = -\frac{m a_8}{32\pi^2 \zeta_3^5 r} \left(1 + 2\zeta_3 r + \frac{4}{3} (\zeta_3 r)^2 \right) \exp[-2\zeta_3 r].$$

The model reference susceptibility is the sum of the two contributions in eqs. (A.6) and (A.7).

The small- r and large- r expansions of this model $F_I^{[3]}(r)$ agree with those given in eq. (4.7) and in eqs. (5.3) and (5.4). The contribution due to $F_I^{[3]^B}(r)$

1178

R. FANTONI and M. P. TOSI

is exponentially small at large r and non-oscillatory terms are absent because even powers only enter the small- p expansion of the model $n_3(p)$ in eq. (A.1).

A.2. Two-dimensional jellium. – For $d = 2$ we obtain, from well-known properties of the Bessel functions [18],

$$(A.8) \quad F_I^{[2]A}(r) = -\frac{m\alpha_2}{\pi r^2} \left\{ \frac{(k_F r)^2}{2} [J_0(k_F r) Y_0(k_F r) + J_1(k_F r) Y_1(k_F r)] \right\} -$$

$$-\frac{m\beta_2}{\pi r^4} \left\{ \frac{(k_F r)^4}{12} [3J_0(k_F r) Y_0(k_F r) + 2J_1(k_F r) Y_1(k_F r) - J_2(k_F r) Y_2(k_F r)] \right\} \xrightarrow{r \rightarrow \infty}$$

$$\xrightarrow{r \rightarrow \infty} m(\alpha_2 + k_F^2 \beta_2) \frac{\sin(2k_F r)}{2(\pi r)^2}$$

and (assuming $\zeta_2 > 0$)

$$(A.9) \quad F_I^{[2]B}(r) = \frac{\pi^2 \alpha_6}{2^5} r \left[\frac{1}{\zeta_2} \frac{d}{d\zeta_2} \right]^2 [H_0^{(1)}(i\zeta_2 r)]^2,$$

where $H_0^{(1)}(x) = J_0(x) + iY_0(x)$ is the zeroth-order Bessel function of the third kind. The asymptotic large- r behaviour of this function is

$$(A.10) \quad [H_0^{(1)}(i\zeta_2 r)]^2 \rightarrow -\frac{2}{\pi \zeta_2 r} \exp[-2\zeta_2 r].$$

Finally, we have the model reference susceptibility

$$(A.11) \quad F_I^{[2]}(r) = F_I^{[2]A}(r) + F_I^{[2]B}(r).$$

It is readily verified that the small- r and large- r expansions of this function agree with those given in eq. (4.8) and in eqs. (5.15) and (5.16). As in the case $d = 3$, the contribution due to $F_I^{[2]B}(r)$ is exponentially small at large r .

A.3. One-dimensional jellium. – For $d = 1$ we obtain

$$(A.12) \quad F_I^{[1]A}(r) = -\frac{2m\alpha_1}{\pi} \text{Si}(2k_F r) + \frac{m\beta_1}{\pi} \left[\frac{k_F \cos(2k_F r)}{r} - \frac{\sin(2k_F r)}{2r^2} \right]$$

and (assuming $\zeta_1 > 0$)

$$(A.13) \quad F_I^{[1]B}(r) = -\frac{m a_w}{\zeta_1^8} \left[1 - \left(1 + \frac{11}{4} \zeta_1 r + \frac{3}{4} (\zeta_1 r)^2 + \frac{1}{6} (\zeta_1 r)^3 \right) \exp[-2\zeta_1 r] \right].$$

Finally, we have the model response function

$$(A.14) \quad F_I^{[1]}(r) = F_I^{[1]A}(r) + F_I^{[1]B}(r).$$

Again it is readily verified that the small- r and large- r expansions of this function agree with those in eq. (4.9) and in eqs. (5.18) and (5.20). Contrary

to the other cases the term $F_I^{[1]B}(r)$ contributes to the leading term in the large- r expansion of $F_I^{[1]}(r)$, its magnitude being $-m c_0^{[1]}$ with $c_0^{[1]} = \alpha_1 + a_w / \zeta_1^8$.

REFERENCES

- [1] SINGWI K. S. and TOSI M. P., *Solid State Phys.*, **36** (1981) 177.
 - [2] NIKLASSON G., *Phys. Rev. B*, **10** (1974) 3052.
 - [3] HOLAS A., in *Strongly Coupled Plasma Physics*, edited by F. J. ROGERS and H. E. DEWITT (Plenum, New York, N.Y.) 1986, p. 463.
 - [4] MARCH A. M. and TOSI M. P., *Philos. Mag. B*, **72** (1995) 295.
 - [5] HOLAS A., MARCH A. H. and TOSI M. P., to be published in *Phys. Chem. Liq.*
 - [6] FANTONI R. and TOSI M. P., to be published in *Physica B*.
 - [7] SANTORO G. E. and GIULIANI G. F., *Phys. Rev. B*, **37** (1988) 4813.
 - [8] PATHAK K. N. and VASHISHTA P., *Phys. Rev. B*, **7** (1973) 3649.
 - [9] IWAMOTO N., *Phys. Rev. A*, **30** (1984) 3289.
 - [10] GRADSHTEIN I. S. and RYZHIK I., *Tables of Integrals, Series and Products* (Academic, New York, N.Y.) 1980.
 - [11] MARCH N. H. and MURRAY A. M., *Phys. Rev.*, **120** (1960) 830.
 - [12] TANATAR B. and CEPERLEY D. M., *Phys. Rev. B*, **39** (1989) 5005.
 - [13] ORTIZ G. and BALLONE P., *Phys. Rev. B*, **50** (1994) 1391.
 - [14] KIMBALL J. C., *Phys. Rev. A*, **7** (1973) 1648.
 - [15] KIMBALL J. C., *J. Phys. A*, **8** (1975) 1513.
 - [16] RAJAGOPAL A. K. and KIMBALL J. C., *Phys. Rev. B*, **15** (1977) 2819.
 - [17] LIGHTHILL M. J., *Introduction to Fourier Analysis and Generalised Functions* (University Press, Cambridge) 1958.
 - [18] WATSON G. S., *Theory of Bessel Functions* (University Press, Cambridge) 1952.
-

Part II
1996

Chapter 3

Some properties of short-range correlations for electrons in quantum wires

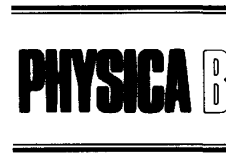
Fantoni R. and Tosi M.P., *Physica B*, **217**, 35 (1996)

Title: “Some properties of short-range correlations for electrons in quantum wires.”

Abstract: The asymptotic behaviours of the momentum distribution, the static structure factor and the local field factor at large momenta are evaluated for the jellium model of an interacting electron fluid confined in a quantum wire. The dependence of the results on the character of the confinement and their relevance to models of the dielectric screening function are discussed.



Physica B 217 (1996) 35–40



Some properties of short-range correlations for electrons in quantum wires

R. Fantoni, M.P. Tosi*

Istituto Nazionale di Fisica della Materia and Classe di Scienze, Scuola Normale Superiore, Piazza dei Cavalieri 7, I-56126 Pisa, Italy

Received 28 June 1995

Abstract

The asymptotic behaviours of the momentum distribution, the static structure factor and the local field factor at large momenta are evaluated for the jellium model of an interacting electron fluid confined in a quantum wire. The dependence of the results on the character of the confinement and their relevance to models of the dielectric screening function are discussed.

1. Introduction

Recent developments in fabrication techniques of quantum wires have made available for experimental study systems in which the conduction electrons can be described by a quasi-one-dimensional Fermi liquid (1DEL) model [1, 2]. The role of the electron–electron interactions in determining the observed electronic excitation spectra in these systems has been accounted for within the random phase approximation (RPA: see Ref. [3] and references given therein).

In such quantum wires the many-body effects are still small, because of the relatively high effective electron density and the relative large effective wire radius. One may expect, however, that with further developments in the production of semiconductor wire structures these system parameters may be varied into a range where the short-range electron–electron correlations that are neglected in the RPA would become relevant.

In the present paper we study some exact asymptotic behaviours of short-range correlations in a 1DEL. Specific attention is given to the behaviour of the momentum distribution at high momenta and to those of the structure factor and of the local field factor in dielectric screening at high wave numbers. Our approach is taken from earlier work on three-dimensional (3D) and two-dimensional (2D) electron liquids [4]. The results emphasize the dependence of short-range correlations in a 1DEL on the nature of the confinement.

2. The model

We consider a quantum wire of length L extending in the \hat{z} direction. It contains N electrons which are free to move along the wire axis in the effective mass sense, but are confined in the \hat{x} – \hat{y} plane by a potential well $U_c(x/a_x, y/a_y)$ where a_x and a_y are the characteristic lengths of the confinement along the \hat{x} and \hat{y} directions. The electronic system at zero temperature is characterized by an effective width

* Corresponding author.

R_0 and by the one-dimensional carrier density $\rho_{\parallel} = N/L$. All vectors will be decomposed into their in-plane and \hat{z} components, with the notations $R \equiv (\mathbf{r}, z)$ for position vectors and $K \equiv (\mathbf{k}, k_z)$ for wave vectors.

The Hamiltonian H is the sum of a transverse part H_{\perp} , a longitudinal part H_{\parallel} and the 3D electron–electron Coulomb interaction V_{e-e} : $H = H_{\parallel} + H_{\perp} + V_{e-e}$. The many-body wave function may be expanded in terms of the eigenfunctions ϕ_i of H_{\parallel} and χ_j of H_{\perp} ,

$$\Psi(R_1, \dots, R_N) = \sum_{i,j} C_{i,j} \phi_i(z_1, \dots, z_N) \chi_j(\mathbf{r}_1, \dots, \mathbf{r}_N). \quad (1)$$

If the combination of energy level spacing due to the confinement and linear carrier density is such that $\langle H_{\perp} \rangle \gg \langle V_{e-e} \rangle$, one may neglect any contribution from excited subband states. The wave function takes the form

$$\Psi(R_1, \dots, R_N) \approx \psi(z_1, \dots, z_N) \prod_i \chi(\mathbf{r}_i), \quad (2)$$

where $\psi(z_1, \dots, z_N) = \sum_i C_{i,0} \phi_i(z_1, \dots, z_N)$ and we have set $\chi_0(\mathbf{r}_1, \dots, \mathbf{r}_N) = \prod_i \chi(\mathbf{r}_i; a_x, a_y)$. The normalized single-particle ground state $\chi(\mathbf{r}_i; a_x, a_y)$ is completely determined by the confining potential. The electron density in the wire is then given by $\rho_w(R) = \rho_{\parallel} \rho_{\perp}(\mathbf{r})$, where $\rho_{\perp}(\mathbf{r}) = |\chi(\mathbf{r}; a_x, a_y)|^2$.

The approximation (2) allows one to formally define a purely one-dimensional jellium problem [5] in terms of the many-body wave function $\psi(z_1, \dots, z_N)$, the effective interactions in the limit $L \rightarrow \infty$ being weighted with $\rho_{\perp}(\mathbf{r})$ according to

$$v(k_z) = 2e^2 \int d^2\mathbf{r} \int d^2\mathbf{r}' \rho_{\perp}(\mathbf{r}) \rho_{\perp}(\mathbf{r}') K_0(k_z |\mathbf{r} - \mathbf{r}'|). \quad (3)$$

Here, $K_0(x)$ is the zeroth-order modified Bessel function of the second kind and $2e^2 K_0(k_z |a|)$ is the Fourier transform of $e^2 / \sqrt{z^2 + a^2}$. We recall that $K_0(x) = -\ln(x)$ for $x \ll 1$ and $K_0(x) = \exp(-x) \sqrt{\pi/2x}$ for $x \gg 1$. For the 1DEL model we define the dimensionless length $r_s = (2\rho_{\parallel} a_0)^{-1}$ with a_0 the Bohr radius and the Fermi wave number $k_F = \pi\rho_{\parallel}/2$.

Eq. (3) can be rewritten as

$$v(k_z) = \frac{e^2}{\pi} \int \frac{|\rho_{\perp}(\mathbf{k})|^2}{k_z^2 + k^2} d^2\mathbf{k}, \quad (4)$$

where we have indicated with $\rho_{\perp}(\mathbf{k})$ the Fourier transform of $\rho_{\perp}(\mathbf{r})$. If both confinement lengths a_x and a_y are non-vanishing, and noticing that $\int |\rho_{\perp}(\mathbf{k})|^2 d^2\mathbf{k} = (2\pi)^2 \int |\rho_{\perp}(\mathbf{r})|^2 d^2\mathbf{r} < \infty$, we can use the dominated convergence theorem [6] to evaluate the asymptotic large- k_z behaviour of the integral in Eq. (4). We obtain

$$v(k_z) \rightarrow \frac{4\pi e^2}{k_z^2} Q_2, \quad (5)$$

where $Q_2 = \int |\rho_{\perp}(\mathbf{r})|^2 d^2\mathbf{r}$. However, if one of the confinement lengths (a_y , say) vanishes, i.e. in the case $\rho_{\perp}(\mathbf{r}) = \rho_x(x) \delta(y)$ we can first perform the k_y integration in Eq. (4) and subsequently apply the dominated convergence theorem. We then obtain

$$v(k_z) \rightarrow \frac{2\pi e^2}{|k_z|} Q_1, \quad (6)$$

where $Q_1 = \int |\rho_x(x)|^2 dx$. We shall refer to these two cases in the following as a 3D-like and a 2D-like quantum wire and use them to emphasize the role of the type of confinement in determining the short-range correlations between the electrons.

3. The static structure factor

The pair distribution function $g_w(R_1, R_2)$ in the quantum wire is the probability of finding a pair of electrons at points R_1 and R_2 , namely

$$g_w(R_1, R_2) = \frac{N(N-1)}{\rho_w(R_1)\rho_w(R_2)} \int |\Psi(R_1, \dots, R_N)|^2 \prod_{i=3}^N d^3R_i. \quad (7)$$

Upon inserting Eq. (2) in Eq. (7) we find the pair distribution function for the 1DEL,

$$g(z_1 - z_2) = \frac{N(N-1)}{\rho_{\parallel}^2} \int |\psi(z_1, \dots, z_N)|^2 \prod_{i=3}^N dz_i. \quad (8)$$

The static structure factor $S_w(K)$ of the quantum wire is related to the pair distribution function by

$$\begin{aligned} & \int [S_w(\mathbf{k}, k_z) - 1] \exp(-i\mathbf{k}R) \frac{d^3K}{(2\pi)^3} \\ &= \frac{1}{\rho_{\parallel}} \int d^2\mathbf{r}_2 \rho_w(\mathbf{r}_2 + \mathbf{r}) \rho_w(\mathbf{r}_2) [g_w(R_2 + R, R_2) - 1] \\ &\equiv \frac{1}{\rho_{\parallel}} [G(R) - I(R)]. \end{aligned} \quad (9)$$

For the 1DEL we define $S(k_z) = S_w(0, k_z)$ so that Eq. (9) becomes

$$\int_{-\infty}^{\infty} [S(k_z) - 1] \exp(-ik_z z) \frac{dk_z}{2\pi} = \rho_{\parallel} [g(z) - 1]. \quad (10)$$

3.1. Large k_z behaviour in the 1DEL

Yasuhara [7] has shown for 3D jellium that the electron–electron ladder interactions at all orders determine the asymptotic form of the structure factor at large momenta. Following his method it is easily shown that $S(k_z)$ in the 1DEL has the following exact asymptotic form for large k_z ($k_z \gg k_F$):

$$1 - S(k_z) = \frac{v(k_z)}{\varepsilon(k_z)} \rho_{\parallel} g(0) + \dots, \quad (11)$$

with $\varepsilon(k_z) = k_z^2/2m$. Therefore, if the 1DEL is confined in a 3D-like quantum wire, by inserting Eq. (5) in Eq. (11) we get

$$1 - S(k_z) = \frac{8\pi\rho_{\parallel}}{a_0} \frac{1}{k_z^4} Q_2 g(0) + \dots. \quad (12)$$

If instead the 1DEL is confined in a 2D-like quantum wire we should use Eq. (6) in Eq. (11), thus obtaining

$$1 - S(k_z) = \frac{4\pi\rho_{\parallel}}{a_0} \frac{1}{|k_z|^3} Q_1 g(0) + \dots. \quad (13)$$

The power law for the asymptotic approach of the structure factor to unity in Eq. (12) resembles that found by Kimball [8] for 3D jellium. Similarly, the form of Eq. (13) resembles that for 2D jellium [9].

3.2. Large k_z behaviour in a quantum wire

More generally, for a 3D quantum wire Eq. (9) yields

$$\begin{aligned} \lim_{t \rightarrow \infty} (tK)^4 [S_w(tk_x, tk_y, tk_z) - 1] \\ = -8\pi\rho_{\parallel} \frac{d}{d|R|} [\hat{G}(|R|) - \hat{I}(|R|)] \Big|_{|R|=0}, \end{aligned} \quad (14)$$

where $\hat{G}(|R|) - \hat{I}(|R|)$ is the average of $G(R) - I(R)$ taken over the sphere of radius $|R|$. The analogous expression for a 2D wire is

$$\begin{aligned} \lim_{t \rightarrow \infty} (tK)^3 [S_w(tk_x, tk_z) - 1] \\ = -2\pi\rho_{\parallel} \frac{d}{d|R|} [\hat{G}(|R|) - \hat{I}(|R|)] \Big|_{|R|=0}. \end{aligned} \quad (15)$$

Since $I(R)$ is completely determined from the knowledge of the confining potential, the same will be true for $(d/d|R|)\hat{I}(|R|)|_{|R|=0}$. On the other hand, $(d/d|R|)\hat{G}(|R|)|_{|R|=0}$ must be proportional to $G(0)$ as a consequence of the cusp theorem [10]. This yields

$$\frac{d}{d|R|} \hat{G}(|R|) \Big|_{|R|=0} = \frac{1}{a_0} G(0) \quad (16)$$

for a 3D-like wire and

$$\frac{d}{d|R|} \hat{G}(|R|) \Big|_{|R|=0} = \frac{2}{a_0} G(0) \quad (17)$$

for a 2D-like one.

4. The momentum distribution

The probability $n_w(K)$ of finding an electron with momentum K in the quantum wire, per unit transverse area, can be written as

$$\begin{aligned} n_w(K) = \rho_{\parallel} \int \exp[iK(R - R')] \Psi^*(R, R_2, \dots, R_N) \\ \times \Psi(R', R_2, \dots, R_N) dR dR' \prod_{i=2}^N dR_i. \end{aligned} \quad (18)$$

In the 1DEL approximation $n_w(K)$ takes the form

$$n_w(K) = |\phi(k)|^2 n(k_z) \quad (19)$$

where $\phi(k)$ is the Fourier transform of the single-particle ground state for the motion in the transverse direction and $n(k_z)$ is the momentum distribution in the 1DEL. From Eq. (2) we have

$$\begin{aligned} n(k_z) = \rho_{\parallel} \int \exp[ik_z(z - z')] \psi^*(z, z_2, \dots, z_N) \\ \times \psi(z', z_2, \dots, z_N) dz dz' \prod_{i=2}^N dz_i. \end{aligned} \quad (20)$$

4.1. Large k_z behaviour in the 1DEL

As was shown for 3D jellium by Yasuhara and Kawazoe [11], the electron–electron ladder diagrams also determine the asymptotic form of the momentum distribution at large momenta. We follow their approach for the one-electron momentum distribution in the 1DEL. It is easily shown that $n(k_z)$ has for large k_z ($k_z \gg k_F$) the asymptotic form

$$n(k_z) = \left(\frac{\rho_{\parallel} v(k_z)}{2\varepsilon(k_z)} \right)^2 g(0) + \dots \quad (21)$$

Therefore, if the 1DEL is confined in a 3D-like quantum wire, using Eq. (5) in Eq. (21) yields

$$n(k_z) = \left(\frac{4\pi\rho_{\parallel}}{a_0} \right)^2 \frac{1}{k_z^8} Q_2^2 g(0) + \dots \quad (22)$$

If instead the 1DEL is confined in a 2D-like quantum wire we should use Eq. (6) in Eq. (21), with the result

$$n(k_z) = \left(\frac{2\pi\rho_{\parallel}}{a_0} \right)^2 \frac{1}{k_z^6} Q_1^2 g(0) + \dots \quad (23)$$

The power-law decays of the momentum distribution in Eqs. (22) and (23) are the same as for 3D and 2D jellium. These were derived by Kimball [12] and by Rajagopal and Kimball [9], respectively, through an alternative argument that we apply to a quantum wire immediately below.

4.2. Large k_z behaviour in a quantum wire

The momentum distribution is obtained from Eq. (18) as the Fourier transform of a function which is bilinear in the many-electron wave function and its asymptotic form at large momenta is determined by the points of non-analyticity in the wave function. On the other hand, when two electrons are very close to each other their mutual repulsion dominates over the interactions with the other electrons and hence the dominant behaviour of the wave function can be determined from the two-body Schrödinger equation. Such a constraint implies that the many-electron wave function is everywhere continuous with its derivative excepts

at points in phase space which correspond to zero interparticle separation.

By developing this argument, which is originally due to Kimball [12], we find

$$n_w(\mathbf{k}, k_z) \xrightarrow[k \text{ fixed}]{k_z \rightarrow \infty} \left(\frac{4\pi\rho_{\parallel}}{a_0} \right)^2 \frac{1}{k_z^8} \int |\rho_{\perp}(\mathbf{r})|^2 g_w(R, R) d\mathbf{r} \quad (24)$$

for a 3D-like quantum wire and

$$n_w(\mathbf{k}, k_z) \xrightarrow[k \text{ fixed}]{k_z \rightarrow \infty} \left(\frac{2\pi\rho_{\parallel}}{a_0} \right)^2 \frac{1}{k_z^6} \int |\rho_{\perp}(\mathbf{r})|^2 g_w(R, R) d\mathbf{r} \quad (25)$$

for a 2D-like one.

5. The local field factor

The linear density response function $\chi(k_z, \omega)$ of the 1DEL can be written in terms of the interacting reference susceptibility $\chi_1(k_z, \omega)$ and of a local field factor $\tilde{G}(k_z, \omega)$ as

$$\chi(k_z, \omega) = \frac{\chi_1(k_z, \omega)}{1 - v(k_z)[1 - \tilde{G}(k_z, \omega)]\chi_1(k_z, \omega)}. \quad (26)$$

The interacting reference susceptibility, first introduced by Niklasson [13] for 3D jellium, is defined in a similar way as the Lindhard free-electron response function but with the ideal Fermi momentum distribution replaced by the true momentum distribution of the interacting electron assembly.

Following the method used by Niklasson [13] it can be shown that for points in the (k_z, ω) plane well outside the region of particle–hole excitations, the local field factor in Eq. (26) satisfies two exact limiting behaviours. These are expressed in terms of the function

$$G^{\text{PV}}(k_z) = \frac{1}{2\pi\rho_{\parallel}} \int_{-\infty}^{\infty} dq \left\{ \frac{q^2 v(q)}{k_z^2 v(k_z)} - \frac{(q + k_z)^2 v(q + k_z)}{k_z^2 v(k_z)} \right\} [S(q) - 1]. \quad (27)$$

$G^{\text{PV}}(k_z)$ is the form taken in the 1DEL by the static local field factor first introduced by Pathak and Vashishta [14] for 3D jellium.

Niklasson's method involves a study of the equations of motion for the single-particle and the two-particle density matrices, which allow a full evaluation of the interacting reference susceptibility in the limit of large K or large ω . It is easily shown that the following limit must hold for $|\omega \pm k_z^2/2m| \gg k_F^2/2m$ and ω finite,

$$\lim_{k_z \rightarrow \infty} \tilde{G}(k_z, \omega) = G^{\text{PV}}(\infty). \quad (28)$$

Using Eqs. (5) and (6) in Eqs. (27) and (28) we find

$$\begin{aligned} \tilde{G}(k_z \rightarrow \infty, \omega) = 1 - g(0) \\ + \frac{1}{8\pi^2 e^2 \rho_{\parallel} Q_2} \int dq q^2 v(q) [S(q) - 1] \end{aligned} \quad (29)$$

for a 1DEL obtained from 3D confinement and

$$\tilde{G}(k_z \rightarrow \infty, \omega) = 1 - g(0) \quad (30)$$

for a 1DEL with 2D confinement. Eq. (30) coincides with the result obtained by Santoro and Giuliani [15] for 2D jellium.

Finally, it is also easily shown by the same method that

$$\lim_{\omega \rightarrow \infty} \tilde{G}(k_z, \omega) = G^{\text{PV}}(k_z) \quad (31)$$

for $|\omega \pm k_z^2/2m| \gg k_F^2/2m$ and k_z finite.

A final remark concerning the asymptotic behaviour of static dielectric screening at large wave numbers is in order. After rewriting Eq. (26) in terms of the Lindhard function $\chi_0(k_z, \omega)$ and of a new local field factor $G(k_z, \omega)$,

$$\chi(k_z, \omega) = \frac{\chi_0(k_z, \omega)}{1 - v(k_z) [1 - G(k_z) \chi_0(k_z, \omega)]}, \quad (32)$$

it is easily shown from our results that $G(k_z, 0)$ increases as k_z^2 at large momenta in a 1DEL with 3D-like confinement and as $|k_z|$ when the confinement is 2D-like. These behaviours reproduce those first pointed out by Holas [16] for 3D and 2D jellium.

6. Concluding remarks

The Coulomb interaction potential between electrons in a quantum wire would not have a Fourier transform if both confinement lengths were taken as vanishingly small, because of its divergence at vanishing separation. The transverse density form factor $\rho_{\perp}(\mathbf{r})$, with Fourier transform $\rho_{\perp}(\mathbf{k})$, therefore is a crucial element of the theory and through it the nature of the confinement enters to determine the effective 1D electron–electron interaction in Eqs. (3) and (4). The Coulomb matrix element at large momentum transfers takes in general a 3D-like form as in Eq. (5), reducing to the 2D-like form of Eq. (6) in the case where one of the confinement lengths can be taken as vanishingly small. These asymptotic forms arise from transverse averaging of the Bessel function in the integrand in Eq. (3), which by itself would lead to an exponential decay factor at large momenta.

The asymptotic behaviours of the momentum distribution, the static structure factor and the local field factor that we have explicitly evaluated at large momenta reflect the above nature of the Coulomb matrix element. Dimensional cross-over in these behaviours is to be expected as one of the confinement lengths is squeezed down. Even in the case of 3D-like confinement, however, the short-range correlations reflect the confinement through the magnitude of the parameter Q_2 .

References

- [1] A.S. Plaut, H. Lage, P. Grambow, D. Heitmann, K. von Klitzing and K. Ploog, Phys. Rev. Lett. 67 (1991) 1642.
- [2] A.R. Goñi, A. Pinczuk, J.S. Weiner, J.M. Calleja, B.S. Dennis, L.N. Pfeiffer and K.W. West, Phys. Rev. Lett. 67 (1991) 3298.
- [3] Q.P. Li and S. Das Sarma, Phys. Rev. B 43 (1991) 11 768.
- [4] K.S. Singwi and M.P. Tosi, Solid State Phys. 36 (1981) 177.
- [5] W.I. Friesen and B. Bergersen, J. Phys. C 13 (1980) 6627.
- [6] The dominated convergence theorem asserts that when integrating a sequence of pointwise convergent functions f_n , it is permissible to bring the limit inside the integral sign if the absolute values of all the f_n are bounded from above by one integrable function. See W. Rudin, Real and Complex Analysis (McGraw-Hill, New York, 1966) p. 26.
- [7] H. Yasuhara, Physica 78 (1974) 420.
- [8] J.C. Kimball, Phys. Rev. A 7 (1973) 1648.

- [9] A.K. Rajagopal and J.C. Kimball, *Phys. Rev. B* 15 (1977) 2819.
- [10] A.E. Carlsson and N.W. Ashcroft, *Phys. Rev. B* 25 (1982) 3474 and references given therein.
- [11] H. Yasuhara and Y. Kawazoe, *Physica A* 85 (1976) 416.
- [12] J.C. Kimball, *J. Phys. A* 8 (1975) 1513.
- [13] G. Niklasson, *Phys. Rev. B* 10 (1974) 3052.
- [14] K.N. Pathak and P. Vashishta, *Phys. Rev. B* 7 (1973) 3649.
- [15] G.E. Santoro and G.F. Giuliani, *Phys. Rev. B* 37 (1988) 4813.
- [16] A. Holas, in: *Strongly Coupled Plasma Physics*, eds. F.J. Rogers and H.E. DeWitt (Plenum, New York, 1986) p. 463.



Part III
2003

Chapter 4

Pressures for a One-Component Plasma on a Pseudosphere

Fantoni R., Jancovici B., and Téllez G., J. Stat. Phys., **112**, 27 (2003)

Title: “Pressures for a One-Component Plasma on a Pseudosphere.”

Abstract: The classical (i.e. non-quantum) equilibrium statistical mechanics of a two-dimensional one-component plasma (a system of charged point-particles embedded in a neutralizing background) living on a pseudosphere (an infinite surface of constant negative curvature) is considered. In the case of a flat space, it is known that, for a one-component plasma, there are several reasonable definitions of the pressure, and that some of them are not equivalent to each other. In the present paper, this problem is revisited in the case of a pseudosphere. General relations between the different pressures are given. At one special temperature, the model is exactly solvable in the grand canonical ensemble. The grand potential and the one-body density are calculated in a disk, and the thermodynamic limit is investigated. The general relations between the different pressures are checked on the solvable model.

Pressures for a One-Component Plasma on a Pseudosphere

R. Fantoni,¹ B. Jancovici,² and G. Téllez^{2,3}

Received July 22, 2002; accepted February 7, 2003

The classical (i.e., non-quantum) equilibrium statistical mechanics of a two-dimensional one-component plasma (a system of charged point-particles embedded in a neutralizing background) living on a pseudosphere (an infinite surface of constant negative curvature) is considered. In the case of a flat space, it is known that, for a one-component plasma, there are several reasonable definitions of the pressure, and that some of them are not equivalent to each other. In the present paper, this problem is revisited in the case of a pseudosphere. General relations between the different pressures are given. At one special temperature, the model is exactly solvable in the grand canonical ensemble. The grand potential and the one-body density are calculated in a disk, and the thermodynamic limit is investigated. The general relations between the different pressures are checked on the solvable model.

KEY WORDS: Pseudosphere; negative curvature; two-dimensional one-component plasma; pressure; exactly solvable models.

1. INTRODUCTION

Coulomb systems such as plasmas or electrolytes are made of charged particles interacting through Coulomb's law. The simplest model of a Coulomb system is the one-component plasma (OCP), also called jellium: an assembly of identical point charges, embedded in a neutralizing uniform

¹ Dipartimento di Fisica Teorica dell' Università and Istituto Nazionale di Fisica della Materia, Strada Costiera 11, 34014 Trieste, Italy; e-mail: rfantoni@ts.infn.it

² Laboratoire de Physique Théorique, Bâtiment 210, Université de Paris-Sud, 91405 Orsay, France (Unité Mixte de Recherche No. 8627-CNRS); e-mail: Bernard.Jancovici@th.u-psud.fr

³ Permanent address: Grupo de Física Teórica de la Materia Condensada, Departamento de Física, Universidad de Los Andes, A.A. 4976, Bogotá, Colombia; e-mail: gtellez@uniandes.edu.co

background of the opposite sign. Here we consider the classical (i.e., non-quantum) equilibrium statistical mechanics of the OCP. Although many features of more realistic systems are correctly reproduced, this model has the peculiarity that there are several reasonable definitions of its pressure, and some of these definitions are not equivalent to each other.^(1,2)

The two-dimensional version (2D OCP) of the OCP has been much studied. Provided that the Coulomb potential due to a point-charge is defined as the solution of the Poisson equation in a two-dimensional world (i.e., is a logarithmic function $-\ln r$ of the distance r to that point-charge), the 2D OCP mimicks many generic properties of the three-dimensional Coulomb systems. Of course, this toy logarithmic model does not describe real charged particles, such as electrons, confined on a surface, which nevertheless interact through the three dimensional Coulomb potential $1/r$. One motivation for studying the 2D OCP is that its equilibrium statistical mechanics is exactly solvable at one special temperature: both the thermodynamical quantities and the correlation functions are available.⁽³⁾

How the properties of a system are affected by the curvature of the space in which the system lives is a question which arises in general relativity. This is an incentive for studying simple models. Thus, the problem of a 2D OCP on a pseudosphere has been considered.⁽⁴⁾ A pseudosphere is a non-compact Riemannian surface of constant negative curvature. Unlike the sphere it has an infinite area and it is not embeddable in the three dimensional Euclidean space. The property of having an infinite area makes it interesting from the point of view of Statistical Physics because one can take the thermodynamic limit on it.

For this 2D OCP on a pseudosphere, the problem of studying and comparing the different possible definitions of the pressure also arises. This is the subject of the present paper. In Section 2, we give some basic properties of the pseudosphere and of a 2D OCP on it. In Section 3, we define the different pressures and derive general relations between them. In Section 4, we illustrate the general properties by considering the special temperature at which all properties can be explicitly and exactly calculated.

2. PSEUDOSPHERE AND ONE-COMPONENT PLASMA

2.1. The Pseudosphere

There are at least three commonly known sets of coordinates to describe a pseudosphere of Gaussian curvature $-1/a^2$. The one which renders explicit the resemblance with the sphere is $\vec{q} = (q^1, q^2) = (q^\tau, q^\varphi) = (\tau, \varphi)$ with $\tau \in [0, \infty[$ and $\varphi \in [0, 2\pi[$, the metric being

$$ds^2 = g_{\alpha\beta} dq^\alpha dq^\beta = a^2(d\tau^2 + \sinh^2 \tau d\varphi^2) \quad (2.1)$$

Another set of coordinates often used is (r, φ) with $r/(2a) = \tanh(\tau/2)$. They are the polar coordinates of a disk of radius $2a$. The metric in terms of these new coordinates is

$$ds^2 = \frac{dr^2 + r^2 d\varphi^2}{[1 - (r^2/4a^2)]^2} \quad (2.2)$$

The disk with such a metric is called the Poincaré disk. Through an appropriate conformal transformation, the Poincaré disk can be mapped onto the upper half-plane with some metric, the Poincaré half-plane, but this latter representation will not be used here. The geodesic distance d_{01} between any two points $\vec{q}_0 = (\tau_0, \varphi_0)$ and $\vec{q}_1 = (\tau_1, \varphi_1)$ on the pseudosphere is given by

$$\cosh(d_{01}/a) = \cosh \tau_1 \cosh \tau_0 - \sinh \tau_1 \sinh \tau_0 \cos(\varphi_1 - \varphi_0) \quad (2.3)$$

Given the set of points at a geodesic distance from the origin less than or equal to d , that we shall call a disk of radius d , we can easily determine its circumference

$$\mathcal{C} = 2\pi a \sinh\left(\frac{d}{a}\right) \underset{d \rightarrow \infty}{\sim} \pi a e^{d/a} \quad (2.4)$$

and its area

$$\mathcal{A} = 4\pi a^2 \sinh^2\left(\frac{d}{2a}\right) \underset{d \rightarrow \infty}{\sim} \pi a^2 e^{d/a} \quad (2.5)$$

The Laplace–Beltrami operator on the pseudosphere is

$$\Delta = \frac{1}{a^2} \left(\frac{1}{\sinh \tau} \frac{\partial}{\partial \tau} \sinh \tau \frac{\partial}{\partial \tau} + \frac{1}{\sinh^2 \tau} \frac{\partial^2}{\partial \varphi^2} \right) \quad (2.6)$$

2.2. The One-Component Plasma

The 2D OCP which is considered here is an ensemble of N identical point particles of charge q , constrained to move in a disk of radius $d = a\tau_0$ by an infinite potential barrier on the boundary of this domain $\tau = \tau_0$. The average particle number density is $n = N/\mathcal{A}$, where \mathcal{A} is the area (2.5). There is a background with a charge density $\rho_b = -qn_b$ uniformly smeared on the disk (ρ_b is 0 outside the disk). It is convenient to introduce the number of elementary charges in the background: $N_b = n_b \mathcal{A}$. The total charge is not necessarily 0, thus in general $n_b \neq n$.

The pair Coulomb potential $v(d)$ between two unit charges, a geodesic distance d apart, satisfies the Poisson equation on the pseudosphere,

$$\Delta v(d) = -2\pi\delta^{(2)}(d) \quad (2.7)$$

where $\delta^{(2)}(d)$ is the Dirac delta function on the curved manifold. This Poisson equation admits a solution vanishing at infinity,

$$v(d) = -\ln \left[\tanh \left(\frac{d}{2a} \right) \right] \quad (2.8)$$

The electrostatic potential of the background $w(\vec{q})$ satisfies

$$\Delta w(\vec{q}) = -2\pi\rho_b \quad (2.9)$$

By symmetry, this electrostatic potential is only a function of τ . Expressing the Laplacian (2.6) in terms of the variable $\cosh \tau$, and requesting the solution to be regular at $\tau=0$ and to have the correct value at $\tau=\tau_0$ (corresponding to the background total charge), one finds the solution

$$w(\tau) = 2\pi a^2 q n_b \left\{ \ln \left[\frac{1 - \tanh^2(\tau_0/2)}{1 - \tanh^2(\tau/2)} \right] + \sinh^2(\tau_0/2) \ln[\tanh^2(\tau_0/2)] \right\} \quad (2.10)$$

Let $dS = 2\pi a^2 \sinh \tau d\tau$ be an area element. The self energy of the background is

$$\begin{aligned} v_0 &= \frac{1}{2} \int_{\tau < \tau_0} \rho_b w(\tau) dS \\ &= (2\pi a^2 q n_b)^2 \left\{ \sinh^2(\tau_0/2) - \ln[\cosh^2(\tau_0/2)] \right. \\ &\quad \left. - \sinh^4(\tau_0/2) \ln[\tanh^2(\tau_0/2)] \right\} \end{aligned} \quad (2.11)$$

The total potential energy of the system is

$$U = v_0 + v_{pb} + v_{pp} \quad (2.12)$$

where v_{pp} is the potential energy due to the interactions between the particles,

$$v_{pp} = \frac{1}{2} \sum_{\substack{i,j=1 \\ i \neq j}}^N q^2 v(d_{ij}) \quad (2.13)$$

and v_{pb} is the potential energy due to the interaction between the particles and the background,

$$v_{pb} = \sum_{i=1}^N qw(\tau_i) \quad (2.14)$$

3. THE DIFFERENT PRESSURES AND THEIR RELATIONS

In the case of a flat system, the pressure which is often considered, termed the thermal pressure, is defined from the free energy F by the standard relation $P^{(\theta)} = -(\partial F / \partial \mathcal{A})_{\beta, N, N_b}$, where β is the inverse temperature. In the case of a flat neutral ($N = N_b$) 2D OCP, this thermal pressure is given by the simple exact expression $\beta P^{(\theta)} = n[1 - (\beta q^2 / 4)]$.^(5,6) Thus, this thermal pressure becomes negative for $\beta q^2 > 4$, i.e., at low temperatures. This pathology of the OCP occurs also in three dimensions; it is related to the presence of an inert background without kinetic energy. Indeed, the uniform background can be considered as the limit of a gas of negative particles of charge $-\epsilon$ and number density ν , when $\epsilon \rightarrow 0$, $\nu \rightarrow \infty$, for a fixed value of the charge density $-\epsilon\nu$. In this limit, the ideal-gas part (kinetic part) of the background average energy density becomes infinite. In the OCP Hamiltonian, this infinite energy density is omitted. The price paid for this omission is that the corresponding (infinite) ideal-gas contribution to the pressure is omitted, and the remaining pressure may be negative.⁴

Unhappy with this negativeness, Choquard *et al.*⁽¹⁾ and Navet *et al.*⁽²⁾ have introduced another pressure, the kinetic pressure $P^{(k)}$, which is the pressure exerted on the wall by the particles of charge q only. This kinetic pressure turns out to be also the one which is obtained through the use of the virial theorem. Although for usual fluids the thermal and kinetic pressures are equivalent, in the presence of a background they are different, with the kinetic pressure being always positive. This positiveness led the above authors to argue that the kinetic pressure is the “right” one. Anyhow, a detailed comparison of the diverse possible definitions of the pressure of a flat OCP has been done.⁽¹⁾

In the present paper, it is this comparison that we extend to the case of a 2D OCP on a pseudosphere. We shall restrict ourselves to the case of a domain in the shape of a disk. We are especially interested in the thermodynamic limit, i.e., when the disk radius becomes infinite, for fixed values of β , n , n_b .

⁴In the case of a two-dimensional *two*-component plasma made of point-particles, the pressure also becomes negative when extrapolated to low temperatures $\beta q^2 > 4$. However, now $\beta q^2 > 4$ is outside the domain of definition of the partition function.

3.1. Kinetic and Virial Pressures

The average force exerted by the particles on a perimeter element ds is $(1/\beta) n^{(1)}(\tau_0) ds$, where $n^{(1)}(\tau)$ is the one-body density at the distance $a\tau$ from the origin. Therefore, the kinetic pressure is

$$P^{(k)} = (1/\beta) n^{(1)}(\tau_0) \quad (3.1)$$

We assume that this quantity has a limit when $\tau_0 \rightarrow \infty$. In Section 4, this assumption will be checked in the special case $\beta q^2 = 2$. It will now be shown that the virial pressure $P^{(v)}$, i.e., the pressure computed from the virial theorem, is the same as $P^{(k)}$.

In terms of the $2N$ coordinate components q^N and $2N$ conjugate momentum components p^N , the Hamiltonian of our OCP of N particles is

$$H(q^N, p^N) = T(q^N, p^N) + \bar{U}(q^N) \quad (3.2)$$

where $\bar{U} = U + \text{confining potential}$ and the kinetic energy T is

$$T = \frac{1}{2m} \sum_{i=1}^N g^{\alpha\beta}(\vec{q}_i) p_{i\alpha} p_{i\beta} \quad (3.3)$$

The Roman indices label the particles, and the lower or upper Greek indices denote covariant or contravariant components, respectively. As usual, a sum over repeated Greek indices is tacitly assumed. The equations of motion for particle i are

$$\begin{cases} \dot{q}_i^\alpha = \frac{\partial H}{\partial p_{i\alpha}} = \frac{1}{m} g^{\alpha\beta}(\vec{q}_i) p_{i\beta} \\ \dot{p}_{i\alpha} = -\frac{\partial H}{\partial q_i^\alpha} = -\frac{1}{2m} \frac{\partial g^{\beta\gamma}}{\partial q_i^\alpha} p_{i\beta} p_{i\gamma} - \frac{\partial \bar{U}}{\partial q_i^\alpha} \end{cases} \quad (3.4)$$

where the dot stands for total derivative with respect to time. If we take the time derivative of $\sum_i q_i^\tau p_{i\tau} = \sum_i \tau_i p_{i\tau}$, we find⁵

$$\frac{d}{dt} \sum_i \tau_i p_{i\tau} = \frac{1}{m} \sum_{i=1}^N g^{\tau\beta}(\vec{q}_i) p_{i\tau} p_{i\beta} - \frac{1}{2m} \sum_{i=1}^N \tau_i \frac{\partial g^{\beta\gamma}}{\partial \tau_i} p_{i\beta} p_{i\gamma} - \sum_{i=1}^N \tau_i \frac{\partial \bar{U}}{\partial \tau_i} \quad (3.5)$$

⁵ One may be tempted to start with the time derivative of $\sum_i q_i^\alpha p_{i\alpha} = \sum_i (\tau_i p_{i\tau} + \varphi_i p_{i\varphi})$. Note however that this quantity does not remain finite at all times. This is because, when one follows the motion of a particle colliding with the boundary, it may go around the origin indefinitely, and φ_i (which must be defined as a continuous variable, without any 2π jumps) may increase indefinitely. Thus the time average of the time derivative of this quantity does not vanish.

where the last term is called the virial of the system. Since the system is confined in a finite domain, the coordinates $\tau_i(t)$ and their canonically conjugated momenta $p_{i\tau}(t)$ remain finite at all times. Thus,

$$\left\langle \frac{d}{dt} \sum_{i=1}^N \tau_i p_{i\tau} \right\rangle_t = 0 \quad (3.6)$$

where $\langle \dots \rangle_t$ denotes a time average. Assuming that the system is ergodic, we can replace time averages by microcanonical averages. Assuming the equivalence of ensembles in the thermodynamic limit, we can as well use canonical or grand-canonical averages $\langle \dots \rangle$. In the present section, we use canonical averages. The average of the r.h.s. of (3.5) vanishes. Separating in the last term of (3.5) the contribution from the forces exerted by the walls, which is, in the average, $-a\tau_0 \mathcal{E}P^{(v)}$, we obtain

$$a\tau_0 \mathcal{E}P^{(v)} = \left\langle \frac{1}{m} \sum_{i=1}^N g^{\tau\beta}(\vec{q}_i) p_{i\tau} p_{i\beta} \right\rangle - \left\langle \frac{1}{2m} \sum_{i=1}^N \tau_i \frac{\partial g^{\beta\gamma}}{\partial \tau_i} p_{i\beta} p_{i\gamma} \right\rangle - \left\langle \sum_{i=1}^N \tau_i \frac{\partial U}{\partial \tau_i} \right\rangle \quad (3.7)$$

We now calculate the three terms in the r.h.s. of (3.7). The first one is the average of twice a contribution to the Hamiltonian, which is quadratic in the N variables $p_{i\tau}$ (g is diagonal); since the average of a quadratic term in the Hamiltonian is $1/(2\beta)$, the first term in the r.h.s. of (3.7) is

$$\left\langle \frac{1}{m} \sum_{i=1}^N g^{\tau\tau}(\vec{q}_i) (p_{i\tau})^2 \right\rangle = \frac{N}{\beta} \quad (3.8)$$

The second term reduces to $-\langle (1/2m) \sum_{i=1}^N \tau_i (\partial g^{\varphi\varphi} / \partial \tau_i) (p_{i\varphi})^2 \rangle$. Averaging first on $p_{i\varphi}$ replaces $(p_{i\varphi})^2/2m$ by $1/[2\beta g^{\varphi\varphi}(\tau_i)]$. The second term becomes

$$\frac{1}{\beta} \left\langle \sum_{i=1}^N \frac{\tau_i}{\tanh \tau_i} \right\rangle = \frac{1}{\beta} \int_{\tau < \tau_0} n^{(1)}(\tau) \frac{\tau}{\tanh \tau} dS \quad (3.9)$$

Finally, since

$$\frac{dn^{(1)}(\tau_1)}{d\tau_1} = -\beta N \frac{\int e^{-\beta U} (\partial U / \partial \tau_1) dS_2 \cdots dS_N}{\int e^{-\beta U} dS_1 dS_2 \cdots dS_N} \quad (3.10)$$

the third term can be written as

$$-N \left\langle \tau_1 \frac{\partial U}{\partial \tau_1} \right\rangle = \frac{1}{\beta} \int_{\tau_1 < \tau_0} \tau_1 \frac{dn^{(1)}(\tau_1)}{d\tau_1} dS_1 \quad (3.11)$$

Putting together the contributions (3.8), (3.9), and (3.11) gives for (3.7)

$$\alpha\tau_0\mathcal{C}P^{(v)} = \frac{N}{\beta} + \frac{1}{\beta} \int_0^{\tau_0} \left[n^{(1)}(\tau) \frac{\tau}{\tanh \tau} + \tau \frac{dn^{(1)}(\tau)}{d\tau} \right] 2\pi a^2 \sinh \tau d\tau \quad (3.12)$$

After an integration by parts, (3.12) becomes

$$P^{(v)} = \frac{1}{\beta} n^{(1)}(\tau_0) = P^{(k)} \quad (3.13)$$

3.2. The Thermal Pressure

The thermal pressure is defined as

$$P^{(\theta)} = - \left(\frac{\partial F}{\partial \mathcal{A}} \right)_{\beta, N, N_b} \quad (3.14)$$

where F is the free energy. This expression is appropriate for the canonical ensemble, since F is related to the canonical partition function Z by $\beta F = -\ln Z$.

3.2.1. The Thermal Pressure in the Grand Canonical Ensemble

In the following, we shall also need an expression of the thermal pressure appropriate for the grand canonical ensemble. It should be remembered that, for a flat OCP in three dimensions, the grand canonical partition function must be defined⁽⁷⁾ as an ensemble of systems with any number N of particles in a fixed volume and *with a fixed background charge density* $-qn_b$ (using an ensemble of neutral systems, i.e., varying n_b together with N would give a divergent grand partition function). In two dimensions, β times the free energy for a neutral flat system⁽³⁾ behaves as $[1 - (\beta q^2/4)] N \ln N$ as $N \rightarrow \infty$, and therefore the neutral grand canonical partition function diverges if $\beta q^2 > 4$. This indicates that, in the present case of a 2D OCP on a pseudosphere, a similar divergence might occur for an ensemble of neutral systems, and we prefer to use an ensemble with a fixed background (which, furthermore, will be seen to be exactly solvable at $\beta q^2 = 2$). Thus, the grand partition function Ξ and the corresponding grand potential $\Omega = -(1/\beta) \ln \Xi$ are functions of β , \mathcal{A} , ζ , n_b , where ζ is the fugacity. The usual Legendre transformation from F to Ω and from N to ζ changes (3.14) into

$$P^{(\theta)} = - \left(\frac{\partial \Omega}{\partial \mathcal{A}} \right)_{\beta, \zeta, N_b} \quad (3.15)$$

We assume that, even on a pseudosphere, the grand potential is extensive, i.e., of the form $\Omega = \mathcal{A}\omega(\beta, \zeta, n_b)$. Since ω depends on \mathcal{A} through $n_b = N_b/\mathcal{A}$, Eq. (3.15) becomes

$$P^{(\theta)} = -\omega + n_b \frac{\partial \omega}{\partial n_b} \quad (3.16)$$

Note the difference with an ordinary fluid, without a background, for which $P^{(\theta)} = -\omega$.

3.2.2. The $P^{(\theta)} - P^{(k)}$ Difference

For a OCP, the thermal pressure is different from the kinetic pressure. In the case of a 2D OCP in a flat disk, in the thermodynamic limit, the boundary becomes a straight line and the difference was found to be⁽¹⁾

$$P^{(\theta)} - P^{(k)} = -2\pi q^2 n_b \int_0^\infty [n^{(1)}(x) - n_b] x dx \quad (3.17)$$

where $n^{(1)}(x)$ is the density at distance x from the boundary. Using the Poisson equation, one can write (3.17) in the equivalent form⁽⁸⁾

$$P^{(\theta)} - P^{(k)} = qn_b [\phi_{\text{surface}} - \phi_{\text{bulk}}] \quad (3.18)$$

where ϕ_{bulk} and ϕ_{surface} are the electric potential in the bulk and on the disk boundary, respectively.⁶

Equation (3.18) can be proven as follows. Either in the flat case, or in the case of a pseudosphere, let us consider a large disk of area \mathcal{A} , filled with a 2D OCP. For compressing it infinitesimally, changing the area by $d\mathcal{A} < 0$, at constant β, N, N_b , we must provide the reversible work $\delta W = -P^{(\theta)} d\mathcal{A}$. We may achieve that compression in two steps. First, one compresses the particles only, leaving the background behind; the corresponding work is $\delta W^{(1)} = -P^{(k)} d\mathcal{A}$, since $P^{(k)}$ is the force per unit length exerted on the wall by the particles alone. Then, one compresses the background, i.e., brings the charge $qn_b d\mathcal{A}$ from a region where the potential is ϕ_{surface} into the plasma where the potential is $\phi(r)$, spreading it uniformly; the corresponding work is $\delta W^{(2)} = qn_b d\mathcal{A} [(1/\mathcal{A}) \int \phi(r) dS - \phi_{\text{surface}}]$, where $\phi(r)$ is the potential at distance r from the center. Therefore,

$$P^{(\theta)} - P^{(k)} = qn_b \left[\phi_{\text{surface}} - \frac{1}{\mathcal{A}} \int \phi(r) dS \right] \quad (3.19)$$

⁶ In the original papers,^(1,8) the derivations of (3.17) and (3.18) have been done in the case of a neutral system. However, these derivations can be easily extended to systems carrying a total non vanishing charge.

We expect $\phi(r)$ to differ from ϕ_{bulk} only in the neighborhood of the boundary circle.

In the case of a flat disk, the contribution of this neighborhood to the integral in (3.19) is negligible in the thermodynamic limit, $\phi(r)$ can be replaced by the constant ϕ_{bulk} , and one obtains (3.18). On a pseudosphere, (3.19) [with $\phi(\tau)$ instead of $\phi(r)$] is still valid. However, now, in the large-disk limit, the integration element $dS = 2\pi a^2 \sinh \tau d\tau$ makes the boundary neighborhood dominant, and we rather have

$$P^{(\theta)} - P^{(k)} \sim qn_b \left[\phi(\tau_0) - e^{-\tau_0} \int_0^{\tau_0} \phi(\tau) e^\tau d\tau \right] \quad (3.20)$$

After some manipulations, in the thermodynamic limit, (3.20) can be shown to be equivalent to

$$P^{(\theta)} - P^{(k)} = -2\pi a^2 n_b q^2 \int_0^\infty [n^{(1)}(\sigma) - n_b] \sigma e^{-\sigma} d\sigma \quad (3.21)$$

where we have introduced the variable $\sigma = \tau_0 - \tau$ and $n^{(1)}(\sigma)$ now denotes the particle density at distance $a\sigma$ from the boundary. Indeed, in (3.21), $n^{(1)}(\tau) - n_b$ can be expressed in terms of $\phi(\tau)$ through the Poisson equation $\Delta\phi(\tau) = -2\pi q[n^{(1)}(\tau) - n_b]$. Since the charge density is localized at large τ , we can use for the Laplacian $\Delta \sim a^{-2}[d^2/d\tau^2 + d/d\tau]$. After integrations by parts, (3.20) is recovered.

In conclusion, (3.17) valid for a large flat disc generalizes into (3.21) on a pseudosphere. In the limit $a \rightarrow \infty$, $\sigma \rightarrow 0$, $a\sigma = x$, Eq. (3.21) does reproduce (3.17).

3.3. The Mechanical Pressure

Choquard *et al.*⁽¹⁾ have also defined a mechanical pressure, in terms of the free energy F , as

$$P^{(m)} = - \left(\frac{\partial F}{\partial \mathcal{A}} \right)_{\beta, N, n_b} \quad (3.22)$$

In terms of the grand potential Ω , a Legendre transformation now gives

$$P^{(m)} = - \left(\frac{\partial \Omega}{\partial \mathcal{A}} \right)_{\beta, \zeta, n_b} \quad (3.23)$$

If the grand potential is extensive, of the form $\Omega = \mathcal{A}\omega(\beta, \zeta, n_b)$, (3.23) gives

$$P^{(m)} = -\omega \quad (3.24)$$

The difference $P^{(m)} - P^{(k)}$ can be obtained by a slight change in the argument of Section 3.2.2. Again, we consider a large disk filled with a 2D OCP of area \mathcal{A} , and we compress it infinitesimally, changing its area by $d\mathcal{A} < 0$, now at constant β, N, n_b , providing the reversible work $\delta W = -P^{(m)} d\mathcal{A}$, in two steps. Again, first one compresses the particles only, leaving the background behind, and the corresponding work is $\delta W^{(1)} = -P^{(k)} d\mathcal{A}$. Then, one must withdraw the leftover background charge $qn_b d\mathcal{A}$, bringing it from the surface where the potential is ϕ_{surface} to infinity where the potential vanishes. The corresponding work is $\delta W^{(2)} = -qn_b d\mathcal{A} \phi_{\text{surface}}$. Therefore, for a disk on a pseudosphere, $P^{(m)} - P^{(k)} = qn_b \phi_{\text{surface}}$.⁷

In the thermodynamic limit, $\phi_{\text{surface}} \rightarrow 2\pi a^2 q(n - n_b)$ and

$$P^{(m)} - P^{(k)} = 2\pi a^2 q^2 n_b (n - n_b) \quad (3.25)$$

This difference vanishes for a neutral system ($n = n_b$).

The relations (3.21) and (3.25) between the different pressures obtained here by means of electrostatic arguments can also be obtained in a more formal way following Choquard *et al.*,⁽¹⁾ using the dilatation method (doing a change of variable $\tau = \tau_0 \tilde{\tau}$ in the partition function to explicitly show the area \mathcal{A} dependence) and the BGY equations to replace the two-body density terms that appear in the calculations by one-body density terms.

3.4. The Maxwell Tensor Pressure

On a pseudosphere, since the area of a large domain is of the same order as the area of the neighborhood of the boundary, all the above definitions of the pressure depend on the boundary conditions. In previous papers, a definition of a bulk pressure independent of the boundary conditions has been looked for. After an erroneous attempt,⁽⁴⁾ it has been

⁷ This result is identical with the one obtained by Choquard *et al.*⁽¹⁾ in the case of a flat disk. However, their general formula might make difficulties in two dimensions, because the Coulomb potential $-\ln(r/L)$ does not vanish at infinity and involves an arbitrary constant length L . These difficulties do not arise on a pseudosphere.

argued^(9,10) that a bulk pressure P_{Maxwell} could be defined from the Maxwell stress tensor⁽¹¹⁾ at some point well inside the fluid. The result was

$$\beta P_{\text{Maxwell}} = n_b \left(1 - \frac{\beta q^2}{4} \right) \quad (3.26)$$

That same equation of state holds for the 2D OCP on a plane, a sphere, or a pseudosphere.

4. EXACT RESULTS AT $\beta q^2 = 2$

When the Coulombic coupling constant is $\beta q^2 = 2$, all the thermodynamic properties and correlation functions of the two-dimensional one-component plasma can be computed exactly in several geometries^(3,12,13) including the pseudosphere.⁽⁴⁾ In ref. 4 the density and correlation functions in the bulk, on a pseudosphere, were computed. Here we are interested in these quantities near the boundary. In ref. 4 the calculations were done for a system with a $-\ln \sinh(d/2a)$ interaction and it was shown that this interaction gives the same results as the real Coulomb interaction $-\ln \tanh(d/2a)$, as far as the bulk properties are concerned. The argument in favor of this equivalence no longer holds for the density and other quantities near the boundary; therefore we shall concentrate on the real Coulomb system with a $-\ln \tanh(d/2a)$ interaction. This system was briefly considered in the Appendix of ref. 4. For the sake of completeness, we revisit here the reduction of the statistical mechanics problem to the study of a certain operator.

4.1. The Grand Potential

Working with the set of coordinates (r, φ) on the pseudosphere (the Poincaré disk representation), the particle i -particle j interaction term in the Hamiltonian can be written as⁽⁴⁾

$$v(d_{ij}) = -\ln \tanh(d_{ij}/2a) = -\ln \left| \frac{(z_i - z_j)/(2a)}{1 - (z_i \bar{z}_j/4a^2)} \right| \quad (4.1)$$

where $z_j = r_j e^{i\varphi_j}$ and \bar{z}_j is the complex conjugate of z_j . This interaction (4.1) happens to be the Coulomb interaction in a flat disc of radius $2a$ with ideal conductor walls. Therefore, it is possible to use the techniques which have been developed^(14,15) for dealing with ideal conductor walls, in the grand canonical ensemble.

The grand canonical partition function of the OCP at fugacity ζ with a fixed background density n_b , when $\beta q^2 = 2$, is

$$\mathcal{E} = C_0 \left[1 + \sum_{N=1}^{\infty} \frac{1}{N!} \int \prod_{k=1}^N \frac{\zeta(r_k) r_k dr_k d\varphi_k}{[1 - (r_k^2/4a^2)]} \prod_{i < j} \left| \frac{(z_i - z_j)/(2a)}{1 - (z_i \bar{z}_j/4a^2)} \right|^2 \right] \quad (4.2)$$

where for $N = 1$ the product $\prod_{i < j}$ must be replaced by 1. We have defined a position-dependent fugacity $\zeta(r) = \zeta [1 - r^2/(4a^2)]^{4\pi n_b a^2 - 1} e^C$ which includes the particle-background interaction (2.10) and only one factor $[1 - r^2/(4a^2)]^{-1}$ from the integration measure $dS = [1 - r^2/(4a^2)]^{-2} d\mathbf{r}$. This should prove to be convenient later. The e^C factor is

$$e^C = \exp \left[4\pi n_b a^2 \left(\ln \cosh^2 \frac{\tau_0}{2} - \sinh^2 \frac{\tau_0}{2} \ln \tanh^2 \frac{\tau_0}{2} \right) \right] \quad (4.3)$$

which is a constant term coming from the particle-background interaction term (2.10) and

$$\ln C_0 = \frac{(4\pi n_b a^2)^2}{2} \left[\ln \cosh^2 \frac{\tau_0}{2} + \sinh^2 \frac{\tau_0}{2} \left(\sinh^2 \frac{\tau_0}{2} \ln \tanh^2 \frac{\tau_0}{2} - 1 \right) \right] \quad (4.4)$$

which comes from the background-background interaction (2.11). Notice that for large domains, when $\tau_0 \rightarrow \infty$, we have

$$e^C \sim \left[\frac{e^{\tau_0 + 1}}{4} \right]^{4\pi n_b a^2} \quad (4.5)$$

and

$$\ln C_0 \sim -\frac{(4\pi n_b a^2)^2 e^{\tau_0}}{4} \quad (4.6)$$

Let us define a set of reduced complex coordinates $u_i = (z_i/2a)$ inside the Poincaré disk and its corresponding images $u_i^* = (2a/\bar{z}_i)$ outside the disk. By using Cauchy identity

$$\det \left(\frac{1}{u_i - u_j^*} \right)_{(i,j) \in \{1, \dots, N\}^2} = (-1)^{N(N-1)/2} \frac{\prod_{i < j} (u_i - u_j)(u_i^* - u_j^*)}{\prod_{i,j} (u_i - u_j^*)} \quad (4.7)$$

the particle-particle interaction term together with the $[1 - (r_i^2/4a^2)]^{-1}$ other term from the integration measure can be cast into the form

$$\prod_{i < j} \left| \frac{(z_i - z_j)/(2a)}{1 - (z_i \bar{z}_j/4a^2)} \right|^2 \prod_{i=1}^N [1 - (r_i^2/4a^2)]^{-1} = \det \left(\frac{1}{1 - u_i \bar{u}_j} \right)_{(i,j) \in \{1, \dots, N\}^2} \quad (4.8)$$

The grand canonical partition function then is

$$\mathcal{E} = \left[1 + \sum_{N=1}^{\infty} \frac{1}{N!} \int \prod_{k=1}^N d^2\mathbf{r}_k \zeta(r_k) \det \left(\frac{1}{1-u_i\bar{u}_j} \right) \right] C_0 \quad (4.9)$$

We shall now show that this expression can be reduced to an infinite continuous determinant, by using a functional integral representation similar to the one which has been developed for the two-component Coulomb gas.⁽¹⁶⁾ Let us consider the Gaussian partition function

$$Z_0 = \int \mathcal{D}\psi \mathcal{D}\bar{\psi} \exp \left[\int \bar{\psi}(\mathbf{r}) M^{-1}(z, \bar{z}') \psi(\mathbf{r}') d^2\mathbf{r} d^2\mathbf{r}' \right] \quad (4.10)$$

The fields ψ and $\bar{\psi}$ are anticommuting Grassmann variables. The Gaussian measure in (4.10) is chosen such that its covariance is equal to⁸

$$\langle \bar{\psi}(\mathbf{r}_i) \psi(\mathbf{r}_j) \rangle = M(z_i, \bar{z}_j) = \frac{1}{1-u_i\bar{u}_j} \quad (4.11)$$

where $\langle \dots \rangle$ denotes an average taken with the Gaussian weight of (4.10). By construction we have

$$Z_0 = \det(M^{-1}) \quad (4.12)$$

Let us now consider the following partition function

$$Z = \int \mathcal{D}\psi \mathcal{D}\bar{\psi} \exp \left[\int \bar{\psi}(\mathbf{r}) M^{-1}(z, \bar{z}') \psi(\mathbf{r}') d^2\mathbf{r} d^2\mathbf{r}' + \int \zeta(r) \bar{\psi}(\mathbf{r}) \psi(\mathbf{r}) d^2\mathbf{r} \right] \quad (4.13)$$

which is equal to

$$Z = \det(M^{-1} + \zeta) \quad (4.14)$$

and then

$$\frac{Z}{Z_0} = \det[M(M^{-1} + \zeta)] = \det[1 + K] \quad (4.15)$$

⁸ Actually the operator M should be restricted to act only on analytical functions for its inverse M^{-1} to exist.

where

$$K(\mathbf{r}, \mathbf{r}') = M(z, \bar{z}') \zeta(r') = \frac{\zeta(r')}{1 - u\bar{u}'} \quad (4.16)$$

The results which follow can also be obtained by exchanging the order of the factors M and $M^{-1} + \zeta$ in (4.15), i.e., by replacing $\zeta(r')$ by $\zeta(r)$ in (4.16), however using the definition (4.16) of K is more convenient. Expanding the ratio Z/Z_0 in powers of ζ we have

$$\frac{Z}{Z_0} = 1 + \sum_{N=1}^{\infty} \frac{1}{N!} \int \prod_{k=1}^N d^2\mathbf{r}_k \zeta(r_k) \langle \bar{\psi}(\mathbf{r}_1) \psi(\mathbf{r}_1) \cdots \bar{\psi}(\mathbf{r}_N) \psi(\mathbf{r}_N) \rangle \quad (4.17)$$

Now, using Wick theorem for anticommuting variables,⁽¹⁶⁾ we find that

$$\langle \bar{\psi}(\mathbf{r}_1) \psi(\mathbf{r}_1) \cdots \bar{\psi}(\mathbf{r}_N) \psi(\mathbf{r}_N) \rangle = \det M(z_i, \bar{z}_j) = \det \left(\frac{1}{1 - u_i \bar{u}_j} \right) \quad (4.18)$$

Comparing Eqs. (4.17) and (4.9) with the help of Eq. (4.18) we conclude that⁹

$$\mathcal{E} = C_0 \frac{Z}{Z_0} = C_0 \det(1 + K) \quad (4.19)$$

The problem of computing the grand canonical partition function has been reduced to finding the eigenvalues of the operator K . The eigenvalue problem for K reads

$$\int \zeta e^C \frac{\left(1 - \frac{r'^2}{4a^2}\right)^{4\pi n_b a^2 - 1}}{1 - \frac{z\bar{z}'}{4a^2}} \Phi(\mathbf{r}') r' dr' d\varphi' = \lambda \Phi(\mathbf{r}) \quad (4.20)$$

For $\lambda \neq 0$ we notice from Eq. (4.20) that $\Phi(\mathbf{r}) = \Phi(z)$ is an analytical function of z . Because of the circular symmetry it is natural to try $\Phi(z) = \Phi_\ell(z) = z^\ell = r^\ell e^{i\ell\varphi}$ with ℓ a non-negative integer (the functions z^ℓ form a complete basis for the analytical functions). Expanding

$$\frac{1}{1 - \frac{z\bar{z}'}{4a^2}} = \sum_{n=0}^{\infty} \left(\frac{z\bar{z}'}{4a^2} \right)^n \quad (4.21)$$

⁹ Actually, the determinants Z_0 and Z are divergent quantities, since the eigenvalues of M (restricted to act on analytical functions) are easily found to be $4\pi a^2/(\ell+1)$, with ℓ any non-negative integer. However, the ratio Z/Z_0 turns out to be finite.

and replacing $\Phi_\ell(z) = z^\ell$ in Eq. (4.20) one can show that Φ_ℓ is actually an eigenfunction of K with eigenvalue

$$\lambda_\ell = 4\pi a^2 \zeta e^C B_{t_0}(\ell + 1, 4\pi n_b a^2) \quad (4.22)$$

with $t_0 = r_0^2/(4a^2) = \tanh^2(\tau_0/2)$ and

$$B_{t_0}(\ell + 1, 4\pi n_b a^2) = \int_0^{t_0} (1-t)^{4\pi n_b a^2 - 1} t^\ell dt \quad (4.23)$$

the incomplete beta function. So we finally arrive to the result for the grand potential

$$\beta\Omega = -\ln \bar{\mathcal{E}} = -\ln C_0 - \sum_{\ell=0}^{\infty} \ln(1 + 4\pi a^2 \zeta e^C B_{t_0}(\ell + 1, 4\pi n_b a^2)) \quad (4.24)$$

with e^C and $\ln C_0$ given by Eqs. (4.3) and (4.4). This result is valid for any disk domain of radius $a\tau_0$. Later, in Section 4.3, we will derive a more explicit expression of the grand potential for large domains $\tau_0 \rightarrow \infty$.

4.2. The Density

As usual one can compute the density by doing a functional derivative of the grand potential with respect to the position-dependent fugacity:

$$n^{(1)}(\mathbf{r}) = \left(1 - \frac{r^2}{4a^2}\right)^2 \zeta(r) \frac{\delta \ln \bar{\mathcal{E}}}{\delta \zeta(r)} \quad (4.25)$$

The factor $[1 - (r^2/4a^2)]^2$ is due to the curvature,⁽⁴⁾ so that $n^{(1)}(\mathbf{r}) dS$ is the average number of particles in the surface element $dS = [1 - (r^2/4a^2)]^{-2} d\mathbf{r}$. Using a Dirac-like notation, one can formally write

$$\ln \bar{\mathcal{E}} = \text{Tr} \ln(1 + K) + \ln C_0 = \int \langle \mathbf{r} | \ln(1 + \zeta(r) M) | \mathbf{r} \rangle d\mathbf{r} + \ln C_0 \quad (4.26)$$

Then, doing the functional derivative (4.25), one obtains

$$\begin{aligned} n^{(1)}(\mathbf{r}) &= \left(1 - \frac{r^2}{4a^2}\right)^2 \zeta(r) \langle \mathbf{r} | (1 + K)^{-1} M | \mathbf{r} \rangle \\ &= 4\pi a \left(1 - \frac{r^2}{4a^2}\right)^2 \zeta(r) \tilde{G}(\mathbf{r}, \mathbf{r}) \end{aligned} \quad (4.27)$$

where we have defined $\tilde{G}(\mathbf{r}, \mathbf{r}')$ by¹⁰ $\tilde{G} = (1 + K)^{-1} M / (4\pi a)$. More explicitly, \tilde{G} is the solution of $(1 + K) \tilde{G} = M / (4\pi a)$, that is

$$\tilde{G}(\mathbf{r}, \mathbf{r}') + \zeta e^C \int \tilde{G}(\mathbf{r}'', \mathbf{r}') \frac{\left(1 - \frac{r''^2}{4a^2}\right)^{4\pi n_b a^2 - 1}}{1 - \frac{z\bar{z}''}{4a^2}} d\mathbf{r}'' = \frac{1}{4\pi a \left[1 - \frac{z\bar{z}'}{4a^2}\right]} \quad (4.28)$$

and the density is given by

$$n^{(1)}(\mathbf{r}) = 4\pi a \zeta e^C \left(1 - \frac{r^2}{4a^2}\right)^{4\pi n_b a^2 + 1} \tilde{G}(\mathbf{r}, \mathbf{r}) \quad (4.29)$$

From the integral Eq. (4.28) one can see that $\tilde{G}(\mathbf{r}, \mathbf{r}')$ is an analytical function of z . Thus the solution is of the form

$$\tilde{G}(\mathbf{r}, \mathbf{r}') = \sum_{\ell=0}^{\infty} a_{\ell}(\mathbf{r}') z^{\ell} \quad (4.30)$$

and Eq. (4.28) yields

$$\tilde{G}(\mathbf{r}, \mathbf{r}') = \frac{1}{4\pi a} \sum_{\ell=0}^{\infty} \left(\frac{z\bar{z}'}{4a^2}\right)^{\ell} \frac{1}{1 + 4\pi a^2 \zeta e^C B_{\ell_0}(\ell + 1, 4\pi n_b a^2)} \quad (4.31)$$

Then the density is given by

$$n^{(1)}(r) = \zeta e^C \left(1 - \frac{r^2}{4a^2}\right)^{4\pi n_b a^2 + 1} \sum_{\ell=0}^{\infty} \left(\frac{r^2}{4a^2}\right)^{\ell} \frac{1}{1 + 4\pi a^2 \zeta e^C B_{\ell_0}(\ell + 1, 4\pi n_b a^2)} \quad (4.32)$$

After some calculation (see Appendix A), it can be shown that, in the limit $a \rightarrow \infty$, the result for the flat disk in the canonical ensemble⁽¹⁷⁾

$$\frac{n^{(1)}(r)}{n_b} = \exp(-\pi n_b r^2) \sum_{\ell=0}^{N_b - 1} \frac{(\pi n_b r^2)^{\ell}}{\gamma(\ell + 1, N_b)} \quad (4.33)$$

is recovered, up to a correction due to the non-equivalence of ensembles in finite systems. In (4.33), γ is the incomplete gamma function

$$\gamma(\ell + 1, x) = \int_0^x t^{\ell} e^{-t} dt \quad (4.34)$$

¹⁰ The factor $4\pi a$ is there just to keep the same notations as in ref. 4.

In that flat-disk case, in the thermodynamic limit (half-space), $n^{(1)}(r_0) = n_{\text{contact}} \rightarrow n_b \ln 2$.

4.3. Large Domains

We are now interested in large domains $\tau_0 \rightarrow \infty$. In this thermodynamic limit we will show that the sums in Eqs. (4.24) and (4.32) can be replaced by integrals. For pedagogical reasons we will first consider the case $4\pi n_b a^2 = 1$ in which the calculations are simpler, and afterwards deal with the general case.

4.3.1. The Case $4\pi n_b a^2 = 1$

In this case the incomplete beta function that appears in Eqs. (4.24) and (4.32) simply is

$$B_{t_0}(\ell + 1, 1) = \frac{t_0^{\ell+1}}{\ell + 1} = \frac{[\tanh^2(\tau_0/2)]^{\ell+1}}{\ell + 1} \quad (4.35)$$

When $\tau_0 \rightarrow \infty$ we have

$$B_{t_0}(\ell + 1, 1) \sim \frac{\exp(-4(\ell + 1) e^{-\tau_0})}{\ell + 1} \quad (4.36)$$

Then the sum appearing in the grand potential (4.24) takes the form

$$\sum_{\ell=0}^{\infty} \ln \left(1 + \frac{\zeta e \exp(-4(\ell + 1) e^{-\tau_0})}{n_b 4(\ell + 1) e^{-\tau_0}} \right) \quad (4.37)$$

where we have used the asymptotic expression (4.5) for e^C . This sum can be seen as a Riemann sum for the variable $x = 4(\ell + 1) e^{-\tau_0}$. Indeed, for large values of τ_0 , the variable x varies in small steps $dx = 4e^{-\tau_0}$. The sum (4.37) then converges, when $\tau_0 \rightarrow \infty$, to the integral

$$\int_0^{\infty} \ln \left(1 + \frac{\zeta e e^{-x}}{n_b x} \right) \frac{dx}{4e^{-\tau_0}} \quad (4.38)$$

This expression together with Eq. (4.6) for the constant $\ln C_0$ gives the grand potential in the thermodynamic limit $\tau_0 \rightarrow \infty$

$$\beta\Omega \sim -\frac{e^{\tau_0}}{4} \left[\int_0^{\infty} \ln \left(1 + \frac{\zeta e e^{-x}}{n_b x} \right) dx - 1 \right] \quad (4.39)$$

We notice that the grand potential is extensive as expected. The area of the system being $\mathcal{A} = 4\pi a^2 \sinh^2(\tau_0/2) \simeq \pi a^2 e^{\tau_0}$, we find that the grand potential per unit area $\omega = \Omega/\mathcal{A}$ is given by

$$\beta\omega = -n_b \left[\int_0^\infty \ln \left(1 + \frac{\zeta e e^{-x}}{n_b x} \right) dx - 1 \right] \quad (4.40)$$

Similar calculations lead from Eq. (4.32) to the density $n^{(1)}(\sigma)$ near the boundary as a function of the distance from that boundary $a\sigma = a(\tau_0 - \tau)$,

$$n^{(1)}(\sigma) = \zeta e e^{2\sigma} \int_0^\infty \frac{e^{-xe^\sigma}}{1 + \frac{\zeta e e^{-x}}{n_b x}} dx \quad (4.41)$$

After the change of variable $xe^\sigma \rightarrow x$, this can be written as

$$\frac{n^{(1)}(\sigma)}{n_b} = \int_0^\infty \frac{xe^{-x} dx}{\frac{xe^{-\sigma}}{(\zeta e/n_b)} + e^{-xe^{-\sigma}}} \quad (4.42)$$

The average density $n = N/\mathcal{A}$ can be obtained integrating the density profile (4.42) or by using the thermodynamic relation $N = -\beta\zeta(\partial\Omega/\partial\zeta)$. We find

$$\frac{n}{n_b} = \int_0^\infty \frac{e^{-x} dx}{\frac{x}{(\zeta e/n_b)} + e^{-x}} \quad (4.43)$$

4.3.2. The General Case

With the case $4\pi n_b a^2 = 1$ we have illustrated the general procedure for computing the thermodynamic limit. Now we proceed to compute it in the more general case where $4\pi n_b a^2$ has any positive value. To simplify the notations let us define $\alpha = 4\pi n_b a^2$. The main difficulty is to find a suitable asymptotic expression of the incomplete beta function

$$B_{t_0}(\ell + 1, \alpha) = \int_0^{t_0} (1-t)^{\alpha-1} t^\ell dt \quad (4.44)$$

when $t_0 \rightarrow 1$ which is valid for large ℓ . As we have noticed in the previous section the main contribution from the sum in ℓ that appears in the grand potential comes from large values of ℓ which are of order e^{τ_0} . For these

values of ℓ the integrand in the definition of the beta function $(1-t)^{\alpha-1} t^\ell$ is very peaked around $t = t_0$ and decays very fast when $t \rightarrow 0$. So the main contribution to the incomplete beta function comes from values of t near t_0 . It is then natural to do the change of variable in the integral $t = t_0 - v$ where with the new variable v the integral is mainly dominated by small values of v . Then we have

$$B_{t_0}(\ell + 1, \alpha) = \int_0^{t_0} (1 - t_0 + v)^{\alpha-1} e^{\ell \ln(t_0 - v)} dv \quad (4.45)$$

Replacing t_0 by its asymptotic value $t_0 \sim 1 - 4e^{-\tau_0}$ and taking into account that v is small (of order $e^{-\tau_0}$), we find, at first order in $e^{-\tau_0}$,

$$B_{t_0}(\ell + 1, \alpha) \sim \frac{1}{\ell^\alpha} \Gamma(\alpha, x) \quad (4.46)$$

where we have introduced once more the variable $x = 4\ell e^{-\tau_0}$ (at first order in $e^{-\tau_0}$ it is the same variable $x = 4(\ell + 1) e^{-\tau_0}$ introduced in the case $\alpha = 1$) and

$$\Gamma(\alpha, x) = \int_x^\infty y^{\alpha-1} e^{-y} dy \quad (4.47)$$

is an incomplete gamma function. With this result and Eq. (4.5) the term $e^C B_{t_0}(\ell + 1, \alpha)$ in the expressions (4.24) and (4.32) appears as a function of the continuous variable $x = 4\ell e^{-\tau_0}$

$$e^C B_{t_0}(\ell + 1, \alpha) \sim e^\alpha \frac{\Gamma(\alpha, x)}{x^\alpha} \quad (4.48)$$

With this result we can replace the sums for ℓ in Eqs. (4.24) and (4.32) by integrals over the variable x and we find the following expressions for the grand potential per unit area

$$\beta\omega = \frac{1}{4\pi a^2} \left\{ (4\pi n_b a^2)^2 - \int_0^\infty \ln \left[1 + 4\pi a^2 \zeta e^{4\pi n_b a^2} \frac{\Gamma(4\pi n_b a^2, x)}{x^{4\pi n_b a^2}} \right] dx \right\} \quad (4.49)$$

and the density

$$n^{(1)}(\sigma) = \zeta e^{4\pi n_b a^2} e^{(4\pi n_b a^2 + 1)\sigma} \int_0^\infty \frac{e^{-xe^\sigma} dx}{1 + 4\pi a^2 \zeta e^{4\pi n_b a^2} \frac{\Gamma(4\pi n_b a^2, x)}{x^{4\pi n_b a^2}}} \quad (4.50)$$

In particular the contact value of the density, that is when $\sigma = 0$, is

$$n_{\text{contact}} = n^{(1)}(0) = \zeta e^{4\pi n_b a^2} \int_0^\infty \frac{e^{-x} dx}{1 + 4\pi a^2 \zeta e^{4\pi n_b a^2} \frac{\Gamma(4\pi n_b a^2, x)}{x^{4\pi n_b a^2}}} \quad (4.51)$$

After some calculation (see Appendix A), it can be shown that, in the limit $a \rightarrow \infty$, the result for the flat disk in the thermodynamic limit $n_{\text{contact}} = n_b \ln 2$ is again recovered.

An alternative expression for the density which we will also use is obtained by doing the change of variable $x e^\sigma \rightarrow x$ and introducing again $\alpha = 4\pi n_b a^2$

$$\frac{n^{(1)}(\sigma)}{n_b} = \int_0^\infty \frac{x^\alpha e^{-x} dx}{\frac{x^\alpha e^{-\alpha\sigma}}{(\zeta e^\alpha/n_b)} + \alpha \Gamma(\alpha, x e^{-\sigma})} \quad (4.52)$$

From this expression it can be seen that in the bulk, when $\sigma \rightarrow \infty$ and $e^{-\sigma} \rightarrow 0$, the density is equal to the background density, $n^{(1)}(\sigma) \rightarrow n_b$. The system is neutral in the bulk. The excess charge, which is controlled by the fugacity ζ , concentrates as usual on the boundary.

The average total number of particles N and the average density $n = N/\mathcal{A}$ can be computed either by using the thermodynamic relation

$$N = -\beta \zeta \frac{\partial \Omega}{\partial \zeta} \quad (4.53)$$

or by integrating the density profile (4.50)

$$N = \int_{\tau < \tau_0} n^{(1)}(\sigma) dS = \pi a^2 e^{\tau_0} \int_0^\infty n^{(1)}(\sigma) e^{-\sigma} d\sigma \quad (4.54)$$

The two methods yield the same result, as expected,

$$n = \frac{N}{\mathcal{A}} = \zeta e^{4\pi n_b a^2} \int_0^\infty \frac{\Gamma(4\pi n_b a^2, x) dx}{x^{4\pi n_b a^2} + 4\pi a^2 \zeta e^{4\pi n_b a^2} \Gamma(4\pi n_b a^2, x)} \quad (4.55)$$

The ratio of the average density and the background density can be put in the form

$$\frac{n}{n_b} = \int_0^\infty \frac{\Gamma(\alpha, x) dx}{\frac{x^\alpha}{(\zeta e^\alpha/n_b)} + \alpha \Gamma(\alpha, x)} \quad (4.56)$$

As seen on Eqs. (4.52) and (4.56) the density profile $n^{(1)}(\sigma)$ and the average density n are functions of the parameter $g = \zeta e^{4\pi n_b a^2} / n_b$. Different values of this parameter g give different density profiles and mean densities. Depending on the value of g the system can be globally positive, negative or neutral. From Eq. (4.56) it can be seen that the average density is a monotonous increasing function of the fugacity, as it should be. Therefore there is one unique value of the fugacity for which the system is globally neutral. For the case $4\pi n_b a^2 = 1$, we have determined numerically the value of g needed for the system to be neutral, $n = n_b$. This value is $g = \zeta e / n_b = 1.80237$.

It may be noted that, in the case of a flat disk in the grand canonical ensemble, the 2D OCP remains essentially neutral (the modulus of its total charge cannot exceed one elementary charge q), whatever the fugacity ζ might be;^(18, 19) this is because the Coulomb interaction $-\ln(r/L)$ becomes infinite at infinity and bringing an excess charge from a reservoir at infinity to the system already carrying a net charge would cost an infinite energy. On the contrary, in the present case of a 2D OCP on a pseudosphere, the Coulomb interaction (2.8) has an exponential decay at large distances, and varying the fugacity does change the total charge of the disk.

Figure 1 shows several plots of the density $n^{(1)}(\sigma)$ as a function of the distance σ from the boundary (in units of a), for different values of g , in the case $\alpha = 4\pi n_b a^2 = 1$. It is interesting to notice that for $g \leq 1$ the density

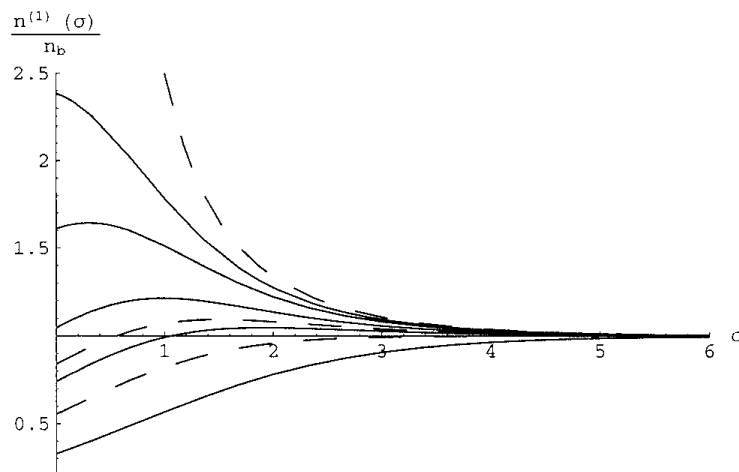


Fig. 1. The density profile $n^{(1)}(\sigma)$ (in units of n_b) as a function of the distance from the boundary σ (in units of a) for different values of the parameter $g = \zeta e / n_b$ in the case $4\pi n_b a^2 = 1$. From bottom to top, in full line $g = 0.5, 1.5, 2.5, 5.0, 10.0$ and in dashed line $g = 1$ (change of behavior between monotonous increasing profile and oscillating profile), $g = 1.80237$ (globally neutral system) and $g \rightarrow \infty$.

is always an increasing function of σ . Far away from the boundary, the density approaches the background density n_b from below. On the other hand when $g > 1$, but not too large, the density profile shows an oscillation: $n^{(1)}(\sigma)$ is no longer a monotonous function of σ . Far away from the boundary, $\sigma \rightarrow \infty$, the density now approaches the background density from above. Finally, when g is large enough, the density profile is again monotonous, now a decreasing function of σ .

The change of behavior as $\sigma \rightarrow \infty$ can actually be shown analytically. Let us define $u = e^{-\sigma}$. From Eq. (4.52) we have

$$\frac{\partial}{\partial u} \left(\frac{n^{(1)}(\sigma)}{n_b} \right) = \int_0^\infty \frac{\alpha x^{2\alpha} u^{\alpha-1} e^{-x-xu}}{\left(\frac{(xu)^\alpha}{g} + \alpha \Gamma(\alpha, xu) \right)^2} \left[1 - \frac{e^{xu}}{g} \right] dx \quad (4.57)$$

The first term in the integral is always positive. The second term, $1 - (e^{xu}/g)$, in the limit $\sigma \rightarrow \infty$ ($u \rightarrow 0$) is $1 - (1/g)$. If $g < 1$ it is negative, then $\partial n^{(1)}/\partial u$ is negative and $n^{(1)}(\sigma)$ is then an increasing function of σ when $\sigma \rightarrow \infty$ as it was noticed in the last paragraph.

Also, in this case $\alpha = 1$, when $\zeta \rightarrow \infty$ the density profile (4.42) can be computed explicitly

$$\frac{n^{(1)}(\sigma)}{n_b} = \frac{1}{(1 - e^{-\sigma})^2} \quad (4.58)$$

It is clearly a monotonous decreasing function of σ .

4.4. Relations Between the Different Pressures

From the explicit expressions (4.49) and (4.52) for the grand potential and the density profile, we can check the relations between the different pressures obtained in Section 3. The mechanical pressure simply is $P^{(m)} = -\omega$ and it is given by Eq. (4.49). This expression can be transformed by doing an integration by parts in the integral giving

$$\beta P^{(m)} = -\frac{1}{4\pi a^2} \left\{ \int_0^\infty \frac{4\pi a^2 x \zeta e^{4\pi n_b a^2} \frac{d}{dx} \left[\frac{\Gamma(4\pi n_b a^2, x)}{x^{4\pi n_b a^2}} \right]}{1 + 4\pi a^2 \zeta e^{4\pi n_b a^2} \frac{\Gamma(4\pi n_b a^2, x)}{x^{4\pi n_b a^2}}} dx + (4\pi n_b a^2)^2 \right\} \quad (4.59)$$

By the replacement

$$\frac{d}{dx} \left[\frac{\Gamma(4\pi n_b a^2, x)}{x^{4\pi n_b a^2}} \right] = -\frac{e^{-x}}{x} - 4\pi n_b a^2 \frac{\Gamma(4\pi n_b a^2, x)}{x^{4\pi n_b a^2 + 1}} \quad (4.60)$$

in Eq. (4.59), one recognizes the expressions (4.51) and (4.55) for the contact density and the average density, thus giving

$$\beta P^{(m)} = n^{(1)}(0) + 4\pi n_b a^2 (n - n_b) \quad (4.61)$$

which is precisely, when $\beta q^2 = 2$, the relation (3.25) between the mechanical pressure $P^{(m)}$ and the kinetic pressure $P^{(k)} = (1/\beta) n^{(1)}(0)$ obtained in Section 3.

The thermal pressure is

$$P^{(\theta)} = -\omega(\zeta, n_b) + n_b \left(\frac{\partial \omega(\zeta, n_b)}{\partial n_b} \right)_\zeta \quad (4.62)$$

The last term in this equation is given by

$$\beta n_b \frac{\partial \omega}{\partial n_b} = \frac{1}{4\pi a^2} \left\{ 2\alpha^2 - \int_0^\infty \frac{4\pi a^2 \zeta}{1 + \frac{4\pi a^2 \zeta e^\alpha \Gamma(\alpha, x)}{x^\alpha}} \alpha \frac{\partial}{\partial \alpha} \left[\frac{e^\alpha \Gamma(\alpha, x)}{x^\alpha} \right] dx \right\} \quad (4.63)$$

Making the replacement

$$\alpha \frac{\partial}{\partial \alpha} \left[\frac{e^\alpha \Gamma(\alpha, x)}{x^\alpha} \right] = \alpha e^\alpha \left(\frac{\Gamma(\alpha, x)}{x^\alpha} + \frac{\partial}{\partial \alpha} \left[\frac{\Gamma(\alpha, x)}{x^\alpha} \right] \right) \quad (4.64)$$

in Eq. (4.63), one recognizes in the first term the average density n , thus obtaining

$$\beta n_b \frac{\partial \omega}{\partial n_b} = \alpha(2n_b - n) - \alpha I \quad (4.65)$$

where

$$I = \int_0^\infty \frac{\zeta e^\alpha}{1 + \frac{4\pi a^2 \zeta e^\alpha \Gamma(\alpha, x)}{x^\alpha}} \frac{\partial}{\partial \alpha} \left[\frac{\Gamma(\alpha, x)}{x^\alpha} \right] dx \quad (4.66)$$

So the thermal pressure is given by

$$\beta P^{(\theta)} = n^{(1)}(0) + \alpha n_b - \alpha I \quad (4.67)$$

On the other hand the integral appearing in the general relation (3.21) between the thermal pressure and the kinetic pressure

$$J = \int_0^\infty (n^{(1)}(\sigma) - n_b) e^{-\sigma} \sigma d\sigma \quad (4.68)$$

can be split into two parts

$$J = -n_b + I' \quad (4.69)$$

with

$$I' = \int_0^\infty n^{(1)}(\sigma) \sigma e^{-\sigma} d\sigma \quad (4.70)$$

Using the actual integral representation for the density profile given by Eq. (4.50) yields

$$I' = \int_0^\infty \frac{\zeta e^\alpha}{1 + \frac{4\pi a^2 \zeta e^\alpha \Gamma(\alpha, x)}{x^\alpha}} \left\{ \int_0^\infty e^{\alpha\sigma} e^{-x e^\sigma} \sigma d\sigma \right\} dx \quad (4.71)$$

The integral over σ can be cast in the form

$$\frac{\partial}{\partial \alpha} \left[\int_0^\infty e^{\alpha\sigma} e^{-x e^\sigma} d\sigma \right] \quad (4.72)$$

By doing the change of variable $y = x e^\sigma$ one immediately recognizes the integral representation of the incomplete gamma function. The above expression is then equal to

$$\frac{\partial}{\partial \alpha} \left[\frac{\Gamma(\alpha, x)}{x^\alpha} \right] \quad (4.73)$$

Thus we have proven that $I' = I$ and finally we have the relation

$$\beta(P^{(\theta)} - P^{(k)}) = -4\pi n_b a^2 \int_0^\infty (n^{(1)}(\sigma) - n_b) e^{-\sigma} \sigma d\sigma \quad (4.74)$$

which is relation (3.21) in the solvable case $\beta q^2 = 2$.

5. CONCLUSION

In a flat space, the neighborhood of the boundary of a large domain has a volume which is a negligible fraction of the whole volume. This is why, for the statistical mechanics of ordinary fluids, usually there is a thermodynamic limit: when the volume becomes infinite, quantities such as the free energy per unit volume or the pressure have a unique limit, independent of the domain shape and of the boundary conditions. However, even in a flat space, the one-component plasma is special. For the OCP, it is possible to define several non-equivalent pressures, some of which, for instance the kinetic pressure, obviously are surface-dependent even in the infinite-system limit.

Even for ordinary fluids, statistical mechanics on a pseudosphere is expected to have special features, which are essentially related to the property that, for a large domain, the area of the neighborhood of the boundary is of the same order of magnitude as the whole area. Although some bulk properties, such as correlation functions far away from the boundary, will exist, extensive quantities such as the free energy or the grand potential are strongly dependent on the boundary neighborhood and surface effects. For instance, in the large-domain limit, no unique limit is expected for the free energy per unit area F/\mathcal{A} or the pressure $-(\partial F/\partial \mathcal{A})_{\beta, N}$.

In the present paper, we have studied the 2D OCP on a pseudosphere, for which surface effects are expected to be important for both reasons: because we are dealing with a one-component plasma and because the space is a pseudosphere. Therefore, although the correlation functions far away from the boundary have unique thermodynamic limits,⁽⁴⁾ many other properties are expected to depend on the domain shape and on the boundary conditions. This is why we have considered a special well-defined geometry: the domain is a disk bounded by a plain hard wall, and we have studied the corresponding large-disk limit. Our results have been derived only for that geometry.

We have been especially interested by different pressures which can be defined for this system. It has been shown that the virial pressure $P^{(v)}$ (defined through the virial theorem) and the kinetic pressure $P^{(k)}$ (the force per unit length that the particles alone exert on the wall) are equal to each other. We have also considered the thermal pressure $P^{(\theta)}$, the definition of which includes contributions from the background. It should be noted that this thermal pressure is also dependent on surface effects, since it is defined by (3.14) and (3.15) in terms of the free energy or the grand potential, and the corresponding partition functions include relevant contributions from the surface region. The thermal pressure is not equal to the previous ones. We have also considered the so-called mechanical pressure $P^{(m)}$ which

differs from the kinetic one only for charged systems. General relations among these different pressures have been established.

One of the referees of the present paper has asked which one of these different pressures is the “right” one, i.e., which one would be measured by a barometer. The answer, based on the previous paragraph, is that it depends on which kind of “barometer” is used. For instance, the measured pressure would not be the same if the barometer, placed on the wall, measures only the force exerted on it by the particles alone, or if it also feels the force exerted by the background.

When $\beta q^2 = 2$, the model is exactly solvable, in the grand canonical ensemble. Explicit expressions have been obtained for the grand potential, the density profile, and the pressures. The general relations between the different pressures have been checked.

A bulk pressure, independent of the surface effects, can be defined from the Maxwell stress tensor. It is not astonishing that this bulk pressure is different from the previous ones, all of which depend on surface effects.

APPENDIX A. THE FLAT LIMIT

In this Appendix we study the flat limit $a \rightarrow \infty$ of the expressions found for the density in Section 4. We shall study the limit $a \rightarrow \infty$ for a finite system and then take the thermodynamic limit and compare to the result of taking first the thermodynamic limit and then the flat limit $a \rightarrow \infty$. Since for a large system on the pseudosphere boundary effects are of the same order as bulk effects it is not clear a priori whether computing these two limits in different order would give the same results. We shall show that, indeed, the same results are obtained.

For a finite disk of radius $d = ar_0$, we have in the flat limit $a \rightarrow \infty$, $d \sim r_0$. In Eq. (4.32), in the limit $a \rightarrow \infty$, the term e^C given by (4.3) becomes

$$e^C \sim \left(\frac{r_0^2}{4a^2} \right)^{-N_b} e^{N_b} \quad (\text{A.1})$$

where $N_b = \pi n_b r_0^2$ is the number of particles in the background in the flat limit. Since for large a , $t_0 = r_0^2/(4a^2)$ is small, the incomplete beta function in Eq. (4.32) is

$$\begin{aligned} B_{t_0}(\ell + 1, \alpha) &= \int_0^{t_0} e^{(\alpha-1)\ln(1-t)} t^\ell dt \\ &\sim \int_0^{t_0} e^{-(\alpha-1)t} t^\ell dt \sim \frac{\gamma(\ell + 1, N_b)}{\alpha^{\ell+1}} \end{aligned} \quad (\text{A.2})$$

Expanding $(1 - (r^2/4a^2))^{4\pi n_b a^2} \sim \exp(-\pi n_b r^2)$ in Eq. (4.32) we finally find the density as a function of the distance r from the center

$$n^{(1)}(r) = n_b e^{-\pi n_b r^2} \sum_{\ell=0}^{\infty} \frac{(\pi n_b r^2)^\ell}{\alpha^{\ell-N_b} N_b^{N_b} e^{-N_b(n_b/\zeta)} + \gamma(\ell+1, N_b)} \quad (\text{A.3})$$

When $\alpha \rightarrow \infty$ the terms for $\ell > N_b$ in the sum vanish because $\alpha^{\ell-N_b} \rightarrow \infty$. Then

$$n^{(1)}(r) = n_b e^{-\pi n_b r^2} \sum_{\ell=0}^{E(N_b)-1} \frac{(\pi n_b r^2)^\ell}{\gamma(\ell+1, N_b)} + \Delta n^{(1)}(r) \quad (\text{A.4})$$

The first term is the density for a flat OCP in the canonical ensemble with a background with $E(N_b)$ elementary charges ($E(N_b)$ is the integer part of N_b). The second term is a correction due to the inequivalence of the ensembles for finite systems and it depends on whether N_b is an integer or not. If N_b is not an integer

$$\Delta n^{(1)}(r) = n_b \frac{(\pi n_b r^2)^{E(N_b)} e^{-\pi n_b r^2}}{\gamma(E(N_b)+1, N_b)} \quad (\text{A.5})$$

and if N_b is an integer

$$\Delta n^{(1)}(r) = n_b \frac{(\pi n_b r^2)^{N_b} e^{-\pi n_b r^2}}{N_b^{N_b} e^{-N_b(n_b/\zeta)} + \gamma(N_b+1, N_b)} \quad (\text{A.6})$$

In any case in the thermodynamic limit $r_0 \rightarrow \infty$, $N_b \rightarrow \infty$, this term $\Delta n^{(1)}(r)$ vanishes giving the known results for the OCP in a flat space in the canonical ensemble.^(3,17) Integrating the profile density (A.4) one finds the average number of particles. For a finite system it is interesting to notice that the average total number of particles N is

$$N = E(N_b) + 1 \quad (\text{A.7})$$

for N_b not an integer and

$$N = N_b + \frac{1}{1 + \frac{N_b^{N_b} e^{-N_b n_b}}{\zeta \gamma(N_b+1, N_b)}} \quad (\text{A.8})$$

for N_b an integer. In both cases the departure from the neutral case $N = N_b$ is at most of one elementary charge as it was noticed before.^(18,19)

Let us now consider the other order of the limits. We start with the expression (4.51) for the contact density in the thermodynamic limit in the pseudosphere and show that in the limit $a \rightarrow \infty$ the value of the contact density reduces to the known expression for a neutral OCP in a flat space at a hard wall.⁽¹⁷⁾ We also show that in that limit the average density is independent of the fugacity and equal to the background density $n = n_b$.

Equation (4.51) can be rewritten as

$$\frac{n_{\text{contact}}}{n_b} = \int_0^\infty \frac{x^\alpha e^{-x} dx}{\frac{n_b}{\zeta} x^\alpha e^{-\alpha} + \alpha \Gamma(\alpha, x)} \quad (\text{A.9})$$

For large α , the numerator of the integrand in (A.9) has a sharp peak at $x = \alpha$ and can be expanded as

$$x^\alpha e^{-x} \sim e^{\alpha \ln \alpha - \alpha - \left(\frac{x-\alpha}{\sqrt{2\alpha}}\right)^2} \quad (\text{A.10})$$

In the denominator, using the large α expansion of the incomplete gamma function,⁽²⁰⁾ and neglecting 1 with respect to α , we obtain

$$\alpha \Gamma(\alpha, x) \sim \alpha^\alpha e^{-\alpha} \sqrt{\frac{\pi\alpha}{2}} \left[1 - \text{erf}\left(\frac{x-\alpha+1}{\sqrt{2\alpha}}\right) \right] \quad (\text{A.11})$$

where

$$\text{erf}(t) = \frac{2}{\sqrt{\pi}} \int_0^t e^{-u^2} du \quad (\text{A.12})$$

is the error function. Using (A.10) and (A.11) in (A.9) gives

$$\frac{n_{\text{contact}}}{n_b} \sim \int_0^\infty \frac{e^{-\left(\frac{x-\alpha}{\sqrt{2\alpha}}\right)^2} dx}{\frac{n_b}{\zeta} \left(\frac{x}{\alpha}\right)^\alpha + \sqrt{\frac{\pi\alpha}{2}} \left[1 - \text{erf}\left(\frac{x-\alpha+1}{\sqrt{2\alpha}}\right) \right]} \quad (\text{A.13})$$

For $x > \alpha$, the first term in the denominator goes to infinity for large α and the integrand goes to zero. On the other hand, when $x < \alpha$, this same first term goes to zero, thus, after the change of variable $t = (x-\alpha)/\sqrt{2\alpha}$,

$$\frac{n_{\text{contact}}}{n_b} \sim \frac{2}{\sqrt{\pi}} \int_{-\sqrt{\alpha/2}}^0 \frac{e^{-t^2} dt}{1 - \text{erf}\left(t + \frac{1}{\sqrt{2\alpha}}\right)} \quad (\text{A.14})$$

Finally, as $\alpha \rightarrow \infty$,

$$\frac{n_{\text{contact}}}{n_b} \rightarrow \int_{-\infty}^0 \frac{d \operatorname{erf}(t)}{1 - \operatorname{erf}(t)} dt = \ln 2 \quad (\text{A.15})$$

This is the known value⁽¹⁷⁾ for the contact density at a hard plain wall for a neutral OCP.

Following the same lines, Eq. (4.56) for the average density becomes in the limit $\alpha \rightarrow \infty$

$$\frac{n}{n_b} \sim \sqrt{\frac{2}{\alpha}} \int_{-\sqrt{\alpha/2}}^0 \frac{[1 - \operatorname{erf}(t)] dt}{1 - \operatorname{erf}(t)} = 1 \quad (\text{A.16})$$

The average density is equal to the background density and it is independent of the fugacity. Whatever value the fugacity has, the system cannot be charged in the flat case in the thermodynamic limit.

ACKNOWLEDGMENTS

R.F. would like to thank F. Benatti for his lectures in Trieste and stimulating discussions. B.J. and G.T. acknowledge support from ECOS Nord/COLCIENCIAS-ICFES-ICETEX action C00P02 of French and Colombian cooperation. G.T. acknowledge partial financial support from COLCIENCIAS and BID through project #1204-05-10078.

REFERENCES

1. Ph. Choquard, P. Favre, and Ch. Gruber, *J. Stat. Phys.* **23**:405 (1980).
2. M. Navet, E. Jamin, and M. R. Feix, *J. Phys. (Paris) Lett.* **41**:L-69 (1980).
3. B. Jancovici, *Phys. Rev. Lett.* **46**:386 (1981).
4. B. Jancovici and G. Téllez, *J. Stat. Phys.* **91**:953 (1998).
5. A. Salzberg and S. Prager, *J. Chem. Phys.* **38**:2587 (1963).
6. E. H. Hauge and P. C. Hemmer, *Phys. Norvegica* **5**:209 (1971).
7. E. H. Lieb and H. Narnhofer, *J. Stat. Phys.* **12**:291 (1975).
8. H. Totsuji, *J. Chem. Phys.* **75**:871 (1981).
9. B. Jancovici, *J. Stat. Phys.* **99**:1281 (2000).
10. B. Jancovici, *J. Stat. Phys.* **102**:1315 (2001).
11. J. D. Jackson, *Classical Electrodynamics* (Wiley, New York, 1962).
12. A. Alastuey and B. Jancovici, *J. Phys. (France)* **42**:1 (1981).
13. J. M. Caillol, *J. Phys. (Paris) Lett.* **42**:L-245 (1981).
14. P. J. Forrester, *J. Chem. Phys.* **95**:4545 (1991).
15. B. Jancovici and G. Téllez, *J. Stat. Phys.* **82**:609 (1996).

Pressures for a One-Component Plasma on a Pseudosphere**57**

16. J. Zinn-Justin, *Quantum Field Theory and Critical Phenomena* (Clarendon, Oxford, 1989).
 17. B. Jancovici, *J. Phys. (Paris) Lett.* **42**:L-223 (1981).
 18. B. Jancovici, *J. Phys. (France)* **47**:389 (1986).
 19. B. Jancovici, *J. Stat. Phys.* **110**:879 (2003).
 20. A. Erdélyi *et al.*, *Higher Transcendental Functions* (McGraw-Hill, New York, 1953), Vol. 3.
-

Chapter 5

Generating functionals, consistency, and uniqueness in the integral equation theory of liquids

Fantoni R. and Pastore G., J. Chem. Phys., **119**, 3810 (2003)

Title: “Generating functionals, consistency, and uniqueness in the integral equation theory of liquids.”

Abstract: We discuss and illustrate through numerical examples the relations between generating functionals, thermodynamic consistency (in particular the virial-free energy one), and uniqueness of the solution, in the integral equation theory of liquids. We propose a new approach for deriving closures automatically satisfying such characteristics. Results from a first exploration of this program are presented and discussed.

Generating functionals, consistency, and uniqueness in the integral equation theory of liquids

R. Fantoni^{a)} and G. Pastore^{b)}

Dipartimento di Fisica Teorica dell' Università and Istituto Nazionale di Fisica della Materia, Strada Costiera 11, 34014 Trieste, Italy

(Received 21 April 2003; accepted 19 May 2003)

We discuss and illustrate through numerical examples the relations between generating functionals, thermodynamic consistency (in particular the virial-free-energy one), and uniqueness of the solution in the integral equation theory of liquids. We propose an approach for deriving closures automatically satisfying such characteristics. Results from a first exploration of this program are presented and discussed. © 2003 American Institute of Physics. [DOI: 10.1063/1.1590642]

I. INTRODUCTION

Integral equation theories (IETs) of liquid-state statistical mechanics are valuable tools for studying structural and thermodynamic properties of pairwise interacting fluid systems.^{1,2} Many of these approximations to the exact relation between pair potential and pair correlation functions have been proposed in the last half century, starting from the pioneering works^{3–5} to the most refined and modern approximations^{6–10} which may approach the accuracy of computer simulation with a negligible computational cost.

The functional method in statistical mechanics¹ provides the most general and sound starting point to introduce IETs as approximations of the exact functional relations, and it is the classical statistical mechanics counterpart of the quantum density functional theory.

Notwithstanding the success of present IETs to describe the structure of simple one-component systems, considerable work is still devoted to derive improved approximations which could accurately describe the thermodynamics as well. Also applications to nonsimple or multicomponent systems are still subject of current studies.

Actually, the description of thermodynamics is one weak point of IET approaches: reasonable and apparently harmless approximations to the potential-correlation relations usually result in a dramatically inconsistent thermodynamics where many, if not all, among the exact sum rules derived from statistical mechanics, are violated.

The problem of thermodynamic inconsistency—i.e., the inequivalence between different routes to thermodynamics—actually plagues the IET approach to the point that the degree of inconsistency between different formulas for the same quantity is used as an intrinsic measurement of the quality of a closure.

In the past, some discussion of the thermodynamic consistency appeared in the literature. The hypernetted chain (HNC) approximation was recognized as a closure directly derivable from an approximation for the free-energy functional,¹¹ thus exhibiting consistency between the virial

formula and the thermodynamic expression for the pressure. However, this limited consistency is not enough to guarantee a unique and faithful description of the phase diagram. Apart from the problem of the remaining inconsistencies, the descriptions of the critical points and spinodal lines are seriously inadequate.

Extensive work on HNC (Refs. 12–14) showed that in place of a true spinodal line, it is more appropriate to describe the numerical results as due to a region in the thermodynamic plane where no real solution of the integral equation exists. In particular, Belloni¹² showed that the disappearance of the solution originates from a branching point where two solutions merge, instead of from a line of diverging compressibility. Thus, we have direct evidence that the HNC approximation may have multiple solutions, at least in part of the phase diagram.

Empirical improvements on HNC have been proposed^{6,9,10} providing in many cases excellent results for one-component simple fluids. However, although reduced, the thermodynamic inconsistency problem remains and the multiple-solution problem is completely untouched.

In this work we start an investigation of a new approach to IETs directly addressing the two points of uniqueness of the solution and thermodynamic consistency. The basic idea is to constrain the search for new closures within the class of generating functionals which are strictly convex free-energy functionals, thus enforcing the virial-energy consistency as well as the uniqueness of the solution.

In particular, in the present paper we try to answer the following questions: (i) Does at least one strictly convex free-energy functional of the pair correlation function exist? (ii) What is the nature of the resulting spinodal line (if any)? (iii) What is the quality of the resulting thermodynamic and structural results? (iv) Does the simultaneous requirement of consistency and uniqueness automatically provide improved results?

As we will show, we have a positive answer for (i), a thorough and interesting characterization for (ii), some interesting indications for (iii), and a partly negative answer for (iv).

However, we can show that it is possible to exploit the

^{a)}Electronic mail: rfantoni@ts.infn.it

^{b)}Electronic mail: pastore@ts.infn.it

control provided by the generating functional approach to easily generate new closures and we feel our procedure could be the basis of a more systematic approach to IETs.

In Sec. II we recall the connections between closures, generating functionals, thermodynamic consistency, and uniqueness of solutions and we illustrate them in the well-known case of HNC approximation. In Sec. III we introduce two straightforward extensions of the HNC approximation intended to cure its problems. In Sec. IV numerical results are presented and discussed. In Sec. V we show two possible improvements of the closures studied.

II. THERMODYNAMIC CONSISTENCY AND UNIQUENESS OF THE SOLUTION OF INTEGRAL EQUATIONS

Since the work by Olivares and McQuarrie,¹⁵ it is known the general method to obtain the generating functional whose extremum with respect to variations of the direct $[c(r)]$ or total $[h(r)]$ correlation functions results in the closure relation, provided the Ornstein–Zernike (OZ) equation is satisfied.

For example, if we have a closure of the form

$$\rho^2 c(r) = \Psi\{h(r), \beta\phi(r)\}, \quad (1)$$

where $\phi(r)$ is the pair interaction potential and Ψ is an arbitrary function, the functional

$$\begin{aligned} Q[h(r), \beta\phi(r)] = & \frac{1}{2\beta\rho} \left(\int \frac{d\mathbf{k}}{(2\pi)^3} \{\rho h(k) - \ln[1 - \rho h(k)]\} \right. \\ & - \int d\mathbf{r} h(r) \\ & \left. \times \int_0^1 dt \Psi\{th(r), \beta\phi(r)\} + \text{const} \right) \quad (2) \end{aligned}$$

is such that the extremum condition

$$\frac{\delta Q}{\delta h(r)} = 0 \quad (3)$$

is equivalent to

$$\begin{aligned} \rho^2 h(r) = & \Psi\{h(r), \beta\phi(r)\} \\ & + \rho \int h(|\mathbf{r}-\mathbf{r}'|) \Psi\{h(r'), \beta\phi(r')\} d\mathbf{r}'. \quad (4) \end{aligned}$$

Olivares and McQuarrie also showed how to find the generating functional if the closure is expressed in the form

$$\rho^2 h(r) = \Psi\{c(r), \beta\phi(r)\}. \quad (5)$$

In Appendix A we discuss the extension of their method to the case of a closure written as

$$\rho^2 c(r) = \Psi\{\gamma(r), \beta\phi(r)\}, \quad (6)$$

where $\gamma(r) = h(r) - c(r)$ is the indirect correlation function. Notice that most of the modern closures correspond to this last case.

The possibility of translating the original integral equation into an extremum problem allows us to get an easy control on two important characteristics of the approxima-

tion: thermodynamic consistency between energy and virial routes to the thermodynamics and uniqueness of the solution.

Indeed, once we get the generating functional Q , due to the approximations induced by the closure, there is no guarantee that its value at the extremum is an excess free energy. In order to be a free energy, the functional should satisfy the condition

$$\frac{\delta Q}{\delta \phi(r)} = \frac{\rho}{2} g(r), \quad (7)$$

where $g(r) = h(r) + 1$ is the pair distribution function.

Even if this condition is not new and mention to it is present in the literature,¹⁶ we discuss it in Appendix B as well as its consequences on the thermodynamic consistency between the virial pressure and the density derivative of the free energy.

Another issue where the generating functional approach is useful is the problem of multiple solutions of the integral equations.¹² In particular, the analysis of the convexity properties of the generating functional is a very powerful tool.^{17,18}

Let us illustrate this technique in the case of HNC closure. It is well known^{11,15} that the HNC equation, with closure

$$c(r) = h(r) - \ln[g(r)e^{\beta\phi(r)}], \quad (8)$$

can be derived from the variational principle

$$\frac{\delta \mathcal{F}[h]}{\delta h(r)} = 0, \quad (9)$$

where

$$\mathcal{F}[h] = \mathcal{F}_{OZ}[h] + \mathcal{F}_{HNC}[h], \quad (10)$$

with

$$\mathcal{F}_{OZ}[h] = \int \frac{d\mathbf{k}}{(2\pi)^3} \{\rho \hat{h}(k) - \ln[1 + \rho \hat{h}(k)]\}, \quad (11a)$$

$$\begin{aligned} \mathcal{F}_{HNC}[h] = & \rho^2 \int d\mathbf{r} \{1 + g(r) (\ln[g(r)e^{\beta\phi(r)}] - 1) \\ & - h^2(r)/2\}. \quad (11b) \end{aligned}$$

Let us call $\bar{h}(r)$ the extremum of \mathcal{F} , solution of the variational principle (9). It can be shown (see Appendix B) that, within an additive constant, $\mathcal{F}[\bar{h}]/(2\beta\rho)$ is the excess Helmholtz free energy per particle of the liquid. This ensures thermodynamic consistency between the route to the pressure going through the partial derivative of the free energy and the one going through the virial theorem (see Appendix B). In addition, it allows us to get a closed expression for the excess chemical potential without further approximations.^{19,20} This feature is highly desirable for applications of IETs to the determination of the phase diagrams.

Moreover, if we can prove that \mathcal{F} , defined on some convex set of trial correlation functions D_c , is a strictly convex functional, then we know that if a solution to Eq. (9) exists,

it corresponds to a minimum and is unique. A functional \mathcal{F} is strictly convex if, for all $y(r) \in D_c$ and $y(r) \neq 0$, we have

$$A = \int y(r) \frac{\delta^2 \mathcal{F}[h]}{\delta h(r) \delta h(r')} y(r') d\mathbf{r} d\mathbf{r}' > 0. \quad (12)$$

We calculate the second functional derivatives as follows:

$$\frac{\delta^2 \mathcal{F}_{OZ}[h]}{\delta h(r) \delta h(r')} = \rho^2 \int \frac{d\mathbf{k}}{(2\pi)^3} e^{-i\mathbf{k} \cdot (\mathbf{r} + \mathbf{r}')} \frac{1}{[1 + \rho \hat{h}(k)]^2}, \quad (13a)$$

$$\frac{\delta^2 \mathcal{F}_{HNC}[h]}{\delta h(r) \delta h(r')} = \rho^2 \delta(\mathbf{r} - \mathbf{r}') \left(\frac{1}{g(r)} - 1 \right). \quad (13b)$$

Recalling that the static structure factor $S(k) = 1 + \rho \hat{h}(k)$, we find, for A ,

$$A/\rho^2 = \int \frac{d\mathbf{k}}{(2\pi)^3} \frac{\hat{y}^2(k)}{S^2(k)} + \int d\mathbf{r} y^2(r) \left(\frac{1}{g(r)} - 1 \right). \quad (14)$$

Now, the most interesting results would be to show the strict convexity of the HNC functional over the convex set of all the admissible pair correlation functions [all the $h(r) \geq -1$ and properly decaying to zero at large distance].

However, this is not the case for HNC. It has not been possible to show the positive definiteness of Eq. (14) and it has been shown¹² that in some region of the thermodynamic plane the HNC approximation does exhibit multiple solutions.

The best we can do is to obtain a more limited result. Calling $g_1 = \text{sup}g(r)$ ($g_1 > 1$ is the height of the first peak of the pair distribution function) and using Parseval theorem, we find

$$A/\rho^2 > \int \frac{d\mathbf{k}}{(2\pi)^3} \hat{y}^2(k) \left(\frac{1}{S^2(k)} - 1 + \frac{1}{g_1} \right), \quad (15)$$

from which we deduce that $A > 0$ on the following set of functions:

$$D = \{h(r) \mid 0 < S(k) < \sqrt{g_1/(g_1 - 1)} \forall k\}. \quad (16)$$

We conclude that \mathcal{F} defined on any convex set of functions $D_c \subset D$ is strictly convex. Near the triple point we are sure we are out from such set since the first peak of the pair distribution function for the Lennard-Jones fluid is $g_1 \approx 3$ (Ref. 21), so that $\sqrt{g_1/(g_1 - 1)} \approx 1.2$. The first peak of the static structure factor is also close to 3. Then we are not inside D and the HNC approximation may have multiple solutions.¹²

Instead, if we are in the weak-coupling regime, the previous conditions tell us that there is a range where the branch of solutions going to the perfect gas limit is unique and quite isolated from other solutions.

III. EXTENSIONS OF THE HNC APPROXIMATION

The generating functional approach can be used in a systematic way to look for better closures. We think that this way we can obtain a less empirical search method for improving closures.

In the following we report some preliminary analysis we have done. As a first test of our program, we have restricted

our investigations to simple modifications of the HNC functional. As we will discuss later, such a choice is certainly not optimal. However, we can learn enough to consider the approach worthwhile of further investigations and we feel the results are interesting in order to reveal more details about the characteristics of the solutions of the highly nonlinear IETs.

A. HNC/H2 approximation

We want to modify the HNC closure in order to have an integral equation with a generating functional which is strictly convex without having to restrict its definition domain. We choose, as our modified HNC (HNC/H2) closure,²²

$$c(r) = h(r) - \ln[g(r)] - \beta\phi(r) - \alpha h^2(r), \quad (17)$$

with α a parameter to be determined. The new closure generating functional is

$$\mathcal{F}_{HNC/H2}[h] = \rho^2 \int d\mathbf{r} \{1 + g(r) (\ln[g(r)] e^{\beta\phi(r)} - 1) - h^2(r)/2 + \alpha h^3(r)/3\}. \quad (18)$$

Its second functional derivative with respect to h is

$$\frac{\delta^2 \mathcal{F}_{HNC/H2}[h]}{\delta h(r) \delta h(r')} = \rho^2 \delta(\mathbf{r} - \mathbf{r}') \left[\frac{1}{g(r)} - 1 + 2\alpha h(r) \right]. \quad (19)$$

Recalling that $h = g - 1$ and $g(r) > 0$ for all r , we see that, for $\alpha = 1/2$,

$$\frac{1}{g} - 1 + 2\alpha h = \frac{(1-g)^2}{g} \geq 0 \quad \forall g. \quad (20)$$

Then $\mathcal{F}_{HNC/H2}$ is a convex functional, and since \mathcal{F}_{OZ} is unchanged and strictly convex (see Appendix C), their sum, the generating functional of the integral equation, is strictly convex.

Moreover, $\{\mathcal{F}_{OZ}[\bar{h}] + \mathcal{F}_{HNC/H2}[\bar{h}]\}/(2\beta\rho)$ continues to be the excess Helmholtz free energy per particle of the liquid since Eq. (7) holds (see Appendix B).

We have then an integral equation which is both thermodynamically consistent (the pressure calculated from the virial theorem coincides with that one calculated from the Helmholtz free energy) and with a solution which, when it exists, is unique.

B. HNC/H3 approximation

In the same spirit as in Sec. III A we can try to add a term h^3 in the HNC/H2 closure

$$c(r) = h(r) - \ln[g(r)] - \beta\phi(r) - \alpha h^2(r) - \gamma h^3(r), \quad (21)$$

with α and γ parameters to be determined. We call this approximation HNC/H3. The closure generating functional is

$$\mathcal{F}_{HNC/H3}[h] = \rho^2 \int d\mathbf{r} \{1 + g(r) (\ln[g(r)] e^{\beta\phi(r)} - 1) - h^2(r)/2 + \alpha h^3(r)/3 + \gamma h^4(r)/4\}. \quad (22)$$

Its second functional derivative with respect to h is

$$\begin{aligned} \frac{\delta^2 \mathcal{F}_{HNC/H3}[h]}{\delta h(r) \delta h(r')} &= \rho^2 \delta(\mathbf{r}-\mathbf{r}') \left[\frac{1}{g(r)} - 1 + 2\alpha h(r) + 3\gamma h^2(r) \right] \\ &= \rho^2 \delta(\mathbf{r}-\mathbf{r}') \frac{1-g(r)}{g(r)} \{1 - 2\alpha g(r) + 3\gamma g(r)\} \\ &\quad \times [1 - g(r)]. \end{aligned} \quad (23)$$

In order to have the right-hand side of this expression positive for $g > 0$ the only choice we have is to set $\alpha = 1/2$. In this way,

$$(1-g)[1 - 2\alpha g + 3\gamma g(1-g)] = (1-g)^2(1 + 3\gamma g), \quad (24)$$

and we see that $\mathcal{F}_{HNC/H3}$ is a convex functional if we additionally choose $\gamma > -1/[3 \sup g(r)]$.

Once again $\{\mathcal{F}_{OZ}[\bar{h}] + \mathcal{F}_{HNC/H3}[\bar{h}]\}/(2\beta\rho)$ is the excess Helmholtz free energy per particle of the liquid and the thermodynamic consistency virial free energy is ensured.

IV. NUMERICAL RESULTS

To solve numerically the OZ plus closure system of nonlinear equations we used Zerah's algorithm²³ and Fourier transforms were done using fast Fourier transform. In the code we always work with adimensional thermodynamic variables $T^* = 1/(\beta\epsilon)$, $\rho^* = \rho\sigma^3$, and $P^* = P\sigma^3/\epsilon$, where σ and ϵ are the characteristic length and characteristic energy of the system, respectively. We always used 1024 grid points and a step size $\Delta r = 0.025\sigma$.

The thermodynamic quantities were calculated according to the statistical mechanics formulas for the excess internal energy per particle,

$$U^{exc}/N = 2\pi\rho \int_0^\infty \phi(r)g(r)r^2 dr; \quad (25)$$

the excess virial pressure

$$\beta P^v/\rho - 1 = -\frac{2}{3}\pi\beta\rho \int_0^\infty \frac{d\phi(r)}{dr} g(r)r^3 dr; \quad (26)$$

the bulk modulus calculated from the compressibility equation,

$$B_c = \frac{\beta}{\rho\chi_T} = \frac{1}{S(k=0)}, \quad (27)$$

where χ_T is the isothermal compressibility; and the bulk modulus calculated from the virial equation,

$$B_p = \beta \frac{\partial P^v}{\partial \rho}.$$

For the calculation of B_p once $g(r)$ and $c(r)$ had been calculated, Lado's scheme for Fourier transforms²⁴ was used to determine $\partial \hat{g}(k)/\partial \rho$. Even if slow, this allows us to explicitly calculate and later invert the coefficients matrix of the linear system of equations which enters the calculation of $\partial \hat{g}(k)/\partial \rho$.

TABLE I. We compare various thermodynamic quantities as obtained from the MC simulation of Hansen and Shiff, the RY, HNC, and HNC/H2 closures, for the inverse 12th-power fluid at the freezing point ($z=0.813$). $U^{exc}/(N\epsilon)$ is the excess internal energy per particle, $\beta P^v/\rho - 1$ the excess virial pressure, and B_c and B_p are the bulk moduli calculated from the compressibility and the virial equations, respectively.

Closure	$U^{exc}/(N\epsilon)$	$\beta P^v/\rho - 1$	B_c	B_p
MC	2.675	18.7	-	72.7
RY ($\alpha=0.603$)	2.626	18.36	69.78	70.13
HNC	3.009	21.04	45.28	80.43
HNC/H2	3.200	22.37	52.66	87.26

A. Inverse power potentials

The general form of the inverse power potential is

$$\phi(r) = \epsilon \left(\frac{\sigma}{r} \right)^n, \quad (28)$$

where $3 < n < \infty$. For this class of fluids the thermodynamics depends only on the dimensionless coupling parameter

$$z = (\rho\sigma^3/\sqrt{2})(\beta\epsilon)^{3/n}. \quad (29)$$

In this paper we choose to fix $\rho^* = 1$ so that Eq. (29) gives the relation between z and T^* .

We performed our calculations on the $n=12, 6$, and 4 fluids at the freezing point. We compared three kind of closures: the one of Rogers and Young²⁵ (RY) with thermodynamic consistency virial compressibility and known to be very close to the simulation results, the hypermetted chain closure, and the HNC/H2 described in Sec. IIIA. In each case we compared our data with the Monte Carlo (MC) results of Hansen and Schiff.²⁶

1. Inverse 12th-power potential

The freezing point for this fluid is at $z=0.813$. The RY α parameter to achieve thermodynamic consistency at this value of z is 0.603. Notice that we express α in units of σ and not of $a=(3/4\pi\rho)^{1/3}$ as in the original Rogers and Young's paper.²⁵

In Table I we compare various thermodynamic quantities (the excess internal energy per particle, excess virial pressure, bulk moduli) obtained from the MC simulation of Hansen and Schiff,²⁶ the RY, HNC, and HNC/H2 closures.

In Fig. 1 we compare the MC, HNC, and HNC/H2 results for the pair distribution function.

2. Inverse 6th-power potential

The freezing point for this fluid is at $z=1.54$. The RY α parameter to achieve thermodynamic consistency at this value of z is 1.209.

In Table II we compare various thermodynamic quantities (the excess internal energy per particle, excess virial pressure, bulk moduli) obtained from the MC simulation of Hansen and Schiff,²⁶ the RY, HNC, and HNC/H2 closures.

3. Inverse 4th-power potential

The freezing point for this fluid is at $z=3.92$. The RY α parameter to achieve thermodynamic consistency at this value of z is 1.794.

3814 J. Chem. Phys., Vol. 119, No. 7, 15 August 2003

R. Fantoni and G. Pastore

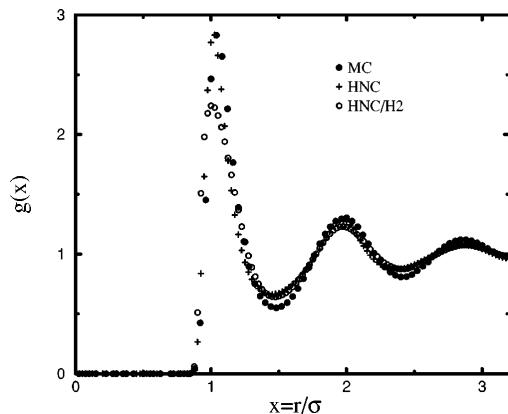


FIG. 1. Comparison of the Monte Carlo (MC), HNC, and HNC/H2 results for the pair distribution function of the inverse 12th-power fluid at $z = 0.813$.

In Table III we compare various thermodynamic quantities (the excess internal energy per particle, excess virial pressure, bulk moduli) obtained from the MC simulation of Hansen and Shiff,²⁶ the RY, HNC, and HNC/H2 closures.

In Fig. 2 we compare the MC, HNC, and HNC/H2 results for the pair distribution function.

B. Spinodal line

In this subsection we study a pair potential with a minimum. In particular we chose the Lennard-Jones potential

$$\phi(r) = 4\epsilon \left[\left(\frac{\sigma}{r} \right)^{12} - \left(\frac{\sigma}{r} \right)^6 \right], \quad (30)$$

where ϵ and σ are positive parameters. The critical point for this fluid is at²⁷ $T_c^* = 1.3120 \pm 0.0007$, $\rho_c^* = 0.316 \pm 0.001$, and $P_c^* = 0.1279 \pm 0.0006$.

Integral equations usually fail to have a solution at low temperature and intermediate densities: i.e., in the two-phases unstable region of the phase diagram. In particular it is well known that the HNC approximation is unable to reproduce the *spinodal line*, the locus of points of infinite compressibility in the phase diagram.¹² This is due to the loss of solution as one approaches the unstable region on an isotherm from high or from low densities. The line of loss of solution, in the phase diagram, is called the *termination line*.

TABLE II. We compare various thermodynamic quantities as obtained from the MC simulation of Hansen and Shiff, the RY, HNC, and HNC/H2 closures, for the inverse 6th-power fluid at the freezing point ($z = 1.54$). $U^{exc}/(N\epsilon)$ is the excess internal energy per particle, $\beta P^{(v)}/\rho - 1$ the excess virial pressure, and B_c and B_p are the bulk moduli calculated from the compressibility and the virial equations, respectively.

Closure	$U^{exc}/(N\epsilon)$	$\beta P^{(v)}/\rho - 1$	B_c	B_p
MC	4.090	38.8	-	110.1
RY ($\alpha = 1.209$)	4.114	39.03	111.0	111.4
HNC	4.235	40.18	84.02	113.7
HNC/H2	4.283	40.64	88.29	115.8

TABLE III. We compare various thermodynamic quantities as obtained from the MC simulation of Hansen and Shiff, the RY (notice that the bulk moduli were not given in the Rogers and Young's paper and the value of the virial pressure as reported in our table was not corrected to take into account the long-range nature of the potential), the HNC and HNC/H2 closures, for the inverse 4th-power fluid at the freezing point ($z = 3.92$). $U^{exc}/(N\epsilon)$ is the excess internal energy per particle, $\beta P^{(v)}/\rho - 1$ the excess virial pressure, and B_c and B_p are the bulk moduli calculated from the compressibility and the virial equations, respectively.

Closure	$U^{exc}/(N\epsilon)$	$\beta P^{(v)}/\rho - 1$	B_c	B_p
MC	8.233	107.7	-	156
RY ($\alpha = 1.794$)	8.001	104.7	250.1	242.9
HNC	8.047	105.3	223.3	244.2
HNC/H2	8.068	105.5	227.0	257.7

According to the discussion of Sec. II, the loss of solution for the HNC approximation can be traced back to the loss of strict convexity of the generating functional.²⁸ Indeed, using the HNC approximation, we computed the bulk modulus from the compressibility equation B_c on several isotherms as a function of the density. At low temperatures we found that at both high density and low density we were unable to continue the isotherm at low values of B_c . Zerah's algorithm either could not get to convergence or it would converge at a nonphysical solution (with a pole in the structure factor at some finite wave vector k). Since HNC/H2 has, by construction, an always strictly convex generating functional, we expect it to be able to approximate a spinodal line (there should be no termination line).

In Fig. 3 we show the behavior of B_c on several isotherms as a function of density, calculated with the HNC/H2 approximation. We see that now there are no termination points. B_c never becomes exactly zero, and the low-temperature isotherms develop a bump in the intermediate-density region. The same plot for the bulk modulus calculated from the virial pressure B_p shows that at low temperatures this bulk modulus indeed becomes zero along the isotherms both at high and low densities.

In Fig. 4 the pressure is plotted as a function of the density on several isotherms for the HNC/H2 approximation. Apart from the fact that we find negative pressures, the isotherms have a van der Waals-like behavior.

The graphical analysis of the pressure plotted as a function of the chemical potential shows that the coexistence of the two phases (points where the curve crosses itself) is possible and is lost between $T^* = 1.1$ and $T^* = 1.2$. There generally are two points of coexistence.

V. IMPROVING THE CLOSURES

The numerical results for HNC/H2 exhibit interesting features as far as the coexistence region is concerned but show unambiguously a worst agreement with the MC structural data in correspondence with a marginal improvement in the thermodynamics.

We feel that the main problem is the difficulty of an accurate description of the bridge functions in terms of powers of the pair correlation function. Recent investigations of improved closures seem to point to the indirect correlation function $\gamma(r)$ or some renormalized version of it as the best

J. Chem. Phys., Vol. 119, No. 7, 15 August 2003

Integral equation theory of liquids 3815

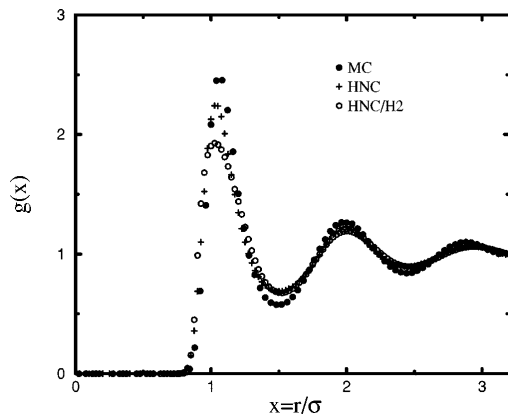


FIG. 2. Comparison of the Monte Carlo (MC), HNC, and HNC/H2 results for the pair distribution function of the inverse 4th-power fluid at $z=3.92$.

starting point for progress. However, before moving to more complex relations or functional dependences, we have explored two possible directions for improving the HNC/H2 closure. In the first approach we have tried to follow the reference hypernetted chain (RHNC) approach by Lado.²⁹ In the second we have explored the possibilities of optimization offered by the numerical coefficient of the cubic term in the generating functional.

A. Pseudobridge functions for HNC/H2

From the graphical analysis of the pair distribution function it is known¹ that $g(r)$ may be written as

$$g(r) = \exp[-\beta\phi(r) + \gamma(r) + B(r)], \quad (31)$$

where $\gamma(r) = h(r) - c(r)$ is the sum of all the series-type diagrams and $B(r)$ the sum of bridge-type diagrams. If we take

$$B(r) = -\frac{1}{2}h^2(r) + G(r), \quad (32)$$

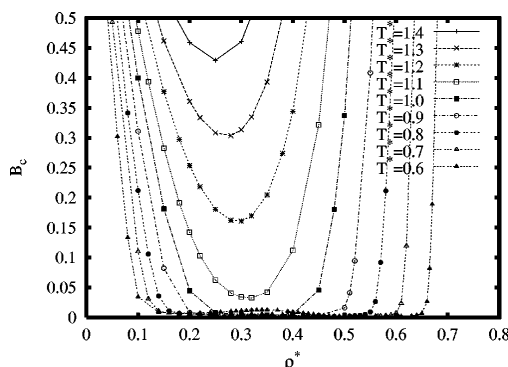


FIG. 3. Behavior of B_c of the Lennard-Jones fluid, on several isotherms as a function of the density for the HNC/H2 approximation.

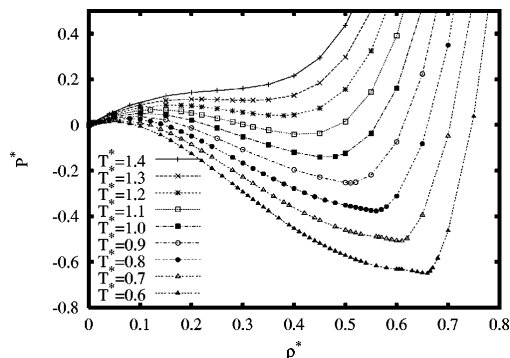


FIG. 4. Behavior of the pressure of the Lennard-Jones fluid, on several isotherms as a function of the density for the HNC/H2 approximation.

we have that our HNC/H2 approximation amounts to setting $G(r)=0$. Rosenfeld and Ashcroft⁶ proposed that $B(r)$ should be essentially the same for all potentials $\phi(r)$. We now make a similar proposal for the G function, and we will refer to it as the *pseudobridge function*. In the same spirit of the RHNC approximation of Lado²⁹ we will approximate $G(r)$ with the G function of a short-range (reference) potential $\phi_0(r)$. Assuming known the properties of the reference system, we can calculate the G function as follows:

$$G_0(r) = \ln[g_0(r)e^{\beta\phi_0(r)}] - \gamma_0(r) + \frac{1}{2}h_0^2(r). \quad (33)$$

The reference HNC/H2 (RHNC/H2) approximation is then

$$g(r) = \exp\left[-\beta\phi(r) + \gamma(r) - \frac{1}{2}h^2(r) + G_0(r)\right]. \quad (34)$$

An expression for the free-energy functional can be obtained *turning on* the potential $\phi(r)$ in two stages: first, from the noninteracting state to the reference potential $\phi_0(r)$ and then from there to the full potential $\phi(r)$. To this end we write

$$\phi(r; \lambda_0, \lambda_1) = \lambda_0\phi_0(r) + \lambda_1\Delta\phi(r), \quad (35)$$

with $\Delta\phi(r) = \phi(r) - \phi_0(r)$. Following the same steps as in Ref. 7 we obtain, for the excess free energy per particle,

$$f^{exc} = f_1 + f_2 + f_3^{(0)} + \Delta f_3, \quad (36)$$

where the first two terms were already encountered in Sec. II:

$$\beta f_1 = \frac{1}{2}\rho \int d\mathbf{r} \{1 + g(r) [\ln[g(r)e^{\beta\phi(r)}] - 1] - h^2(r)/2 + h^3(r)/6\}, \quad (37)$$

$$\beta f_2 = \frac{1}{2\rho} \int \frac{d\mathbf{k}}{(2\pi)^3} \{\rho\hat{h}(k) - \ln[1 + \rho\hat{h}(k)]\}. \quad (38)$$

The third term is assumed known:

$$\begin{aligned} \beta f_3^{(0)} &= -\frac{1}{2}\rho \int d\mathbf{r} \int_0^1 d\lambda_0 G(r; \lambda_0, 0) \frac{\partial g(r; \lambda_0, 0)}{\partial \lambda_0} \\ &= \beta(f^{(0)} - f_1^{(0)} - f_2^{(0)}); \end{aligned} \quad (39)$$

here, $f^{(0)}$ is the excess free energy per particle of the refer-

ence system and $f_1^{(0)}, f_2^{(0)}$ are defined as in Eqs. (37), (38) for the reference potential and its corresponding correlation functions. The last term is

$$\beta\Delta f_3 = -\frac{1}{2}\rho \int d\mathbf{r} \int_0^1 d\lambda_1 G(r; 1, \lambda_1) \frac{\partial g(r; 1, \lambda_1)}{\partial \lambda_1}. \quad (40)$$

According to our proposal, G is insensitive to a change in potential from ϕ_0 to ϕ . We may then approximate this last term as follows:

$$\beta\Delta f_3 \approx -\frac{1}{2}\rho \int d\mathbf{r} G_0(r) [g(r) - g_0(r)]. \quad (41)$$

Now that we have the free energy we may consider it as a functional of both $h(r)$ and $G_0(r)$ and take its variation with respect to these functions. We find

$$\begin{aligned} \beta\delta f^{exc} = & \frac{1}{2}\rho \int d\mathbf{r} \{c(r) - h(r) + h^2(r)/2 + \ln[g(r)e^{\beta\phi(r)}] \\ & - G_0(r)\} \delta h(r) - \frac{1}{2}\rho \int d\mathbf{r} [g(r) - g_0(r)] \delta G_0(r). \end{aligned} \quad (42)$$

It follows that the free energy is minimized when both the RHNC/H2 closure [Eq. (34)] is satisfied and when the constraint

$$\int d\mathbf{r} [g(r) - g_0(r)] \delta G_0(r) = 0 \quad (43)$$

is fulfilled.

Taking the second functional derivative of f^{exc} with respect to $h(r)$ we find that also this free energy is a strictly convex functional of the total correlation function. This property was lacking in the RHNC theory and constitutes the main feature of the RHNC/H2 closure. As already stressed in Sec. III A it ensures that if a solution to the integral equation exists it has to be unique.

The constraint, as for RHNC, gives a certain thermodynamic consistency to the theory (see Ref. 7). If we choose a hard sphere reference potential $\phi_0(r) = \phi_0(r; \sigma)$ which depends on the length scale σ , the optimum values of the parameters that makes the generating functional a free energy can be determined by the constraint (43) which becomes

$$\int d\mathbf{r} [g(r) - g_0(r)] \frac{\partial G_0(r)}{\partial \sigma} = 0. \quad (44)$$

However, neither the hard-sphere pseudobridge functions nor some empirical attempt to model the unknown function via a Yukawa function provided useful results.

B. Optimized HNC/H3 approximation

For $\gamma=0$ HNC/H3 reduces to HNC/H2. For $\gamma>0$ the first peak of the pair distribution function is dumped with respect to the one of the pair distribution function calculated with HNC/H2. For $\gamma<0$ the first peak increases giving in general a better fit to the simulation data.

In Fig. 5 we compare the pair distribution function of the Lennard-Jones fluid near its triple point, calculated with a molecular dynamic simulation,²¹ the HNC/H2 approxima-

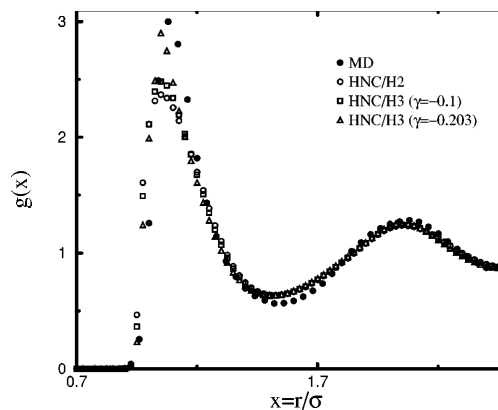


FIG. 5. Comparison of the pair distribution function of a Lennard-Jones fluid at $\rho^*=0.85$ and $T^*=0.719$, computed from the molecular dynamic (MD) simulation of Verlet, the HNC/H2 approximation, and the HNC/H3 approximation. For HNC/H3 we present results obtained setting $\gamma=-0.1$ (when the generating functional of the approximation is still strictly convex) and $\gamma=-0.203$ (which gives the best fit possible to the simulation data but does not ensure the strict convexity of the generating functional).

tion, the approximation HNC/H3 with $\gamma=-0.203$ (at lower values of γ Zerah's algorithm would fail to converge), and the approximation HNC/H3 with $\gamma=-0.1$ (when the generating functional of HNC/H3 is still strictly convex). As we can see HNC/H3 fits the simulation data better than HNC/H2 even if the first peak is still slightly displaced to the left of the simulation data, a well-known problem of the HNC approximation.⁶

The best results are given by HNC/H3 with $\gamma=-0.203$. Note that the HNC/H3 generating functional at this value of γ is not strictly convex (strict convexity is lost for $\gamma \lesssim -1/9$). The first peak of the static structure factor is at $k\sigma=6.75$ and has a magnitude of 2.41, a quite low value for a liquid near the triple point. We have calculated the pressure and the internal energy. We found $\beta P/\rho \approx 3.87$ and $U^{exc}/(N\epsilon) \approx -5.72$ [very close to the HNC results $\beta P/\rho \approx 3.12$ and $U^{exc}/(N\epsilon) \approx -5.87$] to be compared with the simulation results³⁰ 0.36 and -6.12 , respectively. The bulk moduli are $B_c \approx 11.74$ and $B_p \approx 36.61$ which shows that at the chosen value of γ we do not have the thermodynamic consistency virial compressibility and we do not improve on HNC inconsistency (using HNC we find $B_c \approx 7.09$ and $B_p \approx 32.72$).

VI. CONCLUSIONS

In this paper we have analyzed the relations between generating functionals, thermodynamic consistency, and uniqueness of the solution of the integral equations of liquid-state theory. We think that the requirement of deriving from a free energy and the uniqueness of the solution are two important ingredients to enforce in the quest for better closures. The former requirement is of course crucial to get virial-energy consistency. But it is also important to get integral equations able to provide a closed formula for the chemical potential without additional approximations. This last issue

looks highly desirable for applications of IET to the determination of phase diagrams. The latter is certainly a useful constraint from the numerical point of view but it is also a very strong condition, probably able to avoid some non physical behavior in the coexistence region, although this point would deserve further investigation. Most of the existing closures fail to satisfy the condition of uniqueness of the solution. Among them, only the optimized random phase approximation by Andersen and Chandler^{18,31} satisfies both constraints although they were not used in the original derivation of the approximation. One obvious question is whether the enforcement of these constraints automatically results in improved closures.

In this work, we have started an exploration of the capabilities of the combined requirement of consistency and uniqueness, starting with simple modifications to the HNC closure, corresponding to the addition of a square and a cubic power of $h(r)$ in the HNC functional. We found a couple of approximations (HNC/H2 and HNC/H3), which have built in the virial-free-energy thermodynamic consistency and have a unique solution.

We numerically tested these closures on inverse power and the Lennard-Jones fluid. From the tests on the inverse-power potential fluids one can see that the HNC/H2 approximation is comparable to HNC for the thermodynamic quantities and performs worse than RY and even HNC for structural properties. The tests on the Lennard-Jones fluid revealed that this approximation does not suffer from the presence of a termination line (present in HNC and almost all the existing closures). This allowed us to follow isotherms from the low-density to the high-density region, and this behavior would be very useful in the study of the phase coexistence. However, the thermodynamic results show only a marginal improvement on HNC and the structure is definitely worse.

Our trials to improve HNC/H2 in the same spirit of the modified HNC approaches did not succeed. We feel that the main reason is in the difficulty of modeling the real bridge functions through a polynomial in the function $h(r)$. In this respect, approaches based on generating functionals depending on the indirect correlation function $\gamma(r)$ look more promising but we have not tried them yet.

Much better results for the structure are found with HNC/H3 as is shown in Fig. 5. However, probably for the same reasons just discussed, one has to give up to have an approximation with a strictly convex generating functional depending on $h(r)$. The thermodynamics reproduced by HNC/H3 is not yet satisfactory: due to the slight left shift of the main peak of the $g(r)$, the calculated pressure misses the simulation result. Nonetheless, the presence of the free parameter γ in HNC/H3 leaves open the possibility of imposing the thermodynamic consistency virial compressibility. If the value of the parameter needed to have the consistency is bigger than $-1/[3\text{supg}(r)]$, then we would have an approximation which is completely thermodynamically consistent and have a unique solution. This strategy may eventually lead us to discover that the price we have to pay to have a completely thermodynamically consistent approximation is the loss of strict convexity of the generating functional.

APPENDIX A: GENERATING FUNCTIONALS OF γ

Often in the numerical solution of the OZ plus closure integral equation use is made of the auxiliary function $\gamma(r) = h(r) - c(r)$. Suppose that the closure relation can be written as

$$\rho^2 c(r) = -\Psi\{\gamma(r)\}, \quad (\text{A1})$$

where Ψ is a local function of the function γ and has a dependence on the value of the pair potential not explicitly shown.

We want to translate the integral equation into a variational principle involving functionals of $\gamma(r)$. Then we introduce a closure functional $\mathcal{F}_{cl}[\gamma]$ such that

$$\frac{\delta \mathcal{F}_{cl}[\gamma]}{\delta \gamma(r)} = \Psi\{\gamma(r)\} \quad (\text{A2})$$

and an OZ functional $\mathcal{F}_{Oz,c}[\gamma]$ such that, when $c(r)$ and $\gamma(r)$ satisfy the OZ equation, we have

$$\frac{\delta \mathcal{F}_{Oz,c}[\gamma]}{\delta \gamma(r)} = \rho^2 c(r). \quad (\text{A3})$$

Then when both the closure and the OZ relations are satisfied, the functional $\mathcal{F} = \mathcal{F}_{cl} + \mathcal{F}_{Oz,c}$ is stationary with respect to variations of $\gamma(r)$: i.e.,

$$\frac{\delta \mathcal{F}[\gamma]}{\delta \gamma(r)} = 0. \quad (\text{A4})$$

This is the variational principle sought.

Now, we want to find $\mathcal{F}_{Oz,c}$. The OZ equation in k space is

$$\rho \hat{c}^2(k) + \rho \hat{\gamma}(k) \hat{c}(k) - \hat{\gamma}(k) = 0. \quad (\text{A5})$$

When we solve it for \hat{c} we find two solutions

$$\hat{c} = \frac{-\hat{\Gamma} \pm \sqrt{\hat{\Gamma}^2 + 4\hat{\Gamma}}}{2\rho}, \quad (\text{A6})$$

where $\hat{\Gamma}(k) = \rho \hat{\gamma}(k)$ is always positive since

$$\hat{\Gamma} = \rho^2 \hat{h} \hat{c} = \rho^2 \frac{\hat{h}^2}{1 + \rho \hat{h}} = \rho^2 \frac{\hat{h}^2}{S(k)}, \quad (\text{A7})$$

$S(k)$ being the liquid static structure factor which is positive definite for all k . Since $\hat{c}(k)$ is a function which oscillates around 0, where \hat{c} is negative we have to choose the solution with the minus sign, where it is positive the one with the plus sign. In particular, if the isothermal compressibility of the liquid χ_T is smaller than the one of the ideal gas, χ_T^0 , we have that

$$\hat{c}(0) = \frac{1}{\rho} \left(1 - \frac{\chi_T^0}{\chi_T} \right) < 0, \quad (\text{A8})$$

and we have to start with the minus sign.

The functional we are looking for is then [see Eq. (30) in Ref. 15, with the constant set equal to zero]

$$\mathcal{F}_{OZ,c}[\gamma] = \int_0^1 dt \int d\mathbf{r} \gamma(r) \int \frac{d\mathbf{k}}{(2\pi)^3} \frac{\rho}{2} e^{i\mathbf{k}\cdot\mathbf{r}} \times [-t\hat{\Gamma}(k) + s_c(k) \sqrt{t^2\hat{\Gamma}^2(k) + 4t\hat{\Gamma}(k)}], \quad (\text{A9})$$

where $s_c(k)$ is +1 when $\hat{c}(k) \geq 0$ and -1 when $\hat{c}(k) < 0$. Rearranging the integrals and making the change of variable $y = t\hat{\Gamma}$ we find

$$\begin{aligned} \mathcal{F}_{OZ,c}[\gamma] &= \frac{1}{2} \int \frac{d\mathbf{k}}{(2\pi)^3} \int_0^{\hat{\Gamma}(k)} dy [-y + s_c(k) \sqrt{y^2 + 4y}] \\ &= \int \frac{d\mathbf{k}}{(2\pi)^3} \{ -\hat{\Gamma}^2/4 + s_c(k) \\ &\quad \times ((1 + \hat{\Gamma}/2) \sqrt{(1 + \hat{\Gamma}/2)^2 - 1} \\ &\quad - \ln[1 + \hat{\Gamma}/2 + \sqrt{(1 + \hat{\Gamma}/2)^2 - 1}]) \}. \end{aligned} \quad (\text{A10})$$

If the closure relation has the form

$$\rho^2 h(r) = -\Psi\{\gamma(r)\}, \quad (\text{A11})$$

we can derive the corresponding functional using the same procedure. The final result is a functional $\mathcal{F}_{OZ,h}[\gamma]$ which differs from Eq. (A10) for a plus sign in front of the first term in the integral.

However, by examining their second functional derivatives, we notice that both $\mathcal{F}_{OZ,c}[\gamma]$ and $\mathcal{F}_{OZ,h}[\gamma]$ are not certainly convex or concave. Thus, any check of the convexity properties of generating functionals of the $\gamma(r)$ function should be done on the full functional.

APPENDIX B: THERMODYNAMIC CONSISTENCY

For a homogeneous liquid interacting through a pair potential $\phi(r)$, the Helmholtz free energy per particle, f , can be considered a functional of ϕ . Indeed, in the canonical ensemble, one has

$$\begin{aligned} \beta f[\phi] &= \beta f_0 \\ &\quad - \frac{1}{N} \ln \left(\frac{1}{V^N} \int \exp \left[-\beta \frac{1}{2} \sum_{i \neq j} \phi(\mathbf{r}_{ij}) \right] d\mathbf{r}_1 \cdots d\mathbf{r}_N \right), \end{aligned} \quad (\text{B1})$$

where f_0 is the free energy per particle of the ideal gas ($\phi=0$) and V is the volume of the liquid. Taking the functional derivative with respect to $\beta\phi(r)$ one finds

$$\frac{\delta\beta f[\phi]}{\delta\beta\phi(r)} = \frac{\rho}{2} g(r). \quad (\text{B2})$$

Imagine that we found a functional $\mathcal{A}([h],[\phi],\rho,\beta)$ that has an extremum for those correlation functions that solve the OZ and the closure system of equations. Suppose further that such functional has the property

$$\frac{\delta\beta\mathcal{A}}{\delta\beta\phi(r)} = \frac{\rho}{2} g(r), \quad (\text{B3})$$

which can be rewritten more explicitly as follows:

$$\left. \frac{\delta\beta\mathcal{A}}{\delta\beta\phi(r)} \right|_{[h],\rho,\beta} + \int d\mathbf{r}' \left. \frac{\delta\beta\mathcal{A}}{\delta h(r')} \right|_{[\phi],\rho,\beta} \frac{\delta h(r')}{\delta\beta\phi(r)} = \frac{\rho}{2} g(r). \quad (\text{B4})$$

Evaluating this expression on the correlation function \bar{h} solution of the OZ plus closure system of equations, which is an extremum for \mathcal{A} , we find

$$\left. \frac{\delta\beta\mathcal{A}}{\delta\beta\phi(r)} \right|_{[\bar{h}],\rho,\beta} = \frac{\rho}{2} \bar{g}(r). \quad (\text{B5})$$

Then we can write

$$\begin{aligned} \beta\mathcal{A}([\bar{h}],[\phi],\rho,\beta) &= \int d\mathbf{r} \left. \frac{\delta\beta\mathcal{A}}{\delta\beta\phi(r)} \right|_{[\bar{h}],\rho,\beta} \beta\phi(r) \\ &\quad + \mathcal{D}([\bar{h}],\rho,\beta), \end{aligned} \quad (\text{B6})$$

with \mathcal{D} a functional independent of ϕ . Changing variables to adimensional ones, $\mathbf{r} = \mathbf{r}^* \rho^{-1/3}$ and using Eq. (B5) we find

$$\begin{aligned} \beta\mathcal{A}([\bar{h}^*],[\phi],\rho,\beta) &= \frac{1}{2} \int d\mathbf{r}^* \bar{g}^*(r^*) \beta\phi(r^* \rho^{-1/3}) \\ &\quad + \mathcal{D}([\bar{h}^*],\rho,\beta), \end{aligned} \quad (\text{B7})$$

where we defined new distribution functions $g^*(r^*) = g(r^* \rho^{-1/3})$. If \mathcal{D} has no explicit dependence on ρ , then one readily finds

$$\begin{aligned} \rho \frac{\partial\beta\mathcal{A}([\bar{h}^*],[\phi],\rho,\beta)}{\partial\rho} &= -\frac{\rho}{6} \int d\mathbf{r}^* \bar{g}^*(r^*) \beta\phi'(r^* \rho^{-1/3}) r^* \rho^{-4/3} \\ &= -\frac{\rho}{6} \int d\mathbf{r} \bar{g}(r) \beta\phi'(r) r = \beta P^{exc}/\rho, \end{aligned} \quad (\text{B8})$$

where again we used the fact that \mathcal{A} has an extremum for $h = \bar{h}$. We used a prime to denote a derivative with respect to the argument, and P^{exc} is the excess pressure of the liquid.

If \mathcal{D} has no explicit dependence on β , we also find

$$\frac{\partial\beta\mathcal{A}([\bar{h}^*],[\phi],\rho,\beta)}{\partial\beta} = \frac{\rho}{2} \int d\mathbf{r} \bar{g}(r) \phi(r) = U^{exc}/N, \quad (\text{B9})$$

where U^{exc} is the excess internal energy.

If \mathcal{D} has no explicit dependence on both β and ρ , $\mathcal{D}([\bar{h}^*],\rho,\beta) = \mathcal{D}([\bar{h}^*])$, we conclude from Eqs. (B8) and (B9) that

$$\mathcal{A}([\bar{h}^*],[\phi],\rho,\beta) = f^{exc}(\rho,\beta) + \text{const}, \quad (\text{B10})$$

where f^{exc} is the excess free energy per particle of the fluid. Under these circumstances we see from Eq. (B8) that we have thermodynamic consistency between the route to the pressure going through the partial derivative of the free energy and the route to the pressure going through the virial theorem.

APPENDIX C: STRICT CONVEXITY OF $\mathcal{F}_{oz}[h]$

It can be proved that the functional

$$\mathcal{F}_{oz}[h] = \int \frac{d\mathbf{k}}{(2\pi)^3} \{ \rho \hat{h}(k) - \ln[1 + \rho \hat{h}(k)] \}, \quad (C1)$$

defined on the convex set

$$D_c = \{ h(r) | S(k) > 0 \quad \forall k \}, \quad (C2)$$

is a strictly convex functional. The strict convexity is a trivial consequence of the strict convexity of the integrand in Eq. (C1).

It remains to prove that D_c is a convex set. Given two elements of this set h' and h'' , we need to show that $h = \lambda h' + (1-\lambda)h''$ is an element of D_c for all $\lambda \in [0,1]$. Since

$$\begin{aligned} S(k) &= 1 + \rho \hat{h}(k) \\ &= 1 + \rho [\lambda \hat{h}'(k) + (1-\lambda) \hat{h}''(k)] \\ &= 1 + \lambda [S'(k) - 1] + (1-\lambda) [S''(k) - 1] \\ &= \lambda S'(k) + (1-\lambda) S''(k) > 0 \quad \forall \lambda \in [0,1], \end{aligned} \quad (C3)$$

then D_c is a convex set.

¹J. P. Hansen and I. R. McDonald, *Theory of Simple Liquids*, 2nd ed. (Academic Press, London, 1986).
²C. Caccamo, Phys. Rep. **274**, 1 (1996).
³M. Born and H. S. Green, Proc. R. Soc. London, Ser. A **188**, 10 (1946).
⁴J. K. Percus and G. J. Yevick, Phys. Rev. **110**, 1 (1958).

⁵J. M. J. van Leeuwen, J. Groenvelde, and J. De Boer, Physica **25**, 792 (1959).
⁶Y. Rosenfeld and N. W. Ashcroft, Phys. Rev. A **20**, 1208 (1979).
⁷F. Lado, S. M. Foiles, and N. W. Ashcroft, Phys. Rev. A **28**, 2374 (1983).
⁸L. Verlet, Mol. Phys. **41**, 183 (1980).
⁹G. A. Martynov and G. N. Sarkisov, Mol. Phys. **49**, 1495 (1983).
¹⁰D.-M. Duh and A. D. J. Haymet, J. Chem. Phys. **103**, 2625 (1995).
¹¹T. Morita and K. Hiroike, Prog. Theor. Phys. **25**, 537 (1961).
¹²L. Belloni, J. Chem. Phys. **98**, 8080 (1993).
¹³P. D. Poll and N. W. Ashcroft, Phys. Rev. A **35**, 5167 (1987).
¹⁴A. Schlijper, M. Telo de Gama, and P. Ferreira, J. Chem. Phys. **98**, 1534 (1993).
¹⁵W. Olivares and D. A. McQuarrie, J. Chem. Phys. **65**, 3604 (1976).
¹⁶S. Høye and G. Stell, J. Chem. Phys. **67**, 439 (1977).
¹⁷G. Pastore, Mol. Phys. **63**, 731 (1988).
¹⁸G. Pastore, O. Akinlade, F. Matthews, and Z. Badirkhan, Phys. Rev. E **57**, 460 (1998).
¹⁹R. Kjellander and S. Sarman, J. Chem. Phys. **90**, 2768 (1989).
²⁰L. Lee, J. Chem. Phys. **97**, 8606 (1992).
²¹L. Verlet, Phys. Rev. **165**, 201 (1968).
²²Our first trial should really be $c = -\ln g - \beta\phi$, which should be called HNC/H1. We have tested numerically this closure, and we found that it performed worse than HNC/H2 for both the structure and thermodynamics of the system under examination.
²³G. Zerah, J. Comput. Phys. **61**, 280 (1985).
²⁴F. Lado, J. Comput. Phys. **8**, 417 (1971).
²⁵F. J. Rogers and D. A. Young, Phys. Rev. A **30**, 999 (1984).
²⁶J. P. Hansen and D. Shiff, Mol. Phys. **25**, 1281 (1973).
²⁷J. J. Potoff and A. Z. Panagiotopoulos, J. Chem. Phys. **109**, 10914 (1998).
²⁸P. G. Ferreira, R. L. Carvalho, M. M. Telo de Gama, and A. G. Schlijper, J. Chem. Phys. **101**, 594 (1994).
²⁹F. Lado, Phys. Rev. A **8**, 2548 (1973).
³⁰L. Verlet, Phys. Rev. **159**, 98 (1967).
³¹H. C. Andersen and D. Chandler, J. Chem. Phys. **57**, 1918 (1972).

Chapter 6

Stability of the iterative solutions of integral equations as one phase freezing criterion

Fantoni R. and Pastore G., Phys. Rev. E, **68**, 046104 (2003)

Title: “Stability of the iterative solutions of integral equations as one phase freezing criterion.”

Abstract: A recently proposed connection between the threshold for the stability of the iterative solution of integral equations for the pair correlation functions of a classical fluid and the structural instability of the corresponding real fluid is carefully analyzed. Direct calculation of the Lyapunov exponent of the standard iterative solution of HNC and PY integral equations for the 1D hard rods fluid shows the same behavior observed in 3D systems. Since no phase transition is allowed in such 1D system, our analysis shows that the proposed one phase criterion, at least in this case, fails. We argue that the observed proximity between the numerical and the structural instability in 3D originates from the enhanced structure present in the fluid but, in view of the arbitrary dependence on the iteration scheme, it seems uneasy to relate the numerical stability analysis to a robust one-phase criterion for predicting a thermodynamic phase transition.

PHYSICAL REVIEW E 68, 046104 (2003)

Stability of the iterative solutions of integral equations as one phase freezing criterion

R. Fantoni* and G. Pastore†

Dipartimento di Fisica Teorica dell' Università and Istituto Nazionale di Fisica della Materia, Strada Costiera 11, 34014 Trieste, Italy

(Received 22 May 2003; published 8 October 2003)

A recently proposed connection between the threshold for the stability of the iterative solution of integral equations for the pair correlation functions of a classical fluid and the structural instability of the corresponding real fluid is carefully analyzed. Direct calculation of the Lyapunov exponent of the standard iterative solution of hypermetted chain and Percus-Yevick integral equations for the one-dimensional (1D) hard rods fluid shows the same behavior observed in 3D systems. Since no phase transition is allowed in such 1D system, our analysis shows that the proposed one phase criterion, at least in this case, fails. We argue that the observed proximity between the numerical and the structural instability in 3D originates from the enhanced structure present in the fluid but, in view of the arbitrary dependence on the iteration scheme, it seems uneasy to relate the numerical stability analysis to a robust one-phase criterion for predicting a thermodynamic phase transition.

DOI: 10.1103/PhysRevE.68.046104

PACS number(s): 05.70.Fh, 61.20.Ne

I. INTRODUCTION

When studying the structure and thermodynamics of classical fluids, one is often faced with the task of solving the nonlinear integral equation which stems out of the combination of the Ornstein-Zernike equation and an approximate relation between pair potential and correlation functions (the closure) [1]. Integral equations can be generally written in the form

$$\gamma(r) = A\gamma(r), \tag{1}$$

where $\gamma(r) \in S$ may be the total correlation function $h(r)$, the direct correlation function $c(r)$, or a combination of the two, S is a set of a metric space of functions, and $A: S \rightarrow S$ is a nonlinear operator mapping S into itself.

Numerical analysis of integral equations suggests the use of the following combination

$$\gamma(r) = h(r) - c(r), \tag{2}$$

since γ is a much smoother function than h or c , especially in the core region.

It has been pointed out by Malescio and co-workers [2-4] that, amongst the different numerical schemes that one may choose to solve (1), the *simple iterative scheme of Picard* plays a special role. Picard's scheme consists in generating successive approximations to the solution through the relationship

$$\gamma_{n+1} = A\gamma_n, \tag{3}$$

starting from some initial value γ_0 . If the sequence of successive approximations $\{\gamma_n\}$ converges toward a value γ^* , then γ^* is a fixed point for the operator A , i.e., it is a solution of Eq. (1), $\gamma^* = A\gamma^*$. Banach's fixed point theorem (see chapter 1 in Ref. [5] especially theorem 1.A) states that, given an operator $A: S \rightarrow S$, where S is a closed nonempty set

in a complete metric space, the simple iteration (3) may converge towards the only fixed point in S (A is k contractive) or it may not converge (A is nonexpansive). So the simple iterative method can be used to signal a fundamental change in the properties of the underlying operator.

The operator A will, in general, depend on the thermodynamic state of the fluid. In order to determine the properties of the operator at a given state we can proceed as follows. First, we find the fixed point γ^* using a numerical scheme (more refined than the Picard's) capable of converging in the high density region. Next, we perturb the fixed point with an arbitrary initial perturbation $\delta_0(r)$ so that

$$A(\gamma^* + \delta_0) \approx A\gamma^* + \left. \frac{\partial A}{\partial \gamma} \right|_{\gamma^*} \delta_0 = \gamma^* + M\delta_0, \tag{4}$$

where we have introduced the Floquet matrix M . Now $\delta_1 = M\delta_0$ may be considered as the new perturbation. We then generate the succession $\{\delta_n\}$ where

$$\delta_n = M\delta_{n-1}. \tag{5}$$

If the succession converges to zero then the operator A is k contractive, if it diverges the operator is nonexpansive. Malescio and co-workers call $\{\delta_n\}$ *fictitious dynamics* and associate it to the resulting fate of the initial perturbation the nature of the *structural equilibrium* of the fluid. If the succession converges to zero they say that the fluid is *structurally stable* and *structurally unstable* otherwise. We will call ρ_{inst} the density where the transition between a structurally stable and unstable fluid occurs.

Following Malescio and co-workers it is possible to define a *measure* for the structural stability of the system as follows. We define

$$S_i = \frac{\|M\delta_i(r)\|}{\|\delta_i(r)\|}, \tag{6}$$

*Electronic address: rfantoni@ts.infn.it

†Electronic address: pastore@ts.infn.it

R. FANTONI AND G. PASTORE

 PHYSICAL REVIEW E **68**, 046104 (2003)

where $\|f(r)\| = \sqrt{\sum_{i=1}^N f^2(r_i)}$ is the norm of a function f defined over a mesh of N points. We assume that the norm of the perturbation depends exponentially on the number of iterations

$$\|\delta_n\| = \|\delta_0\| 2^{\lambda n}, \quad (7)$$

where λ is the Lyapunov exponent related to the fictitious dynamics. Then one can write the average exponential stretching of initially nearby points as

$$\lambda = \lim_{n \rightarrow \infty} \frac{1}{n} \log_2 \left(\prod_{i=0}^{n-1} S_i \right). \quad (8)$$

Malescio and co-workers have calculated the dependence of λ on the density for various simple three-dimensional liquids (and various closures): hard spheres [2], Yukawa, inverse power, and Lennard-Jones potentials [3]. For all these systems they found that λ increases with the density and the density at which λ becomes positive, ρ_{inst} , falls close to the freezing density ρ_f of the fluid system. This occurrence leads them to propose this kind of analysis as a one-phase criterion to predict the freezing transition of a dense fluid and to estimate ρ_f . However, we think that there are some practical and conceptual difficulties with such one-phase criterion.

First of all, it does not depend only on the closure adopted but also on the kind of algorithm used to solve the integral equation. Indeed, different algorithms give different ρ_{inst} and Malescio and co-workers choose to use as instability threshold for their criterion the one obtained using Picard algorithm, thus giving it a special status. However, it is hard to understand why the particular algorithm adopted in the solution of the integral equation should be directly related to a phase boundary.

Moreover, one would expect that the estimate of ρ_{inst} would improve in connection with improved closures. This is not the case, at least in the one-component hard-sphere fluid.

Even a more serious doubt about the validity of the proposed criterion comes from its behavior in one-dimensional systems. In this paper we present the same Lyapunov exponent analysis on a system of hard rods in one dimension treated using either the Percus-Yevick (PY) or the hypernetted chain (HNC) approximations. What we find is that the Lyapunov exponent as a function of density has the same behavior as that of the three-dimensional system (hard spheres): it becomes positive beyond a certain ρ_{inst} . Since it is known [6] that a one-dimensional fluid of hard rods does not have a phase transition, our result sheds some doubts on the validity of the proposed criterion.

II. TECHNICAL DETAILS

As numerical scheme to calculate the fixed point we used Zerah's algorithm [7] for the three-dimensional systems and a modified iterative method for the hard rods in one dimension. In the modified iterative method input and output are mixed at each iteration

$$\gamma_{n+1} = A_{mix} \gamma_n + \alpha A \gamma_n + (1 - \alpha) \gamma_n, \quad (9)$$

where α is a real parameter $0 < \alpha < 1$. Note that while for a nonexpansive operator A the Picard iterative method (3) needs not converge, one can prove convergence results on an Hilbert space for the modified iterative method with fixed α (see proposition 10.16 in Ref. [5]). In all the computations we used a uniform grid of $N=1024$ points with a spacing $\delta r=0.025$. Generally, we observed a marginal increase of ρ_{inst} by lowering N .

A method to find a Lyapunov exponent, equivalent but more accurate than the one of Malescio co-workers (8), goes through the diagonalization of the Floquet matrix. Note that in general this matrix is nonsymmetric, thus yielding complex eigenvalues. A Lyapunov exponent can then be defined as [8]

$$\lambda' = \log \left[\max_i \left(\sqrt{\text{Re}(e_i)^2 + \text{Im}(e_i)^2} \right) \right], \quad (10)$$

where e_i is the i th eigenvalue. In our numerical computations we always used Eq. (10) to calculate the Lyapunov exponents since it is explicitly independent from the choice of an initial perturbation.

We constructed the Floquet matrix in the following way [9]. In a Picard iteration we start from $\gamma(r)$, we calculate $c(r)$ from the closure approximation, we calculate its Fourier transform $\tilde{c}(k)$, we calculate $\tilde{\gamma}(k)$ from the OZ equation, and finally we antitransform $\tilde{\gamma}$ to get $\gamma'(r)$. For example for a three-dimensional system a PY iteration in discrete form can be written as follows:

$$c_i = (1 + \gamma_i)(e^{-\beta\phi_i} - 1), \quad (11)$$

$$\tilde{c}_j = \frac{4\pi\delta r}{k_j} \sum_{i=1}^{N-1} r_i \sin(k_j r_i) c_i, \quad (12)$$

$$\tilde{\gamma}_j = \rho \tilde{c}_j^2 / (1 - \rho \tilde{c}_j), \quad (13)$$

$$\gamma'_i = \frac{\delta k}{2\pi^2 r_i} \sum_{j=1}^{N-1} k_j \sin(k_j r_i) \tilde{\gamma}_j, \quad (14)$$

where $r_i = i \delta r$ are the N mesh points in r space, $k_j = j \delta k$ are the N mesh points in k space, with $\delta k = \pi / (N \delta r)$, $c_i = c(r_i)$, $\gamma_i = \gamma(r_i)$, $\tilde{c}_j = \tilde{c}(k_j)$, $\tilde{\gamma}_j = \tilde{\gamma}(k_j)$, and $\phi_i = \phi(r_i)$ is the interparticle potential calculated on the grid points. The Floquet matrix will then be

$$\begin{aligned} M_{ij} &= \frac{\partial \gamma'_i}{\partial \gamma_j} = \sum_{m=1}^{N-1} \frac{\partial \gamma'_i}{\partial \tilde{\gamma}_m} \frac{\partial \tilde{\gamma}_m}{\partial \tilde{c}_m} \frac{\partial \tilde{c}_m}{\partial c_j} \frac{\partial c_j}{\partial \gamma_j} \\ &= \frac{\delta r \delta k}{\pi} \left(\frac{r_j}{r_i} \right) (e^{-\beta\phi_j} - 1) (D_{i-j} - D_{i+j}), \end{aligned} \quad (15)$$

where

$$D_i = \sum_{m=1}^{N-1} \cos(k_m r_i) \left[\frac{2\rho \tilde{c}_m}{1 - \rho \tilde{c}_m} + \left(\frac{\rho \tilde{c}_m}{1 - \rho \tilde{c}_m} \right)^2 \right]. \quad (16)$$

STABILITY OF THE ITERATIVE SOLUTIONS OF . . .

The HNC case can be obtained replacing in Eq. (15) $[\exp(-\beta\phi_j)-1]$ with $[\exp(-\beta\phi_j+\gamma_j)-1]$.

To derive the expression for the Floquet matrix valid for the one-dimensional system and consistent with a trapezoidal discretization of the integrals, we need to replace Eqs. (11) and (13) with

$$\tilde{c}_j = 2\delta r \left(\sum_{i=1}^{N-1} \cos(k_j r_i) c_i + \frac{1}{2} c_0 \right), \quad (17)$$

$$\tilde{\gamma}'_i = \frac{\delta k}{\pi} \left(\sum_{i=1}^{N-1} \cos(k_j r_i) \tilde{\gamma}_i + \frac{1}{2} \tilde{\gamma}_0 \right). \quad (18)$$

III. NUMERICAL RESULTS

We checked our procedure for a three-dimensional hard-spheres fluid and a Lennard-Jones fluid at a reduced temperature $T^*=2.74$. Our results, obtained using Eq. (10), were in good agreement with those of Malescio *et al.* [2,3] which used recipe (8) instead (another difference between our analysis and theirs is that we used for γ the indirect correlation function (2) while they were using the total correlation function h). For the Lennard-Jones fluid our results were indistinguishable from those of Malescio *et al.* [3]. We found a reduced instability density ρ_{inst}^* around 1.09 in the PY approximation and around 1.06 in the HNC approximation. For the three-dimensional hard-sphere fluid we found slightly larger (4%) values for ρ_{inst} . We found a $\eta_{inst} = \rho_{inst} \pi d^3/6$ of about 0.445 in the PY approximation and around 0.461 in the HNC approximation. We also checked the value corresponding to the Martynov-Sarkisov [10] closure and we found $\eta_{inst} = 0.543$.

We feel that the differences are within what we can expect on the basis of small numerical differences in different implementations. We think that it is more worthy of notice that closures providing better structural and thermodynamic properties, like PY or MS do not provide a better value of η_{inst} .

We looked at the structure of the Floquet matrix too but from direct inspection we can conclude that it is not diagonally dominated.

Then, we have calculated the Lyapunov exponent (10) as a function of the density for a fluid of hard rods in one dimension using both PY and HNC closures. The results of the calculation are shown in Fig. 1 and Fig. 2. The curves show the same qualitative behavior as the ones for the three-dimensional fluid. From Fig. 1 we can see how the slope of the curves starts high at low densities and decreases rapidly with ρ . At high densities the Lyapunov exponent becomes zero at ρ_{inst} . As expected, to find the fixed point for $\rho \geq \rho_{inst}$ it is necessary to choose $\alpha < 1$ in the modified iterative scheme (9). Before reaching the instability threshold the curves show a rapid change in their slope at $\rho_c < \rho_{inst}$. Figure 2 shows a magnification of the region around ρ_c from which we are led to conclude that, within the numerical accuracy of the calculations, the slope of the curves $d\lambda'/d\rho$ undergoes a jump at ρ_c .

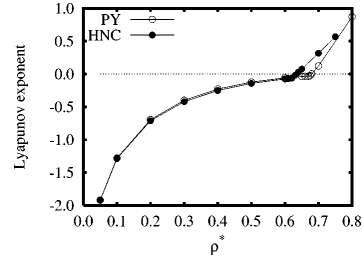
 PHYSICAL REVIEW E **68**, 046104 (2003)


FIG. 1. For a fluid of hard rods in one dimension, we show the Lyapunov exponent as a function of the reduced density ($\rho^* = \rho\sigma$ where σ is the rods width) as calculated using the PY and the HNC closures.

IV. CONCLUSIONS

The fictitious dynamics associated to the iterative solution of an integral equation can signal the transition of the map of the integral equation from k contractive to nonexpansive. If the Lyapunov exponent is negative the map is k contractive, if it is positive the map is nonexpansive.

Since it is possible to modify, in an arbitrary way, the fictitious dynamics keeping the same fixed point, it is difficult to understand a deep direct connection between the stability properties of the map and a one-phase criterion for a thermodynamic transition.

Admittedly, the correlations shown by Malescio *et al.* are striking. We calculated the Lyapunov exponent as a function of the density for various fluids (hard spheres in one and three-dimensions and three-dimensional Lennard-Jones fluid) both in the HNC and PY approximations. For the three-dimensional fluids the instability density falls close to the freezing density ρ_f . For example, the Lennard-Jones fluid studied with HNC should undergo a freezing transition at $\rho^* \approx 1.06$ or at $\rho^* \approx 1.09$, if studied with PY, rather close to the freezing density $\rho_f^* \approx 1.113$. For hard spheres ρ_{inst}^* is about 10% smaller than $\rho_f^* \approx 0.948$. The Hansen-Verlet “rule” states that a simple fluid freezes when the maximum of the structure factor is about 2.85 [11]. According to this rule the three-dimensional hard-spheres fluid studied with HNC should undergo a freezing transition at $\rho = 1.01$ while when studied with PY the transition should be at $\rho = 0.936$.

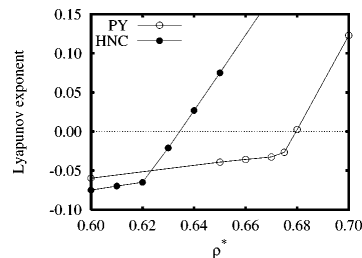


FIG. 2. We show a magnification of Fig. 1 in a neighborhood of the instability threshold.

R. FANTONI AND G. PASTORE

PHYSICAL REVIEW E **68**, 046104 (2003)

The corresponding estimates obtained through ρ_{inst}^* , 0.879 (HNC) and 0.850 (PY) are poorer and, more importantly, are not consistent with the well known better performance of PY in the case of hard spheres.

In one dimension, a fluid of hard spheres (hard rods), cannot undergo a phase transition [6]. From Fig. 1 we see that the system still becomes structurally unstable. This can be explained by observing that the structural stability as defined by Malescio *et al.* is a property of the map A and in particular of the algorithm used to get the solution of the integral equation under study. As such, it is not directly related to the thermodynamic properties even at the approxi-

mate level of the theory (there is no direct relation between the contractiveness properties of A and the thermodynamics). It looks more reasonable that the increase of the correlations would be the common origin of the numerical instability of the Picard iteration and, whenever it is possible, of thermodynamic phase transitions.

ACKNOWLEDGMENTS

G.P. would like to acknowledge preliminary exploratory work on this subject carried on in collaboration with Matteo Mosangini and Waheed Adeniyi Adeagbo.

-
- [1] J.P. Hansen and I.R. McDonald, *Theory of Simple Liquids*, 2nd ed. (Academic Press, London, 1986).
 - [2] G. Malescio, P.V. Giaquinta, and Y. Rosenfeld, *Phys. Rev. E* **57**, R3723 (1998).
 - [3] G. Malescio, P.V. Giaquinta, and Y. Rosenfeld, *Phys. Rev. E* **61**, 4090 (2000).
 - [4] G. Malescio and P.V. Giaquinta, *Phys. Rev. E* **62**, 4439 (2000).
 - [5] E. Zeidler, *Nonlinear Functional Analysis and its Applications* (Springer-Verlag, New York, 1986), Vol. 1.
 - [6] L.V. Hove, *Physica* (Amsterdam) **16**, 137 (1950).
 - [7] G. Zerah, *J. Comput. Phys.* **61**, 280 (1985).
 - [8] R.Z. Sagdeev, D.A. Usikov, and G.M. Zaslavsky, *Nonlinear Physics: From The Pendulum To Turbulence and Chaos* (Chur: Harwood Academic Publishers, London, 1988).
 - [9] M.J. Gillan, *Mol. Phys.* **38**, 1781 (1979).
 - [10] G.A. Martynov and G.N. Sarkisov, *Mol. Phys.* **49**, 1495 (1983).
 - [11] J.P. Hansen and L. Verlet, *Phys. Rev.* **184**, 151 (1969).

Part IV

2004

Chapter 7

Direct correlation functions of the Widom-Rowlinson model

Fantoni R. and Pastore G., *Physica A*, **332**, 349 (2004)

Title: “Direct correlation functions of the Widom-Rowlinson model.”

Abstract: We calculate, through Monte Carlo numerical simulations, the partial total and direct correlation functions of the three dimensional symmetric Widom-Rowlinson mixture. We find that the differences between the partial direct correlation functions from simulation and from the Percus-Yevick approximation (calculated analytically by Ahn and Lebowitz) are well fitted by Gaussians. We provide an analytical expression for the fit parameters as function of the density. We also present Monte Carlo simulation data for the direct correlation functions of a couple of non additive hard sphere systems to discuss the modification induced by finite like diameters.

Available online at www.sciencedirect.com

SCIENCE @ DIRECT®

Physica A 332 (2004) 349–359

PHYSICA A

www.elsevier.com/locate/physa

Direct correlation functions of the Widom–Rowlinson model

R. Fantoni*, G. Pastore

*Dipartimento di Fisica Teorica dell' Università and Istituto Nazionale di Fisica della Materia,
Strada Costiera 11, Trieste 34014, Italy*

Received 8 September 2003

Abstract

We calculate, through Monte Carlo (MC) numerical simulations, the partial total and direct correlation functions of the three dimensional symmetric Widom–Rowlinson mixture. We find that the differences between the partial direct correlation functions from simulation and from the Percus–Yevick approximation (calculated analytically by Ahn and Lebowitz) are well fitted by Gaussians. We provide an analytical expression for the fit parameters as function of the density. We also present MC simulation data for the direct correlation functions of a couple of non-additive hard sphere systems to discuss the modification induced by finite like diameters. © 2003 Elsevier B.V. All rights reserved.

PACS: 61.20.Ja; 61.20.Gy*Keywords:* Widom–Rowlinson model; Direct correlation function

1. Introduction

Fluid binary mixtures may exhibit the phenomenon of phase separation. The simplest system able to undergo a demixing phase transition is the model introduced by Widom and Rowlinson [1] some years ago. Consider a binary mixture of non-additive hard spheres (NAHS). This is a fluid made of hard spheres of species 1 of diameter R_{11} and number density ρ_1 and hard spheres of species 2 of diameter R_{22} and number density ρ_2 , with a pair interaction potential between species i and j that can be written as

* Corresponding author. Tel.: +39-040-2240608; fax: +39-040-224601.

E-mail addresses: rfantoni@ts.infn.it (R. Fantoni), pastore@ts.infn.it (G. Pastore).

350

R. Fantoni, G. Pastore / Physica A 332 (2004) 349–359

follows:

$$v_{ij}(r) = \begin{cases} \infty, & r < R_{ij}, \\ 0, & r > R_{ij}, \end{cases} \quad (1)$$

where $R_{12} = (R_{11} + R_{22})/2 + \alpha$. The Widom-Rowlinson (WR) model is obtained choosing the diameters of the spheres equal to 0,

$$R_{11} = R_{22} = 0, \quad (2)$$

so that there is no interaction between like spheres and there is a hard core repulsion of diameter α between unlike spheres. The symmetry of the system induces the symmetry of the unlike correlations [$h_{12}(r) = h_{21}(r)$, $c_{12}(r) = c_{21}(r)$]. The WR model has been studied in the past by exact [2] and approximate [3–6] methods and it has been shown that it exhibits a phase transition at high density. More recently, additional studies have appeared and theoretical predictions have been confirmed by Monte Carlo (MC) computer simulations [7–10].

In this paper we will study the three-dimensional symmetric Widom-Rowlinson mixture for which $\rho_1 = \rho_2 = \rho/2$, where ρ is the total number density of the fluid, and

$$h_{11}(r) = h_{22}(r), \quad (3)$$

$$c_{11}(r) = c_{22}(r). \quad (4)$$

Moreover, we know from (1) that the partial pair correlation function $g_{ij} = h_{ij} + 1$ must obey

$$g_{ij}(r) = 0 \quad \text{for } r < R_{ij}. \quad (5)$$

Our main goal is to focus on the direct correlation functions (dcf) of the WR model as a simplified prototype of NAHS systems. The reasons to focus on the dcf's is twofold: on the one hand, they are easier functions to model and fit. On the other hand, they play a central role in approximate theories like the Percus-Yevick approximation or mean spherical approximation (MSA) [11]. We hope that a better understanding of the dcf's properties in the WR model, could help in developing accurate analytical theories for the NAHS systems.

We calculate through MC simulations the like $g_{11}^{(MC)}(r)$ and unlike $g_{12}^{(MC)}(r)$ pair distribution functions for a system large enough to allow a meaningful determination of the correspondent partial dcf $c_{11}^{(MC)}(r)$ and $c_{12}^{(MC)}(r)$, using the Ornstein-Zernike equation [11]. We compare the results for the unlike dcf with the results of the Percus-Yevick (PY) analytic solution found by Ahn and Lebowitz [3,4]. In the same spirit as the work of Grundke and Henderson [12] for a mixture of additive hard spheres, we propose a fit for the functions $\Delta_{11}^c(r) = c_{11}^{(MC)}(r)$ and $\Delta_{12}^c(r) = c_{12}^{(MC)}(r) - c_{12}^{(PY)}(r)$.

At the end of the paper, we also show the results from two MC simulations on a mixture of NAHS with equal diameter spheres $R_{11} = R_{22} = R_{12}/2$ and on one with different diameter spheres $R_{11} = 0$ and $R_{22} = R_{12}$ to study the effect of non zero like diameters on the WR dcf's.

2. MC simulation and PY solution

The MC simulation was performed with a standard NVT metropolis algorithm [13] using $N = 4000$ particles. Linked lists [13] have been used to reduce the computational cost. We generally used 5.2×10^8 MC steps where one step corresponds to the attempt to move a single particle. The typical CPU time for each density was around 20 h (runs at higher densities took longer than runs at smaller densities) on a Compaq Alpha Server 4100 5/533.

We run the simulation of WR model at 6 different densities $\bar{\rho} = \rho\alpha^3 = 0.28748, 0.4, 0.45, 0.5, 0.575,$ and 0.65 . Notice that the most recent computer simulation calculations [9,10] give consistent estimates of the critical density around 0.75 . Our data at the highest density (0.65) are consistent with a one-phase system.

The MC simulation returned the $g_{ij}(r)$ over a range not less than 9.175α for the densest system. In all the studied cases, pair distribution functions attained their asymptotic value well inside the maximum distance they were evaluated. Thus, it has been possible to obtain accurate Fourier transforms of the correlation functions $[h_{ij}(k)]$. To obtain the $c_{ij}(r)$ we used Ornstein–Zernike equation as follows:

$$c_{11}(k) = \frac{h_{11}(k)[1 + (\rho/2)h_{11}(k)] - (\rho/2)h_{12}^2(k)}{[1 + (\rho/2)h_{11}(k)]^2 - [(\rho/2)h_{12}(k)]^2}, \tag{6}$$

$$c_{12}(k) = \frac{h_{12}(k)}{[1 + (\rho/2)h_{11}(k)]^2 - [(\rho/2)h_{12}(k)]^2}. \tag{7}$$

From the $h_{ij}(k)$ and $c_{ij}(k)$, we get the difference $\gamma_{ij}(k) = h_{ij}(k) - c_{ij}(k)$ which is the Fourier transform of a continuous function in real space. So it is safe to transform back into real space [to get $\gamma_{ij}(r)$]. Finally, the dcf's are obtained from the differences $h_{ij}(r) - \gamma_{ij}(r)$.

While for a system of NAHS in three-dimensions a closed-form solution to the PY approximation is still lacking, Ahn and Lebowitz have found an analytic solution of this approximation for the WR model (in one and three dimensions).

The PY approximation consists of the assumption that $c_{ij}(r)$ does not extend beyond the range of the potential

$$c_{ij}(r) = 0 \quad \text{for } r > R_{ij}. \tag{8}$$

Combining this with the exact relation (5) and using the Ornstein–Zernike equation, we are left with a set of equations for $c_{ij}(r)$ and $g_{ij}(r)$ which have been solved analytically by Ahn and Lebowitz.

Their solution is parameterized by a parameter z_0 . They introduce the following two functions of z_0 (which can be written in terms of elliptic integrals of the first and third kind):

$$I_1 \equiv \int_{z_0}^{\infty} \frac{dz}{z\sqrt{z^3 + 4z/z_0 - 4}}, \tag{9}$$

$$I_2 \equiv \int_{z_0}^{\infty} \frac{dz}{\sqrt{z^3 + 4z/z_0 - 4}} \tag{10}$$

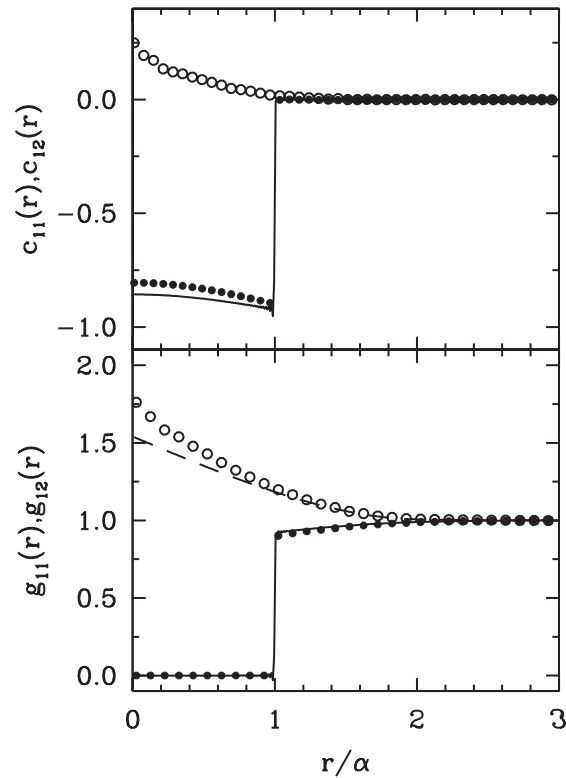


Fig. 1. Top panel: partial dcf's obtained from the MC simulation (points) with the $c_{12}^{(PY)}(r)$ obtained from the PY approximation (line) at a density $\rho\alpha^3=0.28748$. Bottom panel: partial pair distribution functions obtained from the MC simulation compared with the ones obtained from the PY approximation at the same density. The open circles and the dashed line: the like correlation functions. Closed circles and the continuous line: the unlike correlation functions.

and define z_0 in terms of the partial densities ρ_1 and ρ_2 as follows:

$$\eta \equiv 2\pi\sqrt{\rho_1\rho_2} = \frac{(I_2/2)^3}{\cos I_1}. \quad (11)$$

They then define the following functions (note that in the last equality of Eq. (3.76) in Ref. [4] there is a misprint):

$$\begin{aligned} \bar{c}_{12}(k) \equiv & -\frac{2}{\sqrt{\rho_1\rho_2}} \sqrt{\frac{1+Y}{z_0^3 Y^3 + 4Y + 4}} \\ & \times \sin \left[\frac{1}{2} \sqrt{z_0^3 Y^3 + 4Y + 4} \int_1^\infty \frac{dz}{(z+Y)\sqrt{z_0^3 z^3 + 4z - 4}} \right], \end{aligned} \quad (12)$$

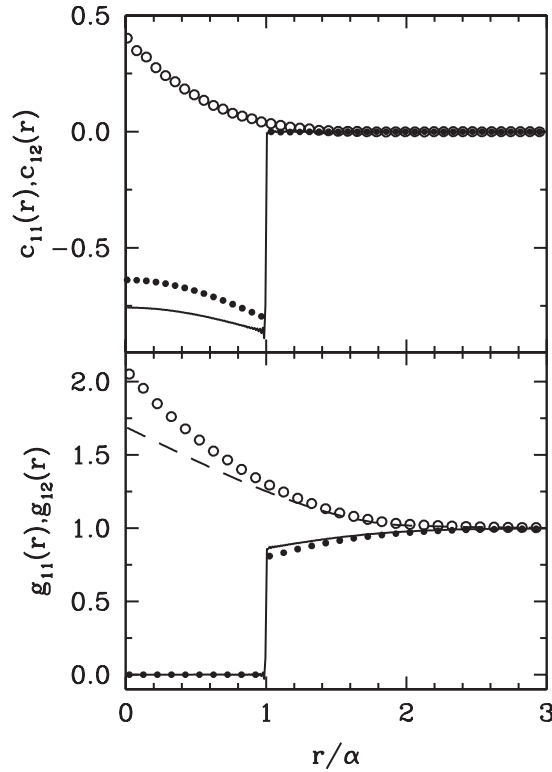


Fig. 2. Same as in Fig. 1 at a density $\rho x^3 = 0.4$.

$$\bar{h}_{12}(k) \equiv \bar{c}_{12}(k)[1 - \rho_1 \rho_2 \bar{c}_{12}(k)], \tag{13}$$

where $Y \equiv (2k/I_2)^2$.

We also realized that some other misprint should be present in the Ahn and Lebowitz paper since we have found empirically that the PY solution (with k in units of α) should be given by

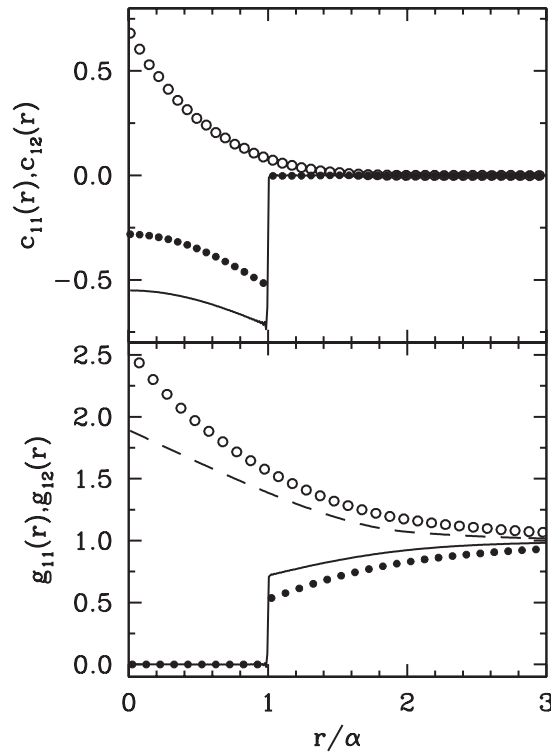
$$c_{12}(k) = \bar{c}_{12}(ks), \tag{14}$$

where s is a scale parameter to be determined as follows:

$$s = -[\bar{h}_{12}(r=0)]^{1/3}. \tag{15}$$

Notice that for the symmetric case $\rho_1 = \rho_2 = \rho/2$ and $\eta = \pi\rho = 0.90316\dots$ we find $z_0 = 1$ and $s = 1$.

In Figs. 1–3 we show three cases corresponding to the extreme and one intermediate density. In the figures, we compare the MC simulation data with the PY solution for the partial pair distribution functions and the partial dcf. Our results for the partial pair distribution functions at $\rho x^3 = 0.65$ are in good agreement with the ones of Shew and Yethiraj [9]. The figures show how the like correlation functions obtained from


 Fig. 3. Same as in Fig. 1 at a density $\rho\alpha^3 = 0.65$.

the PY approximation are the ones that differ most from the MC simulation data. The difference is more marked in a neighborhood of $r = 0$ and becomes more pronounced as the density increases.

3. Fit of the data

From the simulations we found that $c_{12}^{(MC)}(r) < 8 \times 10^{-3}$ for $r > \alpha$ at all the densities studied. This allows us to say that $\Delta_{12}^c(r) \simeq 0$ for $r > \alpha$. Moreover we found that both $\Delta_{12}^c(r)$ for $r < \alpha$, and $\Delta_{11}^c(r)$ are very well fitted by Gaussians

$$\Delta_{11}^c(r) \simeq b_{11} \exp[-a_{11}(r + d_{11})^2] \quad \text{for all } r > 0, \quad (16)$$

$$\Delta_{12}^c(r) \simeq b_{12} \exp[-a_{12}r^2] \quad \text{for } 0 < r < \alpha. \quad (17)$$

In Figs. 4 and 5 we show the behaviors of the parameters of the best fit (16) and (17), with density. In order to check the quality of the fit, we did not use the data at $\bar{\rho} = 0.45$ in the determination of the parameters. The points for a_{12} and b_{12} are well

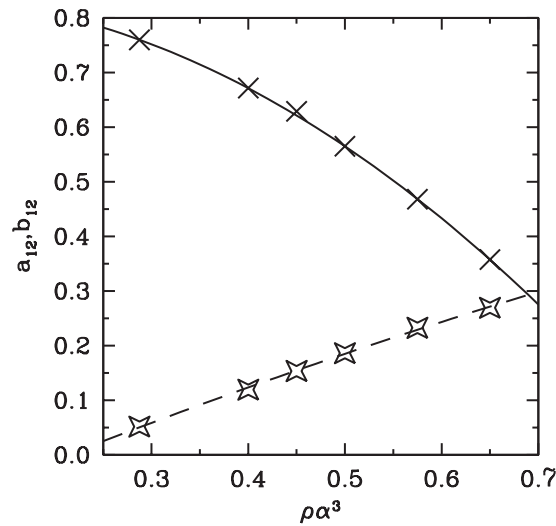


Fig. 4. We plot, for five different values of the density, the parameters a_{12} (diagonal crosses) and b_{12} (starred crosses) of the best Gaussian fit (17) to $\Delta_{12}^c(r)$ for $r < \alpha$, and fit them with parabolae (lines). The parameters at $\rho\alpha^3 = 0.45$ where not used for the parabolic fit and give an indication of the quality of the fit.

fitted by a straight line or a parabola. As shown in Fig. 4 the best parabolae are

$$a_{12}(\bar{\rho}) = 0.839 + 0.096\bar{\rho} - 1.287\bar{\rho}^2, \tag{18}$$

$$b_{12}(\bar{\rho}) = -0.155 + 0.759\bar{\rho} - 0.159\bar{\rho}^2. \tag{19}$$

Fig. 5 shows how the parameters for $\Delta_{11}^c(r)$ are much more scattered and hard to fit. The quartic polynomial going through the five points, for each coefficient, are

$$a_{11}(\bar{\rho}) = -55.25 + 504.8\bar{\rho} - 1659.\bar{\rho}^2 + 2364.\bar{\rho}^3 - 1236.\bar{\rho}^4, \tag{20}$$

$$b_{11}(\bar{\rho}) = 171.4 - 1556.\bar{\rho} + 5166.\bar{\rho}^2 - 7421.\bar{\rho}^3 + 3906.\bar{\rho}^4, \tag{21}$$

$$d_{11}(\bar{\rho}) = 128.9 - 1144.\bar{\rho} + 3747.\bar{\rho}^2 - 5328.\bar{\rho}^3 + 2782.\bar{\rho}^4. \tag{22}$$

The difficulty in finding a good fit for these parameters may be twofold: first we are fitting $\Delta_{11}^c(r)$ with a three (instead of two) parameter curve and second, the partial pair distribution functions obtained from the MC simulation are less accurate in a neighborhood of the origin (due to the reduced statistics there). This inaccuracy is amplified in the process of finding the partial dcf's. Such inaccuracy will not affect significantly $\Delta_{12}^c(r)$ which has a derivative very close or equal to zero near the origin, but it will significantly affect $\Delta_{11}^c(r)$, which is very steep near the origin.

In order to estimate the quality of the fit we have used the simulation data at $\bar{\rho} = 0.45$. From Fig. 4 we can see how the parabolic fit is a very good one. In Fig. 5 the point at $\bar{\rho} = 0.45$ gives an indication of the accuracy of the quartic fit. We have

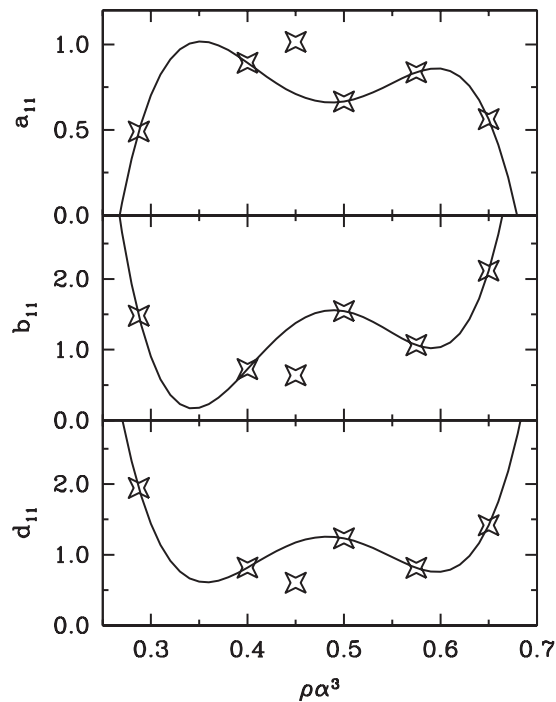


Fig. 5. We plot, for five different values of the density, the parameters a_{11} , b_{11} and d_{11} (stars) of the best Gaussian fit (16) to $\Delta_{11}^c(r)$, and draw the quartic polynomial (lines) through them. The parameters at $\rho\alpha^3 = 0.45$ were not used to determine the quartic polynomial and give an indication of the quality of the fit.

also compared the pair distribution and dcf's obtained from the fit with those from MC: both the like and unlike distribution functions are well reproduced, while there is a visible discrepancy in the dcf from the origin up to $r = 0.5\alpha$. However we expect that moving on the high-density or low-density regions (where the quartic polynomial becomes more steep), the quality of the fit will get worse. In particular, the predicted negative values for a_{11} , in those regions, are completely unphysical and the fit should not be used to extrapolate beyond the range $0.28 < \bar{\rho} < 0.65$.

4. From WR to NAHS

In order to see how the structure, and in particular the dcf's of the WR model change as one switches on the spheres diameters we have made two additional MC simulations. In the first one we chose $\rho_1 = \rho_2 = 0.65/R_{12}^3$ and $R_{11} = R_{22} = R_{12}/2$. The resulting partial pair distribution functions and partial dcf are shown in Fig. 6. From a comparison with Fig. 3, we see how in this case the switching on of the like diameters

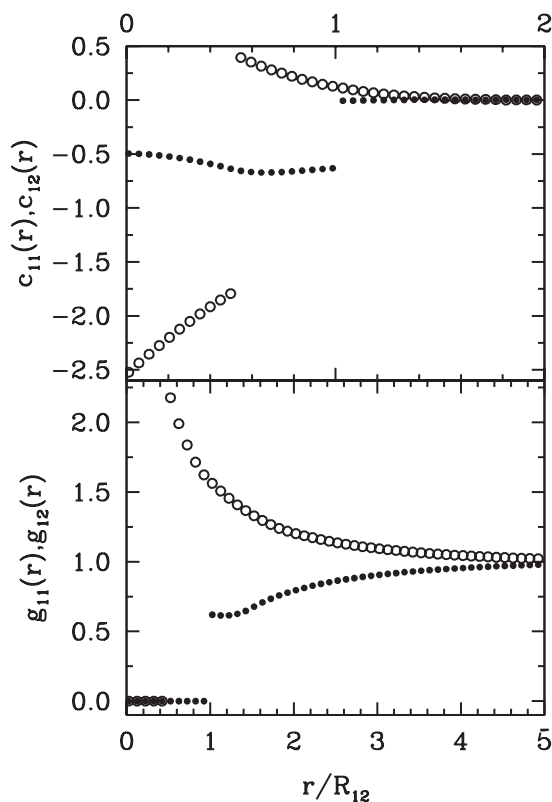


Fig. 6. Monte Carlo results at a density $\rho = \rho_1 = \rho_2 = 0.65/R_{12}^3$ for the partial dcf's (on top) and the partial pair distribution function (below) of a mixture of NAHS with $R_{11} = R_{22} = R_{12}/2$. The open circles denote the like correlation functions. The closed circles denote the unlike correlation functions.

causes both $c_{12}(r)$ for $r < R_{12}$ and $g_{12}(r)$ for $r > R_{12}$ to approach $r = R_{12}$ with a slope close to zero.

In the second simulation we chose $\rho_1 = \rho_2 = 0.65/R_{12}^3$ and $R_{11} = 0$, $R_{22} = R_{12}$. The resulting partial pair distribution functions and partial dcf's are shown in Fig. 7. From a comparison with Fig. 3 we see how in this case the switching on of the like diameters causes both $g_{11}(0)$ and $c_{11}(0)$ to increase, and $c_{12}(r)$ to lose the nearly zero slope at $r = 0$. As in the previous case, $g_{12}(r)$ for $r > R_{12}$ approaches $r = R_{12}$ with a slope close to zero. The like 22 correlation functions for $r > R_{12}$ vary over a range comparable to the one over which vary the like 11 correlation functions of the WR model.

For both these cases, there is no analytic solution of the PY approximation available and a better understanding of the behavior of the direct correlation functions may help in finding approximate expressions [14].

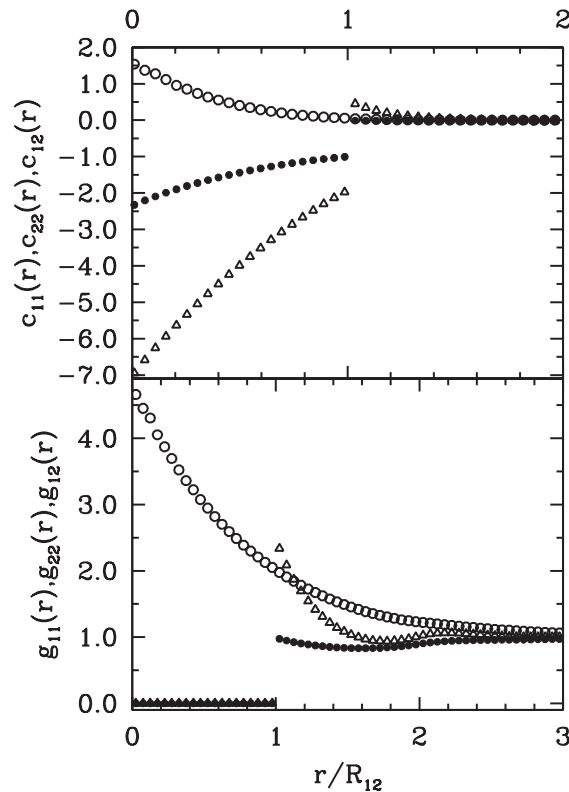


Fig. 7. MC results at a density $\rho = \rho_1 = \rho_2 = 0.65/R_{12}^3$ for the partial dcf's (on top) and the partial pair distribution function (below) of a mixture of NAHS with $R_{11}=0$ and $R_{22}=R_{12}$. The open circles denote the like 11 correlation functions. The open triangles denote the like 22 correlation functions. The closed circles denote the unlike correlation functions.

5. Conclusions

In this paper, we have evaluated the direct correlation functions (dcf) of a Widom-Rowlinson mixture at different densities through Monte Carlo (MC) simulation and we have studied the possibility of fitting the difference between MC data and the PY dcf's. We found a very good parameterization of $c_{12}(r)$ for $r < \alpha$ (see Eqs. (17)–(19)) and a poorer one for $c_{11}(r)$ (see Eqs. (16) and (20)–(22)). The difficulty in this last case probably arises from the necessity of using three parameters [instead of just two needed for parameterizing $c_{12}(r)$], although it cannot be completely excluded some effect of the decreasing precision of the simulation data near the origin.

In the last part of the paper, we have illustrated with additional MC data the changes induced in the WR dcf's by a finite size of the excluded volume of like correlations. These results are meant to provide a guide in the search of a manageable, simple

analytical parameterization of the structure of mixtures of non additive hard spheres which is still not available although highly desirable.

References

- [1] B. Widom, J. Rowlinson, *J. Chem. Phys.* 15 (1970) 1670.
- [2] D. Ruelle, *Phys. Rev. Lett.* 16 (1971) 1040.
- [3] S. Ahn, J.L. Lebowitz, *Phys. Lett.* 44A (1973) 424.
- [4] S. Ahn, J.L. Lebowitz, *J. Chem. Phys.* 60 (1974) 523.
- [5] E. Bergmann, *Mole. Phys.* 32 (1976) 237.
- [6] J. Karkheck, G. Stell, *J. Chem. Phys.* 71 (1979) 3620.
- [7] H. Luo, C. Hoheisel, J. Karkheck, *Phys. Rev. A* 42 (1976) 4690.
- [8] R. Dickman, G. Stell, *J. Chem. Phys.* 102 (1995) 8674.
- [9] C.-Y. Shew, A. Yethiraj, *J. Chem. Phys.* 104 (1996) 7665.
- [10] G. Johnson, H. Gould, J. Machta, L.K. Chayes, *Phys. Rev. Lett.* 79 (1997) 2612.
- [11] J.P. Hansen, I.R. McDonald, *Theory of Simple Liquids*, 2nd Edition, Academic Press, London, 1986.
- [12] E.W. Grundke, D. Henderson, *Mole. Phys.* 24 (1972) 269.
- [13] M.P. Allen, F.J. Tildesley, *Computer Simulation of Liquids*, Clarendon Press, Oxford, 1987.
- [14] D. Gazzillo, G. Pastore, *Chem. Phys. Lett.* 159 (1989) 388.

Chapter 8

Computer simulation study of the closure relations in hard sphere fluids

Fantoni R. and Pastore G., J. Chem. Phys., **120**, 10681 (2004)

Title: “Computer simulation study of the closure relations in hard sphere fluids.”

Abstract: We study, using Monte Carlo simulations, the cavity and the bridge functions of various hard sphere fluids: one component system, equimolar additive and non additive binary mixtures. In particular, we numerically check the assumption of local dependency of the bridge functions from the indirect correlation functions, on which most of the existing integral equation theories hinge. We find that this condition can be violated either in the region around the first and second neighbors shell, or inside the hard core, for the systems here considered. The violations manifest themselves clearly in the so called Duh-Haymet plots of the bridge functions versus the indirect correlation functions and become amplified as the coupling of the system increases.

[HTML ABSTRACT + LINKS](#)

JOURNAL OF CHEMICAL PHYSICS

VOLUME 120, NUMBER 22

8 JUNE 2004

Computer simulation study of the closure relations in hard sphere fluidsR. Fantoni^{a)}*Dipartimento di Fisica Teorica dell' Università and Istituto Nazionale di Fisica della Materia, Strada Costiera 11, 34014 Trieste, Italy*G. Pastore^{b)}*Dipartimento di Fisica Teorica dell' Università and INFN DEMOCRITOS National Simulation Center, Strada Costiera 11, 34014 Trieste, Italy*

(Received 19 February 2004; accepted 19 March 2004)

We study, using Monte Carlo simulations, the cavity and the bridge functions of various hard sphere fluids: one component system, equimolar additive, and nonadditive binary mixtures. In particular, we numerically check the assumption of local dependency of the bridge functions from the indirect correlation functions, on which most of the existing integral equation theories hinge. We find that this condition can be violated either in the region around the first and second neighbors shell, or inside the hard core, for the systems here considered. The violations manifest themselves clearly in the so-called Duh–Haymet plots of the bridge functions versus the indirect correlation functions and become amplified as the coupling of the system increases. © 2004 American Institute of Physics. [DOI: 10.1063/1.1739392]

I. INTRODUCTION

A central problem in the theory of the static structure of classical liquids is to find a simple and efficient way to obtain the pair correlation functions from the interparticle forces in pairwise interacting fluids. Exact statistical mechanics^{1,2} allows us to write the formal solution of such problems as the coupled set of equations:

$$1 + h_{ij}(r) = \exp[-\beta\phi_{ij}(r) + h_{ij}(r) - c_{ij}(r) + B_{ij}(r)] \quad (1)$$

and

$$h_{ij}(r) = c_{ij}(r) + \sum_l \rho_l \int d\mathbf{r}' c_{il}(r') h_{lj}(|\mathbf{r} - \mathbf{r}'|), \quad (2)$$

where $h_{ij}(r)$ and $c_{ij}(r)$ are the (total) and direct correlation functions for atomic pairs of species i and j , ρ_l is the number density of the l th component and $\beta = 1/kT$. The functions $B_{ij}(r)$, named bridge functions after their diagrammatic characterization¹ are *functionals* of the total correlation functions, i.e., their value at distance r depends on the values of all the correlation functions at all distances.

The basic difficulty with Eqs. (1) and (2) is that we do not have an explicit and computationally efficient relation between $B_{ij}(r)$ and the correlation functions, so we have to resort to approximations. The results of the last three decades of research have shown that it is possible to make progress by approximating the bridge functionals $B_{ij}(r)$ by *functions* of the indirect correlation functions $\gamma_{ij}(r) = h_{ij}(r) - c_{ij}(r)$ (approximate closures). Once we have an explicit form for $B_{ij}(\gamma_{ij}(r))$, the resulting integral Eqs. (1) and (2), although approximate, can provide excellent results for the static structure of liquids. Moreover, besides the original focus on

the structural properties, in recent years interest has grown toward using approximate integral equations to obtain thermodynamics and the phase diagrams of liquids and liquid mixtures.³

In particular, Kjellander and Sarman⁴ and Lee⁵ have derived an approximate but useful formula for the chemical potential of a fluid requiring only the knowledge of the correlation functions at the thermodynamic state of interest. Their formula is based on two main approximations. The first is the same assumption from which integral equations are derived, i.e., that the bridge functions $B_{ij}(r)$ are local functions of the corresponding indirect correlation functions. The second stronger assumption is that the only dependence of the bridge functions from the thermodynamic state is through the indirect correlation functions. Thus, the functional dependence of $B_{ij}(\gamma_{ij})$ is the same for all the states.

In this paper we want to investigate via direct numerical computer simulation the two approximations.

Up to now, numerical studies of the bridge functions and of the accuracy of the local approximation have been limited to the case of one component systems^{6,7} or electrolytic solutions.⁸ We feel that two-component systems deserve more interest for many reasons: (i) there are strong indications that the approximate universality of the bridge functions⁹ is not valid in multicomponent systems, (ii) the phase diagrams of multicomponent systems are richer and more interesting than those of pure fluids, and (iii) it turns out that modeling the bridge functions for multicomponent systems is much more difficult than for pure systems.

We have studied, through Monte Carlo simulation, the bridge functions of a few systems of nonadditive hard spheres (NAHS) mixtures, including the limiting cases of additive (AHS) mixtures and one component system. In particular we are interested in a direct check of the local hypothesis for the functional relations between bridge and correlation functions in binary mixtures. To this aim we use the so

^{a)}Electronic mail: rfantoni@ts.infn.it^{b)}Electronic mail: pastore@ts.infn.it

called Duh–Haymet plots.⁸ These are plots of the partial bridge functions B_{ij} as a function of the partial indirect correlation functions γ_{ij} .

The paper is organized as follows: In Sec. II we summarize the equations we used to evaluate the cavity correlation functions from which the bridge functions can be easily obtained and we provide the relevant technical details of the numerical calculations. In Sec. III we present and discuss our numerical results.

II. CALCULATION OF THE CAVITY AND BRIDGE FUNCTIONS

A. Theory

The binary NAHS system is a fluid made of hard spheres of two species. One specie, here named 1, with diameter R_{11} and number density ρ_1 and another specie (2) with diameter R_{22} and number density ρ_2 , with a pair interaction potential that can be written as follows:

$$\phi_{ab}(r) = \begin{cases} \infty & r < R_{ab}, \\ 0 & r > R_{ab}, \end{cases} \quad (3)$$

where $R_{12} = (R_{11} + R_{22})/2 + \alpha$, with α being the nonadditivity parameter. We will also study various special cases as the one component system, and the binary mixture of additive hard spheres (AHS) $\alpha=0$. We can rewrite Eq. (1) to obtain the partial bridge functions

$$B_{ab}(r) = \ln y_{ab}(r) - \gamma_{ab}(r), \quad (4)$$

where $y_{ab}(r)$ are the partial cavity functions

$$y_{ab}(r) = g_{ab}(r) \exp[\beta \phi_{ab}(r)]. \quad (5)$$

Here $g_{ij}(r) = 1 + h_{ij}(r)$ are the partial radial distribution functions. Notice that both the cavity functions and the indirect correlation functions are everywhere continuous, and so is the bridge.

In the region outside the hard cores, in a hard sphere (HS) system, the cavity correlation functions coincide with the pair distribution functions $g_{ij}(r)$. In order to determine

the relationship between the partial bridge functions and the partial indirect correlation functions within the hard cores, we need to calculate the partial cavity functions. There are two distinct methods for calculating them:⁶ the one which uses Henderson's equation¹⁰ and the direct simulation method of Torrie and Patey.¹¹ We decided to use the first method which is accurate at small r .

For a binary mixture the like cavity functions can be obtained from the following canonical average:

$$y_{aa}(r_{1_a 2_a}) = \frac{V z_a}{N_a} \bar{y}_{aa}(r_{1_a 2_a}) = \frac{V z_a}{N_a} \left\langle \exp \left\{ -\beta \left[\sum_{i_a > 2}^{N_a+1} \phi_{aa}(r_{1_a i_a}) + \sum_{i_b=1}^{N_b} \phi_{ab}(r_{1_a i_b}) \right] \right\} \right\rangle_{N_1, N_2, V, T}, \quad (6)$$

where $a, b=1, 2$ with $b \neq a$, $r_{i_a j_b}$ is the distance between particle i of specie a and particle j of specie b , $z_a = \exp(\beta \mu_a)/\Lambda^3$ is the activity of specie a , μ_a its chemical potential, and Λ the de Broglie thermal wavelength, V is the volume, N_a the number of particles of specie a , so that the prefactor $V z_a / N_a = \exp(\beta \mu_a^{\text{exc}})$, where μ_a^{exc} is the excess chemical potential of specie a . The notation $\langle \dots \rangle_{N_1, N_2, V, T}$ indicates the canonical average at fixed number of particles, volume, and temperature.

So to calculate $\bar{y}_{aa}(r)$ we need to introduce in the system of $N_a + N_b$ particles labeled $1_b, \dots, N_b, 2_a, \dots, (N+1)_a$ a test particle 1_a placed a distance r from particle 2_a and calculate, at each Monte Carlo step, the interaction of this particle with all the particles of the system except particle 2_a .

We immediately realize that when $r=0$ we must have

$$\bar{y}_{aa}(0) = 1, \quad (7)$$

since the configurations where particle 2_a overlaps with other particles of the system are forbidden. Moreover, by

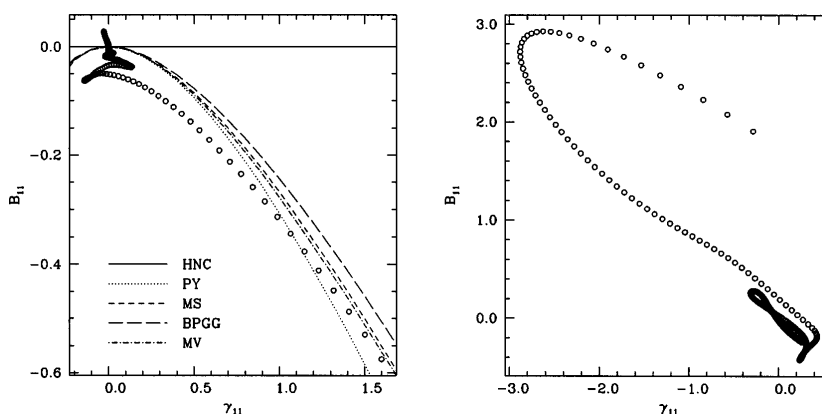


FIG. 1. The first two graphs are Duh–Haymet plots (dots), outside the hard core region, for the one component HS system (the lines show the behavior of integral equation closures). On the left $\rho=0.650$, on the right $\rho=0.925$.

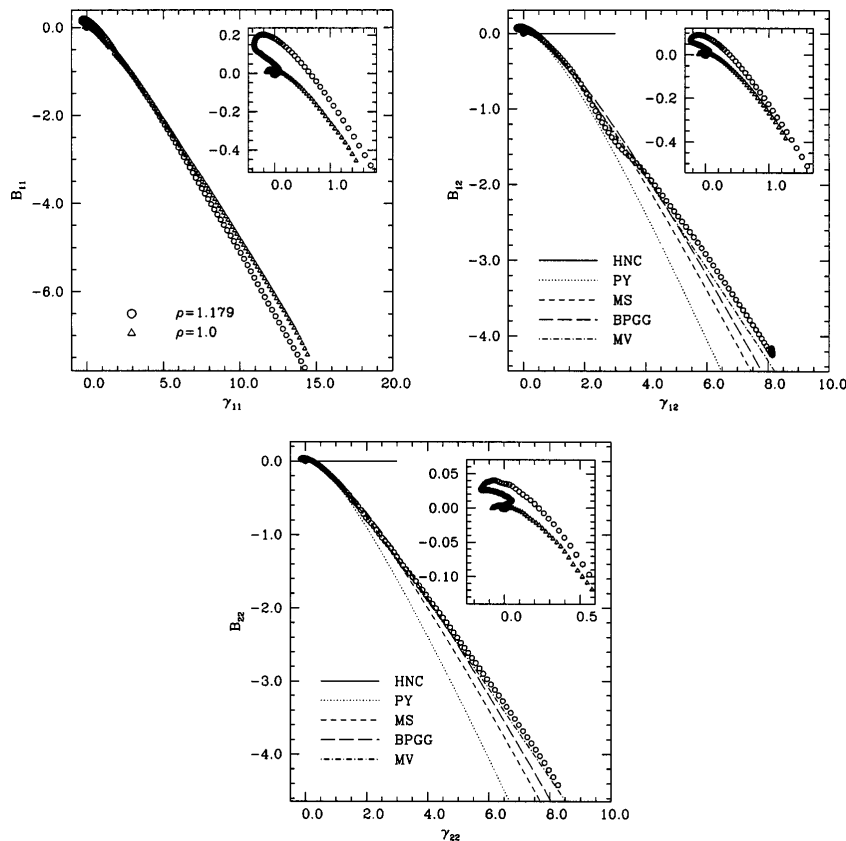


FIG. 2. Full Duh-Haymet plots obtained by the inversion of the Monte Carlo simulation data (dots) compared with some of the most common integral equation theories (lines) for the equimolar binary mixture of AHS at two different densities (in the second and third plot only results at the highest density are shown). $R_{11}=1$, $R_{12}=0.8$, and $R_{22}=0.6$. The insets show the portion of the bridge function outside the hard cores.

taking into account that $y_{ab}(r) = g_{ab}(r)$ for $r > R_{ab}$ and from the asymptotic value of the partial pair distribution functions follows that

$$\lim_{r \rightarrow \infty} \bar{y}_{aa}(r) = e^{-\beta \mu_a^{\text{exc}}} \quad (8)$$

The unlike cavity functions can be obtained from the following canonical average:

$$\begin{aligned} y_{12}(r_{1,1_2}) &= \frac{Vz_1}{N_1} \bar{y}_{12}(r_{1,1_2}) \\ &= \frac{Vz_1}{N_1} \left\langle \exp \left[-\beta \left(\sum_{i_2=1}^{N_2} \phi_{12}(r_{1,i_2}) + \sum_{i_1=1}^{N_1+1} \phi_{11}(r_{1,i_1}) \right) \right] \right\rangle_{N_1, N_2, V, T} \end{aligned} \quad (9)$$

So to calculate $\bar{y}_{12}(r)$ we need to introduce in the system of $N_1 + N_2$ particles labeled $1_2, \dots, N_2, 2_1, \dots, (N+1)_1$ a test particle 1_1 placed a distance r from particle 1_2 and calculate,

at each Monte Carlo step, the interaction of this particle with all the particles of the system except particle 1_2 .

Now there is no simple argument to guess the contact value of \bar{y}_{12} . All we can say is that we must have $\bar{y}_{12}(0) \leq 1$. At large r we still have

$$\lim_{r \rightarrow \infty} \bar{y}_{12}(r) = e^{-\beta \mu_1^{\text{exc}}} \quad (10)$$

B. Numerical implementation

Monte Carlo simulations were performed with a standard NVT Metropolis algorithm¹² using $N=4000$ particles. Linked lists¹² have been used to reduce the computational cost. To calculate the partial pair distribution functions we generally used 5.2×10^8 Monte Carlo steps, where one step corresponds to the attempt to move a single randomly chosen particle, and incremented the histograms once every 20×4000 steps. To calculate the partial cavity functions we

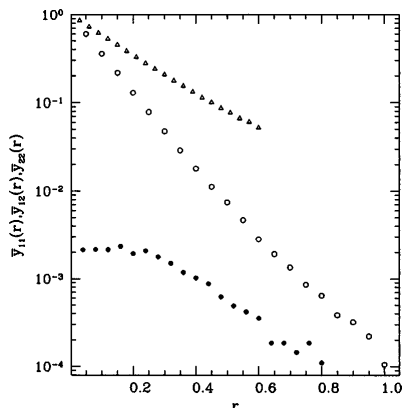


FIG. 3. Cavity functions inside the hard core for the equimolar binary mixture of AHS (at the same conditions as in Fig. 2 at the highest density). The plot shows the behavior of the functions defined in Eqs. (6) and (9) (notice the logarithmic scale on the ordinates), the triangles denote the 22 function, the open circles the 11 function, and the closed circle the 12 function.

used 1.6×10^9 Monte Carlo steps and incremented the histograms once every 2×4000 steps. The acceptance ratio was adjusted to values between 10% and 40%.

The Monte Carlo simulation returned the $g_{ab}(r)$ over a range not less than $8.125R_{11}$ for the densest system. In all the studied cases, the pair distribution functions attained their asymptotic value well inside the maximum distance they were evaluated. Thus, it has been possible to obtain accurate Fourier transforms of the total correlation functions $[\hat{h}_{ab}(k)]$ [it was necessary to cure the cusps at contact in the partial pair distribution functions by adding to them $H(R_{ab} - r)g_{ab}(R_{ab})$, H being the Heaviside step function, before taking the Fourier transform and removing its analytical Fourier transform afterwards]. To obtain the partial indirect correlation functions we first calculated the partial direct correlation functions $[\hat{c}_{ab}(k)]$ using the Fourier transform of the Ornstein–Zernike Eq. (2) and then we got the Fourier transform of the indirect correlation functions $\hat{\gamma}_{ij}(k) = \hat{h}_{ij}(k) - \hat{c}_{ij}(k)$ which is the transform of a continuous function in real space and then is safe to transform back numerically to obtain $\gamma_{ab}(r)$.

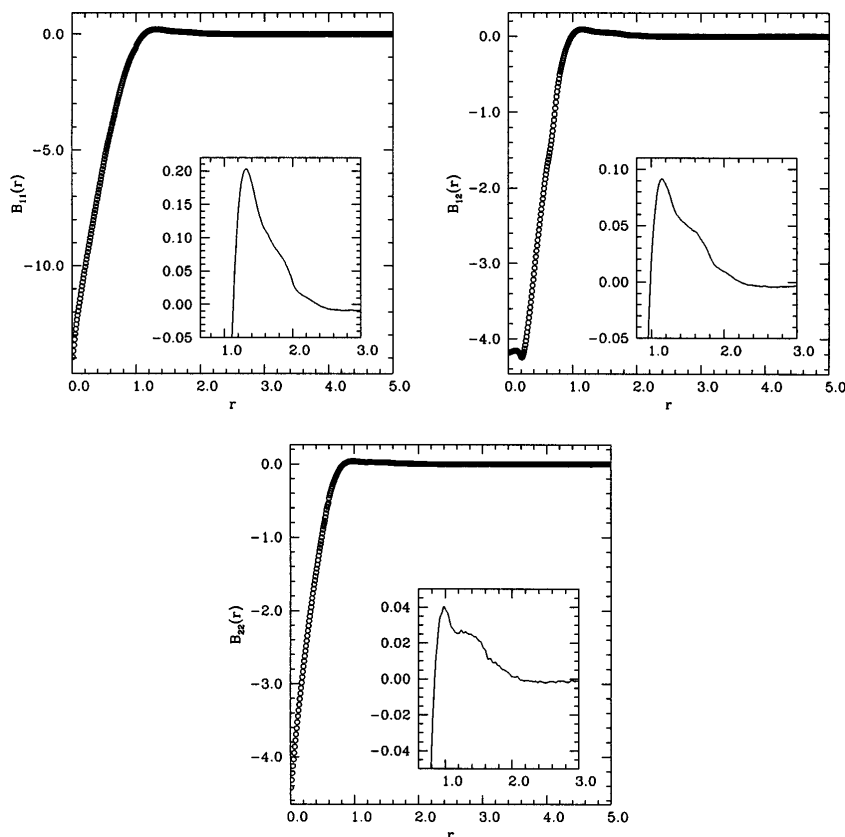


FIG. 4. Bridge functions $B_{ab}(r)$ for the equimolar binary mixture of AHS (at the same conditions as in Fig. 2 at the highest density). The insets show magnifications of the regions just outside of the hard cores.

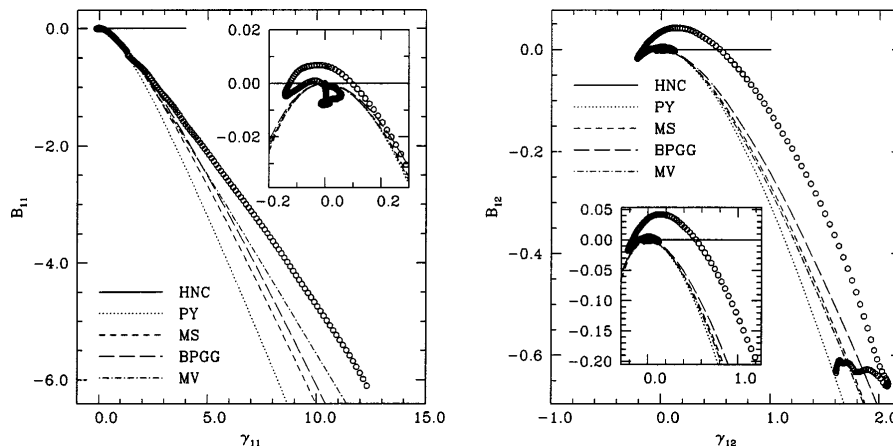


FIG. 5. Full Duh-Haymet plots obtained by the inversion of the Monte Carlo simulation data (dots) and by some of the most common integral equation theories (lines) for the equimolar binary mixture of NAHS with equal like diameters and negative nonadditivity $\alpha = -0.351$, at $\rho_1 = 0.589$. $R_{11} = R_{22} = 1$ and $R_{12} = 0.649$. The insets shows the portion of the bridge function outside the hard cores.

III. NUMERICAL RESULTS

We carried on simulations on the following systems: (A), one component HS; (B), equimolar binary mixture of AHS; (C), equimolar binary mixture of NAHS with equal like diameters and negative nonadditivity; (D), equimolar binary mixture of NAHS with equal like diameters and positive nonadditivity; and (E), equimolar binary mixture of NAHS with different like diameters. In all these cases we have drawn the corresponding Duh-Haymet plots, i.e., we plot, for each distance, the pairs $(B_{ij}(r), \gamma_{ij}(r))$.

When we are outside the hard core the partial bridge functions (4) reduces to

$$B_{ab}(r) = \ln g_{ab}(r) - \gamma_{ab}(r) \tag{11}$$

and we can obtain the bridge functions directly from the pair correlation functions solving the OZ Eq. (2) to get the partial indirect correlation functions γ_{ab} .

To realize the Duh-Haymet plots when we are within the hard core regions, we first calculated the cavity functions \bar{y}_{ab} as explained in Sec. II and then the bridge functions (up to an additive constant, the excess chemical potential $\beta\mu_a^{exc}$) from their definition (4). Estimating the excess chemical potential from the long range behavior of the cavity functions [see Eqs. (8) and (10)] we were able to find the full bridge functions. Since the cavity functions in proximity of R_{ab} becomes very small, they are subject to statistical errors. In order to obtain smooth Duh-Haymet plots we needed to smooth the cavity functions obtained from the simulation. We did this by constructing the cubic smoothing spline which has as small a second derivative as possible.

A. One component HS

We carried out two simulations at $\rho_1 = 0.650$ (with a packing fraction of $\eta = \pi\rho_1 R_{11}^3/6 = 0.340$) and $\rho_1 \approx 0.925$ ($\eta = 0.484$), the former corresponding to an intermediate density case and the latter to a liquid close to the freezing point. In our simulations we use R_{11} as a unit of length.

Inside the hard core, the bridge and the indirect correlation functions are monotonic and, for the cases here considered, there are no nonlocalities in the Duh-Haymet plots inside the core. Thus, to search for nonlocalities it is enough to analyze results in the external region. The resulting curves in the (B, γ) plane corresponding to points outside the hard core region are shown in Fig. 1. On the left the intermediate density case and on the right the high density one. We see that, as the density increases, the nonlocality becomes more accentuated. Of course, the quality of a local approximation does depend on the choice of the correlation functions used

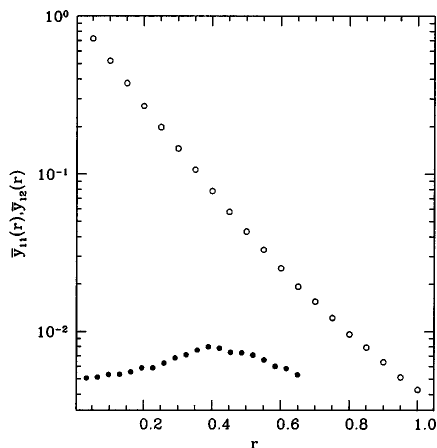


FIG. 6. Cavity functions for the equimolar binary mixture of NAHS with equal like diameters and negative nonadditivity (at the same conditions as in Fig. 5). The graph shows the behavior of the functions defined in Eqs. (6) and (9) (notice the logarithmic scale on the ordinates), the open circle denotes the like functions and the closed circle the unlike one.

10686 J. Chem. Phys., Vol. 120, No. 22, 8 June 2004

R. Fantoni and G. Pastore

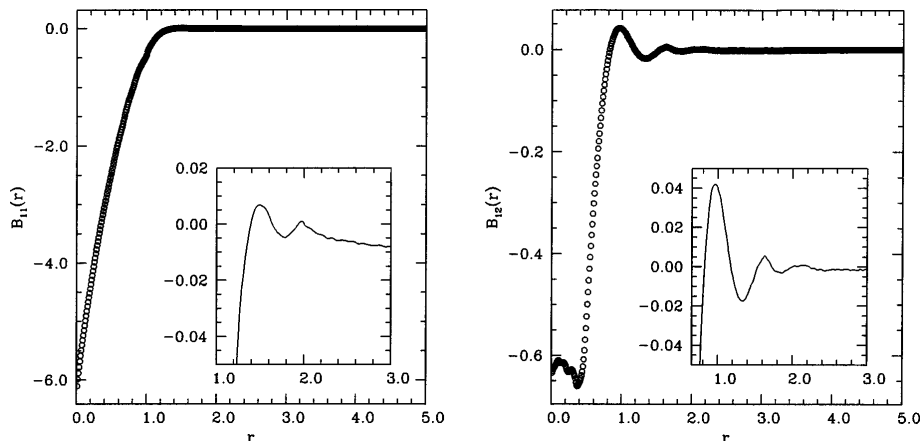


FIG. 7. Bridge functions $B_{ab}(r)$ for the equimolar binary mixture of NAHS with equal like diameters and negative nonadditivity (at the same conditions as in Fig. 5). The insets shows magnifications of the regions just outside of the hard cores.

as independent variable: plotting the bridge function as a function of the direct correlation function we observed the opposite behavior.

In order to compare the computer simulation results with the local approximate $B(\gamma)$ relations used in the integral equations, we have plotted the curves corresponding to different closures: the hypernetted chain (HNC):¹

$$B(\gamma) = 0, \quad (12)$$

the Percus–Yevick (PY):¹

$$B(\gamma) = \log(1 + \gamma) - \gamma, \quad (13)$$

the Martynov Sarkisov (MS),¹³ and its generalization by Balone, Pastore, Galli, and Gazzillo (BPGG):¹⁴

$$B(\gamma) = (1 + \alpha\gamma)^{1/\alpha} - \gamma - 1, \quad (14)$$

(MS) corresponds to $\alpha=2$, in the BPGG generalization α could be used as state dependent parameter to enforce thermodynamic consistence, here a fixed value of 15/8 has been used as suggested in (Ref. 14), and the modified Verlet (MV):¹⁵

$$B(\gamma) = \frac{-\gamma^2}{2[1 + 0.8\gamma]}. \quad (15)$$

We can see that the best closures (MS, BPGG, and MV), although not passing through the simulation curve, tend to follow its slope and curvature. When looking at Fig. 1 one should also bear in mind that the values of the bridge func-

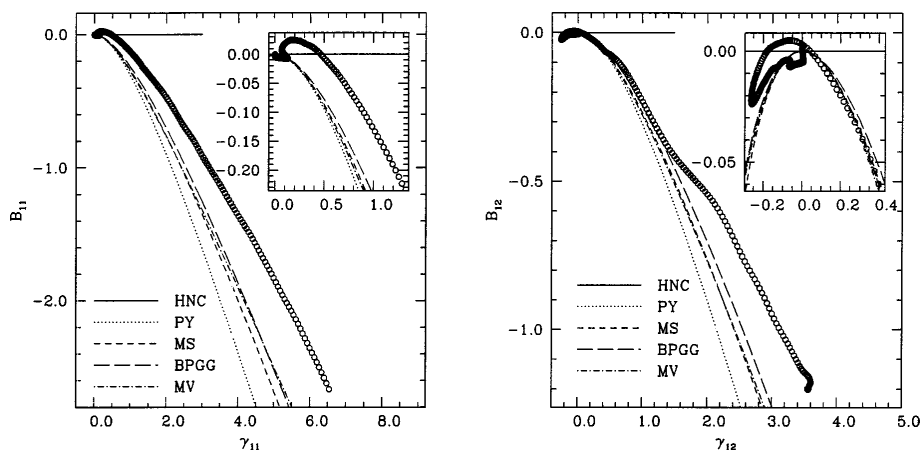


FIG. 8. Full Duh–Haymet plots obtained by the inversion of the Monte Carlo simulation data (dots) and by some of the most common integral equation theories (lines) for the equimolar binary mixture of NAHS with equal like diameters and positive nonadditivity $\alpha=+0.2$, at $\rho_1=0.200$. $R_{11}=R_{22}=1$ and $R_{12}=1.2$. The insets shows the portion of the bridge function outside the hard cores.

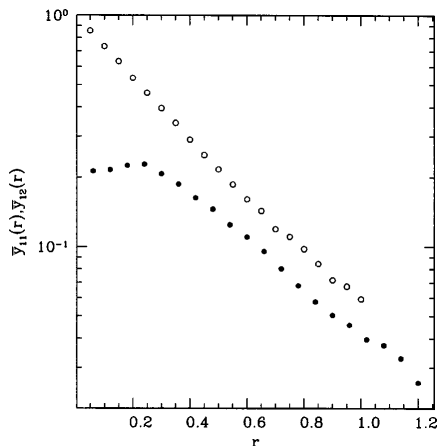


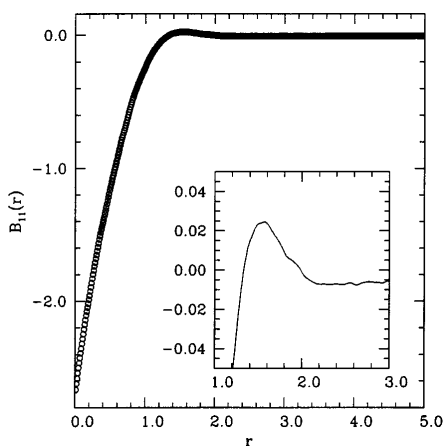
FIG. 9. Cavity functions for the equimolar binary mixture of NAHS with equal like diameters and positive nonadditivity (at the same conditions as in Fig. 8). The graph shows the behavior of the functions defined in Eqs. (6) and (9) (notice the logarithmic scale on the ordinates), the open circle denotes the like functions, and the closed circle the unlike functions.

tion outside the hard core are not the most relevant for the quality of the structural and thermodynamic results of the closures.

B. Equimolar binary mixture of AHS

We carried out a simulation at $\rho_1 = \rho_2 \approx 0.589$ [$\eta = \pi(\rho_1 R_{11}^3 + \rho_2 R_{22}^3)/6 = 0.375$] and $\rho_1 = 0.5$. We chose $R_{11} = 1$, $R_{12} = 0.8$, and $R_{22} = 0.6$.

The results outside the hard core region are shown in the insets of the plots of Fig. 2. There are non-localities in a neighborhood of the origin which corresponds to the large r region. These are more evident in the high density case.



The most interesting feature shown in the figure is the difference between the curves at the two different densities. If the hypothesis of closures defined by a unique function $B(\gamma)$ would be exact data for different densities should collapse into a unique curve in these plots. The data shown in Figs. 1 and 2 indicate clearly that this is not strictly true. However, at low and intermediate densities the quantitative effect of the changing functional form is not dramatic. And even at the highest liquid densities, the success of closures such as MV, MS, or BPGG can be probably explained in term of a higher sensitivity of the theory to localized (near the contact) features of the bridge functions more than to the behavior over the whole range of distances.

Inside the hard core region the Duh–Haymet plots do not have nonlocalities. In Fig. 3 we show the results for the cavity functions \bar{y}_{ab} for the system at the highest density. The plot for the unlike functions is more noisy than the plots for the like functions because \bar{y}_{12} being smaller than \bar{y}_{aa} for $a = 1, 2$ is more subject to statistical error.

In Fig. 2 we show the full Duh–Haymet plots for the system at the highest density, from the simulation (dots) and from integral equation theories (lines). The plots show how the MV approximation is the best one for this system. The unlike bridge function starts at $r=0$ close to the MV approximation, stays close to this approximation as r increases and at some point have a smooth change in behavior and get closer to the PY curve.

Figure 4 shows the full bridge functions as a function of r for the system at the highest density. It is worth of notice the almost flat region of the unlike bridge near the origin.

C. Equimolar binary mixture of NAHS: $R_{11} = R_{22}$, $\alpha < 0$

We carried out a simulation at $\rho_1 = \rho_2 = 0.573$ ($\eta = 0.6$). We chose $R_{11} = R_{22} = 1$ and $R_{12} = 0.649$ ($\alpha = -0.351$). These radii values would be suitable for a reference system to model correlation in molten NaCl.¹⁶

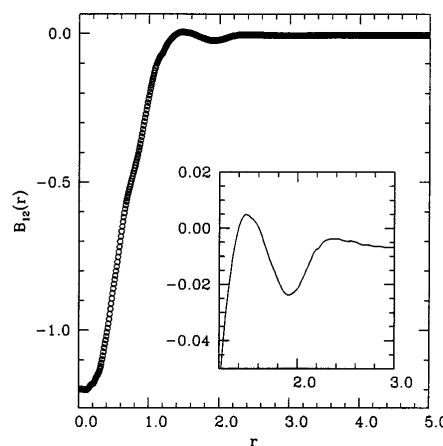


FIG. 10. Bridge functions $B_{ab}(r)$ for the equimolar binary mixture of NAHS with equal like diameters and positive nonadditivity (at the same conditions as in Fig. 8). The insets shows magnifications of the regions just outside of the hard cores.

10688 J. Chem. Phys., Vol. 120, No. 22, 8 June 2004

R. Fantoni and G. Pastore

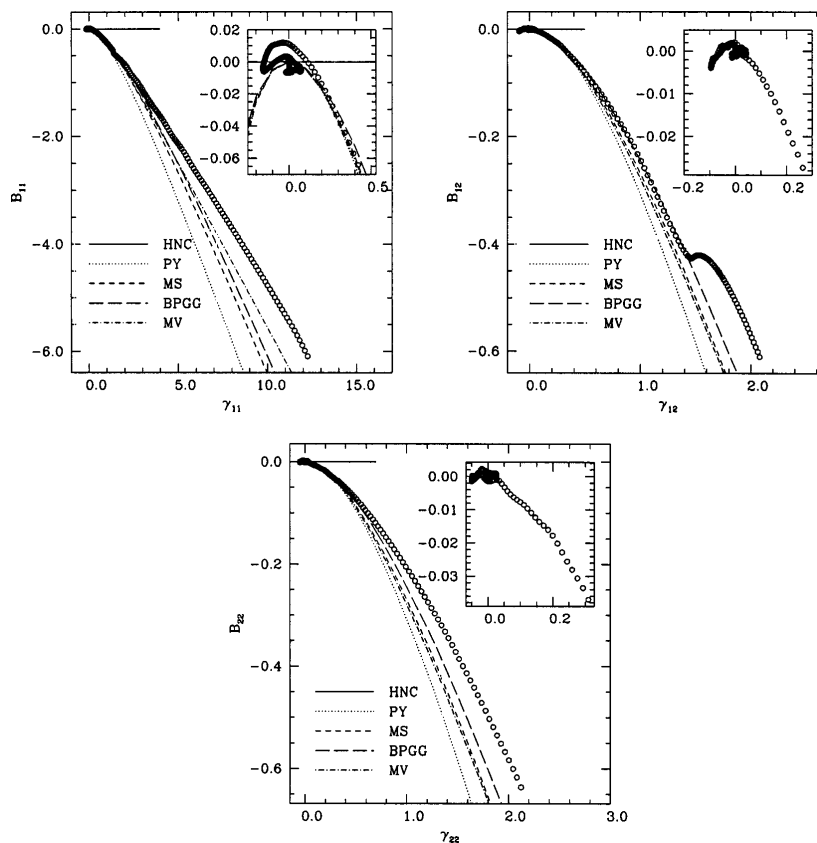


FIG. 11. Full Duh–Haymet plots obtained by the inversion of the Monte Carlo simulation data (dots) and by some of the most common integral equation theories (lines) for the equimolar binary mixture of NAHS with different like diameters $R_{11}=1$ and $R_{12}=R_{22}=0.6$, at $\rho_1=0.589$. The insets shows the portion of the bridge function outside the hard cores.

The results outside the hard core region are shown in the insets of the plots of Fig. 5. There are nonlocalities in the neighborhood of the origin corresponding to the large r region.

In Fig. 6 we show the results for the cavity functions \bar{y}_{ab} .

In Fig. 5 we show the full Duh–Haymet plots from the Monte Carlo simulation (dots) and from the most common integral equation theories (lines). The approximation which seems to be closer to the like bridge function is MV: only at big r the bridge functions is well approximated by PY, MS, BPGG, and MV. The unlike bridge function starts at $r=0$ close to the PY approximation but as r increases it has a sudden change in behavior which displaces it away from all the approximations. Inside the hard core region the Duh–Haymet plots for the unlike functions exhibit significant nonlocalities in correspondence with the non monotonic behavior of the unlike cavity function (black dots in Fig. 6).

Figure 7 shows the full bridge functions as a function of

r . The unlike bridge function shows oscillations in a neighborhood of the origin.

D. Equimolar binary mixture of NAHS: $R_{11}=R_{22}$, $\alpha>0$

We carried out a simulation at $\rho_1=\rho_2=0.200$ ($\eta=0.209$). We chose $R_{11}=R_{22}=1$ and $R_{12}=1.2$ ($\alpha=+0.2$). Notice that this system undergoes phase separation when $\rho=2\rho_1>0.42$.

The results outside the hard core region are shown in the insets of the plots of Fig. 8. There are nonlocalities in a neighborhood of the origin corresponding to large distances.

Also for this system, inside the hard core region the Duh–Haymet plots for the unlike functions have nonlocalities in a neighborhood of $r=0$. These are smaller in extent than the ones found for system C. In Fig. 9 we show the results for the cavity functions \bar{y}_{ab} .

In Fig. 8 we show the full Duh–Haymet plots from the simulation (dots) and from the most common integral equa-

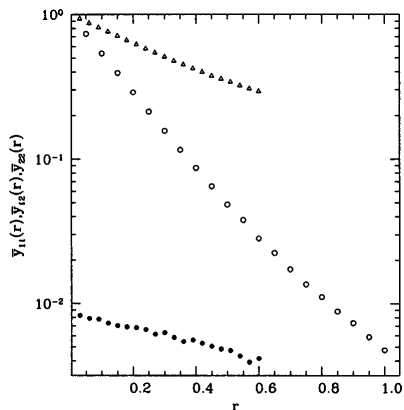


FIG. 12. Cavity functions for the equimolar binary mixture of NAHS with different like diameters (at the same conditions as in Fig. 11). The graph shows the behavior of the functions defined in Eqs. (6) and (9) (notice the logarithmic scale on the ordinates), the triangles denote the 22 function, the open circles the 11 function, and the closed circle the 12 function.

tions (lines). The approximations which seem to be closer to the like bridge function is MV and BPGG even if there is always a gap between the approximations and the simulation. The unlike bridge function starts at $r=0$ far away from all the approximations but as r increases it has a smooth change in behavior approaching the BPGG curve.

Figure 10 shows the full bridge functions as a function of r . Again, the unlike bridge function have an almost flat behavior in a neighborhood of the origin.

E. Equimolar binary mixture of NAHS: $R_{11} \neq R_{22}$

We carried out a simulation at $\rho_1 = \rho_2 = 0.589$ ($\eta = 0.375$). We chose $R_{11} = 1$ and $R_{12} = R_{22} = 0.6$ ($\alpha = -0.2$).

The results outside the hard core region are shown in the insets of the plots of Fig. 11. There are nonlocalities in a neighborhood of the origin which corresponds to the big r region.

Inside the hard core region the Duh–Haymet plots have no nonlocalities. In Fig. 12 we show the results for the cavity functions \bar{y}_{ab} .

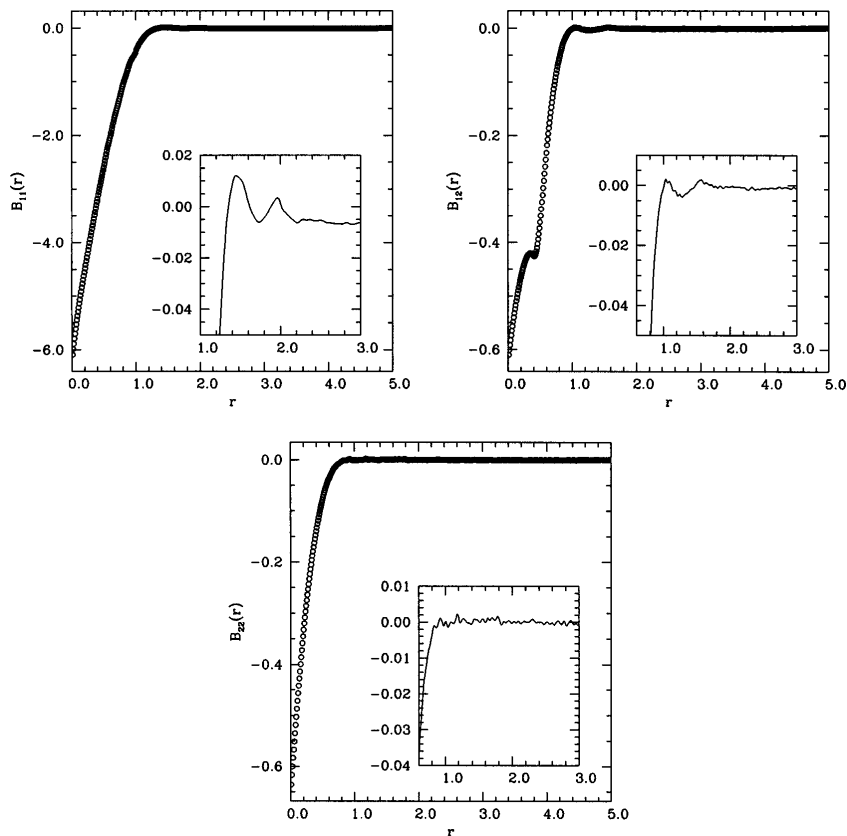


FIG. 13. Bridge functions $B_{ab}(r)$ for the equimolar binary mixture of NAHS with different like diameters (at the same conditions as in Fig. 11). The insets shows magnifications of the regions just outside of the hard cores.

In Fig. 11 we show the full Duh–Haymet plots from the simulation (dots) and from the most common integral equations (lines). The approximation which is closer to the 11 bridge function is the MV. The one that is closer to the 22 bridge function is the BPGG. The 12 bridge function starts at $r=0$ far away from all the 5 approximations and as r increases has a sudden change in behavior and starts following the BPGG approximation.

Figure 13 shows the full bridge functions as a function of r . The unlike bridge function shows again a qualitatively different behavior near the origin.

IV. CONCLUSIONS

From our analysis it follows that the nonlocalities in the function relationship between the bridge functions and the indirect correlation functions may appear either outside of the hard core regions or inside of it. While the nonlocalities outside the hard core appear both in the like and in the unlike functions, the ones inside the hard core appear only in the unlike functions (see Fig. 5 and Fig. 8), for the systems that we have studied. Their appearance can be directly related to the peculiar behavior of the unlike cavity correlation function inside the hard core.

As is shown by a comparison of the plots of Fig. 1 and from Fig. 2 the nonlocalities become more accentuated as we increase the coupling (the density) of the system. Nonetheless Fig. 8 shows that the nonlocalities may appear even in a weakly coupled system (in this case symmetric NAHS with positive non additivity). Among the systems studied the one which presents the worst nonlocalities is the equimolar symmetric NAHS with negative nonadditivity (see Fig. 5). For this system the Duh–Haymet plot for the unlike bridge function is nonlocal both in the hard core region (in a neighborhood of $r=0$) and outside of it (at large r).

We can conclude that the two hypothesis of a local function approximation for the bridge functionals of the indirect correlation functions and the stronger hypothesis of unique functional form independent on the state, are not strictly supported by the numerical data. For the one component system, this finding is consistent with the observed density dependence of the bridge function reported in Ref. 17. We observe clear violations of both the assumptions increasing with the density. This negative statement should be somewhat mitigated by realizing that the violations of the locality, in the

systems studied, are limited to the small and large distances regions. The latter, corresponding to the region of the fast vanishing of the bridge functions affect very little the thermodynamic and structural properties of the systems. The former are presumably more important for the level of thermodynamic consistence of the theory but have small effect on quality of the structural results. The well known success of closures like MS, BPGG, and MV supports such point of view.

From comparison with the simulation data in the cases we have studied, we conclude that the best approximations of the true hard sphere bridge functions are provided by the MV and BPGG even if, especially in the unlike bridge functions, there are a wide variety of characteristic behaviors which are not captured by any of the most popular integral equation approximations. In this respect, we feel that a final comment on the local functional approximation in the case of multicomponent systems is in order. Indeed, density functional theory allows to say that the bridge function B_{ij} should be a functional of all the pair correlation functions, not only the (i,j) one. Thus, we could have a function approximation $B_{ij}(\gamma_{11}(r), \gamma_{12}(r), \gamma_{22}(r))$ which would be local in space but not with respect to the components. At the best of our knowledge, up to now no attempt has been done to explore this additional freedom to improve the modeling of the bridge functions in multicomponent systems.

- ¹J. P. Hansen and I. R. McDonald, *Theory of Simple Liquids*, 2nd ed. (Academic, London, 1986).
- ²J. Caillol, *J. Phys. A* **35**, 4189 (2002).
- ³C. Caccamo, *Phys. Rep.* **274**, 1 (1996).
- ⁴R. Kjellander and S. Sarman, *J. Chem. Phys.* **90**, 2768 (1989).
- ⁵L. L. Lee, *J. Chem. Phys.* **97**, 8606 (1992).
- ⁶M. Llano-Restrepo and W. G. Chapman, *J. Chem. Phys.* **97**, 2046 (1992).
- ⁷D.-M. Duh and A. D. J. Haymet, *J. Chem. Phys.* **103**, 2625 (1995).
- ⁸D.-M. Duh and A. D. J. Haymet, *J. Chem. Phys.* **97**, 7716 (1992).
- ⁹Y. Rosenfeld and N. W. Ashcroft, *Phys. Rev. A* **20**, 1208 (1979).
- ¹⁰J. R. Henderson, *Mol. Phys.* **48**, 389 (1983).
- ¹¹G. Torrie and G. N. Patey, *Mol. Phys.* **34**, 1623 (1977).
- ¹²M. P. Allen and D. J. Tildesley, *Computer Simulation of Liquids* (Clarendon, Oxford, 1987).
- ¹³G. A. Martynov and G. N. Sarkisov, *Mol. Phys.* **49**, 1495 (1983).
- ¹⁴P. Ballone, G. Pastore, G. Galli, and D. Gazzillo, *Mol. Phys.* **59**, 275 (1986).
- ¹⁵L. Verlet, *Mol. Phys.* **41**, 183 (1980).
- ¹⁶P. Ballone, G. Pastore, and M. P. Tosi, *J. Chem. Phys.* **81**, 3174 (1984).
- ¹⁷A. Malijevsky and S. Labik, *Mol. Phys.* **60**, 663 (1987).

Part V
2005

Chapter 9

Stability boundaries, percolation threshold, and two phase coexistence for polydisperse fluids of adhesive colloidal particles

Fantoni R., Gazzillo D., Giacometti A., J. Chem. Phys., **122**, 034901 (2005)

Title: “Stability boundaries, percolation threshold, and two phase coexistence for polydisperse fluids of adhesive colloidal particles.”

Abstract: We study the polydisperse Baxter model of sticky hard spheres (SHS) in the modified Mean Spherical Approximation (mMSA). This closure is known to be the zero-order approximation (C0) of the Percus-Yevick (PY) closure in a density expansion. The simplicity of the closure allows a full analytical study of the model. In particular we study stability boundaries, the percolation threshold, and the gas-liquid coexistence curves. Various possible sub-cases of the model are treated in details. Although the detailed behavior depends upon the particularly chosen case, we find that, in general, polydispersity inhibits instabilities, increases the extent of the non percolating phase, and diminishes the size of the gas-liquid coexistence region. We also consider the first-order improvement of the mMSA (C0) closure (C1) and compare the percolation and gas-liquid boundaries for the one-component system with recent Monte Carlo simulations. Our results provide a qualitative understanding of the effect of polydispersity on SHS models and are expected to shed new light on the applicability of SHS models for colloidal mixtures.

[HTML ABSTRACT + LINKS](#)THE JOURNAL OF CHEMICAL PHYSICS **122**, 034901 (2005)

Stability boundaries, percolation threshold, and two-phase coexistence for polydisperse fluids of adhesive colloidal particles

Riccardo Fantoni,^{a)} Domenico Gazzillo,^{b)} and Achille Giacometti^{c)}*Istituto Nazionale per la Fisica della Materia and Dipartimento di Chimica Fisica, Università di Venezia, S. Marta DD 2137, I-30123 Venezia, Italy*

(Received 17 September 2004; accepted 20 October 2004; published online 28 December 2004)

We study the polydisperse Baxter model of sticky hard spheres (SHS) in the modified mean spherical approximation (mMSA). This closure is known to be the zero-order approximation C0 of the Percus-Yevick closure in a density expansion. The simplicity of the closure allows a full analytical study of the model. In particular we study stability boundaries, the percolation threshold, and the gas-liquid coexistence curves. Various possible subcases of the model are treated in details. Although the detailed behavior depends upon the particularly chosen case, we find that, in general, polydispersity inhibits instabilities, increases the extent of the nonpercolating phase, and diminishes the size of the gas-liquid coexistence region. We also consider the first-order improvement of the mMSA (C0) closure (C1) and compare the percolation and gas-liquid boundaries for the one-component system with recent Monte Carlo simulations. Our results provide a qualitative understanding of the effect of polydispersity on SHS models and are expected to shed new light on the applicability of SHS models for colloidal mixtures. © 2005 American Institute of Physics. [DOI: 10.1063/1.1831275]

I. INTRODUCTION

In sterically stabilized colloidal mixtures, particles are coated with polymer brushes to prevent irreversible flocculation due to van der Waals attraction.¹ If the solvent is a moderate one, a lowering of the temperature yields very strong attraction with a range much less than the typical colloidal size. In microemulsions of polydispersed spherical water droplets each coated by a monolayer of sodium di-2-ethylhexylsulfosuccinate dispersed in a continuum of oil, the droplets interact with each other via a hard core plus a short range attractive potential, the strength of which increases with temperature.² For these systems, a very useful theoretical model is the sticky hard sphere (SHS) model proposed by Baxter³ long time ago for atomic liquids. In the original Baxter solution^{3,4} the one-component Ornstein-Zernike (OZ) integral equation was analytically solved within the Percus-Yevick (PY) approximation. Successive extension to mixtures,⁵ however, proved to be a formidable task in view of the fact that a large [infinite (Ref. 6)] number of coupled quadratic equations ought to be solved numerically in order to have a complete understanding of both thermodynamics and structure of the model. This is the reason why, to the best of our knowledge, only binary mixtures have been explicitly discussed so far in this framework.⁵ Moreover it has been proven by Stell⁷ that sticky spheres of equal diameter in the Baxter limit are not thermodynamically stable and size polydispersity can be expected to restore thermodynamic stability.

Motivated by this scenario, it was recently proposed⁸ a

simpler approximation [modified mean spherical approximation (mMSA) closure] having the advantage that also the multicomponent case could be worked out analytically.^{9,10} Further analysis and comparison with both Monte Carlo (MC) and PY results^{8,11,12} in the one-component case, have shown that the mMSA closure for Baxter model is a reliable one up to experimentally significant densities. The price to pay for this simplification is that only the energy equation of state gives rise to a critical behavior, the other two routes yielding either a noncritical behavior (compressibility), or a diverging equation of state (virial).

In this work we pursue this investigation by studying the multicomponent version of the model proposed in Ref. 8, and analyzing various consequences. We first solve the multicomponent version of Baxter model within the mMSA closure, and show that the solution is equivalent to the one derived in Ref. 9 for a companion SHS model. The solution, derived in terms of an auxiliary function called Baxter factor correlation, turns out to be formally similar to that derived with the PY closure. However, and this is the crux of the matter, the matrix function representing the stickiness parameters is unconstrained, unlike the PY counterpart. In order to make further progress and derive the multicomponent energy equation of state, a further assumption is necessary on the matrix representing the stickiness parameters. As discussed previously (see Ref. 9 for details) a remarkable simplification occurs when the general element of this matrix has the form of a sum of dyads (i.e., it is dyadic). In these cases the necessary matrix inversion can be carried out analytically and all measurable quantities can then be computed. Physically, this reduction to a dyadic form amounts to assume a relation among polydispersity in size and polydispersity in stickiness, that is on the adhesion forces. In addition to the two cases

^{a)}Electronic mail: rfantoni@unive.it^{b)}Electronic mail: gazzillo@unive.it^{c)}Electronic mail: achille@unive.it

034901-2 Fantoni, Gazzillo, and Giacometti

J. Chem. Phys. 122, 034901 (2005)

proposed in Ref. 9 (denoted as cases I and II in the following) and that proposed in Ref. 13 (case IV), we shall consider two further cases. The first one (case III) is a physically motivated variant of case I, whereas the second one (case V) has its main justification in the simplifying features occurring when one attempts to go beyond the mMSA closure with a density perturbative approach (to first order this will be called C1, as in Ref. 8, for reasons which will become apparent in the rest of the paper).

The main results of our analysis are the following. We derive the instability curves in three of the considered cases (cases I–III) within the mMSA approximation and analyze the effect of polydispersity in some detail. In order to test the reliability of the mMSA approximation, we also consider the first-order correction C1 in the one-component case and compare with the PY result.

Next we consider the effect of polydispersity on the percolation threshold. This is an interesting phenomenon on its own right and has attracted considerable attention recently,^{11,12,14–16} being a paradigmatic example of flocculation instability. In particular, recent Monte Carlo simulations^{11,12} on monodisperse (one-component) spheres with sticky adhesion have clearly tested the performance of analytical calculations based on the PY approximation.^{15,16} We then study the percolation transition as a function of polydispersity in all above mentioned cases within mMSA. Again we can discriminate the effect of polydispersity on the percolation line, and also compare it with the first-order correction C1, the PY approximation, and MC simulations in the one-component case.

Next we consider phase equilibrium. A major obstacle to the analysis of phase transition in polydisperse systems is posed by the fact that, in principle, one has to deal with a large (infinite) number of integral nonlinear equations corresponding to the coexistence conditions among various phases. In this model, however, as it also occurs in other simpler models such as hard spheres (HS),¹⁷ van der Waals fluids¹⁸ and in more complex cases such as factorizable hard-sphere Yukawa potentials,^{19,20} the task can be carried out in full detail in view of the fact that the (excess) free energy depends upon only a finite number of moments of the size distribution function. In the particular case of two-phase coexistence, we derive the cloud and shadow curves of all cases in the mMSA approximation. We compare the results with those derived earlier for a polydisperse van der Waals fluid,¹⁷ and discuss analogies and differences in this respect. Finally we compare the results of the mMSA one-component case with the first-order correction, the PY approximation, and the results of MC simulations.

The plan of the paper is as follows. In Sec. II we define the multicomponent SHS model, give the solution for Baxter factor correlation function in the mMSA (C0) approximation,

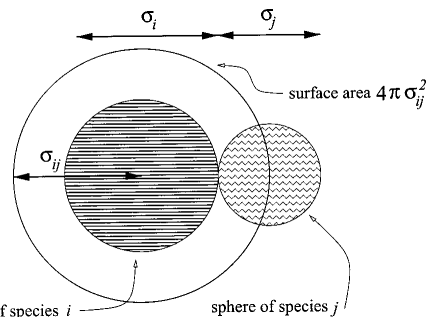


FIG. 1. Schematic diagram showing the area of the contact surface between a particle of species i and a particle of species j .

and define the various cases of polydispersion models taken under exam; in Sec. III we give the solution for Baxter factor correlation function in the C1 approximation and show how case V is particularly suitable to study the polydisperse system analytically; in Sec. IV we analytically derive the instability boundaries; in Sec. V we find analytically the percolation thresholds; in Sec. VI we derive numerically the two-phase coexistence curves; in Sec. VII we lay down our conclusions and further developments.

II. BAXTER MODEL AND MODIFIED MSA SOLUTION

In Baxter model of SHS1, one starts adding to the HS potential a square-well tail with²¹

$$\phi_{ij}(r) = -k_B T \ln \left(\frac{1}{12\tau_{ij}} \frac{R_{ij}}{R_{ij} - \sigma_{ij}} \right), \quad \sigma_{ij} \leq r \leq R_{ij}, \quad (1)$$

where $\sigma_{ij} = (\sigma_i + \sigma_j)/2$ (σ_i being the HS diameter of species i), $R_{ij} - \sigma_{ij}$ denotes the well width, k_B is Boltzmann constant, T the temperature, and the dimensionless parameter $\tau_{ij}^{-1} \geq 0$ measures the strength of surface adhesiveness or “stickiness” between particles of species i and j (τ_{ij} is also an unspecified increasing function of T). The sticky limit corresponds to taking $\{R_{ij}\} \rightarrow \{\sigma_{ij}\}$.

The Baxter form of the OZ integral equations for this model admits a very simple analytic solution if one uses the following mMSA:

$$c_{ij}(r) = f_{ij}(r) \quad \text{for } r \geq \sigma_{ij}, \quad (2)$$

where $c_{ij}(r)$ and $f_{ij}(r) = \exp[-\beta\phi_{ij}(r)] - 1$ are the direct correlation function and the Mayer function, respectively [$\beta = (k_B T)^{-1}$]. This can be easily inferred by using the formalism introduced in Ref. 8. As pointed out in that reference, the mMSA closure can be reckoned as a zero-order approximation in a perturbative expansion, and hence it will also be denoted as C0 henceforth. In terms of Baxter factor correlation functions $q_{ij}(r)$, its extension to mixtures reads

$$q_{ij}(r) = \begin{cases} \frac{1}{2} a_i (r - \sigma_{ij})^2 + (b_i + a_i \sigma_{ij})(r - \sigma_{ij}) + K_{ij}, & L_{ij} = (\sigma_i - \sigma_j)/2 \leq r \leq \sigma_{ij}, \\ 0, & \text{elsewhere,} \end{cases} \quad (3)$$

$$a_i = \frac{1}{\Delta} + \frac{3\xi_2\sigma_i}{\Delta^2} - \frac{12\xi_i}{\Delta}, \quad b_i = \left(\frac{1}{\Delta} - a_i\right) \frac{\sigma_i}{2}, \quad (4)$$

$$\xi_n = \frac{\pi}{6} \sum_{i=1}^p \rho_i \sigma_i^n, \quad \zeta_i = \frac{\pi}{6} \sum_{m=1}^p \rho_m \sigma_m K_{im}, \quad \Delta = 1 - \xi_3, \quad (5)$$

with p being the number of components, ρ_i the number density of species i , and

$$K_{ij}^{(\text{mMSA})} = \frac{1}{12\tau_{ij}} \sigma_{ij}^2 \equiv K_{ij}^0. \quad (6)$$

We remark that although Eqs. (3)–(5) are formally identical to their PY counterpart, this result is in fact simpler in such they differ in the quantity K_{ij} , which in the PY approximation reads²¹

$$K_{ij}^{(\text{PY})} = K_{ij}^0 y_{ij}^{(\text{PY})}(\sigma_{ij}) \equiv \frac{1}{12} \lambda_{ij} \sigma_{ij}^2, \quad (7)$$

where $y_{ij}^{(\text{PY})}(\sigma_{ij})$ is the contact value of the PY cavity function. In general, the parameters λ_{ij} can be determined only numerically by solving a set of $p(p+1)/2$ coupled quadratic equations,^{5,21} and this makes the multicomponent PY solution of limited interest from the practical viewpoint. In particular, a global analysis of the phase diagram proves to be a formidable task within the PY approximation.⁵ On the other hand, in view of the simplicity of Eq. (6) with respect to its PY counterpart Eq. (7), this is indeed possible within the mMSA (C0) approximation. The above results is, moreover, fully equivalent to a parallel but different sticky HS model (SHS3) studied by us in previous work.^{8,9} Hence, as discussed in those references, this analysis can be pursued analytically provided that K_{ij} has a dyadic form. To this aim, we consider polydisperse fluids with HS diameters distributed according to a Schulz distribution.²²

As regards stickiness, we choose to keep it either constant or related to the particle size. There are two main reasons for this. First, one expects the adhesion forces to depend upon the area of the contact surface between two particles (see Fig. 1), and hence on their sizes. Second and more practical reason is that this is a simple way of obtaining the required factorization. As the stickiness-size relation is not clearly understood, we consider five different possibilities, denoted as cases I–V henceforth. The three simplest choices are

$$\frac{1}{\tau_{ij}} = \frac{1}{\tau} \frac{\langle \sigma \rangle^2}{\sigma_{ij}^2}, \Rightarrow [K_{ij}^{(\text{mMSA})}]_{\text{case I}} = \frac{1}{12\tau} \langle \sigma \rangle^2, \quad (8)$$

$$\frac{1}{\tau_{ij}} = \frac{1}{\tau} \frac{\sigma_i \sigma_j}{\sigma_{ij}^2}, \Rightarrow [K_{ij}^{(\text{mMSA})}]_{\text{case II}} = \frac{1}{12\tau} \sigma_i \sigma_j, \quad (9)$$

$$\frac{1}{\tau_{ij}} = \frac{1}{\tau} \frac{\langle \sigma^2 \rangle}{\sigma_{ij}^2}, \Rightarrow [K_{ij}^{(\text{mMSA})}]_{\text{case III}} = \frac{1}{12\tau} \langle \sigma^2 \rangle, \quad (10)$$

where $\langle \sigma \rangle$ is the average HS diameter ($\langle F \rangle \equiv \sum_i x_i F_i$, here $x_i = \rho_i / \rho$ is the molar fraction of species i with $\rho = \sum_i \rho_i$ the total number density), and τ is assumed to depend only on the temperature, while the remaining factor in τ_{ij}^{-1} is a measure of stickiness strength and is related to the particle sizes.

The physical interpretation of these choices is the following. In case I the stickiness is assumed to be proportional to the surface contact area of two colloidal particles having average size $\langle \sigma \rangle$, whereas in case II the adhesion of each particle is linearly related to its size. Case III, finally, is a variant of case I where one considers an average stickiness rather than the stickiness of an average particle.

In all these cases the $K_{ij}^{(\text{mMSA})}$ matrix can be factorized as

$$K_{ij}^{(\text{mMSA})} = Y_i Y_j, \quad (11)$$

with Y_i having dimensions of length [$Y_i = (\sqrt{12\tau})^{-1} \langle \sigma \rangle$, $Y_i = (\sqrt{12\tau})^{-1} \sigma_i$, and $Y_i = (\sqrt{12\tau})^{-1} \langle \sigma^2 \rangle^{1/2}$ in cases I, II, and III, respectively]. Note that cases I and II have already been exploited by us in previous work.⁹

We also consider a case similar to that proposed by Tutschka and Kahl¹³ (henceforth denoted as case IV)

$$\frac{1}{\tau_{ij}} = \frac{1}{\tau}. \quad (12)$$

In this case the $K_{ij}^{(\text{mMSA})}$ matrix can be written as a sum of three factorized terms [as it can be immediately inferred by expanding the square $\sigma_{ij}^2 = (\sigma_i + \sigma_j)^2/4$] and has the interesting physical interpretation of being proportional to the area of the actual contact surface $4\pi\sigma_{ij}^2$ between particles of species i and j . Finally, and for reasons related to the C1 approximation that will be further elaborated below, we consider case V defined by the linear (rather than quadratic) dependence

$$\frac{1}{\tau_{ij}} = \frac{1}{\tau} \frac{\langle \sigma \rangle}{\sigma_{ij}}, \quad (13)$$

in this case the $K_{ij}^{(\text{mMSA})}$ parameters can be written as a sum of two factorized terms.

III. THE C1 APPROXIMATION

It was recently argued⁸ in the one-component case, that the mMSA (C0) approximation can be improved by including the next order term in the density expansion of the direct correlation function. Its extension to multicomponent mixtures reads

$$c_{ij}(r) = f_{ij}(r) \left[1 + \sum_m \rho_m \gamma_{imj}^{(1)}(r) \right], \quad r \geq \sigma_{ij}, \quad (14)$$

where

$$\begin{aligned} \gamma_{imj}^{(1)}(r) &= \int f_{im}(|\mathbf{r}-\mathbf{r}'|) f_{mj}(r') d\mathbf{r}' \\ &= \frac{2\pi}{r} \int_0^\infty ds s f_{im}(s) \int_{|r-s|}^{r+s} dt t f_{mj}(t), \end{aligned} \quad (15)$$

is the first-order coefficient in the density expansion of the partial indirect correlation functions $\gamma_{ij}(r)$. As discussed in Ref. 8, if we retain in the PY closure only the terms corresponding to the zero- and first-order expansion in density we recover the C1 approximation (14). It turns out that Baxter factor correlation function can still be cast in the form, Eqs. (3)–(5) but the K_{ij} parameters have the form

034901-4 Fantoni, Gazzillo, and Giacometti

 J. Chem. Phys. **122**, 034901 (2005)

$$K_{ij}^{(C1)} = K_{ij}^0 \gamma_{ij}^{(C1)}(\sigma_{ij}), \quad (16)$$

where the partial cavity functions at contact for this closure are

$$\gamma_{ij}^{(C1)}(\sigma_{ij}) = 1 + \sum_m \rho_m \gamma_{imj}^{(1)}(\sigma_{ij}). \quad (17)$$

Using in Eq. (15) $f_{ij}(r) = -\theta(\sigma_{ij} - r) + \delta(r - \sigma_{ij})\sigma_{ij}/(12\tau_{ij})$, we find after some algebra the following result

$$\begin{aligned} \gamma_{imj}^{(1)}(\sigma_{ij}) = & \frac{2\pi}{\sigma_{ij}} \left\{ \frac{\sigma_{im}^2}{12\tau_{im}} \left[-\frac{1}{2}(\sigma_{mj}^2 - L_{jm}^2) + \frac{\sigma_{mj}^2}{12\tau_{mj}} \right] \right. \\ & + \frac{2}{3}\sigma_{ij}L_{mi}^3 + \frac{\sigma_{mj}^2}{12\tau_{mj}} \frac{1}{2}(L_{mi}^2 - \sigma_{mi}^2) \\ & + \frac{1}{4}(\sigma_{mj}^2 - \sigma_{ij}^2)(\sigma_{mi}^2 - L_{mi}^2) \\ & \left. + \frac{1}{3}\sigma_{ij}(\sigma_{mi}^3 - L_{mi}^3) - \frac{1}{8}(\sigma_{mi}^4 - L_{mi}^4) \right\}. \quad (18) \end{aligned}$$

Because of the presence of the factor $1/\sigma_{ij}$ in Eq. (18), $K_{ij}^{(C1)}$ cannot be expressed as a sum of factorized terms if we use any of the cases I, II, or III. Case IV, on the other hand, would be tractable, but it would yield $K_{ij}^{(C1)}$ as a sum of 14 factorized terms (proportional to $\sigma_i^n \sigma_j^m$ with $n, m = 0, 1, 2, 3$ except $n = m = 0, 3$) which is unmanageable in practice. In case V, on the other hand, a great simplification occurs and we find

$$K_{ij}^{(C1)} = k_0 + (\sigma_i + \sigma_j)k_1 + \sigma_i \sigma_j k_2, \quad (19)$$

where

$$k_0 = \eta \frac{1}{576} \frac{\langle \sigma \rangle^3 \langle \sigma^2 \rangle}{\langle \sigma^3 \rangle} \frac{1}{\tau^3}, \quad (20)$$

$$\begin{aligned} k_1 = & \frac{1}{24} \langle \sigma \rangle \frac{1}{\tau} + \eta \left(\frac{1}{576} \frac{\langle \sigma \rangle^4}{\langle \sigma^3 \rangle} \frac{1}{\tau^3} \right. \\ & \left. - \frac{1}{48} \frac{\langle \sigma \rangle^2 \langle \sigma^2 \rangle}{\langle \sigma^3 \rangle} \frac{1}{\tau^2} + \frac{1}{24} \langle \sigma \rangle \frac{1}{\tau} \right), \quad (21) \end{aligned}$$

$$k_2 = \eta \left(\frac{1}{576} \frac{\langle \sigma \rangle^3}{\langle \sigma^3 \rangle} \frac{1}{\tau^3} - \frac{1}{24} \frac{\langle \sigma \rangle^3}{\langle \sigma^3 \rangle} \frac{1}{\tau^2} + \frac{1}{8} \frac{\langle \sigma \rangle \langle \sigma^2 \rangle}{\langle \sigma^3 \rangle} \frac{1}{\tau} \right), \quad (22)$$

where $\eta = \xi_3$ is the packing fraction. The expression (19) is slightly more complicated than the $K_{ij}^{(mMSA)}$ treated with case IV, because of the k_0 term. This noteworthy feature is the main justification for the particular form of case V.

IV. PHASE INSTABILITIES

Our first task is the analysis of the phase instabilities for the polydisperse system only in the mMSA using cases I, II, and III.

The next level of approximation C1 is considerably more laborious (since the calculations for the C1 approximation

even in the simple case of case V requires determinants of n -dyadic matrices with $n > 4$) and we shall limit ourselves to the one-component case for simplicity.

A. mMSA approximation for the discrete polydisperse system

For p -component mixtures, one can define the following generalization of the Bhatia-Thornton concentration-concentration structure factor:²³⁻²⁵

$$S_{CC}(k) / \left(\prod_m x_m \right) = |\mathbf{S}(k)| \sum_{i,j=1}^p (x_i x_j)^{1/2} S_{ij}^{-1}(k), \quad (23)$$

where $|\mathbf{S}(k)|$ denotes the determinant of the matrix $\mathbf{S}(k)$ whose elements are the Ashcroft-Langreth partial structure factors.²⁶ Furthermore, the $S_{ij}^{-1}(k)$ functions are the elements of the inverse of $\mathbf{S}(k)$, which can be expressed as

$$S_{ij}^{-1}(k) = \delta_{ij} - (\rho_i \rho_j)^{1/2} \bar{c}_{ij}(k) = \sum_m \hat{Q}_{mi}(-k) \hat{Q}_{mj}(k), \quad (24)$$

with $\bar{c}_{ij}(k)$ three-dimensional Fourier transform of $c_{ij}(r)$, $\hat{Q}_{ij}(k) = \delta_{ij} - 2\pi(\rho_i \rho_j)^{1/2} \hat{q}_{ij}(k)$, and $\hat{q}_{ij}(k)$ being the unidimensional Fourier transform of $q_{ij}(r)$ (k is the magnitude of the exchanged wave vector, δ_{ij} the Kronecker delta).

Phase instability corresponds to the divergence of the long wavelength limit $S_{CC}(k=0)$, which is related to the concentration fluctuations. Taking into account the relations

$$\sum_{i,j} (x_i x_j)^{1/2} S_{ij}^{-1}(0) = \sum_i x_i a_i^2 = (\rho k_B T K_T)^{-1} = \left(\frac{\partial \beta P}{\partial \rho} \right)_T, \quad (25)$$

$$|\mathbf{S}(0)| = |\mathbf{I} - \mathbf{C}(0)|^{-1} = |\hat{\mathbf{Q}}(0)|^{-2}, \quad (26)$$

[where K_T is the isothermal compressibility, \mathbf{I} the unit matrix of order p , and \mathbf{C} has elements $(\rho_i \rho_j)^{1/2} \bar{c}_{ij}(k)$], $S_{CC}(k=0)$ can be reexpressed as

$$\frac{S_{CC}(0)}{\prod_m x_m} = \frac{1}{|\hat{\mathbf{Q}}(0)|^2 (\rho k_B T K_T)}. \quad (27)$$

For a one-component system the divergence of K_T signals mechanical instability, associated with a gas-liquid phase transition or condensation. However, a multicomponent fluid usually becomes unstable while K_T remains finite and different from zero. In this case, it is the vanishing of $|\hat{\mathbf{Q}}(0)|$ which causes the divergence of $S_{CC}(0)$ and produces a phase instability.^{24,25} Indeed if one tries to calculate the locus of points in the phase diagram (τ, η) where $\sum_i x_i a_i^2 = 0$, using cases I, II, or III, discovers that such curves disappear (the quadratic equations in τ have a negative discriminant) as soon as we switch on the size polydispersity letting $\langle \sigma^2 \rangle \neq \langle \sigma \rangle^2$. We remark that the exact nature of this instability requires a more involved analysis and it will be deferred to a future work.

The computation of $|\hat{\mathbf{Q}}(0)|$, which usually becomes a formidable task with increasing p , is rather simple for the

mMSA solution of Baxter model when K_{ij} is factorized as in Eq. (11). In fact, $\hat{Q}(k)$ becomes an n -dyadic (or Jacobi) matrix

$$\hat{Q}_{ij} = \delta_{ij} + \sum_{\nu=1}^n A_i^{(\nu)} B_j^{(\nu)} \quad (i, j = 1, \dots, p), \quad (28)$$

with the remarkable property that its determinant, which is of order p , turns out to be equal to a determinant of order n ($\ll p$ for polydisperse fluids).⁹ The necessary expressions are reported in Appendix A.

For factorized K_{ij} 's, one finds

$$\hat{Q}_{ij}(0) = \delta_{ij} + \frac{\pi}{6} (\rho_i \rho_j)^{1/2} \left[\frac{1}{\Delta} \sigma_j^3 + \sigma_i \frac{3}{\Delta} \left(\xi_2 \frac{1}{\Delta} \sigma_j^3 + \sigma_j^2 \right) - 12 Y_i \left(\xi_{1,1} \frac{1}{\Delta} \sigma_j^3 + \sigma_j Y_j \right) \right], \quad (29)$$

with

$$\xi_{m,n} = \frac{\pi}{6} \rho \langle \sigma^m Y^n \rangle, \quad (30)$$

($\langle \dots \rangle$) denotes a compositional average, i.e., $\langle FG \rangle \equiv \sum_i x_i F_i G_i$. Note that $\xi_{m,0} = \xi_m$.

We emphasize that the decomposition of Eq. (29) into $A_i^{(\nu)}$ and $B_j^{(\nu)}$ is not unique. However, $\hat{Q}_{ij}(0)$ of cases I and III is 3-dyadic (i.e., it contains $n=3$ dyadic terms), while $\hat{Q}_{ij}(0)$ of case II is simply 2-dyadic. As a consequence, one has to calculate at most a determinant of order 3. The general result for all three cases is

$$|\hat{Q}(0)| = \frac{1}{\Delta^2} [(1 + 2\xi_3)(1 - 12\xi_{1,2}) + 36\xi_{2,1}^2]. \quad (31)$$

Physically admissible states must satisfy the inequality $|\hat{Q}(0)| > 0$ (Ref. 27) and the stability boundary is reached when $|\hat{Q}(0)| = 0$, which yields

$$\tau = \begin{cases} \frac{\langle \sigma \rangle^3 \eta - \left(\frac{\langle \sigma \rangle \langle \sigma^2 \rangle}{\langle \sigma^3 \rangle} \right)^2 \frac{3\eta^2}{1+2\eta}}{\langle \sigma^3 \rangle} & \text{(case I),} \\ \frac{\eta(1-\eta)}{1+2\eta} & \text{(case II),} \\ \frac{\langle \sigma \rangle \langle \sigma^2 \rangle \eta - \frac{\langle \sigma^2 \rangle^3}{\langle \sigma^3 \rangle^2} \frac{3\eta^2}{1+2\eta}}{\langle \sigma^3 \rangle} & \text{(case III).} \end{cases} \quad (32)$$

If the HS diameters follow a Schulz distribution, then the stability boundary of cases I and III can be expressed as

$$\tau = \begin{cases} \eta \left(\frac{1}{M_1 M_2} - \frac{1}{M_2^2} \frac{3\eta}{1+2\eta} \right) & \text{(case I),} \\ \eta \left(\frac{1}{M_2} - \frac{M_1}{M_2^2} \frac{3\eta}{1+2\eta} \right) & \text{(case III),} \end{cases} \quad (33)$$

where $M_j = 1 + j s^2$ with $s = [\langle \sigma^2 \rangle - \langle \sigma \rangle^2]^{1/2} / \langle \sigma \rangle$ measuring the degree of size polydispersity.

The fluid is stable at "temperatures" τ higher than those given by the previous equations (since $|\hat{Q}(0)| > 0$). Let us now compare two mixtures with the same packing fraction η but different polydispersity degree s . As depicted in Fig. 2 at

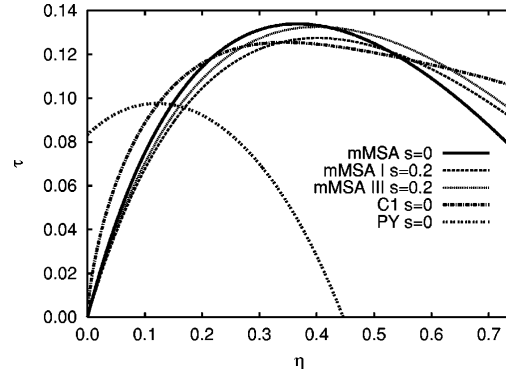


FIG. 2. Curves for the onset of phase instability (the fluid is stable above the curves shown) as obtained from the mMSA approximation for a monodisperse $s=0$ system, and for a polydisperse system with $s=0.2$, and polydispersity chosen as in cases I, II, and III [see Eq. (32)]. We also show for the one-component system the curve for the onset of mechanical instability predicted by the C1 approximation [see Eq. (34)] and the one predicted by the PY approximation [see Eq. (37)].

small η values, increasing s at fixed η lowers the stability curve of cases I and III. As shown by the left branch of the curve (the opposite trend on the right-hand side of the figure is not acceptable, since the mMSA closure can be a reasonable approximation only in the low density regime) the onset of instability occurs at lower τ . As expected, polydispersity renders the mixture more stable with respect to concentration fluctuations. Quite surprisingly, on the other hand, the stability boundary does not depend on s at fixed η in case II, and all mixtures with different polydispersity have the same stability boundary as the one-component case ($s=0$).

B. C1 approximation for the one-component system

As remarked, the C1 approximation yields rather more complex expressions and here we restrict to the one-component case. Yet, this example provides a flavor of how this approximation would work in the multicomponent case and could be compared with the result given by $|\hat{Q}(0)| = 0$. For the one-component system phase instability coincides with the divergence of K_T . As from Eq. (25)

$$(\rho k_B T K_T)^{-1} = a^2 = \left[\frac{1+2\eta}{(1-\eta)^2} - \frac{1}{\tau} y^{(C1)}(\sigma) \frac{\eta}{1-\eta} \right] = 0, \quad (34)$$

where [see Eqs. (17) and (18)]

$$y^{(C1)}(\sigma) = 1 + y_1(\tau) \eta, \quad (35)$$

with

$$y_1(\tau) = \frac{5}{2} - \frac{1}{\tau} + \frac{1}{12\tau^2}. \quad (36)$$

The curve for the onset of mechanical instability is shown in Fig. 2 and compared with the PY one

$$\tau = \frac{10 - 9(1-\eta) + 14\eta}{12(1+2\eta)}. \quad (37)$$

One clearly sees that the C1 stability boundary lowers and shifts to the left in agreement with the PY result.

V. PERCOLATION THRESHOLD

In view of the simplicity of the mMSA (C0) solution, one might expect that other quantities, besides those discussed so far, can be computed analytically. We now show that this is indeed the case. The problem we address in this section is *continuum percolation*. This problem is far from being new.²⁸ However, new activity along this line has been stirred by recent and precise Monte Carlo results for the one-component case,^{11,12} and it is then rather interesting to consider its multicomponent extension. For the sake of completeness we now recall the basic necessary formalism.¹⁴⁻¹⁶

In the sticky limit the partial Boltzmann factors read

$$e_{ij}(r) = \theta(r - \sigma_{ij}) + \frac{K_{ij}^0}{\sigma_{ij}} \delta(r - \sigma_{ij}), \quad (38)$$

where θ is the Heaviside step function and δ the Dirac delta function.

When studying percolation problems in the continuum is useful to rewrite the Boltzmann factor as the sum of two terms^{14,28} $e_{ij}(r) = e_{ij}^*(r) + e_{ij}^+(r)$, where

$$e_{ij}^*(r) = \theta(r - \sigma_{ij}), \quad (39)$$

$$e_{ij}^+(r) = \frac{K_{ij}^0}{\sigma_{ij}} \delta(r - \sigma_{ij}). \quad (40)$$

The corresponding Mayer functions will be $f_{ij}(r) = f_{ij}^*(r) + f_{ij}^+(r)$, with

$$f_{ij}^*(r) = e_{ij}^*(r) - 1, \quad (41)$$

$$f_{ij}^+(r) = e_{ij}^+(r). \quad (42)$$

The procedure to obtain equations of *connectedness* and *blocking* functions from the usual pair correlation functions and direct correlation functions is best described through the use of graphical language. If we substitute f_{ij}^* and f_{ij}^+ bonds for f_{ij} bonds in the density expansions for these functions, then the connectedness functions, which we will indicate with a cross superscript, are expressed as the sums of those terms that have at least one f_{ij}^+ bond path connecting the two root vertices. The sums of the remaining terms in the expansions give the blocking functions.

The percolation threshold corresponds to the existence of an infinite cluster of particles and is given by the divergence of the mean cluster size^{14,28}

$$S_{\text{cluster}} = 1 + \rho \sum_{i,j} x_i x_j \int d\mathbf{r} h_{ij}^+(r) = S_{NN}^+(k=0) \\ \equiv \sum_{i,j} (x_i x_j)^{1/2} S_{ij}^+(k=0), \quad (43)$$

where $h_{ij}^+(r)$ is the pair connectedness function (related to the joint probability of finding a particle of species i and a particle of species j at a distance r and that these two particles are connected) and

$$S_{ij}^+(k) \equiv \delta_{ij} + (\rho_i \rho_j)^{1/2} \tilde{h}_{ij}^+(k). \quad (44)$$

Since $h_{ij}^+(r)$ is related to the so called direct connectedness function $c_{ij}^+(r)$ through an OZ equation, one can use Baxter formalism again, introducing a factor function $q_{ij}^+(r)$. If we now define $\hat{Q}_{+,ij}(k) = \delta_{ij} - 2\pi(\rho_i \rho_j)^{1/2} q_{ij}^+(k)$, then it results that

$$S_{ij}^+(k) = \sum_m \hat{Q}_{+,im}^{-1}(k) \hat{Q}_{+,jm}^{-1}(-k) \quad (45)$$

and thus

$$S_{\text{cluster}} = \sum_m s_m^2(0), \quad (46)$$

where

$$s_m(0) = \sum_i \sqrt{x_i} \hat{Q}_{+,im}^{-1}(0). \quad (47)$$

Clearly $\hat{Q}_{+,im}^{-1}(0)$ diverges to infinity when $|\hat{Q}_{+,im}(0)| = 0$, and this relation defines the percolation threshold.

Another interesting and related quantity is the average coordination number

$$\bar{Z} = 4\pi\rho \sum_{i,j} x_i x_j \int_0^{\sigma_{ij}} h_{ij}^+(r) r^2 dr. \quad (48)$$

A. mMSA approximation

The mMSA closure for $c_{ij}^+(r)$ is

$$c_{ij}^+(r) = f_{ij}^+(r) = 0, \quad r > \sigma_{ij}. \quad (49)$$

On the other hand when $r \leq \sigma_{ij}$ we have $e_{ij}^*(r) = 0$ and $f_{ij}^+(r) = e_{ij}(r)$, so we must have exactly

$$h_{ij}^+(r) = e_{ij}^*(r) y_{ij}^+(r) + f_{ij}^+(r) y_{ij}(r) \\ = e_{ij}(r) y_{ij}(r) = \frac{K_{ij}^0}{\sigma_{ij}} y_{ij}(\sigma_{ij}) \delta(r - \sigma_{ij}) \quad r \leq \sigma_{ij}. \quad (50)$$

Within the mMSA we have for the cavity function at contact⁷

$$y_{ij}(\sigma_{ij}) = 1 \quad \text{for all } i, j. \quad (51)$$

Following the same steps of Chiew and Glandt,^{15,16} we then find (see Appendix B for details)

$$q_{ij}^+(r) = K_{ij} \theta(r - L_{ij}) \theta(\sigma_{ij} - r). \quad (52)$$

From which it follows

$$\hat{Q}_{+,ij}(0) = \delta_{ij} - 2\pi(\rho_i \rho_j)^{1/2} K_{ij} \sigma_j. \quad (53)$$

Within cases I, II, and III

$$\hat{Q}_{+,ij}(0) = \delta_{ij} + a_i^+ b_j^+, \quad (54)$$

$$a_i^+ = -2\pi\rho \sqrt{x_i} Y_i, \quad (55)$$

$$b_j^+ = \sqrt{x_j} Y_j \sigma_j. \quad (56)$$

Now from Eq. (54) follows that $\hat{Q}_{+,ij}(0)$ is a 1-dyadic form. Using the properties of dyadic matrices (see Appendix A) we then find

$$\hat{Q}_{+,ij}^{-1}(0) = \frac{1}{|\hat{Q}_+(0)|} \begin{vmatrix} \delta_{ij} & b_j^+ \\ a_i^+ & 1 + \mathbf{a}^+ \cdot \mathbf{b}^+ \end{vmatrix}, \quad (57)$$

where

$$|\hat{Q}_+(0)| = 1 + \mathbf{a}^+ \cdot \mathbf{b}^+ = 1 - 12\xi_{1,2}. \quad (58)$$

From Eq. (47) we find

$$s_m(0) = \frac{1}{|\hat{Q}_+(0)|} \left[\sqrt{x_m}(1 + \mathbf{a}^+ \cdot \mathbf{b}^+) - b_m^+ \sum_i \sqrt{x_i} a_i^+ \right], \quad (59)$$

and from Eq. (46)

$$S_{\text{cluster}} = 1 + \frac{24}{\xi_0} \frac{\xi_{1,1}\xi_{0,1}}{1 - 12\xi_{1,2}} + \frac{144}{\xi_0} \frac{\xi_{2,2}\xi_{0,1}^2}{(1 - 12\xi_{1,2})^2}. \quad (60)$$

The percolation transition occurs when

$$\tau = \begin{cases} \frac{\langle \sigma \rangle^3}{\langle \sigma^3 \rangle} \eta = \frac{1}{M_1 M_2} \eta & \text{(case I),} \\ \eta & \text{(case II),} \\ \frac{\langle \sigma \rangle \langle \sigma^2 \rangle}{\langle \sigma^3 \rangle} \eta = \frac{1}{M_2} \eta & \text{(case III).} \end{cases} \quad (61)$$

The threshold is independent of s at fixed η for case II, but lowers with increasing size polydispersity in cases I and III. The curve is simply a straight line, as a consequence of the mean-field character of the mMSA (C0) closure. The qualitative result found with cases I and III is, however, interesting. For the average coordination number we find from Eqs. (48) and (50)

$$\begin{aligned} \bar{Z} &= 4\pi\rho \sum_{i,j} x_i x_j K_{ij} \sigma_{ij} \\ &= \frac{24}{\xi_0} \xi_{1,1} \xi_{0,1} \\ &= \begin{cases} 2 \frac{\eta}{\tau} \frac{\langle \sigma \rangle^3}{\langle \sigma^3 \rangle} & \text{(case I),} \\ 2 \frac{\eta}{\tau} \frac{\langle \sigma \rangle \langle \sigma^2 \rangle}{\langle \sigma^3 \rangle} & \text{(cases II and III).} \end{cases} \end{aligned} \quad (62)$$

At the percolation transition we then find

$$\bar{Z} = \begin{cases} 2 & \text{(case I and III),} \\ 2/M_2 & \text{(case II).} \end{cases} \quad (63)$$

Using case IV $\hat{Q}_{+,ij}(0)$ turns out to be 3-dyadic; the percolation transition occurs when $|\hat{Q}_+(0)| = 0$, i.e.,

$$1 - \frac{\eta}{\tau} - \frac{s^2(4+7s^2)}{8(1+3s^2+2s^4)} \left(\frac{\eta}{\tau} \right)^2 + \frac{s^6}{16(1+s^2)(1+2s^2)^2} \left(\frac{\eta}{\tau} \right)^3 = 0. \quad (64)$$

The solution $\eta/\tau = p(s)$ such that $p(0) = 1$ is a monotonously decreasing function with

$$\lim_{s \rightarrow \infty} p(s) = 0.756431 \dots \quad (65)$$

Then with this case we find that increasing the polydispersity the nonpercolating region of the phase diagram diminishes.

With case V $\hat{Q}_{+,ij}(0)$ turns out to be 2-dyadic, and the percolation transition occurs when

$$\tau = \left(\frac{\langle \sigma \rangle \langle \sigma^2 \rangle}{\langle \sigma^3 \rangle} + \sqrt{\frac{\langle \sigma \rangle^3}{\langle \sigma^3 \rangle}} \right) \frac{\eta}{2} = \left(\frac{1}{M_2} + \sqrt{\frac{1}{M_1 M_2}} \right) \frac{\eta}{2}, \quad (66)$$

which has the physical behavior already found with cases I, II, and III.

B. C1 approximation with case V

As remarked, in case V we can work out the percolation threshold equation even within the C1 approximation. From Eq. (51) we have exactly

$$h_{ij}^+(r) = \frac{K_{ij}^0}{\sigma_{ij}} y_{ij}^{(C1)}(\sigma_{ij}) \delta(r - \sigma_{ij}), \quad r \leq \sigma_{ij}, \quad (67)$$

where $y_{ij}^{(C1)}(\sigma_{ij})$ is given by Eq. (17). For the closure condition of the direct connectedness function we find again

$$\begin{aligned} c_{ij}^+(r) &= f_{ij}^+(r) + f_{ij}^+(r) \sum_m \rho_m \gamma_{imj}^{(1)}(r) \\ &\quad + f_{ij}^{*+}(r) \sum_m \rho_m \gamma_{ijm}^{(1)+}(r) = 0, \quad r > \sigma_{ij}, \end{aligned} \quad (68)$$

since $f_{ij}^+(r) = f_{ij}^{*+}(r) = 0$ for $r > \sigma_{ij}$. To determine $f_{ij}^+(r)$ we then follow the same steps as for the mMSA case and we find

$$q_{ij}^+(r) = K_{ij}^0 y_{ij}^{(C1)}(\sigma_{ij}) \theta(r - L_{ij}) \theta(\sigma_{ij} - r). \quad (69)$$

When we insert K_{ij} from Eq. (19) into the expression for $\hat{Q}_{+,ij}(0)$ [see Eq. (53)] this becomes a 4-dyadic matrix whose determinant is

$$|\hat{Q}_+(0)| = 1 + \sum_{i=1}^6 q_i(s, \eta) / \tau^i, \quad (70)$$

where the coefficients $q_i(s, \eta)$ are given in Appendix C.

The percolation threshold is the solution of $|\hat{Q}_+(0)| = 0$. This is an algebraic equation of order 6 in τ . We can plot the correct root $\tau(\eta)$ for different values of polydispersity, as reported in Fig. 3. We see that increasing the polydispersity increases the nonpercolating phase. One can clearly observe a clear improvement from the mMSA (C0) approximation although the $\eta \rightarrow 0$ limit is still qualitatively different from the PY one-component case. It would be interesting to study if the ‘‘true’’ percolation threshold passes through the origin ($\eta = 0, \tau = 0$) (as occur in the C0 or C1 approximations) or has a finite limit ($\eta = 0, \tau = \tau_0$) (as it occur for monodisperse fluids in the PY approximation with $\tau_0 = 1/12$). Even if the Monte Carlo results of Refs. 11 and 12 are inconclusive in this respect, physically it is plausible to assume that at very low density the average number of bonds per particle is not sufficient to support large clusters at all and we would tend to favor the first scenario.²⁹

For the one-component system the average cluster size is

034901-8 Fantoni, Gazzillo, and Giacometti

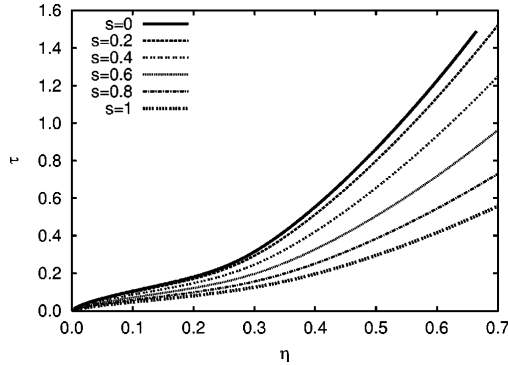
 J. Chem. Phys. **122**, 034901 (2005)


FIG. 3. Dependence of the percolation threshold, as calculated from the C1 approximation using case V (see Sec. V B), from the polydispersity.

$$S_{\text{cluster}} = 1 + \rho \bar{h}^+(0) = \frac{1}{1 - \rho \bar{c}^+(0)}$$

$$= \frac{1}{[\hat{Q}_+(0)]^2} = \frac{1}{[1 - \eta y^{(C1)}(\sigma)/\tau]^2}.$$
(71)

The percolation transition occurs when $\eta y^{(C1)}(\sigma) = \tau$ or

$$\eta = \frac{2(-3\tau^2 + \sqrt{3}\tau^{3/2}\sqrt{1-9\tau+30\tau^2})}{1-12\tau+30\tau^2}.$$
(72)

In Fig. 4 we compare our result for the one-component ($s=0$) system with the PY result of Chiew and Glandt¹⁵ and the Monte Carlo simulation of Miller and Frenkel.^{11,12}

The average coordination number becomes

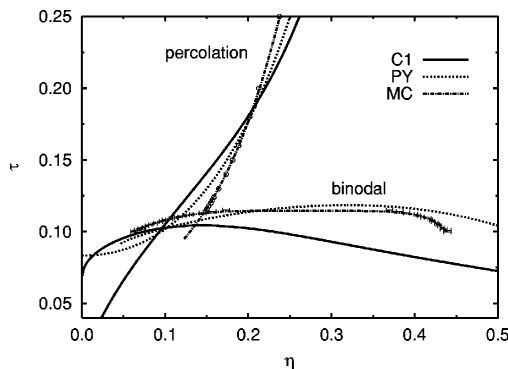


FIG. 4. Binodal curve and percolation threshold [see Eq. (73)], for a one-component system, in the C1 approximation. For comparison we also show the percolation threshold of the Percus-Yevick approximation (Ref. 15) (which exists for $\tau \geq 1/12$), the one from the Monte Carlo simulation of Miller and Frenkel (Ref. 12) (circles are the simulation results and the fit, the dot-dashed line, is only valid for $\tau \geq 0.095$), the binodal curve of the Percus-Yevick approximation (from the energy route) (Ref. 4), and the binodal curve from the Monte Carlo simulation of Miller and Frenkel (Ref. 12) (points with errorbars are the simulation results and the fit, the dot-dashed line, is merely to guide the eye).

$$\bar{Z} = 2 \frac{\eta}{\tau} y^{(C1)}(\sigma)$$
(73)

and at the percolation transition we find $\bar{Z} = 2$.

VI. PHASE EQUILIBRIUM

Phase equilibrium is another interesting aspect which can be analyzed in full details within our model. It was pointed out in Ref. 10 that the equation of state derived from the energy route for a one-component system of sticky hard spheres in the mMSA approximation is van der Waals-like. The same holds true for the system studied with the C1 approximation. It is worth stressing that the equation of state derived from the compressibility route cannot yield a van der Waals loop since from Eq. (25) $[\partial(\beta P)/\partial \rho]_{\tau} > 0$.³⁰ On the other hand the equation of state derived from the virial equation has been shown to diverge for the mMSA approximation⁸ and we anticipate that it also diverges for the C1 approximation. This is the reason why we focus our analysis on the energy route in the present work.

In this section we will find the binodal curves for the polydisperse system treated with the mMSA (C0) approximation and for the one-component system treated with the C1 approximation. The coexistence problem for a polydisperse system is, in general, a much harder task than its one-component counterpart, since it involves the solution of a large (infinite) number of integral nonlinear equations. But we will see that since our excess free energy is expressed in terms of a finite number of moments of the size distribution function (a similar feature occurs for polydisperse van der Waals models,¹⁸ for polydisperse HS (Ref. 17) and for Yukawa-like potentials^{19,20}) the coexistence problem can be simplified and becomes numerically solvable through a simple Newton-Raphson algorithm [see Eqs. (79)–(81)]. The necessary formalism to this aim can be found in a recent review,¹⁷ and we will briefly recall it next.

A. From a discrete to a continuous polydisperse mixture

Consider a mixture made of p components labeled $i = 1, \dots, p$, containing $N^{(0)}$ particles and with density $\rho^{(0)}$, which separates, at a certain temperature τ , into m daughter phases, where each phase, labeled $\alpha = 1, \dots, m$, has a number of particles $N^{(\alpha)}$ and density $\rho^{(\alpha)}$. Let the molar fraction of the particles of species i of phase α be $x_i^{(\alpha)}$, $\alpha=0$ corresponding to the parent phase. At equilibrium the following set of constraints must be fulfilled: (i) volume conservation, (ii) conservation of the total number of particles of each species, (iii) equilibrium condition for the pressures $P^{(\alpha)}(\tau, \rho^{(\alpha)}, \{x_i^{(\alpha)}\})$, and (iv) equilibrium condition for the chemical potentials $\mu_i^{(\alpha)}(\tau, \rho^{(\alpha)}, \{x_i^{(\alpha)}\})$. This set of constraints form a closed set of equations (see Appendix D for details) for the $(2+p)m$ unknowns $\rho^{(\alpha)}$, $x_i^{(\alpha)} = N_i^{(\alpha)}/N^{(0)}$, and $x_i^{(\alpha)}$ with $i = 1, \dots, p$ and $\alpha = 1, \dots, m$. Extension to the polydisperse case with an infinite number of components is achieved by switching from the discrete index variable i to the continuous variable σ using the following replacement rule:

$$x_i \rightarrow F(\sigma) d\sigma, \quad (74)$$

where $F(\sigma)d\sigma$ is the fraction of particles with diameter in the interval $(\sigma, \sigma+d\sigma)$. The function $F(\sigma)$ will be called *molar fraction density function* or more simply size distribution function. Note that, due to this replacement rule, we also have

$$P^{(\alpha)}(\tau, \rho^{(\alpha)}, \{x_i^{(\alpha)}\}) \rightarrow P^{(\alpha)}(\tau, \rho^{(\alpha)}; [F^{(\alpha)}]), \quad (75)$$

$$\mu_i^{(\alpha)}(\tau, \rho^{(\alpha)}, \{x_i^{(\alpha)}\}) \rightarrow \mu^{(\alpha)}(\sigma, \tau, \rho^{(\alpha)}; [F^{(\alpha)}]), \quad (76)$$

i.e., the thermodynamic quantities become functionals of the size distribution function and the equilibrium conditions (ii)–(iv) has to be satisfied for all values of the continuous variable σ . The phase coexistence problem that now consists in solving the constraints (i)–(iv) for the unknowns $\rho^{(\alpha)}$, $x^{(\alpha)}$, and $F^{(\alpha)}(\sigma)$ for $\alpha=1, \dots, m$, turns out to be a rather formidable task hardly solvable from a numerical point of view. Fortunately, as outlined in the following section, for our model a remarkable simplification occurs.

B. Truncatable excess free energy

As is described in the following section, the excess free energy of our system is *truncatable*: it is only a function of the three moments ξ_i , $i=1,2,3$ of the size distribution function [see Eq. (86) for cases I, II, III, IV, and V treated with mMSA, and Eq. (100) for case V treated with C1]. So we have the following simplification

$$P^{(\alpha)}(\tau, \rho^{(\alpha)}; [F^{(\alpha)}]) \rightarrow P^{(\alpha)}(\tau, \rho^{(\alpha)}; \{\xi_i^{(\alpha)}\}), \quad (77)$$

$$\mu^{(\alpha)}(\sigma, \tau, \rho^{(\alpha)}; [F^{(\alpha)}]) \rightarrow \mu^{(\alpha)}(\sigma, \tau, \rho^{(\alpha)}; \{\xi_i^{(\alpha)}\}), \quad (78)$$

where $\{\xi_i^{(\alpha)}\}$ is a short-hand notation for $\xi_1^{(\alpha)}, \xi_2^{(\alpha)}, \xi_3^{(\alpha)}$. It turns out that the two-phase ($m=2$) coexistence problem, the one in which we are interested (we are thus concentrating on the high temperature portion of the phase diagram), reduces to the solution of the following eight equations in the eight unknowns $\rho^{(1)}, \rho^{(2)}, \{\xi_i^{(1)}\}$, and $\{\xi_i^{(2)}\}$,

$$\xi_i^{(\alpha)} = \frac{\pi}{6} \rho^{(\alpha)} \int Q^{(\alpha)}(\sigma, \tau, \rho^{(0)}, \rho^{(1)}, \rho^{(2)}; \{\xi_i^{(1)}\}, \{\xi_i^{(2)}\}) \times F^{(0)}(\sigma) \sigma^i d\sigma, \quad i=1,2,3 \quad \alpha=1,2, \quad (79)$$

$$1 = \int Q^{(\alpha)}(\sigma, \tau, \rho^{(0)}, \rho^{(1)}, \rho^{(2)}; \{\xi_i^{(1)}\}, \{\xi_i^{(2)}\}) F^{(0)}(\sigma) d\sigma, \quad (80)$$

$$\alpha=1 \text{ or } 2, \quad (80)$$

$$P^{(1)}(\tau, \rho^{(1)}; \{\xi_i^{(1)}\}) = P^{(2)}(\tau, \rho^{(2)}; \{\xi_i^{(2)}\}), \quad (81)$$

with

$$\rho^{(\alpha)} Q^{(\alpha)} = \rho^{(0)} \frac{(\rho^{(1)} - \rho^{(2)})(1 - \delta_{1\alpha} + \delta_{1\alpha} e^{\beta \Delta \mu^{\text{exc}}})}{(\rho^{(1)} - \rho^{(0)}) + (\rho^{(0)} - \rho^{(2)}) e^{\beta \Delta \mu^{\text{exc}}}}, \quad (82)$$

and

$$\Delta \mu^{\text{exc}} = \mu^{\text{exc}(2)}(\sigma, \tau, \rho^{(2)}; [F^{(2)}]) - \mu^{\text{exc}(1)}(\sigma, \tau, \rho^{(1)}; [F^{(1)}]), \quad (83)$$

where we indicate with the superscript exc the excess part (over the ideal) of the chemical potential. For a complete derivation of Eqs. (79)–(81) see Appendix D.

C. Thermodynamic properties

In order to obtain the equation of state of our model Eq. (1) from the energy route, one exploits the following exact result (if $\tau_{ij} = \tau/\epsilon_{ij}$ with the ϵ_{ij} independent of τ);

$$\begin{aligned} \frac{\partial(\beta A^{\text{exc}}/N)}{\partial \tau} &= 2\pi\rho \sum_{i,j} x_i x_j \int \frac{\partial[\beta \phi_{ij}(r)]}{\partial \tau} g_{ij}(r) r^2 dr \\ &= 2\pi\rho \sum_{i,j} x_i x_j \int_{\sigma_{ij}}^{R_{ij}} \frac{1}{\tau} e_{ij}(r) y_{ij}(r) r^2 dr \\ &= 2\pi\rho \sum_{i,j} x_i x_j \frac{1}{\tau} \int_{\sigma_{ij}}^{R_{ij}} \frac{1}{12\tau_{ij}} \frac{R_{ij}}{R_{ij} - \sigma_{ij}} y_{ij}(r) r^2 dr. \end{aligned}$$

Upon taking the sticky limit we find

$$\frac{\partial(\beta A^{\text{exc}}/N)}{\partial \tau} = \frac{\eta}{\langle \sigma^3 \rangle} \frac{1}{\tau} \sum_{i,j} x_i x_j \frac{1}{\tau_{ij}} \sigma_{ij}^3 y_{ij}(\sigma_{ij}). \quad (84)$$

1. mMSA approximation

Within the mMSA approximation the partial cavity functions at contact are all equal to 1 so from Eq. (84), after integration over τ from $\tau=\infty$ (hard sphere case), we find

$$\begin{aligned} \frac{\beta(A_{\text{SHS}}^{\text{exc}} - A_{\text{HS}}^{\text{exc}})}{N} \xi_0 &= \begin{cases} -\frac{1}{\tau} \frac{\xi_1^3}{\xi_0} & \text{(case I),} \\ -\frac{1}{\tau} \xi_2 \xi_1 & \text{(cases II and III),} \\ -\frac{1}{\tau} \frac{1}{4} (3\xi_1 \xi_2 + \xi_0 \xi_3) & \text{(case IV),} \\ -\frac{1}{\tau} \frac{1}{2} \left(\xi_1 \xi_2 + \frac{\xi_1^3}{\xi_0} \right) & \text{(case V).} \end{cases} \quad (85) \end{aligned}$$

The pressure can be found, from $\beta P/\rho = \eta \partial(\beta A/N)/\partial \eta$

$$\begin{aligned} \frac{\pi}{6} \beta [P_{\text{SHS}}(\tau, \rho; \{\xi_i\}) - P_{\text{HS}}(\tau, \rho; \{\xi_i\})] &= \frac{\beta(A_{\text{SHS}}^{\text{exc}} - A_{\text{HS}}^{\text{exc}})}{N} \xi_0, \quad (86) \end{aligned}$$

where for P_{HS} we use an equation due to Boublík, Mansoori, Carnahan, Starling, and Leland (Refs. 31 and 32) which reduces to the Carnahan-Starling one when $s=0$,

$$\begin{aligned} \frac{\pi}{6} \beta P_{\text{HS}}(\tau, \rho; \{\xi_i\}) \\ = Z_{\text{HS}} \xi_0 = \frac{\xi_0}{1-\xi_3} + 3 \frac{\xi_1 \xi_2}{(1-\xi_3)^2} + 3 \frac{\xi_2^3}{(1-\xi_3)^3} \\ - \frac{\xi_3 \xi_2^3}{(1-\xi_3)^3} = \xi_0 \left\{ \frac{1}{1-\eta} + \frac{3\eta}{(1-\eta)^2} \frac{1}{M_2} \right. \\ \left. + \left[\frac{3\eta^2}{(1-\eta)^3} - \frac{\eta^3}{(1-\eta)^3} \right] \frac{M_1}{M_2^2} \right\}. \end{aligned} \quad (87)$$

The excess free energy of the polydisperse hard sphere system is obtained integrating $(Z_{\text{HS}}-1)/\eta$ over η , from $\eta=0$, and recalling that the excess free energy is zero when $\eta=0$. We then find³³

$$\begin{aligned} \frac{\beta A_{\text{HS}}^{\text{exc}}}{N} &= \frac{\eta}{(1-\eta)^2} \frac{M_1}{M_2^2} + \frac{3\eta}{1-\eta} \frac{1}{M_2} + \left[\frac{M_1}{M_2^2} - 1 \right] \ln(1-\eta) \\ &= \frac{\xi_2^3}{\xi_0 \xi_3 (1-\xi_3)^2} + 3 \frac{\xi_1 \xi_2}{\xi_0 (1-\xi_3)} \\ &\quad + \left(\frac{\xi_2^3}{\xi_0 \xi_3^2} - 1 \right) \ln(1-\xi_3). \end{aligned} \quad (88)$$

Note that both $A_{\text{HS}}^{\text{exc}}$ and $A_{\text{HS}}^{\text{exc}}$ depend upon only a finite number of moments ξ_i , and this is the crucial feature for the feasibility of the phase equilibrium, as remarked.

For the chemical potential $\beta \mu_i = \partial(\beta A/V)/\partial \rho_i$ we find after some algebra

$$\begin{aligned} \beta \mu^{\text{exc}}(\sigma, \tau, \rho; \{\xi_i\}) \\ = (\mu_{\text{HS}}^{[0]} + \Delta \mu^{[0]}) + (\mu_{\text{HS}}^{[1]} + \Delta \mu^{[1]}) \sigma \\ + (\mu_{\text{HS}}^{[2]} + \Delta \mu^{[2]}) \sigma^2 + (\mu_{\text{HS}}^{[3]} + \Delta \mu^{[3]}) \sigma^3, \end{aligned} \quad (89)$$

where

$$\mu_{\text{HS}}^{[0]} = -\ln(1-\xi_3), \quad (90)$$

$$\mu_{\text{HS}}^{[1]} = 3\xi_2/(1-\xi_3), \quad (91)$$

$$\begin{aligned} \mu_{\text{HS}}^{[2]} &= \left(3 \frac{\xi_2^2}{\xi_3^2} \right) \ln(1-\xi_3) \\ &\quad + 3\xi_1/(1-\xi_3) + \left(3 \frac{\xi_2^2}{\xi_3} \right) / (1-\xi_3)^2, \end{aligned} \quad (92)$$

$$\begin{aligned} \mu_{\text{HS}}^{[3]} &= \left(-2 \frac{\xi_2^3}{\xi_3^3} \right) \ln(1-\xi_3) + \left(\xi_0 - \frac{\xi_2^3}{\xi_3^2} \right) / (1-\xi_3) \\ &\quad + \left(3\xi_1 \xi_2 - \frac{\xi_2^3}{\xi_3} \right) / (1-\xi_3)^2 + \left(2 \frac{\xi_2^3}{\xi_3} \right) / (1-\xi_3)^3. \end{aligned} \quad (93)$$

and

$$\Delta \mu^{[0]} = \begin{cases} \frac{1}{\tau} \frac{\xi_1^3}{\xi_0^2} & \text{(case I),} \\ 0 & \text{(cases II and III),} \\ -\frac{1}{\tau} \frac{\xi_3}{4} & \text{(case IV),} \\ \frac{1}{\tau} \frac{\xi_1^3}{2\xi_0^2} & \text{(case V),} \end{cases} \quad (94)$$

$$\Delta \mu^{[1]} = \begin{cases} -\frac{1}{\tau} \frac{3\xi_1^2}{\xi_0} & \text{(case I),} \\ -\frac{1}{\tau} \xi_2 & \text{(cases II and III),} \\ -\frac{1}{\tau} \frac{3\xi_2}{4} & \text{(case IV),} \\ -\frac{1}{\tau} \frac{1}{2} \left(\xi_2 + \frac{3\xi_1^2}{\xi_0} \right) & \text{(case V),} \end{cases} \quad (95)$$

$$\Delta \mu^{[2]} = \begin{cases} 0 & \text{(case I),} \\ -\frac{1}{\tau} \xi_1 & \text{(cases II and III),} \\ -\frac{1}{\tau} \frac{3\xi_1}{4} & \text{(case IV),} \\ -\frac{1}{\tau} \frac{\xi_1}{2} & \text{(case V),} \end{cases} \quad (96)$$

$$\Delta \mu^{[3]} = \begin{cases} 0 & \text{(case I),} \\ 0 & \text{(cases II and III),} \\ -\frac{1}{\tau} \frac{\xi_0}{4} & \text{(case IV),} \\ 0 & \text{(case V).} \end{cases} \quad (97)$$

It is noteworthy that if we retain in the expression (87) for P_{HS} , only the first term, then our case IV coincides with the van der Waals model of Bellier-Castella *et al.*¹⁸ with $n=1$, $l=0$, upon identifying 4τ with the temperature used by these authors.

2. C1 approximation with case V

In analogy with what we have done before, we now consider the C1 approximation for case V. Using Eq. (17) into Eq. (84)

$$\begin{aligned} \frac{\partial(\beta A^{\text{exc}}/N)}{\partial \tau} &= 12 \frac{\eta}{\tau} \left[k_0 \frac{\langle \sigma \rangle}{\langle \sigma^3 \rangle} + k_1 \left(\frac{\langle \sigma^2 \rangle + \langle \sigma \rangle^2}{\langle \sigma^3 \rangle} \right) \right. \\ &\quad \left. + k_2 \frac{\langle \sigma^2 \rangle \langle \sigma \rangle}{\langle \sigma^3 \rangle} \right]. \end{aligned} \quad (98)$$

Integrating from $\tau=\infty$ we find

034901-11 Polydisperse fluids of adhesive colloidal particles

 J. Chem. Phys. **122**, 034901 (2005)

TABLE I. For the one-component system, we compare the critical parameters obtained from the mMSA, C1, and PY (Ref. 4) approximations with the ones from the Monte Carlo simulation of Miller and Frenkel (Ref. 12).

	τ_c	η_c	$(Z_{\text{SHS}})_c$
mMSA	0.0943	0.13	0.36
C1	0.1043	0.14	0.37
PY	0.1185	0.32	0.32
MC	0.1133	0.27	---

$$\begin{aligned}
 & \frac{\beta(A_{\text{SHS}}^{\text{exc}} - A_{\text{HS}}^{\text{exc}})}{N} \\
 &= -\frac{\eta}{2} \frac{1}{\tau} \left(\frac{\langle \sigma \rangle^3}{\langle \sigma^3 \rangle} + \frac{\langle \sigma \rangle \langle \sigma^2 \rangle}{\langle \sigma^3 \rangle} \right) + \frac{\eta^2}{2} \left[-\frac{1}{\tau} \left(\frac{\langle \sigma \rangle \langle \sigma^2 \rangle}{\langle \sigma^3 \rangle} \right) \right. \\
 & \quad + \frac{\langle \sigma \rangle^3}{\langle \sigma^3 \rangle} + 3 \frac{\langle \sigma \rangle^2 \langle \sigma^2 \rangle}{\langle \sigma^3 \rangle^2} + \frac{1}{\tau^2} \left(\frac{1}{4} \frac{\langle \sigma \rangle^2 \langle \sigma^2 \rangle^2}{\langle \sigma^3 \rangle^2} \right) \\
 & \quad \left. + \frac{3}{4} \frac{\langle \sigma \rangle^4 \langle \sigma^2 \rangle}{\langle \sigma^3 \rangle^2} - \frac{1}{\tau^3} \left(\frac{1}{72} \frac{\langle \sigma \rangle^6}{\langle \sigma^3 \rangle^2} + \frac{1}{24} \frac{\langle \sigma \rangle^4 \langle \sigma^2 \rangle}{\langle \sigma^3 \rangle^2} \right) \right]. \quad (99)
 \end{aligned}$$

For this case we limit ourselves to study the coexistence problem for the one-component system. In Table I we compare the critical parameters obtained through the energy route for the mMSA, C1, PY approximations and MC simulation, for the one-component system.

Note that, as already pointed out in Ref. 8, a density expansion of $y(\sigma)$ within the PY approximation gives to zero order the $y(\sigma)$ of the mMSA approximation and to first order the $y(\sigma)$ of the C1 approximation (as should be expected comparing the density expansions of the closures corresponding to these approximations). So at low densities Z_{SHS} from mMSA, C1, and PY should be comparable. From Table I we see that the true critical parameters are between the PY and the C1 ones.

In Fig. 4 we depict the binodal curve obtained from the C1 approximation for the one-component system and we compare it with the PY binodal curve (obtained from the energy route) Ref. 4 and the one resulting from the MC simulation of Miller and Frenkel.¹² Remarkably, the gas-liquid coexistence curve predicted by C1 lies closer to the MC data than the one predicted by PY on the gas branch and further on the liquid branch.

D. Numerical results

In this section we describe the numerical results obtained from the solution of Eqs. (79)–(81) for the SHS in the mMSA, through a Newton-Raphson algorithm.

We first determined the *cloud* and *shadow* curves by solving Eqs. (79)–(81) for the particular case in which we set $\rho^{(0)} = \rho^{(1)}$ so that $F^{(1)}(\sigma) = F^{(0)}(\sigma)$. The cloud curve $\rho_c(\tau)$ is such that the solutions $\rho^{(1)}(\tau)$, $\rho^{(2)}(\tau)$ of the full coexistence problem given by Eqs. (79)–(81), for a fixed $\rho^{(0)}$ (the coexistence or binodal curves), have the property that for a certain temperature τ_0 , $\rho^{(1)}(\tau_0) = \rho_c(\tau_0) = \rho^{(0)}$, i.e. the density of phase 1 ends on the cloud curve. The shadow curve is the set of points $\rho_s(\tau)$ in equilibrium with the corresponding

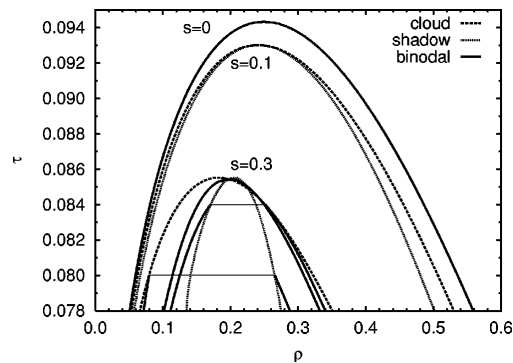


FIG. 5. Cloud and shadow curves for case I in the mMSA at two values of polydispersity: $s=0.1$ and $s=0.3$. For the case $s=0.3$ we also show three coexistence curves (continuous lines) obtained setting $\rho^{(0)}=0.08$, $\rho^{(0)}=0.25$, and $\rho^{(0)}=0.197=\rho_{cr}$. For comparison the binodal of the monodisperse ($s=0$) system has also been included.

cloud curve, i.e., $\rho^{(2)}(\tau_0) = \rho_s(\tau_0)$, the density of phase 2 ends on the shadow curve. The interception between the cloud and the corresponding shadow curve gives the critical point (τ_{cr}, ρ_{cr}) : when $\rho^{(0)} = \rho_{cr}$ the two solutions $\rho^{(1)}(\tau)$, $\rho^{(2)}(\tau)$ meet at the critical point.

In order to find the cloud and shadow curves we choose as the parent distribution $F^{(0)}(\sigma)$ a Schulz distribution with $\langle \sigma \rangle = 1$, and the initial conditions, for the Newton-Raphson algorithm, in the high temperature τ_* and low polydispersity s_* region. Our starting conditions for the solution are

$$\rho^{(\alpha)} = \rho_{oc}^{(\alpha)}, \quad (100)$$

$$\xi_1^{(\alpha)} = \frac{\pi}{6} \rho^{(\alpha)}, \quad (101)$$

$$\xi_2^{(\alpha)} = \frac{\pi}{6} \rho^{(\alpha)} (1 + s_*^2), \quad (102)$$

$$\xi_3^{(\alpha)} = \frac{\pi}{6} \rho^{(\alpha)} (1 + s_*^2) (1 + 2s_*^2), \quad (103)$$

for $\alpha=1,2$, where $\rho_{oc}^{(1)}$ and $\rho_{oc}^{(2)}$ are the coexistence densities at a temperature τ_* for the one-component system. Once the cloud and shadow curves are determined we proceed to find the coexistence curves for a given mother density.

In Fig. 5 we depict the cloud and shadow curves obtained with our case I for two representative values of polydispersity, $s=0.1$ and $s=0.3$. For comparison the coexistence curve of the one-component system ($s=0$) is also reported. As polydispersity increases, the critical point moves to lower densities and lower temperatures ($\tau_{cr} \approx 0.094$, $\rho_{cr} \approx 0.249$ at $s=0$, $\tau_{cr} \approx 0.093$, $\rho_{cr} \approx 0.24$ at $s=0.1$, and $\tau_{cr} \approx 0.085$, $\rho_{cr} \approx 0.197$ at $s=0.3$). Let us now fix $s=0.3$, a value corresponding to a moderate polydispersity. Again in Fig. 5 we depict three coexistence curves upon changing the mother density $\rho^{(0)}=0.08$, $\rho^{(0)}=0.25$, and $\rho^{(0)}=0.197=\rho_{cr}$.

All these curves closely resemble the corresponding ones obtained for the polydisperse van der Waals model,¹⁸ in

034901-12 Fantoni, Gazzillo, and Giacometti

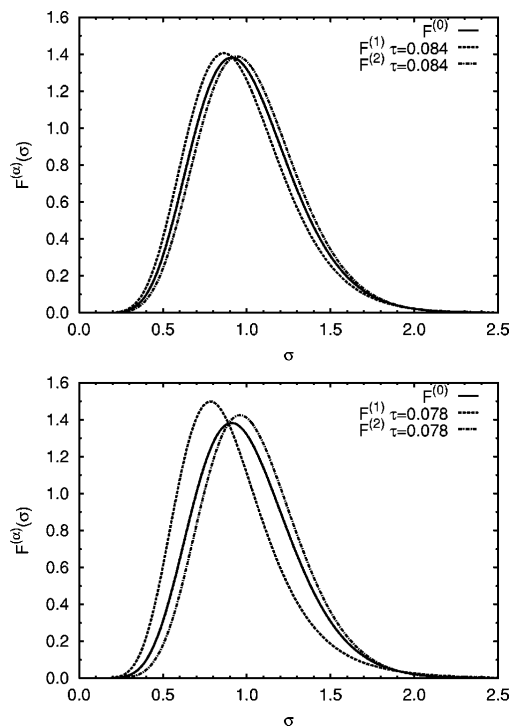
 J. Chem. Phys. **122**, 034901 (2005)


FIG. 6. Evolution of the size distribution of the coexisting phases $F^{(1)}(\sigma)$ and $F^{(2)}(\sigma)$, with temperature along the critical binodal of Fig. 5 ($s=0.3$, $\rho^{(0)}=0.197=\rho_{cr}$). For comparison also the parent Schulz distribution is shown (continuous line).

agreement with previous results. In Fig. 6 we show how the two daughter distribution functions (at $s=0.3$ and $\rho^{(0)}=\rho_{cr}$) differ from the parent Schulz distribution (a process usually called *fractionation*), for two different values of temperature $\tau=0.084$ and $\tau=0.078$.

Next we consider differences in the critical behavior with respect to change in the case. In Fig. 7 we show the cloud and shadow curves obtained using cases I, IV, and V at $s=0.3$. While for cases I and V the critical point is displaced at lower temperature and lower density respect to the monodisperse system, the critical point of case IV is displaced at higher temperatures and lower density. The cloud curves of cases II and III have a low density branch that does not meet the high density one as soon as $s>0$; moreover, the cloud curve does not meet the corresponding shadow curve, so there is no critical point. We are not aware of similar features in other polydisperse models, although this is of course to be expected in other cases as well.

VII. CONCLUSIONS

In this work we have performed an extensive analysis of the phase diagram for Baxter SHS model in the presence of polydispersity. In spite of its simplicity, this model has been proven to be extremely useful in the theoretical characteriza-

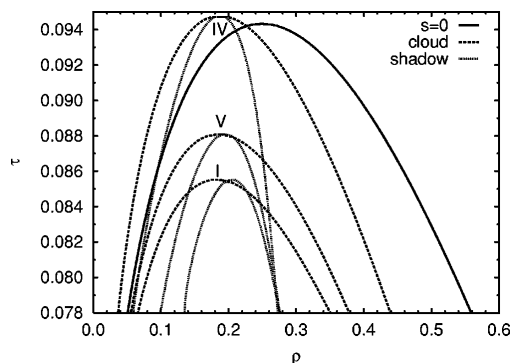


FIG. 7. Cloud and shadow curves for cases I, IV, and V in the mMSA at $s=0.3$. For comparison the binodal of the monodisperse ($s=0$) system has also been included (continuous line).

tion of sterically stabilized colloids. These systems are, however, affected by intrinsic polydispersity in some of their physical properties (size, species, etc.) and hence the effect of polydispersity on the corresponding theoretical models cannot be overlooked and is then a rather interesting point to address. As only formal manipulations⁵ can be carried out for the multicomponent Baxter SHS model within the PY approximation, we have resorted to a simpler closure mMSA to which the PY closure reduces in the limit of zero density and that was recently shown⁸ to reproduce rather precisely many of the interesting features of its PY counterpart. Our analysis has also been inspired by recent results by Miller and Frankel¹² who showed that Baxter SHS model coupled with PY closure reproduced fairly well their MC data in the one-component case. We have studied the effect of polydispersity on phase stability boundaries, the percolation phase transition, and the gas-liquid phase transition. We have considered five different cases of polydispersity. This is because there is no general agreement on the way in which adhesion forces are depending on the size of particles. Cases I and II had already been discussed in previous work by us,⁹ case III is a variant of case I, whereas a case similar to case IV had been employed by Tutschka and Kahl.¹³ Finally case V has been specifically devised to cope with approximation C1. In spite of the apparent redundancy of all these subcases, we believe that each of these examples has a reasonable interest on its own, and hence we have included them all in our discussion.

We studied the instability boundaries and the two-phase coexistence problem of polydisperse SHS system in the mMSA (C0). The next level of approximation C1 would still be feasible, but significantly more lengthly. We have laid down the necessary formalism in Secs. III and VI.C.2, and tested its effect on the one-component case, by comparing the results against the PY approximation and MC data. We derived the percolation threshold of the polydisperse system both within mMSA (C0) closure (for all five cases) and in the C1 approximation (using case V).

We found that the effect of polydispersity on the stability and phase boundaries slightly depends upon the chosen case, but there are general features shared by all of them: polydis-

persity renders the mixture more stable with respect to concentration fluctuations (in the small density region, see Fig. 2) with the exception of case II for which the stability boundary is independent from the polydispersity; Eqs. (61), (64), and (66) (in the mMSA), and Eq. (70) (in the C1), describe its effect on the percolation threshold (see Figs. 4 and 3). Polydispersity increases the region of the phase diagram where we have a nonpercolating phase, with the exception of case IV, for which the opposite trend is observed, and of case II for which the percolation threshold is independent from the polydispersity; polydispersity reduces the region of the phase diagram where we have a gas-liquid coexistence for cases I and V, while the opposite trend is observed for case IV (see Fig. 7). For cases II and III we obtained cloud curves with a gap at high temperature, moreover the cloud curve does not meet the corresponding shadow curve, so there is no critical point, as soon as polydispersity is introduced.

In conclusion, the typical effect of polydispersity is to reduce the size of the unstable region, the percolating region, and the two-phase region of the phase diagram, although exceptions to this general rule have been observed for cases II, III, and IV.

For the one-component case we also compared the percolation threshold and binodal curve obtained from the C1 approximation with the results from the PY approximation^{4,15} and the results from the Monte Carlo simulation of Miller and Frenkel¹² (see Fig. 4). The percolation threshold from C1 appears to approach that from PY, but is still significantly different from the results from the Monte Carlo simulation (the zero density limit, on the other hand, appears to be more physically sound than the PY one, and this feature remains to be elucidated). The gas-liquid coexistence curve predicted by C1 is better than the one given by PY on the gas branch and worse on the liquid branch. Table I shows how the true (from the Monte Carlo simulation of Miller and Frenkel¹²) critical temperature and density for the gas-liquid coexistence should lay between the ones predicted by PY and the ones predicted by C1.

Future developments of the present work can be envisaged along the following lines: (i) as pointed out in Ref. 24 on defining $\psi_G = \Pi_m x_m / S_{CC}(0)$ and $\psi_A = \Pi_m x_m / [(pk_B T K_T) S_{CC}(0)]$, the condition $\psi_G > 0$ is necessary but not sufficient for the material stability of the system and the condition $\psi_A > 0$ is necessary but not sufficient for the mixed material and mechanical stability. It could happen that those two conditions are satisfied but the system is nonetheless unstable as occurs, for example, in the binary mixture stud-

ied by Chen and Forstmann.³⁴ Even though a characterization of the instability boundary in the spirit of Chen and Forstmann seems unattainable for a polydisperse system, it would be desirable, in the future, a more precise location of the instability boundaries. Moreover the way we found the instability boundaries for the polydisperse system was to start from the instability condition valid for a discrete mixture and take the limit of a continuous mixture on the instability boundaries of the discrete mixture. It would be interesting to compare our analysis with the one given by Bellier-Castella *et al.* (see Sec. IIC in Ref. 18) who take the continuous limit from the outset; (ii) all the percolation thresholds that we have calculated have a low density branch that enters the gas-liquid coexistence region. The same feature is observed for the one-component system studied through Monte Carlo simulation.^{11,12} While it is clear that continuum percolation is, strictly speaking, not a thermodynamic phase transition, one could expect, from a “dynamical” point of view, an interference between the formation of infinite clusters of particles and phase separation, and a clarification of this point would have interesting experimental applications; and (iii) the polydisperse system is expected to display, in the low temperature region, other critical points signaling the onset of $m > 2$ phase coexistence,¹⁸ and it would be interesting to study their evolution with polydispersity for our system.

ACKNOWLEDGMENT

This work was supported by the Italian MIUR (PRIN-COFIN 2004/2005).

APPENDIX A: DETERMINANT AND INVERSE OF A DYADIC MATRIX

Given the n -dyadic matrix of Eq. (28), its determinant is

$$|\hat{Q}| = \begin{vmatrix} 1 + \mathbf{A}^{(1)} \cdot \mathbf{B}^{(1)} & \mathbf{A}^{(1)} \cdot \mathbf{B}^{(2)} & \dots & \mathbf{A}^{(1)} \cdot \mathbf{B}^{(n)} \\ \mathbf{A}^{(2)} \cdot \mathbf{B}^{(1)} & 1 + \mathbf{A}^{(2)} \cdot \mathbf{B}^{(2)} & \dots & \mathbf{A}^{(2)} \cdot \mathbf{B}^{(n)} \\ \vdots & \vdots & \ddots & \vdots \\ \mathbf{A}^{(n)} \cdot \mathbf{B}^{(1)} & \mathbf{A}^{(n)} \cdot \mathbf{B}^{(2)} & \dots & 1 + \mathbf{A}^{(n)} \cdot \mathbf{B}^{(n)} \end{vmatrix} \quad (A1)$$

Furthermore, any dyadic matrix \hat{Q} admits *analytic* inverse for any number p of components, with elements given by

$$\hat{Q}_{ij}^{-1} = \frac{1}{|\hat{Q}|} \begin{vmatrix} \delta_{ij} & B_j^{(1)} & B_j^{(2)} & \dots & B_j^{(n)} \\ A_i^{(1)} & 1 + \mathbf{A}^{(1)} \cdot \mathbf{B}^{(1)} & \mathbf{A}^{(1)} \cdot \mathbf{B}^{(2)} & \dots & \mathbf{A}^{(1)} \cdot \mathbf{B}^{(n)} \\ A_i^{(2)} & \mathbf{A}^{(2)} \cdot \mathbf{B}^{(1)} & 1 + \mathbf{A}^{(2)} \cdot \mathbf{B}^{(2)} & \dots & \mathbf{A}^{(2)} \cdot \mathbf{B}^{(n)} \\ \vdots & \vdots & \vdots & \ddots & \vdots \\ A_i^{(n)} & \mathbf{A}^{(n)} \cdot \mathbf{B}^{(1)} & \mathbf{A}^{(n)} \cdot \mathbf{B}^{(2)} & \dots & 1 + \mathbf{A}^{(n)} \cdot \mathbf{B}^{(n)} \end{vmatrix} \quad (A2)$$

APPENDIX B: DERIVATION OF EQ. (52)

The closure condition (49) justify the usual generalized Wiener-Hopf factorization³⁵

$$rc_{ij}^+(|r|) = -q_{ij}^+(r) + 2\pi \sum_m \rho_m \int_{L_{mi}}^{\infty} dt q_{mi}^+(t) q_{mj}^+(r+t), \quad (\text{B1})$$

$$rh_{ij}^+(|r|) = -h_{ij}^+(r) + 2\pi \sum_m \rho_m \int_{L_{im}}^{\infty} dt q_{im}^+(t)(r-t) \times h_{mj}^+(|r-t|), \quad (\text{B2})$$

where $r > L_{ij}$, the prime denotes differentiation, and $q_{ij}^+(r)$ are real functions with support on $[L_{ij}, \sigma_{ij}]$ and zero everywhere else.

Let us determine $q_{ij}^+(r)$. Using the exact condition (50) in Eq. (B2) we find for $L_{ij} < r \leq \sigma_{ij}$

$$q_{ij}^+(r) = -K_{ij} \delta(|r| - \sigma_{ij}) + 2\pi \sum_m \rho_m \int_{L_{im}}^{\sigma_{im}} dt q_{im}^+(t) \times (r-t) \frac{K_{mj}}{\sigma_{mj}} \delta(|r-t| - \sigma_{mj}). \quad (\text{B3})$$

The second term on the right end side is equal to $2\pi \sum_m \rho_m q_{im}^+(r - \sigma_{mj}) K_{mj}$ which is zero when $r < \sigma_{ij}$. So we simply have

$$q_{ij}^+(r) = -K_{ij} \delta(|r| - \sigma_{ij}), \quad L_{ij} < r \leq \sigma_{ij}. \quad (\text{B4})$$

Integrating this equation gives Eq. (52).

APPENDIX C: COEFFICIENTS OF EQ. (70)

The coefficients in Eq. (70) are as follows:

$$q_1(s, \eta) = -\frac{\eta(2+5\eta)(1+3s^2+2s^4)^3}{2(1+s^2)^3(1+2s^2)^4}, \quad (\text{C1})$$

$$q_2(s, \eta) = -\frac{\eta^2\{-4 + [\eta(2+\eta) - 5]s^2\}(1+3s^2+2s^4)^2}{4(1+s^2)^3(1+2s^2)^4}, \quad (\text{C2})$$

$$q_3(s, \eta) = \frac{\eta^2\{-2 + [6\eta(1+\eta) - 5]s^2 - 2s^4\}}{24(1+s^2)(1+2s^2)^3}, \quad (\text{C3})$$

$$q_4(s, \eta) = -\frac{\eta^3 s^2 [2 + 5\eta + (4 + 7\eta)s^2]}{96(1+s^2)^2(1+2s^2)^4}, \quad (\text{C4})$$

$$q_5(s, \eta) = 0, \quad (\text{C5})$$

$$q_6(s, \eta) = \frac{\eta^4 s^4}{2304(1+s^2)^3(1+2s^2)^4}. \quad (\text{C6})$$

APPENDIX D: PHASE COEXISTENCE CONDITIONS

In this Appendix we give a complete derivation of Eqs. (79)–(81) in the main text.

Consider a p -component mixture. Each species i has number density $\rho_i^{(0)} = N_i^{(0)}/V^{(0)}$, where $N_i^{(0)}$ is the number of particles of type i and $V^{(0)}$ the volume of the system.

We assume that at a certain temperature τ the system separates into m daughter phases, where each phase $\alpha = 1, \dots, m$ is characterized by a volume $V^{(\alpha)}$ and a number of particles of species i , $N_i^{(\alpha)}$.

At equilibrium the following set of constraints must be fulfilled.

(1) Volume conservation

$$V^{(0)} = \sum_{\alpha=1}^m V^{(\alpha)}, \quad (\text{D1})$$

(2) Conservation of the total number of particles of each species

$$N_i^{(0)} = \sum_{\alpha=1}^m N_i^{(\alpha)}, \quad i = 1, \dots, p, \quad (\text{D2})$$

(3) equilibrium condition for the pressures

$$P^{(\alpha)}(\tau, V^{(\alpha)}, \{N_i^{(\alpha)}\}) = P^{(\beta)}(\tau, V^{(\beta)}, \{N_i^{(\beta)}\}); \quad (\text{D3})$$

(4) equilibrium condition for the chemical potentials

$$\mu_i^{(\alpha)}(\tau, V^{(\alpha)}, \{N_i^{(\alpha)}\}) = \mu_i^{(\beta)}(\tau, V^{(\beta)}, \{N_i^{(\beta)}\}), \quad i = 1, \dots, p, \quad (\text{D4})$$

where $\{N_i^{(\alpha)}\}$ is a short-hand notation for $N_1^{(\alpha)}, \dots, N_p^{(\alpha)}$.

It is convenient to use the following set of variables: τ , $\rho^{(\alpha)} = N^{(\alpha)}/V^{(\alpha)}$, $x_i^{(\alpha)} = N_i^{(\alpha)}/N^{(\alpha)}$, $i = 1, \dots, p$ with $N^{(\alpha)} = \sum_i N_i^{(\alpha)}$. Introducing $x^{(\alpha)} = N^{(\alpha)}/N^{(0)}$ Eqs. (D1)–(D4) can be rewritten as follows:

$$\frac{1}{\rho^{(0)}} = \sum_{\alpha} \frac{1}{\rho^{(\alpha)}} x^{(\alpha)}, \quad (\text{D5})$$

$$x_i^{(0)} = \sum_{\alpha} x_i^{(\alpha)} x^{(\alpha)}, \quad (\text{D6})$$

$$P^{(\alpha)}(\tau, \rho^{(\alpha)}, \{x_i^{(\alpha)}\}) = P^{(\beta)}(\tau, \rho^{(\beta)}, \{x_i^{(\beta)}\}), \quad (\text{D7})$$

$$\mu_i^{(\alpha)}(\tau, \rho^{(\alpha)}, \{x_i^{(\alpha)}\}) = \mu_i^{(\beta)}(\tau, \rho^{(\beta)}, \{x_i^{(\beta)}\}), \quad (\text{D8})$$

with the normalization condition

$$\sum_i x_i^{(\alpha)} = 1, \quad \alpha = 1, \dots, m. \quad (\text{D9})$$

Equations (D5)–(D9) form a set of closed equations for the $(2+p)m$ unknowns $\rho^{(\alpha)}$, $x^{(\alpha)}$, $x_i^{(\alpha)}$ with $i = 1, \dots, p$ and $\alpha = 1, \dots, m$. Note that when $m = p + 1$ the densities of the various phases $\rho^{(\alpha)}$ will be independent of $\rho^{(0)}$, since relations (D7), (D8), and (D9) form a closed set of equations for the unknowns $\rho^{(\alpha)}$, $x_i^{(\alpha)}$.

In the continuous polydisperse limit ($p \rightarrow \infty$) we have to take into account the substitution rule (74). Then the thermodynamic quantities will be rewritten as in Eqs. (75) and (76), and Eqs. (D5)–(D8) become

$$\frac{1}{\rho^{(0)}} = \sum_{\alpha} \frac{1}{\rho^{(\alpha)}} x^{(\alpha)}, \quad (\text{D10})$$

$$F^{(0)}(\sigma) = \sum_{\alpha} F^{(\alpha)}(\sigma) x^{(\alpha)}, \quad (\text{D11})$$

$$P^{(\alpha)}(\tau, \rho^{(\alpha)}; [F^{(\alpha)}]) = P^{(\beta)}(\tau, \rho^{(\beta)}; [F^{(\beta)}]), \quad (D12)$$

$$\mu^{(\alpha)}(\sigma, \tau, \rho^{(\alpha)}; [F^{(\alpha)}]) = \mu^{(\beta)}(\sigma, \tau, \rho^{(\beta)}; [F^{(\beta)}]), \quad (D13)$$

with the normalization condition

$$\int F^{(\alpha)}(\sigma) d\sigma = 1, \quad \alpha = 1, \dots, m. \quad (D14)$$

Integrating Eq. (D11) over σ and using Eq. (D14) we find

$$\sum_{\alpha} x^{(\alpha)} = 1. \quad (D15)$$

The set of Eqs. (D10)–(D14) forms a closed set of equations for the unknowns $\rho^{(\alpha)}$, $x^{(\alpha)}$, and $F^{(\alpha)}(\sigma)$ with $\alpha = 1, \dots, m$. Note that, due to the substitution rule (74), sum over i becomes integration over σ and thermodynamic quantities become functionals of the distribution function. We have indicated such dependence with square brackets.

Two-phase coexistence

Let us now specialize ourselves to the two-phase ($m = 2$) coexistence. We are thus concentrating on the high temperature portion of the phase diagram, since coexistence with $m > 2$ (Gibbs phase rule does not restrict the value of m in a system of infinitely many species) is expected to occur at low temperatures. From Eqs. (D15) and (D10) we find

$$x^{(1)} = \frac{\rho^{(0)} - \rho^{(2)}}{\rho^{(1)} - \rho^{(2)}} \frac{\rho^{(1)}}{\rho^{(0)}}, \quad (D16)$$

$$x^{(2)} = \frac{\rho^{(1)} - \rho^{(0)}}{\rho^{(1)} - \rho^{(2)}} \frac{\rho^{(2)}}{\rho^{(0)}}. \quad (D17)$$

Note that $x^{(1)}$ and $x^{(2)}$ must be positive. So if $\rho^{(1)} < \rho^{(2)}$, then $\rho^{(0)}$ must lie between $\rho^{(1)}$ and $\rho^{(2)}$, if $\rho^{(2)} < \rho^{(1)}$, it must lie between $\rho^{(2)}$ and $\rho^{(1)}$. Substituting these expressions in Eq. (D11) we find

$$\rho^{(2)} F^{(2)} = \rho^{(0)} F^{(0)} \frac{\rho^{(1)} - \rho^{(2)}}{\rho^{(1)} - \rho^{(0)}} + \rho^{(1)} F^{(1)} \frac{\rho^{(0)} - \rho^{(2)}}{\rho^{(0)} - \rho^{(1)}}. \quad (D18)$$

Next we divide the chemical potentials in their ideal and excess components $\mu = \mu^{\text{id}} + \mu^{\text{exc}}$ where

$$\beta \mu^{\text{id}(\alpha)}(\sigma, \tau, \rho^{(\alpha)}; [F^{(\alpha)}]) = \ln[\Lambda^3 \rho^{(\alpha)} F^{(\alpha)}(\sigma)], \quad (D19)$$

with Λ being the de Broglie thermal wavelength. Now Eq. (D13) becomes

$$F^{(1)}(\sigma) = F^{(2)}(\sigma) \frac{\rho^{(2)}}{\rho^{(1)}} e^{\beta \Delta \mu^{\text{exc}}}, \quad (D20)$$

$$\Delta \mu^{\text{exc}} = \mu^{\text{exc}(2)}(\sigma, \tau, \rho^{(2)}; [F^{(2)}]) - \mu^{\text{exc}(1)}(\sigma, \tau, \rho^{(1)}; [F^{(1)}]). \quad (D21)$$

From Eqs. (D18) and (D20) we find

$$F^{(\alpha)}(\sigma) = F^{(0)}(\sigma) Q^{(\alpha)}(\sigma, \tau, \rho^{(0)}, \rho^{(1)}, \rho^{(2)}; [F^{(1)}], [F^{(2)}]), \quad (D22)$$

where the $Q^{(\alpha)}$ are defined by Eq. (82).

Formally Eqs. (D18), (D20), and (D12) with $\alpha = 1, \beta = 2$, and (D14) with $\alpha = 1$ or 2 , form a closed set of equations for the unknowns $\rho^{(1)}, \rho^{(2)}, F^{(1)}(\sigma)$, and $F^{(2)}(\sigma)$. In our case the free energy of the system [cases I, II, III, IV, and V treated with mMSA, see Eq. (85), or case V treated with C1, see Eq. (99)] is *truncatable*: it is only a function of the three moments ξ_i , $i = 1, 2, 3$ of the size distribution function F . So the problem is mapped into the solution of the eight Eqs. (79)–(81) in the eight unknowns $\rho^{(1)}, \rho^{(2)}, \xi_1^{(1)}, \xi_2^{(1)}, \xi_3^{(1)}, \xi_1^{(2)}, \xi_2^{(2)},$ and $\xi_3^{(2)}$.

- ¹H. Löwen, Phys. Rep. **237**, 249 (1994).
- ²S. H. Chen, J. Rouch, F. Sciortino, and P. Tartaglia, J. Phys.: Condens. Matter **6**, 10855 (1994).
- ³R. J. Baxter, J. Chem. Phys. **49**, 2770 (1968).
- ⁴R. O. Watts, D. Henderson, and R. J. Baxter, Adv. Chem. Phys. **21**, 421 (1971).
- ⁵B. Barbooy and R. Tenne, Chem. Phys. **38**, 369 (1979).
- ⁶Strictly speaking we should distinguish between *discrete polydispersity* (multicomponent mixture with a large number of components $p \approx 10^2 - 10^3$) and a *continuous polydispersity* corresponding to $p \rightarrow \infty$ with a continuous distribution of sizes or other properties. This distinction will be specified in more details in Sec. VI.
- ⁷G. Stell, J. Stat. Phys. **63**, 1203 (1991).
- ⁸D. Gazzillo and A. Giacometti, J. Chem. Phys. **120**, 4742 (2004).
- ⁹D. Gazzillo and A. Giacometti, J. Chem. Phys. **113**, 9837 (2000).
- ¹⁰D. Gazzillo and A. Giacometti, Mol. Phys. **101**, 2171 (2003).
- ¹¹M. A. Miller and D. Frenkel, Phys. Rev. Lett. **90**, 135702 (2003).
- ¹²M. A. Miller and D. Frenkel, J. Chem. Phys. **121**, 535 (2004).
- ¹³C. Tutschka and G. Kahl, J. Chem. Phys. **108**, 9498 (1998).
- ¹⁴A. Coniglio, U. De Angelis, and A. Forlani, J. Phys. A **10**, 1123 (1977).
- ¹⁵Y. C. Chiew and E. D. Glandt, J. Phys. A **16**, 2599 (1983).
- ¹⁶Y. C. Chiew and E. D. Glandt, J. Phys. A **22**, 3969 (1989).
- ¹⁷P. Sollich, J. Phys.: Condens. Matter **14**, R79 (2002).
- ¹⁸L. Bellier-Castella, H. Xu, and M. Baus, J. Chem. Phys. **113**, 8337 (2000).
- ¹⁹Y. V. Kalyuzhnyi and G. Kahl, J. Chem. Phys. **119**, 7335 (2003).
- ²⁰Y. V. Kalyuzhnyi, G. Kahl, and P. T. Cummings, J. Chem. Phys. **120**, 10133 (2004).
- ²¹J. W. Perram and E. R. Smith, Chem. Phys. Lett. **35**, 138 (1975).
- ²²Here, for simplicity, we disregard possible complications arising from the fact that unphysically large particles are included in this analysis. These were discussed in Ref. 19.
- ²³A. B. Bhatia and D. E. Thornton, Phys. Rev. B **2**, 3004 (1970).
- ²⁴D. Gazzillo, Mol. Phys. **83**, 1171 (1994).
- ²⁵D. Gazzillo, Mol. Phys. **84**, 303 (1995).
- ²⁶N. W. Ashcroft and D. C. Langreth, Phys. Rev. **156**, 685 (1967).
- ²⁷B. Barbooy, Chem. Phys. **11**, 357 (1975).
- ²⁸T. L. Hill, J. Chem. Phys. **23**, 617 (1955).
- ²⁹In this respect both C0 and C1 would be more precise than the PY closure and this is a remarkable feature.
- ³⁰Even though it may happen that one has loss of solution of $\sum_{i,j} a_i^2$ for certain values of the density, as occurs for the Percus-Yevick closure (Ref. 3).
- ³¹T. Boublik, J. Chem. Phys. **53**, 471 (1970).
- ³²G. A. Mansoori, N. F. Carnahan, K. E. Starling, and T. W. Leland, Jr., J. Chem. Phys. **54**, 1523 (1971).
- ³³J. J. Salacuse and G. Stell, J. Chem. Phys. **77**, 3714 (1982).
- ³⁴X. S. Chen and F. Forstmann, J. Chem. Phys. **97**, 3696 (1992).
- ³⁵R. J. Baxter, J. Chem. Phys. **52**, 4559 (1970).

Chapter 10

The thermodynamic instabilities of a binary mixture of sticky hard spheres

Fantoni R., Gazzillo D., Giacometti A., Phys. Rev. E, **72**, 011503 (2005)

Title: “The thermodynamic instabilities of a binary mixture of sticky hard spheres.”

Abstract: The thermodynamic instabilities of a binary mixture of sticky hard spheres (SHS) in the modified Mean Spherical Approximation (mMSA) and the Percus-Yevick (PY) approximation are investigated using an approach devised by X. S. Chen and F. Forstmann [J. Chem. Phys. 97, 3696 (1992)]. This scheme hinges on a diagonalization of the matrix of second functional derivatives of the grand canonical potential with respect to the particle density fluctuations. The zeroes of the smallest eigenvalue and the direction of the relative eigenvector characterize the instability uniquely. We explicitly compute three different classes of examples. For a symmetrical binary mixture, analytical calculations, both for mMSA and for PY, predict that when the strength of adhesiveness between like particles is smaller than the one between unlike particles, only a pure condensation spinodal exists; in the opposite regime, a pure demixing spinodal appears at high densities. We then compare the mMSA and PY results for a mixture where like particles interact as hard spheres (HS) and unlike particles as SHS, and for a mixture of HS in a SHS fluid. In these cases, even though the mMSA and PY spinodals are quantitatively and qualitatively very different from each other, we prove that they have the same kind of instabilities. Finally, we study the mMSA solution for five different mixtures obtained by setting the stickiness parameters equal to five different functions of the hard sphere diameters. We find that four of the five mixtures exhibit very different type of instabilities. Our results are expected to provide a further step toward a more thoughtful application of SHS models to colloidal fluids.

PHYSICAL REVIEW E 72, 011503 (2005)

Thermodynamic instabilities of a binary mixture of sticky hard spheres

Riccardo Fantoni,* Domenico Gazzillo,† and Achille Giacometti‡

Istituto Nazionale per la Fisica della Materia and Dipartimento di Chimica Fisica, Università di Venezia, S. Marta DD 2137, I-30123 Venezia, Italy

(Received 4 March 2005; published 19 July 2005; corrected 19 August 2005)

The thermodynamic instabilities of a binary mixture of sticky hard spheres (SHS) in the modified mean spherical approximation (mMSA) and the Percus–Yevick (PY) approximation are investigated using an approach devised by Chen and Forstmann [J. Chem. Phys. 97, 3696 (1992)]. This scheme hinges on a diagonalization of the matrix of second functional derivatives of the grand canonical potential with respect to the particle density fluctuations. The zeroes of the smallest eigenvalue and the direction of the relative eigenvector characterize the instability uniquely. We explicitly compute three different classes of examples. For a symmetrical binary mixture, analytical calculations, both for mMSA and for PY, predict that when the strength of adhesiveness between like particles is smaller than the one between unlike particles, only a pure condensation spinodal exists; in the opposite regime, a pure demixing spinodal appears at high densities. We then compare the mMSA and PY results for a mixture where like particles interact as hard spheres (HS) and unlike particles as SHS, and for a mixture of HS in a SHS fluid. In these cases, even though the mMSA and PY spinodals are quantitatively and qualitatively very different from each other, we prove that they have the same kind of instabilities. Finally, we study the mMSA solution for five different mixtures obtained by setting the stickiness parameters equal to five different functions of the hard sphere diameters. We find that four of the five mixtures exhibit very different type of instabilities. Our results are expected to provide a further step toward a more thoughtful application of SHS models to colloidal fluids.

DOI: 10.1103/PhysRevE.72.011503

PACS number(s): 64.70.Fx, 64.60.−i, 64.60.Ak

I. INTRODUCTION

Thermodynamic instabilities are important to locate on the phase diagram of a fluid system those regions where the system cannot exist as a single phase.

For a one-component system with Helmholtz free energy A , pressure P , in a volume V , at a temperature T , the condition for phase stability is $(\partial^2 A / \partial V^2)_{T,N} = -(\partial P / \partial V)_{T,N} = 1 / (V \chi_T) > 0$. The points where the isothermal compressibility χ_T diverges define the so called spinodal line, or phase instability boundary [1], that separates the stable from the unstable region of the phase diagram. In the stable region, where $\chi_T > 0$, the system can exist in a single phase, while inside the other region the free energy can be lowered by phase separation into two phases with different densities. This kind of instability is usually referred to as mechanical instability, associated with a gas-liquid transition or condensation [1–4].

In a binary mixture the situation is more complex [1–6]. The thermodynamic instability is located on the points of the phase diagram where $(\partial^2 G / \partial x^2)_{T,P,N} / \chi_T = 0$, where x is the concentration of one of the two species, and G is the Gibbs free energy. The points where $\chi_T^{-1} = 0$ are instabilities of pure condensation (and the Bhatia-Thornton [7] density-density structure factor, $S_{\rho\rho}(k)$, diverges at $k=0$). The points where $(\partial^2 G / \partial x^2)_{T,P,N} = 0$ are again instabilities of pure condensation when $\delta = \rho(v_1 - v_2) = (\partial V / \partial x)_{T,P,N} / V$ diverges (ρ is the total

number density, v_i the partial molar volume, per particle, of species i . In this case all Bhatia-Thornton structure factors diverge at $k=0$) and are instabilities of pure demixing when $\delta=0$ (in this case the Bhatia-Thornton concentration-concentration structure factor, $S_{xx}(k)$, diverges at $k=0$). But, in general (for an asymmetric mixture), the kind of instability may be in between one of pure condensation and one of pure demixing, with δ finite and different from zero (also in this case all Bhatia-Thornton structure factors diverge at $k=0$). For the particular case of a binary symmetric mixture the only allowed instabilities are the ones of pure condensation and of pure demixing, since $\delta=0$.

A different route was followed by Chen and Forstmann [5] to characterize the instability uniquely in terms of an angle α , function of the density and x .

The purpose of this work is to investigate the nature of instabilities for a binary mixture of sticky hard spheres (SHS). The SHS one-component model was originally proposed by Baxter [8–10], who showed how it admitted an analytic solution in the Percus–Yevick (PY) approximation. The PY solution was later extended to mixtures [11–14] and it is nowadays regarded as extremely useful in colloidal systems. In the SHS model one accounts for a very short range attractive potential by defining an infinitely narrow and deep square well. This limit is carried out in a suitable way so that the second virial coefficient is finite. Due to its highly idealized nature, the one-component SHS model is not free of pathologies [15]. Nonetheless this model has recently regained considerable attention in studies of colloidal suspensions [16–19] especially in its polydisperse version. Since the PY solution of a p -component SHS mixture requires the solution of $p(p+1)/2$ coupled quadratic equations which are

*Email address: rfantoni@unive.it

†Email address: gazzillo@unive.it

‡Email address: achille@unive.it

FANTONI, GAZZILLO, AND GIACOMETTI

PHYSICAL REVIEW E 72, 011503 (2005)

hard to solve for high p , attempts have been made to treat the model with “simpler” approximations [20,21], which would allow analytic solution even for polydisperse systems. One of these approximations, that we will consider in this work, is the modified mean spherical approximation (mMSA) [22].

In the present work we apply the Chen and Forstmann formalism to a binary SHS mixture, using both the mMSA and the PY approximation. The former can be regarded as the zero density limit of the latter and, hence, its predictions must be accepted with care. However, it has its main merit in the fact that it entitles analytical predictions even in the multicomponent case, unlike the PY closure.

Three classes of systems will be discussed in details. First we consider the symmetric mixture, where equal-size equimolar components interact with variable strength only in the unlike part. This simplified case was already studied by Chen and Forstmann for hard core particles with attractive Yukawa interactions within the reference hypernetted chain approximation. In this particular SHS case we are able to perform a full characterization of the mixture both for mMSA and PY. In a second class we discuss two paradigmatic cases: (i) A fluid having HS interactions among like particles and SHS interactions for the unlike (system A) and (ii) a fluid formed by one SHS species and another HS one (system B). For PY both cases have been previously discussed by Barboy and Tenne [14], by Penders and Vrij [23], and by Regnaut, Amokrane, and Heno [24,25] without, however, tackling the issue of the stability nature. Even in these two cases a detailed analytical investigation can be carried out. Building upon our recent work [26], we finally discuss a third class of examples involving a general binary mixture where, however, the stickiness parameters are related to the sizes of the particles according to some plausible prescriptions [26]. Within the mMSA, we are then able to discuss the nature of the instabilities previously calculated in Ref. [26], by evaluating numerically the Chen and Forstmann angle α .

The remainder of the paper is organized as follows. In Sec. II we briefly outline Chen and Forstmann’s approach, in Sec. III we report the PY and mMSA solutions for the Baxter factor correlation function of the SHS mixture. Sec. IV is dedicated to the binary symmetric mixture, whereas Secs. V is dedicated to systems A and B. Section VI deals with five binary mixtures obtained setting the stickiness parameters equal to five different functions of the sphere diameters.

II. METHOD FOR ANALYZING THE INSTABILITY

For the sake of completeness, we briefly recall the main steps of the method reported in Ref. [5]. In doing this, however, we shall follow the general density functional formalism outlined in Ref. [27] which yields a clearer viewpoint.

A. The Chen and Forstmann formalism

Consider a binary mixture with N_1 particles of species 1 with coordinates $\mathbf{r}_1^1, \dots, \mathbf{r}_{N_1}^1$ and N_2 particles of species 2 with coordinates $\mathbf{r}_1^2, \dots, \mathbf{r}_{N_2}^2$ interacting through spherically symmetric pair potentials. Define the microscopic densities to be

$$\rho_i(\mathbf{r}) \equiv \sum_{\nu=1}^{N_i} \delta(\mathbf{r} - \mathbf{r}_\nu^i) \quad i = 1, 2 \quad (1)$$

for each one of the two species.

Consider now the nonhomogeneous system with an external potential $\phi_1(\mathbf{r})$ acting on the particles of species 1 and an external potential $\phi_2(\mathbf{r})$ acting on the particles of species 2. Let μ_i and Λ_i be the chemical potential and the de Broglie thermal wavelength, respectively, for species i , $N = N_1 + N_2$ the total number of particles, and $\mathbf{r}^N = (\{\mathbf{r}_\nu^1\}, \{\mathbf{r}_\nu^2\})$ a shorthand notation for the total set of coordinates. The grand partition function of the system with total internal energy $W(\mathbf{r}^N)$ is a functional of the generalized potentials $u_i(\mathbf{r}) = \beta[\mu_i - \phi_i(\mathbf{r})]$

$$\Theta[u_1, u_2] \equiv \sum_{N_1=0}^{\infty} \sum_{N_2=0}^{\infty} \frac{1}{\Lambda_1^{3N_1} N_1!} \frac{1}{\Lambda_2^{3N_2} N_2!} \times \int e^{-\beta W(\mathbf{r}^N) + \sum_{i=1}^2 \int u_i(\mathbf{r}) \rho_i(\mathbf{r}) d\mathbf{r}} d\mathbf{r}^N = e^{-\beta \Omega[u_1, u_2]}, \quad (2)$$

where Ω is the grand free energy. It can be proven [27] that the functional Ω is strictly concave in u_1 and u_2 (if we opportunistically restrict its domain of definition). The equilibrium number density of species i is given by

$$\rho_i(\mathbf{r}) \equiv \langle \rho_i(\mathbf{r}) \rangle = - \frac{\delta \beta \Omega[u_1, u_2]}{\delta u_i(\mathbf{r})}. \quad (3)$$

It follows that the following functional of $\{\rho_i\}$ and $\{u_i\}$

$$\beta A[\rho_1, \rho_2, u_1, u_2] \equiv \sum_{i=1}^2 \int \rho_i(\mathbf{r}) u_i(\mathbf{r}) d\mathbf{r} + \beta \Omega[u_1, u_2], \quad (4)$$

is also strictly concave in u_1 and u_2 , so it admits a unique maximum for $u_i = \bar{u}_i$, $i = 1, 2$, where the $\{\bar{u}_i\}$ can be determined univocally from Eq. (3) once the equilibrium densities $\{\rho_i\}$ are known.

We now set $\bar{A}[\rho_1, \rho_2] \equiv A[\rho_1, \rho_2, \bar{u}_1, \bar{u}_2]$. Again one can prove [27] that this Helmholtz free energy is a strictly convex functional in ρ_1 and ρ_2 .

Introduce the following “grand free energy functional” of the densities

$$\beta \Omega'[\rho_1, \rho_2] \equiv \beta \bar{A}[\rho_1, \rho_2] - \sum_{i=1}^2 \int \rho_i(\mathbf{r}) v_i(\mathbf{r}) d\mathbf{r}, \quad (5)$$

where $\{v_i\}$ are some given generalized potentials, independent of the densities. Clearly only when $v_i = \bar{u}_i$, $i = 1, 2$, we have $\Omega' = \Omega$, i.e., equilibrium.

Taking the first functional derivative of Ω' with respect to the densities we find

$$\frac{\delta \beta \Omega'[\rho_1, \rho_2]}{\delta \rho_i(\mathbf{r})} = \frac{\delta \beta \bar{A}[\rho_1, \rho_2]}{\delta \rho_i(\mathbf{r})} - v_i(\mathbf{r}) = \bar{u}_i(\mathbf{r}) - v_i(\mathbf{r}), \quad (6)$$

where in the second equality Eqs. (3) and (4) were used. At equilibrium we then have that the first functional derivatives

of Ω' vanish and Ω' attains its minimum value.

The second functional derivatives of Ω' with respect to the densities at equilibrium are [27]

$$\left. \frac{\delta^2 \beta \Omega'[\rho_1, \rho_2]}{\delta \rho_i(\mathbf{r}_1) \delta \rho_j(\mathbf{r}_2)} \right|_{\text{equil.}} = \left. \frac{\delta \bar{u}_i(\mathbf{r}_1)}{\delta \rho_j(\mathbf{r}_2)} \right|_{\text{equil.}} = \frac{\delta_{ij} \delta(\mathbf{r}_1 - \mathbf{r}_2)}{\rho_i(\mathbf{r}_1)} - c_{ij}(\mathbf{r}_1, \mathbf{r}_2), \quad (7)$$

where $c_{ij}(\mathbf{r}_1, \mathbf{r}_2)$ are the partial direct correlation functions of the system.

So a Taylor expansion, up to the second order terms, yields the fluctuation of Ω' around the equilibrium caused by small density fluctuations

$$\begin{aligned} \delta \Omega' &= \Omega'[\rho_1 + \delta \rho_1, \rho_2 + \delta \rho_2] - \Omega'[\rho_1, \rho_2] \\ &= \frac{1}{2\beta} \int \int \sum_{i,j} \left[\frac{\delta_{ij} \delta(\mathbf{r}_1 - \mathbf{r}_2)}{\rho_i(\mathbf{r}_1)} - c_{ij}(\mathbf{r}_1, \mathbf{r}_2) \right] \delta \rho_i(\mathbf{r}_1) \delta \rho_j(\mathbf{r}_2) d\mathbf{r}_1 d\mathbf{r}_2. \end{aligned} \quad (8)$$

If the system is homogeneous and isotropic at equilibrium [i.e., $\bar{u}_i(\mathbf{r}) = \beta \mu_i$, $i=1, 2$], so that

$$\rho_i(\mathbf{r}) = \frac{N_i}{V} = \rho_i, \quad (9)$$

$$c_{ij}(\mathbf{r}_1, \mathbf{r}_2) = c_{ij}(|\mathbf{r}_1 - \mathbf{r}_2|), \quad (10)$$

where V is the volume (assumed large enough), then we can rewrite the integral of Eq. (8), which is a convolution, as a \mathbf{k} integral of a product of Fourier transforms. Replacing the \mathbf{k} integral $[(2\pi)^{-3} \int d\mathbf{k} \dots]$ by a sum over discrete \mathbf{k} values $[V^{-1} \sum_{\mathbf{k}} \dots]$, one obtains

$$\delta \Omega' = \frac{1}{2\beta V} \sum_{\mathbf{k}} \sum_{i,j} \delta \bar{\rho}_i^*(\mathbf{k}) \tilde{A}_{ij}(\mathbf{k}) \delta \bar{\rho}_j(\mathbf{k}), \quad (11)$$

where $\delta \bar{\rho}_i(\mathbf{k}) = \delta \bar{\rho}_i(\mathbf{k}) / \sqrt{\rho_i}$ and the asterisk indicates complex conjugation, having denoted with the tilde the Fourier transform

$$\tilde{f}(\mathbf{k}) \equiv \int_V f(\mathbf{r}) e^{i\mathbf{k}\cdot\mathbf{r}} d\mathbf{r}, \quad (12)$$

so that

$$\tilde{A}_{ij}(k) = \delta_{ij} - \sqrt{\rho_i \rho_j} \tilde{c}_{ij}(k). \quad (13)$$

Notice that, due to the symmetry of the direct correlation functions under exchange of species indexes, the matrix $\tilde{\mathbf{A}}(k)$ is symmetric.

The probability distribution for the density fluctuations $\delta \rho_i$ (at constant T , V , and $\{\mu_i\}$) is proportional to $e^{-\beta \delta \Omega'}$ [28]. We therefore get for the mean values of the fluctuation products

$$\langle \delta \bar{\rho}_i^*(\mathbf{k}) \delta \bar{\rho}_j(\mathbf{k}) \rangle = V [\tilde{\mathbf{A}}^{-1}]_{ij}(k) = V [\delta_{ij} + \sqrt{\rho_i \rho_j} \tilde{h}_{ij}(k)], \quad (14)$$

where the last equality exploits the Ornstein-Zernike (OZ) equations between the partial total correlation functions h_{ij} and the partial direct correlation functions.

Next define the molar fraction of species i to be $x_i = \rho_i / \rho$, with $\rho = \sum_i \rho_i$ being the total density of the mixture. One usually introduces [7] two linear combinations of fluctuations of partial densities, i.e., the fluctuation of total density, $\delta \bar{\rho}(\mathbf{k})$, and the fluctuation of concentration of species 1, $\delta \bar{x}(\mathbf{k})$,

$$\delta \bar{\rho}(\mathbf{k}) = \delta \bar{\rho}_1(\mathbf{k}) + \delta \bar{\rho}_2(\mathbf{k}) = \sqrt{\rho} [\sqrt{x_1} \delta \bar{\rho}_1(\mathbf{k}) + \sqrt{x_2} \delta \bar{\rho}_2(\mathbf{k})], \quad (15)$$

$$\begin{aligned} \delta \bar{x}(\mathbf{k}) &= \frac{1}{\rho} [\rho_2 \delta \bar{\rho}_1(\mathbf{k}) - \rho_1 \delta \bar{\rho}_2(\mathbf{k})] = \sqrt{\frac{x_1 x_2}{\rho}} [\sqrt{x_2} \delta \bar{\rho}_1(\mathbf{k}) \\ &\quad - \sqrt{x_1} \delta \bar{\rho}_2(\mathbf{k})], \end{aligned} \quad (16)$$

so that, if $\delta \bar{\rho}_1$ and $\delta \bar{\rho}_2$ change in proportion to their respective mean concentration, then $\delta \bar{x} = 0$.

We also introduce

$$\delta \bar{\rho}(\mathbf{k}) = \frac{1}{\sqrt{\rho}} \delta \bar{\rho}(\mathbf{k}), \quad (17)$$

$$\delta \bar{x}(\mathbf{k}) = \sqrt{\frac{\rho}{x_1 x_2}} \delta \bar{x}(\mathbf{k}), \quad (18)$$

so that, in terms of the following two column vectors

$$\mathbf{u}(\mathbf{k}) = \begin{pmatrix} \delta \bar{\rho}_1(\mathbf{k}) \\ \delta \bar{\rho}_2(\mathbf{k}) \end{pmatrix}, \quad \mathbf{v}(\mathbf{k}) = \begin{pmatrix} \delta \bar{\rho}(\mathbf{k}) \\ \delta \bar{x}(\mathbf{k}) \end{pmatrix}, \quad (19)$$

Eqs. (15) and (16) can be written in compact notation as $\mathbf{u} = \mathbf{U} \mathbf{v}$ where

$$\mathbf{U} = \begin{pmatrix} \sqrt{x_1} & \sqrt{x_2} \\ \sqrt{x_2} & -\sqrt{x_1} \end{pmatrix}, \quad (20)$$

notice that $\mathbf{U}^2 = \mathbf{I}$, where \mathbf{I} is the identity matrix.

We find then from Eq. (11) (superscript T indicating the transpose)

$$\delta \Omega' = \frac{1}{2\beta V} \sum_{\mathbf{k}} \mathbf{v}^{T*}(\mathbf{k}) \mathbf{M}(k) \mathbf{v}(\mathbf{k}), \quad (21)$$

where $\mathbf{M}(k)$ is the following symmetric matrix:

$$\mathbf{M}(k) = \mathbf{U} \tilde{\mathbf{A}}(k) \mathbf{U} = \begin{pmatrix} M_{\rho\rho} & M_{\rho x} \\ M_{x\rho} & M_{xx} \end{pmatrix}, \quad (22)$$

with

$$M_{\rho\rho} = 1 - \rho [x_1^2 \tilde{c}_{11} + x_2^2 \tilde{c}_{22} + 2x_1 x_2 \tilde{c}_{12}], \quad (23)$$

$$M_{xx} = 1 - \rho x_1 x_2 [\tilde{c}_{11} + \tilde{c}_{22} - 2\tilde{c}_{12}], \quad (24)$$

FANTONI, GAZZILLO, AND GIACOMETTI

PHYSICAL REVIEW E 72, 011503 (2005)

$$M_{\rho x} = M_{xp} = \rho \sqrt{x_1 x_2} [x_2 \tilde{c}_{22} - x_1 \tilde{c}_{11} - (x_2 - x_1) \tilde{c}_{12}]. \quad (25)$$

The elements of the $\mathbf{M}(0)$ matrix are related to thermodynamic quantities [5], as shown in the Appendix. In particular the determinant of \mathbf{M} is

$$\det(\mathbf{M}) = x_1 x_2 \frac{(\chi_T^0)^2}{\chi_T V} \left(\frac{\partial^2 G}{\partial x_1^2} \right)_{T,P,N}, \quad (26)$$

where χ_T is the isothermal compressibility, and $\chi_T^0 = \beta/\rho$ is the isothermal compressibility of the ideal gas.

For the particular systems that we shall consider in the following, it turns out that the matrix $\tilde{\mathbf{A}}$ can be written, using the Wiener–Hopf factorization in terms of the Baxter factor matrix $\hat{\mathbf{Q}}$ [11]

$$\tilde{\mathbf{A}}(k) = \hat{\mathbf{Q}}^{T*}(k) \hat{\mathbf{Q}}(k). \quad (27)$$

Hence $\det[\mathbf{M}(k)] = \det[\tilde{\mathbf{A}}(k)] = |\det[\hat{\mathbf{Q}}(k)]|^2 \geq 0$ and $\text{trace}[\mathbf{M}(k)] = \text{trace}[\tilde{\mathbf{A}}(k)] \geq 0$.

The inverse of $\mathbf{M}(k)$ yields the mean square fluctuations of total density and concentration, i.e., the density-density structure factor $S_{\rho\rho}(k)$, the concentration-concentration structure factor $S_{xx}(k)$, and the cross term $S_{\rho x}(k)$ [7]

$$S_{\rho\rho}(k) = \frac{1}{V} \langle \delta\bar{\rho}^*(\mathbf{k}) \delta\bar{\rho}(\mathbf{k}) \rangle = [\mathbf{M}^{-1}]_{\rho\rho}(k), \quad (28)$$

$$S_{xx}(k) = \frac{x_1 x_2}{V} \langle \delta\bar{x}^*(\mathbf{k}) \delta\bar{x}(\mathbf{k}) \rangle = x_1 x_2 [\mathbf{M}^{-1}]_{xx}(k), \quad (29)$$

$$S_{\rho x}(k) = \frac{\sqrt{x_1 x_2}}{V} \langle \delta\bar{\rho}^*(\mathbf{k}) \delta\bar{x}(\mathbf{k}) \rangle = \sqrt{x_1 x_2} [\mathbf{M}^{-1}]_{\rho x}(k). \quad (30)$$

Now, since $\mathbf{M}(k)$ is a symmetric matrix, it can be diagonalized through an orthogonal change of basis and it will have real eigenvalues

$$\lambda_{\pm}(k) = \frac{\text{tr}[\mathbf{M}(k)] \pm \sqrt{\{\text{tr}[\mathbf{M}(k)]\}^2 - 4 \det[\mathbf{M}(k)]}}{2}, \quad (31)$$

with $\lambda_+(k) \geq \lambda_-(k) \geq 0$. For the normalized eigenvectors we find

$$\mathbf{z}_{\pm}(k) = \begin{pmatrix} a_{\pm}(k) \\ b_{\pm}(k) \end{pmatrix}, \quad (32)$$

with

$$a_{\pm}(k) = 1 / \sqrt{1 + \left[\frac{M_{\rho\rho}(k) - \lambda_{\pm}(k)}{M_{\rho x}(k)} \right]^2}, \quad (33)$$

$$b_{\pm}(k) = -a_{\pm} \frac{M_{\rho\rho}(k) - \lambda_{\pm}(k)}{M_{\rho x}(k)}. \quad (34)$$

The transition matrix to the base formed by the eigenvectors will be

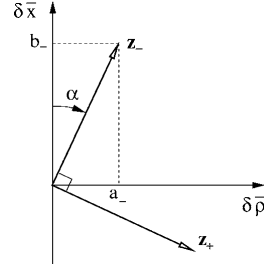


FIG. 1. Schematic representation of the two orthonormal vectors \mathbf{z}_{\pm} defined in Eq. (32) and of the angle α defined in Eq. (41) when $\alpha \in [0, \pi/2]$. When $\alpha \in [-\pi/2, 0]$ the angle shown in the figure corresponds to $|\alpha|$ and $\delta\bar{x}$ to $-\delta\bar{x}$.

$$\mathbf{Z}(k) = \begin{pmatrix} a_+(k) & a_-(k) \\ b_+(k) & b_-(k) \end{pmatrix}, \quad (35)$$

Eq. (21) can then be recast into the form

$$\delta\Omega'[\delta\rho_1, \delta\rho_2] = \frac{1}{2\beta V} \sum_{\mathbf{k}} [\lambda_+(k) |\delta\bar{\rho}_+(\mathbf{k})|^2 + \lambda_-(k) |\delta\bar{\rho}_-(\mathbf{k})|^2], \quad (36)$$

where $\delta\bar{\rho}_{\pm}$ are the Fourier components of the vector for the total density and concentration fluctuation in the eigenvector base, namely

$$\mathbf{Z}^{-1}\mathbf{v} = \begin{pmatrix} \delta\bar{\rho}_+ \\ \delta\bar{\rho}_- \end{pmatrix}, \quad (37)$$

or

$$\delta\bar{\rho}_+(\mathbf{k}) = a_+(k) \delta\bar{\rho}(\mathbf{k}) + b_+(k) \delta\bar{x}(\mathbf{k}), \quad (38)$$

$$\delta\bar{\rho}_-(\mathbf{k}) = a_-(k) \delta\bar{\rho}(\mathbf{k}) + b_-(k) \delta\bar{x}(\mathbf{k}). \quad (39)$$

B. Characterization of the instability

We wish to know which combination of density and concentration fluctuations, $(\delta\bar{\rho}, \delta\bar{x})$ or $(\delta\bar{\rho}_+, \delta\bar{\rho}_-)$, yields the smallest increase $\delta\Omega'$ of grand free energy. The border of a stability region (spinodal line) will be determined by the smaller eigenvalue $\lambda_-(k)$ going to zero. It is important to remark that the minimum eigenvalue will vanish if and only if $\det[\mathbf{M}(k)] = \lambda_-(k)\lambda_+(k) = |\det[\hat{\mathbf{Q}}(k)]|^2$ vanishes. The spinodal equation thus corresponds to

$$\lambda_-(k) = 0 \quad \text{or} \quad \det[\hat{\mathbf{Q}}(k)] = 0. \quad (40)$$

For all $\bar{\mathbf{k}}$ vectors with $\bar{k} = |\bar{\mathbf{k}}|$ being a solution of the spinodal equation, we can calculate the related eigenvector $\mathbf{z}_-(\bar{\mathbf{k}})$ and find, from Eq. (39), one nonzero linear combination $\delta\bar{\rho}_-(\bar{\mathbf{k}})$ of density and concentration fluctuations for which $\delta\Omega' = 0$. Thus $\mathbf{z}_-(\bar{\mathbf{k}}) = [a_-(\bar{k}), b_-(\bar{k})]^T$ characterizes the phase transition uniquely. On defining the angle (see Fig. 1)

$$\alpha = \arctan\left(\frac{a_-}{b_-}\right)_{k=\bar{k}} = \arctan\left[\frac{\hat{Q}_{12}(\bar{k})\sqrt{x_1} - \hat{Q}_{11}(\bar{k})\sqrt{x_2}}{\hat{Q}_{12}(\bar{k})\sqrt{x_2} + \hat{Q}_{11}(\bar{k})\sqrt{x_1}}\right], \quad (41)$$

the instability will be predominantly of the demixing type when α is close to 0 (i.e., only concentration fluctuations occur) and predominantly of the condensation type when α is close to $\pm\pi/2$ (i.e., only density fluctuates at fixed concentration).

The same feature can be seen in real space. When $\lambda_-(\bar{k})=0$ and $\alpha=0$ ($\Rightarrow a_-=0, b_-=0$, and therefore $\delta\bar{\rho}_+=a_+\delta\bar{\rho}, \delta\bar{\rho}_-=b_-\delta\bar{x}$), one can get $\delta\Omega'=0$ only if $\delta\bar{\rho}_+(\bar{\mathbf{k}})=0$, which requires $\delta\bar{\rho}(\bar{\mathbf{k}})=0$, i.e., the fluctuations that do not increase the "grand free energy" can be expressed as

$$\delta\rho_1(\mathbf{r}) = \frac{1}{V} \sum_{\substack{\mathbf{k} \\ |\mathbf{k}|=\bar{k}}} \delta\rho_1(\mathbf{k})e^{-i\mathbf{k}\cdot\mathbf{r}}, \quad (42)$$

$$\delta\rho_2(\mathbf{r}) = -\delta\rho_1(\mathbf{r}). \quad (43)$$

On the other hand, when $\lambda_-(\bar{k})=0$ and $\alpha=\pm\pi/2$ ($\Rightarrow \delta\bar{\rho}_+=b_+\delta\bar{x}, \delta\bar{\rho}_-=a_-\delta\bar{\rho}$), $\delta\bar{\rho}_+(\bar{\mathbf{k}})=0$ now requires $\delta\bar{x}(\bar{\mathbf{k}})=0$, which corresponds to

$$\delta\rho_2(\mathbf{r}) = +\frac{\rho_2}{\rho_1}\delta\rho_1(\mathbf{r}). \quad (44)$$

Equation (42) yields oscillating partial density fluctuations for species 1 on the spinodal line, whereas Eqs. (43) and (44) represent the two different behaviors of the species 2 in correspondence to the two extreme values of α (0 and $\pm\pi/2$, respectively). For $\alpha=0$, the fluctuations of species 2 must be in opposition of phase compared to those of species 1, [see Eq. (43)], and this can be clearly interpreted as related to spatial demixing. In the opposite case ($\alpha=\pm\pi/2$), Eq. (44) means that an increase of species 1 in some region drives an increase of species 2 in the same region, a clear indication of a condensation type of instability. When α varies from zero to $\pm\pi/2$ the allowed fluctuations will continuously vary from the pure demixing to the pure condensation type.

For a class of approximations (closures) having the partial direct correlation functions vanishing beyond a finite range, it was proven in [11] that $\hat{\mathbf{Q}}(k)$ is nonsingular for any $k>0$,

so we can limit our search for the zeroes of the minimum eigenvalue to the case $k=0$. Moreover, since $\lim_{k\rightarrow\infty} \det[\hat{\mathbf{Q}}(k)]=1$ and $\det[\hat{\mathbf{Q}}(k)]$ is a continuous function of k , we must also have $\det[\hat{\mathbf{Q}}(k=0)]$ non-negative, otherwise $\det[\hat{\mathbf{Q}}(k)]$ would vanish for some finite k . We can use this last condition to determine which regions of the phase diagram are unstable. We cannot in fact gather this information by just looking at the matrix $\hat{\mathbf{A}}$, which is always positive definite when nonsingular. In the following, whenever we omit the dependence from the wave vector k , we shall refer to the case $k=0$.

III. THE BINARY STICKY HARD SPHERE FLUID

We consider the SHS mixture described in the introduction by the following square-well interaction potential between a sphere of species i and one of species j [8,9,13,14]

$$\beta\phi_{ij}(r) = \begin{cases} +\infty & 0 < r < \sigma_{ij}, \\ -\ln\left(\frac{1}{12\tau_{ij}}\frac{R_{ij}}{R_{ij}-\sigma_{ij}}\right) & \sigma_{ij} \leq r \leq R_{ij}, \\ 0 & r > R_{ij}, \end{cases} \quad (45)$$

where $\beta=1/(k_B T)$ (k_B being Boltzmann constant and T the temperature), $\sigma_{ij}=(\sigma_i+\sigma_j)/2$ (σ_i being the diameter of a sphere of species i), $R_{ij}-\sigma_{ij}$ denotes the well width, and the dimensionless parameter

$$\frac{1}{\tau_{ij}} = \frac{\epsilon_{ij}}{\tau} = \frac{\nu_{ij}}{\tau^*} \geq 0, \quad (46)$$

measures the strength of surface adhesiveness or "stickiness" between particles of species i and j . In (46), τ is an unspecified increasing function of T , and we introduced the dimensionless quantities $\nu_{ij}=\epsilon_{ij}/\epsilon_{11}$ and $\tau^*=\tau/\epsilon_{11}$. The next step which defines the SHS model consists in taking the sticky limit $\{R_{ij}\}\rightarrow\{\sigma_{ij}\}$. Notice that the logarithm in the initial square-well potential (45) is chosen so to have a simple expression for the Boltzmann factor, which reduces to a combination of an Heaviside step function and a Dirac delta function in the sticky limit.

Within a class of mixed closures for which the partial direct correlation functions $c_{ij}(r)$ after the sticky limit vanish beyond σ_{ij} {generalized PY (GPY) approximation [21]}, the model can be analytically solved for the Baxter factor correlation function

$$q_{ij}(r) = \begin{cases} \frac{1}{2}a_i(r-\sigma_{ij})^2 + (b_i + a_i\sigma_{ij})(r-\sigma_{ij}) + K_{ij}, & L_{ij} = (\sigma_i - \sigma_j)/2 \leq r \leq \sigma_{ij}, \\ 0, & \text{elsewhere,} \end{cases} \quad (47)$$

FANTONI, GAZZILLO, AND GIACOMETTI

PHYSICAL REVIEW E 72, 011503 (2005)

$$a_i = \frac{1}{\Delta} + \frac{3\xi_2\sigma_i}{\Delta^2} - \frac{12\xi_1}{\Delta}, \quad b_i = \left(\frac{1}{\Delta} - a_i\right)\frac{\sigma_i}{2}, \quad (48)$$

$$\xi_n = \frac{\pi}{6} \sum_i \rho_i \sigma_i^n, \quad \xi_i = \frac{\pi}{6} \sum_m \rho_m \sigma_m K_{im}, \quad \Delta = 1 - \xi_3. \quad (49)$$

The Baxter factor matrix $\hat{\mathbf{Q}}(k)$ first introduced in Eq. (27) is related to Baxter factor correlation function through

$$\hat{Q}_{ij}(k) = \delta_{ij} - 2\pi\sqrt{\rho_i\rho_j}\hat{q}_{ij}(k), \quad (50)$$

where $\hat{q}_{ij}(k)$ is the one-dimensional Fourier transform of $q_{ij}(r)$. It can be expressed in terms of spherical Bessel functions of the zeroth and first order and its explicit expression can be found in Eq. (27) of Ref. [20], and will not be reproduced here.

The symmetric matrix K_{ij} is given by

$$K_{ij} = \frac{\sigma_{ij}^2}{12\tau_{ij}}\bar{y}_{ij}, \quad (51)$$

where $\bar{y}_{ij}=y_{ij}(\sigma_{ij}^+)$ are the contact values of the partial cavity functions. For this kind of system a more natural parameter to use in place of the total density $\rho=\sum_i\rho_i$ is the total packing fraction $\eta=\xi_3$.

In the modified mean spherical approximation [$c_{ij}(r)=f_{ij}(r)$ when $r>\sigma_{ij}$, where $f_{ij}(r)=\exp[-\beta\phi_{ij}(r)]-1$ are the Mayer functions] one can show [21] that [29]

$$\bar{y}_{ij}=1 \quad \text{for all } i \text{ and } j, \quad (52)$$

In the Percus–Yevick approximation [$c_{ij}(r)=f_{ij}(r)y_{ij}(r)$] one can show that the \bar{y}_{ij} have to satisfy the following set of coupled quadratic equations [13]

$$\bar{y}_{ij}\sigma_{ij} = a_i\sigma_{ij} + b_i + 2\pi\sum_k \rho_k \frac{\sigma_{ki}^2}{12\tau_{kj}}\bar{y}_{kj}q_{ki}(L_{ki}). \quad (53)$$

It is worth stressing that the above expressions are valid for both the mMSA and the PY closures, provided that the correct values of \bar{y}_{ij} are inserted into the matrix K_{ij} given in Eq. (51) [20,26]. All the results gathered so far in this section are valid for a generic p -component SHS mixture. In the rest of the work we will specialize to two-component ($p=2$) mixtures. For a binary mixture the determinant of $\hat{\mathbf{Q}}(0)$ can be reduced to the following simple expression [30]

$$\det[\hat{\mathbf{Q}}(0)] = \frac{1+2\eta}{(1-\eta)^2} - \frac{\eta_1\lambda_{11}^{BT} + \eta_2\lambda_{22}^{BT}}{(1-\eta)^2} - \frac{\eta_1\eta_2}{(1-\eta)^3} [3(\lambda_{11}^{BT} + \lambda_{22}^{BT} - 2\lambda_{12}^{BT}) - \lambda_{11}^{BT}\lambda_{22}^{BT} + (\lambda_{12}^{BT})^2], \quad (54)$$

where

$$\eta_i = \frac{\pi}{6}\rho_i\sigma_i^3, \quad (55)$$

$$\lambda_{ij} = \frac{\bar{y}_{ij}}{\tau_{ij}}, \quad (56)$$

$$\lambda_{ij}^{BT} = (1-\eta)\lambda_{ij}\frac{\sigma_{ij}^2}{\sigma_i\sigma_j}. \quad (57)$$

Our task is the determination of the spinodal line and of the nature of the instability. These can be expressed respectively by the reduced temperature $\tau^*=f_r(\rho\sigma_1^3, x_1, \zeta, \{v_{ij}\})$ and the angle $\alpha=f_\alpha(\rho\sigma_1^3, x_1, \zeta, \{v_{ij}\})$, where $\zeta=\sigma_2/\sigma_1$. Sometimes it also proves convenient to use another set of independent variables, namely $\eta, x_1, \zeta, \{v_{ij}\}$.

We anticipate that, while f_r will in general depend on the particular chosen closure, f_α need not mirror this feature. An example is the case studied in Section V, where two ϵ_{ij} are zero and $\epsilon_{\bar{i}\bar{j}}>0$. Then $\lambda_{ij}=0$ for $i\neq\bar{i}$ or $j\neq\bar{j}$ and the spinodal equation

$$\lambda_-(0)=0 \quad \text{or} \quad \det[\hat{\mathbf{Q}}(0)]=0. \quad (58)$$

is sufficient for determining the third λ , which turns out to be a function $\lambda_{\bar{i}\bar{j}}(\eta, x_1, \zeta)$, independent from the particular closure within the class we are considering. Since in each matrix element of $\hat{\mathbf{Q}}$ the quantities \bar{y}_{ij} and τ_{ij} appear only in the ratios λ_{ij} it follows that the angle α [see Eq. (41)] will also be independent of the particular closure.

In the case of a general binary mixture (with two or three nonvanishing ϵ_{ij}) we expect a dependence of the angle from the closure, even if this point would deserve further investigation.

IV. THE SYMMETRIC BINARY MIXTURE

The PY approximation leads, even in the simple binary case, to the solution of two coupled quartic equations. We then start with a simpler task, akin to the one already discussed by Chen and Forstmann [5] for a different potential, of finding the spinodal line and angle α predicted by the mMSA and PY for the symmetric binary mixture. In this case $x_1=x_2=1/2$, $\sigma_1=\sigma_2=\sigma$, and $\epsilon_{11}=\epsilon_{22}$. By symmetry we must have $\bar{c}_{11}=\bar{c}_{22}$ and from Eq. (25) it follows that \mathbf{M} is diagonal, the cross term M_{px} being identically zero and

$$\lambda_- = \min\{M_{pp}, M_{xx}\}. \quad (59)$$

Therefore the symmetric mixture can only have either pure condensation ($\alpha=\pm\pi/2$) or pure demixing ($\alpha=0$) instabilities.

Moreover for the symmetric mixture we have from Eqs. (28)–(30)

$$S_{pp} = \frac{1}{M_{pp}}, \quad (60)$$

$$S_{xx} = \frac{1}{4M_{xx}}, \quad (61)$$

$$S_{px} = 0. \quad (62)$$

We see then that on a pure condensation instability $S_{pp}(0)\rightarrow\infty$ or $\tilde{h}_{11}(0)+\tilde{h}_{12}(0)\rightarrow\infty$, whereas on a pure demixing instability $S_{xx}(0)\rightarrow\infty$ or $\tilde{h}_{11}(0)-\tilde{h}_{12}(0)\rightarrow\infty$, and each

THERMODYNAMIC INSTABILITIES OF A BINARY...

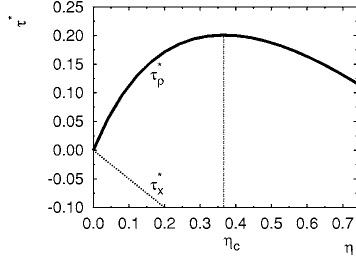


FIG. 2. Spinodal line (continuous curve) for the symmetric mixture in the mMSA with $\nu_{12}=2$. The kind of instability is of pure condensation along the whole spinodal.

type of instability shows a distinct form of long-range behavior in the correlation functions.

A. Symmetric mixture in the mMSA

Let us first consider the symmetric mixture within the mMSA. The spinodal line will be of pure condensation when $M_{\rho\rho}=0$, that is

$$\tau^* = \tau_p^* = (1 + \nu_{12}) \frac{1}{2} \eta \frac{1 - \eta}{1 + 2\eta}, \quad (63)$$

whose maximum in the (τ^*, η) plane occurs at $\eta = \eta_c^{mMSA} = (\sqrt{3}-1)/2 = 0.3660\dots$ (independently of ν_{12}). On the other hand the spinodal will be a line of pure demixing when $M_{xx}=0$ which has as solution

$$\tau^* = \tau_x^* = (1 - \nu_{12}) \frac{1}{2} \eta. \quad (64)$$

Note that the allowed packing fractions are the ones smaller than the close packed packing fraction $\eta_0 = \pi\sqrt{2}/6 = 0.7404\dots$

For the determinant of $\hat{Q}(0)$ we find from Eq. (54)

$$\det[\hat{Q}(0)] = \frac{(\tau - \tau_p)(\tau - \tau_x)}{\tau^2} \frac{1 + 2\eta}{(1 - \eta)^2}, \quad (65)$$

so that the system is unstable when τ lies between the two roots τ_p and τ_x , at a given packing fraction.

While the condensation line is always present, the existence of a demixing line depends upon the value of ν_{12} , as expected. When $\nu_{12} \geq 1$ the demixing line $\tau^* = \tau_x^*$ lies below the η axis, and hence, the spinodal in the phase diagram (τ^*, η) is the curve $\tau^* = \tau_p^*$ (see Fig. 2), with the instability being of pure condensation at all densities. Notice that this would be the case for Lorentz–Berthelot mixtures for which we have $\epsilon_{12} \equiv \sqrt{\epsilon_{11}\epsilon_{22}} = \epsilon_{11}$, which corresponds to $\nu_{12}=1$, that is the one-component case.

When $\nu_{12} < 1$ the two roots $\tau^* = \tau_p^*$ and $\tau^* = \tau_x^*$ intercept at a point [31] (see Fig. 3) having packing fraction

$$\eta = \eta_{px} = \frac{2\nu_{12}}{3 - \nu_{12}} < 1, \quad (66)$$

so the instability is of pure condensation for $\eta < \eta_{px}$ and of pure demixing for $\eta > \eta_{px}$.

PHYSICAL REVIEW E 72, 011503 (2005)

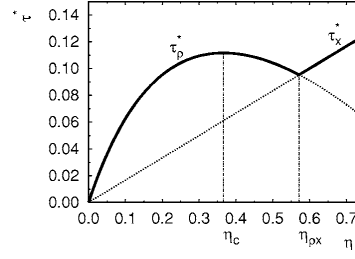


FIG. 3. Spinodal line (continuous curve) for the symmetric mixture in the mMSA with $\nu_{12}=2/3$. In this case the instability is of pure condensation for $\eta < \eta_{px}$ along $\tau^* = \tau_p^*$ and of pure demixing for $\eta > \eta_{px}$ along $\tau^* = \tau_x^*$.

B. Symmetric mixture in the PY

In the PY approximation we first need to determine the cavity functions at contact. Equation (53) for the binary symmetric mixture can be recast into the following form

$$\lambda_{11}\tau_{11} - \frac{1}{2}\eta\left(\frac{1}{12}\lambda_{11}^2 - \frac{1}{\Delta}\lambda_{11}\right) = \bar{y}_{11}^{HS} + \frac{1}{2}\eta\left(\frac{1}{12}\lambda_{12}^2 - \frac{1}{\Delta}\lambda_{12}\right), \quad (67)$$

$$\lambda_{12}\tau_{12} \left[1 + \frac{1}{\tau_{12}} \left(\frac{\eta}{2\Delta} - \frac{1}{12}\eta\lambda_{11} \right) \right] = \bar{y}_{12}^{HS} - \frac{\eta}{2\Delta}\lambda_{11}, \quad (68)$$

where

$$\bar{y}_{11}^{HS} = \bar{y}_{12}^{HS} = \bar{y}^{HS} = \frac{2 + \eta}{2(1 - \eta)^2}, \quad (69)$$

is the HS expression for the cavity functions at contact. Substitution of Eq. (68) into Eq. (67) leads to a quartic equation for λ_{11} . The solution for the cavity functions at contact can then be written as

$$\frac{\bar{y}_{11}}{\tau_{11}} = R, \quad (70)$$

$$\frac{\bar{y}_{12}}{\tau_{12}} = \frac{\bar{y}^{HS} - \frac{\eta}{2\Delta}R}{\tau_{12} \left[1 + \frac{1}{\tau_{12}} \left(\frac{\eta}{2\Delta} - \frac{1}{12}\eta R \right) \right]}, \quad (71)$$

where R is a solution of the quartic equation.

In order to find the physically meaningful zeroes of $M_{\rho\rho}$ and M_{xx} we proceed as follows. First we compute all the four roots R_i , $i=a,b,c,d$ of the quartic equation and, hence, $(\bar{y}_{11})_i = (\bar{y}_{11})_i(\tau^*, \eta, \nu_{12})$, and $(\bar{y}_{12})_i = (\bar{y}_{12})_i(\tau^*, \eta, \nu_{12})$ are the cavity functions at contact obtained using the root R_i , while $(M_{\rho\rho})_i$ and $(M_{xx})_i$ are the diagonal elements of \mathbf{M} obtained using for the cavity functions at contact $(\bar{y}_{11})_i$ and $(\bar{y}_{12})_i$. As it turns out, only two roots R_i will give physically admissible cavity functions at contact. Then we compute the zeroes of

FANTONI, GAZZILLO, AND GIACOMETTI

PHYSICAL REVIEW E 72, 011503 (2005)

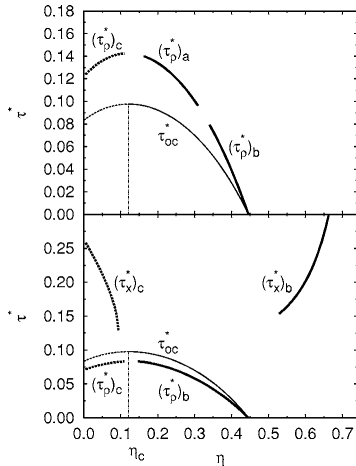


FIG. 4. Spinodal line for the symmetric mixture in the PY approximation with $\nu_{12}=2$ in the top panel and with $\nu_{12}=2/3$ in the bottom panel. At $\nu_{12}=2$ the instability is of pure condensation along $\tau^*=(\tau_\rho^*)_i$, $i=a,b$ and of pure demixing along $\tau^*=(\tau_x^*)_i$, $i=a,b$. The zeroes labeled c are unphysical. The gaps between the curves $\tau^*=(\tau_\rho^*)_i$ are numerical artifacts. At $\nu_{12}=2/3$ there is the appearance of a pure demixing spinodal at high η which does not cross the pure condensation one. For reference we also plot in both panels the spinodal of the one component system τ_{oc}^* [see Eq. (76)] which is physical only for $\eta > \eta_c = (3\sqrt{2}-4)/2 = 0.1213\dots$

$(M_{\rho\rho})_i$, denoted as $\tau^*=(\tau_\rho^*)_i(\eta, \nu_{12})$, and of $(M_{xx})_i$, denoted as $\tau^*=(\tau_x^*)_i(\eta, \nu_{12})$. Then physical zeroes are then selected by the requirement that

$$\lim_{\nu_{12} \rightarrow 1} (\bar{y}_{11})_i((\tau_\alpha^*)_i, \eta, \nu_{12}) = \lim_{\nu_{12} \rightarrow 1} (\bar{y}_{12})_i((\tau_\alpha^*)_i, \eta, \nu_{12}) = \bar{y}_+^{oc}((\tau_\alpha^*)_i, \eta) \quad \alpha = \rho, x, \quad (72)$$

where \bar{y}_+^{oc} is the physical cavity function at contact for the one-component system

$$\bar{y}_\pm^{oc}(\tau, \eta) = \frac{1}{2} \left[1 + \frac{\eta}{\Delta} \frac{1}{\tau} \pm \sqrt{\left(1 + \frac{\eta}{\Delta} \frac{1}{\tau}\right)^2 - \frac{\eta}{3} \frac{y^{HS}}{\tau^2}} \right]. \quad (73)$$

Using constraint (72) we find that the correct physical solution is $R=R_b$ at high η , the only one such that

$$\lim_{\tau \rightarrow \infty} (\bar{y}_{11})_b = \lim_{\tau \rightarrow \infty} (\bar{y}_{12})_b = \bar{y}^{HS}, \quad (74)$$

$$\lim_{\eta \rightarrow 0} (\bar{y}_{11})_b = \lim_{\eta \rightarrow 0} (\bar{y}_{12})_b = 1, \quad (75)$$

while at small η the solution to use is $R=R_a$ such that condition (72) is satisfied. As for the one-component system there is an interval $[0, \eta_e]$ where there are no physical zeroes. For the one-component case the spinodal

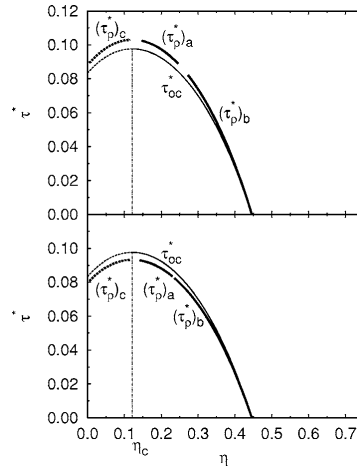


FIG. 5. Same as Fig. 4 with $\nu_{12}=1/0.9$ in the top panel and $\nu_{12}=1/1.1$ in the bottom panel. In this last case the expected line of pure demixing would start at $\eta > \eta_0 = 0.7404\dots$ in the unphysical range of densities.

$$\tau^* = \tau_{oc}^* = \frac{1 + 4\eta - 14\eta^2}{12(1-\eta)(1+2\eta)}, \quad (76)$$

exists only if $\eta > \eta_c$ where $\eta_c = \eta_c^{PY} = (3\sqrt{2}-4)/2 = 0.1213\dots$ and η_c^{PY} is the PY critical packing fraction. For the binary symmetric mixture, numerical results strongly suggest the coincidence of η_c with the critical packing fraction (see Figs. 4 and 5) but we have not succeeded in proving it (nor in determining an expression for it). The unphysical continuation of the pure condensation spinodal in the range $[0, \eta_c]$ is given by the root $R=R_c$ such that

$$\lim_{\nu_{12} \rightarrow 1} (\bar{y}_{11})_c((\tau_\alpha^*)_c, \eta, \nu_{12}) = \lim_{\nu_{12} \rightarrow 1} (\bar{y}_{12})_c((\tau_\alpha^*)_c, \eta, \nu_{12}) = \bar{y}_-^{oc}((\tau_\alpha^*)_c, \eta) \quad \alpha = \rho, x. \quad (77)$$

Notice that this solution would also give, in the same range of η , an unphysical spinodal of pure demixing whenever $\nu_{12} < 1$.

The zeroes $\tau^*=(\tau_\rho^*)_i$ and $\tau^*=(\tau_x^*)_i$ are shown in Fig. 4 for $\nu_{12}=2$, and for $\nu_{12}=2/3$ (the same conditions as in Figs. 2 and 3, respectively). As it happened in the mMSA, for $\nu_{12} > 1$ there is only a spinodal of pure condensation, while for $\nu_{12} < 1$ a spinodal of pure demixing appears at high η , as expected on physical grounds. However, unlike the mMSA case, the pure demixing and the pure condensation lines do not merge. Also the shapes and numerical values of the PY spinodals significantly differ from the mMSA ones. In Fig. 5 we select ν_{12} slightly above 1 and slightly below 1 in order to check the correct convergence towards the one-component case. At $\nu_{12}=1/1.1$ the line of pure demixing appears in the physically non-accessible region $\eta > \eta_0$.

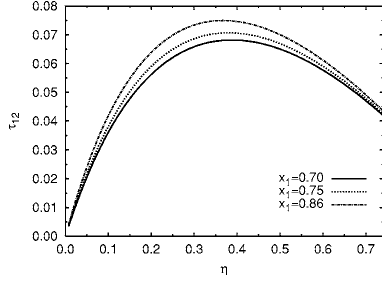


FIG. 6. For system A the mMSA spinodal [see Eq. (84)] for $\zeta = 2$ and three different values of x_1 .

V. TWO PARADIGMATIC SYSTEMS

The next two mixtures can be regarded as paradigmatic examples of a system where one expects to have a predominant condensation or predominant demixing type of thermodynamic instability. The thermodynamics of these mixtures have been previously investigated by Barboy and Tenne [14] within the PY approximation. In the following we shall extend this analysis of the instability type both within mMSA and PY closures. The two systems are defined as follows: (system A) $\epsilon_{12} > 0, \epsilon_{11} = \epsilon_{22} = 0$; (system B) $\epsilon_{11} > 0, \epsilon_{12} = \epsilon_{22} = 0$. System A corresponds to a fluid where the HS potential acts between like particles and the SHS potential between unlike particles, while system B corresponds to HS (species 2) in a SHS fluid (species 1). Alternatively, on regarding the large spheres as the “solvent” and the small spheres as the “solvent,” systems A and B can be reckoned as a schematic model mimicking a “good” and a “poor” solvent, respectively [23].

For system A we have $\lambda_{11}^{BT} = \lambda_{22}^{BT} = 0$, so Eq. (53) reduces to a linear equation for \bar{y}_{12} with the following solution [which corrects Eq. (64) of Barboy and Tenne]

$$\bar{y}_{12} = \frac{\bar{y}_{12}^{HS}}{1 + \frac{\xi_2 \sigma_{12}}{2\Delta \tau_{12}}}, \quad (78)$$

where

$$\bar{y}_{12}^{HS} = \frac{1}{\Delta} + \frac{3 \xi_2 \sigma_1 \sigma_2}{2 \Delta^2 \sigma_{12}}, \quad (79)$$

is the HS expression for the contact cavity function.

For system B we have $\lambda_{12}^{BT} = \lambda_{22}^{BT} = 0$, so Eq. (53) reduces to a quadratic equation for \bar{y}_{11} . The only solution which reduces to the HS expression for $\tau_{11} \rightarrow \infty$, is [identical to Eq. (57) of Barboy and Tenne]

$$\bar{y}_{11} = \frac{\bar{y}_{11}^{HS}}{\frac{1}{2} \left[1 + \frac{\eta_1}{\Delta} \frac{1}{\tau_{11}} + \sqrt{\left(1 + \frac{\eta_1}{\Delta} \frac{1}{\tau_{11}} \right)^2 - \frac{\eta_1}{3} \bar{y}_{11}^{HS} \frac{1}{\tau_{11}^2}} \right]}, \quad (80)$$

where

$$\bar{y}_{11}^{HS} = \frac{1}{\Delta} + \frac{3 \xi_2}{2 \Delta^2} \sigma_1, \quad (81)$$

is the HS expression for the contact cavity function. The instability lines are again given by Eq. (58).

Let $\lambda_{ij}(\eta, x_1, \zeta)$ be the solution of the spinodal Eq. (58) for the only nonvanishing λ_{ij} . As the cavity functions must be positive, the spinodal exists only for those values of η, x, ζ for which $\lambda_{ij} > 0$. It may also happen (and it does in the PY case) that the spinodal equation

$$\lambda_{ij}^{(closure)} = \frac{\bar{y}_{ij}^{(closure)}(\tau_{ij}, \eta, x_1, \zeta)}{\tau_{ij}} = \lambda_{ij}(\eta, x_1, \zeta), \quad (82)$$

upon choosing the correct physical solution for $\bar{y}_{ij}^{(closure)}$, does not have any real positive solutions for τ , at certain values of η, x, ζ . For these values the spinodal predicted by the particular closure has loss of solution and the predicted value for the angle α has clearly no physical meaning.

A. Instabilities for system A

On setting

$$\lambda_A^{BT} = 3 + \sqrt{\left(3 + \frac{\Delta}{\eta_1} \right) \left(3 + \frac{\Delta}{\eta_2} \right)}, \quad (83)$$

for system A the solution of Eq. (58) within the mMSA approximation is

$$\tau_{12}^{mMSA} = \frac{\Delta}{\lambda_A^{BT}} \frac{\sigma_{12}^2}{\sigma_1 \sigma_2}, \quad (84)$$

while in the PY is

$$\tau_{12}^{PY} = \bar{y}_{12}^{HS} \tau_{12}^{mMSA} - \frac{\xi_2 \sigma_{12}}{2\Delta}, \quad (85)$$

and, in the limit of high dilution while keeping τ_{12}^{mMSA} constant, one finds $\tau_{12}^{PY} \rightarrow \tau_{12}^{mMSA}$, as expected in view of the fact that the PY contact cavity functions converge towards the mMSA contact cavity functions.

In order to exist, the instability line must clearly lie on the $\tau_{12} > 0$ side of the (τ_{12}, η) plane. It is easy to see that, while

$$\left. \frac{d\tau_{12}^{mMSA}}{d\eta} \right|_{\eta=0} > 0 \quad \text{for any choice of } x_1 \text{ and } \zeta, \quad (86)$$

we have that $(\sigma_1 < \sigma_2)$

$$\left. \frac{d\tau_{12}^{PY}}{d\eta} \right|_{\eta=0} > 0 \quad \text{only when} \quad \frac{\sigma_2}{\sigma_1 + \sigma_2} < x_1 < \frac{\sigma_2^3}{\sigma_1^3 + \sigma_2^3}. \quad (87)$$

So in the PY approximation the thermodynamic instability disappears as x_1 falls outside the range indicated in Eq. (87).

In Figs. 6 and 7 we depict the mMSA and PY spinodals, respectively, at a given value of ζ and three different values of x_1 for which the PY spinodal does exist. One clearly sees that conditions (86) and (87) result in a large scale difference between the two plots.

FANTONI, GAZZILLO, AND GIACOMETTI

PHYSICAL REVIEW E 72, 011503 (2005)

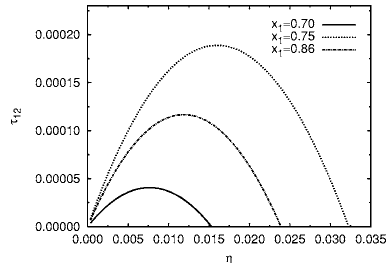


FIG. 7. For system A the PY spinodal [see Eq. (85)] under the same conditions considered in Fig. 6.

As regards the angle α , we know, from the discussion at the end of Sec. III, that the angles predicted by the two approximations are the same, and from Fig. 8 we see that the kind of instability is mainly of condensation type in accord with what we expected from the outset. Two exact limits are worth mentioning. First, the infinite dilute limit

$$\lim_{\eta \rightarrow 0} \alpha = \arctan \left[\frac{\sqrt{x_2/x_1} + \sqrt{\sigma_2/\sigma_1}}{\sqrt{\sigma_2 x_2/(\sigma_1 x_1)} - 1} \right], \quad (88)$$

provides an analytical check of the numerical results reported in Fig. 8. Second, when $\sigma_2 \gg \sigma_1$ one obtains

$$\lim_{\zeta \rightarrow \infty} \alpha = \arctan \sqrt{x_1/x_2}. \quad (89)$$

This result bears an interesting physical interpretation. As the fraction x_2 of large particles decreases, the angle α tends to $\pi/2$, that is to a condensation instability. This is in striking contrast with what one would expect for HS on the basis of an entropic depletion mechanism [32,33], which would tend to favor demixing in a system with a small number of large spheres. The reason for this can be traced back to the fact that in system A unlike particles have attractive interactions, thus preventing smaller particles to slip out from the interstitial region between two larger spheres. This interpretation

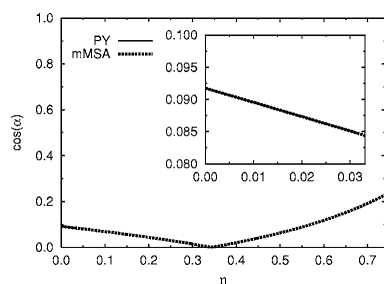


FIG. 8. Behavior of the angle α of Eq. (41) predicted by the mMSA and PY for system A when $x_1=0.75$, $\zeta=2$. In this case the PY spinodal has no solutions when $\eta > 0.03227\dots$. In the inset we show the region of η where the PY spinodal exists. Note that here and in the following $\cos \alpha$ rather than the angle α itself is depicted for visual convenience.

also holds true if one regards system A as a good solvent.

B. Instabilities for system B

Denoting

$$\lambda_B^{BT} = \frac{(1+2\eta)(1-\eta)}{\eta_1(1-\eta) + 3\eta_1\eta_2}, \quad (90)$$

for system B the solution of Eq. (58) within the mMSA is

$$\tau_{11}^{mMSA} = \frac{\Delta}{\lambda_B^{BT}}, \quad (91)$$

while in the PY approximation is

$$\tau_{11}^{PY} = \gamma_{11}^{HS} \tau_{11}^{mMSA} + \frac{\eta_1}{12\tau_{11}^{mMSA}} - \frac{\eta_1}{\Delta}, \quad (92)$$

for

$$\tau_{11}^{PY} > \frac{\eta_1}{\Delta} \left(\frac{\lambda_B^{BT}}{6} - 1 \right). \quad (93)$$

In view of the above constraint, there is an interval $\eta \in [0, \eta_c]$ where no physical spinodal exists. We stress that only for the one-component SHS limit ($x_2=0$) one finds that $\eta_c = \eta_c$, with η_c being the critical packing fraction, whereas in the more general case, studied here, this occurrence is no longer true, as shown in Fig. 10. Once again τ_{11}^{PY} , as given in Eq. (92), reduces to τ_{11}^{mMSA} , in the limit of high dilution, with τ_{11}^{mMSA} kept constant. However, unlike τ_{11}^{mMSA} , which is always a concave function of η for any choice of x_1 and ζ , τ_{11}^{PY} , it may display a van der Waals loop (see Fig. 10) as a function of η . The shape of the spinodal is strongly dependent on the content of the HS component in the mixture. When $x_1 < \bar{x}_1$ ($\bar{x}_1 \approx 0.8681\dots$ when $\zeta=1$) the spinodal is a monotonously increasing function of η , while for $x_1 > \bar{x}_1$ a loop appears. This point has already been emphasized by Barbooy and Tenne [14].

As previously remarked, even in this case both mMSA and PY results for α coincide in the respective range of existence. In Fig. 11 we see that the instability for system B tends to pure demixing for $\zeta=1$ and large η . As ζ is increased, one finds the same limit (89) as for system A. Once again the osmotic depletion mechanism fails because of the presence of stickiness this time among the small particles. As a further support to this interpretation, one also finds in the opposite limit

$$\lim_{\zeta \rightarrow 0} \alpha = \arctan \left(\frac{x_1 - \eta}{\sqrt{x_1 x_2}} \right). \quad (94)$$

In this case, when $x_1 = \eta$ the instability of the system is of a pure demixing type, so the solvent (particles of species 2) is a poor one. This is because the smaller particles (species 2) interact as HS both with larger spheres (species 1) and with each other. Hence, not only the depletion mechanism is not opposed in the present case, but, quite on the contrary, is favored by the attraction occurring between two big spheres (see Fig. 9). This results into the possibility for the existence of a demixing instability even if the HS binary mixture,

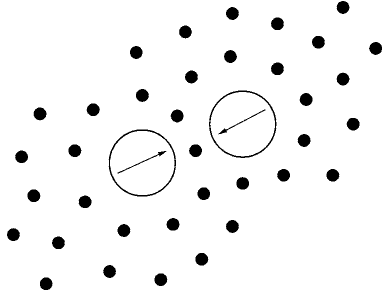


FIG. 9. In system B, when we have a small number of large particles of species 1, the demixing instability [see Eq. (94)] should be favored by the osmotic depletion mechanism, since the small spheres interact through a HS potential both among themselves and with the big spheres.

within the closures considered here, does not have any instability [see Eq. (98)]. One can also show that

$$\lim_{\eta \rightarrow 0} \alpha^{mMSA} = \arctan \sqrt{x_1/x_2}, \quad (95)$$

where α^{mMSA} is the angle predicted by the mMSA, whose spinodal does not have loss of solution at small η , or, upon using η_1, η_2, y as independent variables, $\lim_{\eta_1 \rightarrow 0} \alpha^{mMSA} = 0$.

Before closing this section, a word of caution should be given on the aforementioned interpretations. In order to have a clear and quantitative understanding of the depletion mechanism discussed in this section (for both systems A and B), the depletion potential, that is the effective potential among the large spheres mediated by the presence of the small ones, should be computed. Hence, the aforementioned scenarios should only be considered as a plausible possibility rather than a definite statement.

VI. FIVE BINARY MIXTURES TREATED WITH MMSA

As a final point it is instructive to consider a more general example. To this aim, it proves convenient to relate the adhesion strengths ϵ_{ij} to the particle sizes $\{\sigma_i\}$. Our past experience [26] suggests to consider five different cases, obtained setting $\epsilon_{ij}/\epsilon_0 = \mathcal{F}_{ij}^\mu(\sigma_1, \sigma_2)$ for $\mu=1, 2, 3, 4$, and 5. The functions \mathcal{F}^μ are selected as follows [26]

$$\frac{\epsilon_{ij}}{\epsilon_0} = \begin{cases} \langle \sigma \rangle^2 / \sigma_{ij}^2 & \text{case I,} \\ \sigma_i \sigma_j / \sigma_{ij}^2 & \text{case II,} \\ \langle \sigma^2 \rangle / \sigma_{ij}^2 & \text{case III,} \\ 1 & \text{case IV,} \\ \langle \sigma \rangle / \sigma_{ij} & \text{case V,} \end{cases} \quad (96)$$

where $\langle F \rangle \equiv \sum_i x_i F_i$. A critical justification leading to the above choice can be found in Ref. [26]. Note that since for all five cases the ϵ_{ij} are homogeneous functions of order zero in the diameters $\{\sigma_i\}$, the corresponding mixtures are invariant under a transformation where $V \rightarrow \lambda V$ and all $\sigma_i \rightarrow \lambda \sigma_i$ with λ a scale factor [34].

We have calculated the angle α defined in Eq. (41) on the spinodal [Eq. (58)] for all the cases listed in (96) within the mMSA closure. The angle α turns out to be the same for cases I and III. The results are shown in Figs. 12 and 13 for $x_1=1/2$ and two different values of ζ . We have only considered packing fractions $\eta \leq \eta_m = \pi\sqrt{2}/6$, where η_m is the maximum packing fraction for a ‘‘completely demixed’’ HS mixture (i.e., the packing fraction of a mixture where the spheres of species 1 are in a close packed configuration occupying a volume V_1 and the spheres of species 2 are in a closed packed configuration occupying a volume V_2 such that $V_2 \cap V_1 = 0$). It gives a lower bound to the true maximum packing fraction.

In cases I and III we have pure condensation as $\eta \rightarrow 0$. Case V display a pure condensation point at small but non-zero values of η . In case II we find a pure demixing point at high η , for sufficiently large ζ in the same region where in case IV we have a pure condensation point. The packing fraction of pure demixing for case II can be easily calculated to be

$$\eta = \frac{\langle \sigma \rangle \langle \sigma^3 \rangle}{\langle \sigma^4 \rangle}, \quad (97)$$

which turns out to be very close, albeit in general not coincident, with the packing fraction at which we find pure condensation in case IV.

We remark that (both for mMSA and PY) the presence of an instability curve for the SHS model is entirely due to the stickiness, since in the HS limit ($\tau \rightarrow \infty$) we have

$$\lim_{\tau \rightarrow \infty} \det[\hat{Q}(0)] = \frac{1 + 2\eta}{(1 - \eta)^2}, \quad (98)$$

which is always a positive quantity. Equation (98) can be derived from Eq. (54) by noticing that the contact values of the partial cavity functions \bar{y}_{ij} must remain finite as $\tau \rightarrow \infty$. So the above statement is actually valid for any closure in which the partial direct correlation functions vanish beyond σ_{ij} . In particular it is valid for the mMSA and the PY [35] approximations. For other, thermodynamically more consistent closures, the statement is no longer true since phase separation has been observed for highly asymmetric HS binary mixtures [36].

VII. CONCLUSIONS

In this work we have applied the method devised by Chen and Forstmann [5] to characterize the kind of thermodynamic instability to a number of carefully selected SHS binary systems. The crucial quantity turns out to be the Chen and Forstmann angle α , see Eq. (41), on the spinodal: when α is close to 0 the instability is of the pure demixing type, whereas a value close to $\pm\pi/2$ indicates a pure condensation instability.

The presence of adhesion between the spheres results in the existence of thermodynamic instabilities for the SHS model when treated within closures having the direct correlation functions vanishing beyond the hard core ranges, whereas it is known that the HS mixture within the same

FANTONI, GAZZILLO, AND GIACOMETTI

PHYSICAL REVIEW E 72, 011503 (2005)

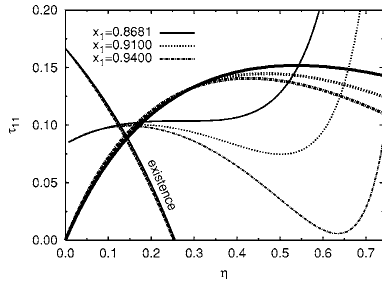


FIG. 10. For system B the spinodals predicted by mMSA [thick lines, see Eq. (91)] and the ones predicted by PY [thin lines, see Eq. (92)] for $\zeta=1$ at three different values of x_1 . The physically meaningful PY spinodals are those lying above the “existence” lines in accord with condition (93).

approximations do not show any instability [see Eq. (98)].

We have first considered the symmetric binary mixture in the mMSA (see Sec. IV A) and in the PY approximation (see Sec. IV B). This latter case was already considered by Chen and Forstmann for a different potential. We have found that when $\epsilon_{11} \leq \epsilon_{12}$ the instability is of pure condensation along the whole spinodal [see Fig. 2 and Eq. (63) for the mMSA, and Figs. 4 and 5 for the PY], while when $\epsilon_{11} > \epsilon_{12}$ a pure demixing spinodal appears at large packing fractions [see Fig. 3 and Eqs. (63) and (64) for the mMSA, and Figs. 4 and 5 for the PY], all within their respective limits of validity. This general behavior appears to be characteristic of symmetric binary mixtures, in the sense that it is observed in systems with pair potentials more “complex” than the SHS potential (hard spheres with Yukawa tails [37], square well [31], Lennard–Jones [38], etc.) which do not admit analytic solutions. The condensation and demixing lines are found to meet at a point in the mMSA, whereas they do not merge within the PY approximation.

Other two interesting examples can be treated in detail from an analytical point of view as discussed in Sec. V. We compared the spinodals and the angles α predicted by mMSA with those predicted by PY for a binary mixture with $\epsilon_{12} > 0$ and $\epsilon_{11} = \epsilon_{22} = 0$ (system A) and one with $\epsilon_{11} > 0$ and $\epsilon_{12} = \epsilon_{22} = 0$ (system B). Being the SHS interaction attractive, one should expect system A to present mainly condensation instabilities and system B mainly demixing instabilities. These choices for the ϵ_{ij} reduce Eq. (53) for the contact values of the cavity functions in the PY approximation at most to a quadratic one, simplifying calculations considerably. We find that the spinodals predicted by the two approximations are very different both quantitatively and qualitatively [see Figs. 6 and 7, and Eqs. (84) and (85) for system A, and Fig. 10 and Eqs. (91) and (92) for system B]. Nonetheless the corresponding angles α do not depend on the closure, when this is chosen within the GPY large class containing mMSA and PY as particular cases. In agreement with our expectations, we find that the instabilities of system A are predominantly of the condensation type (see Fig. 8), while the ones of system B of the demixing type when $\zeta=1$ (see Fig. 11). For system B when we have a small number of

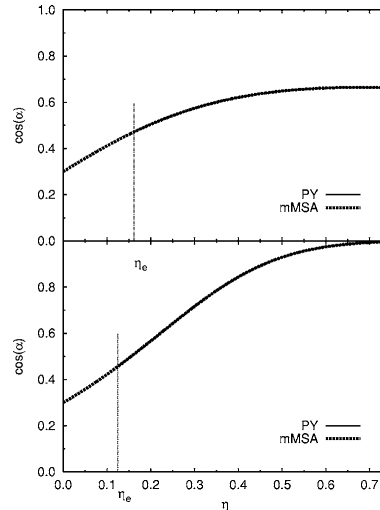


FIG. 11. For system B behavior of the angle α of Eq. (41) predicted by mMSA and PY for $x_1=0.91$ and $\zeta=1$ in the bottom panel (in this case the PY spinodal has loss of solution for $\eta < \eta_e \approx 0.1248\dots$) and $\zeta=2$ in the top panel (in this case the PY spinodal has loss of solution for $\eta < \eta_e \approx 0.1614\dots$).

large spheres of species 1, the demixing instability may be favored by both the osmotic depletion mechanism [32] and the stickiness between the large spheres (see Fig. 9).

In the more general case, the pair potential depends in general on three parameters: the ratio of the sphere diameters of the two species, $\zeta = \sigma_2 / \sigma_1$, and two dimensionless parameters which measure the relative strength of surface adhesiveness, $\nu_{22} = \epsilon_{22} / \epsilon_{11}$ and $\nu_{12} = \epsilon_{12} / \epsilon_{11}$. A reduction occurs when the latter are connected to the former through plausible relationships $\epsilon_{ij} = \epsilon_0 \mathcal{F}_{ij}(\sigma_1, \sigma_2)$. Following our previous work [26], we have considered five possible cases [see Sec. IV and Eq. (96)]. We find that four of the five cases exhibit very distinct types of instabilities (see Figs. 12 and 13): Cases I and III have the same angle α , with pure condensation at $\eta \rightarrow 0$ and predominant demixing for $\eta > 0$; case V has a pure condensation instability point at low packing frac-

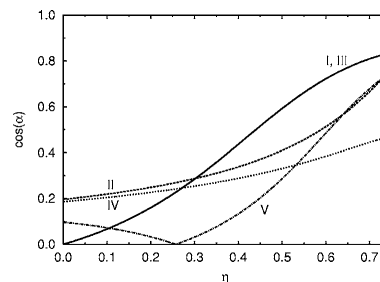


FIG. 12. Behavior of the angle α of Eq. (41) for cases I, II, III, IV, and V when $x_1=1/2$ and $\zeta=3/2$.

THERMODYNAMIC INSTABILITIES OF A BINARY...

PHYSICAL REVIEW E 72, 011503 (2005)

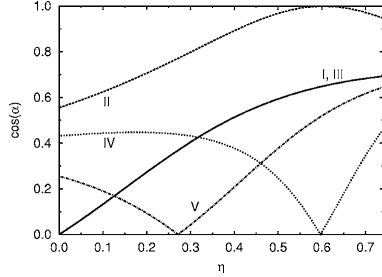


FIG. 13. Behavior of the angle α of Eq. (41) for cases I, II, III, IV, and V when $x_1=1/2$ and $\zeta=5$.

tions; case IV has a pure condensation instability point at high packing fractions provided that ζ is sufficiently large, whereas case II has a pure demixing instability point under the same conditions.

It would be desirable to extend the present study in two respects. First it would be interesting to consider different, more sophisticated, closures, in view of our results on the two examples (denoted as systems A and B) where the angle α is shown to be independent of the particular closure within the GPY class, in spite of a large difference in the corresponding instability curves. Second, it would be nice to test the analytical predictions given in this work against numerical simulations, with a particular attention to what concerns the depletion mechanism. We plan to address both issues in a future work.

ACKNOWLEDGMENT

This work was supported by the Italian MIUR (PRIN-COFIN 2004/2005).

APPENDIX: THERMODYNAMIC RELATIONS FOR THE ELEMENTS OF THE M MATRIX

In this appendix we gather together some well known relationships between thermodynamic quantities and the results obtained in the main text. The Ashcroft–Langreth partial structure factors [39] of an homogeneous and isotropic p -component mixture are related to the partial total correlation functions as

$$S_{ij}(k) = \delta_{ij} + \rho \sqrt{x_i x_j} \tilde{h}_{ij}(k), \tag{A1}$$

where $x_i = \langle N_i \rangle / \langle N \rangle$ is the molar fraction of particles of species i and ρ the total density of the mixture. From the normalization condition for the partial pair distribution functions of the grand canonical ensemble follows

$$S_{ij}(0) = \sqrt{\frac{x_i}{x_j}} \left(\frac{\langle N_i N_j \rangle - \langle N_i \rangle \langle N_j \rangle}{\langle N_i \rangle} \right), \tag{A2}$$

The matrix $\tilde{\mathbf{A}}$, defined in Eq. (13) of the text, is related to the structure factors by

$$S_{ij}(k) = [\tilde{\mathbf{A}}^{-1}]_{ij}(k). \tag{A3}$$

We now relate composition fluctuations to thermodynamic quantities. The grand partition function is

$$e^{-\beta\Omega} = \sum_{N_1, \dots, N_p=0}^{\infty} e^{\beta[\sum_{i=1}^p N_i \mu_i - A(T, V, \{N_i\})]}, \tag{A4}$$

where $A(T, V, \{N_i\})$ is the Helmholtz free energy of a member of the grand canonical ensemble with given number of particles of each species, and the chemical potentials $\{\mu_i\}$ are to be determined from the average number of particles of each species

$$\langle N_i \rangle = \sum_{N_1, \dots, N_p=0}^{\infty} N_i e^{\beta[\Omega + \sum_{i=1}^p N_i \mu_i - A(T, V, \{N_i\})]}. \tag{A5}$$

We immediately find

$$\left(\frac{\partial \Omega}{\partial \mu_i} \right)_{T, V, \{\mu_{\bar{i}}\}} = - \langle N_i \rangle, \tag{A6}$$

and

$$\begin{aligned} \frac{1}{\beta} \left(\frac{\partial N_i}{\partial \mu_j} \right)_{T, V, \{\mu_{\bar{i}}\}} &= \langle N_i \rangle \left(\frac{\partial \Omega}{\partial \mu_j} \right)_{T, V, \{\mu_{\bar{i}}\}} + \langle N_i N_j \rangle \\ &= \langle N_i N_j \rangle - \langle N_i \rangle \langle N_j \rangle = \sqrt{x_i x_j} S_{ij}(0) \langle N \rangle, \end{aligned} \tag{A7}$$

where the index \bar{i} denotes all species different from i . Since the thermodynamic derivatives $(\partial N_i / \partial \mu_j)_{T, V, \{\mu_{\bar{i}}\}}$ are the elements of the inverse of the matrix whose elements are $(\partial \mu_i / \partial N_j)_{T, V, \{N_{\bar{i}}\}}$ we can invert the above relation to read

$$\beta \left(\frac{\partial \mu_i}{\partial N_j} \right)_{T, V, \{N_{\bar{i}}\}} = \frac{1}{\langle N \rangle \sqrt{x_i x_j}} [\mathbf{S}^{-1}]_{ij}(0) = \frac{1}{V \rho \sqrt{x_i x_j}} \tilde{\mathbf{A}}_{ij}(0), \tag{A8}$$

where we indicated with \mathbf{S} the matrix whose elements are the partial structure factors.

We now define the partial volumes as

$$v_i = \left(\frac{\partial V}{\partial N_i} \right)_{T, P, \{N_{\bar{i}}\}}. \tag{A9}$$

Since the total volume is an homogeneous function of order one in the extensive variables we must have

$$\sum_{i=1}^p N_i v_i = V, \tag{A10}$$

since the Gibbs free energy $G = G(T, P, \{N_i\})$ is an homogeneous function of order one in the extensive variables we must have

FANTONI, GAZZILLO, AND GIACOMETTI

PHYSICAL REVIEW E **72**, 011503 (2005)

$$\sum_{i=1}^p N_i \mu_i = G, \quad (\text{A11})$$

so in particular the chemical potentials will be homogeneous functions of order zero in the variables $\{N_i\}$, we can then write $\mu_i = \mu_i(T, P, \{\{N_{ij}\}\})$ where with the symbol $\{\{N_{ij}\}\}$ we mean that the variables $\{N_j\}$ can appear only as ratios. We also find

$$\left(\frac{\partial \mu_i}{\partial N_j}\right)_{T, V, \{N_{\bar{j}}\}} = \left(\frac{\partial \mu_i}{\partial N_j}\right)_{T, P, \{\{N_{\bar{j}}\}\}} + \frac{v_i v_j}{V \chi_T}, \quad (\text{A12})$$

where χ_T is the isothermal compressibility

$$\chi_T = -\frac{1}{V} \left(\frac{\partial V}{\partial P}\right)_{T, \{N_{\bar{j}}\}}. \quad (\text{A13})$$

Notice also that taking the partial derivative of Eq. (A11) with respect to N_j at constant T, P , and we find the following Gibbs–Duhem relation

$$\sum_{i=1}^p N_i \left(\frac{\partial \mu_i}{\partial N_j}\right)_{T, P, \{\{N_{\bar{j}}\}\}} = 0. \quad (\text{A14})$$

We want now find thermodynamic relations for the matrix elements M_{pp} , M_{xx} , and M_{px} of the binary mixture. We will do the calculation explicitly for M_{pp} and quote the final result for the other two elements. So from Eq. (23) we find for M_{pp}

$$\begin{aligned} M_{pp} &= x_1(1 - \rho x_1 \bar{c}_{11}) + x_2(1 - \rho x_2 \bar{c}_{22}) - \rho x_1 x_2 (\bar{c}_{12} + \bar{c}_{21}) \\ &= V \rho \beta \sum_{i,j=1}^2 x_i x_j \left(\frac{\partial \mu_i}{\partial N_j}\right)_{T, V, \{N_{\bar{j}}\}} = \frac{\rho \beta}{\chi_T} \sum_{i,j=1}^2 x_i x_j v_i v_j = \frac{\chi_T^0}{\chi_T}, \end{aligned} \quad (\text{A15})$$

where $\chi_T^0 = \beta/\rho$ is the isothermal compressibility of the ideal gas, in the second equality Eqs. (13) and (A8) were used, in the third equality we used Eqs. (A12) and (A14) and in the last equality Eq. (A10). For M_{px} we find

$$M_{px} = \sqrt{x_1 x_2} \delta \frac{\chi_T^0}{\chi_T}, \quad (\text{A16})$$

where

$$\delta \equiv \rho(v_1 - v_2) = \frac{1}{V} \left(\frac{\partial V}{\partial x_1}\right)_{T, P, N}, \quad (\text{A17})$$

and for M_{xx}

$$M_{xx} = x_1 x_2 \delta^2 \frac{\chi_T^0}{\chi_T} + x_1 x_2 \frac{\chi_T^0}{V} \left(\frac{\partial^2 G}{\partial x_1^2}\right)_{T, P, N}. \quad (\text{A18})$$

The determinant factorizes

$$\det(\mathbf{M}) = \det(\tilde{\mathbf{A}}) = [\det(\hat{\mathbf{Q}})]^2 = x_1 x_2 \frac{(\chi_T^0)^2}{\chi_T} \left(\frac{\partial^2 G}{\partial x_1^2}\right)_{T, P, N},$$

thus yielding Eq. (26) in the main text.

- [1] J. S. Rowlinson, *Liquids and Liquid Mixtures*, 2nd ed. (Butterworths, London, 1969).
- [2] C. H. P. Lupis, *Chemical Thermodynamics of Materials* (North-Holland, Dordrecht, 1983).
- [3] D. Gazzillo, *Mol. Phys.* **83**, 1171 (1994).
- [4] D. Gazzillo, *Mol. Phys.* **84**, 303 (1995).
- [5] X. S. Chen and F. Forstmann, *J. Chem. Phys.* **97**, 3696 (1992).
- [6] C. P. Ursenbach and G. N. Patey, *J. Chem. Phys.* **100**, 3827 (1994).
- [7] A. B. Bhatia and D. E. Thornton, *Phys. Rev. B* **2**, 3004 (1970).
- [8] R. J. Baxter, *J. Chem. Phys.* **49**, 2770 (1968).
- [9] R. J. Baxter, in *Physical Chemistry, an Advanced Treatise*, edited by D. Henderson (Academic Press, New York, 1971) Vol. 8A, Chap. 4.
- [10] R. O. Watts, D. Henderson, and R. J. Baxter, *Adv. Chem. Phys.* **21**, 421 (1971).
- [11] R. J. Baxter, *J. Chem. Phys.* **52**, 4559 (1970).
- [12] B. Barbo, *Chem. Phys.* **11**, 357 (1975).
- [13] J. W. Perram and E. R. Smith, *Chem. Phys. Lett.* **35**, 138 (1975).
- [14] B. Barbo and R. Tenne, *Chem. Phys.* **38**, 369 (1979).
- [15] G. Stell, *J. Stat. Phys.* **63**, 1203 (1991).
- [16] C. Robertus, W. H. Philipse, J. G. H. Joosten, and Y. K. Levine, *J. Chem. Phys.* **90**, 4482 (1989).
- [17] S. H. Chen, J. Rouch, F. Sciortino, and P. Tartaglia, *J. Phys.: Condens. Matter* **6**, 10855 (1994).
- [18] H. Löwen, *Phys. Rep.* **237**, 249 (1994).
- [19] G. Nägele, *Phys. Rep.* **272**, 215 (1996).
- [20] D. Gazzillo and A. Giacometti, *J. Chem. Phys.* **113**, 9837 (2000).
- [21] D. Gazzillo and A. Giacometti, *J. Chem. Phys.* **120**, 4742 (2004).
- [22] Note that the mMSA solution for the Baxter factor function of the SHS binary model can also be obtained (see Ref. [40]) from the model of a mixture of hard spheres interacting through Yukawa potentials in the MSA (see Ref. [41]) upon taking the limit of a vanishing screening length.
- [23] M. H. G. M. Penders and A. Vrij, *Physica A* **173**, 532 (1991).
- [24] C. Regnaut, S. Amokrane, and Y. Heno, *J. Chem. Phys.* **102**, 6230 (1995).
- [25] S. Amokrane and C. Regnaut, *J. Chem. Phys.* **106**, 376 (1997).
- [26] R. Fantoni, D. Gazzillo, and A. Giacometti, *J. Chem. Phys.* **122**, 034901 (2005).
- [27] J. M. Caillol, *J. Phys. A* **35**, 4189 (2002).
- [28] L. D. Landau and E. M. Lifshitz, *Statistical Physics*, 3rd ed. (Butterworth-Heinemann, 2001), Part 1.
- [29] Note that in the mMSA, unlike in the PY, $y_{ij}(\sigma_{ij}^+)$ differs from $y_{ij}(R_{ij}^+)$ even in the sticky limit, in view of the fact that $y_{ij}(r)$ is not continuous at R_{ij} . This feature allows to obtain the correct HS result in the limit of no adhesion.
- [30] Our Eq. (54) corrects Eq. (60) of Barbo and Tenne (see Ref. [14]) where a sign is misprinted. Note also that these authors

THERMODYNAMIC INSTABILITIES OF A BINARY...

PHYSICAL REVIEW E **72**, 011503 (2005)

use the symbol d_{ij} in place of our σ_{ij} and $\tau_{ij}^{BT}=6\tau_{ij}$ where the superscript *BT* indicates that the symbol is the one used by Barboy and Tenne.

- [31] N. B. Wilding, F. Schmid, and P. Nielaba, *Phys. Rev. E* **58**, 2201 (1998).
- [32] S. Asakura and F. Oosawa, *J. Chem. Phys.* **22**, 1255 (1954).
- [33] J. L. Barrat and J. P. Hansen, *Basic Concepts for Simple and Complex Liquids* (Cambridge University Press, Cambridge, 2003).
- [34] P. Sollich (unpublished), after the submission of this work it has been brought to our attention [P. Sollich (private communication)] that cases I, III, and V have a pair interaction potential [see Eq. (45)] which might include many-body effects due to the presence of the averages. This is because, for instance, the interaction between two particles of species 1 depends also on the diameter of the particles of species 2. As a complement to this observation, we also note that as the diameter of one species of particles, say $\sigma_1 \rightarrow 0$, vanishes, then -according to Eq. (45)—those pointwise particles are noninteracting among themselves thus requiring $K_{11} \rightarrow 0$ as well. This constraint would rule out cases I and III.
- [35] J. L. Lebowitz and J. S. Rowlinson, *J. Chem. Phys.* **41**, 133 (1964).
- [36] T. Biben and J.-P. Hansen, *Phys. Rev. Lett.* **66**, 2215 (1991).
- [37] C. Jędrzejek, J. Konior, and M. Streszewski, *Phys. Rev. A* **35**, 1226 (1987).
- [38] O. Antonevych, F. Forstmann, and E. Diaz-Herrera, *Phys. Rev. E* **65**, 061504 (2002).
- [39] N. W. Ashcroft and D. C. Langreth, *Phys. Rev.* **156**, 685 (1967).
- [40] D. Gazzillo and A. Giacometti, *Mol. Phys.* **101**, 2171 (2003).
- [41] L. Blum and J. S. Høye, *J. Stat. Phys.* **19**, 317 (1978).

Part VI

2006

Chapter 11

Multicomponent adhesive hard sphere models and short-ranged attractive interactions in colloidal or micellar solutions

Gazzillo D., Giacometti A., **Fantoni R.**, and Sollich P., Phys. Rev. E. **74**, 051407 (2006)

Title: “Multicomponent adhesive hard sphere models and short-ranged attractive interactions in colloidal or micellar solutions”

Abstract: We investigate the dependence of the stickiness parameters $t_{ij} = 1/(12\tau_{ij})$ where the τ_{ij} are the conventional Baxter parameters on the solute diameters σ_i and σ_j in multicomponent sticky hard sphere (SHS) models for fluid mixtures of mesoscopic neutral particles. A variety of simple but realistic interaction potentials, utilized in the literature to model short-ranged attractions present in real solutions of colloids or reverse micelles, is reviewed. We consider: (i) van der Waals attractions, (ii) hard-sphere-depletion forces, (iii) polymer-coated colloids, and (iv) solvation effects (in particular hydrophobic bonding and attractions between reverse micelles of water-in-oil microemulsions). We map each of these potentials onto an equivalent SHS model by requiring the equality of the second virial coefficients. The main finding is that, for most of the potentials considered, the size-dependence of $t_{ij}(T, \sigma_i, \sigma_j)$ can be approximated by essentially the same expression, i.e., a simple polynomial in the variable $\sigma_i\sigma_j/\sigma_{ij}^2$, with coefficients depending on the temperature T , or for depletion interactions on the packing fraction η_0 of the depletant particles.

PHYSICAL REVIEW E 74, 051407 (2006)

Multicomponent adhesive hard sphere models and short-ranged attractive interactions in colloidal or micellar solutions

Domenico Gazzillo,^{1,*} Achille Giacometti,¹ Riccardo Fantoni,¹ and Peter Sollich²

¹Istituto Nazionale per la Fisica della Materia and Dipartimento di Chimica Fisica, Università di Venezia, S. Marta DD 2137, I-30123 Venezia, Italy

²Department of Mathematics, King's College London, Strand, London WC2R 2LS, United Kingdom

(Received 12 July 2006; published 22 November 2006)

We investigate the dependence of the stickiness parameters $t_{ij}=1/(12\tau_{ij})$ —where the τ_{ij} are the conventional Baxter parameters—on the solute diameters σ_i and σ_j in multicomponent sticky hard sphere (SHS) models for fluid mixtures of mesoscopic neutral particles. A variety of simple but realistic interaction potentials, utilized in the literature to model *short-ranged attractions* present in real solutions of colloids or reverse micelles, is reviewed. We consider: (i) van der Waals attractions, (ii) hard-sphere-depletion forces, (iii) polymer-coated colloids, and (iv) solvation effects (in particular hydrophobic bonding and attractions between reverse micelles of water-in-oil microemulsions). We map each of these potentials onto an equivalent SHS model by requiring the equality of the second virial coefficients. The main finding is that, for most of the potentials considered, the size-dependence of $t_{ij}(T, \sigma_i, \sigma_j)$ can be approximated by essentially the same expression, i.e., a simple polynomial in the variable $\sigma_i\sigma_j/\sigma_{ij}^2$, with coefficients depending on the temperature T , or—for depletion interactions—on the packing fraction η_0 of the depletant particles.

DOI: 10.1103/PhysRevE.74.051407

PACS number(s): 82.70.Dd, 82.70.Uv, 64.60.-i

I. INTRODUCTION

Theoretical investigation of solutions of *mesoscopic* particles—with sizes within the range $10-10^4$ Å—such as colloids, micelles, and globular proteins, is more problematic than the study of fluids with atomic or simple molecular constituents—with sizes within the range $1-10$ Å [1–4]. The main difficulties are due to the large difference between solute and solvent molecular sizes, as well to the possible presence of high electric charges and large charge-asymmetries. Treating mixtures of macroions and microions, with strong long-ranged Coulombic forces, represents a challenge for the most typical methods of the modern statistical-mechanical theory of fluids, namely Monte Carlo (MC) or molecular dynamics (MD) computer simulations and integral equations (IE) based on the Ornstein-Zernike equation coupled with approximate “closures” [5]. Large size-asymmetries entail very different time scales in MD simulations and may lead to ergodicity problems both in MC and MD calculations. Moreover, large size differences imply several difficulties even when using IE theories.

For simplicity, the present paper will be restricted to fluids of *neutral* particles with spherically symmetric interactions, neglecting all Coulombic forces due to net electric charges. Starting from a fluid mixture with one or more solute species (big particles, or macroparticles) and one “solvent” species (much smaller molecules or microparticles, which might be either a true solvent or polymer coils, smaller colloidal particles, etc.), we will adopt an *effective fluid* approach, which eliminates all large size asymmetries by averaging out the microscopic degrees of freedom corresponding to the solvent [6,7]. As a consequence, the influence of the solvent is incorporated into an *effective* potential for the interaction be-

tween big particles, and the initial mixture is reduced to a fluid made up of only solute molecules (one or more components). Usually, at the simplest level of description the effective potential includes, in addition to a steeply repulsive part, a very *short-ranged attractive* one, whose range is a small fraction of the macroparticle size. Recall that a force is said to be “short-ranged” if it derives from a potential $\phi_{ij}(r)$ which vanishes as r^{-n} with $n \geq 4$ when $r \rightarrow \infty$ [8,9]; the force $-\partial\phi_{ij}/\partial r$ then decays as $r^{-(n+1)}$. This definition of short-ranged potentials is clearly related to the second virial coefficient $B_{2,ij}$, which is a central quantity in our paper: when the forces are short-ranged in the above-mentioned sense, the integral which defines $B_{2,ij}$ [see Eq. (1) below] is finite, whereas it diverges for long-ranged interactions, i.e., when $r \leq 3$. Note that the definition of short-ranged forces is not unique in the literature. For instance, in Hirschfelder’s classical reference book [10] short-range forces are the “valence or chemical forces,” arising from overlap of electron clouds at very short intermolecular separations. The potential of such repulsive, and often highly directional, forces varies exponentially with the distance r . On the other hand, all potentials proportional to inverse powers of r are called “long-ranged” by Hirschfelder [11].

Once a reasonable approximation to the effective potential is known, it could be employed in both computer simulations or IE calculations. Unfortunately, IEs can be solved analytically only in very specific cases, for some potentials and within particular “closures” [5]. The simplest model with both repulsion and attraction which is analytically tractable refers to a fluid made up of hard spheres (HS) with an infinitely narrow and infinitely deep attractive tail. This highly idealized model of *adhesive* or *sticky hard spheres* (SHS) was proposed by Baxter [12], and admits an analytical solution within the Percus-Yevick (PY) approximation [12–14]. Notwithstanding its crudeness and known shortcomings [15], the SHS model is not a purely academic exercise. In fact, it

*Electronic address: gazzillo@unive.it

GAZZILLO *et al.*

PHYSICAL REVIEW E **74**, 051407 (2006)

has seen continuously growing interest in the last two decades because of its ability to describe semiquantitatively many properties of real fluids of neutral spherical particles, such as colloidal suspensions, micelles, protein solutions, microemulsions, and systems exhibiting phase transitions of several types (see, for example, Refs. [15–18] and references therein). Accurate simulation data for one-component SHS have recently been reported by Miller and Frenkel [19].

Because of the simplicity of the SHS model, it has often been suggested to model potentials comprising a hard core and short-ranged attractive tail by means of sticky potentials. To achieve this one needs to define an appropriate *equivalence* between the actual interaction and its *sticky representation*. This *mapping* of a generic short-ranged potential onto a SHS interaction is usually accomplished by requiring the two different models to have equal second virial coefficients [16,20]. Moreover, when applied to mixtures, this approach requires a further step, and this is the main point addressed in the present work.

In a series of earlier papers [21–25], we investigated the multicomponent SHS model, focusing on its possible application to *polydisperse* colloidal suspensions, namely to mixtures where the number p of components is so *large* that it can effectively be regarded as stemming from a continuous distribution. This is, for instance, the case of size polydispersity, where—in the discrete notation—a SHS mixture is fully characterized by two sets of parameters, i.e., the HS diameters $\{\sigma_i\}$ and the “stickiness” coefficients $\{t_{ij}=1/(12\tau_{ij})\}$ (τ_{ij} are Baxter’s parameters); the latter depend on temperature T and the strength of the interparticle adhesion. Intuitively, one expects t_{ij} to depend on the diameters σ_i and σ_j of the interacting particles i and j , but it is not easy to specify *a priori* the correct functional form, and in our previous papers we attempted some reasonably motivated choices for such a dependence.

The main purpose of the present paper is to investigate the relationship between stickiness coefficients and particle sizes, and thus to get new insights into the possible forms of the function $t_{ij}=t_{ij}(T, \sigma_i, \sigma_j)$, starting from a physically sound basis. To achieve this, we will present an overview of the most important short-ranged attractive interactions occurring in real solutions of colloids or micelles. In doing this, our claim is not to be fully exhaustive, but rather to gather sufficient physical information about the mechanisms which cause short-ranged attractive interactions in solutions of mesoscopic particles, and the corresponding simplest model potentials used for their representation.

By considering several different systems—dispersion forces, depletion forces, polymer-coated colloids, solvation forces (in particular, hydrophobic interactions and reverse micelles in water-in-oil microemulsions)—we have surprisingly found strong similarities among the simplest models employed to represent this wide variety of physical phenomena. By constructing, for each of the relevant potentials, an equivalent SHS representation, we will deduce and compare the corresponding expressions for $t_{ij}=t_{ij}(T, \sigma_i, \sigma_j)$.

The paper is organized as follows. In Sec. II we will introduce the basic formalism, concerning the second virial coefficient, the Baxter SHS model, and the mapping rule for getting the equivalent SHS potential from a given short-

range attraction. Section III is dedicated to the direct van der Waals interaction, while Secs. IV–VI survey the most important short-ranged attractions that are indirect, i.e., mediated by the solvent. The hydrophobic effect and interactions between reverse micelles will be considered in Sec. VI, as particular cases of solvation forces. For each model potential, a reasonable approximation to the corresponding $t_{ij}=t_{ij}(T, \sigma_i, \sigma_j)$ will be calculated. Finally, a summary, with a brief discussion, and our conclusions will be given in Sec. VII.

II. BASIC FORMALISM

A. Second virial coefficient

For a multicomponent fluid, the second virial coefficient of the osmotic pressure reads $B_2=\sum_{i,j}x_i x_j B_{2,ij}$, where x_i is the molar fraction of species i , and the partial second virial coefficient for the i - j interaction is given by

$$B_{2,ij} = -\frac{1}{2} \int f_{ij}(r) d\mathbf{r} = -2\pi \int_0^{+\infty} f_{ij}(r) r^2 dr, \quad (1)$$

with

$$f_{ij}(r) = \exp[-\beta\phi_{ij}(r)] - 1 \quad (2)$$

being the Mayer function, $\beta=(k_B T)^{-1}$, k_B the Boltzmann constant, and T the absolute temperature.

When the actual potential consists of a hard core plus a short-ranged attractive tail, i.e., $\phi_{ij}(r)=\phi_{ij}^{\text{HS}}(r)+\phi_{ij}^{\text{tail}}(r)$, one gets

$$B_{2,ij} = B_{2,ij}^{\text{HS}} + B_{2,ij}^{\text{tail}}, \quad (3)$$

$$B_{2,ij}^{\text{tail}} = -2\pi \int_{\sigma_{ij}}^{+\infty} f_{ij}^{\text{tail}}(r) r^2 dr = B_{2,ij}^{\text{HS}} \left[-3 \int_1^{+\infty} f_{ij}^{\text{tail}}(\sigma_{ij} x) x^2 dx \right], \quad (4)$$

where σ_i is the HS diameter for particles of species i and we set $\sigma_{ij}=(\sigma_i+\sigma_j)/2$ as usual, introducing also the shorthands $B_{2,ij}^{\text{HS}}=(2\pi/3)\sigma_{ij}^3$ and $f_{ij}^{\text{tail}}(r)=\exp[-\beta\phi_{ij}^{\text{tail}}(r)]-1$.

Often, the required integration cannot be performed analytically, but if $\phi_{ij}^{\text{tail}}(r)$ is sufficiently small compared to the thermal energy $k_B T$, then approximate analytical expressions may be obtained after expanding the Mayer function $f_{ij}^{\text{tail}}(r)$ in powers of $Y \equiv -\beta\phi_{ij}^{\text{tail}}(r)$. A numerical estimate of the range of applicability and the maximum relative error $\Delta_{\text{max}} = \max|1-f_{\text{approx}}/f|$, for each of the three simplest approximations, is

$$f = e^Y - 1 \approx \begin{cases} Y, & 0 < Y \leq 0.1, & \Delta_{\text{max}} \sim 5\% \\ Y + Y^2/2, & 0 < Y \leq 0.6, & \Delta_{\text{max}} \sim 5\% \\ Y + Y^2/2 + Y^3/6, & 0 < Y \leq 1, & \Delta_{\text{max}} \leq 3\%. \end{cases} \quad (5)$$

B. Adhesive hard spheres as a limiting case of square-well model

Probably, the simplest two-parameter representation of a spherically symmetric interaction with steeply repulsive core and short-ranged attractive tail is the *square-well* (SW) potential

$$\phi_{ij}^{SW}(r) = \begin{cases} +\infty, & 0 < r < \sigma_{ij} \\ -\epsilon_{ij}, & \sigma_{ij} \leq r \leq \sigma_{ij} + w_{ij} \\ 0, & r > \sigma_{ij} + w_{ij}, \end{cases} \quad (6)$$

with $\epsilon_{ij} > 0$ and w_{ij} being the depth and width of the well, respectively. The corresponding partial second virial coefficient reads

$$\begin{aligned} B_{2,ij}^{SW} &= B_{2,ij}^{HS} \{1 - (e^{\beta\epsilon_{ij}} - 1)[(1 + \Delta_{ij})^3 - 1]\} \\ &= B_{2,ij}^{HS} \left[1 - 3(e^{\beta\epsilon_{ij}} - 1) \left(\Delta_{ij} + \Delta_{ij}^2 + \frac{1}{3}\Delta_{ij}^3 \right) \right] \end{aligned} \quad (7)$$

with $\Delta_{ij} = w_{ij}/\sigma_{ij} \geq 0$. Equation (7) shows that, if the well is narrow ($\Delta_{ij} \ll 1$), $B_{2,ij}^{SW}$ can be significantly different from $B_{2,ij}^{HS}$ only when the attraction is strong enough ($e^{\beta\epsilon_{ij}} \gg 1$).

Unfortunately, despite the simplicity of the SW model, no satisfactory analytical solution of the resulting IEs has been found so far. However, such a solution *can* be found within the Percus-Yevick (PY) approximation for a special limiting case, when the well width Δ_{ij} goes to zero but the depth ϵ_{ij} goes to infinity in such a way that the contribution of the attraction to the second virial coefficient remains finite and different from zero (Baxter's sticky limit) [12]. The short-ranged attraction becomes a surface adhesion, and the particles of the resulting model are thus named *adhesive* or *sticky hard spheres*. From Eq. (7) one sees that Baxter's condition on $B_{2,ij}^{SW}$ requires the product $(e^{\beta\epsilon_{ij}} - 1)\Delta_{ij} \equiv t_{ij}$ to be independent of Δ_{ij} for small Δ_{ij} , and this leads to the following condition for the SW depth:

$$\epsilon_{ij}^{\text{Baxter SW}} = k_B T \ln \left(1 + \frac{t_{ij}}{\Delta_{ij}} \right). \quad (8)$$

As previously mentioned, our t_{ij} is simply related to Baxter's original parameter τ_{ij} by

$$t_{ij} = \frac{1}{12\tau_{ij}} \geq 0. \quad (9)$$

Here, t_{ij} measures the strength of surface adhesiveness or "stickiness" between particles of species i and j , and must be an unspecified *decreasing* function of T . In fact, as $T \rightarrow \infty$ one must also have $\tau_{ij} \rightarrow \infty$, in order to recover the correct HS limit. The SHS models must therefore satisfy the *high-temperature condition*

$$\lim_{T \rightarrow \infty} t_{ij} = 0. \quad (10)$$

A consequence of Eq. (8) is a very simple expression for the SW Mayer function

$$f_{ij}^{\text{Baxter SW}}(r) = \begin{cases} -1, & 0 < r < \sigma_{ij} \\ t_{ij}\sigma_{ij}/w_{ij}, & \sigma_{ij} \leq r \leq \sigma_{ij} + w_{ij} \\ 0, & r > \sigma_{ij} + w_{ij}. \end{cases} \quad (11)$$

Baxter focused on f_{ij} , since this quantity directly determines $B_{2,ij}$ and, furthermore, the coefficients in the cluster expansion of thermodynamic properties and correlation functions can be expressed in terms of multidimensional integrals of products of Mayer functions [5]. The simple functional form of $f_{ij}^{\text{Baxter SW}}(r)$ then allows one to calculate analytically many quantities of interest. In the "sticky limit" $\{w_{ij}\} \rightarrow \{0\}$, the Mayer function becomes

$$f_{ij}^{\text{SHS}}(r) = [\theta(r - \sigma_{ij}) - 1] + t_{ij}\sigma_{ij}\delta_+(r - \sigma_{ij}) \quad (12)$$

with $\theta(x)$ being the Heaviside function ($=0$ when $x < 0$, and $=1$ when $x > 0$) and $\delta_+(x)$ an asymmetric Dirac distribution [26], while the SHS second virial coefficient is simply

$$B_{2,ij}^{\text{SHS}} = B_{2,ij}^{\text{HS}}(1 - 3t_{ij}). \quad (13)$$

C. Mapping onto equivalent SHS model

On comparing Eqs. (13) and (4), one has

$$t_{ij}^{\text{eq(tail)}} = -\frac{B_{2,ij}^{\text{tail}}}{3B_{2,ij}^{\text{HS}}}, \quad (14)$$

and hence the following *mapping rule*: the parameters t_{ij} of the *equivalent* SHS model must be given by

$$t_{ij}^{\text{eq(tail)}} = \frac{1}{\sigma_{ij}^3} \int_{\sigma_{ij}}^{+\infty} f_{ij}^{\text{tail}}(r)r^2 dr = \int_1^{+\infty} f_{ij}^{\text{tail}}(\sigma_{ij}x)x^2 dx. \quad (15)$$

This is the main relation used in the remaining part of the paper. The superscript in $t_{ij}^{\text{eq(tail)}}$ means: this t_{ij} yields *the SHS potential equivalent to ϕ_{ij}^{tail}* .

III. VAN DER WAALS ATTRACTION

The main *direct* attraction between two *neutral* molecules i and j is the *van der Waals* (vdW) interaction, represented by the potential $\phi_{ij}^{\text{vdW}}(r) = -C_{ij}^{\text{vdW}}r^{-6}$, which is, in general, the sum of three different contributions. For most simple molecules—except the small highly polar ones—the vdW attraction is almost exclusively determined by the dispersion forces; the latter are in fact the only contribution to the vdW forces if both molecules are nonpolar.

A. Dispersion forces

The *dispersion* or *London* forces are *induced-dipole/induced-dipole* interactions, whose potential is given by the London formula [10]

$$\phi_{ij}^{\text{disp}}(r) = -\frac{C_{ij}}{r^6}, \quad C_{ij} = \frac{3}{2} \frac{I_i I_j}{I_i + I_j} \alpha'_i \alpha'_j \quad \text{for large } r, \quad (16)$$

where I_i and α'_i are, respectively, the ionization energy and *polarizability volume* for molecules of species i . As the name

GAZZILLO *et al.*

 PHYSICAL REVIEW E **74**, 051407 (2006)

suggests, α'_i has the dimensions of volume. It can also be written as $\alpha'_i/(4\pi\epsilon_0)$, where ϵ_0 is the permittivity of the vacuum and α_i is the polarizability of species i , which increases with increasing molecular size and number of electrons. Hence the polarizability volume is proportional to the molecular volume, i.e., $\alpha'_i \propto \sigma_i^3$.

This *polarizability effect* alone can produce considerable molecular attraction, and is responsible for the formation of liquid phases from gases of nonpolar substances (argon, hydrogen, nitrogen, etc.). The name “dispersion forces” stems from the fact that the electronic oscillations producing the London attraction are also responsible for the dispersion of light.

B. Hamaker’s macroscopic approximation

Colloids, micelles, and globular proteins are mesoscopic particles formed by a very large number of polarizable molecules (typically 10^{10} in micrometer-sized particles) [1]. As a consequence, the total attraction energy between such macroparticles can be obtained by pairwise summation of London energies between all molecules of the two interacting bodies. Hamaker [27] performed an approximate calculation [2] for the energy of interaction of two fully *macroscopic* bodies i and j in a vacuum, with densities ρ_i and ρ_j and occupying volumes V_i and V_j . Replacing the discrete distribution of molecules inside each body with a continuous one, Hamaker obtained for two spheres of arbitrary size [2]

$$\begin{aligned} \phi_{ij}^H(r) &= -\frac{A_{ij}^H}{12} \left[\frac{\sigma_i\sigma_j}{r^2 - \sigma_{ij}^2} + \frac{\sigma_i\sigma_j}{r^2 - L_{ij}^2} + 2 \ln \left(\frac{r^2 - \sigma_{ij}^2}{r^2 - L_{ij}^2} \right) \right] \\ &= -\frac{A_{ij}^H}{12} \left[\frac{\sigma_i\sigma_j}{r^2} \left(\frac{1}{1 - \sigma_{ij}^2/r^2} + \frac{1}{1 - L_{ij}^2/r^2} \right) \right. \\ &\quad \left. + 2 \ln \left(\frac{1 - \sigma_{ij}^2/r^2}{1 - L_{ij}^2/r^2} \right) \right], \end{aligned} \quad (17)$$

where $L_{ij} = |\sigma_i - \sigma_j|/2$, and $\sigma_{ij} < r < +\infty$. Here, $A_{ij}^H = \pi^2 \rho_i \rho_j C_{ij}$ [4] is referred to as Hamaker’s constant, and has dimensions of energy. As $C_{ij} \propto \alpha'_i \alpha'_j \propto \sigma_i^3 \sigma_j^3$, and $\rho_i \rho_j \propto \sigma_i^{-3} \sigma_j^{-3}$, A_{ij}^H is nearly independent of i and j . In the case where all mesoscopic particles are made up of the same material but have different diameters (discrete size polydispersity) A_{ij}^H reduces to $A_H = \pi^2 \rho^2 C$, which is a property of the material itself.

Hamaker’s macroscopic result has also been applied to mesoscopic particles, with the justification that the potential (17) has a *scaling property*: if r, σ_i, σ_j are all multiplied by a factor γ , the attraction energy remains unaltered, i.e., $\phi_{ij}^H(\gamma r, \gamma \sigma_i, \gamma \sigma_j) = \phi_{ij}^H(r, \sigma_i, \sigma_j)$. Note, however, that Hamaker’s formula refers to two spheres in free space, i.e., it neglects the screening of London forces due to the suspending medium.

In the limit $r \rightarrow +\infty$, a series expansion of Eq. (17) yields

$$\phi_{ij}^H(r) \approx -\frac{A_{ij}^H \sigma_i^3 \sigma_j^3}{36 r^6} \quad \text{for } r \gg \sigma_{ij} > L_{ij}, \quad (18)$$

which means that at large distances the two spheres behave, to leading order, like point-particles even though the factors σ_i^3 and σ_j^3 stem from HS volumes.

On the other hand, the Hamaker potential is singular at contact, i.e., when $r \rightarrow \sigma_{ij}$. This is due to the approximation of regarding the two spheres as continuous distributions of *point-particles*, neglecting all intermolecular repulsions. The leading divergence is

$$\begin{aligned} \phi_{ij}^H(r) &\approx -\frac{A_{ij}^H \sigma_i \sigma_j}{12 r^2 - \sigma_{ij}^2} \\ &\approx -\frac{A_{ij}^H \sigma_i \sigma_j}{24 \sigma_{ij}} \frac{1}{r - \sigma_{ij}} \quad \text{for } 0 < r - \sigma_{ij} \ll \min(\sigma_i, \sigma_j). \end{aligned} \quad (19)$$

This divergence simply means that the continuum picture must break down and molecular granularity, with excluded-volume effects, cannot be neglected once the closest distance $r - \sigma_{ij}$ between the two spherical surfaces becomes very small.

Such a deep attractive potential would lead to irreversible association or “floculation” of the suspended particles. This effect can be avoided in one of two different ways, namely by *charge stabilization* or *steric stabilization*. In the first case, some surface chemical groups of the particles become partially ionized in water, and the resulting electrostatic repulsion makes close contact impossible. In the second case, stabilization is achieved by grafting polymer chains (“hair”) to the particle surfaces. Both stabilization mechanisms—extensively used for colloidal suspensions—imply that the closest approach distance between i and j becomes larger than σ_{ij} , i.e., $\sigma_{ij}^{\text{eff}} = \sigma_{ij} + \delta$, with $\delta > 0$ being an additional characteristic length. The Hamaker singularity at contact is thus avoided, and the vdW attraction may then be treated as a small *perturbation*, if the effective HS diameter is sufficiently large compared to the bare one (in sterically stabilized colloidal suspensions, σ^{eff} exceeds σ typically by 10%). Moreover, it is possible to strongly reduce the value of the Hamaker constant by “refractive index matching” [2].

A numerical estimate of the strength of the Hamaker attraction is given, in the one-component case, for simplicity, by the quantity

$$Y_{\text{max}} \equiv -\beta \phi^H(\sigma + \delta) = 3H(1 + \lambda) \frac{T_H}{T}, \quad (20)$$

where $\lambda \equiv \delta/\sigma$,

$$H(u) = \frac{1}{u^2 - 1} + \frac{1}{u^2} + 2 \ln \left(1 - \frac{1}{u^2} \right), \quad (21)$$

and, from Eq. (18), we have defined a *Hamaker temperature* as

$$T_H = \frac{A_H}{36k_B}, \quad (22)$$

which depends on the material which constitutes the particles. In most cases, A_H lies between 10^{-20} and 10^{-19} J, i.e., $2k_B T \lesssim A_H \lesssim 20k_B T$, where $T = 298.15$ K. A typical value A_H

MULTICOMPONENT ADHESIVE HARD SPHERE MODELS...

PHYSICAL REVIEW E 74, 051407 (2006)

TABLE I. Approximate lower bound T^{\min}/K for the applicability of the linear, quadratic, cubic approximation to the Mayer function f_{ij} , as a function of the parameter $\lambda = \sigma_0/\sigma$ (see text).

Approximation	$\lambda=0.1$	$\lambda=0.2$	$\lambda=0.3$
Linear	6300	1800	700
Quadratic	1050	300	117
Cubic	630	180	70

$=0.5 \times 10^{-20} \text{ J}$ ($=10k_B T$) yields $T_H = 100 \text{ K}$, and thus, at room temperature,

$$\phi^H(\sigma + \delta) \approx \begin{cases} -2k_B T & \text{if } \lambda = 0.1 \\ -0.6k_B T & \text{if } \lambda = 0.2 \\ -0.2k_B T & \text{if } \lambda = 0.3. \end{cases}$$

Using Eq. (20) for Y_{\max} together with the criteria in Eq. (5), one finds the approximate lower bound T^{\min}/K for the applicability, respectively, of the linear, quadratic, and cubic approximations to the Mayer function, as reported in Table I.

Thus, whereas the linear approximation works only at high temperatures, the quadratic one is already sufficient even at room temperature if $\lambda \geq 0.2$.

Unfortunately, analytical integration of the expression (17) is not possible, and consequently no result for $f_{ij}^{\text{eq(H)}}$ can be obtained directly from $\phi_{ij}^H(r)$. Nevertheless, in order to get a rough approximation to $f_{ij}^{\text{eq(H)}}$, we propose an analytically integrable interpolation of the correct behavior of $\phi_{ij}^H(r)$ at short and large distances, i.e.,

$$\phi_{ij}^{\text{H-interp}}(r) = -\frac{A_{ij}^H}{36} \left\{ \frac{3\sigma_i\sigma_j}{2\sigma_{ij}} \frac{1}{r-\sigma_{ij}} \exp\left(-\frac{r-\sigma_{ij}}{L}\right) + \frac{\sigma_i^3\sigma_j^3}{r^6} \left[1 - \exp\left(-\frac{r-\sigma_{ij}}{L}\right) \right] \right\}, \quad (23)$$

where $\sigma_{ij} + \delta \leq r < +\infty$, and L acts as a screening length. When $\delta = 0.1\sigma$, $L = 0.108\sigma \approx \delta$ yields a satisfactory contact value, i.e., $\phi_{ij}^{\text{H-interp}}(\sigma_{ij} + \delta) \approx \phi_{ij}^H(\sigma_{ij} + \delta)$. Using the linear approximation, valid at high temperatures, one gets

$$f_{ij}^{\text{eq(H-interp)}} \approx \frac{1}{k_B T} \frac{A_{ij}^H \sigma_i \sigma_j}{24 \sigma_{ij}^2} \left[E_1\left(\frac{\delta}{L}\right) + 2e^{-\delta/L} \frac{L}{\sigma_{ij}} + \left(1 + \frac{\delta}{L}\right) e^{-\delta/L} \left(\frac{L}{\sigma_{ij}}\right)^2 \right],$$

where $E_1(z) = \int_z^{+\infty} \frac{e^{-u}}{u} du$ is the exponential integral. However, since the factors $L/\sigma_{ij}^2 \approx \delta/\sigma_{ij}^2$ refer to big particles, the leading term, at least within the linear approximation, is

$$f_{ij}^{\text{eq(H-interp)}} \approx \frac{3}{2} E_1\left(\frac{\delta}{L}\right) \left(\frac{T_H \sigma_i \sigma_j}{T \sigma_{ij}^2}\right). \quad (24)$$

C. Polarizable hard spheres: Sutherland model

Focusing only on the r^{-6} part of the Hamaker potential, which represents the long-distance polarizability, one could

define a simpler model, corresponding to a mixture of *mesoscopic* HS with dispersion attractions, called *polarizable* hard spheres (PHS), i.e.,

$$\phi_{ij}^{\text{PHS}}(r) = \begin{cases} +\infty, & 0 < r < \sigma_{ij} \\ -A_{ij}\sigma_i^3\sigma_j^3/r^6, & r \geq \sigma_{ij}, \end{cases} \quad (25)$$

where the choice

$$A_{ij} = \frac{A_{ij}^H}{36} \quad (26)$$

ensures the mesoscopic size of the particles. If all particles are made up of the same material substance, then $\phi_{ij}^{\text{PHS}}(r) = -A\sigma_i^3\sigma_j^3/r^6$ for $r \geq \sigma_{ij}$.

The potential (25) may be regarded as a special case of the *Sutherland model*, which represents rigid spheres which attract one another according to an inverse-power law, i.e., $\phi^{\text{Sutherland}}(r) = -\epsilon(\sigma/r)^b$ for $r \geq \sigma$ ($\epsilon > 0$) [10]. Indeed, one could rewrite it as $\phi_{ij}^{\text{PHS}}(r) = -\epsilon_{ij}^{\text{PHS}}(\sigma_{ij}/r)^6$, with $\epsilon_{ij}^{\text{PHS}} = A(\sigma_i\sigma_j/\sigma_{ij}^2)^3$ for particles with the same material composition.

The strength of this interaction, in the one-component case, is then given by

$$Y_{\max} \equiv -\beta\phi^{\text{PHS}}(\sigma) = \frac{T_H}{T} \approx \frac{100 \text{ K}}{T},$$

after taking $T_H \approx 100 \text{ K}$. From the results outlined in Eq. (5), a linearization of the Mayer function makes sense for $T \geq 1000 \text{ K}$. A quadratic approximation is feasible when $T \geq 167 \text{ K}$. Finally, the cubic approximation holds for $T \geq 100 \text{ K}$.

Therefore, in the multicomponent case, one can safely adopt the cubic approximation to $f_{ij}^{\text{PHS}}(r)$ and perform the integration in Eq. (15), obtaining

$$f_{ij}^{\text{eq(PHS)}} = 12 \frac{T_H}{T} \left(\frac{\sigma_i\sigma_j}{\sigma_{ij}^2}\right)^3 + 15 \left[\frac{T_H}{T} \left(\frac{\sigma_i\sigma_j}{\sigma_{ij}^2}\right)^3\right]^2 + 8 \left[\frac{T_H}{T} \left(\frac{\sigma_i\sigma_j}{\sigma_{ij}^2}\right)^3\right]^3. \quad (27)$$

In the one-component case this expression reduces to

$$f^{\text{eq(PHS)}} = 12 \frac{T_H}{T} + 15 \left(\frac{T_H}{T}\right)^2 + 8 \left(\frac{T_H}{T}\right)^3.$$

For $T_H \approx 100 \text{ K}$, this results, at $T \approx 300 \text{ K}$, in a value $f^{\text{eq(PHS)}} \approx 5.96$, which corresponds in Baxter's parametrization to

$$\tau = \frac{1}{12t} \approx 0.014,$$

and lies well below the critical temperature of the SHS fluid, $\tau_c = 0.1133 \pm 0.0005$ [19].

IV. EXCLUDED VOLUME DEPLETION FORCES

In general, the *indirect, solvent-mediated*, solute-solute interactions depend on both the solute-solvent and solvent-

TABLE II. Approximate upper bound η_0^{\max} for the applicability of the linear, quadratic, cubic approximation to the Mayer function f_{ij} , as a function of λ defined above.

Approximation	$\lambda=0.1$	$\lambda=0.3$	$\lambda=0.5$	$\lambda=0.7$	$\lambda=0.9$	$\lambda=1.0$
Linear	0.006	0.017	0.025	0.03	0.0375	0.04
Quadratic	0.04	0.10	0.15	0.19	0.23	0.24
Cubic	0.06	0.17	0.25	0.32	0.38	0.4

solvent ones, and thus may be very difficult to evaluate [6,7,20,28,29]. We will now report several very simplified cases.

Asakura and Oosawa (AO) [30], and independently Vrij [31], first showed that two big (colloidal, or solute) particles, immersed in a sea of small particles, feel a mutual attraction when their surfaces get closer than the size of the smaller particles (*depletion attraction*). This effect is an indirect attraction originating from the interactions of the two big particles with the small ones of the environment, even if these latter consist of, say, hard spheres. In mixtures with neutral components, the small particles—hereafter referred to also as *depletant* particles—may correspond, for example, to solvent molecules, nonadsorbing polymer coils, or smaller colloidal particles.

Upon adding, for instance, polymers to a stable colloidal suspension, the colloidal particles tend to aggregate. The polymer-induced depletion forces between the colloidal particles can cause formation of colloidal crystals or flocculation.

In the AO model, originally designed to describe colloid-polymer mixtures, the big-big (colloid-colloid) interactions as well as the big-small ones are modeled as excluded-volume HS interactions, while the small-small interactions are assumed to be zero (ideal gas approximation, corresponding to mutually interpenetrable, noninteracting depletant molecules). In particular, polymer coils are assumed to have an effective HS diameter equal to twice their radius of gyration.

Consider two big HS of species i and j at distance r , with radii R_i and R_j , in a dilute suspension of depletant spheres of species 0, with radius R_0 . The solute molecule i produces a spherical *excluded-volume* region of radius $\sigma_{i0}=R_i+R_0$ around itself where the centers of the depletant particles cannot penetrate; this is also called the *depletion zone*. When the shortest distance $r-(R_i+R_j)=r-\sigma_{ij}$ between the surfaces of i and j becomes less than the diameter $\sigma_0=2R_0$, the two depletion spheres surrounding i and j overlap and the small particles are expelled from the region between the big molecules. This implies that the thermal impact forces on the pair i and j from the “outside” are only partially compensated by those from the “inside” (see Fig. 8 of Ref. [31]). The depletion effect is due to this unbalanced pressure difference, which pushes the big particles together, resulting in a net attraction. From another point of view, the overlapping of excluded volumes implies that the total *free volume* accessible to small particles increases, leading to a gain in the

system entropy with a consequent decrease of the Gibbs free energy. This trend to decrease free energy produces an effective indirect attraction between the big spheres. AO and Vrij [30,31] evaluated the *HS-depletion* (HS-depl) potential as

$$\phi_{ij}^{\text{HS-depl}}(r) = \begin{cases} +\infty, & 0 < r < \sigma_{ij} \\ -\rho_0 k_B T V_{ij}^{\text{overlap}}(r), & \sigma_{ij} \leq r \leq D_{ij} \\ 0, & r > D_{ij}, \end{cases} \quad (28)$$

$$V_{ij}^{\text{overlap}}(r) = \frac{\pi}{12} \frac{1}{r} (D_{ij} - r)^2 \times [3D_{ii}D_{jj} - 4D_{ij}(D_{ij} - r) + (D_{ij} - r)^2], \quad (29)$$

where ρ_0 is the number density of the depletant molecules, $D_{ij} \equiv \sigma_{ij} + \sigma_0$, and $V_{ij}^{\text{overlap}}(r)$ denotes the lens-shaped overlap volume of two spheres with radii $\sigma_{i0}=(\sigma_i+\sigma_0)/2$ and $\sigma_{0j}=(\sigma_j+\sigma_0)/2$, at distance r (see Appendix). The attraction increases linearly with temperature and with the concentration of depletant particles. Since the AO model includes only HS interactions, the corresponding depletion forces have a purely entropic origin. Finally, it should be emphasized that the AO approximation is valid only for dilute suspensions of depletant molecules, i.e., at low ρ_0 values; formally, this last restriction can be removed by replacing ρ_0 by the density of polymer in a large reservoir connected to the system.

The tail of $\phi_{ij}^{\text{HS-depl}}(r)$ has a finite range, equal to the diameter σ_0 of the depletant molecules. The attraction strength can be estimated from

$$Y_{ij,\max} \equiv -\beta \phi_{ij}^{\text{HS-depl}}(\sigma_{ij}) = \eta_0 \left(1 + \frac{3}{2} \frac{\sigma_i \sigma_j}{\sigma_{ij} \sigma_0} \right), \quad (30)$$

where $\eta_0=(\pi/6)\rho_0\sigma_0^3$ is the packing fraction of the depletant particles. Note that $Y_{ij,\max}$ does not depend on temperature, but the attraction strength may be tuned by varying η_0 .

For one-component solutes, $Y_{ij,\max}$ reduces to $Y_{\max} = \eta_0(1 + 1.5/\lambda)$ with $\lambda \equiv \sigma_0/\sigma$. In this case—following again the criteria given in Eq. (5)—the upper boundary η_0^{\max} for the applicability of the linear, quadratic, and cubic approximations to the Mayer function given as a function of λ , respectively, is reported in Table II.

The quadratic approximation result for the equivalent SHS model is

$$t_{ij}^{\text{eq(HS-depl)}} \approx \frac{\eta_0}{2} \left[\frac{\sigma_i \sigma_j}{\sigma_{ij}^2} + \left(1 + \frac{1}{4} \frac{\sigma_i \sigma_j}{\sigma_{ij}^2} \right) \lambda_{ij} + \frac{1}{2} \lambda_{ij}^2 + \frac{1}{12} \lambda_{ij}^3 \right] + \frac{1}{10} \left(\frac{\eta_0}{2} \right)^2 \left[9 \left(\frac{\sigma_i \sigma_j}{\sigma_{ij}^2} \right)^2 \frac{1}{\lambda_{ij}} + 16 \frac{\sigma_i \sigma_j}{\sigma_{ij}^2} + \frac{4}{7} \left(\frac{13}{7} + 4 \frac{\sigma_i \sigma_j}{\sigma_{ij}^2} \right) \lambda_{ij} + \frac{17}{7} \lambda_{ij}^2 + \frac{17}{63} \lambda_{ij}^3 \right],$$

where $\lambda_{ij} \equiv \sigma_0 / \sigma_{ij}$. As remarked, this expression does not depend on T , since the solute-solvent interactions are of purely HS character. If $\lambda_{ij} \ll 1$, then the leading terms are

$$t_{ij}^{\text{eq(HS-depl)}} \approx \left[\frac{\eta_0}{2} + \frac{8}{5} \left(\frac{\eta_0}{2} \right)^2 \right] \left(\frac{\sigma_i \sigma_j}{\sigma_{ij}^2} \right) + \frac{9}{10} \left(\frac{\eta_0}{2} \right)^2 \frac{1}{\lambda_{ij}} \left(\frac{\sigma_i \sigma_j}{\sigma_{ij}^2} \right)^2.$$

Generalizing from the form of the quadratic approximation for general λ_{ij} , one expects the *cubic* approximation to yield a result of the form

$$t_{ij}^{\text{eq(HS-depl)}} \approx C_1 \left(\frac{\sigma_i \sigma_j}{\sigma_{ij}^2} \right) + C_2 \left(\frac{\sigma_i \sigma_j}{\sigma_{ij}^2} \right)^2 + C_3 \left(\frac{\sigma_i \sigma_j}{\sigma_{ij}^2} \right)^3. \quad (31)$$

Several other studies of depletion forces, which go beyond the entropic HS approach by taking into account more refined representations of the solute-solvent and solvent-solvent interactions, are also available in the recent literature [6,7,20,28,29].

V. POLYMER-COATED COLLOIDS OR HAIRY SPHERES

If the intermolecular attractive forces are strong enough, a colloidal suspension phase-separates, or even flocculates or gels. As explained above, stability against flocculation may be ensured by steric or charge stabilization. In steric stabilization, the colloidal molecules are coated with grafted polymers—the “hair”—which can prevent particles from coming sufficiently close to experience a strong vdW-attraction.

However, changing the solvent or the temperature may turn the effective interaction from repulsion (HS-behavior) to attraction [32–34]. When sterically stabilized colloidal particles are immersed in a *good* solvent for the polymer brushes, the solutes behave like HS, independently of temperature; this is the case, for example, of silica particles covered with a layer of octadecyl chains, when immersed in cyclohexane. On the other hand, for each *poor* solvent there exists a Flory’s *theta-temperature* T_θ [35], which is characteristic of the given solvent-polymer pair and has the following property: the solute particles behave like HS at $T > T_\theta$, whereas an attraction occurs at $T < T_\theta$. This occurs with, e.g.,

silica particles with octadecyl chains, when dispersed in benzene. The term “ θ -solvent” indicates a poor solvent at $T = T_\theta$.

These effects originate from a competition between polymer-solvent and polymer-polymer interactions. First, the nature of the solvent influences the polymer conformation. In fact, in a good solvent the interactions between polymer elements—monomer units—and adjacent solvent molecules are strongly attractive and thus predominate over possible intrachain polymer attractions. Consequently, the polymer will assume an “extended-chain” configuration, so as to reduce the number of intrachain contacts between monomer units. Polymer-coated colloidal particles will have fully extended hair and thus the largest HS diameter possible, corresponding to the strongest solute-solute repulsion.

In a poor solvent, on the other hand, the polymer-solvent attractions are weak. Now it is the temperature that determines the solute-solute interaction. At $T > T_\theta$ the hair will be fully extended, as in good solvents (HS behavior). At low temperatures $T < T_\theta$ the polymer segments find their own environment more satisfying than that provided by the solvent. This preference may produce more compact “globular” configurations, in which intrachain polymer-polymer contacts occur more frequently (“curly hair”). In an alternative view, when two solute particles are in close contact, a high number of polymer-polymer attractions is favored by the interpenetration of the two polymeric layers.

In the literature on sterically stabilized colloids [32–34], the attractive part of the potential for one-component *hairy hard spheres* (HHS)—due to the polymer-polymer interactions between surface layers of different particles—was described by a SW, with a depth proportional to the (maximum) *overlap volume* of the layers and temperature-dependent in analogy with the Flory-Krigbaum model for polymer segments [36]. The SW width equals the length of interpenetration of the stabilizing chains, whose maximum value coincides with the thickness ℓ of the polymeric layer.

For mixtures, we could consider the most direct extension of the one-component SW model. In such a case, using Eq. (15), a SW potential could immediately be mapped onto a SHS one:

$$t_{ij}^{\text{eq(SW)}} = [\exp(\beta \epsilon_{ij}^{\text{SW}}) - 1] \frac{1}{3} [(1 + \Delta_{ij}^{\text{SW}})^3 - 1]. \quad (32)$$

When the SW is very narrow ($\Delta_{ij}^{\text{SW}} \ll 1$), one can approximate

$$t_{ij}^{\text{eq(SW)}} \approx [\exp(\beta \epsilon_{ij}^{\text{SW}}) - 1] \Delta_{ij}^{\text{SW}}. \quad (33)$$

However, instead of a discontinuous SW model, we prefer to propose a potential with a similar but continuous attractive tail of finite range, i.e.,

$$\phi_{ij}^{\text{HHS}}(r) = \begin{cases} +\infty, & r < \sigma_{ij} \\ -k_B T F(T) \rho_\ell V^{\text{overlap}}(R_i + \ell, R_j + \ell, r), & \sigma_{ij} \leq r \leq \sigma_{ij} + 2\ell \\ 0, & r > \sigma_{ij} + 2\ell, \end{cases} \quad (34)$$

GAZZILLO *et al.*

 PHYSICAL REVIEW E **74**, 051407 (2006)

where

$$F(T) = \begin{cases} 0, & T > T_0 \\ T_0/T - 1, & T < T_0. \end{cases} \quad (35)$$

Here, we call $F(T)$ Flory's temperature-function, and $\phi_{ij}^{\text{HHS}}(r)$ is assumed to be proportional to the overlap volume between polymeric layers of the two HHS at separation r , with ρ_ℓ being a number density proportional to the polymer density in the stabilizing layer.

Within the linear approximation, one finds for the equivalent SHS model

$$t_{ij}^{\text{eq(HHS)}} \approx F(T) \frac{\eta_\ell}{2} \left[\frac{\sigma_i \sigma_j}{\sigma_{ij}^2} + \left(1 + \frac{1}{4} \frac{\sigma_i \sigma_j}{\sigma_{ij}^2} \right) \frac{2\ell}{\sigma_{ij}} + \frac{1}{2} \left(\frac{2\ell}{\sigma_{ij}} \right)^2 + \frac{1}{12} \left(\frac{2\ell}{\sigma_{ij}} \right)^3 \right],$$

where $\eta_\ell \equiv \frac{\pi}{6} \rho_\ell (2\ell)^3$. Since the thickness ℓ is much smaller than the particle sizes, one may expect—by analogy with the HS-depletion model—that the cubic approximation reads

$$t_{ij}^{\text{eq(HHS)}} \approx C_1 \left[F(T) \eta_\ell \frac{\sigma_i \sigma_j}{\sigma_{ij}^2} \right] + C_2 \left[F(T) \eta_\ell \frac{\sigma_i \sigma_j}{\sigma_{ij}^2} \right]^2 + C_3 \left[F(T) \eta_\ell \frac{\sigma_i \sigma_j}{\sigma_{ij}^2} \right]^3. \quad (36)$$

Note that, since $F(T)=0$ when $T > T_0$, then $\lim_{T \rightarrow +\infty} F(T) = 0$. Thus the form of $F(T)$ ensures that the high-temperature condition (10) is satisfied.

VI. SOLVATION FORCES: GURNEY-FRIEDMAN MODEL

An indirect interaction between solute particles may also arise from solvation. To picture solvation effects, Gurney [37] and Frank and Evans [38] introduced the physically intuitive concept of *cosphere* or *solvation layer*. One supposes that any isolated solute particle is surrounded by some region in which the solvent has different properties than the bulk solvent, since its structure is markedly affected by the presence of the solute: some of the solvent-solute bonds have been broken by the introduction of the “foreign” particle. Clearly, such a region has no well-defined boundary, but Gurney's model assumes that significant effects come from only the few solvent molecules that are directly next to the solute particles, i.e., in a spherical shell whose thickness δ is taken to be a few solvent diameters or even the size of only one solvent molecule (for water, a molecular diameter of 2.76 Å is acceptable). This picture was first applied to electrolyte solutions by Friedman and co-workers [39]. In the ionic case, however, the previous definition of cosphere, with the same thickness for every ionic species, may be too restrictive, since the solvation region may extend even outside the cosphere, as occurs for very small ions (Li^+ , and polyvalent ions such as Mg^{2+} , Ca^{2+} , etc.).

When two solute particles i and j approach sufficiently closely for their solvation layers to overlap, some of the cosphere solvent is displaced. Furthermore, the overlapping re-

gion contains solvent molecules which are now affected by the combined force field of two solutes, so that its structure might even differ from that of each isolated cosphere. The whole process, in which the sum of the cosphere volumes is reduced by overlap and the solvent relaxes to its normal bulk state, will be accompanied by a Gibbs free energy change. If the solvent molecules in the isolated solvation layers are in a state of lower free energy than those in the bulk, the overlap of two cospheres with the consequent expulsion of solvent gives rise to a free energy increase, and the resulting contribution to the interaction between two solutes is repulsive. When the solvent molecules in the solvation layers are in a state of higher free energy than those in the bulk, the expulsion of solvent from the overlapping region leads to a free energy decrease. In this case, both the free energy and the disruption of solvent structure are minimized when two solute particles i and j are brought close together, causing a net $i-j$ attraction.

Because of the lack of knowledge about the properties of the solvent in the solvation region, it is difficult to construct a detailed and physically sound microscopic model of the effects described above. Adopting a heuristic approach, Friedman and co-workers [39] proposed that the free energy change accompanying the cosphere overlapping of two HS solute particles i and j gives rise to the *Gurney potential*, defined by

$$\phi_{ij}^{\text{Gurney}}(r) = A_{ij}(T, p) \frac{V^{\text{overlap}}(R_i + \delta, R_j + \delta, r)}{v_0}. \quad (37)$$

Here the Gurney parameter A_{ij} is in general a function of temperature T and pressure p and represents the molar free energy of transfer of solvent from the overlapping region of the $i-j$ cospheres to the bulk. As previously discussed, $A_{ij} < 0$ corresponds to attraction. Furthermore, v_0 is the mean volume of a solvent molecule, while the volume of solvent returning to the bulk is given by the intersection volume of the cospheres surrounding the two solute HS at distance r , namely $V^{\text{overlap}}(R_i + \delta, R_j + \delta, r)$. The free-energy parameters A_{ij} were determined numerically by fitting the model to experimental data.

The close resemblance of $\phi_{ij}^{\text{Gurney}}(r)$ to both $\phi_{ij}^{\text{HHS}}(r)$ and $\phi_{ij}^{\text{HS-depl}}(r)$ is apparent. By analogy one obtains immediately

$$t_{ij}^{\text{eq(Gurney-solvation)}} \approx C_1 \left[E_{ij}(T, p) \frac{\sigma_i \sigma_j}{\sigma_{ij}^2} \right] + C_2 \left[E_{ij}(T, p) \frac{\sigma_i \sigma_j}{\sigma_{ij}^2} \right]^2 + C_3 \left[E_{ij}(T, p) \frac{\sigma_i \sigma_j}{\sigma_{ij}^2} \right]^3, \quad (38)$$

where

$$E_{ij}(T, p) = \frac{1}{2} \frac{|A_{ij}(T, p)|}{k_B T} \left[\frac{\pi}{6} \frac{(2\delta)^3}{v_0} \right]. \quad (39)$$

This expression may be applied, in particular, to both cases of solvation interactions—hydrophobic bonding and interactions between reverse micelles—whose physical origin will be illustrated in the following.

A. Hydrophobic interaction

The *hydrophobic interaction* (or *hydrophobic bonding*) consists in the tendency shown by nonpolar portions of molecules or ions with long nonpolar chains or aromatic groups, for example, surfactants, phospholipids, glycerides, and dye-stuffs, to aggregate in aqueous solutions, partially or completely removing such parts from contact with the solvent [2,40,41]. This *hydrophobic attraction* between nonpolar entities, which occurs exclusively in water, has, to a large extent, an *entropic* origin, related to the strong tendency of water molecules to form hydrogen bonds and associate [4].

The physical mechanisms underlying the solvation forces are rather well-understood when the solvent is water. Polar molecules or polar groups of a solute feel strong attraction towards water molecules, and thus are said to be *hydrophilic* (“water-loving”). On the other hand, nonpolar molecules or nonpolar groups “dislike” water, and are called *hydrophobic* (“water-hating,” or “water-avoiding”).

The *hydrophobic effect* means that nonpolar particles have an extremely weak solubility in water, since inserting one of them—a noble gas atom, a chlorine or oxygen molecule, a hydrocarbon molecule, etc.—into water may actually lead to an increase of Gibbs free energy, i.e., $\Delta G_{\text{solution}} > 0$. Indeed, the formation of a new cavity requires the breaking of many water-water hydrogen bonds with a considerable $\Delta G > 0$, which cannot be compensated by the small $\Delta G < 0$ provided by the new solute-water vdW interactions (the nonpolar solute cannot participate in the formation of hydrogen bonds). Then, in order to get a further decrease of G , the water molecules close to the solute reorient themselves, so as to create as many hydrogen bonds with adjacent water molecules as possible. The result is the formation of a “cage”—or hydration layer—around the solute, with more rigid water-water bonds than in the bulk. Such an additional *ordering* in the solvent, brought about by the introduction of a solute molecule, implies a significant entropy decrease, $\Delta S < 0$, and thus a strong positive contribution $-T\Delta S$ to the total $\Delta G = \Delta H - T\Delta S$ of solution at constant T and p . This explains why nonpolar particles are hydrophobic: one gets $\Delta G_{\text{solution}} > 0$, when the entropic contribution dominates over the enthalpic one ΔH , which is usually small and may be positive or negative. On the other hand, at higher temperatures the solubility increases, and one may find $\Delta G_{\text{solution}} < 0$. In fact, ΔS becomes much smaller because the molecular thermal motion struggles more efficiently against the structure formation around a nonpolar solute.

The same hydrophobic effect is responsible for the above-mentioned *hydrophobic bonding*, where nonpolar parts of molecules or ions tend to aggregate. In fact, the solvent molecules prefer mutual contacts over those with the “foreign” substance (solute), while the aggregation of solutes reduces the total volume of their “cages,” minimizing the loss of entropy. The hydrophobic interaction arises when overlap of hydration-layers occurs, and becomes increasingly attractive as the distance between two solute particles decreases.

This phenomenon in aqueous solutions of alcohols was studied by Friedman and Krishnan [42], who used a model potential containing a repulsive term of the r^{-9} form, plus an attractive Gurney term given by Eq. (37), representing the

overlap between cospheres. For the substances they considered, these authors found values of the Gurney coefficient A_{xx} in the range -190 to -60 cal mol $^{-1}$. The cosphere thickness δ was taken to be 2.76 Å, corresponding to one molecular layer of water.

Clark *et al.* [43] investigated the same physical systems with a more refined model, including a core potential based upon Lennard-Jones potentials for individual atom-atom interactions and again a Gurney term for the hydrophobic attraction. They found a minimum $\approx -0.5k_B T$ in their potentials of average force that implies an overall tendency for those alcohols to associate when in an aqueous environment.

Hydrophobic bonding is very important in interface and colloid science. It is often the driving force behind the way in which biomolecules organize themselves and it is responsible for the formation of micelles, bimolecular layers, and lamellar structures.

B. Reverse micelles in water-in-oil microemulsions

Molecules having both hydrophilic and hydrophobic parts are said to be *amphiphilic* (“dual-loving,” in the sense of being both “water-loving” and “water-hating;” from the Greek $\alpha\mu\phi\iota\lambda\iota\varsigma$ = “on both sides”). An important example is provided by relatively short chain molecules with an ionizable or polar (thus hydrophilic) head-group and a nonpolar (thus hydrophobic) tail, consisting of one or several flexible hydrocarbon chain(s). Since these molecules can significantly lower the surface tension of a solution, they are generically called *surfactants* or *surface-active agents* [1,2,41]. When immersed in water, the head-group may become negatively or positively charged, or it remains polar with no net electric charge. Accordingly, the surfactants are classified as *anionic*, *cationic*, or *nonionic*.

Clearly, it is the hydrophilic head-group that keeps a surfactant solute dissolved in the water. The hydrophobic tail tends to avoid contact with water and to seek, as far as possible, a nonaqueous environment. The longer the hydrophobic tail, the poorer the solubility in water and, hence, the greater the tendency of the surfactant to escape from the aqueous solution. Consequently, as the solute concentration increases, a phase-separation may occur. Alternatively, the surfactant molecules accumulate at interfaces between water and other liquids or gases, or spontaneously *self-assemble* into supramolecular aggregates of mesoscopic size that minimize the number of contacts between water and hydrocarbon tails and maximize the number of tail-tail interactions.

If a surfactant is added to pure water under atmospheric pressure, its molecules first form a monolayer film at the water-air interface, with polar heads pointing towards the water and tails exposed to the air. Above a certain concentration of surfactant (*critical micellization concentration*), one finds an abrupt change in the properties of the solution; in fact, now the solute particles in the bulk begin to form supramolecular aggregates like micelles, planar lamellar bilayers, and vesicles, whose size and shape are, to a large extent, determined by the geometric properties of the surfactant molecules [1,2]. These (*direct micelles*) have a nearly spherical structure, in which the head-groups are placed at

GAZZILLO *et al.*

PHYSICAL REVIEW E **74**, 051407 (2006)

the surface and are thus exposed to the aqueous environment, whereas the nonpolar tails occupy the interior of the micelle, avoiding any contact with water.

A surfactant, when added to a mixture of water and oil (an organic liquid immiscible with water), forms monolayers at every water-oil interface. Several disordered or partially ordered phases are possible, depending on temperature and surfactant concentration. In particular, one can get a *microemulsion*, which is a two-phase suspension of finely divided droplets of *oil in water* (O/W), or *water in oil* (W/O), depending on the relative concentration of the two liquids. Each droplet is coated with a monolayer film of surfactant, which separates water from oil. In W/O microemulsions one finds *reverse* (or *inverted*) *micelles*, where the core is formed by a droplet of water, and the surrounding surfactant molecules now have the head-groups inside the micelle, in contact with water, while their hydrocarbon tails point towards the outside oil phase [44–47]. Clearly, such flexible tails resemble the polymer-hair of sterically stabilized colloids, but in reverse micelles the number of chains is lower and thus a large amount of oil can penetrate the surfactant layer. For the sake of simplicity, we do not consider the possible presence of a cosurfactant, which is generally an alcohol and mixes with surfactant in the outside layer.

In most models for W/O microemulsions the suspending medium, containing mainly oil, is treated as a continuous phase, and the reverse micelles are represented as composed of two parts. The internal one, including both the water droplet and surfactant head-groups, is assumed to be a spherical and impenetrable core, with HS radius R . The external part consists of a concentric, *penetrable* spherical layer, with thickness equal to the length ℓ of the aliphatic chains of surfactant in their fully extended conformation. Thus the total radius of a micelle is $R' = R + \ell$. Because of the flexibility of the chains, ℓ has sometimes been allowed to depend on temperature, i.e., $\ell = \ell(T)$ [46].

The short-ranged attraction between reverse micelles seems to be mainly determined by the overlapping of the penetrable surfactant layers during collisions [44,45,47]. The interpenetration of the aliphatic chains of the surfactant induces oil removal. Now, the partial molar volume of oil inside the surfactant layer is expected to be larger than in the pure oil-phase (this effect is related to the volume of CH_2 and CH_3 groups in the aliphatic layers). A difference of 0.2 \AA^3 seems to be sufficient to explain an interaction potential compatible with light scattering experiments [45].

Roux and Bellocq [45] proposed the simplest model for equal-sized micelles, assuming that the interaction potential is proportional to the overlap volume. The extension of their formula to mixtures is immediate. According to our terminology, the resulting expression is equivalent to a particular Gurney potential, i.e.,

$$\begin{aligned} \phi_{ij}^{\text{rev.micel}}(r) &= \begin{cases} +\infty, & r < \sigma_{ij} \\ -k_B T \Delta\rho V^{\text{overlap}}(R_i + \ell, R_j + \ell, r), & \sigma_{ij} \leq r \leq \sigma_{ij} + 2\ell \\ 0, & r > \sigma_{ij} + 2\ell, \end{cases} \end{aligned} \quad (40)$$

where $\Delta\rho$ is an adjustable parameter which depends only on the oil.

More refined models also include a Hamaker-vdW attraction between water cores. Electrostatic contributions and other more complicated terms have not been considered in the present paper.

VII. CONCLUSIONS

We have started from the problem of building up statistical mechanical models for fluid mixtures of mesoscopic particles, like colloids, micelles, or globular proteins, by using very simple *effective* potentials containing a HS repulsion plus a short-ranged attractive tail that represent the interaction between big particles after averaging out the microscopic degrees of freedom related to much smaller molecules (solvent, added polymers, etc.). The simplest tail corresponds to the highly idealized *surface adhesion*, modeled through a δ_s -term, of the SHS potential. Since we are interested in multicomponent SHS fluids, and in the past difficulties had been encountered in choosing their stickiness parameters t_{ij} , the present paper has focused on the relationship between t_{ij} and particle sizes, i.e., on the possible functional forms of $t_{ij}(T, \sigma_i, \sigma_j)$. To elucidate this issue we have regarded the SHS potentials as models that may be derived, with some simplification, from more realistic interactions. The idea of associating an *equivalent* SHS representation to a realistic interaction, by requiring the equality of the second virial coefficients, is already known and widely accepted. We have chosen this mapping based upon the virial equivalence because of its simplicity and partial analytical tractability. Since B_2 yields only the first correction of pressure with respect to ideality, one can reasonably expect that the performance of the resulting SHS model should worsen with increasing density. By requiring the equivalence of quantities different from B_2 , one could obtain alternative mappings and generally different values for the effective parameters, leading to more successful results at high densities. An application of such an idea was given, for example, in Ref. [47], where the solvent molecules were modeled as SHS by requiring the equivalence of structural properties, i.e., the solvent-solvent structure factor and the coordination number. Unfortunately, this approach does not admit an analytical treatment, and a comparison with it goes beyond the scope of the present paper.

Our aim was to investigate the most interesting cases of short-ranged attractive interactions for some paradigmatic physical systems. To provide a physically sound basis for the choice of t_{ij} and, in particular, its dependence on the particle diameters, we have presented a detailed and self-contained overview on several topics related to short-ranged attractive interactions in real mixtures of neutral mesoscopic particles. We have considered: (i) the van der Waals or dispersion forces—direct interactions—and three cases with indirect, solvent-mediated, attractions: (ii) depletion forces, (iii) polymer-coated colloids, and (iv) solvation forces (in particular, hydrophobic bonding and interactions between reverse micelles in water-in-oil microemulsions).

Due to obvious analytical difficulties, our analysis has been restricted to the determination of the leading terms of t_{ij} . These have been evaluated by series expansion of the

MULTICOMPONENT ADHESIVE HARD SPHERE MODELS...

PHYSICAL REVIEW E 74, 051407 (2006)

Mayer function that appears in the second virial coefficient. We have discussed in particular the linear, quadratic, and cubic approximations and their respective ranges of validity.

The main result is that, in almost all cases considered, the leading contributions to t_{ij} can be expressed as

$$t_{ij}^{\text{eg(tail)}} \approx C_1 \left[M_{ij}(X, \dots) \frac{\sigma_i \sigma_j}{\sigma_{ij}^2} \right] + C_2 \left[M_{ij}(X, \dots) \frac{\sigma_i \sigma_j}{\sigma_{ij}^2} \right]^2 + \dots, \quad (41)$$

where, in most scenarios, X is the temperature T , and the property

$$\lim_{T \rightarrow +\infty} M_{ij}(T, \dots) = 0 \quad (42)$$

ensures that the *high-temperature condition* of Eq. (10) is satisfied. In the case of the depletion attraction, X coincides with the packing fraction η_0 of the depletant particles. For

hairy HS, both T and η_ℓ are variables included in M_{ij} . As regards the dependence of t_{ij} on the big particle sizes, which was the basic question of the present work, it is remarkable that t_{ij} can be expressed as a simple polynomial in the variable $(\sigma_i \sigma_j / \sigma_{ij}^2)$. A quadratic approximation may already be sufficient. The only case in which the expression for t_{ij} differs from that given in Eq. (41) is the Sutherland model for polarizable HS, which yields

$$t_{ij}^{\text{eg(PHS)}} = 12 \frac{T_H}{T} \left(\frac{\sigma_i \sigma_j}{\sigma_{ij}^2} \right)^3 + 15 \left[\frac{T_H}{T} \left(\frac{\sigma_i \sigma_j}{\sigma_{ij}^2} \right)^3 \right]^2 + 8 \left[\frac{T_H}{T} \left(\frac{\sigma_i \sigma_j}{\sigma_{ij}^2} \right)^3 \right]^3. \quad (43)$$

It is pleasant that even here we find powers of the same *basic size-dependent factor*, $(\sigma_i \sigma_j / \sigma_{ij}^2)$. Note that this factor has the property that the sticky attraction vanishes when at least

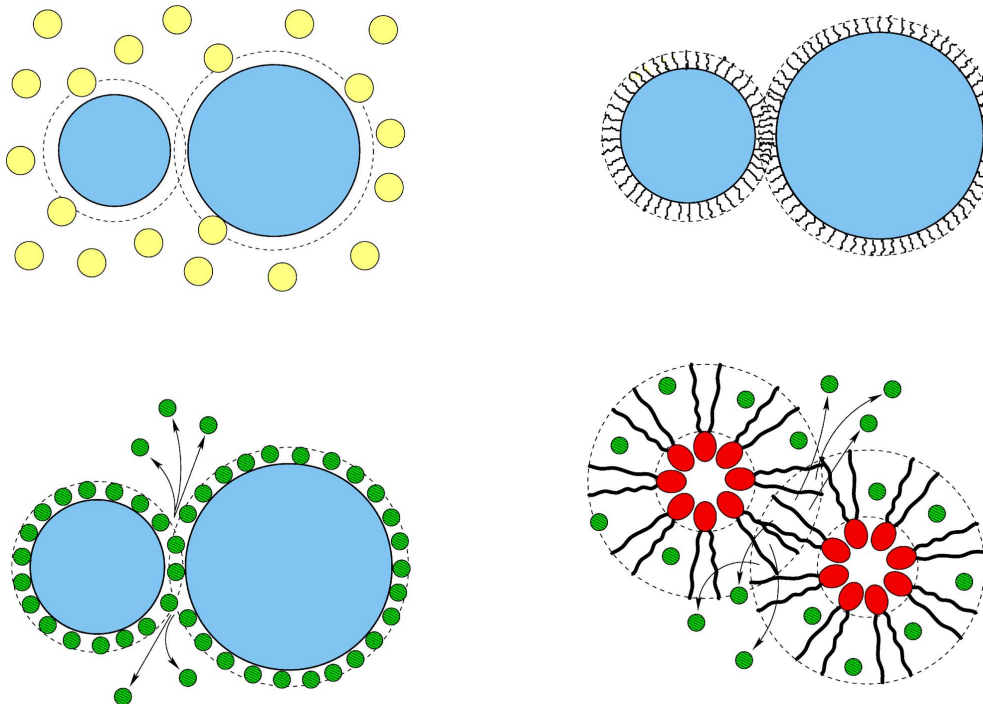


FIG. 1. (Color online) Schematic representation of some systems described by SHS equivalent models in the text. Upper left panel: Excluded-volume depletion attraction between big spheres (solutes) in a sea of smaller depletant particles (light-gray). The dashed curves represent the excluded-volume regions where the centers of the depletant particles cannot penetrate. Upper right panel: Polymer-coated colloids or hairy spheres, when their sterically stabilizing layers of grafted polymers overlap. Lower left panel: Overlap of solvation layers (“cospheres”) in the Gurney-Friedman model, and expulsion of solvent from the overlapping region. The small spheres (dark-gray) represent solvent molecules. Lower right panel: Interaction between reverse micelles in water-in-oil microemulsions. In each micelle the internal dashed curve indicates the impenetrable core, formed by a droplet of water where the head-groups of the surfactant molecules are immersed. The region between the core and the external dashed curve is the penetrable part of the micelle, corresponding to the hydrocarbon tails and containing some oil molecules (small spheres). The micellar attraction is mainly due to oil removing from the overlapping region and its transfer to the bulk.

GAZZILLO *et al.*

PHYSICAL REVIEW E **74**, 051407 (2006)

one of the two particles i and j becomes a point, i.e., it satisfies the *point-limit condition*

$$\lim_{\sigma_i, \text{ or } \sigma_j \rightarrow 0} t_{ij}(T, \sigma_i, \sigma_j) = 0. \quad (44)$$

This condition would be expected to hold for any interaction of “adhesive” type which in the limit involves a particle surface of vanishing area [48].

The similarity among most of the resulting expressions for $t_{ij}^{\text{eq(tail)}}$ can easily be understood. In fact, most of the different short-ranged attractions considered here have been explained, by different authors, in terms of quite similar models, where mesoscopic particles are represented as hard spheres with a surrounding, concentric spherical layer (see Fig. 1). In the AO case this layer is characterized somewhat indirectly by the fact that the density of the centers of mass of the depletant polymers is zero inside the layer but has a nonzero value outside it. In the other cases, the layer has a clearer physical reality. For polymer-coated colloids, for example, the layer is the polymeric film grafted on the colloidal surface. In the hydrophobic bonding the layer is formed by the solvation water molecules. For reverse micelles, the core comprising the water droplet and the polar heads of surfactants is surrounded by a layer made up of hydrocarbon tails of surfactants plus a certain quantity of oil.

It is very appealing, and somewhat surprising, that the factor $\sigma_i \sigma_j / \sigma_{ij}^2$ appears even in our result for the Hamaker potential, which refers to a direct interaction where no spherical layer around the solutes is involved. Note that this dependence on the particle diameters is clearly due to the Hamaker integration, since for point-dipoles at the center of hard spheres (polarizable HS) we have found a different factor, i.e., $(\sigma_i \sigma_j / \sigma_{ij}^2)^3$.

We remark that the models we have considered can be divided into two different classes. The first one includes the two models of dispersion forces (Hamaker potential and polarizable HS), with the common feature of having an attractive r^{-6} tail. The second class refers to the solvent-mediated attractions (depletion effects, polymer-coated colloids, solvation forces). Here, we have reported the simplest examples, which can be regarded as variants of one single model: hard spheres with a penetrable concentric spherical layer (“cosphere,” in a wider sense). As a consequence, since the attraction depends on the volume overlap of the cospheres, the potentials of all these models are “truncated,” i.e., they are rigorously zero beyond some characteristic distance.

The main difference between the above-mentioned classes—infinite tail in the first, finite tail in the second—might suggest that the idea of representing realistic potentials by an equivalent SHS model is justifiable for the second class, but somewhat more questionable when the tail is infinite. In particular, since a proper treatment of long tails is essential for thermodynamics, the SHS-mapping of the Hamaker and Sutherland potentials might introduce some qualitative differences in such a kind of properties. This viewpoint is certainly correct and Hamaker and Sutherland potentials should be appropriately distinguished from the remaining models of this paper. In fact, an “exact” treatment of all these models would surely yield very different thermodynamic and structural predictions. Nevertheless, in our context the B_2 -mapping onto SHS can be expected to yield a representation of realistic interactions that is simple, analytically tractable, and reliable in appropriate regimes, at low and intermediate densities.

In a companion paper [49], we have applied a perturbative approach to the solution of the polydisperse SHS model within the Percus-Yevick approximation. The suggestions put forward in the present paper regarding the relationship between stickiness and size could help to improve the necessary input to that kind of scheme.

In conclusion, the present paper suggests—for multicomponent SHS models—the expression for t_{ij} given by Eq. (41) as a simple choice that is physically justified by its relation to the above-mentioned models of real interactions. Clearly, Eq. (41) is an *approximate* result, but we believe that it correctly includes the *leading terms* of the dependence of t_{ij} on the particle sizes. In spite of the rather drastic approximations used here, this could be useful with the rationale of having a simple and tractable representation of rather complex interactions, at the simplest possible level of description.

ACKNOWLEDGMENTS

We are grateful to Andrés Santos and Saïd Amokrane for enlightening discussions and critical reading of the paper. The work in Italy was supported by a MIUR-COFIN 2006-2007 grant (*Colloidal mixtures, globular proteins and liquid crystal-like phases of biopolymers*).

APPENDIX: VOLUME OVERLAP BETWEEN SPHERES

The volume of the intersection between HS with radii a and b , at distance r , is

$$V^{\text{overlap}}(a, b, r) = \begin{cases} (4\pi/3)\min(a^3, b^3), & 0 < r < |a - b|, \\ \frac{\pi}{12} \left[-3(a^2 - b^2)^2 \frac{1}{r} + 8(a^3 + b^3) - 6(a^2 + b^2)r + r^3 \right], & |a - b| < r < a + b, \\ 0, & r > a + b. \end{cases} \quad (\text{A1})$$

For $|a-b| < r < a+b$ this expression can conveniently be rewritten as

$$V^{\text{overlap}}(a,b,r) = \frac{\pi}{12} [12ab(r-a-b)^2 + 4(a+b)(r-a-b)^3 + (r-a-b)^4] \frac{1}{r}. \quad (\text{A2})$$

Taking $a = \sigma_{i0} = (\sigma_i + \sigma_0)/2$ and $b = \sigma_{j0} = (\sigma_j + \sigma_0)/2$, one gets $V^{\text{overlap}}(\sigma_{i0}, \sigma_{j0}, r) = V_{ij}^{\text{overlap}}(r)$ of Eq. (29).

- [1] J. L. Barrat and J. P. Hansen, *Basic Concepts for Simple and Complex Liquids* (Cambridge University Press, Cambridge, England, 2003).
- [2] J. Lyklema, *Fundamentals of Interface and Colloid Science* (Academic Press, London, 2000), Vol. 1.
- [3] D. Frenkel, in *Soft and Fragile Matter. Nonequilibrium Dynamics, Metastability and Flow*, edited by M. E. Cates and M. R. Evans (SUSSP Publications, Edinburg, and Institute of Physics Publishing, London, 2000).
- [4] M. Kleman and O. D. Lavrentovich, *Soft Matter Physics: An Introduction* (Springer-Verlag, New York, 2003).
- [5] J. P. Hansen and I. R. McDonald, *The Theory of Simple Liquids* (Academic, London, 1986).
- [6] S. Amokrane, A. Ayadim, P. Germain, J. G. Malherbe, and C. Regnaut, *Trends Chem. Phys.* **11**, 119 (2004).
- [7] A. A. Louis, E. Allahyarov, H. Löwen, and R. Roth, *Phys. Rev. E* **65**, 061407 (2002).
- [8] B. Widom, *Statistical Mechanics. A Concise Introduction for Chemists* (Cambridge University Press, Cambridge, England, 2002), p. 98.
- [9] H. L. Friedmann, *A Course in Statistical Mechanics* (Prentice-Hall, Englewood Cliffs, NJ, 1985), p. 135.
- [10] J. O. Hirschfelder, C. F. Curtiss, and R. B. Bird, *Molecular Theory of Gases and Liquids* (Wiley, New York, 1965).
- [11] Note that, as a consequence of the two different definitions of short-ranged forces, the classical Lennard-Jones (LJ) potential, with r^{-6} tail, should be considered short-ranged according to Widom's definition, but long-ranged according to Hirschfelder's one. In our opinion, this discrepancy in terminology at the level of potentials may be disconcerting but is not essential, while the consequent differences at the level of mechanical-statistical properties should be emphasized. In fact, fluids with potentials "decaying exponentially or faster" with r may exhibit undoubtedly different physical behaviors compared to systems characterized by longer-ranged r^{-n} potentials (like LJ). This can be argued by considering, for instance, the wetting at attractive walls, as well as the asymptotic decay of their pair correlation function at large distances.
- [12] R. J. Baxter, *J. Chem. Phys.* **49**, 2270 (1968); R. J. Baxter, in *Physical Chemistry, An Advanced Treatise, Vol. 8A*, edited by D. Henderson (Academic Press, New York, 1971), Chap. 4; R. O. Watts, D. Henderson, and R. J. Baxter, *Adv. Chem. Phys.*, **21**, 421 (1971).
- [13] J. W. Perram and E. R. Smith, *Chem. Phys. Lett.* **35**, 138 (1975).
- [14] B. Barbois and R. Tenne, *Chem. Phys.* **38**, 369 (1979).
- [15] G. Stell, *J. Stat. Phys.* **63**, 1203 (1991).
- [16] C. Regnaut and J. C. Ravey, *J. Chem. Phys.* **91**, 1211 (1989).
- [17] A. Jamnik, *J. Chem. Phys.* **105**, 10511 (1996); **114**, 8619 (2001).
- [18] A. Santos, S. Bravo Yuste, and M. L. De Haro, *J. Chem. Phys.* **109**, 6814 (1998).
- [19] M. A. Miller and D. Frenkel, *Phys. Rev. Lett.* **90**, 135702 (2003); *J. Chem. Phys.* **121**, 535 (2004); *J. Phys.: Condens. Matter* **16**, S4901 (2004).
- [20] C. Regnaut, S. Amokrane, and Y. Heno, *J. Chem. Phys.* **102**, 6230 (1995).
- [21] D. Gazzillo and A. Giacometti, *J. Chem. Phys.* **113**, 9837 (2000); *Physica A* **304**, 202 (2002).
- [22] D. Gazzillo and A. Giacometti, *Mol. Phys.* **100**, 3307 (2002).
- [23] D. Gazzillo and A. Giacometti, *Mol. Phys.* **101**, 2171 (2003); *J. Appl. Crystallogr.* **36**, 832 (2003).
- [24] D. Gazzillo and A. Giacometti, *J. Chem. Phys.* **120**, 4742 (2004).
- [25] R. Fantoni, D. Gazzillo, and A. Giacometti, *J. Chem. Phys.* **122**, 034901 (2005); *Phys. Rev. E* **72**, 011503 (2005).
- [26] Taking the limit $w \rightarrow 0$ of the function $\phi_w(x) = w^{-1}$ for $x_0 < x < x_0 + w$, and $=0$ elsewhere, one gets the asymmetric Dirac delta distribution $\delta_+(x)$, which has the property: $\int_A^B dx F(x) \delta_+(x - x_0) = F(x_0^+)$, if $A \leq x_0 < B$, and $=0$, if $x_0 < A$ or $x_0 \geq B$.
- [27] H. C. Hamaker, *Physica (Amsterdam)* **4**, 1058 (1937).
- [28] S. Amokrane, *J. Chem. Phys.* **108**, 7459 (1998).
- [29] J. G. Malherbe, C. Regnaut, and S. Amokrane, *Phys. Rev. E* **66**, 061404 (2002).
- [30] S. Asakura and F. Oosawa, *J. Chem. Phys.* **22**, 1255 (1954); *J. Polym. Sci.* **33**, 183 (1958).
- [31] A. Vrij, *Pure Appl. Chem.* **48**, 471 (1976).
- [32] C. G. de Kruif, P. W. Rouw, W. J. Briels, M. H. G. Duits, A. Vrij, and R. P. May, *Langmuir* **5**, 422 (1989).
- [33] H. Verduin and J. K. G. Dhont, *J. Colloid Interface Sci.* **172**, 425 (1995).
- [34] M. H. G. Duits, R. P. May, A. Vrij, and C. G. de Kruif, *Langmuir* **7**, 62 (1991).
- [35] P. J. Flory, *Principles of Polymer Chemistry* (Cornell University Press, Ithaca, 1953).
- [36] P. J. Flory and W. R. Krigbaum, *J. Chem. Phys.* **18**, 1086 (1950).
- [37] R. W. Gurney, *Ionic Processes in Solution* (Dover, New York, 1953).
- [38] H. S. Frank and M. W. Evans, *J. Chem. Phys.* **13**, 507 (1945).
- [39] P. S. Ramanathan and H. L. Friedman, *J. Chem. Phys.* **54**, 1086 (1971); H. L. Friedman and C. V. Krishnan, in *Water, A Comprehensive Treatise*, edited by F. Franks (Plenum Press, New York, 1973), Vol. 3; H. L. Friedman and W. D. T. Dale, in *Statistical Mechanics, Part A: Equilibrium Techniques*, edited by B. J. Berne (Plenum Press, New York, 1977).
- [40] F. Franks, in *Water, A Comprehensive Treatise*, edited by F.

GAZZILLO *et al.*

PHYSICAL REVIEW E **74**, 051407 (2006)

- Franks (Plenum Press, New York, 1978), Vol. 4.
- [41] A. Ben-Naim, *Hydrophobic Interactions* (Plenum Press, New York, 1980).
- [42] H. L. Friedman and C. V. Krishnan, in *The Physical Chemistry of Aqueous Systems*, edited by R. L. Kay (Plenum Press, New York, 1973).
- [43] A. H. Clark, F. Franks, M. D. Pedley, and D. S. Reid, *J. Chem. Soc., Faraday Trans. 1* **73**, 290 (1977).
- [44] B. Lemaire, P. Bothorel, and D. Roux, *J. Phys. Chem.* **87**, 1023 (1983); S. Brunetti, D. Roux, A. M. Bellocq, G. Fourche, and P. Bothorel, *ibid.* **87**, 1028 (1983).
- [45] D. Roux and A. M. Bellocq, in *Physics of Amphiphiles: Micelles, Vesicles, and Microemulsions*, edited by V. Degiorgio and M. Corti (Academic Press, New York, 1985), p. 842.
- [46] M. Bouaskarne, S. Amokrane, and C. Regnaut, *J. Chem. Phys.* **114**, 2442 (2001).
- [47] S. Amokrane and C. Regnaut, *J. Chem. Phys.* **106**, 376 (1997).
- [48] B. Barbov, *Chem. Phys.* **11**, 357 (1975).
- [49] R. Fantoni, D. Gazzillo, A. Giacometti, and P. Sollich, *J. Chem. Phys.* **125**, 164504 (2006).

Chapter 12

Phase behavior of polydisperse sticky hard spheres: analytical solutions and perturbation theory

Gazzillo D., Giacometti A., and **Fantoni R.**, Mol. Phys. **104**, 3451 (2006)

Title: “Phase behavior of polydisperse sticky hard spheres: analytical solutions and perturbation theory”

Abstract: We discuss phase coexistence of polydisperse colloidal suspensions in the presence of adhesion forces. The combined effect of polydispersity and Baxter’s sticky-hard-sphere (SHS) potential, describing hard spheres interacting via strong and very short-ranged attractive forces, give rise, within the Percus-Yevick (PY) approximation, to a system of coupled quadratic equations which, in general, cannot be solved either analytically or numerically. We review and compare two recent alternative proposals, which we have attempted to bypass this difficulty. In the first one, truncating the density expansion of the direct correlation functions, we have considered approximations simpler than the PY one. These C_n approximations can be systematically improved. We have been able to provide a complete analytical description of polydisperse SHS fluids by using the simplest two orders C_0 and C_1 , respectively. Such a simplification comes at the price of a lower accuracy in the phase diagram, but has the advantage of providing an analytical description of various new phenomena associated with the onset of polydispersity in phase equilibria (e.g. fractionation). The second approach is based on a perturbative expansion of the polydisperse PY solution around its monodisperse counterpart. This approach provides a sound approximation to the real phase behavior, at the cost of considering only weak polydispersity. Although a final settlement on the soundness of the latter method would require numerical simulations for the polydisperse Baxter model, we argue that this approach is expected to keep correctly into account the effects of polydispersity, at least qualitatively.

Phase behaviour of polydisperse sticky hard spheres: analytical solutions and perturbation theory

DOMENICO GAZZILLO*, RICCARDO FANTONI and ACHILLE GIACOMETTI

Istituto Nazionale per la Fisica della Materia and Dipartimento di Chimica Fisica,
Università di Venezia, S. Marta DD 2137, I-30123 Venezia, Italy

(Received 27 July 2006; in final form 13 September 2006)

We discuss the phase coexistence of polydisperse colloidal suspensions in the presence of adhesion forces. The combined effect of polydispersity and Baxter's sticky-hard-sphere (SHS) potential, describing hard spheres interacting via strong and very short-ranged attractive forces, give rise, within the Percus–Yevick (PY) approximation, to a system of coupled quadratic equations which, in general, cannot be solved either analytically or numerically. We review and compare two recent alternative proposals that have attempted to by-pass this difficulty. In the first, truncating the density expansion of the direct correlation functions, we have considered approximations simpler than the PY one. These C_n approximations can be systematically improved. We have been able to provide a complete analytical description of polydisperse SHS fluids using the simplest two orders C_0 and C_1 . Such a simplification comes at the price of a lower accuracy in the phase diagram, but has the advantage of providing an analytical description of various new phenomena associated with the onset of polydispersity in phase equilibria (e.g., fractionation). The second approach is based on a perturbative expansion of the polydisperse PY solution around its monodisperse counterpart. This approach provides a sound approximation to the real phase behaviour, at the cost of considering only weak polydispersity. Although a final determination of the soundness of the latter method would require numerical simulations for the polydisperse Baxter model, we argue that this approach is expected to correctly take into account the effects of polydispersity, at least qualitatively.

1. Introduction

New technological advances in the physico-chemical manipulation of colloidal mixtures have re-ignited the issue of gaining a theoretical understanding of the phase behaviour of polydisperse systems [1]. 'Polydispersity' in colloidal solutions means that, due to the production process, suspended macroparticles with the same chemical composition cannot be exactly identical to each other, but, in general, have different sizes, and possibly different surface charges, shapes, etc. In practice, a polydisperse system can be viewed as a mixture with a very large—or essentially infinite—number M of different species or components, identified by one or several parameters (M large but finite refers to *discrete polydispersity*, whereas $M \rightarrow \infty$ with a continuous distribution of polydisperse parameters corresponds to *continuous polydispersity*). The present paper considers the discrete polydispersity of spherical colloidal particles, with their

diameter being the only polydisperse attribute (size-polydispersity).

When polydispersity is not negligible, the phase behaviour becomes much richer, but determination of the phase transition boundaries requires a much more involved formalism compared with the monodisperse counterpart. In fact, the coexistence condition in terms of intensive variables requires that all phases must have equal temperature, pressure and chemical potentials of the M components. In the presence of polydispersity, one should thus solve a number of equations of the order of M^2 , a task that is practically impossible for M large or infinite.

However, the study of phase equilibria can conveniently start from the appropriate thermodynamic potential, which is the Helmholtz free energy A when the experimentally controlled variables are temperature, volume and number of different colloidal species. In the one-component case, the coexistence condition of equal pressure and chemical potential has a simple geometrical interpretation in terms of free energy density a : the densities of two coexisting phases are determined

*Corresponding author. Email: gazzillo@unive.it

by constructing a double-tangent to a plotted versus particle density. This recipe leads to the well-known Maxwell construction, which connects suitably selected points along a van der Waals (vdW) subcritical isotherm, in order to 'reduce' its unphysical loop to a constant-pressure line characteristic of a first-order phase transition.

In the polydisperse case, significant progress in the very difficult problem of predicting phase equilibria can be obtained for models with *truncatable* free energies [1]. Here, 'truncatable' means that the excess free energy of the polydisperse system turns out to depend only on a *finite* number of moments of the distribution corresponding to the polydisperse attribute (the diameter σ in the simplest case). For spherical colloids, the excess free energy of the vdW model extended to polydisperse fluids has such a truncatable structure. Due to this property, this vdW theory has often been employed as the simplest model to investigate the effects of polydispersity on the gas-liquid transition [1, 2]. On the other hand, the influence of polydispersity on freezing has been addressed by using the hard-sphere (HS) mixture model, which also admits a truncatable free energy [1] (for the fluid phase, the Boublik-Mansoori-Carnahan-Starling-Leland (BMCSSL) [3] expression was employed). It is worth recalling that it is currently believed that size-polydispersity might destabilize crystallization, eventually inhibiting freezing above a certain 'terminal' value of polydispersity [1].

The present paper focuses on—and reviews—a number of recent attempts to investigate polydisperse phase equilibria, at least within some approximations, for another prototype model useful for studying colloidal suspensions, namely Baxter's sticky-hard-spheres (SHS) model [4]. Here the particles are hard spheres with surface adhesion, and the corresponding potential can be obtained as a limit of an attractive square-well which becomes infinitely deep and narrow, according to a particular prescription which ensures a finite non-zero contribution of adhesion to the second virial coefficient ('sticky limit'). For the one-component version of this model, Baxter and collaborators [4] solved the Ornstein-Zernike (OZ) integral equation coupled with the Percus-Yevick (PY) approximation ('closure'). This *fully analytical* solution allows the determination of all structural and thermodynamical properties of the SHS fluid. On the other hand, the multi-component PY solution, which soon followed Baxter's work [5, 6], is practically inapplicable in the presence of significant polydispersity. In fact, it requires the computation of a set of parameters $\{\Lambda_{ij}\}$ determined by a system of $M(M+1)/2$ quadratic equations, which, in general, cannot be solved even numerically for a mixture with a large number of components. Moreover,

even in the presence of a general solution for this nonlinear algebraic system, the problem of phase coexistence would still remain out of reach in view of the previous remarks.

In a series of recent papers [7–9, 11–13], we attempted to make some progress along two different lines.

First, starting from the *density* expansion of the cavity function at contact, we considered a sequence of simpler approximations (compared with the PY one) [7–11]. Within the two simplest of these approximations, denoted C_0 and C_1 (for reasons that will become clear below), we were able to derive analytically all relevant information regarding structure and thermodynamics, including the phase coexistence, in view of the fact that the corresponding free energy turns out to be truncatable [11]. Due to the simplicity of C_0 and C_1 , it is however reasonable to expect these approximations to fail at high packing fractions, with a consequent incomplete or even incorrect description of the effects of polydispersity on the phase diagram.

Therefore, in collaboration with Peter Sollich, we recently explored a second approach [12], where the expansion variable (which must be small) is an appropriate polydispersity index. In such a way, we tried to solve the nonlinear algebraic system—involved in the PY result—*perturbatively in polydispersity*, starting from the monodisperse PY solution.

2. Baxter's SHS model and PY solution

The SHS model is defined as a limiting case of a particular square-well (SW) model [4], based upon a potential including steeply repulsive core and short-ranged attractive tail, i.e.

$$\phi_{ij}^{\text{Baxter SW}}(r) = \begin{cases} +\infty, & 0 < r < \sigma_{ij} \equiv (\sigma_i + \sigma_j)/2, \\ -\epsilon_{ij}^{\text{Baxter SW}}, & \sigma_{ij} \leq r \leq R_{ij} \equiv \sigma_{ij} + w_{ij}, \\ 0, & r > R_{ij}, \end{cases} \quad (1)$$

with

$$\epsilon_{ij}^{\text{Baxter SW}} = k_B T \ln \left(1 + t_{ij} \frac{\sigma_{ij}}{w_{ij}} \right), \quad (2)$$

where σ_i is the HS diameter of species i , $\epsilon_{ij}^{\text{Baxter SW}} > 0$ and w_{ij} are the depth and width of the well, respectively, k_B denotes Boltzmann's constant, and T is the temperature. Moreover,

$$t_{ij} = \frac{1}{12\tau_{ij}} \geq 0, \quad (3)$$

where the conventional Baxter parameter τ_{ij} is an unspecified increasing function of T , and τ_{ij}^{-1} measures the strength of the surface adhesion or ‘stickiness’ between particles of species i and j .

The ‘sticky limit’ of $\phi_{ij}^{\text{Baxter SW}}(r)$ corresponds to taking $w_{ij} \rightarrow 0$. While the SW width goes to zero, its depth $e_{ij}^{\text{Baxter SW}}$ diverges, giving rise to a Dirac delta function in the Boltzmann factor [4], i.e.

$$e^{-\beta\phi_{ij}^{\text{HS}}(r)} = \theta(r - \sigma_{ij}) + t_{ij}\sigma_{ij}\delta(r - \sigma_{ij}), \tag{4}$$

where $\beta = (k_B T)^{-1}$, and θ and δ are the Heaviside step function and the Dirac delta function, respectively.

The advantage of the sticky limit is that one effectively deals with a single parameter τ_{ij} for each pair, rather than a combination of energy and length scales (as occurs in the square-well model, for which no analytical solution is known). On the one hand, this particular limit has the disadvantage of introducing some pathologies into the model, notably in the one-component case [14]. On the other hand, Baxter’s model represents the simplest paradigmatic example of a combination of steep repulsion and short-range attraction which entails a complete analytical solution in the one-component case, within a robust approximation such as the PY closure.

In the multi-component case, the PY solution of the OZ equation in terms of Baxter’s factor correlation function reads [5, 6]

$$q_{ij}(r) = \begin{cases} \left(\frac{1}{2}a_i(r - \sigma_{ij})^2 + (b_i + a_i\sigma_{ij}) \right) & (\sigma_i - \sigma_j)/2 \leq r \leq \sigma_{ij}, \\ (r - \sigma_{ij}) + \Lambda_{ij}, & \\ 0, & \text{elsewhere,} \end{cases} \tag{5}$$

where the expressions for the parameters a_i and b_i may be found in [7], while the quantity

$$\Lambda_{ij} = t_{ij}y_{ij}(\sigma_{ij})\sigma_{ij}^2, \tag{6}$$

which depends on the cavity function at contact $y_{ij}(\sigma_{ij})$, must be a solution of the following system of quadratic equations:

$$\Lambda_{ij} = \alpha_{ij} + \beta_{ij} \sum_m x_m \left[\Lambda_{im}\Lambda_{jm} - \frac{1}{2}(\Lambda_{im}\Gamma_{mj} + \Lambda_{jm}\Gamma_{mi}) \right], \tag{7}$$

$$i, j = 1, 2, \dots, M.$$

Here, x_m is the molar fraction of the m th species ($m = 1, \dots, M$), and $\alpha_{ij} = t_{ij}y_{ij}^{\text{HS-PY}}(\sigma_{ij})\sigma_{ij}^2$, $\beta_{ij} = 12\rho t_{ij}\sigma_{ij}$ (ρ is the total number density), and $\Gamma_{ij} = \sigma_i\sigma_j/(1 - \eta)$,

with η being the packing fraction [12]. The solution of these equations for $\{\Lambda_{ij}\}$ is the real bottleneck of the multi-component PY result, as mentioned in the Introduction: for large M (and, in particular, for $M \rightarrow \infty$), this calculation is next to impossible, analytically and numerically.

As a consequence, although the PY closure is commonly believed to be very sound for short-range potentials (for one-component SHS fluids this was confirmed by recent numerical simulations [15]), one has to conclude that, in the multi-component (poly-disperse) case, the PY solution has very limited practical usefulness, since its solution scheme cannot be fully accomplished. This is the reason why other possible routes have been attempted, as we discuss next.

3. Simplified closures: the class of C_n approximations

A ‘closure’ is a relationship, added to the OZ equation, between the direct correlation function $c_{ij}(r)$ and $h_{ij}(r) = g_{ij}(r) - 1$ or $\gamma_{ij}(r) = h_{ij}(r) - c_{ij}(r)$ ($g_{ij}(r)$ being the radial distribution function) [16].

Let us return to Baxter’s SW model given by equation (1) (i.e. *before* the ‘sticky limit’), and consider the following general class of ‘closures’ [10]:

$$c_{ij}(r) = \begin{cases} -1 - \gamma_{ij}(r), & 0 < r < \sigma_{ij}, \\ c_{ij}^{\text{shrink}}(r), & \sigma_{ij} \leq r \leq R_{ij}, \\ 0, & r > R_{ij}. \end{cases} \tag{8}$$

The expression $c_{ij}(r) = -1 - \gamma_{ij}(r)$ inside the core ($r < \sigma_{ij}$) is exact and dictated by the HS potential. The form outside the well ($r > R_{ij}$) may then be identified with the PY approximation,

$$c_{ij}^{\text{PY}}(r) = f_{ij}(r)[1 + \gamma_{ij}(r)], \tag{9}$$

since, for Baxter’s potential, the Mayer function, $f_{ij}(r) = \exp[-\beta\phi_{ij}(r)] - 1$, vanishes for $r > R_{ij}$.

The choice of $c_{ij}^{\text{shrink}}(r)$ inside the well (region which ‘shrinks’ in the sticky limit) defines one particular closure within the proposed class. Of course, $c_{ij}^{\text{shrink}}(r) = c_{ij}^{\text{PY}}(r)$ corresponds to the PY approximation. On the other hand, when $c_{ij}^{\text{shrink}}(r) \neq c_{ij}^{\text{PY}}(r)$, we are in the presence of *mixed closures*, which have frequently appeared in the literature [17]. In order to define mixed closures simpler than the PY approximation, we consider the *density* expansion of the exact direct correlation function [16], and denote by the

3454

D. Gazzillo et al.

C_n approximation a truncation of this series to order $O(\rho^n)$. The simplest two approximations are

$$\begin{aligned} c_{ij}^{\text{shrink}}(r) &= f_{ij}(r) && (C_0 \text{ closure}), \\ c_{ij}^{\text{shrink}}(r) &= f_{ij}(r)[1 + (\sum_k \rho_k f_{ik} * f_{kj})(r)] && (C_1 \text{ closure}), \end{aligned} \quad (10)$$

where ρ_k is the number density of species k , and $*$ denotes convolutive integration [10].

In the 'sticky limit' $R_{ij} \rightarrow \sigma_{ij}^+$ the well region shrinks, but a 'memory' of the approximation chosen for c_{ij}^{shrink} remains in the solution of the OZ integral equation. In fact, although all solutions $q_{ij}(r)$ corresponding to closures belonging to the class given by equation (8) have the same functional form as the PY solution (equation (5)), each closure is characterized by its own approximation to $y_{ij}(\sigma_{ij})$, which is involved in the expressions of the parameters a_i , b_i and Λ_{ij} . For instance, the C_0 and C_1 approximations correspond to

$$\begin{aligned} y_{ij}(\sigma_{ij}) &= 1 && (C_0 \text{ closure}), \\ y_{ij}(\sigma_{ij}) &= 1 + y_{ij}^{(1)}(\sigma_{ij})\eta && (C_1 \text{ closure}), \end{aligned} \quad (11)$$

which are, respectively, the zeroth- and first-order truncations of the density expansion for the exact cavity function at contact (see [10] for details).

While a brute-force truncation of the above density expansions leads to analytical expressions sufficiently simple to be applied to the multi-component (polydisperse) case, one should reasonably expect less

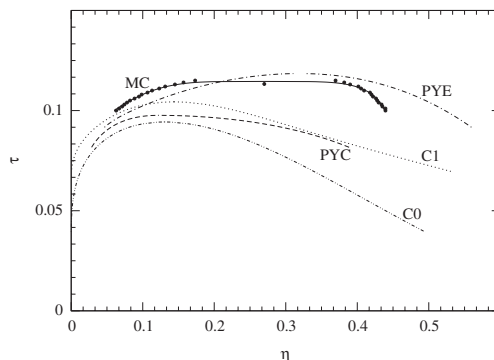


Figure 1. Coexistence (binodal) curves for the one-component Baxter model. Both the compressibility (PYC) and the energy (PYE) results as obtained from the Percus–Yevick approximation [4] are reported and compared with the C_0 and C_1 approximations from [11] and with Monte Carlo simulations (MC) from [15]. In the MC case the continuous line is simply a guide to the eye.

accuracy, especially in the high-density regime. In the one-component case, we can carefully check this point.

In figure 1, coexistence curves obtained from the C_0 and C_1 approximations are compared with the PY ones (using both compressibility and energy routes), and with Monte Carlo simulations from [15]. It is apparent how the PY energy route (PYE) yields a rather precise representation of the MC results, unlike the compressibility route (PYC). It is worth noting that the results stemming from the C_1 approximation, although rather close to the MC data in the low-density branch, clearly fail to accurately reproduce them for higher densities, as expected.

In spite of their lack of accuracy, the C_0 and C_1 approximations provide a rather sound basis for obtaining insight into the phase equilibria of polydisperse SHS fluids, since they allow simple analytical, or semi-analytical, treatments.

A first important feature of the C_0 and C_1 approximations for polydisperse SHS is that the corresponding free energy has a *truncatable* structure, that is it depends upon a few (four at most) moments of the (discrete) size distribution, $\xi_\nu = (\pi/6)\rho \sum_j x_j \sigma_j^\nu$, with $\nu=0, 1, 2, 3$.

A second remarkable fact is that the C_0 and C_1 approximations are able to describe the so-called *fractionation* phenomena characteristic in phase equilibria of polydisperse systems. While we refer to a recent review [1] for a detailed description of the increased complexity in the polydisperse phase diagrams, here we just mention two important points. First, fractionation means that the daughter phases, obtained from the demixing of a parent homogeneous phase, need not have the same composition as the parent phase. As a consequence, there is no single coexistence line ('binodal') as in the one-component case, but one rather finds a *cloud curve*, representing the temperature–density dependence line of the low-density majority phase ('gas'), and a *shadow curve*, representing the temperature–density dependence of the high-density minority phase (incipient 'liquid'). While for one-component systems these two curves are identical, for polydisperse systems in general they are not, with the exception of the critical point, where they coincide by definition.

However, in order to apply the C_0 and C_1 approximations to the multi-component SHS model, we have to tackle a further important problem, that is the definition of the stickiness parameters τ_{ij} .

4. Size dependence of stickiness parameters

In mixtures, τ_{ij} will depend on the particular pair i, j considered, and should reasonably be expected to be related to the particle sizes. Assuming that we are

dealing only with size-polydispersity, we can always decouple temperature and adhesion as

$$\frac{1}{\tau_{ij}} = \frac{1}{\tau} \epsilon_{ij} = \frac{1}{\tau} F(\sigma_i, \sigma_j), \quad (12)$$

where the last equality stems from the assumption of size-polydispersity and of a purely pairwise potential. Unfortunately, the exact form of the size dependence of these stickiness parameters is still an open problem, due to the lack of experimental and theoretical insights [13]. On the other hand, a few guidelines—based on arguments discussed in [11, 12]—provide, as reasonable and plausible, the following dependencies:

$$\epsilon_{ij} = F(\sigma_i, \sigma_j) = \begin{cases} \sigma_0^2/\sigma_{ij}^2, & \text{Case I,} \\ \sigma_i\sigma_j/\sigma_{ij}^2, & \text{Case II,} \\ 1, & \text{Case IV,} \\ \sigma_0/\sigma_{ij}, & \text{Case V.} \end{cases} \quad (13)$$

Here, σ_0 is a characteristic reference length (e.g., the parental mean diameter) and the numbering of the various cases follows the convention of previous work [11, 12].

Figure 2 reports the results of the calculation of the cloud and shadow curves for polydisperse SHS within the simple C_0 approximation. Here and below, polydispersity is measured by an index s , which is the normalized standard deviation of the size distribution. Hence, $s=0$ corresponds to a mono-disperse case, whereas $s=0.1$ and $s=0.3$ indicate moderate and significant polydispersity, respectively. The top panel of figure 2 depicts the results for case I of the size dependence of the stickiness parameters. As s increases, the coexistence region shrinks, thus suggesting that polydispersity *disfavours* the phase transition. On the other hand, this trend is markedly case dependent, as illustrated in the bottom panel of figure 2, where the cloud-shadow pairs with polydispersity $s=0.3$ are displayed for different size dependence cases. It can clearly be seen that, whereas for cases I and V the same trend is observed, case IV seems to suggest a *widening* of the phase coexistence region (hence favouring the phase transition).

In view of the lack of numerical simulations for polydisperse SHS in order to make a comparison, we have no way, at the present stage, of checking how realistic these results are. On the other hand, we might suspect, based on the comparison in the one-component case, C_0 to fail to provide an accurate representation in the region of low temperatures and high densities. This is the reason why other possible approaches have recently been tested. We now illustrate a different

perturbative approach that has proved to be promising in this context.

5. Perturbative treatment of the SHS-PY solution

The main difficulty in dealing with the PY solution for polydisperse SHS stems from the solution of the coupled quadratic system of equations (7). As the one-component case has a well-defined solution, one might then suspect that—for weak polydispersity—a perturbative expansion around this solution might include the main effects of polydispersity. This is, in fact, what happens, as recently shown [12] by exploiting a general perturbation theory due to Evans [18]. The main idea is that, for weak polydispersity, size distributions are narrowly peaked around a mean reference value (σ_0 in the present case), and hence all quantities such as

$$\delta_i = \frac{\sigma_i - \sigma_0}{\sigma_0} \ll 1 \quad (14)$$

are small. Therefore, one might expand both ϵ_{ij} , and all quantities appearing in Λ_{ij} , in powers of δ_i . A similar expansion can be performed in the free energy, and hence all thermodynamic quantities can be computed. The entire procedure is described in detail in [1, 12, 18]. Here, we just summarize the main results.

The approximate range of validity of the perturbation expansion can be envisaged by considering the polydisperse HS case where the ‘exact’ BMCSL approximation [3] can be compared with the corresponding perturbative solution based on the one-component ($s=0$) counterpart. This is reported in the top-left part of figure 3, where the quantity $\beta P v_0$ ($v_0 = \pi\sigma_0^3/6$) is plotted against the packing fraction η for increasing values of polydispersity. It is apparent that the perturbative solution remains rather close to the ‘exact’ polydisperse BMCSL solution even for moderate polydispersity $s \leq 0.3$, which is the maximum value considered in the remaining part of this work. The remaining plots in figure 3 display the effect of polydispersity on the PY pressure equation of state as obtained from the energy route and for decreasing values of the temperature τ . In the one-component case $s=0$, a van der Waals loop starts to appear when we cross the critical temperature $\tau_c \sim 0.1185$ coming from the high τ regime. Obviously, this signals the onset of a liquid-gas phase transition, and the corresponding phase diagram can be obtained by a standard Maxwell construction by connecting appropriate points with the same pressure. In the presence of polydispersity (here represented by choice IV for the size dependence of the stickiness

3456

D. Gazzillo et al.

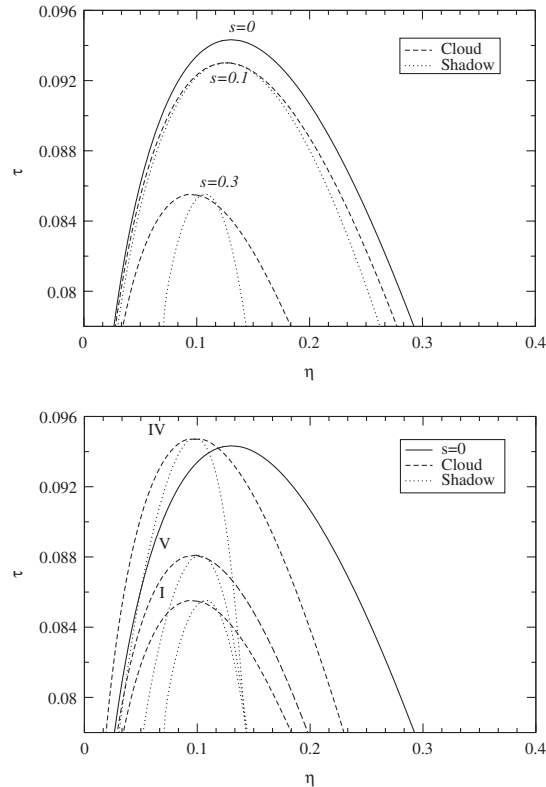


Figure 2. (Top) Cloud and shadow curve for model I within the C_0 approximation at increasing polydispersity: $s=0$, $s=0.1$ and $s=0.3$. (Bottom) Same as above but for a fixed value of polydispersity $s=0.3$ and different choices for the stickiness adhesion (models I, IV and V).

parameters), the same procedure *cannot* be applied due to fractionation, as already discussed. Nevertheless, we can clearly see that, as s increases, the van der Waals loop region (when present) expands, thus suggesting that a phase transition is favoured by the presence of polydispersity. A similar feature occurs for the polydisperse van der Waals model [2] and for the numerical results of the PY compressibility equation of state [19] (note that, in the latter, a *gap* rather than a *loop* signals the onset of the transition). A somewhat surprising feature is that, at fixed packing fraction η , the pressure decreases with increasing polydispersity *less* in the presence of adhesion rather than in its absence (i.e. for the HS case). An intuitive plausible interpretation of this feature can be found in [12].

The same perturbative approach allows the determination of the cloud and shadow curves for the various size dependence cases of τ_{ij}^{-1} . This is reported in figure 4

for cases II, IV (top panel) and I, V (bottom panel). In the first case, the cloud and shadow lines collapse into a single curve, and this can be understood on the basis of the particular scaling properties of the free energy to this order in perturbation theory [12]. In all cases, there is a breakdown of the perturbation theory on approaching the critical point, and this is a known general drawback of Evans' perturbative scheme. Nevertheless, in all cases and to this order in perturbation theory, there is a tendency of the phase coexistence region to *increase* with polydispersity, in qualitative agreement with the intuitive picture obtained from figure 3.

It is worth stressing the difference with respect to previous non-perturbative results stemming from the C_0 solution, where all different cases (with the notable exception of IV) predicted a reduction of the phase coexistence region. While in the C_0 description we have provided a careful treatment of polydispersity at the

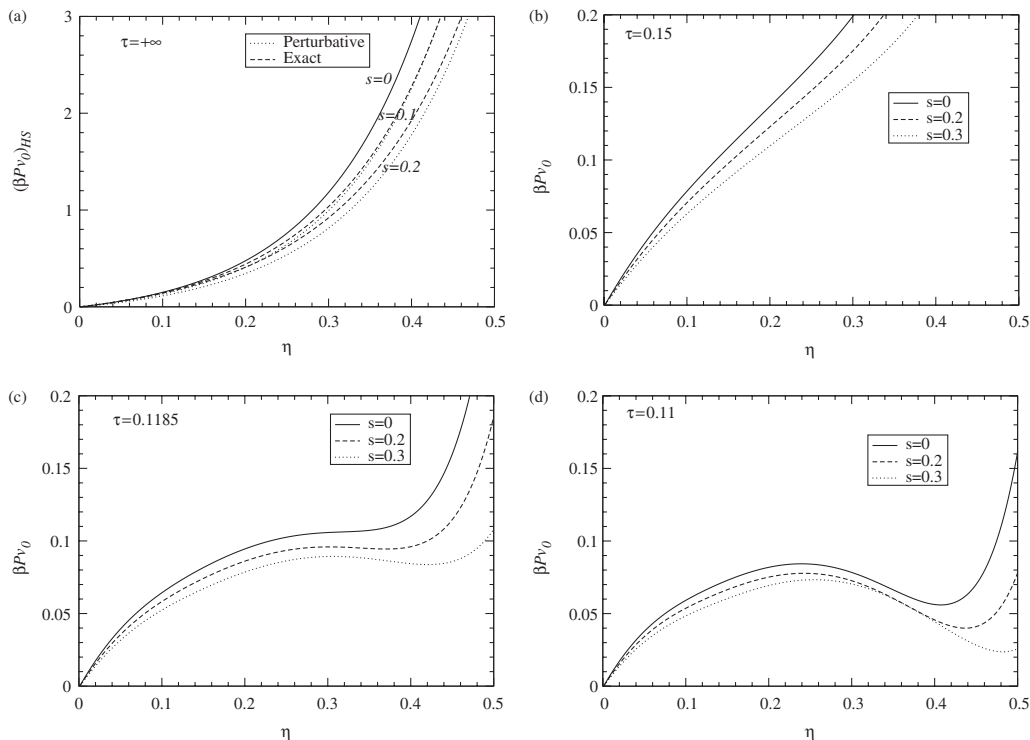


Figure 3. Behaviour of the energy equation of state within our perturbative scheme. In all cases the quantity $\beta P v_0$ is plotted against the packing fraction η . In clockwise order, the first curve (left, top) reports a comparison of the perturbative versus the 'exact' BMCSL solution in the equation of state for polydisperse HS ($\tau = +\infty$). The other curves report the perturbative solution for the energy equation of state within the PY approximation for the SHS Baxter model. Results are depicted for three values of temperature, $\tau = 0.15 > \tau_c$, $\tau = 0.1185 \sim \tau_c$ and $\tau = 0.1 < \tau_c$, and for different degrees of polydispersity. The choice for the size dependence of the stickiness parameters corresponds to model IV.

expense of the accuracy of the exploited approximation, in the perturbative description of the PY solution, polydispersity is assumed to be small and hence one might suspect that solutions with large polydispersities cannot fit within this picture. On balance, however, we would favour the latter rather than the former description. An almost correct representation of the one-component counterpart is a necessary requirement for checking the effect of polydispersity, and we are not aware of any physical or experimental system where the effects of polydispersity are so strong that they could not be taken into account, at least at the simplest qualitative level, by the perturbative scheme proposed here. Along this line, some further proposals have been put forward in [12] to derive a phenomenological BMCSL-like approximation for SHS, which might be regarded as our 'best and simplest guess' to the *exact* phase

behaviour of polydisperse SHS. Even on the size dependence of τ_{ij}^{-1} some possible support of the proposed forms may be put forward [12, 13].

6. Conclusions

In this work, we have summarized recent advances in predicting, theoretically, the phase diagram for polydisperse suspensions of colloidal particles with surface adhesion, within the simple description of Baxter's model. Emphasis was placed on the crucial—unsolved—step required to obtain the multi-component SHS-PY solution, and the proposed recipes to deal with this problem. The first is based on a simplification of the closure. It has the

3458

D. Gazzillo et al.

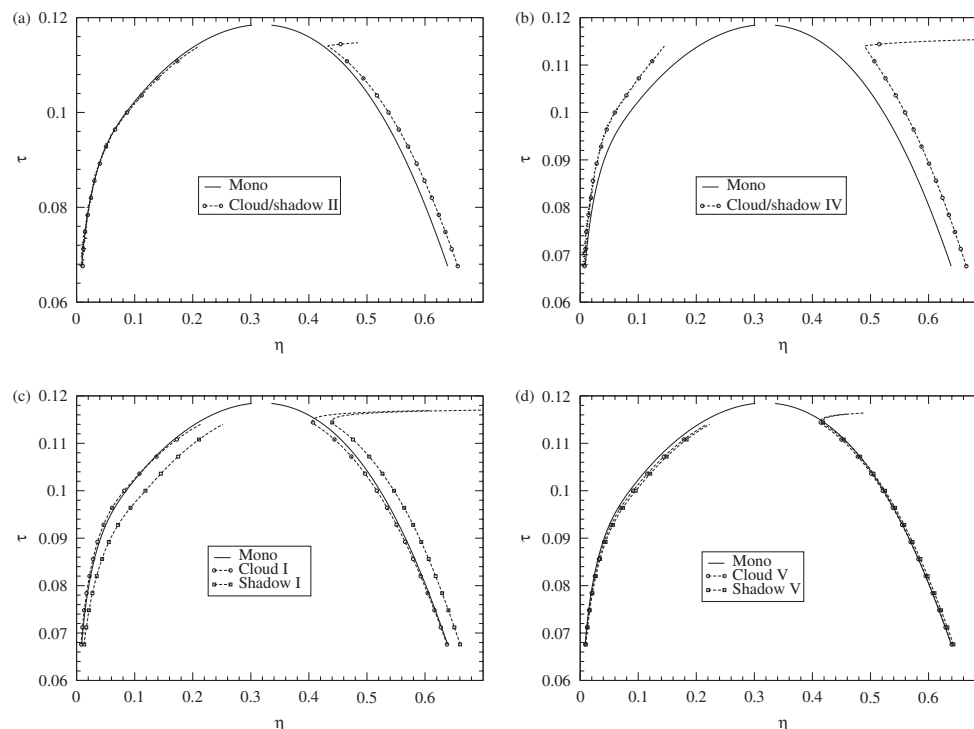


Figure 4. Cloud/shadow pairs from the perturbative results for the PY solution of the SHS Baxter model. In clockwise order, the results for choices II, IV (top) and I, V (bottom) are depicted. In the top two panels, the cloud and shadow curves coincide to this order in perturbation, whereas in the bottom panels they are different. In order to have all pictures on the same scale, the selected value for polydispersity is $s=0.3$ for models II and IV (top) and $s=0.1$ for models I and V (bottom). In all cases, the continuous curve represents the monodisperse ($s=0$) result.

advantage of allowing a complete analytical analysis on the effects of polydispersity, including fractionation, but has the disadvantage of very questionable accuracy. The second is based on a perturbative method, starting from the energy PY one-component solution, which is known to provide an accurate description of the phase diagram. The drawback of this scheme is that it works for mild polydispersity, but it cannot describe the changes in the critical point region. Notwithstanding these limitations, this novel approach is expected to find practical application in the interpretation of all those phenomena where Baxter's model and polydispersity both play a role.

Acknowledgements

We thank Peter Sollich for ongoing collaboration on the subject of this paper.

References

- [1] P. Sollich, *J. Phys.: Condens. Matter* **14**, R79 (2002).
- [2] L. Bellier-Castella, H. Xu, and M. Baus, *J. Chem. Phys.* **113**, 8337 (2000).
- [3] T. Boublik, *J. Chem. Phys.* **53**, 471 (1970); G. A. Mansoori, N. F. Carnahan, K. E. Starling, and T. W. Leland Jr, *J. Chem. Phys.* **54**, 1523 (1971); J. J. Salacuse and G. Stell, *J. Chem. Phys.* **77**, 3714 (1982).
- [4] R. J. Baxter, *J. Chem. Phys.* **49**, 2270 (1968); R. J. Baxter, in *Physical Chemistry, An Advanced Treatise*, edited by D. Henderson (Academic Press, New York, 1971), Vol. 8A, chapt. 4; R. O. Watts, D. Henderson, and R. J. Baxter, *Adv. Chem. Phys.* **21**, 421 (1971).
- [5] J. W. Perram and E. R. Smith, *Chem. Phys. Lett.* **35**, 138 (1975).
- [6] B. Barbooy and R. Tenne, *Chem. Phys.* **38**, 369 (1979).
- [7] D. Gazzillo and A. Giacometti, *J. Chem. Phys.* **113**, 9837 (2000); *ibid.* *Physica A* **304**, 202 (2002).
- [8] D. Gazzillo and A. Giacometti, *Molec. Phys.* **100**, 3307 (2002).

- [9] D. Gazzillo and A. Giacometti, *Molec. Phys.* **101**, 2171 (2003).
- [10] D. Gazzillo and A. Giacometti, *J. Chem. Phys.* **120**, 4742 (2004).
- [11] R. Fantoni, D. Gazzillo, and A. Giacometti, *J. Chem. Phys.* **122**, 034901 (2005); *ibid.* *Phys. Rev. E* **72**, 011503 (2005).
- [12] R. Fantoni, D. Gazzillo, A. Giacometti, and P. Sollich, *J. Chem. Phys.*, **125**, 164504 (2006).
- [13] D. Gazzillo, A. Giacometti, R. Fantoni, and P. Sollich, *Phys. Rev. E*, in press.
- [14] G. Stell, *J. Statist. Phys.* **63**, 1203 (1991).
- [15] M. A. Miller and D. Frenkel, *Phys. Rev. Lett.* **90**, 135702 (2003); *ibid.* *J. Chem. Phys.* **121**, 535 (2004); *ibid.* *J. Phys.: Condens. Matter* **16**, S4901 (2004).
- [16] J. L. Barrat and J. P. Hansen, *Basic Concepts for Simple and Complex Liquids* (Cambridge University Press, Cambridge, 2003); J. P. Hansen and I. R. McDonald, *The Theory of Simple Liquids* (Academic Press, London, 1986).
- [17] J. N. Herrera and L. Blum, *J. Chem. Phys.* **94**, 5077 (1991).
- [18] M. L. Evans, *J. Chem. Phys.* **114**, 1915 (2001).
- [19] C. Robertus, W. H. Philipse, J. G. Joosten, and Y. K. Levine, *J. Chem. Phys.* **90**, 4482 (1989).

Chapter 13

Phase behavior of weakly polydisperse sticky hard spheres: Perturbation theory for the Percus-Yevick solution

Fantoni R., Gazzillo D., Giacometti A., and Sollich P. J. Chem. Phys., **125**, 164504 (2006)
Title:“Phase behavior of weakly polydisperse sticky hard spheres: Perturbation theory for the Percus-Yevick solution”

Abstract: We study the effects of size polydispersity on the gas-liquid phase behavior of mixtures of sticky hard spheres. To achieve this, the system of coupled quadratic equations for the contact values of the partial cavity functions of the Percus-Yevick solution [R. J. Baxter, J. Chem. Phys. **49**, 2770 (1968)] is solved within a perturbation expansion in the polydispersity, i.e., the normalized width of the size distribution. This allows us to make predictions for various thermodynamic quantities which can be tested against numerical simulations and experiments. In particular, we determine the leading order effects of size polydispersity on the cloud curve delimiting the region of two-phase coexistence and on the associated shadow curve; we also study the extent of size fractionation between the coexisting phases. Different choices for the size dependence of the adhesion strengths are examined carefully; the Asakura-Oosawa model [J. Chem. Phys. **22**, 1255 (1954)] of a mixture of polydisperse colloids and small polymers is studied as a specific example.

THE JOURNAL OF CHEMICAL PHYSICS **125**, 164504 (2006)

Phase behavior of weakly polydisperse sticky hard spheres: Perturbation theory for the Percus-Yevick solution

Riccardo Fantoni,^{a)} Domenico Gazzillo,^{b)} and Achille Giacometti^{c)}
*Istituto Nazionale per la Fisica della Materia and Dipartimento di Chimica Fisica,
Università Ca' Foscari di Venezia, Santa Marta DD 2137, I-30123 Venezia, Italy*

Peter Sollich^{d)}
Department of Mathematics, King's College London, Strand, London WC2R 2LS, United Kingdom

(Received 9 August 2006; accepted 5 September 2006; published online 23 October 2006)

We study the effects of size polydispersity on the gas-liquid phase behavior of mixtures of sticky hard spheres. To achieve this, the system of coupled quadratic equations for the contact values of the partial cavity functions of the Percus-Yevick solution [R. J. Baxter, *J. Chem. Phys.* **49**, 2770 (1968)] is solved within a perturbation expansion in the polydispersity, i.e., the normalized width of the size distribution. This allows us to make predictions for various thermodynamic quantities which can be tested against numerical simulations and experiments. In particular, we determine the leading order effects of size polydispersity on the cloud curve delimiting the region of two-phase coexistence and on the associated shadow curve; we also study the extent of size fractionation between the coexisting phases. Different choices for the size dependence of the adhesion strengths are examined carefully; the Asakura-Oosawa model [*J. Chem. Phys.* **22**, 1255 (1954)] of a mixture of polydisperse colloids and small polymers is studied as a specific example. © 2006 American Institute of Physics. [DOI: 10.1063/1.2358136]

I. INTRODUCTION

In the context of soft matter, a number of systems are known to display a combination of a very steep repulsion and a short ranged attraction. This includes, for instance, polymer-coated colloids,^{1,2} globular proteins,³ and microemulsions.⁴ In spite of the notable differences in the details of the interactions among these systems, most of the common essential features are captured by a paradigmatic model known as the adhesive or sticky hard sphere model. Sticky hard spheres are impenetrable particles of diameters $\{\sigma_i\}$ with adhesive surfaces. The simplest way of describing the adhesion properties, in the framework of atomic fluids, was originally proposed by Baxter⁵ in terms of a potential where energy and length scales were combined into a single parameter, thus defining the so-called sticky hard sphere (SHS) potential. Baxter showed that for this model the Ornstein-Zernike integral equation determining the correlation functions in the liquid state admitted an analytic solution within the Percus-Yevick (PY) approximation. Together with his collaborators, he predicted from this solution (via both the compressibility and the energy routes of liquid state theory) that the model displays a gas-liquid transition.^{6,7} This PY solution was soon extended to mixtures^{8–11} and has since found a number of interesting applications in the area of colloidal suspensions.^{1,2,12–15} When studying the phase behavior of such fluids an important issue to deal with is the fact that colloidal particles are generally not identical but

may have different characteristics (size, charge, chemical species, etc). Often, the distribution of the relevant parameter is effectively continuous, and the fluid is then referred to as polydisperse. We will focus in this paper on *size polydispersity*, i.e., a fluid with a distribution of particle diameters. (A small degree of size polydispersity is, in fact, required to resolve thermodynamic pathologies which occur in the case of strictly equal-sized, i.e., monodisperse, sticky hard spheres.¹⁶) The particle size distribution is fixed when the particles are synthesized. Thereafter, only the overall density can be modified by adding or removing a solvent, while keeping constant all ratios of densities of particles of different sizes; this traces out a so-called “dilution line” in the phase diagram.

Given the success of the PY closure for the monodisperse SHS model, it is natural to try to extend it to the polydisperse case. Unfortunately, the PY approximation is tractable only for mixtures of a small number of particle species: the case of a binary mixture can be solved analytically,¹¹ and for mixtures with a limited number of components (ten or fewer) a numerical solution is feasible.¹² The polydisperse case requires one to keep track of an effectively infinite number of particles species, one for each size, and cannot be tackled directly. An alternative, which we have explored in previous work, is to use simpler integral equation theories such as the modified mean spherical approximation (mMSA or C0). Between this and the PY approximation⁵ lies a set of increasingly accurate approximations denoted as C_n , with $n=1, 2, \dots$. They are based on a density expansion of the direct correlation function outside the hard core and can be shown to improve, order by order, the various virial coefficients.¹⁷ These C_n approximations *can* be extended to

^{a)}Electronic mail: rfantoni@unive.it

^{b)}Electronic mail: gazzillo@unive.it

^{c)}Electronic mail: achille@unive.it

^{d)}Electronic mail: peter.sollich@kcl.ac.uk

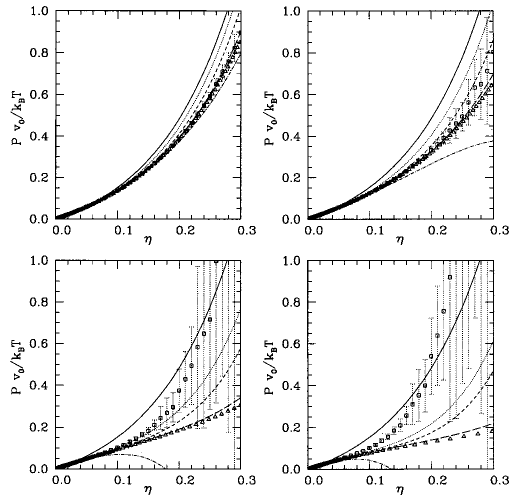
164504-2 Fantoni *et al.*J. Chem. Phys. **125**, 164504 (2006)

FIG. 1. Equation of state, from the energy route, for a one-component fluid of SHS. From left to right and top to bottom the four panels refer to a reduced temperature of $\tau=1.00, 0.50, 0.20$, and 0.15 , respectively. The continuous line corresponds to the MSA approximation, the dotted line to the mMSA approximation, the short dashed line to the C1 approximation, the long dashed line to the PY approximation, the dot-dashed line to the WCA first order perturbation theory, squares to the WCA second order perturbation theory (with error bars indicating the range where the true value should lie with probability of 99.7%), and triangles to the MC simulations of Miller and Frenkel (Ref. 20). In all cases the HS component of the pressure was chosen to be the one obtained from the compressibility route of the PY approximation (Ref. 39).

the polydisperse case with relative ease, provided a particular factorization holds for the matrices appearing in the solution of Baxter's equations. This has allowed us to perform a comprehensive analysis of polydispersity effects on the gas-liquid phase separation.¹⁸

The tractability of the C_n approximations for the polydisperse SHS model does, however, come at the price of lower accuracy. Indeed, for the monodisperse case accurate Monte Carlo simulation data recently published by Miller and Frenkel^{19–21} show that the equation of state of the fluid lies very close to the one derived from the energy route of the PY closure. Both the C0 and C1 approximations, on the other hand, yield precise results only within a rather limited region of the phase diagram, corresponding to high temperatures or low densities¹⁷ (see Fig. 1 below).

The above considerations show that another attack on the PY closure for polydisperse SHS fluids is worthwhile in order to get accurate predictions for the gas-liquid phase behavior. Rather than try to tackle the most general case of a fluid with a potentially wide distribution of particle sizes, which for now remains out of reach, we exploit the idea of Evans²² to treat size polydispersity as a perturbation to the monodisperse phase behavior. For this method to apply, the size distribution only has to be sufficiently narrow, but its shape is otherwise arbitrary. Our approach is also of sufficient generality to consider arbitrary dependences of the adhesion strengths on the particle sizes, including those considered in previous work on the C_n approximations.^{18,23}

Throughout, we consider gas-liquid phase coexistence only. It has been argued²⁴ that even in the presence of polydispersity this is metastable with respect to phase separation into colloidal gas and solid. However, the latter may be unobservable on realistic time scales when formation of the polydisperse solid is hindered by large nucleation barriers²⁵ or an intervening kinetic glass transition;²⁶ the gas-liquid phase splits we calculate will then control the physically observable behavior. Even where the kinetics does allow formation of solid phases, the metastable gas-liquid phase behavior can play a role, e.g., in determining phase ordering pathways.²⁷

This paper is organized as follows. In Sec. II we describe the polydisperse SHS model and discuss various routes for predicting the thermodynamics of this system, comparing their accuracy for the better understood monodisperse case. In the polydisperse setting one needs to model how the strength of the adhesion between two particles depends on their size; we discuss some possible choices for this in Sec. III. Section IV describes our perturbation expansion of the PY closure for the weakly polydisperse SHS model. We first define the perturbation expansion of the free energy used by Evans (Sec. IV A) and summarize the relevant consequences for two-phase coexistence and the attendant size fractionation effects. The basic equations that need to be solved in order to determine thermodynamic properties within the PY approximation are then described and solved perturbatively in Sec. IV B, while Sec. IV C derives from this, via the energy route, the excess Helmholtz free energy. In Sec. V we evaluate numerically the consequences of polydispersity for two-phase coexistence and fractionation for a number of example scenarios, and compare the results with those of alternative approximation schemes. Section VI gives concluding remarks.

II. THE SHS MODEL

The p -component SHS mixture model is made up of hard spheres (HSs) of different diameters σ_i , where $i=1, 2, \dots, p$, interacting through a particular pair potential defined via the following limit procedure. One starts with a pair interaction potential $\phi_{ij}(r)$ with a hard core extending out to distance $r=\sigma_{ij}=(\sigma_i+\sigma_j)/2$, followed by a square well potential of width $R_{ij}-\sigma_{ij}$,

$$\phi_{ij}(r) = \begin{cases} +\infty, & 0 < r < \sigma_{ij} \\ -\ln\left(\frac{1}{12\tau_{ij}} \frac{R_{ij}}{R_{ij}-\sigma_{ij}}\right), & \sigma_{ij} \leq r \leq R_{ij} \\ 0, & r > R_{ij}. \end{cases} \quad (1)$$

Here the dimensionless parameter

$$\frac{1}{\tau_{ij}} = \frac{\epsilon_{ij}}{\tau} \geq 0 \quad (2)$$

measures the surface adhesion strength or "stickiness" between particles of species i and j . In Eq. (2) the reduced temperature τ is an unspecified increasing function of the physical temperature T ; the coefficients ϵ_{ij} specify how stickiness depends on which particle species are in contact and are discussed more fully in the next section. The proce-

dure which defines the SHS model then consists in taking the “sticky limit” $R_{ij} \rightarrow \sigma_{ij}$. The logarithm in the initial square well potential (1) is chosen to give a simple expression for the Boltzmann factor $\exp[-\phi_{ij}(r)]$, which is reduced to a combination of a Heaviside step function and a Dirac delta function in the sticky limit. Here and in the following we measure all energies in units of $k_B T$ to simplify the notation.

A fully polydisperse system is obtained from the above discrete mixture by replacing the molar fractions $x_i = N_i/N$, where N_i is the number of particles of species i and N the total number of particles, with a normalized size distribution function $p(\sigma)$,

$$x_i \rightarrow p(\sigma)d\sigma.$$

Here $p(\sigma) d\sigma$ is the fraction of spheres with diameters in the interval $(\sigma, \sigma+d\sigma)$. Similarly, given a quantity a_i that depends on the species index, one replaces

$$a_i \rightarrow a(\sigma),$$

$$\langle a \rangle = \sum_i x_i a_i \rightarrow \int_0^\infty a(\sigma)p(\sigma)d\sigma.$$

We next consider the possible methods for predicting the thermodynamic behavior of SHS fluids. As pointed out in the Introduction, a good approximation to the effectively exact Monte Carlo (MC) equation of state²⁰ of the *monodisperse* SHS model is obtained by calculating the pressure from the energy route within the PY approximation.⁷ In the case of mixtures no comparable Monte Carlo data exists, nor is a direct solution of the PY closure feasible, so that finding a reliable approximation to the equation of state remains an important open challenge. As described in the Introduction, we have tackled this in previous work within an approximate theory based on a density expansion of the direct correlation function around the MSA solution.^{17,18,23} Another possible route is thermodynamic perturbation theory. For the Baxter SHS model it is easy to convince oneself that only the scheme proposed by Weeks, Chandler, and Anderson²⁸ (WCA) can be applied. We have explored this possibility in the monodisperse case, where Monte Carlo simulations provide reliable reference data. In Fig. 1 we compare the simulation data with the predictions of the MSA, the mMSA, and the C1 approximation [as discussed in (Ref. 17)]; the results from the first and second order WCA (Ref. 28) perturbation theory are also shown. It is clear that the mMSA and the C1 approximation are fairly reliable for low and intermediate densities, even at low reduced temperatures, while the second-order WCA approximation breaks down already at temperatures significantly above the critical point ($\tau_c \approx 0.11$, depending on the approximation used). The WCA method therefore offers little hope of providing the basis for an accurate equation of state for mixtures. One also sees readily from Fig. 1 that the PY closure provides by far the most accurate of all the approximation methods. This is why we return to the problem of solving the PY approximation for SHS mixtures in this paper.

A major challenge in calculating phase equilibria in polydisperse SHS, or indeed any polydisperse fluid, arises

from the fact that its Helmholtz free energy is a functional of the distribution $p(\sigma)$ of the polydisperse attribute.²⁹ However, in simple systems or approximations this functional dependence is reduced, for the *excess* free energy, to one on a finite number of moments of the distribution. In these cases the free energy is called truncatable,^{30,31} and the phase coexistence problem is reduced to the solution of a finite number of coupled nonlinear equations. For example, for the size-polydisperse SHS mixture the mMSA and the C1 approximation yield such a truncatable form for the excess free energy involving only three moments, ρ_1 , ρ_2 , and ρ_3 , and the two-phase coexistence problem can easily be solved numerically.¹⁸ The relevant moments are defined here, including factors of density, as

$$\rho_m = \rho \int_0^\infty \sigma^m p(\sigma) d\sigma \quad (3)$$

for $m=1, 2, 3$; for later reference we note that ρ_3 is proportional to the hard sphere volume fraction.

When the more accurate PY approximation is used, the presence of polydispersity renders an analytical calculation of the free energy impossible (see Sec. IV B). In addition, even if the free energy could be calculated in closed form, it would almost certainly not have a truncatable form, and so predictions for the phase behavior would remain difficult to extract. We therefore propose to consider a small degree of polydispersity as a perturbation²² around the well-understood monodisperse reference system (see Ref. 29 for an overview of earlier work in this perturbative spirit). We denote by σ_0 a characteristic sphere diameter, which will be taken as the mean diameter of the overall or “parent” size distribution $p^{(0)}(\sigma)$ in the system. We then focus on fluids with a narrow size distribution centered on σ_0 , for which the relative particle size deviations

$$\delta = \frac{\sigma - \sigma_0}{\sigma_0} \quad (4)$$

are small for all particle sizes σ . Following Evans, we will expand up to second order in these size deviations.²² The leading order phase boundary shifts and fractionation effects then turn out to be proportional to s^2 , where $s = [\langle \delta^2 \rangle^{(0)}]^{1/2}$ is the normalized standard deviation—also referred to simply as polydispersity—of the parent distribution. Before proceeding to the calculation, we address in the next section the choice of the stickiness coefficients ϵ_{ij} from Eq. (2). These are irrelevant for monodisperse SHS but can have important effects on the behavior of mixtures, as we will see.

III. THE STICKINESS COEFFICIENTS ϵ_{ij}

A. General arguments

At a reduced temperature τ the Boltzmann factor $\exp[-\phi_{ij}(r)]$ for the interaction of two SHS particles depends only on the ratio ϵ_{ij}/τ (and, of course, on σ_{ij}). Physically, the stickiness coefficients ϵ_{ij} represent dimensionless adhesion energies between pairs of particles identified by the species indices i and j . (We revert to the notation for the discrete mixture here; the same considerations obviously apply to the

164504-4 Fantoni *et al.*J. Chem. Phys. **125**, 164504 (2006)

polydisperse system.) The ϵ_{ij} have no analog in the monodisperse case, where only the reduced temperature τ features and ϵ can be set to unity. For (discrete or polydisperse) mixtures, on the other hand, one needs to make an appropriate choice for the dependence, $\epsilon_{ij} = \mathcal{F}(\sigma_i, \sigma_j)$, of the stickiness coefficients on the particle sizes. We discuss possibilities for this choice in this section.

Clearly the appropriate form of the function $\mathcal{F}(\sigma_i, \sigma_j)$ will depend on the kind of physical problem one is studying. Nevertheless, it should satisfy some general requirements: (i) Adhesion should be a purely pairwise property, and so \mathcal{F} should depend only on σ_i and σ_j as anticipated by our notation; \mathcal{F} must clearly also be symmetric under interchange of σ_i and σ_j . (ii) Since the ϵ_{ij} are dimensionless, so must \mathcal{F} be. If it does not contain a separate length scale, it is therefore a homogeneous function of degree zero in (σ_i, σ_j) . The latter case is interesting because it can be seen as the sticky limit of a scalable (i.e., purely size-polydisperse) interaction,²² where, by definition, $\phi_{ij}(r)$ remains unchanged when r , σ_i , and σ_j are all scaled by a common factor. (The square well potential of Eq. (1) can be put into this form by choosing $R_{ij} = \sigma_{ij}[1 + 1/(A\epsilon_{ij} - 1)]$; the sticky limit is obtained by letting $A \rightarrow \infty$.) The presence of pure size polydispersity has important simplifying effects on the phase behavior^{32,33} which we discuss further in Sec. V below. (iii) If the adhesion depends on the surface area of the spheres, one might expect \mathcal{F} to depend on ratios of homogeneous functions of degree 2 in (σ_i, σ_j) . (iv) If the adhesive interaction vanishes when at least one of the two particles i and j degenerates to a point, we need to require $\lim_{\sigma_i \rightarrow 0} \mathcal{F}(\sigma_i, \sigma_j) = 0$; the limit for $\sigma_j \rightarrow 0$ is then also zero, by the symmetry of \mathcal{F} .

In Ref. 18 plausibility and convenience arguments were adduced to suggest the following choices for the quantities ϵ_{ij} :

$$\epsilon_{ij} = \mathcal{F}(\sigma_i, \sigma_j) = \begin{cases} \sigma_0^2 / \sigma_{ij}^2 & \text{case I} \\ \sigma_i \sigma_j / \sigma_{ij}^2 & \text{case II} \\ 1 & \text{case IV} \\ \sigma_0 / \sigma_{ij} & \text{case V.} \end{cases} \quad (5)$$

Here σ_0 is a characteristic reference length for the sizes, taken, as mentioned above, to be the parental mean diameter. In the forms originally suggested,¹⁸ this length was chosen as a moment of the size distribution, $\langle \sigma^n \rangle^{1/n}$ with either $n=1$ or 2. (Case I here corresponds to cases I and III in Ref. 18; we have kept the original numbering for the remaining cases II, IV, and V for ease of reference.) However, this identification has the drawback of introducing many-body effects into the pair potential, as the moments $\langle \sigma^n \rangle$ depend on the thermodynamic state of the fluid and, in particular, on the concentrations of *all* particle species. This is why we have chosen the fixed reference length σ_0 above, consistent with the notion of a purely pairwise interaction. Numerically, the actual choice of σ_0 turns out to have only very minor effects; this can be shown by calculations (not reproduced here) comparing case I (with fixed σ_0) with case III from Ref. 18, obtained by replacing $\sigma_0 \rightarrow \langle \sigma^2 \rangle^{1/2}$.

The form of the $1/\sigma_{ij}^2$ denominator for cases I and II in Eq. (5) is forced by technical constraints detailed in Ref. 18,

TABLE I. Coefficient of the perturbative expansion (6) of the adhesion parameters ϵ_{ij} for the four cases listed in Eq. (5).

	Case I	Case II	Case IV	Case V
ϵ_0	1	1	1	1
ϵ_{1a}	-1	0	0	-1/2
ϵ_{2a}	3/2	1/2	0	1/2
ϵ_{2b}	3/4	-1/4	0	1/4

but these still leave some flexibility in the choice of numerator; cases I and II assume mean-field-like and decoupled dependences, respectively, on stickiness and size. Case IV corresponds to the choice of constant coefficients (independent of particle sizes), while case V is selected in Ref. 18 specifically to permit analytical solution within the C1 closure. Note that not all four cases have all of the properties [(ii)–(iv)] listed above as possible requirements. For example, only cases II and IV are homogeneous functions of (σ_i, σ_j) as required by (ii) when no additional length scale such as σ_0 is involved; they are therefore purely size polydisperse. The properties (iii) and (iv) hold only for case II. It can be argued³⁴ that the dependence on $\sigma_i \sigma_j / \sigma_{ij}^2$ assumed in case II is quite generic for solutions of colloids, micelles, or globular proteins, at least in the high-temperature regime where a linearized approximation for the Boltzmann factor is sufficient. While this favors case II, for phase coexistence we are interested in lower temperatures where it is less clear which case is physically more appropriate; we will therefore include all four cases in our analysis.

For our perturbative analysis we only need to know the coefficients in the expansion of the ϵ_{ij} around the typical particle size $\sigma_i = \sigma_j = \sigma_0$, up to quadratic order in the relative particle size deviations $\delta_i = (\sigma_i - \sigma_0) / \sigma_0$,

$$\epsilon_{ij} = \epsilon_0 + \epsilon_{1a}(\delta_i + \delta_j) + \epsilon_{2a}\delta_i\delta_j + \epsilon_{2b}(\delta_i^2 + \delta_j^2) + \dots \quad (6)$$

The coefficients ϵ_0 , ϵ_{1a} , ϵ_{2a} , and ϵ_{2b} of this expansion are given in Table I for the four cases listed above. Note that $\epsilon_0 = 1$ always so that in the monodisperse limit the ϵ_{ij} are irrelevant, as they should be.

B. Stickiness coefficients for the Asakura-Oosawa model

So far we have considered choices for the stickiness coefficients suggested by rather general arguments. One may wonder whether the ϵ_{ij} can be derived more directly from a physical picture. We shall pursue this here for the well-known Asakura-Oosawa model of colloid-polymer mixtures, which for small polymers leads to a short ranged attractive depletion potential acting between the colloids.³⁵ We shall show that, while a formal sticky limit cannot be taken in general when colloids of different sizes are present, an effective SHS model can still be derived when the polymer size is small but kept as nonzero. This is then simplified further in the perturbative approach for weak polydispersity adopted here.

Consider two colloidal particles represented by impenetrable spheres of diameters σ_i and σ_j immersed in a solution of noninteracting polymers. Within the Asakura-Oosawa

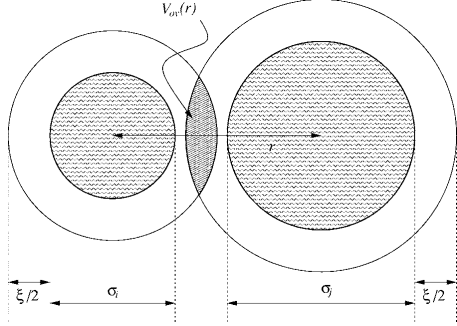


FIG. 2. The overlap volume $V_{ov}(r)$ of the two exclusion zones around colloid particles of diameter σ_i and σ_j which cannot be accessed by polymers of diameter ξ .

model, the polymers are simplified to spheres of diameter ξ which can fully penetrate each other but have a hard sphere interaction with the colloids. It is well known that such a system develops an entropically driven effective attraction between the colloidal particles. This arises due to a reduction in the volume from which the polymers are excluded when the exclusion zones around the colloids overlap (see Fig. 2). This overlap volume as a function of the distance r between the sphere centers is

$$V_{ov}(r) = \frac{\pi}{12} \left[r^3 - 6(R_i^2 + R_j^2)r + 8(R_i^3 + R_j^3) - 3(R_i^2 - R_j^2) \frac{1}{r} \right] \times \theta(\sigma_{ij} + \xi - r), \quad (7)$$

where $R_k = (\sigma_k + \xi)/2$ and only distances $r > \sigma_{ij}$ are allowed because of the hard colloid-colloid repulsion. The effective colloid-colloid attraction induced by the presence of the polymers is then just the overlap volume times the polymer osmotic pressure,^{35,36} giving the overall Asakura-Oosawa (AO) interaction potential

$$\phi_{ij}^{AO}(r) = \begin{cases} +\infty, & 0 < r < \sigma_{ij} \\ -\rho_p V_{ov}(r), & \sigma_{ij} \leq r < \sigma_{ij} + \xi \\ 0, & r \geq \sigma_{ij} + \xi \end{cases} \quad (8)$$

This expression can be obtained formally by integrating out the polymer degrees of freedom from the partition function at fixed polymer chemical potential. The latter is conveniently parameterized by the density ρ_p of polymers in a reservoir connected to the system; because the polymers are taken as ideal, their osmotic pressure is then $k_B T \rho_p$ and the $k_B T$ is absorbed by our choice of units. The effective colloid-colloid interaction will, in general, also contain many-body terms, but these vanish in the limit of small polymers (for monodisperse colloids the condition is $\xi < 0.1547\sigma_0$) that we are interested in.

To map to an equivalent SHS potential, which should be physically reasonable for a small polymer-to-colloid size ratio ξ/σ_0 , one equates the corresponding second virial coefficients. The hard core makes the same contribution ($B_{2,HS}^{ij}$

$= 2\pi\sigma_{ij}^3/3$) in the SHS and the original AO potential, so one can focus on the normalized deviation of the second virial coefficient from this HS value,

$$\Delta B_{2,AO}^{ij} = \frac{B_{2,AO}^{ij} - B_{2,HS}^{ij}}{B_{2,HS}^{ij}} = \frac{3}{\sigma_{ij}^3} \int_{\sigma_{ij}}^{\sigma_{ij} + \xi} [1 - e^{-\phi_{ij}^{AO}(r)}] r^2 dr.$$

For the SHS potential this quantity equals $-1/(4\tau_{ij})$, so the stickiness parameters in the mapped SHS system are assigned as

$$\frac{1}{12\tau_{ij}} = \frac{1}{\sigma_{ij}^3} \int_{\sigma_{ij}}^{\sigma_{ij} + \xi} [e^{-\phi_{ij}^{AO}(r)} - 1] r^2 dr. \quad (9)$$

We now proceed to simplify this expression for small ξ ; in the limit $\xi \rightarrow 0$, the original AO model should become fully equivalent to the mapped SHS system. We will see that for mixtures of colloids of different sizes this strict mathematical limit cannot be taken consistently; nevertheless, as long as ξ/σ_0 is small, we expect the SHS mixture to give a reasonably accurate description of the underlying AO model.

To simplify Eq. (9) we change the integration variable from r to $z = (r - \sigma_{ij})/\xi$, expand the attractive tail of the AO potential in ξ as

$$-\phi_{ij}^{AO}(z) = \frac{\pi}{4} \rho_p \xi^2 \frac{\sigma_i \sigma_j}{\sigma_{ij}} (z - 1)^2 + O(\xi^3), \quad (10)$$

and retain only the leading term. Similarly, approximating $r^2 = (\sigma_{ij} + \xi z)^2 = \sigma_{ij}^2 + O(\xi)$ yields

$$\frac{1}{12\tau_{ij}} = \frac{\xi}{\sigma_{ij}} \int_0^1 [e^{\gamma_{ij}(1-z)^2} - 1] dz = \frac{\xi}{\sigma_{ij}} \left[\frac{1}{2} \sqrt{\frac{\pi}{\gamma_{ij}}} \operatorname{erfi}(\sqrt{\gamma_{ij}}) - 1 \right], \quad (11)$$

where

$$\gamma_{ij} = \frac{\pi}{4} \rho_p \xi^2 \frac{\sigma_i \sigma_j}{\sigma_{ij}}$$

is the value of the attractive potential at contact and $\operatorname{erfi}(z) = \operatorname{erf}(iz)/i$ is the imaginary error function. Because of the prefactor ξ/σ_{ij} in Eq. (11), γ_{ij} has to grow as ξ decreases if we want to keep τ_{ij} finite. For large argument the error function behaves as $\operatorname{erfi}(z) = e^{z^2} [1/z + O(1/z^3)]/\sqrt{\pi}$, and so

$$\frac{1}{12\tau_{ij}} \approx \frac{\xi}{\sigma_{ij}} \frac{e^{\gamma_{ij}}}{2\gamma_{ij}} = \frac{2}{\pi \rho_p \xi \sigma_i \sigma_j} e^{(\pi/4) \rho_p \xi^2 (\sigma_i \sigma_j / \sigma_{ij})}.$$

A nonzero limit value of τ_{ij} for $\xi \rightarrow 0$ thus requires that γ_{ij} grows logarithmically as $\gamma_{ij} = \ln(\sigma_{ij}/\xi)$ to leading order. The corresponding polymer reservoir density, likewise to leading order, goes as

$$\rho_p = \frac{4}{\pi} \frac{\sigma_{ij}}{\sigma_i \sigma_j} \frac{\ln(\sigma_{ij}/\xi)}{\xi^2}. \quad (12)$$

The dominant dependence $\rho_p \propto \xi^{-2}$ in this expression arises because the value of the AO potential at contact scales as $\rho_p \xi^2$; the additional logarithmic factor increases this interac-

164504-6 Fantoni *et al.*J. Chem. Phys. **125**, 164504 (2006)

tion strength to compensate for the decreasing range of the attraction as $\xi \rightarrow 0$. Note that even though the polymer density diverges, the polymers do in fact become very dilute, as one sees from the (reservoir) volume fraction $\eta_p = (\pi/6)\rho_p \xi^3 \sim \xi \ln(\sigma_0/\xi)$ occupied by the polymer spheres.

For monodisperse colloids, the above procedure produces an unambiguous sticky limit for $\xi \rightarrow 0$. The explicit form of Eq. (12) shows, however, that this limit cannot be taken straightforwardly for mixtures: the prefactors $\sigma_{ij}/(\sigma_i \sigma_j)$ of the required leading order divergences of the polymer density are incompatible with each other for different pairs of particle species. In other words, if the ξ dependence of the polymer density is chosen to keep one specific τ_{ij} finite and nonzero, then the others would either tend to zero or grow to infinity in the sticky limit. The example of a binary mixture illustrates this. Suppose that $\sigma_1 > \sigma_2$ and that the polymer density is tuned to keep the τ_{11} finite. Then $1/\tau_{22}$ would both tend to zero for $\xi \rightarrow 0$ so that all interactions involving particles of species 2 become purely HS-like, without any attractive contributions (this is system *B* studied in Ref. 23).

In the absence of a strict sticky limit, we will content ourselves with applying the mapping (11) for small but nonzero polymer-to-colloid size ratios ξ/σ_0 . The properties of the resulting SHS mixture should then still give a good approximation to those of the original AO model. In the perturbative setting of this paper we can then expand Eq. (11) in the small relative deviations $\delta_i = (\sigma_i - \sigma_0)/\sigma_0$ of the particle sizes from the parental mean. In the decomposition $1/\tau_{ij} = \epsilon_{ij}/\tau$ of Eq. (2) we fix the scale of the ϵ_{ij} by requiring, as was done before, that $\epsilon_{ij} = 1$ for particles of the reference size $\sigma_i = \sigma_j = \sigma_0$. This gives

$$\frac{1}{\tau} = \frac{12\xi}{\sigma_0} \left[\frac{1}{2} \sqrt{\frac{\pi}{\gamma}} \operatorname{erfi}(\sqrt{\gamma}) - 1 \right] \approx \frac{6\xi e^\gamma}{\sigma_0 \gamma} \quad (13)$$

for the reduced temperature, where

$$\gamma = \frac{\pi}{4} \rho_p \xi^2 \sigma_0.$$

The second, approximate equality in Eq. (13) holds for large γ as before. To find the perturbative expansion of the stickiness coefficients ϵ_{ij} , we note first that the potentials at contact expand as

$$\gamma_{ij} = \gamma \left[1 + \frac{1}{2}(\delta_i + \delta_j) + \frac{1}{2}\delta_i \delta_j - \frac{1}{4}(\delta_i^2 + \delta_j^2) \right].$$

Since the erfi in Eq. (11) grows at most as $\exp(\gamma_{ij})$, a second order Taylor expansion will give an accurate approximation as long as the perturbations in γ_{ij} are $\ll 1$. This requires $\delta_i \ll 1/\gamma$, which then automatically enforces $\delta_i \ll 1$ since we expect γ to be at least of order unity for the mapping to a SHS mixture to make sense. Under these conditions one then has a valid perturbation expansion of the ϵ_{ij} . The coefficients defined in Eq. (6) are found as $\epsilon_0 = 1$ (by our choice of τ) and

$$\epsilon_{11} = \frac{-1 + g_1}{2}, \quad \epsilon_{2a} = \frac{1 + g_2}{2}, \quad \epsilon_{2b} = \frac{1 - 2g_1 + g_2}{4},$$

where

$$g_1 = \frac{e^\gamma - 1}{\sqrt{\pi/\gamma} \operatorname{erfi}(\sqrt{\gamma}) - 2} - \frac{1}{2},$$

$$g_2 = \frac{[3 + e^\gamma(2\gamma - 3)]/4}{\sqrt{\pi/\gamma} \operatorname{erfi}(\sqrt{\gamma}) - 2} + \frac{3}{8}.$$

From Eq. (13) one sees that the reduced temperature is set by the contact potential γ , which itself is proportional to the polymer reservoir density. Unlike the more *ad hoc* choices of Eq. (5), the expansion of the ϵ_{ij} in terms of the δ_i depends on the reduced temperature τ via γ . For large γ one can use the leading order approximations $g_1 \approx \gamma - 1$ and $g_2 \approx (\gamma^2 - 2\gamma + 1)/2$ to evaluate this dependence. However, since typical values of γ are only logarithmically large in σ_0/ξ , it is generally safer to work with the full expressions.

IV. PERTURBATION THEORY FOR THE POLYDISPERSE PY CLOSURE

In this section we come to the core of our analysis. We first review Evans' perturbative framework for slightly polydisperse systems. To apply this to the PY approximation for SHS mixtures we will need the perturbative expansion of certain correlation function values at contact; from these we can then finally find the excess free energy.

A. Evans' perturbative expansion

The starting point for an analysis of the phase behavior of polydisperse systems is the excess free energy density. In general this is a functional of the size distribution $p(\sigma)$ in the system. It is also a function of the particle density ρ and of temperature; we do not write the latter explicitly below. For slightly polydisperse systems it is expedient to switch from σ to the relative deviations δ from the reference size σ_0 . By the fundamental assumption of a narrow size distribution, the δ are small quantities, and one can expand the excess free energy density f^{ex} , measured again in units of $k_B T$, in terms of moments of $p(\delta)$,²²

$$f^{\text{ex}}(\rho, [p(\delta)]) = f_0^{\text{ex}}(\rho) + \rho a(\rho) \langle \delta \rangle + \rho b(\rho) \langle \delta^2 \rangle + \rho c(\rho) \langle \delta^3 \rangle + \dots \quad (14)$$

Here terms up to second order in δ have been retained; these give the leading effects on the phase boundaries.²² Our functions a , b , and c differ by factors of ρ from those defined in Ref. 22, so that, e.g., a equals Evans' A/ρ ; this simplifies the statement of Eqs. (15)–(17) below. The leading term f_0^{ex} is the excess free energy density of the monodisperse reference system where all particles have $\delta = 0$.

Given the above expansion of the excess free energy, the conditions for two-phase equilibria of the near-monodisperse fluid can be solved perturbatively.²² We briefly recall the main results. The fluid is initially in a parent phase of density $\rho^{(0)}$, with a parent size distribution function $p^{(0)}(\delta)$, where $\langle \delta \rangle^{(0)} = 0$ by our choice of the reference size σ_0 as the parental mean. In order to lower its free energy, the fluid can split into two daughter phases of densities $\rho^{(1)}$ and $\rho^{(2)}$, with distribution functions $p^{(1)}(\delta)$ and $p^{(2)}(\delta)$ which are, in general, different from the parent distribution, a phenomenon referred

to as *fractionation*.²⁹ The densities and size distributions can be worked out perturbatively at any point inside the coexistence region;²² we focus on the properties at the *onset* of phase coexistence, which are most easily accessible experimentally.

Suppose the system is just starting to phase separate, with all of the volume except for an infinitesimal fraction still occupied by phase 1, with density $\rho^{(1)}$. Conservation of particle number then requires that $p^{(1)}(\delta) = p^{(0)}(\delta)$; i.e., the size distribution in this *cloud* phase equals the parent. The coexisting *shadow* phase 2, on the other hand, will generally have $p^{(2)}(\delta) \neq p^{(0)}(\delta)$. Evans²² showed that the cloud and shadow densities, $\rho^{(1)} = \rho_0^{(1)} + \delta\rho^{(1)}$ and $\rho^{(2)} = \rho_0^{(2)} + \delta\rho^{(2)}$, respectively, are shifted from their monodisperse values $\rho_0^{(1)}$ and $\rho_0^{(2)}$ by

$$\delta\rho^{(1)} = -s^2\rho_0^{(1)}\kappa(\rho_0^{(1)}) \left[(\rho_0^{(1)})^2 b'(\rho_0^{(1)}) + \frac{(\Delta a)^2 + 2\Delta b}{2\Delta(1/\rho)} \right], \quad (15)$$

$$\delta\rho^{(2)} = -s^2\rho_0^{(2)}\kappa(\rho_0^{(2)}) \left[(\rho_0^{(2)})^2 b'(\rho_0^{(2)}) + \frac{(\Delta a)^2 + 2\Delta b}{2\Delta(1/\rho)} + (\rho_0^{(2)})^2 a'(\rho_0^{(2)})\Delta a \right]. \quad (16)$$

Here $a' \equiv \partial a / \partial \rho$, $b' \equiv \partial b / \partial \rho$, and $\kappa(\rho) = 1 / [\rho + \rho^2(\partial / \partial \rho)^2 f_0^{\text{HS}}(\rho)]$, which is the isothermal compressibility of the monodisperse reference system. The shorthand Δ indicates differences between the two monodisperse reference phases, e.g., $\Delta a = a(\rho_0^{(1)}) - a(\rho_0^{(2)})$. Finally, recall that s is the parent polydispersity: the phase boundary shifts are, to leading order, quadratic in s .

It is worth noting that Eqs. (15) and (16) are not symmetric in $\rho_0^{(1)}$ and $\rho_0^{(2)}$; by interchanging the two densities one therefore obtains a different cloud-shadow pair. Physically, this corresponds to approaching the onset of phase separation from low or high densities; in a polydisperse system the coexisting phases are different in the two situations since only the respective majority (cloud) phase has the parental size distribution. The size distribution in the corresponding shadow reads, to leading order in δ ,²²

$$p^{(2)}(\delta) = p^{(0)}(\delta)[1 + (\Delta a)\delta]. \quad (17)$$

Overall, the monodisperse binodal delimiting the coexistence region splits into separate cloud and shadow curves, which intersect in the critical point.²⁹ Quantitative information about the critical region is not accessible within the perturbative expansion of Eqs. (15) and (16), however, since the compressibility κ diverges as the critical point is approached.

The above summary shows that knowledge of the functions a , b , and c is sufficient to calculate the leading order phase boundary shifts and fractionation effects for weakly polydisperse systems. In the next two subsections we calculate these functions for the SHS mixture within the PY approximation.

B. Perturbative analysis of the PY closure

To lighten the notation in the rest of the paper, we make all densities dimensionless by measuring them in units of v_0^{-1} , where

$$v_0 = (\pi/6)\sigma_0^3$$

is the volume of a particle with the reference diameter. The third moment ρ_3 defined in Eq. (3) is then identical to the hard sphere volume fraction η . We also measure all particle sizes σ in terms of σ_0 , so that the relation between σ and the fractional deviation from the parental mean diameter becomes simply $\sigma = 1 + \delta$. In the monodisperse case, where all particles have $\delta = 0$, all moments (3) are then identical and equal to the density ρ (which also equals the volume fraction η). Finally, for notational simplicity we again revert temporarily to the case of a discrete p -component SHS mixture; the final results will be expressed in terms of averages over the size distribution and so will be generalized immediately to fully polydisperse systems.

In order to extract the desired thermodynamic quantities from the PY closure, the following set of $p(p+1)/2$ coupled quadratic equations needs to be solved first.¹⁰

$$L_{ij} = \alpha_{ij} + \beta_{ij} \sum_m x_m \left[\frac{1}{12} L_{im} L_{jm} - \frac{1}{2} (L_{im} \phi_{mj} + L_{jm} \phi_{mi}) \right], \quad (18)$$

$$i, j = 1, 2, \dots, p,$$

where the unknowns are

$$L_{ij} = \frac{y_{ij}(\sigma_{ij})\sigma_{ij}^2\epsilon_{ij}}{\tau}.$$

Here $y_{ij}(\sigma_{ij})$ is the partial cavity function at contact which is proportional to the probability of finding a particle of species j touching any given particle of species i . In Eq. (18) the coefficients α_{ij} , β_{ij} , and ϕ_{ij} are given by

$$\alpha_{ij} = y_{ij}^{\text{HS}}(\sigma_{ij})\sigma_{ij}^2\epsilon_{ij}/\tau, \quad (19)$$

$$\beta_{ij} = \rho\sigma_{ij}\epsilon_{ij}/\tau, \quad (20)$$

$$\phi_{ij} = \sigma_i\sigma_j/\Delta. \quad (21)$$

Here the quantities

$$y_{ij}^{\text{HS}}(\sigma_{ij}) = \frac{1}{\Delta} + \frac{3}{2} \frac{\rho_2}{\Delta^2} \frac{\sigma_i\sigma_j}{\sigma_{ij}} \quad (22)$$

are the PY partial cavity functions at contact for the HS fluid (to which the SHS fluid is reduced at infinite reduced temperature τ), and we abbreviate $\Delta = 1 - \eta$, with $\eta \equiv \rho_3$ the HS packing fraction as before. Notice that all four sets of coefficients L_{ij} , α_{ij} , β_{ij} , and ϕ_{ij} are symmetric under exchange of the species indices i and j .

For one-component fluids, the system (18) is reduced to a single quadratic equation. Baxter⁵ showed that only the smaller of the two real solutions (provided such solutions exist at all) is physically significant; it is given explicitly in Eq. (24) below. For true mixtures ($p > 1$), an explicit solution

164504-8 Fantoni *et al.*J. Chem. Phys. **125**, 164504 (2006)

of the rather complicated system (18) of algebraic equations is feasible at best numerically (except for special cases^{12,23}) and is the computational bottleneck of the PY solution. For large p , and certainly for the polydisperse limit $p \rightarrow \infty$, it is impossible in practice. However, progress can be made for near-monodisperse fluids by solving (18) perturbatively. The L_{ij} will generically depend on the reduced temperature τ , the overall number density ρ , the sizes σ_i and σ_j of the particles at contact, and all the molar fractions x_i [or their polydisperse analog, the size distribution $p(\delta)$]. For small δ_i we can therefore expand to quadratic order as

$$L_{ij} = L_0 + L_{1a}(\delta_i + \delta_j) + L_{1b}(\delta) + L_{2a}\delta_i\delta_j + L_{2b}(\delta_i^2 + \delta_j^2) + L_{2c}\langle\delta\rangle(\delta_i + \delta_j) + L_{2d}\langle\delta\rangle^2 + L_{2e}\langle\delta^2\rangle. \quad (23)$$

The idea now is to insert this expansion, and the analogous expansions of the known coefficients α_{ij} , β_{ij} , and ϕ_{ij} , into the right-hand side of Eq. (18). Having done this, one reexpands to quadratic order in δ_i , δ_j , δ_m , and $\langle\delta\rangle$, and to linear order in $\langle\delta^2\rangle$. Finally, one replaces $\sum_m x_m = 1$ and $\sum_m x_m \delta_m^n = \langle\delta^n\rangle$, for $n=1, 2$. Comparing terms of the same form on the left and right of Eq. (18), one then finds a relatively simple set of equations for the coefficients L_0, \dots, L_{2e} , as outlined in the Appendix. To order zero in polydispersity one, of course, retrieves Baxter's original quadratic equation [Eq. (A5)], whose physically relevant solution is

$$L_0 = \frac{\alpha_0}{\frac{1}{2}[1 + \beta_0/\Delta_0 + \sqrt{(1 + \beta_0/\Delta_0)^2 - \beta_0\alpha_0/3}]}, \quad (24)$$

where $\Delta_0 = 1 - \rho$ is the value of Δ in a monodisperse system with density ρ . Since we are perturbing around the physical solution (24) for the monodisperse case, the results we find for slightly polydisperse mixtures will automatically have the correct physical behavior. In a nonperturbative solution, one would need to check separately that the solution branch with the correct low-density limit $L_{ij} \rightarrow \sigma_{ij}^2/\tau_{ij}$ has been selected; this condition arises since $y_{ij}(\sigma_{ij}) \rightarrow 1$ at low density.

The conditions imposed by Eq. (18) for the higher order expansion coefficients L_{1a}, \dots, L_{2e} turn out to be *linear* and can be straightforwardly solved order by order (see the Appendix). The region in the density-temperature plane where Eq. (18) has no physical solution therefore remains as in the monodisperse case, being delimited by $\rho_- < \rho < \rho_+$ with

$$\rho_{\pm} = \frac{1 - 6(\tau - \tau^2) \pm \sqrt{1 - 12\tau + 18\tau^2}}{5 - 12\tau + 6\tau^2} \quad (25)$$

for $\tau < (2 - \sqrt{2})/6$. This is clearly an artifact of our finite-order perturbation theory, given that we know from numerical solutions of Eq. (18) that the region where solutions exist does change with increasing polydispersity.¹² To reproduce this effect within our approach, a resummation of the perturbation theory to all orders would be needed.

C. Excess free energy

Given the perturbative expansion for L_{ij} , we can determine the free energy of weakly polydisperse SHS mixtures

in the PY approximation. There are three known thermodynamic routes (via the energy, compressibility, and virial) that could potentially be used.¹¹ We focus on the one that gives the most reliable equation of state for the monodisperse system (see Fig. 1), i.e., the energy route. It predicts, in general, for the τ derivative of the excess free energy density

$$\frac{\partial f^{\text{ex}}}{\partial \tau} = \frac{\rho^2}{\tau} \sum_{ij} x_i x_j \sigma_{ij} L_{ij}.$$

Inserting the expansion (23) of L_{ij} and reexpanding to quadratic order yields

$$\frac{\partial f^{\text{ex}}}{\partial \tau} = \frac{\rho^2}{\tau} [\Gamma_0 + \Gamma_1 \langle\delta\rangle + \Gamma_2 \langle\delta\rangle^2 + \Gamma_3 \langle\delta^2\rangle],$$

where

$$\Gamma_0 = L_0,$$

$$\Gamma_1 = L_0 + 2L_{1a} + L_{1b},$$

$$\Gamma_2 = L_{1a} + L_{1b} + L_{2a} + 2L_{2c} + L_{2d},$$

$$\Gamma_3 = L_{1a} + 2L_{2b} + L_{2e}.$$

We can then integrate from the desired value of τ to the hard sphere limit $\tau \rightarrow \infty$ to find

$$\Delta f^{\text{ex}} \equiv f^{\text{ex}} - f_{\text{HS}}^{\text{ex}} = \Delta f_0^{\text{ex}} + \Delta f_1^{\text{ex}} \langle\delta\rangle + \Delta f_2^{\text{ex}} \langle\delta\rangle^2 + \Delta f_3^{\text{ex}} \langle\delta^2\rangle,$$

where

$$\Delta f_i^{\text{ex}} = -\rho^2 \int_{\tau}^{\infty} \Gamma_i(\tau') \frac{d\tau'}{\tau'}, \quad i = 0, 1, 2, 3.$$

and $f_{\text{HS}}^{\text{ex}}$ is the excess free energy density of the HS fluid. For the latter we use the standard Boublík,³⁷ Mansoori, Carnahan, Starling, and Leland³⁸ (BMCSL) expression.³⁹ Expanded to second order in polydispersity, this reads

$$f_{\text{HS}}^{\text{ex}} = f_{\text{HS},0}^{\text{ex}} + f_{\text{HS},1}^{\text{ex}} \langle\delta\rangle + f_{\text{HS},2}^{\text{ex}} \langle\delta\rangle^2 + f_{\text{HS},3}^{\text{ex}} \langle\delta^2\rangle,$$

where

$$f_{\text{HS},0}^{\text{ex}} = \frac{\rho^2(4 - 3\rho)}{\Delta_0^2},$$

$$f_{\text{HS},1}^{\text{ex}} = \frac{6\rho^2(2 - \rho)}{\Delta_0^3},$$

$$f_{\text{HS},2}^{\text{ex}} = 3\rho \left[\frac{\rho(1 + 2\rho)(3 + \rho - \rho^2)}{\Delta_0^4} + \ln \Delta_0 \right],$$

$$f_{\text{HS},3}^{\text{ex}} = 3\rho \left[\frac{\rho(1 + 3\rho - 2\rho^2)}{\Delta_0^3} - \ln \Delta_0 \right].$$

Altogether we therefore have, for the perturbative expansion (14) of the excess free energy density of the SHS mixture,

164504-9 Phase behavior of sticky hard spheres

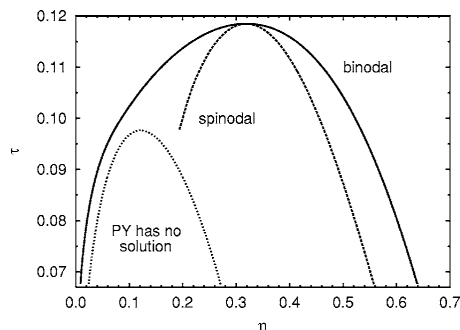
J. Chem. Phys. **125**, 164504 (2006)

FIG. 3. Phase diagram of the monodisperse SHS fluid obtained with the PY closure and the energy route to thermodynamics. Shown are the binodal and spinodal curves and the region where the PY equation has no solution [see Eq. (25)].

$$\begin{aligned}
 f_0^{\text{ex}} &= f_{\text{HS},0}^{\text{ex}} + \Delta f_0^{\text{ex}}, \\
 a\rho &= f_{\text{HS},1}^{\text{ex}} + \Delta f_1^{\text{ex}}, \\
 b\rho &= f_{\text{HS},3}^{\text{ex}} + \Delta f_3^{\text{ex}}, \\
 c\rho &= f_{\text{HS},2}^{\text{ex}} + \Delta f_2^{\text{ex}}.
 \end{aligned}
 \quad (26)$$

With these results we can now proceed to apply Evans' general results to study cloud and shadow curves and fractionation effects in polydisperse SHS mixtures.

Inspection of the lengthy explicit expressions for a - c shows that the dependence on the stickiness expansion coefficients ϵ_{1a} , ϵ_{2a} , and ϵ_{2b} is, in fact, rather simple. For a one finds the form

$$a = a_0 + \epsilon_{1a} a_1, \quad (27)$$

with a_0 and a_1 as functions of ρ and τ only. This is reasonable since a is the coefficient of a first order (in δ) term in the excess free energy and should therefore only depend on the expansion of the ϵ_{ij} to the same order. Function b involves, in addition, terms proportional to ϵ_{1a}^2 and ϵ_{2b} , while the remaining coefficient ϵ_{2a} occurs only in function c . Since c does not feature in the expressions for the phase boundary shifts or fractionation effects to $O(s^2)$, all results we show below are therefore independent of ϵ_{2a} .

V. PHASE BEHAVIOR

In this section we show our results for the phase behavior of polydisperse SHS mixtures. We will explore the various choices of stickiness coefficients discussed in Sec. III, i.e., cases I-V as well as the AO model for small values of the polymer-to-colloid size ratio. Section V A has the main results from our perturbation theory in polydispersity for the PY closure in Sec. V B we then compare these predictions with those from other approximation schemes.

A. PY closure

We start by recalling in Fig. 3 the phase diagram of the monodisperse SHS fluid as obtained within the PY approxi-

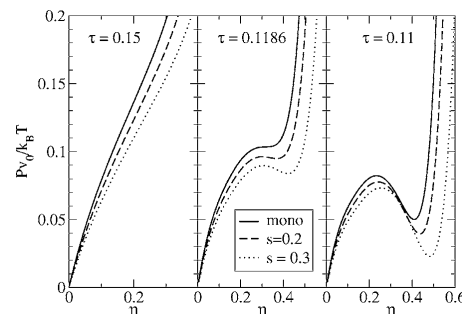


FIG. 4. Pressure from the energy route of the PY approximation for a single (parent) phase with case IV stickiness coefficients, plotted against volume fraction. Results are shown for several small values of the polydispersity s (see legend) and well above, just above, and below (from left to right) the critical point of the monodisperse system. The pressure was determined using Eq. 9 of Ref. 22.

mation and by using the energy route to thermodynamics. Along with the binodal we show the spinodal, where the curvature of the free energy vanishes and a homogeneous phase becomes unstable to local density fluctuations, and the region (25) where Baxter's PY equation has no physical solution. Here and in the following we use on the x axis the volume fraction η rather than the density ρ . In our units, these two quantities are identical for monodisperse systems, but differ to order s^2 in the presence of size polydispersity. For parent phases specifically, Eq. (A4) gives $\eta^{(0)} = \rho^{(0)}(1 + 3s^2)$ to quadratic order. Cloud phases, which share the parental size distribution, have similar $\rho^{(1)} = \rho_0^{(1)}(1 + 3s^2) + \delta\rho^{(1)}$, while for shadow phases one finds using Eq. (17) that $\rho^{(2)} = \rho_0^{(2)}[1 + 3(1 + \Delta a)s^2] + \delta\rho^{(2)}$.²²

To get some initial intuition for the effects of polydispersity, it is useful to consider first the single-phase equation of state. Figure 4 shows plots of the dimensionless pressure against volume fraction at several values of the polydispersity and for three choices of the reduced temperature τ . We consider here constant stickiness coefficients (case IV) to allow a comparison with numerical work for discrete mixtures.¹² It is gratifying that we find qualitatively the same trend, with the pressure decreasing with increasing polydispersity. Quantitatively, however, the results are not directly comparable because in Ref. 12 the less accurate compressibility (rather than energy) route was used to evaluate the pressure.

To interpret physically why the pressure decreases with polydispersity s at fixed packing fraction η , we note first that such a decrease is found also in the absence of adhesion (i.e., for HS). This has been established in simulations⁴⁰ and is reproduced qualitatively by the BMCSL equation of state; the intuitive reason is that in a fluid (gas or liquid) phase a spread of sizes allows for a more efficient packing of the particles. In such a less "jammed" particle arrangement one expects to find fewer interparticle contacts and so, in the presence of adhesion, fewer particle pairs interacting attractively. This will *increase* the pressure, counteracting the reduction, that one would expect for HS, resulting from the

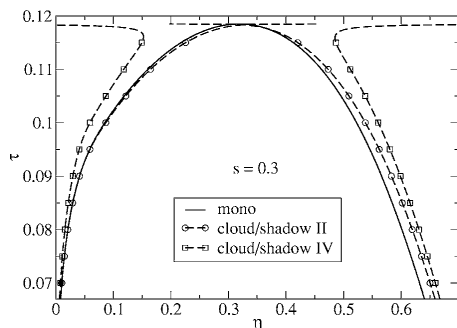
164504-10 Fantoni *et al.*J. Chem. Phys. **125**, 164504 (2006)

FIG. 5. Cloud and shadow curves for SHS mixtures with polydispersity $s=0.3$, as obtained within the PY approximation and the energy route to thermodynamics, for coefficients ϵ_j chosen according to cases II and IV from Eq. (5). The shifts from the binodal of the monodisperse system (labeled “mono”) were calculated using Eq. (15) and give the leading $[O(s^2)]$ corrections in a perturbative treatment of polydispersity. Note the collapse of the cloud and shadow curves, as expected from this order of the perturbation theory for purely size-polydisperse models (Refs. 32 and 33), and the divergence of the perturbation theory at the monodisperse critical point.

more efficient packing. Our results are quite consistent with this: at finite τ , we find that the pressure decreases *less* with polydispersity than in the HS limit $\tau \rightarrow \infty$.

The curves shown for the polydisperse cases in Fig. 4 cannot be used to infer phase coexistence properties directly by, e.g., a Maxwell construction: fractionation means that two coexisting phases do not have properties represented by a single relation between pressure and volume fraction. This remark holds true quite generally for single-phase equations of state in polydisperse systems, including, e.g., the results obtained in Ref. 12 within the PY compressibility route to the equation of state. However, some more limited information on single-phase stability can be deduced. Specifically, a single phase cannot be stable where the pressure decreases with volume fraction. In the middle graph of Fig. 4, for example, where $\tau=0.1186$ is just above the monodisperse critical point and so a monodisperse system is still stable at all densities, the polydisperse mixtures with $s=0.2$ and 0.3 are already unstable in some range of densities. This means that the region where phase separation occurs must extend to larger values of τ for polydisperse than for monodisperse SHS, a result which—for case IV, as considered here—we will find confirmed very shortly.

We next turn to explicit results for the phase behavior, starting in Fig. 5 with cases II and IV for the stickiness coefficients, illustrated here for parent polydispersity $s=0.3$. The cloud curve gives the boundary of the region where phase coexistence occurs. The shadow curve, which records the density of the coexisting phase at each point of incipient phase separation, is normally distinct from this. However, for the purely size-polydisperse cases considered here it is known on general grounds that when represented in terms of volume fraction rather than density the cloud and shadow curves *coincide* to $O(s^2)$.^{32,33} It is reassuring that, as Fig. 5 shows, this property is preserved by the PY approximation.

Turning to more detailed features of Fig. 5, we observe that in case IV the coexistence region is broadened towards

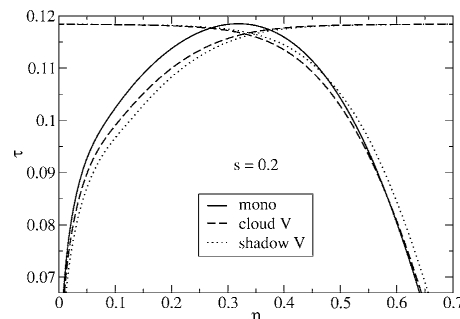


FIG. 6. Cloud and shadow curves for the SHS model with polydispersity $s=0.2$ and case V stickiness coefficients. The binodal of the monodisperse system is shown for comparison.

both lower and higher volume fractions. As the monodisperse critical point is approached, the perturbation expansion breaks down as expected and the cloud/shadow curves diverge. No quantitative information can then be extracted in this regime, but the fact that the divergence is *outwards* still tells us that the coexistence region in the polydisperse case extends to *larger* values of τ than for monodisperse SHS. This is consistent with our inference from the single-phase equation of state above.

Comparing cases II and IV in Fig. 5 one sees first that the phase boundary shifts are rather smaller in the former than in the latter. Also the (slight) broadening of the phase separation region towards lower η is now restricted to τ below around 0.093, while above this value the opposite trend is observed. The divergence of the curves at the monodisperse critical point is now *inwards* so that phase coexistence must terminate at values of τ below the monodisperse τ_c .

Figure 6 shows the cloud and shadow curves for case V. We find that the shifts away from the monodisperse binodal are rather larger than in the previous two cases, and therefore show results for a smaller polydispersity $s=0.2$ rather than for $s=0.3$. Cloud and shadow curves no longer collapse, consistent with expectation as case V is not purely size polydisperse. The cloud curve shows that the coexistence region *narrows* in this case, except on the high-density branch for τ below ≈ 0.085 . The inward divergence of the cloud curve shows that the coexistence region also shrinks towards lower τ . The shadow phases are more dense throughout than the phases on the same branch of the cloud curve. Except for the last point, these trends agree with the nonperturbative results of Ref. 18 derived within the C0 closure.

Case I, shown in Fig. 7, has even stronger polydispersity effects, and we show predictions for a correspondingly smaller polydispersity $s=0.1$. For τ not too far below the critical point the behavior is otherwise qualitatively similar to case V; for lower τ the coexistence region is displaced towards lower rather than, as in case V, higher volume fractions. The shrinking of the coexistence region towards lower τ is again in qualitative agreement with results from the simpler C0 closure.¹⁸

Finally, we turn to the phase behavior predicted for the AO model with a small polymer-to-colloid size ratio ξ/σ_0

164504-11 Phase behavior of sticky hard spheres

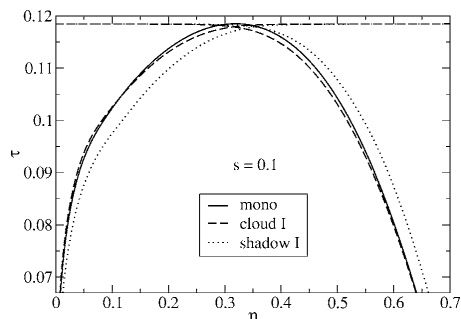
J. Chem. Phys. **125**, 164504 (2006)

FIG. 7. Cloud and shadow curves for the SHS model with polydispersity $s=0.1$ and case I stickiness coefficients. The binodal of the monodisperse system is shown for comparison.

$=0.1$ and polydispersity $s=0.07$, as shown in Fig. 8. For this choice of ξ we have $\gamma \approx 3.97$ at the critical point of the monodisperse system, and the condition $\delta_i \sim s \ll 1/\gamma$ for the validity of the expansion in particle size of the stickiness coefficients ϵ_j is reasonably well obeyed. Here the coexistence region is broadened in all directions by the introduction of polydispersity: towards low and high densities, and also towards larger values of τ . The shadow phases are again more densely packed than the analogous cloud phases.

We conclude this section by considering fractionation effects. These are illustrated in Fig. 9 for cases II and I, for a parent distribution of the Schulz form and with values of the polydispersity s as in the corresponding Figs. 5 and 7. When phase separation is approached from low densities, a gas cloud phase with the parental size distribution coexists with an infinitesimal amount of a liquid shadow phase with a different size distribution. At the high-density boundary of the coexistence region, a liquid cloud phase similarly coexists with a distinct gas shadow phase. Figure 9 shows that for case II the liquid phase contains more larger particles than the coexisting gas in both of these situations (and therefore presumably throughout the whole coexistence range of parent densities at the chosen τ). Case I exhibits the opposite behavior: here the liquid phases contain more *smaller* particles than their coexisting gas counterparts.

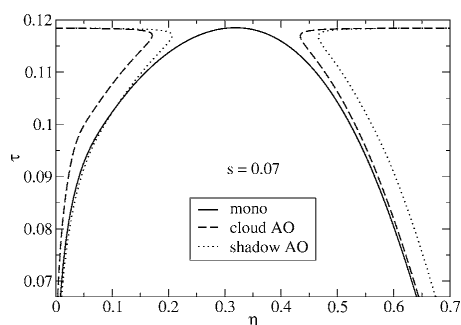


FIG. 8. Cloud and shadow curves for the AO model with polymer-to-colloid size ratio $\xi/\sigma_0=0.1$ and (colloid) polydispersity $s=0.07$. The binodal of the monodisperse system is shown for comparison.

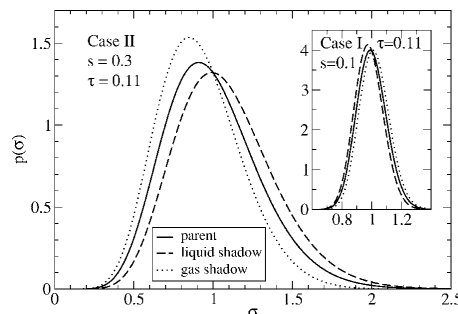


FIG. 9. Fractionation in SHS mixtures with stickiness coefficients chosen according to cases II and I, at $\tau=0.11$ and for polydispersities s as in the corresponding Figs. 5 and 7. Shown are the cloud (parent) size distribution $p(\sigma)$, taken to be of the Schulz form, and the size distributions in the liquid shadow and gas shadow phases that form when coexistence is approached from low densities (gas cloud phase) and high densities (liquid cloud phase), respectively. For case II (main graph) the larger particles tend to accumulate in the liquid phase, while for case I (inset) the opposite is true.

To understand this difference between cases I and II, we return to Eq. (17). Consider the gas cloud point, where $\rho_0^{(1)}$ and $\rho_0^{(2)}$ are the densities of coexisting gas and liquid in the monodisperse system; Δa then is the difference in the values of a between gas and liquid. If this is positive, then Eq. (17) says that the liquid shadow has an enhanced concentration of larger particles. By reversing the role of the two densities one then sees easily that also at the liquid cloud point the liquid phase will contain more of the larger particles than the gas (shadow) phase. In summary, the liquid contains predominantly the larger particles if $\Delta a > 0$, and the smaller particles if $\Delta a < 0$. But from Eq. (27), $\Delta a = \Delta a_0 + \epsilon_{1a} \Delta a_1$ so that different choices of stickiness coefficients affect the direction and strength of fractionation only via ϵ_{1a} . The functions Δa_0 and Δa_1 are shown in Fig. 10 and are both positive; as a result, Δa is positive when $\epsilon_{1a} > -\Delta a_0/\Delta a_1$ and negative otherwise. The ratio occurring on the right-hand side is almost constant and remains close to 1/3 over a large range of τ , as the inset of Fig. 10 demonstrates. We can now

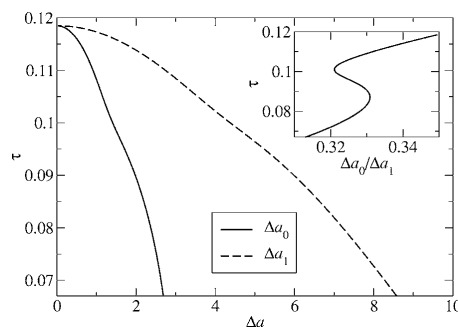


FIG. 10. Decomposition $\Delta a = \Delta a_0 + \epsilon_{1a} \Delta a_1$ of the difference in a between gas and liquid phases. The two contributions Δa_0 and Δa_1 are plotted separately against τ , the latter quantity is graphed on the vertical rather than the horizontal axis for ease of comparison with Figs. 5–8. Inset: ratio of $\Delta a_0/\Delta a_1$.

164504-12 Fantoni *et al.*J. Chem. Phys. **125**, 164504 (2006)

rationalize the difference between cases I and II observed above: for case I, $\epsilon_{1a} = -1 < -1/3$, hence $\Delta a < 0$ and fractionation will enrich the liquid in small particles; for case II, $\epsilon_{1a} = 0 > -1/3$ and one has the opposite situation. Referring to Table I we also conclude that case IV will have the same fractionation behavior as case II, while case V will produce the same “direction” of fractionation (smaller particles in the liquid) as case I but with quantitatively weaker effects. In the AO case ϵ_{1a} depends on τ as discussed in Sec. III B, but this effect turns out to be weak quantitatively, with (for $\xi/\sigma_0 = 0.1$) ϵ_{1a} ranging from ≈ 0.95 at the critical point to ≈ 1.24 at $\tau = 0.065$. Taking for simplicity $\epsilon_{1a} \approx 1$ one infers that fractionation effects will be qualitatively similar to cases II and IV, but quantitatively Δa will be larger by a factor of around 4. All of these conclusions can be confirmed by detailed examination of the explicit results for the various cases.

B. Other approximation schemes

Once one accepts the PY closure, the results shown above are exact in their treatment of polydispersity, certainly within the perturbative setting of weakly polydisperse mixtures. However, the PY closure itself—while more accurate than its competitors—does remain an approximation. It is therefore useful to compare with the predictions of other approximation schemes to assess the robustness of our predictions. We do this first for case II, where an approximate free energy of BMCSL type can be constructed, and then for the AO model, which can be analyzed using the free volume theory of Refs. 41 and 42.

To construct the alternative approximation for case II one starts from a virial expansion of the excess free energy density up to the third virial coefficient. This is easily found as

$$f^{\text{ex}} = \rho \rho_3 + (3 - 12t)\rho_1 \rho_2 + \frac{1}{2}[\rho \rho_3^2 + 3(1 - 12t + 48t^2 - 32t^3)\rho_3^3 + 6(1 - 4t)\rho_1 \rho_2 \rho_3], \quad (28)$$

where $t = 1/(12\tau)$; the terms of second order in density agree with the energy route of the CO approximation.¹⁸ The interesting feature of this result is that the fourth order moment ρ_4 does not appear, in contrast to the analogous expansions for the other cases I, IV, and V that we have considered. Furthermore, the only modification compared to the pure HS case is in the t dependence of the coefficients. These observations suggest that it should be possible to construct a modified free energy expression of BMCSL type which matches the above virial expansion to third order in density. Remarkably, if the desired modified BMCSL form is parametrized in a fairly general manner as

$$f^{\text{ex}} = \left(A_1 \frac{\rho_2^3}{\rho_3} - A_2 \rho \right) [\ln(1 - D\rho_3) + E] + \frac{3B\rho_1 \rho_2}{1 - D\rho_3} + \frac{C\rho_2^3}{\rho_3(1 - D\rho_3)^2}, \quad (29)$$

then by expanding to third order in density and matching to the expansion (28) one finds a *unique* solution for the coefficients,

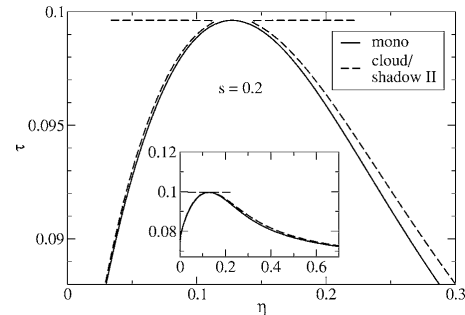


FIG. 11. Cloud and shadow curves for case II stickiness coefficients and with polydispersity $s=0.3$, calculated using the BMCSL-type free energy [Eq. (29)] rather than the PY approximation, as in Fig. 5. The binodal of the monodisperse system, which differs from the PY result, is shown for comparison. Main graph: region around the critical point. Inset: global view of the results on the same scale as in Fig. 5.

$$E = 0, \quad D = A_2 = 1, \quad B = 1 - 4t, \quad C = A_1 = B^3 + 32t^3.$$

The presence of polydispersity is crucial here: for a monodisperse system, the matching conditions to third order in density would not constrain the coefficients sufficiently.

One can now apply the perturbative scheme used throughout this paper to obtain from the excess free energy of Eq. (29) the functions a and b , and hence the cloud and shadow curves. [Note that the perturbative approach is used here mainly for ease of comparison with our other results; since the free energy (29) is truncatable, a full solution of the phase equilibrium conditions would be fairly straightforward.] The results are shown in Fig. 11; note that not just the polydisperse cloud/shadow curves but also the monodisperse binodal are different from the ones obtained from the PY approximation. Looking at the polydispersity-induced shifts, one sees that on the high-density branch of the cloud/shadow curve these are quite comparable to those from the PY approximation (Fig. 5), even semiquantitatively. Polydispersity effects on the low-density branch are rather smaller, again as found within the PY closure. Near the critical point, however, the trends are reversed: the BMCSL-type approximation predicts an extension of the coexistence region towards larger τ and smaller η , whereas the PY approximation leads to the opposite result.

The second case where we have an alternative approximation scheme available for comparison is the AO model. The free volume theory of Ref. 11 effectively linearizes the excess free energy in the polymer (reservoir) potential ρ_p , and the same is true for its generalization to polydisperse colloids.⁴² It is therefore most accurate when the depletion interaction between the colloids, which is proportional to ρ_p , is small (in units of $k_B T$). In order to still get gas-liquid phase separation, the polymer size ξ must then not be too small. This is the opposite limit as for our SHS mapping, which will work best when $\xi \ll \sigma_0$ and the depletion attraction is large at contact. If anything, one therefore expects the best agreement between the two approximations for intermediate values of ξ ; a suitable choice is $\xi/\sigma_0 = 0.1$, as investigated above. Figure 12 compares the two sets of cloud and shadow

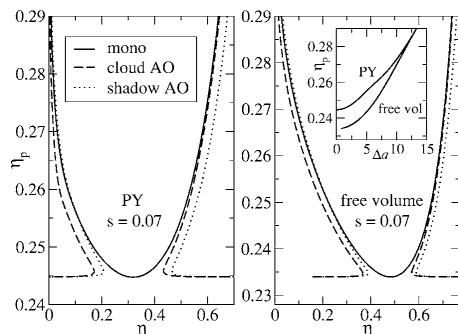


FIG. 12. Comparison of predictions for the AO model with polymer-to-colloid size ratio $\xi/\sigma_0=0.1$. Left: results of SHS mapping analyzed within the PY approximation; as in Fig. 8 cloud and shadow curves are shown for colloid polydispersity $s=0.07$, along with the monodisperse binodal for comparison. The vertical axis now shows the polymer volume fraction rather than the reduced temperature τ . Right: analogous results obtained from free volume theory. Inset, right: fractionation coefficient Δa for the two approximation schemes.

curves predicted. On the vertical axis we plot the polymer (reservoir) volume fraction η_p . This equals $\rho_p \xi^3$ in our dimensionless units and is the conventional variable used in phase diagrams of colloid-polymer mixtures.⁴¹ Comparison of the two panels of Fig. 12 reveals that the qualitative agreement between the two theories is surprisingly good. In particular, the qualitative changes caused by the presence of polydispersity (broadening of coexistence region to lower and higher colloid volume fractions, and lower polymer volume fraction) are in full agreement. For the relevant range of polymer volume fractions there is an even quite good quantitative agreement (but note the slightly different axis ranges on left and right), and the shifts of cloud and shadow curves away from the monodisperse binodal are also quite comparable. Even the predicted fractionation effects agree well: as the inset on the right of Fig. 12 demonstrates, the calculated values of Δa are, apart from the slight shift in the critical point values of the polymer volume fraction, quite consistent with each other.

We note briefly that in order to calculate the free volume theory data shown in Fig. 12 we took the excess free energy for fully polydisperse colloids (at fixed polymer chemical potential) derived in Ref. 42 and then found the functions a and b by expanding explicitly, as in Eq. (14). This gives for a the same result as obtained by Evans,²² while b differs from his expression in terms of approximate correlation functions.²² One might expect that our approach of deriving a and b from one unified polydisperse excess free energy would be somewhat more accurate than Evans' procedure of finding a and b by quite different routes. We have checked that for larger polymer sizes $\xi/\sigma_0=0.4$ our method predicts similar trends to those reported in Ref. 22, but quantitatively the effects of polydispersity are less pronounced.

VI. CONCLUSIONS

We have presented a perturbative approach to the determination of the gas-liquid phase behavior of polydisperse

sticky hard spheres (SHS), studied within the Percus-Yevick (PY) integral equation theory. For arbitrary size polydispersity, the calculation of phase diagrams analogous to those reported here would normally require the solution of a large (or infinite) system of quadratic coupled equations, a task which in practice can be accomplished neither analytically nor numerically. To get around this bottleneck of the PY closure we focused on weakly polydisperse mixtures, where the overall size distribution is narrow in the sense that its normalized (by the mean) standard deviation s is small compared to unity. This allowed us to calculate in closed form the leading order [$O(s^2)$] shifts of cloud and shadow curves away from the monodisperse binodal, and the corresponding fractionation effects. The thermodynamics was derived from the PY solution via the energy route because in the monodisperse case this method gives the best match to Monte Carlo simulation results, even for low reduced temperatures τ around and below the critical point.

In order to specify the properties of a SHS mixture one needs to know how the stickiness coefficients ϵ_{ij} depend on the sizes of the two interacting particles. We discussed a number of plausible constraints on this size dependence. In obtaining explicit results we considered specifically cases I–V (excluding III which, with our now more appropriate choice of reference length, becomes identical to I) previously suggested within exact solutions of simpler closures such as C0 and C1. Of these, cases II and IV are special since they can be seen as the sticky limit of purely size-polydisperse interactions, in which scaling of both particle sizes by a common factor only changes the range but not the strength of the interaction. We have also considered the AO model of a mixture of polydisperse colloids and polymers, which for small polymer size can be mapped to a good approximation onto a SHS model. The stickiness coefficients can be derived in this case rather than postulated; in contrast to the simpler *ad hoc* prescriptions of cases I–V, they are functions of τ .

In the simplest case (case IV) of constant stickiness coefficients we first investigated the single-phase equation of state, finding qualitative agreement with a numerical solution of the compressibility equation of state for a small number of components by Robertus *et al.*¹² Moving on to phase coexistence proper, we found for cases II and IV that cloud and shadow curves coincide in the volume fraction representation and to $O(s^2)$, as expected on general grounds; less obviously, our results also show that in these two cases the deviations of the polydisperse cloud/shadow curves away from the monodisperse binodal are quantitatively small. In all the other cases considered the shadow curves are located at higher volume fractions than the cloud curves, a trend observed in many other polydisperse systems.^{22,29}

Summarizing our findings regarding the effect of polydispersity on the extent of the coexistence region as delimited by the cloud curve, it is simplest initially to group the different scenarios according to their behavior near the critical point. For case IV and the AO model (with a polymer-to-colloid size ratio of 0.1) the coexistence region is shifted to higher reduced temperatures τ ; conversely, at fixed τ it covers a wider range of parent volume fractions η . Cases I,

164504-14 Fantoni *et al.*J. Chem. Phys. **125**, 164504 (2006)

II, and V, on the other hand, show the opposite behavior, with the coexistence region shrinking towards lower τ .

The trends in case IV and AO remain unchanged as one moves to lower values of τ , with the coexistence region continuing to broaden towards lower and higher values of η at the two ends (gas and liquid). In the other cases the shrinking trend near the critical point can be reversed at lower τ . For example, for case II one also eventually sees a broadening to lower (gas branch) and higher (liquid branch) η . For case V the coexistence region is shifted to *higher* η at both ends (gas and liquid) at low τ ; case I shows the opposite behavior.

We have analyzed also the fractionation effects that accompany polydisperse phase separation, where coexisting phases have different particle size distributions. Depending on the stickiness coefficients considered, the liquid phase contains predominantly the larger (as in cases II and IV and AO) or the smaller particles (as in cases I and V). We rationalized this result by showing that the fractionation effects depend on the stickiness coefficients only via the expansion coefficient ϵ_{1a} ; where this is above $\approx -1/3$, the larger particles accumulate in the liquid phase; otherwise, they accumulate in the gas phase.

Finally, we have compared our results with the predictions from other available approximation schemes to check their robustness. Case II is important here because a variety of simple but realistic interaction potentials, used in the literature to model short ranged attractions in real solutions of colloids, reverse micelles, or globular proteins, can be mapped onto this model.³⁴ We constructed an approximate excess free energy by allowing various coefficients within the BMCSL free energy for hard spheres to become τ dependent and to match the (for case II, particularly simple) third order virial expansion. The resulting binodal in the monodisperse limit is rather different from the one obtained from the PY closure with the energy route. The polydispersity-induced shifts of the (coincident) cloud/shadow curves are nevertheless comparable to those predicted by our PY analysis, but only sufficiently far below the critical point. Near the critical point the BMCSL-type excess free energy predicts an enlargement of the coexistence region towards higher τ , while the PY closure gives the opposite result. Given that in the monodisperse case the PY binodal is rather closer to simulation results than the BMCSL-type one, we would expect that the PY predictions are more accurate also for the polydispersity effects.

The second model for which we considered an alternative approximation scheme was the AO model. Here a direct comparison with free volume theory is straightforward since for the latter a generalization to polydisperse colloids has recently been derived.⁴² Even though one expects the two approaches to be valid in complementary regions (small polymer size ξ for the SHS mapping and larger ξ for free volume theory), we found very good qualitative and even semiquantitative agreement of the predictions from the two routes for an intermediate value (0.1) of the polymer-to-colloid size ratio.

In future work, direct simulations of polydisperse SHS mixtures would obviously be of interest to test our predictions and resolve any differences with other approximation

schemes, e.g., in case II. Simulations would be ideal here since in contrast to experiment they would allow one to probe directly different choices for the stickiness coefficients. Because of the presence of polydispersity, a grand canonical Monte Carlo approach^{32,43–45} may be the simulation method of choice, possibly supplemented by specific cluster algorithms tailored to sticky interactions.^{19–21} For the physically more realistic AO model, our predictions should be more accurate than those of free volume theory for small polymer-to-colloid size ratios. Detailed experimental or simulation tests in this regime would be welcome. In simulations one could work directly with the AO depletion potential for the colloids, without ever representing the polymers explicitly. For comparison with experiment one would need to work out the actual volume fraction of polymer in the system rather than in a reservoir; this should, in principle, be a straightforward exercise once our excess free energy has been rewritten as a function of polymer chemical potential. On the experimental side one would require that the colloids are sufficiently polydisperse (beyond a terminal polydispersity around $s=0.07$; see the discussion and bibliography in Ref. 46) to suppress kinetically any solid phases, thus allowing stable observation of the gas-liquid phase splits we have calculated.

APPENDIX: PERTURBATIVE EXPANSION OF L_{ij}

For the perturbative expansion of Eq. (18) one needs the expansions of α_{ij} , β_{ij} , and ϕ_{ij} . These involve the trivial expansions

$$\sigma_i = 1 + \delta_i, \quad (\text{A1})$$

$$\sigma_{ij} = 1 + \frac{1}{2}(\delta_i + \delta_j), \quad (\text{A2})$$

$$\sigma_i \sigma_j = 1 + (\delta_i + \delta_j) + \delta_i \delta_j. \quad (\text{A3})$$

One also needs the expansions to quadratic order of the moments

$$\rho_m = \rho \langle (1 + \delta)^m \rangle = \rho \left(1 + m \langle \delta \rangle + \frac{1}{2} m(m-1) \langle \delta^2 \rangle + \dots \right), \quad (\text{A4})$$

giving in particular $\rho_2 = \rho(1 + 2\langle \delta \rangle + \langle \delta^2 \rangle)$ and $\Delta = 1 - \eta = 1 - \rho_3 = \Delta_0 - 3\rho \langle \delta \rangle - 3\rho \langle \delta^2 \rangle$, with $\Delta_0 = 1 - \rho$ as defined in the main text. The final ingredient is the expansion (6) for the ϵ_{ij} , which is left in general form to allow different possible choices of the stickiness coefficients to be considered together. Altogether one gets the following expansion coefficients for the α_{ij} :

$$\alpha_0 \tau = \frac{1}{\Delta_0} + \frac{3}{2} \frac{\rho}{\Delta_0^2},$$

$$\alpha_{1a} \tau = (1 + \epsilon_{1a}) \frac{1}{\Delta_0} + \left(\frac{9}{4} + \frac{3}{2} \epsilon_{1a} \right) \frac{\rho}{\Delta_0^2},$$

$$\alpha_{1b} \tau = 6 \frac{\rho}{\Delta_0^2} + 9 \frac{\rho^2}{\Delta_0^3},$$

$$\alpha_{2a}\tau = \left(\frac{1}{2} + 2\epsilon_{1a} + \epsilon_{2a}\right)\frac{1}{\Delta_0} + \left(3 + \frac{9}{2}\epsilon_{1a} + \frac{3}{2}\epsilon_{2a}\right)\frac{\rho}{\Delta_0^2},$$

$$\alpha_{2b}\tau = \left(\frac{1}{4} + \epsilon_{1a} + \epsilon_{2b}\right)\frac{1}{\Delta_0} + \left(\frac{3}{4} + \frac{9}{4}\epsilon_{1a} + \frac{3}{2}\epsilon_{2b}\right)\frac{\rho}{\Delta_0^2},$$

$$\alpha_{2c}\tau = \left(\frac{15}{2} + 6\epsilon_{1a}\right)\frac{\rho}{\Delta_0^2} + \left(\frac{27}{2} + 9\epsilon_{1a}\right)\frac{\rho^2}{\Delta_0^3},$$

$$\alpha_{2d}\tau = 27\frac{\rho^2}{\Delta_0^3} + \frac{81}{2}\frac{\rho^3}{\Delta_0^4},$$

$$\alpha_{2e}\tau = \frac{9}{2}\frac{\rho}{\Delta_0^2} + 9\frac{\rho^2}{\Delta_0^3}.$$

Similarly one has for the β_{ij}

$$\beta_0\tau = \rho,$$

$$\beta_{1a}\tau = \left(\frac{1}{2} + \epsilon_{1a}\right)\rho,$$

$$\beta_{1b}\tau = 0,$$

$$\beta_{2a}\tau = (\epsilon_{1a} + \epsilon_{2a})\rho,$$

$$\beta_{2b}\tau = \left(\frac{1}{2}\epsilon_{1a} + \epsilon_{2b}\right)\rho,$$

$$\beta_{2c}\tau = 0,$$

$$\beta_{2d}\tau = 0,$$

$$\beta_{2e}\tau = 0,$$

and for the ϕ_{ij}

$$\phi_0 = \frac{1}{\Delta_0},$$

$$\phi_{1a} = \frac{1}{\Delta_0},$$

$$\phi_{1b} = \frac{3\rho}{\Delta_0^2},$$

$$\phi_{2a} = \frac{1}{\Delta_0},$$

$$\phi_{2b} = 0,$$

$$\phi_{2c} = \frac{3\rho}{\Delta_0^2},$$

$$\phi_{2d} = \frac{9\rho^2}{\Delta_0^3},$$

$$\phi_{2e} = \frac{3\rho}{\Delta_0^2}.$$

One now inserts these expansions into Eq. (18) and proceeds as explained in the main text to obtain the desired conditions on the expansion coefficients L_0, \dots, L_{2e} of the L_{ij} . To state these, it is helpful to define the quantities

$$M_{\alpha,\beta} \equiv \frac{1}{12}L_\alpha L_\beta - \frac{1}{2}(L_\alpha \phi_\beta + L_\beta \phi_\alpha),$$

where Greek indices stand for the labels 0, 1a, 1b, 2a, 2c, 2d, and 2e of the coefficients of the perturbative expansions. The desired conditions are then

$$L_0 = \alpha_0 + \beta_0 M_{0,0}, \quad (\text{A5})$$

$$L_{1a} = \alpha_{1a} + \beta_{1a} M_{0,0} + \beta_0 M_{0,1a}, \quad (\text{A6})$$

$$L_{1b} = \alpha_{1b} + \beta_{1b} M_{0,0} + 2\beta_0 (M_{0,1a} + M_{0,1b}), \quad (\text{A7})$$

$$L_{2a} = \alpha_{2a} + \beta_{2a} M_{0,0} + 2\beta_{1a} M_{0,1a} + \beta_0 M_{1a,1a}, \quad (\text{A8})$$

$$L_{2b} = \alpha_{2b} + \beta_{2b} M_{0,0} + \beta_{1a} M_{0,1a} + \beta_0 M_{0,2b}, \quad (\text{A9})$$

$$L_{2c} = \alpha_{2c} + \beta_{2c} M_{0,0} + 2\beta_{1a} (M_{0,1a} + M_{0,1b}) + \beta_{1b} M_{0,1a} + \beta_0 (M_{1a,1a} + M_{1a,1b} + M_{0,2a} + M_{0,2c}), \quad (\text{A10})$$

$$L_{2d} = \alpha_{2d} + \beta_{2d} M_{0,0} + 2\beta_{1b} (M_{0,1a} + M_{0,1b}) + \beta_0 (2M_{0,2c} + 2M_{0,2d} + 2M_{1a,1b} + M_{1b,1b}), \quad (\text{A11})$$

$$L_{2e} = \alpha_{2e} + \beta_{2e} M_{0,0} + \beta_0 (M_{1a,1a} + 2M_{0,2b} + 2M_{0,2e}). \quad (\text{A12})$$

The first of these determines L_0 and leads back to Baxter's solution (24) for the monodisperse case. All other equations involve the desired coefficient on the left at most linearly on the right hand side and so are trivial to solve; e.g., Eq. (A6) has L_{1a} on the left and implicitly via $M_{0,1a}$ on the right. Running through the equations in order, all expansion coefficients can then be found.

¹H. Löwen, Phys. Rep. **237**, 249 (1994).

²G. Nägele, Phys. Rep. **272**, 215 (1996).

³J. Lyklema, *Fundamental of Interface and Colloid Science* (Elsevier, New York, 2005).

⁴J. Lyklema, *Fundamental of Interface and Colloid Science* (Elsevier, New York, 2000).

⁵R. J. Baxter, J. Chem. Phys. **49**, 2770 (1968).

⁶R. J. Baxter, in *Physical Chemistry: An Advanced Treatise*, edited by D. Henderson (Academic, New York, 1971), Vol. 84, Chap. 4.

⁷R. O. Watts, D. Henderson, and R. J. Baxter, Adv. Chem. Phys. **21**, 421 (1971).

⁸R. J. Baxter, J. Chem. Phys. **52**, 4559 (1970).

⁹B. Barbooy, Chem. Phys. **11**, 357 (1975).

¹⁰J. W. Perram and E. R. Smith, Chem. Phys. Lett. **35**, 138 (1975).

¹¹B. Barbooy and R. Tenne, Chem. Phys. **38**, 369 (1979).

¹²C. Robertus, W. H. Philipse, J. G. H. Joosten, and Y. K. Levine, J. Chem. Phys. **90**, 4482 (1989).

¹³S. H. Chen, J. Rouch, F. Sciortino, and P. Tartaglia, J. Phys.: Condens. Matter **6**, 10855 (1994).

¹⁴R. Piazza, V. Peyre, and V. Degiorgio, Phys. Rev. E **58**, R2733 (1998).

¹⁵P. Prinsen and T. Odijk, J. Chem. Phys. **121**, 6525 (2004).

¹⁶G. Stell, J. Stat. Phys. **63**, 1203 (1991).

¹⁷D. Gazzillo and A. Giacometti, J. Chem. Phys. **120**, 4742 (2004).

¹⁸R. Fantoni, D. Gazzillo, and A. Giacometti, J. Chem. Phys. **122**, 034901 (2005).

¹⁹M. A. Miller and D. Frenkel, Phys. Rev. Lett. **90**, 135702 (2003).

164504-16 Fantoni *et al.*J. Chem. Phys. **125**, 164504 (2006)

- ²⁰M. A. Miller and D. Frenkel, J. Chem. Phys. **121**, 535 (2004).
- ²¹M. A. Miller and D. Frenkel, J. Phys.: Condens. Matter **16**, S4901 (2004).
- ²²R. M. L. Evans, J. Chem. Phys. **114**, 1915 (2001).
- ²³R. Fantoni, D. Gazzillo, and A. Giacometti, Phys. Rev. E **72**, 011503 (2005).
- ²⁴R. P. Sear, Mol. Phys. **96**, 1013 (1999).
- ²⁵S. Auer and D. Frenkel, Nature (London) **413**, 711 (2001).
- ²⁶P. N. Pusey and W. van Meegen, Phys. Rev. Lett. **59**, 2083 (1987).
- ²⁷W. C. K. Poon, F. Renth, R. M. L. Evans, D. J. Fairhurst, M. E. Cates, and P. N. Pusey, Phys. Rev. Lett. **83**, 1239 (1999).
- ²⁸H. C. Andersen, J. D. Weeks, and D. Chandler, Phys. Rev. A **4**, 1597 (1971).
- ²⁹P. Sollich, J. Phys.: Condens. Matter **14**, R79 (2002).
- ³⁰P. Sollich and M. E. Cates, Phys. Rev. Lett. **80**, 1365 (1998).
- ³¹P. Sollich, P. B. Warren, and M. E. Cates, Adv. Chem. Phys. **116**, 265 (2001).
- ³²N. B. Wilding, M. Fasolo, and P. Sollich, J. Chem. Phys. **121**, 6887 (2004).
- ³³P. Sollich (unpublished).
- ³⁴D. Gazzillo, A. Giacometti, R. Fantoni, and P. Sollich, Phys. Rev. E (in press).
- ³⁵S. Asakura and F. Oosawa, J. Chem. Phys. **22**, 1255 (1954).
- ³⁶J. L. Barrat and J. P. Hansen, *Basic Concepts for Simple and Complex Liquids* (Cambridge University Press, Cambridge, 2003).
- ³⁷T. Boublík, J. Chem. Phys. **53**, 471 (1970).
- ³⁸G. A. Mansoori, N. F. Carnahan, K. E. Starling, and T. W. Leland, Jr., J. Chem. Phys. **54**, 1523 (1971).
- ³⁹Note that the energy route to the equation of state of HS fluids is ill defined since the internal energy is just that of the ideal gas. So in the PY approximation one could use (Ref. 47) either the compressibility pressure $P^{PY(c)}$ or the virial pressure $P^{PY(v)}$. For a mixture of a discrete number of species it is known that the BMCSL pressure $P^{BMCSL}=(2P^{PY(c)}+P^{PY(v)})/3$ is more accurate than either of these two limits. Recently, the equivalence between the energy and virial routes to the equation of state for the one-component HS fluid has been shown in Ref. 48. We use the BMCSL expression throughout, except in Fig. 1, where the PY compressibility pressure is used for ease of comparison with earlier work (Ref. 18).
- ⁴⁰S. E. Phan, W. B. Russel, J. X. Zhu, and P. M. Chaikin, J. Chem. Phys. **108**, 9789 (1998).
- ⁴¹H. N. W. Lekkerkerker, W. C. K. Poon, P. N. Pusey, A. Stroobants, and P. B. Warren, Europhys. Lett. **20**, 559 (1992).
- ⁴²M. Fasolo and P. Sollich, J. Chem. Phys. **122**, 074904 (2005).
- ⁴³N. B. Wilding and P. Sollich, J. Chem. Phys. **116**, 7116 (2002).
- ⁴⁴N. B. Wilding and P. Sollich, Europhys. Lett. **67**, 219 (2004).
- ⁴⁵N. B. Wilding, P. Sollich, and M. Fasolo, Phys. Rev. Lett. **95**, 155701 (2005).
- ⁴⁶M. Fasolo and P. Sollich, Phys. Rev. E **70**, 041410 (2004).
- ⁴⁷J. J. Salacuse and G. Stell, J. Chem. Phys. **77**, 3714 (1982).
- ⁴⁸A. Santos, J. Chem. Phys. **123**, 104102 (2005).

Part VII
2007

Chapter 14

Patchy sticky hard spheres: analytical study and Monte Carlo simulations

Fantoni R., Gazzillo D., Giacometti A., Miller M. A., and Pastore G., J. Chem. Phys. **127**, 234507 (2007)

Title: “Patchy sticky hard spheres: analytical study and Monte Carlo simulations”

Abstract: We consider a fluid of hard spheres bearing one or two uniform circular adhesive patches, distributed so as not to overlap. Two spheres interact via a “sticky” Baxter potential if the line joining the centers of the two spheres intersects a patch on each sphere, and via a hard sphere potential otherwise. We analyze the location of the fluid-fluid transition and of the percolation line as a function of the size of the patch (the fractional coverage of the sphere’s surface) and of the number of patches within a virial expansion up to third order and within the first two terms (C0 and C1) of a class of closures C_n hinging on a density expansion of the direct correlation function. We find that the locations of the two lines depend sensitively on both the total adhesive coverage and its distribution. The treatment is almost fully analytical within the chosen approximate theory. We test our findings by means of specialized Monte Carlo (MC) simulations and find the main qualitative features of the critical behaviour to be well captured in spite of the low density perturbative nature of the closure. The introduction of anisotropy is a first step towards a more realistic model of globular proteins in solution.

Patchy sticky hard spheres: Analytical study and Monte Carlo simulationsRiccardo Fantoni,^{a)} Domenico Gazzillo,^{b)} and Achille Giacometti^{c)}
*Dipartimento di Chimica Fisica, Università di Venezia, S. Marta DD 2137, I-30123 Venezia, Italy*Mark A. Miller^{d)}
*University Chemical Laboratory, Lensfield Road, Cambridge CB2 1EW, United Kingdom*Giorgio Pastore^{e)}
Dipartimento di Fisica Teorica, Università di Trieste, Strada Costiera 11, 34100 Trieste, Italy

(Received 26 July 2007; accepted 12 October 2007; published online 19 December 2007)

We consider a fluid of hard spheres bearing one or two uniform circular adhesive patches, distributed so as not to overlap. Two spheres interact via a “sticky” Baxter potential if the line joining the centers of the two spheres intersects a patch on each sphere, and via a hard sphere potential otherwise. We analyze the location of the fluid-fluid transition and of the percolation line as a function of the size of the patch (the fractional coverage of the sphere’s surface) and of the number of patches within a virial expansion up to third order and within the first two terms (C_0 and C_1) of a class of closures C_n hinging on a density expansion of the direct correlation function. We find that the locations of the two lines depend sensitively on both the total adhesive coverage and its distribution. The treatment is almost fully analytical within the chosen approximate theory. We test our findings by means of specialized Monte Carlo simulations and find the main qualitative features of the critical behavior to be well captured in spite of the low density perturbative nature of the closure. The introduction of anisotropic attractions into a model suspension of spherical particles is a first step toward a more realistic description of globular proteins in solution. © 2007 American Institute of Physics. [DOI: 10.1063/1.2805066]

I. INTRODUCTION

The idea of modeling fluids as systems of spherical particles with orientationally dependent attraction dates back at least as far as Boltzmann, who envisaged chemical attraction between atoms only when “their sensitive regions are in contact.”¹ Models of this type, featuring patchy interactions, are currently experiencing renewed relevance in the context of colloidal and biological matter in contrast to their original conception in connection with fluids of atoms and small molecules.^{2–17}

The new interest arises for various reasons. On the technological side, patchy particles give the possibility of designing self-assembling nanoscale devices through anisotropic decorations of the particle surface by means of organic or biological molecules.^{13–15} Nature provides inspiration for what might be achieved in this area, a particularly elegant example being the self-assembly of virus capsids. These protein shells are monodisperse and highly symmetric and are composed of identical subunits. Simplified descriptions of icosahedral virus capsids are currently being formulated using spherical subunits with directional interactions^{18,19} and the possibility of adopting similar schemes to self-assemble other target structures is being explored.¹³ This level of organization inevitably requires a certain specificity in the in-

teractions between the subunits as well as measures to prevent further aggregation of the assembled objects.

Less specific patchy interactions give rise to associating fluids containing a distribution of cluster sizes or extended gel-like networks. The key feature of such systems is a set of pointlike sites on the particle surface, leading to strongly directional bonding with a maximum of one bond per site.^{3,8,10,11,16,17} This type of interaction has proven invaluable in elucidating the interplay between fluid-fluid and sol-gel transitions. One advantage of these models is that powerful analytical tools are available for them, such as Wertheim’s thermodynamic perturbation theory,²⁰ which yields accurate results under experimentally realistic conditions.^{21,22}

In contrast to these models with attractive spots, one can envisage particles that interact through larger attractive regions on their surface, for example, globular proteins with patches of hydrophobic (nonpolar) amino acids exposed at the surface. Isotropic potentials have been remarkably successful in modeling the phase diagrams of certain proteins,^{23–25} but it seems that not all features of their coexistence curves can be properly explained by such simple interactions.²⁶ In this sort of system, it seems more appropriate to consider regions with short-range attractive forces^{2,4–7,9,12} rather than site-site bonds. These attractive patches are capable of sustaining as many “bonds” as permitted by geometry. The size of the patch therefore becomes an important new parameter that does not arise in most work

^{a)}Electronic mail: rfantoni@unive.it.^{b)}Electronic mail: gazzillo@unive.it.^{c)}Electronic mail: achille@unive.it.^{d)}Electronic mail: mam1000@cam.ac.uk.^{e)}Electronic mail: pastore@ts.infn.it.

234507-2 Fantoni *et al.*

 J. Chem. Phys. **127**, 234507 (2007)

on associating fluids. We note, however, that for sufficiently narrow patches, the two models become essentially equivalent.

In the present work, we focus on a simple yet physical model which is a variation of those treated in Ref. 12. We consider uniform circular patches distributed on the surface of the sphere in such a way that they do not overlap. The patches are delimited by circles which can be defined by the associated solid angles. Two particles experience an adhesive attraction only when a patch on one sphere touches a patch on the other. The adhesion is of Baxter's type,²⁷ i.e., the attraction has infinitesimal range, acting only when the particles are exactly in contact, as described in the next section. This model has the advantage that it can be tackled with analytical tools, unlike most other models for which not even the isotropic analog bears this appealing feature. Various issues arise in this sort of model relating to the stability of the liquid phase with respect to crystalline solid phases, and these points have been studied in Refs. 28 and 29.

The integral equation theory of fluids with an angularly dependent pair potential is complicated by the fact that the pair distribution function is also angularly dependent.³⁰ In the general case one must appeal to the symmetries of the fluid (translational invariance, rotational invariance, invariance under permutation of like particles, and invariance under the symmetry operations of the individual particles and of the correlation functions) in order to simplify the problem.^{31–33} In some cases, it is possible to factorize the angular dependence of the Ornstein–Zernike (OZ) equation. For example, the factorization for a fluid of dipolar particles has long been known³⁴ and in Ref. 35 it is shown how to solve the dipole-dipole angular distribution of attraction in the adhesive limit within the Percus–Yevick framework. However, the dipolar case hinges on exploiting a special property of this particular angular distribution that is particularly useful for the angular convolution in the OZ equation. In contrast, for an angular dependence with discontinuities, such as the circular patches treated here, any approach relying on a spherical harmonic expansion would prove a formidable task due to the large number of terms necessary to capture the discontinuities.

In the present model we therefore follow a different route based on two parallel and related schemes. We first perform a virial expansion up to the third virial coefficient. We then proceed to study a class of closures (denoted C_0 , C_1, \dots) which were proposed in Ref. 36 and are based on a density expansion of the direct correlation function. In particular, the zeroth-order term (C_0) turns out to be equivalent to a modified mean spherical approximation, whereas the first-order (C_1) is known to provide the correct third virial coefficient.³⁶ Within both schemes we study the thermodynamics, radial distribution function and percolation threshold, and compare with specialized Monte Carlo simulations which were recently devised to this aim.³⁷ By varying the size of the adhesive patches and by selecting between one patch and two diametrically opposite patches, we are able to investigate the roles of both the total surface coverage and the geometrical distribution of the adhesion. In both the one- and two-patch cases we can change smoothly between small

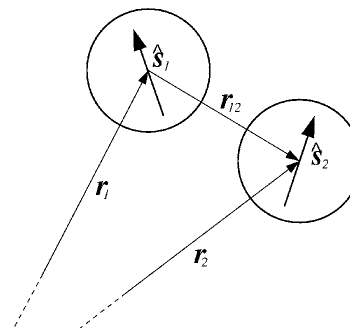


FIG. 1. Summary of the vector notation used to define the model.

sticky spots, capable of making only one bond each, and the isotropic adhesive sphere. We find that the position of the critical fluid-fluid transition line and the percolation threshold are both sensitive to the surface coverage. At fixed coverage, there is also a dependence on the way in which this adhesion is distributed.

Our results can be compared and contrasted with the recent work of Bianchi *et al.*,¹⁷ who consider the maximum number of bonds per particle, rather than the fractional surface coverage, as the key parameter controlling the location of the critical point. In the present work we are able to tune both effects, thus illuminating their specific roles in the location of critical points.

The remainder of the paper is organized as follows. In Sec. II we introduce the model while Sec. III contains a description of the analytical and numerical tools used. Results for the radial distribution function, fluid-fluid transition, and percolation threshold are included in Secs. IV–VI, respectively. Finally, in Sec. VII the inclusion of an adhesive background is discussed, and conclusions and an outlook are contained in Sec. VIII.

II. DEFINITION OF THE MODEL

A. Baxter model with orientationally dependent adhesion

We start with some general remarks on the orientational dependence of a three-dimensional homogeneous fluid of hard spheres with adhesive pairwise interactions. Let \mathbf{r}_i be the coordinates of the i th particle ($i=1, 2, 3, \dots$) and assume that the patch distribution on the sphere has cylindrical symmetry so that its orientation in space is determined by a unit vector $\hat{\mathbf{s}}_i$ rigidly attached to it. Then $\hat{\mathbf{s}}_i = (\sin \theta_i \cos \varphi_i, \sin \theta_i \sin \varphi_i, \cos \theta_i)$ where θ_i and φ_i are the polar and the azimuthal angles with respect to a fixed reference frame (see Fig. 1). As usual, we introduce the relative coordinates $\mathbf{r}_{12} = \mathbf{r}_2 - \mathbf{r}_1$ and the associated distance $r_{12} = |\mathbf{r}_{12}|$, and work with the following short-hand notation: $(1, 2) = (\mathbf{r}_{12}, \theta_1, \varphi_1, \theta_2, \varphi_2)$ and $\Omega_i = (\theta_i, \varphi_i)$ for the orientation of $\hat{\mathbf{s}}_i$. The orientation of $\hat{\mathbf{r}}_{ij} = \mathbf{r}_{ij}/r_{ij}$ with respect to the same frame of reference will be denoted by $\Omega_{ij} = (\theta_{ij}, \varphi_{ij})$.

The particles interact through a pair potential $\phi(1, 2)$,

defined later, which is a generalization of Baxter's sticky hard sphere (SHS) limit²⁷ to orientationally dependent interactions. We start with

$$\beta\Phi(1,2) = \begin{cases} +\infty & 0 < r < \sigma \\ -\ln \left[\frac{\epsilon(1,2) R}{12\tau R - \sigma} \right] & \sigma \leq r \leq R \\ 0 & r > R, \end{cases} \quad (1)$$

where $\beta=1/(k_B T)$ (k_B being Boltzmann's constant and T being the temperature), σ is the diameter of the spheres, and $\epsilon(1,2)/\tau$ is a dimensionless adhesion coefficient. We define $\phi(1,2)$ through the following limit on the Boltzmann factor e :

$$\begin{aligned} e(1,2) &= \exp[-\beta\phi(1,2)] \\ &= \lim_{R \rightarrow \sigma} \exp[-\beta\Phi(1,2)] \\ &= \Theta(r_{12} - \sigma) + \frac{\epsilon(1,2) \sigma}{\tau} \frac{\delta(r_{12} - \sigma)}{12}, \end{aligned} \quad (2)$$

where $\Theta(\cdot)$ is the Heaviside step function and $\delta(\cdot)$ is the Dirac delta function. When $\epsilon(1,2)=1$ we recover the usual Baxter SHS model and, hence, the only orientational dependence is included in the definition of $\epsilon(1,2)$. It is easy to see that $\epsilon(1,2)$ cannot be a simple function of \hat{s}_1 and \hat{s}_2 but must also include a dependence on $\hat{r}_{12}=\mathbf{r}_{12}/r_{12}$ in order to avoid a trivial corresponding states rescaling. This point is discussed in Appendix A. In the present work we shall address a type of orientational dependence which was introduced by Kern and Frenkel¹² following a previous suggestion by Jackson *et al.*²

B. Patchy sticky hard spheres

Consider a single hard sphere having one or more identical adhesive circular patches distributed on its surface in such a way that they do not overlap with one another. The size of the patch can be specified by the angular amplitude 2δ as shown in Fig. 2. The unit vector $\hat{s}_i^{(p)}$ identifies the

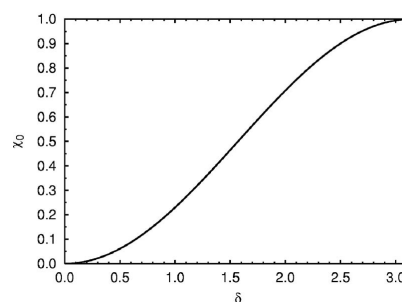
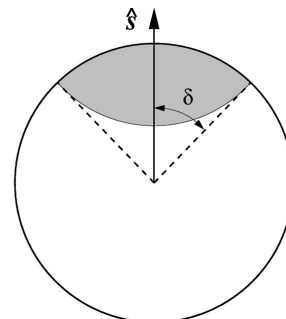


FIG. 2. Top panel: the adhesive patch model of Kern and Frenkel (Ref. 12). Bottom panel: patch surface coverage χ_0 as a function of the patch angle δ .

direction from the center of particle i to the center of patch p on the surface ($p=1, \dots, n$, the total number of patches). The sticky area is then given by points $\hat{\mathbf{r}}$ on the surface of the particle such that the angle between $\hat{s}_i^{(p)}$ and $\hat{\mathbf{r}}$ is smaller than δ .

In conjunction with Eq. (2), the adhesive part of the interaction between two particles acts only if their point of contact lies inside a patch on each particle, as depicted in Fig. 3 for the case of a single patch ($n=1$). Therefore, $\epsilon(1,2) \equiv \epsilon(\hat{s}_1, \hat{s}_2, \hat{\mathbf{r}}_{12})$ can be written as

$$\epsilon(1,2) = \begin{cases} 1 & \text{if } \hat{s}_1^{(p_1)} \cdot \hat{\mathbf{r}}_{12} \geq \cos \delta \text{ and } -\hat{s}_2^{(p_2)} \cdot \hat{\mathbf{r}}_{12} \geq \cos \delta \text{ for some combination } (p_1, p_2) \\ 0 & \text{otherwise.} \end{cases} \quad (3)$$

Each patch occupies a portion of the sphere's surface covered by the solid angle $2\pi(1 - \cos \delta)$ and a fundamental role will be played in our discussion by the fraction of solid angle (i.e., the coverage) associated with δ , namely

$$\chi_0(\delta) = \frac{1}{2}(1 - \cos \delta) = \sin^2\left(\frac{\delta}{2}\right). \quad (4)$$

III. ANALYSIS OF THE MODEL

A. Analytical solution

We now tackle the analytical solution of this problem based on two simple approximations: the virial expansion and the Cn class of closures.

1. Virial expansion

As shown in Appendix B, the first two virial coefficients for this model are

234507-4 Fantoni *et al.*

J. Chem. Phys. **127**, 234507 (2007)

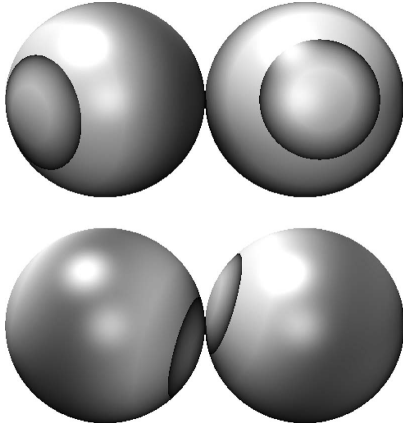


FIG. 3. Adhesion requires simultaneous alignment of patches (dark shading) on both spheres with the vector between their centers. The spheres in the upper panel do not adhere, while those in the lower panel do.

$$b_2 = B_2/v_0 = 4 - 12 \frac{\chi_1}{12\tau}, \quad (5)$$

$$b_3 = B_3/v_0^2 = 10 - 60 \frac{\chi_1}{12\tau} + 144 \frac{\chi_2}{(12\tau)^2} - 96 \frac{\chi_3}{(12\tau)^3}, \quad (6)$$

where $v_0 = \pi\sigma^3/6$ is the volume of a sphere and

$$\chi_2(\delta, n) = 4 \left\langle \epsilon(1,3)\epsilon(2,3)\Theta\left(\frac{\pi}{3} - \theta_{13}\right) \right\rangle_{\Omega_1, \Omega_2, \Omega_3, \Omega_{13}}, \quad (8)$$

$$\chi_3(\delta, n) = \langle \epsilon(1,2)\epsilon(1,3)\epsilon(2,3) \rangle_{\Omega_1, \Omega_2, \Omega_3 | \theta_{12}=\pi/3, \theta_{23}=2\pi/3}, \quad (9)$$

where we have defined the angular average (with $d\tilde{\Omega} = d\Omega/4\pi$),

$$\langle \dots \rangle_{\Omega} = \int d\tilde{\Omega} \dots \quad (10)$$

Here, θ_{ij} is the angle between $\hat{\mathbf{r}}_{ij}$ and $\hat{\mathbf{r}}_{13}$ (which can be chosen along the z axis), and $\epsilon(i, j)$ is always associated with a delta function that forces spheres i and j to be in contact. Note that in Eq. (6) the effect of anisotropy is embedded in the parameters χ_1, χ_2, χ_3 defined in Eqs. (7)–(9), and that these parameters are therefore functions of δ and n . The isotropic case is recovered when all χ 's equal 1. We remark that the expression for χ_2 involves an average over the relative orientations Ω_{13} while there is an overlap between spheres 1 and 2, each of which is simultaneously in contact with sphere 3. Under such conditions there is always a maximum possible angle $\pi/3$ for θ_{13} and this gives rise to the normalization factor of 4 in Eq. (8).

If one limits the expansion to the second virial coefficient, a law of corresponding states based on the rescaling

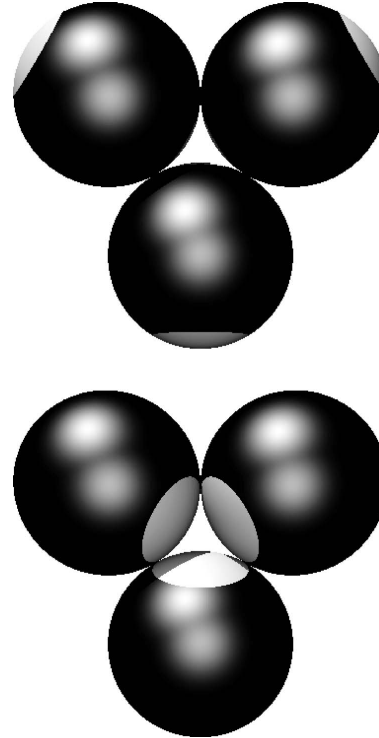


FIG. 4. Configurations of three mutually bonded spheres, each possessing a large single patch (dark shading). The patch vectors point inward in the top panel and outward in the bottom panel. The latter case is only possible for $\delta > 5\pi/6$. Combinations of these arrangements are also possible.

$\tau \rightarrow \tau/\chi_1$ between the patchy and the isotropic SHS models holds true. This correspondence breaks down even at the level of the third virial.

It is easy to see that $\chi_1 = n^2\chi_0^2$ as this is simply the product of the separate coverages on each sphere. A calculation of χ_2 and χ_3 is much more laborious and can be found in Appendix C for the case of a single patch. The final result in this case is

$$\chi_1 = \chi_0^2, \quad (11)$$

$$\chi_2 = \chi_0^2 Q_1(\delta), \quad (12)$$

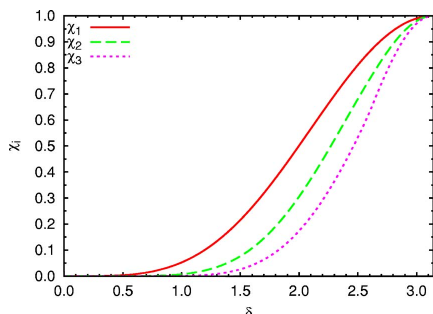
$$\chi_3 = R_1^3(\delta), \quad (13)$$

where the coefficients Q_1 and R_1 are given in Appendix C. For $\delta \geq 5\pi/6$ it is possible to have three mutually bonded spheres with the patch vectors pointing either inward or outward (see Fig. 4). Note that for the isotropic limit $\delta = \pi$ all χ_i ($i=1, 2, 3$) are equal to 1 as they should be. The three χ_i coefficients are plotted in Fig. 5 as functions of δ .

For spheres with two diametrically opposite patches, each of width δ , one finds

$$\chi_1 = 4\chi_0^2, \quad (14)$$

234507-5 Patchy sticky hard spheres

 J. Chem. Phys. **127**, 234507 (2007)

 FIG. 5. (Color online) Dependence of the coefficients χ_i ($i=1,2,3$) on δ for the one-patch model.

$$\chi_2 = 4\chi_0^2 Q_2(\delta), \quad (15)$$

$$\chi_3 = R_2^3(\delta), \quad (16)$$

where the coefficients Q_2 and R_2 are given in Appendix D. Note that in this case when $\delta > \pi/3$ it is also possible to have sphere 1 in contact with spheres 2 and 3 through different patches as shown in Fig. 6. The three χ_i coefficients are plotted in Fig. 7 as functions of δ .

The virial expansion of the excess free energy density is

$$\beta f^{\text{ex}} v_0 = b_2 \eta^2 + \frac{1}{2} b_3 \eta^3 + \dots, \quad (17)$$

where $\eta = \rho v_0$ is the hard sphere packing fraction. This allows the calculation of the corresponding pressure and chemical potential

$$\beta P(\tau, \eta) v_0 = \eta + b_2 \eta^2 + b_3 \eta^3 + \dots,$$

$$\beta \mu(\tau, \eta) = \ln(\Lambda^3/v_0) + \ln \eta + 2b_2 \eta + \frac{3}{2} b_3 \eta^2 + \dots,$$

where Λ is the de Broglie wavelength.

2. Integral equations within the Cn closures

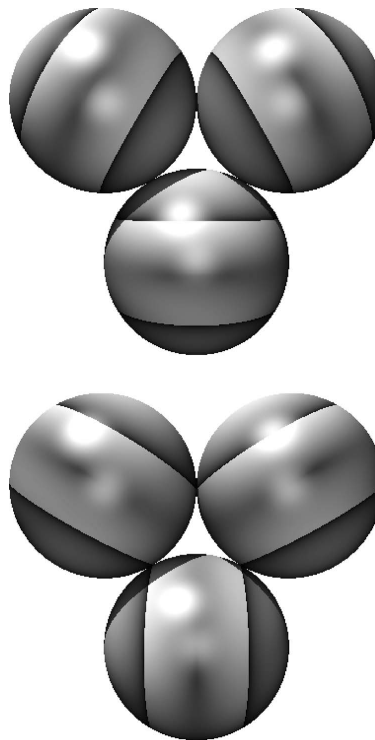
While the virial expansion only allows a limited low-density region of the phase diagram to be probed, the integral equation approach is much more powerful in this respect. The trade-off is, of course, that since the OZ equation involves the total correlation function h and direct correlation function c , both of which are unknown, it can be solved only after adding a closure, that is a second, approximate, relationship involving h , c , and the pair potential. In this section we discuss a particular class of these closures (denoted Cn hereafter) which have already been exploited in the isotropic case and have proven to provide reasonably good predictions even for intermediate densities.³⁶

The OZ equation for a homogeneous fluid of molecules interacting through anisotropic pair potentials is

$$h(1,2) = c(1,2) + \rho \int d(3) c(1,3) h(3,2), \quad (18)$$

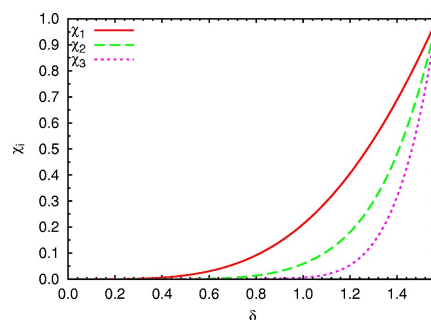
where $d(i) \equiv d\mathbf{r}_i d\tilde{\Omega}_i$. More explicitly [see Eq. (10)],

$$h(1,2) = c(1,2) + \rho \int d\mathbf{r}_3 \langle c(1,3) h(3,2) \rangle_{\Omega_3}, \quad (19)$$


 FIG. 6. Configurations of three mutually bonded spheres, each possessing two patches (dark shading). In the upper panel only one patch on each sphere is involved in the bonds; in the lower panel both patches on each sphere are involved. The latter case is only possible for $\delta \geq \pi/3$. Combinations of these arrangements are also possible.

In a homogeneous fluid, translational invariance of any correlation function implies that one can introduce reduced coordinates $\mathbf{r}_{12} = \mathbf{r}_2 - \mathbf{r}_1$ and $\mathbf{r}_{13} = \mathbf{r}_3 - \mathbf{r}_1$,

$$h(\mathbf{r}_{12}, \Omega_1, \Omega_2) = c(\mathbf{r}_{12}, \Omega_1, \Omega_2) + \rho \int d\mathbf{r}_3 \langle c(\mathbf{r}_{13}, \Omega_1, \Omega_3) h(\mathbf{r}_{32}, \Omega_3, \Omega_2) \rangle_{\Omega_3}, \quad (20)$$


 FIG. 7. (Color online) Dependence of the coefficients χ_i ($i=1,2,3$) on δ for the two-patch model.

The presence of the convolution makes it convenient to Fourier transform this equation with respect to the position variable \mathbf{r} . This yields for the corresponding functions (indicated with a hat) in Fourier space \mathbf{k} ,

$$\hat{h}(\mathbf{k}, \Omega_1, \Omega_2) = \hat{c}(\mathbf{k}, \Omega_1, \Omega_2) + \rho \langle \hat{c}(\mathbf{k}, \Omega_1, \Omega_3) \hat{h}(\mathbf{k}, \Omega_3, \Omega_2) \rangle_{\Omega_3}, \quad (21)$$

The additional complication with respect to the isotropic case is the presence of the orientational average of the product appearing in Eq. (21). In order to make progress, we use a simple angular decoupling approximation

$$\langle \hat{c}(\mathbf{k}, \Omega_1, \Omega_3) \hat{h}(\mathbf{k}, \Omega_3, \Omega_2) \rangle_{\Omega_3} \approx \langle \hat{c}(\mathbf{k}, \Omega_1, \Omega_3) \rangle_{\Omega_3} \langle \hat{h}(\mathbf{k}, \Omega_3, \Omega_2) \rangle_{\Omega_3}. \quad (22)$$

As discussed in Ref. 36, Cn closures are based on a density expansion of the cavity function $y(1,2)$ which is related to the radial distribution function $g(1,2)$ by $g(1,2) = y(1,2)e(1,2)$.

In the presence of anisotropy, all correlation functions clearly depend upon the solid angles $\Omega_1, \Omega_2, \Omega_{12}$. It is then customary to consider³⁰ the corresponding angular averaged quantities $g(r \equiv r_{12}) = \langle g(1,2) \rangle_{\Omega_1, \Omega_2, \Omega_{12}}$ and similarly for $y(r \equiv r_{12})$. Within Cn closures, for $r > \sigma$, the radial distribution function $g(r)$ coincides with the cavity function $y(r)$. A density expansion of the cavity function yields

$$y(r) = 1 + \rho y_1(r) + \dots, \quad (23)$$

where

$$y_1(r_{12}) = \int d\mathbf{r}_3 \langle f(1,3) f(3,2) \rangle_{\Omega_1, \Omega_2, \Omega_3, \Omega_{12}}. \quad (24)$$

Calculation of Eq. (24) proceeds using arguments akin to those presented in Appendix B, which are based on the decomposition in Eq. (B2). The integral in Eq. (24) then splits into three integrals containing the various combinations of the HS and the sticky parts of the Mayer function as in Eq. (B2).

B. Monte Carlo algorithms for Baxter-like potentials

Monte Carlo simulations of adhesive hard spheres require particular care even in the isotropic case because of the singular nature of the potential. For completeness we summarize the main ideas below, deferring to Ref. 37 for the details.

Conventional Monte Carlo displacements of a SHS would fail because the bonded states between particles occupy an infinitesimal volume of configuration space (and so would never be located by random displacements) but have infinite strength (and so would never be broken). The solution is to compare the integrated weights of the various bonded and unbonded states, which are finite. Specialized algorithms that exploit this approach have been devised for the canonical ensemble^{38,39} and were subsequently extended to the grand canonical ensemble.^{40,41} The latter is particularly convenient for identifying the critical point.⁴²

The Monte Carlo algorithm for isotropic adhesive spheres can be modified to deal with the patchy case by incorporating the anisotropy in the acceptance criterion for trial moves. Trial moves are attempted as described in detail in Ref. 41 as though the spheres were uniformly adhesive. Once the trial position of the displaced particle has been chosen, a uniformly distributed random orientation is selected. The move is then accepted only if an overlap of hard cores is not generated (as in the isotropic case) and if all contacts specified in the trial configuration have patches suitably aligned to make the required bonds. This scheme produces the desired Boltzmann distribution³⁷ and is applicable to an arbitrary arrangement of patches. However, it becomes inefficient when the total adhesive coverage of the sphere is small because the random generation of orientations is then unlikely to lead to patches being aligned with bonds, leading to a high rejection rate.

IV. STRUCTURE

In the following we shall compare predictions from the combined C1-orientational mean field approximation and virial expansion with the results of Monte Carlo simulations.

One finds that $y_1(r)$ is different from zero only in the region $0 \leq r \leq 2\sigma$ and

$$y_1(r) = \frac{\pi}{12} \left(\frac{r}{\sigma} + 4 \right) \left(\frac{r}{\sigma} - 2 \right)^2 + \frac{\chi_1}{12\tau} 2\pi \left(\frac{r}{\sigma} - 2 \right) + \frac{\bar{\chi}_2(r)}{(12\tau)^2} 2\pi \frac{\sigma}{r}, \quad (25)$$

where

$$\bar{\chi}_2(r) = \langle \epsilon(1,2) \epsilon(1,3) \rangle_{\Omega_1, \Omega_2, \Omega_3 | \theta_{12} = 2 \arcsin(r/2\sigma)}. \quad (26)$$

In order to compute the angularly averaged radial distribution function $g(r)$ we have solved the full OZ Eq. (20) within the C1 closure supplemented with the decoupling approximation (22). The Wertheim-Baxter method²⁷ and the C1 closure combine such that only the cavity function at contact depends upon the angular coefficients χ_1, χ_2, χ_3 . The solution for Baxter function is

$$q(r) = [a(r^2 - \sigma^2)/2 + b\sigma(r - \sigma) + q_\sigma \sigma^2] \Theta(\sigma - r) \quad r > 0, \quad (27)$$

where

$$a = \frac{1 + 2\eta}{(1 - \eta)^2} - \frac{12q_\sigma \eta}{1 - \eta}, \quad (28)$$

$$b = -\frac{3\eta}{2(1 - \eta)^2} + \frac{6q_\sigma \eta}{1 - \eta}, \quad (29)$$

$$q_\sigma = \frac{\bar{y}^{C1}}{12\tau}, \quad (30)$$

$$\bar{y}^{C1} = \langle y^{C1}(r_{12} = \sigma, \Omega_1, \Omega_2, \Omega_{12}) \epsilon(1,2) \rangle_{\Omega_1, \Omega_2, \Omega_{12}} = y_0 + y_1 \eta. \quad (31)$$

The coefficients $y_{0,1} = y_{0,1}(\tau)$ are related to the reduced virial

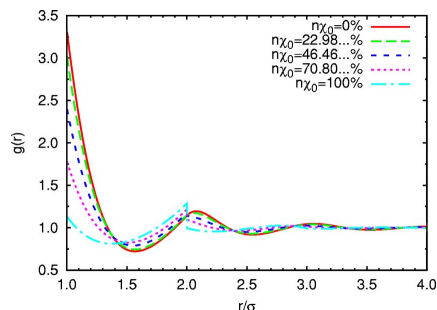


FIG. 8. (Color online) Radial distribution function for the one-patch model ($n=1$) at $\eta=0.4$ and $\tau=0.2$ within the C1 approximation and for various values of the adhesive coverage $n\chi_0$.

coefficients $b_{2,3}$ by Eq. (41), later. Therefore, we can read off their values

$$y_0 = \chi_1, \quad (32)$$

$$y_1 = \left(30 \frac{\chi_1}{12\tau} - 144 \frac{\chi_2}{(12\tau)^2} + 144 \frac{\chi_3}{(12\tau)^3} \right) \tau. \quad (33)$$

In order to extract the numerical behavior of the radial distribution function $g(r)$ we have employed a discretization method due to Perram⁴³ to compute the numerical integral

$$rh(r) = -q'(r) + 2\pi\rho \int_0^{\infty} du q(u)(r-u)h(|r-u|). \quad (34)$$

For the one-patch spheres the result is reported in Fig. 8 for various values of δ , at $\eta=0.4$ and $\tau=0.2$. The choices $\delta=0$ and $\delta=\pi$ correspond to the limiting cases of pure HS and isotropic SHS, respectively. Upon decreasing the size of the patch, the behavior smoothly interpolates between these two cases, as expected. The characteristic jump in $g(r)$ at $r=2\sigma$ in the isotropic SHS model⁴¹ can be explicitly computed within the C1 integral equation closure to be

$$g(2\sigma^+) - g(2\sigma^-) = -6\eta[\bar{y}^{C1}/(12\tau)]^2. \quad (35)$$

The jump is also present for intermediate values of δ and gradually fades out toward the HS result as illustrated in Fig. 8. In order to assess the precision of the predictions of the Cn closures, in Fig. 9 we compare the radial distribution generated by both C0 and C1 closures with Monte Carlo simulations (lower panel) and with the corresponding isotropic case (upper panel). The C1 closure is seen to follow the Monte Carlo behavior well over the range of the ratio r/σ considered, in both the isotropic and anisotropic cases.

Like the Percus–Yevick solution of the isotropic model, the C0 and C1 closures fail to capture certain δ function and step discontinuities in the radial distribution function,⁴⁴ such as those visible in the Monte Carlo results in the range $\sigma < r < 2\sigma$ in Fig. 9. These features arise from clusters in which the distance between two particles is fixed or limited indirectly by a sequence of adhesive bonds, for example, the outermost pair of particles in face-sharing tetrahedra. These clusters are sampled correctly by the Monte Carlo simulations.⁴⁵

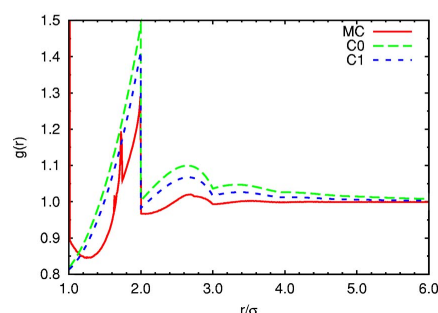
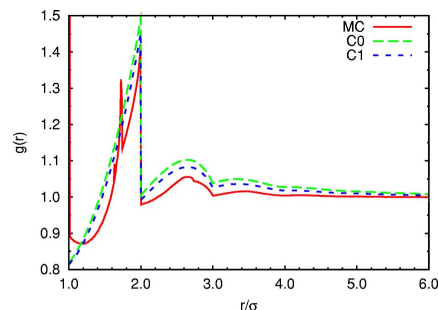


FIG. 9. (Color online) Comparison between the radial distribution function from MC simulations and from the C0 and C1 approximations in the isotropic case ($n\chi_0=100\%$, top panel) and for an intermediate value of the single patch ($n=1$) case with $n\chi_0=80\%$ (bottom panel). Both sets of calculations were performed at $\tau/(n\chi_0)^2=0.125$ and $\rho\sigma^3=0.35$ corresponding to $\eta=0.183\dots$

V. FLUID-FLUID COEXISTENCE CURVE

An interesting issue, both from the theoretical view point and for the possible implications in predictions of experimental phase transitions in solutions of globular proteins, is the determination of the fluid-fluid coexistence curve for the patchy sticky hard spheres, which we now address. We note that the dense fluid (liquid) phase, though often long-lived, is generally only metastable for systems of particles interacting through sufficiently short-ranged isotropic attractive forces. However, it has recently been predicted that a thermodynamically stable liquid will be recovered if the coordination number of the particles is restricted to a maximum of 6 or less.²⁹ Nevertheless, it seems that the specific details of the interactions must be taken into account before a firm conclusion can be drawn for a particular model.⁴⁶

A. Virial expansion

In order to find the coexistence or binodal line we need to solve for $\eta_1(\tau)$ and $\eta_2(\tau)$ the following set of equations:

$$P(\tau, \eta_1) = P(\tau, \eta_2),$$

$$\mu(\tau, \eta_1) = \mu(\tau, \eta_2).$$

A straightforward use of Eq. (17) for the excess free energy density to this aim, however, yields meaningless results even at moderate densities as one could have expected

234507-8 Fantoni *et al.*

J. Chem. Phys. **127**, 234507 (2007)

from the outset. A way out of this problem was proposed in Ref. 47 in the context of polydisperse SHS fluids. The idea hinges on a modification of the Carnahan–Starling expression for the HS excess free energy density⁴⁸

$$\beta f_{cs}^{\text{ex}} v_0 = \frac{4 - 3\eta}{(1 - \eta)^2} \eta^2, \quad (36)$$

so that it matches the patchy SHS result up to the third order in density. A possible choice is

$$\beta f_{cs}^{\text{ex}} v_0 = (c - 1)\eta \ln(1 - \eta) + 3d \frac{\eta^2}{1 - \eta} + c \frac{\eta^2}{(1 - \eta)^2}, \quad (37)$$

where c and d are parameters to be determined by expanding to the third order in density and matching to Eq. (17). We then find

$$c = \frac{b_3 - 2b_2 + 1}{3}, \quad (38)$$

$$d = \frac{b_2 - 1}{3}. \quad (39)$$

The pressure and the chemical potential are then

$$\beta P v_0 = \eta + \eta^2 \frac{1 + 3d(1 - \eta) + \eta[\eta - 2 + c(3 - \eta)]}{(1 - \eta)^3},$$

$$\beta \mu = \ln(\Lambda^3/v_0) + \ln \eta + (c - 1)\ln(1 - \eta) + \frac{(1 + c + 6d)\eta - (2 - 2c + 9d)\eta^2 + (1 - c + 3d)\eta^3}{(1 - \eta)^3},$$

respectively. In the limit $c=d=1$ Eq. (37) reduces to Eq. (36) as expected.

The behavior of the binodal line as a function of δ is shown in Fig. 10. As δ decreases, the coexistence region shrinks as expected, since HS fluids ($\delta=0$) admit only a single phase.⁴⁹

B. C1 integral equation

An alternative route is to start from the excess free energy stemming from the energy route of the C1 approximation³⁶

$$\beta f_{cs}^{\text{ex}} v_0 = \beta f_{cs}^{\text{ex}} v_0 - (b_2 - b_2^{\text{HS}})\eta^2 + (b_3 - b_3^{\text{HS}})\frac{\eta^3}{2}, \quad (40)$$

where $b_n^{\text{HS}} = b_n(\tau \rightarrow \infty)$. The rescaled virial coefficients $b_n = b_n(\tau)$ can be related to the values of the corresponding coefficients of the expansion for the cavity function at contact $\bar{y} = y_0 + y_1\eta + y_2\eta^2 + \dots$ by means of the relation (see, e.g., Ref. 36, and references therein)

$$y_{n-2}(\tau)/\tau^2 = \frac{1}{n-1} \frac{d[b_n(\tau) - b_n^{\text{HS}}]}{d\tau}, \quad n \geq 2. \quad (41)$$

Hence, we have

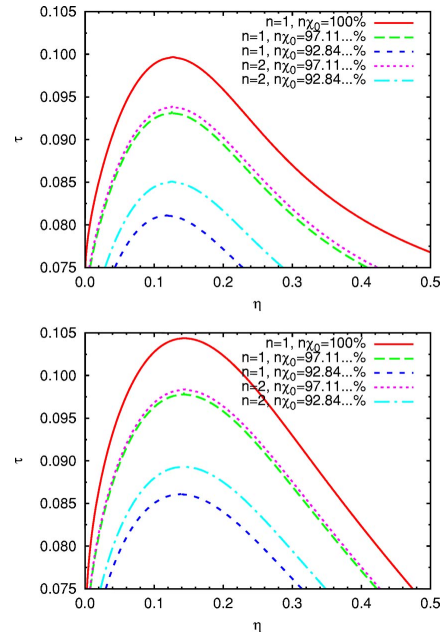


FIG. 10. (Color online) Dependence on the adhesive coverage $n\chi_0$ of the binodal line calculated from the modified Carnahan–Starling free energy of Eq. (37) (top panel) and from the C1 approximation of Eq. (40) (bottom panel). The one-patch ($n=1$) and two-patch ($n=2$) systems are compared at the same total coverage.

$$\beta P v_0 = \eta + 2\eta^2 \frac{\eta - 2}{(\eta - 1)^3} - \frac{\chi_1}{\tau} \eta^2 + \left(-5 \frac{\chi_1}{\tau} + \frac{\chi_2}{\tau^2} - \frac{1}{18} \frac{\chi_3}{\tau^3} \right) \eta^3, \quad (42)$$

$$\beta \mu = \ln(\Lambda^3/v_0) + \ln \eta + \eta \frac{8 + 3(\eta - 3)}{(1 - \eta)^3} - \frac{\chi_1}{\tau} 2\eta + \left(-5 \frac{\chi_1}{\tau} + \frac{\chi_2}{\tau^2} - \frac{1}{18} \frac{\chi_3}{\tau^3} \right) \frac{3\eta^2}{2}. \quad (43)$$

We remark that these results need no further orientational approximations as all effects of anisotropy are exactly included in $\chi_{1,2,3}$.

The results for the binodals are shown in Fig. 10. For each of the adhesive coverages depicted, both theoretical treatments predict that the binodal line for the two-patch model lies above its counterpart for a single patch. This could be expected on physical grounds, since a more distributed region of adhesion usually facilitates the aggregation process. A closer analysis, however, indicates that this is not always the case. This is shown in Fig. 11 where we report the change in the critical point as a function of the adhesive coverage $n\chi_0$ of the sphere surface. The difference between one and two patches decreases as δ increases, as expected, but it is clearly visible through the whole range of existence. Remarkably, there is an inversion of the two curves around

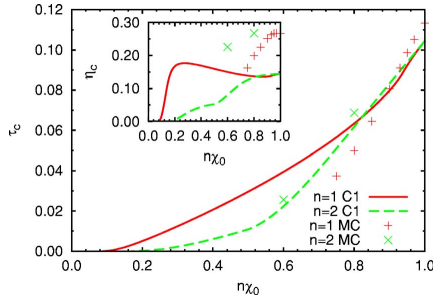


FIG. 11. (Color online) Dependence of the critical reduced temperature on the total adhesive coverage $n\chi_0$ for $n=1$ and 2 patches, calculated from the C1 approximation of Eq. (40) and from MC. The inset shows the critical packing fraction.

80% coverage. For approximately $n\chi_0 \geq 0.8$ the critical temperature for two patches lies above its one-patch counterpart. This means that the fluid-fluid transition line is encountered at higher temperature when an identical adhesive coverage is distributed over two spots rather than consolidated into a single big patch. However, this is no longer true when the size of the patch becomes too small. The reason is that under such conditions, it is then possible to bind three or more particles within a single patch, whereas at most two particles (one on each of the two opposite patches) can be attached in the two-patch case.

An additional noteworthy feature of Fig. 11 is the existence of a kink at $\delta = \pi/3$ (50% coverage) in the two-patch case. The kink is related to the degeneracy illustrated in Fig. 6. A similar kink occurs in the single-patch curve at $\delta = 5\pi/6$ (93.3% coverage). Again, this stems from degeneracy, as illustrated in Fig. 4.

Due to the inherent difficulty of tracing out critical temperatures to low coverage, we have been unable to verify the crossing of the one- and two-patch critical temperatures by Monte Carlo (MC) simulations. Figure 11 reports MC results down to around 60% coverage and the two-patch critical temperature is always above the one-patch case. We suspect, however, that an inversion might still occur in MC simulations, but at lower values of χ_0 , as yet inaccessible to our simulations.

The sensitivity of the shape and location of the coexistence curve to the geometry of the adhesive distribution is quite a remarkable feature of this archetypal patchy model. It seems likely, therefore, that a proper understanding of experimentally determined phase diagrams of globular proteins should take into account the nonuniformity of their surfaces and consequently of their interactions.

VI. PERCOLATION

A further interesting issue, already discussed in the context of the isotropic model, is the percolation threshold,^{42,50} to which we now turn.

A. Virial expansion

In one-patch systems only dimers can form for δ up to $\pi/6$, while clusters of any size are in principle possible above this threshold. In order to study the percolation threshold we can use the strategy devised in Ref. 51. Based on the definition of the connectedness correlation function (see later), the percolation threshold is signaled by the divergence of the mean cluster size

$$S = 1 + \rho \int d\mathbf{r}_{12} \langle h^+(\mathbf{r}_{12}, \Omega_1, \Omega_2) \rangle_{\Omega_1, \Omega_2}, \quad (44)$$

where h^+ is the pair connectedness function, which is related to the direct connectedness function c^+ by the Ornstein-Zernike equation. Both are related to the connected part of the Mayer function $f^+(1,2) = f(1,2) - f_{\text{HS}}(1,2)$ as given in Eq. (B2), $f_{\text{HS}}(1,2)$ being the HS part as given by Eq. (B3). As in the case of Eq. (22) we assume that

$$\begin{aligned} \langle \hat{c}^+(\mathbf{k}, \Omega_1, \Omega_3) \hat{h}^+(\mathbf{k}, \Omega_3, \Omega_2) \rangle_{\Omega_3} \\ \simeq \langle \hat{c}^+(\mathbf{k}, \Omega_1, \Omega_3) \rangle_{\Omega_3} \langle \hat{h}^+(\mathbf{k}, \Omega_3, \Omega_2) \rangle_{\Omega_3}. \end{aligned} \quad (45)$$

The average Fourier transform of the direct connectedness function $\hat{c}^+(k) = \langle \hat{c}^+(k, \Omega_1, \Omega_2) \rangle_{\Omega_1, \Omega_2}$ at $k=0$ then identifies the threshold by the equation

$$\rho \hat{c}^+(0) = 1. \quad (46)$$

Upon power expansion in the density we have

$$\hat{c}^+(0) = \sum_{n=2}^{\infty} \hat{c}_n^+(0) \rho^{n-2} = \hat{c}_2^+(0) + \rho \hat{c}_3^+(0) + O(\rho^2). \quad (47)$$

Using the earlier decomposition of the Mayer function the first two coefficients are found to be

$$\hat{c}_2^+(0) = \int d\mathbf{r}_{12} \langle f^+(1,2) \rangle_{\Omega_1, \Omega_2}, \quad (48)$$

$$\begin{aligned} \hat{c}_3^+(0) = \int d\mathbf{r}_{12} d\mathbf{r}_{13} \langle [f^+(1,2) f_{\text{HS}}(1,3) f_{\text{HS}}(2,3) \\ + 3f_{\text{HS}}(1,2) f^+(1,3) f^+(2,3) \\ + f^+(1,2) f^+(1,3) f^+(2,3)] \rangle_{\Omega_1, \Omega_2, \Omega_3}. \end{aligned} \quad (49)$$

An analysis following that in Appendix B then yields

$$\hat{c}_2^+(0)/v_0 = 24 \frac{\chi_1}{12\tau}, \quad (50)$$

$$\hat{c}_3^+(0)/v_0^2 = 60 \frac{\chi_1}{12\tau} - 432 \frac{\chi_2}{(12\tau)^2} + 288 \frac{\chi_3}{(12\tau)^3}. \quad (51)$$

To first order in the density, the percolation threshold is then given by a straight line

$$\tau = 2\chi_1 \eta. \quad (52)$$

The next order already yields a more complex solution involving both χ_2 and χ_3 ,

234507-10 Fantoni *et al.*

 J. Chem. Phys. **127**, 234507 (2007)

$$\eta = \frac{-6\chi_1\tau^2 + \sqrt{6\tau^{3/2}\sqrt{\chi_3 + 6\chi_1^2\tau - 18\chi_2\tau + 30\chi_1\tau^2}}}{\chi_3 - 18\chi_2\tau + 30\chi_1\tau^2}. \quad (53)$$

We then see that for $\eta_- \leq \eta \leq \eta_+$ with

$$\eta_{\pm} = \frac{-6(\chi_1^2 - 3\chi_2) \pm \sqrt{36(\chi_1^2 - 3\chi_2)^2 - 120\chi_1\chi_3}}{60\chi_1^2}, \quad (54)$$

Equation (53) has no real solutions. Clearly, the acceptable part of the solution is that for $\eta \leq \eta_-$.

B. C1 integral equation

The unphysical loss of the solution for the percolation threshold as obtained from the virial expansion is present also in the isotropic SHS model ($\delta = \pi$). This shortcoming does not occur in an integral equation approach.⁵⁰ Within the Cn class of closures a crucial role is played by the angular average of the cavity function at contact $\bar{y} = \langle y(r_{12} = \sigma, \Omega_1, \Omega_2, \Omega_{12}) \epsilon^2(1, 2) \rangle_{\Omega_1, \Omega_2, \Omega_{12}}$. Its density expansion reads

$$\bar{y}^{Cn} = y_0 + y_1\eta + y_2\eta^2 + \dots, \quad (55)$$

where $y_n = y_n(\tau)$ is related to the reduced virial coefficients b_n by Eq. (41). For y_0 and y_1 they have already been computed in Eq. (33). The percolation threshold is then given by $\eta \bar{y}^{Cn} = \tau$ where $\bar{y}^{Cn} = \langle y^{Cn}(r_{12} = \sigma, \Omega_1, \Omega_2, \Omega_{12}) \epsilon^2(1, 2) \rangle_{\Omega_1, \Omega_2, \Omega_{12}}$ and $y^{Cn}(r_{12} = \sigma, \Omega_1, \Omega_2, \Omega_{12})$ is the contact cavity function within the Cn approximation.

Since $\epsilon^2 = \epsilon$ then $\bar{y} = \bar{y}$ and within the C0 approximation ($\bar{y}^{C0} = y_0$) we find

$$\tau = \chi_1\eta. \quad (56)$$

whereas within the C1 approximation ($\bar{y}^{C1} = y_0 + y_1\eta$) we find

$$\eta = \frac{-6\chi_1\tau^2 + \sqrt{12\tau^{3/2}\sqrt{\chi_3 + 3\chi_1^2\tau - 12\chi_2\tau + 30\chi_1\tau^2}}}{\chi_3 - 12\chi_2\tau + 30\chi_1\tau^2}. \quad (57)$$

Now the loss of solution occurs between

$$\eta_{\pm} = \frac{-3(\chi_1^2 - 4\chi_2) \pm \sqrt{9(\chi_1^2 - 4\chi_2)^2 - 120\chi_1\chi_3}}{30\chi_1^2}. \quad (58)$$

Note that at small values of δ a gap may also appear in the C1 percolation threshold for $\delta \leq 1.21$ in the one-patch model and for $\delta \leq 1.22$ in the two-patch case. Figure 12 summarizes our findings and compares with MC simulations. From the figure we see that for δ close to π the percolation threshold of the two-patch model lies above that of the one-patch case at same total surface adhesive coverage, while the opposite trend is observed at lower δ . This mirrors our previous results for the coexistence curve.

Another quantity which is useful to assess the onset of a phase transition is the average coordination number, defined by

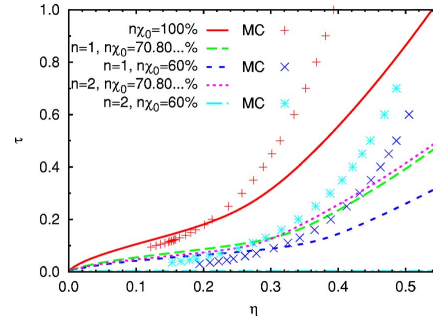


FIG. 12. (Color online) Percolation thresholds for various total adhesive coverages as calculated from the C1 approximation (lines), Eq. (57), and MC simulation (points). The one-patch ($n=1$) and two-patch ($n=2$) cases are compared at the same total coverage.

$$Z = \rho \int d\mathbf{r}_{12} \langle h^+(1, 2) \rangle_{\Omega_1, \Omega_2, \Omega_{12}}. \quad (59)$$

One finds

$$Z = 2 \frac{\eta}{\tau} \bar{y}^{Cn}, \quad (60)$$

which on the percolation threshold gives $Z=2$. This prediction is compared with MC results in Fig. 13 where we show the average coordination number at the percolation threshold obtained from the MC simulations for the one- and two-patch models at 60% coverage.

We are now in a position to summarize the phase diagram for one and two patches within the C1 approximation. This is reported in Fig. 14. For two patches, the C1 phase diagram (coexistence curve and percolation line) is compared with MC results in Fig. 15 both for the full isotropic case (100% coverage) and for 60% coverage. Note that while the percolation line terminates at the point shown, the coexistence curve has a solution for the whole range of packing fraction considered. However, we have chosen to terminate the plot for the same value of η as the percolation line.

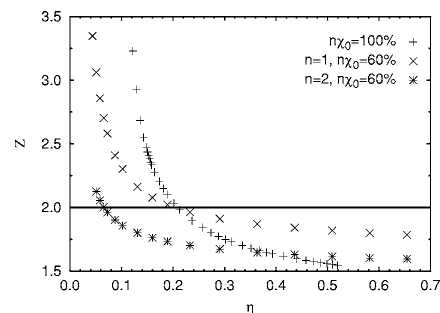


FIG. 13. Average coordination numbers at the percolation threshold for the one- and two-patch models at 60% coverage, obtained through MC. The continuous line is the prediction from the integral equation theory. The isotropic case is also reported for comparison.

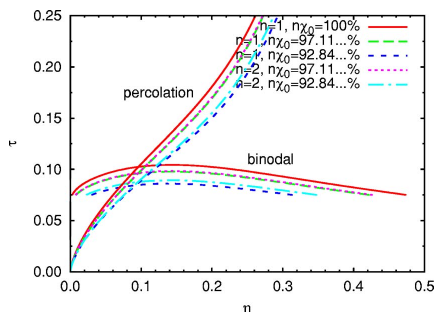


FIG. 14. (Color online) Phase diagram in the C1 approximation, for various values of the adhesive coverage $n\chi_0$. The one-patch ($n=1$) and two-patch ($n=2$) models are compared at the same total coverage.

VII. PHASE DIAGRAM AND ADDITION OF ADHESIVE BACKGROUND

So far we have considered the case of adhesive patches on hard spheres. The disadvantage of this model is that there is no fluid-fluid transition below a certain surface coverage χ_0 . We have also shown that at fixed surface coverage the liquid more easily forms if the adhesion is distributed in different patches on the sphere surface for sufficiently large patches and we expect the opposite to be true for low coverage.

One could argue that a more physical model should have a strongly directional potential mimicking, e.g., active sites in a globular protein, in addition to an underlying isotropic attractive potential favoring a general fluid-fluid phase transition. To this aim, we modify our potential by adding a uniform adhesive background to each sphere on top of which a patchy potential of the type considered so far is active. This effect can be obtained by a simple substitution $\epsilon \rightarrow 1 + \lambda\epsilon$ with λ measuring the strength of adhesion on the patches, yielding

$$\chi_1 \rightarrow 1 + \lambda\chi_1, \tag{61}$$

$$\chi_2 \rightarrow 1 + 2\lambda\chi_1 + \lambda^2\chi_2, \tag{62}$$

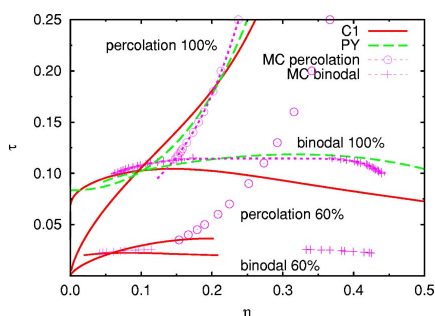


FIG. 15. (Color online) Comparison of the C1 approximation with MC simulation (dots) for the phase diagram of particles with two patches. The MC isotropic phase diagram is taken from Ref. 42.

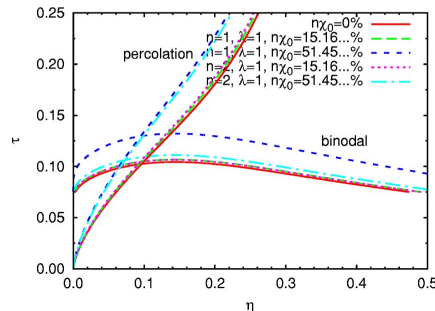
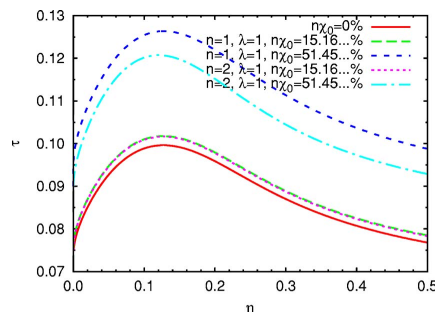


FIG. 16. (Color online) Dependence of the binodal line of patchy adhesive spheres with a background adhesion on the total surface coverage $n\chi_0$ of the patches: in the upper panel as calculated from the modified Carnahan–Starling free energy of Eq. (37); in the lower panel as calculated from the C1 approximation, Eq. (40).

$$\chi_3 \rightarrow 1 + 3\lambda\chi_1 + 3\lambda^2\chi_2 + \lambda^3\chi_3, \tag{63}$$

where

$$\bar{\chi}_2 = \langle \epsilon(1,2)\epsilon(1,3) \rangle_{\Omega_1, \Omega_2, \Omega_3} \Big|_{\theta_{12}=\pi/3}. \tag{64}$$

The phase diagram is now modified as depicted in Fig. 16 where we have set $\lambda=1$ to be the strength of the patches throughout. In this case we see that even a small sticky patch (of amplitude $\delta \sim 0.5$) is sufficient to raise both the binodal and percolation threshold of the isotropic model. At equal coverage, the binodal and percolation threshold of the two-patch model lie below their one-patch counterparts, in agreement with the observed trend in the absence of background adhesion.

Note that the critical point is now less sensitive to the size of the patches because an isotropic SHS—rather than a hard sphere—is now the limiting case as $\delta \rightarrow 0$. Indeed, the critical point does not move along η while it covers the whole range $\tau_c < \tau < 2\tau_c$ ($\lambda=1$), where τ_c is the critical reduced temperature of the isotropic model (see Fig. 17). The critical point shifts of the one- and two-patch models are now almost indistinguishable even though the crossing at 80% coverage still remains.

VIII. CONCLUSIONS

In this work we have studied, through integral equation theories and Monte Carlo simulations, the structure, percola-

234507-12 Fantoni *et al.*

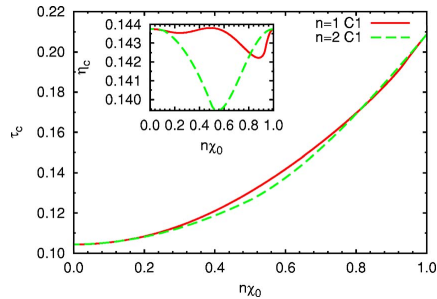
 J. Chem. Phys. **127**, 234507 (2007)


FIG. 17. (Color online) Dependence of the critical reduced temperature on the adhesive coverage in the patchy model with a uniform adhesive background, calculated from the C1 approximation, Eq. (40). The inset shows the behavior of the critical packing fraction.

tion, and fluid-fluid coexistence curves of a model of hard spheres with one or two uniform sticky patches on their surface. Particles interact through an adhesive Baxter potential only if patches on different spheres are suitably oriented and as hard spheres otherwise. Unlike most previous studies, we have been able to analyze in some detail the dependence of the aforementioned properties on the size of the patch and its interplay with the number of patches.

The integral equation theory is based on the first two approximations (C0 and C1) of a class of closures C_n which have already proved to provide a good qualitative representation of the exact behavior and are almost fully analytical. The comparison between the analytical work and Monte Carlo simulations indicates that C1 yields a gratifying qualitative description of the phase diagram notwithstanding the expected limitation due to its low density nature. While for the thermodynamics the results from the integral equation theories are exact within the given closure, for the percolation problem and the structure an additional orientational mean field approximation is necessary to decouple the orientational average.

Radial distribution functions within the C0 and C1 integral equation theories exhibit a characteristic jump at $r=2\sigma$ (whose magnitude depends on the patch angle δ) and a cusp at $r=3\sigma$. The coexistence and percolation lines move to lower temperature as the patch angle decreases from π (the isotropic case) to zero (hard spheres). For a fixed surface coverage above approximately 80%, the curves of the two-patch case lie above the corresponding single-patch ones, while the opposite trend is observed below that point. We have suggested that this is due to two patches of sufficiently large size being able to form bonds to more particles than can a single patch. We have also argued that this reasoning does not apply at low coverage, and that, in fact, the opposite situation might be expected. The crossover is not observed in the MC simulations within the range of adhesive coverage studied here (about 60%), but we cannot exclude the possibility for lower coverage, where the simulations converge very slowly. When an adhesive background is included in addition to the patches, both the liquid and percolating phase of the system are favored with respect to the isotropic case even in the presence of very small patches.

In spite of the limited number of cases (one or two patches) addressed in the present work, our analysis suggests that both the total fraction of the surface covered by adhesion and the number of patches are crucial parameters in controlling the location of the critical point. In the limit of a single bond per patch, our analysis is consistent with a recent suggestion⁵² of a generalized law of corresponding states for anisotropic patchy interactions. We remark that, from the purely theoretical point of view, there exist only few paradigmatic toy models with anisotropic interactions amenable to analytical or semianalytical treatment.

Our analysis can be regarded as complementary to recent investigations of the phase diagrams of globular proteins^{8,53,54} in that our starting point is the isotropic sticky hard sphere from which some adhesion is removed, rather than a hard sphere to which highly localized attractive spots are added. This approach goes beyond the limitation of one bond per patch, which is an essential feature of Wertheim thermodynamic perturbation theory. The price to pay is, of course, that only a qualitative agreement with MC simulations can be achieved.

It would be interesting to extend the present work in some respects. In view of the difficulties of MC simulations in probing low coverage, a comparison with a numerical solution of a more robust closure such as, for instance, the Percus–Yevick approximation which has a full analytical description in the isotropic case, would provide a more quantitative assessment of the results presented here. Such a solution would also help to evaluate the (uncontrolled) angular decoupling approximation exploited in the present analysis of structure and the percolation threshold. Work along these lines is in progress and will be presented in a future publication.

ACKNOWLEDGMENTS

This work was supported by the Italian MIUR (PRIN-COFIN 2006/2007). M.A.M. thanks the Royal Society of London and EPSRC (United Kingdom) for financial support.

APPENDIX A: THE LAW OF CORRESPONDING STATES

Consider the simplest possible dependence $\Delta(\hat{s}_1, \hat{s}_2) = \hat{s}_1 \cdot \hat{s}_2$ and assume that $\epsilon(1,2) = \Delta(\hat{s}_1, \hat{s}_2)$, i.e., the adhesion coefficient does not depend on $\hat{\mathbf{r}}_{12} = \mathbf{r}_{12}/r_{12}$. Within the Weeks–Chandler–Andersen perturbative expansion⁵⁵ of the Helmholtz free energy A^{SHS} one finds

$$\begin{aligned} \frac{\beta(A^{\text{SHS}} - A^{\text{HS}})}{N} = & \int d(1)d(2)a^{(1)}(\mathbf{r}_1, \mathbf{r}_2; \eta)\Delta\epsilon(1,2) \\ & + \int d(1)d(2)d(3)d(4) \\ & \times a^{(2)}(\mathbf{r}_1, \mathbf{r}_2, \mathbf{r}_3, \mathbf{r}_4; \eta)\Delta\epsilon(1,2)\Delta\epsilon(3,4) \\ & + \dots, \end{aligned} \quad (\text{A1})$$

where $d(i)$ is a short-hand notation for $d\mathbf{r}_i d\tilde{\Omega}_i$, with $d\tilde{\Omega}_i$ the average solid angle $\sin\theta_i d\theta_i d\varphi_i / (4\pi)$, A^{HS} the Helmholtz free energy of the reference hard sphere (HS) system

$$\Delta\epsilon(1,2) = \frac{\epsilon(1,2)}{12\tau} \delta(r_{12} - \sigma), \quad (\text{A2})$$

and the functions $a^{(n)}$ are expressed in terms of the correlation functions of the reference system which only depend on the packing fraction $\eta = \pi\rho\sigma^3/6$, with ρ as the density. We see then that the angular dependence in ϵ factorizes and one finds

$$\frac{\beta(A^{\text{SHS}} - A^{\text{HS}})}{N} = \sum_i A^{(i)}(\eta) \left(\frac{\chi_i}{12\tau}\right)^i, \quad (\text{A3})$$

where $\chi_i = \int d\tilde{\Omega}_1 d\tilde{\Omega}_2 \epsilon(1,2)$. This analysis shows how, in this case, the law of corresponding states holds. For example, if $\tau = g(\eta)$ is the spinodal or binodal of the SHS system with isotropic interaction ($\epsilon=1$),^{27,56,57} then the spinodal or binodal of the SHS with directional adhesion will be $\tau = \chi_1 g(\eta)$, which will lie above that of the isotropic system if $\chi_1 > 1$ and below otherwise.

APPENDIX B: THE THIRD VIRIAL COEFFICIENT

In this appendix we provide a derivation of Eqs. (6)–(9). We start from the usual definition of the third virial coefficient

$$B_3 = -\frac{1}{3V} \int d\mathbf{r}_1 d\mathbf{r}_2 d\mathbf{r}_3 \langle f(1,2)f(1,3)f(2,3) \rangle_{\Omega_1, \Omega_2, \Omega_3}, \quad (\text{B1})$$

where, in line with Eq. (2), the Mayer function can split into two terms

$$f(i,j) = f_{\text{HS}}(i,j) + \frac{\sigma}{12\tau} \epsilon(i,j) \delta(r_{ij} - \sigma). \quad (\text{B2})$$

In the earlier equation we have set the HS part to the usual form

$$f_{\text{HS}}(i,j) = -\Theta(\sigma - r_{ij}). \quad (\text{B3})$$

Upon expanding the product, one can easily find

$$\Delta B_3 = B_3 - B_3^{\text{HS}} = \Delta B_3^{(1)} + \Delta B_3^{(2)} + \Delta B_3^{(3)}, \quad (\text{B4})$$

where $B_3^{\text{HS}} = 5\pi^2\sigma^6/18$ is the HS result and

$$\Delta B_3^{(1)} = -\frac{1}{V} \left(\frac{\sigma}{12\tau}\right) \int d\mathbf{r}_1 d\mathbf{r}_2 d\mathbf{r}_3 \langle f_{\text{HS}}(1,2)f_{\text{HS}}(1,3) \times \epsilon(2,3) \delta(r_{23} - \sigma) \rangle_{\Omega_1, \Omega_2, \Omega_3}, \quad (\text{B5})$$

$$\Delta B_3^{(2)} = -\frac{1}{V} \left(\frac{\sigma}{12\tau}\right)^2 \int d\mathbf{r}_1 d\mathbf{r}_2 d\mathbf{r}_3 \langle f_{\text{HS}}(1,2) \times \epsilon(1,3) \delta(r_{13} - \sigma) \epsilon(2,3) \delta(r_{23} - \sigma) \rangle_{\Omega_1, \Omega_2, \Omega_3}, \quad (\text{B6})$$

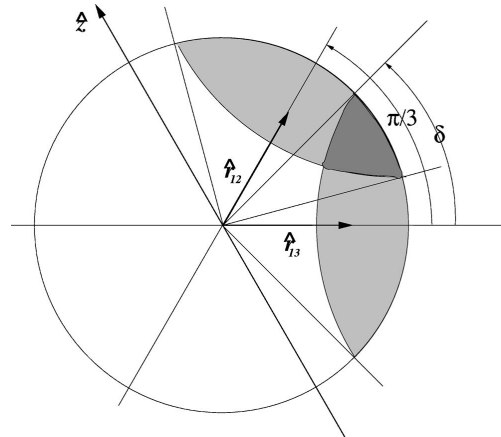


FIG. 18. Basic geometry for the calculation of $R_1(\delta)$ in Eq. (C1). The required solid angle is the overlap of the two cones of width δ (the darkly shaded region in the sketch).

$$\Delta B_3^{(3)} = -\frac{1}{3V} \left(\frac{\sigma}{12\tau}\right)^3 \int d\mathbf{r}_1 d\mathbf{r}_2 d\mathbf{r}_3 \langle \epsilon(1,2) \delta(r_{12} - \sigma) \times \epsilon(1,3) \delta(r_{13} - \sigma) \epsilon(2,3) \delta(r_{23} - \sigma) \rangle_{\Omega_1, \Omega_2, \Omega_3}. \quad (\text{B7})$$

The earlier integrals are most conveniently evaluated in bipolar coordinates by introducing $\mathbf{r}_{12} = \mathbf{r}_2 - \mathbf{r}_1$ and $\mathbf{r}_{13} = \mathbf{r}_3 - \mathbf{r}_1$. This leads to $r_{23} = \sqrt{r_{12}^2 + r_{13}^2 - 2r_{12}r_{13}\hat{\mathbf{r}}_{12} \cdot \hat{\mathbf{r}}_{13}}$ where it is most convenient to choose $\hat{\mathbf{r}}_{13}$ as the z axis. For $\Delta B_3^{(1)}$ one finds

$$\Delta B_3^{(1)} = -\left(\frac{\sigma}{12\tau}\right) \int d\mathbf{r}_{23} d\mathbf{r}_{12} \Theta(\sigma - r_{12}) \Theta(\sigma - |\mathbf{r}_{12} - \mathbf{r}_{23}|) \times \delta(r_{23} - \sigma) \langle \epsilon(2,3) \rangle_{\Omega_2, \Omega_3}. \quad (\text{B8})$$

Here one first performs the integration over \mathbf{r}_{12} , which covers twice a spherical cap of height $\sigma/2$ and then the straightforward integration over \mathbf{r}_{23} . Clearly the anisotropic part decouples, thus yielding the isotropic part times χ_1 as claimed. For $\Delta B_3^{(2)}$ a little more care is necessary. One first obtains

$$\Delta B_3^{(2)} = \left(\frac{\sigma}{12\tau}\right)^2 \int_0^\infty dr_{12} r_{12}^2 \Theta(\sigma - r_{12}) \times \int_0^\infty dr_{13} r_{13}^2 \delta(\sigma - r_{13}) \int d\Omega_{12} d\Omega_{13} \times \delta(\sqrt{r_{12}^2 + r_{13}^2 - 2r_{12}r_{13} \cos \theta_{12} - \sigma}) \times \langle \epsilon(1,3) \epsilon(2,3) \rangle_{\Omega_1, \Omega_2, \Omega_3}. \quad (\text{B9})$$

After a first integration over r_{13} , an additional integration over $\cos \theta_{12}$ then requires $\theta_{13} \leq \pi/3$ (corresponding to the maximum available angle for all three particles in reciprocal contact). This also yields a normalization factor $4 = 1/\sin^2(\pi/6)$ in order to have the correct limit $\epsilon(i,j) \rightarrow 1$ for all (i,j) . The final result is

234507-14 Fantoni *et al.*

J. Chem. Phys. **127**, 234507 (2007)

$$\Delta B_3^{(2)} = \frac{\pi^2 \sigma^6}{36\tau^2} \frac{1}{4\pi} \int d\Omega_{13} \times 4 \left\langle \epsilon(1,2)\epsilon(2,3)\Theta\left(\frac{\pi}{3} - \theta_{13}\right) \right\rangle_{\Omega_1, \Omega_2, \Omega_3}, \quad (\text{B10})$$

thus yielding the isotropic part times χ_2 as reported in Eq. (8). An almost identical procedure also gives

$$\Delta B_3^{(3)} = - \left(\frac{\sigma}{12\tau} \right)^3 \frac{8\pi^2 \sigma^2}{3} \int_0^\infty dr_{12} r_{12}^2 \delta(r_{12} - \sigma) \times \int_{-1}^{+1} d(\cos \theta_{12}) \delta(\sqrt{r_{12}^2 + \sigma^2 - 2r_{12}\sigma \cos \theta_{12}} - \sigma) \times \langle \epsilon(1,2)\epsilon(1,3)\epsilon(2,3) \rangle_{\Omega_1, \Omega_2, \Omega_3}, \quad (\text{B11})$$

which, after an integration over the angular variables, leads to the desired decoupling for the anisotropic part χ_3 as given in Eq. (9). Note that in this configuration all three spheres are necessarily touching and this fixes the angles θ_{ij} to a well defined value given in Eq. (9). This completes the derivation of Eq. (6).

APPENDIX C: COEFFICIENTS χ_2 AND χ_3 FOR THE ONE-PATCH CASE

Here we give the analytic expressions for the coefficients Q_1 and R_1 used in Eqs. (12) and (13) of the main text in terms of characteristic integrals which are then evaluated numerically. The basic procedure follows a similar analysis carried out in a different context,⁵⁸ which requires the calculation of the solid angle associated with the intersection of two identical patches on the same sphere as indicated in Fig. 18. For χ_3 , one can easily see that for $\delta < \pi/6$ there is no possibility of intersection, even in the close-packed configuration. For $\delta \geq \pi/6$ the form of the resulting integral can be most conveniently written in slightly different ways depending on the amplitude δ of the patch

$$R_1(\delta) = \alpha_{b,1}(\delta)\Theta\left(\delta - \frac{\pi}{6}\right)\Theta\left(\frac{2\pi}{3} - \delta\right) + \beta_{b,1}(\delta)\Theta\left(\delta - \frac{2\pi}{3}\right)\Theta\left(\frac{5\pi}{6} - \delta\right) + \gamma_{b,1}(\delta)\Theta\left(\delta - \frac{5\pi}{6}\right), \quad (\text{C1})$$

where the various terms are given in terms of the integrals

$$\alpha_{b,1}(\delta) = \frac{1}{\pi} \int_{2\pi/3-\delta}^{\pi/2} d\theta \sin \theta \arccos\left(\frac{\cos \delta - \cos \theta \cos 2\pi/3}{\sin \theta \sin 2\pi/3}\right), \quad (\text{C2})$$

$$\beta_{b,1}(\delta) = 1 - \frac{1}{\pi} \int_{\delta-2\pi/3}^{\pi/2} d\theta \sin \theta \arccos\left(\frac{\cos(\pi - \delta) - \cos \theta \cos \pi/3}{\sin \theta \sin \pi/3}\right), \quad (\text{C3})$$

$$\gamma_{b,1}(\delta) = 1 - 2 \sin^2\left(\frac{\pi - \delta}{2}\right). \quad (\text{C4})$$

For example $\alpha_{b,1}$ given in Eq. (C2) is the simplest integral resulting from the calculation of the overlapping region of the two cones of width δ as depicted in Fig. 18.

For χ_2 an additional complication arises from the additional degree of freedom given by the fact that only two of the three spheres are (in general) in contact. One finds

$$Q_1(\delta) = \alpha_{a,1}(\delta)\Theta\left(\frac{\pi}{6} - \delta\right) + \beta_{a,1}(\delta)\Theta\left(\delta - \frac{\pi}{6}\right)\Theta\left(\frac{\pi}{2} - \delta\right) + \gamma_{a,1}(\delta)\Theta\left(\delta - \frac{\pi}{2}\right)\Theta\left(\frac{5\pi}{6} - \delta\right) + \delta_{a,1}(\delta)\Theta\left(\delta - \frac{5\pi}{6}\right), \quad (\text{C5})$$

with

$$\alpha_{a,1}(\delta) = \frac{2}{\pi} \int_0^{2\delta} d\theta' \sin \theta' \int_{\pi/2+\theta'/2-\delta}^{\pi/2} d\theta \sin \theta \arccos\left(\frac{\cos \delta - \cos \theta \cos(\pi/2 + \theta'/2)}{\sin \theta \sin(\pi/2 + \theta'/2)}\right), \quad (\text{C6})$$

$$\beta_{a,1}(\delta) = \frac{2}{\pi} \int_0^{\pi/3} d\theta' \sin \theta' \int_{\pi/2+\theta'/2-\delta}^{\pi/2} d\theta \sin \theta \arccos\left(\frac{\cos \delta - \cos \theta \cos(\pi/2 + \theta'/2)}{\sin \theta \sin(\pi/2 + \theta'/2)}\right), \quad (\text{C7})$$

$$\gamma_{a,1}(\delta) = \frac{2}{\pi} \left[\frac{\pi}{2} - \int_0^{\pi/3} d\theta' \sin \theta' \int_{\delta-\pi/2-\theta'/2}^{\pi/2} d\theta \sin \theta \arccos\left(\frac{\cos(\pi - \delta) - \cos \theta \cos(\pi/2 - \theta'/2)}{\sin \theta \sin(\pi/2 - \theta'/2)}\right) \right], \quad (\text{C8})$$

$$\delta_{a,1}(\delta) = \frac{2}{\pi} \left[2\pi \sin^2 \delta + \int_0^{2(\pi-\delta)} d\theta' \sin \theta' \int_{\delta-\pi/2-\theta'/2}^{\pi/2} d\theta \sin \theta \arccos \left(\frac{\cos(\pi-\delta) - \cos \theta \cos(\pi/2 - \theta'/2)}{\sin \theta \sin(\pi/2 - \theta'/2)} \right) + \left[1 - 2 \sin^2 \left(\frac{\pi-\delta}{2} \right) \right] \frac{\pi}{2} [2 \cos(2\delta) - 1] \right]. \quad (C9)$$

APPENDIX D: COEFFICIENTS χ_2 AND χ_3 FOR THE TWO-PATCH CASE

Here we give the analytic expressions for the coefficients Q_2 and R_2 used in Eqs. (15) and (16) of the main text

$$Q_2(\delta) = \alpha_{a,2}(\delta)\Theta\left(\frac{\pi}{6} - \delta\right) + \beta_{a,2}(\delta)\Theta\left(\delta - \frac{\pi}{6}\right)\Theta\left(\frac{\pi}{3} - \delta\right) + \gamma_{a,2}(\delta)\Theta\left(\delta - \frac{\pi}{3}\right)\Theta\left(\frac{\pi}{2} - \delta\right), \quad (D1)$$

$$R_2(\delta) = \alpha_{b,2}(\delta)\Theta\left(\delta - \frac{\pi}{6}\right)\Theta\left(\frac{\pi}{3} - \delta\right) + \beta_{b,2}(\delta)\Theta\left(\delta - \frac{\pi}{3}\right)\Theta\left(\frac{\pi}{2} - \delta\right), \quad (D2)$$

with

$$\alpha_{a,2}(\delta) = \frac{4}{\pi} \int_0^{2\delta} d\theta' \sin \theta' \int_{\pi/2+\theta'/2-\delta}^{\pi/2} d\theta \sin \theta \arccos \left(\frac{\cos \delta - \cos \theta \cos(\pi/2 + \theta'/2)}{\sin \theta \sin(\pi/2 + \theta'/2)} \right), \quad (D3)$$

$$\beta_{a,2}(\delta) = \frac{4}{\pi} \int_0^{\pi/3} d\theta' \sin \theta' \int_{\pi/2+\theta'/2-\delta}^{\pi/2} d\theta \sin \theta \arccos \left(\frac{\cos \delta - \cos \theta \cos(\pi/2 + \theta'/2)}{\sin \theta \sin(\pi/2 + \theta'/2)} \right), \quad (D4)$$

$$\gamma_{a,2}(\delta) = \frac{4}{\pi} \left[\int_0^{\pi/3} d\theta' \sin \theta' \int_{\pi/2+\theta'/2-\delta}^{\pi/2} d\theta \sin \theta \arccos \left(\frac{\cos \delta - \cos \theta \cos(\pi/2 + \theta'/2)}{\sin \theta \sin(\pi/2 + \theta'/2)} \right) + \int_0^{\pi/3} d\theta' \sin \theta' \int_{\pi/2}^{\theta'/2+\delta} d\theta \sin \theta \arccos \left(\frac{\cos \delta - \cos \theta \cos(\theta'/2)}{\sin \theta \sin(\theta'/2)} \right) \right], \quad (D5)$$

$$\alpha_{b,2}(\delta) = \frac{2}{\pi} \int_{2\pi/3-\delta}^{\pi/2} d\theta \sin \theta \arccos \left(\frac{\cos \delta - \cos \theta \cos 2\pi/3}{\sin \theta \sin 2\pi/3} \right), \quad (D6)$$

$$\beta_{b,2}(\delta) = \frac{2}{\pi} \int_{2\pi/3-\delta}^{\pi/2} d\theta \sin \theta \arccos \left(\frac{\cos \delta - \cos \theta \cos 2\pi/3}{\sin \theta \sin 2\pi/3} \right) + \frac{2}{\pi} \int_{\pi/2}^{\pi/6+\delta} d\theta \sin \theta \arccos \left(\frac{\cos \delta - \cos \theta \cos \pi/6}{\sin \theta \sin \pi/6} \right). \quad (D7)$$

¹L. Boltzmann, *Lectures on Gas Theory* (Dover, New York, 1995), Chap. 6.
²G. Jackson, W. G. Chapman, and K. E. Gubbins, *Mol. Phys.* **65**, 1 (1988).
³L. Blum, P. T. Cummings, and D. Bratko, *J. Chem. Phys.* **92**, 3741 (1990).
⁴N. A. Busch, M. S. Wertheim, Y. C. Chiew, and M. L. Yarmush, *J. Chem. Phys.* **101**, 3147 (1994).
⁵D. Ghonasgi and W. G. Chapman, *J. Chem. Phys.* **102**, 2585 (1995).
⁶N. A. Busch, M. S. Wertheim, and M. L. Yarmush, *J. Chem. Phys.* **104**, 3962 (1996).
⁷A. Lomakin, N. Asherie, and G. B. Benedek, *Proc. Natl. Acad. Sci. U.S.A.* **96**, 9465 (1999).
⁸R. P. Sear, *J. Chem. Phys.* **111**, 4800 (1999).
⁹E. Mileva and G. T. Evans, *J. Chem. Phys.* **113**, 3766 (2000).
¹⁰F. Sciortino, *Nat. Mater.* **1**, 145 (2002).
¹¹F. W. Starr and J. F. Douglas, *J. Chem. Phys.* **119**, 1777 (2003).
¹²N. Kern and D. Frenkel, *J. Chem. Phys.* **118**, 9882 (2003).
¹³Z. Zhang and S. C. Glotzer, *Nano Lett.* **4**, 1407 (2004).
¹⁴S. C. Glotzer, *Science* **306**, 419 (2004).
¹⁵Y. S. Cho, G. R. Yi, J. M. Lim, S. H. Kim, V. N. Maniharan, D. J. Pine, and S. M. Yang, *J. Am. Chem. Soc.* **127**, 15968 (2005).
¹⁶F. Sciortino, P. Tartaglia, and E. Zaccarelli, *J. Phys. Chem. B* **109**, 21942 (2005).
¹⁷E. Bianchi, J. Largo, P. Tartaglia, E. Zaccarelli, and F. Sciortino, *Phys. Rev. Lett.* **97**, 168301 (2006).
¹⁸M. F. Hagan and D. Chandler, *Biophys. J.* **91**, 42 (2006).
¹⁹A. W. Wilber, J. P. K. Doye, A. A. Louis, E. G. Noya, M. A. Miller, and P. Wong, *J. Chem. Phys.* **127**, 085106 (2007).
²⁰M. Wertheim, *J. Stat. Phys.* **35**, 19 (1984).
²¹Yu. V. Kalyuzhnyi, M. F. Holovko, and A. D. J. Haymet, *J. Chem. Phys.* **95**, 9151 (1991).
²²Yu. V. Kalyuzhnyi, G. Stell, M. L. Llano-Rastrepo, W. G. Chapman, and M. F. Holovko, *J. Chem. Phys.* **101**, 7939 (1994).
²³R. Piazza, V. Peyre, and V. Degiorgio, *Phys. Rev. E* **58**, R2733 (1998).
²⁴A. Giacometti, D. Gazzillo, G. Pastore, and T. K. Das, *Phys. Rev. E* **71**, 031108 (2005).
²⁵G. Pellicane, D. Costa, and C. Caccamo, *J. Phys. Chem. B* **108**, 7538 (2004).
²⁶A. Lomakin, N. Asherie, and G. B. Benedek, *J. Chem. Phys.* **104**, 1646 (1996).
²⁷R. J. Baxter, *J. Chem. Phys.* **49**, 2770 (1968).
²⁸G. Stell, *J. Stat. Phys.* **63**, 1203 (1991).
²⁹P. Charbonneau and D. Frenkel, *J. Chem. Phys.* **126**, 196101 (2007).
³⁰C. G. Gray and K. E. Gubbins, *Theory of Molecular Fluids* (Clarendon, New York, 1984).

234507-16 Fantoni *et al.*

J. Chem. Phys. **127**, 234507 (2007)

- ³¹L. Blum and A. J. Torruella, J. Chem. Phys. **56**, 303 (1972).
³²L. Blum, J. Chem. Phys. **57**, 1862 (1972).
³³L. Blum, J. Chem. Phys. **58**, 3295 (1973).
³⁴M. S. Wertheim, J. Chem. Phys. **55**, 4291 (1971).
³⁵D. Gazzillo, R. Fantoni, and A. Giacometti (unpublished).
³⁶D. Gazzillo and A. Giacometti, J. Chem. Phys. **120**, 4742 (2004).
³⁷M. A. Miller and D. Frenkel (unpublished).
³⁸N. A. Seaton and E. D. Glandt, J. Chem. Phys. **87**, 1785 (1987).
³⁹W. G. T. Kranendonk and D. Frenkel, Mol. Phys. **64**, 403 (1988).
⁴⁰A. Jamnik and D. Bratko, Phys. Rev. E **50**, 1151 (1994).
⁴¹M. A. Miller and D. Frenkel, J. Chem. Phys. **121**, 535 (2004).
⁴²M. A. Miller and D. Frenkel, Phys. Rev. Lett. **90**, 135702 (2003).
⁴³J. W. Perram, Mol. Phys. **30**, 1505 (1975).
⁴⁴P. T. Cummings, J. W. Perram, and W. R. Smith, Mol. Phys. **31**, 535 (1976).
⁴⁵M. A. Miller and D. Frenkel, J. Phys.: Condens. Matter **16**, S4901 (2004).
⁴⁶F. Romano, P. Tartaglia, and F. Sciortino, J. Phys.: Condens. Matter **19**, 322101 (2007).
⁴⁷R. Fantoni, D. Gazzillo, A. Giacometti, and P. Sollich, J. Chem. Phys. **125**, 164504 (2006).
⁴⁸N. F. Carnahan and K. E. Starling, J. Chem. Phys. **51**, 635 (1969).
⁴⁹B. J. Alder and T. E. Wainwright, J. Chem. Phys. **27**, 1208 (1957).
⁵⁰R. Fantoni, D. Gazzillo, and A. Giacometti, J. Chem. Phys. **122**, 034901 (2005).
⁵¹U. Alon, A. Drory, and I. Balberg, Phys. Rev. A **42**, 4634 (1990).
⁵²G. Foffi and F. Sciortino, J. Phys. Chem. B **111**, 9702 (2007).
⁵³P. R. ten Wolde and D. Frenkel, Science **277**, 1975 (1997).
⁵⁴J. F. Lutsko and G. Nicolis, J. Chem. Phys. **122**, 244907 (2005).
⁵⁵H. C. Andersen, J. D. Weeks, and D. Chandler, Phys. Rev. A **4**, 1597 (1971).
⁵⁶R. J. Baxter, in *Physical Chemistry, an Advanced Treatise*, edited by D. Henderson (Academic, New York, 1971), Vol. 8A, Chap. 4.
⁵⁷R. O. Watts, D. Henderson, and R. J. Baxter, Adv. Chem. Phys. **21**, 421 (1971).
⁵⁸S. M. Oversteegen and H. N. W. Lekkerkerker, Phys. Rev. E **68**, 021404 (2003).

Part VIII
2008

Chapter 15

Fluids of spherical molecules with dipolarlike nonuniform adhesion: an analytically solvable anisotropic model

Gazzillo D., **Fantoni R.**, and Giacometti A., Phys. Rev. E **78**, 021201 (2008)

Title: “Fluids of spherical molecules with dipolarlike nonuniform adhesion: an analytically solvable anisotropic model”

Abstract: We consider an anisotropic version of Baxter’s model of ‘sticky hard spheres’, where a nonuniform adhesion is implemented by adding, to an isotropic surface attraction, an appropriate ‘dipolar sticky’ correction (positive or negative, depending on the mutual orientation of the molecules). The resulting nonuniform adhesion varies continuously, in such a way that in each molecule one hemisphere is ‘stickier’ than the other.

We derive a complete analytic solution by extending a formalism [M. S. Wertheim, J. Chem. Phys. **55**, 4281 (1971)] devised for dipolar hard spheres. Unlike Wertheim’s solution which refers to the ‘mean spherical approximation’, we employ a *Percus-Yevick closure with orientational linearization*, which is expected to be more reliable.

We obtain analytic expressions for the orientation-dependent pair correlation function $g(1, 2)$. Only one equation for a parameter K has to be solved numerically. We also provide very accurate expressions which reproduce K as well as some parameters, Λ_1 and Λ_2 , of the required Baxter factor correlation functions with a relative error smaller than 1%. We give a physical interpretation of the effects of the anisotropic adhesion on the $g(1, 2)$.

The model could be useful for understanding structural ordering in complex fluids within a unified picture.

PHYSICAL REVIEW E 78, 021201 (2008)

**Fluids of spherical molecules with dipolarlike nonuniform adhesion:
An analytically solvable anisotropic model**

Domenico Gazzillo, Riccardo Fantoni, and Achille Giacometti

Dipartimento di Chimica Fisica, Università di Venezia, S. Marta DD 2137, I-30123 Venezia, Italy

(Received 12 December 2007; revised manuscript received 10 April 2008; published 7 August 2008)

We consider an anisotropic version of Baxter's model of "sticky hard spheres," where a nonuniform adhesion is implemented by adding, to an isotropic surface attraction, an appropriate "dipolar sticky" correction (positive or negative, depending on the mutual orientation of the molecules). The resulting nonuniform adhesion varies continuously, in such a way that in each molecule one hemisphere is "stickier" than the other. We derive a complete analytic solution by extending a formalism [M. S. Wertheim, *J. Chem. Phys.* **55**, 4281 (1971)] devised for dipolar hard spheres. Unlike Wertheim's solution, which refers to the "mean spherical approximation," we employ a *Percus-Yevick closure with orientational linearization*, which is expected to be more reliable. We obtain analytic expressions for the orientation-dependent pair correlation function $g(1,2)$. Only one equation for a parameter K has to be solved numerically. We also provide very accurate expressions which reproduce K as well as some parameters, Λ_1 and Λ_2 , of the required Baxter factor correlation functions with a relative error smaller than 1%. We give a physical interpretation of the effects of the anisotropic adhesion on the $g(1,2)$. The model could be useful for understanding structural ordering in complex fluids within a unified picture.

DOI: 10.1103/PhysRevE.78.021201

PACS number(s): 61.20.Gy, 61.20.Qg, 61.25.Em

I. INTRODUCTION

Anisotropy of molecular interactions plays an important role in many physical, chemical, and biological processes. Attractive forces are responsible for the tendency toward particle association, while the directionality of the resulting bonds determines the geometry of the resulting clusters. Aggregation may thus lead to very different structures: in particular, chains, globular forms, and bi- or three-dimensional networks. Understanding the microscopic mechanisms underlying such phenomena is clearly very important both from a theoretical and a technological point of view. Polymerization of inorganic molecules, phase behavior of nonspherical colloidal particles, building up of micelles, gelation, formation of α helices from biomolecules, DNA strands, and other ordered structures in living organisms, protein folding and crystallization, self-assembly of nanoparticles into composite objects designed for new materials, are all subjects of considerable interest, belonging to the same class of systems with anisotropic interactions.

Modern studies on these complex systems strongly rely upon computer simulations, which have provided a great deal of useful information about many properties of molecular fluids. Nevertheless, analytic models with explicit expressions for structural and thermodynamic properties still represent an irreplaceable tool, in view of their ability to capture the essential features of the investigated physical systems.

At the lowest level in this hierarchy of minimal models on assembling particles, lies the problem of the formation of linear aggregates, from dimers [1,2] up to polymer chains. This topic has been extensively investigated, through both computer simulations and analytical methods. In the latter case a remarkable example is Wertheim's analytic solution of the *mean spherical approximation* (MSA) integral equation for dipolar hard spheres (DHS), i.e., hard spheres (HS) with a point dipole at their center [3] (hereafter referred to as Ref.

[1]). For the DHS model, several studies predict chain formation, whereas little can be said about the existence of a fluid-fluid coexistence line, since computer simulations and mean field theories provide contradictory results [4–8]. On the other hand, for mesoscopic fluids the importance of combining *short-ranged* anisotropic attractions and repulsions has been well established [9,10], and hence the long range of the dipolar interaction is less suited for the mesoscopic systems considered here, at variance with their atomistic counterpart.

The aim of the present paper is to address both the above points, by studying a model with anisotropic surface adhesion that is amenable to an analytical solution, within an approximation which is expected to be valid at significant experimental regimes.

In the isotropic case, the first model with "surface adhesion" was introduced a long time ago by Baxter [11,12]. The interaction potential of these "sticky hard spheres" (SHS) includes a HS repulsion plus a spherically symmetric attraction, described by a square well (SW), which becomes infinitely deep and narrow, according to a limiting procedure (Baxter's sticky limit) that keeps the second virial coefficient finite.

Possible anisotropic variations include "sticky points" [13–21], "sticky patches" [10,22–27] and, more recently, "Gaussian patches" [28,29]. The most common version of patchy sticky models refers to HS with one or more "uniform circular patches," all of the same species. This kind of patch has a well-defined circular boundary on the particle surface, and is always attractive, with a "uniform" strength of adhesion, which does not depend on the contact point within the patch [22].

In the present paper we consider a "dipolarlike" SHS model, where the sum of a uniform surface adhesion (isotropic background) plus an appropriate dipolar sticky correction—which can be both positive or negative, depend-

GAZZILLO, FANTONI, AND GIACOMETTI

PHYSICAL REVIEW E 78, 021201 (2008)

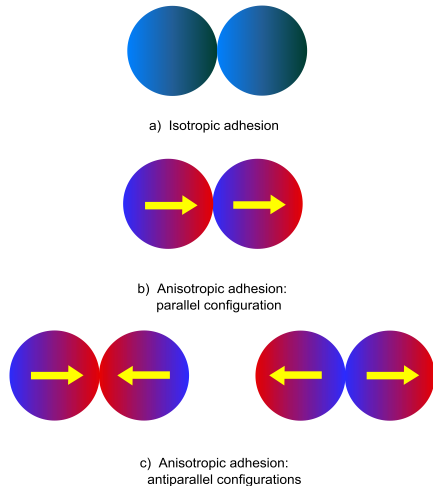


FIG. 1. (Color online) Illustration of the dipolarlike adhesion. In the top panel (a) the adhesion is isotropic, with $\epsilon(1,2)=1$. In the two other cases the adhesion is anisotropic and (i) stronger and maximum in the head-to-tail parallel configuration (b), where $\epsilon(1,2)=1+2\alpha$; and (ii) weaker and minimum in the two antiparallel configurations (c) [head-to-head and tail-to-tail orientations, both with $\epsilon(1,2)=1-2\alpha$].

ing on the orientations of the particles—yields a nonuniform adhesion. Although the adhesion varies continuously and no discontinuous boundary exists, the surface of each molecule may be regarded as formed by two hemispherical “patches” (colored red and blue, respectively, in the online Fig. 1). One of these hemispheres is ‘stickier’ than the other, and the entire molecular surface is adhesive, but its stickiness is nonuniform and varies in a dipolar fashion. By varying the dipolar contribution, the degree of anisotropy can be changed, in such a way that the total sticky potential can be continuously tuned from very strong attractive strength (twice the isotropic one) to vanishing adhesion (HS limit). The physical origin of this model may be manifold (nonuniform distribution of surface charges, or hydrophobic attraction, or other physical mechanisms), one simple realization being as due to an “extremely screened” attraction. The presence of a solvent together with a dense ionic atmosphere could induce any electrostatic interaction to vanish close to the molecular surface, and—in the idealized sticky limit—to become *truncated* exactly at contact.

For this model, we solve analytically the molecular Ornstein-Zernike (OZ) integral equation, by using a truncated *Percus-Yevick* (PY) approximation, with orientational linearization (PY-OL), since it retains only the lowest order terms in the expansions of the correlation functions in angular basis functions. This already provides a clear indication of the effects of anisotropy on the adhesive adhesion.

The idea of an anisotropic surface adhesion is not new. In a series of papers on hydrogen-bonded fluids such as water, Blum and co-workers [30–32] already studied models of spherical molecules with anisotropic pair potentials, includ-

ing both electrostatic multipolar interactions and sticky adhesive terms of multipolar symmetry. Within appropriate closures, these authors outlined the general features of the analytic solutions of the OZ equation by employing a very powerful formalism based upon expansions in rotational invariants. In particular, Blum, Cummings, and Bratko [32] obtained an analytic solution within a mixed MSA/PY closure (extended to mixtures by Protsykevich [34]) for molecules which have surface adhesion of dipolar symmetry and at most dipole-dipole interactions. From the physical point of view, our model—with “dipolarlike” adhesion resulting from the sum of an isotropic plus a dipolar term—is different and more specifically characterized with respect to the one of Ref. [32], whose adhesion has a simpler, strictly “dipolar,” symmetry. From the mathematical point of view, however, the same formalism employed by Blum *et al.* [32] could also be applied to our model. Unfortunately, the solution given in Ref. [32] is not immediately usable for the actual computation of correlation functions, since the explicit determination of the parameters involved in their analytical expressions is lacking.

In the present paper we adopt a simpler solution method, by extending the elegant approach devised by Wertheim for DHS within the MSA closure [3], and, most importantly, we aim at providing a *complete* analytic solution—including the determination of all required parameters—within our PY-OL approximation.

The paper is organized as follows. Section II defines the model. In Sec. III we recall the molecular OZ integral equation and the basic formalism. In Sec. IV we present the analytic solution. Numerical exact results for some necessary parameters, as well as very accurate analytic approximations for them, will be shown in Sec. V. Some preliminary plots illustrating the effects of the anisotropic adhesion on the local structure are reported in Sec. VI. Phase stability is briefly discussed in Sec. VII, while final remarks and conclusions are offered in Sec. VIII.

II. HARD SPHERES WITH ADHESION OF DIPOLARLIKE SYMMETRY

Let the symbol $i \equiv (\mathbf{r}_i, \Omega_i)$ (with $i=1, 2, 3, \dots$) denote both the position \mathbf{r}_i of the molecular center and the orientation Ω_i of molecule i ; for linear molecules, $\Omega_i \equiv (\theta_i, \varphi_i)$ includes the usual polar and azimuthal angles. Translational invariance for uniform fluids allows one to write the dependence of the pair correlation function $g(1, 2)$ as

$$(1, 2) = (\mathbf{r}_{12}, \Omega_1, \Omega_2) = (r, \Omega_1, \Omega_2, \hat{\mathbf{r}}_{12}) = (r, \Omega_1, \Omega_2, \Omega_r),$$

with $\mathbf{r}_{12} = \mathbf{r}_2 - \mathbf{r}_1$, $r = |\mathbf{r}_{12}|$, and Ω_r being the solid angle associated with $\hat{\mathbf{r}}_{12} = \mathbf{r}_{12}/r$.

In the spirit of Baxter’s isotropic counterpart [11,39], our model is defined by the Mayer function given by

$$f^{\text{HS}}(1, 2) = f^{\text{HS}}(r) + t\epsilon(1, 2)\sigma\delta(r - \sigma), \quad (1)$$

where $f^{\text{HS}}(r) = \Theta(r - \sigma) - 1$ is its HS counterpart, Θ is the Heaviside step function [$\Theta(x < 0) = 0$, $\Theta(x > 0) = 1$] and $\delta(r - \sigma)$ is the Dirac delta function, which ensures that the adhesive interaction occurs only at contact (σ being the hard

FLUIDS OF SPHERICAL MOLECULES WITH...

PHYSICAL REVIEW E 78, 021201 (2008)

sphere diameter). An appropriate limit of the following particular square-well potential of width $R - \sigma$,

$$\Phi^{\text{SW}}(1,2) = \begin{cases} +\infty, & 0 < r < \sigma \\ -k_B T \ln \left[1 + t \epsilon(1,2) \frac{\sigma}{R - \sigma} \right], & \sigma < r < R \\ 0, & r > R, \end{cases}$$

can be shown to lead to Eq. (1).

The angular dependence is buried in the angular factor

$$\epsilon(1,2) = 1 + \alpha D(1,2), \quad (2)$$

including the dipolar function

$$D(1,2) = D(\Omega_1, \Omega_2, \Omega_r) = 3(\mathbf{u}_1 \cdot \hat{\mathbf{r}})(\mathbf{u}_2 \cdot \hat{\mathbf{r}}) - \mathbf{u}_1 \cdot \mathbf{u}_2,$$

which stems from the dipole-dipole potential $\phi^{\text{dip-dip}}(1,2) = -\mu^2 D(1,2)/r^3$ (μ is the magnitude of the dipole moment) and is multiplied by the tunable *anisotropy parameter* α . In the isotropic case $\alpha=0$, one has $\epsilon(1,2)=1$. Here and in the following, $\hat{\mathbf{r}}$ coincides with $\hat{\mathbf{r}}_{12} = -\hat{\mathbf{r}}_{21}$, while \mathbf{u}_i is the versor attached to molecule i (drawn as the yellow arrow in Fig. 1), which completely determines its orientation Ω_i . Note the symmetry $D(2,1)=D(1,2)$.

The condition $\epsilon(1,2) \geq 0$ must be enforced in order to preserve a correct definition of the sticky limit, ensuring that the total sticky interaction remains attractive for all orientations, and the range of variability $-2 \leq D(1,2) \leq 2$ yields the limitation $0 \leq \alpha \leq \frac{1}{2}$ on the anisotropy degree. The stickiness parameter t —equal to $(12\tau)^{-1}$ in Baxter's original notation [11]—measures the strength of surface adhesion relative to the thermal energy $k_B T$ (k_B being the Boltzmann constant, T being the absolute temperature) and increases with decreasing temperature.

If we adopt an “intermolecular reference frame” (with both polar axis and Cartesian z axis taken along \mathbf{r}_{12}), then the Cartesian components of $\hat{\mathbf{r}}$ and \mathbf{u}_i are $(0, 0, 1)$ and $(\sin \theta_i \cos \varphi_i, \sin \theta_i \sin \varphi_i, \cos \theta_i)$, respectively, and thus

$$D(1,2) = 2 \cos \theta_1 \cos \theta_2 - \sin \theta_1 \sin \theta_2 \cos(\varphi_1 - \varphi_2). \quad (3)$$

The strength of adhesion between two particles 1 and 2 at contact depends—in a continuous way—on the relative orientation of \mathbf{u}_1 and \mathbf{u}_2 as well as on the versor $\hat{\mathbf{r}}_{12}$ of the intermolecular distance. We shall call *parallel* any configuration with $\mathbf{u}_1 \cdot \mathbf{u}_2 = 1$, while *antiparallel* configurations are those with $\mathbf{u}_1 \cdot \mathbf{u}_2 = -1$ (see Fig. 1). For all configurations with $D(1,2) > 0$, the anisotropic part of adhesion is attractive and adds to the isotropic one. Thus, the surface adhesion is maximum, and larger than in the isotropic case, when $\mathbf{u}_1 = \mathbf{u}_2 = \hat{\mathbf{r}}_{12}$ and thus $\epsilon(1,2) = 1 + 2\alpha$ [head-to-tail parallel configuration, shown in Fig. 1(b)]. On the contrary, when $D(1,2) < 0$ the anisotropic contribution is repulsive and subtracts from the isotropic one, so that the total sticky interaction still remains attractive. Then, the stickiness is minimum, and may even vanish for $\alpha = 1/2$, when $\mathbf{u}_1 = -\mathbf{u}_2 = \hat{\mathbf{r}}_{12}$ and thus $\epsilon(1,2) = 1 - 2\alpha$ [head-to-head or tail-to-tail antiparallel configurations, reported in Fig. 1(c)]. The intermediate case of *orthogonal* configuration (\mathbf{u}_2 perpendicular to \mathbf{u}_1) corresponds to $D(1,2) = 0$, which is equivalent to the isotropic SHS interaction.

TABLE I. Angular convolutions of the basis functions 1, Δ , and D_k .

	1	Δ	D_k
1	1	0	0
Δ	0	$\Delta/3$	$D_k/3$
D_k	0	$D_k/3$	$(D_k + 2\Delta)/3$

It proves convenient to “split” $f^{\text{SHS}}(1,2)$ as

$$f^{\text{SHS}}(1,2) = f_0(r) + f_{\text{ex}}(1,2), \quad (4)$$

$$f_0(r) = f^{\text{HS}}(r) + t\sigma\delta(r - \sigma) \equiv f^{\text{iso-SHS}}(r),$$

$$f_{\text{ex}}(1,2) = (\alpha t)\sigma\delta(r - \sigma)D(1,2), \quad (5)$$

where the spherically symmetric $f_0(r)$ corresponds to the “reference” system with isotropic background adhesion, while $f_{\text{ex}}(1,2)$ is the orientation-dependent “excess” term.

We remark that, as shown in Ref. [1] (see also Table I in Appendix A of the present paper), convolutions of f^{SHS} functions generate correlation functions with a more complex angular dependence. Therefore, in addition to $D(1,2)$, it is necessary to consider also

$$\Delta(1,2) = \mathbf{u}_1 \cdot \mathbf{u}_2 = \cos \theta_1 \cos \theta_2 + \sin \theta_1 \sin \theta_2 \cos(\varphi_1 - \varphi_2), \quad (6)$$

where the last equality holds true in the intermolecular frame. The limits of variation for $\Delta(1,2)$ are clearly $-1 \leq \Delta(1,2) \leq 1$.

III. BASIC FORMALISM

This section, complemented by Appendix A, presents the main steps of Wertheim's formalism, as well as its extension to our model.

A. Molecular Ornstein-Zernike equation

The molecular OZ integral equation for a pure and homogeneous fluid of molecules interacting via nonspherical pair potentials is

$$h(1,2) = c(1,2) + \rho \int d\mathbf{r}_3 \langle c(1,3)h(3,2) \rangle_{\Omega_3}, \quad (7)$$

where $h(1,2)$ and $c(1,2)$ are the total and direct correlation functions, respectively, ρ is the number density, and $g(1,2) = 1 + h(1,2)$ is the pair distribution function [36–38]. Moreover, the angular brackets with subscript Ω denote an average over the orientations, i.e., $\langle \dots \rangle_{\Omega} = (4\pi)^{-1} \int d\Omega \dots$

The presence of convolution makes this equation convenient to Fourier transform (FT), by integrating with respect to the space variable \mathbf{r} alone, according to

$$\hat{F}(\mathbf{k}, \Omega_1, \Omega_2) = \int d\mathbf{r} F(\mathbf{r}, \Omega_1, \Omega_2) \exp(i\mathbf{k} \cdot \mathbf{r}). \quad (8)$$

The \mathbf{r} -space convolution becomes a product in \mathbf{k} space, thus leading to

GAZZILLO, FANTONI, AND GIACOMETTI

PHYSICAL REVIEW E 78, 021201 (2008)

$$\hat{h}(\mathbf{k}, \Omega_1, \Omega_2) = \hat{c}(\mathbf{k}, \Omega_1, \Omega_2) + \rho \langle \hat{c}(\mathbf{k}, \Omega_1, \Omega_3) \hat{h}(\mathbf{k}, \Omega_3, \Omega_2) \rangle_{\Omega_3}, \quad (9)$$

As usual the OZ equation involves two unknown functions h and c , and can be solved only after adding a closure, that is, a second (approximate) relationship among c , h , and the potential.

B. Splitting of the OZ equation: Reference and excess part

The particular form of our potential, as defined by the Mayer function of Eq. (1), gives rise to a remarkable exact splitting of the original OZ equation. Using diagrammatic methods [36–38] it is easy to see that both c and h can be expressed as a graphical series containing the Mayer function f as a *bond function*. If $f^{\text{SHS}} = f_0 + f_{\text{ex}}$ is substituted into all graphs of the above series, each diagram with n f -bonds will generate 2^n new graphs. In the cluster expansion of c , the sum of all graphs having only f_0 -bonds will yield $c_0(r) = c^{\text{iso-SHS}}(r)$, i.e., the direct correlation function (DCF) of the reference fluid with isotropic adhesion. On the other hand, all remaining diagrams have at least one f_{ex} -bond, whose expression is given by Eq. (5). Thus, in the sum of this second subset of graphs it is possible to factorize αt , and we can write

$$c^{\text{SHS}}(1,2) = c_0(r) + c_{\text{ex}}(1,2), \quad (10)$$

$$c_0(r) = c^{\text{iso-SHS}}(r),$$

$$c_{\text{ex}}(1,2) = (\alpha t) c^{\ddagger}(1,2). \quad (11)$$

Similarly, for h we get

$$h^{\text{SHS}}(1,2) = h_0(r) + h_{\text{ex}}(1,2), \quad (12)$$

$$h_0(r) = h^{\text{iso-SHS}}(r),$$

$$h_{\text{ex}}(1,2) = (\alpha t) h^{\ddagger}(1,2). \quad (13)$$

Note that this useful separation into reference and excess parts may also be extended to other correlation functions, such as $\gamma(1,2) \equiv h(1,2) - c(1,2)$, $g(1,2) = 1 + h(1,2)$, and the “cavity” function $y(1,2) = g(1,2)/e(1,2)$. The function γ coincides with the OZ convolution integral, without singular δ terms. Similarly, y is also “regular,” and its exact expression reads $y(1,2) = \exp[\gamma(1,2) + B(1,2)]$, where the “bridge” function B is defined by a complicated cluster expansion [36–38].

From Eqs. (10)–(13), which are merely a consequence of the particular form of f_{ex} in the splitting of f^{SHS} , one immediately sees that, if the anisotropy degree α tends to zero, then

$$\lim_{\alpha \rightarrow 0} c_{\text{ex}}(1,2) = \lim_{\alpha \rightarrow 0} h_{\text{ex}}(1,2) = \lim_{\alpha \rightarrow 0} y_{\text{ex}}(1,2) = 0. \quad (14)$$

Note that the spherically symmetric parts c_0 and h_0 must be related through the OZ equation for the reference fluid with isotropic adhesion (reference OZ equation)

$$h_0(r) = c_0(r) + \rho \int d\mathbf{r}_3 c_0(r_{13}) h_0(r_{32}). \quad (15)$$

Thus, substituting c and h of Eq. (7) with $c_0 + c_{\text{ex}}$ and $h_0 + h_{\text{ex}}$, respectively, and subtracting Eq. (15), we find that c_{ex} and h_{ex} must obey the following relation:

$$h_{\text{ex}}(1,2) = c_{\text{ex}}(1,2) + \rho \int d\mathbf{r}_3 [c_0(r_{13}) \langle h_{\text{ex}}(3,2) \rangle_{\Omega_3} + \langle c_{\text{ex}}(1,3) \rangle_{\Omega_3} h_0(r_{32}) + \langle c_{\text{ex}}(1,3) h_{\text{ex}}(3,2) \rangle_{\Omega_3}],$$

and when

$$\langle c_{\text{ex}}(1,3) \rangle_{\Omega_3} = \langle h_{\text{ex}}(3,2) \rangle_{\Omega_3} = 0, \quad (16)$$

the orientation-dependent excess parts c_{ex} and h_{ex} satisfy the equality

$$h_{\text{ex}}(1,2) = c_{\text{ex}}(1,2) + \rho \int d\mathbf{r}_3 \langle c_{\text{ex}}(1,3) h_{\text{ex}}(3,2) \rangle_{\Omega_3}, \quad (17)$$

which is decoupled from that of the reference fluid and may be regarded as an OZ equation for the excess part (excess OZ equation). As we shall see, condition (16) is satisfied in our scheme.

We stress that, in principle, the closures for Eqs. (15) and (17), respectively, might be different. In addition, although the two OZ equations are decoupled, a suitably selected closure might establish a relationship between F_0 and $F(F = c, h)$.

C. Percus-Yevick closure with orientational linearization

For hard-core fluids, h and c inside the core are given by

$$h(1,2) = -1 \quad \text{for } 0 < r < \sigma,$$

$$c(1,2) = -[1 + \gamma(1,2)] \quad \text{for } 0 < r < \sigma. \quad (18)$$

At the same time, we have the following *exact* relations:

$$h(1,2) = g(1,2) - 1 = e(1,2)y(1,2) - 1,$$

$$c(1,2) = f(1,2)[1 + \gamma(1,2)] + e(1,2)[y(1,2) - 1 - \gamma(1,2)].$$

Since c , h , and g are discontinuous for hard-core fluids and involve δ terms for sticky particles, it is more convenient to define closures in terms of y and γ , which are still continuous and without δ singularities. The Percus-Yevick approximation for molecular fluids with orientation-dependent interactions corresponds to assuming

$$y^{\text{PY}}(1,2) = 1 + \gamma(1,2) \quad \text{everywhere}, \quad (19)$$

and thus, for the DCF,

$$c^{\text{PY}}(1,2) = f(1,2)[1 + \gamma(1,2)], \quad (20)$$

which implies that c vanishes beyond the range of the potential.

However, the dependence of $\gamma(1,2)$ on angles may still be very complex. A possible procedure is to perform a series expansion of all correlation functions in terms of an *infinite*

FLUIDS OF SPHERICAL MOLECULES WITH...

PHYSICAL REVIEW E 78, 021201 (2008)

set of *rotational invariants*, which are angular basis functions—related to the spherical harmonics—having the property of rotational invariance valid for homogeneous fluids [33]. Unfortunately, the full PY approximation requires an infinite number of expansion coefficients for both $c(1,2)$ and $h(1,2)$. This approach is usually impracticable, but sometimes even unnecessary, as it is possible that the most significant angular basis functions are included in a small closed subset of that infinite set. Indeed this happens, for instance, in the DHS model within the MSA [3], where the set $\{1, \Delta, D\}$ is the required subset. Although this does not happen in our model, we shall argue that the same truncation is sufficient due to the dipolar symmetry of the anisotropic adhesion.

Indeed, a natural assumption is that the only nonzero harmonics in $c(1,2)$ and $h(1,2)$ are those contained in $f(1,2)$ and those which can be obtained from that set by convolution [30]. Now, the angular basis functions included in our f bond are only 1 and D , but the convolution of two f bonds involves the angular average of two D 's, which yields [3]

$$\begin{aligned} &\langle D(\mathbf{k}, \Omega_1, \Omega_3) D(\mathbf{k}, \Omega_3, \Omega_2) \rangle_{\Omega_3} \\ &= \frac{1}{3} [D(\mathbf{k}, \Omega_1, \Omega_2) + 2\Delta(\mathbf{k}, \Omega_1, \Omega_2)] \end{aligned}$$

in \mathbf{k} space, and thus generates also Δ . Consequently, we will expand any angle-dependent correlation function F as

$$F(1,2) = F_0(r) + F_\Delta(r)\Delta(1,2) + F_D(r)D(1,2) + \dots, \quad (21)$$

neglecting all higher-order terms. In other words, we assume that all angular series expansions can be *truncated* after these first three terms, *linear* with respect to the angular basis functions. Using this spirit in the PY approximation, given by Eq. (20), we obtain the following PY correlation functions with *orientational linearization* (OL):

$$\begin{aligned} c^{\text{PY-OL}}(1,2) &= c_0(r) + c_\Delta(r)\Delta(1,2) + c_D(r)D(1,2) \\ &= c_0(r) + (\alpha t) [c_\Delta^\dagger(r)\Delta(1,2) + c_D^\dagger(r)D(1,2)], \end{aligned} \quad (22)$$

and

$$\begin{aligned} h^{\text{PY-OL}}(1,2) &= h_0(r) + h_\Delta(r)\Delta(1,2) + h_D(r)D(1,2) \\ &= h_0(r) + (\alpha t) [h_\Delta^\dagger(r)\Delta(1,2) + h_D^\dagger(r)D(1,2)], \end{aligned} \quad (23)$$

where

$$\left. \begin{aligned} c_0(r) &= \Lambda_0 \sigma \delta(r - \sigma) \\ c_\Delta(r) &= \Lambda_\Delta \sigma \delta(r - \sigma) \\ c_D(r) &= \Lambda_D \sigma \delta(r - \sigma) \end{aligned} \right\} \text{ for } r \geq \sigma, \quad (24)$$

with

$$\begin{aligned} \Lambda_0 &= y_0^{\text{PY}}(\sigma)t, \\ \Lambda_\Delta &= y_\Delta^{\text{PY}}(\sigma)t, \end{aligned}$$

$$\Lambda_D = [y_D^{\text{PY}}(\sigma) + \alpha y_0^{\text{PY}}(\sigma)], \quad t = y_D^{\text{PY}}(\sigma)t + \alpha \Lambda_0, \quad (25)$$

$$y_0^{\text{PY}}(r) = 1 + \gamma_0(r),$$

$$y_\Delta^{\text{PY}}(r) = \gamma_\Delta(r) = (\alpha t) y_\Delta^\dagger(r),$$

$$y_D^{\text{PY}}(r) = \gamma_D(r) = (\alpha t) y_D^\dagger(r). \quad (26)$$

Clearly for $f(1,2)$ no truncation is required, as the expansion

$$f_0(r) = f^{\text{iso-SHS}}(r) = f^{\text{HS}}(r) + t\sigma\delta(r - \sigma),$$

$$f_\Delta(r) = 0,$$

$$f_D(r) = (\alpha t)\sigma\delta(r - \sigma) \quad (27)$$

is exact. It can be shown that $c(1,2)$ and $h(1,2)$ must have the same approximate form in view of the OZ equation, Eq. (7).

The solution of the original OZ equation (7) is then equivalent to the calculation of the radial coefficients $c_0(r)$, $c_\Delta(r)$, $c_D(r)$ and $h_0(r)$, $h_\Delta(r)$, $h_D(r)$, which are the projections of $c(1,2)$ and $h(1,2)$ onto the angular basis $\{1, \Delta, D\}$. The *core condition* on h , Eq. (18), becomes

$$\left. \begin{aligned} h_0(r) &= -1 \\ h_\Delta(r) &= 0 \\ h_D(r) &= 0 \end{aligned} \right\} \text{ for } 0 < r < \sigma. \quad (28)$$

Note that in the zero density limit $\gamma(1,2) = \rho \int d\mathbf{r}_3 \langle c(1,3)h(3,2) \rangle_{\Omega_3}$ must vanish, and thus $y^{\text{PY}}(1,2) \rightarrow 1$, i.e.,

$$\lim_{\rho \rightarrow 0} y_0^{\text{PY}}(r) = 1, \quad \lim_{\rho \rightarrow 0} y_\Delta^{\text{PY}}(r) = \lim_{\rho \rightarrow 0} y_D^{\text{PY}}(r) = 0,$$

while both $c(1,2)$ and $h(1,2)$ must reduce to $f(1,2)$ as follows:

$$\lim_{\rho \rightarrow 0} F_0(r) = f_0(r),$$

$$\lim_{\rho \rightarrow 0} F_\Delta(r) = 0$$

$$\lim_{\rho \rightarrow 0} F_D(r) = f_D(r) \quad (F = c, h),$$

and

$$\lim_{\rho \rightarrow 0} \Lambda_0 = t, \quad \lim_{\rho \rightarrow 0} \Lambda_\Delta = 0, \quad \lim_{\rho \rightarrow 0} \Lambda_D = \alpha t. \quad (29)$$

Moreover, as $\alpha \rightarrow 0$ all Δ and D coefficients of c , h , and y vanish, so that the isotropic adhesion case is recovered. Finally, it is also worth stressing that the *same* δ term arises in c , h , and g , that is,

$$F(1,2) = F_{\text{reg}}(1,2) + F_{\text{sing}}(1,2) \quad (F = c, h, g),$$

where F_{reg} is the “regular” part (i.e., the part with no δ singularity, and—at most—some step discontinuities), while $F_{\text{sing}}(1,2) = \sigma\delta(r - \sigma)\Lambda(1,2)$ is the singular term representing the anisotropic surface adhesion [with $\Lambda(1,2) = \Lambda_0 + \Lambda_\Delta\Delta(1,2) + \Lambda_D D(1,2)$].

D. Integral equations for the projections of c and h

In the following, we extend Wertheim theory [3] to our model, in order to obtain the radial projections of c and h . The PY-OL approximation to the excess anisotropic part of the correlation functions is

$$c_{\text{ex}}^{\text{PY-OL}}(1,2) = c_{\Delta}(r)\Delta(1,2) + c_D(r)D(1,2),$$

$$h_{\text{ex}}^{\text{PY-OL}}(1,2) = h_{\Delta}(r)\Delta(1,2) + h_D(r)D(1,2), \quad (30)$$

thus verifying the required property $\langle c_{\text{ex}}(1,3) \rangle_{\Omega_3} = \langle h_{\text{ex}}(3,2) \rangle_{\Omega_3} = 0$ described in Sec. III, and allowing the splitting of the molecular OZ equation into a reference and an excess part.

The first part is the reference PY equation, and coincides with that solved by Baxter for the fluid with isotropic adhesion [11,12] as follows:

$$\begin{aligned} h_0(r) &= c_0(r) + \rho(h_0 \star c_0) \\ h_0(r) &= -1, \quad 0 < r < \sigma \\ c_0(r) &= \Lambda_0 \sigma \delta(r - \sigma), \quad r \geq \sigma, \end{aligned} \quad (31)$$

where the symbol \star denotes spatial convolution, i.e., $(A \star B)(r_{12}) = \int A(r_{13})B(r_{32})d\mathbf{r}_3$.

The second part is the excess PY-OL equation, given by Eq. (17) coupled with the PY-OL closure. Following an extension of Wertheim's approach, as described in detail in Appendix A, Eq. (17) can be split into the following system for the Δ and D projections of c and h :

$$\begin{aligned} h_{\Delta}(r) &= c_{\Delta}(r) + \frac{1}{3}\rho(c_{\Delta} \star h_{\Delta} + 2c_D^0 \star h_D^0), \\ h_D^0(r) &= c_D^0(r) + \frac{1}{3}\rho(c_{\Delta} \star h_D^0 + c_D^0 \star h_{\Delta} + c_D^0 \star h_D^0), \end{aligned} \quad (32)$$

where $c_D^0(r)$ and $h_D^0(r)$ are defined by the relationship

$$F_D^0(r) = F_D(r) - 3 \int_r^{\infty} \frac{F_D(x)}{x} dx \quad (F = c, h), \quad (33)$$

whose inverse is [3]

$$F_D(r) = F_D^0(r) - \frac{3}{r^3} \int_0^r F_D^0(x)x^2 dx. \quad (34)$$

The core conditions become

$$\left. \begin{aligned} h_{\Delta}(r) &= 0 \\ h_D^0(r) &= -3K \end{aligned} \right\} \text{for } 0 < r < \sigma, \quad (35)$$

with

$$K = \int_{\sigma^-}^{\infty} \frac{h_D(x)}{x} dx = K_{\text{reg}} + \Lambda_D, \quad (36)$$

$$K_{\text{reg}} = \int_{\sigma}^{\infty} \frac{h_{D,\text{reg}}(r)}{r} dr. \quad (37)$$

Note that the presence of the δ singularity in $h_D(x)$ requires the specification of σ^- as the lower integration limit, unlike the case of Ref. [1] where only the regular part K_{reg} is present. Moreover, since $h_D(r) = \alpha h_D^{\dagger}(r)$, from Eq. (36) one could also write

$$K = \alpha t \mathcal{K}, \quad (38)$$

which shows that K is related to the anisotropy degree, and vanishes both in the symmetric adhesion case ($\alpha=0$) and in the HS limit ($t=0$). Since $h_D(r) \rightarrow f_D(r) = (\alpha t)\sigma\delta(r-\sigma)$ in the zero density limit, one then finds that

$$\lim_{\eta \rightarrow 0} K = \alpha t. \quad (39)$$

Finally, the PY-OL closure for the new DCFs reads

$$\left. \begin{aligned} c_{\Delta}(r) &= \Lambda_{\Delta} \sigma \delta(r - \sigma) \\ c_D^0(r) &= \Lambda_D \sigma \delta(r - \sigma) \end{aligned} \right\} r \geq \sigma \quad (40)$$

(for simplicity, here and in the following we omit the superscript PY-OL).

E. Decoupling of the integral equations

It is possible to *decouple* the two equations for Δ and D coefficients by introducing two new unknown functions which are linear combinations of the previous ones. As shown in Appendix A, if we define $F_1(r)$ and $F_2(r)$ ($F = c, h$) through the relations

$$F_1(r) = (3\mathcal{L}_1)^{-1}[F_{\Delta}(r) - F_D^0(r)],$$

$$F_2(r) = (3\mathcal{L}_2)^{-1}[F_{\Delta}(r) + 2F_D^0(r)] \quad (F = c, h),$$

then we get the OZ equations

$$h_1(r) = c_1(r) + \rho_1(h_1 \star c_1),$$

$$h_2(r) = c_2(r) + \rho_2(h_2 \star c_2),$$

with the following densities and core conditions:

$$\rho_1 = \mathcal{L}_1 \rho,$$

$$\rho_2 = \mathcal{L}_2 \rho,$$

$$\left. \begin{aligned} h_1(r) &= K/\mathcal{L}_1, \\ h_2(r) &= -2K/\mathcal{L}_2 \end{aligned} \right\} \text{for } 0 < r < \sigma.$$

The decoupling of the three different projections of c and h is remarkable: the molecular anisotropic OZ equation reduces to a set of three radial integral relations, which may be regarded as OZ equations for three "hypothetical" fluids (labeled as 0, 1, 2) with *spherically symmetric* interactions. We stress that there is not a unique solution to the decoupling problem, since—in principle—there exist infinite possible choices for $(\mathcal{L}_1, \mathcal{L}_2)$. The final results are clearly independent of the values of $(\mathcal{L}_1, \mathcal{L}_2)$.

In the present paper, we adopt Wertheim's choice, i.e., $\mathcal{L}_1 = -K$ and $\mathcal{L}_2 = 2K$, which leads to

$$F_1(r) = \frac{1}{3K}[F_D^0(r) - F_\Delta(r)]$$

$$F_2(r) = \frac{1}{3K}\left[F_D^0(r) + \frac{1}{2}F_\Delta(r)\right] \quad (F=c,h), \quad (41)$$

$$\rho_1 = -K\rho$$

$$\rho_2 = 2K\rho,$$

$$h_1(r) = -1$$

$$h_2(r) = -1 \quad \text{for } 0 < r < \sigma \quad (42)$$

(in Ref. [1], F_1 and F_2 were denoted as F_- and F_+ , respectively).

Note that the auxiliary fluids have densities different from that of the reference fluid (the negative sign of ρ_1 poses no special difficulty).

We can also write

$$F_m(r) = F_{m,\text{reg}}(r) + \Lambda_m \sigma \delta(r - \sigma), \quad (43)$$

with

$$F_{1,\text{reg}}(r) = \frac{1}{3K}[F_{D,\text{reg}}^0(r) - F_{\Delta,\text{reg}}(r)],$$

$$F_{2,\text{reg}}(r) = \frac{1}{3K}\left[F_{D,\text{reg}}^0(r) + \frac{1}{2}F_{\Delta,\text{reg}}(r)\right], \quad (44)$$

and

$$h_{D,\text{reg}}(r) = \begin{cases} 0, & 0 < r < \sigma, \\ h_{D,\text{reg}}^0(r) + 3r^{-3}\left[K_{\text{reg}}\sigma^3 - \int_\sigma^r h_{D,\text{reg}}^0(x)x^2 dx\right], & r > \sigma. \end{cases} \quad (48)$$

At $r = 2\sigma h_{D,\text{reg}}$ and $h_{D,\text{reg}}^0$ have the same discontinuity. We also get

$$h_{D,\text{reg}}(\sigma^+) = h_{D,\text{reg}}^0(\sigma^+) + 3K_{\text{reg}}. \quad (49)$$

Clearly, these results must agree with those obtained from Eq. (33), i.e.,

$$h_D^0(r) = h_D(r) - 3\psi(r),$$

$$\psi(r) \equiv \int_r^\infty h_D(x)x^{-1} dx = \Lambda_D \theta(\sigma - r) + \int_r^\infty h_{D,\text{reg}}(x)x^{-1} dx.$$

In order to recover Eq. (49) along this second route, note that $\psi(r)$ is not continuous at $r = \sigma$. In fact, from Eqs. (36) and (37) follows $\psi(\sigma^-) = K$ whereas $\psi(\sigma^+) = K_{\text{reg}}$.

$$\Lambda_1 = \frac{1}{3K}(\Lambda_D - \Lambda_\Delta)$$

$$= \frac{1}{3K}[h_{D,\text{reg}}(\sigma^+) - h_{\Delta,\text{reg}}(\sigma^+)]t + \alpha \frac{1}{3K}\Lambda_0,$$

$$\Lambda_2 = \frac{1}{3K}\left(\Lambda_D + \frac{1}{2}\Lambda_\Delta\right)$$

$$= \frac{1}{3K}\left[h_{D,\text{reg}}(\sigma^+) + \frac{1}{2}h_{\Delta,\text{reg}}(\sigma^+)\right]t + \alpha \frac{1}{3K}\Lambda_0 \quad (45)$$

(since $\gamma_{\dots}(\sigma) = h_{\dots,\text{reg}}(\sigma^+) - c_{\dots,\text{reg}}(\sigma^+)$, and $c_{\dots,\text{reg}}(\sigma^+) = 0$ within the PY-OL closure).

Knowing the correlation functions $F_1(r)$ and $F_2(r)$ (with $F=c,h$), one can derive $F_\Delta(r)$, $F_D^0(r)$, i.e.,

$$F_\Delta(r) = 2K[F_2(r) - F_1(r)],$$

$$F_D^0(r) = 2K\left[F_2(r) + \frac{1}{2}F_1(r)\right], \quad (46)$$

and

$$\Lambda_\Delta = 2K(\Lambda_2 - \Lambda_1),$$

$$\Lambda_D = K(2\Lambda_2 + \Lambda_1). \quad (47)$$

Finally, from $F_\Delta(r)$, $F_D^0(r)$ one has to evaluate $F_\Delta(r)$, $F_D(r)$, by employing Eq. (34). We note the following points:

(i) Insertion of $h_D^0(r) = h_{D,\text{reg}}^0(r) + \Lambda_D \sigma \delta(r - \sigma)$ into Eq. (34) yields $h_D(r) = h_{D,\text{reg}}(r) + \Lambda_D \sigma \delta(r - \sigma)$, with

(ii) Similarly, for $c_D(r)$ we obtain $c_D(r) = c_{D,\text{reg}}(r) + \Lambda_D \sigma \delta(r - \sigma)$, with

$$c_{D,\text{reg}}(r) = c_{D,\text{reg}}^0(r) - 3r^{-3}\left[\int_0^r c_{D,\text{reg}}^0(x)x^2 dx + \Lambda_D \sigma^3 \theta(r - \sigma)\right], \quad (50)$$

since $\int_0^r \delta(x - \sigma)x^2 dx = \sigma^2 \theta(r - \sigma)$. On the other hand, from Eq. (33) one easily finds that

$$c_D(r) = c_D^0(r) \quad \text{for } r \geq \sigma. \quad (51)$$

(iii) By applying the relationship (34) to $c_D(r)$, using Eq. (51) and noticing that $c_D(x) = 0$ for $r > \sigma$ within the PY-OL approximation, leads to a *sum rule* as follows:

GAZZILLO, FANTONI, AND GIACOMETTI

PHYSICAL REVIEW E 78, 021201 (2008)

$$\int_0^\infty c_D^0(x)x^2 dx = \int_0^\sigma c_{D,\text{reg}}^0(x)x^2 dx + \Lambda_D \sigma^3 = 0, \quad (52)$$

that we will exploit later.

IV. ANALYTIC SOLUTION

We have seen that the molecular PY-OL integral equation (IE) for our *anisotropic*-SHS model splits into three IE's,

$$\begin{aligned} h_m(r) &= c_m(r) + \rho_m(h_m \star c_m), \\ h_m(r) &= -1, \quad 0 < r < \sigma \quad (m=0,1,2), \\ c_m(r) &= \Lambda_m \sigma \delta(r-\sigma), \quad r \geq \sigma, \end{aligned} \quad (53)$$

where

$$\begin{aligned} \rho_0 &= \rho, \\ \rho_1 &= -K\rho, \\ \rho_2 &= 2K\rho, \end{aligned} \quad (54)$$

 and the “amplitudes” of the adhesive δ terms are

$$\begin{aligned} \Lambda_0 &= [1 + h_{0,\text{reg}}(\sigma^+)]t = y_0^{\text{PY}}(\sigma)t, \\ \Lambda_m &= h_{m,\text{reg}}(\sigma^+)t + \mathcal{P} = y_m^{\text{PY}}(\sigma)t + \mathcal{P} \quad (m=1,2), \end{aligned} \quad (55)$$

with

$$\mathcal{P} = \frac{1}{3} \frac{\alpha t y_0^{\text{PY}}(\sigma)}{K} + \frac{K_{\text{reg}} t}{K} = \frac{1}{3} \frac{\alpha \Lambda_0}{K} + \frac{K_{\text{reg}} t}{K}. \quad (56)$$

Here, the new expressions of Λ_1 and Λ_2 have been obtained from Eqs. (45) with the help of Eqs. (49) and (44).

The essential difference with respect to Ref. [1] lies in the closure, which is—of course—related to the model potential. While Wertheim's paper on DHS [3] employed the MSA closure, which performs properly for long-ranged electrostatic potentials at a low strength of interaction, our PY-OL closure is more appropriate for the short-ranged potential of the present model.

The first integral equation IE0 is fully independent, whereas IE1 and IE2 depend on the solution of IE0 (unlike the case of Ref. [1]), because of the presence of Λ_0 inside Λ_1 and Λ_2 . While IE0 is exactly the PY equation for the reference SHS with *isotropic* adhesion solved by Baxter [11,12], IE1 and IE2 are different from both Wertheim's MSA solution for DHS and Baxter's PY solution for SHS. We remark that the closures for IE1 and IE2 are not PY as Λ_1 and Λ_2 —given by Eq. (55)—differ, by the term \mathcal{P} , from those appropriate for the PY choice, corresponding to $\Lambda_m^{\text{PY}} = y_m^{\text{PY}}(\sigma)t$.

Consequently, IE1 and IE2 can be reckoned as belonging to a class of *generalized PY* (GPY) *approximations*, introduced in Ref. [39], which admit an analytic solution. Thus, the PY-OL closure for $c(1,2)$ leads to a PY integral equation for $c_0(r)$, coupled to two GPY integral equations for $c_1(r)$ and $c_2(r)$ [which are linear combinations of $c_\Delta(r)$ and $c_D^0(r)$].

On comparing the three IE's and their closures given by Eq. (53), it is apparent that they have exactly the same form, but differ by the density ρ_m and the expression for Λ_m . The first integral equation IE0 corresponds to an isotropic SHS fluid with density ρ . On the other hand, IE1 and IE2 refer to “auxiliary” isotropic SHS fluids with densities ρ_1 and ρ_2 , and adhesion parameters Λ_1 and Λ_2 , respectively. Note that, according to Eqs. (45), Λ_m is not evaluated at the actual density ρ_m of the auxiliary fluid, but at the real density ρ . These remarks strongly suggest that the solutions of IE0, IE1, and IE2 can be expressed in terms of a *unique* solution—the PY one for isotropic SHS—by changing only ρ_m and Λ_m . This can be achieved by the formal mapping

$$\begin{aligned} F_0(r) &= F^{\text{iso-SHS}}(r; \eta_0, \Lambda_0) \\ F_1(r) &= F^{\text{iso-SHS}}(r; \eta_1, \Lambda_1) \quad (F = q, c, h), \\ F_2(r) &= F^{\text{iso-SHS}}(r; \eta_2, \Lambda_2) \end{aligned} \quad (57)$$

where $\eta_0 = \eta$ is the *real* volume fraction, while η_1 and η_2 are “modified volume fractions” of the auxiliary fluids 1 and 2, i.e.,

$$\begin{aligned} \eta_0 &= \eta \equiv (\pi/6)\rho\sigma^3, \\ \eta_1 &= -K\eta, \\ \eta_2 &= 2K\eta. \end{aligned} \quad (58)$$

In Eqs. (57) $q(r)$ denotes the Baxter factor correlation function, introduced in the next section.

It is worth noting that this result for SHS mirrors the analog of the MSA solution for DHS [3] where all three harmonic coefficients can be expressed similarly, in terms of a single PY solution for the reference HS fluid.

A. Baxter factorization

We shall now solve Eqs. (53) by using the Wiener-Hopf factorization due to Baxter [12]. Let us recall its basic steps. After Fourier transforming the OZ equation for a one-component fluid with spherically symmetric interactions, one assumes the following factorization:

$$\begin{aligned} 1 - \rho \tilde{c}(k) &= Q(k)Q(-k), \\ Q(k) &= 1 - 2\pi\rho \int_0^\infty q(r)e^{ikr} dr. \end{aligned} \quad (59)$$

Then it can be shown that the introduction of the “factor correlation function” $q(r)$ allows the OZ equation to be cast into the form [12]

$$\begin{aligned} rc(r) &= -q'(r) + 2\pi\rho \int_0^\infty du q(u)q'(r+u), \\ rh(r) &= -q'(r) + 2\pi\rho \int_0^\infty du q(u)(r-u)h(|r-u|), \end{aligned} \quad (60)$$

where the prime denotes differentiation with respect to r . Solving these Baxter equations is tantamount to

FLUIDS OF SPHERICAL MOLECULES WITH...

PHYSICAL REVIEW E 78, 021201 (2008)

determining—within a chosen closure—the function $q(r)$, from which $c(r)$ and $h(r)$ can be easily calculated. It is also necessary to remember that, for *all* closures leading to $c(r) = 0$ for $r > \sigma$, one finds $q(r) = 0$ for $r > \sigma$ [39].

On applying Baxter's factorization to Eqs. (53), we get

$$rh_m(r) = -q'_m(r) + 2\pi\rho_m \int_0^\sigma du q_m(u)(r-u)h_m(r-u). \quad (61)$$

with $m=0,1,2$. Now the closure $c_m(r) = \Lambda_m \sigma \delta(r-\sigma)$ for $r \geq \sigma$ implies that the same δ term must appear in $h_m(r)$. Thus, for $0 \leq r \leq \sigma$, using $h_m(r) = -1 + \Lambda_m \sigma \delta(r-\sigma)$, we find

$$q'_m(r) = a_m r + b_m \sigma - \Lambda_m \sigma^2 \delta(r-\sigma),$$

with

$$\begin{aligned} a_m &= 1 - 2\pi\rho_m \int_0^\sigma du q_m(u), \\ b_m \sigma &= 2\pi\rho_m \int_0^\sigma du q_m(u)u. \end{aligned} \quad (62)$$

The δ term of $q'_m(r)$ means that $q_m(r)$ has a discontinuity $q_m(\sigma^+) - q_m(\sigma^-) = -\Lambda_m \sigma^2$, with $q_m(\sigma^+) = 0$. Integrating $q'_m(r)$, substituting this result into Eqs. (62), and solving the corresponding algebraic system, we find the following solution:

$$q_m(r) = \begin{cases} \frac{1}{2} a_m (r-\sigma)^2 + (a_m + b_m) \sigma (r-\sigma) + \Lambda_m \sigma^2, & 0 \leq r \leq \sigma \\ 0 & \text{otherwise,} \end{cases} \quad (63)$$

$$a_m = a^{\text{HS}}(\eta_m) - \frac{12\eta_m \Lambda_m}{1-\eta_m}, \quad (64)$$

$$b_m = b^{\text{HS}}(\eta_m) + \frac{6\eta_m \Lambda_m}{1-\eta_m}, \quad (65)$$

$$\eta_m = (\pi/6)\rho_m \sigma^3, \quad (66)$$

$$a^{\text{HS}}(x) = \frac{1+2x}{(1-x)^2}, \quad b^{\text{HS}}(x) = -\frac{3x}{2(1-x)^2}. \quad (67)$$

From the first of Eqs. (60) we get the DCFs $c_m(r) = c_{m,\text{reg}}(r) + \Lambda_m \sigma \delta(r-\sigma)$, where $c_{m,\text{reg}}(r) = 0$ for $r \geq \sigma$, and for $0 < r < \sigma$,

$$c_{m,\text{reg}}(r) = -\frac{1}{2} \eta_m a_m^2 \left(\frac{r}{\sigma}\right)^3 + 6\eta_m [(a_m + b_m)^2 - 2a_m \Lambda_m] \left(\frac{r}{\sigma}\right) - a_m^2 - 12\eta_m \Lambda_m^2 \left(\frac{r}{\sigma}\right)^{-1}. \quad (68)$$

The second of Eqs. (60) yields the total correlation functions $h_m(r) = h_{m,\text{reg}}(r) + \Lambda_m \sigma \delta(r-\sigma)$. For $r > \sigma$, Eq. (61) becomes

$$H_{m,\text{reg}}(r) = 12\eta_m \sigma^{-3} \begin{cases} \int_0^{r-\sigma} du q_m(u) H_{m,\text{reg}}(r-u) + \int_{r-\sigma}^\sigma du q_m(u)(u-r) + \Lambda_m \sigma^2 q_m(r-\sigma), & \sigma < r < 2\sigma \\ \int_0^\sigma du q_m(u) H_{m,\text{reg}}(r-u), & r > 2\sigma, \end{cases} \quad (69)$$

where $H_m(r) \equiv r h_m(r)$. Due to the last term of Eq. (69) and the discontinuity of $q_m(r)$ at $r = \sigma$, $h_{m,\text{reg}}(r)$ has a jump of at $r = 2\sigma$ [40,41]: $h_{m,\text{reg}}(2\sigma^+) - h_{m,\text{reg}}(2\sigma^-) = -6\eta_m \Lambda_m^2$.

B. An important relationship

In Appendix B it is shown that a remarkable consequence of the sum rule (52) is the condition

$$a_2 = a_1, \quad (70)$$

which will play a significant role in the determination of the unknown parameters Λ_1 , Λ_2 , and K (see Appendix B).

C. Reference fluid coefficients

The $m=0$ case corresponds to Baxter's PY results for the reference fluid of isotropic SHS particles [11,12]. We have $q_0(r) = q^{\text{iso-SHS}}(r; \eta, \Lambda_0)$, and

GAZZILLO, FANTONI, AND GIACOMETTI

PHYSICAL REVIEW E 78, 021201 (2008)

$$c_0(r) = c^{\text{iso-SHS}}(r; \eta, \Lambda_0) = c_{\text{reg}}^{\text{iso-SHS}}(r; \eta, \Lambda_0) + \Lambda_0 \sigma \delta(r - \sigma),$$

$$h_0(r) = h^{\text{iso-SHS}}(r; \eta, \Lambda_0) = h_{\text{reg}}^{\text{iso-SHS}}(r; \eta, \Lambda_0) + \Lambda_0 \sigma \delta(r - \sigma) \quad (71)$$

(for simplicity, we omit—here and in the following—the superscript PY).

D. Δ and D coefficients

We write $q_m(r) = q^{\text{iso-SHS}}(r; \eta_m, \Lambda_m)$ with $m=1,2$. Then,

(i) For the Δ coefficients, after recalling Eq. (43) and exploiting Eqs. (47), we end up with

$$c_\Delta(r) = 2K[c_{0,\text{reg}}(r; 2K\eta, \Lambda_2) - c_{0,\text{reg}}(r; -K\eta, \Lambda_1)] + \Lambda_\Delta \sigma \delta(r - \sigma),$$

$$h_\Delta(r) = 2K[h_{0,\text{reg}}(r; 2K\eta, \Lambda_2) - h_{0,\text{reg}}(r; -K\eta, \Lambda_1)] + \Lambda_\Delta \sigma \delta(r - \sigma). \quad (72)$$

(ii) For the D coefficients, we get

$$c_D^0(r) = 2K \left[c_{0,\text{reg}}(r; 2K\eta, \Lambda_2) + \frac{1}{2} c_{0,\text{reg}}(r; -K\eta, \Lambda_1) \right] + \Lambda_D \sigma \delta(r - \sigma),$$

$$h_D^0(r) = 2K \left[h_{0,\text{reg}}(r; 2K\eta, \Lambda_2) + \frac{1}{2} h_{0,\text{reg}}(r; -K\eta, \Lambda_1) \right] + \Lambda_D \sigma \delta(r - \sigma). \quad (73)$$

Finally, from $c_D^0(r)$ and $h_D^0(r)$ we can calculate $c_D(r)$ and $h_D(r)$, as described by Eqs. (50) and (48), respectively.

In short, (a) our PY-OL solution— $\{c_0, c_\Delta, c_D\}$ and $\{h_0, h_\Delta, h_D\}$ —satisfies both the PY closures and the core conditions; (b) all coefficients contain a surface adhesive δ term; and (c) $\{h_0, h_\Delta, h_D\}$ all exhibit a step discontinuity at $r=2\sigma$.

V. EVALUATION OF THE PARAMETERS K , Λ_1 , AND Λ_2

 Λ_2

The calculation of the Baxter functions q_m 's ($m=0,1,2$) requires the evaluation of K , Λ_1 , and Λ_2 , for a given set of α , η , and t values, a task that we address next.

A. Exact expressions

Four equations are needed to find the three quantities $\Lambda_m = q_m(\sigma^-)/\sigma^2$ ($m=0,1,2$), as well as the parameter $K(\eta, t, \alpha)$. We stress that the *almost fully analytical* determination of these unknown parameters was lacking in Ref. [32] and represents an important part of the present work. Our detailed analysis is given in Appendix B, and we quote here the main results.

(i) For Λ_0 , the same PY equation found by Baxter for isotropic SHS [11,12]

$$12\eta t \Lambda_0^2 - \left(1 + \frac{12\eta}{1-\eta} t\right) \Lambda_0 + y_\sigma^{\text{HS}}(\eta) t = 0. \quad (74)$$

Only the smaller of the two real solutions (when they exist) is physically significant [11,12], and reads

$$\Lambda_0 = y_0^{\text{PY}}(\sigma) t = \frac{y_\sigma^{\text{HS}}(\eta) t}{\frac{1}{2} \left[1 + \frac{12\eta}{1-\eta} t + \sqrt{\left(1 + \frac{12\eta}{1-\eta} t\right)^2 - 48\eta y_\sigma^{\text{HS}}(\eta) t^2} \right]}. \quad (75)$$

(ii) For Λ_1 and Λ_2 , two other quadratic equations, i.e.,

$$12\eta_m t \Lambda_m^2 - \left(1 + \frac{12\eta_m}{1-\eta_m} t\right) \Lambda_m + h_\sigma^{\text{HS}}(\eta_m) t = -\mathcal{P} \quad (m=1,2). \quad (76)$$

(iii) The fourth equation is the following linear relationship between Λ_1 and Λ_2 :

$$\frac{12\eta_2 \Lambda_2}{1-\eta_2} - \frac{12\eta_1 \Lambda_1}{1-\eta_1} = \frac{\eta_2(4-\eta_2)}{(1-\eta_2)^2} - \frac{\eta_1(4-\eta_1)}{(1-\eta_1)^2}, \quad (77)$$

which stems from the condition $a_2 = a_1$.

The analysis of Appendix B gives

$$\Lambda_2(\eta_1, \eta_2, t, \alpha) = \Lambda_1(\eta_2, \eta_1, t, \alpha), \quad (78)$$

with

$$\Lambda_m = \Lambda + \Lambda_m^{\text{ex}} \quad (m=1,2), \quad (79)$$

$$\Lambda = \frac{1}{3} + \frac{1}{4} \left(\frac{\eta_1}{1-\eta_1} + \frac{\eta_2}{1-\eta_2} \right) = \frac{1}{3} + \frac{x(1+4x)}{4(1+x)(1-2x)}, \quad (80)$$

$$\Lambda_1^{\text{ex}} = \frac{\eta_2}{4(1-\eta_2)} W_0^{\text{ex}}, \quad \Lambda_2^{\text{ex}} = \frac{\eta_1}{4(1-\eta_1)} W_0^{\text{ex}}, \quad (81)$$

where we have introduced $\eta_1 = -x$, $\eta_2 = 2x$ ($x \equiv K\eta$), and W_0^{ex} is defined in Appendix B. All these quantities are analytic functions of $x=K\eta$. Thus, to complete the solution, we need an equation for K , which can be written as

$$K = \alpha t \mathcal{K}, \quad \text{with } \mathcal{K} = \frac{y_0^{\text{PY}}(\sigma)}{Z(\eta_1, \eta_2, t)}, \quad (82)$$

$$Z = \frac{3}{2}(\Lambda_1 + \Lambda_2) - 3 \left\{ \frac{1}{2} \sum_{m=1}^2 \left[12\eta_m \Lambda_m^2 - \frac{12\eta_m \Lambda_m}{1-\eta_m} + h_\sigma^{\text{HS}}(\eta_m) \right] + \frac{K_{\text{reg}}}{K} \right\} t, \quad (83)$$

and $\lim_{\eta \rightarrow 0} Z(\eta_1, \eta_2, t) = 1$. Insertion of found expressions for Λ_1 , Λ_2 , and K_{reg} (see Appendix B) into Eq. (82) yields a single equation for K that we have solved numerically, although some further analytic simplifications are probably possible. Our solution is then almost fully analytical, as only the final equation for K is left to be solved numerically.

B. Approximate expressions

For practical use we next derive very accurate analytical approximations to K , Λ_1 , and Λ_2 , which provide a useful tool

FLUIDS OF SPHERICAL MOLECULES WITH...

PHYSICAL REVIEW E 78, 021201 (2008)

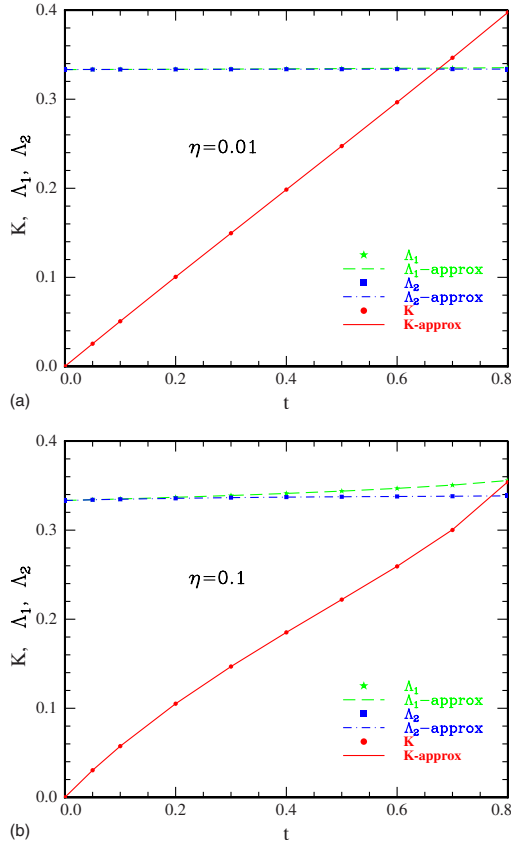


FIG. 2. (Color online) Comparison between exact numerical and approximate analytical results for the parameters K , Δ_1 , and Δ_2 as a function of t , for anisotropy degree $\alpha=1/2$ and two values of the packing fraction: $\eta=0.01$ (top panel) and $\eta=0.1$ (bottom panel).

for fully analytical calculations. Since in all cases of our interest we always find $x=K\eta \ll 1$, a series expansion leads to

$$W_0^{\text{ex}} = \frac{2}{3}(1+5x)t + \mathcal{O}(x^2), \quad (84)$$

and, consequently,

$$\Lambda_1^{\text{ex}} = \frac{x(1+5x)}{3(1-2x)}t + \mathcal{O}(x^3), \quad \Lambda_2^{\text{ex}} = -\frac{x(1+5x)}{6(1+x)}t + \mathcal{O}(x^3). \quad (85)$$

Similarly we can expand Z in Eq. (83) as

$$Z(x,t) = 1 + z_1(t)x + z_2(t)x^2 + \mathcal{O}(x^3), \quad (86)$$

with

$$z_1(t) = \frac{1}{4}(3+11t),$$

$$z_2(t) = \frac{1}{4}(15+61t-4t^2). \quad (87)$$

Insertion of this result into Eq. (82) yields a cubic equation for K ,

$$z_2(t)\eta^2 K^3 + z_1(t)\eta K^2 + K - \alpha t y_0^{\text{PY}}(\sigma) = 0,$$

which, again with the help of Eq. (82), is equivalent to a cubic equation for Z ,

$$Z^3 - Z^2 + z_1(t)[\alpha t y_0^{\text{PY}}(\sigma)\eta]Z + z_2(t)[\alpha t y_0^{\text{PY}}(\sigma)\eta]^2 = 0. \quad (88)$$

The physically acceptable solution then reads

$$Z(\eta,t) = \frac{1}{3}\left(1 + \sqrt[3]{B + \sqrt{B^2 - C^3}} + \sqrt[3]{B - \sqrt{B^2 - C^3}}\right), \quad (89)$$

where

$$B = 1 + \frac{9}{2}z_1(t)[\alpha t y_0^{\text{PY}}(\sigma)\eta] + \frac{27}{2}z_2(t)[\alpha t y_0^{\text{PY}}(\sigma)\eta]^2,$$

$$C = 1 + 3z_1(t)[\alpha t y_0^{\text{PY}}(\sigma)\eta]. \quad (90)$$

In conclusion, our approximate analytic solution for K , Δ_1 , and Δ_2 includes three simple steps: (i) calculate K by using Eqs. (82), (89), (90), and (87); (ii) evaluate $x=K\eta$; and (iii) solve for Δ_1 and Δ_2 by means of Eqs. (80) and (85).

C. Numerical comparison

In order to assess the precision of previous approximations, we have calculated K , Δ_1 , and Δ_2 by two methods: (i) solving numerically Eqs. (B8), and (ii) using our analytic approximations. After fixing $\alpha=1/2$, we have increased the adhesion strength (or decreased the temperature) from $t=0$ (HS limit) up to $t=0.8$, for some representative values of the volume fraction ($\eta=0.01, 0.1, 0.2$, and 0.4). The maximum value of t corresponds to $\tau=1/(12t) \approx 0.1$, which lies close to the critical temperature of the isotropic SHS fluid. On the other hand, $\eta=0.01$ has been chosen to illustrate the fact that, as $\eta \rightarrow 0$, the parameter K tends to αt . The linear dependence of K on t in this case is clearly visible in the top panel of Fig. 2.

In Figs. 2 and 3 the exact and approximate results for K , Δ_1 , and Δ_2 are compared. The agreement is excellent: at $\eta=0.1, 0.2$, and 0.4 , the relative error on K does not exceed 0.1%, 0.4%, and 1%, respectively, while the maximum of the absolute relative errors on Δ_1 and Δ_2 always remain less than 0.05, 0.2, and 0.6% in the three above-mentioned cases. It is worth noting that, as η increases, the variations of Δ_1 and Δ_2 are always relatively small; on the contrary, K experiences a marked change, with a progressive lowering of the relevant curve.

GAZZILLO, FANTONI, AND GIACOMETTI

PHYSICAL REVIEW E 78, 021201 (2008)

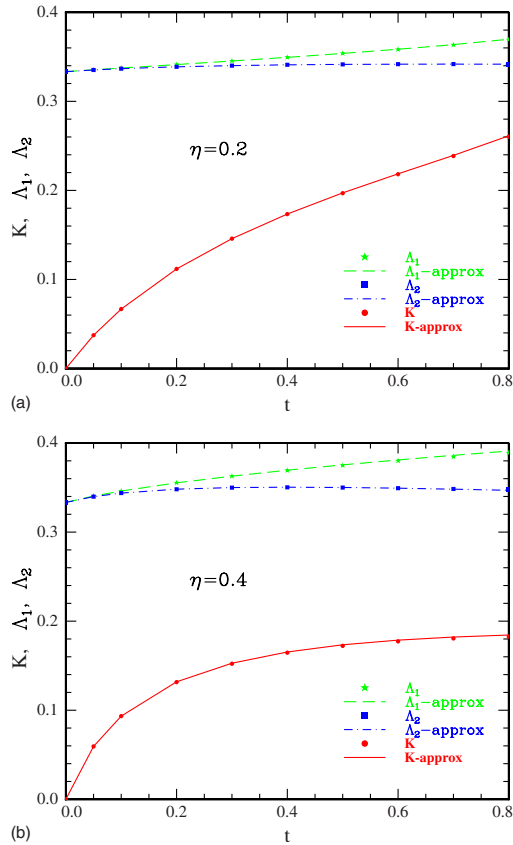


FIG. 3. (Color online) Same as in Fig. 2, but for $\eta=0.2$ (top panel) and $\eta=0.4$ (bottom panel).

VI. SOME ILLUSTRATIVE RESULTS ON THE LOCAL ORIENTATIONAL STRUCTURE

Armed with the knowledge of the analytic expression for the q_m 's a rapid numerical calculation of the three harmonic coefficients $\{h_0, h_\Delta, h_D\}$ appearing in

$$g^{\text{PY-OL}}(1,2) = 1 + h_0(r) + h_\Delta(r)\Delta(1,2) + h_D(r)D(1,2) \quad (91)$$

can be easily obtained as follows. From the second Baxter IE (60), one can generate $h(r)$ directly from $q(r)$, avoiding the passage through $c(r)$. From $\{q_0, q_1, q_2\}$ one first obtains $\{h_0, h_1, h_2\}$ by applying a slight extension of Perram's numerical method [42] and then derives $\{h_0, h_\Delta, h_D\}$, according to the above-mentioned recipes.

The main aim of the present paper was to present the necessary mathematical machinery to investigate thermophysical properties. We now illustrate the interest of the model by reporting some preliminary numerical results on the orientational dependence of $g^{\text{PY-OL}}(1,2)$ —i.e., on the lo-

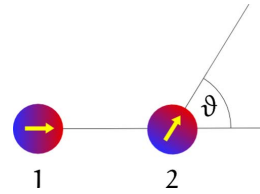


FIG. 4. (Color online) Illustration of the simple configuration discussed in the text and chosen to define some radial sections through the multidimensional plot of $g(1,2)$.

cal orientational structure—as a consequence of the anisotropic adhesion. A more detailed analysis will be reported in a forthcoming paper.

Consider the configuration depicted in Fig. 4. Let a generic particle 1 be fixed at a position \mathbf{r}_1 in the fluid with orientation \mathbf{u}_1 , and consider another particle 2 located along the straight half-line, which originates from the center of 1 and with direction \mathbf{u}_1 . This second particle has then a fixed distance r from 1, but can assume all possible orientations \mathbf{u}_2 , which—by axial symmetry—can be described by a single polar angle $\theta \equiv \theta_2$ (i.e., the angle between \mathbf{u}_1 and \mathbf{u}_2) with respect to the intermolecular reference frame. Within this geometry, we have $(\theta_1, \varphi_1) = (0, 0)$ and $\varphi_2 = 0$, obtaining $\Delta(1,2) = \cos \theta$, $D(1,2) = 2 \cos \theta$. Consequently, $g(1,2) = g(r, \theta_1, \varphi_1, \theta_2, \varphi_2)$ reduces to

$$g(r, \theta) = g_0(r) + [h_\Delta(r) + 2h_D(r)] \cos \theta, \quad (92)$$

where $\theta \equiv \theta_2$, and $g_0(r) = 1 + h_0(r)$ is the radial distribution function of the reference isotropic SHS fluid.

Clearly, $g(r, \theta)$ is proportional to the probability of finding, at a distance r from a given molecule 1, a molecule 2 having a *relative* orientation θ . We consider the three most significant values of this angle: (i) $\theta=0$, which corresponds to the “parallel” configuration of \mathbf{u}_1 and \mathbf{u}_2 ; (ii) $\theta=\pi/2$, for the “orthogonal” configuration; and (iii) $\theta=\pi$, for the two “antiparallel” (head-to-head and tail-to-tail) configurations. From Eq. (92) it follows that

$$g^{\text{par}}(r) = g(r, 0) = g_0(r) + [h_\Delta(r) + 2h_D(r)],$$

$$g^{\text{ortho}}(r) = g(r, \pi/2) = g_0(r),$$

$$g^{\text{antipar}}(r) = g(r, \pi) = g_0(r) - [h_\Delta(r) + 2h_D(r)]. \quad (93)$$

Note that $g^{\text{ortho}}(r)$ coincides with the isotropic result $g_0(r)$.

In Fig. 5 we depict the above sections through the three-dimensional surface corresponding to $g(r, \theta)$, i.e., $g^{\text{par}}(r)$, $g^{\text{ortho}}(r)$, and $g^{\text{antipar}}(r)$, for $\eta=0.3$ with $t=0.2$ and $t=0.6$, respectively, at the highest asymmetry value admissible in the present model, i.e., $\alpha=1/2$. The most significant features from these plots are (i) $g^{\text{antipar}}(\sigma^+) > g^{\text{par}}(\sigma^+)$ and (ii) for $r > 2\sigma_B^{\text{antipar}}(r) \approx g^{\text{par}}(r) \approx g_0(r)$, i.e., the anisotropic adhesion seems to affect only the first coordination layer $\sigma < r < 2\sigma$, around each particle.

The interpretation of these results is the following. In view of (i) we see that the parallel configuration is less probable than the antiparallel one at contact. Such a finding, to-

FLUIDS OF SPHERICAL MOLECULES WITH...

PHYSICAL REVIEW E 78, 021201 (2008)

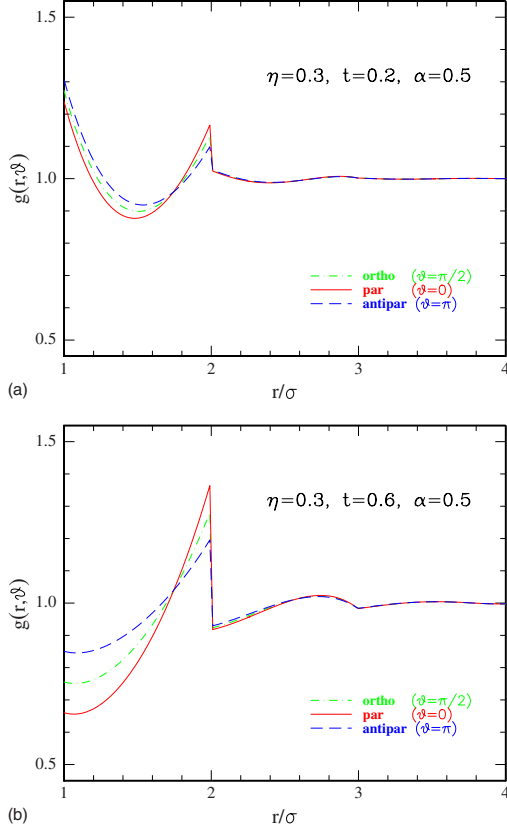


FIG. 5. (Color online) Sections through $g(1,2)$, with particles 1 and 2 in the configuration shown by the previous figure, calculated as a function of r for fixed relative orientations: $\theta=0$ (parallel configuration), $\theta=\pi/2$ (orthogonal configuration), and $\theta=\pi$ (antiparallel configurations).

gether with (ii), means that chain formation characteristic of polymerization is inhibited by the short-ranged anisotropic adhesion exploited here. This strictly contrasts with the case of long-ranged DHS fluids, where it is believed [7,8] that chaining phenomena might preempt the gas-liquid transition. This specific feature of the present model is extremely interesting and we plan a throughout investigation on this topic in a future publication.

VII. PHASE STABILITY

In view of previous findings, a very natural question is whether the addition of our anisotropic sticky term to the potential changes phase stability and phase transition curves with respect to the corresponding isotropic case. We believe the answer to be positive. This is strongly suggested by the results obtained for similar anisotropic models, such as hard

spheres with sticky points [13–21] or sticky patches [10,22–27].

We now briefly comment on this issue. Within our formalism, this problem of stability can be conveniently analyzed using standard formalism devised for this aim [44–47]. We start from the stability condition with respect to small but arbitrary fluctuations of the one-particle density $\rho(1)$ from the equilibrium configuration, denoted as “eq” [45–47],

$$\int d(1) \int d(2) \left[\frac{\delta(1,2)}{\rho(1)} - c(1,2) \right]_{\text{eq}} \delta\rho(1) \delta\rho(2) > 0. \quad (94)$$

Here $d(i)$ stands for $d\mathbf{r}_i d\Omega_i$, $i=1,2$, and we assume the equilibrium one-particle density to be $\rho/4\pi$ [45–47].

We expand the fluctuations both in Fourier modes and in spherical harmonics [44]

$$\delta\rho(j) \equiv \delta\rho(\mathbf{r}_j, \Omega_j) = \int \frac{d\mathbf{k}}{(2\pi)^3} e^{i\mathbf{k}\cdot\mathbf{r}_j} \sum_{l=0}^{+\infty} \sum_{m=-l}^{+l} \delta\tilde{\rho}(\mathbf{k}) Y_{lm}(\Omega_j). \quad (95)$$

Using the orthogonality relation [44]

$$\int d\Omega Y_{lm}^*(\Omega) Y_{l'm'}(\Omega) = \delta_{ll'} \delta_{mm'}, \quad (96)$$

standard manipulations [47] show that condition (94) can be recast into the form

$$\sum_{l_1, l_2=0}^{+\infty} \sum_{m_1=-l_1}^{+l_1} \sum_{m_2=-l_2}^{+l_2} \int \frac{d\mathbf{k}}{(2\pi)^3} \delta\tilde{\rho}_{l_1 m_1}(\mathbf{k}) \delta\tilde{\rho}_{l_2 m_2}^*(\mathbf{k}) \tilde{A}_{l_1 m_1 l_2 m_2}(\mathbf{k}) > 0, \quad (97)$$

where the matrix elements $\tilde{A}_{l_1 m_1 l_2 m_2}(\mathbf{k})$ are given by

$$\begin{aligned} \tilde{A}_{l_1 m_1 l_2 m_2}(\mathbf{k}) = & (-1)^{m_1} \frac{4\pi}{\rho} \delta_{l_1 l_2} \delta_{m_1, -m_2} \\ & - \int d\Omega_1 \int d\Omega_2 Y_{l_1 m_1}(\Omega_1) Y_{l_2 m_2}(\Omega_2) \\ & \times \int d\mathbf{r} e^{i\mathbf{k}\cdot\mathbf{r}} c(\mathbf{r}, \Omega_1, \Omega_2). \end{aligned} \quad (98)$$

The problem of the stability has been reported to the character of the eigenvalues of matrix (98). This turns out to be particularly simple in our case. Using the results (A3) it is easy to see that

$$\begin{aligned} \int d\mathbf{r} e^{i\mathbf{k}\cdot\mathbf{r}} c(\mathbf{r}, \Omega_1, \Omega_2) = & \tilde{c}_0(k) + \tilde{c}_\Delta(k) \Delta(\Omega_1, \Omega_2) \\ & + \tilde{c}_D(k) D(\Omega_1, \Omega_2, \Omega_k). \end{aligned} \quad (99)$$

Insertion of Eq. (99) into Eq. (98) leads to

GAZZILLO, FANTONI, AND GIACOMETTI

PHYSICAL REVIEW E 78, 021201 (2008)

$$\begin{aligned} \tilde{A}_{l_1 m_1 l_2 m_2}(\mathbf{k}) = & (-1)^{m_1} \frac{4\pi}{\rho} \delta_{l_1 l_2} \delta_{m_1 - m_2} - [\tilde{c}_0(k) I_{l_1 m_1 l_2 m_2}^{(0)} \\ & + \tilde{c}_\Delta(k) I_{l_1 m_1 l_2 m_2}^{(\Delta)} + \tilde{c}_D(k) I_{l_1 m_1 l_2 m_2}^{(D)}], \end{aligned} \quad (100)$$

where we have introduced the following integrals, which can be evaluated in the intermolecular frame, using standard properties of the spherical harmonics [44]:

$$\begin{aligned} I_{l_1 m_1 l_2 m_2}^{(0)} & \equiv \int d\Omega_1 \int d\Omega_2 Y_{l_1 m_1}(\Omega_1) Y_{l_2 m_2}(\Omega_2) \\ & = 4\pi \delta_{l_1 0} \delta_{l_2 0} \delta_{m_1 0} \delta_{m_2 0}, \\ I_{l_1 m_1 l_2 m_2}^{(\Delta)} & \equiv \int d\Omega_1 \int d\Omega_2 Y_{l_1 m_1}(\Omega_1) Y_{l_2 m_2}(\Omega_2) \Delta(\Omega_1, \Omega_2) \\ & = \frac{4}{3} \pi \delta_{l_1 1} \delta_{l_2 1} \delta_{m_1 0} \delta_{m_2 0}, \\ I_{l_1 m_1 l_2 m_2}^{(D)}(\cos \theta) & \equiv \int d\Omega_1 \int d\Omega_2 Y_{l_1 m_1}(\Omega_1) Y_{l_2 m_2}(\Omega_2) D(\Omega_1, \Omega_2, \Omega_k) \\ & = \frac{4}{3} \pi \delta_{l_1 1} \delta_{l_2 1} \delta_{m_1 0} \delta_{m_2 0} 2P_2(\cos \theta), \end{aligned} \quad (101)$$

and where $P_2(x) = (3x^2 - 1)/2$ is the second Legendre polynomial.

Hence, the matrix (98) is diagonal and the relevant terms are

$$\tilde{A}_{0000}(k) = 4\pi \left[\frac{1}{\rho} - \tilde{c}_0(k) \right], \quad (102)$$

whose positiveness is recognized as the isotropic stability condition, and

$$\tilde{A}_{1010}(\mathbf{k}) = 4\pi \left\{ \frac{1}{\rho} - \frac{1}{3} [\tilde{c}_\Delta(k) + 2P_2(\cos \theta) \tilde{c}_D(k)] \right\}. \quad (103)$$

All remaining diagonal terms have the form $\tilde{A}_{l_0 l_0} = 4\pi/\rho > 0$.

In order to test for possible angular instabilities, we consider the limit $k \rightarrow 0$ of Eq. (103), namely,

$$\tilde{A}_{1010}(0) = \frac{4\pi}{\rho} \left\{ 1 - \frac{\rho}{3} [\tilde{c}_\Delta(0) + 2P_2(\cos \theta) \tilde{c}_D(0)] \right\}. \quad (104)$$

This can be quickly computed with the aid of Eqs. (46) and (59), the fact that $\tilde{c}_D(0) = \tilde{c}_D^0(0)$ and the identity (70). We find

$$\tilde{A}_{1010}(0) = \frac{4\pi}{\rho} a_1^2, \quad (105)$$

which is independent of the angle θ . This value is found to be always positive as $a_1 > 0$ (see Fig. 6). Within this first-

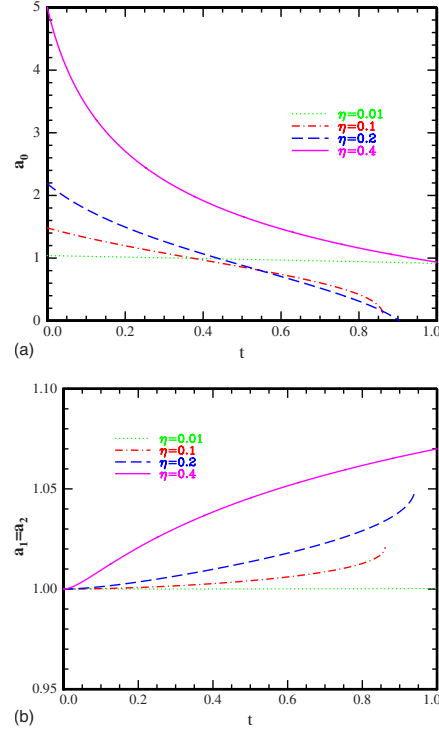


FIG. 6. (Color online) Evaluation of quantities a_0 (top panel) and $a_1 = a_2$ (bottom panel) as a function of t for various packing fractions ranging from $\eta = 0.01$ to $\eta = 0.4$. These are computed from Eq. (64) with $m = 0, 1$. Note that for both $\eta = 0.1$ and $\eta = 0.2$, $a_0 = 0$ corresponds to the onset of isotropic instability.

order approximation, therefore, the only instability in the system stems from the isotropic compressibility. The reason for this can be clearly traced back to the first-order approximation to the angular dependence of the correlation functions. If quadratic terms in Δ and D were included into the series expansion for correlation functions, the particular combination leading to a cancellation of the angular dependence in the stability matrix $\tilde{A}_{l_1 m_1 l_2 m_2}(0)$ would not occur, leading to a different result.

This fact is consistent with the more general statement that, in any approximate theory, thermodynamics usually requires a higher degree of theoretical accuracy than the one sufficient for obtaining significant structural data. Conceptually, the need for distinguishing structural results from thermodynamical ones is rather common. For instance, in statistical mechanics of liquids it is known that approximating the model potential only with its repulsive part (for instance, the hard sphere term) can account for all essential features of the structure, but yields unsatisfactory thermodynamics. On the other hand, the present paper refers to a *simplified* statistical-mechanical tool, i.e., the OZ equation within our PY-OL closure, which has been explicitly selected to allow an analyti-

cal solution. Our results, however, indicate that the first-order expansion used in the PY-OL closure can give reasonable information about structure, but not on thermodynamics, where a higher level of sophistication is required.

VIII. CONCLUDING REMARKS

In this paper we have discussed an anisotropic variation of the original Baxter model of hard spheres with surface adhesion. In addition to the HS potential, molecules of the fluid interact via an isotropic sticky attraction plus an additional anisotropic sticky correction, whose strength depends on the orientations of the particles in dipolar way. By varying the value of a parameter α , the anisotropy degree can be changed. Consequently, the strength of the total sticky potential can vary from twice the isotropic one down to the limit of no adhesion (HS limit). These particles may be regarded as having two nonuniform, hemispherical, “dipolarlike patches,” thus providing a link with uniformly adhesive patches [10,22–27].

We have obtained a full analytic solution of the molecular OZ equation, within the PY-OL approximation, by using Wertheim’s technique [3]. Our PY-OL approximation should be tested against exact computer simulations, in order to assess its reliability. Nevertheless, we may reasonably expect the results to be reliable even at experimentally significant densities, notwithstanding the truncation of the higher-order terms in the angular expansion. Only one equation, for the parameter K , has to be solved numerically. In addition, we have provided analytic approximations to K , Λ_1 , and Λ_2 so accurate that, in practice, the whole solution can really be regarded as fully analytical. From this point of view, the present paper complements the above-mentioned previous work by Blum *et al.* [32].

We have also seen that thermophysical properties require a more detailed treatment of the angular part than the PY-OL closure. Nonetheless, even within the PY-OL oversimplified framework, our findings are suggestive of a dependence of the fluid-fluid coexistence line on anisotropy.

Our analysis envisions a number of interesting perspectives, already hinted at by the preliminary numerical results reported here. It would be very interesting to compare the structural and thermodynamical properties of this model with those stemming from truly dipolar hard spheres [45–47]. The possibility of local orientational ordering can be assessed by computing the pair correlation function $g(1,2)$ for the most significant interparticle orientations. We have shown that this task can be easily performed within our scheme. This should provide important information about possible chain formation and its subtle interplay with the location of the fluid-fluid transition line. The latter bears a particular interest in view of the fact that computer simulations on DHS are notoriously difficult and their predictions regarding the location of such a transition line have proven so far inconclusive [43]. The long-range nature of DHS interactions may in fact promote polymerization preempting the usual liquid-gas transition [8]. Our preliminary results on the present model strongly suggest that this is not the case for sufficiently short-ranged interactions, thus allowing the location of such

a transition line to be studied as a function of the anisotropy degree of the model. Our sticky interactions have only attractive adhesion, the only repulsive part being that pertinent to hard spheres, whereas the DHS potential is both attractive and repulsive, depending on the orientations.

Finally, information about the structural ordering in the present model would neatly complement those obtained by us in a recent parallel study on a SHS fluid with one or two uniform circular patches [10]. Work along this line is in progress and will be reported elsewhere.

ACKNOWLEDGMENTS

We acknowledge financial support from PRIN Grant No. 2005027330. It is our pleasure to thank Giorgio Pastore and Mark Miller for enlightening discussions on the subject.

APPENDIX A: EXTENSION OF WERTHEIM’S APPROACH

The Fourier transform of the excess PY-OL equation, Eq. (17), reads

$$\begin{aligned} \hat{h}_{\text{ex}}(\mathbf{k}, \Omega_1, \Omega_2) &= \hat{c}_{\text{ex}}(\mathbf{k}, \Omega_1, \Omega_2) \\ &+ \rho \langle \hat{c}_{\text{ex}}(\mathbf{k}, \Omega_1, \Omega_3) \hat{h}_{\text{ex}}(\mathbf{k}, \Omega_3, \Omega_2) \rangle_{\Omega_3} \end{aligned} \quad (\text{A1})$$

(the superscripts have been omitted for simplicity). In order to evaluate the angular average, we first need the FT of c and h . The FT integral (8) may be rewritten as

$$\begin{aligned} &\int_0^\infty dr r^2 \int d\Omega_r \exp(i\mathbf{k} \cdot \mathbf{r}) [\dots] \\ &= \int_0^\infty dr r^2 \int_0^{2\pi} d\phi \int_{-1}^{+1} d(\cos \theta) e^{ikr \cos \theta} [\dots]. \end{aligned}$$

Let us now apply this operator to $F_{\text{ex}}(1,2)$ ($F=c, h$), expressed as

$$F_{\text{ex}}(\mathbf{r}, \Omega_1, \Omega_2) = F_\Delta(r) \Delta(\Omega_1, \Omega_2) + F_D(r) D(\Omega_1, \Omega_2, \Omega_r), \quad (\text{A2})$$

and first perform the angular integration $\int d\Omega_r$, recalling that [3]

$$\begin{aligned} &\int d\Omega_r \exp(i\mathbf{k} \cdot \mathbf{r}) 1 = 4\pi j_0(kr) 1, \\ &\int d\Omega_r \exp(i\mathbf{k} \cdot \mathbf{r}) \Delta(\Omega_1, \Omega_2) = 4\pi j_0(kr) \Delta(\Omega_1, \Omega_2), \\ &\int d\Omega_r \exp(i\mathbf{k} \cdot \mathbf{r}) D(\Omega_1, \Omega_2, \Omega_r) = -4\pi j_2(kr) D(\Omega_1, \Omega_2, \Omega_k), \end{aligned} \quad (\text{A3})$$

where $j_0(x) = x^{-1} \sin x$ and $j_2(x) = 3x^{-3} \sin x - 3x^{-2} \cos x - j_0(x)$ are Bessel functions, and

GAZZILLO, FANTONI, AND GIACOMETTI

PHYSICAL REVIEW E 78, 021201 (2008)

$$D(\Omega_1, \Omega_2, \Omega_k) = 3(\mathbf{u}_1 \cdot \hat{\mathbf{k}})(\mathbf{u}_2 \cdot \hat{\mathbf{k}}) - \mathbf{u}_1 \cdot \mathbf{u}_2 \equiv D_k(1, 2),$$

 with $\hat{\mathbf{k}} = \mathbf{k}/k$. We get

$$\hat{F}_{\text{ex}}(\mathbf{k}, \Omega_1, \Omega_2) = \tilde{F}_\Delta(k)\Delta(\Omega_1, \Omega_2) + \tilde{F}_D(k)D(\Omega_1, \Omega_2, \Omega_k),$$

where $\tilde{F}_\Delta(k)$ is the usual FT of the spherically symmetric function $F_\Delta(r)$: $\tilde{F}_\Delta(k) = 4\pi \int_0^\infty dx x^2 j_0(kx) F_\Delta(x)$. On the other hand, $\tilde{F}_D(k) = -4\pi \int_0^\infty dx x^2 j_2(kx) F_D(x)$, which is the Hankel transform of $F_D(r)$, may conveniently be considered as the FT of a “modified” function $F_D^0(r)$, i.e., $\tilde{F}_D(k) = \tilde{F}_D^0(k)$. Taking the inverse FT of $\tilde{F}_D^0(k)$ yields

$$F_D^0(r) = \frac{1}{2\pi^2} \int_0^\infty dk k^2 j_0(kr) \tilde{F}_D^0(k) = F_D(r) - 3 \int_r^\infty \frac{F_D(x)}{x} dx, \quad (\text{A4})$$

with the help of the identity

$$\int_0^\infty dk k^2 j_0(kr) j_2(kx) = \frac{\pi}{2} \left[\frac{3\theta(x-r)}{x^3} - \frac{\delta(x-r)}{x^2} \right].$$

 In conclusion, the FT of $F_{\text{ex}}(1, 2)$ reads

$$\hat{F}_{\text{ex}}(\mathbf{k}, \Omega_1, \Omega_2) = \tilde{F}_\Delta(k)\Delta(\Omega_1, \Omega_2) + \tilde{F}_D^0(k)D(\Omega_1, \Omega_2, \Omega_k), \quad (\text{A5})$$

 with F standing for h or c .

 Let us now define the *angular convolution* of two functions as

$$A \circ B = B \circ A \equiv \langle A(\Omega_1, \Omega_3) B(\Omega_3, \Omega_2) \rangle_{\Omega_3}.$$

Wertheim [3] demonstrated that the rotational invariants 1, Δ , and D form a closed group under angular convolution; that is, the angular convolution of any two members of this set yields only a function in the same set, or zero, according to Table I.

Substituting the expressions for \hat{c}_{ex} and \hat{h}_{ex} given by Eq. (A5) into the angular average $\hat{c}_{\text{ex}} \circ \hat{h}_{\text{ex}} = \langle \hat{c}_{\text{ex}}(\mathbf{k}, \Omega_3, \Omega_2) \hat{h}_{\text{ex}}(\mathbf{k}, \Omega_3, \Omega_2) \rangle_{\Omega_3}$, with the help of Table I we obtain

$$\begin{aligned} \hat{c}_{\text{ex}} \circ \hat{h}_{\text{ex}} &= \tilde{c}_\Delta \tilde{h}_\Delta \frac{1}{3} \Delta + \tilde{c}_\Delta \tilde{h}_D \frac{1}{3} D_k \\ &+ \tilde{c}_D^0 \tilde{h}_\Delta \frac{1}{3} D_k + \tilde{c}_D^0 \tilde{h}_D \frac{1}{3} (2\Delta + D_k). \end{aligned}$$

Inserting this result into Eq. (A1) and equating the coefficients of Δ and D separately, one finds that the \mathbf{k} -space excess PY-OL equation splits into two coupled integral equations, i.e.,

$$\tilde{h}_\Delta - \tilde{c}_\Delta = \frac{1}{3} \rho (\tilde{c}_\Delta \tilde{h}_\Delta + 2\tilde{c}_D^0 \tilde{h}_D^0),$$

$$\tilde{h}_D^0 - \tilde{c}_D^0 = \frac{1}{3} \rho (\tilde{c}_\Delta \tilde{h}_D^0 + \tilde{c}_D^0 \tilde{h}_\Delta + \tilde{c}_D^0 \tilde{h}_D^0). \quad (\text{A6})$$

Coming back to the \mathbf{r} space, one gets the following equations:

$$h_\Delta(r) = c_\Delta(r) + \frac{1}{3} \rho (c_\Delta \star h_\Delta + 2c_D^0 \star h_D^0),$$

$$h_D^0(r) = c_D^0(r) + \frac{1}{3} \rho (c_\Delta \star h_D^0 + c_D^0 \star h_\Delta + c_D^0 \star h_D^0). \quad (\text{A7})$$

In particular, since $h_D(r) = 0$ for $0 < r < \sigma$, Eq. (33) yields $h_D^0(r) = -3K$ for $0 < r < \sigma$, with K being a dimensionless parameter defined by

$$K = \int_{\sigma^-}^\infty \frac{h_D(x)}{x} dx. \quad (\text{A8})$$

The exact core conditions for Eqs. (A7) are

$$\left. \begin{aligned} h_\Delta(r) &= 0 \\ h_D^0(r) &= -3K \end{aligned} \right\} \text{ for } 0 < r < \sigma. \quad (\text{A9})$$

Now, in the PY-OL closure for the DCFs, Eqs. (24), the closure for $c_D(r)$ must be replaced with that corresponding to $c_D^0(r)$ (for simplicity, here and in the following we omit the superscript PY-OL). In order to derive this, let us start from $c_D(r) = c_{D,\text{reg}}(r) + \Lambda_D \sigma \delta(r - \sigma)$, where $c_{D,\text{reg}}(r) = f^{\text{HS}}(r) y_D^{\text{PY}}(r) = 0$ for $r \geq \sigma$. Then Eq. (33) yields

$$c_D^0(r) = c_D(r) - 3 \int_r^\sigma \frac{c_{D,\text{reg}}(x)}{x} dx - 3\Lambda_D \theta(\sigma - r),$$

since $\int_r^\infty \delta(x - \sigma) x^{-1} dx = \sigma^{-1} \theta(\sigma - r)$ [35]. So we get

$$c_D^0(r) = c_D(r) \quad \text{for } r \geq \sigma, \quad (\text{A10})$$

and the required new closures are

$$\left. \begin{aligned} c_\Delta(r) &= \Lambda_\Delta \sigma \delta(r - \sigma) \\ c_D^0(r) &= \Lambda_D \sigma \delta(r - \sigma) \end{aligned} \right\} r \geq \sigma. \quad (\text{A11})$$

In order to *decouple* the two integral equations for Δ and D coefficients, we then introduce two new unknown functions, which are linear combinations of the previous ones. Defining

$$\tilde{F}_{\text{new}} = \lambda_1 \tilde{F}_\Delta + \lambda_2 \tilde{F}_D^0 \quad (F = c, h),$$

and using Eqs. (A6) leads to

$$\begin{aligned} \tilde{h}_{\text{new}} - \tilde{c}_{\text{new}} &= \lambda_1 (\tilde{h}_\Delta - \tilde{c}_\Delta) + \lambda_2 (\tilde{h}_D^0 - \tilde{c}_D^0) \\ &= \frac{1}{3} \rho [\lambda_1 \tilde{c}_\Delta \tilde{h}_\Delta + \lambda_2 (\tilde{c}_\Delta \tilde{h}_D^0 + \tilde{c}_D^0 \tilde{h}_\Delta) + (2\lambda_1 \\ &+ \lambda_2) \tilde{c}_D^0 \tilde{h}_D^0]. \end{aligned}$$

Requiring the second member of this equation to be proportional to $\rho \tilde{c}_{\text{new}} \tilde{h}_{\text{new}}$ —that is, equal to $\mathcal{L} \rho (\lambda_1 \tilde{c}_\Delta + \lambda_2 \tilde{c}_D^0)$ ($\lambda_1 \tilde{h}_\Delta + \lambda_2 \tilde{h}_D^0$), with \mathcal{L} being the proportionality constant—yields the following conditions:

FLUIDS OF SPHERICAL MOLECULES WITH...

PHYSICAL REVIEW E 78, 021201 (2008)

$$\frac{1}{3}\lambda_1 = \mathcal{L}\lambda_1^2,$$

$$\frac{1}{3}\lambda_2 = \mathcal{L}\lambda_1\lambda_2,$$

$$\frac{1}{3}(2\lambda_1 + \lambda_2) = \mathcal{L}\lambda_2^2.$$

An infinite number of solutions are possible, and correspond to

$$(\lambda_1, \lambda_2) = \frac{1}{3\mathcal{L}_1}(1, -1), \quad \text{and} \quad (\lambda_1, \lambda_2) = \frac{1}{3\mathcal{L}_2}(1, 2),$$

since there is no need for the proportionality constant to have the same value in the two cases, i.e., ξ_2 can differ from ξ_1 . As a consequence, we can write the two new $h_{\text{new}}(r)$ as

$$\begin{aligned} h_1(r) &= (3\mathcal{L}_1)^{-1}[h_\Delta(r) - h_D^0(r)], \\ h_2(r) &= (3\mathcal{L}_2)^{-1}[h_\Delta(r) + 2h_D^0(r)], \end{aligned} \quad (\text{A12})$$

while similar expressions hold for c_1 and c_2 . From Eqs. (A9) it follows that $h_1(r) = K/\mathcal{L}_1$ and $h_2(r) = -2K/\mathcal{L}_2$ for $0 < r < \sigma$.

In Ref. [1] Wertheim chose $\mathcal{L}_1 = -K$ and $\mathcal{L}_2 = 2K$ [3], which leads to

$$\begin{aligned} F_1(r) &= \frac{1}{3K}[F_D^0(r) - F_\Delta(r)] \\ F_2(r) &= \frac{1}{3K}\left[F_D^0(r) + \frac{1}{2}F_\Delta(r)\right] \end{aligned} \quad (F = c, h), \quad (\text{A13})$$

$$\rho_1 = -K\rho,$$

$$\rho_2 = 2K\rho,$$

$$\begin{aligned} h_1(r) &= -1 \\ h_2(r) &= -1 \end{aligned} \quad \text{for } 0 < r < \sigma \quad (\text{A14})$$

(in Ref. [1], F_1 and F_2 were denoted as F_- and F_+ , respectively). Clearly, Wertheim's choice has the advantage of providing, for all the three hypothetical fluids, core conditions of the typical HS form: $h_m(r) = -1$ for $0 < r < \sigma$ ($m=0, 1, 2$). The cost to pay is the introduction of "modified densities" for the auxiliary fluids 1 and 2 (the negative sign of ρ_1 poses no special difficulty).

On the other hand, it would be equally proposable to choose $\mathcal{L}_1 = \mathcal{L}_2 = 1$, which leads to

$$\begin{aligned} F_1(r) &= \frac{1}{3}[F_\Delta(r) - F_D^0(r)] \\ F_2(r) &= \frac{1}{3}[F_\Delta(r) + 2F_D^0(r)] \end{aligned} \quad (F = c, h),$$

$$\rho_1 = \rho,$$

$$\rho_2 = \rho,$$

$$\begin{aligned} h_1(r) &= K \\ h_2(r) &= -2K \end{aligned} \quad \text{for } 0 < r < \sigma.$$

The advantage of this second possibility would be that all the three "hypothetical" fluids have the same *real* density, while the cost is represented by the less usual core conditions, which, however, pose no particular difficulty.

APPENDIX B: EQUATIONS FOR THE UNKNOWN PARAMETERS

Three *quadratic* equations for the Λ_m 's ($m=0, 1, 2$) can be obtained from Eqs. (55) and (56), after deriving from Eq. (69) the following expressions for the PY-OL *contact values*:

$$h_{m,\text{reg}}(\sigma^+) = h_\sigma^{\text{HS}}(\eta_m) - \frac{12\eta_m}{1-\eta_m}\Lambda_m + 12\eta_m\Lambda_m^2, \quad (\text{B1})$$

where

$$\begin{aligned} h_\sigma^{\text{HS}}(x) &= y_\sigma^{\text{HS}}(x) - 1, \\ y_\sigma^{\text{HS}}(x) &= \left(1 + \frac{1}{2}x\right)(1-x)^{-2}. \end{aligned} \quad (\text{B2})$$

Substituting Eq. (B1) into the expressions for Λ_m given by Eqs. (55), we get

(i) for Λ_0 , the same PY equation found by Baxter for isotropic SHS [11,12]

$$12\eta t\Lambda_0^2 - \left(1 + \frac{12\eta}{1-\eta}t\right)\Lambda_0 + y_\sigma^{\text{HS}}(\eta)t = 0. \quad (\text{B3})$$

Only the smaller of the two real solutions (when they exist) is physically significant [11,12], and reads

$$\Lambda_0 = \frac{y_\sigma^{\text{HS}}(\eta)t}{2\left[1 + \frac{12\eta}{1-\eta}t + \sqrt{\left(1 + \frac{12\eta}{1-\eta}t\right)^2 - 48\eta y_\sigma^{\text{HS}}(\eta)t^2}\right]}. \quad (\text{B4})$$

(ii) For Λ_1 and Λ_2 , the equations

$$12\eta_m t\Lambda_m^2 - \left(1 + \frac{12\eta_m}{1-\eta_m}t\right)\Lambda_m + h_\sigma^{\text{HS}}(\eta_m)t = -\mathcal{P} \quad (m=1, 2). \quad (\text{B5})$$

It is remarkable that the right-hand member of these equations does not depend on the index m . This fact means that Λ_2 obeys exactly the same equation as Λ_1 , but with η_2 replacing η_1 ; as will be confirmed later, such a property implies that, if one writes $\Lambda_1 = \Lambda_1(\eta_1, \eta_2, t, \alpha)$, then Λ_2 must have the same functional form with η_2 interchanged with η_1 , i.e., $\Lambda_2(\eta_1, \eta_2, t, \alpha) = \Lambda_1(\eta_2, \eta_1, t, \alpha)$.

Now the system of equations for Λ_1 , Λ_2 , and K must be completed by a further relationship, which can be obtained from the sum rule, Eq. (52). Taking into account that $c_D^0 = K(2c_2 + c_1)$, and multiplying Eq. (52) by $4\pi\rho$ yields

GAZZILLO, FANTONI, AND GIACOMETTI

PHYSICAL REVIEW E 78, 021201 (2008)

$$4\pi\rho_2 \int_0^\infty c_2(x)x^2 dx = 4\pi\rho_1 \int_0^\infty c_1(x)x^2 dx. \quad (\text{B6})$$

On the other hand, putting $k=0$ into Eq. (59) gives

$$1 - \rho_m \bar{c}_m(k=0) = 1 - 4\pi\rho_m \int_0^\infty c_m(r)r^2 dr = Q_m^2(k=0) = a_m^2,$$

since $Q_m(k=0) \equiv a_m$ [as shown by the first of Eqs. (62)]. Then Eq. (B6) becomes $a_2^2 = a_1^2$, which splits into two equations: $a_2 = a_1$ and $a_2 = -a_1$. From the expression for a_m , one can easily realize that the second equation does not satisfy the $t \rightarrow 0$ limit, whereas the first one, $a_2 = a_1$ [or, equivalently, $a^{\text{iso-SHS}}(\eta_2, \Lambda_2) = a^{\text{iso-SHS}}(\eta_1, \Lambda_1)$], leads to the following linear relationship between Λ_1 and Λ_2 :

$$\frac{12\eta_2\Lambda_2}{1-\eta_2} - \frac{12\eta_1\Lambda_1}{1-\eta_1} = a^{\text{HS}}(\eta_2) - a^{\text{HS}}(\eta_1). \quad (\text{B7})$$

Note that the two Eqs. (B5) are coupled [since $K_{\text{reg}}/K = 1 - \Lambda_D/K = 1 - (2\Lambda_2 + \Lambda_1)$], but with the help of Eq. (B7) they could be easily decoupled. However, since the right-hand members of Eqs. (B5) coincide, we can get a new relationship by equating their first members, and exploiting Eq. (B7). So we arrive at the following equations for the three unknowns Λ_1 , Λ_2 , and K :

$$12\eta_2 t \Lambda_2^2 - \Lambda_2 + b^{\text{HS}}(\eta_2)t = 12\eta_1 t \Lambda_1^2 - \Lambda_1 + b^{\text{HS}}(\eta_1)t,$$

$$\frac{12\eta_2\Lambda_2}{1-\eta_2} - \frac{12\eta_1\Lambda_1}{1-\eta_1} = \frac{\eta_2(4-\eta_2)}{(1-\eta_2)^2} - \frac{\eta_1(4-\eta_1)}{(1-\eta_1)^2},$$

$$12\eta_1 t \Lambda_1^2 - \left(1 + \frac{12\eta_1}{1-\eta_1}t\right)\Lambda_1 + h_\sigma^{\text{HS}}(\eta_1)t = -\mathcal{P}. \quad (\text{B8})$$

The first two equations form a closed system for Λ_1 and Λ_2 . The second one suggests that we can assume

$$\frac{12\eta_m\Lambda_m}{1-\eta_m} = \frac{\eta_m(4-\eta_m)}{(1-\eta_m)^2} + W,$$

or, equivalently,

$$\Lambda_m = \frac{1}{3} + \frac{\eta_m}{4(1-\eta_m)} + \frac{1-\eta_m}{12\eta_m}W \quad (m=1,2), \quad (\text{B9})$$

where $W = W(\eta_1, \eta_2, t)$ is an unknown function, which must be proportional to $\eta_1\eta_2$. In fact, Eqs. (B5) require that

$$\lim_{\eta \rightarrow 0} \Lambda_1 = \lim_{\eta \rightarrow 0} \Lambda_2 = \frac{1}{3}, \quad (\text{B10})$$

since, from Eq. (56), one has $\lim_{\eta \rightarrow 0} \mathcal{P} = \frac{1}{3}$ ($\lim_{\eta \rightarrow 0} K_{\text{reg}} = 0$). If Λ_1 and Λ_2 in the first of Eqs. (B8) are replaced with the new expressions (B9), then one gets a quadratic equation for W as follows:

$$(1-\eta_1\eta_2)tW^2 - (1-2\eta_1\eta_2t)W + \frac{3\eta_1\eta_2}{(1-\eta_1)(1-\eta_2)}M = 0, \quad (\text{B11})$$

with

$$\begin{aligned} M &= 1 + \left[\frac{1+2(\eta_1+\eta_2)-5\eta_1\eta_2}{(1-\eta_1)(1-\eta_2)} - \frac{1}{3}(1-\eta_1)(1-\eta_2) \right] t \\ &= 1 + \left[\frac{1+2x+10x^2}{(1+x)(1-2x)} - \frac{1}{3}(1+x)(1-2x) \right] t, \end{aligned} \quad (\text{B12})$$

where we have put $\eta_1 = -x$, $\eta_2 = 2x$ ($x \equiv K\eta$). The acceptable solution is

$$\begin{aligned} W &= \frac{1-2\eta_1\eta_2t}{2(1-\eta_1\eta_2)t} (1-\sqrt{\mathcal{D}}) \\ &= \frac{3\eta_1\eta_2}{(1-\eta_1)(1-\eta_2)} W_0 = -\frac{6x^2}{(1+x)(1-2x)} W_0, \end{aligned} \quad (\text{B13})$$

with

$$W_0 = \frac{M}{\frac{1}{2}(1-2\eta_1\eta_2t)(1+\sqrt{\mathcal{D}})} = \frac{M}{\frac{1}{2}(1+4x^2t)(1+\sqrt{\mathcal{D}})}, \quad (\text{B14})$$

$$\begin{aligned} \mathcal{D} &= 1 - \frac{12\eta_1\eta_2(1-\eta_1\eta_2)}{(1-\eta_1)(1-\eta_2)(1-2\eta_1\eta_2t)^2} Mt \\ &= 1 + \frac{24x^2(1+2x^2)}{(1+x)(1-2x)(1+4x^2t)^2} Mt. \end{aligned} \quad (\text{B15})$$

Note that $\lim_{\eta \rightarrow 0} W_0 = \lim_{\eta \rightarrow 0} M = 1 + (2/3)t$.

The functions W , W_0 , D , and M are symmetrical with respect to the exchange of η_1 and η_2 ; in particular, $W(\eta_2, \eta_1, t) = W(\eta_1, \eta_2, t)$, and this property implies that

$$\Lambda_2(\eta_1, \eta_2, t) = \Lambda_1(\eta_2, \eta_1, t), \quad (\text{B16})$$

confirming our previous guess.

Moreover, if we put

$$W_0 = 1 + W_0^{\text{ex}}, \quad (\text{B17})$$

then

$$\Lambda_m = \Lambda + \Lambda_m^{\text{ex}}, \quad (\text{B18})$$

with

$$\Lambda = \frac{1}{3} + \frac{1}{4} \left(\frac{\eta_1}{1-\eta_1} + \frac{\eta_2}{1-\eta_2} \right) = \frac{1}{3} + \frac{x(1+4x)}{4(1+x)(1-2x)}, \quad (\text{B19})$$

$$\Lambda_1^{\text{ex}} = \frac{\eta_2}{4(1-\eta_2)} W_0^{\text{ex}}, \quad \Lambda_2^{\text{ex}} = \frac{\eta_1}{4(1-\eta_1)} W_0^{\text{ex}}. \quad (\text{B20})$$

Here, both Λ and W_0^{ex} are symmetric with respect to η_1 and η_2 , whereas Λ_m^{ex} represents the asymmetric part of Λ_m .

Note that the knowledge of Λ_1 and Λ_2 allows one to calculate Λ_Δ and Λ_D immediately. In fact, Eqs. (47) lead to

FLUIDS OF SPHERICAL MOLECULES WITH...

PHYSICAL REVIEW E 78, 021201 (2008)

$$\begin{aligned}\Lambda_\Delta &= 2K(\Lambda_2 - \Lambda_1) \\ &= -K \frac{3x}{2(1+x)(1-2x)} W_0^{\text{ex}},\end{aligned}$$

$$\begin{aligned}\Lambda_D &= K(2\Lambda_2 + \Lambda_1) \\ &= K \left\{ 1 + \frac{3x}{4(1+x)(1-2x)} [1 + 2x(2 + W_0^{\text{ex}})] \right\}.\end{aligned}\tag{B21}$$

Now we must find an equation for K . We can regard the third of Eqs. (B8) as the required relationship. However, in order to derive a more symmetric expression, we prefer to start from Eqs. (B5), rewritten as

$$\begin{aligned}12\eta_1 t \Lambda_1^2 - \left(1 + \frac{12\eta_1}{1-\eta_1} t \right) \Lambda_1 + h_\sigma^{\text{HS}}(\eta_1) t + \frac{K_{\text{reg}}}{K} t \\ + \frac{1}{3} \frac{\alpha t}{K} y_0^{\text{PY}}(\sigma) = 0,\end{aligned}$$

$$\begin{aligned}12\eta_2 t \Lambda_2^2 - \left(1 + \frac{12\eta_2}{1-\eta_2} t \right) \Lambda_2 + h_\sigma^{\text{HS}}(\eta_2) t + \frac{K_{\text{reg}}}{K} t \\ + \frac{1}{3} \frac{\alpha t}{K} y_0^{\text{PY}}(\sigma) = 0,\end{aligned}\tag{B22}$$

and we get

$$K = \alpha t \mathcal{K}, \quad \text{with } \mathcal{K} = \frac{y_0^{\text{PY}}(\sigma)}{Z(\eta_1, \eta_2, t)},\tag{B23}$$

$$\begin{aligned}Z = \frac{3}{2}(\Lambda_1 + \Lambda_2) - 3 \left\{ \frac{1}{2} \sum_{m=1}^2 \left[12\eta_m \Lambda_m^2 - \frac{12\eta_m \Lambda_m}{1-\eta_m} \right. \right. \\ \left. \left. + h_\sigma^{\text{HS}}(\eta_m) \right] + \frac{K_{\text{reg}}}{K} \right\} t,\end{aligned}\tag{B24}$$

and $\lim_{\eta \rightarrow 0} Z(\eta_1, \eta_2, t) = 1$. Replacing the found expressions for Λ_1 , Λ_2 , and Λ_D into Eq. (B23) yields an equation for K that we have solved numerically, although some further analytic simplifications are probably possible.

-
- [1] F. Spinozzi, D. Gazzillo, A. Giacometti, P. Mariani, and F. Carsughi, *Biophys. J.* **82**, 2165 (2002).
 [2] A. Giacometti, D. Gazzillo, G. Pastore, and T. K. Das, *Phys. Rev. E* **71**, 031108 (2005).
 [3] M. S. Wertheim, *J. Chem. Phys.* **55**, 4291 (1971).
 [4] J. J. Weis and D. Levesque, *Phys. Rev. Lett.* **71**, 2729 (1993).
 [5] M. E. van Leeuwen and B. Smit, *Phys. Rev. Lett.* **71**, 3991 (1993).
 [6] R. P. Sear, *Phys. Rev. Lett.* **76**, 2310 (1996).
 [7] P. J. Camp, J. C. Shelley, and G. N. Patey, *Phys. Rev. Lett.* **84**, 115 (2000).
 [8] T. Tlusty and S. A. Safran, *Science* **290**, 1328 (2000).
 [9] D. Gazzillo, A. Giacometti, R. Fantoni, and P. Sollich, *Phys. Rev. E* **74**, 051407 (2006).
 [10] R. Fantoni, D. Gazzillo, A. Giacometti, M. A. Miller, and G. Pastore, *J. Chem. Phys.* **127**, 234507 (2007).
 [11] R. J. Baxter, *J. Chem. Phys.* **49**, 2770 (1968).
 [12] R. J. Baxter, in *Physical Chemistry, an Advanced Treatise*, edited by D. Henderson (Academic, New York, 1971), Vol. 8A, Chap. 4.
 [13] F. Sciortino, P. Tartaglia, and E. Zaccarelli, *J. Phys. Chem. B* **109**, 21942 (2005).
 [14] E. Bianchi, J. Largo, P. Tartaglia, E. Zaccarelli, and F. Sciortino, *Phys. Rev. Lett.* **97**, 168301 (2006).
 [15] C. De Michele, S. Gabrielli, P. Tartaglia, and F. Sciortino, *J. Phys. Chem. B* **110**, 8064 (2006).
 [16] A. Lomakin, N. Asherie, and G. B. Benedek, *Proc. Natl. Acad. Sci. U.S.A.* **96**, 9645 (1999).
 [17] F. W. Starr and J. F. Douglas, *J. Chem. Phys.* **119**, 1777 (2003).
 [18] Z. Zhang and S. C. Glotzer, *Nano Lett.* **4**, 1407 (2004).
 [19] S. C. Glotzer, *Science* **306**, 419 (2004).
 [20] S. C. Glotzer, M. J. Solomon, and N. A. Kotov, *AIChE J.* **50**, 2978 (2004).
 [21] F. Sciortino, E. Bianchi, J. F. Douglas, and P. Tartaglia, *J. Chem. Phys.* **126**, 194903 (2007).
 [22] G. Jackson, W. G. Chapman, and K. E. Gubbins, *Mol. Phys.* **65**, 1 (1988).
 [23] D. Ghonasgi and W. G. Chapman, *J. Chem. Phys.* **102**, 2585 (1995).
 [24] R. P. Sear, *J. Chem. Phys.* **111**, 4800 (1999).
 [25] E. Mileva and G. T. Evans, *J. Chem. Phys.* **113**, 3766 (2000).
 [26] N. Kern and D. Frenkel, *J. Chem. Phys.* **118**, 9882 (2003).
 [27] Z. Zhang, A. S. Keys, T. Chen, and S. C. Glotzer, *Langmuir* **21**, 11547 (2005).
 [28] A. W. Wilber, J. P. K. Doye, A. A. Louis, E. G. Noya, M. A. Miller, and P. Wong, *J. Chem. Phys.* **127**, 085106 (2007).
 [29] J. P. K. Doye, A. A. Louis, I-C. Lin, L. R. Allen, E. G. Noya, A. W. Wilber, H. C. Kok, and R. Lyus, *Phys. Chem. Chem. Phys.* **9**, 2197 (2007).
 [30] P. T. Cummings and L. Blum, *J. Chem. Phys.* **84**, 1833 (1986).
 [31] D. Wei and L. Blum, *J. Chem. Phys.* **89**, 1091 (1988).
 [32] L. Blum, P. T. Cummings, and D. Bratko, *J. Chem. Phys.* **92**, 3741 (1990).
 [33] L. Blum and A. J. Torruella, *J. Chem. Phys.* **56**, 303 (1971).
 [34] I. A. Protsykevich, *Condens. Matter Phys.* **6**, 629 (2003).
 [35] Recall that the Dirac delta function is defined by $\int_a^b \delta(x)$

GAZZILLO, FANTONI, AND GIACOMETTI

PHYSICAL REVIEW E **78**, 021201 (2008)

- $-x_0)F(x)dx=F(x_0)$ if $a \leq x_0 \leq b$ ($=0$ otherwise), for any F continuous at $x=x_0$.
- [36] H. L. Friedman, *A Course in Statistical Mechanics* (Prentice-Hall, Englewood Cliffs, NJ, 1985).
- [37] L. L. Lee, *Molecular Thermodynamics of Nonideal Fluids* (Butterworths, Boston, 1988).
- [38] J. P. Hansen and I. R. McDonald, *Theory of Simple Liquids*, 3rd ed. (Academic Press, Amsterdam, 2006).
- [39] D. Gazzillo and A. Giacometti, *J. Chem. Phys.* **120**, 4742 (2004).
- [40] W. G. T. Kranendonk and D. Frenkel, *Mol. Phys.* **64**, 403 (1988).
- [41] M. A. Miller and D. Frenkel, *J. Phys.: Condens. Matter* **16**, S4901 (2004).
- [42] J. W. Perram, *Mol. Phys.* **30**, 1505 (1975).
- [43] D. Frenkel and B. Smit, *Understanding Molecular Simulation. From Algorithms to Applications* (Academic Press, San Diego, 2002), p. 221.
- [44] C. G. Gray and K. E. Gubbins, *Theory of Molecular Fluids* (Clarendon Press, Oxford, 1984), Vol. I, Appendix 3E.
- [45] J. Stecki and A. Kloczkowski, *Mol. Phys.* **42**, 51 (1981).
- [46] X. S. Chen and F. Forstmann, *Mol. Phys.* **76**, 1203 (1992).
- [47] S. Klapp and F. Forstmann, *J. Chem. Phys.* **106**, 9742 (1997).

Chapter 16

Penetrable Square-Well fluids: exact results in one dimension

Santos A., **Fantoni R.**, and Giacometti A., Phys. Rev. E **77**, 051206 (2008)

Title: “Penetrable square-well fluids: Exact results in one dimension.”

Abstract: We introduce a model of attractive penetrable spheres by adding a short-range attractive square well outside a penetrable core, and we provide a detailed analysis of structural and thermodynamical properties in one dimension using the exact impenetrable counterpart as a starting point. The model is expected to describe star polymers in regimes of good and moderate solvent under dilute conditions. We derive the exact coefficients of a low-density expansion up to second order for the radial distribution function and up to fourth order in the virial expansion. These exact results are used as a benchmark to test the reliability of approximate theories (Percus-Yevick and hypernetted chain). Notwithstanding the lack of an exact solution for arbitrary densities, our results are expected to be rather precise within a wide range of temperatures and densities. A detailed analysis of some limiting cases is carried out. In particular, we provide a complete solution of the sticky penetrable-sphere model in one dimension up to the same order in density. The issue of Ruelle’s thermodynamics stability is analyzed and the region of a well-defined thermodynamic limit is identified.

Appears in the SklogWiki:

http://www.sklogwiki.org/SklogWiki/index.php/Penetrable_square_well_model

PHYSICAL REVIEW E 77, 051206 (2008)

Penetrable square-well fluids: Exact results in one dimension

Andrés Santos*

Departamento de Física, Universidad de Extremadura, E-06071 Badajoz, Spain

Riccardo Fantoni† and Achille Giacometti‡

Dipartimento di Chimica Fisica, Università di Venezia, Calle Larga S. Marta DD2137, I-30123 Venezia, Italy

(Received 5 February 2008; published 19 May 2008)

We introduce a model of attractive penetrable spheres by adding a short-range attractive square well outside a penetrable core, and we provide a detailed analysis of structural and thermodynamical properties in one dimension using the exact impenetrable counterpart as a starting point. The model is expected to describe star polymers in regimes of good and moderate solvent under dilute conditions. We derive the exact coefficients of a low-density expansion up to second order for the radial distribution function and up to fourth order in the virial expansion. These exact results are used as a benchmark to test the reliability of approximate theories (Percus-Yevick and hypernetted chain). Notwithstanding the lack of an exact solution for arbitrary densities, our results are expected to be rather precise within a wide range of temperatures and densities. A detailed analysis of some limiting cases is carried out. In particular, we provide a complete solution of the sticky penetrable-sphere model in one dimension up to the same order in density. The issue of Ruelle's thermodynamics stability is analyzed and the region of a well-defined thermodynamic limit is identified.

DOI: 10.1103/PhysRevE.77.051206

PACS number(s): 61.20.Gy, 61.20.Ne, 05.20.Jj, 05.70.Ce

I. INTRODUCTION

Unlike simple liquids, where two-body potentials describe interactions at the atomistic level, complex liquid interactions are always a result of an average process over the microscopic degrees of freedom. As a result, highly simplified models often accurately describe a number of experimental features ranging from structural to thermophysical properties. Examples include colloidal dispersions, macromolecules, and combinations of the two [1]. A noteworthy feature of these systems is that the hard-core repulsive barrier for very short range is not an essential ingredient of the model. In the case of highly ramified polymers in good solvents (star polymers), for instance, the centers of mass of two polymer chains can be at a distance much smaller than their respective radii of gyration and they are well described by an effective Gaussian interaction [2]. The simplest of this class of minimal bounded potentials is the so-called penetrable-sphere (PS) model [3] which has attracted considerable attention in the last few years (see, e.g., Ref. [4] and references therein). In this case the infinite barrier of the hard-sphere (HS) potential is replaced by a finite one, thus allowing for a finite probability of penetrating inside the core.

A major advantage of the PS potential is, of course, simplicity. On the other hand, it lacks an attractive part which is expected to be relevant in such a complex environment in view of the ubiquity of van der Waals dispersion forces. The purpose of the present work is to address this point by proposing a variation of the PS model in which a square well (SW) is added outside the core. This model, hereafter referred to as the penetrable square-well (PSW) model, has an

extremely rich phenomenology notwithstanding its simplicity, including a number of interesting limiting cases as will be discussed later on.

One-dimensional bounded interactions do not belong to the class of nearest-neighbor fluids for which the total potential energy can be written as

$$U_N(x_1, \dots, x_N) = \sum_{i=1}^{N-1} \phi(|x_{i+1} - x_i|), \quad (1.1)$$

where $\phi(r)$ is the pair potential and $\{x_i, i=1, \dots, N\}$ are the coordinates of the N particles confined in a segment of length L , which eventually may be let to go to infinity. A necessary (but not sufficient) condition for a one-dimensional fluid to satisfy Eq. (1.1) is to be a hard-core fluid, i.e., a fluid made of particles which cannot penetrate one another due to the existence of an infinite repulsive potential barrier in $\phi(r)$.

Nearest-neighbor fluids admit an analytic exact statistical-mechanical solution in one dimension [5]: the partition function, equation of state, and correlation functions of any order can be calculated analytically from the knowledge of the pair potential. Both structural and thermophysical properties can be analytically obtained in one dimension for Baxter's sticky hard-sphere (SHS) potential [6,7], and for the SW potential [8], in addition to the HS potential [5,9–13], but the technique permits in principle the analysis of a large class of nearest-neighbor one-dimensional potentials.

In the absence of the nearest-neighborhood constraint (as happens with bounded potentials), the situation is far more complex, and we are not aware of any general analytical approach to the problem, even in one dimension. As a matter of fact there exist only a few examples of analytically solvable one-dimensional models of this type, which include the Kac potential [14] and the Coulomb potential [15,16]. For PSs, it was observed [4,17] that the exact analytic solution for HSs can be efficiently exploited to build a rather precise,

*andres@unex.es; URL: <http://www.unex.es/fisteor/andres/>

†rfantoni@unive.it

‡achille@unive.it

SANTOS, FANTONI, AND GIACOMETTI

PHYSICAL REVIEW E 77, 051206 (2008)

albeit approximate, solution of the penetrable counterpart. This analysis is here extended to PSW interactions. Using a low-density expansion and the corresponding exact solution for the SW problem, we derive the exact result up to the second order in a density expansion of the radial distribution function and up to fourth order in the virial expansion of the equation of state. These exact low-density calculations are contrasted with approximate theories such as the Percus-Yevick (PY) and the hypernetted chain (HNC) closures, thus providing an assessment of the relative reliability of both approximations and the low-density expansion. As a preliminary simplified step in our calculation, we also examine the penetrable counterpart of the SHS problem, denoted as sticky penetrable spheres (SPS) in the following, which provides a guideline to tackling the more difficult PSW problem.

The introduction of an attractive part of the potential into a penetrable interaction raises the important issue of the existence of a well-defined thermodynamic limit [18,19]. We address this problem for the PSW model and provide compelling arguments to identify the stability region, which is guaranteed for a sufficiently small (≈ 0.5) ratio between the attractive and repulsive energy scales and arbitrary values of the other parameters.

The remaining of the paper is structured as follows. In Sec. II we introduce the model along with all its limiting cases (including the SPS fluid) and we study its stability. Section III briefly accounts for the main equations necessary for the analytical solution of the nearest-neighbor class of fluids with arbitrary interactions. The exact solution of the one-dimensional SHS potential is derived within this general approach in Sec. III B and this is used to obtain the corresponding low-density solution of the SPS model in Sec. IV. A similar analysis is carried out in Sec. V for the PSW potential and the results are contrasted with those stemming from PY and HNC closures. Section VII contains some closing remarks, whereas some of the more technical details are confined in suitable appendixes.

II. THE PENETRABLE SQUARE-WELL MODEL

The penetrable square-well model is defined by the following pair potential (see Fig. 1):

$$\phi(r) = \begin{cases} +\epsilon_r, & r < \sigma, \\ -\epsilon_a, & \sigma < r < \sigma + \Delta, \\ 0, & r > \sigma + \Delta, \end{cases} \quad (2.1)$$

where ϵ_r and ϵ_a are two positive constants accounting for the repulsive and attractive parts of the potential, respectively. Here σ is the diameter of the sphere (length of the rod in one dimension) and $\Delta < \sigma$ is the width of the well. This model has a number of relevant limiting cases. When $\epsilon_r \rightarrow \infty$ it reduces to a square-well fluid, whereas $\epsilon_a \rightarrow 0$ yields the penetrable-sphere model studied in Ref. [4] in the one-dimensional case. In addition it gives rise to an interesting variation, referred to as sticky penetrable spheres, within an appropriate limit of a well of infinite depth and vanishing width (see below). Finally, we recover the hard-sphere fluid in the combined limit $\epsilon_r \rightarrow \infty$ and $\epsilon_a \rightarrow 0$.

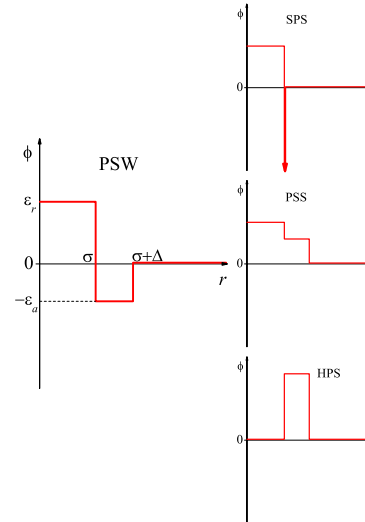


FIG. 1. (Color online) Sketch of the penetrable square-well (PSW) potential (left column). The right column shows a few limiting cases: the sticky penetrable-sphere (SPS) potential ($\epsilon_r \rightarrow \infty$ and $\Delta \rightarrow 0$), the penetrable square-shoulder (PSS) potential ($\epsilon_r > -\epsilon_a > 0$), and the hollow penetrable-sphere (HPS) potential ($\epsilon_r = 0$ and $\epsilon_a < 0$).

It is worthwhile to note that the PSW model (and its variants) considered here is different from other apparently similar models like the Widom-Rowlinson model of interpenetrating spheres [20], the concentric-shell model [21], or the permeable-sphere model [22].

As usual, a very important role is played by the Mayer function

$$f(r) = e^{-\beta\phi(r)} - 1, \quad (2.2)$$

where $\beta = 1/k_B T$ is the inverse of the thermal energy (k_B is the Boltzmann constant and T is the absolute temperature). In the present model, this becomes

$$f(r) = \begin{cases} -\gamma_r, & r < \sigma, \\ +\gamma_a, & \sigma < r < \sigma + \Delta, \\ 0, & r > \sigma + \Delta, \end{cases} \quad (2.3)$$

$$= \gamma_r f_{\text{HS}}(r) + \gamma_a [\Theta(r - \sigma) - \Theta(r - \sigma - \Delta)],$$

where

$$\gamma_r = 1 - e^{-\beta\epsilon_r} \quad (2.4)$$

is the parameter measuring the degree of penetrability varying between 0 (free penetrability) and 1 (impenetrability) and

$$\gamma_a = e^{\beta\epsilon_a} - 1 \quad (2.5)$$

plays a similar role for the attractive part. Here $f_{\text{HS}}(r) = \Theta(r - \sigma) - 1$ is the Mayer function for a HS model, which can then be recovered in the limit $\gamma_r \rightarrow 1$ and $\gamma_a \rightarrow 0$, and $\Theta(r)$ is the usual step function equal to 1 for $r > 0$ and 0 otherwise. It

PENETRABLE SQUARE-WELL FLUIDS: EXACT RESULTS...

PHYSICAL REVIEW E 77, 051206 (2008)

also proves convenient to introduce the ratio $\gamma = \gamma_a / \gamma_r$, which is a measure of the depth of the attractive well, relative to the “penetrability” of the core. In that way, Eq. (2.3) can be rewritten as

$$f(r) = \gamma_r \{f_{\text{HS}}(r) + \gamma [\Theta(r - \sigma) - \Theta(r - \sigma - \Delta)]\} = \gamma_r f_{\text{SW}}(r), \quad (2.6)$$

where $f_{\text{SW}}(r)$ is the Mayer function of a SW fluid with the change $\gamma_a \rightarrow \gamma$.

Although the PSW model can be defined for any dimensionality of the system, throughout the remainder of this paper we will specialize to the one-dimensional case.

A. The thermodynamic stability issue

As anticipated in the Introduction, in our model we need to make sure that the system is always *stable* in the sense that the total energy is always bounded from below by $-NB$, N being the number of particles and B an arbitrary positive constant [19]. The physical origin of this instability can be traced back to the fact that a soft core allows the possibility of a “collapsed state” where the energy is no longer proportional to the number of particles N and a well-defined thermodynamic limit may not exist. In a classic paper, Fisher and Ruelle [18] provided a set of conditions on the pair potentials which are sufficient for stability, but the actual implementation of such conditions in soft-core systems is far from being trivial, as was recently shown for Gaussian-core models [23] and Lennard-Jones fluids [24].

In the PSW model, the issue is clearly related to the interplay between the two energy scales ϵ_r and ϵ_a for the repulsive and attractive parts of the potential. As shown in Appendix A, we predict that the system *might be unstable* when $\epsilon_r < 2\epsilon_a$ whereas we prove that it is *certainly stable* in the opposite case $\epsilon_r > 2\epsilon_a$.

B. The sticky limit: The SPS model

It is instructive at this point to consider a particular limit of the PSW model which will be referred to as the sticky penetrable-sphere model (see Fig. 1). This is a variation of a widely used sticky hard-sphere model introduced a long time ago by Baxter [25], which has proven to be extremely useful in the framework of complex fluids, recently even in its anisotropic version [26]. The simplest way of introducing it is at the level of the Mayer function [see Eq. (2.3)], which becomes

$$f_{\text{SHS}}(r) = f_{\text{HS}}(r) + \alpha \sigma \delta_+(r - \sigma), \quad (2.7)$$

where

$$\delta_+(r) = \lim_{a \rightarrow 0^+} \frac{\Theta(r) - \Theta(r - a)}{a}. \quad (2.8)$$

The relation with the SPS model is then provided by

$$f_{\text{SPS}}(r) = \gamma_r f_{\text{SHS}}(r). \quad (2.9)$$

In the original SHS model [25], $\alpha = 1/12\tau > 0$ (τ playing the role of an effective temperature) but the connection with the

TABLE I. Summary of the models.

Model	Acronym	ϵ_r	ϵ_a	Δ
Penetrable spheres	PS	>0	0	>0
Penetrable square well	PSW	>0	>0	>0
Sticky penetrable sphere	SPS	>0	$\rightarrow +\infty$	$\rightarrow 0$
Penetrable square shoulder	PSS	>0	<0	>0
Hollow penetrable sphere	HPS	0	<0	>0
Hollow hard sphere	HHS	0	$\rightarrow -\infty$	>0

PSW model is readily achieved from Eq. (2.6) by considering the limits $\Delta \rightarrow 0$ and $\epsilon_r \rightarrow \infty$ so that $\alpha = (\gamma_a / \gamma_r)(\Delta / \sigma)$ remains finite. In spite of its usefulness, the SHS model is known to suffer from some mathematical drawbacks, the most important of them being that it is unstable in spatial dimensions greater than 1, as pointed out by Stell [27], in view of the divergence of the virial coefficient corresponding to a close-packed configuration. For the SPS model we will be able to achieve a number of exact results which can be exploited as a guideline for the more complex PSW model.

C. Other limiting cases

In all previous cases, we have tacitly assumed $\epsilon_a > 0$. In principle, however, nothing prevents one from considering the opposite case $\epsilon_a < 0$ (which implies $\gamma_a < 0$). In this case the PSW potential gives rise to an interesting class of models, at least from an academic point of view, with two positive energy scales (ϵ_r and $|\epsilon_a|$). If $\epsilon_r > |\epsilon_a|$, we get a purely repulsive potential that could be called the penetrable square-shoulder (PSS) model (see Fig. 1). A peculiar situation occurs if $\epsilon_r < |\epsilon_a|$: when two particles approach they have first to overcome the barrier $|\epsilon_a|$ at $r = \sigma + \Delta$; once this is done, they experience an attractive well of depth $|\epsilon_a| - \epsilon_r$ for $r < \sigma$. Thus the potential is attractive for short distances and repulsive for larger distances. The simplest version of models with $\epsilon_a < 0$ and $\epsilon_r < |\epsilon_a|$ corresponds to $\epsilon_r = 0$, which will be referred to as the hollow penetrable-sphere (HPS) model (see Fig. 1). If, in addition, the limit $|\epsilon_a| \rightarrow \infty$ is taken, one gets an *athermal* potential that will be referred to as the hollow hard-sphere (HHS) model since the particles look like hard spheres of diameter $\sigma + \Delta$ with a “hole” of diameter σ inside. If two particles are separated by a distance larger than $\sigma + \Delta$, they behave as hard spheres and the holes have no effect. On the other hand, if the separation between them is smaller than σ , they can never separate a distance larger than σ . In the HHS model, $\gamma_a \rightarrow -1$ and $\gamma_r \rightarrow 0$, so that the functions $y_2(r)$ and $g_2(r)$ are well defined (see below). In Sec. VI we will discuss the results for representative values of the parameters. A summary of the penetrable models treated in this paper, along with the corresponding values for ϵ_r , ϵ_a , and Δ characterizing them, is reported in Table I.

III. BASIC FORMALISM FOR EXACT PROPERTIES OF NEAREST-NEIGHBOR POTENTIALS

A. General scheme

The great advantage of dealing with one-dimensional models is that they are usually amenable to exact solutions,

SANTOS, FANTONI, AND GIACOMETTI

PHYSICAL REVIEW E 77, 051206 (2008)

at least in the limit of sufficiently short-range interactions [14]. The trade-off is, of course, the fact that these models do not have phase transitions. In the context of fluids, this translates into the fact that there exist exact solutions for the HS, SHS, and SW models [5,6,8,10,11,28,29]. The same formalism allows one to tackle non-nearest-neighbor one-dimensional fluids [4], thus leading to an approximate solution. Let us recall the main results of this approach, referring to Ref. [8] for a self-contained treatment. The main quantity to be computed is the Laplace transform of the Boltzmann factor $e^{-\beta\phi(r)}$:

$$\tilde{\Omega}(s) = \int_0^\infty ds e^{-sr} e^{-\beta\phi(r)}. \quad (3.1)$$

This is directly related to the Laplace transform of the radial distribution function $g(r)$,

$$\tilde{G}(s) = \int_0^\infty ds e^{-sr} g(r). \quad (3.2)$$

The relation is (see Refs. [8,10] for details)

$$\tilde{G}(s) = \frac{1}{\rho} \left(\frac{\tilde{\Omega}(s)}{\tilde{\Omega}(s+\xi)} - 1 \right)^{-1}, \quad (3.3)$$

where $\rho=N/L$ is the density of the one-dimensional fluid. Here ξ is a solution of the equation

$$\left. \frac{\partial \ln \tilde{\Omega}(s)}{\partial s} \right|_{s=\xi} = -\frac{1}{\rho}. \quad (3.4)$$

Finally, the equation of state (EOS) (and hence the whole thermodynamics) can be cast into the very simple form

$$\beta P = \xi, \quad (3.5)$$

where P is the pressure.

In practice, the scheme goes as follows. Evaluate $\tilde{\Omega}(s)$ from the Boltzmann factor by a Laplace transform, Eq. (3.1); solve for ξ from Eq. (3.4); insert the result into Eq. (3.3); invert the Laplace transform (3.2) to obtain $g(r)$ and, in parallel, compute the EOS from (3.5).

As a final remark, we anticipate that, when dealing with discontinuous potentials (or Boltzmann factors), it is convenient to introduce the cavity function $y(r)$ which is related to the radial distribution function $g(r)$ and the pair potential $\phi(r)$ by the general relation

$$g(r) = e^{-\beta\phi(r)} y(r). \quad (3.6)$$

Moreover, it can be expanded in powers of the density,

$$y(r) = 1 + \sum_{n=1}^{\infty} \rho^n y_n(r). \quad (3.7)$$

In principle, knowledge of all y_n coefficients provides the exact solution to the cavity function $y(r)$ (provided that the above series converges) and hence to the problem. This also allows us to assess the reliability of well-known approximations involving the direct correlation function $c(r)$ and the cavity function [30], such as the Percus-Yevick closure

$$c(r) = f(r)y(r) \quad (3.8)$$

and the hypernetted chain closure

$$c(r) = f(r)y(r) + y(r) - 1 - \ln y(r). \quad (3.9)$$

B. Exact solution of the SHS model in one dimension

Let us particularize the above procedure to derive the exact solution of Baxter's SHS model in one dimension. Starting from the Boltzmann factor

$$e^{-\beta\phi(r)} = \Theta(r-\sigma) + \alpha\sigma\delta_+(r-\sigma), \quad (3.10)$$

its Laplace transform (3.1) yields

$$\tilde{\Omega}(s) = \left(\alpha\sigma + \frac{1}{s} \right) e^{-s\sigma}. \quad (3.11)$$

Equation (3.4) can then be arranged to get the following quadratic equation:

$$\xi^2\sigma^2\alpha(1-\rho\sigma) + \xi\sigma(1-\rho\sigma) - \rho\sigma = 0. \quad (3.12)$$

Its physical solution is

$$\xi = \frac{\sqrt{1+4\alpha\rho\sigma/(1-\rho\sigma)} - 1}{2\alpha\sigma}, \quad (3.13)$$

which can be substituted into Eq. (3.5) to give

$$\frac{\beta P}{\rho} = \frac{\sqrt{1+4\alpha\rho\sigma/(1-\rho\sigma)} - 1}{2\alpha\rho\sigma}, \quad (3.14)$$

which represents the EOS for this system. In order to get the exact radial distribution function, we exploit Eq. (3.3) to get

$$\tilde{G}(s) = \frac{1}{\rho} \sum_{n=1}^{\infty} \left(\frac{\tilde{\Omega}(s+\xi)}{\tilde{\Omega}(s)} \right)^n = \frac{1}{\rho} \sum_{n=1}^{\infty} \frac{(\alpha\sigma + \frac{1}{s+\xi})^n e^{-ns\sigma}}{(\alpha\sigma + \frac{1}{\xi})^n}. \quad (3.15)$$

We can now use the binomial theorem to expand $(\alpha\sigma + \frac{1}{s+\xi})^n$ and invert the Laplace transform (3.2) term by term by using the residue theorem, to obtain

$$g(r) = \sum_{n=1}^{\infty} \psi_n(r-n\sigma)\Theta(r-n\sigma), \quad (3.16)$$

$$\begin{aligned} \psi_n(r) = & \frac{1}{\rho} \frac{1}{(\alpha\sigma + 1/\xi)^n} \left[(\alpha\sigma)^n \delta_+(r) + \sum_{k=1}^n \binom{n}{k} \right. \\ & \left. \times (\alpha\sigma)^{n-k} \frac{r^{k-1} e^{-\xi r}}{(k-1)!} \right], \end{aligned} \quad (3.17)$$

which is the correct result found in Ref. [6] with a different method.

IV. EXACT PROPERTIES OF THE SPS MODEL

Next we turn our attention to the corresponding penetrable SPS counterpart. Following Ref. [4], the basic idea hinges on deducing the exact low-density orders of the SPS model from those of the SHS model, which can be evaluated

exactly. Each term $y_n(r)$ can be represented as a sum of suitable diagrams, whose forms for $y_1(r)$ and $y_2(r)$ were given in Ref. [4] and will not be repeated here. Each bond in the diagrams corresponds to a Mayer function $f(r)$ and the ones for the SPS and SHS models are related by Eq. (2.9). For the SHS model previously discussed, the exact cavity function $y(r)$ does not have a Dirac δ function at $r=\sigma$ and the regular part is continuous at that point. Neither of these two properties is any longer true for the SPS model, as further elaborated below. Here and in the following we set $\sigma=1$ for simplicity.

The result is

$$y_1^{(SPS)}(r) = \gamma_r^2 y_1^{(SHS)}(r), \tag{4.1}$$

$$y_2^{(SPS)}(r) = \gamma_r^3 y_{2A}^{(SHS)}(r) + 2\gamma_r^4 y_{2B}^{(SHS)}(r) + \frac{\gamma_r^4}{2} y_{2C}^{(SHS)}(r) + \frac{\gamma_r^5}{2} y_{2D}^{(SHS)}(r), \tag{4.2}$$

where the first-order density term is

$$y_1^{(SHS)}(r) = (2 - r - 2\alpha)\Theta(2 - r) + \alpha^2[2\delta_+(r) + \delta_+(r - 2)]. \tag{4.3}$$

Note that this has a δ singularity at $r=0$ and is continuous at $r=1$. For the second order in density we have

$$y_{2A}^{(SHS)}(r) = [-(3 - r^2) + 6\alpha(1 - \alpha)]\Theta(1 - r) + \left(-\frac{1}{2}(3 - r)^2 + 3\alpha(3 - \alpha - r)\right)[\Theta(3 - r) - \Theta(1 - r)] + \alpha^3[3\delta_+(r - 1) + \delta_+(r - 3)], \tag{4.4}$$

$$y_{2B}^{(SHS)}(r) = \left(\frac{1}{2}(6 - 2r - r^2) - \alpha(6 - 6\alpha - r)\right)\Theta(1 - r) + \left(\frac{1}{2}(2 - r)(4 - r) - \alpha(8 - 4\alpha - 3r)\right) \times [\Theta(2 - r) - \Theta(1 - r)] + \alpha^2(1 - 2\alpha)[2\delta_+(r) + \delta_+(r - 2)] - 2\alpha^3\delta_+(r - 1), \tag{4.5}$$

$$y_{2C}^{(SHS)}(r) = [y_1^{(SHS)}(r)]^2, \tag{4.6}$$

$$y_{2D}^{(SHS)}(r) = [-(3 - 2r) + 2\alpha(3 - 3\alpha - r)]\Theta(1 - r) + [-(2 - r)^2 + 4\alpha(2 - \alpha - r)][\Theta(2 - r) - \Theta(1 - r)] + 2\alpha^3[6\delta_+(r) + \delta_+(r - 1) + 3\delta_+(r - 2)] - \alpha^4[4\delta_+^2(r) + \delta_+^2(r - 2)]. \tag{4.7}$$

The functions (4.4)–(4.7) present some peculiar properties. In particular, (i) the regular parts of $y_{2A}^{(SHS)}(r)$, $y_{2B}^{(SHS)}(r)$, and $y_{2D}^{(SHS)}(r)$ are discontinuous at $r=1$; (ii) $y_{2A}^{(SHS)}(r)$, $y_{2B}^{(SHS)}(r)$, and $y_{2D}^{(SHS)}(r)$ have a δ singularity at $r=1$; and (iii) $y_{2C}^{(SHS)}(r)$ and $y_{2D}^{(SHS)}(r)$ present δ^2 singularities at $r=0$ and 2. However, these three classes of singularities cancel out when setting $\gamma_r=1$ in Eq. (4.2) to obtain the total second-order function $y_2^{(SHS)}(r)$ [31]. On the other hand, since for SPS $y_{2A}^{(SHS)}(r)$, $y_{2B}^{(SHS)}(r)$, $y_{2C}^{(SHS)}(r)$, and $y_{2D}^{(SHS)}(r)$ are weighted by different powers of γ_r (3, 4, 4, and 5, respectively), the corresponding exact second-order cavity function is discontinuous at $r=1$ and has a δ singularity at $r=1$ and δ^2 singularities at $r=0$ and 2. The δ singularity at $r=1$ is responsible for a diverging fourth virial coefficient of the SPS model (see Sec. V B below).

V. EXACT PROPERTIES OF THE PSW MODEL

A. Calculation of y_1 and y_2

As already mentioned, the SPS model suffers from the same drawbacks as the original SHS model plus some additional ones, so that it can hardly be regarded as a sound model in higher dimensions. However it has served as a test bench for analytical techniques. Armed with these tools, we can now tackle the more difficult PSW model, which has the SW fluid as a reference model. We recall that the latter does not have an exact solution in higher dimensions but it is amenable to an exact treatment in one dimension [8]. The discussion follows closely the route already introduced for the SPS model, namely, the density expansion, Eq. (3.7). The radial distribution function $g(r)$ is related to the cavity function $y(r)$ by Eq. (3.6) which with the help of Eqs. (2.2) and (2.3) yields

$$g(r) = \begin{cases} (1 - \gamma_r)y(r), & r < 1, \\ (1 + \gamma\gamma_r)y(r), & 1 < r < 1 + \Delta, \\ y(r), & r > 1 + \Delta. \end{cases} \tag{5.1}$$

As in the SPS model, the cavity function can be exactly computed up to second order in density, this time by reducing the problem to the solution of the SW model.

The first-order term reads ($\Delta < 1$)

$$y_1(r) = \gamma_r^2 \begin{cases} 2(1 + \gamma^2\Delta) - r(1 + 2\gamma + 2\gamma^2), & 0 \leq r \leq \Delta, \\ 2 - 2\gamma\Delta - r, & \Delta \leq r \leq 2, \\ \gamma(2 + \gamma)(r - 2) - 2\gamma\Delta, & 2 \leq r \leq 2 + \Delta, \\ (2 + 2\Delta - r)\gamma^2, & 2 + \Delta \leq r \leq 2 + 2\Delta, \\ 0, & 2 + 2\Delta \leq r. \end{cases} \tag{5.2}$$

SANTOS, FANTONI, AND GIACOMETTI

PHYSICAL REVIEW E 77, 051206 (2008)

The second order can be reduced to the calculation of the corresponding diagrams of the SW model as anticipated. We find

$$y_2(r) = \gamma_r^3 y_{2A}^{(SW)}(r) + 2\gamma_r^4 y_{2B}^{(SW)}(r) + \frac{\gamma_r^4}{2} y_{2C}^{(SW)}(r) + \frac{\gamma_r^5}{2} y_{2D}^{(SW)}(r), \quad (5.3)$$

where the explicit calculation of the various terms is described in Appendix B and is given by Eqs. (B1), (B2), (B4), and (B8). It can be checked that these expressions reduce to those of the SPS model, Eqs. (4.4)–(4.7), in the limit $\gamma \rightarrow \infty$ and $\Delta \rightarrow 0$ with $\alpha = \gamma\Delta/\sigma = \text{const}$.

B. Computation of B_2 , B_3 , and B_4

The EOS can be obtained from the knowledge of the radial distribution function $g(r)$ through a number of routes. The most common ones are the virial route

$$\frac{\beta P}{\rho} \equiv Z(\rho, \beta) = 1 + 2^{d-1} v_d \rho \int_0^\infty dr r^d y(r) \frac{\partial}{\partial r} f(r), \quad (5.4)$$

the compressibility route

$$\left(\beta \frac{\partial P}{\partial \rho} \right)^{-1} \equiv \chi(\rho, \beta) = 1 + 2^d v_d \rho \int_0^\infty dr r^{d-1} [g(r) - 1], \quad (5.5)$$

and the energy route

$$\frac{U}{N} \equiv u(\rho, \beta) = \frac{d}{2\beta} \left(1 + 2^d v_d \rho \beta \int_0^\infty dr r^{d-1} \phi(r) g(r) \right), \quad (5.6)$$

where d is the dimensionality of the system and $v_d = (\pi/4)^{d/2} / \Gamma(1+d/2)$ is the volume of a d -dimensional sphere of unit diameter. Thermodynamic consistency for the exact $g(r)$ requires the three routes to be completely equivalent and hence

$$\chi^{-1}(\rho, \beta) = \frac{\partial}{\partial \rho} [\rho Z(\rho, \beta)], \quad (5.7)$$

$$\rho \frac{\partial}{\partial \rho} u(\rho, \beta) = \frac{\partial}{\partial \beta} Z(\rho, \beta). \quad (5.8)$$

For an approximate $g(r)$, on the other hand, the consistency is no longer guaranteed and different routes (or combinations of them) may lead to different results.

Let us specialize to the one-dimensional case of the PSW model, where we have just derived the exact $g(r)$ up to second order in a density expansion. Equations (5.4)–(5.6) become, using the potential (2.1),

$$Z(\rho, \beta) = 1 + \rho \gamma_r [(1 + \gamma)y(1) - \gamma(1 + \Delta)y(1 + \Delta)], \quad (5.9)$$

$$\chi(\rho, \beta) = 1 + 2\rho \left(\int_0^1 dr [(1 - \gamma_r)y(r) - 1] + \int_1^{1+\Delta} dr [(1 + \gamma_r\gamma)y(r) - 1] + \int_{1+\Delta}^{+\infty} dr [y(r) - 1] \right), \quad (5.10)$$

$$u(\rho, \beta) = \frac{1}{2\beta} + \rho \left(\epsilon_r (1 - \gamma_r) \int_0^1 dr y(r) - \epsilon_a (1 + \gamma_r\gamma) \int_1^{1+\Delta} dr y(r) \right). \quad (5.11)$$

Inserting the expansion (3.7) for the cavity function $y(r)$, we find

$$Z = 1 + B_2 \rho + B_3 \rho^2 + B_4 \rho^3 + \dots, \quad (5.12)$$

$$\chi = 1 + \chi_2 \rho + \chi_3 \rho^2 + \chi_4 \rho^3 + \dots, \quad (5.13)$$

$$u = \frac{1}{2\beta} + u_2 \rho + u_3 \rho^2 + u_4 \rho^3 + \dots. \quad (5.14)$$

Clearly Eq. (5.12) is the virial expansion for the compressibility factor Z , whereas (5.13) and (5.14) are the analogous expansions for the isothermal compressibility χ and the energy per particle u . If the exact coefficients y_n appearing in Eq. (3.7) are known, the above three quantities provide the identical exact EOS.

On starting from the second-order values B_2 , χ_2 , and u_2 one can obtain perturbatively higher orders term by term from the knowledge of $y_n(r)$. The result can be cast into the form

$$B_2 = \gamma_r (1 - \gamma\Delta), \quad \chi_2 = -2B_2,$$

$$u_2 = \epsilon_r (1 - \gamma_r) - \epsilon_a (1 + \gamma_r\gamma)\Delta, \quad (5.15)$$

$$B_n = \gamma_r [(1 + \gamma)y_{n-2}(1) - \gamma(1 + \Delta)y_{n-2}(1 + \Delta)], \quad n \geq 3, \quad (5.16)$$

$$\chi_n = 2 \left((1 - \gamma) \int_0^1 dr y_{n-2}(r) + (1 + \gamma_r\gamma) \int_1^{1+\Delta} dr y_{n-2}(r) + \int_{1+\Delta}^\infty dr y_{n-2}(r) \right), \quad n \geq 3, \quad (5.17)$$

$$u_n = \epsilon_r (1 - \gamma_r) \int_0^1 dr y_{n-2}(r) - \epsilon_a (1 + \gamma_r\gamma) \times \int_1^{1+\Delta} dr y_{n-2}(r), \quad n \geq 3. \quad (5.18)$$

Note that B_n depends upon y_{n-2} so that knowledge of the exact y_1 and y_2 allows the computation of the exact virial coefficients up to B_4 . The third- and fourth-order results can be obtained from Eqs. (5.2) and (5.3). After some algebra, one gets

PENETRABLE SQUARE-WELL FLUIDS: EXACT RESULTS...

PHYSICAL REVIEW E 77, 051206 (2008)

$$B_3 = \gamma_r^3 [1 - \gamma\Delta(2 - \Delta - 2\gamma\Delta)], \quad (5.19)$$

$$\chi_3 = 4B_2^2 - 3B_3, \quad (5.20)$$

$$u_3 = \frac{\epsilon_r}{2} \gamma_r^2 (1 - \gamma_r) [3 - 2\gamma\Delta(2 - \Delta - \gamma\Delta)] - \frac{\epsilon_a}{2} \gamma_r^2 (1 + \gamma_r \gamma) \Delta(2 - \Delta - 4\gamma\Delta) = \frac{1}{2} \frac{\partial}{\partial \beta} B_3, \quad (5.21)$$

$$B_4 = -\frac{\gamma_r^6}{2} [1 - \gamma\Delta(3 - 3\Delta - 6\gamma\Delta + \Delta^2 + 4\gamma\Delta^2 + 3\gamma^2\Delta^2 - \gamma^3\Delta^2)] + \frac{\gamma_r^5}{2} [7 - \gamma\Delta(21 - 15\Delta - 36\gamma\Delta + 3\Delta^2 + 16\gamma\Delta^2 - 16\gamma^2\Delta^2 - 4\gamma^3\Delta^2)] - \frac{\gamma_r^4}{2} [4 - \gamma\Delta(12 - 6\Delta - 18\gamma\Delta + \Delta^2 + 3\gamma\Delta^2 + 3\gamma^2\Delta^2 - 3\gamma^3\Delta^2)], \quad (5.22)$$

$$\chi_4 = -4(2B_2^3 - 3B_2B_3 + B_4), \quad (5.23)$$

$$u_4 = \frac{1}{3} \frac{\partial}{\partial \beta} B_4. \quad (5.24)$$

The three routes provide consistently identical results for B_3 and B_4 , i.e., the relations (5.7) and (5.8) are verified, as they should be. In the energy case the following identity is needed:

$$\begin{aligned} \frac{\partial}{\partial \beta} &= \frac{\partial \gamma_r}{\partial \beta} \frac{\partial}{\partial \gamma_r} + \frac{\partial \gamma}{\partial \beta} \frac{\partial}{\partial \gamma} \\ &= \epsilon_r (1 - \gamma_r) \frac{\partial}{\partial \gamma_r} + \frac{\epsilon_a (1 + \gamma_r \gamma) - \epsilon_r \gamma (1 - \gamma_r)}{\gamma_r} \frac{\partial}{\partial \gamma}. \end{aligned} \quad (5.25)$$

Equation (5.22) gives the exact fourth virial coefficient as a function of the three relevant parameters of the PSW model, namely, γ_r , γ , and Δ . The results for the PS and SW models are recovered as

$$\lim_{\epsilon_a \rightarrow 0} B_4 = \lim_{\epsilon_a \rightarrow \epsilon_r} \frac{B_4}{(1 + \Delta)^3} = \gamma_r^4 \left(-\frac{\gamma_r^2}{2} + \frac{7\gamma_r}{2} - 2 \right), \quad (5.26)$$

$$\lim_{\epsilon_r \rightarrow \infty} B_4 = 1 - \gamma\Delta \left(3 - 3\Delta - 6\gamma\Delta + \frac{1}{2}\Delta^2 + \frac{9}{2}\gamma\Delta^2 + 5\gamma^2\Delta^2 \right), \quad (5.27)$$

respectively. On the other hand, while B_2 and B_3 are well defined in the SPS limit ($\gamma \rightarrow \infty$ and $\Delta \rightarrow 0$ with $\alpha = \gamma\Delta = \text{finite}$) [see Eqs. (5.15) and (5.19)], the presence of the terms $\gamma^3\Delta^2$ in Eq. (5.22) implies that $B_4 \rightarrow \infty$ in the SPS model. Equation (5.16) shows that this is a direct consequence of the divergence of $y_2^{(\text{SPS})}(r)$ at $r=1$. However,

$y_2^{(\text{SHS})}(1) = \text{finite}$, so that B_4 is well defined in the SHS model ($\gamma_r=1$), as shown by Eq. (5.27).

The second, third, and fourth virial coefficients for the PSS model ($\epsilon_a < 0$) are still given by Eqs. (5.15), (5.19), and (5.22), except that $\gamma < 0$. In the case of the HPS model ($\epsilon_a < 0$ and $\epsilon_r \rightarrow 0$ or, equivalently, $\gamma_a < 0$, $\gamma = \gamma_a / \gamma_r$, and $\gamma_r \rightarrow 0$), one gets

$$\lim_{\epsilon_r \rightarrow 0} B_2 = -\gamma_a \Delta, \quad \lim_{\epsilon_r \rightarrow 0} B_3 = 0, \quad \lim_{\epsilon_r \rightarrow 0} B_4 = -\frac{3}{2} \gamma_a^4 \Delta^3. \quad (5.28)$$

The special case of the HHS model is obtained by further taking the limit $\epsilon_a \rightarrow \infty$ ($\gamma_a \rightarrow -1$).

VI. SOME ILLUSTRATIVE CASES AND COMPARISON WITH THE PY AND HNC APPROXIMATIONS

The approximate character of a given closure can be typically inferred by looking at $g_2(r) = e^{-\beta\phi(r)} y_2(r)$ along with the corresponding fourth virial coefficient B_4 . Being coefficients in a density expansion, both can be either positive or negative. We now plot the exact $g_2(r)$ and B_4 for some illustrative cases and compare them with the PY and HNC theories (3.8) and (3.9). The PY and HNC results corresponding to Eq. (5.3) are [30]

$$y_2^{\text{PY}}(r) = \gamma_r^3 y_{2A}^{(\text{SW})}(r) + 2\gamma_r^4 y_{2B}^{(\text{SW})}(r), \quad (6.1)$$

$$y_2^{\text{HNC}}(r) = \gamma_r^3 y_{2A}^{(\text{SW})}(r) + 2\gamma_r^4 y_{2B}^{(\text{SW})}(r) + \frac{\gamma_r^4}{2} y_{2C}^{(\text{SW})}(r). \quad (6.2)$$

Comparison with Eq. (5.3) shows that the HNC theory neglects $y_{2D}^{(\text{SW})}(r)$ and the PY theory neglects, in addition, $y_{2C}^{(\text{SW})}(r)$. As a consequence, the expression for the fourth virial coefficient in the PY and HNC approximations depends on the thermodynamic route. The corresponding results can be found in Appendix C.

Let us start with $g_2(r)$. As a prototypical PSW system we have chosen $\epsilon_a / \epsilon_r = 0.25$ and $\Delta = 0.5$. Figure 2 shows $g_2(r)$ for $k_B T / \epsilon_r = 0.5$ and 1. It can be observed that the HNC and PY approximations tend to overestimate and underestimate, respectively, the values of $g_2(r)$ in the overlapping region $r < 1$. This is due to the fact that $y_{2D}^{(\text{SW})}(r)$ is generally negative in the region $r < 1$, while $y_{2C}^{(\text{SW})}(r)$ is positive definite and larger than the magnitude of $y_{2D}^{(\text{SW})}(r)$. Inside the well ($1 < r < 1 + \Delta$) the PY and HNC curves practically coincide at $k_B T / \epsilon_r = 0.5$, both being rather inaccurate, while at the higher temperature $k_B T / \epsilon_r = 1$ the PY prediction is quite good. Moreover, the PY theory is a better approximation than the HNC theory for $r > 2$. This is explained by the fact that $y_{2C}^{(\text{SW})}(r) + y_{2D}^{(\text{SW})}(r) = 0$ in the region $r > 2$, so that $g_2^{\text{PY}}(r)$ coincides with the exact $g_2(r)$ for $r > 2$ in the case of the SW model ($\gamma_r = 1$). If $\gamma_r < 1$ the combination $y_{2C}^{(\text{SW})}(r) + \gamma_r y_{2D}^{(\text{SW})}(r)$ does not vanish for $r > 2$ but is still rather small for the cases of Fig. 2. For $r > 2 + 2\Delta$, both $g_2^{\text{HNC}}(r)$ and $g_2^{\text{PY}}(r)$ become exact since $y_{2C}^{(\text{SW})}(r)$ and $y_{2D}^{(\text{SW})}(r)$ vanish in that region.

Figure 3 depicts the function $g_2(r)$ for a representative case of the PSS model (see Sec. II C). Most of the preceding

SANTOS, FANTONI, AND GIACOMETTI

PHYSICAL REVIEW E 77, 051206 (2008)

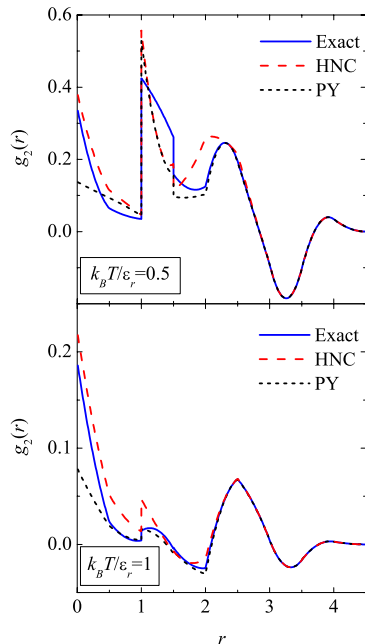


FIG. 2. (Color online) Second-order radial distribution function $g_2(r)$ for a PSW model with $\epsilon_a/\epsilon_r=0.25$, $\Delta=0.5$, and $k_B T/\epsilon_r=0.5$ (top panel) and 1 (bottom panel). The solid, long-dashed, and short-dashed lines correspond to the exact result, the HNC approximation, and the PY approximation, respectively.

comments in connection with Fig. 2 apply here as well. Finally, the function $g_2(r)$ corresponding to the HPS model is shown in Fig. 4 for $\Delta=0.5$ and two temperatures: $k_B T/|\epsilon_a| = 0$ and 0.5. Note that the zero-temperature case is equivalent to the HHS limit. It is interesting to note that the curves corresponding to both temperatures are quite similar, except for a change of scale. In the HPS model the HNC theory gives the exact $g_2(r)$ because, for large $|\gamma|$, $y_{2D}^{(SW)}(r)$ scales with γ^4 , while it has a weight γ^5 and so does not contribute to $y_2(r)$. Similarly, $y_{2B}^{(SW)}(r)$ scales with γ^3 and so it does not contribute to $y_2(r)$ either. On the other hand, $\gamma_r^4 y_{2C}^{(SW)}(r)$ is different from zero in the regions $0 \leq r \leq \Delta$ and $2 \leq r \leq 2 + 2\Delta$ and it is there where the PY theory fails, yielding $g_2^{PY}(r)=0$.

In order to have a feeling of the behavior of the exact B_4 , we now plot them for some representative values of the parameters. Figure 5 shows the exact [see Eq. (5.22)] and the approximate (see Appendix C) values of the fourth virial coefficient as functions of temperature for the same PSW model as considered in Fig. 2, i.e., the one defined by $\epsilon_a/\epsilon_r=0.25$ and $\Delta=0.5$. While the exact B_4 goes to $-\infty$ as $T \rightarrow 0$, the HNC and PY theories artificially predict a divergence to $+\infty$. We can observe that the best agreement with the exact curve corresponds to $B_4^{\text{HNC},c}$ up to $k_B T/\epsilon_r \approx 0.5$ and to $B_4^{\text{PY},c}$ thereafter. The worst behaviors correspond to $B_4^{\text{HNC},v} = B_4^{\text{HNC},e}$ and $B_4^{\text{PY},v}$.

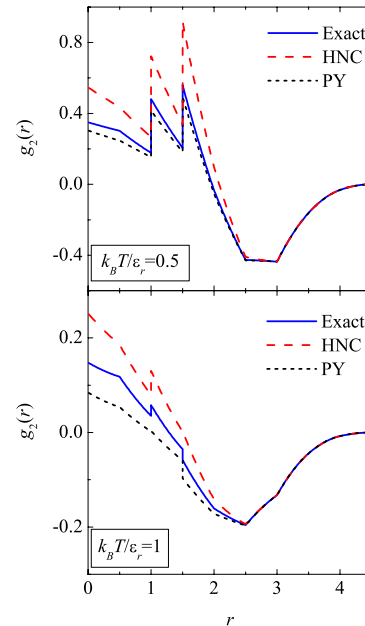


FIG. 3. (Color online) Second-order radial distribution function $g_2(r)$ for a PSS model with $\epsilon_a/\epsilon_r=-0.5$, $\Delta=0.5$, and $k_B T/\epsilon_r=0.5$ (top panel) and 1 (bottom panel). The solid, long-dashed, and short-dashed lines correspond to the exact result, the HNC approximation, and the PY approximation, respectively.

The results for the PSS model considered in Fig. 3, namely, $\epsilon_a/\epsilon_r=-0.5$ and $\Delta=0.5$, are displayed in Fig. 6. For low temperatures this model reduces to the HS model of diameter $1+\Delta$. It is found that $B_4^{\text{PY},v}$ and, especially, $B_4^{\text{PY},e}$ present an excellent agreement with the exact B_4 . On the other hand, the poorest performances are presented by $B_4^{\text{HNC},v} = B_4^{\text{HNC},e}$ and $B_4^{\text{PY},e}$.

We have also evaluated B_4 for the HPS model at various values of $k_B T/|\epsilon_a|$, as depicted in Fig. 7, and compared with the PY approximation (compressibility route). As said before, the HNC theory becomes exact for the HPS model. Interestingly, in this case both the virial and the energy routes from the PY approximation yield exact results, even though $y_2^{\text{PY}}(r)$ is not exact.

It is worthwhile noting that B_4 is not a monotonic function of temperature in the PSW model (see Fig. 5): it is negative for low temperatures, reaches a positive maximum value at an intermediate temperature, and then decays, reaching a very small negative minimum value at a certain temperature, and finally going to zero from below. Although hardly apparent in Fig. 6, the behavior of B_4 is also non-monotonic in the PSS model: it is generally positive and decays as the temperature increases, but eventually reaches a very small negative minimum value and thereafter tends to zero from below. In contrast, the fourth virial coefficient of the HPS model (see Fig. 7) is negative definite and monotonically increases with increasing temperature.

PENETRABLE SQUARE-WELL FLUIDS: EXACT RESULTS...

PHYSICAL REVIEW E 77, 051206 (2008)

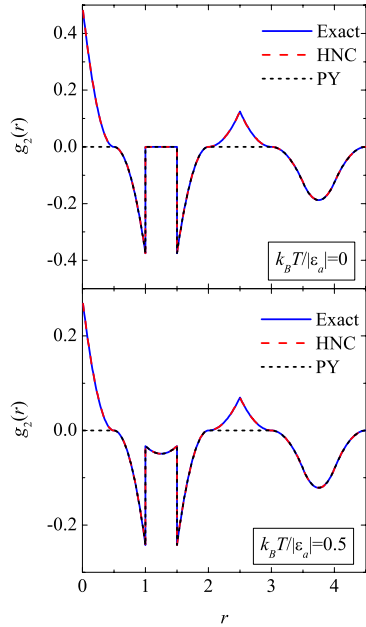


FIG. 4. (Color online) Second-order radial distribution function $g_2(r)$ for the HPS model with $\Delta=0.5$ and $k_B T/|\epsilon_a|=0.5$ (bottom panel) and 0 (top panel, corresponding to the HHS model). The solid, long-dashed, and short-dashed lines correspond to the exact result, the HNC approximation, and the PY approximation, respectively. Note that the HNC approximation provides the exact result in the HPS model.

VII. CONCLUSIONS AND OUTLOOK

In this paper, we have introduced the PSW model and outlined a number of exact results for this model in one

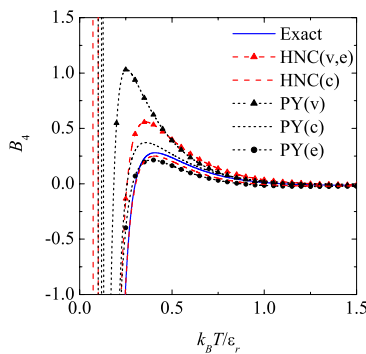


FIG. 5. (Color online) Fourth virial coefficient B_4 as a function of $k_B T/\epsilon_r$ for a PSW model with $\epsilon_a/\epsilon_r=0.25$ and $\Delta=0.5$. The solid, dashed, and dotted lines correspond to the exact result, the HNC approximation (virial-energy and compressibility routes), and the PY approximation (virial, compressibility, and energy routes), respectively.

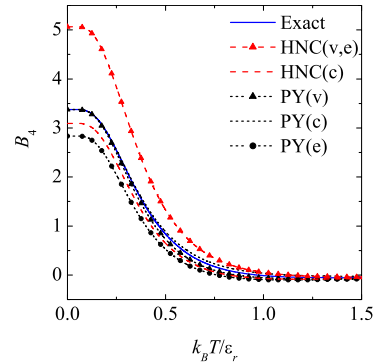


FIG. 6. (Color online) Fourth virial coefficient B_4 as a function of $k_B T/\epsilon_r$ for a PSS model with $\epsilon_a/\epsilon_r=-0.5$ and $\Delta=0.5$. The solid, dashed, and dotted lines correspond to the exact result, the HNC approximation (virial-energy and compressibility routes), and the PY approximation (virial, compressibility, and energy routes), respectively.

dimension. The potential contains two energy scales (the core barrier ϵ_r and the well depth ϵ_a) and two length scales (the core diameter σ and the well width Δ). This model is a variation of the widely used square-well one with a finite energy barrier replacing the hard core. As such, this is not a nearest-neighbor system and there exists no general approach leading to an exact solution even in the one-dimensional case. In spite of this we have been able to obtain the exact first few coefficients in the density expansions of the relevant structural and thermodynamical properties. Specifically, we have computed both the cavity and radial distribution functions up to second order in density and the virial expansion up to fourth order. As a stringent test of the calculations, we have explicitly checked that different routes to thermodynamics (virial, compressibility, and energy) are consistent with one another up to this order.

This model includes a variety of other models as special cases. By taking the limit of an infinitely narrow and deep

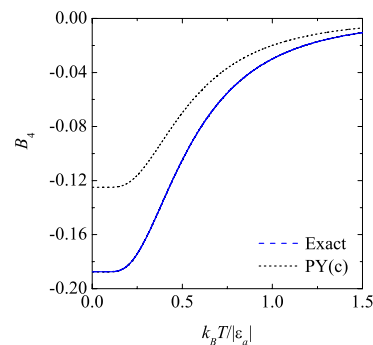


FIG. 7. (Color online) Fourth virial coefficient B_4 as a function of $k_B T/|\epsilon_a|$ for a HPS model with $\Delta=0.5$. The dashed line corresponds to the exact result whereas the dotted line corresponds to the PY approximation (compressibility route).

SANTOS, FANTONI, AND GIACOMETTI

PHYSICAL REVIEW E 77, 051206 (2008)

well ($\epsilon_a \rightarrow \infty$, $\Delta \rightarrow 0$) we obtain the SPS model which can be also reckoned as a variant of the SHS model with penetrable core. Upon reversing the sign of the attractive energy scale ϵ_a we obtain a PSS model with successive soft repulsive barriers of decreasing height. If the second barrier is higher than the first ($-\epsilon_a > \epsilon_r > 0$), we find a potential that is attractive for short distances and repulsive for larger distances. An interesting situation, that we have denoted as the HPS model, corresponds to $-\epsilon_a > \epsilon_r = 0$. In the limit of zero temperature (or, equivalently, $\epsilon_a \rightarrow -\infty$) the HPS model becomes the HHS model, characterized by an infinitely high barrier between σ and $\sigma + \Delta$. Here the equilibrium state consists of "chains" of connected particles: two adjacent particles of the same chain move freely, provided that the distance between their centers does not exceed σ ; on the other hand, particles of different chains behave as hard spheres of diameter $\sigma + \Delta$. In the limit $|\epsilon_a| \rightarrow 0$ (and also if $-\epsilon_a = \epsilon_r > 0$) the PSW fluid reduces to the PS one, and all results obtained here are consistent with previous analysis on the PS model within this limit. Finally, all results smoothly converge to the HS limit when $\epsilon_r \rightarrow \infty$ and $|\epsilon_a| \rightarrow 0$ (or $-\epsilon_a = \epsilon_r \rightarrow \infty$), as expected.

The combined effect of the absence of a hard core and the presence of a finite attractive part of the PSW potential raises the issue of the existence of a well-defined thermodynamic limit of the system. We have analyzed this issue in detail and we have assessed the limits of stability as a function of the ratio between the attractive and repulsive energy scales: when $\epsilon_a/\epsilon_r \leq \frac{1}{2}$ the system is stable, whereas in the opposite case the system might be unstable (when $\epsilon_r > 0$ and $\epsilon_a < 0$ the system is always stable independently of the energy scales). The SPS limit turns out to be always unstable since the exact fourth-order virial coefficient diverges, unlike the corresponding SHS counterpart which is well behaved.

A main advantage of exact relations is that one can assess the reliability of approximate theories. A comparison with PY and HNC closures unveils the corresponding strengths and weaknesses of both. We have found that each of them has a domain in space where it outperforms the other, and we have explained why this is so in terms of the exact and approximate behavior of the second-order cavity function $\gamma_2(r)$. As a general feature, the HNC approach tends to overestimate the cavity function within the core whereas the PY method has the opposite tendency. On the other hand, the PY method is consistently superior in the large- r region. Both approximate theories produce artifacts in the low-temperature region of the fourth virial coefficients.

It would be extremely interesting to extend the present work in some respects. While our analysis has provided a careful comparison of the PY and HNC approximate theories with respect to the exact result, we have not attempted a detailed physical interpretation of the results. This is because our exact analysis was limited to the lowest orders in density, which are expected to be valid only within a rather limited region of the phase diagram. It turns out, however, that even this limited knowledge can be exploited to construct rather precise approximations for the PSW model in the limits of low ($1 - \gamma_r \ll 1$) and high penetrability ($\gamma_r \ll 1$), for arbitrary value of the density. This analysis mirrors that already performed for the PS model [4,17], can be tested against numerical simulations, and nicely complements the exact low-

density results presented here. The boundedness of the class of penetrable-sphere potentials raises the possibility of a phase transition even in a one-dimensional system [32,33] and the presence of the attractive part might also give rise to additional transitions in the fluid phase. We plan to address this point in future work.

It is worth stressing that the large number of parameters present in the PSW fluid (two energy scales, two characteristic lengths, density, and temperature) may render the phase diagram analysis quite problematic, so an exact understanding of the low-dimensional behavior, where the analysis can be carried out almost fully analytically, is always welcome. Having done this, the extension to three dimensions should be facilitated, and our results predict an extremely rich phase diagram which might be useful to describe complex fluids with soft cores within a unified picture.

ACKNOWLEDGMENTS

We are grateful to C. Likos for suggesting that we look at the problem of Ruelle's instability. The research of A.S. has been supported by the Ministerio de Educación y Ciencia (Spain) through Grant No. FIS2007-60977. A.G. and R.F. acknowledge support from the Italian MIUR (PRIN-COFIN).

APPENDIX A: RUELLE'S STABILITY CRITERION

According to Ruelle's criterion, a sufficient condition of thermodynamic stability is [18,19]

$$U_N(x_1, \dots, x_N) = \sum_{i=1}^{N-1} \sum_{j=i+1}^N \phi(|x_i - x_j|) \geq -NB \quad (\text{A1})$$

for all configurations $\{x_i\}$, where B is a fixed bound.

Let us first demonstrate that for small repulsion ($\epsilon_r < 2\epsilon_a$) there exists at least one configuration violating the stability constraint. We consider a particular configuration where the N particles are distributed into N/s clusters of s overlapping particles each, so that the centers of the s particles belonging to the same cluster coincide (with a tolerance $\Delta/2$). Next, the centers of two adjacent clusters are separated by a distance between σ and $\sigma + \Delta$. The potential energy corresponding to this configuration is

$$U_N(s) = \frac{Ns(s-1)}{s-2} \epsilon_r - \left(\frac{N}{s} - 1\right) s^2 \epsilon_a. \quad (\text{A2})$$

The first term on the right-hand side represents the repulsive energy of the $s(s-1)/2$ pairs of each cluster, times the number of clusters. The second term is the attractive energy of the interaction between the s particles of each cluster and the s particles of its neighbor cluster, times the number of pairs of adjacent clusters. Obviously, the value of the total potential energy U_N depends on the value of s . The extreme cases are $s=1$ and N . We then see that the value that minimizes $U_N(s)$ is

PENETRABLE SQUARE-WELL FLUIDS: EXACT RESULTS...

PHYSICAL REVIEW E 77, 051206 (2008)

$$s_* = \frac{N}{2} \left(1 - \frac{\epsilon_r}{2\epsilon_a} \right), \quad (\text{A3})$$

which is meaningful only if $\epsilon_r < 2\epsilon_a$. The corresponding minimum value of $U_N(s)$ is

$$U_N(s_*) = -N \left[\frac{\epsilon_r}{2} + \frac{N}{16} \epsilon_a \left(2 - \frac{\epsilon_r}{\epsilon_a} \right)^2 \right], \quad \epsilon_r < 2\epsilon_a. \quad (\text{A4})$$

The quantity enclosed between square brackets grows linearly with N and so it is not bounded. Therefore, if $\epsilon_r < 2\epsilon_a$, there exists at least a configuration that violates Ruelle's criterion. On the other hand, we note that if $\epsilon_r > 2\epsilon_a$ the minimum of $U_N(s)$ is reached at $s=1$, in which case

$$U_N(s) \geq U_N(s=1) = -(N-1)\epsilon_a, \quad \epsilon_r > 2\epsilon_a, \quad (\text{A5})$$

so that all these special configurations are consistent with Ruelle's criterion. Indeed, we now show that no other configurations violate Ruelle's criterion if $\epsilon_r > 2\epsilon_a$ so that the model is thermodynamically stable if the above condition is satisfied.

Without loss of generality we can see any given configuration of N particles as a set of M clusters ($1 \leq M \leq N$), each cluster i being made of s_i overlapping particles (i.e., any pair of particles of a given cluster are separated a distance smaller than σ). For fixed M and $\{s_i\}$, the total potential energy can be decomposed as

$$U_N(\{s_i\}; M) = U_N^{\text{intra}}(\{s_i\}; M) + U_N^{\text{inter}}(\{s_i\}; M), \quad (\text{A6})$$

where

$$U_N^{\text{intra}}(\{s_i\}; M) = \frac{\epsilon_r}{2} \sum_{i=1}^M s_i(s_i - 1) \quad (\text{A7})$$

is the contribution associated with pairs of particles inside each cluster and U_N^{inter} is the contribution associated with pairs of particles belonging in different clusters. Note that in the latter contribution the energy for each pair can be ϵ_r (if the separation is smaller than σ), $-\epsilon_a$ (if the separation lies between σ and $\sigma+\Delta$), or zero (if the separation is larger than $\sigma+\Delta$). It is clear that the minimum value of U_N^{inter} is achieved when all the particles of a cluster interact attractively with all the particles of the neighbor cluster:

$$U_N^{\text{inter}}(\{s_i\}; M) \geq -\epsilon_a \sum_{i=1}^{M-1} s_i s_{i+1} > -\epsilon_a \sum_{i=1}^{M-1} s_i s_{i+1} - \epsilon_a s_1 s_M. \quad (\text{A8})$$

Therefore,

$$\begin{aligned} U_N(\{s_i\}; M) &> \frac{\epsilon_r}{2} \sum_{i=1}^M s_i(s_i - 1) - \frac{\epsilon_a}{2} \sum_{i=1}^M s_i(s_{i-1} + s_{i+1}) \\ &\equiv W_N(\{s_i\}; M), \end{aligned} \quad (\text{A9})$$

where $s_0 = s_M$ and $s_{M+1} = s_1$. Given M , what is the set of population numbers $\{s_i\}$ that minimizes W_N subject to the constraint that $\sum_{i=1}^M s_i = N$? Using a Lagrange multiplier λ , the problem reduces to solving

$$\begin{aligned} \frac{\partial}{\partial s_j} \left(W_N(\{s_i\}; M) - \lambda \sum_{i=1}^M s_i \right) &= \frac{\epsilon_r}{2} (2s_j - 1) - \epsilon_a (s_{j-1} + s_{j+1}) - \lambda \\ &= 0, \quad 1 \leq j \leq M. \end{aligned} \quad (\text{A10})$$

The solution is $s_i = N/M$ and $\lambda = (N/M)(\epsilon_r - 2\epsilon_a) - \epsilon_r/2$. This could have been expected by symmetry arguments. Therefore, given M clusters, the minimum W_N is obtained with a uniform distribution $s_i = N/M$. For $\epsilon_r > 2\epsilon_a$ we can thus write

$$\begin{aligned} U_N(\{s_i\}; M) &> W_N(\{s_i = N/M\}; M) \\ &= \frac{\epsilon_r}{2} M(N/M)(N/M - 1) - \epsilon_a M(N/M)^2 \\ &= (\epsilon_r/2 - \epsilon_a) N^2/M - N\epsilon_r/2 > -N\epsilon_r/2, \end{aligned} \quad (\text{A11})$$

which proves that Ruelle's stability criterion is satisfied.

APPENDIX B: SECOND-ORDER CAVITY FUNCTIONS FOR THE SW MODEL

The first-order term $y_1^{(\text{SW})}(r)$ (for $\Delta < \sigma \equiv 1$) is given by Eq. (5.2) with $\gamma_r = 1$. This allows for a straightforward determination of $y_{2C}^{(\text{SW})}(r)$ as

$$y_{2C}^{(\text{SW})}(r) = [y_1^{(\text{SW})}(r)]^2. \quad (\text{B1})$$

Next, one can also evaluate the Fourier transform of the integral corresponding to the 2A diagram. Going back to real space, the result is

$$\begin{aligned} y_{2A}^{(\text{SW})}(r) &= -\frac{3}{2} \gamma (1 + \gamma)^2 (1 - \Delta - r)^2 \Theta(1 - \Delta - r) + \frac{3}{2} (1 + \gamma) \\ &\quad \times (1 + 2\gamma + 3\gamma^2) (1 - r)^2 \Theta(1 - r) - \frac{3}{2} \gamma (2 + 4\gamma \\ &\quad + 3\gamma^2) (1 + \Delta - r)^2 \Theta(1 + \Delta - r) + \frac{3}{2} \gamma^2 (1 + \gamma) (1 \\ &\quad + 2\Delta - r)^2 \Theta(1 + 2\Delta - r) - \frac{1}{2} (1 + \gamma)^3 (3 - r)^2 \Theta(3 \\ &\quad - r) + \frac{3}{2} \gamma (1 + \gamma)^2 (3 + \Delta - r)^2 \Theta(3 + \Delta - r) - \frac{3}{2} \gamma^2 (1 \\ &\quad + \gamma) (3 + 2\Delta - r)^2 \Theta(3 + 2\Delta - r) + \frac{1}{2} \gamma^3 (3 + 3\Delta \\ &\quad - r)^2 \Theta(3 + 3\Delta - r). \end{aligned} \quad (\text{B2})$$

For $y_{2B}^{(\text{SW})}(r)$ we can make use of the identity

$$y_{2B}(r) = \int_{-\infty}^{\infty} ds y_1(s) f(s) f(|r-s|), \quad (\text{B3})$$

which leads to the result

$$\begin{aligned} y_{2B}^{(\text{SW})}(r) &= \gamma (1 + \gamma) (2 - \Delta - 4\gamma\Delta) (\Delta - r) \Theta(\Delta - r) + \gamma (1 \\ &\quad + \gamma)^2 (1 - \Delta - r)^2 \Theta(1 - \Delta - r) - (1 + 3\gamma + 5\gamma^2 \\ &\quad + 3\gamma^3) (1 - r)^2 \Theta(1 - r) + \gamma (2 + 4\gamma + 3\gamma^2) (1 + \Delta \end{aligned}$$

SANTOS, FANTONI, AND GIACOMETTI

PHYSICAL REVIEW E 77, 051206 (2008)

$$\begin{aligned}
 & -r)^2\Theta(1+\Delta-r)-\gamma^2(1+\gamma)(1+2\Delta-r)^2\Theta(1 \\
 & +2\Delta-r)+\frac{1}{2}(1+\gamma)^2(4-r-4\gamma\Delta)(2-r)\Theta(2-r) \\
 & -\gamma(1+\gamma)(4-r-4\gamma\Delta)(2+\Delta-r)\Theta(2+\Delta-r) \\
 & +\frac{1}{2}\gamma^2(4-r-4\gamma\Delta)(2+2\Delta-r)\Theta(2+2\Delta-r).
 \end{aligned} \tag{B4}$$

Computation of $y_{2D}^{(SW)}(r)$ is much more laborious and requires a different route. We go back to the general formalism and compute the exact $\tilde{\Omega}(s)$ from the Laplace transform (3.1), which is

$$\tilde{\Omega}(s) = \frac{e^{-s}}{s}(1 + \gamma - \gamma e^{-s\Delta}). \tag{B5}$$

Equation (3.4) then yields for the parameter ξ the following density expansion:

$$\xi = \rho + (1 - \gamma\Delta)\rho^2 + [1 - \gamma\Delta(2 - \Delta - 2\gamma\Delta)]\rho^3 + \dots \tag{B6}$$

Inserting this solution into Eq. (3.3) and inverting the Laplace transform (3.2), we can obtain the corresponding radial distribution function $g_2(r)$ correct up to second order in density. Use of Eq. (5.1) then yields the corresponding cavity function $y_2(r)$ and then $y_{2D}^{(SW)}(r)$ is given by the difference

$$y_{2D}^{(SW)}(r) = 2y_2(r) - 2y_{2A}^{(SW)}(r) - 4y_{2B}^{(SW)}(r) - 4y_{2C}^{(SW)}(r). \tag{B7}$$

This provides the result for $r \geq 1$. Inside the core we have three different regions under the assumption that $\Delta \leq 1$, namely, $0 \leq r \leq \Delta$, $\Delta \leq r \leq 1 - \Delta$, and $1 - \Delta \leq r \leq 1$. The quadratic expression in each region can be obtained by imposing continuity conditions and with some help from numerical evaluation. The final analytic result is

$$\begin{aligned}
 y_{2D}^{(SW)}(r) = & -2\gamma(1+\gamma)[(1+\gamma+\gamma^2)r-2+\Delta(1+3\gamma-\gamma^2)](\Delta \\
 & -r)\Theta(\Delta-r)-\gamma(1+\gamma)^2(1-\Delta-r)^2\Theta(1-\Delta-r) \\
 & +(1+3\gamma+5\gamma^2+3\gamma^3)(1-r)^2\Theta(1-r)-\gamma(2+4\gamma \\
 & +3\gamma^2)(1+\Delta-r)^2\Theta(1+\Delta-r)+\gamma^2(1+\gamma)(1+2\Delta \\
 & -r)^2\Theta(1+2\Delta-r)+(1+\gamma)^2[r(1-2\gamma-\gamma^2)-2 \\
 & +4\gamma+2\gamma^2+4\gamma\Delta](2-r)\Theta(2-r)+4\gamma^2(1+\gamma)(r \\
 & -2-\Delta+\gamma\Delta)(2+\Delta-r)\Theta(2+\Delta-r)-\gamma^4(2+2\Delta \\
 & -r)^2\Theta(2+2\Delta-r).
 \end{aligned} \tag{B8}$$

Note that the first derivative $y'(r)$ is discontinuous at $r = \Delta$, 2 , $2 + \Delta$, and $2 + 2\Delta$, as can be inferred from its explicit computation at this order in density.

APPENDIX C: CALCULATION OF B_4 FOR THE PSW MODEL IN THE PY AND HNC APPROXIMATIONS

Here the fourth virial coefficient predicted by the PY and HNC approximations via the various thermodynamic routes

(u =virial, c =compressibility, e =energy) are given.

1. PY approximation

Using Eq. (6.1), along with the recursion relations (5.15)–(5.18), we have

$$\begin{aligned}
 B_4^{PY,v} = & \gamma_r^5[3 - \gamma\Delta(9 - 7\Delta - 16\gamma\Delta + \Delta^2 + 6\gamma\Delta^2 + 6\gamma^2\Delta^2 \\
 & - 2\gamma^3\Delta^2)] - \frac{\gamma_r^4}{2}[4 - \gamma\Delta(12 - 6\Delta - 18\gamma\Delta + \Delta^2 + 3\gamma\Delta^2 \\
 & + 3\gamma^2\Delta^2 - 3\gamma^3\Delta^2)],
 \end{aligned} \tag{C1}$$

$$\chi_4^{PY} = -4(2B_2^3 - 3B_2B_3 + B_4^{PY,c}), \tag{C2}$$

$$\begin{aligned}
 B_4^{PY,c} = & \frac{\gamma_r^5}{3}[7 - \gamma\Delta(21 - 15\Delta - 36\gamma\Delta + 3\Delta^2 + 16\gamma\Delta^2 \\
 & + 16\gamma^2\Delta^2 - 4\gamma^3\Delta^2)] \\
 & - \frac{\gamma_r^4}{3}[4 - \gamma\Delta(12 - 6\Delta - 18\gamma\Delta + \Delta^2 + 3\gamma\Delta^2 + 3\gamma^2\Delta^2 \\
 & - 3\gamma^3\Delta^2)],
 \end{aligned} \tag{C3}$$

$$\begin{aligned}
 u_4^{PY} = & \frac{\gamma_r^3}{6}(1 + \gamma_r\gamma)\Delta[12 - 18\gamma_r - 6\Delta(1 - 2\gamma_r + 6\gamma - 10\gamma_r\gamma) \\
 & + \Delta^2(1 - 2\gamma_r + 6\gamma - 26\gamma_r\gamma + 9\gamma^2 - 36\gamma_r\gamma^2 - 12\gamma^3 \\
 & + 16\gamma_r\gamma^3)]\epsilon_a - \frac{\gamma_r^3}{6}(1 - \gamma_r)\Delta[16 - 28\gamma_r - 6\gamma\Delta(6 \\
 & - 11\gamma_r) + 6\gamma\Delta^2(3 - 8\gamma_r + 6\gamma - 14\gamma_r\gamma) - \gamma(1 + \gamma)\Delta^3(3 \\
 & - 10\gamma_r + 3\gamma - 28\gamma_r\gamma)]\epsilon_r.
 \end{aligned} \tag{C4}$$

The fourth virial coefficient associated with the energy route, $B_4^{PY,e}$, is obtained from Eq. (C4) as

$$B_4^{PY,e} = 3 \int_0^B d\beta' u_4^{PY}(\beta'). \tag{C5}$$

Its expression is quite long and so it is omitted here. In addition to its dependence on γ_r and γ , $B_4^{PY,e}$ depends on $\epsilon_a/(n_a\epsilon_a - n_r\epsilon_r)$ with $(n_a, n_r) = (1, 1), (1, 2), (1, 3), (1, 4), (2, 1), (2, 3), (3, 1), (3, 2), (4, 1)$.

It is instructive to consider some special cases. First, the results for the PS model correspond to the limit $\epsilon_a \rightarrow 0$ ($\gamma \rightarrow 0$) or $\epsilon_a \rightarrow -\epsilon_r$ ($\gamma \rightarrow -1$):

$$\lim_{\epsilon_a \rightarrow 0} B_4^{PY,v} = \lim_{\epsilon_a \rightarrow -\epsilon_r} \frac{B_4^{PY,v}}{(1 + \Delta)^3} = \gamma_r^4(3\gamma_r - 2), \tag{C6}$$

$$\lim_{\epsilon_a \rightarrow 0} B_4^{PY,c} = \lim_{\epsilon_a \rightarrow -\epsilon_r} \frac{B_4^{PY,c}}{(1 + \Delta)^3} = \gamma_r^4 \left(\frac{7\gamma_r}{3} - \frac{4}{3} \right), \tag{C7}$$

$$\lim_{\epsilon_a \rightarrow 0} B_4^{PY,e} = \lim_{\epsilon_a \rightarrow -\epsilon_r} \frac{B_4^{PY,e}}{(1 + \Delta)^3} = \gamma_r^4 \left(\frac{14\gamma_r}{5} - 2 \right). \tag{C8}$$

In the special case of the HPS model ($\epsilon_a < 0$ and $\epsilon_r \rightarrow 0$) one finds that $B_4^{PY,v}$ and $B_4^{PY,e}$ reduce to the exact result [see Eq. (5.28)] but $\lim_{\epsilon_r \rightarrow 0} B_4^{PY,c} = -\gamma_a^4\Delta^3$.

PENETRABLE SQUARE-WELL FLUIDS: EXACT RESULTS...

PHYSICAL REVIEW E 77, 051206 (2008)

The conventional SW model corresponds to $\epsilon_r \rightarrow \infty$ ($\gamma \rightarrow 1$):

$$\lim_{\epsilon_r \rightarrow \infty} B_4^{\text{PY},v} = 1 - \gamma\Delta \left(3 - 4\Delta - 7\gamma\Delta + \frac{1}{2}\Delta^2 + \frac{9}{2}\gamma\Delta^2 + \frac{9}{2}\gamma^2\Delta^2 - \frac{1}{2}\gamma^3\Delta^2 \right), \quad (\text{C9})$$

$$\lim_{\epsilon_r \rightarrow \infty} B_4^{\text{PY},c} = 1 - \gamma\Delta \left(3 - 3\Delta - 6\gamma\Delta + \frac{2}{3}\Delta^2 + \frac{13}{3}\gamma\Delta^2 + \frac{13}{3}\gamma^2\Delta^2 - \frac{1}{3}\gamma^3\Delta^2 \right), \quad (\text{C10})$$

$$\lim_{\epsilon_r \rightarrow \infty} B_4^{\text{PY},e} = \frac{4}{5} - \gamma\Delta \left(3 - 3\Delta - 6\gamma\Delta + \frac{1}{2}\Delta^2 + 5\gamma\Delta^2 + \frac{9}{2}\gamma^2\Delta^2 - \frac{1}{2}\gamma^3\Delta^2 \right). \quad (\text{C11})$$

If, furthermore, the SHS limit ($\gamma \rightarrow \infty$ and $\Delta \rightarrow 0$ with $\gamma\Delta = \text{const}$) is taken in Eqs. (C9)–(C11), an artificial divergence of B_4 is obtained.

The results corresponding to HS are obtained by taking either the limit $\epsilon_r \rightarrow \infty$ ($\gamma_r \rightarrow 1$) in Eqs. (C6)–(C8) or the limit $\epsilon_a \rightarrow 0$ ($\gamma \rightarrow 0$) in Eqs. (C9)–(C11). In either case one sees that the virial and compressibility routes yield the exact result, while the energy route value is wrong by a factor 4/5. A third possibility consists of taking the limit $\epsilon_a \rightarrow -\infty$ ($\gamma \rightarrow -1$) in Eqs. (C9)–(C11). However, in this last case the energy route yields an incorrect dependence on Δ :

$$\lim_{\epsilon_a \rightarrow -\infty} \lim_{\epsilon_r \rightarrow \infty} B_4^{\text{PY},e} = \frac{4}{5} + \frac{\Delta}{2}(6 + 6\Delta + \Delta^2). \quad (\text{C12})$$

The fact that the right-hand side of Eq. (C12) is not proportional to $(1+\Delta)^3$ implies that if one starts from $B_4^{\text{PY},e}$ for the PSS model of shoulder height and width $-\epsilon_a$ and Δ , respectively, and then one takes the limit $\epsilon_a \rightarrow -\infty$ to get the HS model of diameter $1+\Delta$, the result has an artificial dependence on Δ . This anomaly of the PY description was discussed in Ref. [34].

2. HNC approximation

Similarly to the preceding analysis, from Eq. (6.2) one gets

$$B_4^{\text{HNC},v} = \frac{3}{2} B_4^{\text{PY},c}, \quad (\text{C13})$$

$$\chi_4^{\text{HNC}} = -4(2B_2^3 - 3B_2B_3 + B_4^{\text{HNC},c}), \quad (\text{C14})$$

$$B_4^{\text{HNC},c} = \frac{5\gamma_r^5}{12} [7 - \gamma\Delta(21 - 15\Delta - 36\gamma\Delta + 3\Delta^2 + 16\gamma\Delta^2 + 16\gamma^2\Delta^2 - 4\gamma^3\Delta^2)] - \frac{\gamma_r^4}{2} [4 - \gamma\Delta(12 - 6\Delta - 18\gamma\Delta + \Delta^2 + 3\gamma\Delta^2 + 3\gamma^2\Delta^2 - 3\gamma^3\Delta^2)], \quad (\text{C15})$$

$$u_4^{\text{HNC}} = \frac{1}{3} \frac{\partial}{\partial \beta} B_4^{\text{HNC},v}. \quad (\text{C16})$$

Equation (C16) implies that $B_4^{\text{HNC},e} = B_4^{\text{HNC},v}$. This confirms that, in general, the energy and virial routes are thermodynamically consistent in the HNC approximation [35]. It is also noteworthy that the fourth virial coefficient predicted by the HNC approximation in the virial and energy routes is exactly three-halves the one predicted by the PY approximation in the compressibility energy route, Eq. (C13). This simple relation is not restricted to one-dimensional (1D) models since it also occurs in the 3D PS model [17]. It would be extremely interesting to check whether relation (C13) is a general property valid for any interaction potential and for any dimensionality.

In the PS and SW limits Eq. (C15) becomes

$$\lim_{\epsilon_a \rightarrow 0} B_4^{\text{HNC},c} = \lim_{\epsilon_a \rightarrow \epsilon_r} \frac{B_4^{\text{HNC},c}}{(1+\Delta)^3} = \gamma_r^4 \left(\frac{35\gamma_r}{12} - 2 \right), \quad (\text{C17})$$

$$\lim_{\epsilon_r \rightarrow \infty} B_4^{\text{HNC},c} = \frac{11}{12} - \gamma\Delta \left(\frac{11}{4} - \frac{13}{4}\Delta - 6\gamma\Delta + \frac{3}{4}\Delta^2 + \frac{31}{6}\gamma\Delta^2 + \frac{31}{6}\gamma^2\Delta^2 - \frac{1}{6}\gamma^3\Delta^2 \right), \quad (\text{C18})$$

respectively.

The three routes in the HNC theory yield the exact result (5.28) in the HPS limit. However, as in the case of the PY theory, an artificial divergence of B_4 is predicted in the SHS limit.

- [1] J. L. Barrat and J. P. Hansen, *Basic Concepts for Simple and Complex Liquids* (Cambridge University Press, Cambridge, U.K., 2003).
 [2] C. N. Likos, Phys. Rep. **348**, 267 (2001).
 [3] C. Marquest and T. A. Witten, J. Phys. (France) **50**, 1267 (1989).
 [4] Al. Malijevský and A. Santos, J. Chem. Phys. **124**, 074508 (2006).
 [5] Z. W. Salsburg, R. W. Zwanzig, and J. G. Kirkwood, J. Chem.

- Phys. **21**, 1098 (1953).
 [6] N. A. Seaton and E. D. Glandt, J. Chem. Phys. **84**, 4595 (1986).
 [7] S. B. Yuste and A. Santos, J. Stat. Phys. **72**, 703 (1993).
 [8] M. Heying and D. S. Corti, Fluid Phase Equilib. **220**, 85 (2004).
 [9] E. Tonks, Phys. Rev. **50**, 955 (1936).
 [10] R. P. Feynman, *Statistical Mechanics* (W.A. Benjamin, Reading, MA, 1972).

SANTOS, FANTONI, AND GIACOMETTI

PHYSICAL REVIEW E 77, 051206 (2008)

- [11] D. S. Corti and P. G. Debenedetti, *Phys. Rev. E* **57**, 4211 (1998).
- [12] J. L. Lebowitz and D. Zomick, *J. Chem. Phys.* **54**, 3335 (1971).
- [13] A. Santos, *Phys. Rev. E* **76**, 062201 (2007).
- [14] E. H. Lieb and D. C. Mattis, *Mathematical Physics in One Dimension* (Academic Press, New York, 1966); D. C. Mattis, *The Many-Body Problem: An Encyclopedia of Exactly Solved Models in One Dimension* (World Scientific, Singapore, 1993).
- [15] R. Fantoni, Ph.D. thesis, University of Trieste, 2003 (unpublished).
- [16] It may be useful to stress that in quantum statistical mechanics the condition of impenetrability in a one-dimensional fluid with periodic boundary conditions is responsible for the impossibility to treat the particles just as fermions or bosons but one necessarily has to introduce the anyonic fractional statistics. In classical statistical mechanics the change in the topology of phase space does not have such a dramatic consequence.
- [17] A. Santos and Al. Malijevský, *Phys. Rev. E* **75**, 021201 (2007).
- [18] M. E. Fisher and D. Ruelle, *J. Math. Phys.* **7**, 260 (1966).
- [19] D. Ruelle, *Statistical Mechanics: Rigorous Results* (Benjamin, London, 1969).
- [20] B. Widom and J. S. Rowlinson, *J. Chem. Phys.* **52**, 1670 (1970).
- [21] S. Torquato, *J. Chem. Phys.* **81**, 5079 (1984).
- [22] P. A. Rikvold and G. Stell, *J. Colloid Interface Sci.* **108**, 158 (1985); P. A. Rikvold and G. Stell, *J. Chem. Phys.* **82**, 1014 (1985).
- [23] A. A. Louis, P. G. Bolhuis, and J. P. Hansen, *Phys. Rev. E* **62**, 7961 (2000).
- [24] D. M. Heyes, M. J. Cass, and G. Rickayzen, *J. Chem. Phys.* **126**, 084510 (2007).
- [25] R. J. Baxter, *J. Chem. Phys.* **49**, 2770 (1968).
- [26] R. Fantoni, D. Gazzillo, A. Giacometti, M. Miller, and G. Pastore, *J. Chem. Phys.* **127**, 234507 (2007).
- [27] G. Stell, *J. Stat. Phys.* **63**, 1203 (1991).
- [28] R. Kikuchi, *J. Chem. Phys.* **23**, 2327 (1955).
- [29] Z. Elkoshi, H. Reiss, and A. D. Hammerich, *J. Stat. Phys.* **41**, 685 (1985).
- [30] J.-P. Hansen and I. R. McDonald, *Theory of Simple Liquids*, 3rd ed. (Academic Press, London, 2006).
- [31] Note that the cancellation of these three singularities does not occur in the HNC approximation, where $y_{2D}^{(SHS)}(r)$ is neglected. In the PY approximation both $y_{2C}^{(SHS)}(r)$ and $y_{2D}^{(SHS)}(r)$ are neglected, so that the singularities (i) and (ii) persist.
- [32] L. Acedo and A. Santos, *Phys. Lett. A* **323**, 427 (2004).
- [33] J. A. Cuesta and A. Sánchez, *J. Stat. Phys.* **115**, 869 (2004).
- [34] A. Santos, *Mol. Phys.* **104**, 3411 (2006).
- [35] T. Morita, *Prog. Theor. Phys.* **23**, 829 (1960); see also J. A. Barker and D. Henderson, *Rev. Mod. Phys.* **48**, 587 (1976).

Chapter 17

Two dimensional one-component plasma on a Flamm's paraboloid

Fantoni R. and Tellez G., J. Stat. Phys. **133**, 449 (2008)

Title: "Two-dimensional one-component plasma on a Flamm's paraboloid."

Abstract: We study the classical non-relativistic two-dimensional one-component plasma at Coulomb coupling $\Gamma = 2$ on the Riemannian surface known as Flamm's paraboloid which is obtained from the spatial part of the Schwarzschild metric. At this special value of the coupling constant, the statistical mechanics of the system is exactly solvable analytically. The Helmholtz free energy asymptotic expansion for the large system has been found. The density of the plasma, in the thermodynamic limit, has been carefully studied in various situations.

J Stat Phys (2008) 133: 449–489
DOI 10.1007/s10955-008-9616-x

Two-Dimensional One-Component Plasma on Flamm's Paraboloid

Riccardo Fantoni · Gabriel Téllez

Received: 5 June 2008 / Accepted: 13 August 2008 / Published online: 8 September 2008
© Springer Science+Business Media, LLC 2008

Abstract We study the classical non-relativistic two-dimensional one-component plasma at Coulomb coupling $\Gamma = 2$ on the Riemannian surface known as Flamm's paraboloid which is obtained from the spatial part of the Schwarzschild metric. At this special value of the coupling constant, the statistical mechanics of the system are exactly solvable analytically. The Helmholtz free energy asymptotic expansion for the large system has been found. The density of the plasma, in the thermodynamic limit, has been carefully studied in various situations.

Keywords Coulomb systems · One-component plasma · Non-constant curvature

1 Introduction

The system under consideration is a classical (non-quantum) two-dimensional one-component plasma: a system composed of one species of charged particles living in a two-dimensional surface, immersed in a neutralizing background, and interacting with the Coulomb potential. The one-component classical Coulomb plasma is exactly solvable in one dimension [1]. In two dimensions, in their 1981 work, B. Jancovici and A. Alastuey [2, 3] showed how the partition function and n -body correlation functions of the two-dimensional one-component classical Coulomb plasma (2dOCP) on a plane can be calculated exactly analytically at the special value of the coupling constant $\Gamma = \beta q^2 = 2$, where β is the inverse temperature and q the charge carried by the particles. This has been a very important result in statistical physics since there are very few analytically solvable models of continuous fluids in dimensions greater than one.

R. Fantoni
Istituto Nazionale per la Fisica della Materia and Dipartimento di Chimica Fisica, Università di Venezia,
S. Marta DD 2137, 30123 Venezia, Italy

G. Téllez (✉)
Grupo de Física Teórica de la Materia Condensada, Departamento de Física, Universidad de Los Andes,
A.A. 4976, Bogotá, Colombia
e-mail: gtellez@uniandes.edu.co

Since then, a growing interest in two-dimensional plasmas has led to study this system on various flat geometries [4–6] and two-dimensional curved surfaces: the cylinder [7, 8], the sphere [9–13] and the pseudosphere [14–16]. These surfaces have constant curvature and the plasma there is homogeneous. Therefore, it is interesting to study a case where the surface does not have a constant curvature.

In this work we study the 2dOCP on the Riemannian surface \mathcal{S} known as Flamm's paraboloid, which is obtained from the spatial part of the Schwarzschild metric. The Schwarzschild geometry in general relativity is a vacuum solution to the Einstein field equation which is spherically symmetric and in a two-dimensional world its spatial part has the form

$$ds^2 = \left(1 - \frac{2M}{r}\right)^{-1} dr^2 + r^2 d\varphi^2. \quad (1.1)$$

In general relativity, M (in appropriate units) is the mass of the source of the gravitational field. This surface has a hole of radius $2M$ and as the hole shrinks to a point (limit $M \rightarrow 0$) the surface becomes flat. It is worthwhile to stress that, while Flamm's paraboloid considered here naturally arises in general relativity, we will study the classical (i.e. non quantum) statistical mechanics of the plasma obeying non-relativistic dynamics. Our approach is to consider that the classical, non-relativistic, particles of the plasma are constrained to move in a curved surface, without any reference to general relativity. Recent developments for a statistical physics theory in special relativity have been made in [17, 18].

The "Schwarzschild wormhole" provides a path from the upper "universe" to the lower one. We will study the 2dOCP on a single universe, on the whole surface, and on a single universe with the "horizon" (the region $r = 2M$) grounded.

The Coulomb potential between two unit charges on this surface is defined as a solution of Poisson equation. Depending on the boundary conditions imposed, several Coulomb potentials can be considered. For example, we find that the Coulomb potential, in a single universe with a hard wall boundary at $r = 2M$, is given by $-\ln|z_1 - z_2| + \text{constant}$, where $z_i = (\sqrt{r_i} + \sqrt{r_i - 2M})^2 e^{i\varphi_i}$. This simple form will allow us to determine analytically the partition function and the n -body correlation functions at $\Gamma = 2$ by extending the original method of Jancovici and Alastuey [2, 3]. We will also compute the thermodynamic limit of the free energy of the system, and its finite-size corrections. These finite-size corrections to the free energy will contain the signature that Coulomb systems can be seen as critical systems in the sense explained in [5, 6].

The work is organized as follows: in Sect. 2, we describe the one-component plasma model and Flamm's paraboloid, i.e. the Riemannian surface \mathcal{S} where the plasma is embedded. In Sect. 3, we find the Coulomb pair potential on the surface \mathcal{S} and the particle-background potential. The Coulomb potential depends on the boundary conditions imposed. We consider three different cases. First, we find the Coulomb potential when the system occupies the whole surface \mathcal{S} . Then, we consider the case when just the upper half of the surface \mathcal{S} is available to the particles, and the lower part is empty, with hard wall boundary conditions between these two regions. At last, we determine the Coulomb potential in the grounded horizon case: the particles live in the upper part of the surface and the lower part is an ideal grounded conductor. In Sect. 4, we determine the exact analytical expression for the partition function and density at $\Gamma = 2$ for the 2dOCP on just one half of the surface, on the whole surface, and on the surface with the horizon grounded. In Sect. 5, we outline the conclusions.

2 The Model

A one-component plasma is a system of N pointwise particles of charge q and density n immersed in a neutralizing background described by a static uniform charge distribution of charge density $\rho_b = -qn_b$.

In this work, we want to study a two-dimensional one-component plasma (2dOCP) on a Riemannian surface S with the following metric

$$ds^2 = g_{\mu\nu}dx^\mu dx^\nu = \left(1 - \frac{2M}{r}\right)^{-1} dr^2 + r^2 d\varphi^2 \tag{2.1}$$

or $g_{rr} = 1/(1 - 2M/r)$, $g_{\varphi\varphi} = r^2$, and $g_{r\varphi} = 0$.

This is an embeddable surface in the three-dimensional Euclidean space with cylindrical coordinates (r, φ, Z) with $ds^2 = dZ^2 + dr^2 + r^2 d\varphi^2$, whose equation is

$$Z(r) = \pm 2\sqrt{2M(r - 2M)}. \tag{2.2}$$

This surface is illustrated in Fig. 1. It has a hole of radius $2M$. We will from now on call the $r = 2M$ region of the surface its "horizon".

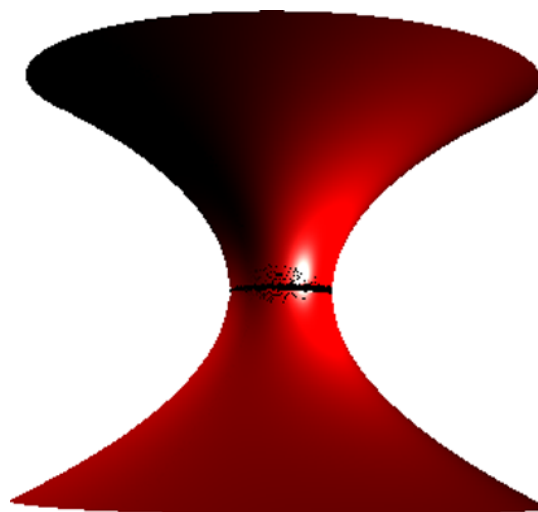
Flamm's Paraboloid S

The surface S whose local geometry is fixed by the metric (1.1) is known as Flamm's paraboloid. It is composed by two identical "universes": S_+ the one at $Z > 0$, and S_- the one at $Z < 0$. These are both multiply connected surfaces with the "Schwarzschild wormhole" providing the path from one to the other.

The system of coordinates (r, φ) with the metric (1.1) has the disadvantage that it requires two charts to cover the whole surface S . It can be more convenient to use the variable

$$u = \frac{Z}{4M} = \pm \sqrt{\frac{r}{2M} - 1} \tag{2.3}$$

Fig. 1 The Riemannian surface S : Flamm's paraboloid



instead of r . Replacing r as a function of Z using equation (2.2) gives the following metric when using the system of coordinates (u, φ) ,

$$ds^2 = 4M^2(1 + u^2)[4du^2 + (1 + u^2)d\varphi^2]. \tag{2.4}$$

The region $u > 0$ corresponds to S_+ and the region $u < 0$ to S_- .

Let us consider that the OCP is confined in a “disk” defined as

$$\Omega_R^+ = \{\mathbf{q} = (r, \varphi) \in S_+ | 0 \leq \varphi \leq 2\pi, 2M \leq r \leq R\}. \tag{2.5}$$

The area of this disk is given by

$$\mathcal{A}_R = \int_{\Omega_R^+} dS = \pi \left[\sqrt{R(R - 2M)}(3M + R) + 6M^2 \ln \left(\frac{\sqrt{R} + \sqrt{R - 2M}}{\sqrt{2M}} \right) \right], \tag{2.6}$$

where $dS = \sqrt{g} dr d\varphi$ and $g = \det(g_{\mu\nu})$. The perimeter is $C_R = 2\pi R$.

The Riemann tensor in a two-dimensional space has only $2^2(2^2 - 1)/12 = 1$ independent component. In our case the characteristic component is

$$R^r_{\varphi r \varphi} = -\frac{M}{r}. \tag{2.7}$$

The scalar curvature is then given by the following indexes contractions

$$\mathcal{R} = R^\mu_{\mu} = R^{\mu\nu}_{\mu\nu} = 2R^r_{\varphi r \varphi} = 2g^{\varphi\varphi} R^r_{\varphi r \varphi} = -\frac{2M}{r^3}, \tag{2.8}$$

and the (intrinsic) Gaussian curvature is $K = \mathcal{R}/2 = -M/r^3$. The (extrinsic) mean curvature of the manifold turns out to be $H = -\sqrt{M}/8r^3$.

The Euler characteristic of the disk Ω_R^+ is given by

$$\chi = \frac{1}{2\pi} \left(\int_{\Omega_R^+} K dS + \int_{\partial\Omega_R^+} k dl \right), \tag{2.9}$$

where k is the geodesic curvature of the boundary $\partial\Omega_R^+$. The Euler characteristic turns out to be zero, in agreement with the Gauss-Bonnet theorem $\chi = 2 - 2h - b$ where $h = 0$ is the number of handles and $b = 2$ the number of boundaries.

We can also consider the case where the system is confined in a “double” disk

$$\Omega_R = \Omega_R^+ \cup \Omega_R^-, \tag{2.10}$$

with $\Omega_R^- = \{\mathbf{q} = (r, \varphi) \in S_- | 0 \leq \varphi \leq 2\pi, 2M \leq r \leq R\}$, the disk image of Ω_R^+ on the lower universe S_- portion of S . The Euler characteristic of Ω_R is also $\chi = 0$.

A Useful System of Coordinates

The Laplacian for a function f is

$$\begin{aligned} \Delta f &= \frac{1}{\sqrt{g}} \frac{\partial}{\partial q^\mu} \left(\sqrt{g} g^{\mu\nu} \frac{\partial}{\partial q^\nu} \right) f \\ &= \left[\left(1 - \frac{2M}{r} \right) \frac{\partial^2}{\partial r^2} + \frac{1}{r^2} \frac{\partial^2}{\partial \varphi^2} + \left(\frac{1}{r} - \frac{M}{r^2} \right) \frac{\partial}{\partial r} \right] f, \end{aligned} \tag{2.11}$$

where $\mathbf{q} \equiv (r, \varphi)$. In Appendix A, we show how, finding the Green function of the Laplacian, naturally leads to consider the system of coordinates (x, φ) , with

$$x = (\sqrt{u^2 + 1} + u)^2. \tag{2.12}$$

The range for the variable x is $]0, +\infty[$. The lower paraboloid \mathcal{S}_- corresponds to the region $0 < x < 1$ and the upper one \mathcal{S}_+ to the region $x > 1$. A point in the upper paraboloid with coordinate (x, φ) has a mirror image by reflection ($u \rightarrow -u$) in the lower paraboloid, with coordinates $(1/x, \varphi)$, since if

$$x = (\sqrt{u^2 + 1} + u)^2 \tag{2.13}$$

then

$$\frac{1}{x} = (\sqrt{u^2 + 1} - u)^2. \tag{2.14}$$

In the upper paraboloid \mathcal{S}_+ , the new coordinate x can be expressed in terms of the original one, r , as

$$x = \frac{(\sqrt{r} + \sqrt{r - 2M})^2}{2M}. \tag{2.15}$$

Using this system of coordinates, the metric takes the form of a flat metric multiplied by a conformal factor

$$ds^2 = \frac{M^2}{4} \left(1 + \frac{1}{x}\right)^4 (dx^2 + x^2 d\varphi^2). \tag{2.16}$$

The Laplacian also takes a simple form

$$\Delta f = \frac{4}{M^2(1 + \frac{1}{x})^4} \Delta_{\text{flat}} f, \tag{2.17}$$

where

$$\Delta_{\text{flat}} f = \frac{\partial^2 f}{\partial x^2} + \frac{1}{x} \frac{\partial f}{\partial x} + \frac{1}{x^2} \frac{\partial^2 f}{\partial \varphi^2} \tag{2.18}$$

is the Laplacian of the flat Euclidean space \mathbb{R}^2 . The determinant of the metric is now given by $g = [M^2 x (1 + x^{-1})^4 / 4]^2$.

With this system of coordinates (x, φ) , the area of a "disk" Ω_R^+ of radius R [in the original system (r, φ)] is given by

$$\mathcal{A}_R = \frac{\pi M^2}{4} p(x_m) \tag{2.19}$$

with

$$p(x) = x^2 + 8x - \frac{8}{x} - \frac{1}{x^2} + 12 \ln x \tag{2.20}$$

and $x_m = (\sqrt{R} + \sqrt{R - 2M})^2 / (2M)$.

3 Coulomb Potential

3.1 Coulomb Potential Created by a Point Charge

The Coulomb potential $G(x, \varphi; x_0, \varphi_0)$ created at (x, φ) by a unit charge at (x_0, φ_0) is given by the Green function of the Laplacian

$$\Delta G(x, \varphi; x_0, \varphi_0) = -2\pi \delta^{(2)}(x, \varphi; x_0, \varphi_0) \tag{3.1}$$

with appropriate boundary conditions. The Dirac distribution is given by

$$\delta^{(2)}(x, \varphi; x_0, \varphi_0) = \frac{4}{M^2 x (1 + x^{-1})^4} \delta(x - x_0) \delta(\varphi - \varphi_0). \tag{3.2}$$

Notice that using the system of coordinates (x, φ) the Laplacian Green function equation takes the simple form

$$\Delta_{\text{flat}} G(x, \varphi; x_0, \varphi_0) = -2\pi \frac{1}{x} \delta(x - x_0) \delta(\varphi - \varphi_0) \tag{3.3}$$

which is formally the same Laplacian Green function equation for flat space.

We shall consider three different situations: when the particles can be in the whole surface \mathcal{S} , or when the particles are confined to the upper paraboloid universe \mathcal{S}_+ , confined by a hard wall or by a grounded perfect conductor.

3.1.1 Coulomb Potential G^{ws} when the Particles Live in the Whole Surface \mathcal{S}

To complement the Laplacian Green function equation (3.1), we impose the usual boundary condition that the electric field $-\nabla G$ vanishes at infinity ($x \rightarrow \infty$ or $x \rightarrow 0$). Also, we require the usual interchange symmetry $G(x, \varphi; x_0, \varphi_0) = G(x_0, \varphi_0; x, \varphi)$ to be satisfied. Additionally, due to the symmetry between each universe \mathcal{S}_+ and \mathcal{S}_- , we require that the Green function satisfies the symmetry relation

$$G^{\text{ws}}(x, \varphi; x_0, \varphi_0) = G^{\text{ws}}(1/x, \varphi; 1/x_0, \varphi_0). \tag{3.4}$$

The Laplacian Green function equation (3.1) can be solved, as usual, by using the decomposition as a Fourier series. Since (3.1) reduces to the flat Laplacian Green function equation (3.3), the solution is the standard one

$$G(x, \varphi; x_0, \varphi_0) = \sum_{n=1}^{\infty} \frac{1}{n} \left(\frac{x_{<}}{x_{>}} \right)^{2n} \cos[n(\varphi - \varphi_0)] + g_0(x, x_0), \tag{3.5}$$

where $x_{>} = \max(x, x_0)$ and $x_{<} = \min(x, x_0)$. The Fourier coefficient for $n = 0$, has the form

$$g_0(x, x_0) = \begin{cases} a_0^+ \ln x + b_0^+, & x > x_0 \\ a_0^- \ln x + b_0^-, & x < x_0. \end{cases} \tag{3.6}$$

The coefficients a_0^\pm, b_0^\pm are determined by the boundary conditions that g_0 should be continuous at $x = x_0$, its derivative discontinuous $\partial_x g_0|_{x=x_0^+} - \partial_x g_0|_{x=x_0^-} = -1/x_0$, and the boundary condition at infinity $\nabla g_0|_{x \rightarrow \infty} = 0$ and $\nabla g_0|_{x \rightarrow 0} = 0$. Unfortunately, the boundary condition at infinity is trivially satisfied for g_0 , therefore g_0 cannot be determined only

with this condition. In flat space, this is the reason why the Coulomb potential can have an arbitrary additive constant added to it. However, in our present case, we have the additional symmetry relation (3.4) which should be satisfied. This fixes the Coulomb potential up to an additive constant b_0 . We find

$$g_0(x, x_0) = -\frac{1}{2} \ln \frac{x_{>}}{x_{<}} + b_0, \tag{3.7}$$

and summing explicitly the Fourier series (3.5), we obtain

$$G^{ws}(x, \varphi; x_0, \varphi_0) = -\ln \frac{|z - z_0|}{\sqrt{|zz_0|}} + b_0, \tag{3.8}$$

where we defined $z = x e^{i\varphi}$ and $z_0 = x_0 e^{i\varphi_0}$. Notice that this potential does not reduce exactly to the flat one when $M = 0$. This is due to the fact that the whole surface S in the limit $M \rightarrow 0$ is not exactly a flat plane \mathbb{R}^2 , but rather it is two flat planes connected by a hole at the origin, this hole modifies the Coulomb potential.

3.1.2 Coulomb Potential G^{hs} when the Particles Live in the Half Surface S_+ Confined by Hard Walls

We consider now the case when the particles are restricted to live in the half surface S_+ , $x > 1$, and they are confined by a hard wall located at the "horizon" $x = 1$. The region $x < 1$ (S_-) is empty and has the same dielectric constant as the upper region occupied by the particles. Since there are no image charges, the Coulomb potential is the same G^{ws} as above. However, we would like to consider here a new model with a slightly different interaction potential between the particles. Since we are dealing only with half surface, we can relax the symmetry condition (3.4). Instead, we would like to consider a model where the interaction potential reduces to the flat Coulomb potential in the limit $M \rightarrow 0$. The solution of the Laplacian Green function equation is given in Fourier series by equation (3.5). The zeroth order Fourier component g_0 can be determined by the requirement that, in the limit $M \rightarrow 0$, the solution reduces to the flat Coulomb potential

$$G^{flat}(\mathbf{r}, \mathbf{r}') = -\ln \frac{|\mathbf{r} - \mathbf{r}'|}{L}, \tag{3.9}$$

where L is an arbitrary constant length. Recalling that $x \sim 2r/M$, when $M \rightarrow 0$, we find

$$g_0(x, x_0) = -\ln x_{>} - \ln \frac{M}{2L} \tag{3.10}$$

and

$$G^{hs}(x, \varphi; x_0, \varphi_0) = -\ln |z - z_0| - \ln \frac{M}{2L}. \tag{3.11}$$

3.1.3 Coulomb Potential G^{gh} when the Particles Live in the Half Surface S_+ Confined by a Grounded Perfect Conductor

Let us consider now that the particles are confined to S_+ by a grounded perfect conductor at $x = 1$ which imposes Dirichlet boundary condition to the electric potential. The Coulomb

potential can easily be found from the Coulomb potential G^{ws} (3.8) using the method of images

$$G^{gh}(x, \varphi; x_0, \varphi_0) = -\ln \frac{|z - z_0|}{\sqrt{|z z_0|}} + \ln \frac{|z - \bar{z}_0^{-1}|}{\sqrt{|z \bar{z}_0^{-1}|}} = -\ln \left| \frac{z - z_0}{1 - z \bar{z}_0} \right|, \tag{3.12}$$

where the bar over a complex number indicates its complex conjugate. We will call this the grounded horizon Green function. Notice how its shape is the same of the Coulomb potential on the pseudosphere [15] or in a flat disk confined by perfect conductor boundaries [6].

This potential can also be found using the Fourier decomposition. Since it will be useful in the following, we note that the zeroth order Fourier component of G^{gh} is

$$g_0(x, x_0) = \ln x_<. \tag{3.13}$$

3.2 The Background

The Coulomb potential generated by the background, with a constant surface charge density ρ_b satisfies the Poisson equation

$$\Delta v_b = -2\pi \rho_b. \tag{3.14}$$

Assuming that the system occupies an area \mathcal{A}_R , the background density can be written as $\rho_b = -q N_b / \mathcal{A}_R = -q n_b$, where we have defined here $n_b = N_b / \mathcal{A}_R$ the number density associated to the background. For a neutral system $N_b = N$. The Coulomb potential of the background can be obtained by solving Poisson equation with the appropriate boundary conditions for each case. Also, it can be obtained from the Green function computed in the previous section

$$v_b(x, \varphi) = \int G(x, \varphi; x', \varphi') \rho_b dS'. \tag{3.15}$$

This integral can be performed easily by using the Fourier series decomposition (3.5) of the Green function G . Recalling that $dS = \frac{1}{4} M^2 x (1 + x^{-1})^4 dx d\varphi$, after the angular integration is done, only the zeroth order term in the Fourier series survives

$$v_b(x, \varphi) = \frac{\pi \rho_b M^2}{2} \int_1^{x_m} g_0(x, x') x \left(1 + \frac{1}{x}\right)^4 dx. \tag{3.16}$$

The previous expression is for the half surface case and the grounded horizon case. For the whole surface case, the lower limit of integration should be replaced by $1/x_m$, or, equivalently, the integral multiplied by a factor 2.

Using the explicit expressions for g_0 , (3.7), (3.10), and (3.13) for each case, we find, for the whole surface,

$$v_b^{ws}(x, \varphi) = -\frac{\pi \rho_b M^2}{8} [h(x) - h(x_m) + 2p(x_m) \ln x_m - 4b_0 p(x_m)] \tag{3.17}$$

where $p(x)$ was defined in (2.20), and

$$h(x) = x^2 + 16x + \frac{16}{x} + \frac{1}{x^2} + 12(\ln x)^2 - 34. \tag{3.18}$$

Notice the following properties satisfied by the functions p and h

$$p(x) = -p(1/x), \quad h(x) = h(1/x) \tag{3.19}$$

and

$$p(x) = xh'(x)/2, \quad p'(x) = 2x\left(1 + \frac{1}{x}\right)^4, \tag{3.20}$$

where the prime stands for the derivative.

The background potential for the half surface case, with the pair potential $-\ln(|z - z'|M/2L)$ is

$$v_b^{hs}(x, \varphi) = -\frac{\pi\rho_b M^2}{8} \left[h(x) - h(x_m) + 2p(x_m) \ln \frac{x_m M}{2L} \right]. \tag{3.21}$$

Also, the background potential in the half surface case, but with the pair potential $-\ln(|z - z'|/\sqrt{|zz'|}) + b_0$ is

$$v_b^{\bar{hs}}(x, \varphi) = -\frac{\pi\rho_b M^2}{8} \left[h(x) - \frac{h(x_m)}{2} + p(x_m) \left(\ln \frac{x_m}{x} - 2b_0 \right) \right]. \tag{3.22}$$

Finally, for the grounded horizon case,

$$v_b^{gh}(x, \varphi) = -\frac{\pi\rho_b M^2}{8} [h(x) - 2p(x_m) \ln x]. \tag{3.23}$$

4 Partition Function and Densities at $\Gamma = 2$

We will now show how, at the special value of the coupling constant $\Gamma = \beta q^2 = 2$, the partition function and n -body correlation functions can be calculated exactly, for the different cases considered below.

In the following we will distinguish four cases labeled by A : $A = hs$, the plasma on the half surface (choosing G^{hs} as the pair Coulomb potential); $A = ws$, the plasma on the whole surface (choosing G^{ws} as the pair Coulomb potential); $A = \bar{hs}$, the plasma on the half surface but with the Coulomb potential G^{ws} of the whole surface case; and $A = gh$, the plasma on the half surface with the grounded horizon (choosing G^{gh} as the pair Coulomb potential).

The total potential energy of the plasma is, in each case

$$V^A = v_0^A + q \sum_i v_b^A(x_i) + q^2 \sum_{i < j} G^A(x_i, \varphi_i; x_j, \varphi_j), \tag{4.1}$$

where (x_i, φ_i) is the position of charge i on the surface, and

$$v_0^A = \frac{1}{2} \int \rho_b v_b^A(x, \varphi) dS \tag{4.2}$$

is the self energy of the background in each of the four mentioned cases. In the grounded case $A = gh$, one should add to V^{gh} in (4.1) the self energy that each particle has due to the polarization it creates on the grounded conductor.

4.1 The 2dOCP on Half Surface with Potential $-\ln|z - z'| - \ln M/(2L)$

4.1.1 Partition Function

For this case, we work in the canonical ensemble with N particles and the background neutralizes the charges: $N_b = N$, and $n = N/\mathcal{A}_R = n_b$. The potential energy of the system takes the explicit form

$$V^{hs} = -q^2 \sum_{1 \leq i < j \leq N} \ln|z_i - z_j| + \frac{q^2}{2} \alpha \sum_{i=1}^N h(x_i) + \frac{q^2}{2} N \ln \frac{M}{2L} - \frac{q^2}{4} N \alpha h(x_m) + \frac{q^2}{2} N^2 \ln x_m - \frac{q^2}{4} \alpha^2 \int_1^{x_m} h(x) p'(x) dx, \tag{4.3}$$

where we have used the fact that $dS = \pi M^2 x(1 + x^{-1})^4 dx/2 = \pi M^2 p'(x) dx/4$, and we have defined

$$\alpha = \frac{\pi n_b M^2}{4}. \tag{4.4}$$

Integrating by parts the last term of (4.3) and using (3.20), we find

$$V^{hs} = -q^2 \sum_{1 \leq i < j \leq N} \ln|z_i - z_j| + \frac{q^2}{2} \alpha \sum_{i=1}^N h(x_i) + \frac{q^2}{2} N \ln \frac{M}{2L} + \frac{q^2}{2} N^2 \ln x_m + \frac{q^2}{2} \alpha^2 \int_1^{x_m} \frac{[p(x)]^2}{x} dx - \frac{q^2}{2} N \alpha h(x_m). \tag{4.5}$$

When $\beta q^2 = 2$, the canonical partition function can be written as

$$Z^{hs} = \frac{1}{\lambda^{2N}} Z_0^{hs} \exp(-\beta F_0^{hs}) \tag{4.6}$$

with

$$-\beta F_0^{hs} = -N \ln \frac{M}{2L} - N^2 \ln x_m - \alpha^2 \int_1^{x_m} \frac{[p(x)]^2}{x} dx + N \alpha h(x_m) \tag{4.7}$$

and

$$Z_0^{hs} = \frac{1}{N!} \int \prod_{i=1}^N dS_i e^{-\alpha h(x_i)} \prod_{1 \leq i < j \leq N} |z_i - z_j|^2, \tag{4.8}$$

where $\lambda = \sqrt{2\pi\beta\hbar^2/m}$ is the de Broglie thermal wavelength. Z_0 can be computed using the original method for the OCP in flat space [2, 3], which was originally introduced in the context of random matrices [19, 20]. By expanding the Vandermonde determinant $\prod_{i < j} (z_i - z_j)$ and performing the integration over the angles, the partition function can be written as

$$Z_0^{hs} = \prod_{k=0}^{N-1} \mathcal{B}_N(k), \tag{4.9}$$

where

$$\mathcal{B}_N(k) = \int x^{2k} e^{-\alpha h(x)} dS \tag{4.10}$$

$$= \frac{\alpha}{n_b} \int_1^{x_m} x^{2k} e^{-\alpha h(x)} p'(x) dx. \tag{4.11}$$

In the flat limit $M \rightarrow 0$, we have $x \sim 2r/M$, with r the radial coordinate of the flat space \mathbb{R}^2 , and $h(x) \sim p(x) \sim x^2$. Then, \mathcal{B}_N reduces to

$$\mathcal{B}_N(k) \sim \frac{1}{n_b \alpha^k} \gamma(k + 1, N), \tag{4.12}$$

where $\gamma(k + 1, N) = \int_0^N t^k e^{-t} dt$ is the incomplete Gamma function. Replacing into (4.9), we recover the partition function for the OCP in a flat disk of radius R [3]

$$\ln Z^{\text{hs}} = \frac{N}{2} \ln \frac{\pi L^2}{n_b \lambda^4} + \frac{3N^2}{4} - \frac{N^2}{2} \ln N + \sum_{k=1}^N \ln \gamma(k, N). \tag{4.13}$$

4.1.2 Thermodynamic Limit $R \rightarrow \infty, x_m \rightarrow \infty$, and Fixed M

Let us consider the limit of a large system when $x_m = (\sqrt{R} + \sqrt{R - 2M})^2 / (2M) \rightarrow \infty$, $N \rightarrow \infty$, constant density n , and constant M . Therefore α is also kept constant. In appendix B, we develop a uniform asymptotic expansion of $\mathcal{B}_N(k)$ when $N \rightarrow \infty$ and $k \rightarrow \infty$ with $(N - k) / \sqrt{N} = O(1)$. Let us define \hat{x}_k by

$$k = \alpha p(\hat{x}_k). \tag{4.14}$$

The asymptotic expansion (B15) of $\mathcal{B}_N(k)$ can be rewritten as

$$\begin{aligned} \mathcal{B}_N(k) &= \frac{1}{2n_b} \sqrt{\pi \alpha \hat{x}_k p'(\hat{x}_k)} e^{2k \ln \hat{x}_k - \alpha h(\hat{x}_k)} [1 + \text{erf}(\epsilon_k)] \\ &\times \left[1 + \frac{1}{12k} + \frac{1}{\sqrt{k}} \xi_1(\epsilon_k) + \frac{1}{k} \xi_2(\epsilon_k) \right], \end{aligned} \tag{4.15}$$

where

$$\epsilon_k = \frac{2p(x_k)}{x_k p'(x_k)} \frac{N - k}{\sqrt{2k}} \tag{4.16}$$

is a order one parameter, and the functions $\xi_1(\epsilon_k)$ and $\xi_2(\epsilon_k)$ can be obtained from the calculation presented in Appendix B. They are integrable functions for $\epsilon_k \in [0, \infty[$. We will obtain an expansion of the free energy up to the order $\ln N$. At this order the functions $\xi_{1,2}$ do not contribute to the result.

Writing down

$$\ln Z_0^{\text{hs}} = \sum_{k=0}^N \ln \mathcal{B}_N(k) - \ln \mathcal{B}_N(N) \tag{4.17}$$

and using the asymptotic expansion (4.15), we have

$$\begin{aligned} \ln Z_0^{\text{hs}} &= -N \ln \frac{n_b}{\sqrt{2\pi}} + S_1^{\text{hs}} + S_2^{\text{hs}} + S_3^{\text{hs}} + \frac{1}{12} \ln N \\ &- \ln \left[\sqrt{\alpha} x_m \left(1 + \frac{1}{x_m} \right)^2 \right] - 2N \ln x_m + \alpha h(x_m) + O(1) \end{aligned} \tag{4.18}$$

with

$$S_1^{\text{hs}} = \sum_{k=0}^N \ln \left[\sqrt{\alpha} \hat{x}_k \left(1 + \frac{1}{\hat{x}_k} \right)^2 \right], \tag{4.19}$$

$$S_2^{\text{hs}} = \sum_{k=0}^N [2k \ln \hat{x}_k - \alpha h(\hat{x}_k)], \tag{4.20}$$

$$S_3^{\text{hs}} = \sum_{k=0}^N \ln \frac{1 + \text{erf}(\epsilon_k)}{2}. \tag{4.21}$$

Notice that the contribution of $\xi_1(\epsilon_k)$ is of order one, since $\sum_k \xi_1(\epsilon_k)/\sqrt{k} \sim \int_0^\infty \xi_1(\epsilon) d\epsilon = O(1)$. Also, $\sum_k \xi_2(\epsilon_k)/k \sim (1/\sqrt{N}) \int_0^\infty \xi_2(\epsilon) d\epsilon = O(1/\sqrt{N})$.

S_3^{hs} gives a contribution of order \sqrt{N} , transforming the sum over k into an integral over the variable $t = \epsilon_k$, we have

$$S_3 = \sqrt{2N} \int_0^\infty \ln \frac{1 + \text{erf}(t)}{2} dt + O(1). \tag{4.22}$$

This contribution is the same as the perimeter contribution in the flat case.

To expand S_1^{hs} and S_2^{hs} up to order $O(1)$, we need to use the Euler-McLaurin summation formula [21, 22]

$$\sum_{k=0}^N f(k) = \int_0^N f(y) dy + \frac{1}{2}[f(0) + f(N)] + \frac{1}{12}[f'(N) - f'(0)] + \dots \tag{4.23}$$

We find

$$S_1^{\text{hs}} = \frac{N}{2} \ln \alpha + \alpha x_m^2 \left(\ln x_m - \frac{1}{2} \right) + \alpha x_m (8 \ln x_m - 4) + \left(14\alpha + \frac{1}{2} \right) \ln x_m + 6(\ln x_m)^2 \tag{4.24}$$

and

$$S_2^{\text{hs}} = N^2 \ln x_m + N \ln x_m - \alpha N h(x_m) + \alpha^2 \int_1^{x_m} \frac{[p(x)]^2}{x} dx - \frac{\alpha}{2} h(x_m) + \frac{1}{6} \ln x_m. \tag{4.25}$$

Summing all terms in $\ln Z_0^{\text{hs}}$ and those from βF_0^{hs} , we notice that all nonextensive terms cancel, as it should be, and we obtain

$$\ln Z^{\text{hs}} = -N\beta f_B + 4x_m\alpha - C_R \beta \gamma_{\text{hard}} + \left(14\alpha - \frac{1}{6} \right) \ln x_m + O(1), \tag{4.26}$$

where

$$\beta f_B = -\frac{1}{2} \ln \frac{2\pi^2 L^2}{n\lambda^4} \tag{4.27}$$

is the bulk free energy of the OCP in the flat geometry [3],

$$\beta\gamma_{\text{hard}} = -\sqrt{\frac{n_b}{2\pi}} \int_0^\infty \ln \frac{1 + \text{erf}(y)}{2} dy \tag{4.28}$$

is the perimeter contribution to the free energy ("surface" tension) in the flat geometry near a plane hard wall [5], and

$$C_R = 2\pi R = \pi M \sqrt{x_m p'(x_m)/2} = \pi M x_m + O(1) \tag{4.29}$$

is the perimeter of the boundary at $x = x_m$.

The region $x \rightarrow \infty$ has zero curvature, therefore in the limit $x_m \rightarrow \infty$, most of the system occupies an almost flat region. For this reason, the extensive term (proportional to N) is expected to be the same as the one in flat space f_B . The largest boundary of the system $x = x_m$ is also in an almost flat region, therefore it is not surprising to see the factor γ_{hard} from the flat geometry appear there as well. Nevertheless, we notice an additional contribution $4\alpha x_m$ to the perimeter contribution, which comes from the curvature of the system.

In the logarithmic correction $\ln x_m$, we notice a $-(1/6) \ln x_m$ term, the same as in a flat disk geometry [5], but also a nonuniversal contribution due to the curvature $14\alpha \ln x_m$. In Refs. [5, 6], it is argued that Coulomb systems should exhibit only a universal logarithmic finite-size corrections $(\chi/6) \ln R$, for a system of typical large size R , and Euler characteristic χ . We do not find this correction in the result (4.26). The reason for this difference is that in [5, 6], the large system limit is taken at fixed shape, contrary to what has been done in this section. So, it is also interesting to consider now the thermodynamic limit keeping the shape of the surface fixed. This is done in the next section.

4.1.3 Thermodynamic Limit at Fixed Shape: $\alpha \rightarrow \infty$ and x_m Fixed

In the previous section we studied a thermodynamic limit case where a large part of the space occupied by the particles becomes flat as $x \rightarrow \infty$ keeping M fixed. Another interesting thermodynamic limit that can be studied is the one where we keep the shape of the space occupied by the particles fixed. This limit corresponds to the situation $M \rightarrow \infty$ and $R \rightarrow \infty$ while keeping the ratio R/M fixed, and of course the number of particles $N \rightarrow \infty$ with the density n fixed. Equivalently, recalling that $N = \alpha p(x_m)$, in this limit x_m is fixed and finite, and $\alpha = \pi M^2 n_b / 4 \rightarrow \infty$. We shall use α as the large parameter for the expansion of the free energy. In this limit, we expect the curvature effects to remain important, in particular the bulk free energy (proportional to α) will not be the same as in flat space.

Using the expansion (B18) of $\mathcal{B}_N(k)$ for the fixed shape situation, we have

$$\ln Z_0^{\text{hs}} = N \ln \frac{\sqrt{\pi}}{n_b} + N \ln \sqrt{\alpha} + S_1^{\text{hs, fixed}} + S_2^{\text{hs, fixed}} + S_3^{\text{hs, fixed}} + O(1), \tag{4.30}$$

where now

$$S_1^{\text{hs, fixed}} = \frac{1}{2} \sum_{k=0}^{N-1} \ln [\hat{x}_k p'(\hat{x}_k)], \tag{4.31}$$

$$S_2^{\text{hs, fixed}} = -\alpha \sum_{k=0}^{N-1} [h(\hat{x}_k) - 2p(\hat{x}_k) \ln \hat{x}_k], \tag{4.32}$$

$$S_3^{\text{hs, fixed}} = \sum_{k=0}^{N-1} \ln \frac{\text{erf}(\epsilon_{k,1}) + \text{erf}(\epsilon_{k,m})}{2} \tag{4.33}$$

with $\epsilon_{k,m}$ and $\epsilon_{k,1}$ given in (B19) and (B20), and \hat{x}_k is given by $k = \alpha p(\hat{x}_k)$. Using the Euler-McLaurin expansion, we obtain

$$S_1^{\text{hs, fixed}} = \alpha \int_1^{x_m} \frac{(1+x)^4}{x^3} \ln \frac{2(x+1)^4}{x^2} dx + O(1), \tag{4.34}$$

$$S_2^{\text{hs, fixed}} = N^2 \ln x_m - \alpha N h(x_m) + \alpha^2 \int_1^{x_m} \frac{[p(x)]^2}{x} dx + \frac{\alpha}{2} h(x_m) - N \ln x_m + O(1). \tag{4.35}$$

For $S_3^{\text{hs, fixed}}$, the relevant contributions are obtained when k is of order \sqrt{N} , where $\epsilon_{k,1}$ is of order one, and when $N - k$ is of order \sqrt{N} , where $\epsilon_{k,m}$ is of order one. In those regions, the sum can be changed into an integral over the variable $t = \epsilon_{k,1}$ or $t = \epsilon_{k,m}$. This gives

$$S_3^{\text{hs, fixed}} = -\sqrt{\frac{4\pi\alpha}{n_b}} \left[x_m \left(1 + \frac{1}{x_m} \right)^2 + 4 \right] \beta \gamma_{\text{hard}} + O(1) \tag{4.36}$$

with γ_{hard} given in (4.28). Once again the nonextensive terms (proportional to α^2) in $S_2^{\text{hs, fixed}}$ cancel out with similar terms in $F_0^{\text{hs, fixed}}$ from (4.7). The final result for the free energy $\beta F^{\text{hs}} = -\ln Z^{\text{hs}}$ is

$$\begin{aligned} \ln Z^{\text{hs}} = & \alpha \left[-p(x_m) \beta f_B + \frac{1}{2} [h(x_m) - 2p(x_m) \ln x_m] + \int_1^{x_m} \frac{(1+x)^4}{x^3} \ln \frac{(x+1)^4}{x^2} dx \right] \\ & - \sqrt{\frac{4\pi\alpha}{n_b}} \left[x_m \left(1 + \frac{1}{x_m} \right)^2 + 4 \right] \beta \gamma_{\text{hard}} + O(1), \end{aligned} \tag{4.37}$$

where f_B , given by (4.27), is the bulk free energy per particle in a flat space. We notice the additional contribution to the bulk free energy due to the important curvature effects [second and third term of the first line of (4.37)] that remain present in this thermodynamic limit.

The boundary terms, proportional to $\sqrt{\alpha}$, turn out to be very similar to those of a flat space near a hard wall [23], with a contribution $\beta \gamma_{\text{hard}} C_b$ for each boundary at $x_b = x_m$ and at $x_b = 1$ with perimeter

$$C_b = \pi M \sqrt{\frac{x_b p'(x_b)}{2}} = \pi M x_b \left(1 + \frac{1}{x_b} \right)^2. \tag{4.38}$$

Also, we notice the absence of $\ln \alpha$ corrections in the free energy. This is in agreement with the general results from Refs. [5, 6], where, using arguments from conformal field theory, it is argued that for two-dimensional Coulomb systems living in a surface of Euler characteristic χ , in the limit of a large surface keeping its shape fixed, the free energy should exhibit a logarithmic correction $(\chi/6) \ln R$ where R is a characteristic length of the size of the surface. For our curved surface studied in this section, the Euler characteristic is $\chi = 0$, therefore no logarithmic correction is expected.

4.1.4 Distribution Functions

Following [2], we can also find the k -body distribution functions

$$n^{(k)\text{hs}}(\mathbf{q}_1, \dots, \mathbf{q}_k) = \det[\mathcal{K}_N^{\text{hs}}(\mathbf{q}_i, \mathbf{q}_j)]_{(i,j) \in \{1, \dots, k\}^2}, \tag{4.39}$$

where $\mathbf{q}_i = (x_i, \varphi_i)$ is the position of the particle i , and

$$\mathcal{K}_N^{\text{hs}}(\mathbf{q}_i, \mathbf{q}_j) = \sum_{k=0}^{N-1} \frac{z_i^k z_j^k e^{-\alpha[h(|z_i|)+h(|z_j|)]/2}}{\mathcal{B}_N(k)}, \tag{4.40}$$

where $z_k = x_k e^{i\varphi_k}$. In particular, the one-body density is given by

$$n^{\text{hs}}(x) = \mathcal{K}_N(\mathbf{q}, \mathbf{q}) = \sum_{k=0}^{N-1} \frac{x^{2k} e^{-\alpha h(x)}}{\mathcal{B}_N(k)}. \tag{4.41}$$

4.1.5 Internal Screening

Internal screening means that at equilibrium, a particle of the system is surrounded by a polarization cloud of opposite charge. It is usually expressed in terms of the simplest of the multipolar sum rules [24]: the charge or electroneutrality sum rule, which for the OCP reduces to the trivial relation

$$\int n^{(2)\text{hs}}(\mathbf{q}_1, \mathbf{q}_2) dS_2 = (N - 1)n^{(1)\text{hs}}(\mathbf{q}_1), \tag{4.42}$$

which is actually satisfied for any fluid.

For our model, it is easy to verify that (4.42) is satisfied because of the particular structure (4.39) of the correlation function expressed as a determinant of the kernel $\mathcal{K}_N^{\text{hs}}$, and the fact that $\mathcal{K}_N^{\text{hs}}$ is a projector

$$\int dS_3 \mathcal{K}_N^{\text{hs}}(\mathbf{q}_1, \mathbf{q}_3) \mathcal{K}_N^{\text{hs}}(\mathbf{q}_3, \mathbf{q}_2) = \mathcal{K}_N^{\text{hs}}(\mathbf{q}_1, \mathbf{q}_2). \tag{4.43}$$

Indeed,

$$\begin{aligned} \int n^{(2)\text{hs}}(\mathbf{q}_1, \mathbf{q}_2) dS_2 &= \int [\mathcal{K}_N^{\text{hs}}(\mathbf{q}_1, \mathbf{q}_1) \mathcal{K}_N^{\text{hs}}(\mathbf{q}_2, \mathbf{q}_2) - \mathcal{K}_N^{\text{hs}}(\mathbf{q}_1, \mathbf{q}_2) \mathcal{K}_N^{\text{hs}}(\mathbf{q}_2, \mathbf{q}_1)] dS_2 \\ &= \int n^{(1)\text{hs}}(\mathbf{q}_1) n^{(1)\text{hs}}(\mathbf{q}_2) dS_2 - \mathcal{K}_N^{\text{hs}}(\mathbf{q}_1, \mathbf{q}_1) \\ &= (N - 1)n^{(1)\text{hs}}(\mathbf{q}_1). \end{aligned} \tag{4.44}$$

4.1.6 External Screening

External screening means that, at equilibrium, for an infinite fluid, an external charge introduced into the system is surrounded by a polarization cloud of opposite charge. When an external infinitesimal point charge Q is added to the system, it induces a charge density $\rho_Q(\mathbf{q})$. External screening means that

$$\int \rho_Q(\mathbf{q}) dS = -Q. \tag{4.45}$$

Using linear response theory we can calculate ρ_Q to first order in Q as follows. Imagine that the charge Q is at \mathbf{q} . Its interaction energy with the system is $\hat{H}_{int} = Q\hat{\phi}(\mathbf{q})$ where $\hat{\phi}(\mathbf{q})$

is the microscopic electric potential created at \mathbf{q} by the system. Then, the induced charge density at \mathbf{q}' is

$$\rho_Q(\mathbf{q}') = -\beta \langle \hat{\rho}(\mathbf{q}') \hat{H}_{int} \rangle_T = -\beta Q \langle \hat{\rho}(\mathbf{q}') \hat{\phi}(\mathbf{q}) \rangle_T, \tag{4.46}$$

where $\hat{\rho}(\mathbf{q}')$ is the microscopic charge density at \mathbf{q}' , $\langle AB \rangle_T = \langle AB \rangle - \langle A \rangle \langle B \rangle$, and $\langle \dots \rangle$ is the thermal average. Assuming external screening (4.45) is satisfied, one obtains the Carnie-Chan sum rule [24]

$$\beta \int \langle \hat{\rho}(\mathbf{q}') \hat{\phi}(\mathbf{q}) \rangle_T dS' = 1. \tag{4.47}$$

Now, in a uniform system starting from this sum rule one can derive the second moment Stillinger-Lovett sum rule [24]. The derivation of Stillinger-Lovett sum rule from (4.47) is done using the fact that for a homogenous system, the correlation function in (4.47) depends only on the distance between \mathbf{q} and \mathbf{q}' . This is not true in the present situation, because our system is not homogeneous since the curvature is not constant throughout the surface but varies from point to point. If we apply the Laplacian with respect to \mathbf{q} to this expression and use Poisson equation

$$\Delta_{\mathbf{q}} \langle \hat{\rho}(\mathbf{q}') \hat{\phi}(\mathbf{q}) \rangle_T = -2\pi \langle \hat{\rho}(\mathbf{q}') \hat{\rho}(\mathbf{q}) \rangle_T, \tag{4.48}$$

we find

$$\int \langle \hat{\rho}(\mathbf{q}') \hat{\rho}(\mathbf{q}) \rangle_T dS' = 0. \tag{4.49}$$

Equation (4.49) is another way of writing the charge sum rule (4.42) in the thermodynamic limit.

4.1.7 Asymptotics of the Density in the Limit $x_m \rightarrow \infty$ and α Fixed, for $1 \ll x \ll x_m$

The formula (4.41) for the one-body density, although exact, does not allow a simple evaluation of the density at a given point in space, as one has first to calculate $B_N(k)$ through an integral and then perform the sum over k . One can then try to determine the asymptotic behaviors of the density.

In this section, we consider the limit $x_m \rightarrow \infty$ and α fixed, and we study the density in the bulk of the system $1 \ll x \ll x_m$.

In the sum (4.41), the dominant terms are the ones for which k is such that $\hat{x}_k = x$, with \hat{x}_k defined in (4.14). Since $1 \ll x \ll x_m$, the dominant terms in the calculation of the density are obtained for values of k such that $1 \ll k \ll N$. Therefore in the limit $N \rightarrow \infty$, in the expansion (4.15) of $B_N(k)$, the argument of the error function is very large, then the error function can be replaced by 1. Keeping the correction $1/(12k)$ from (4.15) allow us to obtain an expansion of the density up to terms of order $O(1/x^2)$. Replacing the sum over k into an integral over \hat{x}_k , we have

$$n^{hs}(x) = \frac{n_b}{\sqrt{\pi}} \int_{-\infty}^{\infty} e^{\Psi(\hat{x}_k)} f(\hat{x}_k) \left(1 - \frac{1}{12\alpha p(\hat{x}_k)} \right) d\hat{x}_k \tag{4.50}$$

with

$$\Psi(\hat{x}_k) = 2\alpha p(\hat{x}_k) \ln \frac{x}{\hat{x}_k} - \alpha [h(x) - h(\hat{x}_k)] \tag{4.51}$$

and

$$f(\hat{x}_k) = \sqrt{\frac{\alpha p'(\hat{x}_k)}{\hat{x}_k}}. \tag{4.52}$$

We proceed now to use the Laplace method to compute this integral. The function $\Psi(\hat{x}_k)$ has a maximum for $\hat{x}_k = x$, with $\Psi(x) = 0$ and

$$\Psi''(x) = -\frac{2\alpha p'(x)}{x}, \tag{4.53a}$$

$$\Psi^{(3)}(x) = -\frac{4\alpha}{x} + O(1/x^2), \tag{4.53b}$$

$$\Psi^{(4)}(x) = \frac{4\alpha}{x^2} + O(1/x^3). \tag{4.53c}$$

Expanding for \hat{x}_k close to x and for $x \gg 1$ up to order $1/x^2$, we have

$$\begin{aligned} n^{hs}(x) &= \frac{n_b}{\sqrt{\pi}} \int_{-\infty}^{+\infty} e^{-\alpha p'(x)(\hat{x}_k-x)^2/x} \left(f(x) + f'(x)(\hat{x}_k-x) + \frac{f''(x)(\hat{x}_k-x)^2}{2} \right) \\ &\times \left(1 + \frac{1}{3!} \Psi^{(3)}(x)(\hat{x}_k-x)^3 + \frac{1}{4!} \Psi^{(4)}(x)(\hat{x}_k-x)^4 + \frac{[\Psi^{(3)}(x)]^2}{3!^2 2} (\hat{x}_k-x)^6 \right) \\ &\times \left(1 - \frac{1}{12\alpha p(x)} + O(1/x^3) \right) d\hat{x}_k. \end{aligned} \tag{4.54}$$

For the expansion of $f(\hat{x}_k)$ around $\hat{x}_k = x$, it is interesting to notice that

$$f'(x) = O(1/x^2), \quad \text{and} \quad f''(x) = O(1/x^3). \tag{4.55}$$

In the integral, the factor containing $f'(x)$ is multiplied by $(\hat{x}_k - x)$ which after integration vanishes. Therefore, the relevant contributions to order $O(1/x^2)$ are

$$\begin{aligned} n^{hs}(x) &= \frac{n_b}{\sqrt{\pi}} \int_{-\infty}^{+\infty} e^{-\alpha p'(x)(\hat{x}_k-x)^2/x} \sqrt{\frac{\alpha p'(x)}{x}} \\ &\times \left(1 + \frac{1}{3!} \Psi^{(3)}(x)(\hat{x}_k-x)^3 + \frac{1}{4!} \Psi^{(4)}(x)(\hat{x}_k-x)^4 + \frac{[\Psi^{(3)}(x)]^2}{3!^2 2} (\hat{x}_k-x)^6 \right) \\ &\times \left(1 - \frac{1}{12\alpha p(x)} \right) d\hat{x}_k + O(1/x^3). \end{aligned} \tag{4.56}$$

Then, performing the Gaussian integrals and replacing the dominant values of $\Psi(x)$ and its derivatives from (4.53) for $x \gg 1$, we find

$$n^{hs}(x) = n_b \left(1 + \frac{1}{12\alpha x^2} \right) \left(1 - \frac{1}{12\alpha x^2} \right) + O(1/x^3) = n_b + O(1/x^3). \tag{4.57}$$

In the bulk of the plasma, the density of particles equal the bulk density, as expected. The above calculation, based the Laplace method, generates an expansion in powers of $1/x$ for the density. The first correction to the background density, in $1/x^2$, has been shown to be zero. We conjecture that this is probably true for any subsequent corrections in powers $1/x$

if the expansion is pushed further, because the corrections to the bulk density are probably exponentially small, rather than in powers of $1/x$, due to the screening effects. In the following subsections, we consider the expansion of the density in other types of limits, and in particular close to the boundaries, and the results suggest that our conjecture is true.

4.1.8 Asymptotics of the Density Close to the Boundary in the Limit $x_m \rightarrow \infty$

We study here the density close to the boundary $x = x_m$ in the limit $x_m \rightarrow \infty$ and M fixed. Since in this limit this region is almost flat, one would expect to recover the result for the OCP in a flat space near a wall [23]. Let $x = x_m + y$ where $y \ll x_m$ is of order 1.

Using the dominant term of the asymptotics (4.15),

$$\mathcal{B}_N(k) = \frac{1}{2n_b} \sqrt{\pi \alpha \hat{x}_k p'(\hat{x}_k)} e^{2k \ln \hat{x}_k - \alpha h(\hat{x}_k)} [1 + \text{erf}(\epsilon_k)], \tag{4.58}$$

we have

$$n^{\text{hs}}(x) = \frac{2n_b}{\sqrt{\pi}} \sum_{k=0}^{N-1} \frac{e^{2k(\ln x - \ln \hat{x}_k) - \alpha[h(x) - h(\hat{x}_k)]}}{\sqrt{\alpha \hat{x}_k p'(\hat{x}_k)} [1 + \text{erf}(\epsilon_k)]}, \tag{4.59}$$

where we recall that $\hat{x}_k = p^{-1}(k/\alpha)$. The exponential term in the sum has a maximum when $\hat{x}_k = x$ i.e. $k = k_{\text{max}} = \alpha p(x)$, and since x is close to $x_m \rightarrow \infty$, the function is very peaked near this maximum. Thus, we can use Laplace method to compute the sum. Expanding the argument of the exponential up to order 2 in $k - k_{\text{max}}$, we have

$$n^{\text{hs}}(x) = \frac{2n_b}{\sqrt{\pi}} \sum_{k=0}^{N-1} \frac{\exp[-\frac{2}{\alpha x p'(x)}(k - k_{\text{max}})^2]}{\sqrt{\alpha x p'(x)} [1 + \text{erf}(\epsilon_k)]}. \tag{4.60}$$

Now, replacing the sum by an integral over $t = \epsilon_k$ and replacing $x = x_m - y$, we find

$$n^{\text{hs}}(x) = \frac{2n_b}{\sqrt{\pi}} \int_0^\infty \frac{\exp[-(t - \sqrt{2\alpha}y)^2]}{1 + \text{erf}(t)} dt. \tag{4.61}$$

Since both $x_m \rightarrow \infty$, and $x \rightarrow \infty$, in that region, the space is almost flat. If s is the geodesic distance from x to the border, then we have $y \sim \sqrt{(\pi n_b/\alpha)} s$, and (4.61) reproduces the result for the flat space [23], as expected.

4.1.9 Density in the Thermodynamic Limit at Fixed Shape: $\alpha \rightarrow \infty$ and x_m Fixed

Using the expansion (B18) of $\mathcal{B}_N(k)$ for the fixed shape situation, we have

$$n^{\text{hs}}(x) = 2n_b \sum_{k=0}^{N-1} \frac{e^{-\alpha[h(x) - 2p(\hat{x}_k) \ln x - h(\hat{x}_k) + 2p(\hat{x}_k) \ln \hat{x}_k]}}{\sqrt{\alpha \pi \hat{x}_k p'(\hat{x}_k)} [\text{erf}(\epsilon_{k,1}) + \text{erf}(\epsilon_{k,m})]}. \tag{4.62}$$

Once again, to evaluate this sum when $\alpha \rightarrow \infty$ it is convenient to use Laplace method. The argument of the exponential has a maximum when k is such that $\hat{x}_k = x$. Transforming the sum into an integral over \hat{x}_k , and expanding the argument of the integral to order $(\hat{x}_k - x)^2$, we have

$$n^{\text{hs}}(x) = \frac{2n_b \sqrt{\alpha}}{\sqrt{\pi}} \int_1^{x_m} \sqrt{\frac{p'(\hat{x}_k)}{\hat{x}_k}} \frac{e^{-\alpha p'(x)(x - \hat{x}_k)^2/x}}{\text{erf}(\epsilon_{k,1}) + \text{erf}(\epsilon_{k,m})} d\hat{x}_k. \tag{4.63}$$

Depending on the value of x the result will be different, since we have to take special care of the different cases when the corresponding dominant values of \hat{x}_k are close to the limits of integration or not.

Let us first consider the case when $x - 1$ and $x_m - x$ are of order one. This means we are interested in the density in the bulk of the system, far away from the boundaries. In this case, since $\epsilon_{k,1}$ and $\epsilon_{k,m}$, defined in (B19) and (B20), are proportional to $\sqrt{\alpha} \rightarrow \infty$, then each error function in the denominator of (4.63) converge to 1. Also, the dominant values of \hat{x}_k , close to x (more precisely, $x - \hat{x}_k$ of order $1/\sqrt{\alpha}$), are far away from 1 and x_m (more precisely, $\hat{x}_k - 1$ and $x_m - \hat{x}_k$ are of order 1). Then, we can extend the limits of integration to $-\infty$ and $+\infty$, and approximate \hat{x}_k by x in the term $p'(\hat{x}_k)/\hat{x}_k$. The resulting Gaussian integral is easily performed, to find

$$n(x) = n_b, \quad \text{when } x - 1 \text{ and } x_m - x \text{ are of order 1.} \tag{4.64}$$

Let us now consider the case when $x - x_m$ is of order $1/\sqrt{\alpha}$, i.e. we study the density close to the boundary at x_m . In this case $\epsilon_{k,m}$ is of order 1 and the term $\text{erf}(\epsilon_{k,m})$ cannot be approximated to 1, whereas $\epsilon_{k,1} \propto \sqrt{\alpha} \rightarrow \infty$ and $\text{erf}(\epsilon_{k,1}) \rightarrow 1$. The terms $p'(\hat{x}_k)/\hat{x}_k$ and $p'(x)/x$ can be approximated to $p'(x_m)/x_m$ up to corrections of order $1/\sqrt{\alpha}$. Using $t = \epsilon_{k,m}$ as new variable of integration, we obtain

$$n^{\text{hs}}(x) = \frac{2n_b}{\sqrt{\pi}} \int_0^{+\infty} \frac{\exp\left[-\left(t - \sqrt{\frac{\alpha p'(x_m)}{x_m}}(x_m - x)\right)^2\right]}{1 + \text{erf}(t)} dt, \quad \text{for } x_m - x \text{ of order } \frac{1}{\sqrt{\alpha}}. \tag{4.65}$$

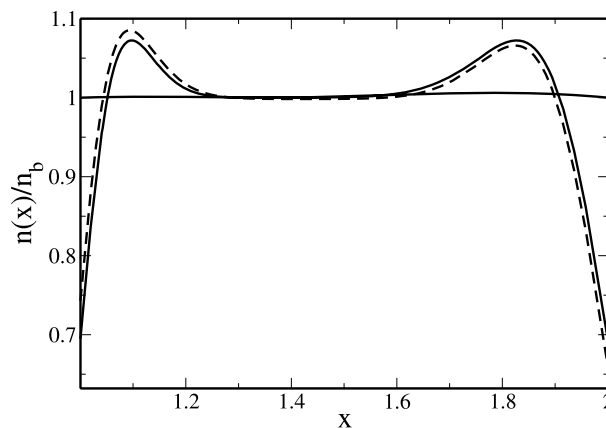
In the case where $x - 1$ is of order $1/\sqrt{\alpha}$, close to the other boundary, a similar calculation yields,

$$n^{\text{hs}}(x) = \frac{2n_b}{\sqrt{\pi}} \int_0^{+\infty} \frac{\exp\left[-\left(t - \sqrt{\alpha p'(1)}(x - 1)\right)^2\right]}{1 + \text{erf}(t)} dt, \quad \text{for } x - 1 \text{ of order } \frac{1}{\sqrt{\alpha}}, \tag{4.66}$$

where $p'(1) = 32$.

Figure 2 compares the density profile for finite $N = 100$ with the asymptotic results (4.64), (4.65) and (4.66). The figure show how the density tends to the background density, n_b , far from the boundaries. Near the boundaries it has a peak, eventually decreasing below n_b when approaching the boundary. In the limit $\alpha \rightarrow \infty$, the value of the density at each boundary is $n_b \ln 2$.

Fig. 2 The normalized one-body density $n^{\text{hs}}(x)/n_b$, for the 2dOCP on just one universe of the surface S . The dashed line corresponds to a numerical evaluation, obtained from (4.41), with $N = 100$, $x_m = 2$ and $\alpha = 4.15493$. The solid line corresponds to the asymptotic result in the fixed shape limit when $\alpha \rightarrow \infty$, and $x_m = 2$ fixed



Interestingly, the results (4.64), (4.65) and (4.66) turn out to be the same as the one for a flat space near a hard wall [23]. From the metric (2.16), we deduce that the geodesic distance to the boundary at x_m is $s = M(x_m - x)\sqrt{p'(x_m)/(8x_m)}$ (when $x_m - x$ is of order $1/\sqrt{\alpha}$), and a similar expression for the distance to the boundary at $x = 1$ replacing x_m by 1. Then, in terms of the geodesic distance s to the border, the results (4.65) and (4.66) are exactly the same as those of an OCP in a flat space close to a plane hard wall [23],

$$n(s) = \frac{2n_b}{\sqrt{\pi}} \int_0^{+\infty} \frac{\exp[-(t - s\sqrt{2\pi n_b})^2]}{1 + \operatorname{erf}(t)} dt. \tag{4.67}$$

This result shows that there exists an interesting universality for the density, because, although we are considering a limit where curvature effects are important, the density turns out to be the same as the one for a flat space. Another way to understand the recovery of density profile in a flat space near a hard wall (4.67), is to notice that in this limit $\alpha \rightarrow \infty$, we have $M \gg n_b^{-1/2}$: the curvature-variation length is much larger than the density-variation scale.

4.2 The 2dOCP on the Whole Surface with Potential $-\ln(|z - z'|/\sqrt{|zz'|}) + b_0$

4.2.1 Partition Function

Until now we studied the 2dOCP on just one universe. Let us find the thermodynamic properties of the 2dOCP on the whole surface S . In this case, we also work in the canonical ensemble with a global neutral system. The position $z_k = x_k e^{i\varphi_k}$ of each particle can be in the range $1/x_m < x_k < x_m$. The total number particles N is now expressed in terms of the function p as $N = 2\alpha p(x_m)$. Similar calculations to the ones of the previous section lead to the following expression for the partition function, when $\beta q^2 = 2$,

$$Z^{\text{ws}} = \frac{1}{\lambda^{2N}} Z_0^{\text{ws}} \exp(-\beta F_0^{\text{ws}}) \tag{4.68}$$

now, with

$$-\beta F_0^{\text{ws}} = Nb_0 + N\alpha h(x_m) - \frac{N^2}{2} \ln x_m - \alpha^2 \int_{1/x_m}^{x_m} \frac{[p(x)]^2}{x} dx \tag{4.69}$$

and

$$Z_0^{\text{ws}} = \frac{1}{N!} \int \prod_{i=1}^N dS_i e^{-\alpha h(x_i)} x_i^{-N+1} \prod_{1 \leq i < j \leq N} |z_i - z_j|^2. \tag{4.70}$$

Expanding the Vandermonde determinant and performing the angular integrals we find

$$Z_0^{\text{ws}} = \prod_{k=0}^{N-1} \tilde{B}_N(k) \tag{4.71}$$

with

$$\tilde{B}_N(k) = \int x^{2k-N+1} e^{-\alpha h(x)} dS \tag{4.72}$$

$$= \frac{\alpha}{n} \int_{1/x_m}^{x_m} x^{2k-N+1} e^{-\alpha h(x)} p'(x) dx. \tag{4.73}$$

The function $\tilde{\mathcal{B}}_N(k)$ is very similar to \mathcal{B}_N , and its asymptotic behavior for large values of N can be obtained by Laplace method as explained in Appendix B.

4.2.2 Thermodynamic Limit $R \rightarrow \infty, x_m \rightarrow \infty$, and Fixed M

Writing the partition function as

$$\ln Z_0^{\text{ws}} = \sum_{k=0}^N \ln \tilde{\mathcal{B}}_N(k) - \ln \tilde{\mathcal{B}}_N(N), \tag{4.74}$$

and using the asymptotic expansion (B31) for $\tilde{\mathcal{B}}_N$, we have

$$\begin{aligned} \ln Z_0^{\text{ws}} = & -\ln \frac{n_b}{\sqrt{2\pi}} + S_1^{\text{ws}} + S_2^{\text{ws}} + S_3^{\text{ws}} + S_4^{\text{ws}} + S_5^{\text{ws}} - \ln \left[\sqrt{\alpha} x_m \left(1 + \frac{1}{x_m} \right)^2 \right] \\ & - \ln x_m - N \ln x_m + \alpha h(x_m), \end{aligned} \tag{4.75}$$

where

$$S_1^{\text{ws}} = \sum_{k=0}^N \ln \left[\sqrt{\alpha} \hat{x}_{k-\frac{N}{2}} \left(1 + \frac{1}{\hat{x}_{k-\frac{N}{2}}} \right)^2 \right], \tag{4.76}$$

$$S_2^{\text{ws}} = \sum_{k=0}^N 2 \left(k - \frac{N}{2} \right) \ln \hat{x}_{k-\frac{N}{2}} - \alpha h \left(\hat{x}_{k-\frac{N}{2}} \right), \tag{4.77}$$

$$S_3^{\text{ws}} = \sum_{k=0}^N \ln \frac{\text{erf}(\epsilon_{k,\text{min}}) + \text{erf}(\epsilon_{k,\text{max}})}{2}, \tag{4.78}$$

$$S_4^{\text{ws}} = \sum_{k=0}^N \ln \hat{x}_{k-\frac{N}{2}}, \tag{4.79}$$

$$S_5^{\text{ws}} = \sum_{k'=1}^{N/2} \left(\frac{1}{12} + \frac{3}{8} \right) \frac{1}{|k'|} + \sum_{k'=-N/2}^{-1} \left(\frac{1}{12} - \frac{1}{8} \right) \frac{1}{|k'|} = \frac{5}{6} \ln x_m + O(1) \tag{4.80}$$

and $\epsilon_{k,\text{min}}$ and $\epsilon_{k,\text{max}}$ are defined in (B33). Notice that $S_4^{\text{ws}} = 0$ due to the symmetry relation $\hat{x}_{-\ell} = 1/\hat{x}_\ell$, therefore only the sums $S_1^{\text{ws}}, S_2^{\text{ws}}, S_3^{\text{ws}}$ and S_5^{ws} contribute to the result. These sums are similar to the ones defined for the half surface case, with the difference that the running index $k' = k - N/2$ varies from $-N/2$ to $N/2$ instead of 0 to N as in the half surface case. This difference is important when considering the remainder terms in the Euler-McLaurin expansion, because now both terms for $k' = -N/2$ and $k' = N/2$ are important in the thermodynamic limit. In the half surface case only the contribution for $k = N$ was important in the thermodynamic limit.

The asymptotic expansion of each sum, for $x_m \rightarrow \infty$, is now

$$S_1^{ws} = \frac{N}{2} \ln \alpha + x_m^2 (2 \ln x_m - 1) + 2x_m (8 \ln x_m - 4) + (28\alpha + 1) \ln x_m + 12\alpha (\ln x_m)^2 + O(1), \tag{4.81}$$

$$S_2^{ws} = \frac{N^2}{2} \ln x_m + \alpha^2 \int_{1/x_m}^{x_m} \frac{[p(x)]^2}{x} dx - \alpha N h(x_m) + N \ln x_m - \alpha h(x_m) + \frac{1}{3} \ln x_m + O(1), \tag{4.82}$$

$$S_3^{ws} = -2x_m \sqrt{\frac{4\pi\alpha}{n_b}} \beta \gamma_{\text{hard}} + O(1), \tag{4.83}$$

where γ_{hard} is defined in (4.28). The free energy is given by $\beta F^{ws} = -\ln Z^{ws}$, with

$$\begin{aligned} \ln Z^{ws} = & 2\alpha x_m^2 \ln x_m + N \left(b_0 + \ln \frac{\sqrt{2\pi\alpha}}{\lambda^2 n_b} \right) - \alpha x_m^2 + 8\alpha x_m (2 \ln x_m - 1) - 2C_R \beta \gamma_{\text{hard}} \\ & + 12\alpha (\ln x_m)^2 + 28\alpha \ln x_m + \frac{1}{6} \ln x_m + O(1). \end{aligned} \tag{4.84}$$

We notice that the free energy for this system turns out to be nonextensive with a term $2\alpha x_m^2 \ln x_m$. This is probably due to the special form of the potential $-\ln(|z - z'|/\sqrt{|zz'|})$: the contribution from the denominator in the logarithm can be written as a one-body term $[(N - 1)/2] \ln x$, which is not intensive but extensive. However, this nonextensivity of the final result is mild, and can be cured by choosing the arbitrary additive constant b_0 of the Coulomb potential as $b_0 = -\ln(Mx_m) + \text{constant}$.

4.2.3 Thermodynamic Limit at Fixed Shape: $\alpha \rightarrow \infty$ and x_m Fixed

For this situation, we use the asymptotic behavior (B34) of \tilde{B}_N

$$\ln Z_0^{ws} = N \ln \frac{\sqrt{\pi\alpha}}{n_b} + S_1^{\text{ws, fixed}} + S_2^{\text{ws, fixed}} + S_3^{\text{ws, fixed}} + S_4^{\text{ws, fixed}}, \tag{4.85}$$

where, now

$$S_1^{\text{ws, fixed}} = \frac{1}{2} \sum_{k=0}^{N-1} \ln [\hat{x}_{k-\frac{N}{2}} p'(\hat{x}_{k-\frac{N}{2}})], \tag{4.86}$$

$$S_2^{\text{ws, fixed}} = -\alpha \sum_{k=0}^{N-1} [h(\hat{x}_{k-\frac{N}{2}}) - 2p(\hat{x}_{k-\frac{N}{2}}) \ln \hat{x}_{k-\frac{N}{2}}], \tag{4.87}$$

$$S_3^{\text{ws, fixed}} = \sum_{k=0}^{N-1} \ln \frac{\text{erf}(\epsilon_{k, \text{min}}) + \text{erf}(\epsilon_{k, \text{max}})}{2}, \tag{4.88}$$

$$S_4^{\text{ws, fixed}} = \sum_{k=0}^{N-1} \ln \hat{x}_{k-\frac{N}{2}}. \tag{4.89}$$

These sums can be computed as earlier using Euler-McLaurin summation formula. We notice that

$$S_4^{ws, fixed} = \alpha \int_{1/x_m}^{x_m} \ln x p'(x) dx + O(1) = 0 + O(1) \tag{4.90}$$

because of the symmetry properties $\ln(1/x) = -\ln x$ and $p'(1/x)d(1/x) = -p'(x)dx$. In the computation of $S_2^{ws, fixed}$ there is an important difference with the case of the half surface section, due to the contribution when $k = 0$, since $\hat{x}_{-N/2} = 1/\hat{x}_{N/2} = 1/x_m$

$$S_2^{ws, fixed} = -\alpha N h(x_m) - \frac{N^2}{2} \ln x_m + \alpha^2 \int_{1/x_m}^{x_m} \frac{[p(x)]^2}{x} dx + O(1). \tag{4.91}$$

There is no $O(\alpha)$ contribution from $S_2^{ws, fixed}$. Finally, the free energy $\beta F^{ws} = -\ln Z^{ws}$ is given by

$$\begin{aligned} \ln Z^{ws} = & \alpha \left[2p(x_m) \left(\ln \frac{\sqrt{2\pi\alpha}}{\lambda^2 n_b} + b_0 \right) + \int_{1/x_m}^{x_m} \frac{(1+x)^4}{x^3} \ln \frac{(x+1)^4}{x^2} dx \right] \\ & - 2\sqrt{\frac{4\pi\alpha}{n_b}} x_m \left(1 + \frac{1}{x_m} \right)^2 \beta \gamma_{hard} + O(1). \end{aligned} \tag{4.92}$$

We notice that the free energy has again a nonextensive term proportional to $\alpha \ln \alpha$, but, once again, it can be cured by choosing the constant b_0 as $b_0 = -\ln(Mx_m) + \text{constant}$. The perimeter correction, $2C_R \beta \gamma_{hard}$, proportional to $\sqrt{\alpha}$, has the same form as for the half surface case, with equal contributions from each boundary at $x = 1/x_m$ and $x = x_m$. Once again, there is no $\ln \alpha$ correction in agreement with the general theory of Ref. [5, 6] and the fact that the Euler characteristic of this manifold is $\chi = 0$.

4.2.4 Density

The density is now given by

$$n^{ws}(x) = \sum_{k=0}^{N-1} \frac{x^{2k-N+1} e^{-\alpha h(x)}}{\tilde{\mathcal{B}}_N(k)}. \tag{4.93}$$

Due to the fact that the asymptotic behavior of $\tilde{\mathcal{B}}_N(k)$ is almost the same as the one of $\mathcal{B}_N(k')$ with $k' = |k - \frac{N}{2}|$, the behavior of the density turn out to be the same as for the half surface case, in the thermodynamic limit $\alpha \rightarrow \infty$, x_m fixed,

$$n(x) = n_b, \quad \text{in the bulk, i.e., when } x - x_m \text{ and } x - \frac{1}{x_m} \text{ are of order 1.} \tag{4.94}$$

And, close to the boundaries, $x \rightarrow x_b$ with $x_b = x_m$ or $x_b = 1/x_m$,

$$n(x) = \frac{2n_b}{\sqrt{\pi}} \int_0^{+\infty} \frac{\exp\left[-\left(t - \sqrt{\frac{\alpha p'(x_b)}{x_b}} |x - x_b|\right)^2\right]}{1 + \text{erf}(t)} dt, \quad \text{for } x_b - x \text{ of order } \frac{1}{\sqrt{\alpha}}. \tag{4.95}$$

If the result is expressed in terms of the geodesic distance s to the border, we recover, once again, the result of the OCP in a flat space near a hard wall (4.67).

4.3 The 2dOCP on the Half Surface with Potential $-\ln(|z - z'|/\sqrt{|zz'|}) + b_0$

4.3.1 Partition Function

In this case, we have $N = \alpha p(x_m)$. Following similar calculations to the ones of the previous cases, we find that the partition function, at $\beta q^2 = 2$, is

$$Z^{\overline{\text{hs}}} = Z_0^{\overline{\text{hs}}} e^{-\beta F_0^{\overline{\text{hs}}}} \tag{4.96}$$

with

$$-\beta F_0^{\overline{\text{hs}}} = \alpha^2 p(x_m)h(x_m) - p(x_m)^2 \ln x_m + \int_1^{x_m} \frac{[p(x)]^2}{x} dx - Nb_0 \tag{4.97}$$

and

$$Z_0^{\overline{\text{hs}}} = \prod_{k=0}^{N-1} \hat{\mathcal{B}}_N(k) \tag{4.98}$$

with

$$\hat{\mathcal{B}}_N(k) = \frac{\alpha}{n_b} \int_1^{x_m} x^{2k+1} e^{-\alpha h(x)} dx. \tag{4.99}$$

4.3.2 Thermodynamic Limit $R \rightarrow \infty$, $x_m \rightarrow \infty$, and Fixed M

The asymptotic expansion of $\hat{\mathcal{B}}_N(k)$ is obtained from (B31) replacing k' by k and considering only the case $k > 0$. As explained in Appendix B, the main difference with the other half surface case (Sect. 4.1), is an additional term \hat{x}_k in each factor of the partition function and the additional term $(3/(8k))$ in the expansion (B31). Therefore, the partition function can be obtained from the one of the half surface with potential $-\ln|z - z'|$ by adding the terms

$$S_4^{\overline{\text{hs}}} = \sum_{k=0}^{N-1} \ln \hat{x}_k, \tag{4.100}$$

$$S_5^{\overline{\text{hs}}} = \sum_{k=1}^{N-1} \frac{3}{8k} = \frac{3}{8} \ln N + O(1) = \frac{3}{4} \ln x_m + O(1). \tag{4.101}$$

Using Euler-McLaurin expansion, we have

$$\begin{aligned} S_4^{\overline{\text{hs}}} &= \sum_{k=0}^N \ln \hat{x}_k - \ln x_m \\ &= \int_1^{x_m} \alpha p'(x) \ln x dx + \frac{1}{2} \ln x_m - \ln x_m + O(1) \\ &= \alpha p(x_m) \ln x_m - \alpha \int_1^{x_m} \frac{p(x)}{x} dx - \frac{1}{2} \ln x_m + O(1) \\ &= \alpha p(x_m) \ln x_m - \frac{1}{2} \alpha h(x_m) - \frac{1}{2} \ln x_m + O(1), \end{aligned} \tag{4.102}$$

where we used the property (3.20). Finally,

$$\begin{aligned} \ln Z^{\text{hs}} &= \alpha x_m^2 \ln x_m + N \left(b_0 + \ln \frac{\sqrt{2\pi\alpha}}{\lambda^2 n_b} \right) - \frac{\alpha}{2} x_m^2 + 4\alpha x_m (2 \ln x_m - 1) \\ &\quad - C_R \beta \gamma_{\text{hard}} + 6\alpha (\ln x_m)^2 + 14\alpha \ln x_m + \frac{1}{12} \ln x_m + O(1). \end{aligned} \tag{4.103}$$

The result is one-half of the one for the full surface, $\ln Z^{\text{ws}}$, as it might be expected.

4.3.3 Thermodynamic Limit at Fixed Shape: $\alpha \rightarrow \infty$ and x_m Fixed

For this case, the asymptotics of $\hat{\mathcal{B}}_N$ are very similar to those of \mathcal{B}_N from (B18)

$$\hat{\mathcal{B}}_N(k) \sim \hat{x}_k \mathcal{B}_N(k). \tag{4.104}$$

Therefore, the only difference from the calculations of the half surface case with potential $-\ln|z - z'| + \text{constant}$, and this case, is the sum

$$S_4^{\text{hs, fixed}} = \sum_{k=0}^{N-1} \ln \hat{x}_k. \tag{4.105}$$

We have

$$\begin{aligned} S_4^{\text{hs, fixed}} &= \int_1^{x_m} \alpha p'(x) \ln x \, dx + O(1) \\ &= \alpha p(x_m) \ln x_m - \frac{1}{2} \alpha h(x_m) + O(1). \end{aligned} \tag{4.106}$$

Here, the term $k = N$ and the remainder of the Euler-McLaurin expansion give corrections of order $O(\alpha^0) = O(1)$, as opposed to the previous section where they gave contributions of order $O(\ln x_m)$.

Finally, we find

$$\begin{aligned} \ln Z^{\text{hs}} &= \alpha \left[p(x_m) \left(\frac{1}{2} \ln \frac{\sqrt{2\alpha\pi}}{n_b \lambda^2} + b_0 \right) + \int_1^\infty \frac{(1+x)^4}{x^3} \ln \frac{(1+x)^4}{x^2} \, dx \right] \\ &\quad - \sqrt{\frac{4\pi\alpha}{n_b}} \left[x_m \left(1 + \frac{1}{x_m} \right) + 4 \right] \beta \gamma_{\text{hard}} + O(1). \end{aligned} \tag{4.107}$$

The bulk free energy, proportional to α , plus the nonextensive term proportional $\alpha \ln \alpha$, are one-half the ones from (4.92) for the full surface case, as expected. The perimeter contribution, proportional to $\sqrt{\alpha}$ is again the same as in all the previous cases of thermodynamic limit at fixed shape, i.e. a contribution $\beta \gamma_{\text{hard}} C_b$ for each boundary at $x_b = x_m$ and at $x_b = 1$ with perimeter C_b (4.38). Once again, there is no $\ln \alpha$ correction in agreement with the fact that the Euler characteristic of this manifold is $\chi = 0$.

4.4 The Grounded Horizon Case with Potential $-\ln(|z - z'|/|1 - z\bar{z}'|)$

4.4.1 Grand Canonical Partition Function

In order to find the partition function for the system in the half space, with a metallic grounded boundary at $x = 1$, when the charges interacting through the pair potential

of (3.12) it is convenient to work in the grand canonical ensemble instead, and use the techniques developed in [6, 25]. We consider a system with a fixed background density ρ_b . The fugacity $\tilde{\zeta} = e^{\beta\mu}/\lambda^2$, where μ is the chemical potential, controls the average number of particles $\langle N \rangle$, and in general the system is nonneutral $\langle N \rangle \neq N_b$, where $N_b = \alpha p(x_m)$. The excess charge is expected to be found near the boundaries at $x = 1$ and $x = x_m$, while in the bulk the system is expected to be locally neutral. In order to avoid the collapse of a particle into the metallic boundary, due to its attraction to the image charges, we confine the particles to be in a “disk” domain $\tilde{\Omega}_R$, where $x \in [1 + w, x_m]$. We introduced a small gap w between the metallic boundary and the domain containing the particles, the geodesic width of this gap is $W = \sqrt{\alpha p'(1)/(2\pi n_b)} w$. On the other hand, for simplicity, we consider that the fixed background extends up to the metallic boundary.

In the potential energy of the system (4.1) we should add the self energy of each particle, that is due to the fact that each particle polarizes the metallic boundary, creating an induced surface charge density. This self energy is $\frac{q^2}{2} \ln|x^2 - 1|/M/2L$, where the constant $\ln(M/2L)$ has been added to recover, in the limit $M \rightarrow 0$, the self energy of a charged particle near a plane grounded wall in flat space.

The grand partition function, when $\beta q^2 = 2$, is

$$\Xi = e^{-\beta F_0^{\text{gh}}} \left[1 + \sum_{N=1}^{\infty} \frac{\zeta^N}{N!} \int \prod_{i=1}^N dS_i \prod_{i<j} \left| \frac{z_i - z_j}{1 - z_i \bar{z}_j} \right|^2 \prod_{i=1}^N \left| |z_i|^2 - 1 \right|^{-1} \prod_{i=1}^N e^{-\alpha[h(x_i) - 2N_b \ln x_i]} \right], \tag{4.108}$$

where for $N = 1$ the product $\prod_{i<j}$ must be replaced by 1. The domain of integration for each particle is $\tilde{\Omega}_R$. We have defined a rescaled fugacity $\zeta = 2L\tilde{\zeta}/M$ and

$$-\beta F_0^{\text{gh}} = \alpha N_b h(x_m) - N_b^2 \ln x_m - \alpha^2 \int_1^{x_m} \frac{[p(x)]^2}{x} dx \tag{4.109}$$

which is very similar to F_0^{hs} , except that here $N_b = \alpha p(x_m)$ is not equal to N the number of particles.

Let us define a set of reduced complex coordinates $u_i = z_i$ and its corresponding images $u_i^* = 1/\bar{z}_i$. By using Cauchy identity

$$\det \left(\frac{1}{u_i - u_j^*} \right)_{(i,j) \in \{1, \dots, N\}^2} = (-1)^{N(N-1)/2} \frac{\prod_{i<j} (u_i - u_j)(u_i^* - u_j^*)}{\prod_{i,j} (u_i - u_j^*)} \tag{4.110}$$

the particle-particle interaction and self energy terms can be cast into the form

$$\prod_{i<j} \left| \frac{z_i - z_j}{1 - z_i \bar{z}_j} \right|^2 \prod_{i=1}^N (|z_i|^2 - 1)^{-1} = (-1)^N \det \left(\frac{1}{1 - z_i \bar{z}_j} \right)_{(i,j) \in \{1, \dots, N\}^2}. \tag{4.111}$$

The grand canonical partition function is then

$$\Xi = e^{-\beta F_0^{\text{gh}}} \left[1 + \sum_{N=1}^{\infty} \frac{1}{N!} \int \prod_{i=1}^N dS_i \prod_{i=1}^N [-\zeta(x_i)] \det \left(\frac{1}{1 - z_i \bar{z}_j} \right) \right], \tag{4.112}$$

with $\zeta(x) = \zeta e^{-\alpha[h(x) - 2N_b \ln x]}$. We shall now recall how this expression can be reduced to a Fredholm determinant [25]. Let us consider the Gaussian partition function

$$Z_0 = \int \mathcal{D}\psi \mathcal{D}\bar{\psi} \exp \left[\int \bar{\psi}(\mathbf{q}) A^{-1}(z, \bar{z}') \psi(\mathbf{q}') dS dS' \right]. \tag{4.113}$$

The fields ψ and $\bar{\psi}$ are anticommuting Grassmann variables. The Gaussian measure in (4.113) is chosen such that its covariance is equal to

$$\langle \bar{\psi}(\mathbf{q}_i)\psi(\mathbf{q}_j) \rangle = A(z_i, \bar{z}_j) = \frac{1}{1 - z_i \bar{z}_j}, \tag{4.114}$$

where $\langle \dots \rangle$ denotes an average taken with the Gaussian weight of (4.113). By construction we have

$$Z_0 = \det(A^{-1}). \tag{4.115}$$

Let us now consider the following partition function

$$Z = \int \mathcal{D}\psi \mathcal{D}\bar{\psi} \exp \left[\int \bar{\psi}(\mathbf{q}) A^{-1}(z, \bar{z}') \psi(\mathbf{q}') dS dS' - \int \zeta(x) \bar{\psi}(\mathbf{q}) \psi(\mathbf{q}) dS \right] \tag{4.116}$$

which is equal to

$$Z = \det(A^{-1} - \zeta) \tag{4.117}$$

and then

$$\frac{Z}{Z_0} = \det[A(A^{-1} - \zeta)] = \det(1 + K), \tag{4.118}$$

where K is an integral operator (with integration measure dS) with kernel

$$K(\mathbf{q}, \mathbf{q}') = -\zeta(x') A(z, \bar{z}') = -\frac{\zeta(x')}{1 - z \bar{z}'}. \tag{4.119}$$

Expanding the ratio Z/Z_0 in powers of ζ we have

$$\frac{Z}{Z_0} = 1 + \sum_{N=1}^{\infty} \frac{1}{N!} \int \prod_{i=1}^N dS_i (-1)^N \prod_{i=1}^N \zeta(x_i) \langle \bar{\psi}(\mathbf{q}_1)\psi(\mathbf{q}_1) \cdots \bar{\psi}(\mathbf{q}_N)\psi(\mathbf{q}_N) \rangle. \tag{4.120}$$

Now, using Wick theorem for anticommuting variables [26], we find that

$$\langle \bar{\psi}(\mathbf{q}_1)\psi(\mathbf{q}_1) \cdots \bar{\psi}(\mathbf{q}_N)\psi(\mathbf{q}_N) \rangle = \det A(z_i, \bar{z}_j) = \det \left(\frac{1}{1 - z_i \bar{z}_j} \right). \tag{4.121}$$

Comparing (4.120) and (4.112) with the help of (4.121) we conclude that

$$\Xi = e^{-\beta F_0^{\text{gh}}} \frac{Z}{Z_0} = e^{-\beta F_0^{\text{gh}}} \det(1 + K). \tag{4.122}$$

The problem of computing the grand canonical partition function has been reduced to finding the eigenvalues λ of the operator K . The eigenvalue problem for K reads

$$-\int_{\Omega_R} \frac{\zeta(x')}{1 - z \bar{z}'} \Phi(x', \varphi') dS' = \lambda \Phi(x, \varphi). \tag{4.123}$$

For $\lambda \neq 0$ we notice from equation (4.123) that $\Phi(x, \varphi) = \Phi(z)$ is an analytical function of $z = x e^{i\varphi}$ in the region $|z| > 1$. Because of the circular symmetry, it is natural to try

$\Phi(z) = \Phi_\ell(z) = z^{-\ell}$ with $\ell \geq 1$ a positive integer. Expanding

$$\frac{1}{1 - z\bar{z}'} = - \sum_{n=1}^{\infty} (z\bar{z}')^{-n} \tag{4.124}$$

and replacing $\Phi_\ell(z) = z^{-\ell}$ in (4.123), we show that Φ_ℓ is indeed an eigenfunction of K with eigenvalue

$$\lambda_\ell = \zeta \mathcal{B}_{N_b}^{\text{gh}}(N_b - \ell), \tag{4.125}$$

where

$$\mathcal{B}_{N_b}^{\text{gh}}(k) = \frac{\alpha}{n_b} \int_{1+w}^{x_m} x^{2k} e^{-\alpha h(x)} p'(x) dx \tag{4.126}$$

which is very similar to \mathcal{B}_N defined in (4.11), except for the small gap w in the lower limit of integration. So, we arrive to the result for the grand potential

$$\beta\Omega = -\ln \Xi = \beta F_0^{\text{gh}} - \sum_{\ell=1}^{\infty} \ln[1 + \zeta \mathcal{B}_{N_b}^{\text{gh}}(N_b - \ell)]. \tag{4.127}$$

4.4.2 Thermodynamic Limit at Fixed Shape: $\alpha \rightarrow \infty$ and x_m Fixed

Let us define $k = N_b - \ell$ for $\ell \in \mathbb{N}^*$, thus k is positive, then negative when ℓ increases. Therefore, it is convenient to split the sum (4.127) in $\ln \Xi$ into two parts

$$S_6^{\text{gh, fixed}} = \sum_{k=-\infty}^{-1} \ln[1 + \zeta \mathcal{B}_{N_b}^{\text{gh}}(k)], \tag{4.128}$$

$$S_7^{\text{gh, fixed}} = \sum_{k=0}^{N_b-1} \ln[1 + \zeta \mathcal{B}_{N_b}^{\text{gh}}(k)]. \tag{4.129}$$

The asymptotic behavior of $\mathcal{B}_{N_b}^{\text{gh}}(k)$ when $\alpha \rightarrow \infty$ can be directly deduced from the one of \mathcal{B}_N found in Appendix B, (B18), taking into account the small gap w near the boundary at $x = 1 + w$. When $k < 0$, we have $\hat{x}_k < 1$, then we notice that $\epsilon_{k,1}$ defined in (B20) is negative, and that the relevant contributions to the sum $S_6^{\text{gh, fixed}}$ are obtained when k is close to 0, more precisely k of order $O(\sqrt{N_b})$. So, we expand \hat{x}_k around $\hat{x}_k = 1$ up to order $(\hat{x}_k - 1)^2$ in the exponential term $e^{-\alpha[h(\hat{x}_k) - 2p(\hat{x}_k)\ln \hat{x}_k]}$ from (B18). Then, we have, for $k < 0$ of order $O(\sqrt{N_b})$,

$$\mathcal{B}_{N_b}^{\text{gh}}(k) = \frac{\sqrt{\alpha\pi p'(1)}}{2n_b} e^{\alpha p'(1)(1-\hat{x}_k)^2} \text{erfc}[\sqrt{\alpha p'(1)}(1+w-\hat{x}_k)], \tag{4.130}$$

where $\text{erfc}(u) = 1 - \text{erf}(u)$ is the complementary error function. Then, up to corrections of order $O(1)$, the sum $S_6^{\text{gh, fixed}}$ can be transformed into an integral over the variable $t = \sqrt{\alpha p'(1)}(1 - \hat{x}_k)$, to find

$$S_6^{\text{gh, fixed}} = \sqrt{\alpha p'(1)} \int_0^\infty \ln \left[1 + \frac{\zeta \sqrt{\alpha\pi p'(1)}}{2n_b} e^{t^2} \text{erfc}(t + \sqrt{2\pi n_b} W) \right] dt + O(1). \tag{4.131}$$

Let $C_1 = \sqrt{2\pi\alpha p'(1)/n_b}$, be total length of the boundary at $x = 1$. We notice that

$$\zeta \frac{\sqrt{\alpha\pi p'(1)}}{2n_b} = \frac{\zeta C_1}{\sqrt{2n_b}} = \frac{2\tilde{\zeta} L}{\sqrt{2n_b}} \frac{C_1}{M} \tag{4.132}$$

is fixed and of order $O(1)$ in the limit $M \rightarrow \infty$, since in the fixed shape limit C_1/M is fixed. Therefore $S_6^{\text{gh, fixed}}$ gives a contribution proportional to the perimeter C_1 .

For $S_7^{\text{gh, fixed}}$, we define

$$\tilde{\epsilon}_{k,1} = \sqrt{\alpha p'(1)} (1 + w - \hat{x}_k), \tag{4.133}$$

and we write

$$\begin{aligned} S_7^{\text{gh, fixed}} &= \sum_{k=0}^{N_b-1} \ln \left[1 + \frac{\zeta \sqrt{\alpha\pi \hat{x}_k p'(\hat{x}_k)}}{2n_b} e^{-\alpha[h(\hat{x}_k) - 2p(\hat{x}_k) \ln \hat{x}_k]} [\text{erf}(\tilde{\epsilon}_{k,1}) + \text{erf}(\epsilon_{k,m})] \right] \\ &= S_8^{\text{gh, fixed}} + S_1^{\text{hs, fixed}} + S_2^{\text{hs, fixed}} + N_b \ln \frac{\zeta \sqrt{\alpha\pi}}{n_b}, \end{aligned} \tag{4.134}$$

where

$$S_8^{\text{gh, fixed}} = \sum_{k=0}^{N_b-1} \ln \left[\frac{n_b e^{\alpha[h(\hat{x}_k) - 2p(\hat{x}_k) \ln \hat{x}_k]}}{\zeta \sqrt{\alpha\pi \hat{x}_k p'(\hat{x}_k)}} + \frac{1}{2} [\text{erf}(\tilde{\epsilon}_{k,1}) + \text{erf}(\epsilon_{k,m})] \right] \tag{4.135}$$

and we see that the sums $S_1^{\text{hs, fixed}}$ and $S_2^{\text{hs, fixed}}$ reappear. These are defined in (4.31) and (4.32) and computed in (4.34) and (4.35). In a similar way to $S_6^{\text{gh, fixed}}$, $S_8^{\text{gh, fixed}}$ gives only boundary contributions when k is close to 0, of order $\sqrt{N_b}$ (grounded boundary at $x = 1$) and when k is close to N_b with $N_b - k$ of order $\sqrt{N_b}$ (boundary at $x = x_m$). We have,

$$\begin{aligned} S_8^{\text{gh, fixed}} &= \sqrt{\alpha p'(1)} \int_0^\infty \ln \left[\frac{n_b e^{-t^2}}{\zeta \sqrt{\alpha\pi p'(1)}} + \frac{1}{2} [\text{erf}(t - \sqrt{2\pi n_b} W) + 1] \right] dt \\ &\quad + \sqrt{\alpha x_m p'(x_m)} \int_0^\infty \ln \left[\frac{\text{erf}(t) + 1}{2} \right] dt. \end{aligned} \tag{4.136}$$

Let us introduce again the perimeter of the outer boundary at $x = x_m$, $C_R = \sqrt{2\pi\alpha x_m p'(x_m)/n_b}$. Putting together all terms, we finally have

$$\begin{aligned} \ln \Xi &= -N_b \beta \omega_B + \frac{\alpha}{2} [h(x_m) - 2p(x_m) \ln x_m] + \alpha \int_1^{x_m} \frac{(1+x)^4}{x^3} \ln \frac{(1+x)^4}{x^2} dx \\ &\quad - C_1 \beta \gamma_{\text{metal}} - C_R \beta \gamma_{\text{hard}} + O(1), \end{aligned} \tag{4.137}$$

where

$$\beta \omega_B = - \ln \frac{2\pi \tilde{\zeta} L}{\sqrt{2n_b}} \tag{4.138}$$

is the bulk grand potential per particle of the OCP near a plane metallic wall in the flat space. The surface (perimeter) tensions γ_{metal} and γ_{hard} associated to each boundary (metallic at

$x_b = 1$, and hard wall at $x_b = x_m$) are given by

$$\beta\gamma_{\text{metal}} = -\sqrt{\frac{n_b}{2\pi}} \int_0^\infty \ln \left[1 + \frac{\zeta \sqrt{\alpha\pi x_b p'(x_b)}}{2n_b} e^{t^2} \operatorname{erfc}(t + \sqrt{2\pi n_b} W) \right] dt - \sqrt{\frac{n_b}{2\pi}} \int_0^\infty \ln \left[\frac{n_b e^{-t^2}}{\zeta \sqrt{\alpha\pi p'(x_b) x_b}} + \frac{1}{2} [\operatorname{erf}(t - \sqrt{2\pi n_b} W) + 1] \right] dt \quad (4.139)$$

with $x_b = 1$, and (4.28) for $\beta\gamma_{\text{hard}}$.

Notice, once again, that the combination

$$\frac{\zeta \sqrt{\alpha\pi x_b p'(x_b)}}{2n_b} = \frac{2\tilde{\zeta} L}{\sqrt{2n_b}} \frac{C_b}{M} \quad (4.140)$$

is finite in this fixed shape limit, since the perimeter C_b of the boundary at x_b scales as M . Up to a rescaling of the fugacity $\tilde{\zeta}$ to absorb the factor C_b/M , the surface tension near the metallic boundary γ_{metal} is the same as the one found in Ref. [6] in flat space. It is also similar to the one found in Ref. [25] with a small difference due to the fact that in that reference the background does not extend up to the metallic boundary, but has also a small gap near the boundary.

There is no $\ln \alpha$ correction in the grand potential in agreement with the fact that the Euler characteristic of the manifold is $\chi = 0$.

Let us decompose $\ln \Xi$ into its bulk and perimeter parts,

$$\ln \Xi = -\beta\Omega_b^{\text{gh}} - C_1\beta\gamma_{\text{metal}} - C_R\beta\gamma_{\text{hard}} + O(1) \quad (4.141)$$

with the bulk grand potential Ω_b^{gh} given by

$$-\beta\Omega_b^{\text{gh}} = -N_b\beta\omega_B + \frac{\alpha}{2} [h(x_m) - 2p(x_m) \ln x_m] + \alpha \int_1^{x_m} \frac{(1+x)^4}{x^3} \ln \frac{(1+x)^4}{x^2} dx. \quad (4.142)$$

The average number of particles is given by the usual thermodynamic relation $\langle N \rangle = \zeta \partial(\ln \Xi) / \partial \zeta$. Following (4.141), it can be decomposed into bulk and perimeter contributions,

$$\langle N \rangle = N_b - C_1\zeta \frac{\partial\beta\gamma_{\text{metal}}}{\partial\zeta}. \quad (4.143)$$

The boundary at $x = x_m$ does not contribute because γ_{hard} does not depend on the fugacity. From this equation, we can deduce the perimeter linear charge density σ which accumulates near the metallic boundary

$$\sigma = -\zeta \frac{\partial\beta\gamma_{\text{metal}}}{\partial\zeta}. \quad (4.144)$$

We can also notice that the bulk Helmholtz free energy $F_b^{\text{gh}} = \Omega_b^{\text{gh}} + \mu N_b$ is the same as for the half surface, with Coulomb potential G^{hs} , given in (4.37).

4.4.3 Thermodynamic Limit $R \rightarrow \infty$, $x_m \rightarrow \infty$, and Fixed M

This limit is of restricted interest, since the metallic boundary perimeter remains of order $O(1)$, we expect to find the same thermodynamic quantities as in the half surface case with

hard wall “horizon” boundary up to order $O(\ln x_m)$. This is indeed the case: let us split $\ln \Xi$ into two sums S_6^{gh} and S_7^{gh} as in (4.128) and (4.129). For $k < 0$, the asymptotic expansion of $\mathcal{B}_{N_b}(k)$ derived in Appendix B should be revised, because the absolute maximum of the integrand is obtained for values of the variable of integration outside the domain of integration. Within the domain of integration the maximum value of the integrand in (4.126) is obtained when $x = 1 + w$. Expanding the integrand around that value, we obtain to first order, for large $|k|$,

$$\mathcal{B}_{N_b}^{\text{gh}}(k) \sim \frac{\alpha p'(1+w)}{2n_b|k|} e^{-2w|k|}. \tag{4.145}$$

Then

$$\begin{aligned} S_6^{\text{gh}} &= \sum_{k=-\infty}^0 \ln[1 + \zeta \mathcal{B}_{N_b}^{\text{gh}}(k)] \\ &= \int_0^\infty dk \ln\left[1 + \zeta \frac{\alpha p'(1+w)}{2n_b|k|} e^{-2w|k|}\right] + O(1) \\ &= O(1), \end{aligned} \tag{4.146}$$

does not contribute to the result at orders greater than $O(1)$. For the other sum, we have

$$\begin{aligned} S_7^{\text{gh}} &= \sum_{k=0}^{N_b} \ln[\zeta \mathcal{B}_{N_b}^{\text{gh}}(k)] + \sum_{k=0}^{N_b} \ln\left[1 + \frac{1}{\zeta \mathcal{B}_{N_b}^{\text{gh}}(k)}\right] \\ &= \sum_{k=0}^{N_b} \ln[\zeta \mathcal{B}_{N_b}^{\text{gh}}(k)] + O(1). \end{aligned} \tag{4.147}$$

The second sum is indeed $O(1)$, because $1/[\zeta \mathcal{B}_{N_b}^{\text{gh}}(k)]$ has a fast exponential decay for large k , therefore the sum can be converted into an finite [order $O(1)$] integral over the variable k .

Now, since the asymptotic behavior of $\mathcal{B}_{N_b}^{\text{gh}}(k)$, for $k > 0$ and large, is essentially the same as the one for $\mathcal{B}_{N_b}(k)$, we immediately find, up to $O(1)$ corrections,

$$\ln \Xi = \beta \mu N_b + \ln Z^{\text{hs}} + O(1), \tag{4.148}$$

where $\ln Z^{\text{hs}}$ is minus the free energy in the half surface case with hard wall boundary, given by (4.26).

4.4.4 The One-Body Density

As usual one can compute the density by doing a functional derivative of the grand potential with respect to a position-dependent fugacity $\zeta(\mathbf{q})$

$$n^{\text{gh}}(\mathbf{q}) = \zeta(\mathbf{q}) \frac{\delta \ln \Xi}{\delta \zeta(\mathbf{q})}. \tag{4.149}$$

For the present case of a curved space, we shall understand the functional derivative with the rule $\frac{\delta \zeta(\mathbf{q}')}{\delta \zeta(\mathbf{q})} = \delta(\mathbf{q}, \mathbf{q}')$ where $\delta(\mathbf{q}, \mathbf{q}') = \delta(x - x')\delta(\varphi - \varphi')/\sqrt{g}$ is the Dirac distribution on the curved surface.

Using a Dirac-like notation, one can formally write

$$\ln \Xi = \text{Tr} \ln(1 + K) - \beta F_0^{\text{gh}} = \int \langle \mathbf{q} | \ln(1 - \zeta(\mathbf{q})A) | \mathbf{q} \rangle dS - \beta F_0^{\text{gh}}. \tag{4.150}$$

Then, doing the functional derivative (4.149), one obtains

$$n^{\text{gh}}(\mathbf{q}) = \zeta \langle \mathbf{q} | (1 + K)^{-1}(-A) | \mathbf{q} \rangle = \zeta G(\mathbf{q}, \mathbf{q}), \tag{4.151}$$

where we have defined $G(\mathbf{q}, \mathbf{q}')$ by $G = (1 + K)^{-1}(-A)$. More explicitly, G is the solution of $(1 + K)G = -A$, that is

$$G(\mathbf{q}, \mathbf{q}') - \int_{\Omega_R} \zeta(x'') \frac{G(\mathbf{q}'', \mathbf{q}')}{1 - z\bar{z}''} dS'' = -\frac{1}{1 - z\bar{z}'}. \tag{4.152}$$

From this integral equation, one can see that $G(\mathbf{q}, \mathbf{q}')$ is an analytical function of z in the region $|z| > 1$. Then, we look for a solution in the form of a Laurent series

$$G(\mathbf{q}, \mathbf{q}') = \sum_{\ell=1}^{\infty} a_{\ell}(\mathbf{r}') z^{-\ell}. \tag{4.153}$$

Replacing into (4.152) yields

$$G(\mathbf{q}, \mathbf{q}') = \sum_{\ell=1}^{\infty} \frac{(z\bar{z}')^{-\ell}}{1 + \lambda_{\ell}}. \tag{4.154}$$

Recalling that $\lambda_{\ell} = \zeta \mathcal{B}_N^{\text{gh}}(N_b - \ell)$, the density is given by

$$n^{\text{gh}}(x) = \zeta \sum_{k=-\infty}^{N_b-1} \frac{x^{2k} e^{-\alpha h(x)}}{1 + \zeta \mathcal{B}_N^{\text{gh}}(k)}. \tag{4.155}$$

4.4.5 Density in the Thermodynamic Limit at Fixed Shape $\alpha \rightarrow \infty$ and x_m Fixed

Using the asymptotic behavior (B18) of $\mathcal{B}_N^{\text{gh}}$, we have

$$n^{\text{gh}}(x) = \zeta \sum_{k=-\infty}^{N_b} \frac{\exp(-\alpha[h(x) - 2p(\hat{x}_k) \ln x - h(\hat{x}_k) + 2p(\hat{x}_k) \ln \hat{x}_k])}{e^{\alpha[h(\hat{x}_k) - 2p(\hat{x}_k) \ln \hat{x}_k]} + \frac{\zeta \sqrt{\alpha \pi \hat{x}_k p'(\hat{x}_k)}}{2n_b} [\text{erf}(\tilde{\epsilon}_{k,1}) + \text{erf}(\epsilon_{k,m})]}. \tag{4.156}$$

Once again, this sum can be evaluated using Laplace method. The exponential in the numerator presents a peaked maximum for k such that $\hat{x}_k = x$. Expanding the argument of the exponential around its maximum, we have

$$n^{\text{gh}}(x) = \zeta \sum_{k=-\infty}^{N_b} \frac{e^{-\alpha p'(x)(x - \hat{x}_k)^2/x}}{e^{\alpha[h(\hat{x}_k) - 2p(\hat{x}_k) \ln \hat{x}_k]} + \frac{\zeta \sqrt{\alpha \pi \hat{x}_k p'(\hat{x}_k)}}{2n_b} [\text{erf}(\tilde{\epsilon}_{k,1}) + \text{erf}(\epsilon_{k,m})]}. \tag{4.157}$$

Now, three cases has to be considered, depending on the value of x .

If x is in the bulk, i.e. $x - 1$ and $x_m - x$ of order 1, the exponential term in denominator vanishes in the limit $\alpha \rightarrow \infty$, and we end up with an expression which is essentially the same

as in the canonical case (4.62) [the difference in the lower limit of summation is irrelevant in this case since the summand vanishes very fast when \hat{x}_k differs from x]. Therefore, in the bulk, $n^{\text{gh}}(x) = n_b$ as expected.

When $x_m - x$ is of order $O(1/\sqrt{\alpha})$, once again the exponential term in the denominator vanishes in the limit $\alpha \rightarrow \infty$. The resulting expression is transformed into an integral over the variable $\epsilon_{k,m}$, and following identical calculations as the ones from Sect. 4.1.9, we find that, $n^{\text{gh}}(x) = n^{\text{hs}}(x)$, that is the same result (4.65) as for the hard wall boundary. This is somehow expected since, the boundary at $x = x_m$ is of the hard wall type. Notice that the density profile near this boundary does not depend on the fugacity ζ .

The last case is for the density profile close to the metallic boundary, when $x - 1$ is of order $O(1/\sqrt{\alpha})$. In this case, contrary to the previous ones, the exponential term in the denominator does not vanish. Expanding it around $\hat{x}_k = 1$, we have

$$n^{\text{gh}}(x) = \zeta \sum_{k=-\infty}^{N_b} \frac{e^{-\alpha p'(x)(x-\hat{x}_k)^2/x}}{e^{-\epsilon_{k,1}^2} + \frac{\zeta \sqrt{\alpha \pi \hat{x}_k p'(\hat{x}_k)}}{2n_b} [\text{erf}(\tilde{\epsilon}_{k,1}) + 1]}. \tag{4.158}$$

Transforming the summation into an integral over the variable $t = -\epsilon_{k,1}$, we find

$$n^{\text{gh}}(x) = \zeta \sqrt{\alpha p'(1)} \int_{-\infty}^{+\infty} \frac{e^{-[t + \sqrt{\alpha p'(1)}(x-1)]^2} dt}{e^{-t^2} + \frac{\zeta \sqrt{\alpha \pi p'(1)}}{2n_b} \text{erfc}(t + \sqrt{2\pi n_b} W)}. \tag{4.159}$$

For purposes of comparison with Ref. [25], this can be rewritten as

$$n^{\text{gh}}(x) = \zeta \sqrt{\alpha p'(1)} e^{-\alpha p'(1)[(x-1-w)^2 - w^2]} \int_{-\infty}^{+\infty} \frac{e^{-2\sqrt{\alpha p'(1)}(x-1)t} dt}{1 + \frac{\zeta \sqrt{\alpha \pi p'(1)}}{2n_b} \text{erfc}(t) e^{(t - \sqrt{2\pi n_b} W)^2}}. \tag{4.160}$$

Which is very similar to the density profile near a plane metallic wall in flat space found in Ref. [25] [there is a small difference, due to the fact that in [25] the background did not extend up to the metallic wall, but also had a gap, contrary to our present model]. Figure 3 shows the density profile for two different values of the fugacity, and compares the asymptotic results with a direct numerical evaluation of the density.

Interestingly, once again, the density profile shows a universality feature, in the sense that it is essentially the same as for a flat space. As in the flat space, the fugacity controls the excess charge which accumulates near the metallic wall, due to the attraction of the charges to their images. Only the density profile close to the metallic wall depends on the fugacity. In the bulk, the density is constant, equal to the background density. Close to the other boundary (the hard wall one), the density profile is the same as in the other models from previous sections, and it does not depend on the fugacity.

5 Conclusions

The two-dimensional one-component classical plasma has been studied on Flamm's paraboloid (the Riemannian surface obtained from the spatial part of the Schwarzschild metric). The three-dimensional one-component classical plasma had long been used as the simplest microscopic model to describe many Coulomb fluids such as electrolytes, plasmas, molten salts [27]. The two-dimensional one-component plasma has been studied in a varieties of geometries, from the simplest planar geometry to curved surfaces as the cylinder,

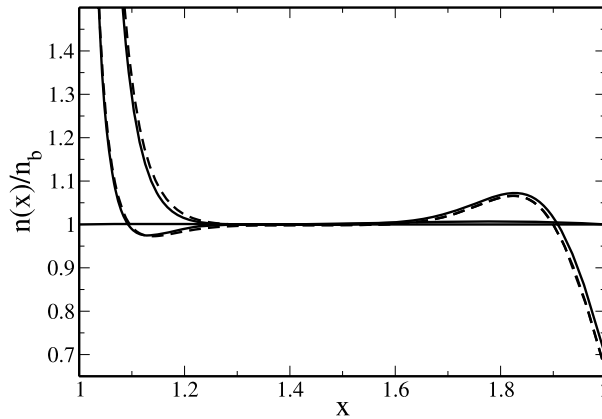


Fig. 3 The normalized one-body density $n^{\text{gh}}(x)/n_b$, in the grounded horizon case. The *dashed lines* correspond to a numerical evaluation, obtained from (4.155), with $N = 100$, $x_m = 2$ and $\alpha = 4.15493$ and truncating the sum to 301 terms (the lower value of k is -200). The gap close to the metallic boundary has been chosen equal to $w = 0.01$. The *solid lines* correspond to the asymptotic result in the fixed shape limit when $\alpha \rightarrow \infty$, and $x_m = 2$ fixed. The two upper curves correspond to a fugacity given by $\zeta \sqrt{\alpha}/(2n_b) = \zeta L \sqrt{\pi}/n_b = 1$, while the two lower ones correspond to $\zeta L \sqrt{\pi}/n_b = 0.1$. Notice how the value of the fugacity only affects the density profile close to the metallic boundary $x = 1$

the sphere, and the pseudosphere. From this point of view, this work presents new results as it describes the properties of the plasma on a surface that had never been considered before in this context.

The Coulomb potential on this surface has been carefully determined. When we limit ourselves to study only the upper or lower half parts (S_{\pm}) of the surface (see Fig. 1) the Coulomb potential is $G^{\text{hs}}(\mathbf{q}, \mathbf{q}') = -\ln|z - z'| + \text{constant}$, with the appropriate set of coordinates (x, φ) defined in Sect. 2, and $z = xe^{i\varphi}$. When the particles live on the whole surface, then the Coulomb potential turns out to be $G^{\text{ws}}(\mathbf{q}, \mathbf{q}') = -\ln(|z - z'|/\sqrt{|zz'|}) + \text{constant}$. When the charges live in the upper part with the horizon grounded, the Coulomb potential can be determined using the method of images form electrostatics, it is $G^{\text{gh}}(\mathbf{q}, \mathbf{q}') = -\ln(|z - z'|/|1 - z\bar{z}'|)$.

Since the Coulomb potential takes a form similar to the one of a flat space, this allows to use the usual techniques [2, 3] to compute the thermodynamic properties when the coupling constant $\Gamma = \beta q^2 = 2$.

Two different thermodynamic limits have been considered: the one where the radius R of the “disk” confining the plasma is allowed to become very big while keeping the surface hole radius M constant, and the one where both $R \rightarrow \infty$ and $M \rightarrow \infty$ with the ratio R/M kept constant (fixed shape limit). In both limits we computed the free energy up to corrections of order $O(1)$.

The plasma on the half surface has an extensive free energy, in both types of thermodynamic limit, upon choosing the arbitrary additive constant in the Coulomb potential equal to $-\ln M + \text{constant}$. The system on the full surface has an extensive free energy upon choosing the constant in the Coulomb potential equal to $-\ln(Mx_m) + \text{constant}$ where $x_m = (\sqrt{R} + \sqrt{R - 2M})^2/(2M)$.

In the limit $R \rightarrow \infty$ while keeping M fixed, most of the surface available to the particles is almost flat, therefore the bulk free energy is the same as in flat space, but corrections from the flat case, due to the curvature effects, appear in the terms proportional to R and the terms proportional to $\ln R$. These corrections are different for each case (half or whole surface).

The asymptotic expansion at fixed shape ($\alpha \rightarrow \infty$) presents a different value for the bulk free energy than in the flat space, due to the curvature corrections. On the other hand, the perimeter corrections to the free energy turn out to be the same as for a flat space. This expansion of the free energy does not exhibit the logarithmic correction, $\ln \alpha$, in agreement with the fact that the Euler characteristic of this surface vanishes.

For completeness, we also studied the system on half surface letting the particles interact through the Coulomb potential G^{ws} . In this mixed case the result for the free energy is simply one-half the one found for the system on the full surface.

In the case where the "horizon" is grounded (metallic boundary), the system is studied in the grand canonical ensemble. The limit $R \rightarrow \infty$ with M fixed, reproduces the same results as the case of the half surface with potential G^{hs} up to $O(1)$ corrections, because the effects of the size of the metallic boundary remain $O(1)$. More interesting is the thermodynamic limit at fixed shape, where we find that the bulk thermodynamics are the same as for the half surface with potential G^{hs} , but a perimeter correction associated to the metallic boundary appears. This turns out to be the same as for a flat space. This perimeter correction ("surface" tension) $\beta \gamma_{\text{metal}}$ depends on the value of the fugacity. In the grand canonical formalism, the system can be nonneutral, in the bulk the system is locally neutral, and the excess charge is found near the metallic boundary. In contrast, the outer hard wall boundary (at $x = x_m$), exhibits the same density profile as in the other cases, independent of the value of the fugacity. This reflects in a perimeter contribution $\beta \gamma_{\text{hard}}$ equal to the one of the previous cases.

When the horizon shrinks to a point the upper half surface reduces to a plane and one recovers the well known result valid for the one-component plasma on the plane. In the same limit the whole surface reduces to two flat planes connected by a hole at the origin.

We carefully studied the one body density for several different situations: plasma on half surface with potential G^{hs} and G^{ws} , plasma on the whole surface with potential G^{ws} , and plasma on half surface with the horizon grounded. When only one-half of the surface is occupied by the plasma, if we use G^{hs} as the Coulomb potential, the density shows a peak in the neighborhoods of each boundary, tends to a finite value at the boundary and to the background density far from it, in the bulk. If we use G^{ws} , instead, the qualitative behavior of the density remains the same. In the thermodynamic limit at fixed shape, we find that the density profile is the same as in flat space near a hard wall, regardless of the Coulomb potential used.

In the grounded horizon case the density reaches the background density far from the boundaries. In this case, the fugacity and the background density control the density profile close to the metallic boundary (horizon). In the bulk and close to the outer hard wall boundary, the density profile is independent of the fugacity. In the thermodynamic limit at fixed shape, the density profile is the same as for a flat space.

Internal and external screening sum rules have been briefly discussed. Nevertheless, we think that systems with non-constant curvature should deserve a revisiting of all the common sum rules for charged fluids.

Acknowledgements Riccardo Fantoni would like to acknowledge the support from the Italian MIUR (PRIN-COFIN 2006/2007). He would also wish to dedicate this work to his wife Ilaria Tognoni who is undergoing a very delicate and reflexive period of her life.

G.T. acknowledges partial financial support from Comité de Investigaciones y Posgrados, Facultad de Ciencias, Universidad de los Andes.

Appendix A: Green Function of Laplace Equation

In this appendix, we illustrate the calculation of the Green function using the original system of coordinates (r, φ) . The Coulomb potential generated at $\mathbf{q} = (r, \varphi)$ by a unit charge placed at $\mathbf{q}_0 = (r_0, \varphi_0)$ with $r_0 > 2M$ satisfies the Poisson equation

$$\Delta G(r, \varphi; r_0, \varphi_0) = -2\pi \delta(r - r_0) \delta(\varphi - \varphi_0) / \sqrt{g}, \tag{A1}$$

where $g = \det(g_{\mu\nu}) = r^2 / (1 - 2M/r)$. To solve this equation, we expand the Green function G and the second delta distribution in a Fourier series as follows

$$G(r, \varphi; r_0, \varphi_0) = \sum_{n=-\infty}^{\infty} e^{in(\varphi-\varphi_0)} g_n(r, r_0), \tag{A2}$$

$$\delta(\varphi - \varphi_0) = \frac{1}{2\pi} \sum_{n=-\infty}^{\infty} e^{in(\varphi-\varphi_0)}, \tag{A3}$$

to obtain an ordinary differential equation for g_n

$$\left[\left(1 - \frac{2M}{r}\right) \frac{\partial^2}{\partial r^2} + \left(\frac{1}{r} - \frac{M}{r^2}\right) \frac{\partial}{\partial r} - \frac{n^2}{r^2} \right] g_n(r, r_0) = -\delta(r - r_0) / \sqrt{g}. \tag{A4}$$

To solve this equation we first solve the homogeneous one for $r < r_0$: $g_{n,-}(r, r_0)$ and $r > r_0$: $g_{n,+}(r, r_0)$. The solution is, for $n \neq 0$,

$$g_{n,\pm}(r, r_0) = A_{n,\pm} (\sqrt{r} + \sqrt{r-2M})^{2n} + B_{n,\pm} (\sqrt{r} + \sqrt{r-2M})^{-2n}, \tag{A5}$$

and, for $n = 0$, one finds

$$g_{0,\pm}(r, r_0) = A_{0,\pm} + B_{0,\pm} \ln(\sqrt{r} + \sqrt{r-2M}). \tag{A6}$$

The form of the solution immediately suggest that it is more convenient to work with the variable $x = (\sqrt{r} + \sqrt{r-2M})^2 / (2M)$. For this reason, we introduced this new system of coordinates (x, φ) which is used in the main text.

Appendix B: Asymptotic Expansions of $\mathcal{B}_N(k)$, $\tilde{\mathcal{B}}_N(k)$ and $\hat{\mathcal{B}}_N(k)$

B.1 Asymptotic Expansion of $\mathcal{B}_N(k)$

B.1.1 Limit $N \rightarrow \infty$, $x_m \rightarrow \infty$, and Fixed α

Doing the change of variable $s = \alpha p(x)$ in the integral (4.11), we have

$$\mathcal{B}_N(k) = \frac{1}{n_b} \int_0^N x^{2k} e^{-\alpha h(x)} ds, \tag{B1}$$

where x is related to the variable of integration s by $s = \alpha p(x)$. The limit $k \rightarrow \infty$ and $N \rightarrow \infty$ can be obtained using Laplace method [28]. To this end, let us write $\mathcal{B}_N(k)$ as

$$\mathcal{B}_N(k) = \frac{k}{n} \int_0^{N/k} e^{k\phi_k(t)} dt, \tag{B2}$$

where we made the change of variable $t = s/k$ and we defined

$$\phi_k(t) = 2 \ln x - \frac{\alpha}{k} h(x), \tag{B3}$$

where

$$x = p^{-1}(kt/\alpha). \tag{B4}$$

The derivative of ϕ_k is

$$\phi'_k(t) = \frac{1}{x} \frac{dx}{dt} (1-t) \tag{B5}$$

$$= \frac{2k}{\alpha x p'(x)} (1-t), \tag{B6}$$

where we have used the definition (B4) of x and the properties (3.20) of h and p .

The maximum of $\phi_k(t)$ is obtained when $t = 1$. At this point we have

$$\phi''_k(1) = -\frac{2k}{\alpha \hat{x}_k p'(\hat{x}_k)} = -1 + O(1/\sqrt{k}), \tag{B7a}$$

$$\phi^{(3)}_k(1) = \frac{4k^2}{\alpha^2} \frac{p'(\hat{x}_k) + x_k p''(\hat{x}_k)}{\hat{x}_k^2 p'(\hat{x}_k)^3} = 2 + O(1/\sqrt{k}), \tag{B7b}$$

$$\phi^{(4)}_k(1) = \frac{6k^3}{\alpha^3 p'(\hat{x}_k)} \frac{d}{dx} \left[\frac{p'(x) + x p''(x)}{x^2 p'(x)^3} \right]_{x=\hat{x}_k} = -6 + O(1/\sqrt{k}), \tag{B7c}$$

where

$$\hat{x}_k = p^{-1}(k/\alpha). \tag{B8}$$

Expanding $\phi_k(t)$ up to order $(t-1)^4$, and defining $v = \sqrt{k|\phi''_k(1)|} (t-1)$, we have

$$\begin{aligned} \mathcal{B}_N(k) &= \frac{\sqrt{k} e^{k\phi_k(1)}}{n \sqrt{|\phi''_k(1)|}} \int_{-\sqrt{k|\phi''_k(1)|}}^{(N-k)\sqrt{k|\phi''_k(1)|/k}} e^{-v^2/2} \\ &\times \left[1 + \frac{v^3 \phi^{(3)}_k(1)}{3! \sqrt{k} |\phi''_k(1)|^{3/2}} + \frac{v^4 \phi^{(4)}_k(1)}{4! k |\phi''_k(1)|^2} + \frac{v^6 [\phi^{(3)}_k(1)]^2}{3!^2 2k |\phi''_k(1)|^3} + o\left(\frac{1}{k}\right) \right] dv. \end{aligned} \tag{B9}$$

Let us define

$$\epsilon_k = \sqrt{|\phi''_k(1)|} \frac{N-k}{\sqrt{2k}} = \frac{N-k}{\sqrt{2N}} + O(1/\sqrt{N}) \tag{B10}$$

which is an order one parameter, since we are interested in an expansion for N and k large with $N-k$ of order \sqrt{N} . Using the integrals

$$\int_{-\infty}^{\epsilon} e^{-v^2/2} dv = \sqrt{\frac{\pi}{2}} \left[1 + \operatorname{erf}\left(\frac{\epsilon}{\sqrt{2}}\right) \right], \tag{B11}$$

$$\int_{-\infty}^{\epsilon} e^{-v^2/2} v^3 dv = -(2 + \epsilon^2) e^{-\epsilon^2/2}, \tag{B12}$$

$$\int_{-\infty}^{\epsilon} e^{-v^2/2} v^4 dv = 3\sqrt{\frac{\pi}{2}} \left[1 + \operatorname{erf}\left(\frac{\epsilon}{\sqrt{2}}\right) \right] - e^{-\epsilon^2/2} \epsilon (3 + \epsilon^2), \tag{B13}$$

$$\int_{-\infty}^{\epsilon} e^{-v^2/2} v^6 dv = 15\sqrt{\frac{\pi}{2}} \left[1 + \operatorname{erf}\left(\frac{\epsilon}{\sqrt{2}}\right) \right] - e^{-\epsilon^2/2} \epsilon (15 + 5\epsilon^2 + \epsilon^4), \quad (\text{B14})$$

where $\operatorname{erf}(z) = (2/\sqrt{\pi}) \int_0^z e^{-u^2} du$ is the error function, we find in the limit $N \rightarrow \infty$, $k \rightarrow \infty$, and finite ϵ_k ,

$$\mathcal{B}_N(k) = \sqrt{\frac{\pi k}{2|\phi_k''(1)|}} \frac{e^{k\phi_k(1)}}{n} [1 + \operatorname{erf}(\epsilon_k)] \left[1 + \frac{1}{12k} + \frac{1}{\sqrt{k}} \xi_1(\epsilon_k) + \frac{1}{k} \xi_2(\epsilon_k) \right]. \quad (\text{B15})$$

The functions $\xi_1(\epsilon_k)$ and $\xi_2(\epsilon_k)$ contain terms proportional $e^{-\epsilon_k^2}$, from the Gaussian integrals above. However, as explained in the main text, these do not contribute to the final result for the partition function up to order $O(1)$, because the exponential term $e^{-\epsilon_k^2}$ make convergent and finite the integrals of these functions that appear in the calculations, giving terms of order $O(1)$ and $O(1/\sqrt{N})$ respectively.

B.1.2 Limit $N \rightarrow \infty$, $\alpha \rightarrow \infty$, Fixed x_m

For the determination of the thermodynamic limit at fixed shape, we also need the asymptotic behavior of $\mathcal{B}_N(k)$ when $\alpha \rightarrow \infty$ at fixed x_m . We write $\mathcal{B}_N(k)$ as

$$\mathcal{B}_N(k) = \frac{\alpha}{n_b} \int_1^{x_m} e^{-\alpha[h(x)-2p(\hat{x}_k)\ln x]} p'(x) dx, \quad (\text{B16})$$

where we have defined once again \hat{x}_k by $k = \alpha p(\hat{x}_k)$. We apply Laplace method for $\alpha \rightarrow \infty$. Let

$$F(x) = h(x) - 2p(\hat{x}_k) \ln x. \quad (\text{B17})$$

F has a minimum for $x = \hat{x}_k$ with $F''(\hat{x}_k) = 2p'(\hat{x}_k)/\hat{x}_k$. Expanding to the order $(x - \hat{x}_k)^2$ the argument of the exponential and following calculations similar to the ones of the previous section, we find

$$\begin{aligned} \mathcal{B}_N(k) &= \frac{\sqrt{\alpha \pi \hat{x}_k p'(\hat{x}_k)}}{2n_b} e^{-\alpha[h(\hat{x}_k)-2p(\hat{x}_k)\ln \hat{x}_k]} [\operatorname{erf}(\epsilon_{k,1}) + \operatorname{erf}(\epsilon_{k,m})] \\ &\times \left(1 + \frac{1}{\alpha} \xi_0(\hat{x}_k) + \frac{1}{\sqrt{\alpha}} [\xi_{1,m}(\epsilon_{k,m}) + \xi_{1,1}(\epsilon_{k,1})] \right), \end{aligned} \quad (\text{B18})$$

where

$$\epsilon_{k,m} = \sqrt{\frac{\alpha p'(x_m)}{x_m}} (x_m - \hat{x}_k), \quad (\text{B19})$$

$$\epsilon_{k,1} = \sqrt{\alpha p'(1)} (\hat{x}_k - 1). \quad (\text{B20})$$

The terms with the error functions come from incomplete Gaussian integral and take into account the contribution of values of k such that $x_m - \hat{x}_k$ (or $\hat{x}_k - 1$) is of order $1/\sqrt{\alpha}$, or equivalently $N - k$ (or k) of order \sqrt{N} .

The functions $\xi_0(\hat{x}_k)$, $\xi_{1,1}(\epsilon_{k,1})$, and $\xi_{1,m}(\epsilon_{k,m})$ can be computed explicitly, pushing the expansion one order further. These next order corrections are different than in the previous section, in particular $(1/\alpha)\xi_0(\hat{x}_k) \neq 1/(12k)$.

However, these next order terms are not needed in the computation of the partition function at order $O(1)$, since they give contributions of order $O(1)$. Note in particular that the term $\xi_0(\hat{x}_k)/\alpha$ gives contributions of order $O(1)$, contrary to the previous limit studied earlier where it gave contributions of order $\ln N$. Indeed, in the logarithm of the partition function, this term gives a contribution

$$\sum_{k=0}^N \frac{\xi_0(\hat{x}_k)}{\alpha} = \frac{1}{\alpha} \int_1^{x_m} \alpha p'(x) \xi_0(x) dx + o(1) = O(1). \tag{B21}$$

B.2 Asymptotic Expansions of $\tilde{\mathcal{B}}_N(k)$ and $\hat{\mathcal{B}}_N(k)$

To study $\tilde{\mathcal{B}}_N(k)$, it is convenient to define $k' = k - \frac{N}{2}$, then

$$\tilde{\mathcal{B}}_N(k) = \frac{\alpha}{n_b} \int_{1/x_m}^{x_m} x^{2k'} e^{-\alpha h(x)} x p'(x) dx, \tag{B22}$$

which is very similar to

$$\hat{\mathcal{B}}_N(k) = \frac{\alpha}{n_b} \int_1^{x_m} x^{2k} e^{-\alpha h(x)} x p'(x) dx, \tag{B23}$$

changing k' by k , and taking into account the extended domain of integration $[1/x_m, 1]$ for $\tilde{\mathcal{B}}_N$. As in the previous section, the asymptotic expansions for $\tilde{\mathcal{B}}_N(k)$ and $\hat{\mathcal{B}}_N(k)$ can be obtained using Laplace method. Notice that for $\tilde{\mathcal{B}}_N(k)$, k' is in the range $[-\frac{N}{2}, \frac{N}{2}]$. When $k' < 0$, the maximum of the integrand is in the region $[1/x_m, 1]$, and when $k' > 0$, the maximum is in the region $[1, x_m]$. Due to the fact that the contribution to the integral from the region $[1/x_m, 1]$ is negligible when $k' > 0$, the asymptotics for $\hat{\mathcal{B}}_N(k)$ will be the same as those for $\tilde{\mathcal{B}}_N(k)$, for $k' > 0$, doing the change $k \rightarrow k'$. Therefore, we present only the derivation of the asymptotics of $\tilde{\mathcal{B}}_N$.

B.2.1 Limit $N \rightarrow \infty, x_m \rightarrow \infty$, and Fixed α

We proceed as for $\mathcal{B}_N(k)$, defining the variable of integration $t = \alpha p(x)/k'$, then

$$\tilde{\mathcal{B}}_N(k) = \frac{|k'|}{n_b} \int_{-\frac{N}{2|k'|}}^{\frac{N}{2|k'|}} x e^{k' \phi_{k'}(t)} dt, \tag{B24}$$

where $\phi_{k'}(t)$ is the same function defined in (B3). Now we apply Laplace method to compute this integral. The main difference with the calculations done for \mathcal{B}_N are the following. First, taking into account that k' can be positive or negative, we should note that

$$\phi_{k'}''(1) = \begin{cases} -1 + O(1/\sqrt{|k'|}) & k' > 0 \\ 1 + O(1/\sqrt{|k'|}) & k' < 0, \end{cases} \tag{B25}$$

$$\phi_{k'}^{(3)}(1) = \begin{cases} 2 + O(1/\sqrt{|k'|}) & k' > 0 \\ -2 + O(1/\sqrt{|k'|}) & k' < 0, \end{cases} \tag{B26}$$

$$\phi_{k'}^{(4)}(1) = \begin{cases} -6 + O(1/\sqrt{|k'|}) & k' > 0 \\ 6 + O(1/\sqrt{|k'|}) & k' < 0. \end{cases} \tag{B27}$$

Second, we also need to expand x close to the maximum which is obtained for $t = 1$,

$$x = \hat{x}_{k'}[1 + a(t - 1) + b(t - 1)^2 + O((t - 1)^3)] \tag{B28}$$

with

$$a = \frac{p(\hat{x}_{k'})}{\hat{x}_{k'} p'(\hat{x}_{k'})} = \begin{cases} \frac{1}{2} + O(1/\sqrt{|k'|}) & k' > 0 \\ -\frac{1}{2} + O(1/\sqrt{|k'|}) & k' < 0 \end{cases} \tag{B29}$$

and

$$b = -\frac{p(\hat{x}_{k'})^2 p''(\hat{x}_{k'})}{2\hat{x}_{k'} p'(\hat{x}_{k'})^3} = \begin{cases} -\frac{1}{8} + O(1/\sqrt{|k'|}) & k' > 0 \\ \frac{3}{8} + O(1/\sqrt{|k'|}) & k' < 0. \end{cases} \tag{B30}$$

Notice in particular that for the term b , the difference between positive and negative values of k' is not only a change of sign. This is to be expected since the function x is not invariant under the change $x \rightarrow 1/x$.

Following very similar calculations to the ones done for \mathcal{B}_N with the appropriate changes mentioned above, we finally find

$$\begin{aligned} \tilde{B}_N(k) &= \frac{\hat{x}_{k'}}{2n_b} \sqrt{\pi \alpha \hat{x}_{k'} p'(\hat{x}_{k'})} e^{-\alpha[h(\hat{x}_{k'}) - 2p(\hat{x}_{k'}) \ln \hat{x}_{k'}]} \\ &\times [\text{erf}(\epsilon_{k,\min}) + \text{erf}(\epsilon_{k,\max})] \left[1 + \left(\frac{1}{12} + c \right) \frac{1}{|k'|} + \dots \right] \end{aligned} \tag{B31}$$

with

$$c = \begin{cases} \frac{3}{8} & k' > 0 \\ -\frac{1}{8} & k' < 0 \end{cases} \tag{B32}$$

and

$$\epsilon_{k,\max} = \sqrt{\frac{\alpha p'(x_m)}{x_m}} (x_m - \hat{x}_{k-\frac{N}{2}}), \tag{B33a}$$

$$\epsilon_{k,\min} = \sqrt{\frac{\alpha p'(1/x_m)}{1/x_m}} \left(\hat{x}_{k-\frac{N}{2}} - \frac{1}{x_m} \right). \tag{B33b}$$

The dots in (B31) represent contributions of lower order and of functions of $\epsilon_{k,\min}$ and $\epsilon_{k,\max}$ that give $O(1)$ contributions to the partition function. Comparing to the asymptotics of \mathcal{B}_N we notice two differences: the factor $\hat{x}_{k'}$ multiplying all the expressions and the correction $c/|k'|$.

B.2.2 Limit $N \rightarrow \infty$, $\alpha \rightarrow \infty$, and Fixed x_m

The asymptotic expansion of \tilde{B}_N in this fixed shape situation is simpler, since we do not need the terms of order $1/\alpha$. Doing similar calculations as the ones done for \mathcal{B}_N taking into account the additional factor x in the integral we find

$$\tilde{B}_N(k) = \frac{\hat{x}_{k'} \sqrt{\alpha \pi \hat{x}_{k'} p'(\hat{x}_{k'})}}{2n_b} e^{-\alpha[h(\hat{x}_{k'}) - 2p(\hat{x}_{k'}) \ln \hat{x}_{k'}]} [\text{erf}(\epsilon_{k,\min}) + \text{erf}(\epsilon_{k,\max})]. \tag{B34}$$

References

1. Edwards, S.F., Lenard, A.: *J. Math. Phys.* **3**, 778 (1962)
2. Jancovici, B.: *Phys. Rev. Lett.* **46**, 386 (1981)
3. Alastuey, A., Jancovici, B.: *J. Phys. (France)* **42**, 1 (1981)
4. Rosinberg, M.L., Blum, L.: *J. Chem. Phys.* **81**, 3700 (1984)
5. Jancovici, B., Manificat, G., Pisani, C.: *J. Stat. Phys.* **76**, 307 (1994)
6. Jancovici, B., Téllez, G.: *J. Stat. Phys.* **82**, 609 (1996)
7. Choquard, P.: *Helv. Phys. Acta* **54**, 332 (1981)
8. Choquard, P., Forrester, P.J., Smith, E.R.: *J. Stat. Phys.* **33**, 13 (1983)
9. Caillol, J.M.: *J. Phys. (Paris) Lett.* **42**, L (1981)
10. Forrester, P.J., Jancovici, B., Madore, J.: *J. Stat. Phys.* **69**, 179 (1992)
11. Forrester, P.J., Jancovici, B.: *J. Stat. Phys.* **84**, 337 (1996)
12. Téllez, G., Forrester, P.J.: *J. Stat. Phys.* **97**, 489 (1999)
13. Jancovici, B.: *J. Stat. Phys.* **99**, 1281 (2000)
14. Jancovici, B., Téllez, G.: *J. Stat. Phys.* **91**, 953 (1998)
15. Fantoni, R., Jancovici, B., Téllez, G.: *J. Stat. Phys.* **112**, 27 (2003)
16. Jancovici, B., Téllez, G.: *J. Stat. Phys.* **116**, 205 (2004)
17. Kaniadakis, G.: *Phys. Rev. E* **66**, 056125 (2002)
18. Kaniadakis, G.: *Phys. Rev. E* **72**, 036108 (2005)
19. Mehta, M.L.: *Random Matrices*. Academic Press, San Diego (1991)
20. Ginibre, J.: *J. Math. Phys.* **6**, 440 (1965)
21. Abramowitz, M., Stegun, A.: *Handbook of Mathematical Functions*. Dover, New York (1965)
22. Wong, R.: *Asymptotic Approximations of Integrals*. Academic Press, San Diego (1989)
23. Jancovici, B.: *J. Stat. Phys.* **28**, 43 (1982)
24. Martin, P.A.: *Rev. Mod. Phys.* **60**, 1075 (1988)
25. Forrester, P.J.: *J. Phys. A: Math. Gen.* **18**, 1419 (1985)
26. Zinn-Justin, J.: *Quantum Field Theory and Critical Phenomena*, 2nd edn. Clarendon Press, Oxford (1993)
27. March, N.H., Tosi, M.P.: *Coulomb Liquids*. Academic Press, San Diego (1984)
28. Bender, C.M., Orzag, S.A.: *Advanced Mathematical Methods for Scientists and Engineers: Asymptotic Methods and Perturbation Theory*. Springer, Berlin (1999)

Part IX
2009

Chapter 18

Penetrable-Square-Well fluids: Analytical study and Monte Carlo simulations

Fantoni R., Giacometti A., Malijevisky A., and Santos A., J. Chem. Phys. **131**, 124106 (2009)

Title: “Penetrable-Square-Well fluids: Analytical study and Monte Carlo simulations”

Abstract: We study structural and thermophysical properties of a one-dimensional classical fluid made of penetrable spheres interacting via an attractive square-well potential. Penetrability of the spheres is enforced by reducing from infinite to finite the repulsive energy barrier in the pair potentials. As a consequence, an exact analytical solution is lacking even in one dimension. Building upon previous exact analytical work in the low-density limit [Santos *et al.*, Phys. Rev. E **77**, 051206 (2008)], we propose an approximate theory valid at any density and in the low-penetrable regime. By comparison with specialized Monte Carlo simulations and integral equation theories, we assess the regime of validity of the theory. We investigate the degree of inconsistency among the various routes to thermodynamics and explore the possibility of a fluid-fluid transition. Finally we locate the dependence of the Fisher-Widom line on the degree of penetrability. Our results constitute the first systematic study of penetrable spheres with attractions as a prototype model for soft systems.

Appears in the SklogWiki:

http://www.sklogwiki.org/SklogWiki/index.php/Penetrable_square_well_model

THE JOURNAL OF CHEMICAL PHYSICS 131, 124106 (2009)

Penetrable-square-well fluids: Analytical study and Monte Carlo simulationsRiccardo Fantoni,^{1,a)} Achille Giacometti,^{1,b)} Alexandr Malijevský,^{2,c)} and Andrés Santos^{3,d)}¹Dipartimento di Chimica Fisica, Università di Venezia, Calle Larga S. Marta DD2137, I-30123 Venezia, Italy²E. Hála Laboratory of Thermodynamics, Academy of Science of the Czech Republic, Prague 6, Czech Republic and Department of Chemical Engineering, Institute of Theoretical Physics, Imperial College London, South Kensington Campus, London SW7 2BZ, United Kingdom³Departamento de Física, Universidad de Extremadura, Badajoz E-06071, Spain

(Received 19 June 2009; accepted 2 September 2009; published online 23 September 2009)

We study structural and thermophysical properties of a one-dimensional classical fluid made of penetrable spheres interacting via an attractive square-well potential. Penetrability of the spheres is enforced by reducing from infinite to finite the repulsive energy barrier in the pair potentials. As a consequence, an exact analytical solution is lacking even in one dimension. Building upon previous exact analytical work in the low-density limit [A. Santos, R. Fantoni, and A. Giacometti, *Phys. Rev. E* **77**, 051206 (2008)], we propose an approximate theory valid at any density and in the low-penetrable regime. By comparison with specialized Monte Carlo simulations and integral equation theories, we assess the regime of validity of the theory. We investigate the degree of inconsistency among the various routes to thermodynamics and explore the possibility of a fluid-fluid transition. Finally we locate the dependence of the Fisher–Widom line on the degree of penetrability. Our results constitute the first systematic study of penetrable spheres with attractions as a prototype model for soft systems. © 2009 American Institute of Physics.
[doi:10.1063/1.3236515]

I. INTRODUCTION

Hard spheres constitute a paradigmatic system for many simple and complex fluids. Steric stabilized colloids, for instance, are suspensions made of colloidal particles coated by short linear polymers suspended in a microscopic solvent fluid. For sufficiently high temperature and/or in the presence of a good solvent, those dressed colloids effectively interact as hard spheres.¹

On the other hand, a number of soft colloidal systems is always penetrable at least to a certain extent.² Notable examples include for instance star-shaped³ or branched-shaped⁴ polymers where each macromolecule can be roughly regarded as a sphere of a given radius (the radius of gyration), but two particles can clearly interpenetrate to a substantially smaller distance.

A necessary (but not sufficient) condition for a one-dimensional fluid to be a *nearest-neighbor* fluid is to be a hard-core fluid, i.e., a fluid made of particles which cannot penetrate one another due to the existence of an infinite repulsive potential barrier in the pair potential $\phi(r)$. Nearest-neighbor fluids admit an analytical exact statistical-mechanical solution.⁵ The partition function, equation of state, and correlation functions of any order can be calculated analytically from the knowledge of the pair potential. This is no longer the case for non-neighbor fluids.⁶

Penetrable spheres (PSs)^{7,8} can be reckoned as the simplest representation of soft colloids where the range of penetrability can be tuned from zero (hard spheres) to infinity (ideal gas). Both limits are amenable to an exact analytical treatment, but the intermediate case is not.

When an attractive, short-range, square well (SW) is added to PS, one obtains the so-called penetrable-SW (PSW) fluid.¹⁰ On one hand, this enriches the model so that it can also account for short-range attractive interactions which are ubiquitous in such systems. On the other hand, it also complicates the treatment due to possible Ruelle instabilities associated with the lack of a well defined thermodynamic limit.^{11,12} As the width of the well vanishes with a constant area under the well, the PSW model reduces to what we denote¹⁰ as the sticky-penetrable-sphere (SPS) model. This model was found to be thermodynamically unstable¹⁰ due to the divergence of the fourth virial coefficient. In fact, SPS model violates the (sufficient) condition for stability (see Appendix A in Ref. 10).

We emphasize that various classes of penetrable systems appeared in the literature with rather different meanings. The Widom–Rowlinson model of nonadditive hard-sphere mixtures,¹³ for instance, is not associated with a well defined pair potential as in the case of the present study. Likewise, the Rikvold–Stell–Torquato “permeable sphere” model^{14,15} is defined through a condition on correlation function which is not equivalent to a constant repulsive potential inside the core region. On the contrary, our PSW model belongs to the same class of bounded potentials as the Gaussian-core mod-

^{a)}Electronic mail: rfantoni@unive.it.^{b)}Electronic mail: achille@unive.it.^{c)}Electronic mail: amali@post.cz.^{d)}Electronic mail: andres@unex.es. URL: <http://www.unex.es/fisteor/andres/>

els originally proposed by Stillinger *et al.*¹⁶ in the late 1970s and exploited more recently by Likos *et al.*,⁸ Lang *et al.*,⁹ and Louis *et al.*¹⁷

In a previous paper,¹⁰ we introduced the PSW fluid model and discussed the conditions under which the model is Ruelle stable. In addition, we also derived an exact low-density expansion up to second order in the radial pair distribution function (corresponding to the fourth order in the virial coefficient) which was shown to compete with standard integral equation approximations such as Percus-Yevick (PY) and hypernetted chain (HNC) over a wide region of the density-temperature phase diagram. These exact results, however, fail to reproduce the correct behavior when the concentration is large, due to their low-density character.

The aim of the present paper is to extend the analysis to these more demanding conditions, by using an approximation already successfully exploited in the PS case. In this case it has been argued⁷ that the exact analytical solution stemming from corresponding hard-sphere particles can be efficiently exploited to implement a low-penetrability approximate solution (called LTA in Ref. 7). The basic idea behind the method is that for sufficiently low penetrability, the functional form of the equations derived in the impenetrable case can be smoothly adapted to the penetrable case by “healing” a few crucial aspects of the original solution. Building on this idea, we here show that this methodology can also be applied to the PSW case by starting from the corresponding impenetrable counterpart (i.e., the SW potential).

We discuss the soundness of this approximation in various ways: First by comparing the low-penetrability approximation (LPA) low-density results against the exact low-density expansion which was computed in Ref. 10 and, second, by comparing with specialized Monte Carlo (MC) simulations and standard integral equations (notably PY and HNC). We show how LPA properly describes a significant part of the phase diagram with a performance comparable with integral equations at a semianalytical level.

The introduction of an attractive part in the PS potential opens the route to some interesting questions that we also address in the present paper. First of all, we question the existence of a fluid-fluid phase separation in addition to the fluid-solid transition, by limiting our analysis within the range of applicability of LPA, that is, we avoid densities so high that a substantial interpenetration among particles is expected.

Within the same LPA, we also investigate modifications on the Fisher-Widom (FW) line, marking the transition from oscillatory to exponential decay regimes for correlation functions, that is known to exist even in the SW one-dimensional fluid.¹⁸ We find an increase in the exponential decay region and we address the physical motivations behind this.

The structure of the paper is as follows. We define the PSW model in Sec. II. In Sec. III we briefly recall the well known general scheme allowing for the exact analytical solution of the class of nearest-neighbor one-dimensional fluids. We then construct the LPA in Sec. IV and show how this reduces to its counterpart within the PS limit⁷ and assess its performance in comparison with known exact results within

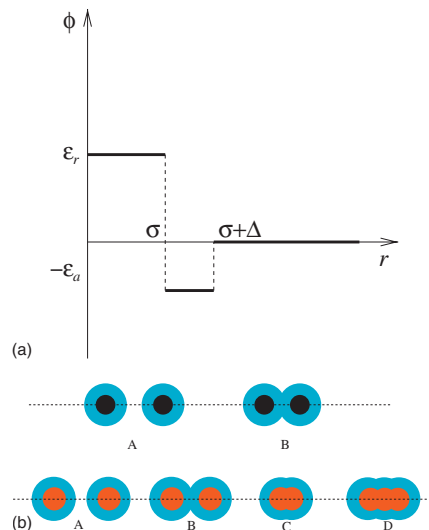


FIG. 1. The PSW potential (top panel). The middle and bottom panels sketch the different behaviors of the SW and PSW models, respectively. In the SW case there exists a hard core (black inner sphere) and an interaction range (light blue outer sphere) so two spheres on a line can either noninteract (A) or attract each other as the corresponding interaction spheres overlap (B). As a consequence, different spheres cannot interchange positions on a one-dimensional line and the problem is analytically solvable. In the PSW the core is soft (red inner sphere) and hence we can have in addition to configurations (A) and (B) identical to the SW case, also the case where the internal cores overlap such as (C) and (D). Different spheres can then interchange position and the problem is a many-body one.

the low-density limit.¹⁰ Sections V and VI contain a discussion on the FW line and on the routes to thermodynamics, as predicted by the LPA, respectively. The regions in the density-temperature diagram where the LPA is only slightly thermodynamically inconsistent (and thus expected to be reliable) are discussed in Sec. VII, where also an improved version of the approximation is proposed. Section VIII includes a very brief description on the numerical methods (MC simulations and integral equations) discussed in the present model. These numerical results are presented and compared with LPA theory in Sec. IX. The paper ends with some concluding remarks in Sec. X.

II. THE PENETRABLE-SQUARE-WELL MODEL

The PSW fluid is defined through the following pair potential¹⁰ (see Fig. 1, top panel),

$$\phi(r) = \begin{cases} \epsilon_r, & r < \sigma, \\ -\epsilon_a, & \sigma < r < \sigma + \Delta, \\ 0, & r > \sigma + \Delta, \end{cases} \quad (1)$$

where ϵ_r and ϵ_a are two positive constants accounting for the repulsive and attractive parts of the potential, respectively. The corresponding Mayer function $f(r) = e^{-\beta\phi(r)} - 1$ (where $\beta = 1/k_B T$ is the inverse temperature parameter) reads

$$f(r) = \gamma_r f_{\text{HS}}(r) + \gamma_a [\Theta(r - \sigma) - \Theta(r - \sigma - \Delta)], \quad (2)$$

where $\gamma_r = 1 - e^{-\beta \epsilon_r}$ is the parameter measuring the degree of penetrability varying between 0 (free penetrability) and 1 (impenetrability) and $\gamma_a = e^{\beta \epsilon_a} - 1 > 0$ plays a similar role for the attractive part. Here $f_{\text{HS}}(r) = \Theta(r - \sigma) - 1$ is the Mayer function for the hard-sphere model which can then be recovered in the limit $\gamma_r \rightarrow 1$ and either $\gamma_a \rightarrow 0$ or $\Delta \rightarrow 0$. $\Theta(r)$ is the usual step function equal to 1 for $r > 0$ and 0 otherwise. It also proves convenient to introduce the ratio $\gamma = \gamma_a / \gamma_r$, which is a measure of the relative depth of the attractive well.

The above potential reduces to the corresponding PS and SW potentials in the limits $\epsilon_a \rightarrow 0$ (or $\Delta \rightarrow 0$) and $\epsilon_r \rightarrow \infty$, respectively. Other interesting limiting cases have already been detailed in Ref. 10.

Consider a SW fluid in one dimension: different particles can be assigned an increasing coordinate on the axis line and the only possible configurations are those indicated with (A) or (B) in Fig. 1 (middle panel), where either the centers of two different spheres are separated a distance greater than the attractive SW range and behave as hard spheres (A) or they are sufficiently close to attract each other (B). PSW spheres, on the other hand, can interpenetrate with some energy cost so they also display configurations such as, for instance, (C) or (D) in Fig. 1 (bottom panel). PSW fluids are then effectively a many-body problem and, as such, not amenable to an analytical solution. In the present paper, our analysis will be limited to the case $\epsilon_r > 2\epsilon_a$ where a well defined thermodynamic limit is ensured.¹⁰

III. GENERAL RECIPE FOR NEAREST-NEIGHBOR INTERACTIONS

In this section we provide a synopsis of the main steps required by the analytical solution of any nearest-neighbor fluid.^{5,19,20} This will be used in the next section to introduce a motivated approximate solution in a particular limit.

- From the Boltzmann factor $e^{-\beta \phi(r)}$ compute its Laplace transform

$$\tilde{\Omega}(s) = \int_0^\infty dr e^{-sr} e^{-\beta \phi(r)}. \quad (3)$$

- The equation of state is given by

$$\beta p = \frac{\xi}{\sigma}, \quad (4)$$

where p is the pressure and the parameter ξ is the solution of the equation,

$$\rho = - \frac{\tilde{\Omega}(\xi/\sigma)}{\tilde{\Omega}'(\xi/\sigma)}, \quad (5)$$

where ρ is the density and $\tilde{\Omega}'(s) = \partial \tilde{\Omega}(s) / \partial s$. This provides all thermodynamics.

- The radial distribution function (RDF) can be obtained from

$$\tilde{G}(s) = \frac{1}{\rho} \frac{\tilde{\Omega}(s + \xi/\sigma)}{\tilde{\Omega}(\xi/\sigma) - \tilde{\Omega}(s + \xi/\sigma)}, \quad (6)$$

which is the Laplace transform of the RDF $g(r)$.

This is sufficient to compute both thermodynamics and structural properties of any one-dimensional system with nearest-neighbor interactions.

At odds to this class of problems, PSs do not possess any analytical solution even in one dimension. This is because it is not possible to convolute appropriate Laplace transform along a one-dimensional axis, which is the essential feature rendering the short-range one-dimensional models solvable. In turn this is due to the existence of multiple “blobs” formed by interpenetrating spheres so that it is no longer possible to “order” them along a line in such a way that they do not cross each other, a key point to the existence of the analytical solution (see Fig. 1, middle panel). Because of this, we now turn our attention to a motivated approximation which amounts to assume a slight decrease from an infinite repulsive barrier, an approximation which will be denoted as low penetrability.

IV. THE LOW-PENETRABILITY APPROXIMATION

A. Construction of the approximation

In Ref. 10 we followed the philosophy of considering a low-density expansion to provide exact analytical results valid up to second order in the RDF $g(r)$ and up to fourth order in the virial expansion. This is a very useful exact limit case to test approximate theories and numerical simulations, but it has the considerable disadvantage of being limited to very low densities. We now consider a different approach where density can in principle be arbitrarily large but we assume low penetrability among different spheres, patterned after a similar idea already used in the PS case.⁷

For notational simplicity, in the following, lengths will be measured in units of σ (so that $\sigma = 1$) and we introduce $\lambda = 1 + \Delta/\sigma$ as a dimensionless measure of the external well boundary. The Laplace transform of the Boltzmann factor $e^{\beta \phi(r)}$ for the PSW model is

$$\tilde{\Omega}(s) = \frac{1 - \gamma_r}{s} + \frac{\gamma_r}{s} [(1 + \gamma)e^{-s} - \gamma e^{-\lambda s}]. \quad (7)$$

The PSW fluid is not a nearest-neighbor fluid, as remarked, but it reduces to the nearest-neighbor SW fluid as $\gamma_r \rightarrow 1$ (and $\Delta < 1$). In this limit, it is natural to use the recipe given in Sec. III for the SW fluid to derive an approximate equation of state and an approximate $g(r)$ from Eqs. (4)–(6), respectively. This, however, must be exercised with care as important general properties of any model, such as, for instance, the continuity of the cavity function $y(r) = g(r)e^{\beta \phi(r)}$, are typically lost by this brute force procedure. The driving idea behind this simple LPA is then to keep the general features of the original SW solution and enforce some specific modifications guided by the accounting of increasingly important constraints.²¹

Our LPA implementation amounts to replacing Eq. (6) with

124106-4 Fantoni *et al.*

J. Chem. Phys. **131**, 124106 (2009)

$$\tilde{G}(s) = \frac{1}{\rho} \frac{\tilde{\Omega}(s + \zeta)}{\tilde{\Omega}_0(\zeta) - \tilde{\Omega}_0(s + \zeta)}, \quad (8)$$

where $\tilde{\Omega}_0(s)$ is (formally) the Laplace transform of the Boltzmann factor of the SW model, which can be obtained from $\tilde{\Omega}(s)$ by discarding the first term on the right-hand side of Eq. (7), i.e.,

$$\tilde{\Omega}_0(s) = \frac{\gamma_r}{s} [(1 + \gamma)e^{-s} - \gamma e^{-\lambda s}]. \quad (9)$$

This simple choice can be shown to be fully equivalent to keeping Eq. (6) but with a replacement $e^{-s} \rightarrow e^{-(s-a)}$ in Eq. (7), where the free parameter a is fixed by the continuity condition of the cavity function $y(r)$ at the hard-core discontinuity $r=1$. This is known to be the most important feature to obtain a correct representation in integral equation theories of SW fluids, both from the analytical and the numerical viewpoints.²²⁻²⁴

We note that, unlike the SW counterpart, $\zeta \neq \beta p$. It is a transcendental function of β and ρ , which can be obtained by ensuring the correct behavior of $g(r) \rightarrow 1$ as $r \rightarrow \infty$, or, equivalently, $s\tilde{G}(s) \rightarrow 1$ as $s \rightarrow 0$. From Eq. (8), this gives

$$\rho = - \frac{\tilde{\Omega}(\zeta)}{\tilde{\Omega}'_0(\zeta)} = \zeta \frac{h + 1 - q}{1 - q + (1 - \lambda q)\zeta}, \quad (10)$$

where in the second equality we introduced the following quantities:

$$q = \frac{\gamma}{1 + \gamma} e^{-\zeta \Delta}, \quad (11)$$

$$h = \frac{1 - \gamma_r}{\gamma_r(1 + \gamma)} e^{\zeta}. \quad (12)$$

For given values of the potential parameters (Δ , ϵ_r , and ϵ_a) and for given values of the inverse temperature β and the auxiliary parameter ζ , the quantities q and h are obtained from Eqs. (11) and (12) and inserted into Eq. (10) to determine the density ρ . The impenetrable SW potential corresponds to the limit $h \rightarrow 0$.

In order to compute the RDF $g(r)$ we first compute explicitly $\tilde{G}(s)$ from Eqs. (6) and (7),

$$\tilde{G}(s) = \frac{1}{\rho} \frac{h + e^{-s}(1 - qe^{-s\Delta})}{(1 - q)(1 + s/\zeta) - e^{-s}(1 - qe^{-s\Delta})}. \quad (13)$$

Upon expanding the denominator in Eq. (13) in powers of $(1 - qe^{-s\Delta})(1 + s/\zeta)$, and inverting the Laplace transform term by term, one gets

$$\rho g(r) = \frac{h\zeta}{1 - q} e^{-\zeta r} + \sum_{n=1}^{\infty} \sum_{k=0}^n \binom{n}{k} (-q)^k \psi_n(r - n - k\Delta) \times \Theta(r - n - k\Delta), \quad (14)$$

where

$$\psi_n(r) = \left(\frac{\zeta}{1 - q}\right)^n \left[\frac{r^{n-1}}{(n-1)!} + \frac{h\zeta}{1 - q} \frac{r^n}{n!} \right] e^{-\zeta r}. \quad (15)$$

We anticipate that the LPA does not capture correctly the $r < \Delta$ trend at high densities, while it works well for $r > \Delta$. The reason for this can be traced back to the failure of the LPA to account for the discontinuous slope of the cavity function $y(r)$ at $r=\Delta$. Moreover, the approximate $y(r)$ turns out to be discontinuous rather than continuous at $r=\lambda$, as detailed in Appendix A. These deficiencies can be accounted for step by step at the price of an increase in the complexity of the approximation and are a consequence of the phenomenological nature of the LPA. This will be further discussed in Sec. VII.

As already remarked, the PSW model reduces in the appropriate limit to the penetrable analog of Baxter's sticky hard spheres, denoted as SPS in Ref. 10. This is further elaborated in Appendix B, where it is also discussed the LPA of the SPS model. We explicitly checked this is indeed the limit for PSW in the limit of very narrow and very deep well. On the other hand, we also found (see Appendix B) that this model is also thermodynamically unstable as it violates the stability criterion $\epsilon_r > 2\epsilon_a$, and hence it will not be further discussed in the remaining of this paper.

B. The penetrable-rod limit

Here we show that either in the limit $\epsilon_a \rightarrow 0$ (which implies $\gamma \rightarrow 0$) or, alternatively, in the limit $\Delta \rightarrow 0$, the LPA that we just found for the PSW model reduces to the corresponding one proposed in Ref. 7 for the PS model.

Taking the limit $\gamma \rightarrow 0$ in Eq. (7) one finds Eq. (2.53) of Ref. 7. Moreover $q \rightarrow 0$ and $h \rightarrow (\gamma_r^{-1} - 1)e^{\zeta}$ and so Eq. (10) reduces to $\rho = [1 + (\gamma_r^{-1} - 1)e^{\zeta}] / (1 + \zeta^{-1})$, which can be rewritten as $(\xi - \zeta)e^{-\xi} / (\gamma_r^{-1} - 1) = \zeta$ with $\xi = \rho(1 + \zeta)$, which coincides with Eq. (4.4) of Ref. 7 where our ζ replaces their ξ' . It is straightforward to check that the same expressions for $\tilde{\Omega}(s)$ and for ρ in terms of ζ and γ_r are obtained in the alternative limit $\Delta \rightarrow 0$. Hence LPA for PS is fully recovered.

C. Comparison with exact low-density expansion

It proves interesting to compare the LPA to order ρ with the exact results derived in Ref. 10 based on a low-density expansion, in order to assess the ability of LPA to reproduce low-density results. The general expansion of $g(r)$ in powers of the density ρ has the following structure:²⁵

$$g(r) = g_0(r) + g_1(r)\rho + \dots \quad (16)$$

The exact results for $g_0(r)$ and $g_1(r)$ have been derived in Ref. 10:

$$g_0^{\text{exact}}(r) = \begin{cases} 1 - \gamma_r, & r < 1, \\ 1 + \gamma\gamma_r, & 1 < r < 1 + \Delta, \\ 1, & r > 1 + \Delta, \end{cases} \quad (17)$$

$$g_1^{\text{exact}}(r) = \gamma_r^2 \begin{cases} (1 - \gamma_r)[2(1 + \gamma^2\Delta) - r(1 + 2\gamma + 2\gamma^2)], & 0 \leq r \leq \Delta, \\ (1 - \gamma_r)(2 - 2\gamma\Delta - r), & \Delta \leq r < 1, \\ (1 + \gamma\gamma_r)(2 - 2\gamma\Delta - r), & 1 < r < 1 + \Delta, \\ 2 - 2\gamma\Delta - r, & 1 + \Delta < r \leq 2, \\ \gamma(2 + \gamma)(r - 2) - 2\gamma\Delta, & 2 \leq r \leq 2 + \Delta, \\ (2 + 2\Delta - r)\gamma^2, & 2 + \Delta \leq r \leq 2 + 2\Delta, \\ 0, & 2 + 2\Delta \leq r. \end{cases} \quad (18)$$

In order to compare $g_0^{\text{exact}}(r)$ and $g_1^{\text{exact}}(r)$ with LPA results, we expand ζ as derived from Eq. (10) to lowest order in density, $\zeta = \zeta_0\rho + \zeta_1\rho^2 + \mathcal{O}(\rho^3)$, and plug the results into Eqs. (14) and (15). This yields Eq. (16), where the coefficients $g_0(r)$ and $g_1(r)$ are computed within the LPA. Whereas $g_0(r) = g_0^{\text{exact}}(r)$, $g_1(r)$ is found to differ from the exact result $g_1^{\text{exact}}(r)$. Analytical expressions for ζ_0 , ζ_1 , and $g_1(r)$ can be found in Appendix C.

Having done this, one can estimate the difference in the cavity function between LPA and exact results to order ρ , which reads (see Appendix C)

$$y_1^{\text{exact}}(r) - y_1(r) = \begin{cases} C_1 + D_1\Delta + E_1(\Delta - 1) + F_1(r - \Delta), & 0 \leq r \leq \Delta, \\ C_1 + D_1\Delta + E_1(r - 1), & \Delta \leq r \leq 1, \\ C_1 + D_1(1 + \Delta - r), & 1 \leq r \leq 1 + \Delta, \end{cases} \quad (19)$$

where

$$C_1 = \gamma\gamma_r^2(1 - \gamma_r)\frac{1 + \gamma}{1 + \gamma\gamma_r}\Delta, \quad (20)$$

$$D_1 = \gamma\gamma_r\frac{(1 - \gamma_r)^2}{1 + \gamma\gamma_r}, \quad (21)$$

$$E_1 = \gamma_r(1 - \gamma_r), \quad (22)$$

$$F_1 = \gamma_r[1 - \gamma_r - 2\gamma\gamma_r(1 + \gamma)]. \quad (23)$$

The right-hand side of Eq. (19) preserves the continuity of $y_1(r)$ at $r = \Delta$ and $r = 1$, but imposes the continuity of $y_1(r)$ at $r = 1 + \Delta$ and that of $y_1'(r)$ at $r = 1$ and $r = 1 + \Delta$, as well as the discontinuity of the exact $y_1'(r)$ at $r = \Delta$. The latter discontinuity is, according to Eqs. (17) and (18),

$$\lim_{\rho \rightarrow 0} \frac{y'(\Delta^+) - y'(\Delta^-)}{\rho y(\Delta)} = 2\gamma\gamma_r^2(1 + \gamma). \quad (24)$$

V. THE FISHER-WIDOM LINE

In a remarkable piece of work,¹⁸ Fisher and Widom argued that the asymptotic decay of the correlation functions is determined by the nature of the poles $s_i = s_i(\beta, \rho)$ ($i = 1, 2, 3, \dots$), with largest real part of the Laplace transform $\tilde{G}(s)$ of the RDF. This asymptotic decay can be of two dif-

ferent types: oscillatory at high densities and/or high pressures and monotonic for low densities and/or pressures. The latter regime can exist only in the presence of competing effects in the potential function, so it cannot exist for purely repulsive short-range potentials, such as HS and PS potentials.

In particular, rather general arguments²⁶ suggest a behavior

$$g(r) - 1 = \sum_i A_i e^{s_i r} \approx A_1 e^{s_1 r}, \quad (25)$$

where we specialized to one-dimensional systems and the sum runs over the discrete sets of poles s_i , A_i being (in general complex) amplitudes. The asymptotic behavior of $g(r)$ is dominated by the pole s_1 having the least negative real part (to ensure stability of the liquid). If s_1 is complex, its conjugate $s_2 = s_1^*$ must also be included in the asymptotic behavior.

Fisher and Widom derived the line—henceforth denoted as Fisher–Widom (FW) line—where this transition takes place, both in the pressure versus temperature and in the density versus temperature diagrams, for the one-dimensional SW potential. On crossing this line, one finds a sharp transition in the character of the RDF $g(r) - 1$: for any fixed temperature in the p - T plane, $g(r)$ has an oscillatory character above the FW line and an exponential decay below it. The transition is a signature of local ordering without any singularities in thermodynamical quantities as there is no phase transition in the one-dimensional SW fluid. In three dimensions, the FW line precedes the coexistence line when lowering the pressure at a fixed temperature. This has been numerically observed for various fluids including SW,²⁶ Lennard–Jones,^{27–29} and other softer potentials.³⁰

In view of the possibility for PSW to display fluid–fluid and fluid–solid phase transitions in spite of their one-dimensional character, it is interesting to wonder what happens to the FW line in the transition from SW to PSW. We now analyze this in the framework of the LPA.

The poles of $\tilde{G}(s)$ (different from $s = 0$) can be read off from Eq. (8):

$$\tilde{\Omega}_0(s + \zeta) = \tilde{\Omega}_0(\zeta). \quad (26)$$

As we are here interested in the pole with the negative real part closest to the origin, we set $s = -x \neq 0$ as the real root of Eq. (26),

124106-6 Fantoni *et al.*

J. Chem. Phys. **131**, 124106 (2009)

$$\tilde{\Omega}_0(\zeta - x) = \tilde{\Omega}_0(\zeta), \quad (27)$$

and $s = -x' \pm iy$ as the complex root with the least negative real part, i.e.,

$$\text{Re } \tilde{\Omega}_0(\zeta - x' \pm iy) = \tilde{\Omega}_0(\zeta), \quad (28)$$

$$\text{Im } \tilde{\Omega}_0(\zeta - x' \pm iy) = 0. \quad (29)$$

The pole s_1 determining the asymptotic behavior is either $s_1 = -x$ (monotonic decay) if $x < x'$ or $s_1 = -x' \pm iy$ (oscillatory decay) if $x > x'$. The FW transition takes place when $x = x'$.

Equation (27) yields the condition

$$e^{-s}(1 - qe^{-s\Delta}) = (1 - q)\left(1 + \frac{s}{\zeta}\right), \quad (30)$$

where q is given by Eq. (11). Quite interestingly, as the parameter h is missing, this equation formally coincides with its SW counterpart, originally studied by Fisher and Widom [see Eq. (3.6) in Ref. 18]. We can rewrite Eqs. (27)–(29) as follows:

$$e^x(1 - qe^{x\Delta}) = (1 - q)\left(1 - \frac{x}{\zeta}\right), \quad (31)$$

$$e^{x'}(\cos y - qe^{x'\Delta}\cos \lambda y) = (1 - q)\left(1 - \frac{x'}{\zeta}\right), \quad (32)$$

$$e^x(\sin y - qe^{x\Delta}\sin \lambda y) = -(1 - q)\frac{y}{\zeta}. \quad (33)$$

At the FW transition ($x = x'$), Eqs. (31)–(33) form a set of three coupled equations whose solution yields x , y , and ζ as functions of q . Use of Eq. (10) then gives the line in the ρ - T plane.

It proves convenient to eliminate ζ from Eqs. (31) and (32) to obtain

$$x = \frac{1}{\Delta} \ln \frac{1 - \cos y}{q(1 - \cos \lambda y)}, \quad (34)$$

so that from Eqs. (31) and (33) we can now get

$$\zeta = x - y \frac{\cos y - \cos \lambda y}{\sin y - \sin \lambda y + \sin y \Delta}. \quad (35)$$

When Eqs. (34) and (35) are inserted into Eq. (31) we get

$$\begin{aligned} \sin y - \sin \lambda y + \sin y \Delta - \frac{y}{x}(\cos y - \cos \lambda y) \\ = -e^{-x}(1 - q)\frac{y}{x}(1 - \cos \lambda y), \end{aligned} \quad (36)$$

where $x(q, y)$ is given by Eq. (34) so that this is a transcendental equation in $y(q)$. Once $y(q)$ is known from Eq. (36),

Eqs. (34) and (35) provide $x(q)$ and $\zeta(q)$, respectively. The parameter $\gamma(q)$ is obtained by inverting Eq. (11),

$$\gamma(q) = \frac{q}{e^{-\zeta(q)\Delta} - q}, \quad (37)$$

and the inverse temperature $\beta(q)$ is obtained from

$$\gamma(q) = \frac{e^{\beta(q)\epsilon_a} - 1}{1 - e^{-\beta(q)\epsilon_r}} \quad (38)$$

on using the definitions of γ , γ_r , and γ_a .

Finally, Eqs. (10) and (12) provide $\rho(q)$ and the combination of $\beta(q)$ and $\rho(q)$ yields the FW line in the ρ - T plane. In order to have it in the p - T plane one needs to get before the equation of state and the result will depend on the chosen route (virial, compressibility, or energy). This is discussed in the following section.

VI. EQUATION OF STATE

As PSW is not an exactly solvable model, thermodynamics will in general depend on the followed route, so we are going to check the three standard routes (virial, compressibility, and energy) for the compressibility factor $Z = \beta p / \rho$, as predicted by the LPA. The virial route is defined by

$$Z = 1 - \rho \beta \int_0^\infty dr r y(r) e^{-\beta \phi(r)} \phi'(r), \quad (39)$$

which, using standard manipulations,²⁵ yields

$$Z = 1 + \rho \gamma_r [(1 + \gamma)y(1) - \gamma \lambda y(\lambda)]. \quad (40)$$

As $y(\lambda^-) \neq y(\lambda^+)$ within LPA (see Appendix A), $y(\lambda) = (1/2)[y(\lambda^-) + y(\lambda^+)]$ is assumed. Thus, using Eqs. (A4) and (A8), we get

$$Z = 1 + \frac{\zeta}{1 - q} \left\{ 1 - \lambda q \left[1 + \gamma_r (1 + \gamma) \frac{1 + \gamma \gamma_r / 2}{1 + \gamma \gamma_r} \frac{h \zeta \Delta}{1 - q} \right] \right\}. \quad (41)$$

It is easy to check using Eqs. (10) and (41) that in the case of the SW model ($h = 0$) one recovers the expected result $Z = \zeta / \rho$.

Next we consider the compressibility route:

$$\begin{aligned} \chi &\equiv \frac{1}{\beta} \left(\frac{\partial \rho}{\partial p} \right)_\beta \\ &= 1 + 2\rho \int_0^\infty dr [g(r) - 1] \\ &= 1 + 2\rho \lim_{s \rightarrow 0} [\tilde{G}(s) - s^{-1}]. \end{aligned} \quad (42)$$

Using Eqs. (10) and (13) the last term of Eq. (42) can be written as

$$2\rho\lim_{s\rightarrow 0}[\tilde{G}(s) - s^{-1}] = \left(\frac{\partial p}{\partial \zeta}\right)_\beta - \frac{\tilde{\Omega}'(\zeta)}{\tilde{\Omega}_0'(\zeta)}. \tag{43}$$

Introducing the quantity

$$X(\zeta) \equiv \frac{1}{(\partial\rho/\partial\zeta)_\beta} \frac{\tilde{\Omega}_0'(\zeta) - \tilde{\Omega}'(\zeta)}{\tilde{\Omega}_0'(\zeta)}, \tag{44}$$

Eq. (42) becomes

$$\chi = \left(\frac{\partial p}{\partial \zeta}\right)_\beta [1 + X(\zeta)], \tag{45}$$

and using the definition of χ we find

$$\beta \left(\frac{\partial p}{\partial \zeta}\right)_\beta = \frac{1}{1 + X(\zeta)}. \tag{46}$$

Therefore the compressibility route yields

$$\beta p(\zeta) = \int_0^\zeta \frac{d\zeta'}{1 + X(\zeta')}. \tag{47}$$

In the SW limit one clearly has $X(\zeta)=0$ and $\beta p=\zeta$, as it should.

The energy route is by far the most delicate. We start from the internal energy per particle

$$\begin{aligned} u &= \frac{1}{2\beta} + \rho \int_0^\infty dr \phi(r) g(r) \\ &= \frac{1}{2\beta} + \epsilon_r \rho \int_0^1 dr g(r) - \epsilon_a \rho \int_1^\lambda dr g(r). \end{aligned} \tag{48}$$

Equation (A1) provides the necessary result for $g(r)$ in the interval $0 < r < \lambda$, so that

$$\begin{aligned} u &= \frac{1}{2\beta} + \epsilon_r \frac{h}{1-q} (1 - e^{-\zeta}) \\ &\quad - \epsilon_a \left[\frac{1}{1-q} (1 - e^{-\zeta\Delta}) \left(1 + \frac{h}{1-q} + h e^{-\zeta} \right) \right. \\ &\quad \left. - \frac{h}{(1-q)^2} e^{-\zeta\Delta} \zeta \Delta \right]. \end{aligned} \tag{49}$$

In order to obtain βp from u we exploit the following thermodynamic relation

$$\rho^2 \left(\frac{\partial u}{\partial \rho}\right)_\beta = \left(\frac{\partial \beta p}{\partial \beta}\right)_\rho, \tag{50}$$

and the identity

$$\left(\frac{\partial u}{\partial \rho}\right)_\beta = \left(\frac{\partial u}{\partial \zeta}\right)_\beta \left(\frac{\partial \zeta}{\partial \rho}\right)_\beta, \tag{51}$$

to obtain

$$\left(\frac{\partial \beta p}{\partial \beta}\right)_\rho = \frac{\rho^2}{(\partial\rho/\partial\zeta)_\beta} \left(\frac{\partial u}{\partial \zeta}\right)_\beta. \tag{52}$$

Once again one can check that Eq. (52) is satisfied by the SW result $\beta p=\zeta$.

The right-hand side of Eq. (52) is a function of β and ρ , which we denote as $R(\beta, \rho)$, as ζ is itself a function of the same variables through Eq. (10). Thus, Eq. (52) gives

$$\beta p(\beta, \rho) = \zeta(\rho, \beta_{\max}) - \int_\beta^{\beta_{\max}} d\beta' R(\beta', \rho), \tag{53}$$

where β_{\max} is a conveniently chosen high value.³¹

VII. RELIABILITY OF LPA AND POSSIBLE IMPROVEMENTS

We are now in the position to draw a qualitative phase diagram in the $\rho\sigma - k_B T / \epsilon_a$ plane indicating the boundary where the LPA can be approximately regarded to be reliable. Of course, a definite reliability test is only possible after comparison with computer simulation results but before that we can use the internal consistency among the three thermodynamic routes as a reliability criterion.

In general, it turns out that thermodynamic inconsistency increases as the temperature and the density increase. To characterize this, let us define a density $\rho_{\text{lim}}(T)$ such that the largest relative deviation among the three routes is smaller than 5% if $\rho < \rho_{\text{lim}}(T)$. Therefore, all the points in the temperature-density plane with $\rho < \rho_{\text{lim}}(T)$ represent states where the LPA is only weakly inconsistent. This boundary line is shown in Fig. 2 for three representative cases of the pair $(\epsilon_r / \epsilon_a$ and $\Delta)$. We observe that the region where the LPA is thermodynamically consistent shrinks as ϵ_r / ϵ_a decreases and/or Δ increases. In any case, it is noteworthy that if the density is smaller than a certain value (which of course depends on ϵ_r / ϵ_a and Δ), the LPA remains thermodynamically consistent even for high temperatures.

The above reliability criterion is based on thermodynamics and thus it is a global one. On the other hand, we know that the LPA has some local shortcomings, such as an artificial discontinuity of the cavity function at the point $r=1 + \Delta$, as shown in Appendix A. Moreover, it does not predict

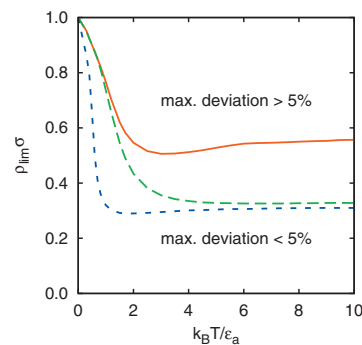


FIG. 2. Phase diagram in the $\rho\sigma - k_B T / \epsilon_a$ space showing the region where LPA can be considered as reliable. The curves correspond, from top to bottom, to the cases $(\epsilon_r / \epsilon_a, \Delta) = (5, 0.5)$, $(5, 1)$, and $(2, 0.5)$. The points below each curve represent states where the relative deviation between the three routes to the pressure is smaller than 5%.

124106-8 Fantoni *et al.*

J. Chem. Phys. **131**, 124106 (2009)

the discontinuity of the slope of the RDF at $r=\Delta$, already present by the exact result to first order in density, as indicated by Eq. (24).

As anticipated in Sec. IV, we can extend the validity of the LPA by a suitable modification of the cavity function $y(r)$ in order to ensure a correct behavior both within the core

region and at the well-edge discontinuity. We outline a possible approach to this issue in the remainder of this section.

Inspired by the comparison with exact low-density results as given in Sec. IV C, we modify the LPA (mLPA) by adding linear terms in the region $0 \leq r \leq 1 + \Delta$, following a form based on that of Eq. (19), namely,

$$g^{\text{mLPA}}(r) = g(r) + \frac{1}{\rho} \begin{cases} (1 - \gamma_r)[C + D\Delta + E(\Delta - 1) + F(r - \Delta)], & 0 \leq r \leq \Delta, \\ (1 - \gamma_r)[C + D\Delta + E(r - 1)], & \Delta \leq r < 1, \\ (1 + \gamma_r\gamma_r)[C + D(1 + \Delta - r)], & 1 < r < 1 + \Delta, \end{cases} \quad (54)$$

where $g(r)$ is the LPA RDF as given Eq. (14). The parameters C , D , and E can be determined by imposing the continuity of $y(r)$ at $r=1+\Delta$ and of $y'(r)$ at $r=1+\Delta$ and $r=1$, respectively. They are given by

$$C = \frac{\gamma_r(1 + \gamma)}{1 + \gamma\gamma_r} \frac{hq\zeta^2}{(1 - q)^2} \Delta, \quad (55)$$

$$D = \frac{1 - \gamma_r}{1 + \gamma\gamma_r} \frac{hq\zeta^2}{(1 - q)^2} + C\zeta, \quad (56)$$

$$E = \frac{1}{1 + \gamma\gamma_r} \frac{h\zeta^2}{(1 - q)^2} - D. \quad (57)$$

The addition of the coefficient F is motivated by the exact results to first order in density, Eq. (18), showing that, as recalled above, $g(r)$ exhibits a change of slope at $r=\Delta$, a feature not accounted for by the LPA. In order to determine the coefficient F we extend the exact low-density condition (24) to finite density. This implies

$$F = E - 2\rho\gamma\gamma_r^2(1 + \gamma) \left[\frac{1 + \gamma}{\gamma(1 - \gamma_r)} \frac{hq\zeta}{1 - q} + C + D\Delta + E(\Delta - 1) \right]. \quad (58)$$

It is straightforward to check that $C = C_1\rho^2 + \mathcal{O}(\rho^3)$, $D = D_1\rho^2 + \mathcal{O}(\rho^3)$, $E = E_1\rho^2 + \mathcal{O}(\rho^3)$, $F = F_1\rho^2 + \mathcal{O}(\rho^3)$, where C_1 , D_1 , E_1 , and F_1 are given by Eqs. (20)–(23). Therefore, the mLPA is exact to first order in density.

The discussed modification of LPA then takes care of the continuity of the cavity function $y(r)$ at both interaction discontinuities $r=1$ (already accounted for within LPA) and $r=\lambda$ (where the original LPA fails to provide continuity), and it correctly matches the exact results for $g(r)$ up to first order in density. A similar modification of the SPS model, discussed in Appendix A, would heal the discontinuity appearing in the corresponding LPA values $y^{\text{SPS}}(1^+) \neq y^{\text{SPS}}(1^-)$, which is a consequence of the combined effects of the LPA discontinuity $y(\lambda^+) \neq y(\lambda^-)$ and the sticky limit. This would provide an expression (not reported here) which is this sticky limit of Eq. (54).

VIII. MONTE CARLO SIMULATIONS AND INTEGRAL EQUATION THEORY

In order to assess the reliability of the LPA, we will compare in Sec. IX with specialized MC simulations. In addition, prompted by the results of Ref. 10, we will also compare LPA with standard integral equation theories, such as PY and HNC.²⁵

A. Monte Carlo simulations

We employed the conventional MC simulation on an NVT ensemble with periodic boundary conditions which in one dimension means that the system is treated as a ring. $N=5 \times 10^4$ penetrable-rod particles were displaced according to the Metropolis algorithm to create an initial sample of configurations. Following the equilibration stage, each run is divided into 20 basic simulation blocks, in which 10^5 measurements are performed to collect correlation functions data. One hundred trial moves per particle are implemented between each measurement, so that 10^{13} equilibrium configurations are generated in each run.

In order to speed up the simulation process the particles are labeled such that they create a consecutive sequence in clockwise order. Calculation of a potential of a particle i in a given configuration then reduces to a searching for the highest label $j > i$ and the lowest label $k < i$ associated with the particles still interacting with the particle i . In contrast with the case of impenetrable spheres in one dimension, the order of particles changes so that a relabeling must be undertaken after each shift of a particle. Obviously, at higher temperatures the number of penetration can be high, which makes the calculations more demanding compared to hard body systems.

There are in general two routes for the evaluation of the pressure. Determination of the pressure using a mechanical (virial) route relies on an ensemble average of a virial, i.e., a quantity involving the forces acting on all the particles. Alternatively, a thermodynamic expression relates pressure to the volume derivative of the free energy and is implemented by calculating the free energy change associated with small virtual change of volume. However, for systems with discontinuous interaction, both mechanical and thermodynamic ap-

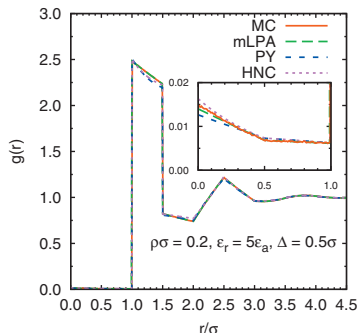


FIG. 3. Results for the RDF $g(r)$ vs r/σ with $\Delta/\sigma=0.5$, $k_B T/\epsilon_a=1$, $\epsilon_r/\epsilon_a=5$, and $\rho\sigma=0.2$. Predictions from the mLPA given by Eq. (54) (long dashed line) are compared with both MC results (solid line) and PY and HNC integral equations (short dashed and dotted lines, respectively). In the inset a magnification of the $r<\sigma$ region is shown.

proaches become identical. Specifically, for the PSW fluid model both approaches reduce on a calculation of distribution function at $r=1$ and $r=\lambda$ [see Eq. (40)].

B. Integral equations

The presence of penetrability does not pose any particular difficulties to standard integral equation theories. As a matter of fact these have been already employed in the PS case⁷ and in the PSW case¹⁰ within standard approximations where the one-dimensional Ornstein-Zernike equation,

$$h(r) = c(r) + \rho \int_{-\infty}^{\infty} dr' c(|r-r'|)h(r'), \tag{59}$$

is associated with a PY closure,

$$c(r) = f(r)y(r), \tag{60}$$

or with an HNC closure

$$c(r) = f(r)y(r) + y(r) - 1 - \ln y(r). \tag{61}$$

We solved the PY and HNC integral equations using a Zerah's algorithm³² with up to 2^{12} grid points depending on the considered state point.

IX. RESULTS WITHIN THE LPA

In this section we compare numerical results stemming from the LPA with MC simulations and integral equation theories (PY and HNC) for both RDF (where we will consider the improved mLPA) and equation of state (at the level of the simple LPA).

A. Results for $g(r)$

As a first approach to assess the performance of the LPA, we consider the RDF $g(r)$ for two representative state points. The well is kept fixed at $\Delta/\sigma=0.5$ and temperature is also fixed by the attractive energy scale so that $k_B T/\epsilon_a=1$. Figure 3 depicts the behavior of $g(r)$ for a density $\rho\sigma=0.2$ and an

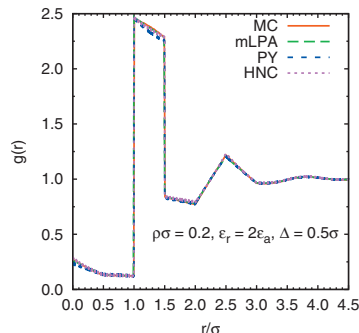


FIG. 4. Same as in Fig. 3 at the instability threshold $\epsilon_r/\epsilon_a=2$. All other parameters are as in Fig. 3.

energy ratio $\epsilon_r/\epsilon_a=5$, which is well above the stability threshold value $\epsilon_r/\epsilon_a=2$.¹⁰ The stability threshold is then probed in Fig. 4, whereas a higher density $\rho\sigma=0.8$ is tested in Fig. 5 with all other parameters identical to those of Fig. 3.

In all cases, mLPA results (that only differ from the LPA ones within the interaction range, $0 < r < \lambda$) are compared with MC simulations and integral equations and follow the expected trend. For low densities ($\rho\sigma=0.2$) and low penetrability ($\epsilon_r/\epsilon_a=5$) mLPA, PY, and HNC all provide very accurate descriptions of MC data with a very tiny difference in the well region $1 \leq r/\sigma \leq 1.5$, where the integral equations predict a slight curvature of $g(r)$, while the mLPA confirms the practically linear shape of the simulation data. Moreover, a blow up of $g(r)$ in the deep core region ($0 \leq r \leq \Delta$) shows that the mLPA is very accurate, while the PY and HNC theories underestimate and overestimate, respectively, the MC data. The same good performance of the mLPA is also observed for a much larger penetrability ($\epsilon_r/\epsilon_a=2$), provided the density is relatively low ($\rho\sigma=0.2$), as shown in Fig. 4. This is consistent with Fig. 2, according to which the density $\rho\sigma=0.2$ lies in the region where the LPA is expected to be accurate for any temperature when $\epsilon_r/\epsilon_a=2$ and $\Delta/\sigma=0.5$. As for the integral equations, they are also rather accurate for the case considered in Fig. 3, although they still show a slight curvature inside the well and slightly deviate from the

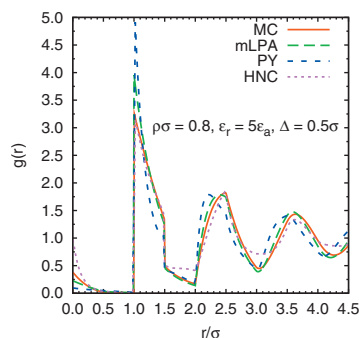


FIG. 5. Same as in Fig. 3 at a higher density $\rho\sigma=0.8$. All other parameters are as in Fig. 3.

124106-10 Fantoni *et al.*

J. Chem. Phys. **131**, 124106 (2009)

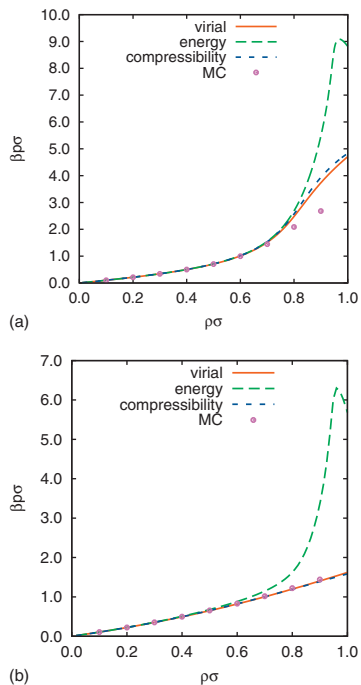


FIG. 6. Plot of $\beta\rho\sigma$ vs $\rho\sigma$ for $\Delta/\sigma=0.5$, $\epsilon_r/\epsilon_a=5$, and $k_B T/\epsilon_a=1$ (top panel) and $k_B T/\epsilon_a=5$ (bottom panel). Different curves refer to different routes. The symbols denote MC simulation results.

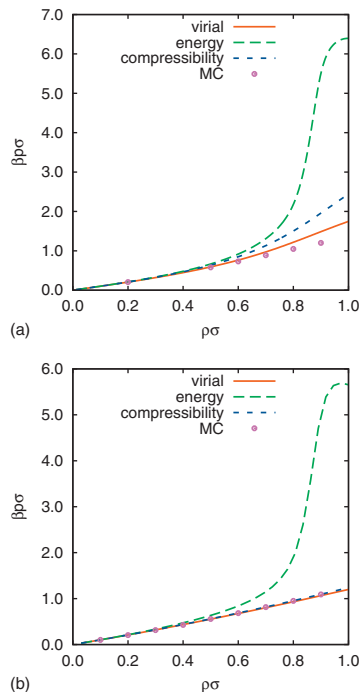


FIG. 7. Same as in Fig. 6, except that $\epsilon_r/\epsilon_a=2$.

MC results for $r < \Delta$. Differences begin to be relevant at high-density ($\rho\sigma=0.8$), mostly inside the core $0 < r/\sigma < 1$ and in the contact values $r=\sigma^+$. Again, this agrees with Fig. 2, which shows that the state $(\rho\sigma, k_B T/\epsilon_a)=(0.8, 1)$ is practically on the boundary line corresponding to $\epsilon_r/\epsilon_a=5$ and $\Delta/\sigma=0.5$. In any case, Fig. 5 shows that the best general agreement with the MC results is presented by the mLPA, followed by the HNC theory, which, however, predicts reasonably well the peaks of $g(r)$, but not the minima. We explicitly checked (not shown) that for smaller values of the well width Δ , PSW results increasingly tend to the SPS counterpart, as anticipated.

B. Results for equation of state

Next we turn to the analysis of thermodynamics within LPA. As anticipated (see Sec. VI), the lack of an exact solution gives rise to thermodynamical inconsistencies where compressibility, virial, and energy routes all give rise to different results. The consistency degree among different routes is a (partial) signature of the LPA performance, as discussed in Sec. VII. In Fig. 6 we report the behavior of βp as a function of the reduced density $\rho\sigma$. Once again, we fix the width of the well $\Delta=0.5\sigma$ and the energy ratio $\epsilon_r/\epsilon_a=5$ and consider two different temperatures $k_B T/\epsilon_a=1$ (top panel) and $k_B T/\epsilon_a=5$ (bottom panel). In the former case different

routes give practically indistinguishable results up to $\rho\sigma \approx 0.8$, whereas in the latter a difference is clearly visible at densities higher than $\rho\sigma \approx 0.6$ with energy, virial, and compressibility routes having decreasing βp for identical values of $\rho\sigma$. Similar results are observed at the stability edge $\epsilon_r/\epsilon_a=2$, as shown in Fig. 7. We remark that higher temperatures effectively correspond to higher penetrability, as particles have relatively more attractive energies, as compared to the positive repulsive barrier, and hence they can penetrate more. Therefore pressure differences among different thermodynamical routes can be reckoned as a rough measure of the breakdown of LPA. On the other hand, consistency among different routes does not necessarily mean “exact” results, as they can all converge to the incorrect value.

A comparison with MC numerical simulations is therefore also included in Figs. 6 and 7. Somewhat surprisingly, this suggests that the virial route is the closest to the true value for the pressure, with both compressibility and energy routes always lying on the opposite side with the latter being the farthest from the MC results.

In order to compare with LPA, we carefully scanned a wide range of temperatures and densities within the region $0 \leq \rho\sigma \leq 1$ where LPA provides consistent thermodynamics as remarked. Within this region we found no signature of fluid-fluid transition line as expected. Our preliminary numerical results for higher densities, where strong overlapping among different particles is enforced, provide a clear evi-

124106-11 Penetrable-square-well fluids

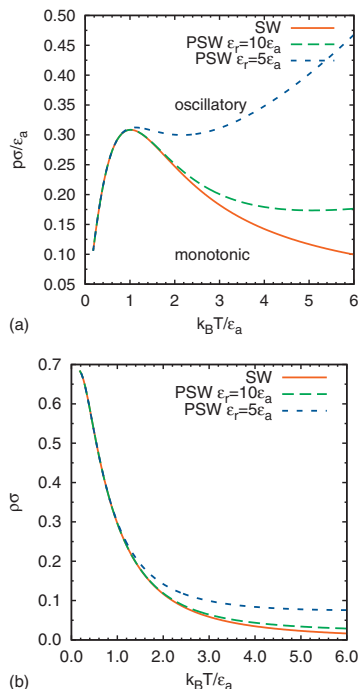
 J. Chem. Phys. **131**, 124106 (2009)


FIG. 8. Plot of the FW transition line in the $p\sigma/\epsilon_a$ vs $k_B T/\epsilon_a$ plane (top panel) and in the $\rho\sigma$ vs $k_B T/\epsilon_a$ plane (bottom panel). Here $\Delta/\sigma=1$ and $\epsilon_r/\epsilon_a=(\infty, 10, 5)$. Note that, except in the SW case ($\epsilon_r/\epsilon_a=\infty$), $\zeta/\sigma \neq \beta p$. Note also that in these cases the three routes to the pressure are not distinguishable one from the other on the graph scale.

dence of phase separation. As the main emphasis of the present paper is on analytical approximations, this point will be discussed in some detail elsewhere.

C. Results for Fisher–Widom line

Let us follow the recipe given in Sec. V to locate the FW line. In Fig. 8 we report the quantities $p\sigma/\epsilon_a$ and $\rho\sigma$ as a function of $k_B T/\epsilon_a$ for $\Delta=\sigma$ and decreasing values of the ratio ϵ_r/ϵ_a . The case $\epsilon_r/\epsilon_a \rightarrow \infty$ is the one addressed in the original FW work on the one-dimensional SW fluid.¹⁸ We remind that above the FW line, $g(r)-1$ has oscillatory behavior, whereas it is exponentially decaying below it, and it is located in the homogeneous fluid region of the phase diagram, above the critical temperature if phase separation is present.

As the repulsive barrier becomes finite, the region of monotonic behavior increases for large $k_B T/\epsilon_a$ whereas it remains essentially unchanged for lower temperatures. This is not surprising as penetrability (i.e., finite repulsive barrier) favors the onset of a critical region. Somewhat more surprising is the fact that this happens in the high- rather than in the low-temperature region. A similar feature is also appearing in the ρ - T plane (see bottom panel). In order to test the effect of different width values, we repeated the same calculation for $\Delta=0.5\sigma$. Results are presented in Fig. 9 and are in agreement

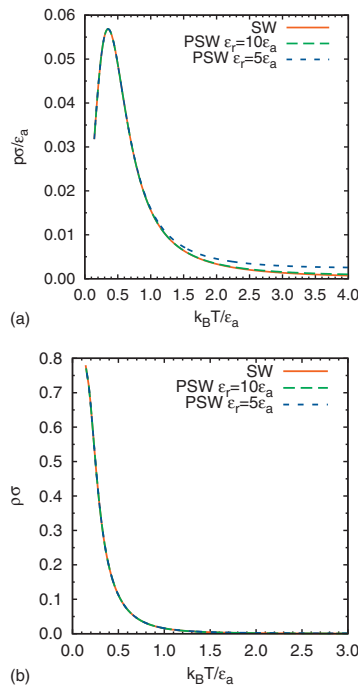


FIG. 9. Same as in Fig. 8, except that $\Delta/\sigma=0.5$.

(in the limit $\epsilon_r/\epsilon_a \rightarrow \infty$) with results for the one-dimensional SW fluid presented in Ref. 33 for a hard-core to well-width ratio equal to 2 (see Fig. 1 in Ref. 33). For this well width the influence of the ratio ϵ_r/ϵ_a on the FW line is much less important.

Although we have been unable to find a simple physical explanation for this behavior, we remark that the sensitivity of the FW line to the barrier height occurs as the density decreases. Consider for instance the density $\rho\sigma=0.1$ for models with $\Delta=\sigma$. In the SW case ($\epsilon_r/\epsilon_a \rightarrow \infty$) the decay of the RDF changes from monotonic to oscillatory as one increases the temperature and crosses the value $k_B T/\epsilon_a \approx 2.2$. In the case of the PSW model with $\epsilon_r/\epsilon_a=5$, according to the LPA, the transition takes place at $k_B T/\epsilon_a \approx 2.8$. If the density is sufficiently low ($\rho\sigma \leq 0.076$ for $\epsilon_r/\epsilon_a=5$), the asymptotic decay of $g(r)-1$ is monotonic for any temperature, while this effect is absent in the impenetrable SW limit. One might argue that this influence of the energy ratio ϵ_r/ϵ_a on the high-temperature branch of the FW line is an artifact of the LPA since the latter approximation is *a priori* restricted to low temperatures. On the other hand, this high-temperature branch also corresponds to low densities, counterbalancing the penetrability effect and making the LPA presumably accurate. As a matter of fact, the FW lines plotted in the top panels of Figs. 8 and 9 are obtained from the three thermodynamic routes but the three curves are, in each case, indistinguishable from each other. In other words, the FW lines are well inside the regions in Fig. 2 where the LPA is thermodynamically consistent from a practical point of view.

X. CONCLUSIONS AND OUTLOOK

One-dimensional fluids with nearest-neighbor interactions admit an exact analytical solution for both structural and thermophysical properties with a well defined protocol.^{5,20} Nearest-neighbor interactions, in turn, require a well defined hard-core term in the pairwise potential preventing superpositions and particle exchanges which is the crucial ingredient necessary for the exact solution. The absence of the above constraint, on the other hand, allows the presence of critical phase transitions, in spite of the one-dimensional character of the system, which are fully absent in the hard-core counterparts.

Effective pair interactions with a soft-repulsive component are well-known features of polymer solutions and colloidal suspensions.^{1,2} Among many different model potentials,² with various degrees of core softness, PSs stands out for its simplicity.⁷ In this model, the infinite repulsive energy is reduced to a finite one, thus introducing an effective “temperature” into an otherwise athermal hard-sphere system. This potential model lacks attractive interactions but these can be accounted for in the PSW companion model where an attractive short-range SW is added to the PS model.¹⁰

At sufficiently low temperatures, thermal energy cannot overcome the repulsive barrier and penetrability is low, whereas at high temperatures different particles can interpenetrate to a significant extent. Hence, within this framework, low- and high-temperature and low- and high-penetrability terminology can be used synonymously.

In this work we studied structural and thermodynamic properties of the PSW model. Using a LPA akin to that discussed for PS,⁷ we considered rather interesting issues specific of the presence of attractive interactions (and thus absent in the PS model) such as fluid-fluid phase separation or the existence of a FW line.¹⁸ This is a pseudotransition associated with a clear-cut change, from oscillatory to monotonic, in the asymptotic decay properties of the RDF, as transition line is approached, even in those cases where the existence of a critical region is prevented by rigorous theorems (e.g., the SW one-dimensional fluid). It requires the simultaneous presence of attractive and repulsive energies and hence it cannot exist for the simpler PS model

Our LPA has been devised to reduce to that of PS in the limit of no well. We assessed its performance by comparing it with exact results¹⁰ in the low-density limit and by comparing with MC simulations and PY and HNC integral equation theories for larger densities where exact analytical results do not exist. We found that it reproduces a significant portion of the T - p parameter space at the level of pair correlation function, the main difference being in the penetrability region $0 < r < \sigma$. At odds with its SW counterpart, PSW thermodynamics depends on the chosen route in view of the inconsistencies introduced by the LPA. We quantified the inconsistencies among virial, compressibility, and energy routes and discussed how they reflect into the computation of the FW line. In all considered cases, we found a magnification at large temperatures of the monotonic regime region as penetrability increases and a much smaller, if any, modifica-

tion, at lower temperatures. In all cases the FW line is found within the region where LPA is expected to be accurate as thermodynamic inconsistencies are small. Within the density region $0 \leq \rho\sigma \leq 1$, we found no sign of a fluid-fluid phase separation, although both fluid-fluid and fluid-solid transitions are expected at higher densities.

In the limit of infinitely narrow and deep well, PSW has been shown to reduce to a penetrable version of Baxter adhesive model,³⁴ which violates the stability condition set for a well defined thermodynamic limit.¹⁰ As the main weaknesses of LPA for the PSW stems mainly from a nonadequate representation of the penetrable region $0 < r/\sigma < 1$, we then discussed how a simple modification of the RDF in this region gives a significant improvement when tested against MC results under rather demanding conditions.

This paper is part of an ongoing effort on PSW outlined in our previous work.¹⁰ Future work will address a complementary approximation (the high-penetrability limit) and its matching with the LPA discussed in the present paper, so that the entire parameter T - p - ρ space can be discussed with some comfortable degree of confidence. This will resolve some of the subtle points with no conclusive answer left by the present paper. In addition, a detailed investigation of the high density region $\rho\sigma > 1$ is underway and will be reported elsewhere.

ACKNOWLEDGMENTS

The work of R.F. and A.G. was supported by the Italian MIUR through a Grant No. PRIN-COFIN 2007B57EAB (2008/2009). A.M. is grateful for the support of the Ministry of Education, Youth, and Sports of the Czech Republic, under Project No. LC512 (Center for Biomolecules and Complex Molecular Systems). The research of A.S. was supported by the Ministerio de Educación y Ciencia (Spain) through Grant No. FIS2007-60977 (partially financed by FEDER funds) and by the Junta de Extremadura through Grant No. GRU09038.

APPENDIX A: ANALYSIS OF THE CONTINUITY OF $y(r)$ WITHIN LPA

From Eq. (14) we have that if $r < 2$,

$$\rho g(r) = \frac{h\zeta}{1-q} e^{-\zeta r} + \begin{cases} 0, & 0 \leq r < 1, \\ \psi_1(r-1), & 1 < r < 1+\Delta, \\ \psi_1(r-1)q - \psi_1(r-1-\Delta), & 1+\Delta < r < 2. \end{cases} \tag{A1}$$

The explicit expressions of $\psi_1(r)$ is, from Eq. (15),

$$\psi_1(r) = \frac{\zeta}{1-q} e^{-\zeta r} \left(1 + \frac{h\zeta}{1-q} r \right). \tag{A2}$$

The continuity condition of $y(r)$ at $r=1$ is then given by condition

$$\frac{1}{1-\gamma_r} \frac{h\zeta}{1-q} e^{-\zeta} = \frac{1}{1+\gamma\gamma_r} \left[\frac{h\zeta}{1-q} e^{-\zeta} + \psi_1(0) \right], \quad (\text{A3})$$

which is identically satisfied, so that

$$\rho y(1) = \frac{\zeta}{(1-q)\gamma_r(1+\gamma)}. \quad (\text{A4})$$

However, $y(r)$ is discontinuous at $r=\lambda=1+\Delta$:

$$\begin{aligned} \rho y(\lambda^-) &= \frac{1}{1+\gamma\gamma_r} \left[\frac{h\zeta}{1-q} e^{-\zeta\lambda} + \psi_1(\Delta) \right] \\ &= \frac{\zeta q}{\gamma_r\gamma(1-q)} \left[1 + \frac{\gamma_r(1+\gamma)}{1+\gamma\gamma_r} \frac{h\zeta\Delta}{1-q} \right], \end{aligned} \quad (\text{A5})$$

$$\begin{aligned} \rho y(\lambda^+) &= \frac{h\zeta}{1-q} e^{-\zeta\lambda} + \psi_1(\Delta) - q\psi_1(0) \\ &= \frac{\zeta q}{\gamma_r\gamma(1-q)} \left[1 + \gamma_r(1+\gamma) \frac{h\zeta\Delta}{1-q} \right]. \end{aligned} \quad (\text{A6})$$

The jump is then given by

$$\rho[y(\lambda^+) - y(\lambda^-)] = \frac{\gamma_r(1+\gamma)}{1+\gamma\gamma_r} \frac{h\zeta\zeta^2\Delta}{(1-q)^2}, \quad (\text{A7})$$

and the value used as an estimate of the point is then given by the average of the left and right limits,

$$\begin{aligned} \rho \frac{y(\lambda^+) + y(\lambda^-)}{2} &= \frac{\zeta q}{\gamma_r\gamma(1-q)} \left[1 + \gamma_r(1+\gamma) \frac{1+\gamma\gamma_r/2}{1+\gamma\gamma_r} \frac{h\zeta\Delta}{1-q} \right]. \end{aligned} \quad (\text{A8})$$

APPENDIX B: THE STICKY-PENETRABLE-SPHERE MODEL

In this appendix, we provide a connection with the SPS introduced in Ref. 10. This is the penetrable analog of Baxter’s sticky-hard-sphere (SHS) well-known model.³⁴ The SPS limit can be obtained by considering the limit $\Delta \rightarrow 0$ and $\epsilon_a \rightarrow \infty$ so that $\alpha = \gamma\Delta$ remains finite, hence playing the role of an adhesivity parameter. We then define SPS by the Mayer function¹⁰

$$f_{\text{SPS}}(r) = \gamma_r f_{\text{SHS}}(r), \quad (\text{B1})$$

where

$$f_{\text{SHS}}(r) = f_{\text{HS}}(r) + \alpha \delta_+(r - \sigma) \quad (\text{B2})$$

is the Mayer functions of the SHS potential and

$$\delta_+(r) \equiv \lim_{a \rightarrow 0^+} \frac{\Theta(r) - \Theta(r-a)}{a}. \quad (\text{B3})$$

The fluid parameters are then the adhesivity coefficient $\alpha > 0$, the penetrability coefficient γ_r , and the density ρ .

As anticipated, the SPS fluid is thermodynamically unstable in the sense discussed in Sec. II. This can be seen both because the required limit does not satisfy the sufficient condition for stability $\epsilon_r > 2\epsilon_a$,¹⁰ and directly using arguments akin to those used by Stell³⁵ to prove the instability of the

original Baxter’s model³⁴ in dimensions greater than one. Nonetheless it provides an overall consistency testbench to the performance of LPA within the well established framework of SHS.

In the combined limit $\gamma \rightarrow \infty$ and $\Delta \rightarrow 0$ with $\alpha = \gamma\Delta$, Eqs. (7) and (9) become

$$\tilde{\Omega}^{\text{SPS}}(s) = \frac{1-\gamma_r}{s} + \gamma_r \left(\alpha + \frac{1}{s} \right) e^{-s}, \quad (\text{B4})$$

$$\tilde{\Omega}_0^{\text{SPS}}(s) = \gamma_r \left(\alpha + \frac{1}{s} \right) e^{-s}. \quad (\text{B5})$$

Using the first equality in Eq. (10) it follows that

$$\rho = \frac{f/\zeta + 1/\zeta + \alpha}{\alpha + 1/\zeta + 1/\zeta^2}, \quad (\text{B6})$$

where

$$f = \frac{1-\gamma_r}{\gamma_r} e^{\zeta}. \quad (\text{B7})$$

We then use the LPA as given in Eq. (8) to find

$$\rho \tilde{G}^{\text{SPS}}(s) = \frac{f/(s+\zeta) + [\alpha + 1/(s+\zeta)]e^{-s}}{(\alpha + 1/\zeta) - [\alpha + 1/(s+\zeta)]e^{-s}}, \quad (\text{B8})$$

whose inverse Laplace transform yields the RDF,

$$\rho g^{\text{SPS}}(r) = \sum_{n=0}^{\infty} \psi_n^{\text{SPS}}(r-n) \Theta(r-n), \quad (\text{B9})$$

where

$$\psi_0^{\text{SPS}}(r) = \frac{f}{\alpha + 1/\zeta} e^{-\zeta r}, \quad (\text{B10})$$

$$\begin{aligned} \psi_n^{\text{SPS}}(r) &= \left(\frac{\alpha}{\alpha + 1/\zeta} \right)^n \left[\frac{f}{\alpha + 1/\zeta} + \sum_{k=1}^n \binom{n}{k} \frac{1}{\alpha^k k!} \right. \\ &\quad \left. \times \left(kr^{k-1} + \frac{f}{\alpha + 1/\zeta} r^k \right) + \delta(r) \right] e^{-\zeta r}. \end{aligned} \quad (\text{B11})$$

In the impenetrable limit $\gamma_r \rightarrow 1$ and $f \rightarrow 0$, Eqs. (B6)–(B11) reduce to the exact one-dimensional SHS counterparts,^{22,36,37} as they should.

A word of caution is in order here. Using Eqs. (B9)–(B11), the cavity function $y(r) = g(r)e^{\beta\phi(r)}$ at contact $r=1$ is found to be discontinuous as

$$\rho y^{\text{SPS}}(1^-) = \frac{1}{\gamma_r} \frac{1}{\alpha + 1/\zeta}, \quad (\text{B12})$$

$$\rho y^{\text{SPS}}(1^+) = \rho y^{\text{SPS}}(1^-) + \frac{\alpha f}{(\alpha + 1/\zeta)^2}. \quad (\text{B13})$$

Note that Eq. (B12) is the sticky limit of the PSW value $\rho y(1)$, Eq. (A4), [recall that $y(r)$ is continuous at $r=1$ within the PSW] and is also the sticky limit of the PSW value $\rho y(\lambda^-)$, Eq. (A5). On the other hand, Eq. (B13) is the sticky limit of the PSW value $y(\lambda^+)$, Eq. (A5). Therefore, the discontinuity of $y^{\text{SPS}}(r)$ at $r=1$ is a direct consequence of the

124106-14 Fantoni *et al.*

J. Chem. Phys. **131**, 124106 (2009)

discontinuity of the PSW cavity function at $r=\lambda$. Both discontinuities are artifacts of the LPA. Again, this can be amended by an improved mLPA approach which is discussed in Sec. VII.

APPENDIX C: LOW-DENSITY EXPANSION OF THE LPA

Let us compare the LPA to order ρ with the exact results. From Eqs. (10)–(12) we easily get

$$g_1(r) = \gamma_r^2 \begin{cases} (1 - \gamma_r) \left[1 - \gamma \frac{1 + \gamma_r}{\gamma_r} \Delta - (r - 1) \frac{1}{\gamma_r} \right], & 0 \leq r < 1, \\ (1 + \gamma \gamma_r) \left[1 - \gamma \frac{1 + \gamma_r}{\gamma_r} \Delta + (r - 1) \frac{\gamma - \gamma_r - 2\gamma \gamma_r}{\gamma_r(1 + \gamma \gamma_r)} \right], & 1 < r < 1 + \Delta, \\ 2 - 2\gamma \Delta - r, & 1 + \Delta < r \leq 2, \\ \gamma(2 + \gamma)(r - 2) - 2\gamma \Delta, & 2 \leq r \leq 2 + \Delta, \\ (2 + 2\Delta - r)\gamma^2, & 2 + \Delta \leq r \leq 2 + 2\Delta, \\ 0, & 2 + 2\Delta \leq r. \end{cases} \quad (C3)$$

Comparison between Eqs. (C3) and (18) shows that the LPA reproduces the exact result for $r \geq 1 + \Delta$. On the other hand, it fails to do so within the potential range. The differences between the first-order exact and LPA cavity functions are given by Eq. (19).

$$\zeta = \zeta_0 \rho + \zeta_1 \rho^2 + \mathcal{O}(\rho^3), \quad (C1)$$

with

$$\zeta_0 = \gamma_r, \quad \zeta_1 = \gamma_r^3(1 - \gamma \Delta). \quad (C2)$$

Upon inserting the result into Eqs. (14) and (15), and after some algebra, we find the correct zeroth order term $g_0(r) = g_0^{\text{exact}}(r)$ as given in Eq. (17), and

¹J.-L. Barrat and J.-P. Hansen, *Basic Concepts for Simple and Complex Liquids* (Cambridge University Press, Cambridge, 2003).
²C. N. Likos, *Phys. Rep.* **348**, 267 (2001).
³M. Watzlawek, C. N. Likos, and H. Löwen, *Phys. Rev. Lett.* **82**, 5289 (1999).
⁴M. Ballauff and C. N. Likos, *Angew. Chem., Int. Ed.* **43**, 2998 (2004).
⁵Z. W. Salsburg, R. W. Zwanzig, and J. G. Kirkwood, *J. Chem. Phys.* **21**, 1098 (1953).
⁶See, e.g., R. Fantoni, Ph.D. thesis, University of Trieste, 2003, and references therein.
⁷A. Malijevský and A. Santos, *J. Chem. Phys.* **124**, 074508 (2006).
⁸C. N. Likos, M. Watzlawek, and H. Löwen, *Phys. Rev. E* **58**, 3135 (1998).
⁹A. Lang, C. N. Likos, M. Watzlawek, and H. Löwen, *J. Phys.: Condens. Matter* **12**, 5087 (2000).
¹⁰A. Santos, R. Fantoni, and A. Giacometti, *Phys. Rev. E* **77**, 051206 (2008).
¹¹D. Ruelle, *Statistical Mechanics: Rigorous Results* (Benjamin, London, 1969).
¹²M. E. Fisher and D. Ruelle, *J. Math. Phys.* **7**, 260 (1966).
¹³B. Widom and J. S. Rowlinson, *J. Chem. Phys.* **52**, 1670 (1970).
¹⁴S. Torquato, *J. Chem. Phys.* **81**, 5079 (1984).
¹⁵P. A. Rikvold and G. Stell, *J. Chem. Phys.* **82**, 1014 (1985).

¹⁶F. H. Stillinger, *J. Chem. Phys.* **65**, 3968 (1976).
¹⁷A. A. Louis, P. G. Bolhuis, and J.-P. Hansen, *Phys. Rev. E* **62**, 7961 (2000).
¹⁸M. E. Fisher and B. Widom, *J. Chem. Phys.* **50**, 3756 (1969).
¹⁹D. S. Corti and P. G. Debenedetti, *Phys. Rev. E* **57**, 4211 (1998).
²⁰M. Heying and D. S. Corti, *Fluid Phase Equilib.* **220**, 85 (2004).
²¹It may be noted that the LPA presented here is identical to the low-temperature approximation introduced in Ref. 7.
²²S. B. Yuste and A. Santos, *J. Stat. Phys.* **72**, 703 (1993).
²³A. Santos, *Mol. Phys.* **104**, 3411 (2006).
²⁴See, e.g., A. Giacometti, G. Pastore, and F. Lado, *Mol. Phys.* **107**, 555 (2009).
²⁵J.-P. Hansen and I. R. McDonald, *Theory of Simple Liquids* (Academic, Amsterdam, 2006).
²⁶R. Evans, J. R. Henderson, D. C. Hoye, A. O. Parry, and Z. A. Suber, *Mol. Phys.* **80**, 755 (1993).
²⁷R. J. F. Leote de Carvalho, R. Evans, D. C. Hoyle, and J. R. Henderson, *J. Phys.: Condens. Matter* **6**, 9275 (1994).
²⁸C. Vega, L. F. Rull, and S. Lago, *Phys. Rev. E* **51**, 3146 (1995).
²⁹M. Dijkstra and R. Evans, *J. Chem. Phys.* **112**, 1449 (2000).
³⁰P. Tarazona, E. Chacón, and E. Velasco, *Mol. Phys.* **101**, 1595 (2003).
³¹It is interesting to remark that $\lim_{\beta \rightarrow \infty} \zeta(\rho, \beta) = 0$ if $\rho < (1 + \Delta/2)^{-1}$, while $\lim_{\beta \rightarrow \infty} \zeta(\rho, \beta) = \zeta_0(\rho) \neq 0$ if $\rho > (1 + \Delta/2)^{-1}$, where $\zeta_0(\rho)$ is the solution of $\rho^{-1} = \zeta_0^{-1} + (1 - \lambda e^{-\beta \Delta}) / (1 - e^{-\beta \Delta})$.
³²G. Zerah, *J. Comput. Phys.* **61**, 280 (1985).
³³P. Perry and S. Fisk, *J. Chem. Phys.* **57**, 4065 (1972).
³⁴R. J. Baxter, *J. Chem. Phys.* **49**, 2770 (1968).
³⁵G. Stell, *J. Stat. Phys.* **63**, 1203 (1991).
³⁶Y. Tago and S. Katsura, *Can. J. Phys.* **53**, 2587 (1975).
³⁷N. A. Seaton and E. D. Glandt, *J. Chem. Phys.* **84**, 4595 (1986).

Chapter 19

Local orientational ordering in fluids of spherical molecules with dipolar-like anisotropic adhesion

Gazzilo D., **Fantoni R.**, and Giacometti A., Phys Rev. E **80**, 061207 (2009)

Title: “Local orientational ordering in fluids of spherical molecules with dipolar-like anisotropic adhesion.”

Abstract: We discuss some interesting physical features stemming from our previous analytical study of a simple model of a fluid with dipolar-like interactions of very short range in addition to the usual isotropic Baxter potential for adhesive spheres. While the isotropic part is found to rule the global structural and thermodynamical equilibrium properties of the fluid, the weaker anisotropic part gives rise to an interesting short-range local ordering into a periodically modulated structure with preferred antiparallel alignment.

Local orientational ordering in fluids of spherical molecules with dipolarlike anisotropic adhesion

Domenico Gazzillo, Riccardo Fantoni, and Achille Giacometti

Dipartimento di Chimica Fisica, Università di Venezia, S. Marta DD 2137, I-30123 Venezia, Italy

(Received 18 August 2009; revised manuscript received 21 October 2009; published 31 December 2009)

We discuss some interesting physical features stemming from our previous analytical study of a simple model of a fluid with dipolarlike interactions of very short range in addition to the usual isotropic Baxter potential for adhesive spheres. While the isotropic part is found to rule the global structural and thermodynamical equilibrium properties of the fluid, the weaker anisotropic part gives rise to an interesting short-range local ordering of nearly spherical condensation clusters, containing short portions of chains having nose-to-tail parallel alignment, which runs antiparallel to adjacent similar chains.

DOI: 10.1103/PhysRevE.80.061207

PACS number(s): 61.20.Gy, 61.20.Qg, 61.25.Em

Even simple hard sphere fluids display a nontrivial phase diagram, as a function of the packing fraction, which can be experimentally probed and theoretically interpreted [1]. Softening the potential and/or increasing its range, leads to a remarkably richer phase diagram, which has attracted considerable attention recently (see, e.g., [2] for a recent review). Yethiraj and van Blaaderen [3] have discussed how it is experimentally possible to tune the interactions from hard sphere to soft and dipolar ones. More recently, Lu *et al.* [4] showed that, contrary to an intuitive expectation, gelation of particles with short-range attractions is intimately connected with its equilibrium phase diagram.

It is widely believed that the addition of a long-range repulsion to a short-range attraction inhibits phase separation, by promoting the formation of an equilibrium gel. The same mechanism can be achieved by reducing the probability of forming a bulk liquid using the concept of limited valency and/or patchy particles [2]. This idea has been recently explored by a number of authors, who have used the so-called Kern and Frenkel model with circular adhesive patches (of nonvanishing area), or that with short-ranged attractive point sites on the surface of hard spheres [5–11].

In spite of their usefulness, the above models share a common shortcoming on the discontinuous dependence of the potential on the particle orientations, which makes them very difficult to investigate from a theoretical point of view. This drawback is not present in molecular interactions where this dependence is continuous, as for instance in dipolar interactions [12], a case which is particularly interesting for various reasons. First, because of their widespread appearance in colloidal suspensions, such as ferrofluids, which have important practical applications. In addition, recent studies [13–15] have shown the existence of a significant influence, in the equilibrium properties of the fluid, of chainlike aggregation characteristic of the dipolar interaction, which strongly competes with a stable fluid-fluid phase separation.

Motivated by this features, in this paper, we then take an extreme alternative of considering a tail with dipolarlike anisotropy combined with a very short-range attraction. The latter is patterned after the well-known Baxter’s sticky hard sphere (SHS) potential, where attraction occurs only at contact [16]. Building upon our previous, almost fully analytical, study on this model within the Percus-Yevick closure with orientational linearization (PY-OL) [17], we discuss here some additional interesting features on the local ordering properties, which were not accounted for in our previous work.

In the same spirit of Baxter’s isotropic counterpart [16], the model is defined by the following Mayer function [17]:

$$f(1,2) = f_{\text{HS}}(r) + t\epsilon(1,2)\sigma\delta(r - \sigma), \quad (1)$$

where $f_{\text{HS}}(r) = \Theta(r - \sigma) - 1$ is its hard sphere (HS) contribution, Θ is the Heaviside step function [$\Theta(x < 0) = 0$, $\Theta(x > 0) = 1$], and the Dirac delta function $\delta(r - \sigma)$ ensures that the adhesive interaction occurs only at contact (σ is the HS diameter). The symbol $i \equiv (\mathbf{r}_i, \Omega_i)$ (with $i = 1, 2$) denotes both the position \mathbf{r}_i of the molecular center and the orientation Ω_i , which combines the usual polar and azimuthal angles (θ_i, φ_i) . Thus, we have $(1, 2) = (\mathbf{r}_{12}, \Omega_1, \Omega_2) = (r, \hat{\mathbf{r}}_{12}, \Omega_1, \Omega_2) = (r, \Omega_r, \Omega_1, \Omega_2)$, with $\mathbf{r}_{12} = \mathbf{r}_2 - \mathbf{r}_1$, $r = |\mathbf{r}_{12}|$, and Ω_r being the solid angle associated with $\hat{\mathbf{r}}_{12} = \mathbf{r}_{12}/r$. Moreover, t is the stickiness parameter, equal to $(12\tau)^{-1}$ in Baxter’s original notation [16], which measures the strength of surface adhesion and increases with decreasing temperature.

Finally, the angular dependence of the surface adhesion is expressed through the angular factor

$$\epsilon(1,2) = 1 + \alpha D(1,2), \quad (2)$$

including the dipolar function

$$D(1,2) = D(\Omega_r, \Omega_1, \Omega_2) = 3(\hat{\mathbf{r}} \cdot \mathbf{u}_1)(\hat{\mathbf{r}} \cdot \mathbf{u}_2) - \mathbf{u}_1 \cdot \mathbf{u}_2. \quad (3)$$

Here and in the following, the unit vector \mathbf{u}_i represents the orientation Ω_i of molecule i , while $\hat{\mathbf{r}}$ coincides with $\hat{\mathbf{r}}_{12} = -\hat{\mathbf{r}}_{21}$.

The anisotropic function $\epsilon(1,2)$, which has the same symmetry as the dipolar interaction, modulates the sticky attraction. The requirement $\epsilon(1,2) \geq 0$ along with $-2 \leq D(1,2) \leq 2$ enforce the limits $0 \leq \alpha \leq \frac{1}{2}$ on the anisotropy degree. This range corresponds to the surface interaction always being attractive. In the isotropic case, one has $\alpha = 0$ and $\epsilon(1,2) = 1$.

As convolutions of Mayer functions generate correlation functions with a more complex angular dependence [12], it is necessary to consider also the angular function

$$\Delta(1,2) = \mathbf{u}_1 \cdot \mathbf{u}_2, \quad (4)$$

whose limits of variation are clearly $-1 \leq \Delta(1,2) \leq 1$.

We note the difference between the dipolar anisotropic adhesion introduced here and the anisotropy belonging to the class of uniform circular “sticky patches” [5,6,18–22]. In the

GAZZILLO, FANTONI, AND GIACOMETTI

 PHYSICAL REVIEW E **80**, 061207 (2009)

latter case, the strength of adhesion is uniform, independent of the contact point inside an attractive patch, whereas in our model the value of the anisotropic correction at $D(1,2)$ changes with the position of the contact point. Moreover, $D(1,2)$ can assume both positive and negative values, depending on the molecular orientations. Consequently, the strength of adhesion between two particles 1 and 2 at contact depends—in a continuous way—on the relative orientation of \mathbf{u}_1 and \mathbf{u}_2 as well as on the unit vector $\hat{\mathbf{r}}_{12}$ of the intermolecular distance. The orientations with $D(1,2) > 0$, and thus, with $\epsilon(1,2) = 1 + \alpha D(1,2) > 1$, correspond to an attraction stronger than the isotropic one [given by $\epsilon(1,2) = 1$], whereas the configurations with $D(1,2) < 0$, and thus with $\epsilon(1,2) < 1$, are characterized by a weaker attraction, which can even reduce to zero (HS limit) in the case of highest anisotropy admissible in the present model, i.e., $\alpha = 1/2$.

In particular, we shall focus on a set of *parallel and antiparallel* configurations with $\Delta(1,2) = \mathbf{u}_1 \cdot \mathbf{u}_2 = 1$, and $\Delta(1,2) = -1$, respectively. The surface adhesion reaches its maximum value when $\mathbf{u}_1 = \mathbf{u}_2 = \hat{\mathbf{r}}_{12}$, which yields $D(1,2) = 2$ and $\epsilon(1,2) = 1 + 2\alpha$ (head-to-tail parallel configuration). On the contrary, the stickiness is minimum, and vanishes for $\alpha = 1/2$, when $\mathbf{u}_1 = -\mathbf{u}_2 = \hat{\mathbf{r}}_{12}$, which corresponds to $D(1,2) = -2$ and $\epsilon(1,2) = 1 - 2\alpha$ (head-to-head or tail-to-tail antiparallel configurations). The intermediate case of *orthogonal* configuration (\mathbf{u}_2 perpendicular to \mathbf{u}_1) corresponds to $D(1,2) = 0$, which is equivalent to the isotropic SHS interaction.

Introducing the orientational average $\langle \dots \rangle_{\mathbf{u}} = (4\pi)^{-1} \int d\mathbf{u} \dots$ we note the following results

$$\begin{aligned} \langle \Delta(1,2) \rangle_{\mathbf{u}_1, \mathbf{u}_2} &= 0 & \langle D(1,2) \rangle_{\mathbf{u}_1, \mathbf{u}_2} &= 0 \\ \langle \Delta(1,2) D(1,2) \rangle_{\mathbf{u}_1, \mathbf{u}_2} &= 0 & \langle D^2(1,2) \rangle_{\mathbf{u}_1, \mathbf{u}_2} &= \frac{2}{3}. \end{aligned} \quad (5)$$

In a previous paper (hereafter referred to as Paper I) [17], we have analytically solved for this model the Percus-Yevick integral equation with an orientational linearization.

We here recall the main results, referring to Paper I for details. We start with the molecular Ornstein-Zernike (OZ) integral equation for homogeneous fluids,

$$h(1,2) = c(1,2) + \rho \int d\mathbf{r}_3 c(1,3) h(3,2)_{\mathbf{u}_3}, \quad (6)$$

where $h(1,2)$ and $c(1,2)$ are the total and direct correlation functions, respectively, and ρ is the number density.

Any angle-dependent correlation function $F(1,2)$ could be expanded in a basis of rotational invariants [23], whose first few terms are

$$F(1,2) = F_0(r) + F_\Delta(r) \Delta(1,2) + F_D(r) D(1,2) + \dots, \quad (7)$$

We stop at the linear terms, assuming [12,17] that the angular basis $\{1, \Delta, D\}$ is sufficient for our purposes.

The *PY-OL closure* [17] is a combination of the PY closure, i.e., $c^{\text{PY}} = f(1 + \gamma)$, with the linear expansion of $\gamma \equiv h - c$ given by $\gamma^{\text{OL}}(1,2) = \gamma_0(r) + \gamma_\Delta(r) \Delta(1,2) + \gamma_D(r) D(1,2)$, which also neglects the $\Delta\Delta$ and D^2 terms stemming from the product $f\gamma$. This leads to

$$c^{\text{PY-OL}}(1,2) = c_0(r) + c_\Delta(r) \Delta(1,2) + c_D(r) D(1,2), \quad (8)$$

$$c_0(r) = f_{\text{HS}}(r) [1 + \gamma_0(r)] + \Lambda_0 \sigma \delta(r - \sigma),$$

$$c_\Delta(r) = f_{\text{HS}}(r) \gamma_\Delta(r) + \Lambda_\Delta \sigma \delta(r - \sigma),$$

$$c_D(r) = f_{\text{HS}}(r) \gamma_D(r) + \Lambda_D \sigma \delta(r - \sigma), \quad (9)$$

$$\Lambda_0 = t[1 + \gamma_0(\sigma)], \quad \Lambda_\Delta = t\gamma_\Delta(\sigma), \quad \Lambda_D = t\gamma_D(\sigma) + \alpha\Lambda_0. \quad (10)$$

The solution of the OZ equation with the above closure then yields the approximate pair distribution function

$$\begin{aligned} g^{\text{PY-OL}}(1,2) &= 1 + h^{\text{PY-OL}}(1,2) \\ &= g_0(r) + h_\Delta(r) \Delta(1,2) + h_D(r) D(1,2), \end{aligned} \quad (11)$$

$$g_0(r) = e_{\text{HS}}(r) [1 + \gamma_0(r)] + \Lambda_0 \sigma \delta(r - \sigma),$$

$$h_\Delta(r) = e_{\text{HS}}(r) \gamma_\Delta(r) + \Lambda_\Delta \sigma \delta(r - \sigma),$$

$$h_D(r) = e_{\text{HS}}(r) \gamma_D(r) + \Lambda_D \sigma \delta(r - \sigma), \quad (12)$$

where $g_0(r) = 1 + h_0(r)$, and $e_{\text{HS}}(r) = 1 + f_{\text{HS}}(r)$ is the HS Boltzmann factor.

The first term in Eqs. (9) corresponds to the well known isotropic Baxter's sticky hard sphere solution [16] and the OZ equation and this closure constitute a self-contained system. The remaining two have a similar form, but they depend in a nontrivial way upon the isotropic term (see Paper I for details).

It is instructive to consider the behavior of the $g(1,2)$ assuming that $\hat{\mathbf{r}}_{12} \cdot \mathbf{u}_1 = 1$. We focus on a generic reference particle 1, with fixed position \mathbf{r}_1 and orientation \mathbf{u}_1 , and consider a particle 2 located along the straight half line, which originates from \mathbf{r}_1 and has the same direction as \mathbf{u}_1 (polar axis). Imagine that 2 has fixed distance r from 1, but can assume all possible orientations \mathbf{u}_2 , which—by axial symmetry—can be described by the single angle $\theta_{12} = \cos^{-1}(\mathbf{u}_1 \cdot \mathbf{u}_2)$. Consequently, $g(1,2)$ reduces to: $g(r, \theta_{12}) = g_0(r) + [h_\Delta(r) + 2h_D(r)](\mathbf{u}_1 \cdot \mathbf{u}_2)$.

Figure 1(a) depicts the behavior of $g_0(r)$, which coincides with the reference isotropic part $g^{\text{isoSHS}}(r)$ of the pair correlation function, at $\eta = (\pi/6)\rho\sigma^3 = 0.4$.

Here, $t=0$ gives the HS limiting case, $g^{\text{HS}}(r)$, and we consider increasing values of t , which correspond to increasing adhesion or decreasing temperature, i.e., $t=0.1, 0.3, 0.5$ and 0.8 . The last t -value yields $\tau = 1/(12t) \approx 0.1$, which lies close to the critical temperature of the isotropic fluid [24].

Two features are noteworthy. First of all, the short-range interactions mainly modify the short-range portions of the pair correlation functions. Very pronounced effects are visible in the range $\sigma < r < 2\sigma$, but significant changes are also present all the way out to $r=4\sigma$ and beyond, while the phase of the oscillations is clearly shifted by the addition of the short-range attraction.

A second interesting feature concerns the t dependence of $g_0(r)$ in the first shell. As the adhesion strength increases from $t=0$ (HS) to $t=0.8$, the contact value monotonically

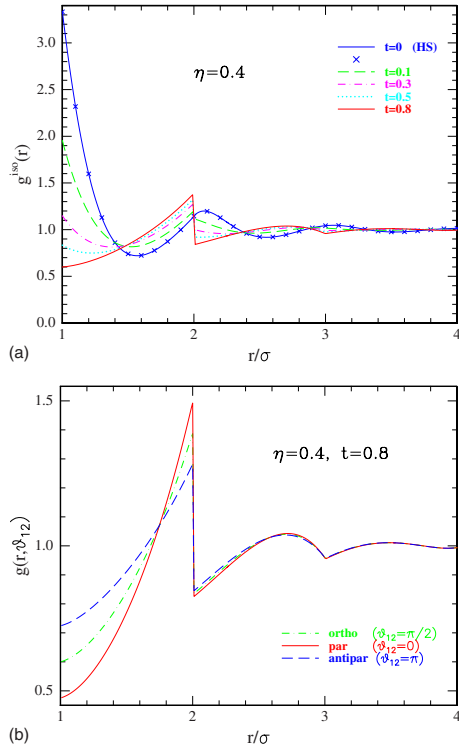


FIG. 1. (Color online) (a) Isotropic part of the pair correlation function, $g_0(r) = g^{\text{isoSHS}}(r)$, at $\eta = 0.4$, for $t = 0, 0.1, 0.3, 0.5$, and 0.8 corresponding to increasing adhesion strength or decreasing temperature. $t = 0$ yields the HS limit. (b) Behavior of $g(r, \theta_{12})$, when $\alpha = 1/2$, at $\eta = 0.4$ and $t = 0.8$, for three representative orientations $\theta_{12} = 0, \pi/2, \pi$ (parallel, orthogonal, and antiparallel configurations).

decreases, whereas a discontinuous peak progressively builds up at $r = (2\sigma)^-$. This somewhat counter-intuitive result can be easily understood in terms of the reduction of the pressure exerted on particles 1 and 2 by the surrounding ones in the presence of increasing attraction, thus, providing an average larger separation among 1 and 2.

Suppose now that we modulate this attraction with the anisotropic dipolarlike dependence described above. When $\alpha = 1/2$ the effect on g is shown in Fig. 1(b) for three representative values of θ_{12} : $\theta_{12} = 0$ (parallel orientation), $\theta_{12} = \pi/2$ (orthogonal orientation), and $\theta_{12} = \pi$ (antiparallel orientation). Note that in the orthogonal case, the dipolar dependence vanishes and one recovers the isotropic behavior. The main differences occur in the first shell, where the orthogonal curve $\theta_{12} = \pi/2$ is bracketed between the antiparallel ($\theta_{12} = \pi$) and the parallel ($\theta_{12} = 0$) results. Similar qualitative results (with different separations among parallel and antiparallel curves) are found when the angle between $\hat{\mathbf{r}}_{12}$ and \mathbf{u}_1 is varied.

From Fig. 1(b) we note that at contact ($r = \sigma^+$) the antipar-

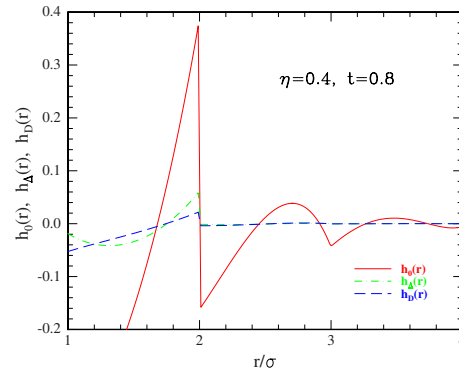


FIG. 2. (Color online) The three components $h_0(r)$, $h_\Delta(r)$, and $h_D(r)$ of the molecular total correlation function for $\alpha = 1/2$, $\eta = 0.4$, and $t = 0.8$. At $r < \sigma$ one has $h_0(r) = -1$ and $h_\Delta(r) = h_D(r) = 0$.

allel configuration is more probable than the nose-to-tail parallel one; conversely, at separations close to $r = 2\sigma^-$ the parallel alignment is predominant. This can also be confirmed by plotting the projections $h_\Delta(r)$ and $h_D(r)$ of the molecular correlation function $h^{\text{PY-OL}}(1, 2)$ on the angular basis $\Delta(12)$ and $D(12)$, respectively. This is depicted in Fig. 2 where the isotropic corresponding contribution $h_0(r)$ is also reported by contrast. One observes a weak negative correlation for both quantities in the region $r \approx \sigma^+$ and, conversely, a positive correlation close to $2\sigma^-$. A crossing occurs approximately around the same value $r \approx 1.7\sigma$ where the parallel component in Fig. 1(b) overtakes the antiparallel one, as expected. As we shall see, however, this is a local ordering which does not affect the condensation process.

In order to get more insight into such an orientational ordering, we compute the number of particles with orientation \mathbf{u}_2 that a generic reference particle 1 with orientation \mathbf{u}_1 “sees” in an appropriate surrounding volume V_{AB} . Assuming \mathbf{u}_1 as polar axis and taking into account the sphere S with center \mathbf{u}_1 and radius R , V_{AB} is defined as the portion of S corresponding to the solid angle $\Omega_{AB} = \{(\theta, \varphi) | \theta_A \leq \theta \leq \theta_B, 0 \leq \varphi \leq 2\pi\}$ (see Fig. 3). Taking for instance $\theta_A = 0$ and $\theta_B = \pi/3$, we can analyze the “forward ordering” as seen by the reference particle, while choice $\theta_A = \pi/3$ and $\theta_B = \pi/2$ allows to discuss the “lateral ordering.”

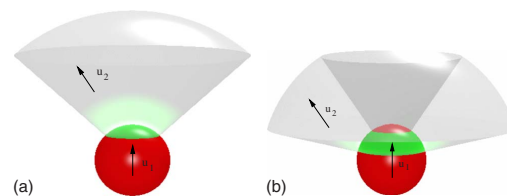


FIG. 3. (Color online) Schematic representation of the volume V_{AB} (included in the shading area) in two different situations: (top panel) $\theta_A = 0$ giving the contribution from the forward region, and (bottom panel) $\theta_A \neq \theta_B \neq 0$ giving information on the lateral adjacent region.

GAZZILLO, FANTONI, AND GIACOMETTI

 PHYSICAL REVIEW E **80**, 061207 (2009)

The number of particles in an infinitesimal spherical cone of height $R=\lambda\sigma$ and infinitesimal solid angle $d\Omega_r$ in a given direction $\hat{\mathbf{r}}$ is $dN(\mathbf{u}_1, \mathbf{u}_2, \hat{\mathbf{r}}) = d\Omega_r \int_0^R dr r^2 \rho g(1, 2)$, where $d\Omega_r = d\hat{\mathbf{r}}$. In a finite solid angle Ω_{AB} ,

$$N(\mathbf{u}_1, \mathbf{u}_2) = \int_{\Omega_{AB}} d\hat{\mathbf{r}} \int_0^R dr r^2 \rho g(1, 2). \quad (13)$$

Using the first line of Eqs. (5) and (11) we see that, within the PY-OL closure, $\langle g(12) \rangle_{\mathbf{u}_1, \mathbf{u}_2} = g_0(r)$ so that the average number is

$$\bar{N} = \langle N(\mathbf{u}_1, \mathbf{u}_2) \rangle_{\mathbf{u}_1, \mathbf{u}_2} = \rho \Omega_{AB} \int_0^R dr r^2 g_0(r) = \rho \Omega_{AB} \sigma^3 I_0, \quad (14)$$

with $\Omega_{AB} = \int_0^{2\pi} d\varphi \int_{\theta_A}^{\theta_B} d\theta \sin \theta = 2\pi(\cos \theta_A - \cos \theta_B)$ and

$$I_0 = (\lambda^3 - 1)/3 + \int_1^\lambda dx x^2 h_{0,\text{reg}}(x) + \Lambda_0. \quad (15)$$

Here, we have used the results of Paper I (see especially Sec. IIID and IIIE), where $h_0(r)$ is decomposed into a ‘‘regular’’ term $h_{0,\text{reg}}(r)$ and a ‘‘singular’’ term proportional to the delta function. A similar decomposition is carried out (see again in Paper I) for the $h_\Delta(r)$ and $h_D(r)$ parts. Using

$$(\Omega_{AB})^{-1} \int_{\Omega_{AB}} d\hat{\mathbf{r}} D(1, 2) = M_{AB}(\mathbf{u}_1 \cdot \mathbf{u}_2), \quad (16)$$

$$M_{AB} = \cos^2 \theta_A + \cos \theta_A \cos \theta_B + \cos^2 \theta_B - 1, \quad (17)$$

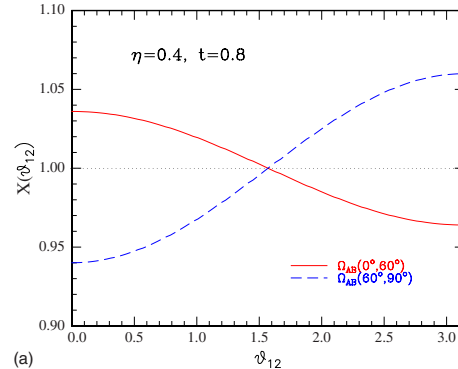
we find that the fraction X of particles with orientation \mathbf{u}_2 in the volume V_{AB} around a reference particle having orientation \mathbf{u}_1 , only depends upon the angle $\theta_{12} = \cos^{-1}(\mathbf{u}_1 \cdot \mathbf{u}_2)$ and is given by

$$X(\theta_{12}) = \frac{N(\mathbf{u}_1, \mathbf{u}_2)}{\bar{N}} = 1 + \frac{I_\Delta + M_{AB} I_D}{I_0} (\mathbf{u}_1 \cdot \mathbf{u}_2), \quad (18)$$

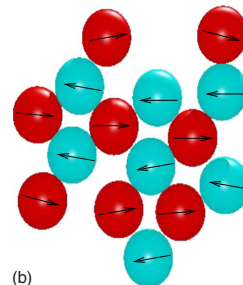
$$I_\Delta = \int_1^\lambda dx x^2 h_{\Delta,\text{reg}}(x) + \Lambda_\Delta,$$

$$I_D = \int_1^\lambda dx x^2 h_{D,\text{reg}}(x) + \Lambda_D. \quad (19)$$

Figure 4(a) depicts X as a function of θ_{12} in the case $\lambda = 2$ (first shell). In the forward region, represented by the solid angle $\Omega_{AB}(0, \pi/3)$, we find $X(0) > X(\pi)$ so there are more particles with parallel orientation, with respect to particle 1. On the contrary, $X(0) < X(\pi)$ in the surrounding lateral region, characterized by $\Omega_{AB}(\pi/3, \pi/2)$, means that here the molecules with antiparallel orientations prevail. Although these effects are rather small, it is reasonable to expect that such differences should grow significantly if the anisotropy parameter α could become much larger than the strength t of isotropic adhesion. Note that, while X_{forward} is larger than X_{lateral} in the interval $0 \leq \theta_{12} \leq \pi/2$, an inversion occurs in the region $\pi/2 < \theta_{12} \leq \pi$ in agreement with the



(a)



(b)

FIG. 4. (Color online) (a) Plot of the fraction X of molecules with orientation θ_{12} contained in the volume V_{AB} defined by $\sigma \leq r \leq 2\sigma$ and by the solid angle Ω_{AB} , with $\theta_A=0$ and $\theta_B=\pi/3$ for the forward direction and $\theta_A=\pi/3$, $\theta_B=\pi/2$ for the lateral direction. Parameters are $\alpha=1/2$, $\eta=0.4$, and $t=0.8$ in all cases. (b) Schematic representation of a globular cluster, with internal chain-like orientational ordering.

results of $g(r, \theta_{12})$ reported above [Fig. 1(b)].

The above results are suggestive of the following physical picture. Because of the limits imposed on the anisotropy parameter ($0 \leq \alpha \leq 1/2$) by the choice of the potential, the contribution of the dipolarlike interaction is significantly weaker compared to the isotropic part, and does not affect the main condensation process with the formation of globule clusters of nearly isotropic shape. This is in sharp contrast with the purely long-range dipolar models which are mainly characterized by chainlike aggregation [13–15]. However a local ordering occurs within these globular agglomerates of condensation, that are mainly formed by short portions of antiparallel chains running next each other and held together essentially by the isotropic attraction. This is schematically depicted in Fig. 4(b).

We note that only particles belonging to different, antiparallel, chains have *direct contact*. Consecutive molecules with parallel nose-to-tail orientation—i.e., belonging to the same chain—are not in contact, but lie with average separations slightly smaller than 2σ as suggested by the behavior of g in Fig. 1(b). Thus antiparallel molecules of adjacent chains ‘‘mediate’’ an *indirect contact* between consecutive particles of a given chain.

Once again, we stress that this phenomena should be considered a local fluctuation with very short range (of the order of one shell, as remarked) and does not extend to the entire fluid. This can be readily checked by considering the limit $\lambda \rightarrow \infty$, in which case one finds $I_D=0$, so that the dependence from $\mathbf{u}_1 \cdot \mathbf{u}_2 = \cos \theta_{12}$ is averaged to zero. As we shall see below, a direct consequence of this is that the coexistence line of the isotropic model is not significantly affected by the anisotropic part, within the PY-OL approximation.

In view of the last remark, one might rightfully wonder whether the anisotropic part plays any role in the thermodynamics of our model. We can convince ourselves that the answer is positive, by considering the exact third virial coefficient as defined by

$$B_3 = -\frac{1}{3V} \int d\mathbf{r}_1 d\mathbf{r}_2 d\mathbf{r}_3 \langle f(1,2)f(1,3)f(2,3) \rangle_{\mathbf{u}_1, \mathbf{u}_2, \mathbf{u}_3}, \quad (20)$$

Note that, in view of Eq. (5), the exact second virial coefficient $B_2 = -\frac{1}{2} \int d\mathbf{r} \langle f(1,2) \rangle_{\mathbf{u}_1, \mathbf{u}_2}$ coincides with its isotropic counterpart. However, this is not the case for B_3 , that can be computed following the method outlined in [6] for patchy sticky hard spheres, a close relative to the present model. One finds

$$b_3 = B_3/v_0^2 = 10 - 60t\chi_1 + 144t^2\chi_2 - 96t^3\chi_3, \quad (21)$$

where $v_0 = (\pi/6)\sigma^3$ and

$$\begin{aligned} \chi_1 &= \langle \epsilon(1,2) \rangle_{\mathbf{u}_1, \mathbf{u}_2} & \chi_2 &= \langle \epsilon(1,2)\epsilon(1,3) \rangle_{\mathbf{u}_1, \mathbf{u}_2, \mathbf{u}_3}, \\ \chi_3 &= \langle \epsilon(1,2)\epsilon(1,3)\epsilon(2,3) \rangle_{\mathbf{u}_1, \mathbf{u}_2, \mathbf{u}_3}. \end{aligned} \quad (22)$$

Again using Eq. (5), we find $\chi_1 = 1 = \chi_2$. The exact value of χ_3 turns out to be

$$\chi_3 = 1 - \frac{11}{72} \alpha^3. \quad (23)$$

The anisotropic contribution is represented by the term $-(11/72)\alpha^3 \approx 0.02$, which is very weak with respect to the isotropic one.

Having assessed the limits of the model, we now turn to discuss the limits of the approximation involved in the PY-OL closure. A simple and direct way to quantify its deviation from the exact results is to consider the first-order density expansion of the exact direct correlation function $c(1,2) = f(1,2) + c^{(1)}(1,2)\rho + \dots$. We find

$$c^{(1)}(1,2) = c_{\text{PY-OL}}^{(1)}(1,2) + c_{\text{ex}}^{(1)}(1,2), \quad (24)$$

with $c_{\text{PY-OL}}^{(1)}(1,2) = c_0^{(1)}(r) + c_\Delta^{(1)}(r)\Delta(1,2) + c_D^{(1)}(r)D(1,2)$, and

$$\begin{aligned} c_{\text{ex}}^{(1)}(1,2) &= (\alpha t) [\gamma_\Delta^{(1)}(\sigma)\Delta(1,2)D(1,2) \\ &+ \gamma_D^{(1)}(\sigma)D^2(1,2)] \sigma \delta(r - \sigma), \end{aligned} \quad (25)$$

whereas the PY closure includes both $c_{\text{PY-OL}}^{(1)}(1,2)$ and $c_{\text{ex}}^{(1)}(1,2)$, thus, reproducing the exact third virial coefficient through $B_3 = -\frac{1}{3} \int d\mathbf{r} \langle c^{(1)}(1,2) \rangle_{\mathbf{u}_1, \mathbf{u}_2}$, the PY-OL approximation omits the contributions included in $c_{\text{ex}}^{(1)}(1,2)$. Consequently, $b_3^{\text{PY-OL}}$ reduces to the purely isotropic contribution: $b_3^{\text{iso}} = 10 - 60t + 144t^2 - 96t^3$. The anisotropic contribution b_3^{aniso}

$= \frac{44}{3}(\alpha t)^3$, stemming from $c_{\text{ex}}^{(1)}(1,2)$, can be easily computed again with the help of Eqs. (5), in agreement with the exact result [Eq. (23)]. Next, we consider the thermodynamics. As in all approximate closures, even within the PY one there exist three standard routes to the equation of state: compressibility, energy, and virial routes.

In the first two cases, it is easy to convince oneself that the result is the same as for the isotropic SHS system calculated in [16]. This is again due to Eq. (5) and is a consequence of the linearity of the expansion in the angular part involved in the PY-OL approximation, Eq. (7), and of the minor role played by the anisotropic part, as testified by the weak α -dependence of the third virial coefficient [Eqs. (22) and (23)]. This is also in agreement with the stability analysis of Paper I, which can also be extended to finite values of the wave vector k .

As often the case, the virial route is more delicate. Here, standard steps lead to

$$\begin{aligned} \frac{\beta p}{\rho} &= 1 + 4\eta y_0(\sigma) - 4\eta t \\ &\times \left\{ 2y_0(\sigma) + Y'_0(\sigma) + \frac{2\alpha}{3} [2y_D(\sigma) + Y'_D(\sigma)] \right\}, \end{aligned} \quad (26)$$

where $\eta = \rho v_0$ is the packing fraction, and $Y_0(r) = r y_0(r)$, $Y_D(r) = r y_D(r)$, with $y^{\text{PY}}(1,2) = 1 + \gamma(1,2)$ being the PY cavity function.

For given t , η , one can calculate $y_0(\sigma)$, $y_D(\sigma)$, $Y'_0(\sigma)$, and $Y'_D(\sigma)$ analytically using expressions from Paper I. However, $Y'_0(\sigma)$ and $Y'_D(\sigma)$ require some care, since space derivative and sticky limit do not commute [16]. So from Eq. (26) one finds the virial pressure. The corresponding results are collected in Fig. 5 for different values of t , at both $\alpha=0$ (isotropic case) and $\alpha=1/2$ (with the anisotropic contribution included). A comparison with the virial expansion up to the third virial coefficient is also added in the case $t=0.9$ and $\alpha=1/2$.

In agreement with the previous structural findings, we find a dependence on the anisotropy. This is very small for $t \leq 0.5$ but increasingly appreciable for larger values of the adhesion strength t . In Fig. 5 one clearly sees that the pressure increases by roughly 10% on going from $\alpha=0$ (no anisotropy) to $\alpha=0.5$ (maximum anisotropy) for $t=0.9$ and $\eta \geq 0.2$.

Despite the strong differences with the pure dipolar case, it proves instructive to get some insight into the competition between the tendency to condensation on the one hand and to chaining on the other hand, by applying to the present model the arguments put forward by Tlusty and Safran [13] in the dipolar case. These authors devised a phenomenological theory, where the two above-mentioned tendencies are represented by the concentrations of ‘‘junctions’’ and ‘‘ends,’’ respectively (see [13]). We have closely followed their arguments to derive the critical parameters τ_c and η_c of the present model in terms of the energies ϵ_1 , ϵ_3 of ends and junctions respectively. One finds [13]

GAZZILLO, FANTONI, AND GIACOMETTI

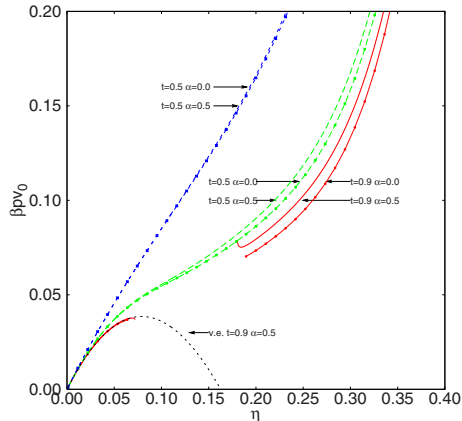
 PHYSICAL REVIEW E **80**, 061207 (2009)


FIG. 5. (Color online) A plot of $\beta p v_0$ versus the packing fraction η for four different values of $t=1/(12\tau)$, with ($\alpha=1/2$) and without ($\alpha=0$) the anisotropic contribution using the virial route to the pressure. The third order virial expansion is also added (v.e.) in the most relevant case $t=0.9$ and $\alpha=0.5$ for comparison. The part of the lines, which are not shown, correspond to a loss of solutions.

$$\tau_c = \frac{\epsilon_1 - 3\epsilon_3}{3 \ln 3 - 2 \ln 2}, \quad \ln \eta_c = - \frac{\epsilon_1(2 \ln 3 - \ln 2) - \epsilon_3 \ln 2}{\epsilon_1 - 3\epsilon_3}, \quad (27)$$

which coincides with the results of [13]. Matching this critical values with the one of the isotropic adhesive spheres of Miller and Frenkel [24], $\tau_c=0.1133$ and $\eta_c=0.266$, we find $\epsilon_1=0.186$ and $\epsilon_3=-0.0102$ (the value $\epsilon_3 < 0$ means that junctions are enhanced with respect to ends, once more favoring condensation). In our results the number of ends ρ_1 and junctions ρ_3 turn out to be equal ($\rho_1=\rho_3$) at the critical point, which is thus a point of connectivity transition in the system. Figure 6 depicts the coexistence line, which does not display the re-entrance characteristic of the pure dipolar case (com-

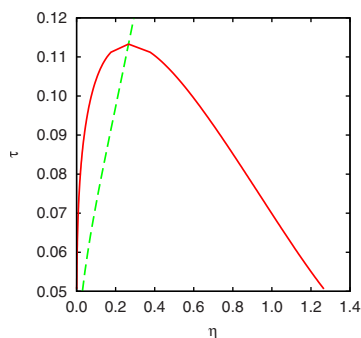


FIG. 6. (Color online) Phase diagram of our dipolarlike sticky hard spheres, calculated for defect energies $\epsilon_1=0.186$ and $\epsilon_3=-0.0102$. At the critical point the binodal curve (continuous line) and the connectivity transition (dashed curve) meet. The line denote the end-rich “gas” with the junction-rich “liquid.”

pare with Fig. 2 of [13]). This is in complete agreement with the remark by Tlustý and Safran that the addition of an isotropic short-range attraction—such as the case of the present model—reports the curve to its characteristic parabolic shape (see also Fig. 3 of [13]). This is also consistent with very recent numerical simulation results [25,26] showing that the addition of a very weak isotropic attraction to the dipolar HS potential makes the condensation transition easily observable. In summary, we have studied structural and thermophysical properties of a particular hard-core fluid where the attractive part of the potential includes an anisotropy of dipolar form infinitesimally short and infinitely strong.

Any two molecules of the fluid interact only at contact with a potential having, in addition to an adhesive isotropic part of the Baxter type, an additional adhesive term, whose intensity depends upon the mutual orientation of the two particles in a dipolar fashion. Our potential belongs to a class of simple anisotropic models that have recently attracted considerable interest in connection with aggregation phenomena in colloidal fluids, polymers and globular proteins, because of their possible experimental relevance for self-assembling materials and biological viruses.

The extremely short-range nature of this peculiar dipolar interaction strongly contrasts with the long-range nature of the dipolar hard sphere model. In the latter case, the formation of chains and long anisotropic agglomerates significantly affects the possibility of a gas-liquid transition. Using a simplified treatment of the angular part, based upon a first-order expansion in angular invariants so to allow an almost fully analytical solution, we have shown that only the local (first few) coordination shells are affected by the anisotropy. This is due to the fact that the orientationally dependent part of the potential has a relatively weak strength with respect to the isotropic attractive term, as forced by the particular choice of the potential associated with the $0 \leq \alpha \leq 1/2$ limits. As a result, all structural and thermodynamical properties are only mildly affected by the anisotropic adhesion.

Nonetheless, the competition of the two adhesive terms (the isotropic and the anisotropic ones) gives rise to an anisotropic local ordering within each (almost isotropic) molecular agglomerate consisting of short chains of molecules with parallel head-to-tail orientation, “glued” to similar chains globally oriented in the opposite direction, thus giving an antiparallel alignment for particles belonging to two adjacent chains. It would be interesting to contrast the present results with more realistic models incorporating a competition between an isotropic and anisotropic short range interactions, such as for instance Stockmayer fluids [27], dipolar Yukawa HS fluids [28] or combination of dipolar and square-well potentials [26]. In spite of its simplicity, the results of the present work suggest that, in the presence of dipolarlike anisotropy, one can continuously tune from situations only affecting the local ordering (such as in the case presented here) to situations where this effect is much more global (such as the real dipolar case), by simply adjusting the range of interaction.

Funding from PRIN-COFIN 2007 is gratefully acknowledged.

LOCAL ORIENTATIONAL ORDERING IN FLUIDS OF ...

PHYSICAL REVIEW E **80**, 061207 (2009)

- [1] E. Zaccarelli, C. Valeriani, E. Sanz, W. C. K. Poon, M. E. Cates, and P. N. Pusey, *Phys. Rev. Lett.* **103**, 135704 (2009).
- [2] E. Zaccarelli, *J. Phys.: Condens. Matter* **19**, 323101 (2007).
- [3] A. Yethiraj and A. van Blaaderen, *Nature (London)* **421**, 513 (2003).
- [4] P. J. Lu, E. Zaccarelli, F. Ciulla, A. B. Schofield, F. Sciortino, and D. Weitz, *Nature (London)* **453**, 499 (2008).
- [5] N. Kern and D. Frenkel, *J. Chem. Phys.* **118**, 9882 (2003).
- [6] R. Fantoni, D. Gazzillo, A. Giacometti, M. A. Miller, and G. Pastore, *J. Chem. Phys.* **127**, 234507 (2007); A. Giacometti, F. Lado, J. Largo, G. Pastore, and F. Sciortino, *ibid.* **131**, 174114 (2009).
- [7] H. Liu, S. K. Kumar, and F. Sciortino, *J. Chem. Phys.* **127**, 084902 (2007).
- [8] G. Foffi and F. Sciortino, *J. Phys. Chem. B* **111**, 9702 (2007).
- [9] E. Bianchi, P. Tartaglia, E. Zaccarelli, and F. Sciortino, *J. Chem. Phys.* **128**, 144504 (2008).
- [10] C. Gögelein, G. Nägele, R. Tuinier, T. Gibaud, A. Stradner, and P. Schurtenberger, *J. Chem. Phys.* **129**, 085102 (2008).
- [11] J. M. Tavares, P. I. C. Teixeira, and M. M. Telo de Gama, *Mol. Phys.* **107**, 453 (2009).
- [12] M. S. Wertheim, *J. Chem. Phys.* **55**, 4291 (1971).
- [13] T. Tlusty and S. A. Safran, *Science* **290**, 1328 (2000).
- [14] P. J. Camp, J. C. Shelley, and G. N. Patey, *Phys. Rev. Lett.* **84**, 115 (2000).
- [15] G. Ganzenmüller and P. J. Camp, *J. Chem. Phys.* **126**, 191104 (2007).
- [16] R. J. Baxter, *J. Chem. Phys.* **49**, 2770 (1968).
- [17] D. Gazzillo, R. Fantoni, and A. Giacometti, *Phys. Rev. E* **78**, 021201 (2008).
- [18] G. Jackson, W. G. Chapman, and K. E. Gubbins, *Mol. Phys.* **65**, 1 (1988).
- [19] R. P. Sear, *J. Chem. Phys.* **111**, 4800 (1999).
- [20] D. Ghonasgi and W. G. Chapman, *J. Chem. Phys.* **102**, 2585 (1995).
- [21] E. Mileva and G. T. Evans, *J. Chem. Phys.* **113**, 3766 (2000).
- [22] Z. Zhang, A. S. Keys, T. Chen, and S. C. Glotzer, *Langmuir* **21**, 11547 (2005).
- [23] C. G. Gray and K. E. Gubbins, *Theory of Molecular Fluids*, (Clarendon Press, Oxford, 1984), Vol. I, Appendix 3E.
- [24] M. Miller and D. Frenkel, *J. Chem. Phys.* **121**, 535 (2004).
- [25] G. Ganzenmüller, G. N. Patey, and P. J. Camp, *Mol. Phys.* **107**, 403 (2009).
- [26] M. Martín-Betancourt, J. M. Romero-Enrique, and L. F. Rull, *Mol. Phys.* **107**, 563 (2009).
- [27] M. E. van Leeuwen and B. Smit, *Phys. Rev. Lett.* **71**, 3991 (1993).
- [28] I. Szalai, D. Henderson, D. Boda, and K. Y. Chan, *J. Chem. Phys.* **111**, 337 (1999).

Chapter 20

Thermodynamic consistency of energy and virial routes: An exact proof within the linearized Debye-Hückel theory

Santos A., **Fantoni R.**, and Giacometti A., J. Chem. Phys. **131**, 181105 (2009)

Title: “Thermodynamic consistency of energy and virial routes: An exact proof within the linearized Debye-Hückel theory.”

Abstract: The linearized Debye-Hückel theory for liquid state is shown to provide thermodynamically consistent virial and energy routes for any potential and for any dimensionality. The importance of this result for bounded potentials is discussed.

Has been among the 14th most downloaded JCP articles in the month of November.

Thermodynamic consistency of energy and virial routes: An exact proof within the linearized Debye–Hückel theory

Andrés Santos,^{1,a)} Riccardo Fantoni,^{2,b)} and Achille Giacometti^{3,c)}

¹Departamento de Física, Universidad de Extremadura, E-06071 Badajoz, Spain

²National Institute for Theoretical Physics (NITheP), Stellenbosch 7600, South Africa

³Dipartimento di Chimica Fisica, Università di Venezia, Calle Larga S. Marta DD2137, I-30123 Venezia, Italy

(Received 5 October 2009; accepted 27 October 2009; published online 13 November 2009)

The linearized Debye–Hückel theory for liquid state is shown to provide thermodynamically consistent virial and energy routes for any potential and for any dimensionality. The importance of this result for bounded potentials is discussed. © 2009 American Institute of Physics. [doi:10.1063/1.3265991]

Integral equations of liquid theory always involve some approximate closure.^{1,2} This is an approximate relation between the pair and the direct correlation functions in addition to the exact Ornstein–Zernike integral equation. Unlike exact theories, these approximate closures introduce well known inconsistencies among different routes to the equation of state. Given the knowledge of the pair correlation function, there are clearly many possible routes leading to the equation of state, but the most frequently used are the energy, the virial (or pressure), and the compressibility routes.

The degree of inconsistency clearly depends upon the goodness of the approximate closure, so that some closures might display weaker differences than others and might even, under some particular circumstances, give no difference at all between two particular routes. The most notable example of this (although rarely mentioned in the literature) is the virial-energy consistency within the hypernetted-chain (HNC) approximation.³ Other more recent examples include the energy and virial routes in the hard-sphere limit of the square-shoulder potential (for any approximation),^{4,5} and again the energy-virial consistency for soft-potentials within the mean-spherical approximation (MSA).⁶

The aim of this communication is to add one more case to this relatively short list by showing that energy and virial routes are completely equivalent within the linearized Debye–Hückel (LDH) approximation for *any potential* in *any dimensionality*. Our interest in this problem has been triggered by recent investigations on bounded potentials,^{7–9} where this consistency is of particular importance, as we shall discuss.

Consider an arbitrary potential $\phi(\mathbf{r})$ for a homogeneous fluid of N particles in d dimensions. Newton's third law of motion implies that $\phi(\mathbf{r}) = \phi(-\mathbf{r})$, but the potential need not be spherically symmetric. The virial equation is associated with the compressibility factor $Z(\rho, \beta)$ as¹

$$Z \equiv \frac{\beta P}{\rho} = 1 + \frac{\rho}{2d} \int d\mathbf{r} \mathbf{y}(\mathbf{r}) \mathbf{r} \cdot \nabla f(\mathbf{r}), \quad (1)$$

where $\beta = 1/k_B T$ is the inverse temperature, ρ and P are the density and the pressure, respectively, and $f(\mathbf{r}; \beta) = e^{-\beta\phi(\mathbf{r})} - 1$ is the Mayer function. In Eq. (1) we have also introduced the cavity function $\mathbf{y}(\mathbf{r}; \rho, \beta)$, which is related to the pair correlation function $g(\mathbf{r}; \rho, \beta)$ by the relation $\mathbf{y}(\mathbf{r}) = e^{\beta\phi(\mathbf{r})} g(\mathbf{r})$. The energy equation is associated with the energy U per particle $u(\rho, \beta)$,

$$u \equiv \frac{U}{N} = \frac{d}{2\beta} - \frac{\rho}{2} \int d\mathbf{r} \mathbf{y}(\mathbf{r}) \frac{\partial f(\mathbf{r})}{\partial \beta}. \quad (2)$$

A standard thermodynamic identity¹⁰ provides the consistency condition between the pressure and energy routes:

$$\rho \left(\frac{\partial u}{\partial \rho} \right)_\beta = \left(\frac{\partial Z}{\partial \beta} \right)_\rho. \quad (3)$$

The explicit notation of the variable being kept fixed and the parameter dependence will be dropped henceforth for notational simplicity. It proves convenient to further introduce the quantity $w(\mathbf{r}; \rho, \beta) = \mathbf{y}(\mathbf{r}; \rho, \beta) - 1$, which is related to the potential of mean force $\psi(\mathbf{r}; \rho, \beta) = -\beta^{-1} \ln g(\mathbf{r}; \rho, \beta)$ by $-\beta[\psi(\mathbf{r}) - \phi(\mathbf{r})] = \ln[1 + w(\mathbf{r})]$. We anticipate that $w(\mathbf{r})$, introduced as a definition at this stage, will assume a particular physical meaning within the LDH approximation later on. Then, identity (3) translates into the following condition:

$$-\frac{\partial}{\partial \rho} \left[\rho \int d\mathbf{r} w(\mathbf{r}) \frac{\partial f(\mathbf{r})}{\partial \beta} \right] = \frac{1}{d} \frac{\partial}{\partial \beta} \left[\int d\mathbf{r} w(\mathbf{r}) \mathbf{r} \cdot \nabla f(\mathbf{r}) \right]. \quad (4)$$

Introducing the Fourier transforms $\tilde{w}(\mathbf{k}; \rho, \beta)$ and $\tilde{f}(\mathbf{k}; \beta)$ of $w(\mathbf{r}; \rho, \beta)$ and $f(\mathbf{r}; \beta)$, respectively, Eq. (4) becomes, after standard manipulations,

^{a)}Electronic mail: andres@unex.es. URL: <http://www.unex.es/fisteor/andres/>.

^{b)}Electronic mail: rfantoni@ts.infn.it.

^{c)}Electronic mail: achille@unive.it.

181105-2 Santos, Fantoni, and Giacometti

 J. Chem. Phys. **131**, 181105 (2009)

$$\begin{aligned} \frac{\partial}{\partial \rho} \left[\rho \int \frac{d\mathbf{k}}{(2\pi)^d} \tilde{w}(\mathbf{k}) \frac{\partial \tilde{f}(\mathbf{k})}{\partial \beta} \right] \\ = \frac{\partial}{\partial \beta} \left[\frac{1}{d} \int \frac{d\mathbf{k}}{(2\pi)^d} \tilde{w}(\mathbf{k}) \nabla_{\mathbf{k}} \cdot (\mathbf{k} \tilde{f}(\mathbf{k})) \right]. \end{aligned} \quad (5)$$

Here we have used $\tilde{w}(-\mathbf{k}) = \tilde{w}(\mathbf{k})$ from the symmetry relation $\phi(-\mathbf{r}) = \phi(\mathbf{r})$. Equation (5) can be recast into a more convenient form by taking into account the mathematical identity

$$\begin{aligned} \frac{\partial}{\partial \beta} [\tilde{w}(\mathbf{k}) \nabla_{\mathbf{k}} \cdot (\mathbf{k} \tilde{f}(\mathbf{k}))] \\ = d \frac{\partial \tilde{w}(\mathbf{k})}{\partial \beta} \tilde{f}(\mathbf{k}) + \nabla_{\mathbf{k}} \cdot \left[\mathbf{k} \tilde{w}(\mathbf{k}) \frac{\partial \tilde{f}(\mathbf{k})}{\partial \beta} \right] \\ + \mathbf{k} \cdot \left[\frac{\partial \tilde{w}(\mathbf{k})}{\partial \beta} \nabla_{\mathbf{k}} \tilde{f}(\mathbf{k}) - \frac{\partial \tilde{f}(\mathbf{k})}{\partial \beta} \nabla_{\mathbf{k}} \tilde{w}(\mathbf{k}) \right]. \end{aligned} \quad (6)$$

Upon integration over \mathbf{k} in Eq. (5) the second surface term of the right-hand side of Eq. (6) can be dropped and hence we find

$$\begin{aligned} \frac{\partial}{\partial \rho} \left[\rho \int \frac{d\mathbf{k}}{(2\pi)^d} \tilde{w}(\mathbf{k}) \frac{\partial \tilde{f}(\mathbf{k})}{\partial \beta} \right] \\ = \int \frac{d\mathbf{k}}{(2\pi)^d} \frac{\partial \tilde{w}(\mathbf{k})}{\partial \beta} \tilde{f}(\mathbf{k}) + \frac{1}{d} \int \frac{d\mathbf{k}}{(2\pi)^d} \mathbf{k} \\ \cdot \left[\frac{\partial \tilde{w}(\mathbf{k})}{\partial \beta} \nabla_{\mathbf{k}} \tilde{f}(\mathbf{k}) - \frac{\partial \tilde{f}(\mathbf{k})}{\partial \beta} \nabla_{\mathbf{k}} \tilde{w}(\mathbf{k}) \right]. \end{aligned} \quad (7)$$

We remark that no approximations have been carried out so far, and that Eq. (7) is completely equivalent to the consistency condition (3). Therefore, *any* $\tilde{w}(\mathbf{k})$ satisfying Eq. (7) gives thermodynamically consistent results via the energy and virial routes.

We now show that this is in fact the case for the LDH theory which is defined by $w(\mathbf{r}) = y(\mathbf{r}) - 1$ where $\tilde{w}(\mathbf{k})$ satisfies the scaling relation¹¹

$$\rho \tilde{w}(\mathbf{k}) = F(\rho \tilde{f}(\mathbf{k})), \quad (8)$$

with $F(z) = z^2 / (1 - z)$. This immediately provides the following expressions

$$\frac{\partial}{\partial \rho} [\rho \tilde{w}(\mathbf{k})] = F'(\rho \tilde{f}(\mathbf{k})) \tilde{f}(\mathbf{k}), \quad (9)$$

$$\frac{\partial \tilde{w}(\mathbf{k})}{\partial \beta} = F'(\rho \tilde{f}(\mathbf{k})) \frac{\partial \tilde{f}(\mathbf{k})}{\partial \beta}, \quad (10)$$

$$\nabla_{\mathbf{k}} \tilde{w}(\mathbf{k}) = F'(\rho \tilde{f}(\mathbf{k})) \nabla_{\mathbf{k}} \tilde{f}(\mathbf{k}). \quad (11)$$

Equations (10) and (11) readily yield

$$\frac{\partial \tilde{w}(\mathbf{k})}{\partial \beta} \nabla_{\mathbf{k}} \tilde{f}(\mathbf{k}) = \frac{\partial \tilde{f}(\mathbf{k})}{\partial \beta} \nabla_{\mathbf{k}} \tilde{w}(\mathbf{k}), \quad (12)$$

so that the second integral on the right-hand side of (7) vanishes identically. In addition, Eqs. (9) and (10) show that the

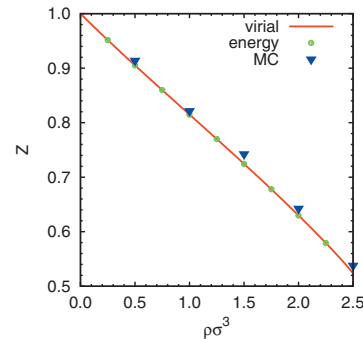


FIG. 1. Equation of state of the three-dimensional PSW model, Eq. (13), as obtained from the virial route, Eq. (1) (solid line) and from the energy route, Eq. (2) (solid circles) for reduced temperature $k_B T / \epsilon_a = 8$, well width $\Delta / \sigma = 0.5$, and energy ratio $\epsilon_r / \epsilon_a = 2$. Also shown are the results obtained from MC simulations (triangles).

remaining terms in Eq. (7) are identical. This closes the proof.

It is useful to put the present result into some perspectives. The LDH theory can be derived from diagrammatic methods¹ by summing all simple chain diagrams to all orders in density ρ . A mathematical device to do this is to formally multiply the Mayer function $f(\mathbf{r})$ by a bookkeeping parameter μ , and then let $\mu \rightarrow 0$, so that the leading diagrams to be retained at each order are the simple chain diagrams, which then give the dominant contribution to the pair correlation function within this approximation. This procedure is physically justified only for *bounded* potentials where $|f(\mathbf{r})|$ can be made arbitrarily small by increasing the temperature, and hence the virial-energy consistency is also representative of the exact behavior of the equation of state, unlike the case of unbounded potentials where this is not the case and consistency does not automatically ensure exact results.¹²

Representative examples of bounded potentials, recently discussed in the literature, include Gaussian potentials,¹³ penetrable spheres,⁷ and penetrable square-well (PSW).^{8,9} These potentials are currently of the greatest interest both from a practical point of view, as they mimic ultrasoft systems such as suitable mixtures of colloids and polymers,¹⁴ and theoretically, as they are compatible with a phase transition even in one-dimensional systems (see for instance discussion in Ref. 9).

We have explicitly numerically checked the virial-energy equation within the PSW model defined by the potential^{8,9}

$$\phi(r) = \begin{cases} \epsilon_r, & r < \sigma \\ -\epsilon_a, & \sigma < r < \sigma + \Delta \\ 0, & r > \sigma + \Delta, \end{cases} \quad (13)$$

where σ is the particle diameter, Δ is the width of the well, and ϵ_r and ϵ_a are two positive constants accounting for the repulsive and attractive parts of the potential, respectively. Two particles then attract each other through a square-well potential of depth $-\epsilon_a < 0$ and width Δ , but can also interpenetrate each other with an energy cost $\epsilon_r > 0$. Figure 1 depicts both the virial and the energy equation of state for the

PSW model at a representative state point, as obtained from a numerical solution within the LDH approximation. As expected, we find complete numerical consistency, in agreement with the analytical proof. The compressibility equation of state (not shown) lies slightly below the energy-virial curve. Figure 1 also includes Monte Carlo (MC) data obtained for the same system and state.¹⁵ We observe that at this relatively high temperature the LDH solution provides an accurate equation of state, in agreement with the previous discussion on bounded potentials.

We close this communication with a few remarks. The analytical proof presented here is patterned after a similar proof on the virial-energy consistency within the MSA for a general class of soft potentials which include bounded interactions treated here.⁶ Given the close relationship between MSA and LDH for soft potentials,¹ the result presented here and in Ref. 6 retrospectively can be cast within a unified framework associated with the existence of a scaling form in Fourier space akin to Eq. (8).

Of different nature appears to be the virial-energy consistency within the HNC closure. This is a direct consequence of the existence of an explicit expression for the free energy, pressure, and chemical potential as a result of a *single* approximation, thus increasing internal consistency.^{3,16,17}

On the other hand, the HNC theory can be alternatively viewed as an approximation to the exact diagrammatic expansion of the pair correlation function which retains the complete class of particular diagrams (chains, both simple and netted, and bundles) and the virial-energy consistency can be also regarded as a direct consequence of this.^{2,18} As the full expansion including all diagrams is of course consistent, an additional further consequence is that the class of diagrams not included within the HNC approximation (the so-called elementary diagrams related to the bridge function) must also be consistent from the virial-energy point of view. Our result builds upon this argument by adding the additional piece of information that the full inclusion of simple chain diagrams only also leads to virial-energy consistency. A profound consequence of our result is therefore that the virial-energy consistency is deeply tied to the retention of all diagrams within a given class.¹⁹

The research of A.S. was supported by the Ministerio de Educación y Ciencia (Spain) through Grant No. FIS2007-60977 (partially financed by FEDER funds) and by the Junta de Extremadura through Grant No. GRU09038. The work of

R.F. and A.G. was supported by the Italian MIUR through a grant PRIN-COFIN Contract No. 2007B57EAB(2008/2009). The authors are grateful to D. Henderson and F. Lado for a critical reading of the manuscript.

¹J.-P. Hansen and I. R. McDonald, *Theory of Simple Liquids*, 3rd ed. (Academic, New York, 2006).

²J. A. Barker and D. Henderson, *Rev. Mod. Phys.* **48**, 587 (1976).

³T. Morita, *Prog. Theor. Phys.* **23**, 829 (1960).

⁴A. Santos, *J. Chem. Phys.* **123**, 104102 (2005).

⁵A. Santos, *Mol. Phys.* **104**, 3411 (2006).

⁶A. Santos, *J. Chem. Phys.* **126**, 116101 (2007).

⁷Al. Malijevský, S. B. Yuste, and A. Santos, *Phys. Rev. E* **76**, 021504 (2007).

⁸A. Santos, R. Fantoni, and A. Giacometti, *Phys. Rev. E* **77**, 051206 (2008).

⁹R. Fantoni, A. Giacometti, Al. Malijevský, and A. Santos, *J. Chem. Phys.* **131**, 124106 (2009).

¹⁰This can be quickly established by starting from the definition of the Helmholtz free energy $F=U-TS$ (S being the entropy), so that $P=-(\partial F/\partial V)_{\beta,N}$, $Z=\rho[\partial(\beta F/N)/\partial\rho]_{\beta}$, and $U=[\partial(\beta F)/\partial\beta]_{N,V}$. Equation (3) then follows immediately.

¹¹In the *nonlinear* Debye-Hückel theory, the potential of mean force follows the relation $-\beta[\psi(\mathbf{r})-\phi(\mathbf{r})]=w(\mathbf{r})$, where $\bar{w}(\mathbf{k})$ is still given by Eq. (8). Note that within the LDH approximation, $h(\mathbf{r})=f(\mathbf{r})+w(\mathbf{r})+w(\mathbf{r})/(\mathbf{r})$. Upon dropping the last nonlinear term, using the Ornstein-Zernike relation in k -space, $\bar{h}(\mathbf{k})=\bar{c}(\mathbf{k})/[1-\rho\bar{c}(\mathbf{k})]$, and transforming back to real space, one finds $c(\mathbf{r})=f(\mathbf{r})$. This can be further reduced to the MSA approximation (extended to all \mathbf{r}) $c(\mathbf{r})=-\beta\phi(\mathbf{r})$ for bounded potentials and high temperatures (see below).

¹²Note that the LDH theory was originally devised for Coulomb potential where it is justified for distances larger than the Debye length (and sufficiently high temperatures). For bounded potentials (and again sufficiently high temperatures), the region of reliability is extended to all distances.

¹³B. M. Mladek, G. Kahl, and M. Neumann, *J. Chem. Phys.* **124**, 064503 (2006); See also B. M. Mladek, M. J. Feraud, G. Kahl, and M. Neumann, *Condens Matter Phys.* **8**, 135 (2005).

¹⁴C. N. Likos, *Phys. Rep.* **348**, 267 (2001).

¹⁵The MC data were generated from standard *NVT* simulations of 108 particles with 8×10^6 MC steps (one particle move per step). The pressure was determined from the virial equation through analysis of the pair correlation function at the singularities of the potential.

¹⁶A. G. Schlijper, M. M. Telo de Gama, and P. G. Ferreira, *J. Chem. Phys.* **98**, 1534 (1993).

¹⁷The HNC closure can also be derived from a variational principle (see Ref. 3). The functional evaluated at its extremum is proportional to the excess Helmholtz free energy of the fluid and this ensures thermodynamic consistency between the virial and energy routes. In this context, see W. Olivares and D. A. McQuarrie, *J. Chem. Phys.* **65**, 3604 (1976); R. Fantoni and G. Pastore, *ibid.* **119**, 3810 (2003).

¹⁸R. Balescu, *Equilibrium and Nonequilibrium Statistical Mechanics* (Wiley, New York, 1975).

¹⁹In this respect, note that the Percus-Yevick theory, which retains all linear chains but only a subset of netted chains in the diagrammatic expansion of $y(\mathbf{r})$, yields in general inconsistent energy and virial equations of state.

Part X
2010

Chapter 21

A Numerical Test of a High-Penetrability Approximation for the One-Dimensional Penetrable-Square-Well Model

Fantoni R., Giacometti A., Malijevsky A., and Santos A., J. Chem. Phys. **133**, 024101 (2010)

Title: “A numerical test of a high-penetrability approximation for the one-dimensional penetrable-square-well model.”

Abstract: The one-dimensional penetrable-square-well fluid is studied using both analytical tools and specialized Monte Carlo simulations. The model consists of a penetrable core characterized by a finite repulsive energy combined with a short-range attractive well. This is a many-body one-dimensional problem, lacking an exact analytical solution, for which the usual van Hove theorem on the absence of phase transition does not apply. We determine a high-penetrability approximation complementing a similar low-penetrability approximation presented in previous work. This is shown to be equivalent to the usual Debye-Hückel theory for simple charged fluids for which the virial and energy routes are identical. The internal thermodynamic consistency with the compressibility route and the validity of the approximation in describing the radial distribution function is assessed by a comparison against numerical simulations. The Fisher-Widom line separating the oscillatory and monotonic large-distance behaviors of the radial distribution function is computed within the high-penetrability approximation and compared with the opposite regime, thus providing a strong indication of the location of the line in all possible regimes. The high-penetrability approximation predicts the existence of a critical point and a spinodal line, but this occurs outside the applicability domain of the theory. We investigate the possibility of a fluid-fluid transition by the Gibbs ensemble Monte Carlo techniques, not finding any evidence of such a transition. Additional analytical arguments are given to support this claim. Finally, we find a clustering transition when Ruelle’s stability criterion is not fulfilled. The consequences of these findings on the three-dimensional phase diagrams are also discussed.

THE JOURNAL OF CHEMICAL PHYSICS 133, 024101 (2010)

A numerical test of a high-penetrability approximation for the one-dimensional penetrable-square-well model

Riccardo Fantoni,^{1,a)} Achille Giacometti,^{2,b)} Alexandr Malijevský,^{3,c)} and Andrés Santos^{4,d)}¹National Institute for Theoretical Physics (NITheP), Stellenbosch 7600, South Africa²Dipartimento di Chimica Fisica, Università Ca' Foscari Venezia, Calle Larga S. Marta DD2137, I-30123 Venezia, Italy³E. Hála Laboratory of Thermodynamics, Institute of Chemical Process Fundamentals of the ASCR, v. v. i., 165 02 Prague 6, Czech Republic and Department of Physical Chemistry,

Institute of Chemical Technology, Prague, 166 28 Praha 6, Czech Republic

⁴Departamento de Física, Universidad de Extremadura, E-06071 Badajoz, Spain

(Received 16 April 2010; accepted 28 May 2010; published online 9 July 2010)

The one-dimensional penetrable-square-well fluid is studied using both analytical tools and specialized Monte Carlo simulations. The model consists of a penetrable core characterized by a finite repulsive energy combined with a short-range attractive well. This is a many-body one-dimensional problem, lacking an exact analytical solution, for which the usual van Hove theorem on the absence of phase transition does not apply. We determine a high-penetrability approximation complementing a similar low-penetrability approximation presented in previous work. This is shown to be equivalent to the usual Debye–Hückel theory for simple charged fluids for which the virial and energy routes are identical. The internal thermodynamic consistency with the compressibility route and the validity of the approximation in describing the radial distribution function is assessed by a comparison against numerical simulations. The Fisher–Widom line separating the oscillatory and monotonic large-distance behaviors of the radial distribution function is computed within the high-penetrability approximation and compared with the opposite regime, thus providing a strong indication of the location of the line in all possible regimes. The high-penetrability approximation predicts the existence of a critical point and a spinodal line, but this occurs outside the applicability domain of the theory. We investigate the possibility of a fluid-fluid transition by the Gibbs ensemble Monte Carlo techniques, not finding any evidence of such a transition. Additional analytical arguments are given to support this claim. Finally, we find a clustering transition when Ruelle's stability criterion is not fulfilled. The consequences of these findings on the three-dimensional phase diagrams are also discussed. © 2010 American Institute of Physics. [doi:10.1063/1.3455330]

I. INTRODUCTION

Recent advances in chemical synthesis have unveiled more and more the importance of soft-matter systems, such as dispersions of colloidal particles, polymers, and their combinations. Besides their practical interest, these new developments have opened up new theoretical avenues in (at least) two instances. First, it is possible to experimentally fine-tune the details of interactions (range, strength,...), making these systems a unique laboratory for testing highly simplified models within an effective-interaction approach where the microscopic degrees of freedom are integrated out in favor of renormalized macroparticle interactions. Second, they offer the possibility of exploring new types of equilibrium phase behaviors not present in the simple-fluid paradigm.

As early as in 1989, Marquest and Witten¹ suggested that the experimentally observed crystallization in some copoly-

mer micellar systems could be rationalized on the basis of a bounded interaction, that is, an interaction that does not diverge at the origin. Successive theoretical work showed that this class of bounded or ultrasoft potentials naturally arises as effective interactions between the centers of mass of many soft and flexible macromolecules, such as polymer chains, dendrimers, star polymers, etc. (see, e.g., Ref. 2 for a reference on the subject). Two well-studied cases belonging to the above class are the Gaussian core model (GCM) introduced by Stillinger³ and the penetrable-sphere (PS) model introduced in Refs. 1 and 4, whose freezing transition turns out to display rather exotic features with no analog in the atomistic fluid realm.

In the present paper, we shall consider a close relative of the PS model, first introduced in Ref. 5, denoted as the penetrable-square-well (PSW) model, where a short-range attractive tail is added to the PS model just outside the core region. In the limit of infinite repulsive energy, the PS and PSW models reduce to the usual hard-sphere (HS) and square-well (SW) models, respectively.

An additional interesting feature common to both PS and PSW, as well as to all bounded potentials, is the fact that

^{a)}Electronic mail: rfantoni@ts.infn.it.

^{b)}Electronic mail: achille@unive.it.

^{c)}Electronic mail: a.malijevsky@imperial.ac.uk.

^{d)}Electronic mail: andres@unex.es. URL: <http://www.unex.es/fisteor/andres/>

even when confined to one-dimensional (1D) systems, they may exhibit a nontrivial phase diagram due to the penetrability which prevents an exact analytical solution.

This is because particles cannot be lined up on a line with a well defined and fixed ordering in view of the possibility of reciprocal interpenetration (with some positive energy cost), thus lacking an essential ingredient allowing for an exact solution in the respective hard-core counterparts (HS and SW). It is then particularly useful to discuss some motivated approximations in the 1D model which can then be benchmarked against numerical simulations and subsequently exploited in the much more complex three-dimensional (3D) case.

The aim of the present paper is to complete a study on the 1D PSW model started in Refs. 5 and 6, as well as the general results presented in Ref. 5, which are particularly relevant in the present context. In the first paper of the series,⁵ we introduced the model and discussed the range of stability in terms of the attractive versus repulsive energy scale. We provided, in addition, exact analytical results in the low-density limit [second order in the radial distribution function (RDF) and fourth order in the virial expansion] and a detailed study of the Percus–Yevick and hypernetted-chain integral equations. These were used in the following paper⁶ to propose a low-penetrability approximation (LPA) at finite density which was then tested against numerical simulation. This LPA is expected to break down in the opposite regime, namely, when temperatures and densities are such that particles easily interpenetrate each other. In the present paper, we address this latter regime by proposing a complementary approximation [the high-penetrability approximation (HPA)] and discussing its range of validity and the relationship with the low-penetrability regime. Note that a similar matching of the LPA and HPA has already been carried out by two of the present authors in the framework of the PS model.^{7,8} It turns out that the HPA in the context of bounded potentials coincides with the linearized Debye–Hückel (LDH) classical approximation originally introduced in the framework of the Coulomb potential.⁹ It has been recently shown¹⁰ that two of the three standard routes to thermodynamics (the energy and the virial routes) are automatically consistent within the LDH approximation, for any potential and dimensionality. This means that a deviation from the third standard route to thermodynamics (the compressibility route) can be exploited to assess the degree of reliability of the high-penetrability (or LDH) approximation. This is indeed discussed in the present paper, where we also discuss the full hierarchy of approximations ranging from the full Debye–Hückel approximation to the simplest mean-spherical approximation (MSA).

In view of the boundedness of the potential, the usual van Hove no-go theorem^{11,12} on the absence of phase transitions in certain 1D fluids does not hold. It is then natural to ask whether a phase transition occurs in the 1D PSW fluid by noting that the addition of an attractive tail to the pair potential of the PS model extends the question to the fluid–fluid transition, in addition to the fluid–solid transition possible even within the PS model. In the present paper we confine our attention to the fluid–fluid case only and discuss this possibility using both analytical arguments and state-of-the-

art numerical simulations.^{13–16} Our results are compatible with the absence of such a transition, as we shall discuss. This is also supported by recent analytical results¹⁷ using a methodology devised for 1D models with long-range interactions.¹⁸ We discuss possible reasons for this and a plausible scenario for the 3D case.

Finally, we note that the approach to a critical point is frequently anticipated by the so-called Fisher–Widom (FW) line¹⁹ marking the borderline between a region with oscillatory behavior in the long-range domain of the correlation function (above the FW line) and a region of exponential decay. We discuss the location of this line within the HPA and again the matching of this result with that stemming from the LPA.

The structure of this paper is as follows. We define the PSW model in Sec. II. We then construct the HPA in Sec. III and in Sec. IV we discuss some approximations related to it. Section V contains a discussion on the routes to thermodynamics, as predicted by the HPA. The structure predicted by the approximation is compared with the Monte Carlo (MC) data in Sec. VI. The FW line and the possibility of a fluid–fluid transition are discussed in Sec. VII. The paper ends with some concluding remarks in Sec. VIII.

II. THE PSW MODEL

The PSW model is defined by the following pair potential:^{5,6}

$$\phi_{\text{PSW}}(r) = \begin{cases} +\epsilon_r, & r < \sigma \\ -\epsilon_a, & \sigma < r < \sigma + \Delta \\ 0, & r > \sigma + \Delta, \end{cases} \quad (2.1)$$

where Δ is the well width and ϵ_r and ϵ_a are two positive constants accounting for the repulsive and attractive parts of the potential, respectively. In the following, we shall restrict our analysis to the case $\Delta/\sigma < 1$ and $\epsilon_r > 2\epsilon_a$, where we know the 1D model to be stable with a well defined thermodynamic limit.⁵ It is shown in Appendix A that more generally, the 1D PSW model is guaranteed to be stable if $\epsilon_r > 2(\ell+1)\epsilon_a$, where ℓ is the integer part of Δ/σ . For lower values of ϵ_r , the model may or may not be stable and we will come back to this point in Sec. VII.

An important role in the following is played by the corresponding Mayer function:

$$f_{\text{PSW}}(r) = \gamma_r f_{\text{HS}}(r) + \gamma_a [\Theta(r - \sigma) - \Theta(r - \sigma - \Delta)], \quad (2.2)$$

where $\gamma_r = 1 - e^{-\beta\epsilon_r}$ is the parameter measuring the degree of penetrability varying between 0 (free penetrability) and 1 (impenetrability), while $\gamma_a = e^{\beta\epsilon_a} - 1 > 0$ measures the strength of the well depth. Here $\beta = 1/k_B T$ with T as the temperature and k_B as the Boltzmann constant, $f_{\text{HS}}(r) = -\Theta(\sigma - r)$ is the Mayer function for HSs and $\Theta(r)$ is the Heaviside step function.

A detailed discussion of the limiting cases of the PSW model can be found in Ref. 5. Here we merely note that the PSW Mayer function $f_{\text{PSW}}(r)$ is immediately related to the usual SW Mayer function by

$$f_{\text{PSW}}(r) = \gamma_r f_{\text{SW}}(r), \quad (2.3)$$

$$f_{\text{SW}}(r) = f_{\text{HS}}(r) + \gamma[\Theta(r - \sigma) - \Theta(r - \sigma - \Delta)], \quad (2.4)$$

where we have introduced the ratio $\gamma = \gamma_a / \gamma_r$. At a given value of ϵ_r / ϵ_a , γ increases quasilinearly with $e^{\beta\epsilon_a}$, its minimum value $\gamma = \epsilon_a / \epsilon_r$, corresponding to $\beta\epsilon_a \rightarrow 0$.

III. THE HPA

In Ref. 6 we discussed a LPA to the PSW model. Within this approximation, one assumes $1 - \gamma_r = e^{-\beta\epsilon_r} \ll 1$ so that the repulsive barrier ϵ_r is sufficiently higher than the thermal energy $k_B T$, penetrability is small, and the system is almost a hard-core one. The advantage of this theoretical scheme is that one can use the general recipe leading to the exact solution for the 1D SW problem—in fact, valid for any potential with a hard-core and short-range attractions—and perform some *ad hoc* adjustments to ensure that some basic physical conditions on the RDF $g(r)$ are satisfied. Comparison with MC simulations showed a good behavior of the LPA even for $\beta\epsilon_r = 2$ ($1 - \gamma_r \approx 0.14$), provided the density was moderate ($\rho\sigma < 0.5$).

The opposite limit $\gamma_r \ll 1$ is also inherently interesting for several reasons. From a physical viewpoint this amounts to starting from the ideal gas limit $\gamma_r \rightarrow 0$ (one of the common reference systems for simple fluids) and progressively building up interactions by increasing γ_r . An additional mathematical advantage stems from the simple observation^{7,8,20} that in the (exact) cluster expansion of $g(r)$ only the dominant chain diagrams need to be retained at all orders, thus leading to the possibility of an exact summation of those leading contributions. As we shall see shortly, this is in fact a procedure known as the Debye–Hückel approximation in the context of charged fluids.^{9,10}

Our main goal is the computation of the cavity function $y(r) \equiv e^{\beta\phi(r)}g(r)$, from which one can immediately compute the RDF $g(r) = y(r)[1 + f(r)]$. In the PSW case one then has from Eq. (2.3),

$$g(r) = \begin{cases} (1 - \gamma_r)y(r), & r < 1 \\ (1 + \gamma_a)y(r), & 1 < r < \lambda \\ y(r), & r > \lambda, \end{cases} \quad (3.1)$$

where $\lambda = 1 + \Delta$ and, in conformity with previous work,^{5,6} we have redefined all lengths in units of σ so we set $\sigma = 1$ in most of the following equations.

As shown in Ref. 20 for the PS case, the exact form of the PSW cavity function in the limit $\gamma_r \rightarrow 0$ at finite $\gamma = \gamma_a / \gamma_r$ and $\rho\gamma_r$ is

$$y(r) = 1 + \gamma_r w(r), \quad (3.2)$$

where the function $w(r)$ is defined through its Fourier transform

$$\tilde{w}(k) = \rho\gamma_r \frac{\tilde{f}_{\text{SW}}^2(k)}{1 - \rho\gamma_r \tilde{f}_{\text{SW}}(k)}, \quad (3.3)$$

with $\tilde{f}_{\text{SW}}(k)$ being the Fourier transform of $f_{\text{SW}}(r)$. Note that in the limit $\gamma_r \rightarrow 0$ one has $\gamma_r \approx \beta\epsilon_r$ and $\gamma \approx \epsilon_a / \epsilon_r$.

Generalizing an analogous approximation in the context of the PS model,^{7,8} our HPA consists of assuming Eqs. (3.2)

and (3.3) for finite, but small, values of γ_r . It is worth noting that the combination of expressions (3.2) and (3.3) defines what is usually referred to, in a different context, as the LDH approximation,^{9,10} and this will be further elaborated below.

Equations (3.2) and (3.3) hold for any dimensionality. In the specific 1D case, and taking into account Eq. (2.4), we have

$$\begin{aligned} \tilde{f}_{\text{SW}}(k) &= 2 \int_0^\infty dr \cos(kr) f_{\text{SW}}(r) \\ &= -\frac{2}{k} [(1 + \gamma) \sin k - \gamma \sin \lambda k]. \end{aligned} \quad (3.4)$$

The function $w(r)$ can be numerically evaluated in real space by the Fourier inversion as

$$w(r) = \frac{\rho\gamma_r}{\pi} \int_0^\infty dk \cos(kr) \frac{\tilde{f}_{\text{SW}}^2(k)}{1 - \rho\gamma_r \tilde{f}_{\text{SW}}(k)}. \quad (3.5)$$

An explicit expression for the density expansion of $w(r)$ within the HPA is reported in Eqs. (B7) and (B8) of Appendix B, where the radius of convergence of the expansion is also analyzed.

From Eqs. (2.3), (3.1), and (3.2) the total correlation function, $h(r) = g(r) - 1$, within the HPA is easily obtained as

$$h(r) = \gamma_r w(r) [1 + \gamma_r f_{\text{SW}}(r)] + \gamma_r f_{\text{SW}}(r) \quad (3.6)$$

or in the Fourier space,

$$\tilde{h}(k) = \gamma_r \frac{\tilde{f}_{\text{SW}}(k)}{1 - \rho\gamma_r \tilde{f}_{\text{SW}}(k)} + \rho\gamma_r^3 \int_{-\infty}^\infty \frac{dk'}{2\pi} \frac{\tilde{f}_{\text{SW}}^2(k') \tilde{f}_{\text{SW}}(|k - k'|)}{1 - \rho\gamma_r \tilde{f}_{\text{SW}}(k')}. \quad (3.7)$$

From this equation it is straightforward to get the structure factor

$$\begin{aligned} S(k) = 1 + \rho\tilde{h}(k) &= \frac{1}{1 - \rho\gamma_r \tilde{f}_{\text{SW}}(k)} \\ &+ \rho^2 \gamma_r^3 \int_{-\infty}^\infty \frac{dk'}{2\pi} \frac{\tilde{f}_{\text{SW}}^2(k') \tilde{f}_{\text{SW}}(|k - k'|)}{1 - \rho\gamma_r \tilde{f}_{\text{SW}}(k')} \end{aligned} \quad (3.8)$$

and the Fourier transform of the direct correlation function $\tilde{c}(k) = \tilde{h}(k) / S(k)$. The zero wavenumber value of the structure factor is

$$S(0) = \frac{1}{1 + 2\rho\gamma_r(1 - \gamma\Delta)} + \rho^2 \gamma_r^3 \int_0^\infty \frac{dk}{\pi} \frac{\tilde{f}_{\text{SW}}^3(k)}{1 - \rho\gamma_r \tilde{f}_{\text{SW}}(k)}, \quad (3.9)$$

where we have taken into account that $\tilde{f}_{\text{SW}}(0) = -2(1 - \gamma\Delta)$. This completes the calculation of the correlation functions within the HPA.

IV. APPROXIMATIONS RELATED TO THE HPA

As anticipated in Sec. III, the HPA is the exact equivalent to the well-known LDH approximation, which is widely

used in the context of charged simple fluids.⁹ The latter is actually an intermediate step of a hierarchy of successive approximations ranging from the simplest MSA to the full nonlinear version of the Debye–Hückel approximation (see Ref. 11 in Ref. 10 for a discussion on this point). For the PSW model—and more generally for any bounded potential—the LDH approximation (the HPA in the present language) is particularly relevant in view of the fact that one can make $f_{\text{PSW}}(r)$ arbitrarily small by letting $\gamma_r \rightarrow 0$, thus justifying the approximation of neglecting nonchain diagrams. It is then interesting to check the performance of the other approximations included in the aforementioned class, which will be translated in the present context for simplicity.

On top of the hierarchy of approximations there is the nonlinear HPA (nlHPA)

$$y(r) = e^{\gamma_r w(r)}, \quad (4.1)$$

which is equivalent to the nonlinear Debye–Hückel approximation, as remarked. The HPA, Eq. (3.2), is obtained upon linearizing the exponential, an approximation valid again in the limit $\gamma_r \ll 1$. An additional approximation—denoted here as the modified HPA (mHPA)—can be considered with the help of Eq. (3.6) by neglecting the quadratic term in γ_r . This yields

$$h(r) = \gamma_r [w(r) + f_{\text{SW}}(r)]. \quad (4.2)$$

This is equivalent to keeping only the first term on the right-hand side of Eq. (3.7), which implies $\tilde{c}(k) = \gamma_r \tilde{f}_{\text{SW}}(k)$ or, in real space,

$$c(r) = f_{\text{PSW}}(r). \quad (4.3)$$

The lowest rank in the hierarchy is occupied by the MSA, which is obtained from Eq. (4.3) upon linearization of the Mayer function $f_{\text{PSW}}(r)$,

$$c(r) = -\beta \phi_{\text{PSW}}(r). \quad (4.4)$$

Since $w(r)$ is a convolution, it must be continuous at $r = 1$ and $r = \lambda$. It follows that the approximations with a continuous cavity function at $r = 1$ and $r = \lambda$ are nlHPA and HPA. For instance, in mHPA (4.2) the cavity function is $y(r) = 1 + \gamma_r w(r) / [1 + \gamma_r f_{\text{SW}}(r)]$ so that one has $y(1^-) - y(1^+) = \gamma_r^2 w(1)(1 + \gamma)(1 - \gamma_r)^{-1}(1 + \gamma \gamma_r)^{-1}$ and $y(\lambda^+) - y(\lambda^-) = \gamma_r^2 w(\lambda) \gamma (1 + \gamma \gamma_r)^{-1}$.

It has been shown in Ref. 10 that the virial and energy routes to thermodynamics (to be discussed below) are consistent with one another within the HPA, for any potential and any dimensionality. A similar statement holds true for soft potentials within the MSA.²¹ This clearly includes the PSW potential in both cases.

It is interesting to make contact with previous work carried out by Likos *et al.*^{22,23} on a general class of unbounded potentials which are free of attractive parts, thus resulting particularly useful in the context of the fluid-solid transition. In Ref. 22, the MSA given in Eq. (4.4) along with the spinodal instability to be discussed in detail in Sec. VII, has been introduced for a general class of unbounded potentials including the PS as a particular case. This has been further elaborated and extended to include the GCM in Ref. 23. In both cases, the authors discuss directly the 3D case so that a

direct comparison with the present work cannot be drawn at the present stage, but they also provide a detailed discussion of various approximations, within the general framework of density functional theory, that provides a unified framework where even the present model could be included.

V. EQUATION OF STATE

Given an approximate solution of a fluid model there are several routes to the equation of state which, in general, give different results. The most common are three:⁹ the virial, the compressibility, and the energy route. The consistency of the outcome of these different routes can be regarded as an assessment on the soundness of the approximation. For some particular approximations it may also happen that the consistency of two of the three routes is automatically enforced (see Ref. 10 and references therein for a detailed discussion on this point). This is the case of the HPA, where the virial and energy routes coincide, as anticipated. Hence, the consistency with the compressibility route will provide a rough estimate of the regime of validity of the HPA within a phase diagram for the PSW potential.

Let us briefly recall⁹ the methods to compute the compressibility factor, $Z = \beta p / \rho$, associated with the three different routes. The virial route is defined by

$$Z = 1 - \rho \beta \int_0^\infty dr r y(r) e^{-\beta \phi(r)} \phi'(r), \quad (5.1)$$

which, using standard manipulations,⁹ yields

$$Z = 1 + \rho \gamma_r [(1 + \gamma)y(1) - \gamma \lambda y(\lambda)]. \quad (5.2)$$

Thus the problem is reduced to the computation of the cavity function $y(r)$ which, in the present context, follows from Eqs. (3.2) and (3.5).

Next, we consider the compressibility route,

$$Z = \frac{1}{\rho} \int_0^\rho \frac{d\rho'}{S(0)}, \quad (5.3)$$

where the integral can be readily evaluated with the help of Eq. (3.9).

Regarding the energy route, we start from the internal energy per particle

$$u = \frac{1}{2\beta} + \rho \int_0^\infty dr \phi(r) g(r), \quad (5.4)$$

which yields

$$u = \frac{1}{2\beta} + \epsilon_r (1 - \gamma_r) \rho \int_0^1 dr y(r) - \epsilon_a (1 + \gamma_a) \rho \int_1^\lambda dr y(r). \quad (5.5)$$

In the above equation, the expressions given by Eqs. (2.1) and (3.1) have been used. In order to obtain βp from u we exploit the following standard thermodynamic identity:¹⁰

$$\rho^2 \left(\frac{\partial u}{\partial \rho} \right)_\beta = \left(\frac{\partial \beta p}{\partial \beta} \right)_\rho, \quad (5.6)$$

thus leading to

024101-5 HPA for penetrable-square-well model

J. Chem. Phys. **133**, 024101 (2010)

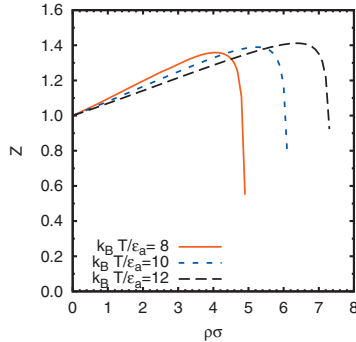


FIG. 1. Plot of the compressibility factor $Z = \beta p / \rho$ as computed from the virial (-energy) route to the pressure for $\epsilon_r / \epsilon_a = 2$ and $\Delta / \sigma = 1$. Results for three different reduced temperatures $k_B T / \epsilon_a = 8, 10, 12$ are displayed.

$$Z = 1 + \rho \int_0^\beta d\beta' \left(\frac{\partial u}{\partial \rho} \right)_{\beta'}. \quad (5.7)$$

We have used the exact consistency between the virial and energy routes within the HPA as a test of the numerical calculations.

Figure 1 depicts the results of the virial—and hence energy, as remarked—route under the condition $\epsilon_r / \epsilon_a = 2$, which constitutes the borderline range of stability of the 1D PSW model with $\Delta / \sigma < 1$.⁵ Under this demanding condition, we have considered three reduced temperatures from $k_B T / \epsilon_a = 8$ to $k_B T / \epsilon_a = 12$, whereas the width of the well has been fixed to the value $\Delta / \sigma = 1$. We remark that $\rho \sigma$ is not limited in values from above due to the boundness of the potential. The clear downturn of all three curves for sufficiently large reduced density $\rho \sigma$ is a consequence of the existence of a maximum density ρ_{\max} [see Eq. (B10)], beyond which the HPA breaks down, as described at the end of Appendix B. In particular, the values of the maximum density for $\epsilon_r / \epsilon_a = 2$ and $\Delta / \sigma = 1$ are $\rho_{\max} \sigma = 4.94, 6.15,$ and 7.36 at $k_B T / \epsilon_a = 8, 10,$ and 12 , respectively, in agreement with Fig. 1.

We compare in Fig. 2 the results from the virial (-energy) and the compressibility routes with MC simulations²⁴ for an intermediate value of the reduced temperature ($k_B T / \epsilon_a = 10$) and other parameters as before. Rather interestingly, the virial (-energy) route appears to reproduce rather well the numerical simulation results up to the region where the artificial downward behavior shows up, whereas the compressibility route begins to deviate for densities $\rho \sigma > 3$.

As the temperature increases the HPA theory clearly remains a good approximation for a larger range of densities. We can naturally measure this by the requirement that virial (-energy) and compressibility routes are consistent within a few percent. This is indeed shown in Fig. 3, where we depict a transition line separating a “reliable” from an “unreliable” regime, as measured by the relative deviation of the two routes (here taken to be 5%), for four choices of the model parameters: $(\epsilon_r / \epsilon_a, \Delta / \sigma) = (2, 1), (2, 0.5), (5, 1),$ and $(5, 0.5)$. The value $\Delta / \sigma = 0.5$ is frequently used in the SW

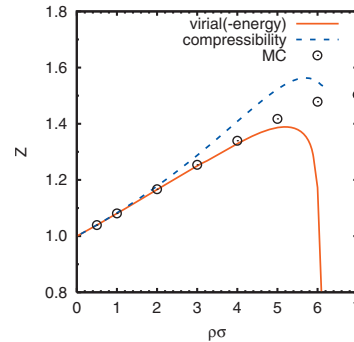


FIG. 2. Comparison between the compressibility factor $Z = \beta p / \sigma$ from the virial (-energy) and the compressibility route to the pressure. The circles represent MC simulation results. Chosen parameters are $\epsilon_r / \epsilon_a = 2, \Delta / \sigma = 1,$ and $k_B T / \epsilon_a = 10$.

counterpart.²⁵ We observe that the region $0 \leq \rho \leq \rho_{\text{lim}}(T)$ where the HPA is reliable is hardly dependent on Δ / σ [compare curves (a), (b) for $\epsilon_r / \epsilon_a = 5$ and (c), (d) for $\epsilon_r / \epsilon_a = 2$ in Fig. 3]. On the other hand, at given values of Δ / σ and $k_B T / \epsilon_a$, the range $0 \leq \rho \leq \rho_{\text{lim}}(T)$ decreases with increasing ϵ_r / ϵ_a [compare curves (a), (d) for $\Delta / \sigma = 0.5$ and (b), (c) for $\Delta / \sigma = 1$ in Fig. 3], as expected. However, this effect is much less important if the increase of ϵ_r / ϵ_a takes place at fixed $k_B T / \epsilon_r$ (see inset of Fig. 3). It is interesting to note that as illustrated in Fig. 2, the HPA virial route keeps being reliable up to a certain density higher than ρ_{lim} .

As said above, in Ref. 6 we introduced a LPA that was accurate for states where the penetrability effects were low or moderate. The LPA is complemented by the HPA presented in this paper. It is then interesting to compare the regions where each approximation can be considered reliable according to the same criterion as in Fig. 3. This is shown in

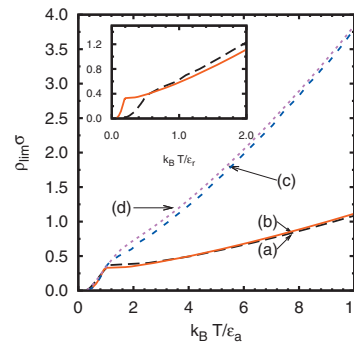


FIG. 3. Rough estimate of the region of reliability for the HPA, on the basis of the consistency between the virial (-energy) and compressibility routes, in the reduced density $\rho \sigma$ vs reduced temperature $k_B T / \epsilon_a$ plane. Here the curves (a)–(d) correspond to $(\epsilon_r / \epsilon_a, \Delta / \sigma) = (5, 0.5), (5, 1), (2, 1),$ and $(2, 0.5)$, respectively. The region below each curve represents states where the relative deviation between the virial (-energy) route and the compressibility one is smaller than 5% and hence regarded as reliable. The inset shows the curves in the $\rho \sigma$ vs $k_B T / \epsilon_r$ plane for $(\epsilon_r / \epsilon_a, \Delta / \sigma) = (2, 1)$ (dashed line) and $(5, 1)$ (solid line).

024101-6 Fantoni *et al.*

J. Chem. Phys. **133**, 024101 (2010)

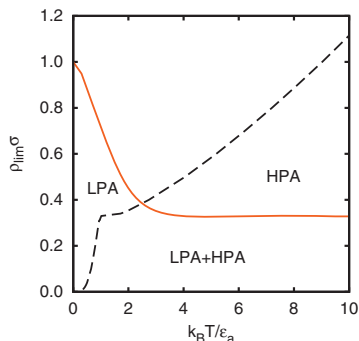


FIG. 4. Regions of reliability for the LPA and the HPA in the reduced density $\rho\sigma$ vs reduced temperature $k_B T/\epsilon_a$ plane. Here $\epsilon_r/\epsilon_a=5$ and $\Delta/\sigma=1$. The labels LPA, HPA, and LPA+HPA indicate the regions where only the LPA, only the HPA, or both approximations are reliable, respectively.

Fig. 4 for the case $\epsilon_r/\epsilon_a=5$ and $\Delta/\sigma=1$. The two transition lines split the plane into four regions: a region where only the LPA is reliable, a region where only the HPA is reliable, a region where both approximations are reliable (and provide equivalent results), and a region where none of them is sufficiently good. The latter region shrinks as ϵ_r/ϵ_a decreases (thanks to the HPA) or Δ/σ decreases (thanks to the LPA).

VI. STRUCTURE

As an additional test of the soundness of the HPA, we also study the RDF $g(r)=h(r)+1$, which can easily be obtained from Eqs. (3.1) and (3.2), or equivalently from Eq. (3.6), once the auxiliary function $w(r)$ has been determined. For a sufficiently high temperature (and hence high penetrability), the HPA is clearly well performing, as can be inferred from Fig. 5, when compared with standard NVT MC results. Here we have considered the same parameters as in the preceding section ($\epsilon_r/\epsilon_a=2$ and $\Delta/\sigma=1$) at a corresponding high-temperature value $k_B T/\epsilon_a=10$ and a density $\rho\sigma=1.5$, where overlappings are unavoidable. Under these conditions, there is no visible difference among the various approximations considered in Sec. IV. The excellent performance of the

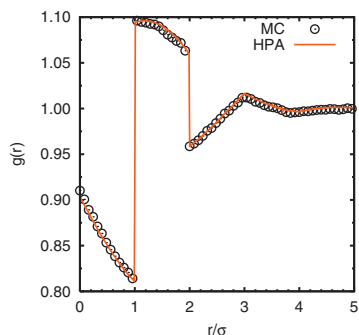


FIG. 5. Results for the RDF $g(r)$ as a function of r/σ with $\epsilon_r/\epsilon_a=2$, $\Delta/\sigma=1$, $k_B T/\epsilon_a=10$, and $\rho\sigma=1.5$. Predictions from the HPA (solid line) are compared with MC results (circles).

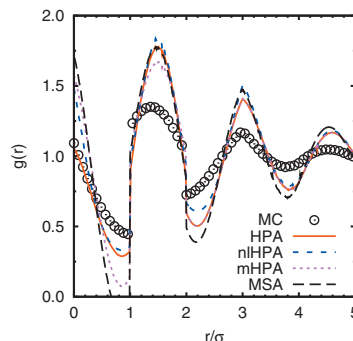
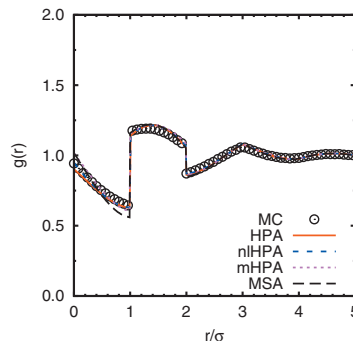


FIG. 6. Comparison of different approximations in the results for the RDF $g(r)$ vs r/σ . Chosen parameters are $\epsilon_r/\epsilon_a=2$, $\Delta/\sigma=1$, and $\rho\sigma=1.5$. MC results (circles) are compared with the HPA (solid line), the nlHPA (dashed line), the mHPA (short dashed line), and the MSA (long dashed line). The two different panels refer to different reduced temperatures: $k_B T/\epsilon_a=5$ (top panel) and $k_B T/\epsilon_a=3$ (bottom panel). Note that both panels are drawn within the same scale.

HPA observed in Fig. 5 agrees with the reliability criterion of Fig. 3 since the state $k_B T/\epsilon_a=10$ and $\rho\sigma=1.5$ is well below the curve (c) corresponding to $\epsilon_r/\epsilon_a=2$ and $\Delta/\sigma=1$.

As we cool down, significant differences among various approximations (HPA, nlHPA, mHPA, and MSA) begin to appear, as depicted in Fig. 6, where results corresponding to temperatures $k_B T/\epsilon_a=5$ (top panel) and $k_B T/\epsilon_a=3$ (bottom panel) are reported within the same scale. The states $k_B T/\epsilon_a=5$ and $\rho\sigma=1.5$ are still lying in the reliable region of Fig. 3, but close to the boundary line (c), while the states $k_B T/\epsilon_a=3$ and $\rho\sigma=1.5$ are clearly outside that region. In the case $k_B T/\epsilon_a=5$ the HPA and its three variants are practically indistinguishable, except in the region $0 < r < \sigma$, which is very important to describe the correct thermodynamic behavior, where the best agreement with MC data corresponds to the nlHPA, followed by the HPA. The two approximations that do not preserve the continuity of the cavity functions (mHPA and MSA) overestimate the jump at $r=\sigma$. In the lower temperature case $k_B T/\epsilon_a=3$ all the approximations overestimate the oscillations of the RDF. Interestingly, the HPA captures quite well the values of $g(r)$ near the origin. The worst overall behavior corresponds again to the MSA, which even predicts negative values of $g(r)$ for $r/\sigma \leq 1$.

024101-7 HPA for penetrable-square-well model

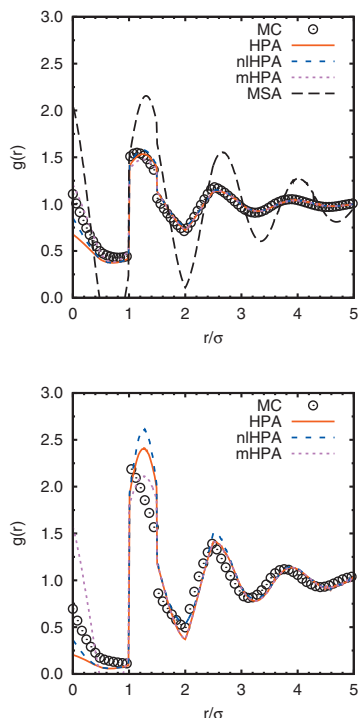
J. Chem. Phys. **133**, 024101 (2010)


FIG. 7. An additional comparison of different approximations in the results for the RDF $g(r)$ vs r/σ . Here fixed parameters are $\epsilon_r/\epsilon_a=5$ and $\Delta/\sigma=0.5$. MC results (circles) are compared with the HPA (solid line), the nHPA (dashed line), the mHPA (short dashed line), and the MSA (long dashed line). The top panel refers to the state $k_B T/\epsilon_a=5$ and $\rho\sigma=1.5$, whereas the bottom panel refers to $k_B T/\epsilon_a=2$ and $\rho\sigma=0.8$. In the bottom panel the MSA is not depicted. Again both panels are on the same scale.

Additional insights can be obtained by decreasing the range of interactions, in close analogy with what we considered in previous work for the complementary LPA.⁶ This is reported in Fig. 7 for cases $\epsilon_r/\epsilon_a=5$ and $\Delta/\sigma=0.5$ with $(k_B T/\epsilon_a, \rho\sigma)=(5, 1.5)$ (top panel) and $(k_B T/\epsilon_a, \rho\sigma)=(2, 0.8)$ (bottom panel). Again we stress that the same scale is used for both panels in order to emphasize the effect of lowering the temperature. Clearly this is a more demanding situation. In fact, both states are above curve (a) of Fig. 3 and thus outside the corresponding reliability region. Therefore, clear deviations from MC results appear in all considered approximations, especially in the lower temperature case $k_B T/\epsilon_a=2$ (bottom panel). Yet, the HPA is still a reasonably good approximation that follows the main qualitative features of the correct $g(r)$. In the higher temperature case $k_B T/\epsilon_a=5$ the only noticeable limitations of the HPA practically take place near the origin, this deficiency being largely corrected by the mHPA.

To conclude this section, it is worthwhile comparing the two complementary approaches HPA and LPA at a case where both are expected to be reliable, according to the diagram of Fig. 4. This is done in Fig. 8 for $\epsilon_r/\epsilon_a=5$, $\Delta/\sigma=1$, $k_B T/\epsilon_a=2$, and $\rho\sigma=0.2$. We observe that both approxima-

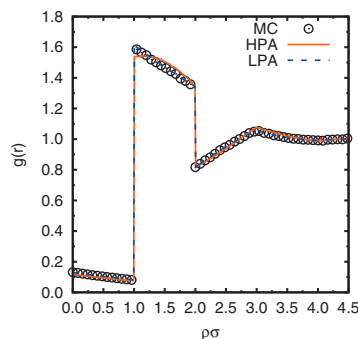


FIG. 8. Comparison of different approximations in the results for the RDF $g(r)$ vs r/σ . Chosen parameters are $\epsilon_r/\epsilon_a=5$, $\Delta/\sigma=1$, $k_B T/\epsilon_a=2$, and $\rho\sigma=0.2$. MC results (circles) are compared with the HPA (solid line) and the LPA (dashed line).

tions agree well each other and with MC data, except in the region $1 < r/\sigma < \Delta/\sigma$, where the HPA RDF presents an artificial curvature.

VII. FW LINE AND FLUID-FLUID TRANSITION

We now turn to an interesting point raised in previous work,⁶ namely, the question of whether the model can display a phase transition in spite of its 1D character. The existence of general theorems—all essentially based on the original van Hove's result¹¹—on the absence of phase transitions for a large class of 1D models with short-range interactions is well established.¹² PSW and PS models, however, do not belong to the class for which these general theorems hold. This is because boundness allows multiple, partial (or even total) overlapping at some energy cost, thus rendering the arguments used in the aforementioned theorems invalid.

On the other hand, none of these theorems provide a general guideline to understand whether a 1D model may or may not display a nontrivial phase transition, and one has then to rely on the specificity of each model. As discussed in our previous work,⁶ it is instructive to first address the simpler question of the location of the FW line. This is a line separating two different regimes for the large-distance behavior of the RDF $g(r)$ in the presence of competing repulsive/attractive interactions.¹⁹ The rationale behind the FW line is that on approaching the critical points where attractions become more and more effective, the behavior of correlation functions must switch from oscillatory (characteristic of repulsive interactions) to exponential with a well defined correlation length ξ . In the previous work, we analyzed the location of this line for PSW within the LPA. Here we extend this analysis to the HPA regime and discuss the compatibility of the two results.

Let us first briefly recall the main points of the analysis, referring to Ref. 6 for details. From Eq. (3.1) we note that the asymptotic behavior of $g(r)$ is the same as that of $y(r)$. In view of Eq. (3.2), this is hence related to $w(r)$, whose asymptotic behavior is governed by the pair of conjugate

024101-8 Fantoni *et al.*

J. Chem. Phys. **133**, 024101 (2010)

poles of $\tilde{w}(k)$ with an imaginary part closest to the origin. If the real part of the pair is zero, the decay is monotonic and oscillatory otherwise.

According to Eq. (3.3), the poles of $\tilde{w}(k)$ are given by

$$\rho\gamma_f\tilde{w}(k) = 1. \quad (7.1)$$

Let $k = \pm ix$ be the imaginary pole and $k = \pm i(x' \pm iy)$ be the pole with the imaginary part closest to the origin. The FW line is determined by the condition $x=x'$. This gives, at a given temperature, three equations in the three unknowns— x , y , and ρ .⁶ More specifically, after some algebra, one gets

$$\begin{aligned} \frac{y}{x} \sinh x \sinh(\lambda x) [\cos y - \cos(\lambda y)] \\ = \sinh x \cosh(\lambda x) \sin(\lambda y) (\cos y - 1) \\ - \sinh(\lambda x) \cosh x \sin y [\cos(\lambda y) - 1], \end{aligned} \quad (7.2)$$

$$\gamma = \left[\frac{\sinh(\lambda x) \cos(\lambda y) - 1}{\sinh x \cos y - 1} - 1 \right]^{-1}, \quad (7.3)$$

$$\rho = \frac{1}{2\gamma_f \gamma \sinh(\lambda x) - (1 + \gamma) \sinh x}. \quad (7.4)$$

The inverse of the parameter x represents the correlation length $\xi = 1/x$. From a practical point of view it is more convenient to use x rather than $k_B T / \epsilon_a$ as a free parameter to construct the FW line. In that way, Eq. (7.2) becomes a transcendental equation that gives y as a function of x ; once $y(x)$ is known, the solution to Eq. (7.3) gives $k_B T / \epsilon_a$ as a function of x ; finally, insertion of $y(x)$ and $k_B T(x) / \epsilon_a$ into Eq. (7.4) provides $\rho(x)$. The corresponding values of the pressure are obtained from either Eq. (5.2) (virial-energy route) or Eq. (5.3) (compressibility route).

We observe that T decreases as x decreases, until a critical value T_c is found in the limit $x \rightarrow 0$. In that limit, Eqs. (7.2)–(7.4) simplify to

$$\begin{aligned} \lambda y_c [\cos y_c - \cos(\lambda y_c)] \\ = \sin(\lambda y_c) (\cos y_c - 1) - \lambda \sin y_c [\cos(\lambda y_c) - 1], \end{aligned} \quad (7.5)$$

$$\gamma_c = \left[\lambda \frac{\cos(\lambda y_c) - 1}{\cos y_c - 1} - 1 \right]^{-1}, \quad (7.6)$$

$$\rho_c = \frac{1}{2\gamma_f \gamma_c \Delta - 1}. \quad (7.7)$$

At the critical point $(T, \rho) = (T_c, \rho_c)$, one has $x=0$ or, equivalently, $\xi \rightarrow \infty$. Therefore, at this point $w(r)$ does not decay for long distances and in the Fourier space one has $\tilde{w}(k) \sim k^{-2}$ and $S(k) \sim k^{-2}$ for short wave numbers. The condition $S(k) \sim k^{-2}$ is also satisfied for $T < T_c$ if $\rho\sigma = [2\gamma_f(\gamma\Delta/\sigma - 1)]^{-1}$, in agreement with Eq. (3.9). This defines in the ρ - T plane a spinodal line or locus of points of infinite isothermal compressibility (within the compressibility route). The spinodal line cannot be extended to temperatures larger than the critical value T_c because $[2\gamma_f(\gamma\Delta/\sigma - 1)]^{-1} \geq \rho_{\max}\sigma$ if $T \geq T_c$,

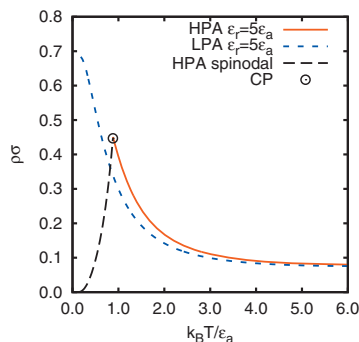
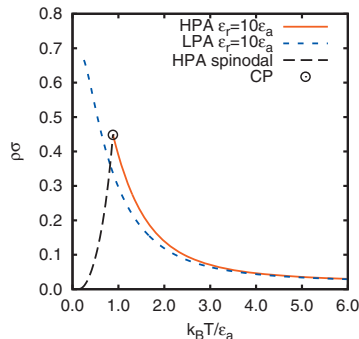


FIG. 9. Plot of the FW transition line in the $\rho\sigma$ vs $k_B T / \epsilon_a$ plane with $\Delta/\sigma=1$ and $\epsilon_r/\epsilon_a=10$ (top panel) and $\epsilon_r/\epsilon_a=5$ (bottom panel). The long dashed curves are the spinodal lines predicted by the HPA. The FW and spinodal lines meet at the critical point (denoted by a circle).

where ρ_{\max} is the maximum density beyond which the HPA is unphysical at a given temperature (see Appendix B). We further note that the spinodal line only has a lower density (or vaporlike) branch, thus hampering the interpretation of (T_c, ρ_c) as a conventional critical point.

The above features are already suggestive of considering the HPA spinodal line as an artifact of the theory when used in a region of parameter space where the approximation is invalid. Additional support to this view stems from the fact that the HPA keeps predicting a spinodal line and a critical point even in the SW case ($\epsilon_r/\epsilon_a \rightarrow \infty$ and $\gamma_f \rightarrow 1$), a clearly incorrect feature. As we shall discuss further below, specialized numerical simulations coupled with a recent analytical study¹⁷ strongly support the absence of any phase transition in the present 1D PSW model.

In Fig. 9 we report the comparison between the FW lines, as predicted by the LPA and the HPA, in the $\rho\sigma$ versus $k_B T / \epsilon_a$ plane for $\Delta/\sigma=1$ and two different energy ratios, $\epsilon_r/\epsilon_a=10$ and $\epsilon_r/\epsilon_a=5$. The spinodal line predicted by the HPA is also included. As said above, the FW and spinodal lines meet at the critical point. While at high temperatures (above $k_B T / \epsilon_a=3$) there is a remarkable agreement between the two approximations (LPA and HPA), deviations occur at lower temperatures.

As in the original work by Fisher and Widom,¹⁹ we also

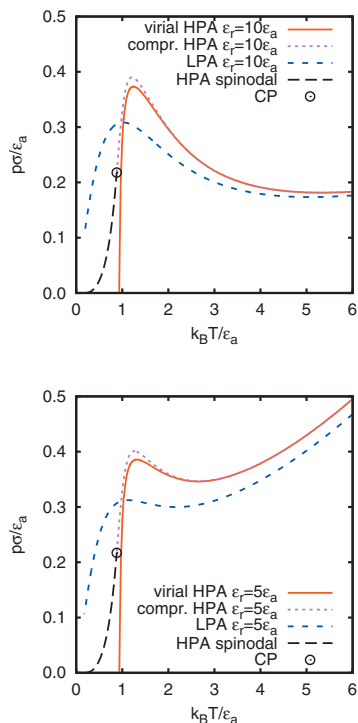


FIG. 10. Same as in Fig. 9, but in the $p\sigma/\epsilon_a$ vs $k_B T/\epsilon_a$ plane. Note that while in the LPA the three routes to the pressure are not distinguishable one from the other on the graph scale, for the HPA the difference between the virial and the compressibility route is noticeable at low temperatures.

report the FW line in the $p\sigma/\epsilon_a$ versus $k_B T/\epsilon_a$ plane (see Fig. 10), where again we compare the lines as derived from the HPA and LPA schemes. For the energy ratio $\epsilon_r/\epsilon_a=10$ (top panel) we see that the HPA and the LPA give qualitative similar forms of the FW line with a significant deviation at low temperatures, where again the HPA FW line is interrupted at $T=T_c$. Note that while all three standard routes give practically identical results within the LPA, the virial (-energy) route in the HPA differs from the compressibility one at low temperatures (more than 5% for $k_B T/\epsilon_a \lesssim 1.2$). For consistency, the HPA spinodal line is obtained via the compressibility route only. Similar features occur for the second lower value of the energy ratio, namely, $\epsilon_r/\epsilon_a=5$ (bottom panel). Again, the LPA and HPA lines are qualitatively similar, the three routes in the LPA provide indistinguishable results, and the virial and energy routes in the HPA deviate more than 5% for $k_B T/\epsilon_a \lesssim 1.2$. The main distinctive feature in this case $\epsilon_r/\epsilon_a=5$ is a marked upswing of the tail of the FW line, absent in the previous case $\epsilon_r/\epsilon_a=10$. This means that on increasing penetrability—that is, on decreasing ϵ_r/ϵ_a —the transition from oscillatory (above the line) to monotonic (below the line) behaviors occurs at a higher pressure and a higher density for a fixed temperature $k_B T/\epsilon_a$.

Despite the important differences in the steps followed to derive the LPA and the HPA, it is noteworthy that they

agree in the qualitative shape of the FW lines (even though the HPA predicts a spurious spinodal line). It is then reasonable to expect that the true FW line should interpolate the LPA line at low temperatures with the HPA line at high temperatures.

Finally, we now tackle the issue of the existence of a phase transition for the PSW 1D model. In view of the HPA results on the seemingly existence of a spinodal line (and hence of a critical point), we consider here the fluid-fluid transition. As we shall see, our numerics is compatible with the absence of such a transition, thus supporting the view that the above findings of a spinodal line is indeed a consequence of the application of the HPA to a regime where the theory is not valid.

As the FW line always anticipates the critical point, as remarked, we can then look for the existence of a fluid-fluid coexistence line in the region predicted by the interpolation of the LPA and HPA FW lines. We have carried out extensive simulations of the PSW fluid using the Gibbs ensemble MC techniques and employing all standard improvements suggested in literature.^{13–16} In order to validate our code, we tested it against the case of the 1D SW potential, where exact analytical predictions for all thermodynamic quantities are available.

We have used up to 1000 particles and carefully scanned the temperature range $0.1 < k_B T/\epsilon_a < 2.0$ and the density range $0.1 < \rho\sigma < 6$, as suggested by the FW line (see Fig. 9). We have also considered different values of ϵ_r/ϵ_a and Δ/σ for cases giving a significant overlapping probability. In all the cases we have not found any signature of a fluid-fluid phase separation.

Although the *absence* of a critical transition is always much more difficult to assess as opposed to its presence, the first scenario is consistent with more than one indication. The first indication stems from a lattice model counterpart of the 1D PSW model. This is discussed in Appendix C, where the lattice version of the PSW model is constructed following standard manipulations with the result that no phase transitions are present for *finite occupancy*. An additional evidence supporting the absence of any fluid-fluid or freezing transition stems from the very recent exact analytical work alluded earlier¹⁷ which, using the methodology presented in Ref. 18, concludes that *no phase transitions* are present for the PSW and PS models in 1D.

In our simulations we have also investigated values of ϵ_r/ϵ_a and Δ/σ which violate Ruelle’s stability criterion (see Appendix A) and thus the 1D PSW model is not necessarily stable in the thermodynamic limit. Here the phenomenology turns out to be much more interesting. For sufficiently low temperatures and sufficiently high densities we observe the formation of a “blob” of many-particle clusters (each made of a large number of overlapping particles) having a well defined and regular distribution on the axis, and occupying only a portion of the system length. In the blob phases the energy per particle grows with the number of particles, thus revealing the absence of a thermodynamic limit. The transition from a “normal” phase to a blob phase if $\epsilon_r/\epsilon_a < 2(\ell + 1)$, where ℓ is the integer part of Δ/σ , is illustrated in Fig. 11. This figure shows the RDF at $\rho\sigma=6$ (top panel) and $\rho\sigma$

024101-10 Fantoni *et al.*

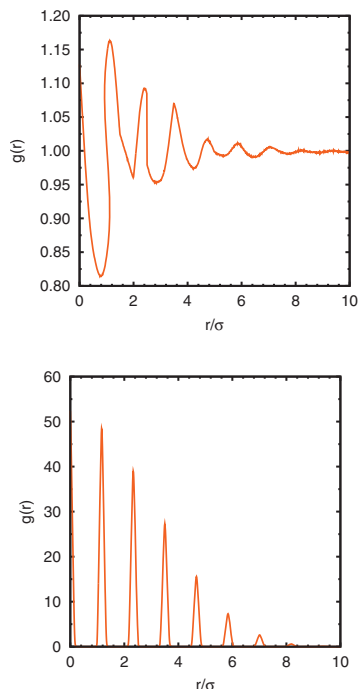
J. Chem. Phys. **133**, 024101 (2010)


FIG. 11. Plot of the RDF $g(r)$ obtained from MC simulations for $\epsilon_r/\epsilon_a=2$, $\Delta/\sigma=1.5$, $k_B T/\epsilon_a=10$, and $\rho\sigma=6$ (top panel) and $\rho\sigma=8$ (bottom panel).

$=8$ (bottom panel) for $\epsilon_r/\epsilon_a=2$, $\Delta/\sigma=1.5$, and $k_B T/\epsilon_a=10$. At the lower density the structure of the PSW fluid is qualitatively not much different from that expected if $\epsilon_r/\epsilon_a > 2(\ell+1)$ (compare, for instance, with Fig. 6). However, the structure at the higher density is reminiscent of that of a solid, except that the distribution of particles does not span the whole length (here $L=N/\rho=62.5\sigma$). Instead, the particles distribute into a few clusters regularly spaced with distance 1.17σ so that the particles of a given cluster interact attractively with all the particles of the nearest- and next-nearest-neighbor clusters. Note that the number of particles within any given cluster is not necessarily identical. It is also worth noticing that in spite of the huge difference in the vertical scales of both panels in Fig. 11, they are consistent with the condition $\int_0^{L/2} dr h(r) = -1/2\rho$.

The decay of the peaks of $g(r)$ is mainly due to the lack of translational invariance, i.e., the first and last clusters have only one nearest-neighbor cluster, the first, second, next-to-last, and last clusters have only one next-nearest-neighbor cluster, and so on.

We stress that the above phenomenon is specific of bounded potentials, such as PSW, and has no counterpart in the hard-core domain. It is then plausible to expect their appearance even in the corresponding 3D versions of these models where freezing transition (and phase separation for SW) is present but could both be hampered by the presence of this clustering phenomenon in the region of parameter space where Ruelle's stability criterion is violated. This

would extend the interesting phenomenology already established for the PS case.²² Work along these lines on the 3D case is underway and will be reported elsewhere.

VIII. CONCLUSIONS

In this paper we have completed the study initiated in previous work^{5,6} on the PSW model in 1D. This is a model combining the three main ingredients present in many colloidal-polymer solutions, namely, repulsions, attractions, and penetrability. While the first two are ubiquitous even in simple fluids, the latter is a peculiarity of complex fluids where there exist many examples of colloid-polymer systems which are penetrable (with some energy cost) to some extent, and they involve both steric repulsions and short-range attractions. This model then captures all these crucial features at the simplest level of description within an implicit solvent description.

The main new point of this paper was to present an additional and complementary approximation, denoted as the HPA, valid in regimes complementary to those valid for the low-penetrability scheme LPA discussed in Ref. 6. While the idea behind the LPA was to modify the *exact* relations valid for the 1D SW fluid—and in fact for any fluid with a hard-core and short-range attraction—to allow penetrability within some reasonable approximation, the driving force behind the HPA is the fact that for bounded potential the Mayer function can be made arbitrarily small by considering sufficiently high temperatures. As a consequence, only the linear chain diagrams need to be retained at each order in the cluster expansion. As it turns out,¹⁰ this is tantamount to considering the celebrated Debye–Hückel theory for charged fluids, and we have considered here the soundness of this approximations at various regimes as compared to specialized MC simulations. The latter were also compared with other approximations which parallel the entire hierarchy of approximations in the framework of charged fluids, ranging from the most sophisticated nonlinear Debye–Hückel theory to the simplest MSA. We have assessed the regime of reliability of these approximations both for thermodynamic and correlation functions by comparison with MC simulations and by internal consistency between different routes to thermodynamics.

Next we have also discussed the location of the FW line, separating oscillatory from monotonic behavior in the correlation function, within the HPA and compared with that obtained from the LPA introduced in previous work.⁶ In agreement with previous findings, we find that penetrability enhances the region where correlation functions have a monotonic regime. The FW lines derived from the HPA and LPA schemes are found to be in qualitative agreement, thus making drawing of a line interpolating the high- and low-temperature regimes possible.

As a final point, we investigated the possibility of a fluid-fluid transition. This possibility arises because the boundness of the potential renders the van Hove theorem on the absence of phase transition for 1D model with short-range interactions nonapplicable. In fact, the HPA is seen to predict a critical point where the FW line meets a spinodal

line. However, this prediction takes place in a region of densities and temperatures where the HPA is not reliable. A careful investigation using both NVT and Gibbs ensemble MC techniques akin to those exploited in the investigations of the analog problem for the 3D SW model yields negative results. These findings are also supported by analytical arguments based on the lattice gas counterpart where the absence of transition can be motivated by the absence of an infinite occupancy of each site, as well as by an exact analytical proof¹⁷ of a no-go theorem proving the absence of any phase transition in this model, which is in agreement with, and beautifully complements, our work.

In our quest for a possible thermodynamic transition in the 1D PSW model we have explored values of the energy ratio ϵ_r/ϵ_a and well width Δ/σ for which the stability of the system in the thermodynamic limit is not guaranteed by Ruelle's criterion.^{26,27} We have found that as the temperature decreases and/or the density increases, a transition from a normal fluid phase to a peculiar solidlike phase takes place. The latter phase is characterized by the formation of clusters of overlapping particles occupying a small fraction of the available space and with nonextensive properties. This clustering transition pre-empts both the fluid-fluid and fluid-solid transitions.

In view of the results presented here, it would be very interesting to discuss the phase diagram of the corresponding 3D PSW model. The phase diagram of the SW model ($\epsilon_r/\epsilon_a \rightarrow \infty$) is indeed well established and includes both a fluid-solid transition—present even in the HS counterpart—and a fluid-fluid transition line. The latter is present for any value of ϵ_a and Δ/σ but is stable against freezing only for $\Delta/\sigma > 0.25$, the depth of the well being irrelevant.²⁸ The results presented here strongly suggest the importance of the additional parameter ϵ_r/ϵ_a . A first interesting issue would be the Ruelle instability in 3D. A straightforward extension of the arguments presented in Appendix A predicts a guaranteed stability for $\epsilon_r/\epsilon_a > 12$ (if $\Delta/\sigma < 1$), but the actual onset of the instability cannot be assessed through these arguments. One could expect that for sufficiently high penetrability (i.e., $\epsilon_r/\epsilon_a < 12$ and high density) a phenomenon akin to the “clustering” transition found here could be present. In the case $\epsilon_r/\epsilon_a > 12$, where the clustering transition is not expected, the interesting point is to assess the influence of the ratio ϵ_r/ϵ_a on the location of the fluid-fluid critical point and coexistence line. All of these open the possibility of a rich and interesting phase diagram which would complement that already present in a general class of bounded potentials with no attractive tails.^{22,23} We note that the high-penetrability regime is indeed the realm of the HPA presented here, which can be obviously extended to 3D. Work on the 3D PSW model including the above points and other aspects is underway and will be reported elsewhere.

ACKNOWLEDGMENTS

One of us (R.F.) wishes to thank M. Kastner for useful discussions and ongoing collaboration. He also gratefully acknowledges the support of the NITheP of South Africa. The support of the PRIN-COFIN under Grant No. 2007B58EAB

is acknowledged. The research of A.S. was supported by the Spanish government through Grant No. FIS2007-60977, partially financed by FEDER funds. A.M. would like to acknowledge the financial support of the MSMT of the Czech Republic under Project No. LC512 and the GAAS of the Czech Republic (Grant No. IAA400720710).

APPENDIX A: RUELLE'S STABILITY CRITERION

Let us consider the 1D PSW model characterized by ϵ_r/ϵ_a and Δ/σ . Let us call ℓ the integer part of Δ/σ , i.e., $\ell \leq \Delta/\sigma < \ell + 1$. According to Ruelle's criterion, a sufficient condition of thermodynamic stability is^{26,27}

$$U_N(x_1, \dots, x_N) = \sum_{i=1}^{N-1} \sum_{j=i+1}^N \phi(|x_i - x_j|) \geq -NB \quad (\text{A1})$$

for all configurations $\{x_i\}$, where B is a fixed bound.

Given the number of particles N , we want to obtain the configuration with the minimum potential energy U_N . Without loss of generality we can see any given configuration as a set of M clusters ($1 \leq M \leq N$), each cluster i being made of s_i overlapping particles (i.e., any pair of particles of a given cluster is separated a distance smaller than σ). In Ref. 5 we proved that for a fixed value of M the minimum energy corresponds to $s_i = s = N/M$, all the particles of each cluster being located at the same point and the centers of two adjacent clusters being separated a distance σ . Therefore, we can restrict ourselves to this class of ordered configurations and use s as the variational variable.

The repulsive contribution to the potential energy is

$$U_N^r(s) = M \frac{s(s-1)}{2} \epsilon_r. \quad (\text{A2})$$

To compute the attractive contribution we need to take into account that all the particles of a given cluster interact attractively with the particles of the $\ell + 1$ nearest clusters. The total number of pairs of interacting clusters are $(\ell + 1)[M - (\ell + 1)] + \ell + (\ell - 1) + (\ell - 2) + \dots + 1 = (\ell + 1)(M - 1 - \ell/2)$. Therefore,

$$U_N^a(s) = -(\ell + 1) \left(M - \frac{\ell + 2}{2} \right) s^2 \epsilon_a. \quad (\text{A3})$$

The total potential energy $U_N = U_N^r + U_N^a$ is

024101-12 Fantoni *et al.*

J. Chem. Phys. **133**, 024101 (2010)

$$U_N(s) = N \frac{s-1}{2} \epsilon_r - (\ell+1) \left(N - \frac{\ell+2}{2} s \right) s \epsilon_a. \quad (\text{A4})$$

$$s_* = \frac{N}{\ell+2} \left[1 - \frac{\epsilon_r}{2(\ell+1)\epsilon_a} \right]. \quad (\text{A5})$$

We then see that the value that minimizes $U_N(s)$ is

This value is only meaningful if $\epsilon_r/2(\ell+1)\epsilon_a < 1$. Otherwise, $s_* = 1$. In summary, the absolute minimum value of U_N is

$$U_N^* = U_N(s_*) = \begin{cases} -\frac{N}{2} \left\{ \epsilon_r + N \frac{\ell+1}{\ell+2} \epsilon_a \left[1 - \frac{\epsilon_r}{2(\ell+1)\epsilon_a} \right]^2 \right\}, & \epsilon_r < 2(\ell+1)\epsilon_a \\ -(\ell+1) \left(N - \frac{\ell+2}{2} \right) \epsilon_a, & \epsilon_r > 2(\ell+1)\epsilon_a. \end{cases} \quad (\text{A6})$$

Therefore, if $\epsilon_r > 2(\ell+1)\epsilon_a$ the potential energy is bounded from below by $-NB$ with $B = (\ell+1)\epsilon_a$ and thus the system is stable in the thermodynamic limit. On the other hand, if $\epsilon_r < 2(\ell+1)\epsilon_a$ there exist configurations that violate Ruelle's criterion and so the thermodynamic stability of the system is not guaranteed.

APPENDIX B: DENSITY EXPANSION OF $w(r)$ WITHIN THE HPA

Starting from Eq. (3.3) and for $\rho\gamma_r |\tilde{f}_{SW}(k)| < 1$, the Fourier transform $\tilde{w}(k)$ can be expanded in power series as

$$\tilde{w}(k) = \sum_{n=2}^{\infty} (\rho\gamma_r)^{n-1} \tilde{f}_{SW}^n(k). \quad (\text{B1})$$

Upon inverse Fourier transform one then has

$$w(r) = \sum_{n=2}^{\infty} (\rho\gamma_r)^{n-1} w_n(r), \quad (\text{B2})$$

where

$$w_n(r) = \int_{-\infty}^{\infty} \frac{dk}{2\pi} e^{ikr} \tilde{f}_{SW}^n(k). \quad (\text{B3})$$

Equation (3.4) can be rewritten as

$$\tilde{f}_{SW}(k) = \frac{i}{k} [(1+\gamma)(e^{ik} - e^{-ik}) - \gamma(e^{ik\lambda} - e^{-ik\lambda})]. \quad (\text{B4})$$

Therefore,

$$\tilde{f}_{SW}^n(k) = \frac{i^n}{k^n} \sum_{m=0}^n \sum_{p=0}^m \sum_{q=0}^{n-m} \binom{n}{m} \binom{m}{p} \binom{n-m}{q} \times (-1)^{m+p+q} (1+\gamma)^m \gamma^{n-m} e^{ik[2p-m+(2q-n+m)\lambda]}. \quad (\text{B5})$$

The origin ($k=0$) is a regular point of $\tilde{f}_{SW}(k)$ and hence of $\tilde{f}_{SW}^n(k)$ [but not of each separate term in Eq. (B5)], so we can choose to save the point $k=0$ in Eq. (B3) either from above or from below. Here we do it from above with the result

$$\lim_{\epsilon \rightarrow 0^+} \int_{\mathcal{L}} \frac{dk}{2\pi} \frac{e^{ikr}}{(k+i\epsilon)^n} = \frac{(-r)^{n-1}}{(n-1)!} \Theta(-r), \quad n > 0, \quad (\text{B6})$$

where the path \mathcal{L} in the complex k plane goes from $k=-\infty$ to $k=+\infty$ and closes itself on the upper plane if $r > 0$ and in the lower one if $r < 0$. In Eq. (B3) we then find

$$w_n(r) = \sum_{m=0}^n \sum_{p=0}^m \sum_{q=0}^{n-m} \binom{n}{m} \binom{m}{p} \binom{n-m}{q} (-1)^{m+p+q} (1+\gamma)^m \gamma^{n-m} \times \frac{[-r-2p+m-(2q-n+m)\lambda]^{n-1}}{(n-1)!} \Theta[-r-2p+m-(2q-n+m)\lambda]. \quad (\text{B7})$$

It is interesting to note that $w_n(r) = 0$ if $r > \lambda n$. Thus Eq. (B2) can be rewritten as

$$w(r) = \sum_{n=\max\{2, [r/\lambda]\}}^{\infty} (\rho\gamma_r)^{n-1} w_n(r), \quad (\text{B8})$$

where $[r/\lambda]$ is the integer part of r/λ .

The radius of convergence of series (B8) depends on temperature and can be obtained by the same arguments as in the PS case.⁷ From the denominator of Eq. (3.3), it follows that the series converges provided that $\rho < \rho_{\text{conv}}$, where

$$(\gamma_r \rho_{\text{conv}})^{-1} = |\tilde{f}_{SW}|_{\text{max}}. \quad (\text{B9})$$

Here $|\tilde{f}_{SW}|_{\text{max}}$ denotes the absolute maximum value of $|\tilde{f}_{SW}(k)|$. From Eq. (3.4) if $\gamma < (\lambda^3 - 1)^{-1}$ that maximum corresponds to $k=0$, i.e., $|\tilde{f}_{SW}|_{\text{max}} = -\tilde{f}_{SW}(0)$, and so $\gamma_r \rho_{\text{conv}} = (1 - \gamma\Delta)^{-1}/2$. On the other hand, if $\gamma > (\lambda^3 - 1)^{-1}$ the maximum value $|\tilde{f}_{SW}|_{\text{max}}$ takes place at $k \neq 0$ and so $\gamma_r \rho_{\text{conv}}$ must be obtained numerically. For sufficiently large values of $\gamma\Delta$ one has $|\tilde{f}_{SW}|_{\text{max}} = \tilde{f}_{SW}(0)$ so that $\gamma_r \rho_{\text{conv}} = (\gamma\Delta - 1)^{-1}/2$ and this coincides with the maximum physical density (see below). Figure 12 shows $\gamma_r \rho_{\text{conv}}$ as a function of $\gamma\Delta$ for two values of Δ/σ . In the PS limit ($\gamma\Delta \rightarrow 0$) one has $\gamma_r \rho_{\text{conv}} = \frac{1}{2}$. As the strength of the attractive part of the potential (measured by the product $\gamma\Delta$) increases, the radius of convergence first grows, reaches a maximum, and then decays.

024101-13 HPA for penetrable-square-well model

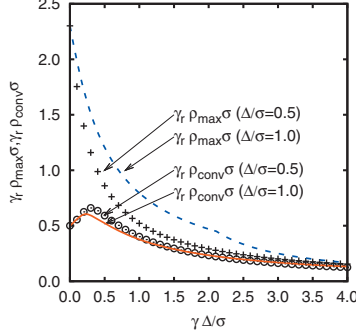
J. Chem. Phys. **133**, 024101 (2010)


FIG. 12. Plot of the radius of convergence $\gamma_r \rho_{conv} \sigma$ and of the maximum density $\gamma_r \rho_{max} \sigma$ vs $\gamma \Delta / \sigma$ for $\Delta / \sigma = 0.5$ and $\Delta / \sigma = 1.0$.

Except when $\gamma \Delta$ is so large that $|\tilde{f}_{SW}|_{max} = \tilde{f}_{SW}(0)$, the maximum $|\tilde{f}_{SW}|_{max}$ corresponds to a negative value of $\tilde{f}_{SW}(k)$ and so the singularity responsible for the radius of convergence is located on the negative real axis. Therefore, $w(r)$ is still well defined beyond the radius of convergence, i.e., for $\rho > \rho_{conv}$. On the other hand, analogous to the PS case,^{20,29} the HPA for the PSW fluid becomes unphysical, at a given temperature, for densities larger than a certain value ρ_{max} given by the condition

$$(\gamma_r \rho_{max})^{-1} = \tilde{f}_{SW}^{max}, \quad (B10)$$

where \tilde{f}_{SW}^{max} is the absolute maximum value of $\tilde{f}_{SW}(k)$. Since $\tilde{f}_{SW}^{max} \leq |\tilde{f}_{SW}|_{max}$, it is obvious that $\rho_{max} \geq \rho_{conv}$. For sufficiently large values of $\gamma \Delta$ (actually, for temperatures below the critical value T_c defined in Sec. VII) one has $\tilde{f}_{SW}^{max} = \tilde{f}_{SW}(0)$, and so $\gamma_r \rho_{max} = (\gamma \Delta - 1)^{-1/2}$. In that case, the line of maximum density becomes a spinodal line, as discussed in Sec. VII. Figure 12 also includes a plot of $\gamma_r \rho_{max}$ as a function of $\gamma \Delta$ for the same two values of Δ / σ . Note the kink of the curve $\gamma_r \rho_{max}$ for $\Delta / \sigma = 1$ at the critical point ($\gamma_c \Delta / \sigma \approx 2.11$ and $\gamma_r \rho_c \approx 0.45$) so that $\gamma_r \rho_{max} = (\gamma \Delta - 1)^{-1/2}$ (spinodal line) if $\gamma \Delta / \sigma > 2.11$.

APPENDIX C: THE PSW LATTICE GAS

Consider the PSW model in 1D. The grand partition function is

$$\Xi(\mu, L, T) = \sum_{N=0}^{\infty} \frac{1}{N!} \left(\frac{e^{\beta \mu}}{\Lambda_T} \right)^N Z_N(L, T), \quad (C1)$$

where Λ_T is the thermal de Broglie's wavelength and

$$Z_N(L, T) = \int_L dr_1, \dots, dr_N \exp \left[-\beta \frac{1}{2} \sum_{i \neq j=1}^N \phi(\mathbf{r}_i - \mathbf{r}_j) \right]. \quad (C2)$$

We now discretize the length L as a sum of $N_c \gg 1$ cells of size $a = L / N_c$ with occupancy n_α , $\alpha = 1, \dots, N_c$. The value of a is chosen in the interval $\sigma < a < \sigma + \Delta$, with $\Delta < \sigma$ so that two particles in the same cell are assumed to interact repulsively and two particles in adjacent cells are assumed to

interact attractively. The integral can then be approximated as $\int_L dr \approx a N_c$ and the configurational partition function Z_N as

$$Z_N(L, T) \approx a^N \sum_{\{n_\alpha\}} \delta_{N, \sum_\alpha n_\alpha} \exp \left[-\beta \frac{1}{2} \sum_{\alpha, \beta=1}^{N_c} \chi_{\alpha\beta} \tilde{\phi}_{\alpha\beta} \right] N!. \quad (C3)$$

In Eq. (C3) the δ function accounts for the constraint $N = \sum_\alpha n_\alpha$ and the factor $N!$ of the indistinguishability of the particles. Also we have introduced $\chi_{\alpha\beta}$ accounting for multi-interactions among cells and $\tilde{\phi}_{\alpha\beta}$ which is equal to ϵ_r if $\alpha = \beta$ and equal to $-\epsilon_a$ for nearest-neighboring (nn) cells. Noting that each particle in an α -cell can either interact with $n_\alpha - 1$ other particles within the same cell or with n_β particles within a nn β -cell, we see that

$$\frac{1}{2} \sum_{\alpha, \beta=1}^{N_c} \chi_{\alpha\beta} \tilde{\phi}_{\alpha\beta} = -\epsilon_a \sum_{(\alpha\beta)} n_\alpha n_\beta + \frac{1}{2} \epsilon_r \sum_\alpha n_\alpha (n_\alpha - 1). \quad (C4)$$

Substituting into Eq. (C1) we then find

$$\Xi(\mu, L, T) = \sum_{N=0}^{\infty} \left(\frac{a}{\Lambda_T} e^{\beta \mu} \right)^N \sum_{\{n_\alpha\}} \delta_{N, \sum_\alpha n_\alpha} \times \exp \left[-\beta \frac{1}{2} \sum_{\alpha, \beta} \chi_{\alpha\beta} \tilde{\phi}_{\alpha\beta} \right]. \quad (C5)$$

Because of the δ , the two sums can be inverted and the sum over N can be explicitly carried out thus obtaining

$$\Xi(\mu, L, T) = \sum_{\{n_\alpha\}} \exp \left[-\beta \left(-\epsilon_a \sum_{(\alpha\beta)} n_\alpha n_\beta + \frac{1}{2} \epsilon_r \sum_\alpha n_\alpha (n_\alpha - 1) - \tilde{\mu} \sum_\alpha n_\alpha \right) \right], \quad (C6)$$

with $\tilde{\mu} = \mu + (1/\beta) \ln(a/\Lambda_T)$.

Assume a finite length L (and hence a finite number of cells N_c) with periodic boundary conditions. The above partition function can then be solved by standard transfer matrix techniques

$$\Xi(\mu, L, T) = \sum_{\{n_1, \dots, n_{N_c}\}} \prod_{\alpha=1}^{N_c} A_{n_\alpha n_{\alpha+1}} = \text{Tr} A^{N_c}, \quad (C7)$$

where we have introduced the matrix

$$A_{n_\alpha n_\beta} = \exp \left[-\beta \left(-\epsilon_a n_\alpha n_\beta + \frac{\epsilon_r}{4} (n_\alpha (n_\alpha - 1) + n_\beta (n_\beta - 1)) - \frac{\tilde{\mu}}{2} (n_\alpha + n_\beta) \right) \right]. \quad (C8)$$

If N_c is finite, one then has in the thermodynamic limit

$$\lim_{L \rightarrow \infty} \frac{1}{L} \log \Xi(\mu, L, T) = \frac{1}{a} \log \lambda_0, \quad (C9)$$

where λ_0 is the largest eigenvalue of the matrix. Clearly this is analytic and no phase transitions are possible for finite occupancy N_c .

024101-14 Fantoni *et al.*J. Chem. Phys. **133**, 024101 (2010)

- ¹C. Marquest and T. A. Witten, *J. Phys. (Paris)* **50**, 1267 (1989).
- ²C. N. Likos, *Phys. Rep.* **348**, 267 (2001).
- ³F. H. Stillinger, *J. Chem. Phys.* **65**, 3968 (1976).
- ⁴C. N. Likos, M. Watzlawek, and H. Löwen, *Phys. Rev. E* **58**, 3135 (1998).
- ⁵A. Santos, R. Fantoni, and A. Giacometti, *Phys. Rev. E* **77**, 051206 (2008).
- ⁶R. Fantoni, A. Giacometti, Al. Malijevský, and A. Santos, *J. Chem. Phys.* **131**, 124106 (2009).
- ⁷Al. Malijevský and A. Santos, *J. Chem. Phys.* **124**, 074508 (2006).
- ⁸Al. Malijevský, S. B. Yuste, and A. Santos, *Phys. Rev. E* **76**, 021504 (2007).
- ⁹J.-P. Hansen and I. R. McDonald, *Theory of Simple Liquids* (Academic, Amsterdam, 2006).
- ¹⁰A. Santos, R. Fantoni, and A. Giacometti, *J. Chem. Phys.* **131**, 181105 (2009).
- ¹¹L. van Hove, *Physica (Amsterdam)* **16**, 137 (1950).
- ¹²J. A. Cuesta and A. Sanchez, *J. Stat. Phys.* **115**, 869 (2004).
- ¹³A. Z. Panagiotopoulos, *Mol. Phys.* **61**, 813 (1987).
- ¹⁴A. Z. Panagiotopoulos, N. Quirk, M. Stapleton, and D. J. Tildesley, *Mol. Phys.* **63**, 527 (1988).
- ¹⁵B. Smit, Ph. De Smedt, and D. Frenkel, *Mol. Phys.* **68**, 931 (1989).
- ¹⁶B. Smit and D. Frenkel, *Mol. Phys.* **68**, 951 (1989).
- ¹⁷R. Fantoni and M. Kastner, "Non-existence of a Phase Transition for the Penetrable Square Wells in One Dimension," JSTAT (submitted).
- ¹⁸M. Kastner, *Rev. Mod. Phys.* **80**, 167 (2008).
- ¹⁹M. E. Fisher and B. Widom, *J. Chem. Phys.* **50**, 3756 (1969).
- ²⁰L. Acedo and A. Santos, *Phys. Lett. A* **323**, 427 (2004).
- ²¹A. Santos, *J. Chem. Phys.* **126**, 116101 (2007).
- ²²C. N. Likos, A. Lang, M. Watzlawek, and H. Löwen, *Phys. Rev. E* **63**, 031206 (2001).
- ²³C. N. Likos, B. M. Mladek, D. Gottwald, and G. Kahl, *J. Chem. Phys.* **126**, 224502 (2007).
- ²⁴MC results were obtained from a standard NVT ensemble calculation with periodic boundary conditions. We used $N=500$ particles and 10^6 MC steps, which were checked to be sufficient for a good accuracy.
- ²⁵C. Vega, L. F. Rull, and S. Lago, *Phys. Rev. E* **51**, 3146 (1995).
- ²⁶M. E. Fisher and D. Ruelle, *J. Math. Phys.* **7**, 260 (1966).
- ²⁷D. Ruelle, *Statistical Mechanics: Rigorous Results* (Benjamin, London, 1969).
- ²⁸W. G. T. Kranendonk and D. Frenkel, *Mol. Phys.* **64**, 403 (1988).
- ²⁹N. Grewe and W. Klein, *J. Math. Phys.* **18**, 1729 (1977); **18**, 1735 (1977); W. Klein and N. Grewe, *J. Chem. Phys.* **72**, 5456 (1980).

Chapter 22

Non existence of a phase transition for the Penetrable Square Well model in one dimension

Fantoni R., J. Stat. Mech., 07030 (2010)

Title: “Non existence of a phase transition for the Penetrable Square Well model in one dimension.”

Abstract: Penetrable Square Wells in one dimension were introduced for the first time in [A. Santos *et. al.*, Phys. Rev. E, **77**, 051206 (2008)] as a paradigm for ultra-soft colloids. Using the Kastner, Schreiber, and Schnetz theorem [M. Kastner, Rev. Mod. Phys., **80**, 167 (2008)] we give strong evidence for the absence of any phase transition for this model. The argument can be generalized to a large class of model fluids and complements the van Hove’s theorem.

Non-existence of a phase transition for penetrable square wells in one dimension

Riccardo Fantoni

National Institute of Theoretical Physics (NITheP) and Institute of Theoretical
Physics, University of Stellenbosch, Stellenbosch 7600, South Africa
E-mail: rfantoni27@sun.ac.za

Received 8 June 2010

Accepted 8 July 2010

Published 30 July 2010

Online at stacks.iop.org/JSTAT/2010/P07030

[doi:10.1088/1742-5468/2010/07/P07030](https://doi.org/10.1088/1742-5468/2010/07/P07030)

Abstract. Penetrable square wells in one dimension were introduced for the first time in Santos *et al* (2008 *Phys. Rev. E* **77** 051206) as a paradigm for ultra-soft colloids. Using the Kastner, Schreiber and Schnetz theorem (Kastner 2008 *Rev. Mod. Phys.* **80** 167) we give strong evidence for the absence of any phase transition for this model. The argument can be generalized to a large class of model fluids and complements van Hove's theorem.

Keywords: rigorous results in statistical mechanics, classical Monte Carlo simulations, classical phase transitions (theory), other numerical approaches

Contents

1. Introduction	2
2. The KSS theorem	3
3. The PSW model	3
4. Absence of a phase transition	4
5. The limit of the normalized determinant	7
6. Conclusions	12
Acknowledgments	12
Appendix. Alternative support to the Szegő result	12
References	14

1. Introduction

The penetrable square well (PSW) model in one dimension was first introduced in [1] as a good candidate for providing a description of star polymers in regimes of good and moderate solvent under dilute conditions. The issue of Ruelle's thermodynamic stability was analyzed and the region of the phase diagram for a well defined thermodynamic limit of the model was identified. A detailed analysis of its structural and thermodynamical properties was then carried through, for low temperatures [2] and high temperatures [3].

The problem of assessing the existence of phase transitions for this one-dimensional model had never been dealt with in a definitive way. Several attempts to find a gas-liquid phase transition were carried through using the Gibbs ensemble Monte Carlo (GEMC) technique [4]–[8] but all gave negative results. Now it is well known that in three dimensions the square well (SW) model admits for a particular choice of the well parameters a gas-liquid transition [9]. As van Hove's theorem shows [10, 12, 13, 11], this disappears in one dimension. Nonetheless the PSW model in one dimension, being a non-nearest neighbor fluid, is not analytically solvable and since we have no hard core, van Hove's theorem no longer holds. It is then interesting to answer the question of whether a phase transition is possible for it. We should also mention that we also used the GEMC technique to probe for the transition in the three-dimensional PSW and we generally found that for a given well width there is a penetrability threshold above which the gas-liquid transition disappears.

In the present work we use the Kastner, Schreiber and Schnetz (KSS) theorem [14, 15] to give strong analytic evidence for the absence of any phase transition for this fluid model.

The argument hinges on a theorem of Szegő [16] on Toeplitz matrices and can be applied to a large class of one-dimensional fluid models and complement van Hove's theorem.

The paper is organized as follows. In section 2 we state the KSS theorem for the exclusion of phase transitions, in section 3 we describe the PSW model, in section 4 we

Non-existence of a phase transition for penetrable square wells in one dimension

show numerically that the PSW model satisfies the KSS theorem, in section 5 we show analytically that the PSW model satisfies the KSS theorem, and the concluding remarks are presented in section 6.

2. The KSS theorem

The Kastner, Schreiber and Schnetz (KSS) theorem [14, 15] states the following.

Theorem. *KSS: Let $V_N : \Gamma_N \subseteq \mathbb{R}^N \rightarrow \mathbb{R}$ be a smooth potential; an analytic mapping from the configuration space Γ_N onto the reals. Let us indicate with $\mathcal{H}^N(\mathbf{q})$ the Hessian of the potential, and indicate with \mathbf{q}_c the critical points (or saddle points) of $V_N(\mathbf{q})$ (i.e. $\nabla_{\mathbf{q}} V_N|_{\mathbf{q}=\mathbf{q}_c} = 0$), with $k(\mathbf{q}_c)$ their index (the number of negative eigenvalues of $\mathcal{H}^N(\mathbf{q}_c)$). Assume that the potential is a Morse function (i.e. the determinant of the Hessian calculated on all its critical points is non-zero). Whenever Γ_N is non-compact, assume V_N to be ‘confining’, i.e. $\lim_{\lambda \rightarrow \infty} V_N(\lambda \mathbf{q}) = \infty, \forall 0 \neq \mathbf{q} \in \Gamma_N$. Consider the Jacobian densities*

$$j_l(v) = \lim_{N \rightarrow \infty} \frac{1}{N} \ln \left[\frac{\sum_{\mathbf{q}_c \in Q_l([v, v+\epsilon])} J(\mathbf{q}_c)}{\sum_{\mathbf{q}_c \in Q_l([v, v+\epsilon])} 1} \right], \tag{1}$$

where

$$J(\mathbf{q}_c) = \left| \det \frac{\mathcal{H}^N(\mathbf{q}_c)}{2} \right|^{-1/2}, \tag{2}$$

and

$$Q_l(v) = \{\mathbf{q}_c | [V_N(\mathbf{q}_c)/N = v] \wedge [k(\mathbf{q}_c) = l(\text{mod}4)]\}. \tag{3}$$

Then a phase transition in the thermodynamic limit is excluded at any potential energy in the interval $(\bar{v} - \epsilon, \bar{v} + \epsilon)$ if: (i) the total number of critical points is limited by $\exp(CN)$, with C a positive constant; (ii) for all sufficiently small ϵ the Jacobian densities are $j_l(\bar{v}) < +\infty$ for $l = 0, 1, 2, 3$.

Generally the number of critical points of the potential grows exponentially with the number of degrees of freedom of the system. The fact that the total number of critical points is limited by an exponential is thought to be generically valid [17]. We then assume that for Morse potentials the first hypothesis of the theorem is satisfied. So the key hypothesis of the theorem is the second one, which can be reformulated as follows: for all sequences of critical points \mathbf{q}_c such that $\lim_{N \rightarrow \infty} V_N(\mathbf{q}_c)/N = \bar{v}$, we have

$$\lim_{N \rightarrow \infty} |\det \mathcal{H}^N(\mathbf{q}_c)|^{\frac{1}{N}} \neq 0. \tag{4}$$

3. The PSW model

The pair potential of the PSW model can be found as the $l \rightarrow \infty$ limit of the following continuous potential:

$$\phi_l(r) = a[b - \tanh(l(r - 1))] + c[\tanh(l(r - \lambda)) + 1], \tag{5}$$

Non-existence of a phase transition for penetrable square wells in one dimension

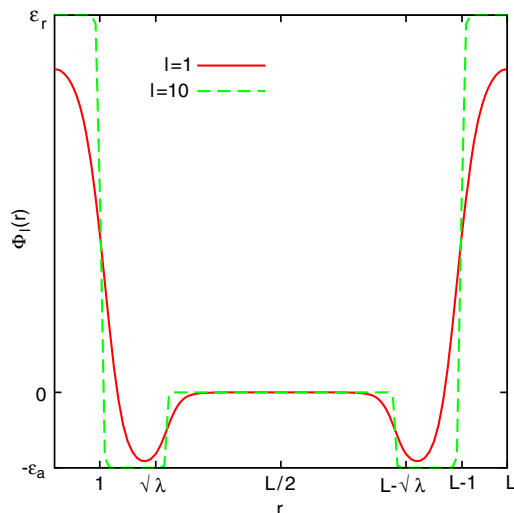


Figure 1. The potential $\Phi_l(|x|)$ for $L \gg 1$. In the plot we used $\epsilon_r = 5, \epsilon_a = 1, \Delta = 4$, and $L = 10$, at two values of the smoothing parameter l .

where $a = (\epsilon_r + \epsilon_a)/2$, $b = (\epsilon_r - \epsilon_a)/(\epsilon_r + \epsilon_a)$, $c = \epsilon_a/2$, with ϵ_r a positive constant which represents the degree of penetrability of the particles, ϵ_a a positive constant representing the depth of the attractive well, and $\lambda = 1 + \Delta$, with Δ the width of the attractive square well. The penetrable spheres (PS) in one dimension are obtained as the $\Delta \rightarrow 0$ limit of the PSW model. In the limit of $\epsilon_r \rightarrow \infty$ the PSW reduces to the SW model.

The PSW model is Ruelle stable for $\epsilon_r/\epsilon_a > 2(n + 1)$ with $n \leq \Delta < n + 1$ [1, 3].

Let us consider a pair potential of the following form:

$$\Phi_l(r) = \phi_l \left(2 \left(\frac{L}{2\pi} \right)^2 \left[1 - \cos \left(2\pi \frac{r}{L} \right) \right] \right). \tag{6}$$

Note that this pair potential is periodic of period L and flat at the origin, $\Phi'_l(0) = 0$. Moreover in the large L limit $\Phi_l(r) \approx \phi_l(r^2)$. In figure 1 we show this potential for different choices of the smoothing parameter l .

4. Absence of a phase transition

In this section we will apply the KSS theorem to give numerical evidence that there is no phase transition for the PSW model introduced above.

The total potential energy is

$$V_N(\mathbf{q}) = \frac{1}{2} \sum_{i,j=1}^N \Phi_l(|x_i - x_j|), \tag{7}$$

where $\mathbf{q} = (x_1, x_2, \dots, x_N)$. If $\lim_{N \rightarrow \infty} V_N(\mathbf{q})/N = v$ one finds $\epsilon_r/2 - \epsilon_a \leq v < +\infty$.

Non-existence of a phase transition for penetrable square wells in one dimension

The saddle points $\mathbf{q}_s = (x_1^s, x_2^s, \dots, x_N^s)$ for the total potential energy ($\nabla_{\mathbf{q}} V_N = 0$), can be various. We will only consider a critical point of the following kind: equally spaced points at fixed density $\rho = N/L$,

$$x_i^s = i/\rho, \quad i = 0, 1, 2, \dots, N - 1. \tag{8}$$

Here we can reach

$$\lim_{N \rightarrow \infty} V_N(\mathbf{q}_\rho)/N = v_\rho, \tag{9}$$

where for large N and up to an additive constant $-\phi_l(0)/2$ we have

$$v_\rho \approx \sum_{i=0}^{N-1} \phi_l \left(2 \left(\frac{L}{2\pi} \right)^2 \left[1 - \cos \left(\frac{2\pi i}{N} \right) \right] \right). \tag{10}$$

If $\rho \gg 1$, in the large N limit we can approximate the sum by an integral such that

$$\begin{aligned} v_\rho &\approx \frac{N}{2\pi} \int_0^{2\pi} \phi_l \left(2 \left(\frac{L}{2\pi} \right)^2 (1 - \cos \alpha) \right) d\alpha \\ &= \frac{N}{\pi} \int_0^2 \frac{\phi_l(2(L/2\pi)^2 x)}{\sqrt{1 - (1-x)^2}} dx, \end{aligned} \tag{11}$$

keeping in mind that $L = N/\rho$ and N is large we find in the $l \rightarrow \infty$ limit

$$\begin{aligned} v_\rho &\approx \frac{N}{\pi} \left\{ \epsilon_r [-\arcsin(1-z)]_0^{1/[2(L/2\pi)^2]} - \epsilon_a [-\arcsin(1-z)]_{1/[2(L/2\pi)^2]}^\lambda \right\} \\ &\approx 2\rho[\epsilon_r - \epsilon_a(\sqrt{\lambda} - 1)] = v_\rho^0, \end{aligned} \tag{12}$$

where we used for small z , $\arcsin(1-z) = \pi/2 - \sqrt{2z} + O[z^{3/2}]$.

For small ρ in the $l \rightarrow \infty$ limit you get

$$v_\rho = \epsilon_r/2, \quad \rho < 1/\sqrt{\lambda} \tag{13}$$

$$v_\rho = \epsilon_r/2 - \epsilon_a, \quad 1/\sqrt{\lambda} < \rho < 1. \tag{14}$$

For intermediate values of the density you will get a stepwise function of the density. A graph of v_ρ is shown in figure 2.

Other stationary points would be the ones obtained by dividing the interval L into $p = N/\alpha$ ($\alpha > 1$) equal pieces and placing α particles at each of the points $x_i^{N,p} = iL/p$, $i = 0, \dots, p - 1$. By doing so we can reach $\lim_{N \rightarrow \infty} V_N(\mathbf{q}_{N,p})/N = v_{N,p}$ where up to an additive constant $-\phi_l(0)/2$ we have

$$v_{N,p} \approx \left(\frac{N}{p} \right) \sum_{i=0}^{p-1} \phi_l \left(2 \left(\frac{L}{2\pi} \right)^2 \left[1 - \cos \left(\frac{2\pi i}{p} \right) \right] \right). \tag{15}$$

We then immediately see that for $\rho \gg \alpha$, $\lim_{N \rightarrow \infty} v_{N,p} = v_\rho^0$ but for small ρ , $v_{N,p} > v_\rho$.

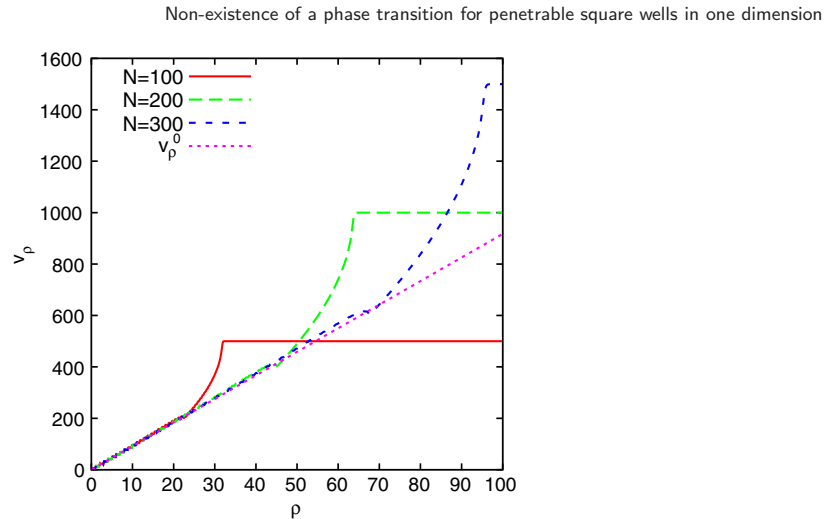


Figure 2. The behavior of v_ρ as a function of the density ρ for $N = 100, 200,$ and 300 when $\epsilon_r = 5, \epsilon_a = 1,$ and $\lambda = 2$ with $l = 100$. Also the theoretical prediction v_ρ^0 at large densities (equation (12)) is shown. Notice that at fixed N, v_ρ will saturate to $\approx N\epsilon_r$ for $4(L/2\pi)^2 < 1$ or $\rho > N/\pi$.

The Hessian $\mathcal{H}_{i,j}^N(\mathbf{q}) = \partial^2 V_N(\mathbf{q})/\partial x_i \partial x_j$ calculated on the saddle points of the first kind can be written as

$$\mathcal{H}_{i,j}^N(\mathbf{q}_\rho) = -\Phi_l''(r_{ij}), \quad i \neq j, \tag{16}$$

$$\mathcal{H}_{i,i}^N(\mathbf{q}_\rho) = \sum_{j \neq i}^N \Phi_l''(r_{ij}), \tag{17}$$

where $\Phi_l''(r)$ is the second derivative of $\Phi_l(r)$ and $r_{ij} = |i - j|/\rho$.

So the Hessian calculated at the saddle point is a circulant symmetric matrix with one zero eigenvalue due to the fact that we have translational symmetry $x_i^p = x_i^p \pm n/\rho$ for any i and any integer n . In order to break the symmetry we need to fix one point, for example the one at x_N^p . So the Hessian becomes a $(N - 1) \times (N - 1)$ symmetric Toeplitz matrix (no longer circulant) which we call $\bar{\mathcal{H}}^{(N-1)}(\mathbf{q}_\rho)$.

In figure 3 we have calculated the $|\det \bar{\mathcal{H}}^N(\mathbf{q}_\rho)|^{1/N}$ as a function of N at $\rho = N/L$ fixed for $\epsilon_a = 1, \epsilon_r = 5, \Delta = 1,$ and $l = 10$. One can see that the normalized determinant of the Hessian does not go to zero in the large N limit. So the Kastner, Schreiber and Schnetz (KSS) criteria [14, 15] are not satisfied and the possibility of a phase transition is excluded. The same holds for the PS model.

In figure 4 we show the dependence of $|\det \bar{\mathcal{H}}^N(\mathbf{q}_\rho)|^{1/N}$ on density for different choices of N .

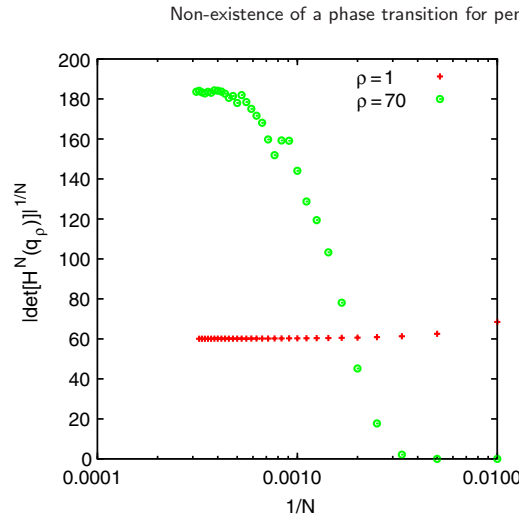


Figure 3. The behavior of $|\det \tilde{\mathcal{H}}^N(\mathbf{q}_\rho)|^{1/N}$ as a function of N at two different densities. Here we chose $\epsilon_a = 1, \epsilon_r = 5, \Delta = 1$, and $l = 10$.

Proved to be a system where there is a phase transition is the self-gravitating ring (SGR) [18] where $\phi_{\text{SGR}}(r) = -1/\sqrt{r + 2(L/2\pi)^2\epsilon}$.¹ In this case one finds $v_\rho^0 = -\rho 2\sqrt{2/\epsilon}\mathcal{A}(2/\epsilon)$, with $\mathcal{A}(x) = \int_0^{\pi/2} d\theta (1 + x \sin^2 \theta)^{-1/2}$. They use the Hadamard upper bound to the absolute value of a determinant to prove that it is indeed the case that $\lim_{N \rightarrow \infty} |\det \tilde{\mathcal{H}}^N(\mathbf{q}_\rho)|^{1/N} = 0$. In figure 5 we show this numerically for a particular choice of the parameters. Actually this result could be expected from what will be proven in the next section, as in the large N limit for any finite ϵ , $\phi_{\text{SGR}} = o(1/N)$ and $|\det \tilde{\mathcal{H}}^N(\mathbf{q}_\rho)|^{1/N} = o(1/N)$. This is a confirmation that the KSS theorem is not violated.

5. The limit of the normalized determinant

In this section we will give analytical evidence that there cannot be a phase transition for the PSW model.

We need to apply to our case Szegő’s theorem [16] for sequences of Toeplitz matrices which deals with the behavior of the eigenvalues as the order of the matrix goes to infinity. In particular we will be using the following proposition.

Proposition. *Let $T_n = \{t_{kj}^n | k, j = 0, 1, 2, \dots, n - 1\}$ be a sequence of Toeplitz matrices with $t_{kj}^n = t_{k-j}^n$ such that $T = \lim_{n \rightarrow \infty} T_n$ and $t_k = \lim_{n \rightarrow \infty} t_k^n$ for $k = 0, 1, 2 \dots$. Let us introduce*

$$f(x) = \sum_{k=-\infty}^{\infty} t_k e^{ikx}, \quad x \in [0, 2\pi]. \tag{18}$$

¹ With this choice the pair potential Φ_{SGR} would be $2\pi\rho$ times the pair potential in the paper of Nardini and Casetti [18].

Non-existence of a phase transition for penetrable square wells in one dimension

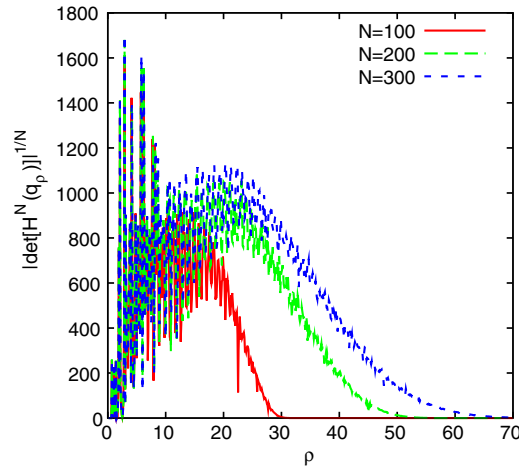


Figure 4. The behavior of $|\det \tilde{\mathcal{H}}^N(\mathbf{q}_\rho)|^{1/N}$ as a function of ρ for various N . Here we chose $\epsilon_a = 1, \epsilon_r = 5, \Delta = 1$, and $l = 10$. Notice that for $\rho \lesssim 1/\sqrt{\lambda}$ then $\mathcal{H}^N(\mathbf{q}_\rho) \approx 0$ and also the normalized determinant is very small, while the approach to zero at large densities is an artifact of the finite sizes of the systems considered.

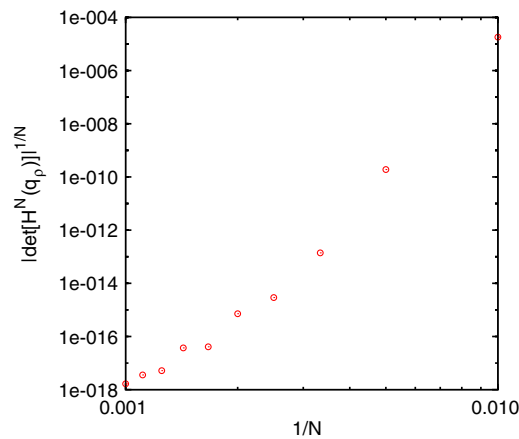


Figure 5. The behavior of $|\det \tilde{\mathcal{H}}^N(\mathbf{q}_\rho)|^{1/N}$ as a function of N for fixed $\rho = 1$ in a bilogarithmic plot. Here we chose $\epsilon = 0.1$.

Then there exists a sequence of Toeplitz matrices $\tilde{T}_n = \{\tilde{t}_{kj} | k, j = 0, 1, 2, \dots, n-1\}$ with $\tilde{t}_{kj} = \tilde{t}_{k-j}$ and

$$\tilde{t}_k = \frac{1}{2\pi} \int_0^{2\pi} f(x) e^{-ikx} dx, \tag{19}$$

Non-existence of a phase transition for penetrable square wells in one dimension

such that

$$\lim_{n \rightarrow \infty} |\det T_n|^{1/n} = \lim_{n \rightarrow \infty} |\det \tilde{T}_n|^{1/n} = \exp\left(\frac{1}{2\pi} \int_0^{2\pi} \ln |f(x)| dx\right), \quad (20)$$

as long as the integral of $\ln |f(x)|$ exists and is finite.

If the Toeplitz matrix is Hermitian then $t_{-k} = t_k^*$ and f is real valued. If moreover the Toeplitz matrix is symmetric then $t_{-k} = t_k$ and additionally $f(x) = f(2\pi - x)$.

By choosing $T_N = \tilde{\mathcal{H}}^N(\mathbf{q}_\rho)$ and defining $t_{i-j}^N = \mathcal{H}_{i,j}^N(\mathbf{q}_\rho)$ we have in the $N \rightarrow \infty$ limit, with $L = N/\rho$ (ρ constant), $t_k = \lim_{N \rightarrow \infty} t_k^N$ and

$$\begin{aligned} f(x) &= \lim_{\substack{N \rightarrow \infty \\ N \text{ odd}}} \left(2 \sum_{k=1}^{(N-1)/2} t_k^N \cos(kx) + t_0^N \right) \\ &= 2 \sum_{k=1}^{\infty} t_k \cos(kx) + t_0, \end{aligned} \quad (21)$$

$$t_k^N = -\Phi_l''(k/\rho), \quad k = 1, 2, \dots, (N-1)/2, \quad (22)$$

$$t_0^N = -2 \sum_{k=1}^{(N-1)/2} t_k^N, \quad (23)$$

So $f(0) = 0$. Notice that in this case the sequence of matrices $\tilde{\mathcal{H}}^N(\mathbf{q}_\rho)$ does not coincide with the sequence used in the proposition; only the limiting matrix for large N coincides. But since Szegő's theorem states that the limit of the normalized determinant exists it should be independent from the sequence chosen. Additional support for the proposition is presented in the appendix.

Now in order to prove the absence of a phase transition we need to prove that $\int_0^{2\pi} \ln |f(x)| dx$ does not diverge to minus infinity. That is, we must control the way f passes through zero. In particular we do not want to have that if x_0 is a zero of f then

$$|f(x)| \sim e^{-1/|x-x_0|^\alpha}, \quad x \sim x_0, \quad (24)$$

with $\alpha \geq 1$, which is faster than any finite power of $(x - x_0)$.

Now for PSW we can write $\Phi_l(r) = \Phi_l^{\text{core}}(r) + \Phi_l^{\text{tail}}(r)$. Choose $\Phi_l^{\text{tail}}(r) = \alpha \exp(-2lr^2)$ with $\alpha = (\epsilon_a + \epsilon_r)e^{2l} - \epsilon_a e^{2\lambda l}$. It is then always possible to redefine the starting potential $\Phi_l(r)$ in such a way that $\Phi_l^{\text{core}}(r)$ exactly vanishes for $r \geq r_{\text{cut}} > \sqrt{\lambda}$ keeping all the derivatives at $r = r_{\text{cut}}$ continuous². Now in equation (21) for f^{core} only a finite number of k contribute to the series, namely the ones for $1 \leq k < \rho r_{\text{cut}}$. So f^{core} will be well behaved on its zeros. For the tail we get $f^{\text{tail}}(x) = -\alpha \sqrt{\pi/2l} x^2 \exp(-x^2/8l)$. So we will never have $|f(x)|$ going through a zero (note that the zeros of f increase in number as ρ increases) with the asymptotically fast behavior of equation (24). This proves the absence of any phase transition for the PSW (or PS) models.

Note that the argument continues to hold for example for the Gaussian core model (GCM) [19] defined by $\phi_{\text{GCM}}(r) = \epsilon \exp[-(r/\sigma)^2]$. In this case by choosing $\phi(r) = \exp(-r)$

² Note that since the potential energy must be a Morse function (on the hypotheses of the KSS theorem), we cannot take the tail potential $\Phi_l^{\text{tail}}(r)$ such that it exactly vanishes for $r > r_{\text{cut}}$. On the other hand the Gaussian decay of $\Phi_l(r)$ for large r is sufficient to guarantee the power law behavior of f on its zeros.

Non-existence of a phase transition for penetrable square wells in one dimension

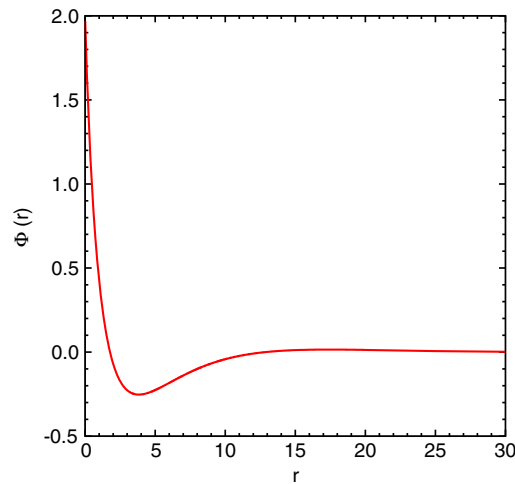


Figure 6. The pair potential $\Phi(r) = 2[\sqrt{-ir}K_1(2\sqrt{-ir}) + \sqrt{ir}K_1(2\sqrt{ir})]$ of the counterexample given in the text. We have $\Phi(0) = 2$ and $\Phi(r) \propto \sin \sqrt{2r} \exp(-\sqrt{2r})$ at large r .

we get in the large L limit $\Phi(r) = \exp(-r^2)$ and the Fourier transform of $\Phi''(r)$ is $-\sqrt{\pi}x^2 \exp(-x^2/4)$ which poses no problems for the zero of $f(x)$ at $x = 0$ (note that in this case $f(x)$ is always positive for $x > 0$).

The argument breaks down if for example $f(x) = -\exp(-1/|x|)$. In this case the pair potential will be given by $\Phi(r) \sim -\int_{-\infty}^{\infty} \exp(ixr)f(x)/x^2 dx$, and one finds $\Phi(r) \sim 2[\sqrt{-ir}K_1(2\sqrt{-ir}) + \sqrt{ir}K_1(2\sqrt{ir})]$, where K_n is the modified Bessel function of the second kind. See figure 6 for a plot. Also the relevant feature in the pair potential, which gives the breakdown of the argument for the absence of a phase transition, is the large r behavior. Notice that in this case we found numerically that the normalized determinant tends to a finite value for large N , in accord with the fact that when the hypotheses of the proposition are not satisfied equation (20) loses its meaning. Considering the normalized determinant for the rescaled potential $\Phi(r)/h(N)$, with $h(N) \rightarrow +\infty$ as $N \rightarrow \infty$, we saw that it does indeed tend to zero, indicating the presence of a phase transition.

We simulated this model fluid and did indeed find that it undergoes a gas-liquid phase transition. The coexisting binodal curve is shown in figure 7 and in table 1 we collect various properties of the two phases. We used GEMC in which two systems can exchange both volume and particles (the total volume V and the total number of particles N are fixed) in such a way as to have the same pressures and chemical potentials. We constructed the binodal for $N = 50$ particles. In the simulation we had $2N$ random particle displacements (with a magnitude of $0.5\sigma_i$, where σ_i is the dimension of the simulation box of system i), $N/10$ volume changes (with a random change of magnitude 0.1 in $\ln[V_1/(V - V_1)]$, where V_1 is the volume of one of the two systems), and N particle swap moves. We observed that in order to obtain the binodals at different system sizes we had to assume a scaling of the following kind: $\beta N^\alpha = \beta_{50} 50^\alpha = \text{constant}$, indicating that the

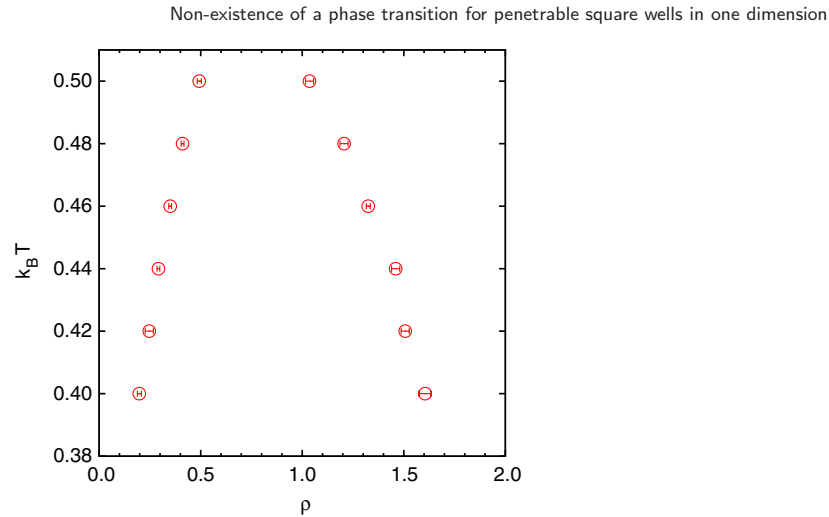


Figure 7. The gas–liquid coexistence line in the temperature–density plane, obtained with the GEMC for $N = 50$ particles³ interacting with the pair potential of figure 6.

Table 1. Gas–liquid coexistence data (T, ρ_i, u_i, μ_i are respectively the temperature, the density, the internal energy per particle, and the chemical potential of the vapor $i = v$ or liquid $i = l$ phase. $\beta = 1/k_B T$ and Λ is the de Broglie thermal wavelength) from GEMC for $N = 50$ particles (see footnote 3).

$k_B T$	ρ_v	ρ_l	u_v	u_l	$-(3 \ln \Lambda)/\beta + \mu_v$	$-(3 \ln \Lambda)/\beta + \mu_l$
0.40	0.20 ± 0.01	1.61 ± 0.03	-0.224 ± 0.009	-0.907 ± 0.007	-0.97 ± 0.01	-0.97 ± 0.01
0.42	0.25 ± 0.02	1.51 ± 0.02	-0.26 ± 0.01	-0.873 ± 0.008	-0.95 ± 0.01	-0.943 ± 0.008
0.44	0.292 ± 0.007	1.46 ± 0.02	-0.290 ± 0.007	-0.854 ± 0.004	-0.938 ± 0.004	-0.921 ± 0.006
0.46	0.350 ± 0.007	1.32 ± 0.01	-0.340 ± 0.004	-0.815 ± 0.006	-0.90 ± 0.01	-0.89 ± 0.02
0.48	0.411 ± 0.007	1.21 ± 0.02	-0.370 ± 0.003	-0.77 ± 0.01	-0.886 ± 0.003	-0.86 ± 0.01
0.50	0.49 ± 0.01	1.04 ± 0.02	-0.420 ± 0.006	-0.71 ± 0.01	-0.87 ± 0.01	-0.862 ± 0.006

model is not Ruelle stable (as may be expected since it has a bounded core and a large attractive region), and $\rho N = \rho_{50} 50 = \text{constant}$, where β_{50} and ρ_{50} are the coexistence data shown in figure 7 and table 1. For $50 \lesssim N \lesssim 100$ we found $\alpha \approx 1/2$, for $N \approx 200$ then $\alpha \approx 2/3$, and for $N \approx 300$ then $\alpha \approx 3/4$.

We then added a hard core to the potential

$$\Phi(r) = \begin{cases} \epsilon & r < 1 \\ 2[\sqrt{-ir}K_1(2\sqrt{-ir}) + \sqrt{ir}K_1(2\sqrt{ir})] & r \geq 1, \end{cases} \quad (25)$$

³ The Monte Carlo simulations were carried out at the Center for High Performance Computing (CHPC), CSIR Campus, 15 Lower Hope St, Rosebank, Cape Town, South Africa. Manufacturer: IBM e1350 Cluster, CPU: AMD Opteron, CPU clock: 2.6 GHz, CPU cores: 2048, memory: 16GB, peak performance: 3.3 Tflops, storage: 94 TB (multiclust), launch date: 2007.

Non-existence of a phase transition for penetrable square wells in one dimension

with ϵ a positive large number, and we saw, through GEMC, that the corresponding fluid still admitted a gas–liquid phase transition (without N scaling of the densities $\rho < 1$) in accord with the expectation that it is the large r tails of the potential that make this model singular from the point of view of our argument.

For fluids with a pair potential Φ given by a hard core and a $-1/r^\alpha$ tail we can take $\Phi''(r) = 0$ for $r < 1$ and $\Phi''(r) = -\alpha(\alpha - 1)/r^{\alpha-2}$ for $r > 1$, and the resulting f function (the Fourier transform of $-\Phi''$) is such that $\ln |f(x)|$ has non-integrable zeros. So this class of models does not fall under the hypotheses of the proposition. And it is well known that when $1 < \alpha < 2$ the corresponding fluid admits a phase transition [12].

6. Conclusions

Using the KSS theorem and a limit theorem of Szegő on Toeplitz matrices we were able to give strong evidence for the exclusion of phase transitions in the phase diagram of the PSW (or PS) fluid. The argument makes use of the fact that the smoothed pair potential amongst the particles has an r cutoff. Even if we just consider two classes of stationary points, i.e. the equally spaced points and equally spaced clusters, we believe that our argument gives strong indications of the absence of a phase transition.

Our argument applies equally well to model fluids with large r tails in the pair potential decaying in such a way that the condition of equation (24) does not hold. For example it applies to the Gaussian core model. We believe this to be a rather large class of fluid models.

We give an example of a model fluid which violates the condition of equation (24) and find through GEMC simulations that it does indeed have a gas–liquid phase transition.

Our argument does not require the fluid to be a nearest neighbor one, for which it is well known that the equation of state can be calculated analytically [20]–[22]. We think that our argument can be a good candidate for complementing the well known van Hove theorem for such systems, violating the hypotheses of the hard core impenetrability of the particles and of the compactness of the support of the tails.

Acknowledgments

We would like to thank Professor Michael Kastner for his careful guidance in the development of the work. Many thanks to Dr Izak Snyman and Professor Robert M Gray for helpful discussions regarding the Toeplitz matrices and Dr Lapo Casetti for proofreading the manuscript before publication.

Appendix. Alternative support to the Szegő result

Our original matrix $\mathcal{H}^N(\mathbf{q}_\rho)$ is a circulant matrix

$$\mathcal{H}^N(\mathbf{q}_\rho) = \begin{pmatrix} h_0^N & h_1^N & h_2^N & h_3^N & \cdots & h_{N-1}^N \\ h_{N-1}^N & h_0^N & h_1^N & h_2^N & \cdots & h_{N-2}^N \\ h_{N-2}^N & h_{N-1}^N & h_0^N & h_1^N & \cdots & h_{N-3}^N \\ \vdots & \vdots & \vdots & \vdots & \ddots & \vdots \\ h_1^N & h_2^N & h_3^N & h_4^N & \cdots & h_0^N \end{pmatrix}. \tag{A.1}$$

J. Stat. Mech. (2010) P07030

Non-existence of a phase transition for penetrable square wells in one dimension

We have checked numerically that the determinant of $\mathcal{H}^N(\mathbf{q}_\rho)$ with one row and one column removed converges in the large N limit to the product of the non-zero eigenvalues of the matrix $\mathcal{H}^N(\mathbf{q}_\rho)$.⁴

Let us assume that $N = 2n + 1$ is odd. Then our matrix has the following additional structure:

$$\begin{aligned} h_i^N &= \tilde{h}_i^N, & i = 1, \dots, n \\ h_{n+i}^N &= \tilde{h}_{n-(i-1)}^N, & i = 1, \dots, n. \end{aligned} \tag{A.2}$$

The eigenvalues of H^N will be given by [23]

$$\psi_m = \sum_{k=0}^{N-1} h_k^N e^{-(2\pi/N)imk}, \quad m = 0, 1, \dots, N - 1 \tag{A.3}$$

with the additional constraint (see equations (16) and (17)) that

$$\psi_0 = \sum_{k=0}^{N-1} h_k^N = 0. \tag{A.4}$$

The eigenvalues can be rewritten as follows:

$$\psi_m = \tilde{h}_0^N + \sum_{k=1}^n \tilde{h}_k^N e^{-(2\pi/N)imk} + \sum_{k=1}^n \tilde{h}_{n-(k-1)}^N e^{-(2\pi/N)im(n+k)}. \tag{A.5}$$

Introducing the summation index $j = n - k + 1$ in the last sum we then obtain

$$\begin{aligned} \psi_m &= \tilde{h}_0^N + \sum_{k=1}^n \tilde{h}_k^N e^{-(2\pi/N)imk} + \sum_{j=n}^1 \tilde{h}_j^N e^{+(2\pi/N)imj} \\ &= \sum_{k=-n}^n t_k^N e^{-(2\pi/N)imk}, \end{aligned} \tag{A.6}$$

with $n = (N - 1)/2$ and $t_k^N = t_{-k}^N = \tilde{h}_k^N$ for $k = 1, 2, \dots, n$.

We take the logarithm of the absolute value of the product of the non-zero eigenvalues to find

$$\mathcal{P} = \frac{1}{N} \ln \left| \prod_{m=1}^N \psi_m \right| = \frac{1}{N} \sum_{m=1}^N \ln |\psi_m|. \tag{A.7}$$

Now in the large N limit we have $t_k = \lim_{N \rightarrow \infty} t_k^N$ for $k = 0, 1, 2, \dots$ and

$$\psi_m \sim \sum_{k=-\infty}^{\infty} t_k e^{-(2\pi/N)imk} \sim f((2\pi/N)m), \tag{A.8}$$

$$\mathcal{P} \sim \frac{1}{N} \sum_{m=1}^N \ln \left| f \left(\frac{2\pi}{N} m \right) \right| \sim \frac{1}{2\pi} \int_0^{2\pi} \ln |f(x)| dx, \tag{A.9}$$

where in the last part we have transformed the sum into an integral.

⁴ We have checked numerically that this property continues to hold as long as the circulant matrix is a symmetric one.

Non-existence of a phase transition for penetrable square wells in one dimension

References

- [1] Santos A, Fantoni R and Giacometti A, 2008 *Phys. Rev. E* **77** 051206
- [2] Fantoni R, Giacometti A, Malijevský A and Santos A, 2009 *J. Chem. Phys.* **131** 124106
- [3] Fantoni R, Giacometti A, Malijevský A and Santos A, 2010 *J. Chem. Phys.* **133** 024101
- [4] Frenkel D and Smit B, 1996 *Understanding Molecular Simulation* (San Diego, CA: Academic)
- [5] Panagiotopoulos A Z, 1987 *Mol. Phys.* **61** 813
- [6] Panagiotopoulos A Z, Quirke N, Stapleton M and Tildesley D J, 1988 *Mol. Phys.* **63** 527
- [7] Smit B, De Smedt Ph and Frenkel D, 1989 *Mol. Phys.* **68** 931
- [8] Smit B and Frenkel D, 1989 *Mol. Phys.* **68** 951
- [9] Liu H, Garde S and Kumar S, 2005 *J. Chem. Phys.* **123** 174505
- [10] van Hove L, 1950 *Physica* **16** 137
- [11] Cuesta J A and Sánchez A, 2004 *J. Stat. Phys.* **115** 869
- [12] Hemmer P C and Stell G, 1970 *Phys. Rev. Lett.* **24** 1284
- [13] Kincaid J M, Stell G and Hall C K, 1976 *J. Chem. Phys.* **65** 2161
- [14] Kastner M and Schnetz O, 2008 *Phys. Rev. Lett.* **100** 160601
- [15] Kastner M, 2008 *Rev. Mod. Phys.* **80** 167
- [16] Grenander U and Szegő G, 1958 *Toeplitz forms and their Applications* (Berkeley: University of California Press) p 65
- [17] Wales D J, 2004 *Energy Landscapes* (Cambridge: Cambridge University Press)
- [18] Nardini C and Casetti L, 2009 *Phys. Rev. E* **80** 060103
- [19] Flory P J and Krigbaum W R, 1950 *J. Chem. Phys.* **18** 1086
- [20] Salsburg Z W, Zwanzig R W and Kirkwood J G, 1953 *J. Chem. Phys.* **21** 1098
- [21] Corti D S and Debenedetti P G, 1998 *Phys. Rev. E* **57** 4211
- [22] Heying M and Corti D S, 2004 *Fluid Phase Equilib.* **220** 85
- [23] Davis P, 1979 *Circulant Matrices* (New York: Wiley)

J. Stat. Mech. (2010) P07030

Part XI

2011

Chapter 23

Cluster theory of Janus particles

Fantoni R., A. Giacometti, F. Sciortino, and G. Pastore, *Soft Matter* **7**, 2419 (2011)

Title: “Cluster theory of Janus particles.”

Abstract: We apply a simple statistical mechanics cluster approximation for studying clustering in the Kern and Frenkel model of Janus fluids. The approach is motivated by recent Monte Carlo simulations work on the same model revealing that the vapor coexisting with the liquid phase contains clusters of different sizes and shapes whose equilibrium concentrations in general depend on the interaction range as well as on thermodynamic parameters. The approximation hinges on a separation between the intra- and inter-cluster interactions, where the former are explicitly computed by Monte Carlo simulations. Two simple liquid theory approximations are exploited for the description of the latter. In the first we use the ideal-gas expressions and obtain a qualitative agreement with extensive Monte Carlo bulk simulations. This can be improved to a semi-quantitative agreement, by using a hard-sphere description for the cluster-cluster interaction.

Has been the 5th most read article in *Soft Matter* on the month of February:

<http://blogs.rsc.org/sm/2011/03/28/>

Appeared as a hot article in the *Soft Matter Blog* in the month of February:

<http://blogs.rsc.org/sm/2011/02/>

Cite this: DOI: 10.1039/c0sm00995d

www.softmatter.org

PAPER

Cluster theory of Janus particles

Riccardo Fantoni,^{*a} Achille Giacometti,^b Francesco Sciortino^c and Giorgio Pastore^d

Received 15th September 2010, Accepted 2nd December 2010

DOI: 10.1039/c0sm00995d

We apply a simple statistical mechanics cluster approximation for studying clustering in the Kern and Frenkel model of Janus fluids. The approach is motivated by recent Monte Carlo simulations work on the same model revealing that the vapor coexisting with the liquid phase contains clusters of different sizes and shapes whose equilibrium concentrations in general depend on the interaction range as well as on thermodynamic parameters. The approximation hinges on a separation between the intra- and inter-cluster contribution to thermodynamics, where only the former is explicitly computed by Monte Carlo simulations. Two level of a simple liquid theory approximations are exploited for the description of the latter. In the first we use the ideal-gas expressions and obtain a qualitative agreement with extensive Monte Carlo bulk simulations. This can be improved to a semi-quantitative agreement, by using a hard-sphere description for the cluster-cluster correlations.

I. Introduction

Recent advances in experimental techniques for chemical synthesis have provided a well defined set of different protocols for obtaining colloidal particles with different shapes, chemical compositions and surface patterns. In particular it is now possible to obtain colloidal particles with a pre-defined number and distribution of solvophobic and solvophilic regions on their surface. These are usually referred to as patchy colloids.^{1–4}

The simplest example within this realm is constituted by the so-called Janus particles, where the surface is partitioned in only two parts with an even distribution of the two philicities. In spite of their apparent simplicity, Janus particles have aroused increasing interest in the last few years both for their potential technological applications and in view of the rather unusual displayed self-assembly properties as compared to conventional isotropic colloidal particles.^{5–8}

A detailed study of the fluid–fluid transition for Janus fluids has recently been carried out by Monte Carlo (MC) simulation^{9,10} using the Kern–Frenkel pair potential.¹¹ Within this model, the solvophobic and solvophilic hemispheres are mimicked by an attractive square-well potential and a repulsive hard-sphere potential respectively, and two spheres attract each other only provided that their centers are within a given distance,

as dictated by the width of the well, and the two attractive patches on each sphere are properly aligned one another, that is, lie within a predefined relative angular range.

The combined features of the equal amplitude of the two philicities coupled with the specificity of the chosen potential types give rise to a micellization process originating in the vapor phase that severely destabilizes the condensation process thus providing a re-entrant vapour coexistence curve that in the temperature–density diagram is skewed toward higher densities as the system is cooled to lower temperatures.⁹ A number of additional unusual features were also found for the vapour phase,¹⁰ including the fact that, for the chosen width of the square-well potential (50% of the particle size), there appeared a predominance of particular clusters formed by single-layer (micelles of about 10 particles) and double-layer (vesicles of about 40 particles) always exposing the hard-sphere part as an external global surface, thus inhibiting the formation of a liquid phase.

It should be emphasized that MC simulations are particularly demanding for this system in that very low temperatures (of the order of 0.25 or less in reduced units) are necessary to observe these phenomena, and this is expected to be even more demanding for decreasing range of the interactions.¹⁰

In this paper, we focus our interest on the study of the vapor phase, following a different approach, hinging on a strategy similar to that devised in the context of associating fluids, where several different theories with different degrees of success have been envisioned.^{12–15}

Our approach has been inspired by the work of Tani and Henderson,¹⁶ extending the Bjerrum theory for association in electrolytic solutions¹⁷ where the total partition function is factorized into an intra- and inter-cluster contribution, so that the original task is reduced to the computation of the partition

^aNational Institute for Theoretical Physics (NITheP) and Institute of Theoretical Physics, Stellenbosch University, Stellenbosch, 7600, South Africa. E-mail: rfantoni27@sun.ac.za

^bDipartimento di Scienze Molecolari e Nanosistemi, Università di Venezia, S. Maria DD2137, I-30123 Venezia, Italy. E-mail: achille@unive.it

^cDipartimento di Fisica, Università di Roma La Sapienza, Piazzale A. Moro 2, 00185 Roma, Italy. E-mail: francesco.sciortino@phys.uniroma1.it

^dDipartimento di Fisica dell'Università, Strada Costiera 11, 34151 Trieste, Italy. E-mail: pastore@ts.infn.it

function for clusters of increasing sizes along with the interaction among them.

While the original approach¹⁶ was limited by the necessity of evaluating analytically even the intra-cluster partition function, in addition to the inter-cluster contribution, we propose to determine the former by explicit Monte Carlo simulations for each cluster and the latter using physically motivated fluid theories. Within MC simulation of each n -cluster, we are then able to determine the energy per particle as a function of temperature and thereby compute the excess free energy of the isolated cluster by thermodynamic integration.

Clearly, this approach is particularly suited to study the vapor phase as once the first n -particle clusters have been simulated the resulting information can be inserted in the inter-cluster theory, and this is enough to determine the partition function of the vapor at all thermodynamic states. We can then follow and predict the dependence of cluster population on thermodynamic conditions and interaction parameters. This is particularly relevant in cases in which spontaneous cluster formation is particularly slow, due for example to the low value of the temperature at which clustering takes place, a common case when the interaction range is very short.

The paper is organized as follows: in section II we describe the model, in sections III and IV we introduce the cluster theory, in section V we describe how we determined the intra-cluster partition function. Additional results are then presented in section VI, and section VII is for final remarks.

II. The Kern and Frenkel model

As in the work of Sciortino *et al.*^{9,10} we used the Kern and Frenkel¹¹ patchy hard sphere model to describe the Janus fluid. Two spherical particles attract *via* a short-range square-well potential only if the line segment joining the centers of the two spheres intercepts a patch on the surface of the first particle and one on the surface of the other. In the case of a single patch per particle, the pair potential reads¹¹

$$\Phi(1,2) = \phi(r_{12})\Psi(\hat{\mathbf{n}}_1, \hat{\mathbf{n}}_2, \hat{\mathbf{r}}_{12}), \quad (1)$$

where

$$\phi(r) = \begin{cases} +\infty & r < \sigma \\ -\varepsilon & \sigma < r < \lambda\sigma \\ 0 & \lambda\sigma < r \end{cases} \quad (2)$$

and

$$\Psi(\hat{\mathbf{n}}_1, \hat{\mathbf{n}}_2, \hat{\mathbf{r}}_{12}) = \begin{cases} 1 & \text{if } \hat{\mathbf{n}}_1 \cdot \hat{\mathbf{r}}_{12} \geq \cos\theta_0 \text{ and } -\hat{\mathbf{n}}_2 \cdot \hat{\mathbf{r}}_{12} \geq \cos\theta_0 \\ 0 & \text{otherwise} \end{cases} \quad (3)$$

where θ_0 is the angular semi-amplitude of the patch. Here $\hat{\mathbf{n}}_1(\omega_1)$ and $\hat{\mathbf{n}}_2(\omega_2)$ are unit vectors giving the directions of the center of the patch in spheres 1 and 2, respectively, with $\omega_1 = (\theta_1, \varphi_1)$ and $\omega_2 = (\theta_2, \varphi_2)$ their corresponding spherical angles in an arbitrary oriented coordinate frame. Similarly, $\hat{\mathbf{r}}_{12}(\Omega)$ is the unit vector of the separation r_{12} between the centers of the two spheres and is defined by the spherical angle Ω . As usual, we have denoted with σ the hard core diameter and $\lambda = 1 + \Delta/\sigma$ with Δ the width of the well.

One can define the fraction of surface covered by the attractive patch as

$$\chi = \Psi(\hat{\mathbf{n}}_1, \hat{\mathbf{n}}_2, \hat{\mathbf{r}}_{12})_{\omega_1, \omega_2}^{1/2} = \sin^2\left(\frac{\theta_0}{2}\right) \quad (4)$$

where we have introduced $\langle \dots \rangle_{\omega} = (1/4\pi) \int d\omega(\dots)$ as the average over the solid angle ω .

Reduced units $k_B T/\varepsilon$ (k_B is the Boltzmann constant) and $\rho\sigma^3$ will be used as a measure of the temperature and density in numerical data.

III. A cluster theory for Janus particles

Following ref. 16, we split the partition function in an inter- and intra-cluster contribution. Let N_n be the number of clusters formed by n particles, where $n = 1, \dots, n_c$ (n_c being the number of different clusters) and $\rho_n = N_n/V$ their density. We then write the total partition function as

$$Q_{tot} = \sum'_{\{N_n\}} \left[\prod_{n=1}^{n_c} \frac{1}{N_n!} (q_n^{intra})^{N_n} \right] Q_{inter}(\{N_n\}, V, T), \quad (5)$$

where the prime indicates that the sum is restricted to all possible configurations satisfying the obvious constraint of conserving the total number of particles N ,

$$\sum_{n=1}^{n_c} nN_n = N. \quad (6)$$

Here q_n^{intra} is the “internal” partition function for an n -particle cluster and $Q_{inter}(\{N_n\}, V, T)$ is the inter-cluster partition function. Additional controlled thermodynamic variables are the total volume V and the temperature T .

The constraint can be dealt with by introducing a Lagrange multiplier so that we minimize the quantity

$$\ln \hat{Q}_{tot} = \ln Q_{tot} + (\ln \lambda) \sum_{n=1}^{n_c} nN_n. \quad (7)$$

In computing the partition function (5) we assume that the sum can be replaced by its largest dominant contribution. With the help of the Stirling approximation $N! \approx (N/e)^N$ one then obtains

$$\ln Q_{tot} \approx \sum_{n=1}^{n_c} [N_n \ln q_n^{intra} - (N_n \ln N_n - N_n)] + \ln Q_{inter}. \quad (8)$$

The correct cluster distribution $\{\bar{N}_n\}$ is then found from the variational condition

$$\left. \frac{\partial}{\partial N_n} \ln \hat{Q}_{tot} \right|_{\{N_n = \bar{N}_n\}} = 0 \quad (9)$$

This allows the calculation of the resulting free energy, $\beta F_{tot} = -\ln Q_{tot}$, in terms of the internal reduced free energy densities, $\beta f_n^{intra} = -\ln q_n^{intra}$, so that

$$\frac{\beta F_{tot}}{V} = \sum_{n=1}^{n_c} [\bar{\rho}_n \ln \bar{\rho}_n - \bar{\rho}_n] + \sum_{n=1}^{n_c} \bar{\rho}_n \beta f_n^{intra} + \sum_{n=1}^{n_c} \bar{\rho}_n \ln V - \frac{1}{V} \ln Q_{inter}. \quad (10)$$

In the above expression, $\beta = 1/(k_B T)$.

IV. Specific models

We now consider two specific cases, where the inter-cluster interaction is not accounted for (the ideal-gas case) or modeled as an effective hard-sphere like interaction between clusters.

A. Ideal gas

The simplest possibility corresponds to considering different clusters as non-interacting ideal particles so that

$$Q_{inter}(\{N_n\}, V, T) = \prod_{n=1}^{n_c} \left(\frac{V}{\Lambda_n^3} \right)^{N_n} \equiv Q_{ideal}, \quad (11)$$

where Λ_n is the de Broglie thermal wavelength associated with each n -cluster.

Using eqn (9) and (11) one easily obtains

$$\bar{\rho}_n = \lambda^n \frac{q_n^{intra}}{\Lambda_n^3}, \quad (12)$$

where $\bar{\rho}_n = \bar{N}_n/V$.

The actual value of the Lagrange multiplier λ can then be numerically obtained upon inverting the constraint (6)

$$\sum_{n=1}^{n_c} n \lambda^n \frac{q_n^{intra}}{\Lambda_n^3} = \rho \equiv \frac{N}{V}. \quad (13)$$

Substitution of eqn (11) into the general expression of the free energy (10) leads to¹⁸

$$\frac{\beta F_{tot}}{V} = \sum_{n=1}^N [\bar{\rho}_n \ln(\bar{\rho}_n \Lambda_n^3) - \bar{\rho}_n] + \sum_{n=1}^N \bar{\rho}_n \beta f_n^{intra}. \quad (14)$$

B. Chemical equilibrium

The above result (14) can be used to compute chemical equilibrium among different clusters. Indeed, on defining μ_n as the chemical potential associated to the n -th cluster, we have

$$\beta \mu_n = \frac{\partial(\beta F_{tot})}{\partial N_n} = \frac{\partial(\beta F_{tot}/V)}{\partial \rho_n} = \ln(\rho_n \Lambda_n^3) + \beta f_n^{intra} \quad (15)$$

We can then impose the equilibrium condition $\mu_n = n\mu_1$ to obtain

$$f_n^{intra} = n f_1^{intra} + k_B T \ln \left[\frac{\rho_n \Lambda_n^3}{(\rho_1 \Lambda_1^3)^n} \right] \quad (16)$$

which can be used to compute the internal free energies, given the cluster distributions. An alternative procedure, based on the explicit computation of the internal energy per particle within each cluster, will be discussed in Section V.

C. Connection with Wertheim association theory

An interesting comparison can be found with Wertheim first-order association theory¹² which is frequently used in this context (see *e.g.* ref. 19 and references therein). Within this theory, the bond contribution to the Helmholtz free energy can be computed from a chemical equilibrium equation under the condition that only a suitable subset of diagrams are included in the cluster expansion and each attractive site is engaged at most in a single bond, the limit of a single-bond per patch in the language of the present paper.

Consider a system formed by only monomers and dimers, that is $n = 1, 2$. Then from eqn (12) and condition (6) limited to $n = 1, 2$ we can obtain a quadratic equation in the Lagrange multiplier λ . The only acceptable root can then be substituted into eqn (12) for $n = 1$ to obtain the fraction of patches that are not bonded, that is the fraction of monomers

$$\frac{\bar{\rho}_1}{\rho} = \frac{2}{1 + \sqrt{1 + 8\rho\Delta}}. \quad (17)$$

Using numerical simulations for $n = 1, 2$ clusters we are able to determine the energy per particle in an n -cluster as a function of temperature and thereby determine the excess free energy of the isolated cluster by integration where $\Delta = (q_2^{intra}/[q_1^{intra}]^2)(\Lambda_1^3/\Lambda_2^3)$. This equation is identical to the result from Wertheim's theory (see eqn (10) in ref. 19) when translated into the appropriate language. Therefore, the present formulation is equivalent to Wertheim's theory provided that temperatures are sufficiently low (see ref. 19 for further details) and the condition single-bond per binding site is satisfied. On the other hand, the present theory allows for an arbitrary amplitude of the patch thus including the possibility of multiple bonding.

Note that while in the case of only two clusters ($n = 1, 2$) requires the solution of a system of 2 coupled equations that results into a quadratic equation for λ , a general case with clusters up to the total number of clusters n_c clearly requires the solution of a system of n_c coupled equation, a task that—in general—has to be carried out numerically.

D. Effective hard sphere inter-cluster interaction

While simple, the ideal gas is clearly rather unphysical even at very low densities. A more physical description amounts to consider all n -particle clusters as identical hard spheres with diameters σ_n and packing fractions $\eta_n = (\pi/6)\rho_n\sigma_n^3$. A rather precise approximate solution in this case is provided by the Boublik, Mansoori, Carnahan, and Starling expression,^{20,21} but for simplicity we here only consider the case $\sigma_n = \sigma_0$ for all n , whose thermodynamics is well described by the simple monodisperse Carnahan–Starling formulae.²² This can be motivated by the fact that only a minor variation is found in the linear cluster dimensions (see Table 1 and discussion further below) and by the observation that instantaneous size variations of an n -particle cluster are comparable with the variation of the average cluster radii for n within a few tens. It is then attempting to approximate the correlations between different shaped populations of clusters by a single effective one-component hard sphere system to take care of the average inter-cluster correlations. Then

$$Q_{inter}(\{N_n\}, V, T) = Q_{ideal} e^{-\beta F_{cs}} \quad (18)$$

where Q_{ideal} is given in eqn (11) and F_{cs} is the Carnahan–Starling²³ excess free energy

$$\frac{\beta F_{cs}(\eta_t)}{N_t} = \frac{\eta_t(4 - 3\eta_t)}{(1 - \eta_t)^2}, \quad (19)$$

where $N_t = \sum_{n=1}^{n_c} N_n$ is the total number of clusters and $\eta_t = \sum_{n=1}^{n_c} \eta_n$ is the total cluster packing fraction. Following the same steps as before one obtains

Table 1 The low temperatures internal energy per particle of the clusters with up to 12 particles when $\Delta = 0.5\sigma$. Also shown is the gyration radius R_g defined in eqn (27)

N	U/n	U	R_g
1	0	0	0
2	-0.5	-1	$\sim 1/2$
3	-1	-3	$\sim 1/\sqrt{3}$
4	-1.5	-6	0.83
5	-2.0	-10	0.76
6	-2.50	-15	0.75
7	-2.71	-19	0.91
8	-2.88	-23	0.93
9	-3.10	-28	0.96
10	-3.20	-32	1.00
11	-3.36	-37	1.04
12	-3.42	-41	1.08

$$\bar{\rho}_n = \lambda^n \frac{q_n^{intra}}{\Lambda_n^3} G(\eta_t), \quad (20)$$

where we have introduced the function

$$G(x) = \exp\left[-\frac{x(8-9x+3x^2)}{(1-x)^3}\right]. \quad (21)$$

For the free energy one obtains from eqn (10)

$$\frac{\beta F_{tot}}{V} = \sum_{n=1}^{n_c} [\bar{\rho}_n \ln(\bar{\rho}_n \Lambda_n^3) - \bar{\rho}_n] + \sum_{n=1}^{n_c} \bar{\rho}_n \beta f_n^{intra} + \frac{\beta F_{cs}(\bar{\eta}_t)}{V}, \quad (22)$$

that differs from the ideal gas counterpart eqn (14) only for the last additional term. Clearly one recovers the ideal gas in the limit $\bar{\rho}_n \rightarrow 0$ as it should. In order to find the correct solution for this system of equation it is important to choose the one that is continuously obtained from the solution of the ideal gas case at $\sigma_0 \rightarrow 0$.

E. Thermodynamic quantities

It proves convenient to express our analysis in terms of reduced partition functions Z rather than of the full partition functions Q used in Section III. This can be conveniently done by the definitions

$$Q_{inter} = \prod_{n=1}^{n_c} \frac{Z_{inter}}{\Lambda_n^{3N_n}}, \quad q_n^{intra} = \Lambda_n^3 Z_n^{intra}. \quad (23)$$

Given the partition function Q_{tot} we can determine the Carahan–Starling excess free energy

$$\beta F^{exc} = -\ln\left(\frac{Q_{tot}}{V^N}\right), \quad (24)$$

the internal energy per particle

$$\begin{aligned} u &= \frac{3}{2\beta} + \frac{1}{N} \frac{\partial(\beta F^{exc})}{\partial\beta} = \frac{3}{2\beta} - \sum_{n=1}^{n_c} \frac{N_n}{N} \frac{\partial(\ln Z_n^{intra})}{\partial\beta} \\ &= \frac{3}{2\beta} + \sum_{n=1}^{n_c} n \frac{N_n}{N} u_n(T), \end{aligned} \quad (25)$$

where u_n is the internal energy per particle of an n -cluster (see Section V). We can also determine the compressibility factor

$$\frac{\beta P}{\rho} = \frac{1}{\rho} \frac{\partial(\ln Q_{tot})}{\partial V} = \frac{1}{\rho} \frac{\partial(\ln Z_{inter})}{\partial V} = \frac{1 + \eta_t + \eta_t^2 - \eta_t^3}{(1 - \eta_t)^3}. \quad (26)$$

V. Computation of the intra-cluster free energy

The simulation were carried out following the same prescription used for the bulk fluid phases.^{9,10} Two kind of moves for each chosen particle—a random translation and a random rotation—were allowed, following standard recipes²⁴ and a standard Metropolis²⁵ algorithm was used to compute the energy per particle of the system of n particles.

Typical runs were of about 5×10^6 steps, one step consisting of n particles moves.

We studied first the case of clusters in the neighborhood of $n = 10$ particles which is expected to be sufficient to observe the micellization process due to the single layer clustering.¹⁰

To this aim we started with an initial configuration of two pentagons with particles at their vertices juxtaposed one above the other. The two pentagons are parallel to the x - y plane, have the z axis passing from their centers, and are one at $z = +\sigma/2$ and the other at $z = -\sigma/2$. The unit vectors attached to the spheres were chosen to connect the origin to the center of the given sphere. We obtained the clusters with a lower number of particles by simply deleting particles and obtained the clusters with a higher number of particles by adding on the z axis a particle just above the upper pentagon and/or just below the lower one. However the results of the simulations are independent of the initial configuration chosen.

In order to compare with previous studies,⁹ we consider the $\Delta = 0.5\sigma$ case first.

We performed the simulations of the isolated cluster and we have explicitly tested that results coincide with the calculation stemming for the bulk low density Janus fluid from which we extract cluster informations by taking all the clusters found with the same size and averaging their properties.

During the simulation we allow all possible moves but we do not count the configurations which are not topologically connected, *i.e.* those configurations where it is not possible to go from one sphere to all the others through a path; the path being allowed or not to move from one particle 1 to particle 2 depending whether $\Phi(12)$ has value $-\varepsilon$ or not.

At high temperatures the limiting value for the energy per particle is $-\varepsilon(n-1)/n$. At low temperature ($k_B T/\sigma < 0.15$) the clusters tend to freeze into certain energy minima. This can be improved by “regularizing” the angular part of the Kern–Frenkel potential into $\Psi(\hat{\mathbf{n}}_1, \hat{\mathbf{n}}_2, \hat{\mathbf{r}}_{12}) = \{\tanh[|(\hat{\mathbf{n}}_1 \cdot \hat{\mathbf{r}}_{12} - \cos\theta_0)| + 1]\} \{\tanh[|(-\hat{\mathbf{n}}_2 \cdot \hat{\mathbf{r}}_{12} - \cos\theta_0)| + 1]\}/4$ and gradually increase l starting from $1/2$ during the simulation up to values where there is no actual difference between the continuous potential and the original stepwise one. This allowed us to reach the configuration with the real minimum energy with a certain confidence.

In Fig. 1 we depict the relative cluster population N_n/N as a function of the reduced density $\rho\sigma^3$ in the ideal-gas case for $n \leq 12$ and two different temperatures $k_B T/\varepsilon = 0.25$ (top panel) and $k_B T/\varepsilon = 0.30$ (bottom panel). Temperature values were selected to bracket the expected critical temperature $k_B T/\varepsilon \approx 0.28$ on transition from a vapor phase mostly formed by

monomers (at higher temperatures) and a vapor phase with predominant clusters (at lower temperatures) in the chosen range of densities.¹⁰

As expected, we observe a predominance of monomers and higher order clusters at low and high density respectively. No significant difference is apparent for the results of the two temperatures. This is most likely due to the ideal-gas nature of the interacting part and can be improved by using the Carnahan–Starling fluid description, as we shall see.

Next we consider the internal energy per particle $u_n = \langle U \rangle/n$ within the n -th cluster along with the gyration radii defined by

$$R_g^2 = \sum_{j=1}^n |\mathbf{r}_j - \mathbf{r}_{av}|^2/n \quad (27)$$

with $\mathbf{r}_{av} = \sum_{j=1}^n \mathbf{r}_j/n$, \mathbf{r}_j being the position of the j -th particle. Results for both internal energy and gyration radii for such configurations are tabulated in Table 1. This provides an additional insight on the morphologies of the obtained clusters, in particular on the relative weak n dependence of the linear size of the obtained clusters.

The results for u_n as a function of temperature are reported in Table 2 and can be conveniently fitted by a Gaussian profile

$$u_n(T) = a_n \exp[-b_n T^2] + c_n, \quad (28)$$

where the fitting parameters a_n , b_n , and c_n for the $n = 2, 3, \dots, 12$ clusters ($u_1 = 0$ by definition) can also be found in Table 2.

From this expression we can determine the excess free energy of the cluster $f_n^{\text{ex.intra}} = \beta F^{\text{ex.intra}}/n$ by thermodynamic integration

Table 2 Fit to a Gaussian of the energy per particle as a function of the temperature (see eqn (28)). c_n values are common to the three cases

n	$\Delta = 0.5\sigma$		$\Delta = 0.25\sigma$		$\Delta = 0.15\sigma$		c_n
	a_n	b_n	a_n	b_n	a_n	b_n	
2	0	1	0	1	0	1	-0.50
3	-0.337	3.880	-0.339	6.905	-0.346	10.780	-0.67
4	-0.778	4.670	-0.771	7.502	-0.774	7.975	-0.75
5	-1.226	5.162	-1.025	5.890	-1.034	9.366	-0.80
6	-1.700	5.600	-1.381	7.361	-1.207	9.214	-0.83
7	-1.899	5.263	-1.423	6.767	-1.480	8.277	-0.86
8	-2.064	5.080	-1.520	4.179	-1.551	8.503	-0.88
9	-2.301	5.478	-1.579	4.367	-1.681	10.160	-0.89
10	-2.394	5.509	-1.725	4.271	-1.551	9.419	-0.90
11	-2.556	5.644	-1.846	4.829	-1.696	9.755	-0.91
12	-2.598	6.077	-1.854	5.723	-1.814	10.567	-0.92

$$f_n^{\text{ex.intra}}(\beta) = \int_0^\beta dx u_n(1/x) \quad (29)$$

So that $f_n^{\text{intra}} = f_n^{\text{ex.intra}} + f_n^{\text{id.intra}}$ with the ideal free energy contribution being

$$f_n^{\text{id.intra}}(\beta) = 3 \ln \Lambda_n + (\ln n!)/n - \ln v_0, \quad (30)$$

where $v_0 = \pi \sigma_0^3/6$ is the volume of one n -cluster, and with the excess part given by

$$f_n^{\text{ex.intra}} = c_n \beta + a_n \sqrt{b_n} \left\{ \frac{e^{-b_n/\beta^2}}{\sqrt{b_n/\beta^2}} + \sqrt{\pi} \left[\text{erf} \left(\sqrt{b_n/\beta^2} \right) - 1 \right] \right\}. \quad (31)$$

The intra-cluster partition function is then $Z_n^{\text{intra}} = v_0^n e^{-n f_n^{\text{intra}}}$ (of course $Z_1^{\text{intra}} = v_0$). As anticipated we here choose $\sigma_n = \sigma_0$, for all n , where σ_0 is the only undetermined parameter in the theory.

VI. Additional results

A. Carnahan–Starling results

In this case the theory depends upon the average diameter of a cluster σ_0 . This is obtained by the requirement that the Carnahan–Starling results best match MC results for the bulk simulations.

To this aim, we consider Monte Carlo results at $\rho \sigma^3 = 0.01$ on the vapor phase, for the distribution of the cluster sizes, with our theory. This is depicted in Fig. 2 where we compare the Carnahan–Starling approximation with the MC data for the distribution of cluster sizes at decreasing values of temperatures starting from $k_B T/\epsilon = 0.5$ which provides a good match with MC results for $\sigma_0 \approx 2.64\sigma$. This value is then used in all subsequent calculations.

It is important to remark that, in order to find the correct solution for this system of equations, it is important to choose the one that is continuously obtained from the solution of the ideal gas case at $\sigma_0 \rightarrow 0$.

At lower temperatures the discrepancy with the MC data for the vapor increases. This was to be expected in view of the fact that the two-layer vesicles (n -clusters with $n = 40$) contribution to

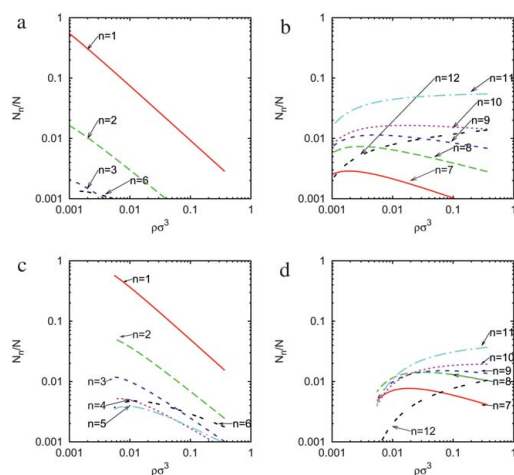


Fig. 1 Values of N_n/N , $n = 1, 2, 3, \dots, 12$ as a function of the density for $\Delta = 0.5\sigma$ and $k_B T/\epsilon = 0.25$ (top panels) and $k_B T/\epsilon = 0.30$ (bottom panels). In both cases curves for $n = 1, \dots, 6$ are on the left panels and those associated with $n = 7, \dots, 12$ are on the right panels. All plots have been reported on the same scale for a better comparison. Clusters associated with values $n = 4, 5$ have curves lying below the lower limit of 0.001 concentration in the case $k_B T/\epsilon = 0.25$.

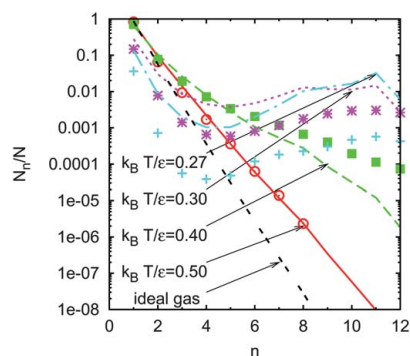


Fig. 2 Comparison between the MC data (points) and our calculations using the effective one component hard sphere inter-cluster partition function within the Carnahan-Starling approximation for $\sigma_0 = 2.64\sigma$ (lines), for N_n/N , $n = 1, 2, 3, \dots, 12$ as a function of the clusters size n at $\rho\sigma^3 = 0.01$, $\Delta = 0.5\sigma$, and various temperatures. Also shown is the ideal gas approximation.

the vapor phase, and not included in the present computation, becomes increasingly important.¹⁰ The agreement could be clearly improved by allowing a temperature dependence of the effective cluster diameter σ_0 , but we have chosen to keep σ_0 fixed to maintain a clear control of the approximations involved in our approach.

In Fig. 3 (top panel) we show the resulting cluster distribution for the N_n/N as a function of density for a temperature ($k_B T/\epsilon = 0.27$) at the onset of the expected critical micelle concentration.¹⁰ Unlike the previous case with an ideal gas, there is now a clear

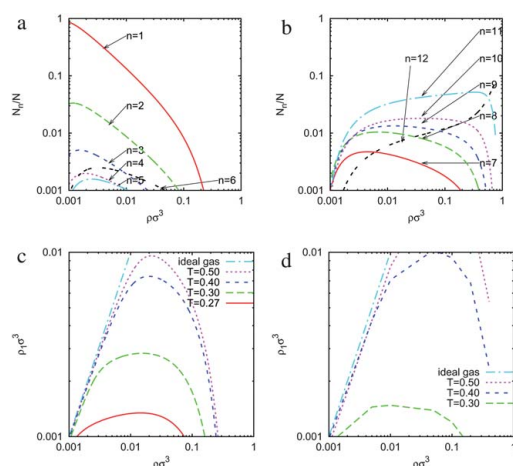


Fig. 3 Values of N_n/N , $n = 1, 2, 3, \dots, 12$ as a function of the density for $k_B T/\epsilon = 0.27$ (top panels). Clusters with $n = 1, \dots, 6$ are on the left, those with $n = 7, \dots, 12$ on the right. The bottom panels depict the monomer concentration $\rho_1\sigma^3$ as a function of the total density $\rho\sigma^3$ for decreasing temperatures. The result of the present approach (left) is contrasted with MC simulations (right). All results refer to the $\Delta = 0.5\sigma$ case with a cluster diameter $\sigma_0 = 2.64\sigma$.

predominance of the $n \approx 10$ clusters in the whole concentration range. Additional insights can be obtained by plotting the monomer density $\rho_1\sigma^3$ versus the total concentration $\rho\sigma^3$ for decreasing temperatures, as reported in the bottom panels of the same figure, where the result of the present approach is contrasted with bulk numerical simulations of the same quantity.¹⁰ This clearly shows the onset of a critical concentration where clusterization becomes the predominant mechanism at each temperature (this can be obtained by extrapolating the flat part of the curves to the vertical axis).

In order to assess the range of reliability of our results, we have also attempted to include in the theory all clusters of size up to 20 particles. Fig. 4 shows how the theory compares with the MC results at $k_B T/\epsilon = 0.4$ for the distribution of the cluster sizes. Note that the vertical axis spans about 8 order of magnitudes. Here we used a slightly different value $\sigma_0 \approx 2.92\sigma$ for the cluster diameters. Our theory nicely follows the MC data for the vapor phase up to $n \leq 12$. For larger clusters discrepancies begin to show up most likely due to the fact isolated clusters tend to frequently disaggregate during the simulation thus providing a very low acceptance ratio. As anticipated, for these larger cluster sizes, a full simulation of the bulk vapor phase begins to be competitive with the present methodology, and this is the main reason why, in the remainder of the paper, we only consider a mixture of n -clusters with $n \leq 12$.

As remarked, the present theory depends upon a free parameter (the average cluster diameter σ_0) that is computed by a best fit with the bulk MC simulations.

Fig. 5 displays the sensitivity of some of the computed quantities to the choice of the average cluster diameter σ_0/σ . In particular, we have considered the compressibility factor $\beta P/\rho$, the internal energy per particle $u = U/N$ and the reduced free energy per particle $\ln(Q_{tot})/N$. In all cases, there is a non-negligible dependence on the σ_0/σ value indicating the importance of selecting the correct effective cluster diameter. This could be improved by considering a distribution of cluster diameters.

Notice that as σ_0 increases the packing fraction of the clusters η , quickly exceeds unity, thus limiting the possible range of

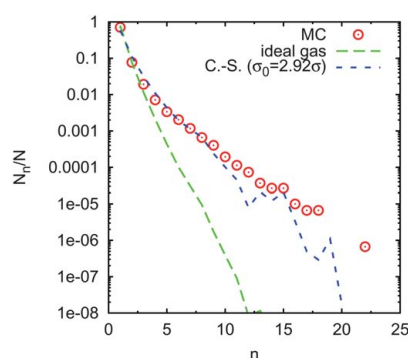


Fig. 4 Comparison between MC data and cluster theory using the Carnahan-Starling approximation (for $\sigma_0/\sigma = 2.92$) for N_n/N , $n = 1, 2, 3, \dots, 20$ as a function of the clusters size n at $k_B T/\epsilon = 0.4$, $\rho\sigma^3 = 0.01$, and $\Delta = 0.5\sigma$.

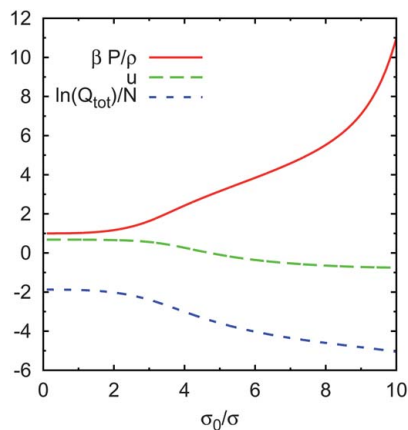


Fig. 5 Values for the compressibility factor, the internal energy per particle, and the logarithm of the total partition function as a function of the n -cluster diameter σ_0/σ at $\rho\sigma^3 = 0.01$, $k_B T/\varepsilon = 0.5$, and $\Delta = 0.5\sigma$.

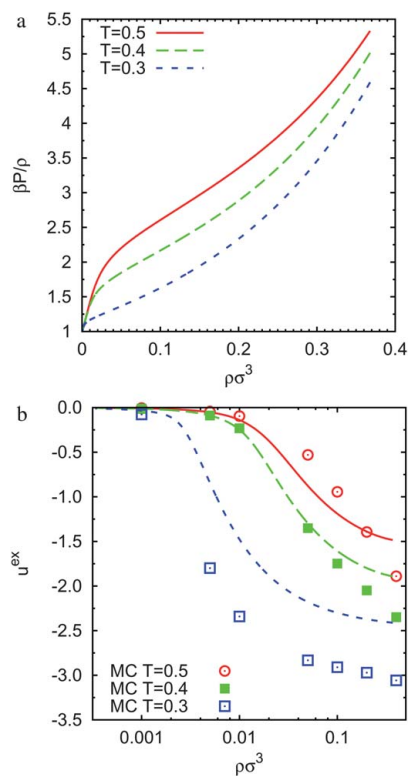


Fig. 6 Compressibility factor as predicted by the Carnahan–Starling ($\sigma_0 = 2.64\sigma$) cluster theory (top panel). In the bottom panel we compare the MC data and the Carnahan–Starling cluster theory (same diameter as above) for the excess internal energy per particle for three different values of temperatures. In all cases $\Delta = 0.5\sigma$.

acceptance for the cluster diameter. Similarly, in Fig. 6 we report the compressibility factor and the excess internal energy per particle. The excess internal energy is compared with the MC data for the vapor phase.⁹

B. Prediction for a different range of the square well

So far, we have considered the case where the range of interaction (the width of the square well) Δ was 50% of the particle size σ . This is the value which has been exploited in details in past MC studies of the bulk Janus fluid.^{9,10} As this range decreases, typical relevant temperatures decrease and simulations become increasingly more demanding from the computational point of view to equilibrate. It is then not surprising that no results have been yet reported in the literature for these ranges. On the other hand, these are the ranges most frequently encountered in the experiments,²⁶ and this is where the usefulness of our method can be assessed.

We have then repeated the calculations for $\Delta/\sigma = 0.25$, that is half of previous value.

Fig. 7 reports the cluster distributions for the ideal and the Carnahan–Starling fluids (lower temperatures), the counterparts of Fig. 1 and 3. Concentrations of the n -clusters are now shifted towards higher densities with respect to the case with the twice as wide range, as expected. Also now the roles of the 10-cluster and the 11-cluster are inverted with respect to before. This means that lower attractive range provides, on average, smaller stable clusters, a results that can be understood on an intuitive basis.

We also found that the thermodynamic quantities considered above are only marginally affected by the reduction of the width well in the considered range of densities and temperature.

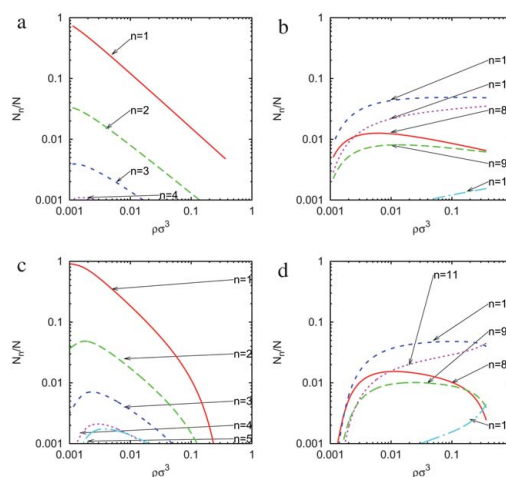


Fig. 7 Cluster distribution in the case of $\Delta = 0.25\sigma$. The top panels report the ideal gas result at $k_B T/\varepsilon = 0.25$ ($n = 1, \dots, 6$ on the left and $n = 7, \dots, 12$ on the right). This is the same as Fig. 1. The bottom panels depict with the same distribution of curves the results obtained with the Carnahan–Starling approximation at $k_B T/\varepsilon = 0.27$ which is the counterpart of Fig. 3.

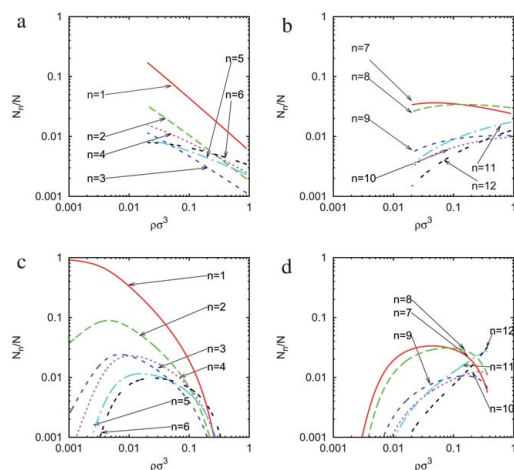


Fig. 8 Same as Fig. 7 for $\Delta = 0.15\sigma$.

We have also considered the case of $\Delta = 0.15\sigma$. From Fig. 8 it is apparent that the concentrations of the n -clusters are once again shifted towards higher densities with respect to the case with $\Delta = 0.25\sigma$. Also now the 7- and 8-clusters seem to be the ones favoured at $T = 0.27$ in a range of densities in a neighborhood of $\rho\sigma^3 = 0.1$. This confirms the trend found in the case of $\Delta = 0.25\sigma$.

VII. Conclusions

In this paper, we have constructed a cluster theory for the vapor of Janus fluid. This is an approach that is complementary to previous studies based on highly demanding MC simulations,^{9,10} with the aim of providing a detailed description of the vapor phase in view of its remarkable unusual micellization properties.

The main idea behind the present approach is to consider the vapor phase as formed by clusters, containing an increasing number of particles, that are weakly interacting among each other so that simple fluid models—such as ideal gas or hard spheres—can be used to mimic their physical properties. The internal degrees of freedom of each cluster are instead obtained through a direct MC simulation of a single isolated cluster, a much simpler task as compared to the bulk simulation, and a procedure akin to those used in the framework of simple fluids¹⁶ is then used to combine the two calculations and obtain the full description of the system.

It is worth noticing that, in the ideal-gas case, a similar procedure has also been already implemented in micellization theories by several groups,^{27,28} and the results we obtain in the present context are quite consistent with those.

There are two basic reasons why we expect this approach to be valuable. First because previous full bulk simulations showed micelles to be only weakly interacting in the vapor density range and hence a simple description for the inter-cluster part is expected to be sufficient. Second, because it has been observed that the vapor properties are mostly dominated by particular cluster sizes corresponding to $n \approx 10$ and $n \approx 40$ particles, so

only a limited number of cluster sizes is necessary to obtain a complete description.

In the present work, we have considered clusters up to 12 particles and compared the ideal-gas description with the description of a gas of hard-spheres, mimicking the original clusters and with an effective cluster diameter σ_0 , using the Carnahan–Starling approximate description. The value of σ_0 has been obtained by a matching of the results for the internal energy with full bulk MC simulations. A good agreement was found at $k_B T \epsilon = 0.5$ and at densities $\rho\sigma^3 = 0.01$ when $\sigma_0 \approx 2.64\sigma$. Results from the Carnahan–Starling theory is found to be far superior as compared to the ideal-gas description, thus emphasizing the importance of inter cluster correlations in the vapor phase.

We also considered higher sizes clusters (of up to 20 particles) but the agreement with the simulations for the larger sizes becomes less satisfactory. The theory becomes less and less accurate as oscillations in the behavior of the concentrations of the big clusters with size appear. This may be due to the difficulty in an accurate determination of the internal energy of isolated big clusters. In this respect in order to be able to observe the vesicles (clusters of around 40 particles⁹) phenomenology we certainly need to include additional insights to avoid the task of the solution of a system of about 40 coupled equations. An additional difficulty consists in the fact that in this case the single diameter effective approximation used for all clusters up to 12 in the present study will no longer be realistic, not even at the simplest possible level of description. Both these problems could be tackled by focussing only on clusters bracketing the interesting ones ($n \approx 10$ and $n \approx 40$ in the present case).

We showed that in accord with the simulation results of ref. 9, at temperatures around $k_B T \epsilon = 0.27$ there is a gap of densities where the number of clusters of 11 particles (micelles) surpasses the number of any other cluster. This gap shrinks as we increase the temperature.

The determined approximation to the partition function of the vapor phase of the Janus fluid can then be used to compute various thermodynamical quantities.

We found reasonable quantitative agreement between the Monte Carlo data of ref. 9 and our theory for the excess internal energy of the vapor phase of the Janus fluid. We additionally computed the compressibility factor for which no simulation data are yet available.

Having validated the model against numerical predictions for $\Delta = 0.5\sigma$ we pursued the analysis for lower widths of the well, values that are closer to the experimental range of interactions.²⁶ In view of the overall decrease in the attractions, characteristic critical temperatures also decrease, thus making numerical simulations increasingly demanding from the computational point of view.

For the case of $\Delta = 0.25\sigma$ we produced new predictions for the concentrations, the compressibility factor, and the internal energy per particle as a function of density. In particular we saw that as the range of the attraction diminishes the Janus fluid prefers to form clusters of a lower number of particles.

Consistent results are also found for the case of $\Delta = 0.15\sigma$, a value which is rather close to those used in experiments.

An attempt to push the cluster theory to bigger cluster sizes showed that the theory becomes less and less accurate as oscillations in the behavior of the concentrations of the big clusters

[View Online](#)

with size appear. This may be due to the difficulty in an accurate determination of the internal energy of isolated big clusters. In this respect in order to be able to observe the vesicles (clusters of around 40 particles⁹) phenomenology we certainly need to include additional insights to avoid the task of the solution of a system of about 40 coupled equations. An additional difficulty consists in the fact that in this case the single diameter effective approximation used for all clusters up to 12 in the present study will no longer be realistic, not even at the simplest possible level of description. Both these problems could be tackled by focusing only on clusters bracketing the interesting ones ($n \approx 10$ and $n \approx 40$ in the present case).

Two additional perspectives will be the subject of a future study. First the dependence on coverage χ could also be tackled using the present approach, and this would provide invaluable information on the micellization mechanism for small coverage, a task that is still out of reach of direct numerical simulations. Secondly, it would be extremely interesting to address the issue of the reentrant phase diagram and the (possible) existence of an additional liquid–liquid critical point. This has been recently attempted in a very recent preprint,²⁹ using a monomer–cluster equilibrium theory in the same spirit as that presented here.

Acknowledgements

RF would like to acknowledge the support of the National Institute of Theoretical Physics of South Africa. AG acknowledges the support of a PRIN-COFIN 2007B58EAB grant. FS acknowledges support from ERC-226207-PATCHY-COLLOIDS and ITN-234810-COMPLOIDS.

References

- 1 V. N. Manoharan, M. T. Elsesser and D. J. Pine, *Science*, 2003, **301**, 483.
- 2 A. B. Pawar and I. Kretzchmar, *Macromol. Rapid Commun.*, 2010, **31**, 150.
- 3 S. C. Glotzer and M. J. Solomon, *Nat. Mater.*, 2007, **6**, 557.
- 4 Z. Zhang and S. C. Glotzer, *Nano Lett.*, 2004, **4**, 1407.
- 5 P. G. de Gennes, *Rev. Mod. Phys.*, 1992, **64**, 645.
- 6 C. Casagrande, P. Fabre, M. Veyssié and E. Raphaël, *Europhys. Lett.*, 1989, **9**, 251.
- 7 L. Hong, A. Cacciuto, E. Luijten and S. Granick, *Nano Lett.*, 2006, **6**, 2510.
- 8 A. Walther and A. H. Müller, *Soft Matter*, 2008, **4**, 663.
- 9 F. Sciortino, A. Giacometti and G. Pastore, *Phys. Rev. Lett.*, 2009, **103**, 237801.
- 10 F. Sciortino, A. Giacometti and G. Pastore, *Phys. Chem. Chem. Phys.*, 2010, **12**, 11869.
- 11 N. Kern and D. Frenkel, *J. Chem. Phys.*, 2003, **118**, 9882.
- 12 M. S. Wertheim, *J. Stat. Phys.*, 1984, **35**, 19; M. S. Wertheim, *J. Stat. Phys.*, 1984, **35**, 35; M. S. Wertheim, *J. Stat. Phys.*, 1986, **42**, 459; M. S. Wertheim, *J. Stat. Phys.*, 1986, **42**, 477.
- 13 G. T. Evans and J. Chem. Phys., 1997, **106**, 9718.
- 14 M. E. Fisher and D. M. Zuckerman, *J. Chem. Phys.*, 1998, **109**, 7961.
- 15 J. Dudowicz, J. F. Douglas and K. F. Freed, *J. Phys. Chem. B*, 2008, **112**, 16193.
- 16 A. Tani and D. Henderson, *J. Chem. Phys.*, 1983, **79**, 2390.
- 17 N. Bjerrum, *Kgl. Danske Vidensk. Selskab*, 1926, **7**, 9.
- 18 J. L. Barrat and J. P. Hansen, *Basic Concepts for Simple and Complex Liquids*, Cambridge University Press, 2003.
- 19 F. Sciortino, E. Bianchi, J. F. Douglas and P. Tartaglia, *J. Chem. Phys.*, 2007, **126**, 194903.
- 20 T. Boublik, *J. Chem. Phys.*, 1970, **53**, 1523.
- 21 G. A. Mansoori, N. F. Carnahan, K. E. Starling and T. W. Leland Jr, *J. Chem. Phys.*, 1971, **54**, 1523.
- 22 N. F. Carnahan and K. E. Starling, *J. Chem. Phys.*, 1969, **51**, 635.
- 23 J. P. Hansen and I. R. McDonald, *Theory of Simple Liquids*, 2nd Ed., Academic Press, 1986.
- 24 M. P. Allen and D. J. Tildesley, *Computer Simulation of Liquids*, Oxford Univ. Press, 1987.
- 25 N. Metropolis, A. W. Rosenbluth, M. N. Rosenbluth, A. H. Teller and E. Teller, *J. Chem. Phys.*, 1953, **21**, 1087.
- 26 L. Hong, A. Cacciuto, E. Luijten and S. Granick, *Langmuir*, 2008, **24**, 621.
- 27 R. Nagarajan and E. Ruckenstein, *Langmuir*, 1991, **7**, 2934.
- 28 J. N. Israelachvili, D. J. Mitchell and B. W. Ninham, *J. Chem. Soc., Faraday Trans. 2*, 1976, **72**, 1525.
- 29 A. Reinhardt, A. J. Williamson, J. P. K. Doyle, J. Carrete, L. M. Varela and A. A. Louis, 2010, arXiv:1010.4676v1 [cond-mat.soft].

Chapter 24

Phase diagram of the penetrable square well-model

Fantoni R., A. Malijevský, A. Santos, and A. Giacometti, EPL **93**, 26002 (2011)

Title: “Phase diagram of the penetrable square well-model”

Abstract: We study a system formed by soft colloidal spheres attracting each other via a square-well potential, using extensive Monte Carlo simulations of various nature. The softness is implemented through a reduction of the infinite part of the repulsive potential to a finite one. For sufficiently low values of the penetrability parameter we find the system to be Ruelle stable with square-well like behavior. For high values of the penetrability the system is thermodynamically unstable and collapses into an isolated blob formed by a few clusters each containing many overlapping particles. For intermediate values of the penetrability the system has a rich phase diagram with a partial lack of thermodynamic consistency.

Appears in the SklogWiki:

http://www.sklogwiki.org/SklogWiki/index.php/Penetrable_square_well_model

Phase diagram of the penetrable-square-well model

R. FANTONI^{1(a)}, A. MALLJEVSKÝ², A. SANTOS³ and A. GIACOMETTI⁴

¹ *National Institute for Theoretical Physics (NITheP) and Institute of Theoretical Physics Stellenbosch 7600, South Africa*

² *E. Hála Laboratory of Thermodynamics, Institute of Chemical Process Fundamentals of the ASCR and Department of Physical Chemistry, Institute of Chemical Technology - Prague, 166 28 Praha 6, Czech Republic, EU*

³ *Departamento de Física, Universidad de Extremadura - E-06071 Badajoz, Spain, EU*

⁴ *Dipartimento di Scienze Molecolari e Nanosistemi, Università Ca' Foscari Venezia - S. Marta DD2137, I-30123 Venezia, Italy, EU*

received 12 October 2010; accepted in final form 3 January 2011

published online 2 February 2011

PACS 64.60.De – Statistical mechanics of model systems (Ising model, Potts model, field-theory models, Monte Carlo techniques, etc.)

PACS 64.60.Ej – Studies/theory of phase transitions of specific substances

PACS 64.70.D- – Solid-liquid transitions

Abstract – We study a system formed by soft colloidal spheres attracting each other via a square-well potential, using extensive Monte Carlo simulations of various nature. The softness is implemented through a reduction of the infinite part of the repulsive potential to a finite one. For sufficiently low values of the penetrability parameter we find the system to be Ruelle stable with square-well-like behavior. For high values of the penetrability the system is thermodynamically unstable and collapses into an isolated blob formed by a few clusters each containing many overlapping particles. For intermediate values of the penetrability the system has a rich phase diagram with a partial lack of thermodynamic consistency.

Copyright © EPLA, 2011

Pair effective interactions in soft-condensed-matter physics can be of various nature and one can often find real systems whose interaction is bounded at small separations as, for instance, in the case of star and chain polymers [1]. In this case, paradigmatic models, such as square-well (SW) fluids, that have been rather successful in predicting thermo-physical properties of simple liquids, are no longer useful. Instead, different minimal models accounting for the boundness of the potential have to be considered, the Gaussian core model [2] and the penetrable-sphere (PS) model [3–5] being well-studied examples. More recently, the penetrable-square-well (PSW) fluid has been added to this category [6–9] with the aim of including the existence of attractive effective potentials. The PSW model is obtained from the SW potential by reducing to a finite value the infinite repulsion at short range,

$$\phi_{\text{PSW}}(r) = \begin{cases} \epsilon_r, & r \leq \sigma, \\ -\epsilon_a, & \sigma < r \leq \sigma + \Delta, \\ 0, & r > \sigma + \Delta, \end{cases} \quad (1)$$

^(a)E-mail: rfantoni@ts.infn.it

where ϵ_r and ϵ_a are two positive energies accounting for the repulsive and attractive parts of the potential, respectively, Δ is the width of the attractive square well, and σ is the width of the repulsive barrier. For $\epsilon_r \rightarrow \infty$ one recovers the SW model, while for $\Delta = 0$ or $\epsilon_a = 0$ one recovers the PS model.

For finite ϵ_a , the ratio ϵ_a/ϵ_r is a measure of the penetrability of the barrier and we shall refer to ϵ_a/ϵ_r as the penetrability ratio. PSW pair potentials can be obtained as effective potentials for instance in polymer mixtures [10,11]. While in the majority of the cases the well depth ϵ_a is much smaller than the repulsive barrier ϵ_r (low penetrability limit) these mesoscopic objects are highly sensitive to external conditions (*e.g.*, quality of the solvent) and may thus in principle exhibit higher values of the penetrability ratio ϵ_a/ϵ_r .

It is well known that three-dimensional SW fluids exhibit a fluid-fluid phase transition for any width of the attractive square well [12–16], the liquid phase becoming metastable against the formation of the solid for a sufficiently narrow well [15]. It is also well established that in the PS fluid (that lacking an attractive component in the pair potential cannot have a fluid-fluid transition) an increase of the density leads to the formation of clusters

R. Fantoni *et al.*

of overlapping particles arranged in an ordered crystalline phase [3,17–19].

While the novel features appearing even in the one-dimensional case have been studied in some details [6–9], no analysis regarding the influence of penetrability and attractiveness on the phase behavior of PSW fluids have been reported, so far, in three dimensions. The present paper aims to fill this vacancy.

A system is defined to be Ruelle stable when the total potential energy U_N for a system of N particles satisfies the condition $U_N \geq -NB$, where B is a finite positive constant [20,21]. In ref. [8] we proved that in the one-dimensional case the PSW model is Ruelle stable if $\epsilon_a/\epsilon_r < 1/2(\ell+1)$, where ℓ is the integer part of Δ/σ . This result can be extended to any dimensionality d by the following arguments. The configuration which minimizes the energy of N particles interacting via the PSW potential is realized when M closed-packed clusters, each consisting of $s = N/M$ particles collapsed into one point, are distributed such that the distance between centers of two neighbor clusters is σ . In such a configuration, all the particles of the same cluster interact repulsively, so the repulsive contribution to the total potential energy is $\epsilon_r Ms(s-1)/2$. In addition, the particles of a given cluster interact attractively with all the particles of those f_Δ clusters within a distance smaller than $\sigma + \Delta$. In the two-dimensional case, $f_\Delta = 6$ and 12 if $\Delta/\sigma < \sqrt{3} - 1$ and $\sqrt{3} - 1 < \Delta/\sigma < 1$, respectively. For $d = 3$, the case we are interested in, one has $f_\Delta = 12, 18$, and 42 if $\Delta/\sigma < \sqrt{2} - 1$, $\sqrt{2} - 1 < \Delta/\sigma < \sqrt{3} - 1$, and $\sqrt{3} - 1 < \Delta/\sigma < 1$, respectively. The attractive contribution to the total potential energy is thus $-\epsilon_a(M/2)[f_\Delta - b_\Delta(M)]s^2$, where $b_\Delta(M)$ accounts for a reduction of the actual number of clusters interacting attractively, due to boundary effects. This quantity has the properties $b_\Delta(M) < f_\Delta$, $b_\Delta(1) = f_\Delta$, and $\lim_{M \rightarrow \infty} b_\Delta(M) = 0$. For instance, in the two-dimensional case with $\Delta/\sigma < \sqrt{3} - 1$ one has $b_\Delta(M) = 2(4\sqrt{M} - 1)/M$. Therefore, the total potential energy is

$$\frac{U_N(M)}{N\epsilon_r} = -\frac{1}{2} + \frac{N}{2M}F(M), \quad (2)$$

where $F(M) \equiv (\epsilon_a/\epsilon_r)b_\Delta(M) + (1 - f_\Delta\epsilon_a/\epsilon_r)$. If $\epsilon_a/\epsilon_r < 1/f_\Delta$, $F(M)$ is positive definite, so $U_N(M)/N$ has a lower bound and the system is stable in the thermodynamic limit. On the other hand, if $\epsilon_a/\epsilon_r > 1/f_\Delta$, one has $F(1) = 1$ but $\lim_{M \rightarrow \infty} F(M) = -(f_\Delta\epsilon_a/\epsilon_r - 1) < 0$. In that case, there must exist a certain *finite* value $M = M_0$ such that $F(M) < 0$ for $M > M_0$. As a consequence, in those configurations with $M > M_0$, $U_N(M)/N$ has no lower bound in the limit $N \rightarrow \infty$ and thus the system may be unstable.

We have performed an extensive analysis of the vapor-liquid phase transition of the system using Gibbs Ensemble Monte Carlo (GEMC) simulations [22–26], starting from the corresponding SW fluid condition and gradually increasing the penetrability ratio ϵ_a/ϵ_r until the transition disappears. A total number of $N = 512$ particles with

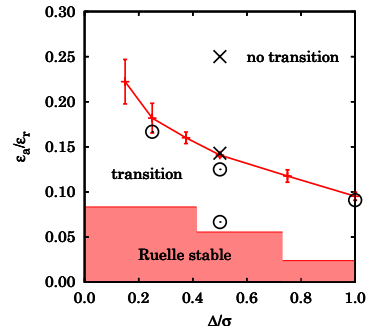


Fig. 1: (Colour on-line) Plot of the penetrability ratio ϵ_a/ϵ_r as a function of Δ/σ . The displayed line separates the parameter region where the PSW model admits a fluid-fluid phase transition from that where it does not. The highlighted region ($\epsilon_a/\epsilon_r \leq 1/12$ for $\Delta/\sigma < \sqrt{2} - 1$, $\epsilon_a/\epsilon_r \leq 1/18$ for $\sqrt{2} - 1 < \Delta/\sigma < \sqrt{3} - 1$, and $\epsilon_a/\epsilon_r \leq 1/42$ for $\sqrt{3} - 1 < \Delta/\sigma < 1$) shows where the model is expected to be thermodynamically stable in the sense of Ruelle for any thermodynamic state. The SW model falls on the horizontal axis ($\epsilon_a/\epsilon_r \rightarrow 0$) and its fluid-fluid transition is expected to be metastable against the freezing transition for $\Delta/\sigma \lesssim 0.25$ [15]. The circles are the points chosen for the calculation of the coexistence lines (see figs. 2 and 5). The crosses are the points chosen for the determination of the boundary between extensive and non-extensive phases (see fig. 3).

$2N$ -particle random displacements, $N/10$ volume changes, and N -particle swap moves between the gas and the liquid box, on average per cycle, were considered. We find that for any given width $\Delta/\sigma < 1$ of the well, there is a limit value of the penetrability ratio ϵ_a/ϵ_r , above which no fluid-fluid phase transition is observed. This is depicted in fig. 1 where it can be observed that (for $\Delta/\sigma < 1$) this line lies outside the Ruelle stable region $\epsilon_a/\epsilon_r < 1/f_\Delta$.

It is instructive to analyze the detailed form of the coexistence curves below (but close to) the limit line of fig. 1. This is presented in fig. 2. We have explicitly checked that our code reproduces completely the results of Vega *et al.* [12] for the SW model. Following standard procedures [12] we fitted the GEMC points near the critical point using the law of rectilinear diameters $(\rho_l + \rho_g)/2 = \rho_c + A(T_c - T)$, where ρ_l (ρ_g) is the density of the liquid (gas) phase, ρ_c is the critical density, and T_c is the critical temperature. Furthermore, the temperature dependence of the density difference of the coexisting phases is fitted to the scaling law $\rho_l - \rho_g = B(T_c - T)^\beta$ where $\beta = 0.32$ is the critical exponent for the three-dimensional Ising model. The amplitudes A and B were determined from the fit. In the state points above the limit line of fig. 1 we have considered temperatures below the critical temperature of the corresponding SW system. The disappearance of the fluid-fluid transition is signaled by the evolution towards an empty gas box and a clustered phase in the liquid box.

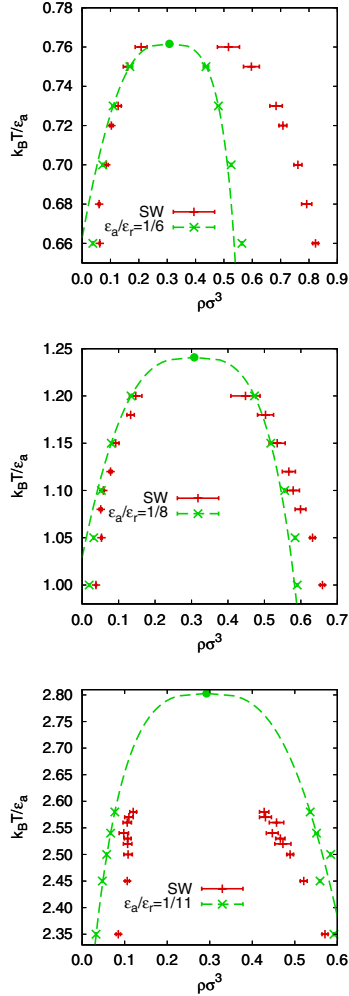


Fig. 2: (Colour on-line) Fluid-fluid coexistence line. The solid circle represents the critical point (ρ_c, T_c) . In the top panel, for $\Delta/\sigma = 0.25$ and $\epsilon_a/\epsilon_r = 1/6$, one has $\rho_c \sigma^3 = 0.307$ and $k_B T_c / \epsilon_a = 0.762$; in the middle panel, below the limit penetrability, for $\Delta/\sigma = 0.5$ and $\epsilon_a/\epsilon_r = 1/8$, one has $\rho_c \sigma^3 = 0.307$ and $k_B T_c / \epsilon_a = 1.241$; and in the bottom panel for $\Delta/\sigma = 1.0$ and $\epsilon_a/\epsilon_r = 1/11$, one has $\rho_c \sigma^3 = 0.292$ and $k_B T_c / \epsilon_a = 2.803$. The lines are the result of the fit with the law of rectilinear diameters. The SW results are the ones of Vega *et al.* [12].

As discussed, the PSW fluid is thermodynamically Ruelle stable when $\epsilon_a/\epsilon_r < 1/f_\Delta$ for all values of the thermodynamic parameters. For $\epsilon_a/\epsilon_r > 1/f_\Delta$ the system is either extensive or non-extensive depending on temperature and density. For a given density, one could then expect that there exists a certain temperature $T_{\text{inst}}(\rho)$, such that the system is metastable if $T > T_{\text{inst}}$ and unstable if

Phase diagram of the penetrable-square-well model

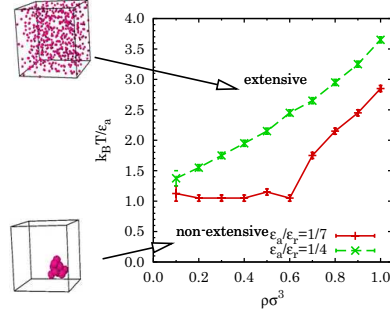


Fig. 3: (Colour on-line) Regions of the phase diagram where the PSW fluid, with $\Delta/\sigma = 0.5$ and two different values of ϵ_a/ϵ_r , is found to be extensive or non-extensive (here we used $N = 512$ particles). Representative snapshots in the two regions are shown on the left-hand side. The instability line corresponding to the higher penetrability case (dashed line) lies above the one corresponding to lower penetrability (continuous line).

$T < T_{\text{inst}}$. We determined the metastable/unstable crossover by performing NVT Monte Carlo simulations with $N = 512$ particles initially uniformly distributed within the simulation box. Figure 3 reports the results in the reduced temperature-density plane for $\Delta/\sigma = 0.5$ and for two selected penetrability ratios $\epsilon_a/\epsilon_r = 1/7$ and $1/4$, the first one lying exactly just above the limit line of fig. 1 while the second deep in the non-transition region. We worked with constant size moves (instead of fixing the acceptance ratios) during the simulation run, choosing the move size of 0.15 in units of the the simulation box side. A crucial point in the above numerical analysis is the identification of the onset of the instability. Clearly the physical origin of this instability stems from the fact that the attractive contribution increases unbounded compared to the repulsive one and particles tend to lump up into clusters of multiply overlapping particles (“blob”). Hence the energy can no longer scale linearly with the total number of particles N and the thermodynamic limit is not well defined (non-extensivity). We define a cluster in the following way. Two particles belong to the same cluster if there is a path connecting them, where we are allowed to move on a path going from one particle to another if the centers of the two particles are at a distance less than σ .

The state points belonging to the unstable region are characterized by a sudden drop of the internal energy and of the acceptance ratios at some points in the system evolution during the MC simulation. Representative snapshots show that a blob structure has nucleated around a certain point and occupies only a part of the simulation box with a few clusters. The number of clusters decreases as one moves away from the boundary line found in fig. 3 towards lower temperatures. Upon increasing ϵ_a/ϵ_r the number of clusters decreases and the number of particles

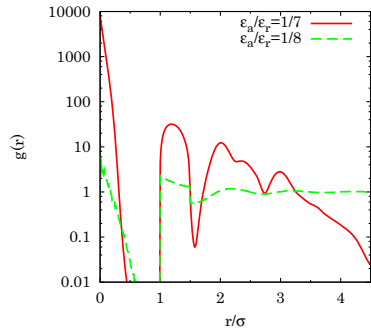
R. Fantoni *et al.*

Fig. 4: (Colour on-line) Radial distribution function for the PSW model at $\Delta/\sigma = 0.5$, $k_B T/\epsilon_a = 1.20$, and $\rho\sigma^3 = 0.7$ for two different values of the penetrability ratio ϵ_a/ϵ_r .

per cluster increases. We assume a state to be metastable if the energy does not undergo the transition after $10^7 N$ -single-particle moves. The fluid-fluid transition above the limit penetrability line of fig. 1 is not possible because the non-extensive phase shows up before the critical point is reached.

The boundary line of fig. 3 is robust with respect to the size of the system, provided that a sufficiently large size ($N \geq 512$) is chosen. When the number of particles in the simulation goes below the number of clusters which would form in the non-extensive phase the system seems to remain extensive. For instance, with $N = 1024$ particles we obtained under the $\epsilon_a/\epsilon_r = 1/7$, $\Delta/\sigma = 0.5$ conditions a threshold temperature $k_B T/\epsilon_a \approx 1.15$ for $\rho\sigma^3 = 0.4$ and 2.25 for $\rho\sigma^3 = 0.8$, which are close to the values obtained with $N = 512$ particles.

There is an apparent hysteresis in forming and melting the non-extensive phase. For example when $\epsilon_a/\epsilon_r = 1/7$, $\Delta/\sigma = 0.5$, and $\rho\sigma^3 = 1.0$ the non-extensive phase starts forming when cooling down to $k_B T/\epsilon_a = 2.75$. Upon increasing the temperature again, we observed a melting transition at significantly higher temperatures ($k_B T/\epsilon_a \gtrsim 4$). We also found the hysteresis to be size dependent; in the same state for $\rho\sigma^3 = 0.6$ the melting temperatures are $k_B T/\epsilon_a \approx 2.5$ for $N = 256$, $k_B T/\epsilon_a \approx 4.5$ for $N = 512$, and $k_B T/\epsilon_a \approx 6.5$ for $N = 1024$. This suggests that the extensive phase in fig. 3 is actually metastable with respect to the non-extensive phase in the thermodynamic limit. However the metastable phase can be stabilized by taking the size of the system finite. In addition we cannot exclude, *a priori*, the possibility of a true extensive stable phase as it is not prevented by the Ruelle criterion. We note that the size dependence of the hysteresis in the melting could be attributed to the fact that the blob occupies only part of the simulation box and therefore a surface term has a rather high impact on the melting temperature.

A convenient way to characterize the structure of the fluid is to consider the radial distribution function $g(r)$.

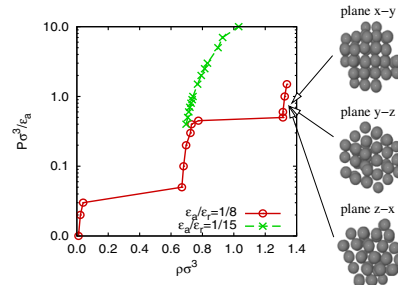


Fig. 5: (Colour on-line) Isotherm $k_B T/\epsilon_a = 1$ for the PSW system with $\Delta/\sigma = 0.5$ and $\epsilon_a/\epsilon_r = 1/8$ and $\epsilon_a/\epsilon_r = 1/15$, as obtained from NPT MC simulation with $N = 108$ particles. The pressure axis is in logarithmic scale. Snapshots of the centers of mass of the clusters in the solid are shown on the right-hand side.

This is depicted in fig. 4 for the cases $\Delta/\sigma = 0.5$, $k_B T/\epsilon_a = 1.20$, and $\rho\sigma^3 = 0.7$ at $\epsilon_a/\epsilon_r = 1/8$ and $\epsilon_a/\epsilon_r = 1/7$. The latter case is in the non-extensive region, according to fig. 3. We can clearly see that there is a dramatic change in the structural properties of the PSW liquid. In the non-extensive case, $\epsilon_a/\epsilon_r = 1/7$, the radial distribution function grows a huge peak at $r = 0$ and decays to zero after the first few peaks, which suggests clustering and confinement of the system.

In order to study the solid phase of the PSW model below the limit penetrability we employed isothermal-isobaric (NPT) MC simulations. A typical run would consist of 10^8 steps (particle moves or volume moves) with an equilibration time of 10^7 steps. We used 108 particles and adjusted the particle moves to have acceptance ratios of ≈ 0.5 and volume changes to have acceptance ratios of ≈ 0.1 . Here we only consider the case of PSW with $\Delta/\sigma = 0.5$ and $\epsilon_a/\epsilon_r = 1/8$ and $1/15$.

For the SW system with a width $\Delta/\sigma = 0.5$ the critical point is known to be at $k_B T_c/\epsilon_a = 1.23$ and $\rho_c \sigma^3 = 0.309$, its triple point being at $k_B T_t/\epsilon_a = 0.508$, $P_t \sigma^3/\epsilon_a = 0.00003$, $\rho_l \sigma^3 = 0.835$, and $\rho_s \sigma^3 = 1.28$ [15]. No solid stable phase was found in ref. [15] for temperatures above the triple point, meaning that the melting curve in the pressure-temperature phase diagram is almost vertical. On the other hand, the phase diagram of the PSW fluid with the same well width and a value of $\epsilon_a/\epsilon_r = 1/8$, just below the limit line of fig. 1, shows that the melting curve has a smooth positive slope in the pressure-temperature phase diagram. In order to establish this, we used NPT simulations to follow the $k_B T/\epsilon_a = 1$ isotherm. From fig. 5 we can clearly see the jumps in density corresponding to the gas-liquid and to the liquid-solid coexistence regions. The presence of a solid phase can be checked by computing the Q_6 order parameter [27], calculated for the center of mass of individual clusters, that in the present case turns out to be $Q_6 \approx 0.35$. The crystal structure is triclinic with a unit cell with

$a = b = c = \sigma$ and $\alpha = \beta = \pi/3$ and $\gamma = \cos^{-1}(1/4)$. There are possibly other solid-solid coexistence regions at higher pressures. Moreover the relaxation time of the MC run in the solid region is an order of magnitude higher than the one in the liquid region.

We also run at the same temperature a set of simulations for the PSW fluid with $\epsilon_a/\epsilon_r = 1/15$. The results (see fig. 5) showed no indication of a stable solid, in agreement with the fact that at this very low value of the penetrability ratio the system is SW-like.

A peculiarity of the PSW in the region below the limit penetrability of fig. 1, but not in the Ruelle stability region, is a violation of the Clausius-Clapeyron equation [28] along the liquid-solid coexistence curve, which represents a partial lack of thermodynamic consistency.

In the intermediate penetrability case (*i.e.*, above Ruelle's threshold but below the limit penetrability), the observed crystal structure is made of clusters of overlapping particles (rarely more than two) located at the sites of a regular crystal lattice. It is precisely this additional degree of penetrability, not present in the SW system, that allows for the coexistence of the liquid and the solid at not excessively large pressures. In this respect qualitative arguments along the lines suggested in ref. [19] could be useful.

In conclusion, we have studied the phase diagram of the three-dimensional PSW system. This model is Ruelle stable for $\epsilon_a/\epsilon_r < 1/f_\Delta$. For $\epsilon_a/\epsilon_r > 1/f_\Delta$ is either metastable or unstable (non-extensive), depending on the values of temperature and density, as shown in fig. 3. The instability is indicated by the collapse of the system in a confined blob made up of a few clusters of several overlapping particles. Moreover, the gas-liquid phase transition disappears, as shown in fig. 1.

For the metastable fluid near the limit penetrability line of fig. 1 we determined the phase diagram comparing it with the corresponding SW case. We determined how the gas-liquid coexistence curves are modified by the presence of penetrability (see fig. 2) and discussed the main features of the phase diagram, including the solid phase, for $\Delta/\sigma = 0.5$.

For the liquid-solid coexistence curves we generally found that the solid density increases with respect to the corresponding SW case, as expected, due to the formation of clusters of overlapping particles in the crystal sites. For $\Delta/\sigma = 0.5$ the PSW model with a sufficient penetrability to have a metastable system, but not a Ruelle stable one, has a melting curve with a positive slope in the pressure-temperature phase diagram with a violation of the Clausius-Clapeyron thermodynamic equation, thus confirming the metastable character of the phases. For sufficient low penetrability the system is in the Ruelle stable region, and behaves as the corresponding SW model.

In summary, by experimentally tuning the repulsive barrier relative to the well depth one could observe a) stable phases resembling those of a normal fluid,

b) metastable phases with fluid-fluid and fluid-solid coexistence, or c) the collapse of the system to a small region.

We thank T. ZYKOVA-TIMAN and B. M. MLADEK for enlightening discussions and useful suggestions. The support of PRIN-COFIN 2007B58EAB, FEDER FIS2010-16587 (Ministerio de Ciencia e Innovación), GAAS IAA400720710 is acknowledged.

REFERENCES

- [1] LIKOS C. N., *Phys. Rep.*, **348** (2001) 267.
- [2] STILLINGER F. H., *J. Chem. Phys.*, **65** (1976) 3968.
- [3] LIKOS C. N., WATZLAWEK M. and LÖWEN H., *Phys. Rev. E*, **58** (1998) 3135.
- [4] MARQUEST C. and WITTEN T. A., *J. Phys. (Paris)*, **50** (1989) 1267.
- [5] MALJEVSKÝ A. and SANTOS A., *J. Chem. Phys.*, **124** (2006) 074508.
- [6] SANTOS A., FANTONI R. and GIACOMETTI A., *Phys. Rev. E*, **77** (2008) 051206.
- [7] FANTONI R., GIACOMETTI A., MALJEVSKÝ A. and SANTOS A., *J. Chem. Phys.*, **131** (2009) 124106.
- [8] FANTONI R., GIACOMETTI A., MALJEVSKÝ A. and SANTOS A., *J. Chem. Phys.*, **133** (2010) 024101.
- [9] FANTONI R., *J. Stat. Mech.*, (2010) P07030.
- [10] BOLHUIS P. G., LOUIS A. A., HANSEN J. P. and MEIJER E. J., *J. Chem. Phys.*, **114** (2001) 4296.
- [11] MCCARTY J., LYUBIMOV I. Y. and GUENZA M. G., *Macromolecules*, **43** (2010) 3964.
- [12] VEGA L., DE MIGUEL E., RULL L. F., JACKSON G. and MCLURE I. A., *J. Chem. Phys.*, **96** (1992) 2296.
- [13] DE MIGUEL E., *Phys. Rev. E*, **55** (1997) 1347.
- [14] DEL RÍO F., ÁVALOS E., ESPÍNDOLA R., RULL L. F., JACKSON G. and LAGO S., *Mol. Phys.*, **100** (2002) 2531.
- [15] LIU H., GARDE S. and KUMAR S., *J. Chem. Phys.*, **123** (2005) 174505.
- [16] GIACOMETTI A., PASTORE G. and LADO F., *Mol. Phys.*, **107** (2009) 555.
- [17] KLEIN W., GOULD H., RAMOS R. A., CLEJAN I. and MEL'CUK A. I., *Physica A*, **205** (1994) 738.
- [18] SCHMIDT M., *J. Phys.: Condens. Matter*, **11** (1999) 10163.
- [19] MLADEK B. M. *et al.*, *J. Phys.: Condens. Matter*, **20** (2008) 494245.
- [20] RUELLE D., *Statistical Mechanics: Rigorous Results* (Benjamin, London) 1969.
- [21] FISHER M. E. and RUELLE D., *J. Math. Phys.*, **7** (1966) 260.
- [22] FRENKEL D. and SMIT B., *Understanding Molecular Simulation* (Academic Press, San Diego) 1996.
- [23] PANAGIOTOPOULOS A. Z., *Mol. Phys.*, **61** (1987) 813.
- [24] PANAGIOTOPOULOS A. Z., QUIRKE N., STAPLETON M. and TILDESLEY D. J., *Mol. Phys.*, **63** (1988) 527.
- [25] SMIT B., PH. DE SMEDT and FRENKEL D., *Mol. Phys.*, **68** (1989) 931.
- [26] SMIT B. and FRENKEL D., *Mol. Phys.*, **68** (1989) 951.
- [27] TEN WOLDE P. R., RUIZ-MONTERO M. J. and FRENKEL D., *J. Chem. Phys.*, **104** (1996) 9932.
- [28] KOFKE D. A., *J. Chem. Phys.*, **98** (1993) 4149.

Chapter 25

Field theoretical approach to a dense polymer with an ideal binary mixture of clustering centers

Fantoni R. and K. K. Müller-Nedebock, Phys. Rev. E **84**, 011808 (2011)

Title: “Field-theoretical approach to a dense polymer with an ideal binary mixture of clustering centers”

Abstract: We propose a field-theoretical approach to a polymer system immersed in an ideal mixture of clustering centers. The system contains several species of these clustering centers with different functionality, each of which connects a fixed number segments of the chain to each other. The fieldtheory is solved using the saddle point approximation and evaluated for dense polymer melts using the Random Phase Approximation. We find a short-ranged effective inter-segment interaction with strength dependent on the the average segment density and discuss the structure factor within this approximation. We also determine the fractions of linkers of the different functionalities.

PHYSICAL REVIEW E **84**, 011808 (2011)**Field-theoretical approach to a dense polymer with an ideal binary mixture of clustering centers**

Riccardo Fantoni*

National Institute for Theoretical Physics (NITheP) and Institute of Theoretical Physics, Stellenbosch 7600, South Africa

Kristian K. Müller-Nedebock†

Institute of Theoretical Physics, Department of Physics, Stellenbosch University, Private Bag XI, Matieland 7602, South Africa

(Received 14 July 2010; revised manuscript received 28 June 2011; published 29 July 2011)

We propose a field-theoretical approach to a polymer system immersed in an ideal mixture of clustering centers. The system contains several species of these clustering centers with different functionality, each of which connects a fixed number segments of the chain to each other. The field theory is solved using the saddle point approximation and evaluated for dense polymer melts using the random phase approximation. We find a short-ranged effective intersegment interaction with strength dependent on the average segment density and discuss the structure factor within this approximation. We also determine the fractions of linkers of the different functionalities.

DOI: [10.1103/PhysRevE.84.011808](https://doi.org/10.1103/PhysRevE.84.011808)

PACS number(s): 61.41.+e, 61.25.hp, 61.25.he, 61.25.H-

I. INTRODUCTION

In this work we consider a system where a single polymer chain is immersed in an ideal binary mixture of clustering centers. The study of the resulting associating polymers has a long history (see, e.g., in [1,2] and references therein). Models for the reversible gelation of polymers range from the consideration of pairwise associations of sticky chain segments [3] to the formation of arbitrary size clusters due to association of dipolar elements in polymer chains [4]. Whereas a large number of theoretical treatments model association with some form of crosslinking, that is, linking of two segments only, or arbitrary size clusters, we present a treatment for a small number of species of clusters consisting of a fixed number of polymer segments. This falls into the so-called closed multimerization scenario [5].

The reversible or permanent linking of polymer chains or sections of polymers has been a topic of extensive investigations for many decades in a wide range of systems. The general statistical physical scenario generally requires evaluating both the statistical physics of the chains within a certain linked scenario as well as a summation over all compatible modes of linking the polymer constituents. Independent of whether the linking (crosslinking, aggregation, clustering, type of polycondensation, etc.) is permanent or reversible the topologically and geometrically permissible combinations of linking or clustering need to be evaluated, albeit with different strategies for quenched or annealed situations [6]. Therefore it is natural to think in terms of the enumeration of graphs, as extensively reviewed by Kuchanov *et al.* [7]. The ideas can then be applied to a variety of systems, such as associating telechelics [8], polycondensation [9], polymers with multiply aggregating groups [10], and general thermally reversible aggregation, clustering, or association [11–19].

There are different possibilities in which the scenario of fixed functionality clustering can be realized. One can think of the segments of the chain connected to particles or sidechains that assemble into structures with closed shells, akin to Janus

particles, where it was recently shown that monodisperse ten-particle micelles, and 40-particle vesicles, are the thermodynamically dominant assembled structures [20–22].

We are interested in the properties of a solution of such a polymer with clustering centers and in the relative dominance of coexisting clusters with different, yet fixed, functionalities. To this end we reformulate a field-theoretical method originally proposed by Edwards for permanent, arbitrary-functional end-linking of chains [23]. The resultant field theory is highly nonlinear, but can be treated analytically and numerically, offering an additional theoretical tool to address questions on the formation of localized, reversible structures of polymer chains.

As already mentioned, in order to compute the partition function or free energy one needs to evaluate the polymer chain conformations subject to the restrictions imposed by the functionalities of the linkers and include all possibilities of linking or cluster formation. This is because we are modeling a strong type of aggregation with fixed functionalities, where the clusters are well-defined and local. In other words, all permissible graphs must be generated, their connectivity restrictions be imposed on the polymer chains and weighted appropriately by Boltzmann factors. Kuchanov *et al.* [7], in their exposition of strategies to do this, also point out the very clear analogy between enumeration of spatially embedded graphs and Feynman diagrams from field theories. The obvious utility of a field-theoretical tactic lies in the large spectrum of available approximation techniques and graphical expansions but also in the freedom to choose the precise manner of implementing the additional fields.

In this paper we introduce additional fields, with the associated functional integration, whose role is to produce the desirable linking, network-formation, or aggregate possibilities as well as enforcing the spatial consequences of this on the appropriate monomers. The current approach is similar to those used in Refs. [7,23] and in work that can be seen as a precursor to the current formalism [24,25]. Whereas the specific systems investigated in Refs. [23] and [7] are addressed such that the ends of polymer chains or of star-like polymer units can associate, respectively, the system under investigation here deals with aggregation of segments of a polymer chain. We show that this system allows a formulation

*rfantoni@ts.infn.it

†kkmn@physics.sun.ac.za

of the field theory that has the mathematically advantageous property that it is *local* in the introduced fields and these additional fields also couple to the density of monomers in a local way.

Clearly the sum over aggregated states, by whatever method derived and approximated, would generally impose a complicated form onto the polymer conformational averages. This is also the case for theories with additional fields following integration over the fields. In approximating the functional integral over fields one expects to find nonlinear integral equations for these fields in the kinds of self-consistent field theory calculation that emerge in models for many systems (as in [7,23]). However, in our formulation the saddle point equations related to the additional fields (and taken before integration over the polymer degrees of freedom) turn out to be only algebraic, albeit nonlinear, providing a significant advantage in tractability in comparison to nonlinear integral equations obtained within other strategies (for other systems). Analysis of the stability, etc. of the resulting theory is also relatively simpler. Completing the integration over the fields incorporates the clustering into the remaining weight for the conformations of the chain (also in a local manner) giving the “structural” contribution that is taken together with the remaining polymer-polymer interactions.

Yet other path integration techniques have made use of generating functional approaches to enumerate tree-like configurations [26–28] in associating systems. Motivated by a wide range of physical scenarios under which polymer chains can aggregate, many different methods (mainly not field theoretical in the sense as here) have been utilized in determining the contribution of certain classes of connections, ranging from summations over a subset of looped conformations [4], sums of tree-like graphs [29], and trees with cycles to analyses for stickers [3,8,30]. Typically the effective polymer-polymer contributions can then be dealt with through a further self-consistent field theory (e.g., [31]) or by determining fluctuations with respect to a reference system (e.g., [32]) or through a mean-field treatment. In principle, before our approximations at least, the field theory introduced here is not restricted to subsets of connectivities or specifically cyclized conformations nor is it *a priori* a mean-field formalism.

In the current calculation we have a single polymer chain that is immersed in an ideal binary mixture of pointwise clustering centers with different functionality (number of links that the center can have with the polymer segments). As a mathematical device we can think of free segments of the chain being part of clusters of functionality one, that is, they cannot connect to any other segments. Moreover, the system is in solution with clustering centers of functionalities a and $b \neq a$. The highly non-Gaussian field theory resulting from the study of the model is quite complicated but can be approached through the saddle point approximation. Assuming the polymer to be highly dense we can then use the random phase approximation (RPA) to describe the polymer degrees of freedom. We are then able to extract the local densities of segments that form part of clusters of different sizes, the effective potential based on small density fluctuations around a background of a given density, and the static structure factor. In the current treatment we develop the formalism and then

investigate properties of the system in the scenario of the uniform polymer segment density with Gaussian fluctuations. However it is also shown where this approximation breaks down. One could certainly expect nonhomogeneous phases to develop which can in principle also be addressed by the formalism together with the consideration of higher orders in density fluctuations [33–35].

We shall refer to “polymer segments” as the *monomeric units* of which the polymer chain is built. “Clustering centers” refer to point-like seeds of “clusters” of segments of the polymer chain. In other words, the clustering centers function so as to attach to a specific number of the segments of the polymer and in so doing to localize these segments at a common point, binding them reversibly into a cluster. Consequently, a polymer segment is also the basic unit to which a single attachment to a single cluster is possible. We shall deal with clustering centers of different functionalities which form a multicomponent system with the polymer and provide a “sea” of centers to form clusters with the polymer segments.

Although our field-theoretical formulation includes no precise model for the mechanism that causes clustering centers of a given functionality to occur, we investigate in Sec. VI the case where the functionalities (10 and 40) of the clustering centers are the same as those determined for Janus particles in recent studies [22]. Indeed there has recently been much development in the techniques for the synthesis of new patchy colloidal particles [36–39]. One particularly simple class of these anisotropic particles, called Janus particles [40–43], seem to form mainly clusters of either 10 or 40 particles. Here Monte Carlo simulations [20,21] indicate that mainly stable micelle (10 particles) or vesicle (40 particles) arrangements of these particles are to be found in the vapor phase. Moreover, it was found that the clusters behave very similarly to an ideal gas, since the particles forming the cluster tend to arrange with their active surfaces toward the cluster center.

Janus chains have been suggested as potentially useful candidates for understanding interesting polymer phenomena [44]. We will apply our formalism to the case of a dense polymer in a Janus fluid and in so doing we hope to add to the recent interest for Janus particles interacting with polymer chains [43–45]. To the best of our knowledge there are no results in the literature that prove the clustering in the Janus fluid in the presence of the polymer. So we will take as a working hypothesis the existence of such a clustering, and make the approximation of treating the Janus fluid as an ideal mixture of Janus particles, micelles of Janus particles, and vesicles of Janus particles (in the spirit of Ref. [22]).

The paper is organized as follows: in Sec. II we describe the model we are studying and formulate the field theory, in Sec. III we perform the saddle point approximation, and discuss when we expect the approximation to be most accurate. Section IV is devoted to an investigation of dense polymer system with clustering. We use the random phase approximation and derive an expression for the free energy density of the system and the effective interaction caused by the clustering centers. In Sec. V we determine the structure factor and its curvature at small wave vectors, in Sec. VI we finally solve the Janus case numerically, and Sec. VII is devoted to the final remarks.

II. THE MODEL

The grand partition function for the ideal binary mixture of clustering centers of functionality a and of functionality b can be written as

$$\Theta = \sum_{N_1=0}^{\infty} \sum_{N_a=0}^{\infty} \sum_{N_b=0}^{\infty} \frac{(z_1 V)^{N_1}}{N_1!} \frac{(z_a V)^{N_a}}{N_a!} \frac{(z_b V)^{N_b}}{N_b!},$$

where we also allowed for a third species of particles, of functionality one, which cannot cause aggregation. z_i are the usual fugacities for species i , V is the volume of the system, and $N_1 + N_a + N_b$ is the total number of clustering centers.

We now wish to connect these to the polymer degrees of freedom and develop a partition function for the system of polymer together with the clustering centers. The “clusters or clustering centers” represents the free *macroparticles* making up the *ideal mixture* (a two component mixture with clusters of two different functionalities that are living in a “sea” of clusters of functionality one: the *particles*) in which the polymer is immersed. These macroparticles are made up of a fixed number of pointwise *particles* (i.e., they have fixed functionality) each of which is *linked* with one polymer segment.

A suitable field-theoretic formalism was developed by Edwards [23] to describe polymer gels. Consider a field $\phi_1 : \mathbb{R}^3 \rightarrow \mathbb{R}$ then the following Wick theorem holds (see Appendix C)

$$\begin{aligned} I(\mathbf{r}_1, \mathbf{r}_2, \dots, \mathbf{r}_{2M}) &= \mathcal{N} \int [d\phi_1] \phi_1(\mathbf{r}_1) \phi_1(\mathbf{r}_2) \dots \phi_1(\mathbf{r}_{2M}) e^{-\frac{1}{2} \int d\mathbf{r} \phi_1^2(\mathbf{r})} \\ &= \sum_{\text{all pairing}} \delta(\mathbf{r}_{l_1} - \mathbf{r}_{l_2}) \delta(\mathbf{r}_{l_3} - \mathbf{r}_{l_4}) \dots \delta(\mathbf{r}_{l_{2M-1}} - \mathbf{r}_{l_{2M}}), \end{aligned} \quad (1)$$

where $l_i = 1, 2, \dots, 2M$ and $l_i \neq l_j$ for all $i \neq j$, and \mathcal{N} is the Gaussian normalization.

If we introduce another field ϕ_2 , in terms of complex fields $\varphi = \phi_1 + i\phi_2$ and $\varphi^* = \phi_1 - i\phi_2$, the following identity follows (see Fig. 1):

$$\begin{aligned} J &= \mathcal{N}' \int [d\phi_1][d\phi_2] \prod_{i=1}^M [\phi_1(\mathbf{r}_i) + i\phi_2(\mathbf{r}_i)] \prod_{j=1}^{M'} [\phi_1(\mathbf{R}_j) \\ &\quad - i\phi_2(\mathbf{R}_j)] e^{-\int d\mathbf{r} \phi_1^2(\mathbf{r}) - \int d\mathbf{r} \phi_2^2(\mathbf{r})} \end{aligned}$$

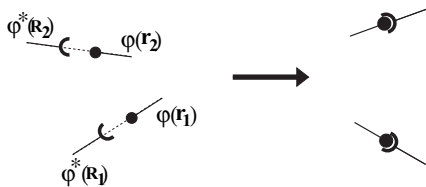


FIG. 1. A schematic representation of the role of the field theory. The fields φ and φ^* are depicted as functions of spatial variables. Multiplication by $\exp(-\int \varphi \varphi^*)$ and subsequent functional integration enforces the linking of the spatial coordinates between pairs of φ and φ^* (in all possible ways).

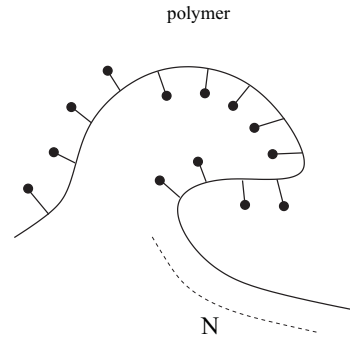


FIG. 2. Shows the polymer made up of N equispaced links that are susceptible to being linked into clusters.

$$\begin{aligned} &= \mathcal{N}' \int [d\varphi][d\varphi^*] \prod_{i=1}^M \varphi(\mathbf{r}_i) \prod_{j=1}^{M'} \varphi^*(\mathbf{R}_j) e^{-\int d\mathbf{r} \varphi(\mathbf{r}) \varphi^*(\mathbf{r})} \\ &= \delta_{M,M'} \sum_{\text{all pairing}} \delta(\mathbf{r}_{l_1} - \mathbf{R}_{m_1}) \delta(\mathbf{r}_{l_2} - \mathbf{R}_{m_2}) \\ &\quad \dots \delta(\mathbf{r}_{l_M} - \mathbf{R}_{m_M}), \end{aligned} \quad (2)$$

where l_i and m_i can vary over $(1, 2, \dots, M)$ with $l_i \neq l_j$ and $m_i \neq m_j$ for all $i \neq j$. This means that each φ is associated with another φ^* through a Dirac δ function in all possible pairwise combinations. As shown in Fig. 1, we can view the fields φ and φ^* as being complementary, since the δ -function connection does not occur between pairs of φ or pairs of φ^* . This Gaussian theory, therefore, enumerates all possible pairs of points \mathbf{r}_i and \mathbf{R}_j and enforces this by inserting a Dirac δ .

We consider a polymer chain consisting of N links (see Fig. 2). Given the Green function $G(\mathbf{r}, \mathbf{r}')$ for the segment of chain between two links, the conformational statistical weight of the polymer, whose conformation is described by the points $\{\mathbf{R}_i\}$, is

$$P(\{\mathbf{R}_i\}) = G(\mathbf{R}_1, \mathbf{R}_2) G(\mathbf{R}_2, \mathbf{R}_3) \dots G(\mathbf{R}_{N-1}, \mathbf{R}_N). \quad (3)$$

The polymer is immersed in an ideal mixture made up of two types of crosslinked particles (see Fig. 3) with

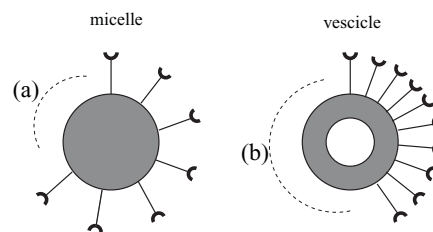


FIG. 3. Shows the clusters of Janus particles: the micelles are made of $a = 10$ links, whereas the vesicles of $b = 40$ links.

RICCARDO FANTONI AND KRISTIAN K. MÜLLER-NEDEBOCK

PHYSICAL REVIEW E **84**, 011808 (2011)

functionalities a and b , respectively. We can also think of the chain segments as forming two types of clusters (closed-shell clusters, as for Janus particles [20]) called micelles and vesicles. What is important is the fixed functionality. The role of these clustering centers is to provide the links of a certain fixed functionality between polymer segments, thereby connecting a given number of segments of the polymer chain together. Then the partition function can be

written as

$$Z_N = \sum_{N_1, N_a, N_b=0}^{\infty} Z_{N_1, N_a, N_b}, \quad (4)$$

where $N = N_1 + aN_a + bN_b$ is the total number of polymer segments or of particles (since the field theory requires that each segment must be paired with a particle) and

$$\begin{aligned} Z_{N_1, N_a, N_b} = \mathcal{N} \int d\mathbf{R}_1 \dots d\mathbf{R}_N e^{-v \sum_{n,m=1}^N \delta(\mathbf{R}_n - \mathbf{R}_m)} \int [d\varphi][d\varphi^*] e^{-\int d\mathbf{r} \varphi(\mathbf{r}) \varphi^*(\mathbf{r})} \varphi^*(\mathbf{R}_1) G(\mathbf{R}_1, \mathbf{R}_2) \varphi^*(\mathbf{R}_2) G(\mathbf{R}_2, \mathbf{R}_3) \\ \dots G(\mathbf{R}_{N-1}, \mathbf{R}_N) \varphi^*(\mathbf{R}_N) \frac{1}{N_1!} \left[\int d\mathbf{r} z_1 \varphi(\mathbf{r}) \right]^{N_1} \frac{1}{N_a!} \left[\int d\mathbf{r} z_a \varphi^a(\mathbf{r}) \right]^{N_a} \frac{1}{N_b!} \left[\int d\mathbf{r} z_b \varphi^b(\mathbf{r}) \right]^{N_b}, \end{aligned} \quad (5)$$

and the z_i are generalized fugacities (that might also contain a multiplicity associated with the functionality). We have explicitly added clusters of functionality one (the single particles) here to represent the sea of particles in which the polymer and the a and b clusters are immersed. Clearly clusters of size one simply link to a single polymer segment and therefore do not cause association as the a and b clusters do. Note that we are not interested in describing the precise model for the mechanism by which the clusters of a given functionality are formed from the aggregation of particles (more on this in Sec. VI); we just assume that this aggregation process takes place. At this level of description the physics of the precise mechanism for the multimerization resides in the fugacities. In our present formalism the clustering centers and the particles are pointlike. In principle it is also possible to extend the current formalism to model clusters of finite extension. We have also added an excluded volume term v to the polymer chain, with the dimensions of a volume.

It is possible to use the formalism without necessarily introducing the essentially inert clusters of functionality one, which turns out to be the fugacity $z_1 = 1$ case of the equations derived below. Appendix D shows the details. We continue with the slightly more general formalism here, noting that $z_1 \rightarrow 1$ will show no effects due to the addition of these convenient clustering centers.

We then find in a short-hand notation, and neglecting for the time being the excluded volume term,

$$\begin{aligned} Z_N = \mathcal{N} \int [d\varphi][d\varphi^*] \left\{ \prod d\mathbf{R} \right\} \left\{ \prod G \right\} \eta^N \\ \times \exp \left\{ - \int d\mathbf{r} \varphi(\mathbf{r}) \varphi^*(\mathbf{r}) + \int d\mathbf{r} \rho(\mathbf{r}) \ln[\varphi^*(\mathbf{r})/\eta] \right. \\ \left. + z_1 \int d\mathbf{r} \varphi(\mathbf{r}) + z_a \int d\mathbf{r} \varphi^a(\mathbf{r}) + z_b \int d\mathbf{r} \varphi^b(\mathbf{r}) \right\}, \end{aligned} \quad (6)$$

$$Z_N = \mathcal{N} \int [d\varphi][d\varphi^*] \left\{ \prod d\mathbf{R} \right\} \left\{ \prod G \right\} \exp\{\mathcal{F}[\varphi, \varphi^*]\}, \quad (7)$$

where we introduced the microscopic density of polymer links $\rho(\mathbf{r}) = \sum_{i=1}^N \delta(\mathbf{r} - \mathbf{R}_i)$ and η is an arbitrary constant with the dimensions of a length to the power $-3/2$. In the rest of the paper we will measure lengths in units of $\eta^{-2/3}$. A natural

choice would be $\eta = \ell^{-3/2}$, with ℓ the Kuhn length of the polymer segment.

A. A simple example

To clarify our formalism we consider here the simple example of a polymer, with four polymer segments, interacting with two clustering centers of functionality $a = 2$. Using the properties of the Gaussian chains, the partition function, neglecting the excluded volume term, is written as

$$\begin{aligned} Z = \mathcal{N} \int [d\varphi][d\varphi^*] \left\{ \prod_{i=1}^4 d\mathbf{R}_i \right\} \left\{ \prod_{i=1}^2 d\mathbf{r}_i \right\} \left\{ \prod_{i=1}^3 G(\mathbf{R}_i, \mathbf{R}_{i+1}) \right\} \\ \times e^{-\int d\mathbf{r} \varphi(\mathbf{r}) \varphi^*(\mathbf{r})} \left\{ \prod_{i=1}^4 \varphi^*(\mathbf{R}_i) \right\} z_2^2 \varphi^2(\mathbf{r}_1) \varphi^2(\mathbf{r}_2) \\ = \mathcal{N} z_2^2 \int d\mathbf{r}_1 d\mathbf{r}_2 \sum' G(\mathbf{r}_{i_1}, \mathbf{r}_{i_2}) G(\mathbf{r}_{i_2}, \mathbf{r}_{i_3}) G(\mathbf{r}_{i_3}, \mathbf{r}_{i_4}). \end{aligned} \quad (8)$$

where we used Eq. (2) and the prime on the last summation symbol indicates that we have to sum over all possible ways of assigning to the indexes (i_1, i_2, i_3, i_4) the set $(1, 1, 2, 2)$. We then see that the result is given by

$$\begin{aligned} Z = \mathcal{N} z_2^2 \left[4 \int d\mathbf{r}_1 d\mathbf{r}_2 G(\mathbf{r}_1, \mathbf{r}_1) G(\mathbf{r}_1, \mathbf{r}_2) G(\mathbf{r}_2, \mathbf{r}_2) \right. \\ \left. + 4 \int d\mathbf{r}_1 d\mathbf{r}_2 G(\mathbf{r}_1, \mathbf{r}_2) G(\mathbf{r}_2, \mathbf{r}_2) G(\mathbf{r}_2, \mathbf{r}_1) \right. \\ \left. + 4 \int d\mathbf{r}_1 d\mathbf{r}_2 G(\mathbf{r}_1, \mathbf{r}_2) G(\mathbf{r}_2, \mathbf{r}_1) G(\mathbf{r}_1, \mathbf{r}_2) \right] \\ = 4 \left[\text{Diagram 1} \right] \\ + 4 \left[\text{Diagram 2} \right] + 4 \left[\text{Diagram 3} \right], \end{aligned} \quad (9)$$

where lines represent polymer segments and black circles represent integration.

III. THE SADDLE POINT APPROXIMATION

We look at the saddle point equations for the fields φ and φ^* for any arbitrary yet fixed conformation of the polymer $\rho = \rho(\mathbf{r}) \geq 0 \forall \mathbf{r} \in \mathbb{R}^3$. The saddle point approximation becomes necessary because the field-theoretical formulation of the system Eq. (6) is certainly highly non-Gaussian. We proceed to calculate the saddle point and note that, for fixed polymer conformation, the resulting condition is a set of algebraic equations, that is, the saddle point depends only on the local density. We shall also see that there always exists exactly one saddle point, corresponding to the physical solution of the equations.

We need to determine the critical point $(\bar{\varphi}, \bar{\varphi}^*)$, which amounts to solving

$$\left. \frac{\delta \mathcal{F}}{\delta \varphi(\mathbf{r})} \right|_{\bar{\varphi}, \bar{\varphi}^*} = 0, \quad \left. \frac{\delta \mathcal{F}}{\delta \varphi^*(\mathbf{r})} \right|_{\bar{\varphi}, \bar{\varphi}^*} = 0 \quad (10)$$

or

$$-\bar{\varphi}^* + z_1 + az_a \bar{\varphi}^{a-1} + bz_b \bar{\varphi}^{b-1} = 0, \quad (11)$$

$$-\bar{\varphi} + \rho / \bar{\varphi}^* = 0. \quad (12)$$

These can be combined to give

$$-\rho / \bar{\varphi} + z_1 + az_a \bar{\varphi}^{a-1} + bz_b \bar{\varphi}^{b-1} = 0. \quad (13)$$

A. Properties of the solutions of the saddle point approximation

From Eq. (13) we can write

$$-\rho + f(\bar{\varphi}) = 0, \quad (14)$$

where $f(x) = z_1 x + az_a x^a + bz_b x^b$. We can then show that there exists at least one positive solution of Eq. (13) for $\rho > 0$. Indeed when $\bar{\varphi} \rightarrow 0$ then $-\rho + f(\bar{\varphi}) = -\rho < 0$, whereas when $\bar{\varphi} > \rho/z_1$ then $-\rho + f(\bar{\varphi}) > 0$. Consequently $-\rho + f(\bar{\varphi})$ goes through a zero when $\bar{\varphi} \in [0, \infty)$. And it is easy to show that there is exactly one positive solution $\bar{\varphi} > 0$ for any $\rho > 0$. $f'(\bar{\varphi}) = z_1 + a^2 z_a \bar{\varphi}^{a-1} + b^2 z_b \bar{\varphi}^{b-1}$ so $f'(\bar{\varphi}) > 0$ for all $\bar{\varphi} \geq 0$. Since the derivative is strictly positive and the polynomial goes from negative to positive, there exists exactly one positive root $\bar{\varphi}$ for any $\rho > 0$. As we show in Sec. IV B the local cluster densities of the saddle point are proportional to $z_1 \bar{\varphi}$, $az_a \bar{\varphi}^a$, and $bz_b \bar{\varphi}^b$, such that $\bar{\varphi}$ must be nonnegative.

B. Solutions for $\bar{\varphi}$ and $\bar{\varphi}^*$

Consider the particular case $a = 2, b = 0$, corresponding to reversible crosslinking, then from Eq. (13) we find for the critical point

$$\bar{\varphi}_{\pm} = \frac{-z_1 \pm \sqrt{z_1^2 + 8z_2 \rho}}{4z_2}, \quad (15)$$

$$\bar{\varphi}_{\pm}^* = \frac{4z_2 \rho}{-z_1 \pm \sqrt{z_1^2 + 8z_2 \rho}}, \quad (16)$$

which rules out the $\bar{\varphi}_-$ solution, as the logarithm of $\bar{\varphi}_-$ is not well defined.

C. Expansion of \mathcal{F} around the critical point

We can expand the function \mathcal{F} around the critical point to second order in the fluctuations $\Delta\varphi = \varphi - \bar{\varphi} = \Delta\phi_1 + i\Delta\phi_2$ and $\Delta\varphi^* = \varphi^* - \bar{\varphi}^* = \Delta\phi_1 - i\Delta\phi_2$,

$$\mathcal{F}[\bar{\varphi} + \Delta\varphi, \bar{\varphi}^* + \Delta\varphi^*] = \mathcal{F}[\bar{\varphi}, \bar{\varphi}^*] + \frac{1}{2} \int d\mathbf{r}_1 \int d\mathbf{r}_2 [\Delta\phi_1(\mathbf{r}_1) \Delta\phi_2(\mathbf{r}_1)] \cdot F_2(\mathbf{r}_1, \mathbf{r}_2) \cdot \begin{pmatrix} \Delta\phi_1(\mathbf{r}_2) \\ \Delta\phi_2(\mathbf{r}_2) \end{pmatrix} + \text{third order terms}, \quad (17)$$

where $F_2(\mathbf{r}_1, \mathbf{r}_2)$ is the following 2×2 matrix:

$$F_2(\mathbf{r}_1, \mathbf{r}_2) = \begin{pmatrix} \left. \frac{\delta^2 \mathcal{F}}{\delta\phi_1(\mathbf{r}_1) \delta\phi_1(\mathbf{r}_2)} \right|_{\bar{\varphi}, \bar{\varphi}^*} & \left. \frac{\delta^2 \mathcal{F}}{\delta\phi_1(\mathbf{r}_1) \delta\phi_2(\mathbf{r}_2)} \right|_{\bar{\varphi}, \bar{\varphi}^*} \\ \left. \frac{\delta^2 \mathcal{F}}{\delta\phi_2(\mathbf{r}_1) \delta\phi_1(\mathbf{r}_2)} \right|_{\bar{\varphi}, \bar{\varphi}^*} & \left. \frac{\delta^2 \mathcal{F}}{\delta\phi_2(\mathbf{r}_1) \delta\phi_2(\mathbf{r}_2)} \right|_{\bar{\varphi}, \bar{\varphi}^*} \end{pmatrix}. \quad (18)$$

We have

$$\left. \frac{\delta^2 \mathcal{F}}{\delta\phi_1(\mathbf{r}_1) \delta\phi_1(\mathbf{r}_2)} \right|_{\bar{\varphi}, \bar{\varphi}^*} = \left[-2 - \frac{\rho}{\bar{\varphi}^{*2}} + a(a-1)z_a \bar{\varphi}^{a-2} + b(b-1)z_b \bar{\varphi}^{b-2} \right] \delta(\mathbf{r}_1 - \mathbf{r}_2), \quad (19)$$

$$\left. \frac{\delta^2 \mathcal{F}}{\delta\phi_1(\mathbf{r}_1) \delta\phi_2(\mathbf{r}_2)} \right|_{\bar{\varphi}, \bar{\varphi}^*} = i \left[\frac{\rho}{\bar{\varphi}^{*2}} + a(a-1)z_a \bar{\varphi}^{a-2} + b(b-1)z_b \bar{\varphi}^{b-2} \right] \delta(\mathbf{r}_1 - \mathbf{r}_2), \quad (20)$$

$$\left. \frac{\delta^2 \mathcal{F}}{\delta\phi_2(\mathbf{r}_1) \delta\phi_2(\mathbf{r}_2)} \right|_{\bar{\varphi}, \bar{\varphi}^*} = \left[-2 + \frac{\rho}{\bar{\varphi}^{*2}} - a(a-1)z_a \bar{\varphi}^{a-2} - b(b-1)z_b \bar{\varphi}^{b-2} \right] \delta(\mathbf{r}_1 - \mathbf{r}_2). \quad (21)$$

We can then introduce the matrix $\mathcal{M}[\rho]$ as

$$\begin{pmatrix} -2 - \frac{\rho}{\bar{\varphi}^{*2}} + a(a-1)z_a \bar{\varphi}^{a-2} + b(b-1)z_b \bar{\varphi}^{b-2} & i \left[\frac{\rho}{\bar{\varphi}^{*2}} + a(a-1)z_a \bar{\varphi}^{a-2} + b(b-1)z_b \bar{\varphi}^{b-2} \right] \\ i \left[\frac{\rho}{\bar{\varphi}^{*2}} + a(a-1)z_a \bar{\varphi}^{a-2} + b(b-1)z_b \bar{\varphi}^{b-2} \right] & -2 + \frac{\rho}{\bar{\varphi}^{*2}} - a(a-1)z_a \bar{\varphi}^{a-2} - b(b-1)z_b \bar{\varphi}^{b-2} \end{pmatrix}, \quad (22)$$

RICCARDO FANTONI AND KRISTIAN K. MÜLLER-NEDEBOCK

 PHYSICAL REVIEW E **84**, 011808 (2011)

Then the partition function can be rewritten as

$$Z_N \approx \mathcal{N}' \int \left\{ \prod d\mathbf{R} \right\} \left\{ \prod G \right\} \exp\{M[\rho]\}, \quad (23)$$

where

$$M[\rho] = \mathcal{F}[\bar{\varphi}, \bar{\varphi}^*] - \frac{1}{2} \int d\mathbf{r} \ln\{\det \mathcal{M}[\rho]\}, \quad (24)$$

and

$$\det \mathcal{M}[\rho] = 4[1 + z_a a(a-1)\bar{\varphi}^a/\rho + z_b b(b-1)\bar{\varphi}^b/\rho]. \quad (25)$$

For finite ρ the determinant is always positive with positive real parts of the eigenvalues, if $\bar{\varphi} > 0$. Hence the saddle point is stable.

As the density ρ increases we note that the free energy calculation due to the saddle point $\mathcal{F}[\bar{\varphi}, \bar{\varphi}^*]$ grows at least as ρ , but that the fluctuation contribution $-\frac{1}{2} \int d\mathbf{r} \ln\{\det \mathcal{M}[\rho]\}$ strives to a constant. Therefore at sufficiently high density we expect the relative contribution of the fluctuations to become negligible.

In the particular case $a = 2, b = 0$ we find

$$\det \mathcal{M}_{\pm}[\rho] = 4(1 + 2z_2 \bar{\varphi}_{\pm}/\bar{\varphi}_{\pm}^*). \quad (26)$$

$$\begin{aligned} \int \left\{ \prod d\mathbf{R} \right\} \left\{ \prod G \right\} \dots &= \mathcal{N}'' \int [d\Delta\rho] \exp \left[-\frac{1}{2} \int d\mathbf{r} \int d\mathbf{r}' \Delta\rho(\mathbf{r}) \frac{\widehat{\mathcal{S}}_0^{-1}(|\mathbf{r}-\mathbf{r}'|)}{V} \Delta\rho(\mathbf{r}') \right] \dots \\ &= \mathcal{N}'' \int [d\Delta\bar{\rho}] \exp \left[-\frac{1}{2} \frac{1}{V} \sum_{\mathbf{k}} \Delta\bar{\rho}(\mathbf{k}) \frac{\widehat{\mathcal{S}}_0^{-1}(k)}{V} \Delta\bar{\rho}(-\mathbf{k}) \right] \dots, \end{aligned} \quad (27)$$

where we denoted with a tilde the Fourier transform [48] and with a hat an inverse Fourier transform. We note that this type of approach is not atypical in calculations for quenched gels [49].

Expanding to second order in the density fluctuations we find, from Eq. (24) and Eqs. (11) and (12),

$$\begin{aligned} M[\bar{\rho} + \Delta\rho] &= AV + B \int d\mathbf{r} \Delta\rho(\mathbf{r}) + C \int d\mathbf{r} [\Delta\rho(\mathbf{r})]^2 + \dots \\ &= AV + C \int d\mathbf{r} [\Delta\rho(\mathbf{r})]^2 + \dots, \end{aligned} \quad (28)$$

where we used the fact that $\int d\mathbf{r} \Delta\rho(\mathbf{r}) = 0$. V is the volume of the box, A , B , and C are given functions of z_1 , z_2 , and $\bar{\rho}$ and for the particular case $a = 2, b = 0$ can be found in Appendix A. Notice that in this case A_- is not defined for any values of the average density so only the A_+ , B_+ , and C_+ solution is physically meaningful, that is, they correspond to the expected positive $\bar{\varphi}$ solution (see Sec. III A).

We then obtain the following approximation for the partition function of Eq. (23):

$$Z_N \approx \mathcal{N}''' e^{AV - \frac{1}{2} \int d\mathbf{r} \ln(\widehat{\mathcal{S}}_0^{-1}/V - 2C)}, \quad (29)$$

IV. THE RANDOM PHASE APPROXIMATION

In this section we express the polymer in terms of a segment density via the so-called random phase approximation. We restrict ourselves to the situations where the polymer segments are presumed to be distributed homogeneously with Gaussian density fluctuations around this value. For sufficiently dense systems this has been treated as a reasonable approximation [6] in permanently networked systems. We do not investigate the cases of possible inhomogeneous phases. In principle we would then need to expand our results in the preceding sections to higher orders in the density fluctuations [33–35] or attempt to express our results in terms of more complex quantities [46,47]. However, we do investigate where our RPA with the homogeneity assumption fails as one indicator for possibly different phase behavior in the system.

A. Basic formulation

Clearly our clustering formalism produces a significantly nontrivial density dependence. Presuming that our system behaves like a highly dense polymer melt, where the fluctuations of $\rho = \bar{\rho} + \Delta\rho$ are small, one can use the following random phase approximation [35] (RPA) (see Appendix B),

where $\widehat{\mathcal{S}}_0^{-1}$ is the operator whose \mathbf{r}, \mathbf{r}' component is given by $\widehat{\mathcal{S}}_0^{-1}(|\mathbf{r}-\mathbf{r}'|)$.

In terms of the free energy density $\beta f = -\ln(Z_N)/V$ we find, in the thermodynamic limit ($V \rightarrow \infty$ with $\bar{\rho} = N/V$ constant),

$$\beta f = -A - \frac{1}{2} \ln(-2C). \quad (30)$$

B. Local clustered segment densities

Following the usual method for grand-canonical ensemble it is possible to calculate the local densities of segments that form part of different sizes of clusters. We then compute

$$n_1 = \frac{z_1}{N} \frac{\partial \ln Z_N}{\partial z_1} \quad (31)$$

for segments of the chain that are not crosslinked, and

$$n_x = x \frac{z_x}{N} \frac{\partial \ln Z_N}{\partial z_x} \quad (32)$$

for the density of segments part of clusters of size x .

Neglecting the logarithmic corrections due to the quadratic fluctuations, we have

$$\ln Z_N = VA = M[\bar{\rho}]. \quad (33)$$

Within the saddle point approximation we split the contributions into parts due to the saddle point above and due to the quadratic fluctuations [notice that this analysis holds also locally at the level of the partition function for an arbitrary $\rho = \rho(\mathbf{r})$ profile of polymer chain density]

$$n_x = x \frac{z_x}{N} \frac{\partial \mathcal{F}[\bar{\varphi}, \bar{\varphi}^*]_{\rho=\bar{\rho}}}{\partial z_x} - x \frac{z_x V}{2N} \frac{\partial \ln \det \mathcal{M}[\bar{\rho}]}{\partial z_x} = n_x^S + n_x^Q, \quad (34)$$

where $x = 1$, $x = a$, or $x = b$. We then find

$$n_x^S = \frac{x z_x \bar{\varphi}^x}{\bar{\rho}}. \quad (35)$$

Since n_x^S 's have to be real and nonnegative, in the saddle point approximation, the solutions $\bar{\varphi}$ also have to be real and nonnegative. Immediately from the saddle point Eq. (13) follows that

$$n_1^S + n_a^S + n_b^S = 1 \quad (36)$$

must hold generally. We also find after some algebra

$$n_1^Q + n_a^Q + n_b^Q = 0. \quad (37)$$

This means that the saddle point approximation conserves the total number of segments for *any* density. Consequently, any average over these density dependent expressions, irrespective of the approximation, must satisfy the conservation. However we note that the conservation laws (36) and (37) do not prevent possibly negative $n_x^S + n_x^Q$ which can arise in the region where the fluctuation part is not sufficiently smaller than the saddle point. As the validity of the saddle point improves with density, this possibility also disappears.

For the special case $a = 2$, $b = 0$ we have

$$n_1^S = \frac{2z_1}{z_1 + \sqrt{z_1^2 + 8z_2\bar{\rho}}}, \quad (38)$$

$$n_1^Q = \frac{z_1(-z_1 + \sqrt{z_1^2 + 8z_2\bar{\rho}})}{2\bar{\rho}(z_1^2 + 8z_2\bar{\rho})}, \quad (39)$$

as a consequence we see that the fraction of monomers not in a crosslink decreases with the density.

C. The effective potential

Upon integrating over the degrees of freedom associated with the clustering centers the remaining integral in the partition function is that over the polymer density degrees of freedom (in the RPA). This permits us to interpret the effective interaction between polymer segments as caused by the clustering. It consists of the typically attractive contribution to the polymer-polymer quadratic density fluctuations from the aggregating fields and any direct polymer-polymer interaction (such as excluded volume interactions).

From Eqs. (23), (27), and (28) we can rewrite the partition function as

$$Z_N \approx \mathcal{N}''' \int [d\Delta\rho] e^{-\frac{1}{2} \int d\mathbf{r} \int d\mathbf{r}' \Delta\rho(\mathbf{r}) \frac{\delta_{\mathbf{r}-\mathbf{r}'}}{V} \Delta\rho(\mathbf{r}')} \times e^{AV} e^{-\frac{1}{2} \int d\mathbf{r} \int d\mathbf{r}' \Delta\rho(\mathbf{r}) W(\mathbf{r}-\mathbf{r}') \Delta\rho(\mathbf{r}')}, \quad (40)$$

where the effective potential between the polymer segments W is given by

$$W(\mathbf{r}-\mathbf{r}') = - \left. \frac{\delta^2 M[\rho]}{\delta\rho(\mathbf{r})\delta\rho(\mathbf{r}')} \right|_{\rho(\mathbf{r})=\bar{\rho}} = -2C(z_1, z_a, z_b; \bar{\rho}) \delta(\mathbf{r}-\mathbf{r}'). \quad (41)$$

We can then split the contribution from the saddle point and the quadratic contribution of Eq. (24) and write

$$C = C_S + C_Q, \quad (42)$$

$$C_S = \frac{1}{2} \left. \frac{\partial^2 f^S(\bar{\varphi}, \rho)}{\partial\rho^2} \right|_{\rho=\bar{\rho}}, \quad (43)$$

$$C_Q = \frac{1}{2} \left. \frac{\partial^2 f^Q(\bar{\varphi}, \rho)}{\partial\rho^2} \right|_{\rho=\bar{\rho}}, \quad (44)$$

where

$$f^S = -\rho + \rho \ln(\rho/\bar{\varphi}) + z_1\bar{\varphi} + z_a\bar{\varphi}^a + z_b\bar{\varphi}^b, \quad (45)$$

$$f^Q = -\frac{1}{2} \ln\{4[1 + a(a-1)z_a\bar{\varphi}^a/\rho + b(b-1)\bar{\varphi}^b/\rho]\}. \quad (46)$$

Now, using Eq. (13), we find $\partial f^S/\partial\rho = \ln\rho - \ln\bar{\varphi}$ and, using the property $\partial\bar{\varphi}/\partial\rho = 1/(z_1 + a^2 z_a \bar{\varphi}^{a-1} + b^2 z_b \bar{\varphi}^{b-1})$, follows $\partial^2 f^S/\partial\rho^2 = 1/\rho - 1/(z_1\bar{\varphi} + z_a a^2 \bar{\varphi}^a + z_b b^2 \bar{\varphi}^b)$. Let us assume for definiteness that $b > a$. Then when ρ is very small $z_1\bar{\varphi} \approx \rho$ and $\partial^2 f^S/\partial\rho^2 \approx a(a-1)(z_a/z_1^a)\rho^{a-2}/[1 - a(z_a/z_1^a)\rho^{a-1}]$, while when ρ is very large $z_b b \bar{\varphi}^b \approx \rho$ so that $\partial^2 f^S/\partial\rho^2 \approx (b-1)/(b\rho)$. Moreover, we find in the large ρ limit that $\partial^2 f^Q/\partial\rho^2$ behaves at least as $1/\rho^2$.

We remark that in the small ρ limit in the $a = 2$, $b = 0$ case $\partial^2 f^Q/\partial\rho^2 \approx 10z_a^2/z_1^4$, whereas in the $a = 10$, $b = 40$ case $\partial^2 f^Q/\partial\rho^2 \approx -3240z_a\rho^7/z_1^{10}$. However we guard against interpreting this as a repulsive interaction as the saddle point approximation to our field theory is not expected to be accurate at small densities. This repulsive contribution in the small density limit for the effective potential of the Janus case (see Sec. VI) explains the fact that here the RPA can be valid (see Sec. IV D) even if we do not add any excluded volume interaction to the polymer.

For the simple case $a = 2$, $b = 0$ we then find that $C_+ = C_S + C_Q$ where

$$C_S = \frac{1}{4\bar{\rho}} \left(1 - \frac{z_1}{\sqrt{z_1^2 + 8z_2\bar{\rho}}} \right), \quad (47)$$

$$C_Q = \frac{1}{8\bar{\rho}^2} \left[\frac{64(\bar{\rho}z_2)^2}{(z_1^2 + 8z_2\bar{\rho})^2} - 1 + \frac{z_1^3 + 12z_1z_2\bar{\rho}}{(z_1^2 + 8z_2\bar{\rho})^{3/2}} \right]. \quad (48)$$

Here we also find in the small $\bar{\rho}$ limit

$$C_S = \frac{z_2}{z_1} - \frac{6z_2^2}{z_1^4} \bar{\rho} + O(\bar{\rho}^2), \quad (49)$$

$$C_Q = \frac{5z_2^2}{z_1^4} - \frac{88z_2^3}{z_1^6} \bar{\rho} + O(\bar{\rho}^2), \quad (50)$$

which tells us that the energy to crosslink goes to a constant proportional to z_2 .

RICCARDO FANTONI AND KRISTIAN K. MÜLLER-NEDEBOCK

PHYSICAL REVIEW E **84**, 011808 (2011)

In the large $\bar{\rho}$ limit

$$C_S = \frac{1}{4\bar{\rho}} - \frac{z_1}{8\sqrt{2z_2}\bar{\rho}^{3/2}} + \frac{z_1^3}{128\sqrt{2z_2^3}\bar{\rho}^{5/2}} + O(\bar{\rho}^{-3}), \quad (51)$$

$$C_Q = \frac{3z_1}{32\sqrt{2z_2}\bar{\rho}^{5/2}} + O(\bar{\rho}^{-3}), \quad (52)$$

which tells us that the energy to crosslink goes to zero as $1/\bar{\rho}$, in accord with the fact that we are in a dense system.

The effective potential calculated here, based on small density fluctuations around a background of a given density, is dependent on the average density. As expected, the clustering produces a local attractive interaction.

However, it is interesting to note that the strength of this interaction decreases with average density. We attribute this to the fact that the fraction of free segments (i.e., those in clusters of size 1) decreases with the average density according to Eq. (38). Therefore, for large $\bar{\rho}$, the number of additional free segments gained by increasing the density from $\bar{\rho}$ to $\bar{\rho} + \Delta$ is proportional to $\bar{\rho}^{-1/2}$ leading to a pairwise contribution $\Delta^2/\bar{\rho}$ as found in Eq. (51).

D. Validity of RPA

The RPA is based on a homogeneity assumption which no longer holds when the RPA itself predicts overly large fluctuations. In order to obtain Eq. (29) we must have that $\tilde{S}_0^{-1}(k)/V - 2C$ is a strictly positive function for all values of the wave vector k . Since $\tilde{S}_0^{-1}(k)$ is a monotonically increasing function of k , the RPA will be valid as long as

$$C < \frac{\tilde{S}_0^{-1}(0)}{2V} = \frac{1}{2V\bar{\rho}^2}. \quad (53)$$

In the thermodynamic limit one would require that $C < 0$ for the validity of RPA.

We can then extend the region of the validity of RPA by adding an excluded volume effect [50] to the polymer which amounts to taking $M[\rho] \rightarrow M[\rho] - v \int d\mathbf{r} \rho^2(\mathbf{r})$ with v a positive constant with the dimensions of a volume. We will then have

$$A \rightarrow A - \bar{\rho}^2 v, \quad B \rightarrow B - 2\bar{\rho} v, \quad C \rightarrow C - v, \quad (54)$$

and the validity of RPA becomes $C < v$.

For the $a = 2, b = 0$ case we have that C_+ is always positive so the RPA cannot be applied without the excluded volume interaction. As a matter of fact we have $\lim_{\bar{\rho} \rightarrow \infty} C_+ = 0$ and $\lim_{\bar{\rho} \rightarrow 0} C_+ = z_2(z_1^2 + 5z_2)/z_1^4$ and C_+ is a monotonically decreasing function of $\bar{\rho}$. So by choosing v any arbitrarily small positive constant we are able to extend the range of validity of RPA to arbitrarily large densities.

In this case choosing $z_1 = 1, z_2 = e^{2\beta}$, and $v = 1$ the validity domain in the phase diagram is determined in Fig. 4.

In Fig. 5 we show the behavior of the free energy density as a function of density in the case $a = 2, b = 0$. Here we choose $z_1 = 1, z_2 = e^{2\beta}$ where $\beta = 1/k_B T$ with k_B Boltzmann constant and T is the temperature and $v = 1$.

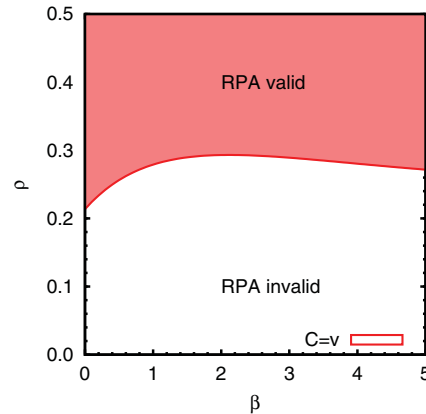


FIG. 4. (Color online) Shows the RPA validity region of the phase diagram, in the $a = 2, b = 0$ case, for $z_1 = 1, z_2 = e^{2\beta}$ and $v = 1$.

V. THE STATIC STRUCTURE FACTOR

The Fourier transform of the pair correlation function is defined as [51]

$$\tilde{g}(\mathbf{k}) = \frac{1}{N} \langle \tilde{\rho}(\mathbf{k}) \tilde{\rho}(-\mathbf{k}) \rangle = \frac{1}{N} \langle \Delta \tilde{\rho}(\mathbf{k}) \Delta \tilde{\rho}(-\mathbf{k}) \rangle, \quad \mathbf{k} \neq 0. \quad (55)$$

The quantity $\tilde{g}(\mathbf{k})$ can be measured experimentally by light scattering. Moreover one can extract some important information on the polymer properties from the small $k = |\mathbf{k}|$ behavior:

$$\tilde{g}(\mathbf{k}) = \tilde{g}(0) \left(1 - \frac{k^2}{3} R_g^2 + \dots \right), \quad (56)$$

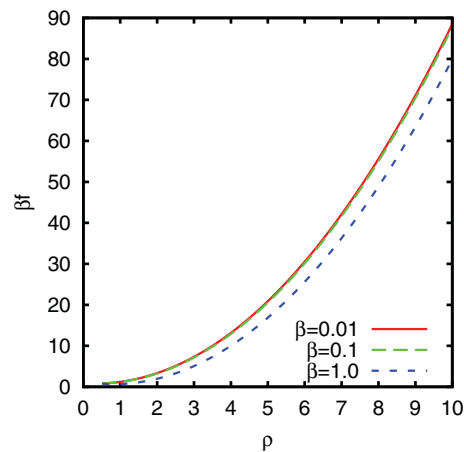


FIG. 5. (Color online) Shows the free energy density as a function of the average density in the $a = 2, b = 0$ case, for $z_1 = 1, z_2 = e^{2\beta}$ and $v = 1$.

where R_g is the radius of gyration of the polymer, namely

$$R_g^2 = \frac{1}{2N^2} \sum_{n=1}^N \sum_{m=1}^N \langle (\mathbf{R}_n - \mathbf{R}_m)^2 \rangle. \quad (57)$$

Now using the result from the RPA we find

$$N\tilde{g}(k) = V[\tilde{\xi}_0^{-1}(k)/V - 2C]^{-1}, \quad (58)$$

which when $C = -v$, agrees with Edwards' result [50,52] for polymer chains with only excluded volume interactions [53]. Notice that the effective potential C is in general a function of $\bar{\rho}$, z_1 , z_a , and z_b . As shown in Sec. IV C, $C + v$ tends to be positive (attractive interaction between polymer segments) in the presence of clustering centers. So we expect there to be a regime of density for which there is a balance between the repulsion due to the excluded volume effect and the attraction due to clustering making $C \approx 0$. In such case our result reproduces the one for the ideal chain (see section 1.2.3 in Ref. [51]).

In the small k limit we find

$$N\tilde{g}(k) = \frac{V^2}{1/\bar{\rho}^2 - 2CV} \left(1 - \frac{k^2}{3}\xi^2 + \dots \right), \quad (59)$$

where $\bar{\rho} = N/V$ is the average polymer segment density for a single long polymer chain and the "curvature" of the structure factor at $k = 0$ is

$$\xi^2 = \frac{\ell^2 \bar{\rho} V}{6 - 12\bar{\rho}^2 CV}, \quad (60)$$

where ℓ is the Kuhn length of the polymer. And in the thermodynamic limit

$$(\xi/\ell)^2 \rightarrow -\frac{1}{12\bar{\rho}C}. \quad (61)$$

So that at large polymer densities the curvature tends to a constant [we note that C now includes the excluded volume as in Eq. (54)].

We also find, in the thermodynamic limit, the following expression for the structure factor:

$$g(k) \rightarrow \frac{12}{(\ell k)^2 - 24\bar{\rho}C}. \quad (62)$$

Notice that in the absence of the effective interaction ($C = 0$) the structure factor diverges at $k = 0$.

In the $a = 2, b = 0$ case, at constant V , in the small N limit we find the free polymer result $\xi^2 = N\ell^2/6 + O(N^3)$. In the large N limit we find

$$(\xi/\ell)^2 = \frac{1}{12v} \frac{V}{N} + \frac{1}{48v^2} \frac{V^2}{N^2} + O(1/N^{5/2}). \quad (63)$$

Given the densest possible filling $N/V \sim 1/v$ the curvature tends to a constant.

VI. THE JANUS CASE

Although our field-theoretical formulation includes no precise model for the mechanism that causes clustering centers of a given functionality to occur, we investigate here the case where the functionalities (10 and 40) of the clustering centers are the same as those determined for Janus particles in recent

studies. Indeed there has recently been much development in the techniques for the synthesis of new patchy colloidal particles [36–39]. One particularly simple class of these anisotropic particles, called Janus particles [40–43], seem to form mainly clusters of either 10 or 40 particles. Here Monte Carlo simulations [20,21] indicate that mainly stable micelle (10 particles) or vesicle (40 particles) arrangements of these particles are to be found in the vapor phase. Moreover it was found that the clusters behave very similarly to an ideal gas, since the particles forming the cluster tend to arrange with their active surfaces toward the cluster center.

Janus chains have been suggested as potentially useful candidates for understanding interesting polymer phenomena [44]. We will apply our formalism to the case of a dense polymer in a Janus fluid and in so doing we hope to add to

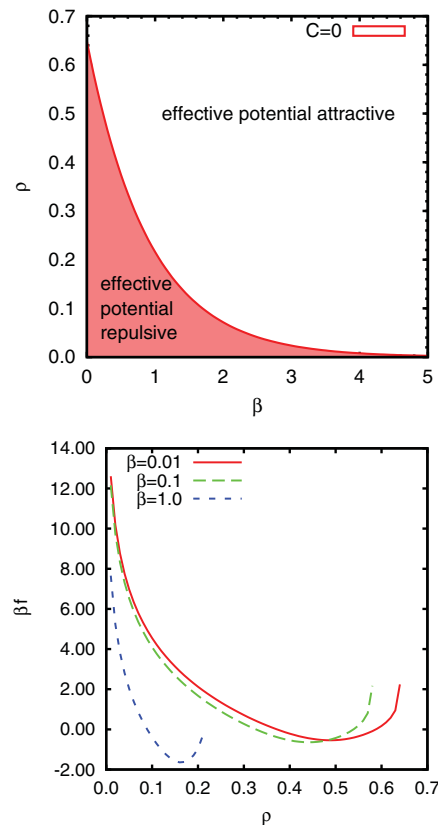


FIG. 6. (Color online) The upper panel shows the RPA validity region of the phase diagram, in the Janus case, for $z_1 = 1, z_{10} = e^{10\beta}, z_{40} = e^{40\beta}$, in the absence of any excluded volume effect. At $\beta = 0$ the $C = 0$ equation has solution $\rho \simeq 0.647933\dots$. Note that the validity region is in the small density region, where the contribution from the quadratic fluctuations of the theory dominates, and the whole theory is expected to be less significant. The lower panel shows the free energy density as a function of the average density. The rapid increase at high density is indicative of the limit of the RPA applicability.

RICCARDO FANTONI AND KRISTIAN K. MÜLLER-NEDEBOCK

PHYSICAL REVIEW E **84**, 011808 (2011)

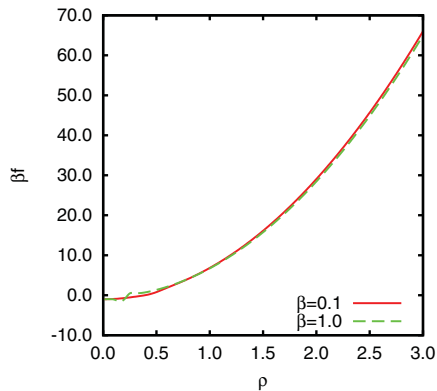


FIG. 7. (Color online) Shows the free energy density as a function of the average density in the Janus case, for $z_1 = 1$, $z_{10} = e^{10\beta}$, $z_{40} = e^{40\beta}$, and $v = 15$.

the recent interest for Janus particles interacting with polymer chains [43–45]. To the best of our knowledge there is no results in the literature that proves the clustering in the Janus fluid in the presence of the polymer. So we will take as a working hypothesis the existence of such a clustering. And make the approximation of treating the backbone units of the polymer (the Janus particles) as an ideal fluid.

Given the general setting described above we can apply our theoretical model to a polymer in a Janus fluid. By this we think of chain segments only clustering to form limited closed shell conformations, that is, micelles and vesicles. As mentioned before, we however do not consider the nature of spacial extent of the clustering in detail and simply presume that it still occurs in the same way as if the Janus particles were not connected to the polymer.

In the Janus case we have to choose $a = 10$ and $b = 40$ (see Fig. 3). We then find for the determination of the critical point

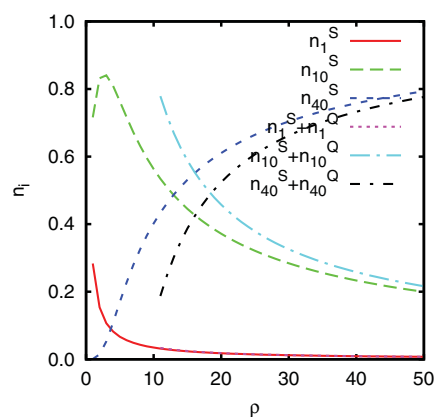


FIG. 8. (Color online) In the Janus case for $z_1 = 1$, $z_{10} = e^{10\beta}$, $z_{40} = e^{40\beta}$, $v = 15$, and $\beta = 1$ shows the concentrations of clusters of 1, 10, and 40 particles as a function of the density.

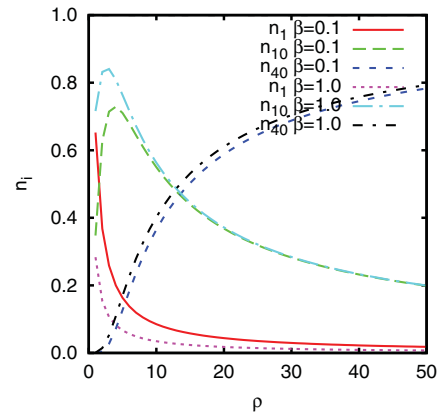


FIG. 9. (Color online) In the Janus case for $z_1 = 1$, $z_{10} = e^{10\beta}$, $z_{40} = e^{40\beta}$, and $v = 15$, shows the concentrations of clusters of 1 (n_1^S), 10 (n_{10}^S), and 40 (n_{40}^S) particles as a function of the density when we do not use the logarithmic correction in Eq. (24).

an algebraic equation of degree 40 Eq. (13). As expected, this equation has just one solution for which A [from Eq. (28)] is real and nonnegative.

We can see the generalized fugacities defined as $z_i \propto \exp(-\beta u_i + \beta \mu_i)$ for $i = 1, 10, 40$, where u_i is the average internal energies of the cluster of i Janus particles and μ_i is the chemical potential of this cluster species. It is moreover reasonable to take $\mu_i \approx \mu$ independent of i (μ being the chemical potential of the vapor phase of the Janus fluid) so that we get $z_i \propto \exp(-\beta u_i)$.

Choosing $z_1 = 1$, $z_{10} = e^{10\beta}$, and $z_{40} = e^{40\beta}$ we find that at small densities (where the theory is expected to be not good) the effective potential is repulsive (due to the quadratic fluctuations in the theory) even without adding an excluded volume to the polymer (see Sec. IV C). The range of validity of RPA in the phase diagram is shown in Fig. 6. In Fig. 6 we show the behavior of the free energy density which clearly shows the signature for the breakdown of the RPA theory at high density.

Notice that, also in this case, $\lim_{\beta \rightarrow \infty} C = 0$ so that by adding a small excluded volume will allow us to reach the high densities domain with RPA. At a fixed temperature C , as a function of density, has a global maximum, so that choosing the excluded volume v bigger than this value, the RPA can be made valid at any density (see Fig. 7). Moreover, we expect the theory to give consistent results in the high density regime.

Our choice for the fugacities is justified *a posteriori* since for $\beta < 1$ we are in the high temperature regime of the Janus vapor [20] where the internal energy of a cluster of i Janus particles is with a good approximation given by $-(i - 1) \approx -i$ (corresponding to a completely stretched cluster).

Since Z_N is a grand canonical in the clusters of Janus particles, we can take derivatives with respect to the generalized fugacity z_i to determine the concentration n_i of clusters of i

Janus particles as follows:

$$n_i = \frac{i(N_i)}{N} = \frac{i}{N} \frac{\partial \ln Z_N}{\partial \ln z_i}, \quad (64)$$

where $\ln Z_N = V[A + \ln(-2C)/2]$.

A graph of the concentrations as a function of the average polymer density is shown in Fig. 8. From Fig. 8 one can see the difference between $n_x = n_x^S$ and $n_x = n_x^S + n_x^Q$ for $x = 1, 10,$ and 40 and $\beta = 1$. Note that the conservation of particles $n_1 + n_{10} + n_{40} = 1$ is exactly satisfied at all densities and temperatures in both cases. In Fig. 9 we show the dependence of the concentrations from the temperature. Thus we would say that at sufficiently high densities the vesicles appear and as a consequence the micelles are reduced.

We conclude that this suggests strong dominance of nonclustering at low densities. As the density is increased smaller clusters and eventually larger clusters dominate the linking behavior.

VII. CONCLUSIONS

In this work we have studied and developed a field-theoretical formalism for a polymer immersed in an ideal mixture of clustering centers. These centers cause clustering of either a particles or b particles, that is, clusters of either species are monodisperse. The field theory couples fields associated with stickers to the polymer chain density and provides a formally exact expression for the partition function (canonical in polymer and grand canonical for the clustering centers). We showed that it is possible to compute quantities using the nonlinear theory by means of a saddle point approximation and we argue that the approximation improves as the density of the polymer chain increases. The current system and the choice of implementation of additional fields enabled us to derive saddle-point equations that are simpler than those

that arise in some other formalisms by not requiring the solution of nonlinear integral equations. The benefit of the local saddle-point equations is that they also enable a relatively simple analysis of the stability and applicability considerations of the theory.

For a homogeneous, dense polymer system, we computed the effective interaction potential (up to quadratic density fluctuations) and computed properties of the structure factor within the random phase approximation. As expected, the addition of an excluded volume interaction will compensate for the attraction due to aggregation effects and extend the validity of the RPA. The effective pairwise potential obtained in this approximation has interesting, nontrivial density dependence. Another clear consequence of increasing chain density is the growing dominance of the higher functional clustering centers.

The nature of the clustering process is definitely of importance in aggregating polymer systems. (Recently, a theory for cluster formation in homopolymer melts was introduced by Semenov [17]). One motivation for our study is the closed multimerization scenario suggested by particles in a Janus fluid, where micelles ($a = 10$) and vesicles ($b = 40$) are known to occur [20,21]. Future work will focus the attention on the stability of such Janus-type multimers when connected to a polymer with more detailed models of the cluster itself.

ACKNOWLEDGMENTS

R.F. gratefully acknowledges support from the NITheP of South Africa. K.K.M.-N. gratefully acknowledges the support of the National Research Foundation.

APPENDIX A: COEFFICIENTS A, B, AND C FOR THE A = 2, B = 0 CASE

The A, B, and C coefficients are given by

$$A_{\pm} = \frac{1}{8z_2} \left\{ -z_1^2 \pm z_1 \sqrt{z_1^2 + 8\bar{\rho}z_2} + 8\bar{\rho}z_2 \ln \left(\frac{4\bar{\rho}z_2}{-z_1 \pm \sqrt{z_1^2 + 8\bar{\rho}z_2}} \right) + 4z_2 \left[\bar{\rho} + \ln \left(1 \pm \frac{z_1}{\sqrt{z_1^2 + 8\bar{\rho}z_2}} \right) - \ln 8 \right] \right\}, \quad (A1)$$

$$B_{\pm} = -\frac{2z_2}{z_1^2 + 8\bar{\rho}z_2} + \frac{1}{4\bar{\rho}} \left(1 \mp \frac{z_1}{\sqrt{z_1^2 + 8\bar{\rho}z_2}} \right) + \ln \left(\frac{4\bar{\rho}z_2}{-z_1 \pm \sqrt{z_1^2 + 8\bar{\rho}z_2}} \right), \quad (A2)$$

$$C_{\pm} = \frac{8z_2^2}{(z_1^2 + 8\bar{\rho}z_2)^2} + \frac{1}{8\bar{\rho}^2} \left[-1 \pm \frac{z_1}{\sqrt{z_1^2 + 8\bar{\rho}z_2}} + \bar{\rho} \left(2 \mp \frac{2z_1(z_1^2 - 2z_2 + 8\bar{\rho}z_2)}{(z_1^2 + 8\bar{\rho}z_2)^{3/2}} \right) \right]. \quad (A3)$$

APPENDIX B: THE RANDOM PHASE APPROXIMATION

For the polymer chain, with a Kuhn length ℓ , we can write

$$\begin{aligned} \int \{ \prod d\mathbf{R} \} \{ \prod G \} &= \int [d\rho] \int [d\zeta] \int [d\mathbf{R}] e^{-\frac{3}{2\ell} \int_0^L ds \mathbf{R}^2(s)} e^{i \int d\mathbf{r} \zeta(\mathbf{r}) (\rho(\mathbf{r}) - \int_0^L \frac{ds}{\ell} \delta[\mathbf{r} - \mathbf{R}(s)])} \\ &= \int [d\rho] \int [d\zeta] \int [d\mathbf{R}] e^{-\frac{3}{2\ell} \int_0^L ds \mathbf{R}^2(s)} e^{i \int d\mathbf{r} \zeta(\mathbf{r}) \rho(\mathbf{r})} \left\{ 1 - i \int d\mathbf{r} \int_0^L \frac{ds}{\ell} \zeta(\mathbf{r}) \delta[\mathbf{r} - \mathbf{R}(s)] \right. \\ &\quad \left. - \frac{1}{2} \int d\mathbf{r} \int_0^L \frac{ds}{\ell} \zeta(\mathbf{r}) \delta[\mathbf{r} - \mathbf{R}(s)] \int d\mathbf{r}' \int_0^L \frac{ds'}{\ell} \zeta(\mathbf{r}') \delta[\mathbf{r}' - \mathbf{R}(s')] + \dots \right\}, \end{aligned} \quad (B1)$$

where $L = N\ell$ is the total polymer length and the dot denotes a derivative with respect to s .

Now the first term gives just a normalization constant \mathcal{N} . To calculate the second term we introduce the polymer center of mass \mathbf{R}_0 so that $\mathbf{R}(s) = \mathbf{R}_0 + \Delta\mathbf{R}(s)$ and write

$$\begin{aligned} & \int [d\zeta] \int [d\mathbf{R}] e^{-\frac{3}{2\ell} \int_0^L ds \dot{\mathbf{R}}^2(s)} e^{i \int d\mathbf{r} \zeta(\mathbf{r}) \rho(\mathbf{r})} \int d\mathbf{r} \int_0^L \frac{ds}{\ell} \zeta(\mathbf{r}) \delta[\mathbf{r} - \mathbf{R}(s)] \\ &= \int [d\zeta] \int [d\mathbf{R}] e^{-\frac{3}{2\ell} \int_0^L ds \dot{\mathbf{R}}^2(s)} e^{i \int d\mathbf{r} \zeta(\mathbf{r}) \rho(\mathbf{r})} \int d\mathbf{r} \int_0^L \frac{ds}{\ell} \zeta(\mathbf{r}) \frac{1}{V} \sum_{\mathbf{k}} e^{i\mathbf{k}\mathbf{r} - i\mathbf{k}\mathbf{R}(s)} \\ &= \int [d\zeta] \int [d\Delta\mathbf{R}] \int d\mathbf{R}_0 e^{-\frac{3}{2\ell} \int_0^L ds \Delta\dot{\mathbf{R}}^2(s)} e^{i \int d\mathbf{r} \zeta(\mathbf{r}) \rho(\mathbf{r})} \int d\mathbf{r} \int_0^L \frac{ds}{\ell} \frac{1}{V} \sum_{\mathbf{k}} \zeta(\mathbf{r}) e^{i\mathbf{k}\mathbf{r}} e^{-i\mathbf{k}(\mathbf{R}_0 + \Delta\mathbf{R}(s))} \\ &= \int [d\zeta] e^{i \int d\mathbf{r} \zeta(\mathbf{r}) \rho(\mathbf{r})} \mathcal{N} \frac{1}{V} \int d\mathbf{r} \int_0^L \frac{ds}{\ell} \sum_{\mathbf{k}} \zeta(\mathbf{r}) \delta_{\mathbf{k},0} \\ &= \int [d\zeta] e^{i \int d\mathbf{r} \zeta(\mathbf{r}) \rho(\mathbf{r})} \mathcal{N} \frac{N}{V} \int d\mathbf{r} \zeta(\mathbf{r}), \end{aligned} \tag{B2}$$

where V is the volume of the box and $\delta_{\mathbf{k},0}$ is the Kronecker delta.

The third term gives

$$\begin{aligned} & \int [d\zeta] e^{i \int d\mathbf{r} \zeta(\mathbf{r}) \rho(\mathbf{r})} \int [d\Delta\mathbf{R}] \int d\mathbf{R}_0 e^{-\frac{3}{2\ell} \int_0^L ds \Delta\dot{\mathbf{R}}^2(s)} \frac{1}{V^2} \sum_{\mathbf{k}} \sum_{\mathbf{k}'} \int d\mathbf{r} \int_0^L \frac{ds}{\ell} \int d\mathbf{r}' \int_0^L \frac{ds'}{\ell} \\ & \quad \times \zeta(\mathbf{r}) \zeta(\mathbf{r}') e^{i\mathbf{k}\mathbf{r}} e^{i\mathbf{k}'\mathbf{r}'} e^{i(\mathbf{k}+\mathbf{k}')\mathbf{R}_0} e^{i\mathbf{k}\Delta\mathbf{R}(s)} e^{i\mathbf{k}'\Delta\mathbf{R}(s')} \\ &= \int [d\zeta] e^{i \int d\mathbf{r} \zeta(\mathbf{r}) \rho(\mathbf{r})} \mathcal{N} \frac{1}{V^2} \int_0^L \frac{ds}{\ell} \int_0^L \frac{ds'}{\ell} \sum_{\mathbf{k}} \tilde{\zeta}(\mathbf{k}) \tilde{\zeta}(-\mathbf{k}) \langle e^{i\mathbf{k}(\mathbf{R}(s) - \mathbf{R}(s'))} \rangle_0, \end{aligned} \tag{B3}$$

where we denoted with the average

$$\langle \dots \rangle_0 = \frac{\int [d\mathbf{R}] e^{-\frac{3}{2\ell} \int_0^L ds \dot{\mathbf{R}}^2(s)} [\dots]}{\int [d\mathbf{R}] e^{-\frac{3}{2\ell} \int_0^L ds \dot{\mathbf{R}}^2(s)}}, \tag{B4}$$

and with the tilde the Fourier transform [48].

Now the average $\langle e^{i\mathbf{k}(\mathbf{R}(s) - \mathbf{R}(s'))} \rangle_0$ can be easily calculated by discretizing the polymer and integrating over the bond vectors $\mathbf{b}_i = \mathbf{R}_{i+1} - \mathbf{R}_i$ as follows:

$$\begin{aligned} \langle e^{i\mathbf{k}(\mathbf{R}(s) - \mathbf{R}(s'))} \rangle_0 &= \frac{\int \prod_i d\mathbf{b}_i e^{-\frac{3}{2\ell^2} \sum_i \mathbf{b}_i^2} e^{i\mathbf{k}(\mathbf{b}_1 + \mathbf{b}_2 + \dots + \mathbf{b}_n)}}{\int \prod_i d\mathbf{b}_i e^{-\frac{3}{2\ell^2} \sum_i \mathbf{b}_i^2}} \\ &= (e^{-\frac{k^2 \ell^2}{6}})^n, \end{aligned} \tag{B5}$$

where $n = |s - s'|/\ell$. Since

$$\int_0^L ds \int_0^L ds' e^{-a|s-s'|} = \frac{2(aL - 1 + e^{-aL})}{a^2}, \tag{B6}$$

we can introduce the function

$$\tilde{\mathcal{S}}_0(k) = \frac{72(k^2 \ell L / 6 - 1 + e^{-\frac{k^2 \ell L}{6}})}{V^2 k^4 \ell^4}, \tag{B7}$$

with $\tilde{\mathcal{S}}_0(0) = (N/V)^2 = \bar{\rho}^2$.

Then the expression we started with in Eq. (B1) can be rewritten, omitting the functional integral over the density collective variable, as

$$\begin{aligned} & \mathcal{N} \int [d\tilde{\zeta}] e^{i \sum_{\mathbf{k}} \tilde{\zeta}(\mathbf{k}) \bar{\rho}(-\mathbf{k})} \left[1 - i \frac{N}{V} \tilde{\zeta}(0) \right. \\ & \quad \left. - \frac{1}{2V} \sum_{\mathbf{k}} \tilde{\zeta}(\mathbf{k}) V \tilde{\mathcal{S}}_0(k) \tilde{\zeta}(-\mathbf{k}) + \dots \right]. \end{aligned} \tag{B8}$$

We can now reconstruct the exponential to obtain

$$\begin{aligned} & \int [d\tilde{\zeta}] e^{i \sum_{\mathbf{k}} \tilde{\zeta}(\mathbf{k}) \bar{\rho}(-\mathbf{k})} e^{-\frac{1}{2V} \sum_{\mathbf{k}} \tilde{\zeta}(\mathbf{k}) V \tilde{\mathcal{S}}_0(k) \tilde{\zeta}(-\mathbf{k}) - i \frac{N}{V} \tilde{\zeta}(0)} \\ &= \mathcal{N}' e^{-\frac{1}{2V} \sum_{\mathbf{k}} \ln[\tilde{\mathcal{S}}_0(k) V]} e^{-\frac{1}{2V} \sum_{\mathbf{k}} \Delta\tilde{\rho}(\mathbf{k}) \frac{\tilde{\mathcal{S}}_0^{-1}(k)}{V} \Delta\tilde{\rho}(-\mathbf{k})}. \end{aligned} \tag{B9}$$

Here $\Delta\tilde{\rho}(\mathbf{k}) = \tilde{\rho}(\mathbf{k}) - \bar{\rho} V \delta_{\mathbf{k},0}$.

APPENDIX C: THE GAUSSIAN DISTRIBUTION

The Gaussian distribution function for a set of real variables x_1, x_2, \dots, x_N is defined as

$$\Psi(x_1, x_2, \dots, x_N) = C \exp\left(-\frac{1}{2} \sum_{n,m} A_{nm} x_n x_m\right), \tag{C1}$$

where A_{nm} is a symmetric positive definite matrix and C is a normalization constant given by the requirement $\int_{-\infty}^{\infty} \dots \int_{-\infty}^{\infty} \prod_n dx_n \Psi = 1$.

Let $\langle \dots \rangle$ be the average of the distribution function of Eq. (C1),

$$\langle \dots \rangle = \int_{-\infty}^{\infty} \dots \int_{-\infty}^{\infty} \prod_n dx_n \dots \Psi(x_1, x_2, \dots, x_N), \tag{C2}$$

then it can be proved [50] that

$$\langle x_n x_m \rangle = [A^{-1}]_{nm}. \tag{C3}$$

In general we have the following formula (Wick's theorem):

$$\begin{aligned} & \langle x_{n_1} x_{n_2} \dots x_{n_{2p}} \rangle \\ &= \sum_{\text{all pairing}} \langle x_{m_1} x_{m_2} \rangle \langle x_{m_3} x_{m_4} \rangle \dots \langle x_{m_{2p-1}} x_{m_{2p}} \rangle. \end{aligned} \tag{C4}$$

If the subscript n of x_n is regarded as a continuous variable, the set of points (x_1, x_2, \dots, x_N) represents a continuous function, and the integral over the set (x_1, x_2, \dots, x_N) reduces to the integration over all the function, and it is called the *functional integral*. It is denoted by the symbol $[dx]$, that is, $\int \prod_n dx_n \dots \rightarrow \int [dx] \dots$.

Consider now the following Gaussian distribution functional:

$$\Psi[\phi] = C \exp \left[-\frac{1}{2} \int_{-\infty}^{\infty} dx \phi^2(x) \right], \quad (C5)$$

where ϕ is a real function, then using the continuous limit of Eq. (C3) we find

$$\langle \phi(x)\phi(x') \rangle = \delta(x - x'), \quad (C6)$$

where δ is the Dirac δ function.

If now $\phi = \phi_1 + i\phi_2$ is a complex function we consider the Gaussian distribution functional

$$\Psi[\phi, \phi^*] = C \exp \left[-\int_{-\infty}^{\infty} dx \phi(x)\phi^*(x) \right]. \quad (C7)$$

Now we find from Eq. (C6)

$$\begin{aligned} \langle \phi(x)\phi^*(x') \rangle &= \langle \phi_1(x)\phi_1(x') + \phi_2(x)\phi_2(x') \rangle \\ &= \frac{1}{2}\delta(x - x') + \frac{1}{2}\delta(x - x') = \delta(x - x') \end{aligned} \quad (C8)$$

and

$$\begin{aligned} \langle \phi(x)\phi(x') \rangle &= \langle \phi_1(x)\phi_1(x') - \phi_2(x)\phi_2(x') \\ &\quad + i\phi_1(x)\phi_2(x') + i\phi_2(x)\phi_1(x') \rangle \\ &= \frac{1}{2}\delta(x - x') - \frac{1}{2}\delta(x - x') = 0. \end{aligned} \quad (C9)$$

APPENDIX D: FIELD THEORY WITHOUT 1 CLUSTERS

An alternative way to formulate the clustering, without the use of clusters of size 1 is presented below. We shall show that a simple mapping reduces again to a special case of Eq. (6).

Consider a system in which we have only clusters of sizes a and b but no “inert” clusters of size 1. As explained in Sec. II the functional integration over the fields φ and φ^* requires matching each φ of a clustering center with a φ^* on the polymer, permitting no unmatched φ and φ^* pairs. Since size a and b clusters do not necessarily attach to each potential site on the polymer, all possible attachment sites have to be generated. The product

$$\prod_{i=1}^N [1 + \varphi^*(\mathbf{R}_i)]$$

produces all equally weighted possibilities of the attaching to the sites $\{\mathbf{R}_i\}, \forall i \in \{1, \dots, N\}$ of a given polymer configuration.

The analog to Eq. (5) then becomes

$$\begin{aligned} Z'_{N_a, N_b} &= \mathcal{N} \int d\mathbf{R}_1 \dots d\mathbf{R}_N e^{-v \sum_{n,m=1}^N \delta(\mathbf{R}_n - \mathbf{R}_m)} \int [d\varphi][d\varphi^*] e^{-\int d\mathbf{r} \varphi(\mathbf{r})\varphi^*(\mathbf{r})} \\ &\quad \times [1 + \varphi^*(\mathbf{R}_1)]G(\mathbf{R}_1, \mathbf{R}_2)[1 + \varphi^*(\mathbf{R}_2)]G(\mathbf{R}_2, \mathbf{R}_3) \dots G(\mathbf{R}_{N-1}, \mathbf{R}_N)[1 + \varphi^*(\mathbf{R}_N)] \\ &\quad \times \frac{1}{N_a!} \left[\int d\mathbf{r} z_a \varphi^a(\mathbf{r}) \right]^{N_a} \frac{1}{N_b!} \left[\int d\mathbf{r} z_b \varphi^b(\mathbf{r}) \right]^{N_b}, \end{aligned} \quad (D1)$$

leading by the same procedure as described in Sec. II to analog of Eq. (6),

$$\begin{aligned} Z'_N &= \mathcal{N} \int [d\varphi][d\varphi^*] \left\{ \prod d\mathbf{R} \right\} \left\{ \prod G \right\} d^N \exp \left[-\int d\mathbf{r} \varphi(\mathbf{r})\varphi^*(\mathbf{r}) \right. \\ &\quad \left. + \int d\mathbf{r} \rho(\mathbf{r}) \ln(1 + \varphi^*(\mathbf{r})/d) + z_a \int d\mathbf{r} \varphi^a(\mathbf{r}) + z_b \int d\mathbf{r} \varphi^b(\mathbf{r}) \right]. \end{aligned} \quad (D2)$$

We see that the trivial transformation $\varphi^* \rightarrow \varphi^* - 1$ in Eq. (D2) above leads to the original field-theoretic equation in the main text Eq. (6) with $z_1 \rightarrow 1$. For this reason we treat the marginally more general case in this paper.

- [1] R. S. Hoy and G. H. Fredrickson, *J. Chem. Phys.* **131**, 224902 (2009).
- [2] M. Rubinstein and A. V. Dobrynin, *Curr. Opin. Colloid Interface Sci.* **4**, 83 (1999).
- [3] A. N. Semenov and M. Rubinstein, *Macromolecules* **31**, 1373 (1998).
- [4] M. Muthukumar, *J. Chem. Phys.* **104**, 691 (1996).
- [5] I. A. Nyrkova and A. N. Semenov, *Eur. Phys. J. E* **17**, 327 (2005).
- [6] R. T. Deam and S. F. Edwards, *Proc. R. Soc. London Ser. A* **280**, 317 (1976).
- [7] S. I. Kuchanov, S. V. Korolev, and S. V. Panyukov, *Adv. Chem. Phys.* **72**, 115 (1988).
- [8] A. V. Ermoshkin and I. Y. Erukhimovich, *J. Chem. Phys.* **110**, 1781 (1999).
- [9] S. Kuchanov, H. Slot, and A. Stroeks, *Prog. Polym. Sci.* **29**, 563 (2004).
- [10] A. Kudlay and I. Y. Erukhimovich, *Macromol. Theory Simul.* **10**, 542 (2001).
- [11] F. Sciortino, E. Bianchi, J. F. Douglas, and P. Tartaglia, *J. Chem. Phys.* **126**, 194903 (2007).
- [12] Yu. V. Kalyuzhnyi, C.-T. Lin, and G. Stell, *J. Chem. Phys.* **108**, 6525 (1998).
- [13] R. Nagarajan, *J. Chem. Phys.* **90**, 1980 (1989).
- [14] F. Ganazzoli, G. Raos, and G. Allegra, *Macromol. Theory Simul.* **8**, 65 (1999).
- [15] F. Tanaka, *Macromolecules* **23**, 3784 (1990).
- [16] B. Xu, A. Yekta, L. Li, Z. Masoumi, and M. A. Winnik, *Colloids Surf. A* **112**, 239 (1996).

RICCARDO FANTONI AND KRISTIAN K. MÜLLER-NEDEBOCK

PHYSICAL REVIEW E **84**, 011808 (2011)

- [17] A. N. Semenov, *Macromolecules* **42**, 6761 (2009).
 [18] S. M. Loverde, A. V. Ermoshkin, and M. Olvera de la Cruz, *J. Polym. Sci., Part B: Polym. Phys.* **43**, 796 (2005).
 [19] I. Y. Erukhimovich and A. V. Ermoshkin, *JETP* **88**, 538 (1999).
 [20] F. Sciortino, A. Giacometti, and G. Pastore, *Phys. Rev. Lett.* **103**, 237801 (2009).
 [21] A. Giacometti, F. Lado, J. Largo, G. Pastore, and F. Sciortino, *J. Chem. Phys.* **131**, 174114 (2009).
 [22] R. Fantoni, A. Giacometti, F. Sciortino, and G. Pastore, *Soft Matter* **7**, 2419 (2011).
 [23] S. F. Edwards, *J. Phys. (France)* **49**, 1673 (1988).
 [24] S. F. Edwards and K. F. Freed, *J. Phys. C* **3**, 739 (1970).
 [25] S. F. Edwards and K. F. Freed, *J. Phys. C* **3**, 750 (1970).
 [26] M. Gordon, *Proc. R. Soc. London Ser. A* **268**, 240 (1962).
 [27] M. Gordon and G. R. Scantlebury, *Trans. Faraday Soc.* **60**, 604 (1964).
 [28] A. Mohan, R. Elliot, and G. H. Fredrickson, *J. Chem. Phys.* **133**, 174903 (2010).
 [29] Y. Bohbot-Raviv, T. M. Snyder, and Z.-G. Wang, *Langmuir* **20**, 7860 (2004).
 [30] M. E. Cates and T. A. Witten, *Macromolecules* **19**, 732 (1986).
 [31] I. Nakamura and A.-C. Shi, *J. Chem. Phys.* **132**, 194103 (2010).
 [32] A. V. Ermoshkin and M. Olvera de la Cruz, *J. Polym. Sci., Part B: Polym. Phys.* **42**, 766 (2004).
 [33] K. M. Hong and J. Noolandi, *Macromolecules* **14**, 727 (1981).
 [34] A. C. Shi, J. Noolandi, and R. C. Desai, *Macromolecules* **29**, 6487 (1996).
 [35] L. Leibler, *Macromolecules* **13**, 1602 (1980).
 [36] V. N. Manoharan, M. T. Elsesser, and D. J. Pine, *Science* **301**, 483 (2003).
 [37] A. B. Pawar and I. Kretzschmar, *Macromol. Rapid Commun.* **31**, 150 (2010).
 [38] S. C. Glotzer and M. J. Solomon, *Nat. Mater.* **6**, 557 (2007).
 [39] Z. Zhang and S. C. Glotzer, *Nano Lett.* **4**, 1407 (2004).
 [40] P. G. de Gennes, *Rev. Mod. Phys.* **64**, 645 (1992).
 [41] C. Casagrande, P. Fabre, M. Veysié, and E. Raphaël, *Europhys. Lett.* **9**, 251 (1989).
 [42] L. Hong, A. Cacciuto, E. Luijten, and S. Granick, *Nano Lett.* **6**, 2510 (2006).
 [43] A. Walther and A. H. Müller, *Soft Matter* **4**, 663 (2008).
 [44] Y. Ding, H. C. Öttinger, A. D. Schlüter, and M. Kröger, *J. Chem. Phys.* **127**, 094904 (2007).
 [45] J. U. Kim and M. W. Matsen, *Phys. Rev. Lett.* **102**, 078303 (2009).
 [46] P. Haronska and T. A. Vilgis, *Phys. Rev. E* **50**, 325 (1994).
 [47] T. A. Vilgis and P. Haronska, *Macromolecules* **27**, 6465 (1994).
 [48] Notice that since the system has a finite volume V the Fourier transform are of the discrete type. In the thermodynamic limit $V \rightarrow \infty$ and $V^{-1} \sum_{\mathbf{k}} \dots \rightarrow \int d\mathbf{k}/(2\pi)^3 \dots$.
 [49] K. K. Müller-Nedebock, S. F. Edwards, and T. C. B. McLeish, *J. Chem. Phys.* **111**, 8196 (1999).
 [50] M. Doi and S. F. Edwards, *The Theory of Polymer Dynamics* (Clarendon, Oxford, 1986).
 [51] M. Doi, *Introduction to Polymer Physics* (Clarendon, Oxford, 1992).
 [52] T. Shimada, M. Doi, and K. Okano, *J. Chem. Phys.* **88**, 2815 (1988).
 [53] Note that for N_p polymer chains this expression should be modified as $\tilde{g}(k) = N_p/[S_0^{-1}(k)/V - 2CN_p]/\bar{\rho}$.

Chapter 26

The penetrable square-well model: extensive versus non-extensive phases

Fantoni R., A. Malijevský, A. Santos, and A. Giacometti, *Mol. Phys.* **109**, 2723 (2011)

Title: “The penetrable square-well model: extensive versus non-extensive phases”

Abstract: The phase diagram of the penetrable square-well fluid is investigated through Monte Carlo simulations of various nature. This model was proposed as the simplest possibility of combining bounded repulsions at short scale and short-range attractions. We prove that the model is thermodynamically stable for sufficiently low values of the penetrability parameter, and in this case the system behaves similarly to the square-well model. For larger penetration, there exists an intermediate region where the system is metastable, with well defined fluid-fluid and fluid-solid transitions, at finite size, but eventually becomes unstable in the thermodynamic limit. We characterize the unstable non-extensive phase appearing at high penetrability, where the system collapses into an isolated blob of a few clusters of many overlapping particles each.

Appears in the SklogWiki:

http://www.sklogwiki.org/SklogWiki/index.php/Penetrable_square_well_model

INVITED ARTICLE

The penetrable square-well model: extensive versus non-extensive phases

Riccardo Fantoni^a, Alexandr Malijevský^b, Andrés Santos^c and Achille Giacometti^{d*}

^aNational Institute for Theoretical Physics (NITheP) and Institute of Theoretical Physics, Stellenbosch 7600, South Africa; ^bE. Hala Laboratory of Thermodynamics, Institute of Chemical Process Fundamentals of the ASCR, Department of Physical Chemistry, Institute of Chemical Technology, Praha 6, Prague 166 28, Czech Republic; ^cDepartamento de Física, Universidad de Extremadura, E-06071 Badajoz, Spain; ^dDipartimento di Scienze Molecolari e Nanosistemi, Università Ca' Foscari Venezia, S. Marta DD2137, I-30123 Venezia, Italy

(Received 27 April 2011; final version received 6 June 2011)

The phase diagram of the penetrable square-well fluid is investigated through Monte Carlo simulations of various nature. This model was proposed as the simplest possibility of combining bounded repulsions at short scale and short-range attractions. We prove that the model is thermodynamically stable for sufficiently low values of the penetrability parameter, and in this case the system behaves similarly to the square-well model. For larger penetration, there exists an intermediate region where the system is metastable, with well-defined fluid–fluid and fluid–solid transitions, at finite size, but eventually it becomes unstable in the thermodynamic limit. We characterize the unstable non-extensive phase appearing at high penetrability, where the system collapses into an isolated blob of a few clusters of many overlapping particles each.

Keywords: penetrable square-well model; thermodynamic stability; phase diagram; Monte Carlo simulations; Gibbs ensemble

1. Introduction

Unlike simple fluids, complex fluids are typically characterized by a significant reduction in the number of degrees of freedom, in view of the hierarchy of different length and energy scales involved. As a result, coarse-grained potentials accounting for effective interactions between a pair of the complex fluid units adopt analytical forms that are often quite different from those considered paradigmatic for simple fluids [1].

An important example of this class of potentials is given by those bounded at small separations, thus indicating the possibility of a partial (or even total) interpenetration. This possibility, completely unphysical in the framework of simple fluids, becomes on the contrary very realistic in the context of complex fluids. While the true two-body interactions always include a hard-core part, accounting for the fact that energies close to contact raise several orders of magnitude, effective interactions obtained upon averaging microscopical degrees of freedom may or may not present this feature, depending on the considered particular system.

Interesting examples with no hard-core part are given by polymer solutions, where effective polymer–polymer interactions can be argued to be of the

Gaussian form [2–4], and star polymers and dendrimers where the so-called penetrable sphere (PS) model is frequently employed [5–7].

In spite of their markedly different phase behaviours [7], both these effective interactions have the common attributes of being bounded at zero separation and lacking an attractive part. The latter feature, however, appears to be particularly limiting in view of the several sources of attractive interactions typical of polymer solution, such as, for instance, depletion forces [4], that are typically accounted through simple attractive square-well (SW) tails.

A tentative combining of both the penetrability at small separation and the attraction at slightly larger scale, led to the introduction of the penetrable square-well (PSW) potential [8–12]. This can be obtained either by starting from the PS model and adding an attractive well, or by starting from the SW model and reducing the infinite repulsive energy to a finite one. In this way, the model is characterized by two length scales (the soft core and the width of the well) and by two energy scales, the height ϵ_r of the repulsive barrier and the depth ϵ_a of the attractive well.

The ratio ϵ_a/ϵ_r , hereafter simply referred to as ‘penetrability’, is a measure of the accessibility of the repulsive barrier and, as we shall see, plays a very

*Corresponding author. Email: achille@unive.it

2724

R. Fantoni et al.

important role in the equilibrium properties of the fluid. When $\epsilon_a/\epsilon_r = 0$, the PSW model reduces to the PS model (if $k_B T/\epsilon_r = \text{finite}$, where T is the temperature) or to the SW model (if $k_B T/\epsilon_a = \text{finite}$). In the latter case, the model exhibits a fluid–fluid phase transition for any width of the attractive square well [13–17], this transition becoming metastable against the formation of the solid for a sufficiently narrow well [17]. As penetrability ϵ_a/ϵ_r increases, different particles tend to interpenetrate more and more because {this becomes} energetically favourable (the precise degree depending on the ϵ_a/ϵ_r ratio). As a result, the total energy {may grow} boundlessly to negative values and the system can no longer be thermodynamically stable. The next question to be addressed is whether this instability occurs for any infinitesimally small value $\epsilon_a/\epsilon_r > 0$ or, conversely, whether there exists a particular value where the transition from stable to unstable regime occurs.

As early as the late 1960s, the concept of a well-behaved thermodynamic limit was translated into a simple rule, known as Ruelle’s criterion [18,19], for the sufficient condition for a system to be stable. In a previous paper [8], we have discussed the validity of Ruelle’s criterion for the one-dimensional PSW case and found that, indeed, there is a well-defined value of penetrability ϵ_a/ϵ_r , that depends upon the range of the attractive tail, below which the system is definitely stable. Within this region, the phase behaviour of the fluid is very similar to that of the SW fluid counterpart. More recently [20], we have tackled the same issue in the three-dimensional fluid. Here we build upon this work by presenting a detailed Monte Carlo study of the phase diagram for different values of penetrability and well width. In this case the PSW fluid is proven to satisfy Ruelle’s criterion below a well-defined value of penetrability that is essentially related to the number of interacting particles for a specific range of attractive interaction. For higher values of penetrability, we find an *intermediate* region where, although the system is thermodynamically unstable (non-extensive) in the limit $N \rightarrow \infty$, it displays a ‘normal’ behaviour, with both fluid–fluid and fluid–solid transitions, for *finite* number of particles N . The actual limit of this intermediate region depends critically upon the considered temperatures, densities, and size of the system. Here the phase diagram is similar to that of the SW counterpart, although the details of the critical lines and point location depend upon the actual penetrability value. For even higher penetrability, the system becomes unstable at any studied value of N and the fluid evolves into clusters of overlapping particles arranged into an ordered phase at high concentration,

with a phenomenology reminiscent of that displayed by the PS model, but with non-extensive properties.

The remainder of the paper is organized as follows. In Section 2 we define the PSW model and in Section 3 we set the conditions for Ruelle’s criterion to be valid. The behaviour of the system outside those conditions is studied in Section 4, where we also determine the fluid–fluid coexistence curves for the PSW model just below the threshold line found before; in Section 5 we determine the instability line, in the temperature–density plane, separating the metastable normal phase from the unstable blob phase. Section 6 is devoted to the fluid–solid transition and in Section 7 we draw some conclusive remarks and perspectives.

2. The penetrable square-well model

The PSW model is defined by the following pair potential

$$\phi(r) = \begin{cases} \epsilon_r, & r \leq \sigma, \\ -\epsilon_a, & \sigma < r \leq \sigma + \Delta, \\ 0, & r > \sigma + \Delta, \end{cases} \quad (1)$$

where ϵ_r and ϵ_a are two positive constants accounting for the repulsive and attractive parts of the potential, respectively, Δ is the width of the attractive square well, and σ is diameter of the repulsive core.

As discussed above, this model encompasses both the possibility of a partial interpenetration, with an energy cost typical of the soft-matter interactions given by ϵ_r , and a short-range attraction typical of both simple and complex fluids given by ϵ_a . Both descriptions can be clearly recovered as limiting cases of the PSW potential: for $\epsilon_r \rightarrow \infty$ it reduces to the SW model, while for $\Delta = 0$ or $\epsilon_a = 0$ one recovers the PS model [21,22]. Figure 1 displays the characteristics of the PSW potential (c), along with the two particular cases, SW (a) and PS (b). The interplay between the two energy scales ϵ_r and ϵ_a gives rise to a number of rather unusual and peculiar features that are the main topic of this paper.

In order to put the PSW model in perspective, let us briefly summarize the main features of the SW and PS potentials.

The SW model has a standard phase diagram typical of a simple fluid, with fluid–fluid and fluid–solid transitions in the intermediate range between the triple and the critical points in the temperature–density plane. The fluid–fluid transition becomes metastable, against crystallization, if the width of the well goes below a certain value that has been estimated to be $\Delta \approx 0.25\sigma$ [17].

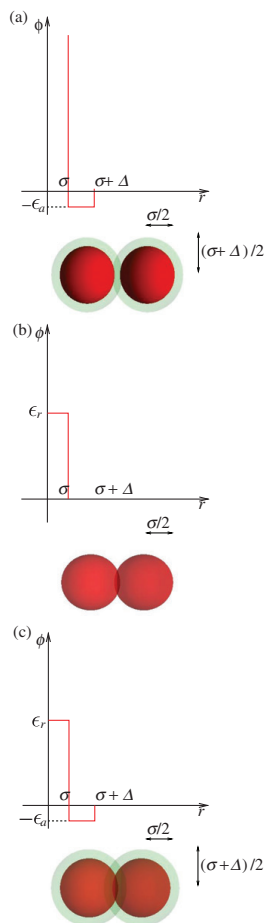


Figure 1. Sketch of the PSW potential used in the present work (c). This potential interpolates between the SW potential (a) and of the PS potential (b). In the SW case (a), spherical particles have a perfect steric hindrance of size σ (the particle diameter) and attractive interactions of range $\sigma + \Delta$ highlighted as a halo in the picture. In the PS case (b), nearest-neighbour particles can partially interpenetrate, with some energy cost ϵ_r , but have no attractive tail. In the PSW there is both the possibility of partial interpenetration (with cost ϵ_r) and short-range SW attraction (with energy gain ϵ_a).

The PS fluid, on the other hand, does not display any fluid–fluid coexistence, in view of the lack of any attractive interactions. The fluid–solid transition is, however, possible and highly unconventional with the formation of multiple occupancy crystals coupled with

possible reentrant melting in the presence of a smoother repulsive interaction, such as a Gaussian form [7,23].

The PSW fluid combines features belonging to both limiting cases within a very subtle interplay between the repulsive and attractive energy scale that affects its thermodynamic stability [8–10].

3. Ruelle’s stability criterion

The issue of thermodynamic stability has a long and venerable history, dating back to the late 1960s [18], and it is nicely summarized in Ruelle’s textbook which is a standard reference for this problem [19].

A system is defined to be (Ruelle) thermodynamically stable [18,19] if there exists a positive number B , such that for the total potential energy Φ_N for a system of N particles it holds

$$\Phi_N \geq -NB. \quad (2)$$

The physical rationale behind this mathematical statement is that the ratio $-\Phi_N/N$ cannot grow unboundedly as N increases if the system is to be well behaved, but must converge to a well-defined limit. This is usually referred to as Ruelle’s stability criterion.

Consider the PSW fluid. As density increases and temperature decreases, particles tend to lump together into clusters (‘blobs’) as they pay some energetic price set by ϵ_r but they gain a (typically larger) advantage due to the attraction ϵ_a . Therefore, as the ratio ϵ_a/ϵ_r increases, one might expect to reach an unstable regime with very few clusters including a large number of significantly overlapping particles, so that Φ_N is no longer proportional to N .

The ratio ϵ_a/ϵ_r (‘penetrability’) plays in PSW fluids a very important role, as we shall see in the following sections. In [10] we proved that the one-dimensional (1D) PSW fluid satisfies Ruelle’s criterion if $\epsilon_a/\epsilon_r \leq 1/2(\ell + 1)$, where ℓ is the integer part of Δ/σ . In this case, we are then guaranteed to have a well-defined equilibrium state.

Here we show that this result can be extended to a three-dimensional (3D) PSW fluid in that Ruelle’s criterion is satisfied if $\epsilon_a/\epsilon_r \leq 1/f_\Delta$, where f_Δ is the maximum number of non-overlapping particles that can be geometrically arranged around a given one within a distance between σ and $\sigma + \Delta$. Of course, f_Δ depends on the width of the attractive interaction Δ . For $\Delta/\sigma < 2^{1/2} - 1$, for instance, one has $f_\Delta = 12$, corresponding to a HCP closed-packed configuration. In the following, we will use a generic d -dimensional notation and consider $d=3$ at the end.

2726

R. Fantoni et al.

The total potential energy of a PSW fluid formed by particles at positions r_1, \dots, r_N can be written in general as

$$\Phi_N(r_1, \dots, r_N) = \frac{1}{2} \sum_{i=1}^N \sum_{j \neq i}^N \phi(|r_i - r_j|). \quad (3)$$

Consider now such a configuration where particles are distributed in M clusters along each direction, each made of s perfectly overlapped particles, and with different clusters arranged in the close-packed configuration. In the Appendix we prove that indeed this is the lowest possible energy configuration in the two-dimensional (2D) case.

The total number of particles is $N = M^d s$. As clusters are in a close-packed configuration, particles of a given cluster interact attractively with all the particles of those f_A clusters within a distance smaller than $\sigma + \Delta$. Consequently, the potential energy has the form

$$\Phi_N(M) = \frac{1}{2} M^d s(s-1)\epsilon_r - \frac{M^d}{2} [f_A - b_A(M)] s^2 \epsilon_a. \quad (4)$$

The first term represents the repulsive energy between all possible pairs of particles in a given s -cluster, while the second term represents the attractive energy between clusters. Here $b_A(M)$ accounts for a reduction of the actual number of clusters interacting attractively, due to boundary effects. This quantity clearly depends upon the chosen value of Δ/σ but we can infer the following general properties

$$b_A(1) = f_A, \quad b_A(M > 2) < f_A, \quad \lim_{M \rightarrow \infty} b_A(M) = 0. \quad (5)$$

In the 1D (with $\Delta/\sigma < 1$) and 2D (with $\Delta/\sigma < 3^{1/2} - 1$) cases, $\Phi_N(M)$ is given by Equations (16) and (23), respectively, so that $b_A(M) = 2M^{-1}$ (1D) and $b_A(M) = 2(4M^{-1} - M^{-2})$ (2D). In general, $b_A(M)$ must be a positive definite polynomial of degree d in M^{-1} with no independent term, its form becoming more complicated as d increases. However, we need not specify the actual form of $b_A(M)$ for our argument, but only the properties given in Equation (5).

Eliminating $s = N/M^d$ in favour of M in Equation (4) one easily gets

$$\frac{\Phi_N(M)}{N} = -\frac{\epsilon_r}{2} + \frac{N}{2} \epsilon_a M^{-d} F(M), \quad (6)$$

where we have introduced the function

$$F(M) \equiv b_A(M) - \left(f_A - \frac{\epsilon_r}{\epsilon_a} \right). \quad (7)$$

Note that $F(M)$ is independent of N . If $\epsilon_a/\epsilon_r < 1/f_A$, $F(M)$ is positive definite and so Φ_N/N has a lower

bound ($-\epsilon_r/2$) and the system is stable in the thermodynamic limit. Let us suppose now that $\epsilon_a/\epsilon_r > 1/f_A$. In that case, $F(1) = \epsilon_r/\epsilon_a > 0$ but $\lim_{M \rightarrow \infty} F(M) = -(f_A - \epsilon_r/\epsilon_a) < 0$. Therefore, there must exist a certain finite value $M = M_0$ such that $F(M) < 0$ for $M > M_0$. In the 1D (with $\Delta/\sigma < 1$) and 2D (with $\Delta/\sigma < 3^{1/2} - 1$) cases the values of M_0 can be explicitly computed:

$$M_0 = \left(1 - \frac{\epsilon_r}{2\epsilon_a} \right)^{-1}, \quad (d = 1), \quad (8)$$

$$M_0 = \frac{2 + (1 + \epsilon_r/2\epsilon_a)^{1/2}}{3} \left(1 - \frac{\epsilon_r}{6\epsilon_a} \right)^{-1}, \quad (d = 2). \quad (9)$$

In general, it is reasonable to expect that $M_0 \sim (1 - \epsilon_r/f_A \epsilon_a)^{-1}$. Regardless of the precise value of M_0 , we have that $\lim_{N \rightarrow \infty} [-\Phi_N(M)]/N = \infty$ for $M > M_0$ and thus the criterion (2) is violated.

This completes the proof that, if $\epsilon_a/\epsilon_r < 1/f_A$, the system is thermodynamically stable as it satisfies Ruelle's stability criterion, Equation (2). Reciprocally, if $\epsilon_a/\epsilon_r > 1/f_A$ there exists a class of blob configurations violating Equation (2). In those configurations the N particles are concentrated on a finite (i.e. independent of N) number of clusters, each with a number of particles proportional to N . For large N the potential energy scales with N^2 and thus the system exhibits non-extensive properties.

In three dimensions, $f_A = 12, 18$, and 42 if $\Delta/\sigma < 2^{1/2} - 1, 2^{1/2} - 1 < \Delta/\sigma < 3^{1/2} - 1$, and $3^{1/2} - 1 < \Delta/\sigma < 1$, respectively, and so the threshold values are $\epsilon_a/\epsilon_r = 1/12, 1/18$, and $1/42$, respectively. There might (and do) exist local configurations with higher coordination numbers, but only those filling the whole space have to be considered in the thermodynamic limit.

In general, Ruelle's criterion (2) is a sufficient but not necessary condition for thermodynamic stability. Therefore, in principle, if $\epsilon_a/\epsilon_r > 1/f_A$ the system may or may not be stable, depending on the physical state (density ρ and temperature T). However, compelling arguments discussed in [19] show that the PSW system with $\epsilon_a/\epsilon_r > 1/f_A$ is indeed unstable (i.e. non-extensive) in the thermodynamic limit for any ρ and T . Notwithstanding this, even if $\epsilon_a/\epsilon_r > 1/f_A$, the system may exhibit 'normal' (i.e. extensive) properties at finite N , provided the temperature is sufficiently high and/or the density is sufficiently low. It is therefore interesting to investigate this regime with the specific goals of (i) defining the stability boundary (if any) and (ii) outlining the fate of the SW-like fluid–fluid and fluid–solid lines as penetrability increases. This will be discussed in the next section, starting from the fluid–fluid coexistence lines.

4. Effect of penetrability on the fluid–fluid coexistence

We have performed an extensive analysis of the fluid–fluid phase transition of the three-dimensional PSW fluid by Gibbs Ensemble Monte Carlo (GEMC) simulations [24–28]. In all cases we have started with the SW fluid ($\epsilon_a/\epsilon_r=0$) and gradually increased penetrability ϵ_a/ϵ_r until disappearance of the transition. Following standard prescriptions [24–28], we construct the fluid–fluid coexistence lines using two systems (the gas and the liquid) that can exchange both volume and particles in such a way that the total volume V and the total number of particles N are fixed and the pressure and chemical potential coincide in both systems. $N=512$ particles were used. By denoting with L_i and V_i ($i=v,l$) the respective sizes and volumes of the vapour and liquid boxes, we used $2N$ particle random displacements of magnitude $0.15L_i$, $N/10$ random volume changes of magnitude 0.1 in $\ln[V_i/(V-V_i)]$, and N particle swaps between the gas and the liquid boxes, on average per cycle.

Our code fully reproduces the results of Vega *et al.* [14] for the SW fluid, as further discussed below. Figure 2 depicts some representative examples of the effect of penetrability on the SW results at different well widths Δ/σ . As Δ/σ increases, the upper limit set by Ruelle’s stability condition $\epsilon_a/\epsilon_r \leq 1/f_{\Delta}$ decreases, and lower penetrability values ϵ_a/ϵ_r have to be used to ensure the existence of the transition line. In Figure 2, values $\epsilon_a/\epsilon_r=1/6, 1/8, 1/11$ were used for $\Delta/\sigma=0.25, 0.5, 1$, respectively. Figure 2 also includes an estimate of the critical points for the PSW fluid obtained from the law of rectilinear diameters, as discussed in [14], that is

$$\frac{\rho_l + \rho_v}{2} = \rho_c + A(T_c - T), \quad (10)$$

where ρ_l (ρ_v) is the density of the liquid (vapour) phase, ρ_c is the critical density and T_c is the critical temperature. Furthermore, the temperature dependence of the density difference of the coexisting phases is fitted to the following scaling form

$$\rho_l - \rho_g = B(T_c - T)^\beta, \quad (11)$$

where the critical exponent for the three-dimensional Ising model $\beta=0.32$ was used to match the universal fluctuations. Amplitudes A and B were determined from the fit.

A detailed collection of the results corresponding to Figures 2(a), (b) and (c) is reported in Table 1.

Note that seemingly stable transition curves are found in all representative cases depicted in Figure 2, thus suggesting a ‘normal’ fluid behaviour for the

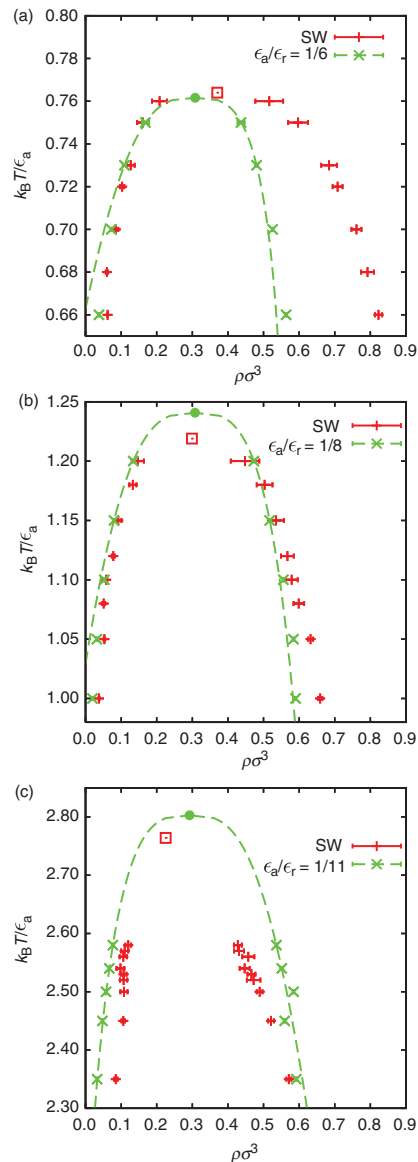


Figure 2. Fluid–fluid coexistence lines for different well widths Δ/σ and penetrabilities ϵ_a/ϵ_r . The SW results are those by Vega *et al.* [14] for the same value of Δ/σ . Circles and boxes represent the estimated critical points for the PSW and the SW fluids, respectively, and the dotted lines represent the coexistence curves for the PSW case. (a) $\Delta/\sigma=0.25$ and $\epsilon_a/\epsilon_r=1/6$; (b) $\Delta/\sigma=0.5$ and $\epsilon_a/\epsilon_r=1/8$; (c) $\Delta/\sigma=1$ and $\epsilon_a/\epsilon_r=1/11$.

2728

R. Fantoni et al.

Table 1. Vapour–liquid coexistence data from GEMC of $N=512$ PSW particles with $\Delta/\sigma=0.25$ and $\epsilon_a/\epsilon_r=1/6$ (top table), $\Delta/\sigma=0.5$ and $\epsilon_a/\epsilon_r=1/8$ (central table) and $\Delta/\sigma=1.0$ and $\epsilon_a/\epsilon_r=1/11$ (bottom table). We used 10^7 MC steps. T , ρ_i , u_i , μ_i are, respectively, the temperature, the density, the internal energy per particle, and the chemical potential of the vapour ($i=v$) or liquid ($i=l$) phase (A being the thermal de Broglie wavelength). Numbers in parentheses correspond to the error on the last digits. The estimated critical points are $k_B T_c/\epsilon_a=0.762$ and $\rho_c \sigma^3=0.307$ (top table), $k_B T_c/\epsilon_a=1.241$ and $\rho_c \sigma^3=0.307$ (central table) and $k_B T_c/\epsilon_a=2.803$ and $\rho_c \sigma^3=0.292$ (bottom table).

$k_B T/\epsilon_a$	$\rho_v \sigma^3$	$\rho_l \sigma^3$	u_v/ϵ_a	u_l/ϵ_a	$\mu_v/\epsilon_a - k_B T/\epsilon_a \ln \Lambda^3$	$\mu_l/\epsilon_a - k_B T/\epsilon_a \ln \Lambda^3$
$\Delta/\sigma=0.25, \epsilon_a/\epsilon_r=1/6$						
0.66	0.0377(6)	0.5634(6)	-0.343(8)	-3.441(13)	-2.410(7)	-2.51(12)
0.70	0.0724(15)	0.5256(15)	-0.614(16)	-3.100(13)	-2.253(5)	-2.27(6)
0.73	0.1093(45)	0.4805(42)	-0.862(38)	-2.920(45)	-2.157(12)	-2.29(8)
0.75	0.1684(95)	0.4368(95)	-1.204(67)	-2.682(27)	-2.211(8)	-2.01(2)
$\Delta/\sigma=0.5, \epsilon_a/\epsilon_r=1/8$						
1.00	0.0194(4)	0.5900(7)	-0.254(7)	-4.687(9)	-4.19(2)	-4.16(5)
1.05	0.0319(5)	0.5841(17)	-0.400(9)	-4.603(14)	-4.00(1)	-4.01(3)
1.10	0.0529(8)	0.5557(8)	-0.651(14)	-4.365(6)	-3.832(6)	-3.83(4)
1.15	0.0799(15)	0.5173(17)	-0.934(18)	-4.087(15)	-3.726(7)	-3.76(4)
1.20	0.1342(37)	0.4728(40)	-1.464(40)	-3.777(26)	-3.642(6)	-3.64(2)
$\Delta/\sigma=1.0, \epsilon_a/\epsilon_r=1/11$						
2.35	0.0327(4)	0.5920(11)	-0.693(8)	-8.931(12)	-8.90(2)	-8.87(6)
2.45	0.0476(5)	0.5593(16)	-1.004(11)	-8.439(21)	-8.66(1)	-8.61(3)
2.50	0.0577(8)	0.5844(12)	-1.201(17)	-8.653(17)	-8.54(2)	-8.59(5)
2.54	0.0670(12)	0.5511(37)	-1.377(25)	-8.231(42)	-8.48(2)	-8.51(2)
2.58	0.0769(9)	0.5361(19)	-1.556(20)	-8.030(22)	-8.41(1)	-8.38(3)

finite-size system studied. Increasing penetrability ϵ_a/ϵ_r at fixed Δ/σ progressively destabilize the transition, until a threshold value $(\epsilon_a/\epsilon_r)_{th}$ is reached where no fluid–fluid transition is observed. Upon changing Δ/σ , one can then draw a line of this values in the ϵ_a/ϵ_r and Δ/σ plane. This is depicted in Figure 3, where the instability line $(\epsilon_a/\epsilon_r)_{th}$ is found to decrease as Δ/σ increases, thus gradually reducing the region where the fluid–fluid transition can be observed, as expected. The shadowed stepwise region identifies the thermodynamically stable region, as guaranteed by Ruelle’s criterion $\epsilon_a/\epsilon_r \leq 1/f_A$ discussed above. Note that points $(\Delta/\sigma=0.25, \epsilon_a/\epsilon_r=1/6)$, $(\Delta/\sigma=0.5, \epsilon_a/\epsilon_r=1/8)$, and $(\Delta/\sigma=1, \epsilon_a/\epsilon_r=1/11)$, corresponding to the values used in Figure 2 and highlighted by circles, lie in the $1/f_A \leq \epsilon_a/\epsilon_r \leq (\epsilon_a/\epsilon_r)_{th}$ region, that is, outside the stable range guaranteed by Ruelle’s criterion.

5. Stable, unstable, and metastable phases

Interestingly, in Ruelle’s textbook [19], the three-dimensional PSW model corresponding to point $(\Delta/\sigma=1, \epsilon_a/\epsilon_r=1/11)$ is exploited as an example of ‘catastrophic’ fluid (see especially Figure 4 and proposition 3.2.2 both in [19]). This is clearly because this state point lies outside the stable region identified by Ruelle’s criterion, as discussed. As already remarked, however, this criterion does not necessarily imply that

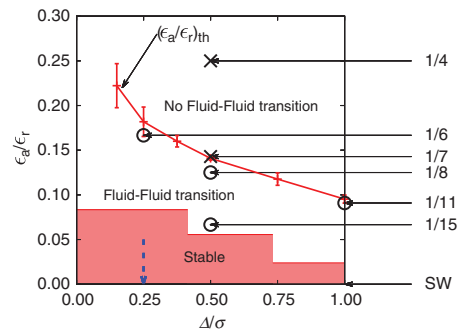


Figure 3. Plot of penetrability ϵ_a/ϵ_r as a function of Δ/σ . The displayed $(\epsilon_a/\epsilon_r)_{th}$ line separates the parameter region where the PSW model, with $N=512$, admits a fluid–fluid phase transition (below this line) from that where it does not. The shadowed stepwise line highlights the region $(\epsilon_a/\epsilon_r \leq 1/12$ for $\Delta/\sigma < 2^{1/2} - 1$, $\epsilon_a/\epsilon_r \leq 1/18$ for $2^{1/2} - 1 < \Delta/\sigma < 3^{1/2} - 1$, and $\epsilon_a/\epsilon_r \leq 1/42$ for $3^{1/2} - 1 < \Delta/\sigma < 1$) where the model is guaranteed to be thermodynamically stable for any thermodynamic state by Ruelle’s criterion. The SW model falls on the $\epsilon_a/\epsilon_r=0$ axis (with finite $k_B T/\epsilon_a$). The vertical dashed arrow points to the SW value $\Delta/\sigma \leq 0.25$ below which the fluid–fluid transition becomes metastable against the freezing transition [17]. The circles are the points chosen for the calculation of the coexistence lines (Figures 2 and 9), while the crosses are the points chosen for the determination of the boundary phases discussed in Figures 5 and 6.

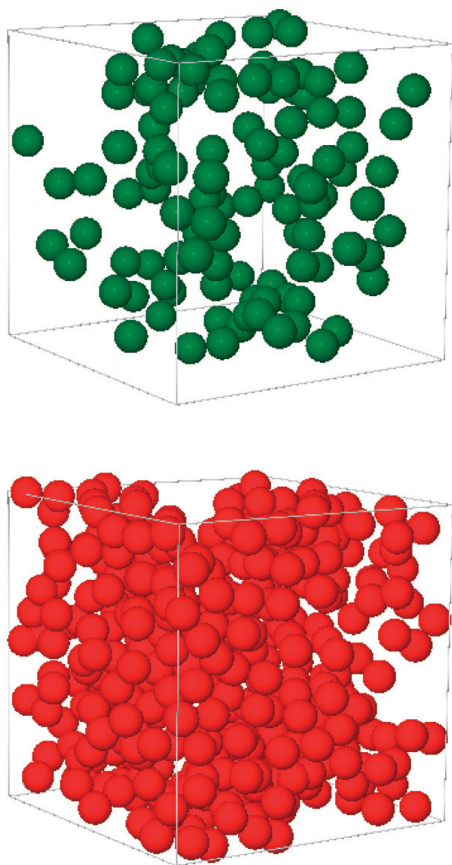


Figure 4. Two GEMC simulation snapshots ($N=512$) at $\Delta/\sigma=0.5$, $\epsilon_a/\epsilon_r=1/8$ (below the threshold value) and $k_B T/\epsilon_a=1.20$. The one on the top panel corresponds to the gas phase ($\rho_v \sigma^3=0.1342$), and the one on the bottom to the liquid phase ($\rho_l \sigma^3=0.4728$).

outside this region the system has to be unstable, but only that it is 'likely' to be so. There are then two possibilities. First, that in the intermediate region $1/f_A \leq \epsilon_a/\epsilon_r \leq (\epsilon_a/\epsilon_r)_{th}$ the system is indeed stable in the thermodynamic limit, a case that is not covered by Ruelle's criterion. Numerical results reported in Figures 2 and 3 appear to support this possibility. The second possibility is that, even in this region, the system is strictly unstable, in the thermodynamic limit, but it appears to be a 'normal' fluid when considered at finite N . This possibility cannot be ruled out by any simulation at finite N , and would be more plausible as hinted by Ruelle's arguments.

In order to illustrate the fact that, at finite N , the system in the intermediate region $1/f_A \leq \epsilon_a/\epsilon_r \leq (\epsilon_a/\epsilon_r)_{th}$ behaves as a normal fluid, in Figure 4 we show two representative snapshots of the gas and the liquid phases at the point ($\Delta/\sigma=0.5$, $\epsilon_a/\epsilon_r=1/8$) that lies just below the $(\epsilon_a/\epsilon_r)_{th}$ line (see Figure 3). In both the gas and the liquid phases, the structure of the fluid presents the typical features of a standard SW fluid, with no significant overlap among different particles.

On the other hand, we have observed that above the threshold line $(\epsilon_a/\epsilon_r)_{th}$ of Figure 3, at a temperature close to the critical temperature of the corresponding SW system, the GEMC simulation evolves towards an empty box and a collapsed configuration in the liquid box.

The second scenario described above can be supported or disproved by a finite-size study of the N -dependence of the transition, as described below.

Assume that at any finite N , the absolute minimum of the internal energy corresponds to the 'collapsed' non-extensive configurations, referred to as 'blob phase' in the following. As discussed in Section 3, the internal energy of these configurations scales with N^2 for large N . However, the system presumably also includes a large number of 'normal' configurations with an internal energy that scales linearly with N . This will be referred to as 'normal phase'.

There is then an energy gap between the total energy associated with the normal and the collapsed configurations with an energy ratio of order N . For finite N and sufficiently high temperature, the Boltzmann statistical factor $\exp(-\Phi_N/k_B T)$ of the collapsed configurations (in spite of the gap) might not be sufficiently large to compensate for the fact that the volume in phase space corresponding to normal configurations has a much larger measure (and hence entropy) than that corresponding to collapsed configurations. As a consequence, the physical properties look normal and one observes a normal phase. Normal configurations have a higher internal energy but also may have a larger entropy. If N is sufficiently small and/or T is high enough, normal configurations might then have a smaller free energy than collapsed configurations. On the other hand, the situation is reversed at larger N and finite temperature, where the statistical weight (i.e. the interplay between the Boltzmann factor and the measure of the phase space volume) of the collapsed configurations becomes comparable to (or even larger than) that of the normal configurations and physical properties become anomalous. This effect could be avoided only if T grows (roughly proportional to N) as N increases, since entropy increases more slowly with N than Φ_N .

2730

R. Fantoni et al.

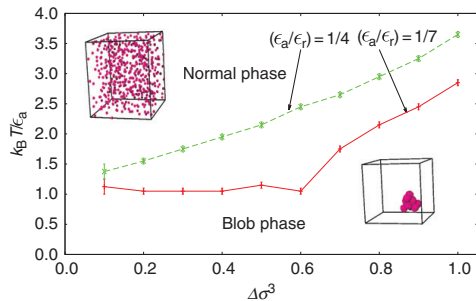


Figure 5. Regions of the phase diagram where the PSW fluid, with $\Delta/\sigma=0.5$ and two different values of ϵ_a/ϵ_r , is expected to exhibit a normal phase (above the instability line) or a blob phase (below the instability line) for $N=512$ particles. Note that the instability line corresponding to the higher penetrability case ($\epsilon_a/\epsilon_r=1/4$, dashed line) lies above the one corresponding to the lower penetrability ($\epsilon_a/\epsilon_r=1/7$, solid line). The two insets depict representative snapshots of respective typical configurations.

In a PSW fluid above the stable region ($\epsilon_a/\epsilon_r > 1/f_\Delta$), we have then to discriminate whether the system is truly stable in the thermodynamic limit $N \rightarrow \infty$, or it is metastable, evolving into an unstable blob phase at a given value of N depending on temperature and density.

In order to shed some more light onto this dual metastable/unstable scenario, we performed NVT Monte Carlo simulations using $N=512$ particles initially distributed uniformly within the simulation box ('regular' initial condition). We carefully monitored the total potential energy of the fluid during the simulation and found that, at any given density, there exists a certain temperature $T_{ins}(\rho)$, such that the system behaves normally after $10^7 N$ single particle moves (normal phase) if $T > T_{ins}$ and collapses to a few clusters of overlapped particles (blob phase) for $T < T_{ins}$.

This is shown in Figure 5 for $\Delta/\sigma=0.5$ and two different penetrability values: $\epsilon_a/\epsilon_r=1/4$ (upper dashed line) and $\epsilon_a/\epsilon_r=1/7$ (lower solid line). The first value lies deeply in the instability region above the threshold $(\epsilon_a/\epsilon_r)_{th}$ value of Figure 3, while the second is sitting right on its top, for this value $\Delta/\sigma=0.5$ of the well width. Also depicted are two snapshots of two representative configurations found under these conditions. While the particles in the normal phase, $T > T_{ins}$, are arranged in a disordered configuration that spans the whole box (see upper snapshot of Figure 5), one can clearly see that for $T < T_{ins}$ a 'blob' structure has nucleated around a certain point within the simulation

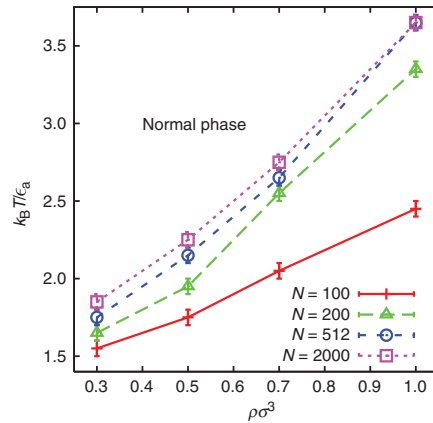


Figure 6. Size dependence of the instability line of Figure 5 for the system $\epsilon_a/\epsilon_r=1/4$ and $\Delta/\sigma=0.5$.

box with a few droplets of several particles each (see lower snapshot of Figure 5).

The three fluid–fluid coexistence phase diagrams displayed in Figure 2 are then representative of a metastable normal phase that persists, for a given N , up to $(\epsilon_a/\epsilon_r)_{th}$ as long as the corresponding critical point (ρ_c, T_c) is such that $T_c > T_{ins}(\rho_c)$, as in the cases reported in Figure 2. Below this instability line, the fluid becomes unstable at any density and a blob phase, where a few large clusters nucleate around certain points and occupy only a part of the simulation, is found. The number of clusters decreases (and the number of particles per cluster increases) as one moves away from the boundary line found in Figure 5 towards lower temperatures. Here a cluster is defined topologically as follows. Two particles belong to the same cluster if there is a path connecting them, where we are allowed to move on a path going from one particle to another if the centers of the two particles are at a distance less than σ .

These results, while not definitive, are strongly suggestive of the fact that even the normal phase is in fact metastable and becomes eventually unstable in the $N \rightarrow \infty$ limit.

This can be further supported by a finite size scaling analysis at increasing N , as reported in Figure 6 in the higher penetrability (and hence most demanding) case $\epsilon_a/\epsilon_r=1/4$. In obtaining these results, we used NVT simulations with 10^{10} single particle moves in all cases.

As expected, the instability temperature line $T_{ins}(\rho)$ moves to higher values as N increases, at fixed density $\rho\sigma^3$, from $N=100$ to $N=2000$, and the normal phase

region significantly shrinks accordingly, being expected to vanish in the thermodynamic limit $N \rightarrow \infty$.

As said before, in all the above computations we started with a regular initial condition having all particles randomly distributed in the entire available simulation box. Under these circumstances, for $T < T_{\text{ins}}$ (where all particles are confined into a blob of a few clusters) a large number of MC steps is required in order to find the true equilibrium distribution. On the other hand, if we have a clustered configuration to start with, a much higher ‘melting’ temperature T_{ins} , above which one recovers a normal phase, is expected. This ‘hysteresis’ effect is indeed observed, as detailed below.

For $\epsilon_a/\epsilon_r = 1/7$, $\Delta/\sigma = 0.5$, and $\rho\sigma^3 = 1.0$ the normal-to-blob transition occurs upon cooling at $k_B T/\epsilon_a \approx 2.75$. Inserting the obtained configuration back in the MC simulation as an initial condition, and increasing the temperature, we find the blob phase to persist up to much higher temperatures $k_B T/\epsilon_a \approx 4$. The hysteresis is also found to be strongly size dependent. With the same system $\epsilon_a/\epsilon_r = 1/7$, $\Delta/\sigma = 0.5$, but for $\rho\sigma^3 = 0.6$, we found the blob-to-normal melting temperatures to be $k_B T/\epsilon_a = 2-3$ for $N = 256$, $k_B T/\epsilon_a = 4-5$ for $N = 512$, and $k_B T/\epsilon_a = 6-7$ for $N = 1024$. Analogously, in the state $\epsilon_a/\epsilon_r = 1/4$, $\Delta/\sigma = 0.5$, and $\rho\sigma^3 = 0.3$, the results are $k_B T/\epsilon_a = 2.1-2.2$, $k_B T/\epsilon_a = 3.7-3.8$, $k_B T/\epsilon_a = 9.0-9.1$, and $k_B T/\epsilon_a = 31-32$ for $N = 100$, $N = 200$, $N = 512$, and $N = 2000$, respectively.

In the interpretation of the size dependence of the hysteresis in the melting, one should also consider the fact that the blob occupies only part of the simulation box and therefore a surface term has a rather high impact on the melting temperature.

Additional insights on the sudden structural change occurring on the fluid upon crossing the threshold line (ϵ_a/ϵ_r)_{th} can be obtained by considering the radial distribution function (RDF) $g(r)$ [29] on two state points above and below this line. We consider a state point at $\Delta/\sigma = 0.5$, $k_B T/\epsilon_a = 1.20$, and $\rho\sigma^3 = 0.7$ and evaluate the RDF at $\epsilon_a/\epsilon_r = 1/8$ (slightly below the threshold line, see Figure 3) and at $\epsilon_a/\epsilon_r = 1/7$. The latter case is sitting right on the top of the threshold line, according to Figure 3. The results are depicted in Figure 7.

Drastic changes in the structural properties of the PSW liquid are clearly noticeable. While in the normal phase ($\epsilon_a/\epsilon_r = 1/8$) the RDF presents the typical features of a standard fluid for a soft-potential and, in particular, converges to unity, in the blob phase ($\epsilon_a/\epsilon_r = 1/7$), the RDF presents a huge peak (note the log-scale) at $r = 0$ and decays to zero after the first few peaks, a behaviour that is suggestive of clustering and

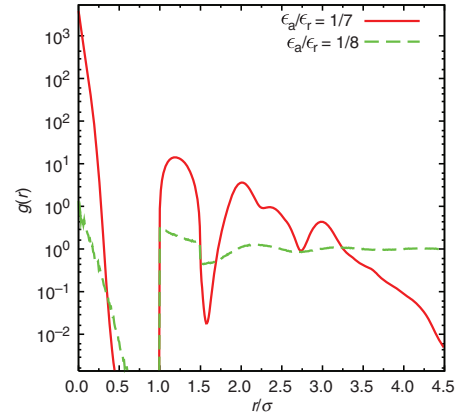


Figure 7. Radial distribution function for the PSW model at $\Delta/\sigma = 0.5$, $k_B T/\epsilon_a = 1.20$, and $\rho\sigma^3 = 0.7$ for two different values of the penetrability parameter ϵ_a/ϵ_r : $\epsilon_a/\epsilon_r = 1/8$ (lying below the threshold line given in Figure 3) and $\epsilon_a/\epsilon_r = 1/7$ (that is on the top of it). The $g(r)$ axis is in a log scale.

confinement of the system. The amplitude of the first maximum in the structure factor grows past the value of 2.85, which is typically reckoned as an indication for a freezing occurring in the system, according to [30].

As a further characterization of the structural ordering of the system, we have also investigated a set of rotationally invariant local order indicators that have been exploited often to quantify order in crystalline solids, liquids, and colloidal gels [29]:

$$Q_l = \left(\frac{4\pi}{2l+1} \sum_{m=-l}^l |\bar{Q}_{lm}|^2 \right)^{1/2}, \quad (12)$$

where \bar{Q}_{lm} is defined as

$$\bar{Q}_{lm} = \frac{\sum_{i=1}^{N_c} N_b(i) \bar{q}_{lm}(i)}{\sum_{i=1}^{N_c} N_b(i)}, \quad (13)$$

where N_c is the number of clusters and

$$\bar{q}_{lm}(i) = \frac{1}{N_b(i)} \sum_{j=1}^{N_b(i)} Y_{lm}(\hat{r}_{ij}). \quad (14)$$

Here $N_b(i)$ is the set of bonded neighbours of the i th cluster, the unit vector \hat{r}_{ij} specifies the orientation of the bond between clusters i and j , and $Y_{lm}(\hat{r}_{ij})$ are the corresponding spherical harmonics.

A particularly useful probe of the possible crystal structure of the system is a value of Q_6 close to unity (see Appendix A of [29]). Results for Q_6 from the PSW

2732

R. Fantoni et al.

Table 2. Number of clusters, Q_6 parameter, and internal energy per particle for the non-extensive phases found in the case $\Delta/\sigma=0.5$ and $\epsilon_a/\epsilon_r=1/4$ (top table) and $\epsilon_a/\epsilon_r=1/7$ (bottom table), just below the curves of Figure 5. The parameter Q_6 was calculated on the final equilibrated particle configuration only, with a neighbour distance of 1.5σ in all cases.

$\rho\sigma^3$	$k_B T/\epsilon_a$	N_c	Q_6	u/ϵ_a
$\epsilon_a/\epsilon_r=1/4$				
0.1	1.0	13	0.04	-60
0.2	1.5	24	0.10	-57
0.3	1.7	115	0.03	-21
0.4	1.9	132	0.05	-19
0.5	2.1	116	0.05	-18
0.6	2.4	98	0.07	-19
0.7	2.6	84	0.04	-18
0.8	2.9	98	0.11	-19
0.9	3.2	74	0.09	-22
1.0	3.6	67	0.05	-23
$\epsilon_a/\epsilon_r=1/7$				
0.1	1.0	51	0.12	-25
0.2	1.0	39	0.06	-37
0.3	1.0	41	0.05	-37
0.4	1.0	42	0.07	-33
0.5	1.1	50	0.29	-24
0.6	1.0	38	0.07	-36
0.7	1.7	55	0.05	-22
0.8	2.1	58	0.11	-22
0.9	2.4	60	0.06	-21
1.0	2.8	62	0.06	-21

model are reported in Table 2 for the two values of penetrability considered in Figure 5 ($\epsilon_a/\epsilon_r=1/4$ and $\epsilon_a/\epsilon_r=1/7$). In order to compute Q_6 , the center of mass of each cluster (as topologically defined before) is identified. Then, the cutoff distance for the nearest-neighbours ‘bonds’ is selected to be approximately equal to the second minimum of $g(r)(r \approx 1.5\sigma)$. As detailed in Table 2, we find $0.03 \leq Q_6 \leq 0.1$ for $\epsilon_a/\epsilon_r=1/4$ (top table) and $0.05 \leq Q_6 \leq 0.12$ for $\epsilon_a/\epsilon_r=1/7$ (bottom table), depending on the considered values of temperature and density. These values have been computed with $N=512$ particles but an increase up to $N=1024$ yields only a slight increase of Q_6 . Besides Q_6 , in Table 2 we report other properties of the blob phases found with $\Delta/\sigma=0.5$ and $\epsilon_a/\epsilon_r=1/4$ and $\epsilon_a/\epsilon_r=1/7$, such as the number of clusters and the internal energy per particle u/ϵ_a . We observe that the number of clusters is rather constant (typically 40–60) for penetrability $\epsilon_a/\epsilon_r=1/7$. For the higher penetrability $\epsilon_a/\epsilon_r=1/4$ the number of clusters is generally larger, as expected, but is quite sensitive to the specific density and temperature values. As for the internal energy per particle, we observe that its magnitude is always more than four times larger than the kinetic contribution $\frac{3}{2}k_B T$.

No conclusive pattern appears from the analysis of results of Table 2, as there seems to be no well-defined behaviour in any of the probes as functions of temperature and density, and this irregular behaviour can be also checked by an explicit observation of the corresponding snapshots. Nonetheless, these results give no indications of the formation of any regular structure.

The final conclusion of the analysis of the fluid–fluid phase diagram region of the PSW model is that the system is strictly thermodynamically stable for $\epsilon_a/\epsilon_r < 1/f_A$ and strictly thermodynamically unstable above it, as dictated by Ruelle’s stability criterion. However, if $\epsilon_a/\epsilon_r > 1/f_A$ there exists an intermediate region where the system looks stable for finite N and becomes increasingly unstable upon approaching the thermodynamic limit.

The next question we would like to address is whether this scenario persists in the fluid–solid transition, where already the PS model displays novel and interesting features. This is discussed in the next section.

6. The fluid–solid transition

It is instructive to contrast the expected phase diagram for the SW model with that of the PSW model.

Consider the SW system with a width $\Delta/\sigma=0.5$ that is a well-studied intermediate case where both a fluid–fluid and a fluid–solid transition have been observed [17]. The corresponding schematic phase diagram is displayed in Figure 8 (top panel), where the critical point is ($k_B T_c/\epsilon_a=1.23$, $\rho_c\sigma^3=0.309$) in the temperature–density plane, and its triple point is ($k_B T_t/\epsilon_a=0.508$, $P_t\sigma^3/\epsilon_a=0.00003$) in the temperature–pressure plane, with $\rho_l\sigma^3=0.835$ and $\rho_s\sigma^3=1.28$ [17]. In [17] no solid stable phase was found for temperatures above the triple point, meaning that the melting curve in the pressure–temperature phase diagram is nearly vertical (see Figure 8, top panel). Motivated by previous findings in the fluid–fluid phase diagram, we consider the PSW model with $\Delta/\sigma=0.5$ and two different penetrability values $\epsilon_a/\epsilon_r=1/15$ and $\epsilon_a/\epsilon_r=1/8$ in the intermediate region $1/f_A \leq \epsilon_a/\epsilon_r \leq (\epsilon_a/\epsilon_r)_{th}$ (see Figure 3), where one expects a normal behaviour for finite N , but with different details depending on the chosen penetrability. In the present case, the first chosen value ($\epsilon_a/\epsilon_r=1/15$) lies very close to the boundary ($\epsilon_a/\epsilon_r=1/f_A$) of the stability region predicted by Ruelle’s criterion, whereas the second chosen value lies, quite on the contrary, close to the threshold curve $(\epsilon_a/\epsilon_r)_{th}$.

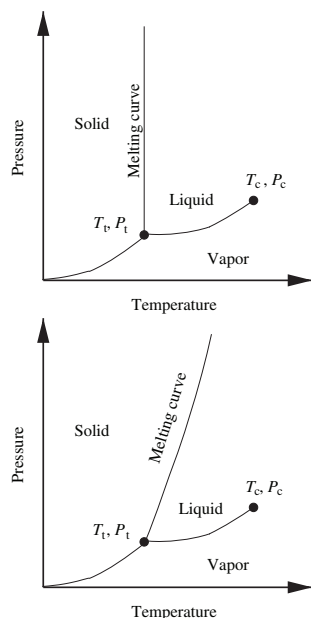


Figure 8. Schematic phase diagram of the SW fluid for $\Delta/\sigma=0.5$ (top panel) and phase diagram of the PSW fluid for $\Delta/\sigma=0.5$ and $\epsilon_a/\epsilon_r=1/8$ (bottom panel).

We have studied the system by isothermal–isobaric (*NPT*) MC simulations, with a typical run consisting of 10^8 MC steps (particle or volume moves) with an equilibration time of 10^7 steps. We considered $N=108$ particles and adjusted the particle moves to have acceptance ratios of approximately 0.5 and volume changes to have acceptance ratios of approximately 0.1. Note that the typical relaxation time in the solid region is an order of magnitude higher than that of the liquid region.

Consider the case $\epsilon_a/\epsilon_r=1/8$ first. The result for the isotherm $k_B T/\epsilon_a=1$ is reported in Figure 9, this temperature being smaller than the critical one $k_B T_c/\epsilon_a=1.241$. From this figure we can clearly see the jumps in the density corresponding to the gas–liquid coexistence region and to the liquid–solid coexistence region. On the basis of the obtained results, we can foresee a phase diagram of the PSW system for this particular value of penetrability to be the one sketched in Figure 8 (bottom panel). In particular, the melting curve has a positive slope in the pressure–temperature phase diagram, unlike the almost vertical slope of the SW counterpart, as discussed. This implies that penetrability allows for a ‘softening’ of the liquid–solid

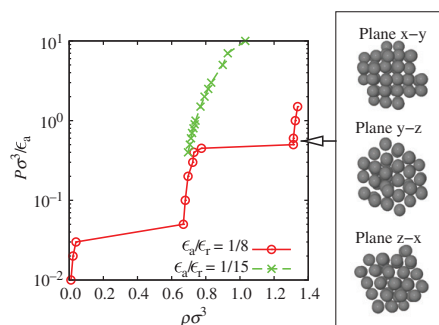


Figure 9. Isotherm $k_B T/\epsilon_a=1$ for the PSW system with $\Delta/\sigma=0.5$ and $\epsilon_a/\epsilon_r=1/8$ and $\epsilon_a/\epsilon_r=1/15$, as obtained from *NPT* MC simulations with $N=108$ particles. The pressure axis is in logarithmic scale. Three views of the same snapshot of the centers of mass of the clusters in the solid are shown on the right-hand side.

transition, so the liquid and the solid can coexist at a temperature higher than the triple one without the need for a huge increase of pressure.

Next we also consider a fluid with $\epsilon_a/\epsilon_r=1/15$, just outside the Ruelle stability region, at the same temperature as before. The results are also reported in Figure 8 and show no indications of a stable solid in the considered range of pressures, in agreement with the fact that at this very low value of penetrability the behaviour of the system is very close to the SW counterpart.

A specific interesting peculiarity of the PSW system in the intermediate region $1/f_A \leq \epsilon_a/\epsilon_r \leq (\epsilon_a/\epsilon_r)_{th}$ of Figure 3 is a lack of full consistency with known thermodynamic relations. In this case, in fact, unlike the SW counterpart, we were unable to trace the coexistence curve between the liquid and the solid using Kofke’s method [31,32], which is equivalent to the numerical integration of the Clausius–Clapeyron equation

$$\left(\frac{d \ln P}{d\beta}\right)_c = -\frac{\Delta h}{\beta P \Delta v}, \quad \beta \equiv \frac{1}{k_B T}, \quad (15)$$

with $\Delta h = h_l - h_s$ and $\Delta v = v_l - v_s$, where h_i and v_i denote, respectively, the molar enthalpy and volume of phase i ($i=1$ for the liquid phase and $i=s$ for the solid phase); the subscript c indicates that the derivative is taken along the coexistence line. Once a single point on the coexistence curve between the two phases is known one can use a trapezoid integration scheme [32] to integrate Equation (15).

In our calculation, we have selected a penetrability $\epsilon_a/\epsilon_r=1/8$ and the isotherm of Figure 8, $k_B T/\epsilon_a=1$,

2734

R. Fantoni et al.

as a reference point. The coexistence pressure at that temperature is $P\sigma^3/\epsilon_a \approx 0.475$ and the molar volume jump is $\Delta v/\sigma^3 \approx 1/0.775 - 1/1.313 \approx 0.529$. We have then calculated the molar enthalpy in the NPT ensemble by computing $(PV + U)/N$ (where U is the total internal energy of the system) with the result $\Delta h/\epsilon_a \approx -5.042 - (-7.593) = 2.551$. Choosing a spacing in β of $-0.05/\epsilon_a$ we get from Equation (15) a predicted coexistence pressure $P\sigma^3/\epsilon_a \approx 0.789$ at $k_B T/\epsilon_a = 1/0.95 = 1.053$. Instead, however, at the latter temperature we found the coexistence pressure between 0.5 and 0.6. Despite this quantitative discrepancy, Equation (15) is useful to understand that the relatively mild slope of the PSW liquid–solid coexistence line in the pressure–temperature phase diagram is essentially due to the fact that the internal energies of the coexisting liquid and solid phases are not too disparate.

A close inspection of several snapshots of the obtained solid phase suggests that, in the intermediate penetrability case, the obtained crystal is made of clusters of overlapping particles located at the sites of a regular crystal lattice with $Q_c \approx 0.35$ [29] and a triclinic structure characterized by a unit cell of sides $a = b = c = \sigma$ and angles $\alpha = \beta = \pi/3$ and $\gamma = \cos^{-1}(1/4)$ (see three views of a common snapshot in Figure 9).

It is worth stressing that the additional degree of penetrability, not present in the SW counterpart, is responsible for the coexistence of the liquid and the solid at not excessively large pressures. Clearly, we cannot rule out the possibility of other additional solid–solid coexistence regions at higher pressures.

7. Conclusions

In this paper, we have studied the phase diagram of the three-dimensional PSW model. This model combines penetrability, a feature typical of effective potential in complex fluids, with a square-well attractive tail, accounting for typical effective attractive interactions that are ubiquitous in soft matter. It can then be regarded as the simplest possible model smoothly interpolating between PS ($\epsilon_a/\epsilon_r \rightarrow 0$, $k_B T/\epsilon_r = \text{finite}$) and SW ($\epsilon_a/\epsilon_r \rightarrow 0$, $k_B T/\epsilon_a = \text{finite}$) fluids, as one changes penetrability ϵ_a/ϵ_r and temperature.

We have proved that the model is thermodynamically stable when $\epsilon_a/\epsilon_r < 1/f_A$, as it satisfies Ruelle's stability criterion [19]. Above this value, the fluid is, strictly speaking, unstable in the thermodynamic limit, exhibiting non-extensive properties. For finite N , however, it displays a rather rich and interesting phenomenology. In particular, there exists an intermediate region $1/f_A \leq \epsilon_a/\epsilon_r \leq (\epsilon_a/\epsilon_r)_{\text{th}}$ in the penetrability–width plane (see Figure 3) where the fluid displays

normal or anomalous behaviour depending on the considered temperatures and densities. For sufficiently large temperatures ($T > T_{\text{ins}}(\rho)$) the fluid presents a metastable normal behaviour with (apparently) stable liquid–liquid and liquid–solid transitions, provided the relative critical temperatures are above the instability line $T = T_{\text{ins}}$. In this case, we have studied the effect of penetrability on the fluid–fluid transition (see Figure 2) close to the threshold line $(\epsilon_a/\epsilon_r)_{\text{th}}$ and found that in general the transition has a higher critical temperature than the SW counterpart. We have attributed this result to the additional degree of freedom given by penetrability that tends to oppose the formation of a crystal until a sufficient large density is achieved.

Below the instability line $T_{\text{ins}}(\rho)$, however, different particles tend to overlap into a few isolated clusters (blobs) confined in a small portion of the available volume and the total energy no longer scales linearly with the number of particles N . As a consequence, the fluid becomes thermodynamically unstable and its properties very anomalous (Figure 5). The metastable region shrinks as either ϵ_a/ϵ_r or N increase (Figure 6).

Above the threshold line $(\epsilon_a/\epsilon_r)_{\text{th}}$ (see Figure 3) the fluid–fluid coexistence disappears, since in this case T_{ins} is too high to allow any phase-separation (for a given N).

An additional interesting feature of the metastable/unstable dualism is included in the hysteresis dependence on the initial condition. When the initial configuration is an unstable one (i.e. a blob) the system melts back to a normal phase at temperatures that are in generally significantly higher than those where the transition normal-to-blob is achieved upon cooling. We have attributed this behaviour to the small statistical weight of the blob configuration in the Boltzmann sampling, in spite of its significantly larger energetic contribution.

We have also studied the fluid–solid transition in the intermediate metastable region $1/f_A \leq \epsilon_a/\epsilon_r \leq (\epsilon_a/\epsilon_r)_{\text{th}}$. We find that the solid density typically increases with respect to the corresponding SW case, due to the formation of clusters of overlapping particles in the crystal sites, as expected on physical grounds. The melting curve is found to have a relatively smooth positive slope, unlike the SW counterpart, and this anomalous behaviour is also reflected in the thermodynamic inconsistency present in the Clausius–Clapeyron thermodynamic equation, thus confirming the metastable character of the phase. When penetrability is sufficiently low to be close to the Ruelle stable region, the system behaves as the corresponding SW system.

One might rightfully wonder whether the finite N metastable phase presented here should have any

experimental consequence at all. We believe the answer to be positive. Imagine being able to craft, through a clever chemical synthesis process, a fluid that may be described by an effective interaction of the PSW form. Our work has then set the boundary for observing a very intriguing normal-to-collapsed phase by either tuning the temperature/density parameters, or by increasing the number of particles in the fluid. In this case, it is the finite N state, rather than the true thermodynamic limit $N \rightarrow \infty$, the relevant one.

Acknowledgements

R.F. would like to thank Giorgio Pastore for useful discussions on the problem. We thank Tatyana Zykova-Timan and Bianca M. Mladek for enlightening discussions and useful suggestions. The support of PRIN-COFIN 2007B58EAB (A.G.), FIS2010-16587 (A.S), and GAAS IAA400720710 (A.M.) is acknowledged. Monte Carlo simulations were carried out at the Center for High Performance Computing (CHPC), CSIR Campus, 15 Lower Hope St., Rosebank, Cape Town, South Africa.

Note added in proofs. After manuscript acceptance, we became aware that the issue of non-extensivity for effective potentials was also studied in the framework of polymers in solution (See V. Krakoviack, J.-P. Hansen, and A. A. Louis, Phys. Rev. E 67, 041801 (2003)).

References

[1] C.N. Likos, Phys. Rep. **348**, 267 (2001).
 [2] F.H. Stillinger, J. Chem. Phys. **65**, 3968 (1976).
 [3] J. McCarty, I.Y. Lyubimov and M.G. Guenza, Macromol. **43**, 3964 (2010).
 [4] P.G. Bolhuis, A.A. Louis, J.P. Hansen and E.J. Meijer, J. Chem. Phys. **114**, 4296 (2001).
 [5] C. Marquest and T.A. Witten, J. Phys. (France) **50**, 1267 (1989).
 [6] C.N. Likos, M. Watzlawek and H. Löwen, Phys. Rev. E **58**, 3135 (1998).
 [7] B.M. Mladek, P. Charbonneau, C.N. Likos, D. Frenkel and G. Kahl, J. Phys.: Condens. Matter **20**, 494245 (2008).
 [8] A. Santos, R. Fantoni and A. Giacometti, Phys. Rev. E **77**, 051206 (2008).
 [9] R. Fantoni, A. Giacometti, A. Malijevský and A. Santos, J. Chem. Phys. **131**, 124106 (2009).
 [10] R. Fantoni, A. Giacometti, A. Malijevský and A. Santos, J. Chem. Phys. **133**, 024101 (2010).
 [11] R. Fantoni, J. Stat. Mech. P07030 (2010).
 [12] D. Mukamel and H.A. Posch, J. Stat. Mech. P03014 (2009).
 [13] A. Giacometti, G. Pastore and F. Lado, Mol. Phys. **107**, 555 (2009).

[14] L. Vega, E. de Miguel, L.F. Rull, G. Jackson and I.A. McLure, J. Chem. Phys. **96**, 2296 (1992).
 [15] E. de Miguel, Phys. Rev. E **55**, 1347 (1997).
 [16] F. del Río, E. Avalos, R. Espindola, L.F. Rull, G. Jackson and S. Lago, Mol. Phys. **100**, 2531 (2002).
 [17] H. Liu, S. Garde and S. Kumar, J. Chem. Phys. **123**, 174505 (2005).
 [18] M.E. Fisher and D. Ruelle, J. Math. Phys. **7**, 260 (1966).
 [19] D. Ruelle, *Statistical Mechanics: Rigorous Results* (Benjamin, 1969), ch. 3.
 [20] R. Fantoni, A. Malijevský, A. Santos and A. Giacometti, Europhys. Lett. **93**, 26002 (2011).
 [21] A. Malijevský and A. Santos, J. Chem. Phys. **124**, 074508 (2006).
 [22] A. Malijevský, S.B. Yuste and A. Santos, Phys. Rev. E **76**, 021504 (2007).
 [23] W. Klein, H. Gould, R.A. Ramos, I. Clejan and A.I. Mel'cuk, Physica A **205**, 738 (1994).
 [24] D. Frenkel and B. Smit, *Understanding Molecular Simulation* (Academic Press, London, 1996).
 [25] A.Z. Panagiotopoulos, Mol. Phys. **61**, 813 (1987).
 [26] A.Z. Panagiotopoulos, N. Quirke, M. Stapleton and D.J. Tildesley, Mol. Phys. **63**, 527 (1988).
 [27] B. Smit, Ph. De Smedt and D. Frenkel, Mol. Phys. **68**, 931 (1989).
 [28] B. Smit and D. Frenkel, Mol. Phys. **68**, 951 (1989).
 [29] P.R. ten Wolde, M.J. Ruiz-Montero and D. Frenkel, J. Chem. Phys. **104**, 9932 (1996).
 [30] J.P. Hansen and L. Verlet, Phys. Rev. **189**, 151 (1969).
 [31] D.A. Kofke, Mol. Phys. **78**, 1331 (1993).
 [32] D.A. Kofke, J. Chem. Phys. **98**, 4149 (1993).

Appendix 1. Ruelle's stability criterion in $d = 2$

Let us consider the two-dimensional PSW model characterized by ϵ_a/ϵ_r and $\Delta/\sigma < 3^{1/2} - 1$. The latter condition implies that in a hexagonal close-packed configuration a particle can interact attractively only with its nearest neighbours, so that $f_\Delta = 6$.

Given the number of particles N , we want to get the configuration with the minimum potential energy Φ_N . We assume that such a configuration belongs to the class of configurations described by m rows, each row made of M clusters, each cluster made of s perfectly overlapped particles. The centers of two adjacent clusters (in the same row or in adjacent rows) are separated a distance σ . The total number of particles is $N = mM_s$. Figure 10 shows a sketch of a configuration with $m = 4$ rows and $M = 6$ clusters per row. The potential energy of an individual row is the same as that of the one-dimensional case [8], namely

$$\Phi^{\text{row}} = Ms \frac{s-1}{2} \epsilon_r - (M-1)s^2 \epsilon_a. \quad (16)$$

The first term accounts for the repulsive energy between all possible pairs of particles in a given s -cluster, while the second term accounts for attractions that are limited to nearest neighbours if $\Delta/\sigma < 3^{1/2} - 1$ in $d = 2$. The potential energy of the whole system is $m\Phi^{\text{row}}$ plus the attractive energy of nearest-neighbour clusters sitting on adjacent rows

2736

R. Fantoni et al.

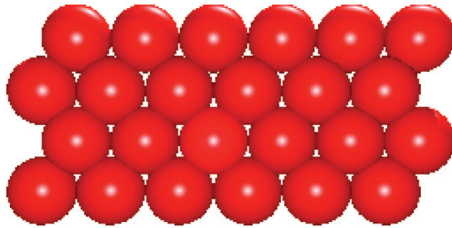


Figure 10. Sketch of a configuration with $m=4$ rows and $M=6$ clusters per row.

(and taking into account the special case of boundary rows). The result is

$$\begin{aligned} \Phi_N(m, s) &= m \left[Ms \frac{s-1}{2} \epsilon_r - (M-1)s^2 \epsilon_a \right] \\ &\quad - (m-1)[1 + 2(M-1)]s^2 \epsilon_a \\ &= N \frac{s-1}{2} \epsilon_r - \left[\frac{3m-2}{m} N - (2m-1)s \right] s \epsilon_a. \end{aligned} \quad (17)$$

For a given number of rows m , the value of s that minimizes $\Phi_N(m, s)$ is found to be

$$s_s(m) = N \frac{3m-2}{2m(2m-1)} \left[1 - \frac{m}{2(3m-2)} \frac{\epsilon_r}{\epsilon_a} \right], \quad (18)$$

which is meaningful only if $\epsilon_a/\epsilon_r > m/2(3m-2) > 1/6$. Otherwise, $s_s(m) = 1$. Therefore, the corresponding minimum value is

$$\begin{aligned} \Phi_N^*(m) &\equiv \Phi_N(m, s_s(m)) \\ &= -\frac{N}{2} \epsilon_r \begin{cases} 1 + N \frac{(3m-2)^2}{2m^2(2m-1)} \frac{\epsilon_a}{\epsilon_r} \left[1 - \frac{m}{2(3m-2)} \frac{\epsilon_r}{\epsilon_a} \right]^2, & \frac{\epsilon_a}{\epsilon_r} > \frac{m}{2(3m-2)}, \\ 2 \left(\frac{3m-2}{m} - \frac{2m-1}{N} \right) \frac{\epsilon_a}{\epsilon_r}, & \frac{\epsilon_a}{\epsilon_r} < \frac{m}{2(3m-2)}. \end{cases} \end{aligned} \quad (19)$$

Let us first suppose that $\epsilon_a/\epsilon_r < 1/6$. In that case, $\epsilon_a/\epsilon_r < m/2(3m-2)$ regardless of the value of $m \geq 1$ and, according to Equation (19), the minimization of $\Phi_N^*(m)$ is achieved with $m = M = N^{1/2}$. As a consequence, Ruelle's stability criterion (2) is satisfied in the thermodynamic limit with $B = 3\epsilon_a$.

Let us now minimize $\Phi_N^*(m)$ with respect to m if $\epsilon_a/\epsilon_r > m/2(3m-2)$. This yields the quadratic equation $(6 - \epsilon_r/\epsilon_a) \times m^2 - 12m + 4 = 0$, whose solution is

$$m_{**} = \frac{2}{3 - (3 + \epsilon_r/\epsilon_a)^{1/2}}. \quad (20)$$

The condition $\epsilon_a/\epsilon_r > m_{**}/2(3m_{**}-2)$ is easily seen to be equivalent to the condition $\epsilon_a/\epsilon_r > 1/6$. Therefore, the absolute minimum of the potential energy in that case is

$$\begin{aligned} \Phi_N^{**} &\equiv \Phi_N^*(m_{**}) \\ &= -\frac{N}{2} \epsilon_r \left[1 + \frac{N \epsilon_a}{8 \epsilon_r} (3 - (3 + \epsilon_r/\epsilon_a)^{1/2})^3 (1 + (3 + \epsilon_r/\epsilon_a)^{1/2}) \right]. \end{aligned} \quad (21)$$

The corresponding value of s_* is

$$s_{**} \equiv s_*(m_{**}) = \frac{N}{4} (3 - (3 + \epsilon_r/\epsilon_a)^{1/2})^2. \quad (22)$$

Comparison between Equations (20) and (22) shows that $N = m_{**}^2 s_{**}$, i.e. the number of clusters per row equals the number of rows, $M_{**} = m_{**}$, as might have been anticipated by symmetry arguments.

Equation (21) shows that, if $\epsilon_a/\epsilon_r > 1/6$, $\lim_{N \rightarrow \infty} (-\Phi_N^{**})/N = \infty$ and thus Ruelle's stability condition (2) is not fulfilled.

We could have restricted to a symmetric arrangement from the very beginning, i.e. $m = M$ and $N = M^2 s$, in which case Equation (17) yields

$$\begin{aligned} \Phi_N(M, s) &= N/M^2 = M^2 s \frac{s-1}{2} \epsilon_r - (3M^2 - 4M + 1)s^2 \epsilon_a \\ &= \frac{N}{2} \left(\frac{N}{M^2} - 1 \right) \epsilon_r - (3M^2 - 4M + 1) \frac{N^2}{M^4} \epsilon_a. \end{aligned} \quad (23)$$

The minimum value (if $\epsilon_a/\epsilon_r > 1/6$) corresponds to the value $M = m_{**}$ given by Equation (20), as expected.

Chapter 27

Nonadditive hard-sphere fluid mixtures. A simple analytical theory

Fantoni R. and Santos A., Phys. Rev. E **84**, 041201 (2011)

Title: “Nonadditive hard-sphere fluid mixtures. A simple analytical theory”

Abstract: We construct a non-perturbative fully analytical approximation for the thermodynamics and the structure of non-additive hard-sphere fluid mixtures. The method essentially lies in a heuristic extension of the Percus-Yevick solution for additive hard spheres. Extensive comparison with Monte Carlo simulation data shows a generally good agreement, especially in the case of like-like radial distribution functions.

PHYSICAL REVIEW E **84**, 041201 (2011)

Nonadditive hard-sphere fluid mixtures: A simple analytical theory

Riccardo Fantoni*

National Institute for Theoretical Physics (NITheP) and Institute of Theoretical Physics, Stellenbosch 7600, South Africa

Andrés Santos†

Departamento de Física, Universidad de Extremadura, E-06071 Badajoz, Spain

(Received 26 July 2011; published 12 October 2011)

We construct a nonperturbative fully analytical approximation for the thermodynamics and the structure of nonadditive hard-sphere fluid mixtures. The method essentially lies in a heuristic extension of the Percus-Yevick solution for additive hard spheres. Extensive comparison with Monte Carlo simulation data shows a generally good agreement, especially in the case of like-like radial distribution functions.

 DOI: [10.1103/PhysRevE.84.041201](https://doi.org/10.1103/PhysRevE.84.041201)

PACS number(s): 61.20.Gy, 61.20.Ne, 61.20.Ja, 51.30.+i

I. INTRODUCTION

The van der Waals ideas [1] show that the most important feature of the pair potential between atoms or molecules is the harsh repulsion that appears at short range and has its origin in the overlap of the outer electron shells. These ideas form the basis of the very successful perturbation theories of the liquid state. This, along with fruitful applications to soft matter [2], explains the continued interest in hard-sphere reference systems [3].

The simplest model for a fluid *mixture* is a system of additive hard spheres (AHSs) for which the like-unlike collision diameter (σ_{ij}) between a particle of species i and one of species j is equal to the arithmetic mean $\sigma_{ij}^{\text{add}} \equiv \frac{1}{2}(\sigma_{ii} + \sigma_{jj})$. A more general model consists of *nonadditive* hard spheres (NAHSs), where the like-unlike collision diameter differs from σ_{ij}^{add} by a quantity $\Delta_{ij} = (\sigma_{ij} - \sigma_{ij}^{\text{add}})/\sigma_{ij}^{\text{add}}$ called the nonadditivity parameter. As mentioned in the paper by Ballone *et al.* [4], where the relevant references may be found, experimental work on alloys, aqueous electrolyte solutions, and molten salts suggests that homocoordination and heterocoordination [5,6] may be interpreted in terms of excluded volume effects due to nonadditivity (positive and negative, respectively) of the repulsive part of the intermolecular potential. NAHS systems are also useful models to describe real physical systems as rare gas mixtures [7] and colloids [8–11]. For a short review of the literature on NAHSs up to 2005 the reader is referred to Ref. [12].

The well-known Percus–Yevick (PY) integral-equation theory [1] is exactly solvable for a mixture of three-dimensional (3D) AHS mixtures [13,14]. The solution has been recently extended to any odd dimensionality [15]. On the other hand, any amount of nonadditivity ($\Delta_{ij} \neq 0$) suffices to destroy the analytical character of the solution and so one needs to resort to numerical methods to solve the PY or other integral equations [4].

The aim of the present paper is to propose a nonperturbative and fully analytical approach for 3D NAHS fluid mixtures, which can be seen as a naïve heuristic *extension* of the PY

solution for AHS mixtures. In doing this, we are guided by the exact solution of the one-dimensional (1D) NAHS model [16–19] and some physical constraints are imposed: the radial distribution function (RDF) $g_{ij}(r)$ must be zero within the diameter σ_{ij} , the isothermal compressibility must be finite, and the zero density limit of the RDF must be satisfied. We find that this strategy gives very good results both for the thermodynamics and the structure, provided that some geometrical constraints on the diameters and the nonadditivity parameter are satisfied. This makes our approach particularly appealing as a reference approximation for integral equation theories and perturbation theories of fluids.

The paper is organized as follows: In Sec. II we describe the NAHS model outlining the physical constraints that we want to embody in our approach. The latter is constructed by a three-stage procedure (approximations RFA, RFA+, and RFA^(m)) in Sec. III. In Sec. IV we present the results for the equation of state from our approximation, comparing them with available Monte Carlo (MC) simulations. The results for the structural properties are presented in Sec. V, where we compare with our own MC simulations. Finally, Sec. VI is devoted to some concluding remarks.

II. THE NAHS MODEL

An n -component mixture of NAHSs in the d -dimensional Euclidean space is a fluid of N_i particles of species i (with $i = 1, 2, \dots, n$), such that there are a total number of particles $N = \sum_{i=1}^n N_i$ in a volume V , and the pair potential between a particle of species i and a particle of species j separated by a distance r is given by

$$U_{ij}(r) = \begin{cases} \infty, & r < \sigma_{ij}, \\ 0, & r > \sigma_{ij}, \end{cases} \quad (2.1)$$

where $\sigma_{ii} = \sigma_i$ and $\sigma_{ij} = \frac{1}{2}(\sigma_i + \sigma_j)(1 + \Delta_{ij})$, so that $\Delta_{ii} = 0$ and $\Delta_{ij} = \Delta_{ji} > -1$. When $\Delta_{ij} = 0$ for all pairs (i, j) we recover the AHS system. In a binary mixture ($n = 2$), $\Delta_{12} = \Delta_{21} = \Delta$ is the only nonadditivity parameter. If $\Delta = -1$ one recovers the case of two independent one-component hard-sphere (HS) systems. In the other extreme case $\sigma_1 = \sigma_2 = 0$ with σ_{12} finite (so that $\Delta \rightarrow \infty$) one obtains the well known Widom-Rowlinson (WR) model [20,21]. Another interesting case is the Asakura-Oosawa model [22,23] (where $\sigma_2 = 0$

 *rfantoni@ts.infn.it, <http://www-dft.ts.infn.it/RFantoni/>

 †andres@unex.es, <http://www.unex.es/eweb/fisteor/andres>

RICCARDO FANTONI AND ANDRÉS SANTOS

 PHYSICAL REVIEW E **84**, 041201 (2011)

and $\Delta > 0$), often used to discuss polymer colloid mixtures and where the notion of a depletion potential was introduced. The NAHS system undergoes a demixing phase transition for positive nonadditivity [24–28]. A demixing transition might also be possible, even for negative nonadditivity [29,30], provided the asymmetry ratio σ_1/σ_2 is sufficiently far from unity. In the present paper we will only consider the NAHS system in its single fluid phase.

Let the number density of the mixture be $\rho = N/V$ and the mole fraction of species i be $x_i = \rho_i/\rho$, where $\rho_i = N_i/V$ is the number density of species i . From these quantities one can define the (nominal) packing fraction $\eta = v_d \rho M_d$, where $v_d = (\pi/4)^{d/2} \Gamma(1 + d/2)$ is the volume of a d -dimensional sphere of unit diameter and

$$M_k \equiv \langle \sigma^k \rangle = \sum_{i=1}^n x_i \sigma_i^k \quad (2.2)$$

denotes the k th moment of the diameter distribution.

The NAHS model, in the thermodynamic limit $N \rightarrow \infty$ with $\rho \equiv N/V$ constant, admits an analytical exact solution for the structure and the thermodynamics in $d = 1$ [16–19]. Moreover, the AHS model in odd dimensions is analytically solvable in the PY approximation [13–15], the result reducing to the exact solution of the problem for $d = 1$ but not for $d \geq 3$.

A. Basic physical constraints on the structure

The RDF $g_{ij}(r)$ must comply with three basic conditions:

(1) $g_{ij}(r)$ must vanish for $r < \sigma_{ij}$. More specifically, for distances near σ_{ij} ,

$$g_{ij}(r) = \Theta(r - \sigma_{ij})[g_{ij}(\sigma_{ij}^+) + g'_{ij}(\sigma_{ij}^+)(r - \sigma_{ij}) + \dots], \quad (2.3)$$

where $\Theta(x)$ is the Heaviside step function.

(2) In the fluid phase the isothermal compressibility χ must be finite. This implies (see below) that the Fourier transform $\tilde{h}_{ij}(q)$ of the total correlation function $h_{ij}(r) \equiv g_{ij}(r) - 1$ has to remain finite at $q = 0$ or, equivalently,

$$\int_0^\infty dr r^\alpha h_{ij}(r) = \text{finite} \quad \text{for} \quad 0 \leq \alpha \leq d - 1. \quad (2.4)$$

(3) In the low-density limit, the RDF is

$$\lim_{\rho \rightarrow 0} g_{ij}(r) = e^{-U_{ij}(r)/k_B T} = \Theta(r - \sigma_{ij}), \quad (2.5)$$

k_B and T being the Boltzmann constant and the absolute temperature, respectively.

As a complement to Eq. (2.5), we give below the exact expression of $g_{ij}(r)$ to first order in density [31]:

$$g_{ij}(r) = \Theta(r - \sigma_{ij}) \left\{ 1 + \frac{\pi \rho}{12r} \sum_{k=1}^n x_k \Theta(\sigma_{ik} + \sigma_{kj} - r) \times (r - \sigma_{ik} - \sigma_{kj})^2 [r^2 + 2(\sigma_{ik} + \sigma_{kj})r - 3(\sigma_{ik} - \sigma_{kj})^2] + \mathcal{O}(\rho^2) \right\}. \quad (2.6)$$

B. The two routes to thermodynamics

For an athermal fluid like NAHSs there are two main routes that lead from the knowledge of the structure to the equation of state (EOS) [1]. These may give different results for an approximate RDF.

The virial route to the EOS of the NAHS mixture requires the knowledge of the contact values $g_{ij}(\sigma_{ij}^+)$ of the RDF,

$$Z^v(\eta) = 1 + \frac{2^{d-1}}{M_d} \eta \sum_{i,j=1}^n x_i x_j \sigma_{ij}^d g_{ij}(\sigma_{ij}^+), \quad (2.7)$$

where $Z = p/\rho k_B T$ is the compressibility factor of the mixture, p being the pressure.

The isothermal compressibility χ , in a mixture, is in general given by

$$\begin{aligned} \chi^{-1} &= \frac{1}{k_B T} \left(\frac{\partial p}{\partial \rho} \right)_{T, \{x_j\}} = \frac{1}{k_B T} \sum_{i=1}^n x_i \left(\frac{\partial p}{\partial \rho_i} \right)_{T, \{x_j\}} \\ &= 1 - \rho \sum_{i,j=1}^n x_i x_j \tilde{c}_{ij}(0), \end{aligned} \quad (2.8)$$

where $\tilde{c}_{ij}(q)$ is the Fourier transform of the direct correlation function $c_{ij}(r)$, which is defined by the Ornstein-Zernike (OZ) equation

$$\tilde{h}_{ij}(q) = \tilde{c}_{ij}(q) + \sum_{k=1}^n \rho_k \tilde{h}_{ik}(q) \tilde{c}_{kj}(q). \quad (2.9)$$

Introducing the quantities $\hat{h}_{ij}(q) \equiv \sqrt{\rho_i \rho_j} \tilde{h}_{ij}(q)$ and $\hat{c}_{ij}(q) \equiv \sqrt{\rho_i \rho_j} \tilde{c}_{ij}(q)$, the OZ relation becomes, in matrix notation,

$$\hat{c}(q) = \hat{h}(q) \cdot [1 + \hat{h}(q)]^{-1}, \quad (2.10)$$

where 1 is the $n \times n$ identity matrix. Thus Eq. (2.8) can be rewritten as

$$\begin{aligned} \chi^{-1} &= \sum_{i,j=1}^n \sqrt{x_i x_j} [\delta_{ij} - \hat{c}_{ij}(0)] \\ &= \sum_{i,j=1}^n \sqrt{x_i x_j} [1 + \hat{h}(0)]_{ij}^{-1}. \end{aligned} \quad (2.11)$$

In Eq. (2.11), and henceforth, we use the notation A_{ij}^{-1} to denote the ij element of the inverse A^{-1} of a given square matrix A .

In the particular case of binary mixtures ($n = 2$), Eq. (2.11) yields

$$\chi = \frac{[1 + \rho x_1 \hat{h}_{11}(0)][1 + \rho x_2 \hat{h}_{22}(0)] - \rho^2 x_1 x_2 \hat{h}_{12}^2(0)}{1 + \rho x_1 x_2 [\hat{h}_{11}(0) + \hat{h}_{22}(0) - 2\hat{h}_{12}(0)]}. \quad (2.12)$$

The compressibility route to the EOS can be obtained from

$$Z^c(\eta) = \int_0^1 dx \chi^{-1}(\eta x). \quad (2.13)$$

C. The one-dimensional system

The exact solution for nonadditive hard rods ($d = 1$) is known [19,32,33]. First, let us introduce the Laplace transform

$$G_{ij}(s) \equiv \int_0^\infty dr e^{-sr} g_{ij}(r). \quad (2.14)$$

In terms of this quantity the exact solution has the form

$$G_{ij}(s) = \frac{1}{\sqrt{x_i x_j}} \sum_{k=1}^n P_{ik}(s) Q_{kj}(s), \quad (2.15)$$

where

$$P_{ij}(s) \equiv \sqrt{x_i x_j} K_{ij} \frac{e^{-\sigma_{ij}(s+\xi)}}{s+\xi} \quad (2.16)$$

is proportional to the Laplace transform of the nearest-neighbor probability distribution and

$$\mathbf{Q}(s) \equiv [1 - \rho \mathbf{P}(s)]^{-1}. \quad (2.17)$$

In Eqs. (2.15) and (2.16), $\xi \equiv p/k_B T = \rho Z$, while $K_{ij} = K_{ji}$ are state-dependent parameters that are determined as functions of ξ from the condition (2.4), which implies $\lim_{s \rightarrow 0} s G_{ij}(s) = 1$, as well as requiring the ratio K_{ij}/K_{ik} to be independent of i [19]. Those conditions also provide the exact EOS in implicit form, i.e., ρ as a function of ξ .

Of course, the above results also hold for additive hard rods. In that case, the additive property $\sigma_{ij} = \sigma_{ij}^{\text{add}} \equiv \frac{1}{2}(\sigma_i + \sigma_j)$ allows us to rewrite the solution in other equivalent ways. To that end, let us define

$$L_{ij} = K_{ij} e^{-\xi \sigma_{ij}^{\text{add}}}, \quad (2.18)$$

so that

$$P_{ij}(s) = \sqrt{x_i x_j} L_{ij} \frac{e^{-\sigma_{ij}^{\text{add}} s}}{s+\xi}, \quad (2.19)$$

$$Q_{ij}^{-1}(s) = e^{a_{ij}s} \sqrt{\frac{x_j}{x_i} \frac{s}{s+\xi}} C_{ij}(s), \quad (2.20)$$

where

$$a_{ij} \equiv \frac{1}{2}(\sigma_i - \sigma_j) \quad (2.21)$$

and

$$C_{ij}(s) \equiv \left(1 + \frac{\xi}{s}\right) \delta_{ij} - \frac{\rho x_i}{s} L_{ij} e^{-\sigma_i s}. \quad (2.22)$$

Here we have made use of the property

$$\sigma_i = \sigma_{ij}^{\text{add}} + a_{ij}. \quad (2.23)$$

It is easy to prove that

$$Q_{ij}(s) = e^{a_{ij}s} \sqrt{\frac{x_j}{x_i} \frac{s+\xi}{s}} C_{ij}^{-1}(s), \quad (2.24)$$

thanks to the property $a_{ik} + a_{kj} = a_{ij}$. Consequently, in the additive case, Eq. (2.15) becomes

$$G_{ij}^{\text{add}}(s) = \frac{e^{-\sigma_{ij}^{\text{add}} s}}{s} \sum_{k=1}^n L_{ik} C_{kj}^{-1}(s), \quad (2.25)$$

where use has been made of the additivity property

$$\sigma_{ik}^{\text{add}} - a_{kj} = \sigma_{ij}^{\text{add}}. \quad (2.26)$$

The additive solution turns out to be

$$L_{ij} = \frac{\xi}{\rho} = \frac{1}{1 - \rho M_1}. \quad (2.27)$$

The fact that $L_{ij} = \text{const}$ allows one to rewrite Eq. (2.25) in yet another equivalent form,

$$G_{ij}^{\text{add}}(s) = \frac{e^{-\sigma_{ij}^{\text{add}} s}}{s} \sum_{k=1}^n L_{ik} B_{kj}^{-1}(s), \quad (2.28)$$

where

$$\begin{aligned} B_{ij}(s) &\equiv \delta_{ij} - \frac{\rho x_i}{s} L_{ij} \varphi_0(\sigma_i s) \\ &= C_{ij}(s) + \frac{\xi}{s} (x_i - \delta_{ij}). \end{aligned} \quad (2.29)$$

In the first equality,

$$\varphi_0(x) \equiv e^{-x} - 1. \quad (2.30)$$

While $\lim_{s \rightarrow 0} s C_{ij}(s) = \xi(\delta_{ij} - x_i) \neq 0$, but $\det[s\mathbf{C}(s)] = \mathcal{O}(s)$, in the case of the matrix $\mathbf{B}(s)$ one has $\lim_{s \rightarrow 0} s B_{ij}(s) = 0$. On the other hand, in both cases, $\lim_{s \rightarrow \infty} C_{ij}(s) = \lim_{s \rightarrow \infty} B_{ij}(s) = \delta_{ij}$, so that $\lim_{s \rightarrow \infty} s e^{\sigma_{ij}^{\text{add}} s} G_{ij}(s) = L_{ij} = \xi/\rho$.

It turns out that Eqs. (2.25), (2.27), and (2.28) are also obtained from the PY solution for additive hard rods. Thus, the PY equation yields the exact solution in the additive case, but not in the nonadditive one.

It is important to bear in mind that, if one inverts the steps, it is possible to formally get Eq. (2.15) from Eq. (2.25). In other words, starting from the form (2.25) of the PY solution for the 1D AHS system, allowing L_{ij} and ξ to be free, and carrying out some formal manipulations, one arrives at an equivalent form, Eq. (2.15), that, if heuristically extended to the NAHS case ($\sigma_{ij} \neq \sigma_{ij}^{\text{add}}$), coincides with the exact solution to the problem. However, it is not possible to recover (2.15) starting from the form (2.28) since the property $L_{ij} = \text{const}$, only valid in the additive case, cannot be reversed.

D. PY solution for three-dimensional AHSs

In this subsection we recall the PY solution for AHSs in three dimensions ($d = 3$) [13,14].

First, one introduces the Laplace transform of $r g_{ij}(r)$,

$$G_{ij}(s) \equiv \int_0^\infty dr e^{-sr} r g_{ij}(r). \quad (2.31)$$

From Eq. (2.3) it follows that

$$\begin{aligned} s e^{\sigma_{ij}s} G_{ij}(s) &= \sigma_{ij} g_{ij}(\sigma_{ij}^+) + [g_{ij}(\sigma_{ij}^+) + \sigma_{ij} g'_{ij}(\sigma_{ij}^+)] s^{-1} \\ &\quad + \mathcal{O}(s^{-2}). \end{aligned} \quad (2.32)$$

Next, Eq. (2.4) implies, for small s ,

$$s^2 G_{ij}(s) = 1 + H_{ij}^{(0)} s^2 + H_{ij}^{(1)} s^3 + \dots \quad (2.33)$$

with $H_{ij}^{(0)} = \text{finite}$ and $H_{ij}^{(1)} = -\tilde{h}_{ij}(0)/4\pi = \text{finite}$, where in general

$$H_{ij}^{(\alpha)} \equiv \frac{1}{\alpha!} \int_0^\infty dr (-r)^\alpha r h_{ij}(r). \quad (2.34)$$

RICCARDO FANTONI AND ANDRÉS SANTOS

 PHYSICAL REVIEW E **84**, 041201 (2011)

Finally, Eq. (2.5) yields

$$\lim_{\rho \rightarrow 0} G_{ij}(s) = \frac{e^{-\sigma_{ij}s}}{s^2} (1 + \sigma_{ij}s). \quad (2.35)$$

Equations (2.31)–(2.35) hold both for NAHSs and AHSs.

The PY solution for AHSs can then be written as [13,14]

$$G_{ij}^{\text{add}}(s) = \frac{e^{-\sigma_{ij}^{\text{add}}s}}{s^2} \sum_{k=1}^n L_{ik}(s) B_{kj}^{-1}(s), \quad (2.36)$$

 where $L(s)$ and $B(s)$ are matrices given by

$$L_{ij}(s) = L_{ij}^{(0)} + L_{ij}^{(1)}s, \quad (2.37)$$

$$B_{ij}(s) = \delta_{ij} + \frac{2\pi\rho x_i}{s^3} [L_{ij}^{(0)}\varphi_2(\sigma_i s) + L_{ij}^{(1)}s\varphi_1(\sigma_i s)], \quad (2.38)$$

where

$$\varphi_1(x) \equiv e^{-x} - 1 + x, \quad (2.39)$$

$$\varphi_2(x) \equiv e^{-x} - 1 + x - \frac{x^2}{2}.$$

 Similarly to the 1D case, $\lim_{s \rightarrow 0} s B_{ij}(s) = 0$. In fact, Eqs. (2.36)–(2.38) are the 3D analogs of Eqs. (2.28) and (2.29). For the general structure of the PY solution with $d = \text{odd}$, the reader is referred to Ref. [15].

 Also as in the 1D case, $\lim_{s \rightarrow \infty} B_{ij}(s) = \delta_{ij}$ and so, according to Eq. (2.32),

$$g_{ij}^{\text{add}}(\sigma_{ij}^+) = \frac{L_{ij}^{(1)}}{\sigma_{ij}^{\text{add}}}. \quad (2.40)$$

 Further, in view of Eq. (2.33), the coefficients of s^0 and s in the power series expansion of $s^2 G_{ij}(s)$ must be 1 and 0, respectively. This yields $2n^2$ conditions that allow us to find [14]

$$L_{ij}^{(0)} = \theta_1 + \theta_2 \sigma_j, \quad L_{ij}^{(1)} = \theta_1 \sigma_{ij}^{\text{add}} + \frac{1}{2} \theta_2 \sigma_i \sigma_j, \quad (2.41)$$

 where $\theta_1 \equiv 1/(1 - \eta)$ and $\theta_2 \equiv 3(M_2/M_3)\eta/(1 - \eta)^2$. It is straightforward to check that Eq. (2.36) complies with the limit (2.35).

The expressions (2.7) and (2.13) which follow from the solution of the PY equation of AHS mixtures are

$$Z_{\text{PY}}^v(\eta) = \frac{1}{1 - \eta} + \frac{M_1 M_2}{M_3} \frac{3\eta}{(1 - \eta)^2} + \frac{M_2^3}{M_3^2} \frac{3\eta^2}{(1 - \eta)^2}, \quad (2.42)$$

$$Z_{\text{PY}}^c(\eta) = \frac{1}{1 - \eta} + \frac{M_1 M_2}{M_3} \frac{3\eta}{(1 - \eta)^2} + \frac{M_2^3}{M_3^2} \frac{3\eta^2}{(1 - \eta)^3}. \quad (2.43)$$

Usually, the virial route underestimates the exact results, while the compressibility route overestimates them.

III. CONSTRUCTION OF THE APPROXIMATIONS

As stated in Sec. I, the main aim of this paper is to construct analytical approximations for the structure and thermodynamics of 3D NAHSs. On the one hand, the approximations will be inspired by the exact solution in the 1D case (see Sec. II C). On the other hand, they will reduce to the AHS PY solution (see Sec. II D). Moreover, as a guide in the construction of the approximations and also to determine the parameters,

the basic physical requirements (2.3)–(2.5) [or, equivalently, (2.32), (2.33), and (2.35)] will be enforced.

 The driving idea is to rewrite Eq. (2.36) in a form akin to that of Eq. (2.15), by inverting the procedure followed in Sec. II C. This method faces several difficulties. One of them is that, as said before, Eq. (2.36) is the 3D analog of Eq. (2.28), but not of Eq. (2.25), and it is not possible to recover directly (i.e., without further assumptions) Eq. (2.15) from Eq. (2.28). One could first try to rewrite Eq. (2.36) in a form akin to that of Eq. (2.25), i.e., a form where the matrix B given by Eq. (2.38) is replaced by a matrix C such that $\lim_{s \rightarrow 0} s C_{ij}(s) \neq 0$. But, given the intricate structure of Eq. (2.38) and the fact that neither $L_{ij}^{(0)}$ nor $L_{ij}^{(1)}$ are constant, this does not seem to be an easy task at all. Therefore, we will work from Eq. (2.36) directly.

A. The AHS PY solution revisited

First, define

$$P_{ij}(s) \equiv \sqrt{x_i x_j} e^{-\sigma_{ij}^{\text{add}}s} L_{ij}(s), \quad (3.1)$$

$$Q_{ij}(s) \equiv e^{a_{ij}s} \sqrt{\frac{x_j}{x_i}} B_{ij}^{-1}(s), \quad (3.2)$$

so that

$$\begin{aligned} Q_{ij}^{-1}(s) &= e^{a_{ij}s} \sqrt{\frac{x_j}{x_i}} B_{ij}(s) \\ &= \delta_{ij} + \frac{2\pi\rho\sqrt{x_i x_j}}{s^3} e^{a_{ij}s} [L_{ij}^{(0)}\varphi_2(\sigma_i s) + L_{ij}^{(1)}s\varphi_1(\sigma_i s)]. \end{aligned} \quad (3.3)$$

Inserting Eqs. (3.1) and (3.2) into Eq. (2.36) we finally get

$$G_{ij}(s) = \frac{s^{-2}}{\sqrt{x_i x_j}} \sum_{k=1}^n P_{ik}(s) Q_{kj}(s), \quad (3.4)$$

where use has been made of the additive property (2.26).

 We emphasize that Eq. (3.4) is fully equivalent to Eq. (2.36) and thus it represents an alternative way of writing the PY solution for AHSs. In both representations the coefficients $L_{ij}^{(0)}$ and $L_{ij}^{(1)}$ are given by Eq. (2.41). On the other hand, since the structure of Eq. (3.4) is formally similar to that of the exact solution for 1D NAHSs, Eq. (2.15), it might be expected that Eq. (3.4) is a reasonable starting point for an extension to 3D NAHSs.

B. Approximation RFA

1. The proposal

A possible proposal for the structural properties of NAHSs is defined by Eq. (3.4) with

$$P_{ij}(s) = \sqrt{x_i x_j} e^{-\sigma_{ij}s} L_{ij}(s), \quad (3.5)$$

$$\begin{aligned} Q_{ij}^{-1}(s) &= \delta_{ij} + \frac{2\pi\rho\sqrt{x_i x_j}}{s^3} e^{a_{ij}s} \\ &\quad \times [L_{ij}^{(0)}\varphi_2(b_{ij}s) + L_{ij}^{(1)}s\varphi_1(b_{ij}s)], \end{aligned} \quad (3.6)$$

 where $L_{ij}(s)$ is still given by Eq. (2.37) [with $L_{ij}^{(0)}$ and $L_{ij}^{(1)}$ yet to be determined] and

$$b_{ij} \equiv \sigma_{ij} + a_{ij}. \quad (3.7)$$

Equations (3.5) and (3.6) are obtained from Eqs. (3.1) and (3.3), respectively, by the extensions $\sigma_{ij}^{\text{add}} \rightarrow \sigma_{ij}$ and $\sigma_i \rightarrow b_{ij}$ [compare Eqs. (2.23) and (3.7)]. Note that Eq. (3.6) can also be written as

$$Q_{ij}^{-1}(s) = \delta_{ij} - \frac{2\pi\rho\sqrt{x_i x_j}}{s^3} [N_{ij}(s)e^{a_{ij}s} - L_{ij}(s)e^{-\sigma_{ij}s}], \quad (3.8)$$

where

$$N_{ij}(s) \equiv L_{ij}^{(0)} \left(1 - b_{ij}s + \frac{b_{ij}^2 s^2}{2} \right) + L_{ij}^{(1)} s(1 - b_{ij}s). \quad (3.9)$$

Of course, the coefficients $L_{ij}^{(0)}$ and $L_{ij}^{(1)}$ are no longer given by Eq. (2.41) but are obtained from the physical conditions

$$\lim_{s \rightarrow 0} s^2 G_{ij}(s) = 1, \quad (3.10)$$

$$\lim_{s \rightarrow 0} s^{-1} [s^2 G_{ij}(s) - 1] = 0, \quad (3.11)$$

which follow from Eq. (2.33). To that purpose, it is convenient to rewrite Eq. (3.4) as

$$s^2 \sum_{k=1}^n \sqrt{x_i x_k} G_{ik}(s) Q_{kj}^{-1}(s) = P_{ij}(s). \quad (3.12)$$

Using Eqs. (3.5) and (3.6), Eq. (3.10) implies

$$1 + \pi\rho \sum_{k=1}^n x_k b_{kj}^2 \left(L_{kj}^{(1)} - \frac{1}{3} L_{kj}^{(0)} b_{kj} \right) = L_{ij}^{(0)}. \quad (3.13)$$

Likewise, Eq. (3.11) gives

$$\pi\rho \sum_{k=1}^n x_k b_{kj}^2 \left[a_{kj} \left(L_{kj}^{(1)} - \frac{1}{3} L_{kj}^{(0)} b_{kj} \right) - \frac{1}{3} b_{kj} \left(L_{kj}^{(1)} - \frac{1}{4} L_{kj}^{(0)} b_{kj} \right) \right] = L_{ij}^{(1)} - \sigma_{ij} L_{ij}^{(0)}. \quad (3.14)$$

Equations (3.13) and (3.14) imply that both $L_{ij}^{(0)}$ and $L_{ij}^{(1)} - \sigma_{ij} L_{ij}^{(0)}$ are independent of the subscript i , i.e.,

$$L_{ij}^{(0)} = S_j, \quad L_{ij}^{(1)} = T_j + \sigma_{ij} S_j, \quad (3.15)$$

where S_j and T_j are determined from Eqs. (3.13) and (3.14). The solution is

$$S_j = \frac{1 - \pi\rho\Psi_j}{(1 - \pi\rho\Lambda_j)(1 - \pi\rho\Psi_j) - \pi^2\rho^2\mu_{j|2,0}\Omega_j}, \quad (3.16)$$

$$T_j = \frac{\pi\rho\Omega_j}{(1 - \pi\rho\Lambda_j)(1 - \pi\rho\Psi_j) - \pi^2\rho^2\mu_{j|2,0}\Omega_j}, \quad (3.17)$$

where we have called

$$\Lambda_j \equiv \mu_{j|2,1} - \frac{1}{3}\mu_{j|3,0}, \quad (3.18)$$

$$\Psi_j \equiv \frac{2}{3}\mu_{j|3,0} - \mu_{j|2,1}, \quad (3.19)$$

$$\Omega_j \equiv \mu_{j|3,1} - \mu_{j|2,2} - \frac{1}{4}\mu_{j|4,0}, \quad (3.20)$$

and

$$\mu_{j|p,q} \equiv \sum_{k=1}^n x_k b_{kj}^p \sigma_{kj}^q. \quad (3.21)$$

In the additive case ($b_{kj} = \sigma_k$) one has $\Lambda_j = \frac{1}{6}M_3 + \frac{1}{2}M_2\sigma_j$, $\Psi_j = \frac{1}{6}M_3 - \frac{1}{2}M_2\sigma_j$, and $\Omega_j = -\frac{1}{4}M_2\sigma_j^2$, so that $S_j = \theta_1 + \theta_2\sigma_j$ and $T_j = -\frac{1}{2}\theta_2\sigma_j^2$, in agreement with Eq. (2.41). In the case of binary nonadditive mixtures ($\Delta \neq 0$), it can be easily checked that the common denominator in Eqs. (3.16) and (3.17) is positive definite. It only vanishes if $\Delta = -2\sigma_2/(\sigma_1 + \sigma_2)$ (assuming $\sigma_2 \leq \sigma_1$) and $\eta = 1 + x_2\sigma_2^3/x_1\sigma_1^3$.

Equation (3.15) closes the approximation (3.4)–(3.6). It relies on the same philosophy as the so-called rational-function approximation used in the past for HS and related systems [15,34] and, therefore, we will use the acronym RFA to refer to it. The explicit forms of $G_{ij}(s)$ for binary mixtures ($n = 2$) are presented in Appendix A.

2. Low-density behavior

To first order in density, Eqs. (3.15)–(3.17) yield

$$L_{ij}^{(0)} = 1 + \pi\rho\Lambda_j + \mathcal{O}(\rho^2), \quad (3.22)$$

$$L_{ij}^{(1)} = \sigma_{ij} + \pi\rho(\sigma_{ij}\Lambda_j + \Omega_j) + \mathcal{O}(\rho^2). \quad (3.23)$$

Thus,

$$Q_{ij}(s) = \delta_{ij} - \frac{2\pi\rho\sqrt{x_i x_j}}{s^3} e^{a_{ij}s} [\varphi_2(b_{ij}s) + \sigma_{ij}s\varphi_1(b_{ij}s)] + \mathcal{O}(\rho^2). \quad (3.24)$$

Insertion into Eq. (3.4) yields

$$G_{ij}(s) = \frac{e^{-\sigma_{ij}s}}{s^2} (1 + \sigma_{ij}s) + \pi\rho \frac{e^{-\sigma_{ij}s}}{s^2} [\Lambda_j + (\sigma_{ij}\Lambda_j + \Omega_j)s] - \frac{2\pi\rho}{s^5} \sum_{k=1}^n x_k e^{-(\sigma_{ik} + \sigma_{kj})s} (1 + \sigma_{ik}s)(1 + \sigma_{kj}s) + \frac{2\pi\rho}{s^5} \sum_{k=1}^n x_k e^{-(\sigma_{ik} - a_{kj})s} (1 + \sigma_{ik}s) \left[1 - a_{kj}s - \frac{1}{2}(\sigma_{kj}^2 - a_{kj}^2)s^2 \right] + \mathcal{O}(\rho^2). \quad (3.25)$$

Laplace inversion gives

$$g_{ij}(r) = \Theta(r - \sigma_{ij}) + \frac{\pi\rho}{r} \Theta(r - \sigma_{ij})(\Lambda_j r + \Omega_j) - \frac{\pi\rho}{12r} \sum_{k=1}^n x_k \Theta(r - \sigma_{ik} - \sigma_{kj})(r - \sigma_{ik} - \sigma_{kj})^2 \times [r^2 + 2(\sigma_{ik} + \sigma_{kj})r - 3(\sigma_{ik} - \sigma_{kj})^2] + \frac{\pi\rho}{12r} \sum_{k=1}^n x_k \Theta(r - \sigma_{ik} + a_{kj})(r - \sigma_{ik} + a_{kj}) [r^3 + (\sigma_{ik} - a_{kj})r^2 - (5\sigma_{ik}^2 + 6\sigma_{kj}^2 + 2\sigma_{ik}a_{kj} - a_{kj}^2)r + 3(\sigma_{ik} + a_{kj})(\sigma_{ik}^2 + a_{kj}^2 - 2\sigma_{kj}^2)] + \mathcal{O}(\rho^2). \quad (3.26)$$

RICCARDO FANTONI AND ANDRÉS SANTOS

 PHYSICAL REVIEW E **84**, 041201 (2011)

As a consequence, approximation RFA is consistent with the exact limits (2.5) and (2.35). To first order in density, the approximation correctly accounts for singularities of $g_{ij}(r)$ at distances $r = \sigma_{ij}$ and $r = \sigma_{ik} + \sigma_{kj}$, $k = 1, \dots, n$ [see Eq. (2.6)]. On the other hand, we see from Eq. (3.25) that, already to first order in density, approximation RFA introduces spurious singularities at $r = \sigma_{ik} - a_{kj} \neq \sigma_{ij}$. One might even have $d_{ij;k} \equiv \sigma_{ik} - a_{kj} - \sigma_{ij} < 0$. In particular, $d_{ii;k} = \sigma_{ik}^{\text{add}} \Delta_{ik}$ becomes negative if $\Delta_{ik} < 0$. Analogously, $d_{ij;i} = -\sigma_{ij}^{\text{add}} \Delta_{ij}$ is negative if $\Delta_{ij} > 0$. Therefore, approximation RFA does not verify in general the condition (2.3). It is worth noting, however, that the hard-core condition (2.3) is also typically violated by density-functional theories [35]. The inability of approximation RFA to guarantee that $g_{ij}(r) = 0$ for $r < \sigma_{ij}$ will be remedied by approximation RFA₊ described in Sec. III C.

3. Short-range behavior

Before presenting approximation RFA₊, we will need to restrict ourselves to cases where the first two singularities of $g_{ij}(r)$, as given by approximation RFA, are σ_{ij} and $\tau_{ij} \equiv \min(\sigma_{ik} - a_{kj}; k = 1, \dots, n; k \neq j)$. As proven in Appendix B, the above requirement in the binary case ($n = 2$) implies the constraint $-\sigma_2/(\sigma_1 + \sigma_2) \leq \Delta \leq 2\sigma_2/(\sigma_1 + \sigma_2)$, where, without loss of generality, it has been assumed $\sigma_2 \leq \sigma_1$. This region of applicability is shown in Fig. 1.

Appendix C gives the expressions for $g_{ij}(r)$ in the range $0 \leq r \leq \max(\sigma_{ij}, \tau_{ij}) + \epsilon$, where ϵ is any positive value smaller than the separation between $\max(\sigma_{ij}, \tau_{ij})$ and the next singularity of $g_{ij}(r)$, provided by approximation RFA for binary mixtures. Extending to general n the arguments presented there, we can write

$$G_{ij}(s) = e^{-\sigma_{ij}s} \Phi_{ij}(s) + 2\pi\rho x_k e^{-\tau_{ij}s} \Gamma_{ikj}(s) + \dots, \quad (3.27)$$

where $k = \kappa$ is the index corresponding to τ_{ij} , i.e., $\tau_{ij} = \sigma_{ik} - a_{kj}$, and the ellipsis denotes terms headed by exponentials of

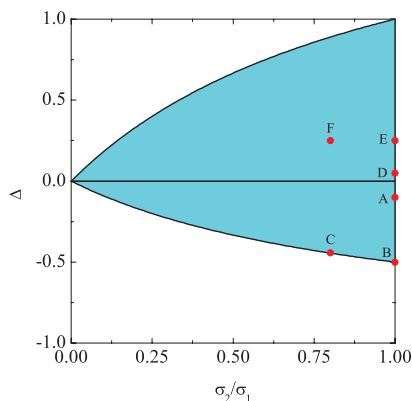


FIG. 1. (Color online) Plane Δ vs σ_2/σ_1 showing the shaded region $-\sigma_2/(\sigma_1 + \sigma_2) \leq \Delta \leq 2\sigma_2/(\sigma_1 + \sigma_2)$ where the first two singularities of $g_{ij}(r)$, according to approximation RFA, are σ_{ij} and $\sigma_{ik} - a_{kj}$ with $k \neq j$. The circles denote the systems analyzed in Sec. V.

the form $e^{-\lambda s}$ with $\lambda > \max(\sigma_{ij}, \tau_{ij})$. In Eq. (3.27),

$$\Phi_{ij}(s) \equiv \frac{1}{s^2} L_{ij}(s) \bar{Q}_{ij}(s), \quad (3.28)$$

$$\Gamma_{ikj}(s) \equiv \frac{1}{s^5} \frac{L_{ik}(s) N_{kj}(s)}{D_0(s)}, \quad (3.29)$$

where

$$\bar{Q}_{ij}^{-1}(s) \equiv \delta_{ij} - \frac{2\pi\rho \sqrt{x_i x_j}}{s^3} N_{ij}(s), \quad (3.30)$$

and $D_0(s)$ is the determinant of the matrix $\bar{Q}^{-1}(s)$. Explicit expressions of $\Phi_{ij}(s)$ and $D_0(s)$ for binary mixtures are given in Appendix C.

Taking the Laplace inversion of Eq. (3.27), one finds that, in the interval $0 \leq r \leq \max(\sigma_{ij}, \tau_{ij}) + \epsilon$,

$$g_{ij}(r) = \frac{1}{r} \Theta(r - \sigma_{ij}) \phi_{ij}(r - \sigma_{ij}) + \frac{2\pi\rho}{r} x_k \Theta(r - \tau_{ij}) \gamma_{ikj}(r - \tau_{ij}), \quad (3.31)$$

where $\phi_{ij}(r)$ and $\gamma_{ikj}(r)$ are the inverse Laplace transforms of $\Phi_{ij}(s)$ and $\Gamma_{ikj}(s)$, respectively.

Note that $\phi_{ij}(0) = \lim_{s \rightarrow \infty} \Phi_{ij}(s) = L_{ij}^{(1)}$, while $\gamma_{ikj}(0) = \lim_{s \rightarrow \infty} \Gamma_{ikj}(s) = 0$. Therefore, the contact values are

$$g_{ij}(\sigma_{ij}^+) = \frac{L_{ij}^{(1)}}{\sigma_{ij}} + \frac{2\pi\rho}{\sigma_{ij}} x_k \Theta(\sigma_{ij} - \tau_{ij}) \gamma_{ikj}(\sigma_{ij} - \tau_{ij}). \quad (3.32)$$

As expected, Eq. (3.32) reduces to Eq. (2.40) in the additive case.

C. Approximation RFA₊

This new option for $g_{ij}(r)$ will differ from approximation RFA only in the region $\min(\sigma_{ij}, \tau_{ij}) \leq r \leq \max(\sigma_{ij}, \tau_{ij})$. More specifically,

$$g_{ij}(r)|_{\text{RFA}_+} = g_{ij}(r)|_{\text{RFA}} + \frac{2\pi\rho}{r} x_k [\Theta(r - \sigma_{ij}) - \Theta(r - \tau_{ij})] \gamma_{ikj}(r - \tau_{ij}). \quad (3.33)$$

On account of Eq. (3.31), Eq. (3.33) can be equivalently rewritten as

$$g_{ij}(r)|_{\text{RFA}_+} = \begin{cases} \Theta(r - \sigma_{ij}) g_{ij}(r)|_{\text{RFA}}, & \tau_{ij} < \sigma_{ij}, \\ g_{ij}(r)|_{\text{RFA}} + \Theta(r - \sigma_{ij}) \Theta(\tau_{ij} - r) \\ \quad \times \frac{2\pi\rho}{r} x_k \gamma_{ikj}(r - \tau_{ij}), & \tau_{ij} > \sigma_{ij}. \end{cases} \quad (3.34)$$

We see from Eq. (3.34) that the idea behind approximation RFA₊ is twofold. On the one hand, it removes the unphysical violation of the property $g_{ij}(r) = 0$ for $r < \sigma_{ij}$ that is present in option RFA when $\tau_{ij} < \sigma_{ij}$. On the other hand, if $\tau_{ij} > \sigma_{ij}$, approximation RFA₊ extrapolates to the region $\sigma_{ij} < r < \tau_{ij}$ the functional form of $g_{ij}(r)$ provided by approximation RFA in the region between τ_{ij} and the next singularity.

In the interval $0 \leq r \leq \max(\sigma_{ij}, \tau_{ij}) + \epsilon$,

$$g_{ij}(r)|_{\text{RFA}_+} = \frac{1}{r} \Theta(r - \sigma_{ij}) [\phi_{ij}(r - \sigma_{ij}) + 2\pi\rho x_k \gamma_{ikj}(r - \tau_{ij})]. \quad (3.35)$$

In particular,

$$g_{ij}(\sigma_{ij}^+) |_{\text{RFA}_+} = \frac{L_{ij}^{(1)}}{\sigma_{ij}} + \frac{2\pi\rho}{\sigma_{ij}} x_k \gamma_{ikj}(\sigma_{ij} - \tau_{ij}). \quad (3.36)$$

D. Approximation RFA₊^(m)

In approximation RFA₊ the full functional form of $\gamma_{ikj}(r)$ is used. This can create some artificial problems in the region $\sigma_{ij} < r < \tau_{ij}$ when $\tau_{ij} > \sigma_{ij}$ and the distance $\tau_{ij} - \sigma_{ij}$ is rather large (as happens in the WR model). Reciprocally, if $\tau_{ij} - \sigma_{ij}$ is not large, it becomes unnecessarily complicated to consider the entire nonlinear function $\gamma_{ikj}(r)$ in the interval $\sigma_{ij} < r < \tau_{ij}$. Thus, we now propose a variant of approximation RFA₊, here denoted as RFA₊^(m), whereby the full true function $\gamma_{ikj}(r)$ is preserved if $\tau_{ij} < \sigma_{ij}$ (in order to enforce the physical constraint of a vanishing RDF for $r < \sigma_{ij}$) but is replaced by its m th degree polynomial approximation $\gamma_{ikj}^{(m)}(r)$

if $\tau_{ij} > \sigma_{ij}$. In summary, option RFA₊^(m) is defined by

$$g_{ij}(r) |_{\text{RFA}_+^{(m)}} = \begin{cases} \Theta(r - \sigma_{ij})g_{ij}(r) |_{\text{RFA}}, & \tau_{ij} < \sigma_{ij}, \\ g_{ij}(r) |_{\text{RFA}} + \Theta(r - \sigma_{ij})\Theta(\tau_{ij} - r) \\ \times \frac{2\pi\rho}{r} x_k \gamma_{ikj}^{(m)}(r - \tau_{ij}), & \tau_{ij} > \sigma_{ij}. \end{cases} \quad (3.37)$$

Consequently, the contact values are

$$g_{ij}(\sigma_{ij}^+) |_{\text{RFA}_+^{(m)}} = \frac{L_{ij}^{(1)}}{\sigma_{ij}} + \frac{2\pi\rho}{\sigma_{ij}} x_k [\Theta(\sigma_{ij} - \tau_{ij})\gamma_{ikj}(\sigma_{ij} - \tau_{ij}) + \Theta(\tau_{ij} - \sigma_{ij})\gamma_{ikj}^{(m)}(\sigma_{ij} - \tau_{ij})]. \quad (3.38)$$

The polynomial $\gamma_{ikj}^{(m)}(r)$ is obtained by truncating after r^m the expansion of $\gamma_{ikj}(r)$ in powers of r . Such an expansion is directly related to that of the Laplace transform $\Gamma_{ikj}(s)$ in powers of s^{-1} . For large s , $\Gamma_{ikj}(s)$ can be shown to be given by

$$\Gamma_{ikj}(s) = s^{-2}L_{ik}^{(1)} \left[L_{kj}^{(0)} \frac{b_{kj}}{2} - L_{kj}^{(1)} \right] b_{kj} + s^{-3} \left\{ L_{ik}^{(0)} \left[L_{kj}^{(0)} \frac{b_{kj}}{2} - L_{kj}^{(1)} \right] b_{kj} - L_{ik}^{(1)} \left[L_{kj}^{(0)} b_{kj} - L_{kj}^{(1)} \right] + 2\pi\rho L_{ik}^{(1)} \left[L_{kj}^{(0)} \frac{b_{kj}}{2} - L_{kj}^{(1)} \right] b_{kj} \sum_{\ell=1}^n x_\ell \left[L_{\ell\ell}^{(0)} \frac{\sigma_\ell}{2} - L_{\ell\ell}^{(1)} \right] \sigma_\ell \right\} + \mathcal{O}(s^{-4}). \quad (3.39)$$

Consequently, the linear and quadratic approximations are

$$\gamma_{ikj}^{(1)}(r) = L_{ik}^{(1)} \left[L_{kj}^{(0)} \frac{b_{kj}}{2} - L_{kj}^{(1)} \right] b_{kj} r, \quad (3.40)$$

$$\gamma_{ikj}^{(2)}(r) = \gamma_{ikj}^{(1)}(r) + \left\{ L_{ik}^{(0)} \left[L_{kj}^{(0)} \frac{b_{kj}}{2} - L_{kj}^{(1)} \right] b_{kj} - L_{ik}^{(1)} \left[L_{kj}^{(0)} b_{kj} - L_{kj}^{(1)} \right] + 2\pi\rho L_{ik}^{(1)} \left[L_{kj}^{(0)} \frac{b_{kj}}{2} - L_{kj}^{(1)} \right] b_{kj} \sum_{\ell=1}^n x_\ell \left[L_{\ell\ell}^{(0)} \frac{\sigma_\ell}{2} - L_{\ell\ell}^{(1)} \right] \sigma_\ell \right\} \frac{r^2}{2}. \quad (3.41)$$

Of course, the three sets of approximations RFA, RFA₊, and RFA₊^(m) reduce to the PY solution in the additive case. Obviously, RFA₊ \equiv RFA₊^(∞). In Sec. V we will generally use RFA₊⁽¹⁾.

IV. COMPARISON WITH MONTE CARLO SIMULATIONS FOR BINARY MIXTURES. THE EQUATION OF STATE

The compressibility factor Z is obtained via the virial and compressibility routes by Eqs. (2.7) and (2.13), respectively. In the case of the virial route one needs the contact values of the RDF, which are given by Eqs. (3.32), (3.36), and (3.38) in approximations RFA, RFA₊, and RFA₊^(m), respectively.

In the compressibility route, the isothermal compressibility χ is obtained from Eq. (2.11), where $\hat{h}_{ij}(0) = \rho \sqrt{x_i x_j} \tilde{h}_{ij}(0) = -4\pi\rho \sqrt{x_i x_j} H_{ij}^{(1)}$, $H_{ij}^{(1)}$ being the coefficient of s^3 in the series expansion of $s^2 G_{ij}(s)$ in powers of s [cf. Eq. (2.33)]. We recall that $G_{ij}(s)$ is given by Eq. (3.4) in approximation RFA.

In approximations RFA₊ and RFA₊^(m), Eqs. (3.33) and (3.37) imply that

$$H_{ij}^{(1)} |_{\text{RFA}_+} = H_{ij}^{(1)} |_{\text{RFA}} - 2\pi\rho x_k \int_{\sigma_{ij}}^{\tau_{ij}} dr r \gamma_{ikj}(r - \tau_{ij}), \quad (4.1)$$

$$H_{ij}^{(1)} |_{\text{RFA}_+^{(m)}} = H_{ij}^{(1)} |_{\text{RFA}} - 2\pi\rho x_k \int_{\sigma_{ij}}^{\tau_{ij}} dr r [\Theta(\sigma_{ij} - \tau_{ij})\gamma_{ikj}(r - \tau_{ij}) + \Theta(\tau_{ij} - \sigma_{ij})\gamma_{ikj}^{(m)}(r - \tau_{ij})]. \quad (4.2)$$

In any case, for the sake of simplicity, we will restrict ourselves in most of this section to approximation RFA.

A. Dependence of the EOS on nonadditivity

Here we study the dependence of the EOS on the nonadditivity parameter Δ by fixing all the other parameters of the mixture (density, composition, and size ratio).

RICCARDO FANTONI AND ANDRÉS SANTOS

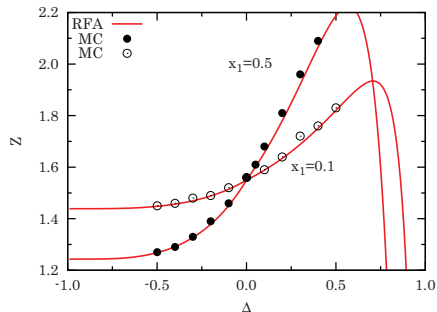
 PHYSICAL REVIEW E **84**, 041201 (2011)


FIG. 2. (Color online) Compressibility factor as a function of the nonadditivity parameter for a symmetric binary mixture of NAHSs at $\rho\sigma^3 = 0.2$ and two different compositions. The MC data are taken from Refs. [36,37].

1. Symmetric binary mixtures

Symmetric mixtures are obtained when $\sigma_1 = \sigma_2 = \sigma$. Therefore, in the additive case ($\Delta = 0$) one recovers the one-component HS system, i.e., $g_{11}(r) = g_{22}(r) = g_{12}(r) = g(r)$, regardless of the value of x_1 .

Figure 2 compares the compressibility factor obtained from MC simulations [36,37] with that predicted by approximation RFA for some representative symmetric systems. We observe that approximation RFA reproduces quite well the exact simulation data at all values of the nonadditivity parameter. At this low density ($\rho\sigma^3 = 0.2, \eta \simeq 0.105$) the virial and compressibility routes are not distinguishable on the scale of the graph.

2. Asymmetric binary mixtures

Asymmetric mixtures correspond to $\sigma_1 \neq \sigma_2$. In that case, when $\Delta = 0$ one recovers the AHS mixture.

Figure 3 shows the Δ dependence of Z for negative nonadditivity and an equimolar ($x_1 = x_2 = \frac{1}{2}$) asymmetric mixture ($\sigma_2/\sigma_1 = 1/3$) at a relatively large density ($\eta = 0.5$).

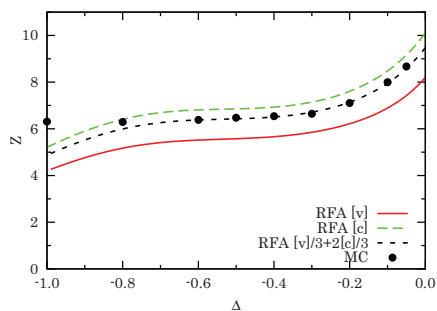


FIG. 3. (Color online) Compressibility factor as a function of the nonadditivity parameter for an equimolar asymmetric binary mixture of NAHSs with a size ratio $\sigma_2/\sigma_1 = 1/3$ at a packing fraction $\eta = 0.5$. The symbols [v] and [c] stand for the virial and compressibility routes, respectively. The MC data are taken from Ref. [38].

In this case the virial route of approximation RFA underestimates the values of Z , while the compressibility route overestimates them. This is also a typical behavior of the PY equation for AHSs. It is thus tempting to try the $Z = \frac{1}{3}Z^v + \frac{2}{3}Z^c$ interpolation recipe [39–42], which is known to work well in the additive case. From Fig. 3 we see that indeed the interpolation formula, as applied to approximation RFA, reproduces quite well the exact simulation data, except for $\Delta \lesssim -0.8$.

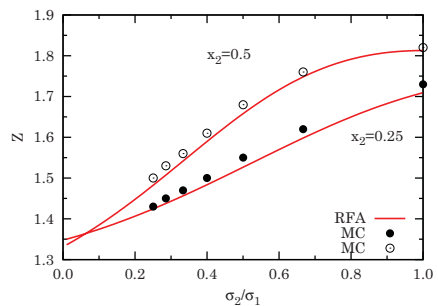
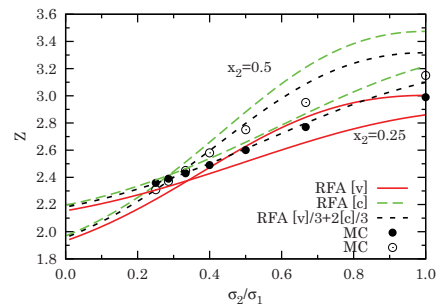
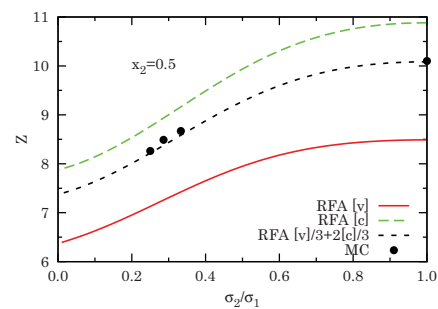


FIG. 4. (Color online) Compressibility factor as a function of the size ratio σ_2/σ_1 for binary asymmetric NAHS mixtures with $x_2 = \frac{1}{2}, \Delta = -0.05$, and $\eta = 0.5$ (top panel); $x_2 = \frac{1}{4}, \Delta = 0.2$, and $\eta = 0.2$ (middle panel); $x_2 = \frac{1}{4}, \Delta = 0.5$, and $\eta = 0.075$ (bottom panel). In the bottom panel only the theoretical data obtained from the virial route are shown since they practically coincide with those obtained from the compressibility route. The MC data are taken from Ref. [38].

B. Dependence of the EOS on the size ratio

Next, we study the dependence of Z on the size ratio σ_2/σ_1 by fixing all the other parameters of the mixture (density, composition, and nonadditivity).

The three panels of Fig. 4 show Z vs σ_2/σ_1 for a slightly negative nonadditivity $\Delta = -0.05$ (top panel), a moderate positive nonadditivity $\Delta = 0.2$ (middle panel), and a larger positive nonadditivity $\Delta = 0.5$ (bottom panel). We observe again that the interpolation recipe $Z = \frac{1}{3}Z^v + \frac{2}{3}Z^c$ for approximation RFA agrees well with the exact simulation data, with the exception of a region close to the size symmetric mixture ($\sigma_2/\sigma_1 = 1$) for positive nonadditivity and moderate density (middle panel).

C. Contact values

In Sec. V we will analyze the RDF $g_{ij}(r)$ predicted by approximations RFA and $\text{RFA}_+^{(1)}$. Before doing so, and as a bridge between the thermodynamic and structural properties, it is worth considering the contact values. Table I provides the contact values for some binary equimolar symmetric NAHS mixtures ($\sigma_1 = \sigma_2 = \sigma$, $x_1 = x_2 = \frac{1}{2}$), as obtained from MC simulations [4], numerical solutions of the PY integral equation [4], and our approximations RFA [Eq. (3.32)] and $\text{RFA}_+^{(1)}$ [Eq. (3.38)]. Since for binary symmetric mixtures $\tau_{11} = \tau_{22} = \sigma_{12} = \sigma(1 + \Delta)$ and $\tau_{12} = \sigma$, it turns out that $g_{11}(\sigma^+) = g_{22}(\sigma^+)$ is common in approximations RFA and $\text{RFA}_+^{(1)}$ if $\Delta < 0$, while $g_{12}(\sigma_{12}^+)$ is common in both approximations if $\Delta > 0$.

TABLE I. Contact values for some binary equimolar symmetric NAHS mixtures. The MC and PY data were taken from Ref. [4]. The labels correspond to systems common to those listed in Table II.

Label	Δ	$\rho\sigma^3$	Source	$g_{11}(\sigma^+)$	$g_{12}(\sigma_{12}^+)$	
D	0.05	0.8	MC	5.305	3.762	
			PY	4.451	3.516	
			RFA	4.006	3.617	
	0.0	0.8	$\text{RFA}_+^{(1)}$	4.580	3.617	
			MC	3.971	3.971	
			PY	3.581	3.581	
	-0.05	0.8	RFA	3.581	3.581	
			$\text{RFA}_+^{(1)}$	3.581	3.581	
			MC	3.117	3.801	
	A	-0.1	1.0	PY	2.925	3.394
				RFA	2.971	3.148
				$\text{RFA}_+^{(1)}$	2.971	3.445
-0.3		1.0	MC	3.394	5.363	
			PY	3.209	4.395	
			RFA	3.497	3.883	
B	-0.5	1.0	$\text{RFA}_+^{(1)}$	3.497	4.763	
			MC	2.168	2.798	
			PY	2.141	2.543	
	0.05	1.0	RFA	2.441	2.251	
			$\text{RFA}_+^{(1)}$	2.441	2.875	
			MC	2.103	1.528	
0.2	1.0	PY	2.060	1.493		
		RFA	2.139	1.407		
		$\text{RFA}_+^{(1)}$	2.139	1.279		

From Table I we observe that approximation $\text{RFA}_+^{(1)}$ is superior to the PY theory in estimating the true contact values, both for positive and negative nonadditivity, except in the cases of $g_{11}(\sigma^+)$ for $\rho\sigma^3 = 1$ and $\Delta = -0.3$ and of $g_{12}(\sigma_{12}^+)$ for $\rho\sigma^3 = 1$ and $\Delta = -0.5$.

V. COMPARISON WITH MONTE CARLO SIMULATIONS FOR BINARY MIXTURES. THE STRUCTURE

The RDF of approximation RFA is analytically and explicitly given in Laplace space by Eqs. (3.4)–(3.6) and (3.15)–(3.21). In real space, $rg_{ij}(r)$ is easily found by taking the inverse Laplace transform of $G_{ij}(s)$ through the numerical scheme described in Ref. [44]. To get $g_{ij}(r)$ in approximation $\text{RFA}_+^{(m)}$, one needs to make use of Eq. (3.37), where $\gamma_{ikj}^{(m)}(r)$ is explicitly given by Eqs. (3.40) and (3.41) for $m = 1$ and $m = 2$, respectively [45]. Notice that, while the true RDF has to be symmetric under exchange of species indices, the RDF obtained from approximation RFA or RFA_+ is, except for symmetric and equimolar mixtures, not symmetric, i.e., $g_{ij}(r) \neq g_{ji}(r)$ if $i \neq j$. Although this artificial asymmetry is generally small from a practical point of view, it represents a penalty we pay for our extension of the AHS solution of the PY equation. To cope with this shortcoming, we just redefine the like-unlike RDF as the symmetrized one $\frac{1}{2}[g_{ij}(r) + g_{ji}(r)]$.

In a binary mixture, $\tau_{11} = \sigma_{12} + a_{12} = \sigma_1 + \frac{1}{2}(\sigma_1 + \sigma_2)\Delta$, $\tau_{22} = \sigma_{12} - a_{12} = \sigma_2 + \frac{1}{2}(\sigma_1 + \sigma_2)\Delta$, and $\tau_{12} = \frac{1}{2}(\sigma_1 + \sigma_2)$. Therefore, $\tau_{11} < \sigma_1$ and $\tau_{22} < \sigma_2$ for $\Delta < 0$, while $\tau_{12} < \sigma_{12}$ for $\Delta > 0$. In what follows, we will truncate $g_{ij}(r)|_{\text{RFA}}$ for $r < \sigma_{ij}$ when $\tau_{ij} < \sigma_{ij}$.

In order to evaluate the merits and limitations of the structural properties predicted by our approximations, we have performed canonical MC simulations of the binary NAHS system with $N = 2196$ particles and $10^5 N$ MC steps per run. The cell index method has been used [46]. The statistical error on the RDF is within the size of the symbols used in the graphs reported.

We have chosen six representative systems, all within the region $-\sigma_2/(\sigma_1 + \sigma_2) \leq \Delta \leq 2\sigma_2/(\sigma_1 + \sigma_2)$ assumed in the construction of approximation RFA_+ . Those six systems are represented in Fig. 1 and their respective values of composition and density are displayed in Table II. Three of the mixtures have a negative nonadditivity (A, B, and C), while the other three have a positive nonadditivity (D, E, and F). Moreover, there are four equimolar symmetric mixtures (A, B, D, and E) and two asymmetric ones (C and F). In those two latter

TABLE II. The six binary NAHS mixtures considered in the analysis of the structure. The last column gives the compressibility factor as obtained from our MC simulations.

Label	σ_2/σ_1	Δ	x_1	$\rho\sigma_1^3$	η	Z_{MC}
A	1	-0.1	1/2	1.0	0.5236	8.648
B	1	-0.5	1/2	1.0	0.5236	3.429
C	4/5	-0.444	1/3	1.0	0.3533	2.335
D	1	0.05	1/2	0.8	0.4189	9.083
E	1	0.25	1/2	0.3	0.1571	2.556
F	4/5	0.25	1/3	0.3	0.1060	1.876

RICCARDO FANTONI AND ANDRÉS SANTOS

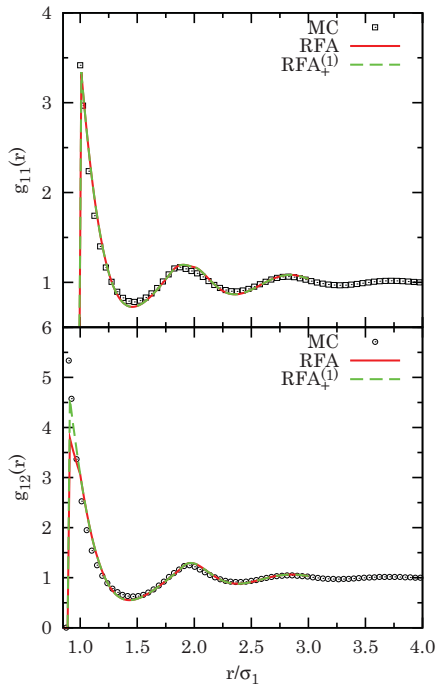
 PHYSICAL REVIEW E **84**, 041201 (2011)


FIG. 5. (Color online) RDF for system A of Table II.

cases, however, both species contribute almost equally to the (nominal) packing fraction η since $x_1\sigma_1^3/x_2\sigma_2^3 = (5/4)^3/2 = 125/128 \simeq 0.98$.

A. Negative nonadditivity

1. Symmetric mixtures

Figures 5 and 6 display the RDF for systems A and B, respectively. System A is only slightly nonadditive and we observe that both approximations RFA and $\text{RFA}_+^{(1)}$ do a very good job. On the other hand, while RFA and $\text{RFA}_+^{(1)}$ coincide for $g_{11}(r)$ with $r > \sigma_1$, they differ for $g_{12}(r)$ in the interval $\sigma_{12} = 0.9\sigma_1 \leq r \leq \tau_{12} = \sigma_1$. In fact, approximation RFA presents an artificial discontinuity of the first derivative $g'_{12}(r)$ at $r = \sigma_1$. This is corrected by approximation $\text{RFA}_+^{(1)}$, which presents a good agreement with the MC results for $r < \sigma_1$. In spite of this, we observe that approximation $\text{RFA}_+^{(1)}$ underestimates the contact value $g_{12}(\sigma_{12}^+)$, in agreement with the entry of Table I corresponding to case A.

In the case of system B the nonadditivity is larger and, according to Fig. 6, the performance of our approximations is still good for $g_{11}(r)$ but worsens for $g_{12}(r)$. In fact, $g_{12}(r)|_{\text{RFA}}$ turns out to be better than $g_{12}(r)|_{\text{RFA}_+^{(1)}}$ in the region $\sigma_{12} = 0.5\sigma_1 \leq r \leq \tau_{12} = \sigma_1$, in agreement with the entry of Table I corresponding to case B. In any case, it is interesting to remark that approximation $\text{RFA}_+^{(1)}$ succeeds in capturing the

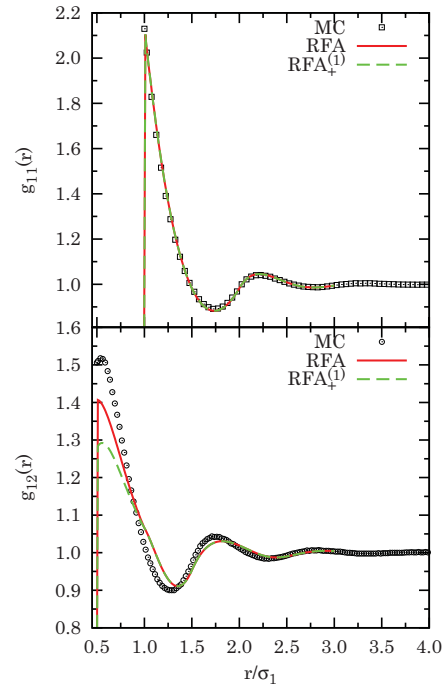


FIG. 6. (Color online) RDF for system B of Table II.

nonmonotonic behavior of $g_{12}(r)$ very near $r = \sigma_{12}$ observed in the simulations.

2. Asymmetric mixture

The only case representing an asymmetric mixture with negative nonadditivity (system C) is shown in Fig. 7. Again, the MC like-like RDF are very well reproduced by the two approximations. In the case of the like-unlike function $g_{12}(r)$, approximation $\text{RFA}_+^{(1)}$ clearly improves approximation RFA in the region $\sigma_{12} = 0.5\sigma_1 \leq r \leq \tau_{12} = 0.9\sigma_1$. Apart from that, both approximations overestimate $g_{12}(r)$ between $r = \tau_{12} = 0.9\sigma_1$ and the location of the first minimum at about $r \simeq 1.25\sigma_1$. In Fig. 7 we have taken $g_{12}(r) \rightarrow \frac{1}{2}[g_{12}(r) + g_{21}(r)]$, as explained at the beginning of this section. Prior to this symmetrization, the maximum relative deviation between $g_{12}(r)$ and $g_{21}(r)$ occurs at $r \simeq 0.75\sigma_1$ and is less than 5%.

B. Positive nonadditivity

1. Symmetric mixtures

Let us consider now positive nonadditivities, starting with symmetric mixtures. Figures 8 and 9 show the results for systems D and E, respectively. For a small nonadditivity $\Delta = 0.05$, both approximations provide very good results, except for $g_{11}(r)$ near contact (see also Table I). Notice, however, that approximation $\text{RFA}_+^{(1)}$ improves approximation RFA in the narrow region $\sigma_1 \leq r \leq \tau_{11} = 1.05\sigma_1$.

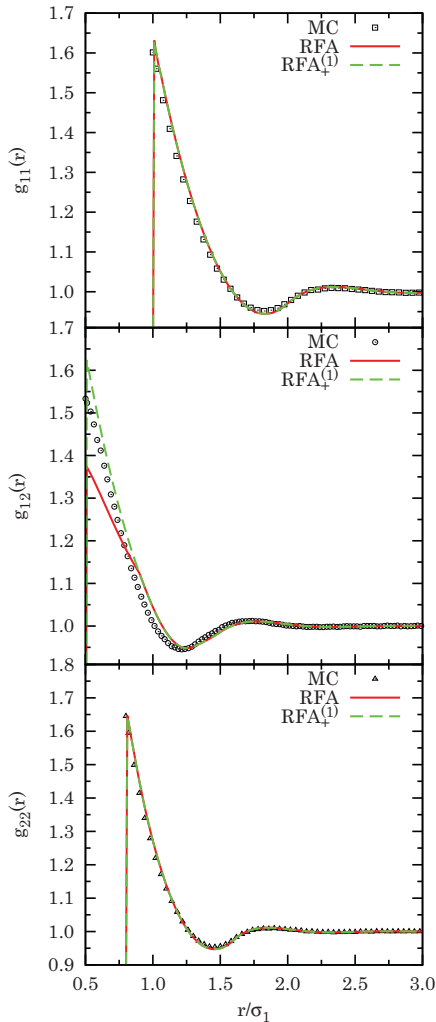


FIG. 7. (Color online) RDF for system C of Table II.

For a larger nonadditivity (system E), Fig. 9 shows the excellent job made by approximation $RFA_+^{(1)}$ in the interval $\sigma_1 \leq r \leq \tau_{11} = 1.25\sigma_1$. In the case of the like-unlike correlation function, however, the approximations overestimate the values between σ_{12} and the first minimum ($r \approx 2\sigma_1$).

2. Asymmetric mixture

Figure 10 displays the three functions $g_{ij}(r)$ for the asymmetric system F. As in case E, approximation $RFA_+^{(1)}$ nicely reproduces the exact results from the simulation for the like-like correlations and corrects the unphysical kink of approximation RFA occurring at $\tau_{11} = 1.225\sigma_1$ and $\tau_{22} = 1.025\sigma_1$. Interestingly enough, although the values of Δ and $\rho\sigma_1^3$ are the same in systems E and F, the performance of the

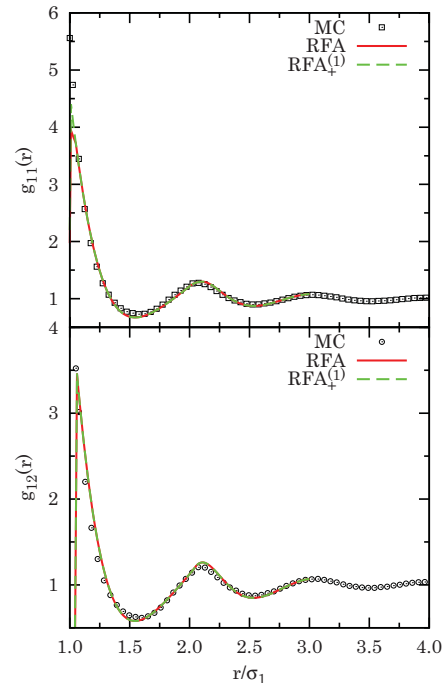


FIG. 8. (Color online) RDF for system D of Table II.

approximations for $g_{12}(r)$ is much better in case F (asymmetric mixture) than in case E (symmetric mixture). This might be partially due to the fact that the packing fraction η is smaller in system F than in system E. For the asymmetric system F, we have found that the maximum relative deviation between $g_{12}(r)$ and $g_{21}(r)$ takes place at $r = \sigma_{12} = \frac{9}{8}\sigma_1$ and is less than 0.5%.

C. The Widom-Rowlinson model

As recalled in Sec. I, the WR model corresponds to an equimolar symmetric binary NAHS mixture where $\sigma_1 = \sigma_2 = 0$ and $\sigma_{12} \neq 0$. The model is then fully characterized by the reduced density, $\rho\sigma_{12}^3$. The critical demixing reduced density for this model is around 0.75 [47,48].

The nonadditivity parameter of the WR model is $\Delta = \sigma_{12}/\sigma_{12}^{add} - 1 \rightarrow \infty$, so it lies well outside the “safe” region for our approximation RFA_+ (see Fig. 1). To compensate for this, we replace here approximation $RFA_+^{(1)}$ by approximation $RFA_+^{(2)}$.

We see from Figs. 11 and 12 that approximation $RFA_+^{(2)}$ does a much better job than expected at the two densities considered. The main drawbacks of the theory are that the contact value $g_{11}(0)$ is dramatically overestimated and the behavior of $g_{12}(r)$ for $r \gtrsim \sigma_{12}$ is qualitatively wrong. In spite of this, it is remarkable that approximation $RFA_+^{(2)}$ captures well the global properties of the RDF in this extreme system.

RICCARDO FANTONI AND ANDRÉS SANTOS

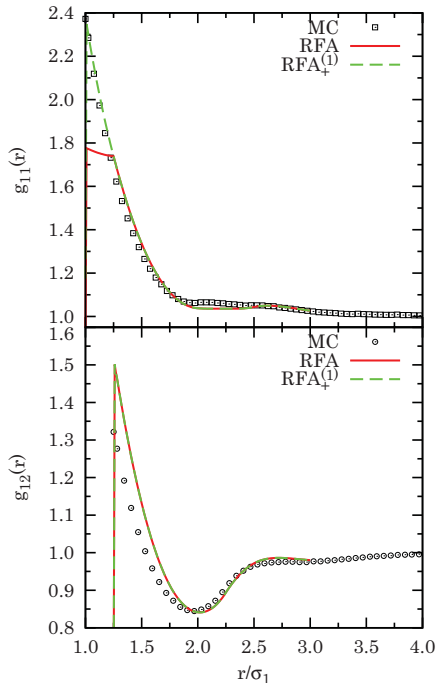
 PHYSICAL REVIEW E **84**, 041201 (2011)


FIG. 9. (Color online) RDF for system E of Table II.

VI. SUMMARY AND CONCLUSIONS

The importance of the NAHS model in liquid state theory cannot be overemphasized. When the reference or effective interaction among the microscopic components (at an atomic or a colloidal level of description) of a statistical system is modeled as of hard-core type, there is no reason to expect that the interaction range σ_{ij} corresponding to the pair (i, j) is enslaved to be the arithmetic mean of the interaction ranges σ_i and σ_j corresponding to the pairs (i, i) and (j, j) , respectively. Therefore, in an n -component NAHS mixture the number of independent interaction ranges is $n(n+1)/2$, in contrast to the number n in an AHS mixture. It is then not surprising that, while an exact solution of the PY theory exists for AHS systems [13], numerical methods are needed when solving the PY and other integral-equation theories for NAHSs [4]. Therefore, analytical approaches to the problem can represent attractive and welcome contributions.

In this paper we have constructed a nonperturbative fully analytical approximation for the Laplace transforms $G_{ij}(s)$ of $rg_{ij}(r)$, where $g_{ij}(r)$ is the set of RDF of a general 3D NAHS fluid mixture. Our approach follows several stages. The starting point is the analytical PY solution for AHSs, Eqs. (2.36)–(2.38). Exploiting the connection between the exact solutions for 1D NAHS and AHS mixtures [see Eqs. (2.15) and (2.28)], the AHS PY solution is rewritten in an alternative form, Eqs. (3.1)–(3.4). Our approximation RFA consists of keeping the form (3.4), except that σ_{ij}^{add} in Eq. (3.1) is replaced by σ_{ij} [cf. Eq. (3.5)] and σ_i in Eq. (3.3) is replaced by $b_{ij} \equiv \sigma_{ij} + a_{ij}$

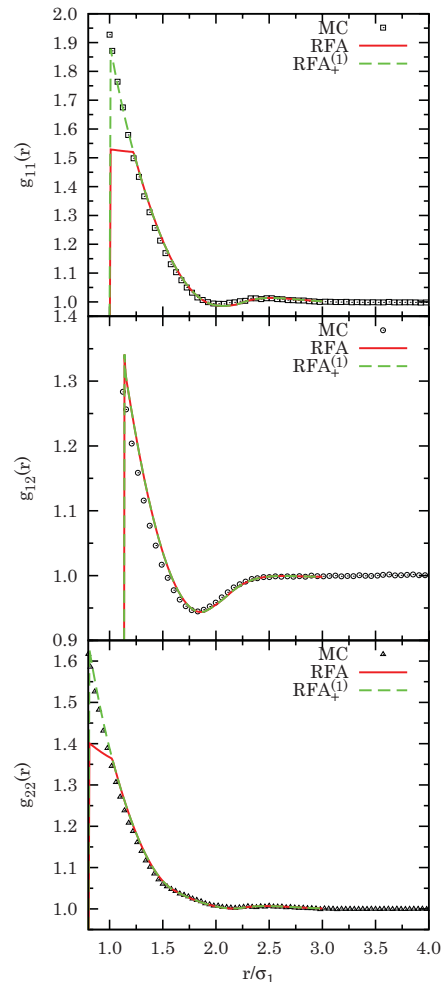


FIG. 10. (Color online) RDF for system F of Table II.

[cf. Eq. (3.6)]. Moreover, the parameters $L_{ij}^{(0)}$ and $L_{ij}^{(1)}$ are no longer given by Eq. (2.41) but are determined by enforcing the condition (2.4) or, equivalently, Eq. (2.33). This results in Eqs. (3.15)–(3.21), and so the problem becomes completely closed and analytical in Laplace space. The equation of state is obtained either via the virial route (2.7) through the contact values (3.32) or via the compressibility route (2.11) through the coefficients $H_{ij}^{(1)}$ in the expansion of $s^2 G_{ij}(s)$ in powers of s , Eq. (2.33).

The penalty we pay for “stretching” the AHS PY solution to the NAHS domain in the way described above is that $g_{ij}(r)$ may not be strictly zero for $r < \sigma_{ij}$ or may exhibit first-order discontinuities at artificial distances. To deal with this problem, we have restricted ourselves to mixtures such that the first two singularities of $g_{ij}(r)$ are σ_{ij} and $\tau_{ij} \equiv \min(\sigma_{ik} - a_{kj})$

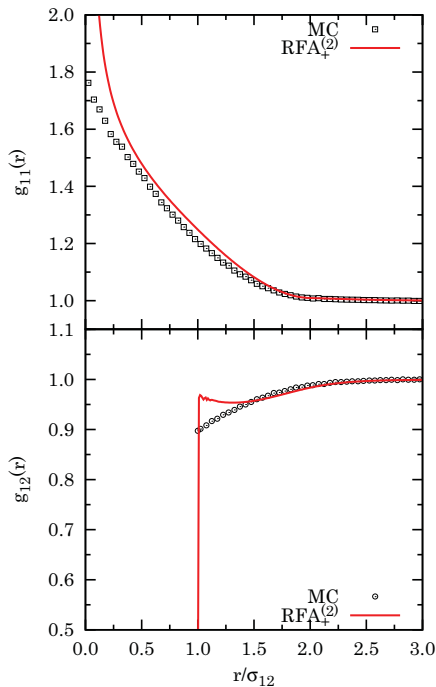


FIG. 11. (Color online) RDF for the WR model at $\rho\sigma_{12}^3 = 0.28748$. The MC data are taken from Ref. [43].

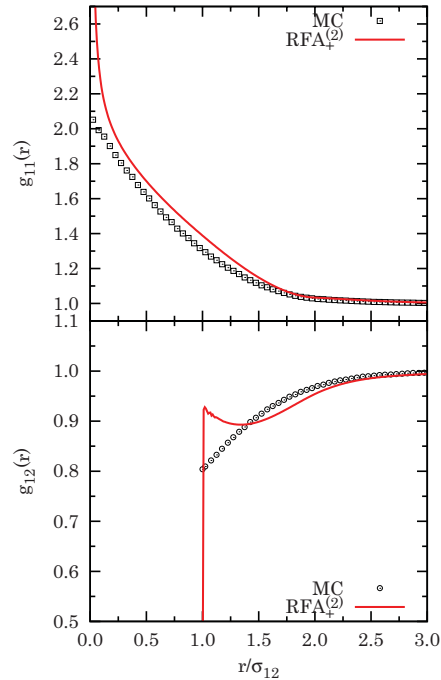


FIG. 12. (Color online) RDF for the WR model at $\rho\sigma_{12}^3 = 0.4$. The MC data are taken from Ref. [43].

$k = 1, \dots, n; k \neq j$). In the binary case ($n = 2$) this restriction corresponds to $-\sigma_2/(\sigma_1 + \sigma_2) \leq \Delta \leq 2\sigma_2/(\sigma_1 + \sigma_2)$ (see Fig. 1). Next, we have constructed a modified approximation RFA_+ whereby either $g_{ij}(r)$ is truncated for $r < \sigma_{ij}$ if $\tau_{ij} < \sigma_j$ or the behavior of $g_{ij}(r)$ for $r \gtrsim \tau_{ij}$ is extrapolated to the interval $\sigma_{ij} < r < \tau_{ij}$ if $\tau_{ij} > \sigma_j$ [cf. Eq. (3.34)]. From a practical point of view, the latter extrapolation can be replaced by a polynomial approximation (e.g., linear or quadratic), yielding approximation $\text{RFA}_+^{(m)}$ [cf. Eq. (3.37)]. This is sufficient to guarantee that the slope of $g_{ij}(r)$ is continuous everywhere for $r > \sigma_{ij}$.

For comparison with MC data of the equation of state we have used approximation RFA since its local limitations at the level of the RDF are largely smoothed out when focusing on the thermodynamic properties. The results show that, if the density is low enough as to make both thermodynamic routes practically coincide, our approximation accurately predicts the MC data, as shown in Fig. 2 and in the bottom panel of Fig. 4. For larger densities, the virial and compressibility routes tend to underestimate and overestimate, respectively, the simulation values, this being a typical PY feature. As in the AHS case, the simple interpolation rule $Z = \frac{1}{3}Z^v + \frac{2}{3}Z^c$ provides very good results, except for large nonadditivities (see Fig. 3 and the top and middle panels of Fig. 4).

Regarding the structural properties, approximation $\text{RFA}_+^{(1)}$ is found to perform quite well. The contact values are generally more accurate than those obtained from the numerical solution

of the PY integral equation, at least for symmetric mixtures, as shown in Table I. Comparison with our own MC simulations shows a very good agreement, except in the case of the like-unlike RDF for distances smaller than the location of the first minimum for large nonadditivities (see Figs. 5–10). On the other hand, even in the case of the WR model ($\Delta \rightarrow \infty$, well beyond the “safe” region of Fig. 1) our approximation $\text{RFA}_+^{(2)}$ does a much better job than expected, as illustrated in Figs. 11 and 12.

In conclusion, one can reasonably argue that our approximation RFA, along with its variants RFA_+ and $\text{RFA}_+^{(m)}$, represent excellent compromises between simplicity and accuracy. We have tried other alternative analytical approaches (simpler as well as more complex) also based on the PY solution for AHSs, but none of them has been found to present a behavior as sound and consistent as those proposed in this paper. We expect that they can be useful in the investigation of such an important statistical-mechanical system (both by itself and also as a reference to other systems) as the NAHS mixture.

The work presented in this paper can be continued along several lines. In particular, we plan to explore in the near future the predictions for the demixing transition from our approximations. It is also worth exploring the NAHS theory that arises when the starting point is not the PY solution for AHSs but the more advanced RFA proposed in Ref. [14], which contains free parameters that can be accommodated to fit any desired EOS in a thermodynamically consistent way.

RICCARDO FANTONI AND ANDRÉS SANTOS

PHYSICAL REVIEW E **84**, 041201 (2011)

ACKNOWLEDGMENTS

The MC simulations presented in Sec. V were carried out at the Center for High Performance Computing (CHPC), CSIR Campus, 15 Lower Hope St., Rosebank, Cape Town, South Africa. RF acknowledges the kind hospitality of the Department of Physics of the University of Extremadura at Badajoz. The research of AS has been supported by the Ministerio de Ciencia e Innovación (Spain) through Grant No.

FIS2010-16587 and the Junta de Extremadura (Spain) through Grant No. GR10158, partially financed by FEDER funds.

APPENDIX A: EXPLICIT EXPRESSIONS OF $G_{ij}(s)$ FOR BINARY MIXTURES IN APPROXIMATION RFA

By performing the inversion of the matrix (3.8) and carrying out the matrix product in Eq. (3.4) one gets

$$G_{11}(s) = \frac{s^{-2}}{D(s)} \left\{ L_{11}(s) \left[1 - \frac{2\pi\rho x_2}{s^3} N_{22}(s) \right] e^{-\sigma_1 s} + \frac{2\pi\rho x_2}{s^3} L_{11}(s) L_{22}(s) e^{-(\sigma_1 + \sigma_2)s} - \frac{2\pi\rho x_2}{s^3} L_{12}(s) L_{21}(s) e^{-2\sigma_{12}s} + \frac{2\pi\rho x_2}{s^3} L_{12}(s) N_{21}(s) e^{-(\sigma_{12} + a_{12})s} \right\}, \tag{A1}$$

$$G_{12}(s) = \frac{s^{-2}}{D(s)} \left\{ L_{12}(s) \left[1 - \frac{2\pi\rho x_1}{s^3} N_{11}(s) \right] e^{-\sigma_{12}s} + \frac{2\pi\rho x_1}{s^3} L_{11}(s) N_{12}(s) e^{-(\sigma_1 + \sigma_2)s/2} \right\}, \tag{A2}$$

where the quadratic functions $N_{kj}(s)$ can be found in Eq. (3.9) and

$$D(s) = \left[1 - \frac{2\pi\rho x_1}{s^3} N_{11}(s) \right] \left[1 - \frac{2\pi\rho x_2}{s^3} N_{22}(s) \right] - \frac{(2\pi\rho)^2 x_1 x_2}{s^6} N_{12}(s) N_{21}(s) + \frac{2\pi\rho x_1}{s^3} L_{11}(s) \left[1 - \frac{2\pi\rho x_2}{s^3} N_{22}(s) \right] e^{-\sigma_1 s} + \frac{2\pi\rho x_2}{s^3} L_{22}(s) \left[1 - \frac{2\pi\rho x_1}{s^3} N_{11}(s) \right] e^{-\sigma_2 s} + \frac{4\pi^2 \rho x_1 x_2}{s^6} [L_{11}(s) L_{22}(s) e^{-(\sigma_1 + \sigma_2)s} - L_{12}(s) L_{21}(s) e^{-2\sigma_{12}s} + L_{12}(s) N_{21}(s) e^{-(\sigma_{12} + a_{12})s} + L_{21}(s) N_{12}(s) e^{-(\sigma_{12} - a_{12})s}] \tag{A3}$$

is the determinant of the matrix \mathbf{Q}^{-1} . The expressions for $G_{22}(s)$ and $G_{21}(s)$ can be obtained by the exchange $1 \leftrightarrow 2$.

APPENDIX B: ORDERING OF SINGULAR DISTANCES IN APPROXIMATION RFA FOR BINARY MIXTURES

By ‘‘singular’’ distances we will refer to those values of r where the RDF $g_{ij}(r)$ or any of its derivatives have a discontinuity. Physical singularities are located, for instance, at $r = \sigma_{ij}$ and $r = \sigma_{ik} + \sigma_{kj}$, $k = 1, \dots, n$. Apart from that, approximation RFA introduces spurious singularities at other distances.

Let us particularize to a binary mixture. The physical leading singularity of $g_{ij}(r)$ should be located at $r = \sigma_{ij}$. However, according to Eq. (A1), the leading singularity of $g_{11}(r)$ takes place at $r = \min(\sigma_1, \sigma_{12} + a_{12}, 2\sigma_{12})$. Analogously, the leading singularity of $g_{22}(r)$ is located at $r = \min(\sigma_2, \sigma_{12} - a_{12}, 2\sigma_{12})$. Finally, Eq. (A2) shows that the leading singularity of $g_{12}(r)$ is $r = \frac{1}{2} \min(2\sigma_{12}, \sigma_1 + \sigma_2)$. Note that we have assumed $\sigma_{12} - a_{12} > 0$, so that the denominator $D(s)$, Eq. (A3), does not affect the leading singularity of $g_{ij}(r)$.

It is thus important to determine the relative ordering of the values σ_1 , σ_2 , $\sigma_{12} - a_{12}$, $\sigma_{12} + a_{12}$, $2\sigma_{12}$, and $\sigma_1 + \sigma_2$. Such an ordering depends on the values of Δ and $R \equiv \sigma_2/\sigma_1$, where, without loss of generality, we assume that $\sigma_2 \leq \sigma_1$. A detailed analysis shows that the Δ - R plane can be split into 13 disjoint regions with distinct order for the above

singular distances. Those regions are indicated in Fig. 13, while Table III shows the order applying within each region.

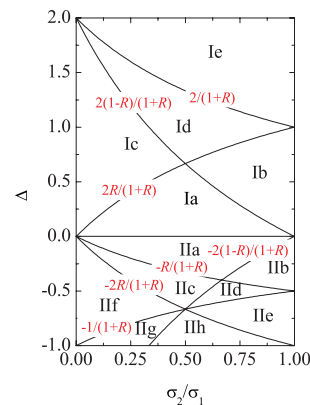


FIG. 13. (Color online) Plane Δ vs $R \equiv \sigma_2/\sigma_1$ showing the regions with different ordering of the distances σ_1 , σ_2 , $\sigma_{12} - a_{12}$, $\sigma_{12} + a_{12}$, $2\sigma_{12}$, and $\sigma_1 + \sigma_2$.

TABLE III. Order of the singular distances $\sigma_1, \sigma_2, \sigma_{12} - a_{12}, \sigma_{12} + a_{12}, 2\sigma_{12}$, and $\sigma_1 + \sigma_2$ in each of the regions of Fig. 13.

Region	Order												
Ia	0	\leq	σ_2	\leq	$\sigma_{12} - a_{12}$	\leq	σ_1	\leq	$\sigma_{12} + a_{12}$	\leq	$\sigma_1 + \sigma_2$	\leq	$2\sigma_{12}$
Ib	0	\leq	σ_2	\leq	σ_1	\leq	$\sigma_{12} - a_{12}$	\leq	$\sigma_{12} + a_{12}$	\leq	$\sigma_1 + \sigma_2$	\leq	$2\sigma_{12}$
Ic	0	\leq	σ_2	\leq	$\sigma_{12} - a_{12}$	\leq	σ_1	\leq	$\sigma_1 + \sigma_2$	\leq	$\sigma_{12} + a_{12}$	\leq	$2\sigma_{12}$
Id	0	\leq	σ_2	\leq	σ_1	\leq	$\sigma_{12} - a_{12}$	\leq	$\sigma_1 + \sigma_2$	\leq	$\sigma_{12} + a_{12}$	\leq	$2\sigma_{12}$
Ie	0	\leq	σ_2	\leq	σ_1	\leq	$\sigma_1 + \sigma_2$	\leq	$\sigma_{12} - a_{12}$	\leq	$\sigma_{12} + a_{12}$	\leq	$2\sigma_{12}$
IIa	0	\leq	$\sigma_{12} - a_{12}$	\leq	σ_2	\leq	$\sigma_{12} + a_{12}$	\leq	σ_1	\leq	$2\sigma_{12}$	\leq	$\sigma_1 + \sigma_2$
IIb	0	\leq	$\sigma_{12} - a_{12}$	\leq	$\sigma_{12} + a_{12}$	\leq	σ_2	\leq	σ_1	\leq	$2\sigma_{12}$	\leq	$\sigma_1 + \sigma_2$
IIc	0	\leq	$\sigma_{12} - a_{12}$	\leq	σ_2	\leq	$\sigma_{12} + a_{12}$	\leq	$2\sigma_{12}$	\leq	σ_1	\leq	$\sigma_1 + \sigma_2$
IId	0	\leq	$\sigma_{12} - a_{12}$	\leq	$\sigma_{12} + a_{12}$	\leq	σ_2	\leq	$2\sigma_{12}$	\leq	σ_1	\leq	$\sigma_1 + \sigma_2$
IIe	0	\leq	$\sigma_{12} - a_{12}$	\leq	$\sigma_{12} + a_{12}$	\leq	$2\sigma_{12}$	\leq	σ_2	\leq	σ_1	\leq	$\sigma_1 + \sigma_2$
IIf	$\sigma_{12} - a_{12}$	\leq	0	\leq	σ_2	\leq	$2\sigma_{12}$	\leq	$\sigma_{12} + a_{12}$	\leq	σ_1	\leq	$\sigma_1 + \sigma_2$
IIg	$\sigma_{12} - a_{12}$	\leq	0	\leq	$2\sigma_{12}$	\leq	σ_2	\leq	$\sigma_{12} + a_{12}$	\leq	σ_1	\leq	$\sigma_1 + \sigma_2$
IIh	$\sigma_{12} - a_{12}$	\leq	0	\leq	$2\sigma_{12}$	\leq	$\sigma_{12} + a_{12}$	\leq	σ_2	\leq	σ_1	\leq	$\sigma_1 + \sigma_2$

Note that $\sigma_{12} - a_{12}$ is negative in Regions IIc, IIg, and IIh, i.e., if $-1 \leq \Delta \leq -2R/(1 + R)$, thus invalidating those regions from the preceding analysis.

We observe that σ_1 and σ_2 are indeed the leading singularities of $g_{11}(r)$ and $g_{22}(r)$, respectively, for positive nonadditivity (regions Ia–Ie). Reciprocally, σ_{12} is the leading singularity of $g_{12}(r)$ for negative nonadditivity (regions IIa–IIh).

In order to construct approximation RFA₊, we want to restrict ourselves to those regions such that the two leading singularities of $g_{11}(r)$ are σ_1 and $\tau_{11} \equiv \sigma_{12} + a_{12}$. Inspection of Table III shows that Regions IIc–IIh are discarded by this criterion. In the remaining regions the leading singularity of $g_{11}(r)$ is $\min(\sigma_1, \sigma_{12} + a_{12})$ but the next one is not necessarily $\max(\sigma_1, \sigma_{12} + a_{12})$ since the latter value competes with $\min(\sigma_1, \sigma_{12} + a_{12}) + \min(\sigma_2, \sigma_{12} - a_{12}, 2\sigma_{12})$, where the term $\min(\sigma_2, \sigma_{12} - a_{12}, 2\sigma_{12})$ comes from the denominator $D(s)$ [cf. Eq. (A3)]. It can be checked that $\max(\sigma_1, \sigma_{12} + a_{12}) \geq \min(\sigma_1, \sigma_{12} + a_{12}) + \min(\sigma_2, \sigma_{12} - a_{12}, 2\sigma_{12})$ in Regions Ic–Ie. Therefore the two first singularities of $g_{11}(r)$ are σ_1 and $\tau_{11} = \sigma_{12} + a_{12}$ in Regions Ia, Ib, IIa, and IIb only. It turns out that in those four regions the two leading singularities of $g_{22}(r)$ are σ_2 and $\tau_{22} \equiv \sigma_{12} - a_{12}$, and the two leading singularities of $g_{12}(r)$ are σ_{12} and $\tau_{12} \equiv \frac{1}{2}(\sigma_1 + \sigma_2)$.

In summary, Regions Ia, Ib, IIa, and IIb are the only ones where the two leading singularities of $g_{ij}(r)$ are σ_{ij} and $\tau_{ij} \equiv \sigma_{ik} - a_{kj}$ with $k \neq j$.

APPENDIX C: SHORT-RANGE FORMS OF $g_{ij}(r)$ FOR BINARY MIXTURES IN APPROXIMATION RFA

In what follows we assume that $-\sigma_2/(\sigma_1 + \sigma_2) \leq \Delta \leq 2\sigma_2/(\sigma_1 + \sigma_2)$, which corresponds to Regions Ia, Ib, IIa, and IIb of Fig. 13. As discussed in Appendix B, this guarantees that the first two singularities of $g_{ij}(r)$ are σ_{ij} and $\tau_{ij} \equiv \sigma_{ik} - a_{kj}$ with $k \neq j$. The aim of this Appendix is to give the expressions of $g_{ij}(r)$ in the region $0 \leq r \leq \max(\sigma_{ij}, \tau_{ij}) + \epsilon$, where ϵ is smaller than the separation between $\max(\sigma_{ij}, \tau_{ij})$ and the next singularity.

It is convenient to assign a bookkeeping parameter z to e^{-s} , so that, for instance, $e^{-\sigma_{ij}s}$ becomes $z^{\sigma_{ij}} e^{-\sigma_{ij}s}$. We will set $z = 1$ at the end of the calculations. Therefore, the denominator $D(s)$

given by Eq. (A3) becomes

$$D(s) = D_0(s) + o(z^0), \tag{C1}$$

where

$$D_0(s) = \left[1 - \frac{2\pi\rho x_1}{s^3} N_{11}(s) \right] \left[1 - \frac{2\pi\rho x_2}{s^3} N_{22}(s) \right] - \frac{(2\pi\rho)^2 x_1 x_2}{s^6} N_{12}(s) N_{21}(s). \tag{C2}$$

In Eq. (C1), $o(z^n)$ denotes terms that are negligible versus z^n in the (formal) limit $z \rightarrow 0$, i.e., $\lim_{z \rightarrow 0} z^{-n} o(z^n) = 0$. From Eq. (A1) we see that the two leading terms in $G_{11}(s)$ are of orders z^{σ_1} and $z^{\sigma_{12} + a_{12}}$:

$$G_{11}(s) = \Phi_{11}(s) e^{-\sigma_1 s} z^{\sigma_1} + 2\pi\rho x_2 \Gamma_{121}(s) e^{-(\sigma_{12} + a_{12})s} \times z^{\sigma_{12} + a_{12}} + o(z^{\sigma_1}) + o(z^{\sigma_{12} + a_{12}}), \tag{C3}$$

where

$$\Phi_{11}(s) \equiv \frac{s^{-2}}{D_0(s)} L_{11}(s) \left[1 - \frac{2\pi\rho x_2}{s^3} N_{22}(s) \right] \tag{C4}$$

and $\Gamma_{ikj}(s)$ is given by Eq. (3.29). Analogously,

$$G_{12}(s) = \Phi_{12}(s) e^{-\sigma_{12} s} z^{\sigma_{12}} + 2\pi\rho x_1 \Gamma_{112}(s) e^{-(\sigma_1 + \sigma_2)s/2} \times z^{(\sigma_1 + \sigma_2)/2} + o(z^{\sigma_{12}}) + o(z^{(\sigma_1 + \sigma_2)/2}), \tag{C5}$$

$$G_{21}(s) = \Phi_{21}(s) e^{-\sigma_{12} s} z^{\sigma_{12}} + 2\pi\rho x_2 \Gamma_{221}(s) e^{-(\sigma_1 + \sigma_2)s/2} \times z^{(\sigma_1 + \sigma_2)/2} + o(z^{\sigma_{12}}) + o(z^{(\sigma_1 + \sigma_2)/2}), \tag{C6}$$

$$G_{22}(s) = \Phi_{22}(s) e^{-\sigma_2 s} z^{\sigma_2} + 2\pi\rho x_1 \Gamma_{212}(s) e^{-(\sigma_{12} - a_{12})s} \times z^{\sigma_{12} - a_{12}} + o(z^{\sigma_2}) + o(z^{\sigma_{12} - a_{12}}), \tag{C7}$$

where

$$\Phi_{12}(s) \equiv \frac{s^{-2}}{D_0(s)} L_{12}(s) \left[1 - \frac{2\pi\rho x_1}{s^3} N_{11}(s) \right], \tag{C8}$$

$$\Phi_{21}(s) \equiv \frac{s^{-2}}{D_0(s)} L_{21}(s) \left[1 - \frac{2\pi\rho x_2}{s^3} N_{22}(s) \right], \tag{C9}$$

$$\Phi_{22}(s) \equiv \frac{s^{-2}}{D_0(s)} L_{22}(s) \left[1 - \frac{2\pi\rho x_1}{s^3} N_{11}(s) \right]. \tag{C10}$$

RICCARDO FANTONI AND ANDRÉS SANTOS

PHYSICAL REVIEW E **84**, 041201 (2011)

Laplace inversion of Eqs. (C3) and (C5)–(C7) shows that in the interval $0 \leq r \leq \max(\sigma_{ij}, \tau_{ij}) + \epsilon$ we obtain

$$g_{11}(r) = \frac{1}{r} \Theta(r - \sigma_1) \phi_{11}(r - \sigma_1) + \frac{2\pi\rho x_2}{r} \Theta(r - \sigma_{12} - a_{12}) \times \gamma_{121}(r - \sigma_{12} - a_{12}), \quad (\text{C11})$$

$$g_{12}(r) = \frac{1}{r} \Theta(r - \sigma_{12}) \phi_{12}(r - \sigma_{12}) + \frac{2\pi\rho x_1}{r} \Theta\left(r - \frac{\sigma_1 + \sigma_2}{2}\right) \times \gamma_{112}\left(r - \frac{\sigma_1 + \sigma_2}{2}\right), \quad (\text{C12})$$

$$g_{21}(r) = \frac{1}{r} \Theta(r - \sigma_{21}) \phi_{21}(r - \sigma_{21}) + \frac{2\pi\rho x_2}{r} \Theta\left(r - \frac{\sigma_1 + \sigma_2}{2}\right) \times \gamma_{221}\left(r - \frac{\sigma_1 + \sigma_2}{2}\right), \quad (\text{C13})$$

$$g_{22}(r) = \frac{1}{r} \Theta(r - \sigma_2) \phi_{22}(r - \sigma_2) + \frac{2\pi\rho x_1}{r} \Theta(r - \sigma_{12} + a_{12}) \times \gamma_{212}(r - \sigma_{12} + a_{12}), \quad (\text{C14})$$

where we have already set $z = 1$. In Eqs. (C11)–(C14), $\phi_{ij}(r)$ and $\gamma_{ikj}(r)$ are the inverse Laplace transforms of $\Phi_{ij}(s)$ and $\Gamma_{ikj}(s)$, respectively.

Since $\phi_{ij}(0) = \lim_{s \rightarrow \infty} \Phi_{ij}(s) = L_{ij}^{(1)}$, the contact values in approximation RFA are

$$g_{11}(\sigma_1^+) = \frac{L_{11}^{(1)}}{\sigma_1}, \quad (\text{C15})$$

$$g_{12}(\sigma_{12}^+) = \frac{L_{12}^{(1)}}{\sigma_{12}} + \frac{2\pi\rho x_1}{\sigma_{12}} \gamma_{112}\left(\sigma_{12} - \frac{\sigma_1 + \sigma_2}{2}\right), \quad (\text{C16})$$

$$g_{21}(\sigma_{21}^+) = \frac{L_{21}^{(1)}}{\sigma_{21}} + \frac{2\pi\rho x_2}{\sigma_{21}} \gamma_{221}\left(\sigma_{21} - \frac{\sigma_1 + \sigma_2}{2}\right), \quad (\text{C17})$$

$$g_{22}(\sigma_2^+) = \frac{L_{22}^{(1)}}{\sigma_2}, \quad (\text{C18})$$

in Regions Ia and Ib ($\Delta > 0$). On the other hand, in Regions IIa and IIb ($\Delta < 0$),

$$g_{11}(\sigma_1^+) = \frac{L_{11}^{(1)}}{\sigma_1} + \frac{2\pi\rho x_2}{\sigma_1} \gamma_{121}(\sigma_1 - \sigma_{12} - a_{12}), \quad (\text{C19})$$

$$g_{12}(\sigma_{12}^+) = \frac{L_{12}^{(1)}}{\sigma_{12}}, \quad (\text{C20})$$

$$g_{21}(\sigma_{21}^+) = \frac{L_{21}^{(1)}}{\sigma_{21}}, \quad (\text{C21})$$

$$g_{22}(\sigma_2^+) = \frac{L_{22}^{(1)}}{\sigma_2} + \frac{2\pi\rho x_1}{\sigma_2} \gamma_{212}(\sigma_2 - \sigma_{12} + a_{12}). \quad (\text{C22})$$

A more compact form is provided by Eq. (3.32).

- [1] J.-P. Hansen and I. R. McDonald, *Theory of Simple Liquids* (Academic Press, London, 2006).
- [2] C. N. Likos, *Phys. Rep.* **348**, 267 (2001).
- [3] A. Mulero, ed., *Theory and Simulation of Hard-Sphere Fluids and Related Systems*, Vol. 753 of Lectures Notes in Physics (Springer, Berlin, 2008).
- [4] P. Ballone, G. Pastore, G. Galli, and D. Gazzillo, *Mol. Phys.* **59**, 275 (1986).
- [5] D. Gazzillo, G. Pastore, and S. Enzo, *J. Phys. Condens. Matter* **1**, 3469 (1989).
- [6] D. Gazzillo, G. Pastore, and R. Frattini, *J. Phys. Condens. Matter* **2**, 3469 (1990).
- [7] J. A. Shouten, *Phys. Rep.* **172**, 33 (1989).
- [8] A. P. Gast, C. K. Hall, and W. B. Russel, *J. Colloid Interface Sci.* **96**, 251 (1983).
- [9] H. N. W. Lekkerkerker, W. C. K. Poon, P. N. Pusey, A. Stroobants, and P. B. Warren, *Europhys. Lett.* **20**, 559 (1992).
- [10] M. Dijkstra, J. M. Brader, and R. Evans, *J. Phys. Condens. Matter* **11**, 10079 (1999).
- [11] E. J. Meijer and D. Frenkel, *J. Chem. Phys.* **100**, 6873 (1994).
- [12] A. Santos, M. López de Haro, and S. B. Yuste, *J. Chem. Phys.* **122**, 024514 (2005).
- [13] J. L. Lebowitz, *Phys. Rev.* **133**, A895 (1964).
- [14] S. B. Yuste, A. Santos, and M. López de Haro, *J. Chem. Phys.* **108**, 3683 (1998).
- [15] R. D. Rohrmann and A. Santos, *Phys. Rev. E* **83**, 011201 (2011).
- [16] Z. W. Salsburg, R. W. Zwanzig, and J. G. Kirkwood, *J. Chem. Phys.* **21**, 1098 (1953).
- [17] J. L. Lebowitz and D. Zomick, *J. Chem. Phys.* **54**, 3335 (1971).
- [18] M. Heying and D. S. Corti, *Fluid Phase Equilib.* **220**, 85 (2004).
- [19] A. Santos, *Phys. Rev. E* **76**, 062201 (2007).
- [20] B. Widom and J. Rowlinson, *J. Chem. Phys.* **15**, 1670 (1970).
- [21] D. Ruelle, *Phys. Rev. Lett.* **16**, 1040 (1971).
- [22] S. Asakura and F. Oosawa, *J. Chem. Phys.* **22**, 1255 (1954).
- [23] S. Asakura and F. Oosawa, *J. Polym. Sci.* **33**, 183 (1958).
- [24] M. Rovere and G. Pastore, *J. Phys. Condens. Matter* **6**, A163 (1994).
- [25] K. Jagannathan and A. Yethiraj, *J. Chem. Phys.* **118**, 7907 (2003).
- [26] W. T. Gózdź, *J. Chem. Phys.* **119**, 3309 (2003).
- [27] A. Buhot, *J. Chem. Phys.* **122**, 024105 (2005).
- [28] E. Lomba, M. Alvarez, L. L. Lee, and N. G. Almarza, *J. Chem. Phys.* **104**, 4180 (1996).
- [29] A. Santos and M. López de Haro, *Phys. Rev. E* **72**, 010501(R) (2005).
- [30] P. Sillrén and J.-P. Hansen, *Mol. Phys.* **105**, 1803 (2010).
- [31] S. B. Yuste, A. Santos, and M. López de Haro, *J. Chem. Phys.* **128**, 134507 (2008).
- [32] J. L. Lebowitz, J. K. Percus, and I. J. Zucker, *Bull. Am. Phys. Soc.* **7**, 415 (1962).
- [33] A. Ben-Naim and A. Santos, *J. Chem. Phys.* **131**, 164512 (2009).
- [34] M. López de Haro, S. B. Yuste, and A. Santos, in *Theory and Simulation of Hard-Sphere Fluids and Related Systems*, edited by A. Mulero, Vol. 753 of Lectures Notes in Physics (Springer, Berlin, 2008), pp. 183–245.
- [35] M. Schmidt, *Phys. Rev. E* **76**, 031202 (2007).
- [36] J. Jung, M. S. Jhon, and F. H. Ree, *J. Chem. Phys.* **100**, 528 (1994).

- [37] J. Jung, M. S. Jhon, and F. H. Ree, *J. Chem. Phys.* **100**, 9064 (1994).
- [38] E. Z. Hamad, *Mol. Phys.* **91**, 371 (1997).
- [39] T. Boublik, *J. Chem. Phys.* **53**, 471 (1970).
- [40] G. A. Mansoori, N. F. Carnahan, K. E. Starlingand, and T. W. Leland, *J. Chem. Phys.* **54**, 1523 (1971).
- [41] E. W. Grundke and D. Henderson, *Mol. Phys.* **24**, 269 (1972).
- [42] L. L. Lee and D. Levesque, *Mol. Phys.* **26**, 1351 (1973).
- [43] R. Fantoni and G. Pastore, *Physica A* **332**, 349 (2004), Note that there is a misprint in Eq. (13), which should read $\bar{h}_{12}(k) = \bar{c}_{12}(k)[1 - \rho_1 \rho_2 \bar{c}_{12}^2(k)]^{-1}$.
- [44] J. Abate and W. Whitt, *Queueing Systems* **10**, 5 (1992).
- [45] See Supplemental Material at <http://link.aps.org/supplemental/10.1103/PhysRevE.84.041201> for a Mathematica notebook with a code to evaluate $g_{ij}(r)$ from approximation $\text{RFA}_+^{(1)}$. The notebook can also be downloaded from [http://www.unex.es/eweb/fisteor/andres/NAHS/gij_NAHS.nb].
- [46] M. P. Allen and D. J. Tildesley, *Computer Simulation of Liquids* (Clarendon Press, Oxford, 1987).
- [47] C.-Y. Shew and A. Yethiraj, *J. Chem. Phys.* **104**, 7665 (1996).
- [48] G. Johnson, H. Gould, J. Machta, and L. K. Chayes, *Phys. Rev. Lett.* **79**, 2612 (1997).

Part XII

2012

Chapter 28

A cluster theory for a Janus fluid

Fantoni R., Eur. Phys. J. B, accepted (2012)

Title: “A cluster theory for a Janus fluid”

Abstract: Recent Monte Carlo simulations on the Kern and Frenkel model of a Janus fluid have revealed that in the vapour phase there is the formation of preferred clusters made up of a well-defined number of particles: the micelles and the vesicles. A cluster theory is developed to approximate the exact clustering properties stemming from the simulations. It is shown that the theory is able to reproduce the micellisation phenomenon.

A cluster theory for a Janus fluid

R. Fantoni^aNational Institute for Theoretical Physics (NITheP) and Institute of Theoretical Physics, Stellenbosch University,
7600 Stellenbosch, South Africa

Received 7 October 2011 / Received in final form 18 December 2011

Published online 28 March 2012 – © EDP Sciences, Società Italiana di Fisica, Springer-Verlag 2012

Abstract. Recent Monte Carlo simulations on the Kern and Frenkel model of a Janus fluid have revealed that in the vapour phase there is the formation of preferred clusters made up of a well-defined number of particles: the micelles and the vesicles. A cluster theory is developed to approximate the exact clustering properties stemming from the simulations. It is shown that the theory is able to reproduce the micellisation phenomenon.

1 Introduction

In the statistical mechanics of fluids [1] the liquid state [2] is a particularly fascinating one. A liquid is neither a gas nor a solid, but the state where correlations really play an important role. The pioneering work of Alder [3] showed that, because of the absence of attractive forces, the hard-sphere fluid admits only a single fluid phase. In order to find the liquid phase it is sufficient to add an attractive square-well to the pair-potential of the hard-spheres. The resulting hard-sphere square-well fluid admits a bell-shaped gas-liquid coexistence curve [4,5] with the critical point moving at low temperatures and high densities as the attractive well width diminishes. Recently Kern and Frenkel [6] studied, through computer experiments, a new fluid model made of hard-spheres with patchy square-well attractions. In its simplest version, the single patch case, the model only depends on the surface coverage χ of the patch and the attraction range. Between the two extreme cases $\chi = 0$, the hard-sphere model, and $\chi = 1$, the hard-sphere square-well model, where the particles pair-potential is isotropic, the particles interaction is directional. The $\chi = 1/2$ model is known as the Janus case, as the particle, like the roman God, has two faces of different functionalities.

Another important process, which may lead to the manifestation of macroscopic phenomena, in certain fluids, is the clustering or association. In 1956, for example, Cooper [7] found that the stable state of the degenerate electron fluid in a metal is one in which particles of opposite spin and opposite momentum form pairs. It was then understood that whereas the electrons in a metal form pairs with relative angular momentum zero, in ^3He this would be prevented by the hard core repulsion, and that

therefore Cooper pairing had to occur in a state of finite angular momentum. In 1961 Lenard [8] proved analytically that a two-component plasma living in one dimension undergoes a transition from the conducting to the insulating state by the formation of neutral dimers made of a positive and a negative charge. A two-component plasma living in two dimensions is only stable at sufficiently high temperatures [9]. But if one adds a hard core to the charges it remains stable even at low temperatures where it undergoes the same transition [10]. The hard core gives rise to anyonic statistics for the quantum fluid living in two dimensions [11]. In three dimensions the two-component plasma with a hard core, the so called restricted-primitive model, also undergoes the clustering transition at low temperature and low densities [12]. An example of a one-component Janus fluid undergoing association is the dipolar hard-sphere fluid. Here a particle can be viewed as the superposition of two uniformly charged spheres: a positive one and a negative one [13].

In their study of the Kern and Frenkel single patch $\chi = 1/2$ Janus case, Sciortino et al. [14] found that the gas branch of the coexistence curve bends at high densities at low temperatures. Below the critical point, the fluid tends to remain in the gas phase for a larger interval of densities respect to the $\chi = 1$ case. This behaviour is due to the tendency of particles to associate due to the directional attractive component in the pair-potential and form clusters. At low temperatures, these clusters interact weakly amongst themselves because the particles of which they are composed tend to expose the hard-sphere hemisphere on the outside of the collapsed cluster.

By studying the clustering properties of the gas phase of the Janus fluid, Sciortino et al. discovered that below the critical temperature there is a range of temperatures where there is formation of two kinds of preferred clusters: the micelles and the vesicles. In the former the particles

^a e-mail: rfantoni27@sun.ac.za

tend to arrange themselves into a spherical shell and in the latter they tend to arrange themselves as two concentric spherical shells.

It is important to confront existing cluster theories with these new findings based on computer experiments. In this work the Bjerrum cluster theory for electrolytes, later extended by Tani and Henderson [15] to include trimers, has been employed (preliminary results appeared in Ref. [16]) for the description of the exact equilibrium cluster concentrations found in the computer experiment of Sciortino et al. The theory is extended to clusters of up to 12 particles in an attempt to reproduce the micellisation phenomenon observed in the simulations around a reduced temperature of 0.27. A different determination of the intra-cluster configurational partition function has been devised in place of the one used by Lee et al. [17].

The Kern and Frenkel fluid has been used to describe soft matter [18] biological and non-biological materials like globular proteins in solution [6,19,20] and colloidal suspensions [6,21], or molecular liquids [22]. Recently there has been a tremendous development in the techniques for the synthesis of patchy colloidal particles [23,24] in the laboratory. These are particles with dimensions of $10\text{--}10^4$ Å in diameter, which obey to Boltzmann statistics¹. From the realm of patchy colloidal particles stems the family of Janus particles for their simplicity [25,26]. It is possible to create Janus particles in the laboratory in large quantities [27] and to study their clustering properties [28,29].

The micelles and the vesicles are complex structures observed in the chemistry of surfactant molecules analogous to those which may be found in the physical biology of the cell [30].

The paper is organized as follows: in Section 2 we describe the fluid model, in Section 3 we present the clustering properties of the fluid found in the Monte Carlo simulations of Sciortino et al., the cluster theory is presented and developed in Sections 4 and 5, in Section 6 we compare the numerical results from our approximation to the exact results of Sciortino et al., and Section 7 is for final remarks.

2 The Kern and Frenkel model

As in the work of Sciortino et al. [14] we use the Kern and Frenkel [6] single patch hard-sphere model of the Janus fluid. Two spherical particles attract via a square-well potential only if the line joining the centers of the two spheres intercepts the patch on the surfaces of both particles. The pair-potential is separated as follows:

$$\Phi(1, 2) = \phi(r_{12})\Psi(\hat{\mathbf{n}}_1, \hat{\mathbf{n}}_2, \hat{\mathbf{r}}_{12}), \quad (1)$$

¹ The quantum effects start playing a role when the de Broglie thermal wavelength $\Lambda = \sqrt{2\pi\hbar^2/(k_B T m)}$ becomes comparable to the particle diameter σ . At room temperature this means that the nanoparticles should have a mass of the order of 10^{-26} kg whereas the microparticles should have a mass of the order of 10^{-32} kg.

where

$$\phi(r) = \begin{cases} +\infty & r < \sigma \\ -\epsilon & \sigma < r < \lambda\sigma \\ 0 & \lambda\sigma < r \end{cases} \quad (2)$$

and

$$\Psi(\hat{\mathbf{n}}_1, \hat{\mathbf{n}}_2, \hat{\mathbf{r}}_{12}) = \begin{cases} 1 & \text{if } \hat{\mathbf{n}}_1 \cdot \hat{\mathbf{r}}_{12} \geq \cos\theta_0 \\ & \text{and } -\hat{\mathbf{n}}_2 \cdot \hat{\mathbf{r}}_{12} \geq \cos\theta_0 \\ 0 & \text{otherwise} \end{cases} \quad (3)$$

where θ_0 is the angular semi-amplitude of the patch. Here $\hat{\mathbf{n}}_i(\omega_i)$ are versors pointing from the center of sphere i to the center of the attractive patch, with ω_i their solid angles and $\hat{\mathbf{r}}_{12}(\Omega)$ is the versor pointing from the center of sphere 1 to the center of sphere 2, with Ω its solid angle. We denote with σ the hard core diameter and $\lambda = 1 + \Delta/\sigma$ with Δ the width of the attractive well.

A particle configuration is determined by its position and its orientation.

We will use σ as the unit of length and ϵ as the unit of energy.

One can determine the fraction of the particle surface covered by the attractive patch as follows

$$\chi = \langle \Psi(\hat{\mathbf{n}}_1, \hat{\mathbf{n}}_2, \hat{\mathbf{r}}_{12}) \rangle_{\omega_1, \omega_2}^{1/2} = \sin^2\left(\frac{\theta_0}{2}\right), \quad (4)$$

where $\langle \dots \rangle_{\omega} = \int \dots d\omega / (4\pi)$.

As in the work of Sciortino et al. [14] we limit ourselves to the Janus case $\chi = 1/2$.

3 Clustering properties

The Janus fluid just described will undergo clustering as there is a directional attractive component in the interaction between its particles. Moreover at low temperatures the collapsed clusters are expected to interact weakly with each other. This is responsible for the bending at high density of the low temperature gas branch of the gas-liquid binodal curve recently determined in reference [14]. Below the critical temperature, in the vapour phase, the appearance of weakly interacting clusters destabilizes the liquid phase in favour of the gas phase. Sciortino et al. during their canonical ensemble (at fixed number of particles N , volume V , and temperature T , with $\rho = N/V$ the density) Monte Carlo simulations of the fluid also studied its clustering properties. In particular they used the following topological definition of a cluster: an ensemble of n particles form a cluster when, starting from one particle, is possible to reach all other particles through a path. The path being allowed to move from one particle to another if there is attraction between the two particles. During the simulation of the fluid they counted the number N_n of clusters of n particles, which depends on the particles configurations, and took a statistical average of this number.

We show in Figure 1 the results they obtained for $\Delta = \sigma/2$ at a reduced density $\rho\sigma^3 = 0.01$ and various reduced

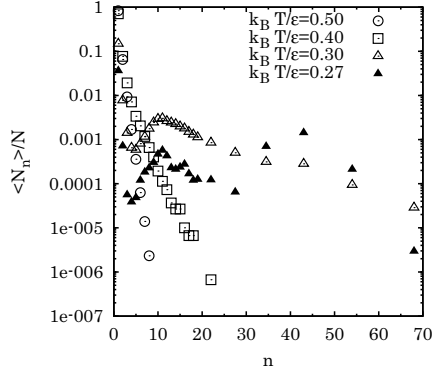


Fig. 1. Exact cluster concentrations of the Janus fluid with $\Delta = \sigma/2$ at a reduced density $\rho\sigma^3 = 0.01$ and various reduced temperatures $k_B T/\epsilon$, from the Monte Carlo simulation of Sciortino et al. [14].

temperatures $k_B T/\epsilon$. From the figure we can see how at a reduced temperature of 0.27, in the vapour phase, there is the formation of two kinds of preferred clusters: one made up of around 10 particles and one made up of around 40 particles.

In their collapsed shape, expected at low temperatures, the particles in the clusters tend to expose their inactive hemisphere on the outside of the cluster, resulting in a weak interaction between pairs of clusters.

In the clusters of around 10 particles the particles tend to arrange themselves into a spherical shell, forming a micellar structure. In the clusters of around 40 particles the particles are arranged into two concentric spherical shells, forming a vesicular structure.

The aim of the present work is to see if we can approximate the exact equilibrium cluster concentrations found in the simulation using a cluster theory. We will restrict ourselves to clusters made of up to 12 particles to see if the theory is able to reproduce the micellisation phenomenon. The theory is described next.

4 A cluster theory for Janus particles

Following reference [15], we describe the fluid of N particles undergoing clustering as a mixture of N species of clusters. Clusters of species $n = 1, \dots, N$, which we call n -clusters, are made up of n particles. We denote with N_n the number of clusters of species n and with $\rho_n = N_n/V$ their density. We assume that the chemical potentials of all the cluster species are zero (there is no cost in energy in the formation or destruction of a cluster). Then the grand-canonical partition function of the fluid can be written as

$$Q_{\text{tot}} = \sum_{\{N_n\}} \prod_{n=1}^N \frac{1}{N_n!} (q_n^{\text{intra}})^{N_n} Q_{\text{inter}}(\{N_n\}, V, T), \quad (5)$$

where one separates the coordinates and momenta relative to the center of mass of a cluster from the ones of the center of mass so that q_n^{intra} will be the intra-cluster partition function of the cluster of species n and Q_{inter} the inter-cluster partition function where we consider the clusters as non identical. The prime indicates that the sum is restricted by the condition that the number of particles of the fluid is N ,

$$\sum_{n=1}^N n N_n = N. \quad (6)$$

We approximate Q_{tot} assuming that the sum can be replaced by its largest dominant contribution. Using the Stirling approximation $N! \approx (N/e)^N$ one then obtains

$$\ln Q_{\text{tot}} \approx \sum_{n=1}^N [N_n \ln q_n^{\text{intra}} - (N_n \ln N_n - N_n)] + \ln Q_{\text{inter}}. \quad (7)$$

The maximum of $\ln Q_{\text{tot}}$ as a function of $\{N_n\}$ on the constraint of equation (6) is given by the point $\{\bar{N}_n\}$ where the gradients of $\ln Q_{\text{tot}}$ and of the constraint have the same direction. Introducing a Lagrange multiplier λ the equilibrium cluster distribution $\{\bar{N}_n\}$ is then found from the conditions

$$\left. \frac{\partial}{\partial N_n} \ln Q_{\text{tot}} \right|_{\{N_n = \bar{N}_n\}} + \ln \lambda^n = 0, \quad n = 1, 2, 3, \dots \quad (8)$$

The resulting Helmholtz free energy, $\beta F_{\text{tot}} = -\ln Q_{\text{tot}}$, can then be written in terms of the intra-cluster free energy, $\beta f_n^{\text{intra}} = -\ln q_n^{\text{intra}}$, and the inter-cluster partition function as follows

$$\frac{\beta F_{\text{tot}}}{V} = \sum_{n=1}^N [\bar{\rho}_n \ln \bar{\rho}_n - \bar{\rho}_n] + \sum_{n=1}^N \bar{\rho}_n \beta f_n^{\text{intra}} + \sum_{n=1}^N \bar{\rho}_n \ln V - \frac{1}{V} \ln Q_{\text{inter}}, \quad (9)$$

where $\beta = 1/k_B T$ with k_B Boltzmann constant and $\bar{\rho}_n = \bar{N}_n/V$.

We expect the equilibrium cluster concentrations, \bar{N}_n/N , to approximate the ones measured in the simulation, $\langle N_n \rangle / N$.

5 Relationship between the configurational partition functions

We will assume that equation (5) also holds at the level of the configurational partition functions Z , as follows

$$Z_{\text{tot}} = \sum_{\{N_n\}} \prod_{n=1}^N \frac{1}{N_n!} (z_n^{\text{intra}})^{N_n} Z_{\text{inter}}(\{N_n\}, V, T). \quad (10)$$

In the calculation we only work at the level of the configurational partition functions.

Since we expect the clusters to be weakly interacting amongst themselves we will approximate the inter-clusters configurational partition function with: (i) the ideal gas approximation for pointwise clusters and (ii) the Carnahan-Starling approximation [31] for clusters of diameter σ_0 . A third possibility, that we have not investigated, would be to use the Boublik et al. approximation [32,33] for clusters of different diameters σ_n .

We will only work with a limited number n_c of different cluster species. Since we are investigating whether the cluster theory is able to reproduce the micellisation phenomenon we will only consider the first n_c clusters: $n = 1, 2, 3, \dots, n_c$. And choosing $n_c = 12$.

We will describe next the two approximations used for the inter-cluster configurational partition function.

5.1 Ideal gas approximation

The simplest possibility is to approximate the mixture of clusters as an ideal one so that

$$Z_{\text{inter}} = V^{N_t}, \quad (11)$$

where $N_t = \sum_n N_n$ is the total number of clusters.

The equations for the equilibrium numbers of clusters are

$$\bar{N}_n = \lambda^n V z_n^{\text{intra}}, \quad n = 1, 2, 3, \dots, n_c \quad (12)$$

$$N = \sum_n n \bar{N}_n, \quad (13)$$

from which we can determine all the concentrations \bar{N}_n/N and the Lagrange multiplier by solving the resulting algebraic equation of order n_c . The case $n_c = 2$ is described in Appendix A.

5.2 Carnahan-Starling approximation

A better approximation is found if we use as the inter-cluster configurational partition function the Carnahan-Starling expression [31] for hard-spheres of diameter σ_0 ,

$$\ln Z_{\text{inter}} = N_t \ln V - N_t \frac{\eta_t(4 - 3\eta_t)}{(1 - \eta_t)^2}, \quad (14)$$

where $\eta_t = (\pi/6)\rho_t\sigma_0^3$ is the clusters packing fraction and $\rho_t = N_t/V$ their density.

In this case one needs to solve a system of $n_c + 1$ coupled transcendental equations,

$$\bar{N}_n = \lambda^n V z_n^{\text{intra}} G(\bar{\eta}_t), \quad i = 1, 2, 3, \dots, n_c \quad (15)$$

$$N = \sum_n n \bar{N}_n, \quad (16)$$

with $\bar{\eta}_t = (\pi/6)\bar{\rho}_t\sigma_0^3$, $\bar{\rho}_t = \bar{N}_t/V$, $\bar{N}_t = \sum_n \bar{N}_n$, and

$$G(x) = \exp \left[-\frac{x(8 - 9x + 3x^2)}{(1 - x)^3} \right]. \quad (17)$$

In order to search for the correct root of this system of equations it is important to choose the one that is continuously obtained from the physical solution of the ideal gas approximation as $\sigma_0 \rightarrow 0$. Giving a volume to the clusters we introduce correlations between them which will prove to be essential for a qualitative reproduction of the micellisation phenomenon though the cluster theory. The Carnahan-Starling approximation amounts to choosing for the sequence of virial coefficients of the hard-spheres, a general term which is a particular second order polynomial and to determine the polynomial coefficients that approximate the third virial coefficient by its closest integer [31]. It could be interesting to repeat the calculation using for the inter-cluster partition function the hard-spheres one choosing all but the first virial coefficient equal to zero, to see if that is sufficient to reproduce the micellisation phenomena.

Note that in order to study the vesicles we would have to solve a system of around 40 coupled equations.

We will describe next how we determine the intra-cluster configurational partition function z_n^{intra} .

5.3 The intra-cluster configurational partition function

To estimate the intra-cluster configurational partition function we performed Monte Carlo simulations of an isolated topological cluster.

We determined the reduced excess internal energy per particle of the n -cluster $u_n^{\text{ex}} = \langle \sum_{i < j} \Phi(i, j) \rangle / (n\epsilon)$ ($u_1^{\text{ex}} = 0$ by definition) as a function of the temperature, and then used thermodynamic integration to determine the intra-cluster configurational partition function.

We found that the results for $u_n^{\text{ex}}(T^*)$ can be fitted by a Gaussian as follows

$$u_n^{\text{ex}}(T^*) = a_n e^{-b_n T^{*2}} + c_n, \quad (18)$$

with $T^* = k_B T / \epsilon$ the reduced temperature.

Given the excess free energy of the n -cluster $F_n^{\text{ex, intra}}$, we can then determine $f_n^{\text{ex, intra}} = \beta F_n^{\text{ex, intra}} / n$ as follows

$$\begin{aligned} f_n^{\text{ex, intra}}(\beta^*) &= \int_0^{\beta^*} u_n^{\text{ex}}(1/x) dx \\ &= c_n \beta^* + a_n \sqrt{b_n} \left\{ \frac{e^{-b_n/\beta^{*2}}}{\sqrt{b_n/\beta^{*2}}} \right. \\ &\quad \left. + \sqrt{\pi} \left[\operatorname{erf} \left(\sqrt{b_n/\beta^{*2}} \right) - 1 \right] \right\}, \quad (19) \end{aligned}$$

with $\beta^* = 1/T^*$ and $v_0 = \pi\sigma_0^3/6$ the volume of the n -cluster. Then the intra-cluster configurational partition function is given by $z_n^{\text{intra}} = v_0^n \exp(-n f_n^{\text{ex, intra}})$ with $z_1^{\text{intra}} = v_0$.

We studied only the first 10 clusters with $n = 3, \dots, 12$. The dimer being trivial. To this end we started with an initial configuration of two pentagons with particles at

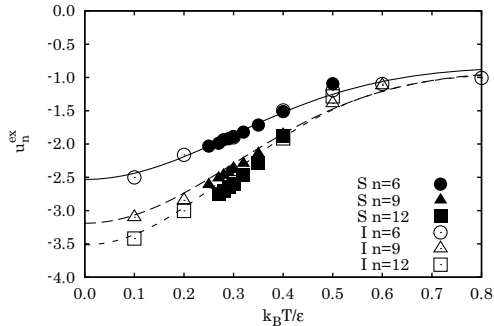


Fig. 2. Reduced excess internal energy per particle as a function of temperature for the 6-, 9-, and 12-cluster. The results from the isolated (I) cluster calculation are compared with the results of Sciortino (S) for the Janus fluid with $\Delta = \sigma/2$ at a reduced density $\rho\sigma^3 = 0.01$. Also shown is the Gaussian fit of equation (18).

their vertexes juxtaposed one above the other. The two pentagons are parallel to the (x, y) plane, have the z axis passing through their centers, and are placed one at $z = +\sigma/2$ and the other at $z = -\sigma/2$. The particles patches all point towards the origin. We formed the clusters with a lower number of particles by simply deleting particles and the clusters with 11 and 12 particles by adding a particle on the z axis just above the upper pentagon and just below the lower one.

We performed the simulations of the isolated cluster at a fictitious reduced density of $\rho\sigma^3 = 0.05$ which ensured a simulation box big enough that the cluster did not percolate through the periodic boundary conditions. We also compared our results for the excess internal energy calculation for the isolated cluster with the results of Sciortino et al. for the low density Janus fluid, from which one extracts cluster information by taking all the clusters found with the same number of particles and averaging their properties, as shown in Figure 2.

At high temperatures the limiting value for the excess internal energy per particle of the isolated n -cluster is $-\epsilon(n-1)/n$ corresponding to the stretched cluster. At low temperature ($T^* < 0.15$) the cluster tends to freeze into certain energy minima. So in order to reach the absolute minimum we used the following smoothing procedure. We smoothed the Kern and Frenkel potential by choosing

$$\Psi(\hat{\mathbf{n}}_1, \hat{\mathbf{n}}_2, \hat{\mathbf{r}}_{12}) = \{\tanh[l(\hat{\mathbf{n}}_1 \cdot \hat{\mathbf{r}}_{12} - \cos\theta_0)] + 1\} \times \{\tanh[l(-\hat{\mathbf{n}}_2 \cdot \hat{\mathbf{r}}_{12} - \cos\theta_0)] + 1\}/4. \quad (20)$$

We then gradually changed the parameter l , during the simulation, starting from $1/2$ and increasing up to values where there is no actual difference between the smoothed potential and the original stepwise one. The reduced excess internal energy per particle and gyration radii for such minimum energy configurations are shown in Table 1.

Table 1. The low temperature reduced excess internal energy per particle $\langle U \rangle / (\epsilon n)$ (U is the potential energy of the cluster) of the clusters with up to 12 particles when $\Delta = \sigma/2$. Also shown is the gyration radius $R_g^2 = \sum_{i=1}^n |\mathbf{r}_i - \mathbf{r}_{cm}|^2 / n$ with $\mathbf{r}_{cm} = \sum_{i=1}^n \mathbf{r}_i / n$, \mathbf{r}_i being the position of the i th particle in the cluster.

n	$\langle U \rangle / (\epsilon n)$	$\langle U \rangle / \epsilon$	R_g
1	0	0	0
2	-0.5	-1	$\sim 1/2$
3	-1	-3	$\sim 1/\sqrt{3}$
4	-1.5	-6	0.83
5	-2.0	-10	0.76
6	-2.50	-15	0.75
7	-2.71	-19	0.91
8	-2.88	-23	0.93
9	-3.10	-28	0.96
10	-3.20	-32	1.00
11	-3.36	-37	1.04
12	-3.42	-41	1.08

In the Metropolis algorithm [34] used to sample the probability distribution function proportional to $e^{-\beta U}$, where U is the potential energy of the cluster, the random walk moves through the configuration space of the particles forming the cluster through two kinds of moves: a displacement of the particle position and a rotation of the particle (through the Marsaglia algorithm [35]). We followed two different strategies in the simulations: (i) we averaged only over the particles configurations that form a cluster and (ii) we explicitly modified the acceptance probability by rejecting moves that break the cluster. So in the second strategy all the moves are counted in the averages. The two strategies turned out to give the same results, as they should. The second strategy is preferable to simulate the bigger clusters at high temperature and for small well widths because there is no loss of statistics.

In Appendix B we present the results for the reduced excess internal energy of the isolated clusters as a function of temperature and their fit of equation (18).

5.4 Thermodynamic quantities

Once the equilibrium cluster distribution $\{\bar{N}_n\}$ has been determined (within the ideal gas or the Carnahan-Starling approximation for the inter-cluster partition function) the configurational partition function Z_{tot} is known. Then the excess free energy is

$$\beta F^{\text{ex}} = -\ln \left(\frac{Z_{\text{tot}}}{V^N} \right), \quad (21)$$

the reduced internal energy per particle of the fluid is

$$u = \frac{3}{2\beta^*} + \frac{1}{N} \frac{\partial(\beta F^{\text{ex}})}{\partial\beta^*} = \frac{3}{2\beta^*} - \sum_n \frac{\bar{N}_n}{N} \frac{\partial \ln z_n^{\text{intra}}}{\partial\beta^*} = \frac{3}{2\beta^*} + \sum_n n \frac{\bar{N}_n}{N} u_n^{\text{ex}}, \quad (22)$$

and its compressibility factor, in the Carnahan-Starling approximation for the inter-cluster configurational partition function, is

$$\frac{\beta P}{\rho} = \frac{1}{\rho} \frac{\partial \ln Z_{\text{tot}}}{\partial V} \approx \frac{1}{\bar{\rho}_t} \frac{\partial \ln Z_{\text{inter}}}{\partial V} = \frac{1 + \bar{\eta}_t + \bar{\eta}_t^2 - \bar{\eta}_t^3}{(1 - \bar{\eta}_t)^3}. \quad (23)$$

Here we have used the approximation $N \approx \bar{N}_t$ which turns out to be reasonable at the chosen value of the cluster diameter, as shown in Figure 4.

In Figure 6 we show the results for the compressibility factor and the reduced excess internal energy per particle. The reduced excess internal energy is compared with the Monte Carlo data of Sciortino et al. (Fig. 1 in Ref. [14]).

6 Results

We present here the numerical results from the cluster theory and compare them with the results of Sciortino et al. from the simulation of the Janus ($\chi = 1/2$) fluid with $\Delta = \sigma/2$.

We studied three different attraction ranges: $\Delta = \sigma/2$, $\Delta = \sigma/4$, and $\Delta = 0.15\sigma$. To the best of our knowledge there are no Monte Carlo results available for the two smaller ranges.

We only present the results obtained from the Carnahan-Starling approximation for the inter-cluster partition function as the ideal gas approximation turned out to be too crude an approximation even for a qualitative description of the exact clustering properties.

6.1 $\Delta = \sigma/2$

For $\Delta = \sigma/2$ we found the following results.

6.1.1 Equilibrium cluster concentrations

In Figure 3 we compare the Monte Carlo data of Sciortino et al. (the results reported in Fig. 1) and our results from the cluster theory. From the figure one can see that the ideal gas approximation for the inter-cluster partition function is not appropriate even at high temperatures in the single fluid phase above the critical point. In order to find agreement with the Monte Carlo data at high temperatures it is sufficient to give a volume to the clusters, treating them as hard-spheres of a diameter σ_0 . In the Carnahan-Starling approximation we gradually increased σ_0 from zero and found that for $\sigma_0 = 2.64\sigma$ the results of the cluster theory were in good agreement with the Monte Carlo data at $k_B T/\epsilon = 0.5$. Using the same cluster diameter at all other temperatures, we saw that the theory is able to qualitatively reproduce the micellisation phenomenon observed in the simulation of Sciortino et al.

The results also suggest that with a temperature-dependent cluster diameter, or more generally with a cluster diameter dependent on the thermodynamic state of the

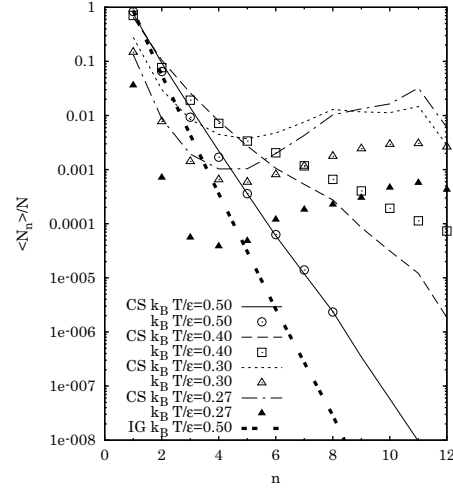


Fig. 3. Comparison between the Monte Carlo (MC) data (points) and the Carnahan-Starling (CS) approximation with $\sigma_0 = 2.64\sigma$ (lines) for the cluster concentrations $\langle N_n \rangle / N$, $n = 1, 2, 3, \dots, 12$, as a function of the cluster size n at $\rho\sigma^3 = 0.01$ and various temperatures. Also shown is the ideal gas (IG) approximation at the same density and the highest temperature $k_B T/\epsilon = 0.5$.

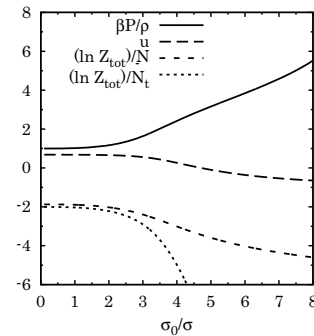


Fig. 4. The compressibility factor, the internal energy per particle, and the logarithm of the total partition function per total number of particles and per total number of clusters as a function of the clusters diameter σ_0 at the thermodynamic state $\rho\sigma^3 = 0.01$ and $k_B T/\epsilon = 0.5$ for $\Delta = 0.5\sigma$.

fluid, we could achieve better agreement between our approximation and the exact results. Our topological definition of a cluster has no direct geometrical interpretation. Other definitions with a geometrical nature are possible. For example Lee et al. in their studies of nucleation define an assembly of particles to be a cluster if they all lie within a sphere of radius σ_0 centered on one of the particles. In our simulations of the isolated clusters these have a globular shape at low temperature and a necklace shape at high temperature. The optimal cluster diameter $\sigma_0 = 2.64\sigma$ (found to give good agreement

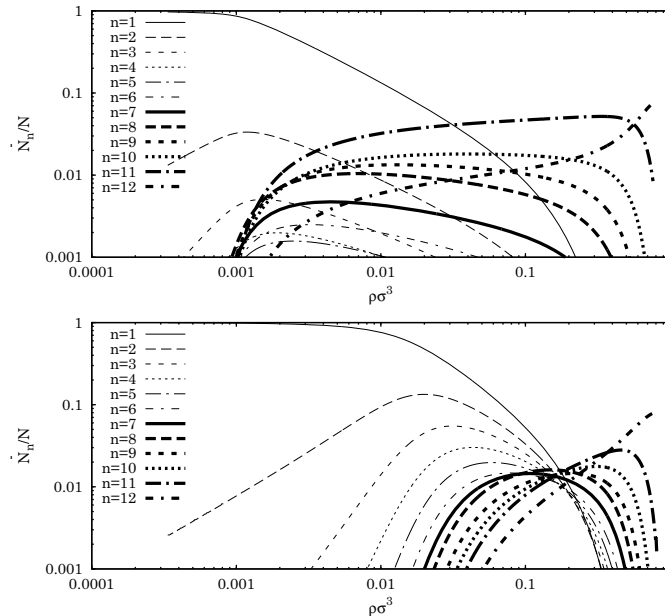


Fig. 5. The equilibrium cluster concentrations \bar{N}_n/N , $n = 1, 2, 3, \dots, 12$, as a function of density for $k_B T/\epsilon = 0.27$ (top panel) and $k_B T/\epsilon = 0.5$ (bottom panel) as obtained from the CS approximation with $\sigma_0 = 2.64\sigma$. Here $\Delta = \sigma/2$.

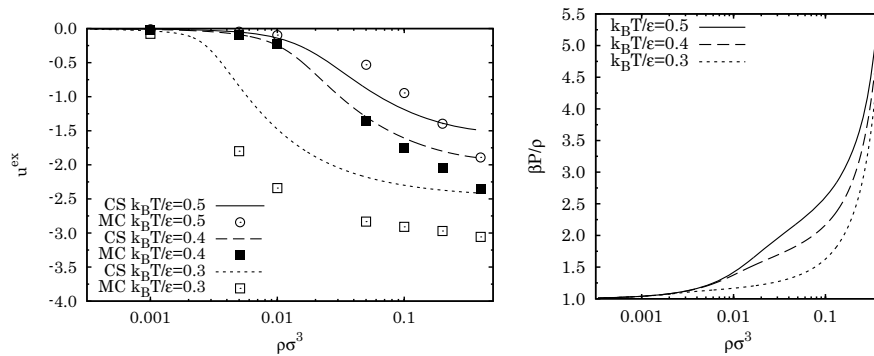


Fig. 6. The top panel shows the reduced excess internal energy per particle for three different values of temperature as a function of density. The results from the Carnahan-Starling (CS) approximation are compared with the Monte Carlo (MC) results of Sciortino et al. [14]. The bottom panel shows the compressibility factor for the same values of temperature as a function of density from the CS approximation (no MC data is available).

between the exact and approximate clusters concentrations at high temperature) suggests necklace clusters made up of around 3 particles or globular clusters made up of around $2\pi(\sigma_0/\sigma)^2/\sqrt{3} \approx 25$ particles placed on a spherical shell. Since σ_0 is the only free parameter of the theory, it is important to estimate how thermodynamic quantities like the compressibility factor $\beta P/\rho$, the reduced internal energy per particle u , and the logarithm of the total configurational partition function per number of particles, $\ln Z_{tot}/N$, or per number of clusters, $\ln Z_{tot}/N_t$, are sensi-

ble to variations in σ_0 . From Figure 4 we can see that for the thermodynamic state $\rho\sigma^3 = 0.01$ and $k_B T/\epsilon = 0.5$, the thermodynamic quantities are roughly independent of σ_0 for $\sigma_0 \lesssim 3\sigma$.

In Figure 5 we show the behaviour of the equilibrium cluster concentrations, from the Carnahan-Starling approximation with $\sigma_0 = 2.64\sigma$, as a function of density at $k_B T/\epsilon = 0.27$.

From the figure we can see that at very low densities there are essentially no clusters. But as the density

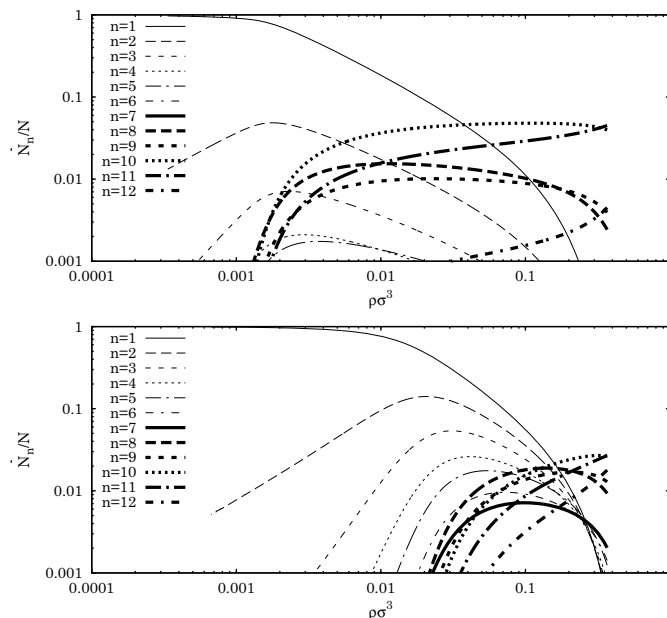


Fig. 7. Same as Figure 5 for $\Delta = \sigma/4$.

increases, clusters of an increasing number of particles appear in the fluid. In particular, at $k_B T/\epsilon = 0.27$ there is an interval of densities where clusters of 11 particles are preferred.

6.1.2 Thermodynamic quantities

Following Section 5.4 we now use the cluster theory within the Carnahan-Starling approximation with $\sigma_0 = 2.64\sigma$ to extract thermodynamic information for the Janus fluid. In Figure 6 we show the results obtained for the excess reduced internal energy per particle and the compressibility factor.

From the figure we see that there is a qualitative agreement between the results of the cluster theory and the Monte Carlo results. No Monte Carlo results are available for the compressibility factor.

6.2 $\Delta = \sigma/4$

Decreasing the width of the attractive well to $\Delta = \sigma/4$ yielded the results shown in Figure 7. We see that now, at the reduced temperature 0.27, the preferred clusters are the ones made up of 10 particles.

6.3 $\Delta = 0.15\sigma$

Decreasing the width of the attractive well even further to $\Delta = 0.15\sigma$, we obtained the results of Figure 8. Now, at the reduced temperature 0.27, there is a range of densities

around $\rho\sigma^3 = 0.1$ where the preferred clusters are made up of 7 or 8 particles.

7 Conclusions

We constructed a cluster theory for a fluid undergoing clustering and showed that it is able to reproduce the micellisation phenomena recently observed in the simulation of the vapour phase of Kern and Frenkel Janus particles [14]. A topological definition of the cluster is used. We determined the intra-cluster configurational partition function through thermodynamic integration of the excess internal energy of the cluster, estimated through Monte Carlo simulations of an isolated cluster. In the simulation we restricted the random walk through the configurations of the particles that compose the cluster by rejecting the moves that break the cluster. Due to the geometrical characteristics of the pair-potential it is expected that the clusters, when in their collapsed shape, will be very weakly interacting amongst themselves as the Janus particles will expose the hard-sphere hemisphere on the outside of the cluster. We thus used for the estimation of the inter-cluster configurational partition function first the simple ideal gas approximation for pointwise clusters and then the Carnahan-Starling approximation for clusters seen as hard-spheres of diameter σ_0 . The equilibrium cluster concentrations obtained with the ideal gas approximation turned out to disagree, even at high temperatures, with the ones obtained from the simulation of the fluid [14] and were not able to reproduce the micellisation phenomenon in the vapour phase. We then gradually

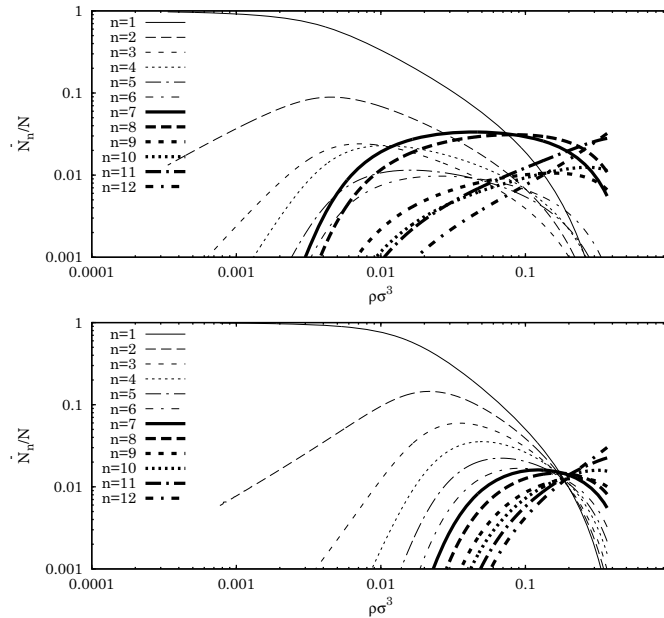


Fig. 8. Same as Figure 5 for $\Delta = 0.15\sigma$.

increased σ_0 from zero until we found good agreement between the equilibrium cluster concentrations obtained with the Carnahan-Starling approximation and the concentrations from the simulation of the fluid [14] at high temperature (above the critical point). Using the same value of σ_0 for lower temperatures (below the critical point) we were able to qualitatively reproduce the micellisation phenomenon observed in the simulation of the fluid [14] around a reduced temperature of 0.27 and a reduced density of 0.01. This result is important for two reasons. Firstly it shows that the clustering fundamentally arising from the canonical ensemble description of the fluid of particles can be approximated by a grand canonical ensemble description of a particular clustered fluid. Secondly the second description, which assumes from the start a clustered structure of the fluid, is much less computationally costly than the first. Unlike most previous works on cluster theories where the aim is usually to avoid the Monte Carlo simulation [15,36], our approach is a hybrid one where we still use the Monte Carlo experiment to determine the intra-cluster properties. Of course our goal can only be a qualitative description of the fluid as we specifically prescribe a particular description of the clusters and this is the source of our approximation.

Studying the behaviour of the equilibrium cluster concentrations as a function of density and temperature, we saw that the micellisation phenomenon only takes place within a particular range of temperatures (below the critical point) and densities (in the vapour phase).

Once the equilibrium concentrations have been found it is possible to determine how the cluster theory approxi-

mates the thermodynamic quantities of the fluid. We find qualitative agreement between the Monte Carlo data of Sciortino et al. [14] and our approximation for the excess internal energy of the vapour phase. For the compressibility factor no Monte Carlo data is available so our results remain a theoretical prediction.

We studied three different values of the attractive square-well width: $\Delta = \sigma/2$, $\Delta = \sigma/4$, and $\Delta = 0.15\sigma$. Monte Carlo results [14] are available only for the largest width. Our study shows that as the range of the attraction diminishes the micelles tend to be made up of a smaller number of particles.

A related interesting problem to that just discussed is the one of trying to give a definition of a liquid drop expected to form in the coexistence region as a result of the condensation instability.

I would like to acknowledge the support of the National Institute for Theoretical Physics of South Africa.

Appendix A: Connection with Wertheim association theory

At small χ , allowing only clusters of one (monomers) and two (dimers) particles, we get

$$\bar{N}_1 = \lambda V z_1^{\text{intra}}, \tag{A.1}$$

$$\bar{N}_2 = \lambda^2 V z_2^{\text{intra}}, \tag{A.2}$$

$$N = \bar{N}_1 + 2\bar{N}_2, \tag{A.3}$$

Table B.1. The tables refer from left to right to clusters made up of $n = 3, 4, \dots, 12$ particles. U is the potential energy of a cluster of n particles. Below $k_B T/\epsilon = 0.1$ the reduced excess internal energy per particle remains roughly constant in all cases: the smoothing procedure described in Section 5.3 was used. The data was obtained with a Monte Carlo simulation over 5 million steps where one step consists of n particles moves. The strategy (i) described in Section 5.3 was used in the simulations.

$k_B T/\epsilon$	$\langle U \rangle/(\epsilon n)$	Error	$k_B T/\epsilon$	$\langle U \rangle/(\epsilon n)$	Error	$k_B T/\epsilon$	$\langle U \rangle/(\epsilon n)$	Error	$k_B T/\epsilon$	$\langle U \rangle/(\epsilon n)$	Error
∞	-0.666	0	∞	-0.75	0	∞	-0.8	0	∞	-0.833	0
0.8	-0.724	0.001	0.8	-0.849	0.004	0.8	-0.942	0.009	0.8	-1.01	0.03
0.6	-0.747	0.001	0.6	-0.898	0.004	0.6	-0.995	0.008	0.6	-1.10	0.02
0.5	-0.769	0.002	0.5	-0.961	0.005	0.5	-1.085	0.008	0.5	-1.19	0.01
0.4	-0.807	0.001	0.4	-1.081	0.004	0.4	-1.322	0.007	0.4	-1.49	0.01
0.3	-0.877	0.001	0.3	-1.278	0.003	0.3	-1.606	0.004	0.3	-1.899	0.009
0.2	-0.9663	0.0008	0.2	-1.460	0.002	0.2	-1.792	0.003	0.2	-2.16	0.01
0.1	-1	≈ 0	0.1	-1.5	≈ 0	0.1	-2.0	≈ 0	0.1	-2.5	0

$k_B T/\epsilon$	$\langle U \rangle/(\epsilon n)$	Error	$k_B T/\epsilon$	$\langle U \rangle/(\epsilon n)$	Error	$k_B T/\epsilon$	$\langle U \rangle/(\epsilon n)$	Error	$k_B T/\epsilon$	$\langle U \rangle/(\epsilon n)$	Error
∞	-0.857	0	∞	-0.875	0	∞	-0.888	0	∞	-0.9	0
0.8	-1.04	0.04	0.8	-1.06	0.05	0.8	-	-	0.8	-	-
0.6	-1.12	0.02	0.6	-1.25	0.05	0.6	-1.12	0.03	0.6	-	-
0.5	-1.28	0.02	0.5	-1.27	0.02	0.5	-1.39	0.03	0.5	-1.36	0.04
0.4	-1.68	0.02	0.4	-1.82	0.02	0.4	-1.87	0.02	0.4	-1.88	0.02
0.3	-2.11	0.04	0.3	-2.26	0.01	0.3	-2.38	0.01	0.3	-2.46	0.02
0.2	-2.39	0.03	0.2	-2.60	0.02	0.2	-2.85	0.02	0.2	-2.94	0.03
0.1	-2.7	≈ 0	0.1	-2.9	≈ 0	0.1	-3.1	≈ 0	0.1	-3.2	≈ 0

$k_B T/\epsilon$	$\langle U \rangle/(\epsilon n)$	Error	$k_B T/\epsilon$	$\langle U \rangle/(\epsilon n)$	Error
∞	-0.909	0	∞	-0.916	0
0.8	-	-	0.8	-	-
0.6	-	-	0.6	-	-
0.5	-1.35	0.03	0.5	-1.28	0.04
0.4	-1.96	0.03	0.4	-1.92	0.04
0.3	-2.55	0.02	0.3	-2.57	0.02
0.2	-3.09	0.09	0.2	-3.00	0.02
0.1	-3.36	≈ 0	0.1	-3.42	≈ 0

which is a quadratic equation in λ . The solution for the fraction of patches that are not bonded (fraction of monomers) is

$$\bar{\rho}_1 = \frac{2}{\rho \sqrt{1 + 8\rho\bar{\Delta}}}, \quad (\text{A.4})$$

with $\bar{\Delta} = z_2^{\text{intra}}/[z_1^{\text{intra}}]^2$ and $\rho = N/V$ the density of the fluid, in accord, at low T , with the recent analysis of Sciortino et al. [37] (compare their X of Eq. (10) with our $\bar{\rho}_1/\rho$ and their Δ with our $\bar{\Delta}$), based on Wertheim association theory [38–41]. Our theory, contrary to the one of Wertheim, allows to consider the case of multiple bonding of the patch.

At high temperature our $\bar{\Delta}$ differs from the Δ of reference [37] but in this limit the clusters begin to dissociate.

Appendix B: Tables for the excess internal energy per particle of the clusters

We present here the results for the reduced excess internal energy per particle as a function of temperature of the

isolated n -cluster with $n = 2, 3, \dots, 12$ as obtained from our Monte Carlo simulations.

In Table B.1 we show the results at $\Delta = 0.5\sigma$ obtained with the strategy (i) described in Section 5.3. The smoothing procedure described in Section 5.3 was used at the lowest temperature. The excess internal energy per particle of the $n = 2$ cluster is always $-\epsilon/2$ given our topological definition of a cluster.

In Table B.2 we show the results at $\Delta = 0.5\sigma$ obtained with strategy (ii) described in Section 5.3. The smoothing procedure described in Section 5.3 was not used at the lowest temperature. Comparing Tables B.1 and B.2 we can see that the two strategies lead to the same results.

In Table B.3 we show the results at $\Delta = 0.25\sigma$ obtained with strategy (i) described in Section 5.3. The smoothing procedure described in Section 5.3 was not used at the lowest temperature.

In Table B.4 we show the results at $\Delta = 0.15\sigma$ obtained with strategy (ii) described in Section 5.3. The smoothing procedure described in Section 5.3 was not used at the lowest temperature.

In Table B.5 we give the fit to the Gaussian of equation (18) of the reduced excess internal energy per particle as a function of the temperature.

Table B.2. The tables refer, from left to right, to clusters made up of $n = 3, 4, 10, 11$ particles. U is the potential energy of a cluster of n particles. The smoothing procedure described in Section 5.3 was not used at the lowest temperature. The strategy (ii) described in Section 5.3 was used in the simulations.

$k_B T/\epsilon$	$\langle U \rangle / (\epsilon n)$	Error	$k_B T/\epsilon$	$\langle U \rangle / (\epsilon n)$	Error	$k_B T/\epsilon$	$\langle U \rangle / (\epsilon n)$	Error	$k_B T/\epsilon$	$\langle U \rangle / (\epsilon n)$	Error
∞	-0.666	0	∞	-0.75	0	∞	-0.9	0	∞	-0.909	0
0.8	-0.7211	0.0002	0.8	-0.8466	0.0005	0.8	-1.066	0.001	0.8	-1.078	0.002
0.6	-0.7437	0.0003	0.6	-0.8995	0.0009	0.6	-1.200	0.003	0.6	-1.215	0.003
0.5	-0.7659	0.0004	0.5	-0.959	0.001	0.5	-1.418	0.009	0.5	-1.423	0.008
0.4	-0.8052	0.0005	0.4	-1.073	0.002	0.4	-1.884	0.009	0.4	-1.90	0.01
0.3	-0.8723	0.0007	0.3	-1.280	0.002	0.3	-2.46	0.01	0.3	-2.52	0.02
0.2	-0.9647	0.0005	0.2	-1.4597	0.0009	0.2	-2.96	0.03	0.2	-3.13	0.04
0.1	-0.99881	0.00005	0.1	-1.49871	0.00006	0.1	-3.1982	0.0006	0.1	-3.16	0.01

Table B.3. Same as Table B.1 but with $\Delta = 0.25\sigma$. The smoothing procedure described in Section 5.3 was not used at the lowest temperature.

$k_B T/\epsilon$	$\langle U \rangle / (\epsilon n)$	Error	$k_B T/\epsilon$	$\langle U \rangle / (\epsilon n)$	Error	$k_B T/\epsilon$	$\langle U \rangle / (\epsilon n)$	Error	$k_B T/\epsilon$	$\langle U \rangle / (\epsilon n)$	Error
∞	-0.666	0	∞	-0.75	0	∞	-0.8	0	∞	-0.833	0
0.7	-0.705	0.002	0.7	-	-	0.7	-0.87	0.02	0.7	-	-
0.5	-0.732	0.002	0.5	-0.866	0.007	0.5	-1.00	0.03	0.5	-0.95	0.01
0.3	-0.832	0.002	0.3	-1.138	0.005	0.3	-1.427	0.008	0.3	-1.63	0.01
0.1	-0.99872	0.00008	0.1	-1.4987	0.0002	0.1	-1.7984	0.0002	0.1	-2.1656	0.0002

$k_B T/\epsilon$	$\langle U \rangle / (\epsilon n)$	Error	$k_B T/\epsilon$	$\langle U \rangle / (\epsilon n)$	Error	$k_B T/\epsilon$	$\langle U \rangle / (\epsilon n)$	Error	$k_B T/\epsilon$	$\langle U \rangle / (\epsilon n)$	Error
∞	-0.857	0	∞	-0.875	0	∞	-0.888	0	∞	-0.9	0
0.7	-	-	0.7	-	-	0.7	-	-	0.7	-	-
0.5	-0.95	0.01	0.5	-	-	0.5	-	-	0.5	-	-
0.3	-1.79	0.01	0.3	-1.91	0.03	0.3	-1.95	0.02	0.3	-2.07	0.04
0.1	-2.22	0.02	0.1	-2.3706	0.0009	0.1	-2.4416	0.0005	0.1	-2.5969	0.0006

$k_B T/\epsilon$	$\langle U \rangle / (\epsilon n)$	Error	$k_B T/\epsilon$	$\langle U \rangle / (\epsilon n)$	Error	$k_B T/\epsilon$	$\langle U \rangle / (\epsilon n)$	Error	$k_B T/\epsilon$	$\langle U \rangle / (\epsilon n)$	Error
∞	-0.909	0	∞	-0.916	0						
0.7	-	-	0.7	-	-						
0.5	-	-	0.5	-	-						
0.3	-2.10	0.04	0.3	-2.01	0.03						
0.1	-2.721	0.002	0.1	-2.730	0.008						

Table B.4. Same as Table B.1 but with $\Delta = 0.15\sigma$. The smoothing procedure described in Section 5.3 was not used at the lowest temperature. The strategy (ii) described in Section 5.3 was used in the simulation.

$k_B T/\epsilon$	$\langle U \rangle / (\epsilon n)$	Error	$k_B T/\epsilon$	$\langle U \rangle / (\epsilon n)$	Error	$k_B T/\epsilon$	$\langle U \rangle / (\epsilon n)$	Error	$k_B T/\epsilon$	$\langle U \rangle / (\epsilon n)$	Error
∞	-0.666	0	∞	-0.75	0	∞	-0.8	0	∞	-0.833	0
0.7	-0.6914	0.0003	0.7	-0.7903	0.0007	0.7	-0.8473	0.0009	0.7	-0.884	0.001
0.5	-0.7114	0.0004	0.5	-0.826	0.002	0.5	-0.895	0.002	0.5	-0.936	0.002
0.3	-0.792	0.001	0.3	-1.138	0.005	0.3	-1.230	0.008	0.3	-1.35	0.01
0.1	-0.9987	0.0002	0.1	-1.49871	0.00006	0.1	-1.7989	0.0001	0.1	-1.9985	0.0004

$k_B T/\epsilon$	$\langle U \rangle / (\epsilon n)$	Error	$k_B T/\epsilon$	$\langle U \rangle / (\epsilon n)$	Error	$k_B T/\epsilon$	$\langle U \rangle / (\epsilon n)$	Error	$k_B T/\epsilon$	$\langle U \rangle / (\epsilon n)$	Error
∞	-0.857	0	∞	-0.875	0	∞	-0.888	0	∞	-0.9	0
0.7	-0.913	0.001	0.7	-0.928	0.001	0.7	-0.945	0.001	0.7	-0.956	0.001
0.5	-0.955	0.002	0.5	-0.980	0.003	0.5	-1.000	0.003	0.5	-1.013	0.004
0.3	-1.61	0.03	0.3	-1.63	0.03	0.3	-1.55	0.06	0.3	-1.56	0.05
0.1	-2.2848	0.0001	0.1	-2.371	0.001	0.1	-2.51	0.04	0.1	-2.396	0.001

$k_B T/\epsilon$	$\langle U \rangle / (\epsilon n)$	Error	$k_B T/\epsilon$	$\langle U \rangle / (\epsilon n)$	Error	$k_B T/\epsilon$	$\langle U \rangle / (\epsilon n)$	Error	$k_B T/\epsilon$	$\langle U \rangle / (\epsilon n)$	Error
∞	-0.909	0	∞	-0.916	0						
0.7	-0.9655	0.0009	0.7	-0.973	0.001						
0.5	-1.022	0.004	0.5	-1.033	0.002						
0.3	-1.61	0.03	0.3	-1.59	0.02						
0.1	-2.5427	0.0004	0.1	-2.66	0.004						

Table B.5. Fit to the Gaussian of equation (18) of the reduced excess internal energy per particle of the first eleven n -clusters as a function of temperature.

n	$\Delta = 0.5\sigma$		$\Delta = 0.25\sigma$		$\Delta = 0.15\sigma$		$c_n = -(n-1)/n$
	a_n	b_n	a_n	b_n	a_n	b_n	
2	0	1	0	1	0	1	-0.5
3	-0.337525	3.88039	-0.33890	6.9050	-0.345587	10.7799	-0.666666
4	-0.778556	4.66976	-0.77059	7.5017	-0.773523	7.97531	-0.75
5	-1.22587	5.16189	-1.0248	5.8901	-1.03428	9.36621	-0.8
6	-1.69844	5.59919	-1.3810	7.3613	-1.20676	9.21365	-0.83333
7	-1.89814	5.26287	-1.4235	6.7666	-1.47964	8.27638	-0.85714
8	-2.06452	5.07916	-1.5201	4.1792	-1.55091	8.50313	-0.875
9	-2.30070	5.47737	-1.5793	4.3672	-1.68144	10.1592	-0.88888
10	-2.39363	5.50909	-1.7253	4.2708	-1.55096	9.41914	-0.9
11	-2.55636	5.64409	-1.8464	4.8294	-1.69591	9.75528	-0.90909
12	-2.59747	6.07744	-1.8541	5.7234	-1.81374	10.5661	-0.91666

References

- T.L. Hill, *Statistical Mechanics* (McGraw-Hill, New York, 1956)
- J.-P. Hansen, I.R. McDonald, *Theory of simple liquids*, 3rd edn. (Elsevier, USA, 2006)
- B.J. Alder, T.E. Wainwright, *J. Chem. Phys.* **27**, 1208 (1957)
- L. Vega, E. de Miguel, L.F. Rull, G. Jackson, I.A. McLure, *J. Chem. Phys.* **96**, 2296 (1992)
- H. Liu, S. Garde, S. Kumar, *J. Chem. Phys.* **123**, 174505 (2005)
- N. Kern, D. Frenkel, *J. Chem. Phys.* **118**, 9882 (2003)
- L.N. Cooper, *Phys. Rev.* **104**, 1189 (1956)
- A. Lenard, *J. Math. Phys.* **2**, 682 (1961)
- E.H. Hauge, P.C. Hemmer, *Physica Norvegica* **5**, 209 (1971)
- J.M. Kosterlitz, D.J. Thouless, *J. Phys. C Solid State Phys.* **6**, 1181 (1973)
- A. Lerda, *Anyons* (Springer-Verlag, New York, 1992)
- C. Valeriani, P.J. Camp, J.W. Zwaniikken, R. Van Roij, M. Dijkstra, *J. Phys.: Condens. Matter* **22**, 104122 (2010)
- L. Rovigatti, J. Russo, F. Sciortino, *Phys. Rev. Lett.* **107**, 237801 (2011)
- F. Sciortino, A. Giacometti, G. Pastore, *Phys. Rev. Lett.* **103**, 237801 (2009)
- A. Tani, D. Henderson, *J. Chem. Phys.* **79**, 2390 (1983)
- R. Fantoni, A. Giacometti, F. Sciortino, G. Pastore, *Soft Matt.* **7**, 2419 (2011)
- J.K. Lee, J.A. Barker, F.F. Abraham, *J. Chem. Phys.* **58**, 3166 (1973)
- P.G. de Gennes, *Rev. Mod. Phys.* **64**, 645 (1992)
- A. Giacometti, F. Lado, J. Largo, G. Pastore, F. Sciortino, *J. Chem. Phys.* **132**, 174110 (2010)
- F. Romano, E. Sanz, F. Sciortino, *J. Chem. Phys.* **132**, 184501 (2010)
- F. Romano, F. Sciortino, *Soft Matt.* **7**, 5799 (2011)
- F. Romano, E. Sanz, F. Sciortino, *J. Chem. Phys.* **134**, 174502 (2011)
- S.C. Glotzer, M.J. Solomon, *Nature Mater.* **6**, 557 (2007)
- A.B. Pawar, I. Kretzchmar, *Macromol. Rapid Comm.* **31**, 150 (2010)
- C. Casagrande, P. Fabre, M. Veyssié, E. Raphaël, *Europhys. Lett.* **9**, 251 (1989)
- A. Walther, A.H. Müller, *Soft Matt.* **4**, 663 (2008)
- L. Hong, S. Jiang, S. Granick, *Langmuir* **22**, 9495 (2006)
- L. Hong, A. Cacciuto, E. Luijten, S. Granick, *Nano Lett.* **6**, 2510 (2006)
- L. Hong, A. Cacciuto, E. Luijten, S. Granick, *Langmuir* **24**, 621 (2008)
- R. Phillips, J. Kondev, J. Theriot, *Physical Biology of the Cell* (Gerland Science, Taylor & Francis Group, 2008), Problem 9.4
- N.F. Carnahan, K.E. Starling, *J. Chem. Phys.* **51**, 635 (1969)
- T. Boublík, *J. Chem. Phys.* **53**, 471 (1970)
- G.A. Mansoori, N.F. Carnahan, K.E. Starling, T.W. Leland Jr., *J. Chem. Phys.* **54**, 1523 (1971)
- M.H. Kalos, P.A. Whitlock, *Monte Carlo Methods* (Wiley-VCH Verlag GmbH & Co., Germany, 2008)
- M.P. Allen, D.J. Tildesley, *Computer Simulation of Liquids* (Oxford University Press, 1987), Appendix G.4
- J.-M. Caillol, J.-J. Weis, *J. Chem. Phys.* **102**, 7610 (1995), and references therein
- F. Sciortino, E. Bianchi, J.F. Douglas, P. Tartaglia, *J. Chem. Phys.* **126**, 194903 (2007)
- M.S. Wertheim, *J. Stat. Phys.* **35**, 19 (1984)
- M.S. Wertheim, *J. Stat. Phys.* **35**, 35 (1984)
- M.S. Wertheim, *J. Stat. Phys.* **42**, 459 (1986)
- M.S. Wertheim, *J. Stat. Phys.* **42**, 477 (1986)

Chapter 29

Two Component Plasma in a Flamm's Paraboloid

Fantoni R., J. Stat. Mech. 04015 (2012)

Title: "Two Component Plasma in a Flamm's Paraboloid"

Abstract: The two component plasma (TCP) living in a Flamm's paraboloid is studied at a value of the coupling constant $\Gamma = 2$ for which an analytic expression for the grand canonical partition function is available. Two cases are considered, the plasma in the half surface with an insulating horizon and the plasma in the whole surface. The Green's function equation necessary to determine the n -particle truncated correlation functions is explicitly found. In both cases this proves too complicated to be solved analytically. So we present the method of solution reducing the problem to finding the two linearly independent solutions of a linear homogeneous second order ordinary differential equation with polynomial coefficients of high degrees. In the flat limit one recovers the solution for the structure of the TCP in a plane in the first case but the collapse of opposite charges at the horizon makes the structure of the plasma physically not well defined in the second case.

Two component plasma in a Flamm's paraboloid

Riccardo Fantoni

National Institute for Theoretical Physics (NITheP) and Institute of Theoretical Physics, University of Stellenbosch, Stellenbosch 7600, South Africa
E-mail: rfantoni27@sun.ac.za

Received 28 February 2012

Accepted 3 April 2012

Published 25 April 2012

Online at stacks.iop.org/JSTAT/2012/P04015

[doi:10.1088/1742-5468/2012/04/P04015](https://doi.org/10.1088/1742-5468/2012/04/P04015)

Abstract. The two component plasma (TCP) living in a Flamm's paraboloid is studied at a value of the coupling constant $\Gamma = 2$ for which an analytic expression for the grand canonical partition function is available. Two cases are considered: the plasma in the half surface with an insulating horizon and the plasma in the whole surface. The Green's function equation necessary to determine the n -particle truncated correlation functions is explicitly found. In both cases this proves too complicated to be solved analytically. Therefore we present a method of solution reducing the problem to finding the two linearly independent solutions of a linear homogeneous second order ordinary differential equation with polynomial coefficients of high degrees. In the flat limit one recovers the solution for the structure of the TCP in a plane in the first case but the collapse of opposite charges at the horizon means that the structure of the plasma is physically not well defined in the second case.

Keywords: algebraic structures of integrable models, classical integrability, correlation functions, rigorous results in statistical mechanics

Contents

1. Introduction	2
2. The Flamm's paraboloid \mathcal{S}	3
3. The Coulomb potential created by a point charge	5
4. The two component plasma model	6
5. TCP in a half surface with an insulating horizon	6
5.1. Symmetries of the Green's function R	8
5.2. Two-body truncated correlation functions and the perfect screening sum rule	8
5.3. From the structure to the thermodynamics	9
5.4. Determination of the Green's function R	9
5.5. Method of solution	11
6. TCP in the whole surface	11
7. Conclusions	14
Acknowledgment	15
References	15

1. Introduction

The two component plasma (TCP) is a neutral mixture of point wise particles of charge $\pm q$. The equation of state of the TCP living in a plane has been known since the work of Salzberg and Prager [1]. In the plasma the attraction between oppositely charged particles competes with the thermal motion and makes the partition function of the finite system diverge when $\Gamma = \beta q^2 \geq 2$, where $\beta = 1/k_B T$ with k_B the Boltzmann constant. The system becomes unstable against the collapse of pairs of oppositely charged particles, and as a consequence all thermodynamic quantities diverge, so that the point particle model is well behaved only for $\Gamma < 2$ [2] when the Boltzmann factor for unlike particles is integrable at small separations of the charges. In this case rescaling the particle coordinates so as to stay in the unit disk one easily proves that the grand canonical partition function is a function of $\sqrt{\lambda_- \lambda_+} V^{(1-\Gamma/4)}$, where V is the volume of the plasma and λ_{\pm} are the fugacities of the two charge species, and as a consequence the equation of state is $\beta P = n(1 - \Gamma/4)$, where $n = n_+ + n_-$ is the total particle number density. It also follows that the ratio $\sqrt{\lambda_- \lambda_+} / n^{(1-\Gamma/4)}$ must be a function of Γ only in the thermodynamic limit [3]. However, if the collapse is avoided by some short range repulsion (hard cores for instance), the model remains well defined for lower temperatures. Then, for $\Gamma > 4$ the long range Coulomb attraction binds positive and negative particles in pairs of finite polarizability. Thus, at

some critical value $\Gamma_c \sim 4$ the system undergoes the Kosterlitz–Thouless transition [4] between a high temperature ($\Gamma < 4$) conductive phase and a low temperature ($\Gamma > 4$) dielectric phase. The same behavior also occurs in the TCP living in one dimension [5].

The structure of the TCP living in a plane at the special value $\Gamma = 2$ of the coupling constant is solvable exactly analytically [6]. Through the use of an external potential it has also been studied in various confined geometries [7]–[10] and in a gravitational field [11, 12].

In curved surfaces it has only been studied in surfaces of constant curvature such as the sphere [13, 14] and the pseudosphere [15]. Unlike the one component plasma where the properties of the Vandermonde determinant allow analytical solution a Cauchy identity is used for the solution of the TCP. Unlike in the one component case where the solution is possible for the plasma confined in a region of the surface now this is not possible anymore without the use of an external potential. In these cases the external potential is rather given by $-(\Gamma/q^2) \ln \sqrt{g}$, where g is the determinant of the metric tensor.

In this work we study the TCP at the special value $\Gamma = 2$ of the coupling constant in a Flamm's paraboloid, a surface of non-constant curvature. In this surface the one component plasma [16] has been studied in various situations: confined to one 'universe' by an insulating or a grounded perfect conductor 'horizon' or in the whole surface. Here we will restrict ourselves to only the first and last situations.

In a curved surface, even though the finite system partition function will still be finite for $\Gamma < 2$ since the surface is locally flat, the structure will change with respect to the flat case. The purpose of the present work is to see how it changes for the special case $\Gamma = 2$ where an exact analytical solution is possible.

2. The Flamm's paraboloid \mathcal{S}

In this work, we want to study a two-dimensional TCP in the Flamm's paraboloid. This is a Riemannian surface \mathcal{S} with the following metric:

$$ds^2 = g_{\mu\nu} dx^\mu dx^\nu = \left(1 - \frac{2M}{r}\right)^{-1} dr^2 + r^2 d\varphi^2, \quad (1)$$

or $g_{rr} = 1/(1 - 2M/r)$, $g_{\varphi\varphi} = r^2$, and $g_{r\varphi} = 0$.

The Flamm's paraboloid is an embeddable surface in the three-dimensional Euclidean space. It is composed of two identical 'universes': \mathcal{S}_+ and \mathcal{S}_- . These are both multiply connected surfaces connected by a hole of radius $2M$. We will from now on call the $r = 2M$ region of the surface its 'horizon'. The scalar curvature is $R = -2M/r^3$.

The system of coordinates (r, φ) with the metric (1) has the disadvantage that it requires two charts to cover the whole surface \mathcal{S} . It can be more convenient to use the variable

$$u = \pm \sqrt{\frac{r}{2M} - 1} \quad (2)$$

instead of r . This gives the following metric when using the system of coordinates (u, φ) :

$$ds^2 = 4M^2(1 + u^2)[4 du^2 + (1 + u^2) d\varphi^2]. \quad (3)$$

The region $u > 0$ corresponds to \mathcal{S}_+ and the region $u < 0$ to \mathcal{S}_- .

The Laplace–Beltrami operator is

$$\begin{aligned}\Delta f &= \frac{1}{\sqrt{g}} \frac{\partial}{\partial q^\mu} \left(\sqrt{g} g^{\mu\nu} \frac{\partial}{\partial q^\nu} \right) f \\ &= \left[\left(1 - \frac{2M}{r} \right) \partial_r^2 + \frac{1}{r^2} \partial_\varphi^2 + \left(\frac{1}{r} - \frac{M}{r^2} \right) \partial_r \right] f,\end{aligned}\quad (4)$$

where $\mathbf{q} \equiv (r, \varphi)$. Finding the Green's function of the Laplacian, naturally [16] leads us to consider the system of coordinates (s, φ) , with

$$s = (\sqrt{u^2 + 1} + u)^2. \quad (5)$$

The range for the variable s is $]0, +\infty[$. The lower paraboloid \mathcal{S}_- corresponds to the region $0 < s < 1$ and the upper one \mathcal{S}_+ to the region $s > 1$. A point in the upper paraboloid with coordinate (s, φ) has a mirror image by reflection ($u \rightarrow -u$) in the lower paraboloid, with coordinates $(1/s, \varphi)$, since if

$$s = (\sqrt{u^2 + 1} + u)^2 \quad (6)$$

then

$$\frac{1}{s} = (\sqrt{u^2 + 1} - u)^2. \quad (7)$$

In the upper paraboloid \mathcal{S}_+ , the new coordinate s can be expressed in terms of the original one, r , as

$$s = \frac{(\sqrt{r} + \sqrt{r - 2M})^2}{2M}. \quad (8)$$

Using this system of coordinates, the metric takes the form of a flat metric multiplied by a conformal factor

$$ds^2 = \frac{M^2}{4} \left(1 + \frac{1}{s} \right)^4 (ds^2 + s^2 d\varphi^2). \quad (9)$$

The Laplacian also takes a simple form

$$\Delta f = \frac{s}{\sqrt{g}} \Delta_{\text{flat}} f, \quad (10)$$

where

$$\Delta_{\text{flat}} f = \partial_s^2 f + \frac{1}{s} \partial_s f + \frac{1}{s^2} \partial_\varphi^2 f \quad (11)$$

is the Laplacian of the flat Euclidean space \mathbb{R}^2 . The square root of the determinant of the metric is now given by $\sqrt{g} = (M/2)^2 s(1 + s^{-1})^4$.

It is useful to keep in mind the following small M behaviors:

$$s = 2 \frac{r}{M} - 2 - \frac{1}{2} \frac{M}{r} - \frac{1}{2} \left(\frac{M}{r} \right)^2 - \frac{5}{8} \left(\frac{M}{r} \right)^3 + O(M^4), \quad (12)$$

$$\sqrt{g} = \frac{rM}{2} + \frac{M^2}{2} + \frac{5M^3}{8r} + O(M^4). \quad (13)$$

3. The Coulomb potential created by a point charge

We here summarize the results found in [16] on the determination of the Coulomb potential between two charges living in a half Flamm's paraboloid with an insulating horizon and between two charges living in the full Flamm's paraboloid.

The Coulomb potential $G(s, \varphi; s_0, \varphi_0)$ created at (s, φ) by a unit charge at (s_0, φ_0) is given by the Green's function of the Laplacian

$$\Delta G(s, \varphi; s_0, \varphi_0) = -2\pi\delta^{(2)}(s, \varphi; s_0, \varphi_0) \quad (14)$$

with appropriate boundary conditions. The Dirac distribution is given by

$$\delta^{(2)}(s, \varphi; s_0, \varphi_0) = \frac{1}{\sqrt{g}}\delta(s - s_0)\delta(\varphi - \varphi_0). \quad (15)$$

Notice that using the system of coordinates (s, φ) the Laplacian Green's function equation takes the simple form

$$\Delta_{\text{flat}} G(s, \varphi; s_0, \varphi_0) = -2\pi\frac{1}{s}\delta(s - s_0)\delta(\varphi - \varphi_0) \quad (16)$$

which is formally the same Laplacian Green's function equation as that for a flat space.

The Laplacian Green's function equation (14) can be solved, as usual, by using the decomposition as a Fourier series. Since equation (14) reduces to the flat Laplacian Green's function equation (16), the solution is the standard one

$$G(s, \varphi; s_0, \varphi_0) = \sum_{n=1}^{\infty} \frac{1}{n} \left(\frac{s_{<}}{s_{>}} \right)^n \cos[n(\varphi - \varphi_0)] + g_0(s, s_0) \quad (17)$$

where $s_{>} = \max(s, s_0)$ and $s_{<} = \min(s, s_0)$.

We consider now the case of particles restricted to live in the half surface (hs) \mathcal{S}_+ , $s > 1$, by a hard wall located at the 'horizon', $s = 1$. The region \mathcal{S}_- , $s < 1$, is empty and has the same dielectric constant as the upper region. We want to consider a model where the interaction potential reduces to the flat Coulomb potential in the flat limit $M \rightarrow 0$. The solution of the Laplacian Green's function equation is given in Fourier series by equation (17). The 0th order Fourier component g_0 can be determined by the requirement that, in the limit $M \rightarrow 0$, the solution reduces to the flat Coulomb potential

$$G^{\text{flat}}(\mathbf{r}, \mathbf{r}') = -\ln \frac{|\mathbf{r} - \mathbf{r}'|}{L}, \quad (18)$$

where L is an arbitrary constant length. Recalling that $s \sim 2r/M$, when $M \rightarrow 0$, we find

$$g_0(s, s_0) = -\ln s_{>} - \ln \frac{M}{2L} \quad (19)$$

and in the half surface

$$G^{\text{hs}}(s, \varphi; s_0, \varphi_0) = -\ln |z - z_0| - \ln \frac{M}{2L}, \quad (20)$$

where we defined $z = se^{i\varphi}$ and $z_0 = s_0e^{i\varphi_0}$. And $\lim_{M \rightarrow 0} G^{\text{hs}} = G^{\text{flat}}$ as desired.

A similar procedure [16] gives the Coulomb potential between charges living in the whole surface (ws) $0 < s < \infty$,

$$G^{\text{ws}}(s, \varphi; s_0, \varphi_0) = -\ln \frac{|z - z_0|}{\sqrt{|zz_0|}} - \ln \frac{L_0}{L}, \quad (21)$$

with L_0 another length scale.

4. The two component plasma model

The TCP is a neutral mixture of two species of point charges of charge $\pm q$. In this work we want to study the plasma in the Flamm's paraboloid. In [16] the Coulomb potential between two charges living in the whole paraboloid, in a half surface with an insulating horizon, and in a half surface with a grounded horizon was found. The first and last cases have been summarized in section 3 as they will be the two cases considered next.

5. TCP in a half surface with an insulating horizon

When the TCP lives in a half surface with an insulating horizon the Coulomb potential is given by equation (20). We will use $u_i = s_i e^{i\varphi_i}$ and $v_j = s_j e^{i\varphi_j}$ to denote the complex coordinates of the positively and negatively charged particles respectively, where $s = (\sqrt{r} + \sqrt{r-2M})^2/2M > 1$. Then, following [6], we use a Cauchy identity [17] to rewrite $e^{-\beta U_{2N}}$, where U_{2N} is the potential energy of a neutral system of N positive and N negative charges, as follows:

$$\begin{aligned} \exp \left\{ 2 \sum_{i < j} \left[\ln \left| \frac{u_i - u_j}{2L/M} \right| + \ln \left| \frac{v_i - v_j}{2L/M} \right| \right] - 2 \sum_{i,j} \ln \left| \frac{u_i - v_j}{2L/M} \right| \right\} \\ = \left(\frac{2L}{M} \right)^{2N} \left| \frac{\prod_{i < j} (u_i - u_j)(v_i - v_j)}{\prod_{i,j} (u_i - v_j)} \right|^2 \\ = \left(\frac{2L}{M} \right)^{2N} \left| \det \left(\frac{1}{u_i - v_j} \right)_{(i,j) \in \{1, \dots, N\}^2} \right|^2, \end{aligned} \quad (22)$$

where we had to choose the particular case of a coupling constant $\Gamma = \beta q^2 = 2$.

Following [6], to avoid divergences we start from a discretized model in which two sub-lattices U and V are introduced. The positive (negative) particles sit on the sub-lattice U (V). Each lattice site is occupied by no or one particle. The grand canonical partition function defined as a sum including only neutral systems is then

$$\Xi = 1 + \sum_{N=1}^{\infty} \left(\frac{2L}{M} \right)^{2N} \lambda_-^N \lambda_+^N \sum_{\substack{u_1, \dots, u_N \in U \\ v_1, \dots, v_N \in V}} \left| \det \left(\frac{1}{u_i - v_j} \right)_{(i,j) \in \{1, \dots, N\}^2} \right|^2, \quad (23)$$

where the sums are defined with the prescription that configurations which differ only by a permutation of identical particles are counted only once, and λ_p is the constant fugacity of the charges of species $p = \pm$. This grand partition function is the determinant of an anti-Hermitian matrix \mathbf{M} explicitly shown in [7].

When passing to the continuum limit in the element \mathbf{M}_{ij} one should replace u_i or v_i by z and u_j or v_j by z' , i.e. $i \rightarrow z$ and $j \rightarrow z'$. Each lattice site is characterized by its complex coordinate z and an isospinor which is $\begin{pmatrix} 1 \\ 0 \end{pmatrix}$ if the site belongs to the positive sub-lattice U and $\begin{pmatrix} 0 \\ 1 \end{pmatrix}$ if it belongs to the negative sub-lattice V . We then define a matrix

\mathcal{M} by

$$\langle z|\mathcal{M}|z'\rangle = \frac{\sigma_x + i\sigma_y}{2} \frac{2L/M}{z - z'} + \frac{\sigma_x - i\sigma_y}{2} \frac{2L/M}{\bar{z} - \bar{z}'}, \quad (24)$$

where the σ s are the 2×2 Pauli matrices operating in the isospinor space, and $z = x + iy$.

The matrix \mathcal{M} can be expressed in terms of a simple Dirac operator

$$\langle z|\mathcal{M}|z'\rangle = \frac{2L}{M} (\sigma_x \partial_x + \sigma_y \partial_y) \ln |z - z'|, \quad (25)$$

and the grand partition function can be rewritten as

$$\begin{aligned} \Xi &= \det \left\{ \mathbf{1} \delta^{(2)}(z; z') + \left[\lambda_+ \frac{\mathbf{1} + \sigma_z}{2} + \lambda_- \frac{\mathbf{1} - \sigma_z}{2} \right] \langle z|\mathcal{M}|z'\rangle \right\} \\ &= \det[\mathbf{I} + \mathbf{K}^{-1}], \end{aligned} \quad (26)$$

with $\mathbf{I} = \mathbf{1} \delta^{(2)}(z; z')$ and

$$\lambda = \lambda_+ \frac{\mathbf{1} + \sigma_z}{2} + \lambda_- \frac{\mathbf{1} - \sigma_z}{2}, \quad (27)$$

$$\mathbf{K}^{-1} = \lambda \mathcal{M}. \quad (28)$$

Then, since $\Delta_{\text{flat}} \ln |z| = 2\pi\delta(s)\delta(\varphi)/s = 2\pi\delta(z)$ (where $s = |z|$ and $\delta(z)$ is the flat Dirac delta function), the inverse operator \mathbf{K} is

$$\mathbf{K} = \mathbf{m}^{-1}(z)\mathbf{O}, \quad (29)$$

where

$$\mathbf{m}(z) = m_+(z) \frac{\mathbf{1} + \sigma_z}{2} + m_-(z) \frac{\mathbf{1} - \sigma_z}{2}, \quad (30)$$

$$\mathbf{O} = \frac{2}{M} (\sigma_x \partial_x + \sigma_y \partial_y). \quad (31)$$

Here $m_{\pm}(z) = (2\pi L \lambda_{\pm} \sqrt{g}/sS)(2/M)^2$ are rescaled position dependent fugacities, $g = \det(g_{\mu\nu})$, and S is the area per lattice site which appears when the discrete sums are replaced by integrals. Notice that in the flat limit $M \rightarrow 0$ we find $m_{\pm} \rightarrow \tilde{m}_{\pm}$, where $\tilde{m}_{\pm} = 2\pi L \lambda_{\pm}/S$ are the rescaled fugacities of the flat system [7, 6]. Moreover S is a local property of the surface independent from its curvature.

We then find

$$\ln \Xi = \text{Tr} \{ \ln [\mathbf{I} + \mathbf{K}^{-1}] \},$$

and the one-body densities and n -body truncated densities can be obtained in the usual way by taking functional derivatives of the logarithm of the grand partition function with respect to the fugacities λ_{\pm} . Marking the sign of the particle charge at z_i by an index $p_i = \pm 1$, and defining the matrix

$$R_{p_1 p_2}(z_1, z_2) = \langle z_1 p_1 | \mathbf{K}^{-1} (\mathbf{I} + \mathbf{K}^{-1})^{-1} | z_2 p_2 \rangle, \quad (32)$$

it can then be shown [6, 7] that they are given by

$$\rho_{p_1}^{(1)}(z_1) = R_{p_1 p_1}(z_1, z_1), \quad (33)$$

$$\rho_{p_1 p_2}^{(2)T}(z_1, z_2) = -R_{p_1 p_2}(z_1, z_2)R_{p_2 p_1}(z_2, z_1), \quad (34)$$

$$\rho_{p_1 p_2, \dots, p_n}^{(n)T}(z_1, z_2, \dots, z_n) = (-)^{n+1} \sum_{(i_1, i_2, \dots, i_n)} R_{p_{i_1} p_{i_2}}(z_{i_1}, z_{i_2}) \cdots R_{p_{i_n} p_{i_1}}(z_{i_n}, z_{i_1}), \quad (35)$$

where $m_p(z) = (2\pi L \lambda_p \sqrt{g}/sS)(2/M)^2 = (\tilde{m}_p \sqrt{g}/s)(2/M)^2$, $\tilde{m}_p = 2\pi L \lambda_p/S$, $\sqrt{g} = (M/2)^2 s(1+1/s)^4$, and the summation runs over all cycles (i_1, i_2, \dots, i_n) built with $\{1, 2, \dots, n\}$.

5.1. Symmetries of the Green's function R

Since $\mathbf{m}^\dagger(z) = \mathbf{m}(z)$ and $\mathbf{O}^\dagger = -\mathbf{O}$ we find

$$\overline{R_{p_1 p_2}(z_1, z_2)} = \langle z_2 p_2 | \mathbf{m}^{-1} \mathbf{O} (\mathbf{I} - \mathbf{m}^{-1} \mathbf{O})^{-1} (\mathbf{m}^{-1} \mathbf{O})^{-1} | z_1 p_1 \rangle. \quad (36)$$

Expanding in \mathbf{O} (by using $(\mathbf{I} - \mathbf{m}^{-1} \mathbf{O})^{-1} = \mathbf{I} + \mathbf{m}^{-1} \mathbf{O} + (\mathbf{m}^{-1} \mathbf{O})^2 + \dots$) and comparing with the definition $R_{p_1 p_2}(z_1, z_2) = \langle z_1 p_1 | (\mathbf{m}^{-1} \mathbf{O})^{-1} (\mathbf{I} + \mathbf{m}^{-1} \mathbf{O})^{-1} \mathbf{m}^{-1} \mathbf{O} | z_2 p_2 \rangle$ we find

$$\overline{R_{pp}(z_1, z_2)} = R_{pp}(z_2, z_1), \quad (37)$$

$$\overline{R_{p-p}(z_1, z_2)} = -R_{-pp}(z_2, z_1), \quad (38)$$

from which it also follows that $R_{pp}(z_1, z_1)$ has to be real. If $\lambda_+ = \lambda_-$ then we additionally must have

$$R_{pp}(z_1, z_2) = R_{-p-p}(z_1, z_2). \quad (39)$$

5.2. Two-body truncated correlation functions and the perfect screening sum rule

For the two-body truncated correlation functions of equation (34) we then find

$$\rho_{++}^{(2)T}(z_1, z_2) = -|R_{++}(z_1, z_2)|^2, \quad (40)$$

$$\rho_{+-}^{(2)T}(z_1, z_2) = |R_{+-}(z_1, z_2)|^2. \quad (41)$$

Notice that the total correlation function for the like particles $h_{++}(z_1, z_2) = \rho_{++}^{(2)T}(z_1, z_2)/\rho_+^{(1)}(z_1)\rho_+^{(1)}(z_2)$ goes to -1 when the particles coincide, $z_1 \rightarrow z_2$, as follows from the structure of equations (33) and (34). Moreover, the truncated densities of any order have to decay to zero as the two groups of particles are infinitely separated. In particular, $|R_{++}(z_1, z_2)| = |R_{++}(s_1, s_2; \varphi)|$, with $\varphi = \varphi_1 - \varphi_2$, has to decay to zero as $|s_1 - s_2| \rightarrow \infty$.

The perfect screening sum rule has to be satisfied for the symmetric mixture

$$\int [\rho_{+-}^{(2)T}(z_1, z_2) - \rho_{++}^{(2)T}(z_1, z_2)] \sqrt{g_1} ds_1 d\varphi_1 = \rho_{\pm}(z_2), \quad (42)$$

where g_1 is g calculated on particle 1.

5.3. From the structure to the thermodynamics

Following [12], we note that if we solve the eigenvalue problem $\mathbf{K}\psi_n = \lambda_n\psi_n$ (here ψ_n is a spinor of components $\psi_{+,n}$ and $\psi_{-,n}$), then

$$\Xi = \prod_n \left(1 + \frac{1}{\lambda_n} \right). \tag{43}$$

Now the eigenvalue problem reads

$$\{m_+(z) + A[m_-(z)]^{-1}A^\dagger\}\psi_-(z) = (m_-(z) - \lambda^2)\psi_-(z), \tag{44}$$

$$\{m_-(z) + A^\dagger[m_+(z)]^{-1}A\}\psi_+(z) = (m_-(z) - \lambda^2)\psi_+(z), \tag{45}$$

where $A = (2/M)(\partial_x + i\partial_y)$ and $A^\dagger = (2/M)(-\partial_x + i\partial_y)$ and the left-hand side is the same as the left-hand side for the Green's functions equations (48) and (49).

Of course we know that the thermodynamic quantities all diverge in our $\Gamma = 2$ case so equation (43), although suggestive, is of small practical interest.

5.4. Determination of the Green's function \mathbf{R}

The Green's function matrix \mathbf{R} is the solution of a system of four coupled partial differential equations, namely

$$(\mathbf{I} + \mathbf{K}^{-1})\mathbf{K}\mathbf{R}(z_1, z_2) = (\mathbf{I} + \mathbf{K})\mathbf{R}(z_1, z_2) = \mathbf{1}\delta^{(2)}(z_1; z_2), \tag{46}$$

where $\delta^{(2)}(z_1; z_2) = \delta^{(2)}(s, \varphi; s_0, \varphi_0) = (\sqrt{g})^{-1}\delta(s - s_0)\delta(\varphi - \varphi_0)$ is the Dirac delta function in the curved surface, $\delta(s - s_0)\delta(\varphi - \varphi_0)/s = \delta(s, \varphi; s_0, \varphi_0) = \delta(z; z_0)$ is the flat Dirac delta function, and $\mathbf{1}$ is the identity matrix. These can be rewritten as follows:

$$[\mathbf{O} + \mathbf{m}(z_1)]\mathbf{R}(z_1, z_2) = \mathbf{m}(z_1)\delta^{(2)}(z_1; z_2).$$

If instead of \mathbf{R} one uses $\mathbf{R} = \mathbf{G}\tilde{\mathbf{m}}$, \mathbf{G} satisfies the equation

$$[\mathbf{O} + \mathbf{m}(z_1)]\mathbf{G}(z_1, z_2) = \frac{4}{M^2}\mathbf{1}\delta(z_1; z_2), \tag{47}$$

where $\delta(z_1; z_2)$ is now the flat Dirac delta function¹.

By combining the components of this equation one obtains decoupled equations for G_{++} and G_{--} as follows:

$$\{m_+(z_1) + A^\dagger[m_-(z_1)]^{-1}A\}G_{++}(z_1, z_2) = \frac{4}{M^2}\delta(s_1, \varphi_1; s_2, \varphi_2), \tag{48}$$

$$\{m_-(z_1) + A[m_+(z_1)]^{-1}A^\dagger\}G_{--}(z_1, z_2) = \frac{4}{M^2}\delta(s_1, \varphi_1; s_2, \varphi_2), \tag{49}$$

while

$$G_{-+}(z_1, z_2) = -[m_-(z_1)]^{-1}AG_{++}(z_1, z_2), \tag{50}$$

$$G_{+-}(z_1, z_2) = +[m_+(z_1)]^{-1}A^\dagger G_{--}(z_1, z_2). \tag{51}$$

¹ The same result could have been reached by noticing that the partition function of equation (23) rewritten in the continuum is equivalent to the partition function of the flat system with position dependent fugacities $\zeta_p(s) = \lambda_p(M/2)^2(1 + 1/s)^4(2L/M)$. This leads naturally [7] to definition of a Green's function $\tilde{\mathbf{G}} = (M/2)\mathbf{G}$ which satisfies the equation $[(M/2)\mathbf{O} + (2\pi/S)\zeta(z)]\tilde{\mathbf{G}}(z, z') = \mathbf{1}\delta(z; z')$, which reduces to equation (47).

Then equation (48) can be rewritten in Cartesian coordinates as

$$\begin{aligned} & \left\{ m_+(z_1)m_-(z_1) - \left(\frac{2}{M}\right)^2 \left[(\partial_{x_1}^2 + \partial_{y_1}^2) - \frac{4(-x_1 + iy_1)}{s_1^2(1+s_1)}(\partial_{x_1} + i\partial_{y_1}) \right] \right\} G_{++}(z_1, z_2) \\ &= \left(\frac{2}{M}\right)^4 \frac{\tilde{m}_-\sqrt{g_1}}{s_1^2} \delta(s_1 - s_2) \delta(\varphi_1 - \varphi_2) = \left(\frac{2}{M}\right)^4 \frac{\tilde{m}_-\sqrt{g_1}}{\sqrt{x_1^2 + y_1^2}} \\ & \quad \times \delta(x_1 - x_2) \delta(y_1 - y_2), \end{aligned} \quad (52)$$

where $s = \sqrt{x^2 + y^2}$. From the expression of the gradient in polar coordinates it follows that

$$\partial_x = \cos \varphi \partial_s - \frac{\sin \varphi}{s} \partial_\varphi, \quad \partial_y = \sin \varphi \partial_s + \frac{\cos \varphi}{s} \partial_\varphi, \quad (53)$$

Which allows us to rewrite equation (52) in polar coordinates as

$$\begin{aligned} & \left[\tilde{m}_+\tilde{m}_- \left(1 + \frac{1}{s_1}\right)^8 - \left(\frac{2}{M}\right)^2 \left(\frac{1}{s_1} \partial_{s_1} (s_1 \partial_{s_1}) + \frac{1}{s_1^2} \partial_{\varphi_1}^2 + \frac{4}{s_1(1+s_1)} \partial_{s_1} + \frac{4i}{s_1^2(1+s_1)} \partial_{\varphi_1} \right) \right] \\ & \quad \times G_{++}(z_1, z_2) = \left(\frac{2}{M}\right)^4 \frac{\tilde{m}_-\sqrt{g_1}}{s_1^2} \delta(s_1 - s_2) \delta(\varphi_1 - \varphi_2). \end{aligned} \quad (54)$$

From this equation we immediately see that $G_{++}(z_1, z_2)$ cannot be real. Notice that in the flat limit $M \rightarrow 0$ we have $s \sim 2r/M$ and equation (54) reduces to

$$\left[\tilde{m}_+\tilde{m}_- - \frac{1}{r_1} \partial_{r_1} (r_1 \partial_{r_1}) - \frac{1}{r_1^2} \partial_{\varphi_1}^2 \right] G_{++}(z_1, z_2) = \frac{\tilde{m}_-}{r_1} \delta(r_1 - r_2) \delta(\varphi_1 - \varphi_2), \quad (55)$$

which, when $\tilde{m}_+ = \tilde{m}_- = \tilde{m}$, has the following well known solution [7, 6]:

$$G_{++}(z_1, z_2) = \frac{\tilde{m}}{2\pi} K_0(\tilde{m}|\mathbf{r}_1 - \mathbf{r}_2|), \quad (56)$$

where K_0 is a modified Bessel function.

Let us from now on restrict ourselves to the case of equal fugacities of the two species. Then $\lambda_- = \lambda_+ = \lambda$ with

$$\tilde{m} = \frac{2\pi L}{S} \lambda = \frac{2\pi L e^{\beta\mu}}{\Lambda^2} = \left(2\pi L \frac{mq^2}{4\pi\hbar^2} \right) e^{2\mu/q^2}, \quad (57)$$

where \hbar is Planck's constant, m is the mass of the particles, and μ is the chemical potential. So \tilde{m} has the dimensions of an inverse length. From the symmetry of the problem we can say that $G_{++} = G_{++}(s_1, s_2; \varphi_1 - \varphi_2)$. We can then express the Green's function as the following Fourier series expansion:

$$G_{++}(s_1, s_2; \varphi) = \frac{1}{2\pi} \sum_{k=-\infty}^{\infty} g_{++}(s_1, s_2; k) e^{ik\varphi}. \quad (58)$$

Then, using the expansion of the Dirac delta function, $\sum_k e^{ik\varphi} = 2\pi\delta(\varphi)$, we find that g_{++} , a continuous real function symmetric under exchange of s_1 and s_2 , has to satisfy

the following equation:

$$[Q_0(k, s_1) + Q_1(s_1)\partial_{s_1} + Q_2(s_1)\partial_{s_1}^2]g_{++}(s_1, s_2; k) = \left(\frac{2}{M}\right)^2 \tilde{m}s_1^3(1 + s_1)^5\delta(s_1 - s_2), \quad (59)$$

where

$$Q_0(k, s) = \tilde{m}^2(1 + s)^9 + \left(\frac{2}{M}\right)^2 ks^6(4 + k(1 + s)),$$

$$Q_1(s) = -\left(\frac{2}{M}\right)^2 s^7(5 + s),$$

$$Q_2(s) = -\left(\frac{2}{M}\right)^2 s^8(1 + s),$$

and the coefficients Q_i are polynomials of up to degree 9.

5.5. Method of solution

We start from the homogeneous form of equation (59). We note that, for a given k , the two linearly independent solutions $f_\alpha(s; k)$ and $f_\beta(s; k)$ of this linear homogeneous second order ordinary differential equation are not available in the mathematical literature to the best of our knowledge. Assuming that we knew these solutions we would then find the Green's function, $g_{++}(s_1, s_2; k)$, writing [18]

$$f(t_1, t_2; k) = c_k f_\alpha(s_<; k) f_\beta(s_>; k), \quad (60)$$

where $s_< = \min(s_1, s_2)$, $s_> = \max(s_1, s_2)$, and f_β has the correct behavior at large s . Then we determine c_k by imposing the kink in f due to the Dirac delta function at $s_1 = s_2$ as follows:

$$\partial_{s_1} f(s_1, s_2; k)|_{s_1=s_2+\epsilon} - \partial_{s_1} f(s_1, s_2; k)|_{s_1=s_2-\epsilon} = -\tilde{m} \frac{(1 + s_2)^4}{s_2^5}, \quad (61)$$

where ϵ is small and positive.

The Green's function, symmetric under exchange of s_1 and s_2 , is reconstructed as follows:

$$G_{++}(z_1, z_2) = G_{++}(s_1, s_2; \varphi) = \frac{1}{2\pi} \sum_{k=-\infty}^{\infty} c_k f_\alpha(s_<; k) f_\beta(s_>; k) e^{ik\varphi}. \quad (62)$$

6. TCP in the whole surface

In the whole surface, using equation (21), we can now write $e^{-\beta U_{2N}}$ at a coupling constant $\Gamma = 2$ as follows:

$$\left| \det \begin{pmatrix} \frac{L}{L_0} \sqrt{|u_j v_j|} \\ u_i - v_j \end{pmatrix}_{(i,j) \in \{1, \dots, N\}^2} \right|^2. \quad (63)$$

The grand partition function will then be

$$\Xi = \det [\mathbf{I} + \mathbf{K}_{\text{ws}}^{-1}], \quad (64)$$

with

$$\mathbf{K}_{\text{ws}}^{-1} = \left(\frac{M}{2L_0} \right) \lambda_{\text{ws}} \mathcal{M}, \quad (65)$$

$$\lambda_{\text{ws}} = \lambda_+ |z| \frac{1 + \sigma_z}{2} + \lambda_- |z| \frac{1 - \sigma_z}{2}. \quad (66)$$

The inverse operator is then given by

$$\mathbf{K}_{\text{ws}} = \left(\frac{2L_0}{M} \right) \mathcal{M}^{-1} \lambda_{\text{ws}}^{-1}, \quad (67)$$

$$\lambda_{\text{ws}}^{-1} = \frac{1}{\lambda_+ |z|} \frac{1 + \sigma_z}{2} + \frac{1}{\lambda_- |z|} \frac{1 - \sigma_z}{2}, \quad (68)$$

$$\mathcal{M}^{-1} = \frac{Ss}{2\pi L \sqrt{g}} \left(\frac{M}{2} \right)^2 \mathbf{O}. \quad (69)$$

Introducing position dependent fugacities²

$$m_p(z) = \frac{2\pi(L/L_0)\lambda_p\sqrt{g}}{Ss} = \tilde{m}_p \frac{\sqrt{g}}{s}, \quad (70)$$

where now $\tilde{m}_p/L_0 \rightarrow \tilde{m}_p$, we can rewrite

$$\mathbf{K}_{\text{ws}} = \frac{\sigma_x + i\sigma_y}{2} a_- + \frac{\sigma_x - i\sigma_y}{2} a_+, \quad (71)$$

with the operators

$$a_- = -\frac{\bar{z}}{m_-(z)|z|^3} + \frac{1}{m_-(z)|z|} (\partial_x - i\partial_y), \quad (72)$$

$$a_+ = -\frac{z}{m_+(z)|z|^3} + \frac{1}{m_+(z)|z|} (\partial_x + i\partial_y). \quad (73)$$

Then the equations for the Green's functions are

$$(1 - a_- a_+) R_{++}(z_1, z_2) = \delta^{(2)}(z_1; z_2), \quad (74)$$

$$(1 - a_+ a_-) R_{--}(z_1, z_2) = \delta^{(2)}(z_1; z_2), \quad (75)$$

$$R_{+-} = -a_- R_{--}, \quad (76)$$

$$R_{-+} = -a_+ R_{++}. \quad (77)$$

² Alternatively we could have left the one-body terms ($\sqrt{|z|}$) outside the determinant, and then considered them as part of the position dependent fugacities, and simply applied the Cornu and Jancovici [7] formalism with these position dependent fugacities.

The equation for R_{++} in the symmetric mixture case is

$$\begin{aligned} & \left[m^2(z_1) - \frac{2}{s_1^4} + \frac{2\partial_{s_1}}{s_1^3} - \frac{\partial_{s_1}^2}{s_1^2} - \frac{-i\partial_{\varphi_1} + \partial_{\varphi_1}^2}{s_1^4} \right] R_{++}(z_1, z_2) \\ & = \frac{m^2(z_1)}{\sqrt{g_1}} \delta(s_1 - s_2) \delta(\varphi_1 - \varphi_2) = \frac{\tilde{m}^2 \sqrt{g_1}}{s_1^2} \delta(s_1 - s_2) \delta(\varphi_1 - \varphi_2). \end{aligned} \tag{78}$$

From this equation we see that $R_{++}(z_1, z_2)$ will now be real.

By expanding equation (78) in a Fourier series in the azimuthal angle we now find

$$[Q_0(k, s_1) + Q_1(s_1)\partial_{s_1} + Q_2(s_1)\partial_{s_1}^2]g_{++}(s_1, s_2; k) = \left(\frac{M}{2}\right)^2 \tilde{m}s_1^3(1+s_1)^4\delta(s_1 - s_2), \tag{79}$$

where

$$\begin{aligned} Q_0(k, s) &= \left(\frac{M}{2}\right)^4 \tilde{m}^2(1+s)^8 + s^4(k^2 - k - 2), \\ Q_1(s) &= 2s^5, \\ Q_2(s) &= -s^6, \end{aligned}$$

and the coefficients Q_i are now polynomials of up to degree 8.

In the flat limit we find, for $G_{++} = R_{++}/\tilde{m}$, the following equation:

$$\left[\tilde{m}^2 - \frac{2}{r_1^4} + \frac{2\partial_{r_1}}{r_1^3} - \frac{\partial_{r_1}^2}{r_1^2} - \frac{-i\partial_{\varphi_1} + \partial_{\varphi_1}^2}{r_1^4} \right] G_{++}(z_1, z_2) = \frac{\tilde{m}}{r_1} \delta(r_1 - r_2) \delta(\varphi_1 - \varphi_2). \tag{80}$$

We then see that we now do not recover the TCP in the plane [7, 6]. This has to be expected because in the flat limit the Flamm's paraboloid reduces to two planes connected by the origin.

After the Fourier expansion of equation (58) we now get

$$[P_0(k, r_1) + P_1(r_1)\partial_{r_1} + P_2(r_1)\partial_{r_1}^2]g_{++}(r_1, r_2; k) = \tilde{m}\delta(r_1 - r_2), \tag{81}$$

where

$$\begin{aligned} P_0(k, r) &= \tilde{m}^2 r + \frac{k^2 - k - 2}{r^3}, \\ P_1(r) &= \frac{2}{r^2}, \quad P_2(r) = -\frac{1}{r}. \end{aligned}$$

The homogeneous form of this equation admits the following two linearly independent solutions:

$$\begin{aligned} f_1(r; -1) &= [D_{-1/2}(i\sqrt{2\tilde{m}r}) + \overline{D_{-1/2}(i\sqrt{2\tilde{m}r})}]/2 & k = -1, \\ f_2(r; -1) &= D_{-1/2}(\sqrt{2\tilde{m}r}) \\ f_1(r; 2) &= [D_{-1/2}((-2)^{1/4}\sqrt{\tilde{m}r}) + \overline{D_{-1/2}((-2)^{1/4}\sqrt{\tilde{m}r})}]/2 & k = 2, \\ f_2(r; 2) &= [D_{-1/2}(i(-2)^{1/4}\sqrt{\tilde{m}r}) + \overline{D_{-1/2}(i(-2)^{1/4}\sqrt{\tilde{m}r})}]/2 \\ f_1(t; k) &= \sqrt{r} I_{-\sqrt{7-4k+4k^2}/4}(\tilde{m}r^2/2) & \text{else,} \\ f_2(t; k) &= \sqrt{r} I_{\sqrt{7-4k+4k^2}/4}(\tilde{m}r^2/2) \end{aligned}$$

where the $D_\nu(x)$ are parabolic cylinder functions and the $I_\mu(x)$ are modified Bessel functions of the first kind which diverge as $e^x/\sqrt{2\pi x}$ for large $x \gg |\mu^2 - 1/4|$.

Again we write $g_{++}(r_1, r_2; k) = c_k f_\alpha(r_<; k) f_\beta(r_>; k)$ and impose the kink condition,

$$\partial_{r_1} g_{++}(r_1, r_2; k)|_{r_1=r_2+\epsilon} - \partial_{r_1} g_{++}(r_1, r_2; k)|_{r_1=r_2-\epsilon} = -\tilde{m}r_2, \quad (82)$$

to find the c_k . The Green's function is then reconstructed using equation (62). But we immediately see that curiously $|G_{++}|$ diverges. Even the structure of the plasma is not well defined in this situation. The collapse of opposite charges at the horizon shrinking to the origin makes the structure of the plasma physically meaningless.

7. Conclusions

An attempt was made to extend the solution of the one component plasma, at the special value of the coupling constant $\Gamma = 2$, living in the Flamm's paraboloid [16] to the two component one, the TCP. The Flamm's paraboloid is a Riemannian surface with non-constant curvature which is asymptotically flat. Its curvature depends on a parameter M ($2M$ being the radius of the horizon) in such a way that for $M \rightarrow 0$ the surface becomes flat: two planes connected by the origin.

The work of Cornu and Jancovici [7, 6] on the TCP in a plane showed that at this particular value of the coupling constant, using a Cauchy identity, it is possible to find an analytic solution to the structure of the plasma starting from a discretized model to avoid divergences and taking the continuous limit in the end. All the n -particle correlation functions with $n > 1$ are well behaved except the particle density which diverges like all the other thermodynamic quantities due to the competition between the attraction of oppositely charged particles and the thermal motion. This can be prevented by adding a hard core to the particles in order to prevent collapse.

In this work we repeated the same calculation for the plasma living in the Flamm's paraboloid, in the half surface case, $s > 1$, with an insulating horizon (at $s = 1$) and in the full surface case, $s > 0$. The solution of the equation determining the structure, the Green's function equation, is reduced to the mathematical problem of finding the two linearly independent solutions of a linear homogeneous second order ordinary differential equation with polynomial coefficients of high degree (9th in the half surface case and 8th in the full surface case). To the best of our knowledge, an analytic solution of these equations turns out to be out of mathematical reach. Nonetheless the many-body problem has been reduced to finding the solutions of a simple differential equation. The further step of finding explicitly the analytical form of the solutions from the given differential equations is a matter of mathematical syntax and we think that it does not add much to the present work.

We discussed the symmetries of the Green's function, the perfect screening sum rule, the relationship between the structure and the thermodynamics, and the method of solution of the Green's function equation.

We found that for the plasma living in the half Flamm's paraboloid with an insulating horizon the flat limit $M \rightarrow 0$ reduces the system to the TCP on a plane [7, 6]. For the plasma living in the full Flamm's paraboloid taking the flat limit one does not recover the plasma in a plane and this has to be expected since the paraboloid in this limit reduces to two planes connected by a hole at the origin. Instead the resulting solution for the

structure turns out to be physically meaningless. The collapse of opposite charges at the horizon as it shrinks to the origin spoils the structure of the plasma.

We leave as an open problem the one of finding approximations to the two linearly independent solutions of the homogeneous counterpart of equation (59), for the half surface case, and of equation (79), for the whole surface case, as a function of the integer k , the further determination of the Green's function in these two cases, through equation (62), the eventual analysis of the solution and discussion about the necessity of the addition of a hard core to the particles (hard 'disks' of diameter D with $\delta s < 2D(1 + 1/s)^{-2}/M$) in order to cure the divergence of the densities ρ_p with the consequent determination of the equation of state. These final steps are necessary in order to have the problem of the structure of the fluid reduced to a closed form. In the present work we limited ourselves to what can be said in an analytical form.

Acknowledgment

I would like to acknowledge the financial support and hospitality from the National Institute for Theoretical Physics of South Africa during the preparation of the work. I would also like to thank Peter Forrester for stimulating the work and Filippo Giraldi for discussions on the solution of the Green's function equation.

References

- [1] Salzberg A and Prager S, 1963 *J. Chem. Phys.* **38** 2587
- [2] Hauge E H and Hemmer P C, 1971 *Phys. Nor.* **5** 209
- [3] Šamaj L and Travěnek I, 2000 *J. Stat. Phys.* **101** 713
- [4] Kosterlitz J M and Thouless D J, 1973 *J. Phys. C: Solid State Phys.* **6** 1181
- [5] Lenard A, 1961 *J. Math. Phys.* **2** 682
- [6] Cornu F and Jancovici B, 1987 *J. Stat. Phys.* **49** 33
- [7] Cornu F and Jancovici B, 1989 *J. Chem. Phys.* **90** 2444
- [8] Forrester P J, 1991 *J. Chem. Phys.* **95** 4545
- [9] Téllez G and Merchán L, 2002 *J. Stat. Phys.* **108** 495
- [10] Merchán L and Téllez G, 2004 *J. Stat. Phys.* **114** 735
- [11] Téllez G, 1997 *J. Chem. Phys.* **106** 8572
- [12] Téllez G, 1998 *J. Phys. A: Math. Gen.* **31** 5277
- [13] Forrester P J, Jancovici B and Madore J, 1992 *J. Stat. Phys.* **69** 179
- [14] Forrester P J and Jancovici B, 1996 *J. Stat. Phys.* **84** 337
- [15] Jancovici B and Téllez G, 1998 *J. Stat. Phys.* **91** 953
- [16] Fantoni R and Téllez G, 2008 *J. Stat. Phys.* **133** 449
- [17] Aitken A C, 1956 *Determinants and Matrices* (New York: Interscience)
- [18] Jackson J D, 1999 *Classical Electrodynamics* 3rd edn (New York: Wiley) sections 3.9 and 3.11

Chapter 30

The structure of colloidosomes with tunable particle density: simulation vs experiment

Fantoni R., Salari J. W. O., Klumperman B., Phys. Rev. E **85**, 061404 (2012)

Title: “The structure of colloidosomes with tunable particle density: simulation vs experiment”

Abstract: Colloidosomes are created in the laboratory from a Pickering emulsion of water droplets in oil. The colloidosomes have approximately the same diameter and by choosing (hairy) particles of different diameters it is possible to control the particle density on the droplets. The experiment is performed at room temperature. The radial distribution function of the assembly of (primary) particles on the water droplet is measured in the laboratory and in a computer experiment of a fluid model of particles with pairwise interactions on the surface of a sphere.

PHYSICAL REVIEW E **85**, 061404 (2012)

Structure of colloidosomes with tunable particle density: Simulation versus experiment

Riccardo Fantoni,^{1,*} Johannes W. O. Salari,^{2,†} and Bert Klumperman^{2,3,‡}

¹National Institute for Theoretical Physics and Institute of Theoretical Physics, University of Stellenbosch, Stellenbosch 7600, South Africa

²Department of Polymer Chemistry, University of Technology Eindhoven, P.O. Box 513, 5600 MB Eindhoven, The Netherlands

³Stellenbosch University, Department of Chemistry and Polymer Science, Private Bag X1, 7602 Matieland, South Africa

(Received 14 February 2012; published 6 June 2012)

Colloidosomes are created in the laboratory from a Pickering emulsion of water droplets in oil. The colloidosomes have approximately the same diameter and by choosing (hairy) particles of different diameters it is possible to control the particle density on the droplets. The experiment is performed at room temperature. The radial distribution function of the assembly of (primary) particles on the water droplet is measured in the laboratory and in a computer experiment of a fluid model of particles with pairwise interactions on the surface of a sphere.

DOI: [10.1103/PhysRevE.85.061404](https://doi.org/10.1103/PhysRevE.85.061404)

PACS number(s): 83.80.Hj, 68.65.-k, 64.70.pv, 64.75.Xc

I. INTRODUCTION

Colloidosomes are hollow spherical structures that are formed by the assembly of colloidal particles at the interfaces of two immiscible liquids [1]. As a result the particles are arranged in a shell that is inherently porous.

The assembly of colloidal particles at liquid interfaces is used in various applications [2]. Moreover, it is a promising technique for the synthesis of novel materials [3] and has recently led to the development of colloidosomes [1], nanocomposite particles [4], porous solids [5], and foams [6].

In this work, we study colloidosomes that are composed of uncharged spherical polystyrene particles of μm size moving on the surface of a water droplet in oil. Similar studies have also been done with charged particles [7]. The study of particles on the surface of a sphere dates back to the old Thomson problem [8] for classical electrons. The statistical physics problem of a one-component plasma on a sphere has been solved exactly analytically at a special value of the temperature [9]. Nonpointwise particles on a sphere have the additional complication of the geometrical frustration, which can be described through the so-called grain boundary scars [10–12]. There have been attempts to formulate a statistical geometry of particle packing [13]. These systems opened up a field of research that studies the effect of curvature and topology of various surfaces on the organization of matter in a more general sense [14]. Structuring at the surface of a droplet can be viewed as a two-dimensional analog to fluid like behavior, crystallization, or glass formation in three-dimensional systems [15].

Fluids on Riemannian surfaces have been the subject of various studies with few exact analytical results [9,16,17], some approximate theories [18], and many Monte Carlo (MC) simulations [19]. Colloidosomes with tunable particle density were synthesized experimentally [20]. A sintering procedure is then used to create capsules, which can be easily handled. The capsules are then dried to obtain colloidal cages. The synthetic details are explained in the next section.

In this work we give the simplest statistical physics description of the colloidosome, where we describe the interaction of the colloidal particles with the surrounding media, water and oil, simply as a holonomic constraint on the particles positions to stay at the water-oil (WO) interface and treat them as a fluid of a fixed number of particles moving on a sphere, the droplet of water in oil, with a mutual pairwise interaction, the pair potential, at a temperature T . Additional frictional effects have been neglected [21]. The assembly of particles on the sphere is studied both in the laboratory and with a computer experiment under certain conditions: number density and temperature. The structural arrangement of the particles is characterized through the radial distribution function. The colloidal particles created in our laboratory are polystyrene solid spherical hairy particles with controllable diameter of the order of $3\ \mu\text{m}$. The particles will then exhibit a hard core interaction. Two types of particle pair potentials were used in the Monte Carlo (MC) simulation of the fluid, namely the hard-sphere one and the polarizable hard-sphere one.

The work is organized as follows: in Sec. II the colloidosome is described; in Sec. III the radial distribution function as a means to probe the structure of the colloidosome is presented in its mathematical definition described in Appendix A, its MC estimator, and its experimental measure; in Sec. IV the MC simulation results are presented; in Sec. V the theoretically exact results of the MC simulation and the experimental results are compared; Section VI is devoted to concluding remarks.

II. EXPERIMENTAL SYSTEM VERSUS STATISTICAL PHYSICS PROBLEM

The details for the synthesis of the colloidosomes can be found in our previous work [20]. Working at room temperature, we first disperse the colloidal particles in a hydrocarbon oil (heptane). Then, water is added while the solution is being stirred vigorously. The function of the shear is two fold. It causes the water to break up into small water droplets and at the same time it allows to overcome the barrier for adsorption of the particles, which are assembled randomly at the WO interface of the droplets. Eventually a stable Pickering emulsion [22] of water droplets covered by polystyrene (pS) particles, the colloidosomes, in oil is formed. The colloidosomes formed have all approximately

*rfantoni@ts.infn.it

†jorissalari@gmail.com

‡bklump@sun.ac.za

FANTONI, SALARI, AND KLUMPERMAN

PHYSICAL REVIEW E **85**, 061404 (2012)

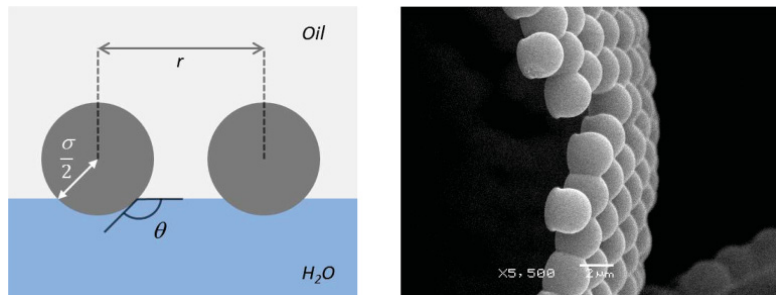


FIG. 1. (Color online) The left panel shows a schematic representation of the equilibrium position of the particles at the WO interface; θ is the three-phase contact angle, r is the particle separation, and σ is the particle diameter. The right panel shows a side view of the particle shell of a colloidosome made with scanning electron microscopy.

the same diameter, and this, as well as the number of colloidal particles on each colloidosome, does not change after the colloidosomes are formed. For further imaging with scanning electron microscopy (SEM) the particles surrounding the droplets need to be (partially) sintered in order to form a continuous and stable shell around the droplet, a capsule. Heating the mixture to 35 °C for 30 minutes proved sufficient to do so. A small amount of the sintered colloidosome dispersion is placed on the SEM sample holder and dried in the fumehood. This removes both the water and heptane remnants and leaves only the capsules, the colloidal cages, which can then be imaged by SEM.

The colloidal polystyrene solid particles are synthesized by the dispersion polymerization of styrene in alcohol and water [20], which is a well-established technique for the formation of highly uniform polymer particles with a narrow size polydispersity. AIBN [azo-bis(isobutyronitrile)] is used as the initiator. The presence of a polymeric stabilizing surface functional group is required for a controlled synthesis of the particles. A nonionic polymeric stabilizer [poly(N-vinylpyrrolidone) (pVP)] is used for this study. Hence, there is no charge on the surface of the particles. During the polymerization, pVP, which efficiently adsorbs on polystyrene, is attached to the particle. In ethanol and water, pVP is soluble. The polymeric chains are extended (with a radius of gyration of $R_g \approx 15$ nm) and are responsible for steric repulsion as two particles get in close contact. This guarantees the steric stabilization of the colloidal suspension. In the oil phase, pVP is insoluble and the polymer chains are collapsed on the surface of the particle, resulting in an attractive potential among the particles. The final dispersion in ethanol and water, therefore, consists of polystyrene particles that are sterically stabilized with a layer of pVP. During the polymerization of styrene, pVP attaches to the particle by both physical adsorption to the particle's surface and chemical grafting. These two mechanisms occur simultaneously, however it is not known to what extent. It is believed that the predominant mechanism for stabilization is the physical adsorption. The particles are washed with pure ethanol by three centrifugation-redispersion cycles in order to remove the residual physically adsorbed pVP. The particles settle due to the centrifugation. The supernatant

solution is decanted and clean ethanol is added to the remaining particles. The particles are then redispersed and the whole procedure is repeated three times. The physically adsorbed pVP is removed, which produces a lower colloidal stability of the particles in ethanol. Large aggregates were observed during this procedure, which is an indication for the presence of an attractive component in the pair potential between the colloidal particles in the suspension. The chemically grafted pVP remains attached to the particle's surface. The remaining particles are dried and redispersed in heptane, before the colloidosomes are synthesized. In conclusion, the surface chemical properties of the particles are mainly determined by polystyrene and the fraction of pVP that is chemically grafted to the surface, although a precise estimate of the grafting density is lacking. It is believed that the grafting density is low, due to the poor colloidal stability of the particles in ethanol after removing the physically adsorbed pVP.

In Pickering emulsions, the particle is adsorbed at the WO interface and is partly immersed in the oil and water phase. The extent of immersion in both phases will eventually have an influence on the particle pair potential. The three-phase contact angle θ is used to denote the position at the interface as shown in Fig. 1.¹ It was determined in our earlier work [20] and is approximately $\theta \approx 130^\circ$, which means that the particle is predominantly immersed in the oil. The surface tension of the particle is altered by the presence of the surface stabilizing groups, which affects the wetting properties and the equilibrium position of the particles at the interface [23]. An atomistic [24] level of description of the core of the solid hairy particles suggests the use of Hamaker [25] calculation for the determination of the interaction between the two spherical cores. The calculation predicts an attractive pair potential which, neglecting the detailed behavior close to contact, is proportional to $(\sigma/r)^6$, r being the distance between the centers of the two cores of diameter σ . Unlike this attraction, which is always present, the steric

¹The right panel of Fig. 1 shows clearly flattening of the particles on the inside of the capsules. We are convinced that this is an artifact of the sintering process. During this process flattening of the particles occurs, which we ascribe to particle deformation to reduce the contact area between particle and water.

repulsion will have a very small range when θ is obtuse since in this case the particle's contact occurs in the oil phase [26]. We thus expect the balance between the attractive interaction and the steric effects to depend on the angle θ . Moreover other kinds of interactions such as depletion, hydrophobic, solvation, or capillary should be taken into account for an accurate description of our system. The simplest description for the pair potential between the particles is the hard-spheres one.

The surface of a sphere of diameter $D = 2R$ is $A = \pi D^2$. The surface area that a particle, with diameter σ , can occupy is approximately $a = \sqrt{3}\sigma^2/2$. The maximum number of particles that can pack the surface of a sphere is approximately

$$N_{\max} \lesssim \frac{A}{a} = \frac{2\pi}{\sqrt{3}} \left(\frac{D}{\sigma}\right)^2, \quad (1)$$

where we assumed that the particles are in a close packing regular hexagonal lattice neglecting curvature effects. The maximum reduced particle density on the sphere will then be $\rho_{\max}\sigma^2 \lesssim 2/\sqrt{3} \approx 1.155$.

Similar experiments [27] make use of water and a liquid of higher density, for the initial solution of the two immiscible liquids. The droplets in the emulsion will now be of the higher density liquid. In the limit of droplets of very high density the particles are expected to be essentially unable to move on the droplet. Our working hypothesis will be, instead, to consider the particles as moving freely on the droplet surface, completely neglecting the presence of the solvent. We then treat the colloidosome of diameter D , number of particles N , and temperature T , through a canonical ensemble classical statistical physics description of the assembly of particles on the water droplet as a fluid of particles constrained to move on the surface of a sphere with a pairwise interaction, the pair potential.

A. Pair potential

Fixing the pair potential completely defines the fluid model, as described in Appendix A and Eq. (8).

The simplest interaction between two colloidal particles is the hard-spheres (HS) pair potential

$$\phi_{\text{HS}}(r) = \begin{cases} +\infty & r < \sigma \\ 0 & r > \sigma \end{cases}, \quad (2)$$

where σ is the diameter of the spheres and r is the Euclidean center to center distance [see Eq. (5)].

The interaction between two neutral particles far apart is dominated by dipolar forces. The simplest model potential, suggested by the London forces [28], corresponds to hard spheres of diameter σ with dispersion attractions, the polarizable hard spheres (PHS),

$$\phi_{\text{PHS}}(r) = \begin{cases} +\infty & r < \sigma \\ -\epsilon_{\text{PHS}} \left(\frac{\sigma}{r}\right)^6 & r > \sigma \end{cases}, \quad (3)$$

where $\epsilon_{\text{PHS}} = A^H/36$ is a positive energy proportional to Hamaker constant [25] A^H , which is a property of the material of which the particles are made and of the environment where the particles are immersed. We here neglect the details of Hamaker's macroscopic approximation [28], which when the

two spheres are close to contact predicts a $-(A^H/24)/(r/\sigma - 1)$ behavior, as we believe they have not much influence on the calculation.

III. RADIAL DISTRIBUTION FUNCTION

In this work we probed the structure of the colloidosome using the radial distribution function (RDF). We compare the experimental RDFs with the ones obtained from MC simulations of a fluid of particles moving on a sphere and interacting with a model pair-potential of the kinds described in Sec. II A. This procedure will allow us to determine which interaction model best describes the experimental assembly of particles. Choosing σ as the unit length, the statistical physics problem only depends on the number of particles N and the reduced density $\rho\sigma^2 = N/[\pi(D/\sigma)^2]$ for the athermal HS model and also on the reduced temperature $k_B T/\epsilon_{\text{PHS}}$ for the PHS one.

A. Monte Carlo simulation

On a sphere, the Monte Carlo simulation [29] solves exactly the statistical physics problem as, since one does not have the additional thermodynamic limit problem, it reduces to an integration, as described in Appendix B.

The particle's positions are $\mathbf{R} = (\mathbf{r}_1, \mathbf{r}_2, \dots, \mathbf{r}_N)$ with

$$\mathbf{r}_i = R[\sin\theta_i \cos\varphi_i \hat{\mathbf{x}} + \sin\theta_i \sin\varphi_i \hat{\mathbf{y}} + \cos\theta_i \hat{\mathbf{z}}]. \quad (4)$$

The Euclidean distance between particles i and j is given by

$$r_{ij} = R\sqrt{2 - 2\hat{\mathbf{r}}_i \cdot \hat{\mathbf{r}}_j}, \quad (5)$$

where $\hat{\mathbf{r}}_i = \mathbf{r}_i/R$ is the versor that from the center of the sphere points towards the center of the i th particle.

The density of particles on the surface of the sphere is

$$\rho = \frac{N}{4\pi R^2}. \quad (6)$$

In the MC simulation [29] the RDF between two points on the sphere, \mathbf{r} and \mathbf{r}' , is calculated through the following histogram estimator [see Eq. (A14)]

$$g(d) = \langle g^{\text{histogram}}(d, \mathbf{R}) \rangle, \quad (7)$$

where $d = 2R \sin[\arccos(\hat{\mathbf{r}} \cdot \hat{\mathbf{r}}')/2]$ is the Euclidean distance between \mathbf{r} and \mathbf{r}' , $\langle \dots \rangle = \int_{S_R} \exp[-\beta U_N(\mathbf{R})] \dots d\mathbf{R} / \int_{S_R} \exp[-\beta U_N(\mathbf{R})] d\mathbf{R}$ is the thermal average, here

$$U_N(\mathbf{R}) = \sum_{i < j} \phi(r_{ij}), \quad (8)$$

is the total potential energy of the fluid of particles, ϕ is the pair potential, and the integrals are taken in such way that $\mathbf{r}_i \in S_R$ for $i = 1, 2, \dots, N$ with S_R the sphere of diameter $D = 2R$, so that $d\mathbf{R} = \prod_i d\mathbf{r}_i$ with $d\mathbf{r}_i = R^2 d\Omega_i = R^2 \sin\theta_i d\theta_i d\varphi_i$, and

$$g^{\text{histogram}}(d, \mathbf{R}) = \sum_{i \neq j} \frac{1_{[d-\Delta/2, d+\Delta/2]}(r_{ij})}{N n_{id}(d)} \quad (9)$$

here $1_{[a,b]}(r) = 1$ if $r \in [a,b]$ and 0 otherwise, and

$$n_{id}(d) = N \left[\left(\frac{d + \Delta/2}{2R}\right)^2 - \left(\frac{d - \Delta/2}{2R}\right)^2 \right], \quad (10)$$

FANTONI, SALARI, AND KLUMPERMAN

PHYSICAL REVIEW E **85**, 061404 (2012)

is the average number of particles on the surface $[d - \Delta/2, d + \Delta/2]$ for the ideal gas of density ρ . $\rho^2 g(d)$ gives the probability that sitting on a particle at \mathbf{r} one has to find another particle at \mathbf{r}' .

B. Experiment

The positional data of the particles in the colloidal cages is directly extracted from SEM images, which allowed the calculation of the particle separation for all visible particle pairs. Δ is set to an arbitrary value of $\sigma/20$. To exclude edge effects, a selection of particles located sufficiently at the center of the SEM image of the colloidal cage is taken into account. The RDF is determined from just one hemisphere. The particle positions from five SEM images of similar colloidal cages were used for the statistical average. The detailed procedure, the selection of particles, and validation of the procedure is described in our previous work [20]. In that work we calculated the radial distribution function from just one SEM image. Here we refined that analysis averaging the results from five SEM images, which is in spirit closer to the procedure used in the MC simulations. Although five images are still a rather small number our present procedure carries nevertheless more information than the one used in Ref. [20]. The absolute error on the experimental $g(r)$ is around 0.3. In the experiment unlike in the simulations each image measurement is uncorrelated from the other.

IV. MONTE CARLO RESULTS

We performed constant N , ρ , and T canonical MC simulations [29]. A typical run would consist of about $5 \times 10^5 N$ single-particle moves, keeping the acceptance ratios constant (≈ 0.3). In all the presented graphs of the simulated RDF the statistical error from the MC integration are not visible on the chosen scale.

We initially chose the PHS model pair potential to see how the RDF would change upon changing the temperature and the density. In order to find agreement with the experimental results it proved necessary to use the simpler HS model, as shown in Sec. V. We then compared the HS results with the soft-sphere model $\phi_{SS}(r) = \epsilon_{SS}(\frac{r}{\sigma})^6$ considered in Ref. [18]. For case “a” of Table I a reduced temperature of $k_B T / \epsilon_{SS} = 0.05$ is sufficient to have similar RDFs for the HS and the SS model on the half hemisphere, but when looking at the RDFs on the whole sphere, the SS RDF, unlike the HS one,

TABLE I. Characteristics of the experimental colloidosomes analyzed. In all cases, the water droplet was of the same diameter $D = 64.8 \mu\text{m}$. Different colloidosomes differed by the diameter σ of the colloidal particles and by the number N of colloidal particles they carried. The same systems, “a”, “b”, “c”, “d”, have been studied through MC simulations.

case	σ (μm)	N	D/σ	$\rho\sigma^2$
a	4.80	561	13.5	0.98
b	3.32	1065	19.5	0.89
c	2.72	1498	23.8	0.84
d	2.56	1449	25.3	0.72

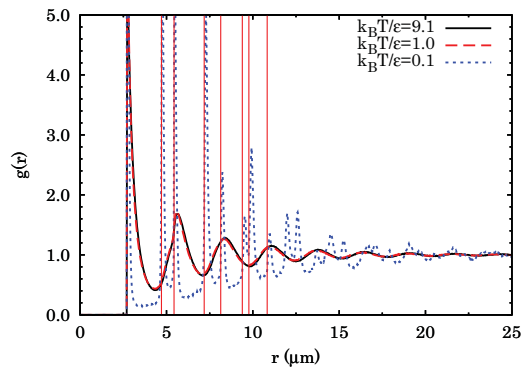


FIG. 2. (Color online) RDF for approximately one hemisphere of the colloidosome “c” of Table I with $N = 1498$, $D/\sigma = 23.8$, and various reduced temperatures, calculated with MC simulations of the PHS fluid. Also shown are the locations (vertical lines) of the first eight coordination shells of a regular planar hexagonal lattice of the hard-core particles (here $\sigma = 2.72 \mu\text{m}$). The mismatch between the peaks of the RDF and these shells is a manifestation of the curvature of the surface.

shows relevant correlations between particles at opposite poles ($|g(2R) - 1| \approx 0.3$).

A. Dependence on temperature

The HS model is athermal so the structure is independent of temperature but only depends on the density. We thus simulated the colloidosome “c” in Table I with the PHS model. We chose different values of the reduced temperature, $k_B T / \epsilon_{PHS}$ to see how the RDF would change.

As expected we found the occurrence of an ordered structure at small reduced temperatures (see Fig. 2). In particular we observe the formation of a regular hexagonal lattice distorted by the curvature of the spherical surface.

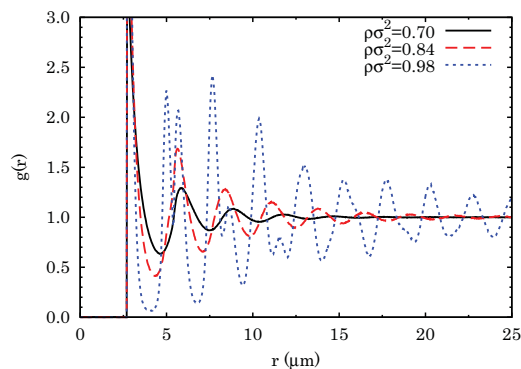


FIG. 3. (Color online) RDF for approximately one hemisphere of the colloidosome with $D/\sigma = 23.8$ and $\sigma = 2.72 \mu\text{m}$ at a reduced temperature $k_B T / \epsilon_{PHS} = 9.1$ and various densities, calculated with a MC simulation of the PHS fluid.

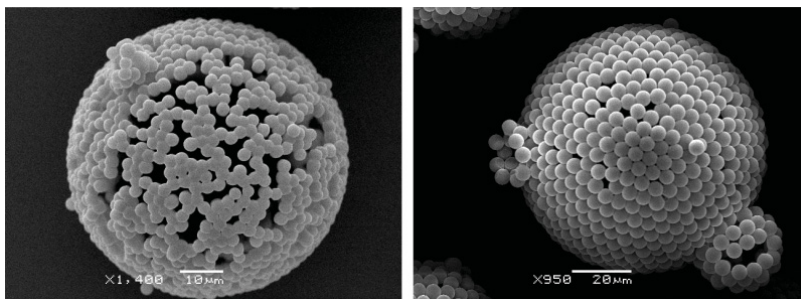


FIG. 4. SEM images of colloidal cages with a fluidlike particle configuration (left panel, $\rho\sigma^2 = 0.84$ and $D/\sigma = 23.8$) and a crystalline-like particle configuration (right panel, $\rho\sigma^2 = 0.98$ and $D/\sigma = 13.5$).

Recall that in a planar perfect hexagonal lattice arrangement of spheres of diameter σ the first coordination shells are as follows: $r/\sigma = 1, \sqrt{3}, 2, \sqrt{7}, 3, 2\sqrt{3}, \sqrt{13}, 4, \sqrt{19}, \sqrt{21}, 5, \dots$

From Fig. 2 we can clearly see how at this reduced density, 0.84, well below the maximum density, the PHS model reduces to the HS model for reduced temperatures $\gtrsim 1$. As we lower the temperature, the attractive tail in the pair potential starts to play a role resulting in a solidification of the fluid. As the fluid

crystallizes, it may experience the cage effect going through glassy phases. The particles become confined in transient cages formed by their neighbors. This prevents them from diffusing freely on the surface of the sphere [30]. A related problem is the extremely long MC equilibration time necessary to draw the RDF of the figure at a temperature of 0.1, starting from a disordered initial configuration. In the limit of $T \rightarrow 0$, in our calculation, the equilibrium configuration of the (classical)

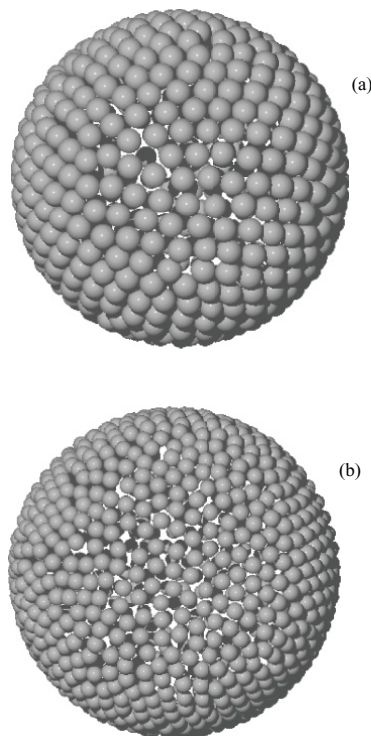
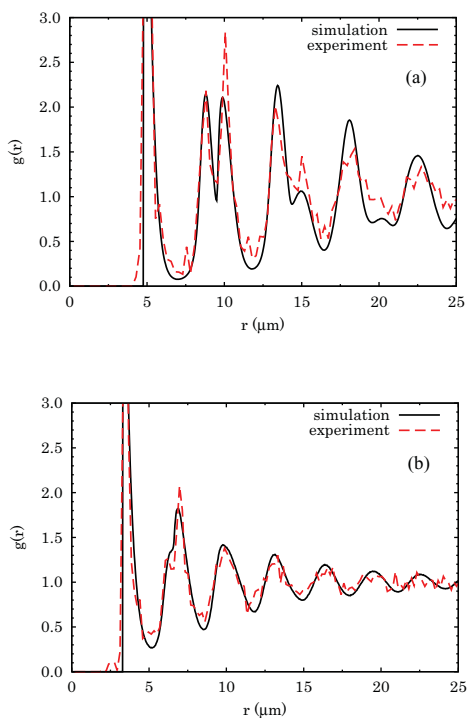


FIG. 5. (Color online) The experimental (dashed red line) and simulated (solid black line) RDF of colloidosomes “a” (top panel) and “b” (bottom panel) of Table I. The fluid model used in the MC simulations was the HS. The graphical representation of a snapshot of the particle positions when the MC has reached equilibrium, shows resemblance with the SEM images.

FANTONI, SALARI, AND KLUMPERMAN

PHYSICAL REVIEW E **85**, 061404 (2012)

particles is the one \mathbf{R}_0 for which $U_N(\mathbf{R})$ has its minimum: the probability density is zero everywhere except on \mathbf{R}_0 . We have a spontaneous breaking of the rotational symmetry (see Appendix A). The monotonously increasing tails in the PHS pair potential produce an equilibrium configuration with the particles forming one cluster of touching spheres. On the contrary, in the SS model the equilibrium configuration will be one where the interparticle spacing depends on the density.

B. Dependence on density

For case “c” in Table I ($D/\sigma = 23.8$ and $\sigma = 2.72 \mu\text{m}$) we chose different values of the density to see how the RDF would change for the PHS model at a relatively high value of the reduced temperature $k_B T / \epsilon_{\text{PHS}} = 9.1$.

We succeeded in reaching high particle densities (without overlaps) by placing one particle at the north pole and then others centered at $\theta = 2n \arcsin(1/2R)$ and $\varphi = 2m \arcsin(1/2R \sin \theta)$ with $n, m = 1, 2, 3, \dots$. This way we were, in particular, able to reach the 0.91 critical density observed by Prestipino Giarritta *et al.* [19] for HS. In doing so we observed the splitting of the second peak into a pair of adjacent peaks corresponding to the second and third coordination shells of a regular hexagonal lattice (see Fig. 3).

From Fig. 3 we can clearly see how the fluid tends to reach an ordered phase at high densities (even at high temperatures). The realization of these ordered phases will go through the formation of colloidal geometrical cages (due to geometrical frustration) on the surface of the water droplet, which is inevitable as the density slowly approaches the maximum density at any temperature.

V. COMPARISON BETWEEN EXPERIMENTAL AND MONTE CARLO SIMULATION RESULTS

The results of the experimental colloidosomes are now compared with the Monte Carlo (MC) simulations. Scanning Electron Microscopy (SEM) images of two different colloidal cages can be found in Fig. 4. The RDF of these colloidal cages and two others are shown in Figs. 5 and 6. The experimental colloidosomes studied differ from one another by particle size and particle density; the water droplets were of the same diameter and the temperature was room temperature, as summarized in Table I. The same values for number of particles, N , and sphere diameter, D/σ , are used in the MC simulations. Our first choice for the pair potential was the HS fluid model, as justified in Sec. II.

It is important to stress that in the experiment we measured the RDF from five images of different colloidal cages. Now,

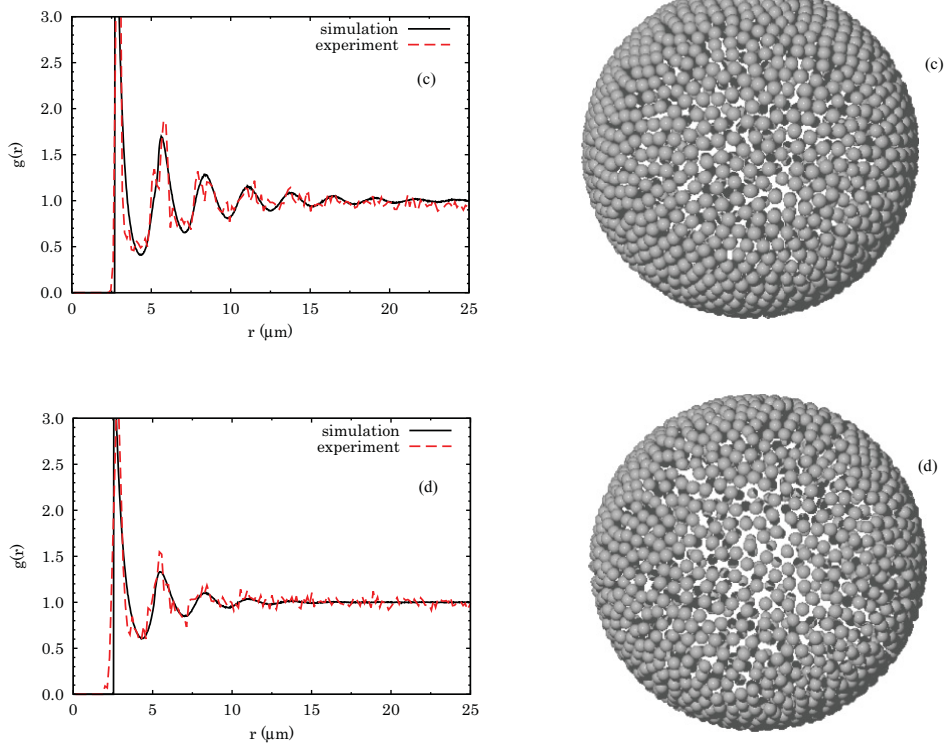


FIG. 6. (Color online) Same as Fig. 5 for the colloidosomes “c” (top panel) and “d” (bottom panel) of Table I.

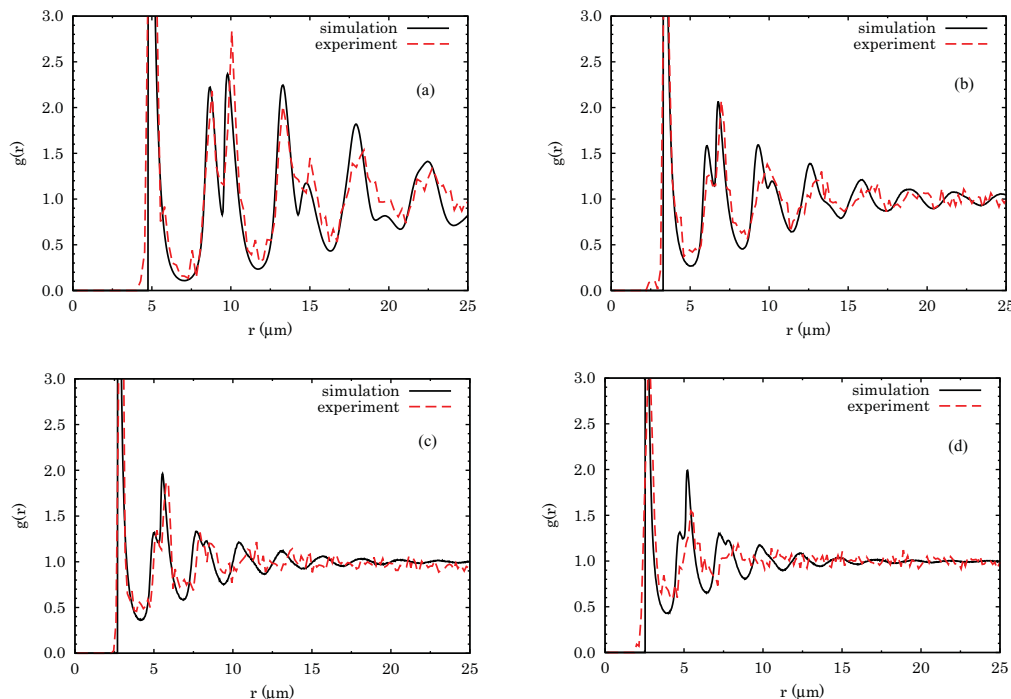


FIG. 7. (Color online) The experimental (dashed red line) and simulated (solid black line) RDF of colloidosomes “a”, “b” (top panel) and “c”, “d” (bottom panel) of Table I. The fluid model used in the MC simulations was the PHS with a reduced temperature of 0.3.

there are two processes responsible for the assembly of the particles on the colloidosome: (i) the adsorption of the particles on the interface at the moment of the formation of the Pickering emulsion and (ii) the motion of the particles on the interface. Our experimental measure is clearly not able to discriminate which one of the two processes is the more relevant, even if we expect that the structure of the colloidal cages obtained after the sintering procedure will carry no history of the former process. Moreover theoretical studies of process (i) are, to the best of our knowledge [31], much less developed than the ones of the latter. Our computer experiment only takes into account the second process assuming that the colloidosome is formed and the particles are in thermal equilibrium on the droplet.

From Figs. 5 and 6 we can see that there is a good agreement between the experimental and the theoretical RDF. This indicates that the HS fluid model gives a good description of the experimental system. The snapshots from the MC simulation of the colloidosome differ from the SEM images of the colloidal cages. The colloidal cages are formed by a network of touching particles. The structure of the experimental fluid points to a pretty strong short-range attraction between the particles mainly as a result of the sintering process. The measure of structure used, $g(r)$, is not sensitive to these structural differences.

We also simulated the experimental colloidosomes with the more realistic PHS model. Initially, the fluid with the

highest particle density (“a”) was used to adjust the reduced temperature. By trial and error we found that $k_B T / \epsilon_{\text{PHS}} = 0.3$ gave a satisfying agreement with the experiment (see Fig. 7). However when we simulated the other colloidal cages with the same reduced temperature (the experimental temperature in all cases did not vary and the Hamaker constant did not change from one colloidosome to the other) we found disagreement between the MC simulation and the experiment as clearly shown by the last panel of Fig. 7. This is an indication that the particles used in the experiment do not interact as PHS. An explanation for this is the balance, in the oil phase, between the steric repulsion of the polymer chains and the Hamaker

TABLE II. Excess internal energy per particle $u^{\text{ex}} = \langle U_N \rangle / N$ for the simulated PHS fluids on the sphere.

$k_B T / \epsilon_{\text{PHS}}$	N	D / σ	$u^{\text{ex}} / \epsilon_{\text{PHS}}$
0.3	561	13.5	-2.1509(6)
0.3	1065	19.5	-1.862(3)
0.3	1498	23.8	-1.732(2)
0.3	1449	25.3	-1.586(3)
0.1	1498	23.8	-2.3484(8)
1.0	1498	23.8	-1.5450(4)
9.1	1498	23.8	-1.5136(3)
9.1	1747	23.8	-2.0932(2)
9.1	1248	23.8	-1.0741(2)

FANTONI, SALARI, AND KLUMPERMAN

PHYSICAL REVIEW E **85**, 061404 (2012)

attraction. However, steric repulsion through the oil phase is unlikely, because pVP is insoluble in heptane. Another, possible explanation is that during emulsification the attractive interaction is balanced by the shear that is applied, and this could be reflected on the capsules structures sintered after the emulsification process.

In Table II we report the excess internal energy per particle measured in the MC simulations of the PHS model in the various systems studied. We can clearly see that as the fluid develops towards a solid phase there is a lowering of the energy.

VI. CONCLUSION

We have studied a colloidosome of polystyrene hairy particles of μm size moving on the surface of a water droplet in oil both experimentally and theoretically through canonical Monte Carlo simulations, which is the ensemble of choice for the description of the experimental system where the number of particles does not vary. In particular we studied the radial distribution function. Agreement was found between the experimental measure and the measure in the computer experiment of the theoretical model of the fluid of pure hard-sphere particles on the surface of a sphere. We did not find agreement between the experiment and the polarizable hard-sphere fluid model.

It would certainly be interesting to pursue a different determination of the radial distribution function through the imaging of the same colloidosome without going through the sintering procedure. This would allow an unbiased determination of the structure of the fluid of particles in their thermal equilibrium on the droplet surface.

Within the Monte Carlo simulation, a wide range of particle densities on the colloidosome was studied. At high density, the particles tend to arrange in a hexagonal lattice, distorted by the curvature of the droplet and the radial distribution function shows clear signatures of the first coordination shells. While at low densities a fluidlike behavior is manifested.

Our Monte Carlo simulation results further show that the addition of an attractive tail to the pure hard-sphere pair potential allows to reach solidification by lowering the temperature even at low densities. We discussed that for pair potentials with support on the whole $[0, 2R]$, crystallization has to be expected at low temperatures at any density.

In our Monte Carlo study we have only considered direct interactions between the colloidal particles and not solvent-mediated indirect interactions, such as excluded volume depletion forces, the hairy hard-spheres interaction [32], or the Gourney solvation interaction, which depend on the thermodynamic state of the system [28]. We have simulated two fluid models on the spherical surface: the athermal HS one and the PHS one. By tuning the reduced temperature in the PHS model so as to get a structure similar to the one of the experimental case “a” of Table I, we were then unable to reproduce the experimental radial distribution function of the other cases “b”, “c”, and “d”. Only the HS model agrees with all four experimental cases.

Our simulations show that the HS fluid model has small correlations between particles at opposite poles even at high densities [19], this is not any more so for particles with a soft core [18]. From the point of view of our work this remains

just a theoretical prediction as our experimental measure of the radial distribution function is only able to probe half hemisphere. Moreover we expect the polystyrene particles used to be well described by the hard-core pair interaction. A further interesting comparison between the experiment and the simulation would be to compute the orientational correlation function Q_6 [33].

A possible further development of the work could be the realization of the binary mixture of small and large particles on the water droplet [34] to find experimental evidences for demixing predicted by the nonadditive hard-sphere model with negative nonadditivity [35]. Or as a possible way to push the fluidlike behavior at larger densities, diminishing the glass gap, as predicted by the additive hard-sphere model [36]. A natural extension would then be the multicomponent mixture, which in its polydisperse limit may leave no space to the glass. It would also be possible to simulate the particles as penetrable-square-well ones [37].

Colloidosomes may be used to isolate viruses when at the moment of the formation of the Pickering emulsion only one is captured inside each droplet. This may be a way to overcome the usual staining procedure. Of course the opposite situation may also be possible when many living cells, for example eukaryotic flagella [38], coordinate themselves in the confined geometry of the drop.

ACKNOWLEDGMENTS

The MC simulations were carried out at the Center for High Performance Computing (CHPC), Council of Scientific and Industrial Research (CSIR) Campus, South Africa. B.K. acknowledges support by the South African Research Chairs Initiative of the Department of Science and Technology and National Research Foundation.

APPENDIX A: PAIR CORRELATION FUNCTION

Given a classical system of N particles of mass m moving in a region \mathcal{R} of a Riemannian manifold of dimension d and metric tensor $g_{\mu\nu}(\mathbf{q})$ with Hamiltonian,

$$\mathcal{H}_N = \mathcal{T}_N + \mathcal{U}_N, \quad (\text{A1})$$

$$\mathcal{T}_N = \frac{1}{2m} \sum_{i=1}^N g^{\mu\nu}(\mathbf{q}_i) p_{i\mu} p_{i\nu}, \quad (\text{A2})$$

$$\mathcal{U}_N = U_N(\mathbf{q}_1, \dots, \mathbf{q}_N), \quad (\text{A3})$$

where we denote with $\mathbf{q} = (q^1, \dots, q^d)$ a point of the manifold, with $\mathbf{q}_i = (q_i^1, \dots, q_i^d)$ the coordinates of particle i and with $\mathbf{p}_i = (p_{i1}, \dots, p_{id})$ its canonically conjugate momenta, and we use the Einstein summation convention to omit the sum over the repeated Greek indices. The canonical ensemble probability density to find the statistical system of distinguishable particles, the fluid, in thermal equilibrium at an inverse temperature $\beta = 1/k_B T$ (with k_B Boltzmann constant) with coordinates $\mathbf{Q} = (\mathbf{q}_1, \dots, \mathbf{q}_N)$ and momenta $\mathbf{P} = (\mathbf{p}_1, \dots, \mathbf{p}_N)$ is

$$\mathcal{F}(\mathbf{Q}, \mathbf{P}, N) = \frac{1}{\Theta} \frac{1}{h^{dN} N!} e^{-\beta(\mathcal{T}_N + \mathcal{U}_N)}, \quad (\text{A4})$$

where h is Planck constant and the normalization factor Θ is the partition function of the canonical ensemble of the

identical particles

$$\begin{aligned} \Theta &= \frac{1}{h^{dN} N!} \int_{\mathcal{R}^N} d\mathbf{Q} \int d\mathbf{P} e^{-\beta(T_N + U_N)} \\ &= \frac{1}{\Lambda^{dN} N!} \int_{\mathcal{R}^N} d\mathbf{V} e^{-\beta U_N} = e^{-\beta F}, \end{aligned} \quad (\text{A5})$$

where in the second equality we performed the Gaussian integral over the conjugated momenta so that $d\mathbf{V} = d\mathbf{v}_1 \cdots d\mathbf{v}_N$ with $d\mathbf{v}_i = \sqrt{g} \prod_{\mu=1}^d dq_i^\mu$ (here $g = \det \|g_{\mu\nu}(\mathbf{q}_i)\| = [\det \|g^{\mu\nu}(\mathbf{q}_i)\|]^{-1}$) the infinitesimal volume element of the manifold and $\Lambda = \sqrt{2\pi\beta\hbar^2/m}$ is the de Broglie thermal wavelength. To justify a classical treatment of the statistical properties it is necessary that Λ be much less than the mean nearest neighbor distance between the particles. In the last equality we used the definition of entropy and F is the Helmholtz free energy.

If the particles move on a sphere of radius one, $\mathcal{R} = S_1$, then the coordinates are the polar coordinates on the sphere $\mathbf{q}_i = (\theta_i, \varphi_i)$ with $\theta_i \in [0, \pi]$ the polar angle and $\varphi_i \in [0, 2\pi]$ the azimuthal angle, and the metric tensor is

$$\|g_{\mu\nu}(\mathbf{q})\| = \begin{pmatrix} 1 & 0 \\ 0 & \sin^2 \theta \end{pmatrix}, \quad (\text{A6})$$

so that $\det \|g_{\mu\nu}(\mathbf{q}_i)\| = \sin^2 \theta_i$ and $d\mathbf{v}_i = \sin \theta_i d\theta_i d\varphi_i \equiv d\Omega_i$ the solid angle spanned by the three-dimensional vector \mathbf{r}_i of the position of particle i in the Euclidean space with origin on the sphere center. Given a physical observable only function of the coordinates $\mathcal{O}_N = \mathcal{O}_N(\mathbf{Q})$, we can then measure its average value as

$$\langle \mathcal{O}_N \rangle = \frac{\int_{\mathcal{R}^N} \mathcal{O}_N(\mathbf{Q}) e^{-\beta U_N(\mathbf{Q})} \prod_{i=1}^N d\mathbf{v}_i}{\int_{\mathcal{R}^N} e^{-\beta U_N(\mathbf{Q})} \prod_{i=1}^N d\mathbf{v}_i}. \quad (\text{A7})$$

For example the one-body correlation function [39] for the particles on a sphere of radius R is measured as

$$\rho(\mathbf{q}) = \left\langle \sum_{i=1}^N \frac{\delta^{(2)}(\mathbf{q}, \mathbf{q}_i)}{R^2} \right\rangle, \quad (\text{A8})$$

where $\delta^{(2)}(\mathbf{q}, \mathbf{q}') = \delta(\theta - \theta') \delta(\varphi - \varphi') / \sqrt{g}$ is the Dirac δ function on the manifold. We now use the fact that our potential energy (8) is invariant under any rotation of the reference frame to say that $\rho(\mathbf{q})$ has to be independent of \mathbf{q} and [by integrating (A8) over $d\mathbf{v}$] we must have $\rho(\mathbf{q}) = \rho = N / (4\pi R^2)$.

The two-body correlation function [39] is measured as

$$g(\mathbf{q}, \mathbf{q}') = \left\langle \sum_{i \neq j} \frac{\delta^{(2)}(\mathbf{q}, \mathbf{q}_i)}{R^2} \frac{\delta^{(2)}(\mathbf{q}', \mathbf{q}_j)}{R^2} \right\rangle / [\rho(\mathbf{q})\rho(\mathbf{q}')]. \quad (\text{A9})$$

Because of rotational invariance g can only depend on the geodesic distance d between \mathbf{q} and \mathbf{q}' . We can then calculate it on a reference frame where $\varphi = \varphi'$ so that $d = R(\theta - \theta')$ and

$$\begin{aligned} g(d) &= \left\langle \sum_{i \neq j} \frac{\delta(\theta - \theta_i)}{R^2 \sin \theta_i} \frac{\delta(\theta' - \theta_j)}{\sin \theta'} \delta(\varphi' - \varphi_i) \delta(\varphi' - \varphi_j) \right\rangle / \\ &\quad \times (R^2 \rho^2). \end{aligned} \quad (\text{A10})$$

If we now choose $\theta = \bar{\theta} + \theta'$ and integrate over $d\mathbf{v}'$ we get

$$g(d) = \left\langle \sum_{i \neq j} \frac{\delta(\bar{\theta} - \theta_{ij})}{R^2 \sin \theta_i} \delta(\varphi_{ij}) \right\rangle / (N\rho), \quad (\text{A11})$$

where $\theta_{ij} = \theta_i - \theta_j$ and $\varphi_{ij} = \varphi_i - \varphi_j$. We can use rotational invariance to choose the sphere north pole sitting on particle j to get further

$$g(d) = \left\langle \sum_{i \neq j} \delta(\bar{\theta} - \theta_{ij}) \delta(\varphi_{ij}) \right\rangle / (N\rho R^2 \sin \bar{\theta}). \quad (\text{A12})$$

In place of the geodesic distance $R\bar{\theta}$ we can use the Euclidean distance $d = 2R \sin(\bar{\theta}/2)$. We can then use the equality $\delta(\bar{\theta} - \theta_{ij}) = \delta(d - d_{ij})R \cos(\bar{\theta}/2)$, here $d_{ij} = 2R \sin(\theta_{ij}/2)$, to write

$$\begin{aligned} g(d) &= \left\langle \sum_{i \neq j} \delta(d - d_{ij}) \delta(\varphi_{ij}) \right\rangle / (N\rho d) \\ &= \left\langle \sum_{i \neq j} \delta(d - r_{ij}) \delta(\varphi_{ij}) \right\rangle / (N\rho d), \end{aligned} \quad (\text{A13})$$

where r_{ij} is defined in Eq. (5) of the main text. Now we use rotational invariance noticing again that given any two point \mathbf{q}_i and \mathbf{q}_j on the sphere one can always find a reference frame in which $\varphi_i = \varphi_j$ to get

$$g(d) = \left\langle \sum_{i \neq j} \delta(d - r_{ij}) \right\rangle / (N\rho 2\pi d). \quad (\text{A14})$$

APPENDIX B: MONTE CARLO SIMULATION

In the Monte Carlo integration one does a random walk [40] in \mathbf{Q} with $\theta_i \in [0, \pi]$, $\varphi_i \in [-\pi/2, \pi/2]$ for all $i = 1, \dots, N$ with periodic boundary conditions: $\varphi = \varphi + 2\pi$ and $\theta = \theta + \pi$. In the Metropolis algorithm [40] one takes as the acceptance probability

$$A[\mathbf{Q} \rightarrow \mathbf{Q}'] = \min \left\{ 1, e^{-\beta(U_N(\mathbf{Q}') - U_N(\mathbf{Q}))} \frac{\prod_{i=1}^N \sin \theta'_i}{\prod_{i=1}^N \sin \theta_i} \right\}. \quad (\text{B1})$$

- [1] A. D. Dinsmore *et al.*, *Science* **298**, 1006 (2002); C. Zeng, H. Bissig, and A. D. Dinsmore, *Solid State Comm.* **139**, 547 (2006); A. B. Subramanian, M. Abkarian, and H. A. Stone, *Nature Mat. Lett.* **4**, 553 (2005).
[2] R. F. Lee, *Spill Science and Technology Bulletin* **5**, 117 (1999); E. Dickinson, *Curr. Opin. Colloid Interface Sci.* **15**, 40 (2010); D. Rousseau, S. Ghosh, and H. Park, *J. Food. Sci.* **74**, E1 (2009); S. Lu, R. J. Pugh, and E. Forssberg, in *Interfacial Separation of*

- Particles*, Vol. 20 (Elsevier, Amsterdam, 2005); J. Frelichowska, M. A. Bolzinger, J. Pelletier, J. P. Valour, and Y. Chevalier, *International Journal of Pharmaceutics* **371**, 56 (2009); P. H. F. Hansen, S. Rödner, and L. Bergström, *Langmuir* **17**, 4867 (2001).
[3] P. Binks and T. S. Horozov, *Colloidal Particles at Liquid Interfaces* (Cambridge University Press, Cambridge, 2006); L. Hong, S. Jiang, and S. Granick, *Langmuir* **22**, 9495 (2006).

- [4] S. A. F. Bon and T. Chen, *Langmuir* **23**, 9527 (2007).
- [5] E. Pitard, M. L. Rosinberg, G. Stell, and G. Tarjus, *Phys. Rev. Lett.* **74**, 4361 (1995).
- [6] Isabelle Cantat, Sylvie Cohen-Addad, Florence Elias, François Graner, Renihard Höhler, Olivier Pitois, Florence Rouyer, and Arnaud Saint-Jalmes, *Les mousses: structure et dynamique* (Belin, Paris, 2010).
- [7] P. Pieranski, *Phys. Rev. Lett.* **45**, 569 (1980); R. Aveyard *et al.*, *ibid.* **88**, 246102 (2002); M. E. Leunissen *et al.*, *Proc. Nat. Acad. Sci. USA* **104**, 2585 (2007); K. Masschaele, B. J. Park, E. M. Furst, J. Fransaer, and J. Vermant, *Phys. Rev. Lett.* **105**, 048303 (2010); J. Guzowski, M. Tasinkevych, and S. Dietrich, *Phys. Rev. E* **84**, 031401 (2011).
- [8] M. Bowick, A. Cacciuto, D. R. Nelson, and A. Travesset, *Phys. Rev. Lett.* **89**, 185502 (2002); M. K.-H. Kiessling, *J. Stat. Phys.* **136**, 275 (2009).
- [9] J. M. Caillol, *J. Phys. Lett.* **42**, L245 (1981).
- [10] A. R. Bausch *et al.*, *Science* **299**, 1716 (2003).
- [11] P. Lipowsky, M. J. Bowick, J. H. Meinke, D. R. Nelson, and A. R. Bausch, *Nature Mat.* **4**, 407 (2005).
- [12] M. J. Bowick, D. R. Nelson, and A. Travesset, *Phys. Rev. B* **62**, 8738 (2000).
- [13] S. Sastry, D. S. Corti, P. G. Debenedetti, and F. H. Stillinger, *Phys. Rev. E* **56**, 5524 (1997).
- [14] M. J. Bowick and L. Giomi, *Adv. Phys.* **58**, 449 (2009).
- [15] C. N. Likos, *Phys. Rep.* **348**, 267 (2001); E. Zaccarelli, *J. Phys.: Condens. Matter* **19**, 323101 (2007).
- [16] R. Fantoni, B. Jancovici, and G. Téllez, *J. Stat. Phys.* **112**, 27 (2003).
- [17] R. Fantoni and G. Téllez, *J. Stat. Phys.* **133**, 449 (2008).
- [18] F. Sausset, G. Tarjus, and D. R. Nelson, *Phys. Rev. E* **81**, 031504 (2010); M. Chávez-Páez *et al.*, *J. Chem. Phys.* **119**, 7461 (2003); P. X. Viveros-Méndez, J. M. Méndez-Alcaraz, and P. González-Mozuelos, *ibid.* **128**, 014701 (2008).
- [19] S. Prestipino Giarritta, M. Ferrario, and P. V. Giaquinta, *Physica A* **187**, 456 (1992); **201**, 649 (1993).
- [20] J. W. O. Salari, G. T. Jemwa, H. M. Wyss, and B. Klumperman, *Soft Matter* **7**, 2033 (2011); J. W. O. Salari, Ph.D. thesis, Eindhoven University of Technology, 2011 (unpublished).
- [21] C. E. Smith, *J. Phys.: Conf. Ser.* **237**, 012021 (2010); L. Bruneau and S. De Bièvre, *Comm. Math. Phys.* **229**, 511 (2002).
- [22] S. U. Pickering, *J. Chem. Soc.* **91**, 2001 (1907).
- [23] J. W. O. Salari, F. A. M. Leermakers, and B. Klumperman, *Langmuir* **27**, 6574 (2011), and references therein.
- [24] L. D. Landau and E. M. Lifshitz, *Quantum Mechanics. Non-relativistic Theory*, 3rd ed., Vol. 3 (Pergamon Press, Oxford, 1977), course of Theoretical Physics. Sec. 89.
- [25] H. C. Hamaker, *Physica* **4**, 1058 (1937).
- [26] Suppose that the particles had a sticky-hard-sphere interaction [41] the surface adhesion would still be canceled by the presence of the hairs.
- [27] S. Jiang and S. Granick, *Langmuir* **24**, 2438 (2008).
- [28] D. Gazzillo, A. Giacometti, R. Fantoni, and P. Sollich, *Phys. Rev. E* **74**, 051407 (2006).
- [29] M. P. Allen and D. J. Tildesley, *Computer Simulation of Liquids* (Clarendon Press, Oxford, 1987); D. Frenkel and B. Smit, *Understanding Molecular Simulation* (Academic Press, San Diego, 1996).
- [30] E. R. Weeks and D. A. Weitz, *Chem. Phys.* **284**, 361 (2002).
- [31] Grazyna Antczak and Gert Ehrlich, *Surface Diffusion: Metals, Metal Atoms, and Clusters* (Cambridge University Press, Cambridge, 2010).
- [32] E. W. Fischer, *Kolloid Z.* **160**, 120 (1958).
- [33] P. R. ten Wolde, M. J. Ruiz-Montero, and D. Frenkel, *J. Chem. Phys.* **104**, 9932 (1996).
- [34] A. D. Law, D. M. A. Buzza, and T. S. Horozov, *Phys. Rev. Lett.* **106**, 128302 (2011).
- [35] A. Santos, M. L. de Haro, and S. B. Yuste, *J. Chem. Phys.* **132**, 204506 (2010); R. Fantoni and A. Santos, *Phys. Rev. E* **84**, 041201 (2011).
- [36] A. Santos, S. B. Yuste, M. L. de Haro, *J. Chem. Phys.* **135**, 181102 (2011).
- [37] R. Fantoni, A. Giacometti, A. Malijevský, and A. Santos, *J. Chem. Phys.* **131**, 124106 (2009).
- [38] R. E. Goldstein, M. Polin, and I. Tuval, *Phys. Rev. Lett.* **107**, 148103 (2011).
- [39] T. L. Hill, *Statistical Mechanics* (McGraw-Hill, New York, 1956).
- [40] M. H. Kalos and P. A. Whitlock, *Monte Carlo Methods* (Wiley, Weinheim, 2008).
- [41] R. Fantoni, D. Gazzillo, and A. Giacometti, *J. Chem. Phys.* **122**, 034901 (2005); *Phys. Rev. E* **72**, 011503 (2005).

Chapter 31

Localization of acoustic polarons at low temperatures: A path integral Monte Carlo approach

Fantoni R., Phys. Rev. B **86**, 144304 (2012)

Title: “Localization of acoustic polarons at low temperatures: A path integral Monte Carlo approach”

Abstract: We calculate the low temperature properties of an acoustic polaron in three dimensions in thermal equilibrium at a given temperature using a specialized path integral Monte Carlo method. In particular we show that the chosen Hamiltonian for the acoustic polaron describes a phase transition from a localized state to an unlocalized state for the electron as the phonon-electron coupling constant decreases. The phase transition manifests itself with a jump discontinuity in the potential energy as a function of the coupling constant. In the weak coupling regime the electron is in an extended state whereas in the strong coupling regime it is found in the self-trapped state.

PHYSICAL REVIEW B **86**, 144304 (2012)

Localization of acoustic polarons at low temperatures: A path-integral Monte Carlo approach

Riccardo Fantoni*

National Institute for Theoretical Physics and Institute of Theoretical Physics, University of Stellenbosch, Stellenbosch 7600, South Africa

(Received 27 April 2012; revised manuscript received 10 August 2012; published 8 October 2012)

We calculate the low-temperature properties of an acoustic polaron in three dimensions in thermal equilibrium at a given temperature using a specialized path-integral Monte Carlo method. In particular we find numerical evidence that the chosen Hamiltonian for the acoustic polaron describes a phase transition from a localized state to an unlocalized state for the electron as the phonon-electron coupling constant decreases. The phase transition manifests itself with a jump discontinuity in the potential energy as a function of the coupling constant. In the weak coupling regime the electron is in an extended state whereas in the strong coupling regime it is found in a self-trapped state.

DOI: 10.1103/PhysRevB.86.144304

PACS number(s): 71.38.Fp, 71.38.Ht

I. INTRODUCTION

An electron in an ionic crystal polarizes the lattice in its neighborhood. An electron moving with its accompanying distortion of the lattice has sometimes been called a “polaron”.^{1,2} Landau addressed the possibility whether an electron can be self-trapped (ST) in a deformable lattice.³⁻⁵ This fundamental problem in solid-state physics has been intensively studied for an optical polaron in an ionic crystal.⁶⁻¹¹ Bogoliubov approached the polaron strong coupling limit with one of his canonical transformations. Feynman used his path-integral formalism and a variational principle to develop an all-coupling approximation for the polaron ground state.¹² Its extension to finite temperatures was studied by Osaka,^{13,14} and more recently by Castrigiano *et al.*¹⁵⁻¹⁷ Recently the polaron problem has gained interest in explaining the properties of the high- T_c superconductors.¹⁸ The polaron problem has been also studied to describe impurities of lithium atoms in Bose-Einstein ultracold quantum gases condensate of sodium atoms.¹⁹ In this context evidence for a transition between free and ST polarons is found whereas for the solid-state optical polaron no ST state has been found yet.⁸⁻¹⁰ The Bogoliubov dispersion at low k is similar to that of acoustic phonons rather than to that of optical phonons.

The acoustic modes of lattice vibration are known to be responsible for the appearance of the ST state.^{1,20,21} Contrary to the optical mode, which interacts with the electron through Coulombic force and is dispersionless, the acoustic phonons have a linear dispersion coupled to the electron through a short-range potential, which is believed to play a crucial role in forming the ST state.²² Acoustic modes have also been widely studied.¹ Sumi and Toyozawa generalized the optical polaron model by including a coupling to the acoustic modes.²³ Using Feynman’s variational approach, they found that the electron is ST with a very large effective mass and small radius as the acoustic coupling exceeds a critical value. Emin and Holstein also reached a similar conclusion within a scaling theory²⁴ in which the Gaussian trial wave function is essentially identical to the harmonic trial action used in the Feynman’s variational approach in the adiabatic limit.²⁵

The ST state distinguishes itself from an extended state (ES) where the polaron has lower mass and a bigger radius. A polaronic phase transition separates the two states with a breaking of translational symmetry in the ST one.¹ The

variational approach is unable to clearly assess the existence of the phase transition.¹ Nevertheless Gerlach and Löwen¹ concluded that no phase transition exists in a large class of polarons. The three-dimensional acoustic polaron is not included in this class but Fisher *et al.*²⁵ argued that its ground state is delocalized.

In this work we employ a particular path-integral (PI) Monte Carlo (MC) method^{26,27} to the continuous, highly nonlocal, acoustic polaron problem at low temperature, which is valid at all values of the coupling strength and solves the problem exactly. Our method differs from previously employed methods²⁸⁻³⁴ since it hinges on the Lévy construction and the multilevel Metropolis method.²⁶ We calculate the potential energy and show that like the effective mass it usefully signals the transition between the ES and the ST state. Our results indicate the existence of the phase transition.

The paper is organized as follows. In Sec. II we describe the acoustic polaron mathematical model. In Sec. III we describe the observables we are interested in. Section IV contains the description of the numerical scheme used to solve the path integral. In Sec. V we report our numerical results. And Sec. VI is for final remarks.

II. MODEL

The acoustic polaron can be described by the following quasicontinuous model:^{7,23}

$$\hat{H} = \frac{\hat{p}^2}{2m} + \sum_k \hbar\omega_k \hat{a}_k^\dagger \hat{a}_k + \sum_k (i\Gamma_k \hat{a}_k e^{ik\hat{x}} + \text{H.c.}).$$

Here \hat{x} and \hat{p} are the electron coordinate and momentum operators respectively and \hat{a}_k is the annihilation operator of the acoustic phonon with wave vector k . The electron coordinate x is a continuous variable, while the phonons wave vector k is restricted by the Debye cutoff k_o . The first term in the Hamiltonian is the kinetic energy of the electron, the second term the energy of the phonons, and the third term the coupling energy between the electron and the phonons with an interaction vertex $\Gamma_k = \hbar u k_o (S/\rho_0)^{1/2} (k/k_o)^{1/2}$, where S is the coupling constant between the electron and the phonons and ρ_0 the number density of unit cells in the crystal

RICCARDO FANTONI

 PHYSICAL REVIEW B **86**, 144304 (2012)

[$\rho_0 = (4\pi/3)(k_o/2\pi)^3$ in the Debye approximation]. The acoustic phonons have a dispersion relation $\omega_k = uk$, u being the sound velocity.

Using the path-integral representation (see Ref. 12, Sec. 8.3), the phonon part in the Hamiltonian can be exactly integrated owing to its quadratic form in phonon coordinates, and one can write the partition function for a polaron in thermal equilibrium at an absolute temperature T ($\beta = 1/k_B T$, with k_B Boltzmann constant) as follows:

$$Z = \int d\mathbf{x} \int_{-}^{\mathbf{x}=\mathbf{x}(\hbar\beta)} e^{-\frac{1}{\hbar} \mathcal{S}[\mathbf{x}(t), \dot{\mathbf{x}}(t), t]} \mathcal{D}\mathbf{x}(t), \quad (1)$$

where the action \mathcal{S} is given by,^{35,36}

$$\begin{aligned} \mathcal{S} &= \frac{m}{2} \int_0^{\hbar\beta} \dot{\mathbf{x}}^2(t) dt - \frac{1}{2\hbar} \int_0^{\hbar\beta} dt \int_0^{\hbar\beta} ds \\ &\quad \times ds \int \frac{d\mathbf{k}}{(2\pi)^3} \Gamma_{\mathbf{k}}^2 e^{i\mathbf{k}\cdot(\mathbf{x}(t)-\mathbf{x}(s))-\omega_{\mathbf{k}}|t-s|}. \end{aligned} \quad (2)$$

$$= \mathcal{S}_f + \mathcal{U}. \quad (3)$$

Here \mathcal{S}_f is the *free particle action*, and \mathcal{U} the *interaction* and we denoted with a dot a time derivative as usual. Setting $\hbar = m = uk_o = k_B = 1$ the inter-action becomes,

$$\mathcal{U} = \int_0^{\beta} dt \int_0^{\beta} ds V_{\text{eff}}(|\mathbf{x}(t) - \mathbf{x}(s)|, |t - s|), \quad (4)$$

with the electron moving subject to an effective *retarded potential*,

$$V_{\text{eff}} = -\frac{S}{2I_D} \int_{q \leq 1} d\mathbf{q} q e^{i\sqrt{\frac{2}{\gamma}} \mathbf{q} \cdot (\mathbf{x}(t) - \mathbf{x}(s)) - q|t-s|}, \quad (5)$$

where $\mathbf{q} = \mathbf{k}/k_o$, $I_D = \int_{q \leq 1} d\mathbf{q} = 4\pi/3$, and we have introduced a nonadiabatic parameter γ defined as the ratio of the average phonon energy, $\hbar uk_o$, to the electron bandwidth, $(\hbar k_o)^2/2m$. This parameter is of order of 10^{-2} in typical ionic crystals with broad band (\sim eV) so that the ST state is well defined.²³ In our simulation we took $\gamma = 0.02$. One can expect two kinds of polarons: Electrons in alkali halides and silver halides are nearly ES while holes in alkali halides are in the ST state.³⁷ The hole is ES in AgBr³⁸ and ST in AgCl.³⁹ The most dramatic observation of the abrupt change of exciton from ES to ST states was made on mixed crystals AgBr_{1-x}Cl_x.⁴⁰

III. OBSERVABLES

The free energy (the ground-state energy, E , in the large β limit) of the polaron is $F = -(\partial Z/\partial\beta)/Z = \langle \mathcal{K} + \mathcal{P} \rangle$, where the first term is the kinetic energy contribution, \mathcal{K} , and the second term is the potential energy contribution, \mathcal{P} . We have,

$$F = -\frac{1}{Z} \int d\mathbf{x} \int_{-}^{\mathbf{x}} \int_{-}^{\mathbf{x}} e^{-\mathcal{S}} \frac{\partial \mathcal{S}}{\partial \beta} \mathcal{D}\mathbf{x} = \left\langle \frac{\partial \mathcal{S}}{\partial \beta} \right\rangle. \quad (6)$$

Scaling the Euclidean time $t = \beta t'$ and $s = \beta s'$ in Eq. (2), deriving \mathcal{U} with respect to β and undoing the scaling in the end we obtain for the potential,

$$\mathcal{P} = -\frac{3S}{2\beta} \int_0^{\beta} dt \int_0^{\beta} ds \int_0^1 dq q^3 \frac{\sin(\sqrt{\frac{2}{\gamma}} q |\mathbf{x}(t) - \mathbf{x}(s)|)}{\sqrt{\frac{2}{\gamma}} q |\mathbf{x}(t) - \mathbf{x}(s)|} e^{-q|t-s|} (2 - q|t-s|).$$

Taking the derivative with respect to β of the action after having scaled both the time as before and the coordinate $\mathbf{x} = \sqrt{\beta} \mathbf{x}'$ and undoing the scaling in the end we obtain for the kinetic energy,

$$\mathcal{K} = -\frac{3S}{4\beta} \int_0^{\beta} dt \int_0^{\beta} ds \int_0^1 dq q^3 \left[\cos\left(\sqrt{\frac{2}{\gamma}} q |\mathbf{x}(t) - \mathbf{x}(s)|\right) - \frac{\sin\left(\sqrt{\frac{2}{\gamma}} q |\mathbf{x}(t) - \mathbf{x}(s)|\right)}{\sqrt{\frac{2}{\gamma}} q |\mathbf{x}(t) - \mathbf{x}(s)|} \right] e^{-q|t-s|}. \quad (7)$$

In the following we will be concerned with a numerical determination of the potential energy.

IV. PATH-INTEGRAL MONTE CARLO

To calculate the PIMC, we first choose a subset of all paths. To do this, we divide the independent variable, Euclidean time, into *steps* of width $\tau = \beta/M$. This gives us a set of *times*, $t_k = k\tau$ spaced a distance τ apart between 0 and β with $k = 0, 1, 2, \dots, M$. At each time t_k we select the special point $\mathbf{x}_k = \mathbf{x}(t_k)$, the *kth time slice*. We construct a path by connecting all points so selected by straight lines. It is possible to define a sum over all paths constructed in this manner by taking a multiple integral over all values of \mathbf{x}_k for $k = 1, 2, \dots, M-1$ where $\mathbf{x}_0 = \mathbf{x}_a$ and $\mathbf{x}_M = \mathbf{x}_b$ are the two fixed ends. The simplest

discretized expression for the action can then be written as follows:

$$S = \sum_{k=1}^M \frac{(\mathbf{x}_{k-1} - \mathbf{x}_k)^2}{2\tau} + \tau^2 \sum_{i=1}^M \sum_{j=1}^M V(t_i, t_j), \quad (8)$$

where $V(t_i, t_j) = V_{\text{eff}}(|\mathbf{x}_i - \mathbf{x}_j|, |i - j|)$ is a symmetric two-variables function. In our simulation we tabulated this function taking $|\mathbf{x}_i - \mathbf{x}_j| = 0, 0.1, 0.2, \dots, 10$ and $|i - j| = 0, 1, \dots, M$. The total configuration space to be integrated over is made of elements $s = \{\mathbf{x}_0, \mathbf{x}_1, \dots, \mathbf{x}_M\}$, where \mathbf{x}_k are the path time slices subject to the periodic boundary condition $\mathbf{x}_M = \mathbf{x}_0$. In order to compute the potential energy $P = \langle \mathcal{P} \rangle$ in the simulation we wish to sample these elements from the

probability distribution, $\pi(s) = e^{-S}/Z$, where the partition function Z normalizes the function π in this space.

In our simulation we chose to use the bisection method, a particular multilevel MC method^{26,41,42} with correlated sampling. The transition probability for the first level is chosen as $T_1 \propto \exp[-(x_{i+m/2} - \bar{x})^2/2\sigma^2(m/2)]$ where $m = 2^l$, l being the number of levels, $\bar{x} = (x_i + x_{i+m})/2$ and $\sigma(t_0/\tau) = \sqrt{[(x(t) - (x(t+t_0) + x(t-t_0))/2)]^2}$ (for the first levels these deviations are smaller than the free particle standard deviations used in the Lévy construction⁴³ $\sigma_f(\ell) = \sqrt{\ell\tau/2}$ with $\ell_k = m/2^k$ in the k th level, much smaller in the ST state). And so on for the other levels: $s_2 = \{x_{i+m/4}, x_{i+3m/4}, \dots, s_l = \{x_{i+1}, x_{i+2}, \dots, x_{i+m-1}\}$. And $s_0 = \{x_0, \dots, x_i, x_{i+m}, \dots, x_{M-1}\}$ where i is chosen randomly. Calling $\tilde{\pi}(s) = e^{-U}/Z$, the level interaction is $\tilde{\pi}_k(s_0, \dots, s_k) = \int ds_{k+1} \dots ds_l \tilde{\pi}(s)$. For the k th level interaction we thus chose the following expression:

$$\tilde{\pi}_k \propto \exp \left[-(\tau \ell_k)^2 \sum_{i=1}^{[M/\ell_k]} \sum_{j=1}^{[M/\ell_k]} V(i \ell_k \tau, j \ell_k \tau) \right]. \quad (9)$$

In the last level $\ell_l = 1$ and the level interaction $\tilde{\pi}_l$ reduces to the exact interaction $\tilde{\pi}$. The acceptance probability for the first level will then be, $A_1 = \min[1, \frac{P_1(s) \tilde{\pi}_1(s) \tilde{\pi}_0(s)}{P_1(s') \tilde{\pi}_1(s') \tilde{\pi}_0(s')}]$ with $P_1 \propto \exp[-(x_{i+m/2} - \bar{x})^2[1/\sigma^2(m/2) - 1/\sigma_f^2(m/2)]]/2$. The initial path was chosen with all time slices set to 0. During the simulation we maintain the acceptance ratios in [0.15, 0.65] by decreasing (or increasing) the number of levels in the multilevel algorithm as the acceptance ratios becomes too low (or too high). We will call Monte Carlo step (MCS) an attempted move.

V. RESULTS

We simulated the acoustic polaron fixing the adiabatic coupling constant $\gamma = 0.02$ and the inverse temperature $\beta = 15$. Such temperature is found to be well suited to extract close to ground-state properties of the polaron.³² For a given coupling constant S we computed the potential energy P extrapolating (with a linear χ square fit) to the continuum time limit, $\tau \rightarrow 0$, three points corresponding to time steps chosen in the interval $\tau \in [1/100, 1/30]$. In Fig. 1 and Table I we show the results for the potential energy as a function of the coupling strength. It is clear the transition between two different regimes, which correspond to the so-called ES and ST states for the weak and strong coupling region, respectively. We found that paths related to ES and ST are characteristically distinguishable. Two typical paths for the ES and ST regimes involved in Fig. 1 are illustrated in Fig. 2. The path in ES state changes smoothly on a large time scale, whereas the path in ST state do so abruptly on a small time scale with a much smaller amplitude, which is an indication that the polaron hardly moves. The local fluctuations of the $x(t)$ and of the potential energy \mathcal{P} (MCS) have an autocorrelation function, which decay much more slowly in the ES state than in the ST one. Moreover the ES simulations are more time consuming than the ST ones.

Concerning the critical property of the transition between the ES and ST states our numerical results are in favor of

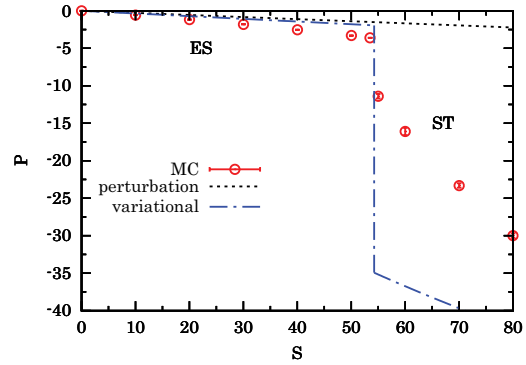


FIG. 1. (Color online) The behavior of the potential energy P as a function of the coupling constant S . The points are the MC results (see Table I), the dashed line is the second-order perturbation theory result (perturbation) and the dot-dashed line is the variational approach from Ref. 23 (variational) in the weak and strong coupling regimes.

the presence of a discontinuity in the potential energy. Even if there is no trace of a translational symmetry breaking as shown by the ST path in Fig. 2 where the initial path was $x(t) = 0$ for all t . With the increase of β , the values for the potential energy P increase in the weak coupling regime but decrease in the strong coupling region. From second-order perturbation theory (see Ref. 12, Sec. 8.2) follows that the energy shift $E(\gamma, S)$ is given by $-3S\gamma[1/2 - \gamma + \gamma^2 \ln(1 + 1/\gamma)]$ from which one extracts the potential energy shift by taking $P(\gamma, S) = \gamma dE(\gamma, S)/d\gamma$. From the Feynman variational approach of Ref. 23 follows that in the weak regime the energy shift is $-3S\gamma[1/2 - \gamma + \gamma \ln(1 + 1/\gamma)]$ and in the strong coupling regime $-S + 3\sqrt{S}/5\gamma$.

Note that since S and τ appear in the combination $S\tau^2$ in \mathcal{U} (and $S\tau$ in \mathcal{P}) the same phase transition from an ES to a ST state will be observed increasing the temperature. With the same Hamiltonian we are able to describe two very different behaviors of the acoustic polaron as the temperature changes.

TABLE I. MC results for P as a function of S at $\beta = 15$ and $\gamma = 0.02$ displayed in Fig. 1. The runs were made of 5×10^5 MCS (with 5×10^4 MCS for the equilibration) for the ES states and 5×10^6 MCS (with 5×10^5 MCS for the equilibration) for the ST states.

S	P
10	-0.573(8)
20	-1.17(2)
30	-1.804(3)
40	-2.53(3)
50	-3.31(4)
53.5	-3.61(1)
55	-11.4(3)
60	-16.1(5)
70	-23.3(3)
80	-30.0(3)

RICCARDO FANTONI

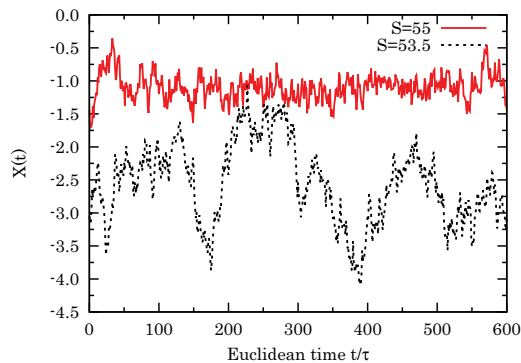
 PHYSICAL REVIEW B **86**, 144304 (2012)


FIG. 2. (Color online) The polaron closed path $\mathbf{x}(t) = [X(t), Y(t), Z(t)]$ as a function of Euclidean time t in units of τ .

VI. CONCLUSION

In conclusion we used a specialized PIMC method to study the low-temperature behavior of an acoustic polaron. At an inverse temperature $\beta = 15$, close to the ground state of the polaron, and at a nonadiabatic parameter $\gamma = 0.02$, typical of ionic crystals, we found numerical evidence for a phase transition between an ES state in the weak coupling regime and a ST one in the strong coupling regime at a value of the phonon-electron coupling constant $S^* = 54.3(7)$ in good agreement with the prediction of Ref. 23, $S^* \sim 1/\gamma$, and the MC simulations of Ref. 32.

To understand the motion of an electron in a deformable lattice we have to consider the fact that the interaction of the electron with the acoustic phonons induces a well barrier proportional to the coupling constant, but it decays due to the retarded property. In the weak coupling region, the electron can easily tunnel through the barrier so that it almost freely moves in the lattice. One can regard the tunneling of the electron as an indication of the motion of the polaron. In this case, a few phonons are involved and the acoustic polaron has a small mass, which has a similar magnitude to the mass of the electron and a large radius. In the strong coupling region, the well barrier becomes sufficiently deep and the electron is temporarily bounded in the polaron and cannot tunnel through the barrier until it gains enough energy from the phonons.

Much more phonons are involved in the polaron and the mass of the polaron becomes much greater than that of the electron with a small radius. In this argument the specific form of the interaction vertex is of fundamental importance.

We used a PIMC with the bisection method and correlated sampling as an unbiased numerical mean to probe the low-temperature properties of the acoustic polaron. This is an independent route to Feynman's variational approach and proved to give reliable results on the existence of the ST state for the electron in a deformable lattice as conceived by Landau. However, the self-trapping we observe in our numerical analysis is not a complete localization of the electron within the polarization cloud of the phonons. The electron path still undergoes small, nearly uncorrelated, fluctuations in Euclidean time in this ST state. Our numerical results support the presence of a discontinuity in the potential energy as a function of the coupling constant and this would be an indication of the existence of a phase transition between the ES and the ST states even if we found no trace of a translational symmetry breaking. Moreover the discontinuity of the ES-ST transition, if it exists, may depend on the cutoff parameter as pointed out by, for example, Ref. 9. In the cold-atom context the role of this parameter is important and the existence of a discontinuous transition is more questionable than in the solid-state polaron case.¹⁹ The present study reports a single-value study of the acoustic polaron case thus restricting the generality of the conclusions.

In a truly localized state the polaron should not diffuse at all (strong localization) or at least should attain a subdiffusive behavior (weak localization). But these properties can be checked by looking at the real-time dynamics of the system and cannot be checked by the Monte Carlo methods such as those used in this work, which deal with polaron properties in imaginary time. Clearly our numerical MC results support the claim of a discontinuity but do not give any proof of a localization transition.

A possible further study could involve the dynamic properties associated with the two different types of motion and bipolarons for short-range interacting systems.

ACKNOWLEDGMENTS

R.F. would like to thank David Ceperley for suggesting the problem and for his guidance during the preparation of the work.

*rfantoni@ts.infn.it

¹B. Gerlach and H. Löwen, *Rev. Mod. Phys.* **63**, 63 (1991).

²J. T. Devreese and A. S. Alexandrov, *Rep. Prog. Phys.* **72**, 066501 (2009).

³L. D. Landau, *Phys. Z. Sowjetunion* **3**, 644 (1933).

⁴L. D. Landau and S. Pekar, *Zh. Eksp. Teor. Fiz.* **16**, 341 (1946).

⁵L. D. Landau and S. I. Pekar, *Zh. Eksp. Teor. Fiz.* **18**, 419 (1948).

⁶H. Fröhlich, H. Pelzer, and S. Zienau, *Philos. Mag.* **41**, 221 (1950).

⁷H. Fröhlich, *Adv. Phys.* **3**, 325 (1954).

⁸R. P. Feynman, *Phys. Rev.* **97**, 660 (1955).

⁹F. M. Peeters and J. T. Devreese, *Phys. Status Solidi* **112**, 219 (1982).

¹⁰T. K. Mitra, A. Chatterjee, and S. Mukhopadhyay, *Phys. Rep.* **91**, 153 (1987).

¹¹B. A. Mason and S. Das Sarma, *Phys. Rev. B* **33**, 1412 (1986).

¹²R. P. Feynman, *Statistical Mechanics* (Benjamin, New York, 1972).

¹³Y. Osaka, *Prog. Theor. Phys.* **22**, 437 (1959).

¹⁴Y. Osaka, *J. Phys. Soc. Jpn.* **21**, 423 (1965).

¹⁵D. P. L. Castrigiano and N. Kokiantonis, *Phys. Lett. A* **96**, 55 (1983).

¹⁶D. P. L. Castrigiano and N. Kokiantonis, *Phys. Lett. A* **104**, 364 (1984).

¹⁷D. C. Khandekar and S. V. Lawande, *Phys. Rep.* **137**, 115 (1986).

- ¹⁸*Proceedings of the International Conference on Materials & Mechanism of Superconductivity, High Temperature Superconductors V*, edited by Y-Sheng He, Pei-Heng Wu, Li-Fang Xu, and Zong-Xian Zhao [Physica (Amsterdam) 282C–287C (1997)].
- ¹⁹J. Tempere, W. Casteels, M. K. Oberthaler, S. Knoop, E. Timmermans, and J. T. Devreese, *Phys. Rev. B* **80**, 184504 (2009).
- ²⁰Y. Toyozawa, *Prog. Theor. Phys.* **26**, 29 (1961).
- ²¹*Polarons and Excitons*, edited by C. G. Kuper and G. D. Whitfield (Oliver and Boyd, Edinburgh, 1963), p. 211.
- ²²F. M. Peeters and J. T. Devreese, *Phys. Rev. B* **32**, 3515 (1985).
- ²³A. Sumi and Y. Toyozawa, *J. Phys. Soc. Jpn.* **35**, 137 (1973).
- ²⁴D. Emin and T. Holstein, *Phys. Rev. Lett.* **36**, 323 (1976).
- ²⁵M. P. A. Fisher and W. Zwerger, *Phys. Rev. B* **34**, 5912 (1986).
- ²⁶D. M. Ceperley, *Rev. Mod. Phys.* **67**, 279 (1995).
- ²⁷J. T. Titantah, C. Pierleoni, and S. Ciuchi, *Phys. Rev. Lett.* **87**, 206406 (2001).
- ²⁸C. Alexandrou, W. Fleischer, and R. Rosenfelder, *Phys. Rev. Lett.* **65**, 2615 (1990).
- ²⁹C. Alexandrou and R. Rosenfelder, *Phys. Rep.* **215**, 1 (1992).
- ³⁰M. Crutz and B. Freedman, *Ann. Phys. (NY)* **132**, 427 (1981).
- ³¹M. Takahashi and M. Imada, *J. Phys. Soc. Jpn.* **53**, 963 (1983).
- ³²X. Wang, *Mod. Phys. Lett. B* **12**, 775 (1998).
- ³³P. E. Kornilovitch, *J. Phys.: Condens. Matter* **9**, 10675 (1997).
- ³⁴P. E. Kornilovitch, *J. Phys.: Condens. Matter* **19**, 255213 (2007).
- ³⁵R. P. Feynman and A. R. Hibbs, *Quantum Mechanics and Path Integrals* (McGraw-Hill, New York, 1965).
- ³⁶This is an approximation as $e^{-\beta\omega_k}$ is neglected. The complete form is obtained by replacing $e^{-\omega_k|t-s|}$ by $e^{-\omega_k|t-s|}/(1 - e^{-\beta\omega_k}) + e^{\omega_k|t-s|}e^{-\beta\omega_k}/(1 - e^{-\beta\omega_k})$. But remember that β is large.
- ³⁷W. Känzig, *Phys. Rev.* **99**, 1890 (1955).
- ³⁸R. C. Hanson and F. C. Brown, *J. Appl. Phys.* **31**, 210 (1960).
- ³⁹M. Höhne and M. Stasiw, *Phys. Status Solidi* **28**, 247 (1968).
- ⁴⁰H. Kanzaki, S. Sakuragi, and K. Sakamoto, *Solid State Commun.* **9**, 999 (1971).
- ⁴¹D. M. Ceperley and E. L. Pollock, *Phys. Rev. Lett.* **56**, 351 (1986).
- ⁴²D. M. Ceperley and E. L. Pollock, *Phys. Rev. B* **39**, 2084 (1989).
- ⁴³P. Lévy, *Compositio Math.* **7**, 283 (1939).

Chapter 32

The density of a fluid on a curved surface

Fantoni R., J. Stat. Mech. 10024 (2012)

Title: “The density of a fluid on a curved surface”

Abstract: We discuss the property of the number density of a fluid of particles living in a curved surface without boundaries to be constant in the thermodynamic limit. In particular we find a sufficient condition for the density to be constant along the Killing vector field generating a given isometry of the surface and the relevant necessary condition. We then show that the Coulomb fluid on any open surface asymptotically flat with a conformal metric with a conformal factor not a function of the azimuthal angle must have constant density in the thermodynamic limit.

The density of a fluid on a curved surface

Riccardo Fantoni

National Institute for Theoretical Physics (NITheP) and Institute of Theoretical Physics, University of Stellenbosch, Stellenbosch 7600, South Africa
E-mail: rfantoni@ts.infn.it

Received 6 June 2012

Accepted 1 October 2012

Published 30 October 2012

Online at stacks.iop.org/JSTAT/2012/P10024

[doi:10.1088/1742-5468/2012/10/P10024](https://doi.org/10.1088/1742-5468/2012/10/P10024)

Abstract. We discuss the property of the number density of a fluid of particles living on a curved surface without boundaries to be constant in the thermodynamic limit. In particular we find a sufficient condition for the density to be constant along the Killing vector field generating a given isometry of the surface, and the relevant necessary condition. We reinterpret the effect of a curvature on the fluid in a physical way as responsible for an external ‘force’ acting on the particles.

Keywords: rigorous results in statistical mechanics

Contents

1. Introduction	2
2. Statement of the problem	3
3. Reinterpretation of the curvature	4
3.1. The Coulomb pair potential	5
3.2. The Coulomb fluid	6
4. The quantum case	7
5. Conclusions	8
Acknowledgments	9
References	9

1. Introduction

The physics of fluids of particles living on surfaces is a well known subject in surface physics. A special role is played by low-dimensional, exactly analytically solvable fluids, as they give approximate solutions in higher dimensions and general sum rules. In the statistical mechanics of continuous fluids, those where the particles are allowed to move in a continuous space, one finds exact solutions for various Coulomb fluids [1]. For example the one-component Coulomb plasma (OCP) is exactly solvable in one dimension [2]. In two dimensions Jancovici and Alastuey [3, 4] proved that the OCP is exactly solvable analytically at a special value of the coupling constant. Since then, a growing interest in two-dimensional plasmas has led to this system being studied on various flat geometries [5]–[7] and two-dimensional curved surfaces, such as cylinders [8, 9], spheres [10]–[14], pseudospheres [15]–[17], and Flamm’s paraboloids [18, 19]. Among these surfaces only the last one is of non-constant curvature. The statistical mechanics of liquids and fluids in curved spaces is a field of growing interest [20].

Here we do not restrict ourselves to those exactly solvable cases but wish to find a general property of any given fluid living on a curved surface without boundaries. A *homogeneous* fluid living on a plane (or in general a Euclidean space) is known [21] to have a *constant density*. This same conclusion holds for a (non-ideal) fluid living on a surface of constant curvature in its thermodynamic limit¹. In this paper we will state what can be said about the constancy of the density for a fluid living on a Riemannian surface without boundaries and embeddable in the three-dimensional Euclidean space, in its thermodynamic limit. It is obvious that an ideal fluid (a gas) has a constant density on any surface, whether or not we are in the thermodynamic limit. But what can be said about a non-ideal fluid?

¹ The notion of thermodynamic limit will become clear further on in the paper.

The study of [18] showed that the OCP on a Flamm’s paraboloid is indeed homogeneous. We expect this occurrence to be due to the long-range nature of the Coulomb potential and argue that it cannot hold in general for other choices of the pair potential or of the surface.

In this work we will give a physical interpretation of the curvature of the surface as an external ‘force’ guiding the particles of the corresponding ‘flat’ fluid. We will show that the Coulomb potential has to be a function of the geodesic distance between the charges and we will restrict ourselves to a definition of a fluid as one made of particles with a pair interaction potential which is a function of the geodesic distance between the two particles. We will then find a necessary and sufficient condition for the density multiplied by the square root of the determinant of the metric tensor to be constant along a certain direction. We will show how this condition holds true both for non-quantum and quantum fluids.

The paper is organized as follows: in section 2 we state the problem we want to solve at the level of non-quantum fluids; in section 3 we reformulate the problem in such way as to make explicit the physical interpretation of the curvature of the surface; section 4 is devoted to the quantum fluid formulation of the problem; section 5 is for final remarks.

2. Statement of the problem

Given a non-quantum fluid of point-like particles *living on* a surface \mathcal{S} embeddable in a three-dimensional Euclidean space (note that we will not take into consideration those surfaces deriving from a Riemannian metric but not embeddable or those not deriving from a metric) and without boundaries one can define the canonical ensemble particle number density as [21]

$$\rho(\mathbf{q}_1) = \frac{N}{Z} \int_{\Omega} e^{-\beta V(\mathbf{q}_1, \dots, \mathbf{q}_N)} \prod_{i=2}^N \sqrt{g(\mathbf{q}_i)} \wedge_{\alpha_i=1}^2 \mathbf{d}q^{\alpha_i}, \tag{1}$$

$$Z = \int_{\Omega} e^{-\beta V(\mathbf{q}_1, \dots, \mathbf{q}_N)} \prod_{i=1}^N \sqrt{g(\mathbf{q}_i)} \wedge_{\alpha_i=1}^2 \mathbf{d}q^{\alpha_i}, \tag{2}$$

where N is the number of particles confined in the region Ω , $\beta = 1/k_B T$ with k_B Boltzmann’s constant and T the absolute temperature. The potential energy of the fluid is $V = \sum_{1 \leq i < j \leq N} v(d(\mathbf{q}_i, \mathbf{q}_j))$ where v is the pair potential and $d(\mathbf{q}, \mathbf{q}')$ is the geodesic distance between the two points \mathbf{q} and \mathbf{q}' . The surface is defined by a metric tensor $g_{\alpha\beta}$ so that the square of the proper length of the infinitesimal line element is given, using the usual Einstein summation convention, by $\mathbf{d}s^2 = g_{\alpha\beta}(\mathbf{q}) \mathbf{d}q^\alpha \otimes \mathbf{d}q^\beta$, where \otimes is the usual tensor product. We denote with $g(\mathbf{q}) = \det \|g_{\alpha\beta}(\mathbf{q})\|$ the Jacobian of the transformation from a locally flat reference frame to the local coordinates system on the surface. Here we use a coordinate basis $\{\mathbf{e}_\alpha = \partial_{q^\alpha}\}$ so that $\mathbf{q} = q^\alpha \mathbf{e}_\alpha$ and the symbol \mathbf{d} stands for the exterior derivative. As usual we use superscript Greek indices for contravariant components and subscript Greek indices for covariant components, and we use a subscript Roman index to denote the (distinguishable) particle number. The symbol \wedge indicates the usual wedge product. In the following we will call $\text{vol}(\Omega) = \int_{\Omega} \sqrt{g(\mathbf{q})} \wedge_{\alpha=1}^2 \mathbf{d}q^\alpha$ the *volume* of the region Ω .

The problem we want to discuss is that of finding continuous transformations that leave unchanged the density $\rho(\mathbf{q})$ in the *thermodynamic limit*. Here we think of the surface \mathcal{S} as an embeddable one without boundaries. And by thermodynamic limit we mean that, if \mathcal{S} extends to infinity, $\text{vol}(\Omega) \rightarrow \infty$ with $\bar{\rho} = N/\text{vol}(\Omega)$ kept constant, or if \mathcal{S} is closed, $\Omega \rightarrow \mathcal{S}$ with $\bar{\rho} = N/\text{vol}(\mathcal{S})$. We want to answer the question: ‘when is $\rho(\mathbf{q})$ constant on \mathcal{S} in the thermodynamic limit?’.

The number density satisfies the following normalization condition

$$\int_{\Omega} \rho(\mathbf{q}) \sqrt{g(\mathbf{q})} \Lambda_{\alpha=1}^2 \mathbf{d}q^{\alpha} = N = \text{vol}(\Omega) \bar{\rho}. \quad (3)$$

So when the density is constant on the surface we must have $\rho = \bar{\rho}$.

3. Reinterpretation of the curvature

Choosing the coordinate basis so that $\xi = \partial_{q^{\alpha}}$ is a Killing vector field [22] generating an *isometry*, then $g_{,\alpha} = 0$, where we use the usual comma convention to indicate a partial directional derivative. We know that if \mathbf{p} is the momentum of a free particle on \mathcal{S} then $\mathbf{p} \cdot \xi$ is a constant of motion $p_{\alpha}(\mathbf{p} \cdot \xi)^{\alpha} = 0$, where we use the usual semicolon convention to indicate a covariant derivative. An ideal gas has constant density on every surface, regardless of the curvature and of the thermodynamic limit. We thus have to worry about the term $\exp(-\beta V)$. Now, if one moves the N particles at $\mathbf{q}_1, \dots, \mathbf{q}_N$ along the vector field ξ , the geodesic distances among the system of particles will stay constant as well as the potential energy V . We then have proved that, given a Killing vector field $\partial_{q^{\alpha}}$, then $\rho_{,\alpha} = 0$. Strictly speaking, before taking the thermodynamic limit, the domain has boundaries, and close to these one might not be able to move the particles along the Killing vector field, invalidating the conclusion near the boundary. When taking the thermodynamic limit, one needs to be able to quantify if these boundary effects will be negligible or not, and how deep they can affect the bulk of the system. This depends on the pair potential v and on the surface. In a flat space it is well known that the boundary effects are negligible (for suitable short-range potentials and for the Coulomb potential for globally neutral systems to have screening). But for a general curved surface, a proper study of what happens in the thermodynamic limit with this boundary effect is needed and it will certainly impose additional conditions on the pair potential v , and probably also on the surface, to keep valid the conclusion that $\rho_{,\alpha} = 0$. The conditions on the surface might appear, for example, in cases similar to the pseudosphere, where it has been shown that boundary effects can be of the same order of magnitude as the bulk properties (see Refs. [15]–[17]). So, additional work in this direction is needed.

This is clearly only a *sufficient* condition, but it is enough to say that on the sphere (or the plane), a surface of constant curvature [23], where $\xi = \partial_{\varphi}$, with φ the azimuthal angle, the density will be constant in the thermodynamic limit. One, in fact, has that the density is constant along parallels. And this, given the symmetries of the sphere, means that the density is indeed everywhere constant over the whole sphere, with $\rho = \bar{\rho}$.

On the other hand a *necessary* condition can be expressed as follows: Say that we find a coordinate system such that, for all v , $(\sqrt{g\rho})_{,\alpha} = 0$, then in particular for $v = 0$ we have $\rho = \text{constant}$ and $g_{,\alpha} = 0$. For a Flamm’s paraboloid [18] we can say that there certainly

exists a fluid (at least one v) such that $(\sqrt{g}\rho)_{,r} \neq 0$, since ∂_r is not a Killing vector of the surface and $g_{,r} \neq 0$. And we know [18] that the OCP is an example.

The problem then reduces to understanding what can be said about surfaces of non-constant curvature. Note that we can as well rewrite equation (1) as follows

$$\sqrt{g(\mathbf{q}_1)}\rho(\mathbf{q}_1) = N \frac{\int_{\Omega} e^{-\beta[V(\mathbf{q}_1, \dots, \mathbf{q}_N) + \sum_{i=1}^N \phi(\mathbf{q}_i; \beta)]} \prod_{i=2}^N \wedge_{\alpha_i=1}^2 \mathbf{d}q^{\alpha_i}}{\int_{\Omega} e^{-\beta[V(\mathbf{q}_1, \dots, \mathbf{q}_N) + \sum_{i=1}^N \phi(\mathbf{q}_i; \beta)]} \prod_{i=1}^N \wedge_{\alpha_i=1}^2 \mathbf{d}q^{\alpha_i}}, \quad (4)$$

where $\phi(\mathbf{q}; \beta) = -[\ln g(\mathbf{q})]/2\beta$ is an ‘external potential’. A form which suggests, on physical grounds, a local dependence of the density on the curvature. The fluid is seen in this formulation as living on a ‘flat space’, the two-dimensional space determined by the local coordinates chart (q^1, q^2) used in the surface, subject to an external potential induced by the metric. This suggestive reinterpretation of the problem can sometimes lead to a wrong intuition. For example, we know that the OCP on a Flamm’s paraboloid (see section 4.2.4 of [18]) has a density that is everywhere constant, even if this surface is only asymptotically flat but curved near the ‘horizon’, the scalar curvature being proportional to the Euclidean distance r from the origin to the power of minus three. Whereas the constancy of the density along the azimuthal direction φ has to be expected from the sufficient condition stated above, the constancy of the density along the radial r direction is not at all intuitive, even more so in the light of the discussion which follows.

For a surface with a conformal metric $g_{\alpha\beta} = \sqrt{g(\mathbf{q})}\delta_{\alpha\beta}$,² the scalar curvature R can be written as

$$R(\mathbf{q}) = e^{\beta\phi(\mathbf{q})}\beta\Delta_{\text{flat}}\phi(\mathbf{q}), \quad (5)$$

where $\Delta_{\text{flat}} = \partial_{q^1}^2 + \partial_{q^2}^2$ is the flat Laplace operator. The external ‘force’ acting on the particles due to the curvature is then $-R \exp(-\beta\phi)/\beta$. For a Flamm’s paraboloid [18] the force acting on the charges turns out to be $4/[\beta s(1+s)^2]$, where $s = \sqrt{(q^1)^2 + (q^2)^2}$. As we have already mentioned above, in this case, the OCP shows a constant density on the surface. In section 3.2 we show that in general one would expect a non-constant density.

On the other hand the formulation of equation (4) suggests that $\sqrt{g}\rho$ should certainly be regarded as a more fundamental quantity than ρ .

3.1. The Coulomb pair potential

Here we want to show that the Coulomb potential between two charged particles living on a given surface \mathcal{S} has to be a function of the geodesic distance between the charges [3, 8, 10, 15, 16, 18].

The Coulomb potential is defined by the Poisson equation,

$$\Delta_{\mathbf{q}} v_{\text{Coul}}(\mathbf{q}, \mathbf{q}') = -2\pi\delta^{(2)}(\mathbf{q}, \mathbf{q}'), \quad (6)$$

where $\Delta_{\mathbf{q}}$ is the Laplace–Beltrami operator and $\delta^{(2)}(\mathbf{q}, \mathbf{q}') = \delta^{(2)}(d(\mathbf{q}, \mathbf{q}'))$ the Dirac delta function, in the surface \mathcal{S} . The Laplace–Beltrami operator is invariant to isometries. This means that if the charge at \mathbf{q} and the one at \mathbf{q}' are moved along the vector field of

² Note that the following are all surfaces of this kind: the sphere embedded in three-dimensional Euclidean space $\sqrt{g} = 4/(1+s^2)^2$, the pseudosphere embedded in three-dimensional Minkowski space $\sqrt{g} = 4/(1-s^2)^2$, the cylinder embedded in three-dimensional Euclidean space $\sqrt{g} = 1$, and a Flamm’s paraboloid embedded in three-dimensional Euclidean space $\sqrt{g} = (1 + 1/s)^4$. Here $s = \sqrt{(q^1)^2 + (q^2)^2}$.

an isometry the Laplace-Beltrami operator will not change. Neglecting eventual additive functions which have a null Laplacian we must have

$$v_{\text{Coul}} = f(d(\mathbf{q}, \mathbf{q}')). \tag{7}$$

For example on the sphere [10] of radius R one finds $f(x) = -\ln(2R \sin(x/2R)/L)$, with L a length scale. The conclusion of equation (7) is in agreement with Fermat's principle for light propagation [24].

3.2. The Coulomb fluid

For an open surface with a conformal metric $g_{\alpha\beta} = (\sqrt{g(s)}/s)\delta_{\alpha\beta}$, $s \in [0, +\infty[$ the Laplace-Beltrami operator can be rewritten as

$$\Delta f = \frac{s}{\sqrt{g}} \Delta_{\text{flat}} f, \tag{8}$$

where Δ_{flat} is the usual Laplace operator in flat space ($x = s \cos \varphi, y = s \sin \varphi$). We can then introduce a complex coordinate $z = se^{i\varphi}$ and the Laplacian Green's function (6)

$$\Delta_{\text{flat}} v_{\text{Coul}}((s, \varphi), (s_0 \varphi_0)) = -2\pi \frac{1}{s} \delta(s - s_0) \delta(\varphi - \varphi_0) \tag{9}$$

can be solved as usual, by using the decomposition as a Fourier series. Since (6) reduces to the flat Laplacian Green's function, the solution is the standard one

$$v_{\text{Coul}}((s, \varphi), (s_0 \varphi_0)) = \sum_{n=1}^{\infty} \frac{1}{n} \left(\frac{s_{<}}{s_{>}} \right)^n \cos[n(\varphi - \varphi_0)] + v_0(s, s_0), \tag{10}$$

where $s_{>} = \max(s, s_0)$ and $s_{<} = \min(s, s_0)$. The Fourier coefficient for $n = 0$ has the form

$$v_0(s, s_0) = \begin{cases} a_0^+ \ln s + b_0^+ & s > s_0 \\ a_0^- \ln s + b_0^- & s < s_0 \end{cases}, \tag{11}$$

and it has to satisfy the boundary conditions that v_0 should be continuous at $s = s_0$, $a_0^+ \ln s_0 + b_0^+ = a_0^- \ln s_0 + b_0^-$, and its derivative discontinuous due to the Dirac delta in (9), $a_0^+/s_0 - a_0^-/s_0 = -1/s_0$. Summing explicitly the Fourier series (10) and requiring additionally that the Coulomb potential $v_{\text{Coul}}(s_1, s_2)$ be symmetric under exchange of 1 and 2 we find

$$v_{\text{Coul}}(s, \varphi; s_0, \varphi_0) = -\ln \frac{|z - z_0|}{h(s, s_0)} + a, \tag{12}$$

with $h(s, s_0) = 1$ or $h(s, s_0) = \sqrt{ss_0}$, and a a constant. Here if we imagine the plasma confined into a disk Ω_R of radius R we can choose

$$v_{\text{Coul}}(s, \varphi; s_0, \varphi_0) = -\ln \frac{|z - z_0|}{h(s, s_0)} + b, \tag{13}$$

with $h(s, s_0) = R$ and $b = a - \ln R$, or $h(s, s_0) = \sqrt{ss_0}$ and $b = a$, so that if we rescale all the s into λs and R into λR the Coulomb potential does not change apart from an additive constant. Imagine now we are on a plane [3], then $h(s, s_0) = R$. Then in the definition of the density (1) at any temperature we can change integration variables in the

The density of a fluid on a curved surface

numerator from (s_i, φ_i) to $(x_i = s_i e^{i(\varphi_i - \varphi_1)}, y_i = \varphi_i - \varphi_1)$ for $i = 2, 3, \dots, N$ with Jacobian 1. Calling $v_b = v_b(s/R) = \bar{\rho} \int_{\Omega_R} v_{\text{Coul}}(s, \varphi; s', \varphi') \sqrt{g(s')} ds' \varphi'$ the neutralizing background potential and v_0 the self energy of the background we can write

$$\rho(s_1, \varphi_1) = \frac{N}{Z} e^{-\beta[v_b(s_1/R) + v_0]} \int_{\Omega_R} \prod_{i>j \geq 2} e^{-\beta v_{\text{Coul}}(\mathbf{q}_i; \mathbf{q}_j)} \prod_{k=2}^N \left(\frac{|x_k - s_1|}{R} \right)^{\beta q^2} \times e^{-\beta v_b(x_k e^{-iy_k}/R)} \sqrt{g(x_k e^{-iy_k})} dx_k dy_k. \tag{14}$$

The integral does not depend on φ_1 , so $\rho(s_1, \varphi_1) = \rho(s_1)$. Now we can make a change of variables where $s_k \rightarrow s_k/s_1$ for $k = 2, 3, \dots, N$ and $R/s_1 \rightarrow T$ so that

$$\rho(s_1) = \frac{N}{Z} e^{-\beta[v_b(1/T) + v_0]} \int_{\Omega_T} \prod_{i>j \geq 2} e^{-\beta v_{\text{Coul}}(\mathbf{q}_i; \mathbf{q}_j)} \prod_{k=2}^N \left(\frac{|x_k - 1|}{T} \right)^{\beta q^2} \times e^{-\beta v_b(s_k/T)} \sqrt{g(s_k s_1)} s_1^{N-1} dx_k dy_k. \tag{15}$$

On a plane $\sqrt{g(ss_1)} = ss_1$, so that in equation (15) there is a multiplicative factor $s_1^{2(N-1)}$. So in the thermodynamic limit $T \rightarrow \infty$ and $N \rightarrow \infty$ we can say that $\rho(s_1) = \text{constant}$, since we know that we must have a well defined thermodynamic limit. The same conclusion holds on a pseudosphere (see section 4.3.2 of [16]), on a cylinder (see equation (12a) of [9]), and on a Flamm’s paraboloid (see section 4.2.4 of [18]). In these cases the explicit analytic expression of the density has been determined for the finite system as a function of the properties of the surface at the special value of the coupling constant $\beta q^2 = 2$. To the best of our knowledge there are no analytical results in the literature where the OCP has been found to have a non-constant number density in the thermodynamic limit on a given curved surface, and probably one has to resort to numerical simulations [25]. It certainly has to be expected that in a general curved surface the OCP in the thermodynamic limit may have a non-constant density, otherwise it would mean that an OCP in the plane has a uniform density for an arbitrary external field. It might actually be true that the effects of the metric and the background potential cancel one another when the potential is determined by Poisson’s equation, but if it is true, it will be necessary to solve for the potential in more detail to prove it.

4. The quantum case

For the quantum fluid we find for the canonical ensemble distinguishable density matrix (the full density matrix for a system of bosons or fermions is then obtained by symmetrization or anti-symmetrization respectively) [26]

$$\rho_D(\mathbf{Q}', \mathbf{Q}; \beta) = \int \rho_D(\mathbf{Q}', \mathbf{Q}((M-1)\tau); \tau) \cdots \rho_D(\mathbf{Q}(\tau), \mathbf{Q}; \tau) \prod_{j=1}^{M-1} \sqrt{\tilde{g}_{(j)}} \prod_{\alpha=1}^{2N} dQ^\alpha(j\tau), \tag{16}$$

where as usual we discretize the imaginary time in bits $\tau = \hbar\beta/M$ and $\mathbf{Q} = (\mathbf{q}_1, \dots, \mathbf{q}_N)$ with

$$\tilde{g}_{(i)} = \det \|\tilde{g}_{\mu\nu}(\mathbf{Q}(i\tau))\|, \tag{17}$$

$$\tilde{g}_{\mu\nu}(\mathbf{Q}) = g_{\alpha_1\beta_1}(\mathbf{q}_1) \otimes \cdots \otimes g_{\alpha_N\beta_N}(\mathbf{q}_N), \tag{18}$$

J. Stat. Mech. (2012) P10024

to get to the path integral formulation, and in the small τ limit for particles of unitary mass it follows that

$$\rho(\mathbf{Q}(2\tau), \mathbf{Q}(\tau); \tau) = (2\pi\hbar)^{-N} \tilde{g}_{(2)}^{-1/4} \sqrt{D(\mathbf{Q}(2\tau), \mathbf{Q}(\tau); \tau)} \tilde{g}_{(1)}^{-1/4} \times e^{\hbar\tau R(\mathbf{Q}(\tau))/12} e^{-(1/\hbar)S(\mathbf{Q}(2\tau), \mathbf{Q}(\tau); \tau)}, \quad (19)$$

where R is the scalar curvature of the surface, S the action and D the van Vleck's determinant

$$D_{\mu\nu} = -\frac{\partial^2 S(\mathbf{Q}(2\tau), \mathbf{Q}(\tau); \tau)}{\partial Q^\mu(2\tau) \partial Q^\nu(\tau)}, \quad (20)$$

$$D(\mathbf{Q}(2\tau), \mathbf{Q}(\tau); \tau) = \det \|D_{\mu\nu}\|. \quad (21)$$

For example for free particles

$$\mathcal{H} = \frac{1}{2} \sum_{i=1}^N g^{\alpha_i \beta_i}(\mathbf{q}_i) p_{\alpha_i} p_{\beta_i} = \frac{1}{2} \sum_{i=1}^N g_{\alpha_i \beta_i}(\mathbf{q}_i) \dot{q}^{\alpha_i} \dot{q}^{\beta_i}, \quad (22)$$

$$S(\mathbf{Q}(2\tau), \mathbf{Q}(\tau); \tau) = K(\mathbf{Q}(2\tau), \mathbf{Q}(\tau); \tau) = \frac{1}{2} \sum_{i=1}^N d^2(\mathbf{q}_i(2\tau), \mathbf{q}_i(\tau))/\tau, \quad (23)$$

and for the fluid

$$S(\mathbf{Q}(2\tau), \mathbf{Q}(\tau); \tau) = K(\mathbf{Q}(2\tau), \mathbf{Q}(\tau); \tau) + \tau V(\mathbf{Q}(\tau)). \quad (24)$$

We then find the partition function through the integral

$$Z = \int \rho_D(\mathbf{Q}, \mathbf{Q}; \beta) \sqrt{\tilde{g}} d\mathbf{Q}, \quad (25)$$

and the number density by

$$\sqrt{g(\mathbf{q}_1)} \rho(\mathbf{q}_1) = N \frac{\int \rho_D(\mathbf{Q}, \mathbf{Q}; \beta) \sqrt{\tilde{g}} \prod_{i=2}^N d\mathbf{q}_i}{Z}. \quad (26)$$

It is then apparent that by choosing the same isometry on each imaginary time slice we reach the same conclusion as in section 3 for the classical (non-quantum) fluid.

5. Conclusions

We showed that in a surface of constant curvature without boundaries the local number density $\rho(\mathbf{q})$ of a non-ideal, ($V \neq 0$), fluid is a constant in the thermodynamic limit. Clearly the ideal gas has constant density on every surface regardless of the curvature and of the thermodynamic limit.

The Coulomb potential for particles living on the surface depends on the metric tensor and is in general a function of the geodesic distance between the two charges. The *Coulomb fluid* density is a constant in the thermodynamic limit in the plane [3] the sphere [10] and the pseudosphere [15]–[17], all surfaces of constant curvature, but also on the Flamm's paraboloid [18], a surface of non-constant curvature.

We proposed a formulation for the number density which gives to the curvature of a surface with a conformal metric (the sphere, the pseudosphere and the Flamm's paraboloid

are three surfaces of this kind) a physical interpretation as an additional external ‘force’ acting on the system of particles moving in the corresponding ‘flat space’. The formulation, although suggestive, partly masks the intuition of the properties of the density because of the fact that the pair potential is inherently related to the properties of the curved surface, *i.e.* the geodesic distance between two points, which cannot be translated in terms of the properties of the corresponding fluid moving in the ‘flat space’ in a straightforward way. On the other hand the formulation suggests that the combination $\sqrt{g}\rho$ is a more fundamental quantity than just ρ itself. One can show both for the non-quantum and the quantum fluid that if ∂_{q^α} is a Killing vector field of the surface then if we can neglect surface effects $[\sqrt{g(\mathbf{q})}\rho(\mathbf{q})]_{,\alpha} = 0$ and if $[\sqrt{g(\mathbf{q})}\rho(\mathbf{q})]_{,\alpha} = 0, \forall v$ then $g_{,\alpha} = 0$. These are the main results of our discussion. We can also say that $g_{,\alpha} = 0$ if and only if $[\sqrt{g(\mathbf{q})}\rho(\mathbf{q})]_{,\alpha} = 0, \forall v$.

The total potential energy of the fluid moving in the ‘flat space’ is $U(\mathbf{Q}) = V(\mathbf{Q}) + \sum_i \phi(\mathbf{q}_i; \beta)$, where the functional dependence on \mathbf{Q} of the first term depends both on the fluid model, through $v(d(\mathbf{q}_i, \mathbf{q}_j))$, and the kind of surface, through d , whereas the functional form of the second term depends *only* on the kind of surface. It is then to be expected that given a fluid model the density can be non-constant on certain surfaces.

The OCP has uniform density on the cylinder (see equation (12a) of [9]), on the pseudosphere (see section 4.3.2 of [16]), and on the Flamm’s paraboloid (see section 4.2.4 of [18]). In these cases the explicit expression of the density has been determined for the finite system as a function of the properties of the surface at the special value of the coupling constant $\beta q^2 = 2$. To the best of our knowledge there are no analytical results in the literature where the OCP has been found to have a non-constant number density in the thermodynamic limit on a given curved surface, and probably one has to resort to numerical simulations [25].

It would be important, in the future, to be able to understand if the surface effects on the finite system have some influence in the conclusion that if ∂_{q^α} is a Killing vector field of the surface then $[\sqrt{g(\mathbf{q})}\rho(\mathbf{q})]_{,\alpha} = 0$ in the thermodynamic limit.

Acknowledgments

I would like to thank the National Institute for Theoretical Physics of South Africa and the Institute of Theoretical Physics of the University of Stellenbosch, where the work was started. Also I would like to thank Karl Möller for stimulating the initiation of this work.

References

- [1] March N H and Tosi M P, 1984 *Coulomb Liquids* (New York: Academic Press)
- [2] Edwards S F and Lenard A, 1962 *J. Math. Phys.* **3** 778
- [3] Jancovici B, 1981 *Phys. Rev. Lett.* **46** 386
- [4] Alastuey A and Jancovici B, 1981 *J. Physique* **42** 1
- [5] Rosinberg M L and Blum L, 1984 *J. Chem. Phys.* **81** 3700
- [6] Jancovici B, Manificat G and Pisani C, 1994 *J. Stat. Phys.* **76** 307
- [7] Jancovici B and Téllez G, 1996 *J. Stat. Phys.* **82** 609
- [8] Choquard Ph, 1981 *Helv. Phys. Acta* **54** 332
- [9] Choquard Ph, Forrester P J and Smith E R, 1983 *J. Stat. Phys.* **33** 13
- [10] Caillol J M, 1981 *J. Physique Lett.* **42** L-245
- [11] Forrester P J, Jancovici B and Madore J, 1992 *J. Stat. Phys.* **69** 179
- [12] Forrester P J and Jancovici B, 1996 *J. Stat. Phys.* **84** 337

The density of a fluid on a curved surface

- [13] Téllez G and Forrester P J, 1999 *J. Stat. Phys.* **97** 489
- [14] Jancovici B, 2000 *J. Stat. Phys.* **99** 1281
- [15] Jancovici B and Téllez G, 1998 *J. Stat. Phys.* **91** 953
- [16] Fantoni R, Jancovici B and Téllez G, 2003 *J. Stat. Phys.* **112** 27
- [17] Jancovici B and Téllez G, 2004 *J. Stat. Phys.* **116** 205
- [18] Fantoni R and Téllez G, 2008 *J. Stat. Phys.* **133** 449
- [19] Fantoni R, 2012 *J. Stat. Mech.* **P04015**
- [20] Tarjus G, Sausset F and Viot P, *Statistical mechanics of liquids and fluids in curved space*, 2011 *Advances in Chemical Physics* vol 148, ed S A Rice and A R Dinner (Hoboken, NJ: John Wiley) ch 4
- [21] Hill T L, 1956 *Statistical Mechanics* (New York: McGraw-Hill)
- [22] Misner C W, Thorne K S and Wheeler J A, 1973 *Gravitation* (New York: Freeman) Section 25.2
- [23] Kühnel W, 2006 *Differential Geometry: Curves-Surfaces-Manifolds* 2nd edn (Providence, RI: American Mathematical Society) Liebmann theorem 4.51
- [24] Rossi B, 1957 *Optics* (London: Addison-Wesley) Section 2-4
- [25] Caillol J M, Levesque D, Weis J J and Hansen J P, 1982 *J. Stat. Phys.* **28** 325
- [26] Schulman L S, 1981 *Techniques and Applications of Path Integrals* (New York: Wiley)

J. Stat. Mech. (2012) P10024

Part XIII
2013

Chapter 33

Low temperature acoustic polaron localization

Fantoni R., Physica B **412**, 112 (2013)

Title: “Low temperature acoustic polaron localization”

Abstract: We calculate the properties of an acoustic polaron in three dimensions in thermal equilibrium at a given low temperature using the path integral Monte Carlo method. The specialized numerical method used is described in full details, thus complementing our previous paper [R. Fantoni, Phys. Rev. B **86**, 144304 (2012)], and it appears to be the first time it has been used in this context. Our results are in favor of the presence of a phase transition from a localized state to an extended state for the electron as the phonon-electron coupling constant decreases. The phase transition manifests itself with a jump discontinuity in the potential energy as a function of the coupling constant and it affects the properties of the path of the electron in imaginary time: In the weak coupling regime the electron is in an extended state whereas in the strong coupling regime it is found in a self-trapped state.



Contents lists available at SciVerse ScienceDirect

Physica B

journal homepage: www.elsevier.com/locate/physb

Low temperature acoustic polaron localization

Riccardo Fantoni*

Dipartimento di Scienze dei Materiali e Nanosistemi, Università Ca' Foscari Venezia, Calle Larga S. Marta DD2137, I-30123 Venezia, Italy

ARTICLE INFO

Article history:

Received 10 October 2012
Received in revised form
12 December 2012
Accepted 21 December 2012
Available online 27 December 2012

Keywords:

Acoustic polaron
Path integral Monte Carlo simulation
Localization

ABSTRACT

We calculate the properties of an acoustic polaron in three dimensions in thermal equilibrium at a given low temperature using the path integral Monte Carlo method. The specialized numerical method used is described in full details, thus complementing our previous paper [R. Fantoni, Phys. Rev. B 86 (2012) 144304], and it appears to be the first time it has been used in this context. Our results are in favor of the presence of a phase transition from a localized state to an extended state for the electron as the phonon–electron coupling constant decreases. The phase transition manifests itself with a jump discontinuity in the potential energy as a function of the coupling constant and it affects the properties of the path of the electron in imaginary time: In the weak coupling regime the electron is in an extended state whereas in the strong coupling regime it is found in a self-trapped state.

© 2012 Elsevier B.V. All rights reserved.

1. Introduction

An electron in a ionic crystal polarizes the lattice in its neighborhood. An electron moving with its accompanying distortion of the lattice has sometimes been called a “polaron” [1,2]. Since 1933 Landau addresses the possibility whether an electron can be self-trapped (ST) in a deformable lattice [3–5]. This fundamental problem in solid state physics has been intensively studied for an optical polaron in an ionic crystal [6–11]. Bogoliubov approached the polaron strong coupling limit with one of his canonical transformations. Feynman used his path integral formalism and a variational principle to develop an all coupling approximation for the polaron ground state [12]. Its extension to finite temperatures appeared first by Osaka [13,14], and more recently by Castrigiano et al. [15–17]. Recently the polaron problem has gained new interest as it could play a role in explaining the properties of the high T_c superconductors [18]. The polaron problem has also been studied to describe an impurity in a Bose–Einstein ultracold quantum gas condensate of atoms [19]. In this context evidence for a transition between free and self-trapped optical polarons is found. For the solid state optical polaron no ST state has been found yet [8,9,11].

The acoustic modes of lattice vibration are known to be responsible for the appearance of the ST state [20,21,1]. Contrary to the optical mode which interacts with the electron through Coulombic force and is dispersionless, the acoustic phonons have a linear dispersion coupled to the electron through a short range potential which is believed to play a crucial role in forming the ST

state [22]. Acoustic modes have also been widely studied [1]. Sumi and Toyozawa generalized the optical polaron model by including a coupling to the acoustic modes [23]. Using Feynman's variational approach, they found that the electron is ST with a very large effective mass as the acoustic coupling exceeds a critical value. Emin and Holstein also reached a similar conclusion within a scaling theory [24] in which the Gaussian trial wave function is essentially identical to the harmonic trial action used in the Feynman's variational approach in the adiabatic limit [25].

The ST state distinguishes itself from an extended state (ES) where the polaron has lower mass and a bigger radius. A polaronic phase transition separates the two states with a breaking of translational symmetry in the ST one [1]. The variational approach is unable to clearly assess the existence of the phase transition [1]. In particular Gerlach and Löwen [1] concluded that no phase transition exists in a large class of polarons. The three-dimensional acoustic polaron is not included in the class but Fisher et al. [25] argued that its ground state is delocalized.

In a recent work [26] we employed for the first time a specialized path integral Monte Carlo (PIMC) method [27,28] to the continuous, highly non-local, acoustic polaron problem at low temperature which is valid at all values of the coupling strength and solves the problem exactly (in a Monte Carlo sense). The method differs from previously employed methods [29–35] and hinges on the Lévy construction and the multilevel Metropolis method with correlated sampling. In such work the potential energy was calculated and it was shown that like the effective mass it usefully signals the transition between the ES and the ST state. Properties of ES and ST states were explicitly shown through the numerical simulation.

Aim of the present paper is to give a detailed description of the PIMC method used in that calculation and some additional numerical results in order to complement the brief paper of Ref. [26].

* Tel.: +39 3384570334.

E-mail addresses: rfantoni3@gmail.com, rfantoni@ts.infn.it

The work is organized as follows: in Section 2 we describe the acoustic polaron model and Hamiltonian, in Section 3 we describe the observables we are going to compute in the simulation, in Section 4 we describe the PIMC numerical scheme employed, in Section 5 we describe the multilevel Metropolis method for sampling the path, in Section 6 we describe the choice of the transition probability and the level action, in Section 7 we describe the correlated sampling. Section 8 is for the results and Section 9 is for final remarks.

2. The model

The acoustic polaron can be described by the following quasi-continuous model [7,23]:

$$\hat{H} = \frac{\hat{p}^2}{2m} + \sum_{\mathbf{k}} \hbar \omega_{\mathbf{k}} \hat{a}_{\mathbf{k}}^\dagger \hat{a}_{\mathbf{k}} + \sum_{\mathbf{k}} (i \Gamma_{\mathbf{k}} \hat{a}_{\mathbf{k}} e^{i\mathbf{k}\cdot\hat{\mathbf{x}}} + \text{H.c.}). \quad (1)$$

Here $\hat{\mathbf{x}}$ and $\hat{\mathbf{p}}$ are the electron coordinate and momentum operators respectively and $\hat{a}_{\mathbf{k}}$ is the annihilation operator of the acoustic phonon with wave vector \mathbf{k} . The first term in the Hamiltonian is the kinetic energy of the electron, the second term the energy of the phonons and the third term the coupling energy between the electron and the phonons. The electron coordinate \mathbf{x} is a continuous variable, while the phonons wave vector \mathbf{k} is restricted by the Debye cut-off k_o . The acoustic phonons have a dispersion relation $\omega_{\mathbf{k}} = u k$ (u being the sound velocity) and they interact with the electron of mass m through the interaction vertex $\Gamma_{\mathbf{k}} = \hbar u k_o (S/N)^{1/2} (k/k_o)^{1/2}$ according to the deformation potential analysis of Ref. [36]. S is the coupling constant between the electron and the phonons and N is the number of unit cells in the crystal with $N/V = (4\pi/3)(k_o/2\pi)^3$ by Debye approximation and V is the crystal volume.

Using the path integral representation (see Ref. [12] Section 8.3), the phonon part in the Hamiltonian can be exactly integrated owing to its quadratic form in phonon coordinates, and one can write the partition function for a polaron in thermal equilibrium at an absolute temperature T ($\beta = 1/k_B T$, with k_B Boltzmann constant) as follows:

$$Z = \int d\mathbf{x} \int_{\mathbf{x}=\mathbf{x}(0)}^{\mathbf{x}=\mathbf{x}(\hbar\beta)} e^{-(1/\hbar)S[\mathbf{x}(t),\dot{\mathbf{x}}(t),t]} \mathcal{D}\mathbf{x}(t), \quad (2)$$

where the action S is given by Ref. [37]¹

$$S = \frac{m}{2} \int_0^{\hbar\beta} \dot{\mathbf{x}}^2(t) dt - \frac{1}{2\hbar} \int_0^{\hbar\beta} dt \int_0^{\hbar\beta} ds \int \frac{d\mathbf{k}}{(2\pi)^3} \Gamma_{\mathbf{k}}^2 e^{i\mathbf{k}\cdot(\mathbf{x}(t)-\mathbf{x}(s)) - \omega_{\mathbf{k}}|t-s|} = S_f + \mathcal{U}. \quad (3)$$

Here S_f is the free particle action and \mathcal{U} is the inter action and we denoted with a dot a time derivative as usual. Using dimensionless units $\hbar = m = u k_o = k_B = V = 1$ the action becomes

$$S = \int_0^{\beta} \frac{\dot{\mathbf{x}}^2(t)}{2} dt + \int_0^{\beta} dt \int_0^{\beta} ds V_{\text{eff}}(|\mathbf{x}(t)-\mathbf{x}(s)|, |t-s|), \quad (4)$$

with the electron moving subject to an effective retarded potential

$$V_{\text{eff}} = -\frac{S}{2I_D} \int_{q \leq 1} d\mathbf{q} q e^{i\sqrt{2/\gamma}\mathbf{q}\cdot(\mathbf{x}(t)-\mathbf{x}(s)) - q|t-s|} \quad (5)$$

$$V_{\text{eff}} = -\frac{3S}{2} \sqrt{\frac{\gamma}{2}} \frac{1}{|\mathbf{x}(t)-\mathbf{x}(s)|} \int_0^1 dq q^2 \sin\left(\sqrt{\frac{2}{\gamma}} q |\mathbf{x}(t)-\mathbf{x}(s)|\right) e^{-q|t-s|}, \quad (6)$$

¹ This is an approximation as $e^{-\beta\omega_{\mathbf{k}}}$ is neglected. The complete form is obtained by replacing $e^{-\omega_{\mathbf{k}}|t-s|}$ by $e^{-\omega_{\mathbf{k}}|t-s|}/(1-e^{-\beta\omega_{\mathbf{k}}}) + e^{\omega_{\mathbf{k}}|t-s|} e^{-\beta\omega_{\mathbf{k}}}/(1-e^{-\beta\omega_{\mathbf{k}}})$. But remember that β is large.

where $\mathbf{q} = \mathbf{k}/k_o$, $I_D = \int_{q \leq 1} d\mathbf{q} = 4\pi/3$, and we have introduced a non-adiabatic parameter γ defined as the ratio of the average phonon energy, $\hbar u k_o$ to the electron band-width, $(\hbar k_o)^2/2m$. This parameter is of order of 10^{-2} in typical ionic crystals with broad band so that the ST state is well-defined [23]. In our simulation we took $\gamma = 0.02$. Note that the integral in Eq. (6) can be solved analytically and the resulting function tabulated.

3. The observables

In particular the internal energy E of the polaron is given by

$$E = -\frac{1}{Z} \frac{\partial Z}{\partial \beta} = \frac{1}{Z} \int d\mathbf{x} \int_{\mathbf{x}} e^{-S} \frac{\partial S}{\partial \beta} \mathcal{D}\mathbf{x} = \left\langle \frac{\partial S}{\partial \beta} \right\rangle, \quad (7)$$

where the internal energy tends to the ground state energy in the large $\beta \rightarrow \infty$ limit.

Scaling the Euclidean time $t = \beta t'$ and $s = \beta s'$ in Eq. (4), deriving S with respect to β , and undoing the scaling, we get

$$\frac{\partial S}{\partial \beta} = -\frac{1}{\beta} \int_0^{\beta} \frac{\dot{\mathbf{x}}^2}{2} dt - \frac{S}{2I_D} \int_0^{\beta} dt \int_0^{\beta} ds \times \int_{q \leq 1} d\mathbf{q} q e^{i\sqrt{2/\gamma}\mathbf{q}\cdot(\mathbf{x}(t)-\mathbf{x}(s)) - q|t-s|} \frac{1}{\beta} (2-q|t-s|), \quad (8)$$

where the first term is the kinetic energy contribution to the internal energy, \mathcal{K} , and the last term is the potential energy contribution, \mathcal{P}

$$\mathcal{P} = -\frac{3S}{2\beta} \int_0^{\beta} dt \int_0^{\beta} ds \int_0^1 dq q^3 \frac{\sin\left(\sqrt{\frac{2}{\gamma}} q |\mathbf{x}(t)-\mathbf{x}(s)|\right)}{\sqrt{\frac{2}{\gamma}} q |\mathbf{x}(t)-\mathbf{x}(s)|} e^{-q|t-s|} \times (2-q|t-s|). \quad (9)$$

So that

$$E = \langle \mathcal{K} + \mathcal{P} \rangle. \quad (10)$$

An expression for \mathcal{K} not involving the polaron speed, can be obtained by taking the derivative with respect to β after having scaled both the time, as before, and the coordinate $\mathbf{x} = \sqrt{\beta} \mathbf{x}'$. Undoing the scaling in the end one gets

$$\mathcal{K} = -\frac{S}{4\beta I_D} \int_0^{\beta} dt \int_0^{\beta} ds \int_{q \leq 1} d\mathbf{q} q e^{i\sqrt{2/\gamma}\mathbf{q}\cdot(\mathbf{x}(t)-\mathbf{x}(s)) - q|t-s|} \times \left[i \sqrt{\frac{2}{\gamma}} \mathbf{q} \cdot (\mathbf{x}(t)-\mathbf{x}(s)) \right] \quad (11)$$

$$\mathcal{K} = -\frac{3S}{4\beta} \int_0^{\beta} dt \int_0^{\beta} ds \int_0^1 dq q^3 \left[\cos\left(\sqrt{\frac{2}{\gamma}} q |\mathbf{x}(t)-\mathbf{x}(s)|\right) - \frac{\sin\left(\sqrt{\frac{2}{\gamma}} q |\mathbf{x}(t)-\mathbf{x}(s)|\right)}{\sqrt{\frac{2}{\gamma}} q |\mathbf{x}(t)-\mathbf{x}(s)|} \right] e^{-q|t-s|}. \quad (12)$$

In the following we will explain how we calculated the potential energy $P = \langle \mathcal{P} \rangle$.

4. Discrete path integral expressions

Generally we are interested in calculating the density matrix $\hat{\rho} = \exp(-\beta\hat{H})$ in the electron coordinate basis, namely

$$\rho(\mathbf{x}_a, \mathbf{x}_b; \beta) = \int_{\mathbf{x}=\mathbf{x}_a}^{\mathbf{x}=\mathbf{x}_b} e^{-S} \mathcal{D}\mathbf{x}(t). \quad (13)$$

To calculate the path integral, we first choose a subset of all paths. To do this, we divide the independent variable, Euclidean

time, into steps of width

$$\tau = \beta/M. \tag{14}$$

This gives us a set of times, $t_k = k\tau$ spaced a distance τ apart between 0 and β with $k=0,1,2,\dots,M$.

At each time t_k we select the special point $\mathbf{x}_k = \mathbf{x}(t_k)$, the k -th time slice. We construct a path by connecting all points so selected by straight lines. It is possible to define a sum over all paths constructed in this manner by taking a multiple integral over all values of \mathbf{x}_k for $k=1,2,\dots,M-1$ where $\mathbf{x}_0 = \mathbf{x}_a$ and $\mathbf{x}_M = \mathbf{x}_b$ are the two fixed ends. The resulting equation is

$$\rho(\mathbf{x}_a, \mathbf{x}_b; \beta) = \lim_{\tau \rightarrow 0} \frac{1}{A} \int_{-\infty}^{\infty} \int_{-\infty}^{\infty} \dots \int_{-\infty}^{\infty} e^{-S} \frac{d\mathbf{x}_1}{A} \dots \frac{d\mathbf{x}_{M-1}}{A}, \tag{15}$$

where the normalizing factor $A = (2\pi\tau)^{3/2}$.

The simplest discretized expression for the action can then be written as follows:

$$S = \sum_{k=1}^M \frac{(\mathbf{x}_{k-1} - \mathbf{x}_k)^2}{2\tau} + \tau^2 \sum_{i=1}^M \sum_{j=1}^M V(t_i, t_j), \tag{16}$$

where $V(t_i, t_j) = V_{\text{eff}}(|\mathbf{x}_i - \mathbf{x}_j|, |i-j|)$ is a symmetric two variables function, $V(s, t) = V(t, s)$. In our simulation we tabulated this function taking $|\mathbf{x}_i - \mathbf{x}_j| = 0, 0.1, 0.2, \dots, 10$ and $|i-j| = 0, 1, \dots, M$.

In writing Eq. (16) we used the following approximate expressions:

$$\dot{\mathbf{x}}_k = \frac{\mathbf{x}_k - \mathbf{x}_{k-1}}{\tau} + O(\tau), \tag{17}$$

$$\int_{t_{k-1}}^{t_k} \dot{\mathbf{x}}^2(t) dt = \dot{\mathbf{x}}_k^2 \tau + O(\tau^2), \tag{18}$$

$$\int_{t_{i-1}}^{t_i} \int_{t_{j-1}}^{t_j} V(s, t) ds dt = V(t_i, t_j) \tau^2 + O(\tau^3). \tag{19}$$

If we take $V=0$ in Eq. (16) the $M-1$ Gaussian integrals in Eq. (15) can be done analytically. The result is the exact free particle density matrix

$$\rho_f(\mathbf{x}_a, \mathbf{x}_b; \beta) = (2\pi\beta)^{-3/2} e^{-(1/2\beta)(\mathbf{x}_a - \mathbf{x}_b)^2}. \tag{20}$$

Thus approximations (17) and (18) allow us to rewrite the polaron density matrix as follows:

$$\rho(\mathbf{x}_a, \mathbf{x}_b; \beta) = \int \dots \int d\mathbf{x}_1 \dots d\mathbf{x}_{M-1} \rho_f(\mathbf{x}_a, \mathbf{x}_1; \tau) \dots \rho_f(\mathbf{x}_{M-1}, \mathbf{x}_b; \tau) \times e^{\tau^2 \sum_i \sum_j V(t_i, t_j)}. \tag{21}$$

In the next section we will see that this expression offers a useful starting point for the construction of an algorithm for the sampling of the path: the Lévy construction and the analogy with classical polymer systems or the classical isomorphism described in Ref. [27]. The partition function is the trace of the density matrix

$$Z = \int d\mathbf{x} \rho(\mathbf{x}, \mathbf{x}; \beta). \tag{22}$$

This restrict the path integral to an integral over closed paths only. In other words the paths we need to consider in calculating Z (and hence F) are closed by the periodic boundary condition, $\mathbf{x}_M = \mathbf{x}_0 = \mathbf{x}$.

To calculate the internal energy we need then to perform the following M -dimensional integral:

$$E = \frac{1}{Z} \int_{-\infty}^{\infty} \int_{-\infty}^{\infty} \dots \int_{-\infty}^{\infty} d\mathbf{x}_0 d\mathbf{x}_1 \dots d\mathbf{x}_{M-1} e^{-S(\mathcal{P} + \mathcal{K})} \Big|_{\mathbf{x}_M = \mathbf{x}_0}. \tag{23}$$

To do this integral we use the Monte Carlo simulation technique described next.

5. Sampling the path

The total configuration space to be integrated over is made of elements $s = [\mathbf{x}_0, \mathbf{x}_1, \dots, \mathbf{x}_M]$ where \mathbf{x}_k are the path time slices subject to the periodic boundary condition $\mathbf{x}_M = \mathbf{x}_0$. In the simulation we wish to sample these elements from the probability distribution

$$\pi(s) = \frac{e^{-S}}{Z}, \tag{24}$$

where the partition function Z normalizes the function π in this space.

The idea is to find an efficient way to move the path in a random walk sampled by π , through configuration space.

In order to be able to make the random walk diffuse fast through configuration space, as τ decreases, is necessary to use multislices moves [27].

In our simulation we chose to use the bisection method (a particular multilevel Monte Carlo sampling method [27]). That is how an l levels move is constructed. Clip out of the path $m = 2^l$ subsequent time slices $\mathbf{x}_i, \mathbf{x}_{i+1}, \dots, \mathbf{x}_{i+m}$ (choosing i randomly). In the first level we keep \mathbf{x}_i and \mathbf{x}_{i+m} fixed and, following Lévy construction for a Brownian bridge [38], we move the bisecting point at $i+m/2$ to:

$$\mathbf{x}_{i+m/2} = \frac{\mathbf{x}_i + \mathbf{x}_{i+m}}{2} + \boldsymbol{\eta}, \tag{25}$$

where $\boldsymbol{\eta}$ is a normally distributed random vector with mean zero and standard deviation $\sqrt{\tau m/4}$. As shown in next section this kind of transition rule samples the path using a transition probability distribution $T \propto \exp(-S_f)$. Thus we will refer to it as *free particle sampling*.

Having sampled $\mathbf{x}_{i+m/2}$, we proceed to the second level bisecting the two new intervals $(0, i+m/2)$ and $(i+m/2, i+m)$ generating points $\mathbf{x}_{i+m/4}$ and $\mathbf{x}_{i+3m/4}$ with the same algorithm. We continue recursively, doubling the number of sampled points at each level, stopping only when the time difference of the intervals is τ .

In this way we are able to partition the full configuration s into l levels, $s = (s_0, s_1, \dots, s_l)$ where $s_0 = [\mathbf{x}_0, \dots, \mathbf{x}_i, \mathbf{x}_{i+m}, \dots, \mathbf{x}_{M-1}]$, unchanged; $s_1 = [\mathbf{x}_{i+m/2}]$, changed in level 1; $s_2 = [\mathbf{x}_{i+m/4}, \mathbf{x}_{i+3m/4}]$, changed in level 2; ...; $s_l = [\mathbf{x}_{i+1}, \mathbf{x}_{i+2}, \dots, \mathbf{x}_{i+m-1}]$ changed in level l .

To construct the random walk we use the multilevel Metropolis method [39,40,27]. Call (s'_1, \dots, s'_l) the new trial positions in the sense of a Metropolis rejection method, the unprimed ones are the corresponding old positions with $s_0 = s'_0$.

In order to decide if the sampling of the path should continue beyond level k , we need to construct the probability distribution π_k for level k . This, usually called the *level action*, is a function of s_0, s_1, \dots, s_k proportional to the reduced distribution function of s_k conditional on s_0, s_1, \dots, s_{k-1} . The optimal choice for the level action would thus be

$$\pi_k^*(s_0, s_1, \dots, s_k) = \int ds_{k+1} \dots ds_l \pi(s). \tag{26}$$

This is only a guideline. Non-optimal choices will lead to slower movement through configuration space. One needs to require only that feasible paths (closed ones) have non-zero level action, and that the action at the last level be exact

$$\pi_i(s_0, s_1, \dots, s_i) = \pi(s). \tag{27}$$

Given the level action $\pi_k(s)$ the optimal choice for the transition probability $T_k(s_k)$, for s_k contingent on the levels already sampled, is given by

$$T_k^*(s_k) = \frac{\pi_k(s)}{\pi_{k-1}(s)}. \tag{28}$$

One can show that T_k^* will be a normalized probability if and only if π_k is chosen as in Eq. (26). In general one need to require only

that T_k be a probability distribution non-zero for feasible paths. In our simulation we used the free particle transition probability of the Lévy construction as a starting point for a more efficient correlated sampling that will be described in a later section.

Once the partitioning and the sampling rule are chosen, the sampling proceeds past level k with probability

$$A_k(s') = \min \left[1, \frac{T_k(s_k)\pi_k(s')\pi_{k-1}(s)}{T_k(s'_k)\pi_k(s)\pi_{k-1}(s')} \right]. \quad (29)$$

That is we compare A_k with a uniformly distributed random number in $(0,1)$, and if A_k is larger, we go on to sample the next level. If A_k is smaller, we make a new partitioning of the initial path, and start again from level 1. Here π_0 needed in the first level can be set equal to 1, since it will cancel out of the ratio.

This acceptance probability has been constructed so that it satisfies a form of “detailed balance” for each level k

$$\frac{\pi_k(s)}{\pi_{k-1}(s)} T_k(s'_k) A_k(s') = \frac{\pi_k(s')}{\pi_{k-1}(s')} T_k(s_k) A_k(s). \quad (30)$$

The moves will always be accepted if the transition probabilities and level actions are set to their optimal values.

The total transition probability for a trial move making it through all l levels is

$$P(s \rightarrow s') = \prod_{k=1}^l T_k(s') A_k(s'). \quad (31)$$

By multiplying Eq. (30) from $k=1$ to $k=l$ and using Eq. (27), one can verify that the total move satisfy the detailed balance condition

$$\pi(s)P(s \rightarrow s') = \pi(s')P(s' \rightarrow s). \quad (32)$$

Thus if there are no barriers or conserved quantities that restrict the walk to a subset of the full configuration space (i.e. assuming the random walk to be ergodic) the algorithm will asymptotically converge to π , independent of the particular form chosen for the transition probabilities, T_k , and the level actions, π_k [41]. We will call *equilibration time* the number of moves needed in the simulation to reach convergence.

Whenever the last level is reached, one calculates the properties (\mathcal{K} and \mathcal{P}) on the new path s' , resets the initial path to the new path, and start a new move. We will call Monte Carlo step (MCS) any attempted move.

6. Choice of T_k and π_k

In our simulation we started moving the path with the Lévy construction described in the preceding section. We will now show that this means that we are sampling an approximate T^* with free particle sampling.

For the free particle case ($U=0$) one can find analytic expressions for the optimal level action π_k^* and the optimal transition rule T_k^* . For examples for the first level, Eq. (26) gives

$$\pi_1^*(\mathbf{x}_{i+m/2}) \propto \rho_f(\mathbf{x}_i, \mathbf{x}_{i+m/2}; \tau m/2) \rho_f(\mathbf{x}_{i+m/2}, \mathbf{x}_{i+m}; \tau m/2), \quad (33)$$

$$\pi_1^*(\mathbf{x}_{i+m/2}) \propto e^{(1/m\tau)(\mathbf{x}_i - \mathbf{x}_{i+m/2})^2} e^{(1/m\tau)(\mathbf{x}_{i+m/2} - \mathbf{x}_{i+m})^2}, \quad (34)$$

$$\pi_1^*(\mathbf{x}_{i+m/2}) \propto e^{(2/m\tau)(\mathbf{x}_{i+m/2} - (\mathbf{x}_i + \mathbf{x}_{i+m})/2)^2}. \quad (35)$$

This justify the Lévy construction and shows that it exactly samples the free particle action (i.e. $A_k=1$ for all k 's). This also imply that for the interacting system we can introduce a *level inter action*, $\tilde{\pi}_k$ such that

$$\tilde{\pi}_k = \int ds_{k+1} \dots ds_l \tilde{\pi}(s), \quad (36)$$

with

$$\tilde{\pi}(s) = \frac{e^{-U}}{Z}. \quad (37)$$

So that the acceptance probability will have the simplified expression

$$A_k(s') = \min \left[1, \frac{\tilde{\pi}_k(s')\tilde{\pi}_{k-1}(s)}{\tilde{\pi}_k(s)\tilde{\pi}_{k-1}(s')} \right]. \quad (38)$$

For the k -th level inter action we chose the following expression:

$$\tilde{\pi}_k \propto \exp \left[-(\tau \ell_k)^2 \sum_{i=1}^{[M/\ell_k]} \sum_{j=1}^{[M/\ell_k]} V(i\ell_k \tau, j\ell_k \tau) \right], \quad (39)$$

where $\ell_k = m/2^k$. In the last level $\ell_l = 1$ and the level inter action $\tilde{\pi}_l$ reduces to the exact inter action $\tilde{\pi}$ thus satisfying Eq. (27).

It is important to notice that during the simulation we never need to calculate the complete level inter action since in the acceptance probabilities enter only ratios of level inter actions calculated on the old and on the new path. For example if for the move we clipped out the interval t_i, \dots, t_{i+m} with $i+m < M$,² we have

$$\ln \frac{\tilde{\pi}_k(s')}{\tilde{\pi}_k(s)} = -(\tau \ell_k)^2 \left\{ \sum_{m=0}^{2^k} \sum_{n=0}^{2^k} V(t_i + m\ell_k \tau, t_i + n\ell_k \tau) + \sum_{m=1}^{i-1} \sum_{n=0}^{2^k} V(m\ell_k \tau, t_i + n\ell_k \tau) + \sum_{m=i+m+1}^M \sum_{n=0}^{2^k} V(m\ell_k \tau, t_i + n\ell_k \tau) \right\}, \quad (40)$$

which is computationally much cheaper than Eq. (39).

7. Correlated sampling

When the path reaches equilibrium (i.e. $P(s \rightarrow s') \approx \pi(s')$) if we calculate

$$\sigma(t_0/\tau) = \sqrt{\left\langle \left[\mathbf{x}(t) - \left(\frac{\mathbf{x}(t+t_0) + \mathbf{x}(t-t_0)}{2} \right) \right]^2 \right\rangle}, \quad (41)$$

we see that these deviations are generally smaller than the free particle standard deviations used in the Lévy construction (see Fig. 1)

$$\sigma_f(\ell_k) = \sqrt{\ell_k \tau/2}. \quad (42)$$

As Fig. 1 shows, the discrepancy gets bigger as ℓ_k increases.

We thus corrected the sampling rule for the correct deviations. For example for the first level we used

$$T_1(\mathbf{x}_{i+m/2}) \propto e^{-(\mathbf{x}_{i+m/2} - \bar{\mathbf{x}})^2/2\sigma^2(m/2)}, \quad (43)$$

where $\bar{\mathbf{x}} = (\mathbf{x}_i + \mathbf{x}_{i+m})/2$. Since the level action is given by

$$\pi_1(\mathbf{x}_{i+m/2}) \propto e^{-(\mathbf{x}_{i+m/2} - \bar{\mathbf{x}})^2/2\sigma_f^2(m/2)} \tilde{\pi}_1(\mathbf{x}_{i+m/2}), \quad (44)$$

we can define a function

$$P_1 \propto e^{-(\mathbf{x}_{i+m/2} - \bar{\mathbf{x}})^2/2(1/\sigma^2(m/2) - 1/\sigma_f^2(m/2))} \quad (45)$$

and write the acceptance probability

$$A_1(s') = \min \left[1, \frac{P_1(s) \tilde{\pi}_1(s') \tilde{\pi}_0(s)}{P_1(s') \tilde{\pi}_1(s) \tilde{\pi}_0(s')} \right], \quad (46)$$

which is a generalization of Eq. (38).

² When $i+m \geq M$ there is a minor problem with the periodic boundary conditions and Eq. (40) will change.

116

R. Fantoni / Physica B 412 (2013) 112–118

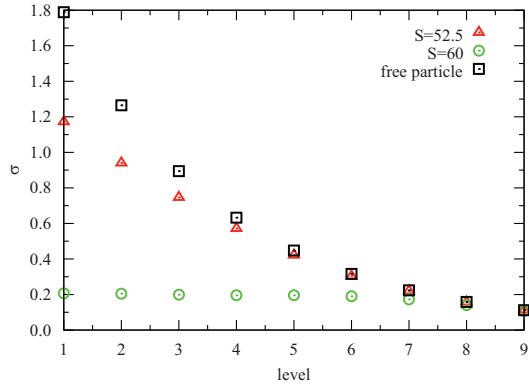


Fig. 1. Shows the deviations (41) for a simulation with $S=60$ and $S=52.5$, $\tau=0.025$, $l=9$. The free particle standard deviations (42) are plotted for comparison. For $S=60$ the path is localized while for $S=52.5$ is unlocalized i.e. closer to the free particle path.

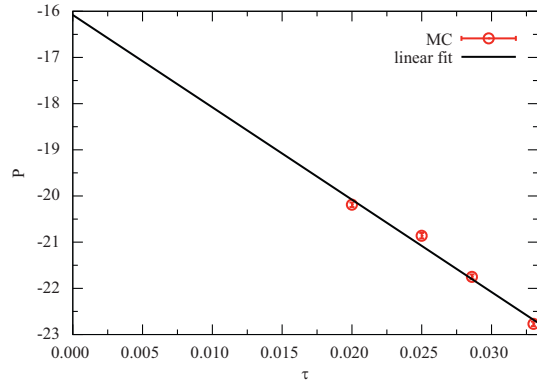


Fig. 2. Shows the time step, τ , extrapolation for the potential energy, $P = \langle \mathcal{P} \rangle$. We run at $\beta = 15$, $\gamma = 0.02$, and $S=60$. The extrapolated value to the continuum limit is in this case $P = -16.1(5)$ which is in good agreement with the result of Ref. [33].

We maintain the acceptance ratios in $[0.15, 0.65]$ by decreasing (or increasing) the number of levels in the multilevel algorithm as the acceptance ratios becomes too low (or too high).

In the Appendix we report some remarks on the error analysis in our MC simulations.

8. Numerical results

We simulated the acoustic polaron fixing the adiabatic coupling constant $\gamma = 0.02$ and the inverse temperature $\beta = 15$. Such temperature is found to be well suited to extract close to ground state properties of the polaron. The path was M time slices long and the time step was $\tau = \beta/M$. For a given coupling constant S we computed the potential energy P extrapolating (with a linear χ square fit) to the continuum time limit, $\tau \rightarrow 0$, three points corresponding to time-steps chosen in the interval $\tau \in [1/100, 1/30]$. An example of extrapolation is shown in Fig. 2 for the particular case $\beta = 15$, $\gamma = 0.02$, and $S=60$.

In Fig. 5 and Table 1 we show that the results for the potential energy as a function of the coupling strength. With the coupling constant $S=52.5$ we generated the equilibrium path which turns out to be unlocalized (see Fig. 4). Changing the coupling constant to $S=60$ and taking the unlocalized path as the initial path we saw the phase transition described in Fig. 3. The path after the phase transition is localized (see Fig. 4).

Note that since S and τ appear in the combination $S\tau^2$ in \mathcal{U} (and $S\tau$ in F) the same phase transition from an ES to a ST state will be observed increasing the temperature. With the same Hamiltonian we are able to describe two very different behavior of the acoustic polaron as the temperature changes.

In Fig. 5 we show that the behavior of the potential energy as a function of the coupling strength. The numerical results suggest the existence of a phase transition regimes which corresponds to the so-called ES and ST states for the weak and strong coupling region respectively. We found that paths related to ES and ST are characteristically distinguishable. Two typical paths for the ES and ST regimes involved in Fig. 5 are illustrated in Fig. 4. The path in ES state changes smoothly in a large time scale, whereas the path in ST state do so abruptly in a small time scale with a much smaller amplitude which is an indication that the polaron hardly moves. The local fluctuations in the results for the potential energy have an autocorrelation

Table 1

MC results for P as a function of S at $\beta = 15$ and $\gamma = 0.02$ displayed in Fig. 5. The runs were made of 5×10^7 MCS (with 5×10^4 MCS for the equilibration) for the ES states and 5×10^6 MCS (with 5×10^3 MCS for the equilibration) for the ST states.

S	P
10	-0.573(8)
20	-1.17(2)
30	-1.804(3)
40	-2.53(3)
50	-3.31(4)
53.5	-3.61(1)
55	-11.4(3)
60	-16.1(5)
70	-23.3(3)
80	-30.0(3)

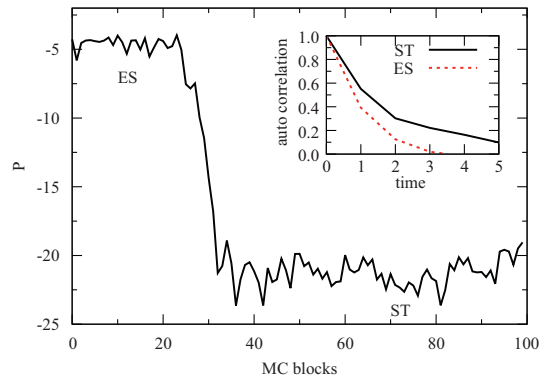


Fig. 3. At $S=60$ the results for the potential energy \mathcal{P} at each MC block (5×10^3 MCS) starting from an initial unlocalized path obtained by a previous simulation at $S=52.5$. We can see that after about 30 blocks there is a transition from the ES state to the ST state. In the inset is shown the autocorrelation function, defined in Eq. (A.8), for the potential energy, for the two states. The correlation time, in MC blocks, is shorter in the unlocalized phase than in the localized one. The computer time necessary to carry on a given number of Monte Carlo steps is longer for the unlocalized phase.

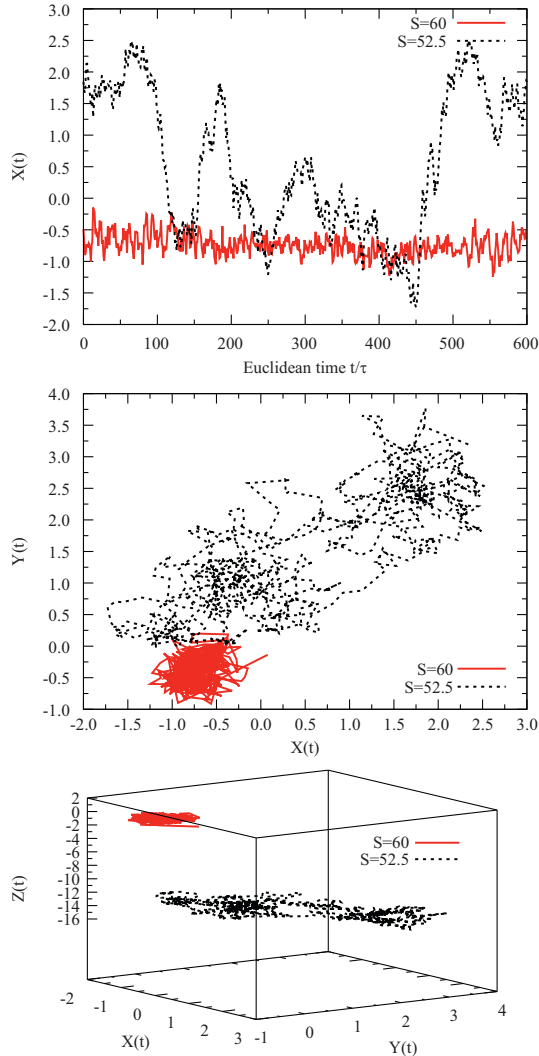


Fig. 4. The top panel shows the polaron (closed) path $x(t)$ as a function of Euclidean time t in units of τ at equilibrium during the simulation. The middle panel shows the projection on the x – y plane of the path. The bottom panel shows the three-dimensional path. We see clearly how both path has moved from the initial path located on the origin but the path at $S=52.5$ is much less localized than the one at $S=60$.

function (defined in Eq. (A.8)) which decay much more slowly in the ES state than in the ST state as shown in the inset of Fig. 3. Concerning the critical property of the transition between the ES and ST states our numerical results are in favor of the presence of a discontinuity in the potential energy. In the large β limit at $\beta = 15$ and fixing the adiabatic coupling constant to $\gamma = 0.02$, the ST state appears at a value of the coupling constant between $S=52.5$ and $S=55$. With the increase of β , the values for the potential energy $P = \langle \mathcal{P} \rangle$ increase in the weak coupling regime but decrease in the strong coupling region.

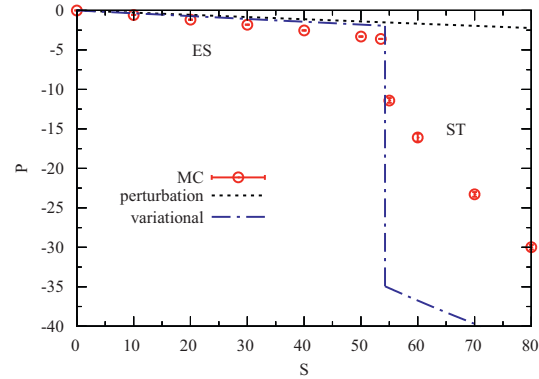


Fig. 5. Shows the behavior of the potential energy P as a function of the coupling constant S . The points are the MC results (see Table 1), the dashed line is the second order perturbation theory result (perturbation) valid in the weak coupling regime and the dot-dashed line is the variational approach from Ref. [23] (variational) in the weak and strong coupling regimes.

From second order perturbation theory (see Ref. [12] Section 8.2) follows that the energy shift $E(\gamma, S)$ is given by $-3S\gamma[1/2 - \gamma + \gamma^2 \ln(1+1/\gamma)]$ from which one extracts the potential energy shift by taking $P(\gamma, S) = \gamma dE(\gamma, S)/d\gamma$. From the Feynman variational approach of Ref. [23] follows that in the weak regime the energy shift is $-3S\gamma[1/2 - \gamma + \gamma \ln(1+1/\gamma)]$ and in the strong coupling regime $-S + 3\sqrt{S/5}\gamma$.

9. Conclusions

We used for the first time a specialized path integral Monte Carlo method to study the low temperature behavior of an acoustic polaron. At an inverse temperature $\beta = 15$ (close to the ground state of the polaron) and at a non-adiabatic parameter $\gamma = 0.02$ typical of ionic crystals we found numerical evidence for a phase transition between an extended state in the weak coupling regime and a self-trapped one in the strong coupling regime at a value of the phonons–electron coupling constant $S = 54.3(7)$. The transition also appears looking at the potential energy as a function of the coupling constant where a jump discontinuity is observed. Comparison with the perturbation theory and the variational calculation of Ref. [23] is also presented.

The specialized path integral Monte Carlo simulation method used as an unbiased way to study the properties of the acoustic polaron has been presented in full detail. It is based on the Lévy construction and the multilevel Metropolis method with correlated sampling. Some remarks on the estimation of the errors in the Monte Carlo calculation are also given in the Appendix. This complements our previous paper [26] where fewer details on the Monte Carlo method had been given.

Our method differs from previously adopted methods [29–34, 28, 35]. Unlike the method of Ref. [29] our path integral is in real space rather than in Fourier space. Refs. [34, 35] put the polaron on a lattice and not on the continuum as we did, while Refs. [33] use PIMC single slice move whereas the multilevel PIMC we used instead is a general sampling method which can efficiently make multislice moves. The efficiency ξ (see the Appendix) for the potential energy increases respect to the single slice sampling because the coarsest movements are sampled and rejected before the finer movements are even constructed. In Ref. [28] the Lévy construction was used as in our case but the Metropolis test was performed after the entire path had been reconstructed, using an

effective action, and not at each intermediate level of the reconstruction. In Ref. [28] the simpler Levy reconstruction scheme was also found to be satisfactory for the efficient sampling of the polaron configuration space even at strong coupling. Even if we have not implemented the method of Ref. [28] we expect our method to be of comparable efficiency to the one of these authors. Infact it is true that the Levy construction is computationally cheap but guiding the path as it is been reconstructed starting already from the first levels as we did should have the advantage of refining the sampling since the path is guided through configuration space starting from the small displacements.

Although our results are of a numerical nature and we only probed the acoustic polaron for one value of the non-adiabatic parameter γ we think that the analysis supports the existence of a localization phase transition as the phonons–electron coupling constant S is increased at constant temperature or as the temperature is decreased at constant S . More so considering the fact that the introduction of a cut-off parameter has shown to work successfully in renormalization treatments.

Appendix A. Estimating errors

Since asymptotic convergence is guaranteed, the main issue is whether configuration space is explored thoroughly in a reasonable amount of computer time. Let us define a measure of the convergence rate and of the efficiency of a given random walk. This is needed to compare the efficiency of different transition rules, to estimate how long the runs should be, and to calculate statistical errors.

The rate of convergence is a function of the property being calculated. Let $\mathcal{O}(s)$ be a given property, and let its value at step k of the random walk be \mathcal{O}_k . Let the estimator for the mean and variance of a random walk with N MCS be

$$O = \langle \mathcal{O}_k \rangle = \frac{1}{N} \sum_{k=0}^{N-1} \mathcal{O}_k, \quad (\text{A.1})$$

$$\sigma^2(\mathcal{O}) = \langle (\mathcal{O}_k - O)^2 \rangle. \quad (\text{A.2})$$

Then the estimator for the variance of the mean will be

$$\sigma^2(O) = \left\langle \left(\frac{1}{N} \sum_k \mathcal{O}_k - \frac{1}{N} \sum_k O \right)^2 \right\rangle, \quad (\text{A.3})$$

$$\sigma^2(O) = \frac{1}{N^2} \left\langle \left[\sum_k (\mathcal{O}_k - O) \right]^2 \right\rangle, \quad (\text{A.4})$$

$$\sigma^2(O) = \frac{1}{N^2} \left\{ \sum_k \langle (\mathcal{O}_k - O)^2 \rangle + 2 \sum_{i < j} \langle (\mathcal{O}_i - O)(\mathcal{O}_j - O) \rangle \right\}, \quad (\text{A.5})$$

$$\sigma^2(O) = \frac{\sigma^2(\mathcal{O})}{N} \left\{ 1 + \frac{2}{N\sigma^2(\mathcal{O})} \sum_{i < j} \langle (\mathcal{O}_i - O)(\mathcal{O}_j - O) \rangle \right\}, \quad (\text{A.6})$$

$$\sigma^2(O) = \frac{\sigma^2(\mathcal{O})k_{\mathcal{O}}}{N}. \quad (\text{A.7})$$

The quantity $k_{\mathcal{O}}$ is called the *correlation time* and can be calculated given the autocorrelation function for $A_k = \mathcal{O}_k - O$. The estimator for the *autocorrelation function*, c_k , can be constructed observing that in the infinite random walk, $\langle A_i A_j \rangle$ has to be a function of $|i-j|$ only. Thus the estimator can be written

$$c_k = \frac{\langle A_0 A_k \rangle}{\sigma^2(\mathcal{O})} = \frac{1}{(N-k)\sigma^2(\mathcal{O})} \sum_{n=1}^{N-k} A_n A_{n+k}. \quad (\text{A.8})$$

So that the estimator for the correlation time will be

$$k_{\mathcal{O}} = 1 + \frac{2}{N} \sum_{k=1}^N (N-k)c_k. \quad (\text{A.9})$$

To determine the true statistical error in a random walk, one needs to estimate this correlation time. To do this, it is very important that the total length of the random walk be much greater than $k_{\mathcal{O}}$. Otherwise the result and the error will be unreliable. Runs in which the number of steps $N \gg k_{\mathcal{O}}$ are called *well converged*.

The correlation time gives the average number of steps needed to decorrelate the property \mathcal{O} . It will depend crucially on the transition rule and has a minimum value of 1 for the optimal rule (while $\sigma(\mathcal{O})$ is independent of the sampling algorithm).

Normally the equilibration time will be at least as long as the equilibrium correlation time, but can be longer. Generally the equilibration time depends on the choice for the initial path. To lower this time is important to choose a physical initial path. Since the polaron system is isotropic, we chose the initial path with all time slices set to $\vec{0}$.

The efficiency of a random walk procedure (for the property \mathcal{O}) is defined as how quickly the error bars decrease as a function of the computer time, $\xi_{\mathcal{O}} = 1/\sigma^2(\mathcal{O})NT = 1/\sigma^2(\mathcal{O})k_{\mathcal{O}}T$ where T is the computer time per step. The efficiency depends not only on the algorithm but also on the computer and the implementation.

References

- [1] B. Gerlach, H. Löwen, Rev. Mod. Phys. 63 (1991) 63.
- [2] J.T. Devreese, A.S. Alexandrov, Rep. Prog. Phys. 72 (2009) 066501.
- [3] L.D. Landau, Phys. Z. Sowjetunion 3 (1933) 644.
- [4] L.D. Landau, S. Pekar, Zh. eksper. teor. Fiz. 16 (1946) 341.
- [5] L.D. Landau, S.I. Pekar, Zh. Eksp. Teor. Fiz. 18 (1948) 419.
- [6] H. Fröhlich, H. Pelzer, S. Zienau, Phil. Mag. 41 (1950) 221.
- [7] H. Fröhlich, Adv. Phys. 3 (1954) 325.
- [8] R.P. Feynman, Phys. Rev. 97 (1955) 660.
- [9] F.M. Peeters, J.T. Devreese, Phys. Stat. Sol. 112 (1982) 219.
- [10] B.A. Mason, S. Das Sarma, Phys. Rev. B 33 (1986) 1412.
- [11] T.K. Mitra, A. Chatterjee, S. Mukhopadhyay, Phys. Rep. 91 (1987) 153.
- [12] R.P. Feynman, Statistical Mechanics, Benjamin, New York, 1972.
- [13] Y. Osaka, Prog. Theor. Phys. 22 (1959) 437.
- [14] Y. Osaka, J. Phys. Soc. Jpn. 21 (1965) 423.
- [15] D.P.L. Castrigiano, N. Kokiantonis, Phys. Lett. 96A (1983) 55.
- [16] D.P.L. Castrigiano, N. Kokiantonis, Phys. Lett. 104A (1984) 364.
- [17] D.C. Khandekar, S.V. Lawande, Phys. Rep. 137 (1986) 115.
- [18] Y-Sheng He, Pei-Heng Wu, Li-Fang Xu, Zong-Xian Zhao (Eds.), Proceedings of the International Conference on Materials & Mechanism of Superconductivity, High Temperature Superconductors V, Physica (Amsterdam) 282C–287C (1997).
- [19] J. Tempere, W. Casteels, M.K. Oberthaler, S. Knoop, E. Timmermans, J.T. Devreese, Phys. Rev. B 80 (2009) 184504.
- [20] Y. Toyozawa, Prog. Theor. Phys. 26 (1961) 29.
- [21] C.G. Kuper, G.D. Whitfield (Eds.), Polarons and Excitons, Oliver and Boyd, Edinburgh, 1963, p. 211.
- [22] F.M. Peeters, J.T. Devreese, Phys. Rev. B 32 (1985) 3515.
- [23] A. Sumi, Y. Toyozawa, J. Phys. Soc. Jpn. 35 (1973) 137.
- [24] D. Emin, T. Holstein, Phys. Rev. Lett. 36 (1976) 323.
- [25] M.P.A. Fisher, W. Zwerger, Phys. Rev. B 34 (1986) 5912.
- [26] R. Fantoni, Phys. Rev. B 86 (2012) 144304.
- [27] D.M. Ceperley, Rev. Mod. Phys. 67 (1995) 279.
- [28] J.T. Titantah, C. Pierleoni, S. Ciuchi, Phys. Rev. Lett. 20 (2001) 206406.
- [29] C. Alexandrou, W. Fleischer, R. Rosenfelder, Phys. Rev. Lett. 65 (1990) 2615.
- [30] C. Alexandrou, R. Rosenfelder, Phys. Rep. 215 (1992) 1.
- [31] M. Crutz, B. Freedman, Ann. Phys. 132 (1981) 427.
- [32] M. Takahashi, M. Imada, J. Phys. Soc. Jpn. 53 (1983) 963.
- [33] X. Wang, Mod. Phys. Lett. B 12 (1998) 775.
- [34] P.E. Kornilovitch, J. Phys.: Condens. Matter 9 (1997) 10675.
- [35] P.E. Kornilovitch, J. Phys.: Condens. Matter 19 (2007) 255213.
- [36] J. Bardeen, W. Shockley, Phys. Rev. 80 (1950) 72.
- [37] R.P. Feynman, A.R. Hibbs, Quantum Mechanics and Path Integrals, McGraw-Hill, New York, 1965.
- [38] P. Lévy, Compos. Math. 7 (1939) 283.
- [39] D.M. Ceperley, E.L. Pollock, Phys. Rev. Lett. 56 (1986) 351.
- [40] D.M. Ceperley, E.L. Pollock, Phys. Rev. B 39 (1989) 2084.
- [41] J.M. Hammersley, C.D. Handscomb, Monte Carlo Methods, Chapman and Hall, London, 1964.

Chapter 34

Hellmann and Feynman theorem versus diffusion Monte Carlo experiment

Fantoni R., Solid State Communications **159**, 106 (2013)

Title: “Hellmann and Feynman theorem versus diffusion Monte Carlo experiment”

Abstract: We discuss about the importance, in a computer experiment, of the choice of suitable estimators to measure a physical quantity. In particular we propose a new direct route to determine estimators for observables which do not commute with the Hamiltonian, which make use of the Hellmann and Feynman theorem. In a diffusion Monte Carlo simulation this introduces a new bias to the measure due to the choice of the auxiliary function which is independent from the bias due to the choice of the trial wave function. We used this route to measure the radial distribution function of a spin one half Fermion fluid.



Contents lists available at SciVerse ScienceDirect

Solid State Communications

journal homepage: www.elsevier.com/locate/ssc



Hellmann and Feynman theorem versus diffusion Monte Carlo experiment

Riccardo Fantoni*

National Institute for Theoretical Physics (NITheP) and Institute of Theoretical Physics, Stellenbosch 7600, South Africa

ARTICLE INFO

Article history:

Received 13 February 2012
 Received in revised form
 27 January 2013
 Accepted 29 January 2013
 by H. Akai
 Available online 8 February 2013

Keywords:

Hellmann and Feynman theorem
 Diffusion Monte Carlo
 Radial distribution function
 Jellium

ABSTRACT

In a computer experiment the choice of suitable estimators to measure a physical quantity plays an important role. We propose a new direct route to determine estimators for observables which do not commute with the Hamiltonian. Our new route makes use of the Hellmann and Feynman theorem and in a diffusion Monte Carlo simulation it introduces a new bias to the measure due to the choice of the auxiliary function. This bias is independent from the usual one due to the choice of the trial wave function. We used our route to measure the radial distribution function of a spin one half Fermion fluid.

© 2013 Elsevier Ltd. All rights reserved.

In a computer experiment of a many particles system, a *fluid*, the determination of suitable estimators to measure, through a statistical average, a given physical quantity, an *observable*, plays an important role. Whereas the average from different estimators must give the same result, the variance, the square of the statistical error can be different for different estimators. We will denote with $\langle O \rangle_f$ the measure of the physical observable O and with $\langle \dots \rangle_f$ the statistical average over the probability distribution f . In this communication we use the word estimator to indicate the function O itself, unlike the more common use of the word to indicate the usual Monte Carlo estimator $\sum_{i=1}^N O_i/N$ of the average, where $\{O_i\}$ is the set obtained by evaluating O over a finite number N of points distributed according to f . This aspect of finding out different ways of calculating quantum properties in some ways resembles experimental physics. The theoretical concept may be perfectly well defined but it is up to the ingenuity of the experimentalist to find the best way of doing the measurement. Even what is meant by “best” is subject to debate.

In this communication we propose a new *direct* route to determine, in a diffusion Monte Carlo simulation, estimators for observables which do not commute with the Hamiltonian. Our new route makes use of the Hellmann and Feynman theorem and it introduces a new *bias* to the measure due to the choice of the auxiliary function. We show how this bias is independent from the usual one due to the choice of the trial wave function. We

then use our route to measure the radial distribution function of a spin one half Fermion fluid.

In ground state Monte Carlo simulations [1,2], unlike classical Monte Carlo simulations [3–5] and path integral Monte Carlo simulations [6], one has to resort to the use of a trial wave function [1], Ψ . While this is not a source of error, *bias*, in a diffusion Monte Carlo simulation [2] of a system of Bosons, it is for a system of Fermions, due to the *sign problem* [7]. Since this is always present in a Monte Carlo simulation of Fermions we will not consider it any further while talking about the bias.

Another source of bias inevitably present in all the three experiments, which we will not take into consideration in the following, is the finite size error. In the rest of the paper we will generally refer to the bias to indicate the error (neglecting the finite size error and the sign problem) that we make when defining different estimators of the same quantity which do not give the same average.

In a ground state Monte Carlo simulation, the energy has the *zero-variance* principle [8]: as the trial wave function approaches the exact ground state, the statistical error vanishes. In a diffusion Monte Carlo simulation of a system of Bosons the local energy of the trial wave function, $E_t(\mathbf{R}) = [H\Psi(\mathbf{R})]/\Psi(\mathbf{R})$, where \mathbf{R} denotes a configuration of the system of particles and H is the Hamiltonian assumed to be real, is an unbiased estimator for the ground state. For Fermions, the ground state energy measurement is biased by the sign problem. For observables O which do not commute with the Hamiltonian, the local estimator, $O_t(\mathbf{R}) = [O\Psi(\mathbf{R})]/\Psi(\mathbf{R})$, is inevitably biased by the choice of the trial wave function. A way of remedy to this bias can be the use of the forward walking method [9,10] or the reptation quantum Monte Carlo method [11] to reach pure estimates. Otherwise this bias can be made of

* Corresponding author.
 E-mail address: rfantoni@ts.infn.it
 URL: <http://www-dft.ts.infn.it/~rfantoni/>

leading order δ^2 , with $\delta = \phi_0 - \Psi$, where ϕ_0 is the ground state wave function, introducing the extrapolated measure, $\bar{O}^{\text{ext}} = 2 \langle O_L \rangle_f - \langle O_L \rangle_{f_{\text{vmc}}}$ where the first statistical average, the *mixed measure*, is over the diffusion Monte Carlo (DMC) stationary probability distribution f and the second, the *variational measure*, over the variational Monte Carlo (VMC) probability distribution f_{vmc} which can also be obtained as the stationary probability distribution of a DMC without branching [12].

One may follow different routes to determine estimators such as the *direct* microscopic route, the *virial* route through the use of the virial theorem, or the *thermodynamic* route through the use of thermodynamic identities. In an unbiased experiment the different routes to the same observable must give the same average.

In this communication we propose to use the Hellmann and Feynman theorem as a direct route for the determination of estimators in a diffusion Monte Carlo simulation. Some attempts in this direction have been tried before [13,14]. The novelty of our approach, in respect to Ref. [13], is a different definition of the correction to the variational measure, necessary in the diffusion experiment, and, in respect to Ref. [14], the fact is that the bias stemming from the sign problem does not exhaust all the bias due to the choice of the trial wave function.

We start with the eigenvalue expression $(H^\lambda - E^\lambda)\Psi^\lambda = 0$ for the ground state of the perturbed Hamiltonian $H^\lambda = H + \lambda O$, by taking the derivative with respect to the parameter λ , multiplying on the right by the ground state at $\lambda = 0$, ϕ_0 , and integrating over the particles configuration to get

$$\int d\mathbf{R} \phi_0 (H^\lambda - E^\lambda) \frac{\partial \Psi^\lambda}{\partial \lambda} = \int d\mathbf{R} \phi_0 \left(\frac{dE^\lambda}{d\lambda} - \frac{dH^\lambda}{d\lambda} \right) \Psi^\lambda.$$

Then we note that due to the Hermiticity of the Hamiltonian the left hand side vanishes at $\lambda = 0$ so that we further get

$$\frac{\int d\mathbf{R} \phi_0 O \Psi^\lambda}{\int d\mathbf{R} \phi_0 \Psi^\lambda} \Big|_{\lambda=0} = \frac{dE^\lambda}{d\lambda} \Big|_{\lambda=0}. \quad (1)$$

This relation holds only in the $\lambda \rightarrow 0$ limit unlike the more common form [15] which holds for any λ . Given $E^\lambda = \int d\mathbf{R} \phi_0 H^\lambda \Psi^\lambda / \int d\mathbf{R} \phi_0 \Psi^\lambda$ the ‘‘Hellmann and Feynman’’ (HF) measure in a diffusion Monte Carlo experiment is then defined as follows:

$$\bar{O}^{\text{HF}} = \frac{dE^\lambda}{d\lambda} \Big|_{\lambda=0} \approx \langle O_L(\mathbf{R}) \rangle_f + \langle \Delta O_L^\alpha(\mathbf{R}) \rangle_f + \langle \Delta O_L^\beta(\mathbf{R}) \rangle_f. \quad (2)$$

The α correction is

$$\Delta O_L^\alpha(\mathbf{R}) = \left[\frac{H\Psi'(\mathbf{R})}{\Psi'(\mathbf{R})} - E_L(\mathbf{R}) \right] \frac{\Psi'(\mathbf{R})}{\Psi(\mathbf{R})}. \quad (3)$$

In a variational Monte Carlo experiment this term, usually, does not contribute to the average (with respect to $f_{\text{vmc}} \propto \Psi^2$) due to the Hermiticity of the Hamiltonian. We will then define a Hellmann and Feynman variational (HFv) estimator as $\bar{O}^{\text{HFv}} = O_L + \Delta O_L^\beta$. The β correction is

$$\Delta O_L^\beta(\mathbf{R}) = [E_L(\mathbf{R}) - E_0] \frac{\Psi'(\mathbf{R})}{\Psi(\mathbf{R})}, \quad (4)$$

where $E_0 = E^\lambda = 0$ is the ground state energy. It should be noticed that our correction differs by a factor 1/2 from the zero-bias correction defined in Ref. [13] because these authors chose $E^\lambda = \int d\mathbf{R} \Psi^\lambda H^\lambda \Psi^\lambda / \int d\mathbf{R} (\Psi^\lambda)^2$ right from the start. This correction is necessary in a diffusion Monte Carlo experiment not to bias the measure. The extrapolated Hellmann and Feynman measure will then be $\bar{O}^{\text{HF-ext}} = 2\bar{O}^{\text{HF}} - \langle O^{\text{HFv}} \rangle_{f_{\text{vmc}}}$. Both corrections α and β to the local estimator depend on the *auxiliary* function, $\Psi' = \partial \Psi^\lambda / \partial \lambda |_{\lambda=0}$. Of course if, on the left hand side of Eq. (2),

we had chosen $\Psi^\lambda = 0$ as the exact ground state wave function, ϕ_0 , instead of the trial wave function, Ψ , then both the corrections would have vanished. When the trial wave function is sufficiently close to the exact ground state function a good approximation to the auxiliary function can be obtained from the first-order perturbation theory for $\lambda \ll 1$. So the Hellmann and Feynman measure is affected by the new source of bias due to the choice of the auxiliary function which is independent from the bias due to the choice of the trial wave function.

We applied the Hellmann and Feynman route to the measurement of the radial distribution function (RDF) of the Fermion fluid studied by Paziani [16]. This is a fluid of spin one-half particles interacting with a bare pair-potential $v_\mu(r) = \text{erf}(\mu r)/r$ immersed in a ‘‘neutralizing’’ background. The pair-potential depends on the parameter μ in such a way that in the limit $\mu \rightarrow 0$ one recovers the ideal Fermi gas and in the limit $\mu \rightarrow \infty$ one finds the Jellium model. We chose this model because it allows to move continuously from a situation where the trial wave function coincides with the exact ground state, in the $\mu \rightarrow 0$ limit, to a situation where the correlations due to the particles interaction become important, in the opposite $\mu \rightarrow \infty$ limit.

We chose as auxiliary function $\Psi' = Q\Psi$, the first one of Toulouse et al. [17] (their Eq. (30))

$$Q_{\sigma,\sigma'}(\mathbf{r},\mathbf{R}) = -\frac{r_s^2}{8\pi V n_\sigma n_{\sigma'}} \sum_{ij \neq i} \delta_{\sigma,\sigma_i} \delta_{\sigma',\sigma_j} \int \frac{d\Omega_{\mathbf{r}}}{4\pi} \frac{1}{|\mathbf{r}-\mathbf{r}_{ij}|}, \quad (5)$$

where σ and σ' denote the spin species, $r = |\mathbf{r}|$ the separation between two particles, r_{ij} the separation between particle i and j , σ_i the spin species of particle i , and $d\Omega_{\mathbf{r}}$ the solid angle element of integration. The particles are in a recipient of volume V at a density $n = n_+ + n_- = 1/[4\pi(a_0 r_s)^3/3]$ with a_0 being the Bohr radius, $a = a_0 r_s$ the lengths unit, and n_σ the density of the spin σ particles. With this choice the α correction partially cancels the histogram estimator $I_{\sigma,\sigma'}(\mathbf{r},\mathbf{R}) = \sum_{ij \neq i} \delta_{\sigma,\sigma_i} \delta_{\sigma',\sigma_j} \int \delta(\mathbf{r}-\mathbf{r}_{ij}) d\Omega_{\mathbf{r}} / (4\pi V n_\sigma n_{\sigma'})$, and one is left with a HFv estimator which goes to zero at large r . This is because the quantity $\langle \Delta I_{\sigma,\sigma'}^2(\mathbf{r},\mathbf{R}) \rangle_{\Psi^2} = -\int_{\partial V^N} \Psi^2(\mathbf{R}) \nabla_{\mathbf{R}} Q_{\sigma,\sigma'}(\mathbf{r},\mathbf{R}) \cdot d\mathbf{S}/r_s^2$ equals minus one for all r with $\mathbf{r} \in V$, instead of zero as normally expected. This is ultimately related to the behavior of the auxiliary function on the border of V^N . The measure of the β correction also goes to zero at large r because one is left with a statistical average of a quantity proportional to $E_L(\mathbf{R}) - E_0$. The Hellmann and Feynman measure then needs to be shifted by +1.

Our variational Monte Carlo experiments showed that in the variational measure the average of the histogram estimator agrees with the average of the HFv estimator within the square root of the variance of the average $\sigma_{\text{av}} = \sqrt{\sigma^2 \mathcal{K}/\mathcal{N}}$ (here σ^2 is the variance, \mathcal{K} the correlation time of the random walk, and \mathcal{N} the number of Monte Carlo steps) and the two σ_{av} are comparable. This is expected since the HFv estimator is defined exactly in Ref. [13] which correctly takes into account the definition of the HF estimator within a variational Monte Carlo simulation. In the fixed nodes diffusion experiment, where one has to add the β correction not to bias the average (note once again that this is defined by us as one half the zero-bias correction of Ref. [13]), the Hellmann and Feynman measure has an average in agreement with the one of the histogram estimator but σ_{av} increases. This is to be expected from the extensive nature of β correction in which the energy appears. Of course the averages from the extrapolated Hellmann and Feynman measure and the extrapolated measure for the histogram estimator also agree.

In the simulation for the Coulomb case, $\mu \rightarrow \infty$, we made extrapolations in time step and number of walkers for each value of r_s . Given a relative precision $\delta_{e_0} = \Delta e_0 / e_0^s$, where $e_0 = \langle E_L \rangle_f / N$,

Δe_0 is the statistical error on e_0 , and e_p^x is the exchange energy, we set relative precision $\delta_{e_0} = 10^{-2}\%$ as our target. The extrapolated values of the time step and number of walkers were then used for all other values of μ . We chose the trial wave function of the Bijl–Dingle–Jastrow [18–20] form as a product of Slater determinants and a Jastrow factor. The pseudo-potential was chosen as in Ref. [21], \mathcal{J}_2 , is expected to give better results for Jellium. Comparison with the simulation of the unpolarized fluid at $r_s=1$ and $\mu=1$ with the pseudo potential of Ref. [22], \mathcal{J}_1 , for

Table 1

Contact values for the unlike RDF of the unpolarized fluid of Pazziani [16] at various r_s and μ from the mixed measure of the histogram estimator (hist) and the HF measure (HF) with the auxiliary function chosen as in Eq. (5), also reported are the two extrapolated measures (ext and HF-ext). The trial wave function used was of the Slater–Jastrow type with the Jastrow of Ref. [21], \mathcal{J}_2 . The last column gives the error on the HF measure. One-hundred sixty two particles were used with 10^5 Monte Carlo steps.

r_s	μ	Hist	Ext	HF	HF-ext	σ_{av} on HF
10	1/2	1.000 (4)	0.91 (1)	1.00	0.92	0.03
10	1	0.644 (3)	0.582 (8)	0.65	0.59	0.03
10	2	0.182 (1)	0.146 (4)	0.18	0.14	0.06
10	4	0.0506 (8)	0.048 (2)	0.05	0.04	0.07
10	∞	0.0096 (3)	0.0118 (8)	0.00	0.00	0.09
5	1/2	1.034 (3)	0.94 (1)	1.03	0.94	0.03
5	1	0.796 (3)	0.743 (9)	0.79	0.73	0.02
5	2	0.405 (2)	0.362 (6)	0.40	0.36	0.02
5	4	0.199 (1)	0.184 (4)	0.20	0.18	0.03
5	∞	0.0799 (8)	0.080 (2)	0.06	0.06	0.03
2	1/2	1.0618 (4)	0.97 (1)	1.05	0.95	0.04
2	1	0.927 (3)	0.852 (9)	0.93	0.86	0.03
2	2	0.697 (3)	0.639 (9)	0.69	0.63	0.02
2	4	0.511 (2)	0.473 (7)	0.51	0.47	0.02
2	∞	0.349 (2)	0.323 (5)	0.32	0.30	0.02
1	1/2	1.077 (3)	0.98 (1)	1.07	0.97	0.02
1	1	0.994 (3)	0.91 (1)	0.99	0.91	0.02
1	2	0.855 (3)	0.787 (9)	0.86	0.81	0.02
1	4	0.730 (2)	0.676 (8)	0.73	0.66	0.01
1	∞	0.602 (2)	0.560 (7)	0.58	0.53	0.01

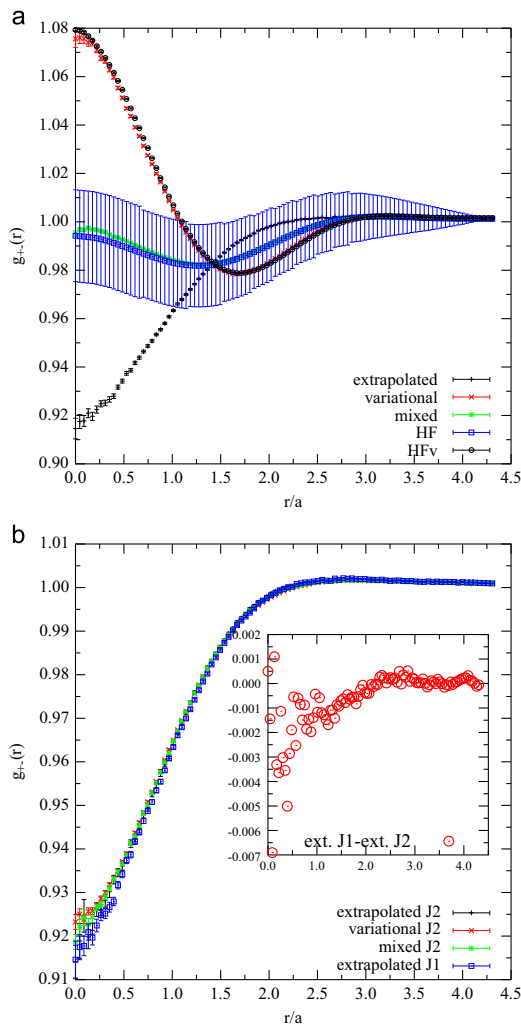


Fig. 1. (Color online) Unlike RDF for the unpolarized fluid of Pazziani [16] at $r_s=1$ and $\mu=1$ with 162 particles. On the left panel the calculation with the Jastrow \mathcal{J}_1 with various measures: variational histogram (variational) and variational HFv (HFv), mixed histogram (mixed) and HF (HF), and extrapolated histogram (extrapolated). On the right panel the calculation with the Jastrow \mathcal{J}_2 with the histogram variational (variational \mathcal{J}_2), mixed (mixed \mathcal{J}_2), and extrapolated (extrapolated \mathcal{J}_2) measures. Also the extrapolated measure with the Jastrow \mathcal{J}_2 is compared with the extrapolated measure with the Jastrow \mathcal{J}_1 . In the inset is shown the difference between the histogram extrapolated measure of the calculation with \mathcal{J}_1 and the histogram extrapolated measure of the calculation with \mathcal{J}_2 . 10^5 Monte Carlo steps were used in the simulations.

which the trial wave function becomes the exact ground state wave function in the $\mu \rightarrow 0$ limit, shows that the two extrapolated measures of the unlike histogram estimator differ one from the other by less than 7×10^{-3} , the largest difference being at contact (see the inset of Fig. 1). The use of more sophisticated trial wave functions, taking into account the effect of backflow and three-body correlations, is found to affect the measure even less. In Table 1 we compare the contact values of the unlike RDF of the unpolarized fluid at various r_s and μ from the measures of the histogram estimator and the HF measures. We see that there is a disagreement between the measure from the histogram estimator and the HF measure only in the Coulomb $\mu \rightarrow \infty$ case at $r_s = 1, 2$.

In conclusions we defined a Hellmann and Feynman estimator to measure a given physical property either in a variational Monte Carlo experiment or in a diffusion Monte Carlo experiment. Our definition coincides with the one of reference [13] in the variational case but is different in the diffusion case. We proof tested our definitions on the calculation of the radial distribution function of a particular Fermion fluid. Our simulations showed that the bias is correctly accounted for in both kinds of experiments but the variance increases in the diffusion experiment relative to the one of the histogram estimator. We believe that the one of determining the relationship between the choice of the auxiliary function and the variance of the Hellmann and Feynman measure is still an open problem.

Acknowledgments

The idea for the work came from discussions with Saverio Moroni. I would also like to acknowledge the hospitality of the National Institute for Theoretical Physics (NITheP) of South Africa where the work was done. The simulations were carried out at the Center for High Performance Computing (CHPC), CSIR Campus, 15 Lower Hope St., Rosebank, Cape Town, South Africa.

References

- [1] W.L. McMillan, *Phys. Rev. A* 138 (1965) 442.
- [2] M.H. Kalos, D. Levesque, L. Verlet, *Phys. Rev. A* 9 (1974) 2178.
- [3] R.W. Hockney, J.W. Eastwood, *Computer Simulation Using Particles*, McGraw-Hill, 1981.
- [4] M.P. Allen, D.J. Tildesley, *Computer Simulation of Liquids*, Clarendon Press, Oxford, 1987.
- [5] D. Frenkel, B. Smit, *Understanding Molecular Simulation*, Academic Press, San Diego, 1996.
- [6] D.M. Ceperley, *Rev. Mod. Phys.* 67 (1995) 279.
- [7] D.M. Ceperley, *J. Stat. Phys.* 63 (1991) 1237.
- [8] D.M. Ceperley, M.H. Kalos, in: K. Binder (Ed.), *Monte Carlo Methods in Statistical Physics*, Springer-Verlag, Heidelberg, 1979, p. 145.
- [9] K.S. Liu, M.H. Kalos, G.V. Chester, *Phys. Rev. A* 10 (1974) 303.
- [10] R.N. Barnett, P.J. Reynolds, W.A. Lester Jr., *J. Comput. Phys.* 96 (1991) 258.
- [11] S. Baroni, S. Moroni, *Phys. Rev. Lett.* 82 (1999) 4745.
- [12] C.J. Umrigar, M.P. Nightingale, K.J. Runge, *J. Chem. Phys.* 99 (1993) 2865.
- [13] R. Assaraf, M. Caffarel, *J. Chem. Phys.* 119 (2003) 10536.
- [14] R. Gaudoin, J.M. Pitarke, *Phys. Rev. Lett.* 99 (2007) 126406.
- [15] L.D. Landau, E.M. Lifshitz, third ed., *Quantum Mechanics. Non-relativistic Theory*, vol. 3, Pergamon Press, 1977. (Course of Theoretical Physics. Eq. (11.16)).
- [16] S. Pazziani, S. Moroni, P. Gori-Giorgi, G.B. Bachelet, *Phys. Rev. B* 73 (2006) 155111.
- [17] J. Toulouse, R. Assaraf, C.J. Umrigar, *J. Chem. Phys.* 126 (2007) 244112.
- [18] A. Bijl, *Physica* 7 (1940) 869.
- [19] R.B. Dingle, *Philos. Mag.* 40 (1949) 573.
- [20] R. Jastrow, *Phys. Rev.* 98 (1955) 1479.
- [21] D.M. Ceperley, in: G.F. Giuliani, G. Vignale (Eds.), *Proceedings of the International School of Physics Enrico Fermi*, IOS Press, Amsterdam, 2004, pp. 3–42. (Course CLVII).
- [22] D. Ceperley, *Phys. Rev. B* 18 (1978) 3126.

Chapter 35

The restricted primitive model of ionic fluids with nonadditive diameters

Fantoni R. and Pastore G., *Europhys. Lett.*, **101**, 46003 (2013)

Title: “The restricted primitive model of ionic fluids with nonadditive diameters”

Abstract: The restricted primitive model with nonadditive hard-sphere diameters is shown to have interesting and peculiar clustering properties. We report accurate calculations of the cluster concentrations. Implementing efficient and ad hoc Monte Carlo algorithms we determine the effect of nonadditivity on both the clustering and the gas-liquid binodal. For negative nonadditivity, tending to the extreme case of completely overlapping unlike ions, the prevailing clusters are made of an even number of particles having zero total charge. For positive nonadditivity, the frustrated tendency to segregation of like particles and the reduced space available to the ions favors percolating clusters at high densities.

The restricted primitive model of ionic fluids with nonadditive diameters

RICCARDO FANTONI¹ and GIORGIO PASTORE²

¹ *Dipartimento di Scienze dei Materiali e Nanosistemi, Università Ca' Foscari Venezia
Calle Larga S. Marta DD2137, I-30123 Venezia, Italy, EU*

² *Dipartimento di Fisica dell'Università and IOM-CNR - Strada Costiera 11, I-34151 Trieste, Italy, EU*

received 7 November 2012; accepted in final form 8 February 2013
published online 5 March 2013

PACS 68.43.Hn – Structure of assemblies of adsorbates (two- and three-dimensional clustering)
PACS 61.20.Qg – Structure of associated liquids: electrolytes, molten salts, etc.
PACS 64.70.pv – Colloids

Abstract – The restricted primitive model with nonadditive hard-sphere diameters is shown to have interesting and peculiar clustering properties. We report accurate calculations of the cluster concentrations. Implementing efficient and *ad hoc* Monte Carlo algorithms we determine the effect of nonadditivity on both the clustering and the gas-liquid binodal. For negative nonadditivity, tending to the extreme case of completely overlapping unlike ions, the prevailing clusters are made of an even number of particles having zero total charge. For positive nonadditivity, the frustrated tendency to segregation of like particles and the reduced space available to the ions favors percolating clusters at high densities.

Copyright © EPLA, 2013

Ionic soft matter [1,2] is a class of conventional condensed soft matter whose interactions are dominated by electrostatics crucially affecting its physical properties. Among the most popular representatives of such a class of materials are natural and synthetic saline environments, like aqueous and nonaqueous electrolyte solutions and molten salts, including room-temperature ionic liquids, as well as a variety of polyelectrolytes and colloidal suspensions. Equally well known are biological systems of proteins.

The simplest fluid modeling an ionic colloidal suspension is the restricted primitive model (RPM) [3] a binary mixture of uniformly charged hard spheres (HS) for which the like-unlike collision diameter between a particle of species 1, of diameter $\sigma_{11} = \sigma$, and a particle of species 2 of diameter $\sigma_{22} = \sigma$, is equal to the arithmetic mean $\sigma_{12}^{\text{add}} = (\sigma_{11} + \sigma_{22})/2 = \sigma$. The two species are of charge $\pm q$ with equal concentrations to ensure charge neutrality, and the particles move in a medium of fixed dielectric constant ϵ . The phase diagram of this model has been widely studied both within computer experiments [4–10] and through analytical theories [11–18].

From these studies emerged how, in the vapor phase of this fluid, and thus in the determination of the phase diagram, an important role is played by association and clustering. In an old paper, [19] one of us studied a more

general RPM fluid where it is allowed for size nonadditivity amongst the particles: the like-unlike collision diameter differs from σ_{12}^{add} by a quantity $\Delta = (\sigma_{12} - \sigma_{12}^{\text{add}})/\sigma_{12}^{\text{add}}$ called the nonadditivity parameter. It was suggested through the use of integral equation theories, that such a fluid might have a dramatic change of its clustering properties. The nonadditivity of the HS diameters does not destroy the simplifying symmetry of the model but it introduces modifications of the properties of the pure RPM model making it a paradigm for the self-assembly of isotropic particles and a challenge to present-day theories of fluids. There seems to be a lack of literature on this subject excepted for ref. [20].

In this letter, we reconsider such a model fluid by using more direct, highly efficient numerical simulations. In particular we analyze the clustering properties outside of the gas-liquid coexistence region. As we will see the clustering turns out to be greatly affected by the nonadditivity parameter. To the best of our knowledge this is the first time that such a model fluid is studied with numerical simulations. The debate on the importance of clustering in the RPM is rejuvenated by studying this new model fluid.

The model system here considered may be realized experimentally through a colloid-star polymer mixture where both species are charged [21,22] and may be relevant

Riccardo Fantoni and Giorgio Pastore

for modeling room temperature ionic liquids [23–26]. It is the RPM of nonadditive charged hard spheres (NACHS). The RPM consists of $N/2$ uniformly charged hard spheres of diameter σ carrying a total charge $+q$ and $N/2$ uniformly charged hard spheres of the same diameter carrying a total charge $-q$. The spheres are moving in a dielectric continuum of dielectric constant ϵ . The interaction between ions of species i and j at a distance r apart is given by

$$\beta\phi_{ij}(r) = \begin{cases} +\infty, & r \leq \sigma_{ij}, \\ \frac{q_i q_j}{k_B T \epsilon r}, & r > \sigma_{ij}, \end{cases} \quad i, j = 1, 2, \quad (1)$$

where $\beta = 1/k_B T$ with T the absolute temperature and k_B Boltzmann's constant, q_i the charge of an ion of species i . The ions form a mixture of NACHS, *i.e.*, $\sigma_{11} = \sigma_{22} = \sigma$ and $\sigma_{12} = \sigma(1 + \Delta)$, with $\Delta > -1$ the nonadditivity parameter. A thermodynamic state is completely specified by the reduced density $\rho^* = \rho\sigma^3 = N\sigma^3/V$, where V is the volume containing the fluid, the reduced temperature $T^* = k_B T \epsilon \sigma / q^2$, and the nonadditivity parameter Δ .

We used canonical NVT Monte Carlo (MC) simulations to study the fluid in a cubic simulation box of volume $V = L^3$ with periodic boundary conditions. The long range of the $1/r$ interaction was accounted for using the Ewald method [27].

We start from a simple cubic configuration of two crystals one made of species 1 and one made of species 2 juxtaposed. The maximum particle displacement, the same along each direction, is determined during the first stage of the equilibration run in such a way to ensure an average acceptance ratio of 50%. We need around 10^5 MC steps (MCS) in order to equilibrate the samples and 10^6 MCS/particle for the statistics.

During the simulation we perform a cluster analysis in the vapor phase. After each 100 MCS we determine the number N_n of clusters made of n particles, so that $\sum_n n N_n = N$. We assume [28,29] that a group of ions forms a cluster if the distance r , calculated using periodic boundary conditions, between a particle of species i of the group and at least one other particle of species j is less than some fixed value, *i.e.*, $r < \sigma_{ij} + \delta\sigma$ where δ is a parameter¹. In all our simulations we chose $\delta = 0.1$ (in ref. [5] a detailed study of the sensitivity of the clustering properties on this parameter is carried out for the pure RPM fluid). Then we take the average of these numbers $\langle N_n \rangle$. Here $Q_n = n \langle N_n \rangle / N$ gives the probability that a particle belongs to a cluster of size n . To establish a criterion for percolation, we also find clusters without using periodic boundary conditions. One of *these* clusters percolates if, amongst its particles, there are two that do not satisfy the cluster condition *as a pair*, but do satisfy the condition if periodic boundary conditions are used.

¹Many different ways of defining a cluster have been proposed [12,15,30–32] since the Bjerrum theory [33] of ionic associations first appeared. Our choice corresponds to the geometric one of Gillan [12].

In fig. 1 we simulated the fluid at a temperature $T^* = 0.1$ above the critical temperature, $T_c^* \approx 0.05$, of the pure RPM [6,9,10]. We see how, at high density, a positive nonadditivity is responsible for a gain of clustering in the fluid, which tends to admit percolating clusters also due to the fact that a positive nonadditivity pushes the fluid at densities closer to the maximum density attainable. It is well known that in the neutral nonadditive hard-sphere fluid a positive nonadditivity tends to demix the mixture at lower densities as Δ increases [34–39], so in our fluid we will have a competition between the tendency to demix in the neutral nonadditive hard-sphere fluid and the tendency to cluster in the RPM fluid. At $\rho^* = 0.45$ both the pure RPM and the $\Delta = +0.3$ have percolating clusters. Lowering the density we first reach a state, at $\rho^* = 0.3$, where the negative nonadditivity gives the same clustering as the RPM and the positive nonadditivity gives higher percolating clustering, then a state, at $\rho^* = 0.1$, where the positive nonadditivity gives the same clustering of RPM and the negative nonadditivity a higher one, and finally a state, at $\rho^* = 0.01$, at low densities where a negative nonadditivity increases the clustering over the RPM fluid and a positive nonadditivity diminishes it. Summarizing, for the fixed values of $|\Delta|$ used, we find, in agreement with ref. [19], that: a) at high density and positive Δ we have more clustering than in the additive model, b) at high density and negative Δ we have less clustering than in the additive model, c) at low density and positive Δ we have less clustering than in the additive model, d) at low densities and negative Δ we have more clustering than in the additive model. These points can be explained observing that a pair of unlike ions have a higher affinity with negative Δ . Thus, in a bulk phase negative Δ favors hetero-coordination. Clusters of a given number of ions tend to be smaller when Δ is negative. As a result, at low density (where excluded volume plays a small role), the extra affinity due to negative Δ enhances cluster formation. By contrast, at high densities, the increase in available volume from the resulting hetero-coordination with negative Δ has an important role, reducing the density-driven imperative to form clusters in the negative Δ case. The same arguments in reverse explain the behavior of a system with positive nonadditivity where now homo-coordination at high density is favored [19].

To qualitatively reproduce the curves with nonpercolating clusters we can use the Tani and Henderson clustering analysis [28,29,40] with an inter-cluster configurational partition function the one of an ideal gas of clusters, in reduced units, $Z_{\text{inter}} \approx (V/\sigma^3)^{N_t}$, where $N_t = \sum_{n=1}^{n_c} N_n$ is the total number of clusters and we assume to have only clusters made of up to n_c particles. Then the equations for the equilibrium cluster concentrations are

$$\langle N_n \rangle / N = \lambda^n z_n^{\text{intra}} / \rho^*, \quad n = 1, 2, \dots, n_c, \quad (2)$$

$$1 = \sum_{n=1}^{n_c} n \langle N_n \rangle / N, \quad (3)$$

The restricted primitive model of ionic fluids with nonadditive diameters

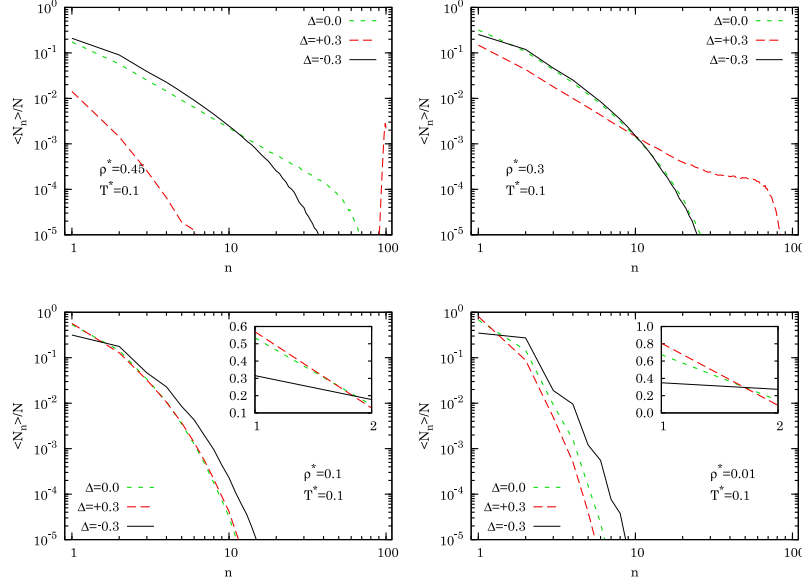


Fig. 1: (Color online) Clustering properties of the fluid at various values of nonadditivity and density. N_n are the number of clusters made of n particles. We chose $\delta = 0.1$. In the MC simulations we used $N = 100$ particles and a number of MCS = 10^7 . The insets allow $\alpha = \langle N_1 \rangle / N$, the degree of dissociation, to be directly read off from the graph.

where z_n^{intra} are the configurational intra-cluster partition functions in reduced units with $z_1^{\text{intra}} = 2$ and $\lambda (= \alpha \rho^* / 2)$ is a Lagrange multiplier to be determined by eq. (3). Moreover neglecting the excess internal energy of the clusters we can approximate $z_n^{\text{intra}} \approx (v_n / \sigma^3)^{(n-1)} 2^n / n!$ where v_n is the volume of an n -cluster. Assuming further the cluster to be in a closed packed configuration we can approximate $v_n \approx n \sigma^3 / \sqrt{2}$. This simple approximation is temperature independent and its usefulness is thereby quite limited.

We checked the size dependence of the curves shown in fig. 1 and saw that when we have no percolating clusters the curve was unaffected by a choice of a higher number of particles (up to 5000), while the curve changed in the presence of percolating clusters. In this case we found that a common curve is given by $\langle N_x \rangle / N$ with $x = n / N \in [0, 1]$. Then, in order to satisfy the normalization condition, $1 = \sum_n n (\langle N_n \rangle / N) \approx \int dx x N^2 (\langle N_x \rangle / N)$, we must have $(\langle N_x \rangle / N') / (\langle N_x \rangle / N'') \approx (N'' / N')^2$ for two different sizes N' and N'' .

In fig. 2 we show the clustering analysis for the fluid with Δ approaching -1 at $T^* = 0.1$ and $\rho^* = 0.45$. We see how letting Δ approach -1 stabilizes small neutrally charged clusters and lowers the degree of dissociation $\alpha = \langle N_1 \rangle / N$. The first stable cluster is the dipole: the “overlap” of a positive and a negative sphere. This are dipoles of moment qr_{12} with $r_{12} < \sigma(1 + \Delta + \delta)$ which

²Clearly a proper analysis of the cluster volume would itself require a MC simulation [12].

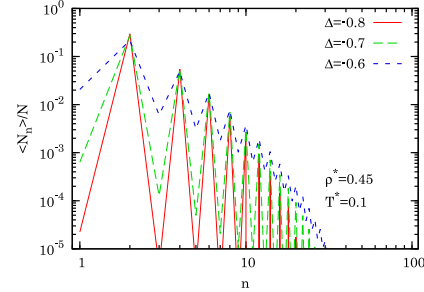


Fig. 2: (Color online) We show the clustering properties of the fluid at $T^* = 0.1$ and $\rho^* = 0.45$ at various values of negative nonadditivity approaching -1 . N_n are the number of clusters made of n particles. We chose $\delta = 0.1$. In the MC simulations we used $N = 100$ particles and a number of MCS = 5×10^7 .

may lack a gas-liquid criticality [41]. We clearly have a transition from a conducting to an insulating phase as Δ goes from 0 to -1 . We expect that in the limiting case of $\Delta = -1$ the system we obtain is the neutral HS fluid of half the density. This is confirmed by a comparison of the like radial distribution functions with the one of the neutral HS even if the $\Delta = -1$ fluid simulation rapidly slows down into the frozen configuration of the overlapping anions and cations. In order to overcome this problem one should alternate single-particle moves with neutrally charged 2-cluster moves.

Riccardo Fantoni and Giorgio Pastore

In order to qualitatively reproduce the curve of fig. 2 we need to use eqs. (2), (3) with $z_n^{\text{intra}} = \sum_{s=0}^n z_{s,n-s}^{\text{intra}}$ where $z_{s,t}^{\text{intra}}$ are the configurational intra-cluster partition functions of a cluster made of s anions and t cations,

$$z_{s,t}^{\text{intra}} = \frac{1}{s!t!} \int_{\Omega_{s,t}} \frac{d\mathbf{r}_2 \dots d\mathbf{r}_{s+t}}{\sigma^{3(s+t-1)}} \times e^{-\beta \sum_{\mu>\nu=1}^{s+t} \phi_{i_\mu j_\nu}(r_{\mu\nu})} \quad (4)$$

$$\approx \frac{(s+t)^{(s+t-1)}}{s!t!} (K/K_0)^{\min\{s,t\}}, \quad (5)$$

$$K/K_0 = \int_{\sigma(1+\Delta)}^{\lambda_B/2} r^2 e^{+\lambda_B/r} dr / \int_{\sigma(1+\Delta)}^{\lambda_B/2} r^2 dr, \quad (6)$$

where the configurational integral goes only over the relative positions and it covers the region $\Omega_{s,t}$ of s anions clusters configuration space, $\lambda_B = \sigma/T^*$ is the Bjerrum length, Roman indices denote the particle species, Greek indices denote the particle labels, a Roman index with a Greek subindex denotes the species of the particle corresponding to the Greek subindex, and $\mathbf{r}_{\mu\nu} = \mathbf{r}_\nu - \mathbf{r}_\mu$ denotes the separation vector between particle μ and particle ν . Equation (5) is justified as follows. Let us call the anions $i_- = 1_-, \dots, s_-$ and the cations $j_+ = 1_+, \dots, t_+$. From eq. (5) it follows that

$$\begin{aligned} z_{t,t}^{\text{intra}} &= \frac{1}{t!^2} \frac{1}{\sigma^{3(2t-1)}} \int_{\Omega_{t,t}} \prod_{l=2}^t d\mathbf{r}_{1+l-} \prod_{k=1}^t d\mathbf{r}_{k+k-} \\ &\times \prod_{i>j=1}^t e^{-2\lambda_B/r_{i+j+}} \prod_{i,j=1}^t e^{+\lambda_B/r_{i+j-}} \\ &\approx \frac{1}{t!^2} \frac{1}{\sigma^{3(2t-1)}} \int_{\Omega_{t,t}} \prod_{l=2}^t d\mathbf{r}_{1+l-} \prod_{k=1}^t d\mathbf{r}_{k+k-} \\ &\times \prod_{i,j=1}^t e^{+\lambda_B/r_{i+j-}}, \end{aligned} \quad (7)$$

where we approximated $e^{-\lambda_B/r} \approx 1$ which is justified at high $T^* < 1/2(1+\Delta)$ or low λ_B . Now we observe that for example $r_{1+2-} = |\mathbf{r}_{1+1-} + \mathbf{r}_{1-2-}|$ with $r_{1-2-} > \sigma$ and $e^{+\lambda_B/r_{1+2-}} \approx 1$. So that for negative nonadditivity we can further approximate

$$\begin{aligned} z_{t,t}^{\text{intra}} &\approx \frac{1}{t!^2} \frac{1}{\sigma^{3(2t-1)}} \int_{\Omega_{t,t}} \prod_{l=2}^t d\mathbf{r}_{1+l-} \prod_{k=1}^t d\mathbf{r}_{k+k-} \\ &\times \prod_{i,j=1}^t e^{+\lambda_B/r_{i+j-}} \\ &\approx \frac{1}{t!^2} \frac{1}{\sigma^{3(2t-1)}} \int_{\Omega_{t,t}} \prod_{l=2}^t d\mathbf{r}_{1+l-} \prod_{k=1}^t d\mathbf{r}_{k+k-} \\ &\times \prod_{i=1}^t e^{+\lambda_B/r_{i+i-}} \\ &\approx \frac{(2t)^{(2t-1)}}{t!^2} (K/K_0)^t, \end{aligned} \quad (8)$$

where the factor $(2t)^{(2t-1)}$ takes into account the volume of $\Omega_{t,t}$. Using the same chain of approximations we reach eq. (5). We immediately see how $z_{1,1}^{\text{intra}} \propto K/\sigma^3$ becomes bigger and bigger as $\Delta \rightarrow -1$ and the same holds for all the $z_{k,k}^{\text{intra}}$ which clearly dominate over all the others $z_{s,t}^{\text{intra}}$ with $s \neq t$. And this qualitatively explains fig. 2.

Sufficiently close to the critical point we determined the qualitative change in the behavior of the gas-liquid coexistence region by switching on a negative or a positive nonadditivity. To this aim we divided the simulation box into m^3 cubes of side $\ell = L/m$ and registered the density inside each cell $\rho_i = \mathcal{N}_i/\ell^3$, where \mathcal{N}_i is the number of particles inside the i -th cell so that $\sum_{i=1}^{m^3} \mathcal{N}_i = N$. Then we calculated the density distribution function $P_m(\rho) = \sum_{i=1}^{m^3} P_m(\rho_i)/m^3$ [42,43], where $P_m(\rho_i)$ is the distribution function for the i -th cell. With $\int P_m(\rho) d\rho = 1$. Above the critical temperature the density probability distribution function can be described by a Gaussian centered at the simulation density, whereas below, it becomes bimodal with two peaks one centered at the gas density and one at the liquid density.

We start from an initial configuration of particles of random species placed on a simple cubic lattice. We equilibrate (melt) the fluid for 10^6 MCS/particle. We then sampled the distribution function every 10 MCS. To enhance the efficiency of the determination of the cell density distribution, every 10 MCS, we choose the subdivision of the simulation box into cells with a random displacement $\mathbf{r} = (r_x, r_y, r_z)$ with $r_x, r_y, r_z \in [0, L]$. And we measured the distribution function on runs of 10^6 MCS/particle.

Choosing $m = 2$ and $N = 100$ the results for the fluid at a temperature $T^* = 0.02$, $\rho^* = 0.2$, well within the coexistence region of the pure RPM fluid, and $\Delta = 0, \pm\mathcal{D}$ with $\mathcal{D} = 10^{-1}, 10^{-2}, 10^{-3}$ are shown in fig. 3. In this case the minimum density that can be registered is $1/\ell^3 = 0.2 \times 8/100 = 0.016$. We see that the pure RPM fluid shows a density distribution function which has three peaks with the first peak, which lies below the minimum density, at approximately the low density of the gas phase, the second peak at the simulation density $\rho^* = 0.2$ which is due to the fact that the fluid develops surfaces between the gas and the liquid phase [44], and the third peak at approximately the high density of the liquid phase. We see from the figure that increasing \mathcal{D} the middle peak is lost first in the positive additive model and then in the negative nonadditive models. Moreover for the biggest \mathcal{D} the peak of the liquid phase is barely visible. This may be due to the fact that one had to choose a proper simulation density closer to the density of the liquid [42,43]. We clearly see how this analysis works like a ‘‘microscope’’ on the degree of nonadditivity predicting an increase(decrease) of the coexistence region for small negative(positive) nonadditivity. This behavior can be explained as follows. Positive nonadditivity increases the effective excluded-volume of ions, thereby reducing the density of the liquid phase, and negative nonadditivity does the opposite.

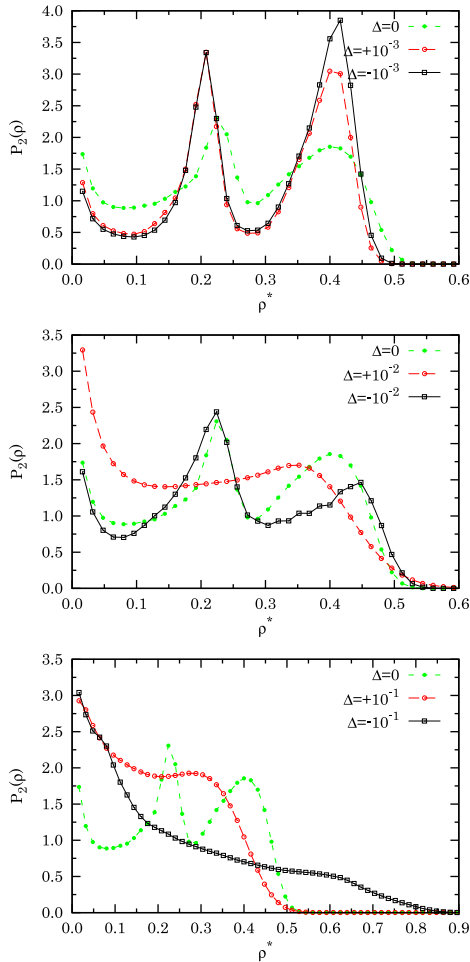


Fig. 3: (Color online) Cell density distribution function for the fluid at $T^* = 0.02$, $\rho^* = 0.2$ and $\Delta = 0, \pm \mathcal{D}$ with $\mathcal{D} = 10^{-3}, 10^{-2}, 10^{-1}$. We used $N = 100$ and $m = 2$ with 10^6 MCS/particle.

We believe that our results could be relevant for the interpretation of experimental work on the phase diagrams of room temperature ionic liquids [25]. In these experimental systems the liquid-liquid binodals shifted above and below the one of the pure RPM are observed depending on the kind of solvent. If on the one hand this can be ascribed to the different dielectric constant of the solvent [24] on the other hand it is clear that depending on the kind of solvent used the anion-cation contact-pairing affinity may vary [45] and thus the different experimental ionic liquids considered should be more correctly described by comparison not just with the pure RPM but with the more realistic primitive model with the addition of either a positive or negative size nonadditivity.

In conclusion, we have performed for the first time a MC simulations study of the vapor phase of the RPM with nonadditive diameters, with particular emphasis on its clustering properties. A density distribution function analysis shows how the gas-liquid coexistence region evolves by switching on the nonadditivity. A negative nonadditivity tends to enlarge the coexistence region while a positive one to shrink it.

From the cluster analysis we were able to distinguish between two kind of behaviors for the cluster concentrations. When we are below the percolation threshold the curves for the cluster concentrations as a function of the cluster size are independent of the number of particles used in the simulation and can be qualitatively explained by a simple clustering theory where one approximates the clusters to form an ideal gas and the n -cluster as formed by n noninteracting particles, for not too small density or nonadditivity. When we are above the percolation threshold the curves depend on the number of particles used in the simulation and obey a simple scaling relationship.

At low density, the negative nonadditive fluid has higher clustering than the pure RPM whereas at high densities the positive nonadditive fluid has a greater degree of clustering. The positive nonadditive fluid is the first one to reach the percolating clusters upon an increase of the density. This is due to the less space available to the ions, for a given density, for positive nonadditivity and to the frustrated tendency to segregation of like particles at high density. A negative nonadditivity tends to greatly enhance the formation of the neutrally charged clusters, starting with the dipole, as can be predicted from the simple clustering theory refined at the intra-cluster level. Traces of these features can also be read from an analysis of the partial radial distribution function and structure factors, which will be presented elsewhere.

In parallel with the density distribution function analysis we are currently planning to perform a Gibbs ensemble MC study of the gas-liquid binodal to establish more accurately the dependence on the nonadditivity parameter.

We hope that the present study could foster additional theoretical and computational studies as well as experimental realizations of these simple but rich fluids.

RF would like to acknowledge the use of the computational facilities of CINECA through the ISCRCA call. Both authors would like to thank the referee for useful comments.

REFERENCES

[1] DE GENNES P. G., *Rev. Mod. Phys.*, **64** (1992) 645.
 [2] HENDERSON D., HOLOVKO M. and TROKHYMCHUK A. (Editors), *Ionic Soft Matter: Modern Trends in Theory and Applications*, *NATO Science Series, Series II: Mathematics, Physics and Chemistry*, Vol. **206** (Springer, Dordrecht) 2004.

Riccardo Fantoni and Giorgio Pastore

- [3] HANSEN J. P. and McDONALD I. R., *Theory of Simple Liquids*, 2nd edition (Academic Press) 1986.
- [4] ORKOULAS G. and PANAGIOTOPOULOS A. Z., *J. Chem. Phys.*, **101** (1994) 1452.
- [5] CAILLOL J.-M. and WEIS J.-J., *J. Chem. Phys.*, **102** (1995) 7610.
- [6] ORKOULAS G. and PANAGIOTOPOULOS A. Z., *J. Chem. Phys.*, **110** (1999) 1581.
- [7] CAMP P. J. and PATEY G. N., *J. Chem. Phys.*, **111** (1999) 9000.
- [8] ROMERO-ENRIQUE J. M., ORKOULAS G., PANAGIOTOPOULOS A. Z. and FISHER M. E., *Phys. Rev. Lett.*, **85** (2000) 4558.
- [9] LUIJTEN E., FISHER M. E. and PANAGIOTOPOULOS A. Z., *Phys. Rev. Lett.*, **88** (2002) 185701.
- [10] CAILLOL J.-M., LEVESQUE D. and WEIS J.-J., *J. Chem. Phys.*, **116** (2002) 10794.
- [11] STELL G., WU K. C. and LARSEN B., *Phys. Rev. Lett.*, **37** (1976) 1369.
- [12] GILLAN M. J., *Mol. Phys.*, **49** (1983) 421.
- [13] GIVEN J. A., *Phys. Rev. A*, **45** (1992) 3849.
- [14] GIVEN J. A. and STELL G., *J. Chem. Phys.*, **96** (1992) 9233.
- [15] FISHER M. E. and LEVIN Y., *Phys. Rev. Lett.*, **71** (1993) 3826.
- [16] ZHOU Y., YEH S. and STELL G., *J. Chem. Phys.*, **102** (1995) 5785.
- [17] GIVEN J. A. and STELL G., *J. Chem. Phys.*, **106** (1997) 1195.
- [18] JIANG J., BLUM L., BERNARD O., PRAUSNITZ J. M. and SANDLER S. I., *J. Chem. Phys.*, **116** (2002) 7977.
- [19] PASTORE G., GIAQUINTA P. V., THAKUR J. S. and TOSI M. P., *J. Chem. Phys.*, **84** (1986) 1827. The relationship between our reduced units and theirs is as follows: $\rho^* = 3\sigma^3/4\pi$ and $T^* = \sigma/\Gamma$.
- [20] ZUCKERMAN D. M., *Analysis, improvement, and extension of electrolyte theories*, PhD Thesis, University of Maryland (1998).
- [21] POON W. C. K., EGELHAAF S. U., STELLBRINK J., ALLGAIER J., SCHOFIELD A. B. and PUSEY P. N., *Philos. Trans. R. Soc. London, Ser. A*, **359** (2001) 897.
- [22] POON W. C. K., *J. Phys.: Condens. Matter*, **14** (2002) R859.
- [23] WEINGÄRTNER H., KLEEMEIER M., WIEGAND S. and SCHÖER W., *J. Stat. Phys.*, **78** (1995) 169.
- [24] KLEEMEIER M., WIEGAND S., SCHRÖER W. and WEINGÄRTNER H., *J. Chem. Phys.*, **110** (1999) 3085.
- [25] SARACAN D., RYBARSCH C. and SCHRÖER W., *Z. Phys. Chem.*, **220** (2006) 1417.
- [26] SCHRÖER W. and VALE V. R., *J. Phys.: Condens. Matter*, **21** (2009) 424119.
- [27] ALLEN M. P. and TILDESLEY D. J., *Computer Simulation of Liquids* (Oxford University Press) 1987.
- [28] FANTONI R., GIACOMETTI A., SCIORTINO F. and PASTORE G., *Soft Matter*, **7** (2011) 2419.
- [29] FANTONI R., *Eur. Phys. J. B*, **85** (2012) 108.
- [30] LEE J. K., BARKER J. A. and ABRAHAM F. F., *J. Chem. Phys.*, **58** (1973) 3166.
- [31] EBELING W. and GRIGO M., *Am. Phys.*, **37** (1980) 21.
- [32] FRIEDMAN H. L. and LARSEN G., *J. Chem. Phys.*, **70** (1979) 92.
- [33] BJERRUM N., *K. Dan. Vidensk. Selsk. Mat.-fys. Medd.*, **7** (1926) 1.
- [34] ROVERE M. and PASTORE G., *J. Phys.: Condens. Matter*, **6** (1994) A163.
- [35] LOMBA E., ALVAREZ M., LEE L. L. and ALMARZA N. G., *J. Chem. Phys.*, **104** (1996) 4180.
- [36] JAGANNATHAN K. and YETHIRAJ A., *J. Chem. Phys.*, **118** (2003) 7907.
- [37] GÓZDŹ W. T., *J. Chem. Phys.*, **119** (2003) 3309.
- [38] BUHOT A., *J. Chem. Phys.*, **122** (2005) 024105.
- [39] SANTOS A., LÓPEZ DE HARO M. and YUSTE S. B., *J. Chem. Phys.*, **132** (2010) 204506.
- [40] TANI A. and HENDERSON D., *J. Chem. Phys.*, **79** (1983) 2390.
- [41] ROVIGATTI L., RUSSO E. and SCIORTINO F., *Phys. Rev. Lett.*, **107** (2011) 237801.
- [42] ROVERE M., HEERMANN D. W. and BINDER K., *Europhys. Lett.*, **6** (1988) 585.
- [43] ROVERE M., HEERMANN D. W. and BINDER K., *J. Phys.: Condens. Matter*, **2** (1990) 7009.
- [44] SMIT B., DE SMEDT PH. and FRENKEL D., *Mol. Phys.*, **68** (1989) 931.
- [45] KALCHER I., SCHULZ J. C. F. and DZUBIELLA J., *Phys. Rev. Lett.*, **104** (2010) 097802.

Chapter 36

Janus fluid with fixed patch orientations: theory and simulations

Maestre M. A. G., **Fantoni R.**, Giacometti A. and Santos A., J. Chem. Phys. **138**, 094904 (2013)

Title: “Janus fluid with fixed patch orientations: theory and simulations”

Abstract: We study thermophysical properties of a Janus fluid with constrained orientations, using analytical techniques and numerical simulations. The Janus character is modeled by means of a Kern-Frenkel potential where each sphere has one hemisphere of square-well and the other of hard-sphere character. The orientational constraint is enforced by assuming that each hemisphere can only point either North or South with equal probability. The analytical approach hinges on a mapping of the above Janus fluid onto a binary mixture interacting via a “quasi” isotropic potential. The anisotropic nature of the original Kern-Frenkel potential is reflected by the asymmetry in the interactions occurring between the unlike components of the mixture. A rational-function approximation extending the corresponding symmetric case is obtained in the sticky limit, where the square-well becomes infinitely narrow and deep, and allows a fully analytical approach. Notwithstanding the rather drastic approximations in the analytical theory, this is shown to provide a rather precise estimate of the structural and thermodynamical properties of the original Janus fluid.



Janus fluid with fixed patch orientations: Theory and simulations

Miguel Ángel G. Maestre,^{1,a)} Riccardo Fantoni,^{2,b)} Achille Giacometti,^{2,c)} and Andrés Santos^{1,d)}

¹*Departamento de Física, Universidad de Extremadura, E-06071 Badajoz, Spain*

²*Dipartimento di Scienze dei Materiali e Nanosistemi, Università Ca' Foscari Venezia, Calle Larga S. Marta DD2137, I-30123 Venezia, Italy*

(Received 20 December 2012; accepted 14 February 2013; published online 5 March 2013)

We study thermophysical properties of a Janus fluid with constrained orientations, using analytical techniques and numerical simulations. The Janus character is modeled by means of a Kern–Frenkel potential where each sphere has one hemisphere of square-well and the other of hard-sphere character. The orientational constraint is enforced by assuming that each hemisphere can only point either North or South with equal probability. The analytical approach hinges on a mapping of the above Janus fluid onto a binary mixture interacting via a “quasi” isotropic potential. The anisotropic nature of the original Kern–Frenkel potential is reflected by the asymmetry in the interactions occurring between the unlike components of the mixture. A rational-function approximation extending the corresponding symmetric case is obtained in the sticky limit, where the square-well becomes infinitely narrow and deep, and allows a fully analytical approach. Notwithstanding the rather drastic approximations in the analytical theory, this is shown to provide a rather precise estimate of the structural and thermodynamical properties of the original Janus fluid. © 2013 American Institute of Physics. [<http://dx.doi.org/10.1063/1.4793626>]

I. INTRODUCTION

Janus fluids refer to colloidal suspensions formed by nearly spherical particles with two different philicities evenly distributed in the two hemispheres.^{1,2} Under typical experimental conditions in a water environment, one of the two hemispheres is hydrophobic, while the other is charged, so that different particles tend to repel each other, hence forming isolated monomers. On the other hand, if repulsive forces are screened by the addition of a suitable salt, then clusters tend to form driven by hydrophobic interactions.³

This self-assembly mechanism has recently attracted increasing attention due to the unprecedented improvement in the chemical synthesis and functionalization of such colloidal particles, that allows a precise and reliable control on the aggregation process that was not possible until a few years ago.⁴ From a technological point of view, this is very attractive as it paves the way to a bottom-up design and engineering of nanomaterials alternative to conventional top-down techniques.⁵

One popular choice of model describing the typical duality characteristic of the Janus fluid is the Kern–Frenkel model.⁶ This model considers a fluid of rigid spheres having their surfaces partitioned into two hemispheres. One of them has a square-well (SW) character, i.e., it attracts other *similar* hemispheres through a SW interaction, thus mimicking the short-range hydrophobic interactions occurring in real Janus fluids. The other part of the surface is assumed to have hard-sphere (HS) interactions with all other hemispheres, i.e.,

with both like HS as well as SW hemispheres. The HS hemisphere hence models the charged part in the limit of highly screened interactions that is required to have aggregation of the clusters.

Although in the present paper only an even distribution between SW and HS surface distributions will be considered (Janus limit), other choices of the coverage, that is the fraction of SW surface with respect to the total one, have been studied within the Kern–Frenkel model.⁷ In fact, one of the most attractive features of the general model stems from the fact that it smoothly interpolates between an isotropic HS fluid (zero coverage) and an equally isotropic SW fluid (full coverage).^{8,9}

The thermophysical and structural properties of the Janus fluid have been recently investigated within the framework of the Kern–Frenkel model using numerical simulations,^{7,10} thus rationalizing the cluster formation mechanism characteristic of the experiments.³ The fluid-fluid transition was found to display an unconventional and particularly interesting phase diagram, with a re-entrant transition associated with the formation of a cluster phase at low temperatures and densities.^{7,10} While numerical evidence of this transition is quite convincing, a minimal theory including all necessary ingredients for the onset of this anomalous behavior is still missing. Two previous attempts are however noteworthy. Reinhardt *et al.*¹¹ introduced a van der Waals theory for a suitable mixture of clusters and monomers that accounts for a re-entrant phase diagram, whereas Fantoni *et al.*^{12,13} developed a cluster theory explaining the appearance of some “magic numbers” in the cluster formation. This notwithstanding, the challenge of an analytical theory fully describing the anomaly occurring in the phase diagram of the Janus fluid still remains.

The aim of the present paper is to attempt a new route in this direction. We will do this by considering a Janus fluid

^{a)}Electronic mail: maestre@unex.es.

^{b)}Electronic mail: rfantoni@ts.infn.it.

^{c)}Electronic mail: achille.giacometti@unive.it.

^{d)}Electronic mail: andres@unex.es. URL: <http://www.unex.es/eweb/fistoeur/andres>.

094904-2 Maestre *et al.*

 J. Chem. Phys. **138**, 094904 (2013)

within the Kern–Frenkel model, where the orientations of the SW hemispheres are constrained to be along either North or South, in a spirit akin to Zwanzig model for the isotropic-nematic transition in liquid crystals.¹⁴

Upon observing that under those conditions, one ends up with only four possible different interactions (North–North, North–South, South–North, and South–South), this constrained model will be further mapped onto a binary mixture interacting via a “quasi” isotropic potential. Here the term “quasi” refers to the fact that a certain memory of the original anisotropic Kern–Frenkel potential is left: after the mapping, one has to discriminate whether a particle with patch pointing North (“spin-up”) is lying above or below that with a patch pointing South (“spin-down”). This will introduce an asymmetry in the unlike components of the binary mixture, as explained in detail below. In order to make the problem tractable from the analytical point of view, the particular limit of an infinitely narrow and deep square-well (sticky limit) will be considered. This limit was originally devised by Baxter and constitutes the celebrated one-component sticky-hard-sphere (SHS) or adhesive Baxter model.¹⁵ By construction, our model reduces to it in the limit of fully isotropic attractive interactions. The latter model was studied within the Percus–Yevick (PY) closure¹⁶ in the original Baxter work and in a subsequent work by Watts *et al.*¹⁷ The extension of this model to a binary mixture was studied by several authors.^{18–22} The SHS model with Kern–Frenkel potential was also studied in Ref. 23, via a virial expansion at low densities.

A methodology alternative to the one used in the above studies hinges on the so-called “rational-function approximation” (RFA),^{24,25} and is known to be equivalent to the PY approximation for the one-component SHS Baxter model¹⁵ and for its extension to symmetric SHS mixtures.^{18,22,24} The advantage of this approach is that it can be readily extended to more general cases, and this is the reason why it will be employed in the present analysis to consider the case of asymmetric interactions. We will show that this approach provides a rather precise estimate of the thermodynamic and structural properties of the Janus fluids with up-down orientations by explicitly testing it against Monte Carlo (MC) simulations of the same Janus fluid.

The remaining part of the paper is envisaged as follows. Section II describes our Janus model and its mapping onto a binary mixture with asymmetric interactions. It is shown in Sec. III that the thermophysical quantities do not require the knowledge of the full (anisotropic) pair correlation functions but only of the functions averaged over all possible North or South orientations. Section IV is devoted to the sticky-limit version of the model, i.e., the limit in which the SW hemisphere has a vanishing well width but an infinite depth leading to a constant value of the Baxter parameter τ . The exact cavity functions to first order in density (and hence exact up to second and third virial coefficients) in the sticky limit are worked out in Appendix A. Up to that point all the equations are formally exact in the context of the model. Then, in Sec. V we present our approximate RFA theory, which hinges on a heuristic extension from the PY solution for mixtures with symmetric SHS interactions to the realm of asymmetric SHS interactions. Some technical aspects are relegated to Ap-

pendices B and C. The prediction of the resulting analytical theory is compared with MC simulations in Sec. VI, where a semi-quantitative agreement is found. Finally, the paper is closed with conclusions and an outlook in Sec. VII.

II. MAPPING THE KERN–FRENKEL POTENTIAL ONTO A BINARY MIXTURE

A. The Kern–Frenkel potential for a Janus fluid

Consider a fluid of spheres with identical diameters σ where the surface of each sphere is divided into two parts. The first hemisphere (the green one in the color code given in Fig. 1) has a SW character, thus attracting another identical hemisphere via a SW potential of width $(\lambda - 1)\sigma$ and depth ϵ . The second hemisphere (the red one in the color code of Fig. 1) is instead a HS potential. The orientational dependent pair potential between two arbitrary particles μ and ν ($\mu, \nu = 1, \dots, N$, where N is the total number of particles in the fluid) has then the form proposed by Kern and Frenkel⁶

$$\Phi(\mathbf{r}_{\mu\nu}, \hat{\mathbf{n}}_\mu, \hat{\mathbf{n}}_\nu) = \phi_{\text{HS}}(r_{\mu\nu}) + \phi_{\text{SW}}(r_{\mu\nu})\Psi(\hat{\mathbf{r}}_{\mu\nu}, \hat{\mathbf{n}}_\mu, \hat{\mathbf{n}}_\nu), \quad (2.1)$$

where the first term is the HS contribution

$$\phi_{\text{HS}}(r) = \begin{cases} \infty, & 0 < r < \sigma, \\ 0, & \sigma < r, \end{cases} \quad (2.2)$$

and the second term is the orientation-dependent attractive part, which can be factorized into an isotropic SW tail

$$\phi_{\text{SW}}(r) = \begin{cases} -\epsilon, & \sigma < r < \lambda\sigma, \\ 0, & \lambda\sigma < r, \end{cases} \quad (2.3)$$

multiplied by an angular dependent factor

$$\Psi(\hat{\mathbf{r}}_{\mu\nu}, \hat{\mathbf{n}}_\mu, \hat{\mathbf{n}}_\nu) = \begin{cases} 1, & \text{if } \hat{\mathbf{n}}_\mu \cdot \hat{\mathbf{r}}_{\mu\nu} \geq 0 \text{ and } \hat{\mathbf{n}}_\nu \cdot \hat{\mathbf{r}}_{\mu\nu} \leq 0, \\ 0, & \text{otherwise.} \end{cases} \quad (2.4)$$

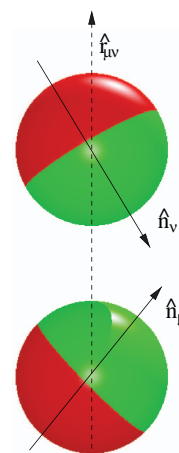


FIG. 1. The Kern–Frenkel potential for Janus fluids.

094904-3 Maestre *et al.*

 J. Chem. Phys. **138**, 094904 (2013)

Here, $\hat{\mathbf{r}}_{\mu\nu} = \mathbf{r}_{\mu\nu}/r_{\mu\nu}$, where $\mathbf{r}_{\mu\nu} = \mathbf{r}_\nu - \mathbf{r}_\mu$, is the unit vector pointing (by convention) from particle μ to particle ν and the unit vectors $\hat{\mathbf{n}}_\mu$ and $\hat{\mathbf{n}}_\nu$ are “spin” vectors associated with the orientation of the attractive hemispheres of particles μ and ν , respectively (see Fig. 1). An attractive interaction then exists only between the two SW portions of the surface sphere, provided that the two particles are within the range of the SW potential.

B. Asymmetric binary mixture

We now consider the particular case where the only possible orientations of particles are with attractive caps pointing only either North or South with equal probability, as obtained by Fig. 1 in the limit $\hat{\mathbf{n}}_\mu = \hat{\mathbf{z}}$, $\hat{\mathbf{n}}_\nu = -\hat{\mathbf{z}}$, and with $\hat{\mathbf{z}}$ pointing North.

Under these conditions, one then notes that the Kern–Frenkel potential (2.1)–(2.4) can be simplified by associating a spin $i = 1$ (up) to particles with SW hemispheres pointing in the North $\hat{\mathbf{z}}$ direction and a spin $j = 2$ (down) to particles with SW hemispheres pointing in the South $-\hat{\mathbf{z}}$ direction, so one is left with only four possible configurations depending on whether particles of type 1 lie above or below particles of type 2, as illustrated in Fig. 2. The relationship between the genuine Janus model (see Fig. 1) and the up-down model (see Fig. 2) is reminiscent to the relationship between the Heisenberg and the Ising model of ferromagnetism. From that point of view, our model can be seen as an Ising-like version of the original Janus model. A similar spirit was also adopted in the Zwanzig model for the isotropic-nematic transition in liquid crystals.¹⁴

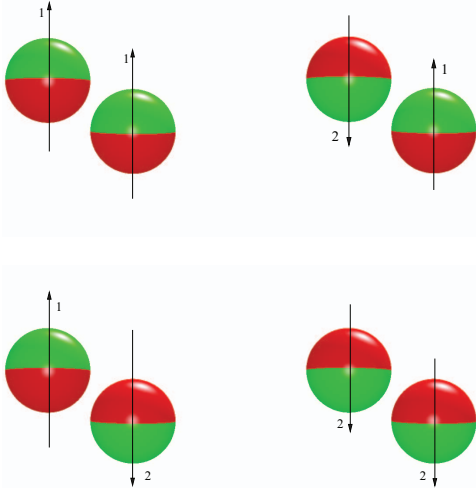


FIG. 2. (Top-left) A particle of type 1 is “below” another particle of type 1 providing SW/HS = HS interactions. (Top-right) A particle of type 1 is “below” a particle of type 2 leading to SW/SW = SW interactions. (Bottom-left) A particle of type 2 is “below” a particle of type 1 yielding HS/HS = HS interactions. (Bottom-right) A particle of type 2 is “below” another particle of type 2 thus leading again to HS/SW = HS interactions.

The advantage of this mapping is that one can disregard the original anisotropic Janus-like nature of the interactions and recast the problem in the form of a binary mixture such that the interaction potential between a particle of species i located at \mathbf{r}_1 and a particle of species j located at \mathbf{r}_2 has the *asymmetric* form

$$\begin{aligned} \phi_{ij}(\mathbf{r}_1, \mathbf{r}_2) &= \phi_{ij}(r_{12}) \\ &= \varphi_{ij}(r_{12}) \Theta(\cos \theta_{12}) + \varphi_{ji}(r_{12}) \Theta(-\cos \theta_{12}), \end{aligned} \quad (2.5)$$

where $\cos \theta_{12} = \hat{\mathbf{r}}_{12} \cdot \hat{\mathbf{z}}$ (recall our convention $\mathbf{r}_{12} = \mathbf{r}_2 - \mathbf{r}_1$) and

$$\varphi_{ij}(r) = \phi_{\text{HS}}(r) + \begin{cases} \phi_{\text{SW}}(r), & \text{if } i = 1 \text{ and } j = 2, \\ 0, & \text{otherwise.} \end{cases} \quad (2.6)$$

In Eq. (2.5) $\Theta(x) = 1$ and 0 for $x > 0$ and $x < 0$, respectively.

It is important to remark that, in general, $\varphi_{12}(r) \neq \varphi_{21}(r)$, as evident from Eq. (2.6). Thus, the binary mixture is not necessarily symmetric [unless $\epsilon = 0$ or $\lambda = 1$ in Eq. (2.3)], unlike standard binary mixtures where this symmetry condition is ensured by construction. In the potential (2.5), there however is still a “memory” of the original anisotropy since the potential energy of a pair of particles of species i and j separated a distance r_{12} depends on whether particle j is “above” ($\cos \theta_{12} > 0$) or “below” ($\cos \theta_{12} < 0$) particle i . In this sense, the binary mixture obtained in this way is “quasi,” and not “fully,” spherically symmetric.

Another important point to be stressed is that, while the *sign* of $\cos \theta_{12}$ represents the only source of anisotropy in the above potential $\phi_{ij}(r_{12})$, this is *not* the case for the corresponding correlation functions, which will explicitly depend upon the relative orientation $\cos \theta_{12}$ and not only upon its sign. This applies, for instance, to the pair correlation functions $g_{ij}(\mathbf{r}) = g_{ij}(r; \theta)$, as shown in Appendix A to first order in density in the sticky limit (see Sec. IV). As an illustration, Fig. 3 shows the first-order pair correlation functions $g_{11}^{(1)}(\mathbf{r})$ and $g_{12}^{(1)}(\mathbf{r})$ as functions of the radial distance r for several orientations θ .

As our aim is to remove the orientational dependence in the original potential altogether, a further simplification is required to reduce the problem to a simple binary mixture having *asymmetric* correlation functions dependent only on distances and not on orientations of spheres. This will be the orientational average discussed in Sec. III.

III. ORIENTATIONAL AVERAGE AND THERMODYNAMICS

A. Orientational average

Most of the content of this section applies to a mixture (with any number of components) characterized by any anisotropic potential $\phi_{ij}(\mathbf{r}) = \phi_{ji}(-\mathbf{r})$ exhibiting the quasi-isotropic form (2.5), where in general $\varphi_{ij}(r) \neq \varphi_{ji}(r)$ if $i \neq j$. In that case, we note that the thermodynamic quantities will generally involve integrals of the general form

$$I_{ij} = \int d\mathbf{r} g_{ij}(\mathbf{r}) \mathcal{F}_{ij}(\mathbf{r}) \quad (3.1)$$

094904-4 Maestre *et al.*

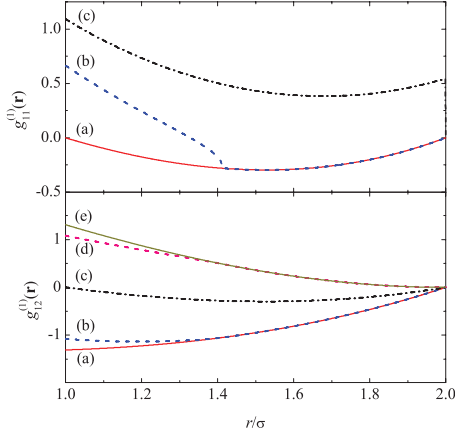
 J. Chem. Phys. **138**, 094904 (2013)


FIG. 3. (Top) Plot of $g_{11}^{(1)}(\mathbf{r})$ as a function of r for (a) $\theta = 0$ and π , (b) $\theta = \frac{\pi}{4}$ and $\frac{3\pi}{4}$, and (c) $\theta = \frac{\pi}{2}$. (Bottom) Plot of the regular part of $g_{12}^{(1)}(\mathbf{r})$ as a function of r for (a) $\theta = 0$, (b) $\theta = \frac{\pi}{4}$, (c) $\theta = \frac{\pi}{2}$, (d) $\theta = \frac{3\pi}{4}$, and (e) $\theta = \pi$. The interaction potential is given by Eq. (2.6) (sketched in Fig. 2), except that the sticky limit with Baxter's temperature $\tau = 0.1$ has been taken (see Sec. IV).

with

$$F_{ij}(\mathbf{r}) = F_{ij}(r)\Theta(\cos\theta) + F_{ji}(r)\Theta(-\cos\theta), \quad (3.2)$$

where in general $F_{ij}(r) \neq F_{ji}(r)$ if $i \neq j$. This strongly suggests that one can define the two orientational averages $g_{ij}^+(\mathbf{r})$ and $g_{ij}^-(\mathbf{r})$ as

$$g_{ij}^+(r) \equiv \bar{g}_{ij}(r) = \int_0^1 d(\cos\theta) g_{ij}(\mathbf{r}), \quad (3.3)$$

$$g_{ij}^-(r) \equiv \bar{g}_{ji}(r) = \int_{-1}^0 d(\cos\theta) g_{ij}(\mathbf{r}). \quad (3.4)$$

Note that $g_{ij}^-(r) = g_{ji}^+(r)$, and this suggests the use of the notation $\bar{g}_{ij}(r)$ and $\bar{g}_{ji}(r)$ instead of $g_{ij}^+(r)$ and $g_{ij}^-(r)$, respectively. Taking into account Eqs. (3.2)–(3.4), Eq. (3.1) becomes

$$I_{ij} = \frac{1}{2} \int d\mathbf{r} [\bar{g}_{ij}(r)F_{ij}(r) + \bar{g}_{ji}(r)F_{ji}(r)]. \quad (3.5)$$

In the case of a double summation over i and j ,

$$\sum_{i,j} x_i x_j I_{ij} = \sum_{i,j} x_i x_j \int d\mathbf{r} \bar{g}_{ij}(r) F_{ij}(r), \quad (3.6)$$

where x_i denotes the mole fraction of species i .

B. Thermodynamics of the mixture: Energy, virial, and compressibility routes

We can now particularize the general result (3.6) to specific cases.

In the case of the internal energy, $\mathcal{F}_{ij}(\mathbf{r}) = \phi_{ij}(\mathbf{r})$ and so the energy equation of state can be written as¹⁶

$$\begin{aligned} u_{\text{ex}} &= \frac{1}{2} \rho \sum_{i,j} x_i x_j \int d\mathbf{r} g_{ij}(\mathbf{r}) \phi_{ij}(\mathbf{r}) \\ &= \frac{1}{2} \rho \sum_{i,j} x_i x_j \int d\mathbf{r} \bar{y}_{ij}(r) \phi_{ij}(r) e^{-\beta\phi_{ij}(r)}, \end{aligned} \quad (3.7)$$

where u_{ex} is the excess internal energy per particle, ρ is the number density, $\beta = 1/k_B T$ (k_B and T being the Boltzmann constant and the temperature, respectively), and $\bar{y}_{ij}(r) \equiv \bar{g}_{ij}(r) e^{\beta\phi_{ij}(r)}$ is the orientational average of the cavity function $y_{ij}(\mathbf{r}) \equiv g_{ij}(\mathbf{r}) e^{\beta\phi_{ij}(r)}$.

A similar result holds for the virial route to the equation of state,

$$\begin{aligned} Z &\equiv \frac{P}{\rho k_B T} \\ &= 1 + \frac{1}{6} \rho \sum_{i,j} x_i x_j \int d\mathbf{r} y_{ij}(\mathbf{r}) \mathbf{r} \cdot \nabla e^{-\beta\phi_{ij}(r)}, \end{aligned} \quad (3.8)$$

where P is the pressure. First, note that

$$\begin{aligned} \nabla\phi_{ij}(\mathbf{r}) &= \left[\frac{d\phi_{ij}(r)}{dr} \Theta(\cos\theta) + \frac{d\phi_{ji}(r)}{dr} \Theta(-\cos\theta) \right] \hat{\mathbf{r}} \\ &\quad - \delta(z) [\varphi_{ij}(r) - \varphi_{ji}(r)] \hat{\mathbf{z}}. \end{aligned} \quad (3.9)$$

Therefore,

$$\mathbf{r} \cdot \nabla\phi_{ij}(\mathbf{r}) = r \left[\frac{d\phi_{ij}(r)}{dr} \Theta(\cos\theta) + \frac{d\phi_{ji}(r)}{dr} \Theta(-\cos\theta) \right], \quad (3.10)$$

and thus

$$Z = 1 + \frac{1}{6} \rho \sum_{i,j} x_i x_j \int d\mathbf{r} \bar{y}_{ij}(r) r \frac{d}{dr} e^{-\beta\phi_{ij}(r)}. \quad (3.11)$$

Finally, let us consider the compressibility route. In a mixture, the (dimensionless) isothermal compressibility χ_T is in general given by

$$\begin{aligned} \chi_T^{-1} &= \frac{1}{k_B T} \left(\frac{\partial p}{\partial \rho} \right)_{T, \{x_j\}} \\ &= \sum_{i,j} \sqrt{x_i x_j} [1 + \hat{h}(0)]_{ij}^{-1}, \end{aligned} \quad (3.12)$$

where $\hat{h}_{ij}(0)$ is proportional to the zero wavenumber limit of the Fourier transform of the total correlation function $h_{ij}(\mathbf{r}) = g_{ij}(\mathbf{r}) - 1$, namely

$$\begin{aligned} \hat{h}_{ij}(0) &= \rho \sqrt{x_i x_j} \int d\mathbf{r} h_{ij}(\mathbf{r}) \\ &= \frac{\rho \sqrt{x_i x_j}}{2} \int d\mathbf{r} [\bar{h}_{ij}(r) + \bar{h}_{ji}(r)]. \end{aligned} \quad (3.13)$$

In the specific case of a binary mixture considered here, Eq. (3.12) becomes

$$\chi_T^{-1} = \frac{1 + x_2 \hat{h}_{11}(0) + x_1 \hat{h}_{22}(0) - 2\sqrt{x_1 x_2} \hat{h}_{12}(0)}{[1 + \hat{h}_{11}(0)][1 + \hat{h}_{22}(0)] - \hat{h}_{12}^2(0)}. \quad (3.14)$$

094904-5 Maestre *et al.*

 J. Chem. Phys. **138**, 094904 (2013)

Equations (3.7) and (3.11)–(3.13) confirm that the knowledge of the two average quantities $\bar{g}_{ij}(r)$ and $\bar{g}_{ji}(r)$ for each pair ij suffices to determine the thermodynamic quantities. In fact, Eqs. (3.7) and (3.11)–(3.13) are formally indistinguishable from those corresponding to mixtures with standard isotropic interactions, except that in our case one generally has $\varphi_{ij}(r) \neq \varphi_{ji}(r)$ and, consequently, $\bar{g}_{ij}(r) \neq \bar{g}_{ji}(r)$.

For future convenience, it is expedient to introduce the Laplace transform of $r\bar{g}_{ij}(r)$:

$$G_{ij}(s) = \int_0^\infty dr e^{-sr} r \bar{g}_{ij}(r). \quad (3.15)$$

Its small- s behavior is of the form²⁵

$$s^2 G_{ij}(s) = 1 + H_{ij}^{(0)} s^2 + H_{ij}^{(1)} s^3 + \dots, \quad (3.16)$$

where

$$H_{ij}^{(n)} \equiv \int_0^\infty dr (-r)^n r \bar{h}_{ij}(r). \quad (3.17)$$

Thus, Eq. (3.13) becomes

$$\hat{h}_{ij}(0) = -2\pi\rho\sqrt{x_i x_j} [H_{ij}^{(1)} + H_{ji}^{(1)}]. \quad (3.18)$$

Note that Eq. (3.16) implies

$$\lim_{s \rightarrow 0} s^2 G_{ij}(s) = 1, \quad (3.19)$$

$$\lim_{s \rightarrow 0} \frac{s^2 G_{ij}(s) - 1}{s} = 0. \quad (3.20)$$

IV. THE STICKY LIMIT

The mapping of the Kern–Frenkel potential with fixed patch orientation along the $\pm\hat{x}$ axis onto a binary mixture represents a considerable simplification. On the other hand, no approximation is involved in this mapping.

The presence of the original SW interactions for the radial part [see Eq. (2.3)] makes the analytical treatment of the problem a formidable task. Progresses can however be made by considering the Baxter SHS limit, for which a well defined approximate scheme of solution is available in the *isotropic* case for both one-component¹⁵ and multi-component^{18–22} fluids. The discussion reported below closely follows the analogue for Baxter symmetric mixtures.^{19,20}

Let us start by rewriting Eq. (2.6) as

$$\varphi_{ij}(r) = \begin{cases} \infty, & r < \sigma, \\ -\epsilon_{ij}, & \sigma < r < \lambda\sigma, \\ 0, & r > \lambda\sigma, \end{cases} \quad (4.1)$$

where $\epsilon_{11} = \epsilon_{22} = \epsilon_{21} = 0$ and $\epsilon_{12} = \epsilon > 0$. However, in this section we will assume generic energy scales ϵ_{ij} . In that case, the virial equation of state (3.11) becomes

$$Z = 1 + 4\eta\bar{y}(\sigma) - 12\eta \sum_{i,j} x_i x_j t_{ij} \frac{\lambda^3 \bar{y}_{ij}(\lambda\sigma) - \bar{y}_{ij}(\sigma)}{\lambda^3 - 1}, \quad (4.2)$$

where $\eta \equiv \frac{\pi}{6}\rho\sigma^3$ is the packing fraction,

$$\bar{y}(r) = \sum_{i,j} x_i x_j \bar{y}_{ij}(r) \quad (4.3)$$

is the orientational average *global* cavity function, and

$$t_{ij} \equiv \frac{1}{12\tau_{ij}} \equiv \frac{1}{3}(\lambda^3 - 1)(e^{\beta\epsilon_{ij}} - 1) \quad (4.4)$$

is a parameter measuring the degree of “stickiness” of the SW interaction $\varphi_{ij}(r)$. This parameter will be used later on to connect results from numerical simulations of the actual Janus fluid with analytical results derived for asymmetric SHS mixtures. Although Baxter’s temperature parameters τ_{ij} are commonly used in the literature, we will employ the inverse temperature parameters $t_{ij} = 1/12\tau_{ij}$ in most of the mathematical expressions.

In the case of the interaction potential (4.1), the energy equation of state (3.7) reduces to

$$u_{\text{ex}} = -12\frac{\eta}{\sigma^3} \sum_{i,j} x_i x_j \epsilon_{ij} e^{\beta\epsilon_{ij}} \int_\sigma^{\lambda\sigma} dr r^2 \bar{y}_{ij}(r). \quad (4.5)$$

The compressibility equation of state (3.12) does not simplify for the SW interaction.

Since the (orientational average) cavity function $\bar{y}_{ij}(r)$ must be continuous, it follows that

$$\bar{g}_{ij}(r) = \bar{y}_{ij}(r)[e^{\beta\epsilon_{ij}} \Theta(r - \sigma) - (e^{\beta\epsilon_{ij}} - 1) \Theta(r - \lambda\sigma)]. \quad (4.6)$$

Following Baxter’s prescription,¹⁵ we now consider the SHS limit

$$\lambda \rightarrow 1, \quad \epsilon_{ij} \rightarrow \infty, \quad t_{ij} \equiv \frac{1}{12\tau_{ij}} \rightarrow (\lambda - 1)e^{\beta\epsilon_{ij}} = \text{finite}, \quad (4.7)$$

so that the well (4.1) becomes infinitely deep and narrow and can be described by a single (inverse) stickiness parameter τ_{ij} . Note that in the present Janus case ($\epsilon_{11} = \epsilon_{22} = \epsilon_{21} = 0$, $\epsilon_{12} = \epsilon > 0$) one actually has $t_{11} = t_{22} = t_{21} = 0$ and $t_{12} = t = 1/12\tau$.

In the SHS limit (4.7), Eqs. (4.2), (4.5), and (4.6) become, respectively,

$$Z = 1 + 4\eta\bar{y}(\sigma) - 4\eta \sum_{i,j} x_i x_j t_{ij} [3\bar{y}_{ij}(\sigma) + \sigma \bar{y}'_{ij}(\sigma)], \quad (4.8)$$

$$u_{\text{ex}} = -12\eta \sum_{i,j} x_i x_j \epsilon_{ij} t_{ij} \bar{y}_{ij}(\sigma), \quad (4.9)$$

$$\bar{g}_{ij}(r) = \bar{y}_{ij}(r)[\Theta(r - \sigma) + t_{ij}\sigma\delta_+(r - \sigma)]. \quad (4.10)$$

In Eq. (4.8), $\bar{y}'_{ij}(\sigma)$ must be interpreted as $\lim_{\lambda \rightarrow 1} \frac{d}{dr} \bar{y}_{ij}(r)|_{r=\sigma}$, which in principle differs from $\frac{d}{dr} \lim_{\lambda \rightarrow 1} \bar{y}_{ij}(r)|_{r=\sigma}$.²⁶ However, both quantities coincide in the one-dimensional case²⁶ and are expected to coincide in the three-dimensional case as well. This is just a consequence of the expected continuity of $\frac{d}{dr} \bar{y}_{ij}(r)$ at $r = \lambda\sigma$ in the SW case.²⁷

094904-6 Maestre *et al.*

 J. Chem. Phys. **138**, 094904 (2013)

Thermodynamic consistency between the virial and energy routes implies

$$\rho \frac{\partial u_{\text{ex}}}{\partial \rho} = \frac{\partial Z}{\partial \beta} = \sum_{i,j} \epsilon_{ij} t_{ij} \frac{\partial Z}{\partial t_{ij}}. \quad (4.11)$$

Using Eqs. (4.8) and (4.9) and equating the coefficients of ϵ_{ij} in both sides, the consistency condition (4.11) yields

$$\begin{aligned} & x_i x_j \left[\sigma \bar{y}'_{ij}(\sigma) - 3\eta \frac{\partial \bar{y}_{ij}(\sigma)}{\partial \eta} \right] \\ &= \sum_{k,\ell} x_k x_\ell \left\{ \frac{\partial \bar{y}_{k\ell}(\sigma)}{\partial t_{ij}} - t_{k\ell} \frac{\partial}{\partial t_{ij}} [3\bar{y}_{k\ell}(\sigma) + \sigma \bar{y}'_{k\ell}(\sigma)] \right\}. \end{aligned} \quad (4.12)$$

For distances $r \gtrsim \sigma$, the orientational averages of the cavity functions can be Taylor expanded as

$$\Theta(r - \sigma) \bar{y}_{ij}(r) = \Theta(r - \sigma) [\bar{y}_{ij}(\sigma) + \bar{y}'_{ij}(\sigma)(r - \sigma) + \dots]. \quad (4.13)$$

Hence, if we denote by $Y_{ij}(s)$ the Laplace transform of $\Theta(r - \sigma) r \bar{y}_{ij}(r)$, Eq. (4.13) yields for large s

$$e^{\sigma s} s Y_{ij}(s) = \sigma \bar{y}_{ij}(\sigma) + [\bar{y}_{ij}(\sigma) + \sigma \bar{y}'_{ij}(\sigma)] s^{-1} + \dots \quad (4.14)$$

According to Eqs. (3.15) and (4.10), the relationship between the Laplace function $G_{ij}(s)$ and $Y_{ij}(s)$ is

$$G_{ij}(s) = Y_{ij}(s) + \sigma^2 t_{ij} \bar{y}_{ij}(\sigma) e^{-\sigma s}. \quad (4.15)$$

Inserting Eq. (4.14) into Eq. (4.15), we obtain the following large- s behavior of $G_{ij}(s)$:

$$\begin{aligned} e^{\sigma s} G_{ij}(s) &= \sigma^2 t_{ij} \bar{y}_{ij}(\sigma) + \sigma \bar{y}_{ij}(\sigma) s^{-1} \\ &+ [\bar{y}_{ij}(\sigma) + \sigma \bar{y}'_{ij}(\sigma)] s^{-2} + \mathcal{O}(s^{-3}). \end{aligned} \quad (4.16)$$

A consequence of this is

$$\frac{\lim_{s \rightarrow \infty} e^{\sigma s} G_{ij}(s)}{\lim_{s \rightarrow \infty} s [e^{\sigma s} G_{ij}(s) - \lim_{s \rightarrow \infty} e^{\sigma s} G_{ij}(s)]} = \sigma t_{ij}. \quad (4.17)$$

V. A HEURISTIC, NON-PERTURBATIVE ANALYTICAL THEORY

A. A simple approximate scheme within the Percus–Yevick closure

The Ornstein–Zernike (OZ) equation for an anisotropic mixture reads¹⁶

$$\begin{aligned} h_{ij}(\mathbf{r}_{12}) &= c_{ij}(\mathbf{r}_{12}) + \rho \sum_k x_k \int d\mathbf{r}_3 h_{ik}(\mathbf{r}_{13}) c_{kj}(\mathbf{r}_{32}) \\ &= c_{ij}(\mathbf{r}_{12}) + \rho \sum_k x_k \int d\mathbf{r}_3 c_{ik}(\mathbf{r}_{13}) h_{kj}(\mathbf{r}_{32}), \end{aligned} \quad (5.1)$$

where $c_{ij}(\mathbf{r})$ is the direct correlation function. The PY closure reads

$$c_{ij}(\mathbf{r}) = g_{ij}(\mathbf{r}) [1 - e^{\beta \phi_{ij}(\mathbf{r})}]. \quad (5.2)$$

Introducing the averages $c_{ij}^+(\mathbf{r}) = \bar{c}_{ij}(\mathbf{r})$ and $c_{ij}^-(\mathbf{r}) = \bar{c}_{ji}(\mathbf{r})$ for $c_{ij}(\mathbf{r})$ in a way similar to Eqs. (3.3) and (3.4), Eq. (5.2) yields

$$\bar{c}_{ij}(\mathbf{r}) = \bar{g}_{ij}(\mathbf{r}) [1 - e^{\beta \phi_{ij}(\mathbf{r})}]. \quad (5.3)$$

Thus, the PY closure for the full correlation functions $c_{ij}(\mathbf{r})$ and $g_{ij}(\mathbf{r})$ translates into an equivalent relation for the orientational average functions $\bar{c}_{ij}(\mathbf{r})$ and $\bar{g}_{ij}(\mathbf{r})$. A similar reasoning, on the other hand, is not valid for the OZ relation. Multiplying both sides of the first equality in Eq. (5.1) by $\Theta(\cos \theta_{12})$ and integrating over $\cos \theta_{12}$ one gets

$$\begin{aligned} \bar{h}_{ij}(r_{12}) &= \bar{c}_{ij}(r_{12}) + \rho \sum_k x_k \int d\mathbf{r}_3 \int_0^1 d(\cos \theta_{12}) \\ &\times h_{ik}(\mathbf{r}_{13}) c_{kj}(\mathbf{r}_{32}). \end{aligned} \quad (5.4)$$

The same result is obtained if we start from the second equality in Eq. (5.1), multiply by $\Theta(-\cos \theta_{12})$, integrate over $\cos \theta_{12}$, and make the changes $\mathbf{r}_{12} \rightarrow -\mathbf{r}_{12}$, $\mathbf{r}_{13} \rightarrow -\mathbf{r}_{13}$, and $i \leftrightarrow j$. Equation (5.4) shows that in the case of anisotropic potentials of the form (2.5) the OZ equation does not reduce to a closed equation involving the averages $\bar{h}_{ij}(\mathbf{r})$ and $\bar{c}_{ij}(\mathbf{r})$ only, as remarked.

In order to obtain a closed theory, we adopt the *heuristic* mean-field decoupling approximation

$$\begin{aligned} & \int d\mathbf{r}_3 \int_0^1 d(\cos \theta_{12}) h_{ik}(\mathbf{r}_{13}) c_{kj}(\mathbf{r}_{32}) \\ & \rightarrow \int d\mathbf{r}_3 \bar{h}_{ik}(r_{13}) \bar{c}_{kj}(r_{32}). \end{aligned} \quad (5.5)$$

Under these conditions, the true OZ relation (5.4) is replaced by the pseudo-OZ relation

$$\bar{h}_{ij}(r_{12}) = \bar{c}_{ij}(r_{12}) + \rho \sum_k x_k \int d\mathbf{r}_3 \bar{h}_{ik}(r_{13}) \bar{c}_{kj}(r_{32}). \quad (5.6)$$

This can then be closed by the PY equation (5.3) and standard theory applies. An alternative and equivalent view is to consider $\bar{c}_{ij}(\mathbf{r})$ not as the orientational average of the true direct correlation function $c_{ij}(\mathbf{r})$ but as exactly defined by Eq. (5.6). Within this interpretation, Eq. (5.3) then represents a pseudo-PY closure not derivable from the true PY closure (5.2).

Within the above interpretation, it is then important to bear in mind that the functions $\bar{g}_{ij}(\mathbf{r})$ obtained from the solution of a combination of Eqs. (5.3) and (5.6) are *not* equivalent to the orientational averages of the functions $g_{ij}(\mathbf{r})$ obtained from the solution of the true PY problem posed by Eqs. (5.1) and complemented by the PY condition (5.2). As a consequence, the solutions to Eqs. (5.3) and (5.6) are *not* expected to provide the exact $\bar{g}_{ij}(\mathbf{r})$ to first order in ρ , in contrast to the true PY problem. This is an interesting nuance that will be further discussed in Sec. V C 3.

The main advantage of the approximate OZ relation (5.6) in the case of anisotropic interactions of the form (2.5) is that it allows to transform the obtention of an *anisotropic* function $g_{ij}(\mathbf{r})$, but *symmetric* in the sense that $g_{ij}(\mathbf{r}) = g_{ji}(-\mathbf{r})$, into the obtention of an *isotropic* function $\bar{g}_{ij}(\mathbf{r})$, but *asymmetric* since $\bar{g}_{ij}(\mathbf{r}) \neq \bar{g}_{ji}(\mathbf{r})$. In the case of the anisotropic SHS potential defined above, we can exploit the known solution of

094904-7 Maestre *et al.*

 J. Chem. Phys. **138**, 094904 (2013)

the PY equation for *isotropic* SHS mixtures to construct the solution of the set made of Eqs. (5.3) and (5.6). This is done in Subsection V B by following the RFA methodology.

B. RFA method for SHS

Henceforth, for the sake of simplicity, we take $\sigma = 1$ as length unit. The aim of this section is to extend the RFA approximation proposed for symmetric SHS mixtures^{24,25} to the asymmetric case.

We start with the one-component case.²⁶ Let us introduce an auxiliary function $F(s)$ related to the Laplace transform $G(s)$ of $rg(r)$ by

$$G(s) = \frac{1}{2\pi} \frac{se^{-s}}{F(s) + \rho e^{-s}}. \quad (5.7)$$

The next step is to approximate $F(s)$ by a *rational function*,

$$F(s) = \frac{S(s)}{L(s)}, \quad (5.8)$$

with $S(s) = S^{(0)} + S^{(1)}s + S^{(2)}s^2 + s^3$ and

$$L(s) = L^{(0)} + L^{(1)}s + L^{(2)}s^2. \quad (5.9)$$

Note that $\lim_{s \rightarrow \infty} F(s)/s = 1/L^{(2)} = \text{finite}$, so that $\lim_{s \rightarrow \infty} e^s G(s) = \text{finite}$, in agreement with Eq. (4.16). Furthermore, Eq. (3.19) requires $F(s) + \rho e^{-s} = \mathcal{O}(s^3)$, so that $S^{(0)} = -\rho L^{(0)}$, $S^{(1)} = \rho(L^{(0)} - L^{(1)})$, $S^{(2)} = \rho(L^{(1)} - \frac{1}{2}L^{(0)} - L^{(2)})$. Taking all of this into account, Eq. (5.7) can be rewritten as

$$G(s) = \frac{e^{-s}}{2\pi s^2} \frac{L(s)}{1 - A(s)}, \quad (5.10)$$

where

$$A(s) = \frac{\rho}{s^3} \left[(1 - e^{-s})L(s) - L^{(0)}s + \left(\frac{1}{2}L^{(0)} - L^{(1)} \right) s^2 \right]. \quad (5.11)$$

In the case of a mixture, $G(s)$, $L(s)$, and $A(s)$ become matrices and Eq. (5.10) is generalized as

$$G_{ij}(s) = \frac{e^{-s}}{2\pi s^2} (\mathbf{L}(s) \cdot [\mathbf{I} - \mathbf{A}(s)]^{-1})_{ij}, \quad (5.12)$$

where \mathbf{I} is the identity matrix and

$$L_{ij}(s) = L_{ij}^{(0)} + L_{ij}^{(1)}s + L_{ij}^{(2)}s^2, \quad (5.13)$$

$$A_{ij}(s) = \rho \frac{x_i}{s^3} \left[(1 - e^{-s})L_{ij}(s) - L_{ij}^{(0)}s + \left(\frac{1}{2}L_{ij}^{(0)} - L_{ij}^{(1)} \right) s^2 \right]. \quad (5.14)$$

Note that $\lim_{s \rightarrow 0} A_{ij}(s) = \text{finite}$, so that $\lim_{s \rightarrow 0} s^2 G_{ij}(s) = \text{finite} \neq 0$ by construction. Analogously, $\lim_{s \rightarrow \infty} e^s G_{ij}(s) = \text{finite}$ also by construction.

The coefficients $L_{ij}^{(0)}$, $L_{ij}^{(1)}$, and $L_{ij}^{(2)}$ are determined by enforcing the exact conditions (3.19), (3.20), and (4.17). The details of the derivation are presented in Appendix B and here we present the final results. The coefficients $L_{ij}^{(0)}$ and $L_{ij}^{(1)}$ do

not depend upon the first index i and can be expressed as linear functions of the coefficients $\{L_{kj}^{(2)}\}$:

$$L_{ij}^{(0)} = 2\pi \frac{1 + 2\eta}{(1 - \eta)^2} - \frac{12\eta}{1 - \eta} \sum_k x_k L_{kj}^{(2)}, \quad (5.15)$$

$$L_{ij}^{(1)} = 2\pi \frac{1 + \eta/2}{(1 - \eta)^2} - \frac{6\eta}{1 - \eta} \sum_k x_k L_{kj}^{(2)}, \quad (5.16)$$

and the coefficients $L_{ij}^{(2)}$ obey the closed set of quadratic equations

$$\begin{aligned} \frac{L_{ij}^{(2)}}{t_{ij}} &= 2\pi \frac{1 + \eta/2}{(1 - \eta)^2} - \frac{6\eta}{1 - \eta} \sum_k x_k (L_{ik}^{(2)} + L_{kj}^{(2)}) \\ &+ \frac{6}{\pi} \eta \sum_k x_k L_{ik}^{(2)} L_{kj}^{(2)}. \end{aligned} \quad (5.17)$$

This closes the problem. Once $L_{ij}^{(2)}$ are known, the contact values are given by

$$\bar{y}_{ij}(1) = \frac{L_{ij}^{(2)}}{2\pi t_{ij}}. \quad (5.18)$$

Although here we have taken into account that all the diameters are equal ($\sigma_{ij} = \sigma = 1$), the above scheme can be easily generalized to the case of different diameters with the additive rule $\sigma_{ij} = (\sigma_i + \sigma_j)/2$. For symmetric interactions (i.e., $t_{ij} = t_{ji}$) one recovers the PY solution of SHS mixtures for any number of components.^{22,24} It is shown in Appendix C that the pair correlation functions $\bar{g}_{ij}(r)$ derived here are indeed the solution to the PY-like problem posed by Eqs. (5.3) and (5.6).

C. Case of interest: $t_{11} = t_{22} = t_{21} = 0$

In the general scheme described by Eqs. (5.12)–(5.18), four different stickiness parameters (t_{11} , t_{12} , t_{21} , and t_{22}) are in principle possible. With the convention that in t_{ij} the particle of species i is always located *below* the particle of species j , we might consider the simplest possibility of having only one SHS interaction $t_{12} = t = 1/12\tau$ and all other HS interactions ($t_{11} = t_{22} = t_{21} = 0$), as illustrated in Fig. 2. This is clearly an intermediate case between a full SHS model ($t_{ij} = t = 1/12\tau$) and a full HS model ($t_{ij} = 0$), with a predominance of repulsive HS interactions with respect to attractive SHS interactions. This is meant to model the intermediate nature of the original anisotropic Kern–Frenkel potential that interpolates between a SW and a HS isotropic potentials upon decreasing the coverage, that is, the fraction of the SW surface patch with respect to the full surface of the sphere.

1. Structural properties

If $t_{11} = t_{22} = t_{21} = 0$, Eq. (5.17) implies $L_{11}^{(2)} = L_{22}^{(2)} = L_{21}^{(2)} = 0$. As a consequence, Eq. (5.17) for $i = 1$ and $j = 2$ yields a *linear* equation for $L_{12}^{(2)}$ whose solution is

$$L_{12}^{(2)} = 2\pi \frac{1 + \eta/2}{1 - \eta} \frac{t}{1 - \eta + 6\eta t}. \quad (5.19)$$

094904-8 Maestre *et al.*

J. Chem. Phys. **138**, 094904 (2013)

According to Eq. (5.18),

$$\bar{y}_{12}(1) = \frac{1 + \eta/2}{(1 - \eta)^2} \left(1 - \frac{6\eta t}{1 - \eta + 6\eta t} \right). \quad (5.20)$$

Next, Eqs. (5.15) and (5.16) yield

$$\frac{L_{11}^{(0)}}{2\pi} = \frac{L_{21}^{(0)}}{2\pi} = \frac{1 + 2\eta}{(1 - \eta)^2}, \quad (5.21)$$

$$\frac{L_{12}^{(0)}}{2\pi} = \frac{L_{22}^{(0)}}{2\pi} = \frac{1 + 2\eta}{(1 - \eta)^2} - \frac{12\eta t}{1 - \eta} x_1 \bar{y}_{12}(1), \quad (5.22)$$

$$\frac{L_{11}^{(1)}}{2\pi} = \frac{L_{21}^{(1)}}{2\pi} = \frac{1 + \eta/2}{(1 - \eta)^2}, \quad (5.23)$$

$$\frac{L_{12}^{(1)}}{2\pi} = \frac{L_{22}^{(1)}}{2\pi} = \frac{1 + \eta/2}{(1 - \eta)^2} - \frac{6\eta t}{1 - \eta} x_1 \bar{y}_{12}(1). \quad (5.24)$$

Once the functions $L_{ij}(s)$ are fully determined, Eq. (5.12) provides the Laplace transforms $G_{ij}(s)$. From Eq. (4.15) it follows that $Y_{11}(s) = G_{11}(s)$, $Y_{22}(s) = G_{22}(s)$, $Y_{21}(s) = G_{21}(s)$, and

$$Y_{12}(s) = G_{12}(s) - t \bar{y}_{12}(1) e^{-s}. \quad (5.25)$$

A numerical inverse Laplace transform²⁸ allows one to obtain $\bar{g}_{11}(r)$, $\bar{g}_{22}(r)$, $\bar{g}_{21}(r)$, and $\bar{y}_{12}(r)$ for any packing fraction η , stickiness parameter $t = 1/12\tau$, and mole fraction x_1 . In what follows, we will omit explicit expressions related to $\bar{g}_{22}(r)$ since they can be readily obtained from $\bar{g}_{11}(r)$ by the exchange $x_1 \leftrightarrow x_2$.

The contact values $\bar{g}_{ij}(1^+) = \bar{y}_{ij}(1)$ with $(i, j) \neq (1, 2)$ cannot be obtained from Eq. (5.18), unless the associated t_{ij} are first assumed to be nonzero and then the limit $t_{ij} \rightarrow 0$ is taken. A more direct method is to realize that, if $t_{ij} = 0$, Eq. (4.16) gives

$$\bar{g}_{ij}(1^+) = \lim_{s \rightarrow \infty} e^s s G_{ij}(s), \quad (i, j) \neq (1, 2). \quad (5.26)$$

The results are

$$\bar{g}_{11}(1^+) = \bar{y}_{11}(1) = \frac{1 + \eta/2}{(1 - \eta)^2} - x_2 \frac{6\eta t}{1 - \eta} \bar{y}_{12}(1), \quad (5.27)$$

$$\bar{g}_{21}(1^+) = \bar{y}_{21}(1) = \frac{1 + \eta/2}{(1 - \eta)^2}, \quad (5.28)$$

$$\bar{y}(1) = \frac{1 + \eta/2}{(1 - \eta)^2} \left(1 - x_1 x_2 \frac{12\eta t}{1 - \eta + 6\eta t} \right). \quad (5.29)$$

It is interesting to note the property $\bar{g}_{11}(1^+) + \bar{g}_{22}(1^+) = \bar{y}_{12}(1) + \bar{g}_{21}(1^+)$.

To obtain the equation of state from the virial route we will need the derivative $\bar{y}'_{12}(1)$. Expanding $e^s G_{12}(s)$ in powers of s^{-1} and using Eq. (4.16), one gets

$$\begin{aligned} \frac{\bar{y}'_{12}(1)}{\bar{y}_{12}(1)} &= \frac{\eta}{(1 - \eta)^2} \left[3t \left(\frac{2 - 4\eta - 7\eta^2}{1 + \eta/2} + 12x_1 x_2 \eta \right) \right. \\ &\quad \left. - \frac{9}{2} \frac{1 - \eta^2}{1 + \eta/2} \right]. \end{aligned} \quad (5.30)$$

2. Thermodynamic properties

a. Virial route. According to Eq. (4.8),

$$\begin{aligned} Z^v &= 1 + 4\eta \bar{y}(1) - 4x_1 x_2 \eta t [3\bar{y}_{12}(1) + \bar{y}'_{12}(1)] \\ &= Z_{\text{HS}}^v - 4x_1 x_2 \eta t \left[3 \frac{1 + 3\eta}{1 - \eta} \bar{y}_{12}(1) + \bar{y}'_{12}(1) \right], \end{aligned} \quad (5.31)$$

where the superscript v denotes the virial route and

$$Z_{\text{HS}}^v = \frac{1 + 2\eta + 3\eta^2}{(1 - \eta)^2} \quad (5.32)$$

is the HS compressibility factor predicted by the virial route in the PY approximation.

b. Energy route. From Eq. (4.9) we have

$$\frac{u_{\text{ex}}}{\epsilon} = -12x_1 x_2 \eta t \bar{y}_{12}(1). \quad (5.33)$$

The compressibility factor can be obtained from u_{ex} via the thermodynamic relation (4.11), which in our case reads

$$\eta \frac{\partial u_{\text{ex}}/\epsilon}{\partial \eta} = \frac{1}{\epsilon} \frac{\partial Z}{\partial \beta} = t \frac{\partial Z}{\partial t}. \quad (5.34)$$

Thus, the compressibility factor derived from the energy route is

$$\begin{aligned} Z^u &= Z_{\text{HS}}^u + \eta \frac{\partial}{\partial \eta} \int_0^t dt' \frac{u_{\text{ex}}(\eta, t')/\epsilon}{t'} \\ &= Z_{\text{HS}}^u - 3x_1 x_2 \frac{\eta}{1 - \eta} \left[4t \bar{y}_{12}(1) + \frac{\ln \left(1 + \frac{6\eta t}{1 - \eta} \right)}{1 - \eta} \right], \end{aligned} \quad (5.35)$$

where Z_{HS}^u plays the role of an integration constant and thus it can be chosen arbitrarily. It can be shown^{29,30} that the energy and the virial routes coincide when the HS system is the limit of a square-shoulder interaction with vanishing shoulder width. From that point of view one should take $Z_{\text{HS}}^u = Z_{\text{HS}}^v$ in Eq. (5.35). On the other hand, a better description is expected from the Carnahan–Starling (CS) equation of state

$$Z_{\text{HS}}^{\text{CS}} = \frac{1 + \eta + \eta^2 - \eta^3}{(1 - \eta)^3}. \quad (5.36)$$

Henceforth we will take $Z_{\text{HS}}^u = Z_{\text{HS}}^{\text{CS}}$.

c. Compressibility route. Expanding $s^2 G_{ij}(s)$ in powers of s it is straightforward to obtain $H_{ij}^{(1)}$ from Eq. (3.16). This allows one to use Eqs. (3.14) and (3.18) to get the inverse susceptibility χ_T^{-1} as

$$\chi_T^{-1} = \frac{1 + 2\eta}{(1 - \eta)^4} \frac{1 + 2\eta - 24x_1 x_2 \eta (1 - \eta) \bar{y}_{12}(1)}{1 - x_1 x_2 \left[\frac{12\eta(1 + \eta/2) \bar{y}_{12}(1)}{1 + 2\eta + 36x_1 x_2 \eta^2 \bar{y}_{12}(1)} \right]^2}, \quad (5.37)$$

that, for an equimolar mixture ($x_1 = x_2 = \frac{1}{2}$), reduces to

$$\chi_T^{-1} = \frac{[(1 - \eta)^2(1 + 2\eta) + 3\eta t (2 + 5\eta - \frac{5}{2}\eta^2)]^2}{(1 - \eta)^5(1 - \eta + 6\eta t)[(1 - \eta)^2 + 3\eta t(4 - \eta)]}. \quad (5.38)$$

The associated compressibility factor is then

$$Z^c = \frac{1}{\eta} \int_0^\eta d\eta' \chi_T^{-1}(\eta'). \quad (5.39)$$

The above integral has an analytical solution, but it is too cumbersome to be displayed here.

3. Low-density expansion

In the standard case of SHS mixtures with symmetric coefficients in the potential parameters, the PY closure is known to reproduce the exact cavity functions to first order in density and thus the third virial coefficient (see Appendix A 2). However, this needs not be the case in the present RFA description for the asymmetric case, as further discussed below. Note that here, “exact” still refers to the simplified problem (orientational average + sticky limit) of Secs. III and IV.

The expansion to first order in density of the Laplace transforms $Y_{ij}(s)$ obtained from Eqs. (4.15), (5.12)–(5.14) and (5.19)–(5.24) is

$$Y_{ij}(s) = e^{-s}(s^{-1} + s^{-2}) + Y_{ij}^{(1)}(s)\rho + \dots, \quad (5.40)$$

where the expressions of the first-order coefficients $Y_{ij}^{(1)}(s)$ will be omitted here. Laplace inversion yields

$$\bar{y}_{ij}^{(1)}(r) = \bar{y}_{ij}^{(1)}(r)|_{\text{exact}} - \Delta\bar{y}_{ij}^{(1)}(r), \quad (5.41)$$

where $y_{ij}^{(1)}(r)|_{\text{exact}}$ are the exact first-order functions given by Eqs. (A37)–(A39) and the deviations $\Delta y_{ij}^{(1)}(r)$ are

$$\Delta\bar{y}_{11}^{(1)}(r) = \Theta(2-r)x_2 \frac{2t^2}{r} \cos^{-1} \frac{r}{2}, \quad (5.42)$$

$$\Delta\bar{y}_{12}^{(1)}(r) = \Theta(2-r)t \left(2\sqrt{1-r^2/4} - r \cos^{-1} \frac{r}{2} \right), \quad (5.43)$$

$$\Delta\bar{y}_{21}^{(1)}(r) = -\Delta\bar{y}_{12}^{(1)}(r). \quad (5.44)$$

In the case of the global quantity $\bar{y}^{(1)}(r)$ the result is

$$\bar{y}^{(1)}(r) = \bar{y}^{(1)}(r)|_{\text{exact}} - \Delta\bar{y}^{(1)}(r), \quad (5.45)$$

where $\bar{y}^{(1)}(r)|_{\text{exact}}$ is given by Eq. (A40) and

$$\Delta\bar{y}^{(1)}(r) = \Theta(2-r)x_1x_2 \frac{2t^2}{r} \cos^{-1} \frac{r}{2}. \quad (5.46)$$

While the main qualitative features of the exact cavity function are preserved, there exist quantitative differences. The first-order functions $\bar{y}_{11}^{(1)}(r)$, $\bar{y}_{22}^{(1)}(r)$, and $\bar{y}^{(1)}(r)$ predicted by the RFA account for the exact coefficient of t but do not include the exact term of order t^2 proportional to $r^{-1}\cos^{-1}(r/2)$. In the case of $\bar{y}_{12}^{(1)}(r)$ and $\bar{y}_{21}^{(1)}(r)$ the exact term of order t proportional to $2\sqrt{1-r^2/4} - r \cos^{-1}(r/2)$ is lacking. Also, while the combination $\bar{y}_{11}^{(1)}(r) + \bar{y}_{22}^{(1)}(r) - \bar{y}_{12}^{(1)}(r) - \bar{y}_{21}^{(1)}(r)$ vanishes in the RFA, the exact result is proportional to $t^2 r^{-1} \cos^{-1}(r/2)$. In short, the RFA correctly accounts for the polynomial terms in $y_{ij}^{(1)}(r)|_{\text{exact}}$ but misses the non-polynomial terms.

As for the thermodynamic quantities, expansion of Eqs. (5.31), (5.35), and (5.39) gives

$$Z^v = 1 + 4(1 - 3x_1x_2t)\eta + 10 \left[1 - 6x_1x_2t \left(1 - \frac{4}{5}t \right) \right] \eta^2 + \mathcal{O}(\eta^3), \quad (5.47)$$

$$Z^u = 1 + 4(1 - 3x_1x_2t)\eta + 10 \left[1 - 6x_1x_2t \left(1 - \frac{6}{5}t \right) \right] \eta^2 + \mathcal{O}(\eta^3), \quad (5.48)$$

$$Z^c = 1 + 4(1 - 3x_1x_2t)\eta + 10 \left[1 - 6x_1x_2t \left(1 - \frac{8}{5}t \right) \right] \eta^2 + \mathcal{O}(\eta^3). \quad (5.49)$$

Comparison with the exact third virial coefficient, Eq. (A50), shows that the coefficient of t^2 is not correct, with the exact factor $4 - 3\sqrt{3}/\pi \simeq 2.35$ replaced by 2, 3, and 4 in Eqs. (5.47)–(5.49), respectively. One consequence is that the virial and energy routes predict the third virial coefficient much better than the compressibility route. A possible improvement is through the interpolation formula

$$Z^{v,u} = \alpha(Z^v + Z_{\text{HS}}^{\text{CS}} - Z_{\text{HS}}^v) + (1 - \alpha)Z^u, \quad (5.50)$$

where $\alpha = 3\sqrt{3}/\pi - 1 \simeq 0.65$ with the proviso that $Z_{\text{HS}}^u = Z_{\text{HS}}^{\text{CS}}$ in Eq. (5.35). Equation (5.50) then reduces to the CS equation of state if $t = 0$ and reproduces the exact third virial coefficient when $t \neq 0$.

4. Phase transition and critical point

In the limit of isotropic interaction ($t_{ij} = t$), our model reduces to the usual SHS Baxter adhesive one-component model. In spite of the fact that the model is, strictly speaking, known to be pathological,³¹ it displays a critical behavior that was numerically studied in some details by MC techniques.^{32,33} The corresponding binary mixture also displays well defined critical properties that, interestingly, are even free from any pathological behavior.²¹ Moreover, the mechanism behind the pathology of the isotropic Baxter model hinges crucially on the geometry of certain close-packed clusters involving 12 or more equal-sized spheres.³¹ On the other hand, our Janus model, having frozen orientations, cannot sustain those pathological configurations.

Within the PY approximation, the critical behavior of the original one-component Baxter SHS model was studied using the compressibility and virial routes,¹⁵ as well as the energy route,¹⁷ in the latter case with the implicit assumption $Z_{\text{HS}}^u = Z_{\text{HS}}^{\text{CS}}$. Numerical simulations indicate that the critical point found through the energy route is the closest to numerical simulation results.^{32,33}

As the present specific model (with, $t_{ij} = t\delta_{i1}\delta_{j2}$) is, in some sense, intermediate between the fully isotropic Baxter SHS one-component model (that has a full, albeit peculiar, gas-liquid transition) and the equally isotropic HS model (that, lacking any attractive part in the potential, cannot have any gas-liquid transition), it is then interesting to ask whether

094904-10 Maestre *et al.*

 J. Chem. Phys. **138**, 094904 (2013)

TABLE I. Location of the critical point in the RFA, according to different routes.

Route	τ_c	η_c	Z_c
Virial, Eq. (5.31)	0.02050	0.1941	0.3685
Energy, Eq. (5.35)	0.0008606	0.2779	0.2906
Hybrid virial-energy, Eq. (5.50)	0.01504	0.1878	0.3441

in the equimolar case ($x_1 = x_2 = \frac{1}{2}$) it still presents a critical gas-liquid transition.

The answer depends on the route followed to obtain the pressure. As seen from Eq. (5.38), the compressibility route yields a positive definite χ_T^{-1} , so that no critical point is predicted by this route. On the other hand, an analysis of the virial [Eq. (5.31)], energy [Eq. (5.35) with $Z_{HS}^u = Z_{HS}^{CS}$], and hybrid virial-energy [Eq. (5.50)] equations of state reveals the existence of van der Waals loops with the respective critical points shown in Table I. The energy route predicts a critical value τ_c about 20 times smaller than the values predicted by the other two routes.

As an illustration, Fig. 4 shows the binodal and a few isotherms, as obtained from the virial route.

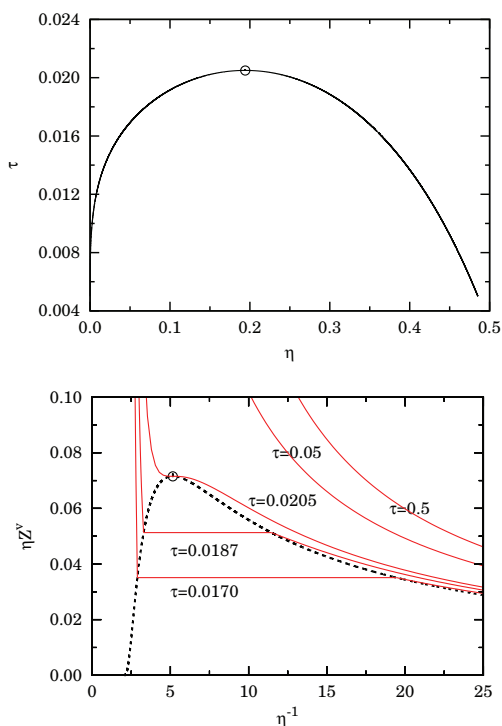


FIG. 4. Binodals from the RFA virial route in the equimolar $x_1 = \frac{1}{2}$ case. The phase diagram is depicted in the (η, τ) plane (solid line, top panel) and in the $(\eta^{-1}, \eta Z^2)$ plane (dashed line, bottom panel). A few characteristic isotherms are plotted in the bottom panel. The critical point is found at $\eta_c \simeq 0.1941$, $\tau_c \simeq 0.02050$, and $\eta_c Z_c \simeq 0.07153$ (indicated by a circle in both panels).

5. A modified approximation

The failure of the RFA to reproduce the exact cavity functions to first order in density (and hence the third virial coefficient) for asymmetric interactions ($t_{ij} \neq t_{ji}$) reveals the price paid for using the orientationally averaged quantities $\bar{g}_{ij}(r)$ instead of the true pair correlation functions $g_{ij}(\mathbf{r})$.

A simple way of getting around this drawback for sufficiently low values of both η and τ consists of modifying the RFA as follows:

$$\bar{y}_{ij}(r) \rightarrow \bar{y}_{ij}(r) + \Delta \bar{y}_{ij}^{(1)}(r)\rho, \quad (5.51)$$

where the functions $\Delta \bar{y}_{ij}^{(1)}(r)$ are given by Eqs. (5.42)–(5.44). We will refer to this as the *modified* rational-function approximation (mRFA). Note that Eq. (5.51) implies that $\bar{g}_{ij}(r) \rightarrow \bar{g}_{ij}(r) + \Delta \bar{y}_{ij}^{(1)}(r)\rho$, except if $(i, j) = (1, 2)$, in which case $\bar{g}_{12}(r) \rightarrow \bar{g}_{12}(r) + \Delta \bar{y}_{12}^{(1)}(r)\rho + \Delta \bar{y}_{12}^{(1)}(1)\delta_+(r-1)\rho t$.

Since the extra terms in Eq. (5.51) are proportional to t or t^2 , this modification can produce poor results for sufficiently large stickiness (say, $t \gtrsim 1$) as, for instance, near the critical point.

VI. NUMERICAL CALCULATIONS

A. Details of the simulations

In order to check the theoretical predictions previously reported, we have performed NVT (isochoric-isothermal) MC simulations using the Kern–Frenkel potential defined in Eqs. (2.1)–(2.4) with a single attractive SW patch (green in the color code of Fig. 1) covering one of the two hemispheres, and with up-down symmetry as depicted in Fig. 2. Particles are then not allowed to rotate around but only to translate rigidly.

The model is completely defined by specifying the relative width $\lambda - 1$, the concentration of one species (mole fraction) $x_1 = 1 - x_2$, the reduced density $\rho^* = \rho\sigma^3$, and the reduced temperature $T^* = k_B T/\epsilon$.

In order to make sensible comparison with the RFA theoretical predictions, we have selected the value $\lambda - 1 = 0.05$ as a well width, which is known to be well represented by the SHS limit,³⁴ and use Baxter's temperature parameter $\tau = [4(\lambda^3 - 1)(e^{1/T^*} - 1)]^{-1}$ [see Eq. (4.4)] instead of T^* . It is interesting to note that, while the unconventional phase diagram found in the simulations of Ref. 7 corresponded to a larger well width ($\lambda = 1.5$), the value $\lambda = 1.05$ is in fact closer to the experimental conditions of Ref. 3.

During the simulations we have computed the orientational averaged pair correlation functions defined by Eqs. (3.3) and (3.4), accumulating separate histograms when $z_2 - z_1 > 0$ or $z_1 - z_2 > 0$ in order to distinguish between functions $\bar{g}_{12}(r) = g_{12}^+(r)$ and $\bar{g}_{21}(r) = g_{12}^-(r)$.

The compressibility factor $Z = \beta P/\rho$ has been evaluated from the values of $\bar{y}_{ij}(r)$ at $r = \sigma$ and $r = \lambda\sigma$ by following Eq. (4.2) with $t_{ij} = (12\tau)^{-1}\delta_{i1}\delta_{j2}$, and the reduced excess internal energy per particle $u_{ex}^* = u_{ex}/\epsilon$ has been evaluated directly from simulations.

In all our simulations, we used $N = 500$ particles, periodic boundary conditions, an equilibration time of around 10^5 MC steps (where a MC step corresponds to a single particle

094904-11 Maestre *et al.*

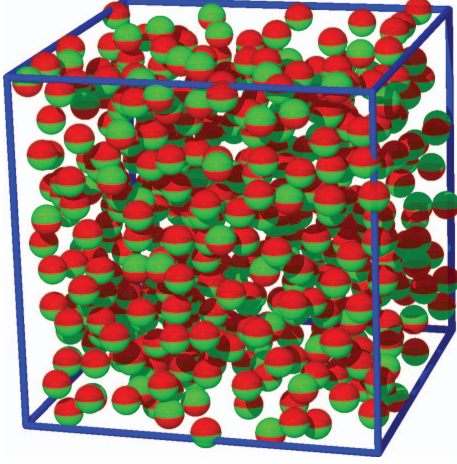
 J. Chem. Phys. **138**, 094904 (2013)


FIG. 5. Snapshot of an equilibrated MC simulation under non-equimolar conditions ($x_1 = 1/5$) with Baxter temperature $\tau = 0.1$ and density $\rho^* = 0.3$. In the simulations we used a total number of particles $N = 500$.

displacement), and a production time of about 10^8 MC steps for the structure calculations and up to 5×10^8 MC steps for the thermophysical calculations. The maximum particle displacement was determined during the first stage of the equilibration run in such a way as to ensure an average acceptance ratio of 50% at production time.

B. Results for non-equimolar binary mixtures

As a preliminary attempt, we consider a binary mixture under non-equimolar conditions, to avoid possible pathologies arising from the symmetry of the two components akin to those occurring in ionic systems. As we shall see below, no such pathologies are found.

In the present case, we consider a system with $x_1 = 1/5$ and $x_2 = 1 - x_1 = 4/5$, so that the majority of the spheres have (green) attractive patches pointing in the direction of $-\hat{z}$.

A snapshot of an equilibrated configuration is shown in Fig. 5. This configuration was obtained using $N = 500$ particles at $\rho^* = 0.3$ and Baxter temperature $\tau = 0.1$ (corresponding to $T^* \simeq 0.354$).

Note that the above chosen state point ($\rho^* = 0.3$ and $\tau = 0.1$) lies well inside the critical region of the full Baxter SHS adhesive model as obtained from direct MC simulations,^{32,33} although of course the present case is expected to display a different behavior as only a fraction of about $x_1 x_2 = 4/25$ of the pair contacts are attractive.

A good insight on the structural properties of the system can be obtained from the computation of the radial distribution functions $\bar{g}_{11}(r)$, $\bar{g}_{12}^+(r) = \bar{g}_{12}(r)$, $\bar{g}_{12}^-(r) = \bar{g}_{21}(r)$, and $\bar{g}_{22}(r)$. This is reported in Fig. 6 for a state point at density $\rho^* = 0.5$ and Baxter temperature $\tau = 0.2$ (corresponding to $T^* \simeq 0.457$). Note that in the case of the pair (1, 2) what is actually plotted is the cavity function $\bar{y}_{12}(r)$ rather than $\bar{g}_{12}(r)$, as explained in the caption of Fig. 6.

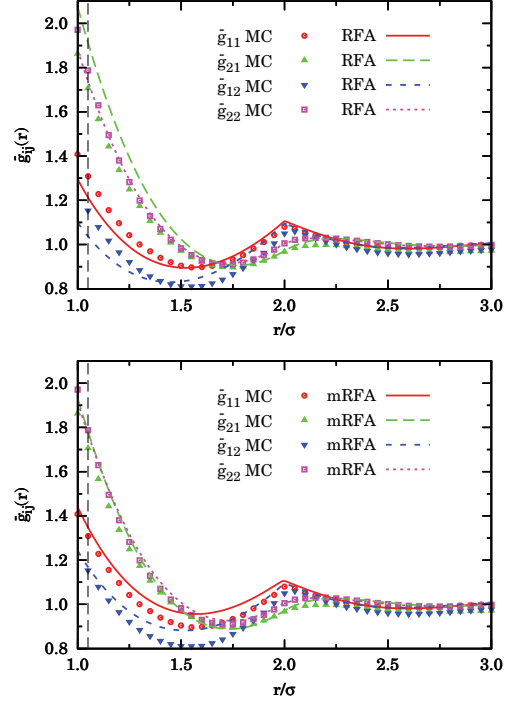


FIG. 6. Comparison between MC simulations and the theoretical predictions from RFA (top) and mRFA (bottom) for the orientational averaged distribution functions $\bar{g}_{11}(r)$, $\bar{y}_{12}(r)$, $\bar{g}_{21}(r)$, and $\bar{g}_{22}(r)$ under non-equimolar conditions ($x_1 = 1/5$) at density $\rho^* = 0.5$ and Baxter temperature $\tau = 0.2$. The dashed vertical line indicates the range $r = \lambda = 1.05$ of the (1, 2) SW interaction used in the simulations. Note that the radial distribution function $\bar{g}_{12}(r)$ is obtained in the MC case by multiplying $\bar{y}_{12}(r)$ in the region $1 \leq r \leq \lambda = 1.05$ by the factor $e^{1/T^*} \simeq 8.93$; in the theoretical cases (SHS limit) $\bar{g}_{12}(r)$ is obtained by adding the singular term $(12\tau)^{-1} \bar{y}_{12}(1) \delta_+(r-1)$ to $\bar{y}_{12}(r)$. The error bars on the MC data are within the size of the symbols used.

The relatively low value $\tau = 0.2$ gives rise to clearly distinct features of the four MC functions $\bar{g}_{ij}(r)$ (which would collapse to a common HS distribution function in the high-temperature limit $\tau \rightarrow \infty$). We observe that $\bar{g}_{22}(r) \simeq \bar{g}_{21}(r) > \bar{g}_{11}(r) > \bar{y}_{12}(r)$ in the region $1 \leq r \lesssim 1.5$. Moreover, $\bar{g}_{11}(r)$ and $\bar{g}_{12}(r)$ exhibit a rapid change around $r = 2$. This is because when a pair (1, 1) is separated a distance $r \approx 2$ there is enough room to fit a particle of species 2 in between and that particle will interact attractively with the particle of the pair (1, 1) below it. In the case of the pair (1, 2) separated a distance $r \approx 2$, the intermediate particle can be either of species 1 (interacting attractively with the particle of species 2 above it) or of species 2 (interacting attractively with the particle of species 1 below it). The same argument applies to a pair (2, 2) separated a distance $r \approx 2$, but in that case the intermediate particle must be of species 1 to produce an attractive interaction; since the concentration of species 1 is four times smaller than that of species 2, the rapid change of $\bar{g}_{22}(r)$ around $r = 2$ is much less apparent than that of $\bar{g}_{11}(r)$ and $\bar{g}_{12}(r)$ in Fig. 6. On the other hand, in a pair (2, 1)

094904-12 Maestre *et al.*

 J. Chem. Phys. **138**, 094904 (2013)

separated a distance $r \approx 2$ an intermediate particle of either species 1 or of species 2 does not create any attraction and thus $\bar{g}_{21}(r)$ is rather smooth at $r = 2$. In short, the pair correlation function $\bar{g}_{21}(r)$ exhibits HS-like features, $\bar{g}_{12}(r)$ exhibits SW-like features (very high values in the region $1 \leq r \leq \lambda$ and discontinuity at $r = \lambda$ due to the direct SW interaction; rapid change around $r = 2$ due to indirect SW interaction), while $\bar{g}_{11}(r)$ and $\bar{g}_{22}(r)$ exhibit intermediate features (rapid change around $r = 2$ due to indirect SW interaction).

It is rewarding to notice how well the MC results are reproduced at a semi-quantitative level by the RFA theory (top panel of Fig. 6), in spite of the various approximations involved. In this respect, it is worth recalling that while MC simulations deal with the real Kern–Frenkel potential, albeit with constrained angular orientations, the RFA theory deals with the asymmetric binary mixture resulting from the mapping described in Sec. II, and this represents an indirect test of the correctness of the procedure. In addition, the RFA does not attempt to describe the true SW interaction (i.e., finite $\lambda - 1$ and T^*) but the SHS limit ($\lambda - 1 \rightarrow 0$ and $T^* \rightarrow 0$ with finite τ). This limit replaces the high jump of $\bar{g}_{12}(r)$ in the region $1 \leq r \leq \lambda$ by a Dirac's delta at $r = 1^+$ and the rapid change of $\bar{g}_{12}(r)$, $\bar{g}_{11}(r)$, and $\bar{g}_{22}(r)$ around $r = 2$ by a kink. Finally, the RFA worked out in Sec. V B results from a heuristic generalization to asymmetric mixtures ($\tau_{ij} \neq \tau_{ji}$) of the PY exact solution for SHS symmetric mixtures ($\tau_{ij} = \tau_{ji}$),^{18–22,24} but it is not the solution of the PY theory for the asymmetric problem, as discussed in Sec. V A. As a matter of fact, the top panel of Fig. 6 shows that some of the drawbacks of the RFA observed to first order in density in Sec. V C 3 [see Eqs. (5.41)–(5.44)] remain at finite density: in the region $1 \leq r \lesssim 1.5$ the RFA underestimates $\bar{y}_{12}(r)$, $\bar{g}_{11}(r)$, and $\bar{g}_{22}(r)$, while it overestimates $\bar{g}_{21}(r)$. These discrepancies are widely remedied, at least in the region $1 \leq r \lesssim 1.25$, by the mRFA approach [see Eq. (5.51)], as shown in the bottom panel of Fig. 6. In particular, the contact values are well accounted for by the mRFA, as well as the property $\bar{g}_{22}(r) \simeq \bar{g}_{21}(r)$. We have observed that the limitations of the correlation functions $\bar{g}_{ij}(r)$ predicted by the RFA become more important as the density and, especially, the stickiness increase and in those cases the mRFA version does not help much since the correction terms $\Delta\bar{y}_{ij}^{(1)}(r)\rho$, being proportional to ρ and to t or t^2 , become too large.

Next we consider thermodynamic quantities, as represented by the compressibility factor $Z = \beta P/\rho$ and the excess internal energy per particle u_{ex}/ϵ , both directly accessible from NVT numerical MC simulations. These quantities are depicted in Fig. 7 as functions of the reduced density ρ^* and for a Baxter temperature $\tau = 0.1$. In both cases, the results for the RFA theory are also included. In the case of the compressibility factor, all four routes are displayed: compressibility [Eqs. (5.20), (5.37), and (5.39)], virial [Eqs. (5.20), (5.30) and (5.31)], energy [Eq. (5.20) and (5.35) with $Z_{\text{HS}}^u = Z_{\text{HS}}^{\text{CS}}$], and hybrid virial-energy [Eq. (5.50)]. In the case of u_{ex}/ϵ , only the genuine energy route, Eq. (5.33), is considered. Note that all RFA thermodynamic quantities, including Eq. (5.39), have explicit analytical expressions.

The top panel of Fig. 7 shows that up to $\rho^* \approx 0.7$ the MC data for the compressibility factor are well predicted by

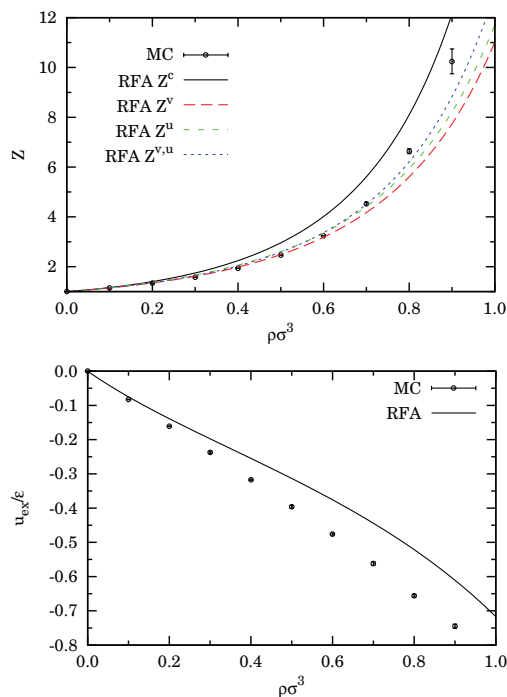
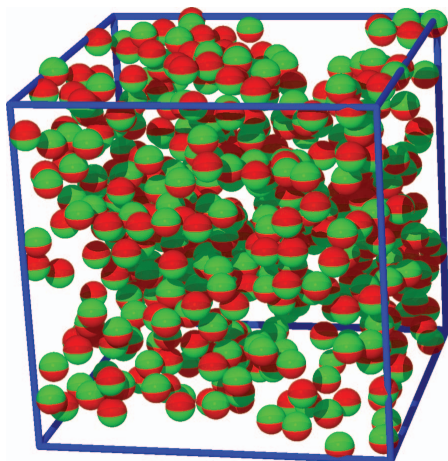


FIG. 7. Comparison of MC simulations and RFA theory for the thermodynamics. Both the compressibility factor $Z = \beta P/\rho$ (top) and the excess internal energy per particle u_{ex}/ϵ (bottom) are displayed as functions of density for the non-equimolar case $x_1 = 1/5$ and for Baxter temperature $\tau = 0.1$. In the case of the compressibility factor (top), results for all four routes (compressibility, virial, energy, and hybrid virial-energy) are reported.

the theoretical Z^v and, especially, Z^u and $Z^{v,u}$. Beyond that point, the numerical results are bracketed by the compressibility route, that overestimates the pressure, and the hybrid virial-energy route, that on the contrary underestimates it. It is interesting to note that, while $Z^v < Z^{v,u} < Z^u$ to second order in density [cf. Eqs. (5.47), (5.48), and (5.50)], the difference $Z^v - Z_{\text{HS}}^v$ grows with density more rapidly than the difference $Z^u - Z_{\text{HS}}^u$ and so both quantities cross at a certain density ($\rho^* \simeq 0.567$ if $x_1 = 1/5$ and $\tau = 0.1$). Therefore, even though $Z^v < Z^u$ (because $Z_{\text{HS}}^v < Z_{\text{HS}}^{\text{CS}}$), $Z^{v,u}$ is no longer bracketed by Z^v and Z^u beyond that density ($\rho^* \simeq 0.567$ in the case of Fig. 7). On balance, the virial-energy route appears to be the most effective one in reproducing the numerical simulations results of the pressure at $x_1 = 1/5$ and $\tau = 0.1$.

As for the internal energy, the bottom panel of Fig. 7 shows that the RFA underestimates its magnitude as a direct consequence of the underestimation of the contact value $\bar{y}_{12}(1)$ [see Eq. (5.33)]. Although not shown in Fig. 7, we have checked that the internal energy per particle obtained from the virial equation of state (5.31) via the thermodynamic relation (5.34) exhibits a better agreement with the simulation data than the direct energy route.

094904-13 Maestre *et al.*

 J. Chem. Phys. **138**, 094904 (2013)

 FIG. 8. Same as in Fig. 5, but for an equimolar mixture ($x_1 = x_2 = 1/2$).

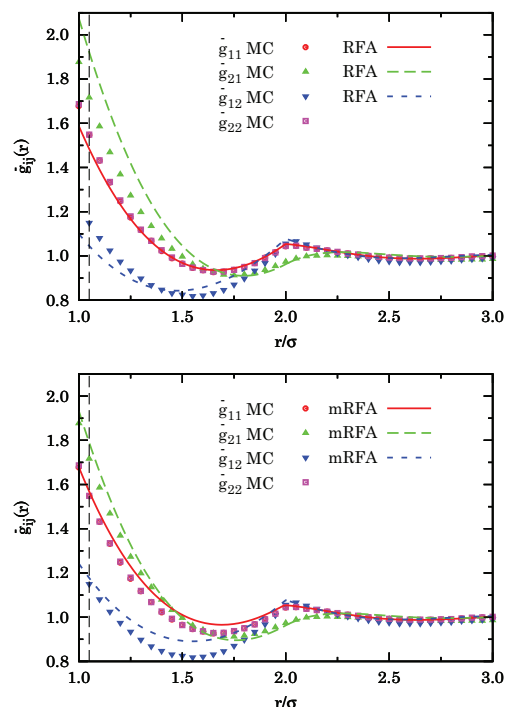
C. Results for equimolar binary mixtures

Having rationalized the non-equimolar case, the equimolar ($x_1 = x_2 = 1/2$) case can now be safely tackled. The equimolarity condition makes the system be more akin to the original Janus model (see Fig. 1) since both spin orientations are equally represented.

We start with the snapshot of an equilibrated configuration at density $\rho^* = 0.3$ and Baxter temperature $\tau = 0.1$, that are the same values used in the non-equimolar case. From Fig. 8 it can be visually inspected that, in contrast to the non-equimolar case of Fig. 5, the number of particles with spin up matches that with spin down. This equimolar condition then facilitates the interpretation of the corresponding structural properties, as illustrated by the radial distribution function $\bar{g}_{ij}(r)$ given in Fig. 9.

This was obtained at a Baxter temperature $\tau = 0.2$ and a density $\rho^* = 0.5$, a state point that is expected to be outside the coexistence curve (see below), but inside the liquid region. Again, this is the same state point as the non-equimolar case previously discussed. Now $\bar{g}_{11}(r) = \bar{g}_{22}(r)$ (independently computed) as it should. Notice that the main features commented before in connection with Fig. 6 persist. In particular, $\bar{g}_{21}(r) > \bar{g}_{11}(r) = \bar{g}_{22}(r) > \bar{y}_{12}(r)$ in the region $1 \leq r \lesssim 1.5$, $\bar{g}_{11}(r) = \bar{g}_{22}(r)$ and $\bar{g}_{12}(r)$ present rapid changes around $r = 2$, and $\bar{g}_{21}(r)$ exhibits a HS-like shape. Also, as before, the RFA captures quite well the behaviors of the correlation functions (especially noteworthy in the case of $\bar{g}_{11} = \bar{g}_{22}$). On the other hand, the RFA tends to underestimate $\bar{y}_{12}(r)$ and $\bar{g}_{11}(r) = \bar{g}_{22}(r)$ and to overestimate $\bar{g}_{21}(r)$ in the region $1 \leq r \lesssim 1.5$. The use of the modified version (mRFA) partially corrects those discrepancies near contact, although the general behavior only improves in the case of $\bar{g}_{21}(r)$.

Comparison between Figs. 6 and 9 shows that $\bar{y}_{12}(r)$ and $\bar{g}_{21}(r)$ are very weakly affected by the change in com-


 FIG. 9. Same as in Fig. 6, but for an equimolar mixture ($x_1 = x_2 = 1/2$).

position. In fact, the spatial correlations between particles of species 1 and 2 mediated by a third particle (i.e., to first order in density) depend strongly on which particle (1 or 2) is above or below the other one but not on the nature of the third intermediate particle, as made explicit by Eqs. (A38) and (A39). Of course, higher-order terms (i.e., two or more intermediate particles) create a composition-dependence on $\bar{y}_{12}(r)$ and $\bar{g}_{21}(r)$, but this effect seems to be rather weak. On the contrary, the minority pair increases its correlation function $\bar{g}_{11}(r)$, while the majority pair decreases its correlation function $\bar{g}_{22}(r)$ in the region $1 \leq r \lesssim 1.5$ when the composition becomes more balanced. Again, this can be qualitatively understood by the exact results to first order in density [see Eq. (A37)].

D. Preliminary results on the critical behavior

One of the most interesting and intriguing predictions of the RFA is the existence of a gas-liquid transition in the equimolar model, despite the fact that only one of the four classes of interactions is attractive (see Sec. V C 4). The elusiveness of this prediction is reflected by the fact that the compressibility route does not account for a critical point and, although the virial and energy routes do, they widely differ in its location, as seen in Table I. In this region of very low values of τ the hybrid virial-energy equation of state is dominated by

094904-14 Maestre *et al.*J. Chem. Phys. **138**, 094904 (2013)

the virial one and thus the corresponding critical point is not far from the virial value.

A simple heuristic argument can be used to support the existence of a true critical point in our model. According to the Noro–Frenkel (NF) generalized principle of corresponding states,³⁵ the critical temperatures of different systems of particles interacting via a hard-core potential plus a short-range attraction are such that the reduced second virial coefficient $B_2^* = B_2/B_2^{\text{HS}}$ has a *common* value $B_2^{*c} \simeq -1.21$. In our model, the reduced second virial coefficient is $B_2^* = 1 - 3t/4 = 1 - 1/16\tau$ [see Eq. (A49)]. Thus, assuming the NF ansatz, the critical point would correspond to $\tau_c^{\text{NF}} \simeq 0.028$, a value higher than but comparable to that listed in Table I from the virial route.

From the computational point of view, a direct assessment on the existence of a gas-liquid transition in the present model is not a straightforward task. Unlike the original SHS Baxter model, a Gibbs ensemble MC (GEMC) calculation for a binary mixture is required to find the coexistence lines. We are currently pursuing this analysis that will be reported elsewhere. As a very preliminary study, we here report NVT results with values of the Baxter temperature close to the critical value $\tau_c^{\text{NF}} \simeq 0.028$ expected on the basis of the NF conjecture. More specifically, we have considered $\tau = 0.030$, 0.0205, and 0.018 (corresponding to $T^* \simeq 0.251$, 0.229, and 0.223, respectively). The numerical results for the pressure, along with the RFA theoretical predictions, are displayed in Fig. 10.

We observe that at $\tau = 0.030$ (top panel) the four theoretical routes clearly indicate a single-phase gas-like behavior with a monotonic increase of the pressure as a function of the density, in consistency with the value $\tau_c \simeq 0.0205$ obtained from the RFA virial route. On the other hand, the MC data show a practically constant pressure between $\rho^* = 0.2$ and $\rho^* = 0.4$, which is suggestive of $\tau = 0.030$ being close to the critical isotherm (remember that $\tau_c^{\text{NF}} \simeq 0.028$). The middle panel has been chosen to represent the critical isotherm predicted by the RFA-virial equation of state. In that case, the simulation data present a clear van der Waals loop with even negative pressures around the minimum. A similar behavior is observed at $\tau = 0.018$ (bottom panel), except that now the RFA-virial isotherm also presents a visible van der Waals loop. Whereas the observation of negative values of isothermal compressibility in the MC simulations can be attributed to finite-size effects and are expected to disappear in the thermodynamic limit, these preliminary results are highly supportive of the existence of a gas-liquid phase transition in our model with a critical (Baxter) temperature $\tau_c \approx 0.03$.

In view of the extremely short-range nature of the potential, the stability of the above liquid phases with respect to the corresponding solid ones may be rightfully questioned.⁷ This is a general issue—present even in the original Baxter model, as well as in the spherically symmetric SW or Yukawa potentials with sufficiently small interaction range^{36–39}—that is clearly outside the scope of the present paper. In any case, it seems reasonable to expect that at sufficiently low temperature and high density the stable phase will consist of an fcc crystal made of layers of alternating species (1-2-1-2-...) along the z direction.

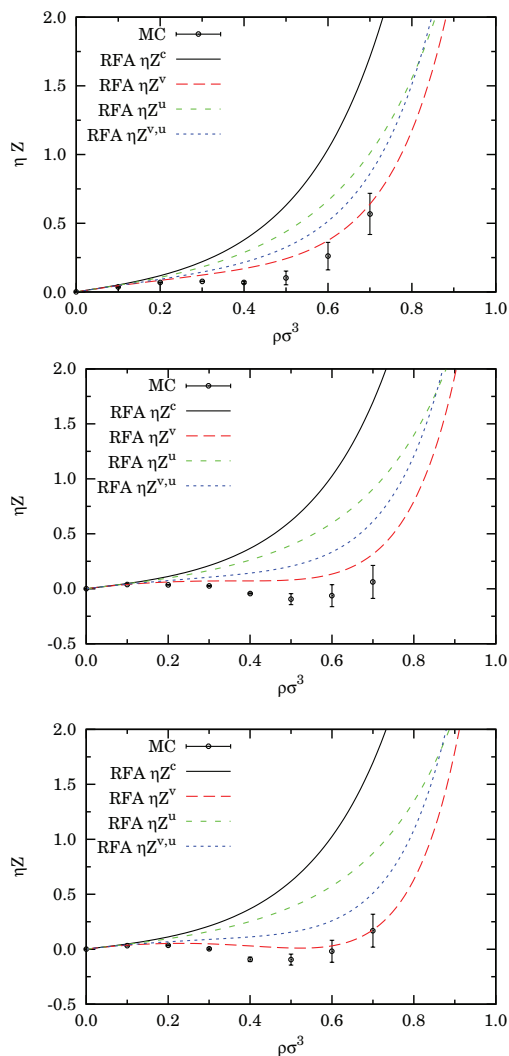


FIG. 10. MC simulation data for the scaled pressure $\eta Z = \frac{\pi}{6}\sigma^3\beta P$ as a function of ρ^* at $\tau = 0.030$ (top panel), 0.0205 (middle panel), and $\tau = 0.018$ (bottom panel) in an equimolar mixture. Densities higher than $\rho^* = 0.7$ are not shown because at these very low temperatures the particles tend to overlap their SW shells and then the calculations slow down considerably. Also shown are the theoretical results for the four routes of the RFA.

VII. CONCLUSIONS AND FUTURE PERSPECTIVES

We have studied thermophysical and structural properties of a Janus fluid having constrained orientations for the attractive hemisphere. The Janus fluid has been modeled using a Kern–Frenkel potential with a single SW patch pointing either up or down, and studied using numerical NVT MC simulations.

The above model has been mapped onto an asymmetric binary mixture where the only memory of the original anisotropic potential stems from the relative position along the z -axis of particles of the two species 1 and 2. In this way, only one [(1, 2) with our choice of labels] out of the four possible interactions is attractive, the other ones [(1, 1), (2, 1), and (2, 2)] being simply HS interactions.

In the limit of infinitely short and deep SW interactions (sticky limit), we discussed how a full analytical theory is possible. We developed a new formulation for asymmetric mixtures of the rational-function approximation (RFA), that is equivalent to the PY approximation in the case of symmetric SHS interactions, but differs from it in the asymmetric case. Results from this theory were shown to be in nice agreement with MC simulations using SW interactions of sufficiently short width (5% of particle size), both for the structural and the thermodynamic properties.

The above agreement is rather remarkable in view of the rather severe approximations involved in the RFA analysis — that are however largely compensated by the possibility of a full analytical treatment— and, more importantly, by the fact that simulations deal with the actual Kern–Frenkel potential with up-down constrained orientations of the patches and SW attractions, while the RFA theory deals with the obtained asymmetric binary mixture and SHS interactions. We regard this agreement as an important indication on the correctness of the mapping.

Within the RFA approximation, all three standard routes to thermodynamics (compressibility, virial, and energy) were considered. To them we added a weighted average of the virial and energy routes with a weight fixed as to reproduce the exact third virial coefficient. Somewhat surprisingly, our results indicate that only the compressibility route fails to display a full critical behavior with a well-defined critical point. The existence of a critical point and a (possibly metastable) gas-liquid phase transition in our model (despite the fact that attractive interactions are partially inhibited) are supported by the NF generalized principle of corresponding states³⁵ and by preliminary simulations results. We plan to carry out more detailed GEMC simulations to fully elucidate this point.

The work presented here can foster further activities toward an analytical theory of the anomalous phase diagram indicated by numerical simulations of the (unconstrained) Janus fluid. We are currently working on the extension of the present model allowing for more general interactions where the red hemispheres in Fig. 2 also present a certain adhesion (e.g., $\tau_{12} < \tau_{11} = \tau_{22} = \tau_{21} < \infty$). This more general model (to which the theory presented in Sec. V B still applies) can be continuously tuned from isotropic SHS ($\tau_{ij} = \tau$) to isotropic HS interactions ($\tau_{ij} \rightarrow \infty$). The increase in the (Baxter) critical temperatures and densities occurring when equating the stickiness of both hemispheres would then mimic the corresponding increase in the location of the critical point upon an increase of the patch coverage in the Kern–Frenkel model.⁷

ACKNOWLEDGMENTS

The research of M.A.G.M. and A.S. has been supported by the Spanish government through Grant No. FIS2010-

16587 and by the Junta de Extremadura (Spain) through Grant No. GR101583, partially financed by FEDER funds. M.A.G.M. is also grateful to the Junta de Extremadura (Spain) for the pre-doctoral fellowship PD1010. A.G. acknowledges financial support by PRIN-COFIN 2010-2011 (Contract No. 2010LKE4CC). R.F. would like to acknowledge the use of the computational facilities of CINECA through the ISCRCA call.

APPENDIX A: EXACT LOW-DENSITY PROPERTIES FOR ANISOTROPIC SHS MIXTURES

1. Cavity function to first order in density

To first order in density, the cavity function of an anisotropic mixture is

$$y_{ij}(\mathbf{r}) = 1 + y_{ij}^{(1)}(\mathbf{r})\rho + \mathcal{O}(\rho^2), \quad (\text{A1})$$

where

$$y_{ij}^{(1)}(\mathbf{r}) = \sum_k x_k y_{ij;k}^{(1)}(\mathbf{r}), \quad (\text{A2})$$

with

$$y_{ij;k}^{(1)}(\mathbf{r}) = \int d\mathbf{r}' f_{ik}(\mathbf{r}') f_{kj}(\mathbf{r} - \mathbf{r}'). \quad (\text{A3})$$

Here, $f_{ij}(\mathbf{r}) = e^{-\beta\phi_{ij}(\mathbf{r})} - 1$ is the Mayer function. In the particular case of the anisotropic SHS potential considered in this paper,

$$\begin{aligned} f_{ij}(\mathbf{r}) &= f_{\text{HS}}(r) + \delta(r-1)[t_{ij}\Theta(\cos\theta) + t_{ji}\Theta(-\cos\theta)] \\ &= f_{ji}^{\text{SHS}}(r) + t_{ij}^{\bar{}}\delta(r-1)\Theta(\cos\theta), \end{aligned} \quad (\text{A4})$$

where $t_{ij}^{\bar{}} \equiv t_{ij} - t_{ji}$,

$$f_{\text{HS}}(r) = -\Theta(1-r), \quad f_{ji}^{\text{SHS}}(r) = f_{\text{HS}}(r) + t_{ji}\delta(r-1). \quad (\text{A5})$$

Inserting Eq. (A4) into Eq. (A3), we get

$$\begin{aligned} y_{ij;k}^{(1)}(\mathbf{r}) &= \Theta(2-r) \left\{ \frac{\pi}{3}(2-r)^2(4+r) - (t_{ki} + t_{jk})\pi(2-r) \right. \\ &\quad \left. + t_{ki}t_{jk}2\pi \left[2\delta(r) + \frac{1}{r} \right] - (t_{i\bar{k}} + t_{k\bar{j}})\mathcal{A}(\mathbf{r}) \right. \\ &\quad \left. + (t_{i\bar{k}}t_{jk} + t_{k\bar{j}}t_{ki})\mathcal{L}(\mathbf{r}) + t_{i\bar{k}}t_{k\bar{j}}\mathcal{L}_0(\mathbf{r}) \right\}, \end{aligned} \quad (\text{A6})$$

where

$$\mathcal{A}(\mathbf{r}) \equiv \int d\mathbf{r}' \delta(r'-1)\Theta(1-|\mathbf{r}-\mathbf{r}'|)\Theta(z'), \quad (\text{A7})$$

$$\mathcal{L}(\mathbf{r}) \equiv \int d\mathbf{r}' \delta(r'-1)\delta(|\mathbf{r}-\mathbf{r}'|-1)\Theta(z'), \quad (\text{A8})$$

$$\mathcal{L}_0(\mathbf{r}) \equiv \int d\mathbf{r}' \delta(r'-1)\delta(|\mathbf{r}-\mathbf{r}'|-1)\Theta(z')\Theta(z-z'). \quad (\text{A9})$$

It can be proved that

$$\mathcal{A}(\mathbf{r}) = \begin{cases} \pi(2-r), & \sqrt{1-r^2/4} \leq \cos\theta \leq 1, \\ A(r/2, \theta), & |\cos\theta| \leq \sqrt{1-r^2/4}, \\ 0, & -1 \leq \cos\theta \leq -\sqrt{1-r^2/4}, \end{cases} \quad (\text{A10})$$

094904-16 Maestre *et al.*

 J. Chem. Phys. **138**, 094904 (2013)

$$\mathcal{L}(\mathbf{r}) = \begin{cases} 2\pi/r, & \sqrt{1-r^2/4} \leq \cos\theta \leq 1, \\ L_0(r/2, \theta), & |\cos\theta| \leq \sqrt{1-r^2/4}, \\ 0, & -1 \leq \cos\theta \leq -\sqrt{1-r^2/4}, \end{cases} \quad (\text{A11})$$

$$\mathcal{L}_0(\mathbf{r}) = \begin{cases} 2\pi/r, & \sqrt{1-r^2/4} \leq \cos\theta \leq 1, \\ L_0(r/2, \theta), & 0 \leq \cos\theta \leq \sqrt{1-r^2/4}, \\ 0, & \cos\theta \leq 0, \end{cases} \quad (\text{A12})$$

where

$$A(\ell, \theta) = 2\pi \Theta(\cos\theta) - \pi\ell - 2\ell \sin^{-1} \frac{\ell \cos\theta}{\sqrt{1-\ell^2} \sin\theta} - 2 \tan^{-1} \frac{\sqrt{\sin^2\theta - \ell^2}}{\cos\theta}, \quad (\text{A13})$$

$$L(\ell, \theta) = -\frac{1}{2\ell} \frac{\partial}{\partial \ell} A(\ell, \theta) = \frac{1}{\ell} \left[\frac{\pi}{2} + \sin^{-1} \frac{\ell \cos\theta}{\sqrt{1-\ell^2} \sin\theta} \right], \quad (\text{A14})$$

$$L_0(\ell, \theta) = L(\ell, \theta) - L(\ell, \pi - \theta) = \frac{2}{\ell} \sin^{-1} \frac{\ell \cos\theta}{\sin\theta \sqrt{1-\ell^2}}. \quad (\text{A15})$$

In Eqs. (A11) and (A12) we have omitted terms proportional to $\delta(r)$ since they will not contribute to $g_{ij}(\mathbf{r})$. Note the symmetry relations $\mathcal{A}(\mathbf{r}) + \mathcal{A}(-\mathbf{r}) = \pi(2-r)$, $\mathcal{L}(\mathbf{r}) + \mathcal{L}(-\mathbf{r}) = 2\pi/r$, $\mathcal{L}(\mathbf{r}) - \mathcal{L}(-\mathbf{r}) = \mathcal{L}_0(\mathbf{r}) - \mathcal{L}_0(-\mathbf{r})$.

The orientational average

$$\bar{y}_{ij;k}^{(1)}(\mathbf{r}) = \int_0^{\pi/2} d\theta \sin\theta y_{ij;k}^{(1)}(\mathbf{r}) \quad (\text{A16})$$

becomes

$$\bar{y}_{ij;k}^{(1)}(\mathbf{r}) = \Theta(2-r) \left\{ \frac{\pi}{3} (2-r)^2 (4+r) - (t_{ki} + t_{jk})\pi(2-r) + t_{ki}t_{jk}2\pi \left[2\delta(r) + \frac{1}{r} \right] - (t_{ik}^- + t_{kj}^-)\bar{\mathcal{A}}(r) + (t_{ik}^-t_{jk} + t_{kj}^-t_{ki})\bar{\mathcal{L}}(r) + t_{ik}^-t_{kj}^-\bar{\mathcal{L}}_0(r) \right\}, \quad (\text{A17})$$

where

$$\bar{\mathcal{A}}(r) = \pi(2-r)(1 - \sqrt{1-r^2/4}) + \bar{\mathcal{A}}(r/2), \quad (\text{A18})$$

$$\bar{\mathcal{L}}(r) = \frac{2\pi}{r}(1 - \sqrt{1-r^2/4}) + \bar{\mathcal{L}}(r/2), \quad (\text{A19})$$

$$\bar{\mathcal{L}}_0(r) = \frac{2\pi}{r}(1 - \sqrt{1-r^2/4}) + \bar{\mathcal{L}}_0(r/2), \quad (\text{A20})$$

with

$$\bar{A}(\ell) = \int_{\sin^{-1}\ell}^{\pi/2} d\theta \sin\theta A(\ell, \theta) = 2\sqrt{1-\ell^2}(\pi - \pi\ell - 1) + 2\ell \cos^{-1}\ell, \quad (\text{A21})$$

$$\bar{L}(\ell) = \int_{\sin^{-1}\ell}^{\pi/2} d\theta \sin\theta L(\ell, \theta) = \frac{1}{\ell}(\pi\sqrt{1-\ell^2} - \cos^{-1}\ell), \quad (\text{A22})$$

$$\bar{L}_0(\ell) = \int_{\sin^{-1}\ell}^{\pi/2} d\theta \sin\theta L_0(\ell, \theta) = \frac{1}{\ell}(\pi\sqrt{1-\ell^2} - 2\cos^{-1}\ell). \quad (\text{A23})$$

2. Second and third virial coefficients

The series expansion of the compressibility factor Z in powers of density defines the virial coefficients:

$$Z = 1 + B_2\rho + B_3\rho^2 + \dots \quad (\text{A24})$$

Using Eq. (A1) in Eq. (4.8), one can identify

$$B_2 = \frac{2\pi}{3} \left(1 - 3 \sum_{i,j} x_i x_j t_{ij} \right), \quad (\text{A25})$$

$$B_3 = \frac{2\pi}{3} \sum_{i,j,k} x_i x_j x_k [(1 - 3t_{ij}\bar{y}_{ij;k}^{(1)}(1) - t_{ij}\bar{y}_{ij;k}^{(1)'}(1))]. \quad (\text{A26})$$

According to Eq. (A17),

$$\bar{y}_{ij;k}^{(1)}(1) = \frac{5\pi}{3} - (t_{ki} + t_{jk})\pi + t_{ki}t_{jk}2\pi - (t_{ik}^- + t_{kj}^-)\bar{\mathcal{A}}(1) + (t_{ik}^-t_{jk} + t_{kj}^-t_{ki})\bar{\mathcal{L}}(1) + t_{ik}^-t_{kj}^-\bar{\mathcal{L}}_0(1), \quad (\text{A27})$$

$$\bar{y}_{ij;k}^{(1)'}(1) = -3\pi + (t_{ki} + t_{jk})\pi - t_{ki}t_{jk}2\pi - (t_{ik}^- + t_{kj}^-)\bar{\mathcal{A}}'(1) + (t_{ik}^-t_{jk} + t_{kj}^-t_{ki})\bar{\mathcal{L}}'(1) + t_{ik}^-t_{kj}^-\bar{\mathcal{L}}_0'(1), \quad (\text{A28})$$

where

$$\bar{\mathcal{A}}(1) = \frac{4\pi}{3} - \sqrt{3}, \quad \bar{\mathcal{A}}'(1) = -\frac{2\pi}{3}, \quad (\text{A29})$$

$$\bar{\mathcal{L}}(1) = \frac{4\pi}{3}, \quad \bar{\mathcal{L}}'(1) = -\frac{2}{3}(2\pi - \sqrt{3}), \quad (\text{A30})$$

$$\bar{\mathcal{L}}_0(1) = \frac{2\pi}{3}, \quad \bar{\mathcal{L}}_0'(1) = -\frac{2}{3}(\pi - 2\sqrt{3}). \quad (\text{A31})$$

The second and third virial coefficients can also be obtained from the compressibility equation (3.14). To that end, note that

$$\hat{h}_{ij}(0) = \hat{h}_{ij}^{(1)}(0)\rho + \hat{h}_{ij}^{(2)}(0)\rho^2 + \dots, \quad (\text{A32})$$

where, according to Eq. (3.13),

$$\hat{h}_{ij}^{(1)}(0) = \sqrt{x_i x_j} 2\pi \left(-\frac{2}{3} + t_{ij} + t_{ji} \right), \quad (\text{A33})$$

094904-17 Maestre *et al.*

 J. Chem. Phys. **138**, 094904 (2013)

$$\begin{aligned} \widehat{h}_{ij}^{(2)}(0) = & \sqrt{x_i x_j} 2\pi \left\{ t_{ij} \overline{y}_{ij}^{(1)}(1) + t_{ji} \overline{y}_{ji}^{(1)}(1) \right. \\ & \left. + \int_1^2 dr r^2 [\overline{y}_{ij}^{(1)}(r) + \overline{y}_{ji}^{(1)}(r)] \right\}. \end{aligned} \quad (\text{A34})$$

Inserting this into Eq. (3.14) and making use of Eqs. (A17)–(A23), one gets $\chi_T^{-1} = 1 + 2B_2\rho + 3B_3\rho^2 + \dots$, with B_2 and B_3 given by Eqs. (A25) and (A26), respectively. Furthermore, it can be checked that the exact consistency condition (4.12) is satisfied by Eqs. (A1), (A2), (A27), and (A28). The verification of these two thermodynamic consistency conditions represent stringent tests on the correctness of the results derived in this appendix.

3. Case $t_{11} = t_{22} = t_{21} = 0$

In the preceding equations of this appendix we have assumed general values for the stickiness parameters t_{ij} . On the other hand, significant simplifications occur in our constrained Janus model, where $t_{ij} = t\delta_{i1}\delta_{j2}$. More specifically,

$$\begin{aligned} y_{11}^{(1)}(\mathbf{r}) = & \Theta(2-r) \left\{ \frac{\pi}{12} (2-r)^2 (4+r) - x_2 t [\pi(2-r) \right. \\ & \left. - t\mathcal{L}(\mathbf{r}) + t\mathcal{L}_0(\mathbf{r})] \right\}, \end{aligned} \quad (\text{A35})$$

$$y_{12}^{(1)}(\mathbf{r}) = \Theta(2-r) \left[\frac{\pi}{12} (2-r)^2 (4+r) - t\mathcal{A}(\mathbf{r}) \right], \quad (\text{A36})$$

$$\begin{aligned} \overline{y}_{11}^{(1)}(r) = & \Theta(2-r) \left[\frac{\pi}{12} (2-r)^2 (4+r) \right. \\ & \left. - x_2 \pi t \left(2-r - \frac{2t}{\pi r} \cos^{-1} \frac{r}{2} \right) \right], \end{aligned} \quad (\text{A37})$$

$$\begin{aligned} \overline{y}_{12}^{(1)}(r) = & \Theta(2-r) \left\{ \frac{\pi}{12} (2-r)^2 (4+r) \right. \\ & \left. - t \left[\pi(2-r) - 2\sqrt{1-r^2/4} + r \cos^{-1} \frac{r}{2} \right] \right\}, \end{aligned} \quad (\text{A38})$$

$$\begin{aligned} \overline{y}_{21}^{(1)}(r) = & \Theta(2-r) \left\{ \frac{\pi}{12} (2-r)^2 (4+r) \right. \\ & \left. - t \left[2\sqrt{1-r^2/4} - r \cos^{-1} \frac{r}{2} \right] \right\}, \end{aligned} \quad (\text{A39})$$

$$\begin{aligned} \overline{y}^{(1)}(r) = & \Theta(2-r) \left[\frac{\pi}{12} (2-r)^2 (4+r) \right. \\ & \left. - x_1 x_2 2\pi t \left(2-r - \frac{t}{\pi r} \cos^{-1} \frac{r}{2} \right) \right], \end{aligned} \quad (\text{A40})$$

$$\overline{y}_{11}^{(1)}(1) = \frac{5\pi}{12} - x_2 \pi t \left(1 - \frac{2t}{3} \right), \quad (\text{A41})$$

$$\overline{y}_{12}^{(1)}(1) = \frac{5\pi}{12} - t \left(\frac{4\pi}{3} - \sqrt{3} \right), \quad (\text{A42})$$

$$\overline{y}_{21}^{(1)}(1) = \frac{5\pi}{12} - t \left(\sqrt{3} - \frac{\pi}{3} \right), \quad (\text{A43})$$

$$\overline{y}_{11}'^{(1)}(1) = -\frac{3\pi}{4} + x_2 t \left[\pi - \frac{2t}{3} (\pi + \sqrt{3}) \right], \quad (\text{A44})$$

$$\overline{y}_{12}'^{(1)}(1) = -\frac{3\pi}{4} + t \frac{2\pi}{3}, \quad (\text{A45})$$

$$\overline{y}_{21}'^{(1)}(1) = -\frac{3\pi}{4} + t \frac{\pi}{3}, \quad (\text{A46})$$

$$\overline{y}^{(1)}(1) = \frac{5\pi}{12} - x_1 x_2 2\pi t \left(1 - \frac{t}{3} \right), \quad (\text{A47})$$

$$\overline{y}^{(1)'}(1) = -\frac{3\pi}{4} + x_1 x_2 2t \left[\pi - \frac{t}{3} (\pi + \sqrt{3}) \right], \quad (\text{A48})$$

$$\frac{6}{\pi} B_2 = 4(1 - 3x_1 x_2 t), \quad (\text{A49})$$

$$\left(\frac{6}{\pi} \right)^2 B_3 = 10 \left\{ 1 - 6x_1 x_2 t \left[1 - \frac{2}{5} \left(4 - 3 \frac{\sqrt{3}}{\pi} \right) t \right] \right\}, \quad (\text{A50})$$

$$\begin{aligned} \frac{u_{\text{ex}}}{\epsilon} = & -12\eta x_1 x_2 t \left\{ 1 + \frac{5}{2} \left[1 - \frac{4}{5} \left(4 - 3 \frac{\sqrt{3}}{\pi} \right) t \right] \eta \right\} \\ & + \mathcal{O}(\eta^2). \end{aligned} \quad (\text{A51})$$

APPENDIX B: EVALUATION OF THE COEFFICIENTS $L_{ij}^{(0)}$, $L_{ij}^{(1)}$, AND $L_{ij}^{(2)}$

In order to apply Eqs. (3.19) and (3.20), it is convenient to rewrite Eq. (5.12) as

$$\frac{1}{2\pi} \mathbf{L}(s) = \mathbf{Q}(s) \cdot [1 - \mathbf{A}(s)], \quad (\text{B1})$$

where we have introduced the matrix \mathbf{Q} as

$$Q_{ij}(s) \equiv e^s s^2 G_{ij}(s). \quad (\text{B2})$$

Thus, Eqs. (3.19) and (3.20) are equivalent to

$$Q_{ij}(s) = 1 + s + \mathcal{O}(s^2). \quad (\text{B3})$$

Expanding $A_{ij}(s)$ in powers of s and inserting the result into Eq. (B1), one gets

$$\frac{1}{2\pi} L_{ij}^{(0)} = 1 - \sum_k A_{kj}^{(0)}, \quad (\text{B4})$$

$$\frac{1}{2\pi} L_{ij}^{(1)} = 1 - \sum_k (A_{kj}^{(1)} + A_{kj}^{(0)}), \quad (\text{B5})$$

094904-18 Maestre *et al.*

 J. Chem. Phys. **138**, 094904 (2013)

where

$$A_{ij}^{(n)} = (-1)^n \rho x_i \left[\frac{L_{ij}^{(0)}}{(n+3)!} - \frac{L_{ij}^{(1)}}{(n+2)!} + \frac{L_{ij}^{(2)}}{(n+1)!} \right]. \quad (\text{B6})$$

Equations (B4) and (B5) constitute a *linear* set of equations which allow us to express the coefficients $L_{ij}^{(0)}$ and $L_{ij}^{(1)}$ in terms of the coefficients $\{L_{kj}^{(2)}\}$. The result is given by Eqs. (5.15) and (5.16).

It now remains the determination of $L_{ij}^{(2)}$. This is done by application of Eq. (4.17), i.e., the ratio first term to second term in the expansion of $e^s G_{ij}(s)$ for large s must be exactly equal to t_{ij} . This is the only point where the stickiness parameters of the mixture appear explicitly.

The large- s behavior from Eq. (5.12) is

$$2\pi e^s G_{ij}(s) = L_{ij}^{(2)} + [L_{ij}^{(1)} + (L^{(2)} \cdot D)_{ij}] s^{-1} + \mathcal{O}(s^{-2}), \quad (\text{B7})$$

where

$$\begin{aligned} D_{ij} &\equiv \rho x_i \left(\frac{1}{2} L_{ij}^{(0)} - L_{ij}^{(1)} + L_{ij}^{(2)} \right) \\ &= \rho x_i \left(L_{ij}^{(2)} - \frac{\pi}{1-\eta} \right). \end{aligned} \quad (\text{B8})$$

Comparison of Eq. (4.16) with Eq. (B7) yields Eq. (5.18) and

$$\frac{12\tau_{ij} L_{ij}^{(2)}}{\sigma_{ij}} = L_{ij}^{(1)} + \sum_{k=1}^m L_{ik}^{(2)} D_{kj}, \quad (\text{B9})$$

$$\frac{L_{ij}^{(2)}}{t_{ij}} = L_{ij}^{(1)} + \sum_k L_{ik}^{(2)} D_{kj}. \quad (\text{B10})$$

Taking into account Eqs. (5.16) and (B8), Eq. (B10) becomes Eq. (5.17).

APPENDIX C: RECOVERY OF THE PSEUDO-PY SOLUTION

The aim of this appendix is to prove that the pair correlation functions $\bar{g}_{ij}(r)$ obtained from the RFA method in Sec. V B satisfy Eqs. (5.3) and (5.6).

First, note that the pseudo-OZ relation (5.6) can be rewritten in the form

$$\widehat{c}(q) = \widehat{h}(q) \cdot [I + \widehat{h}(q)]^{-1}, \quad (\text{C1})$$

where I is the unit matrix and

$$\widehat{c}_{ij}(q) = \rho \sqrt{x_i x_j} \int d\mathbf{r} e^{-i\mathbf{q}\cdot\mathbf{r}} \bar{c}_{ij}(r), \quad (\text{C2})$$

$$\widehat{h}_{ij}(q) = \rho \sqrt{x_i x_j} \int d\mathbf{r} e^{-i\mathbf{q}\cdot\mathbf{r}} \bar{h}_{ij}(r). \quad (\text{C3})$$

Note that $\widehat{h}_{ij}(0) = \frac{1}{2}[\widehat{h}_{ij}(0) + \widehat{h}_{ji}(0)]$, where $\widehat{h}_{ij}(0)$ is defined by Eq. (3.13).

The Fourier transform $\widehat{h}_{ij}(q)$ of the (orientational average) total correlation function $\bar{h}_{ij}(r) = \bar{g}_{ij}(r) - 1$ is related to the Laplace transform $G_{ij}(s)$ [see Eq. (3.15)] by

$$\widehat{h}_{ij}(q) = -2\pi\rho\sqrt{x_i x_j} \left[\frac{G_{ij}(s) - G_{ij}(-s)}{s} \right]_{s=iq}. \quad (\text{C4})$$

Making use of Eqs. (5.12)–(5.14), it is possible to obtain, after some algebra,

$$\begin{aligned} \frac{\widehat{c}_{ij}(q)}{\rho\sqrt{x_i x_j}} &= \frac{4\pi}{q^3} C_{ij}^{(0)} (\sin q - q \cos q) + \frac{4\pi}{q^4} C_{ij}^{(1)} [2q \sin q \\ &\quad - 2 - (q^2 - 2) \cos q] + \frac{4\pi}{q^6} C_{ij}^{(3)} [4q(q^2 - 6) \\ &\quad \times \sin q + 24 - (24 - 12q^2 + q^4) \cos q] \\ &\quad + 4\pi t_{ij} y_{ij}(1) \frac{\sin q}{q}, \end{aligned} \quad (\text{C5})$$

where the coefficients $C_{ij}^{(0)}$, $C_{ij}^{(1)}$, and $C_{ij}^{(3)}$ are independent of q but depend on the density, the composition, and the stickiness parameters. Fourier inversion yields

$$\begin{aligned} \bar{c}_{ij}(r) &= [C_{ij}^{(0)} + C_{ij}^{(1)} r + C_{ij}^{(3)} r^3] \Theta(1-r) \\ &\quad + y_{ij}(1) t_{ij} \delta_+(r-1). \end{aligned} \quad (\text{C6})$$

Taking into account Eq. (4.10) we see that Eq. (C6) has the structure

$$\bar{c}_{ij}(r) = \bar{g}_{ij}(r) - \bar{y}_{ij}(r). \quad (\text{C7})$$

But this is not but the PY closure relation (5.3). In passing, we get the cavity function inside the core:

$$y_{ij}(r) \Theta(1-r) = -[C_{ij}^{(0)} + C_{ij}^{(1)} r + C_{ij}^{(3)} r^3] \Theta(1-r). \quad (\text{C8})$$

- ¹A. B. Pawar and I. Kretschmar, *Macromol. Rapid Commun.* **31**, 150 (2010).
- ²A. Walther and H. E. Müller, *Soft Matter* **4**, 663 (2008).
- ³L. Hong, A. Cacciuto, E. Luijten, and S. Granick, *Langmuir* **24**, 621 (2008).
- ⁴E. Bianchi, R. Blaak, and C. N. Likos, *Phys. Chem. Chem. Phys.* **13**, 6397 (2011).
- ⁵Z. L. Zhang and S. C. Glotzer, *Nano Lett.* **4**, 1407 (2004).
- ⁶N. Kern and D. Frenkel, *J. Chem. Phys.* **118**, 9882 (2003).
- ⁷F. Sciortino, A. Giacometti, and G. Pastore, *Phys. Chem. Chem. Phys.* **12**, 11869 (2010).
- ⁸A. Giacometti, F. Lado, J. Largo, G. Pastore, and F. Sciortino, *J. Chem. Phys.* **131**, 174114 (2009).
- ⁹A. Giacometti, F. Lado, J. Largo, G. Pastore, and F. Sciortino, *J. Chem. Phys.* **132**, 174110 (2010).
- ¹⁰F. Sciortino, A. Giacometti, and G. Pastore, *Phys. Rev. Lett.* **103**, 237801 (2009).
- ¹¹A. Reinhardt, A. J. Williamson, J. P. K. Doyle, J. Carrete, L. M. Varela, and A. A. Louis, *J. Chem. Phys.* **134**, 104905 (2011).
- ¹²R. Fantoni, A. Giacometti, F. Sciortino, and G. Pastore, *Soft Matter* **7**, 2419 (2011).
- ¹³R. Fantoni, *Eur. Phys. J. B* **85**, 108 (2012).
- ¹⁴R. Zwanzig, *J. Chem. Phys.* **39**, 1714 (1963).
- ¹⁵R. J. Baxter, *J. Chem. Phys.* **49**, 2770 (1968).
- ¹⁶J. P. Hansen and I. R. McDonald, *Theory of Simple Liquids* (Academic, New York, 1986).
- ¹⁷R. O. Watts, D. Henderson, and R. J. Baxter, *Adv. Chem. Phys.* **21**, 421 (1971).
- ¹⁸J. W. Perram and E. R. Smith, *Chem. Phys. Lett.* **35**, 138 (1975).
- ¹⁹B. Barbooy, *Chem. Phys.* **11**, 357 (1975).
- ²⁰B. Barbooy and R. Tenne, *Chem. Phys.* **38**, 369 (1979).

094904-19 Maestre *et al.*J. Chem. Phys. **138**, 094904 (2013)

- ²¹E. Zaccarelli, G. Foffi, P. Tartaglia, F. Sciortino, and K. A. Dawson, *Progr. Colloid Polym. Sci.* **115**, 371 (2000).
- ²²C. Tutschka, G. Kahl, and E. Riegler, *Mol. Phys.* **100**, 1025 (2002).
- ²³R. Fantoni, D. Gazzillo, A. Giacometti, M. A. Miller, and G. Pastore, *J. Chem. Phys.* **127**, 234507 (2007).
- ²⁴A. Santos, S. B. Yuste, and M. López de Haro, *J. Chem. Phys.* **109**, 6814 (1998).
- ²⁵M. López de Haro, S. B. Yuste, and A. Santos, in *Theory and Simulations of Hard-Sphere Fluids and Related Systems*, Lecture Notes in Physics Vol. 753, edited by A. Mulero (Springer, Berlin 2008), pp. 183–245.
- ²⁶S. B. Yuste and A. Santos, *Phys. Rev. E* **48**, 4599 (1993).
- ²⁷L. Acedo, *J. Stat. Phys.* **99**, 707 (2000).
- ²⁸J. Abate and W. Whitt, *Queueing Syst.* **10**, 5 (1992).
- ²⁹A. Santos, *J. Chem. Phys.* **123**, 104102 (2005).
- ³⁰A. Santos, *Mol. Phys.* **104**, 3411 (2006).
- ³¹G. Stell, *J. Stat. Phys.* **63**, 1203 (1991).
- ³²M. A. Miller and D. Frenkel, *Phys. Rev. Lett.* **90**, 135702 (2003).
- ³³M. A. Miller and D. Frenkel, *J. Chem. Phys.* **121**, 535 (2004).
- ³⁴A. Malijevský, S. B. Yuste, and A. Santos, *J. Chem. Phys.* **125**, 074507 (2006).
- ³⁵M. G. Noro and D. Frenkel, *J. Chem. Phys.* **113**, 2941 (2000).
- ³⁶P. Bolhuis, M. Hagen, and D. Frenkel, *Phys. Rev. E* **50**, 4880 (1994).
- ³⁷E. Lomba and N. G. Almarza, *J. Chem. Phys.* **100**, 8367 (1994).
- ³⁸M. H. J. Hagen and D. Frenkel, *J. Chem. Phys.* **101**, 4093 (1994).
- ³⁹L. Mederos and G. Navascués, *J. Chem. Phys.* **101**, 9841 (1994).

Chapter 37

Multicomponent fluid of nonadditive hard spheres near a wall

Fantoni R. and Santos A., Phys. Rev. E **87**, 042102 (2013)

Title: “Multicomponent fluid of nonadditive hard spheres near a wall”

Abstract: A recently proposed rational-function approximation [Phys. Rev. E **84**, 041201 (2011)] for the structural properties of nonadditive hard spheres is applied to evaluate analytically (in Laplace space) the local density profiles of multicomponent nonadditive hard-sphere mixtures near a planar nonadditive hard wall. The theory is assessed by comparison with *NVT* Monte Carlo simulations of binary mixtures with a size ratio 1 : 3 in three possible scenarios: a mixture with either positive or negative nonadditivity near an additive wall, an additive mixture with a nonadditive wall, and a nonadditive mixture with a nonadditive wall. It is observed that, while the theory tends to underestimate the local densities at contact (especially in the case of the big spheres) it captures very well the initial decay of the densities with increasing separation from the wall and the subsequent oscillations.

PHYSICAL REVIEW E **87**, 042102 (2013)**Multicomponent fluid of nonadditive hard spheres near a wall**

Riccardo Fantoni*

Dipartimento di Scienze dei Materiali e Nanosistemi, Università Ca' Foscari Venezia, Calle Larga S. Marta DD2137, I-30123 Venezia, Italy

Andrés Santos†

Departamento de Física, Universidad de Extremadura, E-06071 Badajoz, Spain

(Received 5 February 2013; revised manuscript received 20 March 2013; published 3 April 2013)

A recently proposed rational-function approximation [Phys. Rev. E **84**, 041201 (2011)] for the structural properties of nonadditive hard spheres is applied to evaluate analytically (in Laplace space) the local density profiles of multicomponent nonadditive hard-sphere mixtures near a planar nonadditive hard wall. The theory is assessed by comparison with *NVT* Monte Carlo simulations of binary mixtures with a size ratio 1:3 in three possible scenarios: a mixture with either positive or negative nonadditivity near an additive wall, an additive mixture with a nonadditive wall, and a nonadditive mixture with a nonadditive wall. It is observed that, while the theory tends to underestimate the local densities at contact (especially in the case of the big spheres) it captures very well the initial decay of the densities with increasing separation from the wall and the subsequent oscillations.

DOI: [10.1103/PhysRevE.87.042102](https://doi.org/10.1103/PhysRevE.87.042102)

PACS number(s): 61.20.Gy, 61.20.Ne, 61.20.Ja, 68.08.De

I. INTRODUCTION

The study of mixtures near a fluid-solid interface is important for the understanding of wetting and adsorption phenomena where competition among different components may occur. A simplified physical picture of adsorption may be obtained at a microscopic level if one considers the solid surface as a planar smooth hard wall confining the particles of the mixture. Thereby, one can describe the expected oscillations of the (partial) local particle densities in the neighborhood of the wall with an abundance of particles right at contact and a depletion nearby. Whereas confined fluid mixtures of additive hard spheres (AHS) have been widely studied within integral equation theories [1–8], Monte Carlo simulations [8–13], and density-functional theories [9,13–23], much less is known in the case of nonadditive hard spheres (NAHS) [24–27].

In a recent paper [28], NAHS mixtures were studied through the so-called rational-function approximation (RFA) technique [29,30], which amounts to choosing simple (rational-function) expressions for the Laplace space representation of the radial distribution functions of the theory of liquids [31,32]. This allowed us to determine a nonperturbative, fully analytical (in Laplace space) approximation. When the nonadditivity is set to zero, the approximation reduces to the Percus-Yevick (PY) approximation for an AHS mixture.

The purpose of the present work is to use the RFA scheme devised in Ref. [28] to determine the structural properties of an n -component NAHS fluid near a hard wall interacting either additively or nonadditively with the particles of the fluid mixture. A realization of the problem is obtained from a $(n + 1)$ -component NAHS mixture, where one of the species, species 0, is taken to have a vanishing concentration and

an infinite diameter. A similar approach was employed by Malijevsky *et al.* [13] to determine through the RFA the structural properties of a multicomponent AHS fluid near an additive hard wall. In the present case, however, not only the particle-particle interaction may be nonadditive (i.e., the closest distance between the centers of two spheres of species i and j is in general different from the arithmetic mean of the respective diameters), but also the particle-wall may be nonadditive as well. The latter possibility means that the closest distance from the planar wall to the center of a sphere may be different from the radius of the sphere. A similar problem has recently been considered by González *et al.* [33], where strong size selectivity is observed in a binary AHS mixture confined in a narrow cylindrical pore such that each species of the mixture sees a different cylinder radius.

We will compare our approximation results for the local density of particles at a distance z from the wall with exact canonical (fixed number of particles N , volume V , and temperature T) Monte Carlo (MC) simulation results for binary mixtures. In the simulation it is necessary to use two hard walls on the opposite far square faces of a parallelepiped simulation box with rectangular lateral faces and to choose the two walls far enough so that bulk properties of the fluid can be extracted by looking at the center of the box.

The agreement between theory and simulations is quite satisfactory. It is worse at contact (similarly to what happens with the PY theory in the additive case [13]) but it rapidly improves as the distance from the wall increases, so that the first minimum (depletion region) and the subsequent oscillations are well predicted by our analytical approach. To the best of our knowledge, our results constitute the first proposal for an analytical expression (in Laplace space) for the density profiles of a NAHS mixture confined by a (nonadditive or additive) hard wall. As such, the theory is expected to be useful to the experimentalist who needs easy formulas to determine profiles to compare with experimental data, thus bypassing the need of numerical experiments.

*rfantoni@ts.infn.it

†andres@unex.es; <http://www.unex.es/eweb/fisteor/andres>

The paper is organized as follows. In Sec. II we describe the model of the confined fluid we are going to study. The RFA used to extract the structural properties of the fluid is presented in Sec. III, where some details of the wall limit are given in the Appendix. In Sec. IV we describe some details of the NVT MC simulation method we employed for confined binary mixtures. The results for the structural properties are presented in Sec. V, where the RFA and our own MC simulation are compared. Finally, Sec. VI is left for concluding remarks.

II. THE MODEL

An n -component NAHS mixture in the d -dimensional Euclidean space is a fluid of N_i particles of species i with $i = 1, 2, \dots, n$, such that there are a total number of particles $N = \sum_{i=1}^n N_i$ in a volume V , and the pair potential between a particle of species i and a particle of species j separated by a distance r is given by

$$\phi_{ij}(r) = \begin{cases} \infty, & r \leq \sigma_{ij}, \\ 0, & r > \sigma_{ij}, \end{cases} \quad (2.1)$$

where $\sigma_{ii} = \sigma_i$ and $\sigma_{ij} = \frac{1}{2}(\sigma_i + \sigma_j)(1 + \Delta_{ij})$, so that $\Delta_{ii} = 0$ and $\Delta_{ij} = \Delta_{ji} > -1$. When $\Delta_{ij} = 0$ for every pair $i-j$ we recover the AHS system. In the present paper we will only consider the NAHS system in its single fluid phase.

Let $\bar{\rho} = N/V$ be the total number density of the mixture and $\bar{x}_i = N_i/N$ be the mole fraction of species i . These are spatially averaged quantities that can differ from local values in confined situations.

The one-dimensional ($d = 1$) NAHS fluid admits an exact analytical solution for the structural and thermophysical properties in the thermodynamic limit $N \rightarrow \infty$ with $\bar{\rho} = N/V = \text{const}$ [34–37]. Moreover, the AHS fluid with $d = \text{odd}$ allows for an analytical solution of the PY approximate theory [38–41]. Such a solution in the case $d = 1$ reduces to the exact solution particularized to the additive mixture.

Inspired by both the exact solution for one-dimensional NAHS mixtures and the PY solution for three-dimensional AHS mixtures, we have recently proposed an analytical approach for the three-dimensional NAHS system [28]. As said in Sec. I, the aim of the present paper is to use that approximation to determine the structural properties of a ternary mixture where one of the species ($i = 0$) is subject to the wall limit: $\bar{x}_0 \rightarrow 0$ and $\sigma_0 \rightarrow \infty$. Such a ternary mixture represents a binary mixture of AHS ($\Delta_{12} = 0$) or NAHS ($\Delta_{12} \neq 0$) in the presence of a hard wall, which, in addition, may interact additively or nonadditively with the fluid particles (see Sec. III B).

III. RATIONAL-FUNCTION APPROXIMATION

A. General scheme

In Ref. [28], the following proposal for the structural properties of an n -component NAHS fluid defined through the Laplace transform $G_{ij}(s)$ of $rg_{ij}(r)$ was given:

$$G_{ij}(s) = s^{-2} \sum_{k=1}^n e^{-\sigma_{ik}s} L_{ik}(s) B_{kj}(s), \quad (3.1)$$

with

$$\mathbf{B}^{-1}(s) = \mathbf{I} - \mathbf{A}(s), \quad (3.2)$$

$$A_{ij}(s) = \frac{2\pi\bar{\rho}\bar{x}_i}{s^3} [N_{ij}(s)e^{a_{ij}s} - L_{ij}(s)e^{-\sigma_{ij}s}], \quad (3.3)$$

where \mathbf{I} is the unit matrix,

$$L_{ij}(s) \equiv L_{ij}^{(0)} + L_{ij}^{(1)}s, \quad (3.4)$$

$$N_{ij}(s) \equiv L_{ij}^{(0)} \left(1 - b_{ij}s + \frac{b_{ij}^2s^2}{2} \right) + L_{ij}^{(1)}s(1 - b_{ij}s), \quad (3.5)$$

$$b_{ij} \equiv \sigma_{ij} + a_{ij}, \quad a_{ij} \equiv \frac{1}{2}(\sigma_i - \sigma_j). \quad (3.6)$$

Equations (3.1)–(3.5) provide the explicit s -dependence of the Laplace transform $G_{ij}(s)$, but it still remains to obtain the two sets of parameters $L_{ij}^{(0)}$ and $L_{ij}^{(1)}$. This is done by enforcing the physical requirements $\lim_{s \rightarrow 0} s^2 G_{ij}(s) = 1$ and $\lim_{s \rightarrow 0} s^{-1} [s^2 G_{ij}(s) - 1] = 0$ [28]. The result is

$$L_{ij}^{(0)} = S_j, \quad L_{ij}^{(1)} = T_j + \sigma_{ij}S_j, \quad (3.7)$$

where

$$S_j \equiv \frac{1 - \pi\bar{\rho}\Psi_j}{(1 - \pi\bar{\rho}\Lambda_j)(1 - \pi\bar{\rho}\Psi_j) - \pi^2\bar{\rho}^2\mu_{j|2,0}\Omega_j}, \quad (3.8)$$

$$T_j \equiv \frac{\pi\bar{\rho}\Omega_j}{(1 - \pi\bar{\rho}\Lambda_j)(1 - \pi\bar{\rho}\Psi_j) - \pi^2\bar{\rho}^2\mu_{j|2,0}\Omega_j}, \quad (3.9)$$

$$\Lambda_j \equiv \mu_{j|2,1} - \frac{1}{3}\mu_{j|3,0}, \quad (3.10)$$

$$\Psi_j \equiv \frac{2}{3}\mu_{j|3,0} - \mu_{j|2,1}, \quad (3.11)$$

$$\Omega_j \equiv \mu_{j|3,1} - \mu_{j|2,2} - \frac{1}{4}\mu_{j|4,0}, \quad (3.12)$$

and we have called

$$\mu_{j|p,q} \equiv \sum_{k=1}^n \bar{x}_k b_{kj}^p \sigma_{kj}^q. \quad (3.13)$$

As discussed in Ref. [28], the inverse Laplace transform $\mathcal{L}^{-1}[G_{ij}(s)](r)$ may present a spurious behavior in the shell $\min(\sigma_{ij}, \tau_{ij}) \leq r \leq \max(\sigma_{ij}, \tau_{ij})$, where τ_{ij} is the minimum of the list of values $\sigma_{ik} - a_{kj}$ ($k = 1, \dots, n$) that are different from σ_{ij} . If $\sigma_{ik} - a_{kj} = \sigma_{ij}$ for all k , then $\tau_{ij} = \sigma_{ij}$. The anomalous behavior of $\mathcal{L}^{-1}[G_{ij}(s)](r)$ for $\min(\sigma_{ij}, \tau_{ij}) \leq r \leq \max(\sigma_{ij}, \tau_{ij})$ can be avoided with a series of corrections, the simplest one of which yields

$$g_{ij}(r) = \Theta(r - \sigma_{ij}) \left\{ \frac{\mathcal{L}^{-1}[G_{ij}(s)](r)}{r} + C_{ij} \Theta(\tau_{ij} - r) \left(\frac{\tau_{ij}}{r} - 1 \right) \right\}, \quad (3.14)$$

where

$$C_{ij} = 2\pi\bar{\rho}\bar{x}_{\kappa_{ij}} L_{i\kappa_{ij}}^{(1)} \left(L_{\kappa_{ij}}^{(1)} - S_j \frac{b_{\kappa_{ij}j}}{2} \right) b_{\kappa_{ij}j}, \quad (3.15)$$

κ_{ij} being the index associated with τ_{ij} ; i.e., $\tau_{ij} = \sigma_{i\kappa_{ij}} - a_{\kappa_{ij}j}$. The contact values are given by [28]

$$g_{ij}(\sigma_{ij}^+) = \frac{L_{ij}^{(1)}}{\sigma_{ij}} + C_{ij} \left(\frac{\tau_{ij}}{\sigma_{ij}} - 1 \right). \quad (3.16)$$

The approximation (3.14) was referred to as RFA₊⁽¹⁾ in Ref. [28]. In the special case of AHS mixtures, one has $\sigma_{ik} - a_{kj} = \sigma_{ij}$, so that $\tau_{ij} = \sigma_{ij}$ and $g_{ij}(r) = r^{-1} \mathcal{L}^{-1}[G_{ij}(s)](r)$ coincides with the PY solution [38,39].

B. Wall limit

Now we assume that a single sphere of diameter σ_0 is introduced in the n -component fluid. This gives rise to an $(n+1)$ -component fluid, where the extra species ($i=0$), being made of a single particle, has a vanishing concentration $\bar{x}_0 = 0$ in the thermodynamic limit $N \rightarrow \infty$. With this proviso, Eq. (3.1) can be easily extended to this $(n+1)$ -component mixture.

According to Eq. (3.3), if $\bar{x}_0 = 0$, the row $i=0$ of the matrix \mathbf{A} is zero. As a consequence, the row $i=0$ and the column $j=0$ of the matrices \mathbf{B}^{-1} and \mathbf{B} have the forms

$$B_{0j}^{-1} = \delta_{j0}, \quad B_{i0}^{-1} = -A_{i0}, \quad i \geq 1, \quad (3.17)$$

$$B_{0j} = \delta_{j0}, \quad B_{i0} = \sum_{k=1}^n B_{ik} A_{k0}, \quad i \geq 1. \quad (3.18)$$

Thus, application of Eq. (3.1) to the pair $i-0$ with $i \geq 1$ yields

$$G_{i0}(s) = s^{-2} e^{-\sigma_0 s} L_{i0}(s) + \sum_{j=1}^n G_{ij}(s) A_{j0}(s). \quad (3.19)$$

Therefore, the cross function $G_{i0}(s)$ (with $i=1, \dots, n$), which is related to the spatial correlation between a particle of species $i \geq 1$ and the single particle $i=0$, is expressed in terms of the matrix $G_{ij}(s)$ of the n -component mixture and the cross elements $L_{i0}(s)$ and $A_{j0}(s)$.

In principle, the nonadditivity of the $i-0$ interaction would be measured by the nonadditivity parameter Δ_{i0} defined by $\sigma_{i0} = \frac{1}{2}(\sigma_0 + \sigma_i)(1 + \Delta_{i0})$. However, the use of Δ_{i0} is not convenient in the wall limit $\sigma_0 \rightarrow \infty$ that we will take at the end. Instead, we define a nonadditivity distance w_i by $\sigma_{i0} = \frac{1}{2}(\sigma_0 + \sigma_i) + w_i$. Note that, since no 0-0 interaction is present, the definition of the diameter σ_0 is somewhat arbitrary. In fact, if all $w_i = w$ are equal, the apparently nonadditive $i-0$ interaction is indistinguishable from an additive interaction with $\sigma_0 \rightarrow \sigma_0 + 2w$. Therefore, a true nonadditive $i-0$ interaction requires, first, that $n \geq 2$ and, second, that not all $\{w_i\}$ are equal. Therefore, without loss of generality, we take $\min(w_i; i=1, \dots, n) = 0$. This defines the diameter σ_0 unambiguously.

As a next step toward the wall limit, we introduce the shifted radial distribution function

$$\gamma_i(z) = g_{i0}(z + \sigma_0/2). \quad (3.20)$$

Thus, while r is the distance between the centers of the pair $i-0$, $z = r - \frac{1}{2}\sigma_0$ represents the distance from the center of a sphere of species i to the surface of the single sphere $j=0$. If we call $\Gamma_i(s)$ the Laplace transform of $\gamma_i(z)$, the following

relationship applies:

$$G_{i0}(s) = e^{-\sigma_0 s/2} \left[\frac{\sigma_0}{2} \Gamma_i(s) - \Gamma_i'(s) \right], \quad (3.21)$$

where $\Gamma_i'(s) = \partial \Gamma_i(s) / \partial s$.

Finally, we take the wall limit $\sigma_0 \rightarrow \infty$. In that case, the function $\gamma_i(z)$ becomes the ratio between the local number density of particles of species i at a distance z from the wall, $\rho_i(z)$, and the corresponding density in the bulk, ρ_i^b . In an infinite system (as implicitly assumed in the theoretical approach), the bulk and average values coincide, i.e., $\rho_i^b = \rho_i(\infty) = \bar{x}_i \bar{\rho}$.

In the wall limit $\Gamma_i'(s)$ can be neglected versus $\sigma_0 \Gamma_i(s)/2$ in Eq. (3.21), so that

$$\begin{aligned} \Gamma_i(s) &= 2 \lim_{\sigma_0 \rightarrow \infty} \sigma_0^{-1} e^{\sigma_0 s/2} G_{i0}(s) \\ &= 2 e^{-(\sigma_i/2 + w_i)s} \frac{\tilde{L}_i(s)}{s^2} + 2 \sum_{j=1}^n G_{ij}(s) \tilde{A}_j(s), \end{aligned} \quad (3.22)$$

where in the second step we have made use of Eq. (3.19) and have defined

$$\tilde{L}_i(s) \equiv \lim_{\sigma_0 \rightarrow \infty} \sigma_0^{-1} L_{i0}(s), \quad (3.23)$$

$$\tilde{A}_j(s) \equiv \lim_{\sigma_0 \rightarrow \infty} \sigma_0^{-1} e^{\sigma_0 s/2} A_{j0}(s). \quad (3.24)$$

These two quantities are evaluated in the Appendix.

Once the Laplace transform $\Gamma_i(s)$ is well defined, let us consider the correction described by the second line of Eq. (3.14). First, we subtract $\frac{1}{2}\sigma_0$ to the distances, so that the shell $\min(\sigma_{i0}, \tau_{i0}) \leq r \leq \max(\sigma_{i0}, \tau_{i0})$ becomes $\min(\frac{1}{2}\sigma_i + w_i, \tilde{\tau}_i) \leq z \leq \max(\frac{1}{2}\sigma_i + w_i, \tilde{\tau}_i)$, where $\tilde{\tau}_i$ is the minimum of the list of values $\sigma_{ik} - \frac{1}{2}\sigma_k$ ($k=1, \dots, n$) that differ from $\frac{1}{2}\sigma_i + w_i$. Again, $\tilde{\tau}_i = \frac{1}{2}\sigma_i + w_i$, if $\sigma_{ik} - \frac{1}{2}\sigma_k = \frac{1}{2}\sigma_i + w_i$ for all k . Finally, in the limit $\sigma_0 \rightarrow \infty$, one obtains

$$\begin{aligned} \gamma_i(z) &= \Theta(z - \frac{1}{2}\sigma_i - w_i) \{ \mathcal{L}^{-1}[\Gamma_i(s)](r) \\ &\quad + 2\tilde{C}_i \Theta(\tilde{\tau}_i - z)(\tilde{\tau}_i - z) \}, \end{aligned} \quad (3.25)$$

with

$$\tilde{C}_i = 2\pi \bar{\rho} \bar{x}_{\kappa_i} L_{i\kappa_i}^{(1)} \left(\tilde{L}_{\kappa_i}^{(1)} - \tilde{L}^{(0)} \frac{\sigma_{\kappa_i} + w_{\kappa_i}}{2} \right) (\sigma_{\kappa_i} + w_{\kappa_i}), \quad (3.26)$$

where κ_i is the index associated with $\tilde{\tau}_i$, i.e., $\tilde{\tau}_i = \sigma_{i\kappa_i} - \frac{1}{2}\sigma_{\kappa_i}$, and the quantities $\tilde{L}^{(0)}$ and $\tilde{L}_i^{(1)}$ are defined in the Appendix.

The inverse Laplace transform in Eq. (3.25) can be easily performed numerically [42]. On the other hand, the density ratio γ_i at the shortest distance from the wall $z = \frac{1}{2}\sigma_i + w_i$ can be derived analytically. From Eq. (3.16) we easily obtain

$$\gamma_i(z = \frac{1}{2}\sigma_i + w_i) = 2\tilde{L}_i^{(1)} + 2\tilde{C}_i(\tilde{\tau}_i - \frac{1}{2}\sigma_i - w_i). \quad (3.27)$$

The fact that the general scheme gives well-defined expressions in the wall limit ($\bar{x}_0 = 0, \sigma_0 \rightarrow \infty$) is a stringent test on the internal consistency of the RFA approach. It also shows the convenience of dealing with explicit, analytical expressions from which the subsequent limits can be taken.

RICCARDO FANTONI AND ANDRÉS SANTOS

 PHYSICAL REVIEW E **87**, 042102 (2013)

TABLE I. Values of the nonadditivity parameters (Δ_{12} , w_1 , and w_2), the average mole fraction (\bar{x}_1), and the average density ($\bar{\rho}$) for the representative systems considered in this work. In all the cases $\sigma_2/\sigma_1 = 3$. The table also includes the values (x_1^b and ρ^b) measured in the bulk region $z \approx L_z/2$ in our MC simulations with $L_z/\sigma_1 = 30$.

Label	Δ_{12}	w_1/σ_1	w_2/σ_1	\bar{x}_1	x_1^b	$\bar{\rho}\sigma_1^3$	$\rho^b\sigma_1^3$	$\bar{\eta}_{\text{eff}}$
A	0.2	0	0	0.5	0.469	$\frac{1}{30}$	0.0337	0.243
B	-0.2	0	0	0.5	0.503	$\frac{1}{20}$	0.0513	0.237
C1	-0.2	0	0	0.9	0.896	$\frac{1}{10}$	0.1025	0.095
C2	-0.2	0	0	0.9	0.898	$\frac{1}{5}$	0.2040	0.190
D	0	0	0.35	0.5	0.475	$\frac{1}{30}$	0.0345	0.192
E	0	0.35	0	0.5	0.511	$\frac{1}{20}$	0.0503	0.288
F	-0.2	0	0.35	0.5	0.486	$\frac{1}{30}$	0.0350	0.158

IV. MONTE CARLO SIMULATIONS

We have simulated a binary mixture ($n = 2$) of NAHS through canonical NVT MC simulations in a box of fixed volume and sides L_x , L_y , and L_z with $L_x = L_y$ and $L_z \gg L_x$. Periodic boundary conditions are enforced along the x and y directions, but two impenetrable hard walls are located at $z = 0$ and $z = L_z$. The particles are initially placed on a simple cubic regular configuration along the z direction with a first crystal layer of particles of species 1 juxtaposed to a crystal layer of particles of species 2. We reject the i th particle move only in case of overlap with any other particle, i.e., if $r_{ij} < \sigma_{ij}$ for some j , or with one of the walls, i.e., if $\min(z_i, L_z - z_i) < \frac{1}{2}\sigma_i + w_i$. The system is then equilibrated for 10^7 MC steps (where a MC step corresponds to a single particle move) and the properties are generally averaged over additional 10^9 MC steps for production. The maximum particle displacement, the same along each direction, is determined during the first stage of the equilibration run in such a way as to ensure an average acceptance ratio of 50% at production time. As a compromise between the condition $L_z \gg L_x$ and the computational need of not having too high a number of particles, we have taken $L_x = 10\sigma_1$ and $L_z = 30\sigma_1$ in all the simulations presented, except a control case with $L_z = 60\sigma_1$ (see below). The local density profiles $\gamma_i(z) = \rho_i(z)/\rho_i^b$ are obtained, for each species, from histograms of the z coordinates of the particles in bins of width $0.01\sigma_1$. The bulk values ρ_i^b are evaluated in the region of the simulation box with $z \approx L_z/2$, where a negligible influence from the walls is expected. Due to the finite value of L_z , the bulk total density $\rho^b = \rho_1^b + \rho_2^b$ and the bulk mole fraction $x_1^b = \rho_1^b/\rho^b$ differ from their respective average values $\bar{\rho}$ and \bar{x}_1 .

V. RESULTS

A. Representative systems

In the binary case, there are five independent dimensionless parameters of the problem: the size ratio σ_2/σ_1 , the particle-particle nonadditivity parameter Δ_{12} , the particle-wall nonadditivity parameter $\max(w_1, w_2)/\sigma_1$ [remember that, by convention, $\min(w_1, w_2) = 0$], the average mole fraction \bar{x}_1 , and the average reduced density $\bar{\rho}\sigma_1^3$. Here, σ_1 is chosen as the diameter of the small spheres and henceforth it will be used to define the length unit.

In order to focus on the nonadditivity parameters, we have chosen $\sigma_2/\sigma_1 = 3$ for all the systems. Next, three classes of systems have been considered: (i) a nonadditive mixture in the presence of an additive wall, (ii) an additive mixture in the presence of a nonadditive wall, and (iii) a nonadditive mixture with a nonadditive wall. As representative examples of class (i) we have chosen an equimolar mixture with either positive (system A of Table I) or negative (system B of Table I) nonadditivity and a mixture with an excess of small spheres and negative nonadditivity at two densities (systems C1 and C2, respectively). As examples of class (ii), we have chosen an equimolar mixture where the wall presents an extra repulsion to either the large spheres (system D) or the small spheres (system E). Finally, class (iii) is represented by system F, which is analogous to system D, except that the mixture has a negative nonadditivity. The reduced densities $\bar{\rho}\sigma_1^3$ range from $\frac{1}{30}$ to $\frac{1}{5}$, so that the total number of particles $N = \bar{\rho}L_x^2L_z$ ranges from 100 to 600. It is also convenient to measure the density in terms of the *effective* packing fraction $\bar{\eta}_{\text{eff}} = \frac{\pi}{6}\bar{\rho}\sum_{i,j}\bar{x}_i\bar{x}_j\sigma_{ij}^3$ related to van der Waals's one-fluid theory [43], whose values are indicated in the last column of Table I. In the low-density regime, two mixtures with the same value of $\bar{\eta}_{\text{eff}}$ would have the same compressibility factor.

B. Bulk values

The bulk values x_1^b and ρ^b measured in the MC simulations with $L_z = 30\sigma_1$ are also included in Table I. In all the cases the bulk density ρ^b is larger than the average density $\bar{\rho}$. This is due to the fact that the effective length available to the spheres of species i is not L_z but $L_z - (\sigma_i + 2w_i)$. As a consequence, the larger deviation between ρ^b and $\bar{\rho}$ takes place for systems D (3.5%) and F (5.0%), i.e., those systems where the walls produce an extra repulsion ($w_2/\sigma_1 = 0.35$) on the big spheres. This compression effect is only partially compensated by the accumulation of particles at contact with the walls. In the case of the bulk mole fraction x_1^b , the situation is less obvious. Note the identity

$$\frac{\bar{x}_1\bar{\rho}}{x_1^b\rho^b} = \frac{1}{L_z/2} \int_{\sigma_1/2+w_1}^{L_z/2} dz \gamma_1(z). \quad (5.1)$$

Even if the right-hand side of Eq. (5.1) is generally smaller than 1, the fact that $\rho^b > \bar{\rho}$ can give rise to $x_1^b < \bar{x}_1$; i.e., the bulk would be richer in big spheres than on average. This is what

MULTICOMPONENT FLUID OF NONADDITIVE HARD ...

PHYSICAL REVIEW E 87, 042102 (2013)

actually happens for systems A, C1, C2, D, and F. This effect is especially important in systems A and D since in those cases the right-hand side of Eq. (5.1) turns out to be larger than 1 (see Figs. 1 and 5 below for a visual confirmation). Exceptions to the property $x_1^b < \bar{x}_1$ are represented by systems B and E. In those cases, the right-hand side of Eq. (5.1) is sufficiently smaller than 1 (see Figs. 3 and 6 below) as to compensate for the ratio $\rho^b/\bar{\rho} > 1$.

Now we turn our attention to the density profiles. When presenting the theoretical RFA results for each system we have used two criteria. In the first criterion, the quantities $\bar{\rho}$ and \bar{x}_1 appearing in the theoretical scheme described in Sec. III have been identified with the average values employed in the simulations. In the second criterion, the RFA quantities $\bar{\rho}$ and \bar{x}_1 have been identified with the bulk values ρ^b and x_1^b found in the MC simulations with $L_z = 30\sigma_1$. As said before, the theoretical approach deals with formally infinite systems ($L_z \rightarrow \infty$) where the average and bulk quantities coincide. However, when making contact with simulation data corresponding to finite L_z , the use of either the average or the bulk values in the RFA may be important.

C. Nonadditive mixture and additive wall

Figure 1 shows the MC and RFA results for the two (relative) density profiles $\gamma_i(z) = \rho_i(z)/\rho_i^b$ ($i = 1, 2$) in the case of system A (positive nonadditivity). In this system $\tilde{\tau}_1 = 0.9\sigma_1 > \frac{1}{2}\sigma_1$ and $\tilde{\tau}_2 = 1.9\sigma_1 > \frac{1}{2}\sigma_2$, so that the correction term given by the second line of Eq. (3.25) is used in the RFA curves.

The inset of Fig. 1 shows the MC results for both density profiles in the whole region $0 < z < L_z = 30\sigma_1$. We can see that the separation between both hard walls is large enough as to identify a well-defined bulk region in the center. We have chosen system A to assess the influence of finite L_z by carrying out a control simulation with $L_z = 60\sigma_1$. The

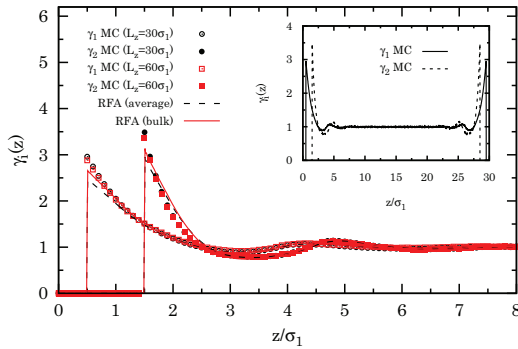


FIG. 1. (Color online) Local density profiles $\gamma_i(z) = \rho_i(z)/\rho_i^b$ for system A ($\sigma_2/\sigma_1 = 3$, $\Delta_{12} = 0.2$, $w_1 = w_2 = 0$, $\bar{x}_1 = 0.5$, $\bar{\rho}\sigma_1^3 = 1/30$). The lines represent the RFA theoretical predictions using the average values \bar{x}_1 and $\bar{\rho}$ (dashed lines) or the empirical bulk values x_1^b and ρ^b (solid lines). The symbols represent our MC simulations with $L_z/\sigma_1 = 30$ (circles) or $L_z/\sigma_1 = 60$ (squares). The inset shows the MC data in the whole domain $0 < z < L_z$ with $L_z/\sigma_1 = 30$. In the MC results, the error bars are within the size of the symbols used in the graph.

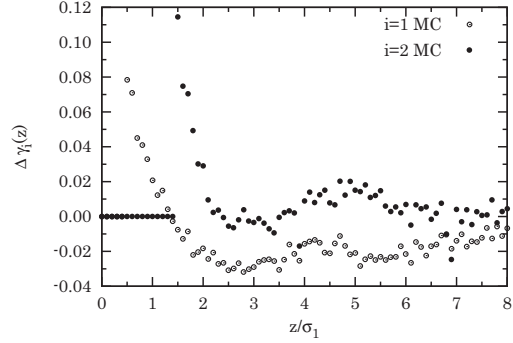


FIG. 2. Differences $\Delta\gamma_i(z) = \gamma_i(z)|_{30} - \gamma_i(z)|_{60}$ between the local densities $\gamma_i(z) = \rho_i(z)/\rho_i^b$ evaluated in MC simulations with $L_z/\sigma_1 = 30$ and those evaluated in MC simulations with $L_z/\sigma_1 = 60$ for system A ($\sigma_2/\sigma_1 = 3$, $\Delta_{12} = 0.2$, $w_1 = w_2 = 0$, $\bar{x}_1 = 0.5$, $\bar{\rho}\sigma_1^3 = 1/30$).

new bulk values are $x_1^b = 0.485$ and $\rho^b\sigma_1^3 = 0.0334$, which, as expected, are closer to the average values than in the case $L_z = 30\sigma_1$ (see Table I). As seen from Fig. 1, the MC data obtained with $L_z = 30\sigma_1$ and $L_z = 60\sigma_1$ are hardly distinguishable, except near contact where the smaller system, having a larger bulk density, presents slightly higher values of $\gamma_i(z)$. A more detailed comparison is made in Fig. 2, where the differences between the values of $\gamma_i(z)$ as obtained with both values of L_z are shown. Figure 2 confirms that the smaller system ($L_z = 30\sigma_1$) presents larger values for the two reduced densities near contact than the larger system ($L_z = 60\sigma_1$). For higher separations the differences are much less important, but yet it is interesting to note that the smaller system tends to present larger values of $\gamma_2(z)$ but smaller values of $\gamma_1(z)$.

Now let us go back to Fig. 1 and comment on the performance of the RFA. We observe that the RFA underestimates the local densities at contact (i.e., at $z = \frac{1}{2}\sigma_i$). On the other hand, the decay of the local densities near the walls and the subsequent oscillations are very well captured by the theory. It is interesting to remark that the agreement with the MC data near contact improves when the bulk values instead of the average ones are used in the theory.

The profiles for system B (negative nonadditivity) are displayed in Fig. 3. In this case $\tilde{\tau}_1 = 0.1\sigma_1$ and $\tilde{\tau}_2 = 1.1\sigma_1$. Since $\tilde{\tau}_1 < \frac{1}{2}\sigma_1$, the correction term in the second line of Eq. (3.25) vanishes. Comparison between Figs. 1 and 3 shows that, in going from system A to system B, the local variation of the density of the big spheres is enhanced, while the local density of the small spheres becomes less structured. Here there are two competing effects at play. On the one hand, at a fixed density, the change from positive to negative nonadditivity produces a weaker density structure near the wall, as the exact result to first order in density clearly shows. On the other hand, at a fixed nonadditivity, an increase in density induces a higher structure. It seems that, in the transition from system A to system B, the latter effect dominates in the case of the big spheres (which are very weakly influenced by the small component) and the former effect does

RICCARDO FANTONI AND ANDRÉS SANTOS

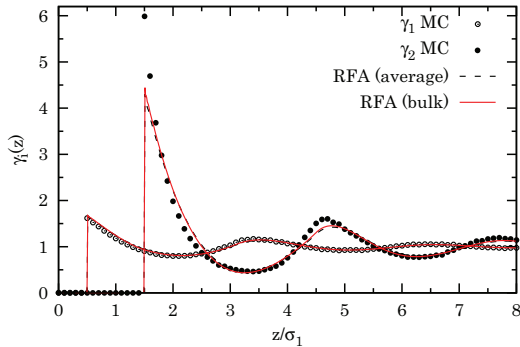
 PHYSICAL REVIEW E **87**, 042102 (2013)


FIG. 3. (Color online) Local density profiles $\gamma_i(z) = \rho_i(z)/\rho_i^b$ for system B ($\sigma_2/\sigma_1 = 3$, $\Delta_{12} = -0.2$, $w_1 = w_2 = 0$, $\bar{x}_1 = 0.5$, $\bar{\rho}\sigma_1^3 = 1/20$). The lines represent the RFA theoretical predictions using the average values \bar{x}_1 and $\bar{\rho}$ (dashed lines) or the empirical bulk values x_1^b and ρ^b (solid lines). The symbols represent our MC simulations with $L_z/\sigma_1 = 30$. In the MC results, the error bars are within the size of the symbols used in the graph.

it in the case of the small spheres (which are strongly influenced by the presence of the large component). It is interesting to note that all these features are very well described by the RFA, especially in the case of $\gamma_1(z)$. The contact value of γ_2 is better estimated in system A than in system B, while the opposite happens for the contact value of γ_1 . Note also that a small discrepancy is observed near the second peak of $\gamma_2(z)$ in Fig. 3. For this system the RFA is practically insensitive to the use of the bulk values instead of the average ones.

In systems A and B the big spheres occupy as much as 27 times more volume than the small ones, so the global properties of the mixture are dominated by species 2. A more balanced situation takes place in systems C1 and C2, where the ratio of partial packing fractions is $\bar{x}_2\sigma_2^3/\bar{x}_1\sigma_1^3 = 3$. In these cases the high concentration asymmetry requires a long simulation run time to reach thermal equilibrium for the big spheres.

The results for systems C1 and C2 are shown in Fig. 4. At the smaller density (system C1) the agreement between theory and simulation is almost perfect. As the density is doubled (system C2), some small deviations are visible, especially in the case of the big spheres. Again, the RFA with the bulk values behaves near contact better than with the average values.

D. Additive mixture and nonadditive wall

Now we consider the cases where the mixture is additive but the wall treats differently both species. The extra repulsion affects the big spheres in system D and the small spheres in system E. In both cases $\tilde{\tau}_i \leq \frac{1}{2}\sigma_i + w_i$, so that again the correction term in Eq. (3.25) does not apply.

The results for systems D and E are shown in Figs. 5 and 6, respectively. In the case of system D, there is much more room for the small spheres to sit between the wall and the big spheres than in the case of system E. As a consequence, the big spheres “feel” the presence of the wall more in the latter case than in the former and, thus, the contact value and the oscillations are more pronounced in system E. These effects are enhanced

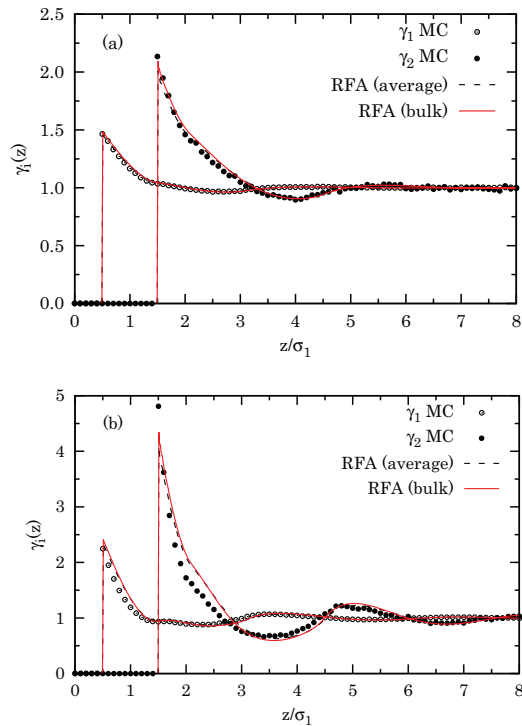


FIG. 4. (Color online) Local density profiles $\gamma_i(z) = \rho_i(z)/\rho_i^b$ for (a) system C1 ($\sigma_2/\sigma_1 = 3$, $\Delta_{12} = -0.2$, $w_1 = w_2 = 0$, $\bar{x}_1 = 0.9$, $\bar{\rho}\sigma_1^3 = 1/10$) and (b) system C2 ($\sigma_2/\sigma_1 = 3$, $\Delta_{12} = -0.2$, $w_1 = w_2 = 0$, $\bar{x}_1 = 0.9$, $\bar{\rho}\sigma_1^3 = 1/5$). The lines represent the RFA theoretical predictions using the average values \bar{x}_1 and $\bar{\rho}$ (dashed lines) or the empirical bulk values x_1^b and ρ^b (solid lines). The symbols represent our MC simulations with $L_z/\sigma_1 = 30$. In the MC results, the error bars are within the size of the symbols used in the graph.

by the larger density of system E relative to that of system D. However, $\gamma_1(z)$ near contact is higher in system D than in system E, so that the effect of wall nonadditivity compensates for the increase of density in the case of the small spheres, analogously to what happens with systems A and B (see Figs. 1 and 3). All these features are correctly accounted for by the RFA, although the quantitative agreement near contact is again worse than that after the first minimum, especially in the case of $\gamma_2(z)$. Note also that the influence on the RFA curves of the use of the bulk versus the average values is noticeable in system D but not in system E.

E. Nonadditive mixture and nonadditive wall

The more general situations where both the particle-particle and the wall-particle interactions are nonadditive is, of course, richer than the preceding classes. As a simple representative system we consider the same case as in system D (wall additionally repelling the big spheres), except that, in addition, species 1 and 2 interact with negative nonadditivity. The

MULTICOMPONENT FLUID OF NONADDITIVE HARD ...

PHYSICAL REVIEW E 87, 042102 (2013)

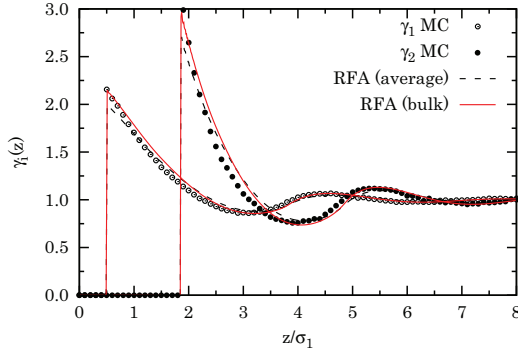


FIG. 5. (Color online) Local density profiles $\gamma_i(z) = \rho_i(z)/\rho_i^b$ for system D ($\sigma_2/\sigma_1 = 3$, $\Delta_{12} = 0$, $w_1 = 0$, $w_2/\sigma_1 = 0.35$, $\bar{x}_1 = 0.5$, $\bar{\rho}\sigma_1^3 = 1/30$). The lines represent the RFA theoretical predictions using the average values \bar{x}_1 and $\bar{\rho}$ (dashed lines) or the empirical bulk values x_1^b and ρ^b (solid lines). The symbols represent our MC simulations with $L_z/\sigma_1 = 30$. In the MC results, the error bars are within the size of the symbols used in the graph.

resulting system F (see Table I) is also close to system B, except that now the wall is nonadditive and the density is smaller. As in systems B–E, the correction term in Eq. (3.25) is not needed.

The local densities for system F are plotted in Fig. 7. Comparison with Fig. 5 shows that the density profile of the big spheres is practically unaffected by the nonadditive character of the 1-2 interaction. This is not surprising taking into account that, as said before, the big spheres occupy 27 times more volume than the small ones and, therefore, the presence of the latter has little impact on the properties of the former. On the contrary, the nonadditivity has a large influence on the local density profile $\gamma_1(z)$. Since spheres of species 1 and

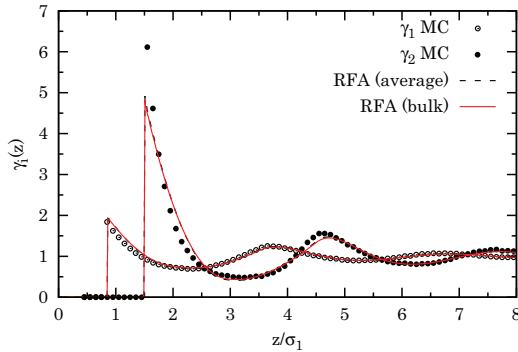


FIG. 6. (Color online) Local density profiles $\gamma_i(z) = \rho_i(z)/\rho_i^b$ for system E ($\sigma_2/\sigma_1 = 3$, $\Delta_{12} = 0$, $w_1/\sigma_1 = 0.35$, $w_2 = 0$, $\bar{x}_1 = 0.5$, $\bar{\rho}\sigma_1^3 = 1/20$). The lines represent the RFA theoretical predictions using the average values \bar{x}_1 and $\bar{\rho}$ (dashed lines) or the empirical bulk values x_1^b and ρ^b (solid lines). The symbols represent our MC simulations with $L_z/\sigma_1 = 30$. In the MC results, the error bars are within the size of the symbols used in the graph.

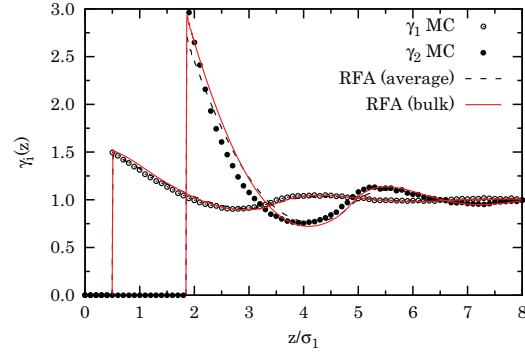


FIG. 7. (Color online) Local density profiles $\gamma_i(z) = \rho_i(z)/\rho_i^b$ for system F ($\sigma_2/\sigma_1 = 3$, $\Delta_{12} = -0.2$, $w_1 = 0$, $w_2/\sigma_1 = 0.35$, $\bar{x}_1 = 0.5$, $\bar{\rho}\sigma_1^3 = 1/30$). The lines represent the RFA theoretical predictions using the average values \bar{x}_1 and $\bar{\rho}$ (dashed lines) or the empirical bulk values x_1^b and ρ^b (solid lines). The symbols represent our MC simulations with $L_z/\sigma_1 = 30$. In the MC results, the error bars are within the size of the symbols used in the graph.

2 can overlap to a certain degree in system F, the big spheres partially alleviate the influence of the wall on the small spheres with respect to the case of system D. As a consequence, the local density of the small spheres is less structured in system F than in system D. Like in system D, the RFA performs very well in system F, especially when the bulk values are used.

VI. CONCLUSIONS

In this work we have developed a simple analytical (in Laplace space) nonperturbative theory for the local density profiles of a multicomponent fluid of NAHS confined by an additive or nonadditive hard wall. The theoretical approach is based on the specialization of the RFA technique recently proposed [28] to the case where an extra single particle of diameter σ_0 is added to the mixture and then the limit of an infinite diameter $\sigma_0 \rightarrow \infty$ is taken. The RFA reduces to the exact solution of the PY approximation for zero nonadditivity, both in the particle-particle and in the particle-wall interactions, but remains analytical even when nonadditivity prevents one from obtaining an analytical solution of the PY theory.

While the theory applies to any number of components, we have focused on a binary mixture with a size ratio 1:3 plus a hard wall. This has allowed us to compare the theoretical results against exact MC simulation. Several representative scenarios have been considered (see Table I): a positive (system A) or negative (systems B, C1, and C2) NAHS fluid with an additive wall, an AHS mixture with a nonadditive wall pushing either the big (system D) or the small (system E) spheres, and a NAHS mixture with a nonadditive wall (system F). In all the cases, a reasonably good agreement between our theory and the MC simulations have been found for the (relative) partial local densities $\gamma_i(z)$. The agreement is worse near contact, where the RFA underestimates the MC values, but rapidly tends to improve for larger distances, so that the initial decay of the local densities and the subsequent oscillations are

RICCARDO FANTONI AND ANDRÉS SANTOS

 PHYSICAL REVIEW E **87**, 042102 (2013)

rather well captured. Note that, since the RFA can be seen as a sort of continuation of the AHS PY solution to the NAHS realm [28], it is not surprising that some of the features of the PY solution remain. One of those features is the underestimation of the contact values [13]. Another PY feature, namely the possibility of predicting a negative first minimum at sufficiently high densities, is also inherited by the RFA.

As shown by Figs. 1 and 3–7, the performance of the RFA is usually better in the case of the small spheres ($i = 1$) than for the large spheres ($i = 2$). This is in part due to the physical observation that the local density structure of species 1 is milder than that of species 2. Another technical reason has to do with the fact that, while the separation between both walls is sufficiently large for the spheres near a wall not to be much influenced by the presence of the other wall, the unavoidable “compression” effect is more important for the big spheres ($L_z/\sigma_2 = 10$) than for the small spheres ($L_z/\sigma_1 = 30$). As Fig. 2 illustrates, when the separation between both walls is doubled, the effect on the density near the walls is more pronounced for the big spheres than for the small ones. Finite-size effects are also related to the small differences between the average densities and their bulk values in the central region $z \approx L_z/2$. We have checked that our theoretical approach exhibits a slightly better agreement with simulations when the empirical bulk values are used instead of the average values.

Our theory, being a simple analytical one, can be efficiently used to easily extract many-body approximate properties for confined fluids under other interesting situations different from the representative ones examined in this work. For instance, extreme cases like the Widom-Rowlinson [44–46] ($\sigma_1 = \sigma_2 = 0$ with σ_{12} finite) or the Asakura-Oosawa [47,48] ($\sigma_1 = 0$ and $\Delta_{12} > 0$) confined fluids can be studied. Another avenue for application of the RFA is the depletion potential between two big spheres immersed in a sea of small spheres [49] interacting nonadditively with them.

ACKNOWLEDGMENTS

The authors are grateful to the referees for suggestions contributing to the improvement of the paper. R.F. would like to acknowledge the use of the computational facilities of CINECA through the ISCRA call. A.S. acknowledges support from the Ministerio de Ciencia e Innovación (Spain) through Grant No. FIS2010-16587 and the Junta de Extremadura (Spain) through Grant No. GR10158, partially financed by Fondo Europeo de Desarrollo Regional (FEDER) funds.

APPENDIX: EVALUATION OF $\tilde{L}_i(s)$ AND $\tilde{A}_j(s)$

Let us recall that $\sigma_{j0} = \frac{1}{2}(\sigma_j + \sigma_0) + w_j$ with $w_j \geq 0$. Therefore, according to Eq. (3.6), $b_{i0} = \sigma_i + w_i$. Thus, Eqs. (3.10)–(3.12) yield

$$\Lambda_0 = \frac{\sigma_0}{2}M_{2,0} + \frac{1}{6}M_{3,0} + \frac{1}{2}M_{2,1}, \quad (\text{A1})$$

$$\Psi_0 = -\frac{\sigma_0}{2}M_{2,0} + \frac{1}{6}M_{3,0} - \frac{1}{2}M_{2,1}, \quad (\text{A2})$$

$$\Omega_0 = -\frac{\sigma_0^2}{4}M_{2,0} - \frac{\sigma_0}{2}M_{2,1} - \frac{1}{4}M_{2,2}, \quad (\text{A3})$$

where

$$M_{p,q} \equiv \sum_{k=1}^n \bar{x}_k (\sigma_k + w_k)^p w_k^q, \quad q \geq 0. \quad (\text{A4})$$

Interestingly enough, the terms proportional to σ_0 and to σ_0^2 in the denominator of Eqs. (3.8) and (3.9) cancel, so that the denominator becomes

$$\tilde{D} \equiv \left(1 - \frac{\pi}{6}\bar{\rho}M_{3,0}\right)^2 - \frac{\pi^2}{4}\bar{\rho}^2(M_{2,1}^2 - M_{2,0}M_{2,2}). \quad (\text{A5})$$

Equations (A1)–(A5) apply to any value of σ_0 . From Eqs. (3.7)–(3.9) it is easy to see that both $L_{i0}^{(0)}$ and $L_{i0}^{(1)}$ are linear functions of σ_0 . Thus, taking the limit (3.23) one gets

$$\tilde{L}_i(s) = \tilde{L}^{(0)} + \tilde{L}_i^{(1)}s \quad (\text{A6})$$

with

$$\tilde{L}^{(0)} = \frac{\pi\bar{\rho}M_{2,0}}{2\tilde{D}}, \quad (\text{A7})$$

$$\tilde{L}_i^{(1)} = \frac{1}{2\tilde{D}} \left[1 - \frac{\pi}{6}\bar{\rho}(M_{3,0} + 3M_{2,1}) + \left(\frac{\sigma_i}{2} + w_i\right)\pi\bar{\rho}M_{2,0} \right]. \quad (\text{A8})$$

Analogously, from Eqs. (3.3) and (3.5), the limit (3.24) becomes

$$\tilde{A}_j(s) = \frac{2\pi\bar{\rho}\bar{x}_j}{s^3} e^{\sigma_j s/2} [\tilde{N}_j(s) - \tilde{L}_j(s)e^{-(\sigma_j + w_j)s}], \quad (\text{A9})$$

where

$$\begin{aligned} \tilde{N}_j(s) = & \tilde{L}^{(0)} \left[1 - (\sigma_j + w_j)s + \frac{(\sigma_j + w_j)^2 s^2}{2} \right] \\ & + \tilde{L}_j^{(1)} s [1 - (\sigma_j + w_j)s]. \end{aligned} \quad (\text{A10})$$

- [1] D. Henderson, F. F. Abraham, and J. A. Barker, *Mol. Phys.* **31**, 1291 (1976).
 [2] D. Henderson, *J. Chem. Phys.* **68**, 780 (1978).
 [3] M. Plischke and D. Henderson, *J. Phys. Chem.* **88**, 6544 (1984).
 [4] M. Plischke and D. Henderson, *J. Chem. Phys.* **84**, 2846 (1985).
 [5] D. Henderson, K.-Y. Chan, and L. Degréve, *J. Chem. Phys.* **101**, 6975 (1994).
 [6] R. Dickman, P. Attard, and V. Simonian, *J. Chem. Phys.* **107**, 205 (1997).
 [7] W. Olivares-Rivas, L. Degréve, D. Henderson, and J. Quintana, *J. Chem. Phys.* **106**, 8160 (1997).
 [8] J. Noworyta, D. Henderson, S. Sokolowski, and J.-Y. Chan, *Mol. Phys.* **95**, 415 (1998).
 [9] Z. Tan, U. Marini Bettolo Marconi, F. van Swol, and K. E. Gubbins, *J. Chem. Phys.* **90**, 3704 (1989).
 [10] I. K. Snook and D. Henderson, *J. Chem. Phys.* **68**, 2134 (1978).
 [11] L. Degréve and D. Henderson, *J. Chem. Phys.* **100**, 1606 (1993).
 [12] M. Rottureau, T. Nicolai, and J. C. Gimel, *Eur. Phys. J. E* **18**, 37 (2005).

- [13] A. Malijevský, S. B. Yuste, A. Santos, and M. López de Haro, *Phys. Rev. E* **75**, 061201 (2007).
- [14] C. N. Patra and S. K. Ghosh, *J. Chem. Phys.* **106**, 2762 (1997).
- [15] C. N. Patra, *J. Chem. Phys.* **111**, 6573 (1999).
- [16] R. Roth and S. Dietrich, *Phys. Rev. E* **62**, 6926 (2000).
- [17] S. Zhou and E. Ruckenstein, *J. Chem. Phys.* **112**, 5242 (2000).
- [18] S. Zhou, *Phys. Rev. E* **63**, 061206 (2001).
- [19] N. Choudhury and S. K. Ghosh, *J. Chem. Phys.* **114**, 8530 (2001).
- [20] C. N. Patra and S. K. Ghosh, *J. Chem. Phys.* **116**, 8509 (2002).
- [21] C. N. Patra and S. K. Ghosh, *J. Chem. Phys.* **116**, 9845 (2002).
- [22] C. N. Patra and S. K. Ghosh, *J. Chem. Phys.* **117**, 8933 (2002).
- [23] C. N. Patra and S. K. Ghosh, *J. Chem. Phys.* **118**, 3668 (2003).
- [24] Y. Duda, E. Vakarin, and J. Alejandre, *J. Colloid Interface Sci.* **258**, 10 (2003).
- [25] A. Patrykiewicz, S. Sokołowski, and O. Pizio, *J. Phys. Chem. B* **109**, 14227 (2005).
- [26] F. Jiménez-Ángeles, Y. Duda, G. Odriozola, and M. Lozada-Cassou, *J. Phys. Chem. C* **112**, 18028 (2008).
- [27] P. Hopkins and M. Schmidt, *Phys. Rev. E* **83**, 050602 (2011).
- [28] R. Fantoni and A. Santos, *Phys. Rev. E* **84**, 041201 (2011). Note that in Eq. (2.12) the hats on the partial correlation functions should be replaced by tildes.
- [29] S. Bravo Yuste, M. López de Haro, and A. Santos, *Phys. Rev. E* **53**, 4820 (1996).
- [30] M. López de Haro, S. B. Yuste, and A. Santos, in *Theory and Simulation of Hard-Sphere Fluids and Related Systems*, edited by A. Mulero, Vol. 753 of Lectures Notes in Physics (Springer-Verlag, Berlin, 2008), pp. 183–245.
- [31] J.-P. Hansen and I. R. McDonald, *Theory of Simple Liquids* (Academic Press, London, 2006).
- [32] R. Fantoni and G. Pastore, *J. Chem. Phys.* **119**, 3810 (2003).
- [33] A. González, J. A. White, F. L. Román, and S. Velasco, *J. Chem. Phys.* **135**, 154704 (2011).
- [34] Z. W. Salsburg, R. W. Zwanzig, and J. G. Kirkwood, *J. Chem. Phys.* **21**, 1098 (1953).
- [35] J. L. Lebowitz and D. Zomick, *J. Chem. Phys.* **54**, 3335 (1971).
- [36] M. Heying and D. S. Corti, *Fluid Phase Equilib.* **220**, 85 (2004).
- [37] A. Santos, *Phys. Rev. E* **76**, 062201 (2007).
- [38] J. L. Lebowitz, *Phys. Rev.* **133**, A895 (1964).
- [39] S. B. Yuste, A. Santos, and M. López de Haro, *J. Chem. Phys.* **108**, 3683 (1998).
- [40] R. D. Rohrmann and A. Santos, *Phys. Rev. E* **83**, 011201 (2011).
- [41] R. D. Rohrmann and A. Santos, *Phys. Rev. E* **84**, 041203 (2011).
- [42] J. Abate and W. Whitt, *Queueing Systems* **10**, 5 (1992).
- [43] D. Henderson and P. J. Leonard, *Proc. Natl. Acad. Sci. USA* **67**, 1818 (1970).
- [44] B. Widom and J. Rowlinson, *J. Chem. Phys.* **15**, 1670 (1970).
- [45] D. Ruelle, *Phys. Rev. Lett.* **16**, 1040 (1971).
- [46] R. Fantoni and G. Pastore, *Physics A* **332**, 349 (2004). Note that there is a misprint in Eq. (13), which should read $\tilde{h}_{12}(k) = \tilde{c}_{12}(k)[1 - \rho_1 \rho_2 \tilde{c}_{12}^2(k)]^{-1}$.
- [47] S. Asakura and F. Oosawa, *J. Chem. Phys.* **22**, 1255 (1954).
- [48] S. Asakura and F. Oosawa, *J. Polym. Sci.* **33**, 183 (1958).
- [49] S. B. Yuste, A. Santos, and M. López de Haro, *J. Chem. Phys.* **128**, 134507 (2008).

Chapter 38

Monte Carlo simulation of the nonadditive restricted primitive model of ionic fluids: Phase diagram and clustering

Fantoni R. and Pastore G., Phys. Rev. E **87**, 052303 (2013)

Title: “Monte Carlo simulation of the nonadditive restricted primitive model of ionic fluids: Phase diagram and clustering”

Abstract: We report an accurate Monte Carlo calculation of the phase diagram and clustering properties of the restricted primitive model with non-additive hard-sphere diameters. At high density the positively non-additive fluid shows more clustering than the additive model and the negatively non-additive fluid shows less clustering than the additive model, at low density the reverse scenario appears. A negative nonadditivity tends to favor the formation of neutrally charged clusters starting from the dipole. A positive nonadditivity favors the pairing of like ions at high density. The critical point of the gas-liquid phase transition moves at higher temperatures and higher densities for a negative nonadditivity and at lower temperatures and lower densities for a positive nonadditivity. The law of corresponding states does not seem to hold strictly. Our results can be used to interpret recent experimental works on room temperature ionic liquids.

Appeared on the Kaleidoscope of PRE on the month of May:

<http://pre.aps.org/kaleidoscope/pre/87/5/052303>

PHYSICAL REVIEW E **87**, 052303 (2013)

Monte Carlo simulation of the nonadditive restricted primitive model of ionic fluids: Phase diagram and clustering

Riccardo Fantoni*

Dipartimento di Scienze dei Materiali e Nanosistemi, Università Ca' Foscari Venezia, Calle Larga S. Marta DD2137, I-30123 Venezia, Italy

Giorgio Pastore†

Dipartimento di Fisica, Università degli Studi di Trieste, Strada Costiera 11, 34151 Trieste, Italy and IOM, CNR, Strada Costiera 11, 34151 Trieste, Italy

(Received 26 September 2012; revised manuscript received 19 March 2013; published 13 May 2013)

We report an accurate Monte Carlo calculation of the phase diagram and clustering properties of the restricted primitive model with nonadditive hard-sphere diameters. At high density the positively nonadditive fluid shows more clustering than in the additive model and the negatively nonadditive fluid shows less clustering than in the additive model; at low density the reverse scenario appears. A negative nonadditivity tends to favor the formation of neutrally charged clusters starting from the dipole. A positive nonadditivity favors the pairing of like ions at high density. The critical point of the gas-liquid phase transition moves at higher temperatures and higher densities for a negative nonadditivity and at lower temperatures and lower densities for a positive nonadditivity. The law of corresponding states does not seem to hold strictly. Our results can be used to interpret recent experimental works on room temperature ionic liquids.

DOI: [10.1103/PhysRevE.87.052303](https://doi.org/10.1103/PhysRevE.87.052303)

PACS number(s): 64.70.pv, 68.43.Hn, 61.20.Qg, 64.60.ah

I. INTRODUCTION

Ionic soft matter [1] is a class of conventional condensed soft matter [2–8] with prevailing contribution from electrostatics, in many cases crucially affecting its physical properties. Among the most popular representatives of such a class of materials are natural and synthetic saline environments, such as aqueous and nonaqueous electrolyte solutions and molten salts as well as a variety of polyelectrolytes and colloidal suspensions. Equally well known are many biologically important proteins.

The simplest theoretical model for ionic colloidal suspensions is the restricted primitive model (RPM) [9], a binary mixture of uniformly charged hard spheres of diameter σ : two species of opposite charge $\pm q$ and equal concentrations to ensure charge neutrality, moving in a medium of fixed dielectric constant ϵ . The phase diagram properties of this model have been widely studied both through analytical theories [10–22] and within computer experiments starting from the seminal works of Friedman and Larsen [23] and Vorontsov-Veliaminov and co-workers [24,25], followed by the pioneering Gibbs ensemble Monte Carlo calculation of Panagiotopoulos [26] and by other numerical simulations [27–34]. The more general primitive model with asymmetry in ion charge [35], ion size [36–38], and both ion charge and size [37,39] has also been studied.

From these studies emerged how, in the vapor phase, an important role is played by association and clustering. In a previous work [40] one of us studied a modified RPM fluid where one allows for size nonadditivity particle diameters. Controlling the nonadditivity, it was suggested through the use of integral equation theories that such a fluid might have a complex behavior due to the possible competition

between clustering tendency due to the Coulomb interaction and demixing tendency due to entropic advantage driven by the nonadditivity. Thus the nonadditivity of the hard-sphere diameters does not destroy the simplifying symmetry of the model, but enriches the properties of the pure RPM, making it a paradigm for the self-assembly of isotropic particles and a challenge to present day theories of fluids. In real systems, the degree of nonadditivity might be directly related to the anion-cation contact-pairing affinity [41], which in turn may be mediated by the solvent.

It is the purpose of this paper to reconsider such a model fluid from the point of view of accurate numerical experiments. In particular, we want to study the clustering properties of the fluid outside the gas-liquid coexistence region. To this aim we determine the gas-liquid coexistence curve through the Gibbs ensemble method after having studied semiquantitatively how the coexistence region changes with the nonadditivity through a density distribution analysis in the canonical ensemble. This way we could be sure that our cluster analysis falls outside the coexistence region in all the cases studied. Clustering turns out to be greatly affected by the nonadditivity parameter, the most striking effect being the prevalence of neutrally charged clusters made up of an even number of particles in the negatively nonadditive fluid. When the nonadditivity allows complete overlap of the two species of particles, the formation of a fluid of neutral hard spheres of half the density is expected and our simulation results clearly show this behavior. In contrast, for a positive nonadditivity, it is known that the neutral hard-sphere mixture tends to demix the two species and the demixing critical density decreases as the nonadditivity increases [42–47]. We expect this property of the neutral system to have some interesting effect on the clustering properties of the charged fluid since demixing cannot occur in a binary charged system: The frustrated tendency to segregate like particles and the reduced space available to the ions favor pairing of like ions and percolating clusters at high densities. Preliminary results from our analysis are presented

*rfantoni@ts.infn.it

†pastore@ts.infn.it

RICCARDO FANTONI AND GIORGIO PASTORE

 PHYSICAL REVIEW E **87**, 052303 (2013)

in [48]; here we extend that analysis and present the gas-liquid binodal of the fluid as a function of the nonadditivity parameter.

The model fluid considered in this paper may be realized experimentally through a colloid-star polymer mixture where both species are charged [49,50] or by room temperature ionic liquids [51–54] as discussed in Sec. III C2. In particular in the latter systems, liquid-liquid binodals shifted above and below the one of the pure RPM are observed, depending on the kind of solvent used. If, on the one hand, this can be ascribed to the different dielectric constant of the solvent [52], on the other hand, it is clear that, depending on the kind of solvent, the anion-cation contact-pairing affinity may vary [41] and thus the different experimental ionic liquids should be more correctly described by comparison not just with the pure RPM, but with the more realistic primitive model with the addition of either a positive or negative size nonadditivity.

The paper is organized as follows. In Sec. II the model for the fluid we want to study is described. In Sec. III the results from the numerical experiments are reported. These are divided into a cluster analysis in Sec. III A, an analysis of the radial distribution function and structure factor in Sec. III B, and an analysis of the gas-liquid coexistence in Sec. III C. Theoretical remarks on the clustering properties are presented in Sec. IV. We summarize in Sec. V.

II. MODEL

The model fluid we want to study is the restricted primitive model of nonadditive hard spheres. The RPM consists of $N/2$ uniformly charged hard spheres of species 1 of diameter σ carrying a total charge $+q$ each and $N/2$ uniformly charged hard spheres of species 2 of the same diameter carrying a total charge $-q$ each. The spheres are moving in a dielectric continuum of dielectric constant ϵ independent of the thermodynamic state. The interaction between an ion of species i and one of species j a distance r apart is given by

$$\beta\phi_{ij}(r) = \begin{cases} +\infty, & r \leq \sigma_{ij} \\ \frac{q_i q_j}{k_B T \epsilon r}, & r > \sigma_{ij} \end{cases} \quad (2.1)$$

for $i, j = 1, 2$, where $\beta = 1/k_B T$, with T the absolute temperature and k_B the Boltzmann constant, and q_i is the charge of an ion of species i . The ions form a mixture of nonadditive hard spheres, i.e.,

$$\sigma_{ij} = \begin{cases} \sigma, & i = j \\ \sigma(1 + \Delta), & i \neq j \end{cases} \quad (2.2)$$

for $i, j = 1, 2$, with the nonadditivity parameter $\Delta > -1$. A thermodynamic state is completely specified by the reduced density $\rho^* = \rho\sigma^3 = N\sigma^3/V$, where V is the volume containing the fluid, the reduced temperature $T^* = k_B T \epsilon \sigma / q^2$ ($q^2/\epsilon\sigma$ is taken as the unit of energy), and the nonadditivity parameter Δ . We will call $x_1 = \rho_-/\rho = 1/2$ and $x_2 = \rho_+/\rho = 1/2$ the anions and cations molar concentrations, respectively.

III. RESULTS

In Fig. 1 we show the phase diagram of the pure RPM fluid, $\Delta = 0$, as obtained from the Gibbs ensemble Monte Carlo

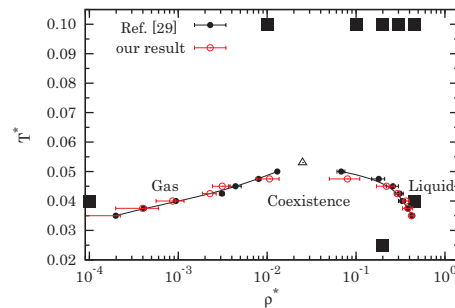


FIG. 1. (Color online) Diagram showing the gas-liquid coexistence curve of the RPM fluid from the Gibbs ensemble MC data of Ref. [29] (closed circles) and ours (open circles), the triangle being the critical point, and the points (closed squares) of the phase diagram where we run our NVT MC simulations.

method by Orkoulas and Panagiotopoulos [29] and by us (see Sec. III C2). The thermodynamic points where we probe the fluid with our NVT Monte Carlo simulations are also shown as closed squares.

In our canonical NVT Monte Carlo (MC) we study the fluid in a simulation box of volume $V = L^3$ with periodic boundary conditions. The long range of the $1/r$ interaction is accounted for using an Ewald sum for the interacting energy in the periodic system [55]. The interaction energy per unit box for $\epsilon = 1$ is calculated as

$$\begin{aligned} \mathcal{U} = & \sum_{\mu < \nu} \sum_{\mathbf{n}} q_{i_\mu} q_{j_\nu} \frac{\text{erfc}(\kappa |\mathbf{r}_{\mu\nu} + L\mathbf{n}|)}{|\mathbf{r}_{\mu\nu} + L\mathbf{n}|} \\ & + \frac{2\pi}{L^3} \sum_{\mathbf{k} \neq \mathbf{0}} \frac{e^{-(k/2\kappa)^2}}{k^2} |\rho_{\mathbf{k}}|^2 - \frac{\kappa}{\sqrt{\pi}} \sum_{\mu} q_{i_\mu}^2 \\ & - \frac{\pi}{2\kappa^2 L^3} \left(\sum_{\mu} q_{i_\mu} \right)^2, \end{aligned} \quad (3.1)$$

where a roman index with a greek subindex denotes the species of the particle labeled by the greek subindex, $\mathbf{r}_{\mu\nu} = \mathbf{r}_\nu - \mathbf{r}_\mu$ with \mathbf{r}_μ the position of particle μ , $\rho_{\mathbf{k}} = \sum_{\mu} q_{i_\mu} e^{-i\mathbf{k}\cdot\mathbf{r}_\mu}$, erfc denotes the complementary error function, $\mathbf{n} = (n_x, n_y, n_z)$ with $n_x, n_y, n_z = 0, \pm 1, \pm 2, \dots$, and $\mathbf{k} = (2\pi/L)(n_x, n_y, n_z)$ are reciprocal lattice vectors. The parameter κ that governs the rate of convergence of the real space and reciprocal space contribution to the energy is taken to be $\kappa \sim 5/L$. With this value of κ , the real space contribution can be restricted to the first term $\mathbf{n} = \mathbf{0}$ only. The reciprocal space term includes all \mathbf{k} vectors such that $n_x^2 + n_y^2 + n_z^2 < 27$. The last term in Eq. (3.1) is zero for the RPM, but it is important in the Gibbs ensemble simulation where a particle exchange between the two boxes can produce systems where there is an unequal number of positive and negative charges. Our choice for the interaction energy takes into account the fact that each charge has a uniform background of neutralizing opposite charge density.

In our NVT MC simulations we used $N = 100$ (except for the test of the size dependence of the clustering analysis, where we considered up to 5000 particles), the acceptance ratio is kept, on average, close to 50% after a preliminary adjustment

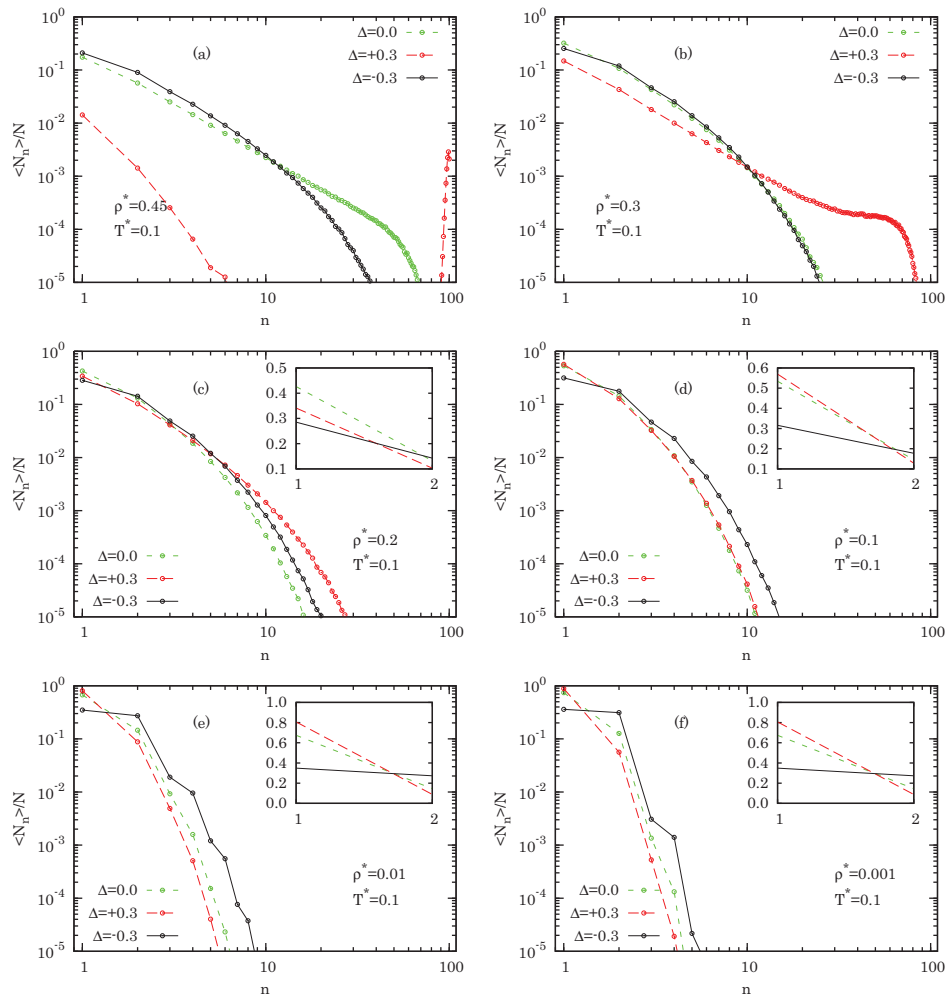


FIG. 2. (Color online) Clustering properties of the fluid at $T^* = 0.1$ at various values of nonadditivity. The N_n are the numbers of clusters made of n particles. In the MC simulations we used $N = 100$ particles and 1×10^7 MCS. The panels are ordered (left to right, top to bottom) in order of decreasing density: $\rho^* = 0.45$ (a), 0.3 (b), 0.2 (c), 0.1 (d), 0.01 (e), and 0.001 (f). The insets allow one to read off the degree of dissociation.

of the maximum particle displacement. We start from a simple cubic configuration of two crystals, one made of species 1 and one made of species 2, juxtaposed in order to avoid overlaps at high densities. We need around 10^5 MC steps (MCS) in order to equilibrate the samples and 10^6 MCS/particle for the statistics.

A. Cluster analysis

During the simulation we perform a cluster analysis. After each 100 MCS we determine the number N_n of clusters made of n particles so that $\sum_n n N_n = N$. We assume [56,57] that a

group of ions forms a cluster if the distance r , calculated using periodic boundary conditions, between a particle of species i of the group and at least one other particle of species j is less than some fixed value, i.e., $r < \sigma_{ij} + \delta^c \sigma$, where δ^c is a parameter.¹ In all our simulations we choose $\delta^c = 0.1$ (in Ref. [30] a detailed study of the sensitivity of the clustering properties

¹Many different ways of defining a cluster have been proposed [12,16,58–60] since the Bjerrum theory [61] of ionic associations first appeared. Our choice corresponds to the one of Gillan [12] and Caillol and Weis [30].

RICCARDO FANTONI AND GIORGIO PASTORE

 PHYSICAL REVIEW E **87**, 052303 (2013)

to this parameter is carried out for the pure RPM fluid). Then we take the average of these numbers $\langle N_n \rangle$. Note that $Q_n = n \langle N_n \rangle / N$ gives the probability that a particle belongs to a cluster of size n . To establish a criterion for percolation we first find the clusters without employing periodic boundary conditions to calculate the distances and then we check whether, among the particles of any of these clusters, there are two that satisfy the cluster condition calculating the distances using periodic boundary conditions. Whenever we find one such cluster the cluster is percolating.

In Fig. 2 we show the results of such an analysis for the fluid at a temperature $T^* = 0.1$ well above the critical temperature $T_c^* \approx 0.05$ of the pure RPM [31,33,34]. In the insets we show a magnification of the region around $n = 1$ from which the degree of dissociation [19,22] $\alpha = \langle N_1 \rangle / N$ can be read off. In the figure we plot the cluster concentrations $\langle N_n \rangle / N$ as a function of the number of particles n in the cluster. We plot n from $n = 1$ (isolated ions) up to $n = N$ (in this case all the particles of the fluid form one big percolating cluster). At $\rho^* = 0.45$ both the pure RPM and the $\Delta = 0.3$ fluid form percolating clusters. Lowering the density, we first reach a state at $\rho^* = 0.3$ where the negative nonadditivity gives the same clustering of the RPM and the positive nonadditivity gives bigger clustering (still with percolating clusters), then a state at $\rho^* = 0.1$ where the positive nonadditivity gives the same clustering of the RPM and the negative nonadditivity a bigger one, and finally a state $\rho^* = 0.01, 0.001$ at low densities where a negative nonadditivity increases the clustering over the RPM fluid and a positive nonadditivity diminishes it. Generally, at high densities we find percolating clusters in the fluids, whereas these disappear at low densities even at a positive nonadditivity. Summarizing, in agreement with Ref. [40], we find, for the fixed values of $|\Delta|$, that at high density and positive Δ we have more clustering than in the additive model since there is a smaller effective volume for the particles, at high density and negative Δ we have less clustering than in the additive model because there is more effective volume for the particles, at low density and positive Δ we have less clustering than in the additive model due to the competition between the tendency to demixing in the corresponding neutral mixture and the tendency to local electroneutrality of the Coulombic systems, and at low densities and negative Δ we have more clustering than in the additive model because neutral clusters are favored, as shown in the next section. We conclude that at high temperature and high density the negative nonadditivity gives lower clustering than in the RPM and by lowering the temperature at constant density or lowering the density at constant temperature it gradually tends to give higher clustering than in the RPM. In contrast, at low density the positive nonadditivity gives lower clustering than in the RPM and by increasing the density it gradually tends to give larger clustering than in the RPM.

We determine the size dependence of the curves shown in Fig. 2 and see that when we have no percolating clusters, for example, the data at $T^* = 0.1, \rho^* = 0.3$, and $\Delta = 0, -0.3$, the curves were unaffected by the choice of a higher number of particles, while when we have percolating clusters, for example, the data at $T^* = 0.1, \rho^* = 0.3$, and $\Delta = 0.3$, the curve $(n, \langle N_n \rangle / N)$ changes with N . In these latter cases we find that a common curve is given by $(x, \langle N_x \rangle / N)$ with $x = n/N \in [0, 1]$.

TABLE I. Fitting parameters a and b in the least-squares fit $\langle N_n \rangle / N = a^n n^{bn} / n!$ for the simulation results of Fig. 2 without percolating clusters (and with the exclusion of the nonsmooth data at $\rho^* = 0.001$). The reduced χ^2 is around 0.5 with greater error approaching $n = 1$. Also shown is the number of particles n_{\max} in the biggest cluster formed in each simulation.

ρ^*	Δ	a	b	n_{\max}
0.45	-0.3	0.220(3)	1.074(4)	64
0.3	0	0.197(4)	1.084(6)	45
0.3	-0.3	0.204(3)	1.069(5)	43
0.2	0	0.206(7)	1.00(1)	23
0.2	0.3	0.200(4)	1.083(5)	45
0.2	-0.3	0.204(7)	1.04(1)	31
0.1	0	0.22(2)	0.86(3)	15
0.1	0.3	0.16(1)	1.01(4)	19
0.1	-0.3	0.15(1)	1.11(2)	29
0.01	0	0.41(7)	0.1(1)	8
0.01	0.3	0.36(8)	0.0(2)	7
0.01	-0.3	0.23(4)	0.72(7)	12

Then, in order to satisfy the normalization condition $1 = \sum_n n \langle N_n \rangle / N \approx \int dx x N^2 \langle N_x \rangle / N$, we must have for two different sizes N' and N'' that $(\langle N_x \rangle / N') / (\langle N_x \rangle / N'') \approx (N'' / N')^2$. We have no general formula to determine when the former behavior is to be expected over the latter. We can only say that the first behavior is generally observed when we do not have percolating clusters, whereas the second is present when we have percolating clusters. In Sec. IV we show that the size-independent curves that we find when there are no percolating clusters can be fitted by $\langle N_n \rangle / N = a^n n^{bn} / n!$ [see Eq. (4.4) with z_n^{intra} obtained from an ideal cluster approximation], with a and b positive fitting parameters. In Table I we show the fitting parameters a and b corresponding to the simulated cases.

In Fig. 3 we show the clustering analysis at the thermodynamic state below the critical temperature of the RPM $T^* = 0.04$ in the gas phase $\rho^* = 5 \times 10^{-5}$ and in the liquid phase $\rho^* = 0.45$. We see how in the gas phase only the first few clusters are present, in agreement with similar results found in Ref. [30], and for a negative nonadditivity the dipoles are clearly the preferred kind of clusters with the smallest degree of dissociation among the three fluids considered. In the liquid phase all three fluids have percolating clusters.

In Fig. 4 we show the clustering analysis for the fluid with Δ approaching -1 at $T^* = 0.1$ and $\rho^* = 0.45$. We see how by letting Δ approach -1 this stabilizes the neutrally charged clusters and lowers the degree of dissociation. The first stable cluster is the dipole: the “overlap” of a positive and a negative sphere. These are dipoles of moment qr_{12} , with $r_{12} < \sigma(1 + \Delta + \delta^c)$, which may lack a gas-liquid criticality [62]. We clearly have a transition from a conducting to an insulating phase as Δ goes from 0 to -1 .

In Fig. 5 we show a snapshot of the equilibrated fluid at $T^* = 0.1, \rho^* = 0.45$, and $\Delta = -0.9$ from which one can see the formation of the dipoles. We expect that in the limiting case of $\Delta = -1$ the fluid we obtain is well reproduced by hard spheres at half the density. This is confirmed by a comparison of the like radial distribution functions with the one of the

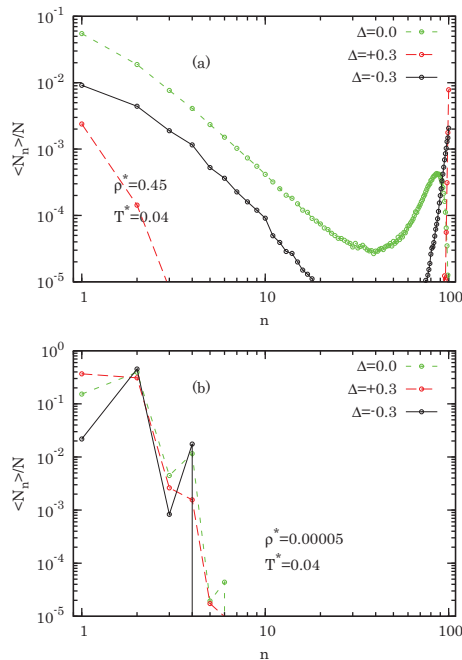


FIG. 3. (Color online) Clustering properties of the fluid at $T^* = 0.04$ and (a) $\rho^* = 0.45$ and (b) $\rho^* = 5 \times 10^{-5}$ at various values of nonadditivity. The N_n are the numbers of clusters made of n particles. In the MC simulations we used $N = 100$ particles and 1×10^7 MCS.

hard spheres even if the $\Delta = -1$ fluid simulation rapidly slows down into the frozen configuration of the overlapping anions and cations. In order to overcome this problem one should alternate single-particle moves and cluster moves where one moves the center of mass of the neutrally charged pairs.

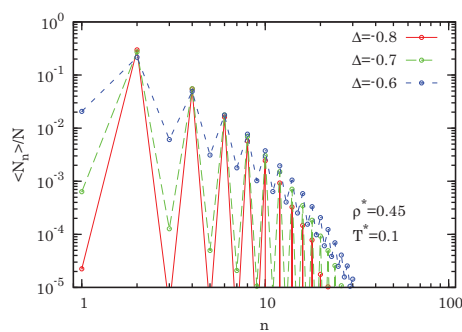


FIG. 4. (Color online) Clustering properties of the fluid at $T^* = 0.1$ and $\rho^* = 0.45$ at various values of negative nonadditivity approaching -1 . The N_n are the numbers of clusters made of n particles. In the MC simulations we used $N = 100$ particles and 5×10^7 MCS.

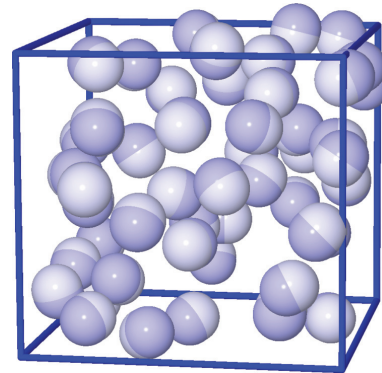


FIG. 5. (Color online) Snapshot of the fluid at $T^* = 0.1, \rho^* = 0.45$, and $\Delta = -0.9$ showing the formation of the dipoles.

B. Radial distribution function and structure factor

In Figs. 6–8 we show the partial radial distribution functions (RDF) $g_{ij}(r) = \langle \sum_{\mu\nu} \delta(\mathbf{r} + \mathbf{r}_\nu^i - \mathbf{r}_\mu^j) \rangle N / \rho x_i x_j$, where \mathbf{r}_μ^i denotes the position of particle μ of species i and the prime to the sum indicates that the terms $\mu = \nu$ when $i = j$ are omitted, and the total RDF $g_{\text{tot}} = \sum_{i,j=1}^2 g_{ij} x_i x_j$ of the three fluids $\Delta = 0, \pm 0.3$ at the thermodynamic states $T^* = 0.1, \rho^* = 0.01, 0.1$ and $T^* = 0.04, \rho^* = 0.45$. Of course, the restrictions $x_1 = x_2$ and $\sigma_{11} = \sigma_{22}$ imply that $g_{11} = g_{22}$. In the simulations we use $N = 100$.

From Fig. 6 we see how the contact value of the like RDF in the $\Delta = -0.3$ case is higher than in the additive case and in the $\Delta = 0.3$ case it is lower than in the additive case. The contact value of the unlike RDF is highest for negative nonadditivity, indicating the tendency to form cation-anion pairs.

From Fig. 7 we see again the same behaviors of the contact values of the like and unlike RDFs. In the negatively additive case we begin to see an alternation of the distribution of oppositely charged shells of ions around a reference ion.

From Fig. 8 we see how at this high density the contact value of the like RDF is highest in the $\Delta = -0.3$ case, but in the $\Delta = 0.3$ case it is still higher than in the additive case. At $\Delta = -0.3$ we see clearly the formation of a second peak in the unlike RDF around $2 + \Delta$ and the expected alternation between the peaks of the like RDF with the ones of the unlike RDF also present in the additive case. This alternation is not present in the positively nonadditive case, indicating now the tendency of like particles to cluster on a microscopic scale: Like particles penetrate the shell of unlike particles around a given reference ion. The contact value of the unlike RDF is highest for negative nonadditivity, indicating the tendency to form cation-anion pairs.

In Fig. 9 we show the Bhatia-Thornton [63] structure factors $S_{NN} = [S_{11} + S_{22} + 2S_{12}]/2$ and $S_{QQ} = [S_{11} + S_{22} - 2S_{12}]/2$, where $S_{ij}(k) = \langle \rho_{\mathbf{k}}^i \rho_{-\mathbf{k}}^j \rangle / N \sqrt{x_i x_j}$ are the partial structure factors and $\rho_{\mathbf{k}}^i = \sum_{\mu} \exp(-i\mathbf{k} \cdot \mathbf{r}_\mu^i)$ is the Fourier transform of the microscopic density of particles of species i . In the figure we chose the same thermodynamic state and nonadditivity considered in Fig. 1 of Ref. [40]. The positive

RICCARDO FANTONI AND GIORGIO PASTORE

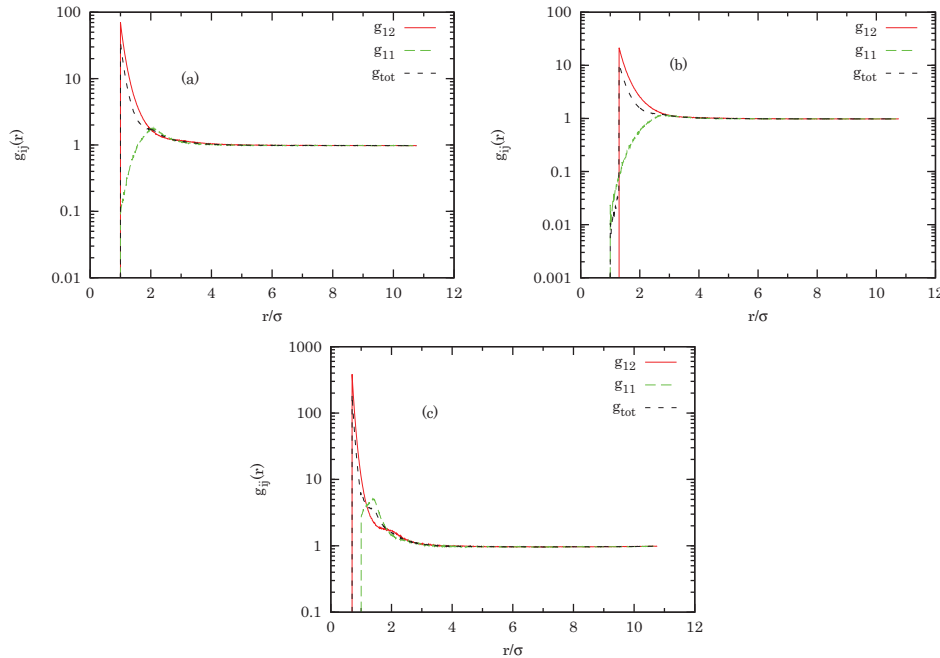
 PHYSICAL REVIEW E **87**, 052303 (2013)


FIG. 6. (Color online) Partial and total RDFs in the simulations at $\rho^* = 0.01, T^* = 0.1$, and (a) $\Delta = 0$, (b) $\Delta = 0.3$, and (c) $\Delta = -0.3$, with the reduced excess internal energy per particle of the fluid $U^{\text{ex}}/N = -0.3924(1)$, $-0.29120(7)$, and $-0.6339(1)$, respectively.

nonadditivity case has percolating clusters. From the figure we see that the charge-charge structure factor S_{QQ} tends to zero at $k = 0$, a consequence of electroneutrality in charged systems [9] that suppresses long-wavelength fluctuations. In order to enforce this condition the structure factor needs to develop a peak at small k that reflects an essentially alternating distribution of the oppositely charged shell of ions around a reference ion. This type of short-range order is an indication of the tendency to cluster. From the figure we see that at high density the positive nonadditive fluid tends to cluster more than the additive fluid and the negative nonadditive fluid tends to cluster less than the additive fluid, in agreement with the results presented in the previous section. With regard to the number-number structure factor S_{NN} , we see that as the nonadditivity decreases, the isothermal compressibility $S_{NN}(0)$ (see the Appendixes of Refs. [63,64]) increases and the short-range order is reduced.

In Table II we report the excess internal energy per particle $U^{\text{ex}}/N = \epsilon\sigma \langle U \rangle / Nq^2$, the compressibility factor $Z = \beta P / \rho$, and the total clusters concentration $\sum_n \langle N_n \rangle / N$ for the cases simulated. The compressibility factor is calculated according to the virial theorem

$$Z = 1 + \frac{U^{\text{ex}}}{3NT^*} + \frac{\pi\rho^*}{3} [g_{11}(\sigma) + (1 + \Delta)^3 g_{12}(\sigma(1 + \Delta))]. \quad (3.2)$$

If the clusters do not interact, as in the independent cluster model (ICM) of Gillan [12], one should have

$Z^{\text{ICM}} = \sum_n \langle N_n \rangle / N$. From Table II we can see how this condition is never satisfied in the cases considered.

C. Gas-liquid coexistence

An important question we try to answer is how the gas-liquid coexistence curve of the pure RPM fluid changes upon switching on of the nonadditivity parameter. To this aim we first perform a density distribution analysis within the NVT ensemble that allows us to easily extract a semiquantitative result and then we use the Gibbs ensemble technique for a careful quantitative determination of the binodals.

1. Density distribution approach

Sufficiently close to the critical point we determine how semiquantitatively the behavior of the gas-liquid coexistence region changes by switching on a negative or a positive nonadditivity. To this aim we divide the simulation box into m^3 cubes of side $L_c = L/m$ and register, as the run progresses, the density inside each cell $\rho_i = \mathcal{N}_i / L_c^3$, where \mathcal{N}_i is the number of particles inside the i th cell so that $\sum_{i=1}^{m^3} \mathcal{N}_i = N$. Then we calculate the density distribution function [65–67] $P_m(\rho) = \sum_{i=1}^{m^3} P_m(\rho_i) / m^3$, where $P_m(\rho_i)$ is the distribution function for the i th cell, with $\int P_m(\rho) d\rho = 1$. Above the critical temperature the density probability distribution function can be described by a Gaussian distribution centered at the simulation

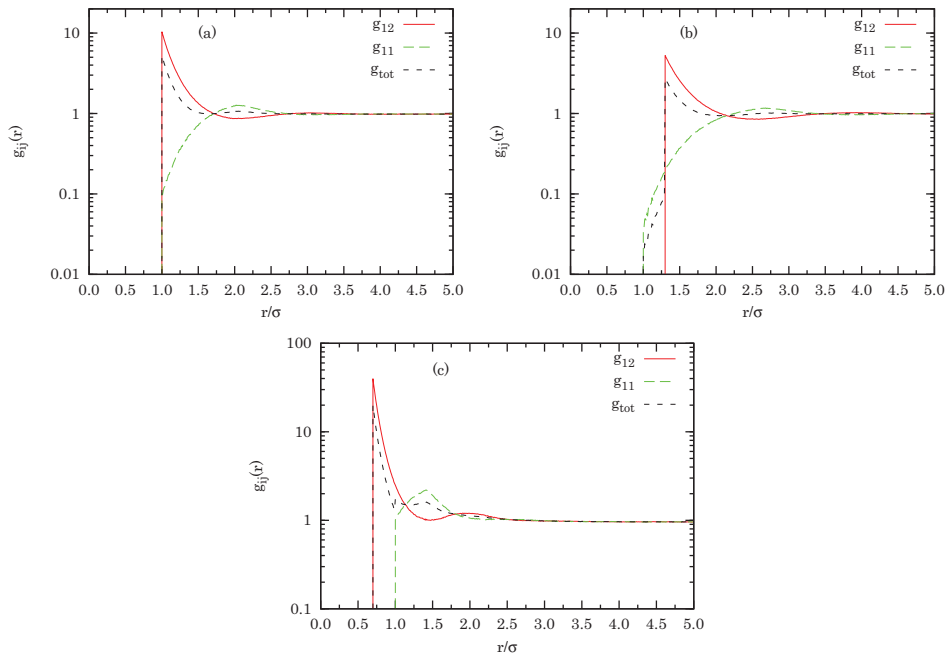


FIG. 7. (Color online) Same as Fig. 6, but at $\rho^* = 0.1$ and $T^* = 0.1$. The reduced excess internal energy per particle of the fluid is (a) $U^{ex}/N = -0.50589(8)$, (b) $U^{ex}/N = -0.41208(6)$, and (c) $U^{ex}/N = -0.7179(1)$.

density, whereas below it becomes bimodal with two peaks, one centered at the gas density and one at the liquid density.

We start from an initial configuration of particles of random species placed on a simple cubic lattice. We equilibrate (melt) the fluid for 10^6 MCS/particle. We then sample the distribution function every 10 MCS. To allow the particles to diffuse out of the cells we choose the subdivision of the simulation box in cells with a random displacement $\mathbf{r} = (r_x, r_y, r_z)$, with $r_x, r_y, r_z \in [0, L]$. This procedure turned out to greatly enhance the efficiency of the determination of the cell density distribution. In addition, we measure the distribution function on runs of 1×10^6 MCS/particle.

Using $m = 2$ and $N = 100$, we obtain the results for the fluid at a temperature $T^* = 0.025$ above the triple point of the RPM [68], a density $\rho^* = 0.2$ well within the coexistence region of the pure RPM fluid, and $\Delta = 0, \pm \mathcal{D}$, with $\mathcal{D} = 10^{-1}, 10^{-2}, 5 \times 10^{-2}$, as shown in Fig. 10. In this case the minimum density that can be registered is $1/L_c^3 = 0.2 \times (8/100) = 0.016$. We see that the pure RPM fluid shows a density distribution function with two peaks: the first one, which lies below the minimum density (and is not visible in our data), at approximately the low density of the gas phase and the second one at approximately the high density of the liquid phase around a reduced density of 0.3. At $\mathcal{D} = 10^{-2}$ the positions of the peaks are roughly the same as for the pure RPM. At $\mathcal{D} = 5 \times 10^{-2}$ the density of the liquid peak in the negatively nonadditive fluid is higher than the one of the pure RPM, whereas the positively nonadditive fluid

has a gas peak, now visible, at higher density than for the pure RPM and a liquid peak at lower density than for the pure RPM. At $\mathcal{D} = 10^{-1}$ this separation tends to increase: In the positively nonadditive model the critical temperature is too close to 0.025 and the bimodal degenerates into a curve with a single peak centered on the simulation density 0.2, whereas in the negatively nonadditive fluid the liquid peak is changed into a broad tail extending up to a density of 0.8. This finding suggests that at a given temperature the width of the coexistence region, relative to the one of the pure RPM, tends to increase for the negatively nonadditive model and decrease for the positively nonadditive model. This result is made more clear and precise in the following section where we present our Gibbs ensemble Monte Carlo calculation.

2. Gibbs ensemble analysis

In order to quantitatively determine the gas-liquid coexistence line of our fluid we use the Gibbs ensemble MC (GEMC) technique [69–73], starting from the pure RPM and gradually switching on the nonadditivity. Here we are interested not in the behavior really close to the critical point, but rather in the shape of the binodal curve and how it moves as a function of Δ .

The GEMC method of Panagiotopoulos is now widely adopted as a standard method for calculating phase equilibria from molecular simulations. According to this method, the simulation is performed in two boxes containing the coexisting phases. Equilibration in each phase is guaranteed by moving

RICCARDO FANTONI AND GIORGIO PASTORE

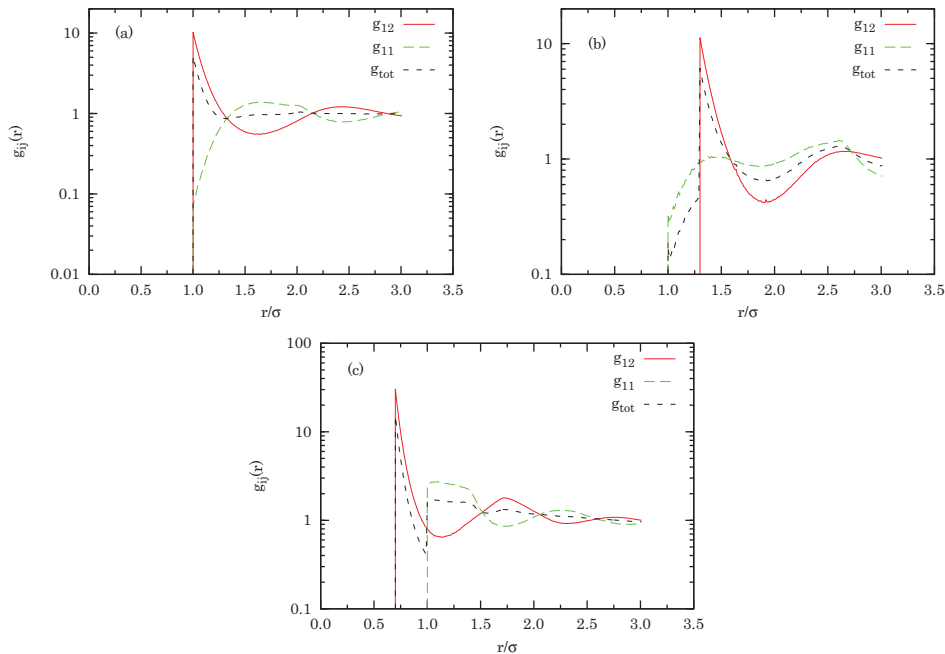
 PHYSICAL REVIEW E **87**, 052303 (2013)


FIG. 8. (Color online) Same as Fig. 6, but at $\rho^* = 0.45$ and $T^* = 0.04$. The reduced excess internal energy per particle of the fluid is (a) $U^{\text{ex}}/N = -0.69094(4)$, (b) $U^{\text{ex}}/N = -0.55242(5)$, and (c) $U^{\text{ex}}/N = -0.96144(7)$.

particles. Equality of pressures is satisfied in a statistical sense by expanding the volume of one of the boxes and contracting the volume of the other. Chemical potentials are equalized by transferring particles from one box to the other. Like the first simulations for the RPM performed by Panagiotopoulos [26], we use single-ion transfer by introducing a background charge density to ensure charge neutrality at all times during the run. This way the system remains overall neutral, but the modified model is similar to a two-component plasma and in a strict sense different from the original RPM, which assumes a zero charge density for the background. To overcome the electroneutrality problem Orkoulas and Panagiotopoulos [29] considered pair transfers.

In the GEMC run we have at each step a probability $a_p/(a_p + a_v + a_s)$ for a particle random displacement, $a_v/(a_p + a_v + a_s)$ for a volume change, and $a_s/(a_p + a_v + a_s)$ for a particle swap move between the gas and the liquid box. We generally choose $a_p = 1$, $a_v = 1/10$, and $a_s = 1$. The maximum particle displacement is kept equal to $L_i/1000$, where L_i is the side of the i th box with $i = 1, 2$. Regarding the volume changes, following Ref. [69] we perform a random walk in $\ln[V_1/V_2]$, with V_i the volume of the i th box choosing a maximum volume displacement of 1%–10%. Volume moves are computationally the cheapest since the energy scales with the length of the box with inverse proportionality. We generally use a total number of $N = 100$ particles, except close to the critical point, where it proves necessary to increase the number of particles in order to avoid large fluctuations in the two

densities. We use $(10\text{--}40) \times 10^6$ MCS for the equilibration and $(100\text{--}200) \times 10^6$ MCS for the production.²

The results are summarized in Table III and Fig. 11. Note that since we get the same coexistence curve as that of Orkoulas and Panagiotopoulos [29] for the pure RPM, as Fig. 1 clearly shows, we consider as equivalent, at the present level of accuracy, our procedure, employing single-neutralized-particle transfers, and the one of Orkoulas and Panagiotopoulos, where pair-particle transfers between the two boxes are used. This can be justified by observing that the fluctuations of charge in the various statistical physics ensembles are expected to decay to zero with the system size and we empirically find that in our case they are already practically irrelevant. The only relevant difference we observe with respect to the calculation of Orkoulas and Panagiotopoulos is the fact that in our case there is a much more considerable emptying of the gas box at low temperatures, which may have some effect on the point at the lowest temperature. We do not carry out a systematic study of the possible system size dependence of the results, but for the pure RPM we repeat the calculation at $T^* = 0.045$ and 0.0475 for two different system sizes with the largest being $N = 370$. The comparison suggests that the critical point tends to shift slightly at higher temperatures upon a

²The GEMC code took ≈ 26 min of CPU time for 10 million steps of a system of size $N = 200$ on an IBM PLX (iDataPlex DX360M3) cluster (2.40 GHz).

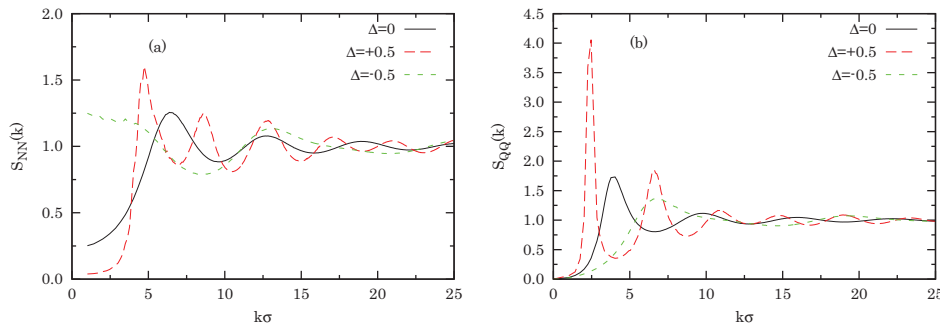


FIG. 9. (Color online) Bhatia-Thornton structure factors (a) $S_{NN}(k)$ and (b) $S_{QQ}(k)$ for $\rho^* = 0.41253, T^* = 0.12$, and $\Delta = 0, \pm 0.5$, as in Fig. 1 of Ref. [40]. Note that our abscissa has to be divided by 1.2 in order to compare with the units used in [40].

system size increase, but far away from the critical point the coexistence curve is not affected appreciably by the system size. However, we stress that an accurate study of critical properties of the present model is beyond the scope of this work.

From the figure we can see clearly the trend: A positive nonadditivity tends to lower the critical temperature, whereas a negative one tends to push the binodal to higher temperatures. This is in agreement with the findings from the density

distribution analysis previously presented. It is well known that RPM condensation is almost identical to that of charged hard dumbbells, underlining the fact that the vapor is essentially already fully associated into dimers and higher neutral clusters and that the liquid structure and thermodynamics are only weakly perturbed by fusing ions together. Hence, if one imagines cooling down on the critical isochore, we can say that the critical point is reached when ion association is complete and then it becomes convenient for the system to phase separate.

TABLE II. Excess internal energy per particle $U^{ex} = \epsilon\sigma \langle U \rangle / q^2$, compressibility factor $Z = \beta P / \rho$, and total clusters concentration $\sum_n \langle N_n \rangle / N$ for the cases simulated.

T^*	ρ^*	Δ	$-U^{ex}/N$	$Z - U^{ex}/3NT^*$	$\sum_n \langle N_n \rangle / N$
0.1	0.45	0	0.627 11(9)	3.764(5)	0.317
0.1	0.45	0.3	0.462 12(9)	9.16(1)	0.026
0.1	0.45	-0.3	0.813 57(9)	3.019(3)	0.410
0.1	0.3	0	0.588 27(6)	2.869(3)	0.528
0.1	0.3	0.3	0.474 93(7)	4.837(6)	0.255
0.1	0.3	-0.3	0.7814(1)	2.797(3)	0.483
0.1	0.2	0	0.553 90(6)	2.445(2)	0.637
0.1	0.2	0.3	0.456 39(6)	3.231(3)	0.540
0.1	0.2	-0.3	0.754 83(9)	2.657(3)	0.530
0.1	0.1	0	0.505 89(8)	2.098(2)	0.730
0.1	0.1	0.3	0.412 08(6)	2.218(2)	0.747
0.1	0.1	-0.3	0.7179(1)	2.539(3)	0.579
0.1	0.01	0	0.3924(1)	1.7373(8)	0.830
0.1	0.01	0.3	0.291 20(7)	1.493(3)	0.900
0.1	0.01	-0.3	0.6339(1)	2.409(2)	0.652
0.1	0.001	0	0.3076(1)	1.582(1)	0.870
0.1	0.001	0.3	0.1971(1)	1.2962(6)	0.943
0.1	0.001	-0.3	0.5992(1)	2.355(2)	0.677
0.04	0.45	0	0.690 94(4)	5.863(8)	0.104
0.04	0.45	0.3	0.552 42(5)	12.83(2)	0.012
0.04	0.45	-0.3	0.961 44(7)	7.09(1)	0.028
0.04	5×10^{-5}	0	0.488 04(2)	4.112(1)	0.563
0.04	5×10^{-5}	0.3	0.353 42(2)	3.254(1)	0.681
0.04	5×10^{-5}	-0.3	0.697 64(1)	5.230(2)	0.493

RICCARDO FANTONI AND GIORGIO PASTORE

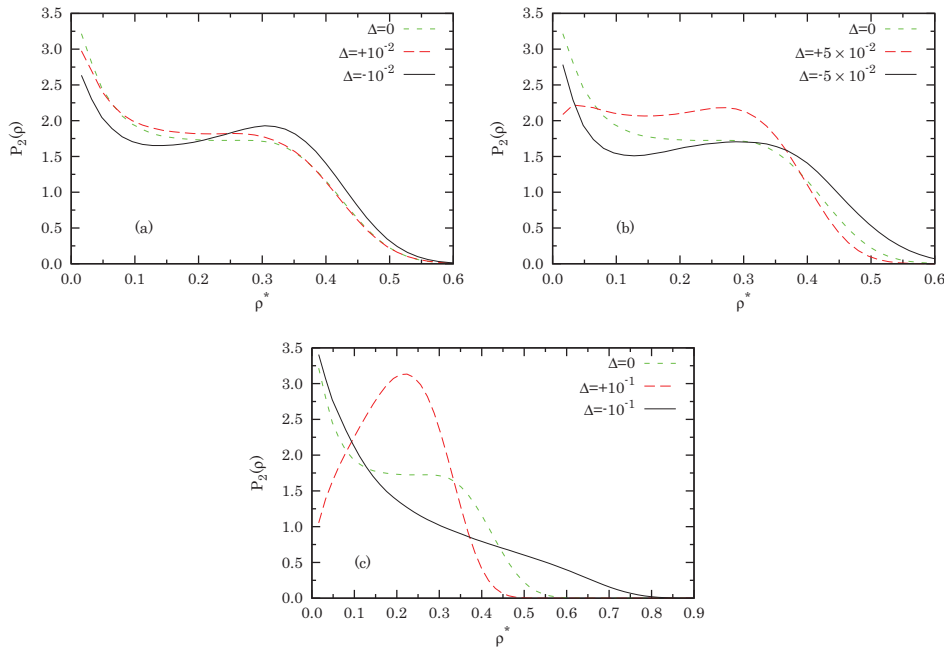
 PHYSICAL REVIEW E **87**, 052303 (2013)


FIG. 10. (Color online) Cell density distribution function for the fluid at $T^* = 0.025, \rho^* = 0.2$, and $\Delta = 0, \pm D$ with (a) $D = 10^{-2}$, (b) $D = 5 \times 10^{-2}$, and (c) $D = 10^{-1}$. We use $N = 100$ and $m = 2$ with 1×10^6 MCSs/particle.

With positive nonadditivity, ion association is less favorable and the critical temperature must go down (association is complete only at lower temperatures); with negative nonadditivity, ion association is more favorable and the critical temperature must go up (association is complete already at higher temperatures).

In order to determine the critical point (T_c^*, ρ_c^*) we empirically fit the binodals using the “diameter” $(\rho_g^* + \rho_l^*)/2$ equation [74]

$$\frac{\rho_g^* + \rho_l^*}{2} = \rho_c^* + A|T^* - T_c^*| + C|T^* - T_c^*|^{2\beta_I} + D|T^* - T_c^*|^{1-\alpha_I} \quad (3.3)$$

and the form of the Wegner expansion [74,75] for the width of the coexistence curve

$$\rho_l^* - \rho_g^* = B|T^* - T_c^*|^{\beta_I} + B_1|T^* - T_c^*|^{\beta_I + \Delta_I} + B_2|T^* - T_c^*|^{\beta_I + 2\Delta_I}, \quad (3.4)$$

where A, C, D , and B, B_1, B_2 are coefficients that we take as fitting parameters as well as ρ_c^*, T_c^* . We stress that our data do not extend sufficiently close to the critical region to allow quantitative estimates of critical exponents and nonuniversal quantities, still we used the above functional forms as convenient fitting formulas, able to capture the typical flatness of the fluid coexistence curves [69]. The pure RPM is believed [33,76–78] to belong to the three-dimensional Ising universality class, so we choose $\beta_I = 0.325, \alpha_I = 0.11$, and $\Delta_I = 0.51$. We are then able to fit the pure RPM case $\Delta = 0$, for which we find

the critical point at $\rho_c^* = 0.0319$ and $T_c^* = 0.0476$; the RPM with positive nonadditivity $\Delta = 0.1$, for which the critical point is found at $\rho_c^* = 0.0275$ and $T_c^* = 0.0432$; and the RPM with negative nonadditivity $\Delta = -0.1$, for which $\rho_c^* = 0.0495$ and $T_c^* = 0.0526$. We stress that these numbers, in particular the values of critical densities, should be considered more as indicative of the dependence of the critical point location on diameter nonadditivity than as accurate estimates.

We believe that our results can be relevant for the interpretation of experimental work on the phase diagrams of room temperature ionic liquids [53] such as the phosphonium halogenide in alkanes solvents and 1-hexyl 3-methyl imidazolium tetrafluoro borate ($C_6\text{mimBF}_4$) in alcohols and water. The degree of nonadditivity seems directly related to the anion-cation contact-pairing affinity [41]. The salts in the (hydrocarbon) solution dissociate in cations (the phosphonium) and anions (the halogen atoms). The contact affinity between anions and cations is mediated by the solvent and different solvents produce different affinities. As a consequence, in the experimental work of Ref. [53], liquid-liquid coexistence curves were observed that, depending on the kind of solvent used in the ionic liquid mixture, can be above ($C_6\text{mimBF}_4$ in alcohols and water) the one of the purely theoretical RPM or below (phosphonium halogenide in alkanes) it in reduced units. Moreover, when plotted onto a corresponding state representation, all the experimental binodals seem to collapse on the same curve even if this occurs very close to the critical point. We then try to see whether or not the law of corresponding states holds for our fluid; we find that far from

TABLE III. Phase coexistence properties for the pure RPM ($\Delta = 0$) and the nonadditive RPM ($\Delta \neq 0$). Here T^* is the reduced temperature, N is the total number of particles in the system for a certain run, N_g is the average number of particles in the gas box during the run, $\mu_i^* = \mu_i \epsilon \sigma / q^2 - T^* \ln \Lambda^3$ is the reduced chemical potential of the liquid box (Λ being the de Broglie thermal wavelength), U_i^{ex} is the total excess internal energy, and ρ_i^* is the reduced density of the gas phase $i = g$ and the liquid phase $i = l$.

Δ	T^*	N	N_g/N	$-\mu_l^*$	$-U_g^{\text{ex}}/N$	$-U_l^{\text{ex}}/N$	ρ_g^*	ρ_l^*
0	0.0475	370	0.51(1)	0.63(1)	0.547(1)	0.609(1)	$5.2(9) \times 10^{-3}$	0.11(3)
0	0.0475	200	0.33(1)	0.63(1)	0.559(2)	0.604(1)	$1.1(3) \times 10^{-2}$	0.08(3)
0	0.045	370	0.26(1)	0.69(3)	0.528(4)	0.6400(7)	$2.3(5) \times 10^{-3}$	0.22(5)
0	0.045	100	0.27(1)	0.63(2)	0.537(4)	0.6393(9)	$3.1(7) \times 10^{-3}$	0.22(5)
0	0.0425	100	0.166(8)	0.65(1)	0.52(1)	0.6576(8)	$2.3(4) \times 10^{-3}$	0.29(2)
0	0.04	100	0.069(5)	0.73(1)	0.50(2)	0.6745(5)	$8(3) \times 10^{-4}$	0.35(3)
0	0.0375	100	0.036(2)	0.72(1)	0.4(1)	0.6835(5)	$4(2) \times 10^{-4}$	0.38(5)
0	0.035	100	0.0020(6)	0.75(2)	0.05(40)	0.6938(5)	$2(20) \times 10^{-5}$	0.42(2)
-0.1	0.0525	200	0.297(9)	0.71(2)	0.602(2)	0.6844(9)	$9(2) \times 10^{-3}$	0.19(5)
-0.1	0.05	100	0.37(1)	0.67(1)	0.609(4)	0.712(1)	$4.8(7) \times 10^{-3}$	0.33(5)
-0.1	0.0475	100	0.094(4)	0.71(2)	0.562(7)	0.7240(8)	$1.7(3) \times 10^{-3}$	0.36(7)
-0.1	0.045	100	0.092(5)	0.69(2)	0.590(9)	0.7380(8)	$1.3(2) \times 10^{-3}$	0.42(5)
-0.1	0.0425	100	0.031(3)	0.85(3)	0.4(1)	0.7503(8)	$5.6(10) \times 10^{-4}$	0.46(4)
-0.1	0.04	100	0.0034(7)	0.83(2)	0.08(40)	0.7582(7)	$5(30) \times 10^{-5}$	0.48(4)
0.1	0.0425	100	0.40(2)	0.58(1)	0.493(3)	0.5620(9)	$5(1) \times 10^{-3}$	0.11(3)
0.1	0.04	100	0.23(1)	0.62(3)	0.487(2)	0.5877(9)	$1.6(4) \times 10^{-3}$	0.19(5)
0.1	0.0375	100	0.068(5)	0.70(2)	0.40(4)	0.6068(5)	$8(1) \times 10^{-4}$	0.24(3)
0.1	0.035	100	0.015(2)	0.72(2)	0.17(26)	0.6157(6)	$1.7(40) \times 10^{-4}$	0.28(2)

the critical point it is not strictly satisfied, as shown by Fig. 12. Interestingly enough, a plot of the RDF between corresponding states shows an almost complete overlap of the three curves upon a shift by $\pm\Delta$ in r , as shown in Fig. 13. We think that the only visible difference, the contact values of the like RDF, is a direct hallmark of the breakup of the corresponding states as a physical consequence of the existence of a third relevant interaction parameter in addition to the unlike hard-sphere diameter and the electric charge. While the Cl^- ion and the BF_4^- anion may be approximated reasonably well by a sphere so that the center of charge is identical to the center of mass, the NTF_2^- anion is by no means spherical. The NTF_2^- anion is flexible and allows for different conformers. The nitrogen

atom in the anion is not necessarily identical to the center of mass and the center of charges [54]. In these cases, instead of the RPM it is better to choose the primitive model with ions of differing sizes as the reference system [36–38].

IV. THEORETICAL REMARKS ON THE CLUSTERING

Under highly diluted conditions [79] we can approximate the fluid as an ideal mixture of cation and anions, anions, and cations with partial densities $\rho_{\pm} = (1 - \alpha)\rho/2$ and $\rho_{-} = \rho_{+} = \alpha\rho/2$, respectively, and for the chemical potentials $\mu_{\pm} = k_B T \ln[(1 - \alpha)\rho\Lambda_{\pm}^3/2K]$, $\mu_{-} = k_B T \ln(\alpha\rho\Lambda_{+}^3/2)$, and $\mu_{+} = k_B T \ln(\alpha\rho\Lambda_{-}^3/2)$, where Λ_{-} and Λ_{+} are the de Broglie thermal wavelengths of the anions and cations, respectively. Here K is the configurational integral of a

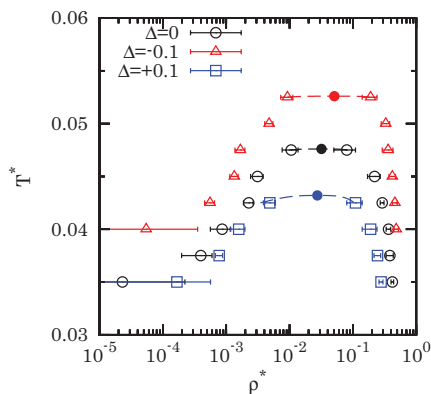


FIG. 11. (Color online) Binodals obtained with the GEMC simulations. The dashed lines are the results of the extrapolation described in the text. The closed circles are the critical points.

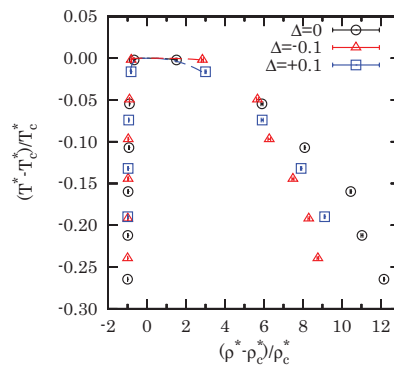


FIG. 12. (Color online) Corresponding state representation of the phase diagram.

RICCARDO FANTONI AND GIORGIO PASTORE

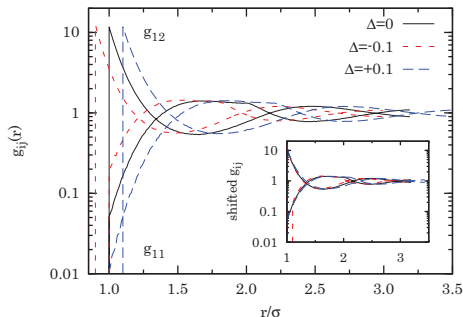
 PHYSICAL REVIEW E **87**, 052303 (2013)


FIG. 13. (Color online) The RDF on corresponding states of the liquid branch at $T^* = 0.0375, \rho^* = 0.38$, and $\Delta = 0$; $T^* = 0.035, \rho^* = 0.28$, and $\Delta = 0.1$; and $T^* = 0.0425, \rho^* = 0.46$, and $\Delta = -0.1$. The inset shows the functions shifted by $\pm\Delta$.

cation-anion pair

$$K = 4\pi \int_{\sigma(1+\Delta)}^{r_c} r^2 e^{\lambda_B/r} dr, \quad (4.1)$$

where $\lambda_B = \sigma/T^*$ is the Bjerrum length and r_c is a cutoff radius conventionally chosen equal to $\lambda_B/2$ corresponding to the minimum of the integrand. At equilibrium $\mu_{\pm} = \mu_+ + \mu_-$, which implies $(1 - \alpha)/\alpha^2 = K\rho/2$. Solving for α yields

$$\alpha = \frac{\sqrt{1 + 2K\rho} - 1}{K\rho}. \quad (4.2)$$

An approximate closed form expression for K valid at low T^* can be obtained by writing for the anion-cation pair distance $r = \sigma(1 + \Delta) + \delta r$ with δr small. Then $\sigma/r \approx 1/(1 + \Delta) - \sigma\delta r/\sigma^2(1 + \Delta)^2 = 2/(1 + \Delta) - r/\sigma(1 + \Delta)^2$. Substituting into Eq. (4.1) and performing the integral with $r_c = \infty$ yields

$$K \approx 4\pi\sigma^3(1 + \Delta)^4 e^{1/T^*(1+\Delta)} T^* \times [1 + 2(1 + \Delta)T^*[1 + (1 + \Delta)T^*]]. \quad (4.3)$$

In our simulations we are never in this very diluted condition and as a consequence we observe the formation of clusters of a higher number of particles than just the dimers. Thus, to estimate the cluster concentrations $x_n^c = \langle N_n \rangle / N$, we need a different analysis closer in spirit to the one of Tani and Henderson [56,57,80]. Simplifying that analysis, we can consider as the intercluster configurational partition function the one of an ideal gas of clusters, in reduced units, $Z_{\text{inter}} \approx (V/\sigma^3)^{N_c}$, where $N_c = \sum_{n=1}^{n^c} N_n$ is the total number of clusters and we assume to have only clusters made of up to n^c particles. Then the equations for the equilibrium cluster concentrations x_n^c are

$$x_n^c = \lambda^n z_n^{\text{intra}} / \rho^*, \quad n = 1, 2, \dots, n^c, \quad (4.4)$$

$$1 = \sum_{n=1}^{n^c} n x_n^c, \quad (4.5)$$

where z_n^{intra} are the configurational intracluster partition functions in reduced units, with $z_1^{\text{intra}} = 2$, and $\lambda (= \alpha\rho^*/2)$ is a Lagrange multiplier. Moreover, neglecting the excess internal energy of the clusters, we can approximate $z_n^{\text{intra}} \approx (v_n/\sigma^3)^{n-1} \sum_{s=0}^n [s!(n-s)!]^{-1} = (v_n/\sigma^3)^{n-1} 2^n/n!$ where v_n

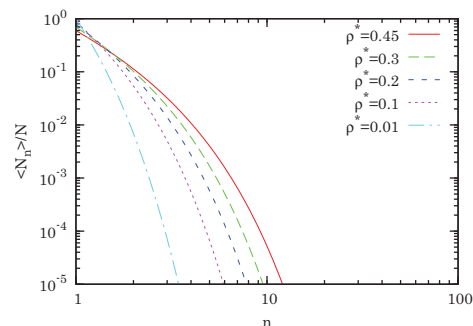


FIG. 14. (Color online) Cluster analysis described in the text for $n^c = 100$ at various densities.

is the volume of an n cluster. Moreover, assuming further the cluster to be in a closed packed configuration, we can approximate, for $\Delta = 0$, $v_n \approx n\sigma^3/\sqrt{2}$. Notice that for $\Delta \neq 0$ we would expect v_n to change by a constant multiplicative factor that would still give the same result for the cluster concentrations. Clearly a proper analysis of the n -cluster volume would require a MC simulation [12]. This temperature-independent approximation gives for $n^c = 100$ the results shown in Fig. 14 (note that the results have a very small dependence on n^c).

From the figure we can say that our simulation results for $T^* = 0.1$ and $\Delta = -0.3$ have qualitatively the same behavior as of our oversimplified analysis. This justifies the fit of Table I where the Laplace multiplier is considered as a fitting parameter. The strong dependence on the nonadditivity (and on temperature) that we observe in the simulation is an indication that the approximation of neglecting the excess internal energy of a cluster is too severe. One should consider $z_n^{\text{intra}} = e^{-n\bar{f}_n^{\text{ex}}/T^*} (v_n/\sigma^3)^{n-1} 2^n/n!$, where $\bar{f}_n^{\text{ex}}(T^*) = \int_0^{1/T^*} u_n^{\text{ex}}(1/x) dx$ is the excess free energy per particle of the n cluster and $\mu_n^{\text{ex}}(T^*) = (\epsilon\sigma/q^2) \langle \sum_{i>j=1}^n \phi_{ij}(r_{ij}) \rangle / n$ is the reduced excess internal energy per particle of the n cluster. Note once again that choosing an \bar{f}_n^{ex} independent of n would lead to the same oversimplified result we described for the cluster concentrations. What really matters is the combined dependence of $\bar{f}_n^{\text{ex}}(T^*)$ on n and T^* , which can be assessed within the MC simulation [12,56,57]. For example, the curves of Figs. 2 and 3 with percolating clusters are better fitted by the three-parameter expression $x_n^c \approx \lambda^{n+an^2} n^{bn}/n!$.

One thing that can be done is to distinguish among the clusters of n particles between the ones formed by s negative particles and t positive particles with $t + s = n$, as done in Ref. [30], in order to be able to approximate analytically the intracluster excess free energy per particle

$$z_n^{\text{intra}} = \sum_{s=0}^n z_{s,n-s}^{\text{intra}}, \quad (4.6)$$

$$z_{s,t}^{\text{intra}} = \frac{1}{s!t!} \frac{1}{\sigma^{3(s+t-1)}} \int_{\Omega_{s,t}} d\mathbf{r}_2 \cdots d\mathbf{r}_{s+t} \times \exp\left(-\beta \sum_{\mu>\nu=1}^{s+t} \phi_{\mu\nu}(r_{\mu\nu})\right), \quad (4.7)$$

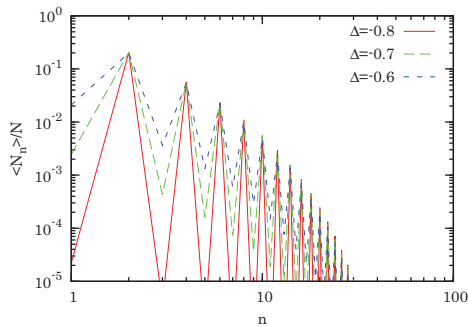


FIG. 15. (Color online) Cluster analysis described in the text for $n^c = 30$, $T^* = 0.1$, $\rho^* = 0.45$, $a = 1.5$, and $b = 0.9$ at various values of Δ .

where the configurational integral goes only over the relative positions and covers the region $\Omega_{s,t}$ of cluster configuration space. This way one can quantitatively [30] estimate how Tani and Henderson's theory [80] deviates from the exact MC results.

We immediately see how $z_{1,1}^{\text{intra}} \propto K/\sigma^3$ becomes increasingly bigger as $\Delta \rightarrow -1$ and the same holds for all the $z_{k,k}^{\text{intra}}$ that clearly dominate over all the other $z_{s,t}^{\text{intra}}$ with $s \neq t$. This qualitatively explains Fig. 4 and is shown in Fig. 15, where we show the results from the approximation described in Appendix for $n^c = 30$, $T^* = 0.1$, $\rho^* = 0.45$, $a = 1.5$, $b = 0.9$, and various values of Δ (note that the results have a very small dependence on n^c).

V. CONCLUSION

We have performed *NVT* MC simulations of the RPM with nonadditive hard-sphere diameters outside the coexistence region with particular emphasis on the clustering properties. In order to establish whether the cluster analysis falls outside the gas-liquid coexistence region for a given value of the nonadditivity, we accurately determined the binodals of the nonadditive fluid using the Gibbs ensemble method after a density distribution function analysis to get insight into the shift of the coexistence region with the nonadditivity. It turned out that a negative nonadditivity tends to shift the critical point to higher temperatures and higher densities whereas a positive one shifts it to lower temperatures and densities. The law of corresponding states does not seem to be strictly fulfilled over an extended region below the critical point for $\Delta = 0, \pm 0.1$. Our results can be used as a theoretical support to the analysis of experimental work on room temperature ionic liquids [52–54] where shifts in the liquid-liquid binodals akin to ours are observed as a function of the kind of solvent used in the ionic mixture.

From the cluster analysis, we were able to distinguish between two kind of behaviors for the cluster concentrations. When we do not observe percolating clusters during the simulation, the curves for the cluster concentrations as a function of the cluster size are independent of the number of

particles used in the simulation. When we observe percolation during the simulation the curves depend on the number of particles used in the simulation, but obey a straightforward scaling with N relationship.

At low densities the negative nonadditive fluid has stronger clustering than in the pure RPM, whereas at high densities the positive nonadditive fluid has the strongest clustering. The positive nonadditive fluid is the first one reaching the percolating clusters upon an increase of density. This certainly depends on the fact that for a positive nonadditivity the ions have less space in which to move at a given density and, due to the presence of two oppositely charged species, there is a competition between the tendency to clustering driven by the Coulomb interaction and the tendency to demixing due to entropic reasons. A negative nonadditivity tends to favor the formation of the neutrally charged clusters starting with dipolar ones. Traces of these features can also be read from an analysis of the partial radial distribution function and structure factors. Our clustering results can be summarized by observing that at high density for a positive deviation from additivity we have more clustering than in the additive model, whereas for a negative deviation from additivity we have less clustering than in the additive model. At low density the reverse behavior is found. These results can be explained by the following arguments: At high density a positive nonadditivity leaves less effective volume to the particles and a negative nonadditivity leaves more effective volume relative to the additive model; at low density a negative nonadditivity favors the formation of neutral clusters and a positive nonadditivity favors the competition between the tendency to demixing in a neutral mixture and the tendency to microscopic intermixing of the two species favored by the Coulombic interactions. These observations are in agreement with the fact that the energy of a cation-anion pair at contact increases for positive nonadditivity and decreases for negative nonadditivity.

A simple temperature-independent clustering theory where we regard the clusters as forming an ideal gas and we approximate the n cluster as an ideal ensemble of n particles in a closed packed configuration can be used to qualitatively explain the cluster concentrations observed at not to high density and absolute value of the nonadditivity. In order to qualitatively explain the prevalence of the neutral clusters in the negatively nonadditive fluid it is necessary to refine the approximation at the intracenter level.

In the future it would be desirable to make quantitative the comparison between clustering theory and MC exact results. The determination of the percolation threshold as a function of nonadditivity would also be interesting. In the temperature density phase diagram, one can determine the percolation threshold by calculating the fraction of configurations with percolating clusters within the *NVT* simulation as a function of density for two systems of different size N . A point of the percolation threshold results then where the curves of the two systems meet.

ACKNOWLEDGMENT

R.F. would like to acknowledge the use of the computational facilities of CINECA through the ISCRRA call.

RICCARDO FANTONI AND GIORGIO PASTORE

PHYSICAL REVIEW E **87**, 052303 (2013)

APPENDIX: APPROXIMATED INTRACLUSTER CONFIGURATIONAL PARTITION FUNCTION FOR NEGATIVE NONADDITIVITY

Let us call the anions $i_- = 1_-, \dots, s_-$ and the cations $j_+ = 1_+, \dots, t_+$. From Eq. (4.7) it follows that

$$z_{t,t}^{\text{intra}} = \frac{1}{t!^2} \frac{1}{\sigma^{3(2t-1)}} \int_{\Omega_{t,t}} \prod_{l=2}^t d\mathbf{r}_{1+l-} \prod_{k=1}^t d\mathbf{r}_{k+k-} \times \prod_{i>j=1}^t e^{-2\lambda_B/r_{i+j-}} \prod_{i,j=1}^t e^{+\lambda_B/r_{i+j-}} \approx \frac{1}{t!^2} \frac{1}{\sigma^{3(2t-1)}} \int_{\Omega_{t,t}} \prod_{l=2}^t d\mathbf{r}_{1+l-} \prod_{k=1}^t d\mathbf{r}_{k+k-} \prod_{i,j=1}^t e^{+\lambda_B/r_{i+j-}}, \quad (\text{A1})$$

where we approximated $e^{-\lambda_B/r} \approx 1$, which is justified at high $T^* < 1/2(1 + \Delta)$ or low λ_B . Now we observe that, for example, $r_{1+2-} = |\mathbf{r}_{1+1-} + \mathbf{r}_{1-2-}|$, with $r_{1-2-} > \sigma$ and $e^{+\lambda_B/r_{1+2-}} \approx 1$. Thus, for negative nonadditivity we can further

approximate

$$z_{t,t}^{\text{intra}} \approx \frac{1}{t!^2} \frac{1}{\sigma^{3(2t-1)}} \int_{\Omega_{t,t}} \prod_{l=2}^t d\mathbf{r}_{1+l-} \prod_{k=1}^t d\mathbf{r}_{k+k-} \prod_{i,j=1}^t e^{+\lambda_B/r_{i+j-}} \approx \frac{1}{t!^2} \frac{1}{\sigma^{3(2t-1)}} \int_{\Omega_{t,t}} \prod_{l=2}^t d\mathbf{r}_{1+l-} \prod_{k=1}^t d\mathbf{r}_{k+k-} \prod_{i=1}^t e^{+\lambda_B/r_{i+i-}} \approx \frac{(2t)^{b(2t-1)}}{t!^2} (K/K_0)^t, \quad (\text{A2})$$

where the factor $(2t)^{b(2t-1)}$ takes into account the volume of $\Omega_{t,t}$ with b a free parameter and

$$K/K_0 = \int_{a\sigma(1+\Delta)}^{\lambda_B/2} r^2 e^{+\lambda_B/r} dr / \int_{a\sigma(1+\Delta)}^{\lambda_B/2} r^2 dr \quad (\text{A3})$$

with a a second free parameter. With the same approximations we can say that

$$z_{s,t}^{\text{intra}} \approx \frac{(s+t)^{b(s+t-1)}}{s!t!} (K/K_0)^{\min\{s,t\}}. \quad (\text{A4})$$

[1] *Ionic Soft Matter: Modern Trends in Theory and Applications*, edited by D. Henderson, M. Holovko, and A. Trokhymchuk, NATO Science Series II: Mathematics, Physics and Chemistry (Springer, Dordrecht, 2004), Vol. 206.

[2] P. G. de Gennes, *Rev. Mod. Phys.* **64**, 645 (1992).

[3] R. Fantoni and G. Pastore, *J. Chem. Phys.* **120**, 10681 (2004).

[4] D. Gazzillo, A. Giacometti, R. Fantoni, and P. Sollich, *Phys. Rev. E* **74**, 051407 (2006).

[5] R. Fantoni, A. Giacometti, A. Malijevský, and A. Santos, *J. Chem. Phys.* **133**, 024101 (2010).

[6] R. Fantoni, A. Giacometti, F. Sciortino, and G. Pastore, *Soft Matter* **7**, 2419 (2011).

[7] R. Fantoni, *Eur. Phys. J. B* **85**, 108 (2012).

[8] R. Fantoni, J. W. O. Salari, and B. Klumperman, *Phys. Rev. E* **85**, 061404 (2012).

[9] J. P. Hansen and I. R. McDonald, *Theory of Simple Liquids*, 2nd ed. (Academic, New York, 1986).

[10] G. Stell, K. C. Wu, and B. Larsen, *Phys. Rev. Lett.* **37**, 1369 (1976).

[11] T. L. Croxton and D. A. McQuarries, *J. Phys. Chem.* **83**, 1840 (1979).

[12] M. J. Gillan, *Mol. Phys.* **49**, 421 (1983).

[13] T. Cartailleur, P. Turq, L. Blum, and N. Condamine, *J. Phys. Chem.* **96**, 6766 (1992).

[14] J. A. Given, *Phys. Rev. A* **45**, 3849 (1992).

[15] J. A. Given and G. Stell, *J. Chem. Phys.* **96**, 9233 (1992).

[16] M. E. Fisher and Y. Levin, *Phys. Rev. Lett.* **71**, 3826 (1993).

[17] M. E. Fisher, *J. Stat. Phys.* **75**, 1 (1994).

[18] G. Stell, *J. Stat. Phys.* **78**, 197 (1995).

[19] Y. Zhou, S. Yeh, and G. Stell, *J. Chem. Phys.* **102**, 5785 (1995).

[20] S. G. Yeh, Y. Q. Zhou, and G. Stell, *J. Phys. Chem.* **100**, 1415 (1996).

[21] J. A. Given and G. Stell, *J. Chem. Phys.* **106**, 1195 (1997).

[22] J. Jiang, L. Blum, O. Bernard, J. M. Prausnitz, and S. I. Sandler, *J. Chem. Phys.* **116**, 7977 (2002).

[23] H. L. Friedman and B. Larsen, *J. Chem. Phys.* **70**, 92 (1979).

[24] P. N. Vorontsov-Veliaminov, A. M. Elashovich, L. A. Morgenshtern, and V. P. Chasovshikh, *High Temp. (USSR)* **8**, 261 (1976).

[25] V. P. Chasovshikh and P. N. Vorontsov-Veliaminov, *High Temp. (USSR)* **14**, 174 (1976).

[26] A. Z. Panagiotopoulos, *Fluid Phase Equilib.* **76**, 97 (1992).

[27] I. S. Graham and J. P. Valleeau, *J. Phys. Chem.* **94**, 7894 (1990).

[28] J.-M. Caillol, *J. Chem. Phys.* **100**, 2161 (1994).

[29] G. Orkoulas and A. Z. Panagiotopoulos, *J. Chem. Phys.* **101**, 1452 (1994).

[30] J.-M. Caillol and J.-J. Weis, *J. Chem. Phys.* **102**, 7610 (1995).

[31] G. Orkoulas and A. Z. Panagiotopoulos, *J. Chem. Phys.* **110**, 1581 (1999).

[32] Q. Yan and J. J. de Pablo, *J. Chem. Phys.* **111**, 9509 (1999).

[33] E. Luijten, M. E. Fisher, and A. Z. Panagiotopoulos, *Phys. Rev. Lett.* **88**, 185701 (2002).

[34] J.-M. Caillol, D. Levesque, and J.-J. Weis, *J. Chem. Phys.* **116**, 10794 (2002).

[35] P. J. Camp and G. N. Patey, *J. Chem. Phys.* **111**, 9000 (1999).

[36] J. M. Romero-Enrique, G. Orkoulas, A. Z. Panagiotopoulos, and M. E. Fisher, *Phys. Rev. Lett.* **85**, 4558 (2000).

[37] A. Z. Panagiotopoulos and M. E. Fisher, *Phys. Rev. Lett.* **88**, 045701 (2002).

[38] Q. Yan and J. J. de Pablo, *Phys. Rev. Lett.* **86**, 2054 (2001).

[39] Q. Yan and J. J. de Pablo, *Phys. Rev. Lett.* **88**, 095504 (2002).

[40] G. Pastore, P. V. Giaquinta, J. S. Thakur, and M. P. Tosi, *J. Chem. Phys.* **84**, 1827 (1986). The relationship between our reduced units and theirs is $\rho^* = 3\sigma^3/4\pi$ and $T^* = \sigma/\Gamma$.

[41] I. Kalcher, J. C. F. Schulz, and J. Dzubiella, *Phys. Rev. Lett.* **104**, 097802 (2010).

MONTE CARLO SIMULATION OF THE NONADDITIVE ...

PHYSICAL REVIEW E **87**, 052303 (2013)

- [42] M. Rovere and G. Pastore, *J. Phys.: Condens. Matter* **6**, A163 (1994).
- [43] E. Lomba, M. Alvarez, L. L. Lee, and N. G. Almarza, *J. Chem. Phys.* **104**, 4180 (1996).
- [44] K. Jagannathan and A. Yethiraj, *J. Chem. Phys.* **118**, 7907 (2003).
- [45] W. T. Gózdź, *J. Chem. Phys.* **119**, 3309 (2003).
- [46] A. Buhot, *J. Chem. Phys.* **122**, 024105 (2005).
- [47] A. Santos, M. López de Haro, and S. B. Yuste, *J. Chem. Phys.* **132**, 204506 (2010).
- [48] R. Fantoni and G. Pastore, *Europhys. Lett.* **101**, 46003 (2013).
- [49] W. C. K. Poon, S. U. Egelhaaf, J. Stellbrink, J. Allgaier, A. B. Schofield, and P. N. Pusey, *Philos. Trans. R. Soc. London Ser. A* **359**, 897 (2001).
- [50] W. C. K. Poon, *J. Phys.: Condens. Matter* **14**, R859 (2002).
- [51] H. Weingärtner, M. Kleemeier, S. Wiegand, and W. Schöer, *J. Stat. Phys.* **78**, 169 (1995).
- [52] M. Kleemeier, S. Wiegand, W. Schröer, and H. Weingärtner, *J. Chem. Phys.* **110**, 3085 (1999).
- [53] D. Saracsan, C. Rybarsch, and W. Schröer, *Z. Phys. Chem.* **220**, 1417 (2006).
- [54] W. Schröer and V. R. Vale, *J. Phys.: Condens. Matter* **21**, 424119 (2009).
- [55] M. P. Allen and D. J. Tildesley, *Computer Simulation of Liquids* (Oxford University Press, Oxford, 1987).
- [56] R. Fantoni, A. Giacometti, F. Sciortino, and G. Pastore, *Soft Matter* **7**, 2419 (2011).
- [57] R. Fantoni, *Eur. Phys. J. B* **85**, 108 (2012).
- [58] J. K. Lee, J. A. Barker, and F. F. Abraham, *J. Chem. Phys.* **58**, 3166 (1973).
- [59] W. Ebeling and M. Grigo, *Am. Phys.* **37**, 21 (1980).
- [60] H. L. Friedman and G. Larsen, *J. Chem. Phys.* **70**, 92 (1979).
- [61] N. Bjerrum, *K. Dan. Vidensk. Selsk. Mat. Fys. Medd.* **7**, 1 (1926).
- [62] L. Rovigatti, J. Russo, and F. Sciortino, *Phys. Rev. Lett.* **107**, 237801 (2011).
- [63] A. B. Bhatia and D. E. Thornton, *Phys. Rev. B* **2**, 3004 (1970).
- [64] R. Fantoni, D. Gazzillo, and A. Giacometti, *Phys. Rev. E* **72**, 011503 (2005).
- [65] M. Rovere, D. W. Heermann, and K. Binder, *Europhys. Lett.* **6**, 585 (1988).
- [66] M. Rovere, D. W. Heermann, and K. Binder, *J. Phys.: Condens. Matter* **2**, 7009 (1990).
- [67] M. Rovere, P. Nielaba, and K. Binder, *Z. Phys. B* **90**, 215 (1993).
- [68] C. Vega, J. L. F. Abascal, C. McBride, and F. Bresme, *J. Chem. Phys.* **119**, 964 (2003).
- [69] D. Frenkel and B. Smit, *Understanding Molecular Simulation* (Academic, San Diego, 1996).
- [70] A. Z. Panagiotopoulos, *Mol. Phys.* **61**, 813 (1987).
- [71] A. Z. Panagiotopoulos, N. Quirke, M. Stapleton, and D. J. Tildesley, *Mol. Phys.* **63**, 527 (1988).
- [72] B. Smit, Ph. De Smedt, and D. Frenkel, *Mol. Phys.* **68**, 931 (1989).
- [73] B. Smit and D. Frenkel, *Mol. Phys.* **68**, 951 (1989).
- [74] J. V. Sengers and J. M. H. Levelt-Sengers, in *Progress in Liquid Physics*, edited by C. A. Croxton (Wiley, Chichester 1978), Chap. 4.
- [75] F. Wegner, *Phys. Rev. B* **5**, 4529 (1972).
- [76] J.-M. Caillol, D. Levesque, and J. J. Weis, *Phys. Rev. Lett.* **77**, 4039 (1996).
- [77] J.-M. Caillol, *Condens. Matter Phys.* **7**, 741 (2004).
- [78] J. V. Sengers and J. G. Shanks, *J. Stat. Phys.* **137**, 857 (2009).
- [79] C. Valeriani, P. J. Camp, J. W. Zwanikken, R. van Roij, and M. Dijkstra, *Soft Matter* **6**, 2793 (2010).
- [80] A. Tani and D. Henderson, *J. Chem. Phys.* **79**, 2390 (1983).

Chapter 39

Radial distribution function in a diffusion Monte Carlo simulation of a Fermion fluid between the ideal gas and the Jellium model

Fantoni R., Eur. Phys. J. B **86**, 286 (2013)

Title: “Radial distribution function in a diffusion Monte Carlo simulation of a Fermion fluid between the ideal gas and the Jellium model”

Abstract: We study, through the diffusion Monte Carlo method, a spin one-half fermion fluid, in the three dimensional Euclidean space, at zero temperature. The point particles, immersed in a uniform “neutralizing” background, interact with a pair-potential which can be continuously changed from zero to the Coulomb potential depending on a parameter μ . We determine the radial distribution functions of the system for various values of density, μ , and polarization. We discuss about the importance, in a computer experiment, of the choice of suitable estimators to measure a physical quantity. The radial distribution function is determined through the usual histogram estimator and through an estimator determined via the use of the Hellmann and Feynman theorem. In a diffusion Monte Carlo simulation the latter route introduces a new bias to the measure of the radial distribution function due to the choice of the auxiliary function. This bias is independent from the usual one due to the choice of the trial wave function. A brief account of the results from this study were presented in a recent communication [R. Fantoni, Solid State Communications, **159**, 106 (2013)].

Radial distribution function in a diffusion Monte Carlo simulation of a Fermion fluid between the ideal gas and the Jellium model

Riccardo Fantoni^a

Dipartimento di Scienze dei Materiali e Nanosistemi, Università Ca' Foscari Venezia, Calle Larga S. Marta DD2137, 30123 Venezia, Italy

Received 12 March 2013 / Received in final form 19 April 2013
Published online 24 June 2013 – © EDP Sciences, Società Italiana di Fisica, Springer-Verlag 2013

Abstract. We study, through the diffusion Monte Carlo method, a spin one-half fermion fluid, in the three dimensional Euclidean space, at zero temperature. The point particles, immersed in a uniform “neutralizing” background, interact with a pair-potential which can be continuously changed from zero to the Coulomb potential depending on a parameter μ . We determine the radial distribution functions of the system for various values of density, μ , and polarization. We discuss about the importance, in a computer experiment, of the choice of suitable estimators to measure a physical quantity. The radial distribution function is determined through the usual histogram estimator and through an estimator determined via the use of the Hellmann and Feynman theorem. In a diffusion Monte Carlo simulation the latter route introduces a new bias to the measure of the radial distribution function due to the choice of the auxiliary function. This bias is independent from the usual one due to the choice of the trial wavefunction. A brief account of the results from this study were presented in a recent communication [R. Fantoni, Solid State Commun. **159**, 106 (2013)].

1 Introduction

The Jellium model is a system of pointwise electrons of charge e and number density n in the three dimensional Euclidean space filled with a uniform neutralizing background of charge density $-en$. The zero temperature, ground-state, properties of the statistical mechanical system thus depends just on the electronic density n or the Wigner-Seitz radius $r_s = (3/4\pi n)^{1/3}/a_0$ where a_0 is Bohr radius. The model can be used for example as a first approximation to describe free electrons in metallic elements [1] ($2 \lesssim r_s \lesssim 4$) or a white dwarf [2] ($r_s \simeq 0.01$).

When an impurity of charge q is added to the system, the screening cloud of electrons will experience the Friedel oscillations. In the Thomas-Fermi description of the static screening an electric potential $qv_H(\mathbf{r})$ (the Hartree potential) is created by the impurity and by the redistribution of the electronic charge $n(\mathbf{r}) - n$. It obeys the Poisson equation $qe\nabla^2 v_H(\mathbf{r}) = 4\pi e[-q\delta(\mathbf{r}) - en(\mathbf{r}) + en]$ and the equilibrium condition on the electrochemical potential, $\mu_c(n(\mathbf{r})) + qev_H(\mathbf{r}) = \text{constant}$. An analytic solution can be obtained for $|q| \ll 1$, when we find $n(\mathbf{r}) - n \simeq -qev_H(\mathbf{r})\partial n/\partial\mu_c$ by expansion of μ around the homogeneous state. Assuming $\partial n/\partial\mu_c$ is positive and with the definition $k_s = \sqrt{4\pi e^2 \partial n/\partial\mu_c}$, the Poisson equation yields

$$v_H(r) = \frac{e^{-k_s r}}{r}. \quad (1)$$

^a e-mail: rfantoni@ts.infn.it

It is clear from this result that the quantity $1/k_s$ measures the distance over which the self consistent potential associated with the impurity penetrates into the electron gas. Thus, $1/k_s$ has the meaning of a screening length. The Thomas-Fermi value of the screening length is obtained by replacing the thermodynamic quantity $\partial n/\partial\mu_c$ by its value for non-interacting fermions, using for μ_c the Fermi energy. Clearly we have that $v_H(r) \rightarrow 1/r$ as $1/k_s \rightarrow \infty$ and $v_H(r) \rightarrow 0$ as $1/k_s \rightarrow 0$. Also v_H is short ranged.

It is important to study the ground-state properties of a model of point fermions of spin one-half interacting with a bare pair-potential $v_\mu(r)$ which can be continuously changed from zero ($\mu \rightarrow 0$, ideal gas) to the Coulomb potential ($\mu \rightarrow \infty$, Jellium model) depending on a parameter μ . We chose the following functional form:

$$v_\mu(r) = \frac{\text{erf}(\mu r)}{r}. \quad (2)$$

Still the fluid is immersed in a static uniform background of continuously distributed point particles which interact with the particles of the fluid with the same pair-potential but of opposite sign.

A major challenge in the Kohn-Sham scheme of density functional theory is to devise approximations to the exchange-correlation functional that accurately describes near-degeneracy or long-range correlation effects such as van der Waals forces. Among recent progresses to circumvent this problem, we mention “range-separated” density functional schemes which combine the Kohn-Sham

formalism with either random-phase approximation [3] or multideterminantal approaches [4]. Such schemes require a local density functional for particles interacting via modified potentials defined in terms of a suitable parameter μ , which either softens the core or suppresses the long-range tail. Further insight into electronic correlations in molecules and materials can be gained through the analysis of the on-top pair correlation function [5].

Within quantum Monte Carlo, the diffusion Monte Carlo is the method of choice for the calculation of ground-state properties of appropriate reference homogeneous systems (the path integral method [6] can be used to extend the study to non-zero temperatures degenerate systems [7]), the most relevant example being the correlation energy of the electron gas obtained by Ceperley and Alder back in 1980 [8]. This is even more so in the present days, since better wavefunctions and optimization methods have been developed, better schemes to minimize finite-size effect have been devised, and vastly improved computational facilities are available.

Recently, Zecca et al. [9] have provided a local density functional for short-range pair potentials $v(r) = \text{erfc}(\mu r)/r$, whereas Paziani et al. [10] have developed a local spin density functional for the softened-core, long range case, $v(r) = \text{erf}(\mu r)/r$.

It is the purpose of this work to build on previous work [9,10] and provide the radial distribution function (RDF), most notably the on-top value, i.e. its value at contact, at a zero radial distance, for the pair potential of reference [10], given in equation (2). A brief account of the results from this study has been presented in a recent communication [11]. Aim of the present work is to give a complete and detailed account of the calculations that has been carried on for such a study.

We performed fixed-nodes diffusion Monte Carlo simulations [12], where we used modern techniques [13] to optimize Slater-Jastrow wavefunctions with backflow and three-body correlations [14] and Hellmann and Feynman (HFM) measures [15] to calculate the RDF, particularly the on-top value, which suffers from poor statistical sampling in its conventional histogram implementation. Twist-averaged boundary conditions [16] and RPA-based corrections [17] to minimize finite-size effects were not found essential for the RDF calculation.

For the fully polarized and unpolarized fluid, we explored a range of densities and of the parameter μ . This required simulating several different systems. We also needed to evaluate and extrapolate out, for representative cases, time-step errors, population control bias, and size effects. We plan to explore intermediate polarizations in a future work.

In the study, we use two kinds of Jastrow-correlation-factors, one better for the near-Jellium systems and one better for the near-ideal systems.

An important component of a computer experiment of a system of many particles, a fluid, is the determination of suitable *estimators* to measure, through a statistical average, a given physical quantity, an observable. Whereas the average from different estimators must give the same re-

sult, the variance, the square of the statistical error, can be different for different estimators. We compare the measure of the histogram estimator for the RDF with a particular HFM one.

In ground state Monte Carlo simulations [18,19], unlike classical Monte Carlo simulations [20–22] and path integral Monte Carlo simulations [6], one has to resort to the use of a trial wavefunction [18], Ψ . While this is not a source of error, bias, in diffusion Monte Carlo simulation [19] of a system of bosons, it is for a system of Fermions, due to the sign problem [23]. Another source of bias inevitably present in all three experiments is the finite size error.

In a ground state Monte Carlo simulation, the energy has the *zero-variance* principle [24]: as the trial wavefunction approaches the exact ground state, the statistical error vanishes. In a diffusion Monte Carlo simulation of a system of bosons the local energy of the trial wavefunction,

$$E_L(\mathbf{R}) = [H\Psi(\mathbf{R})]/\Psi(\mathbf{R}),$$

where \mathbf{R} denotes a configuration of the system of particles and H is the Hamiltonian, which we will here assume to be real, is an unbiased estimator for the ground state. For fermions the ground state energy measurement is biased by the sign problem. For observables O which do not commute with the Hamiltonian the local estimator

$$O_L(\mathbf{R}) = [O\Psi(\mathbf{R})]/\Psi(\mathbf{R}),$$

is inevitably biased by the choice of the trial wavefunction. A way to remedy to this bias can be the use of the forward walking method [25,26] or the reptation quantum Monte Carlo method [27], to reach pure estimates. Otherwise this bias can be made of leading order δ^2 with $\delta = \phi_0 - \Psi$, where ϕ_0 is the ground state wavefunction, introducing the extrapolated measure $\bar{O}^{\text{ext}} = 2\langle O_L \rangle_f - \langle O_L \rangle_{f_{\text{vmc}}}$, where the first statistical average, the mixed measure, is over the diffusion Monte Carlo (DMC) stationary probability distribution f and the second, the variational measure, over the variational Monte Carlo (VMC) probability distribution f_{vmc} , which can also be obtained as the stationary probability distribution of a DMC without branching [28].

One may follow different routes to determine estimators as the *direct* microscopic one, the *virial* route through the use of the virial theorem, or the *thermodynamic* route through the use of thermodynamic identities. This aspect of finding out different ways of calculating quantum properties in some ways resembles experimental physics. The theoretical concept may be perfectly well defined but it is up to the ingenuity of the experimentalist to find the best way of doing the measurement. Even what is meant by “best” is subject to debate. In an unbiased experiment the different routes to the same observable must give the same average.

In this work, we propose to use the Hellmann and Feynman theorem as a direct route for the determination of estimators in a diffusion Monte Carlo simulation. Some attempts in this direction have been tried before [29,30]. The novelty of our approach is a different definition of the

correction to the variational measure, necessary in the diffusion experiment, respect to reference [29] and the fact that the bias stemming from the sign problem does not exhaust all the bias due to the choice of the trial wavefunction, respect to reference [30].

The work is organized as follows: in Section 2, we introduce the fluid model; in Section 3, we describe the Ewald sums technique to treat the long range pair-potential; in Section 4, we describe the fixed-nodes diffusion Monte Carlo (DMC) method; in Section 5, we describe several different ways to evaluate expectation values in a DMC calculation; in Section 6, we describe the choice of the trial wavefunction; in Section 7, we define the RDF and describe some of its exact properties; the numerical results for the RDF are presented in Section 8; Section 9 is for final remarks.

2 The model

The Jellium is an assembly of N electrons of charge e moving in a neutralizing background. The average particle number density is $n = N/\Omega$, where Ω is the volume of the fluid. In the volume Ω there is a uniform neutralizing background with a charge density $\rho_b = -en$. So that the total charge of the system is zero.

In this paper lengths will be given in units of $a = (4\pi n/3)^{-1/3}$. Energies will be given in Rydbergs $\hbar^2/(2ma_0^2)$, where m is the electron mass and $a_0 = \hbar^2/(me^2)$ is the Bohr radius.

In these units the Hamiltonian of Jellium is

$$H = -\frac{1}{r_s^2} \sum_{i=1}^N \nabla_{\mathbf{r}_i}^2 + V(\mathbf{R}), \quad (3)$$

$$V = \frac{1}{r_s} \left(2 \sum_{i<j} \frac{1}{|\mathbf{r}_i - \mathbf{r}_j|} + \sum_{i=1}^N r_i^2 + v_0 \right), \quad (4)$$

where $\mathbf{R} = (\mathbf{r}_1, \mathbf{r}_2, \dots, \mathbf{r}_N)$ with \mathbf{r}_i the coordinate of the i th electron, $r_s = a/a_0$, and v_0 a constant containing the self energy of the background.

The kinetic energy scales as $1/r_s^2$ and the potential energy (particle-particle, particle-background, and background-background interaction) scales as $1/r_s$, so for small r_s (high electronic densities), the kinetic energy dominates and the electrons behave like an ideal gas. In the limit of large r_s , the potential energy dominates and the electrons crystallize into a Wigner crystal [8,31]. No liquid phase is realizable within this model as the pair-potential has no attractive parts even though a superconducting state [32] may still be possible (see Chapt. 8.9 of Ref. [33]).

Modified long range pair-potential

The fluid model studied in this work is obtained modifying the Jellium by replacing the $1/r$ Coulomb potential

between the electrons with the following long range bare pair-potential [10]

$$v_\mu(r) = \frac{\text{erf}(\mu r)}{r}, \quad (5)$$

whose Fourier transform is

$$\tilde{v}_\mu(k) = \frac{4\pi}{k^2} e^{-\frac{k^2}{4\mu^2}}. \quad (6)$$

When $\mu \rightarrow \infty$, we recover the standard Jellium model; in the opposite limit $\mu \rightarrow 0$, we recover the non-interacting electron gas. Notice that v_μ is a long range pair-potential with a penetrable core, $v_\mu(0) = 2\mu/\sqrt{\pi}$. So μ controls the penetrability of two particles. For this kind of system it is lacking a detailed study of the RDF. In this work, we will only be concerned about the fluid phase.

3 Ewald sums

Periodic boundary conditions are necessary for extrapolating results of the finite system to the thermodynamic limit. Suppose the bare pair-potential, in infinite space, is $v(r)$,

$$v(r) = \int \frac{d\mathbf{k}}{(2\pi)^3} e^{-i\mathbf{k}\cdot\mathbf{r}} \tilde{v}(k), \quad \tilde{v}(k) = \int d\mathbf{r} e^{i\mathbf{k}\cdot\mathbf{r}} v(r). \quad (7)$$

The best pair-potential of the finite system is given by the image potential

$$v_I(r) = \sum_{\mathbf{L}} v(|\mathbf{r} + \mathbf{L}|) - \tilde{v}(0)/\Omega \quad (8)$$

where the \mathbf{L} sum is over the Bravais lattice of the simulation cell $\mathbf{L} = (m_x L, m_y L, m_z L)$, where m_x, m_y, m_z range over all positive and negative integers and $\Omega = L^3$. We have also added a uniform background of the same density but opposite charge. Converting this to k -space and using the Poisson sum formula we get

$$v_I(r) = \frac{1}{\Omega} \sum_{\mathbf{k}}' \tilde{v}(k) e^{-i\mathbf{k}\cdot\mathbf{r}}, \quad (9)$$

where the prime indicates that we omit the $\mathbf{k} = 0$ term; it cancels out with the background. The \mathbf{k} sum is over reciprocal lattice vectors of the simulation box

$$\mathbf{k}_{\mathbf{n}} = (2\pi n_x/L, 2\pi n_y/L, 2\pi n_z/L),$$

where n_x, n_y, n_z range over all positive and negative integers.

Because both sums, equations (8) and (9), are so poorly convergent [21] we follow the scheme put forward by Natoli and Ceperley [34] for approximating the image potential by a sum in k -space and a sum in r -space,

$$v_a(\mathbf{r}) = \sum_{\mathbf{L}} v_s(|\mathbf{r} + \mathbf{L}|) + \sum_{|\mathbf{k}| \leq k_c} v_I(k) e^{i\mathbf{k}\cdot\mathbf{r}} - \tilde{v}(0)/\Omega, \quad (10)$$

where $v_s(r)$ is chosen to vanish smoothly as r approaches r_c , where r_c is less than half of the distance across the simulation box in any direction. If either r_c or k_c go to infinity then $v_a \rightarrow v_I$. Natoli and Ceperley show that in order to minimize the error in the potential, it is appropriate to minimize $\chi^2 = \int_{\Omega} [v_I(r) - v_a(r)]^2 d\mathbf{r}/\Omega$, and choose for $v_s(r)$ an expansion in a fixed number of radial functions. This same technique has also been applied to treat the Jastrow-correlation-factor described in Section 6.1.

Now let us work with N particles of charge e in a periodic box and let us compute the total potential energy of the unit cell. Particles i and j are assumed to interact with a potential $e^2 v(r_{ij}) = e^2 v(|\mathbf{r}_i - \mathbf{r}_j|)$. The potential energy for the N particle system is

$$V = \sum_{i < j} e^2 v_I(r_{ij}) + \sum_i e^2 v_M, \quad (11)$$

where $v_M = \frac{1}{2} \lim_{r \rightarrow 0} [v_I(r) - v(r)]$ is the interaction of a particle with its own images; it is a Madelung constant [35] for particle i interacting with the perfect lattice of the simulation cell. If this term were not present, particle i would only see $N - 1$ particles in the surrounding cells instead of N .

4 The fixed-nodes diffusion Monte Carlo (DMC) method

Consider the Schrödinger equation for the many-body wavefunction, $\phi(\mathbf{R}, t)$ (the wavefunction can be assumed to be real, since both the real and imaginary parts of the wavefunction separately satisfy the Schrödinger equation), in imaginary time, with a constant shift E_T in the zero of the energy. This is a diffusion equation in a $3N$ -dimensional space [36]. If E_T is adjusted to be the ground-state energy, E_0 , the asymptotic solution is a steady state solution, corresponding to the ground-state eigenfunction $\phi_0(\mathbf{R})$ (provided $\phi(\mathbf{R}, 0)$ is not orthogonal to ϕ_0).

Solving this equation by a random-walk process with branching is inefficient, because the branching rate, which is proportional to the total potential $V(\mathbf{R})$, can diverge to $+\infty$. This leads to large fluctuations in the weights of the diffusers and to slow convergence when calculating averages. However, the fluctuations, and hence the statistical uncertainties, can be greatly reduced [19] by the technique of importance sampling [37].

One simply multiplies the Schrödinger equation by a known trial wavefunction $\Psi(\mathbf{R})$ that approximate the unknown ground-state wavefunction, and rewrites it in terms of a new probability distribution

$$f(\mathbf{R}, t) = \phi(\mathbf{R}, t) \Psi(\mathbf{R}), \quad (12)$$

whose normalization is given in equation (A.1). This leads to the following diffusion equation:

$$-\frac{\partial f(\mathbf{R}, t)}{\partial t} = -\lambda \nabla^2 f(\mathbf{R}, t) + [E_L(\mathbf{R}) - E_T] f(\mathbf{R}, t) + \lambda \nabla [f(\mathbf{R}, t) \mathbf{F}(\mathbf{R})]. \quad (13)$$

Here $\lambda = \hbar^2/(2m)$, t is the imaginary time measured in units of \hbar , $E_L(\mathbf{R}) = [H\Psi(\mathbf{R})]/\Psi(\mathbf{R})$ is the local energy of the trial wavefunction, and

$$\mathbf{F}(\mathbf{R}) = \nabla \ln \Psi^2(\mathbf{R}). \quad (14)$$

The three terms on the right hand side of equation (13) correspond, from left to right, to diffusion, branching, and drifting, respectively.

At sufficiently long times the solution to equation (13) is

$$f(\mathbf{R}, t) \approx N_0 \Psi(\mathbf{R}) \phi_0(\mathbf{R}) \exp[-(E_0 - E_T)t], \quad (15)$$

where $N_0 = \int \phi_0(\mathbf{R}) \phi(\mathbf{R}, 0) d\mathbf{R}$. If E_T is adjusted to be E_0 , the asymptotic solution is a stationary solution and the average $\langle E_L(\mathbf{R}) \rangle_f$ of the local energy over the stationary distribution gives the ground-state energy E_0 . If we set the branching to zero $E_L(\mathbf{R}) = E_T$ then this average would be equal to the expectation value $\int \Psi(\mathbf{R}) H \Psi(\mathbf{R}) d\mathbf{R}$, since the stationary solution to equation (13) would then be $f = f_{\text{vmc}} = \Psi^2$. In other words, without branching we would obtain the variational energy of Ψ , rather than E_0 , as in a variational Monte Carlo (VMC) calculation.

The time evolution of $f(\mathbf{R}, t)$ is given by:

$$f(\mathbf{R}', t + \tau) = \int d\mathbf{R} G(\mathbf{R}', \mathbf{R}; \tau) f(\mathbf{R}, t), \quad (16)$$

where the Green's function

$$G(\mathbf{R}', \mathbf{R}; \tau) = \Psi(\mathbf{R}') \langle \mathbf{R}' | \exp[-\tau(H - E_T)] | \mathbf{R} \rangle \Psi^{-1}(\mathbf{R})$$

is a transition probability for moving the set of coordinates from \mathbf{R} to \mathbf{R}' in a time τ . Thus, G is a solution of the same differential equation (Eq. (13)), but with the initial condition $G(\mathbf{R}', \mathbf{R}; 0) = \delta(\mathbf{R}' - \mathbf{R})$. For short times τ an approximate solution for G is

$$G(\mathbf{R}', \mathbf{R}; \tau) = (4\pi\lambda\tau)^{-3N/2} e^{-|\mathbf{R}' - \mathbf{R} - \lambda\tau\mathbf{F}(\mathbf{R})|^2/4\lambda\tau} \times e^{-\tau\{[E_L(\mathbf{R}) + E_L(\mathbf{R}')]/2 - E_T\}} + O(\tau^2). \quad (17)$$

To compute the ground-state energy and other expectation values, the N -particle distribution function $f(\mathbf{R}, t)$ is represented, in diffusion Monte Carlo, by an average over a time series of generations of walkers each of which consists of a fixed number of n_w walkers. A walker is a pair $(\mathbf{R}_\alpha, \omega_\alpha)$, $\alpha = 1, 2, \dots, n_w$, with \mathbf{R}_α a $3N$ -dimensional particle configuration with statistical weight ω_α . At time t , the walkers represent a random realization of the N -particle distribution, $f(\mathbf{R}, t) = \sum_{\alpha=1}^{n_w} \omega_\alpha^t \delta(\mathbf{R} - \mathbf{R}_\alpha^t)$. The ensemble is initialized with a VMC sample from $f(\mathbf{R}, 0) = \Psi^2(\mathbf{R})$, with $\omega_\alpha^0 = 1/n_w$ for all α . Note that if the trial wavefunction were the exact ground-state then there would be no branching and it would be sufficient $n_w = 1$. A given walker (\mathbf{R}^t, ω^t) is advanced in time (diffusion and drift) as:

$$\mathbf{R}^{t+\tau} = \mathbf{R}^t + \chi + \lambda\tau \nabla \ln \Psi^2(\mathbf{R}^t)$$

where χ is a normally distributed random $3N$ -dimensional vector with variance $2\lambda\tau$ and zero mean [38]. In order to satisfy detailed balance we accept the move with a probability

$$A(\mathbf{R}, \mathbf{R}'; \tau) = \min[1, W(\mathbf{R}, \mathbf{R}')],$$

where

$$W(\mathbf{R}, \mathbf{R}') = [G(\mathbf{R}, \mathbf{R}'; \tau)\Psi^2(\mathbf{R}')] / [G(\mathbf{R}', \mathbf{R}; \tau)\Psi^2(\mathbf{R})].$$

This step would be unnecessary if G were the exact Green's function, since W would be unity. Finally, the weight ω_α^t is replaced by $\omega_\alpha^{t+\tau} = \omega_\alpha^t \Delta\omega_\alpha^t$ (branching), with

$$\Delta\omega_\alpha^t = \exp \{-\tau[(E_L(\mathbf{R}_\alpha^t) + E_L(\mathbf{R}_\alpha^{t+\tau}))/2 - E_T]\}.$$

However, for the diffusion interpretation to be valid, f must always be positive, since it is a probability distribution. But we know that the many-fermions wavefunction $\phi(\mathbf{R}, t)$, being antisymmetric under exchange of a pair of particles of the parallel spins, must have nodes, i.e. points \mathbf{R} where it vanishes. In the fixed-nodes approximation one restricts the diffusion process to walkers that do not change the sign of the trial wavefunction. One can easily demonstrate that the resulting energy, $\langle E_L(\mathbf{R}) \rangle_f$, will be an upper bound to the exact ground-state energy; the best possible upper bound with the given boundary condition [23].

A detailed description of the algorithm used for the DMC calculation can be found in reference [28].

5 Expectation values in DMC

In a DMC calculation there are various different possibilities to measure the expectation value of a physical observable, as for example the RDF. If $\langle \mathcal{O} \rangle_f$ is the measure and $\langle \dots \rangle_f$ the statistical average over the probability distribution f we will, in the following, use the word *estimator* to indicate the function \mathcal{O} itself, unlike the more common use of the word to indicate the usual Monte Carlo estimator $\sum_{i=1}^N \mathcal{O}_i / N$ of the average, where $\{\mathcal{O}_i\}$ is the set obtained evaluating \mathcal{O} over a finite number N of points distributed according to f . Whereas the average from different estimators must give the same result, the variance, the square of the statistical error, can be different for different estimators.

5.1 The local estimator and the extrapolated measure

To obtain ground-state expectation values of quantities \mathcal{O} that do not commute with the Hamiltonian we introduce the local estimator $O_L(\mathbf{R}) = [O\Psi(\mathbf{R})]/\Psi(\mathbf{R})$ and then compute the average over the DMC walk, the so-called mixed measure,

$$\overline{O}^{\text{mix}} = \langle O_L(\mathbf{R}) \rangle_f = \int \phi_0(\mathbf{R}) O \Psi(\mathbf{R}) d\mathbf{R} / \int \phi_0(\mathbf{R}) \Psi(\mathbf{R}) d\mathbf{R}.$$

This is inevitably biased by the choice of the trial wavefunction. A way to remedy to this bias is the use of the forward walking method [25,26] or the reptation quantum Monte Carlo method [27] to reach pure estimates. Otherwise, this bias can be made of leading order δ^2 , with $\delta = \phi_0 - \Psi$, introducing the extrapolated measure

$$\overline{O}^{\text{ext}} = 2\overline{O}^{\text{mix}} - \overline{O}^{\text{var}}, \quad (18)$$

where $\overline{O}^{\text{var}} = \langle O_L \rangle_{f_{\text{vmc}}}$ is the variational measure. If the mixed measure equals the variational measure then the trial wavefunction has maximum overlap with the ground-state.

5.2 The Hellmann and Feynman measure

Toulouse et al. [15] and Assaraf and Caffarel [29] observed that the *zero-variance* property of the energy [24] can be extended to an arbitrary observable, O , by expressing it as an energy derivative through the use of the Hellmann-Feynman theorem.

In a DMC calculation the Hellmann-Feynman theorem takes a form different from the one in a VMC calculation. Namely we start with the eigenvalue expression $(H^\lambda - E^\lambda)\Psi^\lambda = 0$ for the ground-state of the perturbed Hamiltonian $H^\lambda = H + \lambda O$, take the derivative with respect to λ , multiply on the right by the ground-state at $\lambda = 0$, ϕ_0 , and integrate over the particle coordinates to get

$$\int d\mathbf{R} \phi_0 (H^\lambda - E^\lambda) \frac{\partial \Psi^\lambda}{\partial \lambda} = \int d\mathbf{R} \phi_0 \left(\frac{\partial E^\lambda}{\partial \lambda} - \frac{\partial H^\lambda}{\partial \lambda} \right) \Psi^\lambda. \quad (19)$$

Then, we notice that due to the hermiticity of the Hamiltonian, at $\lambda = 0$ the left hand side vanishes, so that we get [11]

$$\left. \frac{\int d\mathbf{R} \phi_0 O \Psi^\lambda}{\int d\mathbf{R} \phi_0 \Psi^\lambda} \right|_{\lambda=0} = \left. \frac{\partial E^\lambda}{\partial \lambda} \right|_{\lambda=0}. \quad (20)$$

This relation holds only in the $\lambda \rightarrow 0$ limit unlike the more common form [39], which holds for any λ . Also it resembles equation (3) of reference [30].

Given

$$E^\lambda = \int d\mathbf{R} \phi_0(\mathbf{R}) H^\lambda \Psi^\lambda(\mathbf{R}) / \int d\mathbf{R} \phi_0(\mathbf{R}) \Psi^\lambda(\mathbf{R}),$$

the ‘‘Hellmann and Feynman’’ (HFM) measure in a DMC calculation is

$$\begin{aligned} \overline{O}^{\text{HFM}} &= \left. \frac{dE^\lambda}{d\lambda} \right|_{\lambda=0} \approx \langle O_L(\mathbf{R}) \rangle_f \\ &+ \langle \Delta O_L^\alpha(\mathbf{R}) \rangle_f + \langle \Delta O_L^\beta(\mathbf{R}) \rangle_f. \end{aligned} \quad (21)$$

The α correction is [11]

$$\Delta O_L^\alpha(\mathbf{R}) = \left[\frac{H\Psi'}{\Psi'} - E_L(\mathbf{R}) \right] \frac{\Psi'(\mathbf{R})}{\Psi(\mathbf{R})}. \quad (22)$$

This expression coincides with equation (18) of reference [15]. In a VMC calculation this term, usually, does not contribute to the average, with respect to $f_{\text{vmc}} = \Psi^2$, due to the hermiticity of the Hamiltonian. This is of course not true in a DMC calculation. We will then define a Hellmann and Feynman variational (HF M v) estimator as $O^{\text{HF}Mv} = O_L(\mathbf{R}) + \Delta O_L^\alpha(\mathbf{R})$. The β correction is [11]

$$\Delta O_L^\beta(\mathbf{R}) = [E_L(\mathbf{R}) - E_0] \frac{\Psi'(\mathbf{R})}{\Psi(\mathbf{R})}, \quad (23)$$

where $E_0 = E^{\lambda=0}$. Which differs from equation (19) of reference [15] by a factor of one half. This term is necessary in a DMC calculation not to bias the measure. The extrapolated Hellmann and Feynman measure will then be

$$\overline{O}^{\text{HF}M\text{-ext}} = 2\overline{O}^{\text{HF}M} - \langle O^{\text{HF}Mv} \rangle_{f_{\text{vmc}}}. \quad (24)$$

Both corrections α and β to the local estimator depend on the auxiliary function, $\Psi' = \partial\Psi^\lambda/\partial\lambda|_{\lambda=0}$. Of course if we had chosen $\Psi^{\lambda=0}$, on the left hand side of equation (21), as the exact ground state wavefunction, ϕ_0 , instead of the trial wavefunction, then both corrections would have vanished. When the trial wavefunction is sufficiently close to the exact ground state function a good approximation to the auxiliary function can be obtained from first order perturbation theory for $\lambda \ll 1$. So, the Hellmann and Feynman measure is affected by the new source of bias due to the choice of the auxiliary function independent from the bias due to the choice of the trial wavefunction.

It is convenient to rewrite equations (22) and (23) in terms of the logarithmic derivative $Q(\mathbf{R}) = \Psi'(\mathbf{R})/\Psi(\mathbf{R})$ as follows:

$$\Delta O_L^\alpha(\mathbf{R}) = -\frac{1}{r_s^2} \sum_{k=1}^N [\nabla_{\mathbf{r}_k}^2 Q(\mathbf{R}) + 2\mathbf{v}_k(\mathbf{R}) \cdot \nabla_{\mathbf{r}_k} Q(\mathbf{R})], \quad (25)$$

$$\Delta O_L^\beta(\mathbf{R}) = [E_L(\mathbf{R}) - E]Q(\mathbf{R}), \quad (26)$$

where $\mathbf{v}_k(\mathbf{R}) = \nabla_{\mathbf{r}_k} \ln \Psi(\mathbf{R})$ is the drift velocity of the trial wavefunction. For each observable a specific form of Q has to be chosen.

6 Trial wavefunction

We chose the trial wavefunction of the Bijl-Dingle-Jastrow [40–42] or product form

$$\Psi(\mathbf{R}) \propto D(\mathbf{R}) \exp\left(-\sum_{i<j} u(r_{ij})\right). \quad (27)$$

The function $D(\mathbf{R})$ is the exact wavefunction of the non-interacting fermions (the Slater determinant) and serves to give the trial wavefunction the desired antisymmetry

$$D(\mathbf{R}) = \frac{1}{\sqrt{N_+!}} \det(\varphi_{n,m}^+) \frac{1}{\sqrt{N_-!}} \det(\varphi_{n,m}^-), \quad (28)$$

where for the fluid phase $\varphi_{n,m}^\sigma = e^{i\mathbf{k}_n \cdot \mathbf{r}_m} \delta_{\sigma_m, \sigma} / \sqrt{\Omega}$ with \mathbf{k}_n a reciprocal lattice vector of the simulation box such that $|\mathbf{k}_n| \leq k_F^\sigma$, σ the z -component of the spin ($\pm 1/2$), \mathbf{r}_m the coordinates of particle m , and σ_m its spin z -component. For the unpolarized fluid there are two separate determinants for the spin-up and the spin-down states because the Hamiltonian is spin independent. For the polarized fluid there is a single determinant. For the general case of N_+ spin-up particles the polarization will be $\zeta = (N_+ - N_-)/N$ and the Fermi wave-vector for the spin-up (spin-down) particles will be $k_F^\pm = (1 \pm \zeta)^{1/3} k_F$ with $k_F = (3\pi^2 n)^{1/3} = (9\pi/4)^{1/3} / (a_0 r_s)$ the Fermi wave-vector of the paramagnetic fluid. On the computer we fill closed shells so that N_σ is always odd. We only store \mathbf{k}_n for each pair $(\mathbf{k}_n, -\mathbf{k}_n)$ and use sines and cosines instead of $\exp(i\mathbf{k}_n \cdot \mathbf{r}_i)$ and $\exp(-i\mathbf{k}_n \cdot \mathbf{r}_j)$.

The second factor (the Jastrow factor) includes in an approximate way the effects of particle correlations, through the ‘‘Jastrow-correlation-factor’’, $u(r)$, which is repulsive.

6.1 The Jastrow-correlation-factor

Neglecting the cross term between the Jastrow and the Slater determinant in equation (A.6) (third term) and the Madelung constant, the variational energy per particle can be approximated as follows:

$$\begin{aligned} e_V &= \frac{\langle E_L(\mathbf{R}) \rangle_f}{N} = \frac{\int \Psi(\mathbf{R}) H \Psi(\mathbf{R}) d\mathbf{R}}{N} \\ &\approx e_F + \frac{1}{2\Omega} \sum_{\mathbf{k}} [e^2 \tilde{v}_\mu(k) - 2\lambda k^2 \tilde{u}(k)] [S(k) - 1] \\ &\quad + \frac{1}{N\Omega^2} \sum_{\mathbf{k}, \mathbf{k}'} \lambda \mathbf{k} \cdot \mathbf{k}' \tilde{u}(k) \tilde{u}(k') \langle \rho_{\mathbf{k}+\mathbf{k}'} \rho_{-\mathbf{k}} \rho_{-\mathbf{k}'} \rangle_f + \dots, \end{aligned} \quad (29)$$

where $e_F = (3/5)\lambda \sum_\sigma N_\sigma (k_F^\sigma)^2 / N$ is the non-interacting fermions energy per particle, $\tilde{u}(k)$ is the Fourier transform of the Jastrow-correlation-factor $u(r)$, $\tilde{v}_\mu(k) = 4\pi \exp(-k^2/4\mu^2)/k^2$ is the Fourier transform of the bare pair-potential, $S(k)$ is the static structure factor for a given $u(r)$ (see Sect. 7.3), $\rho_{\mathbf{k}} = \sum_{i=1}^N \exp(i\mathbf{k} \cdot \mathbf{r}_i)$ is the Fourier transform of the total number density $\rho(\mathbf{r}) = \sum_i \delta(\mathbf{r} - \mathbf{r}_i)$, and the trailing dots stand for the additional terms coming from the exclusion of the $j = k$ term in the last term of equation (A.6). Next, we make the random phase approximation [43] and we keep only the terms with $\mathbf{k} + \mathbf{k}' = \mathbf{0}$ in the last term. This gives

$$\begin{aligned} e_V &\approx e_F + \frac{1}{2\Omega} \sum_{\mathbf{k}} \left\{ [e^2 \tilde{v}_\mu(k) - 2\lambda k^2 \tilde{u}(k)] \right. \\ &\quad \left. \times [S(k) - 1] - 2n\lambda [k\tilde{u}(k)]^2 S(k) \right\} + \dots \end{aligned} \quad (30)$$

In the limit $k \rightarrow 0$, we have to cancel the Coulomb singularity and we get

$$\begin{aligned}\tilde{u}(k) &= me^2 \tilde{v}_\mu(k) / (\hbar^2 n k^2) \\ &\simeq [(4\pi e^2 / k^2) / (\hbar \omega_p)]^2\end{aligned}$$

(where $\omega_p = \sqrt{4\pi n e^2 / m}$ is the plasmon frequency) or in adimensional units

$$\tilde{u}(k) = \sqrt{\frac{r_s}{3}} \frac{4\pi}{k^2}, \quad \text{small } k. \quad (31)$$

This determines the correct behavior of $\tilde{u}(k)$ as $k \rightarrow 0$ or the long range behavior of $u(r)$

$$u(r) = \sqrt{\frac{r_s}{3}} \frac{1}{r}, \quad \text{large } r. \quad (32)$$

Now to construct the approximate Jastrow-correlation-factor, we start from the expression

$$\epsilon = e_F + \frac{1}{2\Omega} \sum_{\mathbf{k}} [e^2 \tilde{v}_\mu(k) - \mathcal{A} \lambda k^2 \tilde{u}(k)] [S(k) - 1], \quad (33)$$

and use the following perturbation approximation, for how $S(k)$ depends on $\tilde{u}(k)$ [44,45],

$$\frac{1}{S(k)} = \frac{1}{S^x(k)} + \mathcal{B} n \tilde{u}(k), \quad (34)$$

where \mathcal{A} and \mathcal{B} are constant to be determined and $S^x(k)$ the structure factor for the non-interacting fermions (see Eq. (62)), which is $S^x = \sum_{\sigma} S_{\sigma,\sigma}^x$ with

$$S_{\sigma,\sigma}^x(k) = \begin{cases} \frac{n_\sigma}{n} \frac{y_\sigma}{2} (3 - y_\sigma^2) & y_\sigma < 1 \\ \frac{n_\sigma}{n} & \text{else} \end{cases} \quad (35)$$

where $n_\sigma = N_\sigma / \Omega$ and $y_\sigma = k / (2k_F^\sigma)$.

Minimizing ϵ with respect to $u(k)$, we obtain [46]

$$\mathcal{B} n \tilde{u}(k) = -\frac{1}{S^x(k)} + \left[\frac{1}{S^x(k)} + \frac{\mathcal{B} n e^2 \tilde{v}_\mu(k)}{\lambda \mathcal{A} k^2} \right]^{1/2}. \quad (36)$$

This form is optimal at both long and short distances but not necessarily in between. In particular, for any value of ζ , the small k behavior of $\tilde{u}(k)$ is $\sqrt{2r_s/3\mathcal{A}\mathcal{B}}(4\pi/k^2)$, which means that

$$u(r) = \sqrt{\frac{2r_s}{3\mathcal{A}\mathcal{B}}} \frac{1}{r}, \quad \text{large } r. \quad (37)$$

The large k behavior of $\tilde{u}(k)$ is $(r_s/\mathcal{A})\tilde{v}_\mu(k)/k^2$, for any value of ζ , which in r space translates into

$$\left. \frac{du(r)}{dr} \right|_{r=0} = \begin{cases} -\frac{r_s}{2\mathcal{A}} & \mu \rightarrow \infty \\ 0 & \mu \text{ finite.} \end{cases} \quad (38)$$

In order to satisfy the cusp condition for particles of antiparallel spins (any reasonable Jastrow-correlation-factor

has to obey to the cusp conditions (see Ref. [13], Sect. 4.F) which prevent the local energy from diverging whenever any two electrons ($\mu = \infty$) come together) we need to choose $\mathcal{A} = 1$, then the correct behavior at large r (31) is obtained fixing $\mathcal{B} = 2^1$. We will call this Jastrow \mathcal{J}_1 in the following.

It turns out that, at small μ , but not for the Coulomb case, a better choice is given by [47]

$$2n\tilde{u}(k) = -\frac{1}{S^x(k)} + \left[\left(\frac{1}{S^x(k)} \right)^2 + \frac{2ne^2\tilde{v}_\mu(k)}{\lambda k^2} \right]^{1/2}, \quad (39)$$

which still has the correct long (37) and short (38) range behaviors. We will call this Jastrow \mathcal{J}_2 in the following. This is expected since, differently from \mathcal{J}_1 , \mathcal{J}_2 satisfies the additional exact requirement $\lim_{\mu \rightarrow 0} u(r) = 0$, as immediately follows from the definition (39). Then, as confirmed by our results (see Sect. 8.5), at small μ (and any r_s), the trial wavefunction is expected to be very close to the stationary solution of the diffusion problem.

6.2 The backflow and three-body correlations

As shown in Appendix A, the trial wavefunction of equation (27) can be further improved by adding three-body (3B) and backflow (BF) correlations [14,48] as follows:

$$\Psi(\mathbf{R}) = \tilde{D}(\mathbf{R}) \exp \left[-\sum_{i<j} \tilde{u}(r_{ij}) - \sum_{l=1}^N \mathbf{G}(l) \cdot \mathbf{G}(l) \right]. \quad (40)$$

Here

$$\tilde{D}(\mathbf{R}) = \frac{1}{\sqrt{N+!}} \det(\tilde{\varphi}_{n,m}^+) \frac{1}{\sqrt{N-!}} \det(\tilde{\varphi}_{n,m}^-), \quad (41)$$

with $\tilde{\varphi}_{n,m}^\sigma = e^{i\mathbf{k}_n \cdot \mathbf{x}_m} \delta_{\sigma_m,\sigma} / \sqrt{\Omega}$ and \mathbf{x}_m quasi-particle coordinates defined as:

$$\mathbf{x}_i = \mathbf{r}_i + \sum_{j \neq i}^N \eta(r_{ij}) (\mathbf{r}_i - \mathbf{r}_j). \quad (42)$$

The displacement of the quasi-particle coordinates \mathbf{x}_i from the real coordinate \mathbf{r}_i , incorporates effects of hydrodynamic backflow [49], and changes the nodes of the trial wavefunction. The backflow correlation function $\eta(r)$, is parametrized as [14]:

$$\eta(r) = \lambda_B \frac{1 + s_B r}{r_B + w_B r + r^4}, \quad (43)$$

¹ Note that the probability distribution in a variational calculation is (from Eq. (27)) $\Psi^2(\mathbf{R}) \propto D^2(\mathbf{R}) \exp[-2U(\mathbf{R})]$ with $U(\mathbf{R}) = \sum_{i<j} u(r_{ij})$. Then, if one formally writes $D^2(\mathbf{R}) = \exp[-2W(\mathbf{R})]$, Ψ^2 becomes the probability distribution for a classical fluid with potential $W + U$ at an inverse temperature $\beta = 2$. Then one sees that with the choice $\mathcal{B} = 2$, equation (34) coincides with the well-known random phase approximation in the theory of classical fluids (see Ref. [57] Sect. 6.5) where W is the potential of the reference fluid and U the perturbation.

Table 1. Optimized variational parameters of backflow and three-body correlation functions for $N = 54$ and $\zeta = 0$ and various combinations of r_s and μ .

r_s	μ	λ_B	s_B	r_B	w_B	a	b	c
10	1/2	-	-	-	-	-	-	-
10	1	8.408d-4	1.658d+2	-1.383d-3	3.168	0.447	-0.212	1.036
10	2	7.189d-5	9.793d+2	9.478d-6	0.446	1.379d+1	-3.688	0.450
10	4	1.116d-4	6.522d+2	-2.553d-5	0.179	5.981d+1	-4.773	0.462
10	∞	0.781	-0.499	0.324	2.958	0.514	0.327	1.358
5	1/2	-	-	-	-	-	-	-
5	1	-	-	-	-	-	-	-
5	2	2.768d-2	-0.420	0.893	-0.673	1.322d+6	-9.003	0.408
5	4	0.331	-0.680	1.467	1.442	2.729d+1	-2.607	0.659
5	∞	0.161	-0.585	0.335	0.841	0.802	-7.310d-2	1.344
2	1/2	-	-	-	-	-	-	-
2	1	-	-	-	-	-	-	-
2	2	-	-	-	-	-	-	-
2	4	5.272d-2	-1.616	1.732	1.687d-2	804.135	-2.875	0.847
2	∞	5.018d-2	-1.221	0.393	0.681	1.655	-0.596	1.229
1	1/2	-	-	-	-	-	-	-
1	1	-	-	-	-	-	-	-
1	2	-	-	-	-	-	-	-
1	4	1.187d-2	-6.834	0.495	1.295	0.186	0.489	4.739
1	∞	2.1945d-2	-3.086	0.320	1.631	0.306	0.367	2.467

which has the long-range behavior $\sim 1/r^3$.

Three-body correlations are included through the vector functions

$$\mathbf{G}(i) = \sum_{j \neq i}^N \xi(r_{ij})(\mathbf{r}_i - \mathbf{r}_j). \quad (44)$$

We call $\xi(r)$ the three-body correlation function which is parametrized as [50]:

$$\xi(r) = a \exp\{-(r-b)c\}^2. \quad (45)$$

To cancel the two-body term arising from $\mathbf{G}(l) \cdot \mathbf{G}(l)$, we use $\tilde{u}(r) = u(r) - 2\xi^2(r)r^2$

The backflow and three-body correlation functions are then chosen to decay to zero with a zero first derivative at the edge of the simulation box.

6.3 Optimized parameters

Optimizing the trial wavefunction (see Ref. [13], Sect. 7) is extremely important for a fixed-nodes DMC calculation as, even if the Jastrow-correlation-factor is parameter free, the backflow changes the nodes. We carefully studied how the RDF depends on the quality of the trial wavefunction choosing a simple Slater determinant (S) (Eq. (27) without the Jastrow factor), a Slater-Jastrow (SJ) (Eq. (27)), and a Slater-Jastrow with the backflow and three-body corrections (SJ+BF+3B) (Eq. (40)).

In Table 1, we report the optimized parameters for the backflow and three-body correlation functions for a system of $N = 54$ and $\zeta = 0$ at various r_s and μ . We have used these values of the parameters in all subsequent calculations, irrespective of the value of ζ .

In Figure 1, we show the optimized η and ξ for $N = 54$, $\zeta = 0$, $r_s = 10$. The optimization of the 7 parameter dependent trial wavefunction gives a backflow correlation η ordered in μ but a three-body correlation ξ erratic in μ . As one moves away from the Coulomb $\mu \rightarrow \infty$ case the system of particles becomes less interacting and the relevance of the backflow and three-body correlations diminishes. This is supported by the fact that at $\mu = 4, 2, 1$, in correspondence of the erratic behavior, the effect of the three-body correlations on the expectation value of the energy is irrelevant.

7 The radial distribution function (RDF)

The main purpose of the present work is to determine the radial distribution function (RDF) of our fluid model through the DMC calculation.

7.1 Definition of the radial distribution function

The spin-resolved RDF is defined as [51,52]:

$$g_{\sigma,\sigma'}(\mathbf{r}, \mathbf{r}') = \frac{\langle \sum_{i,j \neq i} \delta_{\sigma,\sigma_i} \delta_{\sigma',\sigma_j} \delta(\mathbf{r} - \mathbf{r}_i) \delta(\mathbf{r}' - \mathbf{r}_j) \rangle}{n_{\sigma}(\mathbf{r}) n_{\sigma'}(\mathbf{r}')}, \quad (46)$$

$$n_{\sigma}(\mathbf{r}) = \left\langle \sum_{i=1}^N \delta_{\sigma,\sigma_i} \delta(\mathbf{r} - \mathbf{r}_i) \right\rangle, \quad (47)$$

where here, and in the following, $\langle \dots \rangle$ will denote the expectation value respect to the ground-state. Two exact

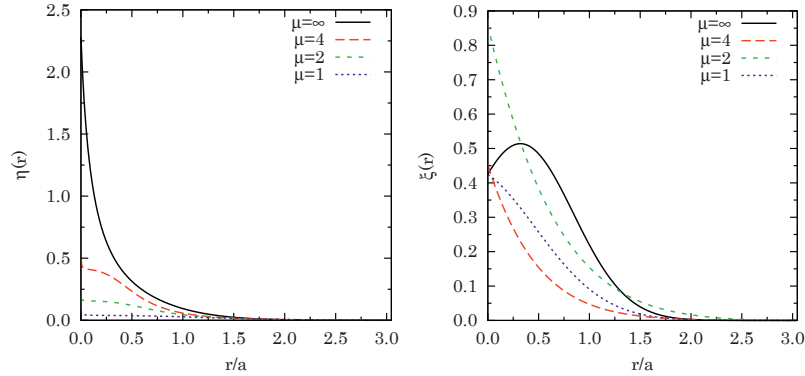


Fig. 1. The optimized correlation functions η and ξ for $N = 54$, $\zeta = 0$, and $r_s = 10$ and different values of μ .

conditions follow immediately from the definition: (i) the zero-moment sum rule

$$\sum_{\sigma, \sigma'} \int d\mathbf{r} d\mathbf{r}' n_{\sigma}(\mathbf{r}) n_{\sigma'}(\mathbf{r}') [g_{\sigma, \sigma'}(\mathbf{r}, \mathbf{r}') - 1] = -N, \quad (48)$$

also known as the charge (monopole) sum rule in the sequence of multipolar sum rules in the framework of charged fluids [53], (ii) $g_{\sigma, \sigma}(\mathbf{r}, \mathbf{r}) = 0$ due to the Pauli exclusion principle.

For the homogeneous and isotropic fluid $n_{\sigma}(\mathbf{r}) = N_{\sigma}/\Omega$ where N_{σ} is the number of particles of spin σ and $g_{\sigma, \sigma'}$ depends only on the distance $r = |\mathbf{r} - \mathbf{r}'|$, so that

$$g_{\sigma, \sigma'}(r) = \frac{1}{4\pi r^2} \frac{\Omega}{N_{\sigma} N_{\sigma'}} \left\langle \sum_{i, j \neq i} \delta_{\sigma, \sigma_i} \delta_{\sigma', \sigma_j} \delta(r - r_{ij}) \right\rangle. \quad (49)$$

The total (spin-summed) radial distribution function will be

$$\begin{aligned} g(r) &= \frac{1}{n^2} \sum_{\sigma, \sigma'} n_{\sigma} n_{\sigma'} g_{\sigma, \sigma'}(r) \\ &= \left(\frac{1+\zeta}{2} \right)^2 g_{+,+}(r) + \left(\frac{1-\zeta}{2} \right)^2 g_{-,-}(r) \\ &\quad + \frac{1-\zeta^2}{2} g_{+,-}(r). \end{aligned} \quad (50)$$

7.2 From the structure to the thermodynamics

As it is well-known the knowledge of the RDF gives access to the thermodynamic properties of the system. The mean potential energy per particle can be directly obtained from $g(r)$ and the bare pair-potential $v_{\mu}(r)$ as follows:

$$e_p = \sum_{\sigma, \sigma'} \frac{n_{\sigma} n_{\sigma'}}{2n} \int d\mathbf{r} e^2 v_{\mu}(r) [g_{\sigma, \sigma'}(r) - 1], \quad (51)$$

where we have explicitly taken into account of the background contribution. Suppose that $e_p(r_s)$ is known as a

function of the coupling strength r_s . The virial theorem for a system with Coulomb interactions ($v_{\infty}(r) = 1/r$) gives $N(2e_k + e_p) = 3P\Omega$ with $P = -d(Ne_0)/d\Omega$ the pressure and $e_0 = e_k + e_p$ the mean total ground-state energy per particle. We then find

$$e_p(r_s) = 2e_0(r_s) + r_s \frac{de_0(r_s)}{dr_s} = \frac{1}{r_s} \frac{d}{dr_s} [r_s^2 e_0(r_s)], \quad (52)$$

which integrates to

$$e_0(r_s) = e_F + \frac{1}{r_s^2} \int_0^{r_s} dr' r'_s e_p(r'_s). \quad (53)$$

We can rewrite the ground-state energy per particle of the ideal Fermi gas, in reduced units, as

$$e_F = \left(\frac{9\pi}{4} \right)^{2/3} \frac{3}{10} \phi_5(\zeta) \frac{1}{r_s^2}, \quad (54)$$

where $\phi_n(\zeta) = (1-\zeta)^{n/3} + (1+\zeta)^{n/3}$. And for the exchange potential energy per particle in the Coulomb case

$$e_p^x = - \left(\frac{2}{3\pi^5} \right)^{1/3} \frac{9\pi}{8} \phi_4(\zeta) \frac{1}{r_s}, \quad (55)$$

which follows from equation (51) and equations (59), (60). The expression for finite μ can be found in reference [10] (see their Eqs. (15), (16)).

7.3 Definition of the static structure factor

If we introduce the microscopic spin dependent number density

$$\rho_{\sigma}(\mathbf{r}) = \sum_{i=1}^N \delta_{\sigma, \sigma_i} \delta(\mathbf{r} - \mathbf{r}_i), \quad (56)$$

and its Fourier transform $\rho_{\mathbf{k}, \sigma}$, then the spin-resolved static structure factors are defined as:

$$S_{\sigma, \sigma'}(\mathbf{k}) = \langle \rho_{\mathbf{k}, \sigma} \rho_{-\mathbf{k}, \sigma'} \rangle / N,$$

which, for the homogeneous and isotropic fluid, can be rewritten as

$$S_{\sigma,\sigma'}(k) = \frac{n_\sigma}{n} \delta_{\sigma,\sigma'} + \frac{n_\sigma n_{\sigma'}}{n} \int [g_{\sigma,\sigma'}(r) - 1] \times e^{-i\mathbf{k}\cdot\mathbf{r}} d\mathbf{r} + \frac{n_\sigma n_{\sigma'}}{n} (2\pi)^3 \delta(\mathbf{k}). \quad (57)$$

From now on we will ignore the delta function at $\mathbf{k} = 0$. The total (spin-summed) static structure factor is $S = \sum_{\sigma,\sigma'} S_{\sigma,\sigma'}$. Due to the charge sum rule (48) we must have $\lim_{k \rightarrow 0} S(k) = 0$. In Section 7.3.2 we will show that the small k behavior of $S(k)$ has to start from the term of order k^2 .

7.3.1 Analytic expressions for the non-interacting fermions

Usually $g_{\sigma,\sigma'}$ is conventionally divided into the (known) exchange and the (unknown) correlation terms

$$g_{\sigma,\sigma'} = g_{\sigma,\sigma'}^x + g_{\sigma,\sigma'}^c, \quad (58)$$

where the exchange term corresponds to the uniform system of non-interacting fermions.

Radial distribution function

We, thus, have (from the definition of the RDF (46) and using Slater determinants for the wavefunction)

$$g_{+,-}^x(r) = 1, \quad (59)$$

$$g_{\sigma,\sigma}^x(r) = 1 - \left[\frac{3j_1(k_F^\sigma r)}{k_F^\sigma r} \right]^2, \quad (60)$$

where $j_1(x) = [\sin(x) - x \cos(x)]/x^2$ is the spherical Bessel function of the first kind and $(k_F^\sigma)^3 = 6\pi^2 n_\sigma$ is the Fermi wave-number for particles of spin σ .

Static structure factor

Again we will have the splitting $S_{\sigma,\sigma'} = S_{\sigma,\sigma'}^x + S_{\sigma,\sigma'}^c$ into the exchange and the correlation parts. So that for the non-interacting fermions we get

$$S_{+,-}^x(k) = 0, \quad (61)$$

$$S_{\sigma,\sigma}^x(k) = \frac{n_\sigma}{n} - \frac{n_\sigma^2}{n} \Theta(2k_F^\sigma - k) \times \frac{3\pi^2}{(k_F^\sigma)^3} \left(1 - \frac{k}{2k_F^\sigma}\right)^2 \left(2 + \frac{k}{2k_F^\sigma}\right) = \frac{n_\sigma}{n} \begin{cases} 1 & k > 2k_F^\sigma \\ \frac{3}{4} \frac{k}{k_F^\sigma} - \frac{1}{16} \left(\frac{k}{k_F^\sigma}\right)^3 & k < 2k_F^\sigma, \end{cases} \quad (62)$$

where $\Theta(x)$ is the Heaviside step function.

7.3.2 RDF sum rules

Both the behaviors of the RDF at small r and at large r have to satisfy to general exact relations or sum rules.

Cusp conditions

When two electrons ($\mu = \infty$) get closer and closer together, the behavior of $g_{\sigma,\sigma'}(r)$ is governed by the exact cusp conditions [54–56]

$$\left. \frac{d}{dr} g_{\sigma,\sigma}(r) \right|_{r \rightarrow 0} = 0, \quad (63)$$

$$\left. \frac{d^3}{dr^3} g_{\sigma,\sigma}(r) \right|_{r \rightarrow 0} = \frac{3}{2a_0} \left. \frac{d^2}{dr^2} g_{\sigma,\sigma}(r) \right|_{r \rightarrow 0}, \quad (64)$$

$$\left. \frac{d}{dr} g_{+,-}(r) \right|_{r \rightarrow 0} = \frac{1}{a_0} g_{+,-}(0), \quad (65)$$

where in the adimensional units $a_0 \rightarrow 1/r_s$. For finite μ , we only have the condition $g_{\sigma,\sigma}(0) = 0$ due to Pauli exclusion principle.

The random phase approximation (RPA) and the long range behavior of the RDF

Within the linear density response theory [57]² one introduces the space-time Fourier transform, $\chi(\mathbf{k}, \omega)$, of the linear density response function. Which is related through the fluctuation dissipation theorem,

$$S(\mathbf{k}, \omega) = -(2\hbar/n)\Theta(\omega)\text{Im}\chi(\mathbf{k}, \omega),$$

to the space-time Fourier transform, $S(\mathbf{k}, \omega)$ (dynamic structure factor), of the van Hove correlation function [58], $\langle \rho(\mathbf{r}, t)\rho(\mathbf{0}, 0) \rangle / n$, where

$$\rho(\mathbf{r}, t) = \exp(iHt/\hbar)\rho(\mathbf{r})\exp(-iHt/\hbar).$$

In the random phase approximation (RPA) we have [59]

$$\frac{1}{\chi_{RPA}(k, \omega)} = \frac{1}{\chi_0(k, \omega)} - e^2 \tilde{v}_\mu(k), \quad (66)$$

where χ_0 is the response function of the non-interacting Fermions (ideal Fermi gas), known as the Lindhard susceptibility [60]. This corresponds to taking the ‘‘proper polarizability’’ (the response to the Hartree potential) equal to the response of the ideal Fermi gas [61]. The RPA static structure factor is then recovered from the fluctuation dissipation theorem as follows:

$$S_{RPA}(k) = -\frac{\hbar}{n} \int_0^\infty \frac{d\omega}{\pi} \text{Im}\chi_{RPA}(k, \omega), \quad (67)$$

² Note that, unlike in the classical case, in quantum statistical physics even the linear response to a static perturbation requires the use of imaginary time correlation functions [53].

where

$$\text{Im}\chi_{RPA} = \frac{\text{Im}\chi_0}{(1 - e^2\tilde{v}_\mu \text{Re}\chi_0)^2 + (e^2\tilde{v}_\mu \text{Im}\chi_0)^2}. \quad (68)$$

The small k behavior of the RPA structure factor is exact [59]. One finds

$$S_{RPA}(k) = \frac{\hbar k^2}{2m\omega_p}, \quad k \ll k_F, \quad (69)$$

where $\omega_p = \sqrt{4\pi n e^2/m}$ is the plasmon frequency [33]. This is also known as the second-moment sum rule for the exact RDF and can be rewritten as: $n \int d\mathbf{r} r^2 [g(r) - 1] = -6(\hbar/2m\omega_p)$. We can then say that $g(r) - 1$ has to decay faster than r^{-5} at large r . The fourth-moment (or compressibility) sum rule links the thermodynamic compressibility, $\chi = [nd(n^2 de_0/dn)/dn]^{-1}$ [61], to the fourth-moment of the RDF. For the equivalent classical system it is well-known that the correlation functions have to decay faster than any inverse power of the distance [53,62,63] (in accord with the Debye-Hückel theory). We are not aware of the existence of a similar result for the zero temperature quantum case.

8 Results of the calculation

We considered fourty systems corresponding to $r_s = 1, 2, 5, 10$, $\mu = \infty, 4, 2, 1, 1/2$, $\zeta = 0, 1$. For each system we calculated the RDF using the histogram estimator in a variational, mixed, and extrapolated measure and a particular HFM measure. Before starting with the simulations we determined the optimal values for the time step τ and the number of walkers n_w for each density.

8.1 Extrapolations

For the Coulomb case, $\mu \rightarrow \infty$, we made extrapolations in time step τ and number of walkers n_w for each value of r_s within our DMC simulations. Given a relative precision $\delta_{e_0} = \Delta e_0/e_p^x$, where $e_0 = \langle E_L \rangle_f/N$, Δe_0 is the statistical error on e_0 , and e_p^x is the exchange energy per particle (see Eq. (55)), we set as our target relative precision $\delta_{e_0} = 10^{-2}\%$.

8.1.1 In time step

Our results are summarized in Table 2. As the characteristic dimension of one particle diffusing walk is $\sigma = \sqrt{2\lambda\tau}$ or $\sqrt{2\tau/r_s^2}$ in dimensional units, this has to remain of the order of the mean nearest neighbor separation a which is chosen to be a constant in our units. Then we expect that at lower r_s one needs to choose smaller time steps τ . For this reason we chose different time steps in the simulations of the table: $\tau = 0.5, 0.1, 0.05$ for $r_s = 10$, $\tau = 0.3, 0.1, 0.05$ for $r_s = 5$, $\tau = 0.05, 0.03, 0.005$ for $r_s = 2$, and $\tau = 0.01, 0.005, 0.001$ for $r_s = 1$. Note that, at fixed r_s , the statistical errors increase as the time step diminishes.

Table 2. Extrapolation in time step for $N = 66$ unpolarized electrons ($\mu = \infty$) at a fixed number of $n_w = 600$ walkers with a trial wavefunction of the SJ type. We run the simulation for 3 different time steps and did a linear fit of the (τ, e_0) data, $e_0 = a + b\tau$. The optimal τ is the largest one compatible with the target precision.

r_s	a	b	χ^2	Optimal τ
10	-0.107456(7)	0.00010(2)	0.9	0.09
5	-0.153352(4)	0.00024(3)	0.1	0.07
2	-0.00416(8)	0.003(2)	4.4	0.01
1	1.14579(7)	0.032(9)	1.1	0.003

Table 3. Extrapolation in number of walkers for $N = 66$ unpolarized electrons ($\mu = \infty$) with a time step $\tau = 0.1$ for $r_s = 10, 5$, $\tau = 0.05$ for $r_s = 2$, and $\tau = 0.01$ for $r_s = 1$ with a trial wavefunction of the SJ type. We run the simulation for 4 different numbers of walkers and did a linear fit of the $(1/n_w, e_0)$ data, $e_0 = a + b/n_w$. The optimal n_w is the smallest one compatible with the target precision.

r_s	a	b	χ^2	optimal n_w
10	-0.107443(3)	0.0032(4)	0.1	354
5	-0.153329(6)	0.0044(7)	0.2	243
2	-0.004036(6)	0.0026(7)	0.2	56
1	1.14609(6)	0.01(1)	1.2	40

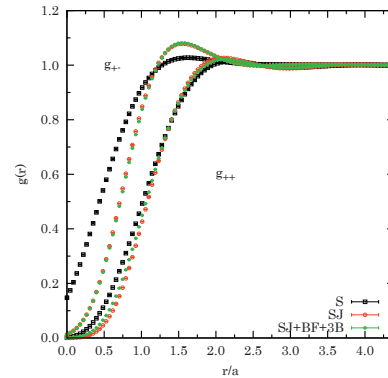


Fig. 2. The mixed measure of the RDF calculated in DMC for $N = 162$, $\zeta = 0$, $\mu = \infty$, $r_s = 10$ with a S, SJ, SJ + BF + 3B trial wavefunction.

8.1.2 In the number of walkers

Our results are summarized in Table 3. The fluctuations of the statistical weight of a walker depend on the fluctuations of the local energy, i.e. by the quality of the trial wavefunction. The quality of the trial wavefunction worsens as r_s becomes larger (for the strongly correlated system), and one expects that the necessary number of walkers increases. This is in agreement with the results of the table. Note that, at fixed r_s , the statistical errors increase as the number of walkers diminishes.

8.2 Effect of backflow and three-body correlations

In Figure 2, we show the mixed measure of the RDF calculated in DMC for $N = 162$, $\zeta = 0$, $\mu = \infty$, $r_s = 10$

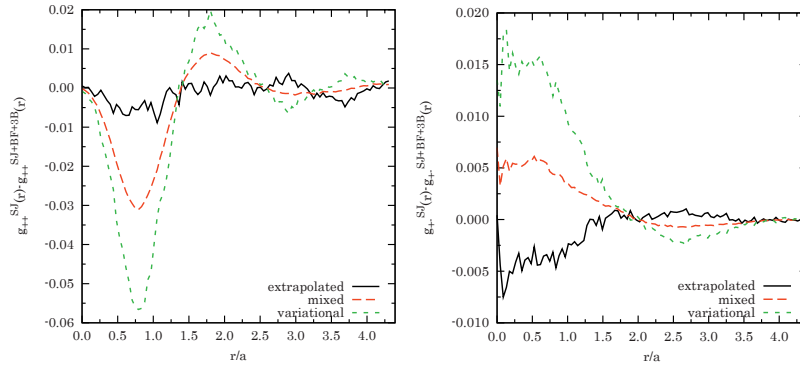


Fig. 3. The difference between the RDF calculated with the SJ wavefunction and the one calculated with the SJ + BF + 3B wavefunction using the variational, the mixed, and the extrapolated measure. The results are for $N = 162$, $\zeta = 0$, $\mu = \infty$. On the left, the like RDF is used at $r_s = 10$, on the right, the unlike RDF at $r_s = 1$.

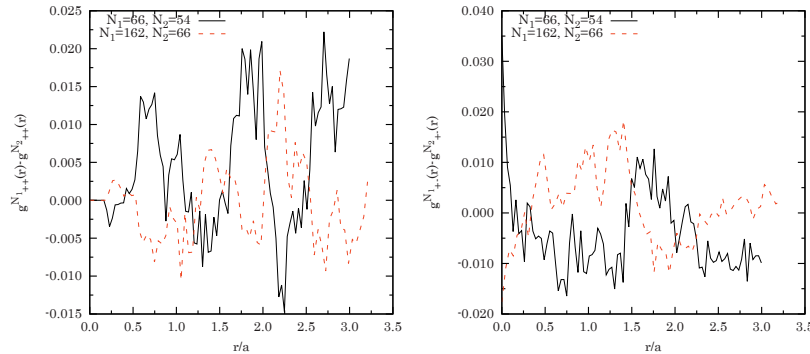


Fig. 4. The difference between the RDF of two systems of electrons ($\mu = \infty$) at $r_s = 10$ and $\zeta = 0$ with different sizes N_1 and N_2 . The RDF are calculated in VMC with the SJ wavefunction. On the left, the difference of the like RDF is shown and on the right, the difference of the unlike RDF is shown.

with different kinds of trial wavefunctions. Of course in a VMC calculation using the Slater determinant wavefunction gives us $g_{\sigma,\sigma'}^x$, the RDF of the ideal gas (see Eqs. (59) and (60)).

In Figure 3, we show the difference between the RDF calculated with the SJ wavefunction and the one calculated with the SJ + BF + 3B wavefunction using the variational, the mixed, and the extrapolated measure.

With the extrapolated measure the results from the SJ computation differs by less than 0.005 from the ones from the SJ + BF + 3B. We then decided to perform our subsequent calculations using the SJ trial wavefunction.

8.3 Size effects

In order to estimate the size effects on the RDF calculation, we performed a series of VMC calculation with the SJ wavefunction on an unpolarized system with different number of particles. The results (see Fig. 4) show that the

size dependence mainly affects the long range behavior of the RDF and the on-top value for the unlike one.

In the simulation the RDF is defined on $r \in [0, r_{\max}]$ with $r_{\max} = L/2$, where $L = \Omega^{1/3} = (4\pi N/3)^{1/3}$ is the size of the simulation box. To minimize size effects we chose to perform our RDF calculation with $N = 162$ in the unpolarized case and $N = 147$ in the polarized case.

8.4 The HFM measure

From the definition (49), we can write the RDF as:

$$g_{\sigma,\sigma'}(r) = \frac{\langle I_{\sigma,\sigma'}(r, \mathbf{R}) \rangle}{\Omega n_{\sigma} n_{\sigma'}}. \quad (70)$$

Since the operator $I_{\sigma,\sigma'}$ is diagonal in coordinate representation then $I_{\sigma,\sigma'} = (I_{\sigma,\sigma'})_L$. Indicating with $\Omega_{\mathbf{r}}$ the solid angle spanned by the \mathbf{r} vector, we can write

$$I_{\sigma,\sigma'}(r, \mathbf{R}) = \sum_{i,j \neq i} \delta_{\sigma,\sigma_i} \delta_{\sigma',\sigma_j} \int \frac{d\Omega_{\mathbf{r}}}{4\pi} \delta(\mathbf{r} - \mathbf{r}_{ij}), \quad (71)$$

which is the usual histogram estimator [21]. Following Toulouse et al. [15], we choose for Q the following expression:

$$Q_{\sigma,\sigma'}(r, \mathbf{R}) = -\frac{r_s^2}{8\pi} \sum_{i,j \neq i} \delta_{\sigma,\sigma_i} \delta_{\sigma',\sigma_j} \int \frac{d\Omega_{\mathbf{r}}}{4\pi} \frac{1}{|\mathbf{r} - \mathbf{r}_{ij}|}, \quad (72)$$

so that (using the identities $\nabla_{\mathbf{r}_{ij}}^2 1/|\mathbf{r} - \mathbf{r}_{ij}| = -4\pi\delta(\mathbf{r} - \mathbf{r}_{ij})$ and $\nabla_{\mathbf{r}_i} f(\mathbf{r}_{kj}) = \nabla_{\mathbf{r}_{kj}} f(\mathbf{r}_{kj})[\delta_{ik} - \delta_{ij}]$, for a given function f) the first term in equation (25) exactly cancels the histogram estimator $I_{\sigma,\sigma'}$. Then the HFMv estimator is

$$\begin{aligned} I_{\sigma,\sigma'}^{\text{HFMv}}(r, \mathbf{R}) &= \frac{1}{2\pi} \sum_{i,j \neq i} \delta_{\sigma,\sigma_i} \delta_{\sigma',\sigma_j} \mathbf{v}_i(\mathbf{R}) \cdot \int \frac{d\Omega_{\mathbf{r}}}{4\pi} \nabla_{\mathbf{r}_{ij}} \\ &\quad \times \frac{1}{|\mathbf{r} - \mathbf{r}_{ij}|} \\ &= -\frac{1}{4\pi} \sum_{i,j \neq i} \delta_{\sigma,\sigma_i} \delta_{\sigma',\sigma_j} \mathbf{v}_i(\mathbf{R}) \cdot \frac{\mathbf{r}_{ij}}{r_{ij}^3} \\ &\quad \times [1 + \text{sgn}(r_{ij} - r)], \end{aligned} \quad (73)$$

which goes to zero at large r ³. The correct (taking care of the missing factor of two in Ref. [15]) β correction is

$$\begin{aligned} \Delta I_{\sigma,\sigma'}^\beta(r, \mathbf{R}) &= -[E_L(\mathbf{R}) - E_0] \frac{r_s^2}{8\pi} \\ &\quad \times \sum_{i,j \neq i} \delta_{\sigma,\sigma_i} \delta_{\sigma',\sigma_j} \int \frac{d\Omega_{\mathbf{r}}}{4\pi} \frac{1}{|\mathbf{r} - \mathbf{r}_{ij}|} \\ &= -[E_L(\mathbf{R}) - E_0] \frac{r_s^2}{16\pi} \\ &\quad \times \sum_{i,j \neq i} \delta_{\sigma,\sigma_i} \delta_{\sigma',\sigma_j} \left(\frac{r_{ij} + r - |r_{ij} - r|}{r_{ij}r} \right). \end{aligned} \quad (74)$$

Note that also $\langle \Delta I_{\sigma,\sigma'}^\beta(r, \mathbf{R}) \rangle$ goes to zero at large r . This particular HFM measure needs to be shifted $g_{\sigma,\sigma'}(r) = g_{\sigma,\sigma'}^{\text{HFM}}(r) + 1$. We chose to do the shift as follows:

$$g_{\sigma,\sigma'}(r) = g_{\sigma,\sigma'}^{\text{HFM}}(r) + g_{\sigma,\sigma'}^{\text{mix}}(L/2) - g_{\sigma,\sigma'}^{\text{HFM}}(L/2).$$

Nonetheless it is expected to give better results for the on-top value of the RDF where the histogram estimator of equation (49), after the necessary discretization of the Dirac delta function, leads, in the measure, to a statistical average divided by zero. Moreover it does not suffer from any discretization error and can be calculated for any value of r .

In Figure 5, we show a comparison for the RDF of the $N = 162, \zeta = 0, \mu = \infty, r_s = 10$ system, calculated in DMC SJ with various kinds of measures. The length of

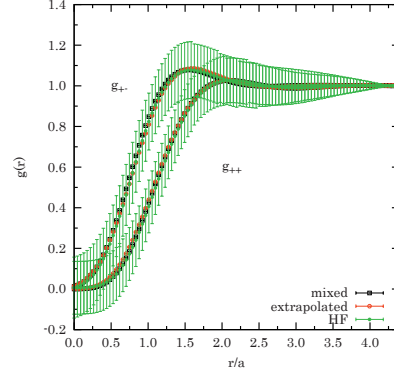


Fig. 5. The RDF of the $N = 162, \zeta = 0, \mu = \infty, r_s = 10$ system, calculated in DMC SJ with various kinds of measures: mixed histogram (mixed), extrapolated histogram (extrapolated), and HFM (HF) with the choice of equation (72).

the run was always the same 50 blocks of 500 steps each. From the figure one can see that with our choice of the β correction the HFM measure has the correct average value (coinciding with the usual histogram estimator). From the figure it is also evident that the HFM measure is much less efficient than the other measures (clearly with a sufficient number of blocks the statistical error on the HFM measure can be made small at will).

This inefficiency is entirely due to the ZB correction (essential in the DMC calculation). From its definition (see Eq. (74)) one can see that it is the small difference of two large terms involving the (extensive) total energy. So the statistical error on the HFM measure is completely dominated by that of the β part, the α part having statistical errors comparable with the ones of the usual histogram estimator, as shown in the left panel of Figure 6.

8.5 Choice of the Jastrow

We noticed that at small r_s, μ , and r the variational measure for the unlike RDF, with the chosen Jastrow \mathcal{J}_1 of equation (36), deviates strongly from the mixed one. This is no longer so with the modified Jastrow \mathcal{J}_2 of equation (39), which at small μ gives also better variational energies (but not for $\mu \rightarrow \infty$ where \mathcal{J}_1 is better. Note that the Jastrow factor does not change the nodes of the wavefunction so the energies calculated from the diffusion with \mathcal{J}_1 or \mathcal{J}_2 coincide). The extrapolated measures do not change appreciably in the two cases apart from near $r = 0$. In Figure 6 we show the difference for the two calculations with \mathcal{J}_1 and \mathcal{J}_2 for the $\zeta = 0, r_s = 1, \mu = 1$ model. From the inset in the left panel, we can see that among the two extrapolated measures there is a difference of the order of 0.005.

Our results with the two Jastrow factors show that \mathcal{J}_1 is better than \mathcal{J}_2 for the near-Jellium systems (μ large) while \mathcal{J}_2 is better than \mathcal{J}_1 for the near-ideal systems (μ small).

³ Note that with the given choice of Q we obtain $\langle \Delta I_{\sigma,\sigma'}^\alpha(r, \mathbf{R}) \rangle_{\Psi^2} = -\int_{\partial\Omega^N} \Psi^2(\mathbf{R}) \nabla Q_{\sigma,\sigma'}(r, \mathbf{R}) \cdot d\mathbf{S}/r_s^2 = -\Omega n_\sigma n_{\sigma'}$, for all r with $\mathbf{r} \in \Omega$, instead of zero as normally expected. This is ultimately related to the behavior of the auxiliary function $\Psi' = Q\Psi$ on the border of Ω^N .

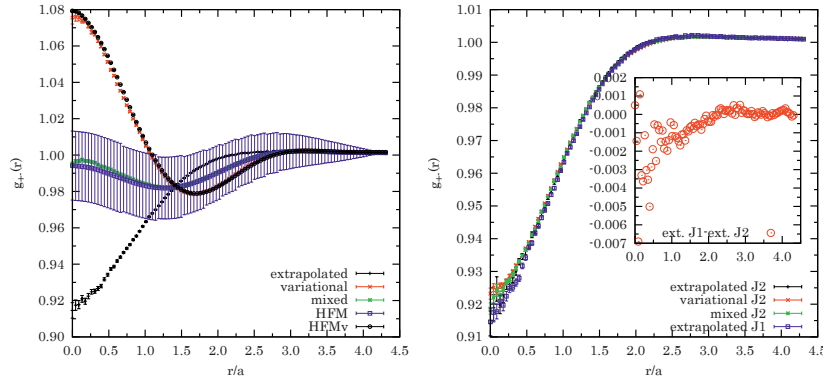


Fig. 6. Unlike RDF for the unpolarized fluid of Paziani et al. [10] at $r_s = 1$ and $\mu = 1$ with $N = 162$. On the left, the calculation with the Jastrow \mathcal{J}_1 of equation (36) with various measures: variational histogram (variational) and variational HFMv (HFMv) using the estimator of equation (73), mixed histogram (mixed) and HFM (HFM), and extrapolated histogram (extrapolated). On the right, the calculation with the Jastrow \mathcal{J}_2 of equation (39) with the histogram variational (variational), mixed (mixed), and extrapolated (extrapolated) measures. In the inset is shown the difference between the histogram extrapolated measure of the calculation with \mathcal{J}_1 and the histogram extrapolated measure of the calculation with \mathcal{J}_2 . 10^5 Monte Carlo steps were used in the simulations.

8.6 The histogram estimator

In Figure 7, we show the DMC results for the histogram extrapolated measure of the RDF of our fluid model at $\zeta = 0$. The time step, τ , and number of walkers, n_w , were chosen according to the indications given in Section 8.1. Figure 8 is for the $\zeta = 1$ case.

In Table 4, we show the on-top values for the unlike RDF, $g_{+-}(0)$, of the unpolarized system, calculated with the histogram variational, the histogram mixed, the histogram extrapolated measure, the HFM measure, and the HFM extrapolated measure (of Eq. (24)).

9 Conclusions

We studied through variational and diffusion Monte Carlo techniques the fluid of spin one-half particles interacting with the bare pair-potential $v_\mu(r) = \text{erf}(\mu r)/r$ and immersed in a uniform counteracting background. When $\mu \rightarrow \infty$ the system reduces to the Jellium model whereas when $\mu \rightarrow 0$ it reduces to the ideal Fermi gas. We performed a detailed analysis of the spin-resolved radial distribution function for this system as a function of the density parameter $r_s = 1, 2, 5, 10$ and the penetrability parameter $\mu = 1/2, 1, 2, 4, \infty$ at two values of the polarization, $\zeta = 0, 1$.

Initially we carefully fine tuned our DMC calculation determining the optimal values for the time step τ and the number of walkers n_w for each value of the density parameter r_s . Increasing the system size N the RDF extends its range $[0, r_{\text{max}}]$ at larger r_{max} . We estimated that for $N \geq 66$ the size dependence of the RDF is lower than 2%. As a compromise between computational cost and reduction of the size effects, the largest uncontrolled source of uncertainty on our RDF measurements, we chose to

perform the RDF calculation with $N = 162$ in the unpolarized case and $N = 147$ in the polarized case.

We calculated the RDF using two different routes: through the usual histogram estimator and through a particular HFM measure. As expected, in the VMC calculations the HFMv estimator gives better results for the on-top value of the RDF. In the DMC calculation the inclusion of the β correction (which must be omitted in the VMC calculation) is indispensable. Moreover, the HFMv estimator is zero for $r > r_{\text{max}}$ so it has to be shifted by +1. From our variational and fixed nodes diffusion Monte Carlo experiments turns out that although in the variational measure the average of the histogram estimator agrees with the average of the HFMv estimator within the square root of the variance of the average $\sigma_{\text{av}} = \sqrt{\sigma^2 \mathcal{K} / \mathcal{N}}$, where σ^2 is the variance, \mathcal{K} the correlation time of the random walk, and \mathcal{N} the number of Monte Carlo steps, and the two σ_{av} are comparable, in the diffusion experiment, where one has to add the β correction not to bias the average, the Hellmann and Feynman measure has an average in agreement with the one of the histogram estimator but the σ_{av} increases. This is to be expected from the extensive nature of the β correction in which the energy appears. Of course the averages from the extrapolated Hellmann and Feynman measure and the extrapolated measure for the histogram estimator also agree.

In the simulation, for the Coulomb case, $\mu \rightarrow \infty$, we made extrapolations in time step and number of walkers for each value of r_s . Given a relative precision $\delta_{e_0} = \Delta e_0 / e_p^x$, where $e_0 = \langle E_L \rangle_f / N$, Δe_0 is the statistical error on e_0 , and e_p^x is the exchange energy, we set as our target relative precision $\delta_{e_0} = 10^{-2}\%$. The extrapolated values of the time step and number of walkers was then used for all other values of μ . We chose the trial wavefunction of the Bijl-Dingle-Jastrow [40–42] form as a product of Slater

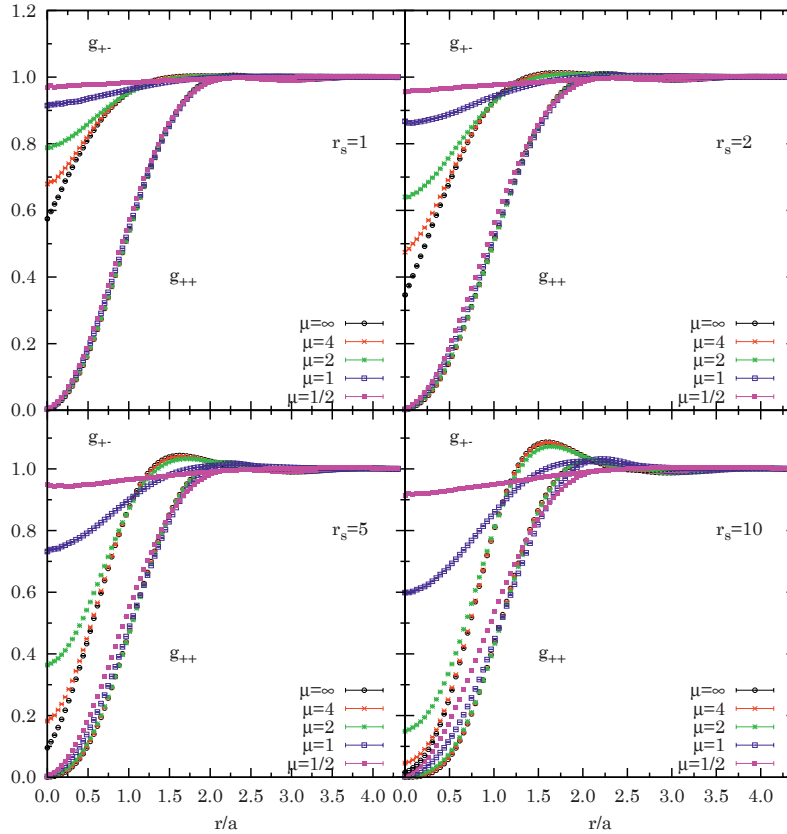


Fig. 7. The histogram extrapolated measure for the RDF of a system of 162 unpolarized ($\zeta = 0$) particles calculated using the SJ trial wavefunction. The VMC calculation was made of 10^6 steps while the DMC by 10^5 . The trial wavefunction used was of the SJ type with the Jastrow \mathcal{J}_1 of equation (36).

determinants and a Jastrow factor. The pseudo potential was chosen as in reference [46], \mathcal{J}_2 , which is expected to give better results for Jellium. Comparison with the simulation of the unpolarized fluid at $r_s = 1$ and $\mu = 1$ with the pseudo potential of reference [47], \mathcal{J}_1 , for which the trial wavefunction becomes the exact ground state wavefunction in the $\mu \rightarrow 0$ limit, show that the two extrapolated measures of the unlike histogram estimator differ one from the other by less than 7×10^{-3} , the largest difference being at contact (see Fig. 1). The use of more sophisticated trial wavefunctions, taking into account the effect of backflow and three-body correlations, is found to affect the measure by even less in the range of densities considered. For the same reason we discarded the use of the twist-averaged boundary conditions [16] and only worked with periodic boundary conditions. In Table 4, we compare the contact values of the unlike RDF of the unpolarized fluid at various r_s and μ from the measures of the histogram estimator and the HFM measures. We see that there is disagreement between the measure from the histogram estimator and

the HFM measure only in the Coulomb $\mu \rightarrow \infty$ case at $r_s = 1, 2$.

Our results complement the ones of Paziani et al. [10], which only reported a limited number of RDF data. We plan, in the future, to complete the calculation at intermediate polarizations, $0 < \zeta < 1$, complementing the work of Ortiz and Ballone [64], and Kwon et al. [14].

We believe it is still an open problem the one of determining the relationship between the choice of the auxiliary function, the bias it introduces in the Hellmann and Feynman measure, and the variance of this measure.

Appendix A: Jastrow, backflow, and three-body

In terms of the stochastic process governed by $f(\mathbf{R}, t)$ one can write, using Kac theorem [65,66]:

$$\int d\mathbf{R} f(\mathbf{R}, \tau) = \left\langle \exp \left[- \int_0^\tau dt E_L(\mathbf{R}^t) \right] \right\rangle_{\text{DRW}}, \quad (\text{A.1})$$

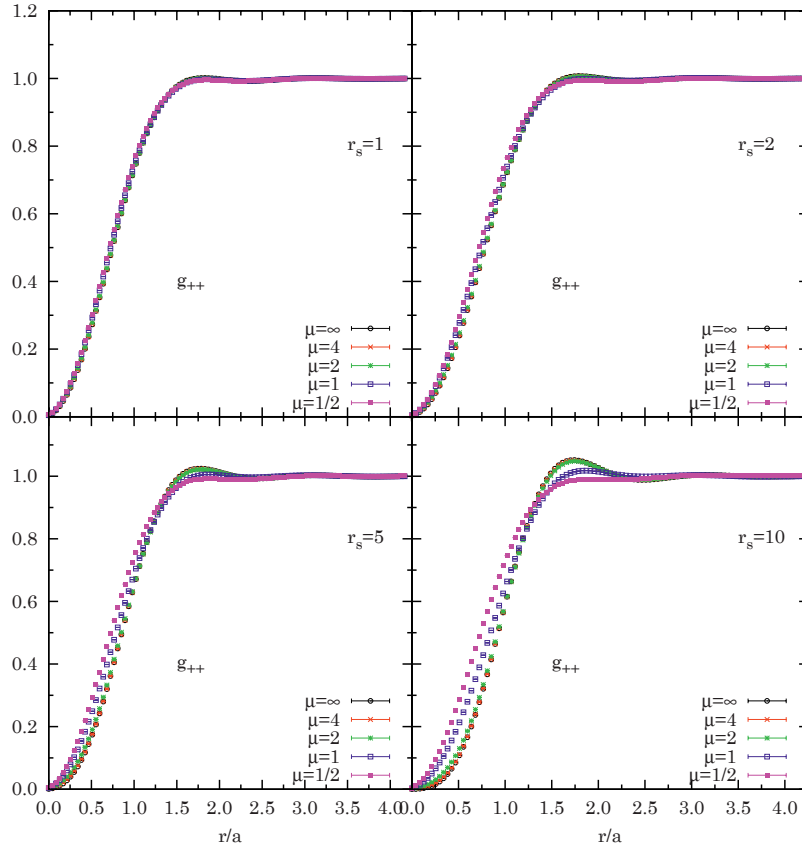


Fig. 8. The histogram extrapolated measure for the RDF of a system of 147 fully polarized ($\zeta = 1$) particles calculated using the SJ trial wavefunction. The VMC calculation was made of 10^6 steps while the DMC by 10^5 . The trial wavefunction used was of the SJ type with the Jastrow \mathcal{J}_1 of equation (36).

where $\langle \dots \rangle_{\text{DRW}}$ means averaging with respect to the diffusing and drifting random walk. Choosing a complete set of orthonormal wavefunctions Ψ_i , we can write for the true time dependent many-body wavefunction:

$$\begin{aligned} \phi(\mathbf{R}, \tau) &= \sum_i \Psi_i(\mathbf{R}) \int d\mathbf{R}' \Psi_i(\mathbf{R}') \phi(\mathbf{R}', \tau) \\ &\approx \Psi(\mathbf{R}) \int d\mathbf{R} f(\mathbf{R}, \tau) \\ &= \Psi(\mathbf{R}) \left\langle \exp \left[- \int_0^\tau dt E_L(\mathbf{R}^t) \right] \right\rangle_{\text{DRW}}, \end{aligned} \quad (\text{A.2})$$

where Ψ is the wavefunction, of the set, of maximum overlap with the true ground-state, the trial wavefunction. Assuming that at time zero we are already close to the stationary solution, for sufficiently small τ we can

approximate

$$\left\langle \exp \left[- \int_0^\tau dt E_L(\mathbf{R}^t) \right] \right\rangle_{\text{DRW}} \approx e^{-\tau E_L(\mathbf{R}^\tau)}. \quad (\text{A.3})$$

By antisymmetrising we get the Fermion wavefunction

$$\phi_F(\mathbf{R}, \tau) \approx \mathcal{A} \left[e^{-\tau E_L(\mathbf{R})} \Psi(\mathbf{R}) \right], \quad (\text{A.4})$$

where given a function $f(\mathbf{R})$, we define the operator (a symmetry of the Hamiltonian)

$$\mathcal{A}[f(\mathbf{R})] = \frac{1}{N_P} \sum_P (-1)^P f(P\mathbf{R}), \quad (\text{A.5})$$

here $N_P = N_+!N_-!$ is the total number of allowed permutations P .

This is called the local energy method to improve a trial wavefunction. Suppose we start from a simple unsymmetrical product of single particle plane waves of N_+

Table 4. Contact values for the unlike RDF of the unpolarized fluid of Piazani et al. [10], at various r_s and μ , from the histogram variational (variational), mixed (mixed), and extrapolated (extrapolated) measures, and the HFM (HFM) and HFM extrapolated (HFM-ext) measures. The trial wavefunction used was of the SJ type with the Jastrow \mathcal{J}_1 of equation (36). The last column gives the error $\sigma_{av} = \sqrt{\sigma^2 \mathcal{K} / \mathcal{N}}$ (σ^2 is the variance, \mathcal{K} the correlation time of the random walk, and \mathcal{N} the number of Monte Carlo steps) on the HFM measure. 162 particles were used with $10^5 \times n_w$ Monte Carlo steps.

r_s	μ	Variational	Mixed	Extrapolated	HFM	HFM-ext	σ_{av} on HFM
10	1/2	1.085(8)	1.000(4)	0.91(1)	1.0006	0.9222	0.03
10	1	0.706(6)	0.644(3)	0.582(8)	0.6474	0.5949	0.03
10	2	0.219(4)	0.182(1)	0.146(4)	0.1798	0.1450	0.06
10	4	0.053(2)	0.0506(8)	0.048(2)	0.0460	0.0394	0.07
10	∞	0.0074(6)	0.0096(3)	0.0118(8)	0.0045	0.0029	0.09
5	1/2	1.129(8)	1.034(3)	0.94(1)	1.0277	0.9381	0.03
5	1	0.850(7)	0.796(3)	0.743(9)	0.7912	0.7325	0.02
5	2	0.448(5)	0.405(2)	0.362(6)	0.4022	0.3565	0.02
5	4	0.214(3)	0.199(1)	0.184(4)	0.1960	0.1782	0.03
5	∞	0.080(2)	0.0799(8)	0.080(2)	0.0625	0.0557	0.03
2	1/2	1.158(8)	1.0618(4)	0.97(1)	1.0545	0.9484	0.04
2	1	1.003(8)	0.927(3)	0.852(9)	0.9270	0.8561	0.03
2	2	0.754(7)	0.697(3)	0.639(9)	0.6919	0.6299	0.02
2	4	0.549(6)	0.511(2)	0.473(7)	0.5127	0.4687	0.02
2	∞	0.376(4)	0.349(2)	0.323(5)	0.3236	0.3030	0.02
1	1/2	1.171(8)	1.077(3)	0.98(1)	1.0705	0.9683	0.02
1	1	1.077(8)	0.994(3)	0.91(1)	0.9938	0.9070	0.02
1	2	0.924(8)	0.855(3)	0.787(9)	0.8640	0.8053	0.02
1	4	0.784(7)	0.730(2)	0.676(8)	0.7295	0.6628	0.01
1	∞	0.645(6)	0.602(2)	0.560(7)	0.5771	0.5263	0.01

spin-up particles with $k < k_F^+$ occupied and N_- spin-up particles with $k < k_F^-$ occupied, for the zeroth order trial wavefunction. Equation (A.4) will give us a first order wavefunction of the Slater-Jastrow type (see Eq. (27)). If we start from an unsymmetrical Hartree-Jastrow trial wavefunction the local energy with the Jastrow factor has the form

$$E_L = V - \lambda \sum_i \left[-k_i^2 - 2i\mathbf{k}_i \cdot \nabla_i \sum_{j < k} u(r_{jk}) - \nabla_i^2 \sum_{j < k} u(r_{jk}) + \left| \nabla_i \sum_{j < k} u(r_{jk}) \right|^2 \right], \quad (\text{A.6})$$

where $V = V(\mathbf{R})$ is the total potential energy and $r_{ij} = |\mathbf{r}_{ij}| = |\mathbf{r}_i - \mathbf{r}_j|$. Then the antisymmetrized second order wavefunction has the form in equation (40), which includes backflow (see the third term), which is the correction inside the determinant and which affects the nodes, and three-body boson-like correlations (see last term) which do not affect the nodes.

The MC simulations presented were carried out at the Center for High Performance Computing (CHPC), CSIR Campus, 15 Lower Hope St., Rosebank, Cape Town, South Africa.

References

1. N.W. Ashcroft, N.D. Mermin, *Solid State Physics* (Harcourt, Inc., Forth Worth, 1976)
2. S.L. Shapiro, S.A. Teukolsky, *Black Holes, White Dwarfs, and Neutron Stars. The Physics of Compact Objects* (John Wiley-VCH Verlag GmbH, Weinheim, 1983)
3. W. Zhu, J. Toulouse, A. Savin, G. Angyan, J. Chem. Phys. **132**, 244108 (2010)
4. J. Toulouse, P. Gori-Giorgi, A. Savin, Theor. Chem. Acc. **114**, 305 (2005)
5. P. Gori-Giorgi, A. Savin, Phys. Rev. A **3**, 032506 (2006)
6. D.M. Ceperley, Rev. Mod. Phys. **67**, 279 (1995)
7. D.M. Ceperley, in *Monte Carlo and Molecular Dynamics of Condensed Matter Systems*, edited by K. Binder, G. Ciccotti (Editrice Compositori, Bologna, 1996)
8. D.M. Ceperley, B.J. Alder, Phys. Rev. Lett. **45**, 566 (1980)
9. L. Zecca, P. Gori-Giorgi, S. Moroni, G.B. Bachelet, Phys. Rev. B **70**, 205127 (2004)
10. S. Piazani, S. Moroni, P. Gori-Giorgi, G.B. Bachelet, Phys. Rev. B **73**, 155111 (2006)
11. R. Fantoni, Solid State Commun. **159**, 106 (2013)
12. J. Kolorenc, L. Mitas, Rep. Prog. Phys. **74**, 026502 (2011)
13. W.M.C. Foulkes, L. Mitas, R.J. Needs, G. Rajagopal, Rev. Mod. Phys. **73**, 33 (2001)
14. Y. Kwon, D.M. Ceperley, R.M. Martin, Phys. Rev. B **58**, 6800 (1998)
15. J. Toulouse, R. Assaraf, C.J. Umrigar, J. Chem. Phys. **126**, 244112 (2007)
16. C. Lin, F.H. Zong, D.M. Ceperley, Phys. Rev. E **64**, 016702 (2001)
17. S. Chiesa, D.M. Ceperley, R.M. Martin, M. Holzmann, Phys. Rev. Lett. **97**, 076404 (2006)
18. W.L. McMillan, Phys. Rev. A **138**, 442 (1965)
19. M.H. Kalos, D. Levesque, L. Verlet, Phys. Rev. A **9**, 2178 (1974)
20. R.W. Hockney, J.W. Eastwood, "Computer Simulation Using Particles" (McGraw-Hill, New York, 1981)

21. M.P. Allen, D.J. Tildesley, *Computer Simulation of Liquids* (Clarendon Press, Oxford, 1987)
22. D. Frenkel, B. Smit, *Understanding Molecular Simulation* (Academic Press, San Diego, 1996)
23. D.M. Ceperley, *J. Stat. Phys.* **63**, 1237 (1991)
24. D.M. Ceperley, M.H. Kalos, in *Monte Carlo Methods in Statistical Physics*, edited by K. Binder (Springer-Verlag, Heidelberg, 1979), p. 145
25. K.S. Liu, M.H. Kalos, G.V. Chester, *Phys. Rev. A* **10**, 303 (1974)
26. R.N. Barnett, P.J. Reynolds, W.A. Lester Jr., *J. Comput. Phys.* **96**, 258 (1991)
27. S. Baroni, S. Moroni, *Phys. Rev. Lett.* **82**, 4745 (1999)
28. C.J. Umrigar, M.P. Nightingale, K.J. Runge, *J. Chem. Phys.* **99**, 2865 (1993)
29. R. Assaraf, M. Caffarel, *J. Chem. Phys.* **119**, 10536 (2003)
30. R. Gaudoin, J.M. Pitarke, *Phys. Rev. Lett.* **99**, 126406 (2007)
31. E. Wigner, *Phys. Rev.* **46**, 1002 (1934)
32. A.J. Leggett, *Rev. Mod. Phys.* **47**, 331 (1975)
33. G.F. Giuliani, G. Vignale, *Quantum Theory of the Electron Liquid* (Cambridge University Press, Cambridge, 2005)
34. V. Natoli, D.M. Ceperley, *Comput. Phys.* **117**, 171 (1995)
35. N.H. March, M.P. Tosi, *Coulomb Liquids* (Academic Press, London, 1984)
36. J.B. Anderson, *J. Chem. Phys.* **65**, 4121 (1976)
37. J.M. Hammersley, D.C. Handscomb, *Monte Carlo Methods* (Chapman and Hall, London, 1964), pp. 57–59
38. M.H. Kalos, P.A. Whitlock, *Monte Carlo Methods* (Wiley-VCH Verlag GmbH & Co., Weinheim, 2008)
39. L.D. Landau, E.M. Lifshitz, *Quantum Mechanics. Non-relativistic Theory*, 3rd edn. course of Theoretical Physics (Pergamon Press, 1977), Vol. 3, Eq. (11.16)
40. A. Bijl, *Physica* **7**, 869 (1940)
41. R.B. Dingle, *Philos. Mag.* **40**, 573 (1949)
42. R. Jastrow, *Phys. Rev.* **98**, 1479 (1955)
43. R.P. Feynman, *Statistical Mechanics: A Set of Lectures* (W.A. Benjamin Inc., London, Amsterdam, Don Mills, Sydney, Tokyo, 1972), Sect. 9.6
44. T. Gaskell, *Proc. Phys. Soc.* **77**, 1182 (1961)
45. T. Gaskell, *Proc. Phys. Soc.* **80**, 1091 (1962)
46. D.M. Ceperley, in *Proceedings of the International School of Physics Enrico Fermi*, edited by G.F. Giuliani, G. Vignale (IOS Press, Amsterdam, 2004), pp. 3–42, course 158
47. D. Ceperley, *Phys. Rev. B* **18**, 3126 (1978)
48. Y. Kwon, D.M. Ceperley, R.M. Martin, *Phys. Rev. B* **48**, 12037 (1993)
49. R.P. Feynman, M. Cohen, *Phys. Rev.* **102**, 1189 (1956)
50. R.M. Panoff, J. Carlson, *Phys. Rev. Lett.* **62**, 1130 (1989)
51. T.L. Hill, *Statistical Mechanics* (McGraw-Hill, New York, 1956)
52. E. Feenberg, *Theory of Quantum Fluids* (Academic Press, New York, 1967)
53. Ph.A. Martin, *Rev. Mod. Phys.* **60**, 1075 (1988)
54. J.C. Kimball, *Phys. Rev. A* **7**, 1648 (1973)
55. A.K. Rajagopal, J.C. Kimball, M. Banerjee, *Phys. Rev. B* **18**, 2339 (1978)
56. M. Hoffmann-Ostenhof, T. Hofmann-Ostenhof, H. Stremnitzer, *Phys. Rev. Lett.* **68**, 3857 (1992).
57. J.P. Hansen, I.R. McDonald, *Theory of simple liquids*, 2nd edn. (Academic Press, London, 1986)
58. L. van Hove, *Phys. Rev.* **95**, 249 (1954)
59. D. Pines, P. Nozières, *Theory of Quantum Liquids* (Benjamin, New York, 1966)
60. J. Lindhard, *Mat.-Fys. Medd.* **28** (1954)
61. M.P. Tosi, in *Electron Correlation in the Solid State*, edited by N.H. March (Imperial College Press, London, 1999), Chap. 1, pp. 1–42
62. A. Alastuey, Ph.A. Martin, *J. Stat. Phys.* **39**, 405 (1985)
63. M.J. Lighthill, *Introduction to Fourier Analysis and Generalized Functions* (Cambridge University Press, 1959), Theorem 19
64. G. Ortiz, P. Ballone, *Phys. Rev. B* **50**, 1391 (1994)
65. M. Kac, *Probability and Related Topics in Physical Sciences* (Interscience Publisher Inc., New York, 1959)
66. M. Kac, in *Proceedings of the Second Berkeley Symposium on Probability and Statistics* (University of California Press, Berkeley, 1951), Sect. 3

Chapter 40

Phase diagrams of Janus fluids with up-down constrained orientations

Fantoni R., Giacometti A., Maestre M. A. G., and Santos A., J. Chem. Phys. **139**, 174902 (2013)

Title: “Phase diagrams of Janus fluids with up-down constrained orientations”

Abstract: A class of binary mixtures of Janus fluids formed by colloidal spheres with the hydrophobic hemispheres constrained to point either up or down are studied by means of Gibbs ensemble Monte Carlo simulations and simple analytical approximations. These fluids can be experimentally realized by the application of an external static electrical field. The gas-liquid and demixing phase transitions in five specific models with different patch-patch affinities are analyzed. It is found that a gas-liquid transition is present in all the models, even if only one of the four possible patch-patch interactions is attractive. Moreover, provided the attraction between like particles is stronger than between unlike particles, the system demixes into two subsystems with different composition at sufficiently low temperatures and high densities.



Phase diagrams of Janus fluids with up-down constrained orientations

Riccardo Fantoni,^{1,a)} Achille Giacometti,^{1,b)} Miguel Ángel G. Maestre,^{2,c)} and Andrés Santos^{2,d)}

¹Dipartimento di Scienze dei Materiali e Nanosistemi, Università Ca' Foscari Venezia, Calle Larga S. Marta DD2137, I-30123 Venezia, Italy

²Departamento de Física, Universidad de Extremadura, E-06071 Badajoz, Spain

(Received 7 August 2013; accepted 17 October 2013; published online 5 November 2013)

A class of binary mixtures of Janus fluids formed by colloidal spheres with the hydrophobic hemispheres constrained to point either up or down are studied by means of Gibbs ensemble Monte Carlo simulations and simple analytical approximations. These fluids can be experimentally realized by the application of an external static electrical field. The gas-liquid and demixing phase transitions in five specific models with different patch-patch affinities are analyzed. It is found that a gas-liquid transition is present in all the models, even if only one of the four possible patch-patch interactions is attractive. Moreover, provided the attraction between like particles is stronger than between unlike particles, the system demixes into two subsystems with different composition at sufficiently low temperatures and high densities. © 2013 AIP Publishing LLC. [<http://dx.doi.org/10.1063/1.4827861>]

I. INTRODUCTION

Engineering new materials through direct self-assembly processes has recently become a new concrete possibility due to the remarkable developments in the synthesis of patchy colloids with different shapes and functionalities. Nowadays, both the synthesis and the aggregation process of patchy colloids can be experimentally controlled with a precision and reliability that were not possible until a few years ago.^{1–5}

Within the general class of patchy colloids, a particularly interesting case is provided by the so-called Janus fluid, where the surface of the colloidal particle is evenly partitioned between the hydrophobic and the hydrophilic moieties, so that attraction between two spheres is possible only if both hydrophobic patches are facing one another.⁶ Several experimental and theoretical studies have illustrated the remarkable properties of this paradigmatic case.^{7,8}

The behavior of patchy particles under external fields has received recent attention.^{9,10} By applying an external electrical or magnetic field, appropriately synthesized dipolar Janus particles may be made to align orientationally, so as to expose their functionally active hemisphere either all up or all down (see Ref. 9, Secs. 1.4.3.1 and 1.4.3.2, and references therein). By mixing the two species one could have in the laboratory a binary mixture of Janus particles where the functionally active patch points in opposite directions for each species.

While theoretical studies have been keeping up with, and sometimes even anticipated, experimental developments, the complexities of the anisotropic interactions in patchy colloids have mainly restricted these investigations to numerical sim-

ulations, which have revealed interesting specificities in the corresponding phase diagrams.

Motivated by the above scenario, we have recently introduced a simplified binary-mixture model of a fluid of Janus spheres (interacting via the anisotropic Kern–Frenkel potential),¹¹ where the hydrophobic patches on each sphere could point only either up (species 1) or down (species 2).¹² This orientational restriction, which is reminiscent of Zwanzig's model for liquid crystals, clearly simplifies the theoretical description while still distilling out the main features of the original Janus model.

In the present paper, we generalize the above Janus fluid model by assuming arbitrary values for the energy scales ϵ_{ij} of the attractive interactions associated with the four possible pair configurations (see Fig. 1), which allows for a free tuning of the strength of the patch-patch attraction. In some cases this can effectively mimic the reduction of the coverage in the original Kern–Frenkel model. Note that, in Fig. 1, ϵ_{ij} is the energy associated with the (attractive) interaction between a particle of species i (at the left) and a particle of species j (at the right) when the former is below the latter, with the arrow always indicating the hydrophobic (i.e., attractive) patch. The original Kern–Frenkel model then corresponds to $\epsilon_{12} > 0$ and $\epsilon_{11} = \epsilon_{22} = \epsilon_{21} = 0$, whereas the full coverage limit is equivalent to $\epsilon_{11} = \epsilon_{22} = \epsilon_{12} = \epsilon_{21} > 0$. On the other hand, the effect of reducing the coverage from the full to the Janus limit, can be effectively mimicked by fixing $\epsilon_{12} > 0$ and progressively decreasing ϵ_{21} and $\epsilon_{11} = \epsilon_{22}$. Moreover, the class of models depicted in Fig. 1 allows for an interpretation more general and flexible than the hydrophobic-hydrophilic one. For instance, one may assume that attraction is only possible when patches of *different* type are facing one another (i.e., $\epsilon_{11} = \epsilon_{22} > 0$ and $\epsilon_{12} = \epsilon_{21} = 0$). As shown below, this will provide a rich scenario of intermediate cases with a number of interesting features in the phase diagram of both the gas-liquid and the demixing transitions.

^{a)}Electronic mail: rfantoni@ts.infn.it

^{b)}Electronic mail: achille.giacometti@unive.it

^{c)}Electronic mail: maestre@unex.es

^{d)}Electronic mail: andres@unex.es. URL: <http://www.unex.es/eweb/fis teor/andres>.

174902-2 Fantoni *et al.*

J. Chem. Phys. **139**, 174902 (2013)

We emphasize the fact that in the simulation part of the present study we will always assume “global” equimolarity, that is, the combined number of particles of species 1 (N_1) is always equal to the combined number of particles of species 2 (N_2), so that $N_1 = N_2 = N/2$, where N is the total number of particles. On the other hand, the equimolarity condition is not imposed on each coexisting phase.

The organization of the paper is as follows. The class of models is briefly described in Sec. II. Next, in Sec. III we present our Gibbs ensemble Monte Carlo (GEMC) results for the gas-liquid and demixing transitions. The complementary theoretical approach is presented in Sec. IV. The paper is closed with some concluding remarks in Sec. V.

II. DESCRIPTION OF THE MODELS

In our class of binary-mixture Janus models, particles of species 1 (with a mole fraction x_1) and 2 (with a mole fraction $x_2 = 1 - x_1$) are dressed with two up-down hemispheres with different attraction properties, as sketched in Fig. 1. The pair potential between a particle of species i at \mathbf{r}_1 and a particle of species j at \mathbf{r}_2 is

$$\phi_{ij}(\mathbf{r}_{12}) = \phi_{ij}(r_{12})\Theta(z_{12}) + \phi_{ji}(r_{12})\Theta(-z_{12}), \quad (1)$$

where $\Theta(z)$ is the Heaviside step function, $\mathbf{r}_{12} = \mathbf{r}_2 - \mathbf{r}_1$, $z_{12} = z_2 - z_1$, and

$$\phi_{ij}(r) = \begin{cases} \infty, & 0 \leq r < \sigma \\ -\epsilon_{ij}, & \sigma \leq r < \sigma + \Delta \\ 0, & \sigma + \Delta \leq r \end{cases} \quad (2)$$

is a standard square-well (SW) potential of diameter σ , width Δ , and energy depth ϵ_{ij} , except that, in general, $\epsilon_{12} \neq \epsilon_{21}$. By symmetry, one must have $\epsilon_{22} = \epsilon_{11}$ (see Fig. 1), so that (for given values of σ and Δ) the space parameter of the interaction potential becomes three-dimensional, as displayed in Fig. 2. Except in the case of the hard-sphere (HS) model ($\epsilon_{ij} = 0$), one can freely choose one of the non-zero ϵ_{ij} to fix the energy scale. Thus, we call $\epsilon = \max_{i,j}\{\epsilon_{ij}\}$ and use the three

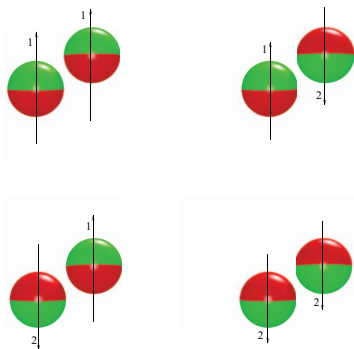


FIG. 1. Sketch of a binary-mixture Janus fluid with up-down constrained orientations. The energy scales of the attractive interactions are (from left to right and from top to bottom) ϵ_{11} , ϵ_{12} , ϵ_{21} , and $\epsilon_{22} = \epsilon_{11}$, respectively. Here we have adopted the convention that ϵ_{ij} is the energy scale when a particle of species i is “below” a particle of species j .

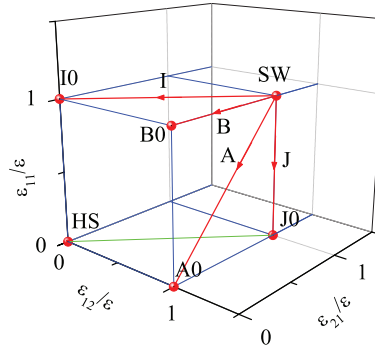


FIG. 2. Parameter space of the class of Janus models defined in the paper.

independent ratios ϵ_{ij}/ϵ as axes in Fig. 2. The model represented by the coordinates (1, 1, 1) is the fully isotropic SW fluid, where species 1 and 2 become indistinguishable. Next, without loss of generality, we choose $\epsilon_{12} \geq \epsilon_{21}$. With those criteria, all possible models of the class lie either inside the triangle SW-I0-B0-SW or inside the square SW-B0-A0-J0-SW. One could argue that any point *inside* the cube displayed in Fig. 2 may represent a distinct model, but this is not so. First, the choice $\epsilon = \max_{i,j}\{\epsilon_{ij}\}$ restricts the models to those lying on one of the three faces $\epsilon_{11}/\epsilon = 1$, $\epsilon_{12}/\epsilon = 1$, or $\epsilon_{21}/\epsilon = 1$. Second, the choice $\epsilon_{12} \geq \epsilon_{21}$ reduces the face $\epsilon_{21}/\epsilon = 1$ to the line SW-J0 and the face $\epsilon_{11}/\epsilon = 1$ to the half-face SW-I0-B0-SW. The vertices SW, I0, B0, A0, and J0 define the five distinguished models we will specifically study. Those models, together with the HS one, are summarized in Table I.

The rationale behind our nomenclature for the models goes as follows. Models with $\epsilon_{12} = \epsilon_{21}$ are isotropic and so we use the letter I to denote the isotropic models with $0 \leq \epsilon_{12}/\epsilon = \epsilon_{21}/\epsilon \leq 1$ and $\epsilon_{11}/\epsilon = 1$. Apart from them, the only additional isotropic models are those with $\epsilon_{12}/\epsilon = \epsilon_{21}/\epsilon = 1$ and $0 \leq \epsilon_{11}/\epsilon \leq 1$, and we denote them with the letter (J) next to I. All the remaining models are anisotropic (i.e., $\epsilon_{12} \neq \epsilon_{21}$). Out of them, we use the letter A to denote the particular subclass of anisotropic models ($0 \leq \epsilon_{11}/\epsilon = \epsilon_{21}/\epsilon \leq 1$ and $\epsilon_{12}/\epsilon = 1$) which can be viewed as the anisotropic counterpart of the isotropic subclass I. Analogously, we employ the letter (B) next to A to refer to the anisotropic counterpart ($\epsilon_{11}/\epsilon = \epsilon_{12}/\epsilon = 1$ and $0 \leq \epsilon_{21}/\epsilon \leq 1$) of the isotropic models J. Finally, the number 0 is used to emphasize that the

TABLE I. Definition of the models.

Model	ϵ_{11}	ϵ_{12}	ϵ_{21}	ϵ_{22}
HS	0	0	0	0
A0	0	ϵ	0	0
I0	ϵ	0	0	ϵ
J0	0	ϵ	ϵ	0
B0	ϵ	ϵ	0	ϵ
SW	ϵ	ϵ	ϵ	ϵ

174902-3 Fantoni *et al.*J. Chem. Phys. **139**, 174902 (2013)

corresponding models are the extreme cases of the subclasses I, J, A, and B, respectively.

Model A0 is the one more directly related to the original Kern–Frenkel potential and was the one analyzed in Ref. 12. Also related to that potential is model B0, where only the interaction between the two hydrophilic patches is purely repulsive. On the other hand, in models I0 and J0 (where $\epsilon_{12} = \epsilon_{21}$) the interaction becomes isotropic and the Janus character of the model is blurred. In model I0 the fluid reduces to a binary mixture with attractive interactions between like components and HS repulsions between unlike ones. This model was previously studied by Zaccarelli *et al.*¹³ using integral equation techniques. In the complementary model J0 attraction exists only between unlike particles. The points A0, B0, I0, and J0 can be reached from the one-component SW fluid along models represented by the lines A, B, I, and J, respectively. Of course, other intermediate models are possible inside the triangle SW-I0-B0-SW or inside the square SW-B0-A0-J0-SW.

In addition to the energy parameters ϵ_{ij} , the number density ρ , and the temperature T , each particular system is specified by the mixture composition (i.e., the mole fraction x_1). In fact, in Ref. 12 the thermodynamic and structural properties of model A0 were studied both under equimolar and non-equimolar conditions.

III. GIBBS ENSEMBLE MONTE CARLO SIMULATIONS

In this paper, we use GEMC techniques^{14–16} to study the gas-liquid condensation process of models SW, A0, B0, I0, and J0 and the demixing transition of models I0 and B0. We have chosen the width of the active attractive patch as in the experiment of Hong *et al.*³ ($\Delta/\sigma = 0.05$). Given the very small width of the attractive wells, we expect the liquid phase to be metastable with respect to the corresponding solid one.^{17–19} Reduced densities $\rho^* = \rho\sigma^3$ and temperatures $T^* = k_B T/\epsilon$ will be employed throughout.

A. Technical details

The GEMC method is widely adopted as a standard method for calculating phase equilibria from molecular simulations. According to this method, the simulation is performed in two boxes (I and II) containing the coexisting phases. Equilibration in each phase is guaranteed by moving particles. Equality of pressures is satisfied in a statistical sense by expanding the volume of one of the boxes and contracting the volume of the other one, keeping the total volume constant. Chemical potentials are equalized by transferring particles from one box to the other one.

In the GEMC run we have on each step a probability $a_p/(a_p + a_v + a_s)$, $a_v/(a_p + a_v + a_s)$, and $a_s/(a_p + a_v + a_s)$ for a particle random displacement, a volume change, and a particle swap move between both boxes, respectively. We generally chose the relative weights $a_p = 1$, $a_v = 1/10$, and $a_s = 20$. To preserve the up-down fixed patch orientation, rotation of particles was not allowed. The maximum particle displacement was kept equal to $10^{-3}L^{(\gamma)}$ where $L^{(\gamma)}$ is the side of the (cubic) box $\gamma = I, II$. Regarding the volume changes, following Ref. 20 we performed a random walk in $\ln(V^{(I)}/V^{(II)})$, with $V^{(\gamma)}$ the volume of the box γ , choosing

a maximum volume displacement of 1%. The volume move is computationally the most expensive one. This is because, after each volume move, it is necessary, in order to determine the next acceptance probability, to perform a full potential energy calculation since *all* the particle coordinates are rescaled by the factor associated with the enlargement or reduction of the boxes. However, this is not necessary for the other two moves since in those cases only the coordinates of a single particle change.

Both in the condensation and in the demixing problems, the Monte Carlo swap move consisted in moving a particle selected randomly in one box into the other box, so that the number of particles of each species in both boxes ($N_1^{(I)}, N_2^{(I)}, N_1^{(II)}$, and $N_2^{(II)}$) were fluctuating quantities. The only constraint was that the *total* number of particles was the same for both species, i.e., $N_1 \equiv N_1^{(I)} + N_1^{(II)} = N_2^{(I)} + N_2^{(II)} \equiv N_2 = N/2$. In the condensation problem we fixed the *global* density $\rho = N/(V^{(I)} + V^{(II)})$ (in all the cases we took $\rho^* = 0.3$, a value slightly below the expected critical density) and then varied the temperature T (below the critical temperature). The measured output quantities were the partial densities $\rho^{(I)} = N^{(I)}/V^{(I)}$ and $\rho^{(II)} = N^{(II)}/V^{(II)}$, where $N^{(\gamma)} = N_1^{(\gamma)} + N_2^{(\gamma)}$ is the total number of particles in box $\gamma = I, II$. Note that $(\rho^{(II)} - \rho)/(\rho - \rho^{(I)}) = V^{(I)}/V^{(II)}$. In contrast, in the demixing problem we fixed T (above the critical temperature) and varied ρ , the output observables being the local mole fractions $x_1^{(I)} = N_1^{(I)}/N^{(I)}$ and $x_1^{(II)} = N_1^{(II)}/N^{(II)}$. In this case, the lever rule is $(x_1^{(II)} - \frac{1}{2})/(\frac{1}{2} - x_1^{(I)}) = N^{(I)}/N^{(II)}$.

The total number of particles of each species was $N_1 = N_2 = 250$, what was checked to be sufficient for our purposes. We used $(50\text{--}100) \times 10^6$ MC steps for the equilibration (longer near the critical point) and $(100\text{--}200) \times 10^6$ MC steps for the production.²¹

B. Gas-liquid coexistence

Results for the gas-liquid transition are depicted in Fig. 3 in the temperature-density plane. Some representative

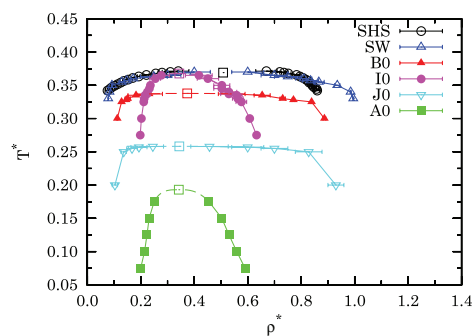


FIG. 3. Gas-liquid binodals for models SW, B0, I0, J0, and A0. The points indicated as SHS in the legend are grand canonical MC (GCMC) results taken from Ref. 22, where the actual one-component SHS model was studied. The remaining results are those obtained in this work from GEMC simulations. In each case, the solid line is a guide to the eye, while the dashed line is the result of the extrapolation to the critical point, which is represented by a square.

TABLE II. Gas-liquid coexistence properties for models A0, B0, I0, and J0, as obtained from our GEMC simulations. T^* is the reduced temperature, ρ_g^* is the reduced density of the gas ($\gamma = g$) and liquid ($\gamma = l$) phases, $N^{(g)}$ is the average number of particles in the gas box, and $U_{\text{ex}}^{(\gamma)}/N^{(\gamma)}$ is the excess internal energy per particle in box γ .

Model	T^*	ρ_g^*	ρ_l^*	$N^{(g)}/N$	$-U_{\text{ex}}^{(g)}/\epsilon N^{(g)}$	$-U_{\text{ex}}^{(l)}/\epsilon N^{(l)}$
A0	0.075	0.1994(6)	0.590(1)	0.493(2)	1.69(1)	1.796(7)
	0.1	0.214(2)	0.559(5)	0.535(4)	1.785(4)	1.780(8)
	0.125	0.223(1)	0.530(6)	0.556(3)	1.63(9)	1.71(5)
	0.15	0.231(1)	0.503(4)	0.574(4)	1.60(1)	1.78(1)
	0.175	0.250(2)	0.455(8)	0.630(6)	1.42(1)	1.632(9)
B0	0.3	0.112(2)	0.887(5)	0.284(5)	1.6(1)	3.27(1)
	0.325	0.128(1)	0.839(3)	0.324(3)	0.761(1)	3.239(7)
	0.328	0.145(5)	0.771(5)	0.363(9)	0.88(2)	2.99(1)
	0.33	0.15(1)	0.73(1)	0.380(1)	0.95(1)	3.016(9)
	0.335	0.18(3)	0.65(3)	0.45(1)	1.0(7)	2.83(2)
	0.337	0.23(5)	0.54(5)	0.59(1)	1.273(4)	2.36(4)
I0	0.3	0.202(3)	0.61(1)	0.5146(7)	2.48(6)	3.04(1)
	0.325	0.211(5)	0.58(2)	0.5371(6)	1.76(4)	2.765(8)
	0.35	0.24(1)	0.50(3)	0.612(3)	1.24(3)	2.30(1)
	0.36	0.25(2)	0.45(4)	0.657(5)	1.01(1)	1.85(5)
	0.365	0.28(3)	0.42(5)	0.71(1)	0.96(2)	1.6(1)
J0	0.2	0.10(1)	0.93(3)	0.249(5)	1.67(2)	2.48(3)
	0.25	0.14(1)	0.83(5)	0.34(1)	0.82(2)	2.25(3)
	0.255	0.17(2)	0.70(5)	0.433(9)	0.90(2)	1.99(2)
	0.257	0.19(3)	0.60(6)	0.62(6)	1.10(7)	1.5(2)

numerical values for models A0, B0, I0, and J0 are tabulated in Table II. In this case, one of the two simulation boxes ($I = g$) contains the gas phase and the other one ($II = l$) contains the liquid phase. Since $\rho_g < \rho < \rho_l$, the choice of the global density ρ establishes a natural bound as to how close to the critical point the measured binodal curve can be. In fact, $N^{(g)} \rightarrow 0$ if $\rho_l \rightarrow \rho$, while $N^{(g)} \rightarrow N$ if $\rho_g \rightarrow \rho$. As is apparent from the values of $N^{(g)}/N$ in Table II, the latter scenario seems to take place in our case $\rho^* = 0.3$.

Although not strictly enforced, we observed that $N_1^{(g)} \simeq N_2^{(g)}$ and $N_1^{(l)} \simeq N_2^{(l)}$ (so both boxes were practically equimolar) in models A0, B0, and J0. On the other hand, in the case of model I0 the final equilibrium state was non-equimolar (despite the fact that, as said before, $N_1 = N_2$ globally), the low-density box having a more disparate composition than the high-density box. The mole fraction values are shown in Table III. Thus, in contrast to models A0, B0, and J0, the GEMC simulations at fixed temperature and global density $\rho^* = 0.3$ spontaneously drove the system I0 into two

coexisting boxes differing both in density and composition. This *spontaneous demixing* phenomenon means that in model I0 the equimolar binodal curve must be metastable with respect to demixing and so it was not observed in our simulations. It is important to remark that, while the equimolar binodal must be robust with respect to changes in the global density ρ (except for the bound $\rho_g < \rho < \rho_l$ mentioned above), the non-equimolar binodal depends on the value of ρ .

In addition to cases SW, B0, I0, J0, and A0, we have also included in Fig. 3, for completeness, numerical results obtained by Miller and Frenkel²² on the one-component Baxter's sticky-hard-sphere (SHS) model.²³ As expected, they agree quite well with our short-range SW results, the only qualitative difference being a liquid branch at slightly larger densities.

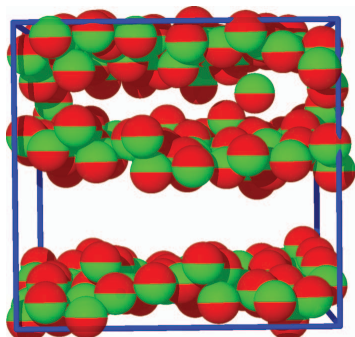
In order to determine the critical point (T_c^*, ρ_c^*) we empirically extrapolated the GEMC binodals using the law of rectilinear "diameters,"²⁴ $\frac{1}{2}(\rho_g^* + \rho_l^*) = \rho_c^* + A|T^* - T_c^*|$, and the Wegner expansion^{24,25} for the width of the coexistence curve, $\rho_l^* - \rho_g^* = B|T^* - T_c^*|^{\beta_l}$. The critical coordinates (T_c^*, ρ_c^*) and the coefficients A and B are taken as fitting parameters. The four points corresponding to the two highest temperatures were used for the extrapolation in each case. We remark that our data do not extend sufficiently close to the critical region to allow for quantitative estimates of critical exponents and non-universal quantities. However, assuming that the models belong to the three-dimensional Ising universality class, we chose $\beta_l = 0.325$. The numerical values obtained by this extrapolation procedure will be presented in Table V below.

The decrease in the critical temperatures and densities in going from the one-component SW fluid to model B0 and

TABLE III. Mole fractions in the gas and liquid boxes in model I0 at different temperatures and with a global density $\rho^* = 0.3$. For the gas and liquid densities, see Table II. Because of the symmetry under label exchange $1 \leftrightarrow 2$, we have adopted the criterion $x_1^{(g)} \leq x_2^{(g)}$ without loss of generality.

T^*	$x_1^{(g)}$	$x_1^{(l)}$
0.3	0.03(1)	0.992(6)
0.325	0.09(2)	0.98(1)
0.35	0.18(3)	0.955(15)
0.36	0.26(3)	0.93(3)
0.365	0.34(3)	0.89(4)

174902-5 Fantoni *et al.*

 J. Chem. Phys. **139**, 174902 (2013)

 FIG. 4. Snapshot of the liquid-phase box in model A0 at $T^* = 0.15$.

then to model A0 is strongly reminiscent of an analogous trend present in the unconstrained one-patch Kern–Frenkel model upon decrease of the coverage.²⁶

It is interesting to remark that, even though the influence of attraction in model A0 is strongly inhibited by the up-down constrained orientation ($\epsilon_{ij} = \epsilon\delta_{i1}\delta_{j2}$), this model exhibits a gas-liquid transition. This surprising result was preliminarily supported by canonical NVT MC simulations in Ref. 12, but now it is confirmed by the new and more appropriate GEMC simulations presented in this paper. Given the patch geometry and interactions in model A0, one might expect the formation of a lamellar-like liquid phase (approximately) made of alternating layers (up-down-up-down...) of particles with the same orientation. This scenario is confirmed by snapshots of the liquid-phase box, as illustrated by Fig. 4.

The Kern–Frenkel analogy is not applicable to the isotropic models I0 and J0. Model J0 presents a critical point intermediate between those of models B0 and A0, as expected. However, while the decrease in the total average attractive strength is certainly one of the main mechanisms dictating the location of the gas-liquid coexistence curves, it cannot be the only discriminating factor, as shown by the results for the isotropic model I0, where the critical temperature is higher and the binodal curve is narrower than that corresponding to the anisotropic model B0. This may be due to the fact that, as said before, the binodal curve in model I0 is not equimolar and this lack of equimolarity is expected to extend to the critical point, as can be guessed from the trends observed in Table III. In other words, two demixed phases can be made to coexist at a higher temperature and with a smaller density difference than two mixed phases.

C. Demixing transition

The bi-component nature of the systems raises the question of a possible demixing transition in which a rich-1 phase coexists with a rich-2 phase at a given temperature T , provided the density is larger than a certain critical consolute density $\rho_{cc}(T)$. The points $\rho_{cc}(T)$ or, reciprocally, $T_{cc}(\rho)$ define the so-called λ -line.²⁷ The interplay between the gas-liquid and demixing transitions is a very interesting issue and was discussed in a general framework by Wilding *et al.*²⁸

Since all the spheres have the same size, a necessary condition for demixing in the case of *isotropic* potentials is that the like attractions must be sufficiently stronger than the unlike attractions.^{28,29} Assuming the validity of this condition to anisotropic potentials and making a simple estimate based on the virial expansion, one finds that demixing requires the coefficient of x_1x_2 in the second virial coefficient to be positive, i.e., $2e^{\epsilon_{11}/k_B T} > e^{\epsilon_{12}/k_B T} + e^{\epsilon_{21}/k_B T}$. While this demixing criterion is only approximate, it suggests that, out of the five models considered, only models B0 and I0 are expected to display demixing transitions. As a matter of fact, we have already discussed the spontaneous demixing phenomenon taking place in model I0 when a low-density phase and a high-density phase are in mutual equilibrium. In this section, however, we are interested in the segregation of the system, at a given T and for $\rho > \rho_{cc}(T)$, into a rich-2 phase I with $x_1^{(I)} = x_d(\rho) < \frac{1}{2}$ and a *symmetric* rich-1 phase II with $x_1^{(II)} = 1 - x_d(\rho) > \frac{1}{2}$, both phases at the *same* density.

Our GEMC simulation results are presented in Fig. 5 and Table IV. We observe that, as expected, $x_1^{(I)} = 1 - x_1^{(II)}$ within statistical fluctuations. We have also checked that $\rho^{(I)} \simeq \rho^{(II)}$, even though this equality is not artificially enforced in the simulations. Such equality is also equivalent to $\rho^{(I)} \simeq \rho$ and we checked that it was satisfied within a standard deviation of $0.02\sigma^{-3}$ in all cases considered in Table IV. To obtain the critical consolute density ρ_{cc}^* for each temperature, we extrapolated the data again according to the Ising scaling relation $\frac{1}{2} - x_d(\rho) = C(\rho - \rho_{cc})^{\beta_I}$.

It is interesting to note that just the absence of attraction when a particle of species 2 is below a particle of species 1 ($\epsilon_{21} = 0$) in model B0 is sufficient to drive a demixing transition. However, as expected, at a common temperature (see $T^* = 0.4$ in Fig. 5), demixing requires higher densities in model B0 than in model I0.

As said above, the interplay of condensation and demixing is an interesting problem by itself.^{28,30} Three alternative scenarios are in principle possible for the intersection of the λ -line and the binodal curve: a critical end point, a triple point, or a tricritical point.²⁸ Elucidation of these scenarios would require grand canonical simulations (rather than GEMC simulations), what is beyond the scope of this paper.

IV. SIMPLE ANALYTICAL THEORIES

Let us now compare the above numerical results with simple theoretical predictions. The solution of integral equation theories for anisotropic interactions and/or multicomponent systems requires formidable numerical efforts, with the absence of explicit expressions often hampering physical insight. Here we want to deal with simple, purely analytical theories that yet include the basic ingredients of the models.

First, we take advantage of the short-range of the attractive well ($\Delta/\sigma = 0.05$) to map the different SW interactions into SHS interactions parameterized by the “stickiness” parameters¹²

$$t_{ij} \equiv \frac{1}{12\tau_{ij}} \equiv \frac{\Delta}{\sigma} \left(1 + \frac{\Delta}{\sigma} + \frac{\Delta^2}{3\sigma^2} \right) (e^{\epsilon_{ij}/k_B T} - 1), \quad (3)$$

174902-6 Fantoni *et al.*

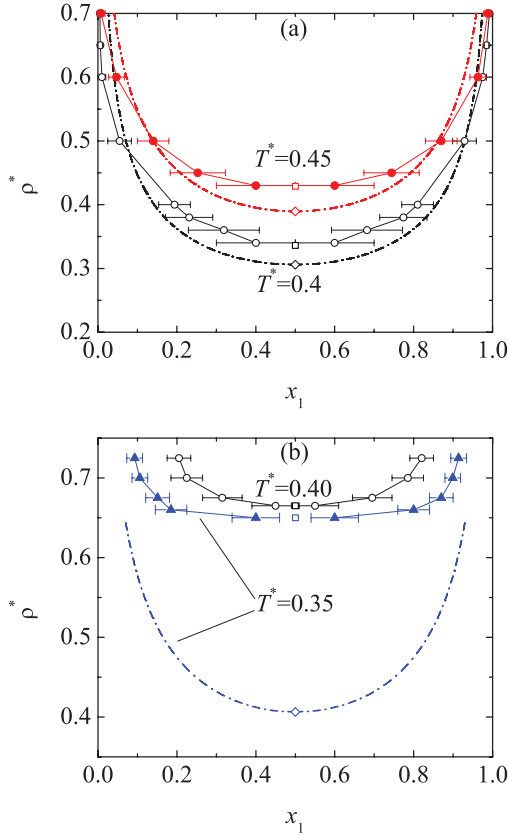
 J. Chem. Phys. **139**, 174902 (2013)


FIG. 5. Demixing curves for models (a) I0 and (b) B0 at two temperatures, as obtained from GEMC simulations, in the density-mole fraction plane. In each case, the solid line is a guide to the eye, while the critical consolute point is represented by a square. For model I0 we found $\rho_{cc}^*(T^* = 0.4) = 0.336$ and $\rho_{cc}^*(T^* = 0.45) = 0.429$; for model B0 the results are $\rho_{cc}^*(T^* = 0.35) = 0.650$ and $\rho_{cc}^*(T^* = 0.4) = 0.665$. The dashed-dotted lines are the theoretical predictions (see Sec. IV C).

which combine the energy and length scales. This mapping preserves the exact second virial coefficient of the genuine SW systems, namely,

$$\frac{B_2}{B_2^{\text{HS}}} = 1 - 3t_{11} + 3x_1x_2(2t_{11} - t_{12} - t_{21}), \quad (4)$$

where $B_2^{\text{HS}} = 2\pi\sigma^3/3$ is the HS coefficient. The exact expression of the third virial coefficient B_3 in the SHS limit for arbitrary t_{ij} is¹²

$$\begin{aligned} \frac{B_3}{B_3^{\text{HS}}} = & 1 - 6t_{11} + \frac{72}{5}t_{11}^2 - \frac{48}{5}t_{11}^3 - \frac{6}{5}x_1x_2[(12t_{11} - 5) \\ & \times (2t_{11} - t_{12} - t_{21}) - 8t_{11}(t_{11}^2 - t_{12}t_{21}) \\ & - 2(4t_{11} - 3)(2t_{11}^2 - t_{12}^2 - t_{21}^2) + 2\alpha(t_{12} - t_{21})^2], \end{aligned} \quad (5)$$

TABLE IV. Demixing coexistence properties for models I0 and B0, as obtained from our GEMC simulations. T^* is the reduced temperature, ρ^* is the reduced density, and $x_1^{(\gamma)}$ is the mole fraction of species 1 in each one of the two coexisting phases $\gamma = \text{I, II}$.

Model	T^*	ρ^*	$x_1^{(\text{I})}$	$x_1^{(\text{II})}$
I0	0.4	0.7	0.005(5)	0.992(5)
		0.65	0.006(6)	0.985(6)
		0.6	0.01(1)	0.97(1)
		0.5	0.05(3)	0.93(3)
		0.4	0.19(4)	0.81(4)
		0.38	0.23(6)	0.77(6)
	0.45	0.36	0.32(9)	0.68(9)
		0.34	0.4(1)	0.6(1)
		0.7	0.01(1)	0.99(1)
		0.6	0.05(2)	0.96(2)
		0.5	0.14(4)	0.87(4)
		0.45	0.25(7)	0.74(7)
B0	0.35	0.725	0.09(2)	0.91(2)
		0.7	0.11(2)	0.90(2)
		0.675	0.15(3)	0.87(3)
		0.66	0.18(4)	0.80(4)
		0.65	0.40(6)	0.60(6)
		0.725	0.20(3)	0.82(3)
	0.4	0.7	0.22(4)	0.78(4)
		0.675	0.31(5)	0.69(5)
		0.665	0.45(6)	0.55(6)

where $B_3^{\text{HS}} = 5\pi^2\sigma^6/18$ and

$$\alpha \equiv \frac{3\sqrt{3}}{\pi} - 1. \quad (6)$$

A. Equations of state

One advantage of the SW \rightarrow SHS mapping is that the Percus–Yevick (PY) integral equation is exactly solvable for SHS mixtures with *isotropic* interactions ($t_{12} = t_{21}$).^{31,32} In principle, that solution can be applied to the models SW, I0, and J0 represented in Fig. 2. On the other hand, if $t_{11} \neq 0$ (models SW and I0), the PY solutions are related to algebraic equations of second (SW) or fourth (I0) degrees, what creates the problem of disappearance of the physical solution for large enough densities or stickiness. In particular, we have observed that the breakdown of the solution preempts the existence of a critical point in model I0. However, in the case of model J0 ($t_{11} = 0$, $t_{12} = t_{21} = t$), the PY solution reduces to a *linear* equation whose solution is straightforward. Following the virial (v) and the energy (u) routes, the respective expressions for the compressibility factor $Z \equiv P/\rho k_B T$ (where P is the pressure) have the form

$$Z_v(\eta, t, x_1) = Z_v^{\text{HS}}(\eta) - x_1x_2Z_v^{(1)}(\eta, t) - x_1^2x_2^2Z_v^{(2)}(\eta, t), \quad (7)$$

$$Z_u(\eta, t, x_1) = Z_u^{\text{HS}}(\eta) - x_1x_2Z_u^{(1)}(\eta, t), \quad (8)$$

174902-7 Fantoni *et al.*

J. Chem. Phys. **139**, 174902 (2013)

where $\eta = \pi \rho^* / 6$ is the packing fraction,

$$Z_v^{\text{HS}}(\eta) = \frac{1 + 2\eta + 3\eta^2}{(1 - \eta)^2} \quad (9)$$

is the HS compressibility factor derived from the PY equation via the virial route, Z_u^{HS} is an indeterminate integration constant, and the explicit expressions for $Z_v^{(1)}$, $Z_v^{(2)}$, and $Z_u^{(1)}$ are

$$Z_v^{(1)}(\eta, t) = \frac{24\eta t}{(1 - \eta + 6\eta t)^2} \left[\frac{1 + 2\eta}{1 - \eta} + 3\eta t \frac{2 + 2\eta - 5\eta^2/2}{(1 - \eta)^2} + 6\eta^2 t^2 \frac{2 - 4\eta - 7\eta^2}{(1 - \eta)^3} \right], \quad (10)$$

$$Z_v^{(2)}(\eta, t) = \frac{288\eta^3 t^2 (2 + \eta)}{(1 - \eta + 6\eta t)^3} \left[\frac{1}{1 - \eta} - t \frac{2 - 11\eta}{(1 - \eta)^2} + t^2 \frac{2 - 10\eta + 61\eta^2/2}{(1 - \eta)^3} \right], \quad (11)$$

$$Z_u^{(1)}(\eta, t) = \frac{6\eta}{(1 - \eta)^2} \left[\frac{2t(2 + \eta)}{1 - \eta + 6\eta t} + \ln \frac{1 - \eta + 6\eta t}{1 - \eta} \right]. \quad (12)$$

To the best of our knowledge, this extremely simple solution of the PY integral equation for a model of SHS mixtures had not been unveiled before.

As apparent from Fig. 2, model A0 is a close relative of model J0. However, the fact that $\epsilon_{12} \neq \epsilon_{21} = 0$ (or $t_{12} \neq t_{21} = 0$) makes the interaction anisotropic and prevents the PY equation from being exactly solvable in this case. On the other hand, we have recently proposed¹² a simple rational-function approximation (RFA) that applies to models with $t_{12} \neq t_{21}$ and reduces to the PY solution in the case of isotropic models ($t_{12} = t_{21}$). The RFA solution for model A0 yields once more a linear equation. The virial and energy equations of state are again of the forms (7) and (8), respectively, with expressions for $Z_v^{(1)}$, $Z_v^{(2)}$, and $Z_u^{(1)}$ given by

$$Z_v^{(1)}(\eta, t) = \frac{12\eta t}{1 - \eta + 6\eta t} \left[\frac{1 + 2\eta}{(1 - \eta)^2} + 2\eta t \frac{1 - 2\eta - 7\eta^2/2}{(1 - \eta)^3} \right], \quad (13)$$

$$Z_v^{(2)}(\eta, t) = \frac{72\eta^3 t^2 (2 + \eta)}{(1 - \eta)^3 (1 - \eta + 6\eta t)}, \quad (14)$$

$$Z_u^{(1)}(\eta, t) = \frac{3\eta}{(1 - \eta)^2} \left[\frac{2t(2 + \eta)}{1 - \eta + 6\eta t} + \ln \frac{1 - \eta + 6\eta t}{1 - \eta} \right]. \quad (15)$$

In the RFA solution for model A0 the exact third virial coefficient (5) is recovered by the interpolation formula

$$\begin{aligned} Z &= Z_{\text{CS}}^{\text{HS}} + \alpha (Z_v - Z_v^{\text{HS}}) + (1 - \alpha) (Z_u - Z_u^{\text{HS}}) \\ &= Z_{\text{CS}}^{\text{HS}} - x_1 x_2 [\alpha Z_v^{(1)} + (1 - \alpha) Z_u^{(1)}] - x_1^2 x_2^2 \alpha Z_v^{(2)}, \end{aligned} \quad (16)$$

where

$$Z_{\text{CS}}^{\text{HS}}(\eta) = \frac{1 + \eta + \eta^2 - \eta^3}{(1 - \eta)^3} \quad (17)$$

is the HS Carnahan–Starling compressibility factor and the interpolation weight α is given by Eq. (6). By consistency, Eq. (16) will also be employed in the PY solution of model J0.

In the cases of models with $\epsilon_{11} \neq 0$ (i.e., SW, B0, and IO), the PY and RFA theories fail to have physical solutions in regions of the temperature-density plane overlapping with the gas-liquid transition. In order to circumvent this problem, we adopt here a simple perturbative approach:

$$Z = Z^{\text{ref}} + (B_2 - B_2^{\text{ref}}) \rho + (B_3 - B_3^{\text{ref}}) \rho^2, \quad (18)$$

where Z^{ref} is the compressibility factor of a reference model and B_2^{ref} and B_3^{ref} are the associated virial coefficients. As a natural choice (see Fig. 2), we take the models J0, A0, and HS (which lie on the plane $\epsilon_{11}/\epsilon = 0$) as reference systems for the models SW, B0, and IO (which lie on the plane $\epsilon_{11}/\epsilon = 1$), respectively. More specifically,

$$Z^{\text{SW}} = Z^{\text{J0}} + (B_2^{\text{SW}} - B_2^{\text{J0}}) \rho + (B_3^{\text{SW}} - B_3^{\text{J0}}) \rho^2, \quad (19)$$

$$Z^{\text{B0}} = Z^{\text{A0}} + (B_2^{\text{B0}} - B_2^{\text{A0}}) \rho + (B_3^{\text{B0}} - B_3^{\text{A0}}) \rho^2, \quad (20)$$

$$Z^{\text{IO}} = Z_{\text{CS}}^{\text{HS}} + (B_2^{\text{IO}} - B_2^{\text{HS}}) \rho + (B_3^{\text{IO}} - B_3^{\text{HS}}) \rho^2. \quad (21)$$

Here, Z^{J0} and Z^{A0} are given by Eq. (16) (with the corresponding expressions of $Z_v^{(1)}$, $Z_v^{(2)}$, and $Z_u^{(1)}$) and the virial coefficients are obtained in each case from Eqs. (4) and (5) with the appropriate values of t_{11} , t_{12} , and t_{21} .

From the explicit knowledge of $Z(\eta, t, x_1)$, standard thermodynamic relations allow one to obtain the free energy per particle $a(\eta, t, x_1)$ and the chemical potentials $\mu_i(\eta, t, x_1)$ as

$$\begin{aligned} \beta a(\eta, t, x_1) &= \int_0^\eta d\eta' \frac{Z(\eta', t, x_1) - 1}{\eta'} + x_1 \ln(x_1 \eta) \\ &\quad + (1 - x_1) \ln[(1 - x_1)\eta] + \text{const}, \end{aligned} \quad (22)$$

$$\begin{aligned} \beta \mu_1(\eta, t, x_1) &= \beta a(\eta, t, x_1) + Z(\eta, t, x_1) \\ &\quad + (1 - x_1) \frac{\partial \beta a(\eta, t, x_1)}{\partial x_1}, \end{aligned} \quad (23)$$

$$\mu_2(\eta, t, x_1) = \mu_1(\eta, t, 1 - x_1), \quad (24)$$

where $\beta \equiv 1/k_B T$.

B. Gas-liquid coexistence

The critical point (η_c, t_c) of the gas-liquid transition is obtained from the well-known condition that the critical isotherm in the pressure-density plane presents an inflection point with horizontal slope at the critical density.³³ In terms

174902-8 Fantoni *et al.*

 J. Chem. Phys. **139**, 174902 (2013)

TABLE V. Comparison between the critical points measured in simulations with those obtained from theoretical approaches.

Method	SW	B0	I0	J0	A0
	T_c^*				
Simulation	0.369 ^a	0.338 ^b	0.368 ^b	0.258 ^b	0.193 ^b
Our theory	0.377	0.341	0.331	0.278	0.214
Noro-Frenkel	0.369	0.335	0.297	0.297	0.247
	ρ_c^*				
Simulation	0.508 ^a	0.373 ^b	0.344 ^b	0.344 ^b	0.342 ^b
Our theory	0.356	0.330	0.366	0.376	0.359

^aGCMC results for the one-component SHS fluid From Ref. 22.

^bOur GEMC simulation results.

 of the compressibility factor Z , this implies

$$\left. \frac{\partial [\eta Z(\eta, t_c, 1/2)]}{\partial \eta} \right|_{\eta=\eta_c} = \left. \frac{\partial^2 [\eta Z(\eta, t_c, 1/2)]}{\partial \eta^2} \right|_{\eta=\eta_c} = 0, \quad (25)$$

where equimolarity ($x_1 = \frac{1}{2}$) has been assumed. For temperatures below the critical temperature (i.e., $t > t_c$) the packing fractions η_g and η_l of the gas and liquid coexisting phases are obtained from the conditions of equal pressure (mechanical equilibrium) and equal chemical potential (chemical equilibrium),³³ i.e.,

$$\eta_g Z(\eta_g, t, 1/2) = \eta_l Z(\eta_l, t, 1/2), \quad (26)$$

$$\mu_1(\eta_g, t, 1/2) = \mu_1(\eta_l, t, 1/2). \quad (27)$$

In order to make contact with the GEMC results, the theoretical values of t_c have been mapped onto those of T_c^* by inverting Eq. (3), namely,

$$\frac{1}{T^*} = \ln \left[1 + \frac{t}{(\Delta/\sigma)(1 + \Delta/\sigma + \Delta^2/3\sigma^2)} \right] \quad (28)$$

with $\Delta/\sigma = 0.05$.

Table V compares the critical points obtained in simulations for the one-component SW fluid (in the SHS limit) and for models B0, I0, J0, and A0 (see Fig. 2) with those stemming from our simple theoretical method. Results from the Noro-Frenkel (NF) corresponding-state criterion,³⁴ according to which $B_2/B_2^{\text{HS}} = -1.21$ at the critical temperature, are also included. We observe that, despite its simplicity and the lack of fitting parameters, our fully analytical theory predicts quite well the location of the critical point, especially in the case of T_c^* . It improves the estimates obtained from the NF criterion, except in the SW case, where, by construction, the NF rule gives the correct value. In what concerns the gas-liquid binodals, Fig. 6 shows that the theoretical curves agree fairly well with the GEMC data, except in the cases of models I0 and A0, where the theoretical curves are much flatter than the simulation ones. The lack of agreement with the binodal curve of model I0 can be partially due to the fact that in the theoretical treatment the two coexisting phases are supposed to be equimolar, while this is not the case in the actual simulations (see Table III).

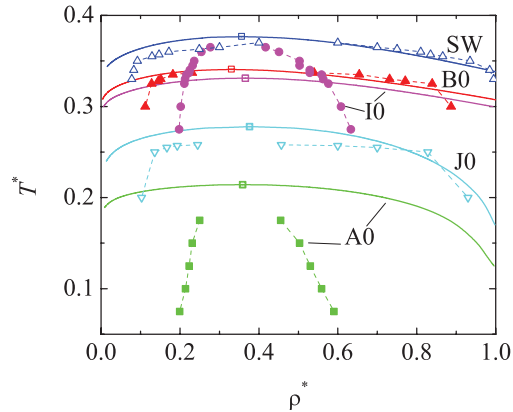


FIG. 6. Gas-liquid binodals for models SW, A0, B0, I0, and J0, as obtained from our theoretical method (solid lines). The critical points are represented by open squares. The symbols joined by dashed lines correspond to our GEMC data (see Fig. 3).

C. Demixing transition

In the case of the demixing transition, the critical consolute density η_{cc} at a given temperature is obtained from

$$\left. \frac{\partial^2 a(\eta_{cc}, t, x_1)}{\partial x_1^2} \right|_{x_1=\frac{1}{2}} = 0. \quad (29)$$

For $\eta > \eta_{cc}$, the demixing mole fraction $x_1 = x_d(\eta)$ is the solution to

$$\mu_1(\eta, t, x_d) = \mu_1(\eta, t, 1 - x_d). \quad (30)$$

In terms of the compressibility factor Z , Eqs. (29) and (30) can be rewritten as

$$\int_0^{\eta_{cc}} d\eta \frac{\partial^2 Z(\eta, t, x_1)/\partial x_1^2|_{x_1=\frac{1}{2}}}{\eta} = -4, \quad (31)$$

$$\int_0^{\eta} d\eta' \frac{\partial Z(\eta', t, x_d)/\partial x_d}{\eta'} = \ln \frac{1 - x_d}{x_d}, \quad (32)$$

respectively.

The perturbative approximations for models I0 and B0 succeed in predicting demixing transitions, even though their respective reference systems (HS and A0) do not demix. In the case of model I0, the critical consolute densities are $\rho_{cc}^*(T^* = 0.4) = 0.306$ and $\rho_{cc}^*(T^* = 0.45) = 0.390$, which are about 9% lower than the values obtained in our GEMC simulations. In the case of model B0, our simple theory predicts a critical consolute point only if $t > 0.7667$, i.e., if $T^* < 0.364$, so no demixing is predicted at $T^* = 0.4$, in contrast to the results of the simulations. At $T^* = 0.35$ the theoretical prediction is $\rho_{cc}^* = 0.406$, a value about 39% smaller than the GEMC one. The theoretical demixing curves at $T^* = 0.4$ and $T^* = 0.45$ for model I0 and at $T^* = 0.35$ for model B0 are compared with the GEMC results in Fig. 5. We can observe a fairly good agreement in the case of model I0, but not for model B0. In the latter case, the theoretical curve spans a

174902-9 Fantoni *et al.*J. Chem. Phys. **139**, 174902 (2013)

density range comparable to that of model I0, while simulations show a much flatter demixing curve.

V. CONCLUDING REMARKS

In conclusion, we have proposed a novel class of binary-mixture Janus fluids with up-down constrained orientations. The class encompasses, as particular cases, the conventional one-component SW fluid, mixtures with isotropic attractive interactions only between like particles (model I0) or unlike particles (model J0), and genuine Janus fluids with anisotropic interactions and different patch-patch affinities (models A0 and B0). Both GEMC numerical simulations and simple theoretical approximations have been employed to analyze the gas-liquid transition under *global* equimolar conditions for the five models and the demixing transition for the two models (I0 and B0) where the attraction between like particles is stronger than between unlike ones. The theoretical analysis employed a mapping onto SHS interactions that were then studied by means of the PY theory (model J0), the RFA (model A0), and low-density virial corrections (models SW, I0, and B0), with semi-quantitative agreement with numerical simulations.

Interestingly, the presence of attraction in only one out of the four possible patch-patch interactions (model A0) turns out to be enough to make the gas-liquid transition possible. Reciprocally, the lack of attraction in only one of the two possible patch-patch interactions between unlike particles (model B0) is enough to produce a demixing transition. Except in model I0, the coexisting gas and liquid phases have an equimolar composition. As the average attraction is gradually decreased, the gas-liquid critical point shifts to lower temperatures (except for an interesting inversion of tendency observed when going from the isotropic model I0 to the anisotropic model B0) and lower densities. Moreover, the coexistence region progressively shrinks, in analogy with what is observed in the unconstrained one-component Janus fluid^{35,36} and in the empty liquid scenario.³⁷ On the other hand, the imposed constraint in the orientation of the attractive patches does not allow for the formation of those inert clusters^{38–40} which in the original Janus fluid are responsible for a re-entrant gas branch.^{26,38,41}

ACKNOWLEDGMENTS

The authors are grateful to J.-P. Hansen for useful suggestions. R.F. acknowledges the use of the PLX computational facility of CINECA through the ISCRA call. A.G. acknowledges funding from PRIN-COFIN2010-2011 (Contract No. 2010LKE4CC). The research of M.A.G.M. and A.S. has been supported by the Spanish government through Grant No. FIS2010-16587 and by the Junta de Extremadura (Spain) through Grant No. GR101583, partially financed by FEDER

funds. M.A.G.M is also grateful to the Junta de Extremadura (Spain) for the pre-doctoral fellowship PD1010.

- ¹S. C. Glotzer and M. J. Solomon, *Nature Mater.* **6**, 557 (2007).
- ²A. Walther and H. E. Müller, *Soft Matter* **4**, 663 (2008).
- ³L. Hong, A. Cacciuto, E. Luijten, and S. Granick, *Langmuir* **24**, 621 (2008).
- ⁴A. B. Pawar and I. Kretzschmar, *Macromol. Rapid Commun.* **31**, 150 (2010).
- ⁵A. Walther and A. H. E. Müller, *Chem. Rev.* **113**, 5194 (2013).
- ⁶E. Bianchi, R. Blaak, and C. N. Likos, *Phys. Chem. Chem. Phys.* **13**, 6397 (2011).
- ⁷*Janus Particle Synthesis, Self-Assembly and Applications*, edited by S. Jiang and S. Granick (Royal Society of Chemistry, London, 2012).
- ⁸R. Fantoni, *The Janus Fluid: A Theoretical Perspective* (Springer, New York, 2013).
- ⁹S. Gangwal, *Directed Assembly and Manipulation of Anisotropic Colloidal Particles by External Fields* (ProQuest, UMI Dissertation Publishing, Ann Arbor, MI, 2011).
- ¹⁰S. Gangwal, A. Pawar, I. Kretzschmar, and O. D. Velev, *Soft Matter* **6**, 1413 (2010).
- ¹¹N. Kern and D. Frenkel, *J. Chem. Phys.* **118**, 9882 (2003).
- ¹²M. A. G. Maestre, R. Fantoni, A. Giacometti, and A. Santos, *J. Chem. Phys.* **138**, 094904 (2013).
- ¹³E. Zaccarelli, G. Foffi, P. Tartaglia, F. Sciortino, and K. Dawson, *Prog. Colloid Polym. Sci.* **115**, 371 (2000).
- ¹⁴A. Z. Panagiotopoulos, *Mol. Phys.* **61**, 813 (1987).
- ¹⁵B. Smit, P. de Smedt, and D. Frenkel, *Mol. Phys.* **68**, 931 (1989).
- ¹⁶B. Smit and D. Frenkel, *Mol. Phys.* **68**, 951 (1989).
- ¹⁷H. Liu, S. Garde, and S. Kumar, *J. Chem. Phys.* **123**, 174505 (2005).
- ¹⁸M. A. Miller and D. Frenkel, *Phys. Rev. Lett.* **90**, 135702 (2003).
- ¹⁹T. Vissers, Z. Preisler, F. Smalburg, M. Dijkstra, and F. Sciortino, *J. Chem. Phys.* **138**, 164505 (2013).
- ²⁰D. Frenkel and B. Smit, *Understanding Molecular Simulation: From Algorithms to Applications*, 2nd ed. (Academic Press, San Diego, 2002).
- ²¹The GEMC code took ≈ 55 s of CPU time for 1×10^6 steps of a system of size $N = 100$ on the IBM iDataPlex DX360M3 Cluster (2.40 GHz).
- ²²M. A. Miller and D. Frenkel, *J. Chem. Phys.* **121**, 535 (2004).
- ²³R. J. Baxter, *J. Chem. Phys.* **49**, 2770 (1968).
- ²⁴J. V. Sengers and J. M. H. Levelt-Sengers, in *Progress in Liquid Physics*, edited by C. A. Croton (Wiley, Chichester, 1978), Chap. 4.
- ²⁵F. Wegner, *Phys. Rev. B* **5**, 4529 (1972).
- ²⁶F. Sciortino, A. Giacometti, and G. Pastore, *Phys. Chem. Chem. Phys.* **12**, 11869 (2010).
- ²⁷N. B. Wilding, *Phys. Rev. E* **52**, 602 (1995).
- ²⁸N. Wilding, F. Schmid, and P. Nielaba, *Phys. Rev. E* **58**, 2201 (1998).
- ²⁹R. Fantoni, D. Gazzillo, and A. Giacometti, *Phys. Rev. E* **72**, 011503 (2005).
- ³⁰W. M. Jacobs and D. Frenkel, *J. Chem. Phys.* **139**, 024108 (2013).
- ³¹J. W. Perram and E. R. Smith, *Chem. Phys. Lett.* **35**, 138 (1975).
- ³²B. Barboy, *Chem. Phys.* **11**, 357 (1975).
- ³³J.-P. Hansen and I. R. McDonald, *Theory of Simple Liquids* (Academic Press, London, 2006).
- ³⁴M. G. Noro and D. Frenkel, *J. Chem. Phys.* **113**, 2941 (2000).
- ³⁵R. Fantoni, D. Gazzillo, A. Giacometti, M. A. Miller, and G. Pastore, *J. Chem. Phys.* **127**, 234507 (2007).
- ³⁶C. Gögelein, F. Romano, F. Sciortino, and A. Giacometti, *J. Chem. Phys.* **136**, 094512 (2012).
- ³⁷E. Bianchi, J. Largo, E. Zaccarelli, and F. Sciortino, *Phys. Rev. Lett.* **97**, 168301 (2006).
- ³⁸F. Sciortino, A. Giacometti, and G. Pastore, *Phys. Rev. Lett.* **103**, 237801 (2009).
- ³⁹R. Fantoni, A. Giacometti, F. Sciortino, and G. Pastore, *Soft Matter* **7**, 2419 (2011).
- ⁴⁰R. Fantoni, *Eur. Phys. J. B* **85**, 108 (2012).
- ⁴¹A. Reinhardt, A. J. Williamson, J. P. K. Doye, J. Carrete, L. M. Varela, and A. A. Louis, *J. Chem. Phys.* **134**, 104905 (2011).

Part XIV

2014

Chapter 41

Depletion force in the infinite-dilution limit in a solvent of nonadditive hard spheres

Fantoni R. and Santos A., J. Chem. Phys. **140**, 244513 (2014)

Title: “Depletion force in the infinite-dilution limit in a solvent of nonadditive hard spheres”

Abstract: The mutual entropic depletion force felt by two solute “big” hard spheres immersed in a binary mixture solvent of nonadditive “small” hard spheres is calculated as a function of the surface-to-surface distance by means of canonical Monte Carlo simulations and through a recently proposed rational-function approximation [Phys. Rev. E **84**, 041201 (2011)]. Four representative scenarios are investigated: symmetric solute particles and the limit where one of the two solute spheres becomes a planar hard wall, in both cases with symmetric and asymmetric solvents. In all cases, the influence on the depletion force due to the nonadditivity in the solvent is determined in the mixed state. Comparison between results from the theoretical approximation and from the simulation shows a good agreement for surface-to-surface distances greater than the smallest solvent diameter.



Depletion force in the infinite-dilution limit in a solvent of nonadditive hard spheres

Riccardo Fantoni^{1,a)} and Andrés Santos^{2,b)}

¹Dipartimento di Scienze dei Materiali e Nanosistemi, Università Ca' Foscari Venezia, Calle Larga S. Marta DD2137, I-30123 Venezia, Italy

²Departamento de Física and Instituto de Computación Científica Avanzada de Extremadura (ICCAEx), Universidad de Extremadura, Badajoz E-06071, Spain

(Received 8 April 2014; accepted 27 May 2014; published online 30 June 2014)

The mutual entropic depletion force felt by two solute “big” hard spheres immersed in a binary mixture solvent of nonadditive “small” hard spheres is calculated as a function of the surface-to-surface distance by means of canonical Monte Carlo simulations and through a recently proposed rational-function approximation [R. Fantoni and A. Santos, Phys. Rev. E **84**, 041201 (2011)]. Four representative scenarios are investigated: symmetric solute particles and the limit where one of the two solute spheres becomes a planar hard wall, in both cases with symmetric and asymmetric solvents. In all cases, the influence on the depletion force due to the nonadditivity in the solvent is determined in the mixed state. Comparison between results from the theoretical approximation and from the simulation shows a good agreement for surface-to-surface distances greater than the smallest solvent diameter. © 2014 AIP Publishing LLC. [<http://dx.doi.org/10.1063/1.4884353>]

I. INTRODUCTION

In chemical physics, one often finds solute particles immersed in a solvent. Even though the solute particles interact through a *true* potential, an important problem consists of reducing the solute-solvent system of particles to an equivalent one made of only the solute particles but interacting through an *effective* potential. This problem has been much studied for the paradigmatic case of an athermal mixture of additive hard spheres (AHS)¹ and for the more general case of nonadditive hard spheres (NAHS).^{2–4} The problem is usually solved in a two-step procedure. Starting from the pioneering work of Asakura and Oosawa,⁵ one first determines the effective *pair* potential, the so-called *depletion entropic potential*, between *two* “big” solute hard spheres (in three^{6–8} or two⁹ dimensions) immersed in a solvent of “small” hard spheres. Once this stage has been carried out, one can study the properties of a fluid of particles interacting with such an effective pair potential.¹⁰ While the assumption of pairwise additivity is essentially uncontrolled, since the presence of a third particle in the vicinity of a pair of solutes will alter the solvent (the depletant) spatial distribution, it is expected that such limitations of the pairwise additivity approximation become progressively less relevant on decreasing the solute density and/or the size ratio between the diameter of a solvent particle and that of a solute particle. The oscillations in the depletion potential, for example, are found to be responsible for gelation in binary mixture of hard spheres¹¹ and for spatial heterogeneity in bimodal colloidal suspensions.¹²

In the present work, we are interested in the first step of such a programme. The depletion potential problem has been

studied in several different scenarios. One can have nonspherical solute¹³ or solvent¹⁴ particles. For spherical solute and solvent particles, the case we are interested in, the solvent itself may be an AHS mixture (binary,¹⁵ multicomponent,¹⁶ or polydisperse^{17,18}). Additionally, the solvent particles may have various kinds of interaction.^{19–22} When the solvent particles interact with a potential which has some attraction, an interesting issue is the one of understanding how the depletion or force will be affected upon approaching the gas-liquid coexistence critical point of the solvent, where the critical fluctuations are expected to give rise to the so-called thermodynamic Casimir forces.^{23–26}

Recently, we constructed an approximate theory for the structure and the thermodynamics of a general NAHS multicomponent mixture,^{27,28} which we called the (first order) rational-function approximation (RFA). The theory provides a fully analytical representation of the radial distribution functions in Laplace space which extends to the nonadditive case the exact solution of the Percus–Yevick (PY) integral equation for AHS mixtures.^{29,30} It is the purpose of the present work to use the RFA theory to predict the depletion force when the solvent is a NAHS binary mixture and to compare our theoretical predictions with Monte Carlo (MC) simulation results. We clearly want to avoid demixing^{31,32} in the solvent. This restricts the combinations of solvent density and (positive) nonadditivity that we are allowed to choose. An interesting open problem, that we leave to a future study, is the study of how the depletion force is affected by approaching the demixing critical point on the critical isochore.

In order to find the depletion force in the simulations, we followed the MC method of Dickman *et al.*³³ In molecular dynamics simulations, however, a different strategy³⁴ is more suitable. We decided not to determine the depletion potential from the force because the spatial integration of the latter can introduce additional uncontrolled uncertainties. On

^{a)}Electronic mail: rfantoni@ts.infn.it

^{b)}Electronic mail: andres@unex.es. URL: <http://www.unex.es/eweb/fisteor/andres/>.

the other hand, it is possible to determine the depletion potential directly in a MC simulation by allowing the two solute impurities to move.²⁶

We will consider four different scenarios: (i) two symmetric solute particles in a symmetric solvent, (ii) two symmetric solute particles in an asymmetric solvent, (iii) extremely asymmetric solutes, in the limit where one of the two solute spheres reduces to a planar hard wall,²⁸ in a symmetric solvent, and (iv) the same situation but in an asymmetric solvent.

The paper is organized as follows. In Sec. II, we introduce the fluid model we set up to study further on, while in Sec. III the observable to be measured in MC simulations and estimated with our RFA theory is described. Details about our MC simulations are given in Sec. IV. Section V presents the numerical and theoretical results for the depletion force and compares them. The paper is closed in Sec. VI with some final remarks.

II. THE MODEL

We consider the following general model. Two solute big hard spheres (the impurities) of species a and b and diameters $\sigma_a = \sigma_{aa}$ and $\sigma_b = \sigma_{bb}$ with $\sigma_{ab} = \frac{1}{2}(\sigma_a + \sigma_b)$ are immersed in a NAHS binary mixture solvent made of N_μ small hard spheres of species $\mu = 1, 2$ of diameter $\sigma_\mu = \sigma_{\mu\mu}$ in a volume V , such that

$$\sigma_{12} = \frac{\sigma_1 + \sigma_2}{2}(1 + \Delta) \quad (2.1)$$

with $\Delta > -1$ measuring the solvent nonadditivity. The solute-solvent interaction is assumed to be additive, i.e., $\sigma_{\mu\alpha} = \frac{1}{2}(\sigma_\mu + \sigma_\alpha)$ with $\mu = 1, 2$ and $\alpha = a, b$.

Without loss of generality, we take $\sigma_1 (\leq \sigma_2)$ as length unit. Thus, we define the solvent/solvent size ratio $\sigma_2/\sigma_1 \geq 1$, the solute/solute size ratio $\sigma_b/\sigma_a \geq 1$, and the solute/solvent size ratio $\sigma_a/\sigma_1 > 1$. The solvent total number density is $\rho = N/V = \sum_{\mu=1}^2 N_\mu/V = \sum_{\mu=1}^2 \rho_\mu$ and the mole fraction of species $\mu = 1, 2$ is $x_\mu = \rho_\mu/\rho$, with $x_1 + x_2 = 1$. From this we can introduce the partial packing fractions $\eta_\mu = \frac{\pi}{6}\rho x_\mu \sigma_\mu^3$ and the nominal total packing fraction $\eta = \sum_\mu \eta_\mu$.

The model is characterized by the following set of six independent dimensionless parameters: η , x_1 , σ_2/σ_1 , and Δ , defining the solvent, and σ_b/σ_a and σ_a/σ_1 , defining the solute. Note that the model can also be obtained from the more general one of a quaternary mixture with $a = 3$, $b = 4$ in the limit of infinite solute dilution $x_3 \rightarrow 0$, $x_4 \rightarrow 0$.⁷

The depletion force is formally independent of the solvent-solvent interaction (see Sec. III).^{33,35} But of course it depends on the local solvent density in the neighborhood of the solute particles and such a density is affected by the solvent-solvent and solvent-solute interactions. A natural question then arises: As the solvent-solvent nonadditivity is switched on, how the induced change in the local solvent density affects the depletion force? Clearly, far away from the solute spheres there will be no change in the almost constant local density, i.e., the bulk density. But the local density in the vicinity of the solute particles would change and thereby so would the force. To first order in density, however, the de-

pletion force is completely independent of the solvent-solvent interaction,⁷ so the influence of nonadditivity is absent. Thus, one can expect the effect to be small for dilute solvents but its impact as the bulk solvent density increases is uncertain.

We could alternatively switch on a solute-solvent nonadditivity,^{2,4,36} but this case is somewhat less interesting than the previous one. For example, in the case of two solute spheres of diameter σ_a immersed in a one-component solvent of spheres of diameter σ_1 with $\sigma_{1a} \neq \frac{1}{2}(\sigma_1 + \sigma_a)$, one can map the problem onto an additive one where the solute particles have an effective diameter $\sigma_a^{\text{eff}} = 2\sigma_{1a} - \sigma_1$, provided that $\sigma_{1a} \geq \frac{1}{2}\sigma_1$. The effective problem determines the depletion force for $r > \sigma_a^{\text{eff}}$, so that the original problem becomes completely solved in the case of negative nonadditivity (since then $\sigma_a > \sigma_a^{\text{eff}}$), while in the case of positive nonadditivity it only remains unsolved in the region $\sigma_a < r < \sigma_a^{\text{eff}}$. For this reason, we will not consider solute-solvent nonadditivity in our analysis.

In this study, we will first restrict ourselves to the particular case of equal solute impurities ($\sigma_b/\sigma_a = 1$) and consider both a symmetric ($\sigma_2/\sigma_1 = 1$, $x_1 = \frac{1}{2}$) and an asymmetric ($\sigma_2/\sigma_1 \neq 1$, $x_1 \neq \frac{1}{2}$) nonadditive solvent. Our aim is to assess in both cases the effect of the solvent nonadditivity on the depletion force. Then, we will consider the case of extremely asymmetric solute impurities in the limit $\sigma_b/\sigma_a \rightarrow \infty$, where one of the two impurities is seen as a hard planar wall both by the other solute sphere and by the solvent species.

III. THE DEPLETION FORCE

We want to determine the force exerted on one big solute sphere immersed in a solvent of small spheres due to the presence of a second big solute sphere, assuming a hard-core repulsion between the solvent and the solute. The solvent in the presence of only one solute sphere at the origin will keep being an isotropic fluid (even if not homogeneous anymore) and the solute sphere will feel a zero net force. However, if we add a second solute sphere in the solvent, the isotropy symmetry will be broken (we are then left with a solvent fluid with axial symmetry around the axis connecting the centers of the two solute spheres) and, as a consequence, each solute sphere will exert an effective force \mathbf{F} on the other one, mediated by the solvent. This force has the form³⁵

$$\beta \mathbf{F}(r) = - \int_S dA \rho^{(r)}(\mathbf{r}_s) \hat{\mathbf{n}}, \quad (3.1)$$

where $\beta = 1/k_B T$ is the inverse temperature parameter, the integral is carried out over the surface S of the sphere centered on the solute particle experiencing the force, dA is an elementary area on S , $\hat{\mathbf{n}}$ is the outward normal unit vector, and $\rho^{(r)}(\mathbf{r}_s)$ is the local density of the solvent (in the presence of the two solute spheres) at the point \mathbf{r}_s on the surface S .

A. Monte Carlo implementation

1. One-component solvent

Let us first assume a one-component solvent made of N spheres of diameter σ_1 and coordinates \mathbf{r}_i ($i = 1, \dots, N$) in

a volume V . The solute particle of species a is centered at \mathbf{r}_a and the solute particle of species b is centered at $\mathbf{r}_b = \mathbf{r}_a + r\hat{\mathbf{r}}$. According to Eq. (3.1), the force $\mathbf{F}_{ab}(r) = F_{ab}(r)\hat{\mathbf{r}}$ felt by sphere b due to the presence of sphere a is then³⁵

$$\beta F_{ab}(r) = -\sigma_{1b}^2 \int d\Omega_s \cos \theta_s \rho^{(r)}(\mathbf{r}_b + \sigma_{1b}\hat{\mathbf{s}}), \quad (3.2)$$

where $d\Omega_s = \sin \theta_s d\theta_s d\varphi_s$ is the elementary solid angle spanned by $\hat{\mathbf{s}}$ taking the polar axis along $\hat{\mathbf{r}}$, $\rho^{(r)}(\mathbf{q}) = \langle \sum_i \delta(\mathbf{q} - \mathbf{r}_i) \rangle$ is the local density of the solvent in the presence of the two solute spheres at a center-to-center distance r , and $\langle \dots \rangle$ is a thermal average.

The expression (3.2) for the depletion force is formally independent of the interaction between the solvent particles and holds as long as we have a hard-sphere interaction between the solvent and the two solute spheres. Clearly, due to the axial symmetry of the solvent fluid, $\rho^{(r)}(\mathbf{r}_b + \sigma_{1b}\hat{\mathbf{s}}) = \langle \sum_i \delta(\sigma_{1b}\hat{\mathbf{s}} - \mathbf{s}_i) \rangle$, with $\mathbf{s}_i = \mathbf{r}_i - \mathbf{r}_b$, is a function of σ_{1b} and θ_s only. Notice that, by Newton's third law, we must have $F_{ab} = -F_{ba}$. In terms of the potential of mean force $\beta u_{ab}(r) = -\ln g_{ab}(r)$, where $g_{ab}(r)$ is the solute-solute radial distribution function in the presence of the solvent, we have

$$\beta F_{ab}(r) = -\beta \frac{du_{ab}(r)}{dr} = \frac{g'_{ab}(r)}{g_{ab}(r)}. \quad (3.3)$$

In MC simulations, we can calculate the force by means of

$$\begin{aligned} \beta F_{ab}(r) &= -\sigma_{1b}^2 \left\langle \sum_i \int d\Omega_s \cos \theta_s \delta(\sigma_{1b}\hat{\mathbf{s}} - \mathbf{s}_i) \right\rangle \\ &\approx -3\sigma_{1b}^2 \left\langle \sum_i \frac{\Pi_{s_i - \frac{\epsilon}{2}, s_i + \frac{\epsilon}{2}}(\sigma_{1b}) \cos \theta_{s_i}}{(s_i + \frac{\epsilon}{2})^3 - (s_i - \frac{\epsilon}{2})^3} \right\rangle, \end{aligned} \quad (3.4)$$

where the boxcar function $\Pi_{a,b}(x) = 1$ if $a \leq x < b$ and zero otherwise, ϵ is a discretization of the s variable, and in the second line of Eq. (3.4) we have discretized the radial part of the Dirac delta function. We can also rewrite Eq. (3.4), by neglecting the term in ϵ^3 in the denominator, as follows:

$$F_{ab}^*(r) \equiv \sigma_{1b} \beta F_{ab}(r) \approx -\sigma_{1b} I^{(r)}(\sigma_{1b}), \quad (3.5)$$

where $F_{ab}^*(r)$ is the dimensionless force and

$$I^{(r)}(s) = \left\langle \sum_i \frac{\Pi_{s - \frac{\epsilon}{2}, s + \frac{\epsilon}{2}}(s_i) \cos \theta_{s_i}}{\epsilon} \right\rangle. \quad (3.6)$$

In the simulations, $I^{(r)}(s)$ is evaluated at $s = s_\kappa = \sigma_{1b} + (2\kappa + 1)\epsilon/2$ with $\kappa = 0, 1, 2, \dots$. The force $F_{ab}^*(r)$ is obtained by extrapolating the data at the contact value $s = \sigma_{1b}$.

2. Multicomponent solvent

In a multicomponent solvent, we have $\rho^{(r)}(\mathbf{q}) = \sum_\mu \rho_\mu^{(r)}(\mathbf{q})$ with $\rho_\mu^{(r)}(\mathbf{q}) = \langle \sum_i \delta_{\mu_i, \mu} \delta(\mathbf{q} - \mathbf{r}_i) \rangle$, where the Greek index stands for the species, the Roman index stands for the particle label, and μ_i denotes the species of particle i . The depletion force is now given by

$$\beta F_{ab}(r) = -\sum_\mu \sigma_{\mu b}^2 \int d\Omega_s \cos \theta_s \rho_\mu^{(r)}(\mathbf{r}_b + \sigma_{\mu b}\hat{\mathbf{s}}). \quad (3.7)$$

The output from the MC simulations are the functions

$$I_\mu^{(r)}(s) = \left\langle \sum_i \delta_{\mu_i, \mu} \frac{\Pi_{s - \frac{\epsilon}{2}, s + \frac{\epsilon}{2}}(s_i) \cos \theta_{s_i}}{\epsilon} \right\rangle, \quad (3.8)$$

calculated at $s = s_\kappa = \sigma_{\mu b} + (2\kappa + 1)\epsilon/2$ with $\kappa = 0, 1, 2, \dots$, so that we now have

$$F_{ab}^*(r) = \sigma_{1b} \beta F_{ab}(r) = -\sigma_{1b} \sum_\mu I_\mu^{(r)}(\sigma_{\mu b}). \quad (3.9)$$

B. Rational-function approximation

Within the RFA^{7,27,28,37} one explicitly obtains the Laplace transform $G_{ab}(s)$ of $rg_{ab}(r)$ in the solute infinite-dilution limit ($x_a \rightarrow 0$ and $x_b \rightarrow 0$) of a quaternary mixture where the solvent is made of species 1 and 2 and the solute is made of species $a = 3$ and $b = 4$. Then, from Eq. (3.3) we have

$$\begin{aligned} \beta F_{ab}(r) &= \frac{[rg_{ab}(r)]'}{rg_{ab}(r)} - \frac{1}{r} \\ &= \frac{\mathcal{L}^{-1}[sG_{ab}(s) - e^{-\sigma_{ab}s} \sigma_{ab} g_{ab}(\sigma_{ab}^+)]}{\mathcal{L}^{-1}[G_{ab}(s)]} - \frac{1}{r}, \end{aligned} \quad (3.10)$$

where \mathcal{L}^{-1} stands for an inverse Laplace transform. In this equation, it is understood that $r > \sigma_{ab}$ since the force is of course singular in the region $0 \leq r \leq \sigma_{ab}$. Thus, given that $\mathcal{L}^{-1}[e^{-\sigma_{ab}s}] = \delta(r - \sigma_{ab})$, we may rewrite

$$\beta F_{ab}(r) = \frac{\mathcal{L}^{-1}[sG_{ab}(s)]}{\mathcal{L}^{-1}[G_{ab}(s)]} - \frac{1}{r}, \quad r > \sigma_{ab}. \quad (3.11)$$

As discussed in Ref. 27, the RFA inverse Laplace transforms for NAHS mixtures could in principle present a spurious behavior in the shell $\min(\sigma_{ab}, \tau_{ab}) \leq r \leq \max(\sigma_{ab}, \tau_{ab})$, where τ_{ab} is the minimum of the list of values $\sigma_{bk} - (\sigma_k - \sigma_a)/2$ ($k = 1-4$) that are different from σ_{ab} . In our case, however, since the solute-solvent interaction is additive, we have $\sigma_{bk} - (\sigma_k - \sigma_a)/2 = \sigma_{ab}$ for all k , so that $\tau_{ab} = \sigma_{ab}$ and the spurious behavior vanishes.

In the limit $\sigma_b/\sigma_a \rightarrow \infty$, the solute sphere b is felt as a planar hard wall by both a solvent particle and by the solute particle a . Before taking the limit we introduce the shifted radial distribution function $\gamma_{ab}(D) = g_{ab}(D + \sigma_{ab})$ for a surface-to-surface distance $D \geq 0$. In Laplace space,

$$G_{ab}(s) = e^{-\sigma_{ab}s} [\sigma_{ab} \Gamma_{ab}(s) - \Gamma'_{ab}(s)], \quad (3.12)$$

where $\Gamma_{ab}(s)$ is the Laplace transform of $\gamma_{ab}(D)$ and $\Gamma'_{ab}(s) = d\Gamma_{ab}(s)/ds$. In the wall limit, Eq. (3.12) yields

$$\Gamma_{aw}(s) = \lim_{\sigma_b/\sigma_a \rightarrow \infty} \frac{2}{\sigma_b} e^{\sigma_{ab}s} G_{ab}(s). \quad (3.13)$$

The corresponding expression for the depletion force is

$$\begin{aligned} \beta F_{aw}(D) &= \frac{\gamma'_{aw}(D)}{\gamma_{aw}(D)} = \frac{\mathcal{L}^{-1}[s\Gamma_{aw}(s) - \gamma_{aw}(0)]}{\mathcal{L}^{-1}[\Gamma_{aw}(s)]} \\ &= \frac{\mathcal{L}^{-1}[s\Gamma_{aw}(s)]}{\mathcal{L}^{-1}[\Gamma_{aw}(s)]}, \end{aligned} \quad (3.14)$$

244513-4 R. Fantoni and A. Santos

 J. Chem. Phys. **140**, 244513 (2014)

where in the last step we have taken into account that $D > 0$ and thus the term coming from $\mathcal{L}^{-1}[1] = \delta(D)$ can be ignored.

Appendix A gives some details on how to carry out the solute infinite-dilution limit analytically, while Appendix B shows how to subsequently carry out the wall limit. Once $G_{ab}(s)$ and $\Gamma_{aw}(s)$ are known, the inverse Laplace transforms may be carried out numerically following the recipe of Ref. 38. When the solvent nonadditivity is switched off ($\Delta = 0$) our RFA approach reduces to the usual PY approximation.^{7,27}

The RFA for NAHS systems inherits from the PY approximation for AHS fluids the possibility of yielding non-physical results near contact for the big-big correlation function in the case of strongly asymmetric mixtures.³⁹⁻⁴¹ As proposed by Henderson,⁴² a simple and convenient way of circumventing this difficulty consists in the replacement $g \rightarrow \exp(g - 1)$. Thus, in order to correct the breakdown of the theory near solute contact, we have also considered an "exponential" RFA (exp-RFA) approximation where²¹

$$g_{ab}^{\text{exp-RFA}}(r) = \exp[g_{ab}^{\text{RFA}}(r) - 1]. \quad (3.15)$$

IV. SIMULATION DETAILS

We performed canonical MC simulations in a parallelepipedal box ($-H/2 < x < H/2$, $-L/2 < y < L/2$, $-L/2 < z < L/2$) with periodic boundary conditions. The two solute spheres a and b are fixed in space, centered at $(-r/2, 0, 0)$ and $(r/2, 0, 0)$, respectively, as shown in Fig. 1. The solvent is in general a binary NAHS mixture, but we will always assume additivity between the solute and the solvent. According to the Metropolis algorithm,⁴³ a solvent particle move is rejected whenever it overlaps with another solvent particle or with any of the two solute spheres. The maximum random particle displacement was chosen so as to have acceptance ratios close to 50%. During the run we measured the shell integrals $I_\mu^{(r)}(s)$ of Eq. (3.8) and the local solvent density. We chose H and L large enough so that away from the two solute spheres the local solvent density shows a bulk-like plateau and thus the

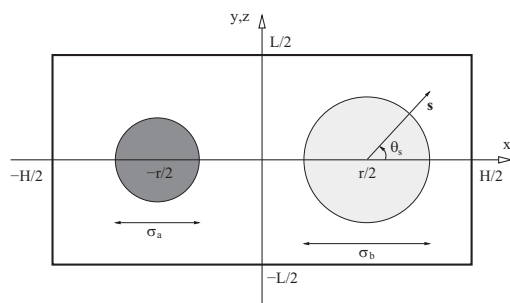


FIG. 1. Schematic simulation arrangement. The simulation box is the parallelepiped $-H/2 < x < H/2$, $-L/2 < y < L/2$, $-L/2 < z < L/2$ with periodic boundary conditions. H and L are chosen large enough so as to have a solvent density exhibiting a bulk-like plateau away from the two solute spheres.

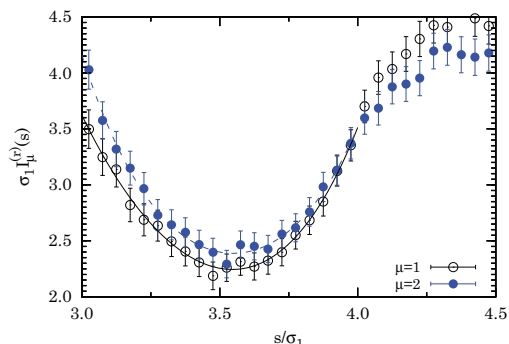


FIG. 2. Shell integrals $I_\mu^{(r)}(s)$ at $r/\sigma_1 = 5$ for the case $x_1 = \frac{1}{2}$, $\sigma_2/\sigma_1 = 1$, $\Delta = 0$, $\sigma_b/\sigma_a = 1$, $\sigma_a/\sigma_1 = 5$. Here, $H/\sigma_1 = 18$, $L/\sigma_1 = 12$, $N = 1134$. The bulk packing fraction is $\eta \approx 0.239(5)$ and the simulation time was $\tau = 4 \times 10^5 N$ single particle moves. The lines are least-square quartic fits on the interval $3 \leq s/\sigma_1 \leq 4$ used to extrapolate $I_\mu^{(r)}(s)$ at contact ($s/\sigma_1 = \sigma_{1b}/\sigma_1 = 3$). The estimated force is then found to be $F_{ab}^*(r) = -\sigma_1 [I_1^{(r)}(\sigma_{1b}) + I_2^{(r)}(\sigma_{2b})] \approx -7.78(8)$. This case is close to the one in Fig. 6(b) of Ref. 33.

solvent density in a cubic cell of side ℓ centered at $(x, y, z) = (-H/2, L/2, L/2)$ can be accepted as a good estimate of the bulk density ρ .

A typical output for the shell integrals from a single simulation is shown in Fig. 2. The uncertainty on each measured value at a given s is determined as $\sqrt{\sigma_v^2 K}/\tau$ where τ is the number of single particle moves, σ_v^2 is the variance of the measures during the run, and K is an estimate of the correlation time of the sequence of measurements assumed as independent from s . In order to determine the depletion force according to Eq. (3.9), we need to find the contact values $I_\mu^{(r)}(\sigma_{\mu b})$. We do this with a least-square quartic fit of the shell integrals near contact, as shown in Fig. 2. Since the solvent binary mixture for the choice of the model parameters in Fig. 2 reduces to a one-component system, no partial demixing is possible, so that the $1 \leftrightarrow 2$ symmetry implies the consequent equality of the two shell integrals. This is reasonably well satisfied within the error estimates. The slight asymmetry observed in Fig. 2 favors one species or the other, in different runs, with equal probabilities.

In the study of the wall limit $\sigma_b/\sigma_a \rightarrow \infty$, we removed the periodic boundary conditions along the x direction and placed a hard wall at $x = -H/2$ and another one at $x = H/2$, rejecting solvent-particle moves producing an overlap with the walls. The solute sphere a was placed on the x axis at $x = -H/2 + D + \sigma_a/2$ and the depletion force felt by the solute impurity $\hat{\mathbf{x}}F_{wa}(D)$ was calculated as a function of $D > 0$. The solvent bulk density was evaluated in a cubic cell of side ℓ centered at $(x, y, z) = (D/2 + \sigma_a/2, L/2, L/2)$.

One can take into account the volume excluded to the solvent particles by the solutes to define a (nominal) average packing fraction $\bar{\eta} = \bar{\eta}_1 + \bar{\eta}_2$, where

$$\bar{\eta}_\mu = \frac{\frac{\pi}{6} N x_\mu \sigma_\mu^3}{HL^2 - \frac{\pi}{6} (\sigma_{a\mu}^3 + \sigma_{b\mu}^3)} \quad (4.1)$$

244513-5 R. Fantoni and A. Santos

 J. Chem. Phys. **140**, 244513 (2014)

 if $\sigma_b/\sigma_a = \text{finite}$ and

$$\bar{\eta}_\mu = \frac{\frac{\pi}{6} N x_\mu \sigma_\mu^3}{(H - \sigma_\mu)L^2 - \frac{\pi}{6} \sigma_\mu^3} \quad (4.2)$$

 if $\sigma_b/\sigma_a = \infty$.

In all the cases presented in Sec. V, we took $N = 500$ solvent particles, box sides $H/\sigma_1 = 18$, $L/\sigma_1 = 12$, a number $\tau = 1.4 \times 10^6 N$ of single particle moves, and a discretization step $\epsilon/\sigma_1 = 0.05$. The side of the cell employed to evaluate the bulk density was $\ell = \sigma_1$.

V. RESULTS

In this section, we present our results for four representative classes of systems: two symmetric solute impurities in a symmetric (class S) or asymmetric (class A) solvent, and a planar wall and a solute impurity in a symmetric (class wS) or asymmetric (class wA) solvent. For each class, we have considered three solvent nonadditivities: zero, positive, and negative. This will allow us to assess the effect of solvent nonadditivity on the depletion force between the impurity particles or between the impurity and the wall. The RFA predictions will be compared with our MC simulations. The parameters characterizing the 12 different systems are given in Table I. The last column gives the average packing fraction $\bar{\eta} = \bar{\eta}_1 + \bar{\eta}_2$ defined by Eqs. (4.1) (solute-solute systems) and (4.2) (wall-solute systems). In the asymmetric-solvent cases ($\sigma_2/\sigma_1 = \frac{3}{2}$), the value of the mole fraction ($x_1 = \frac{193}{250}$) has been chosen such that both species occupy practically equal volumes ($x_1 \sigma_1^3 / x_2 \sigma_2^3 = 1.003$).

As an illustration, Fig. 3 shows a snapshot of an equilibrated MC configuration of system S_0 with the two identical solute particles at contact.

A. Symmetric solvent and symmetric solute impurities

We first consider a symmetric $1 \leftrightarrow 2$ solvent (systems S_0 , S_+ , S_-). In general, for positive nonadditivity ($\Delta > 0$) and sufficiently high densities, the solvent may undergo demixing,³² so that in the simulation we would get $I_1^{(r)}(s) \neq I_2^{(r)}(s)$ by spontaneous symmetry breaking. On the other

TABLE I. Values of the parameters defining the 12 systems considered in this work.

Label	σ_b/σ_a	σ_a/σ_1	x_1	σ_2/σ_1	Δ	$\bar{\eta}$
S_0	1	5	$\frac{1}{2}$	1	0	0.1021
S_+					$\frac{1}{4}$	
S_-					$-\frac{1}{4}$	
A_0	1	5	$\frac{193}{250}$	$\frac{3}{2}$	0	0.1576
A_+					$\frac{1}{5}$	
A_-					$-\frac{1}{5}$	
w S_0	∞	5	$\frac{1}{2}$	1	0	0.1076
w S_+					$\frac{1}{4}$	
w S_-					$-\frac{1}{4}$	
w A_0	∞	5	$\frac{193}{250}$	$\frac{3}{2}$	0	0.1685
w A_+					$\frac{1}{5}$	
w A_-					$-\frac{1}{5}$	

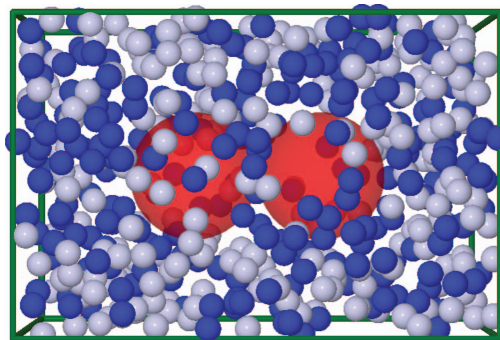


FIG. 3. Snapshot of an equilibrated MC configuration of system S_0 . The solutes are the two big red spheres while the solvent binary mixture is made of small light and dark blue spheres.

hand, if, at a given density, the positive nonadditivity is not too large, the solvent will be in a mixed state and the equality of the two shell integrals is expected. However, we found that, even in states with a mixed solvent in the bulk, the solvent may be partially demixed in the region between the two solute particles because of density compression effects.³⁵ This may be responsible for an asymmetry in the two shell integrals, which is expected to be maximal near a surface-to-surface distance of the two solute impurities equal to one solvent diameter. In order to avoid this effect, we chose a sufficiently small value for the nonadditivity (system S_+).

The first columns of Table II present the simulation results for the depletion force and for the bulk packing fraction of systems S_0 , S_+ , and S_- as functions of the surface-to-surface distance $D = r - \sigma_{ab}$. We observe that the bulk packing fraction is weakly dependent on D and on Δ , being slightly larger than the average value $\bar{\eta}$.

The MC results for the depletion force are compared with the semi-analytical RFA predictions in Fig. 4. We recall that the RFA theory reduces to the PY theory in the additive case ($\Delta = 0$), so the middle solid and dashed lines in Fig. 4 actually represent the PY and exp-PY predictions, respectively. As we can see, those curves for the additive system S_0 agree quite well with the simulation data at and beyond a surface-to-surface separation between the two solute impurities equal to half the solvent diameter, $D \gtrsim \sigma_1/2$. In that region, our RFA theory successfully accounts for the influence of the solvent nonadditivity on the depletion force. A specially good agreement is observed at $D = \sigma_1$, where the theory predicts a kink in the force stemming from the first spatial derivative of the solute-solute radial distribution function. On the other hand, a less satisfactory result is observed near contact of the impurities ($D < \sigma_1/2$), where both the PY (system S_0) and the RFA (systems S_+ and S_-) theories exhibit an artificial upward bending of the curves (instead of the correct quasilinear behavior), implying a force less attractive than it should be. This is, at least qualitatively, corrected by the exp-PY and exp-RFA versions of the theories. Another possible correction could be to develop the second-order RFA,⁴⁴ which is known to work well in the additive solvent case.⁷

TABLE II. MC results for the symmetric cases S_0 , S_+ , S_- , and the asymmetric cases A_0 , A_+ , A_- (see Table I). D is the surface-to-surface separation between the two solutes and η is the bulk packing fraction of the solvent.

D/σ_1	S_0		S_+		S_-		A_0		A_+		A_-	
	F_{ab}^*	η										
0.00	-2.35(3)	0.109(1)	-2.59(2)	0.108(1)	-2.22(2)	0.110(1)	-3.09(3)	0.167(1)	-3.39(3)	0.169(1)	-2.86(2)	0.168(1)
0.25	-1.71(2)	0.109(1)	-1.73(3)	0.109(1)	-1.59(2)	0.110(1)	-2.26(2)	0.166(1)	-2.43(4)	0.169(1)	-2.23(3)	0.171(1)
0.50	-1.03(2)	0.109(1)	-0.93(3)	0.109(1)	-1.01(3)	0.110(1)	-1.40(3)	0.168(1)	-1.33(3)	0.170(1)	-1.41(2)	0.169(1)
0.75	-0.30(3)	0.109(1)	-0.00(2)	0.109(1)	-0.40(2)	0.110(1)	-0.56(3)	0.169(1)	-0.24(3)	0.169(1)	-0.68(3)	0.170(1)
0.84	-0.03(2)	0.109(1)	0.25(3)	0.108(1)	-0.12(3)	0.110(1)	-0.22(3)	0.168(1)	0.13(3)	0.168(1)	-0.35(3)	0.169(1)
0.92	0.26(2)	0.109(1)	0.49(3)	0.108(1)	0.06(3)	0.110(1)	0.10(2)	0.168(1)	0.55(3)	0.168(1)	-0.10(3)	0.170(1)
1.00	0.36(3)	0.109(1)	0.66(3)	0.109(1)	0.21(3)	0.109(1)	0.45(2)	0.171(1)	0.95(4)	0.168(1)	0.17(2)	0.169(1)
1.08	0.32(4)	0.110(1)	0.63(4)	0.109(1)	0.27(3)	0.110(1)	0.50(4)	0.169(1)	0.76(6)	0.171(1)	0.15(4)	0.170(1)
1.16	0.17(4)	0.109(1)	0.28(3)	0.108(1)	0.08(3)	0.110(1)	0.21(4)	0.169(1)	0.36(5)	0.165(1)	0.03(3)	0.170(1)
1.25	-0.02(4)	0.109(1)	0.01(4)	0.108(1)	-0.02(3)	0.110(1)	0.07(5)	0.168(1)	0.23(4)	0.170(1)	-0.07(3)	0.170(1)
1.50	-0.01(4)	0.110(1)	0.02(4)	0.109(1)	-0.03(3)	0.110(1)	0.22(4)	0.169(1)	0.48(5)	0.166(1)	0.14(4)	0.170(1)
1.75	0.01(2)	0.109(1)	-0.13(4)	0.109(1)	-0.05(3)	0.109(1)	-0.07(4)	0.169(1)	-0.20(5)	0.168(1)	0.01(4)	0.170(1)
2.00	0.01(3)	0.109(1)	-0.11(3)	0.109(1)	-0.00(2)	0.110(1)	-0.10(3)	0.169(1)	-0.04(3)	0.168(1)	-0.02(3)	0.170(1)
2.25	-0.03(3)	0.109(1)	-0.06(3)	0.108(1)	-0.02(3)	0.110(1)	-0.04(3)	0.170(1)	-0.12(4)	0.171(1)	-0.06(3)	0.171(1)
2.50	0.02(2)	0.109(1)	0.04(2)	0.109(1)	-0.00(2)	0.109(1)	-0.00(3)	0.169(1)	0.09(3)	0.167(1)	-0.02(2)	0.169(1)

The positive nonadditivity enhances the depletion force and the negative nonadditivity inhibits it. These trends for the effect of the solvent nonadditivity on the depletion force could be expected from the following simple argument. To first order in density, the bulk compressibility factor of the solvent is $1 + B_2\rho$, with $B_2 = (2\pi/3) \sum_{i,j} x_i x_j \sigma_{ij}^3$ being the second virial coefficient. Therefore, in the low-density regime, one would expect the NAHS solvent with a packing fraction η to behave similarly to an effective AHS solvent with an effective packing fraction

$$\eta_{\text{eff}} = \eta \frac{\sum_{i,j} x_i x_j \sigma_{ij}^3}{\sum_{i,j} x_i x_j [(\sigma_i + \sigma_j)/2]^3}. \quad (5.1)$$

Thus, introducing a positive nonadditivity in the solvent is qualitatively analogous to increasing its density, which in turn produces an enhancement of the solute-solute depletion force. Of course, a negative nonadditivity produces the opposite effect.

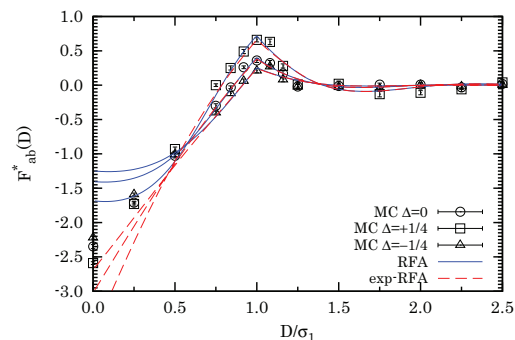


FIG. 4. Depletion force between two identical big hard spheres immersed in a solvent binary mixture of small hard spheres, as a function of their surface-to-surface separation, for systems S_0 , S_+ , and S_- (see Table I). The bulk packing fraction used to obtain the (exp-)RFA results was taken as $\eta = 0.109$ in all cases. The MC results are the ones of Table II.

B. Asymmetric solvent and symmetric solute impurities

Next, we consider the asymmetric-solvent systems A_0 , A_+ , and A_- . In those cases, the two shell integrals are obviously different, i.e., $I_1^{(r)}(s) \neq I_2^{(r)}(s)$. As before, we want to measure the effect on the depletion force of adding a certain nonadditivity to the solvent.

The MC values for the depletion force and the bulk packing fraction are given in Table II. As in the symmetric-solvent cases, the bulk packing fractions are slightly larger than the nominal average values, but now the influence of the solute-solute separation on the bulk values is more pronounced.

Figure 5 compares the MC and RFA results for systems A_0 , A_+ , and A_- . As in the symmetric case, RFA=PY for the AHS solvent ($\Delta = 0$). Now, in addition to a kink in the depletion force at $D = \sigma_1$, the RFA predicts a second kink at $D = \sigma_2$, with smooth oscillations around zero beyond that point. Again, the variation of the depletion force with distance

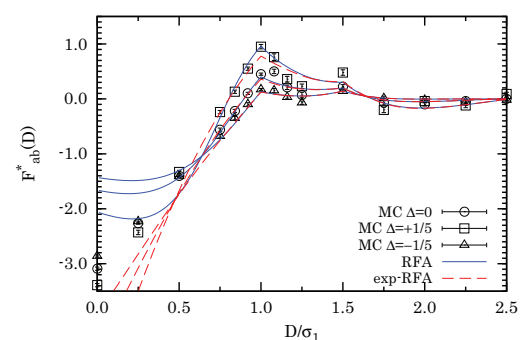


FIG. 5. Depletion force between two identical big hard spheres immersed in a solvent binary mixture of small hard spheres, as a function of their surface-to-surface separation, for systems A_0 , A_+ , and A_- (see Table I). The bulk packing fraction used to obtain the (exp-)RFA results was taken as $\eta = 0.170$ in all cases. The MC results are the ones of Table II.

TABLE III. MC results for the symmetric cases wS_0 , wS_+ , wS_- , and the asymmetric cases wA_0 , wA_+ , wA_- (see Table I). D is the surface-to-surface separation between the wall and the solute sphere and η is the bulk packing fraction of the solvent.

D/σ_1	wS_0		wS_+		wS_-		wA_0		wA_+		wA_-	
	F_{aw}^*	η										
0.00	-4.44(3)	0.110(1)	-4.68(3)	0.108(1)	-4.10(2)	0.111(1)	-5.73(2)	0.172(1)	-6.20(2)	0.169(1)	-5.20(2)	0.170(1)
0.25	-3.29(2)	0.109(1)	-3.30(2)	0.108(1)	-3.11(2)	0.110(1)	-4.34(3)	0.168(1)	-4.49(3)	0.168(1)	-4.02(1)	0.172(1)
0.50	-1.99(2)	0.109(1)	-1.82(3)	0.108(1)	-2.01(2)	0.111(1)	-2.70(2)	0.171(1)	-2.55(3)	0.165(1)	-2.69(2)	0.171(1)
0.75	-0.66(2)	0.109(1)	-0.11(3)	0.108(1)	-0.79(3)	0.110(1)	-1.03(3)	0.170(1)	-0.32(4)	0.168(1)	-1.26(3)	0.172(1)
0.84	-0.06(2)	0.110(1)	0.60(3)	0.108(1)	-0.38(3)	0.111(1)	-0.30(3)	0.170(1)	0.56(3)	0.170(1)	-0.72(3)	0.172(1)
0.92	0.42(3)	0.109(1)	0.60(3)	0.108(1)	0.05(2)	0.110(1)	0.28(3)	0.169(1)	1.24(3)	0.169(1)	-0.22(3)	0.172(1)
1.00	0.95(3)	0.110(1)	1.66(2)	0.108(1)	0.59(3)	0.110(1)	1.00(3)	0.168(1)	2.01(3)	0.167(1)	0.34(3)	0.171(1)
1.08	0.83(5)	0.109(1)	1.42(6)	0.108(1)	0.52(4)	0.110(1)	0.92(7)	0.168(1)	1.91(10)	0.165(1)	0.43(5)	0.172(1)
1.16	0.33(5)	0.109(1)	0.44(7)	0.108(1)	0.19(4)	0.110(1)	0.41(8)	0.168(1)	0.99(10)	0.168(1)	0.16(5)	0.172(1)
1.25	-0.06(5)	0.110(1)	0.04(7)	0.109(1)	-0.05(5)	0.110(1)	0.11(8)	0.169(1)	0.54(10)	0.167(1)	-0.04(7)	0.171(1)
1.50	0.08(6)	0.110(1)	-0.02(7)	0.109(1)	0.12(5)	0.110(1)	0.55(7)	0.171(1)	0.93(9)	0.165(1)	0.38(7)	0.172(1)
1.75	-0.06(5)	0.109(1)	-0.17(6)	0.109(1)	-0.07(4)	0.110(1)	-0.15(7)	0.170(1)	-0.56(8)	0.167(1)	-0.07(6)	0.171(1)
2.00	-0.00(2)	0.110(1)	-0.06(3)	0.108(1)	0.01(2)	0.110(1)	-0.04(5)	0.171(1)	-0.28(5)	0.167(1)	-0.02(3)	0.171(1)
2.25	-0.03(3)	0.109(1)	0.05(3)	0.108(1)	0.00(2)	0.110(1)	-0.05(4)	0.168(1)	-0.16(4)	0.167(1)	-0.00(3)	0.172(1)
2.50	0.05(2)	0.109(1)	0.03(3)	0.108(1)	-0.03(2)	0.111(1)	0.07(3)	0.170(1)	-0.01(3)	0.165(1)	0.01(2)	0.172(1)

increases (decreases) if a positive (negative) nonadditivity is included, as expected from the argument behind Eq. (5.1). Analogous to Fig. 4, a reasonable agreement between our theoretical approximation and the simulation results is observed for $D \gtrsim \sigma_1/2$, but the agreement breaks down when the solutes are near contact. On the other hand, the exp-RFA approximation has the correct linear behavior near contact, even if it underestimates the contact values. Note also that, while RFA and exp-RFA are practically indistinguishable for $D \gtrsim \sigma_1/2$ in Fig. 4, both approximations are slightly different in the region near the kink at $D = \sigma_1$ in the case A_+ , RFA being more accurate than exp-RFA.

C. A wall and one solute impurity in a symmetric solvent

We now explore the cases of extreme solute asymmetry in the limit $\sigma_b/\sigma_a \rightarrow \infty$, where sphere b becomes a planar hard wall.

We start with the cases of a symmetric solvent (systems wS_0 , wS_+ , and wS_-). The MC data for the depletion force and the bulk packing fraction are listed in the first columns of Table III. Since the solvents in systems wS_0 , wS_+ , and wS_- are in the same bulk state (except for small changes of η) as in systems S_0 , S_+ , and S_- , respectively, we can test the Derjaguin approximation⁴⁵ $F_{aa}^*(D) \approx \frac{1}{2}F_{aw}^*(D)$. As can be seen from comparison of Tables II and III, the Derjaguin approximation is rather well satisfied in our simulations, even in the cases of NAHS solvents, $\frac{1}{2}F_{aw}^*(D)$ being typically 1%–10% smaller than $F_{aa}^*(D)$.

Theory and simulation are compared in Fig. 6. Not surprisingly, our RFA approximation (which is again equivalent to the PY approximation in the case $\Delta = 0$) performs quite well for $D \gtrsim \sigma_1/2$ but it breaks down near contact between the wall and the solute spherical impurity, this effect being now more important than in the cases of two identical solutes (Fig. 4). On the other hand, the exp-RFA approximation ex-

hibits a better (quasilinear) behavior near contact, although it underestimates the contact values. Also, analogous to what is observed in Fig. 5, exp-RFA is less accurate than RFA near the kink at $D = \sigma_1$ when a positive nonadditivity is present.

D. A wall and one solute impurity in an asymmetric solvent

To complete the picture, we finally consider the wall-solute force in a NAHS solvent (systems wA_0 , wA_+ , and wA_-). The corresponding MC data can be found in Table III. The Derjaguin approximation $F_{aa}^*(D) \approx \frac{1}{2}F_{aw}^*(D)$ is again well satisfied, although the deviations are slightly larger than in the wS cases, $\frac{1}{2}F_{aw}^*(D)$ being about 4%–10% smaller than $F_{aa}^*(D)$.

As Fig. 7 shows, in contrast to the cases S_+ , A_+ , and wS_+ plotted in Figs. 4–6, respectively, the RFA for a positive

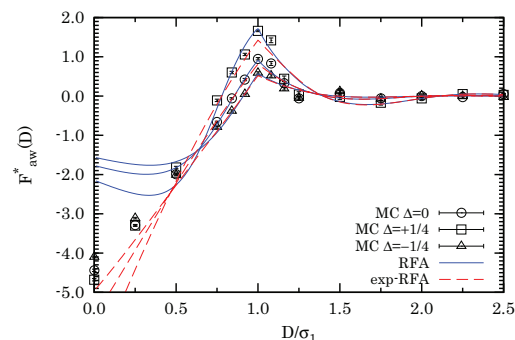


FIG. 6. Depletion force between a hard wall and a big hard sphere immersed in a solvent binary mixture of small hard spheres, as a function of their surface-to-surface separation, for systems wS_0 , wS_+ , and wS_- (see Table I). The bulk packing fraction used to obtain the (exp-)RFA results was taken as $\eta = 0.109$ in all cases. The MC results are the ones of Table III.

244513-8 R. Fantoni and A. Santos

J. Chem. Phys. **140**, 244513 (2014)

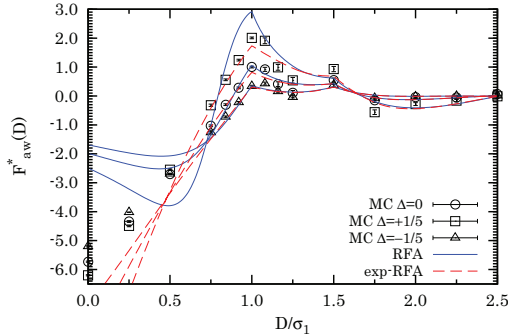


FIG. 7. Depletion force between a hard wall and a big hard sphere immersed in a solvent binary mixture of small hard spheres, as a function of their surface-to-surface separation, for systems wA_0 , wA_+ , and wA_- (see Table I). The bulk packing fraction used to obtain the (exp-)RFA results was taken as $\eta = 0.170$ in all cases. The MC results are the ones of Table III.

nonadditivity (system wA_+) is not able to capture accurately the values of the depletion force in the region near the first kink at $D = \sigma_1$, while the related approximation exp-RFA does. Moreover, the artificial upward bend of the PY curve ($\Delta = 0$) and of the two RFA curves ($\Delta = \pm \frac{1}{5}$) in the region $D \lesssim \sigma_1/2$ is much more dramatic than in Figs. 4–6. Again, the exp-RFA lines tend to correct this behavior but they underestimate the contact values.

VI. CONCLUSIONS

We have studied in this paper the mutual depletion force acting on two solute hard spheres immersed in a solvent consisting in a binary NAHS mixture. We have employed two complementary tools: canonical MC simulations and the semi-analytical RFA (which is fully equivalent to the PY solution when the solvent nonadditivity is switched off). Four different settings have been considered: two symmetric solutes in a symmetric and in an asymmetric solvent, and two extremely asymmetric solutes (in the limit where one of the two spheres reduces to a planar hard wall) again in a symmetric and in an asymmetric solvent. For each class of systems, we have chosen three possibilities: zero nonadditivity, positive nonadditivity, and negative nonadditivity. In all the systems, the solvent remained in a mixed state.

We have found that the RFA performs reasonably well in all cases for a surface-to-surface distance D greater than the radius of the smallest solvent particles, except in the case wA_+ of a wall with an asymmetric solvent with positive nonadditivity, where the theory overestimates the height of the first kink. The approximation in all cases breaks down at and near contact ($D = 0$). To correct this, we have also considered an exp-RFA, which shows the correct quasilinear behavior near contact, even if it is still not able to quantitatively capture the contact values. The approximations correctly predict kinks in the depletion force when D equals any of the two solvent diameters. Our results show how in all cases a positive solvent nonadditivity enhances the depletion force whereas a

negative one inhibits it. Moreover, the Derjaguin approximation is well satisfied in our simulations, even for the nonadditive solvent.

As possible further developments of our study, we plan to try to correct the theoretical approximation near contact and to study the behavior of the force as one approaches the demixing transition of the solvent on the critical isochore.

ACKNOWLEDGMENTS

R.F. acknowledges the hospitality of the University of Extremadura in Badajoz, where the work was carried out, and the use of the CINECA computational facilities under the IS-CRA grant. The research of A.S. was supported by the Spanish Government through Grant No. FIS2010-16587 and by the Junta de Extremadura (Spain) through Grant No. GR10158, both partially financed by FEDER funds.

APPENDIX A: THE SOLUTE INFINITE-DILUTION LIMIT IN THE RFA

For convenience, we here use Roman indexes for the species instead of Greek indexes as done in the main text. In Ref. 27, the following proposal for the structural properties of an n -component NAHS fluid defined through the Laplace transform $G_{ij}(s)$ of $rg_{ij}(r)$ was given:

$$G_{ij}(s) = s^{-2} \sum_{k=1}^n e^{-\sigma_{ik}s} L_{ik}(s) B_{kj}(s), \quad (\text{A1})$$

with

$$B^{-1}(s) = I - A(s), \quad (\text{A2})$$

$$A_{ij}(s) = \frac{2\pi\rho x_i}{s^3} [N_{ij}(s)e^{a_{ij}s} - L_{ij}(s)e^{-\sigma_{ij}s}], \quad (\text{A3})$$

where I is the unit matrix,

$$L_{ij}(s) \equiv L_{ij}^{(0)} + L_{ij}^{(1)}s, \quad (\text{A4})$$

$$N_{ij}(s) \equiv L_{ij}^{(0)} \left(1 - b_{ij}s + \frac{b_{ij}^2s^2}{2} \right) + L_{ij}^{(1)}s(1 - b_{ij}s), \quad (\text{A5})$$

$$b_{ij} \equiv \sigma_{ij} + a_{ij}, \quad a_{ij} \equiv \frac{1}{2}(\sigma_i - \sigma_j). \quad (\text{A6})$$

Equations (A1)–(A5) provide the explicit s -dependence of the Laplace transform $G_{ij}(s)$, but it still remains to determine the two sets of parameters $L_{ij}^{(0)}$ and $L_{ij}^{(1)}$. This is done by enforcing the physical requirements²⁷ $\lim_{s \rightarrow 0} s^2 G_{ij}(s) = 1$ and $\lim_{s \rightarrow 0} s^{-1} [s^2 G_{ij}(s) - 1] = 0$. The results are

$$L_{ij}^{(0)} = S_j, \quad L_{ij}^{(1)} = T_j + \sigma_{ij} S_j, \quad (\text{A7})$$

where

$$S_j \equiv \frac{1 - \pi\rho\Psi_j}{(1 - \pi\rho\Lambda_j)(1 - \pi\rho\Psi_j) - \pi^2\rho^2\mu_{j|2,0}\Omega_j}, \quad (\text{A8})$$

244513-9 R. Fantoni and A. Santos

J. Chem. Phys. **140**, 244513 (2014)

$$T_j \equiv \frac{\pi\rho\Omega_j}{(1 - \pi\rho\Lambda_j)(1 - \pi\rho\Psi_j) - \pi^2\rho^2\mu_{j|2,0}\Omega_j}, \quad (\text{A9})$$

$$\Lambda_j \equiv \mu_{j|2,1} - \frac{1}{3}\mu_{j|3,0}, \quad (\text{A10})$$

$$\Psi_j \equiv \frac{2}{3}\mu_{j|3,0} - \mu_{j|2,1}, \quad (\text{A11})$$

$$\Omega_j \equiv \mu_{j|3,1} - \mu_{j|2,2} - \frac{1}{4}\mu_{j|4,0}, \quad (\text{A12})$$

and we have called

$$\mu_{j|p,q} \equiv \sum_{k=1}^n x_k b_{kj}^p \sigma_{kj}^q. \quad (\text{A13})$$

We now choose our quaternary mixture ($n = 4$) in such a way that the first two species ($i = 1$ and $i = 2$) describe the solvent and the last two species ($i = 3 = a$ and $i = 4 = b$) describe the solute. Then, in the infinite-dilution limit $x_a \rightarrow 0$ and $x_b \rightarrow 0$ we have that

$$\mathbf{B}^{-1} = \begin{pmatrix} (\mathbf{B}^{-1})_{11} & (\mathbf{B}^{-1})_{12} & -A_{1a} & -A_{1b} \\ (\mathbf{B}^{-1})_{21} & (\mathbf{B}^{-1})_{22} & -A_{2a} & -A_{2b} \\ 0 & 0 & 1 & 0 \\ 0 & 0 & 0 & 1 \end{pmatrix}, \quad (\text{A14})$$

and thus

$$\mathbf{B} = \begin{pmatrix} B_{11} & B_{12} & C_{1a} & C_{1b} \\ B_{21} & B_{22} & C_{2a} & C_{2b} \\ 0 & 0 & 1 & 0 \\ 0 & 0 & 0 & 1 \end{pmatrix}, \quad (\text{A15})$$

where

$$C_{ij} = \sum_{k=1}^2 B_{ik} A_{kj}, \quad i = 1, 2 \text{ and } j = a, b. \quad (\text{A16})$$

We have reduced the inversion of the original 4×4 matrix \mathbf{B}^{-1} to the inversion of just the 2×2 submatrix corresponding to the solvent.

We then find

$$s^2 G_{ab}(s) = e^{-\sigma_{ab}s} L_{ab}(s) + \sum_{k=1}^2 e^{-\sigma_{ak}s} L_{ak}(s) C_{kb}(s), \quad (\text{A17})$$

where now $\mu_{j|p,q} = \sum_{k=1}^2 x_k b_{kj}^p \sigma_{kj}^q$.

APPENDIX B: THE WALL LIMIT IN THE RFA

Taking the limit $\sigma_b \rightarrow \infty$, we find from Eq. (A17),

$$\begin{aligned} \Gamma_{aw}(s) &= \lim_{\sigma_b \rightarrow \infty} \frac{2}{\sigma_b} e^{\sigma_{ab}s} G_{ab}(s) \\ &= \frac{2}{s^2} \left[\tilde{L}_{aw}(s) + \sum_{k=1}^2 L_{ak}(s) \tilde{C}_{kw}(s) \right], \end{aligned} \quad (\text{B1})$$

where

$$\tilde{L}_{aw}(s) \equiv \lim_{\sigma_b \rightarrow \infty} \frac{L_{ab}(s)}{\sigma_b}, \quad (\text{B2})$$

$$\tilde{C}_{kw}(s) \equiv \lim_{\sigma_b \rightarrow \infty} \frac{e^{\sigma_{kb}s} C_{kb}(s)}{\sigma_b}, \quad k = 1, 2. \quad (\text{B3})$$

¹M. Dijkstra, R. van Roij, and R. Evans, *Phys. Rev. Lett.* **82**, 117 (1999).

²R. Roth, R. Evans, and A. A. Louis, *Phys. Rev. E* **64**, 051201 (2001).

³A. A. Louis and R. Roth, *J. Phys.: Condens. Matter* **13**, L777 (2001).

⁴C. D. Estrada-Alvarez, E. López-Sánchez, G. Pérez-Ángel, P. González-Mozuelos, J. M. Méndez-Alcaraz, and R. Castañeda Priego, *J. Chem. Phys.* **140**, 026101 (2014).

⁵S. Asakura and F. Oosawa, *J. Chem. Phys.* **22**, 1255 (1954).

⁶R. Roth, R. Evans, and S. Dietrich, *Phys. Rev. E* **62**, 5360 (2000).

⁷S. B. Yuste, A. Santos, and M. López de Haro, *J. Chem. Phys.* **128**, 134507 (2008); **140**, 179901 (2014).

⁸D. J. Ashton, N. B. Wilding, R. Roth, and R. Evans, *Phys. Rev. E* **84**, 061136 (2011).

⁹R. Castañeda-Priego, A. Rodríguez-López, and J. M. M. Alcaraz, *J. Phys.: Condens. Matter* **15**, S3393 (2003).

¹⁰T. Biben, P. Bladon, and D. Frenkel, *J. Phys.: Condens. Matter* **8**, 10799 (1996).

¹¹P. Germain and S. Amokrane, *Phys. Rev. Lett.* **102**, 058301 (2009).

¹²M. Sikorski, A. R. Sandy, and S. Narayanan, *Phys. Rev. Lett.* **106**, 188301 (2011).

¹³P.-M. König, R. Roth, and S. Dietrich, *Phys. Rev. E* **74**, 041404 (2006).

¹⁴W. Li, T. Yang, and H. Ma, *J. Chem. Phys.* **128**, 044910 (2008).

¹⁵D. Henderson, A. D. Trokhymchuk, and D. T. Wasan, *J. Mol. Liq.* **112**, 21 (2004).

¹⁶R. Roth and M. Kinoshita, *J. Chem. Phys.* **125**, 084910 (2006).

¹⁷Y. Mao, *J. Phys. II* **5**, 1761 (1995).

¹⁸X. L. Chu, A. D. Nikolov, and D. T. Wasan, *Langmuir* **12**, 5004 (1996).

¹⁹S. A. Egorov, *Phys. Rev. E* **70**, 031402 (2004).

²⁰G. Cinacchi, Y. Martínez-Ratón, L. Mederos, G. Navascués, A. Tani, and E. Velasco, *J. Chem. Phys.* **127**, 214501 (2007).

²¹A. Lajovic, M. Tomšič, and A. Jamnik, *J. Chem. Phys.* **130**, 104101 (2009).

²²A. Jamnik, *J. Chem. Phys.* **131**, 164111 (2009).

²³C. Bauer, T. Bieker, and S. Dietrich, *Phys. Rev. E* **62**, 5324 (2000).

²⁴C. Hertlein, L. Heden, A. Gambassi, S. Dietrich, and C. Bechinger, *Nature (London)* **451**, 172 (2007).

²⁵N. Gnan, E. Zaccarelli, P. Tartaglia, and F. Sciortino, *Soft Matter* **8**, 1991 (2012).

²⁶N. Gnan, E. Zaccarelli, and F. Sciortino, *J. Chem. Phys.* **137**, 084903 (2012).

²⁷R. Fantoni and A. Santos, *Phys. Rev. E* **84**, 041201 (2011). Note that in Eq. (2.12) the hats on the partial correlation functions should be replaced by tildes.

²⁸R. Fantoni and A. Santos, *Phys. Rev. E* **87**, 042102 (2013).

²⁹J. L. Lebowitz, *Phys. Rev.* **133**, A895 (1964).

³⁰S. B. Yuste, A. Santos, and M. López de Haro, *J. Chem. Phys.* **108**, 3683 (1998).

³¹T. Biben and J.-P. Hansen, *Phys. Rev. Lett.* **66**, 2215 (1991).

³²A. Santos, M. López de Haro, and S. B. Yuste, *J. Chem. Phys.* **132**, 204506 (2010).

³³R. Dickman, P. Attard, and V. Simonian, *J. Chem. Phys.* **107**, 205 (1997).

³⁴E. Allahyarov and H. Löwen, *Phys. Rev. E* **63**, 041403 (2001).

³⁵P. Attard, *J. Chem. Phys.* **91**, 3083 (1989).

³⁶R. Roth and R. Evans, *Europhys. Lett.* **53**, 271 (2001).

³⁷S. B. Yuste, M. López de Haro, and A. Santos, *Phys. Rev. E* **53**, 4820 (1996).

³⁸J. Abate and W. Whitt, *Queueing Syst.* **10**, 5 (1992).

³⁹A. Jamnik, D. Bratko, and D. J. Henderson, *J. Chem. Phys.* **94**, 8210 (1991).

⁴⁰A. Jamnik, *J. Chem. Phys.* **105**, 10511 (1996).

⁴¹D. Henderson and M. Lozada-Cassou, *J. Colloid Interface Sci.* **114**, 180 (1986).

⁴²D. Henderson, *J. Colloid Interface Sci.* **121**, 486 (1988).

⁴³M. H. Kalos and P. A. Whitlock, *Monte Carlo Methods* (John Wiley and Sons, New York, 1986).

⁴⁴M. López de Haro, S. B. Yuste, and A. Santos, in *Theory and Simulation of Hard-Sphere Fluids and Related Systems*, Lectures Notes in Physics Vol. 753, edited by A. Mulero (Springer-Verlag, Berlin, 2008), pp. 183–245.

⁴⁵B. V. Derjaguin, *Kolloid Z.* **69**, 155 (1934).

Chapter 42

Wertheim and Bjerrum-Tani-Henderson theories for associating fluids: a critical assessment

Fantoni R. and Pastore G., J. Chem. Phys **141**, 074108 (2014)

Title: “Wertheim and Bjerrum-Tani-Henderson theories for associating fluids: a critical assessment”

Abstract: Two theories for associating fluids recently used to study clustering in models for self-assembling patchy particles, Wertheim’s and Bjerrum-Tani-Henderson theories, are carefully compared. We show that, for a fluid allowing only for dimerization, Wertheim theory is equivalent to the Bjerrum-Tani-Henderson theory neglecting intercluster correlations. Nonetheless, while the former theory is able to account for percolation and condensation, the latter is not. For the Bjerrum-Tani-Henderson theory we also rigorously prove the uniqueness of the solution for the cluster’s concentrations and the reduction of the system of equations to a single one for a single unknown. We carry out Monte Carlo simulations of two simple models of dimerizing fluids and compare quantitatively the predictions of the two theories with the simulation data.



Wertheim and Bjerrum-Tani-Henderson theories for associating fluids: A critical assessment

Riccardo Fantoni^{1,a)} and Giorgio Pastore^{2,b)}

¹Dipartimento di Scienze Molecolari e Nanosistemi, Università Ca' Foscari Venezia, Calle Larga S. Marta DD2137, I-30123 Venezia, Italy

²Dipartimento di Fisica dell'Università and IOM-CNR, Strada Costiera 11, 34151 Trieste, Italy

(Received 8 June 2014; accepted 31 July 2014; published online 18 August 2014)

Two theories for associating fluids recently used to study clustering in models for self-assembling patchy particles, Wertheim's and Bjerrum-Tani-Henderson theories, are carefully compared. We show that, for a fluid allowing only for dimerization, Wertheim theory is equivalent to the Bjerrum-Tani-Henderson theory neglecting intercluster correlations. Nonetheless, while the former theory is able to account for percolation and condensation, the latter is not. For the Bjerrum-Tani-Henderson theory we also rigorously prove the uniqueness of the solution for the cluster's concentrations and the reduction of the system of equations to a single one for a single unknown. We carry out Monte Carlo simulations of two simple models of dimerizing fluids and compare quantitatively the predictions of the two theories with the simulation data. © 2014 AIP Publishing LLC. [<http://dx.doi.org/10.1063/1.4892878>]

I. INTRODUCTION

Recent advances in the experiments and modeling of patchy colloids,^{1,2} i.e., colloidal particles whose interaction is dominated by the presence of selective, short range interaction sites on their surface, have renewed interest in theories able to describe liquid and vapour phases of associating fluids.

Fluid phase theories able to cope with the strong attractions of associating fluids have been developed starting from the seventies, when hydrogen bond in molecular liquids was a prototype problem. Two of the approximations developed a few decades ago, namely, the approach developed by Tani and Henderson,³ extending Bjerrum's theory⁴ for electrolytic solutions, and the more ambitious statistical mechanics approach by Wertheim⁵ have been recently applied to the study of simple models of patchy colloids.⁶⁻¹⁹ The novelty introduced by applications to self-assembling colloids is the huge variety of interactions which can be engineered and consequently the richness of the behaviors as far as the cluster population and its dependence on the thermodynamic state are concerned. Both approaches identify in the fluid and predict populations of suitably defined clusters.

In both theories, a cluster is defined on the basis of bonding in configuration space. For example, if we describe the fluid, as made by particles interacting with a certain pair-potential $\phi(12)$ between particles 1 and 2, we may consider two particles as bonded whenever their pair-potential is less than a given negative value $-\epsilon_{bond}$. Clusters made of one particle are called "monomers," the ones formed by two particles "dimers," the ones formed of three particles "trimers," ... and the ones formed by a higher but small number of particles "oligomers." A cluster made of a number i of particles

can also be denoted as an i -mer. If we measure the concentrations of the i -mers in an associating fluid we will find that these are functions of the thermodynamic state: The temperature T and the density ρ of the fluid. One can give various definitions of a cluster²⁰ either of a geometrical nature or of a topological one, depending on the spatial arrangement of the bonded particles. A more physical approach would require to introduce the concept of physical cluster^{21,22} but virtually all the existing calculations have been based on clusters defined in configuration space.

In this work we will compare Wertheim's theory⁵ and the one of Bjerrum-Tani-Henderson (BTH).^{3,4} The former one starts from a thorough theoretical analysis, from which it is possible to derive a thermodynamic perturbation theory. Here, we will only discuss the first order term. At high temperature the associating fluid reduce to the "reference" fluid that can also be considered as the one obtained from the associating fluid sending to zero all attractions. The theory is only applicable when some "steric incompatibility" conditions are fulfilled by the associating fluid. The latter starts already by the description of the associating fluid as a mixture of n_c different species of oligomers where the numbers N_i of i -mers are allowed to vary subject to the constraint of a fixed total number of particles. One only assumes that the canonical partition function as a function of all the N_i , the volume and the temperature be factorisable into the product of n_c intra-cluster partition functions and an inter-cluster partition function. Moreover the clusters are assumed to interact weakly with each other.

We will show that for $n_c = 2$ Wertheim theory coincides with the Bjerrum-Tani-Henderson theory when the clusters are described as an ideal gas. Bjerrum-Tani-Henderson theory, on the other hand, allows to improve on this first level of approximation since one can always build better approximations to describe the inter-cluster partition function.

^{a)}Electronic mail: rfantoni@ts.infn.it

^{b)}Electronic mail: pastore@ts.infn.it

In this work we will only consider the Carnahan-Starling approximation,²³ i.e., we approximate intercluster correlations with effective spherically symmetric ones. On the other hand the simple and elegant theory of Wertheim is able, unlike the Bjerrum-Tani-Henderson theory, to describe fluids with percolating ($n_c \rightarrow \infty$) clusters. Due to this fact Wertheim's theory is able to describe in a consistent way the liquid phase while the Bjerrum-Tani-Henderson one is not. So, for n_c finite, Bjerrum-Tani-Henderson theory is expected to be more powerful and flexible than Wertheim theory since it allows to have more accurate results and it is not restricted to systems obeying the steric incompatibility conditions. Instead, Wertheim's theory is the method of choice whenever a consistent picture of the phase diagram is required.

We will then present a comparison and a critical assessment of the two theories by comparison with new Monte Carlo simulation results for two model fluids with $n_c = 2$: a binary mixture and a one-component system, both particularly suitable for comparing theories for association. In particular we will show an, apparently unavoidable, subtle short-come that may appear in the Bjerrum-Tani-Henderson when applied to multicomponent fluid mixtures: At high temperatures, when the fluid is dissociated, in the Bjerrum-Tani-Henderson theory one is left with a one-component mixture of monomers which may differ strongly from the original multicomponent mixture.

The paper is organized as follows: In Sec. II we introduce the thermodynamic quantities we will take in consideration in the following; in Sec. III we describe the two association theories discussing the problem of finite and infinite clusters (Sec. III B 1) and the problem of one attractive site (Sec. III B 2); in Sec. III C we introduce the problem of the gas-liquid coexistence; in Sec. III D we comment on the relevance of the pair-potential microscopic level of description; in Sec. IV we summarize some results obtained applying Wertheim theory to specific fluids with identical sites and sites of two different kinds; in Sec. V we apply the two theories to two simple dimerizing associating fluids (a binary mixture (Sec. V A 1) and a one-component fluid (Sec. V A 2)) and compare them with our Monte Carlo simulation results; in Sec. V B we consider again the problem of infinite clusters for the Bjerrum-Tani-Henderson theory; Sec. VI summarizes the main results and contains a few final remarks.

II. THERMODYNAMICS

Consider a one-component fluid of N associating particles in a volume V at an absolute temperature $T = 1/\beta k_B$ with k_B Boltzmann constant. The inter-particle interaction is assumed to include a hard sphere (HS) part, an isotropic attraction, and localized bonding interaction, in general anisotropic.

The Helmholtz free energy A of a hard-sphere associating fluid can be written as a sum of separate contributions²⁴

$$A = A_{HS} + A_{bond}, \tag{2.1}$$

where A_{HS} is the free energy due to the hard-sphere repulsive cores and A_{bond} is the change in the free energy due to the bonding interaction responsible for association. We will gen-

erally use the notation $a(\rho, T) = a = A/N$ for the free energy per particle, where $\rho = N/V$ is the density of the fluid.

The excess hard-sphere free energy per particle can be modeled by the Carnahan and Starling²³

$$\beta a_{HS}^{ex} = \frac{4\eta - 3\eta^2}{(1 - \eta)^2}, \tag{2.2}$$

where $\eta = (\pi/6)\rho\sigma^3$ is the packing fraction of the hard-spheres of diameter σ . So that adding the ideal gas contribution $\beta a_{id} = \ln(\rho\Lambda^3/e)$, with Λ the de Broglie thermal wavelength, we obtain $a_{HS} = a_{id} + a_{HS}^{ex}$.

We can always define a unit of length, \mathcal{S} , and a unit of energy, \mathcal{E} , so that we can introduce a reduced density, $\rho^* = \rho\mathcal{S}^3$, and a reduced temperature, $T^* = k_B T/\mathcal{E}$.

The association contribution A_{bond} will be discussed in Sec. III.

III. BJERRUM-TANI-HENDERSON VS WERTHEIM

We present now the two association theories of BTH³ and of Wertheim (W).⁵ We derive in each case the bond free energy per particle a_{bond} such that the full free energy per particle of the associating fluid can be written as $a = a_0 + a_{bond}$, where $a_0 = a_{id} + a_0^{ex}$ is the contribution of the reference fluid, the one obtained from the associating fluid setting to zero all the bonding localized attractions.

A. Bjerrum-Tani-Henderson thermodynamic theory

We assume that our fluid is composed of n_c species of clusters. The species i contains N_i clusters each made of i particles. Tani and Henderson^{3,15-19} assumed that the total partition function of the fluid can be written factorizing the n_c intra-cluster partition functions of the single clusters known *a priori* as functions of the temperature T alone. Moreover, assuming that the inter-cluster partition function can be approximated treating the (weakly interacting) clusters as hard-spheres of diameter σ_c , they find the following solution as a result of an extremum procedure,

$$N_1 = N\lambda z_1/\rho G(\eta_c), \tag{3.1}$$

$$N_i = N_1 \lambda^{i-1} z_i/z_1, \quad i = 1, 2, \dots, n_c \tag{3.2}$$

with

$$N = \sum_{i=1}^{n_c} i N_i, \tag{3.3}$$

$$N_c = \sum_{i=1}^{n_c} N_i < N, \tag{3.4}$$

where N is the total number of particles, $\rho = N/V$ is the density of the fluid, N_c the total number of clusters, $\rho_c = N_c/V$ is the density of the clusters, $\eta_c = (\pi/6)\rho_c\sigma_c^3$ is the packing fraction of the clusters of diameter σ_c , $z_i > 0$ the intra-cluster configuration partition function for the species i ($z_1 = 1$ by definition), and $\lambda > 0$ is determined through the constraint of

Eq. (3.3),

$$0 = \sum_{i=1}^{n_c} i \lambda^i z_i - \rho G(\eta_c), \quad (3.5)$$

$$G(x) = \exp \left[\frac{d(x\beta a_0^{ex}(x))}{dx} \right] = \exp \left[\frac{x(8-9x+3x^2)}{(1-x)^3} \right], \quad (3.6)$$

where $a_0^{ex}(\eta) = a_{HS}^{ex}$. This equation for the unknown parameter λ always admits a unique solution. In fact, $G(x)$ is a strictly monotonous increasing function of $0 \leq x < 1$ with $G(0) = 1$ and $\lim_{x \rightarrow 1^-} G(x) = +\infty$. We introduce the concentration of clusters of species i , the i -mers, as $x_i = N_i/N$, and the total concentration of clusters $x_c = N_c/N = \sum_{i=1}^{n_c} x_i = \sum_{i=1}^{n_c} \lambda^i z_i / \sum_{i=1}^{n_c} i \lambda^i z_i$. Then we notice that $\lim_{\lambda \rightarrow 0} x_c = 1$, $\lim_{\lambda \rightarrow \infty} x_c = 1/n_c < 1$, and x_c is a strictly monotonous decreasing function of λ .²⁵ So $G(\eta_c)$ is a strictly monotonous decreasing function of λ with $\lim_{\lambda \rightarrow 0} G(\eta_c) = G[(\pi/6)\rho\sigma_c^3]$ and $\lim_{\lambda \rightarrow \infty} G(\eta_c) = G[(\pi/6n_c)\rho\sigma_c^3]$. We also notice that we must require $(\pi/6)\rho\sigma_c^3 < 1$. Observing next that $\sum_{i=1}^{n_c} i \lambda^i z_i$ is a strictly monotonous increasing function of λ which is zero at $\lambda = 0$, we conclude that Eq. (3.5) must admit always only one solution $\lambda > 0$ such that $\lim_{\rho \rightarrow 0} \lambda = 0$ and $\lim_{\rho \rightarrow 0} x_1 = 1$.

The total partition function Q_{tot} of the fluid is given then by

$$\begin{aligned} \ln Q_{tot} &= \sum_i [N_i \ln z_i - (N_i \ln N_i - N_i)] + \ln Z_c \\ &= N_c - N_c \ln N_1 - (N - N_c) \ln \lambda + \ln Z_c, \end{aligned} \quad (3.7)$$

where Z_c is the inter-cluster configurational partition function and $\beta A_c^{ex} = -\ln(Z_c/V^{N_c})$ is the inter-cluster excess free energy.

Introducing the concentration of monomers $x_1 = N_1/N$ and the concentration of clusters $x_1 < x_c = N_c/N < 1$ (note that $1/x_c$ can be considered as a measure of the average cluster size), we can rewrite

$$\begin{aligned} \beta a_{bond}^{BTH} &= \beta [a - (a^{id} + a_0^{ex})] \\ &= x_c \ln x_1 + (1 - x_c) \ln(\lambda e/\rho) \\ &\quad + \beta (a^{ex} - a_0^{ex}) + constants, \end{aligned} \quad (3.8)$$

where $\beta a = -(\ln Q_{tot})/N$ is the associating fluid total free energy per particle and $a_0^{ex} + a^{id}$ is the reference system total free energy per particle. Note that, in the absence of attractions and therefore in the presence of monomers only $x_1 = x_c = 1$, in order to have $a_{bond}^{BTH} = 0$ we must have $a_0^{ex} = \lim_{x_c \rightarrow 1} a_c^{ex}$. Only for $\sigma_c = \sigma$ this condition is satisfied by the Carnahan-Starling reference system, a_{HS}^{ex} of Eq. (2.2). In the most general case we may think at σ_c as a function of the thermodynamic state of the associating fluid. In the present work we will always restrict to the case of a constant σ_c .

At high temperatures all $z_i \rightarrow 0$ for $i > 1$ and $x_1 \rightarrow x_c \rightarrow 1$ or $\lambda \rightarrow \rho G[(\pi/6)\rho\sigma_c^3]/z_1$, which means we have complete dissociation. At low temperatures all $z_i \rightarrow \infty$ for $i > 1$ and $x_1 \rightarrow 0$ or $\lambda \rightarrow 0$, which means that we have association.

B. Wertheim thermodynamic theory

In Wertheim theory⁵ one assumes that each hard-sphere of the one-component fluid (the case of a mixture will be considered in detail in Sec. V A) is decorated with a set Γ of M attractive sites. Under the assumptions of (i) a single bond per site, (ii) no more than one bond between any two particles, and (iii) no closed loop of bonds, one can write in a first order thermodynamic perturbation theory framework, valid at reasonably high temperatures,

$$\beta a_{bond}^W = \sum_{\alpha \in \Gamma} \left(\ln x_\alpha - \frac{x_\alpha}{2} \right) + \frac{M}{2}, \quad (3.9)$$

where $x_\alpha = N_\alpha/N$ is the fraction of sites α that are not bonded (not to be confused with x_i the concentration of clusters made of a number i of particles. We will always use a Greek index to denote a specific site) and can be solved by the ‘‘law of mass action,’’

$$x_\alpha = \frac{1}{1 + \rho \sum_{\beta \in \Gamma} x_\beta \Delta_{\alpha\beta}}, \quad \alpha \in \Gamma, \quad (3.10)$$

where the probability to form a bond, once the available sites of the two particles are chosen, is given by $\rho \Delta_{\alpha\beta} = \rho \Delta_{\beta\alpha}$ and approximated as

$$\Delta_{\alpha\beta} = \int_{v_{\alpha\beta}} g_0(r_{12}) \langle f_{\alpha\beta}(12) \rangle_{\Omega_1, \Omega_2} d\mathbf{r}_{12}. \quad (3.11)$$

Here the integral is over the volume $v_{\alpha\beta}$ of the bond $\alpha\beta$, g_0 is the radial distribution function of the reference system, $f_{\alpha\beta}$ is the Mayer function between site α on particle 1 and site β on particle 2 (see Sec. III D), and $\langle \dots \rangle_{\Omega_1, \Omega_2}$ denotes an angular average over all orientations of particles 1 and 2 at a fixed relative distance r_{12} . Equation (3.10) should be solved for the real physically relevant solution such that $\lim_{\rho \rightarrow 0} x_\alpha = 1$.

At high temperatures $\Delta_{\alpha\beta} \rightarrow 0$ and $x_\alpha \rightarrow 1$, which means we have complete dissociation. At low temperatures (Wertheim theory is a high temperature expansion but here we just mean the formal low T limit of the first order Wertheim results) $\Delta_{\alpha\beta} \rightarrow \infty$ and $x_\alpha \rightarrow 0$, which means that we have complete association.

The number of attractive sites controls the physical behavior. Models with one site allow only dimerization. The presence of two sites permits the formation of chain and ring polymers. Additional sites allow formation of branched polymers and amorphous systems.

1. Finite vs infinite clusters

Wertheim theory, unlike BTH one, allows for the existence of infinite clusters in the fluid: The percolation phenomenon. In particular, in Wertheim theory one can define¹⁰ $P_s = \sum_i i x_i$ as the probability to have a particle in a finite cluster (in BTH theory $P_s = 1$ by construction). One can then define the mean cluster size, or number averaged size of the finite clusters, $N_n = \sum_i i x_i / \sum_i x_i$, the mean size of a cluster to which a randomly chosen particle belongs, or weight averaged cluster size, $N_w = \sum_i i^2 x_i / \sum_i i x_i$, or higher moments of the cluster size distribution x_i .

074108-4 R. Fantoni and G. Pastore

J. Chem. Phys. **141**, 074108 (2014)

The interplay between condensation and clustering in associating fluids has been the subject of many studies.¹⁰ In particular, Coniglio *et al.*²² proposed a general theory of the equilibrium distribution of clusters, establishing a relation between percolation and condensation. Percolation is generally believed to be a prerequisite for condensation. As a matter of fact in Sec. V B we will show explicitly that BTH theory is unable to account for condensation.

2. One attractive site

The simplest case we can consider in Wertheim theory is the one with a single site α , $M = 1$. In this case only monomers and dimers can ever form. Solving the law of mass action for $x = x_\alpha$, the fraction of non-bonded sites α which coincides with the concentration of monomers x_1 , we find

$$x = \frac{2}{1 + \sqrt{1 + 4\rho\Delta}}, \tag{3.12}$$

with $\Delta = \Delta_{AA}$, which has the correct low density limit $\lim_{\rho \rightarrow 0} x = 1$.

Analogously we can solve this simple case in BTH theory allowing only for monomers and dimers, $n_c = 2$, and choosing the ideal gas approximation for the inter-cluster configurational partition function, $G = 1$ (the $\sigma_c \rightarrow 0$ limit of Eq. (3.6)). Then we should solve for $\lambda > 0$ in the following quadratic equation:

$$x_1 = \lambda z_1 / \rho, \tag{3.13}$$

$$x_2 = \lambda^2 z_2 / \rho, \tag{3.14}$$

$$1 = x_1 + 2x_2. \tag{3.15}$$

The solution for the monomers concentration is

$$x_1 = \frac{2}{1 + \sqrt{1 + 8\rho z_2 / z_1^2}}. \tag{3.16}$$

We then see that we have agreement between the two theories if we choose

$$\Delta = 2z_2 / z_1^2 = 2z_2. \tag{3.17}$$

Already for this simple case we see that the bond contribution to the free energy predicted by the two theories, Eqs. (3.9) and (3.8), coincide. In fact, from BTH theory of Eq. (3.8), since the excess free energy of the reference system and the inter-cluster excess free energy are both zero, we find, up to an additive constant,

$$\begin{aligned} \beta a_{bond}^{BTH} &= x_c \ln x_1 + (1 - x_c) \ln(\lambda e / \rho) \\ &= \ln x_1 + (1 - x_c) \\ &= \ln x_1 - x_1 / 2 + 1/2 = \beta a_{bond}^W, \end{aligned} \tag{3.18}$$

where the second equality follows from Eq. (3.13), the third one from observing that $x_2 = (1 - x_1)/2$, and the last one from Eq. (3.9).

BTH theory, on the other hand, allows to be more accurate and to treat the fluid of clusters instead of just as an ideal

gas as a fluid of hard-spheres of diameter σ_c . In this case one should solve numerically Eqs. (3.1), (3.2), and (3.5) with G given by Eq. (3.6). And the inter-cluster excess free energy will be given by

$$\beta a_c^{ex} = \frac{4\eta_c - 3\eta_c^2}{(1 - \eta_c)^2}, \tag{3.19}$$

whereas the excess free energy per particle of the reference system will be the usual Carnahan-Starling one of Eq. (2.2).²⁶

Taking $a = a_{HS} + a_{bond}$ and choosing $z_2 = \Delta/2$ we compared the behavior of the two theories. Following Ref. 7 and approximating the radial distribution function of the reference system, in Eq. (3.31) which appears next in the text, with its zero density limit, we choose $\Delta = K^0[\exp(\beta\epsilon) - 1]$ with $K^0 = \pi d^4(15\sigma + 4d)/30\sigma^2 \approx 0.332 \times 10^{-3}\sigma^3$. This choice is dictated by the fact that Wertheim theory gives only a semi-quantitative agreement with simulation data and we did not find any substantial improvement, at least in the density ranges we considered, by choosing a better refined low density approximation, as is done in other works.^{7,12} In Fig. 1 we show the comparison of the behavior of the pressure (from Eq. (3.20) which appears next in the text) and dimers concentration as functions of density calculated analytically in Wertheim theory and numerically in BTH theory with $\sigma_c = \sigma$, on several isotherms. As expected even at very small

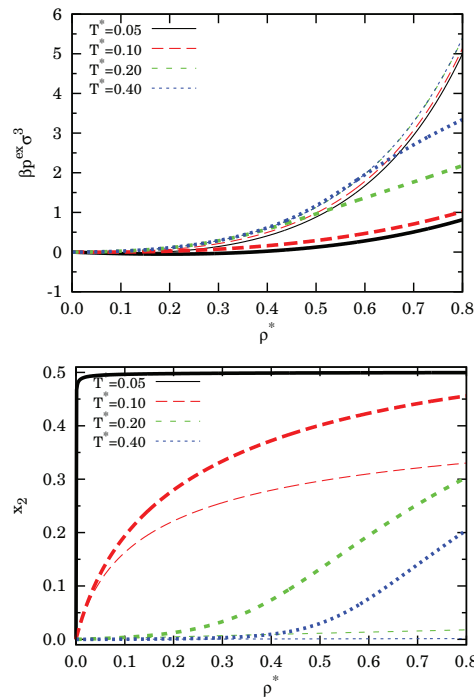


FIG. 1. Comparison of the behavior of the excess pressure, $\beta p^{ex} = \beta p - \rho$ (top panel) and dimers concentration (bottom panel) as functions of density for the BTH theory (thick lines), for $\sigma_c = \sigma$, and the W theory (thin lines), on several isotherms.

temperatures there is no sign of a gas-liquid coexistence, the pressure being a monotonously increasing function of density. We have just shown that at low density the two theories must coincide since $\lim_{\rho \rightarrow 0} G = 1$, but from the figure we see that the interval of densities over which the two theories agree increases of width as T increases. The figure shows how at high temperatures the two theories tend to become coincident but at low temperatures they differ strongly. This raises the question of which one of the two theories is a better approximation when compared to the exact Monte Carlo results. We will delay the answer to this legitimate question until Sec. V A 2. BTH theory naturally demands an approximation for the intra-cluster partition functions. In this work, unlike previous ones,^{3,15-19} we will always use the relation (3.17) when comparing the two theories.

Nonetheless we expect Wertheim theory to become more simple and elegant than BTH theory for $M > 1$. As a matter of fact we expect in these cases the presence in the fluid of i -mers of any size i . So that using BTH theory we will necessarily introduce the additional approximation of the maximum number of cluster species $i \leq n_c$, an artificial cutoff not needed in Wertheim theory.

C. The gas-liquid coexistence

In order to determine the gas-liquid coexistence line (the binodal) one needs to find the compressibility factor $z = \beta p / \rho$, with p the pressure, and the chemical potential μ of the associating fluid according to the thermodynamic relations

$$z(\rho, T) = \rho \left(\frac{\partial \beta a}{\partial \rho} \right)_{T,N}, \quad (3.20)$$

$$\beta \mu(\rho, T) = \left(\frac{\partial \beta a \rho}{\partial \rho} \right)_{T,V} = z + \beta a. \quad (3.21)$$

The coexistence line is then given by the Gibbs equilibrium condition of equality of the pressures and chemical potentials of the two phases

$$\rho_g z(\rho_g, T) = \rho_l z(\rho_l, T), \quad (3.22)$$

$$\beta \mu(\rho_g, T) = \beta \mu(\rho_l, T), \quad (3.23)$$

from which one can find the coexistence density of the gas $\rho_g(T)$ and of the liquid $\rho_l(T)$ phases.

The critical point (ρ_c, T_c) is determined by solving the following system of equations:

$$\left. \frac{\partial z \rho}{\partial \rho} \right|_{\rho_c, T_c} = 0, \quad (3.24)$$

$$\left. \frac{\partial^2 z \rho}{\partial \rho^2} \right|_{\rho_c, T_c} = 0. \quad (3.25)$$

D. Microscopic description: Importance of the pair potential

The fluid is assumed to be made of particles interacting only through a pair-potential $\phi(12) = \phi(\mathbf{r}_1, \Omega_1, \mathbf{r}_2, \Omega_2)$,

where \mathbf{r}_i and Ω_i are the position vector of the center of particle i and the orientation of particle i , respectively.

To give structure to the fluid we further assume that the particles have an isotropic hard-core of diameter σ with

$$\phi(12) = \phi_{HS}(r_{12}) + \Phi(12), \quad (3.26)$$

where $r_{12} = |\mathbf{r}_{12}| = |\mathbf{r}_2 - \mathbf{r}_1|$ is the separation between the two particles 1 and 2 and

$$\phi_{HS}(r) = \begin{cases} +\infty & r \leq \sigma \\ 0 & r > \sigma \end{cases}. \quad (3.27)$$

The anisotropic part $\Phi(12)$ in Wertheim theory is generally chosen as

$$\Phi(12) = \sum_{\alpha \in \Gamma} \sum_{\beta \in \Gamma} \psi_{\alpha\beta}(r_{\alpha\beta}), \quad (3.28)$$

where

$$\mathbf{r}_{\alpha\beta} = \mathbf{r}_2 + \mathbf{d}_\beta(\Omega_2) - \mathbf{r}_1 - \mathbf{d}_\alpha(\Omega_1) \quad (3.29)$$

is the vector connecting site α on particle 1 with site β on particle 2. Here \mathbf{d}_α is the vector from the particle center to site α with $d_\alpha < \sigma/2$. The site-site interactions $\psi_{\alpha\beta} \leq 0$ are assumed to be purely attractive. The Mayer functions introduced in Sec. III B are then defined as $f_{\alpha\beta}(12) = \exp[-\beta \psi_{\alpha\beta}(r_{\alpha\beta})] - 1$.

Wertheim theory depends on the specific form of the site-site potential only through the quantity $\Delta_{\alpha,\beta}$ of Eq. (3.11), as long as the three conditions of a single bond per site, no more than one bond between any two particles, and no closed loop of bonds, are satisfied. A common choice, for example, is a square-well form

$$\psi_{\alpha\beta}(r) = \begin{cases} -\epsilon_{\alpha\beta} & r \leq d_{\alpha\beta} \\ 0 & r > d_{\alpha\beta} \end{cases}, \quad (3.30)$$

where $\epsilon_{\alpha\beta} > 0$ are site-site energy scales, the wells depths, and $d_{\alpha\beta}$ are the wells widths. In this case we must have $d_\alpha + d_\beta > \sigma - d_{\alpha\beta}$ moreover we will have

$$\Delta_{\alpha\beta} = K_{\alpha\beta}(\sigma, d_{\alpha\beta}, \eta)(e^{\beta \epsilon_{\alpha\beta}} - 1). \quad (3.31)$$

We will also call $\lim_{\rho \rightarrow 0} K_{\alpha\beta} = K_{\alpha\beta}^0$ some purely geometric factors. Remember that $\lim_{\rho \rightarrow 0} g_0(r) = \Theta(r - \sigma)$ with Θ the Heaviside step function. Another common choice is the Kern-Frenkel patch-patch pair-potential model.²⁷

In BTH theory on the other hand, we are allowed to relax these conditions and the choice of the pair-potential is more flexible as long as it includes some attractive component responsible for the association.

IV. SOME RESULTS FROM WERTHEIM THEORY

Wertheim theory of associating fluids has been recently tested extensively by Sciortino and co-workers. In a series of papers, they have studied fluids of hard-spheres with identical sites allowing for “chaining”⁶⁻⁹ and with sites of two different kinds allowing for “branching”¹⁰⁻¹² and for

“rings” formation.^{13,14} They showed how the parameter-free Wertheim theory is flexible enough to accommodate a vast number of different microscopic pair-potentials descriptions and nonetheless pointed out some relevant classes of microscopic features giving rise to specific macroscopic behaviors at the level of the clustering, the percolation threshold, and the gas-liquid coexistence.

In all these cases $n_c \rightarrow \infty$ so they cannot be treated with the BTH theory which as we will see in Sec. V B is unable to account for the gas-liquid coexistence. Thus, in order to compare the two theories we have to choose different systems.

V. COMPARISON BETWEEN WERTHEIM THEORY AND BJERRUM-TANI-HENDERSON THEORY

In order to test the accuracy of the Wertheim and BTH theories we carried out some Monte Carlo (MC) simulations on simple models of associating fluids.

A. One attractive site, $n_c = 2$

We limit ourselves to the case $n_c = 2$ and we consider two different realizations of this scenario: A binary mixture and a one-component fluid.

1. A binary mixture

To test the single site case we considered a symmetric binary mixture of particles with the following pair-potential between a particle of species $\bar{\alpha}$ (in this section a Greek index with an over-bar labels the particle species) and one of species $\bar{\beta}$ a center-to-center distance r apart

$$\phi_{\bar{\alpha}\bar{\beta}}(r) = \begin{cases} +\infty & r \leq \sigma_{\bar{\alpha}\bar{\beta}} \\ -(1 - \delta_{\bar{\alpha}\bar{\beta}})\epsilon & \sigma_{\bar{\alpha}\bar{\beta}} < r \leq \sigma_{\bar{\alpha}\bar{\beta}} + \mathcal{W} \\ 0 & r > \sigma_{\bar{\alpha}\bar{\beta}} + \mathcal{W} \end{cases}, \quad (5.1)$$

where $\sigma_{\bar{\alpha}\bar{\beta}} = (1/2)(\sigma_{\bar{\alpha}} + \sigma_{\bar{\beta}})(1 + \mathcal{D}_{\bar{\alpha}\bar{\beta}})$ with $\sigma_{\bar{\alpha}} = \sigma$ and $\mathcal{D}_{\bar{\alpha}\bar{\beta}} = -(1 - \delta_{\bar{\alpha}\bar{\beta}})$ with $\bar{\alpha}$ and $\bar{\beta}$ equal to 1, 2 and δ the Kronecker delta. So that $\sigma_{\bar{\alpha}\bar{\beta}} = \sigma \delta_{\bar{\alpha}\bar{\beta}} \cdot \epsilon > 0$ and $\mathcal{W} > 0$ are, respectively, the square well depth and width for the attraction of unlike particles. Also we choose the symmetric case where the concentrations of particles of species $\bar{\alpha}$, $\mathcal{X}_{\bar{\alpha}} = 1/2$ for $\bar{\alpha} = 1, 2$. In this case the ideal part of the free energy will be given by $\beta a_{id} = \ln(\rho \Lambda^3 / e) + \mathcal{X}_1 \ln \mathcal{X}_1 + \mathcal{X}_2 \ln \mathcal{X}_2$, where the entropy of mixing, the last two terms, is just an additive constant.

It is then clear that, for $\mathcal{W} < \sigma/2$, this model fluid allows for dimerization only, just as the $M = 1$ case of Wertheim. In fact, whenever two unlike particles bind, a third particle can never bind to the formed dimer because of the hard-core repulsion between like particles. Moreover by choosing \mathcal{W} small at will we may reach the ideal condition of $\sigma_c = \sigma$ with σ_c the diameter of the dimers in the BTH theory. The reference fluid, the one with $\epsilon = 0$, is a symmetric non-additive-hard-sphere (NAHS) mixture with non-additivity $\mathcal{D}_{12} = -1$.

We will then take

$$\beta a_0^{ex} = \frac{2\eta - (3/4)\eta^2}{[1 - (1/2)\eta]^2}. \quad (5.2)$$

Wertheim theory has been extended to multicomponent mixtures by Chapman *et al.*²⁸ For a mixture with a number n_s of species and $N_{\bar{\alpha}} = N \mathcal{X}_{\bar{\alpha}}$ particles of species $\bar{\alpha} = 1, 2, \dots, n_s$, we have

$$\beta a_{bond}^W = \sum_{\bar{\alpha}=1}^{n_s} \mathcal{X}_{\bar{\alpha}} [\ln x_{\bar{\alpha}} - x_{\bar{\alpha}}/2 + 1/2], \quad (5.3)$$

where $x_{\bar{\alpha}} = N_{\bar{\alpha}}^{\alpha} / N_{\bar{\alpha}}$ is the monomer fraction of species $\bar{\alpha}$, with $N_{\bar{\alpha}}^{\alpha}$ the number of monomers of species $\bar{\alpha}$, and is determined by the following law of mass action,

$$x_{\bar{\alpha}} = \frac{1}{1 + \rho \sum_{\bar{\beta}=1}^{n_s} \mathcal{X}_{\bar{\beta}} x_{\bar{\beta}} \Delta_{\bar{\alpha}\bar{\beta}}}, \quad (5.4)$$

where

$$\Delta_{\bar{\alpha}\bar{\beta}} = \Delta_{\bar{\beta}\bar{\alpha}} = \int_{v_{\bar{\alpha}\bar{\beta}}} g_{\bar{\alpha}\bar{\beta}}^0(r_{12}) (f_{\bar{\alpha}\bar{\beta}}(12))_{\Omega_1, \Omega_2} d\mathbf{r}_{12}, \quad (5.5)$$

with $g_{\bar{\alpha}\bar{\beta}}^0$ the partial radial distribution of the reference fluid and $f_{\bar{\alpha}\bar{\beta}}(12) = e^{-\beta(\phi_{\bar{\alpha}\bar{\beta}}(r_{12}) - \phi_{\bar{\alpha}\bar{\beta}}^0(r_{12}))} - 1$ the Mayer function between particle 1 of species $\bar{\alpha}$ and particle 2 of species $\bar{\beta}$, with $\phi_{\bar{\alpha}\bar{\beta}}^0$ the pair-potential of the reference fluid.

In our symmetric binary case $x_{\bar{\alpha}=1} = x_{\bar{\alpha}=2} = x$ and $\Delta = \Delta_{12} = K_{12}(e^{\beta\epsilon} - 1)$ (with $\Delta_{\bar{\alpha}\bar{\alpha}} = 0$ for $\bar{\alpha} = 1, 2$), where, since the unlike radial distribution function of the reference system is the one of the ideal gas, equal to one everywhere, we have exactly $K_{12} = (4/3)\pi \mathcal{W}^3$. The solution of Eq. (5.4) is

$$x = \frac{2}{1 + \sqrt{1 + 2\rho\Delta}}. \quad (5.6)$$

Here we will choose $\mathcal{W} = 0.1\sigma$.

On the other hand BTH theory continues to hold just as in its one component fluid formulation given in Sec. III A. We expect the cluster diameter to vary within the interval $\sigma \leq \sigma_c \leq \sigma + \mathcal{W}$ even if for the comparison with the simulation data we will need to consider $\sigma_c < \sigma$. We will now choose $z_2 = \Delta/4$.

At high temperatures $z_2 = \Delta/4 \rightarrow 0$ and $x_1 \rightarrow 1$, $x_c \rightarrow 1$ so $\beta a^W = \beta a_{id} + [2\eta - (3/4)\eta^2]/[1 - (1/2)\eta]^2$, whereas $\beta a^{BTH} = \beta a_{id} + [4\eta_c - 3\eta_c^2]/[1 - \eta_c]^2$. Then for $\sigma_c \neq \sigma/2^{1/3}$ the parameter free Wertheim theory is certainly a better approximation than BTH. At low temperatures $z_2 = \Delta/4 \rightarrow \infty$ and $x_1 \rightarrow 0$, $x_c \rightarrow 1/2$, and the two theories become equivalent for $\sigma_c = \sigma$ (see the Appendix). Within BTH one is free to choose σ_c in such way to get more accurate results.

The opposite behavior was observed for the one-component case of Sec. III B 2 where the two theories, for $\sigma_c = \sigma$, become equivalent at high temperature and at low temperature they differ and BTH is expected to become better than W.

We carried out MC simulations of this mixture in the canonical ensemble using a total number $N = 500$ of particles. In the simulation we measure the pressure from the virial

074108-7 R. Fantoni and G. Pastore

J. Chem. Phys. **141**, 074108 (2014)

theorem as²⁹

$$z^{MC} = 1 + \frac{1}{3}\pi\rho [\sigma^3 g_{11}(\sigma^+) - (e^{\beta\epsilon} - 1)\mathcal{W}^3 g_{12}(\mathcal{W}^+)], \quad (5.7)$$

where $g_{\alpha\beta}$ are the partial radial distribution functions. In the simulation we define a dimer as any two particles for which the pair-potential equals $-\epsilon$. So, we measure the dimers concentration $x_2^{MC} = -u^{ex}/\epsilon$, where u^{ex} is the excess internal energy per particle of the fluid. As usual we choose σ as the unit of length and ϵ as the unit of energy. At the lowest temperature studied, $T^* = 0.1$, the probability of breaking a bond is of the order of $\exp(1/0.1)$, thus requiring 2×10^4 MC attempts to break such a bond. Our simulations were of the order of 4×10^5 MC steps long, with a MC step made by N single particle moves.

We compare the simulation data with the dimers concentrations, x_2^W and x_2^{BTH} , and pressures, ρz^W and ρz^{BTH} , predicted by Wertheim and BTH theories, where

$$z^W = 1 + \rho \frac{\partial\beta (a_0^{ex} + a_{bond}^W)}{\partial\rho}, \quad (5.8)$$

$$z^{BTH} = 1 + \rho \frac{\partial\beta (a_0^{ex} + a_{bond}^{BTH})}{\partial\rho}, \quad (5.9)$$

with a_0^{ex} given by Eq. (5.2), a_{bond}^W given by Eq. (5.3), and a_{bond}^{BTH} given by Eq. (3.8) with $n_c = 2$ and $z_2 = \Delta/4$.

In Fig. 2 we compare the equation of state and the dimers concentration as a function of density predicted by Wertheim and BTH theories with the MC results at a low reduced temperature $T^* = 0.1$. We see that by choosing the cluster diameter opportunely, $\sigma_c < \sigma$, one can get the BTH results for the pressure to overlap with MC data over a wide range of densities. Fig. 3 shows the same comparison at the high temperature $T^* = 0.4$ for the optimal $\sigma_c = \sigma/2^{1/3}$. From the figures we conclude that BTH theory, with the optimal σ_c for the equation of state, improves at low temperatures, where it becomes more accurate than Wertheim theory, but fails a correct descriptions of the clusters concentration at high temperatures and high densities. By appropriately tuning the cluster diameter σ_c it is possible to get better agreement for the dimer concentration but then the theory would fail to reproduce the pressure correctly. So it is never possible to get good agreement for both the pressure and the dimer concentration.

In Fig. 4 we compare the pressure and the dimers concentration as functions of temperature predicted by the two theories, when $\sigma_c = \sigma/2^{1/3}$ in BTH, with the MC results at a low reduced density $\rho^* = 0.6$. The figure shows how in this case the Wertheim theory is better than BTH.

2. A one-component fluid

As a one-component fluid we chose the single patch Kern-Frenkel model^{15,27} where the particles interact with the following pair-potential

$$\phi(r_{12}) = \phi_{HS}(r_{12}) + \phi_{SW}(r_{12})\gamma(\hat{\mathbf{n}}_1, \hat{\mathbf{n}}_2, \hat{\mathbf{r}}_{12}), \quad (5.10)$$

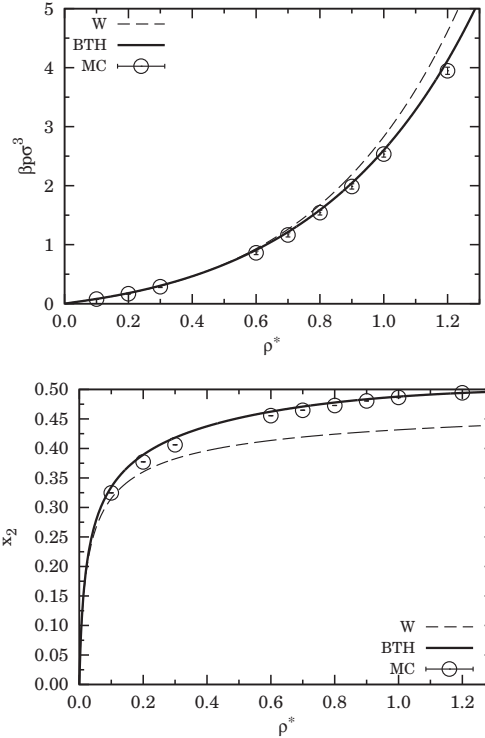


FIG. 2. Pressure (top panel) and dimers concentration (bottom panel) as a function of density on the $T^* = 0.1$ isotherm for $\mathcal{W} = 0.1\sigma$. The broken line is the prediction of W theory, the continuous line the one of BTH theory with $\sigma_c = 0.98\sigma$, and the points are the exact MC data.

where

$$\phi_{SW}(r) = \begin{cases} -\epsilon & \sigma < r \leq \sigma + \mathcal{W} \\ 0 & \text{else} \end{cases}, \quad (5.11)$$

and

$$\gamma(\hat{\mathbf{n}}_1, \hat{\mathbf{n}}_2, \hat{\mathbf{r}}_{12}) = \begin{cases} 1 & \hat{\mathbf{n}}_1 \cdot \hat{\mathbf{r}}_{12} \geq \cos\theta_0 \quad \text{and} \quad -\hat{\mathbf{n}}_2 \cdot \hat{\mathbf{r}}_{12} \geq \cos\theta_0 \\ 0 & \text{else} \end{cases}, \quad (5.12)$$

here $\hat{\mathbf{n}}_i$ is a unit vector pointing from the center of particle i towards the center of her attractive patch and θ_0 is the angular semi-amplitude of the patch. The fraction of the particle surface covered by the attractive patch will then be $\chi = \sqrt{\langle\gamma\rangle_{\Omega_1, \Omega_2}} = \sin^2(\theta_0/2)$.

In order to have $n_c = 2$ we must choose $\theta_0 < \pi/6$ or $\chi < (\sqrt{3} - 1)^2/8 \approx 0.0670$ in the sticky limit $\mathcal{W} \rightarrow 0$ and

$$\cos 2\theta_0 > \frac{1}{2} + \frac{1}{2\sigma(\sigma + \mathcal{W})} \times \sqrt{6\sigma^3\mathcal{W} - \sigma^2\mathcal{W}^2 - 4\sigma\mathcal{W}^3 - \mathcal{W}^4}, \quad (5.13)$$

074108-8 R. Fantoni and G. Pastore

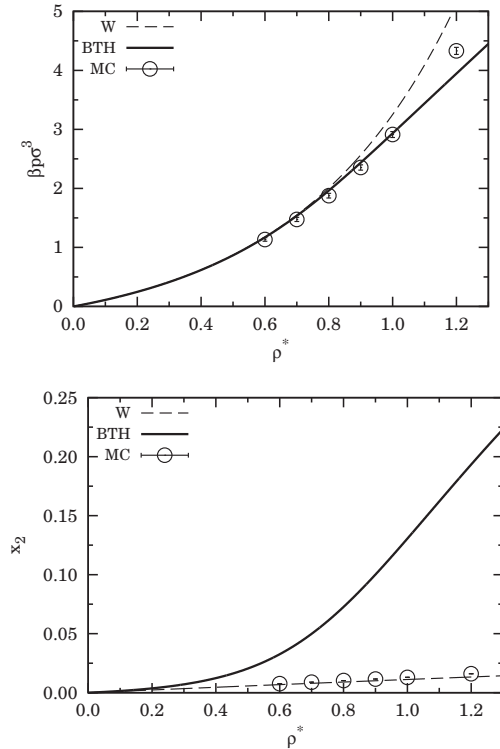
 J. Chem. Phys. **141**, 074108 (2014)


FIG. 3. Pressure (top panel) and dimers concentration (bottom panel) as a function of density on the $T^* = 0.4$ isotherm for $\mathcal{W} = 0.1\sigma$. The broken line is the prediction of W theory, the continuous line the one of BTH theory with $\sigma_c = \sigma/2^{1/3}$, and the points are the exact MC data.

more generally, for small \mathcal{W} . As before we choose $\mathcal{W} = 0.1\sigma$ and in order to fulfill the single bond per patch condition (5.13) we take $\theta_0 = \pi/12$ or $\chi = 0.0170$. This choice corresponds to a patch-patch bonding volume $v_{pp} = (\pi/3)[(\sigma + \mathcal{W})^3 - \sigma^3](1 - \cos \theta_0)^2 \approx 0.402 \times 10^{-3} \sigma^3$. We then choose for Δ its zero density limit approximation $\Delta = v_{pp}(e^{\beta\epsilon} - 1)$.

We carried out MC simulations of this one-component fluid in the canonical ensemble using a number $N = 500$ of particles. The pressure is calculated during the simulation from the virial theorem as follows,²⁷

$$z^{MC} = 1 + \frac{2\pi}{3} \rho \sigma^3 [g(\sigma^+) - (1 + \mathcal{W}/\sigma)^3 \{g_{pp}[(\sigma + \mathcal{W})^-] - g_{pp}[(\sigma + \mathcal{W})^+]\}], \quad (5.14)$$

where $g_{pp}(r)$ is the radial patch-patch distribution function: The partial radial distribution function which considers only particles with facing patches. Again, we measure the dimers concentration as $x_2^{MC} = -u^{\epsilon\sigma}/\epsilon$. As usual we choose σ as the unit of length and ϵ as the unit of energy. A MC move here consisted of both a random displacement of the center of

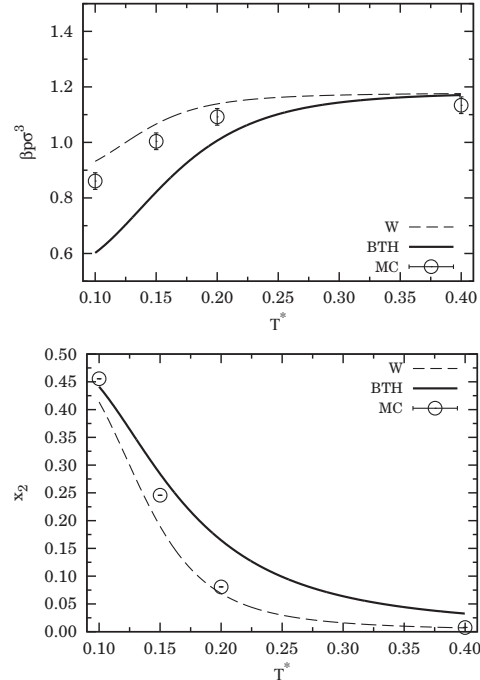


FIG. 4. Pressure (top panel) and dimers concentration (bottom panel) as a function of temperature on the $\rho^* = 0.6$ isochore for $\mathcal{W} = 0.1\sigma$. The broken line is the prediction of W theory, the continuous line the one of BTH theory with $\sigma_c = \sigma/2^{1/3}$, and the points are the exact MC data.

particle and a random rotation of the particle (according to the Marsaglia algorithm³⁰).

In Figs. 5 and 6 we compare the simulation data on two different isotherms, at low temperature $T^* = 0.1$ and high temperature $T^* = 0.4$, with the dimers concentrations, x_2^W and x_2^{BTH} , and pressures, ρz^W and ρz^{BTH} , predicted by Wertheim and BTH theories as shown in Sec. III B 2. From the comparison emerges that at low temperatures one can adjust σ_c in the BTH theory to obtain good agreement either with the pressure or with the dimers concentration data, but not with both simultaneously. In the high temperature limit the two theories coincide for $\sigma_c = \sigma$, but again BTH fails at high densities at large but finite temperature.

For this system we also tried to use in the BTH theory an intercluster partition function derived from the Freasier *et al.*³¹ equation of state for dumbbells with a center-to-center distance equal to σ . But we soon discovered that such an equation of state is very similar to a Carnahan-Starling with a $\sigma_c \approx 2.5\sigma$. This implied that we could study only a density range $\rho^* < 6\sigma^3/(\pi\sigma_c^3) \approx 0.1222$. At such low densities the fluid tends to dissociate into monomers and as a consequence such refined BTH becomes worse than the usual BTH with a Carnahan-Starling intercluster partition function with σ_c close to σ .

074108-9 R. Fantoni and G. Pastore

J. Chem. Phys. **141**, 074108 (2014)

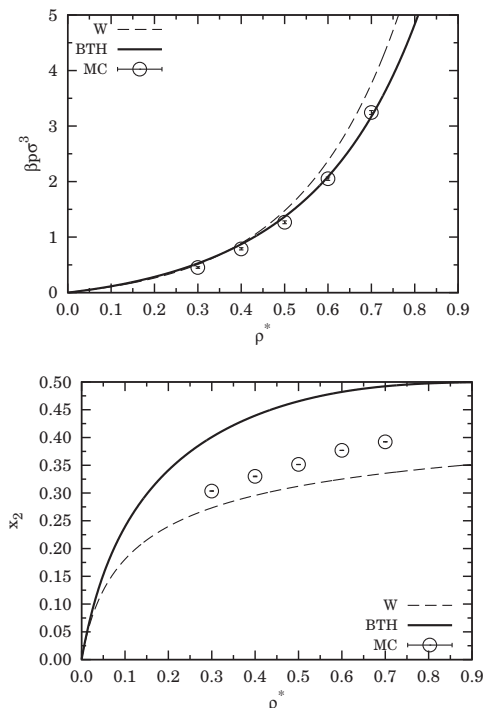


FIG. 5. Pressure (top panel) and dimers concentration (bottom panel) as a function of density on the $T^* = 0.1$ isotherm for $\mathcal{W} = 0.1\sigma$ and $\theta_0 = \pi/12$. The broken line is the prediction of W theory, the continuous line the one of BTH theory with $\sigma_c = 1.23\sigma$, and the points are the exact MC data.

B. Number of cluster species $n_c > 2$

We have seen in various ways that as long as $n_c \leq 2$ we expect, either from the Wertheim theory or from the BTH theory, the absence of the liquid phase. So now we want to understand if there exists a critical n_c, \bar{n}_c , such that for $n_c > \bar{n}_c$ we may have the appearance of the liquid in the associating fluid.

According to Wertheim:⁵ “As long as $[n_c]$ is finite, or at least a reasonably small number, we would expect increasing association with decreasing T , but no gas-liquid transition. On this basis one may conjecture that the gas-liquid transition is related to the catastrophic increase with s of allowed s -mer[s] [...] when no cutoff [...] is provided.”

Wertheim also suggests that, releasing the single bond per site condition, a pair-potential of the form given by Eqs. (3.26)–(3.30) allows to have fluids with $n_c > 2$ finite. If Wertheim is correct we would be unable to predict the liquid phase within the BTH theory.

In order to understand better this point we looked if it is possible to have the appearance of a van der Waals loop in $\beta p^{BTH} = \rho z^{BTH} = \rho^2 \partial \beta a^{BTH} / \partial \rho$ for $n_c > 2$. We looked then at the low temperature $T \rightarrow 0$ and large number of cluster species $n_c \rightarrow \infty$ limit. We choose the $z_i \rightarrow \infty$ for $i > 1$ in the low temperature limit, in such a way to fulfill complete

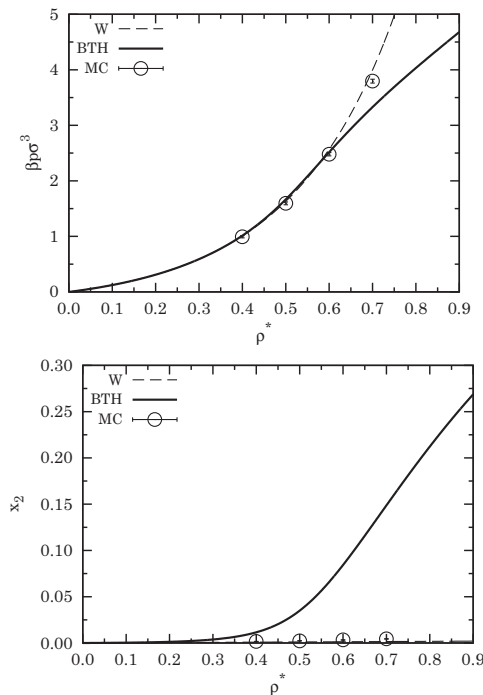


FIG. 6. Pressure (top panel) and dimers concentration (bottom panel) as a function of density on the $T^* = 0.4$ isotherm for $\mathcal{W} = 0.1\sigma$ and $\theta_0 = \pi/12$. The broken line is the prediction of W theory, the continuous line the one of BTH theory with $\sigma_c = \sigma$, and the points are the exact MC data.

association, i.e., $\lim_{T \rightarrow 0} x_{n_c} = 1/n_c$. Specifically we realized this by the choice $z_i = (z_2)^{i-1}$, which can be justified from the extensive property of the intra-cluster excess free energy. Then, due to the complete association, we have

$$x_c \xrightarrow{T \rightarrow 0} \frac{1}{n_c} \xrightarrow{n_c \rightarrow \infty} 0, \tag{5.15}$$

so $a_c^{ex} \rightarrow 0$. Moreover, it is easy to see, either from a numerical analysis or analytically, that

$$-\rho < \alpha(n_c) = \lim_{T \rightarrow 0} \rho^2 \frac{\partial [x_c \ln x_1 + (1 - x_c) \ln(\lambda e / \rho)]}{\partial \rho} \leq -\frac{\rho}{2}, \tag{5.16}$$

with $\alpha(n_c) = (1/n_c - 1)\rho$ (remember that $\lim_{T \rightarrow 0} \lambda = 0$ and temperature and density are two independent variables) and $\lim_{n_c \rightarrow \infty} \alpha(n_c) = -\rho$ and $\alpha(2) = -\rho/2$ (see the Appendix). So that, in particular,

$$\lim_{n_c \rightarrow \infty} \lim_{T \rightarrow 0} p^{BTH} = 0. \tag{5.17}$$

This result strongly suggests that BTH will never be able to account for the liquid phase, contrary to the Wertheim theory.^{6,11,14}

VI. CONCLUSIONS

We compared Wertheim and BTH association theories. Whereas Wertheim theory is able to account for fluids with an infinite number of cluster species, BTH is not. As a result, only Wertheim’s approach is able to account for the percolation and the condensation phenomena.

For the special case of fluids allowing for dimerization only, Wertheim theory becomes equivalent to BTH provided an ideal gas description of the inter-cluster partition function is used. For the Bjerrum-Tani-Henderson theory we also rigorously proved the uniqueness of the solution for the cluster’s concentrations and the reduction of the system of equations to a single one for a single unknown.

To assess the accuracy of Wertheim and the full BTH using a hard-sphere (Carnahan-Starling) description of the inter-cluster partition function, we performed some MC simulations of two dimerizing systems: a binary mixture of associating non-additive hard-spheres and a one component single patch Kern-Frenkel fluid. Our results show that the parameter free Wertheim’s theory captures well, at low density, the behavior of the MC data, both for the pressure and the concentration of dimers, and the range of densities where it is valid increases with increasing temperature. BTH, on the other hand, has the dimer diameter as a free parameter which can be adjusted to find more accurate agreement with the simulation data, even if the breakdown of its validity at high density still remains.

ACKNOWLEDGMENTS

R.F. would like to acknowledge the use of the PLX computational facility of CINECA through the ISCR grant. G.P. acknowledges financial support by PRIN-COFIN 2010-2011 (Contract No. 2010LKE4CC). It is also a pleasure for G.P. to acknowledge help by Ms. Serena Alfarano to check the proof that it is always possible to reduce BTH equations to a single equation.

APPENDIX: LOW TEMPERATURE LIMIT OF BTH AND W THEORIES

For the case studied in Sec. V A, from W theory we find, for the compressibility factor,

$$z_{bond}^W = \rho \frac{\partial \beta a_{bond}^W}{\partial \rho} = - \frac{\Delta \rho}{(1 + \sqrt{1 + 2\Delta \rho})^2}, \quad (A1)$$

so, in the low temperature limit, we have

$$\lim_{\Delta \rightarrow \infty} z_{bond}^W = -1/2. \quad (A2)$$

In BTH theory instead

$$z_{bond}^{BTH} = \rho \frac{\partial \beta a_{bond}^{BTH}}{\partial \rho}. \quad (A3)$$

Recalling that $x_c = (1 + \lambda z_2)/(1 + 2\lambda z_2)$, we find, in the low temperature limit, $\lim_{z_2 \rightarrow \infty} x_c = 1/2$. Then, for $\sigma_c = \sigma$, we have $a_c^{ex} \rightarrow a_0^{ex}$. So, since z_2 and ρ are independent variables,

we find

$$\lim_{z_2 \rightarrow \infty} z_{bond}^{BTH} = \lim_{z_2 \rightarrow \infty} \rho \frac{\partial [x_c \ln x_1 + (1 - x_c) \ln(\lambda e/\rho)]}{\partial \rho}. \quad (A4)$$

Observing further that $\lim_{z_1 \rightarrow \infty} \lambda = 0$ we then find $\lim_{z_2 \rightarrow \infty} z_{bond}^{BTH} = -1/2$ as for Wertheim.

¹A. B. Pawar and I. Kretschmar, *Macromol. Rapid Commun.* **31**, 150 (2010).
²E. Bianchi, R. Blaak, and C. N. Likos, *Phys. Chem. Chem. Phys.* **13**, 6397 (2011).
³A. Tani and D. Henderson, *J. Chem. Phys.* **79**, 2390 (1983).
⁴N. Bjerrum, *Kgl. Dan. Vidensk. Selsk. Mat.-Fys. Medd.* **7**, 1 (1926).
⁵M. S. Wertheim, *J. Stat. Phys.* **35**, 19 (1984); **35**, 35 (1984); **42**, 459 (1986); **42**, 477 (1986).
⁶E. Bianchi, J. Largo, P. Tartaglia, E. Zaccarelli, and F. Sciortino, *Phys. Rev. Lett.* **97**, 168301 (2006).
⁷F. Sciortino, E. Bianchi, J. F. Douglas, and P. Tartaglia, *J. Chem. Phys.* **126**, 194903 (2007).
⁸E. Bianchi, P. Tartaglia, E. Zaccarelli, and F. Sciortino, *J. Chem. Phys.* **128**, 144504 (2008).
⁹H. Liu, S. K. Kumar, F. Sciortino, and G. T. Evans, *J. Chem. Phys.* **130**, 044902 (2009).
¹⁰J. M. Tavares, P. I. C. Teixeira, M. M. Telo de Gama, and F. Sciortino, *J. Chem. Phys.* **132**, 234502 (2010).
¹¹J. Russo, J. M. Tavares, P. I. C. Teixeira, M. M. Telo de Gama, and F. Sciortino, *Phys. Rev. Lett.* **106**, 085703 (2011).
¹²J. Russo, J. M. Tavares, P. I. C. Teixeira, M. M. Telo de Gama, and F. Sciortino, *J. Chem. Phys.* **135**, 034501 (2011).
¹³J. M. Tavares, L. Rovigatti, and F. Sciortino, *J. Chem. Phys.* **137**, 044901 (2012).
¹⁴L. Rovigatti, J. M. Tavares, and F. Sciortino, *Phys. Rev. Lett.* **111**, 168302 (2013).
¹⁵R. Fantoni, A. Giacometti, F. Sciortino, and G. Pastore, *Soft Matter* **7**, 2419 (2011).
¹⁶R. Fantoni, *Eur. Phys. J. B* **85**, 108 (2012).
¹⁷R. Fantoni, *The Janus Fluid: A Theoretical Perspective*, SpringerBriefs in Physics (Springer, New York, 2013).
¹⁸R. Fantoni and G. Pastore, *Europhys. Lett.* **101**, 46003 (2013).
¹⁹R. Fantoni and G. Pastore, *Phys. Rev. E* **87**, 052303 (2013).
²⁰J. K. Lee, J. A. Barker, and F. F. Abraham, *J. Chem. Phys.* **58**, 3166 (1973); W. Ebeling and M. Grigo, *Ann. Phys.* **492**, 21 (1980); M. J. Gillan, *Mol. Phys.* **49**, 421 (1983); J.-M. Caillol and J.-J. Weis, *J. Chem. Phys.* **102**, 7610 (1995); M. E. Fisher and Y. Levin, *Phys. Rev. Lett.* **71**, 3826 (1993); H. L. Friedman and G. Larsen, *J. Chem. Phys.* **70**, 92 (1979).
²¹T. L. Hill, *J. Chem. Phys.* **23**, 617 (1955).
²²A. Coniglio, U. de Angelis, A. Forlani, and G. Lauro, *J. Phys. A* **10**, 219 (1977).
²³N. F. Carnahan and K. E. Starling, *J. Chem. Phys.* **51**, 635 (1969).
²⁴G. Jackson, W. G. Chapman, and K. E. Gubbins, *Mol. Phys.* **65**, 1 (1988).
²⁵In fact $dx_c/d\lambda < 0$ if $\sum_{ij} ij\lambda^{i+j-1} z_i z_j < \sum_{ij} i^2 \lambda^{i+j-1} z_i z_j$. This can be proven observing that for $i \neq j$ we have $(i - j)^2 > 0$ or $2ij < ii + jj$ or $ija_{ij} + jia_{ji} < iia_{ij} + jja_{ji}$ for any $a_{ij} = a_{ji}$. Then we must also have $\sum_{ij} ija_{ij} < \sum_{ij} iia_{ij}$.
²⁶Note that the reference system, the one without attractions and therefore with only monomers, will in general differ in the two theories if $\sigma_c \neq \sigma$.
²⁷N. Kern and D. Frenkel, *J. Chem. Phys.* **118**, 9882 (2003).
²⁸W. G. Chapman, K. E. Gubbins, C. G. Joslin, and C. G. Gray, *Fluid Phase Equilib.* **29**, 337 (1986); C. G. Joslin, C. G. Gray, W. G. Chapman, and K. E. Gubbins, *Mol. Phys.* **62**, 843 (1987).
²⁹J.-P. Hansen and I. R. McDonald, *Theory of Simple Liquids*, 2nd ed. (Academic Press, 1986).
³⁰M. P. Allen and D. J. Tildesley, *Computer Simulation of Liquids* (Oxford University Press, 1987), Appendix G.4.
³¹D. Levesque, J. J. Weis, and J. P. Hansen in *Monte Carlo Methods in Statistical Physics*, Topics in Current Physics, edited by K. Binder (Springer-Verlag, New York, 1979), Vol. 7, Chap. 2, p. 47. See also Eq. (2.27) page 100.

Chapter 43

Gas-liquid coexistence for the bosons square-well fluid and the ^4He binodal anomaly

Fantoni R., Phys. Rev. E **90**, 020102(R) (2014)

Title: “Gas-liquid coexistence for the bosons square-well fluid and the ^4He binodal anomaly”

Abstract: The binodal of a boson square-well fluid is determined as a function of the particle mass through the newly devised quantum Gibbs ensemble Monte Carlo algorithm [R. Fantoni and S. Moroni, *to be published*]. In the infinite mass limit we recover the classical result. As the particle mass decreases the gas-liquid critical point moves at lower temperatures. We explicitly study the case of a quantum delocalization de Boer parameter close to the one of ^4He . For comparison we also determine the gas-liquid coexistence curve of ^4He for which we are able to observe the binodal anomaly below the λ -transition temperature.

Gas-liquid coexistence for the boson square-well fluid and the ^4He binodal anomaly

Riccardo Fantoni*

Dipartimento di Scienze Molecolari e Nanosistemi, Università Ca' Foscari Venezia, Calle Larga Santa Marta DD2137, I-30123 Venezia, Italy

(Received 7 May 2014; published 18 August 2014)

The binodal of a boson square-well fluid is determined as a function of the particle mass through a quantum Gibbs ensemble Monte Carlo algorithm devised by R. Fantoni and S. Moroni [J. Chem. Phys. (to be published)]. In the infinite mass limit we recover the classical result. As the particle mass decreases, the gas-liquid critical point moves at lower temperatures. We explicitly study the case of a quantum delocalization de Boer parameter close to the one of ^4He . For comparison, we also determine the gas-liquid coexistence curve of ^4He for which we are able to observe the binodal anomaly below the λ -transition temperature.

DOI: 10.1103/PhysRevE.90.020102

PACS number(s): 05.30.Jp, 64.70.F-, 67.10.Fj

Soon after Feynman rewrote quantum mechanics and quantum statistical physics in terms of the path integral [1,2] it was realized that this new mathematical object could be used as a powerful numerical instrument. The statistical physics community soon realized that a path integral could be calculated using the Monte Carlo method [3].

Consider a fluid of N bosons at a given absolute temperature $T = 1/k_B\beta$, with k_B the Boltzmann constant. Let the system of particles have a Hamiltonian $\hat{H} = -\lambda \sum_{i=1}^N \nabla_i^2 + \sum_{i<j} \phi(|\mathbf{r}_i - \mathbf{r}_j|)$ symmetric under particle exchange, with $\lambda = \hbar^2/2m$, m the mass of the particles, and $\phi(|\mathbf{r}_i - \mathbf{r}_j|)$ the pair potential of the interaction between particle i at \mathbf{r}_i and particle j at \mathbf{r}_j . The many-particle system will have spatial configurations $\{R\}$, with $R \equiv (\mathbf{r}_1, \dots, \mathbf{r}_N)$ the coordinates of the N particles. The partition function of the fluid can be calculated [3] as a sum over the $N!$ possible particle permutations \mathcal{P} of a path integral over many-particle closed paths $X \equiv (R_0, \dots, R_P)$ in the imaginary time interval $\tau \in [0, \beta = P\epsilon]$, discretized into P intervals of equal length ϵ , the time step, with $R_P = \mathcal{P}R_0$ the β -periodic boundary condition.

More recently a grand-canonical ensemble algorithm has been devised by Boninsegni *et al.* [4] for the path integral Monte Carlo method. This paved the way to the development of a quantum Gibbs ensemble Monte Carlo algorithm (QGEMC) to study the gas-liquid coexistence of a generic boson fluid [5]. This algorithm is the quantum analog of the Panagiotopoulos [6] method, which has now been successfully used for several decades to study first-order phase transitions in classical fluids [7]. However, as simulations in the grand-canonical ensemble, the method does rely on a reasonable number of successful particle insertions to achieve compositional equilibrium. As a consequence, the Gibbs ensemble Monte Carlo method cannot be used to study equilibria involving very dense phases. Unlike previous extensions of the Gibbs ensemble Monte Carlo that include quantum effects (some [8] only consider fluids with internal quantum states; others [9] successfully exploit the path integral Monte Carlo isomorphism between quantum particles and classical ring polymers, but lack the structure of particle exchanges which underlies the Bose or Fermi statistics), the QGEMC scheme is viable even for systems with strong quantum delocalization in the degenerate regime

of temperature. Details of the QGEMC algorithm will be presented elsewhere [5].

In this Rapid Communication we will apply the QGEMC method to the fluid of square-well (SW) bosons in three spatial dimensions as an extension of the work of Vega *et al.* [10] on the classical fluid. The de Boer quantum delocalization parameter $\Lambda = \hbar/\sigma(m\mathcal{E})^{1/2}$, with \mathcal{E} and σ measures of the energy and length scale of the potential energy, can be used to estimate the quantum mechanical effects on the thermodynamic properties of nearly classical liquids [11]. We will consider square-well fluids with two values of the particle mass m : $\Lambda = 1/\sqrt{50}$, close but different from zero, and $\Lambda = 1/\sqrt{5}$. In the first case we compare our result with the one of Vega and in the second case with the one of ^4He , which we consider in our second application. When studying the binodal of ^4He in three spatial dimensions we are able to reproduce the binodal anomaly appearing below the λ point, where the liquid branch of the coexistence curve shows a reentrant behavior.

In our implementation of the QGEMC [5] algorithm we choose the primitive approximation to the path integral action discussed in Ref. [3]. The simulation is performed in two boxes (representing the two coexisting phases) of varying volumes V_1 and $V_2 = V - V_1$ and numbers of particles $N_1 = V_1\rho_1$ and $N_2 = V_2\rho_2 = N - N_1$ with V and $N = V\rho$ constants. The Gibbs equilibrium conditions of pressure and chemical potential equality between the two boxes is enforced by allowing changes in the volumes of the two boxes (the *volume move*, $q = 5$) and by allowing exchanges of particles between the two boxes (the *open-insert move*, $q = 1$, plus the complementary *close-remove move*, $q = 2$, plus the *advance-recede move*, $q = 3$) while at the same time sampling the closed path configuration space (the *swap move*, $q = 4$, plus the *displace move*, $q = 6$, plus the *wiggle move*, $q = 7$). We thus have a menu of seven, $q = 1, 2, \dots, 7$, different Monte Carlo moves where a single random attempt of any one of them with a probability $G_q = g_q / \sum_{q=1}^7 g_q$ constitutes a Monte Carlo step.

We denote with \mathcal{V} the maximum displacement of $\ln(V_1/V_2)$ in the volume move, with $\mathcal{L}^{(p)}$ the maximum particle displacement in box $p = 1, 2$ in the displacement move, and with $\mathcal{M}_q < P$ the maximum number of time slices involved in the $q \neq 5, 6$ move. In order to fulfill a detailed balance we must choose $\mathcal{M}_1 = \mathcal{M}_2$.

*rfantoni@ts.infn.it

RICCARDO FANTONI

PHYSICAL REVIEW E **90**, 020102(R) (2014)

Letting the system evolve at a given absolute temperature T from a given initial state (for example, we shall take $\rho_1 = \rho_2 = \rho$), we measure the densities of the two coexisting phases, $\rho_1 < \rho$ and $\rho_2 > \rho$, which soon approach the coexistence equilibrium values.

First we study a system of bosons in three dimensions interacting with a square-well pair potential,

$$\phi(r) = \begin{cases} +\infty, & r < \sigma, \\ -A, & \sigma \leq r < \sigma(1 + \Delta), \\ 0, & \sigma(1 + \Delta) \leq r, \end{cases} \quad (1)$$

which, for example, can be used as an effective potential for cold atoms [12] with a scattering length $a = \sigma(1 + \Delta)[1 - \tan(\sigma \Delta \sqrt{A/2\lambda})/\sigma(1 + \Delta)\sqrt{A/2\lambda}]$. We choose $A > 0$ as the unit of energies and σ as the unit of length. We then introduce a reduced temperature $T^* = k_B T/A$ and a reduced density $\rho^* = \rho\sigma^3$. When the mass of the boson is very large, i.e., $\lambda^* = \lambda/(A\sigma^2) \ll 1$, we are in the classical limit. The classical fluid has been studied originally by Vega *et al.* [10], who found that the critical point of the gas-liquid coexistence moves at lower temperatures and higher densities as Δ gets smaller. The quantum mechanical effects on the thermodynamic properties of nearly classical liquids can be estimated by the de Boer quantum delocalization parameter $\Lambda = \sqrt{2\lambda^*}$.

During the subcritical temperature runs we register the densities of the gas, ρ_g , and of the liquid, ρ_l ($> \rho_g$), phase (box). When the densities of the two boxes are too close to one another, we may observe the curves crossing, which implies that the two boxes exchange identity. It is then necessary to compute the density probability distribution function, created using the densities of both boxes. When we are at temperatures sufficiently below the critical point, this distribution appears to be bimodal, i.e., it has two peaks approximated by Gaussians. In some representative cases we checked that the peaks of the bimodal calculated thusly occur at the same densities as the peaks of the bimodal obtained from the single density distribution of the worm algorithm after a careful tuning of the chemical potential [13].

We study the model with $\Delta = 0.5$ near their classical limit $\lambda^* = 1/100$ ($\Lambda \approx 0.14, a^* = a/\sigma \approx 1.44$) and at an intermediate case $\lambda^* = 1/10$ ($\Lambda \approx 0.45, a^* \approx 0.58$). We choose $N = 50$, $\rho^* = 0.3$, $\mathcal{L}^{(p)} = V_p^{1/3}/10$, $\mathcal{V} = 1/10$, and we take all \mathcal{M}_q equal, adjusted so as to have the acceptance ratios of the wiggle move close to 50%, $g_1 = g_2 = g_3 = g_4 = g_7 = 1$, $g_5 = 0.0001$, and $g_6 = 0.1$. Moreover, we choose the relative weight of the Z and G sectors of our extended worm algorithm C [4] so as to have the Z -sector acceptance ratios close to 50%. We started from an initial configuration where we have an equal number of particles in boxes of equal volumes at a total density $\rho^* = 0.3$.

All our runs were made of 10^5 blocks of 10^5 MC steps with property measurements every 10^2 steps [14]. The time needed to reach the equilibrium coexistence increases with P and in general with a lowering of the temperature.

If we choose $\lambda^* = 1/100$ and $P = 2$, $\mathcal{M}_q = 1$ (in this case the advance-recede move cannot occur), we find that our algorithm gives results close to the ones of Vega [10] obtained with the classical statistical mechanics ($\lambda^* = 0$) algorithm of Panagiotopoulos [6,15]. As we diminish the time step

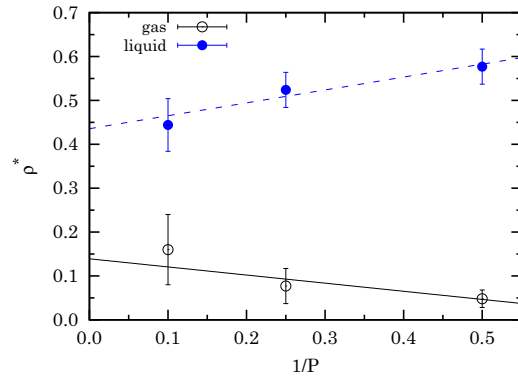


FIG. 1. (Color online) Linear fit to the zero time-step limit $P \rightarrow \infty$ for $T^* = 1$ and $\lambda^* = 1/100$.

$\epsilon^* = 1/PT^*$ at a given temperature, we can extrapolate to the zero time-step limit $P \rightarrow \infty$ as shown in Fig. 1. We thus obtain the fully quantum statistical mechanics result for the binodal shown in Fig. 2, which turns out to exist for $T^* \lesssim 1$. This shows that the critical point due to the effect of the quantum statistics moves at lower temperatures. For the temperatures studied the superfluid fraction [16] of the system was always negligible as in the systems studied in Ref. [9], such as neon ($\Lambda \approx 0.095$) and molecular hydrogen ($\Lambda \approx 0.276$).

In order to extrapolate the binodal to the critical point we used the law of “rectilinear diameters,” $\rho_l + \rho_g = 2\rho_c + a|T - T_c|$, and the Fisher expansion [17], $\rho_l - \rho_g = b|T - T_c|^{\beta_1}(|T - T_c| + c)^{\beta_0 - \beta_1}$, with $\beta_1 = 1/2$ and $\beta_0 = 0.3265$, and a, b, c fitting parameters with $c = 0$ for $\lambda = 0$ and $c \neq 0$ for $\lambda \neq 0$.

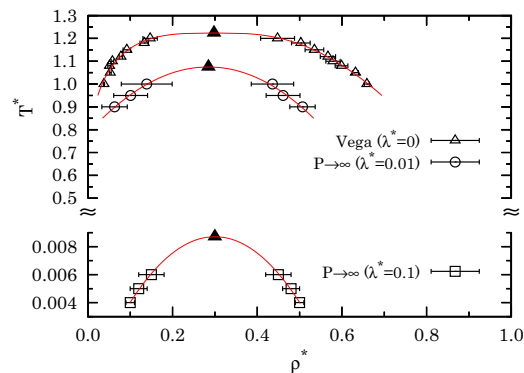


FIG. 2. (Color online) Binodal for the square-well fluid in three dimensions. Shown are the classical results of Vega *et al.* [10] at $\lambda^* = 0$ and our results in the $P \rightarrow \infty$ limit for $\lambda^* = 1/100, 1/10$. In the simulations we used $N = 50$ and for the extrapolation to the zero time-step limit up to $P = 20$ for $\lambda^* = 1/100$ and $P = 500$ for $\lambda^* = 1/10$. The curves extrapolating to the critical point are obtained as described in the text. The solid triangles are the expected critical points.

Upon increasing λ^* to 1/10, the binodal now appears at $T^* \lesssim 0.008$, where we had a non-negligible superfluid fraction [16] [$\rho_s/\rho \approx 0.32(2)$] at $T^* = 0.006$ on the liquid branch]. As a consequence it proves necessary to use larger P in the extrapolation to the zero time-step limit. Notice also that at lower temperature it is necessary to run longer simulations due to the longer paths and equilibration times. We generally expect that by increasing λ^* the gas-liquid critical temperature decreases and the normal-superfluid critical temperature increases. So the window of temperature for the normal liquid tends to close.

Our second study is on ^4He , for which $\lambda^* = 6.0596$. We now take 1 Å as the unit of length and k_B K as the unit of energy. In this case $\sigma \approx 2.5$ Å, $\mathcal{E} \approx 10.9$ K, and $\Lambda \approx 0.42$. This situation is comparable to a square-well case with $\lambda^* = 1/10$. We use $N = 128$ and the Aziz HFDHE2 pair potential [18]

$$\phi(r) = \begin{cases} \epsilon\phi^*(x), & r < r_{\text{cut}}, \\ 0, & r \geq r_{\text{cut}}, \end{cases} \quad (2)$$

$$\phi^*(x) = A \exp(-\alpha x) - \left(\frac{C_6}{x^6} + \frac{C_8}{x^8} + \frac{C_{10}}{x^{10}} \right) F(x), \quad (3)$$

$$F(x) = \begin{cases} \exp[-(D/x - 1)^2], & x < D, \\ 1, & x \geq D, \end{cases} \quad (4)$$

where $x = r/r_m$, $r_m = 2.9673$, $\epsilon/k_B = 10.8$, $A = 0.5448504$, $\alpha = 13.353384$, $C_6 = 1.3732412$, $C_8 = 0.4253785$, $C_{10} = 0.178100$, $D = 1.241314$, and $r_{\text{cut}} = 6$ Å (here we explicitly checked that during the simulation the conditions $V_p^{1/3} > 2r_{\text{cut}}$ for $p = 1, 2$ are always satisfied). In this case it proves convenient to choose $\rho^* = 0.01$, $\mathcal{L}^{(p)} = V_p^{1/3}/10$, $\mathcal{V} = 1/10$, $g_1 = g_2 = g_3 = g_4 = g_7 = 1$, $g_5 = 0.0001$, and $g_6 = 0.1$. As for the SW case we observe a decrease in the width of the coexistence curve $\rho_l - \rho_g$ as the number of time slices increases. We thus work at a small (fixed) time step $\epsilon^* = 0.002$, about 1/1000 of the superfluid transition temperature, as advised in Ref. [3] to be necessary when studying helium with the primitive approximation for the action.

The results for the binodal are shown in Fig. 3. The experimental critical point is at $T_c = 5.25$ K and $\rho_c = 17.3$ mol/l [19]. Factors explaining the discrepancy with experiment could be the size error or the choice of the pair potential. Choosing larger sizes N it is possible to increase r_{cut} and this shifts the simulated critical temperature to higher values. For the three-dimensional ^4He we expect to have the superfluid below a λ temperature $T_\lambda^* = 2.193(6)$ [4], so our results again show that our method works well even in the presence of a non-negligible superfluid fraction. Moreover, as shown by the points, at the two lowest temperatures we observe the expected [20] binodal anomaly below the λ point.

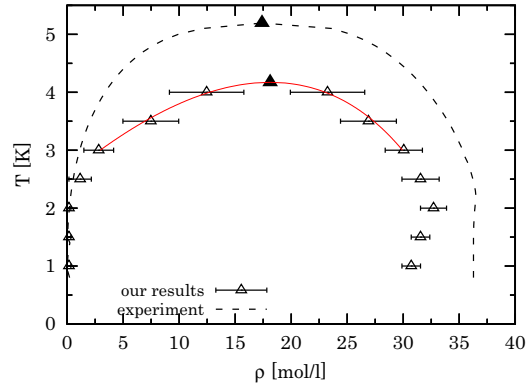


FIG. 3. (Color online) Binodal for the ^4He of Aziz [18] in three dimensions. In our simulations we used $N = 128$, $r_{\text{cut}}^* = 6$, and a time step $\epsilon^* = 0.002$. The continuous (red) curve extrapolating to the critical point is obtained as described in the text. The solid triangle is the estimated critical point. The experimental results from Ref. [19] are also shown as a dashed curve.

In conclusion, we determined the gas-liquid binodal of a square-well fluid of bosons as a function of the particle mass and of ^4He , in three spatial dimensions, from first principles. The critical point of the square-well fluid moves to lower temperatures as the mass of the particles decreases, or as the de Boer parameter increases, while the critical density stays approximately constant.

Our results for ^4He compare well with the experimental critical density even if a lower critical temperature is observed in the simulation. We expect this to be due mainly to a finite-size effect that is unavoidable in the simulation. Nonetheless, we are able to determine the binodal anomaly [20] occurring below the λ -transition temperature. The anomaly that we observe in the simulation appears to be more accentuated than in the experiment and the liquid branch of the binodal falls at slightly lower densities.

Even if our QGEMC method is more efficient at high temperatures, it is able to detect the liquid phase at low temperatures even below the superfluid transition temperature. This numerical method is extremely simple to use and, unlike current methods, does not need the matching of free energies calculated separately for each phase or the simulation of large systems containing both phases and their interface.

R.F. would like to acknowledge the use of the PLX computational facility of CINECA through the ISCR grant. We are grateful to Michael Ellis Fisher for correspondence and helpful comments.

[1] R. P. Feynman, *Rev. Mod. Phys.* **20**, 367 (1948).
 [2] R. P. Feynman, in *Statistical Mechanics: A Set of Lectures*, edited by J. Shaham, Frontiers in Physics Vol. 36 (Benjamin, New York, 1972).

[3] D. M. Ceperley, *Rev. Mod. Phys.* **67**, 279 (1995).
 [4] M. Boninsegni, N. Prokof'ev, and B. Svistunov, *Phys. Rev. Lett.* **96**, 070601 (2006); *Phys. Rev. E* **74**, 036701 (2006).
 [5] R. Fantoni and S. Moroni, *J. Chem. Phys.* (to be published).

RICCARDO FANTONI

PHYSICAL REVIEW E **90**, 020102(R) (2014)

- [6] A. Z. Panagiotopoulos, *Mol. Phys.* **61**, 813 (1987); A. Z. Panagiotopoulos, N. Quirke, M. Stapleton, and D. J. Tildesley, *ibid.* **63**, 527 (1988); B. Smit, Ph. De Smedt, and D. Frenkel, *ibid.* **68**, 931 (1989); B. Smit and D. Frenkel, *ibid.* **68**, 951 (1989); D. Frenkel and B. Smit, *Understanding Molecular Simulation* (Academic, San Diego, 1996).
- [7] A. Z. Panagiotopoulos, *Mol. Sim.* **9**, 1 (1992); F. Sciortino, A. Giacometti, and G. Pastore, *Phys. Rev. Lett.* **103**, 237801 (2009); R. Fantoni and G. Pastore, *Phys. Rev. E* **87**, 052303 (2013); R. Fantoni, A. Maliješský, A. Santos, and A. Giacometti, *Europhys. Lett.* **93**, 26002 (2011); *Mol. Phys.* **109**, 2723 (2011); R. Fantoni, A. Giacometti, M. A. G. Maestre, and A. Santos, *J. Chem. Phys.* **139**, 174902 (2013).
- [8] F. Schneider, D. Marx, and P. Nielaba, *Phys. Rev. E* **51**, 5162 (1995); P. Nielaba, *Int. J. Thermophys.* **17**, 157 (1996).
- [9] Q. Wang and J. K. Johnson, *Fluid Phase Equilib.* **132**, 93 (1997); I. Georgescu, S. E. Brown, and V. A. Mandelshtam, *J. Chem. Phys.* **138**, 134502 (2013); P. Kowalczyk, P. A. Gauden, A. P. Terzyk, E. Pantatosaki, and G. K. Papadopoulos, *J. Chem. Theory Comput.* **9**, 2922 (2013).
- [10] L. Vega, E. de Miguel, L. F. Rull, G. Jackson, and I. A. McLure, *J. Chem. Phys.* **96**, 2296 (1992); H. Liu, S. Garde, and S. Kumar, *ibid.* **123**, 174505 (2005).
- [11] R. A. Young, *Phys. Rev. Lett.* **45**, 638 (1980).
- [12] C. J. Pethik and H. Smith, *Bose-Einstein Condensation in Dilute Gases* (Cambridge University Press, Cambridge, UK, 2002), Chap. 5.
- [13] N. B. Wilding, *Phys. Rev. E* **52**, 602 (1995).
- [14] Our QGEMC code took ≈ 90 s of CPU time for 1 000 000 steps of a system of size $N = 50$, $P = 10$, $\mathcal{M}_q = 5$, calculating properties every 100 steps, on an IBM iDataPlex DX360M3 Cluster (2.40 GHz). The algorithm scales as N^2 , due to the potential energy calculation, and as P , due to the volume move.
- [15] Note that there is no difference between our algorithm in the limit $P = 2$, $\mathcal{M}_q = 1$, and $\lambda^* \rightarrow 0$ and the one of Panagiotopoulos [6].
- [16] E. L. Pollock and D. M. Ceperley, *Phys. Rev. B* **36**, 8343 (1987).
- [17] M. E. Fisher, *Phys. Rev. Lett.* **16**, 11 (1966).
- [18] R. A. Aziz, V. P. S. Nain, J. S. Carley, W. L. Taylor, and G. T. McConville, *J. Chem. Phys.* **70**, 4330 (1979).
- [19] R. D. McCarty, *J. Phys. Chem. Ref. Data* **2**, 923 (1973); V. D. Arp and R. D. McCarty, Natl. Inst. Stand. Technol. Tech. Note (US) No. 1334 (1989).
- [20] H. Stein, C. Porthun, and G. Röpke, *Eur. Phys. J. B* **2**, 393 (1998).

Chapter 44

Quantum Gibbs ensemble Monte Carlo

Fantoni R. and Moroni S., J. Chem. Phys. **141**, 114110 (2014)

Title: “Quantum Gibbs ensemble Monte Carlo”

Abstract: We present a path integral Monte Carlo method which is the full quantum analogue of the Gibbs ensemble Monte Carlo method of Panagiotopoulos to study the gas-liquid coexistence line of a classical fluid. Unlike previous extensions of Gibbs ensemble Monte Carlo to include quantum effects, our scheme is viable even for systems with strong quantum delocalization in the degenerate regime of temperature. This is demonstrated by an illustrative application to the gas-superfluid transition of ^4He in two dimensions.



Quantum Gibbs ensemble Monte Carlo

Riccardo Fantoni^{1,a)} and Saverio Moroni^{2,b)}

¹Dipartimento di Scienze Molecolari e Nanosistemi, Università Ca' Foscari Venezia,
Calle Larga S. Marta DD2137, I-30123 Venezia, Italy

²DEMOCRITOS National Simulation Center, Istituto Officina dei Materiali del CNR and SISSA
Scuola Internazionale Superiore di Studi Avanzati, Via Bonomea 265, I-34136 Trieste, Italy

(Received 30 July 2014; accepted 8 September 2014; published online 18 September 2014)

We present a path integral Monte Carlo method which is the full quantum analogue of the Gibbs ensemble Monte Carlo method of Panagiotopoulos to study the gas-liquid coexistence line of a classical fluid. Unlike previous extensions of Gibbs ensemble Monte Carlo to include quantum effects, our scheme is viable even for systems with strong quantum delocalization in the degenerate regime of temperature. This is demonstrated by an illustrative application to the gas-superfluid transition of ⁴He in two dimensions. © 2014 AIP Publishing LLC. [<http://dx.doi.org/10.1063/1.4895974>]

I. INTRODUCTION

Monte Carlo (MC) simulations¹ in the Gibbs ensemble (GEMC) of Panagiotopoulos² have now been extensively used for several years to study first order phase transitions in classical fluids. According to the GEMC method, the simulation is performed in two boxes each of which contains one of two coexisting phases. Equilibration in each phase is guaranteed by moving particles within the respective box. Equality of pressures is satisfied in a statistical sense by expanding the volume of one of the boxes and contracting the volume of the other. Chemical potentials are equalized by transferring particles from one box to the other. This procedure avoids either the laborious search for matching free energies calculated separately for each phase, or the simulation of a system large enough to contain both phases and their interface.

Notwithstanding the isomorphism between quantum particles and classical ring polymers underlying the path integral formulation of quantum statistical physics,³ and the recognition that path integral Monte Carlo (PIMC) is a tremendously useful numerical tool⁴ to extract unbiased statistical properties of quantum systems, the development of Monte Carlo methods for quantum systems is more complex, and correspondingly less complete, than for classical ones. Putting aside the well known sign problem for fermions⁵ an important aspect is the development of methods able to simulate a given quantum system in different statistical ensembles.

Recently, a new approach to continuous space PIMC simulation was devised⁶ which makes use of the “Worm Algorithm” (WA) previously employed to study lattice models.⁷ The WA is formulated in an enlarged configuration space, which features the possible presence of an open world-line, the worm. It can simulate a system either in the grand canonical or the canonical ensemble, and it enjoys a favorable scaling of the computational cost with the system size for the calculation of properties related to the formation of long permutation cycles,⁸ such as the superfluid fraction or the one-body density matrix.

It is the purpose of the present work to exploit the WA⁶ to obtain an algorithm that is the full quantum analogue of the GEMC and thus can be used to study the gas-liquid phase transition of any (bosonic) quantum fluid.⁹ Several quantum generalizations of GEMC have appeared. However, some of them only consider particles which have internal quantum states but are otherwise classical,¹⁰ others¹¹ are limited to particles isomorph to relatively compact classical polymers (hence, high enough temperature and/or small enough quantumness); none of them features the structure of particle exchanges which underlies Bose (or Fermi) statistics. We apply the quantum Gibbs ensemble Monte Carlo (QGEMC) method to the liquid-gas coexistence of two-dimensional ⁴He where strong quantum effects, including superfluidity, are present.

II. CLASSICAL GIBBS ENSEMBLE MONTE CARLO

We begin with a brief summary of the Gibbs Ensemble Monte Carlo method that we deem useful for the subsequent quantum generalization. A detailed presentation is given in Ref. 12.

The system comprises a box of volume Ω_1 containing N_1 particles and a box of volume Ω_2 containing N_2 particles. The temperature T , the total number of particles $N = N_1 + N_2$, and the total volume $\Omega = \Omega_1 + \Omega_2$ are fixed, and there is no interaction between particles enclosed in different boxes. Starting from the partition function for the Gibbs ensemble

$$Z_G(N, \Omega, T) = \frac{1}{\Omega} \sum_{N_1=0}^N \int d\Omega_1 Z(N_1, \Omega_1, T) Z(N_2, \Omega_2, T), \quad (1)$$

where Z is the canonical partition function, the probability density for the coordinates $R = \{\mathbf{r}_1, \dots, \mathbf{r}_N\}$ of the particles, the number N_1 , and the volume Ω_1 can be cast in the form

$$P_{N,\Omega,T}(R, N_1, \Omega_1) \propto \frac{\Omega_1^{N_1+1} \Omega_2^{N_2+1}}{N_1! N_2!} e^{-\beta V(R)}. \quad (2)$$

^{a)}Electronic mail: rfantoni@ts.infn.it

^{b)}Electronic mail: moroni@democritos.it

Here, $\beta = 1/k_B T$ and the potential energy in the Boltzmann weight, assuming a central pair potential $v(r)$, is

$$V(R) = \sum_{i=1}^{N_1-1} \sum_{j=i+1}^{N_1} v(r_{ij}) + \sum_{i=N_1+1}^{N-1} \sum_{j=i+1}^N v(r_{ij}). \quad (3)$$

The Monte Carlo simulation proceeds via three kinds of moves:

- (1) Displace the position \mathbf{r}_i of a randomly selected particle within its own box; this is done as in standard canonical ensemble simulations.
- (2) Change the volumes; this is done by uniformly sampling a displacement of the quantity $\ln(\Omega_1/\Omega_2)$, with Ω kept fixed.
- (3) Exchange particles; this is done by transferring a randomly chosen particle to a random position in the other box.

The acceptance probabilities are obtained imposing detailed balance.¹² After equilibration, provided N/Ω is within the coexistence region at the temperature T , each of the two boxes will contain one of the coexisting phases.

III. QUANTUM GIBBS ENSEMBLE MONTE CARLO

The QGEMC is based on the Path Integral Monte Carlo method in the Worm Algorithm implementation. We refer to the literature^{4,6} for a full account of these techniques, giving here only a brief discussion of some aspects relevant to the quantum generalization of the classical GEMC.

A. Path integral Monte Carlo

We consider an assembly of N identical particles obeying Bose statistics. In the position representation, the canonical partition function is

$$Z = \frac{1}{N!} \sum_{\mathcal{P}} \int dR \rho(R, \mathcal{P}R; \beta), \quad (4)$$

where $\rho(R, R'; \beta) = \langle R | e^{-\beta H} | R' \rangle$ is the thermal density matrix for distinguishable particles, and the sum over the permutations \mathcal{P} accounts for Bose symmetry. The density matrix can be expressed in a form amenable to Monte Carlo simulation in terms of discretized path integrals

$$\rho(R, R'; \beta) \simeq \int dR_1 \dots dR_{K-1} \prod_{j=1}^K \tilde{\rho}(R_{j-1}, R_j; \epsilon), \quad (5)$$

with $R_0 = R, R_K = R'$, and $\{R_1, \dots, R_{K-1}\}$ a sequence (path) of intermediate configurations. An adjacent pair $\{R_{j-1}, R_j\}$ is called a *link*. In Eq. (5), the factors $\tilde{\rho}$ have an argument $\epsilon = \beta/K$ which corresponds to a temperature K times higher than T , and for high temperature the unknown many-body density matrix can be accurately approximated by an explicit expression of the general form

$$\tilde{\rho}(R, R'; \epsilon) = \rho_F(R, R'; \epsilon) e^{-U(R, R'; \epsilon)}, \quad (6)$$

where

$$\rho_F(R, R'; \epsilon) = (4\pi\lambda\epsilon)^{-dN/2} \prod_{i=1}^N e^{-\epsilon(\mathbf{r}_i - \mathbf{r}'_i)^2/4\lambda\epsilon} \quad (7)$$

is the density matrix for N non-interacting particles in d spatial dimensions, and the function U takes into account the effect of correlations. In the limit $\epsilon \rightarrow 0$, $\tilde{\rho}(R, R', \epsilon)$ approaches $\rho(R, R', \epsilon)$ and the approximate equality (5) becomes exact.

For each particle, Eq. (5) defines a trajectory, or world line (WL), $\{\mathbf{r}_{i,0}, \mathbf{r}_{i,1}, \dots, \mathbf{r}_{i,K}\}$, where the *bead* $\mathbf{r}_{i,j}$ is the position of the i th particle at the j th “time” discretization index. In the calculation of thermal averages, $\langle A \rangle = \text{Tr} \rho A / Z$, the presence of the traces and the Bose symmetry of Eq. (4) require periodic boundary conditions in time, $\mathbf{r}_{i,K} = \mathbf{r}_{i,0}$: the trajectory of a particle ends in the initial position of either the same or another particle, according to the permutation cycles contained in the permutation \mathcal{P} . All the interlinked trajectories of a permutation cycle of k particles form a single WL with kK steps, so that all WLs are closed. The WL of a single particle has a spatial extent limited by the thermal wavelength, while the WL of a long permutation cycle can span the whole system.

The simulation proceeds by sampling a density probability proportional to the integrand of Eq. (5). Specific techniques are devised to update not only the particle positions along the WLs, but also the permutations.

The WLs can be mapped onto classical ring polymers, with peculiar interactions defined through Eq. (5) by viewing the integrand as a Boltzmann weight. Thus, it seems possible to apply the GEMC method to the quantum system as well. However, an issue arises with the exchange move: a quantum particle corresponds, in the classical mapping, to a whole polymer, and the acceptance rate for transferring a polymer to the other box can be expected to be low, particularly at low temperature when the thermal wavelength increases and the spatial extension of the polymers grows. The problem is further compound by the presence of interlinked trajectories belonging to a permutation cycle. This is why quantum applications of GEMC have been limited to relatively high temperature and/or relatively low quantumness.¹¹ We will show how to overcome these difficulties using the WA.

B. Worm algorithm

The WA enlarges the configuration space: along with the closed WLs of Sec. III A, there are configurations with an open WL in which one particle is created in \mathbf{r}_M at time $j_M \epsilon$ and destroyed in \mathbf{r}_I at a later time $j_I \epsilon$. The difference $j_I - j_M$ is intended modulo K , and the open WL can belong to a permutation cycle involving other particles. The points \mathbf{r}_I and \mathbf{r}_M are called Ira and Masha, respectively, and the WL connecting them is called the *worm*. Configurations with only closed WLs belong to the “Z sector” and contribute to the partition function. Configurations with a worm belong to the “G sector” and contribute to the one-body Green function $g(\mathbf{r}_M, \mathbf{r}_I; (j_I - j_M)\epsilon) / Z$. All physical properties, with the exception of the Green function, are calculated only on configurations of the Z sector. The full set of configurations corresponds to the extended partition function

$$Z_W = Z + Z', \quad (8)$$

114110-3 R. Fantoni and S. Moroni

J. Chem. Phys. **141**, 114110 (2014)

where Z can be either the canonical or the grand partition function,

$$Z' = C \sum_{J_I, J_M} \int d\mathbf{r}_I d\mathbf{r}_M g(\mathbf{r}_M, \mathbf{r}_I; (J_I - j_M)\epsilon), \quad (9)$$

and the arbitrary parameter C defines the relative weight of the Z and G sectors. The discretized path integral expression of Eq. (9) is obtained in close analogy with Sec. III A in terms of $\tilde{\rho}(R_{j-1}, R_j; \epsilon)$.

The simulation proceeds via a set of local moves – the complementary pairs *Open* and *Close*, *Insert* and *Remove*, *Advance* and *Recede*, and the self-complementary *Swap* – which guarantee ergodic sampling of the enlarged configuration space by switching between the Z and the G sectors and displacing the coordinates of the particles.⁶

The usefulness of the WA for the implementation of the QGEMC can be appreciated by considering the process of adding a particle to the system (we assume here that Z is the grand partition function): starting from the Z sector, a worm may be *inserted*; once in the G sector, the worm may *advance*, possibly *swap* with existing closed WLs, and eventually get *closed*, thus switching back to the Z sector with one more particle. Each single move is a local update that involves only a limited number of time steps, so that the acceptance rate can be high even in a dense system.

C. Gibbs ensemble

We consider N_1 particles in a volume Ω_1 and N_2 particles in a volume Ω_2 , with Ω , N , and T fixed (see Sec. II). The configurations of the system in the Gibbs ensemble are distributed according to the partition function Z_G of Eq. (1), with each of the canonical partition functions Z of the two subsystems expressed as discretized path integrals with closed WLs, as in Sec. III A. These configurations define the Z sector.

Following the strategy of the WA we enlarge the configuration space allowing for open WLs, while strictly enforcing the constraint of fixed N : whenever there is a worm in box 1, with Masha at $\mathbf{r}_{M1;j}$ and Ira at $\mathbf{r}_{I1;j'}$, there is a worm in box 2 as well, with Masha at $\mathbf{r}_{M2;j'}$ and Ira at $\mathbf{r}_{I2;j}$, as schematically illustrated in Fig. 1. These configurations define the G sector. In the G sector, the number of particles in box α ($\alpha = 1, 2$) varies between N_α and $N_\alpha - 1$, with $N_1 + N_2 = N + 1$, and the total number of particles within each link is N .

The extended partition function is $Z_W = Z_G + Z'$, where

$$Z' = \frac{1}{\Omega} \sum_{N_1} \int d\Omega_1 C \sum_{j,j'=1}^K F_1(j, j') F_2(j', j). \quad (10)$$

The primed summation excludes the terms with $j = j'$ to make sure there is a worm per box in the G sector, and the function F_α – the integral of Eq. (9) for box α – is expressed in terms of density matrices as

$$F_\alpha(j, j') = \frac{1}{N_\alpha!} \sum_{\mathcal{P}_\alpha} \int \rho(\{R_\alpha, \mathbf{r}_{M\alpha}\}, \mathcal{P}_\alpha \{R'_\alpha, \mathbf{r}_{I\alpha}\}; \tau_{j,j'}) \times \rho(R'_\alpha, R_\alpha; \tau_{j',j}) dR'_\alpha dR_\alpha d\mathbf{r}_{M\alpha} d\mathbf{r}_{I\alpha}. \quad (11)$$

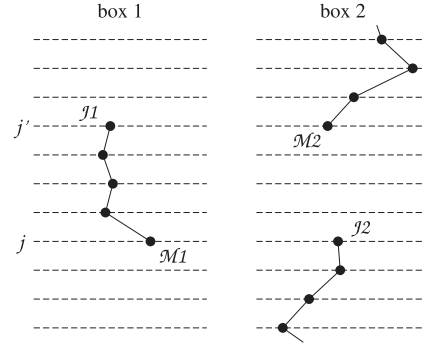


FIG. 1. Schematic illustration of open WLs in the G sector.

Here, the pair $\{R_\alpha, \mathbf{r}_{M\alpha}\}$ indicates the coordinates of Masha and of all the other particles of box α at time index j (the first argument of F_α) and $\{R'_\alpha, \mathbf{r}_{I\alpha}\}$ the coordinates of Ira and of the other particles at j' . The argument $\tau_{j,j'}$ of the density matrices ρ is the positive interval from $j\epsilon$ to $j'\epsilon$ – possibly wrapping around the periodic boundary condition, i.e., $\tau_{j,j'} = [(j' - j + K) \text{mod } K] \epsilon$. Finally, the density matrices are expanded in discretized path integrals using the high temperature approximation $\tilde{\rho}$ as in Sec. III A.

The probability density for all the coordinates X in the system, the number N_1 and the volume Ω_1 is¹³

$$P_{N,\Omega,T}(X) \propto C^{\delta_G} \prod_{j=1}^K \tilde{\rho}(X_{j-1}, X_j; \epsilon), \quad (12)$$

where δ_G is 1 (0) in the G (Z) sector, X_j indicates the positions of all the particles in either box at time $j\epsilon$, and the dependence on N_1 and Ω_1 , as well as all possible permutations of particle labels, are implicitly contained in the configuration X . No sums over permutations appear in P because the symmetrizations of Eq. (11) or (4) are carried out concurrently with the Monte Carlo integration over the coordinates, through updates of the permutation cycles.

We next describe a set of moves which sample the configuration space with probability density $P_{N,\Omega,T}(X)$. They are the standard moves of PIMC and the WA, in some cases combined in pairs to preserve the two-worm structure of the G sector illustrated in Fig. 1, and the volume change move specific of the GEMC method; the particles exchange move of GEMC builds spontaneously through a sequence of WA moves. The acceptance probabilities are obtained by enforcing detailed balance according to the generalized Metropolis algorithm¹² (if the current configuration is in a sector where the proposed move is not applicable, the move is rejected immediately).

(1a) *Open-insert*. This move, schematically illustrated in Fig. 2, is applicable only in the Z sector. It switches from the Z to the G sector by opening an existing closed WL in one box and inserting a new open WL in the other box. A particle is picked randomly, and the links of its WL from j to $j + M$ are removed. The time index j is uniformly sampled in $[1, K]$, and the number of removed links M is uniformly sampled in $[1, \bar{M}]$, where $\bar{M} < K$ is a parameter of the simulation which

114110-4 R. Fantoni and S. Moroni

J. Chem. Phys. **141**, 114110 (2014)

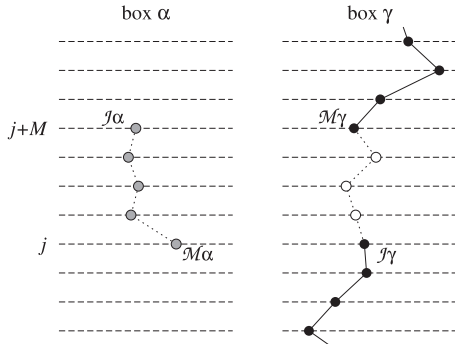


FIG. 2. Schematic illustration of the open-insert move. Two worms are created by removing the white beads and inserting the grey beads.

controls the size of the move. Let α be the label of the other box. The initial bead $\mathbf{r}_{M\alpha,j}$ of the new WL is placed at a position \mathbf{r}_0 randomly sampled in Ω_α , and M further beads are sampled from $\prod_{v=1}^M \rho_0(\mathbf{r}_{v-1}, \mathbf{r}_v; \epsilon)$, where

$$\rho_0(\mathbf{r}, \mathbf{r}'; \epsilon) = (4\pi\lambda\epsilon)^{-d/2} e^{-\frac{(\mathbf{r}-\mathbf{r}')^2}{4\lambda\epsilon}} \quad (13)$$

is the one-particle free propagator. The acceptance probability is $p_{\text{op-in}} = \min\{1, e^{\Delta_U} \pi_{\text{op-in}}\}$, where

$$\pi_{\text{op-in}} = \frac{C M K \Omega_\alpha N}{2 \rho_0(\mathbf{r}_{T\gamma}, \mathbf{r}_{M\gamma}; M\epsilon)} \quad (14)$$

and $\Delta_U = \sum_{v=1}^M [U(X_{v-1}, X_v; \epsilon) - U(X_{v-1}^*, X_v^*; \epsilon)]$ is the change of the interacting part of the action U between the initial configuration X and the proposed configuration X^* .

(1b) *Close-remove* is the complementary move of *open-insert*. A box – say γ – is selected at random. If $M = \tau_{T\gamma, M\gamma}/\epsilon > \bar{M}$, the move is rejected. Otherwise, a WL of M links connecting $\mathbf{r}_0 = \mathbf{r}_{T\gamma}$ to $\mathbf{r}_M = \mathbf{r}_{M\gamma}$ is sampled from $\prod_{v=1}^M \rho_0(\mathbf{r}_{v-1}, \mathbf{r}_v; \epsilon)$. If the open WL in the other box contains more than \bar{M} links the move is rejected, otherwise the worm is removed. The acceptance probability is $p_{\text{cl-rm}} = \min\{1, e^{\Delta_U}/\pi_{\text{op-in}}\}$.

(2) *Advance-recede*. This move is self-complementary, as are all the remaining moves. It applies only to the G sector, and we refer to Fig. 1 for a representation of the initial configuration. A box – say γ – is selected at random. An integer M is uniformly sampled in $[1, \bar{M}]$ and a time direction is selected at random. If the time direction is positive, a new portion of WL sampled from a product of M free-particle propagators is added in box γ starting from $\mathbf{r}_{T\gamma}$, and a corresponding, M -link portion of the open WL existing in box α is removed, starting from $\mathbf{r}_{M\alpha}$. If the time direction is negative, the new portion of WL is added in box γ starting from $\mathbf{r}_{M\gamma}$ and going backwards in time, and the WL in box α is shortened starting from $\mathbf{r}_{T\alpha}$. The move is rejected if $M \geq \tau_{T\gamma, M\gamma}/\epsilon$ (this restriction could be avoided using more elaborate combinations of the WA moves). The acceptance probability of *advance-recede* is $p_{\text{ad-re}} = \min\{1, e^{\Delta_U}\}$.

(3) *Swap*. This move applies only to the G sector. A box is selected at random, and within the chosen box the move proceeds in the same way as in the WA.⁶

(4) *Volume change*. We choose to apply this move only to configurations of the Z sector. For the classical GEMC update of the volumes, it proves convenient to make the dependence on N_1 and Ω_1 explicit. This is achieved¹² by rescaling all lengths in box α by $\Omega_\alpha^{-1/d}$ and formally performing the Monte Carlo integration over the rescaled coordinates $\Xi(X)$. Furthermore, the move is usually implemented¹² by changing the quantity $\ln(\Omega_1/\Omega_2)$, rather than Ω_1 itself, by an amount uniformly sampled in $[-\Delta_\Omega, \Delta_\Omega]$ with Δ_Ω a parameter which controls the size of the move. A factor $\Omega_1^{N_1} \Omega_2^{N_2}$ appears in $P_{N, \Omega, T}$ as a result of rescaling the coordinates, and another factor $\Omega_1 \Omega_2$ as a result of updating the logarithm of the volume (cf. Eq. (2)). In the quantum case, we adopt the same changes of variables. Since each particle is mapped onto K beads, each of which gets rescaled coordinates, the probability density is

$$P_{N, \Omega, T}(\Xi, N_1, \Omega_1) \propto \Omega_1^{KN_1+1} \Omega_2^{KN_2+1} \times \prod_j \tilde{\rho}(X_{j-1}(\Xi), X_j(\Xi); \epsilon). \quad (15)$$

The acceptance probability for a move from Ω_1 to Ω_2^* is

$$p_{\text{vol}} = \min \left\{ 1, \left(\frac{\Omega_2^*}{\Omega_1} \right)^{KN_1+1} \left(\frac{\Omega_2^*}{\Omega_2} \right)^{KN_2+1} e^{\Delta_S} \right\}, \quad (16)$$

where Δ_S is the change of the *full* action between the initial configuration X and the proposed configuration X^*

$$\Delta_S = - \sum_{v=1}^K \ln[\tilde{\rho}(X_{v-1}, X_v; \epsilon)/\tilde{\rho}(X_{v-1}^*, X_v^*; \epsilon)]. \quad (17)$$

The proposed configuration is $X^* = (\Omega_\alpha^*/\Omega_\alpha)^{1/d} X$, with $\alpha = 1$ or 2 as appropriate to the particle index of each component of X . Hence, both the equal-time interparticle distances, $|\mathbf{r}_{i,j} - \mathbf{r}_{k,j}|$, and the single-particle displacements along the WL, $|\mathbf{r}_{i,j-1} - \mathbf{r}_{i,j}|$, are modified upon volume changes. This prescription departs from that recommended for classical systems of composite particles,¹² where only the center of mass follows the variation of the volume while the internal structure remains unchanged (in the quantum analogue, only the centroid of each ring polymer would change while the size and shape of the polymers would stay fixed¹¹). The reason for the prescription chosen here is that for polymers interlinked through permutation cycles the equal-time interparticle distance and the single-particle paths are not independent.

In our implementation, we also include moves which *wiggle* an existing portion of a WL, or *displace* the whole WL of a particle. These moves are standard in PIMC⁴ and since they are not strictly needed for the QGEMC we do not describe them here.

IV. TWO-DIMENSIONAL ⁴He

The phase diagram of ⁴He in two dimensions has been studied in Ref. 14 by PIMC simulations of individual phases

114110-5 R. Fantoni and S. Moroni

J. Chem. Phys. **141**, 114110 (2014)

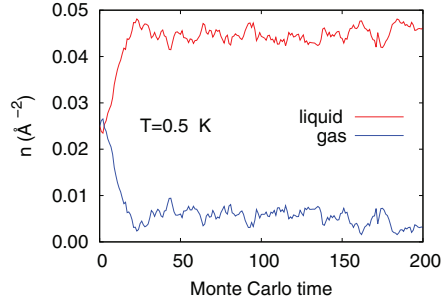


FIG. 3. Data trace of the densities of the gas (blue) and the liquid (red) in the initial stages of the simulation for $T = 0.5$ K.

for many values of density and temperature. A gas-liquid coexistence region is found below 0.87 K. At these temperatures, on account of the large De Boer parameter of ^4He , $\Lambda = 0.429$,⁹ quantum exchange of particles is an important effect:^{4,8} in the thermodynamic limit the normal-superfluid transition temperature at saturated vapour pressure is 0.65 K,⁶ and for finite systems of a few hundred particles the superfluid fraction is non-zero even for $T = 1$ K. Therefore, the gas-liquid coexistence of two-dimensional ^4He is a telling test of the QGEMC algorithm for a degenerate quantum system. An application to a square well model and ^4He in three dimensions has also appeared.¹⁵

We simulate a two-dimensional system of $N = 64$ ^4He atoms distributed between two square boxes with periodic boundary conditions. Within each box, the atoms interact with the HFDHE2 pair potential.¹⁶ We use the primitive approximation

$$\tilde{\rho}(R, R'; \epsilon) = \rho_F(R, R'; \epsilon) e^{-\epsilon[V(R)+V(R')]/2} \quad (18)$$

to the high temperature density matrix, with $\epsilon = 0.002 \text{ K}^{-1}$. The acceptance rate of the moves can be varied by tuning the relevant parameters. In this calculation, we set $\bar{M} = 125$, with acceptances between 35% and 75% for the close-remove, advance-recede, swap and wiggle moves, but only a few percent for the open-insert move. The acceptances of the volume move are between 20% and 40% with $\Delta_\Omega = 10^{-2}$, across the

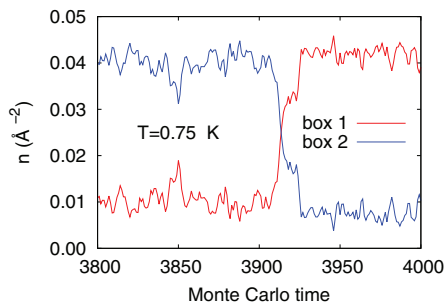


FIG. 4. A portion of the data trace of the densities for the simulation at $T = 0.75$ K, showing an exchange of identity between the two boxes.

TABLE I. The densities n_g and n_l of the coexisting gas and liquid phases as a function of the temperature T .

T (K)	n_g (\AA^{-2})	n_l (\AA^{-2})
	This work	
0.125	$< 10^{-6}$	0.0422(2)
0.250	0.0009(2)	0.0424(4)
0.500	0.0016(2)	0.0416(4)
0.750	0.0106(6)	0.0396(7)
0.875	0.0209(9)	0.0343(10)
	Ref. 14	
0.250	0.000(2)	0.044(2)
0.500	0.000(2)	0.044(2)
0.750	0.009(2)	0.043(2)
0.860	0.020(2)	0.030(2)

whole temperature range. We also adjust the parameter C to maintain the fraction of configurations in the Z sector between 0.15 and 0.55. In principle, a different value of \bar{M} should be used for each move, and all these parameters, as well as the relative frequency of the moves, should be optimized by maximizing the efficiency. We study the temperature range between 0.125 K and 1 K. For each temperature, the simulation starts from a configuration with boxes of equal volume containing 32 atoms each at a density 0.025 \AA^{-2} .

After equilibration, deep in the subcritical temperature regime one of the boxes contains a gas of very low density n_g , and the other a superfluid liquid with a density n_l close to the equilibrium density of the system at $T = 0$ (see Fig. 3). For temperatures closer to the critical point, n_g and n_l approach each other, and we frequently observe that the two boxes exchange identity, i.e., the phase of the system in each box switches back and forth between gas and liquid (see Fig. 4). In this case, the density has a bimodal distribution peaked at the values n_g and n_l of the coexisting phases. This bimodal distribution can be obtained in a grand canonical simulation of a single box, but this requires a fine tuning of the chemical potential.¹⁷ For $T = 1$ K, the two peaks merge into a single gaussian centered at the average density 0.025 \AA^{-2} .

Our results for the densities n_g and n_l of the coexisting phases are listed in Table I and displayed in Fig. 5. They compare favorably with the results of Ref. 14. For each T ,

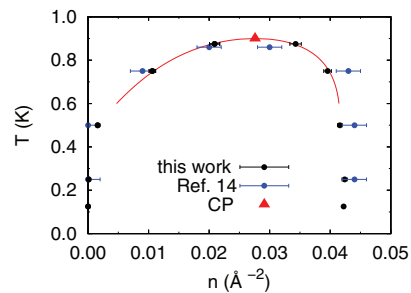


FIG. 5. The binodal line of ^4He in two dimensions. Black points: QGEMC. Blue points: Ref. 14. Red line: extrapolation of the QGEMC results to the critical point (red triangle).

114110-6 R. Fantoni and S. Moroni

J. Chem. Phys. **141**, 114110 (2014)TABLE II. The superfluid fraction n_s in the coexisting gas and liquid phases as a function of T .

T (K)	n_s	
	Gas	Liquid
1.000		0.032(1)
0.875	0.14(3)	0.36(2)
0.750	0.06(3)	0.63(3)
0.500	0.0014(5)	0.938(7)
0.250	$< 10^{-3}$	0.963(10)
0.125	0	0.985(16)

latter are obtained from an integral of the isothermal pressure calculated in the canonical ensemble for several values of the density across the coexistence region; the QGEMC method is simpler because n_g and n_l are obtained with a single simulation, either directly or via the analysis of a bimodal distribution. Each of the present QGEMC calculations took ~ 300 CPU hours on a 2 GHz processor. If needed, the efficiency could be significantly improved using a better approximation to the high temperature density matrix.⁴

The boundary of the gas-liquid coexistence region is called the binodal line. It can be extrapolated to the critical point (CP) using the law of “rectilinear diameters,”¹⁸ $\rho_l + \rho_g = 2\rho_c + a|T - T_c|$, and the expansion¹⁹ $\rho_l - \rho_g = b|T - T_c|^{\beta_1}(|T - T_c| + c)^{\beta_0 - \beta_1}$. Here, $\beta_1 = 1/2$ and $\beta_0 = 1/8$, while ρ_c , T_c , a , b , and c are fitting parameters. We find $\rho_c = 0.028 \text{ \AA}^{-2}$ and $T_c = 0.90 \text{ K}$.

Finally, we list in Table II the winding number estimator⁸ of the superfluid fraction n_s for the two phases as a function of the temperature. A non-zero value on the liquid branch of the binodal over the full range of temperatures considered is a clear indication of the importance of quantum exchanges. On the gas branch of the binodal a finite superfluid fraction also appears, but only at $T \gtrsim 0.5 \text{ K}$, where the density begins to increase significantly entailing a corresponding increase of the degeneracy temperature (although, as mentioned, a finite value of n_s for $T > 0.65 \text{ K}$ is a finite size effect⁶).

V. CONCLUSIONS

We have presented the QGEMC method, a full quantum extension of classical Gibbs Ensemble Monte Carlo based

on the Worm Algorithm. The method is demonstrated for the binodal of ^4He in two dimensions, a physical property of a strongly quantum system in the degenerate temperature regime. Good agreement is found with the results of previous PIMC simulations in the canonical ensemble. In analogy with applications of GEMC to classical fluids,^{20–22} the QGEMC method offers a convenient approach for problems such as gas-liquid coexistence in quantum systems and phase equilibria in quantum mixtures.

ACKNOWLEDGMENTS

We are grateful to M. E. Fisher for correspondence and helpful comments.

- ¹M. H. Kalos and P. A. Whitlock, *Monte Carlo Methods* (Wiley-VCH Verlag GmbH & Co. KGaA, Weinheim, 2008).
- ²A. Z. Panagiotopoulos, *Mol. Phys.* **61**, 813 (1987); B. Smit, Ph. De Smedt, and D. Frenkel, *ibid.* **68**, 931 (1989); B. Smit and D. Frenkel, *ibid.* **68**, 951 (1989).
- ³R. P. Feynman, *Rev. Mod. Phys.* **20**, 367 (1948).
- ⁴D. M. Ceperley, *Rev. Mod. Phys.* **67**, 279 (1995).
- ⁵D. M. Ceperley, *J. Stat. Phys.* **63**, 1237 (1991).
- ⁶M. Boninsegni, N. V. Prokof'ev, and B. V. Svistunov, *Phys. Rev. Lett.* **96**, 070601 (2006); *Phys. Rev. E* **74**, 03670 (2006).
- ⁷N. V. Prokof'ev, B. V. Svistunov, and I. S. Tupitsyn, *Phys. Lett. A* **238**, 253 (1998); *JETP* **87**, 310 (1998).
- ⁸E. L. Pollock and D. M. Ceperley, *Phys. Rev. B* **36**, 8343 (1987).
- ⁹R. A. Young, *Phys. Rev. Lett.* **45**, 638 (1980).
- ¹⁰F. Schneider, D. Marx, and P. Nielaba, *Phys. Rev. E* **51**, 5162 (1995); P. Nielaba, *Int. J. Thermophys.* **17**, 157 (1996).
- ¹¹Q. Wang and J. K. Johnson, *Fluid Phase Equilib.* **132**, 93 (1997); I. Georgescu, S. E. Brown, and V. A. Mandelshtam, *J. Chem. Phys.* **138**, 134502 (2013); P. Kowalczyk, P. A. Gauden, A. P. Terzyk, E. Pantatosaki, and G. K. Papadopoulos, *J. Chem. Theory Comput.* **9**, 2922 (2013).
- ¹²D. Frenkel and B. Smit, *Understanding Molecular Simulation* (Academic Press, San Diego, 1996), Appendix G.
- ¹³The link density matrix $\tilde{\rho}(X, X'; \epsilon)$ of the whole system is the product $\tilde{\rho}(R_\alpha, R'_\alpha; \epsilon)\tilde{\rho}(R_\beta, R'_\beta; \epsilon)$ over the two boxes; particle labels are only permuted within each box.
- ¹⁴M. C. Gordillo and D. M. Ceperley, *Phys. Rev. B* **58**, 6447 (1998).
- ¹⁵R. Fantoni, *Phys. Rev. E* **90**, 020102(R) (2014).
- ¹⁶R. A. Aziz, V. P. S. Nain, J. S. Carley, W. L. Taylor, and G. T. McConville, *J. Chem. Phys.* **70**, 4330 (1979).
- ¹⁷N. B. Wilding, *Phys. Rev. E* **52**, 602 (1995).
- ¹⁸E. A. Guggenheim, *J. Chem. Phys.* **13**, 253 (1945).
- ¹⁹M. E. Fisher, *Phys. Rev. Lett.* **16**, 11 (1966).
- ²⁰R. Fantoni, A. Malijevský, A. Santos, and A. Giacometti, *Europhys. Lett.* **93**, 26002 (2011).
- ²¹R. Fantoni, A. Giacometti, M. A. G. Maestre, and A. Santos, *J. Chem. Phys.* **139**, 174902 (2013).
- ²²R. Fantoni and G. Pastore, *Phys. Rev. E* **87**, 052303 (2013).

Part XV
2015

Chapter 45

Wertheim perturbation theory: thermodynamics and structure of patchy colloids

Fantoni R. and Pastore G., Mol. Phys. **113**, 2593 (2015)

Title: “Wertheim perturbation theory: thermodynamics and structure of patchy colloids”

Abstract: We critically discuss the application of the Wertheim’s theory to classes of complex associating fluids that can be today engineered in the laboratory as patchy colloids and to the prediction of their peculiar gas-liquid phase diagrams. Our systematic study, stemming from perturbative version of the theory, allows us to show that, even at the simplest level of approximation for the inter-cluster correlations, the theory is still able to provide a consistent and stable picture of the behavior of interesting models of self-assembling colloidal suspension. We extend the analysis of a few cases of patchy systems recently introduced in the literature. In particular, we discuss for the first time in detail the consistency of the structural description underlying the perturbative approach and we are able to prove a consistency relationship between the valence as obtained from thermodynamics and from the structure for the one-site case. A simple analytical expression for the structure factor is proposed.

SPECIAL ISSUE IN HONOUR OF JEAN-PIERRE HANSEN

Wertheim perturbation theory: thermodynamics and structure of patchy colloids

Riccardo Fantoni^a and Giorgio Pastore^{b,*}

^aDipartimento di Scienze Molecolari e Nanosistemi, Università Ca' Foscari Venezia, Venezia, Italy; ^bDipartimento di Fisica, Università di Trieste, Trieste, Italy

(Received 30 January 2015; accepted 25 May 2015)

We critically discuss the application of the Wertheim's theory to classes of complex associating fluids that can be today engineered in the laboratory as patchy colloids and to the prediction of their peculiar gas–liquid phase diagrams. Our systematic study, stemming from perturbative version of the theory, allows us to show that, even at the simplest level of approximation for the inter-cluster correlations, the theory is still able to provide a consistent and stable picture of the behaviour of interesting models of self-assembling colloidal suspension. We extend the analysis of a few cases of patchy systems recently introduced in the literature. In particular, we discuss for the first time in detail the consistency of the structural description underlying the perturbative approach and we are able to prove a consistency relationship between the valence as obtained from thermodynamics and from the structure for the one-site case. A simple analytical expression for the structure factor is proposed.

Keywords: colloidal suspensions; Wertheim thermodynamic perturbation theory; associating fluids; structure of fluids

1. Introduction

Recently, there have been interesting developments of techniques for the synthesis of new colloidal patchy particles in the laboratory [1], including seeded growth, swelling, and phase separation. Whereas in the laboratory, relatively less work has been done on the thermodynamic characterisation of self-assembly of these particles, from a theoretical point of view, or in recent computer experiments, these kind of associating fluids [2] and their clustering and phase behaviour are actively studied [3–9].

In principle, statistical mechanics should be able to describe all equilibrium phases. However, the strong and confined attractions responsible of association call for a more clever approach than brute force. In particular, it has been found useful to describe an associating fluid as one where there are n_c species of clusters made of a number i of particles, denoted i -mers. Many definitions of cluster are possible [10–15] either of a geometric nature or of a topological one, depending on the spatial arrangement of the bonded particles. If we measure the concentrations of the i -mers in an associating fluid, we will find that they are functions of the thermodynamic state: for one-component systems, the temperature T and the density ρ of the fluid. Then, special statistical mechanics approaches have been developed to obtain such information and phase diagrams from models of interactions.

In our previous work [2], we compared two theories for cluster equilibria, the Wertheim association theory [16–19]

and the Bjerrum-Tani-Henderson theory [20–26] and we showed that for $n_c = 2$, the two approaches coincide when inter-cluster correlation are ignored, i.e. the system behaves as an ideal gas of clusters. Nonetheless, the simple and elegant perturbation theory described in Wertheim's work is able, unlike the one of Bjerrum-Tani-Henderson, to describe the case of $n_c \rightarrow \infty$ fluids. Due to this fact, Wertheim theory is able to describe the liquid phase, thus giving access to the study of liquid–gas coexistence in a coherent way, while the Bjerrum-Tani-Henderson one is not. The first order in the Wertheim perturbation theory approximation is a simple but very useful tool. At high temperature, the associating fluid reduces to the 'reference' fluid that can also be considered as the one obtained from the associating fluid switching off all attractions. However, in its original form, the theory is only applicable when some 'steric incompatibility' conditions are fulfilled by the associating fluid: a single bond per site, no more than one bond between any two particles, and no closed loop, or ring, of bonds.

Patchy colloids are systems of current experimental and theoretical [1,27] interest. Simple models for their interactions, for example fluids of hard-spheres (HSs) decorated with attractive sites distributed on their surface, are well suited for application of Wertheim theory. For particles with M identical bonding sites, Bianchi *et al.* [3–5] discovered the 'empty liquid' scenario as M approaches two, i.e. when the clusters allowed in the fluid are just the 'chains'. Even more rich phenomenology is found when there are

* Corresponding author. Email: pastore@ts.infn.it

sites of two different kinds [6,7] and ‘junctions’ formation becomes possible. Such structures become responsible for a re-entrance of the liquid branch of the binodal, and for ‘rings’ formation [8,9]. Moreover, extending Wertheim theory beyond its steric incompatibility conditions, the rings formation has been found to be responsible for a re-entrance also in the gas branch and the appearance of a second lower critical point (recently appeared studies which further extend Wertheim theory to allow also for doubly bonded sites [28–30]). From all these studies emerged how Wertheim theory has very good semi-quantitative agreement with exact Monte Carlo (MC) simulations, when applied to these one-component patchy particle fluids (especially so at the level of the clusters concentrations behavior). Far from being a purely theoretical speculation, these fluids can be engineered in the laboratory [1] from patchy colloids.

In the present work, while critically reviewing such theoretical results, in particular elucidating the role of the accuracy of inter cluster correlations, we will discuss the solution of the Wertheim theory applied to HSs with M identical bonding sites and with sites of two different kinds. Our analysis is intended to be as simple and systematic as possible while re-analysing the many works found in the literature on various particular highly idealised associating colloidal suspension models. This will allow us to treat the ring forming systems of Rovigatti *et al.* [8,9] fully analytically as freely jointed chains. We show that also the results in Ref. [31], extending Russo *et al.* [6,7] results to take into account the ‘X-junctions’ formation, and in particular, the existence of characteristic ‘R’-shaped spinodals, are largely independent on the choice of the reference system correlations. Moreover, we find the indication of a gas–liquid coexistence with a critical point at extremely low densities and temperatures at $r < 1/3$, with r the ratio between the gain in energy between the bond of two unlike sites and the one between two like sites.

We also study in detail the relationship between structural and thermodynamic information within Wertheim theory, and in particular between the effective valence as obtained from the thermodynamics and from the structure.

The paper is organised as follows: in Section 2, we introduce the thermodynamic quantities we will take under consideration in the rest of the work; in Section 3, we will review Wertheim association theory in the light of the present work needs, the problem of identical attractive site (Section 3.1.2), and the problem of attractive sites of two different kinds (Section 3.1.3); in Section 3.2, we introduce the problem of the gas–liquid coexistence; in Section 3.3, we comment on the relevance of the pair-potential microscopic level of description; and in Section 4, we systematically re-analyse many results obtained applying Wertheim theory to specific fluids with identical sites (Section 4.1) and sites of two different kinds (Section 4.2). We show, in a systematic way, that all the results present in the literature are structurally stable with respect

to changes in the reference system accuracy; in Section 6, we determine a simple analytical expression for the radial distribution function which we then use to calculate the valence; in Section 7, we determine a simple analytical expression for the structure factor; and Section 8 is for final remarks.

2. Thermodynamics

Consider a one-component fluid of N associating HS particles in a volume V at an absolute temperature $T = 1/\beta k_B$ with k_B Boltzmann constant.

The Helmholtz free energy A of a HS associating fluid can be written as a sum of separate contributions [32]

$$A = A_0 + A_{mf} + A_{\text{bond}}, \quad (1)$$

where A_0 is the free energy of a HS fluid at a density $\rho = N/V$, A_{mf} is the mean-field contribution due to the dispersion forces, and A_{bond} is the change in the free energy due to association. We will generally use the notation $a(\rho, T) = A/N$ for the free energy per particle.

The HS free energy per particle in excess of the ideal gas one is accurately given by the Carnahan and Starling expression [33]

$$\beta a_0^{\text{ex}} = \frac{4\eta - 3\eta^2}{(1 - \eta)^2}, \quad (2)$$

where $\eta = (\pi/6)\rho\sigma^3$ is the packing fraction of the HSs of diameter σ . So that adding the ideal gas contribution $\beta a_{id} = \ln(\rho\Lambda^3/e)$, with Λ the de Broglie thermal wavelength, we obtain $a_0 = a_{id} + a_0^{\text{ex}}$.

The mean-field contribution has the van der Waals form

$$\beta a_{mf} = -\frac{\epsilon_{mf}\rho}{k_B T}, \quad (3)$$

where the constant ϵ_{mf} is the measure of the strength of the mean-field attractions. The addition of this contribution to A_0 is essential to have a gas–liquid coexistence.

From a microscopic point of view, one can see, for example, the mean-field contribution as arising from the first order in β in a high-temperature expansion of a thermodynamic perturbation theory treatment of the square-well (SW) fluid, with the HS taken as the reference system. So, the free energy of the corresponding associating fluid will be given by $A = A_{SW} + A_{\text{bond}}$. But, as we will see in Section 4, one can have gas–liquid coexistence with just $A = A_0 + A_{\text{bond}}$ for a properly chosen A_{bond} .

We can define a unit of length, \mathcal{S} , and a unit of energy, \mathcal{E} , so that we can introduce a reduced density, $\rho^* = \rho\mathcal{S}^3$, and a reduced temperature, $T^* = k_B T/\mathcal{E}$.

The association contribution A_{bond} will be discussed in the next section.

3. Associating fluids

We recall here the main result of Wertheim association theory [16–19]. We write the bond free energy per particle a_{bond} such that the full free energy per particle of the associating fluid can be written as $a = a_0 + a_{\text{bond}}$, where a_0 is the contribution of the reference fluid, the one obtained from the associating fluid setting to zero all the bonding attractions. We discuss the importance of the choice of a proper pair-potential for the fulfillment of the steric incompatibility conditions in the microscopic description of the fluid. And we discuss the problem of the determination of the gas–liquid coexistence line (the binodal) in our one-component fluid.

3.1. Wertheim statistical thermodynamic theory

In Wertheim theory [16–19], one assumes that each HS of the one-component fluid is decorated with a set Γ of M attractive sites. Under the assumptions of: (1) a single bond per site, (2) no more than one bond between any two particles, and (3) no closed loop, or ring, of bonds, one can write in a first-order thermodynamic perturbation theory framework, valid at reasonably high temperatures,

$$\beta a_{\text{bond}}^W = \sum_{\alpha \in \Gamma} \left(\ln x_\alpha - \frac{x_\alpha}{2} \right) + \frac{M}{2}, \quad (4)$$

where $x_\alpha = N_\alpha/N$ is the fraction of sites α that are not bonded. We will also introduce the symbol x_i to denote the concentration of clusters made of a number i of particles. We will always use a Greek index to denote a specific site. We can solve for the x_α from the ‘law of mass action’

$$x_\alpha = \frac{1}{1 + \rho \sum_{\beta \in \Gamma} x_\beta \Delta_{\alpha\beta}}, \quad \alpha \in \Gamma \quad (5)$$

where the probability to form a bond, once the available sites of the two particles are chosen, is given by $\rho \Delta_{\alpha\beta} = \rho \Delta_{\beta\alpha}$ and approximated as

$$\Delta_{\alpha\beta} = \int g_0(r_{12}) \langle f_{\alpha\beta}(12) \rangle_{\Omega_1, \Omega_2} d\mathbf{r}_{12}. \quad (6)$$

Here, g_0 is the radial distribution function of the reference system, $f_{\alpha\beta}$ is the Mayer function between site α on particle 1 and site β on particle 2 (see Section 3.3), and $\langle \dots \rangle_{\Omega_1, \Omega_2}$ denotes an angular average over all orientations of particles 1 and 2 at a fixed relative distance r_{12} . Equation (5) should be solved for the real physically relevant solution such that $\lim_{\rho \rightarrow 0} x_\alpha = 1$. Even if we cannot exclude the possibility of having multiple solutions satisfying to this condition, we never encountered such a case in the present work. Clearly, we cannot assign any physical value to the branches with $x_\alpha \notin [0, 1]$.

At high temperatures $\Delta_{\alpha\beta} \rightarrow 0$ and $x_\alpha \rightarrow 1$, which means we have complete dissociation. At low temperatures (Wertheim theory is a high-temperature expansion but here we just mean the formal low T limit of the first-order Wertheim results) $\Delta_{\alpha\beta} \rightarrow \infty$ and $x_\alpha \rightarrow 0$, which means that we have complete association.

The number of attractive sites controls the physical behaviour. Models with one site allow only dimerisation. The presence of two sites permits the formation of chain and ring polymers. Additional sites allow formation of branched polymers and amorphous systems.

3.1.1. One attractive site

The case of a single attractive site was carefully considered in our previous work [2] where a comparison between the Wertheim theory and the Bjerrum-Tani-Henderson theory [20–26] was made.

3.1.2. Identical attractive sites

Another simple case we can consider in Wertheim theory is the one with M identical attractive sites of kind A (we will always use a capital letter to denote a site kind). Now, the law of mass action for $x = x_A$ (the fraction of unbonded specific sites of kind A) is solved by

$$x = \frac{2}{1 + \sqrt{1 + 4M\rho\Delta}}, \quad (7)$$

with $\Delta = \Delta_{AA}$.

The free energy contribution due to association is now given by

$$\beta a_{\text{bond}}^W = M(\ln x - x/2) + M/2. \quad (8)$$

In this case, $x_1 = x^M$.

3.1.3. Attractive sites of two kinds

A more complex case in Wertheim theory is the one with M_A identical attractive sites of kind A and M_B identical attractive sites of kind B . Now, the law of mass action reduces to the following system of two coupled quadratic equations

$$x_A + M_A \rho \Delta_{AA} x_A^2 + M_B \rho \Delta_{AB} x_A x_B = 1, \quad (9)$$

$$x_B + M_B \rho \Delta_{BB} x_B^2 + M_A \rho \Delta_{AB} x_A x_B = 1, \quad (10)$$

which admits in general a set of four different solutions for (x_A, x_B) from which it is necessary to single out the physically relevant one. In the event that there is no attraction between a site of kind A and a site of kind B , then $\Delta_{AB} = 0$ and the system simplifies to

4

R. Fantoni and G. Pastore

$$x_A = \frac{2}{1 + \sqrt{1 + 4M_A\rho\Delta_{AA}}}, \quad (11)$$

$$x_B = \frac{2}{1 + \sqrt{1 + 4M_B\rho\Delta_{BB}}}. \quad (12)$$

In the event that there is no attraction between sites of the same kind, it simplifies to

$$x_A = 2/\{1 + (M_B - M_A)\rho\Delta_{AB} + \sqrt{[1 + (M_B - M_A)\rho\Delta_{AB}]^2 + 4M_A\rho\Delta_{AB}}\}, \quad (13)$$

and x_B obtained exchanging $A \leftrightarrow B$ in the equation above.

The free energy contribution due to association is now given by

$$\beta a_{\text{bond}}^W = M_A(\ln x_A - x_A/2) + M_A/2 + M_B(\ln x_B - x_B/2) + M_B/2. \quad (14)$$

In this case, $x_1 = x_A^{M_A} x_B^{M_B}$.

3.2. The gas–liquid coexistence

In order to determine the gas–liquid coexistence line (the binodal), one needs to find the compressibility factor $z = \beta p/\rho$, with p the pressure, and the chemical potential μ of the associating fluid according to the thermodynamic relations

$$z(\rho, T) = \rho \left(\frac{\partial \beta a}{\partial \rho} \right)_{T,N}, \quad (15)$$

$$\beta \mu(\rho, T) = \left(\frac{\partial \beta a \rho}{\partial \rho} \right)_{T,V} = z + \beta a. \quad (16)$$

The coexistence line is then given by the Gibbs equilibrium condition of equality of the pressures and chemical potentials of the two phases

$$\rho_g z(\rho_g, T) = \rho_l z(\rho_l, T), \quad (17)$$

$$\beta \mu(\rho_g, T) = \beta \mu(\rho_l, T), \quad (18)$$

from which one can find the coexistence density of the gas $\rho_g(T)$ and of the liquid $\rho_l(T)$ phases.

The critical point (ρ_c, T_c) is determined by solving the following system of equations

$$\left. \frac{\partial z \rho}{\partial \rho} \right|_{\rho_c, T_c} = 0, \quad (19)$$

$$\left. \frac{\partial^2 z \rho}{\partial \rho^2} \right|_{\rho_c, T_c} = 0. \quad (20)$$

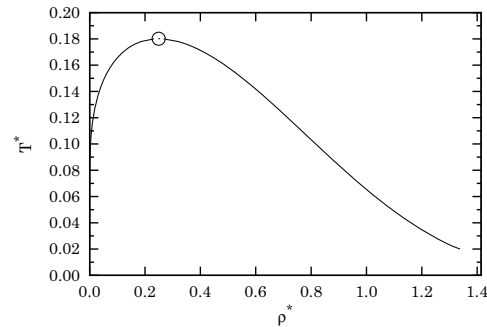


Figure 1. Gas–liquid binodal for the HS plus the van der Waals mean-field term. The circle is the critical point at $\rho_c^* \approx 0.249129$, $T_c^* \approx 0.180155$, and $z_c \approx 0.358956$ [34].

3.2.1. The mean-field case

For the HS fluid in the presence of just a van der Waals mean-field free energy contribution, described by Equation (1) without the last association term, the thermodynamics is parameter free. We take the diameter of the spheres σ as the unit of length (so that $\rho^* \in [0, \sqrt{2}]$ with $\sqrt{2}$ the close-packing reduced density) and ϵ_{mf} as the unit of energy. Solving the Gibbs equilibrium conditions of Equations (17) and (18), we find the binodal of Figure 1 and from Equations (19) and (20), we find the critical point.

We can see this case as describing a thermodynamic perturbation theory approximation for a SW fluid to first order in β small [35]. MC simulations of the SW fluid are well known to show a gas–liquid binodal with the critical point shifting at lower temperatures and higher densities as the width of the attractive well decreases [36,37].

Recently [38], it was shown through numerical simulation and theoretical approaches that a binodal with two maxima, implying the existence of a low-density liquid and a high-density liquid, can arise solely from an isotropic interaction potential with an attractive part and with two characteristic short-range repulsive distances.

We consider the binodal of Figure 1 as ‘standard’ in the sense that the gas branch $T_g(\rho)$ is a monotonously increasing function of density and the liquid branch $T_l(\rho)$ a monotonously decreasing function of density. We will see in the next section that using Wertheim association theory, it is possible to obtain non-standard binodals by replacing the mean-field contribution A_{mf} with a proper association contribution A_{bond} .

3.3. Microscopic description: importance of the pair-potential

The fluid is assumed to be made of particles interacting only through a pair-potential $\phi(12) = \phi(\mathbf{r}_1, \Omega_1, \mathbf{r}_2, \Omega_2)$ where \mathbf{r}_i

and Ω_i are the position vector of the centre of particle i and the orientation of particle i , respectively.

To give structure to the fluid, we further assume that the particles have an isotropic hard-core of diameter σ with

$$\phi(12) = \phi_0(r_{12}) + \Phi(12), \quad (21)$$

where $r_{12} = |\mathbf{r}_{12}| = |\mathbf{r}_2 - \mathbf{r}_1|$ is the separation between the two particles 1 and 2 and

$$\phi_0(r) = \begin{cases} +\infty & r \leq \sigma \\ 0 & r > \sigma \end{cases}, \quad (22)$$

The anisotropic part $\Phi(12)$ in Wertheim theory is generally chosen as

$$\Phi(12) = \sum_{\alpha \in \Gamma} \sum_{\beta \in \Gamma} \psi_{\alpha\beta}(r_{\alpha\beta}), \quad (23)$$

where

$$\mathbf{r}_{\alpha\beta} = \mathbf{r}_2 + \mathbf{d}_\beta(\Omega_2) - \mathbf{r}_1 - \mathbf{d}_\alpha(\Omega_1), \quad (24)$$

is the vector connecting site α on particle 1 with site β on particle 2. Here, \mathbf{d}_α is the vector from the particle centre to site α with $d_\alpha < \sigma/2$. The site–site interactions $\psi_{\alpha\beta} \leq 0$ are assumed to be purely attractive. The Mayer functions introduced in Section 3.1 are then defined as $f_{\alpha\beta}(12) = \exp[-\beta\psi_{\alpha\beta}(r_{\alpha\beta})] - 1$.

Wertheim theory depends on the specific form of the site–site potential only through the quantity $\Delta_{\alpha\beta}$ of Equation (6), as long as the three conditions of a single bond per site, no more than one bond between any two particles, and no closed loop of bonds, are satisfied. A common choice, for example, is a SW form

$$\psi_{\alpha\beta}(r) = \begin{cases} -\epsilon_{\alpha\beta} & r \leq d_{\alpha\beta} \\ 0 & r > d_{\alpha\beta} \end{cases}, \quad (25)$$

where $\epsilon_{\alpha\beta} > 0$ are site–site energy scales, the wells depths, and $d_{\alpha\beta}$ are the wells widths. In this case, we must have $d_\alpha + d_\beta > \sigma - d_{\alpha\beta}$, moreover we will have

$$\Delta_{\alpha\beta} = K_{\alpha\beta}(\sigma, d_{\alpha\beta}, \eta)(e^{\beta\epsilon_{\alpha\beta}} - 1). \quad (26)$$

We will also call $\lim_{\rho \rightarrow 0} K_{\alpha\beta} = K_{\alpha\beta}^0$ some purely geometric factors. Remember that $\lim_{\rho \rightarrow 0} g_0(r) = \Theta(r - \sigma)$ with Θ the Heaviside step function.

Another common choice is the Kern–Frenkel patch–patch pair-potential model [39].

4. Structural stability of Wertheim theory

There has recently been some relevant progress on the study of several complex associating fluids through MC simula-

tions and theoretically through the Wertheim theory outlined above. The comparison between the two approaches shows semi-quantitative agreement, between the exact MC results and the approximated theoretical results, at the level of description of clusters concentrations and of gas–liquid binodal. We will here return on some of the systems studied from Bianchi *et al.* [3–5], Russo *et al.* [6,7], and Rovigatti *et al.* [8,9] from a unified perspective, and concentrating ourselves on the structural stability of the Wertheim theory, i.e. we will show that all the qualitative non-standard features of the phase diagrams at a large extent do not depend on the accuracy of description of the reference system.

4.1. Identical sites

The case of HSs with a number M of identical attractive sites in various geometries on the surface of the spherical particle has been studied by Bianchi *et al.* [3–5]. They showed that the properties of the resulting fluid are largely independent from the sites geometry [5]. And the gas–liquid binodal has a liquid branch moving at lower densities as M decreases. In particular, the binodal vanishes for $M \rightarrow 2$, a scenario that they called ‘empty liquid’: the critical temperature $T_c(M)$ and critical density $\rho_c(M)$ are such that $\lim_{M \rightarrow 2} T_c = \bar{T}_c > 0$ and $\lim_{M \rightarrow 2} \rho_c = 0$. There is then the formation of a homogeneous disordered material at small densities below \bar{T}_c , i.e. a stable equilibrium gel. Moreover, in their fluid with $M = 2$, Bianchi *et al.* observed linear ‘chains’ formation: ‘chaining’.

This is quite different from what happens in fluids of Kern and Frenkel patchy HSs varying the patches surface coverages [40]. In Ref. [40], a study of criticality similar to the one of Bianchi was made varying the attractive patch surface coverage χ . As the surface coverage χ vanishes, $\lim_{\chi \rightarrow 0} T_c = \lim_{\chi \rightarrow 0} \rho_c = 0$ was found in such cases.

Liu *et al.* [35] repeated Bianchi study for a system of SWs, instead of HSs as in the Bianchi case, with a number M of identical attractive sites. In their study, the gas–liquid coexistence remains also for $M \rightarrow 0$, as expected in view of the comments of Section 3.2.1.

4.1.1. Gas–liquid binodal

With M identical sites of kind A , we have in the site–site interaction $\epsilon_{AA} = \epsilon$ which we take as unit of energy and again we take σ as unit of length.

We now choose $a = a_0 + a_{\text{bond}}$ with the association part given by the Wertheim theory Equation (4) with M identical sites (see Section 3.1.2).

Following Ref. [4], we choose the identical sites distributed on the surface of the spherical particle and

$$d_{AA} = d = \left(\sqrt{5 - 2\sqrt{3}} - 1 \right) \sigma / 2 \approx 0.120\sigma, \quad (27)$$

which guarantees that each site is engaged at most in one bond. Moreover, we approximate the radial distribution

function of the reference system with its zero density limit taking $\Delta_{AA} = \Delta = K^0[e^{\beta\epsilon} - 1]$ and using, in Equation (26), the following expressions

$$\langle f_{AA}(12) \rangle = (e^{\beta\epsilon} - 1)m_{AA}(r_{12}) \quad r_{12} > \sigma, \quad (28)$$

$$m_{AA}(r) = \begin{cases} \frac{(d + \sigma - r)^2(2d - \sigma + r)}{6r\sigma^2} & \sigma < r < \sigma + d \\ 0 & r > \sigma + d \end{cases}, \quad (29)$$

$$\begin{aligned} K_{AA}^0 &= K^0 = 4\pi \int_{\sigma}^{\sigma+d} m_{AA}(r)r^2 dr \\ &= \pi d^4(15\sigma + 4d)/30\sigma^2 \\ &\approx 0.332 \times 10^{-3} \sigma^3. \end{aligned} \quad (30)$$

In Figure 2, we show the evolution of the gas–liquid binodal as a function of M , the only free parameter in Wertheim thermodynamic perturbation theory. Compared with Figure 4 of Bianchi *et al.* [3], we see how the qualitative behaviour stays the same even if the two figures differ slightly quantitatively due to our further approximation of taking the radial

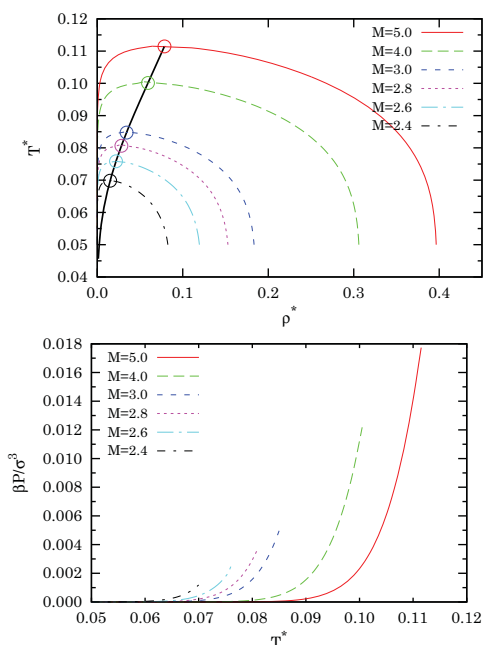


Figure 2. Top panel: evolution of the gas–liquid binodal as a function of M . The continuous thick black line is the locus of the critical points for $M \in [2, 5]$. Bottom panel: pressure–temperature diagram.

distribution of the reference system equal to one in the range where bonding occurs. This shows how the Wertheim theory is robust in its qualitative phase diagram predictions. The binodal appears to be always a standard one. And, as we can see from the figure, upon approaching $M \rightarrow 2$, the coexistence disappears. Bianchi *et al.* [3] called this phenomenon the empty liquid scenario. It in particular tells us that the fluid with $M = 2$, with the two sites chosen at the spherical particle poles in order to avoid the formations of rings (closed loops of bonds), is made only by chains and does not admit a gas–liquid coexistence. The non-integer M cases can be realised through a binary mixture [3,41,42].

From the point of view of Wertheim theory, the reason for this scenario can be explained simply by looking at the low-temperature limit for the bond contribution to the pressure

$$\begin{aligned} \beta P_{\text{bond}}^W &= \rho z_{\text{bond}}^W = \rho^2 \frac{\partial \beta a_{\text{bond}}^W}{\partial \rho} \\ &= -\frac{2M^2 \Delta \rho^2}{(1 + \sqrt{1 + 4M \Delta \rho})^2} \xrightarrow{\Delta \rightarrow \infty} -\frac{M}{2} \rho. \end{aligned} \quad (31)$$

From which immediately follows that for $M > 2$, the pressure as a function of density on a low-temperature isotherm shows a van der Waals loop at low densities, which implies the occurrence of a gas–liquid coexistence region.

4.2. Sites of two kinds

Tavares *et al.* [43,44] studied the case of HS with three sites, two identical A sites at the poles and a third B one. In addition to chaining, here they observe the formation of ‘junctions’: ‘branching’; rings formation is inhibited in these cases since the A sites at the poles have very small well widths and the B site position is chosen so as to avoid small bond loops, i.e. triangular and square arrangements of bonded particles. Two types of junctions are possible in models where AA bonds are responsible for the chaining: X-shaped junctions, due to BB bonds, and Y-shaped junctions, due to AB bonds. They found that when two of the three interaction strengths vanish simultaneously, there can be no liquid–vapour coexistence. These correspond to the limits of non-interacting linear chains ($\epsilon_{AA} \neq 0$, $\epsilon_{BB} = \epsilon_{AB} = 0$), dimers ($\epsilon_{BB} \neq 0$, $\epsilon_{AA} = \epsilon_{AB} = 0$), and hyperbranched polymers ($\epsilon_{AB} \neq 0$, $\epsilon_{AA} = \epsilon_{BB} = 0$) of Equation (13). They also showed that the phase transition always disappears as $\epsilon_{AA} \rightarrow 0$. Moreover, they showed that whereas ‘X-junctions’ only yield a critical point if their formation is energetically favourable, fluids with ‘Y-junctions’ will exhibit a critical point, even if forming them raises the energy, provided this increase is below a certain threshold.

Russo *et al.* [6,7] extended Tavares study to the case of two identical small A sites at the poles and nine equispaced identical big B sites on the equator. Killing the interaction

between two B sites ($\epsilon_{BB} = 0$), they observed the formation of chains and Y-junctions (and possibly hyperbranched polymers for $\epsilon_{AB}/\epsilon_{AA}$ large enough) and eventually a re-entrant behaviour of the liquid branch of the gas–liquid binodal pinched at low temperatures.

Rovigatti *et al.* [8,9] extended Russo model selecting an off-pole position of the A sites, thus adding the possibility of ‘rings’ formation, and observed re-entrance both in the gas and in the liquid branch of the binodal with a second lower critical point where the coexistence curves close itself at low temperatures without the pinch. They needed to relax assumption (3) in Wertheim theory [45–47].

4.2.1. Gas–liquid binodal

Russo *et al.* [6] studied the case of sites of two different kinds when the site–site interaction is restricted to $\epsilon_{BB} = 0$ (no X-junctions). Then, choosing as unit of energy ϵ_{AA} and again σ as the unit of length, the Wertheim theory depends on only five parameters: $r = \epsilon_{AB}/\epsilon_{AA} > 0$ and M_A, M_B, K_{AA}, K_{AB} .

We now choose $a = a_0 + a_{\text{bond}}$ with the association part given by the Wertheim theory Equation (4) with sites of two different kinds (see Section 3.1.3). In particular with the condition $\epsilon_{BB} = 0$, Equations (9) and (10) admit just a set of three different solutions for (x_A, x_B) from which it is necessary to single out the real physically relevant one such that $\lim_{\rho \rightarrow 0} x_A = \lim_{\rho \rightarrow 0} x_B = 1$.

Following Ref. [6], we choose $M_A = 2, M_B = 9$ (see Figure 3) and $K_{AA}^0 = 1.80 \times 10^{-4} \sigma^3, K_{AB}^0 = 1.56 \times 10^{-2} \sigma^3$. In order to fulfil the Wertheim condition [(1), of a single bond per site, the small A sites are meant to reside at the particle poles and the big B sites equispaced on the particle equator. The choice of $K_{AA}^0 \ll K_{AB}^0$ and the large M_B make

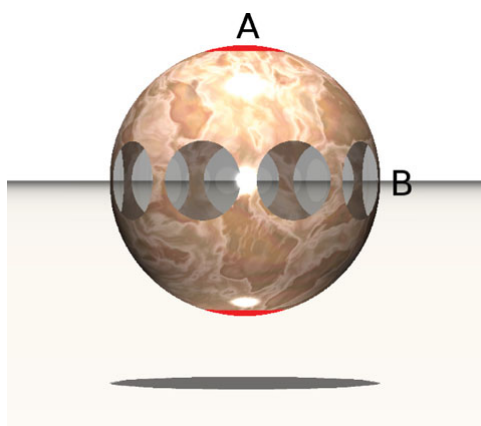


Figure 3. (color online) Pictorial view of a colloidal particle with attractive sites of two different kinds: two A sites on the poles and nine B sites on the equator.

branching entropically favourable. We then approximate $\Delta_{AA} = K_{AA}^0 (e^{\beta \epsilon_{AA}} - 1)$ and $\Delta_{AB} = K_{AB}^0 (e^{\beta \epsilon_{AB}} - 1)$.

In Figure 4, we show the evolution of the gas–liquid binodal as a function of r . Once again, comparing with Figure 3 of Russo *et al.* [6], we observe a complete qualitative agreement, even if in our calculation we further approximated the radial distribution of the reference system equal to one independently of density. We see that for $r < 1/2$, we

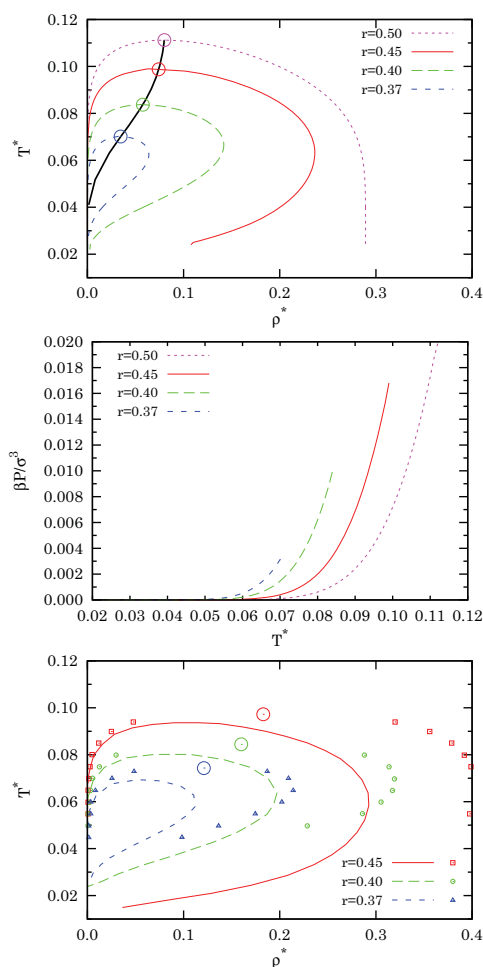


Figure 4. Top panel: evolution of the gas–liquid binodal as a function of r . The continuous thick black line is the locus of the critical points for $r \in]1/3, 1/2]$. Middle panel: pressure–temperature diagram. Bottom panel: binodals of Russo *et al.* [7] Figure 4 as obtained from their analysis (lines) of the Wertheim theory and from their MC simulations (points); the big circles are their predicted critical points.

have a non-standard binodal with a re-entrant liquid branch and a ‘pinched’ shape evidence that indeed the topological phase separation of Tlusty and Safran [48] is observed. Russo *et al.* [6] were able to provide a qualitative explanation for this behaviour by analysing the energetic of the junction formation process: since the energy cost of forming a chain end is $\epsilon_{\text{chain}} = \epsilon_{AA}/2 > 0$ and the energy cost of forming a Y-junction is $\epsilon_{Y\text{-junction}} = -\epsilon_{AB} + \epsilon_{AA}/2 = \epsilon_{AA}(1/2 - r)$, for $r < 1/2$ we have $\epsilon_{Y\text{-junction}} < 0$, and at low temperatures only chains, which we already saw that do not phase separate, are present.

They are also able to conclude that phase separation occurs only if $r > 1/3$. For $r < 1/3$, the energy cost of forming junctions being too high or, alternatively, the entropy gain being too small to offset the loss of translational entropy of chains in the liquid phase.

This behaviour can be understood by looking at $f(T, \rho; r) = d\beta p/d\rho = d\beta(p_0 + p_{\text{bond}}^W)/d\rho$. Differently from Bianchi *et al.* case, now we have $\lim_{\rho \rightarrow 0} d\beta p_{\text{bond}}^W/d\rho = 0$. The zeroes of f are two lines in the (ρ, T) plane, one for the minima of the pressure and one for the maxima. The union of the two lines is called the spinodal line for the coexistence. The equal area construction tells us that the binodal line and the two lines are tangent at the critical point. In Figure 5, we show a tridimensional plot of f for $r = 0.36, 2/5, 1/2$ as a function of temperature and density. Clearly, the three different scenarios do not depend on the specific values of K_{AA}, K_{AB}, M_A, M_B which only influence the region in the phase diagram (ρ, T) where we have the van der Waals loop.

The cluster populations for the chain ends, $2x_A$, and Y-junctions, $9(1 - x_B)$, along the binodal were studied in Ref. [6] and are shown in their Figure 4. From Figure 9 of Ref. [7], we see how the mean value of the number of bonds per particle (the valence), $2(1 - x_A) + 9(1 - x_B)$, tends to 2 at low temperatures, i.e. the fluid tends to be formed essentially by chains which, in agreement with Bianchi *et al.* analysis, are unable to sustain the gas–liquid coexistence.

The study of Russo *et al.* differs substantially from the Janus fluid case [22–24,49] where it is found a re-entrant gas branch for the gas–liquid binodal.

Rovigatti *et al.* [9] extended Russo study to take account of rings formation. In this case, the expression for the Wertheim bond free energy per particle of Equation (14) with $M_A = 2$ should be corrected as follows:

$$\beta a_{\text{bond}}^W = \ln(y x_B^{M_B}) - x_A - \frac{M_B}{2} x_B + 1 + \frac{M_B}{2} - \frac{G_0}{\rho}, \quad (32)$$

where G_n is the n th moment of the rings size distribution

$$G_n = \sum_{i=i_{\text{min}}}^{\infty} i^n W_i(2\rho \Delta_{AA} y)^i, \quad (33)$$

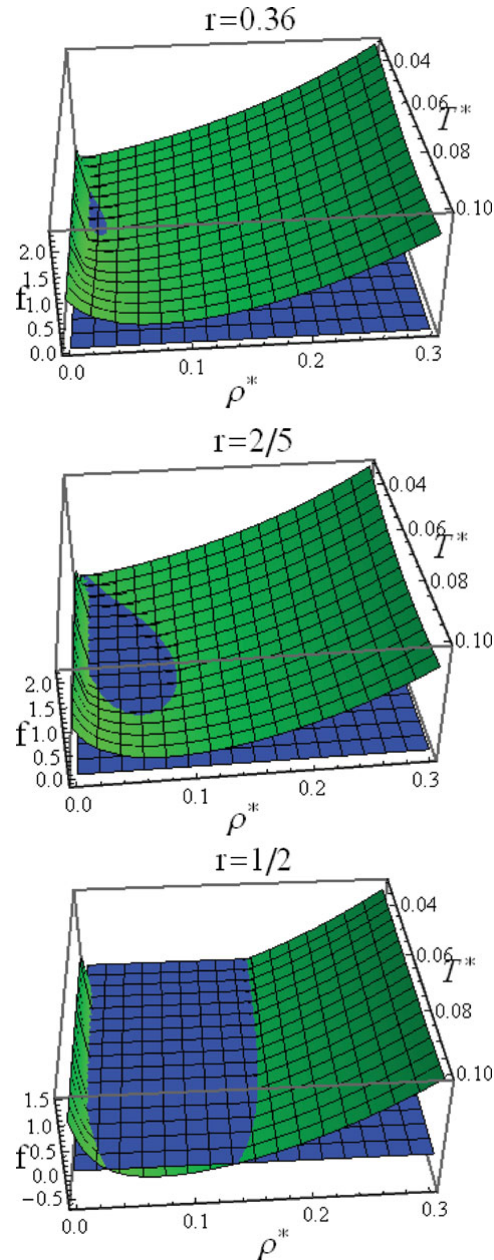


Figure 5. Tridimensional plots of $f(T, \rho; r) = d\beta p/d\rho$ (green surface) for $r = 0.36, 2/5, 1/2$ from top to bottom. Also, shown is the plane $f = 0$ (blue surface). For $r = 1/3$, the two surfaces become tangent at small temperatures and small densities. For $r > 1/2$, the minimum in the pressure moves at larger densities at smaller temperatures.

here i_{\min} is the minimum ring size, y is the fraction of particles with the two A sites unbonded, and W_i is the number of configurations of a ring of size i . Assuming for the rings the freely jointed chain level of description, we can approximate [45]

$$(i+1)W_{i+1} = \frac{i(i-1)}{8\pi} \sum_{j=0}^i \frac{(-1)^j}{j!(i-j)!} \left(\frac{i-1-2j}{2} \right)^{i-2}, \quad (34)$$

for l the smallest integer which satisfies $l \geq (i-1)/2 - 1$. Expression (34) is due to Treloar [50] and is the value of the end-to-end distribution function for a freely jointed chain of i links, when the end links are the length of one link apart (the link length is equal to the diameter of a sphere which we take to be our unit of length). For $i \gg 1$, it has the following asymptotic behaviour [50]

$$(i+1)W_{i+1} \approx \left(\frac{3}{2\pi i} \right)^{3/2} e^{-3/2i}, \quad i \gg 1, \quad (35)$$

The laws of mass action of Equations (9) and (10), for $\epsilon_{BB} = 0$, should now be corrected to take into account of the $G_n \neq 0$ as follows:

$$x_A^2 = y(1 - G_1/\rho), \quad (36)$$

$$1 - x_A = M_B \rho \Delta_{AB} x_B x_A + 2\rho \Delta_{AA} x_A^2 + G_1/\rho, \quad (37)$$

$$1 - x_B = 2\rho \Delta_{AB} x_A x_B. \quad (38)$$

Note that solving for x_A Equation (36) and for x_B Equation (38) and substituting into Equation (37), one finds an equation in y only, which always admits just one solution \bar{y} with the properties $0 \leq \bar{y} \leq 1$ and $\lim_{T \rightarrow 0} \bar{y} = 0$.

In Figure 6, we show our theoretical numerical results for the gas–liquid binodal of the ring forming fluid. A comparison with Figure 1 of Rovigatti *et al.* [9] shows again a good qualitative agreement between the two calculations. In our calculation, we retained the first 50 terms in the convergent series of Equation (33) and chose $M_B = 9$ and Δ_{AA} , Δ_{AB} as before. As we can see, the rings formation is responsible for the re-entrance in both the gas and liquid branches of the binodal and for the appearance of a second lower critical point. At $r = 0.37$, we could not find a coexistence line, leaving a system for which self-assembly is the only mechanism for aggregation.

In particular, upon approaching the upper critical point, at $T = T_c^u$, if we make a reversible transformation going from the liquid phase to the vapour phase on an isotherm, at $T < T_c^u$, we will have, as usual

$$\Delta S = \int \frac{\delta Q}{T} = \frac{\lambda_v m}{T} > 0, \quad (39)$$

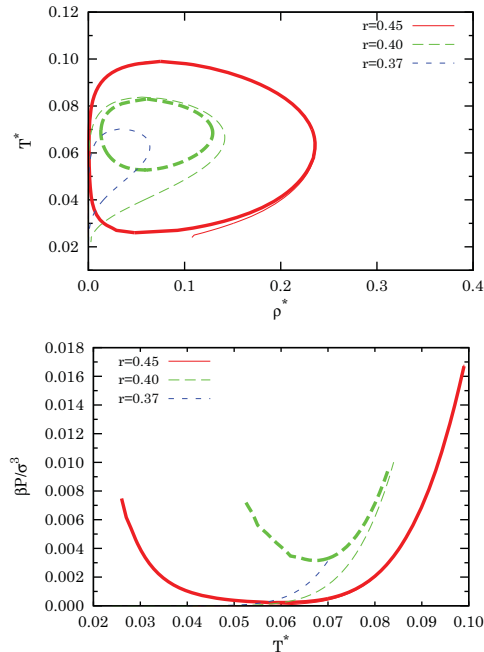


Figure 6. Top panel: evolution of the gas–liquid binodal as a function of r . The thin lines are the binodals of Figure 4. The thick lines are the results obtained for the rings forming fluid. Bottom panel: pressure–temperature diagram.

with ΔS the change in entropy $S = -(\partial A / \partial T)_{N,V}$, δQ the infinitesimal heat exchanges along the path of the transformation, λ_v the ‘latent’ heat of vaporisation, and m the mass of the fluid. Whereas Rovigatti *et al.* [9] show that upon approaching the lower critical point, at $T = T_c^l$, in the same transformation at $T > T_c^l$, one finds

$$\int \frac{\delta Q}{T} = \frac{\lambda_v m}{T} = \Delta S < 0, \quad (40)$$

so that the ‘latent’ heat of vaporisation changes sign as T varies from T_c^u to T_c^l . This can be seen directly from our pressure–temperature diagram of Figure 6 using the Clapeyron–Clausius formula [51].

Rovigatti analysis neglects the rings with AB bonds. We think that their inclusions may have dramatic effects on the phase diagram.

4.2.2. A possible extension

It is possible to extend Russo *et al.* [6,7] results allowing for the $\epsilon_{BB} \neq 0$ condition, responsible for the X-junctions formation [31]. The analysis for just three sites, two of kind

A and one of kind B , can be found in Refs. [43,44] were, interestingly enough, it is found the disappearance of criticality as $\epsilon_{AA} \rightarrow 0$. In our extension, we can introduce an additional parameter $s = \epsilon_{BB}/\epsilon_{AA} > 0$. One immediately verifies that the law of mass action of Equations (9) and (10) admits now four solutions (x_A, x_B) from which one has to determine the physical one such that $x_A, x_B \in [0, 1]$ and $\lim_{\rho \rightarrow 0} x_A = \lim_{\rho \rightarrow 0} x_B = 1$. Clearly, in the limit $r \rightarrow 0$, the problem is similar to the one of Bianchi *et al.* [3] (compare Equations (11) and (12) and Equation (7)) and in the limit $s \rightarrow 0$, we fall back to Russo *et al.* [6,7] case. We are interested in the non-trivial case: $\Delta_{AA} \neq \Delta_{BB}$ or $M_A \neq M_B$. We will choose for M_A, M_B, K_{AA}^0 , and K_{AB}^0 , the same values of the Russo's case of Section 4.2.1. Moreover, we will choose $K_{BB}^0 = K_{AA}^0$. Again, one has $\lim_{\rho \rightarrow 0} d\beta p_{\text{bond}}^W/d\rho = 0$. For s small, we are still able to see the re-entrant liquid scenario contrary to the predictions of Ref. [44]. In other words, we are able to observe a re-entrant liquid branch even in the presence of X-junctions in the fluid, as long as the energy cost for their formation, $\epsilon_{X\text{-junction}} = \epsilon_{AA}(1-s)$, is positive and big enough. This is shown in Figure 7. The figure also shows how an 'R'-shaped spinodal is possible in these cases with a majority of Y-junctions in correspondence of the coexistence region at high temperature, a majority of X-junctions in correspondence of the coexistence region at low temperature, and a majority of chains in between in correspondence of the bottleneck in the 'R', in agreement with the study of Tavares *et al.* [31]. Moreover, we find gas-liquid coexistence also for $r < 1/3$ as long as s is large enough. This is shown in Figure 8 from which it is also apparent the existence of a gas-liquid coexistence with a critical point at extremely low densities and temperatures, unpredicted by the study of Tavares *et al.* [31]. As a matter of fact, the critical temperature can be made small at will by a proper choice of the control parameters s ; the spinodal being essentially independent from r .

5. Break-down of the theory

Apart from the necessity to fulfil the steric incompatibility conditions, the Wertheim theory will break-down in the following cases:

5.1. Low temperature limit

Both the Wertheim theory and the canonical MC simulation break-down at low temperatures. The Wertheim theory is a high-temperature perturbation theory. The first-order version that we have been using until now clearly breaks-down at low temperature when from the mass action law (5) follows that $x_\alpha \rightarrow 0$ which in turn produces an undefined bond free energy (4). Also, the usual MC simulation will break-down at very low temperatures. In fact, imagine we have to break a bond with a single particle move. Then, the total energy difference between the final configuration

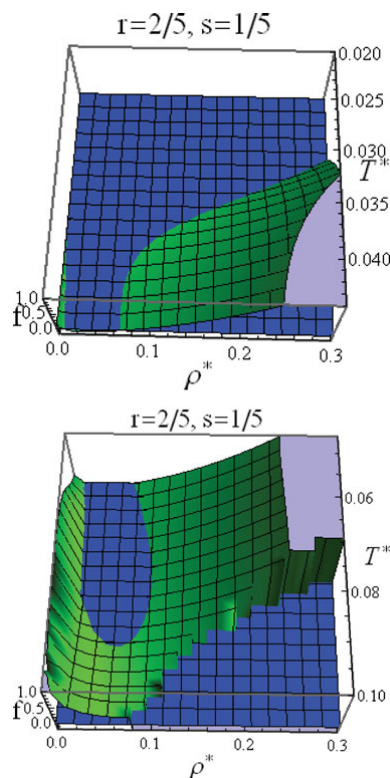


Figure 7. Tridimensional plots of $f(T, \rho; r, s) = d\beta p/d\rho$ (green surface) and of the plane $f = 0$ (blue surface) for $(r, s) = (2/5, 1/5)$. We show two plots one at high temperature and one at low temperature because the (x_A, x_B) physical solution determination changes in the two regions of the phase diagram. The negative f in the high temperature and high density corner of the lowest plot is due to another change in the physical solution determination.

and the initial one would be ϵ and we would need around $1/e^{-\beta\epsilon}$ single particle moves. So, at low temperatures, we would need a very long simulation in order to fully explore configuration space. Depending from the computational resources at one disposal, the range of inaccessible temperatures, before the solidification at zero temperature where the fluid chooses spontaneously the minimum potential energy configuration, may vary. Even if it is possible that patchy fluids, with short-ranged and tunable pair-interactions and with limited valence, will not crystallise at zero temperature [52] remaining a liquid in that limit.

5.2. Infinite number of attractive sites

The Wertheim theory will not be applicable anymore to particles decorated with too many attractive sites. In the

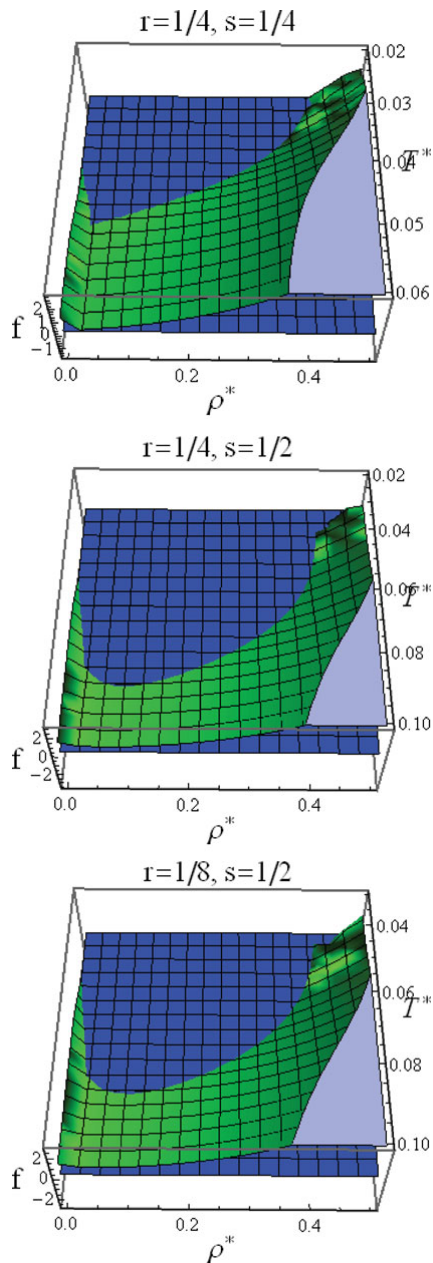


Figure 8. Tridimensional plots of $f(T, \rho; r, s) = d\beta p/d\rho$ (green surface) for $(r, s) = (1/4, 1/4), (1/4, 1/2), (1/8, 1/2)$. Also shown is the plane $f=0$ (blue surface). As we can see, the spinodals of the two cases $(r, s) = (1/4, 1/2), (1/8, 1/2)$ look essentially the same.

limit of an infinite number of sites uniformly distributed over the particle surface, one recovers the SW fluid or the mean-field solution of Section 3.2.1.

6. The radial distribution function

Using the fact that the angular average of the functional derivative of the free energy per particle respect to the angle dependent pair-potential is equal to $\rho/2V$ times the radial distribution function of colloid centres, we can write

$$g(r) = g_0(r) + \frac{2V}{\rho} \left\langle \frac{\delta \alpha_{\text{bond}}^W}{\delta \phi(1, 2)} \right\rangle \quad (41)$$

$$= g_0(r) + \frac{2}{\rho} \frac{1}{4\pi r^2} \sum_{\gamma \in \Gamma} \left(\frac{1}{x_\gamma} - \frac{1}{2} \right) \times \left\langle \frac{\delta x_\gamma}{\delta [\sum_{\alpha, \beta \in \Gamma} \beta \psi_{\alpha\beta}(r_{\alpha\beta})]} \right\rangle, \quad (42)$$

where we denote with $\langle \dots \rangle$ the orientational average, and in the second equality, we used Equations (4) and (21).

To make some progress, we use the following property

$$\left\langle \frac{\delta \langle f_{\alpha\beta} \rangle}{\delta \beta \psi_{\alpha\beta}} \right\rangle = -m_{\alpha\beta}(r) e^{\beta \epsilon_{\alpha\beta}} = -m_{\alpha\beta}(r) - \langle f_{\alpha\beta} \rangle \quad (43)$$

where in the last equality, we used Equations (28) and (29). From Equation (6) follows

$$\delta \Delta_{\alpha\beta} / \delta \langle f_{\alpha\beta} \rangle = 4\pi r_{12}^2 g_0(r_{12}) I_{\alpha\beta}(r_{12}), \quad (44)$$

where $I_{\alpha\beta}(r)$ is equal to one on the support of $\langle f_{\alpha\beta} \rangle$ and zero otherwise. Next, we observe that

$$\begin{aligned} \left\langle \frac{\delta x_\gamma}{\delta [\sum_{\alpha, \beta \in \Gamma} \beta \psi_{\alpha\beta}]} \right\rangle &= \left\langle \frac{1}{M^2} \sum_{\alpha, \beta \in \Gamma} \frac{\delta x_\gamma}{\delta \beta \psi_{\alpha\beta}} \right\rangle \\ &= -4\pi r^2 g_0(r) \frac{1}{M^2} \sum_{\alpha, \beta \in \Gamma} m_{\alpha\beta}(r) e^{\beta \epsilon_{\alpha\beta}} \frac{\partial x_\gamma}{\partial \Delta_{\alpha\beta}}, \end{aligned} \quad (45)$$

where M is the total number of sites per particle and in the last equality, we used the chain rule. So, we obtain

$$g(r) = g_0(r) \left[1 + \frac{1}{M^2 \rho} \sum_{\alpha, \beta, \gamma \in \Gamma} \left(1 - \frac{2}{x_\gamma} \right) \frac{\partial x_\gamma}{\partial \Delta_{\alpha\beta}} m_{\alpha\beta}(r) e^{\beta \epsilon_{\alpha\beta}} \right], \quad (46)$$

where the terms $\frac{\partial x_\gamma}{\partial \Delta_{\alpha\beta}}$ can be determined from the law of mass action, Equation (5). In particular, using the symmetry

12

R. Fantoni and G. Pastore

$\Delta_{\alpha\beta} = \Delta_{\beta\alpha}$, it follows

$$\frac{1}{\rho} \sum_{\gamma \in \Gamma} \left(1 - \frac{2}{x_\gamma}\right) \frac{\partial x_\gamma}{\partial \Delta_{\alpha\beta}} = x_\alpha x_\beta. \quad (47)$$

From Equation (46), we can extract the contact value for the radial distribution function

$$g(\sigma^+) = g_0(\sigma^+) \times \left[1 + \frac{1}{M^2 \rho} \sum_{\alpha, \beta, \gamma \in \Gamma} \left(1 - \frac{2}{x_\gamma}\right) \frac{\partial x_\gamma}{\partial \Delta_{\alpha\beta}} m_{\alpha\beta}(\sigma) e^{\beta \epsilon_{\alpha\beta}} \right], \quad (48)$$

where $m_{\alpha\beta}(\sigma)$ is the product of the two solid angle fractions for the $\alpha\beta$ bond when two particles are located at relative centre-to-centre distance σ . For example, for the Kern and Frenkel pair-potential [39], we would have $m_{\alpha\beta} = \chi_\alpha \chi_\beta$ with χ_{patch} the patch surface coverage. In the Bianchi *et al.* case [4] of Section 4.1, we have instead $m_{\alpha\alpha}(\sigma) = (d/\sigma)^3/3$, from Equation (29). For $g_0(\sigma^+)$, we can use the analytic solution to the Percus–Yevick approximation for the HS fluid [34], namely

$$g_0(\sigma^+) = (1 + \eta/2)/(1 - \eta)^2. \quad (49)$$

Next, we observe that, since $\rho g(r) 4\pi r^2 dr$ gives the number of particles in the spherical shell $[r, r + dr]$ around a particle fixed on the origin, the coordination number can be estimated as follows:

$$C_n = \rho \int_\sigma^{\sigma+d} 4\pi r^2 g_0(r) \times \left[1 + \frac{1}{M^2 \rho} \sum_{\alpha, \beta, \gamma \in \Gamma} \left(1 - \frac{2}{x_\gamma}\right) \frac{\partial x_\gamma}{\partial \Delta_{\alpha\beta}} m_{\alpha\beta}(r) e^{\beta \epsilon_{\alpha\beta}} \right] dr, \quad (50)$$

where $d = \min\{d_{\alpha\beta}\}$. The mean number of bonds per particle (the valence), $v_T = \sum_{\alpha \in \Gamma} (1 - x_\alpha)$, can be also estimated from the structure as follows:

$$v_S = C_n - \lim_{T \rightarrow \infty} C_n = \frac{1}{M^2} \sum_{\alpha, \beta, \gamma \in \Gamma} \left(1 - \frac{2}{x_\gamma}\right) \frac{\partial x_\gamma}{\partial \Delta_{\alpha\beta}} \Delta_{\alpha\beta}. \quad (51)$$

Then, using Equation (47) we immediately find

$$v_S = \frac{\rho}{M^2} \sum_{\alpha, \beta \in \Gamma} x_\alpha x_\beta \Delta_{\alpha\beta} = \frac{1}{M^2} \sum_{\alpha \in \Gamma} (1 - x_\alpha), \quad (52)$$

where the last equality follows from the law of mass action, Equation (5). The sought for consistency between the valence calculated from the thermodynamics and the valence

calculated from the structure only holds in the single site per particle case, $M = 1$.

For example, for M identical sites, we find $v_T = M(1 - x)$ and, choosing Kern–Frenkel patches for which d represents the width of the attractive SW of each patch and χ the patch surface coverage, from Equation (47) follows

$$C_n = \rho \int_\sigma^{\sigma+d} 4\pi r^2 g_0(r) [1 + x^2 \chi^2 e^{\beta \epsilon}] dr. \quad (53)$$

7. The structure factor

We then determined the structure factor $S(k) = 1 + \rho \hat{h}(k)$ with $h(r) = g(r) - 1$ the total correlation function and the hat denotes the Fourier transform.

7.1. Identical sites

For the case of Bianchi *et al.* of Section 4.1, we find

$$S(k) = 1 + 4\pi \rho \int_0^\infty \{g_0(r) [1 + x^2 m(r) e^{\beta \epsilon}] - 1\} \times \frac{\sin(kr)}{k} r dr, \quad (54)$$

where x is given by Equation (7) and $m(r)$ is given by Equation (29). Choosing for $g_0(r) = \Theta(r - \sigma)$, the one obtained from the zero density limit of the HS fluid, we find the ‘triangular’ approximation result of Equation (A1) of Appendix. From this result follows immediately

$$\lim_{k \rightarrow 0} S(k) = 1 + 20\eta \left[(e^{\beta \epsilon} - 8M\eta(e^{\beta \epsilon} - 1))(15d^4 + 4d^5) - 4 \left(5 + \sqrt{5\sqrt{5 + 4d^4 M\eta(e^{\beta \epsilon} - 1)(15 + 4d)}} \right) \right] / \left(5 + \sqrt{5\sqrt{5 + 4d^4 M\eta(e^{\beta \epsilon} - 1)(15 + 4d)}} \right)^2. \quad (55)$$

Moreover, we find

$$\lim_{T \rightarrow 0} S(0) = 1 - 8\eta + \frac{1}{M}, \quad (56)$$

$$\lim_{T \rightarrow \infty} S(0) = 1 - 8\eta + \left(3d^4 + \frac{4}{5}d^5 \right) \eta, \quad (57)$$

whereas for the structure factor of the reference system, we have $S_0(0) = 1 - 8\eta$.

In Figure 9, we show the structure factor of Equation (A1) for $M = 4$ and $T^* = 0.1$, $\eta = 0.1$.

A comparison with the simulation results of Sciortino *et al.* [4] (see their Figure 13) at $M = 2$ and $T^* = 0.055$ shows that approximation (55) breaks-down at high densities. This is shown in Figure 10 where the data of Sciortino

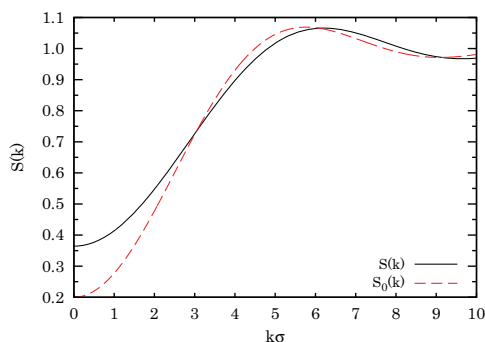


Figure 9. Structure factor for $M = 4$ and $T^* = 0.1$, $\eta = 0.1$ in the Bianchi *et al.* case using for the radial distribution function of the reference system, g_0 , the zero density limit of the hard-sphere fluid. Also shown, for comparison, is the structure factor of the reference system, $S_0(k) = 1 + 24\eta(k\cos(k) - \sin(k))/k^3$.

et al. simulations are compared with the isothermal compressibility sum rule,

$$S(0) = \left[\frac{\partial}{\partial \rho} \left(\rho^2 \frac{\partial \beta a}{\partial \rho} \right) \right]^{-1}, \quad (58)$$

and the relationship between the activity $\Lambda^{-3} e^{\beta \mu}$ and the density is obtained through Equation (16). We think that the fact that the structure as determined by the Equation (54) does not satisfy the isothermal compressibility sum rule of Equation (58) is a thermodynamical inconsistency not universally recognised for the Wertheim theory. In order to find accurate results for the structure, one needs to solve the

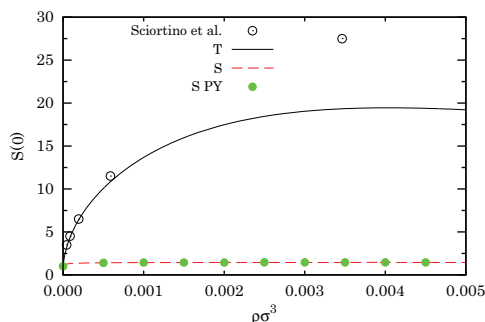


Figure 10. Structure factor at zero wave-number as a function of density for $M = 2$ and $T^* = 0.055$ in the Sciortino *et al.* simulations of Ref. [4], from the thermodynamic route (T) of the isothermal compressibility of Equation (58), from the structure route (S) of Equation (55), and from the zero wave-number limit of Equation (54) taking as a reference system the Percus–Yevick analytic solution for hard-spheres (S PY).

Wertheim Ornstein–Zernike equation with an appropriate closure [53].

8. Conclusions

We have critically analysed some recent applications of the Wertheim perturbation theory to classes of associating fluids of with non-standard phase diagrams and increasing complexity which can be today engineered in the laboratory [1]. In particular, we have illustrated the strong structural stability of the theory, which allows to get a first correct qualitative understanding of the resulting phase diagrams, even at the simplest level where all correlations of the reference system are neglected.

For fluids of HSS with M identical bonding sites, Bianchi *et al.* [3–5] discovered the ‘empty liquid’ scenario as M approaches two, i.e. in the presence of ‘chains’ only. The phenomenology when there are sites of two different kinds is more rich [6,7] and one can have ‘junctions’, responsible for a re-entrance of the liquid branch of the binodal, and ‘rings’ [8,9], responsible for a re-entrance also in the gas branch and the appearance of a second lower critical point.

In our detailed analysis of these results, we show that all the important conclusions on the qualitative behaviour of the phase diagrams can be derived uniquely from theoretical analytical considerations without the need of inputs from simulation results. For example, for the case of rings forming fluids we used as the partition function of an isolated ring the Treloar analytic expression for a freely jointed chain, unlike Rovigatti *et al.* [8,9] who use a fit of the MC data. This approximation makes immediately available a useful tool of analysis of complex phase diagrams even in the absence of more accurate but heavy numerical results.

Also, in the case of the more demanding condition of the presence of X-junctions we find that, when the energy gain for an X-junction formation, s , is low enough, we still observe a re-entrant liquid branch for $r < 1/2$ in the fluid, eventually with an ‘R’-shaped spinodal in agreement with the study of Tavares *et al.* [31]. When s is sufficiently large, we observe gas–liquid coexistence also at $r < 1/3$ in agreement with the predictions of Ref. [44]. In these latter cases, a gas–liquid coexistence with a critical point at an extremely low density and temperature, unpredicted by the work of Tavares *et al.* [31], can be observed.

Moreover, we have discussed in detail the consistency between structural and thermodynamic description within Wertheim perturbation theory and in particular, the valence as obtained from the thermodynamics and from the structure. We can conclude that while the overall structural information underlying the first order perturbative level is not accurate, the theory provides a consistency condition on the estimate of bonded particles, which is satisfied only in the one-site case. An analytical expression for the radial distribution function and the structure factor has also been proposed.

Acknowledgements

We are grateful to José Maria Cantista de Castro Tavares for correspondence and helpful comments. Giorgio Pastore acknowledges financial support by PRIN-COFIN 2010–2011 (contract 2010LKE4CC).

Disclosure statement

No potential conflict of interest was reported by the authors.

Funding

PRIN-COFIN 2010–2011 (Giorgio Pastore) (contract 2010LKE4CC).

References

[1] Gi-Ra Yi, D.J. Pine, and S. Sacanna, *J. Phys. Condens. Matter* **25**, 193101 (2013).
 [2] R. Fantoni and G. Pastore, *J. Chem. Phys.* **141**, 074108 (2014).
 [3] E. Bianchi, J. Largo, P. Tartaglia, E. Zaccarelli, and F. Sciortino, *Phys. Rev. Lett.* **97**, 168301 (2006).
 [4] F. Sciortino, E. Bianchi, J.F. Douglas, and P. Tartaglia, *J. Chem. Phys.* **126**, 194903 (2007).
 [5] E. Bianchi, P. Tartaglia, E. Zaccarelli, and F. Sciortino, *J. Chem. Phys.* **128**, 144504 (2008).
 [6] J. Russo, J.M. Tavares, P.I.C. Teixeira, M.M. Telo da Gama, and F. Sciortino, *Phys. Rev. Lett.* **106**, 085703 (2011).
 [7] J. Russo, J.M. Tavares, P.I.C. Teixeira, M.M. Telo da Gama, and F. Sciortino, *J. Chem. Phys.* **135**, 034501 (2011).
 [8] J.M. Tavares, L. Rovigatti, and F. Sciortino, *J. Chem. Phys.* **137**, 044901 (2012).
 [9] L. Rovigatti, J.M. Tavares, and F. Sciortino, *Phys. Rev. Lett.* **111**, 168302 (2013).
 [10] J.K. Lee, J.A. Barker, and F.F. Abraham, *J. Chem. Phys.* **58**, 3166 (1973).
 [11] W. Ebeling and M. Grigo, *Am. Phys.* **37**, 21 (1980).
 [12] M.J. Gillan, *Mol. Phys.* **49**, 421 (1983).
 [13] J.-M. Caillol and J.-J. Weis, *J. Chem. Phys.* **102**, 7610 (1995).
 [14] M.E. Fisher and Y. Levin, *Phys. Rev. Lett.* **71**, 3826 (1993).
 [15] H.L. Friedman and G. Larsen, *J. Chem. Phys.* **70**, 92 (1979).
 [16] M.S. Wertheim, *J. Stat. Phys.* **35**, 19 (1984).
 [17] M.S. Wertheim, *J. Stat. Phys.* **35**, 35 (1984).
 [18] M.S. Wertheim, *J. Stat. Phys.* **42**, 459 (1986).
 [19] M.S. Wertheim, *J. Stat. Phys.* **42**, 477 (1986).
 [20] N. Bjerrum, *Kgl. Dan. Vidensk. Selsk. Mat.-Fys. Medd.* **7**, 1 (1926).
 [21] A. Tani and D. Henderson, *J. Chem. Phys.* **79**, 2390 (1983).
 [22] R. Fantoni, A. Giacometti, F. Sciortino, and G. Pastore, *Soft Matter* **7**, 2419 (2011).
 [23] R. Fantoni, *Eur. Phys. J. B* **85**, 108 (2012).
 [24] R. Fantoni, *The Janus Fluid: A Theoretical Perspective* (SpringerBriefs in Physics) (Springer, New York, 2013).
 [25] R. Fantoni and G. Pastore, *Europhys. Lett.* **101**, 46003 (2013).
 [26] R. Fantoni and G. Pastore, *Phys. Rev. E* **87**, 052303 (2013).
 [27] E. Bianchi, R. Blaak, and C. N. Likos, *Phys. Chem. Chem. Phys.* **13**, 6397 (2011).

[28] B.D. Marshall, D. Ballal, and W.G. Chapman, *J. Chem. Phys.* **137**, 104909 (2012).
 [29] B.D. Marshall and W.G. Chapman, *J. Chem. Phys.* **138**, 044901 (2013).
 [30] B.D. Marshall and W.G. Chapman, *Phys. Rev. E* **87**, 052307 (2013).
 [31] J.M. Tavares and P.I. Teixeira, *J. Phys. Condens. Matter* **24**, 284108 (2012).
 [32] G. Jackson, W.G. Chapman, and K.E. Gubbins, *Mol. Phys.* **65**, 1 (1988).
 [33] N.F. Carnahan and K.E. Starling, *J. Chem. Phys.* **51**, 635 (1969).
 [34] J.-P. Hansen and I.R. McDonald, *Theory of Simple Liquids*, 3rd ed. (Academic Press, London, 2005).
 [35] H. Liu, S.K. Kumar, F. Sciortino, and G.T. Evans, *J. Chem. Phys.* **130**, 044902 (2009).
 [36] L. Vega, E. de Miguel, L.F. Rull, G. Jackson, and I.A. McLure, *J. Chem. Phys.* **96**, 2296 (1992).
 [37] H. Liu, S. Garde, and S. Kumar, *J. Chem. Phys.* **123**, 174505 (2005).
 [38] G. Malescio, G. Franzese, G. Pellicane, A. Skibinsky, S.V. Buldyrev, and H.E. Stanley, *J. Phys. Condens. Matter* **14**, 2193 (2002).
 [39] N. Kern and D. Frenkel, *J. Chem. Phys.* **118**, 9882 (2003).
 [40] R. Fantoni, D. Gazzillo, A. Giacometti, M.A. Miller, and G. Pastore, *J. Chem. Phys.* **127**, 234507 (2007).
 [41] D. de las Heras, J.M. Tavares, and M.M. Telo da Gama, *J. Chem. Phys.* **134**, 104904 (2011).
 [42] D. de las Heras, J.M. Tavares, and M.M. Telo da Gama, *Soft Matter* **7**, 5615 (2011).
 [43] J.M. Tavares, P.I.C. Teixeira, and M.M. Telo da Gama, *Phys. Rev. E* **80**, 021506 (2009).
 [44] J.M. Tavares, P.I.C. Teixeira, M.M. Telo da Gama, and F. Sciortino, *J. Chem. Phys.* **132**, 234502 (2010).
 [45] R.P. Sear and G. Jackson, *Phys. Rev. E* **50**, 386 (1994).
 [46] A. Galindo, S. Burton, G. Jackson, D. Visco, and D.A. Kofke, *Mol. Phys.* **100**, 2241 (2002).
 [47] A. Avlund, G. Kontogeorgis, and W. Chapman, *Mol. Phys.* **109**, 1759 (2011).
 [48] T. Tlusty and S.A. Safran, *Science* **290**, 1328 (2000).
 [49] F. Sciortino, A. Giacometti, and G. Pastore, *Phys. Rev. Lett.* **103**, 237801 (2009).
 [50] P.J. Flory, *Statistical Mechanics of Chain Molecules* (Interscience Publishers, New York, 1969), Chap. VIII, Section 3.
 [51] E. Fermi, *Termodinamica* (Bollati Boringhieri, Torino, 1958), §18.
 [52] F. Smalenburg and F. Sciortino, *Nature Phys.* **9**, 554 (2013).
 [53] J. Chang and S.I. Sandler, *J. Chem. Phys.* **102**, 437 (1995).

Appendix. The structure factor in the ‘triangular’ approximation

Choosing $g_0(r) = \Theta(r - \sigma)$ in Equation (54) with $m(r)$ defined as in Equation (29), we find

$$S(k) = 1 + 80\eta \left[(15k^3 - 90d^4k^3M\eta - 24d^5k^3M\eta) \cos(k) + (90d^4k^3M\eta + 24d^5k^3M\eta + 10d^3k^3e^{\beta\epsilon} \cos(k) + 3\sqrt{5}k^3\sqrt{5 + 4d^4M\eta(e^{\beta\epsilon} - 1)}(15 + 4d) \cos(k) + (-15k^2 + 90d^4k^2M\eta + 24d^5k^2M\eta) \sin(k) + (-90d^4k^2M\eta - 24d^5k^2M\eta)e^{\beta\epsilon} \sin(k) \right]$$

$$\begin{aligned}
 & + (15d^2k^2 + 30)e^{\beta\epsilon} \sin(k) \\
 & + \frac{-3\sqrt{5}k^2\sqrt{5 + 4d^4M\eta(e^{\beta\epsilon} - 1)(15 + 4d)} \sin(k)}{+ 30(dk \cos(k(1 + d)) - \sin(k(1 + d)))e^{\beta\epsilon}} \Bigg] / \\
 & \left[k^5 \left(5 + \sqrt{5\sqrt{5 + 4d^4M\eta(e^{\beta\epsilon} - 1)(15 + 4d)}} \right)^2 \right].
 \end{aligned}
 \tag{A1}$$

From this expression, one immediately sees that the high-temperature limit, $\beta \rightarrow 0$, of the structure factor is independent from the number of sites, M .

Chapter 46

Bridging and depletion mechanisms in colloid-colloid effective interactions: A reentrant phase diagram?

Fantoni R., Giacometti A., and Santos A., *J. Chem. Phys.* **142**, 224905 (2015)

Title: “Bridging and depletion mechanisms in colloid-colloid effective interactions: A reentrant phase diagram?”

Abstract: A general class of nonadditive sticky-hard-sphere binary mixtures, where small and large spheres represent the solvent and the solute, respectively, is introduced. The solute-solute and solvent-solvent interactions are of hard-sphere type, while the solute-solvent interactions are of sticky-hard-sphere type with tunable degrees of size nonadditivity and stickiness. Two particular and complementary limits are studied using analytical and semi-analytical tools. The first case is characterized by zero nonadditivity, lending itself to a Percus–Yevick approximate solution from which the impact of stickiness on the spinodal curves and on the effective solute-solute potential is analyzed. In the opposite nonadditive case, the solvent-solvent diameter is zero and the model can then be reckoned as an extension of the well-known Asakura–Oosawa model with additional sticky solute-solvent interaction. This latter model has the property that its exact effective one-component problem involves only solute-solute pair potentials for size ratios such that a solvent particle fits inside the interstitial region of three touching solutes. In particular, we explicitly identify the three competing physical mechanisms (depletion, pulling, and bridging) giving rise to the effective interaction. Some remarks on the phase diagram of these two complementary models are also addressed through the use of the Noro–Frenkel criterion and a first-order perturbation analysis. Our findings suggest reentrance of the fluid-fluid instability as solvent density (in the first model) or adhesion (in the second model) is varied. Some perspectives in terms of the interpretation of recent experimental studies of microgels adsorbed onto large polystyrene particles are discussed.



Bridging and depletion mechanisms in colloid-colloid effective interactions: A reentrant phase diagram

Riccardo Fantoni,^{1,a)} Achille Giacometti,^{2,b)} and Andrés Santos^{2,c)}

¹Dipartimento di Scienze Molecolari e Nanosistemi, Università Ca' Foscari Venezia, Calle Larga S. Maria DD2137, I-30123 Venezia, Italy

²Departamento de Física and Instituto de Computación Científica Avanzada (ICCAEx), Universidad de Extremadura, E-06071 Badajoz, Spain

(Received 16 March 2015; accepted 27 May 2015; published online 10 June 2015)

A general class of nonadditive sticky-hard-sphere binary mixtures, where small and large spheres represent the solvent and the solute, respectively, is introduced. The solute-solute and solvent-solvent interactions are of hard-sphere type, while the solute-solvent interactions are of sticky-hard-sphere type with tunable degrees of size nonadditivity and stickiness. Two particular and complementary limits are studied using analytical and semi-analytical tools. The first case is characterized by zero nonadditivity, lending itself to a Percus–Yevick approximate solution from which the impact of stickiness on the spinodal curves and on the effective solute-solute potential is analyzed. In the opposite nonadditive case, the solvent-solvent diameter is zero and the model can then be reckoned as an extension of the well-known Asakura–Oosawa model with additional sticky solute-solvent interaction. This latter model has the property that its exact effective one-component problem involves only solute-solute pair potentials for size ratios such that a solvent particle fits inside the interstitial region of three touching solutes. In particular, we explicitly identify the three competing physical mechanisms (depletion, pulling, and bridging) giving rise to the effective interaction. Some remarks on the phase diagram of these two complementary models are also addressed through the use of the Noro–Frenkel criterion and a first-order perturbation analysis. Our findings suggest reentrance of the fluid-fluid instability as solvent density (in the first model) or adhesion (in the second model) is varied. Some perspectives in terms of the interpretation of recent experimental studies of microgels adsorbed onto large polystyrene particles are discussed. © 2015 AIP Publishing LLC. [<http://dx.doi.org/10.1063/1.4922263>]

I. INTRODUCTION

Many years ago, Asakura and Oosawa¹ (AO) provided an explanation of the clustering and gelation phenomenon occurring when small nonadsorbing polymers, such as polystyrene (PS), were added to a solution of large spherical colloids, say polymethylmethacrylate (PMMA). The basic idea is illustrated in Fig. 1 considering two PMMA colloids, modeled as big spheres, immersed in a fluid formed by a uniform background (that we will neglect henceforth) as well as by PS particles, assumed to be small *noninteracting spheres* that, however, experience a hard-sphere (HS) interaction with the larger ones. Under these conditions, when the separation between the two large spheres is less than the diameter of the small spheres (see Fig. 1), there is an unbalanced pressure of the “sea” of small spheres, providing an entropic gain compared to the case when the separation is large, which can be reckoned as an *effective* attractive interaction driving the clustering of large colloidal spheres.

In real systems, however, the solvent particles do not always behave as an ideal gas or interact only sterically.

Typically, they experience an additional short-range attraction (or repulsion) with the solute, usually due to dispersion forces.^{3–6} The simplest way of accounting for a short-range solute-solvent attraction is by means of Baxter’s sticky-hard-sphere (SHS) model⁷ characterized by a stickiness parameter τ_{sl} . Both issues (solvent-solvent repulsion and solute-solvent short-range attraction) were recently addressed by two experimental studies^{8,9} on adsorbing microgels (MGs) to large PS latex suspension. In this case, the expected mechanism will be clearly different, as illustrated by Fig. 2, inspired by a similar figure of Ref. 8.

Let σ_l and σ_s be the diameters of the large and small spheres, respectively, and suppose we fix the volume fraction η_l of the large colloidal spheres and gradually increase the volume fraction η_s of the small solvent spheres. In the absence of solvent particles, the solute particles will behave essentially as HSs, as depicted in Fig. 2(a). Now imagine we gradually add the small solvent particles. Because of the solute-solvent attraction, they will tend to get adsorbed on the surface of the larger particles and mediate an effective attraction between them. This *bridging* mechanism destabilizes the solution as the large colloidal spheres tend to form aggregates, as schematically illustrated in Fig. 2(b). The global effect is the formation of a *gel* phase caused by a free-energy driven phase separation of the large and small spheres. As η_s increases, solvent

^{a)}Electronic mail: rfantoni@ts.infn.it

^{b)}Electronic mail: achille.giacometti@unive.it

^{c)}Electronic mail: andres@unex.es. URL: <http://www.unex.es/eweb/fisteor/andres>.

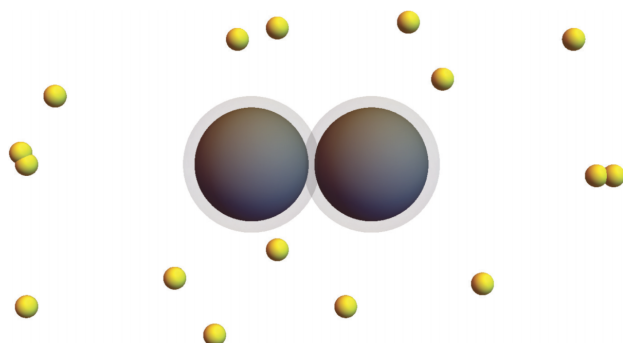


FIG. 1. Cartoon of the AO depletion interaction. The shaded region around each solute represents the volume excluded to the centers of the solvent particles.²

particles tend to progressively cover the solute surface, as depicted in Fig. 2(c). We can easily estimate¹⁰ the critical value η_s^* at which all large spheres will be completely covered to be $\eta_s^* \approx \eta_l(2\pi/\sqrt{3})\sigma_s/\sigma_l$, as discussed in Appendix A. At this point, all the solute colloids can be “fully covered” by solvent particles and they will behave essentially again as HSs with an effective diameter $\sigma_l + \sigma_s$, with a few additional free solvent particles. This situation is pictured in Fig. 2(c). Upon adding further solvent particles, however, depletion forces between the small and the covered colloids set in Fig. 2(d) and phase separation occurs again, this time entropically rather than free-energetically, as in the case of Fig. 2(b). A useful way to represent the phase diagram of such a binary mixture is through an (η_l, η_s) diagram at fixed values of size ratio $q = \sigma_s/\sigma_l$ and stickiness τ_{sl}^{-1} . In this diagram, there will be geometrically inaccessible regions, for example, for η_s or η_l larger than $\pi/3\sqrt{2}$, and lines separating the various phase coexistence regions. The topology of the phase diagram would be controlled by q , while η_s would play the role of an inverse temperature.

Motivated by these new experimental perspectives, recently Chen *et al.*¹¹ considered a HS-SHS binary mixture where one can tune the attraction parameter τ_{sl} between the unlike spheres, with like spheres only interacting via HS interactions. Note that this is the same model already studied by Fantoni *et al.*,¹² as well as by other groups.²⁹ The study of Ref. 11 provided a well defined framework to rationalize the experimental results obtained in Refs. 8 and 9.

In the present work, we will build upon this idea and go further to introduce also an additional—and, to the best of our knowledge, new—model that has the interesting feature

of including the standard AO model^{1,11} as a particular case. In both cases, we will illustrate how an effective one-component solute-solute interaction potential can be obtained and the merits and drawbacks of this procedure.

Both models can be seen as extreme realizations of a general class of nonadditive sticky-hard-sphere (NASHS) binary mixtures where the small-small (or solvent-solvent) and large-large (or solute-solute) interactions are of HS type with diameters σ_{ss} and $\sigma_{ll} = \sigma_l$, respectively, while the small-large (or solvent-solute) interactions are of SHS type characterized by a cross diameter $\sigma_{sl} = (\sigma_s + \sigma_l)/2 = \sigma_l(1 + q)/2$ and an inverse stickiness τ_{sl} . Note that here we denote by $\sigma_s = q\sigma_l$ the diameter of the small spheres *as seen* by the large ones, while σ_{ss} is the diameter of the small spheres as seen by themselves. Thus, the nonadditivity of the unlike interactions is monitored by the ratio $\sigma_{ss}/\sigma_s \leq 1$ (where we have restricted ourselves to zero or positive nonadditivity). The NASHS class reduces to the nonadditive hard-sphere (NAHS) class if the solute-solvent stickiness is switched off.

In the first model that we will study, one has $\sigma_{ss}/\sigma_s = 1$, so that the HS interactions are additive. This model, denoted henceforth as the additive sticky-hard-sphere (ASHS) model, is the one depicted in Fig. 2 and considered in Refs. 11 and 12. Interestingly, the ASHS model can be solved exactly within the Percus–Yevick (PY) approximation^{12–15} and the instability region in the (η_s, η_l) plane enclosed by the spinodal line can be computed. This will be found to form a closed region, in agreement with previous results.¹¹

The second model represents an extreme case of positive nonadditivity, namely, $\sigma_{ss}/\sigma_s = 0$, i.e., the solvent spheres

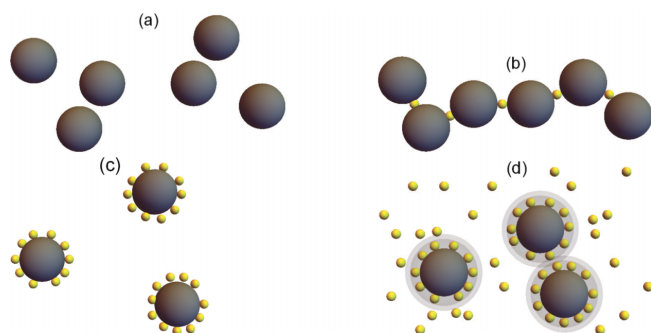


FIG. 2. Different mechanisms occurring in the presence of a short-range attraction between solvent and solute, as the solvent concentration increases: (a) $\eta_s = 0$, HS behavior; (b) $0 < \eta_s < \eta_s^*$, the small fraction of solvent particles act as bridges connecting the solute into a cluster; (c) $\eta_s \approx \eta_s^*$, most of the solute colloids are covered and again behave as HSs with an effective diameter $\sigma_s + \sigma_l$; (d) $\eta_s > \eta_s^*$, the “dressed” solutes feel an effective depletion attraction. The dark and light shaded regions around the solute particles in panel (d) represent the effective solute size and the effective volume excluded to the centers of the solvent particles, respectively.

behave among themselves as an ideal gas. This particular case of the general class of NASHS models reduces to the conventional AO model if the stickiness is switched off (i.e., $\tau_{sl} \rightarrow \infty$). Because of that, we will term this model as the sticky Asakura–Oosawa (SAO) model. The need of supplementing the AO model with a short-range solute-solvent attraction has been recognized, for instance, in Ref. 5. While, in contrast to the ASHS model, the SAO model does not allow for an analytical solution in the PY approximation, its associated *effective* solute-solute pair potential can be exactly derived in the semi-grand-canonical ensemble, analogously to the case of the pure AO model.^{16–18} Moreover, and also in analogy with the AO model,^{17,19–21} such a pair potential turns out to be the only one contributing to the exact effective interaction among the solutes if the size ratio $q = \sigma_s/\sigma_l$ is smaller than the threshold value $q_0 = 2/\sqrt{3} - 1 \approx 0.1547$. A careful comparison between the results of the two models (ASHS and SAO) allows us to pave the way for an improved theoretical understanding of the above experiments.

It is interesting to observe that when the solute-solvent adhesion is set to zero, the model ASHS reduces to a size-asymmetric additive HS (AHS) binary mixture, while the SAO model becomes the original AO model, these two mixtures having quite different critical behaviors upon varying q .^{16,17,22} The metastable fluid-fluid demixing coexistence, responsible for the broadening at $\eta_s > 0$ of the stable fluid-solid coexistence ($0.492 \leq \eta_l \leq 0.543$) for pure HSs ($\eta_s \rightarrow 0$),^{23,24} remains always metastable and exists at small enough q in the AHS case, whereas it becomes stable at large q in the AO case, where a triple point appears. Figure 3 sketches (in the plane σ_{ss}/σ_s vs τ_{sl}^{-1}) the different models referred to above.

The organization of this paper is as follows. Section II presents the problem of the effective solute interaction mediated by the solvent particles within a general framework. This is followed by Sec. III, where the PY solution for the ASHS model is exploited to find the spinodal curves of the original mixture and the effective solute-solute pair potential. The exact derivation of the effective potential in the SAO model with a size ratio $q < q_0$ is addressed in Sec. IV, its three contributions being clearly identified. Next, the different scenarios for criticality in the ASHS and SAO effective systems are analyzed

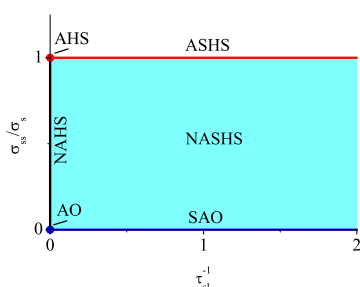


FIG. 3. Plane σ_{ss}/σ_s vs τ_{sl}^{-1} sketching different models mentioned in the text. The general class of NASHS models includes, as limiting cases, ASHS ($\sigma_{ss}/\sigma_s = 1$), SAO ($\sigma_{ss}/\sigma_s = 0$), and NAHS ($\tau_{sl}^{-1} = 0$). The intersection of the NAHS line with the ASHS and SAO lines defines the AHS and AO models, respectively. In this paper, we will be concerned with the ASHS and SAO models.

via the second virial coefficient and the Noro–Frenkel (NF) criterion²⁵ in Sec. V. A more detailed analysis for the SAO model is performed via a first-order perturbation theory in Sec. VI. Finally, our findings are discussed and put in perspective in Sec. VII. The most technical details are relegated to four appendices.

II. GENERAL FRAMEWORK

Consider a colloidal binary mixture of N_s small (solvent) and N_l large (solute) particles, identified by the coordinates $\{\mathbf{r}_1^{(s)}, \mathbf{r}_2^{(s)}, \dots, \mathbf{r}_{N_s}^{(s)}\}$ and $\{\mathbf{r}_1^{(l)}, \mathbf{r}_2^{(l)}, \dots, \mathbf{r}_{N_l}^{(l)}\}$, respectively, in a volume V .

Assuming pair interactions, i.e., assuming the particles are nondeformable, nonpolarizable, . . . , (see Ref. 26 for a recent discussion on the reliability of this assumption), the total potential U can be written as $U = U_{ss} + U_{ll} + U_{sl}$, where

$$U_{ss} = \sum_{i=1}^{N_s-1} \sum_{j=i+1}^{N_s} \varphi_{ss}(|\mathbf{r}_i^{(s)} - \mathbf{r}_j^{(s)}|), \quad (2.1)$$

$$U_{ll} = \sum_{i=1}^{N_l-1} \sum_{j=i+1}^{N_l} \varphi_{ll}(|\mathbf{r}_i^{(l)} - \mathbf{r}_j^{(l)}|), \quad (2.2)$$

$$U_{sl} = \sum_{i=1}^{N_s} \sum_{j=1}^{N_l} \varphi_{sl}(|\mathbf{r}_i^{(s)} - \mathbf{r}_j^{(l)}|). \quad (2.3)$$

The canonical free energy $F(N_s, N_l, V, T)$ is then given by

$$e^{-\beta F} = \frac{\Lambda_s^{-3N_s} \Lambda_l^{-3N_l}}{N_s! N_l!} \int d\mathbf{r}^{N_s} \int d\mathbf{r}^{N_l} e^{-\beta(U_{ss} + U_{ll} + U_{sl})}, \quad (2.4)$$

where $\beta = 1/k_B T$ (k_B being the Boltzmann constant), Λ_s and Λ_l are the de Broglie thermal wavelengths associated with the small and large particles, respectively, and we have used the short-hand notation $d\mathbf{r}^{N_\alpha} = d\mathbf{r}_1^{(\alpha)} \dots d\mathbf{r}_{N_\alpha}^{(\alpha)}$ with $\alpha = s, l$.

Following standard prescriptions,^{16,19,27} one can in principle trace out all the microscopic degrees of freedom associated with the solvent particles and recast Eq. (2.4) in a form of an *effective* one-component system for only the solute particles with a potential energy $U_{ll}^{\text{eff}}(\mathbf{r}_1^{(l)}, \mathbf{r}_2^{(l)}, \dots, \mathbf{r}_{N_l}^{(l)})$. More specifically,

$$e^{-\beta U_{ll}^{\text{eff}}} = \frac{e^{-\beta U_{ll}}}{N_s! \Lambda_s^{3N_s}} \int d\mathbf{r}^{N_s} e^{-\beta(U_{ss} + U_{sl})}, \quad (2.5)$$

so that Eq. (2.4) becomes

$$e^{-\beta F} = \frac{1}{N_l! \Lambda_l^{3N_l}} \int d\mathbf{r}^{N_l} e^{-\beta U_{ll}^{\text{eff}}}. \quad (2.6)$$

In general, however, the effective potential U_{ll}^{eff} is not pairwise additive, meaning that apart from pair-interaction terms (and less relevant zero- and one-body terms), it requires three-body, four-body, . . . terms. Thus, the general structure of U_{ll}^{eff} would be

$$U_{ll}^{\text{eff}} = N_l v_{ll}^{(0)} + \sum_{i=1}^{N_l} v_{ll}^{(1)}(\mathbf{r}_i^{(l)}) + \sum_{i < j}^{N_l} v_{ll}^{(2)}(|\mathbf{r}_i^{(l)} - \mathbf{r}_j^{(l)}|) + \sum_{i < j < k}^{N_l} v_{ll}^{(3)}(\mathbf{r}_i^{(l)}, \mathbf{r}_j^{(l)}, \mathbf{r}_k^{(l)}) + \dots \quad (2.7)$$

224905-4 Fantoni, Giacometti, and Santos

J. Chem. Phys. 142, 224905 (2015)

The physically most relevant contribution is expected to be the one associated with the effective pair potential $v_{ll}(r) \equiv v_{ll}^{(2)}(r)$, in which case one can approximately neglect $v_{ll}^{(n)}$ with $n \geq 3$.

Now we specialize to the general class of NASHS models described in Sec. I. The $\varphi_{ss}(r)$ and $\varphi_{ll}(r)$ pair interactions are of HS type characterized by diameters σ_{ss} and σ_{ll} , respectively, while the small-large interaction $\varphi_{sl}(r)$ is of SHS type^{7,28} with a hard-core distance σ_{sl} and a stickiness parameter τ_{sl}^{-1} , the latter measuring the strength of surface adhesiveness. Therefore, the relevant Mayer functions $f_{\alpha\gamma}(r) = e^{-\beta\alpha\gamma(r)} - 1$ are

$$f_{ss}(r) = -\Theta(\sigma_{ss} - r), \quad (2.8)$$

$$f_{ll}(r) = -\Theta(\sigma_{ll} - r), \quad (2.9)$$

$$f_{sl}(r) = -\Theta(\sigma_{sl} - r) + \frac{\sigma_{sl}}{12\tau_{sl}}\delta(r - \sigma_{sl}). \quad (2.10)$$

Here, $\Theta(x)$ is the Heaviside step function and $\delta(x)$ is the Dirac delta function. To simplify the notation, we adopt the viewpoint of the large spheres by calling $\sigma_l = \sigma_{ll}$ their diameter and defining σ_s as the diameter of the small spheres as felt by the large ones, so that $\sigma_{sl} = (\sigma_s + \sigma_l)/2$. Thus, the size asymmetry of the mixture (again from the viewpoint of the solute particles) is measured by the ratio $q = \sigma_s/\sigma_l < 1$, while the nonadditivity of the hard-core interactions is measured by the ratio $\sigma_{ss}/\sigma_s \leq 1$ (where, as said before, we discard here the case of negative nonadditivity). For later use, let us introduce the partial packing fraction of species α as $\eta_\alpha = \pi\rho_\alpha\sigma_\alpha^3/6$, where $x_\alpha = N_\alpha/N$ is the concentration of species $\alpha = s, l$ and $\rho_\alpha = N_\alpha/V$ is its density. The total number of particles and number density of the fluid mixture are $N = N_l + N_s$ and $\rho = N/V$, respectively.

As discussed in Sec. I, we now particularize to two interesting particular cases that are identified by the ratio σ_{ss}/σ_s : the ASHS model (where $\sigma_{ss}/\sigma_s = 1$) and the SAO model (where $\sigma_{ss}/\sigma_s = 0$). The first model was studied before by two of us (it was called system A in Sec. V of Ref. 12) and has been rejuvenated by a recent study by Chen *et al.*¹¹ The second model is an extension of the well-known AO model, except that a sticky (or adhesive) interaction exists between the solvent and the solute particles. To the best of our knowledge, it has not been studied before. In both cases, we will be able to derive the effective pair potential $v_{ll}(r) = v_{ll}^{(2)}(r)$ [see Eq. (2.7)] either within the PY approximation in the canonical ensemble (ASHS model) or in an exact way in the semi-grand-canonical ensemble (SAO model).

III. THE PY APPROXIMATE SOLUTION OF THE ASHS MODEL

The solution of the PY approximation for the ASHS model was recently studied in Ref. 12. The PY solution actually extends to the more general formulation where the Baxter stickiness coefficient^{7,28} between a particle of species α and one of species γ is $\tau_{\alpha\gamma}^{-1}$.^{13–15} Since here we choose $\tau_{ss} \rightarrow \infty$ and $\tau_{ll} \rightarrow \infty$, we can only have adhesion between unlike particles and $\tau_{sl}^{-1} > 0$ measures its strength.

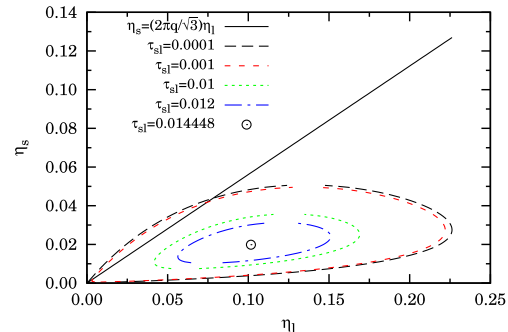


FIG. 4. PY spinodal for $q = q_0$ and several values of τ_{sl} . The straight line is $\eta_s = \eta_s^*$ and the circle is the critical point at $\tau_{sl} = 0.014448$.

A. Spinodal curve

From Eq. (85) of Ref. 12, we find the following expression for the spinodal of the full binary mixture in the (η_s, η_l) plane, as obtained from the PY approximation:

$$\tau_{sl}^{\text{sp}}(\eta_s, \eta_l) = \left[\frac{1 + (1+q)(1-\eta_s-\eta_l)/3(\eta_s+q\eta_l)}{1 + \sqrt{\left(1 + \frac{1-\eta_s-\eta_l}{3\eta_s}\right)\left(1 + \frac{1-\eta_s-\eta_l}{3\eta_l}\right)}} - 1 \right] \times \frac{(1+q)(\eta_s+q\eta_l)}{4q(1-\eta_s-\eta_l)}, \quad (3.1)$$

which, as it should, is symmetric under the exchanges $\eta_s \leftrightarrow \eta_l$ and $q \leftrightarrow 1/q$. For a fixed q , there is a maximum value of τ_{sl}^{sp} for which Eq. (3.1) admits a solution with $\eta_s > 0$ and $\eta_l > 0$. We will denote this maximum value with $\bar{\tau}_{sl}$ and the corresponding solution, the critical point, with $(\bar{\eta}_s, \bar{\eta}_l)$. In particular, at $q = q_0$, we find $\bar{\tau}_{sl} = 0.014448$, $\bar{\eta}_s = 0.019839$, and $\bar{\eta}_l = 0.101645$. For $\tau_{sl} < \bar{\tau}_{sl}$, the solution of Eq. (3.1) is a closed curve in the (η_s, η_l) plane within which the thermodynamically unstable region lies, as shown in Fig. 4. As we can see, the spinodal curve does not change much for $\tau_{sl} < 0.001$, where it is crossed by the straight line representing the critical packing fraction $\eta_s = \eta_s^*$. These findings are in complete agreement with those reported in Ref. 11.

Note that Eq. (3.1) is a particular case of an equation for a general mixture derived by Barboy and Tenne,²⁹ which should however be handled with great care.³⁰

B. Approximate effective one-component fluid

As explained in Sec. II, one could in principle integrate out the solvent degrees of freedom to obtain the effective solute potential U_{ll}^{eff} [see Eqs. (2.5) and (2.7)]. Here, we want to focus on the pair interaction potential $v_{ll}(r) = v_{ll}^{(2)}(r)$. This function can be identified from the solute-solute radial distribution function $g_{ll}(r)$ in the infinite dilution limit ($x_l \rightarrow 0$) since in that limit only pair interactions contribute to $g_{ll}(r)$. Therefore, $g_{ll}(r) \rightarrow e^{-\beta v_{ll}(r)}$, and hence,

$$\beta v_{ll}(r) = - \lim_{x_l \rightarrow 0} \ln g_{ll}(r). \quad (3.2)$$

In the limit of no adhesion ($\tau_{sl} \rightarrow \infty$), $v_{ll}(r)$ becomes the usual depletion potential.^{31,32} For further use, we will refer to

entropic regime as the one with $\tau_{sl} \gg 1$, close to a size-asymmetric binary HS mixture. Reciprocally, the *nonentropic* regime will refer to a system with a small τ_{sl} . The *transitional* regime will correspond to $\tau_{sl} \sim 1$.

Since η_s is supposed to be finite in Eq. (3.2), it is not possible to obtain the exact effective pair potential $v_{ll}(r)$. On the other hand, it can be obtained again from the PY solution, as described in Appendix B. Note that although the infinite dilution limit is applied as a short-cut to derive the pair potential $v_{ll}(r)$, at a nonzero solute concentration, the full effective many-body potential U_{ll}^{eff} includes nonpairwise terms, as represented by $v_{ll}^{(3)}(\mathbf{r}_i, \mathbf{r}_j, \mathbf{r}_k)$ and higher-order terms in Eq. (2.7).

In Fig. 5, we report a few representative examples of the effective solute-solute pair potential corresponding to the ASHS model in the PY approximation (see Appendix B). Figure 5(a) shows the influence of the solute-solvent stickiness at fixed $\eta_s = 0.1$ and $q = q_0$. One can clearly observe the different shape of the potential in the entropic ($\tau_{sl} = 10^4$), transitional ($\tau_{sl} = 1$), and nonentropic ($\tau_{sl} = 0.12$) regimes. In the former case ($\tau_{sl} = 10^4$), the potential is essentially attractive (except for a slight hump in the region $r/\sigma_l \lesssim 1 + q$), thus reflecting the depletion mechanisms (see Fig. 1). Moreover, at this very high value of τ_{sl} , the discontinuity of the potential at $r/\sigma_l = 1 + q$ [see Eq. (B15)] is not visible. In the transitional regime ($\tau_{sl} = 1$), however, the discontinuity at $r/\sigma_l = 1 + q$ is already noticeable and the potential in most of the inner region

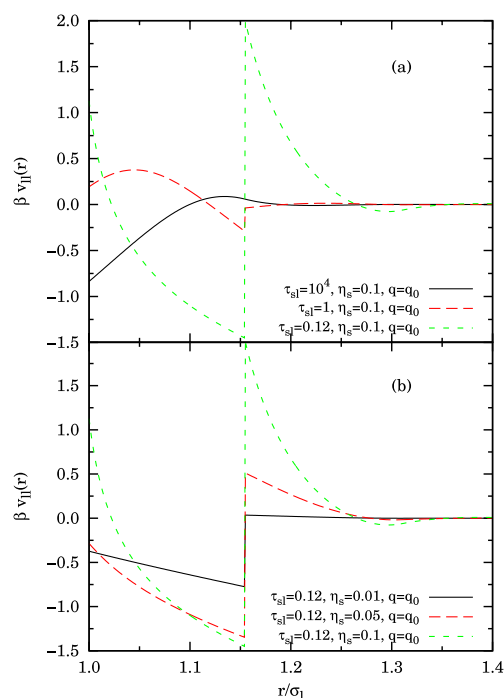


FIG. 5. Effective solute-solute pair potential in the ASHS model, as obtained from the PY approximation (see Appendix B). In panel (a), the stickiness parameter is varied at a fixed solvent packing fraction $\eta_s = 0.1$, while in panel (b), η_s is varied at fixed $\tau_{sl} = 0.12$. In all the cases, the size ratio is $q = q_0$.

$1 < r/\sigma_l < 1 + q$ has changed from attractive to repulsive. These two features are widely enhanced in the nonentropic regime ($\tau_{sl} = 0.12$): there is a high discontinuity at $r/\sigma_l = 1 + q$ and the effective potential is strongly repulsive in the whole region $1 < r/\sigma_l < 1 + q$. Furthermore, a strong repulsion appears as well in the outer region $r/\sigma_l \gtrsim 1 + q$. Figure 5(b) shows that an increase of the solvent density magnifies the characteristic features of the effective potential in the nonentropic regime. The physical origin of the repulsive regions in the nonentropic regime can be ascribed to the net *pulling* role played by the solvent particles attached to the two solutes. This effect will be identified more clearly in the SAO model (see Sec. IV). As for the (attractive) discontinuity at $r/\sigma_l = 1 + q$, it can be attributed to the *bridging* effect of solvent particles attached to both solutes. This bridging mechanism is absent if $r/\sigma_l = (1 + q)^+$ but appears if $r/\sigma_l = (1 + q)^-$.

Dijkstra *et al.*^{16,27} already showed that the effective potential in the entropic regime is unable to produce a stable demixing phase transition with reasonably small q . On the other hand, the step attraction at $r/\sigma_l = 1 + q$ in the potential associated with the nonentropic regime can lead to a demixing transition, as shown in Ref. 12. This is the phase instability studied in the (η_s, η_l) plane in Sec. III A.

With all due cares, the shape of the effective potential in the nonentropic regime depicted in Fig. 5(b) can be *schematically* represented as a square-well (SW) potential of width $q\sigma_l$ and depth $\epsilon \sim |v_{ll}(\sigma_l(1 + q)^-)|$, with an additional repulsive tail starting at $r = \sigma_l(1 + q)^+$. We can then exploit the fact that the phase behavior of a one-component SW fluid is well established.^{33–36} For example, it is sufficient to heuristically consider the approximate critical value³⁵ of the reduced temperature $T^* = k_B T/\epsilon$ to find the appearance of an open phase coexistence region at high η_s (well separated from the closed one predicted in Sec. III A at low η_s). This coexistence region is known to be present in the highly asymmetric AHS mixture^{16,27} (i.e., for small q in the limit $\tau_{sl} \rightarrow \infty$). The effective problem procedure that we followed suggests that, quite intuitively, such a region will not disappear when the attraction is switched on at small τ_{sl} . It is interesting to observe that such a reentrance at large η_s is not predicted by an analysis of the behavior of the effective second virial coefficient B_2^{eff} [see Eq. (B16)], according to which $1/T^* = \ln[1 + (1 - B_2^{\text{eff}}/B_2^{\text{HS}})/(3q + 3q^2 + q^3)]$, where $B_2^{\text{HS}} = \frac{2\pi}{3}\sigma_l^3$. The two heuristic criteria based on an effective SW temperature T^* agree quite well for small values of η_s [as expected from the curve $\eta_s = 0.01$ in Fig. 5(b)], but the B_2^{eff} criterion presents a diverging T^* at a value of η_s such that $B_2^{\text{eff}} = B_2^{\text{HS}}$ and becomes meaningless thereafter (i.e., when $B_2^{\text{eff}} > B_2^{\text{HS}}$). For instance, if $q = q_0$ and $\tau_{sl} = 0.12$, the condition $B_2^{\text{eff}} > B_2^{\text{HS}}$ is satisfied for $\eta_s > 0.274$. The fact that $B_2^{\text{eff}} > B_2^{\text{HS}}$ if η_s is large enough is directly related to the increase of the effective size of the *dressed* solute particles, as depicted in Figs. 2(c) and 2(d).

Of course, the effective one-component fluid is not fully equivalent to the original binary mixture, as we are neglecting three-body (and higher) terms in the effective total potential [see Eq. (2.7)]. Moreover, the potentials of Fig. 5 are the outcome of the PY approximation. Yet, they are expected to give reasonable approximate results in the spirit of an effective fluid. Chen *et al.*¹¹ devised a similar approximate mapping

of the PY solution for the true binary mixture onto a one-component SHS model, from which they were able to read-off the binodal using accurate Monte Carlo (MC) results by Miller and Frenkel.³⁷

While some caution must be exercised when using the pairwise potential formally obtained in the limit $\eta_l \rightarrow 0$ to predict the phase diagram at finite η_l , this keeps being a useful procedure to reduce the complexity of the binary mixture problem,³⁸ allowing one to get additional physical insight without the need, for example, of performing computer simulations of the full binary mixture.

IV. THE SAO MODEL

As shown in Sec. III, the ASHS model ($\sigma_{ss}/\sigma_s = 1$) admits a PY analytical solution but only an approximate reduction to an effective one-component fluid. The SAO model ($\sigma_{ss}/\sigma_s = 0$) is, in some sense, complementary to it, as it does not admit an analytical solution, not even in the PY approximation, but it does admit an exact reduction to an effective one-component fluid for $q < q_0 = 2/\sqrt{3} - 1 \approx 0.1547$, when a solvent particle can fit into the inner volume created by three solutes at contact,³⁹ so that a solvent particle cannot overlap simultaneously with more than two (nonoverlapping) solute particles. This corresponds to $q < 1$ in one spatial dimension.⁴⁰

To proceed, it is convenient to change from the canonical (N_s, N_l, V, T) ensemble to the semi-grand-canonical (μ_s, N_l, V, T) ensemble,^{16,17} where μ_s is the chemical potential of the solvent component. The corresponding thermodynamic potential $\mathcal{F}(\mu_s, N_l, V, T)$ is constructed via the Legendre transform,

$$\mathcal{F}(\mu_s, N_l, V, T) = F(\langle N_s \rangle, N_l, V, T) - \mu_s \langle N_s \rangle. \quad (4.1)$$

Thus, the counterpart of canonical equation (2.4) is

$$\begin{aligned} e^{-\beta\mathcal{F}} &= \sum_{N_s=0}^{\infty} \frac{z_s^{N_s}}{N_s! N_l! \Lambda_l^{3N_l}} \int d\mathbf{r}^{N_s} \int d\mathbf{r}^{N_l} e^{-\beta(U_{ll} + U_{sl})} \\ &= \frac{1}{N_l! \Lambda_l^{3N_l}} \int d\mathbf{r}^{N_l} e^{-\beta U_{ll}^{\text{eff}}}, \end{aligned} \quad (4.2)$$

where

$$z_s = \frac{e^{\beta\mu_s}}{\Lambda_s^3} \quad (4.3)$$

is the solvent fugacity and

$$e^{-\beta U_{ll}^{\text{eff}}} = e^{-\beta U_{ll}} \sum_{N_s=0}^{\infty} \frac{z_s^{N_s}}{N_s!} \int d\mathbf{r}^{N_s} e^{-\beta U_{sl}}. \quad (4.4)$$

Note that in Eq. (4.2) we have taken into account that $U_{ss} = 0$ in the SAO model.

Inserting Eq. (2.3) into Eq. (4.4), it is easy to obtain¹⁷

$$\beta\Omega = -z_s \int d\mathbf{r} \prod_{i=1}^{N_l} [1 + f_{sl}(|\mathbf{r} - \mathbf{r}_i^{(l)}|)], \quad (4.5)$$

where $\Omega = U_{ll}^{\text{eff}} - U_{ll}$ represents the grand potential of an ideal gas of solvent particles in the external field of a fixed configuration of N_l solute particles with coordinates $\{\mathbf{r}_i^{(l)}\}$. Expanding

in products of Mayer functions, Ω can be written as

$$\Omega = \sum_{n=0}^{n_{\max}(q)} \Omega_n. \quad (4.6)$$

Here, Ω_n is the contribution to Ω stemming from the product of n Mayer functions f_{sl} . The upper limit $n_{\max}(q)$ is the maximum number of nonoverlapping solutes that can simultaneously overlap with a single solvent particle. For $n > n_{\max}(q)$, at least one of the factors f_{sl} vanishes and so does Ω_n . If $q < q_0$, then $n_{\max}(q) = 2$, implying that the exact effective potential U_{ll}^{eff} does not include three-body (or higher order) terms. In the interval $q_0 < q \leq 1$, $n_{\max}(q)$ grows by steps as q increases, reaching a maximum value $n_{\max}(q) = 11$ (since a solvent particle can simultaneously overlap with 12 nonoverlapping solutes only if $q > 1$). The first few terms in Eq. (4.6) are

$$\beta\Omega_0 = -z_s V, \quad (4.7)$$

$$\beta\Omega_1 = -z_s \sum_{i=1}^{N_l} \int d\mathbf{r} f_{sl}(|\mathbf{r} - \mathbf{r}_i^{(l)}|), \quad (4.8)$$

$$\begin{aligned} \beta\Omega_2 &= -z_s \sum_{i < j}^{N_l} \int d\mathbf{r} f_{sl}(|\mathbf{r} - \mathbf{r}_i^{(l)}|) f_{sl}(|\mathbf{r} - \mathbf{r}_j^{(l)}|) \\ &= \beta \sum_{i < j}^{N_l} [v_{ll}(|\mathbf{r}_i^{(l)} - \mathbf{r}_j^{(l)}|) - \varphi_{ll}(|\mathbf{r}_i^{(l)} - \mathbf{r}_j^{(l)}|)]. \end{aligned} \quad (4.9)$$

Equation (4.9) allows us to identify the exact effective pair potential as

$$\beta v_{ll}(r) = \beta \varphi_{ll}(r) - z_s \int d\mathbf{r}_s f_{sl}(r_s) f_{sl}(|\mathbf{r}_s - \mathbf{r}|). \quad (4.10)$$

Now, making use of Eq. (2.10), one can obtain

$$\beta\Omega_1 = z_s \eta_l V (1 + q)^3 \left(1 - \frac{1}{4\tau_{sl}}\right), \quad (4.11)$$

$$\beta v_{ll}(r) = \eta_s^{(r)} \begin{cases} \infty, & r < \sigma_l, \\ \psi(r), & \sigma_l < r < \sigma_l(1 + q), \\ 0, & r > \sigma_l(1 + q), \end{cases} \quad (4.12)$$

where $\eta_s^{(r)} = z_s(\pi/6)\sigma_s^3$ is the (nominal) solvent packing fraction of a reservoir made of noninteracting solvent particles and

$$\psi(r) = \psi_d(r) + \psi_p(r) + \psi_b(r), \quad (4.13)$$

with

$$\begin{aligned} \psi_d(r) &= -\frac{6}{\pi\sigma_s^3} \int d\mathbf{r}_s \Theta(\sigma_{sl} - r_s) \Theta(\sigma_{sl} - |\mathbf{r}_s - \mathbf{r}|) \\ &= -\frac{(1 + q - r/\sigma_l)^2 (2 + 2q + r/\sigma_l)}{2q^3}, \end{aligned} \quad (4.14)$$

$$\begin{aligned} \psi_p(r) &= \frac{\sigma_{sl}}{\pi\sigma_s^3 \tau_{sl}} \int d\mathbf{r}_s \delta(r_s - \sigma_{sl}) \Theta(\sigma_{sl} - |\mathbf{r}_s - \mathbf{r}|) \\ &= \frac{(1 + q)^2 (1 + q - r/\sigma_l)}{4q^3 \tau_{sl}}, \end{aligned} \quad (4.15)$$

$$\begin{aligned} \psi_b(r) &= -\frac{\sigma_{sl}^2}{24\pi\sigma_s^3 \tau_{sl}^2} \int d\mathbf{r}_s \delta(r_s - \sigma_{sl}) \delta(|\mathbf{r}_s - \mathbf{r}| - \sigma_{sl}) \\ &= -\frac{(1 + q)^4}{192q^3 \tau_{sl}^2 r/\sigma_l}. \end{aligned} \quad (4.16)$$

The effective solute-solute force $f_{ll}(r) = -\partial v_{ll}(r)/\partial r$ (outside the hard core, $r > \sigma_l$) is

$$\frac{\beta f_{ll}(r)}{\eta_s^{(r)}} = - \left[\psi'_d(r) + \psi'_p(r) + \psi'_b(r) \right] \Theta(1 + q - r/\sigma_l) - \frac{(1+q)^3}{192q^3\tau_{sl}^2} \delta(r - \sigma_l(1+q)), \quad (4.17)$$

where the delta term reflects the discontinuity of $v_{ll}(r)$ at $r = \sigma_l(1+q)$ and

$$\psi'_d(r) = \frac{3}{2q^3\sigma_l} \left[(1+q)^2 - \frac{r^2}{\sigma_l^2} \right], \quad (4.18)$$

$$\psi'_p(r) = -\frac{(1+q)^2}{4q^3\sigma_l\tau_{sl}}, \quad \psi'_b(r) = \frac{(1+q)^4}{192q^3\tau_{sl}^2r^2/\sigma_l}. \quad (4.19)$$

If $q < q_0$, the general relationship between the reservoir packing fraction $\eta_s^{(r)}$ (or, equivalently, the fugacity z_s) and the values η_s and η_l of the binary mixture is derived in Appendix C with the result

$$\eta_s = \eta_s^{(r)} \left[1 - \eta_l(1+q)^3 \left(1 - \frac{1}{4\tau_{sl}} \right) - \frac{12\eta_l^2q^3}{\sigma_l^3} \times \int_{\sigma_l}^{\sigma_l(1+q)} dr r^2 \psi(r) g_{\text{eff}}(r|\eta_l, \eta_s^{(r)}) \right], \quad (4.20)$$

where $g_{\text{eff}}(r|\eta_l, \eta_s^{(r)})$ is the radial distribution function of a pure fluid of large particles interacting via the effective pair potential $v_{ll}(r)$ at a packing fraction η_l . Up to second order in η_l , Eq. (4.20) becomes

$$\eta_s \approx \eta_s^{(r)} \left[1 - \eta_l(1+q)^3 \left(1 - \frac{1}{4\tau_{sl}} \right) - \frac{12\eta_l^2q^3}{\sigma_l^3} \times \int_{\sigma_l}^{\sigma_l(1+q)} dr r^2 \psi(r) e^{-\eta_s^{(r)}\psi(r)} \right]. \quad (4.21)$$

Interestingly, exact effective pair-potential (4.12) can be equivalently obtained from a density expansion of the approximate PY effective potential of the ASHS model described in Sec. III, upon neglecting terms of order higher than linear in η_s and identifying η_s with $\eta_s^{(r)}$, that is correct

in the solute infinite dilution limit [see Eq. (4.20)]. This is not a coincidence³¹ because the PY theory gives the exact radial distribution function to first order in density (and therefore it gives the exact effective potential to that order) and the relevant Mayer diagram, containing only one solvent particle, is the same whether the mixture is additive or not.

The three terms appearing in Eq. (4.13) bear a particularly simple and instructive physical interpretation. The first term, $\psi_d(r)$ [see Eqs. (4.14) and (4.18)], is the conventional AO effective potential.¹⁶ If $r < \sigma_l(1+q)$, no solvent particles fit in the line joining the centers of the two solute particles. This is the typical configuration of *depletion* when the solute-solvent interactions are of HS type, giving rise to an effective *attraction* between the solutes (with a force decreasing its strength quadratically with increasing distance). Now imagine we switch the stickiness on. Interestingly, this produces two competing effects. First, the solvent particles attached to the outer surfaces of each facing solute tend to *pull* the solutes apart, producing an effective solute-solute *repulsion* with a constant force strength. This is represented by the “pulling” term $\psi_p(r)$ [see Eqs. (4.15) and (4.19)]. Second, the solvent particles attached to *both* facing solutes (the “bridges”) tend to increase *attraction* (with a Coulomb-like force strength decreasing with increasing distance), this bridging effect being represented by the term $\psi_b(r)$ [see Eqs. (4.16) and (4.19)]. These three effects are schematically synthesized in Fig. 6.

It is interesting to remark that the SAO model can be easily extended by replacing the solute-solvent sticky surface by a finite-width (Δ_{sl}) SW interaction. The resulting square-well Asakura–Oosawa (SWAO) model is worked out in Appendix D. In this case, the condition for an exact reduction of the effective solute interaction to pairwise terms is $q(1 + \Delta_{sl}) + \Delta_{sl} < q_0$.

The interplay of the three contributions to $\psi(r)$ gives rise to interesting transitions in the shape of the depletion potential, as illustrated in Fig. 7 for the SAO and SWAO models. Let us comment the curves corresponding to the SAO model. For relatively weak stickiness, $\tau_{sl}^{-1} < \tau_c^{-1} \equiv 24(1 - \sqrt{1 - q - q^2/2})/(1+q)^2$, the pulling effect dominates over

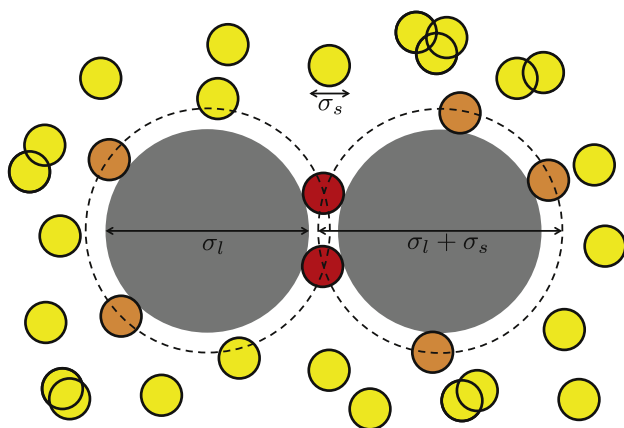


FIG. 6. Cartoon describing the three effects (depletion, pulling, and bridging) contributing to the effective solute-solute interaction in the SAO model. The grey large spheres represent the solutes of diameter σ_l at a distance $r < \sigma_l + \sigma_s = \sigma_l(1+q)$. They are surrounded by a sea of smaller spheres (the solvent) of diameter $\sigma_s = q\sigma_l$ ($q = 0.2$ in the cartoon) that can overlap among themselves and have a sticky surface (represented by a thick perimeter). Some of the solvent particles (the yellow ones) do not touch the solutes and so they contribute to the (attractive) depletion effect, which is represented by $\psi_d(r)$, a volumetric term independent of τ_{sl} . Other solvent particles (the orange ones) are adhered to one of the big spheres, thus contributing to the (repulsive) pulling effect, represented by $\psi_p(r)$, which is a surface term proportional to τ_{sl}^{-1} . Finally, some other small particles (the red ones) are adhered to both solutes, giving rise to the (attractive) bridging effect, represented by $\psi_b(r)$, which is a line (intersection of two surfaces) term proportional to τ_{sl}^{-2} .

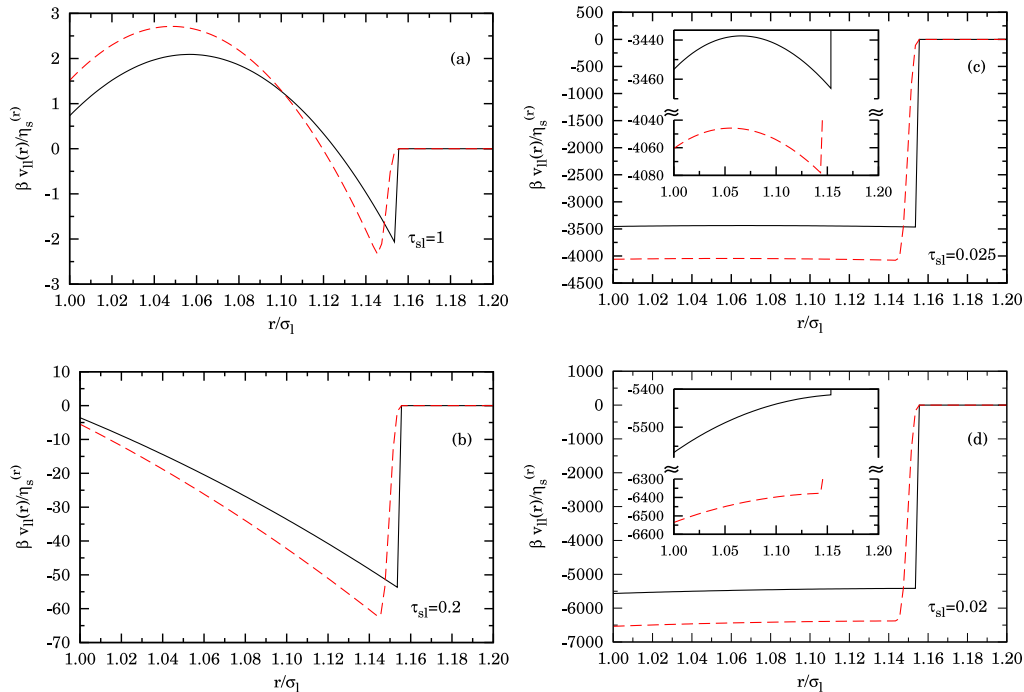


FIG. 7. Plot of $\psi(r) \equiv \beta v_{II}(r)/\eta_s^r$ for (a) $\tau_{sl}=1$, (b) $\tau_{sl}=0.2$, (c) $\tau_{sl}=0.025$, and (d) $\tau_{sl}=0.02$. The solid lines correspond to the SAO model at the threshold value $q=q_0$, while the dashed lines correspond to the SWAO model with $q=q_0-\xi$, $\Delta_{sl}=\xi/(1+q)$, $\xi=10^{-2}$. The insets in panels (c) and (d) show magnified views of the curves for $r/\sigma_1 < 1+q_0$.

the bridging effect for all distances but is dominated by the depletion effect, except for distances close to $r = \sigma_I(1+q)$. Consequently, the effective potential is attractive near $r = \sigma_I$ and repulsive near $r = \sigma_I(1+q)$, as happens in Fig. 7(a). Next, in the intermediate regime $\tau_{sl}^{-1} < \tau_{sl}^{-1} < \tau_{sl}^{-1} \equiv 24(1 + \sqrt{1 - q - q^2/2})/(1+q)^2$, the pulling effect dominates for all distances and the potential is purely repulsive, except for the discontinuous jump at $r = \sigma_I(1+q)$. This is represented by the case of Fig. 7(b). In the strong stickiness regime $\tau_{sl}^{-1} < \tau_{sl}^{-1} < 48$, the depletion effect is practically irrelevant and the pulling effect is dominated by the bridging one, except in the region $r \lesssim \sigma_I(1+q)$. As a consequence, the effective potential is *slightly* attractive near $r = \sigma_I$ and *slightly* repulsive near $r = \sigma_I(1+q)$, as happens in Fig. 7(c). Finally, for very strong stickiness ($\tau_{sl}^{-1} > 48$), the bridging dominates over the pulling for all distances and the potential is purely attractive. This is the case displayed in Fig. 7(d). Those features are essentially preserved in the case of the SWAO model, except that the jump at $r = \sigma_I(1+q)$ is replaced by a rapid (but continuous) increase of the potential between $r = \sigma_I(1+q)$ and $r = \sigma_I(1+q)(1 + \Delta_{sl})$.

From Eqs. (4.14)–(4.19), it is easy to see that in the SAO model the effective potential and force are positive if

$$\frac{6\hat{r} - \sqrt{6\hat{r}(5\hat{r} - 2)}}{24\hat{r}(1 - \hat{r})(2 + \hat{r})} \leq \tau_{sl} \leq \frac{6\hat{r} + \sqrt{6\hat{r}(5\hat{r} - 2)}}{24\hat{r}(1 - \hat{r})(2 + \hat{r})} \quad (4.22)$$

and

$$\frac{2\hat{r} - \sqrt{2(3\hat{r}^2 - 1)}}{24\hat{r}(1 - \hat{r}^2)} \leq \tau_{sl} \leq \frac{2\hat{r} + \sqrt{2(3\hat{r}^2 - 1)}}{24\hat{r}(1 - \hat{r}^2)}, \quad (4.23)$$

respectively, where $\hat{r} \equiv r/[\sigma_I(1+q)]$. Figure 8 shows the region in the plane τ_{sl} vs r where $\psi(r) > 0$ for the threshold value $q = q_0$.

As can be seen from Figs. 7(c) and 7(d), the effective potential in the regime of strong stickiness clearly resembles that of a SW potential of width $q\sigma_I$ and depth $\beta\epsilon = \eta_s^r|\psi(\sigma_I$

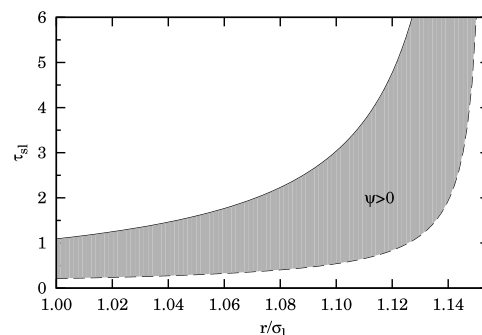


FIG. 8. Plane τ_{sl} vs r showing the region where the effective pair potential in the SAO model for the threshold value $q = q_0$ takes positive values. Outside the shaded region the potential is negative.

$(1+q)| = \eta_s^{(r)}(1+q^{-1})^3/192\tau_{sl}^2$. In this case, the effective phase behavior of an equivalent SW fluid would suggest that for a given $q < q_0$ and a sufficiently small τ_{sl} , we have the appearance of just one lower critical point ($\eta_s^{(r)c}, \eta_l^c$) and the instability region does not close itself again at $\eta_s^{(r)} > \eta_s^{(r)c}$. This is a scenario quite different from the one in the model ASHS, where we found at least one closed island with a lower and an upper critical point (see Sec. III A). It would then be sufficient to switch on a hard-core repulsion (with $\sigma_{ss} = \sigma_s$) among the solvent particles to have a closed spinodal. Along similar lines, it is also interesting to observe that the threshold packing fraction η_s^* defined in Sec. I clearly diverges in the SAO model because the solvent particles can freely overlap.

V. THE NORO–FRENKEL CRITICALITY CRITERION

In 2000, NF²⁵ argued that the reduced second virial coefficient B_2/B_2^{HS} , rather than the range and the strength of the attractive interactions, could be the most convenient quantity to estimate the location of the critical point for a wealth of different colloidal suspensions. Their criticality criterion for particles with variable range attractions,²⁵ complemented by the simulation value of the critical temperature obtained in Ref. 37 for the SHS model, yields $B_2/B_2^{\text{HS}} \simeq -1.21$.

In this section, we apply the NF criterion to the two models discussed before: the ASHS model (see Sec. III) and the SAO model (see Sec. IV). In both cases, if $v_{ll}(r)$ is the effective solute-solute pair potential, the associated second virial

coefficient B_2^{eff} is given by

$$\frac{B_2^{\text{eff}}}{B_2^{\text{HS}}} = 1 - \frac{3}{\sigma_1^3} \int_{\sigma_1}^{\infty} dr r^2 [e^{-\beta v_{ll}(r)} - 1], \quad (5.1)$$

where $B_2^{\text{HS}} = 2\pi\sigma_1^3/3$ is the virial coefficient for HSs of diameter σ_1 . Paradoxically, while the explicit PY expression of $\beta v_{ll}(r)$ in the ASHS model is rather cumbersome (see Appendix B), its associated second virial coefficient B_2^{eff} is much easier to obtain thanks to properties of the Laplace representation. The result can be found in Eq. (B16). In contrast, in the SAO model, the exact expression of $\beta v_{ll}(r)$ is very simple [see Eqs. (4.12)–(4.16)] but the computation of B_2^{eff} needs to be done numerically.

It is particularly instructive to observe that the NF criterion confirms the very different critical behavior between the ASHS model ($\sigma_{ss}/\sigma_s = 1$) and the SAO model ($\sigma_{ss}/\sigma_s = 0$). In Figs. 9(a) and 9(b), we compare the second effective virial coefficients for the two models as functions of τ_{sl} for $q = q_0$ and several values of $\eta_s^{(r)}$. Here, we have identified $\eta_s \rightarrow \eta_s^{(r)}$ in the ASHS case, in consistency with the fact that the effective potential is derived in the infinite solute dilution limit. The loci of points in the plane $\eta_s^{(r)}$ vs τ_{sl} where $B_2^{\text{eff}}/B_2^{\text{HS}} = -1.21$ are displayed in Figs. 9(c) and 9(d). Inside the shaded regions one has $B_2^{\text{eff}}/B_2^{\text{HS}} < -1.21$ and thus phase coexistence is possible, according to the NF criterion.

As we already knew from the results of Sec. III A, Figs. 9(a) and 9(c) show criticality in the ASHS model only for

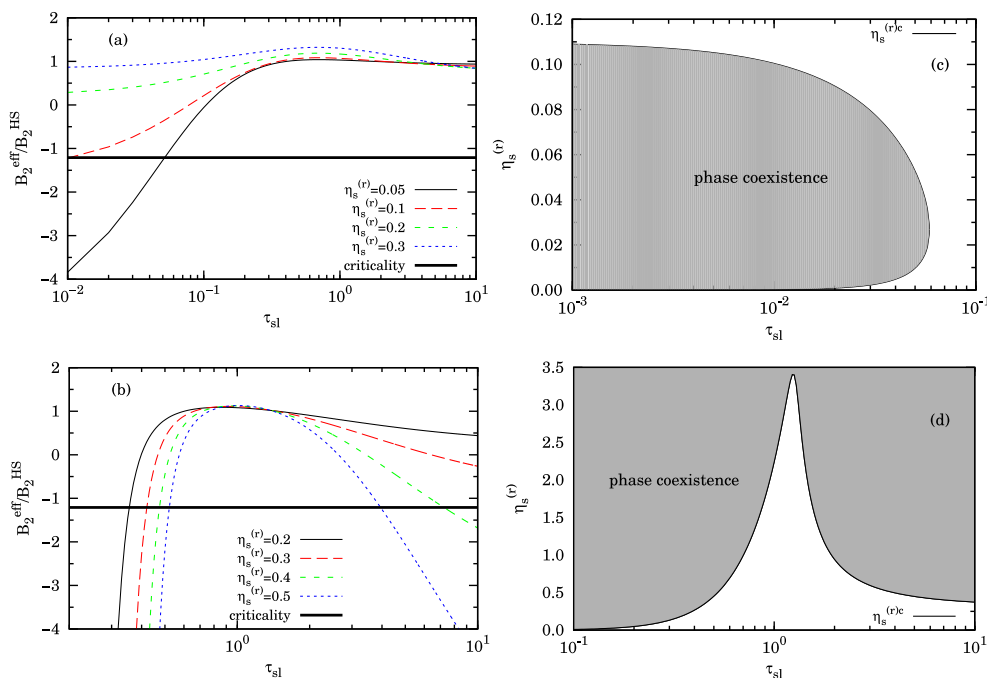


FIG. 9. Second effective virial coefficient as a function of τ_{sl} for $q = q_0$ and several values of $\eta_s^{(r)}$ for (a) ASHS and (b) SAO models. The thick horizontal line corresponds to the NF criticality criterion $B_2^{\text{eff}}/B_2^{\text{HS}} = -1.21$. Panels (c) and (d) show the dependence of the critical value $\eta_s^{(r)} = \eta_s^{(r)c}$ (according to the NF criterion) as a function of τ_{sl} for the ASHS and SAO models, respectively. Note that a logarithmic scale is used on the abscissas.

sufficiently small τ_{sl} and $\eta_s^{(r)}$. On the other hand, the scenario present in the SAO model is completely different. It is easy to check that a critical point in the pure AO model ($\tau_{sl} \rightarrow \infty$) exists only, according to the NF criterion, if $\eta_s^{(r)} \gtrsim 0.318$. However, the presence of stickiness (finite τ_{sl}) dramatically changes the picture. For any $\eta_s^{(r)}$, there exists a critical point if τ_{sl} is small enough. Beyond a certain threshold value, criticality abruptly disappears and then (only if $\eta_s^{(r)} \gtrsim 0.318$) it *re-enters* at a sufficiently large value of τ_{sl} . Thus, if $\eta_s^{(r)} \gtrsim 0.318$, there exists a window of values of τ_{sl} where no phase separation is possible. Note that values of $\eta_s^{(r)} > 1$, as displayed in Fig. 9(d), are not unphysical in the SAO model since the reservoir consists in an ideal gas of noninteracting small particles.

It must be remarked that the bridging and pulling effects are more important in the nonadditive SAO case than in the ASHS one, since in the latter the mutual exclusion of solvent particles interferes with their ability to attach to the solutes. As illustrated in Fig. 9, this leads to paramount differences in the critical behavior of the two extreme models. For intermediate NASHS models with $0 < \sigma_{ss}/\sigma_s < 1$ (see Fig. 3), a transition from Figs. 9(b) and 9(d) to Figs. 9(a) and 9(c), respectively, can be expected as the excluded volume among the solvent spheres is gradually increased.

Note also that in the ASHS model [Fig. 9(a)], the results are approximate (PY) and the solute concentration is zero. On the contrary, in the SAO model [Fig. 9(b)], the results are exact and valid for any finite solute and solvent concentrations. While both models coincide in the limit of vanishing solvent concentration, in practice this equivalence requires extremely small values of $\eta_s^{(r)}$. For instance, at $\eta_s^{(r)} = 10^{-5}$, both values of B_2^{eff} differ by nearly 2%.

VI. PERTURBATION THEORY FOR THE SAO MODEL

From Sec. V we conclude that the “hidden” fluid-fluid phase separation observed by Dijkstra *et al.*¹⁶ in their study of the AO model could be stabilized by adding adhesion, as in our SAO model. This can be quantified more precisely using a first-order thermodynamic perturbation theory.³⁹

Assuming the HS fluid as reference system, we can write the Helmholtz free energy per particle of the effective solute system as

$$\frac{\beta F^{\text{eff}}}{N_l} = \frac{\beta F_{\text{HS}}}{N_l} + 12\eta_l \eta_s^{(r)} \int_{\sigma_l}^{\sigma_l(1+q)} dr r^2 \psi(r) g_{\text{HS}}(r|\eta_l), \quad (6.1)$$

where $\beta F_{\text{HS}}/N_l = (4\eta_l - 3\eta_l^2)/(1 - \eta_l)^2 + \ln(\eta_l) + \text{const}$ is the Carnahan–Starling⁴¹ HS expression, $\psi(r)$ is given by Eqs. (4.13)–(4.16), and g_{HS} is the HS radial distribution function in the PY approximation,⁴² which in the interval $\sigma_l < r < \sigma_l(1+q) < 2$ can be written as

$$g_{\text{HS}}(r|\eta_l) = \sum_{n=1}^3 \lim_{t \rightarrow t_n(\eta_l)} \frac{[t - t_n(\eta_l)] t L(t|\eta_l) e^{t(r-1)}}{S(t|\eta_l) r}, \quad (6.2)$$

where we are measuring lengths in units of σ_l ,

$$S(t|\eta_l) = (1 - \eta_l)^2 t^3 + 6\eta_l(1 - \eta_l)t^2 + 18\eta_l^2 t - 12\eta_l(1 + 2\eta_l), \quad (6.3)$$

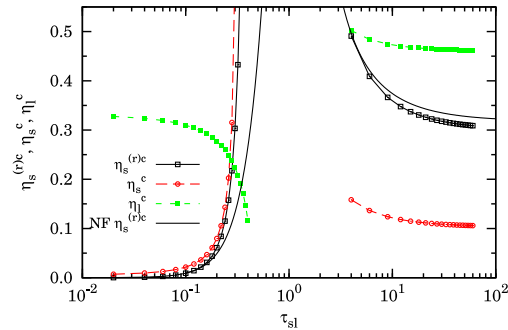


FIG. 10. Critical point for the fluid-fluid coexistence in the SAO model for $q = q_0$ as a function of τ_{sl} . The lines with symbols are obtained from perturbation theory, while the solid line corresponds to the NF criterion [see Fig. 9(d)]. A logarithmic scale is used on the abscissa. Equation (4.21) is used for the conversion between the reservoir and the solvent densities.

$$L(t|\eta_l) = (1 + \eta_l/2)t + 1 + 2\eta_l, \quad (6.4)$$

and $t_n(\eta_l)$ ($n = 1, 2, 3$) are the zeros of $S(t|\eta_l)$. The first-order Helmholtz free energy of Eq. (6.1) can thus be calculated analytically.

The compressibility factor $Z = \beta p/\rho$ and chemical potential μ are then found through

$$Z^{\text{eff}} = \eta_l \left. \frac{\partial(\beta F^{\text{eff}}/N_l)}{\partial \eta_l} \right|_{\eta_s^{(r)c}}, \quad (6.5)$$

$$\beta \mu^{\text{eff}} = Z^{\text{eff}} + \frac{\beta F^{\text{eff}}}{N_l}. \quad (6.6)$$

The critical point $(\eta_s^{(r)c}, \eta_l^c)$ is determined by numerically solving the following set of equations:

$$\left. \frac{\partial(\eta_l Z^{\text{eff}})}{\partial \eta_l} \right|_{\eta_s^{(r)c}, \eta_l^c} = 0, \quad (6.7)$$

$$\left. \frac{\partial^2(\eta_l Z^{\text{eff}})}{\partial \eta_l^2} \right|_{\eta_s^{(r)c}, \eta_l^c} = 0. \quad (6.8)$$

In Fig. 10, we show the critical point $(\eta_s^{(r)c}, \eta_l^c)$ for the fluid-fluid coexistence in the SAO model at the threshold value $q = q_0$ as a function of τ_{sl} . The figure confirms the scenario predicted in Sec. V from the NF criterion. In fact, Fig. 10 shows a relevant mutual consistency between the curves for $\eta_s^{(r)c}$ as obtained from both independent approaches. There is a range of adhesion for which there is no criticality. For high adhesions (small τ_{sl}), we have phase coexistence in the region of low $\eta_s^{(r)}$ region, while for low adhesions (large τ_{sl}), the criticality exists in the region of high $\eta_s^{(r)}$. Of course, we expect a breakdown of the perturbation theory treatment as soon as stickiness becomes too strong. Also, as soon as $q > q_0$, we are neglecting three-body (and higher) terms.

VII. CONCLUSIONS

In this paper, we have studied two complementary models of a binary mixture of (small) solvent and (large) solute particles, where in both cases unlike particles experience an

attractive adhesion interaction of Baxter's type.⁷ We studied the derivation of an effective solute-solute pair-potential for the two models in the regime of large size asymmetry ($q = \sigma_s/\sigma_l \ll 1$) and discussed analogies and differences of the corresponding phase behaviors, as obtained from the resulting effective one-component fluid.

In the first model, which we dubbed ASHS, both solute-solute and solvent-solvent particles interact as HSs and the reduction to an effective one-component fluid can be carried out only approximately via a small solute density expansion. By contrast, this model admits an exact analytical solution within the PY approximation. In the limit of vanishing solute-solvent adhesive attraction, this model reduces to the usual AHS binary mixture, which is known not to display any phase separation within the PY approximation. This might, however, be ascribed to the limitations of the PY closure, as other more sophisticated theories, as well as numerical simulations, support the existence of phase separation, albeit metastable with respect to freezing, at sufficiently large concentrations and size asymmetry (in this context, nevertheless, see Ref. 43). In this case, our analysis of the ASHS model confirms previous findings of a similar study by Chen *et al.*¹¹ in predicting a closed region in the (η_s, η_l) plane where phase separation occurs.

While the ASHS model has been around for some time,¹² the second model (denoted as SAO) is, to the best of our knowledge, new. In this case, solvent particles behave as an ideal gas within each other—but still they experience a SHS interaction with the solutes. In the limit of no adhesion between solute and solvent, this model reduces to the well-known AO one, and we have extended the analysis performed by Dijkstra *et al.*¹⁷ to the present case. As in the AO case, even in the SAO case, the solvent degrees of freedom can be traced out exactly above a well defined size asymmetry (that is, below a critical value q_0 of the size ratio q), so that the resulting effective one-component pair potential is *exact*. By contrast, it is not possible in this case to obtain an exact analytical solution of the binary problem (not even within the PY approximation), so we resorted to study a first-order thermodynamic perturbation theory of the corresponding exact effective solute-solute pair potential.

In both models, effective potentials can be explained in terms of “pulling” and “bridging” effects in addition to the usual “depletion” mechanism. In the SAO case, the analytical expressions of the effective potential derived in Eqs. (4.12)–(4.16) allow for an interesting direct physical interpretation. The pulling effect is represented by the term proportional to τ_{sl}^{-1} [see Eq. (4.15)], as the same (solvent) particle must be in contact with one of the solutes and outside the exclusion volume of the other solute. On the other hand, the bridging effect is represented by the term proportional to τ_{sl}^{-2} [see Eq. (4.16)], as the same (solvent) particle must be in contact with both solute particles. These effects are present in both models, but they are more important in the SAO case than in the ASHS case, since in the latter, the mutual exclusion of solvent particles interferes with their ability to be attached to the solutes. In fact, the situation sketched in Fig. 2(d) is inhibited in the SAO model, as represented by Fig. 9(d), which shows always phase coexistence at increasing $\eta_s^{(r)}$ for any fixed τ_{sl} .

The derivation of the exact SAO effective potential has allowed us to clearly assess the dramatic influence of

solute-solvent attraction on the conventional AO depletion potential. This complements a recent study,⁴⁴ where softness in the solute-solvent repulsion was seen to strongly enhance the depletion mechanism.

Leaving aside the issue of the metastability with respect to the fluid-solid transition, the resulting picture confirms the significant impact of nonadditivity on the fluid-fluid phase diagram, as synthesized by Fig. 9. Within the NF criticality criterion, the SAO model is expected to display a reentrant phase transition in terms of τ_{sl} , whereas the ASHS model is not. On the other hand, the results for the ASHS model are compatible with a reentrant phase transition in terms of η_s , not observed in the SAO model. A first-order perturbation theory on the SAO model confirms this picture.

Our findings nicely confirm and complement those by Chen *et al.*¹¹ but extend them to encompass a *direct* connection with the AO original model, which was missing in the above study, thus paving the way to a more direct interpretation of the experimental results reported in Refs. 8 and 9.

While direct numerical simulations of binary mixtures with large size asymmetries are notoriously difficult, it would be interesting to study with numerical experiments whether adhesion gives rise to the appearance of a metastable fluid-fluid coexistence at large solvent densities for the ASHS model with large q and for the SAO model with very small q . In addition, they open a number of interesting perspectives for future studies. Even without resorting to a direct numerical simulation calculations, a number of different theoretical approaches can be exploited to make further progresses.

As the attraction between the unlike spheres vanishes ($\tau_{sl} \rightarrow \infty$), the PY solution of the ASHS model reduces to the well-known PY solution for a binary AHS mixture,⁴⁵ which does not show phase separation for any size ratio, in spite of the possible depletion interactions. As said above, this seems to be an artifact of the PY approximation, as shown by numerical simulations of the (approximate) effective one-component fluid¹⁶ and by numerical solutions of the Rogers and Young (RY) closure.⁴⁶ Thus, one possibility would be to use the RY closure on a binary mixture with HS interactions between like particles and a short-range SW attraction (in the regimes where this can be considered sticky-like^{47,48}) between unlike spheres. Work along these lines is in progress and will be reported elsewhere.

Another possibility would be to consider a binary ASHS mixture with HS interactions between small spheres, weak SHS interactions between the large spheres, and stronger SHS interactions between small and big spheres. This two-component model (which is known to be free from the thermodynamic inconsistency affecting the one-component model⁴⁹) could be solved rather easily within the PY approximation, as done for instance by Zaccarelli *et al.*⁵⁰

Finally, it would be nice to extend the study reported here for the ASHS and SAO models to a more general NASHS model where one could tune the solvent-solvent diameter from zero (SAO model) to the additive value (ASHS model), thus encompassing both models into a unified framework. MC simulations for a binary ASHS mixture have been performed by Jamnik,⁵¹ but not for the determination of the phase diagram, which has been studied for the one-component SHS fluid

by Miller and Frenkel.^{37,52} To the best of our knowledge, no numerical experiment has ever been tried on the NASHS binary mixture.

ACKNOWLEDGMENTS

A.G. gratefully acknowledges support from PRIN-MIUR 2010-2011 project (Contract No. 2010LKE4CC). The research of A.S. has been partially supported by the Spanish Government through Grant No. FIS2013-42840-P and by the Regional Government of Extremadura (Spain) through Grant No. GR15104 (partially financed by ERDF funds).

APPENDIX A: A SIMPLE GEOMETRICAL ARGUMENT RELATED TO FIG. 2

We first estimate how many small spheres of diameter σ_s are necessary to cover the surface of a large sphere of diameter σ_l . Assuming $q = \sigma_s/\sigma_l \ll 1$, the small spheres will be distributed on the large sphere surface approximately with a hexagonal packing corresponding to an area fraction $\eta_{\text{hex}} = \pi/2\sqrt{3} \approx 0.907$. Thus, $\eta_{\text{hex}} = \phi a/A$, where ϕ is the number of the adsorbed small spheres, $a = (\pi/4)\sigma_s^2$ is the area of the projected disk associated with each solvent sphere, and $A = \pi\sigma_l^2$ is the surface area of the solute particle. Therefore,

$$\phi = \eta_{\text{hex}} \frac{A}{a} = \frac{2\pi}{\sqrt{3}} q^{-2}. \tag{A1}$$

The critical volume fraction η_s^* at which all large colloidal spheres, distributed with a volume fraction $\eta_l = (\pi/6)\rho_l\sigma_l^3$, can be covered is

$$\eta_s^* = \eta_l q^3 \phi \tag{A2}$$

and this leads to the expression reported in Sec. I.

APPENDIX B: ANALYTICAL PY EXPRESSIONS FOR THE ASHS MODEL IN THE LIMIT $x_l \rightarrow 0$

The Rational-Function Approximation (RFA) methodology^{15,31,53} is known to give access to analytical formulas of the PY solution for the ASHS model.^{7,12,28} In this appendix, we assume the infinite dilution limit for the solutes ($x_l \rightarrow 0$).

According to Eq. (36) of Ref. 31, the Laplace transform $G_{ll}(s) = \int_0^\infty dr e^{-sr} r g_{ll}(r)$ of $rg_{ll}(r)$ is, in the limit $x_l \rightarrow 0$,

$$G_{ll}(s) = \frac{e^{-s}}{s^2} \left[L_{ll}(s) + L_{ls}(s) \frac{A_{ss}(s)}{1 - A_{ss}(s)} \right], \tag{B1}$$

where $\sigma_l = 1$ has been chosen as length unit and¹⁵

$$L_{ll}(s) = L_{ll}^{(0)} + L_{ll}^{(1)} s, \tag{B2}$$

$$L_{ls}(s) = L_{ls}^{(0)} + L_{ls}^{(1)} s + L_{ls}^{(2)} s^2, \tag{B3}$$

$$A_{sl}(s) = 12\eta_s \left[\phi_2(qs) L_{sl}^{(0)} + \frac{\phi_1(qs)}{q} L_{sl}^{(1)} + \frac{\phi_0(qs)}{q^2} L_{sl}^{(2)} \right], \tag{B4}$$

$$A_{ss}(s) = 12\eta_s \left[\phi_2(qs) L_{ss}^{(0)} + \frac{\phi_1(qs)}{q} L_{ss}^{(1)} \right]. \tag{B5}$$

Here, $\phi_n(x) \equiv -x^{-(n+1)} \left[e^{-x} - \sum_{j=0}^n (-x)^j / j! \right]$. The coefficients $L_{\alpha\gamma}^{(k)}$ are given by¹⁵

$$L_{ll}^{(0)} = L_{sl}^{(0)} = \frac{1 - (12\eta_s/q^2)L_{sl}^{(2)}}{1 - \eta_s} + \frac{3\eta_s}{q(1 - \eta_s)^2}, \tag{B6}$$

$$L_{ls}^{(0)} = L_{ss}^{(0)} = \frac{1}{1 - \eta_s} + \frac{3\eta_s}{(1 - \eta_s)^2}, \tag{B7}$$

$$L_{ll}^{(1)} = \frac{1 - (6\eta_s/q^2)L_{sl}^{(2)}}{1 - \eta_s} + \frac{3\eta_s}{2q(1 - \eta_s)^2}, \tag{B8}$$

$$L_{sl}^{(1)} = \frac{1 + q - (12\eta_s/q)L_{sl}^{(2)}}{2(1 - \eta_s)} + \frac{3\eta_s}{2(1 - \eta_s)^2}, \tag{B9}$$

$$L_{ls}^{(1)} = \frac{1 + q}{2(1 - \eta_s)} + \frac{3\eta_s}{2(1 - \eta_s)^2}, \tag{B10}$$

$$L_{ss}^{(1)} = q \frac{1 + \eta/2}{(1 - \eta)^2}, \tag{B11}$$

$$L_{ls}^{(2)} = L_{sl}^{(2)} = \frac{1}{12} \frac{1 + q + \frac{3\eta_s}{1 - \eta_s}}{4\tau_{sl} \frac{1 - \eta_s}{1 + q} + \eta_s/q}. \tag{B12}$$

This closes the determination of $G_{ll}(s)$ for given values of η_s , q , and τ_{sl} . Then, by numerical inverse transform, one can easily obtain $g_{ll}(r)$. On the other hand, pure analytical expressions are also possible for the different layers $1 < r < 1 + q$, $1 + q < r < 1 + 2q$, $1 + 2q < r < 1 + 3q$, ... The trick consists in formally attaching a bookkeeping factor ε to any exponential in $G_{ll}(s)$. Then, by expanding in powers of ε , we can write

$$G_{ll}(s) = \sum_{n=0}^\infty \varepsilon^{-(1+nq)s} \Gamma_n(s), \tag{B13}$$

where we have made $\varepsilon = 1$. From Eq. (B13), we get

$$g_{ll}(r) = \frac{1}{r} \sum_{n=0}^\infty \Theta(r - 1 - nq) \gamma_n(r - 1 - nq), \tag{B14}$$

where $\gamma_n(r)$ is the inverse Laplace transform of $\Gamma_n(s)$. The functions $\gamma_n(r)$ can then be expressed in terms of the three roots of a cubic equation, analogously to the case of Eq. (6.2). Therefore, if we are only interested in the interval $1 \leq r \leq 1 + kq$, we just need to keep the first k terms in the sum of Eq. (B14).

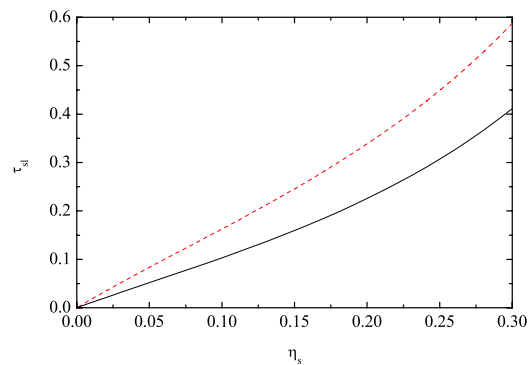


FIG. 11. Loci in the plane τ_{sl} vs η_s where the PY approximation predicts $g_{ll}(r) = 0$ at $r = (1 + q)^+$ for $q = 0.12$ (upper curve) and $q = q_0$ (lower curve). The radial distribution function $g_{ll}(r)$ is not positive definite below each curve.

From a practical point of view, it is sufficient to determine $g_{ll}(r)$ in the interval $1 \leq r \leq 1 + 3q$, in which case only $\gamma_0(r)$, $\gamma_1(r)$, and $\gamma_2(r)$ are needed. Their analytical expressions are easily obtained with a computational software program but are too lengthy to be reproduced here. In general, $\gamma_1(0) \neq 0$, what implies a jump discontinuity of $g_{ll}(r)$ at $r = 1 + q$,

$$\begin{aligned} \delta g_{ll} &\equiv g_{ll}((1+q)^-) - g_{ll}((1+q)^+) = -\frac{\gamma_1(0)}{1+q} \\ &= \frac{(1+q)\eta_s[1+q+(2-q)\eta_s]^2}{12q(1-\eta_s)^2[(1+q)\eta_s+4q\tau_{sl}(1-\eta_s)]^2}. \end{aligned} \quad (\text{B15})$$

Note that $r = 1 + q$ is the threshold distance beyond which no bridges are possible (see Fig. 2). This is clearly reflected by a strong decrease of $g_{ll}(r)$ when going from $r = (1+q)^-$ (bridges are possible) to $r = (1+q)^+$ (no bridging effect). This physical phenomenon can give rise, as an artifact of the PY approximation, to a negative value of $g_{ll}(r)$ at $r = (1+q)^+$ if η_s is sufficiently large or τ_{sl} is sufficiently small. This is illustrated in Fig. 11 for $q = 0.12$ and $q = q_0$.

Once $g_{ll}(r)$ is known, Eq. (3.2) gives the pair potential $v_{ll}(r)$ in the PY approximation, as depicted in Fig. 5. The effective second virial coefficient can also be determined analytically as follows:

$$\begin{aligned} B_2^{\text{eff}} &= -2\pi \int_0^\infty dr r^2 [g_{ll}(r) - 1] = 2\pi \lim_{s \rightarrow 0} \frac{\partial}{\partial s} [G_{ll}(s) - s^{-2}] \\ &= \frac{\pi}{12(1+2\eta_s)^2} \left\{ 8 + (20 - 15q - 6q^2 - q^3)\eta_s + 2(4 - 6q + 3q^2 + q^3)\eta_s^2 - q^3\eta_s^3 \right. \\ &\quad + \frac{2(1+q)\eta_s(1+q+2\eta_s-q\eta_s)[6(1+2\eta_s)+q^2(1-\eta_s)^2+2q(1-\eta_s)(2+\eta_s)]}{(1-\eta_s)[(1+q)\eta_s+4q\tau_{sl}(1-\eta_s)]} \\ &\quad \left. - \frac{(1+q)^2\eta_s(1+q+2\eta_s-q\eta_s)^2(2+q+4\eta_s-q\eta_s)}{(1-\eta_s)[(1+q)\eta_s+4q\tau_{sl}(1-\eta_s)]^2} \right\}. \end{aligned} \quad (\text{B16})$$

APPENDIX C: DERIVATION OF THE RELATIONSHIP BETWEEN η_s , η_l , AND $\eta_s^{(r)}$ IN THE SAO MODEL

In the semi-grand-canonical ensemble (z_s, N_l, V, T) , the average number of small particles can be obtained from the associated thermodynamic potential \mathcal{F} as

$$\langle N_s \rangle_{z_s, N_l} = -z_s \frac{\partial \beta \mathcal{F}}{\partial z_s}. \quad (\text{C1})$$

Now, from Eq. (4.2) and the equality $U_{ll}^{\text{eff}} = U_{ll} + \Omega$, we can write

$$e^{-\beta \mathcal{F}} = \langle e^{-\beta \Omega} \rangle_{N_l} \frac{\int d\mathbf{r}^{N_l} e^{-\beta U_{ll}}}{N_l! \Lambda_l^{3N_l}}, \quad (\text{C2})$$

where

$$\langle \dots \rangle_{N_l} = \frac{\int d\mathbf{r}^{N_l} \dots e^{-\beta U_{ll}}}{\int d\mathbf{r}^{N_l} e^{-\beta U_{ll}}} \quad (\text{C3})$$

denotes a canonical average over the bare solutes. Then, taking into account that $\Omega \propto z_s$, Eq. (C1) reduces to

$$\langle N_s \rangle_{z_s, N_l} = -\frac{\langle e^{-\beta \Omega} \beta \Omega \rangle_{N_l}}{\langle e^{-\beta \Omega} \rangle_{N_l}}. \quad (\text{C4})$$

Next, if $q < q_0$, $\Omega = \Omega_0 + \Omega_1 + \Omega_2$, so that

$$\langle N_s \rangle_{z_s, N_l} = -\beta \Omega_0 - \beta \Omega_1 - \frac{\langle e^{-\beta \Omega_2} \beta \Omega_2 \rangle_{N_l}}{\langle e^{-\beta \Omega_2} \rangle_{N_l}}. \quad (\text{C5})$$

Note that the last term on the right-hand side can be rewritten as

$$\frac{\langle e^{-\beta \Omega_2} \beta \Omega_2 \rangle_{N_l}}{\langle e^{-\beta \Omega_2} \rangle_{N_l}} = \frac{\rho_l^2}{2} V \int d\mathbf{r} \beta v_{ll}(r) g_{\text{eff}}(r | \eta_l, \eta_s^{(r)}), \quad (\text{C6})$$

where

$$g_{\text{eff}}(r_{12}^{(l)} | \eta_l, \eta_s^{(r)}) = \frac{V^2 \int d\mathbf{r}_3^{(l)} \dots \int d\mathbf{r}_{N_l}^{(l)} e^{-\beta U_{ll}^{\text{eff}}}}{\int d\mathbf{r}^{N_l} e^{-\beta U_{ll}^{\text{eff}}}} \quad (\text{C7})$$

and we have taken into account that $N_l(N_l - 1) \approx N_l^2$ in the thermodynamic limit. Finally, applying Eqs. (4.7), (4.11), and (C6) in Eq. (C5), it is easy to obtain Eq. (4.20).

The first two terms on the right-hand side of Eq. (4.20) can also be obtained from the canonical ensemble (N_s, N_l, V, T) . Up to the level of the second virial coefficient, the free energy F is

$$\begin{aligned} \frac{\beta F}{V} &= \rho_s \ln(\rho_s \Lambda_s^3) + \rho_l \ln(\rho_l \Lambda_l^3) - \rho_s - \rho_l + \frac{2\pi}{3} \rho_l^2 \\ &\quad + 2B_{sl} \rho_s \rho_l + O(\rho^3), \end{aligned} \quad (\text{C8})$$

where $B_{sl} = \frac{\pi}{12} \sigma_l^3 (1+q)^3 \left(1 - \frac{1}{4\tau_{sl}}\right)$. The solvent chemical potential is $\mu_s = [\partial(F/V)/\partial \rho_s]_{\rho_l}$, so that

$$z_s \equiv \frac{e^{\beta \mu_s}}{\Lambda_s^3} = \rho_s [1 + 2B_{sl} \rho_l + O(\rho^2)], \quad (\text{C9})$$

which is consistent with Eq. (4.20).

APPENDIX D: SWAO MODEL

In the SWAO model, Eq. (2.10) is replaced by

$$f_{sl}(r) = \begin{cases} -1, & r < \sigma_{sl}, \\ e^{\beta \epsilon_{sl}} - 1, & \sigma_{sl} < r < \sigma_{sl}(1 + \Delta_{sl}), \\ 0, & r > \sigma_{sl}(1 + \Delta_{sl}), \end{cases} \quad (\text{D1})$$

where ϵ_{sl} and $\sigma_{sl} \Delta_{sl}$ are the depth and width, respectively, of the attractive well. One can define an effective stickiness

parameter⁴⁷ $\tau_{sl}^{-1} = 12(e^{\beta\epsilon_{sl}} - 1)\Delta_{sl}$, so that the SWAO model reduces to the SAO one in the double limit $\epsilon_{sl} \rightarrow \infty$, $\Delta_{sl} \rightarrow 0$ at fixed τ_{sl} .

All the steps in Sec. IV up to Eq. (4.10) are still valid for the SWAO model. However, the condition for having $\Omega_n = 0$ if $n \geq 3$ is not $\sigma_{sl} < \sigma_l(1 + q_0)/2$ (or $q < q_0$) but $\sigma_{sl}(1 + \Delta_{sl}) < \sigma_l(1 + q_0)/2$, what is equivalent to $q(1 + \Delta_{sl}) + \Delta_{sl} < q_0$.

To simplify the expressions, in this appendix we take again $\sigma_l = 1$ as the length unit. Inserting Eq. (D1) into Eq. (4.10), one obtains

$$\beta v_{ij}(r) = \eta_s^{(r)} \begin{cases} \infty, & r < 1, \\ \psi(r), & 1 < r < (1 + q)(1 + \Delta_{sl}), \\ 0, & r > (1 + q)(1 + \Delta_{sl}), \end{cases} \quad (\text{D2})$$

where the function $\psi(r)$ can again be decomposed into three terms (depletion + pulling + bridging), as given by Eq. (4.13), except that now

$$\psi_p(r) = \frac{(\tau_{sl}\Delta_{sl})^{-1}}{8\pi q^3} [C(r_-, 1 + q) + C(r_+, (1 + q)(1 + \Delta_{sl})) - 2C(r, 1 + q)], \quad (\text{D3})$$

$$\psi_b(r) = -\frac{(\tau_{sl}\Delta_{sl})^{-2}}{96\pi q^3} [C(r, 1 + q) + C(r, (1 + q)(1 + \Delta_{sl})) - C(r_-, 1 + q) - C(r_+, (1 + q)(1 + \Delta_{sl}))], \quad (\text{D4})$$

where

$$C(r, a) = \frac{\pi}{3}(a - r)^2(2a + r)\Theta(a - r) \quad (\text{D5})$$

is the volume of a spherical cap of height $a - r$ in a sphere of radius a and

$$r_{\pm} \equiv r \pm \frac{(1 + q)^2}{2r}\Delta_{sl} \left(1 + \frac{\Delta_{sl}}{2}\right). \quad (\text{D6})$$

The depletion term is still given by Eq. (4.14), i.e., $\psi_d(r) = -(3/2\pi q^3)C(r, 1 + q)$.

The ranges of the contributions $\psi_d(r)$, $\psi_p(r)$, and $\psi_b(r)$ are $1 + q$, $(1 + q)(1 + \Delta_{sl}/2)$, and $(1 + q)(1 + \Delta_{sl})$, respectively. It can be easily verified that in the sticky limit $\Delta_{sl} \rightarrow 0$, the potential of Eq. (D2) reduces to the one of Eq. (4.12). One can also verify that the jump discontinuity at $r = 2\sigma_{sl} = 1 + q$ of the SAO model disappears in the SWAO one, which is everywhere continuous.

¹S. Asakura and F. Oosawa, *J. Chem. Phys.* **22**, 1255 (1954).

²Usually, when talking about the AO model, one refers to a colloid-polymer mixture where the depletants are linear homopolymers of radius of gyration $\sigma_s/2$ in a good solvent. After tracing out the monomer degrees of freedom and replacing each chain with a particle at its center of mass, the homopolymers can be considered, to a first level of approximation, as noninteracting among themselves but unable to penetrate a sphere of diameter $\sigma_l + \sigma_s$ around each colloidal particle. In this work, however, we will rather talk about a solvent-solute mixture.

³L. Sapir and D. Harries, *J. Phys. Chem. Lett.* **5**, 1061 (2014).

⁴L. Sapir and D. Harries, *Curr. Opin. Colloid Interface Sci.* **20**, 3 (2015).

⁵C. Bechinger, D. Rudhardt, P. Leiderer, R. Roth, and S. Dietrich, *Phys. Rev. Lett.* **83**, 3960 (1999).

⁶Y. C. Kim and J. Mittal, *Phys. Rev. Lett.* **110**, 208102 (2013).

⁷R. J. Baxter, *J. Chem. Phys.* **49**, 2770 (1968).

⁸C. Zhao, G. Yuan, D. Jia, and C. C. Han, *Soft Matter* **8**, 7036 (2012).

⁹C. Zhao, G. Yuan, and C. C. Han, *Macromolecules* **45**, 9468 (2012).

¹⁰R. Fantoni, J. W. O. Salari, and B. Klumperman, *Phys. Rev. E* **85**, 061404 (2012).

¹¹J. Chen, S. R. Kline, and Y. Liu, *J. Chem. Phys.* **142**, 084904 (2015); Erratum, *ibid.* **142**, 149901 (2015).

¹²R. Fantoni, D. Gazzillo, and A. Giacometti, *Phys. Rev. E* **72**, 011503 (2005).

¹³J. W. Perram and E. R. Smith, *Chem. Phys. Lett.* **35**, 138 (1975).

¹⁴B. Barboy, *Chem. Phys.* **11**, 357 (1975).

¹⁵A. Santos, S. B. Yuste, and M. López de Haro, *J. Chem. Phys.* **109**, 6814 (1998).

¹⁶M. Dijkstra, R. van Roij, and R. Evans, *Phys. Rev. E* **59**, 5744 (1999).

¹⁷M. Dijkstra, J. M. Brader, and R. Evans, *J. Phys.: Condens. Matter* **11**, 10079 (1999).

¹⁸K. Binder, P. Virnau, and A. Statt, *J. Chem. Phys.* **141**, 140901 (2014).

¹⁹D. J. Ashton and N. B. Wilding, *Phys. Rev. E* **89**, 031301(R) (2014).

²⁰D. J. Ashton and N. B. Wilding, *J. Chem. Phys.* **140**, 244118 (2014).

²¹A. Santos, M. López de Haro, G. Fiumara, and F. Saija, *J. Chem. Phys.* **142**, 224903 (2015).

²²T. Zykova-Timan, *J. Chem. Phys.* **133**, 014705 (2010).

²³E. G. Noya, C. Vega, and E. de Miguel, *J. Chem. Phys.* **128**, 154507 (2008).

²⁴L. A. Fernández, V. Martín-Mayor, B. Seone, and P. Verrocchio, *Phys. Rev. Lett.* **108**, 165701 (2012).

²⁵M. G. Noro and D. Frenkel, *J. Chem. Phys.* **113**, 2941 (2000).

²⁶R. Menichetti, A. Pelissetto, G. D. Adamo, and C. Pierleoni, "Integral equation analysis of single-site coarse-grained models for polymer-colloid mixtures," *Mol. Phys.* (published online 2015).

²⁷M. Dijkstra, R. van Roij, and R. Evans, *Phys. Rev. Lett.* **82**, 117 (1999).

²⁸R. J. Baxter, *J. Chem. Phys.* **52**, 4559 (1970).

²⁹B. Barboy and R. Tenne, *Chem. Phys.* **38**, 369 (1979).

³⁰D. Gazzillo and A. Giacometti, *J. Chem. Phys.* **120**, 4742 (2004).

³¹S. B. Yuste, A. Santos, and M. López de Haro, *J. Chem. Phys.* **128**, 134507 (2008).

³²R. Fantoni and A. Santos, *J. Chem. Phys.* **140**, 244513 (2014).

³³L. Vega, E. de Miguel, L. F. Rull, G. Jackson, and I. A. McLure, *J. Chem. Phys.* **96**, 2296 (1992).

³⁴H. Liu, S. Garde, and S. Kumar, *J. Chem. Phys.* **123**, 174505 (2005).

³⁵L. Acedo and A. Santos, *J. Chem. Phys.* **115**, 2805 (2001).

³⁶R. Espíndola-Heredia, F. del Río, and A. Malijevský, *J. Chem. Phys.* **130**, 024509 (2009).

³⁷M. Miller and D. Frenkel, *J. Chem. Phys.* **121**, 535 (2004).

³⁸A. Statt, P. Virnau, and K. Binder, "Crystal nuclei in melts: A Monte Carlo simulation of a model for attractive colloids," *Mol. Phys.* (published online 2015).

³⁹A. P. Gast, C. K. Hall, and W. B. Russel, *J. Colloid Interface Sci.* **96**, 251 (1983).

⁴⁰J. M. Brader and R. Evans, *Physica A* **306**, 287 (2002).

⁴¹N. F. Carnahan and K. E. Starling, *J. Chem. Phys.* **51**, 635 (1969).

⁴²W. R. Smith and D. Henderson, *Mol. Phys.* **19**, 411 (1970).

⁴³M. López de Haro, C. F. Tejero, and A. Santos, *J. Chem. Phys.* **138**, 161104 (2013).

⁴⁴L. Rovigatti, N. Gnan, A. Parola, and E. Zaccarelli, *Soft Matter* **11**, 692 (2015).

⁴⁵J. L. Lebowitz and J. S. Rowlinson, *J. Chem. Phys.* **41**, 133 (1964).

⁴⁶T. Biben and J.-P. Hansen, *Phys. Rev. Lett.* **66**, 2215 (1991).

⁴⁷A. Malijevský, S. B. Yuste, and A. Santos, *J. Chem. Phys.* **125**, 074507 (2006).

⁴⁸J. Largo, M. A. Miller, and F. Sciortino, *J. Chem. Phys.* **128**, 134513 (2008).

⁴⁹G. Stell, *J. Stat. Phys.* **63**, 1203 (1991).

⁵⁰E. Zaccarelli, G. Foffi, P. Tartaglia, F. Sciortino, and K. Dawson, *Prog. Colloid Polym. Sci.* **115**, 371 (2000).

⁵¹A. Jannik, *J. Chem. Phys.* **128**, 234504 (2008).

⁵²M. Miller and D. Frenkel, *Phys. Rev. Lett.* **90**, 135702 (2003).

⁵³M. López de Haro, S. B. Yuste, and A. Santos, in *Theory and Simulation of Hard-Sphere Fluids and Related Systems*, Lecture Notes in Physics Vol. 753, edited by A. Mulero (Springer-Verlag, Berlin, 2008), pp. 183–245.

Chapter 47

Two phase coexistence for the hydrogen-helium mixture

Fantoni R., Phys. Rev. E **92**, 012133 (2015)

Title: “Two phase coexistence for the hydrogen-helium mixture”

Abstract: We use our newly constructed quantum Gibbs ensemble Monte Carlo algorithm to perform computer experiments for the two phase coexistence of a hydrogen-helium mixture. Our results are in quantitative agreement with the experimental results of C. M. Sneed, W. B. Streett, R. E. Sonntag, and G. J. Van Wylen. The difference between our results and the experimental ones is in all cases less than 15% relative to the experiment, reducing to less than 5% in the low helium concentration phase. At the gravitational inversion between the vapor and the liquid phase, at low temperatures and high pressures, the quantum effects become relevant. At extremely low temperature and pressure the first component to show superfluidity is the helium in the vapor phase.

PHYSICAL REVIEW E **92**, 012133 (2015)**Two-phase coexistence for hydrogen-helium mixtures**

Riccardo Fantoni*

Dipartimento di Scienze Molecolari e Nanosistemi, Università Ca' Foscari Venezia, Calle Larga S. Marta DD2137, I-30123 Venezia, Italy
(Received 7 January 2015; revised manuscript received 29 June 2015; published 24 July 2015)

We use our quantum Gibbs ensemble Monte Carlo algorithm to perform computer experiments for the two-phase coexistence of a hydrogen-helium mixture. Our results are in quantitative agreement with the experimental results of Sneed, Street, Sonntag, and Van Wylen. The difference between our results and the experimental ones is in all cases less than 15% relative to the experiment, reducing to less than 5% in the low helium concentration phase. At the gravitational inversion between the vapor and the liquid phase, at low temperatures and high pressures, the quantum effects become relevant. At extremely low temperature and pressure, the first component to show superfluidity is the helium in the vapor phase.

DOI: [10.1103/PhysRevE.92.012133](https://doi.org/10.1103/PhysRevE.92.012133)

PACS number(s): 05.30.Rt, 64.60.-i, 64.70.F-, 67.10.Fj

I. INTRODUCTION

Hydrogen and helium are the most abundant elements in the Universe. They are also the most simple. At ambient conditions, helium is an inert gas with a large band gap. Because of its low mass and weak interatomic interactions, it has fascinating properties at low temperatures, one of which is superfluidity. The molecular hydrogen and helium mixture is therefore of special theoretical importance since it is made by the two lightest elements in nature that have the lowest critical temperatures. This mixture is found to make up the atmosphere of giant planets such as Jupiter, and it is essential in stars.

An important problem to study is the phase coexistence of the fluid mixture and the determination of its coexistence properties. Some early experimental studies [1–3] have shown that at coexistence, at low temperature, the mixture shows a strong asymmetry in species concentrations in the liquid relative to the vapor phase, with an abundance of helium atoms in the vapor. This phenomenon results in the liquid floating above its vapor [3] since helium has approximately twice the molecular weight of hydrogen. Such experimental coexistence studies were later extended at higher temperature and pressure [4,5], allowing us to determine a quite complete picture for the coexistence phase diagram of this mixture in the temperature range from 15.5 to 360 K and in the pressure range from 5 bars to 75 kbars. Another interesting issue is whether this system exhibits fluid-fluid solubility at extremely high pressure [6–12], a situation that is hard to achieve in the laboratory.

In this work, we perform a numerical experiment for the two-phase coexistence problem of the hydrogen-helium mixture at low temperatures and pressures using the quantum Gibbs ensemble Monte Carlo (QGEMC) method recently devised [13,14] to solve the coexistence of a generic quantum boson fluid where the particles interact with a given effective pair potential. We will be concerned with situations in which the absolute temperature, T , and the number density, ρ_α , of each of the two components $\alpha = a, b$ of mass m_α are such that at least one of the two components is close to its degeneracy temperature $(T_D)_\alpha = \rho_\alpha^{2/3} \hbar^2 / m_\alpha k_B$, with k_B the Boltzmann constant. For temperatures much higher than

$\max\{(T_D)_\alpha\}$, quantum statistics is not very important. This path-integral Monte Carlo simulation enables us to study the quantum fluid mixture from first principles, leaving the effective pair potentials between the two species, the hydrogen molecules, and the helium atoms as the only source of external information. There are studies on reproducing such coexistence from an equation-of-state approach [15]. Our QGEMC method is expected to break down at high densities near the solid phase. Moreover, clearly our approach becomes infeasible at extremely high pressures when the hydrogen is ionized, and one is left with delocalized metallic electrons [6–12].

Our binary mixture of particles of two species labeled by a Greek index, with coordinates $R \equiv \{\mathbf{r}_\alpha | i_\alpha = 1, 2, \dots, N_\alpha \text{ and } \alpha = a, b\}$ and interacting with a central effective pair-potential $\phi_{\alpha\beta}(r)$, has a Hamiltonian

$$\hat{H} = - \sum_{\alpha=1}^2 \sum_{i_\alpha=1}^{N_\alpha} \lambda_\alpha \nabla_{i_\alpha}^2 + \frac{1}{2} \sum_{\alpha, \beta=1}^2 \sum_{i_\alpha, j_\beta}^{\prime} \phi_{\alpha\beta}(|\mathbf{r}_{i_\alpha} - \mathbf{r}_{j_\beta}|), \quad (1)$$

where the prime on the summation indicates that we must exclude the terms with $i_\alpha = j_\beta$ when $\alpha = \beta$ and $\lambda_\alpha = \hbar^2 / 2m_\alpha$.

The density matrix for the binary mixture at equilibrium at an absolute temperature T is then $\hat{\rho} = e^{-\beta \hat{H}}$ with $\beta = 1/k_B T$. Its coordinate representation $\rho(R, R', \beta)$ can be expressed as a path $[R(\tau)]$ integral in imaginary time (τ) extending from $R = R(0)$ to $R' = R(\beta)$ [16]. The many-particle path is made of $N = N_a + N_b$ single-particle world lines, which constitute the configuration space one needs to sample. Since the Hamiltonian is symmetric under exchange of like particles, we can project over the bosonic states by taking $\rho_B(R, R', \beta) = \sum_{\mathcal{P}} \rho(R, \mathcal{P}R', \beta) / (N_a! N_b!)$, where \mathcal{P} indicates a permutation of particles of the same species.

If we call ρ the number density of the mixture, x_α the molar concentration of species α ($x_b = 1 - x_a$), $P = P(T, \rho, x_a)$ the mixture pressure, and $\mu_\alpha = \mu_\alpha(T, P, x_a)$ the chemical potential of species α , we want to solve the two-phase, I and II, coexistence problem,

$$\mu_a(T, P, x_a^{(I)}) = \mu_a(T, P, x_a^{(II)}), \quad (2)$$

$$\mu_b(T, P, x_a^{(I)}) = \mu_b(T, P, x_a^{(II)}) \quad (3)$$

*rfantoni@ts.infn.it

RICCARDO FANTONI

PHYSICAL REVIEW E **92**, 012133 (2015)TABLE I. Pair-potential parameters: ϕ_{pair} .

Pair	ε^*	r_m^*	α	β	γ	C_6	C_8	C_{10}	D
He-He	10.8	2.9673	13.208	13.353	0	1.3732	0.425 38	0.17810	1.2413
H ₂ -H ₂	315 778	3.41	1.713	10.098	0.412 34	1.6955×10^{-4}	7.2379×10^{-5}	3.8984×10^{-5}	1.28
H ₂ -He	14.76	3.375	13.035	13.22	0	1.8310	0	0	0.798 02

for the concentrations $x_a^{(l)}$ and $x_a^{(h)}$ (and the densities $\rho^{(l)}$ and $\rho^{(h)}$) in the two phases. Since our mixture is not symmetric under exchange of the two species, a and b , we expect in general $x_a^{(h)} \neq 1 - x_a^{(l)}$.

Our QGEMC algorithm [14] uses two boxes maintained in thermal equilibrium at a temperature T and containing the two different phases. It employs a menu of seven different Monte Carlo moves: the *volume* move ($q = 1$) allows changes in the volumes of the two boxes assuring the equality of the pressures between the two phases, the *open-insert* ($q = 2$), *close-remove* ($q = 3$), and *advance-recede* ($q = 4$) allow the swap of a single-particle world line between the two boxes assuring the equality of the chemical potentials between the two phases, the *swap* ($q = 5$) allows us to sample the particle permutations, and the *wiggle* ($q = 6$) and *displace* ($q = 7$) allow us to sample the configuration space. We thus have a menu of seven, $q = 1, 2, \dots, 7$, different Monte Carlo moves with a single random attempt of any one of them occurring with probability $G_q = g_q / \sum_{q=1}^7 g_q$.

The paper is organized as follows: In Sec. II we describe the particular binary mixture studied, in Sec. III we describe the simulation method employed, in Sec. IV we present our numerical results, and Sec. V contains our final remarks.

II. THE H₂-He MIXTURE

We consider a binary fluid mixture of molecular hydrogen (H₂) and the isotope helium four (⁴He), which are two bosons. We take 1 Å as the unit of length and k_B K as the unit of energy. An asterisk over a quantity indicates its reduced adimensional

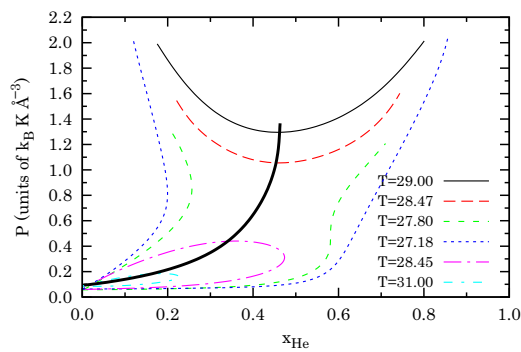


FIG. 1. (Color online) Schematic pressure-composition phase diagram for six isotherms of the hydrogen-helium mixture at low temperatures and low pressures as obtained in the experimental work by Streett *et al.* [4]. The thick continuous black line is the mixture critical line.

value. We have the following for the parameter $\lambda_\alpha = \hbar^2/2m_\alpha$ of the two species $\alpha = \text{H}_2, {}^4\text{He}$:

$$\lambda_{\text{H}_2}^* = 12.032, \quad (4)$$

$$\lambda_{\text{He}}^* = 6.0596. \quad (5)$$

The pair-potential between two helium atoms is the Aziz *et al.* [17] HFDHE2, the one between two hydrogen molecules is that of Silvera *et al.* [18], and the one between a hydrogen molecule and a helium atom is that of Roberts [19,20]. All can be put in the following central form:

$$\phi(r) = \varepsilon \Phi(x), \quad (6)$$

$$\Phi(x) = \exp(\alpha - \beta x - \gamma x^2) - \left(\frac{C_6}{x^6} + \frac{C_8}{x^8} + \frac{C_{10}}{x^{10}} \right) F(x), \quad (7)$$

$$F(x) = \begin{cases} \exp[-(D/x - 1)^2], & x < D, \\ 1, & x \geq D, \end{cases} \quad (8)$$

where $x = r/r_m$, with r_m the position of the minimum, and the various parameters are given in Table I. We have $\phi_{\text{HeHe}}^*(r_m) = -10.8$, $\phi_{\text{H}_2\text{H}_2}^*(r_m) = -34.3$, and $\phi_{\text{H}_2\text{He}}^*(r_m) = -14.8$. Moreover, we have a slight positive nonadditivity: $[r_m^*]_{\text{H}_2\text{He}} = 3.375 > ([r_m^*]_{\text{HeHe}} + [r_m^*]_{\text{H}_2\text{H}_2})/2 = 3.189$.

The experimental coexistence data [1,3,4] are given in Table I of the Supplemental Material [21] and represented schematically in Fig. 1. For example, the mixture at $T = 31$ K has a lower critical state at $P = (0.207k_B) \text{K} \text{Å}^{-3}$, $x_{\text{He}} = 0.214$ and an upper critical state at $P = (1.96k_B) \text{K} \text{Å}^{-3}$, $x_{\text{He}} = 0.49$. The set of all critical states constitutes the x line, $T = T_x(P)$,

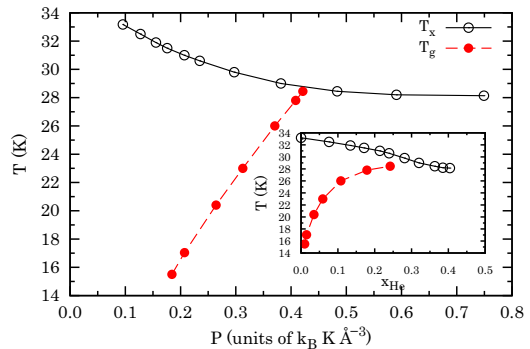


FIG. 2. (Color online) Reproduction of Fig. 3 of Sneed *et al.* [3] for the x line and the g line [see Eq. (11)]. The inset shows the two lines in the temperature-composition plane.

such that for $T > T_x$, then $x_{\text{He}}^{(l)} = x_{\text{He}}^{(ll)}$. The experimental x line of Sneed *et al.* [3] is shown in Fig. 2 for the low-temperature and low-pressure mixture. In the figure, we also show the experimental line for the gravitational inversion described in Sec. III A.

For temperatures higher than the hydrogen critical point $T_{\text{H}_2} = 33.19$ K [$P_{\text{H}_2} = (0.094k_B)$ K \AA^{-3}] there is only an upper critical point [4]. At the temperature at which $T_x(P)$ reaches its minimum, there is no unanimous consensus among the various experimental works.

III. SIMULATION METHOD

We use our QGEMC method, described in Ref. [14], where we monitor the number densities of the two coexisting phases, $\rho^{(i)} = N^{(i)}/V^{(i)} = (N_{\text{He}}^{(i)} + N_{\text{H}_2}^{(i)})/V^{(i)}$ with $i = \text{I,II}$, the concentrations of He in the two phases, $x_{\text{He}}^{(i)} = N_{\text{He}}^{(i)}/(N_{\text{He}}^{(i)} + N_{\text{H}_2}^{(i)}) < 1$, and the pressure P . We shall conventionally order $\rho^{(l)} < \rho^{(ll)}$ so that I will be the vapor phase and II the liquid phase, unless $\rho^{(l)} = \rho^{(ll)}$, in which case we have a fluid-fluid phase coexistence. In the simulation, we fix $N = N_{\text{He}}^{(l)} + N_{\text{He}}^{(ll)} + N_{\text{H}_2}^{(l)} + N_{\text{H}_2}^{(ll)}$ with $N_{\text{H}_2}^{(l)} + N_{\text{H}_2}^{(ll)} = \chi[N_{\text{He}}^{(l)} + N_{\text{He}}^{(ll)}]$ and $V = V^{(l)} + V^{(ll)}$. Otherwise, $N_{\text{He}}^{(l)}, N_{\text{He}}^{(ll)}, N_{\text{H}_2}^{(l)}, N_{\text{H}_2}^{(ll)}$ and $V^{(l)}, V^{(ll)}$ are allowed to fluctuate keeping $V^{(l)} + V^{(ll)}$ and $N_{\text{He}}^{(l)} + N_{\text{He}}^{(ll)}, N_{\text{H}_2}^{(l)} + N_{\text{H}_2}^{(ll)}$ constants. The Gibbs phase rule for a two-phase coexistence of a binary mixture assures that one has two independent thermodynamic quantities [22]. So our control parameters will be the absolute temperature T and the global number density $\rho = N/V$ (instead of the pressure as in the experimental case). As usual, a finite N sets the size error for our calculation, whereas $\chi > 0$ will regulate the size asymmetry numerical effect, so that for

$$N_{\text{He}}^{(l)} = \frac{N x_{\text{He}}^{(l)} [1 - x_{\text{He}}^{(ll)} (1 + \chi)]}{(1 + \chi)(x_{\text{He}}^{(l)} - x_{\text{He}}^{(ll)})} > 0, \quad (9)$$

$$N_{\text{He}}^{(ll)} = \frac{N}{1 + \chi} - N_{\text{He}}^{(l)} > 0, \quad (10)$$

if $x_{\text{He}}^{(ll)} < x_{\text{He}}^{(l)}$, we must have $0 < x_{\text{He}}^{(ll)} < 1/(1 + \chi) < x_{\text{He}}^{(l)} < 1$, and if $x_{\text{He}}^{(l)} < x_{\text{He}}^{(ll)}$, then $0 < x_{\text{He}}^{(l)} < 1/(1 + \chi) < x_{\text{He}}^{(ll)} < 1$. Moreover, we must also always have $\rho^{(l)} < \rho < \rho^{(ll)}$. The initial condition we chose for our simulations was always as follows: $\rho^{(l)} = \rho^{(ll)} = \rho$ and $x_{\text{He}}^{(l)} = x_{\text{He}}^{(ll)} = 1/(1 + \chi)$.

Due to the short-range nature of the effective pair potentials of Eq. (6), we will approximate, during the simulation, $\phi(r) = 0$ for $r > r_{\text{cut}} \gg [r_m]_{\text{H}_2\text{H}_2}$ (this corresponds to the truncated *and* not shifted choice in Ref. [23]). To comply with the minimum image convention for the potential energy calculation, we make sure that the conditions $[V^{(i)}]^{1/3} > 2r_{\text{cut}}$ for $i = \text{I,II}$ are always satisfied during the simulation. This approximation is the only other source of error apart from the size error. The two are related because in the fluid-fluid coexistence, for instance, when $V^{(l)} \approx V^{(ll)} \approx V/2$ during the simulation, we require $r_{\text{cut}} \approx (N/2\rho)^{1/3}/2 \gg [r_m]_{\text{H}_2\text{H}_2}$ for some given ρ .

The path-integral discretization imaginary time step $\delta\tau = \beta/K$, with K the number of time slices, is chosen so that

$\delta\tau^* = 0.002$, which is considered sufficiently small to justify the use of the primitive approximation of the interaction [16]. The parameters \vec{M} , defined in [14], will be called \vec{M}_q for each relevant move q , and the parameter $\Delta\Omega$, also defined in [14], is always chosen equal to 0.01. To fulfill detailed balance, we must choose $\vec{M}_2 = \vec{M}_3$. In particular, we always chose $\vec{M}_2 = 5, \vec{M}_3 = 5, \vec{M}_4 = 5, \vec{M}_5 = 5, \text{ and } \vec{M}_6 = 5$. Regarding the frequency of each move attempt, we always chose $g_1 = 0.001, g_2 = 1, g_3 = 1, g_4 = 1, g_5 = 1, g_6 = 1, \text{ and } g_7 = 0.1$. The parameter C defining the relative weight of the Z and G sectors [14] is adjusted, through short test runs, so as to have a Z -sector frequency as close as possible to 50%. We accumulate averages over 10^5 blocks each made of 10^5 attempted moves with quantities measured every 10^3 attempts. Since the volume move is the most computationally expensive one, we chose its frequency as the lowest. During the simulation, we monitored the acceptance ratios of each move. The various simulations took no more than ~ 150 CPU hours on a 3 GHz processor.

A. Barotropic phenomenon and gravitational inversion

The condition for the gravitational inversion observed experimentally [3] is

$$\rho^{(l)}(m_{\text{He}}x_{\text{He}}^{(l)} + m_{\text{H}_2}x_{\text{H}_2}^{(l)}) > \rho^{(ll)}(m_{\text{He}}x_{\text{He}}^{(ll)} + m_{\text{H}_2}x_{\text{H}_2}^{(ll)}), \quad (11)$$

where $m_{\text{He}}/m_{\text{H}_2} = 1.98553$. When this condition on the mass density inversion with respect to the number density is satisfied, the liquid phase will float on top of the vapor phase. The condition of Eq. (11) can also be rewritten as

$$\rho^{(l)}(1 + kx_{\text{He}}^{(l)}) > \rho^{(ll)}(1 + kx_{\text{He}}^{(ll)}), \quad (12)$$

where $k = m_{\text{He}}/m_{\text{H}_2} - 1 = 0.98553$. This condition may be satisfied when the concentration of He in the vapor phase is bigger than that in the liquid phase at low temperatures, and the number density of the liquid is close to that of the vapor at high pressure. We expect quantum effects to become important in this regime before solidification, which is expected to occur for $T < T_s(P)$. The gravitational inversion of Eq. (12) will be satisfied for $T < T_g(P)$. The experimental s -line $T = T_s(P)$ and g -line $T = T_g(P)$ have been determined in Fig. 3 of Sneed *et al.* [3] in the laboratory.

B. Pressure calculation

We will use the virial estimator for the pressure [see Eq. (6.18) of Ref. [16]] with long-range corrections [24] that can be quite big in the liquid phase. More details on the pressure calculation are given in the Supplemental Material [21].

IV. NUMERICAL RESULTS

Our results are summarized in Table II and compared in Fig. 3 with the experimental data of Refs. [1,3,4] (summarized in a table in the Supplemental Material [21]).

In all of the studied cases, we chose $N = 128$ and $\delta\tau^* = 0.002$. We explored the vapor-liquid coexistence (in this work, we will denote as ‘‘vapor-liquid’’ coexistence the one in which $\rho^{(l)} \neq \rho^{(ll)}$ at five temperatures, $T = 2, 5, 15.5, 26, \text{ and } 31$ K), and the fluid-fluid coexistence (we will denote as ‘‘fluid-fluid’’

RICCARDO FANTONI

PHYSICAL REVIEW E 92, 012133 (2015)

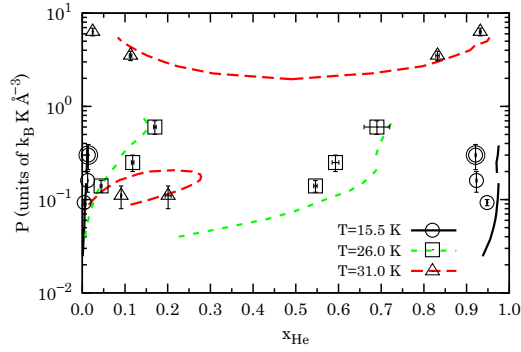


FIG. 3. (Color online) Comparison between the results of our numerical experiments (points from Table II) and of the laboratory experiments (lines from Table I in the Supplemental Material [21]) for the pressure-composition of three isotherms of the hydrogen-helium mixture phase diagram. A logarithmic scale is conveniently used on the ordinates. The double circled points at $T = 15.5$ K denote the case in which we observed gravity inversion in the numerical experiment.

coexistence the one in which $\rho^{(I)} = \rho^{(II)}$ at $T = 31$ K. For the first two lower temperatures studied, we could not find any experimental data for comparison. In these two cases, when we put a number with trailing dots in the table, it means that after the initial equilibration period, the measured property did not change anymore during the rest of the simulation.

For the temperature $T = 15.5$ K, as can be readily verified using the relation of Eq. (12), we observe gravitational inversion on the point at $\rho = 0.02 \text{ \AA}^{-3}$ when the component with the highest degeneracy temperature is the hydrogen in the liquid phase with $T_D \approx 2$ K. Clearly when choosing higher pressures, quantum statistics will become more and more important for the fluid mixture before reaching the solid state.

For the points at $T = 26$ K, $T = 31$ K, $\rho = 0.006 \text{ \AA}^{-3}$, $\chi = 116/12$, $T = 31$ K, $\rho = 0.03 \text{ \AA}^{-3}$, and $\chi = 1$ we observed exchanges of identity between the two phases during the simulation.

TABLE II. Numerical isothermal pressure composition at coexistence. We always used $N = 128$ and $\delta\tau^* = 0.002$. All the pressures are in units of $k_B K \text{ \AA}^{-3}$.

T (K)	ρ (\AA^{-3})	χ	P	$x_{\text{He}}^{(II)}$	$x_{\text{He}}^{(I)}$	$\rho^{(II)}$ (\AA^{-3})	$\rho^{(I)}$ (\AA^{-3})
2.0	0.015	1	-0.08(7)	0.214...	0.639...	0.024 56(1)	0.012 605(2)
5.0	0.010	1	0.014(2)	0.1787(1)	1.000...	0.025 910(6)	0.005 113(1)
15.5	0.010	1	0.093(7)	0.00457(9)	0.948(1)	0.024 10(1)	0.006 544(5)
15.5	0.015	1	0.16(4)	0.0125(3)	0.923(1)	0.023 04(2)	0.011 525(7)
15.5	0.020	1	0.30(9)	0.0142(4)	0.921(1)	0.023 73(2)	0.017 619(5)
26.0	0.010	90/38	0.14(2)	0.044(2)	0.546(4)	0.018 90(5)	0.006 69(1)
26.0	0.015	90/38	0.25(5)	0.118(3)	0.593(8)	0.018 88(7)	0.011 05(5)
26.0	0.020	90/38	0.6(1)	0.170(3)	0.69(3)	0.021 15(2)	0.017 59(8)
31.0	0.006	116/12	0.11(3)	0.091(1)	0.201(7)	0.014(2)	0.005 64(6)
31.0	0.008	1	0.21(2)	0.5025(6)	0.511(1)	0.008 016(7)	0.007 95(1)
31.0	0.030	1	3.5(4)	0.832(4)	0.113(3)	0.031 98(4)	0.028 05(1)
31.0	0.035	1	6.3(6)	0.932(2)	0.0243(9)	0.039 55(5)	0.031 11(1)

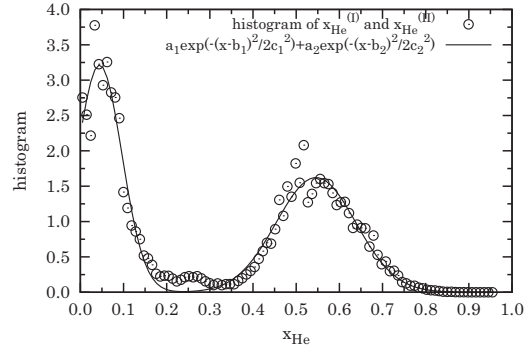


FIG. 4. Fit of the histogram for the block averages of both $x_{\text{He}}^{(I)}$ and $x_{\text{He}}^{(II)}$ with the sum of two Gaussians with six parameters. This is the case $T = 26$ K, $\rho = 0.01 \text{ \AA}^{-3}$, and $\chi = 90/38$, where we had box identity exchanges.

At a temperature $T = 31$ K and a pressure of $P = [0.07(2)k_B] K \text{ \AA}^{-3}$, we found a vapor-liquid coexistence, choosing $\chi = 116/12$. This point should be subject to greater size error than all other points simulated, and thus should be less reliable, since we only have, in the two boxes, a total of 12 helium atoms. Increasing the pressure to $P = [0.21(2)k_B] K \text{ \AA}^{-3}$, in agreement with the experiment, we did not find coexistence, and we observed $\rho^{(I)} \approx \rho^{(II)} \approx \rho$ and $x_{\text{He}}^{(I)} \approx x_{\text{He}}^{(II)} \approx 1/(1 + \chi)$. Increasing the pressure to $P = [3.5(4)k_B] K \text{ \AA}^{-3}$, we did not observe exactly $\rho^{(I)} = \rho^{(II)}$, as measured in the fluid-fluid transition observed in the laboratory [4]. The same holds true for the point at the same temperature but higher pressure, $P = [6.3(6)k_B] K \text{ \AA}^{-3}$.

For all measured points except the one at the lower temperature, $T = 2$ K of Table II, the superfluid fraction [25] of the two components in either phase was negligibly small. At $T = 2$ K of Table II, below the helium lambda-temperature, we observed a negligible superfluid fraction of both components in the liquid phase and of the hydrogen in the vapor phase.

TABLE III. Numerical isothermal pressure-composition coexistence at $T = 31$ K, $\rho = 0.03 \text{ \AA}^{-3}$, and $\chi = 1$ as a function of the number of particles N . We always used $\delta\tau^* = 0.002$. All the pressures are in units of $k_B \text{K \AA}^{-3}$.

N	$r_{\text{cut}} (\text{\AA})$	P	$x_{\text{He}}^{(\text{II})}$	$x_{\text{He}}^{(\text{I})}$	$\rho^{(\text{II})} (\text{\AA}^{-3})$	$\rho^{(\text{I})} (\text{\AA}^{-3})$
64	5	2.4(8)	0.83(3)		0.03144(7)	0.02782(3)
128	6	3.5(4)	0.832(4)	0.113(3)	0.03198(4)	0.02805(1)
256	8	3.4(2)	0.840(3)	0.098(3)	0.03180(3)	0.028170(9)

The helium in the vapor phase was found to have a superfluid fraction of 0.012(3), indicating a tendency to superfluidity.

When we do not observe exchanges of identity between the two phases during the simulation, we are able to find accurate average values for the various measured quantities. Otherwise a histogram analysis of the data is necessary with a nonlinear fit using the superpositions of two shifted Gaussians. For example, in Fig. 4 we show the procedure used to extract the helium concentrations of the two coexisting phases for the case $T = 26$ K, $\rho = 0.01 \text{ \AA}^{-3}$, and $\chi = 90/38$.

The measured property that is less accurate is the pressure due to the size error and the long-range correction dependent on the r_{cut} choice. This problem could be overcome by using the N, P, T version of the Gibbs ensemble algorithm instead of its N, V, T one [26].

A. Finite-size effects

We studied the finite-size effects at $T = 31$ K, $\rho = 0.03 \text{ \AA}^{-3}$, and $\chi = 1$. In Table III, we show the results for the isothermal pressure-composition coexistence at $N = 64$, 128, and 256. As the number of particles increases, we observe a decrease in the ratio of the number of exchanges of identity between the two phases and the total number of particles: For $N = 64$, the exchanges occurred many times, for $N = 128$ only once, and for $N = 256$ never. For the case $N = 64$, we found the peak of the first Gaussian for the histogram of x_{He} with a negative value. The simulation with $N = 64$ took 1.0×10^5 s, the one with $N = 128$ took 1.6×10^5 s, and the one with $N = 256$ took 4.0×10^6 s. From the comparison we see that there is not much difference between $N = 128$ and 256. Apart from the smaller statistical errors in the latter case, the concentrations differ slightly in the two cases.

TABLE IV. Numerical isothermal pressure-composition coexistence at $T = 15.5$ K, $\rho = 0.02 \text{ \AA}^{-3}$, and $\chi = 1$ in a simulation with the full QGEMC algorithm with the Bose-Einstein statistics ($\delta\tau^* = 0.002$), with the QGEMC algorithm with Boltzmann statistics ($\delta\tau^* = 0.002$), and with the GEMC limit (see the main text) of the QGEMC algorithm. We always used $N = 128$. All the pressures are in units of $k_B \text{K \AA}^{-3}$.

Statistics	P	$x_{\text{He}}^{(\text{II})}$	$x_{\text{He}}^{(\text{I})}$	$\rho^{(\text{II})} (\text{\AA}^{-3})$	$\rho^{(\text{I})} (\text{\AA}^{-3})$
QGEMC: Bose-Einstein	0.30(9)	0.0142(4)	0.921(1)	0.02373(2)	0.017619(5)
QGEMC: Boltzmann	0.30(9)	0.0143(4)	0.919(1)	0.02373(2)	0.017638(5)
GEMC: classical limit	0.13(4)	0.000...	1.000...	0.035953(5)	0.0138552(7)

B. Importance of the particle exchanges and of the quantum effects

Setting to zero the frequency of the swap move attempts, our algorithm reduces to a path-integral calculation for distinguishable particles obeying the Boltzmann statistics. On the other hand, choosing $K = 2$ (with $\bar{M}_q = 1$ for all q) and $\lambda_{\text{He}}^* = \lambda_{\text{He}}^* \rightarrow 0$, our algorithm reduces to the classical Gibbs ensemble Monte Carlo (GEMC) algorithm of Panagiotopoulos [27].

For the state point $T = 15.5$ K and $\rho = 0.02 \text{ \AA}^{-3}$ with $N = 128$, we performed two simulations for each of the two cases suggested above to estimate the importance of particle exchanges, which underlie the Bose-Einstein statistics, and of quantum effects, respectively. To reach the GEMC limit from our QGEMC algorithm, we chose, in particular, $\lambda_{\text{He}}^* = \lambda_{\text{He}}^* = 10^{-3}$. The results are shown in Table IV. The acceptance ratio for the swap move was around 0.5 in the full quantum case and imposed zero in the other two simulations.

As we can see from the table, for this state point, there is a very small difference between the path-integral simulation with the full Bose-Einstein statistics and the one with the Boltzmann statistics. In particular, only the densities of the vapor phase are different in the two cases. In both of these simulations, we observe the gravitational inversion. We expect that upon increasing the pressure and thereby the density or reducing the temperature, the particle exchanges will become increasingly important.

On the other hand, there is a large difference between these two simulations and the classical GEMC one. In particular, the gravitational inversion is not observed in the classical limit simulation, even if after a short equilibration time the simulation converged toward the condition $x_{\text{He}}^{(\text{I})} = 1$, i.e., all helium atoms, the heaviest species in the mixture, were found in the less dense phase.

V. CONCLUSIONS

In conclusion, we performed path-integral Monte Carlo simulations using our QGEMC method for the two-phase coexistence of a hydrogen-helium mixture away from freezing. At low temperature, this asymmetric mixture displays a big concentration asymmetry in the two coexisting phases, whereas the densities of the two phases tend to become equal at high pressure. This is responsible for a gravitational inversion, where the liquid, the more dense phase, with an abundance of

RICCARDO FANTONI

PHYSICAL REVIEW E **92**, 012133 (2015)

hydrogen, floats above the vapor, the less dense phase, with an abundance of helium. In this coexistence region of the temperature-pressure diagram, quantum statistics is expected to play an important role, and in our simulations we are able to observe such gravitational inversion. Our numerical experiments are also in good quantitative agreement with the experimental results of Sneed, Streett, Sonntag, and Van Wylen from the late 1960s and early 1970s. The difference between our results on the helium concentration in the two phases and the experimental ones is in all cases less than 15% in the high helium concentration phase and less than 5% in the low helium concentration phase, relative to the experiment.

These results for the hydrogen-helium mixture can be of interest for the study of cold exoplanets with an atmosphere composed predominantly of such a fluid mixture and with the right temperature and pressure conditions for there to be coexistence. In such cases, it could be possible to observe the

gravitational inversion phenomenon and consequent changes in the planet moment of inertia, depending on the atmospheric and climatic conditions. At extremely low temperature and pressure, we find that the first component to show superfluidity is the helium in the vapor phase.

Our QGEMC method [14] is extremely simple to use, reduces to the Gibbs ensemble method of Panagiotopoulos [27] in the classical regime, and gives an exact numerical solution of the statistical physics phase coexistence problem for boson fluids.

An open problem currently under examination is the influence of the finite-size effects on the determination of the binodal curves close to the lower strongly asymmetric critical points, such as, for example, in our case $T = 31$ K, $\rho = 0.006 \text{ \AA}^{-3}$, and $\chi = 116/12$. This requires additional simulations at a higher and lower number of particles.

-
- [1] W. B. Streett, R. E. Sonntag, and G. J. Van Wylen, *J. Chem. Phys.* **40**, 1390 (1964).
 - [2] R. E. Sonntag, G. J. Van Wylen, and R. W. Crain, Jr., *J. Chem. Phys.* **41**, 2399 (1964).
 - [3] C. M. Sneed, R. E. Sonntag, and G. J. Van Wylen, *J. Chem. Phys.* **49**, 2410 (1968).
 - [4] W. B. Streett, *Astrophys. J.* **186**, 1107 (1973).
 - [5] L. C. Van Den Bergh, J. A. Schouten, and N. J. Trappeniers, *Physica A* **141**, 524 (1987).
 - [6] B. Militzer, *J. Low Temp. Phys.* **139**, 739 (2005).
 - [7] M. A. Morales, E. Schwegler, D. Ceperley, C. Pierleoni, S. Hamel, and K. Caspersen, *Proc. Natl. Acad. Sci. (USA)* **106**, 1324 (2009).
 - [8] W. Lorenzen, B. Holst, and R. Redmer, *Phys. Rev. Lett.* **102**, 115701 (2009).
 - [9] W. Lorenzen, B. Holst, and R. Redmer, *Phys. Rev. B* **84**, 235109 (2011).
 - [10] J. M. McMahon, M. A. Morales, C. Pierleoni, and D. M. Ceperley, *Rev. Mod. Phys.* **84**, 1607 (2012).
 - [11] M. A. Morales, S. Hamel, K. Caspersen, and E. Schwegler, *Phys. Rev. B* **87**, 174105 (2013).
 - [12] F. Soubiran, S. Mazevet, C. Winisdoerffer, and G. Chabrier, *Phys. Rev. B* **87**, 165114 (2013).
 - [13] R. Fantoni, *Phys. Rev. E* **90**, 020102(R) (2014).
 - [14] R. Fantoni and S. Moroni, *J. Chem. Phys.* **141**, 114110 (2014).
 - [15] Y. S. Wei and R. J. Sadus, *Fluid Phase Equilibria* **122**, 1 (1996).
 - [16] D. M. Ceperley, *Rev. Mod. Phys.* **67**, 279 (1995).
 - [17] R. A. Aziz, V. P. S. Nain, J. S. Carley, W. L. Taylor, and G. T. McConville, *J. Chem. Phys.* **70**, 4330 (1979).
 - [18] I. F. Silvera and V. V. Goldman, *J. Chem. Phys.* **69**, 4209 (1978).
 - [19] E. A. Mason and W. E. Rice, *J. Chem. Phys.* **22**, 522 (1954).
 - [20] C. S. Roberts, *Phys. Rev.* **131**, 203 (1963).
 - [21] See Supplemental Material at <http://link.aps.org/supplemental/10.1103/PhysRevE.92.012133> for additional details on experimental data and calculations.
 - [22] L. D. Landau and E. M. Lifshitz, *Statistical Physics*, Pt. 1, 3rd ed., Course of Theoretical Physics (Butterworth Heinemann, Oxford, 1951), Sec. 86.
 - [23] B. Smit, *J. Chem. Phys.* **96**, 8639 (1992).
 - [24] M. P. Allen and D. J. Tildesley, *Computer Simulation of Liquids* (Clarendon, Oxford, 1987), Sec. 2.8.
 - [25] E. L. Pollock and D. M. Ceperley, *Phys. Rev. B* **36**, 8343 (1987).
 - [26] D. Frenkel and B. Smit, *Understanding Molecular Simulation* (Academic, San Diego, 1996), Chap. 8.
 - [27] A. Z. Panagiotopoulos, *Mol. Phys.* **61**, 813 (1987).

Part XVI

2016

Chapter 48

Supercooled superfluids in Monte Carlo simulations

Fantoni R., Eur. Phys. J. B **89**, 1 (2016)

Title: “Supercooled superfluids in Monte Carlo simulations”

Abstract: We perform path integral Monte Carlo simulations to study the imaginary time dynamics of metastable supercooled superfluid states and nearly superglassy states of a one component fluid of spinless bosons square wells. Our study shows that the identity of the particles and the exchange symmetry is crucial for the frustration necessary to obtain metastable states in the quantum regime. Whereas the simulation time has to be chosen to determine whether we are in a metastable state or not, the imaginary time dynamics tells us if we are or not close to an arrested glassy state.

Supercooled superfluids in Monte Carlo simulations

Riccardo Fantoni^a

Università di Trieste, Dipartimento di Fisica, strada Costiera 11, 34151 Grignano (Trieste), Italy

Received 23 October 2015 / Received in final form 26 November 2015
 Published online 8 February 2016 – © EDP Sciences, Società Italiana di Fisica, Springer-Verlag 2016

Abstract. We perform path integral Monte Carlo simulations to study the imaginary time dynamics of metastable supercooled superfluid states and nearly superglassy states of a one component fluid of spinless bosons square wells. Our study shows that the identity of the particles and the exchange symmetry is crucial for the frustration necessary to obtain metastable states in the quantum regime. Whereas the simulation time has to be chosen to determine whether we are in a metastable state or not, the imaginary time dynamics tells us if we are or not close to an arrested glassy state.

If a liquid can be cooled below its melting temperature T_m without the occurrence of crystallization, it is called a good glass former, and when the temperature is less than T_m the system is called supercooled. The static and dynamical properties of such systems can be studied over a large temperature range below T_m and it is found that their relaxation times increase very quickly by many decades if the temperature is lowered. At a certain temperature the relaxation time exceeds the timescale of the experiment and therefore the system will fall out of equilibrium. It is this falling out of equilibrium that is called the glass transition. At temperatures well below this glass transition temperature no relaxation seems to take place any longer, on any reasonable timescale, and it is customary to call this material a glass. This transition temperature will in general depend on the type of experiment, since its definition involves the timescale of the experiment. Understanding the transition from a supercooled liquid to a glass, or a disordered solid, is one of the major open problems in condensed matter.

In a liquid of number density ρ , made of mass m particles, moving in a d -dimensional space, the quantum effects will become important when the temperature T is comparable or smaller than the degeneracy temperature $T_D = 2\lambda\rho^{2/d}$, where $\lambda = \hbar^2/2m$ and \hbar is the reduced Planck constant. A liquid such that $T_D > T_m$ is therefore likely to form a quantum glass.

At a temperature $T_{MCT} < T_m$ a kinetic glass transition towards an arrested state is predicted by the mode coupling theory (MCT) [1,2]. Many of the qualitative predictions of this theory have been confirmed in experiments and computer simulations, and thus MCT can currently be regarded as the best available theory of the dynamics of supercooled liquids.

Our aim in this letter is to use path integral Monte Carlo (PIMC) simulations [3] to gain an understanding of

the very general question of the search for an arrested state when the temperature approaches T_{MCT} . Since we are interested in a universal property of glassy systems, our simulations are carried out with a very simple and unrealistic model liquid, namely the square-well bosons [4]. We will be working at very low temperatures $T \approx T_m < T_D$. We will find metastable supercooled superfluid states and evidence for development towards a superglass state [5–7] which should appear at even lower temperatures $T \approx T_{MCT}$.

Using the terminology of reference [3] we are then looking for local minima of the action of the primitive approximation, up to thermal activation according to the Metropolis algorithm [8]. These may differ from the ones of the *inter-action* due to quantum tunneling. In particular we will be interested in how the identity of the particles and their exchange permutation cycles which forms in a PIMC simulation frustrates the development towards the global minimum of the action favoring the formation of the metastable supercooled states [9].

Consider a fluid (homogeneous and isotropic) of N bosons in a volume V and density $\rho = N/V$ at a given absolute temperature $T = 1/k_B\beta$, with k_B Boltzmann constant, with a Hamiltonian

$$\mathcal{H} = -\lambda \sum_{i=1}^N \nabla_i^2 + \sum_{i < j \leq N} \phi(|\mathbf{r}_i - \mathbf{r}_j|)$$

symmetric under particle exchange, with $\lambda = \hbar^2/2m$, m the mass of the particles, and $\phi(|\mathbf{r}_i - \mathbf{r}_j|)$ the pair-potential of interaction between particle i at \mathbf{r}_i and particle j at \mathbf{r}_j . The dynamic structure factor is defined as follows:

$$\begin{aligned} S(k, \omega) &= \frac{1}{2\pi N} \int_{-\infty}^{\infty} dt e^{-i\omega t} \langle \rho_{-\mathbf{k}}(0) \rho_{\mathbf{k}}(t) \rangle \\ &= \int_{-\infty}^{\infty} dt e^{-i\omega t} F(k, t), \end{aligned}$$

^a e-mail: rfantoni@ts.infn.it

where

$$\rho(\mathbf{r}) = \sum_{i=1}^N \delta(\mathbf{r} - \mathbf{r}_i)$$

with $\langle \rho(\mathbf{r}) \rangle = \rho$, $\rho(\mathbf{r}, t) = e^{i\mathcal{H}t/\hbar} \rho(\mathbf{r}) e^{-i\mathcal{H}t/\hbar}$, $\rho_{\mathbf{k}}(t) = \int d\mathbf{r} e^{i\mathbf{k}\cdot\mathbf{r}} \rho(\mathbf{r}, t)$, and $\rho_{\mathbf{k}}(0) = \rho_{\mathbf{k}}$. Given an observable \mathcal{O} we define the statistical average as $\langle \mathcal{O} \rangle = \text{Tr}(\mathcal{O} e^{-\beta\mathcal{H}}) / Z$ with $Z = \text{Tr}(e^{-\beta\mathcal{H}})$ the partition function.

We introduce the analytic continuation of $F(k, t) = \int_{-\infty}^{\infty} d\omega e^{-i\omega t} S(k, \omega)$ in imaginary time as follows

$$F_k(t) = \frac{1}{NZ} \text{Tr} \left(\rho_{-\mathbf{k}} e^{-t\mathcal{H}} \rho_{\mathbf{k}} e^{-(\beta-t)\mathcal{H}} \right). \quad (1)$$

So that $F_k(0) = 2\pi F(k, 0) = \int_{-\infty}^{\infty} d\omega S(k, \omega) = S(k)$ is the static structure factor such that $\lim_{k \rightarrow \infty} S(k) = 1$.

Clearly we have that $F_k(t) = 2\pi F(k, iht)$ is defined for $t \in [0, \beta]$ being symmetric respect to $t = \beta/2$ since $S(k, -\omega) = e^{-\beta\omega} S(k, \omega)$.

The calculation of $F_k(t)$ of equation (1) becomes straightforward in path integral Monte Carlo (PIMC) [3] where it is sufficient to average the product of $\rho_{-\mathbf{k}}$ on the first time-slice with $\rho_{\mathbf{k}}$ at a time-slice a time t later.

The dynamic structure factor for the ideal Bose gas for particles of spin s at a temperature T below the critical temperature $k_B T_c = 4\pi\lambda\{\rho/[(2s+1)\zeta(3/2)]\}^{2/3}$, where ζ is the Riemann zeta function, is given by equation (18) in reference [10]¹, where their λ is our $\sqrt{4\pi\lambda\beta}$, the de Broglie wavelength.

In particular one finds

$$\left. \frac{dF_k(t)}{dt} \right|_{t=0} = - \int_{-\infty}^{\infty} d\omega \hbar\omega S(k, \omega) = -\lambda k^2.$$

In Figure 1 we show how $F_k(t)$ is well-approximated by a pure exponential decay $S(k)e^{-\lambda k^2 t}$ for $t \in [0, \beta/2]$.

We performed grand canonical PIMC with the ‘‘worm’’ algorithm [11] for a system of spin zero square-well bosons in three spatial dimensions. As usual the path $\mathbf{R}(t)$ is discretized in imaginary time t extending from $t = 0$ to $t = \beta = n_\tau\tau$ with a time-step τ . It is made of Nn_τ beads of coordinates $\mathbf{R}(t) = \{(x_i(t), y_i(t), z_i(t)) \quad \forall i = 1, \dots, N\}$ at each time-slice $t = t_j = j\tau$. The particles pair-potential is as follows

$$\phi(r) = \begin{cases} +\infty & r < \sigma \\ -\varepsilon & \sigma \leq r < \sigma(1 + \Delta) \\ 0 & \sigma(1 + \Delta) \leq r. \end{cases} \quad (2)$$

We choose $\varepsilon > 0$ as the unit of energies and σ as the unit of lengths. We then introduce a reduced temperature $T^* = k_B T / \varepsilon$ (with $\beta^* = 1/T^*$), a reduced density $\rho^* = \rho\sigma^3$, and a reduced chemical potential $\mu^* = \mu/\varepsilon$. When the mass m of the bosons and/or the depth of their attractive well ε are sufficiently large, i.e. $\lambda^* = \lambda/(\varepsilon\sigma^2) \ll 1$ we are in the classical limit. The classical fluid has been

¹ There is a misprint in equation (18) where the denominator of the term containing the Dirac delta functions should read $1 - e^{-\omega/\omega_T}$.

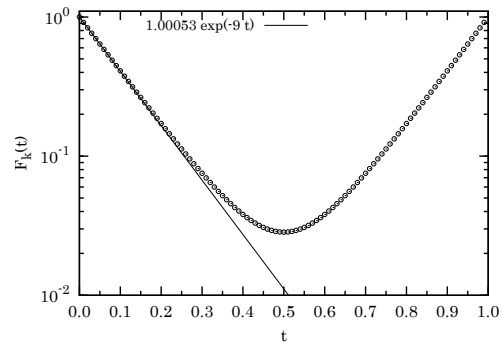


Fig. 1. Behavior of $F_k(t)$, as a function of the imaginary time $t \in [0, \beta]$, for an ideal Bose gas below its critical temperature at $k = 3$, $\lambda = 1$, $k_B T = 1$, $\rho = 0.4$, and $s = 0$. The critical temperature is $k_B T_c = 3.597$. The points are the numerical results from equations (1) and equation (18) of reference [10]. On the ordinates axis we use a logarithmic scale.

studied originally by Vega et al. [12] who found that the critical point of the gas-liquid coexistence moves at lower temperatures and higher densities as Δ gets smaller. The quantum mechanical effects on the thermodynamic properties of nearly classical liquids can be estimated by the de Boer quantum delocalization parameter $\ell = \sqrt{2\lambda^*}$ [13]. The phase diagram of the system in the quantum regime, $T^* \lesssim T_D^* = 2\lambda^*(\rho^*)^{2/3}$, has recently been studied by us [4] with our quantum Gibbs ensemble MC algorithm [14].

Unlike the work of Biroli et al. [6] we will work far away from the sticky limit [15] obtained by setting the stickiness parameter $\mathcal{T}^{-1} = 12e^{\beta\varepsilon}\Delta$ and taking the double limit $\varepsilon \rightarrow \infty$ and $\Delta \rightarrow 0$ at fixed \mathcal{T} . We could reach numerically such limit by taking Δ small enough [16–18]. Instead we will fix $\Delta = 0.5$ in all cases as was done in the previous analysis of reference [4].

In the present letter we want to study the relaxation to zero of the $F_k(t)$ in the quantum regime, so we must choose $\lambda^* \gg 0$ and $T^* \lesssim T_D^*$. Choosing $\lambda^* = 1$ we must choose a sufficiently small temperature and a sufficiently high density. For $T^* = 1$ we need a reduced density $\rho^* \gtrsim (1/2)^{3/2} = 0.35$. The maximum reduced density allowed for our system is $\sqrt{2} = 1.41$ for the close packed configuration of the hard cores. The small attraction between the particles will be responsible for a shift at lower packing fractions, $\eta = \pi\rho\sigma^3/6$, of the melting value for pure hard-sphere (which in the classical limit is approximately 0.54).

In our PIMC we had to choose a discretization time-step, $\tau^* = \beta^*/n_\tau$, for the imaginary time extending from $t\varepsilon = 0$ to $t\varepsilon = \beta^*$. We then chose $n_\tau = 100$ time-slices [3]. The ‘‘worm’’ algorithm uses a menu of 9 different moves: advance, recede, insert, remove, open, close, swap, wiggle, and displace. Labeling each of these moves with $q = 1, 2, \dots, 9$ respectively, a single random attempt of any one of them with probability $G_q = g_q / \sum_{q=1}^9 g_q$ constitutes a MC step. In our simulations we always chose

Table 1. Reduced properties of the simulated system with $\Delta = 0.5$ at $\lambda^* = 1$, $V = 100\sigma^3$ and different μ^* . For the simulation at $T^* = 0.5$, $\mu^* = 80$ (stable) we considered the first 20 000 blocks as equilibration time and they were therefore discarded from the averaging. In all the other cases the equilibration time was taken equal to 1000 blocks, i.e. the ones necessary to bring the system from the empty box to the equilibrium number of particles.

T^*	μ^*	$e_{\text{tot}}/\varepsilon$	$e_{\text{kin}}/\varepsilon$	$e_{\text{pot}}/\varepsilon$	$p\sigma^3/\varepsilon$	$\langle N \rangle$	$\rho\sigma^3$	ρ_s/ρ
1.0	50 (stable)	12.81(6)	17.70(7)	-1.889(6)	3.33(2)	33.92(7)	0.3392(7)	1.05(8)
1.0	80 (stable)	19.20(7)	21.94(8)	-2.734(8)	6.20(3)	42.41(8)	0.4241(8)	1.1(1)
1.0	100 (stable)	24.12(6)	27.46(7)	-3.335(7)	8.75(3)	47.79(6)	0.4779(6)	0.03(1)
0.5	80 (stable)	17.029(8)	20.325(8)	-3.297(3)	6.504(3)	48	0.48	0.013(4)
0.4	80 (metastable)	13.64(4)	17.09(5)	-3.446(5)	5.72(2)	50.19(5)	0.5019(5)	1.2(1)
0.4	90 (metastable)	15.23(4)	18.98(5)	-3.744(6)	6.73(2)	53.16(5)	0.5316(5)	1.05(8)

$g_q = 1$ for $q = 1, 2, \dots, 7, 9$, and $g_8 = 10$. For each move, except the displace one, a maximum number of time-slices involved, \overline{m} , is also defined [11] to control their acceptance ratios. We always chose $\overline{m}_q = 5$ for all q . For the displace move we chose a displacement of the path of the order of $V^{1/3}/1000$. We always chose the C parameter defined in reference [11] equal to 0.1. This value ensured an acceptance ratio for the Z -sector [11] lower but close to 1/2 even if in the simulations converging towards the solid state this increased passed 1/2.

Our simulations were 5×10^4 blocks long with one block made by 100 steps where we did not accumulate the averages and by 100 steps where we did. This sets the simulation (experiment) time.

We studied the model with $\Delta = 0.5$ and $\lambda^* = 1$ at $T^* = 1$, $V = 100\sigma^3$, and $\mu^* = 50, 80, 100$. Starting from the empty box we reached a stable superfluid for $\mu^* = 50$ (stable), 80 (stable) and a stable normal solid for $\mu^* = 100$ (stable). Then we lowered the temperature at $T^* = 0.5$ and we studied the model with $\mu^* = 80$. Now *quenching* from the empty box we reached a metastable superfluid at $\mu^* = 80$ (metastable) for the first 20 000 blocks which later converged towards its stable normal solid state: $\mu^* = 80$ (stable). We then quenched from the empty box at a slightly lower temperature $T^* = 0.4$ keeping the chemical potential at $\mu^* = 80$ (metastable) (which resulted in a slightly higher density respect to the case at the higher temperature $T^* = 0.5$) and we observed that the system, instead of entering the stable solid phase, stayed, for the whole length of our numerical experiment, in a metastable supercooled superfluid state.

In Table 1 we report some properties of the simulated system such as: the total energy per particle e_{tot} , the kinetic energy per particle e_{kin} , the potential energy per particle e_{pot} , the pressure p , the average number of particles $\langle N \rangle$, the density $\rho = \langle N \rangle/V$, and the superfluid fraction ρ_s/ρ , as calculated according to reference [3]. All the presented simulation were *well converged* and the correlation simulation time $k_{\mathcal{O}}$ was never bigger than 500 blocks in any simulation for any property \mathcal{O} . The statistical error was as usual calculated as $\sqrt{\sigma^2(\mathcal{O})k_{\mathcal{O}}/N_s}$, where $\sigma^2(\mathcal{O})$ is the estimator of the variance of the random walk and N_s the number of MC steps.

In Figure 2 we show the static structure factor of the first five systems. This clearly shows how the $T^* = 0.5$, $\mu^* = 80$ (stable) case is a solid state (the structure

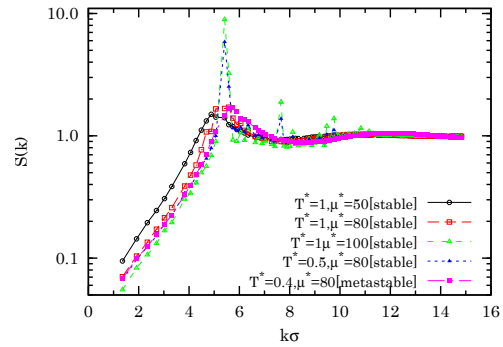


Fig. 2. Static structure factor $F_k(0) = S(k)$ at $\lambda^* = 1$ and $T^* = 1$, $\mu^* = 50$ (stable), 80 (stable), 100 (stable) and $T^* = 1/2$, $\mu^* = 80$ (stable), 80 (metastable). On the ordinates axis we use a logarithmic scale.

factor peak is between 6 and 7) whereas the $T^* = 0.4$, $\mu^* = 80$ (metastable) one is a fluid state (the structure factor peak is here between 1.6 and 1.8). Note that in all cases the simulation was 5×10^4 blocks long and the acceptance ratio of the Z -sector comparable. The difference between the two cases immediately also appears by looking at the evolution of the superfluid fraction during the progress of the simulations, as shown in Figure 4. We clearly see how the $T^* = 0.5$, $\mu^* = 80$ (stable) case has a transition from a superfluid state, before block 20 000, to a normal solid, after. The behavior of $F_k(t)$ as a function of the imaginary time for some chosen reciprocal wave-numbers around the first peak of the correspondent static structure factor for the system with $T^* = 0.4$ and $\mu^* = 80$, which is a precursor of a superfluid glass, a superglass [5,6,19], is such that we observe exponential decays going below 10^{-2} for $t\varepsilon > 0.6$. Whereas for the systems in the solid state at $T^* = 1$, $\mu^* = 100$ (stable) and $T^* = 0.5$, $\mu^* = 80$ (stable) we observe an almost constant value for $F_k(t)$ at the wave-number of the first peak of the correspondent static structure factor and exponentially decaying the other wave-numbers.

In Figure 3 we show the $(x_i(t), y_i(t))$ particles positions at all time-slices at the end of the simulation for the cases $T^* = 0.5$, $\mu^* = 80$ (stable) and $T^* = 0.4$, $\mu^* = 80$ (metastable), respectively.

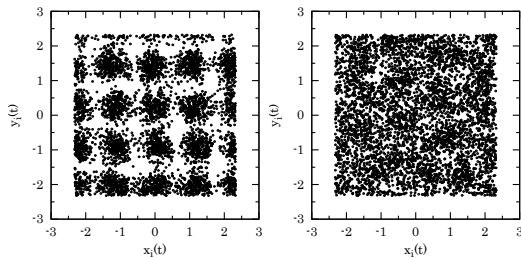


Fig. 3. The $(x_i(t), y_i(t))$ particles positions at all time-slices at the end of the simulation with: $\lambda^* = 1, T^* = 0.5, \mu^* = 80$ (stable) (left panel) and $\lambda^* = 1, T^* = 0.4, \mu^* = 80$ (metastable) (right panel).

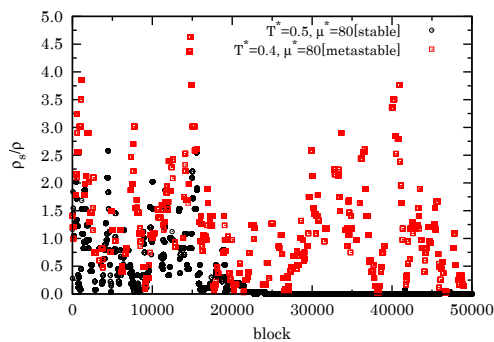


Fig. 4. Superfluid fraction at each PIMC block during the simulation at $\lambda^* = 1$ and $T^* = 0.5, \mu^* = 80$ (stable) and $T^* = 0.4, \mu^* = 80$ (metastable).

Regarding the size effects we can say that the solid state we observed has a triclinic lattice structure with a unit cell with base vectors $\mathbf{a} = (0, 0, a)$, $\mathbf{b} = (a, 0, a/2)$, $\mathbf{c} = (0, a, a/2)$ accommodating approximately 48 particles. At $T^* = 0.4$, a chemical potential of $\mu^* = 80$ is sufficient to reach approximately 50 particles which could be adjusted in a different unit cell with the same crystal structure. Thus we think that the size effects should not be considered as responsible for the observed metastability.

In order to get closer to an arrested metastable state we restarted from the the equilibrated supercooled superfluid configuration of $T^* = 0.4, \mu^* = 80$ (metastable) and increased μ^* by 10. This allowed us to reach another metastable supercooled superfluid state closer to an arrested state where the $F_k(t)$, for the k around the first peak of the static structure factor at 2, shows an initial exponential decay followed by a plateau. This is clearly shown in Figure 5 taken at the end of the simulation and is in accord with the MCT predictions. In order to observe the plateau it is essential the restarting or *aging* procedure.

In conclusion, we proved, for the idealized model of spinless square well bosons, that superfluidity is able to sustain metastability at low temperature and high density. In order to define whether we are on a metastable state

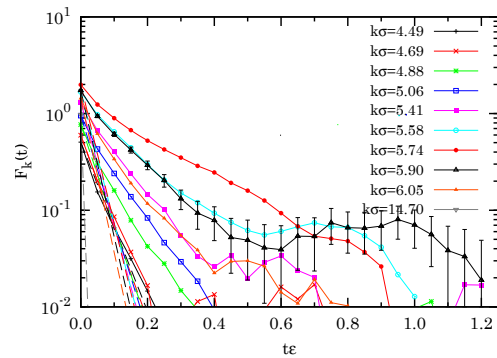


Fig. 5. The behavior of $F_k(t)$ as a function of the imaginary time for various values of k around the first peak of the structure factor. We used $\lambda^* = 1, T^* = 0.4$, and $\mu^* = 90$ (metastable). The dashed lines are the approximate ideal gas results. On the ordinates axis we use a logarithmic scale. For $k\sigma = 5.90$ also the statistical errors are shown.

we need to fix a simulation time interval much longer than the correlation simulation time. We were able to maintain the system in a metastable supercooled superfluid state for a rather long simulation time. The metastable state may not be unique and there may be many of those for a given set of thermodynamic conditions (e.g. μ, V, T in the grand canonical ensemble) all different from one another depending from the kind of quench. The real (diffusive) dynamical (imaginary) time of the physical system can be used to define the insurgence of an arrested glassy state through the aging procedure, even if it is limited to the interval $[0, \beta/2]$.

We should mention here that the simulation time for a classical molecular dynamic and for a MC numerical experiment have profoundly different meanings. The first one can be mapped into the real dynamical time of the classical physical system whereas the second one has nothing to do with it but is merely the number of stochastic moves made to sample the configuration space of the system within the Metropolis algorithm. In the quantum regime one has at his disposal only simulations of the MC type but, as we showed, the simulation time can give an indication of metastability. Whereas the imaginary time real dynamics of the system tells us if we are close to an arrested glassy state.

We are presently implementing a better hard-core propagator [20] to substitute to the primitive approximation which would allow us to use fewer time-slices.

References

1. J.P. Hansen, I.R. McDonald, *Theory of Simple Liquids*, 4th edn. (Elsevier, Amsterdam, 2013)
2. W. Götze, *Complex Dynamics of Glass-forming Liquids: a Mode-Coupling Theory* (Oxford University Press, Oxford, 2009)
3. D.M. Ceperley, Rev. Mod. Phys. **67**, 279 (1995)

4. R. Fantoni, Phys. Rev. E **90**, 020102(R) (2014)
5. M. Boninsegni, N. Prokof'ev, B. Svistunov, Phys. Rev. Lett. **96**, 105301 (2006)
6. G. Biroli, C. Chamon, F. Zamponi, Phys. Rev. B **78**, 224306 (2008)
7. B. Hunt, E. Pratt, V. Grdagkar, M. Yamashita, A.V. Balatsky, J.C. Davis, Science **324**, 632 (2009)
8. N. Metropolis, A.W. Rosenbluth, M.N. Rosenbluth, A.H. Teller, E. Teller, J. Chem. Phys. **21**, 1087 (1953)
9. M. Boninsegni, L. Pollet, N. Prokof'ev, B. Svistunov, Phys. Rev. Lett. **109**, 025302 (2012)
10. K. Baerwinkel, Phys. Kondens. Mater. **12**, 287 (1971)
11. M. Boninsegni, N. Prokof'ev, B. Svistunov, Phys. Rev. Lett. **96**, 070601 (2006)
12. L. Vega, E. de Miguel, L.F. Rull, G. Jackson, I.A. McLure, J. Chem. Phys. **96**, 2296 (1992)
13. R.A. Young, Phys. Rev. Lett. **45**, 638 (1980)
14. R. Fantoni, S. Moroni, J. Chem. Phys. **141**, 114110 (2014)
15. R.J. Baxter, J. Chem. Phys. **49**, 2770 (1968)
16. M.A.G. Maestre, R. Fantoni, A. Giacometti, A. Santos, J. Chem. Phys. **138**, 094904 (2013)
17. R. Fantoni, A. Giacometti, M.A.G. Maestre, A. Santos, J. Chem. Phys. **139**, 174902 (2013)
18. R. Fantoni, A. Giacometti, A. Santos, J. Chem. Phys. **142**, 224905 (2015)
19. D.R. Reichman, P. Charbonneau, J. Stat. Mech. **2005** P05013 (2005)
20. J. Cao, B.J. Berne, J. Chem. Phys. **97**, 2382 (1992)

Chapter 49

Fourth moment sum rule for the charge correlations of a two-component classical plasma

Alastuey A. and **Fantoni R.**, J. Stat. Phys. **163**, 887 (2016)

Title: “Fourth moment sum rule for the charge correlations of a two-component classical plasma”

Abstract: We consider an ionic fluid made with two species of mobile particles carrying either a positive or a negative charge. We derive a sum rule for the fourth moment of equilibrium charge correlations. Our method relies on the study of the system response to the potential created by a weak external charge distribution with slow spatial variations. The induced particle densities, and the resulting induced charge density, are then computed within density functional theory, where the free energy is expanded in powers of the density gradients. The comparison with the predictions of linear response theory provides a thermodynamical expression for the fourth moment of charge correlations, which involves the isothermal compressibility as well as suitably defined partial compressibilities. The familiar Stillinger-Lovett condition is also recovered as a by-product of our method, suggesting that the fourth moment sum rule should hold in any conducting phase. This is explicitly checked in the low density regime, within the Abe-Meeron diagrammatical expansions. Beyond its own interest, the fourth-moment sum rule should be useful for both analyzing and understanding recently observed behaviours near the ionic critical point.



Fourth Moment Sum Rule for the Charge Correlations of a Two-Component Classical Plasma

Angel Alastuey¹ · Riccardo Fantoni²

Received: 3 February 2016 / Accepted: 24 March 2016
© Springer Science+Business Media New York 2016

Abstract We consider an ionic fluid made with two species of mobile particles carrying either a positive or a negative charge. We derive a sum rule for the fourth moment of equilibrium charge correlations. Our method relies on the study of the system response to the potential created by a weak external charge distribution with slow spatial variations. The induced particle densities, and the resulting induced charge density, are then computed within density functional theory, where the free energy is expanded in powers of the density gradients. The comparison with the predictions of linear response theory provides a thermodynamical expression for the fourth moment of charge correlations, which involves the isothermal compressibility as well as suitably defined partial compressibilities. The familiar Stillinger–Lovett condition is also recovered as a by-product of our method, suggesting that the fourth moment sum rule should hold in any conducting phase. This is explicitly checked in the low density regime, within the Abe–Meeron diagrammatical expansions. Beyond its own interest, the fourth-moment sum rule should be useful for both analyzing and understanding recently observed behaviours near the ionic critical point.

Keywords Two-component plasmas · Sum rules · Charge correlations · Critical behaviours

1 Introduction

Sum rules have been playing an important role in the study of charged systems for many years. In general, a sum rule provides a relation between microscopic correlations on the one hand, and macroscopic or universal quantities on the other hand. For charged systems, sum rules often express screening properties, so they shed light on the fundamental mechanisms

✉ Angel Alastuey
alastuey@ens-lyon.fr

¹ Laboratoire de Physique de l’Ecole Normale Supérieure de Lyon, Université de Lyon and CNRS, 46, allée d’Italie, 69007 Lyon, France

² Dipartimento di Fisica, Università di Trieste, strada Costiera 11, 34151 Grignano, Trieste, Italy

at work. Furthermore, they also provide useful constraints for approximate theories. Sum rules have been derived for a large variety of charged systems, including classical, quantum and relativistic plasmas, while they concern both static and dynamic properties in the bulk or near interfaces. For instance, let us mention the last work [1] by Bernard Jancovici, devoted to the study of the time-displaced charge correlations of a relativistic one-component plasma coupled to radiation. Other examples can be found in two reviews [2,3].

One of the most well-known sum rules for classical ionic fluids was derived long ago by Stillinger and Lovett [4], who shown that the second moment of equilibrium charge correlations is given by a simple universal expression, valid in any plasma phase and independent of the microscopic details of the considered models. That second-moment sum rule expresses the perfect screening of weak external charges. A few years later, Vieillefosse and Hansen [5] derived another sum rule for the fourth moment of the charges correlations of the one-component plasma (OCP), where identical positively charged particles move in a rigid uniform neutralizing background. That fourth moment is expressed in terms of the isothermal compressibility. Soon after that work, there was an attempt [6] to extend such a fourth-moment sum rule to the two-component plasma (TCP) where both positive and negative charges are mobile. The corresponding expression for the fourth moment involves ill-defined thermodynamic quantities, so its validity remained quite doubtful. A more convincing approach for that TCP was introduced by van Beijeren and Felderhof [7]. However, the thermodynamical quantities involved in the expression of the fourth moment are defined through the application of suitable external potentials which are not explicit, while the derivation itself is rather tough. In fact, a similar expression was obtained later by Suttorp and van Wonderen [8] for a multicomponent ionic mixture (MIM), where all mobile charges have the same sign and interact *via* the pure Coulomb potential, while a rigid uniform background of opposite charge ensures overall neutrality. Then, all involved thermodynamic quantities become well defined within the considered MIM.

The main goal of the present paper is to derive a fourth moment sum rule for a general TCP, namely to express such moment in terms of suitably defined thermodynamical quantities, similarly to the formulae derived for the OCP [5] or the MIM [8,9]. Our strategy, inspired by Jancovici's style, consists in studying the response of the TCP to a weak external charge distribution with a plane wave structure. In the long wavelength limit, the induced local particle densities vary on macroscopic scales. This allows us to compute the response within some hydrostatic-like approach which involves local equilibrium states with arbitrary densities. As a crucial point, a proper definition of equilibrium homogeneous non-neutral states with arbitrary densities naturally emerges within the framework of density functional theory (DFT). Then the induced charge density is expressed in terms of well-behaved thermodynamical quantities of an auxiliary system, which is nothing but a TCP immersed in a rigid uniform neutralizing background. Comparing that expression with the general linear response formula, we obtain the required fourth moment sum rule for the charge correlations of the genuine unperturbed TCP.

According to the previous strategy, we first introduce in Sect. 2 the various systems which intervene in our analysis. Of course, we start by defining the TCP, where a short-range regularization of the pure Coulomb interactions is essential for avoiding the classical collapse between oppositely charged particles. Two examples of such regularizations are provided, associated with either soft or hard spheres. After recalling that the TCP is always neutral and homogeneous in the absence of any external action on the particles, we show how the application of a suitable external potential produces homogeneous non-neutral states. This leads to the introduction of an auxiliary system, the TCP immersed in a charged background, for which equilibrium states are well defined for any set of particle densities.

The general framework of DFT is exposed in Sect. 3, where we provide the fundamental DFT equation which relates particle densities to the applied external potentials. The central object in that relation is the free energy, which is a functional of particle densities. For slow spatial variations, that free energy functional can be expanded in powers of the gradients of particle densities, where the local ingredients are equilibrium quantities of the above homogeneous auxiliary system. Let us mention that the idea of using density-gradient expansions was introduced a long time ago by van der Waals [10] for studying capillarity.

In Sect. 4, within DFT, we compute the induced particle densities of the TCP submitted to a weak external charge distribution with a plane wave structure and wavenumber k . The resulting induced charge density exactly cancels the external charge distribution in the long wavelength limit $k \rightarrow 0$, as expected from perfect screening arguments. Furthermore, its amplitude at the order k^2 included only depends on thermodynamical quantities of the auxiliary system. In other words the square-gradient corrections in the free energy functional, which intervene in the corresponding amplitudes of each induced particle density at this order, do not contribute anymore when forming the charge density thanks to cancellations. Then, by comparing this exact expression of the induced charge density obtained by DFT with the linear response formula, we obtain the required sum rule for the fourth moment of the charges correlations of the homogeneous neutral TCP. The corresponding thermodynamical expression of that fourth moment involves not only the isothermal compressibility of the TCP, but also partial compressibilities specific to the auxiliary system. We briefly discuss the content of previous approaches [6,7], and we show how the known results for the OCP [5] and the MIM [9] can be easily recovered within our general method.

It is worthy to check explicitly the fourth moment sum rule for specific models where exact calculations can be carried out for both microscopic and thermodynamical quantities. In Sect. 5, we consider a model of charged soft spheres in the low density limit at fixed temperature. Within the Abe–Meeron resummations of the familiar Mayer diagrammatics for particle correlations, we first compute the lowest order terms in the density expansion of the fourth moment of charge correlations, namely the terms of order $1/\rho$, $1/\rho^{1/2}$, $\rho \ln \rho$ and ρ^0 in the density ρ . Abe–Meeron resummed diagrammatics also provide the low density expansion of the thermodynamical quantities involved in the fourth moment sum rule : the corresponding expansion of the thermodynamical expression of the fourth moment exactly coincides with the previous purely microscopic calculation up to order ρ^0 included. That remarkable agreement holds for any values of the microscopic parameters defining the model.

In Sect. 6, we provide some additional comments about the derivation itself and its underlying assumptions, as well as extensions to three and more component systems. Beyond its own conceptual interest, we also discuss a possible use of the fourth moment sum rule for a better understanding of the conductor or dielectric nature of the critical point of the liquid-gas transition of an ionic fluid. It turns out that recent Monte Carlo simulations [11] strongly suggest that the fourth moment of charge correlations diverge when approaching the critical point, in a way close to that of the isothermal compressibility. That observation was one of the motivations for the present work.

2 The Systems of Interest

2.1 Examples of Two-Component Plasmas

We consider a two-component classical plasma (TCP) made with two species $\alpha = 1, 2$ of mobile particles carrying positive or negative charges, let us say $q_1 = Z_1 q > 0$ and

A. Alastuey, R. Fantoni

$q_2 = -Z_2q < 0$ with Z_1 and Z_2 positive integers. The corresponding Hamiltonian for a total number of particles $N = N_1 + N_2$ reads

$$H_{N_1, N_2} = \sum_{i=1}^N \frac{\mathbf{p}_i^2}{2m_{\alpha_i}} + \frac{1}{2} \sum_{i \neq j} u_{\alpha_i \alpha_j}(\mathbf{r}_i, \mathbf{r}_j) \tag{1}$$

where $\alpha_i = 1, 2$ is the species of particle i . The two-body potential $u_{\alpha_i \alpha_j}(\mathbf{r}_i, \mathbf{r}_j)$ only depends on the relative distance $r = |\mathbf{r}_i - \mathbf{r}_j|$, and it includes some short-range regularization of the Coulomb interaction, which is crucial for avoiding the classical collapse between oppositely charged particles. A first soft regularization is embedded in the simple expression

$$u_{\alpha\gamma}(r) = \frac{q_\alpha q_\gamma}{r} [1 - \exp(-r/d_{\alpha\gamma})] \tag{2}$$

which remains finite at $r = 0$. The lengths $d_{\alpha\gamma}$ control the exponential decay at large distances of the short-range part of the two-body potential.

A second regularization amounts to introduce hard cores, namely

$$u_{\alpha\gamma}(r) = \infty \text{ for } r < \sigma_{\alpha\gamma} \text{ and } u_{\alpha\gamma}(r) = \frac{q_\alpha q_\gamma}{r} \text{ for } r > \sigma_{\alpha\gamma} . \tag{3}$$

The corresponding TCP of charged hard spheres is suitable for describing many ionic mixtures, where the hard-core interaction mimics the effective repulsion between the electronic clouds of two ions. If σ_{11} and σ_{22} can be viewed as the effective diameters of the ions, the characteristic crossed lengths $\sigma_{12} = \sigma_{21}$ differ in general from the average $(\sigma_{11} + \sigma_{22})/2$ which would arise if particles really were billiard balls. This so-called non-additivity can be understood by noticing that the $\sigma_{\alpha\gamma}$'s are the typical ranges of the repulsions between electronic clouds for which no pure geometrical considerations apply. The simplest version of that general asymmetric TCP is the celebrated Restrictive Primitive Model, which is fully symmetric with respect to the charges and the hard-core diameters, namely $|q_1| = |q_2| = q$ and $\sigma_{11} = \sigma_{22} = \sigma_{12} = \sigma$.

Other short-range regularizations of the Coulomb interaction can be introduced. The corresponding most general TCP will be denoted \mathcal{S} . The following derivations are valid for any \mathcal{S} , beyond the above two examples.

2.2 The Homogeneous Neutral TCP

Let us first consider that \mathcal{S} is enclosed in a box with volume Λ , while no external potential is applied to the particles. At equilibrium, all statistical ensembles should become equivalent in the thermodynamic limit which is also assumed to exist. Furthermore, in a fluid phase, the bulk is overall neutral, that is the homogeneous particle densities ρ_1 and ρ_2 far from the boundaries satisfy the local neutrality relation

$$q_1 \rho_1 + q_2 \rho_2 = 0 . \tag{4}$$

Strictly speaking, these remarkable results have been only proved in the Debye regime, namely at sufficiently high temperatures and sufficiently low densities, for rather general regularized interactions and rational ratios q_2/q_1 [12]. Moreover, there exists a proof for charge symmetric systems, *i.e.* $q_1 = -q_2$, for any values of the thermodynamic parameters [13]. Let us also mention the beautiful proof for the quantum version with pure Coulomb interactions by Lieb and Lebowitz [14]. According to all those rigorous results, it can be reasonably expected that both the existence of the thermodynamic limit and the local neutrality are valid for any classical TCP in the whole fluid phase.

Fourth Moment Sum Rule for the Charge Correlations...

Important features of the various statistical ensembles are associated with the neutrality relation (4). In the grand-canonical ensemble, the intensive thermodynamical parameters are the inverse temperature β and the chemical potentials μ_α . It turns out that only the linear combination $\mu = (Z_2\mu_1 + Z_1\mu_2)/(Z_1 + Z_2)$ is relevant and entirely determines the total particle density $\rho = \rho_1 + \rho_2$. This can be readily understood within the following simple heuristic arguments. Let us introduce, for any arbitrary configuration, the total number of particles $N = N_1 + N_2$ and the corresponding total charge $Q = Mq$ with $M = Z_1N_1 - Z_2N_2$. According to the decomposition

$$\mu_1N_1 + \mu_2N_2 = \mu N + \nu M \tag{5}$$

with $\nu = (\mu_1 - \mu_2)/(Z_1 + Z_2)$, we see that μ controls the grand-canonical average $\langle N \rangle_{GC}$ of the total particle number, while ν determines the grand-canonical average $\langle Q \rangle_{GC} = q \langle M \rangle_{GC}$ of the net charge. In the thermodynamic limit (TL), $\Lambda \rightarrow \infty$ with β and μ_α fixed, the contributions of non-neutral configurations with Q proportional to the volume Λ become negligible, because the corresponding Boltzmann factors involve a positive self-electrostatic energy which diverges faster than Λ itself. Accordingly, the total charge density in the bulk

$$q_1\rho_1 + q_2\rho_2 = \lim_{TL} \langle Q \rangle_{GC} / \Lambda \tag{6}$$

vanishes for any given ν , while the total particle density $\rho = \rho_1 + \rho_2$ is indeed entirely determined by μ and β .

In the canonical ensemble, the TL is defined by letting $\Lambda \rightarrow \infty$ and $N_\alpha \rightarrow \infty$, keeping β and N_α/Λ fixed. All excess charges go to the boundaries in the TL, and the remaining bulk is always neutral. The bulk thermodynamic quantities and bulk distribution functions computed within the canonical ensemble then become identical to their grand canonical counterparts. In particular the free-energy density in thermal units of this homogeneous neutral phase, which only depends on ρ and $\beta = 1/(k_B T)$, can be computed through

$$f(\rho, \beta) = \lim_{TL} \left(\beta \sum_\alpha \mu_\alpha \langle N_\alpha \rangle_{GC} - \ln \Xi \right) / \Lambda, \tag{7}$$

where Ξ is the grand-canonical partition function. This provides the familiar thermodynamic identity

$$f(\rho, \beta) = \beta(\rho\mu - P), \tag{8}$$

with the pressure $P = \lim_{TL} k_B T \Lambda^{-1} \ln \Xi$. Since the pressure is also given by the thermodynamic relation

$$\beta P = \rho \frac{\partial f}{\partial \rho} - f(\rho, \beta), \tag{9}$$

we infer

$$\beta\mu = \frac{\partial f}{\partial \rho}, \tag{10}$$

which is analogous to the standard thermodynamical identity expressing the chemical potential for a one-component system with short-range interactions.

2.3 The Homogeneous Non-neutral TCP in an External Potential

In order to obtain a non-neutral homogeneous state of S with arbitrary uniform densities, one must apply a non-vanishing external potential on the particles. Let us introduce the electrostatic potential $\varphi_B(\mathbf{r})$ created by an uniform charge density c_B , and the corresponding external potentials $U_\alpha^B(\mathbf{r}) = q_\alpha \varphi_B(\mathbf{r})$ seen by the particles. At equilibrium, the total electrostatic field inside the bulk should identically vanish. According to that simple electrostatic argument, the induced particle densities should be homogeneous, while the resulting charge density $q_1 \rho_1 + q_2 \rho_2$ carried by the particles should cancel the external charge density c_B .

Interestingly, the above quite plausible scenario has been exactly demonstrated within a solvable model by Jancovici [15]. He considered identical point particles in two dimensions with pure Coulomb interactions, which then take a logarithmic form. In addition the particles are submitted to a confining parabolic potential, associated with a fixed external uniform charge density. For a special value of the temperature, all equilibrium distribution functions can be exactly computed. The resulting particle density is indeed uniform in the bulk and such that the total charge density vanishes. Furthermore, all higher-order distribution functions in the bulk become translationally invariant in the TL.

2.4 The Auxiliary System in a Neutralizing Rigid Background

As suggested by the previous considerations, and for further purposes, it is convenient to introduce an auxiliary system S^* , where now the mobile positive and negative charges of the TCP are immersed in an uniform rigid background with charge density c_B . The corresponding Hamiltonian of S^* reads

$$H_{N_1, N_2}^* = \sum_{i=1}^N \frac{\mathbf{p}_i^2}{2m_{\alpha_i}} + \frac{1}{2} \sum_{i \neq j} u_{\alpha_i \alpha_j}(\mathbf{r}_i, \mathbf{r}_j) + \sum_{i=1}^N \int_{\Lambda} d\mathbf{r} \frac{q_{\alpha_i} c_B}{|\mathbf{r}_i - \mathbf{r}|} + \frac{1}{2} \int_{\Lambda^2} d\mathbf{r} d\mathbf{r}' \frac{c_B^2}{|\mathbf{r}' - \mathbf{r}|}, \tag{11}$$

when the system is enclosed in a box with volume Λ . That system can be viewed as an extension of the well-known One-Component Plasma (OCP) made of identical charged particles immersed in a neutralizing rigid background. Now, there are two species which are immersed in the background, similarly to the case of a Binary Ionic Mixture (BIM). However, notice that here we do need a short-range regularization of the Coulomb interaction in order to avoid the collapse between oppositely charged particles, while the BIM can be defined with pure $1/r$ Coulomb interactions because all mobile charges have the same sign.

Like the OCP or the BIM, the system S^* should have a well-behaved thermodynamic limit, which is now taken with a fixed background charge density c_B . Now, in the bulk region, which is again electrically neutral, the homogeneous particle densities satisfy the neutrality relation

$$q_1 \rho_1 + q_2 \rho_2 + c_B = 0. \tag{12}$$

The corresponding free-energy density f^* of the homogeneous neutral system now depends on β , c_B and one particle density. Equivalently, f^* depends on β and on the two particle densities ρ_1 and ρ_2 . For any given set (ρ_1, ρ_2) , the charge background density is adjusted in order to satisfy the neutrality relation (12). This defines the function $f^*(\rho_1, \rho_2, \beta)$, where now ρ_1 and ρ_2 are independent variables. That procedure is analogous to that which defines the free-energy density $f_{\text{OCP}}(\rho, \beta)$ of the OCP for any value of the particle density ρ where a suitable background charge density always ensure overall neutrality.

Fourth Moment Sum Rule for the Charge Correlations...

The homogeneous neutral TCP can be viewed as a particular realization of \mathcal{S}^* for densities (ρ_1, ρ_2) satisfying the neutrality relation (4) in the absence of any background. For such neutral sets, each particle density can be expressed in terms of the total particle number density as

$$\rho_1 = \frac{Z_2}{Z_1 + Z_2} \rho \quad \text{and} \quad \rho_2 = \frac{Z_1}{Z_1 + Z_2} \rho . \tag{13}$$

The thermodynamic quantities of the homogeneous neutral TCP can then be inferred from their counterparts of \mathcal{S}^* for the neutral set of densities (13). For instance, the free-energy density of the homogeneous neutral TCP is given by

$$f(\rho, \beta) = f^*(Z_2\rho/(Z_1 + Z_2), Z_1\rho/(Z_1 + Z_2), \beta) . \tag{14}$$

For further purposes, it is useful to consider the isothermal compressibility defined by

$$\chi_T = -\lim_{TL} \Lambda^{-1} \frac{\partial \Lambda}{\partial P} = \left[\rho \frac{\partial P}{\partial \rho} \right]^{-1} = \beta \left[\rho^2 \frac{\partial^2 f}{\partial \rho^2} \right]^{-1} , \tag{15}$$

where all partial derivatives are taken at fixed β . According to identity (14), χ_T can be recast as

$$\chi_T = \frac{\beta(Z_1 + Z_2)^2}{\rho^2} \left[Z_2^2 \frac{\partial^2 f^*}{\partial \rho_1^2} + Z_1^2 \frac{\partial^2 f^*}{\partial \rho_2^2} + 2Z_1 Z_2 \frac{\partial^2 f^*}{\partial \rho_1 \partial \rho_2} \right]^{-1} , \tag{16}$$

where the second order partial derivatives of f^* are evaluated at the neutral set (13). Eventually, all distribution functions of the homogeneous neutral TCP obviously reduce to those of \mathcal{S}^* for that set of densities.

3 Density Functional Theory

3.1 Grand-Canonical Description

Now we consider a general inhomogeneous state of \mathcal{S} , where each particle of species α is submitted to an external potential $U_\alpha(\mathbf{r})$. We define the inhomogeneous fugacity of each species by

$$z_\alpha(\mathbf{r}) = \frac{\exp[\beta(\mu_\alpha - U_\alpha(\mathbf{r}))]}{(2\pi\lambda_\alpha^2)^{3/2}} . \tag{17}$$

where $\lambda_\alpha = (\beta\hbar^2/m_\alpha)^{1/2}$ is the de Broglie thermal wavelength of species α . The classical grand-canonical partition function of \mathcal{S} enclosed in a box with volume Λ reads

$$\Xi = \sum_{N_1, N_2=0}^{\infty} \frac{1}{N_1! N_2!} \int \prod_{i=1}^N d\mathbf{r}_i z_{\alpha_i}(\mathbf{r}_i) \exp(-\beta V_{N_1, N_2}) , \tag{18}$$

where V_{N_1, N_2} is the potential part of the Hamiltonian (1). The inhomogeneous particle density $\rho_\alpha(\mathbf{r})$ can be expressed as a functional derivative of Ξ with respect to $z_\alpha(\mathbf{r})$, namely

$$\rho_\alpha(\mathbf{r}) = z_\alpha(\mathbf{r}) \frac{\delta \ln \Xi}{\delta z_\alpha(\mathbf{r})} \tag{19}$$

A. Alastuey, R. Fantoni

while parameters Λ and β are kept fixed. The free-energy \mathcal{F} in thermal units of S is given by the Legendre transformation

$$\mathcal{F} = \sum_{\alpha} \int_{\Lambda} d\mathbf{r} \rho_{\alpha}(\mathbf{r}) \beta(\mu_{\alpha} - U_{\alpha}(\mathbf{r})) - \ln \Xi . \tag{20}$$

The grand-partition function Ξ , as well as the free-energy \mathcal{F} , can be considered as functionals of either $z_{\alpha}(\mathbf{r})$ or $\rho_{\alpha}(\mathbf{r})$. The functional derivative of \mathcal{F} with respect to $\rho_{\alpha}(\mathbf{r})$ is readily computed as

$$\frac{\delta \mathcal{F}}{\delta \rho_{\alpha}(\mathbf{r})} = \beta(\mu_{\alpha} - U_{\alpha}(\mathbf{r})) \tag{21}$$

where we have used identity (19) as well as standard calculation rules for functional differentiation. The relation (21) will play a key role in the following. The density profiles $\rho_{\alpha}(\mathbf{r})$ for each given sets $(\mu_{\alpha} - U_{\alpha}(\mathbf{r}))$ can be determined from that relation if one knows the functional dependence of \mathcal{F} with respect to the inhomogeneous densities : this is the strategy of density functional theories (DFT). However, the main difficulty of DFT is that the free-energy functional is not exactly known, except for hard rods in one dimension [16]. In general, approximate forms are used. Here, we will use exact asymptotic expansions for densities with infinitely slow spatial variations.

3.2 Homogeneous Systems

As argued in the previous Section, homogeneous states of S with arbitrary densities (ρ_1, ρ_2) are obtained by applying the external potentials

$$U_{\alpha}^B(\mathbf{r}) = q_{\alpha} \varphi_B(\mathbf{r}) = q_{\alpha} \int_{\Lambda} d\mathbf{r}' \frac{c_B}{|\mathbf{r}' - \mathbf{r}|} \tag{22}$$

with the external charge density $c_B = -(q_1 \rho_1 + q_2 \rho_2)$. If we introduce the potential part V_{N_1, N_2}^* of the Hamiltonian (11) for the auxiliary system S^* with background charge density c_B , we can rewrite

$$V_{N_1, N_2} + \sum_{i=1}^N U_{\alpha_i}^B(\mathbf{r}_i) = V_{N_1, N_2}^* - W_B \tag{23}$$

where

$$W_B = \frac{1}{2} \int_{\Lambda^2} d\mathbf{r} d\mathbf{r}' \frac{c_B^2}{|\mathbf{r}' - \mathbf{r}|} \tag{24}$$

is the self-electrostatic energy of the background charge density c_B . Inserting relation (23) into the general expression (18), we obtain for the grand-partition function of S submitted to the external potentials $U_{\alpha}^B(\mathbf{r})$,

$$\Xi \{ \mu_1 - U_1^B(\cdot), \mu_2 - U_2^B(\cdot) \} = \Xi^* \{ \mu_1, \mu_2 \} \exp(\beta W_B) , \tag{25}$$

where Ξ^* is the grand-partition function S^* for the same chemical potentials μ_{α} and a background charge density c_B , without any applied external potentials, *i.e.* $U_{\alpha}(\mathbf{r}) = 0$. In the derivation of identity (25), we have used that W_B is a pure constant which does not depend on the particle degrees of freedom. This also implies that all the grand-canonical averages for S submitted to $U_{\alpha}^B(\mathbf{r})$ are identical to those for S^* . In particular, both particle densities are identical, so the particle densities of S submitted to $U_{\alpha}^B(\mathbf{r})$ are indeed homogeneous and

Fourth Moment Sum Rule for the Charge Correlations...

they are merely related to c_B via the neutrality condition (12) valid for S^* . Moreover, all particle correlations of both systems are identical.

If we insert expression (25) of Ξ into definition (20) of the free energy of S submitted to $U_\alpha^B(\mathbf{r})$, we obtain in the TL

$$\mathcal{F}\{\rho_1, \rho_2\} - \frac{\beta}{2} \int_{\Lambda^2} d\mathbf{r}d\mathbf{r}' \frac{(q_1\rho_1 + q_2\rho_2)^2}{|\mathbf{r}' - \mathbf{r}|} \sim \mathcal{F}^*\{\rho_1, \rho_2\} \tag{26}$$

while c_B has also been replaced by $-(q_1\rho_1 + q_2\rho_2)$ thanks to the neutrality condition (12). Thus, if we define, in general, the reduced free energy \mathcal{F}_{red} of S by subtracting to \mathcal{F} the self-electrostatic energy of the charge distribution $(q_1\rho_1(\mathbf{r}) + q_2\rho_2(\mathbf{r}))$, namely

$$\mathcal{F}_{\text{red}} = \mathcal{F} - \frac{\beta}{2} \int_{\Lambda^2} d\mathbf{r}d\mathbf{r}' \frac{(q_1\rho_1(\mathbf{r}) + q_2\rho_2(\mathbf{r}))(q_1\rho_1(\mathbf{r}') + q_2\rho_2(\mathbf{r}'))}{|\mathbf{r}' - \mathbf{r}|}, \tag{27}$$

we find the remarkable identity

$$\mathcal{F}_{\text{red}}\{\rho_1, \rho_2\} \sim \mathcal{F}^*\{\rho_1, \rho_2\}, \tag{28}$$

which can be rewritten for the corresponding free-energy densities as

$$f_{\text{red}}(\rho_1, \rho_2, \beta) = f^*(\rho_1, \rho_2, \beta). \tag{29}$$

Notice that this subtraction from the free-energy functional of the self-electrostatic energy was first introduced by Hohenberg and Kohn [17] for studying the quantum electron gas.

3.3 Density Functional Expansions for Almost Homogeneous Systems

For states of S with slow spatial variations of the particle densities, the corresponding reduced free-energy $\mathcal{F}_{\text{red}}\{\rho_1(\cdot), \rho_2(\cdot)\}$ can be expanded in powers of the gradients of $\rho_1(\mathbf{r})$ and $\rho_2(\mathbf{r})$. The leading term in that systematic expansion is purely local and reduces to

$$\int d\mathbf{r} f^*(\rho_1(\mathbf{r}), \rho_2(\mathbf{r}), \beta), \tag{30}$$

where we have used identity (29) for the reduced free-energy density of an homogeneous system. The first correction, the so-called square-gradient term, reads [18, 19]

$$\frac{1}{12} \sum_{\alpha, \gamma} \int d\mathbf{r} M_{\alpha\gamma}^*(\rho_1(\mathbf{r}), \rho_2(\mathbf{r}), \beta) \nabla\rho_\alpha(\mathbf{r}) \cdot \nabla\rho_\gamma(\mathbf{r}), \tag{31}$$

where $M_{\alpha\gamma}^*(\rho_1, \rho_2, \beta)$ is the second moment of the short-range part of the direct two-body correlations, namely $c_{\alpha\gamma}^{\text{SR}}(r) = c_{\alpha\gamma}(r) + \beta q_\alpha q_\gamma / r$, for S^* with homogeneous densities (ρ_1, ρ_2) . Similarly to the emergence of the free-energy density of S^* in the purely local term (30), the direct correlations of S^* arise in the square-gradient term because all the respective distribution functions of S^* and S with the same homogeneous densities are identical as established above. Notice that for systems with short-range interactions, the square-gradient expansion of the free energy \mathcal{F} involves second moments of the direct correlations themselves. Here, thanks to the subtraction (27) of the electrostatic self-energy, the square-gradient expansion of the reduced free energy \mathcal{F}_{red} involves second moments of the short-range part $c_{\alpha\gamma}^{\text{SR}}(r)$, which do converge thanks to the large-distance behaviour $c_{\alpha\gamma}(r) \sim -\beta q_\alpha q_\gamma / r$ when $r \rightarrow \infty$.

The second correction to the purely local contribution (30) involves fourth-order spatial derivatives of the densities, and it has been explicitly computed in Ref. [20]. The corresponding local ingredients are fourth moments of two-, three- and four-body direct correlations of

A. Alastuey, R. Fantoni

S^* with homogeneous densities. Higher-order corrections would exhibit similar structures with well-behaved local ingredients defined for the same system.

4 Linear Response to a Weak Slowly-Varying External Charge Distribution

We start with S in the absence of any applied external potential, namely that realization of S is nothing but the homogeneous neutral TCP. In a second step, let us introduce an external charge distribution $c_{\text{ext}}(\mathbf{r}) = q_{\text{ext}} \exp(i\mathbf{k} \cdot \mathbf{r})$, with an infinitesimal amplitude q_{ext} . Our aim here is to determine the induced charge density in S by DFT and compare to its linear response expression. This will provide the required fourth moment sum rule for the charge correlations of the homogeneous neutral TCP. In a first step, within DFT, we compute the density responses $\delta\rho_\alpha(\mathbf{r})$ to the external potentials, $U_\alpha(\mathbf{r}) = q_\alpha \varphi_{\text{ext}}(\mathbf{r})$ with $\varphi_{\text{ext}}(\mathbf{r})$ the electrostatic potential created by $c_{\text{ext}}(\mathbf{r})$, at leading order in q_{ext} and in the limit of small wave-numbers $k \rightarrow 0$.

4.1 Analysis Within Density Functional Theory

Since the applied external potential varies on an infinitely large scale length, the particle densities should also display infinitely slow spatial variations. Then, the free-energy functional can be replaced by its density-gradient expansion introduced above, namely

$$\begin{aligned} \mathcal{F}\{\rho_1(\cdot), \rho_2(\cdot)\} &= \frac{\beta}{2} \int d\mathbf{r}d\mathbf{r}' \frac{(q_1\rho_1(\mathbf{r}) + q_2\rho_2(\mathbf{r}))(q_1\rho_1(\mathbf{r}') + q_2\rho_2(\mathbf{r}'))}{|\mathbf{r}' - \mathbf{r}|} \\ &+ \int d\mathbf{r} f^*(\rho_1(\mathbf{r}), \rho_2(\mathbf{r}), \beta) \\ &+ \frac{1}{12} \sum_{\alpha,\gamma} \int d\mathbf{r} M_{\alpha\gamma}^*(\rho_1(\mathbf{r}), \rho_2(\mathbf{r}), \beta) \nabla\rho_\alpha(\mathbf{r}) \cdot \nabla\rho_\gamma(\mathbf{r}) + \dots, \end{aligned} \quad (32)$$

where the terms left over do not contribute to the deviations $\delta\rho_\alpha(\mathbf{r})$ at the considered lowest orders in k , as shown further on. The fundamental equation (21) of DFT then becomes for each species,

$$\begin{aligned} \frac{\partial f^*}{\partial \rho_1} - \frac{1}{6} [M_{11}^* \Delta\rho_1(\mathbf{r}) + M_{12}^* \Delta\rho_2(\mathbf{r})] \\ - \frac{1}{12} \left[\frac{\partial M_{11}^*}{\partial \rho_1} (\nabla\rho_1(\mathbf{r}))^2 + 2 \frac{\partial M_{11}^*}{\partial \rho_2} \nabla\rho_1(\mathbf{r}) \cdot \nabla\rho_2(\mathbf{r}) + \left(2 \frac{\partial M_{12}^*}{\partial \rho_2} - \frac{\partial M_{22}^*}{\partial \rho_1} \right) (\nabla\rho_2(\mathbf{r}))^2 \right] + \dots \\ = \beta\mu_1 - \beta q_1 \varphi_{\text{tot}}(\mathbf{r}) \end{aligned} \quad (33)$$

and

$$\begin{aligned} \frac{\partial f^*}{\partial \rho_2} - \frac{1}{6} [M_{22}^* \Delta\rho_2(\mathbf{r}) + M_{12}^* \Delta\rho_1(\mathbf{r})] \\ - \frac{1}{12} \left[\frac{\partial M_{22}^*}{\partial \rho_2} (\nabla\rho_2(\mathbf{r}))^2 + 2 \frac{\partial M_{22}^*}{\partial \rho_1} \nabla\rho_1(\mathbf{r}) \cdot \nabla\rho_2(\mathbf{r}) + \left(2 \frac{\partial M_{12}^*}{\partial \rho_1} - \frac{\partial M_{11}^*}{\partial \rho_2} \right) (\nabla\rho_1(\mathbf{r}))^2 \right] + \dots \\ = \beta\mu_2 - \beta q_2 \varphi_{\text{tot}}(\mathbf{r}), \end{aligned} \quad (34)$$

where $\varphi_{\text{tot}}(\mathbf{r})$ is the total electrostatic potential created by the charge distribution $(q_1\rho_1(\mathbf{r}) + q_2\rho_2(\mathbf{r}) + c_{\text{ext}}(\mathbf{r}))$. In Eqs. (33,34) all involved quantities of S^* are evaluated for homogeneous

Fourth Moment Sum Rule for the Charge Correlations...

densities identical to the local densities $(\rho_1(\mathbf{r}), \rho_2(\mathbf{r}))$ and inverse temperature β . Moreover, all terms left over involve at least fourth-order spatial derivatives of $\rho_1(\mathbf{r})$ and $\rho_2(\mathbf{r})$.

In order to compute the induced densities at lowest order in q_{ext} , we can linearize Eqs. (33,34) with respect to $\delta\rho_\alpha(\mathbf{r})$. The third terms in the l.h.s. of those Eqs. do not contribute anymore since they are at least of order q_{ext}^2 . The resulting deviations take the form of plane waves, like the forcing external charge $c_{\text{ext}}(\mathbf{r})$, namely

$$\delta\rho_1(\mathbf{r}) = A_1(k) \exp(i\mathbf{k} \cdot \mathbf{r}) \quad \text{and} \quad \delta\rho_2(\mathbf{r}) = A_2(k) \exp(i\mathbf{k} \cdot \mathbf{r}) \tag{35}$$

where the amplitudes $A_\alpha(k)$ are proportional to q_{ext} . The total electrostatic potential $\varphi_{\text{tot}}(\mathbf{r})$ satisfies Poisson equation

$$\Delta\varphi_{\text{tot}}(\mathbf{r}) = -4\pi [q_1\rho_1(\mathbf{r}) + q_2\rho_2(\mathbf{r}) + c_{\text{ext}}(\mathbf{r})] = -4\pi [q_1\delta\rho_1(\mathbf{r}) + q_2\delta\rho_2(\mathbf{r}) + c_{\text{ext}}(\mathbf{r})] \tag{36}$$

where the second equality follows from the overall neutrality of the unperturbed system \mathcal{S} . In order to eliminate $\varphi_{\text{tot}}(\mathbf{r})$ in favor of the induced density deviations, it is then sufficient to take the Laplacian of the linearized versions of Eqs. (33,34). This provides

$$\begin{aligned} & \left[4\pi\beta q_1^2 + \chi_{11}^{-1}k^2 + a_{11}k^4 + O(k^6) \right] A_1(k) + \left[4\pi\beta q_1q_2 + \chi_{12}^{-1}k^2 + a_{12}k^4 + O(k^6) \right] A_2(k) \\ & = -4\pi\beta q_1\delta q_{\text{ext}} \end{aligned} \tag{37}$$

$$\begin{aligned} & \left[4\pi\beta q_1q_2 + \chi_{21}^{-1}k^2 + a_{21}k^4 + O(k^6) \right] A_1(k) + \left[4\pi\beta q_2^2 + \chi_{22}^{-1}k^2 + a_{22}k^4 + O(k^6) \right] A_2(k) \\ & = -4\pi\beta q_2\delta q_{\text{ext}} \end{aligned} \tag{38}$$

with $\chi_{\alpha\gamma}^{-1} = \partial^2 f^* / \partial\rho_\alpha \partial\rho_\gamma$ and $a_{\alpha\gamma} = M_{\alpha\gamma}^* / 6$. Those reference quantities are evaluated for the set (ρ_1, ρ_2) ensuring overall neutrality of the unperturbed system \mathcal{S} . Notice that if the thermodynamic function $\chi_{\alpha\gamma}^{-1}$ is specific to the enlarged auxiliary system \mathcal{S}^* , the microscopic second moments $a_{\alpha\gamma}$ entirely depend on the direct correlations of the genuine system \mathcal{S} of interest.

The linear Eqs. (37,38) are straightforwardly solved in terms of the determinant of the associated two by two matrix which reads

$$\begin{aligned} D(k) &= 4\pi\beta \left(q_2^2\chi_{11}^{-1} + q_1^2\chi_{22}^{-1} - 2q_1q_2\chi_{12}^{-1} \right) k^2 \\ &+ \left[\chi_{11}^{-1}\chi_{22}^{-1} - \chi_{12}^{-2} + 4\pi\beta (q_2^2a_{11} + q_1^2a_{22} - 2q_1q_2a_{12}) \right] k^4 + O(k^6) . \end{aligned} \tag{39}$$

The amplitudes $A_\alpha(k)$ are then found to be

$$A_1(k) = \frac{4\pi\beta}{D(k)} \left[\left(q_2\chi_{12}^{-1} - q_1\chi_{22}^{-1} \right) k^2 + (q_2a_{12} - q_1a_{22})k^4 + O(k^6) \right] \delta q_{\text{ext}} \tag{40}$$

and

$$A_2(k) = \frac{4\pi\beta}{D(k)} \left[\left(q_1\chi_{12}^{-1} - q_2\chi_{11}^{-1} \right) k^2 + (q_1a_{12} - q_2a_{11})k^4 + O(k^6) \right] \delta q_{\text{ext}} . \tag{41}$$

Therefore the proportionality coefficient between a given amplitude and δq_{ext} , behaves in the limit $k \rightarrow 0$ as a constant, which depends only on the thermodynamic quantities $\chi_{\alpha\gamma}^{-1}$, plus a term of order k^2 which depends on both $\chi_{\alpha\gamma}^{-1}$ and $a_{\alpha\gamma}$. Now, if we form the induced charge density

$$\delta c(\mathbf{r}) = q_1\delta\rho_1(\mathbf{r}) + q_2\delta\rho_2(\mathbf{r}) = c_{\text{ind}}(k) \exp(i\mathbf{k} \cdot \mathbf{r}) \tag{42}$$

with the charge amplitude

$$c_{\text{ind}}(k) = q_1 A_1(k) + q_2 A_2(k), \tag{43}$$

we find

$$c_{\text{ind}}(k) = -\delta q_{\text{ext}} \left[1 - \frac{(\chi_{11}^{-1} \chi_{22}^{-1} - \chi_{12}^{-2})}{4\pi\beta(q_2^2 \chi_{11}^{-1} + q_1^2 \chi_{22}^{-1} - 2q_1 q_2 \chi_{12}^{-1})} k^2 + O(k^4) \right]. \tag{44}$$

Remarkably, the proportionality coefficient between the induced and external charges goes to -1 when $k \rightarrow 0$, in relation with perfect screening properties, as discussed further. Furthermore the term of order k^2 in its small- k expansion now depends only on the thermodynamical functions $\chi_{\alpha\gamma}^{-1}$, and no longer on the microscopic quantities $a_{\alpha\gamma}$.

4.2 The Fourth Moment Sum Rule

The resulting induced charge density, can be also determined within linear response theory, which provides

$$\delta c(\mathbf{r}) = -\frac{4\pi\beta}{k^2} \tilde{S}(k) \delta q_{\text{ext}} \exp(i\mathbf{k} \cdot \mathbf{r}) \tag{45}$$

In the linear response formula (45), $\tilde{S}(k)$ is the Fourier transform of the charge correlations of the unperturbed system S , i.e. the homogeneous neutral TCP,

$$\tilde{S}(k) = \int d\mathbf{r} \exp(i\mathbf{k} \cdot \mathbf{r}) \left[\sum_{\alpha,\gamma} q_\alpha q_\gamma \rho_{\alpha\gamma}(r) + \sum_\alpha q_\alpha^2 \rho_\alpha \delta(\mathbf{r}) \right] \tag{46}$$

with $\rho_{\alpha\gamma}(r)$ the two-body probability density for the spatial configuration where one particle of species α is fixed at the origin, while another particle of species γ is fixed at \mathbf{r} .

The small- k expansion of the amplitude $c_{\text{ind}}(k)$ can be inferred from the linear response formula (45) by inserting the corresponding expansion of $\tilde{S}(k)$,

$$\tilde{S}(k) = I_0 + I_2 k^2 + I_4 k^4 + \dots, \tag{47}$$

which only involves powers of k^2 thanks to the expected exponential decay of charge correlations in real space. If we compare the resulting expansion of $c_{\text{ind}}(k)$ with the DFT result (44), we readily find

$$I_0 = 0 \quad \text{and} \quad I_2 = \frac{1}{4\pi\beta} \tag{48}$$

which follow from respectively the absence of a $1/k^2$ -term, and the identification of the constant terms. The vanishing of I_0 accounts for the perfect screening of internal charges. The universal value of I_2 , first demonstrated a long ago by Stillinger and Lovett [4], ensures the perfect screening of weak external charges. Beyond those well-known results for the zeroth and second moments of $S(r)$, the DFT expression (44) also provides a new sum rule for the fourth moment, namely

$$I_4 = -\frac{\rho^2}{(4\pi(q_1 - q_2))^2 \beta^3} (\chi_{11}^{-1} \chi_{22}^{-1} - \chi_{12}^{-2}) \chi_T, \tag{49}$$

Fourth Moment Sum Rule for the Charge Correlations...

which follows from the identification of the k^2 -terms. The compressibility χ_T emerges in that sum rule, thanks to the identity (16) rewritten in terms of the charges $q_1 = Z_1q$ and $q_2 = -Z_2q$.

4.3 Related Sum Rules for Other Models

Let us first consider the case of the OCP. A fourth moment sum rule for the corresponding charge correlations $S_{\text{OCP}}(r)$ was derived by Vieillefosse and Hansen [5] through a macroscopic analysis of fluctuations. In their textbook [21], Hansen and Mac Donald propose a simple derivation which is similar to ours. They compute the charge density induced by a weak external plane wave charge distribution within an hydrostatic approach, where the force associated with the local pressure gradient is balanced by the total electrostatic force created by both the external and induced charges. Notice that the corresponding equation can be merely obtained by taking the gradient of the fundamental DFT equation (33) restricted to a single species and where all non-local contributions, including that involving the second moment of the direct correlations, are omitted. Moreover, the corresponding f^* can then be obviously replaced by f_{OCP} . The fourth moment of $S_{\text{OCP}}(r)$ then reduces to [5,21],

$$I_4^{\text{OCP}} = -\frac{1}{(4\pi q\rho)^2\beta\chi_T^{\text{OCP}}} \tag{50}$$

Notice that this expression has been recovered through manipulations of the BGY hierarchy, for pure Coulomb interactions [22] and also including short-range interactions [23].

The OCP result has been extended to a multicomponent ionic mixture (MIM) of all positive point charges immersed in a rigid neutralizing background [8,9]. Interestingly, the derivation is intrinsic and does not rely on the response of the system to a weak external charge distribution. Like the analysis [22] carried out for the OCP, it is based on suitable manipulations of the BGY hierarchy equations for the distribution functions of the infinite homogeneous neutral system. *A priori* the derivation is only valid for pure Coulomb interactions, without any short range regularization which is unnecessary here since all mobile charges repel together. It makes an explicit use of the remarkable homogeneity property of the resulting pair interactions. The fourth moment of charge correlations in real space is then given by formula (7.3) in Ref. [9], which reduces in three dimensions ($d = 3$) to

$$\int d\mathbf{r} r^4 S_{\text{MIM}}(r) = -\frac{120}{\beta \sum_{\alpha,\gamma} q_\alpha q_\gamma \partial\rho_\gamma / \partial\mu_\alpha} \tag{51}$$

where we have used that $q_v = \sum_\alpha q_\alpha \rho_\alpha$, while $\mu_\alpha = \beta^{-1} \partial f_{\text{MIM}} / \rho_\alpha$. Each partial derivative $\partial\rho_\gamma / \partial\mu_\alpha$ is computed by fixing the inverse temperature β as well as all μ_δ 's with $\delta \neq \alpha$. Straightforward manipulations of the multi-variable functions $\rho_\gamma(\beta, \{\mu_\alpha\})$ and $\mu_\alpha(\beta, \{\rho_\gamma\})$ allow us to express all partial derivatives $\partial\rho_\gamma / \partial\mu_\alpha$ in terms of partial derivatives $\partial\mu_\alpha / \partial\rho_\gamma$. In the binary case, we find

$$\begin{aligned} \frac{\partial\rho_1}{\partial\mu_1} &= \frac{\partial\mu_2}{\partial\rho_2} \left[\frac{\partial\mu_1}{\partial\rho_1} \frac{\partial\mu_2}{\partial\rho_2} - \frac{\partial\mu_1}{\partial\rho_2} \frac{\partial\mu_2}{\partial\rho_1} \right]^{-1} ; & \frac{\partial\rho_2}{\partial\mu_2} &= \frac{\partial\mu_1}{\partial\rho_1} \left[\frac{\partial\mu_1}{\partial\rho_1} \frac{\partial\mu_2}{\partial\rho_2} - \frac{\partial\mu_1}{\partial\rho_2} \frac{\partial\mu_2}{\partial\rho_1} \right]^{-1} \\ \frac{\partial\rho_1}{\partial\mu_2} &= -\frac{\partial\mu_1}{\partial\rho_2} \left[\frac{\partial\mu_1}{\partial\rho_1} \frac{\partial\mu_2}{\partial\rho_2} - \frac{\partial\mu_1}{\partial\rho_2} \frac{\partial\mu_2}{\partial\rho_1} \right]^{-1} ; & \frac{\partial\rho_2}{\partial\mu_1} &= -\frac{\partial\mu_2}{\partial\rho_1} \left[\frac{\partial\mu_1}{\partial\rho_1} \frac{\partial\mu_2}{\partial\rho_2} - \frac{\partial\mu_1}{\partial\rho_2} \frac{\partial\mu_2}{\partial\rho_1} \right]^{-1} . \end{aligned} \tag{52}$$

Using the identity

$$I_4 = \frac{1}{120} \int d\mathbf{r} r^4 S(r) \tag{53}$$

and inserting relations (52) into formula (51), we find that the corresponding I_4^{BIM} exactly coincides with our general expression (49) specified to the BIM, where the free-energy density f^* merely reduces to f_{BIM} . Indeed, our derivation also applies to the BIM where q_1 and q_2 now have the same sign, while the auxiliary system \mathcal{S}^* becomes identical to the genuine BIM of interest with the background charge density $c_B = -q_v = -\sum_{\alpha} q_{\alpha} \rho_{\alpha}$.

4.4 About Other Approaches

To our knowledge, in the literature, there exist two attempts to derive a sum rule for the fourth moment of the charge correlations of the TCP. First, the hydrodynamic approach carried out in Ref. [6] provides an expression for the fourth moment, different from formula (49), which involves ill-defined thermodynamic quantities as well as particle masses. Its validity is then quite doubtful, in particular because classical equilibrium charge correlations do not depend on particle masses.

Second, van Beijeren and Felderhof [7] proceed to an intrinsic analysis of charge correlations within the grand-canonical ensemble, where they combine the Ornstein-Zernicke equations with DFT manipulations. In agreement with results previously derived by Mitchell et al. [24], who shown that the fourth moment cannot be expressed in terms of thermodynamic quantities of the sole TCP, they find that it is necessary to introduce non-neutral states of the TCP which can be realized through the application of a suitable external potential. However, they did not provide any scheme which determines that external potential. Thus their free-energy density f^0 , from which the thermodynamical chemical potentials are inferred through the usual identity written in formula (3.12) of Ref. [7], remains a formal quantity, with no prescriptions for explicit calculations. This ambiguity might explain why their work is not always cited. According to our analysis, it can be easily clarified as follows. In fact, as shown in Sect. 2, the external potential mentioned in Ref. [7] is nothing but our potential $U_{\alpha}^B(\mathbf{r}) = q_{\alpha} \varphi_B(\mathbf{r})$ where $\varphi_B(\mathbf{r})$ is the electrostatic potential created by an homogeneous background density. Therefore, f^0 is identical to our free-energy density f^* of the TCP immersed in an uniform rigid background. Then, the relation between partial derivatives (52) allows us to exactly recast formula (6.26) of Ref. [7] as our expression (49), similarly to what occurs for the corresponding formula obtained for the BIM by Suttorp [9].

5 Asymptotic Expansions at Low Densities

It is instructive to check the fourth moment sum rule for specific models and various ranges of thermodynamical parameters. Here, we consider the model of charged soft spheres with the pair interaction $u_{\alpha\gamma}(r)$ given by formula (2). First, we briefly describe how the pair correlations of \mathcal{S}^* can be represented by an infinite series of resummed Mayer graphs. Such resummed diagrammatics constitute a quite suitable framework for deriving low-density expansions of the quantities of interest. From the diagrammatic representation of charge correlations, we infer the low-density expansion of I_4 defined as the coefficient of the k^4 -term in the small- k expansion (47) of $\tilde{S}(k)$. The diagrammatics for the pair correlations also give access to the free energy density f^* through thermodynamical identities. The low-

density expansion of the thermodynamical expression (49) is then computed, and it is shown to exactly match that of I_4 , as expected.

5.1 Exploiting the Principle of Topological Reduction

Let $\rho_{\alpha\gamma,T}^*(r) = \rho_{\alpha\gamma}^*(r) - \rho_\alpha\rho_\gamma$ be the truncated pair distribution functions of \mathcal{S}^* , also called pair correlations, for an arbitrary set of densities (ρ_1, ρ_2) . As argued above, the distributions function of \mathcal{S}^* , which includes a background with charge density $c_B = -(q_1\rho_1 + q_2\rho_2)$, are identical to that of a purely two-component system where the mobile particles are submitted to the external potential (22) $U_\alpha^B(\mathbf{r})$ created by the background. Therefore, pair correlations $\rho_{\alpha\gamma,T}^*(r)$ are represented by series of Mayer diagrams [25] made with two root (white) points respectively fixed at the origin $\mathbf{0}$ and at \mathbf{r} , and an arbitrary number of black points whose positions are integrated over. Each point carries a statistical weight

$$z_\alpha = \frac{\exp[\beta(\mu_\alpha - U_\alpha^B)]}{(2\pi\lambda_\alpha^2)^{3/2}}, \tag{54}$$

while two points are connected by at most one Mayer bond

$$b_M = \exp(-\beta u_{\alpha\gamma}) - 1. \tag{55}$$

Each diagram is simply connected, namely there exists at least one path connecting two arbitrary points.

The previous Mayer diagrams are difficult to handle because the fugacity weights (54) are inhomogeneous and depend on the positions of the points. A great simplification can be achieved by virtue of the principle of topological reduction, nicely exposed in Ref. [21], which consists in removing all articulation points. An articulation point is such that there exists at least one subdiagram attached to it and not connected to the rest of the diagram. In other words, the suppression of the articulation point leaves that subdiagram disconnected from the two root points. If one sums all those subdiagrams attached to a given articulation point, all articulation points are removed, while simultaneously all fugacity weights (54) are replaced by density weights ρ_α [21]. Furthermore, the topological structure of the diagrams is conserved through that reduction. Accordingly, the pair correlations $\rho_{\alpha\gamma,T}^*(r)$ are represented by Mayer diagrams made with the two root points fixed at $\mathbf{0}$ and \mathbf{r} , and an arbitrary number of black points, where the point statistical weights are now the densities ρ_α . Two point are still connected at most by one Mayer bond (55). Each diagram is again simply connected but is now free of any articulation point.

Thanks to the translational invariance of both density weights and Mayer bonds, the Mayer density diagrams reveal quite useful for explicit calculations as described further. Notice that, remarkably, the background does not show in such diagrams, its effects being implicitly and entirely taken into account by the introduction of the homogeneous densities ρ_α .

5.2 Abe–Meeron Resummations

Because of the long-range non-integrable decay of two-body interactions $u_{\alpha\gamma}$, every Mayer diagram diverges. All those divergencies can be removed via chain resummations, as first noticed by Mayer [26] and Salpeter [27], and then performed in a systematic way for the whole diagrammatical series by Abe [28] and Meeron [29]. A simplified presentation of that method can be found in Refs. [30] and [31]. It starts with the decomposition of each Mayer

bond (55) as

$$b_M = b_M^T - \beta q_\alpha q_\gamma v_C \tag{56}$$

with the truncated bond

$$b_M^T = \exp(-\beta u_{\alpha\gamma}) - 1 + \beta q_\alpha q_\gamma v_C \tag{57}$$

and the Coulomb potential $v_C(r) = 1/r$. After inserting the decomposition (56) into every Mayer diagram, one proceeds to systematic resummations of convolution chains of Coulomb bonds $-\beta q_\alpha q_\gamma v_C$. Thanks to remarkable combinatorial properties [31], all those resummations can be performed in terms of a single effective potential, which is nothing but the well-known Debye potential

$$\phi_D(r) = \frac{\exp(-\kappa_D r)}{r} \tag{58}$$

with the Debye inverse length $\kappa_D = (\sum_\alpha 4\pi\beta q_\alpha^2 \rho_\alpha)^{1/2}$. The chain resummations give rise to two bonds [30], the Debye bond

$$b_D = -\beta q_\alpha q_\gamma \phi_D \tag{59}$$

and the short-range dressed bond

$$b_R = \exp\left(-\beta\left(u_{\alpha\gamma}^{SR} + q_\alpha q_\gamma \phi_D\right)\right) - 1 + \beta q_\alpha q_\gamma \phi_D, \tag{60}$$

with the short-range part of pair interactions $u_{\alpha\gamma}^{SR} = u_{\alpha\gamma} - q_\alpha q_\gamma v_C$. The topological structure of the genuine Mayer diagrams remain unchanged, with bonds which can be either b_D or b_R , and with the additional rule excluding convolutions $b_D * b_D$ in order to avoid double counting.

Within the Abe–Meeron resummations, the genuine whole set of Mayer diagrams representing $\rho_{\alpha\gamma, T}^*(r)$ is then exactly transformed into

$$\rho_{\alpha\gamma, T}^*(r) = \rho_\alpha \rho_\gamma \sum_{\mathcal{G}} \frac{1}{S_{\mathcal{G}}} \int \left[\prod_{i=1}^n \sum_{\alpha_i} d\mathbf{r}_i \rho_{\alpha_i} \right] \left[\prod b_D \prod b_R \right]_{\mathcal{G}}. \tag{61}$$

The so-called prototype graphs \mathcal{G} are made with the two root points respectively fixed at $\mathbf{0}$ and \mathbf{r} , and an arbitrary number of n black points with density weights. Two points are connected at most by one bond (59) or (60). Each diagram is simply connected, with no articulation points, while convolutions $b_D * b_D$ are forbidden. The symmetry factor $S_{\mathcal{G}}$ is defined as the number of permutations of labelled black points which leave the product of bonds $[\prod b_D \prod b_R]_{\mathcal{G}}$ unchanged. The summation is carried out over all topologically different graphs \mathcal{G} , including the two graphs with no black points.

In the diagrammatic representation (61), the contribution of every graph \mathcal{G} is finite. Indeed, at large distances, integrability is ensured by the fast decays of both the Debye potential and the short-range part of pair interactions. At short distances, the Debye bond remains integrable despite its $1/r$ singularity, while the short-range dressed bond includes the short-range regularization which also guarantees its integrability. We stress that representation (61) holds for any set (ρ_1, ρ_2) of densities, and then appears to be quite useful for computing equilibrium quantities of \mathcal{S}^* . Moreover it is valid for any short-range regularization $u_{\alpha\gamma}^{SR}$, including of course that describing soft or hard spheres.

Fourth Moment Sum Rule for the Charge Correlations...



Fig. 1 The Debye diagram in the resummed diagrammatic representation (61) of particle correlations. The two root (white points) are fixed at $\mathbf{0}$ and \mathbf{r} respectively. The straight line represents a Debye bond b_D (59)

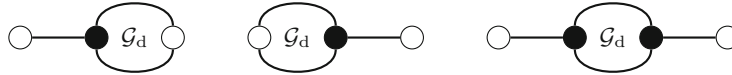


Fig. 2 The three dressed Debye diagrams associated with a given diagram \mathcal{G}_d in the resummed diagrammatic representation (61) of particle correlations

5.3 Charge Correlations

The Fourier transform (46) of the charge correlations of the homogeneous TCP can be recast as

$$\tilde{S}(k) = \sum_{\alpha, \gamma} q_\alpha q_\gamma \tilde{\rho}_{\alpha\gamma}(k) + \sum_{\alpha} q_\alpha^2 \rho_\alpha \tag{62}$$

where the Fourier transform $\tilde{\rho}_{\alpha\gamma}(k)$ of pair correlations is given by the sum of the Fourier transforms of the contributions of all graphs \mathcal{G} in the representation (61). Let us first consider the contribution of the simplest graph \mathcal{G}_D shown in Fig. 1, where the two root points are connected by a Debye bond. Its contribution to $\tilde{S}(k)$ added to the constant term $\sum_{\alpha} q_\alpha^2 \rho_\alpha$ in the formula (62) provides the well-known Debye charge correlations

$$\tilde{S}_D(k) = \frac{\kappa_D^2}{4\pi\beta} \frac{k^2}{k^2 + \kappa_D^2}, \tag{63}$$

which can be derived within a mean-field treatment of correlations, without any diagrammatic considerations. Now we stress that $\tilde{S}_D(k)$ saturates the first two moments sum rules for I_0 and I_2 , since $\tilde{S}_D(k) \sim k^2/(4\pi\beta)$ when $k \rightarrow 0$. Therefore all the remaining graphs in the representation (61) give no contributions to I_0 and I_2 . That remarkable property is related to the following reorganization of the series of graphs, which turns out to be also quite useful for computing the fourth moment I_4 .

Let \mathcal{G}_d be a graph in the representation (61) such that the root points $\mathbf{0}$ and \mathbf{r} are not connected to rest of the diagram by a single Debye bond b_D , or in other words each root point is connected to the rest of the diagram by either a bond b_R or at least two bonds. Such a graph can be dressed by Debye bonds in the sense that the three graphs shown in Fig. 2 also intervene in the representation (61). In \mathcal{G}_{Dd} (\mathcal{G}_{dD}), the black point \mathbf{r}_1 is connected to the root point $\mathbf{0}$ (\mathbf{r}) by a Debye bond b_D , while the subdiagram connecting that black point to the other root point \mathbf{r} ($\mathbf{0}$) is identical to \mathcal{G}_d itself. In \mathcal{G}_{DdD} , the two black points \mathbf{r}_1 and \mathbf{r}_2 are respectively connected to the root points $\mathbf{0}$ and \mathbf{r} by Debye bonds b_D , while they are connected together by a subdiagram identical to \mathcal{G}_d . Clearly, all possible graphs \mathcal{G}_d together with their dressed Debye family generate all graphs in the representation (61) beyond the Debye graph \mathcal{G}_D .

Now, let us consider the total contribution to representation (61) of a given graph \mathcal{G}_d and of its dressed Debye diagrams. After defining

$$K_{\alpha\gamma, \mathcal{G}_d}(r) = \int \left[\prod_{i=1}^n \sum_{\alpha_i} d\mathbf{r}_i \rho_{\alpha_i} \right] \left[\prod b_D \prod b_R \right]_{\mathcal{G}_d} \tag{64}$$

A. Alastuey, R. Fantoni

and noticing that all four graphs $\mathcal{G}_d, \mathcal{G}_{Dd}, \mathcal{G}_{dD}$ and \mathcal{G}_{DdD} have the same symmetry factor $S_{\mathcal{G}_d}$, we can rewrite that total contribution as $\rho_\alpha \rho_\gamma / S_{\mathcal{G}_d}$ times

$$\begin{aligned} &K_{\alpha\gamma, \mathcal{G}_d}(r) - \sum_{\alpha_1} \rho_{\alpha_1} \int d\mathbf{r}_1 \left[\beta q_\alpha q_{\alpha_1} \phi_D(r_1) K_{\alpha_1\gamma, \mathcal{G}_d}(|\mathbf{r} - \mathbf{r}_1|) \right. \\ &\quad \left. + K_{\alpha\alpha_1, \mathcal{G}_d}(r_1) \beta q_{\alpha_1} q_\gamma \phi_D(|\mathbf{r} - \mathbf{r}_1|) \right] \\ &+ \sum_{\alpha_1, \alpha_2} \rho_{\alpha_1} \rho_{\alpha_2} \int d\mathbf{r}_1 d\mathbf{r}_2 \beta q_\alpha q_{\alpha_1} \phi_D(r_1) K_{\alpha_1\alpha_2, \mathcal{G}_d}(|\mathbf{r}_2 - \mathbf{r}_1|) \beta q_{\alpha_2} q_\gamma \phi_D(|\mathbf{r} - \mathbf{r}_2|) \end{aligned} \quad (65)$$

The corresponding contribution to $\tilde{S}(k)$ in formula (62) can be readily computed by using the convolution theorem and $\tilde{\phi}_D(k) = 4\pi/(k^2 + \kappa_D^2)$, with the result

$$\frac{k^4}{(k^2 + \kappa_D^2)^2} \sum_{\alpha, \gamma} \rho_\alpha \rho_\gamma q_\alpha q_\gamma \tilde{K}_{\alpha\gamma, \mathcal{G}_d}(k) \quad (66)$$

divided by the symmetry factor $S_{\mathcal{G}_d}$. Since that expression is at least of order k^4 when $k \rightarrow 0$ for any \mathcal{G}_d , all the graphs beyond the Debye graph \mathcal{G}_D do not contribute neither to I_0 , nor to I_2 . Moreover, because of the prefactor of order k^4 , the resulting contribution to I_4 makes $\tilde{K}_{\alpha\gamma, \mathcal{G}_d}(0)$ appear. After adding the simple contribution of \mathcal{G}_D computed from the Debye formula (63), we eventually obtain the diagrammatic representation of I_4 ,

$$I_4 = -\frac{1}{4\pi\beta\kappa_D^2} + \frac{1}{\kappa_D^4} \sum_{\mathcal{G}_d} \frac{1}{S_{\mathcal{G}_d}} \sum_{\alpha, \gamma} \rho_\alpha \rho_\gamma q_\alpha q_\gamma \tilde{K}_{\alpha\gamma, \mathcal{G}_d}(0). \quad (67)$$

Representation (67) is well-suited for computing the low-density expansion of I_4 . Indeed, and as usual, because of the density weights carried by the black points, only a finite number of graphs contribute up to a given order. However, here we have to take care of the dependence on the density of the bonds b_D and b_R through the Debye wavenumber $\kappa_D = (\sum_\alpha 4\pi\beta q_\alpha^2 \rho_\alpha)^{1/2}$. Consequently, the order of a contribution is not merely given by counting the number of black points on the one hand, while half-integer powers and logarithmic terms arise in the expansion on the other hand. We have computed the first three terms of that expansion, up to constant terms of order ρ^0 included. In the Appendix, we provide some technical details, as well as the complete list of graphs \mathcal{G}_d which contribute up to the considered order. The resulting expansion reads

$$\begin{aligned} I_4 = &-\frac{1}{4\pi\beta\kappa_D^2} + \frac{\pi\beta^2}{\kappa_D^5} \sum_{\alpha, \gamma} q_\alpha^3 q_\gamma^3 \rho_\alpha \rho_\gamma + \frac{2\pi\beta^3}{3\kappa_D^4} \sum_{\alpha, \gamma} q_\alpha^4 q_\gamma^4 \rho_\alpha \rho_\gamma \ln(8\kappa_D d_{\alpha\gamma}) \\ &+ \frac{4\pi\beta}{\kappa_D^4} \sum_{\alpha, \gamma} q_\alpha^2 q_\gamma^2 \rho_\alpha \rho_\gamma d_{\alpha\gamma}^2 - \frac{3\pi\beta^2}{\kappa_D^4} \sum_{\alpha, \gamma} q_\alpha^3 q_\gamma^3 \rho_\alpha \rho_\gamma d_{\alpha\gamma} \\ &+ \frac{1}{\kappa_D^4} \sum_{\alpha, \gamma} q_\alpha q_\gamma \rho_\alpha \rho_\gamma \int d\mathbf{r} \left[\exp(-\beta u_{\alpha\gamma}) - 1 + \beta u_{\alpha\gamma} - \beta^2 u_{\alpha\gamma}^2 / 2 + \beta^3 u_{\alpha\gamma}^3 / 6 \right] \\ &+ \frac{11\pi^2\beta^4}{3\kappa_D^6} \sum_{\alpha, \gamma, \delta} q_\alpha^3 q_\gamma^3 q_\delta^4 \rho_\alpha \rho_\gamma \rho_\delta - \frac{52\pi^3\beta^5}{9\kappa_D^8} \sum_{\alpha, \gamma, \delta, \eta} q_\alpha^3 q_\gamma^3 q_\delta^3 q_\eta^3 \rho_\alpha \rho_\gamma \rho_\delta \rho_\eta + o(\rho^0). \end{aligned} \quad (68)$$

Not surprisingly, the leading term in the expansion (68) is the purely Debye contribution, and it behaves as $1/\rho$. The next correction is of order $1/\rho^{1/2}$ and is independent of the short-

range part of the interactions. Those short-range parts arise in further corrections of order $\ln \rho$ and ρ^0 . The last two terms of order ρ^0 are purely Coulomb contributions. The expansion is valid for any set of densities (ρ_1, ρ_2) , including of course the neutral sets defining the neutral TCP. For other short-range interactions, like hard cores for instance, the structure of the low-density expansion of I_4 is identical to that (68) explicitly computed for charged soft spheres.

5.4 Free Energy Density

The excess free energy of \mathcal{S}^* for any set of homogeneous densities, can be obtained through the usual integration over the inverse temperature of the equilibrium average of the potential part of Hamiltonian (11). The resulting free energy density in thermal units $f^*(\rho_1, \rho_2, \beta)$ reduces to

$$f^*(\rho_1, \rho_2, \beta) = f_{id}(\rho_1, \rho_2, \beta) + \frac{1}{2} \sum_{\alpha, \gamma} \int_0^\beta d\tau \int d\mathbf{r} \rho_{\alpha\gamma, T}^*(r) u_{\alpha\gamma}(r) + \frac{\beta}{2} \sum_{\alpha, \gamma} \rho_\alpha \rho_\gamma \int d\mathbf{r} u_{\alpha\gamma}^{SR}(r). \tag{69}$$

In that formula, the first term takes the familiar form

$$f_{id}(\rho_1, \rho_2, \beta) = \rho_1 \left[\ln \left(\rho_1 (2\pi\lambda_1^2)^{3/2} \right) - 1 \right] + \rho_2 \left[\ln \left(\rho_2 (2\pi\lambda_2^2)^{3/2} \right) - 1 \right] \tag{70}$$

which describes a mixture of ideal gases. The next two terms account for interactions. The second term involving pair correlations $\rho_{\alpha\gamma, T}^*(r)$ is obtained by adding and subtracting $u_{\alpha\gamma}^{SR}$ to the purely Coulomb interactions in the particle-background and background-background parts of the potential energy of Hamiltonian (11). This also provides the third term which merely reduces to

$$\frac{\beta}{2} \sum_{\alpha, \gamma} \rho_\alpha \rho_\gamma \int d\mathbf{r} u_{\alpha\gamma}^{SR}(r) = -2\pi\beta \sum_{\alpha, \gamma} q_\alpha q_\gamma \rho_\alpha \rho_\gamma d_{\alpha\gamma}^2. \tag{71}$$

It is implicitly understood that pair correlations $\rho_{\alpha\gamma, T}^*(r)$ in formula (69) are evaluated at inverse temperature τ .

The contribution of pair correlations $\rho_{\alpha\gamma, T}^*(r)$ to f^* follows by inserting its resummed diagrammatic representation (61) into the second term of formula (69). The contribution of a given diagram \mathcal{G} reads

$$\frac{1}{2S_{\mathcal{G}}} \sum_{\alpha, \gamma} \rho_\alpha \rho_\gamma \int_0^\beta d\tau \int d\mathbf{r} u_{\alpha\gamma}(r) K_{\alpha\gamma, \mathcal{G}}^{(\tau)}(r) \tag{72}$$

where $K_{\alpha\gamma, \mathcal{G}}^{(\tau)}(r)$ is the integral (64) over black points with \mathcal{G} in place of \mathcal{G}_d and bonds evaluated at inverse temperature τ . In the low-density limit, up to a given order in the density, only a finite number of contributions (72) needs to be retained. In the Appendix, we provide a few technical details of the calculations, as well as the list of graphs \mathcal{G} which contribute to f^* up

A. Alastuey, R. Fantoni

to order ρ^2 included. Adding the simple ideal (70) and background (71) contributions, we eventually obtain the low-density expansion of f^* ,

$$\begin{aligned}
 f^* = & \rho_1 \left[\ln \left(\rho_1 \left(2\pi\lambda_1^2 \right)^{3/2} \right) - 1 \right] + \rho_2 \left[\ln \left(\rho_2 \left(2\pi\lambda_2^2 \right)^{3/2} \right) - 1 \right] - \frac{\kappa_D^3}{12\pi} \\
 & - 2\pi\beta \sum_{\alpha,\gamma} q_\alpha q_\gamma \rho_\alpha \rho_\gamma d_{\alpha\gamma}^2 + \frac{3\pi\beta^2}{2} \sum_{\alpha,\gamma} q_\alpha^2 q_\gamma^2 \rho_\alpha \rho_\gamma d_{\alpha\gamma} - \frac{\pi\beta^3}{3} \sum_{\alpha,\gamma} q_\alpha^3 q_\gamma^3 \rho_\alpha \rho_\gamma \ln(8\kappa_D d_{\alpha\gamma}) \\
 & - \frac{1}{2} \sum_{\alpha,\gamma} \rho_\alpha \rho_\gamma \int \mathbf{dr} \left[\exp(-\beta u_{\alpha\gamma}) - 1 + \beta u_{\alpha\gamma} - \beta^2 u_{\alpha\gamma}^2 / 2 + \beta^3 u_{\alpha\gamma}^3 / 6 \right] + o(\rho^2). \quad (73)
 \end{aligned}$$

The leading terms of order $\rho \ln \rho$ in the expansion (73) are ideal contributions. The next correction of order $\rho^{3/2}$ arises from pure Coulomb interactions, and is nothing but the well-known Debye term. Contributions from the short range part of the interactions appear in the terms of order $\rho^2 \ln \rho$ and ρ^2 . The terms left over are least of order $\rho^{5/2} \ln \rho$. Expansion (73) is valid for any set of densities (ρ_1, ρ_2) , and it gives access to all the other thermodynamical functions of \mathcal{S}^* through suitable partial derivatives with respect to the independent parameters β, ρ_1 or ρ_2 defining an homogeneous equilibrium state of \mathcal{S}^* .

For other short-range regularizations, the low-density expansion of f^* has the same structure as (73). However, notice that for hard core potentials, the ideal term in the decomposition (69) of the corresponding f^* must be replaced by the free energy density of hard spheres, $f_{HS}(\rho_1, \rho_2, \beta)$. In the low-density limit, $f_{HS}(\rho_1, \rho_2, \beta)$ can be expanded in entire powers of ρ around the ideal term (70). In the resulting full expansion of f^* , there are terms which depend only on the hard core diameters $\sigma_{\alpha\gamma}$ and not on the particles charges.

5.5 Checking the Sum Rule at Lowest Orders

In order to check the sum rule (49), we first have to compute the low-density expansion of the partial compressibilities $\chi_{\alpha\gamma}^{-1} = \partial^2 f^* / \partial \rho_\alpha \partial \rho_\gamma$. Using expansion (73) of f^* , we find

$$\begin{aligned}
 \chi_{11}^{-1} = & \frac{1}{\rho_1} - \frac{\pi\beta^2 q_1^4}{\kappa_D} + 3\pi\beta^2 q_1^4 d_{11} - 4\pi\beta q_1^2 d_{11}^2 - \frac{2\pi\beta^3 q_1^6}{3} \ln(8\kappa_D d_{11}) \\
 & - \frac{8\pi^2 \beta^4 q_1^5}{3\kappa_D^2} \sum_{\alpha} q_\alpha^3 \rho_\alpha + \frac{8\pi^3 \beta^5 q_1^4}{3\kappa_D^4} \sum_{\alpha\gamma} q_\alpha^3 q_\gamma^3 \rho_\alpha \rho_\gamma \\
 & - \int \mathbf{dr} \left[\exp(-\beta u_{11}) - 1 + \beta u_{11} - \beta^2 u_{11}^2 / 2 + \beta^3 u_{11}^3 / 6 \right] + o(\rho^0), \quad (74)
 \end{aligned}$$

$$\begin{aligned}
 \chi_{22}^{-1} = & \frac{1}{\rho_2} - \frac{\pi\beta^2 q_2^4}{\kappa_D} + 3\pi\beta^2 q_2^4 d_{22} - 4\pi\beta q_2^2 d_{22}^2 - \frac{2\pi\beta^3 q_2^6}{3} \ln(8\kappa_D d_{22}) \\
 & - \frac{8\pi^2 \beta^4 q_2^5}{3\kappa_D^2} \sum_{\alpha} q_\alpha^3 \rho_\alpha + \frac{8\pi^3 \beta^5 q_2^4}{3\kappa_D^4} \sum_{\alpha\gamma} q_\alpha^3 q_\gamma^3 \rho_\alpha \rho_\gamma \\
 & - \int \mathbf{dr} \left[\exp(-\beta u_{22}) - 1 + \beta u_{22} - \beta^2 u_{22}^2 / 2 + \beta^3 u_{22}^3 / 6 \right] + o(\rho^0), \quad (75)
 \end{aligned}$$

and

$$\begin{aligned} \chi_{12}^{-1} = \chi_{21}^{-1} = & -\frac{\pi\beta^2 q_1^2 q_2^2}{\kappa_D} + 3\pi\beta^2 q_1^2 q_2^2 d_{12} - 4\pi\beta q_1 q_2 d_{12}^2 - \frac{2\pi\beta^3 q_1^3 q_2^3}{3} \ln(8\kappa_D d_{12}) \\ & - \frac{\pi\beta^3 q_1^3 q_2^3}{3} - \frac{4\pi^2\beta^4 q_1^2 q_2^2}{3\kappa_D^2} \sum_{\alpha} q_{\alpha}^4 \rho_{\alpha} + \frac{8\pi^3\beta^5 q_1^2 q_2^2}{3\kappa_D^4} \sum_{\alpha\gamma} q_{\alpha}^3 q_{\gamma}^3 \rho_{\alpha} \rho_{\gamma} \\ & - \int dr [\exp(-\beta u_{12}) - 1 + \beta u_{12} - \beta^2 u_{12}^2/2 + \beta^3 u_{12}^3/6] + o(\rho^0). \end{aligned} \tag{76}$$

Notice that the leading contributions of order $1/\rho$ in both χ_{11}^{-1} and χ_{22}^{-1} arise from the ideal terms in f^* , while the next correction of order $1/\rho^{1/2}$ comes from the Debye term in expansion (73). The leading contribution of order $1/\rho^{1/2}$ in χ_{12}^{-1} is also provided by that Debye correction. All terms which are left over in expansions (74), (75) and (76) are at least of order $\rho^{1/2} \ln \rho$.

According to the expression (16) of the isothermal compressibility, the thermodynamical quantity in the right hand side of sum rule (49) can be rewritten as

$$-\frac{\rho^2}{(4\pi(q_1 - q_2))^2 \beta^3} (\chi_{11}^{-1} \chi_{22}^{-1} - \chi_{12}^{-2}) \chi_T = -\frac{(\chi_{11}^{-1} \chi_{22}^{-1} - \chi_{12}^{-2})}{(4\pi\beta)^2 (q_2^2 \chi_{11}^{-1} + q_1^2 \chi_{22}^{-1} - 2q_1 q_2 \chi_{12}^{-1})}. \tag{77}$$

The low-density expansion of that thermodynamical expression is straightforwardly computed by using the expansions (74), (75) and (76) of the $\chi_{\alpha\gamma}^{-1}$'s. Its leading behaviour is immediately obtained by noticing that both χ_{11}^{-1} and χ_{22}^{-1} diverge faster than χ_{12}^{-1} in the zero-density limit, and the corresponding purely ideal behaviours $\chi_{11}^{-1} \sim 1/\rho_1$ and $\chi_{22}^{-1} \sim 1/\rho_2$ provide

$$-\frac{(\chi_{11}^{-1} \chi_{22}^{-1} - \chi_{12}^{-2})}{(4\pi\beta)^2 (q_2^2 \chi_{11}^{-1} + q_1^2 \chi_{22}^{-1} - 2q_1 q_2 \chi_{12}^{-1})} \sim -\frac{\rho_1^{-1} \rho_2^{-1}}{(4\pi\beta)^2 (q_2^2 \rho_1^{-1} + q_1^2 \rho_2^{-1})} = -\frac{1}{4\pi\beta\kappa_D^2}, \tag{78}$$

which coincides with the leading term in expansion (68) of I_4 . The calculation of the next correction of order $1/\rho^{1/2}$ remains simple, since it requires to retain only the first Debye corrections of order $1/\rho^{1/2}$ to the ideal terms in both χ_{11}^{-1} and χ_{22}^{-1} , while χ_{12}^{-1} can be replaced by its leading Debye behaviour. The determination of the terms of order ρ^0 and $\rho^0 \ln \rho$ is still straightforward but more cumbersome. Eventually, we find that all those corrections to the ideal behaviour (78) of the thermodynamical quantity (77) exactly match the low-density expansion (68) of I_4 inferred from its microscopic definition. Thus, the fourth moment sum rule perfectly works, at least up to the considered order in the density.

6 Concluding Comments and Perspectives

In this paper, we have derived a new sum rule for the fourth moment of charge correlations of a TCP. Since the Stillinger–Lovett second moment sum rule naturally emerges as a by-product of our analysis, we believe that this new sum rule holds in any conducting phase, although all the steps of its derivation are not under a complete mathematical control at the moment.

In particular, we expect that the free energy functional can be safely expanded around homogeneous states inside the conducting phase. We stress that all the partial compressibilities of the auxiliary system, namely second partial derivatives with respect to particle densities of the free energy density, have then to be well defined. Thus critical points must be dealt with some care, since singularities in the thermodynamical quantities arise on the one hand, while perfect screening properties can be lost on the other hand, as mentioned below.

Our derivation also involves implicit assumptions about the existence of the thermodynamic limit, and of intrinsic bulk properties with bulk densities which become homogeneous far from the boundaries. Strictly speaking, to our knowledge, this has been only proved for the general three-dimensional TCP in the Debye regime [12] and for its charge-symmetric version [13]. In two dimensions, where the Coulomb potential takes a logarithmic form, both the neutrality and homogeneity of a TCP of point charges have been proved [32]. Extensions of such results to all the systems introduced here would be quite valuable of course, and might constitute the first steps towards a complete proof of our sum rule. Meanwhile, physical arguments, in particular related to the beautiful proof for quantum Coulomb matter [14], strongly suggest that the classical TCP, as well as its version immersed in a charged uniform background, do sustain a well-behaved TL. Furthermore, there are strong evidences, arising either from specific models or mean-field approaches, that screening properties in the bulk can be disentangled from the reorganization of charges at the surface, so any boundary effects can be indeed *a priori* ignored.

In the absence of a complete mathematical proof, checking the sum rule within exact calculations for specific models or thermodynamical regimes is particularly valuable. Here, such checking has been carried out for charged soft spheres in the low density regime, through the explicit calculation of the lowest order terms in density expansions of the quantities of interest. This illustrates the subtle interplay between short-range and screened Coulomb contributions which ultimately ensure the validity of the fourth moment sum rule at the considered orders. If there exists a simple reorganization of the Abe–Meeron diagrams which shows the validity of the second moment Stillinger Lovett sum rule at any order in the density expansion, a similar trick for the fourth moment sum rule, certainly more cumbersome, remains to be discovered.

If our derivation of the fourth moment sum rule is based on the response to external perturbations, more intrinsic derivations would be of great interest, both for enforcing its expected validity on the one hand, and for shedding light on the internal mechanisms at work on the other hand. For instance, the second moment Stillinger Lovett sum rule can be retrieved within suitable manipulations of the BGY hierarchy equations for the equilibrium distribution functions of the unperturbed homogeneous TCP, as shown by Gruber and Martin [33]. Moreover, the BGY hierarchy equations have been also used for deriving the fourth moment sum rule for the OCP [23] and for the BIM with pure Coulomb interactions [9]. We are looking for extending such derivations to the TCP case, where the presence of short-range interactions requires further manipulations. Notice, that a full reorganization of Abe–Meeron diagrammatics as described above could be also seen as an intrinsic derivation. In the same spirit, let us mention that a sixth moment sum rule for the charge correlations of the two-dimensional OCP with logarithmic interactions was established through a full term by term analysis of the Abe–Meeron diagrammatics for the short-range part of the direct correlation function [34]. It turns out that, as a consequence of specific properties of the pure logarithmic interaction, only the simplest graph built with the screened two-dimensional Debye potential contributes to the small- k expansion up to order k^2 included in the Fourier transform of that quantity. The sixth moment of particle correlations, which then coincide with charge correlations, straightforwardly follows by applying the Ornstein-Zernicke equation.

The fourth moment sum rule obviously extends to the TCP immersed in a charged background, namely the thermodynamical expression (49) of the fourth moment of charge correlations is not restricted to densities satisfying overall neutrality, but it is valid for any set of densities (ρ_1, ρ_2). This is well illustrated by the low density calculations for charged soft spheres. Moreover, a similar DFT analysis combined with linear response theory can be carried out for an arbitrary number n of components. This would lead to formulae analogous to the thermodynamical expression (49), but with a more complicated structure arising from the inversion of a $n \times n$ matrix. In the case of the MIM, they should be equivalent to those derived by Suttorp [9]. Eventually, within our formalism, one can obtain sum rules for the zeroth and second moment of particle-charge correlations, by comparing the DFT calculation of a given particle density to its linear response expression. Such sum rules are again equivalent to those obtained for the MIM [9].

Among the various possible applications of our new sum rule, we would like to emphasize its usefulness for a better understanding of the plausible lack of screening properties at the ionic critical point. The liquid-gas transition of a TCP has been widely studied the last twenty years. Let us mention for instance two recent works [35,36]. Numerical simulations have convincingly shown that both liquid and gas phases display perfect screening properties, namely the second moment Stillinger–Lovett sum rule is satisfied. However, a first suspicion about the violation of that sum rule at the critical point was pointed out by Caillol [37]. Meanwhile, such violation was also observed for a solvable asymmetric mean-spherical model by Aqua and Fisher [38], which is expected to share common properties with an asymmetric TCP. More recently, and contrarily to various theoretical expectations, the violation of the Stillinger Lovett sum rule at the critical point was also observed for the fully symmetric RPM by Das, Kim and Fisher [11]: they provide strong numerical evidences by combining refined Monte Carlo simulations in the grand-canonical ensemble with finite-size scaling methods. Furthermore, they also show that the fourth moment of charge correlations diverges when approaching the critical point, in a way analogous to the isothermal compressibility. Clearly, our thermodynamical expression (49) of that fourth moment constitutes a promising tool for analyzing its behaviour near the critical point, as well as the underlying coupling between charge and mass fluctuations. In a similar spirit, let us quote a recent work by Piasecki et al. [39] where the Kirkwood superposition approximation is shown to be inconsistent with the divergency of the compressibility at the critical point for a system with short-range interactions.

Eventually, let us conclude by a few comments regarding the two dimensional (2D) case. The sum rule for the fourth moment of charge-charge correlations derived here explicitly in three dimensions (3D), can be straightforwardly extended to the 2D case: this leads to the simple replacement of the factor 4π in formula (49) by the factor 2π , a direct consequence of the modification of Poisson equation when changing from 3D to 2D. In 2D, the Coulomb potential takes the well-known logarithmic form. Since the corresponding singularity at the origin is relatively weak, the TCP of point charges is well behaved for coupling constants $\Gamma < 2$, namely at sufficiently high temperatures [40]. Then, thanks to scaling properties of the logarithmic interaction, the corresponding equation of state can be exactly computed, providing a simple explicit expression for the compressibility, *i.e.* the zeroth moment of density-density correlations. The sum rules for particle-charge correlations analogous to that derived in Ref.[9] also take simple explicit forms [41]. Moreover, the diagrammatic analysis of the direct correlation function for the 2D OCP introduced in Ref. [34], can be extended to the sum of the two direct correlation functions for the 2D fully symmetric TCP of point charges [42]. After use of the Ornstein-Zernicke equation, this provides an exact explicit expression for the second moment of the density-density corre-

A. Alastuey, R. Fantoni

lations. Checking our new sum rule in that case requires further calculations, in particular because this involves the difference of the two direct correlation functions instead of their sum.

The 2D TCP of point charges collapses at $\Gamma = 2$, so short-range interactions need to be introduced for $\Gamma \geq 2$. At $\Gamma = 2$, Cornu and Jancovici [43] exploited a mapping with a field theory model valid for pure Coulomb interactions, which allowed them to derive analytical expressions for particle correlations of the 2D TCP immersed in a background. Those results obtained in a planar geometry were retrieved by Forrester and Jancovici [44] by working on a sphere and using a more general formalism. Such expressions are expected to become exact in the zero density limit for the well-behaved TCP including short-range interactions. Thus, they constitute a reliable starting point for further checking of the fourth moment sum rule at $\Gamma = 2$, which nevertheless requires an additional detailed analysis of short-range contributions at low densities. Similarly to its application to the study of ionic criticality in 3D, the fourth moment sum rule should also bring new insights for the celebrated Kosterlitz-Thouless transition [45,46]: in the temperature-density plane, there appears a line of critical points separating a high-temperature conducting phase from a low-temperature dielectric phase [47]. The implications of the fourth moment sum rule should complete the results of a previous work [48], where a plausible scenario for the large-distance decay of particle correlations in the dielectric phase was constructed in a way consistent with various sum rules.

Acknowledgments This work was presented at the conference in the memory of Bernard Jancovici (Institut Henri Poincaré, Paris, 5 and 6 november 2015), and it is dedicated to him. We would also like to thank Michael Fisher for his stimulating interest and useful discussions.

Appendix

In Fig. 3, we list the seven diagrams \mathcal{G}_d which contribute to the diagrammatic series (67) for the fourth moment I_4 up to order ρ^0 included.

When computing the Fourier transform $\tilde{K}_{\alpha\gamma, \mathcal{G}_d}(0)$ for each of those diagrams, we can apply the convolution theorem at various places, namely with intermediate points which reduce either to the black points for graphs $\mathcal{G}_d^{(2)}$ and $\mathcal{G}_d^{(3)}$, or to the root white points for graphs $\mathcal{G}_d^{(4-7)}$ by exploiting translational invariance. Two key quantities turn then to be the inverse Fourier transform of $[\tilde{\phi}_D(k)]^2$ and $[\tilde{\phi}_D(k)]^3$ which reduce respectively to

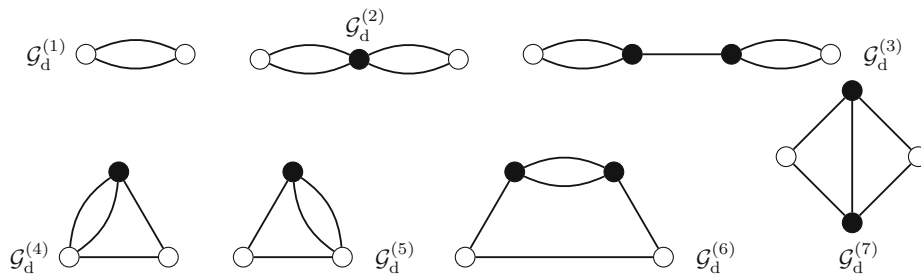


Fig. 3 The seven diagrams \mathcal{G}_d which contribute to I_4 up to order ρ^0 included in the diagrammatic series (67). The bubbles represent short-range dressed bonds b_R (60)

Fourth Moment Sum Rule for the Charge Correlations...

$$\frac{1}{(2\pi)^3} \int d\mathbf{k} \exp(-i\mathbf{k} \cdot \mathbf{r}) \frac{16\pi^2}{(k^2 + \kappa_D^2)^2} = \frac{2\pi}{\kappa_D} \exp(-\kappa_D r) \tag{79}$$

and

$$\frac{1}{(2\pi)^3} \int d\mathbf{k} \exp(-i\mathbf{k} \cdot \mathbf{r}) \frac{64\pi^3}{(k^2 + \kappa_D^2)^3} = \frac{2\pi^2}{\kappa_D^3} (1 + \kappa_D r) \exp(-\kappa_D r), \tag{80}$$

after a straightforward application of the theorem of residues. Another useful trick relies on the decomposition

$$b_R = b_R^{(T)} - \beta u_{\alpha\gamma}^{SR} + \frac{\beta^2}{2} (u_{\alpha\gamma}^{SR} + q_\alpha q_\gamma \phi_D)^2 - \frac{\beta^3}{6} (u_{\alpha\gamma}^{SR} + q_\alpha q_\gamma \phi_D)^3 \tag{81}$$

with the truncated bond

$$b_R^{(T)} = \exp\left(-\beta (u_{\alpha\gamma}^{SR} + q_\alpha q_\gamma \phi_D)\right) - 1 + \beta (u_{\alpha\gamma}^{SR} + q_\alpha q_\gamma \phi_D) - \frac{\beta^2}{2} (u_{\alpha\gamma}^{SR} + q_\alpha q_\gamma \phi_D)^2 + \frac{\beta^3}{6} (u_{\alpha\gamma}^{SR} + q_\alpha q_\gamma \phi_D)^3. \tag{82}$$

Indeed, the corresponding contribution of the truncated bond $b_R^{(T)}$ in graphs $\mathcal{G}_d^{(1-5)}$ can be computed at lowest order in the density by merely replacing $u_{\alpha\gamma}^{SR} + q_\alpha q_\gamma \phi_D$ by the bare pair potential $u_{\alpha\gamma}$ since $(\exp(-\beta u_{\alpha\gamma}) - 1 + \beta u_{\alpha\gamma} - \beta^2 u_{\alpha\gamma}^2/2 + \beta^3 u_{\alpha\gamma}^3/6)$ is integrable in the whole space. The next density-dependent corrections to that leading contribution behave as $\rho^{1/2}$ and can thus be neglected in the considered calculation of I_4 up to order ρ^0 . The contributions of the other terms in the decomposition (81) are easily computed thanks to the simple analytic expressions of $u_{\alpha\gamma}^{SR}$ and ϕ_D . Eventually, combining the above convolution and decomposition tricks, we obtain formula (68) for I_4 .

The five graphs in the series (61) for particle correlations which provide contributions (72) to the free-energy density f^* are listed in Fig. 4. Each contribution follows from formula (72), so the value $K_{\alpha\gamma, \mathcal{G}}^{(\tau)}(r)$ of each graph is first computed with bonds b_D and b_R evaluated at temperature τ . After multiplication of $K_{\alpha\gamma, \mathcal{G}}^{(\tau)}(r)$ by the pair potential $u_{\alpha\gamma}(r)$, the further integrals over \mathbf{r} in the whole space are readily computed by using decomposition (81) with τ in place of β , as well as the inverse Fourier transforms of $[\tilde{\phi}_D(k)]^2$ given by expression (79), and of $\tilde{\phi}_D(k)4\pi/k^2$ which reduces to

$$\frac{1}{(2\pi)^3} \int d\mathbf{k} \exp(-i\mathbf{k} \cdot \mathbf{r}) \frac{16\pi^2}{k^2 (k^2 + \kappa_D^2)} = \frac{4\pi}{\kappa_D^2 r} (1 - \exp(-\kappa_D r)). \tag{83}$$

The final integrals over τ from 0 to β are then easily and explicitly performed for all terms which reduce to combinations of powers laws and logarithmic terms. It remains a term involving

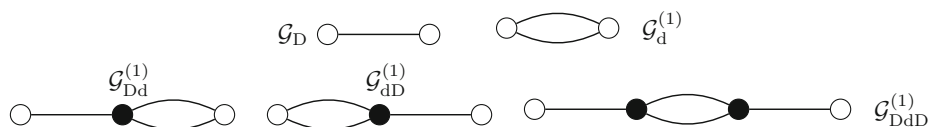


Fig. 4 The five diagrams \mathcal{G} which contribute to f^* up to order ρ^2 included

A. Alastuey, R. Fantoni

$$\int d\mathbf{r} u_{\alpha\gamma} \left[\exp(-\tau u_{\alpha\gamma}) - 1 + \tau u_{\alpha\gamma} - \frac{\tau^2}{2} u_{\alpha\gamma}^2 \right], \quad (84)$$

whose integration over τ leads to the last correction of order ρ^2 in the formula (73) for f^* .

References

1. Jancovici, B., Samaj, L.: Charge and current sum rules in quantum media coupled to radiation II. *J. Stat. Phys.* **139**(3), 432–453 (2010)
2. Martin, PhA: Sum rules in charged fluids. *Rev. Mod. Phys.* **60**, 1075–1127 (1988)
3. Brydges, D.C., Martin, PhA: Coulomb systems at low density. *J. Stat. Phys.* **96**, 1163–1330 (1999)
4. Stillinger Jr., F.H., Lovett, R.: General restriction on the distribution of ions in electrolytes. *J. Chem. Phys.* **49**(5), 1991–1994 (1968)
5. Vieillefosse, P., Hansen, J.P.: Statistical mechanics of dense ionized matter. Hydrodynamic limit and transport coefficients of the classical one-component plasma. *Phys. Rev. A* **12**, 1106–1116 (1975)
6. Giaquinta, P.V., Parrinello, M., Tosi, M.P.: Hydrodynamic correlation functions for molten salts. *Phys. Chem. Liq.* **5**, 305–324 (1976)
7. van Beijeren, H., Felderhof, B.U.: Thermodynamics and correlation functions of plasmas and electrolyte solutions. *Mol. Phys.* **38**(4), 1179–1199 (1979)
8. Suttorp, L.G., van Wonderen, A.J.: Equilibrium properties of a multi-component ionic mixture: I. Sum rules for correlation functions. *Phys. A* **145**, 533–556 (1987)
9. Suttorp, L.G.: Sum rules for correlation functions of ionic mixtures in arbitrary dimension $d \geq 2$. *J. Phys. A* **41**, 495001 (2008)
10. van der Waals, J.D.: The thermodynamic theory of capillarity under the hypothesis of a continuous variation of density. *Z. Phys. Chem.* **13**, 657–725 (1894)
11. Das, S.K., Kim, Y.C., Fisher, M.E.: When is a conductor not perfect? Sum rules fail under critical fluctuations. *Phys. Rev. Lett.* **107**, 215701 (2011)
12. Brydges, D.C., Federbush, P.: Debye screening. *Commun. Math. Phys.* **73**, 197–246 (1980)
13. Frohlich, J., Park, Y.M.: Correlation inequalities and the thermodynamic limit for classical and quantum continuous systems. *Commun. Math. Phys.* **59**, 235–266 (1978)
14. Lieb, E.H., Lebowitz, J.: The constitution of matter: existence of thermodynamics for systems composed of electrons and nuclei. *Adv. Math.* **9**, 316–398 (1972)
15. Jancovici, B.: Exact results for the two-dimensional one-component plasma. *Phys. Rev. Lett.* **46**(6), 386–388 (1981)
16. Percus, J.K.: Equilibrium state of a classical fluid of hard rods in an external field. *J. Stat. Phys.* **15**(6), 505–511 (1976)
17. Hohenberg, P., Kohn, W.: Inhomogeneous electron gas. *Phys. Rev. B* **136**(3), 864–871 (1964)
18. Yang, A.J.M., Fleming, P.D., Gibbs, J.H.: Molecular theory of surface tension. *J. Chem. Phys.* **64**(9), 3732–3747 (1976)
19. Bongiorno, V., Scriven, L.E., Davis, H.T.: Molecular theory of fluid interfaces. *J. Colloid Interface Sci.* **57**(3), 462–475 (1976)
20. Alastuey, A.: Contribution of the three-particle and higher order correlations to the computation of interface density profiles by density functional theories, for two-dimensional plasmas. *Mol. Phys.* **52**(3), 637–675 (1984)
21. Hansen, J.P.: *Mac Donald. Theory of simple liquids.* Academic Press, Cambridge (2006)
22. Vieillefosse, P.: Sum rules and perfect screening conditions for the one-component plasma. *J. Stat. Phys.* **41**(5), 1015–1035 (1985)
23. Vieillefosse, P., Brajon, M.: Sum rules for the one-component plasma with additional short-range forces. *J. Stat. Phys.* **55**(5/6), 1169–1183 (1989)
24. Mitchell, D.J., McQuarrie, D.A., Szabo, A., Groeneveld, J.: On the second-moment condition of Stillinger and Lovett. *J. Stat. Phys.* **17**(1), 15–20 (1977)
25. Mayer, J.E., Mayer, M.G.: *Statistical Mechanics.* Wiley, New York (1940)
26. Mayer, J.E.: The theory of ionic solutions. *J. Chem. Phys.* **18**, 1426–1436 (1950)
27. Salpeter, E.E.: On Mayer's theory of cluster expansions. *Ann. Phys. (N.Y.)* **5**(3), 183–223 (1958)
28. Abe, R.: Giant cluster expansion theory and its application to high temperature plasma. *Prog. Theor. Phys.* **22**(2), 213–226 (1959)
29. Meeron, E.: *Plasma Physics.* Mac Graw-Hill, New York (1961)

30. Alastuey, A., Cornu, F., Perez, A.: Virial expansions for quantum plasmas: Diagrammatic resummations. *Phys. Rev. E* **49**(2), 1077–1093 (1994)
31. Alastuey, A., Ballenegger, V., Cornu, F., Martin, PhA: Screened cluster expansions for partially ionized gases. *J. Stat. Phys.* **113**(3/4), 455–503 (2003)
32. Leblé, T., Serfaty, S., Zeitouni, O., Wu, W.: Large deviations for the two-dimensional two-component plasma. [arXiv:1510.01955v2](https://arxiv.org/abs/1510.01955v2) (2015)
33. Martin, PhA, Gruber, Ch.: A new proof of the Stillinger-Lovett complete shielding condition. *J. Stat. Phys.* **31**(3), 691–710 (1983)
34. Kalinay, P., Markos, P., Samaj, L., Travenec, I.: The sixth-moment sum rule for the pair correlations of the two-dimensional one-component plasma: Exact results. *J. Stat. Phys.* **98**(3), 639–666 (2000)
35. Das, S.K., Kim, Y.C., Fisher, M.E.: Near critical electrolytes: Are the charge-charge sum rules obeyed? *J. Chem. Phys.* **137**, 074902 (2012)
36. Caillol, J.M., Levesque, D.: Liquid-vapor transition and critical behaviour of the ultrasoft restricted primitive model of polyelectrolytes: A Monte Carlo study. *J. Chem. Phys.* **140**, 214505 (2014)
37. Caillol, J.M.: A Monte Carlo study of the dielectric constant of the restricted primitive model of electrolytes on the vapor branch of the coexistence line. *J. Chem. Phys.* **102**, 5471–5479 (1995)
38. Aqua, J.N., Fisher, M.E.: Ionic criticality: an exactly soluble model. *Phys. Rev. Lett.* **92**(13), 135702 (2004)
39. Piasecki, J., Szymczak, P., Kozak, J.J.: Non-existence of a critical point within the Kirkwood superposition approximation. *J. Chem. Phys.* **139**, 141101 (2013)
40. Deutsch, C., Lavaud, M.: The partition function of a two-dimensional plasma. *Phys. Lett. A* **39**(4), 253–254 (1972)
41. Jancovici, B., Samaj, L.: Guest charge and potential fluctuations in two-dimensional classical Coulomb systems. *J. Stat. Phys.* **131**, 613–629 (2008)
42. Jancovici, B., Kalinay, P., Samaj, L.: Another derivation of a sum rule for the two-dimensional two-component plasma. *Phys. A* **279**, 260–267 (2000)
43. Cornu, F., Jancovici, B.: Two-dimensional Coulomb systems: a larger class of solvable models. *Europhys. Lett.* **5**(2), 125–128 (1988)
44. Forrester, P.J., Jancovici, B.: The two-dimensional two-component plasma plus background on a sphere: exact results. *J. Stat. Phys.* **84**(3/4), 337–357 (1996)
45. Kosterlitz, J.M., Thouless, D.J.: Ordering, metastability and phase transitions in two-dimensional systems. *J. Phys. C* **6**, 1181–1203 (1973)
46. Minnhagen, P.: The two-dimensional Coulomb gas, vortex unbinding, and superfluid-superconductive thin films. *Rev. Mod. Phys.* **59**(4), 1001–1066 (1987)
47. Alastuey, A., Cornu, F.: Critical line near the zero-density critical point of the Kosterlitz-Thouless transition. *J. Stat. Phys.* **87**(3/4), 891–895 (1997)
48. Alastuey, A., Cornu, F.: Correlations in the Kosterlitz-Thouless phase of the two-dimensional Coulomb gas. *J. Stat. Phys.* **66**(1/2), 165–231 (1992)

Chapter 50

The Square-Shoulder-Asakura-Oosawa model

Fantoni R., *Physica A* **457**, 406 (2016)

Title: “The Square-Shoulder-Asakura-Oosawa model”

Abstract: A new model for a colloidal size-asymmetric binary mixture is proposed: The Square-Shoulder-Asakura-Oosawa. This belongs to the larger class of non-additive hard-spheres models and has the property that its effective pair formulation is exact whenever the solvent particle fits inside the interstitial region of three touching solute particles. Therefore one can study its properties from the equivalent one-component effective problem. Some remarks on the phase diagram of this new model are also addressed.

Physica A 457 (2016) 406–412



Contents lists available at ScienceDirect

Physica A

journal homepage: www.elsevier.com/locate/physa

The Square-Shoulder-Asakura–Oosawa model



Riccardo Fantoni

Università di Trieste, Dipartimento di Fisica, strada Costiera 11, 34151 Grignano (Trieste), Italy

HIGHLIGHTS

- A new model for a colloidal size-asymmetric binary mixture is proposed: The Square-Shoulder-Asakura–Oosawa.
- Whenever the solvent particle fits inside the interstitial region of three touching solute particles, its properties can be studied from the equivalent analytically exact one-component effective problem.
- The presence of the soft unlike repulsion augments the depletion mechanism and this, in turn, enlarges the metastable fluid–fluid phase coexistence region.

ARTICLE INFO

Article history:

Received 7 January 2016

Received in revised form 7 February 2016

Available online 11 April 2016

Keywords:

Colloidal suspension

Size-asymmetric non-additive binary mixture

Asakura–Oosawa

Square-shoulder

Effective potential

Phase diagram

ABSTRACT

A new model for a colloidal size-asymmetric binary mixture is proposed: The Square-Shoulder-Asakura–Oosawa. This belongs to the larger class of non-additive hard-spheres models and has the property that its effective pair formulation is exact whenever the solvent particle fits inside the interstitial region of three touching solute particles. Therefore one can study its properties from the equivalent one-component effective problem. Some remarks on the phase diagram of this new model are also addressed.

© 2016 Elsevier B.V. All rights reserved.

1. Introduction

Hard-sphere mixtures, additive or non-additive, sticky or not, etc., have very rich phase diagrams showing all three phases of matter: gas, liquid, and solid as well as mixed or demixed and percolating or glass. In some soft-matter laboratories [1–3], experimentalist are engineering always new kinds of (Boltzmann) particles and materials which sometimes show phase diagrams akin to the ones of hard-spheres. It is then very important to be able to predict with great accuracy the theoretical critical phenomena of hard-spheres. Whereas the properties of additive (sticky-)hard-spheres, non-additive (sticky-)hard-spheres have been carefully studied in the past. The same attention has not been given to non-additive square-shoulder-spheres. The one-component Square-Shoulder (SS) fluid model has been used for the first time by Hemmer and Stell [4,5]. It may lead to an isostructural solid–solid transition [6], to a fluid–solid coexisting line with a maximum melting temperature [7], to unusual phase behaviors [8–10] as the reentrance of a hexatic phase in two dimensions [11,12], and to a rich variety of (self-organized) ordered structures [13–16]. It has been used to describe the behavior of metallic glasses [17,7], micellar [18] or granular [19] systems, colloidal suspensions [20,21], primitive models of silica [22], aqueous solutions of electrolytes [23], and water [24,25]. The SS model is the simplest of the class of core-softened potentials models for fluids [26] that can be used.

E-mail address: rfantoni@ts.infn.it.

<http://dx.doi.org/10.1016/j.physa.2016.03.024>

0378-4371/© 2016 Elsevier B.V. All rights reserved.

Recently it has been shown that augmenting the purely steric repulsion of the Asakura–Oosawa [27] model with a *soft* repulsion shell gives rise to temperature dependent interactions which in turn give rise to more realistic effective attractions for cosolute-macromolecule and specifically protective osmolytes systems [28,29].

In the present work, following closely the theoretical framework of Ref. [30], we will study a highly size asymmetric binary mixture of Asakura–Oosawa where the unlike species pair-interaction has a square-shoulder character.

2. Discussion

An important problem in chemical physics is that of understanding how the behavior of the solute is influenced by the presence of the solvent. When there is a clear distinction between which are the solvent particles it is possible to describe the mixture as a binary one. Imagine for example that the solvent particles are the small “s” ones and the solute particles are the large “l” ones, then for a statistical physics description of the mixture we need to know the potential energy of interaction between the various particles, $U(\mathbf{r}_1^{(s)}, \mathbf{r}_2^{(s)}, \dots, \mathbf{r}_1^{(l)}, \mathbf{r}_2^{(l)}, \dots)$ where $\{\mathbf{r}_i^{(s)}\}$ are the coordinates of the small particles and $\{\mathbf{r}_i^{(l)}\}$ the ones of the large particles. It is always possible to write $U = U_{ss}(\mathbf{r}_1^{(s)}, \mathbf{r}_2^{(s)}, \dots) + U_{ll}(\mathbf{r}_1^{(l)}, \mathbf{r}_2^{(l)}, \dots) + U_{sl}(\mathbf{r}_1^{(s)}, \mathbf{r}_2^{(s)}, \dots, \mathbf{r}_1^{(l)}, \mathbf{r}_2^{(l)}, \dots)$, and, neglecting three bodies interactions (i.e. assuming the particles are non-deformable, non-polarizable, ...), we can say that U_{ss} contains all pair interactions between two small particles, U_{ll} contains all pair interactions between two large particles, and U_{sl} contains all pair interactions between a small and a large particle. Then, the influence of the solvent on the behavior of the solute has to be due to U_{sl} and U_{ss} . Clearly the problem simplifies when we can assume $U_{ss} = 0$ and under certain conditions [31] it can even be rewritten exactly in terms of an *effective* one-component one for only the large particle with a potential energy $U_{ll}^{\text{eff}}(\mathbf{r}_1^{(l)}, \mathbf{r}_2^{(l)}, \dots)$ with only pairwise interactions.

In a fluid binary mixture of small and large nonoverlapping hard bodies the small particles may induce a *depletion* entropic attraction between the big particles [27,32,33] when two of these are closer than the dimensions of the small bodies since in this case no small particle fits in the space between the two large particles but there will still be an osmotic pressure due to the small particles surrounding the two big particles pushing them together.

This depletion force serves an important stabilizing role in many biological and technological processes. Specifically, many osmolytes and polymeric crowders that are excluded from protein surfaces stabilize the more compact folded state [28,29].

Following the framework of Ref. [30], in order to understand theoretically this phenomenon we will introduce the following model size-asymmetric binary mixtures: A non-additive hard-sphere binary mixture [34–36,30] with the solvent particles non interacting among themselves, $\sigma_{ss} = 0$, the solute particles interacting as hard-spheres of diameter $\sigma_{ll} = \sigma_l$, and a square-shoulder interaction between the solvent particles and the solute particles where $\sigma_s = q\sigma_l$ is the diameter of the small spheres *as seen by* the large ones. The square-shoulder interaction occurs in a spherical shell of diameter between $\sigma_{sl} = \sigma_l(1 + q)/2$ and $\sigma_{sl}(1 + \lambda_{sl})$, the small and large particles are otherwise interacting as hard-spheres at distances smaller than σ_{sl} . Our size parameter q here plays the role of the usual non-additivity parameter $\Delta = \sigma_{sl}/\sigma_{sl}^{\text{add}} - 1 = q$ with $\sigma_{sl}^{\text{add}} = (\sigma_{ss} + \sigma_{ll})/2$.

This model being non-additive (with positive non-additivity) does not admit an analytical solution for the Percus–Yevick (PY) closure of the Ornstein–Zernike equations but under certain geometrical condition it admits an exact effective pair formulation [30].

We called this model the Square-Shoulder-Asakura–Oosawa (SSAO) model [27,32,33]. Of course, the more general formulation of the model is when one has σ_{ss}/σ_s different from 0, but in this more complicated case of an interacting solvent we would not be able to solve exactly and analytically for the effective one-component problem [30].

Usually when talking about the AO model one refers to a colloid–polymer mixture where the depletants are linear homopolymers in a good solvent of radius of gyration $\sigma_s/2$, which, after tracing out the monomers degrees of freedom and replacing each chain with a particle coinciding with its center of mass [37], can be considered, for $\eta_s \lesssim 1$, to a first level of approximation, as non interacting among themselves but unable to penetrate a sphere of diameter $\sigma_s + \sigma_l$ around each colloidal particle. The colloidal particles are treated as hard spheres of diameter σ_l . In this work we will rather talk always about a solvent–solute mixture.

It is interesting to observe that when the temperature is set to infinity the SSAO model reduces to the usual AO one with a depletion range between σ_l and $2\sigma_{sl}$, whereas when it is set to zero it reduces to an AO model with a larger depletion range extending from σ_l to $2\sigma_{sl}(1 + \lambda_{sl})$.

To the best of our knowledge no numerical experiment has ever been tried on the full SSAO binary mixture.

We will now first discuss the derivation of the effective one-component problem of the SSAO model.

3. The SSAO model

Our SSAO binary mixture model is defined as follows

$$U_{ss} = \sum_{i < j} \varphi_{ss}(|\mathbf{r}_i^{(s)} - \mathbf{r}_j^{(s)}|), \quad (3.1)$$

408

R. Fantoni / Physica A 457 (2016) 406–412

$$U_{ll} = \sum_{i < j} \varphi_{ll}(|\mathbf{r}_i^{(l)} - \mathbf{r}_j^{(l)}|), \tag{3.2}$$

$$U_{sl} = \sum_{i,j} \varphi_{sl}(|\mathbf{r}_i^{(s)} - \mathbf{r}_j^{(l)}|), \tag{3.3}$$

$$f_{ss}(r) = e^{-\beta\varphi_{ss}(r)} - 1 = 0, \tag{3.4}$$

$$f_{ll}(r) = e^{-\beta\varphi_{ll}(r)} - 1 = -\theta(\sigma_{ll} - r), \tag{3.5}$$

$$f_{sl}(r) = e^{-\beta\varphi_{sl}(r)} - 1 = -\theta(\sigma_{sl} - r) + f_0(r), \tag{3.6}$$

where $\beta = 1/k_B T$ with T the absolute temperature, $\varphi_{ss}, \varphi_{ll}, \varphi_{sl}$ are the bare solvent–solvent, solute–solute, and solvent–solute pair-potentials respectively, f_{ss}, f_{ll}, f_{sl} the corresponding Mayer functions, $\sigma_{sl} = \sigma_l(1+q)/2$, θ is the Heaviside step function, and the square-shoulder is

$$f_0(r) = \begin{cases} 0 & r < \sigma_{sl} \\ e^{-\beta\epsilon_{sl}} - 1 & \sigma_{sl} < r < \sigma_{sl}(1 + \lambda_{sl}) \\ 0 & r > \sigma_{sl}(1 + \lambda_{sl}) \end{cases}, \tag{3.7}$$

where $\epsilon_{sl} > 0$ is a positive constant. We can then introduce a reduced temperature as $T^* = 1/\beta\epsilon_{sl}$.

Model SSAO does not admit a PY analytic solution but admits an exact effective one-component description for $q < q_0 = 2/\sqrt{3} - 1 = 0.15470\dots$, when a solvent can fit into the inner volume created by three solutes at contact (or $q < 1$ in one spatial dimension [38]), so that a solvent particle cannot overlap simultaneously with more than two (nonoverlapping) solutes at contact. Following the derivation of Dijkstra et al. [31], we describe the mixture in a mixed canonical (for the solutes) and grand canonical (for the solvent) ensemble, which they call semi-grand-canonical (z_s, N_l, V, T) ensemble. It is then easy to show [30] that in this case, after integrating out the degrees of freedom of the solvent, the effective potential $\beta v_{ll}(r)$ is

$$\beta v_{ll}(r) = \beta\varphi_{ll}(r) - z_s \int d\mathbf{r}_s f_{sl}(r_s) f_{sl}(|\mathbf{r}_s - \mathbf{r}|), \tag{3.8}$$

which upon using Eq. (3.6) gives

$$\beta v_{ll}(r) = \begin{cases} +\infty & r < \sigma_l \\ v_0(r) & \sigma_l < r < 2\sigma_{sl}(1 + \lambda_{sl}) \\ 0 & r > 2\sigma_{sl}(1 + \lambda_{sl}), \end{cases} \tag{3.9}$$

with

$$-v_0(r)/z_s = 2\mathcal{C}(r/2, \sigma_{sl}) - 2(e^{-\beta\epsilon_{sl}} - 1) [\mathcal{C}(r_<, \sigma_{sl}) + \mathcal{C}(r_>, \sigma_{sl}(1 + \lambda_{sl})) - 2\mathcal{C}(r/2, \sigma_{sl})] + 2(e^{-\beta\epsilon_{sl}} - 1)^2 \{\mathcal{C}(r/2, \sigma_{sl}(1 + \lambda_{sl})) - [\mathcal{C}(r_<, \sigma_{sl}) + \mathcal{C}(r_>, \sigma_{sl}(1 + \lambda_{sl})) - \mathcal{C}(r/2, \sigma_{sl})]\}, \tag{3.10}$$

where we denoted with $\mathcal{C}(R, \sigma)$ the volume of a spherical cap of height $\sigma - R$ in a sphere of radius σ , i.e.

$$\mathcal{C}(R, \sigma) = \frac{2\pi\sigma^3}{3} \left[1 - \frac{3R}{2\sigma} + \frac{1}{2} \left(\frac{R}{\sigma} \right)^3 \right] \theta(\sigma - R), \tag{3.11}$$

and $r_< + r_> = r$ with

$$r_< = \frac{r^2 + \sigma_{sl}^2 - \sigma_{sl}^2(1 + \lambda_{sl})^2}{2r}, \tag{3.12}$$

$$r_> = \frac{r^2 + \sigma_{sl}^2(1 + \lambda_{sl})^2 - \sigma_{sl}^2}{2r}. \tag{3.13}$$

In this case, from Dijkstra et al. [31] derivation, one finds that the exact cancellation of all Meyer diagrams higher than the two body one, occurs when [30]

$$\begin{aligned} \frac{\sigma_{sl}(1 + \lambda_{sl}) - \sigma_l/2}{\sigma_l/2} &= q + \lambda_{sl} + q\lambda_{sl} < q_0 \\ &= \frac{2}{\sqrt{3}} - 1. \end{aligned} \tag{3.14}$$

It is easy to show [30] that in the range $\sigma_l < r < 2\sigma_{sl}(1 + \lambda_{sl})$ one finds the result of Eq. (3.9) for the effective potential.

This is formally the same effective potential found in model SWAO of Ref. [30] where we change $\epsilon_{sl} \rightarrow -\epsilon_{sl}$. In the present case the sticky limit procedure would give the same AO model.

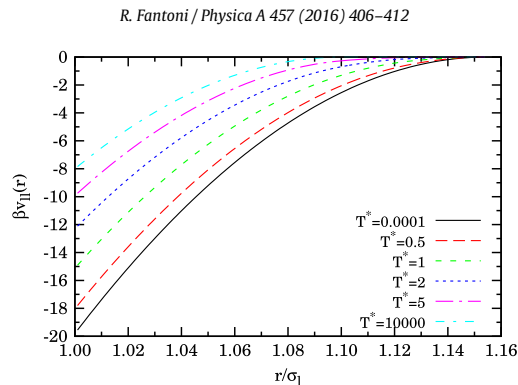


Fig. 1. (Color online) Effective potential for the SSAO mixture at various reduced temperatures and $q = 0.1$, $\lambda_{sl} = (q_0 - q)/(1 + q)$, $\eta_s^{(r)} = 1/2$.

In Fig. 1 we show the effective potential for the SSAO binary mixture at various temperatures. From the figure we see how at infinite temperature the SSAO reduces to the usual AO model with a range $2\sigma_{sl}$ whereas at zero temperature it reduces to an AO model with a wider range extending to $2\sigma_{sl}(1 + \lambda_{sl})$. At intermediate temperatures the effective potential lies continuously between the two extreme cases. Thus, the soft shoulder repulsion enhances the depletion mechanism and the solute stabilization.

Here z_s is the solvent fugacity. We can introduce a solvent reservoir packing fraction $\eta_s^{(r)} = \pi z_s \sigma_s^3 / 6 = \eta_s e^{\beta \mu_s^{\text{ex}}}$, with μ_s^{ex} the excess (over the ideal gas) solvent chemical potential. The solvent reservoir is at the same temperature of the solute. $\eta_s^{(r)}$ is the packing fraction of the reservoir made of non interacting solvent particles. The relationship between $\eta_s^{(r)}$ and η_s can be found calculating the average number of small solvent particles (see Appendix C in Ref. [30]). Up to second order in η_l one finds

$$\eta_s \approx \eta_s^{(r)} \left[1 + \eta_l (1 + q)^3 (\lambda_{sl} (3 + \lambda_{sl} (3 + \lambda_{sl})) e^{-\frac{1}{T^*}} - (1 + \lambda_{sl})^3) - \frac{12 \eta_l^2 q^3}{\sigma_l^3} \times \int_{\sigma_l}^{\sigma_l(1+q)(1+\lambda_{sl})} dr r^2 (v_0/\eta_s^{(r)}) e^{-v_0(r)} \right]. \quad (3.15)$$

4. The Noro and Frenkel criterion

Noro and Frenkel [39] argued that the reduced second virial coefficient B_2/B_2^{HS} , rather than the range and the strength of the attractive interactions, could be the most convenient quantity to estimate the location of the gas–liquid critical point for many different colloidal suspensions. Their criticality criterion for particles with variable range attractions, complemented by the simulation value of the critical temperature obtained in Ref. [40] for the SHS model, yields $B_2/B_2^{\text{HS}} \approx -1.21$.

Applying Noro and Frenkel criticality criterion for particles with variable range attractions [39], complemented by the simulation value of the critical temperature obtained in Ref. [40] for the Sticky–Hard–Sphere model, to our effective one-component problem, we are led to conclude that criticality requires $B_2^{\text{eff}}/B_2^{\text{HS}} = -1.21$ where B_2^{eff} is the second virial coefficient of our effective solute–solute problem

$$B_2^{\text{eff}} = \frac{2\pi}{3} \left\{ \sigma_l^3 - 3 \int_{\sigma_l}^{\infty} dr r^2 [e^{-\beta v_{II}(r)} - 1] \right\}, \quad (4.1)$$

and $B_2^{\text{HS}} = 2\pi \sigma_l^3 / 3$ is the virial coefficient for HS of diameter σ_l . Note that B_2^{eff} can only be calculated numerically.

In Fig. 2 we show the coexistence curves for the phase diagram stemming from the Noro–Frenkel empirical criterion in the $(T^*, \eta_s^{(r)})$ plane, for the SSAO model with $q = 0.1$ for four values of $\lambda_{sl} = 0.001, 0.01, (q_0 - q)/(1 + q), 0.1$. For the last $\lambda_{sl} = 0.1$ case the effective potential of Eq. (3.9) is only an approximation. From the figure we see how even a small shoulder produces dramatic effects in the phase diagram, widening the fluid–fluid coexistence region.

5. Perturbation theory for the SSAO model

From the previous section we understood that the *hidden* or metastable fluid–fluid phase separation observed by Dijkstra et al. [31] in their study of the AO model could be enlarged by adding a soft unlike repulsion as in our SSAO model. Now we want to quantify this more precisely through first order perturbation theory [41]. Taking the HS as reference system we can write the Helmholtz free energy per particle, $a = A/N$, as follows

$$\beta a_{II} = \beta a_{\text{HS}} + 12 \eta_l \int_{\sigma_l}^{\sigma_l(1+q)(1+\lambda_{sl})} \beta v_{II}(r) g_{\text{HS}}(r) r^2 dr, \quad (5.1)$$

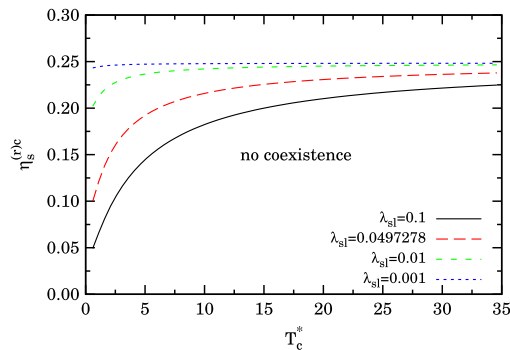


Fig. 2. (Color online) Phase diagram stemming from the Noro and Frenkel empirical criterion in the $(T^*, \eta_s^{(r)})$ plane, for a highly asymmetric, $q = 0.1$, SSAO for four values of λ_{sl} .

where $\beta a_{HS} = (4\eta_l - 3\eta_l^2)/(1 - \eta_l)^2 + \ln(\eta_l) + \text{constants}$ is the Carnahan–Starling [42] expression for HS, βv_{ll} the effective pair-potential of the SSAO model of Eq. (3.9), and g_{HS} is the HS radial distribution function in the PY approximation [43], which in the interval $1 < r < (1 + q)(1 + \lambda_{sl}) < 2$ can be written as follows

$$r g_{HS}(r) = \sum_{i=0}^2 \lim_{t \rightarrow t_i} (t - t_i) t \frac{L(t)}{S(t)} e^{t(r-1)}, \tag{5.2}$$

where we are measuring lengths in units of σ_l ,

$$S(t) = (1 - \eta_l)^2 t^3 + 6\eta_l(1 - \eta_l)t^2 + 18\eta_l^2 t - 12\eta_l(1 + 2\eta_l), \tag{5.3}$$

$$L(t) = (1 + \eta_l/2)t + 1 + 2\eta_l, \tag{5.4}$$

and t_i ($i = 0, 1, 2$) are the zeros of $S(t)$. The first order Helmholtz free energy of Eq. (5.1) can thus be calculated analytically.

The compressibility factor $Z = \beta p/\rho$ and chemical potential μ are then found through

$$Z_l = \eta_l \left. \frac{\partial \beta a_{ll}}{\partial \eta_l} \right|_{\eta_s^{(r)}}, \tag{5.5}$$

$$\beta \mu_l = Z_l + \beta a_{ll}. \tag{5.6}$$

The critical point $(\eta_s^{(r)c}, \eta_l^c)$ is determined by numerically solving the following system of equations

$$\left. \frac{\partial Z_l \eta_l}{\partial \eta_l} \right|_{\eta_s^{(r)c}, \eta_l^c} = 0, \tag{5.7}$$

$$\left. \frac{\partial^2 Z_l \eta_l}{\partial \eta_l^2} \right|_{\eta_s^{(r)c}, \eta_l^c} = 0. \tag{5.8}$$

In Fig. 3 we show the critical point $(\eta_s^{(r)c}, \eta_l^c)$ for the fluid–fluid coexistence of the SSAO model for $q = 0.1$ and $\lambda_{sl} = 0.001$, near to the AO, and $\lambda_{sl} = (q_0 - q)/(1 + q)$, the full SSAO, as a function of the reduced temperature, T^* . The figure confirms the scenario predicted in the previous section from the Noro–Frenkel criterion but gives additional information on the critical solvent and solute packing fractions, η_s^c and η_l^c respectively. Of course we expect a breakdown of the perturbation theory treatment as soon as the depletion mechanism becomes too strong. Also as soon as $q > q_0$ we are neglecting three-body (and higher) terms.

6. Conclusions

We studied a new colloidal strongly asymmetric binary mixture of (small) solvent and (large) solute particles, where unlike particles interact through the repulsive Square-Shoulder (SS) pair-potential, that we called the Square-Shoulder-Asakura–Oosawa (SSAO) model. Whenever the solvent particle fits inside the interstitial region of three touching solute particles we were able to derive exactly and analytically an effective solute–solute pair-potential and discussed the corresponding phase behaviors, as obtained from the resulting effective one-component system.

We found that the mere presence of the soft repulsion in the spherical shell of the SS unlike pair-interaction augments the depletion mechanism typical of the underlying Asakura–Oosawa (AO) mixture. Applying the Noro and Frenkel criterion

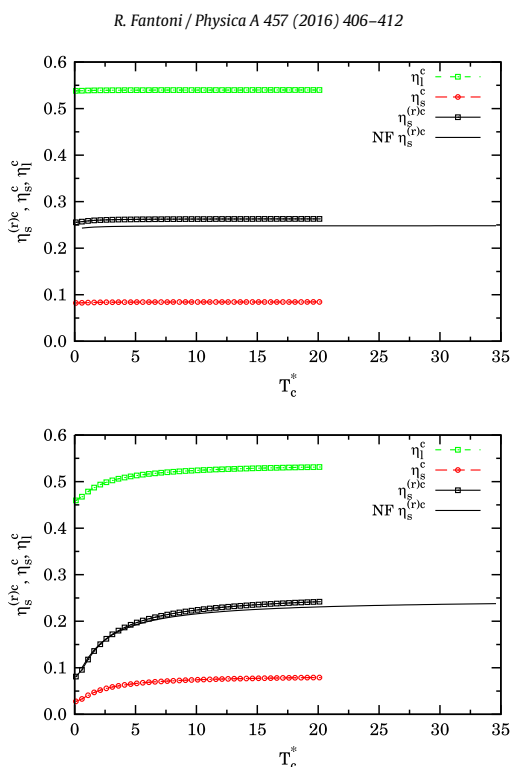


Fig. 3. (Color online) Critical point for the fluid–fluid coexistence in SSAO for $q = 0.1$ and $\lambda_{sl} = 0.001$ (top panel) and $\lambda_{sl} = (q_0 - q)/(1 + q)$ (bottom panel) as a function of T_c^* . The lines with symbols are obtained from thermodynamic perturbation theory, whereas the solid line corresponds to the Noro and Frenkel criterion of Fig. 2. Eq. (3.15) is used for the conversion between the reservoir density and the solvent density.

we saw that this, in turn, enlarges (and may stabilize) the metastable fluid–fluid phase coexistence region typical of the strongly asymmetric AO model at large reservoir packing fractions. A first order thermodynamic perturbation theory nicely confirms the scenario depicted by such criterion.

This phenomenon can be relevant in the experimental study of colloidal suspensions undergoing a fluid–fluid phase transition in the laboratory. Whenever the mathematical mixture just described represents a good model for a real mixture it should be expected that the main effect of the presence of the additional repulsive shell in the unlike species pair-interaction is to increase the depletion mechanism and in turn to enlarge the phase coexistence region of the phase diagram.

Acknowledgment

We acknowledge fruitful discussions with Andrés Santos.

References

- [1] S.M. Anthony, L. Hong, M. Kim, S. Granick, *Langmuir* 22 (2006) 9812.
- [2] J.M. Lynch, G.C. Cianci, E.R. Weeks, *Phys. Rev. E* 78 (2008) 031410.
- [3] E.R. Russel, F. Spaepen, D.A. Weitz, *Phys. Rev. E* 91 (2015) 032310.
- [4] P.C. Hemmer, G. Stell, *Phys. Rev. Lett.* 24 (1970) 1284.
- [5] G. Stell, P.C. Hemmer, *J. Chem. Phys.* 56 (1972) 4274.
- [6] P. Bolhuis, D. Frenkel, *Phys. Rev. Lett.* 72 (1994) 2211.
- [7] D.A. Young, B.J. Alder, *Phys. Rev. Lett.* 38 (1977) 1213.
- [8] C. Rascón, E. Velasco, L. Mederos, G. Navascués, *J. Chem. Phys.* 106 (1997) 6689.
- [9] L. Mederos, *J. Mol. Liq.* 76 (1998) 139.
- [10] S.B. Buldyrev, G. Malescio, C.A. Angell, N. Giovanbattista, S. Prestipino, F. Saija, H.E. Stanley, L. Xu, *J. Phys.: Condens. Matter* 21 (2009) 504106.
- [11] S. Prestipino, F. Saija, P. Giaquinta, *Phys. Rev. Lett.* 106 (2011) 235701.
- [12] S. Prestipino, F. Saija, P. Giaquinta, *J. Chem. Phys.* 137 (2012) 104503.
- [13] P. Ziherl, R.D. Kamien, *J. Chem. Phys.* B 105 (2001) 10147.
- [14] G. Malescio, G. Pellicane, *Nature Mater.* 2 (2003) 97.
- [15] G.J. Pauschenwein, G. Kahl, *J. Chem. Phys.* 129 (2008) 174107.
- [16] J. Formleitner, G. Kahl, *J. Phys.: Condens. Matter* 22 (2010) 104118.
- [17] M. Silbert, W.H. Young, *Phys. Lett. A* 58 (1976) 469.

- [18] N. Osterman, D. Babic, I. Poberaj, J. Dobnikar, P. Zihnerl, *Phys. Rev. Lett.* 99 (2007) 248301.
- [19] J. Duran, *Sands and Powders and Grains: An Introduction to the Physics of Granular Materials*, Springer, New York, 1999.
- [20] H. Löwen, G. Kramposthuber, *Europhys. Lett.* 23 (1993) 673.
- [21] A.A. Louis, E. Allahyarov, H. Löwen, R. Roth, *Phys. Rev. E* 65 (2002) 061407.
- [22] J. Horbach, *J. Phys.: Condens. Matter* 20 (2008) 244118.
- [23] A. Galindo, A. Gil-Villegas, G. Jackson, N. Burgess, *J. Phys. Chem. B* 103 (1999) 10272.
- [24] E.A. Jagla, *J. Chem. Phys.* 111 (1999) 8980.
- [25] N.M. Barraz Jr., E. Salcedo, M.C. Barbosa, *J. Chem. Phys.* 131 (2009) 094504.
- [26] L. Rovigatti, N. Gnan, A. Parola, E. Zaccarelli, *Soft Matter* 11 (2015) 692.
- [27] S. Asakura, F. Oosawa, *J. Chem. Phys.* 22 (1954) 1255.
- [28] L. Sapir, D. Harries, *J. Phys. Chem. Lett.* 5 (2014) 1061.
- [29] L. Sapir, D. Harries, *Curr. Opin. Colloid Interface Sci.* 20 (2015) 3.
- [30] R. Fantoni, A. Giacometti, A. Santos, *J. Chem. Phys.* 142 (2015) 224905.
- [31] M. Dijkstra, J.M. Brader, R. Evans, *J. Phys.: Condens. Matter* 11 (1999) 10079.
- [32] M.L. de Haro, C.F. Tejero, A. Santos, S.B. Yuste, G. Fiumara, F. Saija, *J. Chem. Phys.* 142 (2014) 014902.
- [33] K. Binder, P. Virnau, A. Statt, *J. Chem. Phys.* 141 (2014) 140901.
- [34] R. Fantoni, A. Santos, *Phys. Rev. E* 84 (2011) 041201.
- [35] R. Fantoni, A. Santos, *Phys. Rev. E* 87 (2013) 042102.
- [36] R. Fantoni, A. Santos, *J. Chem. Phys.* 140 (2014) 244513.
- [37] R. Menichetti, A. Pelissetto, G.D. Adamo, C. Pierleoni, *Integral equation analysis of single-site coarse-grained models for polymer-colloid mixtures*, *Mol. Phys.* (2015), published online.
- [38] J.M. Brader, R. Evans, *Physica A* 306 (2002) 287.
- [39] M.G. Noro, D. Frenkel, *J. Chem. Phys.* 113 (2000) 2941.
- [40] M. Miller, D. Frenkel, *J. Chem. Phys.* 121 (2004) 535.
- [41] A.P. Gast, C.K. Hall, W.B. Russel, *J. Colloid Interface Sci.* 96 (1983) 251.
- [42] N.F. Carnahan, K.E. Starling, *J. Chem. Phys.* 51 (1969) 635.
- [43] W.R. Smith, D. Henderson, *Mol. Phys.* 19 (1970) 411.

Chapter 51

Exact results for one dimensional fluids through functional integration

Fantoni R., J. Stat. Phys. **163**, 1247 (2016)

Title: “Exact results for one dimensional fluids through functional integration”

Abstract: We review some of the exactly solvable one dimensional continuum fluid models of equilibrium classical statistical mechanics under the unified setting of functional integration in one dimension. We make some further developments and remarks concerning fluids with penetrable particles. We then apply our developments to the study of the Gaussian core model for which we are unable to find a well defined thermodynamics.



Exact Results for One Dimensional Fluids Through Functional Integration

Riccardo Fantoni¹

Received: 4 January 2016 / Accepted: 22 March 2016
© Springer Science+Business Media New York 2016

Abstract We review some of the exactly solvable one dimensional continuum fluid models of equilibrium classical statistical mechanics under the unified setting of functional integration in one dimension. We make some further developments and remarks concerning fluids with penetrable particles. We then apply our developments to the study of the Gaussian core model for which we are unable to find a well defined thermodynamics.

Keywords Exact results in one dimensional fluids · Functional integration · Wiener measure · Gaussian process · Ornstein–Uhlenbeck and Wiener processes · Gaussian core model

1 Introduction

The physics of one dimensional systems is simpler than that one of higher dimensional ones. Specifically the free energy of an interacting gas, a *fluid*, has had an exact solution only in one dimension. The apparent simplicity of restricting motion to one spatial dimension is well known and has had much appeal. But what is the relation between the exactly soluble models of the one dimensional world and the richer and puzzling problems of the three dimensional one? A one dimensional gas was once thought to be incapable even of condensation. Later with the introduction of infinite range forces it has been made to condense, but even so this liquid can never freeze. What one finds is that these models are useful tests of approximate mathematical methods, the solutions of these models are surprisingly complex and interesting, physical applications are often and unexpectedly discovered, and more importantly they educate us to the need of rigorous and exact analysis with which one can have a better definition of reality. The fact that particles can get around each other is responsible for much of the structure of the ordinary world, and is also responsible for the difficulties which the

✉ Riccardo Fantoni
rfantoni@ts.infn.it

¹ Dipartimento di Fisica, Università di Trieste, Strada Costiera 11, Grignano, 34151 Trieste, Italy

mathematical physicist encounter in studying it. In one dimension we renounce to some of the structure in favor of the possibility of obtaining an exact solution.

The importance of one dimensional physics also lies in the fact that a number of many-body problems in higher dimensions can be accurately mapped into one dimensional problems.

One dimensional models with short range two particles forces do not have a phase transition at a non zero temperature [6].

In this work I will describe a way of simplifying the calculation of the grand canonical partition function of an ensemble of classical particles living in a one dimensional world and interacting with a given pair-potential v , originally described by Edwards and Lenard in their paper [3] which I will call EL from now on. Using the notion of a general Gaussian random process and Kac's theorem, they show how it is possible to express the grand partition function as a one dimensional integral of the fundamental solution of a given partial differential equation. The kind of partial differential equation will be fixed by the kind of *diffusion equation* satisfied by the Gaussian random process. In Sects. 2, 3, and 4 I will present EL's functional integration technique. In Sect. 5.2 I will show how, in EL, the properties of the Wiener process are used to solve "Edwards' model" or "Lenard's model". I will then show, in Sect. 5.1, how one can use the properties of the Ornstein–Uhlenbeck process to solve the "Kac-Baker's model", and, in Sect. 8, how the generalized Ornstein–Uhlenbeck process can be used to solve models with a more general penetrable pair interaction potential. Even though in EL is mentioned the generality of their technique they just apply it to the "Edwards' model". In Sect. 6 I show how EL propose to extract thermodynamical informations from their treatment and in Sect. 7 I show, following EL, how it is possible to reduce the search of the grand partition function, to a characteristic value problem, when the diffusion equation is independent of time. In Sect. 8 I show how one has to renounce to this reduction since the original partial differential equation is not separable anymore. In Sect. 8.1 I then apply the theoretical framework of such section to the Gaussian core model. In particular I will prove that this model is thermodynamically unstable in its attractive version (which is also not H-stable) and I will find an approximate expression for the grand partition function of the repulsive version (which clearly is H-stable) in terms of a triple series one of which is alternating.

More recently [2] the functional integral technique of Edwards and Lenard has been used to solve the statistical mechanics of a one dimensional Coulomb gas with boundary interactions as a one dimensional model for a colloidal and soap film.

I think that the success of the functional integration method described in this work to find exact solutions of the equilibrium classical (non-quantum) statistical mechanics problem of one dimensional fluids has certainly been one of the motivations for the popularity acquired by functional integration after the pioneering developments of Marc Kac and Richard Feynman. The link with the theory of stochastic processes is just a beautiful example of how many different theoretical frameworks come together in the few exact solutions of classical many-body problems.

2 The Problem

The problem is to simplify the calculation of the grand canonical partition function of a system of particles in the segment $[0, L]$ whose positions are labeled by x_i with $i = 1, 2, \dots, N$, in thermal equilibrium at a reduced temperature θ , namely,

Exact Results for One Dimensional Fluids Through Functional...

$$\Omega = \sum_{N=0}^{\infty} \frac{z^N}{N!} \int_0^L dx_N \cdots \int_0^L dx_1 e^{-\frac{V_N(x_1, \dots, x_N)}{\theta}}. \tag{1}$$

EL consider the total potential energy of the system to be,

$$V_N(x_1, \dots, x_N) = \sum_{i=1}^N \sum_{j=1}^N w(x_i, x_j), \tag{2}$$

where $w(x_i, x_j)$ is a function of two variables depending on the pair-potential $v(|x_i - x_j|)$ and the kind of reservoir exchanging particles with the system.

The main idea of EL, is to rewrite the grand partition function as a functional average,

$$\begin{aligned} \Omega &= \left\langle e^{\int_0^L dx' F(\phi(x'))} \right\rangle \\ &= \left\langle \sum_{N=0}^{\infty} \frac{1}{N!} \int_0^L dx_N \cdots \int_0^L dx_1 \prod_{i=1}^N F(\phi(x_i)) \right\rangle. \end{aligned} \tag{3}$$

And then choose $F(\phi) = z \exp(i\sigma\phi)$, to get,

$$\Omega = \sum_{N=0}^{\infty} \frac{z^N}{N!} \int_0^L dx_N \cdots \int_0^L dx_1 \left\langle e^{i\sigma \sum_{i=1}^N \phi(x_i)} \right\rangle, \tag{4}$$

where in interchanging the average with the sum and the integrals they use the linearity of the average. we haven't defined the average yet so we will do it next.

3 Averaging Over a General Gaussian Random Process

A general Gaussian random process $\phi(x)$ is defined by the postulate that for any finite number of points x_1, \dots, x_N the joint probability density for $\phi(x_k)$ in $d\phi_k$ (we will often make use of the abbreviation $\phi_i \equiv \phi(x_i)$) is of the form,

$$P(\phi_1, \dots, \phi_N) = \frac{\sqrt{\det B}}{(2\pi)^{N/2}} e^{-\frac{1}{2} \sum_{k=1}^N \sum_{l=1}^N B_{kl} \phi_k \phi_l}, \tag{5}$$

where $B_{ij} = B_{ij}(x_1, \dots, x_N)$ are the elements of the positive definite matrix B .

Let α_k be N arbitrary real numbers. Then,

$$\begin{aligned} \left\langle e^{i \sum_{i=1}^N \alpha_i \phi_i} \right\rangle &= e^{-\frac{1}{2} \sum_{k=1}^N \sum_{l=1}^N C_{kl} \alpha_k \alpha_l}, \\ \text{where } C &= B^{-1}. \end{aligned} \tag{6}$$

Differentiating with respect to α_k and α_l (not excluding $k = l$) and then setting all α to zero, one obtains,

$$\langle \phi(x_k) \phi(x_l) \rangle = C_{kl} = C(x_k, x_l), \tag{7}$$

where C is a function of two variables only, called the *covariance function*. From equations (6) and (7) follows that also $B_{ij} = B(x_i, x_j)$ is a function of just two variables. The covariance completely characterizes the statistical nature of $\phi(x)$

R. Fantoni

Replacing all the α 's in Eq. (6) with σ and comparing (6) and (4) with (1) and (2) one recognizes that,

$$C(x_1, x_2) = \frac{2}{\theta\sigma^2} w(x_1, x_2). \tag{8}$$

This imposes a restriction to the systems that one can treat. Namely we need w to be positive definite.

Why is all this useful is explained in the next section.

4 Kac's Theorem

Consider a Markoffian process $\phi(x)$, i.e. one for which, given any increasing sequence of "times" x_0, x_1, \dots, x_n , with $x_0 \leq x_1 \leq \dots \leq x_n$, the probability density that $\phi(x_k)$ is in $d\phi_k$ (with $k = 0, 1, \dots, n$) is the product,

$$P(\phi_1, \dots, \phi_n) = \int_{-\infty}^{\infty} \prod_{k=1}^n P(\phi_k, x_k | \phi_{k-1}, x_{k-1}) R(\phi_0, x_0) d\phi_0, \tag{9}$$

where $P(\phi_1, x_1 | \phi_0, x_0)$ is the conditional probability that $\phi(x_1)$ is in an element $d\phi_1$ around ϕ_1 given that $\phi(x_0) = \phi_0$ and $R(\phi, x)$ is the initial probability distribution for the process.¹ Both the conditional probabilities and the initial distribution are assumed to be normalized to unity over the interval $\phi \in [-\infty, +\infty]$,

$$\int_{-\infty}^{\infty} d\phi_1 P(\phi_1, x_1 | \phi_0, x_0) = \int_{-\infty}^{\infty} d\phi R(\phi, x) = 1. \tag{10}$$

Any quantity which is an expression involving $\phi(x)$ is a random variable whose average value may be determined using the probability (9).

One is interested in averages of the form,

$$\begin{aligned} W(x, x_0) &= \left\langle e^{\int_{x_0}^x dx' F(\phi(x'), x')} \right\rangle \\ &= 1 + \sum_{n=1}^{\infty} \frac{1}{n!} \int_{x_0}^x dx_n \int_{x_0}^{x_n} dx_{n-1} \cdots \int_{x_0}^{x_1} dx_1 \langle F(\phi_n, x_n) \cdots F(\phi_1, x_1) \rangle \\ &= 1 + \sum_{n=1}^{\infty} \int_{x_0}^x dx_n \int_{x_0}^{x_n} dx_{n-1} \cdots \int_{x_0}^{x_2} dx_1 \langle F(\phi_n, x_n) \cdots F(\phi_1, x_1) \rangle. \end{aligned} \tag{11}$$

Kac's theorem takes advantage of the Markoffian property (9) to relate to each other the successive terms of this series by an integral-recursion formula. It can be seen by inspection that,

¹ Equation (9) defines what is often called a *Wiener measure* in the space of continuous functions $\phi(x)$.

Exact Results for One Dimensional Fluids Through Functional...

$$W(x, x_0) = \int_{-\infty}^{\infty} d\phi Q(\phi, x|\phi_0, x_0), \tag{12}$$

$$Q = \sum_{n=0}^{\infty} Q_n,$$

$$Q_0(\phi, x|\phi_0, x_0) = \int_{-\infty}^{\infty} d\phi_0 P(\phi, x|\phi_0, x_0)R(\phi_0, x_0)$$

$$Q_n(\phi, x|\phi_0, x_0) = \int_{x_0}^x dx' \int_{-\infty}^{\infty} d\phi' P(\phi, x|\phi', x')F(\phi', x')Q_{n-1}(\phi', x'|\phi_0, x_0)$$

Then one can write the following integral equation for Q ,

$$\begin{aligned} Q(\phi, x|\phi_0, x_0) &= Q_0 + \sum_{n=1}^{\infty} Q_n = \int d\phi_0 PR + \sum_{n=1}^{\infty} \int dx' \int d\phi' PFQ_{n-1} \\ &= \int_{-\infty}^{\infty} d\phi_0 P(\phi, x|\phi_0, x_0)R(\phi_0, x_0) \\ &\quad + \int_{x_0}^x dx' \int_{-\infty}^{\infty} d\phi' P(\phi, x|\phi', x')F(\phi', x')Q(\phi', x'|\phi_0, x_0). \end{aligned} \tag{13}$$

This is the main result of Kac’s theorem.

Now assuming that the stochastic process $\phi(x)$ satisfies a forward Fokker–Planck equation,

$$\begin{aligned} \frac{\partial}{\partial x} P(\phi, x|\phi_0, x_0) &= \mathcal{L}(\phi, x)P(\phi, x|\phi_0, x_0) \\ P(\phi, x_0|\phi_0, x_0) &= \delta(\phi - \phi_0) \quad \text{initial condition} \end{aligned} \tag{14}$$

it immediately follows from the integral formula (13), that Q satisfies,

$$\begin{aligned} \frac{\partial}{\partial x} Q(\phi, x|\phi_0, x_0) &= [\mathcal{L}(\phi, x) + F(\phi, x)]Q(\phi, x|\phi_0, x_0) \\ Q(\phi, x_0|\phi_0, x_0) &= R(\phi, x_0) \quad \text{initial condition} \end{aligned} \tag{15}$$

If we now further assume $\phi(x)$ to be a Gaussian process (so that Eq. (9) is of the form (5)) then we can put together the result of the previous section (8) and Kac’s theorem, to say that,

$$\Omega = W(L, 0) = \int_{-\infty}^{\infty} d\phi Q(\phi, L|0, 0), \tag{16}$$

where $Q = Q(\phi, x|\phi_0, x_0)$ is the solution of the partial differential equation (15) with $F(\phi, x) = F(\phi) = z \exp(i\sigma\phi)$. This is the simplification found by EL.

Note the following points:

- This certainly is a simplification from a computational point of view and establishes a bridge between non-equilibrium statistical mechanics and the theory of stochastic processes and equilibrium statistical mechanics in one dimension.
- When the operator \mathcal{L} is independent of “time” (we keep calling x time because it comes natural from the notion of random process. In the present context though x is the position of a particle along his one dimensional world) then both $P(\phi, x|\phi_0, x_0)$ and $Q(\phi, x|\phi_0, x_0)$ depend only on $|x - x_0|$ since F does not depend explicitly on x .

R. Fantoni

- For a non-stationary random process $\phi(x)$ it is often possible to choose a delta function as initial distribution, i.e. $R(\phi, x_0) = \delta(\phi - \phi_0)$, where $\phi_0 = \phi(x_0)$. In this case Q is the *fundamental solution* of the partial differential Eq. (15).
- For a non-stationary random process the covariance function $C(x_1, x_2) = \langle \phi(x_1)\phi(x_2) \rangle$ is not a function of $|x_2 - x_1|$ alone. The identification of the covariance with the pair-potential v demands that the process be stationary because the pair-potential is a function of the difference of the two position variables. But in some cases (due for example to the presence of the reservoir) w may differ from v (see Sect. 5.2).

As a final remark, in EL is stressed the importance of the Markoffian nature of the process. They observe that the concept of a Markoffian process involves the idea of a succession in “time” and this is meaningless when there is more than one independent variable. So it seems to be hard to extend the technique just described even to a two dimensional system.

In the following section we will apply the functional integration technique just described to some concrete example.

5 Examples

Note that due to the Markoffian nature of the stochastic process the following two properties should be required for $x_0 \leq x_1 \leq x_2$,

$$R(\phi_1, x_1) = \int_{-\infty}^{\infty} d\phi_0 P(\phi_1, x_1 | \phi_0, x_0) R(\phi_0, x_0), \tag{17}$$

$$P(\phi_2, x_2 | \phi_0, x_0) = \int_{-\infty}^{\infty} d\phi_1 P(\phi_2, x_2 | \phi_1, x_1) P(\phi_1, x_1 | \phi_0, x_0). \tag{18}$$

Let us see now how all this works for two well known Markoffian, Gaussian stochastic processes.

5.1 The Ornstein–Uhlenbeck Process

The *Ornstein–Uhlenbeck process* is a stationary process defined as follows,

$$R(\phi_0, x_0) = \frac{e^{-\frac{\phi_0^2}{2}}}{\sqrt{2\pi}}, \tag{19}$$

$$P(\phi, x | \phi_0, x_0) = \frac{e^{-\frac{(\phi - \phi_0 e^{-\gamma \Delta x})^2}{2S(\Delta x)}}}{\sqrt{2\pi S(\Delta x)}}, \tag{20}$$

$$\begin{aligned} \text{with } \Delta x &= |x - x_0|, \\ S(\Delta x) &= 1 - e^{-2\gamma \Delta x}, \end{aligned}$$

where γ is the inverse of the characteristic time constant of the process, i.e. a positive real number.

The covariance for this process is,

$$C(x_1, x_2) = e^{-\gamma|x_1 - x_2|}. \tag{21}$$

The Fokker–Planck equation satisfied by the process is the Smoluchowski diffusion equation for an harmonic oscillator,

$$\mathcal{L}(\phi) = \gamma \left(\frac{\partial^2}{\partial \phi^2} + \frac{\partial}{\partial \phi} \phi \right). \tag{22}$$

So this process can be used to describe a system of particles whose potential energy is,

$$w(x_1, x_2) = \frac{\theta \sigma^2}{2} e^{-\gamma |x_1 - x_2|}. \tag{23}$$

Adding a hard-core part to this long range potential and making it attractive by choosing σ pure imaginary, gives the so called “Kac-Baker model”. Yang and Lee showed that the presence of the hard core part is sufficient to ensure the existence of the thermodynamic potential for the infinite system ($L \rightarrow \infty$). This was calculated exactly by Kac who also proved that the model has no phase transitions (because of the infinite range of the potential, L. Van Hove’s proof is not applicable here). Later Baker showed that if one sets,

$$\sigma = i \sqrt{\frac{\alpha_0 \gamma}{\theta}}, \tag{24}$$

(so that the integral of the potential is independent of γ) and then takes the limit $\gamma \rightarrow 0$ after the limit $L \rightarrow \infty$, then a phase transition of the classical Van der Waals type is obtained. A model with exponential repulsive pair-potential (exactly like the one in (23)) was studied by D. S. Newman, who concluded that it did not show phase transitions in the long range limit $\gamma \rightarrow 0$ [8].

5.2 The Wiener Process

We follow EL and introduce the *Wiener process*. It is a non-stationary process defined by (if $x \geq x_0 > 0$),

$$R(\phi_0, x_0) = \frac{e^{-\frac{\phi_0^2}{4Dx_0}}}{\sqrt{4\pi D x_0}} \tag{25}$$

$$P(\phi, x | \phi_0, x_0) = \frac{e^{-\frac{\Delta \phi^2}{4D \Delta x}}}{\sqrt{4\pi D \Delta x}}, \tag{26}$$

$$\begin{aligned} \text{with } \Delta x &= x - x_0, \\ \Delta \phi &= \phi - \phi_0, \end{aligned}$$

where D is the diffusion constant of the Brownian process, i.e. a positive real number.

The covariance for this process is,

$$C(x_1, x_2) = 2D \min(x_1, x_2). \tag{27}$$

Although this process cannot be differentiated it can be seen as the integral, $\phi(x) = \int_0^x ds \xi(s)$, of the Gaussian white noise process, $\xi(x)$, defined by $\langle \xi(x) \rangle = 0$ and $\langle \xi(x_1) \xi(x_0) \rangle = \zeta^2 \delta(x_1 - x_0)$ and the attribute Gaussian implies that all cumulants higher than of second order vanish. One just needs to set $2D = \zeta^2$.

The Fokker–Planck equation satisfied by the process is the Einstein diffusion equation,

$$\mathcal{L}(\phi) = D \frac{\partial^2}{\partial \phi^2}. \tag{28}$$

R. Fantoni

So this process can be used to describe a system of particles whose potential energy is,

$$w(x_1, x_2) = D\theta\sigma^2 \min(x_1, x_2). \tag{29}$$

It was S. F. Edwards, see EL, who first realized that this is a Coulomb system: electrons of charge q living in the segment $[0, L]$ are in contact with an infinite reservoir (in the region $x < 0$, say). The reservoir exchanges particles with the system of electrons giving rise to the statistical fluctuations in particle number. Take the system plus reservoir electrically neutral as a whole and imagine the system containing N electrons. Then there is a total charge $-Nq$ in the reservoir. Gauss theorem then tells that in the region $x \geq 0$ there is a constant electric field of magnitude $2\pi Nq$, due to the presence of the reservoir. Now choosing,

$$D = \frac{2\pi}{\theta}, \tag{30}$$

$$\sigma = q, \tag{31}$$

one can rewrite the total potential energy of the system as,

$$\begin{aligned} V_N &= 2\pi q^2 \sum_{k=1}^N \sum_{l=1}^N \min(x_k, x_l) \\ &= 2\pi q^2 \sum_{k=1}^N \sum_{l=1}^N \left[-\frac{|x_k - x_l|}{2} + \frac{x_k + x_l}{2} \right] \\ &= -2\pi q^2 \sum_{k < l} |x_k - x_l| + 2\pi q^2 \sum_{k=1}^N \sum_{l=1}^N x_l \\ &= -2\pi q^2 \sum_{k < l} |x_k - x_l| + 2\pi Nq^2 \sum_{l=1}^N x_l. \end{aligned} \tag{32}$$

Which is readily recognized as the expected result for the ‘‘Edwards’ model’’. We are assuming that the line is the real world in which each charge lives. So that also its field lines cannot escape from the line. Then the electric potential of each charge is the solution of $d^2\psi(x)/dx^2 = -4\pi\delta(x)$, i.e. $\psi(x) = -2\pi|x|$.

Note that due to the presence of the neutralizing reservoir, w is not just a function of $|x_i - x_j|$ and consequently the random process is not just a stationary one as in the Kac-Baker example.

In this case Edwards has not been able to answer in a definite way to the problem of continuity of the thermodynamic functions.

6 Thermodynamics

Following EL, we want now comment briefly on the relevance of all this from the point of view of the thermodynamics of the system of particles. Given the grand canonical partition function $\Omega = \Omega(z, L, \theta)$ the equation of state follows from eliminating z between the two following equations,

$$\frac{P}{\theta} = \frac{1}{L} \ln \Omega(z, L, \theta), \tag{33}$$

$$n = z \frac{\partial}{\partial z} \frac{1}{L} \ln \Omega(z, L, \theta). \tag{34}$$

where P is the pressure and n the number density of particles. Sometimes one talks about *chemical potential* μ (of the one-component system), instead of z . The two are related by,

$$z = \left(\frac{m\theta}{2\pi\hbar^2} \right)^{1/2} e^{\mu/\theta} > 0, \tag{35}$$

where m is the mass of the particles. All the other thermodynamic functions can be obtained from the internal energy,

$$U(N, L, S) = -\frac{\partial}{\partial(1/\theta)} \ln \Omega(z, L, \theta) + \frac{1}{2}N\theta, \tag{36}$$

where S is the entropy of the system. Or alternatively from the Helmholtz free energy,

$$A(N, L, \theta) = \mu N - \theta \ln \Omega(z, L, \theta). \tag{37}$$

It is often useful to simplify the problem by studying just the asymptotic behavior of Ω in the infinite system limit $L \rightarrow \infty$. This usually allows the recognition of eventual phase transitions (as in the Yang and Lee theory and L. Van Hove theorem) as singularities in the equation of state. The equation of state for the infinite system becomes then,

$$\left\{ \begin{array}{l} \frac{P}{\theta} = \Phi(z, v, \theta) = \lim_{L \rightarrow \infty} \left[\frac{1}{L} \ln \Omega(z, L, \theta) \right], \\ n = \frac{1}{v} = \lim_{L \rightarrow \infty} \left[z \frac{\partial}{\partial z} \frac{1}{L} \ln \Omega(z, L, \theta) \right], \end{array} \right. \tag{38}$$

where the limit may not be freely interchanged with the differentiation.

7 Characteristic Value Problem

Both the examples described have the common feature that \mathcal{L} is independent of time x . Under this circumstance the problem of calculating the grand canonical partition function Ω may be simplified even further, as shown in EL.

Letting $\phi \rightarrow \phi/\sigma$, the coefficient function $F(\phi)$ in Eq. (15) is periodic with period 2π . It is then possible to reduce the problem (15) to the characteristic value problem of an ordinary differential operator on a finite interval of the independent variable ϕ . Let,

$$\tilde{Q}(\phi, x) = \sum_{n=-\infty}^{\infty} Q(\phi + 2\pi n, x|0, 0). \tag{39}$$

This function is the *periodic solution* of the partial differential Eq. (15) and for $x = 0$ it reduces to,

$$\tilde{Q}(\phi, 0) = \sum_{n=-\infty}^{\infty} R(\phi + 2\pi n, 0). \tag{40}$$

For the ‘‘Kac-Baker model’’ one finds for example

$$\tilde{Q}(\phi, 0) = \theta_3 \left(i\pi\phi/\sigma^2, e^{-2\pi^2/\sigma^2} \right) e^{-\phi^2/2\sigma^2} / \sqrt{2\pi\sigma^2}, \tag{41}$$

where θ_3 is an elliptical theta function [1], and for the ‘‘Edwards’ model’’ $\tilde{Q}(\phi, 0) = \sum_{n=-\infty}^{\infty} \delta(\phi + 2\pi n)$. So, for this latter case, \tilde{Q} is the *periodic fundamental solution* of (15). It then follows that,

R. Fantoni

$$\Omega = \int_{-\pi}^{\pi} d\phi \tilde{Q}(\phi, L). \tag{42}$$

Since F and \mathcal{L} do not depend on x , in solving (15) for \tilde{Q} , one may use the method of separation of variables. This leads to the characteristic value problem,

$$\begin{aligned} [\mathcal{L}(\phi) + F(\phi)] y(\phi) &= \lambda y(\phi), \\ y(\phi + 2\pi) &= y(\phi). \end{aligned} \tag{43}$$

Then one looks for a complete orthonormal set of eigenfunctions y_m with relative eigenvalues λ_m ($m = 0, 1, 2, \dots$),

$$\int_{-\pi}^{\pi} d\phi y_m(\phi) y_{m'}(\phi) = \delta_{m,m'}. \tag{44}$$

The expansion of \tilde{Q} in terms of these functions is,

$$\tilde{Q}(\phi, x) = \sum_{m=0}^{\infty} e^{\lambda_m x} B_m y_m(\phi), \tag{45}$$

$$B_m = \int_{-\pi}^{\pi} d\phi \tilde{Q}(\phi, 0) y_m(\phi). \tag{46}$$

For example $B_m = y_m(0)$ for the ‘‘Edwards’ model’’. The grand partition function becomes,

$$\Omega(L) = \sum_{m=0}^{\infty} A_m e^{\lambda_m L}, \tag{47}$$

$$A_m = B_m \int_{-\pi}^{\pi} d\phi y_m(\phi). \tag{48}$$

The λ_m and the y_m depends parametrically on z which enters into the definition of $F(\phi)$. Moreover since $F(\phi) = F^*(-\phi)$ the λ_m are either real or occur in complex conjugate pairs.

Now assume that among the sequence of eigenvalue λ_m there is one λ_0 that is real and is bigger than the real part of all the others then the following simplification holds,

$$\boxed{\Omega(L \rightarrow \infty) \sim A_0 e^{\lambda_0 L}}. \tag{49}$$

The equation of state for the infinite system then becomes,

$$P = \theta \lambda_0(z), \tag{50}$$

$$\begin{aligned} n &= \lim_{L \rightarrow \infty} \left[z \frac{\partial}{\partial z} \left(\frac{\ln A_0(z)}{L} + \lambda_0(z) \right) \right] \\ &= z \frac{\partial}{\partial z} \lambda_0(z). \end{aligned} \tag{51}$$

For example for the ideal gas, $\sigma \rightarrow 0$ and $\lambda_0(z) = az$, with a a constant.

Let us summarize the characteristic value problem for the examples described. Denoting with a dash a first derivative respect to ϕ ($\dots' \equiv d \dots / d\phi$) we have:

- (i) ‘‘Kac-Baker model’’ repulsive [8],

$$\gamma [\sigma^2 y'' + (\phi y)'] + z e^{i\phi} y = \lambda y, \tag{52}$$

(ii) “Edwards’ model” [3],

$$\frac{2\pi q^2}{\theta} y'' + ze^{i\phi} y = \lambda y, \tag{53}$$

this is a one component plasma.

(iii) “Lenard’s model” [7],

$$\frac{2\pi q^2}{\theta} y'' + 2z \cos(\phi) y = \lambda y, \tag{54}$$

this is a two component plasma system of two kinds of particles with charges $\pm q$ and the corresponding values of z that by symmetry may be assumed equal without loss of generality.

In all cases $y(\phi)$ is a function of period 2π (for the attractive Kac-Baker model the periodicity is lost but the characteristic value problem is still valid).

Unfortunately there is no simple way to solve explicitly Eq. (52) for the Kac-Baker model. Nonetheless it is apparent the existence of the thermodynamic limit for the repulsive model, as was proved by Newman [9].

In the Edwards’ model the presence of the neutralizing reservoir is responsible (the potential energy of interaction between the particles and the reservoir being proportional to $+x$) for the charges all of the same sign to accumulate at the origin resulting in a system with zero density and pressure in accord with the fact that Eq. (53) admits solutions in terms of modified Bessel functions of the first kind $I_{\pm i\sqrt{2\theta\lambda/\pi q^2}}(\sqrt{2\theta z e^{i\phi}/\pi q^2})$ which form a complete set for $\lambda = -m^2$ with $m = 0, 1, 2, \dots$, so that $\lambda_0 = 0$.

In the Lenard’s model the solutions of Eq. (54) is in terms of even and odd Mathieu functions with characteristic value $a = -2\lambda\theta/\pi q^2$, parameter $q = -2\theta z/\pi q^2$, and argument $\phi/2$. According to Floquet’s theorem, any Mathieu function of argument ϕ can be written in the form $e^{ir\phi} f(\phi)$, where f has period 2π and r is the *Mathieu characteristic exponent*. For nonzero q the Mathieu functions are only periodic for certain values of a . Such *Mathieu characteristic values* are given by $a_r = A(r, q)$ with r integer or rational and $A(0, q) \leq A(r, q)$ for all r, q . Then we will have $\lambda_0 = -(\pi q^2/2\theta)A(0, -2\theta z/\pi q^2)$. In Fig. 1 we show the equation of state of the Lenard model at various temperatures θ for $q = 1$.

We are then led to conclude that this system does not admit any phase transition, condensation (gas–liquid) or freezing (liquid–solid).

8 General Penetrable Pair-Potential

In the examples described we started from known stochastic processes to find which physical model they may be able to describe. Actually one wants to do the reverse: given a physical model, i.e. given w (a positive definite function (8)), determine the stochastic process that allows the desired simplification for the grand canonical partition function. It turns out that this is quite easily accomplished when w is a function of the inter particles distance alone.

R. Fantoni

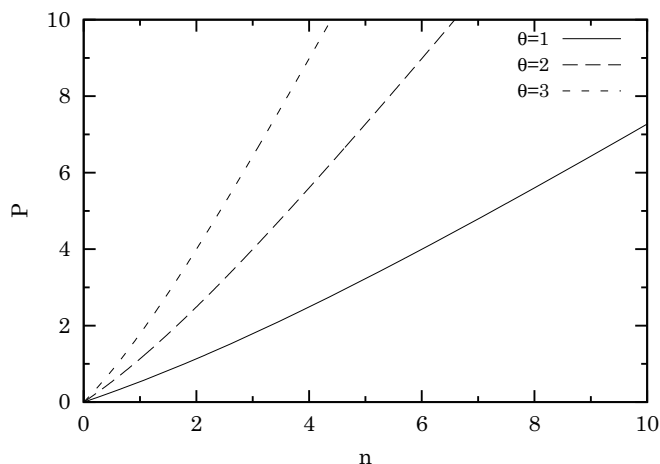


Fig. 1 The equation of state for the Lenard's model at various temperatures θ for $q = 1$

For this purpose it is useful to reconsider the Ornstein–Uhlenbeck process in a more general way. Consider the following stationary stochastic process,

$$R(\phi_0, x_0) = \frac{e^{-\frac{\phi_0^2}{2}}}{\sqrt{2\pi}}, \tag{55}$$

$$P(\phi, x|\phi_0, x_0) = \frac{e^{-\frac{(\phi-\phi_0 A(\Delta x))^2}{2S(\Delta x)}}}{\sqrt{2\pi S(\Delta x)}}, \tag{56}$$

with $\Delta x = |x - x_0|$,
 $S(\Delta x) = 1 - A^2(\Delta x)$,

where the last definition assures the validity of the Markoffian property (17). Clearly, in order to satisfy the Markoffian property (18) we need to require $A(x)A(y) = A(x + y)$ which is only satisfied by choosing A as an exponential as in the Ornstein–Uhlenbeck process. Here we willingly violate this second property and choose A as an arbitrary function. In order to have $P(\phi, x_0|\phi_0, x_0) = \delta(\phi - \phi_0)$ we must also require that $\lim_{x \rightarrow 0} A(x) = 1$.

The covariance for this process is,

$$C(x_1, x_2) = \frac{2}{\theta\sigma^2} w(x_1, x_2) = A(|x_1 - x_2|). \tag{57}$$

It can be readily verified that the transition density of this process satisfies the following forward Fokker–Planck equation,

$$\mathcal{L}(\phi, x) = -\frac{\dot{A}}{A} \left(\frac{\partial^2}{\partial \phi^2} + \frac{\partial}{\partial \phi} \phi \right), \tag{58}$$

where the dot denotes differentiation with respect to time ($\dot{} \equiv d \dots / dx$). All the properties of Sect. 4 continue to hold. All this allows for example to simplify the thermodynamics of a system of particles interacting with a pair-potential,

$$v = \frac{\theta\sigma^2}{4} A, \tag{59}$$

with $v(0) = v_0 = \theta\sigma^2/4$, i.e. *penetrable* particles.

Unfortunately in this case we cannot use the method of separation of variables described in Sect. 7 since \mathcal{L} is time dependent.

In the more general case one has to deal with w 's which are not functions of the pair-potential alone, as happened in the case of Edwards' model. For example one may be interested in modifying Edwards' model for the case of a Coulomb system moving but not living in $[0, L]$ with field lines allowed to exit the segment and interacting with the full three dimensional pair-potential $v(x) = 1/\sqrt{x^2 + \varepsilon^2}$, with ε a small positive quantity so that $v_0 = 1/\varepsilon$ or $\sigma = 2/\sqrt{\varepsilon\theta}$. A neutralizing uniform background in this case gives rise to quadratic terms making even the one-component system stable. To obtain the purely one dimensional case it is necessary to take the $\varepsilon \rightarrow 0$ limit at the end of the analysis of the *quasi one dimensional* case. This problem has been solved by Baxter [8] who developed a method for finding the partition function when the pair-potential satisfies a linear differential equation with constant coefficients. His method still leads to an eigenvalue problem but does not employ functional averaging.

Introducing the function $B^2(x) = -2d \ln A(x)/dx$ one can then say that according to Ito or Stratonovich calculus [5] the process defined by Eqs. (55), (56) satisfies the following stochastic differential equation,

$$\dot{\phi}(x) = -\frac{B^2(x)}{2}\phi(x) + B(x)\xi(x), \tag{60}$$

where $\xi(x)$ is Gaussian white noise with $\zeta = 1$. The $\xi(x)$ can be generated on a computer as pseudo random numbers on a large interval $\xi \in [-a, a]$ with a big enough.

8.1 Example: The Gaussian Core Model

For example we want to simplify the model fluid with $v(x) = v_0e^{-\gamma x^2}$, $\gamma > 0$, the so called Gaussian core model. In this case we have $A(x) = e^{-\gamma x^2}$ and $B^2(x) = 4\gamma x$. For this model we expect that the attractive, $\sigma^2 = 4v_0/\theta < 0$, case is thermodynamically unstable in agreement with the fact that the particles will tend to collapse at a same point since the system is not H-stable in the sense of Ruelle [13]. On the other hand we do not know anything yet about the repulsive, $\sigma^2 > 0$, case, which is H-stable and therefore we must have $P/\theta < z$. For example, we know that there cannot be any condensation but an interesting question is whether there can be freezing [4].

The problem (15) becomes

$$\frac{\partial}{\partial x} \tilde{Q}(\phi, x) = \left[2\gamma x \left(\sigma^2 \frac{\partial^2}{\partial \phi^2} + \frac{\partial}{\partial \phi} \phi \right) + ze^{i\phi} \right] \times \tilde{Q}(\phi, x), \tag{61}$$

$$\tilde{Q}(\phi, 0) = \theta_3 \left(i\pi\phi/\sigma^2, e^{-2\pi^2/\sigma^2} \right) \frac{e^{-\frac{\phi^2}{2\sigma^2}}}{\sqrt{2\pi\sigma^2}}, \tag{62}$$

with $\tilde{Q}(\phi + 2\pi, x) = \tilde{Q}(\phi, x)$. This is a non-separable partial differential equation. Again the grand canonical partition function is given by Eq. (42),

$$\Omega = \int_{-\pi}^{\pi} d\phi \tilde{Q}(\phi, L).$$

Clearly, approximating $F(\phi) \approx z$ or, equivalently, setting $\sigma \rightarrow 0$, we get the ideal gas behavior. In fact the solution to Eq. (61) is, in this simple case,

R. Fantoni

$Q(\phi, x|0, 0) = P(\phi, x|0, 0)e^{zx}$, since $\partial P/\partial x = \mathcal{L}P$. So that from Eqs. (16) and (10) immediately follows $\Omega = e^{zL}$.

In order to make some progress towards the solution of the full Eq. (61) we define $\mathcal{L} \equiv x\mathcal{R}$ and $\mathcal{H}(x) = x\mathcal{R} + F$. Since \mathcal{H} at different times do not commute we use the following Dyson series

$$Q(\phi, x|0, 0) = \mathcal{U}(x, 0)R(\phi, 0), \tag{63}$$

$$\mathcal{U}(x, x_0) = 1 + \sum_{n=1}^{\infty} \int_{x_0}^x dx_n \int_{x_0}^{x_n} dx_{n-1} \cdots \int_{x_0}^{x_2} dx_1 \mathcal{H}(x_n) \cdots \mathcal{H}(x_1),$$

Where R is given by Eq. (55). So that we find $\Omega = 1 + \sum_{n=1}^{\infty} c_n$ with

$$c_n = \int_0^L dx_n \int_0^{x_n} dx_{n-1} \cdots \int_0^{x_2} dx_1 \int_{-\infty}^{\infty} d\phi \mathcal{H}(x_n) \cdots \mathcal{H}(x_1)R(\phi, 0). \tag{64}$$

Solving for c_n we easily find $c_n = \sum_{k=1}^n a_{n,k}$ with

$$a_{n,k} = \frac{e^{-k^2\sigma^2/2} f_{n,k}(\sigma^2) \gamma^{n-k} L^{2n-k} z^k}{k!}, \tag{65}$$

with $f_{n,n} = 1$, $f_{n,1} = 0$ for $n > 1$ and $f_{n,k}(\psi)$ a polynomial of degree $n - k$ in ψ beginning with the monomial of degree one and the others of alternating signs. So

$$\begin{aligned} \Omega &= 1 + \sum_{n=1}^{\infty} \sum_{k=1}^n a_{n,k} = 1 + \sum_{k=1}^{\infty} \sum_{n=k}^{\infty} a_{n,k} \\ &= 1 + \sum_{k=1}^{\infty} \frac{e^{-k^2\sigma^2/2} (zL)^k}{k!} \sum_{n=k}^{\infty} f_{n,k}(\sigma^2) (\gamma L^2)^{n-k} \\ &= 1 + \sum_{k=1}^{\infty} \frac{(zL)^k}{k!} h_k(\sigma^2, \gamma L^2) = \Omega(zL, \sigma^2, \gamma L^2), \end{aligned} \tag{66}$$

where we defined

$$h_k(\psi, \eta) \equiv e^{-k^2\psi/2} g_k(\psi, \eta), \tag{67}$$

$$g_k(\psi, \eta) \equiv \sum_{m=0}^{\infty} f_{k+m,k}(\psi) \eta^m. \tag{68}$$

First of all notice that, if the thermodynamic limit exists, we must have $P = O(z^2/\gamma, \sigma^2)z\theta$ with O a given function of two variables such that $\lim_{\sigma \rightarrow 0} O(a, \sigma^2) = 1$. Note that when there is no interaction between the particles $v_0 \rightarrow 0$ and/or at very high temperature $\theta \rightarrow \infty$, then $\sigma \rightarrow 0$ and we end up with an ideal gas.

Then, if it was $h_k = 1$ we would immediately find the ideal gas behavior. On the other hand if it was $g_k = 1$ we would find an unstable system for $v_0 < 0$ and a stable system with $P = 0 = n$ for $v_0 > 0$ since

$$\frac{1}{L} \ln \left[\sum_{k=0}^{\infty} \frac{e^{-k^2\sigma^2/2} (zL)^k}{k!} \right] \rightarrow \begin{cases} 0 & \sigma^2 > 0 \text{ for } L \rightarrow \infty \\ \infty & \sigma^2 < 0 \text{ for any } L \end{cases}. \tag{69}$$

We then need to find the true h_k or g_k . We already know that $g_1 = 1$. What can we say about $g_k(\psi, \eta)$ for $k > 1$? By inspection of the first few terms of the Dyson series we find

Exact Results for One Dimensional Fluids Through Functional...

that $g_k(\psi, \eta) = 1 + \sum_{m=1}^{\infty} f_{k+m,k}(\psi)\eta^m$ with $f_{k+m,k}(\psi) = \sum_{i=1}^m (-1)^{m+i} d_{k+m,k,i} \psi^i$ and $d_{k+m,k,i}$ some positive coefficients. So that of course $h_k(0, \eta) = 1$ for all k , as it should. Now we can write

$$\begin{aligned} g_k(\psi, \eta) &= 1 + \sum_{m=1}^{\infty} \sum_{i=1}^m d_{k+m,k,i} (-\psi)^i (-\eta)^m \\ &= 1 + \sum_{i=1}^{\infty} (-\psi)^i \sum_{m=i}^{\infty} d_{k+m,k,i} (-\eta)^m \\ &= 1 + \sum_{i=1}^{\infty} l_{k,i}(\eta) (-\psi)^i, \end{aligned} \tag{70}$$

where we defined

$$l_{k,i}(\eta) \equiv \sum_{m=i}^{\infty} d_{k+m,k,i} (-\eta)^m. \tag{71}$$

We start looking for the coefficients for $i = 1$. By inspection of the first seven n we find, for $2 \leq k \leq n - 1$,

$$d_{n,k,1} = 2^n \frac{k!}{n!} b_{n,k}, \tag{72}$$

$$\frac{b_{n,k}}{b_{n,k+1}} = (k - 1) R_{n-k+2}, \tag{73}$$

$$b_{n,n-1} = \binom{n}{n-3} \frac{1}{2^n}. \tag{74}$$

So that

$$b_{n,k} = b_{n,n-1} \frac{(n-3)!}{(k-2)!} \prod_{q=k}^{n-2} R_{n-q+2}, \tag{75}$$

and

$$d_{n,k,1} = \frac{k(k-1)}{3!} r_{n-k}, \tag{76}$$

with, for $2 \leq k \leq n - 2$,

$$r_{n-k} = \prod_{p=4}^{n-k+2} R_p, \tag{77}$$

$$r_2 = 4/(2 \cdot 2 + 1)!!,$$

$$r_3 = 8 \cdot 3/4(2 \cdot 3 + 1)!!,$$

$$r_4 = 16 \cdot 3/5(2 \cdot 4 + 1)!!,$$

$$r_5 = 32 \cdot 3/6(2 \cdot 5 + 1)!!,$$

and so on. We can then guess that

$$r_m = \frac{2^m 3}{(2m + 1)!!(m + 1)}. \tag{78}$$

Then we can easily re-sum the series of Eq. (71) to say that

$$l_{k,1}(\eta) = k(k-1) \times \frac{{}_2F_2(\{1, 1\}, \{3/2, 2\}, -x) - 1}{2}, \tag{79}$$

with ${}_2F_2$ a hyper-geometric function. We also find $\lim_{\eta \rightarrow \infty} l_{k,1}(\eta) = -k(k-1)/2$. What about $l_{k,i}(\eta)$ for $i > 1$?

Their determination is quite laborious but let us suppose first that we had found for $l_{k,i}$,

$$l_{k,i}(\eta) = \frac{1}{i!} \left(\frac{k^2}{2}\right)^i \left(\frac{-\eta}{1+\eta}\right)^i. \tag{80}$$

Then it would follow

$$h_k(\psi, \eta) = e^{-\frac{k^2}{2}\psi} e^{\frac{k^2}{2}\frac{\psi\eta}{1+\eta}} = e^{-\frac{k^2}{2}\frac{\psi}{1+\eta}}, \tag{81}$$

and for the partition function we would find

$$\Omega_L(z) = \sum_{k=0}^{\infty} \frac{(zL)^k}{k!} e^{-\frac{k^2}{2}\frac{\sigma^2}{1+\gamma L^2}}. \tag{82}$$

We could then immediately say that the attractive, $\sigma^2 < 0$, case would be thermodynamically unstable since the series in Eq. (82) would be not summable, whereas the repulsive, $\sigma^2 > 0$, case would be stable. In this latter case $O = \lim_{L \rightarrow \infty} \ln \Omega_L/L$ would be finite and the system would admit a well defined thermodynamic limit without phase transitions. The equation of state would be

$$\frac{P}{\theta} = \lim_{L \rightarrow \infty} \frac{\ln \Omega_L(z)}{L} = O(z/\sqrt{\gamma}, \sigma^2)\sqrt{\gamma}, \tag{83}$$

$$n = \lim_{L \rightarrow \infty} z \frac{\Omega_L\left(ze^{-\frac{\sigma^2}{1+\gamma L^2}}\right)}{\Omega_L(z)} e^{-\frac{\sigma^2}{2(1+\gamma L^2)}} = z, \tag{84}$$

so that $P = O(n^2/\gamma, v_0/\theta)n\theta$ and for small n one would have $P \approx n\theta$.

In order to make some progress towards the exact solution we can then write $d_{n,k,i} = d_{n,k,1}E_{n,k,i}$ and note that $E_{n,k,1} = 1$ and by inspection $E_{2+i,2,i} = 1$. Now if we had $E_{n,k,i} = 1$ for all n, k, i then we would get

$$l_{k,i}(\eta) = \frac{k(k-1)2^{i-1}(-\eta)^i}{(i+1)(2i+1)!!} \times {}_2F_2(\{1, 1+i\}, \{3/2+i, 2+i\}, -\eta). \tag{85}$$

We can then use the following limit

$$\lim_{\eta \rightarrow \infty} {}_2F_2(\{1, 1+i\}, \{3/2+i, 2+i\}, -\eta)\eta = \frac{(i+1)(2i+1)}{2i}, \tag{86}$$

to say that

$$\lim_{\eta \rightarrow \infty} \frac{l_{k,i}(\eta)}{(-\eta)^{i-1}} = -\frac{k(k-1)2^{i-2}}{i(2i-1)!!}. \tag{87}$$

Since, according to Eqs. (87) and (70), in the large η limit,

$$g_k(\psi, \eta) \rightarrow 1 + k(k-1)\psi \times {}_2F_2(\{1, 1\}, \{3/2, 2\}, \psi\eta)/2, \tag{88}$$

for the repulsive, $\sigma^2 > 0$, system we would find

$$\begin{aligned} \frac{P}{\theta} &= \lim_{L \rightarrow \infty} \frac{\ln [{}_2F_2(\{1, 1\}, \{3/2, 2\}, \sigma^2 \gamma L^2)]}{L} \\ &= \begin{cases} \infty & \sigma^2 \gamma & \text{independent of } L \\ \alpha & \sigma^2 \gamma L = \alpha & \text{independent of } L \\ 0 & \sigma^2 \gamma L^2 & \text{independent of } L \end{cases} \end{aligned} \tag{89}$$

and $n = 0$. So that in the first two cases we would violate the H-stability condition according to which $P/\theta < z$. This is a signal that our approximation is too brute.

In the appendix we report the first few exact $E_{n,k,i}$. Even if we found it too hard to guess the full analytic expression from the first few of them, the results of the appendix can be used to refine our analysis.

Our final expression for the partition function is

$$\begin{aligned} \Omega &= \sum_{k=0}^{\infty} \frac{e^{-\sigma^2 k^2 / 2} (zL)^k}{k!} \left(1 + k(k-1) \sum_{i=1}^{\infty} (\sigma^2 \gamma L^2)^i \times \right. \\ &\quad \left. \sum_{l=0}^{\infty} (-\gamma L^2)^l \frac{E_{k+l+i,k,i} 2^{l+i}}{2(l+i+1)(2(l+i)+1)!!} \right) \end{aligned} \tag{90}$$

$$\begin{cases} < e^{zL} & \sigma^2 > 0, \\ = \infty & \sigma^2 < 0, \end{cases} \tag{91}$$

Note that the dependence of $E_{k+m,k,i}$ on k is crucial because otherwise we could immediately conclude that the pressure would be independent from z . And this fact, added to the H-stability condition $P/\theta < z$, would be enough to say that the repulsive Gaussian core model only admits a zero pressure zero density state. Note also that the dependence of $E_{n,k,i}$ on i is also crucial because otherwise for $\sigma = 1$ the argument of the first two series would be symmetric under exchange of i and l which would mean that the two models with $\gamma > 0$ and with $\gamma < 0$ would have the same thermodynamics which is clearly absurd [14].

The first alternating series has very slow numerical convergence as L grows. We then found it difficult to extract even a numerical equation of state. Nonetheless we found that the triple series is convergent at least in the high temperature regime, $0 < \sigma^2 \ll 1$.

From the H-stability condition (90) we find that for any L and $k > 1$ we must have

$$\begin{aligned} &\frac{-1}{k(k-1)} \\ &\leq \sum_{i=1}^{\infty} (\sigma^2 \gamma L^2)^i \sum_{l=0}^{\infty} (-\gamma L^2)^l \frac{E_{k+l+i,k,i} 2^{l+i}}{2(l+i+1)(2(l+i)+1)!!} \\ &= \sum_{m=1}^{\infty} (-\gamma L^2)^m \frac{2^m \sum_{i=1}^m (-\sigma^2)^i E_{k+m,k,i}}{2(m+1)(2m+1)!!} = G_k(\sigma^2, \gamma L^2) \\ &< \frac{e^{\sigma^2 k^2 / 2} - 1}{k(k-1)}. \end{aligned} \tag{92}$$

R. Fantoni

Then, we find $\sum_{i=1}^m (-\sigma^2)^i E_{k+m,k,i} = -\sigma^2 + F_{m,k}(\sigma^2)$ for $m \geq 2$ with $F_{m,k}(\sigma^2) = \sum_{i=2}^m (-\sigma^2)^i E_{k+m,k,i}$. In the large L limit we then have, for $\gamma > 0$,

$$G_k(\sigma^2, \gamma L^2) \rightarrow \sigma^2/2 + \lim_{L \rightarrow \infty} H_k(\sigma^2, \gamma L^2), \tag{93}$$

$$\begin{aligned} H_k(\sigma^2, \gamma L^2) &= \sum_{m=2}^{\infty} (-\gamma L^2)^m \frac{2^{m-1} F_{m,k}(\sigma^2)}{(m+1)(2m+1)!!} \\ &= (\gamma L^2)^2 M_k(\sigma^2, \gamma L^2), \end{aligned} \tag{94}$$

$$M_k(\sigma^2, \gamma L^2) = \sum_{m=0}^{\infty} (-\gamma L^2)^m \frac{2^{m+1} F_{m+2,k}(\sigma^2)}{(m+3)(2m+5)!!}.$$

In view of the H-stability upper bound of Eq. (92), M_k should be decaying as $1/L^4$ or faster, at large L . If it decays faster, then G_k is independent of k and the only possible state is a zero pressure one. If it decays as $1/L^4$, from the results of the appendix we can say that it does not increase with k and again the zero pressure state is the only one possible in the thermodynamic limit. So, in the end, we were unable to find a regular thermodynamics even for the repulsive stable case with positive γ . Everything is pointing towards a zero pressure state in the thermodynamic limit. This would be in agreement with the observation that as $\theta \rightarrow 0$ the only configurations contributing to the integral in Eq. (1) are the ones with minimum $V_N - \mu N$ which are those where the particles are infinitely spaced one another with $n \rightarrow 0$. Moreover the result of Penrose and Ruelle [10, 12] on the convergence radius of the Mayer series for stable and tempered pair-potentials would not be violated since for any finite L our triple series is convergent in the high temperature regime $0 < \sigma^2 \ll 1$.

8.2 Observation

Now, we can observe that the same conclusion would be expected for the easier Kac-Baker model, $v(x) = v_0 e^{-\gamma|x|}$, $\gamma > 0$, for which the structure of the solution for the partition function reads

$$\begin{aligned} \Omega &= 1 + \sum_{k=1}^{\infty} \frac{e^{-k^2 \sigma^2/2} (zL)^k}{k!} \sum_{n=k}^{\infty} f_{n,k}(\sigma^2) (\gamma L)^{n-k} \\ &= \Omega(zL, \sigma^2, \gamma L), \end{aligned} \tag{95}$$

with some given polynomials $f_{n,k}$. Again we can definitely say that the attractive model is thermodynamically unstable and that the repulsive one is thermodynamically stable but only admits the $P = 0 = n$ state for $\gamma \propto L^{-1}$. For the rest, also for this case we expect a situation similar to the one of the Gaussian core model. Should this behavior be generally expected for any positive, purely repulsive, penetrable pair-potential with non-compact² support? This will be studied in a forthcoming work.

² It is in fact clear that for a positive repulsive pair-potential with compact support we would have a partition function bounded below by the partition function of the hard-rods fluid which being a nearest neighbor fluid has a well defined thermodynamics with an exact analytical solution [11].

9 Conclusions

We reviewed, under the unified setting of functional integration in one dimension, some of the exactly solvable one dimensional continuum fluid models of equilibrium classical statistical mechanics. Following the original idea of Marc Kac we write the partition function of each model as a path integral over particular Markoffian, Gaussian stochastic processes. Following the idea of Sam Edwards we further reduce the thermodynamic problem for such fluids to the solution of a second order ordinary differential equation, the characteristic value problem.

In the work of Edwards and Lenard [3] it is also given a detailed analysis of how one can extend this method to get solutions for the pair- and higher orders static correlation functions.

We propose a generalization of the method which allows to treat other models with a rather generic pair-potential of interaction between the constituent penetrable particles of the fluid. The characteristic value problem of Edwards cannot be used anymore but the simplification of Kac remains valid. We apply this further developments to the simple case of the Gaussian core fluid model for which we prove that the attractive system is thermodynamically unstable, in agreement with the fact that it is not H-stable in the sense of Ruelle [13], and find an approximate expression for the exact partition function in terms of a triple series one of which is alternating. We were unable to find a well defined thermodynamics even for the repulsive system. Everything suggest that the only admitted state in the thermodynamic limit is the zero pressure one. If this conclusion was confirmed it would mean that a Monte Carlo simulation carried on the Gaussian core model would just observe finite size effects.

Acknowledgments I would like to thank Prof. Klaus Shulten whose course in non-equilibrium statistical mechanics held at Urbana in 1999 in the Loomis laboratory, stimulated the study of the EL paper as a final individual project. I would also like to thank Prof. Giorgio Pastore and Andres Santos for many useful discussions.

Appendix: The Coefficients $E_{n,k,i}$

In Table 1 we list the first exact $E_{n,k,i}$ coefficients for $i = 2, 3, 4$ and the first seven n .

Table 1 Exact $E_{n,k,i}$ for $i = 2, 3, 4$.

$E_{n,k,2}$	$n = 7$	$n = 6$	$n = 5$	$n = 4$
$k = 2$	15	7	3	1
$k = 3$	5105/352	79/12	33/14	
$k = 4$	211/18	243/56		
$k = 5$	389/56			
$E_{n,k,3}$	$n = 7$	$n = 6$	$n = 5$	
$k = 2$	25	6	1	
$k = 3$	4923/176	31/6		
$k = 4$	17			
$E_{n,k,4}$	$n = 7$	$n = 6$		
$k = 2$	10	1		
$k = 3$	965/88			

R. Fantoni

Table 1 continued

$E_{n,k,2}$	$n = 7$	$n = 6$	$n = 5$	$n = 4$
$k = 2$	15	7	3	1
$k = 3$	14.5	6.6	2.4	
$k = 4$	11.7	4.3		
$k = 5$	6.9			
$E_{n,k,3}$	$n = 7$	$n = 6$	$n = 5$	
$k = 2$	25	6	1	
$k = 3$	28.0	5.2		
$k = 4$	17			
$E_{n,k,4}$	$n = 7$	$n = 6$		
$k = 2$	10	1		
$k = 3$	11.0			

From the table we can see how there is a very weak dependence on k . So we can on a first ground assume that $E_{n,k,i} \approx E_{n,2,i} = e_{n-i,i}$ for all k . Moreover the entries of the table satisfy the following recurrence relation

$$e_{2,i} = 1, \tag{96}$$

$$e_{j,2} = 2^{j-1} - 1, \tag{97}$$

$$e_{j,i} = ie_{j-1,i} + e_{j,i-1}, \tag{98}$$

with $j = n - i$. So that introducing the generating function $\varphi(x, i) = \sum_{j=2}^{\infty} e_{j,i} x^j$ we easily find

$$\varphi(x, 2) = x^2/(x - 1)(2x - 1), \tag{99}$$

$$\varphi(x, i)/x = i\varphi(x, i) + \varphi(x, i - 1)/x, \tag{100}$$

with solution

$$\varphi(x, i) = \frac{x^3}{(x - 1)(-x)^i (2 - 1/x)_{i-1}}, \tag{101}$$

with $(a)_i = a(a + 1) \cdots (a + i - 1) = \Gamma(a + i)/\Gamma(a)$ the Pochhammer symbol. The desired coefficient $e_{j,i}$ is the j th coefficient in the series expansion of $\varphi(x, i)$ around $x = 0$.

More precisely we can then write $E_{n,k,i} = h_{n,k,i} e_{n-i,i}$ with $h_{n,2,i} = 1$ and $E_{2+i,2,i} = 1$. We can also observe that $E_{n,k,i}$ tends to decrease with k at fixed n and i .

References

1. Abramowitz, M., Stegun, I.A.: Handbook of Mathematical Functions. Dover, New York (1972)
2. Dean, D.S., Horgan, R.R., Sentenac, D.: Boundary effects in the one-dimensional coulomb gas. J. Stat. Phys. **90**, 899 (1998)
3. Edwards, S.F., Lenard, A.: Exact statistical mechanics of a one-dimensional system with coulomb forces. II. The method of functional integration. J. Math. Phys. **3**, 778 (1962)
4. Fantoni, R.: Non-existence of a phase transition for penetrable square wells in one dimension. J. Stat. Mech. **2010**, P07030 (2010)
5. Gardiner, C.W.: Handbook of Stochastic Methods. Springer, New York (1983)

Exact Results for One Dimensional Fluids Through Functional...

6. Hove, L.V.: Sur l'intégrale de configuration pour les systèmes de particules à une dimension. *Physica* **16**, 137 (1950)
7. Lenard, A.: Exact statistical mechanics of a one-dimensional system with coulomb forces. *J. Math. Phys.* **2**, 682 (1961)
8. Lieb, E.H., Mattis, D.C.: *Mathematical Physics in One Dimension*. Academic Press, New York (1966)
9. Newman, D.: Equation of state for a gas with a weak, long-range positive potential. *J. Math. Phys.* **5**, 1153 (1964)
10. Penrose, O.: Convergence of fugacity expansions for fluids and lattice gases. *J. Math. Phys.* **4**, 1312 (1963)
11. Prigogine, I.: *The Molecular Theory of Solutions*. Interscience, New York (1957)
12. Ruelle, D.: Correlation functions of classical gases. *Ann. Phys.* **5**, 109 (1963)
13. Ruelle, D.: *Statistical Mechanics: Rigorous Results*. Benjamin, London (1969)
14. Rybicki, G.B.: Exact statistical mechanics of a one-dimensional self-gravitating system. *Astrphys. Space Sci.* **14**, 56 (1971)

Part XVII
2017

Chapter 52

One-dimensional fluids with positive potentials

Fantoni R., J. Stat. Phys. **166**, 1334 (2017)

Title: “One-dimensional fluids with positive potentials”

Abstract: We study a class of one-dimensional classical fluids with penetrable particles interacting through positive, purely repulsive, pair-potentials. Starting from some lower bounds to the total potential energy, we draw results on the thermodynamic limit of the given model.



One-Dimensional Fluids with Positive Potentials

Riccardo Fantoni¹

Received: 7 September 2016 / Accepted: 21 December 2016 / Published online: 5 January 2017
© Springer Science+Business Media New York 2017

Abstract We study a class of one-dimensional classical fluids with penetrable particles interacting through positive, purely repulsive, pair-potentials. Starting from some lower bounds to the total potential energy, we draw results on the thermodynamic limit of the given model.

Keywords Exact results · One-dimensional fluids · Thermodynamic limit

1 Introduction

Recently we found evidence that a non pairwise-additive interaction fluid model for penetrable classical particles living in one-dimension does not admit a well defined thermodynamics [1], but can only exist in a zero pressure state.

We know that physical pairwise-additive models could also have the same thermodynamic singularity. Whereas the Ruelle stability principle [2] tells us only that a fluid of N particles with a total potential energy, V_N , bounded from below, $V_N > NB$ with B a constant, cannot have a divergent pressure, it does not tell us whether it can only have a zero pressure in the thermodynamic limit. This happens for example for models with penetrable particles interacting with a positive, purely repulsive, long-range pair-potential v .

We will consider some lower bounds to the total potential energy V_N which will allow us to prove some important results regarding the thermodynamic limit of the underlying one-dimensional fluid model.

✉ Riccardo Fantoni
rfantoni@ts.infn.it

¹ Dipartimento di Fisica, Università di Trieste, strada Costiera 11, 34151 Grignano, Trieste, Italy

Author's personal copy

2 The Problem

The grand canonical partition function of a system of particles in the segment $[0, L]$ whose positions are labeled by x_i with $i = 1, 2, \dots, N$, in thermal equilibrium at a reduced temperature θ , is given by

$$\Omega = \sum_{N=0}^{\infty} \frac{z^N}{N!} \int_0^L dx_N \cdots \int_0^L dx_1 e^{-\frac{V_N(x_1, \dots, x_N)}{\theta}}, \tag{2.1}$$

where $z > 0$ is the activity. The total potential energy of the system is

$$\begin{aligned} V_N(x_1, \dots, x_N) &= \sum_{i < j} v(|x_i - x_j|) \\ &= \sum_{i=1}^{N-1} \sum_{j=i+1}^N v(|x_i - x_j|), \end{aligned} \tag{2.2}$$

where $v(x)$ is the pair-potential. We will assume that $v(x) \leq v(0) = v_0 < \infty$ for all x , i.e. penetrable particles. For $v = 0$ we have the ideal gas (id).

Since $\Omega > 1$ we must have for the fluid pressure P

$$\frac{P}{\theta} = \lim_{L \rightarrow \infty} \frac{\ln \Omega}{L} > 0, \tag{2.3}$$

so the pressure cannot be negative. In addition we will assume that $v(x)$ is a positive function, $v(x) > 0$ for all x , then

$$\begin{aligned} \frac{P}{\theta} &= \lim_{L \rightarrow \infty} \frac{\ln \Omega}{L} \\ &< \lim_{L \rightarrow \infty} \frac{\ln \left[\sum_{N=0}^{\infty} \frac{(zL)^N}{N!} \right]}{L} = z. \end{aligned} \tag{2.4}$$

So $0 < P < \theta z$.

Let us furthermore assume that $v(x)$ has tails decaying to zero at large x and such that, for all x in $[0, L]$,

$$v(x) > v(L), \tag{2.5}$$

with

$$\lim_{L \rightarrow \infty} v(L) = 0. \tag{2.6}$$

Then we find

$$\Omega < \sum_{N=0}^{\infty} \frac{(zL)^N}{N!} e^{-\frac{v(L)N(N-1)}{2\theta}}, \tag{2.7}$$

and for the pressure,

$$\begin{aligned} \frac{P}{\theta} &= \lim_{L \rightarrow \infty} \frac{\ln \Omega}{L} \\ &< \lim_{L \rightarrow \infty} \frac{\ln \left[\sum_{N=0}^{\infty} \frac{(zL)^N}{N!} e^{-\frac{v(L)N(N-1)}{2\theta}} \right]}{L} \\ &= \lim_{L \rightarrow \infty} \frac{\ln \left[\int_0^{\infty} dy \frac{(zL)^{y/\sqrt{v(L)}}}{[y/\sqrt{v(L)}]!} e^{-\frac{y(y-\sqrt{v(L)})}{2\theta}} \right] - \ln[\sqrt{v(L)}]}{L}, \end{aligned} \tag{2.8}$$

where we introduced the new continuous variable $y = N\sqrt{v(L)}$ to transform the series into an integral over y . Clearly if we had $\lim_{L \rightarrow \infty} v(L) = v_{\infty}$ with $v_{\infty} > 0$ a constant, we could immediately conclude that the limit in Eq. (2.8) is zero (see Eq. (5.5)) and the fluid has a singular thermodynamic limit. Since the pair-potential is defined always up to an additive constant, in this case, in order to find a reasonable result, one needs to properly scale the chemical potential as follows: $\ln(z) \rightarrow \ln(z) + v_{\infty}(N - 1)/2\theta$.

Let us now introduce the Inverse Power Law Model (IPLM- α), $v(x) = v_0/[(|x|/\sigma)^\alpha + 1]$, with v_0, σ , and α three positive constants, and the Generalized Exponential Model (GEM- α), $v(x) = v_0 e^{-\gamma(|x|/\sigma)^\alpha}$, with γ a fourth positive constant. For the IPLM- α with $\alpha < 1$ the limit on the right hand side of Eq. (2.8) is equal to zero (see Eq. (5.15)) and the fluid can only exist in its zero pressure state. For $1 \leq \alpha < 2$ it is non-zero smaller than z . For $\alpha \geq 2$ it is equal to z (see Eq. (5.14)), i.e. it has the ideal gas behavior. For the GEM- α the limit is also always equal to z .

On the other hand we can obtain a more stringent upper bound to the pressure observing that for models with a pair-potential with monotonically decaying tails, i.e. with $v'(x) < 0$ for all x or purely repulsive, like the ones we just introduced, the configuration of minimum potential energy is approximately the one with all particles equally spaced on the segment, so

$$\begin{aligned} \min(V_N) &= [1 + a(\alpha, N, L)] \sum_{i < j} v \left[\frac{(j-i)L}{N-1} \right] \\ &= [1 + a(\alpha, N, L)](N-1) \sum_{k=1}^N v \left[\frac{kL}{N-1} \right] \\ &> [1 + a(\alpha, N, L)](N-1) v \left(\frac{L}{N-1} \right). \end{aligned} \tag{2.9}$$

For example we find, in Eq. (2.9), $a(\alpha, 3, L) = 0$ and for $N > 3$ we generally have $a < 0$. Moreover,

$$\lim_{\alpha \rightarrow \infty} a = \lim_{L \rightarrow \infty} a = 0, \tag{2.10}$$

$$\lim_{\alpha \rightarrow 0} a = \lim_{L \rightarrow 0} a = 0. \tag{2.11}$$

Clearly $\lim_{N \rightarrow 0} a = 0$ and we must also have

$$0 < \lim_{N \rightarrow \infty} [1 + a(\alpha, N, L)] \leq 1. \tag{2.12}$$

So $a(\alpha, N, L)$ remains finite for all α, L , and N since it must be a continuous function.

Author's personal copy

Then we will have

$$\frac{P}{\theta} < \lim_{L \rightarrow \infty} \frac{\ln \left[\sum_{N=0}^{\infty} \frac{(zL)^N}{N!} e^{-\frac{[1+\alpha] \sum_{i < j} v \left[\frac{(j-i)L}{N-1} \right]}{\theta}} \right]}{L}. \tag{2.13}$$

We want to study the limit on the right hand side

$$\mathcal{L} = \lim_{L \rightarrow \infty} \frac{\ln \left[\sum_{N=0}^{\infty} \frac{(zL)^N}{N!} e^{-\frac{[1+\alpha] \sum_{i < j} v \left[\frac{(j-i)L}{N-1} \right]}{\theta}} \right]}{L}. \tag{2.14}$$

Now we observe that for finite L ,

$$\begin{aligned} \lim_{N \rightarrow \infty} \frac{L}{N^2} \sum_{i < j} v \left[\frac{(j-i)L}{(N-1)} \right] &= \int_0^L dx v(x) \\ &= b(\alpha, L), \end{aligned} \tag{2.15}$$

where $b(\alpha, L)$ diverges at large L for the IPLM- α with $\alpha \leq 1$. Then the limit of Eq. (2.14) can be easily found for the IPLM- α with $\alpha \leq 1$, as

$$\mathcal{L} = \lim_{L \rightarrow \infty} \frac{\ln \left[\sum_{N=0}^{\infty} \frac{(zL)^N}{N!} e^{-\frac{[1+\alpha]bL^{-1}N^2}{\theta}} \right]}{L} = 0. \tag{2.16}$$

So we conclude that also the IPLM- α with $\alpha = 1$ does not have a well defined thermodynamic limit. A pair-potential such that $\lim_{L \rightarrow \infty} b$ is a finite constant, is said to be *short range*.

Note that the GEM- α for $\alpha = 1$ reduces to the Exponential Model (EM), for $\alpha = 2$ to the Gaussian Core Model (GCM), and taking the $\alpha \rightarrow \infty$ limit of either the GEM- α or the IPLM- α ,

$$\lim_{\alpha \rightarrow \infty} v(x) = \begin{cases} v_0 & |x| < \sigma \\ 0 & |x| > \sigma \end{cases} \tag{2.17}$$

we find the Penetrable Rods Model (PRM). For the PRM the thermodynamics is well defined as follows from the analytic solution of the Tonks gas [3] for the Hard Rods Model (HRM). In fact we must have

$$\Omega_{HRM} < \Omega_{PRM} < \Omega_{id} = e^{zL}. \tag{2.18}$$

According to our analysis, the IPLM- α and the GEM- α are non-singular for $\alpha \rightarrow \infty$ and the IPLM- α is singular for $\alpha \leq 1$.

Moreover as already noticed in Ref. [1] the GEM- α with $\gamma \propto L^{-\alpha}$ are singular as immediately follows from Eq. (2.8) and Eq. (5.5).

3 External Potential

In order to regularize the models introduced in the previous section, the IPLM- α for $\alpha \leq 1$, which have a long-range pair-potential, it is necessary to introduce a confining negative external potential which will prevent the particles to “escape” to infinity on the line.

Then we will have

$$V_N(x_1, \dots, x_N) = \sum_{i < j} v(|x_i - x_j|) + N \sum_i \phi(x_i) \tag{3.1}$$

with ϕ the external potential such that $\phi(x) < -v_0/2$ for all x in $[0, L]$. So that we must now have $P/\theta > ze^{-v_0/2\theta}$.

4 Thermodynamic Regularity

In this section we want to discuss about the thermodynamic regularity of the IPLM- α for $\alpha > 1$, which are *short-range*. We know that $P < \theta z$. So we should look for a non-zero lower bound to the pressure. We also know that the IPLM- ∞ is equivalent to the PRM which is regular. So we can assume the IPLM- α to remain regular in a neighborhood of $\alpha \rightarrow \infty$. The property that $v(x) \leq v_0$ implies $V_N \leq N(N - 1)v_0/2$ which in turn implies $P \geq 0$ which is not enough to say that P must be non-zero.

Even if it looks plausible to assume that short-range models should admit a regular thermodynamic limit we are unable to find a general principle rigorously proving such an assumption.

5 A Particular Non Pairwise-Additive Model

In Ref. [1] we studied the fluid model with

$$V_N = \sum_{i < j} w(x_i, x_j), \tag{5.1}$$

$$w(x_i, x_j) = v_0 \prod_{k=i}^{j-1} A(|x_k - x_{k+1}|), \tag{5.2}$$

$$A(x) = v(x)/v_0, \tag{5.3}$$

where $x_1 \leq x_2 \leq \dots \leq x_N$. Proceeding as in Sect. 2 we may assume that for equally spaced particles

$$V_N \gtrsim \text{constant} (N - 1) \sum_{k=1}^N \left[A \left(\frac{L}{N - 1} \right) \right]^k,$$

so that from the properties of the geometric series in the large N limit

$$\sum_{k=1}^N \left[A \left(\frac{L}{N - 1} \right) \right]^k \sim \frac{1 - [A(L/N)]^N}{1 - A(L/N)}, \tag{5.4}$$

and choosing for v the GEM- α , this behaves as N for $\alpha > 1$ as $(1 - e^{-L})N/L$ for $\alpha = 1$, and as $(N/L)^\alpha$ for $\alpha < 1$. So from the limit in Eq. (5.5) we conclude immediately that the model is thermodynamically singular for $\alpha > 1$ with a zero pressure, in agreement with the results of Ref. [1]. Nothing can be said for $\alpha \leq 1$. The case $\alpha = 1$ reduces to the physical pairwise additive model.

6 Ensemble Equivalence

In this section we discuss the equivalence of the three thermodynamic ensembles of statistical physics, *i.e.* the grand canonical, the canonical, and the microcanonical. The argument for the equivalence can be found in any textbook on statistical physics, as for example in the Course of Theoretical Physics of Landau and Lifshitz [4]. We briefly retrace the argument below and in the next two subsections.

We divide a closed system, after a period of time long enough respect to its relaxation time, in many microscopic parts and consider one in particular. We call $\rho(q, p) = w(E(q, p))$ the distribution function for such part, where $q = (x_1, x_2, \dots)$ are the particles coordinates and $p = (p_1, p_2, \dots)$ their momenta. In order to obtain the probability $W(E)dE$ that the subsystem has an energy between E and $E + dE$ we must multiply $w(E)$ by the number of states with energies in this interval. We call $\Gamma(E)$ the number of states with energies less or equal to E . Then the required number of states between E and $E + dE$ can be written $(d\Gamma(E)/dE)dE \propto dqdp$ and the energy probability distribution is $W(E) = (d\Gamma(E)/dE)w(E)$. With the normalization condition $\int W(E)dE = 1$. The function $W(E)$ has a well defined maximum in $E = \bar{E}$ and a typical width ΔE such that $W(\bar{E})\Delta E = 1$ or $w(\bar{E})\Delta\Gamma = 1$, where $\Delta\Gamma = (d\Gamma(\bar{E})/dE)\Delta E$ is the number of states corresponding to the energy interval ΔE . This is also called the *statistical weight* of the macroscopic state of the subsystem, and its logarithm $S = \ln \Delta\Gamma$, is called *entropy* of the subsystem. The *microcanonical* distribution function for the closed system is $dw \propto \delta(E - E_0) \prod_i (d\Gamma_i/dE_i)dE_i \propto \delta(E - E_0)e^S \prod_i dE_i$, where E_0 is the constant energy of the closed system and we used the fact that the various subsystems are statistically independent so that $\Delta\Gamma = \prod_i \Delta\Gamma_i$ and $S = \sum_i S_i$. We know that the most probable values of the energies E_i are the mean values \bar{E}_i . This means that $S(E_1, E_2, \dots)$ must have its maximum when $E_i = \bar{E}_i$. But the \bar{E}_i are the energy values of the subsystems which corresponds to the complete statistical equilibrium of the system. So we reach the important conclusion that the entropy of the closed system, in a state of complete statistical equilibrium, has its maximum value, for a given energy E_0 of the closed system.

6.1 Canonical vs Microcanonical

Let us now come back to the problem of finding the distribution function of the subsystem, *i.e.* of any small macroscopic part of the big closed system. We then apply the microcanonical distribution to the whole system, $dw \propto \delta(E + E' - E_0)d\Gamma d\Gamma'$, where $E, d\Gamma$ and $E', d\Gamma'$ refer to the subsystem and to the *rest* respectively, and $E_0 = E + E'$. Our aim is to find the probability $w(q, p)$ of a state of the system in such way for the subsystem be in a well defined state (with energy $E(q, p)$), *i.e.* in a well defined macroscopic state. We then choose $d\Gamma = 1$, pose $E = E(q, p)$ and integrate respect to $\Gamma', w(q, p) \propto \int \delta(E(q, p) + E' - E_0)d\Gamma' \propto (e^{S'})_{E'=E_0-E(q,p)}$. We use the fact that since the subsystem is small then its energy $E(q, p)$ will be small respect to E_0 , $S'(E_0 - E(q, p)) \approx S'(E_0) - E(q, p)dS'(E_0)/dE_0$. The derivative of the entropy respect to the energy is just $\beta = 1/\theta$ where θ is the reduced temperature of the closed system which corresponds with that of the subsystem in equilibrium. Then we find $w(q, p) \propto e^{-\beta E(q,p)}$ which is the well known *canonical* distribution.

6.2 Grand Canonical vs Canonical

We want now generalize the canonical distribution to a subsystem with a variable number of particles. Now the distribution function will depend both on the energy and on

Author's personal copy

1340

R. Fantoni

the number of particles N . The energies $E(q, p, N)$ will be different for different values of N . The probability that the subsystem contains N particles and be in the state (q, p) will be $w(q, p, N) \propto e^{S'(E_0 - E(q, p, N), N_0 - N)}$. Let then expand S' in powers of $E(q, p, N)$ and N keeping just the linear terms, so that $S'(E_0 - E(q, p, N), N_0 - N) \approx S'(E_0, N_0) - \beta E(q, p, N) + \beta \mu N$, where the chemical potential μ and the temperature of the subsystem and the rest are the same, since we require equilibrium. So we obtain for the distribution function $w(q, p, N) \propto e^{\beta(\mu N - E(q, p, N))}$. We can define the activity as $z = e^{\beta\mu}$. This is the grand canonical distribution we chose to use throughout our discussion.

6.3 On the Ensemble Equivalence in our Models

The ensemble equivalence may fail when approaching a phase transition when the fluctuations become so large that the linear approximation used above fails [5,6]. This is not the case for the models studied in the present work which do not admit a gas-liquid phase transition since the pair-potential is lacking a negative part (even if we cannot exclude a liquid-solid transition). All three distribution described above, the microcanonical, the canonical, and the grand canonical are in principle suitable for determining the thermodynamic properties of our models. The only difference from this point of view lies in the degree of mathematical convenience. In proactive the microcanonical distribution is the least convenient and is never used for this purpose. The grand canonical distribution is usually the most convenient. For example the Ruelle stability principle [2] holds only in this ensemble. This justifies our choice throughout the work.

7 Conclusions

For a one-dimensional fluid model we consider some lower bounds to the total potential energy V_N which allow us to prove some results regarding its thermodynamic limit. In particular we study fluids of penetrable particles interacting with a positive purely repulsive pair-potential with tails decaying to zero at infinite separations. We study two kinds of models: The IPLM- α and the GEM- α . For the long-range models, i.e. the IPLM- α for $\alpha \leq 1$, the fluid can only exist in its zero pressure state. For the short-range models we are not able to draw any conclusion.

We find good evidence that a particular non pairwise-additive model already introduced in a recent previous work [1] is thermodynamically singular.

Our results could give some insights to prove the thermodynamic limit of more complex fluids such as the ones described in [7–11].

Appendix 1: Some Limits

We have

$$\lim_{L \rightarrow \infty} \frac{\ln \left[\sum_{N=0}^{\infty} \frac{(zL)^N}{N!} e^{-N^{1+\epsilon}} \right]}{L} = \begin{cases} z & \epsilon \leq -1 \\ l & -1 < \epsilon < 0 \\ z/e & \epsilon = 0 \\ 0 & \epsilon > 0 \end{cases} \tag{5.5}$$

Author's personal copy

with $z/e < l < z$. For example to prove the last case $\epsilon > 0$ we can observe that

$$\frac{(zL)^N}{N!} e^{-N^{1+\epsilon}} = \frac{(zL/e^d)^N}{N!} e^{-N(N^\epsilon-d)} \tag{5.6}$$

$$< \frac{(zL/e^d)^N}{N!}, \text{ for } N > d^{1/\epsilon}. \tag{5.7}$$

Then for any finite $d > 0$ we will find

$$0 < \lim_{L \rightarrow \infty} \frac{\ln \left[\sum_{N=0}^{\infty} \frac{(zL)^N}{N!} e^{-N^{1+\epsilon}} \right]}{L} < \frac{z}{e^d}. \tag{5.8}$$

Since d can be chosen very large but finite, then the limit of Eq. (5.5) must be zero.

Also

$$\lim_{L \rightarrow \infty} \frac{\ln \left[\sum_{N=0}^{\infty} \frac{(zL)^N}{N!} e^{-N/L} \right]}{L} = \lim_{L \rightarrow \infty} z e^{-1/L} = z. \tag{5.9}$$

And

$$\sum_{N=0}^{\infty} \frac{(zL)^N}{N!} e^{-(N/L)^2} \tag{5.10}$$

$$= \sum_{N=0}^{\infty} \frac{(zL)^N}{N!} \sum_{k=0}^{\infty} \frac{(-)^k (N/L)^{2k}}{k!} \tag{5.11}$$

$$= \sum_{k=0}^{\infty} \frac{(-)^k (z^2)^k}{k!} \sum_{N=0}^{\infty} \frac{(zL)^{N-2k}}{N!/N^{2k}} \xrightarrow{L \gg \sigma} \tag{5.12}$$

$$\sum_{k=0}^{\infty} \frac{(-)^k (z^2)^k}{k!} \sum_{N=2k}^{\infty} \frac{(zL)^{N-2k}}{N!/N^{2k}} = e^{-z^2} e^{zL}, \tag{5.13}$$

so

$$\lim_{L \rightarrow \infty} \frac{\ln \left[\sum_{N=0}^{\infty} \frac{(zL)^N}{N!} e^{-(N/L)^2} \right]}{L} = \lim_{L \rightarrow \infty} z - z^2/L = z. \tag{5.14}$$

Proceeding as above we can also prove that for the IPLM- α with $\alpha > 2$ and all the GEM- α we must have $P < \theta z$.

Moreover we have

$$\begin{aligned} 0 &< \frac{\ln \left[\sum_{N=0}^{\infty} \frac{(zL)^N}{N!} e^{-v(L)N^2} \right]}{L} \\ &< \frac{\ln \left[\sum_{N=0}^{\infty} (zL)^N e^{-v(L)N^2} \right]}{L} \\ &= \frac{\ln \left[e^{[\ln(zL)]^2/4v(L)} \sum_{N=0}^{\infty} e^{-v(L)[N-\ln(zL)/2v(L)]^2} \right]}{L} \end{aligned}$$

Author's personal copy

1342

R. Fantoni

$$\begin{aligned}
&< \frac{\ln \left[e^{[\ln(zL)]^2/4v(L)} \sum_{N=0}^{\infty} e^{-v(L)N^2} \right]}{L} \\
&= \frac{[\ln(zL)]^2}{4v(L)L} + \frac{\ln \left[\int_0^{\infty} dy e^{-y^2} \right]}{L} - \frac{\ln[v(L)]}{2L}. \quad (5.15)
\end{aligned}$$

Then, since for the IPLM- α with $\alpha < 1$ the limit of the last expression is zero, its pressure must be zero as mentioned in the main text.

References

1. Fantoni, R.: Exact results for one dimensional fluids through functional integration. *J. Stat. Phys.* **163**, 1247–1267 (2016)
2. Ruelle, D.: *Statistical Mechanics: Rigorous Results*. Benjamin, London (1969)
3. Tonks, L.: The complete equation of state of one, two and three-dimensional gases of hard elastic spheres. *Phys. Rev.* **50**, 955 (1936)
4. Landau, L.D., Lifshitz, E.M.: *Statistical Physics*. In: Lifshitz, E.M., Pitaevskii, L.P. (eds.) *Course of Theoretical Physics*, vol. 5. Butterworth-Heinemann, Oxford (1980). translated from the Russian by J. B. Sykes and M. J. Kearsley
5. Touchette, H.: Equivalence and nonequivalence of ensembles: thermodynamic, macrostate, and measure levels. *J. Stat. Phys.* **159**, 987–1016 (2015)
6. Costeniuc, M., Ellis, H.T.R.S., Turkington, B.: Generalized canonical ensembles and ensemble equivalence. *Phys. Rev. E* **73**, 026105 (2006)
7. Fantoni, R.: A cluster theory for a Janus fluid. *Eur. Phys. J. B.* **85**, 108 (2012)
8. Fantoni, R., Malijevský, A., Santos, A., Giacometti, A.: Phase diagram of the penetrable square well-model. *Europhys. Lett.* **93**, 26002 (2011)
9. Gazzillo, D., Fantoni, R., Giacometti, A.: Fluids of spherical molecules with dipolarlike nonuniform adhesion: an analytically solvable anisotropic model. *Phys. Rev. E.* **78**, 021201 (2008)
10. Maestre, M.A.G., Fantoni, R., Giacometti, A., Santos, A.: Janus fluid with fixed patch orientations: theory and simulations. *J. Chem. Phys.* **138**, 094904 (2013)
11. Fantoni, R., Giacometti, A., Maestre, M.A.G., Santos, A.: Phase diagrams of Janus fluids with up-down constrained orientations. *J. Chem. Phys.* **139**, 174902 (2013)

Chapter 53

The moment sum-rules for ionic liquids at criticality

Fantoni R., *Physica A* **477C**, 187 (2017)

Title: “The moment sum-rules for ionic liquids at criticality”

Abstract: We discuss the first three well known moment charge-charge sum-rules for a general ionic liquid. For the special symmetric case of the Restricted Primitive Model, Das, Kim, and Fisher (2011) has recently discovered, through Monte Carlo simulations, that the Stillinger-Lovett or second-moment sum-rule fails at criticality. We critically discuss a possible explanation for this unexpected behavior. On the other hand the fourth-moment sum-rule turns out to be able to account for the results of the simulations at criticality.

Physica A 477 (2017) 187–194



Contents lists available at ScienceDirect

Physica A

journal homepage: www.elsevier.com/locate/physa

The moment sum-rules for ionic liquids at criticality



Riccardo Fantoni

Università di Trieste, Dipartimento di Fisica, strada Costiera 11, 34151 Grignano (Trieste), Italy

ARTICLE INFO

Article history:

Received 7 November 2016

Received in revised form 3 January 2017

Available online 28 February 2017

Keywords:

Ionic liquid

Electrolyte

Moment sum-rule

Stillinger–Lovett sum-rule

Criticality

Clustering

ABSTRACT

We discuss the first three well known moment charge–charge sum-rules for a general ionic liquid. For the special symmetric case of the Restricted Primitive Model, Das, Kim, and Fisher (2011) has recently discovered, through Monte Carlo simulations, that the Stillinger–Lovett or second-moment sum-rule fails at criticality. We critically discuss a possible explanation for this unexpected behavior. On the other hand the fourth-moment sum-rule turns out to be able to account for the results of the simulations at criticality.

© 2017 Elsevier B.V. All rights reserved.

1. Introduction

It is well known that among all possible long-range pair-potentials, it is only in the Coulomb case that the decay law of the correlations faster than any inverse power is compatible with the structure of equilibrium equations (such as the Born–Green–Yvon). Under the exponential clustering hypothesis for charged fluids, a number of exact sum-rules on the correlation functions can be obtained [1]. Of particular relevance is the Stillinger–Lovett second-moment charge–charge sum-rule which is equivalent to the property that the inverse dielectric function vanishes in the limit of small wavenumbers. When this condition holds the fluid completely shields any external charge inhomogeneity and behaves as a conducting medium.

In a recent work Das, Kim, and Fisher [2,3] found out, through finely discretized grand canonical Monte Carlo simulations, that in the Restricted Primitive Model (RPM) of an electrolyte, the second- and fourth-moment charge–charge sum-rules, typical for ionic fluids, are violated at criticality. For a 1:1 equisized charge-symmetric hard-sphere electrolyte their grand canonical simulations, with a new finite-size scaling device, confirm the Stillinger–Lovett second-moment sum-rule except, contrary to current theory [4], for its failure at the critical point (T_c, ρ_c) . Furthermore, the k^4 term in the charge–charge correlation or structure factor $S_{ZZ}(k)$ expansion is found to diverge like the compressibility when $T \rightarrow T_c$ at ρ_c . These findings are in evident disagreement with available theory for *charge-symmetric* models and, although their results are qualitatively similar to behavior expected for *charge-asymmetric* systems [4], even a semiquantitative understanding has eluded them.

Starting from the Ornstein–Zernike equation and extending at all densities the small density diagrammatic [5] property for the partial direct correlation functions of behaving as $1/r$ in the $r \rightarrow \infty$ limit, it is possible to arrive quickly to the second- and fourth-moment sum rules even if the fourth-moment one will not be expressed in terms of just thermodynamic functions.

The second- and fourth-moment sum-rules are rigorously derived starting from the Born–Green–Yvon equations and the exponential clustering hypothesis by Suttrop and van Wonderen [6–8] for a thermodynamically stable ionic mixture made of pointwise particles of charges all of the same sign immersed in a neutralizing background, the “Jellium”. The same

E-mail address: rfantoni@ts.infn.it.

<http://dx.doi.org/10.1016/j.physa.2017.02.064>

0378-4371/© 2017 Elsevier B.V. All rights reserved.

sum-rules must hold also when we allow in the ionic mixture the presence of mobile charges of *both signs*, which requires to consider a pair-potential regularization in order to prevent opposite charges collapse.

In this work we critically discuss the numerical findings of Das, Kim, and Fisher [2] at the light of the above mentioned analytical work of Suttorp and van Wonderen [6–8] and of a recent result of Santos and Piasecki [9] proving the long range behavior of the *n*-body correlation functions of a general fluid at his gas–liquid critical point.

2. The ionic fluids model

A multi-component ionic mixture of an electrolyte is made of mobile charges whose μ component (the particles of species μ) has molar fraction x_μ and charge $z_\mu e$, here e is the unit of charge and z_μ are integer numbers. So we may, in general, have charges of both signs. One is generally interested in studying a neutral state (since matter around us is neutrally charged). This can be obtained in the event that $\sum_\mu x_\mu z_\mu = 0$. Otherwise is necessary the addition of a neutralizing uniform background of charge density $-\rho e \sum_\mu x_\mu z_\mu$, with ρ the number density of the system of charges. A particularly simple case is the Restricted Primitive Model (RPM) where we have only two components with $x_1 = x_2 = 1/2$ and $z_1 = -z_2 = 1$ (without a background).

The Hamiltonian of a multi-component ionic mixture consisting of *s* components, confined in a region $\Omega \subset \mathbb{R}^3$ of volume V , is

$$H = \sum_{i=1}^N \frac{p_i^2}{2m_{\alpha_i}} + U(\mathbf{r}_1, \dots, \mathbf{r}_N), \tag{2.1}$$

$$U = \frac{1}{2} \sum_{i,j} z_{\alpha_i} z_{\alpha_j} v_{\alpha_i \alpha_j}(|\mathbf{r}_i - \mathbf{r}_j|), \tag{2.2}$$

with $p = |\mathbf{p}|$ and the pair-potential

$$v_{\mu\nu}(r) = v^c(r) + v^{sr}_{\mu\nu}(r), \tag{2.3}$$

where $r = |\mathbf{r}|$, v^c is the bare Coulomb potential

$$v^c(r) = \frac{e^2}{V} \sum_{\mathbf{k}(\neq \mathbf{0})} \frac{4\pi}{k^2} e^{i\mathbf{k}\cdot\mathbf{r}}, \tag{2.4}$$

and v^{sr} is a short-range regularization assumed integrable on \mathbb{R}^3 which includes the local repulsion effect needed to enforce thermodynamic stability [10] when we allow for the presence of particles of opposite charge in the mixture. A first soft regularization can be chosen as

$$v^{sr}_{\mu\nu}(r) = -\frac{e^2}{r} e^{-r/d_{\mu\nu}}, \tag{2.5}$$

where the lengths $d_{\mu\nu}$ control the exponential decay at large distances. A second regularization amounts to introduce hard-cores, namely

$$v^{sr}_{\mu\nu}(r) = \begin{cases} \infty & r < \sigma_{\mu\nu} \\ 0 & r > \sigma_{\mu\nu}, \end{cases} \tag{2.6}$$

where $\sigma_{\mu\nu} = (\sigma_\mu + \sigma_\nu)/2$ and σ_μ is the diameter of the hard-sphere particles of species μ . In Eq. (2.4) we used periodic boundary conditions just to stress the fact that we are interpreting the Monte Carlo simulations of Das, Kim, and Fisher [2], but of course our theoretical arguments apply to the continuous system as well.

The system contains N_μ particles of species μ . We will denote by $\mathbf{q} = (\alpha, \mathbf{r})$ the species α and the position \mathbf{r} of a particle of this species. The particle i of species μ has mass m_{μ_i} , charge $z_{\mu_i} e$ with e the unit of charge and $z_{\mu_i} = 0, \pm 1, \pm 2, \dots$, position \mathbf{r}_i , and momentum \mathbf{p}_i . The symbol \sum' means that one should sum over all particles under the restriction $i \neq j$ when $\alpha_i = \alpha_j$. Periodic boundary conditions have been assumed in the definition of the pair-potential. Each charge in the region Ω is neutralized by a uniform background of opposite charge density. On account of the presence of the neutralizing background the term $\mathbf{k} = \mathbf{0}$ is excluded in Eq. (2.4). The potential energy of Eq. (2.2) is defined up to an additive constant, the Madelung constant $\sum_i z_{\alpha_i}^2 \lim_{r \rightarrow 0} [v^c(r) - e^2/r]/2$, which takes into account the interaction of a particle with its own images, and which becomes important in a grand-canonical calculation. We will generally use a Greek index to denote the species label and a Roman index to denote the particle label.

Moreover we impose the constraint

$$Q = Ne \sum_{\mu=1}^s x_\mu z_\mu = \text{constant}, \tag{2.7}$$

where $N = \sum_\mu N_\mu$ is the total number of particles and $x_\mu = N_\mu/N$ are the molar fractions of particles of species μ . We also have that $\rho = N/V$ is the particles density and $\rho_\mu = \rho x_\mu$ are the partial densities of the ionic mixture. The neutralizing background has a uniform charge density $-e\rho_Z$ with $\rho_Z = \rho \sum_\mu x_\mu z_\mu$.

Table 1
Critical point estimates for the RPM model from several computer simulation studies. The reduced temperature is $T^* = k_B T \sigma / e^2$, with k_B Boltzmann constant, and the reduced density is $\rho^* = \rho \sigma^3$.

Reference	Year	T_c^*	ρ_c^*
Valleau [12]	1991	0.070	0.07
Panagiotopoulos [13]	1992	0.056	0.04
Orkoulas [14]	1994	0.053	0.025
Caillol [15,16]	1997	0.0488(2)	0.080(5)
Orkoulas [17]	1999	0.0490(3)	0.070(5)
Yan [18]	1999	0.0492(3)	0.062(5)
Caillol [19]	2002	0.04917(2)	0.080(5)

The 1:1 equisized charge-symmetric hard sphere electrolyte, the RPM model, is obtained as the particular case with $s = 2$, $x_1 = x_2 = 1/2$, $\sigma_1 = \sigma_2 = \sigma$, $z_1 = -z_2 = 1$. So that $Q = 0$ and the neutralizing background vanishes.

The RPM has been carefully studied through several computer simulations and the critical point of the gas-liquid coexistence has been given various estimates during the years as summarized in Table 1. On the coexistence spinodal line the isothermal compressibility $\chi_T = (\partial \rho / \partial p)_{(N,\mu),T} / \rho \rightarrow \infty$, with p the pressure of the mixture. On approaching the critical point, the amplitude of density fluctuations increases and local fluctuations become correlated over increasingly long distances. Anomalies in the intensity of light scattered from a fluid near its critical point, particularly the phenomenon known as critical opalescence, were first studied theoretically by Ornstein and Zernike as far back as 1914 [11].

3. The moment sum-rules

While the thermodynamic stability of the fluid model ensures the existence of the correlation functions in the thermodynamic limit,

$$\begin{aligned} \rho^{(n)}(\mathbf{q}_1, \dots, \mathbf{q}_n) &= \rho_1 \dots \rho_n g_{\alpha_1 \dots \alpha_n}^{(n)}(\mathbf{r}_1, \dots, \mathbf{r}_n) \\ &= \left\langle \sum_{i_1, \dots, i_n} \delta(\mathbf{r}_1 - \mathbf{r}_{i_1}) \delta_{\alpha_1, \alpha_{i_1}} \dots \delta(\mathbf{r}_n - \mathbf{r}_{i_n}) \delta_{\alpha_n, \alpha_{i_n}} \right\rangle, \quad n = 1, 2, \dots, \end{aligned} \tag{3.1}$$

where $\langle \dots \rangle$ is a thermal average defined for an infinitely extended system, sum-rules are exact relationships that the correlation functions must obey and can be derived from the microscopic constituent equations like for example the Born-Green-Yvon (BGY) hierarchy [5] under appropriate plausible assumptions.

Sometimes it proves convenient to introduce another set of correlation functions, namely the Ursell's functions $h^{(n)}$,

$$g_{\alpha_1 \alpha_2}^{(2)}(\mathbf{r}_1, \mathbf{r}_2) = h_{\alpha_1 \alpha_2}^{(2)}(\mathbf{r}_1, \mathbf{r}_2) + 1, \tag{3.2}$$

$$g_{\alpha_1 \alpha_2 \alpha_3}^{(3)}(\mathbf{r}_1, \mathbf{r}_2, \mathbf{r}_3) = h_{\alpha_1 \alpha_2 \alpha_3}^{(3)}(\mathbf{r}_1, \mathbf{r}_2, \mathbf{r}_3) + h_{\alpha_1 \alpha_2}^{(2)}(\mathbf{r}_1, \mathbf{r}_2) + h_{\alpha_1 \alpha_3}^{(2)}(\mathbf{r}_1, \mathbf{r}_3) + h_{\alpha_2 \alpha_3}^{(2)}(\mathbf{r}_2, \mathbf{r}_3) + 1, \tag{3.3}$$

$$\begin{aligned} g_{\alpha_1 \alpha_2 \alpha_3 \alpha_4}^{(4)}(\mathbf{r}_1, \mathbf{r}_2, \mathbf{r}_3, \mathbf{r}_4) &= h_{\alpha_1 \alpha_2 \alpha_3 \alpha_4}^{(4)}(\mathbf{r}_1, \mathbf{r}_2, \mathbf{r}_3, \mathbf{r}_4) + h_{\alpha_1 \alpha_2 \alpha_3}^{(3)}(\mathbf{r}_1, \mathbf{r}_2, \mathbf{r}_3) + h_{\alpha_1 \alpha_2 \alpha_4}^{(3)}(\mathbf{r}_1, \mathbf{r}_2, \mathbf{r}_4) \\ &\quad + h_{\alpha_1 \alpha_3 \alpha_4}^{(3)}(\mathbf{r}_1, \mathbf{r}_3, \mathbf{r}_4) + h_{\alpha_2 \alpha_3 \alpha_4}^{(3)}(\mathbf{r}_2, \mathbf{r}_3, \mathbf{r}_4) \\ &\quad + h_{\alpha_1 \alpha_2}^{(2)}(\mathbf{r}_1, \mathbf{r}_2) h_{\alpha_3 \alpha_4}^{(2)}(\mathbf{r}_3, \mathbf{r}_4) + h_{\alpha_1 \alpha_3}^{(2)}(\mathbf{r}_1, \mathbf{r}_3) h_{\alpha_2 \alpha_4}^{(2)}(\mathbf{r}_2, \mathbf{r}_4) \\ &\quad + h_{\alpha_1 \alpha_4}^{(2)}(\mathbf{r}_1, \mathbf{r}_4) h_{\alpha_2 \alpha_3}^{(2)}(\mathbf{r}_2, \mathbf{r}_3) + h_{\alpha_1 \alpha_2}^{(2)}(\mathbf{r}_1, \mathbf{r}_2) \\ &\quad + h_{\alpha_1 \alpha_3}^{(2)}(\mathbf{r}_1, \mathbf{r}_3) + h_{\alpha_1 \alpha_4}^{(2)}(\mathbf{r}_1, \mathbf{r}_4) \\ &\quad + h_{\alpha_2 \alpha_3}^{(2)}(\mathbf{r}_2, \mathbf{r}_3) + h_{\alpha_2 \alpha_4}^{(2)}(\mathbf{r}_2, \mathbf{r}_4) + h_{\alpha_3 \alpha_4}^{(2)}(\mathbf{r}_3, \mathbf{r}_4) + 1, \end{aligned} \tag{3.4}$$

It has been shown by Alastuey and Martin [20] that among all possible long-range potentials, it is only the Coulomb case that a decay law of the Ursell correlations faster than any inverse power is compatible with the structure of equilibrium BGY equations. We may then assume, at least far away from a critical point, that these Ursell functions tend to zero faster than any power r_{ij}^{-m} with integer m , if the separation r_{ij} between the positions \mathbf{r}_i and \mathbf{r}_j goes to infinity. This assumption is the usual exponential clustering hypothesis for charged systems.

Introducing the notation $\int d\mathbf{q} \dots = \int d\mathbf{r} \sum_{\alpha=1}^s \dots$ we must have the following normalization properties for the two sets,

$$\lim_{N \rightarrow \infty} \frac{1}{N^n} \int d\mathbf{q}_1 \dots d\mathbf{q}_n \rho^{(n)}(\mathbf{q}_1, \dots, \mathbf{q}_n) = 1, \tag{3.5}$$

$$\lim_{N \rightarrow \infty} \frac{1}{N^n} \int d\mathbf{q}_1 \dots d\mathbf{q}_n \rho_1 \dots \rho_n h_{\alpha_1 \dots \alpha_n}^{(n)}(\mathbf{r}_1, \dots, \mathbf{r}_n) = 0. \tag{3.6}$$

In the following we will drop the superscript on the correlation functions when not leading to confusion. Note also that $\rho(\mathbf{q}) = \langle \sum_i \delta(\mathbf{r} - \mathbf{r}_i) \delta_{\alpha, \alpha_i} \rangle = \rho_\alpha$ in a homogeneous mixture whereas $h_{\alpha_1 \alpha_2}^{(2)}(\mathbf{r}_1, \mathbf{r}_2) = h_{\alpha_1 \alpha_2}(|\mathbf{r}_1 - \mathbf{r}_2|)$ in a homogeneous and isotropic mixture.

3.1. The Ornstein–Zernike approach

The Ornstein–Zernike (OZ) equation in reciprocal-space for a fluid mixture is given by

$$\hat{h}_{\mu\nu}(k) = \hat{c}_{\mu\nu}(k) + \rho \sum_{\lambda} x_{\lambda} \hat{c}_{\mu\lambda}(k) \hat{h}_{\lambda\nu}(k), \tag{3.7}$$

where $k = |\mathbf{k}|$, $\hat{h}_{\mu\nu}(k)$ is the Fourier transform of the partial total correlation functions $h_{\mu\nu}(r) = g_{\mu\nu}(r) - 1$ with $g_{\mu\nu}$ the partial radial distribution functions

$$g_{\mu\nu}(r) = \frac{1}{N \rho x_{\mu} x_{\nu}} \left\langle \sum'_{i,j} \delta_{\mu, \alpha_i} \delta_{\nu, \alpha_j} \delta(\mathbf{r} - \mathbf{r}_i - \mathbf{r}_j) \right\rangle, \tag{3.8}$$

and $\hat{c}_{\mu\nu}(k)$ are the Fourier transform of the partial direct correlation functions [5].

The partial structure factors are defined as

$$S_{\mu\nu}(k) = x_{\mu} \delta_{\mu\nu} + \rho x_{\mu} x_{\nu} \hat{h}_{\mu\nu}(k). \tag{3.9}$$

Given a partial function $f_{\mu\nu}$ we can now introduce the following number–number, number–charge, and charge–charge functions

$$\begin{cases} f_{NN} = \sum_{\mu, \nu} f_{\mu\nu} \\ f_{NZ} = \sum_{\mu, \nu} z_{\mu} f_{\mu\nu} \\ f_{ZZ} = \sum_{\mu, \nu} z_{\mu} z_{\nu} f_{\mu\nu} \end{cases} \tag{3.10}$$

where in the RPM case $f_{NZ} = 0$.

We can moreover introduce the following definitions

$$\begin{cases} \tilde{h}_{\mu\nu} = \sqrt{x_{\mu} x_{\nu}} \hat{h}_{\mu\nu} \\ \tilde{c}_{\mu\nu} = \sqrt{x_{\mu} x_{\nu}} \hat{c}_{\mu\nu} \\ \tilde{S}_{\mu\nu} = S_{\mu\nu} / \sqrt{x_{\mu} x_{\nu}} = \delta_{\mu\nu} + \rho \tilde{h}_{\mu\nu} \end{cases} \tag{3.11}$$

with which the OZ equation can be written in a simple matrix form

$$\tilde{\mathbf{S}} - \mathbf{I} = \rho \tilde{\mathbf{S}} \tilde{\mathbf{c}}, \tag{3.12}$$

where \mathbf{I} is the identity matrix. Eq. (3.12) can also be rewritten as follows

$$\tilde{\mathbf{S}} = (\mathbf{I} - \rho \tilde{\mathbf{c}})^{-1}. \tag{3.13}$$

It is natural [5] to separate the direct correlation functions into a short-range and a Coulombic part

$$\hat{c}_{\mu\nu}(k) = \hat{c}_{\mu\nu}^{sr}(k) - \frac{4\pi \beta z_{\mu} z_{\nu} e^2}{k^2}, \tag{3.14}$$

where $\hat{c}_{\mu\nu}^{sr}(k)$ is a regular function in the $k \rightarrow 0$ limit. We then see, after some algebra, that in the small k limit, it must be $S_{NN} \sim k^0$, $S_{NZ} \sim k^2$, and $S_{ZZ} \sim k^2$. Moreover, It is a simple algebraic task, starting from the matrix form $\tilde{\mathbf{S}} = k^2(k^2 \mathbf{I} - \rho k^2 \tilde{\mathbf{c}})^{-1}$, to show that for the RPM case

$$S_{ZZ}(k) = \frac{k^2}{(k_D/\bar{z}_2)^2} + \left(\frac{\rho}{4} \hat{c}_{ZZ}^{sr}(0) - 1 \right) \frac{k^4}{(k_D/\bar{z}_2)^4} + O(k^6), \tag{3.15}$$

where $k_D = \sqrt{4\pi \beta \rho \bar{z}_2^2 e^2}$ is the Debye wave-number with $\bar{z}_2^2 = \sum_{\mu} x_{\mu} z_{\mu}^2$. In the RPM $\bar{z}_2^2 = 1$. Since we have $S_{ZZ}(k) = \sum_{\mu} x_{\mu} z_{\mu}^2 + \rho \sum_{\mu, \nu} x_{\mu} x_{\nu} z_{\mu} z_{\nu} \hat{h}_{\mu\nu}(k)$, using spherical symmetry, from Eq. (3.15) follow the following first three charge–charge

moment sum-rules

$$\rho \sum_{\mu, \nu} x_{\mu} x_{\nu} z_{\mu} z_{\nu} \int d\mathbf{r} h_{\mu\nu}(r) = -\bar{z}_2^2 \tag{3.16}$$

$$\rho \sum_{\mu, \nu} x_{\mu} x_{\nu} z_{\mu} z_{\nu} \int d\mathbf{r} r^2 h_{\mu\nu}(r) = -\frac{6}{(k_D/\bar{z}_2)^2} \tag{3.17}$$

$$\rho \sum_{\mu, \nu} x_{\mu} x_{\nu} z_{\mu} z_{\nu} \int d\mathbf{r} r^4 h_{\mu\nu}(r) = -\frac{120}{(k_D/\bar{z}_2)^4} \left(1 - \frac{\rho}{4} \hat{c}_{ZZ}^{st}(0)\right). \tag{3.18}$$

The first identity, the zeroth-moment sum-rule, is a consequence of the normalization conditions of the correlation functions (3.8)

$$\rho \sum_{\mu} x_{\mu} z_{\mu} \int d\mathbf{r} h_{\mu\nu}(r) = \sum_{\mu} z_{\mu} \frac{\langle N_{\mu} N_{\nu} \rangle - \langle N_{\mu} \rangle \langle N_{\nu} \rangle - \delta_{\mu\nu} \langle N_{\mu} \rangle}{\langle N_{\nu} \rangle} = -z_{\nu} \tag{3.19}$$

and reflects internal screening (or bulk electroneutrality). The second, the second-moment sum-rule, is commonly known as the Stillingers–Lovett (SL) condition [21] and reflects external screening. The third is the fourth-moment sum-rule.

In view of the exponential clustering expected to hold in ionic fluids away from criticality (see next section) we may assume the following small k expansions

$$S_{NN}(k)/S_{NN}(0) = 1 + \sum_{p \geq 1} (-)^p \xi_{N,p}^{2p}(T, \rho) k^{2p}, \tag{3.20}$$

$$S_{ZZ}(k)/\bar{z}_2^2 = 0 + \xi_{Z,1}^2 k^2 - \sum_{p \geq 2} (-)^p \xi_{Z,p}^{2p}(T, \rho) k^{2p}, \tag{3.21}$$

where working in the grand-canonical ensemble [5] $S_{NN}(0) = \chi_T/\chi_T^0$ with $\chi_T^0 = \beta/\rho$ the isothermal compressibility of the ideal gas.

Das, Kim, and Fisher [2] has calculated through grand-canonical Monte Carlo simulations the second S_2 and fourth S_4 moments: $S_{ZZ}(k)/\bar{z}_2^2 = 0 + S_2 k^2 - S_4 k^4 + \dots$ for the RPM, and found a deviation of about 16% on the SL condition, $S_2 = 1/k_D^2$, at criticality. Moreover S_4 appears to diverge to $+\infty$ upon approaching the RPM critical point. At criticality, density correlations are long ranged and [11] $S_{NN}(k) \sim 1/k^{2-\eta}$ for $k \rightarrow 0$ with $0 < \eta < 1$ the anomalous critical-point decay exponent [22] (equal to zero in the Ornstein–Zernike theory) [23]. Equivalently, in real-space, in three dimensions, $\sum_{\mu, \nu} x_{\mu} x_{\nu} h_{\mu\nu}(r) \sim 1/r^{1+\eta}$ for $r \rightarrow \infty$. Then according to Proposition 1 of Ref. [24] we cannot say anything about the SL sum-rule; the fact that the SL sum rule is found to fail means that the density correlations must decay as $1/r^5$ or slower. Evidently the development of clustering or association amongst the particles of the mixture upon approaching the critical point inhibits the external screening. Or in other words, the diverging density fluctuations that characterize criticality destroy perfect screening at (T_c, ρ_c) .

3.2. The Born–Green–Yvon approach [6–8]

Suttorp and van Wonderen [6] study a thermodynamically stable ionic mixture with pointwise mobile charges all of the same sign ($z_{\mu} \leq 0$ for all μ) with the pair-potential of Eq. (2.3) without the short-range term v^{st} . Starting from the Born–Green–Yvon hierarchy [5] and using the hypothesis of exponential clustering of the Ursell’s functions they are able to show that independently of the statistical ensemble used to describe the ionic liquid the internal screening and SL conditions (3.16)–(3.17) hold. In order to make progress for subsequent relationships one has to specify the ensemble. In a grand-canonical ensemble with the constraint (2.7) the independent variables are β, V , the $s - 1$ chemical potentials, and $q = Q/V$. They are able to prove the following additional sum-rules for the partial pair Ursell’s functions

$$\rho \sum_{\mu, \nu} x_{\mu} x_{\nu} \int d\mathbf{r} h_{\mu\nu}(r) = \frac{2}{3} \frac{\beta}{\rho} \frac{\partial \rho}{\partial \beta} - 2 \frac{q}{\rho} \frac{\partial \rho}{\partial q} + 1, \tag{3.22}$$

$$\rho \sum_{\mu, \nu} x_{\mu} x_{\nu} z_{\mu} z_{\nu} \int d\mathbf{r} r^2 h_{\mu\nu}(r) = -\frac{6}{(k_D/\bar{z}_2)^2} e \frac{\partial \rho}{\partial q}, \tag{3.23}$$

$$\rho \sum_{\mu, \nu} x_{\mu} x_{\nu} z_{\mu} z_{\nu} \int d\mathbf{r} r^4 h_{\mu\nu}(r) = -\frac{120}{(k_D/\bar{z}_2)^4} \frac{e^2 \beta \rho}{q} \frac{\partial p}{\partial q}, \tag{3.24}$$

where p is the pressure and in the partial derivatives all others independent variables are kept constant. For example, we see that from Eq. (3.22) follows

$$S_{NN}(0) = \frac{\chi_T}{\chi_T^0} = \frac{2}{3} \frac{\beta}{\rho} \frac{\partial \rho}{\partial \beta} + 2 \left(1 - \frac{q}{\rho} \frac{\partial \rho}{\partial q}\right). \tag{3.25}$$

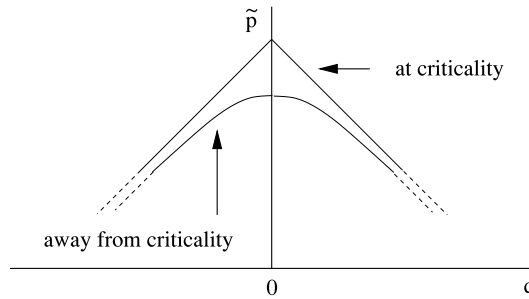


Fig. 1. Sketch of $\tilde{p}(q)$ near $q = 0$ upon approaching criticality.

For an ionic mixture with positive and negative mobile charges, made thermodynamically stable by the addition of the short-range pair-potential v^{sr} , the zeroth-moment of Eqs. (3.22) and (3.16) clearly continue to hold as well as the second-moment SL sum-rule of Eqs. (3.18)–(3.23) as it is shown in Ref. [24]. Note that in order to derive the SL sum-rule a weaker condition than the exponential clustering hypothesis is actually needed as shown in Ref. [24]. That is, one just needs to require a certain short-range behavior of the Ursell functions. For the fourth-moment condition of Eq. (3.24) we also expect there to be no effect due to the short-range regularization as shown in Refs. [25–27] and in Appendix. So we can say that the Suttorp and van Wonderen sum-rules hold generally for the more general ionic liquid model of a mixture with positive and negative mobile charges opportunely regularized.

On the other hand from the work of Santos and Piasecki [9] follows that the Ursell functions of any order have a long-range behavior on a critical point, thus violating the exponential clustering hypothesis necessary to prove the Suttorp and van Wonderen sum rules. In this sense the numerical result found by Fisher et al. of the violation of the second and fourth moment of the charge–charge structure factor of the Restricted Primitive Model at criticality, is not in contradiction with the result of Suttorp and van Wonderen. But is instead telling us something that goes beyond the analysis of the sum-rules based on the exponential clustering hypothesis.

Note that we can write the partial derivative on the right hand side of Eq. (3.23) as follows

$$\begin{aligned} \frac{\partial \rho}{\partial q} &= \frac{\partial(\rho, \mu_1, T, V)}{\partial(q, \mu_1, T, V)} \\ &= \frac{\partial(\rho, \mu_1, T, V)}{\partial(N_1, N_2, T, V)} \frac{\partial(N_1, N_2, T, V)}{\partial(q, \mu_1, T, V)} \\ &= \frac{1}{V} \left[\left(\frac{\partial \mu_1}{\partial N_2} \right)_{N_1} - \left(\frac{\partial \mu_1}{\partial N_1} \right)_{N_2} \right]_{T,V} \left[\left(\frac{\partial N_1}{\partial q} \right)_{\mu_1} \left(\frac{\partial N_2}{\partial \mu_1} \right)_q - \left(\frac{\partial N_1}{\partial \mu_1} \right)_q \left(\frac{\partial N_2}{\partial q} \right)_{\mu_1} \right]_{T,V}. \end{aligned} \tag{3.26}$$

So that for the symmetric RPM where $\mu_1 = \mu_2$, using the $1 \leftrightarrow 2$ symmetry, we find $\partial \rho / \partial q = 0$, since the first Jacobian vanishes. Whereas, for a one component system, where $q = e\rho$, we find $\partial \rho / \partial q = 1/e$.

From the analysis of Suttorp and van Wonderen we also deduce that

$$\bar{z}_2^2 S_4 = \left(\frac{\bar{z}_2}{k_D} \right)^4 \frac{e^2 \beta \rho}{q} \frac{\partial p}{\partial q} = - \left(\frac{\bar{z}_2}{k_D} \right)^4 e^2 \beta \rho \frac{\partial^2 \tilde{p}}{\partial q^2}, \tag{3.27}$$

where $\tilde{p} = p - q\tilde{\mu}_q$ with $\tilde{\mu}_q = -\partial \tilde{p} / \partial q$ the Lagrange multiplier which takes into account of the constraint (2.7). The RPM results of Das, Kim, and Fisher [2] show how $(k_D/\bar{z}_2)^4 \bar{z}_2^2 S_4 \rightarrow 0$ for $\rho \rightarrow 0$ (their Fig. 3). This is easily explained observing that as $\rho \rightarrow 0$ we must have $\beta p \rightarrow \rho$ so that from Eq. (3.27) follows

$$(k_D/\bar{z}_2)^4 \bar{z}_2^2 S_4 \rightarrow e^2 \frac{\partial \rho^2}{\partial q^2} = 0. \tag{3.28}$$

This result also implies that, in view of Eq. (3.18), $\rho \hat{c}_{ZZ}^{sr}(0) \rightarrow 4$.

Moreover from Das, Kim, and Fisher [2] Fig. 4, follows that in the RPM we must have

$$\lim_{q \rightarrow 0} \frac{\partial^2 \tilde{p}}{\partial q^2} = -\infty \tag{3.29}$$

when one approaches the critical point. Notice that by charge symmetry we must have that both p and \tilde{p} are even functions of q . So a sketch of $\tilde{p}(q)$ near $q = 0$ must look as in Fig. 1. The figure aims to give a very qualitative sketch of $\tilde{p}(q)$ only in a very narrow neighborhood of $q = 0$. Away from criticality we must have $\partial p / \partial q|_{q=0} = 0$ and S_4 is finite. But near

criticality $\partial p/\partial q|_{q=0} > 0$ and S_4 diverges. This means that near criticality there is a non negligible variation of the pressure of the fluid upon switching on a charge asymmetry ($q \neq 0$) keeping overall neutrality with the neutralizing background. So notwithstanding the fact that the exponential clustering hypothesis breaks down near criticality the results of Das, Kim, and Fisher [2] do not tell us anything about the failure of the fourth-moment sum-rule. On the other hand their Figs. 1 and 2 indicate the failure of the SL condition upon approaching the critical point, as already observed in the previous section.

4. Conclusions

We studied a general ionic mixture with particles of different mass, diameter, and charge immersed in a neutralizing background so that the mixture is globally neutral. When we allow for the presence of mobile charges of opposite sign we need to add either a soft- or a hard-core regularization to the pair-potential in order to make the mixture thermodynamically stable.

We derived a series of sum-rules on the first three moments of the charge–charge correlation functions starting from the Ornstein–Zernike theory [5]. Then we showed that the sum-rules derived by Suttorp and van Wonderen [6] for an ionic mixture made of particles all of the same sign immersed in a neutralizing background remain valid if one allows the particles to carry charges of opposite sign and adds a soft or a hard-core repulsion in order to ensure thermodynamic stability. In particular they remain valid for the symmetric RPM case when the neutralizing background vanishes. Suttorp and van Wonderen derivation relies on the assumption of the exponential clustering in the mixture [1].

We interpreted recent results of Das, Kim, and Fisher [2] reporting the failure of the charge–charge second-moment sum-rules for the RPM of a ionic liquid at criticality and the divergence of the charge–charge fourth-moment at criticality. In particular the divergence of the fourth moment S_4 at the critical point of the RPM seems to still be in agreement with the fourth-moment sum-rule (even if the exponential clustering of the Ursell’s function breaks down there as shown in Ref. [9]) if one assumes that at criticality there is a non negligible variation of the pressure of the fluid upon switching on a charge asymmetry ($q \neq 0$) keeping overall neutrality with the neutralizing background. The observed violation of the second-moment sum-rule on the other hand seems to indicate that at criticality the clustering phenomenon occurring in the ionic mixture is responsible for the break down of the external screening and the system behaves as an insulator [1]. At criticality we do not have anymore an exponential or short-range clustering but a long-range clustering as shown by the results of Ref. [9].

Our results could be helpful to a better understanding of Refs. [28,29] and Refs. [30–32]. Moreover our results could give some insights to study the critical behavior of more complex fluids such as the ones described in Refs. [33–45].

Acknowledgments

We are grateful to Michael Ellis Fisher and Angel Alastuey for correspondence and helpful comments.

Appendix. Invariance in form of the moment sum-rules under the addition of a hard-core

Let us call PWE the point-wise particle electrolyte considered by Suttorp and van Wonderen [6] and HSE the hard-sphere electrolyte obtained by our model of Eqs. (2.1)–(2.6). The configurations space of PWE is Ω^N whereas the one of HSE is $\mathcal{O}_N = \{\mathbf{R} \equiv (\mathbf{r}_1, \dots, \mathbf{r}_N) \in \Omega^N \mid \forall i, j \neq i \quad |\mathbf{r}_i - \mathbf{r}_j| > \sigma_{\alpha_i \alpha_j}\} \subset \Omega^N$. In particular it is well known from electrostatics that HSE is equivalent to the PWE restricted to the configuration space \mathcal{O}_N . We then conclude that the sum-rules of Eqs. (3.23) and (3.24) must hold also for the HSE. In any case the thermodynamic quantities on both sides of the sum-rule will remain unchanged after the restriction. Infact, calling the complementary set $\mathcal{O}_N^c = \Omega^N - \mathcal{O}_N = \{\mathbf{R} \equiv (\mathbf{r}_1, \dots, \mathbf{r}_N) \in \Omega^N \mid \exists i, j \neq i \quad |\mathbf{r}_i - \mathbf{r}_j| \leq \sigma_{\alpha_i \alpha_j}\}$ we have for a generic thermal average of an everywhere finite physical observable

$$\begin{aligned} \langle \dots \rangle_{\text{PWE}} &= \frac{\int_{\Omega^N} \dots e^{-\beta U} d\mathbf{R}}{\int_{\Omega^N} e^{-\beta U} d\mathbf{R}} = \frac{\int_{\mathcal{O}_N} \dots e^{-\beta U} d\mathbf{R} + \int_{\mathcal{O}_N^c} \dots e^{-\beta U} d\mathbf{R}}{\int_{\mathcal{O}_N} e^{-\beta U} d\mathbf{R} + \int_{\mathcal{O}_N^c} e^{-\beta U} d\mathbf{R}} \\ &= \frac{\int_{\mathcal{O}_N} \dots e^{-\beta U} d\mathbf{R} \left(1 + \int_{\mathcal{O}_N^c} \dots e^{-\beta U} d\mathbf{R} / \int_{\mathcal{O}_N} \dots e^{-\beta U} d\mathbf{R} \right)}{\int_{\mathcal{O}_N} e^{-\beta U} d\mathbf{R} \left(1 + \int_{\mathcal{O}_N^c} e^{-\beta U} d\mathbf{R} / \int_{\mathcal{O}_N} e^{-\beta U} d\mathbf{R} \right)} \\ &\rightarrow \frac{\int_{\mathcal{O}_N} \dots e^{-\beta U} d\mathbf{R}}{\int_{\mathcal{O}_N} e^{-\beta U} d\mathbf{R}} = \langle \dots \rangle_{\text{HSE}}, \end{aligned} \tag{A.1}$$

in the thermodynamic limit $\Omega \rightarrow \mathbb{R}^3$ and $N = \rho V$. Since the measure of \mathcal{O}_N is an infinite of higher order than the measure of \mathcal{O}_N^c . This does not mean of course that the Ursell functions themselves will be equal for the PWE and the HSE and in fact they will be different generally.

This argument suggests that Suttorp and van Wonderen analysis [6] continues to hold also for an ionic mixture with mobile charges of opposite sign opportunely regularized. This has recently been proved semi-heuristically by Alastuey and Fantoni [27] for the fourth moment of the charge–charge structure factor of such an ionic mixture.

References

- [1] Ph.A. Martin, *Rev. Modern Phys.* 60 (1988) 1075.
- [2] S.K. Das, Y.C. Kim, M.E. Fisher, *Phys. Rev. Lett.* 107 (2011) 215701.
- [3] S.K. Das, Y.C. Kim, M.E. Fisher, *J. Chem. Phys.* 137 (2012) 074902.
- [4] G. Stell, *J. Stat. Phys.* 78 (1995) 197.
- [5] J.-P. Hansen, I.R. McDonald, *Theory of Simple Liquids*, second ed., Academic Press, London, 1986.
- [6] L.G. Suttorp, A.J. van Wonderen, *Physica A* 145 (1987) 533.
- [7] A.J. van Wonderen, L.G. Suttorp, *Physica A* 145 (1987) 557.
- [8] L.G. Suttorp, *J. Phys. A* 41 (2008) 495001.
- [9] A. Santos, J. Piasecki, *Mol. Phys.* 113 (2015) 2855.
- [10] D. Ruelle, *Statistical Mechanics*, W. A. Benjamin, Inc., New York, 1969.
- [11] M.E. Fisher, *J. Math. Phys.* 5 (1964) 944.
- [12] J.P. Valleau, *J. Chem. Phys.* 95 (1991) 584.
- [13] A.Z. Panagiotopoulos, *Fluid Phase Equilib.* 76 (1992) 97.
- [14] G. Orkoulas, A.Z. Panagiotopoulos, *J. Chem. Phys.* 101 (1994) 1452.
- [15] J.-M. Caillol, D. Levesque, J.J. Weis, *Phys. Rev. Lett.* 77 (1996) 4039.
- [16] J.-M. Caillol, D. Levesque, J.J. Weis, *J. Chem. Phys.* 107 (1997) 1565.
- [17] G. Orkoulas, A.Z. Panagiotopoulos, *J. Chem. Phys.* 110 (1999) 1581.
- [18] Q. Yan, J.J. de Pablo, *J. Chem. Phys.* 111 (1999) 9509.
- [19] J.-M. Caillol, D. Levesque, J.-J. Weis, *J. Chem. Phys.* 116 (2002) 10794.
- [20] A. Alastuey, P.A. Martin, *J. Stat. Phys.* 39 (1985) 405.
- [21] F.H. Stillinger Jr., R. Lovett, *J. Chem. Phys.* 49 (1968) 1991.
- [22] M.E. Fisher, *Rev. Modern Phys.* 70 (1998) 653.
- [23] The value of η is difficult to determine experimentally, but the available evidence suggests that it is a small, positive number, approximately equal to 0.05. Independent of dimensionality one finds [22] the following relationship between critical exponents $\nu(2 - \eta) = \gamma$.
- [24] Ph.A. Martin, Ch. Gruber, *J. Stat. Phys.* 31 (1983) 691.
- [25] P. Vieillefosse, *J. Stat. Phys.* 41 (1985) 1015.
- [26] P. Vieillefosse, M. Brajon, *J. Stat. Phys.* 55 (1988) 1169.
- [27] A. Alastuey, R. Fantoni, *J. Stat. Phys.* 163 (2016) 887.
- [28] R. Fantoni, G. Pastore, *Europhys. Lett.* 101 (2013) 46003.
- [29] R. Fantoni, G. Pastore, *Phys. Rev. E* 87 (2013) 052303.
- [30] R. Fantoni, *J. Stat. Mech.* (2012) P04015.
- [31] R. Fantoni, B. Jancovici, G. Téllez, *J. Stat. Phys.* 112 (2003) 27.
- [32] R. Fantoni, G. Téllez, *J. Stat. Phys.* 133 (2008) 449.
- [33] R. Fantoni, *Eur. Phys. J. B* 85 (2012) 108.
- [34] R. Fantoni, A. Malijevský, A. Santos, A. Giacometti, *Europhys. Lett.* 93 (2011) 26002.
- [35] D. Gazzillo, R. Fantoni, A. Giacometti, *Phys. Rev. E* 78 (2008) 021201.
- [36] M.A.G. Maestre, R. Fantoni, A. Giacometti, A. Santos, *J. Chem. Phys.* 138 (2013) 094904.
- [37] R. Fantoni, A. Giacometti, M.A.G. Maestre, A. Santos, *J. Chem. Phys.* 139 (2013) 174902.
- [38] R. Fantoni, D. Gazzillo, A. Giacometti, *Phys. Rev. E* 72 (2005) 011503.
- [39] R. Fantoni, D. Gazzillo, A. Giacometti, *J. Chem. Phys.* 122 (2005) 034901.
- [40] R. Fantoni, A. Giacometti, A. Santos, *J. Chem. Phys.* 142 (2015) 224905.
- [41] R. Fantoni, G. Pastore, *Mol. Phys.* 113 (2015) 2593.
- [42] R. Fantoni, G. Pastore, *J. Chem. Phys.* 141 (2014) 074108.
- [43] R. Fantoni, D. Gazzillo, A. Giacometti, M.A. Miller, G. Pastore, *J. Chem. Phys.* 127 (2007) 234507.
- [44] D. Gazzillo, R. Fantoni, A. Giacometti, *Mol. Phys.* 104 (2006) 3451.
- [45] R. Fantoni, D. Gazzillo, A. Giacometti, P. Sollich, *J. Chem. Phys.* 125 (2006) 164504.

Chapter 54

Andersen-Weeks-Chandler perturbation theory and one-component sticky-hard-sphere

Fantoni R., J. Stat. Phys. **168**, 652 (2017)

Title: “Andersen-Weeks-Chandler perturbation theory and one-component sticky-hard-sphere”

Abstract: We apply second order Andersen-Weeks-Chandler perturbation theory to the one-component sticky-hard-spheres fluid. We compare the results with the mean spherical approximation, the Percus-Yevick approximation, two generalized Percus-Yevick approximations, and the Monte Carlo simulations.

Author's personal copy

J Stat Phys
DOI 10.1007/s10955-017-1810-2



Andersen–Weeks–Chandler Perturbation Theory and One-Component Sticky-Hard-Spheres

Riccardo Fantoni¹

Received: 20 March 2017 / Accepted: 3 May 2017
© Springer Science+Business Media New York 2017

Abstract We apply second order Andersen–Weeks–Chandler perturbation theory to the one-component sticky-hard-spheres fluid. We compare the results with the mean spherical approximation, the Percus–Yevick approximation, two generalized Percus–Yevick approximations, and the Monte Carlo simulations.

Keywords Andersen–Weeks–Chandler thermodynamic perturbation theory · Sticky-hard-spheres · Colloidal suspension · Mean spherical approximation · Generalized Percus–Yevick approximation · Monte Carlo simulation

1 Introduction

The sticky-hard-sphere (SHS) model introduced by Baxter in [1] plays an important role in soft matter offering a description of a sterically stabilized colloidal suspension [2–8].

In this work we apply Andersen–Weeks–Chandler (AWC) thermodynamic-perturbation-theory (TPT) [9] to treat the SHS three-dimensional fluid and we compare the results for the equation of state of our calculation with the ones for the mean-spherical-approximation (MSA) [9], for the Percus–Yevick (PY) approximation [9], for two generalized-Percus–Yevick (GPY) approximations (C0 and C1 in Ref. [10]), and for the Monte Carlo simulations of Miller and Frenkel [11].

We are then able to show how the TPT breaks down at low reduced temperature and high density. Our analysis gives a reference benchmark for the behavior of the SHS system when treated with the AWC TPT scheme.

Electronic supplementary material The online version of this article (doi:10.1007/s10955-017-1810-2) contains supplementary material, which is available to authorized users.

Riccardo Fantoni
rfantoni@ts.infn.it

¹ Dipartimento di Fisica, Università di Trieste, strada Costiera 11, 34151 Grignano, Trieste, Italy

Our analysis also clarifies the role played by the reducible Mayer diagrams in the second order AWC TPT.

The work is organized as follows. In Sect. 2 we introduce the AWC TPT scheme, in Sect. 3 we define the SHS fluid model, in Sect. 4 we outline our calculation of the AWC TPT for the SHS fluid, in Sect. 5 we clarify the role played by the reducible integrals, in Sect. 6 we discuss some technical details regarding our Monte Carlo calculation of the various order terms of the TPT, in Sect. 7 we present our results, and Sect. 8 is for our conclusive discussion.

2 The Andersen-Weeks-Chandler Thermodynamic Perturbation Scheme

Following AWC perturbation theory [12] we consider the Helmholtz free energy A as a functional of the Boltzmann factor $e(1, 2) = \exp[-\beta\phi(1, 2)]$ ($\phi(1, 2)$ being the pair interaction potential of the fluid under exam) and expand it in a Taylor series around the Boltzmann factor, $e_0(1, 2)$, of a given reference system. Working in the grand-canonical ensemble we obtain the following perturbative expansion in $\Delta e = e - e_0$

$$\beta[A[e] - A[e_0]] = \beta[\Delta A]_{(1)} + \beta[\Delta A]_{(2)} + \dots, \tag{1}$$

$$\beta[\Delta A]_{(1)} = -\frac{1}{2} \int d1d2 \frac{\rho_0(1, 2)}{e_0(1, 2)} \Delta e(1, 2), \tag{2}$$

$$\begin{aligned} \beta[\Delta A]_{(2)} = & -\frac{1}{2} \left[\int d1d2d3 \frac{\rho_0(1, 2, 3)}{e_0(1, 2)e_0(1, 3)} \Delta e(1, 2)\Delta e(1, 3) \right. \\ & \left. + \frac{1}{4} \int d1d2d3d4 \frac{\rho_0(1, 2, 3, 4) - \rho_0(1, 2)\rho_0(3, 4)}{e_0(1, 2)e_0(3, 4)} \Delta e(1, 2)\Delta e(3, 4) \right] \\ & + \frac{1}{2N} \left(\rho^2 \frac{\chi_T^0}{\chi_T^{id}} \right) \left\{ \frac{\partial}{\partial \rho} \beta[\Delta A]_{(1)} \right\}^2. \end{aligned} \tag{3}$$

where $\beta = 1/(k_B T)$ (with k_B Boltzmann constant and T absolute temperature), \bar{N} average number of particles, $\rho = \bar{N}/V$ (with V volume of the system), $\chi_T^{id} = \beta/\rho$ isothermal compressibility of the ideal gas, χ_T^0 isothermal compressibility of the reference system, $\rho_0(1, \dots, n)$ the grand-canonical ensemble n -body correlation function of the reference system, and in the last term of Eq. (3) the density derivative is taken at constant temperature, volume, and chemical potential. In order to derive these expressions one can adapt the details found in Appendix D of Hansen and McDonald book [9] where their expression (6.2.14) is found. It is then an easy task to pass from their expansion in terms of the pair-potential variation to our expansion in terms of the Boltzmann factor variation.

3 One-Component Sticky-Hard-Spheres

For the Baxter [1] one-component sticky-hard-spheres (SHS) model one has

$$e(r) = \theta(r - \sigma) + \frac{\sigma}{12\tau} \delta(r - \sigma), \tag{4}$$

where σ is the spheres diameter, τ the reduced temperature, θ is the Heaviside step function, and δ the Dirac delta function.

Choosing as reference system the hard-spheres (HS) model one has

$$e_0(r) = \theta(r - \sigma), \tag{5}$$

Author's personal copy

Andersen-Weeks-Chandler Perturbation Theory...

so that

$$\Delta e(r) = \frac{\sigma}{12\tau} \delta(r - \sigma). \tag{6}$$

So one sees that AWC expansion (1) reduces to an expansion in powers of $1/\tau$.

4 Calculation

Before expression (3) can be used some approximation must be introduced for the three- and four-body distribution functions. The most widely used approximation is Kirkwood superposition approximation [13]. This has previously successfully applied to the second order thermodynamic perturbation study of the square well potential by Henderson and Barker [14].

Using the Kirkwood superposition approximation (KSA) [13] one can express the n -body correlation functions $\rho_0(1, \dots, n) = \rho^n g_0(1, \dots, n)$ in terms of pair distribution functions according to

$$g_0(1, \dots, n) \approx \prod_{i < j}^n g_0(i, j). \tag{7}$$

The idea is to use for the pair distribution function of the reference HS system the analytic solution of the Ornstein-Zernike equation with the Percus-Yevick closure.

The first two terms in the perturbative expansion (1) reduce to

$$\beta \frac{[\Delta A]_{(1)}}{\bar{N}} = -\frac{I_2}{\rho}, \tag{8}$$

$$\beta \frac{[\Delta A]_{(2)}}{\bar{N}} = -\frac{1}{2} \left(\frac{I_3}{\rho} + \frac{I_4}{\rho} \right) + \frac{1}{2} \left(\frac{\chi_T^0}{\chi_T^{id}} \right) \left(\frac{\partial I_2}{\partial \rho} \right)^2, \tag{9}$$

where

$$\frac{I_2}{\rho} = \frac{1}{2\rho} \frac{1}{V} \int d1d2 \frac{\rho_0(1, 2)}{e_0(1, 2)} \Delta e(1, 2) = \frac{1}{\tau} (\eta \bar{y}_0), \tag{10}$$

where $\eta = \frac{\pi}{6} \rho \sigma^3$ is the hard sphere packing fraction, $y_0(1, 2) = g_0(1, 2)/e_0(1, 2)$ is the cavity function of the reference system and $\bar{y}_0 = y_0(|\mathbf{r}_1 - \mathbf{r}_2| = \sigma)$. Upon using KSA one finds,

$$\frac{I_3}{\rho} = \frac{1}{\rho} \frac{1}{V} \int d1d2d3 \frac{\rho_0(1, 2, 3)}{e_0(1, 2)e_0(1, 3)} \Delta e(1, 2) \Delta e(1, 3) \tag{11}$$

$$\approx \frac{\rho^2}{V} \int d1d2d3 y_0(1, 2) y_0(1, 3) J_3(1, 2, 3) \Delta e(1, 2) \Delta e(1, 3),$$

$$\frac{I_4}{\rho} = \frac{1}{4\rho} \frac{1}{V} \int d1d2d3d4 \frac{\rho_0(1, 2, 3, 4) - \rho_0(1, 2)\rho_0(3, 4)}{e_0(1, 2)e_0(3, 4)} \Delta e(1, 2) \Delta e(3, 4) \tag{12}$$

$$\approx \frac{\rho^3}{4V} \int d1d2d3d4 y_0(1, 2) y_0(3, 4) J_4(1, 2, 3, 4) \Delta e(1, 2) \Delta e(3, 4),$$

Author's personal copy

R. Fantoni

where we have introduced

$$\begin{aligned}
 J_3(1, 2, 3) &= 1 + h_0(2, 3), \\
 J_4(1, 2, 3, 4) &= 4h_0(1, 3) \\
 &\quad + 4h_0(1, 3)h_0(1, 4) \\
 &\quad + 2h_0(1, 4)h_0(2, 3) \\
 &\quad + 4h_0(1, 3)h_0(1, 4)h_0(2, 3) \\
 &\quad + h_0(1, 3)h_0(1, 4)h_0(2, 3)h_0(2, 4),
 \end{aligned}
 \tag{13}$$

where $h_0(1, 2) = g_0(1, 2) - 1$ is the total correlation function of the reference system. Note that the first term in J_3 and the first and second terms in J_4 give rise to *reducible* integrals (i.e. integrals that can be reduced into products of simpler integrals).

It is convenient to perform the calculation of I_3 and I_4 in reciprocal space, to get,

$$\frac{I_3}{\rho} \approx \frac{1}{\tau^2} (2\eta\bar{y}_0)^2 \left(1 + \frac{1}{12\pi} \frac{1}{\eta} g_1 \right),
 \tag{15}$$

$$\frac{I_4}{\rho} \approx \frac{1}{\tau^2} (2\eta\bar{y}_0)^2 \frac{1}{4} \left[4 \left(\frac{1}{a^2} - 1 \right) + \frac{1}{3\pi} \frac{1}{\eta} h_2^a + \frac{1}{6\pi} \frac{1}{\eta} h_2^b + \frac{1}{72\pi^2} \frac{1}{\eta^2} h_3 + \frac{1}{6^3 2^6 \pi^4} \frac{1}{\eta^3} h_4 \right],
 \tag{16}$$

and

$$g_1 = \int_0^\infty dz z^2 j_0^2(z) H(z),
 \tag{17}$$

$$h_2^a = \int_0^\infty dz z^2 j_0(z) H^2(z),
 \tag{18}$$

$$h_2^b = \int_0^\infty dz z^2 j_0^2(z) H^2(z),
 \tag{19}$$

$$h_3 = \int_0^\infty dz_1 z_1^2 \int_0^\infty dz_2 z_2^2 \int_{-1}^1 dx j_0(z_1) j_0(z_2) H(z_1) H(z_2) H \left(\sqrt{z_1^2 + z_2^2 - 2z_1 z_2 x} \right),
 \tag{20}$$

$$\begin{aligned}
 h_4 &= \int_0^\infty dz_1 z_1^2 \int_0^\infty dz_2 z_2^2 \int_0^\infty dz_3 z_3^2 \int_0^\pi d\theta_1 \sin \theta_1 \int_0^\pi d\theta_2 \sin \theta_2 \int_0^{2\pi} d\phi \\
 &\quad j_0(z_1) j_0 \left(\sqrt{z_2^2 + z_3^2 - 2z_2 z_3 \cos \theta_2} \right) H(z_2) H(z_3) H \left(\sqrt{z_1^2 + z_2^2 - 2z_1 z_2 \cos \delta} \right) \\
 &\quad H \left(\sqrt{z_1^2 + z_3^2 - 2z_1 z_3 \cos \theta_1} \right),
 \end{aligned}
 \tag{21}$$

where in the integrand of h_4

$$\cos \delta = \cos \theta_1 \cos \theta_2 + \sin \theta_1 \sin \theta_2 \cos \phi.
 \tag{22}$$

Author's personal copy

Andersen-Weeks-Chandler Perturbation Theory...

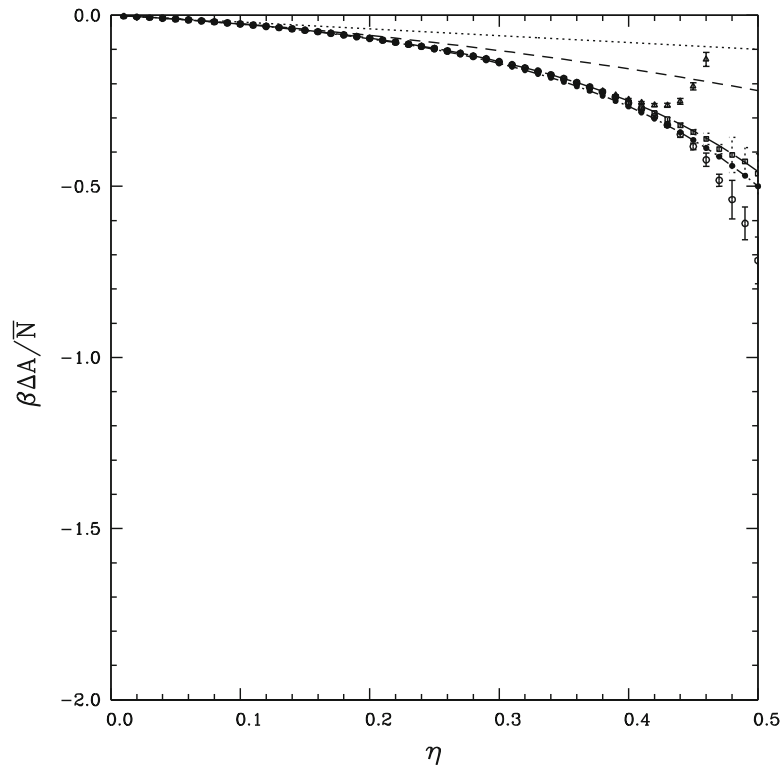


Fig. 1 We show $\beta \Delta A / \bar{N} = \beta(A^{SHS} - A^{HS}) / \bar{N}$ as a function of the packing fraction at $\tau = 5$ for various approximations: (in the MSA $\Delta A = 0$) C0 (dotted line) [10], C1 (short dashed line) [10], PY (long dashed line) [9], $\beta[\Delta A]_{(1)} / \bar{N}$ (dotted dashed line and filled circles), $\beta([\Delta A]_{(1)} + [\Delta A]_{(2)}) / \bar{N}$ (empty circles), $\beta([\Delta A]_{(1)} + [\Delta A]_{(2)}) / \bar{N}$ (empty squares), and $\beta([\Delta A]_{(1)} + [\Delta A]_{(2)}') / \bar{N}$ (empty triangles).

In all these expressions we have introduced the following notation

$$a^2 = \frac{\chi_T^{id}}{\chi_T^0} = 1 - \rho \tilde{c}_0(0), \tag{23}$$

$$\bar{y}_0 = y_0(\sigma) = g_0(\sigma) / e_0(\sigma), \tag{24}$$

$$H(z) = \rho \tilde{h}_0(z/\sigma) = \frac{\rho \tilde{c}_0(z/\sigma)}{1 - \rho \tilde{c}_0(z/\sigma)}, \tag{25}$$

$$j_0(z) = \frac{\sin z}{z}, \tag{26}$$

where $g_0(r)$, $y_0(r)$, $\tilde{h}_0(k)$, $\tilde{c}_0(k)$ are respectively the hard spheres radial distribution function, cavity function, the Fourier transform of the total correlation function and the Fourier transform of the direct correlation function, and j_0 is the zeroth order spherical Bessel function of the first kind.

Finally the Fourier transform of the HS direct correlation function calculated through the Percus-Yevick closure is given by [15]

$$\rho \tilde{c}_0(z/\sigma) \approx -24\eta \int_0^1 ds s^2 j_0(sz)(\alpha + \beta s + \gamma s^3), \tag{27}$$

Author's personal copy

R. Fantoni

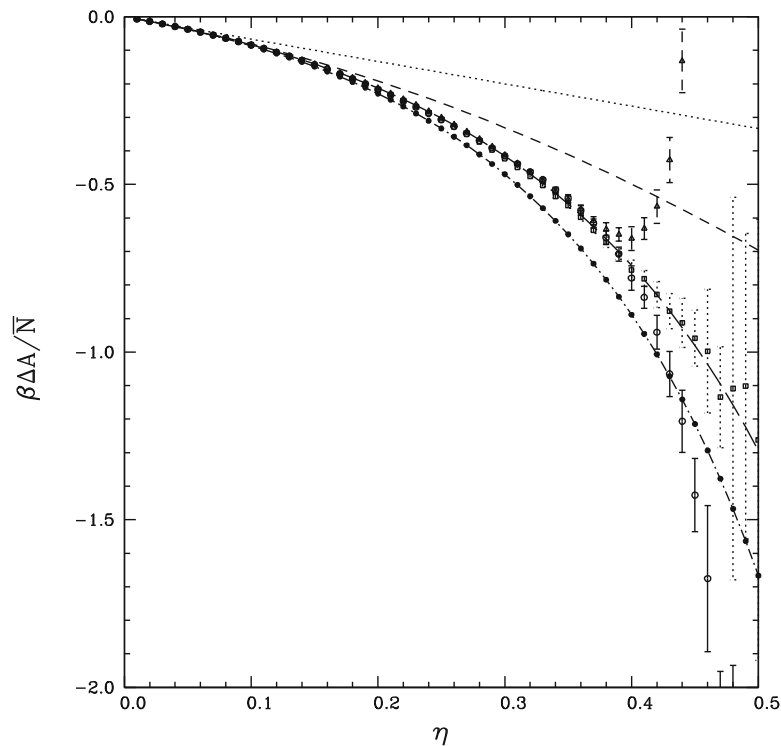


Fig. 2 Same as Fig. 1 at $\tau = 1.5$.

where

$$\alpha = \left[\frac{1 + 2\eta}{(1 - \eta)^2} \right]^2, \tag{28}$$

$$\beta = -6\eta \left[\frac{1 + \eta/2}{(1 - \eta)^2} \right]^2, \tag{29}$$

$$\gamma = \frac{\eta}{2} \left[\frac{1 + 2\eta}{(1 - \eta)^2} \right]^2. \tag{30}$$

and it is easily verified that under such approximation one has

$$a \approx \frac{1 + 2\eta}{(1 - \eta)^2}, \tag{31}$$

$$\bar{y}_0 \approx \frac{1 + \eta/2}{(1 - \eta)^2}. \tag{32}$$

5 Neglecting Reducible Integrals

It has been observed by Henderson and Barker [14] that the role of the last term in Eq. (3)

Author's personal copy

Andersen-Weeks-Chandler Perturbation Theory...

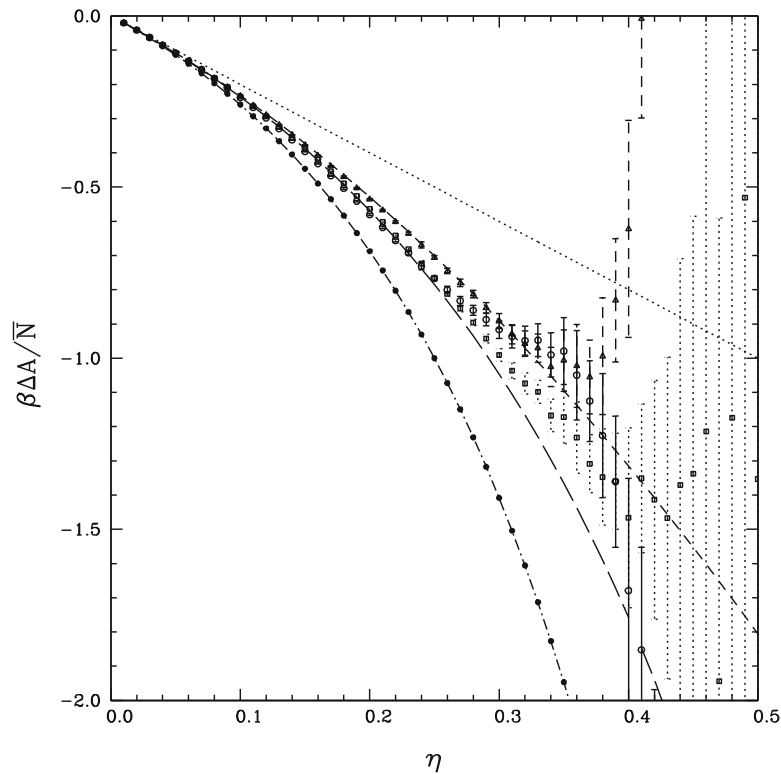


Fig. 3 Same as Fig. 1 at $\tau = 0.5$.

$$c\bar{N} = \frac{1}{2\bar{N}} \left(\rho^2 \frac{\chi_T^0}{\chi_T^{id}} \right) \left\{ \frac{\partial}{\partial \rho} \beta[\Delta A]_{(1)} \right\}^2, \tag{33}$$

is to cancel in the second order term of the perturbative expansion, $[\Delta A]_{(2)}$, all reducible integrals appearing in I_3 and I_4 . So that the final expression for the second order term of expansion (1) would be (exactly the expression found in [12])

$$\beta \frac{[\Delta A]_{(2)}}{\bar{N}} = -\frac{1}{2} \left(\frac{I'_3}{\rho} + \frac{I'_4}{\rho} \right), \tag{34}$$

where

$$\frac{I'_3}{\rho} = \frac{I_3}{\rho} - \frac{1}{\tau^2} (2\eta\bar{y}_0)^2, \tag{35}$$

$$\frac{I'_4}{\rho} = \frac{I_4}{\rho} - \frac{1}{\tau^2} (2\eta\bar{y}_0)^2 \frac{1}{4} \left[4 \left(\frac{1}{a^2} - 1 \right) + \frac{1}{3\pi} \frac{1}{\eta} h_2^a \right]. \tag{36}$$

Alternatively one may use the sum rule

$$\frac{\partial \rho_0(1, 2)}{\partial \rho} = \frac{1}{\rho} \frac{\chi_T^{id}}{\chi_T^0} \left\{ 2\rho_0(1, 2) + \int d3 [\rho_0(1, 2, 3) - \rho\rho_0(1, 2)] \right\}, \tag{37}$$

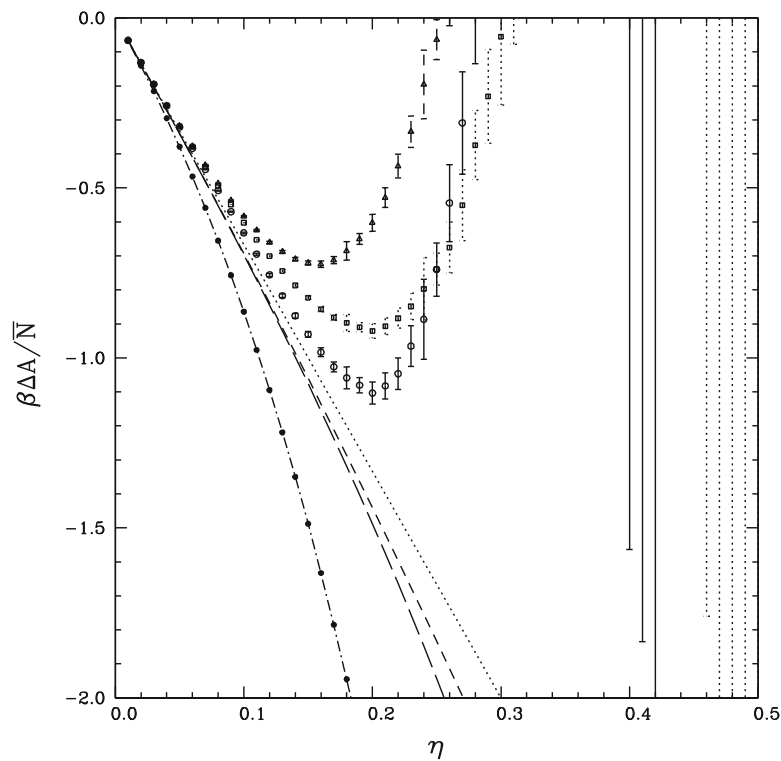


Fig. 4 Same as Fig. 1 at $\tau = 0.15$.

to rewrite \mathcal{C} (Eq. 33) in terms of two and three body correlation functions and upon using the superposition approximation one finds

$$\beta \frac{[\Delta A]_{(2)}'}{\bar{N}} = -\frac{1}{2} \left(\frac{I'_3}{\rho} + \frac{I'_4}{\rho} \right) + \frac{1}{\tau^2} \frac{a^2}{8} (2\eta\bar{y}_0)^2 \left(\frac{1}{12\pi} \frac{1}{\eta} h_2^a \right)^2, \quad (38)$$

6 Technical Details

The five integrals (17–21) were all calculated using Monte Carlo technique [16] averaging the various integrands on 10^6 randomly sampled points. Since all of those integrals are improper (extending up to infinity in the z variables) it was necessary to split each integration on the z variables into an integral over $[0, 1]$ plus an integral over $[1, \infty]$. This latter integral was then reduced through a change of variable $z \rightarrow 1/z$ into an integral over $[0, 1]$.

The errors on the estimate of a given integral was calculated so that the true value of the integral would lie 99.7% of the time within the estimate plus or minus the error.

7 Results

Figures 1, 2, 3, and 4 show the results for $\beta\Delta A/N$ as a function of η . Amongst the three expressions used: (8), (34), and (38), the more accurate is $[\Delta A]_{(2)}'$, the one suggested in [12]

Author's personal copy

Andersen-Weeks-Chandler Perturbation Theory...

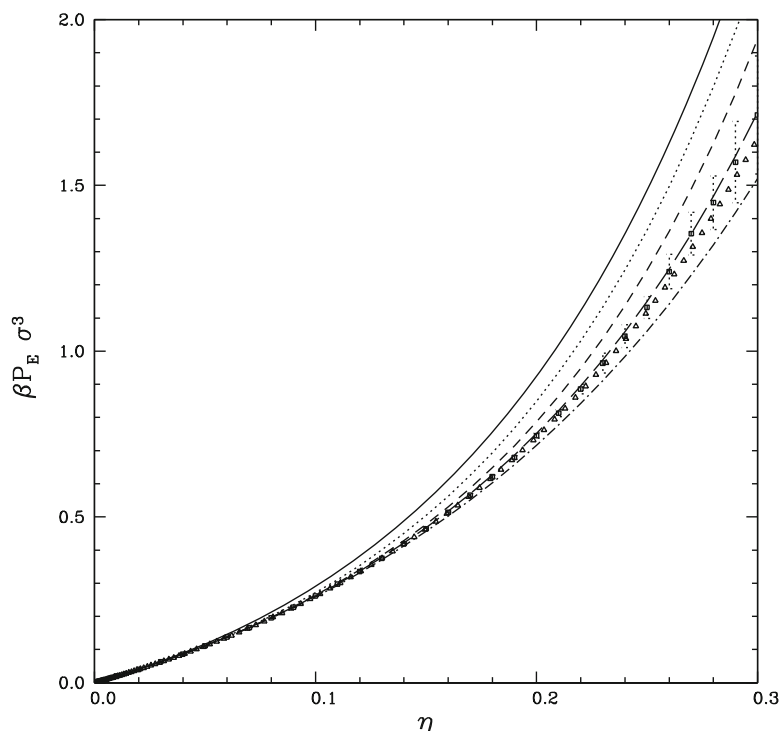


Fig. 5 We show $\beta P\sigma^3$ as a function of the packing fraction at $\tau = 1$ for various approximations: MSA (continuous line), C0 (dotted line) [10], C1 (short dashed line) [10], PY (long dashed line) [9], AWC 1st order (dotted dashed line), AWC 2nd order (empty squares), and Monte Carlo results of Miller and Frenkel (empty triangles) [11].

and it falls on the PY approximation for big τ and small η . At high η the error bars become more relevant.

Figures 5, 6, 7, and 8 show the results for

$$\beta P\sigma^3 = \beta P_{HS}\sigma^3 + \frac{6}{\pi}\eta^2 \frac{\partial\beta\Delta A/N}{\partial\eta}, \tag{39}$$

as a function of η , where for the pressure of the HS reference system we chose the PY result from the compressibility route, i.e.

$$\beta P_{HS}\sigma^3 = \frac{6}{\pi}\eta \left[\frac{1 + \eta + \eta^2}{(1 - \eta)^3} \right]. \tag{40}$$

The second order AWC TPT is taken from the (34) calculation.

8 Discussion

Our first calculation, the one using $[\Delta A]_{(2)}$ (see Eq. (8)) is certainly not correct because we are using the KSA only on the integrands of the first two integrals of Eq. (3) calculating the last term exactly; this certainly leads to an inconsistency in the use of KSA.

Author's personal copy

R. Fantoni

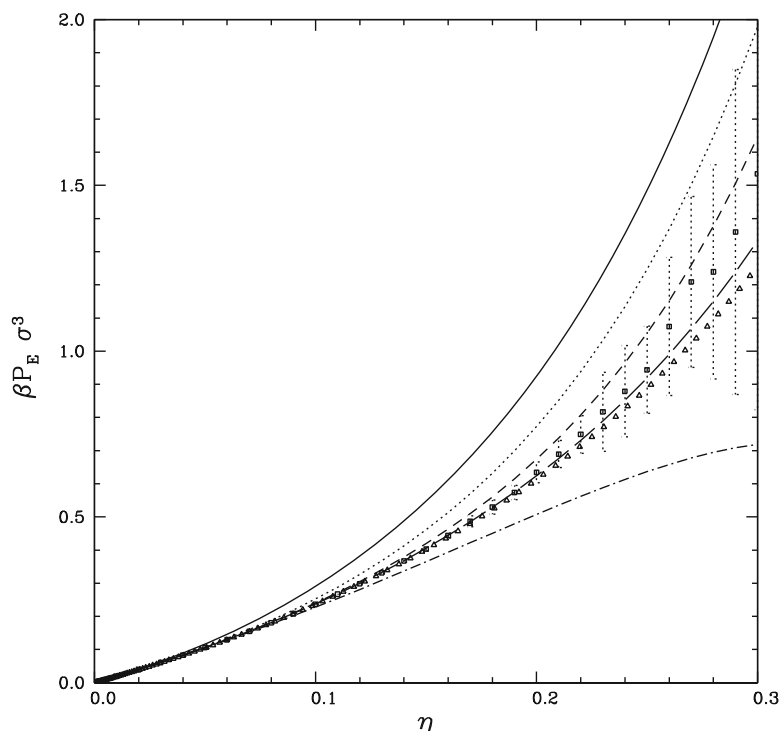


Fig. 6 Same as Fig. 5 at $\tau = 0.5$.

Our third calculation, the one using $[\Delta A]''_{(2)}$ (see Eq. (38)) is also not correct. This can be understood as follows. It is well known that KSA fails to satisfy the sum rule (37). Using KSA in the left hand side of Eq. (37) one finds

$$\frac{1}{\rho} \frac{\chi_T^{id}}{\chi_T^0} \left\{ 2\rho_0(1, 2) + \int d3 [\rho_0(1, 2, 3) - \rho\rho_0(1, 2)] \right\} \approx \gamma_1 + \gamma_2, \tag{41}$$

where

$$\gamma_1 = g_0(1, 2)2\rho, \tag{42}$$

$$\gamma_2 = g_0(1, 2) \frac{\chi_T^{id}}{\chi_T^0} \int d3 [\rho h_0(1, 3)][\rho h_0(2, 3)], \tag{43}$$

and we used the compressibility sum rule,

$$\frac{\chi_T^0}{\chi_T^{id}} = 1 + \rho \int h_0(1, 2) d1. \tag{44}$$

Eq. (41) can be also rewritten as,

$$\frac{\partial \ln g_0(1, 2)}{\partial \rho} \approx \frac{\chi_T^{id}}{\chi_T^0} \int d3 h_0(1, 3)h_0(2, 3). \tag{45}$$

This approximation is certainly valid in the limit of small densities when $\chi_T^0 \rightarrow \chi_T^{id}$ and $h_0 \rightarrow e_0 - 1 = f_0$ (f_0 being the Mayer function of the reference system), after all the

Author's personal copy

Andersen-Weeks-Chandler Perturbation Theory...

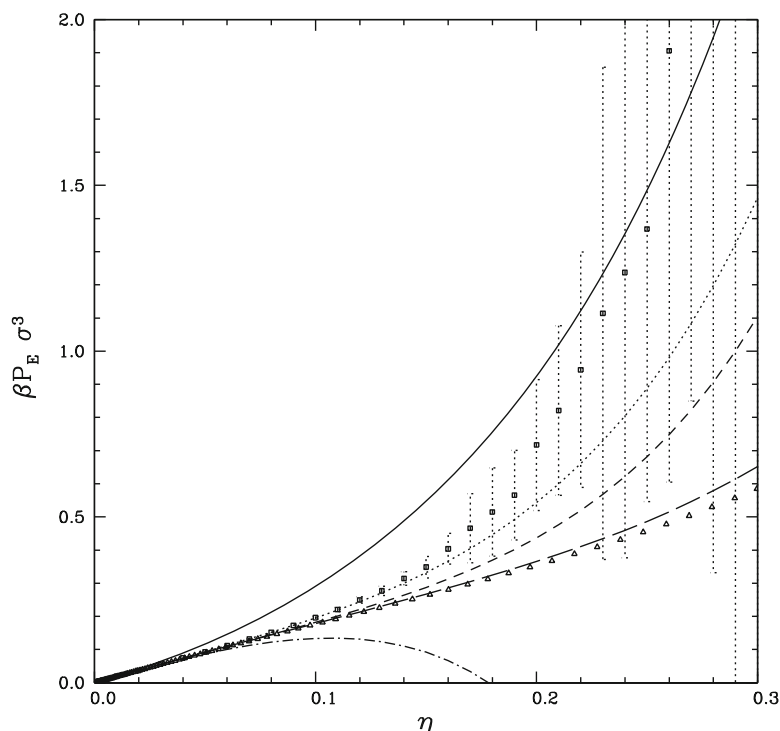


Fig. 7 Same as Fig. 5 at $\tau = 0.2$.

KSA becomes exact in such limit (as the potential of mean force tends to the pair interaction potential). Otherwise the correction term $\gamma_3/(\rho^2 g_0)$ would be of order ρ as $\rho \rightarrow 0$ (see the ‘‘Appendix A’’). So that the exact expression for the density derivative of the two body correlation function would be

$$\frac{\partial \rho_0(1, 2)}{\partial \rho} = \gamma_1(1, 2) + \gamma_2(1, 2) + \gamma_3(1, 2), \tag{46}$$

where $\gamma_i = O(\rho^i)$ as $\rho \rightarrow 0$. It is then clear that in calculating the square

$$\left[\frac{\partial}{\partial \rho} \frac{1}{2} \int d1d2 \frac{\rho_0(1, 2)}{e_0(1, 2)} \Delta e(1, 2) \right]^2, \tag{47}$$

in the \mathcal{C} term, the term stemming from

$$\left[\frac{1}{2} \int d1d2 \frac{\gamma_2(1, 2)}{e_0(1, 2)} \Delta e(1, 2) \right]^2, \tag{48}$$

which gives rise to the last term in Eq. (38), will be of the same leading order (ρ^4) as the one coming from

$$\left[\frac{1}{2} \int d1d2 \frac{\gamma_1(1, 2)}{e_0(1, 2)} \Delta e(1, 2) \right] \left[\frac{1}{2} \int d1d2 \frac{\gamma_3(1, 2)}{e_0(1, 2)} \Delta e(1, 2) \right], \tag{49}$$

in the small density limit. But since in KSA this last term is neglected, in order to be consistent (up to orders ρ^3 in the small density limit) one needs to neglect also the term of

Author's personal copy

R. Fantoni

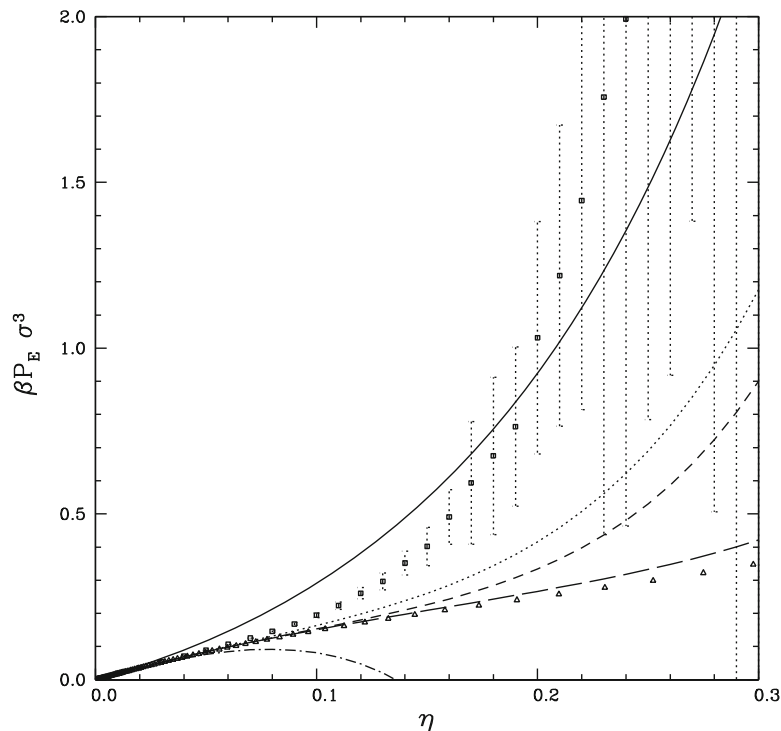


Fig. 8 Same as Fig. 5 at $\tau = 0.15$.

Eq. (48). Moreover it can be easily verified that the two terms coming from γ_1 times γ_1 cancel the first reducible integral in I_3 and the first reducible integral in I_4 whereas the term coming from γ_1 times γ_2 cancels the second reducible integral in I_4 . So that Eq. (34) (the original AWC expression) for the second order perturbative term in the AWC theory, is recovered.

The correct second order AWC calculation, $[\Delta A]_{(2)}$ (see Eq. (34)) shows that the TPT breaks down at small reduced temperatures τ and large packing fractions η , as expected.

While the superposition approximation has long been used for lack of anything better it is known to introduce significant errors in certain applications like that leading to the Yvon–Born–Green integral equation. With that in mind, it could be interesting to use the MC method to directly evaluate the terms in the basic expression (3) for the second order term in the AWC expansion. This would require the simulation of the three and four-body distribution functions of the reference HS system. That would provide a direct test of the accuracy of the second order AWC perturbation expression (1). One may in fact suspect that errors from superposition in Eq. (3) are probably larger than the intrinsic errors resulting from truncating the expansion that leads to Eq. (3). We plan to address this point in a forthcoming work and we leave this question as an open problem for the time being.

The results of the present work could be used to complement the studies in the following Refs. [17–23].

Author's personal copy

Andersen-Weeks-Chandler Perturbation Theory...

Appendix A: Correction to Approximation (45)

One can understand that Eq. (45) is not an exact relation by comparing the small density expansion of the left and right hand side. For the left hand side we have [9]

$$\frac{\partial \ln g_0(1, 2)}{\partial \rho} = \text{diagram} + \left(\text{diagram} + \text{diagram} + \text{diagram} + \text{diagram} \right) 2\rho + O(\rho^2), \tag{A1}$$

where in the Mayer graphs the filled circles are field points of weight 1 and connecting bonds are Mayer functions of the reference system f_0 . And using

$$h_0(1, 2) = \text{diagram} + \left(\text{diagram} + \text{diagram} \right) \rho + O(\rho^2), \tag{A2}$$

in the right hand side one finds,

$$\frac{\chi_T^{id}}{\chi_T^0} \int d3 h_0(1, 3)h_0(2, 3) = \frac{\int d3 h_0(1, 3)h_0(2, 3)}{1 + \frac{\rho}{V} \int d1d2 h_0(1, 2)} \tag{A3}$$

$$= \frac{\text{diagram} + \left(\text{diagram} + \text{diagram} + \text{diagram} \right) 2\rho + O(\rho^2)}{1 + \left(\frac{\text{diagram}}{V} \right) 2\rho + O(\rho^2)}$$

$$= \text{diagram} + \left[\text{diagram} + \text{diagram} + \text{diagram} + \text{diagram} - \left(\text{diagram} \right) \cdot \left(\frac{\text{diagram}}{V} \right) \right] 2\rho + O(\rho^2)$$

$$= \alpha_0(1, 2) + \alpha_1(1, 2) + O(\rho^2),$$

So that the correction term is of order ρ , namely,

$$\alpha'_1(1, 2) = \left[\text{diagram} + \left(\text{diagram} \right) \cdot \left(\frac{\text{diagram}}{V} \right) \right] 2\rho. \tag{A4}$$

The correct small density expansion for the density derivative of the two body correlation function is

$$\frac{\partial \rho_0(1, 2)}{\partial \rho} = g_0(1, 2) [2\rho + \rho^2 \alpha_0(1, 2) + \rho^2 \alpha_1(1, 2) + \rho^2 \alpha'_1(1, 2) + O(\rho^4)], \tag{A5}$$

where the first term neglected in KSA is $\rho^2 \alpha'_1 = O(\rho^3)$.

References

1. Baxter, R.J.: Percus–Yevick equation for hard spheres with surface adhesion. *Chem. Phys.* **49**, 2770–2774 (1968)
2. Fantoni, R., Gazzillo, D., Giacometti, A.: The thermodynamic instabilities of a binary mixture of sticky hard spheres. *Phys. Rev. E* **72**, 011503-1,14 (2005)
3. Gazzillo, D., Giacometti, A., Fantoni, R., Sollich, P.: Multicomponent adhesive hard sphere models and short-ranged attractive interactions in colloidal or micellar solutions. *Phys. Rev. E* **74**, 051407-1,14 (2006)
4. Gazzillo, D., Fantoni, R., Giacometti, A.: Phase behavior of polydisperse sticky hard spheres: analytical solutions and perturbation theory. *Mol. Phys.* **104**, 3451–3459 (2006)
5. Fantoni, R., Gazzillo, D., Giacometti, A., Sollich, P.: Phase behavior of weakly polydisperse sticky hard spheres: Perturbation theory for the Percus–Yevick solution. *J. Chem. Phys.* **125**, 164504-1,16 (2006)
6. Fantoni, R., Gazzillo, D., Giacometti, A., Miller, M.A., Pastore, G.: Patchy sticky hard spheres: analytical study and Monte Carlo simulations. *J. Chem. Phys.* **127**, 234507-1,16 (2007)
7. Gazzillo, D., Fantoni, R., Giacometti, A.: Fluids of spherical molecules with dipolarlike nonuniform adhesion: an analytically solvable anisotropic model. *Phys. Rev. E* **78**, 021201-1,20 (2008)
8. Gazzillo, D., Fantoni, R., Giacometti, A.: Local orientational ordering in fluids of spherical molecules with dipolar-like anisotropic adhesion. *Phys. Rev. E* **80**, 061207-1,7 (2009)
9. Hansen, J.P., McDonald, I.R.: *Theory of Simple Liquids*, 2nd edn. Academic Press, Amsterdam (1986)
10. Gazzillo, D., Giacometti, A.: Analytic solutions for Baxter’s model of sticky hard sphere fluids within closures different from the Percus–Yevick approximation. *J. Chem. Phys.* **120**, 4742–4754 (2004)
11. Miller, M.A., Frenkel, D.: Competition of percolation and phase separation in a fluid of adhesive hard spheres. *Phys. Rev. Lett.* **90**, 135702 1,4 (2003)
12. Andersen, H.C., Weeks, J.D., Chandler, D.: Relationship between the hard-sphere fluid and fluids with realistic repulsive forces. *Phys. Rev. A* **4**, 1597–1607 (1971)
13. Kirkwood, J.G.: Statistical mechanics of fluid mixtures. *J. Chem. Phys.* **3**, 300–313 (1935)
14. Henderson, D., Barker, J.A.: Perturbation theories. In: H. Eyring, D. Henderson, W. Jost (eds.) *Physical Chemistry: An Advanced Treatise*, vol. VIII, chap. 6. Academic Press, New York (1971)
15. Ashcroft, N.W., Lekner, J.: Structure and resistivity of liquid metals. *Phys. Rev.* **145**, 83–90 (1966)
16. Kalos, M.H., Whitlock, P.A.: *Monte Carlo Methods*, vol. I. Wiley, New York (1986)
17. Fantoni, R., Gazzillo, D., Giacometti, A.: Stability boundaries, percolation threshold, and two phase coexistence for polydisperse fluids of adhesive colloidal particles. *J. Chem. Phys.* **122**, 034,901–1,15 (2005)
18. Maestre, M.A.G., Fantoni, R., Giacometti, A., Santos, A.: Janus fluid with fixed patch orientations: theory and simulations. *J. Chem. Phys.* **138**, 094,904–1,19 (2013)
19. Fantoni, R., Giacometti, A., Maestre, M.A.G., Santos, A.: Phase diagrams of Janus fluids with up-down constrained orientations. *J. Chem. Phys.* **139**, 174,902–1,9 (2013)
20. Fantoni, R., Pastore, G.: Wertheim and Bjerrum–Tani–Henderson theories for associating fluids: a critical assessment. *J. Chem. Phys.* **141**, 074,108–1,10 (2014)
21. Fantoni, R., Pastore, G.: Wertheim perturbation theory: thermodynamics and structure of patchy colloids. *Mol. Phys.* **113**, 2593–2607 (2015)
22. Fantoni, R., Giacometti, A., Santos, A.: Bridging and depletion mechanisms in colloid–colloid effective interactions: a reentrant phase diagram. *J. Chem. Phys.* **142**, 224,905–1,14 (2015)
23. Fantoni, R.: The square-shoulder–Asakura–Oosawa model. *Physica A* **457**, 406–412 (2016)



Chapter 55

One-Dimensional Fluids with Second Nearest-Neighbor Interactions

Fantoni R. and Santos A., J. Stat. Phys. **169**, 1171 (2017)

Title: “One-Dimensional Fluids with Second Nearest-Neighbor Interactions”

Abstract: As is well known, one-dimensional systems with interactions restricted to first nearest neighbors admit a full analytically exact statistical-mechanical solution. This is essentially due to the fact that the knowledge of the first nearest-neighbor probability distribution function, $p_1(r)$, is enough to determine the structural and thermodynamic properties of the system. On the other hand, if the interaction between second nearest-neighbor particles is turned on, the analytically exact solution is lost. Not only the knowledge of $p_1(r)$ is not sufficient anymore, but even its determination becomes a complex many-body problem. In this work we systematically explore different approximate solutions for one-dimensional second nearest-neighbor fluid models. We apply those approximations to the square-well and the attractive two-step pair potentials and compare them with Monte Carlo simulations, finding an excellent agreement.

Author's personal copy

J Stat Phys
DOI 10.1007/s10955-017-1908-6



One-Dimensional Fluids with Second Nearest-Neighbor Interactions

Riccardo Fantoni¹ · Andrés Santos² 

Received: 5 September 2017 / Accepted: 27 October 2017
© Springer Science+Business Media, LLC 2017

Abstract As is well known, one-dimensional systems with interactions restricted to first nearest neighbors admit a full analytically exact statistical-mechanical solution. This is essentially due to the fact that the knowledge of the first nearest-neighbor probability distribution function, $p_1(r)$, is enough to determine the structural and thermodynamic properties of the system. On the other hand, if the interaction between second nearest-neighbor particles is turned on, the analytically exact solution is lost. Not only the knowledge of $p_1(r)$ is not sufficient anymore, but even its determination becomes a complex many-body problem. In this work we systematically explore different approximate solutions for one-dimensional second nearest-neighbor fluid models. We apply those approximations to the square-well and the attractive two-step pair potentials and compare them with Monte Carlo simulations, finding an excellent agreement.

Keywords One-dimensional fluids · Nearest-neighbors · Square-well model · Two-step model · Radial distribution function · Fisher-Widom line

1 Introduction

It is well known that equilibrium systems confined in one-dimensional geometries with interactions restricted to first nearest neighbors (1st nn) admit a full exact statistical-mechanical solution [5, 15, 26, 27, 29–37, 39, 42, 43, 52, 53]. Apart from its undoubtful pedagogical and illustrative values [6, 8, 11, 12, 25, 44–47], this exact solution can also be exploited as a benchmark for approximations [2, 3, 7, 10, 13, 14, 16, 43, 51] or simulation methods [9].

Andrés Santos
andres@unex.es

Riccardo Fantoni
rfantoni@ts.infn.it

¹ Dipartimento di Fisica, Università di Trieste, strada Costiera 11, 34151 Grignano, Trieste, Italy

² Departamento de Física and Instituto de Computación Científica Avanzada (ICCAEX), Universidad de Extremadura, 06006 Badajoz, Spain

Exact solutions are also possible for a few one-dimensional systems with interactions extending beyond 1st nn, as happens, for example, in the one- and two-component plasma, the Kac–Baker model, or isolated self-gravitating system [19,20,41]. However, most one-dimensional non-1st nn fluids do not admit an analytical exact solution but only an approximate one, as happens, for example, to the penetrable-square-well model [18,22,48].

While a fair amount of simplification of relevant questions occurs in a lattice gas or Ising model context [15], here we will be concerned with spatially continuous fluid systems. The two main ingredients allowing for an exact statistical-mechanical treatment of one-dimensional fluids (in the isothermal-isobaric ensemble) are [47]: (i) the pair interaction potential diverges as the two particles approach each other, so that the ordering of the particles cannot change, and (ii) each particle interacts only with its two 1st nn. In that case, it is possible to obtain the exact 1st nn probability distribution function, $p_1(r)$, whose knowledge is in turn enough to determine all the structural and thermodynamic properties of the system.

On the other hand, even if the ordering property (i) is maintained, as soon as the interaction extends to second nearest neighbors (2nd nn) the exact solution is generally lost. First, the determination of $p_1(r)$ becomes a complex many-body problem. Second, even if $p_1(r)$ were known, the convolution property relating $p_1(r)$ to the more general correlation functions is no longer valid and one is again faced with a many-body correlation coupling. Nonetheless, the problem is in general more tractable than the one of a generic non-1st nn fluid since the potential energy now contains only the interactions between 1st and 2nd nn pairs. It is therefore interesting to find reasonable approximate solutions in this particular case. This is the objective of the present work.

After revising the exact expressions for the ℓ th-order nn distribution functions in the isothermal-isobaric ensemble and their structure, we devise a sequence of approximations (by means of a diagrammatic description) at various increasing orders of accuracy. Our sequence gives the exact solution only at infinite order, but we will discover that already at second order it does a very good job. As illustrations, we will apply our approach to two particular cases: the square-well (SW) and the attractive two-step (TS) models.

As for the thermodynamic properties, the equation of state is determined from three alternative routes: the virial and compressibility routes, and the consistency condition that the radial distribution function (RDF) must tend to 1 at large distances. This gives us useful thermodynamic consistency tests on our approximations. Of course, the van Hove theorem [28,40,54] states that in our case there cannot be a phase transition for the fluid and, in particular, the isothermal susceptibility cannot diverge. We check this by computing the isothermal susceptibility through two different thermodynamic routes. Another relevant thermodynamic consistency test refers to the internal energy per particle.

We carry on a detailed analysis of the RDF and compare the behavior of our approximations with the results from canonical Monte Carlo (MC) simulations for both the SW and TS models. Also, within our approximate theory, we compute the Fisher–Widom (FW) line [23] for the SW model at various ranges.

The work is organized as follows. In Sect. 2 the problem of the 2nd nn fluid is presented and the exact solution in the 1st nn case is recalled. In Sect. 3 we introduce the sequence of approximations used to solve the 2nd nn problem. This is followed by Sects. 4 and 5, where the approximations are particularized to the SW and TS fluids, and compared with our own MC simulations. In Sect. 6 we calculate the FW line for the SW model. Finally, Sect. 7 presents our concluding remarks.

Author's personal copy

One-Dimensional Fluids with Second Nearest-Neighbor Interactions

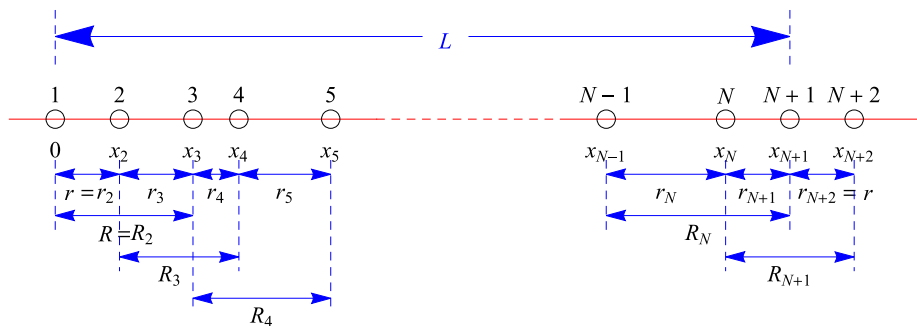


Fig. 1 Illustration of the one-dimensional fluid and of the distances used in the main text. For simplicity, particle $i = 1$ defines the origin of coordinates (i.e., $x_1 = 0$)

2 The Problem

Let us consider a one-dimensional system of N particles in a box of length L (so that the number density is $n = N/L$) subject to a pair interaction potential $\phi(r)$ such that:

- i. $\lim_{r \rightarrow 0} \phi(r) = \infty$. This implies that the *order* of the particles in the line does not change, i.e., the particles are assumed to be *impenetrable*.
- ii. $\phi(r) = 0$ for $r > D$. Thus, the interaction has a *finite range* D .
- iii. Each particle interacts *only* with its 1st and 2nd nn, i.e., with the four particles closer to it.

The total potential energy is then

$$\Phi_N(\mathbf{r}^N) = \sum_{i=1}^N [\phi(x_{i+1} - x_i) + \gamma \phi(x_{i+2} - x_i)], \quad (2.1)$$

where $\mathbf{r}^N = \{x_1, x_2, \dots, x_N\}$ are the coordinates of the N particles ordered in such way that $x_1 < x_2 < \dots < x_N$, and periodic boundary conditions (pbc) are assumed, so that $x_{N+1} = x_1 + L$ and $x_{N+2} = x_2 + L$. A sketch of the system is shown in Fig. 1. In Eq. (2.1) we have introduced the bookkeeping factor γ simply to keep track of the 2nd nn contribution to the total potential energy. At the end of the calculations $\gamma = 1$ will be taken.

2.1 General Relations

2.1.1 Nearest-Neighbor and Pair Correlation Functions

Given a reference particle at a certain position, let $p_1(r)dr$ be the *conditional* probability of finding its 1st nn at a distance between r and $r + dr$ to its right. More in general, we can define $p_\ell(r)dr$ as the conditional probability of finding its (right) ℓ th neighbor ($1 \leq \ell \leq N - 1$) at a distance between r and $r + dr$ [47]. Since the ℓ th neighbor of the reference particle must be somewhere, the normalization condition, in the thermodynamic limit ($N \rightarrow \infty, L \rightarrow \infty, n = \text{const}$), is

$$\int_0^\infty dr p_\ell(r) = 1. \quad (2.2)$$

The physical meaning of the RDF [4, 24, 28, 47] implies that $ng(r)dr$ is the *total* number of particles at a distance between r and $r + dr$, regardless of whether those particles correspond

Author's personal copy

R. Fantoni, A. Santos

to the 1st nn, the 2nd nn, . . . of the reference particle. Thus, again in the thermodynamic limit,

$$ng(r) = \sum_{\ell=1}^{\infty} p_{\ell}(r). \tag{2.3}$$

2.1.2 Thermodynamic Quantities

Apart from characterizing the equilibrium spatial correlations, the RDF allows one to obtain the thermodynamic quantities by means of well-known statistical-mechanical formulas [47]. For instance, the excess internal energy per particle is given by

$$\beta u = \beta n \int_0^{\infty} dr \phi(r)g(r) = \beta \int_0^{\infty} dr \phi(r) [p_1(r) + p_2(r)], \tag{2.4}$$

where $\beta \equiv 1/k_B T$ is the (reduced) inverse temperature (k_B and T being the Boltzmann constant and the absolute temperature, respectively) and we have taken into account that $\phi(r)$ vanishes beyond 2nd nn.

Moreover, from the virial theorem we find

$$\frac{\beta p}{n} = 1 - \beta n \int_0^{\infty} dr r \phi'(r)g(r) = 1 + n \int_0^{\infty} dr r f'(r)y(r), \tag{2.5}$$

where p is the pressure, $\dots' \equiv d\dots/dr$, $f(r) = e^{-\beta\phi(r)} - 1$ is the Mayer factor, and $y(r) = g(r)e^{\beta\phi(r)}$ is the cavity function. A thermodynamic consistency test comes from the following Maxwell relation

$$\left(\frac{\partial\beta u}{\partial\beta p}\right)_{\beta} = \beta \left(\frac{\partial n^{-1}}{\partial\beta}\right)_{\beta p}. \tag{2.6}$$

Of course, for an exact solution this is an identity.

The isothermal susceptibility is defined as

$$\chi_T = \left(\frac{\partial n}{\partial\beta p}\right)_{\beta}. \tag{2.7}$$

Alternatively, it can also be obtained via the compressibility route as [47]

$$\chi_T = 1 + 2n \int_0^{\infty} dr [g(r) - 1] = 1 + 2n \lim_{s \rightarrow 0} \left[\widehat{G}(s) - \frac{1}{s} \right], \tag{2.8}$$

where

$$\widehat{G}(s) \equiv \int_0^{\infty} dr e^{-rs} g(r) \tag{2.9}$$

is the Laplace transform of the RDF. Again, the two routes (2.7) and (2.8) give identical results if the exact RDF is used. Note that the physical condition $\lim_{r \rightarrow \infty} g(r) = 1$ and Eq. (2.8) imply the small- s behavior

$$\widehat{G}(s) = \frac{1}{s} + \frac{\chi_T - 1}{2n} + \mathcal{O}(s). \tag{2.10}$$

Author's personal copy

One-Dimensional Fluids with Second Nearest-Neighbor Interactions

2.1.3 Isothermal-Isobaric Ensemble

We will see that retaining in the potential energy of the fluid up to the 2nd nn interactions involves an N -body coupling in any of the ℓ th nn distribution functions. This renders the one-dimensional problem extremely more complicated than the 1st nn fluid, for which a general analytical solution can be found [47] due to the decoupling of each pair of nn (see Sect. 2.2).

In the isothermal-isobaric (or NpT) ensemble, the N -body configurational probability density function is [47]

$$\rho(\mathbf{r}^N) \propto e^{-\beta pL - \beta \Phi_N(\mathbf{r}^N)}. \tag{2.11}$$

As a consequence, we find for $p_1(r)$ (see Fig. 1)

$$p_1(r) \propto \int_r^\infty dL e^{-\beta pL} \int_{x_2}^L dx_3 \int_{x_3}^L dx_4 \cdots \int_{x_{N-1}}^L dx_N e^{-\beta \Phi_N(\mathbf{r}^N)}, \tag{2.12}$$

where we have taken particles $i = 1$ (at $x_1 = 0$) and $i = 2$ (at $x_2 = r$) as the representative 1st nn pair. The proportionality constant in Eq. (2.12) is obtained from the normalization condition (2.2).

Using Eq. (2.1) and the pbc we find (see Fig. 1 for notation)

$$\begin{aligned} \Phi_N(\mathbf{r}^N) = & \phi(r) + \gamma\phi(R) + \phi(r_3) + \gamma\phi(R_3) + \phi(r_4) \\ & + \gamma\phi(R_4) + \cdots + \phi(r_{N+1}) + \gamma\phi(R_{N+1}), \end{aligned} \tag{2.13}$$

with $R = x_3 = r + r_3$ and $r_i = x_i - x_{i-1}$, $R_i = x_{i+1} - x_{i-1} = r_i + r_{i+1}$ for $i = 3, 4, \dots, N + 1$. It is proved in Appendix A that, after an adequate change of variables, Eq. (2.12) becomes

$$\begin{aligned} p_1(r) \propto & e^{-\beta[pr + \phi(r)]} \int_0^\infty dr_3 e^{-\beta[pr_3 + \phi(r_3)]} e^{-\gamma\beta\phi(r+r_3)} \\ & \times \int_0^\infty dr_4 e^{-\beta[pr_4 + \phi(r_4)]} e^{-\gamma\beta\phi(r_3+r_4)} \dots \\ & \times \int_0^\infty dr_N e^{-\beta[pr_N + \phi(r_N)]} e^{-\gamma\beta\phi(r_{N-1}+r_N)} \\ & \times \int_0^\infty dr_{N+1} e^{-\beta[pr_{N+1} + \phi(r_{N+1})]} e^{-\gamma\beta\phi(r_N+r_{N+1})} e^{-\gamma\beta\phi(r_{N+1}+r)}. \end{aligned} \tag{2.14}$$

We clearly see that all the $N - 1$ spatial integrals are coupled, so that we cannot proceed any further without introducing approximations. This many-body coupling can be conveniently visualized by means of a diagrammatic representation, as shown in the first row of Table 1.

For the 2nd nn distribution we have

$$p_2(R) \propto \int_R^\infty dL e^{-\beta pL} \int_0^R dx_2 \int_R^L dx_4 \int_{x_4}^L dx_5 \cdots \int_{x_{N-1}}^L dx_N e^{-\beta \Phi_N(\mathbf{r}^N)}. \tag{2.15}$$

As proved in Appendix A, this becomes

$$\begin{aligned} p_2(R) \propto & e^{-\beta[pR + \gamma\phi(R)]} \int_0^R dr_2 e^{-\beta\phi(r_2)} e^{-\beta\phi(R-r_2)} \\ & \times \int_0^\infty dr_4 e^{-\beta[pr_4 + \phi(r_4)]} e^{-\gamma\beta\phi(R-r_2+r_4)} \end{aligned}$$

Author's personal copy

R. Fantoni, A. Santos

Table 1 Diagrammatic representation

Label	Function	Diagram
exact	$p_1(1,2)$	∞
exact	$p_2(1,3)$	∞
exact	$p_3(1,4)$	∞
$1^{(00)}$	$p_1^{(00)}(1,2)$	∞
$1^{(01)}$	$p_1^{(01)}(1,2)$	∞
$1^{(11)}$	$p_1^{(11)}(1,2)$	∞
$2^{(00)}$	$p_2^{(00)}(1,3)$	∞
$2^{(01)}$	$p_2^{(01)}(1,3)$	∞
$2^{(11)}$	$p_2^{(11)}(1,3)$	∞
$3^{(00)}$	$p_3^{(00)}(1,4)$	∞
$3^{(01)}$	$p_3^{(01)}(1,4)$	∞
$3^{(11)}$	$p_3^{(11)}(1,4)$	∞

We indicate with (i, j) the distance $r_{ij} = |x_i - x_j|$. The open circles denote the root points (not integrated out) i and j , while the filled circles (enclosed by open ones) denote field points (integrated out). The thick straight lines represent a link $\exp\{-\beta[pr + \phi(r)]\}$ between 1st nn, while the thin curved lines represent a link $\exp[-\gamma\beta\phi(r)]$ between 2nd nn. In this representation, the dashed lines link two root points, while the solid lines link two field points or one root and one field point

$$\begin{aligned}
 & \times \int_0^\infty dr_5 e^{-\beta[pr_5 + \phi(r_5)]} e^{-\gamma\beta\phi(r_4+r_5)} \dots \int_0^\infty dr_N e^{-\beta[pr_N + \phi(r_N)]} e^{-\beta\phi(r_{N-1}+r_N)} \\
 & \times \int_0^\infty dr_{N+1} e^{-\beta[pr_{N+1} + \phi(r_{N+1})]} e^{-\gamma\beta\phi(r_N+r_{N+1})} e^{-\gamma\beta\phi(r_{N+1}+r_2)}. \tag{2.16}
 \end{aligned}$$

Author's personal copy

One-Dimensional Fluids with Second Nearest-Neighbor Interactions

Once again, the expression above depends on all the N -body terms. It is represented by the second row in Table 1.

In the case of the 3rd nn distribution, its formal expression is

$$p_3(\bar{R}) \propto \int_{\bar{R}}^{\infty} dL e^{-\beta pL} \int_0^{\bar{R}} dx_2 \int_{x_2}^{\bar{R}} dx_3 \int_{\bar{R}}^L dx_5 \cdots \int_{x_{N-1}}^L dx_N e^{-\beta \Phi_N(\mathbf{r}^N)}, \quad (2.17)$$

where we have denoted by \bar{R} the distance between the reference particles 1 and 4. Equation (2.17) is equivalent to (see Appendix A)

$$\begin{aligned} p_3(\bar{R}) &\propto e^{-\beta p\bar{R}} \int_0^{\bar{R}} dr_2 e^{-\beta\phi(r_2)} e^{-\gamma\beta\phi(\bar{R}-r_2)} \int_0^{\bar{R}-r_2} dr_3 e^{-\beta\phi(r_3)} e^{-\gamma\beta\phi(r_2+r_3)} e^{-\beta\phi(\bar{R}-r_2-r_3)} \\ &\times \int_0^{\infty} dr_5 e^{-\beta[pr_5+\phi(r_5)]} e^{-\gamma\beta\phi(\bar{R}-r_2-r_3+r_5)} \int_0^{\infty} dr_6 e^{-\beta[pr_6+\phi(r_6)]} e^{-\gamma\beta\phi(r_5+r_6)} \dots \\ &\times \int_0^{\infty} dr_N e^{-\beta[pr_N+\phi(r_N)]} e^{-\gamma\beta\phi(r_{N-1}+r_N)} \\ &\times \int_0^{\infty} dr_{N+1} e^{-\beta[pr_{N+1}+\phi(r_{N+1})]} e^{-\gamma\beta\phi(r_N+r_{N+1})} e^{-\gamma\beta\phi(r_{N+1}+r_2)}. \end{aligned} \quad (2.18)$$

The diagram representing Eq. (2.18) is displayed as the third row of Table 1.

The process can be continued in a similar way to get $p_\ell(\bar{R})$ with $\ell = 4, \dots, N - 1$ and $\bar{R} = x_{\ell+1} - x_1$. In particular,

$$\begin{aligned} p_{N-1}(\bar{R}) &\propto e^{-\beta p\bar{R}} \int_0^{\bar{R}} dr_2 e^{-\beta\phi(r_2)} \int_0^{\bar{R}-r_2} dr_3 e^{-\beta\phi(r_3)} e^{-\gamma\beta\phi(r_2+r_3)} \\ &\times \int_0^{\bar{R}-r_2-r_3} dr_4 e^{-\beta\phi(r_4)} e^{-\gamma\beta\phi(r_3+r_4)} \dots \\ &\times \int_0^{\bar{R}-r_2-r_3-\dots-r_{N-2}} dr_{N-1} e^{-\beta\phi(r_{N-1})} e^{-\gamma\beta\phi(r_{N-2}+r_{N-1})} e^{-\beta\phi(\bar{R}-r_2-r_3-\dots-r_{N-1})} e^{-\gamma\beta\phi(\bar{R}-r_2-r_3-\dots-r_{N-2})} \\ &\times \int_0^{\infty} dr_{N+1} e^{-\beta[pr_{N+1}+\phi(r_{N+1})]} e^{-\gamma\beta\phi(\bar{R}-r_2-r_3-\dots-r_{N-1}+r_{N+1})} e^{-\gamma\beta\phi(r_{N+1}+r_2)}. \end{aligned} \quad (2.19)$$

2.2 First Nearest-Neighbor Fluids: Exact Solution

Let us suppose now that the 2nd nn interactions are switched off. This is equivalent to setting $\gamma = 0$ in Eqs. (2.1) and (2.13). In that case, the curved lines in the three first rows of Table 1 disappear and most of the integrals in Eqs. (2.14), (2.16), and (2.18) can be absorbed into the proportionality constants:

$$p_1(r) = K_1 e^{-\beta[pr+\phi(r)]}, \quad (2.20a)$$

$$p_2(R) \propto e^{-\beta pR} \int_0^R dr_2 e^{-\beta\phi(r_2)} e^{-\beta\phi(R-r_2)}, \quad (2.20b)$$

$$p_3(\bar{R}) \propto e^{-\beta p\bar{R}} \int_0^{\bar{R}} dr_2 e^{-\beta\phi(r_2)} \int_0^{\bar{R}-r_2} dr_3 e^{-\beta\phi(r_3)} e^{-\beta\phi(\bar{R}-r_2-r_3)}, \quad (2.20c)$$

where in Eq. (2.20a) K_1 is the normalization constant. In the case of Eq. (2.19), even though only the integral over r_{N+1} can be absorbed into the proportionality constant so that $N - 2$ integrals still remain, they acquire a simple convolution structure:

Author's personal copy

R. Fantoni, A. Santos

$$\begin{aligned}
 p_{N-1}(\bar{R}) \propto & e^{-\beta p \bar{R}} \int_0^{\bar{R}} dr_2 e^{-\beta \phi(r_2)} \int_0^{\bar{R}-r_2} dr_3 e^{-\beta \phi(r_3)} \int_0^{\bar{R}-r_2-r_3} dr_4 e^{-\beta \phi(r_4)} \dots \\
 & \times \int_0^{\bar{R}-r_2-r_3-\dots-r_{N-2}} dr_{N-1} e^{-\beta \phi(r_{N-1})} e^{-\beta \phi(\bar{R}-r_2-r_3-\dots-r_{N-1})}. \quad (2.21)
 \end{aligned}$$

Thus, in the case of a pure 1st nn fluid, the following recurrence relation holds

$$p_\ell(r) = \int_0^r dr' p_1(r') p_{\ell-1}(r-r') \equiv (p_1 * p_{\ell-1})(r). \quad (2.22)$$

It is straightforward to check that Eqs. (2.20) and (2.21) are consistent with Eq. (2.22). The convolution structure of the integral in Eq. (2.22) suggests the introduction of the Laplace transform

$$\hat{p}_\ell(s) \equiv \int_0^\infty dr e^{-rs} p_\ell(r), \quad (2.23)$$

so that Eq. (2.22) becomes

$$\hat{p}_\ell(s) = \hat{p}_1(s) \hat{p}_{\ell-1}(s) = [\hat{p}_1(s)]^\ell. \quad (2.24)$$

The normalization condition (2.2) is equivalent to

$$\hat{p}_\ell(0) = 1. \quad (2.25)$$

Note that this condition is automatically satisfied by Eq. (2.24) provided that $\hat{p}_1(0) = 1$. In fact, the Laplace transform of Eq. (2.20a) is

$$\hat{p}_1(s) = K_1 \hat{\Omega}(s + \beta p), \quad K_1 = \frac{1}{\hat{\Omega}(\beta p)}, \quad (2.26)$$

where

$$\hat{\Omega}(s) \equiv \int_0^\infty dr e^{-sr} e^{-\beta \phi(r)} \quad (2.27)$$

is the Laplace transform of the pair Boltzmann factor $e^{-\beta \phi(r)}$.

In this case of a 1st nn fluid, the RDF in Laplace space is exactly given by [see Eqs. (2.3) and (2.9)]

$$\hat{G}(s) = \frac{1}{n} \sum_{\ell=1}^\infty [\hat{p}_1(s)]^\ell = \frac{1}{n} \frac{\hat{p}_1(s)}{1 - \hat{p}_1(s)}. \quad (2.28)$$

Finally, the number density n is obtained as a function of pressure and temperature by enforcing the condition $\lim_{s \rightarrow 0} sG(s) = 1$ [see Eq. (2.10)]. The result is [47]

$$n = -\frac{\hat{\Omega}(\beta p)}{\hat{\Omega}'(\beta p)}, \quad (2.29)$$

where

$$\hat{\Omega}'(s) \equiv \frac{\partial \hat{\Omega}(s)}{\partial s} = -\int_0^\infty dr e^{-rs} r e^{-\beta \phi(r)}. \quad (2.30)$$

Obviously, Eqs. (2.20)–(2.22), (2.24), (2.26), (2.28), and (2.29) cease to be exactly valid as soon as the interactions extend to 2nd nn (i.e., $\gamma = 1$).

3 Our Approximations

3.1 First Nearest-Neighbor Distribution

As discussed above, the exact expression (2.14) for p_1 is not amenable for an analytical treatment of the problem. We will then introduce a hierarchy of successive approximations.

In Eq. (2.14) we observe that, apart from the prefactor $\exp\{-\beta[pr + \phi(r)]\}$, the distance r appears explicitly in the first integral (over r_3) and, because of the pbc, in the last integral (over r_{N+1}). The dependence on r propagates as well to the remaining integrals (over r_4, \dots, r_N) due to the nested structure of the integrals induced by the 2nd nn terms of the form $\exp[-\gamma\beta\phi(r_i + r_{i+1})]$, as diagrammatically illustrated in the first row of Table 1. On the other hand, the r -dependence becomes more and more indirect and attenuated as the integrals involve particles farther and farther from the pair (1, 2), either to its right or (because of the pbc) to its left. Thus, by truncating the integrals at a certain order and incorporating their values into the normalization constant, one can construct a hierarchy of approximations to $p_1(r)$ involving only a finite number of particles in the environment of the pair (1, 2).

The crudest approximation would consist in just neglecting the r -dependence in all the integrals of Eq. (2.14), i.e.,

$$p_1^{(00)}(r) = K_1^{(00)} e^{-\beta[pr + \phi(r)]}, \tag{3.1}$$

where $K_1^{(00)}$ is the normalization constant. Henceforth, a factor of the form $K_\ell^{(k_1 k_2)}$ will denote a normalization constant. In the zeroth-order approximation (3.1), represented by the diagram with the label 1⁽⁰⁰⁾ in Table 1, $p_1(r)$ is assumed to be given by the exact solution (2.20a) for the 1st nn fluid. It can reasonably be expected that this is a very poor approximation for the 2nd nn fluid.

A less trivial approximation is obtained by including the integral over r_3 but not the other ones, i.e.,

$$p_1^{(01)}(r) = K_1^{(01)} e^{-\beta[pr + \phi(r)]} \int_0^\infty dr_3 e^{-\beta[pr_3 + \phi(r_3)]} e^{-\beta\phi(r+r_3)}, \tag{3.2}$$

where henceforth $\gamma = 1$ is already set. This first-order approximation to the exact $p_1(r)$ is represented by the diagram with the label 1⁽⁰¹⁾ in Table 1. If, instead of including the integral over r_3 (i.e., the distance between the root particle 2 and the particle to its right) we include the integral over r_{N+1} (i.e., the distance between the root particle 1 and the particle to its left, according to the pbc) we have

$$p_1^{(10)}(r) = K_1^{(10)} e^{-\beta[pr + \phi(r)]} \int_0^\infty dr_{N+1} e^{-\beta[pr_{N+1} + \phi(r_{N+1})]} e^{-\beta\phi(r_{N+1}+r)}. \tag{3.3}$$

Since r_3 and r_{N+1} are dummy integration variables, it is obvious that $p_1^{(10)}(r) = p_1^{(01)}(r)$, as expected by symmetry arguments.

The first-order approximation $p_1^{(01)}(r)$, while more reliable than $p_1^{(00)}(r)$, is asymmetric as it treats one side of the pair (1, 2) differently from the other side. This is remedied by the second-order approximation

$$p_1^{(11)}(r) = K_1^{(11)} e^{-\beta[pr + \phi(r)]} \left[\int_0^\infty dr_3 e^{-\beta[pr_3 + \phi(r_3)]} e^{-\beta\phi(r+r_3)} \right]^2, \tag{3.4}$$

where we have exploited the fact that the integrals over r_3 and over r_{N+1} are identical. A diagram for this approximation is shown with the label 1⁽¹¹⁾ in Table 1.

Obviously, the same scheme could be followed by introducing the approximations $p_1^{(12)}$, $p_1^{(22)}$, $p_1^{(33)}$, and so on. They become increasingly more accurate at the expense of becoming increasingly more involved. In fact, the exact 1st nn distribution is recovered, in the thermodynamic limit, as $p_1 = \lim_{k \rightarrow \infty} p_1^{(kk)}$. As a compromise between accuracy and simplicity we stop at the second-order approximation $p_1^{(11)}$.

3.2 Second Nearest-Neighbor Distribution

A similar process can be followed for the 2nd nn distribution $p_2(R)$. Here, particles 1 and 3 are fixed and one needs to integrate over all the positions of the intermediate particle 2. If one ignores in Eq. (2.16) the R -dependence of the integrals over those field particles to the right of 3 or to the left of 1, one finds

$$\begin{aligned}
 p_2^{(00)}(R) &= K_2^{(00)} e^{-\beta[pR+\phi(R)]} \int_0^R dr_2 e^{-\beta\phi(r_2)} e^{-\beta\phi(R-r_2)} \\
 &= \frac{K_2^{(00)}}{[K_1^{(00)}]^2} e^{-\beta\phi(R)} \int_0^R dr_2 p_1^{(00)}(r_2) p_1^{(00)}(R-r_2). \tag{3.5}
 \end{aligned}$$

A diagram for this zeroth-order approximation is shown with the label $2^{(00)}$ in Table 1, where we have used the fact that the point 2 is an articulation point to simplify the diagram as the convolution of two sub-diagrams.

The asymmetric first-order approximation for p_2 is

$$\begin{aligned}
 p_2^{(01)}(R) &= K_2^{(01)} e^{-\beta[pR+\phi(R)]} \int_0^R dr_2 e^{-\beta\phi(r_2)} e^{-\beta\phi(R-r_2)} \\
 &\quad \times \int_0^\infty dr_4 e^{-\beta[pr_4+\phi(r_4)]} e^{-\beta\phi(R-r_2+r_4)} \\
 &= \frac{K_2^{(01)}}{K_1^{(00)} K_1^{(01)}} e^{-\beta\phi(R)} \int_0^R dr_2 p_1^{(00)}(r_2) p_1^{(01)}(R-r_2). \tag{3.6}
 \end{aligned}$$

This approximation is described by the diagram with the label $2^{(01)}$ in Table 1, where again the convolution property is used.

The symmetrization of $p_2^{(01)}$ gives rise to the second-order approximation

$$\begin{aligned}
 p_2^{(11)}(R) &= K_2^{(11)} e^{-\beta[pR+\phi(R)]} \int_0^R dr_2 e^{-\beta\phi(r_2)} e^{-\beta\phi(R-r_2)} \\
 &\quad \times \int_0^\infty dr_4 e^{-\beta[pr_4+\phi(r_4)]} e^{-\beta\phi(R-r_2+r_4)} \\
 &\quad \times \int_0^\infty dr_{N+1} e^{-\beta[pr_{N+1}+\phi(r_{N+1})]} e^{-\beta\phi(r_{N+1}+r_2)}. \\
 &= \frac{K_2^{(11)}}{[K_1^{(01)}]^2} e^{-\beta\phi(R)} \int_0^R dr_2 p_1^{(01)}(r_2) p_1^{(01)}(R-r_2). \tag{3.7}
 \end{aligned}$$

A diagram for this approximation is shown with label $2^{(11)}$ in Table 1. Again, the point 2 is an articulation point so that the diagram simplifies as the convolution of two sub-diagrams.

Author's personal copy

One-Dimensional Fluids with Second Nearest-Neighbor Interactions

As in the case of p_1 , one could define $p_2^{(22)}$, $p_2^{(33)}$, ..., but for simplicity we stop at the level of the $2^{(11)}$ approximation (3.7).

3.3 Third Nearest-Neighbor Distribution

Regarding the 3rd nn probability distribution, we can proceed by starting from Eq. (2.18) and introducing the zeroth-, first-, and second-order approximations. They are given by

$$p_3^{(00)}(\bar{R}) = K_3^{(00)} e^{-\beta p \bar{R}} \int_0^{\bar{R}} dr_2 e^{-\beta \phi(r_2)} e^{-\beta \phi(\bar{R}-r_2)} \times \int_0^{\bar{R}-r_2} dr_3 e^{-\beta \phi(r_3)} e^{-\beta \phi(r_2+r_3)} e^{-\beta \phi(\bar{R}-r_2-r_3)}, \tag{3.8}$$

$$p_3^{(01)}(\bar{R}) = K_3^{(01)} e^{-\beta p \bar{R}} \int_0^{\bar{R}} dr_2 e^{-\beta \phi(r_2)} e^{-\beta \phi(\bar{R}-r_2)} \times \int_0^{\bar{R}-r_2} dr_3 e^{-\beta \phi(r_3)} e^{-\beta \phi(r_2+r_3)} e^{-\beta \phi(\bar{R}-r_2-r_3)} \times \int_0^\infty dr_5 e^{-\beta [pr_5 + \phi(r_5)]} e^{-\beta \phi(\bar{R}-r_2-r_3+r_5)}, \tag{3.9}$$

$$p_3^{(11)}(\bar{R}) = K_3^{(11)} e^{-\beta p \bar{R}} \int_0^{\bar{R}} dr_2 e^{-\beta \phi(r_2)} e^{-\beta \phi(\bar{R}-r_2)} \times \int_0^{\bar{R}-r_2} dr_3 e^{-\beta \phi(r_3)} e^{-\beta \phi(r_2+r_3)} e^{-\beta \phi(\bar{R}-r_2-r_3)} \times \int_0^\infty dr_5 e^{-\beta [pr_5 + \phi(r_5)]} e^{-\beta \phi(\bar{R}-r_2-r_3+r_5)} \times \int_0^\infty dr_{N+1} e^{-\beta [pr_{N+1} + \phi(r_{N+1})]} e^{-\beta \phi(r_{N+1}+r_2)}. \tag{3.10}$$

These approximations are represented by the diagrams labeled $3^{(00)}$, $3^{(01)}$, and $3^{(11)}$, respectively, in Table 1. Since there are no articulation points, the diagrams cannot be simplified any further.

By following the same process one could construct similar approximations for p_4 , p_5 , ..., but they become increasingly more intricate as they would involve at least three, four, ... nested integrals.

3.4 Radial Distribution Function

As clearly seen from Eq. (2.3), the knowledge (even if it were exact) of $p_1(r)$, $p_2(r)$, and $p_3(r)$ is not enough to get the RDF $g(r)$, as we need $p_\ell(r)$ for $\ell \geq 4$ as well. Thus, additional approximations are required.

Assume first that we want to construct an approximate function $\hat{G}(s)$ based on $\hat{p}_1(s)$ and $\hat{p}_2(s)$ only (since it is essential to keep at least those two quantities in a 2nd nn fluid). How can we estimate $\hat{p}_\ell(s)$ with $\ell \geq 3$ from $\hat{p}_1(s)$ and $\hat{p}_2(s)$? A simple possibility consists in extending the exact convolution property (2.24) of 1st nn fluids as an approximation to 2nd nn fluids. Two main possibilities arise:

$$\hat{p}_{2\ell+1}(s) = \hat{p}_1(s) [\hat{p}_2(s)]^\ell, \quad \hat{p}_{2\ell+2}(s) = [\hat{p}_2(s)]^{\ell+1}, \quad \ell \geq 1, \tag{3.11a}$$

$$\hat{p}_\ell(s) = [\hat{p}_1(s)]^\ell, \quad \ell \geq 3. \tag{3.11b}$$

Then, application of Eq. (2.3) yields, respectively,

$$\widehat{G}(s) = \frac{1}{n} \frac{\widehat{p}_1(s) + \widehat{p}_2(s)}{1 - \widehat{p}_2(s)}, \quad n = \frac{2}{\widetilde{p}_2}, \tag{3.12a}$$

$$\widehat{G}(s) = \frac{1}{n} \left\{ \frac{\widehat{p}_1(s)}{1 - \widehat{p}_1(s)} + \widehat{p}_2(s) - [\widehat{p}_1(s)]^2 \right\}, \quad n = \frac{1}{\widetilde{p}_1}. \tag{3.12b}$$

Here, we have used the condition $\lim_{s \rightarrow 0} s \widehat{G}(s) = 1$ [see Eq. (2.10)] to determine the number density n in terms of

$$\widetilde{p}_\ell \equiv - \left. \frac{\partial \widehat{p}_\ell(s)}{\partial s} \right|_{s=0} = \int_0^\infty dr r p_\ell(r). \tag{3.13}$$

Regardless of whether Eqs. (3.12a) or (3.12b) is used, a different approximation for $\widehat{G}(s)$ is made depending on which approximation is chosen for p_1 (see Sect. 3.1) and p_2 (see Sect. 3.2). We introduce the notation $[1^{(\alpha_1)2^{(\alpha_2)}}]_a$ and $[1^{(\alpha_1)2^{(\alpha_2)}}]_b$ to refer to Eqs. (3.12a) and (3.12b), respectively, complemented with the approximations $1^{(\alpha_1)}$ for p_1 and $2^{(\alpha_2)}$ for p_2 , where $(\alpha_1), (\alpha_2) = (00), (01),$ or (11) .

In Eq. (3.12) $\widehat{p}_3(s)$ is expressed in terms of $\widehat{p}_1(s)$ and $\widehat{p}_2(s)$. On the other hand, if the 3rd nn probability distribution is described, with independence of $\widehat{p}_1(s)$ and $\widehat{p}_2(s)$, by any of the approximation of Sect. 3.3 we can construct $\widehat{p}_\ell(s)$ with $\ell \geq 4$ as any of the following three possibilities:

$$\begin{aligned} \widehat{p}_{3\ell+1}(s) &= \widehat{p}_1(s) [\widehat{p}_3(s)]^\ell, & \widehat{p}_{3\ell+2}(s) &= \widehat{p}_2(s) [\widehat{p}_3(s)]^\ell, \\ \widehat{p}_{3\ell+3}(s) &= [\widehat{p}_3(s)]^{\ell+1}, & \ell &\geq 1, \end{aligned} \tag{3.14a}$$

$$\widehat{p}_{2\ell}(s) = [\widehat{p}_2(s)]^\ell, \quad \widehat{p}_{2\ell+1}(s) = \widehat{p}_1(s) [\widehat{p}_2(s)]^\ell, \quad \ell \geq 2, \tag{3.14b}$$

$$\widehat{p}_\ell(s) = [\widehat{p}_1(s)]^\ell, \quad \ell \geq 4. \tag{3.14c}$$

This gives rise, respectively, to

$$\widehat{G}(s) = \frac{1}{n} \frac{\widehat{p}_1(s) + \widehat{p}_2(s) + \widehat{p}_3(s)}{1 - \widehat{p}_3(s)}, \quad n = \frac{3}{\widetilde{p}_3}, \tag{3.15a}$$

$$\widehat{G}(s) = \frac{1}{n} \left\{ \frac{\widehat{p}_1(s) + \widehat{p}_2(s)}{1 - \widehat{p}_2(s)} + \widehat{p}_3(s) - \widehat{p}_1(s) \widehat{p}_2(s) \right\}, \quad n = \frac{2}{\widetilde{p}_2}, \tag{3.15b}$$

$$\widehat{G}(s) = \frac{1}{n} \left\{ \frac{\widehat{p}_1(s)}{1 - \widehat{p}_1(s)} + \widehat{p}_2(s) + \widehat{p}_3(s) - [\widehat{p}_1(s)]^2 - [\widehat{p}_1(s)]^3 \right\}, \quad n = \frac{1}{\widetilde{p}_1}. \tag{3.15c}$$

As before, we will denote as $[1^{(\alpha_1)2^{(\alpha_2)3^{(\alpha_3)}}]_a$, $[1^{(\alpha_1)2^{(\alpha_2)3^{(\alpha_3)}}]_b$, and $[1^{(\alpha_1)2^{(\alpha_2)3^{(\alpha_3)}}]_c$ the approximations (3.15a), (3.15b), and (3.15c), respectively, complemented with the approximations $1^{(\alpha_1)}$ for p_1 , $2^{(\alpha_2)}$ for p_2 , and $3^{(\alpha_3)}$ for p_3 .

Note that Eqs. (3.12) and (3.15) are fully equivalent in the case of a 1st nn fluid, as a consequence of Eq. (2.24). This is not so, however, for 2nd nn fluids. On physical grounds, the approximations of the form $[1^{(\alpha_1)2^{(\alpha_2)}}]_a$, where $\widehat{p}_3(s) \approx \widehat{p}_1(s) \widehat{p}_2(s)$, are expected to be more accurate than those of the form $[1^{(\alpha_1)2^{(\alpha_2)}}]_b$, where $\widehat{p}_3(s) \approx [\widehat{p}_1(s)]^3$. Likewise, the approximations of the form $[1^{(\alpha_1)2^{(\alpha_2)3^{(\alpha_3)}}]_a$ are expected to be better than those of the form $[1^{(\alpha_1)2^{(\alpha_2)3^{(\alpha_3)}}]_b$ or, even more, of the form $[1^{(\alpha_1)2^{(\alpha_2)3^{(\alpha_3)}}]_c$.

We will now apply our approximations to two specific 2nd nn fluid models and assess the results by MC simulations.

Author's personal copy

One-Dimensional Fluids with Second Nearest-Neighbor Interactions

4 The Square-Well Potential

As a simple prototype potential to test our approach, let us consider the SW potential,

$$\phi(r) = \begin{cases} \infty, & r < \sigma, \\ -\varepsilon, & \sigma \leq r < \lambda\sigma, \\ 0, & \lambda\sigma \leq r. \end{cases} \tag{4.1}$$

The physical properties of the fluid will depend on the dimensionless range λ , the reduced temperature $T^* \equiv k_B T / \varepsilon$, and either the reduced density $n^* \equiv n\sigma$ or the reduced pressure $p^* \equiv p\sigma / \varepsilon$. Of course, for $\lambda \leq 2$ the fluid is a 1st nn one so it admits an exact solution [29,45,47]. Our results for the 2nd nn fluid will allow us to extend such an exact solution, in an approximate way, to the range $2 < \lambda \leq 3$.

4.1 Structural Properties

Clearly, due to the hard core at $r = \sigma$, one has $p_\ell(r) = 0$ for $r < \ell\sigma$. Therefore,

$$ng(r) = \begin{cases} p_1(r), & \sigma < r < 2\sigma, \\ p_1(r) + p_2(r), & 2\sigma < r < 3\sigma, \\ p_1(r) + p_2(r) + p_3(r), & 3\sigma < r < 4\sigma, \\ \vdots & \vdots \end{cases} \tag{4.2}$$

All the approximations for the 1st nn, 2nd nn, and 3rd nn distributions described in Sects. 3.1–3.3 have fully analytical (albeit too long to be displayed here) expressions in the case of the SW potential, both in real space and in Laplace space. This allows one to obtain analytical expressions for the Laplace transform $\widehat{G}(s)$ in any of the approximations described in Sect. 3.4. The RDF in real space, $g(r)$, can then be found up to $r = 4\sigma$ by application of Eq. (4.2) and, for longer distances, by a numerical inverse Laplace transform using the algorithm described in Ref. [1].

Henceforth, unless stated otherwise, we take $\sigma = 1$ as the length unit and particularize to $\lambda = 3$, which is the largest range consistent with 2nd nn interactions.

Before comparing with MC simulations, let us analyze the convergence of the approximations presented in Sects. 3.1–3.3. Figure 2a shows $p_1^{(00)}(r)$, $p_1^{(01)}(r)$, $p_1^{(11)}(r)$, and $p_1^{(12)}(r)$ (the latter quantity not explicitly defined in Sect. 3.1) at the state $T^* = 1$, $p^* = 1$. We observe that the second-order approximation $p_1^{(11)}(r)$ is almost indistinguishable from the third-order one $p_1^{(12)}(r)$. We have also checked that the fourth order approximation $p_1^{(22)}(r)$ differs from the third-order one by about 0.1%. Therefore, we can conclude that convergence has been practically reached already at second order.

The 2nd nn functions $p_2^{(00)}(r)$, $p_2^{(01)}(r)$, $p_2^{(11)}(r)$, and $p_2^{(12)}(r)$ at the same thermodynamic state are plotted in Fig. 2b. Again we find that a good convergence has been reached with the second-order approximation $p_2^{(11)}(r)$.

Figure 3a is equivalent to Fig. 2 but for the 3rd nn distribution. Once more, we observe that the second-order approximation $p_3^{(11)}(r)$ is hardly distinguishable from the third-order approximation $p_3^{(12)}(r)$. The convolution approximations $(p_1^{(11)} * p_1^{(11)} * p_1^{(11)})(r)$ and $(p_1^{(11)} * p_2^{(11)})(r)$ are compared with $p_3^{(11)}(r)$ in Fig. 3b. As expected, the convolution functions $p_1 * p_1 * p_1$ and $p_1 * p_2$ are only qualitatively correct in describing the 3rd nn distribution. In fact, $p_1 * p_1 * p_1$ fails in capturing the kink of p_3 at $r = 4$. All of this confirms that, in

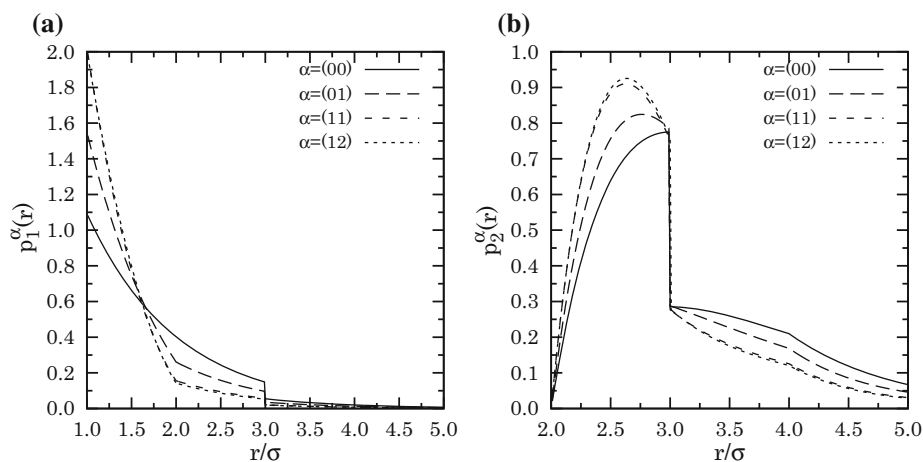


Fig. 2 **a** Plot of $p_1^{(00)}(r)$ (—), $p_1^{(01)}(r)$ (---), $p_1^{(11)}(r)$ (- - -), and $p_1^{(12)}(r)$ (· · ·) at $T^* = 1$ and $p^* = 1$. **b** Plot of $p_2^{(00)}(r)$ (—), $p_2^{(01)}(r)$ (---), $p_2^{(11)}(r)$ (- - -), and $p_2^{(12)}(r)$ (· · ·) for the SW fluid ($\lambda = 3$) at $T^* = 1$ and $p^* = 1$

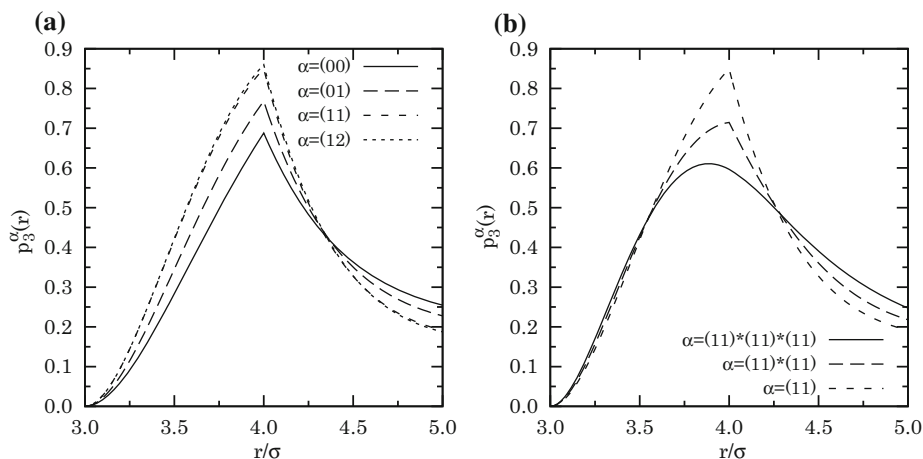


Fig. 3 **a** Plot of $p_3^{(00)}(r)$ (—), $p_3^{(01)}(r)$ (---), $p_3^{(11)}(r)$ (- - -), and $p_3^{(12)}(r)$ (· · ·) at $T^* = 1$ and $p^* = 1$. **b** Plot of $(p_1^{(11)} * p_1^{(11)} * p_1^{(11)})(r)$ (—), $(p_1^{(11)} * p_2^{(11)})(r)$ (---), and $p_3^{(11)}(r)$ (- - -) for the SW fluid ($\lambda = 3$) at $T^* = 1$ and $p^* = 1$

principle, Eq. (3.12a) is a better approximation than Eq. (3.12b) but it is worse than any of Eqs. (3.15), at least in the range $1 < r < 4$.

Once we have seen that the second-order approximations for $p_1(r)$, $p_2(r)$, and $p_3(r)$ represent a good balance between simplicity and accuracy, we consider now the RDF and compare the theoretical approximations of Sect. 3.4 with our own canonical MC simulations (with $N = 1024$ particles).

In Fig. 4 we show the RDF calculated from the approximation $[1^{(11)}2^{(11)}]_a$ [see Eq. (3.12a)] compared with our MC simulations, at several values of the reduced temperature and density. It is apparent that the approximation $[1^{(11)}2^{(11)}]_a$ works very well in the region

Author's personal copy

One-Dimensional Fluids with Second Nearest-Neighbor Interactions

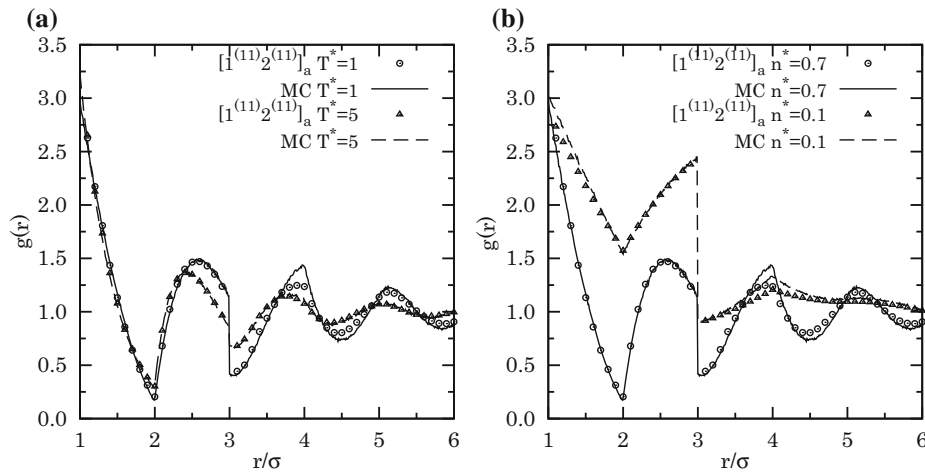


Fig. 4 Plot of $g(r)$ as obtained from MC simulations (— and - -) and from the approximation $[1^{(11)}2^{(11)}]_a$ [see Eq. (3.12a)] (\circ and Δ) for the SW fluid ($\lambda = 3$) at $n^* = 0.7$ and two temperatures ($T^* = 1$ and $T^* = 5$, respectively) and **b** $T^* = 1$ and two densities ($n^* = 0.7$ and $n^* = 0.1$, respectively)

$1 < r < 3$, where $ng(r) = p_1(r) + p_2(r)$, and keeps being generally good for larger distances, even though p_3 is approximated by $p_1 * p_2$.

In view of Fig. 3b, the quality of the approximations in the region $r > 3$ is expected to improve if p_3 is approximated with independence of p_1 and p_2 , as done in Eqs. (3.15). This is confirmed by Fig. 5, where the approximation $[1^{(11)}2^{(11)}3^{(11)}]_a$ [see Eq. (3.15a)] is compared with MC data for the same three states as in Fig. 4 plus the more stringent state $T^* = 0.5$ and $n^* = 0.7$. A very good agreement is observed, although, not surprisingly, the quality of the approximation worsens as the temperature decreases and the density increases [see Fig. 5d].

4.2 Thermodynamic Properties

The approximations for the 1st, 2nd, and 3rd nn probability distribution functions and for the RDF worked out in Sect. 3 can also be used to obtain the thermodynamic properties, as presented in Sect. 2.1.2. We focus on the equation of state (i.e., the relationship between pressure, density, and temperature), the isothermal susceptibility, and the excess internal energy per particle. Given the approximate character of our proposals, the results will in general depend on the route followed to obtain those thermodynamic quantities. In fact, the degree of thermodynamic inconsistency will be used as a test of our approach.

The most direct way of determining the equation of state is as $n = \ell / \tilde{p}_\ell$, with $\ell = 1, 2, 3$, in accordance with Eqs. (3.12) and (3.15). This gives the number density as an explicit function of pressure and temperature, i.e., $n(\beta, \beta p)$. If we prefer to express the pressure as a function of density and temperature, $p(n, T)$, we need to solve numerically the equation $n = n(\beta, \beta p)$. In either choice of independent variables, the compressibility factor is obtained as $Z \equiv \beta p / n$. We will use the superscript (A), i.e., $n^{(A)}$ and $Z^{(A)}$, to denote this “direct” route to the equation of state. From it, the excess internal energy per particle (u) and the isothermal susceptibility (χ_T) can be obtained via the thermodynamic properties (2.6) and (2.7), respectively, namely

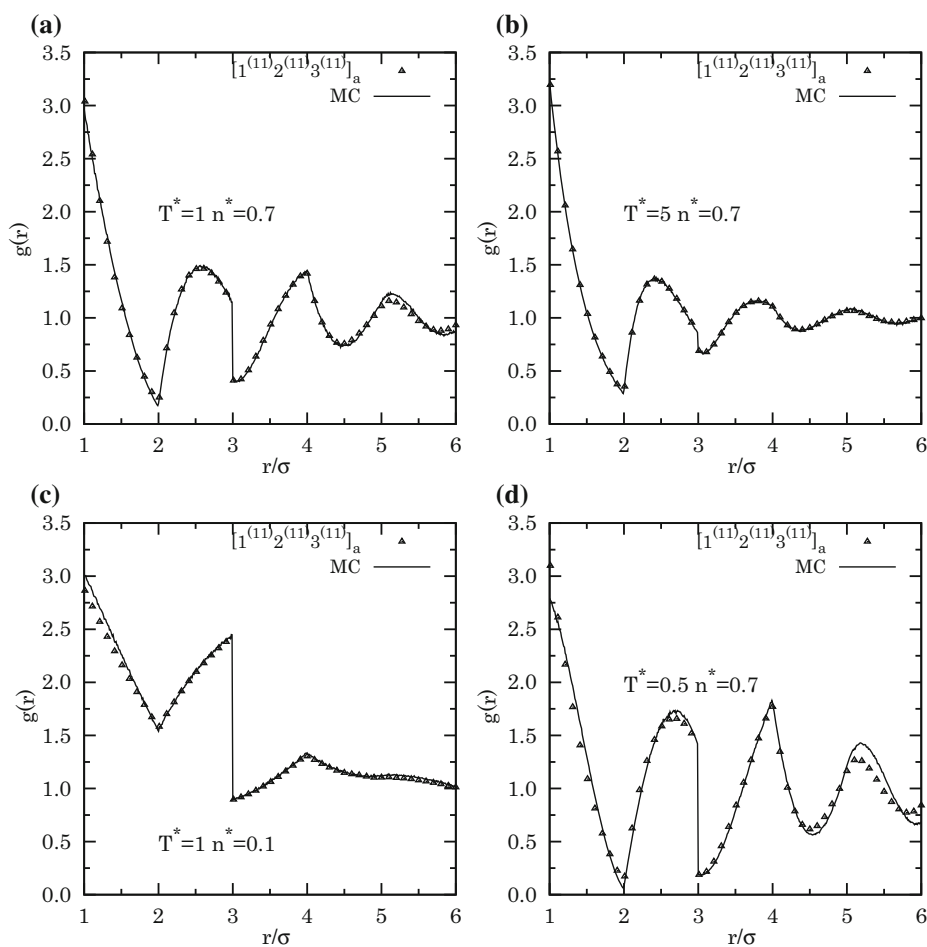


Fig. 5 Plot of $g(r)$ as obtained from MC simulations (—) and from the approximation $[1^{(11)}2^{(11)}3^{(11)}]_a$ [see Eq. (3.15a)] (Δ) for the SW fluid ($\lambda = 3$) at **a** $T^* = 1$ and $n^* = 0.7$, **b** $T^* = 5$ and $n^* = 0.7$, **c** $T^* = 1$ and $n^* = 0.1$, and **d** $T^* = 0.5$ and $n^* = 0.7$

$$u^{(A)}(\beta, \beta p) = \beta p \int_0^1 dt \left(\frac{\partial 1/n^{(A)}(\beta, t\beta p)}{\partial \beta} \right)_{\beta p}, \tag{4.3a}$$

$$\chi_T^{(A)} = \left(\frac{\partial n^{(A)}}{\partial \beta p} \right)_\beta = \frac{1}{(\partial n Z^{(A)} / \partial n)_T}. \tag{4.3b}$$

Alternatively, u , Z , and χ_T can be obtained from the energy (e), virial (v), and compressibility (c) routes, respectively, as given by Eqs. (2.4), (2.5), and (2.8). In particular, for the SW potential (4.1) one has

$$\frac{u^{(e)}}{\varepsilon} = - \int_1^\lambda dr p_1(r) - \int_2^\lambda dr p_2(r), \tag{4.4}$$

Author's personal copy

One-Dimensional Fluids with Second Nearest-Neighbor Interactions

$$\begin{aligned} Z^{(v)} &= 1 + n [g(1^+) - \lambda (e^{\beta\epsilon} - 1) g(\lambda^+)] \\ &= 1 + p_1(1^+) - \lambda (e^{\beta\epsilon} - 1) [p_1(\lambda^+) + p_2(\lambda^+)]. \end{aligned} \tag{4.5}$$

As for the isothermal susceptibility, application of the approximations (3.12) and (3.15) into Eq. (2.8) yields

$$\chi_T^{(c)} = \frac{3\tilde{p}_3}{\tilde{p}_3^2} - \frac{2(\tilde{p}_1 + \tilde{p}_2)}{\tilde{p}_3} - 1, \tag{4.6a}$$

$$\chi_T^{(c)} = \frac{2\tilde{p}_2}{\tilde{p}_2^2} - \frac{2\tilde{p}_1}{\tilde{p}_2} - 1, \tag{4.6b}$$

$$\chi_T^{(c)} = \frac{\tilde{p}_1}{\tilde{p}_1^2} - 1, \tag{4.6c}$$

where

$$\tilde{p}_\ell \equiv \left. \frac{\partial^2 \hat{p}_\ell(s)}{\partial s^2} \right|_{s=0} = \int_0^\infty dr r^2 p_\ell(r). \tag{4.7}$$

Equation (4.6a) applies to Eq. (3.15a), while Eq. (4.6b) applies to Eqs. (3.12a) and (3.15b), and Eq. (4.6c) applies to Eqs. (3.12b) and (3.15c). From Eq. (2.7) and $\chi_T^{(c)}$, the compressibility factor can be obtained as

$$Z^{(c)}(\beta, \beta p) = \frac{1}{\int_0^1 dt \chi_T^{(c)}(\beta, t\beta p)}. \tag{4.8}$$

The thermodynamic quantities $Z^{(A)}$, $u^{(A)}$, $\chi_T^{(A)}$, $Z^{(v)}$, $u^{(e)}$, $\chi_T^{(e)}$, and $Z^{(c)}$ are common to those approximations (3.12) and (3.15) having the same denominator of the form $1 - \hat{p}_\ell(s)$. In our notation, this means that $[1^{(\alpha_1)2^{(\alpha_2)}}]_a = [1^{(\alpha_1)2^{(\alpha_2)}3^{(\alpha_2)}}]_b$ and $[1^{(\alpha_1)2^{(\alpha_2)}}]_b = [1^{(\alpha_1)2^{(\alpha_2)}3^{(\alpha_3)}}]_c$ in what concerns the thermodynamic properties. Thus, here we will refer to the thermodynamic properties associated with the three approximations $[1^{(11)2^{(11)}3^{(11)}}]_{a,b,c}$.

Figure 6 presents thermodynamic consistency tests for the different routes within the approximations $[1^{(11)2^{(11)}3^{(11)}}]_{a,b,c}$. As expected, $[1^{(11)2^{(11)}3^{(11)}}]_a$ is the most consistent approximation, the thermodynamic quantities deviating typically less than 10% at the relatively low temperature $T^* = 1$.

The theoretical values are compared with MC simulation results for a few thermodynamic states in Table 2. We can observe that the best agreement in the case of the compressibility factor is generally reached with the direct route, $Z^{(A)}$, in the $[1^{(11)2^{(11)}3^{(11)}}]_a$ approximation. The compressibility route, however, tends to overestimate the value of Z . In what refers to the excess internal energy, the energy route is generally better than the direct route. By a fortuitous cancellation of errors, the approximations $[1^{(11)2^{(11)}3^{(11)}}]_{b,c}$ can in some cases outperform the approximation $[1^{(11)2^{(11)}3^{(11)}}]_a$ in estimating u .

In Fig. 7 we show the behavior of the compressibility factor and of the excess internal energy per particle as functions of density at temperatures $T^* = 1$ and $T^* = 5$. At the latter temperature the three approximations $[1^{(11)2^{(11)}3^{(11)}}]_{a,b,c}$ provide practically indistinguishable results. As can be observed, the agreement with our MC results is very satisfactory.

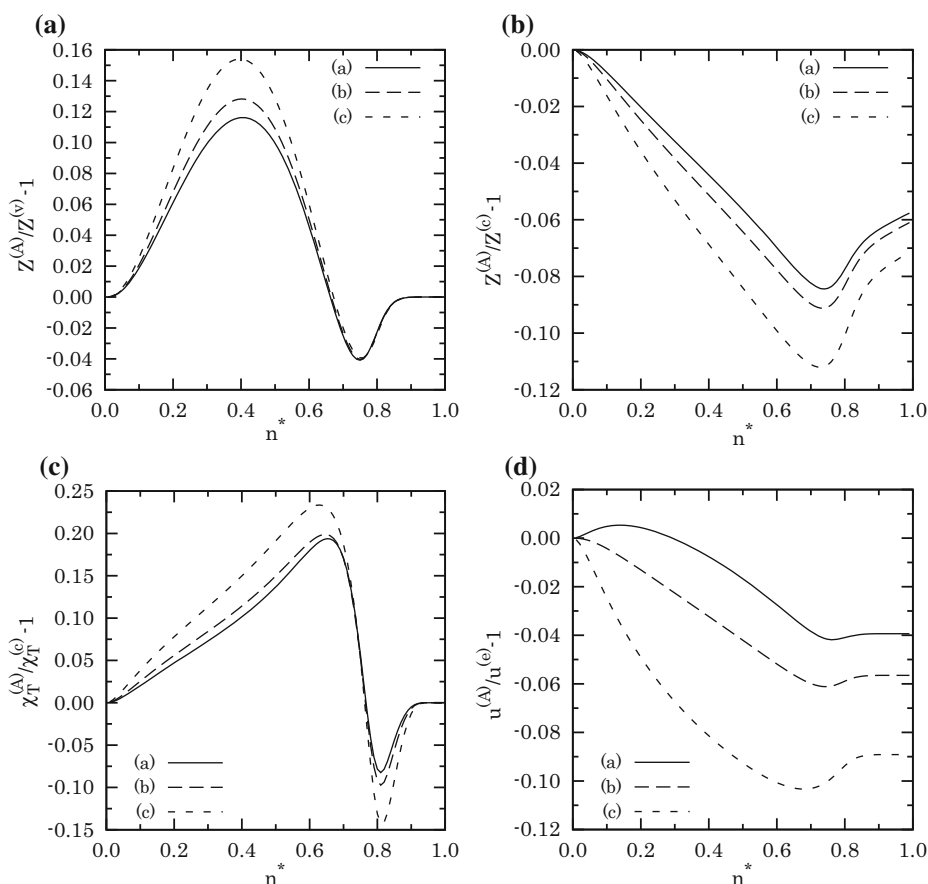


Fig. 6 Plot of the relative differences **a** $Z^{(A)}/Z^{(v)} - 1$, **b** $Z^{(A)}/Z^{(c)} - 1$, **c** $\chi_T^{(A)}/\chi_T^{(c)} - 1$, and **d** $u^{(A)}/u^{(e)} - 1$ as functions of density for the SW fluid ($\lambda = 3$) at $T^* = 1$. The curves correspond to the approximations $[1^{(11)}2^{(11)}3^{(11)}]_a$ (—), $[1^{(11)}2^{(11)}3^{(11)}]_b$ (---), and $[1^{(11)}2^{(11)}3^{(11)}]_c$ (-.-)

5 The Two-Step Potential

Let us now consider the following TS fluid defined by the potential

$$\phi(r) = \begin{cases} \infty, & r < \sigma, \\ -\varepsilon, & \sigma \leq r < \lambda_1\sigma, \\ -\varepsilon_2, & \lambda_1\sigma \leq r < \lambda\sigma, \\ 0, & \lambda\sigma \leq r. \end{cases} \tag{5.1}$$

Clearly, for $\varepsilon_2 = \varepsilon$, or $\lambda_1 = 1$, or $\lambda_1 = \lambda$ we recover the SW fluid of Sect. 4. More in general, playing with the signs and the magnitudes of the two energy scales, ε and ε_2 , several classes of piece-wise constant potentials can be described [49,50]. Here, we will restrict ourselves just to the case of full attraction with $\varepsilon > \varepsilon_2 > 0$. Analogously to the SW case, we define the reduced density and temperature as $n^* \equiv n\sigma$ and $T^* \equiv k_B T/\varepsilon$, respectively.

Obviously, if $\lambda \leq 2$ the TS interaction cannot extend beyond 1st nn and therefore the exact solution described in Sect. 2.2 applies. On the other hand, if $2 < \lambda \leq 3$, the interaction

Author's personal copy

One-Dimensional Fluids with Second Nearest-Neighbor Interactions

Table 2 Some thermodynamic quantities for the SW fluid ($\lambda = 3$) at several values of T^* and n^*

Method	$Z^{(A)}$	$Z^{(v)}$	$Z^{(c)}$	$\chi_T^{(A)}$	$\chi_T^{(c)}$	$u^{(A)}/\varepsilon$	$u^{(e)}/\varepsilon$
$T^* = 1, n^* = 0.1$							
MC	0.8402 (6)			–		–0.434 (1)	
$[1^{(11)}2^{(11)}3^{(11)}]_a$	0.8427	0.8271	0.8494	1.3381	1.3117	–0.4273	–0.4252
$[1^{(11)}2^{(11)}3^{(11)}]_b$	0.8441	0.8269	0.8529	1.3309	1.2978	–0.4241	–0.4259
$[1^{(11)}2^{(11)}3^{(11)}]_c$	0.8474	0.8263	0.8614	1.3151	1.2667	–0.4169	–0.4274
$T^* = 1, n^* = 0.4$							
MC	0.785 (1)			–		–1.168 (1)	
$[1^{(11)}2^{(11)}3^{(11)}]_a$	0.8087	0.7246	0.8461	0.9596	0.8713	–1.1213	–1.1299
$[1^{(11)}2^{(11)}3^{(11)}]_b$	0.8200	0.7269	0.8643	0.9347	0.8389	–1.1014	–1.1381
$[1^{(11)}2^{(11)}3^{(11)}]_c$	0.8450	0.7322	0.9073	0.8822	0.7672	–1.0618	–1.1559
$T^* = 1, n^* = 0.7$							
MC	1.575 (3)			–		–1.752 (1)	
$[1^{(11)}2^{(11)}3^{(11)}]_a$	1.6263	1.6680	1.7725	0.1268	0.1083	–1.6772	–1.7442
$[1^{(11)}2^{(11)}3^{(11)}]_b$	1.6480	1.6875	1.8103	0.1278	0.1092	–1.6440	–1.7487
$[1^{(11)}2^{(11)}3^{(11)}]_c$	1.6980	1.7324	1.9102	0.1304	0.1098	–1.5774	–1.7587
$T^* = 5, n^* = 0.1$							
MC	1.0669 (1)			–		–0.2373 (4)	
$[1^{(11)}2^{(11)}3^{(11)}]_a$	1.0671	1.0670	1.0674	0.8724	0.8715	–0.2368	–0.2368
$[1^{(11)}2^{(11)}3^{(11)}]_b$	1.0671	1.0670	1.0676	0.8723	0.8711	–0.2367	–0.2368
$[1^{(11)}2^{(11)}3^{(11)}]_c$	1.0671	1.0670	1.0681	0.8723	0.8698	–0.2366	–0.2368
$T^* = 5, n^* = 0.4$							
MC	1.4733 (5)			–		–0.9230 (8)	
$[1^{(11)}2^{(11)}3^{(11)}]_a$	1.4769	1.4738	1.4840	0.4230	0.4172	–0.9188	–0.9217
$[1^{(11)}2^{(11)}3^{(11)}]_b$	1.4775	1.4740	1.4875	0.4226	0.4147	–0.9169	–0.9220
$[1^{(11)}2^{(11)}3^{(11)}]_c$	1.4789	1.4746	1.4973	0.4216	0.4075	–0.9116	–0.9225
$T^* = 5, n^* = 0.7$							
MC	2.940 (2)			–		–1.683 (1)	
$[1^{(11)}2^{(11)}3^{(11)}]_a$	2.9592	2.9613	2.9915	0.09464	0.09345	–1.6697	–1.6843
$[1^{(11)}2^{(11)}3^{(11)}]_b$	2.9602	2.9620	3.0040	0.09470	0.09317	–1.6623	–1.6845
$[1^{(11)}2^{(11)}3^{(11)}]_c$	2.9627	2.9638	3.0397	0.09486	0.09237	–1.6423	–1.6849

involves both 1st and 2nd nn, so that only approximate treatments are possible. The aim of this section is to test the performance of the approximations of Sect. 3 against our MC simulations (again with $N = 1024$ particles) in the case of the TS potential. To that end, we will fix $\lambda_1 = 1.5$, $\lambda = 3$, and $\varepsilon_2 = \varepsilon/2$. This means that the strength of the 2nd nn interactions is weaker in this TS potential than in the SW potential considered in Sect. 4. Therefore, at common values of T^* and n^* , our approximations may be expected to be more accurate for the TS fluid than for the SW fluid.

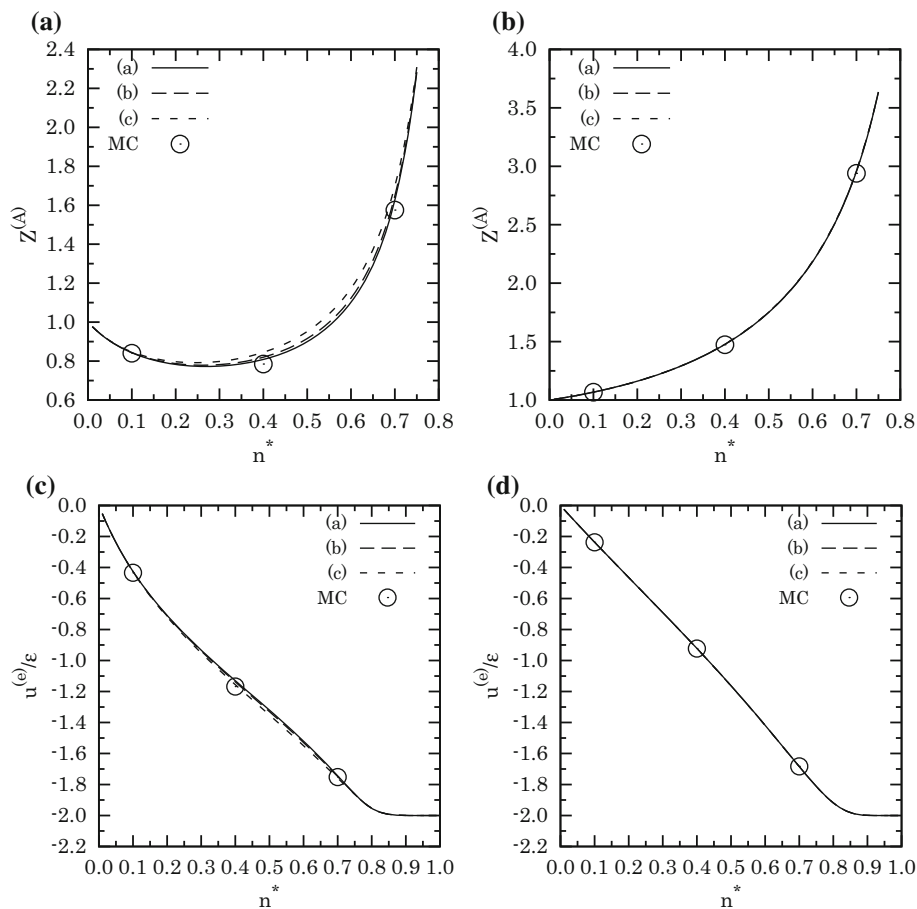


Fig. 7 Plot of the compressibility factor Z [panels **a** and **b**] and of the excess internal energy per particle u [panels **c** and **d**] as functions of density for the SW fluid ($\lambda = 3$) at $T^* = 1$ [panels **a** and **c**] and $T^* = 5$ [panels **b** and **d**]. The curves are theoretical results $Z^{(A)}$ and $u^{(e)}$, as obtained from the approximations $[1^{(11)}2^{(11)}3^{(11)}]_a$ (—), $[1^{(11)}2^{(11)}3^{(11)}]_b$ (---), and $[1^{(11)}2^{(11)}3^{(11)}]_c$ (- - -), while the circles represent MC data. Note that in panels **c**–**d** the three approximations $[1^{(11)}2^{(11)}3^{(11)}]_{a,b,c}$ yield practically indistinguishable results

5.1 Structural Properties

As happened in the case of the SW potential, the approximations described in Sects. 3.1–3.3 lend themselves to analytical implementations in the case of the TS potential. Moreover, due to the hard core at $r = \sigma$, Eq. (4.2) still applies.

Figure 8 shows the RDF obtained from our approximation $[1^{(11)}2^{(11)}]_a$ at several values of n^* and T^* and tests it with the result of our MC simulations. From comparison with Fig. 4, we see that, as expected, the agreement between the theoretical approximation $[1^{(11)}2^{(11)}]_a$ and the MC simulations improves with respect to the SW case treated in Sect. 4. The more sophisticated approximation $[1^{(11)}2^{(11)}3^{(11)}]_a$ does an even better job (not shown). The improvement of the theoretical approximation $[1^{(11)}2^{(11)}3^{(11)}]_a$ when applied to the TS fluid rather than to the SW fluid is confirmed by Fig. 9 at a low temperature ($T^* = 0.5$) and high density ($n^* = 0.7$) [compare with Fig. 5d].

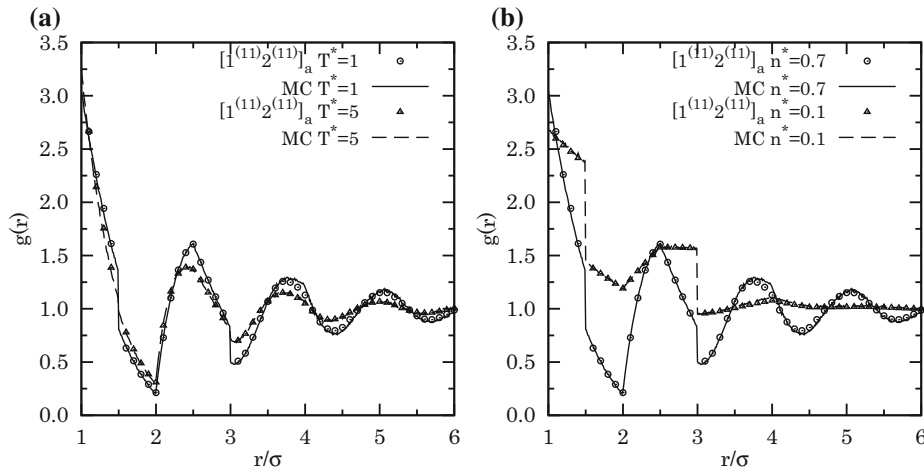
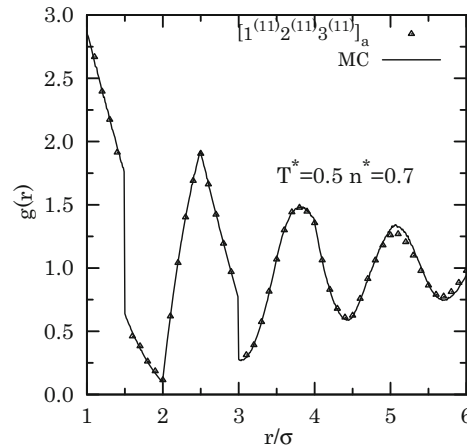


Fig. 8 Plot of $g(r)$ as obtained from MC simulations (— and --) and from the approximation $[1^{(11)}2^{(11)}]_a$ [see Eq. (3.12a)] (\circ and Δ) for the TS fluid ($2\lambda_1 = \lambda = 3, \epsilon_2/\epsilon = \frac{1}{2}$) at **a** $n^* = 0.7$ and two temperatures ($T^* = 1$ and $T^* = 5$, respectively) and **b** $T^* = 1$ and two densities ($n^* = 0.7$ and $n^* = 0.1$, respectively)

Fig. 9 Plot of $g(r)$ as obtained from MC simulations (—) and from the approximation $[1^{(11)}2^{(11)}3^{(11)}]_a$ [see Eq. (3.15a)] (Δ) for the TS fluid ($2\lambda_1 = \lambda = 3, \epsilon_2/\epsilon = \frac{1}{2}$) at $T^* = 0.5$ and $n^* = 0.7$



5.2 Thermodynamic Properties

As discussed in Sect. 4.2, the “direct” route $n = \ell/\tilde{p}_\ell$ allows one to obtain $Z^{(A)}, u^{(A)}$, and $\chi_T^{(A)}$. The compressibility route yields $\chi_T^{(c)}$ and $Z^{(c)}$ again from Eqs. (4.6) and (4.8). As for $u^{(e)}$ and $Z^{(v)}$, the counterparts of Eqs. (4.4) and (4.5) are

$$\frac{u^{(e)}}{\epsilon} = - \int_1^{\lambda_1} dr [p_1(r) + p_2(r)] - \frac{\epsilon_2}{\epsilon} \int_{\lambda_1}^{\lambda} dr [p_1(r) + p_2(r)], \tag{5.2}$$

$$\begin{aligned} Z^{(v)} &= 1 + n \left[g(1^+) - \lambda_1 \left(e^{\beta(\epsilon - \epsilon_2)} - 1 \right) g(\lambda_1^+) - \lambda \left(e^{\beta\epsilon_2} - 1 \right) g(\lambda^+) \right] \\ &= 1 + p_1(1^+) - \lambda_1 \left(e^{\beta(\epsilon - \epsilon_2)} - 1 \right) [p_1(\lambda_1^+) + p_2(\lambda_1^+)] \\ &\quad - \lambda \left(e^{\beta\epsilon_2} - 1 \right) [p_1(\lambda^+) + p_2(\lambda^+)]. \end{aligned} \tag{5.3}$$

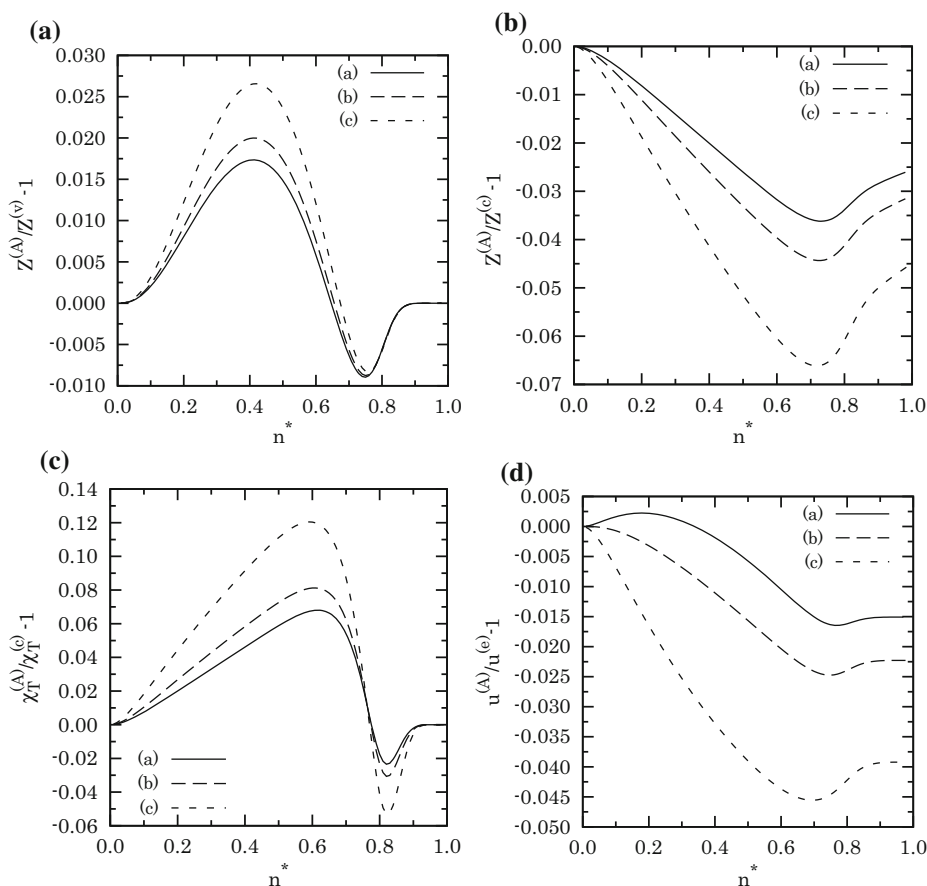


Fig. 10 Plot of the relative differences **a** $Z^{(A)}/Z^{(v)} - 1$, **b** $Z^{(A)}/Z^{(c)} - 1$, **c** $\chi_T^{(A)}/\chi_T^{(c)} - 1$, and **d** $u^{(A)}/u^{(e)} - 1$ as functions of density for the TS fluid ($2\lambda_1 = \lambda = 3$, $\varepsilon_2/\varepsilon = \frac{1}{2}$) at $T^* = 1$. The curves correspond to the approximations $[1^{(11)}2^{(11)}3^{(11)}]_a$ (—), $[1^{(11)}2^{(11)}3^{(11)}]_b$ (- -), and $[1^{(11)}2^{(11)}3^{(11)}]_c$ (- · -)

Of course, since $p_2(r) = 0$ for $r < 2$, the term $p_2(r)$ in the first integral of Eq. (5.2) and the term $p_2(\lambda_1^+)$ in Eq. (5.3) can be removed if $\lambda_1 < 2$, as happens in our specific case ($\lambda_1 = 1.5$, $\lambda = 3$).

From Fig. 10 we see again that the approximation $[1^{(11)}2^{(11)}3^{(11)}]_a$ is thermodynamically more consistent than $[1^{(11)}2^{(11)}3^{(11)}]_b$, and the latter is more consistent than $[1^{(11)}2^{(11)}3^{(11)}]_c$. Also comparison between Figs. 6 and 10 shows that, as expected, our approximations are much more consistent for the TS fluid than for the SW fluid at common values of T^* and n^* .

Table 3 and Fig. 11 show a comparison with our MC simulation data. The conclusions are similar to those drawn from Table 2 and Fig. 7 in the SW case, except that now the performance of the approximations are even better. In fact, from Fig. 11 one can notice that the three approximations $[1^{(11)}2^{(11)}3^{(11)}]_{a,b,c}$ are practically indistinguishable, even at $T^* = 1$.

Author's personal copy

One-Dimensional Fluids with Second Nearest-Neighbor Interactions

Table 3 Some thermodynamic quantities for the TS fluid ($2\lambda_1 = \lambda = 3, \varepsilon_2/\varepsilon = \frac{1}{2}$) at several values of T^* and n^*

Method	$Z^{(A)}$	$Z^{(v)}$	$Z^{(c)}$	$\chi_T^{(A)}$	$\chi_T^{(c)}$	$u^{(A)}/\varepsilon$	$u^{(e)}/\varepsilon$
$T^* = 1, n^* = 0.1$							
MC	0.9425 (5)			–		–0.2341 (6)	
$[1^{(11)}2^{(11)}3^{(11)}]_a$	0.9440	0.9421	0.9467	1.0964	1.0882	–0.2324	–0.2320
$[1^{(11)}2^{(11)}3^{(11)}]_b$	0.9443	0.9421	0.9481	1.0954	1.0841	–0.2319	–0.2321
$[1^{(11)}2^{(11)}3^{(11)}]_c$	0.9445	0.9420	0.9518	1.0927	1.0730	–0.2306	–0.2322
$T^* = 1, n^* = 0.4$							
MC	1.0075 (8)			–		–0.750 (1)	
$[1^{(11)}2^{(11)}3^{(11)}]_a$	1.0193	1.0019	1.0401	0.7279	0.6958	–0.7391	–0.7404
$[1^{(11)}2^{(11)}3^{(11)}]_b$	1.0228	1.0028	1.0501	0.7231	0.6832	–0.7338	–0.7420
$[1^{(11)}2^{(11)}3^{(11)}]_c$	1.0317	1.0051	1.0761	0.7111	0.6515	–0.7214	–0.7459
$T^* = 1, n^* = 0.7$							
MC	1.905 (3)			–		–1.2302 (8)	
$[1^{(11)}2^{(11)}3^{(11)}]_a$	1.9182	1.9304	1.9895	0.1269	0.1204	–1.2105	–1.2290
$[1^{(11)}2^{(11)}3^{(11)}]_b$	1.9240	1.9349	2.0126	0.1272	0.1197	–1.2003	–1.2300
$[1^{(11)}2^{(11)}3^{(11)}]_c$	1.9392	1.9468	2.0761	0.1280	0.1177	–1.1763	–1.2325
$T^* = 5, n^* = 0.1$							
MC	1.0831 (1)			–		–0.1441 (2)	
$[1^{(11)}2^{(11)}3^{(11)}]_a$	1.0832	1.0832	1.0833	0.8493	0.8489	–0.1445	–0.1445
$[1^{(11)}2^{(11)}3^{(11)}]_b$	1.0832	1.0832	1.0834	0.8493	0.8487	–0.1445	–0.1445
$[1^{(11)}2^{(11)}3^{(11)}]_c$	1.0832	1.0832	1.0837	0.8493	0.8481	–0.1444	–0.1445
$T^* = 5, n^* = 0.4$							
MC	1.5287 (4)			–		–0.6090 (5)	
$[1^{(11)}2^{(11)}3^{(11)}]_a$	1.5311	1.5304	1.5347	0.4064	0.4038	–0.6076	–0.6083
$[1^{(11)}2^{(11)}3^{(11)}]_b$	1.5312	1.5304	1.5364	0.4063	0.4025	–0.6072	–0.6084
$[1^{(11)}2^{(11)}3^{(11)}]_c$	1.5316	1.5306	1.5415	0.4061	0.3989	–0.6057	–0.6085
$T^* = 5, n^* = 0.7$							
MC	3.003 (2)			–		–1.188 (1)	
$[1^{(11)}2^{(11)}3^{(11)}]_a$	3.0270	3.0275	3.0421	0.09520	0.09470	–1.1845	–1.1882
$[1^{(11)}2^{(11)}3^{(11)}]_b$	3.0272	3.0277	3.0487	0.09522	0.09453	–1.1826	–1.1882
$[1^{(11)}2^{(11)}3^{(11)}]_c$	3.0279	3.0282	3.0680	0.09526	0.09403	–1.1771	–1.1883

6 The Fisher–Widom Line of the Square-Well Model

Rather general arguments [17,23] suggest a behavior of the one-dimensional $g(r)$ at large r of the following form,

$$g(r) - 1 = \sum_i A_i e^{s_i r} \simeq A_1 e^{s_1 r} + A_2 e^{s_2 r} + A_3 e^{s_3 r} + \dots, \tag{6.1}$$

where the sum runs over the discrete set of nonzero poles s_i of the Laplace transform $\widehat{G}(s)$, the amplitudes $A_i = \text{Res} [\widehat{G}(s)]_{s_i}$ being the associated (in general complex) residues, and the

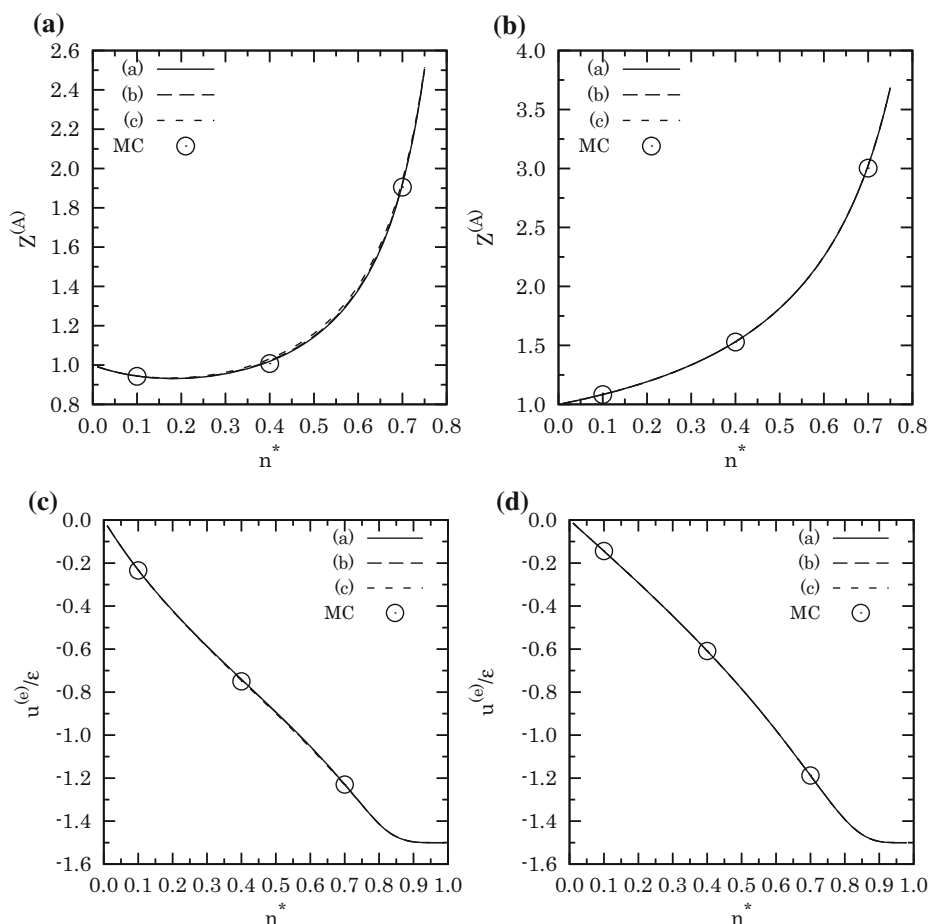


Fig. 11 Plot of the compressibility factor Z [panels **a** and **b**] and of the excess internal energy per particle u [panels **c** and **d**] as functions of density for the TS fluid ($2\lambda_1 = \lambda = 3, \epsilon_2/\epsilon = \frac{1}{2}$) at $T^* = 1$ [panels **a** and **c**] and $T^* = 5$ [panels **b** and **d**]. The curves are theoretical results $Z^{(A)}$ and $u^{(e)}$, as obtained from the approximations $[1^{(11)}2^{(11)}3^{(11)}]_a$ (—), $[1^{(11)}2^{(11)}3^{(11)}]_b$ (- -), and $[1^{(11)}2^{(11)}3^{(11)}]_c$ (- · -), while the circles represent MC data. Note that the three approximations $[1^{(11)}2^{(11)}3^{(11)}]_{a,b,c}$ yield practically indistinguishable results

ordering $0 > \text{Re}(s_1) \geq \text{Re}(s_2) \geq \text{Re}(s_3) \geq \dots$ is adopted. Note that in Eq. (6.1) the poles are assumed to be single. In case of s_i being a multiple pole, the corresponding term $A_i e^{s_i r}$ must be replaced by $\text{Res} [e^{sr} \widehat{G}(s)]_{s_i}$. For the discussion below it is sufficient to assume that the pole with the largest real part is single.

Equation (6.1) shows that the asymptotic decay of the total correlation function $h(r) = g(r) - 1$ is determined by the nature of the pole(s) with the largest real part of the Laplace transform $\widehat{G}(s)$ of the RDF. If $s_1 = -\kappa + i\omega$ and $s_2 = -\kappa - i\omega$ make a pair of complex conjugates, then the asymptotic decay of $h(r)$ is *oscillatory*:

$$h(r) \approx 2|A_1|e^{-\kappa r} \cos(\omega r + \delta), \tag{6.2}$$

Author's personal copy

One-Dimensional Fluids with Second Nearest-Neighbor Interactions

where δ is the argument of A_1 , i.e., $A_{1,2} = |A_1|e^{\pm i\delta}$. On the other hand, if $s_1 = -\kappa'$ is a real pole, the decay is *monotonic*, namely

$$h(r) \approx A_1 e^{-\kappa' r}. \tag{6.3}$$

In general, the oscillatory decay (6.2) reflects the correlating effects of the repulsive part of the interaction potential, while the correlating effects of the attractive part are reflected by the monotonic decay (6.3). At a given temperature, the first type of decay takes place at sufficiently high values of pressure (or density), whereas the monotonic decay occurs at sufficiently low values of pressure (or density). Following Fisher and Widom [23], the locus of transition points from one type to the other one ($\kappa' = \kappa$) defines a line (the so-called FW line) in the pressure (or density) versus temperature plane, with a maximum defining a sort of pseudocritical point.

If the interactions are restricted to the 1st nn, the exact solution is given by Eq. (2.28), so that the poles of $\widehat{G}(s)$ are the roots of $\widehat{p}_1(s) - 1$ [21,23]. Due to the property (2.24), those are also roots of $\widehat{p}_\ell(s) - 1$ with $\ell = 2, 3, \dots$. On the other hand, this equivalence is broken if the interactions involve 2nd nn and we use our approximations (3.12) and (3.15). Thus, the poles of $\widehat{G}(s)$ are determined by the roots of $\widehat{p}_1(s) - 1$ in the approximations (3.12b) and (3.15c), the roots of $\widehat{p}_2(s) - 1$ in the approximations (3.12a) and (3.15b), and the roots of $\widehat{p}_3(s) - 1$ in the approximation (3.15a). In each case, the FW line is obtained by solving the set of coupled equations

$$\widehat{p}_\ell(s = -\kappa) - 1 = 0, \tag{6.4a}$$

$$\text{Re} [\widehat{p}_\ell(s = -\kappa \pm i\omega)] - 1 = 0, \tag{6.4b}$$

$$\text{Im} [\widehat{p}_\ell(s = -\kappa \pm i\omega)] = 0, \tag{6.4c}$$

where in Eq. (6.4a) we have taken into account that $\kappa' = \kappa$ on the FW line. At given T , the solution to Eqs. (6.4) (with $\ell = 1, 2$, or 3) gives p , κ , and ω on the FW line. We see that, as happened with the thermodynamic quantities, $[1^{(\alpha_1)2^{(\alpha_2)}}]_a = [1^{(\alpha_1)2^{(\alpha_2)}3^{(\alpha_2)}}]_b$ and $[1^{(\alpha_1)2^{(\alpha_2)}}]_b = [1^{(\alpha_1)2^{(\alpha_2)}3^{(\alpha_3)}}]_c$ in what concerns the FW line. Again, we can focus on the three approximations $[1^{(11)2^{(11)}3^{(11)}}]_{a,b,c}$.

Now we apply the above general description to the SW potential (4.1) with varying range λ . In Fig. 12a we show a comparison between the three approximations $[1^{(11)2^{(11)}3^{(11)}}]_{a,b,c}$ at $\lambda = 2.1$. They agree well up to approximately the location of the pseudocritical point, i.e., for $T^* \gtrsim 1$. At lower temperatures, however, the two approximations $[1^{(11)2^{(11)}3^{(11)}}]_{b,c}$ [i.e., the solutions to Eq. (6.4) with $\ell = 1, 2$] exhibit an unphysical increase of the pressure as temperature decreases. This may be regarded as an artifact of the approximations, which break down at small temperatures when the particles of the fluid are highly coupled. Nevertheless, the approximation $[1^{(11)2^{(11)}3^{(11)}}]_a$ is qualitatively correct.

The influence of λ on the FW line is analyzed in Fig. 12b, where the exact results for $\lambda = 1.5$ and 2 are contrasted with those resulting from our approximation $[1^{(11)2^{(11)}3^{(11)}}]_a$ for $\lambda = 2.1, 2.2$, and 2.3 . We can see that the most relevant trends observed when increasing λ in the “safe” exact domain ($\lambda \leq 2$) are extended to the domain $\lambda > 2$. In particular, the location of the pseudocritical point moves to larger values of temperature and, especially, of pressure as the range λ increases. Also, at a given T^* (larger than the pseudocritical value), the oscillatory–monotonic transition takes place at noticeably higher values of p^* , even if λ is increased very little. Nonetheless, the approximation $[1^{(11)2^{(11)}3^{(11)}}]_a$ predicts too sharp a decay of the FW line below the pseudocritical temperature, even crossing the lines of smaller λ . We believe this to be an artifact of the approximation, which becomes less reliable as temperature decreases.

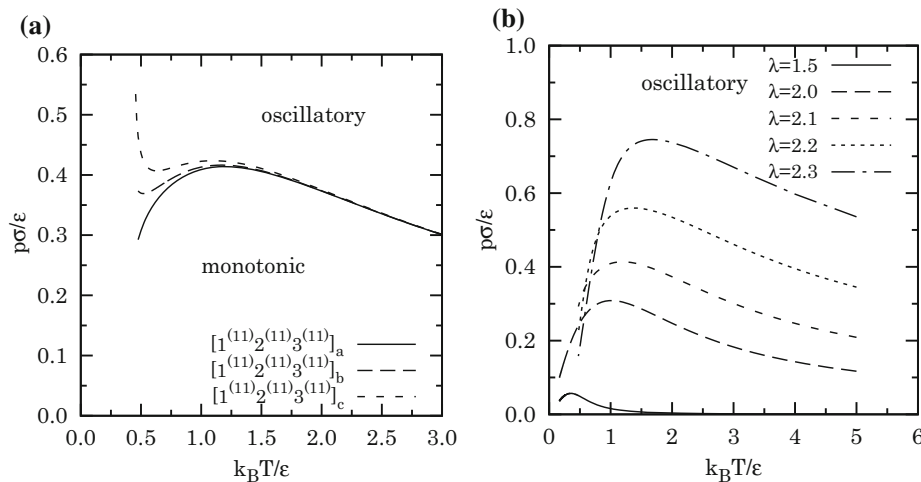


Fig. 12 **a** FW line for the SW fluid with $\lambda = 2.1$, as calculated from the approximations $[1^{(11)}2^{(11)}3^{(11)}]_a$ (—), $[1^{(11)}2^{(11)}3^{(11)}]_b$ (---), and $[1^{(11)}2^{(11)}3^{(11)}]_c$ (- - -). **b** FW lines for the SW fluid with $\lambda = 1.5$ (—), 2 (---), 2.1 (- - -), 2.2 (· · ·), and 2.3 (- · -); the lines corresponding to $\lambda = 1.5$ and 2 are exact, while those corresponding to $\lambda > 2$ were calculated from the approximation $[1^{(11)}2^{(11)}3^{(11)}]_a$

7 Conclusions

In this work we have proposed a detailed analysis of approximate analytical extensions to 2nd nn fluids of the exact analytical solution of 1st nn fluids confined in one spatial dimension. The inclusion of the 2nd nn interactions renders the calculation of the partition function and the various correlation functions extremely more cumbersome than in the 1st nn case. In particular, the exact solution is not tractable anymore. A detailed diagrammatic analysis of the exact structure of the correlation functions and of their various approximations has also been carried out in the spirit of the Mayer cluster diagrams.

Two stages have been followed to determine the RDF $g(r)$. In the first stage, attention is focused on the ℓ th nn probability distribution function $p_\ell(r)$. The exact $p_\ell(r)$, which involves a many-body problem, is approximated by $p_\ell^{(k_1 k_2)}(r)$, where only integrals involving the k_1 particles to the left of particle 1 and the k_2 particles to the right of particle $\ell + 1$ are incorporated. In the second stage, a finite number of functions $\hat{p}_1(s), \hat{p}_2(s), \dots, \hat{p}_\ell(s)$ (in Laplace space) are used to approximate the Laplace transform of the RDF, $\hat{G}(s)$. This double sequence of approximations becomes the exact solution only in the infinite order limit, i.e., if $\ell \rightarrow \infty$ in the construction of $\hat{G}(s)$ and $k_1, k_2 \rightarrow \infty$ in the construction of $p_\ell^{(k_1 k_2)}(r)$. Here we have restricted ourselves to $k_1, k_2 \leq 1$ in the construction of $p_\ell^{(k_1 k_2)}(r)$ and to $\ell = 3$ in the construction of $\hat{G}(s)$. Out of this, our recommended approximation is given by Eq. (3.15a) complemented by Eqs. (3.4), (3.7), and (3.10). We have denoted this combined approximation as $[1^{(11)}2^{(11)}3^{(11)}]_a$.

Our theoretical approach has been assessed by comparison with our own MC simulations for the SW and TS fluids, in both cases with the largest potential range compatible with 2nd nn interactions. The comparison has been made both at the level of the most common thermodynamic quantities, such as the equation of state and the internal energy per particle, and at the level of the RDF. Also some internal thermodynamic consistency tests (three different routes to the equation of state, two to the isothermal susceptibility, and two to

Author's personal copy

One-Dimensional Fluids with Second Nearest-Neighbor Interactions

the internal energy) have been carefully addressed. We have found that $[1^{(11)}2^{(11)}3^{(11)}]_a$ is a sufficiently good approximation for the SW fluid, while the simpler approximation $[1^{(11)}2^{(11)}]_a$ is already good enough for the TS potential (at least when the depth of the second step, affecting also the 2nd nn, is one half the depth of the first step, affecting only the 1st nn).

Finally, we have calculated the FW line (separating states where the correlation function decays monotonically from those where it decays in an oscillatory way) of the SW model for various ranges. Although the reliability of the approximation $[1^{(11)}2^{(11)}3^{(11)}]_a$ is expected to worsen at temperatures lower than the pseudocritical one, the results clearly show that the FW line is rather sensitive to changes in the potential range, the pseudocritical point moving to higher temperatures and, especially, pressures as the range increases

The analysis presented here can become a useful tool, as an approximate extension to the 2nd nn fluid of the exact 1st nn fluid analytical solution, whenever one wants to find an easy, albeit approximate, solution for the fluid properties, both structural and thermodynamic. It can avoid having to resort to simulations or serve as a guide to them, with the necessary caution of keeping in mind that the reliability of the approach is expected to worsen at very low temperatures.

Our general scheme can be easily generalized to the inclusion of any number of nn interactions, but one must treat each case independently. This is an alternative procedure to the eigenvalue route used, for example, in Ref. [19] towards the analytical solution of a generic (non-quantum) one-dimensional fluid of impenetrable particles interacting through pair interactions which reflect the fact that the particles are “living” on the line or simply moving on the line but embedded in a higher dimensional space. It is also worth mentioning that the isothermal-isobaric ensemble results can be regarded as evaluation of a generating function; embedding in an overcomplete density functional formalism [38] makes extension to non-1st nn interactions possible.

On the other hand, the method cannot be easily generalized to more than one spatial dimension since a crucial ingredient is the ordering of the particles on the line, which is lost in dimensions higher than one. Of course, following a bottom-up strategy, one is free to blindly adapt our approximation scheme, for example, to the more realistic three-dimensional case (where even the SW potential with $\lambda < 2$ cannot be solved exactly), but the result remains uncertain.

Acknowledgements R.F. is grateful to the Departamento de Física, Universidad de Extremadura, for its hospitality during a two-month stay in early 2017, when this work was initiated. A.S. acknowledges the financial support of the Ministerio de Economía y Competitividad (Spain) through Grant No. FIS2016-76359-P and the Junta de Extremadura (Spain) through Grant No. GR15104, both partially financed by “Fondo Europeo de Desarrollo Regional” funds.

A Derivation of Eqs. (2.14), (2.16), and (2.18)

A.1 Equation (2.14)

By a change of variables from absolute coordinates ($\{x_i\}$) to relative coordinates ($\{r_i\}$), we find that Eq. (2.12) can be rewritten as

$$p_1(r) \propto e^{-\beta\phi(r)} \int_r^\infty dL e^{-\beta p L} \int_0^{L-r} dr_3 e^{-\beta\phi(r_3)} e^{-\gamma\beta\phi(r+r_3)} \\ \times \int_0^{L-r-r_3} dr_4 e^{-\beta\phi(r_4)} e^{-\gamma\beta\phi(r_3+r_4)} \dots$$

Author's personal copy

R. Fantoni, A. Santos

$$\begin{aligned} & \times \int_0^{L-r-r_3-\dots-r_{N-1}} dr_N e^{-\beta\phi(r_N)} e^{-\gamma\beta\phi(r_{N-1}+r_N)} \\ & \times e^{-\beta\phi(r_{N+1})} e^{-\gamma\beta\phi(r_N+r_{N+1})} e^{-\gamma\beta\phi(r_{N+1}+r)}, \end{aligned} \tag{A.1}$$

where $r_{N+1} = L - r - r_3 - \dots - r_N$ and we have taken into account that $r_{N+2} = r$. The change of variables $L \rightarrow L' = L - r$ implies that a factor $e^{-\beta pr}$ comes out of the integrals. Exchanging the integral over L' and the integral over r_3 we get

$$\begin{aligned} p_1(r) & \propto e^{-\beta[pr+\phi(r)]} \int_0^\infty dr_3 e^{-\beta\phi(r_3)} e^{-\gamma\beta\phi(r+r_3)} \int_{r_3}^\infty dL' e^{-\beta pL'} \\ & \times \int_0^{L'-r_3} dr_4 e^{-\beta\phi(r_4)} e^{-\gamma\beta\phi(r_3+r_4)} \dots \\ & \times \int_0^{L'-r_3-\dots-r_{N-1}} dr_N e^{-\beta\phi(r_N)} e^{-\gamma\beta\phi(r_{N-1}+r_N)} e^{-\beta\phi(r_{N+1})} \\ & \times e^{-\gamma\beta\phi(r_N+r_{N+1})} e^{-\gamma\beta\phi(r_{N+1}+r)}. \end{aligned} \tag{A.2}$$

Next, changing variables $L' \rightarrow L'' = L' - r_3$ and exchanging the integral over L'' and the integral over r_4 we find

$$\begin{aligned} p_1(r) & \propto e^{-\beta[pr+\phi(r)]} \int_0^\infty dr_3 e^{-\beta[pr_3+\phi(r_3)]} e^{-\gamma\beta\phi(r+r_3)} \\ & \times \int_0^\infty dr_4 e^{-\beta\phi(r_4)} e^{-\gamma\beta\phi(r_3+r_4)} \int_{r_4}^\infty dL'' e^{-\beta pL''} \dots \\ & \times \int_0^{L''-r_4-\dots-r_{N-1}} dr_N e^{-\beta\phi(r_N)} e^{-\gamma\beta\phi(r_{N-1}+r_N)} e^{-\beta\phi(r_{N+1})} \\ & \times e^{-\gamma\beta\phi(r_N+r_{N+1})} e^{-\gamma\beta\phi(r_{N+1}+r)}. \end{aligned} \tag{A.3}$$

This process can be continued with $L'' \rightarrow L''' = L'' - r_4$, $L''' \rightarrow L^{IV} = L''' - r_5, \dots$, until arriving to $L^{(N-1)} = L - r - r_3 - \dots - r_N = r_{N+1}$ (see Fig. 1). After performing all these changes it is easy to see that Eq. (2.14) is finally obtained.

A.2 Equation (2.16)

Using Eq. (2.1) and the pbc, Eq. (2.15) can be rewritten as

$$\begin{aligned} p_2(R) & \propto e^{-\gamma\beta\phi(R)} \int_R^\infty dL e^{-\beta pL} \int_0^R dr_2 e^{-\beta\phi(r_2)} e^{-\beta\phi(R-r_2)} \\ & \times \int_0^{L-R} dr_4 e^{-\beta\phi(r_4)} e^{-\gamma\beta\phi(R-r_2+r_4)} \int_0^{L-R-r_4} dr_5 e^{-\beta\phi(r_5)} e^{-\gamma\beta\phi(r_4+r_5)} \dots \\ & \times \int_0^{L-R-r_4-\dots-r_{N-1}} dr_N e^{-\beta\phi(r_N)} e^{-\gamma\beta\phi(r_{N-1}+r_N)} e^{-\beta\phi(r_{N+1})} \\ & \times e^{-\gamma\beta\phi(r_N+r_{N+1})} e^{-\gamma\beta\phi(r_{N+1}+r_2)}. \end{aligned} \tag{A.4}$$

Analogously to the case of $p_1(r)$, the change of variables $L \rightarrow L' = L - R$ implies that a factor $e^{-\beta pR}$ comes out of the integrals. Exchanging the integral over L' and the integral over r_4 we get

Author's personal copy

One-Dimensional Fluids with Second Nearest-Neighbor Interactions

$$\begin{aligned}
 p_2(R) &\propto e^{-\beta[pR+\gamma\phi(R)]} \int_0^R dr_2 e^{-\beta\phi(r_2)} e^{-\beta\phi(R-r_2)} \\
 &\times \int_0^\infty dr_4 e^{-\beta\phi(r_4)} e^{-\gamma\beta\phi(R-r_2+r_4)} \int_{r_4}^\infty dL' e^{-\beta p L'} \\
 &\times \int_0^{L'-r_4} dr_5 e^{-\beta\phi(r_5)} e^{-\gamma\beta\phi(r_4+r_5)} \dots \\
 &\times \int_0^{L'-r_4-\dots-r_{N-1}} dr_N e^{-\beta\phi(r_N)} e^{-\gamma\beta\phi(r_{N-1}+r_N)} e^{-\beta\phi(r_{N+1})} \\
 &\times e^{-\gamma\beta\phi(r_N+r_{N+1})} e^{-\gamma\beta\phi(r_{N+1}+r_2)}. \tag{A.5}
 \end{aligned}$$

Successive changes of variables $L' \rightarrow L'' = L' - r_4$, $L'' \rightarrow L''' = L'' - r_5$, $L''' \rightarrow L^{IV} = L''' - r_6, \dots$, until $L^{(N-2)} = L - R - r_4 - \dots - r_N = r_{N+1}$ allows one to derive Eq. (2.16).

A.3 Equation (2.18)

As before, use of Eq. (2.1) and of the pbc yields

$$\begin{aligned}
 p_3(\bar{R}) &\propto \int_{\bar{R}}^\infty dL e^{-\beta p L} \int_0^{\bar{R}} dr_2 e^{-\beta\phi(r_2)} e^{-\gamma\beta\phi(\bar{R}-r_2)} \int_0^{\bar{R}-r_2} dr_3 \\
 &\times e^{-\beta\phi(r_3)} e^{-\gamma\beta\phi(r_2+r_3)} e^{-\beta\phi(\bar{R}-r_2-r_3)} \\
 &\times \int_0^{L-\bar{R}} dr_5 e^{-\beta\phi(r_5)} e^{-\gamma\beta\phi(\bar{R}-r_2-r_3+r_5)} \\
 &\times \int_0^{L-\bar{R}-r_5} dr_6 e^{-\beta\phi(r_6)} e^{-\gamma\beta\phi(r_5+r_6)} \dots \\
 &\times \int_0^{L-\bar{R}-r_5-\dots-r_{N-1}} dr_N e^{-\beta\phi(r_N)} e^{-\gamma\beta\phi(r_{N-1}+r_N)} \\
 &\times e^{-\beta\phi(r_{N+1})} e^{-\gamma\beta\phi(r_N+r_{N+1})} e^{-\gamma\beta\phi(r_{N+1}+r_2)}. \tag{A.6}
 \end{aligned}$$

Again, the change of variables $L \rightarrow L' = L - \bar{R}$ implies that a factor $e^{-\beta p \bar{R}}$ comes out of the integrals. Exchanging the integral over L' and the integral over r_5 , changing variables to $L' \rightarrow L'' = L' - r_5$, and continuing this process we finally reach Eq. (2.18).

References

1. Abate, J., Whitt, W.: The Fourier-series method for inverting transforms of probability distributions. *Queueing Syst.* **10**, 5–88 (1992)
2. Archer, A.J., Evans, R.: Relationship between local molecular field theory and density functional theory for non-uniform liquids. *J. Chem. Phys.* **138**, 014,502 (2013)
3. Archer, A.J., Chacko, B., Evans, R.: The standard mean-field treatment of inter-particle attraction in classical DFT is better than one might expect. *J. Chem. Phys.* **147**, 034,501 (2017)
4. Barker, J.A., Henderson, D.: What is “liquid”? Understanding the states of matter. *Rev. Mod. Phys.* **48**, 587–671 (1976)
5. Ben-Naim, A., Santos, A.: Local and global properties of mixtures in one-dimensional systems. II. Exact results for the Kirkwood-Buff integrals. *J. Chem. Phys.* **131**, 164–512 (2009)
6. Bishop, M.: Virial coefficients for one-dimensional hard rods. *Am. J. Phys.* **51**, 1151–1152 (1983)
7. Bishop, M.: WCA perturbation theory for one-dimensional Lennard-Jones fluids. *Am. J. Phys.* **52**, 158–161 (1984)

8. Bishop, M.: A kinetic theory derivation of the second and third virial coefficients of rigid rods, disks, and spheres. *Am. J. Phys.* **57**, 469–471 (1989)
9. Bishop, M., Berne, B.J.: Molecular dynamics of one-dimensional hard rods. *J. Chem. Phys.* **60**, 893–897 (1974)
10. Bishop, M., Boonstra, M.A.: Comparison between the convergence of perturbation expansions in one-dimensional square and triangle-well fluids. *J. Chem. Phys.* **79**, 1092–1093 (1983)
11. Bishop, M., Boonstra, M.A.: Exact partition functions for some one-dimensional models via the isobaric ensemble. *Am. J. Phys.* **51**, 564–566 (1983)
12. Bishop, M., Boonstra, M.A.: A geometrical derivation of the second and third virial coefficients of rigid rods, disks, and spheres. *Am. J. Phys.* **51**, 653–654 (1983)
13. Bishop, M., Boonstra, M.A.: The influence of the well width on the convergence of perturbation theory for one-dimensional square-well fluids. *J. Chem. Phys.* **79**, 528–529 (1983)
14. Bishop, M., Swamy, K.N.: Perturbation theory of one-dimensional triangle- and square-well fluids. *J. Chem. Phys.* **85**, 3992–3994 (1986)
15. Borzi, C., Ord, G., Percus, J.K.: The direct correlation function of a one-dimensional Ising model. *J. Stat. Phys.* **46**, 51–66 (1987)
16. Brader, J.M., Evans, R.: An exactly solvable model for a colloid-polymer mixture in one-dimension. *Physica A* **306**, 287–300 (2002)
17. Evans, R., Henderson, J.R., Hoyle, D.C., Parry, A.O., Sabeur, Z.A.: Asymptotic decay of liquid structure: oscillatory liquid-vapour density profiles and the Fisher-Widom line. *Mol. Phys.* **80**, 755–775 (1993)
18. Fantoni, R.: Non-existence of a phase transition for penetrable square wells in one dimension. *J. Stat. Mech.* P07030 (2010)
19. Fantoni, R.: Exact results for one dimensional fluids through functional integration. *J. Stat. Phys.* **163**, 1247–1267 (2016)
20. Fantoni, R.: One-dimensional fluids with positive potentials. *J. Stat. Phys.* **166**, 1334–1342 (2017)
21. Fantoni, R., Giacometti, A., Malijevský, A., Santos, A.: Penetrable-square-well fluids: analytical study and Monte Carlo simulations. *J. Chem. Phys.* **131**, 124106 (2009)
22. Fantoni, R., Giacometti, A., Malijevský, A., Santos, A.: A numerical test of a high-penetrability approximation for the one-dimensional penetrable-square-well model. *J. Chem. Phys.* **133**, 024101 (2010)
23. Fisher, M.E., Widom, B.: Decay of correlations in linear systems. *J. Chem. Phys.* **50**, 3756–3772 (1969)
24. Hansen, J.P., McDonald, I.R.: *Theory of Simple Liquids*, 3rd edn. Academic Press, London (2006)
25. Harnett, J., Bishop, M.: Monte Carlo simulations of one dimensional hard particle systems. *Comput. Educ. J.* **18**, 73–78 (2008)
26. Herzfeld, K.F., Goepfert-Mayer, M.: On the states of aggregation. *J. Chem. Phys.* **2**, 38–44 (1934)
27. Heying, M., Corti, D.S.: The one-dimensional fully non-additive binary hard rod mixture: exact thermophysical properties. *Fluid Phase Equil.* **220**, 85–103 (2004)
28. Huang, K.: *Statistical Mechanics*. Wiley, New York (1963)
29. Katsura, S., Tago, Y.: Radial distribution function and the direct correlation function for one-dimensional gas with square-well potential. *J. Chem. Phys.* **48**, 4246–4251 (1968)
30. Kikuchi, R.: Theory of one-dimensional fluid binary mixtures. *J. Chem. Phys.* **23**, 2327–2332 (1955)
31. Korteweg, D.T.: On van der Waals's isothermal equation. *Nature* **45**, 152–154 (1891)
32. Lebowitz, J.L., Zomick, D.: Mixtures of hard spheres with nonadditive diameters: some exact results and solution of PY equation. *J. Chem. Phys.* **54**, 3335–3346 (1971)
33. Lebowitz, J.L., Percus, J.K., Zucker, I.J.: Radial distribution functions in crystals and fluids. *Bull. Am. Phys. Soc.* **7**, 415–415 (1962)
34. Nagayima, T.: Statistical mechanics of one-dimensional substances i. *Proc. Phys.-Math. Soc. Jpn.* **22**, 705–720 (1940)
35. Nagayima, T.: Statistical mechanics of one-dimensional substances ii. *Proc. Phys.-Math. Soc. Jpn.* **22**, 1034–1047 (1940)
36. Percus, J.K.: Equilibrium state of a classical fluid of hard rods in an external field. *J. Stat. Phys.* **15**, 505–511 (1976)
37. Percus, J.K.: One-dimensional classical fluid with nearest-neighbor interaction in arbitrary external field. *J. Stat. Phys.* **28**, 67–81 (1982)
38. Percus, J.K.: Density functional theory of single-file classical fluids. *Mol. Phys.* **100**, 2417–2422 (2002)
39. Rayleigh, Lord: On the virial of a system of hard colliding bodies. *Nature* **45**, 80–82 (1891)
40. Ruelle, D.: *Statistical Mechanics: Rigorous Results*. World Scientific, Singapore (1999)
41. Rybicki, G.B.: Exact statistical mechanics of a one-dimensional self-gravitating system. *Astrophys. Space Sci.* **14**, 56–72 (1971)
42. Salsburg, Z.W., Zwanzig, R.W., Kirkwood, J.G.: Molecular distribution functions in a one-dimensional fluid. *J. Chem. Phys.* **21**, 1098–1107 (1953)

Author's personal copy

One-Dimensional Fluids with Second Nearest-Neighbor Interactions

43. Santos, A.: Exact bulk correlation functions in one-dimensional nonadditive hard-core mixtures. *Phys. Rev. E* **76**, 062201 (2007)
44. Santos, A.: Radial distribution function for sticky hard rods. Wolfram Demonstrations Project (2012). <http://demonstrations.wolfram.com/RadialDistributionFunctionForStickyHardRods/>
45. Santos, A.: Radial distribution function for one-dimensional square-well and square-shoulder fluids. Wolfram Demonstrations Project (2015). <http://demonstrations.wolfram.com/RadialDistributionFunctionForOneDimensionalSquareWellAndSqua/>
46. Santos, A.: Radial distribution functions for nonadditive hard-rod mixtures. Wolfram Demonstrations Project (2015). <http://demonstrations.wolfram.com/RadialDistributionFunctionsForNonadditiveHardRodMixtures/>
47. Santos, A.: A Concise Course on the Theory of Classical Liquids. Basics and Selected Topics. Lecture Notes in Physics, vol. 923. Springer, New York (2016)
48. Santos, A., Fantoni, R., Giacometti, A.: Penetrable square-well fluids: exact results in one dimension. *Phys. Rev. E* **77**, 051206 (2008)
49. Santos, A., Yuste, S.B., López de Haro, M.: Rational-function approximation for fluids interacting via piece-wise constant potentials. *Condens. Matter Phys.* **15**, 23602 (2012)
50. Santos, A., Yuste, S.B., López de Haro, M., Bárcenas, M., Orea, P.: Structural properties of fluids interacting via piece-wise constant potentials with a hard core. *J. Chem. Phys.* **139**, 074503 (2013)
51. Schmidt, M.: Fundamental measure density functional theory for nonadditive hard-core mixtures: the one-dimensional case. *Phys. Rev. E* **76**, 031202 (2007)
52. Takahasi, H.: Eine einfache methode zur behandlung der statistischen mechanik eindimensionaler substanzen. *Proc. Phys. Math. Soc. Jpn.* **24**, 60–62 (1942)
53. Tonks, L.: The complete equation of state of one, two, and three-dimensional gases of elastic spheres. *Phys. Rev.* **50**, 955–963 (1936)
54. van Hove, L.: Sur l'intégrale de configuration pour les systèmes de particules à une dimension. *Physica* **16**, 137–143 (1950)

Chapter 56

White-dwarf equation of state and structure: the effect of temperature

Fantoni R., J. Stat. Mech. 113101 (2017)

Title: “White-dwarf equation of state and structure: the effect of temperature”

Abstract: We study the effect of having a finite temperature on the equation of state and structure of a white dwarf. In order to keep the treatment as general as possible we carry out our discussion for ideal quantum gases obeying both the Fermi-Dirac and the Bose-Einstein statistics even though we only use the results for the free electron gas inside a white dwarf. We discuss the effect of temperature on the stability of the star and on the Fermi hole.

PAPER: Quantum statistical physics, condensed matter, integrable systems

White-dwarf equation of state and structure: the effect of temperature

Riccardo Fantoni

Dipartimento di Fisica, Università di Trieste, strada Costiera 11, 34151
Grignano (Trieste), Italy
E-mail: rfantoni@ts.infn.it

Received 2 July 2017

Accepted for publication 17 September 2017

Published 6 November 2017

Online at stacks.iop.org/JSTAT/2017/113101

<https://doi.org/10.1088/1742-5468/aa9339>



CrossMark

Abstract. We study the effect of having a finite temperature on the equation of state and structure of a white dwarf. In order to keep the treatment as general as possible we carry out our discussion for ideal quantum gases obeying both the Fermi–Dirac and the Bose–Einstein statistics even though we only use the results for the free electron gas inside a white dwarf. We discuss the effect of temperature on the stability of the star and on the Fermi hole.

Keywords: quantum gases

J. Stat. Mech. (2017) 113101

Contents

1. Introduction	2
2. The thermodynamics of the ideal quantum gas	4
2.1. Relativistic effects at high density in a gas of fermions.	7
2.2. The onset of quantum statistics.	8
2.3. The Chandrasekhar limit.	10
3. The structure of the ideal quantum gas	12
4. Conclusions	15
Appendix. The adiabatic equation of state for a relativistic ideal electron gas at finite temperature	16
References	16

1. Introduction

A *white dwarf* below the regime of neutron drip, at mass densities less than $4 \times 10^{11} \text{ g cm}^{-3}$, are stars that emit light of a white color due to their relatively high surface temperature of about 10^4 K . Because of their small radii R , luminous white dwarfs, radiating away their residual thermal energy, are characterized by much higher effective temperatures, T , than normal stars even though they have lower luminosities (which vary as $R^2 T^4$). In other words, white dwarfs are much ‘whiter’ than normal stars, hence their name [1–3].

The life of white dwarfs begins when a star dies, they are, therefore, *compact objects* [4]. Star death begins when most of the nuclear fuel has been consumed. A white dwarfs has about one solar mass M_\odot with characteristic radii of about 5000 km and mean densities of around 10^6 g cm^{-3} . They are no longer burning nuclear fuel and are slowly cooling down as they radiate away their residual thermal energy.

They support themselves against gravity by the pressure of cold electrons, near their degenerate, zero temperature state. In 1932 Landau [5] presented an elementary explanation of the equilibrium of a white dwarf that had been previously discovered by Chandrasekhar in 1931 [6–8], building, on the formulation of the Fermi–Dirac statistics in August 1926 [9] and the work of Fowler in December 1926 [10], on the role of the *electron degeneracy pressure* to keep the white dwarf from gravitational collapse. Landau’s explanation can be found in section 3.4 of the book of Shapiro and Teukolsky [4], and fixes the equilibrium maximum mass of the white dwarf at $M_{\text{max}} \sim 1.5M_\odot$, whereas Chandrasekhar’s result was $M_{\text{Ch}} = 1.456M_\odot$ for completely ionized matter made of elements with a ratio between mass number and atomic number equal to 2. Strictly speaking, one would have a matter made of a fluid of electrons and a fluids of nuclei. In the work of Chandrasekhar the fluid of electrons is treated as an ideal gas where the electrons are not interacting among themselves and the nuclei, thousands times heavier, are neglected.

White-dwarf equation of state and structure: the effect of temperature

Despite their high surface temperature, these stars are still considered cold, however, because on a first approximation temperature does not affect the equation of state of its matter. White dwarfs are described as faint stars below the main sequence in the Hertzsprung–Russell diagram. In other words, white dwarfs are less luminous than main-sequence stars of corresponding colors. While slowly cooling, the white dwarfs change in color from white to red and finally to black. White dwarfs can be considered as one possibility for the final stage of stellar evolution since they are considered static over the lifetime of the Universe.

White dwarfs were established in the early 20th century and have been studied and observed ever since. They comprise an estimated 3% of all the stars of our galaxy. Because of their low luminosity, white dwarfs (except the very nearest ones) have been very difficult to detect at any reasonable distance and that is why there was very little observational data supporting the theory at the time of them being discovered. The companion of Sirius, discovered in 1915 by Adams [11, 12], was among the earliest to become known. The cooling of white dwarfs is not only a fascinating phenomenon but in addition offers information of many body physics in a new setting since the circumstances of an original star cannot be built up in a laboratory. Moreover, the evolution and the equation of state for white dwarfs can be useful on Earth, providing us with more understanding of matter and physics describing the Universe.

In this work, we discuss how the Chandrasekhar analysis at zero temperature should be changed in order to take into account the effect of having a quantum ideal gas at finite (non-zero) temperature. For the sake of generality we will treat in parallel the case of the Fermi and the Bose ideal gases. Only the Fermi case is appropriate for the description of the white dwarf interior made of ionized matter characterized by a sea of free cold electrons (as Chandrasekhar did, we will neglect the Coulomb interaction between the electrons and disregard the nuclei in order to keep the treatment analytically solvable. We will also use Newtonian gravity to study the star stability disregarding general relativistic effects). At the typical surface temperature and density of a white dwarf the momentum thermal average fraction of particles having momentum $\hbar\mathbf{k}$ and a full relativistic dispersion relation ($\mathcal{C}_k/\mathcal{C}_0$ where \mathcal{C}_k is given by equation (2.25) below) varies appreciably over a k range that is a fraction of 0.933¹ of the k range where it is different from zero. So we generally expect the effect of temperature to play a role in the behavior of the ideal quantum gas. We will pursue our analysis for both the thermodynamic properties: as the validity of the various polytropic adiabatic equation of state as a function of density, and for the structural properties, such as the Fermi hole.

The paper is organized as follows: in section 2 we review the thermodynamic properties of the ideal quantum gases at finite temperatures. This section contains three subsections, in the first one, section 2.1, we discuss the importance of a full relativistic treatment at high densities, in the second one, section 2.2, we discuss the onset of quantum statistics as the star collapses, and in the third one, section 2.3, we present the revised Chandrasekhar analysis. In section 3 we present our study of the structure of the ideal quantum gases at finite temperature and in the full relativistic regime.

¹This value will get smaller as the star cools down in view of equation (2.20) and will eventually become close to zero as the momentum thermal average fraction approaches a step function.

2. The thermodynamics of the ideal quantum gas

We want to find the thermodynamic grand potential of a system of many free fermions or bosons with a rest mass m in thermodynamic equilibrium at an inverse temperature $\beta = 1/k_B T$.

The Hamiltonian of the system is

$$\mathcal{H} = \sum_i (-\hbar^2 c^2 \Delta_i + m^2 c^4)^{1/2}, \tag{2.1}$$

with Δ the Laplacian and c the speed of light.

Assuming the many particles are distinguishable (Boltzmannons) the density matrix operator, $\hat{\rho}_D$, satisfies the Bloch equation

$$\frac{\partial \hat{\rho}_D(\beta)}{\partial \beta} = -\mathcal{H} \hat{\rho}_D(\beta), \tag{2.2}$$

$$\hat{\rho}_D(0) = \mathcal{I}, \tag{2.3}$$

where \mathcal{I} is the identity operator. The solution of equation (2.2) in coordinate representation $\mathbf{R} = (\mathbf{r}_1, \dots, \mathbf{r}_N)$, where \mathbf{r}_i is the position of the i th spinless particle in three-dimensional space, has the following solution

$$\rho_D(R_0, R_1; \beta) = \langle R_0 | e^{-\beta \mathcal{H}} | R_1 \rangle = \int \frac{d\mathbf{K}}{(2\pi)^{3N}} e^{-i\mathbf{K} \cdot (\mathbf{R}_0 - \mathbf{R}_1)} e^{-\beta \sum_i (\hbar^2 c^2 \mathbf{k}_i^2 + m^2 c^4)^{1/2}}, \tag{2.4}$$

where $\mathbf{K} = (\mathbf{k}_1, \dots, \mathbf{k}_N)$ and $\mathbf{R}_n = (\mathbf{r}_1^n, \dots, \mathbf{r}_N^n)$. A very simple calculation yields the propagator ρ_D in closed form. The result can be cast in the following form

$$\rho_D = \prod_i \mathcal{R}(\mathbf{r}_i^1, \mathbf{r}_i^0), \tag{2.5}$$

where \mathcal{R} in one dimension is

$$\mathcal{R}_{1d}(\mathbf{r}^1, \mathbf{r}^0) = \frac{mc^2 \beta}{\pi \Psi^{1/2}} K_1 \left(\frac{mc}{\hbar} \Psi^{1/2} \right), \tag{2.6}$$

where $\Psi = (\mathbf{r}^1 - \mathbf{r}^0)^2 + (\hbar c \beta)^2$ and K_ν is the familiar modified Bessel functions of order ν . In three dimensions we thus find

$$\begin{aligned} \mathcal{R}(\mathbf{r}^1, \mathbf{r}^0) &= -\frac{1}{2\pi |\mathbf{r}^1 - \mathbf{r}^0|} \frac{d\mathcal{R}_{1d}(\mathbf{r}^1, \mathbf{r}^0)}{d|\mathbf{r}^1 - \mathbf{r}^0|} \\ &= \frac{mc^2 \beta}{4\pi^2 \Psi^{3/2}} \left[\frac{mc}{\hbar} \Psi^{1/2} K_0 \left(\frac{mc}{\hbar} \Psi^{1/2} \right) + 2K_1 \left(\frac{mc}{\hbar} \Psi^{1/2} \right) + \frac{mc}{\hbar} \Psi^{1/2} K_2 \left(\frac{mc}{\hbar} \Psi^{1/2} \right) \right]. \end{aligned} \tag{2.7}$$

Note that for the non-relativistic gas, when $\mathcal{H} = -\lambda \sum_i \Delta_i$, ρ_D would have been the usual Gaussian $\Lambda^{-3N} e^{-(\mathbf{R}_1 - \mathbf{R}_0)^2 / 4\lambda\beta}$, with $\lambda = \hbar^2 / 2m$ and $\Lambda = \sqrt{4\pi\beta\lambda}$, the de Broglie thermal wavelength.

Taking care of the indistinguishability of the particles we can describe a system of bosons and fermions with spin $s = (g - 1)/2$ through density matrices, $\hat{\rho}_{B,F}$, which are obtained from the distinguishable one opportunely symmetrized or antisymmetrized,

White-dwarf equation of state and structure: the effect of temperature

respectively. The corresponding grand canonical partition functions can then be found through a standard procedure [13] from $\Theta_{B,F} = e^{-\beta\Omega_{B,F}} = \sum_{N=0}^{\infty} Z_{B,F}^N e^{N\mu}$ where $Z_{B,F}^N = e^{-\beta F_{B,F}^N}$ is the trace of $\hat{\rho}_{B,F}$. Here $\mu = (\ln z)/\beta$ is the chemical potential, F is the Helmholtz free energy, and Ω is the grand thermodynamic potential.

If V is the volume occupied by the system of particles, the pressure is given by $P = -\Omega/V$, and the average number of particles, $N = nV = -z\partial\beta\Omega/\partial z$, where n is the number density. We find for bosons

$$\beta P = \frac{gm^2c}{2\pi^2\beta\hbar^3} \sum_{\nu=1}^{\infty} \frac{z^\nu}{\nu^2} K_2(\beta mc^2\nu), \tag{2.8}$$

$$n = \frac{gm^2c}{2\pi^2\beta\hbar^3} \sum_{\nu=1}^{\infty} \frac{z^\nu}{\nu} K_2(\beta mc^2\nu), \tag{2.9}$$

and for fermions

$$\beta P = \frac{gm^2c}{2\pi^2\beta\hbar^3} \sum_{\nu=1}^{\infty} \frac{(-1)^{\nu-1} z^\nu}{\nu^2} K_2(\beta mc^2\nu), \tag{2.10}$$

$$n = \frac{gm^2c}{2\pi^2\beta\hbar^3} \sum_{\nu=1}^{\infty} \frac{(-1)^{\nu-1} z^\nu}{\nu} K_2(\beta mc^2\nu). \tag{2.11}$$

Clearly in the zero temperature limit ($\beta \rightarrow \infty$) these reduce to (see section 2.3 of [4] and our appendix)

$$P = \frac{g}{2} \frac{mc^2}{\lambda^3} \phi(x), \tag{2.12}$$

$$n = \frac{g}{2} \frac{x^3}{3\pi^2\lambda^3}, \tag{2.13}$$

$$\phi(x) = \frac{1}{8\pi^2} \left[x\sqrt{1+x^2} \left(\frac{2}{3}x^2 - 1 \right) + \ln \left(x + \sqrt{1+x^2} \right) \right], \tag{2.14}$$

where $\lambda = \hbar/mc$, with m the electron mass, is the electron Compton wavelength.

We can then introduce the polylogarithm, b_μ , of order μ and the companion f_μ function,

$$b_\mu(z) = \sum_{\nu=1}^{\infty} \frac{z^\nu}{\nu^\mu}, \tag{2.15}$$

$$f_\mu(z) = \sum_{\nu=1}^{\infty} \frac{(-1)^{\nu-1} z^\nu}{\nu^\mu} = -b_\mu(-z) = (1 - 2^{1-\mu}) b_\mu(z). \tag{2.16}$$

J. Stat. Mech. (2017) 113101

White-dwarf equation of state and structure: the effect of temperature

At finite temperatures, in the extreme relativistic case, we find for bosons

$$\beta P = \frac{g}{\pi^2(\beta\hbar c)^3} b_4(z), \tag{2.17}$$

$$n = \frac{g}{\pi^2(\beta\hbar c)^3} b_3(z), \tag{2.18}$$

where we used the property $z db_\mu(z)/dz = b_{\mu-1}(z)$, and for fermions

$$\beta P = \frac{g}{\pi^2(\beta\hbar c)^3} f_4(z), \tag{2.19}$$

$$n = \frac{g}{\pi^2(\beta\hbar c)^3} f_3(z). \tag{2.20}$$

In agreement with section 61 of Landau [14]. And in the non-relativistic case, we find for bosons

$$\beta P = \frac{g}{\Lambda^3} b_{5/2}(z), \tag{2.21}$$

$$n = \frac{g}{\Lambda^3} b_{3/2}(z), \tag{2.22}$$

and for fermions

$$\beta P = \frac{g}{\Lambda^3} f_{5/2}(z), \tag{2.23}$$

$$n = \frac{g}{\Lambda^3} f_{3/2}(z), \tag{2.24}$$

in agreement with section 56 of Landau [14]. Recalling that the internal energy of the system is given by $E = -\partial \ln \Theta / \partial \beta$, we find in the extreme relativistic case $E = 3PV$ and in the non-relativistic case $E = 3PV/2$. At very low density n , and high temperature T , when $n/T^{3/2}$ is very small, $b_{3/2}(z) \approx f_{3/2}(z)$ is very small and z is also very small. In this case $b_{3/2}(z) \approx b_{5/2}(z) \approx f_{3/2}(z) \approx f_{5/2}(z) \approx z$ and we find for the quantum gas $E/V \approx (3/2)K_B T n$. That is, the non-relativistic classical limit. For the bosons, as the temperature gets small at fixed density, $b_{3/2}(z)$ increases (see equation (2.22)) and z gets close to 1. $b_\mu(z)$ is a monotonically increasing function of z , which is only defined in $0 \leq z \leq 1$, so the boson ideal gas must have a chemical potential less than zero. $b_{3/2}(1) = \zeta(3/2) \approx 2.612$ and $b_{5/2}(1) = \zeta(5/2) \approx 1.341$, where ζ is the Riemann zeta function. The temperature $T_c = \frac{2\pi\hbar^2}{mk_B} \left(\frac{n/g}{\zeta(3/2)} \right)^{2/3}$ at which $z = 1$ is called the *critical temperature* for the Bose–Einstein condensation in the non-relativistic case. For $T < T_c$ the number of bosons with energy greater than zero will then be $N_> = N(T/T_c)^{3/2}$. The rest $N_0 = N[1 - (T/T_c)^{3/2}]$ bosons are in the lowest energy state, i.e. have zero energy. For the fermions the activity is allowed to vary in $0 \leq z < \infty$ and the functions $f_\mu(z)$ can be extended at $z > 1$ by using the following integral representation $f_x(z) = [\int_0^\infty dy y^{x-1} / (e^y/z + 1)] / \Gamma(x)$, where Γ is the usual gamma function.

J. Stat. Mech. (2017) 113101

White-dwarf equation of state and structure: the effect of temperature

Given the entropy $S = -\partial\Omega/\partial T$ we immediately see that, in both the extreme relativistic and the non-relativistic cases, S/N must be a homogeneous function of order zero in z , and that along an adiabatic process (S/N constant) we must have z constant. Then, on an adiabatic, in the extreme relativistic case, $P \propto n^{1+1/3}$, a polytrope of index 3, and in the non-relativistic case, $P \propto n^{1+2/3}$, a polytrope of index 3/2. This conclusion clearly continues to hold at zero temperature when $z \rightarrow \infty$ and the entropy is zero.

2.1. Relativistic effects at high density in a gas of fermions

The thermal average fraction of particles having momentum $\mathbf{p} = \hbar\mathbf{k}$ is given by

$$C_k = \frac{g}{N} \frac{1}{e^{\beta[\epsilon(k)-\mu]} - \xi} = \frac{g}{N\xi} b_0 (\xi z e^{-\beta\epsilon_k}), \quad V \int \frac{d\mathbf{k}}{(2\pi)^3} C_k = 1, \tag{2.25}$$

where $\xi = +1, -1$ and 0 refer to the Bose, Fermi and Boltzmann gases, respectively.

In a degenerate ($T=0$) Fermi gas we can define the Fermi energy as $\epsilon_F = \mu = \sqrt{p_F^2 c^2 + m^2 c^4}$, in terms of the Fermi momentum p_F . From equation (2.25) it follows that the thermal average fraction of particles having momentum $\mathbf{p} = \hbar\mathbf{k}$ is $C_k = (g/N)\Theta[\mu - \epsilon(k)]$, where Θ is the Heaviside unit step function and $\epsilon(k) = \sqrt{\hbar^2 k^2 c^2 + m^2 c^4}$ is the full relativistic dispersion relation. We will then have for the density

$$n = \frac{g}{h^3} \int_0^{p_F} 4\pi p^2 dp = \frac{4\pi g}{3h^3} p_F^3. \tag{2.26}$$

We then see immediately that at high density the Fermi momentum is also large, and as a consequence the Fermi gas becomes relativistic. By contrast, the degenerate Bose gas will undergo Bose–Einstein condensation and have all the particles in the zero energy state.

At finite temperature, from the results of the previous section, we find that since $f_\mu(z)$ is a monotonously increasing function of z then at large density n , z is also large and at fixed temperature this implies that the chemical potential μ is also large. In view of equation (2.25) this means that in the gas there are fermions of ever increasing momentum so that a relativistic treatment becomes necessary.

From equations (2.10) and (2.11) it is possible (see appendix) to extract the full relativistic adiabatic equation of state as a function of temperature and observe the transition from the low density regime to the high density extreme relativistic one. In figure 1 we show the exponent $\Gamma = d \ln P / d \ln n$ for the adiabatic full relativistic equation of state as a function of density. For the sake of the calculation it may be convenient to use natural units $\hbar = c = k_B = 1$. From the figure we see how at high density (which implies high activity) $\Gamma \rightarrow 4/3$. This figure should be compared with figure 2.3 of [4] for the degenerate Fermi gas. In particular we see how at a temperature of $T = 20\,000$ K the Fermi gas can already be considered extremely relativistic at an electron number density $n \gtrsim 10^{25} \text{ cm}^{-3}$. While we know (see [4] and equations (2.12)–(2.14)) that the completely degenerate gas becomes extremely relativistic for $n \gtrsim 10^{31} \text{ cm}^{-3}$.

J. Stat. Mech. (2017) 113101

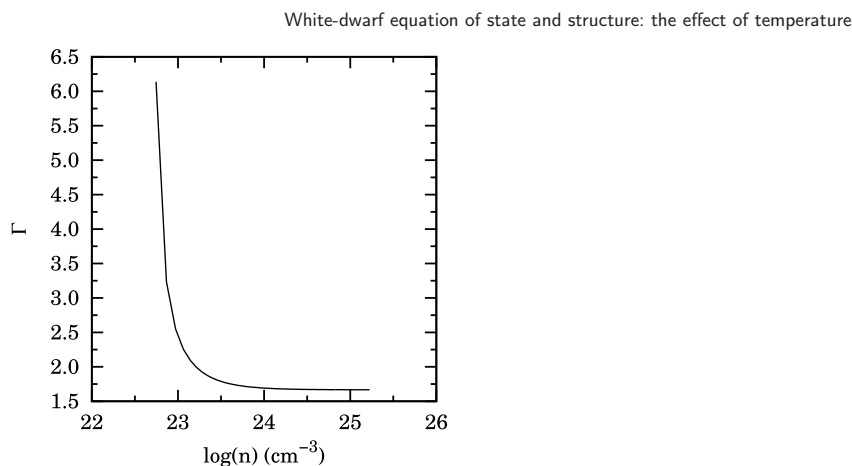


Figure 1. The exponent $\Gamma = d \ln P / d \ln n$ for the adiabatic full relativistic equation of state as a function of density. We chose a temperature $T = 20\,000$ K and zero entropy, $g = 2$, and m is the mass of an electron. n is in cm^{-3} .

2.2. The onset of quantum statistics

For a spherically symmetric distribution of matter, the mass interior to a radius r is given by

$$m(r) = \int_0^r \rho 4\pi r'^2 dr', \quad \text{or} \quad \frac{dm(r)}{dr} = 4\pi r^2 \rho. \tag{2.27}$$

Here, since we are considering non-relativistic matter made of completely ionized elements of atomic number Z and mass number A , $\rho = \rho_0 = \mu_e m_u n$ is the rest mass density with $\mu_e = A/Z$ the mean molecular weight per electron and $m_u = 1.66 \times 10^{-24}$ g the atomic mass unit. If the star is in a steady state, the gravitational force balances the pressure force at every point. To derive the *hydrostatic equilibrium* equation, consider an infinitesimal fluid element lying between r and $r + dr$ and having an area dA perpendicular to the radial direction. The gravitational attraction between $m(r)$ and the mass $dm = \rho dA dr$ is the same as if $m(r)$ were concentrated at a point at the center, while the mass outside exerts no force on dm . The net outward pressure force on dm is $-[P(r + dr) - P(r)]dA$, where P is the pressure. So, in equilibrium,

$$\frac{dP}{dr} = -\frac{Gm(r)\rho}{r^2}, \tag{2.28}$$

where G is the universal gravitational constant².

A consequence of the hydrostatic equilibrium is the *virial theorem*. The gravitational potential energy of the star of radius R is

² Here we are assuming Newtonian theory of gravity. For the general relativistic stability analysis see for example section 6.9 of [4].

White-dwarf equation of state and structure: the effect of temperature

$$\begin{aligned}
 W &= - \int_0^R \frac{Gm(r)}{r} \rho 4\pi r^2 dr \\
 &= \int_0^R \frac{dP}{dr} 4\pi r^3 dr \\
 &= -3 \int_0^R P 4\pi r^2 dr,
 \end{aligned}
 \tag{2.29}$$

where we have integrated by parts.

Now we assume that the gas of fermions is characterized by an adiabatic equation of state

$$P = K \rho_0^\Gamma, \quad K, \quad \Gamma = 1 + \frac{1}{n} \text{ constants},
 \tag{2.30}$$

which is also called a *polytrope* of polytropic index n . For example, for fermions in the extreme relativistic limit we find

$$K = \frac{P}{\rho^{4/3}} = \frac{\pi^{2/3} \hbar c}{g^{1/3} (\mu_e m_u)^{4/3}} \frac{f_4(z)}{f_3^{4/3}(z)},
 \tag{2.31}$$

where z depends on the temperature and density and goes to infinity in the degenerate limit ($\lim_{z \rightarrow \infty} f_4(z)/f_3^{4/3}(z) = 3^{1/3}/2^{5/3}$). At the temperature and density typical of a white dwarf z is very large so the equation of state is practically indistinguishable from the one in the degenerate limit.

Calling u' the energy density of the gas, excluding the rest mass energy, we must have from the first law of thermodynamics, assuming adiabatic changes,

$$d(u/\rho_0) = -Pd(1/\rho_0),
 \tag{2.32}$$

and integration leads to

$$u = \rho_0 c^2 + \frac{P}{\Gamma - 1},
 \tag{2.33}$$

which gives $u' = P/(\Gamma - 1)$. Now equation (2.29) can be rewritten as

$$W = -3(\Gamma - 1)U,
 \tag{2.34}$$

where $U = \int_0^R u' 4\pi r^2 dr$ is the total internal energy of the star. The total energy of the star, $E = W + U$, is then

$$E = -\frac{3\Gamma - 4}{3(\Gamma - 1)} |W|.
 \tag{2.35}$$

If equation (2.30) holds everywhere inside the star of total mass M and constant density, then the gravitational potential energy is given by

$$W = -3 \int_0^M \frac{P}{\rho} dm(r) = -\frac{3(\Gamma - 1)}{5\Gamma} \frac{GM^2}{R},
 \tag{2.36}$$

J. Stat. Mech. (2017) 113101

where we used $d(P/\rho) = [(\Gamma - 1)/\Gamma]Gm(r)d(1/r)$ and integrated by parts using $\Gamma > 1$.

Without nuclear fuel, E decreases due to radiation. According to equations (2.35) and (2.36), $\Delta E < 0$ implies $\Delta R < 0$ whenever $\Gamma > 4/3$. That is, the star contracts and the gas will soon become quantum (see [4] section 3.2). Can the star contract forever, extracting energy from the infinite supply of gravitational potential energy until R goes to zero or until the star undergoes total collapse? The answer is no for stars with $M \sim M_\odot$, as is demonstrated by Chandrasekhar [15] or in the book of Shapiro and Teukolsky [4]. We will reproduce their treatments in the next section.

2.3. The Chandrasekhar limit

The hydrostatic equilibrium equations (2.27) and (2.28) can be combined to give

$$\frac{1}{r^2} \frac{d}{dr} \left(\frac{r^2 dP}{\rho dr} \right) = -4\pi G\rho. \tag{2.37}$$

Substituting the equation of state (2.30) and reducing the result to dimensionless form with

$$\rho = \rho_c \theta^n, \tag{2.38}$$

$$r = a\eta, \tag{2.39}$$

$$a = \sqrt{\frac{(n+1)K\rho_c^{1/n-1}}{4\pi G}}, \tag{2.40}$$

where $\rho_c = \rho(r=0)$ is the central density, we find

$$\frac{1}{\eta^2} \frac{d}{d\eta} \eta^2 \frac{d\theta}{d\eta} = -\theta^n. \tag{2.41}$$

This is the *Lane–Emden equation* for the structure of a polytrope of index n . The boundary conditions at the center of a polytropic star are

$$\theta(0) = 1, \tag{2.42}$$

$$\theta'(0) = 0. \tag{2.43}$$

The condition (2.42) follows directly from equation (2.38). Equation (2.43) follows from the fact that near the center $m(r) \approx 4\pi\rho_c r^3/3$, so that, using equation (2.27), $d\rho/dr = 0$.

Equation (2.41) can be easily integrated numerically, starting at $\eta = 0$ with the boundary conditions (2.42) and (2.43). One finds that for $n < 5$ ($\Gamma > 6/5$), the solutions decreases monotonically and have a zero at a finite value $\eta = \eta_n$: $\theta(\eta_n) = 0$. This point corresponds to the surface of the star, where $P = \rho = 0$. Thus the radius of the star is

$$R = a\eta_n, \tag{2.44}$$

J. Stat. Mech. (2017) 113101

while the mass is

$$\begin{aligned}
 M &= \int_0^R 4\pi r^2 \rho \, dr \\
 &= 4\pi a^3 \rho_c \int_0^{\eta_n} \eta^2 \theta^n \, d\eta \\
 &= -4\pi a^3 \rho_c \int_0^{\eta_n} \frac{d}{d\eta} \left(\eta^2 \frac{d\theta}{d\eta} \right) \, d\eta \\
 &= 4\pi a^3 \rho_c \eta_n |\theta'(\eta_n)|.
 \end{aligned} \tag{2.45}$$

Eliminating ρ_c between equations (2.44) and (2.45) gives the mass–radius relation for polytropes

$$M = 4\pi R^{(3-n)/(1-n)} \left[\frac{(n+1)K}{4\pi G} \right]^{n/(n-1)} \eta_n^{(3-n)/(1-n)} \eta_n^2 |\theta'(\eta_n)|. \tag{2.46}$$

The solutions we are particularly interested in are

$$\Gamma = \frac{5}{3}, \quad n = \frac{3}{2}, \quad \eta_{3/2} = 3.653\,75, \quad \eta_{3/2}^2 |\theta'(\eta_{3/2})| = \omega_{3/2} = 2.714\,06, \tag{2.47}$$

$$\Gamma = \frac{4}{3}, \quad n = 3, \quad \eta_3 = 6.896\,85, \quad \eta_3^2 |\theta'(\eta_3)| = \omega_3 = 2.018\,24, \tag{2.48}$$

which, as explained in section 2.1, corresponds to the low density non-relativistic case and to the high density relativistic case, respectively. Note that for $\Gamma = 4/3$, M is independent of ρ_c and hence R . We conclude that as $\rho_c \rightarrow \infty$, the electrons become more and more relativistic throughout the star, and the mass asymptotically approaches the value

$$M_{\text{Ch}} = 4\pi \omega_3 \left(\frac{K}{\pi G} \right)^{3/2}, \tag{2.49}$$

as $R \rightarrow 0$. The mass limit (2.49) is called the *Chandrasekhar limit* (see equation (36) in [6], equation (58) in [16], or equation (43) in [17]) and represents the maximum possible mass of a white dwarf.

In figure 2 we show the temperature dependence of the Chandrasekhar limit at $\mu_e = 2$.

For the dependence of the star mass on the central density as it develops through the various polytropes, as shown in figure 1, see for example figure 3.2 of [4]. Clearly in the high $\rho_c \rightarrow \infty$ limit we will have in the degenerate limit $z \rightarrow \infty$, from equation (2.31),

$$M \rightarrow M_{\text{Ch}} = 1.456\,39 \left(\frac{2}{\mu_e} \right)^2 M_{\odot}, \tag{2.50}$$

where μ_e can be taken approximately equal to 2 or to $56/26$, assuming that all the elements have been subject to nuclear fusion in the stable iron ^{56}Fe .

The star will not become a black hole if $R > r_s$ (see figure 1.1 of [4]), with $r_s = 2GM_{\text{Ch}}/c^2$ the Schwarzschild radius in the Chandrasekhar limit, i.e.

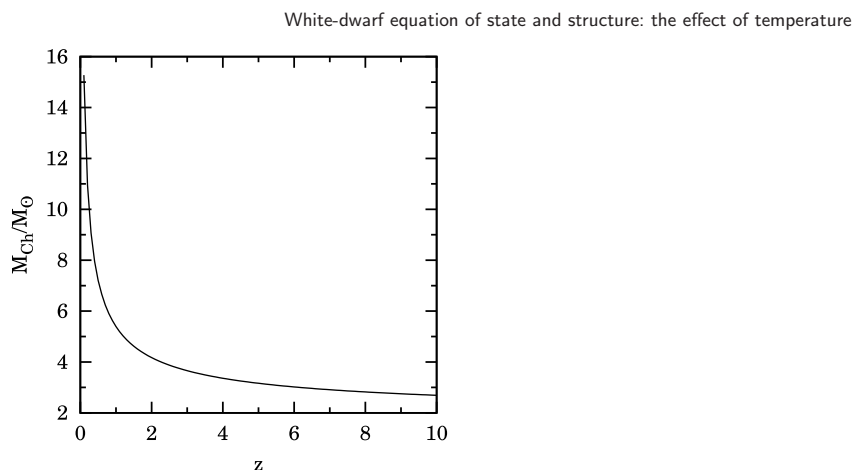


Figure 2. Temperature dependence of the Chandrasekar limit at $\mu_e = 2$. We recall that $z = e^{\beta\mu}$.

$$K < \frac{\eta_3 c^2}{2^3 \omega_3 \rho_c^{1/3}}, \tag{2.51}$$

where K is given by (2.31). This suggests that at high enough central densities the star’s fate is to become a black hole. The critical central density is given in the degenerate $z \rightarrow \infty$ limit by $\bar{\rho}_c = g(\mu_e/2)^4 (2.3542 \times 10^{17} \text{ g cm}^{-3})$ which is well above the one required for the neutron drip.

If the star has a mass lower than M_{Ch} it will not reach the Chandrasekhar limit but will remain on a polytrope with $n < 3$. If the star has a mass higher than M_{Ch} it will eventually evolve through a supernovae explosion into a more compact object as a neutron star (when electrons are captured by protons to form neutrons by β^+ decay), a quark star, or a black hole.

3. The structure of the ideal quantum gas

The radial distribution function $g(r)$ is related to the structure factor $S(k)$ by the following Fourier transform

$$n[g(r) - 1] = \frac{1}{V} \sum_{\mathbf{k}} e^{i\mathbf{k}\cdot\mathbf{r}} [S(k) - 1]. \tag{3.1}$$

Taking into account that the operator of the particle number N_0 is a constant of motion, the fluctuation–dissipation theorem (see appendix of [18]) $\chi''(k, \omega) = (n\pi/\hbar)(1 - e^{-\beta\hbar\omega})S(k, \omega)$, can be solved for the van Hove function

$$S(k, \omega) = \frac{\hbar}{n\pi} [1 - \delta_{\mathbf{k}}] \frac{\chi''(k, \omega)}{1 - e^{-\beta\hbar\omega}} + \left\langle \frac{(\delta N)^2}{N} \right\rangle \delta_{\mathbf{k}} \delta(\omega), \tag{3.2}$$

White-dwarf equation of state and structure: the effect of temperature

where $\langle \dots \rangle$ represents averaging in the grand canonical ensemble. The static structure factor $S(k) = \int_{-\infty}^{\infty} d\omega S(k, \omega)$ is then

$$S(k) = \frac{\hbar}{n\pi} [1 - \delta_{\mathbf{k}}] \int_0^{\infty} d\omega \chi''(k, \omega) \coth\left(\frac{\beta\hbar\omega}{2}\right) + \left\langle \frac{(\delta N)^2}{N} \right\rangle \delta_{\mathbf{k}} \delta(\omega), \quad (3.3)$$

where the last term does not contribute in the thermodynamic limit [19]. We substitute (see appendix of [18])

$$\chi''(k, \omega) = N\pi \int \frac{d\mathbf{k}'}{(2\pi)^3} \mathcal{C}_{k'} \{ \delta[\hbar\omega - \Delta_{\mathbf{k}'}(\mathbf{k})] - \delta[\hbar\omega + \Delta_{\mathbf{k}'}(\mathbf{k})] \}, \quad (3.4)$$

with $\Delta_{\mathbf{k}'}(\mathbf{k}) = \epsilon(|\mathbf{k}' + \mathbf{k}|) - \epsilon(k')$, and obtain for $\mathbf{k} \neq \mathbf{0}$

$$S(k) = V \int \frac{d\mathbf{k}'}{(2\pi)^3} \mathcal{C}_{k'} \coth\left\{ \frac{1}{2} \beta [\epsilon(|\mathbf{k}' + \mathbf{k}|) - \epsilon(k')] \right\}, \quad k > 0, \quad (3.5)$$

where \mathcal{C}_k denotes the thermal average fraction of particles having momentum $\hbar\mathbf{k}$ defined in equation (2.25).

For further analytical manipulation we rewrite

$$\frac{\beta}{2} [\epsilon(k) - \mu] = \ln \sqrt{\frac{g}{N\mathcal{C}_k} + \xi}. \quad (3.6)$$

One rewrites equation (3.5) changing variables first $\mathbf{k} + \mathbf{k}' \rightarrow \mathbf{k}$ and subsequently $\mathbf{k} \rightarrow -\mathbf{k}$ to find

$$S(k) = V \int \frac{d\mathbf{k}'}{(2\pi)^3} \mathcal{C}_{|\mathbf{k}+\mathbf{k}'|} \coth\left\{ \frac{1}{2} \beta [\epsilon(k) - \epsilon(|\mathbf{k} + \mathbf{k}'|)] \right\}. \quad (3.7)$$

Adding equations (3.5) and (3.7) and making use of the fact that the hyperbolic cotangent is an odd function, one finds

$$2S(k) = V \int \frac{d\mathbf{k}'}{(2\pi)^3} (\mathcal{C}_{k'} - \mathcal{C}_{|\mathbf{k}+\mathbf{k}'|}) \coth\left\{ \frac{1}{2} \beta [\epsilon(|\mathbf{k}' + \mathbf{k}|) - \epsilon(k')] \right\}. \quad (3.8)$$

Now using equation (3.6) we find

$$\begin{aligned} S(k) &= \frac{V}{2} \int \frac{d\mathbf{k}'}{(2\pi)^3} (\mathcal{C}_{k'} - \mathcal{C}_{|\mathbf{k}+\mathbf{k}'|}) \coth\left[\ln \sqrt{\frac{g}{N\mathcal{C}_{|\mathbf{k}+\mathbf{k}'|}} + \xi} - \ln \sqrt{\frac{g}{N\mathcal{C}_{k'}} + \xi} \right] \\ &= \frac{V}{2} \int \frac{d\mathbf{k}'}{(2\pi)^3} \left(\mathcal{C}_{k'} + \mathcal{C}_{|\mathbf{k}+\mathbf{k}'|} + \frac{2N\xi}{g} \mathcal{C}_{k'} \mathcal{C}_{|\mathbf{k}+\mathbf{k}'|} \right) \\ &= 1 + \frac{VN\xi}{g} \int \frac{d\mathbf{k}'}{(2\pi)^3} \mathcal{C}_{k'} \mathcal{C}_{|\mathbf{k}+\mathbf{k}'|}, \quad k > 0, \end{aligned} \quad (3.9)$$

where $\coth[\ln \sqrt{x}] = (x + 1)/(x - 1)$ was used in the middle step. From this follows

$$\frac{1}{V} \sum_{\mathbf{k} \neq \mathbf{0}} e^{i\mathbf{k}\cdot\mathbf{r}} [S(k) - 1] = \frac{n\xi}{g} \left\{ 2\mathcal{C}_0 \sum_{\mathbf{k} \neq \mathbf{0}} \mathcal{C}_k e^{i\mathbf{k}\cdot\mathbf{r}} + \left| \sum_{\mathbf{k} \neq \mathbf{0}} \mathcal{C}_k e^{i\mathbf{k}\cdot\mathbf{r}} \right|^2 \right\}, \quad (3.10)$$

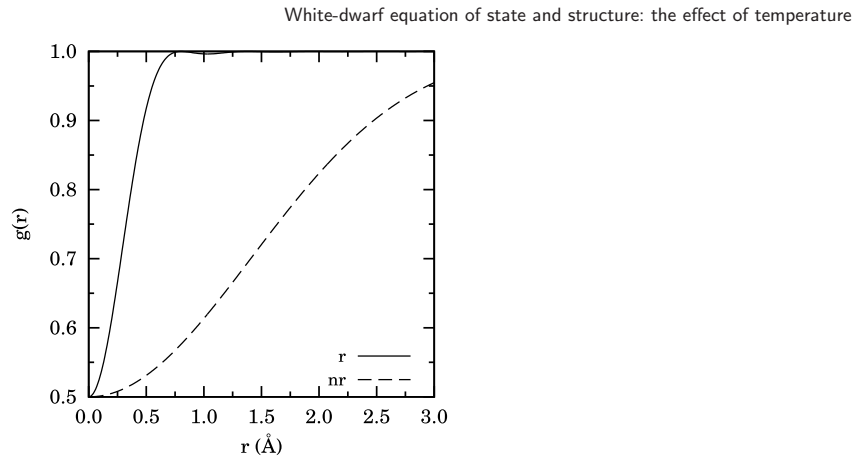


Figure 3. The radial distribution function for ideal electrons ($\xi = -1, g = 2$) in the relativistic and the non-relativistic cases. Here we chose $T = 20\,000$ K and $n = 1.04 \times 10^{22} \text{ cm}^{-3}$ in the non-relativistic case and $n = 5.93 \times 10^{24} \text{ cm}^{-3}$ in the relativistic case. r is in angstroms.

where $\mathcal{C}_0 = \delta_{\xi,1} \Theta(T_c - T) N_0 / N$, with Θ the Heaviside step function, denotes the fraction of particles that occupy the zero momentum state. We then introduce the function $F(r) = \sum_{\mathbf{k}} \mathcal{C}_k e^{i\mathbf{k}\cdot\mathbf{r}}$. This assume the following forms

$$F_r(r) = \mathcal{C}_0(T) + \frac{g}{2\pi^2 n (\beta \hbar c)^2 \xi} \int_0^\infty \kappa d\kappa b_0 \left(\xi z e^{-\sqrt{\kappa^2 + \beta^2 m^2 c^4}} \right) \sin\left(\frac{1}{\beta \hbar c} \kappa r\right) / r, \quad (3.11)$$

$$F_{er}(r) = \mathcal{C}_0(T) + \frac{g}{2\pi^2 n (\beta \hbar c)^2 \xi} \int_0^\infty \kappa d\kappa b_0 \left(\xi z e^{-\kappa} \right) \sin\left(\frac{1}{\beta \hbar c} \kappa r\right) / r, \quad (3.12)$$

$$F_{nr}(r) = \mathcal{C}_0(T) + \frac{2g}{\pi n \Lambda^2 \xi} \int_0^\infty \kappa d\kappa b_0 \left(\xi z e^{-\kappa^2} \right) \sin\left(\frac{2\sqrt{\pi}}{\Lambda} \kappa r\right) / r. \quad (3.13)$$

in the relativistic $\epsilon(k) = \sqrt{\hbar^2 k^2 c^2 + m^2 c^4}$, extreme relativistic $\epsilon(k) = c \hbar k$, and non-relativistic $\epsilon(k) = \lambda k^2$ cases, respectively. Inserting equations (3.9) into (3.1) we find

$$g(r) = 1 + \frac{\xi}{g} [F^2(r) - \mathcal{C}_0^2(T)]. \quad (3.14)$$

which generalizes equation (117.8) of Landau [14]. In figure 3 we show the radial distribution function for fermions in the relativistic and the non-relativistic cases. From the figure we see how the Fermi hole becomes larger in the non relativistic case at smaller number densities. Increasing the temperature by one order of magnitude (see figure 3.3 of [4]), keeping the density fixed produces a change in the radial distribution function of the order of 10^{-2} , with the Fermi hole getting smaller.

For the electron gas we should include the Coulomb interaction between the particles: the *jellium*. The radial distribution function of the jellium cannot of course be calculated exactly analytically; for a Monte Carlo simulation of the degenerate ($T = 0$)

J. Stat. Mech. (2017) 113101

White-dwarf equation of state and structure: the effect of temperature

jellium see, for example, [20] and for the jellium at finite temperature see, for example, [21].

Actually a more accurate result could be found by treating the white dwarf matter as a binary mixture of electrons and nuclei, which can today be done exactly with Monte Carlo simulation techniques such as the one devised in [22].

From these numerical studies one could extract a more accurate value for the constant K in the adiabatic equation of state and thus the critical central density $\bar{\rho}_c = (\eta_3 c^2 / 2^3 \omega_3 K)^3$.

4. Conclusions

In this work we studied the importance of temperature dependence on ideal quantum gases relevant for white dwarf interiors. Even if the temperature of the star is six orders of magnitude smaller than the Fermi energy of the electron gas inside the star, we find that the temperature effects are quite relevant at white dwarf densities and temperatures. In particular we show that the adiabatic equation of state becomes extremely relativistic, with $\Gamma = 4/3$, at densities six orders of magnitude lower than the ones required for the completely degenerate, $T = 0$, case. Even if the polytropic form of the adiabatic equation of state remains the same as that at zero temperature, the proportionality constant K changing by just a 10^{-10} relative factor between the finite temperature case and the zero temperature case, we think that an accurate analysis of the star evolution, at least at the level of the ideal electron gas approximation in the absence of nuclei, should properly take into account the temperature effects. This gives us a complete exactly solvable analytic approximation for the compact star interior at a finite temperature. We could comment that the temperature effects are smaller than the corrections necessary to take into account the Coulomb interactions between the electrons and of the presence of the nuclei, but from a calculation point of view it is still desirable to keep under control the magnitude of the temperature corrections alone. Since this can be done analytically we think that their analysis is relevant by itself.

We gave the generalization to finite temperature of all the zero temperature results used by Chandrasekhar and, in order to keep the treatment as general as possible, we studied in parallel the Fermi and the Bose gases. Clearly, only the Fermi gas results were used for the description of the ideal electron gas in the star interior.

We then studied the structure of the ideal quantum gas as a function of temperature. We found the Fermi hole for the cold electron gas in a white dwarf, which turned out to be of the order of 1 \AA in the full relativistic regime at a number density of the order of $n \sim 10^{26} \text{ cm}^{-3}$ and bigger in the non-relativistic regime at smaller densities and fixed temperature. The radial distribution function was also affected by the temperature and the Fermi hole gets smaller as the temperature increases at fixed density.

We also pointed out that in order to correct our result for the Coulomb interaction among the electrons and for the presence of the nuclei, it is necessary to abandon the analytic treatment in favor of a numerical simulation. We gave some relevant references for Monte Carlo methods that are important to adopt to solve this fascinating subject. These corrections to the Chandrasekhar result or to our temperature

White-dwarf equation of state and structure: the effect of temperature

dependent treatment are important more from a philosophical point of view rather than an experimental or observational point of view. They would lead us to the exact knowledge of the properties of a mixture of electrons and nuclei at astrophysical conditions such as the ones found in white dwarfs.

Moreover, let us observe that only a general relativistic statistical physics theory would give us fully correct results for the stability of a white dwarf. But since this theory has not yet been formulated [23] we will have to wait until the theory becomes available.

Appendix. The adiabatic equation of state for a relativistic ideal electron gas at finite temperature

Using the dispersion relation $\epsilon(k) = \sqrt{\hbar^2 k^2 c^2 + m^2 c^4}$, with m the rest mass of an electron, we find the pressure and the density from,

$$\beta P = g \int \frac{d\mathbf{k}}{(2\pi)^3} \ln(1 + ze^{-\beta\epsilon(k)}), \tag{A.1}$$

$$n = g \int \frac{d\mathbf{k}}{(2\pi)^3} \frac{1}{e^{\beta\epsilon(k)}/z + 1}. \tag{A.2}$$

Integrating by parts the pressure equation and changing variable $\kappa = \beta\hbar ck$ we find

$$\beta P = \frac{g}{(\beta\hbar c)^3} \frac{1}{2\pi^2} \frac{1}{3} \int d\kappa \frac{\kappa^3 / \sqrt{\kappa^2 + (\beta mc^2)^2}}{e^{\sqrt{\kappa^2 + (\beta mc^2)^2}/z} + 1}, \tag{A.3}$$

$$n = \frac{g}{(\beta\hbar c)^3} \frac{1}{2\pi^2} \int d\kappa \frac{\kappa^2}{e^{\sqrt{\kappa^2 + (\beta mc^2)^2}/z} + 1}. \tag{A.4}$$

These equations are equivalent to equations (2.10) and (2.11) in the main text. Then the entropy is given by

$$S/Vk_B = g \int \frac{d\mathbf{k}}{(2\pi)^3} \ln(1 + ze^{-\beta\epsilon(k)}) - g \int \frac{d\mathbf{k}}{(2\pi)^3} \frac{\ln z - \beta\epsilon(k)}{e^{\beta\epsilon(k)}/z + 1}. \tag{A.5}$$

On an adiabatic the entropy per particle $s = S/Nk_B$ is constant, and from equation (A.1) it follows that

$$\beta P = g \int \frac{d\mathbf{k}}{(2\pi)^3} \frac{\ln z - \beta\epsilon(k)}{e^{\beta\epsilon(k)}/z + 1} + sn. \tag{A.6}$$

References

- [1] Balian R and Blaizot J P 1999 *Am. J. Phys.* **67** 1189
- [2] Silbar R and Reddy S 2004 *Am. J. Phys.* **72** 892
- [3] Jackson C B, Taruna J, Pouliot S L, Ellison B W, Lee D D and Piekarewicz J 2005 *Eur. J. Phys.* **26** 695
- [4] Shapiro S L and Teukolsky S A 1983 *Black Holes, White Dwarfs and Neutro Stars, the Physics of Compact Objects* (New York: Wiley)

White-dwarf equation of state and structure: the effect of temperature

- [5] Landau L D 1932 *Phys. Z. Sowjetunion* **1** 285
- [6] Chandrasekhar S 1931 *Mon. Not. R. Astron. Soc.* **91** 456
- [7] Chandrasekhar S 1931 *Phil. Mag.* **11** 592
- [8] Chandrasekhar S 1931 *Astrophys. J.* **74** 81
- [9] Dirac P A M 1926 *Proc. R. Soc. A* **112** 661
- [10] Fowler R H 1926 *Mon. Not. R. Astron. Soc.* **87** 114
- [11] Adams W S 1915 *Publ. Astron. Soc. Pac.* **27** 236
- [12] Adams W S 1925 *Proc. Natl Acad. Sci. USA* **11** 382
Adams W S 1925 *Observatory* **49** 88 (erratum)
- [13] Feynman R P 1972 *Statistical Mechanics: a Set of Lectures (Frontiers in Physics vol 36)* (New York: Benjamin) (notes taken by R Kikuchi and H A Feiveson, edited by Jacob Shaham)
- [14] Landau L D and Lifshitz E M 1980 *Statistical Physics, Part I (Course of Theoretical Physics vol 5)* 3rd edn (Portsmouth, NH: Butterworth Heinemann) (translated from the Russian by J B Sykes and M J Kearsley, edited by E M Lifshitz and L P Pitaevskii)
- [15] Chandrasekhar S 1938 *An Introduction to the Study of Stellar Structure* (Chicago, IL: University of Chicago Press)
- [16] Chandrasekhar S 1935 *Mon. Not. R. Astron. Soc.* **95** 207
- [17] Chandrasekhar S 1983 Nobel prize lecture
- [18] March N H and Tosi M P 1984 *Coulomb Liquids* (New York: Academic)
- [19] Bosse J, Pathak K N and Singh G S 2011 *Phys. Rev. E* **84** 042101
- [20] Fantoni R 2013 *Eur. Phys. J. B* **86** 286
- [21] Militzer B, Pollock E L and Ceperley D M 2003 arXiv:0310401 [cond-mat]
- [22] Dewing M and Ceperley D M 2002 *Recent Advances in Quantum Monte Carlo Methods*, II ed W A Lester *et al* (Singapore: World Scientific)
- [23] Rovelli C 2013 *Phys. Rev. D* **87** 084055

J. Stat. Mech. (2017) 113101

Part XVIII

2018

Chapter 57

Effect of quantum dispersion on the radial distribution function of a one-component sticky-hard-sphere fluid

Fantoni R., J. Stat. Mech. 043101 (2018)

Title: “Effect of quantum dispersion on the radial distribution function of a one-component sticky-hard-sphere fluid”

Abstract: In this short communication we present a possible scheme to study the radial distribution function of the quantum slightly polydisperse Baxter sticky hard sphere liquid at finite temperature through a semi-analytical method devised by Chandler and Wolynes.

PAPER: Quantum statistical physics, condensed matter, integrable systems

Effect of quantum dispersion on the radial distribution function of a one-component sticky-hard-sphere fluid

Riccardo Fantoni

Dipartimento di Fisica, Università di Trieste, strada Costiera 11,
34151 Grignano (Trieste), Italy
E-mail: rfantoni@ts.infn.it

Received 29 October 2017
Accepted for publication 13 March 2018
Published 16 April 2018

Online at stacks.iop.org/JSTAT/2018/043103
<https://doi.org/10.1088/1742-5468/aab690>



Abstract. In this short communication we present a possible scheme to study the radial distribution function of the quantum slightly polydisperse Baxter sticky hard sphere liquid at finite temperature through a semi-analytical method devised by Chandler and Wolynes.

Keywords: correlation functions, quantum fluids, rigorous results in statistical mechanics

J. Stat. Mech. (2018) 043103

Contents

Acknowledgments 6
 Appendix. The primitive action 6
 References 8

It is well known that a one-component classical sticky-hard-sphere (SHS) liquid [1] is thermodynamically unstable [2].

Nonetheless, when studied with a Monte Carlo computer simulation the fluid is stable [3]. This is due to the fact that a computer can only work with numbers with a finite number of decimal figures. The computer arithmetics in fact differs from the arithmetics of real number because the standard representation of numbers must use a finite and fixed number of bits. So that the fluid studied through the computer simulation will necessarily be polydisperse (in size). And it has been proven that the polydisperse SHS fluid is indeed thermodynamically stable [2].

It is then legitimate to pose the following questions: what would the outcome for the radial distribution function of a quantum SHS fluid, obeying to Boltzmann statistics (for the sake of simplicity), calculated through the path integral Monte Carlo simulation, be? Can one find a reasonable approximation for it, through other means? The relevant parameters of the problem will be the inverse temperature $\beta = 1/K_B T$, the density ρ , the spheres mass m and diameter σ , and α the adhesion coefficient.

The aim of the note is to show how one may try to answer these questions using an approach devised by Chandler and Wolynes [4] which relies on an *isomorphism* between the quantum statistical mechanics of a many body system and the classical statistical mechanics of a particular *polyatomic* fluid. Using the path integral formulation of quantum statistical mechanics it can be shown (see appendix) that the canonical partition function of a system of N quantum identical particles of mass m obeying to Boltzmann statistics and interacting through a pair potential $v(r)$, at absolute temperature T , is approached in the $P \rightarrow \infty$ limit by the classical partition function of N indistinguishable ring *molecules* made up of P distinguishable *atoms*, at temperature TP , with a total potential energy

$$V(R_0, \dots, R_{P-1}) = \sum_{t=0}^{P-1} \left\{ \frac{|R_t - R_{t+1}|^2}{4\lambda\varepsilon^2} + \sum_{i<j}^N v(|\mathbf{r}_i^{(t)} - \mathbf{r}_j^{(t)}|) \right\}, \tag{1}$$

where $R_t \equiv (\mathbf{r}_1^{(t)}, \dots, \mathbf{r}_N^{(t)})$ are the positions of the atoms at *site* (imaginary thermal time slice) t of the N molecules, with $R_p = R_0$, and

$$\lambda = \frac{\hbar^2}{2m}, \tag{2}$$

$$\varepsilon = \frac{\beta}{P}. \tag{3}$$

Effect of quantum dispersion on the radial distribution function of a one-component sticky-hard-sphere fluid

This is known as the primitive action as explained in the appendix.

Note that for the SHS Baxter model [1] one has

$$e^{-\beta v(r)} - 1 \xrightarrow{\text{sticky limit}} -\theta(\sigma - r) + \sigma\alpha\delta(r - \sigma), \tag{4}$$

where the adhesion coefficient $\alpha = \epsilon/\epsilon_0 = 1/12\tau$, with ϵ_0 a characteristic energy scale, is a *monotonous function* of β . We can say that $\tau = \tau(\beta)$ is a monotonously increasing function of the absolute temperature T representing a reduced temperature. The problem is then well set only upon assigning the function $\tau(\beta)$.

The radial distribution function of the quantum system is then given by

$$g(r; \beta) = \lim_{P \rightarrow \infty} \frac{1}{P} \sum_{t=0}^{P-1} g_{0t}(r; \beta/P), \tag{5}$$

where $g_{tt'}$ is the intermolecular site-site radial distribution function of the isomorphic classical system.

The idea of Chandler and Wolynes is to use the reference interaction site model (RISM) theory [5] to determine the g_{0t} for $t = 0, \dots, P - 1$ for a given P ($P = 2$ being the simplest but less accurate approximation). That is, one needs to solve the following integral equation subject to a given closure

$$\hat{\mathbf{h}}(k; \epsilon) = \hat{\boldsymbol{\omega}}(k; \epsilon) \hat{\mathbf{c}}(k; \epsilon) [1 - \rho \hat{\boldsymbol{\omega}}(k; \epsilon) \hat{\mathbf{c}}(k; \epsilon)]^{-1} \hat{\boldsymbol{\omega}}(k; \epsilon), \tag{6}$$

where $\hat{\mathbf{h}}(k; \epsilon)$ and $\hat{\mathbf{c}}(k; \epsilon)$ are the matrices whose elements are the Fourier transform of the intermolecular site-site total correlation function $h_{tt'}(r; \epsilon) = g_{tt'}(r; \epsilon) - 1$ and direct correlation function $c_{tt'}(r; \epsilon)$ respectively and the elements of $\hat{\boldsymbol{\omega}}(k; \epsilon)$ are the Fourier transform of

$$\begin{aligned} \omega_{tt'}(\mathbf{r}; \epsilon) &= \delta_{tt'} \delta(\mathbf{r}) + (1 - \delta_{tt'}) s_{tt'}(r; \epsilon), \\ &= \begin{cases} \delta(\mathbf{r}) & t = t' \\ s_{tt'}(r; \epsilon) & t \neq t' \end{cases} \end{aligned} \tag{7}$$

where $s_{tt'}(r; \epsilon)$ are the intramolecular site-site radial distribution functions of the isomorphic classical system, for which a reasonable approximation is

$$s_{tt'}(r; \epsilon) \approx \gamma_{tt'} e^{-\frac{r^2}{4\lambda|t-t'|\epsilon}} y_{\text{SHS}}(r; \tau(|t-t'|\epsilon)), \tag{8}$$

where the normalization constant $\gamma_{tt'}$ should be determined from the condition

$$\int s_{tt'}(r; \epsilon) \, d\mathbf{r} = 1, \tag{9}$$

and $y_{\text{SHS}}(r; \tau)$ is the cavity radial distribution function of a system of classical SHS of diameter σ , with reduced temperature τ at a packing fraction $\eta = \pi\rho\sigma^3/6$, $\rho = N/V$ being the density. That is $y_{\text{SHS}}(r; \tau) = g_{\text{SHS}}(r; \tau) \exp[\tau v(r)]$ which is a continuous function of r even when the radial distribution function of the SHS model, g_{SHS} , and/or v are discontinuous.

In equation (8) the exponential factor stems from the kinetic part of the action and again we used the functional dependence of the adhesion coefficient τ on the inverse temperature $|t - t'|\epsilon$.

Effect of quantum dispersion on the radial distribution function of a one-component sticky-hard-sphere fluid

Clearly we will have $y_{\text{SHS}}(r; \tau) = g_{\text{SHS}}(r; \tau)$ for $r > \sigma$. The Laplace transform of $rg_{\text{SHS}}(r; \tau)$ in the Percus–Yevick approximation for the SHS system is given by [6]

$$\begin{aligned} \widehat{G}_{\text{SHS}}(s) &= \int_0^\infty dr e^{-sr} r g_{\text{SHS}}(r; \tau) \\ &= \frac{e^{-s}}{s^2} \frac{\Lambda_0 + \Lambda_1 s + \Lambda_2 s^2}{1 - 12\eta[\varphi_2(s)\Lambda_0 + \varphi_1(s)\Lambda_1 + \varphi_0(s)\Lambda_2]}, \end{aligned} \quad (10)$$

where,

$$\varphi_k(x) = x^{-(k+1)} \left(\sum_{l=0}^k \frac{(-x)^l}{l!} - e^{-x} \right), \quad (11)$$

and

$$\Lambda_0 = \frac{1 + 2\eta}{(1 - \eta)^2} - \frac{12\eta}{1 - \eta} \Lambda_2, \quad (12)$$

$$\Lambda_1 = \frac{1 + \eta/2}{(1 - \eta)^2} - \frac{6\eta}{1 - \eta} \Lambda_2. \quad (13)$$

$$\begin{aligned} \Lambda_2 &= \frac{1 - (1 - \tau^{-1})\eta - w}{2\tau^{-1}(1 - \eta)\eta}, \\ w &= \sqrt{(1 - \eta) \left[1 - \eta \left(1 - 2\tau^{-1} + \frac{\tau^{-2}}{3} \right) \right] + \frac{\tau^{-2}}{2}\eta^2}. \end{aligned} \quad (14)$$

In figure 1 we show the intramolecular site-site radial distribution functions of the isomorphous classical system assuming an adhesion coefficient independent from temperature.

For the closure one may use the modified mean spherical approximation (mMSA) [7]

$$c_{tt'}(r) = f_{tt'}(r) = e^{-\beta v_{tt'}(r)} - 1, \quad r > d_{tt'}, \quad (15)$$

where

$$v_{tt'}(r) = \begin{cases} v(r) & t = t' \\ 0 & t \neq t' \end{cases}, \quad (16)$$

and

$$d_{tt'} = \begin{cases} \sigma & t = t' \\ 0 & t \neq t' \end{cases}. \quad (17)$$

Here we are neglecting the fact that the size of a path (or polymer), its thermal wavelength, is $\Lambda_\beta = \sqrt{\beta \hbar^2 / m}$. Combined with the exact relation valid for $r \leq d_{tt'}$

¹ One may take into account of the size of the path by taking for example $d_{tt'} = \{\sigma \text{ for } t = t', \{0 \text{ for } \sigma < \Lambda_\beta, \sigma - \Lambda_\beta \text{ for } \sigma > \Lambda_\beta\} \text{ for } t = t' \pm 1, 0 \text{ otherwise}\}$.

Effect of quantum dispersion on the radial distribution function of a one-component sticky-hard-sphere fluid

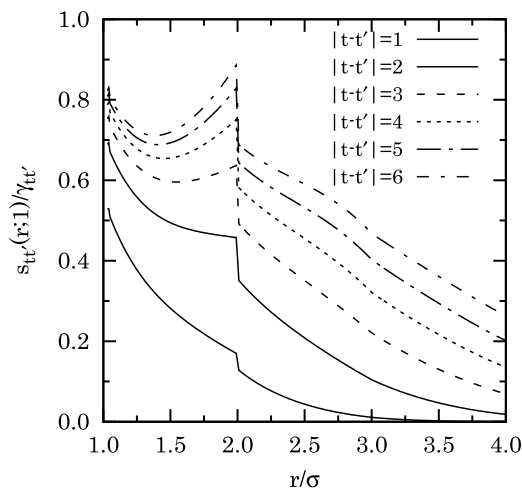


Figure 1. The intramolecular site-site radial distribution functions of the isomorphic classical system $s_{tt'}(r;1)$ for $\lambda = 1$, $\eta = 0.32$, and $\tau = 0.2$.

$$h_{tt'}(r) = \begin{cases} \frac{\sigma}{12\tau} y_{tt}(d_{tt}) \delta(r - d_{tt}) - 1 & t = t' \\ -1 & t \neq t' \end{cases}, \quad (18)$$

where $y_{tt}(d_{tt})$ are the intermolecular site-site cavity functions at contact which in the mMSA are [7]

$$y_{tt}(d_{tt}) = 1, \quad t = 0, \dots, P - 1. \quad (19)$$

Then, for the closure, we will have

$$c_{tt'}(r) = 0, \quad r > d_{tt'}, \quad (20)$$

$$h_{tt'}(r) = \begin{cases} \frac{\sigma}{12\tau} \delta(r - \sigma) - 1 & t = t' \\ -1 & t \neq t' \end{cases}, \quad r \leq d_{tt'}. \quad (21)$$

The RISM integral equation (6) can be rewritten as the following Ornstein–Zernike-like relation,

$$\hat{\mathbf{h}}(k; \varepsilon) = \hat{\boldsymbol{\omega}}(k; \varepsilon) \hat{\mathbf{c}}(k; \varepsilon) \hat{\boldsymbol{\omega}}(k; \varepsilon) + \rho \hat{\boldsymbol{\omega}}(k; \varepsilon) \hat{\mathbf{c}}(k; \varepsilon) \hat{\mathbf{h}}(k; \varepsilon). \quad (22)$$

The main obstacle in solving this integral equation reside in the fact that the intramolecular site-site radial distribution function of the isomorphic classical system, $s_{tt'}(r; \varepsilon)$, is known only numerically through Laplace inversion of equation (10) obtained for example using the algorithm of Abate and Whitt [8].

The uncontrolled approximations in this treatment reside in: (i) equation (8), where we have approximated the full equilibrium distribution function for P cavities forming a molecule with the cavity pair distribution function of the SHS classical fluid (this approximation becomes worse and worse as P decreases). Since the primitive

Effect of quantum dispersion on the radial distribution function of a one-component sticky-hard-sphere fluid

approximation error goes like $\lambda\varepsilon^2$ [9] it is reasonable to expect that a good enough approximation would require $\lambda\beta^2/P^2 \sim 0.01$. Of course one reasonably expects that solving RISM equations numerically becomes rapidly a difficult task (including non-convergence problems) as P increases; (ii) equation (17), where we are neglecting the thermal wavelength of a polymer.

To our knowledge the quantum slightly polydisperse Baxter sticky hard spheres liquid has never been studied before either through computer simulations of the one-component system or through other means. To assess the existence of thermodynamic and structural properties of such a physical model from a rigorous mathematical point of view seems to be a quite formidable task. In this respect the theory of path integrals should probably be the place to start to look at. It is infact out of doubt that at any finite P the classical isomorphic system is thermodynamically ($N \rightarrow \infty$ at constant ρ) well defined, but understanding the effect of the slightly polydisperse adhesion (the last term in equation (4)) in the $P \rightarrow \infty$ (Feynman–Kac-)limit does not seem so easy. There are three different limits we have to deal with: (i) the sticky limit, (ii) the path integral limit, and (iii) the thermodynamic limit. While it is quite customary to take the thermodynamic limit in the end, the order of the first two limits should be immaterial. Moreover we expect the path integral solution to depend crucially on the choice of the function $\tau(T)$.

We plan to adopt the present scheme to obtain semi-analytical quantitative results for the radial distribution function of the extension to the quantum regime of some of the classical fluids studied in [10–24], in the near future.

Acknowledgments

I would like to acknowledge fruitful discussions with Professor Domenico Gazzillo during my stay at the Chemical Physics department of the University Ca’ Foscari of Venice.

Appendix. The primitive action

In this appendix we give a brief review of the derivation of the primitive approximation given in [9]. Suppose the Hamiltonian is split into two pieces $\mathcal{H} = \mathcal{T} + \mathcal{V}$, where \mathcal{T} and \mathcal{V} are the kinetic and potential operators. Recall the exact Baker–Campbell–Hausdorff formula to expand $\exp(-\varepsilon\mathcal{H})$ into the product $\exp(-\varepsilon\mathcal{T})\exp(-\varepsilon\mathcal{V})$. As $\varepsilon \rightarrow 0$ the commutator terms which are of order higher than ε^2 become smaller than the other terms and thus can be neglected. This is known as the *primitive approximation*

$$e^{-\varepsilon(\mathcal{T}+\mathcal{V})} \approx e^{-\varepsilon\mathcal{T}}e^{-\varepsilon\mathcal{V}} \tag{A.1}$$

hence we can approximate the exact density matrix by product of the density matrices for \mathcal{T} and \mathcal{V} alone. One might worry that this would lead to an error as $P \rightarrow \infty$, with small errors building up to a finite error. According to the Trotter [25] formula, one does not have to worry

$$e^{-\beta(\mathcal{T}+\mathcal{V})} = \lim_{P \rightarrow \infty} [e^{-\varepsilon\mathcal{T}}e^{-\varepsilon\mathcal{V}}]^P. \tag{A.2}$$

Effect of quantum dispersion on the radial distribution function of a one-component sticky-hard-sphere fluid

The Trotter formula holds if the three operators \mathcal{T} , \mathcal{V} , and $\mathcal{T} + \mathcal{V}$ are self-adjoint and make sense separately, for example, if their spectrum is bounded below. [26] This is the case for the Hamiltonian describing SHS.

Let us now write the primitive approximation in position space $R = (\mathbf{r}_1, \mathbf{r}_2, \dots, \mathbf{r}_N)$ with \mathbf{r}_i the coordinate of the i th particle,

$$\rho(R_0, R_2; \varepsilon) \approx \int dR_1 \langle R_0 | e^{-\varepsilon \mathcal{T}} | R_1 \rangle \langle R_1 | e^{-\varepsilon \mathcal{V}} | R_2 \rangle, \tag{A.3}$$

and evaluate the kinetic and potential density matrices. Since the potential operator is diagonal in the position representation, its matrix elements are trivial

$$\langle R_1 | e^{-\varepsilon \mathcal{V}} | R_2 \rangle = e^{-\varepsilon V(R_1)} \delta(R_2 - R_1). \tag{A.4}$$

The kinetic matrix can be evaluated using the eigenfunction expansion of \mathcal{T} . Consider, for example, the case of distinguishable particles in a cube of side L with periodic boundary conditions. Then the exact eigenfunctions and eigenvalues of \mathcal{T} are $L^{-3N/2} e^{iK_n R}$ and λK_n^2 , with $K_n = 2\pi \mathbf{n} / L$ and \mathbf{n} a $3N$ -dimensional integer vector. We are using here dimensional units. Then

$$\langle R_0 | e^{-\varepsilon \mathcal{T}} | R_1 \rangle = \sum_{\mathbf{n}} L^{-3N} e^{-\varepsilon \lambda K_n^2} e^{-iK_n (R_0 - R_1)} \tag{A.5}$$

$$= (4\pi \lambda \varepsilon)^{-3N/2} \exp \left[-\frac{(R_0 - R_1)^2}{4\lambda \varepsilon} \right], \tag{A.6}$$

where $\lambda = \hbar^2 / 2m$. Equation (A.6) is obtained by approximating the sum by an integral. This is appropriate only if the thermal wavelength of one step is much less than the size of the box, $\lambda \varepsilon \ll L^2$. In some special situations this condition could be violated, in which case one should use equation (A.5) or add periodic ‘images’ to equation (A.6). The exact kinetic density matrix in periodic boundary conditions is a theta function, $\prod_{i=1}^{3N} \theta_3(z_i, q)$, where $z_i = \pi(R_0^i - R_1^i) / L$, R^i is the i th component of the $3N$ dimensional vector R , and $q = e^{-\lambda \varepsilon (2\pi / L)^2}$ (see chapter 16 of [27]). Errors from ignoring the boundary conditions are $O(q)$, exponentially small at large P .

A *link* m is a pair of time slices (R_{m-1}, R_m) separated by a *time step* $\varepsilon = \beta / P$. The *action* S^m of a link is defined as minus the logarithm of the exact density matrix. Then the exact path-integral expression becomes

$$\rho(R_0, R_P; \beta) = \int dR_1 \dots dR_{P-1} \exp \left[-\sum_{m=1}^P S^m \right]. \tag{A.7}$$

It is convenient to separate out the *kinetic action* from the rest of the action. The exact kinetic action for link m will be denoted K^m

$$K^m = \frac{3N}{2} \ln(4\pi \lambda \varepsilon) + \frac{(R_{m-1} - R_m)^2}{4\lambda \varepsilon}. \tag{A.8}$$

The *inter-action* is then defined as what is left

$$U^m = U(R_{m-1}, R_m; \varepsilon) = S^m - K^m. \tag{A.9}$$

Effect of quantum dispersion on the radial distribution function of a one-component sticky-hard-sphere fluid

In the primitive approximation the inter-action is

$$U_1^m = \frac{\varepsilon}{2}[V(R_{m-1}) + V(R_m)], \quad (\text{A.10})$$

where we have symmetrized U_1^m with respect to R_{m-1} and R_m , since one knows that the exact density matrix is symmetric and thus the symmetrized form is more accurate.

A capital letter U refers to the total link inter-action. One should not think of the exact U as being strictly the potential action. That is true for the primitive action but, in general, is only correct in the small- ε limit. The exact U also contains kinetic contributions of higher order in ε . If a subscript is present on the inter-action, it indicates the order of approximation; the primitive approximation is only correct to order ε . No subscript implies the exact inter-action.

The *residual energy* of an approximate density matrix is defined as

$$E_A(R, R'; t) = \frac{1}{\rho_A(R, R'; t)} \left[\mathcal{H} + \frac{\partial}{\partial t} \right] \rho_A(R, R'; t). \quad (\text{A.11})$$

The residual energy for an exact density matrix vanishes; it is a local measure of the error of an approximate density matrix. The Hamiltonian \mathcal{H} is a function of R ; thus the residual energy is not symmetric in R and R' .

It is useful to write the residual energy as a function of the inter-action. We find

$$E_A(R, R'; t) = V(R) - \frac{\partial U_A}{\partial t} - \frac{(R - R') \cdot \nabla U_A}{t} + \lambda \nabla^2 U_A - \lambda (\nabla U_A)^2. \quad (\text{A.12})$$

The terms on the right hand side are ordered in powers of ε , keeping in mind that $U(R)$ is of order ε , and $|R - R'|$ is of order $\varepsilon^{1/2}$. One obtains the primitive action by setting the residual energy to zero and dropping the last three terms on the right hand side.

The residual energy of the primitive approximation is

$$E_1(R, R'; t) = \frac{1}{2} [V(R) - V(R')] - \frac{1}{2} (R - R') \cdot \nabla V + \frac{\lambda t}{2} \nabla^2 V - \frac{\lambda t^2}{4} (\nabla V)^2. \quad (\text{A.13})$$

With a leading error of $\sim \lambda \varepsilon^2$.

References

- [1] Baxter R J 1968 *J. Chem. Phys.* **49** 2770
- [2] Stell G 1991 *J. Stat. Phys.* **63** 1203
- [3] Miller M A and Frenkel D 2003 *Phys. Rev. Lett.* **90** 135702
- [4] Chandler D and Wolynes P G 1981 *J. Chem. Phys.* **74** 4078
- [5] Hansen J P and McDonald I R 1986 *Theory of Simple Liquids* 2nd edn (New York: Academic)
- [6] Santos A 2016 *A Concise Course on the Theory of Classical Liquids (Lecture Notes in Physics vol 923)* (Heidelberg: Springer)
- [7] Gazzillo D and Giacometti A 2004 *J. Chem. Phys.* **120** 4742
- [8] Abate J and Whitt W 1992 *Queueing Syst.* **10** 5
- [9] Ceperley D M 1995 *Rev. Mod. Phys.* **67** 279
- [10] Fantoni R, Gazzillo D and Giacometti A 2005 *J. Chem. Phys.* **122** 034901
- [11] Fantoni R, Gazzillo D and Giacometti A 2005 *Phys. Rev. E* **72** 011503

Effect of quantum dispersion on the radial distribution function of a one-component sticky-hard-sphere fluid

- [12] Gazzillo D, Giacometti A, Fantoni R and Sollich P 2006 *Phys. Rev. E* **74** 051407
- [13] Gazzillo D, Fantoni R and Giacometti A 2006 *Mol. Phys.* **104** 3451
- [14] Fantoni R, Gazzillo D, Giacometti A and Sollich P 2006 *J. Chem. Phys.* **125** 164504
- [15] Fantoni R, Gazzillo D, Giacometti A, Miller M A and Pastore G 2007 *J. Chem. Phys.* **127** 234507
- [16] Gazzillo D, Fantoni R and Giacometti A 2008 *Phys. Rev. E* **78** 021201
- [17] Gazzillo D, Fantoni R and Giacometti A 2009 *Phys. Rev. E* **80** 061207
- [18] Fantoni R, Giacometti A, Sciortino F and Pastore G 2011 *Soft Matter* **7** 2419
- [19] Fantoni R 2012 *Eur. Phys. J. B* **85** 108
- [20] Fantoni R, Giacometti A, Maestre M A G and Santos A 2013 *J. Chem. Phys.* **139** 174902
- [21] Fantoni R and Pastore G 2014 *J. Chem. Phys.* **141** 074108
- [22] Fantoni R, Giacometti A and Santos A 2015 *J. Chem. Phys.* **142** 224905
- [23] Fantoni R and Pastore G 2015 *Mol. Phys.* **113** 2593
- [24] Fantoni R 2016 *Physica A* **457** 406
- [25] Trotter H F 1959 *Proc. Am. Math. Soc.* 10 545
- [26] Simon B 1979 *Functional Integration and Quantum Physics* (New York: Academic)
- [27] Abramowitz M and Stegun I A 1970 *Handbook of Mathematical Functions* (New York: Dover)

Chapter 58

Two component boson-fermion plasma at finite temperature

Fantoni R., Int. J. Mod. Phys. C **29**, 1850028 (2018)

Title: “Two component boson-fermion plasma at finite temperature”

Abstract: We discuss thermodynamic stability of neutral real (quantum) matter from the point of view of a computer experiment at finite, nonzero, temperature. We perform (restricted) path integral Monte Carlo simulations of the two component plasma where the two species are both bosons, both fermions, and one boson and one fermion. We calculate the structure of the plasma and discuss about the formation of binded couples of oppositely charged particles. The purely bosonic case is thermodynamically unstable. In this case we find an undetermined size-dependent contact value unlike partial radial distribution function. For the purely fermionic case, we find a demixing transition with binding also of like species.

International Journal of Modern Physics C
Vol. 29, No. 3 (2018) 1850028 (11 pages)
© World Scientific Publishing Company
DOI: [10.1142/S0129183118500286](https://doi.org/10.1142/S0129183118500286)



Two component boson-fermion plasma at finite temperature

Riccardo Fantoni

*Dipartimento di Fisica, Università di Trieste
strada Costiera 11, 34151 Grignano (Trieste), Italy
rfantoni@ts.infn.it*

Received 14 January 2018

Accepted 12 March 2018

Published 29 March 2018

We discuss thermodynamic stability of neutral real (quantum) matter from the point of view of a computer experiment at finite, nonzero, temperature. We perform (restricted) path integral Monte Carlo simulations of the two component plasma where the two species are both bosons, both fermions, and one boson and one fermion. We calculate the structure of the plasma and discuss about the formation of binded couples of oppositely charged particles. The purely bosonic case is thermodynamically unstable. In this case we find an undetermined size-dependent contact value unlike partial radial distribution function. For the purely fermionic case, we find a demixing transition with binding also of like species.

Keywords: Two component plasma; Monte Carlo simulation; finite temperature; restricted path integral; worm algorithm; fermions sign problem; structure; thermodynamic stability.

PACS Nos.: 02.70.Ss, 05.10.Ln, 05.30.Fk, 05.70.-a, 61.20.Ja, 61.20.Ne.

1. Introduction

For matter to be stable it must be globally neutral. It is well known that in order for a system of an equal number N of oppositely charged point particles to be stable against collapse, quantum mechanics is required, and furthermore at least one of the species of particles must be a fermion. Without the exclusion principle, the ground state energy per particle of the system diverges as $N^{7/5}$ and the thermodynamic limit is not well defined.¹ As a matter of fact, in the classical limit one is forced to introduce a short-range regularization (like an hard core or others)² of the pair-potential between the particles in order to prevent the collapse of the negative charges on the positive ones.^{3,4} All this is at the heart of the fundamental question of whether the matter we live in is stable or not.

In this work, we want to explore the structure of a two-component mixture of particles with two opposite charge species. We will consider particles of charge $\pm e$ with e the charge of an electron. Furthermore, we will assume that the two species both have the mass of an electron m . We will consider explicitly the cases where

R. Fantoni

both species have spin 1/2 (purely fermionic), when they both have spin 1 (purely bosonic) and when one species has spin 1/2 and one species has spin 1 (fermions–bosons mixture). In all cases, we assume that each species has polarization equal to 1. Doing so, we will be able to determine the thermodynamic instability of the purely bosonic case as opposed to the other two cases. We will work at high temperatures and intermediate densities, when the quantum effects are not very important. The path integral Monte Carlo computer experiment is only exact in the purely bosonic case apart from the usual finite size and imaginary time discretization errors. For the other two cases, it is necessary to resort to an approximation due to the *fermions sign problem*.^{5,6} We will choose the restricted path integral approximation with a restriction based on the nodes of the ideal density matrix, which is known to perform reasonably well for the one component (Jellium) case from the pioneering work of Brown *et al.*^{7,8} Other methods have been implemented recently in order to reach high densities: Bonitz *et al.*^{9,10} combine configuration path integral Monte Carlo and permutation blocking path integral Monte Carlo. Malone *et al.*¹¹ agrees well with the one of Bonitz at high densities and the direct path integral Monte Carlo one of Filinov *et al.*¹² that agrees well with Brown at low density and moderate temperature. Our method is alternative to all previously employed ones.

In our simulations, we use the *worm algorithm*^{13,14} which is able to sample the necessary permutations of the indistinguishable particles without the need of explicitly sampling the permutations' space treating the paths as “worms” with a tail (*Masha*) and a head (*Ira*) in the β -periodic imaginary time, which can be attached one with the other in different ways or swap some of their portions. We explicitly and efficiently applied the restriction to the worms and this allowed us to treat the fermionic or mixed case explicitly, albeit only approximately. The approximation is expected to become better at low density and high temperature, i.e. when correlation effects are weak.

Possible physical realizations of interest to our work for the case of both species of spin 1/2 are a nonrelativistic electron–positron plasmas created in the laboratory¹⁵ or an electron–hole plasma which is important in the realm of low-temperature semiconductor physics. Conduction electrons and holes in semiconductors interact with Coulomb force and can have very similar effective masses.^{16,17}

The work is organized as follows: In Sec. 2, we describe the physical model we want to study, in Sec. 3, we describe the computer experiment method and techniques, in Sec. 4, we describe our numerical results, and Sec. 5 is for final remarks.

2. The Model

Setting lengths in units of the Bohr radius $a_0 = \hbar^2/me^2$ and energies in Rydberg's units, $\text{Ry} = \hbar^2/2ma_0^2$, where m is the electron mass, the Hamiltonian of the two

component nonrelativistic electron–positron mixture is

$$\mathcal{H} = \mathcal{T} + \mathcal{V} = -\lambda \sum_{i=1}^{N_+} \nabla_{\mathbf{r}_i^+}^2 - \lambda \sum_{i=1}^{N_-} \nabla_{\mathbf{r}_i^-}^2 + V(R), \quad (2.1)$$

$$V = 2 \left(\sum_{i < j}^{N_+} \frac{1}{|\mathbf{r}_i^+ - \mathbf{r}_j^+|} + \sum_{i < j}^{N_-} \frac{1}{|\mathbf{r}_i^- - \mathbf{r}_j^-|} - \sum_{i=1}^{N_+} \sum_{j=1}^{N_-} \frac{1}{|\mathbf{r}_i^+ - \mathbf{r}_j^-|} \right), \quad (2.2)$$

where $\lambda = \hbar^2/2ma_0^2 = Ry$, $R = (\mathbf{r}_1^+, \dots, \mathbf{r}_{N_+}^+, \mathbf{r}_1^-, \dots, \mathbf{r}_{N_-}^-)$ with \mathbf{r}_i^+ the coordinates of the i th positron and \mathbf{r}_i^- the ones of the i th electron. We will choose $N_+ = N_- = N$, since the system must be neutrally charged in order to be thermodynamically stable. We will not introduce any short-range regularization of the Coulomb potential. And we will treat the Coulomb long-range potential using the Ewald sums technique¹⁸ in order to treat it in the periodic box of side L of the simulation.

We will treat explicitly the electron–positron case where the two particles are both fermions, the case where both species are bosons, and the case where only one species is a fermion. Of course, there is no charged boson in nature with the mass and the charge of the electron, so this will remain a speculative analysis, to explore the thermodynamic stability and statistical properties of the mixture.

We will carry on a grand canonical simulation at fixed chemical potentials of the two species μ^+, μ^- , volume $\Omega = L^3$, and absolute temperature $T = 1/k_B\beta$, with k_B the Boltzmann constant.

3. Simulation Method

We carry on a (restricted) path integral Monte Carlo computer experiment¹⁹ using the *worm algorithm*^{13,14} to simulate the behavior of the quantum mixture at finite temperature.

The *density matrix* of a system of many distinguishable bodies at temperature $k_B T = \beta^{-1}$ can be written as an integral over all paths $\{R_t\}$

$$\rho(R_\beta, R_0; \beta) = \oint_{R_0 \rightarrow R_\beta} dR_t \exp(-S[R_t]). \quad (3.1)$$

The path R_t begins at R_0 and ends at R_β . For nonrelativistic particles interacting with a potential $V(R)$, the *action* of the path, $S[R_t]$, is given by the Feynman–Kac formula

$$S[R_t] = \int_0^\beta dt \left[\frac{1}{4\lambda} \left| \frac{dR_t}{dt} \right|^2 + V(R_t) \right]. \quad (3.2)$$

Thermodynamic properties, such as the radial distribution function (RDF), are related to the diagonal part of the density matrix, so that the path returns to its starting place after a time β .

To perform Monte Carlo calculations of the integrand, one makes imaginary thermal time discrete with a *time step* τ , so that one has a finite (and hopefully small)

R. Fantoni

number of time slices and thus a classical system of N particles in $M = \beta/\tau$ time slices; an equivalent NM particle classical system of “polymers”.¹⁹

Thermodynamic properties are averages over the thermal $2N$ -body density matrix which is defined as a thermal occupation of the exact eigenstates $\phi_i(R)$

$$\rho(R, R'; \beta) = \sum_i \phi_i^*(R) e^{-\beta E_i} \phi_i(R'). \quad (3.3)$$

The partition function is the trace of the density matrix

$$Z(\beta) = e^{-\beta F} = \int dR \rho(R, R; \beta) = \sum_i e^{-\beta E_i}, \quad (3.4)$$

with F Helmholtz’s free energy. Other thermodynamic averages are obtained as

$$\langle \mathcal{O} \rangle = Z(\beta)^{-1} \int dR dR' \langle R | \mathcal{O} | R' \rangle \rho(R', R; \beta). \quad (3.5)$$

Path integrals are constructed using the product property of density matrices

$$\rho(R_2, R_0; \beta_1 + \beta_2) = \int dR_1 \rho(R_2, R_1; \beta_2) \rho(R_1, R_0; \beta_1), \quad (3.6)$$

which holds for any sort of density matrix. If the product property is used M times, we can relate the density matrix at a temperature β^{-1} to the density matrix at a temperature $M\beta^{-1}$. The sequence of intermediate points $\{R_1, R_2, \dots, R_{M-1}\}$ is the path, and the *time step* is $\tau = \beta/M$. As the time step gets sufficiently small, the Trotter theorem tells us that we can assume that the kinetic \mathcal{T} and potential \mathcal{V} operator commute so that: $e^{-\tau \mathcal{H}} = e^{-\tau \mathcal{T}} e^{-\tau \mathcal{V}}$ (strictly speaking this is only possible when \mathcal{V} is bounded from below²⁰ but this is always satisfied by our simulation since we use a radial discretization of the pair Coulomb potential) and the *primitive approximation* for the Boltzmann density matrix is found¹⁹

$$\rho(R_0, R_M; \beta) = \int dR_1 \dots dR_{M-1} \exp \left[- \sum_{m=1}^M S^m \right], \quad (3.7)$$

$$K^m = \frac{3N}{2} \ln(4\pi\lambda\tau) + \frac{(R_{m-1} - R_m)^2}{4\lambda\tau}, \quad (3.8)$$

$$S^m - K^m \approx U_{\text{primitive}}^m = \frac{\tau}{2} [V(R_{m-1}) + V(R_m)]. \quad (3.9)$$

The Feynman–Kac formula for the Boltzmann density matrix results from taking the limit $M \rightarrow \infty$. The price we have to pay for having an explicit expression for the density matrix is additional integrations; all together $3N(M-1)$. Without techniques for multidimensional integration, nothing would have been gained by expanding the density matrix into a path. Fortunately, simulation methods can accurately treat such integrands. It is feasible to make M rather large, say in the hundreds or thousands, and thereby systematically reduce the time-step error. The leading error of the primitive approximation goes like $\sim \lambda\tau^2$.¹⁹

In addition to sampling the path, one also needs to sample all the various necessary permutations of the indistinguishable particles (bosons or fermions) and this is accomplished on the fly through the use of the worm algorithm.^{13,14}

When we are dealing with bosons or fermions $\rho_{B,F}(R_\beta, R_0; \beta) = \mathcal{A}_\mathcal{P} \rho(R_\beta, \mathcal{P}R_0; \beta)$ is the density matrix corresponding to some set of quantum numbers which are obtained by using the projection operator $\mathcal{A}_\mathcal{P} = \frac{1}{N!} \sum \mathcal{P}(\pm)^\mathcal{P}$, where \mathcal{P} is a permutation of particle labels and the permutation sign is a plus for bosons (B) and a minus for fermions (F), on the distinguishable particle density matrix. Then, for bosons we can carry on the Monte Carlo calculation without further approximations, but for fermions the following *Restricted Path Integral* approximation is also necessary in order to overcome the ubiquitous sign problem^{5,6}

$$\rho_F(R_\beta, R_0; \beta) = \int dR' \rho_F(R', R_0; 0) \oint_{R' \rightarrow R_\beta \in \gamma_T(R_0)} dR_t e^{-S[R_t]}, \quad (3.10)$$

where the subscript means that we restrict the path integration to paths starting at R' , ending at R_β and avoiding the nodes (the zeroes) of a known *trial density matrix*, ρ_T , assumed to have nodes, $\partial\gamma_T$, close to the true ones. The weight of the walk is $\rho_F(R', R_0; 0) = (N!)^{-1} \sum \mathcal{P}(-)^\mathcal{P} \delta(R' - \mathcal{P}R_0)$. It is clear that the contribution of all the paths for a single element of the density matrix will be of the same sign, thus avoiding the sign problem. On the diagonal, the density matrix is positive and on the path restriction $\rho_F(R, R_0; \beta) > 0$, then, only even permutations are allowed since $\rho_F(R, \mathcal{P}R; \beta) = (-)^\mathcal{P} \rho_F(R, R; \beta)$. It is then possible to use a bosonic calculation to get the approximate fermionic case.

The restriction is implemented choosing as the trial density matrix the ideal density matrix: we just reject the move (*remove, close, wiggle* and *displace* in the Z -sector, and *advance* and *swap* in the G -sector),^{13,14} whenever the proposed path is such that the ideal fermionic or fermionic-bosonic density matrix calculated between the reference point and any of the time slices subject to newly generated particles positions has a negative value.

The ideal fermionic or fermionic-bosonic density matrix is given by

$$\rho_0(R, R'; t) \propto \mathcal{A} \begin{pmatrix} e^{-\frac{(r_i^+ - r_j^+)^2}{4\lambda t}} & e^{-\frac{(r_i^+ - r_k^-)^2}{4\lambda t}} \\ e^{-\frac{(r_i^- - r_j^+)^2}{4\lambda t}} & e^{-\frac{(r_i^- - r_k^-)^2}{4\lambda t}} \end{pmatrix}, \quad (3.11)$$

where $\lambda = \hbar^2/2m$ and \mathcal{A} is the (anti)symmetrization operator for the positive and negative species (purely fermionic mixture) or for the positive species only (fermionic-bosonic mixture). We expect this approximation to be best at high temperatures and low densities when the correlation (the particles coupling and their quantum nature) effects are weak. Clearly in a simulation of the ideal gas ($V = 0$), this restriction returns the exact result for fermions, otherwise, it is just an approximation.

The restriction or the fixed nodes path integral may have an influence on the thermodynamic stability of the fluid under study, especially at low temperatures

R. Fantoni

when quantum effects become more relevant. On the other hand, if this were the case, it would have an influence on the stability of the fluid under all thermodynamic states which we can clearly exclude since as soon as we include at least one fermionic species in the binary mixture, the system becomes thermodynamically stable even at moderately low temperatures when the restriction is not very effective.

4. Results

In our simulations, we chose $k_B T = 10 \text{ Ry}$ and $L = 5a_0$. Going to lower temperatures, the contact value for the unlike partial RDF tends to increase since the

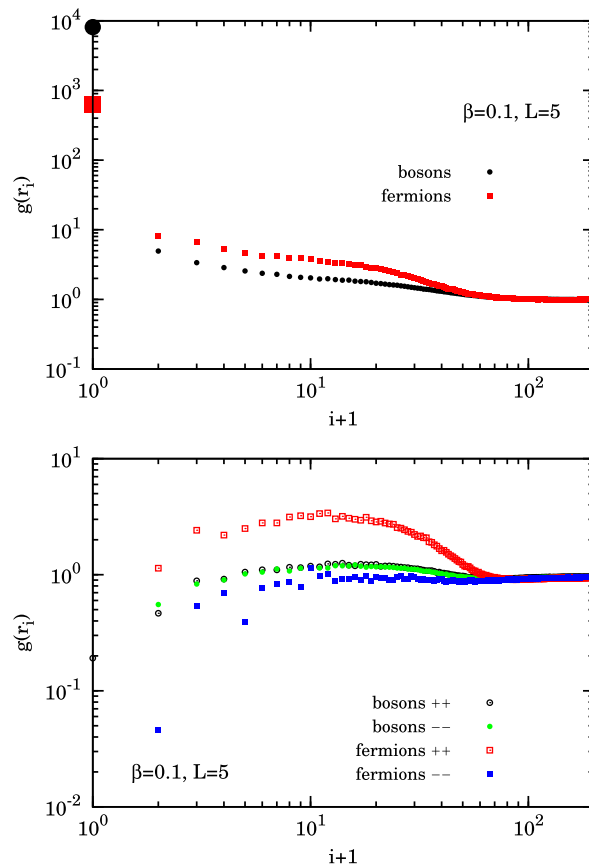


Fig. 1. (Color online) We show the partial RDF on a log-log scale. For the mixture of bosons and the fluid with one bosonic species and one fermionic species, we show $g_{+-}(r_i)$ in the upper panel and $g_{++}(r_i)$, $g_{--}(r_i)$ in the bottom panel. In all cases, we have $L/2 = r_{\text{cut}} a_0 = 2.5a_0$ and the RDF are calculated on 200 radial points $r_i = idr$ with $dr = r_{\text{cut}}/200$. The simulation was carried on at $\beta = 0.1 \text{ Ry}^{-1}$ with $M = 10$ time slices and an average of approximately 36 particles for the fermions case and 39 for the bosons case. The simulation was 15 000 blocks of 500 steps taking averages every 100 moves. But $g_{+-}(0)$ for the purely bosonic case continued to grow afterwards.

binding between a positive and a negative charge increases. This is because the coupling constant of the mixture is $\Gamma = \beta e^2/a_0$. For the purely bosonic case, the contact value never reaches an equilibrium during the simulation evolution unlike for the purely fermionic case or the fermions–bosons mixture where a positive charge binds with a negative charge in a stable way at low densities.²¹

It is also useful to introduce a degeneracy temperature $\Theta = T/T_F$, where $T_F = T_D 2\pi^2/\alpha_3^{2/3}$ is the Fermi temperature, here $\alpha_3 = 4\pi/3$, and

$$T_D = \frac{2n^{2/3}}{k_B} \text{ Ry}, \quad (4.1)$$

with $n = Na_0^3/V$, the density is the degeneracy temperature. For temperatures higher than T_D , as in our simulations, quantum effects are less relevant. For this reason, we chose $M = 10$ in all cases giving a $\tau = 0.01 \text{ Ry}^{-1}$. So the primitive approximation is a good one.

Another relevant parameter is the Wigner–Seitz radius $r_s = (3/4\pi n)^{1/3}$ which in the degenerate regime $\Theta \ll 1$ regulates whether the system of particles is dominated by the potential energy or by the kinetic energy. At high r_s , the potential energy dominates and the system tends to crystallize.¹⁷

From Fig. 1, we see how the binary mixture is stable when the particles are fermions and unstable when they are bosons. This is manifested by a contact value of the unlike partial RDF, for the purely bosonic case, which is one order of magnitude higher than the one for the purely fermionic case. It varies wildly during the simulation evolution, with variations of one or more orders of magnitudes upon

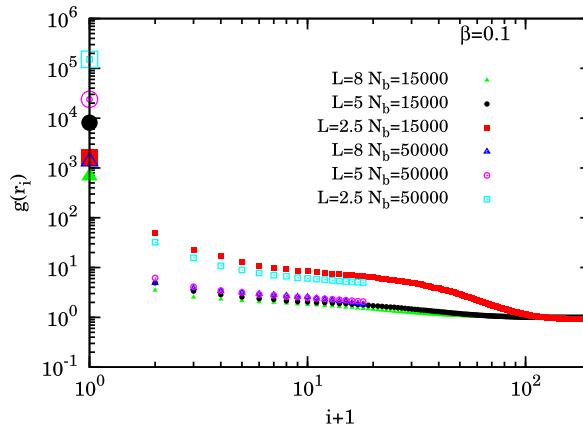


Fig. 2. (Color online) We show the unlike partial RDF on a log–log scale for the purely bosonic case at three different values of $L/2 = r_{\text{cut}}a_0$ and approximately same density and at two times during the simulation, after $N_b = 15\,000$ blocks (of 50 000 worm moves) and after $N_b = 50\,000$ blocks. The RDF are calculated on 200 radial points $r_i = idr$ with $dr = r_{\text{cut}}/200$. The simulation was carried on at $\beta = 0.1 \text{ Ry}^{-1}$ with $M = 10$ time slices. The simulation was 15 000 blocks of 500 steps taking averages every 100 moves. But $g_{+-}(0)$ continued to grow afterwards.

R. Fantoni

inspections of the simulation at different time intervals of 10 000 blocks of 50 000 worm moves each. The like partial RDF for the purely fermionic case shows a spontaneous symmetry breaking, where the positive–positive RDF differs from the negative–negative one and presents a broad shoulder near the origin which suggests the formation of like positive pairs. The contact value in the bosonic case has huge variations upon changes of the size of the system as shown by Fig. 2. This also means that there is no well-defined thermodynamic limit of the RDF which in turn is a manifestation of the system instability.¹ This does not occur when at least one of the two species is a fermion. In this case, a slight shoulder near the origin in the

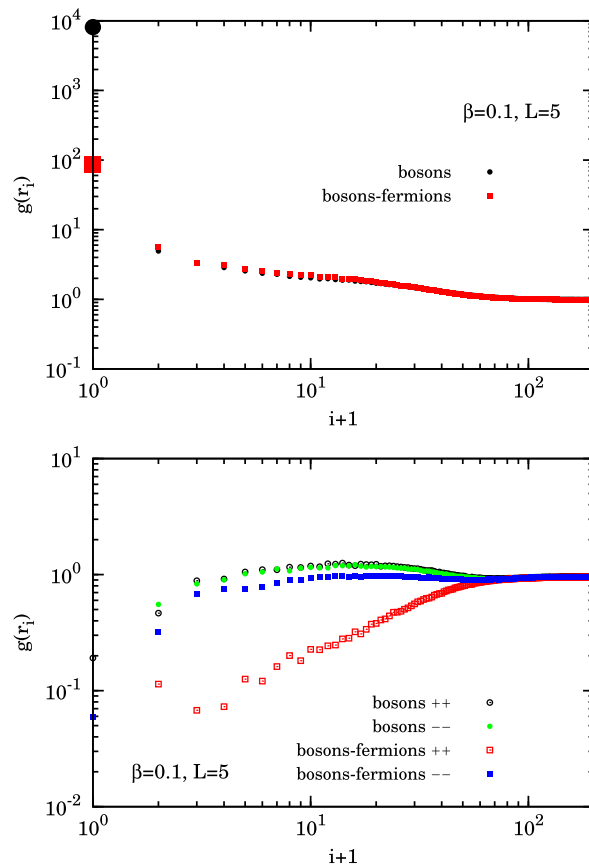


Fig. 3. (Color online) We show the partial RDF on a log–log scale. For the mixture of bosons and the fluid with one bosonic species and one fermionic species, we show $g_{+-}(r_i)$ in the upper panel and $g_{++}(r_i), g_{--}(r_i)$ in the bottom panel. In all cases, we have $L/2 = r_{\text{cut}}a_0 = 2.5a_0$ and the RDF are calculated on 200 radial points $r_i = idr$ with $dr = r_{\text{cut}}/200$. The simulation was carried on at $\beta = 0.1 \text{ Ry}^{-1}$ with $M = 10$ time slices and an average of approximately 38 particles for the mixed fermionic–bosonic case and 39 for the purely bosonic case. The simulation was 15 000 blocks of 500 steps taking averages every 100 moves. But $g_{+-}(0)$ for the purely bosonic case continued to grow afterwards.

unlike partial RDF indicates the stable pairing between a positive and a negative charge. The shoulder grows at lower temperature and lower density.

In order to have stability, it is sufficient to have at least one of the two particle species to be a fermion as is shown in Fig. 3. In this case, the like partial RDF for the bosonic species is comparable with the one of the purely bosonic case and the one for the fermionic component is lower. No like pair formation is visible from the structure analysis. The unlike partial RDF is superposed to the one of the purely fermionic case but presents an on top value two orders of magnitudes smaller.

The difference between the purely fermionic mixture and the fermions–bosons had to be expected also from the point of view of the fact that our spin polarized fermions, unlike the bosons, do not have a state with zero total angular momentum.

5. Conclusions

In conclusion, we carried on some computer experiments for the binary mixture of oppositely charged pointwise particle species when both species are bosons, both fermions, and one boson and one fermion. We chose the charge and the mass equal to the ones of the electron and only considered fully polarized species. We used the worm algorithm to perform (restricted) path integral Monte Carlo simulations, at finite temperatures.

We simulated the mixture with a weak degree of degeneracy $\Theta \sim 1.4$ and a weak coupling $\Gamma = 0.2$. The Wigner–Seitz radius for each species was $r_s \sim 1$.

During the simulations, we measured the radial distribution function of the three mixtures and found that the purely bosonic one is thermodynamically unstable toward the collapse of oppositely charged particles upon the others. Whereas, in the other two mixtures, the Pauli exclusion principle restores the stability producing stable bindings: like pairs form for the purely fermionic case as a result of a spontaneous symmetry breaking in a demixing transition and unlike pairs form in both cases. The instability manifests itself through a pronounced peak in the contact value of the unlike partial RDF which is strongly size-dependent in the experiment and keeps growing as the simulation evolves without ever reaching convergence towards a stable value. This observation tells us that the fermionic character of the simplest constituent of matter is essential in nature to be able to have a stable matter. On the other hand, if one uses nonquantum statistical mechanics, one must regularize the Coulomb potential at short range, for example through the addition of a hard core to the otherwise pointwise particles.^{3,4} Even if in the relativistic regime it is plausible to talk about an electron radius, attempts to model the electron as a nonpoint particle are considered ill-conceived and counter-pedagogic.²²

In order to have a stable matter, it is necessary that it is globally neutral and that it is made up of at least one fermionic species. Physical realizations of our model are nonrelativistic electron–positron plasma produced in the laboratory¹⁵ and electron–hole plasma in semiconductors.¹⁶ Of course, in the numerical experiment we do not have the physical limitations that occur in a laboratory. This allowed us to inquire

R. Fantoni

into also the mixture with one bosonic or even both bosonic components. Another interesting issue where our study could become relevant is atom and molecule formation. In its simplest setting it involves the study of an electron–proton mixture. Since the mass of an electron is three orders of magnitude smaller than the mass of a proton, the degeneracy temperature of the electron species is three orders of magnitude smaller than the one of the nuclei, at a given density. Therefore, it is very unlikely that an electron, with a world-line with many particle exchanges will bind to a nucleus which has a world-line with many less particle exchanges. In order for this to occur we have to go down to temperatures $k_B T_I \sim e^2/2a_0 = 1 \text{ Ry}$ and electron densities such that $T_F \sim T_I$, i.e. $n \sim 0.048$ or $r_s \sim 1.7$.²¹ Molecules may form at even lower temperatures. Nonetheless in our stable purely fermionic mixture with an equal species mass, we see already at the chosen thermodynamic state, the unlike species binding and a spontaneous symmetry breaking for like species bindings in a demixing transition.^{23–25}

We intend to adopt this method to simulate the two-component plasma in a curved surface^{26–29} in the near future. For example, it could be interesting to study the two-component plasma on the surface of a sphere with a magnetic monopole at the center.³⁰

References

1. E. Lieb, *Rev. Mod. Phys.* **48**, 553 (1976).
2. A. Alastuey and R. Fantoni, *J. Stat. Phys.* **163**, 887 (2016).
3. R. Fantoni and G. Pastore, *Europhys. Lett.* **101**, 46003 (2013).
4. R. Fantoni and G. Pastore, *Phys. Rev. E* **87**, 052303 (2013).
5. D. M. Ceperley, *J. Stat. Phys.* **63**, 1237 (1991).
6. D. M. Ceperley, in *Monte Carlo and Molecular Dynamics of Condensed Matter Systems*, eds. K. Binder and G. Ciccotti (Editrice Compositori, Italy, 1996).
7. E. W. Brown, B. K. Clark, J. L. DuBois and D. M. Ceperley, *Phys. Rev. Lett.* **110**, 146405 (2013).
8. E. Brown, M. A. Morales, C. Pierleoni and D. M. Ceperley, in *Frontiers and Challenges in Warm Dense Matter*, eds. F. G. *et al.* (Springer, 2014), pp. 123–149.
9. T. Dornheim, S. Groth, T. Sjostrom, F. D. Malone, W. M. C. Foulkes and M. Bonitz, *Phys. Rev. Lett.* **117**, 156403 (2016).
10. S. Groth, T. Dornheim, T. Sjostrom, F. D. Malone, W. M. C. Foulkes and M. Bonitz, *Phys. Rev. Lett.* **119**, 135001 (2017).
11. F. D. Malone, N. S. Blunt, E. W. Brown, D. K. K. Lee, J. S. Spencer, W. M. C. Foulkes and J. J. Shepherd, *Phys. Rev. Lett.* **117**, 115701 (2016).
12. V. S. Filinov, V. E. Fortov, M. Bonitz and Z. Moldabekov, *Phys. Rev. E* **91**, 033108 (2015).
13. M. Boninsegni, N. Prokof'ev and B. Svistunov, *Phys. Rev. Lett.* **96**, 070601 (2006).
14. M. Boninsegni, N. V. Prokof'ev and B. V. Svistunov, *Phys. Rev. E* **74**, 036701 (2006).
15. N. Iwamoto, *Phys. Rev. E* **47**, 604 (1993).
16. J. P. Wolfe, J. L. Lin and D. W. Snoke, in *Bose Einstein Condensation*, ed. A. Griffin, D. W. Snoke and S. Stringari (Cambridge, New York, 1995), pp. 281–329.
17. J. Shunway and D. M. Ceperley, in *Proc. Int. Conf. Strongly Coupled Coulomb Systems* (St. Malo, France, 1999).

Two component boson-fermion plasma at finite temperature

18. V. D. Natoli and D. M. Ceperley, *J. Comput. Phys.* **117**, 171 (1995).
19. D. M. Ceperley, *Rev. Mod. Phys.* **67**, 279 (1995).
20. B. Simon, *Functional Integration and Quantum Physics* (Academic, New York, 1979).
21. C. Pierleoni, B. Bernu, D. M. Ceperley and W. R. Magro, *Phys. Rev. Lett.* **73**, 2145 (1994).
22. L. J. Curtis, *Atomic Structure and Lifetimes: A Conceptual Approach* (Cambridge University Press, 2003), p. 74.
23. R. Fantoni and A. Santos, *Phys. Rev. E* **84**, 041201 (2011).
24. R. Fantoni and A. Santos, *Phys. Rev. E* **87**, 042102 (2013).
25. R. Fantoni and A. Santos, *J. Chem. Phys.* **140**, 244513 (2014).
26. R. Fantoni, B. Jancovici and G. Téllez, *J. Stat. Phys.* **112**, 27 (2003).
27. R. Fantoni and G. Téllez, *J. Stat. Phys.* **133**, 449 (2008).
28. R. Fantoni, *J. Stat. Mech.* P04015 (2012).
29. R. Fantoni, *J. Stat. Mech.* P10024 (2012).
30. V. Melik-Alaverdian, G. Ortiz and N. E. Bonesteel, *J. Stat. Phys.* **104**, 449 (2001).

Chapter 59

One-component fermion plasma on a sphere at finite temperature

Fantoni R., Int. J. Mod. Phys. C **29**, 1850064 (2018)

Title: “One-component fermion plasma on a sphere at finite temperature”

Abstract: We study through a computer experiment, using the restricted path integral Monte Carlo method, a one-component fermion plasma on a sphere at finite, non-zero, temperature. We extract thermodynamic properties like the kinetic and internal energy per particle and structural properties like the radial distribution function. This study could be relevant for the characterization and better understanding of the electronic properties of hollow graphene spheres.

International Journal of Modern Physics C
Vol. 29, No. 8 (2018) 1850064 (14 pages)
© World Scientific Publishing Company
DOI: [10.1142/S012918311850064X](https://doi.org/10.1142/S012918311850064X)



One-component fermion plasma on a sphere
at finite temperature

Riccardo Fantoni

*Dipartimento di Fisica, Università di Trieste
Strada Costiera 11, 34151 Grignano (Trieste), Italy
rfantoni@ts.infn.it*

Received 1 May 2018
Accepted 5 June 2018
Published 11 July 2018

We study through a computer experiment, using the restricted path integral Monte Carlo method, a one-component fermion plasma on a sphere at finite, nonzero, temperature. We extract thermodynamic properties like the kinetic and internal energy per particle and structural properties like the radial distribution function. This study could be relevant for the characterization and better understanding of the electronic properties of hollow graphene spheres.

Keywords: One-component plasma; hollow graphene sphere; Monte Carlo simulation; finite temperature; restricted path integral; worm algorithm; fermions sign problem; structure; radial distribution function; thermodynamics; internal energy.

PACS Nos.: 02.70.Ss, 05.10.Ln, 05.30.Fk, 05.70.-a, 61.20.Ja, 61.20.Ne.

1. Introduction

We want to study the one-component fermion plasma on the surface of a sphere of radius a at finite, nonzero, temperature, as an evolution of the Thomson problem. The plasma is an ensemble of point-wise electrons which interact through the Coulomb potential assuming that the electric field lines can permeate the tridimensional space where the sphere is embedded. The system of particles is thermodynamically stable even if the pair-potential is purely repulsive because the particles are confined to the compact surface of the sphere, and we do not need to add a uniform neutralizing background as in the Wigner *Jellium* model. Therefore, our spherical plasma made of N spinless indistinguishable electrons of charge $-e$ and mass m will carry a total negative charge $-Ne$, a total mass Nm , and will have a radius a .

Note that in the limit $a \rightarrow \infty$ with a fixed surface density $\sigma = N/4\pi a^2$ our system becomes thermodynamically unstable since all the particles tend to escape to infinity. In order to prevent this pathological scenario one would have to add a uniform neutralizing background on the spherical surface of positive surface charge density $+\sigma e$. This amounts to replacing the Coulomb potential e^2/r with the corrected one

R. Fantoni

$e^2/r - B$ with $B = \int_{\text{sphere}} (e^2/r) dA / (4\pi a^2) = e^2$, where the integral is over the surface of the sphere $dA = a^2 \sin \theta d\theta d\varphi$ and $r = a\sqrt{2 - 2 \cos \theta}$ is the Euclidean distance between the north pole and another point on the sphere, with polar angle θ . The constant D is chosen to make sure that the average value of the interaction is zero and must be subtracted from the self-energy which would otherwise be zero. We would then obtain the Wigner Jellium system on the sphere which has received much attention from the point of view of path integral Monte Carlo recently in the Euclidean tridimensional space.¹⁻⁸

We want to study the structural and thermodynamic properties at finite, nonzero, temperature of the spherical fermion plasma through restricted path integral Monte Carlo. In particular, we will calculate the radial distribution function of the particles on the surface of the sphere and their kinetic and internal energy per particle.

Even if impenetrable identical particles on the surface of a sphere admit a fractional anyonic statistics,⁹ we will just study their fermionic nature, leaving the implementation of the anyonic statistics to a subsequent work. This amounts to distinguishing only among even and odd permutations rather than among the larger elements of the braid group. We will then consider the union of all the topologically disjoint portions of the particles configuration space belonging just to each of the two fermionic sections. This simplifies the problem considerably since the braid group is much larger and complex than the permutation group.⁹

A quantum fluid on a Riemannian surface has been studied before in relation to the quantum Hall effect.¹⁰⁻¹² A generalized stochastic method has also been implemented for the many-body ground state.^{13,14} We are not aware of any path integral Monte Carlo attempt in the spirit of our work. We expect our work to be relevant for the characterization of the electronic properties of hollow graphene spheres^{15,16} constructed in the laboratory and for their implementation as electrodes for supercapacitors and batteries, as superparamagnetic materials, as electrocatalysts for oxygen reduction, as drug deliverers, and as a conductive catalyst for photovoltaic applications.¹⁷⁻²⁵ Our numerical experiments, albeit idealized, are capable of exploring the properties of these systems under the most various thermodynamic conditions, even extreme conditions otherwise not accessible in the laboratory. Therefore we are able to explore and characterize the phenomenology of these systems with cost-free computer experiments that can later be used as guides for the laboratory set up.

The paper is organized as follows: in Sec. 2, we describe the problem we want to solve and the method used for its resolution, in Sec. 3, we present our numerical results, and Sec. 4 is for the concluding discussion.

2. The Problem

A point \mathbf{q} on the sphere of radius a , the surface of constant positive curvature, is given by

$$\mathbf{r}/a = \sin \theta \cos \varphi \hat{\mathbf{x}} + \sin \theta \sin \varphi \hat{\mathbf{y}} + \cos \theta \hat{\mathbf{z}}, \quad (1)$$

One-component fermion plasma on a sphere at finite temperature

with θ the polar angle and φ the azimuthal angle. The N particles positions are at $\mathbf{R} = (\mathbf{r}_1, \mathbf{r}_2, \dots, \mathbf{r}_N)$. The surface density of the plasma will then be $\sigma = N/4\pi a^2$. On the sphere we have the following metric:

$$ds^2 = g_{\mu\nu} dq^\mu dq^\nu = a^2 [d\theta^2 + \sin^2 \theta d\varphi^2], \tag{2}$$

where Einstein summation convention on repeated indices is assumed, we will use Greek indices for either the surface components or the surface components of each particle coordinate and roman indices for either the particle index or the time-slice index, $q^1 = \theta \in [0, \pi)$, $q^2 = \varphi \in [-\pi, \pi)$, and the positive definite and symmetric metric tensor is given by

$$g_{\mu\nu} = \begin{pmatrix} a^2 & 0 \\ 0 & a^2 \sin^2 \theta \end{pmatrix}. \tag{3}$$

We have periodic boundary conditions in $\theta + \pi = \theta$ and in $\varphi + 2\pi = \varphi$. We will not need to implement explicitly the periodic boundary conditions as all that is needed in the simulation is the geodesic and the Euclidean distance which are expressed in terms of trigonometric functions which are periodic in the coordinates θ and φ . We will also define $\mathbf{Q} = (\mathbf{q}_1, \mathbf{q}_2, \dots, \mathbf{q}_N)$ which will be the coordinates used in the code. The geodesic distance between two infinitesimally close points \mathbf{Q} and \mathbf{Q}' is $ds^2(\mathbf{Q}, \mathbf{Q}') = \sum_{i=1}^N ds^2(\mathbf{q}_i, \mathbf{q}'_i)$, where the geodesic distance between the points \mathbf{q} and \mathbf{q}' on the sphere is

$$s(\mathbf{q}, \mathbf{q}') = a \arccos[\cos(q^1) \cos(q'^1) \tag{4}$$

$$+ \sin(q^1) \sin(q'^1) \cos(q^2 - q'^2)]. \tag{5}$$

On a computer the haversine formula is numerically better conditioned for small distances. Moreover, to avoid rounding errors for the special case of antipodal points the Vincenty formula for an ellipsoid with equal major and minor axes may be used.

The Hamiltonian of the N nonrelativistic indistinguishable particles of the one-component spinless fermion plasma is given by

$$\mathcal{H} = \mathcal{T} + \mathcal{V} = -\lambda \sum_{i=1}^N \Delta_i + \sum_{i<j} v_{ij}, \tag{6}$$

with $\lambda = \hbar^2/2m$, where m is the electron mass, and $\Delta_i = g_i^{-1/2} \partial(g_i^{1/2} g_i^{\mu\nu} \partial/\partial q_i^\nu) / \partial q_i^\mu$ the Laplace–Beltrami operator for the i th particle on the sphere of radius a in local coordinates, where $g_{\mu\alpha} g^{\alpha\nu} = \delta_\mu^\nu$ and $g_i = \det ||g_{\mu\nu}(\mathbf{q}_i)||$. We have assumed that \mathcal{H} in curved space has the same form as in flat space. For the pair-potential, v , we will choose

$$v_{ij} = e^2/r_{ij}, \tag{7}$$

where e is the electron charge and r_{ij} is the Euclidean distance between two particles at \mathbf{q}_i and \mathbf{q}_j , which is given by

$$r_{ij} = a \sqrt{2 - 2\hat{\mathbf{r}}_i \cdot \hat{\mathbf{r}}_j} = 2a \sin[\arccos(\hat{\mathbf{r}}_i \cdot \hat{\mathbf{r}}_j)/2], \tag{8}$$

R. Fantoni

where $\hat{\mathbf{r}}_i = \mathbf{r}_i/a$ is the versor that from the center of the sphere points towards the center of the i th particle.

Given the antisymmetrization operator \mathcal{A} , and the inverse temperature $\beta = 1/k_B T$, with k_B Boltzmann's constant, the one-component fermion plasma density matrix, $\rho_F = \mathcal{A}e^{-\beta\mathcal{H}}$, in the coordinate representation, on a generic Riemannian manifold of metric g ,^{26,27} is

$$\rho_F(\mathbf{Q}', \mathbf{Q}; \beta) = \int \rho_F(\mathbf{Q}', \mathbf{Q}((M-1)\tau); \tau) \cdots \rho_F(\mathbf{Q}(\tau), \mathbf{Q}; \tau) \times \prod_{j=1}^{M-1} \sqrt{\tilde{g}_{(j)}} \prod_{i=1}^N dq_i^1(j\tau) \wedge dq_i^2(j\tau), \tag{9}$$

where as usual we discretize the *imaginary thermal time* in bits $\tau = \hbar\beta/M$. We will often use the following shorthand notation for the *path integral* measure: $\prod_{j=1}^{M-1} \sqrt{\tilde{g}_{(j)}} \prod_{i=1}^N dq_i^1(j\tau) \wedge dq_i^2(j\tau) \rightarrow \mathcal{D}\mathbf{Q}$ as $M \rightarrow \infty$. The path of the i th particle is given by $\{\mathbf{q}_i(t)|t \in [0, \hbar\beta]\}$ with t the imaginary thermal time. Each $\mathbf{q}_i(j\tau)$ with $i = 1, \dots, N$ and $j = 1, \dots, M$ represents the various *beads* forming the discretized path. The N particle path is given by $\{\mathbf{Q}(t)|t \in [0, \hbar\beta]\}$. Moreover,

$$\tilde{g}_{(j)} = \det \|\tilde{g}_{\mu\nu}(\mathbf{Q}(j\tau))\|, \quad j = 1, 2, \dots, M-1, \tag{10}$$

$$\tilde{g}_{\mu\nu}(\mathbf{Q}) = g_{\alpha_1\beta_1}(\mathbf{q}_1) \otimes \dots \otimes g_{\alpha_N\beta_N}(\mathbf{q}_N). \tag{11}$$

In the small τ limit we have

$$\rho_F(\mathbf{Q}(2\tau), \mathbf{Q}(\tau); \tau) = (2\pi\hbar)^{-N} \mathcal{A}[\tilde{g}_{(2)}^{-1/4} \sqrt{D(\mathbf{Q}(2\tau), \mathbf{Q}(\tau); \tau)} \tilde{g}_{(1)}^{-1/4} \times e^{\lambda\tau R(\mathbf{Q}(\tau))/6\hbar} e^{-\frac{1}{\hbar}S(\mathbf{Q}(2\tau), \mathbf{Q}(\tau); \tau)}], \tag{12}$$

where \mathcal{A} can act on the first, or on the second, or on both *time slices*, $R(\mathbf{Q})$ the scalar curvature of the curved manifold, S the action and D the van Vleck's determinant

$$D_{\mu\nu} = -\frac{\partial^2 S(\mathbf{Q}(2\tau), \mathbf{Q}(\tau); \tau)}{\partial Q^\mu(2\tau) \partial Q^\nu(\tau)}, \tag{13}$$

$$\det \|D_{\mu\nu}\| = D(\mathbf{Q}(2\tau), \mathbf{Q}(\tau); \tau), \tag{14}$$

where the Greek index denotes the two components of each particle coordinate.

For the *action* and the *kinetic-action* we have

$$S(\mathbf{Q}', \mathbf{Q}) = K(\mathbf{Q}', \mathbf{Q}) + U(\mathbf{Q}', \mathbf{Q}), \tag{15}$$

$$K(\mathbf{Q}', \mathbf{Q}) = \frac{3N\hbar}{2} \ln(4\pi\lambda\tau/\hbar) + \frac{\hbar^2 s^2(\mathbf{Q}', \mathbf{Q})}{4\lambda\tau}, \tag{16}$$

where in the *primitive approximation*²⁸ we find the following expression for the *interaction*,

$$U(\mathbf{Q}', \mathbf{Q}) = \frac{\tau}{2} [V(\mathbf{Q}') + V(\mathbf{Q})], \tag{17}$$

One-component fermion plasma on a sphere at finite temperature

$$V(\mathbf{Q}) = \sum_{i < j} v_{ij}. \tag{18}$$

In particular, the kinetic-action is responsible for a diffusion of the random walk with a variance of $2\lambda\tau g^{\mu\nu}/\hbar$.

On the sphere we have $R = N\mathcal{R}$ with $\mathcal{R} = 2/a^2$, the scalar curvature of the sphere of radius a , and in the $M \rightarrow \infty$ limit $s(\mathbf{Q}', \mathbf{Q}) \rightarrow ds(\mathbf{Q}', \mathbf{Q})$ and $\tilde{g}_{(2)}^{-1/4} \sqrt{D(\mathbf{Q}(2\tau), \mathbf{Q}(\tau); \tau)} \tilde{g}_{(1)}^{-1/4} \rightarrow (\hbar^2/2\lambda\tau)^N$. We recover the Feynman–Kac path integral formula on the sphere in the $\tau \rightarrow 0$ limit. In a computer experiment calculation it is enough to take M sufficiently large, of the order of 100 or 1000,²⁸ so to keep $\tau \sim 0.01$, recalling the primitive approximation error scales as $\sim \lambda\tau^2$. We will then have to deal with $2NM$ multidimensional integrals for which Monte Carlo is a suitable computational method. For example to measure an observable \mathcal{O} we need to calculate the following quantity:

$$\langle \mathcal{O} \rangle = \frac{\int O(\mathbf{Q}, \mathbf{Q}') \rho_F(\mathbf{Q}', \mathbf{Q}; \beta) d\mathbf{Q} d\mathbf{Q}'}{\int \rho_F(\mathbf{Q}, \mathbf{Q}; \beta) d\mathbf{Q}}, \tag{19}$$

where $\sqrt{\tilde{g}} \prod_{i=1}^N dq_i^1 \wedge dq_i^2 \equiv d\mathbf{Q}$. Note that most of the properties that we will measure are diagonal in coordinate representation, requiring then just the diagonal density matrix, $\rho_F(\mathbf{Q}, \mathbf{Q}; \beta)$. For example, for the radial distribution function, $g(r) = \langle \mathcal{O} \rangle$ with r the Euclidean distance between points \mathbf{q} and \mathbf{q}' , $r = 2a \sin[\arccos(\hat{\mathbf{q}} \cdot \hat{\mathbf{q}}')/2]$, we have the following histogram estimator:

$$O(\mathbf{Q}; r) = \sum_{i \neq j} \frac{1_{[r-\Delta/2, r+\Delta/2[}(q_{ij})}{N n_{id}(r)}, \tag{20}$$

where Δ is the histogram bin, $1_{[a,b[}(x) = 1$ if $x \in [a, b[$ and 0 otherwise, and

$$n_{id}(r) = N \left[\left(\frac{r + \Delta/2}{2a} \right)^2 - \left(\frac{r - \Delta/2}{2a} \right)^2 \right], \tag{21}$$

is the average number of particles on the spherical crown $[r - \Delta/2, r + \Delta/2[$ for the ideal gas of density σ . We have that $\sigma^2 g(r)$ gives the probability that sitting on a particle at \mathbf{q} one has to find another particle at \mathbf{q}' .

Fermions' properties cannot be calculated exactly with path integral Monte Carlo because of the fermions sign problem.^{29,30} We then have to resort to an approximated calculation. The one we chose was the restricted path integral approximation^{29,30} with a “free fermions restriction”. The trial density matrix used in the restriction is chosen as the one reducing to the ideal density matrix in the limit of $t \ll 1$ and is given by

$$\rho_0(\mathbf{Q}', \mathbf{Q}; t) \propto \mathcal{A} \left\| e^{-\frac{\hbar\sigma^2(\mathbf{q}', \mathbf{q}_j)}{4\lambda t}} \right\|. \tag{22}$$

R. Fantoni

The *restricted path integral identity* that we will use states^{29,30}

$$\rho_F(\mathbf{Q}', \mathbf{Q}; \beta) \propto \int \sqrt{\bar{g}''} d\mathbf{Q}'' \rho_F(\mathbf{Q}'', \mathbf{Q}; 0) \times \oint_{\mathbf{Q}'' \rightarrow \mathbf{Q} \in \gamma_0(\mathbf{Q})} \mathcal{D}\mathbf{Q}''' e^{-S[\mathbf{Q}''']/\hbar}, \quad (23)$$

where S is the Feynman–Kac action.

$$S[\mathbf{Q}] = \int_0^{\hbar\beta} dt \left[\frac{\hbar^2}{4\lambda} \dot{\mathbf{Q}}_\mu \dot{\mathbf{Q}}^\mu + V(\mathbf{Q}) \right]. \quad (24)$$

Here, the dot indicates a total derivative with respect to the imaginary thermal time, and the subscript in the path integral of Eq. (2) means that we restrict the path integration to paths starting at \mathbf{Q}'' , ending at \mathbf{Q}' and avoiding the nodes of ρ_0 , that is *the reach of \mathbf{Q}* . The nodes are on the reach boundary $\partial\gamma_0$. The weight of the walk is $\rho_F(\mathbf{Q}'', \mathbf{Q}; 0) = \mathcal{A}\delta(\mathbf{Q}'' - \mathbf{Q}) = (N!)^{-1} \sum_{\mathcal{P}} (-)^{\mathcal{P}} \delta(\mathbf{Q}'' - \mathcal{P}\mathbf{Q})$, where the sum is over all the permutations \mathcal{P} of the N fermions, $(-)^{\mathcal{P}}$ is the permutation sign, positive for an even permutation and negative for an odd permutation, and the Dirac’s delta function is on the sphere. It is clear that the contribution of all the paths for a single element of the density matrix will be of the same sign, thus solving the sign problem; positive if $\rho_F(\mathbf{Q}'', \mathbf{Q}; 0) > 0$, negative otherwise. On the diagonal the density matrix is positive and on the path restriction $\rho_F(\mathbf{Q}', \mathbf{Q}; \beta) > 0$, then only even permutations are allowed since $\rho_F(\mathbf{Q}, \mathcal{P}\mathbf{Q}; \beta) = (-)^{\mathcal{P}} \rho_F(\mathbf{Q}, \mathbf{Q}; \beta)$. It is then possible to use a bosons calculation to get the fermions case. Clearly the restricted path integral identity with the free fermions restriction becomes exact if we simulate free fermions, but otherwise is just an approximation. The approximation is expected to become better at low density and high temperature, i.e. when correlation effects are weak. The implementation of the restricted, fixed nodes, path integral identity within the worm algorithm has been the subject of a recent study on the tridimensional Euclidean Jellium.

We will use the *worm algorithm*^{31,32} to generate spontaneously the needed permutations for the antisymmetrization operator \mathcal{A} . The permutations on the sphere will generate paths with different braiding properties. Identical impenetrable (scalar) particles on a sphere are, in general, anyons with fractional statistics.⁹ Here we will just project out the fermionic component of the broader braid group by just looking at the sign of the trial free fermions density matrix. The object of study is still the realization of the simulation of the anyonic system. The worm algorithm is able to sample the necessary permutations of the indistinguishable particles without the need of explicitly sampling the permutations space treating the paths as “worms” with a tail (*Masha*) and a head (*Ira*) in the β -periodic imaginary time, which can be attached one with the other in different ways or swap some of their portions.

We will work in the grand canonical ensemble with fixed chemical potential μ , surface area $A = 4\pi a^2$, and absolute temperature T . At a higher value of the

chemical potential we will have a higher number of particles on the surface and a higher density. On the other hand, increasing the radius of the sphere at constant chemical potential will produce a plasma with lower surface density. The *Coulomb coupling constant* is $\Gamma = \beta e^2 / a_0 r_s$ with $a_0 = \hbar^2 / me^2$ the Bohr radius and $r_s = (4\pi\sigma)^{-1/2} / a_0$. At weak coupling, $\Gamma \ll 1$, the plasma becomes weakly correlated and approaches the ideal gas limit. This will occur at high temperature and/or low density. The *electron degeneracy parameter* is $\Theta = T / T_D$, where the degeneracy temperature $T_D = \sigma \hbar^2 / mk_B$. For temperatures higher than T_D , $\Theta \gg 1$, quantum effects are less relevant.

3. Results

Choosing length in Wigner–Seitz’s radius, $a_0 r_s$, units and energies in Rydberg’s, $\text{Ry} = \hbar^2 / 2ma_0^2$, units we have $\lambda = \text{Ry} / r_s^2$, $\Gamma = \beta(2/r_s)$, and $\Theta = (2\pi r_s^2) / \beta$. We then see immediately that when quantum effects are relevant, at $\Theta \lesssim 1$, and at low density or high r_s the potential energy dominates in the Hamiltonian (6) and the electron plasma tends to crystallize in a Wigner’s crystal. On the other hand at $\Theta \gg 1$, in the classical regime, the system tends to crystallize at high density. In our grand canonical simulation it is rather convenient to choose the length unit to be just the Bohr radius since r_s is not an input parameter.

We use a free fermion trial density matrix restriction for the fixed nodes path integral calculation from the worm algorithm^{32,33} to the reach of the reference point in moves ending in the Z sector: remove, close, wiggle, and displace. We will use the primitive approximation of Eq. (17). Our algorithm has been recently described in Ref. 34. Here we do not randomize the reference point time slice and we do not restrict the G sector. We choose the probability of being in the G sector ($\propto C_0$ in Ref. 32) so as to have Z sector’s acceptance ratio close to 8/10. The restriction implementation is rather simple: we just reject the move whenever the proposed path is such that the ideal fermion density matrix (22) calculated between the reference point and any of the time slices subject to newly generated particles positions has a negative value. The algorithm will spontaneously choose the optimal needed τ , in the sense that for bigger τ it will not be able to come back and forth between the Z and the G sector remaining stuck in the G sector.

The restricted worm algorithm simulations length was $n \times 10^3$ blocks, with $n \in [0, 10]$ an integer. Each block was made of 500 steps during which 100 moves were made and measures and averages taken. The moves were of nine kinds: advance, recede, insert, open and swap ending in the G sector; remove, close, wiggle and displace ending in the Z sector.³⁵ Each move involved no more than 20 time slices. And they were chosen from a menu with equal probabilities. The integration measures factors \sqrt{g} were only used in the acceptance probabilities of the self-complementary moves: wiggle, swap and displace.

In Table 1 we show the cases studied in our simulations. The first case A is at a temperature of about 3946 K below the graphene melting temperature.³⁶ From the

R. Fantoni

Table 1. Thermodynamic states treated in our simulations: μ (Ry) chemical potential, β (Ry⁻¹) inverse temperature, \bar{N} average number of particles, \bar{r}_s average value of r_s , e_K (Ry) kinetic energy per particle from the thermodynamic estimator as explained in Ref. 28, and e_V (Ry) potential energy per particle. The other quantities were introduced in the main text. We chose length in Bohr radius' units and energy in Rydberg's units. We chose M such as to have $\tau = 0.01$ or less in all cases except case A where we have $\tau = 0.02$.

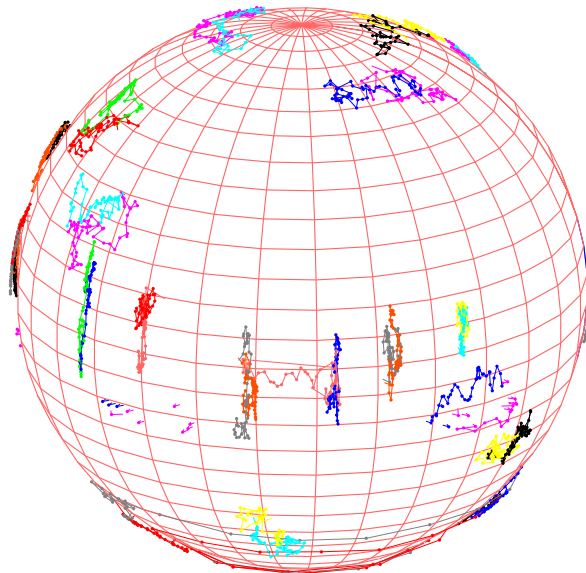
Case	M	μ	a/a_0	β	\bar{N}	\bar{r}_s	Γ	Θ	e_K	e_V
A	2000	4	5	40	15.03(3)	1.29	62.0	0.261	24.9(3)	2.67(3)
B	500	8	5	5	20.80(8)	1.10	9.12	1.51	48.97(4)	3.857(6)
C	100	10	5	1	29.2(2)	0.925	2.16	5.38	48.5(2)	6.08(5)
D	50	8	5	1/2	31.0(1)	0.898	1.11	10.1	47.84(6)	6.43(3)
E	10	-13	5	1/10	61.8(3)	0.636	0.314	25.4	51(1)	12.83(6)
F	2	-300	5	2/100	58.9(1)	0.651	6.14×10^{-2}	133	61(4)	11.86(2)
G	2	-250	5	0.015	48.00(3)	0.722	4.16×10^{-2}	218	-9(4)	9.412(5)
H	100	4	10	1	35.3(2)	1.68	1.19	17.8	-38(36)	3.90(2)
I	100	0	20	1	50.5(4)	2.81	0.711	49.8	42(3)	3.02(3)
L	100	-8	200	1	17.7(2)	47.5	4.21×10^{-2}	1.42×10^4	45(3)	0.118(1)

table we see how the potential energy per particle diminishes as the density of the system decreases.

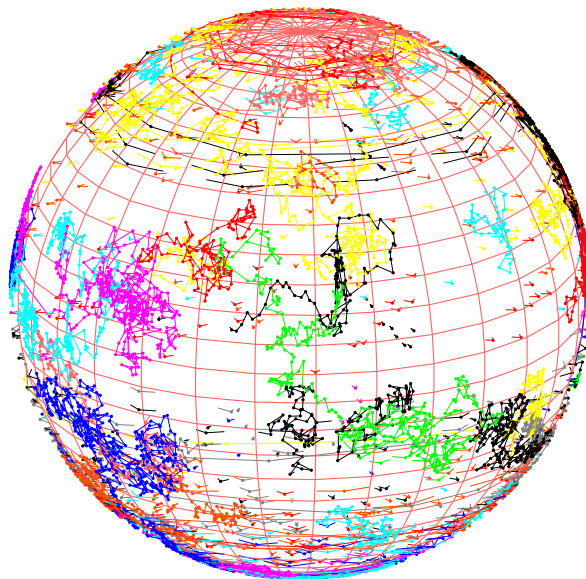
In Fig. 1 we show a snapshot of the macroscopic path during an equilibrated simulation of cases B and C of Table 1. We see how the particles tend to cover the sphere surface isotropically. As it should be since there is nothing able to break the symmetry. Regarding the paths configuration we see immediately that the ones in case B, at lower temperature, are more extended than the ones in case C, at higher temperature, in agreement with the fact that the de Broglie thermal wavelength, the size of a path in absence of interactions, is bigger in case B. We can distinguish between several kinds of conformations. There are the localized paths and the un-localized path covering a large portion of the sphere surface. Paths tend to avoid the poles at low temperature. They tend to wind around the sphere running along the parallels in proximity of the poles and to run along the meridians in proximity of the equator. This is because these are the paths favored by the kinetic-action which is expressed in terms of the square of the geodesic distance of Eq. (4) which, unlike the Euclidean distance, is homogeneous only in the azimuthal angle, the q^2 local coordinate, but not in the polar angle, the q^1 local coordinate. At lower temperature, when the path size increases, the worm diffuses more and we can have paths covering a larger part of the sphere with longer links between two beads. If we rotate the sphere moving its \hat{z} axis, the paths configuration will also rotate.

In Fig. 2 we show the radial distribution function for the cases shown in Table 1. Note that here we are plotting against the Euclidean distance instead of the geodesic one so the value of $g(r)$ on the diameter is at $r = a\sqrt{2}$, the top value is at $r = 0$, and the antipodal value is at $r = 2a$. We then see the effect of curvature on the Coulomb and Fermi hole near contact as they evolve by increasing the temperature. The extent of the Coulomb and Fermi hole at the lowest temperature amounts to roughly 2.5 Bohr's radii. In the limit of very high temperature, the radial distribution

One-component fermion plasma on a sphere at finite temperature



(a)



(b)

Fig. 1. (Color online) Snapshot of the macroscopic path during the simulation of case C in Table 1 in the top panel and case B in Table 1 in the bottom panel. The different worms have different colors. Some paths penetrate through the surface of the sphere and appear as broken links.

R. Fantoni

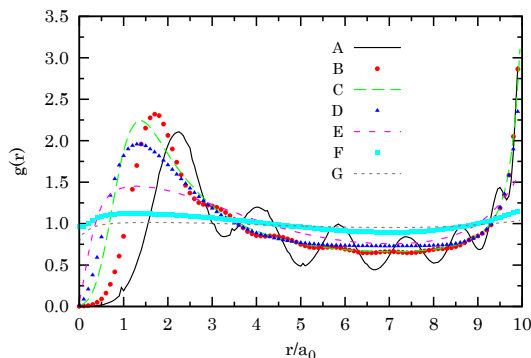


Fig. 2. (Color online) The radial distribution function for the spinless fermion plasma on the sphere of radius $a = 5a_0$ at an inverse temperature β and a chemical potential μ for the cases A-G shown in Table 1.

function tends to the constant function everywhere equal to unity (see case G of Table 1). Another feature of the radial distribution function is the first peak which is produced due to the Pauli exclusion principle, responsible for the Fermi hole, for the Coulomb repulsion, responsible for the Coulomb hole, and for the temperature effect which tends to make particles bump one on the other. From Fig. 2 we clearly see how at small Θ , when the Pauli exclusion becomes strong, the peak tends to shift at larger distances. At very high Θ , the Pauli exclusion becomes very weak and the Fermi hole tends to disappear. Curiously enough the height of the first peak, the probability that sitting on a particle we find one in its neighborhood, is lower than the antipodal value, probability of finding a particle to the particle antipodes. The first peak height and the antipodal value have a nonmonotonic behavior with temperature. Since there are no attractions in the pair-potential, we only observe oscillations in the radial distribution function at very low temperature.

In Fig. 3 we show the radial distribution function of the plasma at the inverse temperature $\beta = 1 \text{ Ry}^{-1}$ on spheres of different diameters and with roughly equal average number of particles, as shown in Table 1 for cases C, H, I and L. Case L corresponds to a sphere of the diameter of 20 nanometers and still presents the Coulomb and Fermi hole. We can see that, as the diameter increases and the density decreases, the first peak height increases. This had to be expected in view of the fact that the system in the semi-quantal regime will tend to crystallize as the density decreases. The peak height tends to become bigger than the antipodal value.

We always worked with no more than 65 electrons which could correspond to the π conduction electrons of the carbon atoms in the graphene sphere. So, the spheres should be made by 10–100 C atoms. The same order of magnitude as in fullerenes where the smallest buckyball cluster is C_{20} and the most common is the buckminsterfullerene C_{60} . Here we are not taking care of the fact that, in graphene, at the Dirac point, electrons have zero effective mass. These graphinos should have a relativistic Hamiltonian rather than the nonrelativistic one we used in Eq. (6).

One-component fermion plasma on a sphere at finite temperature

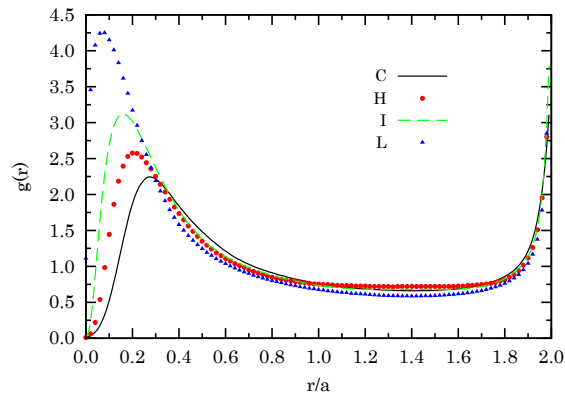


Fig. 3. (Color online) The radial distribution function for the spinless fermion plasma on the sphere of different radii at an inverse temperature $\beta = 1 \text{ Ry}^{-1}$ and a chemical potential μ for the cases shown in Table 1.

4. Conclusions

We simulated a one-component spinless fermion plasma at finite, nonzero, temperature on the surface of a sphere. The Coulomb interaction is e^2/r with r the Euclidean distance between the two electrons of elementary charge e . Here we could as well have chosen instead of r the geodesic distance, s , within the sphere. We used a new implementation of the restricted fixed nodes path integral identity within the worm Monte Carlo algorithm. This gives us an approximated numerical solution of the many-body problem. The exact solution cannot be accessed due to the fermion sign catastrophe. Impenetrable indistinguishable particles on the surface of a sphere admit, in general, anyonic statistics. Here we just project the larger braid group onto the permutation group and choose the fermion sector for our study.

The path integral Monte Carlo method chosen uses the primitive approximation for the action which could be improved for example by the use of the pair-product action.²⁸ The restriction is carried on choosing as the trial density matrix the one of ideal free fermion. This choice would return an exact solution for the simulation of ideal fermions but it furnishes just an approximation for the interacting coulombic plasma.

Our results extend to the quantum regime the previous nonquantum results obtained for the analytically exactly solvable plasma on curved surfaces³⁷⁻⁴² and for its numerical Monte Carlo experiment.⁴³ Here we just study the geometry of the sphere leaving the more complex surfaces with a nonconstant curvature to a further study. As is shown by the snapshot of the macroscopic path, the configuration space appears much more complicated than in the classical case (see Figs. 5 and 6 of Ref. 43). A first notable phenomena is that whereas the particles distribution is certainly isotropic the paths conformation is not, with beads distributed in such way to avoid the poles at low temperature. Some paths tend to wind around the sphere

R. Fantoni

running along the parallels in proximity of the poles, others to run along the meridians in proximity of the equator. This is a direct consequence of the coordinate dependence of the variance of the diffusion. If we rotate the sphere the path configuration will also rotate with the sphere. We have several kinds of worms configurations. At high and low temperature: the localized ones, those winding around the sphere along parallels, and those penetrating through the surface of the sphere, at low temperature, the unlocalized ones distributed over a larger part of the surface with long links between the beads of the path.

The structure of the plasma on the sphere reveals how the curvature influences the Coulomb and Fermi holes as they evolve in temperature and density. In particular we observe a monotonic increase of the extent of the Fermi hole as the temperature diminishes. Our analysis shows how the probability of finding a particle nearby another particle is lower than the probability of finding a particle at the antipodes unless for spheres of large diameter. At a higher degeneracy parameter the Pauli exclusion effect becomes less important and the Fermi hole tends to disappear. In the high temperature limit the particles will tend to cover the sphere more uniformly. Decreasing the surface density at fixed low temperature the first peak of the radial distribution function grows monotonically in height, tends to become bigger than its antipodal value, and shifts at smaller distances.

Our computer experiment could be used to predict the properties of a metallic spherical shell, as for example a spherical shell of graphene. Today we assisted the rapid development of the laboratory realization of graphene hollow spheres with many technological interests like the employment as electrodes for supercapacitors and batteries, as superparamagnetic materials, as electrocatalysts for oxygen reduction, as drug deliverers, as a conductive catalyst for photovoltaic applications. Of course, with simulation we can access the more various and extreme conditions otherwise not accessible in a laboratory.

A possible further study would be the simulation of the neutral sphere where we model the plasma of electrons as embedded in a spherical shell that is uniformly positively charged in such a way that the system is globally neutrally charged. This can easily be done by changing the Coulomb pair-potential into $e^2/r \rightarrow e^2/(1/r - 1)$. In the $a \rightarrow \infty$ limit, this would reduce to the Wigner Jellium model which has been receiving much attention lately, from the point of view of a path integral Monte Carlo simulation.¹⁻⁸ Alternatively, we could study the two-component plasma on the sphere as has recently been done in the tridimensional Euclidean space.⁴⁴ Another possible extension of our work is the realization of the simulation of the full anyonic plasma on the sphere taking care appropriately of the fractional statistics and the phase factors to append to each disconnected region of the path integral expression for the partition function. This could become important in a study of the quantum Hall effect by placing a magnetic Dirac monopole at the center of the sphere.^{13,14} Also the adaptation of our study to a fully relativistic Hamiltonian could be of some interest for the treatment of the Dirac points graphinos.

Acknowledgments

I would like to dedicate this work to my daughter Alice and to my wife Laure without whose support all this could not have been accomplished. I would like to acknowledge relevant discussions with Saverio Moroni whose comments and suggestions have been invaluable through the whole creation of the work.

References

1. E. W. Brown, B. K. Clark, J. L. DuBois and D. M. Ceperley, *Phys. Rev. Lett.* **110**, 146405 (2013).
2. E. Brown, M. A. Morales, C. Pierleoni and D. M. Ceperley, in *Frontiers and Challenges in Warm Dense Matter*, ed. F. Graziani *et al.* (Springer, 2014), pp. 123–149.
3. T. Dornheim, S. Groth, T. Sjostrom, F. D. Malone, W. M. C. Foulkes and M. Bonitz, *Phys. Rev. Lett.* **117**, 156403 (2016).
4. T. Dornheim, S. Groth, T. Schoof, C. Hann and M. Bonitz, *Phys. Rev. B* **93**, 205134 (2016).
5. S. Groth, T. Schoof, T. Dornheim and M. Bonitz, *Phys. Rev. B* **93**, 085102 (2016).
6. S. Groth, T. Dornheim, T. Sjostrom, F. D. Malone, W. M. C. Foulkes and M. Bonitz, *Phys. Rev. Lett.* **119**, 135001 (2017).
7. F. D. Malone, N. S. Blunt, E. W. Brown, D. K. K. Lee, J. S. Spencer, W. M. C. Foulkes and J. J. Shepherd, *Phys. Rev. Lett.* **117**, 115701 (2016).
8. V. S. Filinov, V. E. Fortov, M. Bonitz and Z. Moldabekov, *Phys. Rev. E* **91**, 033108 (2015).
9. A. Lerda, *Anyons. Quantum Mechanics of Particles with Fractional Statistics*, Lecture Notes in Physics (Springer-Verlag, Berlin Heidelberg, 1992).
10. C. T. Prieto, *J. Phys. Conf. Ser.* **175**, 012014 (2009).
11. H. R. Lee, *J. Korean Phys. Soc.* **34**, S189 (1999).
12. M. Bergeron and G. Semenoff, *Ann. Phys.* **245**, 1 (1996).
13. V. Melik-Alaverdian, N. E. Bonesteel and G. Ortiz, *Phys. Rev. Lett.* **79**, 5286 (1997).
14. V. Melik-Alaverdian, G. Ortiz and N. E. Bonesteel, *J. Stat. Phys.* **104**, 449 (2001).
15. A. Rashid and M. Yusoff, *Graphene-Based Energy Devices* (Wiley-VCH, Weinheim, 2015).
16. A. Tiwari and M. Syväjärvi, *Graphene Materials: Fundamentals and Emerging Applications* (Scrivener Publishing, Massachusetts, 2015).
17. P. Guo, H. Song and X. Chena, *J. Mater. Chem.* **20**, 4867 (2010).
18. J. Cao, Y. Wang, P. Xiao, Y. Chen, Y. Zhou, J.-H. Ouyang and D. Jia, *Carbon* **56**, 389 (2013).
19. L. Wu, H. Feng, M. Liu, K. Zhang and J. Li, *Nanoscale* **5**, 10839 (2013).
20. Q. Shao, J. Tang, Y. Lin, F. Zhang, J. Yuan, H. Zhang, N. Shinyaa and L.-C. Qinc, *J. Mater. Chem. A* **1**, 15423 (2013).
21. Y. Zhao, M. Chen and L. Wu, *Nanotechnology* **27**, 342001 (2016).
22. J. S. Cho, J.-K. Lee and Y. C. Kang, *Sci. Rep.* **6** (2016).
23. D. Hao, C. Xuefen, Q. Liangdong and Z. Xiaohui, *Rare Met. Mater. Eng.* **45**, 1669 (2016).
24. W. Huang, S. Ding, Y. Chen, W. Hao, X. Lai, J. Peng, J. Tu, Y. Cao and X. Li, *Sci. Rep.* **7** (2017).
25. E. Bi, H. Chen, X. Yang, F. Ye, M. Yin and L. Han, *Sci. Rep.* **5** (2017).
26. R. Fantoni, *J. Stat. Mech.* 10024 (2012).
27. L. S. Schulman, *Techniques and Applications of Path Integrals* (John Wiley & Sons, 1981).

R. Fantoni

28. D. M. Ceperley, *Rev. Mod. Phys.* **67**, 279 (1995).
29. D. M. Ceperley, *J. Stat. Phys.* **63**, 1237 (1991).
30. D. M. Ceperley, in *Monte Carlo and Molecular Dynamics of Condensed Matter Systems*, ed. K. Binder and G. Ciccotti (Editrice Compositori, Italy, 1996).
31. N. V. Prokof'ev, B. V. Svistunov and I. S. Tupitsyn, *J. Exp. Theor. Phys.* **87**, 310 (1998).
32. M. Boninsegni, N. Prokof'ev and B. Svistunov, *Phys. Rev. Lett.* **96**, 070601 (2006).
33. M. Boninsegni, N. V. Prokof'ev and B. V. Svistunov, *Phys. Rev. E* **74**, 036701 (2006).
34. R. Fantoni, *Eur. Comp. Phys. Comm.* (2018), in preparation.
35. R. Fantoni and S. Moroni, *J. Chem. Phys.* **141**, 114110 (2014).
36. J. H. Los, K. V. Z. and M. I. Katsnelson and A. Fasolino, *Phys. Rev. B* **91**, 045415 (2015).
37. R. Fantoni, B. Jancovici and G. Téllez, *J. Stat. Phys.* **112**, 27 (2003).
38. R. Fantoni and G. Téllez, *J. Stat. Phys.* **133**, 449 (2008).
39. R. Fantoni, *J. Stat. Mech.* 04015 (2012).
40. R. Fantoni, *J. Stat. Mech.* 10024 (2012).
41. R. Fantoni, *J. Stat. Phys.* **163**, 1247 (2016).
42. R. Fantoni, *Physica A* **477C**, 187 (2017).
43. R. Fantoni, J. W. O. Salari and B. Klumperman, *Phys. Rev. E* **85**, 061404 (2012).
44. R. Fantoni, *Int. J. Mod. Phys. C* **29**, 1850028 (2018).

Chapter 60

From the Liouville to the Smoluchowski equation for a colloidal solute particle in a solvent

Fantoni R., Physica A **5**, 682 (2018)

Title: “From the Liouville to the Smoluchowski equation for a colloidal solute particle in a solvent”

Abstract: We show how the Smoluchowski dynamics of a colloidal Brownian particle suspended in a molecular solvent can be reached starting from the microscopic Liouvillian evolution of the full classical model in the high friction limit. The integration of the solvent degrees of freedom goes through a multiple time scale perturbation expansion which removes the secular divergences. A simple dynamical Monte Carlo scheme is then proposed to solve the resulting evolution equation for the colloid solute particle. In particular we study the approach to the equilibrium Boltzmann distribution at late times and its resilience behavior at shorter times as influenced by the steepness of the external potential and the friction coefficient around their respective minima. This is very important to understand the fate of the Brownian particle’s random walk and its evolution history.

Physica A 515 (2019) 682–692



Contents lists available at ScienceDirect

Physica A

journal homepage: www.elsevier.com/locate/physa



From the Liouville to the Smoluchowski equation for a colloidal solute particle in a solvent



Riccardo Fantoni

Università di Trieste, Dipartimento di Fisica, strada Costiera 11, 34151 Grignano (Trieste), Italy

HIGHLIGHTS

- We reach the Smoluchowski dynamics of a colloidal Brownian particle suspended in a molecular solvent starting from the microscopic Liouvillian evolution of the full classical model in the high friction limit.
- The integration of the solvent degrees of freedom goes through a multiple time scale perturbation expansion which removes the secular divergences.
- A simple dynamical Monte Carlo scheme is then proposed to solve the resulting evolution equation for the colloid solute particle.
- In particular we study the approach to the equilibrium Boltzmann distribution at late times and its resilience behavior at shorter times.

ARTICLE INFO

Article history:

Received 11 May 2017

Received in revised form 5 August 2018

Available online xxxx

Keywords:

Colloidal suspension

Solvent

Solute

Brownian dynamics

Liouville

Fokker–Planck

Smoluchowski

Monte Carlo

ABSTRACT

We show how the Smoluchowski dynamics of a colloidal Brownian particle suspended in a molecular solvent can be reached starting from the microscopic Liouvillian evolution of the full classical model in the high friction limit. The integration of the solvent degrees of freedom goes through a multiple time scale perturbation expansion which removes the secular divergences. A simple dynamical Monte Carlo scheme is then proposed to solve the resulting evolution equation for the colloid solute particle. In particular we study the approach to the equilibrium Boltzmann distribution at late times and its resilience behavior at shorter times as influenced by the steepness of the external potential and the friction coefficient around their respective minima. This is very important to understand the fate of the Brownian particle's random walk and its evolution history.

© 2018 Elsevier B.V. All rights reserved.

1. Introduction

The dynamics of a many-body system can be given in terms of the time evolution of the probability phase space density of the chosen ensemble of particles. We must require that the total time derivative of the probability density vanishes so that the probability density as seen by an observer moving with a phase point along its phase space trajectory, is independent of time. Phase points of the statistical ensemble are neither created nor destroyed as time evolves.

The Liouvillian dynamics gives rise to the famous kinetic equation discovered by Boltzmann in 1872 (where the assumption of two body collisions only and of uncorrelated successive collisions are only valid at sufficiently low density) or to the exact Born–Bogoliubov–Green–Kirkwood–Yvon (BBGKY) hierarchical equations.

According to BBGKY the dynamics of a single particle requires the knowledge of the two-body probability density. But if we additionally require that the particle we are looking upon has mass much larger than that of all the other particles it is

E-mail address: rfantoni@ts.infn.it.

<https://doi.org/10.1016/j.physa.2018.09.107>

0378-4371/© 2018 Elsevier B.V. All rights reserved.

possible to expand perturbatively such dynamics so to find a closed equation for just the single massive particle probability phase space density.

A colloidal suspension is made of colloidal particles immersed in a solvent. The solvent (which may be water or other liquids) is in general a molecular liquid which can be described at a microscopic level by particles much smaller and lighter than the macromolecular colloidal particle. The problem of the dynamics of the big colloidal solute particle subject to its interaction with the smaller solvent molecules in statistical equilibrium at a given absolute temperature T is an interesting one. Starting from the observation in 1827 by Robert Brown of the motion of pollen grains in water and the interpretation of Albert Einstein in 1905 which was later verified experimentally by Jean Baptiste Perrin in 1908, the Brownian motion began to occupy an important role in non-equilibrium statistical physics. Even if the initial description of the colloid solute particle dynamics was an empirical one it soon became clear the microscopic origin of the Brownian motion. A complete microscopic description has to take into account the solvent in a proper way. The challenge is to be able to “remove” the degrees of freedom of the solvent in favor of the ones of the solute particle. So as to have a mesoscopic description of the dynamics of the colloid solute particle dressed by the solvent.

In the second half of last century it had been discovered [1] that it is indeed possible to derive the Brownian motion equations starting from the Liouvillian evolution, $\mathcal{L} \equiv i\{\mathcal{H}, \dots\}$, with $\{\dots\}$ the Poisson brackets and \mathcal{H} the model classical Hamiltonian, of the probability density in the phase space of a model of N solvent particles and the colloidal particle, $f^{(N+1)}(t) = \exp(-i\mathcal{L}t)f^{(N+1)}(0)$, to the Fokker–Planck equation [2,3] for the dynamics of the dressed solute particle alone subject to friction. The friction coefficient ξ is expressed in terms of an equilibrium average over the phase space of the solvent in the external field of the solute particle of a particular term containing the microscopic force exerted by the solvent on the colloidal particle. At the end of last century it was shown furthermore that a high friction expansion, in turn, brings [4] to the Smoluchowski equation for the colloid solute particle or its equivalent stochastic Langevin equation. Some related literature to the present framework can be found in the following references [5–8].

In this work we outline a simple Monte Carlo scheme that may be used to solve the resulting Smoluchowski equation that we call Dynamical Monte Carlo (DynMC). The realistic case of a colloidal suspension of poly(methyl methacrylate) (PMMA) particles in water [9] is taken as an example. In particular we study the approach to the equilibrium Boltzmann distribution at late times and its resilience behavior at shorter times as influenced by the steepness of the external potential and the friction coefficient around their respective minima. This is very important to understand the fate of the Brownian particle's random walk and its evolution history. We test our new algorithm on the case of a harmonic one dimensional external potential for which the analytic exact solution of the Smoluchowski equation is known.

Of course a more realistic treatment of the molecular solvent would be through a quantum statistical mechanics description where $\mathcal{L} \equiv i[\hat{\mathcal{H}}, \dots]/\hbar$, with $[\dots]$ the commutator and $\hat{\mathcal{H}}$ the model Hamiltonian operator. Then we would have a mixed evolution where the solvent is treated quantum mechanically and the massive colloid solute particle is treated classically (see for example Ref. [10] or Ref. [11] where the full quantum mechanical treatment is considered). We leave this as an open future problem.

The paper is organized as follows: In Section 2 we present the reduction from the Liouville equation to the Fokker–Planck equation, in Section 3 we present the reduction from the Fokker–Planck equation to the Smoluchowski equation, in Section 4 we present the Dynamical Monte Carlo algorithm (DynMC), in Section 5 we carry on a computer experiment with the newly developed algorithm to solve for the time dependence of the mean Brownian particle position under the influence of an external harmonic potential in one spatial solution, Section 6 is for final remarks.

2. From the Liouville to the Fokker–Planck equation

In this section we will reproduce and discuss the multiple time scale perturbation expansion presented in Ref. [12] which brings from the microscopic Liouville equation for a solute particle in a solvent to its mesoscopic Fokker–Planck equation.

We consider a colloidal solute particle of diameter Σ and mass M immersed in a colloidal suspension of small solvent particles of diameter σ and mass $m \ll M$. The Hamiltonian of the system of $N + 1$ particles can thus be written as

$$\mathcal{H} = \frac{P^2}{2M} + \sum_{i=1}^N \frac{p_i^2}{2m} + V_N(\mathbf{r}^N) + V_b(\mathbf{R}, \mathbf{r}^N), \quad (1)$$

where V_N is the total interaction energy of the N solvent particles of coordinates $\mathbf{r}^N = (\mathbf{r}_1, \mathbf{r}_2, \dots, \mathbf{r}_N)$ and momenta $\mathbf{p}^N = (\mathbf{p}_1, \mathbf{p}_2, \dots, \mathbf{p}_N)$, and V_b is the potential energy of the solvent particles in the field of a Brownian solute particle placed at \mathbf{R} with momentum \mathbf{P} . The Liouville operator splits naturally into a solvent and a Brownian terms: $\mathcal{L} = \mathcal{L}_s + \mathcal{L}_b$, with

$$\mathcal{L}_s = -i \sum_{i=1}^N \left(\frac{\mathbf{p}_i}{m} \cdot \frac{\partial}{\partial \mathbf{r}_i} + \mathbf{f}_i \cdot \frac{\partial}{\partial \mathbf{p}_i} \right), \quad (2)$$

$$\mathcal{L}_b = -i \left(\frac{\mathbf{P}}{M} \cdot \frac{\partial}{\partial \mathbf{R}} + \mathbf{F} \cdot \frac{\partial}{\partial \mathbf{P}} \right), \quad (3)$$

where $\mathbf{f}_i = -\partial(V_N + V_b)/\partial\mathbf{r}_i$ is the force acting on the solvent particle i and $\mathbf{F} = -\partial V_b/\partial\mathbf{R}$ is the force exerted on the solute particle by the solvent particles. The Liouville equation for the phase space probability density of the system of $N + 1$ particles is therefore

$$\frac{\partial}{\partial t} f^{[N+1]}(\mathbf{B}, \mathbf{b}^N; t) = -i(\mathcal{L}_s + \mathcal{L}_b) f^{[N+1]}(\mathbf{B}, \mathbf{b}^N; t), \tag{4}$$

where we use the following notation: $\mathbf{B} \equiv \{\mathbf{R}, \mathbf{P}\}$ and $\mathbf{b}^N \equiv \{\mathbf{r}^N, \mathbf{p}^N\}$.

We now introduce a perturbation parameter $\epsilon = \sqrt{m/M} \ll 1$ and rescale the solute particle momenta accordingly as follows: $\mathbf{P}' = \epsilon\mathbf{P}$, so that

$$\mathcal{L}_b = -i\epsilon \left(\frac{\mathbf{P}'}{m} \cdot \frac{\partial}{\partial \mathbf{R}} + \mathbf{F} \cdot \frac{\partial}{\partial \mathbf{P}'} \right) \equiv \epsilon \mathcal{L}'_b. \tag{5}$$

We want to find now the Liouville equation for the one-particle distribution function

$$f_b(\mathbf{B}, t) \equiv f^{[1]}(\mathbf{R}, \mathbf{P}'; t) = \int f^{[N+1]}(\mathbf{B}, \mathbf{b}^N; t) d\mathbf{b}^N. \tag{6}$$

Integrating then Eq. (4) over the coordinates and momenta of the solvent we find

$$\frac{\partial}{\partial t} f_b(\mathbf{B}, t) = -\epsilon \frac{\mathbf{P}'}{m} \cdot \frac{\partial}{\partial \mathbf{R}} f_b(\mathbf{B}, t) - \epsilon \int \mathbf{F} \cdot \frac{\partial}{\partial \mathbf{P}'} f^{[N+1]}(\mathbf{B}, \mathbf{b}^N; t) d\mathbf{b}^N, \tag{7}$$

where the term containing \mathcal{L}_s vanishes because we assume zero net flow of probability at infinity in phase space.

The perturbation expansion in ϵ over a *multiple time scale* is necessary in order to extract the mesoscopic time evolution from the microscopic one due to secular divergences of the solution at sufficiently long times, irrespective of how small ϵ may be. We then introduce an auxiliary distribution function

$$f_\epsilon^{[N+1]}(\mathbf{B}, \mathbf{b}^N; t_0, t_1, t_2, \dots) = f_{\epsilon 0}^{[N+1]} + \epsilon f_{\epsilon 1}^{[N+1]} + \epsilon^2 f_{\epsilon 2}^{[N+1]} + \dots, \tag{8}$$

which is a function of multiple time variables

$$t_0 = t, \quad t_1 = \epsilon t, \quad t_2 = \epsilon^2 t, \quad \dots, \quad t_n = \epsilon^n t. \tag{9}$$

Eq. (8) indicates that the dependence of the distribution function on t_n characterizes the evolution on the time scale $t \sim \epsilon^n$ for $n = 0, 1, 2, \dots$. So, the original Liouville Eq. (4) is replaced by

$$\left(\frac{\partial}{\partial t_0} + \epsilon \frac{\partial}{\partial t_1} + \epsilon^2 \frac{\partial}{\partial t_2} + \dots \right) f_\epsilon^{[N+1]} = -i(\mathcal{L}_s + \epsilon \mathcal{L}'_b) f_\epsilon^{[N+1]}, \tag{10}$$

and the Liouville equation for the Brownian motion by

$$\left(\frac{\partial}{\partial t_0} + \epsilon \frac{\partial}{\partial t_1} + \epsilon^2 \frac{\partial}{\partial t_2} + \dots \right) f_{b\epsilon} = -\epsilon \frac{\mathbf{P}'}{m} \cdot \frac{\partial}{\partial \mathbf{R}} f_{b\epsilon} - \epsilon \int \mathbf{F} \cdot \frac{\partial}{\partial \mathbf{P}'} f_\epsilon^{[N+1]} d\mathbf{b}^N. \tag{11}$$

Term by term integration of this equation shows that also $f_{b\epsilon}$ can be expanded in the form: $f_{b\epsilon} = f_{b0} + \epsilon f_{b1} + \epsilon^2 f_{b2} + \dots$. The crucial difference between Eq. (8) and a conventional perturbation expansion is the fact that the auxiliary function has a physical meaning only along the so-called physical line defined by (9). We are therefore free to impose whatever boundary conditions are needed to ensure that the expansion is free of secular divergences at successive powers of ϵ at large times. The same is true of the expansion for $f_{b\epsilon}$.

We will work up to order ϵ^2 , retaining only the three time variables t_0, t_1 , and t_2 . Substituting the perturbation expansion for $f_\epsilon^{[N+1]}$ and $f_{b\epsilon}$ in Eq. (11) and equating coefficients of equal powers of ϵ , we arrive at the following results.

[0.] To zeroth order in ϵ :

From Eq. (11) we find immediately

$$\frac{\partial}{\partial t_0} f_{b0} = 0, \tag{12}$$

so that $f_{b0} = f_{b0}(\mathbf{R}, \mathbf{P}'; t_1, t_2, \dots)$. From Eq. (10) we find

$$\frac{\partial}{\partial t_0} f_{\epsilon 0}^{[N+1]} = -i\mathcal{L}_s f_{\epsilon 0}^{[N+1]}. \tag{13}$$

Since the equilibrium phase space probability density of the solvent in the presence of the Brownian solute particle at \mathbf{R} satisfies the relation $\mathcal{L}_s f_0^{[N]}(\mathbf{b}^N|\mathbf{R}) = 0$, the solution to Eq. (13) is simply

$$f_{\epsilon 0}^{[N+1]} = f_{b0}(\mathbf{R}, \mathbf{P}'; t_1, t_2) f_0^{[N]}(\mathbf{b}^N|\mathbf{R}), \tag{14}$$

where

$$\int f_0^{[N]}(\mathbf{b}^N|\mathbf{R}) d\mathbf{b}^N = 1, \quad f_0^{[N]}(\mathbf{b}^N|\mathbf{R}) \propto e^{-\beta\mathcal{H}}, \quad \frac{\partial}{\partial \mathbf{R}} f_0^{[N]} = \beta \mathbf{F} f_0^{[N]}, \tag{15}$$

here $\beta = 1/k_B T$ with T the absolute temperature. We now employ the freedom of choice of boundary condition on the auxiliary function $f_{b\epsilon}$ imposing the following initial condition: $f_{b\epsilon}(\mathbf{R}, \mathbf{P}'; t_0 = 0, t_1, t_2) = f_{b0}(\mathbf{R}, \mathbf{P}'; t_1, t_2)$, which in turn implies that $f_{bn}(\mathbf{R}, \mathbf{P}'; t_0 = 0, t_1, t_2) = 0$ for $n = 1, 2$.

[1.] To first order in ϵ :

From Eqs. (10) and (11) we find

$$\frac{\partial}{\partial t_0} f_{\epsilon 1}^{[N+1]} + \frac{\partial}{\partial t_1} f_{\epsilon 0}^{[N+1]} = -i\mathcal{L}_s f_{\epsilon 1}^{[N+1]} - i\mathcal{L}'_b f_{\epsilon 0}^{[N+1]} \tag{16}$$

and

$$\frac{\partial}{\partial t_0} f_{b1} + \frac{\partial}{\partial t_1} f_{b0} = \int (-i\mathcal{L}'_b) f_{\epsilon 0}^{[N+1]} d\mathbf{b}^N, \tag{17}$$

respectively. Eqs. (12) and (14) show that f_{b0} and $f_{\epsilon 0}^{[N+1]}$ are both independent of t_0 . To avoid secular growth of f_{b1} in (17) it is necessary to impose $\partial f_{b1} / \partial t_0 = 0$, which combined with the initial condition for f_{b1} implies that $f_{b1} = 0$ identically, and

$$\frac{\partial}{\partial t_1} f_{b0} = \int (-i\mathcal{L}'_b) f_{\epsilon 0}^{[N+1]} d\mathbf{b}^N = -i\mathcal{L}'_b f_{b0}, \tag{18}$$

where in the last equality we used Eq. (14). We therefore focus on the time evolution of f_{b0} . Eq. (18) shows that on the time scale t_1 the evolution of the distribution function of the Brownian particle is the same as that of a single particle in the field of the solvent. Eq. (16) can now be rearranged as follows

$$\begin{aligned} \left(\frac{\partial}{\partial t_0} + i\mathcal{L}_s \right) f_{\epsilon 1}^{[N+1]} &= - \left(\frac{\partial}{\partial t_1} + i\mathcal{L}'_b \right) f_{\epsilon 0}^{[N+1]} \\ &= -\mathbf{F} \cdot \left(\frac{\beta \mathbf{P}'}{m} + \frac{\partial}{\partial \mathbf{P}'} \right) f_{b0} f_0^{[N]}, \end{aligned} \tag{19}$$

which, upon choosing the boundary condition $f_{\epsilon 1}^{[N+1]}(\mathbf{R}, \mathbf{P}', \mathbf{b}^N; t_0 = 0, t_1, t_2) = 0$, has the formal solution

$$\begin{aligned} f_{\epsilon 1}^{[N+1]}(\mathbf{R}, \mathbf{P}', \mathbf{b}^N; t_0, t_1, t_2) &= \\ - \int_0^{t_0} ds e^{-i\mathcal{L}_s s} \mathbf{F} \cdot \left(\frac{\beta \mathbf{P}'}{m} + \frac{\partial}{\partial \mathbf{P}'} \right) f_{b0}(\mathbf{R}, \mathbf{P}'; t_1, t_2) f_0^{[N]}(\mathbf{b}^N | \mathbf{R}), \end{aligned} \tag{20}$$

as can be checked by direct substitution in (20).

[2.] To second order in ϵ :

From Eq. (11) and the fact that $f_{b1} = 0$ we find

$$\frac{\partial}{\partial t_0} f_{b2} + \frac{\partial}{\partial t_2} f_{b0} = \int (-i\mathcal{L}'_b) f_{\epsilon 1}^{[N+1]} d\mathbf{b}^N. \tag{21}$$

Since f_{b0} is independent of t_0 , secular growth is again suppressed by setting $\partial f_{b2} / \partial t_0 = 0$. Substituting the solution (20) into Eq. (21) we obtain a closed equation for the evolution of $f_{b0}(\mathbf{R}, \mathbf{P}'; t_1, t_2)$:

$$\begin{aligned} \frac{\partial}{\partial t_2} f_{b0} &= \lim_{t_0 \rightarrow \infty} \int d\mathbf{b}^N f_0^{[N]}(\mathbf{b}^N | \mathbf{R}) i\mathcal{L}'_b \\ &\times \int_0^{t_0} ds e^{-i\mathcal{L}_s s} \mathbf{F} \cdot \left(\frac{\beta \mathbf{P}'}{m} + \frac{\partial}{\partial \mathbf{P}'} \right) f_{b0}, \end{aligned} \tag{22}$$

where the limit $t_0 \rightarrow \infty$ can be easily taken because f_{b0} is independent of t_0 . Recognizing that $e^{-i\mathcal{L}_s s} \mathbf{F}$ is the time evolution $\mathbf{F}(-s)$ we then find

$$\begin{aligned} \frac{\partial}{\partial t_2} f_{b0} &= \lim_{t_0 \rightarrow \infty} \int_0^{t_0} ds \langle \mathcal{L}'_b \mathbf{F}(-s) \rangle_b \cdot \left(\frac{\beta \mathbf{P}'}{m} + \frac{\partial}{\partial \mathbf{P}'} \right) f_{b0} \\ &= \frac{1}{3} \int_0^\infty ds \langle \mathbf{F} \cdot \mathbf{F}(-s) \rangle_b \frac{\partial}{\partial \mathbf{P}'} \cdot \left(\frac{\beta \mathbf{P}'}{m} + \frac{\partial}{\partial \mathbf{P}'} \right) f_{b0}, \end{aligned} \tag{23}$$

where $\langle \dots \rangle_b = \int \dots f_0^{[N]}(\mathbf{b}^N | \mathbf{R}) d\mathbf{b}^N$ denotes an equilibrium average over the phase space variables of the solvent particles in the external field of the solute particle.

Putting together the results obtained so far and going back to physical time and to the original momentum variable \mathbf{P} , we arrive finally to the Fokker–Planck (or Klein [2] and Kramers [3]) equation for $f_b(\mathbf{R}, \mathbf{P}; t)$:

$$\frac{\partial}{\partial t} f_b(\mathbf{R}, \mathbf{P}; t) = \left(\epsilon \frac{\partial}{\partial t_1} + \epsilon^2 \frac{\partial}{\partial t_2} \right) \Big|_{t_1=\epsilon t, t_2=\epsilon^2 t} f_{b0}(\mathbf{R}, \mathbf{P}; t_1, t_2)$$

$$= \left[-\frac{\mathbf{P}}{M} \cdot \frac{\partial}{\partial \mathbf{R}} + \xi \frac{\partial}{\partial \mathbf{P}} \cdot \left(\mathbf{P} + \frac{M}{\beta} \frac{\partial}{\partial \mathbf{P}} \right) \right] f_b(\mathbf{R}, \mathbf{P}; t), \tag{24}$$

where the friction coefficient

$$\xi = \frac{\beta}{3M} \int \langle \mathbf{F} \cdot \mathbf{F}(-s) \rangle_b ds. \tag{25}$$

3. From the Fokker–Planck to the Smoluchowski equation

We now introduce a dimensionless friction $\xi_d = \xi \tau_T$ with $\tau_T = \Sigma/v_T$ a thermal time and $v_T = \sqrt{1/\beta M}$ the thermal velocity. In the high friction limit one can carry on a multiple time scale perturbation expansion in the small $\epsilon_b \equiv 1/\xi_d \ll 1$ parameter [4], which multiplies the time derivative in the Fokker–Planck equation (24), to finally reach the Smoluchowski [13] equation, governing the time evolution of the probability density in configuration space:

$$\rho_b(\mathbf{R}, t) = \int f_b(\mathbf{R}, \mathbf{P}; t) d\mathbf{P}. \tag{26}$$

We then repeat the same multiple time scale perturbation analysis performed in the previous section replacing now ϵ with ϵ_b . If we use the following notation

$$\mathcal{L}_{FP} \equiv \frac{\partial}{\partial \mathbf{P}} \cdot \left(\mathbf{P} + \frac{M}{\beta} \frac{\partial}{\partial \mathbf{P}} \right), \tag{27}$$

the identification of different powers of ϵ_b in the Fokker–Planck equation gives the following relations:

$$\mathcal{L}_{FP} f_{b0} = 0, \tag{28}$$

$$\mathcal{L}_{FP} f_{b1} = \tau_T \left[\frac{\partial}{\partial t_0} + \frac{\mathbf{P}}{M} \cdot \frac{\partial}{\partial \mathbf{R}} \right] f_{b0}, \tag{29}$$

$$\mathcal{L}_{FP} f_{b2} = \tau_T \left[\frac{\partial}{\partial t_0} + \frac{\mathbf{P}}{M} \cdot \frac{\partial}{\partial \mathbf{R}} \right] f_{b1} + \tau_T \frac{\partial}{\partial t_1} f_{b0}. \tag{30}$$

The zeroth order equation imposes a Maxwellian distribution

$$f_{b0}(\mathbf{R}, \mathbf{P}; t_0, t_1, \dots) = \Phi(\mathbf{R}; t_0, t_1, \dots) e^{-\beta P^2/2M}. \tag{31}$$

The first order equation imposes then

$$\mathcal{L}_{FP} f_{b1} = \tau_T \frac{\partial \Phi}{\partial t_0} e^{-\beta P^2/2M} + \tau_T \frac{\mathbf{P}}{M} \cdot \frac{\partial \Phi}{\partial \mathbf{R}} e^{-\beta P^2/2M}. \tag{32}$$

In order to eliminate secular divergences we must require $\partial \Phi / \partial t_0 = 0$, and the first correction for the distribution function is now given by

$$f_{b1}(\mathbf{R}, \mathbf{P}; t_0, t_1, \dots) = -\tau_T \frac{\mathbf{P}}{M} \cdot \frac{\partial \Phi}{\partial \mathbf{R}} e^{-\beta P^2/2M} + \Psi(\mathbf{R}; t_0, t_1, \dots) e^{-\beta P^2/2M}. \tag{33}$$

The second order equation becomes

$$\begin{aligned} \mathcal{L}_{FP} f_{b2} = & \left[\tau_T \frac{\partial \Psi}{\partial t_0} + \tau_T \frac{\partial \Phi}{\partial t_1} - (v_T \tau_T)^2 \frac{\partial}{\partial \mathbf{R}} \cdot \frac{\partial \Phi}{\partial \mathbf{R}} \right] e^{-\beta P^2/2M} + \tau_T \frac{\mathbf{P}}{M} \cdot \frac{\partial \Psi}{\partial \mathbf{R}} e^{-\beta P^2/2M} + \\ & \left[\tau_T^2 \left(v_T^2 \frac{\partial}{\partial \mathbf{R}} \cdot \frac{\partial}{\partial \mathbf{R}} - \frac{\mathbf{P}}{M} \cdot \frac{\partial \mathbf{P}}{\partial \mathbf{R}} \frac{\partial}{\partial \mathbf{R}} \right) \Phi \right] e^{-\beta P^2/2M}. \end{aligned} \tag{34}$$

In order to remove the secular divergences as t_0 grows to infinity, we must impose $\partial \Psi / \partial t_0 = 0$. Moreover it is easy to show that the eigenfunctions of \mathcal{L}_{FP} are the functions $H_n \exp(-\beta P^2/2M)$ where H_n is the n th Hermite polynomial. Since the Maxwellian is associated with a null eigenvalue, in order to require that the integral of the right hand side of Eq. (34) in $d\mathbf{P}$ vanishes, we must impose that all terms multiplying the Maxwellian vanish, due to the orthogonality condition between the eigenfunctions. We must then have

$$\frac{\partial \Phi}{\partial t_1} = v_T^2 \tau_T \frac{\partial}{\partial \mathbf{R}} \cdot \frac{\partial \Phi}{\partial \mathbf{R}}. \tag{35}$$

We now can collect the results obtained so far to obtain the distribution function to order ϵ_b^2 as follows

$$f_b(\mathbf{R}, \mathbf{P}; t) = \left[\Phi - \epsilon_b \tau_T \frac{\mathbf{P}}{M} \cdot \frac{\partial \Phi}{\partial \mathbf{R}} + \epsilon_b \Psi + O(\epsilon_b^2) \right] e^{-\beta P^2/2M}, \tag{36}$$

and from Eq. (26) it follows immediately

$$\rho_b(\mathbf{R}, t) = \left(\frac{2M\pi}{\beta}\right)^{3N/2} [\Phi + \epsilon_b \Psi + O(\epsilon_b^2)]. \quad (37)$$

Then the time evolution for ρ_b is obtained restricting the different variables t_i to the physical line as follows

$$\begin{aligned} & \frac{\partial}{\partial t} \rho_b(\mathbf{R}, t) \\ &= \left(\frac{\partial}{\partial t_0} + \epsilon_b \frac{\partial}{\partial t_1}\right) \left(\frac{2M\pi}{\beta}\right)^{3N/2} [\Phi(\mathbf{R}; t_1, \dots) + \epsilon_b \Psi(\mathbf{R}; t_1, \dots) + O(\epsilon_b^2)]_{t_0=t, t_1=\epsilon_b t, \dots} \\ &= \epsilon_b \frac{\partial}{\partial t_1} \left(\frac{2M\pi}{\beta}\right)^{3N/2} \Phi(\mathbf{R}; t_1, \dots)_{t_0=t, t_1=\epsilon_b t, \dots} + O(\epsilon_b^2). \end{aligned} \quad (38)$$

Then using Eq. (35) we finally find the diffusion equation

$$\frac{\partial \rho_b(\mathbf{R}, t)}{\partial t} = \frac{v_T^2}{\xi} \frac{\partial}{\partial \mathbf{R}} \cdot \frac{\partial \rho_b(\mathbf{R}, t)}{\partial \mathbf{R}} + O(1/\xi_d^2). \quad (39)$$

If we had an external field $\mathbf{F}_e(\mathbf{R}) = -\partial V_e(\mathbf{R})/\partial \mathbf{R}$ acting on the Brownian solute particle then the initial Hamiltonian would have been

$$\mathcal{H} = \frac{P^2}{2M} + \sum_{i=1}^N \frac{p_i^2}{2m} + V_N(\mathbf{r}^N) + V_b(\mathbf{R}, \mathbf{r}^N) + V_e(\mathbf{R}), \quad (40)$$

and the Smoluchowski equation [13] becomes

$$\frac{\partial \rho_b(\mathbf{R}, t)}{\partial t} = \frac{v_T^2}{\xi} \frac{\partial}{\partial \mathbf{R}} \cdot \left(\frac{\partial}{\partial \mathbf{R}} - \beta \mathbf{F}_e(\mathbf{R})\right) \rho_b(\mathbf{R}, t), \quad (41)$$

which can also be written as

$$\frac{\partial \rho_b(\mathbf{R}, t)}{\partial t} = \frac{v_T^2}{\xi} \frac{\partial}{\partial \mathbf{R}} \cdot e^{-\beta V_e(\mathbf{R})} \frac{\partial}{\partial \mathbf{R}} e^{\beta V_e(\mathbf{R})} \rho_b(\mathbf{R}, t), \quad (42)$$

which shows immediately that $\rho_b \propto \exp[-\beta V_e(\mathbf{R})]$ is a stationary solution. So that calling

$$\beta v_T^2 / \xi = 1/\gamma, \quad (43)$$

where γ is usually known as the *mobility*, we can rewrite the Smoluchowski Eq. (41) as

$$\frac{\partial \rho_b(\mathbf{R}, t)}{\partial t} = \frac{\partial}{\partial \mathbf{R}} \cdot \left(\frac{\partial}{\partial \mathbf{R}} \frac{v_T^2}{\xi} - \frac{\mathbf{F}_e(\mathbf{R})}{\gamma}\right) \rho_b(\mathbf{R}, t), \quad (44)$$

which through Ito's calculus [14] can be proved to be equivalent to the following stochastic differential equation, the Langevin equation

$$\gamma \dot{\mathbf{R}} = \mathbf{F}_e(\mathbf{R}) + \sqrt{2(\gamma v_T)^2 / \xi} \zeta(t), \quad (45)$$

where we denote with the dot a time derivative and ζ is a white noise. In this respect Eq. (43) is considered as a case of *fluctuation and dissipation theorem*. It is then straightforward to show that for $\mathbf{F}_e = 0$ we find $\langle |\mathbf{R}(t) - \mathbf{R}(0)|^2 \rangle = 6Dt$ with $D = v_T^2 / \xi$ the *diffusion constant*. Eq. (43) is known as the Einstein relation. The fluctuations of the particle as it undergoes its random walk are related to the drag force (or dissipation of momentum) that the particle feels as it moves through the solvent.

The Einstein relation gives an excellent way to determine Boltzmann's constant experimentally. Watch a particle perform a Brownian jitter. After time t , the distance traveled by the particle should be $\langle R^2 \rangle = 2k_B T / \pi \eta \Sigma$, where we have used the Stokes formula $\gamma = 3\pi \eta \Sigma$ to relate the mobility to the viscosity η . This experiment was done in 1908 by the French physicist Jean Baptiste Perrin and won him the 1926 Nobel prize.

The full form of the Langevin equation is the one with the acceleration term. Then using the relation $\mathbf{P}/M = \mathbf{V} = \dot{\mathbf{R}}$ we should have in a less viscous fluid the equation $M\dot{\mathbf{V}} = -\gamma\mathbf{V} + \mathbf{F}_e + \gamma\sqrt{2D}\zeta$ for which we still find for $\mathbf{F} = 0$, $\langle |\mathbf{R}(t) - \mathbf{R}(0)|^2 \rangle = 6Dt$ and $\langle \mathbf{V}(t) \cdot \mathbf{V}(t) \rangle = 3D\gamma/M$ at late times. This stochastic differential equation leads through Ito's calculus to the Fokker–Planck equation for $f_b(\mathbf{R}, \mathbf{P}; t)$. This Eq. (24) is sometimes also called the Klein and Kramers equation and sometimes the Chandrasekhar equation.

4. The dynamical Monte Carlo method

We now want to show how the Smoluchowski evolution equation can be solved by stochastic means. In nature, equilibrium distributions are generated by an evolution process. The Smoluchowski equation

$$\frac{\partial \rho_b(\mathbf{R}, t)}{\partial t} = \nabla \cdot \mathbf{D}(\mathbf{R}) \cdot [\nabla - \beta \mathbf{F}_e(\mathbf{R})] \rho_b(\mathbf{R}, t), \quad (46)$$

is the unique “master” equation which is:

- local in space
- goes to the Boltzmann distribution
- is Markovian

Here $\mathbf{D}(\mathbf{R})$ is, in general, a many-body tensor. In the previous section we saw that for the one-body problem it is sufficient to take it as a constant diagonal tensor $D_{ij} = \delta_{ij}D$ and $\mathbf{F}_e = -\nabla V_e$ is the external force.

The asymptotic solution of $\rho_b(\mathbf{R}, t)$ will be $\rho_0(\mathbf{R}) \propto \exp[-\beta V_e(\mathbf{R})]$. It is easy to see that this distribution satisfies $d\rho_0/dt = 0$. If we assume the process is ergodic, since it is Markovian, this must be the only solution.

Let us define Green’s function: $G(\mathbf{R}, \mathbf{R}_0; t) = G(\mathbf{R}_0 \rightarrow \mathbf{R}; t)$ is the solution to Eq. (46) with the boundary condition at zero time: $G(\mathbf{R}, \mathbf{R}_0; 0) = \delta(\mathbf{R} - \mathbf{R}_0)$. We can prove that the Green’s function satisfies *detailed balance*:

$$\rho_0(\mathbf{R})G(\mathbf{R} \rightarrow \mathbf{R}'; t) = \rho_0(\mathbf{R}')G(\mathbf{R}' \rightarrow \mathbf{R}; t), \tag{47}$$

for any value of t . To do that one writes the evolution equation for the symmetrized Green’s function: $[\rho_0(\mathbf{R})/\rho_0(\mathbf{R}')]^{1/2} G(\mathbf{R} \rightarrow \mathbf{R}'; t)$, and sees that the right hand side of the master equation is a Hermitian operator (see Appendix) which implies that the symmetrized Green’s function is symmetric in \mathbf{R} and \mathbf{R}' . Then the random walk must eventually have ρ_0 as its equilibrium distribution [15]. G can be used for a transition probability and it will always give an acceptance probability of unity [16]. Also it gives the interesting dynamics of a viscous particles always in contact with a heat bath.

The Smoluchowski equation leads to an interesting process but we can only calculate G in the short time limit. In the following we explain a general procedure for devising an algorithm of sampling G . Let us calculate the moments of G ,

$$I_n(\mathbf{R}_0, t) = \int d\mathbf{R} (\mathbf{R} - \mathbf{R}_0)^n G(\mathbf{R}_0 \rightarrow \mathbf{R}; t). \tag{48}$$

Take the time derivative of this equation, use the master equation on the right hand side, and integration by parts to get a simple integral over G on the right hand side. We interpret this as an average $\langle \dots \rangle$. We assume there are no absorbing surfaces of the random walks. Then,

$$dI_0/dt = 0. \tag{49}$$

This implies the normalization of G is always one, so the evolution describes a process which neither creates nor destroys walks. The next moment is:

$$d[I_1]_k/dt = \langle \nabla_j D_{kj} + D_{kj}[F_e]_j \beta \rangle, \tag{50}$$

where we use the Einstein summation convention over the repeated indexes. Let us assume that \mathbf{F}_e and $\nabla \mathbf{D}$ are slowly varying. Then we can replace them by the values at the initial point and integrate in time:

$$[R_t]_k = \langle R_k \rangle = [R_0]_k + t \langle \nabla_j D_{kj}(\mathbf{R}) + D_{kj}(\mathbf{R})[F_e]_j(\mathbf{R}) \beta \rangle_{\mathbf{R}=\mathbf{R}_0} + O(t^2), \tag{51}$$

where $\langle \dots \rangle_g$ is an average respect to the small time Green’s function G_g of Eq. (54). The equation for the second moment is:

$$dI_2/dt = 2 \langle D_{ii} + (\mathbf{R} - \mathbf{R}_0)_i (\nabla_j D_{ij} + D_{ij}[F_e]_j \beta) \rangle, \tag{52}$$

Integrating in time we then find

$$\langle (\mathbf{R} - \mathbf{R}_0)^2 \rangle = 2 \langle D_{ii}(\mathbf{R}) \rangle_{\mathbf{R}=\mathbf{R}_0} t + O(t^2). \tag{53}$$

The solution at small time is a Gaussian distribution with the above mean and covariance, namely

$$G_g(\mathbf{R}, \mathbf{R}_0; t) = \frac{e^{-(\mathbf{R}-\mathbf{R}_0)(4\langle D_{ij}(\mathbf{R}) \rangle_{\mathbf{R}=\mathbf{R}_0} t)^{-1}(\mathbf{R}-\mathbf{R}_0)}}{\sqrt{4\pi \langle D_{ii}(\mathbf{R}) \rangle_{\mathbf{R}=\mathbf{R}_0} t^{3N}}}. \tag{54}$$

According to the central limit theorem, Eqs. (51) and (53) are all that is needed to simulate the random walk if the time step t is sufficiently small. The effect of the external field is to push the mean position of the Brownian particle away from its current position. An outward push in directions where the external force is positive. The cage of the surrounding solvent is also present whenever the diffusion tensor is \mathbf{R} dependent.

5. A simple Monte Carlo simulation

For some simple forms of the external potential V_e the Smoluchowski equation admits an analytical solution. For example the one-dimensional Smoluchowski equation in empty space (which requires the probability density to vanish at spatial infinity faster than any inverse power of R) can be solved analytically for

- A linear potential $V_e(x) = cx$ [17],

$$G(x, x_0; t) = \frac{e^{-\frac{(x-x_0+D\beta ct)^2}{4Dt}}}{\sqrt{4\pi Dt}}. \tag{55}$$

- A harmonic potential $V_e(x) = cx^2/2$ [18],

$$G(x, x_0; t) = \frac{e^{-\frac{(x-x_0 e^{-2t/\tilde{t}})^2}{2S(t)/\beta c}}}{\sqrt{2\pi S(t)/\beta c}}, \tag{56}$$

$$S(t) = 1 - e^{-4t/\tilde{t}},$$

$$\tilde{t} = 2/\beta cD.$$

In each one of these cases a proper change of time dependent coordinates is used to reduce the Smoluchowski equation to the free diffusion equation.

Except for these simple cases in order to extract the evolution of the Green's function we must resort to a simulation. We can then use the Markovian property as follows

$$G(\mathbf{R}, \mathbf{R}_0; t - t_0) = \int G_g(\mathbf{R}, \mathbf{R}_n; t - t_n) G_g(\mathbf{R}_n, \mathbf{R}_{n-1}; t_n - t_{n-1}) \cdots G_g(\mathbf{R}_1, \mathbf{R}_0; t_1 - t_0) d\mathbf{R}_1 d\mathbf{R}_2 \cdots d\mathbf{R}_n, \tag{57}$$

where $t_n - t_{n-1} = \tau$ is a small time step. At fixed \mathbf{R}, \mathbf{R}_0 , and $t - t_0 = (n + 1)\tau$ we can then easily compute the Green's function $G(\mathbf{R}, \mathbf{R}_0; t)$ through a Monte Carlo integration sampling the successive G_g of Eq. (54) with the Box–Müller method (see Ref. [15] section 3.1). For small enough τ we sample $G_g(\mathbf{R}_1, \mathbf{R}_0; \tau)$ at fixed \mathbf{R}_0 generating \mathbf{R}_1 then we sample $G_g(\mathbf{R}_2, \mathbf{R}_1; \tau)$ generating \mathbf{R}_2 and so on for the remaining $n - 2$ factors ending with the generated \mathbf{R}_n . We can then evaluate $G_g(\mathbf{R}, \mathbf{R}_n; \tau)$ at fixed \mathbf{R} on \mathbf{R}_n with a Monte Carlo integration to find $G(\mathbf{R}, \mathbf{R}_0; (n + 1)\tau)$. Clearly we will have to control the convergence of the algorithm as τ gets smaller and smaller.

Eq. (57) suggests a path integral representation of the Green's function solution of the Smoluchowski equation, namely

$$G(\mathbf{R}, \mathbf{R}_0; t - t_0) \propto \iint_{\mathbf{R}_0}^{\mathbf{R}} e^{-S} \mathcal{D}\mathbf{R}(t), \tag{58}$$

with an action

$$S = \int_{t_0}^t dt' \sum_k [\dot{R}_k(t') - \langle \nabla_j D_{kj} + D_{kj} [F_e]_j \beta \rangle |_{\mathbf{R}=\mathbf{R}(t')}]^2 / 4 \langle D_{ii} \rangle |_{\mathbf{R}=\mathbf{R}(t')}, \tag{59}$$

where the dot denotes a total derivative with respect to time.

If the colloidal particle is initially localized around $\bar{\mathbf{R}}_0 = \int \mathbf{R} \rho_{b0}(\mathbf{R}) d\mathbf{R}$ where we assume to be given $\rho_{b0}(\mathbf{R}) = \rho_b(\mathbf{R}, t_0)$ we may want to find its average position at a later time

$$\bar{\mathbf{R}}(t) = \int \mathbf{R} G(\mathbf{R}, \mathbf{R}_0; t - t_0) \rho_{b0}(\mathbf{R}_0) d\mathbf{R} d\mathbf{R}_0. \tag{60}$$

Relevant mesoscopic time scales are the time $\tau_b = 1/\xi$ over which the velocity of a Brownian particle relaxes. At room temperature, for typical values of ξ , we find $\tau_b \approx 10^{-9}$ s. Taking $\Sigma \approx 1 \mu\text{m}$ and $M \approx 10^{-21}$ kg [9,19] at room temperature $1/\beta \approx 10^{-21}$ J we have $v_T \approx 1$ m/s and $\tau_T \approx 10^{-6}$ s. Another relevant time scale is the time required for an isolated Brownian particle to diffuse over a distance equal to its diameter $\tau_c = \Sigma^2/D = \xi \beta M \Sigma^2 \approx 10^{-3}$ s $> \tau_T > \tau_b$. On the microscopic level the shortest time scale is the Enskog mean collision time $\tau_E = 1/\Gamma_E = \sqrt{\beta m/\pi}/4\rho_s \sigma^2 g(\sigma)$ where $g(r)$ (see Ref. [12] section 2.5) is the radial distribution function of the solvent. For a solvent such as water $\sigma = \Sigma/10^4$, and $\tau_E \approx 10^{-12}$ s. We already know that for $t \gg \tau_E$ the Smoluchowski solution tends to the equilibrium Boltzmann distribution which remains then stable on a large subsequent time scale. For example, for the one dimensional harmonic potential with an initial Gaussian distribution centered on x_0 we find

$$\bar{x}(t) = \frac{\sqrt{2}x_0 e^{-\beta cDt}}{\sqrt{(1 - e^{-2\beta cDt})[1 + \coth(\beta cDt)]}}, \tag{61}$$

showing that the relaxation time is proportional to $1/\beta cD$. In Fig. 1 we show a DynMC simulation of this case for $\beta cD = 1 \text{ s}^{-1}$, $x_0 = 2$ m, and fixed $\tau = 0.001$ s. Clearly at long enough times the solute particle will reach the equilibrium average position

$$\bar{\mathbf{R}}_e = \frac{\int \mathbf{R} e^{-\beta V_e(\mathbf{R})} d\mathbf{R}}{\int e^{-\beta V_e(\mathbf{R})} d\mathbf{R}}. \tag{62}$$

The natural time scale over which the Smoluchowski evolution approach equilibrium is τ_b . What may be interesting to observe is whether a proper control of the external fields allows the approach to equilibrium to happens more rapidly, thus indicating a “persistence” of the Boltzmann distribution since early times. Clearly if $V_e(\mathbf{R}) = V_e(R)$ one must end up in $\bar{\mathbf{R}}_e = 0$, by symmetry. For a single Brownian particle Eq. (51) becomes

$$\dot{\mathbf{R}}_t \simeq \mathbf{R}_0 + \tau D \beta \langle \mathbf{F}_e \rangle_g |_{\mathbf{R}=\mathbf{R}_0}, \tag{63}$$

690

R. Fantoni / Physica A 515 (2019) 682–692

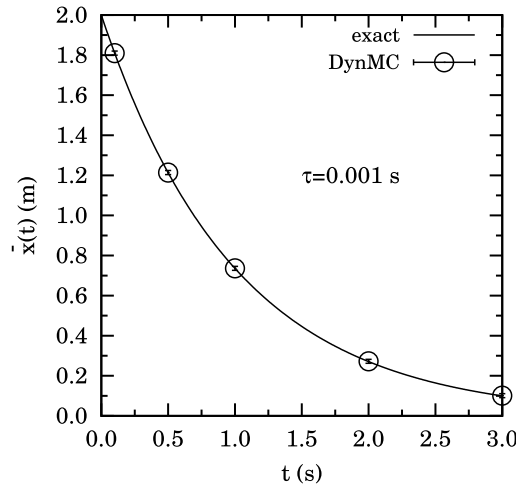


Fig. 1. DynMC simulation for the one dimensional harmonic potential with an initial Gaussian distribution centered on $x_0 = 2$ m with $\beta cD = 1$ s⁻¹ and $\tau = 0.001$ s. In this case $\langle F_e(x) \rangle_g = -cx/(1 + \beta cD\tau)$. The continuous line is the exact analytical solution of Eq. (61) and the symbols are the results of the simulation.

so that, if $\langle \mathbf{F}_e \rangle_g = 0$ we will have $\mathbf{R}_t = \mathbf{R}_0$ at all time slices and

$$\bar{\mathbf{R}}(t) = \int \mathbf{R} G_g(\mathbf{R}, \mathbf{R}_0; t - t_0) \rho_{b0}(\mathbf{R}_0) d\mathbf{R} d\mathbf{R}_0. \tag{64}$$

We also immediately see that the persistence will be the more important the steeper the external potential approaches its minimum. On an unstable equilibrium point of the potential (a maximum) the Green's function will be swallowed and eventually vanish in time.

Another interesting question is to determine the influence on the evolution of a spatially dependent diffusion coefficient $D(\mathbf{R}) = v_T^2/\xi(\mathbf{R})$ rather than a constant. From Eq. (51) we see that around an equilibrium point for the external potential we will still have

$$\mathbf{R}_\tau \simeq \mathbf{R}_0 + \tau \langle \nabla D \rangle_g |_{\mathbf{R}=\mathbf{R}_0}. \tag{65}$$

We will call this the “cage effect” of the solvent on the evolution of the solute particle.

In addition to the empty space boundary conditions other kinds are possible. Calling $\mathcal{I} \equiv D(\nabla - \beta \mathbf{F}_e)$ the flux operator and $\partial\Omega$ the boundary of the space Ω where the solute particle is confined, the most general case are the radiation boundary conditions, namely

$$\hat{\mathbf{n}}(\mathbf{R}) \cdot \mathcal{I}(\mathbf{R}) G(\mathbf{R}, \mathbf{R}_0; t - t_0) = \omega G(\mathbf{R}, \mathbf{R}_0; t - t_0), \quad \mathbf{R} \in \partial\Omega, \tag{66}$$

where $\hat{\mathbf{n}}(\mathbf{R})$ denotes a unit vector normal to the surface $\partial\Omega$. The reactivity is measured by the ω parameter. For $\omega = 0$ we have a non-reactive or reflective boundary condition and for $\omega \rightarrow \infty$ we have a reaction boundary condition. So for a confined case we have to choose the required boundary condition and then determine the proper small time step Green's function G_g . For example for the solution in half space $X \geq 0$ with a reaction boundary condition at $X = 0$, $G((0, Y, Z), \mathbf{R}_0; t - t_0) = 0$, we may use the image technique as follow

$$G_g(\mathbf{R}, \mathbf{R}_0; \tau) = \frac{e^{-[(X-X_t)^2+(Y-Y_t)^2+(Z-Z_t)^2]/4\langle D_{ii}(\mathbf{R}) \rangle_g |_{\mathbf{R}=\mathbf{R}_0} \tau}}{\sqrt{4\pi \langle D_{ii}(\mathbf{R}) \rangle_g |_{\mathbf{R}=\mathbf{R}_0} \tau}^{-3N}} - \frac{e^{-[(X+X_t)^2+(Y-Y_t)^2+(Z-Z_t)^2]/4\langle D_{ii}(\mathbf{R}) \rangle_g |_{\mathbf{R}=\mathbf{R}_0} \tau}}{\sqrt{4\pi \langle D_{ii}(\mathbf{R}) \rangle_g |_{\mathbf{R}=\mathbf{R}_0} \tau}^{-3N}}. \tag{67}$$

6. Conclusions

In conclusion, for a colloidal suspension made up of one solute big and heavy particle and N solvent small and light particles we show how it is possible to reduce the Liouville dynamics to the Fokker–Planck dynamics by integrating over the coordinates and momenta of the solvent particles. And how integrating furthermore on the momenta of the solute particle

it is possible to reduce the Fokker–Planck equation to the Smoluchowski equation in the high friction regime. The two successive reductions are based on a multiple time scale perturbation expansions. The first reduction was discovered in the second half of last century and the second reduction at the end of last century a simple Dynamical Monte Carlo (DynMC) algorithm is presented to solve the Smoluchowski equation for the Brownian motion of the solute particle in empty space and a thought computer experiment illustrated.

We discuss how a steep external potential around its minimum will drive the approach to equilibrium more rapidly than the natural time scale τ_b and the cage effect due to the solvent. In particular we present a DynMC simulation on the harmonic case with a constant diffusion which well reproduces the exact analytical solution of the Smoluchowski equation. The simplicity of the simulation makes it very useful for the treatment of problems which do not have an analytic solution. We presented results for the average position of the solute particle as a function of time, but other quantities can be computed as for example the full Green's function starting from Eq. (57).

We discuss the proper boundary conditions to be imposed on the Smoluchowski second order partial differential equation in order to have a radiation, reflective, or reaction boundary and we give the small time expression for the Green's function in half space with a reaction boundary condition on the plane of separation using the image technique. An interesting progress that could be made at the level of the Fokker–Planck description is to derive the expression for the friction coefficient for a colloidal patchy sticky hard sphere in a solvent of isotropic sticky hard spheres, in the spirit of Refs. [20–36]. Or in a solvent of penetrable square well particles, in the spirit of Refs. [37–42]. Or fluid mixtures adsorbed in porous disordered materials with random confinement, as in Refs. [43,44].

We leave as an open problem the generalization of the present treatment to the case of a classical Brownian solute macromolecule in a quantum solvent.

Appendix. Hermiticity of the Smoluchowski operator

We will work in empty space. Then we introduce the Smoluchowski operator $\mathcal{L}_S(\mathbf{R}) = \nabla \mathbf{D} \rho_0(\mathbf{R}) \nabla \rho_0^{-1}(\mathbf{R})$. For any two functions $g(\mathbf{R})$ and $h(\mathbf{R})$ decaying to zero at spatial infinity faster than any inverse power we can write, using two times an integration by parts,

$$\begin{aligned} & \int d\mathbf{R} \frac{1}{\sqrt{\rho_0(\mathbf{R})}} g(\mathbf{R}) \mathcal{L}_S(\mathbf{R}) \sqrt{\rho_0(\mathbf{R})} h(\mathbf{R}) = \\ & - \int d\mathbf{R} \rho_0(\mathbf{R}) \nabla \left(\frac{1}{\sqrt{\rho_0(\mathbf{R})}} g(\mathbf{R}) \right) \mathbf{D} \nabla \frac{1}{\sqrt{\rho_0(\mathbf{R})}} h(\mathbf{R}) = \\ & \int d\mathbf{R} \frac{1}{\sqrt{\rho_0(\mathbf{R})}} h(\mathbf{R}) \mathcal{L}_S(\mathbf{R}) \sqrt{\rho_0(\mathbf{R})} g(\mathbf{R}), \end{aligned} \tag{A.1}$$

which proves the Hermiticity, $[\sqrt{\rho_0}^{-1} \mathcal{L}_S \sqrt{\rho_0}]^\dagger = \sqrt{\rho_0}^{-1} \mathcal{L}_S \sqrt{\rho_0}$, of the Smoluchowski operator. So that, from the Chapman–Kolmogorov relation

$$G(\mathbf{R}_0 \rightarrow \mathbf{R}; t) = \int d\mathbf{R}_1 G(\mathbf{R}_1 \rightarrow \mathbf{R}; \tau) G(\mathbf{R}_0 \rightarrow \mathbf{R}_1; t - \tau), \tag{A.2}$$

follows

$$\begin{aligned} \frac{\partial}{\partial t} G(\mathbf{R}_0 \rightarrow \mathbf{R}; t) &= \mathcal{L}_S(\mathbf{R}) G(\mathbf{R}_0 \rightarrow \mathbf{R}; t) \\ &= \int d\mathbf{R}_1 G(\mathbf{R}_1 \rightarrow \mathbf{R}; \tau) \mathcal{L}_S(\mathbf{R}_1) G(\mathbf{R}_0 \rightarrow \mathbf{R}_1; t - \tau) \\ &= \int d\mathbf{R}_1 \frac{G(\mathbf{R}_0 \rightarrow \mathbf{R}_1; t - \tau)}{\rho_0(\mathbf{R}_1)} \mathcal{L}_S(\mathbf{R}_1) \rho_0(\mathbf{R}_1) G(\mathbf{R}_1 \rightarrow \mathbf{R}; \tau) \\ &\xrightarrow{\tau \rightarrow t} \frac{1}{\rho_0(\mathbf{R}_0)} \mathcal{L}_S(\mathbf{R}_0) \rho_0(\mathbf{R}_0) G(\mathbf{R}_0 \rightarrow \mathbf{R}; t), \end{aligned} \tag{A.3}$$

where in the last limit we used the initial condition $G(\mathbf{R}_0 \rightarrow \mathbf{R}_1; 0) = \delta(\mathbf{R}_0 - \mathbf{R}_1)$. And, using the symmetry of the left hand side of Eq. (A.3) respect to exchange of $\mathbf{R}_0 \leftrightarrow \mathbf{R}$, we finally find the detailed balance relation $\rho_0(\mathbf{R}_0) G(\mathbf{R}_0 \rightarrow \mathbf{R}; t) = \rho_0(\mathbf{R}) G(\mathbf{R} \rightarrow \mathbf{R}_0; t)$.

References

[1] R.I. Cukier, J.M. Deutch, Phys. Rev. 177 (1969) 240.
 [2] O. Klein, Ark. Mat. Astron. Fys. 16 (1921) 1.
 [3] H.A. Kramers, Physica 7 (1940) 284.
 [4] L. Bocquet, Amer. J. Phys. 65 (1997) 140.
 [5] R.C. Balescu, Equilibrium and Non-Equilibrium Statistical Mechanics, Wiley, 1975.
 [6] G.F. Mazenko, Nonequilibrium Statistical Mechanics, Wiley, 2008.
 [7] L.E. Reichl, A Modern Course in Statistical Physics, Wiley, 2009.

- [8] U.M.B. Marconi, S. Melchionna, *J. Chem. Phys.* 126 (2007) 184109.
- [9] C. Wang, W. Yang, S. Fu, Functionalization of colloidal particles, in: A. Elaissari (Ed.), *Colloidal Polymers: Synthesis and Characterization*, Marcel Dekker Inc., 2003.
- [10] K. Schulten, M. Tesch, Coupling of protein motion to electron transfer: Molecular dynamics and stochastic quantum mechanics study of photosynthetic reaction centers, *Chem. Phys.* 158 (1991) 421.
- [11] D. Xu, K. Schulten, *Chem. Phys.* 182 (1992) 91.
- [12] J.-P. Hansen, I.R. McDonald, *Theory of Simple Liquids: With Applications to Soft Matter*, fourth ed., Academic Press, 2013.
- [13] M. von Smoluchowski, *Ann. Phys.* 48 (1916) 1103.
- [14] C.W. Gardiner, *Handbook of Stochastic Methods*, Springer, New York, 1983.
- [15] M.H. Kalos, P.A. Whitlock, *Monte Carlo Methods*, John Wiley & Sons, 1986.
- [16] N. Metropolis, A.W. Rosenbluth, M.N. Rosenbluth, A.H. Teller, E. Teller, *J. Chem. Phys.* 21 (1953) 1087.
- [17] R. Kubo, *Adv. Chem. Phys.* 15 (1969) 101.
- [18] S. Xiao-Jun, L. Xiao-Xia, Y. Yu-Liang, D. Jun-Feng, Z. Jing-Shang, *Commun. Theor. Phys. (Beijing China)* 43 (2005) 1099.
- [19] S.M. Klein, V.N. Manoharan, D.J. Pine, F.F. Lange, *Colloid Polym. Sci.* 282 (2003) 7.
- [20] R. Fantoni, D. Gazzillo, A. Giacometti, *J. Chem. Phys.* 122 (2005) 034901.
- [21] R. Fantoni, D. Gazzillo, A. Giacometti, *Phys. Rev. E* 72 (2005) 011503.
- [22] D. Gazzillo, A. Giacometti, R. Fantoni, P. Sollich, *Phys. Rev. E* 74 (2006) 051407.
- [23] D. Gazzillo, R. Fantoni, A. Giacometti, *Mol. Phys.* 104 (2006) 3451.
- [24] R. Fantoni, D. Gazzillo, A. Giacometti, P. Sollich, *J. Chem. Phys.* 125 (2006) 164504.
- [25] R. Fantoni, D. Gazzillo, A. Giacometti, M.A. Miller, G. Pastore, *J. Chem. Phys.* 127 (2007) 234507.
- [26] D. Gazzillo, R. Fantoni, A. Giacometti, *Phys. Rev. E* 78 (2008) 021201.
- [27] D. Gazzillo, R. Fantoni, A. Giacometti, *Phys. Rev. E* 80 (2009) 061207.
- [28] R. Fantoni, A. Giacometti, F. Sciortino, G. Pastore, *Soft Matter* 7 (2011) 2419.
- [29] R. Fantoni, *Eur. Phys. J. B* 85 (2012) 108.
- [30] R. Fantoni, J.W.O. Salari, B. Klumperman, *Phys. Rev. E* 85 (2012) 061404.
- [31] M.A.G. Maestre, R. Fantoni, A. Giacometti, A. Santos, *J. Chem. Phys.* 138 (2013) 094904.
- [32] R. Fantoni, G. Pastore, *Europhys. Lett.* 101 (2013) 46003.
- [33] R. Fantoni, G. Pastore, *Phys. Rev. E* 87 (2013) 052303.
- [34] R. Fantoni, A. Giacometti, M.A.G. Maestre, A. Santos, *J. Chem. Phys.* 139 (2013) 174902.
- [35] R. Fantoni, A. Giacometti, A. Santos, *J. Chem. Phys.* 142 (2015) 224905.
- [36] R. Fantoni, G. Pastore, *Mol. Phys.* 113 (2015) 2593.
- [37] A. Santos, R. Fantoni, A. Giacometti, *Phys. Rev. E* 77 (2008) 051206.
- [38] R. Fantoni, A. Giacometti, A. Malijevský, A. Santos, *J. Chem. Phys.* 131 (2009) 124106.
- [39] R. Fantoni, A. Giacometti, A. Malijevský, A. Santos, *J. Chem. Phys.* 133 (2010) 024101.
- [40] R. Fantoni, *J. Stat. Mech.* (2010) P07030.
- [41] R. Fantoni, A. Malijevský, A. Santos, A. Giacometti, *Europhys. Lett.* 93 (2011) 26002.
- [42] R. Fantoni, A. Malijevský, A. Santos, A. Giacometti, *Mol. Phys.* 109 (2011) 2723.
- [43] P.G.D.S. Lucentini, G. Pellicane, *Phys. Rev. Lett.* 101 (2008) 246101.
- [44] G. Pellicane, R.L.C. Vink, C. Caccamo, H. Löwen, *Phys. Rev. Lett.* 101 (2008) 115101.

Part XIX

2019

Chapter 61

Plasma living in a curved surface at some special temperature

Fantoni R., Physica A **524**, 177 (2019)

Title: “Plasma living in a curved surface at some special temperature”

Abstract: The simplest statistical mechanics model of a Coulomb plasma in two spatial dimensions admits an exact analytic solution at some special temperature in several (curved) surfaces. We present in a unifying perspective these solutions for the (non-quantum) plasma, made of point particles carrying an absolute charge e , in thermal equilibrium at a temperature $T = e^2/2k_B$, with k_B Boltzmann’s constant, discussing the importance of having an exact solution, the role of the curvature of the surface, and the densities of the plasma.

Physica A 524 (2019) 177–220



Contents lists available at ScienceDirect

Physica A

journal homepage: www.elsevier.com/locate/physa



Minireview

Plasma living in a curved surface at some special temperature

Riccardo Fantoni

Università di Trieste, Dipartimento di Fisica, strada Costiera 11, 34151 Grignano (Trieste), Italy



ARTICLE INFO

Article history:
Received 23 August 2018
Available online 27 April 2019

Keywords:
Classical statistical physics
Plasma
Riemannian surfaces
Curvature
Coulomb potential
Partition function
Densities
Exact analytic solution

ABSTRACT

The simplest statistical mechanics model of a Coulomb plasma in two spatial dimensions admits an exact analytic solution at some special temperature in several (curved) surfaces. We present in a unifying perspective these solutions for the (non-quantum) plasma, made of point particles carrying an absolute charge e , in thermal equilibrium at a temperature $T = e^2/2k_B$, with k_B Boltzmann's constant, discussing the importance of having an exact solution, the role of the curvature of the surface, and the densities of the plasma.

© 2019 Elsevier B.V. All rights reserved.

Contents

1. The surface	179
2. The Coulomb potential	180
3. The background	180
4. The total potential energy	180
5. The densities and distribution functions	181
6. The plane	181
6.1. The Coulomb potential	181
6.2. The background	182
6.3. The total potential energy	182
6.4. Partition function and densities at a special temperature	182
7. The cylinder	183
7.1. The Coulomb potential	183
7.2. The background	184
7.3. The total potential energy	184
7.4. Partition function and densities at a special temperature	184
8. The sphere	185
8.1. The Coulomb potential	185
8.2. The background	185
8.3. The total potential energy	185
8.4. Partition function and densities at a special temperature	185
9. The pseudosphere	186
9.1. The Coulomb potential	188
9.2. The background	188
9.3. Ergodicity	188

E-mail address: rfantoni@ts.infn.it.

<https://doi.org/10.1016/j.physa.2019.04.222>
0378-4371/© 2019 Elsevier B.V. All rights reserved.

9.4.	Calculation of the curvature of \mathcal{M}	189
9.5.	Ergodicity of the semi-ideal Coulomb plasma	190
9.6.	Partition function and densities at a special temperature	190
10.	The Flamm paraboloid	194
10.1.	Coulomb potential in the whole surface (ws).....	196
10.2.	Coulomb potential in the half surface (hs) confined by hard walls.....	197
10.3.	Coulomb potential on half surface with a grounded horizon (gh).....	197
10.4.	The background.....	197
10.5.	Partition function and densities at a special temperature	198
10.5.1.	The 2D OCP on half surface with potential $-\ln z - z' - \ln M/(2L)$	198
10.5.2.	Internal screening.....	200
10.5.3.	External screening.....	200
10.5.4.	The 2D OCP on the whole surface with potential $-\ln(z - z' /\sqrt{ zz' })$	200
10.5.5.	The 2D OCP on the half surface with potential $-\ln(z - z' /\sqrt{ zz' })$	201
10.5.6.	The grounded horizon case.....	202
11.	The plane.....	204
11.1.	Symmetries of Green's function R	206
11.2.	Two-body truncated correlation functions and perfect screening sum rule.....	206
11.3.	Determination of Green's function R	207
12.	The sphere.....	208
12.1.	Thermodynamic properties.....	208
12.2.	Determination of Green's function G	208
13.	The pseudosphere.....	209
13.1.	Determination of Green's function G	209
13.2.	Thermodynamic properties.....	209
14.	The Flamm paraboloid	209
14.1.	Half surface with an insulating horizon	209
14.2.	Determination of Green's function R	210
14.3.	Method of solution	211
14.4.	Whole surface	211
	Appendix A. Electrostatic potential of the background for the OCP in the pseudosphere	214
	Appendix B. The flat limit for the OCP in the pseudosphere	215
	Appendix C. Green's function of Laplace equation in Flamm's paraboloid.....	216
	C.1. Laplace equation	216
	C.2. Green's function of Laplace equation.....	217
	C.3. The grounded horizon case	218
	Appendix D. The geodesic distance on the Flamm paraboloid	218
	References	219

Part I

Introduction

The physics of fluids of particles living in (curved) surfaces is a well known chapter of surface physics. It arises in situations in which particles are adsorbed or confined on a substrate with nonzero curvature, be it the wall of a porous material, or a membrane, a vesicle, a micelle for example made of amphiphilic surfactant molecules such as lipids, or a biological membrane, or the surface of a large solid particle, or an interface in an oil–water emulsion [1]. On the other hand it often occurs that by lowering the number of spatial dimensions, the statistical mechanics problem of a given fluid in the whole space, greatly simplifies, to the point of becoming, in certain cases, exactly solvable analytically in the continuum. A relevant feature of such low dimensional exactly solvable fluids is that they often play an important role as exact standards and guides to test approximate solutions and numerical experiments for (higher dimensional) fluid's models. In a more general context, the few exact analytical results have helped form new qualitative insights given by sum rules and in clarifying the nature of the long distance asymptotic decay of the truncated two (or more) particle distribution functions [2,3].

In the statistical physics of continuous fluids, those where the particles are allowed to move in a continuous space, one finds examples of exactly solvable ones especially among the non-quantum in lower dimensions (one and two).

Coulomb systems [4,5] such as plasmas, electrolytes, or generally ionic materials are made of charged particles interacting through the long-range Coulomb law. They are an important chapter of ionic condensed matter (in systems like molten salts, transition metal ions in solution, molten alkali halides, ...) or ionic soft matter (in systems like natural or synthetic saline environments like aqueous and non aqueous electrolyte solutions, polyelectrolytes, colloidal suspensions, ...). The simplest model of a Coulomb system is the one-component plasma (OCP), also called *jellium*: an assembly of identical point charges of charge e , embedded in a neutralizing uniform background of the opposite sign. Here we consider the classical (i.e. non-quantum) equilibrium statistical mechanics of the OCP. According to the proof of Sari and Merlini [6]

which goes through “H-stability” and the “cheese theorem”, the OCP must have a well behaved thermodynamic limit. Though this model might seem, at first sight, oversimplified as to bear little resemblance to molten salts or liquid metals, it is nevertheless of great value in clarifying general effects which emerge as a direct consequence of long-range Coulomb’s interaction. This model constitutes the basic link between the microscopic description and the phenomenology of ionic condensed and soft matter.

The two-dimensional version (2D OCP) of the OCP has been much studied. Provided that the Coulomb potential due to a point-charge is defined as the solution of the Poisson equation “in” a two-dimensional world, i.e., is a logarithmic function $-\ln r$ of the distance r to that point-charge, the 2D OCP mimics many generic properties of the three-dimensional Coulomb systems. In this case the electric field lines are not allowed to leave the surface as it happens in the satirical novella of Edwin Abbott Abbott [7]. Of course, this toy logarithmic model does not describe real charged particles, such as electrons, confined on a surface, which nevertheless interact through the three dimensional Coulomb potential $1/r$. One motivation for studying the 2D OCP is that its equilibrium statistical mechanics is analytically exactly solvable at one special temperature: both the thermodynamical quantities and the correlation functions are available.

The OCP is exactly solvable in one dimension [8,9]. In two dimensions, Jancovici and Alastuey [10–13] proved that the OCP is exactly solvable analytically at a special value of the coupling constant, $\Gamma = \beta e^2 = 2$ where $\beta = 1/k_B T$ with k_B Boltzmann’s constant and T the absolute temperature, on a plane. Since then, a growing interest in two-dimensional plasmas has led to study this system on various flat geometries [14–16] and two-dimensional curved surfaces like the cylinder [17,18], the sphere [19–22], the pseudosphere [23–25], and Flamm paraboloid [26]. Among these surfaces only the last one is of non-constant curvature.

How the properties of a system are affected by the curvature of the space in which the system lives is a question which arises in general relativity. This is an incentive for studying simple models.

The two-component plasma (TCP) is a neutral mixture of point-wise particles of charge $\pm e$. The equation of state of the TCP living in a plane is known since the work of Salzberg and Prager [27]. In the plasma the attraction between oppositely charged particles competes with the thermal motion and makes the partition function of the finite system diverge when $\Gamma = \beta e^2 \geq 2$, where $\beta = 1/k_B T$ with k_B Boltzmann constant. The system becomes unstable against the collapse of pairs of oppositely charged particles, and as a consequence all thermodynamic quantities diverge, so that the point particle model is well behaved only for $\Gamma < 2$ [28] when the Boltzmann factor for unlike particles is integrable at small separations of the charges. In this case rescaling the particles coordinates so as to stay in the unit disk one easily proves that the grand canonical partition function is a function of $\sqrt{\zeta_- \zeta_+} V^{(1-\Gamma/4)}$, where V is the volume occupied by the plasma and ζ_{\pm} the fugacities of the two charge species, and as a consequence the equation of state is $\beta p = n(1 - \Gamma/4)$ where $n = \rho_+ + \rho_-$ is the total particle number density. However, if the collapse is avoided by some short range repulsion (hard cores for instance), the model remains well defined for lower temperatures. Then, for $\Gamma > 4$ the long range Coulomb attraction binds positive and negative particles in pairs of finite polarizability. Thus, at some critical value $\Gamma_c \sim 4$ the system undergoes the Kosterlitz–Thouless transition [29] between a high temperature ($\Gamma < 4$) conductive phase and a low temperature ($\Gamma > 4$) dielectric phase. For $\Gamma \geq 2$ it is necessary to regularize the system of point charges allowing for a short-range strong repulsion between unlike charge which may be modeled as hard (impenetrable) disks, i.e. giving a physical dimension to the particles to prevent the collapse. The same behavior also occurs in the TCP living in one dimension [9,30].

The structure of the TCP living in a plane at the special value $\Gamma = 2$ of the coupling constant is also exactly solvable analytically [31,32]. Through the use of an external potential it has also been studied in various confined geometries [33–36] and in a gravitational field [37,38]. It has been studied in surfaces of constant curvature as the sphere [39,40] and the pseudosphere [23] and on the Flamm paraboloid of non-constant curvature [41]. Unlike the OCP where the properties of the Vandermonde determinant allowed the analytical solution a Cauchy identity is used for the solution of the TCP. Unlike in the one-component case where the solution was possible for the plasma confined in a region of the surface now this is not possible, anymore, without the use of an external potential. In these cases the external potential is rather given by $-(\Gamma/e^2) \ln \sqrt{g}$ where g is the determinant of the metric tensor of the Riemannian surface [42]. On a curved surface, even though the finite system partition function will still be finite for $\Gamma < 2$ since the surface is locally flat, the structure will change respect to the flat case.

Purpose of this review is to describe the state of the art for the studies on the exactly solvable statistical physics models of a plasma on a (curved) surface. In Section 2 we will treat the OCP in the various surfaces and in Section 3 the TCP in the various surfaces. Except for the OCP on the plane we will stop at the solution for the partition function and the densities of the finite OCP. If the reader wishes he can refer to the original papers for the resulting expressions in the thermodynamic limit. The solutions for the TCP do not give the results for the finite system but only its thermodynamic limit. For the OCP we use the canonical ensemble for the plane, the cylinder and the sphere, and the grand canonical ensemble for the pseudosphere and the Flamm paraboloid on half surface with grounded horizon. For the TCP we only use the grand canonical ensemble. When appropriate we point out the ensemble inequivalence which arise for the finite system.

1. The surface

We will generally consider *Riemannian surfaces* S with a coordinate frame $\mathbf{q} = (x^1, x^2)$ and with a metric

$$ds^2 = g_{\mu\nu}(\mathbf{q}) dx^\mu dx^\nu, \quad (1.1)$$

with $g_{\mu\nu}$ the metric tensor and Einstein's summation convention on repeated index has been adopted. We will denote with $g(\mathbf{q})$ the Jacobian of the transformation to an orthonormal coordinate reference frame, i.e. the determinant of the metric tensor $g_{\mu\nu}$. The surface may be embeddable in the three dimensional space or not. It is important to introduce a disk Ω_R of radius R and its boundary $\partial\Omega_R$. The torsion-less connection coefficients compatible with the metric, the Christoffel symbols, in a coordinate frame are

$$\Gamma_{\mu\beta\gamma} = \frac{1}{2}(g_{\mu\beta,\gamma} + g_{\mu\gamma,\beta} - g_{\beta\gamma,\mu}), \tag{1.2}$$

where the comma denotes a partial derivative as usual. The Riemann tensor in a coordinate frame reads

$$R^\alpha{}_{\beta\gamma\delta} = \Gamma^\alpha{}_{\beta\delta,\gamma} - \Gamma^\alpha{}_{\beta\gamma,\delta} + \Gamma^\alpha{}_{\mu\gamma}\Gamma^\mu{}_{\beta\delta} - \Gamma^\alpha{}_{\mu\delta}\Gamma^\mu{}_{\beta\gamma}, \tag{1.3}$$

in a two-dimensional space has only $2^2(2^2 - 1/12) = 1$ independent component. The scalar curvature is then given by the following indexes contractions (the trace of the Ricci curvature tensor),

$$\mathcal{R} = R^\mu{}_\mu = R^{\mu\nu}{}_{\mu\nu}, \tag{1.4}$$

and the (intrinsic) Gaussian curvature is $K = \mathcal{R}/2$. In an embeddable surface we may define also a (extrinsic) mean curvature $H = (k_1 + k_2)/2$, where the principal curvatures k_i , $i = 1, 2$ are the eigenvalues of the shape operator or equivalently the second fundamental form of the surface and $1/k_i$ are the principal radii of curvature. The Euler characteristic of the disk Ω_R is given by

$$\chi = \frac{1}{2\pi} \left(\int_{\Omega_R} K dS + \int_{\partial\Omega_R} k dl \right), \tag{1.5}$$

where k is the geodesic curvature of the boundary $\partial\Omega_R$.

2. The Coulomb potential

The Coulomb potential $G(\mathbf{q}, \mathbf{q}_0)$ created at \mathbf{q} by a unit charge at \mathbf{q}_0 is given by the Green function of the Laplacian

$$\Delta G(\mathbf{q}, \mathbf{q}_0) = -2\pi \delta^{(2)}(\mathbf{q}; \mathbf{q}_0), \tag{2.1}$$

with appropriate boundary conditions. Here Δ is the Laplace–Beltrami operator. This equation can often be solved by using the decomposition of G as a Fourier series.

3. The background

The Coulomb potential generated by the background, with a constant surface charge density $\rho_b = -en_b$ satisfies the Poisson equation

$$\Delta v_b = -2\pi \rho_b. \tag{3.1}$$

The Coulomb potential of the background can be obtained by solving Poisson equation with the appropriate boundary conditions. Also, it can be obtained from the Green function computed in the previous section

$$v_b(\mathbf{q}) = \int G(\mathbf{q}, \mathbf{q}') \rho_b(\mathbf{q}') dS'. \tag{3.2}$$

This integral can be performed easily by using the Fourier series decomposition of Green's function G .

4. The total potential energy

The total potential energy of the plasma is then

$$V_N = V_N^{pp} + V_N^{pb} + V_N^0 = \frac{e^2}{2} \sum_{i \neq j} G(|\mathbf{q}_i - \mathbf{q}_j|) + e \sum_i \int_{\Omega_R} v_b(|\mathbf{q} - \mathbf{q}_i|) d\mathbf{q} + \frac{1}{2} \iint_{\Omega_R} \rho_b v_b(|\mathbf{q} - \mathbf{q}'|) d\mathbf{q} d\mathbf{q}', \tag{4.1}$$

where the last term V_N^0 is the self energy of the background and the first two terms V_N^{pp} and V_N^{pb} are the interaction potential energy between the charges at \mathbf{q}_i , $i = 1, \dots, N$ and between the charges and the background, respectively.

5. The densities and distribution functions

Given either the canonical partition function in a fixed region $\Omega \in \mathcal{S}$ of a Riemannian surface \mathcal{S} , $Z_N(\Gamma)$ with $\Gamma = \beta e^2$ the coupling constant, or the grand canonical one $\mathcal{E}[\{\lambda_p(\mathbf{q})\}, \Gamma]$, with λ_p some position dependent fugacities, we can define the n -body density functions. Denoting with $\mathbf{p} = (p, \mathbf{q})$ the species p and the position \mathbf{q} of a particle of this species, we have,

$$\begin{aligned} \rho^{(n)}(\mathbf{p}_1, \dots, \mathbf{p}_n; N, \Gamma) &= \rho(\mathbf{p}_1; N, \Gamma) \cdots \rho(\mathbf{p}_n; N, \Gamma) g_{p_1 \dots p_n}(\mathbf{q}_1, \dots, \mathbf{q}_n; N, \Gamma) \\ &= \left\langle \sum_{i_1, \dots, i_n}^{DP} \delta^{(2)}(\mathbf{q}_1; \mathbf{q}_{i_1}) \delta_{p_1, p_{i_1}} \cdots \delta^{(2)}(\mathbf{q}_n; \mathbf{q}_{i_n}) \delta_{p_n, p_{i_n}} \right\rangle_{N, \Gamma}, \end{aligned} \tag{5.1}$$

where $\delta_{p,q}$ is the Kronecker delta, $\delta^{(2)}$ is the Dirac delta function on the curved surface such that $\int \delta^{(2)}(\mathbf{q}; \mathbf{q}') d\mathcal{S} = 1$ with $d\mathcal{S} = \sqrt{g(\mathbf{q})} d\mathbf{q}$ the elementary surface area on \mathcal{S} , $\langle \dots \rangle_{N, \Gamma} = \sum_{p_1, \dots, p_n} \int_{\Omega} \cdots e^{-\beta V_N} d\mathcal{S}_1 \cdots d\mathcal{S}_N / Z_N$ is the thermal average in the canonical ensemble, \sum^{DP} denotes the inclusion in the sum only of addends containing the product of delta functions relative to different particles, and we omitted the superscript (1) in the one-body densities. The g_{p_1, \dots, p_n} are known as the n -body distribution functions. It is convenient to introduce another set of correlation functions which decay to zero as two groups of particles are largely separated [2], namely the truncated (Ursell) correlation functions,

$$\rho^{(n)T}(\mathbf{p}_1, \dots, \mathbf{p}_n; N, \Gamma) = \rho^{(n)}(\mathbf{p}_1, \dots, \mathbf{p}_n; N, \Gamma) - \sum_{m < n} \prod \rho^{(m)T}(\mathbf{p}_{i_1}, \dots, \mathbf{p}_{i_m}; N, \Gamma), \tag{5.2}$$

where the sum of products is carried out over all possible partitions of the set $(1, \dots, n)$ into subsets of cardinal number $m < n$.

In terms of the grand canonical partition function we will have,

$$\rho^{(n)}(\mathbf{p}_1, \dots, \mathbf{p}_n; \{\lambda_p\}, \Gamma) = \prod_{i=1}^n \lambda_{p_i}(\mathbf{q}_i) \frac{1}{\mathcal{E}[\{\lambda_p\}, \Gamma]} \frac{\delta^{(n)} \mathcal{E}[\{\lambda_p\}, \Gamma]}{\delta \lambda_{p_1}(\mathbf{q}_1) \cdots \delta \lambda_{p_n}(\mathbf{q}_n)}, \tag{5.3}$$

and

$$\rho^{(n)T}(\mathbf{p}_1, \dots, \mathbf{p}_n; \{\lambda_p\}, \Gamma) = \prod_{i=1}^n \lambda_{p_i}(\mathbf{q}_i) \frac{\delta^{(n)} \ln \mathcal{E}[\{\lambda_p\}, \Gamma]}{\delta \lambda_{p_1}(\mathbf{q}_1) \cdots \delta \lambda_{p_n}(\mathbf{q}_n)}. \tag{5.4}$$

We may also use the notation $\rho^{(n)}(\mathbf{p}_1, \dots, \mathbf{p}_n; \{\lambda_p\}, \Gamma) = \rho_{p_1 \dots p_n}^{(n)}(\mathbf{q}_1, \dots, \mathbf{q}_n; \{\lambda_p\}, \Gamma)$ where for example in the two-component mixture each $p = \pm$ denotes either a positive or a negative charge. And sometimes we may omit the dependence from the number of particles, the fugacities, and the coupling constant. From the structure it is possible to derive the thermodynamic properties of the plasma (but not the contrary).

Part II

The one-component plasma

An *one-component plasma* is a system of N identical particles of charge e embedded in a uniform neutralizing background of opposite charge.

6. The plane

The metric tensor in the Cartesian coordinates $\mathbf{q} = (x, y)$ of the *plane* is,

$$\mathbf{g} = \begin{pmatrix} 1 & 0 \\ 0 & 1 \end{pmatrix}, \tag{6.1}$$

and the curvature is clearly zero. We will use polar coordinates $\mathbf{q} = (r, \varphi)$ with $r = \sqrt{x^2 + y^2}$ and $\varphi = \arctan(y/x)$.

6.1. The Coulomb potential

The Coulomb interaction potential between a particle at \mathbf{q} and a particle at \mathbf{q}_0 a distance $r = |\mathbf{q} - \mathbf{q}_0|$ from one another is

$$G(\mathbf{q}, \mathbf{q}_0) = -\ln(|\mathbf{q} - \mathbf{q}_0|/L), \tag{6.2}$$

where L is a length scale.

6.2. The background

If one assumes the particles to be confined in a disk $\Omega_R = \{\mathbf{q} \in \mathcal{S} | 0 \leq \varphi \leq 2\pi, 0 \leq r \leq R\}$ of area $\mathcal{A}_R = \pi R^2$ the background potential is

$$v_b(r) = en_b \frac{\pi}{2} \left(r^2 - R^2 + 2R^2 \ln \frac{R}{L} \right), \tag{6.3}$$

where $r = |\mathbf{q}|$.

6.3. The total potential energy

The total potential energy of the system is then given by Eq. (4.1). Developing all the terms and using $n_b = n = N/\mathcal{A}_R$ (this is not a necessary condition since we can imagine a situation where $n_b \neq n$. In this case the system would not be electrically neutral) we then find

$$V_N/e^2 = - \sum_{i<j} \ln \left(\frac{r_{ij}}{L} \right) + \frac{n_b \pi}{2} \sum_i r_i^2 + n_b^2 \pi^2 R^4 \left(-\frac{3}{8} + \frac{1}{2} \ln \frac{R}{L} \right), \tag{6.4}$$

where $r_{ij} = |\mathbf{q}_i - \mathbf{q}_j|$ and $r_i = |\mathbf{q}_i|$. This can be rewritten as follows

$$V_N/e^2 = - \sum_{i<j} \ln \left(\frac{r_{ij}}{R} \right) + \frac{N}{2} \sum_i \left(\frac{r_i}{R} \right)^2 + N^2 \left(-\frac{3}{8} + \frac{1}{2} \ln \frac{R}{L} \right) - \frac{N(N-1)}{2} \ln \left(\frac{R}{L} \right). \tag{6.5}$$

We can then introduce the new variables [12] $\mathbf{z}_i = \sqrt{N} \mathbf{q}_i / R$ to find

$$V_N/e^2 = f(\{\mathbf{z}_i\}) + f_c \tag{6.6}$$

$$f = - \sum_{i<j} \ln z_{ij} + \frac{1}{2} \sum_i z_i^2, \tag{6.7}$$

$$f_c = \frac{N(N-1)}{4} \ln(n\pi L^2) + N^2 \left(-\frac{3}{8} + \frac{1}{2} \ln \frac{R}{L} \right). \tag{6.8}$$

We can always choose $L = R$ so that in the thermodynamic limit $\lim_{N \rightarrow \infty} f_c/N = -\ln(n\pi L^2)/4$ and the excess Helmholtz free energy per particle

$$a_{exc} = F_{exc}/N \rightarrow -\frac{e^2}{4} \ln(n\pi L^2) + a_0(T), \tag{6.9}$$

with a_0 some function of the temperature T alone. Therefore, the equation of state has the simple form

$$p = (1/\beta - e^2/4)n, \tag{6.10}$$

where $\beta = 1/k_B T$ with k_B Boltzmann's constant.

6.4. Partition function and densities at a special temperature

At the special temperature $T_0 = e^2/2k_B$ the partition function can be found exactly analytically using the properties of the Vandermonde determinant [12,13]. Using polar coordinates $\mathbf{z}_i = (z_i, \theta_i)$, one obtains at T_0 a Boltzmann factor

$$e^{-\beta V_N} = A_N e^{-\sum_i z_i^2} \left| \prod_{i<j} (Z_i - Z_j) \right|^2, \tag{6.11}$$

where A_N is a constant and $Z_i = z_i \exp(i\theta_i)$. This expression can be integrated upon variables \mathbf{z}_i ($0 \leq z_i \leq \sqrt{N}$) by expanding the Vandermonde determinant $\prod (Z_i - Z_j)$. One obtains the partition function

$$Z_N(2) = \int e^{-\beta V_N} d\mathbf{z}_1 \dots d\mathbf{z}_N = A_N \pi^N N! \prod_{j=1}^N \gamma(j, N), \tag{6.12}$$

where

$$\gamma(j, N) = \int_0^{\sqrt{N}} e^{-z^2} z^{2(j-1)} 2z dz = \int_0^N e^{-t} t^{j-1} dt, \tag{6.13}$$

is the incomplete gamma function. Taking the thermodynamic limit of $-\ln(Z_N(2)/A_R^N)/N \rightarrow \beta a_{\text{exc}}(2)$ we obtain the Helmholtz free energy per particle

$$a_{\text{exc}}(2) = -\frac{e^2}{4} \ln(\pi n L^2) + \frac{e^2}{2} \left[1 - \frac{1}{2} \ln(2\pi) \right]. \tag{6.14}$$

One can also obtain the n -body distribution functions from the truncated densities [2] as follows

$$g(1, \dots, n; N) = e^{-\sum_{i=1}^n z_i^2} \det [K_N(Z_i \bar{Z}_j)]_{i,j=1,\dots,n}, \tag{6.15}$$

where \bar{Z} is the complex conjugate of Z and

$$K_N(x) = \sum_{i=1}^N \frac{x^{i-1}}{\gamma(i, N)}. \tag{6.16}$$

In the thermodynamic limit $N \rightarrow \infty$, $\gamma(i, N) \rightarrow (i - 1)!$, and $K_N(x) \rightarrow e^x$. In this limit, one obtains from Eq. (6.15) the following explicit distribution functions [12]

$$g(1) = 1, \tag{6.17}$$

$$g(1, 2) = 1 - e^{-\pi n r_{12}^2}, \tag{6.18}$$

$$g(1, 2, 3) = \dots \tag{6.19}$$

This *Gaussian falloff* is in agreement with the general result according to which, among all possible long-range pair potentials, it is only in the Coulomb case that a decay of correlations faster than any inverse power is compatible with the structure of equilibrium equations like the Born–Green–Yvon hierarchic set (see Ref. [2] section II.B.3). A somewhat surprising result is that the correlations does not have the typical exponential falloff typical of the high-temperature Debye–Hückel approximation [43]. One easily checks that the distribution functions obey the perfect screening and other sum rules.

Expansions around $\Gamma = 2$ suggests that the pair correlation function changes from the exponential form to an oscillating one for a region with $\Gamma > 2$. This behavior of the pair correlation function as the coupling is stronger has been observed in Monte Carlo simulations [44]. For sufficient high values of Γ (low temperatures) the 2D OCP begins to crystallize and there are several works where the freezing transition is found. For the case of the sphere Caillol et al. [44] localized the coupling parameter for melting at $\Gamma \approx 140$. In the limit $\Gamma \rightarrow \infty$ the 2D OCP becomes a Wigner crystal. In particular, the spatial configuration of the charges which minimizes the energy at zero temperature for the 2D OCP on a plane is the usual hexagonal lattice. Nowadays, the corresponding Wigner crystal of the 2D OCP on sphere or Thomson problem may be solved numerically [1].

7. The cylinder

The *cylinder* may be useful to compare an exactly soluble fluid with the results from its Monte Carlo simulation for example, where one needs to use periodic boundary conditions. The two dimensional system studied in the simulation would actually live on a torus but the cylinder is already a relevant step forward in this direction.

The metric tensor in the cartesian coordinates $\mathbf{q} = (x, y)$ is,

$$\mathbf{g} = \begin{pmatrix} 1 & 0 \\ 0 & 1 \end{pmatrix}, \tag{7.1}$$

and again the curvature is zero.

7.1. The Coulomb potential

We now consider [17,18] a rectangular disk $\Omega_{L,W} = \{\mathbf{q} \in S | -L/2 \leq x \leq L/2, -W/2 \leq y \leq W/2\}$. We then solve Eq. (2.1) imposing periodicity in y with period W expanding G in a Fourier series in y where the coefficients are functions of x and written as inverse Fourier transforms. The solution is

$$G(\mathbf{q}_1, \mathbf{q}_2) = -\frac{\pi}{W} |x_1 - x_2| + \frac{\text{sgn}(x_1 - x_2)}{2} \ln \left\{ 1 - 2e^{-\frac{2\pi}{W} |x_1 - x_2|} \cos \frac{2\pi}{W} (y_1 - y_2) + e^{-\frac{4\pi}{W} |x_1 - x_2|} \right\}, \tag{7.2}$$

where $\text{sgn}(x) = |x|/x$ is the sign of x . The term proportional to $|x_1 - x_2|$ comes from the constant term in the Fourier series solution, while the other terms sum to give the logarithmic part.

7.2. The background

The potential of the background (3.1) is then

$$v_b(x) = en_b \frac{\pi}{4} (L^2 + 4x^2), \tag{7.3}$$

since the second term on the right hand side of Eq. (7.2) is an odd function of $x_1 - x_2$.

7.3. The total potential energy

The total potential energy (4.1) for $n_b = n = N/WL$ can then be written as

$$V_N/e^2 = \sum_{i<j} G(\mathbf{q}_i, \mathbf{q}_j) + \pi n \sum_i x_i^2 + B_N, \tag{7.4}$$

where B_N is a constant irrelevant to the distribution function.

7.4. Partition function and densities at a special temperature

The energy of Eq. (7.4) can be inserted into the formula for the canonical partition function $Z_N(\Gamma)$ at $\Gamma = \beta e^2 = 2$ to obtain

$$Z_N(2) = A_N \int_{-L/2}^{L/2} dx_N \int_{-L/2}^{x_N} dx_{N-1} \cdots \int_{-L/2}^{x_2} dx_1 e^{-2\pi n \sum_i x_i^2} \times \int_{-W/2}^{W/2} dy_1 \cdots \int_{-W/2}^{W/2} dy_N \prod_{i<j} \left(e^{\frac{2\pi}{W}(x_i+x_j)} \left| e^{-\frac{2\pi}{W}(x_i-iy_i)} - e^{-\frac{2\pi}{W}(x_j-iy_j)} \right|^2 \right), \tag{7.5}$$

where A_N is a constant. Now we notice that the y -dependent part of the integrand is contained in the square modulus of a Vandermonde determinant. We use the permutation notation to write the expansion of the determinant and its conjugate as follows

$$\int_{-W/2}^{W/2} dy_1 \cdots \int_{-W/2}^{W/2} dy_N \prod_{i<j} \left| e^{-\frac{2\pi}{W}(x_i-iy_i)} - e^{-\frac{2\pi}{W}(x_j-iy_j)} \right|^2 = \sum_{P,Q} \epsilon(P)\epsilon(Q) \prod_{i=1}^N \left(e^{-\frac{2\pi x_i}{W}[P(i)+Q(i)-2]} \int_{-W/2}^{W/2} dy_i e^{-\frac{2\pi iy_i}{W}[P(i)-Q(i)]} \right), \tag{7.6}$$

where the sums are over the $N!$ permutations, $\epsilon(P)$ denotes the sign of permutation P . Only permutations for which $P(i) = Q(i)$, $1 \leq i \leq N$ contribute. Recalling that $n = N/WL$ we obtain

$$Z_N(2) = A_N W^N \sum_P \int_{-L/2}^{L/2} dx_N \int_{-L/2}^{x_N} dx_{N-1} \cdots \int_{-L/2}^{x_2} dx_1 \times \prod_{i=1}^N e^{-2\pi n \left[x_i^2 - 2x_i \frac{1}{2} \left[1 - 2 \frac{P(i)-1}{N} \right] \right]}. \tag{7.7}$$

For permutation P , make the substitution $x_i = z_{P(i)}$, $1 \leq i \leq N$. We then have a sum over ordered integrals over the z_i . The integrand is the same for each permutation and each possible ordering of the z_i occurs exactly once. Hence, the sum over ordered integrals may be written as an unrestricted multiple integral over $[-L/2, L/2]^N$. Renaming $z_i = x_i$ for $1 \leq i \leq N$ and using the appropriately defined B_N , we obtain

$$Z_N(2) = B_N W^N \prod_{i=1}^N \int_{-L/2}^{L/2} dx_i e^{-2\pi n \left[x_i - \frac{1}{2} \left(1 - 2 \frac{i-1}{N} \right) \right]^2} \tag{7.8}$$

This equation describes the canonical partition function for an assembly of N independent harmonic oscillators with mean position evenly spaced on $[-L/2, L/2]$. Using the correct form of B_N we may now take the thermodynamic limit of $-\ln(Z_N(2)/A_N^N)/N$ to obtain for the excess free energy per particle $\beta a_{exc}(2) = \beta a_{exc,plane}(2) + M$ where $a_{exc,plane}(2)$ is expression (6.14) with the choice $L = W/2\pi$ and $M = \pi/6nW^2$ is a Madelung constant for the potential in the semiperiodic boundary conditions used.

To calculate the one-particle distribution function in the finite system we simply leave out the integrations over x_1 and y_1 . Define $x_0 = -L/2$, $x_{N+1} = L/2$, and the ordering of the x variables with $x_0 \leq x_2 \leq x_3 \leq \cdots \leq x_p \leq x_1 < x_{p+1} \leq \cdots \leq x_N \leq x_{N+1}$. There are $(N-1)!$ orderings, each giving the same contribution to $g(1; N)$. We use the Vandermonde determinant representation of the integrand and carry out the integrations over y_2, \dots, y_N giving $P(i) = Q(i)$, $2 \leq i \leq N$,

and so $P(1) = Q(1)$ by default. Collect all the integrals with $P(1) = q$ and change variables with $x_i = z_{p(i)}$, $2 \leq i \leq N$; $P(i) \neq q$ and $x_1 = z_q$. This generates ordered integrals with respect to $(N - l)$ of the z_i , all possible orderings occurring exactly once. An unrestricted integral over

$$\{z_1, \dots, z_{q-1}, z_{q+1}, \dots, z_N\} \in [-L/2, L/2]^{N-1}, \tag{7.9}$$

results. The final form for the one-particle distribution function is then

$$g(1; N) = \frac{1}{Wn} \sum_{q=1}^N e^{-2\pi n [x_1 - \frac{1}{2}(1 - 2\frac{q-1}{N})]^2} / I(q, L, N), \tag{7.10}$$

$$I(i, L, N) = \int_{-L/2}^{L/2} dx e^{-2\pi n [x_1 - \frac{1}{2}(1 - 2\frac{i-1}{N})]^2}. \tag{7.11}$$

The higher orders distribution functions are determined in Ref. [18].

8. The sphere

The metric tensor in the polar coordinates $\mathbf{q} = (\theta, \varphi)$ is now,

$$\mathbf{g} = \begin{pmatrix} a^2 & 0 \\ 0 & a^2 \sin^2 \theta \end{pmatrix}, \tag{8.1}$$

where a is the radius of the sphere. The sphere is embeddable in the three dimensional Euclidean space. The intrinsic Gaussian curvature of the sphere is a constant $K = 1/a^2$ and the surface area of the sphere is $\mathcal{A}_S = 4\pi a^2$. So the sphere is the surface of constant positive curvature by Liebmann’s theorem. Also by Minding’s theorem we know that surfaces with the same constant curvature are locally isometric.

8.1. The Coulomb potential

The Coulomb interaction between a particle at \mathbf{r}_i and a particle at \mathbf{r}_j is

$$G(\mathbf{r}_i, \mathbf{r}_j) = -\ln(r_{ij}/L), \tag{8.2}$$

$$r_{ij} = 2a \sin(\theta_{ij}/2), \tag{8.3}$$

$$\varphi_{ij} = \arccos(\mathbf{r}_i \cdot \mathbf{r}_j / a^2), \tag{8.4}$$

where \mathbf{r}_k is the three-dimensional vector from the center of the sphere to particle k on the sphere surface and r_{ij} is the length of the chord joining \mathbf{r}_i and \mathbf{r}_j .

8.2. The background

The background potential is then a constant

$$v_b = en_b 2\pi a^2 \left(-1 + \ln \frac{4a^2}{L^2} \right). \tag{8.5}$$

8.3. The total potential energy

The total potential energy of the system (4.1) is then

$$V_N / e^2 = -\frac{1}{2} \sum_{i < j} \ln \left[\frac{2a^2}{L^2} (1 - \cos \theta_{ij}) \right] - \frac{N^2}{4} \left(1 - \ln \frac{4a^2}{L^2} \right). \tag{8.6}$$

8.4. Partition function and densities at a special temperature

At $\Gamma = \beta e^2 = 2$ the excess canonical partition function is

$$Z_N(2) = e^{N^2/2} \left(\frac{L}{2a} \right)^N \int \prod_{i=1}^N d\mathbf{q}_i \prod_{j < k} \left(\frac{1 - \cos \theta_{jk}}{2} \right), \tag{8.7}$$

where denoting with $g = \det[g_{\mu\nu}]$ we have $d\mathbf{q} = dS = \sqrt{g} dq^1 dq^2 = a^2 \sin \theta d\theta d\varphi$. Introducing the Cayley-Klein parameters defined by

$$\alpha_i = \cos \frac{\theta_i}{2} e^{i\varphi_i/2}, \tag{8.8}$$

$$\beta_i = -i \sin \frac{\theta_i}{2} e^{-i\varphi_i/2}, \tag{8.9}$$

we can write

$$1 - \cos \theta_{ij} = 2|\alpha_i \beta_j - \alpha_j \beta_i|^2. \tag{8.10}$$

The integrand of Eq. (8.7) takes the form

$$\prod_{i<j} \left(\frac{1 - \cos \theta_{jk}}{2} \right) = \left| \prod_{k=1}^N \beta_k^{N-1} \prod_{i<j} \left(\frac{\alpha_i}{\beta_i} - \frac{\alpha_j}{\beta_j} \right) \right|^2. \tag{8.11}$$

The second product in the right hand side of this equation is a van der Monde determinant. Expanding it and inserting in Eq. (8.7) we find

$$Z_N(2) = e^{N^2/2} (2\pi L)^N a^N N! \prod_{k=1}^N \frac{(k-1)!(N-k)!}{N!}. \tag{8.12}$$

This result is similar to the result (6.12) on the plane apart from the fact that now only complete gamma functions are involved. The excess free energy per particle is identical to the result (6.14) for the plane.

For the distribution functions we find [19]

$$g(1, 2, \dots, n; N) = \det[(\alpha_i \bar{\alpha}_j + \beta_i \bar{\beta}_j)^{N-1}], \tag{8.13}$$

where $\bar{\alpha}$ is the complex conjugate of α . In particular

$$g(1; N) = 1, \tag{8.14}$$

$$g(1, 2; N) = 1 - \left(\frac{1 + \cos \theta_{12}}{2} \right)^{N-1}. \tag{8.15}$$

The system appears to be homogeneous for all N and the distribution functions are invariant under a rotation of the sphere.

The thermodynamic limit is obtained defining $\rho_i = R\theta_i$ and taking the limit $N \rightarrow \infty$ and $R \rightarrow \infty$ at n constant, keeping ρ_i and φ_i constant for each particle i . For an infinitely large sphere the particles will be situated in the tangent plane at the North pole and there positions will be characterized by the polar coordinates (ρ_i, φ_i) . The solution for the planar geometry of Section 6 is thereby recovered.

9. The pseudosphere

The pseudosphere is non-embeddable in the three dimensional Euclidean space and it is a non-compact Riemannian surface of constant negative curvature. Unlike the sphere it has an infinite area and this fact makes it interesting from the point of view of statistical physics because one can take the thermodynamic limit on it.

Riemannian surfaces of negative curvature play a special role in the theory of dynamical systems [45]. Hadamard study of the geodesic flow of a point particle on a such surface [46] has been of great importance for the future development of ergodic theory and of modern chaos theory. In 1924 the mathematician Emil Artin [47] studied the dynamics of a free point particle of mass m on a pseudosphere closed at infinity by a reflective boundary (a billiard). Artin’s billiard belongs to the class of the so called Anosov systems. All Anosov systems are ergodic and possess the mixing property [48]. Sinai [49] translated the problem of the Boltzmann–Gibbs gas into a study of the by now famous “Sinai’s billiard”, which in turn could relate to Hadamard’s model of 1898. Recently, smooth experimental versions of Sinai’s billiard have been fabricated at semiconductor interfaces as arrays of nanometer potential wells and have opened the new field of mesoscopic physics [50].

The following important theorem holds for Anosov systems [51,52]:

Theorem 9.1. *Let M be a connected, compact, orientable analytic surface which serves as the configurational manifold of a dynamical system whose Hamiltonian is $H = K + U$. Let the dynamical system be closed and its total energy be h . Consider the manifold \mathcal{M} defined by the Maupertuis Riemannian metric $ds^2 = 2(h - U)K dt^2$ on M , where t is time. If the curvature of \mathcal{M} is negative everywhere then the dynamical system is an Anosov system and in particular is ergodic on $M_h = \{h = H\}$.*

If the dynamical system is composed of N particles, the same conclusions hold, we need only require that the curvature be negative when we keep the coordinates of all the particles but anyone constant.

The metric tensor of the pseudosphere in the coordinates $\mathbf{q} = (\theta, \varphi)$ with $\theta \in [0, \infty[$ is,

$$\mathbf{g} = \begin{pmatrix} a^2 & 0 \\ 0 & a^2 \sinh^2 \theta \end{pmatrix}, \tag{9.1}$$

where a is the “radius” of the pseudosphere.

Introducing the alternative coordinates $\mathbf{q} = (r, \varphi)$ with $r/2a = \tanh(\theta/2)$ we find

$$\mathbf{g} = \begin{pmatrix} [1 - (r/2a)^2]^{-2} & 0 \\ 0 & r^2[1 - (r/2a)^2]^{-2} \end{pmatrix}. \tag{9.2}$$

These are the polar coordinates $\omega = (r/2a, \varphi)$ of a disk of the unitary disk, $\mathcal{D} = \{\omega \in \mathbb{C} \mid |\omega| < 1\}$, which with such a metric is called the *Poincaré disk*.

A third set of coordinates used is $\mathbf{q} = (x, y)$ obtained from $(r/2a, \varphi)$ through the Cayley transformation,

$$z = x + iy = \frac{\omega + i}{1 + i\omega}. \tag{9.3}$$

which establishes a bijective transformation between the unitary disk and the complex half plane,

$$\mathcal{H} = \{z = x + iy \mid x \in \mathbb{R}, y > 0\}. \tag{9.4}$$

The center of the unitary disk corresponds to the point $z_0 = i$, “the center of the plane”. The metric becomes,

$$\mathbf{g} = \begin{pmatrix} a^2/y^2 & 0 \\ 0 & a^2/y^2 \end{pmatrix}. \tag{9.5}$$

The complex half plane with such a metric is called the *hyperbolic plane*, and the metric the *Poincaré’s metric*.

Cayley transformation is a particular Möbius transformation. Poincaré metric is invariant under Möbius transformations. And any transformation that preserves Poincaré metric is a Möbius transformation.

The geodesic distance d_{01} between any two points $\mathbf{q}_0 = (\tau_0, \varphi_0)$ and $\mathbf{q}_1 = (\tau_1, \varphi_1)$ on the pseudosphere \mathcal{S} is given by,

$$\cosh(d_{01}/a) = \cosh \tau_1 \cosh \tau_0 - \sinh \tau_1 \sinh \tau_0 \cos(\varphi_1 - \varphi_0). \tag{9.6}$$

Given the set of points Ω_d at a geodesic distance from the origin less or equal to d ,

$$\Omega_d = \{(\tau, \varphi) \in \mathcal{S} \mid \tau a \leq d, \varphi \in [0, 2\pi)\}, \tag{9.7}$$

that we shall call a disk of radius d , we can determine its circumference,

$$\begin{aligned} C &= \mathcal{L}(\partial\Omega_d) = a \int_{\tau=d/a}^{\infty} \sqrt{\dot{\tau}^2 + \sinh^2 \tau} \dot{\varphi}^2 dt \\ &= 2\pi a \sinh\left(\frac{d}{a}\right) \underset{d \rightarrow \infty}{\sim} \pi a e^{d/a}, \end{aligned} \tag{9.8}$$

and its area,

$$\begin{aligned} \mathcal{A} &= \mathcal{V}(\Omega_d) = \int_0^{2\pi} d\varphi \int_0^{d/a} d\tau a^2 \sinh \tau \\ &= 4\pi a^2 \sinh^2\left(\frac{d}{2a}\right) \underset{d \rightarrow \infty}{\sim} \pi a^2 e^{d/a}. \end{aligned} \tag{9.9}$$

The Laplace–Beltrami operator on \mathcal{S} is,

$$\begin{aligned} \Delta &= \frac{1}{\sqrt{g}} \frac{\partial}{\partial q^\mu} \left(\sqrt{g} g^{\mu\nu} \frac{\partial}{\partial q^\nu} \right) \\ &= \frac{1}{a^2} \left(\frac{1}{\sinh \tau} \frac{\partial}{\partial \tau} \sinh \tau \frac{\partial}{\partial \tau} + \frac{1}{\sinh^2 \tau} \frac{\partial^2}{\partial \varphi^2} \right), \end{aligned} \tag{9.10}$$

where g is the determinant of the metric tensor $g = \det[g_{\mu\nu}]$.

The characteristic component of the Riemann tensor is,

$$R^\tau_{\varphi\tau\varphi} = -\sinh^2 \tau. \tag{9.11}$$

The Gaussian curvature is given by

$$R^\tau_{\varphi\tau\varphi} = g^{\varphi\varphi} R^\tau_{\varphi\tau\varphi} = -\frac{1}{a^2}, \tag{9.12}$$

except at its singular cusp, in agreement with Hilbert’s theorem. Contraction gives the components of the Ricci tensor,

$$R^\tau_{\tau} = R^\varphi_{\varphi} = -\frac{1}{a^2}, \quad R^\tau_{\varphi} = 0, \tag{9.13}$$

and further contraction gives the scalar curvature,

$$R = -\frac{2}{a^2}. \tag{9.14}$$

The ensemble of N identical point-wise particles of charge e are constrained to move in a connected and compact domain $\Omega \subset S$ by an infinite potential barrier on the boundary of the domain $\partial\Omega$ with a number density $n = N/\mathcal{V}(\Omega)$.

9.1. The Coulomb potential

The pair Coulomb potential between two unit charges a geodesic distance d apart, satisfies Poisson equation on S ,

$$\Delta G(d) = -2\pi\delta^{(2)}(d), \tag{9.15}$$

where $\delta^{(2)}(d_{01}) = \delta(\mathbf{q}_0 - \mathbf{q}_1)/\sqrt{g}$ is the Dirac delta function on the curved manifold. Poisson equation admits a solution vanishing at infinity,

$$G(d_{ij}) = -\ln \left[\tanh \left(\frac{d_{ij}}{2a} \right) \right]. \tag{9.16}$$

9.2. The background

If we choose $\Omega = \Omega_{a\tau_0}$, the electrostatic potential of the background inside Ω can be chosen (see Appendix A) to be just a function of τ ,

$$v_b(\tau) = en_b 2\pi a^2 \left\{ \ln \left[\frac{1 - \tanh^2(\tau_0/2)}{1 - \tanh^2(\tau/2)} \right] + \sinh^2(\tau_0/2) \ln[\tanh^2(\tau_0/2)] \right\}. \tag{9.17}$$

9.3. Ergodicity

Consider a closed one component Coulomb plasma of N charges and total energy h , confined in the domain $\Omega_{a\tau_0} \subset S$. Let the coordinates of particle i be $\mathbf{q}_i = q_{(i)\alpha} \vec{e}_\alpha = (q_{(i)1}, q_{(i)2}) \in \Omega_{a\tau_0}$, where $\vec{e}_\alpha = \partial/\partial q^\alpha$ ($\alpha = 1, 2$) is a coordinate basis for S . The trajectory of the dynamical system,

$$\mathcal{T}_{\tau_0} = \{q^N(t) \equiv (\mathbf{q}_1, \dots, \mathbf{q}_N) \mid t \in [0, t_0]\}, \tag{9.18}$$

is a geodesic on the $2N$ dimensional manifold \mathcal{M} defined by the metric,

$$\mathcal{G}_{\alpha\beta} = (h - V_N)g_{\mu\nu}(\mathbf{q}_i) \otimes \dots \otimes g_{\mu\nu}(\mathbf{q}_N), \tag{9.19}$$

on S^N . We now assume $n_b = n$ and rewrite $V_N^{pb} = v_1 + v_{pb}$ where

$$v_1 = N 2\pi a^2 e^2 n \{ \ln[1 - \tanh^2(\tau_0/2)] + \sinh^2(\tau_0/2) \ln[\tanh^2(\tau_0/2)] \}, \tag{9.20}$$

is a constant. Since the interaction between the particles is repulsive we conclude that, up to an additive constant ($V_N^0 + v_1$), the potential V_N is a positive function of the coordinates of the particles. Since v_{pb} and V_N^{pp} are positive on $\Omega_{a\tau_0}$ we have,

$$\mathcal{G}'_{\alpha\beta} < \mathcal{G}'_{\alpha\beta} = (h - V_N^0 - v_1)g_{\mu\nu}(\mathbf{q}_i) \otimes \dots \otimes g_{\mu\nu}(\mathbf{q}_N), \tag{9.21}$$

where \mathcal{G}' has a negative curvature along the coordinates of any given particle. In the next subsection we will calculate the curvature of \mathcal{G} along the coordinates of one particle. According to the theorem stated in the introduction we will require the curvature to be negative everywhere on S^N . This will determine a condition on the kinetic and potential energy of the system, sufficient for its ergodicity to hold on M_h .

Let $\tilde{\mathbf{p}}_i = p_{(i)\alpha} \tilde{\omega}^\alpha$ be the momentum of charge i , where $\tilde{\omega}^\alpha = \tilde{d}q^\alpha$ are the 1-forms of the dual coordinate basis, and define $p^N(t) \equiv (\tilde{p}_1, \dots, \tilde{p}_N)$, $q^N(t) \equiv (\mathbf{q}_1, \dots, \mathbf{q}_N)$. The ergodicity of the system tells us that given any dynamical quantity $A(q^N, p^N)$, its time average,

$$\langle A \rangle_t = \lim_{T \rightarrow \infty} \frac{1}{T} \int_0^T A(q^N, p^N) dt, \tag{9.22}$$

coincides with its microcanonical phase space average,

$$\langle A \rangle_h = \frac{\int_{M_{ps}} A(q^N, p^N) \delta(h - H) d^{4N} \mu_{ps}}{\int_{M_{ps}} \delta(h - H) d^{4N} \mu_{ps}}, \tag{9.23}$$

where the phase space of the system is,

$$M_{ps} = \{(q^N, p^N) \mid \mathbf{q}_i \in S \ i = 1, \dots, N; \\ p_{(i)\alpha} \in [-\infty, \infty] \ i = 1, \dots, N, \alpha = 1, 2\}, \tag{9.24}$$

the phase space measure is,

$$d^{4N} \mu_{ps} = \prod_{\alpha=1}^2 dq_{(1)\alpha} \cdots dq_{(N)\alpha} dp_{(1)\alpha} \cdots dp_{(N)\alpha}, \tag{9.25}$$

and δ is the Dirac delta function.

9.4. Calculation of the curvature of \mathcal{M}

We calculate the curvature of \mathcal{M} along particle 1 using Cartan structure equations. Let $K = h - U(\tau, \varphi)$ be the kinetic energy of the N particle system of total energy h , as a function of the coordinates of particle 1 (all the other particles having fixed coordinates). We choose an orthonormal basis,

$$\begin{cases} \tilde{\omega}^{\hat{\tau}} = a\sqrt{K}d\tau \\ \tilde{\omega}^{\hat{\varphi}} = a \sinh(\tau)\sqrt{K}d\varphi \end{cases} \tag{9.26}$$

By Cartan second theorem we know that the connection 1-form satisfies $\tilde{\omega}_{\hat{\alpha}\hat{\beta}} + \tilde{\omega}_{\hat{\beta}\hat{\alpha}} = 0$. Then we must have,

$$\begin{cases} \tilde{\omega}^{\hat{\tau}}_{\hat{\tau}} = \tilde{\omega}^{\hat{\varphi}}_{\hat{\varphi}} = 0 \\ \tilde{\omega}^{\hat{\tau}}_{\hat{\varphi}} = -\tilde{\omega}^{\hat{\varphi}}_{\hat{\tau}} = -\tilde{\omega}^{\hat{\varphi}}_{\hat{\tau}} \end{cases} \tag{9.27}$$

We use Cartan first theorem to calculate $\tilde{\omega}^{\hat{\tau}}_{\hat{\varphi}}$,

$$\begin{aligned} d\tilde{\omega}^{\hat{\tau}} &= -\tilde{\omega}^{\hat{\varphi}}_{\hat{\varphi}} \wedge \tilde{\omega}^{\hat{\tau}} \\ &= d(a\sqrt{K}d\tau) \\ &= aK^{\frac{1}{2}}_{,\varphi} d\varphi \wedge d\tau = 0, \end{aligned} \tag{9.28}$$

where in the last equality we used the fact that the pair interaction is a function of $\varphi_i - \varphi_j$ and that the interaction with the background is a function of τ only (being the system confined in a domain which is symmetric under translations of φ). We must then conclude that $\tilde{\omega}^{\hat{\tau}}_{\hat{\varphi}}$ is either zero or proportional to $\tilde{\omega}^{\hat{\varphi}}$. We proceed then calculating,

$$\begin{aligned} d\tilde{\omega}^{\hat{\varphi}} &= -\tilde{\omega}^{\hat{\tau}}_{\hat{\tau}} \wedge \tilde{\omega}^{\hat{\varphi}} \\ &= d(a \sinh(\tau)\sqrt{K}d\varphi) \\ &= a(\sinh(\tau)K^{\frac{1}{2}})_{,\tau} d\tau \wedge d\varphi, \end{aligned} \tag{9.29}$$

which tells us that indeed,

$$\tilde{\omega}^{\hat{\varphi}}_{\hat{\tau}} = \frac{(\sinh(\tau)K^{\frac{1}{2}})_{,\tau}}{a \sinh(\tau)K} \tilde{\omega}^{\hat{\varphi}}. \tag{9.30}$$

Next we calculate the characteristic component of the curvature 2-form $\mathcal{R}^{\hat{\alpha}}_{\hat{\beta}} = d\tilde{\omega}^{\hat{\alpha}}_{\hat{\beta}} + \tilde{\omega}^{\hat{\alpha}}_{\hat{\gamma}} \wedge \tilde{\omega}^{\hat{\gamma}}_{\hat{\beta}}$,

$$\begin{aligned} \mathcal{R}^{\hat{\tau}}_{\hat{\varphi}} &= d\tilde{\omega}^{\hat{\tau}}_{\hat{\varphi}} \\ &= d[-(\sinh(\tau)K^{\frac{1}{2}})_{,\tau} K^{-\frac{1}{2}} d\varphi] \\ &= -\frac{[(\sinh(\tau)K^{\frac{1}{2}})_{,\tau} K^{-\frac{1}{2}}]_{,\tau}}{a^2 \sinh(\tau)K} \tilde{\omega}^{\hat{\tau}} \wedge \tilde{\omega}^{\hat{\varphi}}. \end{aligned} \tag{9.31}$$

and use Cartan third theorem to read off the characteristic component of the Riemann tensor,

$$R^{\hat{\tau}}_{\hat{\varphi}\hat{\tau}\hat{\varphi}} = -\frac{[(\sinh(\tau)K^{\frac{1}{2}})_{,\tau} K^{-\frac{1}{2}}]_{,\tau}}{a^2 \sinh(\tau)K}. \tag{9.32}$$

We find then for the scalar curvature,

$$\begin{aligned} R &= R^{\hat{\alpha}\hat{\beta}}_{\hat{\alpha}\hat{\beta}} = 2R^{\hat{\tau}\hat{\varphi}}_{\hat{\tau}\hat{\varphi}} \\ &= -\frac{2}{a^2} \left\{ \frac{[(\sinh(\tau)K^{\frac{1}{2}})_{,\tau} K^{-\frac{1}{2}}]_{,\tau}}{\sinh(\tau)K} \right\}, \end{aligned} \tag{9.33}$$

which can be rewritten in terms of the Laplacian as follows,

$$R = -\frac{2}{a^2 K} \left\{ 1 + \frac{1}{2K} \left[-a^2 \Delta U + \frac{U_{,\varphi\varphi}}{\sinh^2 \tau} - \frac{(U_{,\tau})^2}{K} \right] \right\}. \tag{9.34}$$

For finite values of h , the condition for R to be negative on all the accessible region of S^N is then,

$$2\pi a^2 q^2 n - \frac{U_{,\varphi\varphi}}{\sinh^2 \tau} + \frac{(U_{,\tau})^2}{K} < 2K. \tag{9.35}$$

9.5. Ergodicity of the semi-ideal Coulomb plasma

Consider a one component Coulomb plasma where we switch off the mutual interactions between the particles, leaving unchanged the interaction between the particles and the neutralizing background ($U = V_N^0 + V_N^{bb}$). We will call it the “semi-ideal” system. Define,

$$\Omega(h, \tau_0) = \{q^N | \mathbf{q}_i \in \Omega_{a\tau_0} \ \forall i, h - U(q^N) \geq 0\}, \tag{9.36}$$

and call $h' = h - V_N^0 - v_1$ and

$$\begin{aligned} f(N) &= -N \ln[1 - \tanh^2(\tau_0/2)] = N \ln[1 + \sinh^2(\tau_0/2)] \\ &= N \ln\left(1 + \frac{N}{4\pi a^2 n}\right). \end{aligned} \tag{9.37}$$

We will have ($\alpha = 2\pi a^2 n e^2$)

$$r = \inf_{q^N \in \Omega(h, \tau_0)} 2K^2 = \begin{cases} 2[h' - \alpha f(N)]^2 & h' > \alpha f(N) \\ 0 & h' \leq \alpha f(N) \end{cases}, \tag{9.38}$$

Notice that for large N , at constant n , we have (see Appendix A),

$$-V_N^0/\alpha = \frac{\alpha}{e^2} \left[-2\frac{N}{4\pi a^2 n} + \ln\left(1 + \frac{N}{4\pi a^2 n}\right) + \frac{1}{2}\right] + O(1/N), \tag{9.39}$$

$$-v_1/\alpha = f(N) + N - \frac{\alpha}{e^2} + O(1/N). \tag{9.40}$$

Using the extensive property of the energy we may assume that $h = Nh_0$, where h_0 is the total energy per particle. Then for large N we will have

$$h' = Nh_0 + \alpha f(N) + \left(\frac{\alpha}{e}\right)^2 \left[\ln\left(1 + \frac{N}{4\pi a^2 n}\right) - \frac{1}{2}\right] + O(1/N) > \alpha f(N), \tag{9.41}$$

if $h_0 \geq 0$.

On the other hand for $h' > \alpha f(N)$ we have

$$\begin{aligned} l &= \sup_{q^N \in \Omega(h, \tau_0)} [\alpha K + (U_{,\tau})^2] \leq \sup_{q^N \in \Omega(h, \tau_0)} [\alpha K] + \sup_{q^N \in \Omega(h, \tau_0)} [(U_{,\tau})^2] \\ &= l_+ = \alpha h' + \alpha^2 \tanh^2(\tau_0/2), \end{aligned} \tag{9.42}$$

Condition (9.35) is always satisfied if $l < r$. Then the semi-ideal system is ergodic if,

$$h' > h'_+ = \alpha f(N) + \frac{\alpha}{4} \left[1 + \sqrt{1 + 8f(N) + 8 \tanh^2(\tau_0/2)}\right], \tag{9.43}$$

where h'_+ is the largest root of the equation $l_+ = r$. Recalling that $\tanh^2(\tau_0/2) \rightarrow 1$ at large N , one can verify that, given Eqs. (9.41), (9.43) must be satisfied at large N if $h_0 > 0$.

We conclude that the semi ideal system is certainly ergodic if the total energy is extensive and the total energy per particle is positive.

9.6. Partition function and densities at a special temperature

Working with the set of coordinates (r, φ) on the pseudosphere (the Poincaré disk representation), the particle i -particle j interaction term in the Hamiltonian can be written as [23]

$$G(d_{ij}) = -\ln \tanh(d_{ij}/2a) = -\ln \left| \frac{(z_i - z_j)/2a}{1 - (z_i \bar{z}_j/4a^2)} \right|, \tag{9.44}$$

where $z_j = r_j e^{i\varphi_j}$ and \bar{z}_j is the complex conjugate of z_j . This interaction (9.44) happens to be the Coulomb interaction in a flat disc of radius $2a$ with ideal conductor walls. Therefore, it is possible to use the techniques which have been developed [16,34] for dealing with ideal conductor walls, in the grand canonical ensemble.

The grand canonical partition function of the OCP at fugacity ζ with a fixed background density n_b , when $\Gamma = \beta e^2 = 2$, is

$$\mathcal{E}(2) = C_0 \left[1 + \sum_{N=1}^{\infty} \frac{1}{N!} \int \prod_{i=1}^N \frac{r_i dr_i d\varphi_i}{[1 - (r_i^2/4a^2)]} \prod_{i<j} \left| \frac{(z_i - z_j)/2a}{1 - (z_i \bar{z}_j/4a^2)} \right|^2 \prod_{i=1}^N \zeta(r_i) \right] \tag{9.45}$$

where for $N = 1$ the product $\prod_{i<j}$ must be replaced by 1. We have defined a position-dependent fugacity $\zeta(r) = \zeta [1 - r^2/4a^2]^{4\pi n_b a^2 - 1} e^C$ which includes the particle-background interaction (9.17) and only one factor $[1 - r^2/4a^2]^{-1}$ from the integration measure $dS = [1 - r^2/4a^2]^{-2} d\mathbf{r}$. This should prove to be convenient later. The e^C factor is

$$e^C = \exp \left[4\pi n_b a^2 \left(\ln \cosh^2 \frac{\tau_0}{2} - \sinh^2 \frac{\tau_0}{2} \ln \tanh^2 \frac{\tau_0}{2} \right) \right] \tag{9.46}$$

which is a constant term coming from the particle-background interaction term (9.17) and

$$\ln C_0 = \frac{(4\pi n_b a^2)^2}{2} \left[\ln \cosh^2 \frac{\tau_0}{2} + \sinh^2 \frac{\tau_0}{2} \left(\sinh^2 \frac{\tau_0}{2} \ln \tanh^2 \frac{\tau_0}{2} - 1 \right) \right] \tag{9.47}$$

which comes from the background-background interaction. Notice that for large domains, when $\tau_0 \rightarrow \infty$, we have

$$e^C \sim \left[\frac{e^{\tau_0+1}}{4} \right]^{4\pi n_b a^2} \tag{9.48}$$

and

$$\ln C_0 \sim - \frac{(4\pi n_b a^2)^2 e^{\tau_0}}{4} \tag{9.49}$$

Let us define a set of reduced complex coordinates $u_i = (z_i/2a)$ inside the Poincaré disk and its corresponding images $u_i^* = (2a/\bar{z}_i)$ outside the disk. By using the following Cauchy identity [53]

$$\det \left(\frac{1}{u_i - u_j^*} \right)_{(i,j) \in \{1, \dots, N\}^2} = (-1)^{N(N-1)/2} \frac{\prod_{i<j} (u_i - u_j)(u_i^* - u_j^*)}{\prod_{i,j} (u_i - u_j^*)} \tag{9.50}$$

the particle-particle interaction term together with the $[1 - (r_i^2/4a^2)]^{-1}$ other term from the integration measure can be cast into the form

$$\prod_{i<j} \left| \frac{(z_i - z_j)/2a}{1 - (z_i \bar{z}_j/4a^2)} \right|^2 \prod_{i=1}^N [1 - (r_i^2/4a^2)]^{-1} = \det \left(\frac{1}{1 - u_i \bar{u}_j} \right)_{(i,j) \in \{1, \dots, N\}^2} \tag{9.51}$$

The grand canonical partition function then is

$$\mathcal{E}(2) = \left[1 + \sum_{N=1}^{\infty} \frac{1}{N!} \int \prod_{i=1}^N d^2 \mathbf{r}_i \prod_{i=1}^N \zeta(r_i) \det \left(\frac{1}{1 - u_i \bar{u}_j} \right) \right] C_0 \tag{9.52}$$

We shall now show that this expression can be reduced to an infinite continuous determinant, by using a functional integral representation similar to the one which has been developed for the two-component Coulomb gas [54]. Let us consider the Gaussian partition function

$$Z_0 = \int \mathcal{D}\psi \mathcal{D}\bar{\psi} \exp \left[\int \bar{\psi}(\mathbf{r}) M^{-1}(z, \bar{z}') \psi(\mathbf{r}') d^2 \mathbf{r} d^2 \mathbf{r}' \right] \tag{9.53}$$

The fields ψ and $\bar{\psi}$ are anticommuting Grassmann variables. The Gaussian measure in (9.53) is chosen such that its covariance is equal to¹

$$\langle \bar{\psi}(\mathbf{r}_i) \psi(\mathbf{r}_j) \rangle = M(z_i, \bar{z}_j) = \frac{1}{1 - u_i \bar{u}_j} \tag{9.54}$$

where $\langle \dots \rangle$ denotes an average taken with the Gaussian weight of (9.53). By construction we have

$$Z_0 = \det(M^{-1}) \tag{9.55}$$

Let us now consider the following partition function

$$Z = \int \mathcal{D}\psi \mathcal{D}\bar{\psi} \exp \left[\int \bar{\psi}(\mathbf{r}) M^{-1}(z, \bar{z}') \psi(\mathbf{r}') d^2 \mathbf{r} d^2 \mathbf{r}' + \int \zeta(r) \bar{\psi}(\mathbf{r}) \psi(\mathbf{r}) d^2 \mathbf{r} \right] \tag{9.56}$$

¹ Actually the operator M should be restricted to act only on analytical functions for its inverse M^{-1} to exist.

192

R. Fantoni / Physica A 524 (2019) 177–220

which is equal to

$$Z = \det(M^{-1} + \zeta) \tag{9.57}$$

and then

$$\frac{Z}{Z_0} = \det[M(M^{-1} + \zeta)] = \det[1 + K] \tag{9.58}$$

where

$$K(\mathbf{r}, \mathbf{r}') = M(z, \bar{z}') \zeta(r') = \frac{\zeta(r')}{1 - u\bar{u}'} \tag{9.59}$$

The results which follow can also be obtained by exchanging the order of the factors M and $M^{-1} + \zeta$ in (9.58), i.e. by replacing $\zeta(r')$ by $\zeta(r)$ in (9.59), however using the definition (9.59) of K is more convenient. Expanding the ratio Z/Z_0 in powers of ζ we have

$$\frac{Z}{Z_0} = 1 + \sum_{N=1}^{\infty} \frac{1}{N!} \int \prod_{i=1}^N d^2\mathbf{r}_i \prod_{i=1}^N \zeta(r_i) \langle \bar{\psi}(\mathbf{r}_1)\psi(\mathbf{r}_1) \cdots \bar{\psi}(\mathbf{r}_N)\psi(\mathbf{r}_N) \rangle \tag{9.60}$$

Now, using Wick theorem for anticommuting variables [54], we find that

$$\langle \bar{\psi}(\mathbf{r}_1)\psi(\mathbf{r}_1) \cdots \bar{\psi}(\mathbf{r}_N)\psi(\mathbf{r}_N) \rangle = \det M(z_i, \bar{z}_j) = \det \left(\frac{1}{1 - u_i\bar{u}_j} \right) \tag{9.61}$$

Comparing Eqs. (9.60) and (9.52) with the help of Eq. (9.61) we conclude that

$$\Xi(2) = C_0 \frac{Z}{Z_0} = C_0 \det(1 + K) \tag{9.62}$$

The problem of computing the grand canonical partition function has been reduced to finding the eigenvalues of the operator K . The eigenvalue problem for K reads

$$\int \zeta e^c \frac{\left(1 - \frac{r'^2}{4a^2}\right)^{4\pi n_b a^2 - 1}}{1 - \frac{z\bar{z}'}{4a^2}} \Phi(\mathbf{r}') r' dr' d\varphi' = \lambda \Phi(\mathbf{r}) \tag{9.63}$$

For $\lambda \neq 0$ we notice from Eq. (9.63) that $\Phi(\mathbf{r}) = \Phi(z)$ is an analytical function of z . Because of the circular symmetry it is natural to try $\Phi(z) = \Phi_\ell(z) = z^\ell = r^\ell e^{i\ell\varphi}$ with ℓ a positive integer. Expanding

$$\frac{1}{1 - \frac{z\bar{z}'}{4a^2}} = \sum_{n=0}^{\infty} \left(\frac{z\bar{z}'}{4a^2}\right)^n \tag{9.64}$$

and replacing $\Phi_\ell(z) = z^\ell$ in Eq. (9.63) one can show that Φ_ℓ is actually an eigenfunction of K with eigenvalue

$$\lambda_\ell = 4\pi a^2 \zeta e^c B_{t_0}(\ell + 1, 4\pi n_b a^2) \tag{9.65}$$

with $t_0 = r_0^2/4a^2 = \tanh^2(\tau_0/2)$ and

$$B_{t_0}(\ell + 1, 4\pi n_b a^2) = \int_0^{t_0} (1 - t)^{4\pi n_b a^2 - 1} t^\ell dt \tag{9.66}$$

the incomplete beta function. So we finally arrive to the result for the grand potential

$$\beta\Omega = -\ln \Xi(2) = -\ln C_0 - \sum_{\ell=0}^{\infty} \ln(1 + 4\pi a^2 \zeta e^c B_{t_0}(\ell + 1, 4\pi n_b a^2)) \tag{9.67}$$

with e^c and $\ln C_0$ given by Eqs. (9.46) and (9.47). This result is valid for any disk domain of radius $a\tau_0$. A more explicit expression of the grand potential for large domains $\tau_0 \rightarrow \infty$ can also be obtained [24].

As usual one can compute the density by doing a functional derivative of the grand potential with respect to the position-dependent fugacity:

$$n^{(1)}(\mathbf{r}) = \left(1 - \frac{r^2}{4a^2}\right)^2 \zeta(r) \frac{\delta \ln \Xi(2)}{\delta \zeta(r)} \tag{9.68}$$

The factor $[1 - (r^2/4a^2)]^2$ is due to the curvature [23], so that $n^{(1)}(\mathbf{r}) dS$ is the average number of particles in the surface element $dS = [1 - (r^2/4a^2)]^{-2} d\mathbf{r}$. Using a Dirac-like notation, one can formally write

$$\ln \Xi(2) = \text{tr} \ln(1 + K) + \ln C_0 = \int \langle \mathbf{r} | \ln(1 + \zeta(r)M) | \mathbf{r} \rangle d\mathbf{r} + \ln C_0 \tag{9.69}$$

Then, doing the functional derivative (9.68), one obtains

$$n^{(1)}(\mathbf{r}) = \left(1 - \frac{r^2}{4a^2}\right)^2 \zeta(r) \langle \mathbf{r} | (1+K)^{-1} M | \mathbf{r} \rangle = 4\pi a \left(1 - \frac{r^2}{4a^2}\right)^2 \zeta(r) \tilde{G}(\mathbf{r}, \mathbf{r}) \tag{9.70}$$

where we have defined $\tilde{G}(\mathbf{r}, \mathbf{r}')$ by² $\tilde{G} = (1+K)^{-1} M / 4\pi a$. More explicitly, \tilde{G} is the solution of $(1+K)\tilde{G} = M / 4\pi a$, that is

$$\tilde{G}(\mathbf{r}, \mathbf{r}') + \zeta e^c \int \tilde{G}(\mathbf{r}'', \mathbf{r}') \frac{\left(1 - \frac{r''^2}{4a^2}\right)^{4\pi n_b a^2 - 1}}{1 - \frac{z\bar{z}''}{4a^2}} d\mathbf{r}'' = \frac{1}{4\pi a \left[1 - \frac{z\bar{z}'}{4a^2}\right]} \tag{9.71}$$

and the density is given by

$$n^{(1)}(\mathbf{r}) = 4\pi a \zeta e^c \left(1 - \frac{r^2}{4a^2}\right)^{4\pi n_b a^2 + 1} \tilde{G}(\mathbf{r}, \mathbf{r}) \tag{9.72}$$

From the integral equation (9.71) one can see that $\tilde{G}(\mathbf{r}, \mathbf{r}')$ is an analytical function of z . Trying a solution of the form

$$\tilde{G}(\mathbf{r}, \mathbf{r}') = \sum_{\ell=0}^{\infty} a_{\ell}(\mathbf{r}') z^{\ell} \tag{9.73}$$

into Eq. (9.71) yields

$$\tilde{G}(\mathbf{r}, \mathbf{r}') = \frac{1}{4\pi a} \sum_{\ell=0}^{\infty} \left(\frac{z\bar{z}'}{4a^2}\right)^{\ell} \frac{1}{1 + 4\pi a^2 \zeta e^c B_{\ell_0}(\ell + 1, 4\pi n_b a^2)} \tag{9.74}$$

Then the density is given by

$$n^{(1)}(r) = \zeta e^c \left(1 - \frac{r^2}{4a^2}\right)^{4\pi n_b a^2 + 1} \sum_{\ell=0}^{\infty} \left(\frac{r^2}{4a^2}\right)^{\ell} \frac{1}{1 + 4\pi a^2 \zeta e^c B_{\ell_0}(\ell + 1, 4\pi n_b a^2)} \tag{9.75}$$

After some calculation (see Appendix B), it can be shown that, in the limit $a \rightarrow \infty$, the result for the flat disk in the canonical ensemble [55]

$$\frac{n^{(1)}(r)}{n_b} = \exp(-\pi n_b r^2) \sum_{\ell=0}^{N_b-1} \frac{(\pi n_b r^2)^{\ell}}{\gamma(\ell + 1, N_b)} \tag{9.76}$$

is recovered, up to a correction due to the non-equivalence of ensembles in finite systems. In (9.76), γ is the incomplete gamma function

$$\gamma(\ell + 1, x) = \int_0^x t^{\ell} e^{-t} dt \tag{9.77}$$

In that flat-disk case, in the thermodynamic limit (half-space), $n^{(1)}(r_0) = n_{\text{contact}} \rightarrow n_b \ln 2$.

In a flat space, the neighborhood of the boundary of a large domain has a volume which is a negligible fraction of the whole volume. This is why, for the statistical mechanics of ordinary fluids, usually there is a thermodynamic limit: when the volume becomes infinite, quantities such as the free energy per unit volume or the pressure have a unique limit, independent of the domain shape and of the boundary conditions. However, even in a flat space, the one-component plasma is special. For the OCP, it is possible to define several non-equivalent pressures, some of which, for instance the kinetic pressure [24], obviously are surface-dependent even in the infinite-system limit.

Even for ordinary fluids, statistical mechanics on a pseudosphere is expected to have special features, which are essentially related to the property that, for a large domain, the area of the neighborhood of the boundary is of the same order of magnitude as the whole area. Although some bulk properties, such as correlation functions far away from the boundary, will exist, extensive quantities such as the free energy or the grand potential are strongly dependent on the boundary neighborhood and surface effects. For instance, in the large-domain limit, no unique limit is expected for the free energy per unit area F/\mathcal{A} or the pressure $-(\partial F/\partial \mathcal{A})_{\beta, N}$.

In the present section, we have studied the 2D OCP on a pseudosphere, for which surface effects are expected to be important for both reasons: because we are dealing with a one-component plasma and because the space is a pseudosphere. Therefore, although the correlation functions far away from the boundary have unique thermodynamic limits [23], many other properties are expected to depend on the domain shape and on the boundary conditions. This is why we have considered a special well-defined geometry: the domain is a disk bounded by a plain hard wall, and we have studied the corresponding large-disk limit. Our results have been derived only for that geometry.

² The factor $4\pi a$ is there just to keep the same notations as in Ref. [23].

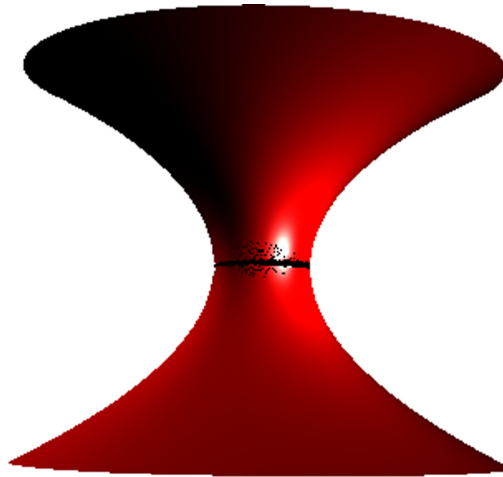


Fig. 1. The Riemannian surface S of Eq. (10.2).

10. The Flamm paraboloid

The metric tensor of Flamm's paraboloid in the coordinates $\mathbf{q} = (r, \varphi)$ is now,

$$\mathbf{g} = \begin{pmatrix} (1 - 2M/r)^{-1} & 0 \\ 0 & r^2 \end{pmatrix}, \tag{10.1}$$

where M is a constant. This is an embeddable surface in the three-dimensional Euclidean space with cylindrical coordinates (r, φ, Z) with $ds^2 = dZ^2 + dr^2 + r^2 d\varphi^2$, whose equation is

$$Z(r) = \pm 2\sqrt{2M(r - 2M)}. \tag{10.2}$$

This surface is illustrated in Fig. 1. It has a hole of radius $2M$. As the hole shrinks to a point (limit $M \rightarrow 0$) the surface becomes flat. We will from now on call the $r = 2M$ region of the surface its "horizon". The Schwarzschild geometry in general relativity is a vacuum solution to the Einstein field equation which is spherically symmetric and in a two dimensional world its spatial part is a Flamm paraboloid S . In general relativity, M (in appropriate units) is the mass of the source of the gravitational field.

The "Schwarzschild wormhole" provides a path from the upper "universe" S_+ ($Z > 0$) to the lower one S_- ($Z < 0$). These are both multiply connected surfaces. We will study the OCP on a single universe, on the whole surface, and on a single universe with the "horizon" (the region $r = 2M$) grounded.

Since the curvature of the surface is not a constant but varies from point to point, the plasma will not be uniform even in the thermodynamic limit.

The system of coordinates (r, φ) with the metric (10.1) has the disadvantage that it requires two charts to cover the whole surface S . It can be more convenient to use the variable

$$u = \frac{Z}{4M} = \pm \sqrt{\frac{r}{2M} - 1} \tag{10.3}$$

instead of r . Replacing r as a function of Z using Eq. (10.2) gives the following metric when using the system of coordinates $\mathbf{q} = (u, \varphi)$,

$$\mathbf{g} = \begin{pmatrix} (4M)^2(1 + u^2) & 0 \\ 0 & 4M^2(1 + u^2)^2 \end{pmatrix}, \tag{10.4}$$

The region $u > 0$ corresponds to S_+ and the region $u < 0$ to S_- .

Let us consider that the OCP is confined in a disk defined as

$$\Omega_R^+ = \{\mathbf{q} = (r, \varphi) \in S_+ | 0 \leq \varphi \leq 2\pi, 2M \leq r \leq R\}. \tag{10.5}$$

The area of this disk is given by

$$\mathcal{A}_R = \int_{\Omega_R} dS = \pi \left[\sqrt{R(R - 2M)}(3M + R) + 6M^2 \ln \left(\frac{\sqrt{R} + \sqrt{R - 2M}}{\sqrt{2M}} \right) \right], \tag{10.6}$$

where $dS = \sqrt{g} dr d\varphi$ and $g = \det[g_{\mu\nu}]$. The perimeter is $C_R = 2\pi R$.

The Riemann tensor characteristic component is

$$R^r_{\varphi r \varphi} = -\frac{M}{r}. \tag{10.7}$$

The scalar curvature is then given by the following indexes contractions

$$\mathcal{R} = R^\mu_{\mu} = R^{\mu\nu}_{\mu\nu} = 2R^r_{\varphi r \varphi} = 2g^{\varphi\varphi}R^r_{\varphi r \varphi} = -\frac{2M}{r^3}, \tag{10.8}$$

and the (intrinsic) Gaussian curvature is $K = \mathcal{R}/2 = -M/r^3$. The (extrinsic) mean curvature of the manifold turns out to be $H = -\sqrt{M/8r^3}$.

The Euler characteristic (1.5) of the disk Ω_R^+ turns out to be $\chi = 0$, in agreement with the Gauss–Bonnet theorem $\chi = 2 - 2h - b$ where $h = 0$ is the number of handles and $b = 2$ the number of boundaries.

We can also consider the case where the system is confined in a “double” disk

$$\Omega_R = \Omega_R^+ \cup \Omega_R^-, \tag{10.9}$$

with $\Omega_R^- = \{\mathbf{q} = (r, \varphi) \in \mathcal{S}_- | 0 \leq \varphi \leq 2\pi, 2M \leq r \leq R\}$, the disk image of Ω_R^+ on the lower universe \mathcal{S}_- portion of \mathcal{S} . The Euler characteristic of Ω_R is also $\chi = 0$.

The fact that the Euler characteristic is zero implies that the asymptotic expansion in the thermodynamic limit of the free energy does not exhibit the logarithmic corrections predicted by Ref. [15].

The Laplacian for a function f is

$$\begin{aligned} \Delta f &= \frac{1}{\sqrt{g}} \frac{\partial}{\partial q^\mu} \left(\sqrt{g} g^{\mu\nu} \frac{\partial}{\partial q^\nu} \right) f \\ &= \left[\left(1 - \frac{2M}{r} \right) \frac{\partial^2}{\partial r^2} + \frac{1}{r^2} \frac{\partial^2}{\partial \varphi^2} + \left(\frac{1}{r} - \frac{M}{r^2} \right) \frac{\partial}{\partial r} \right] f, \end{aligned} \tag{10.10}$$

where $\mathbf{q} \equiv (r, \varphi)$. In Appendix C, we show how, finding the Green function of the Laplacian, naturally leads to consider the system of coordinates (x, φ) , with

$$x = (\sqrt{u^2 + 1} + u)^2. \tag{10.11}$$

The range for the variable x is $]0, +\infty[$. The lower paraboloid \mathcal{S}_- corresponds to the region $0 < x < 1$ and the upper one \mathcal{S}_+ to the region $x > 1$. A point in the upper paraboloid with coordinate (x, φ) has a mirror image by reflection ($u \rightarrow -u$) in the lower paraboloid, with coordinates $(1/x, \varphi)$, since if

$$x = (\sqrt{u^2 + 1} + u)^2 \tag{10.12}$$

then

$$\frac{1}{x} = (\sqrt{u^2 + 1} - u)^2. \tag{10.13}$$

In the upper paraboloid \mathcal{S}_+ , the new coordinate x can be expressed in terms of the original one, r , as

$$x = \frac{(\sqrt{r} + \sqrt{r - 2M})^2}{2M}. \tag{10.14}$$

Using this system of coordinates, the metric takes the form of a flat metric multiplied by a conformal factor

$$\mathbf{g} = \begin{pmatrix} (M/2)^2(1 + 1/x)^4 & 0 \\ 0 & (M/2)^2(1 + 1/x)^4 x^2 \end{pmatrix}, \tag{10.15}$$

The Laplacian also takes a simple form

$$\Delta f = \frac{4}{M^2 \left(1 + \frac{1}{x}\right)^4} \Delta_{\text{flat}} f \tag{10.16}$$

where

$$\Delta_{\text{flat}} f = \frac{\partial^2 f}{\partial x^2} + \frac{1}{x} \frac{\partial f}{\partial x} + \frac{1}{x^2} \frac{\partial^2 f}{\partial \varphi^2} \tag{10.17}$$

is the Laplacian of the flat Euclidean space \mathbb{R}^2 . The determinant of the metric is now given by $g = [M^2 x (1 + x^{-1})^4 / 4]^2$.

With this system of coordinates (x, φ) , the area of a disk Ω_R^+ of radius R , in the original system (r, φ) , is given by

$$\mathcal{A}_R = \frac{\pi M^2}{4} p(x_m) \tag{10.18}$$

196

R. Fantoni / Physica A 524 (2019) 177–220

with

$$p(x) = x^2 + 8x - \frac{8}{x} - \frac{1}{x^2} + 12 \ln x \tag{10.19}$$

and $x_m = (\sqrt{R} + \sqrt{R - 2M})^2 / (2M)$.

The Coulomb potential $G(x, \varphi; x_0, \varphi_0)$ created at (x, φ) by a unit charge at (x_0, φ_0) is given by the Green function of the Laplacian

$$\Delta G(x, \varphi; x_0, \varphi_0) = -2\pi \delta^{(2)}(x, \varphi; x_0, \varphi_0) \tag{10.20}$$

with appropriate boundary conditions. The Dirac distribution on S is given by

$$\delta^{(2)}(x, \varphi; x_0, \varphi_0) = \frac{4}{M^2 x (1 + x^{-1})^4} \delta(x - x_0) \delta(\varphi - \varphi_0) \tag{10.21}$$

Notice that using the system of coordinates (x, φ) the Laplacian Green function equation takes the simple form

$$\Delta_{\text{nat}} G(x, \varphi; x_0, \varphi_0) = -2\pi \frac{1}{x} \delta(x - x_0) \delta(\varphi - \varphi_0) \tag{10.22}$$

which is formally the same Laplacian Green function equation for flat space.

We shall consider three different situations: when the particles can be in the whole surface S , or when the particles are confined to the upper paraboloid universe S_+ , confined by a hard wall or by a grounded perfect conductor.

The geodesic distance on the Flamm paraboloid is determined in [Appendix D](#).

10.1. Coulomb potential in the whole surface (ws)

To complement the Laplacian Green function equation (10.20), we impose the usual boundary condition that the electric field $-\nabla G$ vanishes at infinity ($x \rightarrow \infty$ or $x \rightarrow 0$). Also, we require the usual interchange symmetry $G(x, \varphi; x_0, \varphi_0) = G(x_0, \varphi_0; x, \varphi)$ to be satisfied. Additionally, due to the symmetry between each universe S_+ and S_- , we require that the Green function satisfies the symmetry relation

$$G^{ws}(x, \varphi; x_0, \varphi_0) = G^{ws}(1/x, \varphi; 1/x_0, \varphi_0) \tag{10.23}$$

The Laplacian Green function equation (10.20) can be solved, as usual, by using the decomposition as a Fourier series, as shown in [Appendix C](#). Since Eq. (10.20) reduces to the flat Laplacian Green function equation (10.22), the solution is the standard one

$$G(x, \varphi; x_0, \varphi_0) = \sum_{n=1}^{\infty} \frac{1}{n} \left(\frac{x_{<}}{x_{>}} \right)^n \cos [n(\varphi - \varphi_0)] + g_0(x, x_0) \tag{10.24}$$

where $x_{>} = \max(x, x_0)$ and $x_{<} = \min(x, x_0)$. The Fourier coefficient for $n = 0$, has the form

$$g_0(x, x_0) = \begin{cases} a_0^+ \ln x + b_0^+, & x > x_0 \\ a_0^- \ln x + b_0^-, & x < x_0. \end{cases} \tag{10.25}$$

The coefficients a_0^\pm, b_0^\pm are determined by the boundary conditions that g_0 should be continuous at $x = x_0$, its derivative discontinuous $\partial_x g_0|_{x=x_0^+} - \partial_x g_0|_{x=x_0^-} = -1/x_0$, and the boundary condition at infinity $\nabla g_0|_{x \rightarrow \infty} = 0$ and $\nabla g_0|_{x \rightarrow 0} = 0$. Unfortunately, the boundary condition at infinity is trivially satisfied for g_0 , therefore g_0 cannot be determined only with this condition. In flat space, this is the reason why the Coulomb potential can have an arbitrary additive constant added to it. However, in our present case, we have the additional symmetry relation (10.23) which should be satisfied. This fixes the Coulomb potential up to an additive constant b_0 . We find

$$g_0(x, x_0) = -\frac{1}{2} \ln \frac{x_{>}}{x_{<}} + b_0, \tag{10.26}$$

and summing explicitly the Fourier series (10.24), we obtain

$$G^{ws}(x, \varphi; x_0, \varphi_0) = -\ln \frac{|z - z_0|}{\sqrt{|zz_0|}} + b_0, \tag{10.27}$$

where we defined $z = xe^{i\varphi}$ and $z_0 = x_0 e^{i\varphi_0}$. Notice that this potential does not reduce exactly to the flat one when $M = 0$. This is due to the fact that the whole surface S in the limit $M \rightarrow 0$ is not exactly a flat plane \mathbb{R}^2 , but rather it is two flat planes connected by a hole at the origin, this hole modifies the Coulomb potential.

10.2. Coulomb potential in the half surface (hs) confined by hard walls

We consider now the case when the particles are restricted to live in the half surface S_+ , $x > 1$, and they are confined by a hard wall located at the “horizon” $x = 1$. The region $x < 1$ (S_-) is empty and has the same dielectric constant as the upper region occupied by the particles. Since there are no image charges, the Coulomb potential is the same G^{ws} as above. However, we would like to consider here a new model with a slightly different interaction potential between the particles. Since we are dealing only with half surface, we can relax the symmetry condition (10.23). Instead, we would like to consider a model where the interaction potential reduces to the flat Coulomb potential in the limit $M \rightarrow 0$. The solution of the Laplacian Green function equation is given in Fourier series by Eq. (10.24). The zeroth order Fourier component g_0 can be determined by the requirement that, in the limit $M \rightarrow 0$, the solution reduces to the flat Coulomb potential

$$G^{flat}(\mathbf{r}, \mathbf{r}') = -\ln \frac{|\mathbf{r} - \mathbf{r}'|}{L} \tag{10.28}$$

where L is an arbitrary constant length. Recalling that $x \sim 2r/M$, when $M \rightarrow 0$, we find

$$g_0(x, x_0) = -\ln x_> - \ln \frac{M}{2L} \tag{10.29}$$

and

$$G^{hs}(x, \varphi; x_0, \varphi_0) = -\ln |z - z_0| - \ln \frac{M}{2L}. \tag{10.30}$$

10.3. Coulomb potential on half surface with a grounded horizon (gh)

Let us consider now that the particles are confined to S_+ by a grounded perfect conductor at $x = 1$ which imposes Dirichlet boundary condition to the electric potential. The Coulomb potential can easily (see Appendix C) be found from the Coulomb potential G^{ws} (10.27) using the method of images

$$G^{gh}(x, \varphi; x_0, \varphi_0) = -\ln \frac{|z - z_0|}{\sqrt{|zz_0|}} + \ln \frac{|z - \bar{z}_0^{-1}|}{\sqrt{|z\bar{z}_0^{-1}|}} = -\ln \left| \frac{z - z_0}{1 - z\bar{z}_0} \right| \tag{10.31}$$

where the bar over a complex number indicates its complex conjugate. We will call this the grounded horizon Green function. Notice how its shape is the same of the Coulomb potential on the pseudosphere [24] or in a flat disk confined by perfect conductor boundaries [16].

This potential can also be found using the Fourier decomposition. Since it will be useful in the following, we note that the zeroth order Fourier component of G^{gh} is

$$g_0(x, x_0) = \ln x_<. \tag{10.32}$$

10.4. The background

The Coulomb potential generated by the background, with a constant surface charge density ρ_b satisfies the Poisson equation, for $r > 2M$,

$$\Delta v_b = -2\pi \rho_b, \tag{10.33}$$

Assuming that the system occupies an area \mathcal{A}_R , the background density can be written as $\rho_b = -qN_b/\mathcal{A}_R = -qn_b$, where we have defined here $n_b = N_b/\mathcal{A}_R$ the number density associated to the background. For a neutral system $N_b = N$. The Coulomb potential of the background can be obtained by solving Poisson equation with the appropriate boundary conditions for each case. Also, it can be obtained from the Green function computed in the previous section

$$v_b(x, \varphi) = \int G(x, \varphi; x', \varphi') \rho_b dS' \tag{10.34}$$

This integral can be performed easily by using the Fourier series decomposition (10.24) of the Green function G . Recalling that $dS = \frac{1}{4}M^2x(1+x^{-1})^4 dx d\varphi$, after the angular integration is done, only the zeroth order term in the Fourier series survives

$$v_b(x, \varphi) = \frac{\pi \rho_b M^2}{2} \int_1^{x_m} g_0(x, x') x' \left(1 + \frac{1}{x'}\right)^4 dx'. \tag{10.35}$$

The previous expression is for the half surface case and the grounded horizon case. For the whole surface case, the lower limit of integration should be replaced by $1/x_m$, or, equivalently, the integral multiplied by a factor two.

Using the explicit expressions for g_0 , (10.26), (10.29), and (10.32) for each case, we find, for the whole surface,

$$v_b^{ws}(x, \varphi) = -\frac{\pi \rho_b M^2}{8} [h(x) - h(x_m) + 2p(x_m) \ln x_m - 4b_0p(x_m)] \tag{10.36}$$

198

R. Fantoni / Physica A 524 (2019) 177–220

where $p(x)$ was defined in Eq. (10.19), and

$$h(x) = x^2 + 16x + \frac{16}{x} + \frac{1}{x^2} + 12(\ln x)^2 - 34. \tag{10.37}$$

Notice the following properties satisfied by the functions p and h

$$p(x) = -p(1/x), \quad h(x) = h(1/x) \tag{10.38}$$

and

$$p(x) = xh'(x)/2, \quad p'(x) = 2x \left(1 + \frac{1}{x}\right)^4 \tag{10.39}$$

where the prime stands for the derivative.

The background potential for the half surface case, with the pair potential $-\ln(|z - z'|M/2L)$ is

$$v_b^{\text{hs}}(x, \varphi) = -\frac{\pi \rho_b M^2}{8} \left[h(x) - h(x_m) + 2p(x_m) \ln \frac{x_m M}{2L} \right]. \tag{10.40}$$

Also, the background potential in the half surface case, but with the pair potential $-\ln(|z - z'|/\sqrt{|zz'|}) + b_0$ is

$$v_b^{\text{hs}}(x, \varphi) = -\frac{\pi \rho_b M^2}{8} \left[h(x) - \frac{h(x_m)}{2} + p(x_m) \left(\ln \frac{x_m}{x} - 2b_0 \right) \right]. \tag{10.41}$$

Finally, for the grounded horizon case,

$$v_b^{\text{gh}}(x, \varphi) = -\frac{\pi \rho_b M^2}{8} [h(x) - 2p(x_m) \ln x]. \tag{10.42}$$

10.5. Partition function and densities at a special temperature

We will now show how at the special value of the coupling constant $\Gamma = \beta e^2 = 2$ the partition function and n -body correlation functions can be calculated exactly.

10.5.1. The 2D OCP on half surface with potential $-\ln|z - z'| - \ln M/(2L)$

For this case, we work in the canonical ensemble with N particles and the background neutralizes the charges: $N_b = N$, and $n = N/\mathcal{A}_R = n_b$. The potential energy of the system takes the explicit form

$$\begin{aligned} V^{\text{hs}} = & -e^2 \sum_{1 \leq i < j \leq N} \ln |z_i - z_j| + \frac{e^2}{2} \alpha \sum_{i=1}^N h(x_i) + \frac{e^2}{2} N \ln \frac{M}{2L} - \frac{e^2}{4} N \alpha h(x_m) \\ & + \frac{e^2}{2} N^2 \ln x_m - \frac{e^2}{4} \alpha^2 \int_1^{x_m} h(x) p'(x) dx \end{aligned} \tag{10.43}$$

where we have used the fact that $dS = \pi M^2 x(1 + x^{-1})^4 dx/2 = \pi M^2 p'(x) dx/4$, and we have defined

$$\alpha = \frac{\pi n_b M^2}{4}. \tag{10.44}$$

Integrating by parts the last term of (10.43) and using (10.39), we find

$$\begin{aligned} V^{\text{hs}} = & -e^2 \sum_{1 \leq i < j \leq N} \ln |z_i - z_j| + \frac{e^2}{2} \alpha \sum_{i=1}^N h(x_i) + \frac{e^2}{2} N \ln \frac{M}{2L} + \frac{e^2}{2} N^2 \ln x_m \\ & + \frac{e^2}{2} \alpha^2 \int_1^{x_m} \frac{[p(x)]^2}{x} dx - \frac{e^2}{2} N \alpha h(x_m). \end{aligned} \tag{10.45}$$

When $\beta e^2 = 2$, the canonical partition function can be written as

$$Z^{\text{hs}} = \frac{1}{\Lambda^{2N}} Z_0^{\text{hs}} \exp(-\beta F_0^{\text{hs}}) \tag{10.46}$$

with

$$-\beta F_0^{\text{hs}} = -N \ln \frac{M}{2L} - N^2 \ln x_m - \alpha^2 \int_1^{x_m} \frac{[p(x)]^2}{x} dx + N \alpha h(x_m) \tag{10.47}$$

and

$$Z_0^{\text{hs}}(2) = \frac{1}{N!} \int \prod_{i=1}^N dS_i e^{-\alpha h(x_i)} \prod_{1 \leq i < j \leq N} |z_i - z_j|^2. \tag{10.48}$$

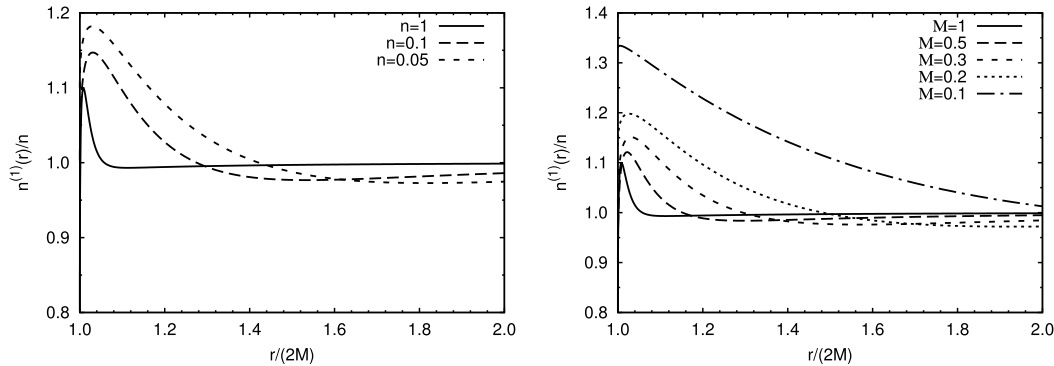


Fig. 2. The one body density $n^{hs}(r)/n$ of Eq. (10.56), for the 2D OCP on just one universe of the surface S , obtained with $N = 300$. On the left at fixed $M = 1$ and on the right at fixed $n = 1$.

where $\Lambda = \sqrt{2\pi\beta\hbar^2/m}$ is the de Broglie thermal wavelength. $Z_0(2)$ can be computed using the original method for the OCP in flat space [12,13], which was originally introduced in the context of random matrices [10,56], and which was presented in Section 6. By expanding the Vandermonde determinant $\prod_{i<j}(z_i - z_j)$ and performing the integration over the angles, the partition function can be written as

$$Z_0^{hs}(2) = \prod_{k=0}^{N-1} \mathcal{B}_N(k), \tag{10.49}$$

where

$$\mathcal{B}_N(k) = \int x^{2k} e^{-\alpha h(x)} dS \tag{10.50}$$

$$= \frac{\alpha}{n_b} \int_1^{x_m} x^{2k} e^{-\alpha h(x)} p'(x) dx. \tag{10.51}$$

In the flat limit $M \rightarrow 0$, we have $x \sim 2r/M$, with r the radial coordinate of flat space \mathbb{R}^2 , and $h(x) \sim p(x) \sim x^2$. Then, \mathcal{B}_N reduces to

$$\mathcal{B}_N(k) \sim \frac{1}{n_b \alpha^k} \gamma(k+1, N) \tag{10.52}$$

where $\gamma(k+1, N) = \int_0^N t^k e^{-t} dt$ is the incomplete Gamma function. Replacing into (10.49), we recover the partition function (6.14) for the OCP in a flat disk of radius R [13]

$$\ln Z^{hs}(2) = \frac{N}{2} \ln \frac{\pi L^2}{n_b \Lambda^4} + \frac{3N^2}{4} - \frac{N^2}{2} \ln N + \sum_{k=1}^N \ln \gamma(k, N). \tag{10.53}$$

Following [12], we can also find the k -body distribution functions

$$n^{(k)hs}(\mathbf{q}_1, \dots, \mathbf{q}_k) = \det[\mathcal{K}_N^{hs}(\mathbf{q}_i, \mathbf{q}_j)]_{(i,j) \in \{1, \dots, k\}^2}, \tag{10.54}$$

where $\mathbf{q}_i = (x_i, \varphi_i)$ is the position of the particle i , and

$$\mathcal{K}_N^{hs}(\mathbf{q}_i, \mathbf{q}_j) = \sum_{k=0}^{N-1} \frac{z_i^k z_j^k e^{-\alpha(h(|z_i|) + h(|z_j|))/2}}{\mathcal{B}_N(k)}. \tag{10.55}$$

where $z_k = x_k e^{i\varphi_k}$. In particular, the one-body density is given by

$$n^{hs}(x) = \mathcal{K}_N(\mathbf{q}, \mathbf{q}) = \sum_{k=0}^{N-1} \frac{x^{2k} e^{-\alpha h(x)}}{\mathcal{B}_N(k)}. \tag{10.56}$$

The density shows a peak in the neighborhoods of each boundary, tends to a finite value at the boundary and to the background density far from it, in the bulk. This is shown in Fig. 2

10.5.2. Internal screening

Internal screening means that at equilibrium, a particle of the system is surrounded by a polarization cloud of opposite charge. It is usually expressed in terms of the simplest of the multipolar sum rules [2]: the charge or electroneutrality sum rule, which for the OCP reduces to the relation

$$\int n^{(2)\text{hs}}(\mathbf{q}_1, \mathbf{q}_2) dS_2 = (N - 1)n^{(1)\text{hs}}(\mathbf{q}_1), \quad (10.57)$$

This relation is trivially satisfied because of the particular structure (10.54) of the correlation function expressed as a determinant of the kernel $\mathcal{K}_N^{\text{hs}}$, and the fact that $\mathcal{K}_N^{\text{hs}}$ is a projector

$$\int dS_3 \mathcal{K}_N^{\text{hs}}(\mathbf{q}_1, \mathbf{q}_3) \mathcal{K}_N^{\text{hs}}(\mathbf{q}_3, \mathbf{q}_2) = \mathcal{K}_N^{\text{hs}}(\mathbf{q}_1, \mathbf{q}_2). \quad (10.58)$$

Indeed,

$$\begin{aligned} \int n^{(2)\text{hs}}(\mathbf{q}_1, \mathbf{q}_2) dS_2 &= \int [\mathcal{K}_N^{\text{hs}}(\mathbf{q}_1, \mathbf{q}_1) \mathcal{K}_N^{\text{hs}}(\mathbf{q}_2, \mathbf{q}_2) - \mathcal{K}_N^{\text{hs}}(\mathbf{q}_1, \mathbf{q}_2) \mathcal{K}_N^{\text{hs}}(\mathbf{q}_2, \mathbf{q}_1)] dS_2 \\ &= \int n^{(1)\text{hs}}(\mathbf{q}_1) n^{(1)\text{hs}}(\mathbf{q}_2) dS_2 - \mathcal{K}_N^{\text{hs}}(\mathbf{q}_1, \mathbf{q}_1) \\ &= (N - 1)n^{(1)\text{hs}}(\mathbf{q}_1). \end{aligned} \quad (10.59)$$

10.5.3. External screening

External screening means that, at equilibrium, an external charge introduced into the system is surrounded by a polarization cloud of opposite charge. When an external infinitesimal point charge Q is added to the system, it induces a charge density $\rho_Q(\mathbf{q})$. External screening means that

$$\int \rho_Q(\mathbf{q}) dS = -Q. \quad (10.60)$$

Using linear response theory we can calculate ρ_Q to first order in Q as follows. Imagine that the charge Q is at \mathbf{q} . Its interaction energy with the system is $\hat{H}_{int} = Q\hat{\phi}(\mathbf{q})$ where $\hat{\phi}(\mathbf{q})$ is the microscopic electric potential created at \mathbf{q} by the system. Then, the induced charge density at \mathbf{q}' is

$$\rho_Q(\mathbf{q}') = -\beta \langle \hat{\rho}(\mathbf{q}') \hat{H}_{int} \rangle_T = -\beta Q \langle \hat{\rho}(\mathbf{q}') \hat{\phi}(\mathbf{q}) \rangle_T, \quad (10.61)$$

where $\hat{\rho}(\mathbf{q})$ is the microscopic charge density at \mathbf{q} , $\langle AB \rangle_T = \langle AB \rangle - \langle A \rangle \langle B \rangle$, and $\langle \dots \rangle$ is the thermal average. Assuming external screening (10.60) is satisfied, one obtains the Carnie–Chan sum rule [2]

$$\beta \int \langle \hat{\rho}(\mathbf{q}') \hat{\phi}(\mathbf{q}) \rangle_T dS' = 1. \quad (10.62)$$

Now in a uniform system starting from this sum rule one can derive the second moment Stillinger–Lovett sum rule [2]. This is not possible here because our system is not homogeneous since the curvature is not constant throughout the surface but varies from point to point. If we apply the Laplacian respect to \mathbf{q} to this expression and use Poisson equation

$$\Delta_{\mathbf{q}} \langle \hat{\rho}(\mathbf{q}') \hat{\phi}(\mathbf{q}) \rangle_T = -2\pi \langle \hat{\rho}(\mathbf{q}') \hat{\rho}(\mathbf{q}) \rangle_T, \quad (10.63)$$

we find

$$\int \rho_e^{(2)}(\mathbf{q}', \mathbf{q}) dS' = 0, \quad (10.64)$$

where $\rho_e^{(2)}(\mathbf{q}', \mathbf{q}) = \langle \hat{\rho}(\mathbf{q}') \hat{\rho}(\mathbf{q}) \rangle_T$ is the excess pair charge density function. Eq. (10.64) is another way of writing the charge sum rule Eq. (10.57) in the thermodynamic limit.

10.5.4. The 2D OCP on the whole surface with potential $-\ln(|z - z'|/\sqrt{|zz'|})$

Until now we studied the 2D OCP on just one universe. Let us find the thermodynamic properties of the 2D OCP on the whole surface \mathcal{S} . In this case, we also work in the canonical ensemble with a global neutral system. The position $z_k = x_k e^{i\varphi_k}$ of each particle can be in the range $1/x_m < x_k < x_m$. The total number particles N is now expressed in terms of the function p as $N = 2\alpha p(x_m)$. Similar calculations to the ones of the previous section lead to the following expression for the partition function, when $\beta e^2 = 2$,

$$Z^{\text{ws}} = \frac{1}{A^{2N}} Z_0^{\text{ws}} \exp(-\beta F_0^{\text{ws}}) \quad (10.65)$$

now, with

$$-\beta F_0^{\text{ws}} = Nb_0 + N\alpha h(x_m) - \frac{N^2}{2} \ln x_m - \alpha^2 \int_{1/x_m}^{x_m} \frac{[p(x)]^2}{x} dx \quad (10.66)$$

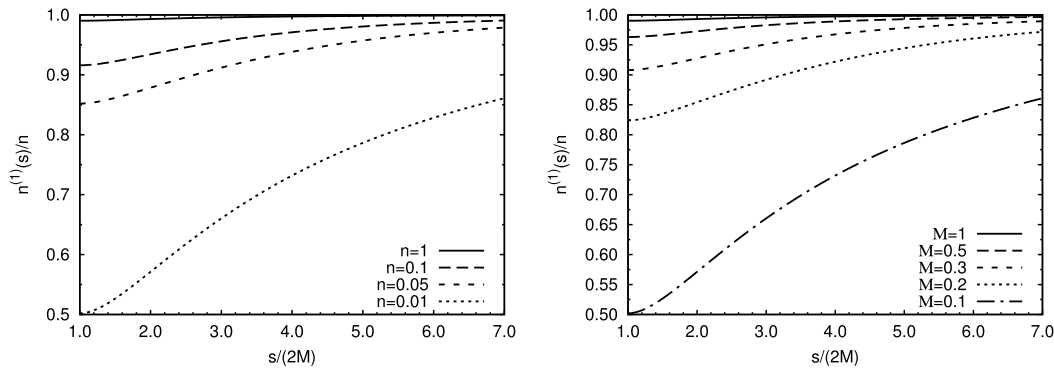


Fig. 3. The one body density $n^{(1)}(s)/n$, where $s = 2Mx$, for the 2D OCP on the whole manifold, obtained using Eq. (10.70) with $N = 300$. On the left at fixed $M = 1$ and on the right at fixed $n = 1$.

and

$$Z_0^{ws}(2) = \frac{1}{N!} \int \prod_{i=1}^N dS_i e^{-\alpha h(x_i)} x_i^{-N+1} \prod_{1 \leq i < j \leq N} |z_i - z_j|^2. \tag{10.67}$$

Expanding the Vandermonde determinant and performing the angular integrals we find

$$Z_0^{ws}(2) = \prod_{k=0}^{N-1} \tilde{\mathcal{B}}_N(k) \tag{10.68}$$

with

$$\tilde{\mathcal{B}}_N(k) = \int x^{2k-N+1} e^{-\alpha h(x)} dS \tag{10.69}$$

$$= \frac{\alpha}{n} \int_{1/x_m}^{x_m} x^{2k-N+1} e^{-\alpha h(x)} p'(x) dx. \tag{10.70}$$

The function $\tilde{\mathcal{B}}_N(k)$ is very similar to \mathcal{B}_N , and its asymptotic behavior for large values of N can be obtained by Laplace method as explained in Ref. [26].

The one body density for the 2D OCP on the whole manifold is drawn in Fig. 3. From the figure we can see how the peaks in the neighborhood of the horizon are now disappeared. The density approaches the horizon with zero slope.

10.5.5. The 2D OCP on the half surface with potential $-\ln(|z - z'|/\sqrt{|zz'|})$

In this case, we have $N = \alpha p(x_m)$. In this case the partition function at $\beta e^2 = 2$ is

$$Z^{\overline{hs}} = Z_0^{\overline{hs}} e^{-\beta F_0^{\overline{hs}}} \tag{10.71}$$

with

$$-\beta F_0^{\overline{hs}} = \alpha^2 p(x_m) h(x_m) - p(x_m)^2 \ln x_m + \int_1^{x_m} \frac{[p(x)]^2}{x} dx - Nb_0 \tag{10.72}$$

and

$$Z_0^{\overline{hs}}(2) = \prod_{k=0}^{N-1} \hat{\mathcal{B}}_N(k) \tag{10.73}$$

with

$$\hat{\mathcal{B}}_N(k) = \frac{\alpha}{n_b} \int_1^{x_m} x^{2k+1} e^{-\alpha h(x)} dx \tag{10.74}$$

In Fig. 4 we compare the one body density obtained in this case with the one of the previous section.

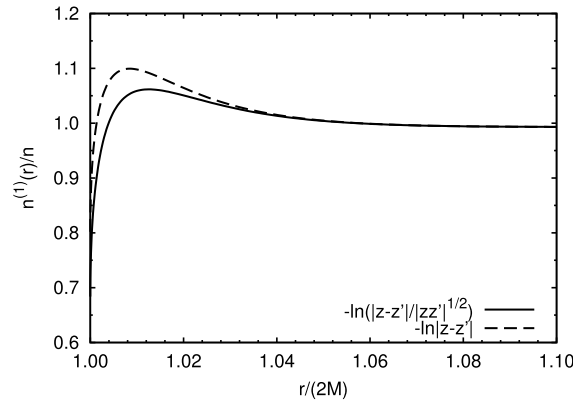


Fig. 4. The one body density $n^{(1)}(r)/n$, for the 2D OCP on just one universe of the surface S , obtained using both the pair potential $-\ln|z-z'|$ and $-\ln(|z-z'|/\sqrt{|zz'|})$ at fixed $M = n = 1$.

10.5.6. The grounded horizon case

In order to find the partition function for the system in the half space, with a metallic grounded boundary at $x = 1$, when the charges interact through the pair potential of Eq. (10.31) it is convenient to work in the grand canonical ensemble instead, and use the techniques developed in Refs. [16,57]. We consider a system with a fixed background density ρ_b . The fugacity $\zeta = e^{\beta\mu}/\Lambda^2$, where μ is the chemical potential, controls the average number of particles $\langle N \rangle$, and in general the system is non-neutral $\langle N \rangle \neq N_b$, where $N_b = \alpha p(x_m)$. The excess charge is expected to be found near the boundaries at $x = 1$ and $x = x_m$, while in the bulk the system is expected to be locally neutral. In order to avoid the collapse of a particle into the metallic boundary, due to its attraction to the image charges, we confine the particles to be in a disk domain $\tilde{\Omega}_R$, where $x \in [1+w, x_m]$. We introduced a small gap w between the metallic boundary and the domain containing the particles, the geodesic width of this gap is $W = \sqrt{\alpha p'(1)/(2\pi n_b)} w$. On the other hand, for simplicity, we consider that the fixed background extends up to the metallic boundary.

In the potential energy of the system (4.1) we should add the self energy of each particle, that is due to the fact that each particle polarizes the metallic boundary, creating an induced surface charge density. This self energy is $\frac{e^2}{2} \ln[|x^2 - 1|/M/2L]$, where the constant $\ln(M/2L)$ has been added to recover, in the limit $M \rightarrow 0$, the self energy of a charged particle near a plane grounded wall in flat space.

The grand partition function, when $\beta e^2 = 2$, is

$$\mathcal{E}(2) = e^{-\beta F_0^{\text{gh}}} \left[1 + \sum_{N=1}^{\infty} \frac{\zeta^N}{N!} \int \prod_{i=1}^N dS_i \prod_{i<j} \left| \frac{z_i - z_j}{1 - z_i \bar{z}_j} \right|^2 \prod_{i=1}^N (|z_i|^2 - 1)^{-1} \prod_{i=1}^N e^{-\alpha \{h(x_i) - 2N_b \ln x_i\}} \right] \tag{10.75}$$

where for $N = 1$ the product $\prod_{i<j}$ must be replaced by 1. The domain of integration for each particle is $\tilde{\Omega}_R$. We have defined a rescaled fugacity $\zeta = 2L\zeta/M$ and

$$-\beta F_0^{\text{gh}} = \alpha N_b h(x_m) - N_b^2 \ln x_m - \alpha^2 \int_1^{x_m} \frac{[p(x)]^2}{x} dx \tag{10.76}$$

which is very similar to F_0^{hs} , except that here $N_b = \alpha p(x_m)$ is not equal to N the number of particles.

Let us define a set of reduced complex coordinates $u_i = z_i$ and its corresponding images $u_i^* = 1/\bar{z}_i$. By using Cauchy identity (9.50),

$$\det \left(\frac{1}{u_i - u_j^*} \right)_{(i,j) \in \{1, \dots, N\}^2} = (-1)^{N(N-1)/2} \frac{\prod_{i<j} (u_i - u_j)(u_i^* - u_j^*)}{\prod_{i,j} (u_i - u_j^*)} \tag{10.77}$$

the particle–particle interaction and self energy terms can be cast into the form

$$\prod_{i<j} \left| \frac{z_i - z_j}{1 - z_i \bar{z}_j} \right|^2 \prod_{i=1}^N (|z_i|^2 - 1)^{-1} = (-1)^N \det \left(\frac{1}{1 - z_i \bar{z}_j} \right)_{(i,j) \in \{1, \dots, N\}^2} \tag{10.78}$$

The grand canonical partition function is then

$$\mathcal{E}(2) = e^{-\beta F_0^{\text{gh}}} \left[1 + \sum_{N=1}^{\infty} \frac{1}{N!} \int \prod_{i=1}^N dS_i \prod_{i=1}^N [-\zeta(x_i)] \det \left(\frac{1}{1 - z_i \bar{z}_j} \right) \right], \tag{10.79}$$

with $\zeta(x) = \zeta e^{-\alpha[h(x) - 2N_b \ln x]}$. We now notice that we already found an analogous expression (9.52) when studying the pseudosphere. We therefore proceed as we did for that case. For ease of reading we repeat here the relevant steps reducing this expression to a Fredholm determinant [57]. Then let us consider the Gaussian partition function

$$Z_0 = \int \mathcal{D}\psi \mathcal{D}\bar{\psi} \exp \left[\int \bar{\psi}(\mathbf{q}) A^{-1}(z, \bar{z}') \psi(\mathbf{q}') dS dS' \right] \tag{10.80}$$

The fields ψ and $\bar{\psi}$ are anticommuting Grassmann variables. The Gaussian measure in (10.80) is chosen such that its covariance is equal to

$$\langle \bar{\psi}(\mathbf{q}_i) \psi(\mathbf{q}_j) \rangle = A(z_i, \bar{z}_j) = \frac{1}{1 - z_i \bar{z}_j} \tag{10.81}$$

where $\langle \dots \rangle$ denotes an average taken with the Gaussian weight of (10.80). By construction we have

$$Z_0 = \det(A^{-1}) \tag{10.82}$$

Let us now consider the following partition function

$$Z = \int \mathcal{D}\psi \mathcal{D}\bar{\psi} \exp \left[\int \bar{\psi}(\mathbf{q}) A^{-1}(z, \bar{z}') \psi(\mathbf{q}') dS dS' - \int \zeta(x) \bar{\psi}(\mathbf{q}) \psi(\mathbf{q}) dS \right] \tag{10.83}$$

which is equal to

$$Z = \det(A^{-1} - \zeta) \tag{10.84}$$

and then

$$\frac{Z}{Z_0} = \det[A(A^{-1} - \zeta)] = \det(1 + K) \tag{10.85}$$

where K is an integral operator (with integration measure dS) with kernel

$$K(\mathbf{q}, \mathbf{q}') = -\zeta(x') A(z, \bar{z}') = -\frac{\zeta(x')}{1 - z \bar{z}'}. \tag{10.86}$$

Expanding the ratio Z/Z_0 in powers of ζ we have

$$\frac{Z}{Z_0} = 1 + \sum_{N=1}^{\infty} \frac{1}{N!} \int \prod_{i=1}^N dS_i (-1)^N \prod_{i=1}^N \zeta(x_i) \langle \bar{\psi}(\mathbf{q}_1) \psi(\mathbf{q}_1) \dots \bar{\psi}(\mathbf{q}_N) \psi(\mathbf{q}_N) \rangle \tag{10.87}$$

Now, using Wick theorem for anticommuting variables [54], we find that

$$\langle \bar{\psi}(\mathbf{q}_1) \psi(\mathbf{q}_1) \dots \bar{\psi}(\mathbf{q}_N) \psi(\mathbf{q}_N) \rangle = \det A(z_i, \bar{z}_j) = \det \left(\frac{1}{1 - z_i \bar{z}_j} \right) \tag{10.88}$$

Comparing Eqs. (10.87) and (10.79) with the help of Eq. (10.88) we conclude that

$$\mathcal{E}(2) = e^{-\beta F_0^{\text{gh}}} \frac{Z(2)}{Z_0(2)} = e^{-\beta F_0^{\text{gh}}} \det(1 + K) \tag{10.89}$$

The problem of computing the grand canonical partition function has been reduced to finding the eigenvalues λ of the operator K . The eigenvalue problem for K reads

$$-\int_{\bar{\Omega}_R} \frac{\zeta(x')}{1 - z \bar{z}'} \Phi(x', \varphi') dS' = \lambda \Phi(x, \varphi) \tag{10.90}$$

For $\lambda \neq 0$ we notice from Eq. (10.90) that $\Phi(x, \varphi) = \Phi(z)$ is an analytical function of $z = x e^{i\varphi}$ in the region $|z| > 1$. Because of the circular symmetry, it is natural to try $\Phi(z) = \Phi_\ell(z) = z^{-\ell}$ with $\ell \geq 1$ a positive integer. Expanding

$$\frac{1}{1 - z \bar{z}'} = -\sum_{n=1}^{\infty} (z \bar{z}')^{-n} \tag{10.91}$$

and replacing $\Phi_\ell(z) = z^{-\ell}$ in Eq. (10.90) we show that Φ_ℓ is indeed an eigenfunction of K with eigenvalue

$$\lambda_\ell = \zeta B_{N_b}^{\text{gh}}(N_b - \ell) \tag{10.92}$$

204

R. Fantoni / Physica A 524 (2019) 177–220

where

$$\mathcal{B}_{N_b}^{\text{gh}}(k) = \frac{\alpha}{n_b} \int_{1+w}^{x_m} x^{2k} e^{-\alpha h(x)} p'(x) dx \tag{10.93}$$

which is very similar to \mathcal{B}_N defined in Eq. (10.51), except for the small gap w in the lower limit of integration. So, we arrive to the result for the grand potential

$$\beta\Omega = -\ln \mathcal{E}(2) = \beta F_0 - \sum_{\ell=1}^{\infty} \ln \left[1 + \zeta \mathcal{B}_{N_b}^{\text{gh}}(N_b - \ell) \right]. \tag{10.94}$$

As usual one can compute the density by doing a functional derivative of the grand potential with respect to a position-dependent fugacity $\zeta(\mathbf{q})$

$$n^{\text{gh}}(\mathbf{q}) = \zeta(\mathbf{q}) \frac{\delta \ln \mathcal{E}(2)}{\delta \zeta(\mathbf{q})}. \tag{10.95}$$

For the present case of a curved space, we shall understand the functional derivative with the rule $\delta \zeta(\mathbf{q}') / \delta \zeta(\mathbf{q}) = \delta^{(2)}(\mathbf{q}; \mathbf{q}')$ where $\delta^{(2)}(\mathbf{q}; \mathbf{q}') = \delta(x - x') \delta(\varphi - \varphi') / \sqrt{g}$ is the Dirac distribution on the curved surface.

Using a Dirac-like notation, one can formally write

$$\ln \mathcal{E}(2) = \text{tr} \ln(1 + K) - \beta F_0^{\text{gh}} = \int \langle \mathbf{q} | \ln(1 - \zeta(\mathbf{q})A) | \mathbf{q} \rangle dS - \beta F_0^{\text{gh}} \tag{10.96}$$

Then, doing the functional derivative (10.95), one obtains

$$n^{\text{gh}}(\mathbf{q}) = \zeta \langle \mathbf{q} | (1 + K)^{-1} (-A) | \mathbf{q} \rangle = \zeta \tilde{G}(\mathbf{q}, \mathbf{q}) \tag{10.97}$$

where we have defined $\tilde{G}(\mathbf{q}, \mathbf{q}')$ by $\tilde{G} = (1 + K)^{-1} (-A)$. More explicitly, G is the solution of $(1 + K)\tilde{G} = -A$, that is

$$\tilde{G}(\mathbf{q}, \mathbf{q}') - \int_{\tilde{\Omega}_R} \zeta(x'') \frac{\tilde{G}(\mathbf{q}'', \mathbf{q}')}{1 - z\bar{z}''} dS'' = -\frac{1}{1 - z\bar{z}'}. \tag{10.98}$$

From this integral equation, one can see that $\tilde{G}(\mathbf{q}, \mathbf{q}')$ is an analytical function of z in the region $|z| > 1$. Then, we look for a solution in the form of a Laurent series

$$\tilde{G}(\mathbf{q}, \mathbf{q}') = \sum_{\ell=1}^{\infty} a_{\ell}(\mathbf{r}') z^{-\ell} \tag{10.99}$$

into Eq. (10.98) yields

$$\tilde{G}(\mathbf{q}, \mathbf{q}') = \sum_{\ell=1}^{\infty} \frac{(z\bar{z}')^{-\ell}}{1 + \lambda_{\ell}}. \tag{10.100}$$

Recalling that $\lambda_{\ell} = \zeta \mathcal{B}_N^{\text{gh}}(N_b - \ell)$, the density is given by

$$n^{\text{gh}}(x) = \zeta \sum_{k=-\infty}^{N_b-1} \frac{x^{2k} e^{-\alpha h(x)}}{1 + \zeta \mathcal{B}_N^{\text{gh}}(k)} \tag{10.101}$$

The density reaches the background density far from the boundaries. In this case, the fugacity and the background density control the density profile close to the metallic boundary (horizon). In the bulk and close to the outer hard wall boundary, the density profile is independent of the fugacity. In Fig. 5 we show the density for various choices of the parameters M , n , and ζ . The figure shows how the density tends to the background density far from the horizon. The value of the density at the horizon depends on n and ζ .

Part III

The two-component plasma

A two-component plasma is a neutral mixture of two species of $2N$ point charges of opposite charge $\pm e$.

11. The plane

We represent the Cartesian components of the position $\mathbf{q} = (x, y)$ of a particle by the complex number $z = x + iy$. For a system of N positive charges with complex coordinates u_i and N negative charges with complex coordinates v_j the Boltzmann factor at $\Gamma = \beta e^2 = 2$ is,

$$e^{2 \sum_{i < j} \left[\ln \frac{|u_i - u_j|}{L} + \ln \frac{|v_i - v_j|}{L} \right] - 2 \sum_{i,j} \ln \frac{|u_i - v_j|}{L}} = L^{2N} \left| \frac{\prod_{i < j} (u_i - u_j)(v_i - v_j)}{\prod_{i,j} (u_i - v_j)} \right|^2$$

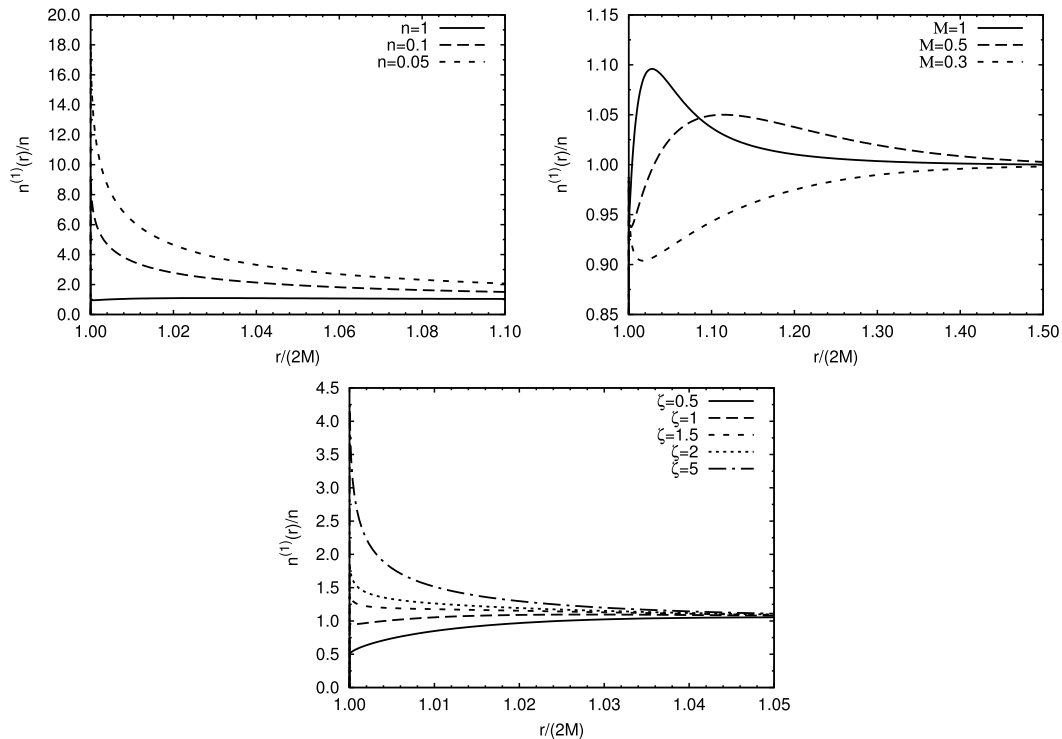


Fig. 5. The one body density $n^{(1)}(r)/n$ obtained truncating the sum of Eq. (10.101) after the first 300 terms and choosing $(\sqrt{R} + \sqrt{R - 2M})^2 / 2M = 10$. On top on the left at fixed $M = \zeta = 1$ and on the right at fixed $n = \zeta = 1$. On the bottom at fixed $M = n = 1$.

$$= L^{2N} \left| \det \left(\frac{1}{u_i - v_j} \right)_{(i,j) \in \{1, \dots, N\}^2} \right|^2, \tag{11.1}$$

where the last equality stems from the Cauchy identity (9.50). Following Ref. [32], it is convenient to start with a discretized model for which there are no divergencies. Two interwoven sublattices U and V are introduced. The positive (negative) particles sit on the sublattice $U(V)$. Each lattice site is occupied no or one particle. A possible external potential is described by position dependent fugacities $\zeta_+(u_i)$ and $\zeta_-(v_i)$. The grand partition function reorganized as a sum including only neutral systems is

$$\mathcal{E}(2) = 1 + \sum_{N=1}^{\infty} L^{2N} \prod_{i=1}^N \zeta_+(u_i) \zeta_-(v_i) \sum_{\substack{u_1, \dots, u_N \in U \\ v_1, \dots, v_N \in V}} \left| \det \left(\frac{1}{u_i - v_j} \right)_{(i,j) \in \{1, \dots, N\}^2} \right|^2, \tag{11.2}$$

where the sums are defined with the prescription that configurations which differ only by a permutation of identical particles are counted only once. This grand partition function is the determinant of an anti-Hermitian matrix \mathbf{M} explicitly shown in Ref. [33].

When passing to the continuum limit in the element \mathbf{M}_{ij} one should replace u_i or v_i by z and u_j or v_j by z' , i.e. $i \rightarrow z$ and $j \rightarrow z'$. Each lattice site is characterized by its complex coordinate z and an isospinor which is $\begin{pmatrix} 1 \\ 0 \end{pmatrix}$ if the site belongs to the positive sublattice U and $\begin{pmatrix} 0 \\ 1 \end{pmatrix}$ if it belongs to the negative sublattice V . We then define a matrix \mathcal{M} by

$$\langle z | \mathcal{M} | z' \rangle = \frac{\sigma_x + i\sigma_y}{2} \frac{L}{z - z'} + \frac{\sigma_x - i\sigma_y}{2} \frac{L}{\bar{z} - \bar{z}'}, \tag{11.3}$$

where the σ are the 2×2 Pauli matrices operating in the isospinor space.

The matrix \mathcal{M} can be expressed in terms of a simple Dirac operator $\mathcal{J} = \sigma_x \partial_x + \sigma_y \partial_y$ as follows,

$$\langle z | \mathcal{M} | z' \rangle = L(\sigma_x \partial_x + \sigma_y \partial_y) \ln |z - z'|, \tag{11.4}$$

and the grand partition function can be rewritten as

$$\begin{aligned} \mathcal{E}(2) &= \det \left\{ \mathbf{1} \delta^{(2)}(z; z') + \left[\zeta_+(z) \frac{\mathbf{1} + \sigma_z}{2} + \zeta_-(z) \frac{\mathbf{1} - \sigma_z}{2} \right] \langle z | \mathcal{M} | z' \rangle \right\} \\ &= \det[\mathbf{1} + \mathcal{K}^{-1}], \end{aligned} \tag{11.5}$$

where $\mathbf{1}$ is the 2×2 identity matrix and

$$\boldsymbol{\lambda} = \zeta_+ \frac{\mathbf{1} + \sigma_z}{2} + \zeta_- \frac{\mathbf{1} - \sigma_z}{2}, \tag{11.6}$$

$$\mathcal{K}^{-1} = \boldsymbol{\lambda} \mathcal{M}. \tag{11.7}$$

Then, since $\Delta \ln |z| = 2\pi \delta(r) \delta(\varphi) / r = 2\pi \delta(z)$, where $(r = |z|, \varphi = \arg z)$ are the polar coordinates in the plane, the inverse operator is $\mathcal{K} = \mathcal{O} \mathbf{m}^{-1}$, where

$$\mathbf{m}(z) = m_+(z) \frac{\mathbf{1} + \sigma_z}{2} + m_-(z) \frac{\mathbf{1} - \sigma_z}{2}, \tag{11.8}$$

$$\mathcal{O} = \sigma_x \partial_x + \sigma_y \partial_y = \mathcal{J}. \tag{11.9}$$

Here $m_{\pm}(z) = 2\pi L \zeta_{\pm}(z) / S$ are rescaled position dependent fugacities and S is the area per lattice site which appears when the discrete sums are replaced by integrals.

We then find

$$\ln \mathcal{E}(2) = \text{tr} \{ \ln [\mathbf{1} + \mathcal{K}^{-1}] \},$$

which expresses the well known equivalence between the 2D OCP at $\Gamma = 2$ and a free Fermi field [58].

The one-body densities and n -body truncated densities [2] can be obtained in the usual way by taking functional derivatives of the logarithm of the grand partition function with respect to the fugacities ζ_{\pm} . Marking the sign of the particle charge at z_i by an index $p_i = \pm$, and defining the matrix

$$R_{p_1 p_2}(z_1, z_2) = \langle z_1 p_1 | \mathcal{K}^{-1} (\mathbf{1} + \mathcal{K}^{-1})^{-1} | z_2 p_2 \rangle, \tag{11.10}$$

it can then be shown [32,33] that they are given by

$$\rho_{p_1}^{(1)}(z_1) = R_{p_1 p_1}(z_1, z_1), \tag{11.11}$$

$$\rho_{p_1 p_2}^{(2)T}(z_1, z_2) = -R_{p_1 p_2}(z_1, z_2) R_{p_2 p_1}(z_2, z_1), \tag{11.12}$$

$$\rho_{p_1 p_2 \dots p_n}^{(n)T}(z_1, z_2, \dots, z_n) = (-)^{n+1} \sum_{(i_1, i_2, \dots, i_n)} R_{p_{i_1} p_{i_2}}(z_{i_1}, z_{i_2}) \dots R_{p_{i_n} p_{i_1}}(z_{i_n}, z_{i_1}), \tag{11.13}$$

where the summation runs over all cycles (i_1, i_2, \dots, i_n) built with $\{1, 2, \dots, n\}$.

11.1. Symmetries of Green's function R

Since $\mathbf{m}^\dagger = \mathbf{m}$ and $\mathcal{O}^\dagger = -\mathcal{O}$ we find

$$\overline{R_{p_1 p_2}(z_1, z_2)} = \langle z_2 p_2 | \mathbf{m}(z) (\mathbf{m}(z) - \mathcal{O})^{-1} | z_1 p_1 \rangle. \tag{11.14}$$

Expanding in \mathcal{O} and comparing with the definition $R_{p_1 p_2}(z_1, z_2) = \langle z_1 p_1 | \mathbf{m}(z) (\mathbf{m}(z) + \mathcal{O})^{-1} | z_2 p_2 \rangle$ we find

$$\overline{R_{pp}(z_1, z_2)} = R_{pp}(z_2, z_1), \tag{11.15}$$

$$\overline{R_{p-p}(z_1, z_2)} = -R_{-pp}(z_2, z_1). \tag{11.16}$$

From which also follows that $R_{pp}(z_1, z_1)$ has to be real. If $\zeta_+ = \zeta_-$ then we additionally must have

$$R_{pp}(z_1, z_2) = R_{-p-p}(z_1, z_2). \tag{11.17}$$

11.2. Two-body truncated correlation functions and perfect screening sum rule

For the two-body truncated correlation functions of Eq. (11.12) we then find

$$\rho_{++}^{(2)T}(z_1, z_2) = -|R_{++}(z_1, z_2)|^2, \tag{11.18}$$

$$\rho_{+-}^{(2)T}(z_1, z_2) = |R_{+-}(z_1, z_2)|^2. \tag{11.19}$$

Notice that the total correlation function for the like particles $h_{++}(z_1, z_2) = \rho_{++}^{(2)T}(z_1, z_2) / \rho_+^{(1)}(z_1)\rho_+^{(1)}(z_2)$ goes to -1 when the particles coincide $z_1 \rightarrow z_2$ as follows from the structure of Eqs. (11.11) and (11.12). Moreover the truncated densities of any order has to decay to zero as two groups of particles are infinitely separated. In particular $|R_{++}(z_1, z_2)| = |R_{++}(r_1, r_2, \varphi_2 - \varphi_1)|$ has to decay to zero as $|\mathbf{q}_1 - \mathbf{q}_2| \rightarrow \infty$.

The perfect screening sum rule has to be satisfied for the symmetric mixture

$$\int [\rho_{+-}^{(2)T}(z_1, z_2) - \rho_{++}^{(2)T}(z_1, z_2)]\sqrt{g_1}dr_1d\varphi_1 = \rho_{\pm}(z_2), \tag{11.20}$$

where g_1 is g calculated on particle 1.

11.3. Determination of Green's function R

The Green function matrix \mathbf{R} is the solution of a system of four coupled partial differential equations, namely

$$(\mathbf{1} + \mathcal{K}^{-1})\mathcal{K}\mathbf{R}(z_1, z_2) = (\mathbf{1} + \mathcal{K})\mathbf{R}(z_1, z_2) = \mathbf{1}\delta^{(2)}(z_1; z_2) \tag{11.21}$$

where $\delta^{(2)}(z_1; z_2) = (\sqrt{g})^{-1}\delta(r - r_0)\delta(\varphi - \varphi_0)$, with $\sqrt{g} = r$ is the Dirac delta function on the plane which we will call $\delta(z_1 - z_2)$ the flat Dirac delta and $\mathbf{1}$ is the 2×2 identity matrix. These coupled equations can be rewritten as follows

$$[\mathcal{O} + \mathbf{m}(z_1)]\mathbf{R}(z_1, z_2) = \mathbf{m}(z_1)\delta^{(2)}(z_1; z_2).$$

If instead of \mathbf{R} one uses $\mathbf{R} = \mathbf{G}\mathbf{m}$, \mathbf{G} satisfies the equation

$$[\mathcal{O} + \mathbf{m}(z_1)]\mathbf{G}(z_1, z_2) = \mathbf{1}\delta^{(2)}(z_1; z_2). \tag{11.22}$$

By combining the components of this equation one obtains decoupled equations for G_{++} and G_{--} as follows

$$\{m_+(z_1) + A^\dagger[m_-(z_1)]^{-1}A\} G_{++}(z_1, z_2) = \delta^{(2)}(r_1, \varphi_1; r_2, \varphi_2), \tag{11.23}$$

$$\{m_-(z_1) + A[m_+(z_1)]^{-1}A^\dagger\} G_{--}(z_1, z_2) = \delta^{(2)}(r_1, \varphi_1; r_2, \varphi_2), \tag{11.24}$$

where $A = \partial_x + i\partial_y$, while

$$G_{-+}(z_1, z_2) = -[m_-(z_1)]^{-1}AG_{++}(z_1, z_2), \tag{11.25}$$

$$G_{+-}(z_1, z_2) = +[m_+(z_1)]^{-1}A^\dagger G_{--}(z_1, z_2), \tag{11.26}$$

Then Eq. (14.6) can be rewritten in Cartesian coordinates as

$$\left[m_+m_- - \frac{1}{r_1}\partial_{r_1}(r_1\partial_{r_1}) - \frac{1}{r_1^2}\partial_{\varphi_1}^2 \right] G_{++}(z_1, z_2) = \frac{m_-}{r_1}\delta(r_1 - r_2)\delta(\varphi_1 - \varphi_2). \tag{11.27}$$

which, when $m_+(z) = m_-(z) = m$, has the following solution [32,33]

$$G_{++}(z_1, z_2) = \frac{m}{2\pi}K_0(m|\mathbf{q}_1 - \mathbf{q}_2|), \tag{11.28}$$

$$G_{-+}(z_1, z_2) = \frac{m}{2\pi}\frac{(x_1 - x_2) + i(y_1 - y_2)}{|\mathbf{q}_1 - \mathbf{q}_2|}K_1(m|\mathbf{q}_1 - \mathbf{q}_2|), \tag{11.29}$$

where K_0 and K_1 are modified Bessel functions. These functions decay at large distances on a characteristic length scale m^{-1} . The n -body truncated densities (11.13) are well defined quantities for the point particle system. The two-body truncated densities, for example, have the simple forms

$$\rho_{++}^{(2)T}(r) = -\left(\frac{m^2}{2\pi}\right)^2 K_0^2(mr), \tag{11.30}$$

$$\rho_{+-}^{(2)T}(r) = -\left(\frac{m^2}{2\pi}\right)^2 K_1^2(mr). \tag{11.31}$$

The one-body densities, however, as given by Eq. (11.11), are infinite since $K_0(mr)$ diverges logarithmically as $r \rightarrow 0$. This divergence can be suppressed by a short distance cutoff R . We replace the point particles by small hard discs of diameter R and use a regularized form of Eq. (11.11),

$$\rho_{\pm} = \frac{m^2}{2\pi}K_0(mR) \sim \frac{m^2}{2\pi}\left[\ln\frac{2}{mR} - \gamma\right], \tag{11.32}$$

where $\gamma = 0.5772$ is Euler's constant. Keeping the point charge expression for the correlation functions for separations larger than R the perfect screening rule (11.20) is satisfied.

Integrating $\rho_+ + \rho_- = m\partial(\beta p)/\partial m$, from Eq. (11.32) one obtains for the pressure p ,

$$\beta p = \frac{1}{2}(\rho_+ + \rho_-) + \frac{m^2}{4\pi}. \tag{11.33}$$

The same result can be obtained by using the regularized form of Eq. (11.5). In the limit $mR \rightarrow 0$ one finds the expected result for an ideal gas of collapsed neutral pairs.

12. The sphere

We consider the stereographic projection [39] of the sphere of radius a on the plane tangent to its south pole. The coordinates of the point $\mathbf{p} = (x, y)$ stereographic projection of a point $\mathbf{q} = (\theta, \varphi)$ of the sphere from the north pole is given in terms of the complex coordinate $z = x + iy$ by $z = 2ae^{i\varphi} \cotan(\theta/2)$. This projection is a conformal transformation. The conformal metric in the new coordinates (x, y) is then

$$\mathbf{g} = \begin{pmatrix} e^\omega & 0 \\ 0 & e^\omega \end{pmatrix}, \tag{12.1}$$

with the conformal factor given by

$$e^\omega = \sin^2 \frac{\theta}{2} = \frac{1}{1 + (|z|/2a)^2}. \tag{12.2}$$

The length r_{ij} (8.3) of the chord joining two particles i and j has a simple relation with its projection $|z_i - z_j|$,

$$r_{ij} = e^{\omega_i/2} |z_i - z_j| e^{\omega_j/2} = \sin \frac{\theta_i}{2} |z_i - z_j| \sin \frac{\theta_j}{2}. \tag{12.3}$$

We can then follow the same steps as in Section 11 with $z - z'$ replaced by $e^{\omega/2}(z - z')e^{\omega'/2}$. In particular the matrix \mathcal{M} will now become,

$$\langle z | \mathcal{M} | z' \rangle = \frac{\sigma_x + i\sigma_y}{2} \frac{L}{e^{\omega/2}(z - z')e^{\omega'/2}} + \frac{\sigma_x - i\sigma_y}{2} \frac{L}{e^{\omega/2}(\bar{z} - \bar{z}')e^{\omega'/2}}, \tag{12.4}$$

In the inverse operator \mathcal{K} we now have

$$\mathcal{O} = e^{-3\omega/2} \not\partial e^{\omega/2} = \not\mathcal{D}, \tag{12.5}$$

since the Dirac delta function on the sphere $\delta^{(2)}(z; z') = e^{-2\omega} \delta(z - z')$ where δ is the flat Dirac delta function.

Thus, the Dirac operator $\not\partial$ in the plane has to be replaced by $\not\mathcal{D}$ defined by (12.5). It turns out that $\not\mathcal{D}$ is the Dirac operator on the sphere. The Dirac operators in curved spaces have been investigated by many authors.

12.1. Thermodynamic properties

If we define $m = 2\pi L\zeta/S$ in terms of the fugacity ζ and the area per lattice site S (a local property of the surface), we have

$$\ln \mathcal{E}(2) = \text{tr} \ln[1 + m\not\mathcal{D}^{-1}]. \tag{12.6}$$

The eigenvalues of $\not\mathcal{D}$ are [59] $\pm in/a$ where n is any positive integer, with multiplicity $2n$. Thus the pressure is given by

$$\beta p = \frac{\ln \mathcal{E}(2)}{4\pi a^2} = \frac{1}{8\pi a^2} \text{tr} \ln[1 - m^2 \not\mathcal{D}^{-2}] = \frac{1}{2\pi a^2} \sum_{n=1}^{\infty} n \ln \left[1 + \frac{m^2 a^2}{n^2} \right], \tag{12.7}$$

and the densities are

$$\rho_+ + \rho_- = m \frac{\partial}{\partial m} (\beta p) = \frac{m^2}{4\pi a^2} \text{tr} \frac{1}{m^2 - \not\mathcal{D}^2} = \frac{m^2}{\pi} \sum_{n=1}^{\infty} \frac{n}{m^2 a^2 + n^2}. \tag{12.8}$$

These pressure and densities are divergent quantities, unless they are regularized by a short distance cutoff, as in the planar case. In the limit $a \rightarrow \infty$, setting $k = n/a$, one retrieves the non-regularized planar results.

12.2. Determination of Green's function G

Eq. (11.22) now becomes

$$(\not\mathcal{D} + \mathbf{m})\mathbf{G}(\mathbf{p}, \mathbf{p}') = e^{-2\omega} \mathbf{1}\delta(\mathbf{p} - \mathbf{p}'), \tag{12.9}$$

which in terms of

$$\tilde{\mathbf{G}}(\mathbf{p}, \mathbf{p}') = e^{\omega/2} \mathbf{G}(\mathbf{p}, \mathbf{p}') e^{\omega'/2}, \tag{12.10}$$

can be rewritten as

$$(\not\partial + \mathbf{m}e^\omega)\tilde{\mathbf{G}}(\mathbf{p}, \mathbf{p}') = \mathbf{1}\delta(\mathbf{p} - \mathbf{p}'). \tag{12.11}$$

This equation has a remarkably simple interpretation. $\tilde{\mathbf{G}}(\mathbf{p}, \mathbf{p}')$ is the Green function of the planar problem with a position dependent fugacity $me^\omega = m/[1 + (r/2a)^2]$. This equation correctly reduces to the flat analogue (11.22) in the $a \rightarrow \infty$ limit. Moreover, it admits solutions in term of some hypergeometric functions [39].

13. The pseudosphere

The pseudosphere has already been discussed in Section 9.

We then observe that the curved system can be mapped onto a flat system in the Poincaré disk. The Boltzmann factor gain a multiplicative contribution $[1 - (r_i/2a)^2]$ for each particle and in the computation of the partition function the area element $dS_i = [1 - (r_i/2a)^2]^{-2} d\mathbf{r}_i$. Thus, the original system with a constant fugacity ζ maps onto a flat system with a position dependent fugacity $\zeta [1 - (r_i/2a)^2]^{-1}$.

The Dirac operator on the pseudosphere is then,

$$\mathcal{D} = \left(1 - \frac{r^2}{4a^2}\right)^{3/2} \not{\partial} \left(1 - \frac{r^2}{4a^2}\right)^{-1/2} \tag{13.1}$$

13.1. Determination of Green's function G

Eq. (12.10) now becomes,

$$\tilde{\mathbf{G}}(z_1, z_2) = \left(1 - \frac{r_1^2}{4a^2}\right)^{-1/2} \mathbf{G}(z_1, z_2) \left(1 - \frac{r_2^2}{4a^2}\right)^{-1/2}, \tag{13.2}$$

and Eq. (12.11) becomes,

$$\left[\not{\partial} + \frac{\mathbf{m}}{1 - (r/2a)^2}\right] \tilde{\mathbf{G}}(z, z') = \mathbf{1}\delta(z - z'). \tag{13.3}$$

where δ is the flat Dirac delta.

Thus \mathbf{G} is the Green function of $\mathcal{D} + \mathbf{m}$ on the pseudosphere. The solution of these coupled partial differential equations can be found in terms of hypergeometric functions [38]. Again the flat limit results by taking $a \rightarrow \infty$ at a fixed value of m .

13.2. Thermodynamic properties

If we define $m = 4\pi a\zeta/S$ in terms of the fugacity ζ and the area per lattice site S (a local property of the surface), we have,

$$\mathcal{E}(2) = \det[1 + m\mathcal{D}^{-1}]. \tag{13.4}$$

Then the equation of state can be obtained integrating $n = m\partial(\beta p)/\partial m$ where $n = 2\rho_+$. The one-body density ρ_+ can be obtained from Eq. (11.11) where $\mathbf{R} = \mathbf{Gm}$. However, the integration cannot be performed in terms of known functions for arbitrary m .

14. The Flamm paraboloid

Flamm's paraboloid has already been discussed in Section 10.

14.1. Half surface with an insulating horizon

When the TCP lives in the half surface with an insulating horizon the Coulomb potential is given by Eq. (10.30). We will use $u_i = s_i e^{i\varphi_i}$ and $v_j = s_j e^{i\varphi_j}$ to denote the complex coordinates of the positively and negatively charged particles respectively, where, according to (10.14), we set $s = (\sqrt{r} + \sqrt{r - 2M})^2/2M > 1$. Note that the following small M behaviors holds: $s = 2r/M - 2 - M/2r + O(M^2)$ and $\sqrt{g} = rM/2 + O(M^2)$.

The Boltzmann factor at $\Gamma = \beta e^2 = 2$ now becomes

$$\left(\frac{2L}{M}\right)^{2N} \left| \det \left(\frac{1}{u_i - v_j} \right)_{(i,j) \in \{1, \dots, N\}^2} \right|^2, \tag{14.1}$$

where L is a length scale.

We can then repeat the analysis of Eqs. (11.1)–(11.20) noticing that now $\delta^{(2)}(z_1; z_2) = (\sqrt{g})^{-1} \delta(s - s_0) \delta(\varphi - \varphi_0)$ is the Dirac delta function on the curved surface and $\delta(s - s_0) \delta(\varphi - \varphi_0)/s = \delta(z - z_0)$ is the flat Dirac delta. Which gives the following,

$$m_{\pm}(z) = (2\pi L \zeta_{\pm} \sqrt{g}/sS)(2/M)^2, \tag{14.2}$$

rescaled position dependent fugacities which tends to $\tilde{m}_{\pm} = 2\pi L \zeta_{\pm}/S$, the ones of the flat system, in the $M \rightarrow 0$ limit. Here S is a local property of the surface independent of its curvature. Moreover Eqs. (11.4) and (11.9) read

$$\langle z | \mathcal{M}_{\text{hs}} | z' \rangle = \frac{2L}{M} (\sigma_x \partial_x + \sigma_y \partial_y) \ln|z - z'|, \tag{14.3}$$

210

R. Fantoni / Physica A 524 (2019) 177–220

$$\mathcal{O}_{hs} = \frac{2}{M}(\sigma_x \partial_x + \sigma_y \partial_y) = \frac{2}{M} \not\partial. \tag{14.4}$$

14.2. Determination of Green's function R

Upon defining $\mathbf{R} = \mathbf{G}\tilde{\mathbf{m}}$, \mathbf{G} satisfies the equation

$$[\mathcal{O} + \mathbf{m}(z_1)]\mathbf{G}(z_1, z_2) = \mathbf{1}(4/M^2)\delta(z_1; z_2). \tag{14.5}$$

which in the flat limit $M \rightarrow 0$ reduces to Eq. (11.22). Unfortunately this equation does not admit an analytical solution for \mathbf{G} . By combining the components of this equation one obtains decoupled equations for G_{++} and G_{--} as follows

$$\{m_+(z_1) + A^\dagger[m_-(z_1)]^{-1}A\}G_{++}(z_1, z_2) = \frac{4}{M^2}\delta(s_1, \varphi_1; s_2, \varphi_2), \tag{14.6}$$

$$\{m_-(z_1) + A[m_+(z_1)]^{-1}A^\dagger\}G_{--}(z_1, z_2) = \frac{4}{M^2}\delta(s_1, \varphi_1; s_2, \varphi_2), \tag{14.7}$$

while

$$G_{-+}(z_1, z_2) = -[m_-(z_1)]^{-1}AG_{++}(z_1, z_2), \tag{14.8}$$

$$G_{+-}(z_1, z_2) = +[m_+(z_1)]^{-1}A^\dagger G_{--}(z_1, z_2), \tag{14.9}$$

Then Eq. (14.6) can be rewritten in Cartesian coordinates as

$$\left\{ m_+(z_1)m_-(z_1) - \left(\frac{2}{M}\right)^2 \left[(\partial_{x_1}^2 + \partial_{y_1}^2) - \frac{4(-x_1 + iy_1)}{s_1^2(1+s_1)}(\partial_{x_1} + i\partial_{y_1}) \right] \right\} G_{++}(z_1, z_2) = \left(\frac{2}{M}\right)^4 \frac{\tilde{m}_- \sqrt{g_1}}{s_1^2} \delta(s_1 - s_2) \delta(\varphi_1 - \varphi_2) = \left(\frac{2}{M}\right)^4 \frac{\tilde{m}_- \sqrt{g_1}}{\sqrt{x_1^2 + y_1^2}} \delta(x_1 - x_2) \delta(y_1 - y_2), \tag{14.10}$$

where $s = \sqrt{x^2 + y^2}$. From the expression of the gradient in polar coordinates follows

$$\begin{cases} \partial_x = \cos \varphi \partial_s - \frac{\sin \varphi}{s} \partial_\varphi, \\ \partial_y = \sin \varphi \partial_s + \frac{\cos \varphi}{s} \partial_\varphi. \end{cases} \tag{14.11}$$

Which allows us to rewrite Eq. (14.10) in polar coordinates as

$$\left[\tilde{m}_+ \tilde{m}_- \left(1 + \frac{1}{s_1}\right)^8 - \left(\frac{2}{M}\right)^2 \left(\frac{1}{s_1} \partial_{s_1} (s_1 \partial_{s_1}) + \frac{1}{s_1^2} \partial_{\varphi_1}^2 + \frac{4}{s_1(1+s_1)} \partial_{s_1} + \frac{4i}{s_1^2(1+s_1)} \partial_{\varphi_1} \right) \right] G_{++}(z_1, z_2) = \left(\frac{2}{M}\right)^4 \frac{\tilde{m}_- \sqrt{g_1}}{s_1^2} \delta(s_1 - s_2) \delta(\varphi_1 - \varphi_2). \tag{14.12}$$

From this equation we immediately see that $G_{++}(z_1, z_2)$ cannot be real. Notice that in the flat limit $M \rightarrow 0$ we have $s \sim 2r/M$ and Eq. (14.12) reduces to

$$\left[\tilde{m}_+ \tilde{m}_- - \frac{1}{r_1} \partial_{r_1} (r_1 \partial_{r_1}) - \frac{1}{r_1^2} \partial_{\varphi_1}^2 \right] G_{++}(z_1, z_2) = \frac{\tilde{m}_-}{r_1} \delta(r_1 - r_2) \delta(\varphi_1 - \varphi_2). \tag{14.13}$$

which, when $\tilde{m}_+ = \tilde{m}_- = \tilde{m}$, has the following well known solution [32,33]

$$G_{++}(z_1, z_2) = \frac{\tilde{m}}{2\pi} K_0(\tilde{m}|\mathbf{r}_1 - \mathbf{r}_2|), \tag{14.14}$$

where K_0 is a modified Bessel function.

Let us from now on restrict to the case of equal fugacities of the two species. Then $\zeta_- = \zeta_+ = \zeta$ with

$$\tilde{m} = \frac{2\pi L}{S} \zeta = \frac{2\pi L e^{\beta\mu}}{\Lambda^2} = \left(2\pi L \frac{m e^2}{4\pi \hbar^2}\right) e^{2\mu/e^2}, \tag{14.15}$$

where \hbar is Planck's constant, m is the mass of the particles, and μ the chemical potential. So \tilde{m} has the dimensions of an inverse length. From the symmetry of the problem we can say that $G_{++} = G_{++}(s_1, s_2; \varphi_1 - \varphi_2)$. We can then express the Green function as the following Fourier series expansion

$$G_{++}(s_1, s_2; \varphi) = \frac{1}{2\pi} \sum_{k=-\infty}^{\infty} g_{++}(s_1, s_2; k) e^{ik\varphi}. \tag{14.16}$$

Then, using the expansion of the Dirac delta function, $\sum_k e^{ik\varphi} = 2\pi \delta(\varphi)$, we find that g_{++} , a continuous real function symmetric under exchange of s_1 and s_2 , has to satisfy the following equation

$$\begin{aligned} [Q_0(k, s_1) + Q_1(s_1) \partial_{s_1} + Q_2(s_1) \partial_{s_1}^2] g_{++}(s_1, s_2; k) = \\ \left(\frac{2}{M}\right)^2 \tilde{m} s_1^3 (1+s_1)^5 \delta(s_1 - s_2), \end{aligned} \tag{14.17}$$

where

$$\begin{aligned} Q_0(k, s) &= \tilde{m}^2 (1+s)^9 + \left(\frac{2}{M}\right)^2 k s^6 (4+k(1+s)), \\ Q_1(s) &= -\left(\frac{2}{M}\right)^2 s^7 (5+s), \\ Q_2(s) &= -\left(\frac{2}{M}\right)^2 s^8 (1+s). \end{aligned}$$

And the coefficients Q_i are polynomials of up to degree 9.

14.3. Method of solution

We start from the homogeneous form of Eq. (14.17). We note that, for a given k , the two linearly independent solutions $f_\alpha(s; k)$ and $f_\beta(s; k)$ of this linear homogeneous second order ordinary differential equation are not available in the mathematical literature to the best of our knowledge. Assuming we knew those solutions we would then find the Green function, $g_{++}(s_1, s_2; k)$, writing [60]

$$f(t_1, t_2; k) = c_k f_\alpha(s_<; k) f_\beta(s_>; k), \tag{14.18}$$

where $s_< = \min(s_1, s_2)$, $s_> = \max(s_1, s_2)$, and f_β has the correct behavior at large s . Then we determine c_k by imposing the kink in f due to the Dirac delta function at $s_1 = s_2$ as follows

$$\partial_{s_1} f(s_1, s_2; k)|_{s_1=s_2+\epsilon} - \partial_{s_1} f(s_1, s_2; k)|_{s_1=s_2-\epsilon} = -\tilde{m} \frac{(1+s_2)^4}{s_2^5}, \tag{14.19}$$

where ϵ is small and positive.

The Green function, symmetric under exchange of s_1 and s_2 , is reconstructed as follows

$$G_{++}(z_1, z_2) = G_{++}(s_1, s_2; \varphi) = \frac{1}{2\pi} \sum_{k=-\infty}^{\infty} c_k f_\alpha(s_<; k) f_\beta(s_>; k) e^{ik\varphi} \tag{14.20}$$

14.4. Whole surface

On the whole surface, using Eq. (10.27) with $b_0 = -\ln(L_0/L)$, we can now write the Boltzmann factor at a coupling constant $\Gamma = \beta e^2 = 2$ as follows,

$$\left| \det \left(\frac{L}{L_0} \frac{\sqrt{|u_i v_j|}}{u_i - v_j} \right)_{(i,j) \in \{1, \dots, N\}^2} \right|^2, \tag{14.21}$$

where L_0 is another length scale.

The grand partition function will then be,

$$\Xi(2) = \det [\mathbf{1} + \kappa_{ws}^{-1}], \tag{14.22}$$

212

R. Fantoni / Physica A 524 (2019) 177–220

where now Eqs. (11.4) and the ones following read,

$$\langle z | \mathcal{M}_{ws} | z' \rangle = \frac{L}{L_0} (\sigma_x \partial_x + \sigma_y \partial_y) \ln |z - z'|, \tag{14.23}$$

$$\mathcal{K}_{ws}^{-1} = \lambda_{ws} \mathcal{M}_{ws}, \tag{14.24}$$

$$\lambda_{ws} = \zeta_+ |z| \frac{\mathbf{1} + \sigma_z}{2} + \zeta_- |z| \frac{\mathbf{1} - \sigma_z}{2}, \tag{14.25}$$

$$\mathbf{K}_{ws} = \mathcal{M}_{ws}^{-1} \lambda_{ws}^{-1}, \tag{14.26}$$

$$\lambda_{ws}^{-1} = \frac{1}{\zeta_+ |z|} \frac{\mathbf{1} + \sigma_z}{2} + \frac{1}{\zeta_- |z|} \frac{\mathbf{1} - \sigma_z}{2}. \tag{14.27}$$

Introducing position dependent fugacities

$$m_{\pm}(z) = \frac{2\pi(L/L_0)\zeta_{\pm}\sqrt{g}}{Ss} = \tilde{m}_{\pm} \frac{\sqrt{g}}{s}, \tag{14.28}$$

where now $\tilde{m}_{\pm}/L_0 \rightarrow \tilde{m}_{\pm}$, we can rewrite

$$\mathcal{K}_{ws} = \frac{\sigma_x + i\sigma_y}{2} a_- + \frac{\sigma_x - i\sigma_y}{2} a_+, \tag{14.29}$$

with the operators

$$a_- = -\frac{\bar{z}}{m_-(z)|z|^3} + \frac{1}{m_-(z)|z|} (\partial_x - i\partial_y), \tag{14.30}$$

$$a_+ = -\frac{z}{m_+(z)|z|^3} + \frac{1}{m_+(z)|z|} (\partial_x + i\partial_y). \tag{14.31}$$

Then the equation for the Green functions are

$$(1 - a_- a_+) R_{++}(z_1, z_2) = \delta^{(2)}(z_1; z_2), \tag{14.32}$$

$$(1 - a_+ a_-) R_{--}(z_1, z_2) = \delta^{(2)}(z_1; z_2), \tag{14.33}$$

$$R_{+-} = -a_- R_{-+}, \tag{14.34}$$

$$R_{-+} = -a_+ R_{++}. \tag{14.35}$$

The equation for R_{++} in the symmetric mixture case is

$$\left[m^2(z_1) - \frac{2}{s_1^4} + \frac{2\partial_{s_1}}{s_1^3} - \frac{\partial_{s_1}^2}{s_1^2} - \frac{-i\partial_{\varphi_1} + \partial_{\varphi_1}^2}{s_1^4} \right] R_{++}(z_1, z_2) = \frac{m^2(z_1)}{\sqrt{g_1}} \delta(s_1 - s_2) \delta(\varphi_1 - \varphi_2) = \frac{\tilde{m}^2 \sqrt{g_1}}{s_1^2} \delta(s_1 - s_2) \delta(\varphi_1 - \varphi_2), \tag{14.36}$$

From this equation we see that $R_{++}(z_1, z_2)$ will now be real.

By expanding Eq. (14.36) in a Fourier series in the azimuthal angle we now find

$$\left[Q_0(k, s_1) + Q_1(s_1) \partial_{s_1} + Q_2(s_1) \partial_{s_1}^2 \right] g_{++}(s_1, s_2; k) = \left(\frac{M}{2} \right)^2 \tilde{m} s_1^3 (1 + s_1)^4 \delta(s_1 - s_2), \tag{14.37}$$

where

$$Q_0(k, s) = \left(\frac{M}{2} \right)^4 \tilde{m}^2 (1 + s)^8 + s^4 (k^2 - k - 2),$$

$$Q_1(s) = 2s^5,$$

$$Q_2(s) = -s^6.$$

And the coefficients Q_i are now polynomials of up to degree 8.

In the flat limit we find, for $G_{++} = R_{++}/\tilde{m}$, the following equation

$$\left[\tilde{m}^2 - \frac{2}{r_1^4} + \frac{2\partial_{r_1}}{r_1^3} - \frac{\partial_{r_1}^2}{r_1^2} - \frac{-i\partial_{\varphi_1} + \partial_{\varphi_1}^2}{r_1^4} \right] G_{++}(z_1, z_2) = \frac{\tilde{m}}{r_1} \delta(r_1 - r_2) \delta(\varphi_1 - \varphi_2). \tag{14.38}$$

We then see that we now do not recover the TCP in the plane [32,33]. This has to be expected because in the flat limit, Flamm's paraboloid reduces to two planes connected by the origin.

After the Fourier expansion of Eq. (14.16) we now get

$$[P_0(k, r_1) + P_1(r_1)\partial_{r_1} + P_2(r_1)\partial_{r_1}^2]g_{++}(r_1, r_2; k) = \tilde{m}\delta(r_1 - r_2), \tag{14.39}$$

where

$$P_0(k, r) = \tilde{m}^2 r + \frac{k^2 - k - 2}{r^3},$$

$$P_1(r) = \frac{2}{r^2},$$

$$P_2(r) = -\frac{1}{r}.$$

The homogeneous form of this equation admits the following two linearly independent solutions

$$\left. \begin{aligned} f_1(r; -1) &= [D_{-1/2}(i\sqrt{2\tilde{m}r}) + D_{-1/2}(i\sqrt{2\tilde{m}r})]/2 \\ f_2(r; -1) &= D_{-1/2}(\sqrt{2\tilde{m}r}) \end{aligned} \right\} k = -1,$$

$$\left. \begin{aligned} f_1(r; 2) &= \frac{[D_{-1/2}((-2)^{1/4}\sqrt{\tilde{m}r}) + D_{-1/2}((-2)^{1/4}\sqrt{\tilde{m}r})]/2}{D_{-1/2}((-2)^{1/4}\sqrt{\tilde{m}r})} \\ f_2(r; 2) &= \frac{[D_{-1/2}(i(-2)^{1/4}\sqrt{\tilde{m}r}) + D_{-1/2}(i(-2)^{1/4}\sqrt{\tilde{m}r})]/2}{D_{-1/2}(i(-2)^{1/4}\sqrt{\tilde{m}r})} \end{aligned} \right\} k = 2,$$

$$\left. \begin{aligned} f_1(t; k) &= \sqrt{r} I_{-\sqrt{7-4k+4k^2}/4}(\tilde{m}r^2/2) \\ f_2(t; k) &= \sqrt{r} I_{\sqrt{7-4k+4k^2}/4}(\tilde{m}r^2/2) \end{aligned} \right\} \text{else},$$

where $D_\nu(x)$ are parabolic cylinder functions and $I_\mu(x)$ are the modified Bessel functions of the first kind which diverge as $e^x/\sqrt{2\pi x}$ for large $x \gg |\mu^2 - 1/4|$.

Again we write $g_{++}(r_1, r_2; k) = c_k f_\alpha(r_<; k) f_\beta(r_>; k)$ and impose the kink condition,

$$\partial_{r_1} g_{++}(r_1, r_2; k)|_{r_1=r_2+\epsilon} - \partial_{r_1} g_{++}(r_1, r_2; k)|_{r_1=r_2-\epsilon} = -\tilde{m}r_2, \tag{14.40}$$

to find the c_k . The Green function is then reconstructed using Eq. (14.20). But we immediately see that curiously $|G_{++}|$ diverges. Even the structure of the plasma is not well defined in this situation. The collapse of opposite charges at the horizon shrinking to the origin makes the structure of the plasma physically meaningless.

Part IV

Conclusions

We presented a review of the analytical exact solutions of the one-component and two-component plasma at the special value of the coupling constant $\Gamma = 2$ in various Riemannian surfaces. Starting from the pioneering work [12] of Bernard Jancovici in 1981 showing the analytic exact solution for the Jellium on the plane, many other curved surfaces with a conformal metric has been considered. Namely: the cylinder, the sphere, the pseudosphere, and the Flamm paraboloid. From a physical point of view we can see the curvature of the surface as an additional external field acting on the system of charges moving in the corresponding flat space [42]. Even if this point of view does not take into account the fact that the Coulomb pair potential always reflect its harmonicity inside the given surface. For this reason we did not try a unifying treatment but rather a detailed presentation of each case individually as characteristic of the diverse scenarios which stem out of the various surfaces so far studied in the literature.

In our review we put light on the description of the surface, of the Coulomb potential (and the background potential for the OCP) in the surface, and of the exact solution for the partition function and for the correlation functions. The surfaces considered exhaust to the best of our knowledge all the cases considered in the literature until now. We hope that the review could be a valuable instrument for the reader who needs to have a broad overview on this fascinating exactly solvable fluid model giving the opportunity of finding in one place a self contained summary of various results appeared in the literature at different times and in different journals. We did our best to fill in all the conceptual gaps between the lines so that the reader can follow the various derivations without needing to refer to the original papers which would require an interruption of the reading. This choice required a certain degree of detail which we thought necessary in place of a more conversational presentation.

We decided to leave out the results of taking the thermodynamic limit of the various finite OCP expressions. If the reader desires he can always go back to the original references to find this lacking piece of information. It is well known that Coulomb systems have to exhibit critical finite-size effects [15]. The last surface considered, Flamm's paraboloid, is the only surface of non-constant curvature considered. Nonetheless the one-body density of the plasma is a constant

even in this surface in the thermodynamic limit [42]. On the Flamm paraboloid two different thermodynamic limits can be considered [26]: the one where the radius R of the disk confining the plasma is allowed to become very big while keeping the surface hole radius M constant, and the one where both $R \rightarrow \infty$ and $M \rightarrow \infty$ with the ratio R/M kept constant (fixed shape limit). When the horizon shrinks to a point the upper half surface reduces to a plane and one recovers the well known result valid for the one-component plasma on the plane. In the same limit the whole surface reduces to two flat planes connected by a hole at the origin. When only one-half of the surface is occupied by the plasma the density shows a peak in the neighborhoods of each boundary, tends to a finite value at the boundary and to the background density far from it, in the bulk. In the thermodynamic limit at fixed shape, we find that the density profile is the same as in flat space near a hard wall. In the grounded horizon case the density reaches the background density far from the boundaries. In this case, the fugacity and the background density control the density profile close to the metallic boundary (horizon). In the bulk and close to the outer hard wall boundary, the density profile is independent of the fugacity. In the thermodynamic limit at fixed shape, the density profile is the same as for a flat space.

The importance of having an exactly soluble many-body systems at least at one special temperature relies in the fact that it can serve as a guide for numerical experiments or for approximate solutions of the same system at other temperatures or for different more realistic systems. For example the 2D OCP thermodynamics and structure can now be efficiently expanded in Jack polynomials for even values of the coupling constant Γ [20,61,62]. And the TCP can be solved in the whole stability range of temperatures [63].

The original 1981 work of Jancovici [12] has been important for the understanding of the fractional quantum Hall effect in the Laughlin development [64] of a Jastrow correlation factor of the variational wave function of the Landau problem [65] for an Hall system in its ground state. We expect the results on the curved surface to be relevant in the developments towards a general relativistic statistical mechanics [66] which is still missing. The main difficulty being the lack of a canonical Hamiltonian in a generally covariant theory where the dynamics is only given relationally rather than in terms of evolution in physical time. And without a Hamiltonian it is difficult to even start doing statistical physics [67].

The quantum 2D OCP does not admit an analytic exact solution but it has been studied through a computer experiment either in its ground state [68,69] or at finite temperature [70–73].

Appendix A. Electrostatic potential of the background for the OCP in the pseudosphere

In this appendix we give the expression for the electrostatic potential of the background,

$$v_b(\mathbf{q}_1) = \int \rho_b G(d_{10}) dS_0 = -n_b e \int_{\Omega} G(d_{10}) dS_0. \tag{A.1}$$

The electric potential of the background satisfies Eq. (3.1). Using the coordinates (r, φ) we have,

$$v_b''(r) + \frac{1}{r} v_b'(r) = \alpha_b \frac{4a^2}{(1-r^2)^2}, \tag{A.2}$$

where $\alpha_b = -2\pi \rho_b$ and we denote with a prime a derivative with respect to r . This differential equation admits the following solution for v_b' ,

$$\begin{aligned} v_b'(r) &= e^{-\int_{r_0}^r \frac{1}{r'} dr'} \left[v_b'(r_0) + 4a^2 \int_{r_0}^r \frac{\alpha_b}{(1-r'^2)^2} e^{\int_{r_0}^{r'} \frac{1}{s} ds} dr' \right] \\ &= \frac{r_0 v_b'(r_0)}{r} + \frac{4a^2}{r} \int_{r_0}^r \alpha_b \frac{r'}{(1-r'^2)^2} dr'. \end{aligned} \tag{A.3}$$

Since the potential has to be chosen continuous at r_0 we set $v_b'(r_0) = 2a^2 \alpha_b r_0 / (1-r_0^2)$ to find,

$$v_b'(r) = 2a^2 \alpha_b \begin{cases} \frac{r}{1-r^2} & r \leq r_0 \\ \frac{r_0^2}{1-r_0^2} \frac{1}{r} & r > r_0 \end{cases},$$

where $r_0 = \tanh(\tau_0/2)$. For the potential inside $\Omega_{a\tau_0}$ we then have,

$$v_b(r) = -\alpha_b a^2 \ln(1-r^2) + \text{constant}, \tag{A.4}$$

or using the coordinates (τ, φ) ,

$$v_b(\tau) = -\alpha_b a^2 \ln[1 - \tanh^2(\tau/2)] + \text{constant}. \tag{A.5}$$

We need to adjust the additive constant in such a way that this potential at $\tau = \tau_0$ has the correct value corresponding to the total background charge. We then have,

$$\text{constant} = v_b(0) = -en \int_{\Omega_{a\tau_0}} G(\tau a) dS$$

$$\begin{aligned}
 &= 2\pi a^2 qn \int_0^{\tau_0} \ln[\tanh(\tau/2)] \sinh \tau \, d\tau \\
 &= \alpha_b a^2 [\ln[1 - \tanh^2(\tau_0/2)] + \sinh^2(\tau_0/2) \ln[\tanh^2(\tau_0/2)]] .
 \end{aligned}
 \tag{A.6}$$

We reach then the following expression for the potential inside $\Omega_{a\tau_0}$,

$$v_b(\tau) = \alpha_b a^2 \left\{ \ln \left[\frac{1 - \tanh^2(\tau_0/2)}{1 - \tanh^2(\tau/2)} \right] + \sinh^2(\tau_0/2) \ln[\tanh^2(\tau_0/2)] \right\} .
 \tag{A.7}$$

The self energy of the background is,

$$\begin{aligned}
 V_N^0 &= \frac{1}{2} \int_S \rho_b v_b \, dS \\
 &= \frac{1}{2} \rho_b \alpha_b a^2 2\pi a^2 \left\{ \int_0^{\tau_0} \ln \left[\frac{1 - \tanh^2(\tau_0/2)}{1 - \tanh^2(\tau/2)} \right] \sinh \tau \, d\tau + \right. \\
 &\quad \left. \sinh^2(\tau_0/2) \ln[\tanh^2(\tau_0/2)] \int_0^{\tau_0} \sinh \tau \, d\tau \right\} \\
 &= -2a^4 (\pi \rho_b)^2 \{ 1 - \cosh \tau_0 + 4 \ln[\cosh(\tau_0/2)] + 2 \sinh^4(\tau_0/2) \ln[\tanh^2(\tau_0/2)] \} .
 \end{aligned}
 \tag{A.8}$$

Notice that if we drop the last term on the right hand side of this equation, i.e. if we adjust the additive constant so that the potential of the background vanishes on the boundary $\partial\Omega_{a\tau_0}$, then in the limit $a \rightarrow \infty$ we recover the self energy of the flat system $N^2 e^2/8$.

Appendix B. The flat limit for the OCP in the pseudosphere

In this Appendix we study the flat limit $a \rightarrow \infty$ of the expressions found for the density in Section 9.6. We shall study the limit $a \rightarrow \infty$ for a finite system and then take the thermodynamic limit. Since for a large system on the pseudosphere boundary effects are of the same order as bulk effects it is not clear a priori whether computing these two limits in different order would give the same results. In Ref. [24] we show that it does.

For a finite disk of radius $d = a\tau_0$, we have in the flat limit $a \rightarrow \infty$, $d \sim r_0$. In Eq. (10.101), in the limit $a \rightarrow \infty$, the term e^C given by (9.46) becomes

$$e^C \sim \left(\frac{r_0^2}{4a^2} \right)^{-N_b} e^{N_b}
 \tag{B.1}$$

where $N_b = \pi n_b r_0^2$ is the number of particles in the background in the flat limit. Since for large a , $t_0 = r_0^2/4a^2$ is small, the incomplete beta function in Eq. (10.101) is

$$B_{t_0}(\ell + 1, \alpha) = \int_0^{t_0} e^{(\alpha-1)\ln(1-t)} t^\ell \, dt \sim \int_0^{t_0} e^{-(\alpha-1)t} t^\ell \, dt \sim \frac{\gamma(\ell + 1, N_b)}{\alpha^{\ell+1}}
 \tag{B.2}$$

Expanding $(1 - (r^2/4a^2))^{4\pi n_b a^2} \sim \exp(-\pi n_b r^2)$ in Eq. (10.101) we finally find the density as a function of the distance r from the center

$$n^{(1)}(r) = n_b e^{-\pi n_b r^2} \sum_{\ell=0}^{\infty} \frac{(\pi n_b r^2)^\ell}{\alpha^{\ell-N_b} N_b^{N_b} e^{-N_b(n_b/\zeta)} + \gamma(\ell + 1, N_b)}
 \tag{B.3}$$

When $\alpha \rightarrow \infty$ the terms for $\ell > N_b$ in the sum vanish because $\alpha^{\ell-N_b} \rightarrow \infty$. Then

$$n^{(1)}(r) = n_b e^{-\pi n_b r^2} \sum_{\ell=0}^{E(N_b)-1} \frac{(\pi n_b r^2)^\ell}{\gamma(\ell + 1, N_b)} + \Delta n^{(1)}(r)
 \tag{B.4}$$

The first term is the density for a flat OCP in the canonical ensemble with a background with $E(N_b)$ elementary charges ($E(N_b)$ is the integer part of N_b). The second term is a correction due to the inequivalence of the ensembles for finite systems and it depends on whether N_b is an integer or not. If N_b is not an integer

$$\Delta n^{(1)}(r) = n_b \frac{(\pi n_b r^2)^{E(N_b)} e^{-\pi n_b r^2}}{\gamma(E(N_b) + 1, N_b)}
 \tag{B.5}$$

and if N_b is an integer

$$\Delta n^{(1)}(r) = n_b \frac{(\pi n_b r^2)^{N_b} e^{-\pi n_b r^2}}{N_b^{N_b} e^{-N_b(n_b/\zeta)} + \gamma(N_b + 1, N_b)}
 \tag{B.6}$$

In any case in the thermodynamic limit $r_0 \rightarrow \infty, N_b \rightarrow \infty$, this term $\Delta n^{(1)}(r)$ vanishes giving the known results for the OCP in a flat space in the canonical ensemble [12,55]. Integrating the profile density (B.4) one finds the average number of particles. For a finite system it is interesting to notice that the average total number of particles N is

$$N = E(N_b) + 1 \tag{B.7}$$

for N_b not an integer and

$$N = N_b + \frac{1}{1 + \frac{N_b^{N_b} e^{-N_b} n_b}{\zeta \gamma(N_b+1, N_b)}} \tag{B.8}$$

for N_b an integer. In both cases the departure from the neutral case $N = N_b$ is at most of one elementary charge as it was noticed before [74,75].

Appendix C. Green’s function of Laplace equation in Flamm’s paraboloid

In this appendix, we illustrate the calculation of the Green function, for the various situations considered, using the original system of coordinates (r, φ) .

C.1. Laplace equation

We first find a solution $v(\mathbf{q})$, not circularly symmetric, to Laplace equation

$$\Delta v = 0, \tag{C.1}$$

through the separation of variables technique. We then write

$$v(r, \varphi) = R(r)\phi(\varphi), \tag{C.2}$$

so that Laplace equation splits into the two ordinary differential equations

$$\phi'' = -k^2 \phi, \tag{C.3}$$

$$(r^2 - 2Mr)R'' + (r - M)R' = k^2 R. \tag{C.4}$$

Taking care of the boundary condition $\phi(\varphi + 2\pi) = \phi(\varphi)$ we find that the first equation admits solution only when k is an integer. The solutions being

$$\phi_n = C_+ e^{in\varphi} + C_- e^{-in\varphi} \quad n = 0, 1, 2, 3, \dots \tag{C.5}$$

The solutions of the second equation are

$$R_n = \begin{cases} C_1 \cosh(na) + C_2 \sinh(na) & r > 2M \\ C_1 \cos(na) + C_2 \sin(na) & r < 2M \end{cases} \tag{C.6}$$

where

$$a = \begin{cases} 2 \arctan \sqrt{\frac{r}{2M - r}} & r < 2M \\ 2 \ln \frac{\sqrt{r} + \sqrt{r - 2M}}{\sqrt{2M}} & r > 2M \end{cases} \tag{C.7}$$

Here C_-, C_+, C_1 , and C_2 are the integration constants.

Then the general solution is real for $C_+ = C_- = C_0$

$$v(r, \varphi) = \sum_{n=0}^{\infty} R_n(r)\phi_n(\varphi) = \begin{cases} C_0 \left(C_1 + C_2 \frac{\sin a}{\cos \varphi - \cos a} \right) & r < 2M \\ C_0 \left(C_1 + C_2 \frac{\sinh a}{\cos \varphi - \cosh a} \right) & r > 2M \end{cases} \tag{C.8}$$

If we require the Coulomb potential to go to zero at $r = \infty$ we must choose $C_1 - C_2 = 0$ so that (for $C_0 = 1$)

$$v(r, \varphi) = \begin{cases} 1 + \frac{\sin a}{\cos \varphi - \cos a} & r < 2M \\ 1 + \frac{\sinh a}{\cos \varphi - \cosh a} & r > 2M \end{cases} \tag{C.9}$$

Moreover $v(2M, \varphi) = 1$.

C.2. Green’s function of Laplace equation

We now want to find the Coulomb potential generated at $\mathbf{q} = (r, \varphi)$ by a charge at $\mathbf{q}_0 = (r_0, \varphi_0)$ with $r_0 > 2M$. We then have to solve the Poisson equation

$$\Delta G(r, \varphi; r_0, \varphi_0) = -2\pi \delta(r - r_0) \delta(\varphi - \varphi_0) / \sqrt{g}, \tag{C.10}$$

where $g = \det(g_{\mu\nu}) = r^2 / (1 - 2M/r)$. To this end we expand the Green function G and the second delta function in a Fourier series as follows

$$G(r, \varphi; r_0, \varphi_0) = \sum_{n=-\infty}^{\infty} e^{in(\varphi-\varphi_0)} g_n(r, r_0), \tag{C.11}$$

$$\delta(\varphi - \varphi_0) = \frac{1}{2\pi} \sum_{n=-\infty}^{\infty} e^{in(\varphi-\varphi_0)}, \tag{C.12}$$

to get an ordinary differential equation for g_n

$$\left[\left(1 - \frac{2M}{r}\right) \frac{\partial^2}{\partial r^2} + \left(\frac{1}{r} - \frac{M}{r^2}\right) \frac{\partial}{\partial r} - \frac{n^2}{r^2} \right] g_n(r, r_0) = -\delta(r - r_0) / \sqrt{g}. \tag{C.13}$$

To solve this equation we first solve the homogeneous one for $r < r_0$: $g_{n,-}(r, r_0)$ and $r > r_0$: $g_{n,+}(r, r_0)$. This equation was already solved in (C.6) for $n \neq 0$

$$g_{n,\pm} = A_{n,\pm} (\sqrt{r} + \sqrt{r-2M})^{2n} + B_{n,\pm} (\sqrt{r} + \sqrt{r-2M})^{-2n} \tag{C.14}$$

and for $n = 0$ one finds

$$g_{0,\pm} = A_{0,\pm} + B_{0,\pm} \ln(\sqrt{r} + \sqrt{r-2M}). \tag{C.15}$$

The form of the solution immediately suggest that it is more convenient to work with the variable $x = (\sqrt{r} + \sqrt{r-2M})^2 / (2M)$. For this reason, we introduced this new system of coordinates (x, φ) which is used in the main text.

We then impose the following boundary conditions: (i) the solution at $r = r_0$ should be continuous, (ii) the first derivative at $r = r_0$ should have a jump due to the delta function, (iii) at $r = 2M$ the solution should tend to the solution of the flat system ($M \rightarrow 0$), and (iv) the solution should vanish at $r = \infty$, namely,

$$g_{n,-}(r_0, r_0) = g_{n,+}(r_0, r_0), \tag{C.16}$$

$$g'_{n,-}(r_0, r_0) = g'_{n,+}(r_0, r_0) + \frac{1}{\sqrt{r_0(r_0 - 2M)}}, \tag{C.17}$$

$$B_{n,-} = 0 \text{ for } n > 0, \quad A_{n,-} = 0 \text{ for } n < 0, \tag{C.18}$$

$$A_{n,+} = 0 \text{ for } n > 0, \quad B_{n,+} = 0 \text{ for } n < 0. \tag{C.19}$$

Performing the Fourier series of Eq. (C.11) then leads to the following result,

$$G^{\text{hs}}(r, \varphi; r_0, \varphi_0) = -\ln|z - z_0|, \tag{C.20}$$

where the complex coordinates $z = (\sqrt{r} + \sqrt{r-2M})^2 e^{i\varphi}$ and $z_0 = (\sqrt{r_0} + \sqrt{r_0-2M})^2 e^{i\varphi_0}$ have been introduced. This solution reduces to the correct Coulomb green function on a plane as $M \rightarrow 0$ and it is the Coulomb potential on one universe of the surface \mathcal{S} .

In order to find the Coulomb potential on the whole surface we can then start from the definition (10.3) and go back to the $s = (\sqrt{r} + \sqrt{r-2M})^2$ variable. If we do this we find as solutions,

$$s_{\pm} = 2M(\sqrt{u^2 + 1} \pm u)^2, \tag{C.21}$$

So that for the Coulomb potential one can choose one of the two definitions depending on which charge is in the upper or lower universe. Neglecting an additive constant we could then set

$$G^{\text{ws}}(u, \varphi; u_0, \varphi_0) = -\ln|z - z_0|, \tag{C.22}$$

where $z = (\sqrt{u^2 + 1} + u)^2 e^{i\varphi}$ and $z_0 = (\sqrt{u_0^2 + 1} + u_0)^2 e^{i\varphi_0}$. Actually this potential as it stands does not have the correct symmetry properties under the exchange of the charges from one universe to the other. It can easily be shown that if z is a point in the upper universe then $1/z$ is its symmetric in the lower universe. Then we should expect that if we take $z_0 = 1$ (in the horizon) the potential created at z should be the same as the one created at $1/z$, by symmetry. More generally, one should have $G^{\text{ws}}(z, z_0) = G^{\text{ws}}(1/z, 1/z_0)$.

We then need to revise the calculations of the Coulomb potential. We define the Coulomb potential as the solution of Poisson equation with the boundary condition that the electric field vanishes at infinity (this also happens for a flat space). However it turns out that with this boundary condition one still have several different solutions, and contrary to

the flat case, there are some that differ in more than a constant term. One can see this by solving Poisson equation using the Fourier transform, the constants of integration for the term which does not depend on the angular variable cannot be determined.

However one can impose some additional conditions. For instance we expect the Coulomb potential to be symmetric in the exchange of z and z_0 . The previous solution $-\ln|z - z_0|$ does satisfy this, but it is not the unique solution with this property. Additionally, we can impose the symmetry relation $G^{ws}(z, z_0) = G^{ws}(1/z, 1/z_0)$. Then one finds the solution

$$G^{ws}(z, z_0) = -\ln(|z - z_0|/\sqrt{|zz_0|}) . \tag{C.23}$$

We have not verified if this is the only solution (up to a constant) satisfying this symmetry, but we think so. For the whole surface we think that we should use this Coulomb potential instead of the original one, which does not treat on the same foot the upper and lower parts of the surface. However we have noticed that this potential does not reduce to the flat one when $M = 0$, but this is normal: if we work with the whole surface the limit $M = 0$ is not exactly the flat one, it is two flat planes connected by a hole at the origin, this hole modifies the Coulomb potential.

C.3. The grounded horizon case

Imagine now that the horizon at $r = 2M$ is a perfect conductor. We then start from

$$g_{n,\pm} = A_{n,\pm} \cosh \left[2n \ln(\sqrt{r} + \sqrt{r - 2M}) \right] + B_{n,\pm} \sinh \left[2n \ln(\sqrt{r} + \sqrt{r - 2M}) \right] . \tag{C.24}$$

We fix the four integration constants, for each n , requiring that: (i) the solution at $r = r_0$ should be continuous, (ii) the first derivative at $r = r_0$ should have a jump due to the delta function, (iii) at $r = 2M$ the solution should vanish, and (iv) the solution has the correct behavior at $r = \infty$, namely,

$$g_{n,-}(r_0, r_0) = g_{n,+}(r_0, r_0) , \tag{C.25}$$

$$g'_{n,-}(r_0, r_0) = g'_{n,+}(r_0, r_0) + \frac{1}{\sqrt{r_0(r_0 - 2M)}} , \tag{C.26}$$

$$g_{n,-}(2M, r_0) = 0 , \tag{C.27}$$

$$A_{n,+} = B_{n,+} \text{ for } n \geq 0 , \quad A_{n,+} = -B_{n,+} \text{ for } n < 0 . \tag{C.28}$$

Performing the Fourier series of Eq. (C.11) then leads to the following result for $r > r_0$

$$G(r, \varphi; r_0, \varphi_0) = -\ln \sqrt{\frac{1 + c^2 - 2c \cos(\varphi - \varphi_0)}{1 + b^2 - 2b \cos(\varphi - \varphi_0)}} + 2 \ln \frac{\sqrt{r_0} + \sqrt{r_0 - 2M}}{\sqrt{2M}} , \tag{C.29}$$

$$b = \left(\frac{\sqrt{r} + \sqrt{r - 2M}}{\sqrt{r_0} + \sqrt{r_0 - 2M}} \right)^2 , \tag{C.30}$$

$$c = \left(\frac{(\sqrt{r} + \sqrt{r - 2M})(\sqrt{r_0} + \sqrt{r_0 - 2M})}{2M} \right)^2 , \tag{C.31}$$

and the solution for $r < r_0$ is obtained by merely exchanging r with r_0 .

In terms of the complex numbers z and z_0 this can be rewritten as follows

$$G^{gh}(r, \varphi; r_0, \varphi_0) = -\ln \left| \frac{(z - z_0)/2M}{1 - z\bar{z}_0/4M^2} \right| \tag{C.32}$$

where the bar over a complex number indicates its complex conjugate. We will call this the grounded horizon green function. Notice how its shape is the same of the Coulomb potential on the pseudosphere [24] M playing the role of the complex radius. This green function could have been found from the Coulomb one (C.20) by using the images method from electrostatics.

Appendix D. The geodesic distance on the Flamm paraboloid

The geodesics are determined by the following equation

$$\ddot{r} + (\Gamma_{rrr}\dot{r}^2 + \Gamma_{r\varphi\varphi}\dot{\varphi}^2)/g_{rr} = 0 , \tag{D.1}$$

$$\ddot{\varphi} + 2\Gamma_{\varphi\varphi r}\dot{\varphi}\dot{r}/g_{\varphi\varphi} = 0 , \tag{D.2}$$

where the dot stands for a total differentiation with respect to time and the Christoffel symbols are as follows

$$\Gamma_{rrr} = g_{rr,r}/2 , \tag{D.3}$$

$$\Gamma_{\varphi\varphi r} = -\Gamma_{r\varphi\varphi} = g_{\varphi\varphi,r}/2 . \tag{D.4}$$

Here the comma means partial differentiation as usual.

The geodesics equation (D.1)–(D.2) is then

$$\ddot{r} - \left[\frac{M}{(r-2M)^2} \dot{r}^2 + r\dot{\phi}^2 \right] \left(1 - \frac{2M}{r} \right) = 0, \quad (\text{D.5})$$

$$\ddot{\phi} + \frac{2}{r} \dot{\phi} \dot{r} = 0, \quad (\text{D.6})$$

The geodesic distance between two points on the surface is

$$d(\mathbf{q}_1, \mathbf{q}_2) = \int_{t_1}^{t_2} \frac{ds}{dt} dt = \int_{r_1}^{r_2} y dr = \int_{r_1}^{r_2} \sqrt{\frac{1}{1 - \frac{2M}{r}} + r^2 x^2} dr$$

where $x(r) = d\phi/dr$ and $y(r) = ds/dr$.

Using $\dot{\phi} = x\dot{r}$ in Eqs. (D.5) and (D.6) we find

$$x' = \left(\frac{2}{r} + \frac{M}{r^2 - 2Mr} \right) x + r \left(1 - \frac{2M}{r} \right) x^3, \quad (\text{D.7})$$

where the prime stands for differentiation with respect to r .

The solution for $x(r)$ and $y(r)$ are as follows

$$x(r) = \pm \sqrt{\frac{15r^3(2M-r)}{r^4(30M^2 - 24Mr + 5r^2) - C}}, \quad (\text{D.8})$$

$$y(r) = \sqrt{r^2 x^2 + \frac{r}{r-2M}}, \quad (\text{D.9})$$

with C the integration constant, so that,

$$d(\mathbf{q}, \mathbf{q}_0) = \int_{r_0}^r y(r') dr', \quad (\text{D.10})$$

$$\phi - \phi_0 = \int_{r_0}^r x(r') dr'. \quad (\text{D.11})$$

References

- [1] R. Fantoni, J.W.O. Salari, B. Klumperman, *Phys. Rev. E* 85 (2012) 061404.
- [2] P.A. Martin, *Rev. Modern Phys.* 60 (1988) 1075.
- [3] G. Tarjus, F. Sausset, P. Viot, *Adv. Chem. Phys.* 148 (2010) 251.
- [4] N.H. March, M.P. Tosi, *Coulomb Liquids*, Academic Press, 1984.
- [5] D. Henderson, M. Holovko, A. Trokhymchuk (Eds.), *Ionic Soft Matter: Modern Trends in Theory and Applications*, in: NATO Science Series, Springer, Dordrecht, 2005.
- [6] R.R. Sari, D. Merlini, *J. Stat. Phys.* 14 (1976) 91.
- [7] E.A. Abbott, *Flatland: A Romance of Many Dimensions*, Seeley & Co., London, 1884.
- [8] S.F. Edwards, A. Lenard, *J. Math. Phys.* 3 (1962) 778.
- [9] R. Fantoni, *J. Stat. Phys.* 163 (2016) 1247.
- [10] J. Ginibre, *J. Math. Phys.* 6 (1965) 440.
- [11] M.L. Mehta, *Random Matrices*, Academic, New York, 1967.
- [12] B. Jancovici, *Phys. Rev. Lett.* 46 (1981a) 386.
- [13] A. Alastuey, B. Jancovici, *J. Phys. (France)* 42 (1981) 1.
- [14] M.L. Rosinberg, L. Blum, *J. Chem. Phys.* 81 (1984) 3700.
- [15] B. Jancovici, G. Manificat, C. Pisani, *J. Stat. Phys.* 76 (1994) 307.
- [16] B. Jancovici, G. Téllez, *J. Stat. Phys.* 82 (1996) 609.
- [17] P. Choquard, *Helv. Phys. Acta* 54 (1981) 332.
- [18] P. Choquard, P.J. Forrester, E.R. Smith, *J. Stat. Phys.* 33 (1983) 13.
- [19] J.M. Caillol, *J. Phys. (Paris) -Lett.* 42 (1981) L.
- [20] G. Téllez, P.J. Forrester, *J. Stat. Phys.* 97 (1999) 489.
- [21] B. Jancovici, *J. Stat. Phys.* 99 (2000) 1281.
- [22] R.P. Salazar, G. Téllez, *J. Stat. Phys.* 164 (2016) 969.
- [23] B. Jancovici, G. Téllez, *J. Stat. Phys.* 91 (1998) 953.
- [24] R. Fantoni, B. Jancovici, G. Téllez, *J. Stat. Phys.* 112 (2003) 27.
- [25] B. Jancovici, G. Téllez, *J. Stat. Phys.* 116 (2004) 205.
- [26] R. Fantoni, G. Téllez, *J. Stat. Phys.* 133 (2008) 449.
- [27] A. Salzberg, S. Prager, *J. Chem. Phys.* 38 (1963) 2587.
- [28] E.H. Hauge, P.C. Hemmer, *Phys. Nor.* 5 (1971) 209.
- [29] J.M. Kosterlitz, D.J. Thouless, *J. Phys. C* 6 (1973) 1181.
- [30] A. Lenard, *J. Math. Phys.* 2 (1961) 682.
- [31] M. Gaudin, *J. Phys. (France)* 46 (1985) 1027.
- [32] F. Cornu, B. Jancovici, *J. Stat. Phys.* 49 (1987) 33.

- [33] F. Cornu, B. Jancovici, *J. Chem. Phys.* 90 (1989) 2444.
- [34] P.J. Forrester, *J. Chem. Phys.* 95 (1991) 4545.
- [35] G. Téllez, L. Merchán, *J. Stat. Phys.* 108 (2002) 495.
- [36] L. Merchán, G. Téllez, *J. Stat. Phys.* 114 (2004) 735.
- [37] G. Téllez, *J. Chem. Phys.* 106 (1997) 8572.
- [38] G. Téllez, *J. Phys. A: Math. Gen.* 31 (1998) 5277.
- [39] P.J. Forrester, B. Jancovici, J. Madore, *J. Stat. Phys.* 69 (1992) 179.
- [40] P.J. Forrester, B. Jancovici, *J. Stat. Phys.* 84 (1996) 337.
- [41] R. Fantoni, *J. Stat. Mech.* (2012a) P04015.
- [42] R. Fantoni, *J. Stat. Mech.* (2012b) 10024.
- [43] P. Debye, E. Hückel, *Phys. Z.* 9 (1923) 185.
- [44] J.M. Caillol, D. Levesque, J.P. Hansen, *J. Stat. Phys.* 28 (1982) 325.
- [45] F. Steiner, (Semestre d'été 1995), Quantum chaos and hyperbolic geometry, Tech. Rep. (Université de Hambourg) troisième cycle de la physique en suisse romande, cours du Professeur Frank Steiner.
- [46] J. Hadamard, *J. Math. Pures Appl.* 4 (1898) 27.
- [47] E. Artin, *Abh. Math. Sem. d.* 3 (1924) 170, hamburgischen Universität.
- [48] V.I. Arnold, A. Avez, *Ergodic Problems of Classical Mechanics*, W. A. Benjamin, Inc, New York, Amsterdam, 1968.
- [49] Y.G. Sinai, *Dokl. Akad. Nauk.* 153 (6) (1963) [Sov. Math. Dokl. 4, 1818–1822 (1963)].
- [50] C.W.J. Beenakker, H. van Houten, *Solid State Phys.* (1991) 44.
- [51] V.I. Arnold, V.V. Kozlov, A.I. Neishtadt, in: R.V. Gamkrelidze, V.I. Arnold (Eds.), *Mathematical Aspects of Classical and Celestial Mechanics* (Springer) 2nd Printing 1997 of the 2nd Edition 1993 Which was Originally Published As *Dynamical Systems III*, in: *Encyclopedia of Mathematical Sciences*. Translated by A. Iacob., vol. 3, 1993, see remark to theorem 20 of chapter 6.
- [52] D.V. Anosov, *Proc. Steklov Inst. Math.* (1967) 90.
- [53] A.C. Aitken, *Determinants and Matrices*, Interscience, New York, 1956.
- [54] J. Zinn-Justin, *Quantum Field Theory and Critical Phenomena*, second ed., Clarendon Press, Oxford, 1993.
- [55] B. Jancovici, *J. Phys. Lett.* 42 (1981b) L.
- [56] M.L. Mehta, *Random Matrices*, Academic Press, 1991.
- [57] P.J. Forrester, *J. Phys. A: Math. Gen.* 18 (1985) 1419.
- [58] S. Samuel, *Phys. Rev. D* 18 (1978) 1916.
- [59] Jayewardena C., *Helv. Phys. Acta* 61 (1988) 636.
- [60] J.D. Jackson, *Classical Electrodynamics*, third ed., John Wiley & Sons, Inc. United States of America, 1999, sections 39 & 311.
- [61] L. Šamaj, *J. Stat. Phys.* 117 (2004) 131.
- [62] G. Téllez, P. Forrester, *J. Stat. Phys.* 148 (2012) 824.
- [63] L. Šamaj, *J. Phys. A* 36 (2003) 5913.
- [64] R.B. Laughlin, *Phys. Rev. Lett.* 50 (1983) 1395.
- [65] L.D. Landau, E.M. Lifshitz, *Quantum Mechanics (Non-Relativistic Theory)*, Vol. 3, third ed., 1958, Pergamon Press course of Theoretical Physics, §112.
- [66] C. Rovelli, *Phys. Rev. D* 87 (2013) 084055.
- [67] C. Rovelli, *Quantum Gravity*, Cambridge University, Cambridge, 2004.
- [68] B. Tanatar, D.M. Ceperley, *Phys. Rev. B* 39 (1989) 5005.
- [69] Y. Kwon, D.M. Ceperley, R.M. Martin, *Phys. Rev. B* 53 (1996) 7376.
- [70] B. Militzer, E.L. Pollock, D.M. Ceperley, 2003. *cond-mat/0310401*.
- [71] D.M. Ceperley, in: G.F. Giuliani, G. Vignale (Eds.), *Proceedings of the International School of Physics Enrico Fermi*, in: series and number CLVII, IOS Press, Amsterdam, 2004, pp. 3–42.
- [72] E.W. Brown, B.K. Clark, D.M. Ceperley, *Phys. Rev. Lett.* 110 (2013a) 146405.
- [73] E.W. Brown, J.L. DuBois, D.M. Ceperley, *Phys. Rev. B* 88 (R) (2013b) 081102.
- [74] B. Jancovici, *J. Phys. (France)* 47 (1986) 389.
- [75] B. Jancovici, *J. Stat. Phys.* 110 (2003) 879.



Part XX
2021

Chapter 62

Form invariance of the moment sum-rules for jellium with the addition of short-range terms in the pair-potential

Fantoni R., Indian J. Phys. **95**, 1027 (2021)

Title: “Form invariance of the moment sum-rules for jellium with the addition of short-range terms in the pair-potential”

Abstract: We find the first three (even) structure factor moments for a (non-quantum) one-component Jellium made of particles living in three dimensions and interacting with a Coulomb pair-potential plus a short-range term with either a finite range or decaying exponentially fast at large distances. Starting from the hierarchical Born-Green-Yvon equations we show that they are all form invariant respect to the addition of the short-range term. We discuss the relevance of the present study to interpret the failure of the moment sum-rules of ionic-liquids at criticality.

Author's personal copy

Indian J Phys
https://doi.org/10.1007/s12648-020-01750-2



ORIGINAL PAPER

Form invariance of the moment sum-rules for jellium with the addition of short-range terms in the pair-potential

R Fantoni*

Dipartimento di Fisica, Università di Trieste, Strada Costiera 11, 34151 Grignano (Trieste), Italy

Received: 08 August 2019 / Accepted: 06 December 2019

Abstract: We find the first three (even) structure factor moments for a (non-quantum) one-component Jellium made of particles living in three dimensions and interacting with a Coulomb pair-potential plus a short-range term with either a finite range or decaying exponentially fast at large distances. Starting from the hierarchical Born-Green-Yvon equations we show that they are all form invariant respect to the addition of the short-range term. We discuss the relevance of the present study to interpret the failure of the moment sum-rules of ionic-liquids at criticality.

Keywords: Sum-rule; Multipolar sum-rule; Structure factor moments; Internal screening; External screening; One-component plasma; Jellium; Short-range interaction

PACS number; 05.70.Fh; 61.20.Qg; 64.60.F-; 64.70

1. Introduction

A prototypical model of solid state physics describing free electrons in metallic elements is the one-component *Jellium*: a statistical mechanics one-component fluid of pointwise charged particles made thermodynamically stable by the addition of a uniform inert neutralizing background. This fluid has been studied in great details in history both in its classical and in its quantum versions. Here we will only deal with the classical version of the model. In particular several plausible exact relationships between the n -point correlations functions, the so called *sum-rules*, has been determined over the years [1]. Of particular interest, due to the direct link with scattering experiments on the fluid, are the even moments of the structure factor, the so called moment sum-rules, which give the coefficients of the even powers of the wavenumber in a large wavelength expansion of the structure factor. The zeroth-moment sum-rule, or charge sum-rule, is commonly known as a consequence of the *internal* screening properties of the Coulomb system and has been known since the work of Debye and Hückel [2]. The second-moment or Stillinger-Lovett [3] sum-rule is due to the *external* screening and has been proved

rigorously for the first time by Martin et al. [4]. The fourth-moment sum-rule has been proved rigorously for the first time by Vieillefosse [5] after it had been established earlier with various heuristic arguments [6–8].

A mixture of charged particles can have species with opposite charges. In these cases in addition to the electrical neutrality of the system with the introduction of a neutralizing background it is necessary to introduce a hard-core on the particles, in order to assure thermodynamical stability. It is then important to understand how the addition of a short-range regularizing term (with compact support or decaying exponentially fast [9]) to the pure Coulomb pair-potential influences the various sum-rules.

In this work we perform this study on the one-component Jellium extending Vieillefosse [5] work to a pair-potential where we add to the Coulomb term a generic short-range term with either a finite support or exponentially decaying at large distances. We work in three spatial dimensions leaving the extension to other dimensions, to a mixture, and to more general short-range potential regularizations to future works. We start from the constituent Born-Green-Yvon hierarchic equations [10] for the n -point correlation functions and with certain assumptions on the decay of the n -particle Ursell functions as subgroups of particles are infinitely separated (the *exponential clustering* hypothesis) we use a series of *multipolar sum-rules* [1] to determine the first three even structure factor moments.

*Corresponding author, E-mail: riccardo.fantoni@istruzione.it

We already know that the forms of the first two even moments are not influenced by the presence of the regularizing short-range term in the pair-potential [1, 4]. We will find that also the fourth-moment is form invariant.

This work is a step forward in the understanding of the failure of the second and fourth moment sum-rules recently observed in the restricted primitive model (RPM) at criticality [11, 12]. In fact, it was only until recently that the previously unknown form of the fourth moment sum-rule for the RPM was established using a semi-heuristic argument [13, 14] claiming form invariance respect to the pure coulombic case. Our present result gives a rigorous first principle proof of the form invariance at least in the weak coupling regime and for the one-component Jellium. This fact, if confirmed for the two-component plasma, relegates the failure of the sum-rules at criticality to the disruption, upon approaching a phase transition, of the *exponential clustering*, i.e. the decay to zero of the truncated correlations faster than any inverse power of distance as groups of particles are separated by an infinite distance. In fact, it has to be expected that at criticality the correlation functions develops long-range tails with monotonous or oscillating inverse power law decay [15].

The work is organized as follows: In Sect. 2 we find again the zeroth moment sum-rule following the original derivation of Martin et al. [1], in Sect. 3 we find again the second moment sum-rule following the original derivation of Martin et al. [1, 4], in Sect. 4 we derive the fourth moment sum-rule with a route alternative to the one of Vieillefosse [5] which explains clearly from the point of view of the BGY why also this moment is form invariant upon the addition of a short-range term to the Coulomb pair-potential, in Sect. 5 we determine the isothermal compressibility of the system, and Sect. 6 is for the concluding remarks.

2. Derivation of the zeroth moment sum-rule

The second order Born-Green-Yvon (BGY) hierarchy [1]

$$\begin{aligned}
 & \nabla_{\mathbf{r}_1} u_2(1, 2) \\
 &= \beta \mathbf{F}_{21} [u_2(1, 2) + 1] \\
 &+ \rho \int d\mathbf{r}_3 [1 + u_2(1, 2) + u_2(1, 3) + u_2(2, 3) \\
 &+ u_3(1, 2, 3)] \beta \mathbf{F}_{31} \\
 &- \rho \int d\mathbf{r}_3 [u_2(1, 2) + 1] \beta \mathbf{F}_{31} \\
 &= \beta \mathbf{F}_{21} [u_2(1, 2) + 1] + \rho \int d\mathbf{r}_3 [u_2(2, 3) \\
 &+ u_3(1, 2, 3)] \beta \mathbf{F}_{31}
 \end{aligned} \tag{1}$$

where $\beta = 1/k_B T$ with k_B Boltzmann's constant and T the absolute temperature, ρ is the density of the fluid, $\mathbf{F}_{21} = -\nabla_{\mathbf{r}_1} v(1, 2)$, with $v(1, 2)$ the pair-potential that is the sum of a Coulomb term $v^c(1, 2) = e^2/|\mathbf{r}_2 - \mathbf{r}_1|$ and a short-range term $v^{sr}(1, 2)$ with compact support or decaying exponentially fast [9]. We will also call $\mathbf{F}_{21}^c = -\nabla_{\mathbf{r}_1} v^c(1, 2)$ and $\mathbf{F}_{21}^{sr} = -\nabla_{\mathbf{r}_1} v^{sr}(1, 2)$. According to Ref. [9] the Ursell functions $u_n(1, 2, \dots, n)$ must satisfy exponential clustering [1], i.e. they should tend to zero (monotonously or oscillating) faster than any inverse power of the distance as the distance between any group of particles at $(\mathbf{r}_1, \mathbf{r}_2, \dots, \mathbf{r}_n)$ tends to infinity. The Ursell functions are assumed to depend only on the shape of the figure formed by the various points (and not on its space orientation) and they are symmetrical in any permutation of the particles. The first assumption is a consequence of the homogeneity and isotropy of the fluid, the second is a consequence of distinguishability of the particles. Of course the exponential clustering assumption is valid for the high temperature (low density) infinite homogeneous phase of the fluid when the correlation functions are believed to obey to the BGY hierarchy. We will generally indicate vectors with a bold-face letter and absolute values of vectors with a normal (Roman) version of the same font $r = |\mathbf{r}|$. We use a hat to denote the unit vector $\hat{\mathbf{r}} = \mathbf{r}/r$.

In the second equality of Eq. (1) we used the fact that $\int d\mathbf{r}_3 u_2(1, 3) \mathbf{F}_{13} = 0$ by symmetry. Now we observe that the left hand side of Eq. (1) tends to zero faster than any inverse power of $x = |\mathbf{x}| = |\mathbf{r}_2 - \mathbf{r}_1|$ as x tends to infinity and the same is true for the first and fourth terms on the right hand side. So the sum of the second and third terms on the right hand side must vanish in the same way, in this limit. Then we require that

$$\int d\mathbf{r}_3 s(2, 3) \mathbf{F}_{31} \tag{2}$$

where $s(2, 3) = \rho u_2(2, 3) + \delta(2, 3)$ and δ is the Dirac delta function, tends to zero faster than any power of the distance x when the latter tends to infinity. Expanding Eq. (2) in powers of $1/x$ in this limit, we deduce

$$\int d\mathbf{r}_3 s(\mathbf{y}) y^l P_l(\hat{\mathbf{x}} \cdot \hat{\mathbf{y}}) = 0, \quad l \geq 1 \tag{3}$$

$$I_0 = \int d\mathbf{r}_3 s(\mathbf{y}) = 0 \tag{4}$$

where $\mathbf{y} = \mathbf{r}_3 - \mathbf{r}_2$ and P_l are the Legendre polynomials. Eq. (4) is the zeroth moment sum-rule also known as the charge or electroneutrality sum-rule [1]. It is the simpler of the multipolar sum-rules (3). We immediately see that in our derivation we did not use the fact that v is purely Coulombic. It is sufficient that it contains the Coulomb potential.

Author's personal copy

Form invariance of the moment sum-rules

3. Derivation of the second moment sum-rule

Following Ref. [4] we may write the second order BGY hierarchy as follows

$$\begin{aligned} \nabla_{\mathbf{r}_2} u_2(1, 2) &= \beta \mathbf{F}_{12} [u_2(1, 2) + 1] + \\ &\rho \int d\mathbf{r}_3 [1 + u_2(1, 2) + u_2(1, 3) + u_2(2, 3) \\ &+ u_3(1, 2, 3)] \beta \mathbf{F}_{32} - \\ &\rho \int d\mathbf{r}_3 [u_2(1, 2) + 1] \beta \mathbf{F}_{32} \end{aligned} \quad (5)$$

where $\mathbf{F}_{12} = -\nabla_{\mathbf{r}_2} v(1, 2)$, with $v(1, 2)$ the pair-potential, and the last line in Eq. (6) is for the neutralizing uniform background. We immediately observe that $\int d\mathbf{r}_3 u_2(2, 3) \mathbf{F}_{23} = 0$ by symmetry.

Multiplying by $\mathbf{r}_{12} = \mathbf{r}_1 - \mathbf{r}_2$ and integrating over \mathbf{r}_1 we find

$$\begin{aligned} \int d\mathbf{r}_1 \mathbf{r}_{12} \cdot \nabla_{\mathbf{r}_2} u_2(1, 2) &= \int d\mathbf{r}_1 \mathbf{r}_{12} \left\{ \beta \mathbf{F}_{12} \right. \\ &+ \rho \int d\mathbf{r}_3 \{ u_2(1, 3) + [\delta(1, 3) + \delta(1, 2)] u_2(2, 3) / \rho \\ &+ u_3(1, 2, 3) \} \beta \mathbf{F}_{32} \left. \right\} \\ &= \int d\mathbf{r}_1 \mathbf{r}_{12} \left\{ \int d\mathbf{r}_3 [\rho u_2(1, 3) + \delta(1, 3)] \beta \mathbf{F}_{32} \right. \\ &+ \rho \int d\mathbf{r}_3 c_3(1|2, 3) \beta \mathbf{F}_{32} \left. \right\}, \end{aligned} \quad (6)$$

where $s(1, 3) = \rho u_2(1, 3) + \delta(1, 3)$ and $c_3(1|2, 3) = u_3(1, 2, 3) + [\delta(1, 2) + \delta(1, 3)] u_2(2, 3) / \rho$ the excess charge density which does not carry multipoles of any order (See Proposition 2.2 in Ref. [1]). Then

$$\begin{aligned} \int d\mathbf{r}_1 \mathbf{r}_{12} \cdot \nabla_{\mathbf{r}_2} u_2(1, 2) &= \int d\mathbf{r}_1 \mathbf{r}_{12} \int d\mathbf{r}_3 s(1, 3) \beta \mathbf{F}_{32} \\ &+ \rho \int d\mathbf{r}_3 \beta \mathbf{F}_{32} \int d\mathbf{r}_1 \mathbf{r}_{12} c_3(1|2, 3). \end{aligned} \quad (7)$$

Now we observe that due to the dipole sum-rule [1] the last line in Eq. (7) must vanish, $\mathbf{F} = \mathbf{F}^{sr} + \mathbf{F}^c$ can be split into a short-range term, \mathbf{F}^{sr} , and a coulombic term, \mathbf{F}^c , where

$$\begin{aligned} \int d\mathbf{r}_1 \mathbf{r}_{12} \int d\mathbf{r}_3 s(1, 3) \beta \mathbf{F}_{32}^{sr} \\ = \int d\mathbf{r}_{23} \beta \mathbf{F}_{32}^{sr} \int d\mathbf{r}_{13} (\mathbf{r}_{13} + \mathbf{r}_{32}) s(1, 3) = 0, \end{aligned} \quad (8)$$

where we used the charge sum-rule and isotropy of the system. This tells us that the result we will find for the second moment is form invariant under the addition to the pair-potential of a generic short-range term. Also, using $\nabla_{\mathbf{r}_1} = -\nabla_{\mathbf{r}_2}$ and $\int d\mathbf{r}_1 \dots = -\int d\mathbf{r}_2 \dots$, we find

$$\int d\mathbf{r}_1 \mathbf{r}_{12} \cdot \nabla_{\mathbf{r}_2} u_2(1, 2) = 3 \int d\mathbf{r}_1 u_2(1, 2) = -3/\rho, \quad (9)$$

where we also used the charge sum-rule. Putting all together, we find

$$\begin{aligned} -\frac{3}{\rho} &= \frac{1}{2} \int d\mathbf{r}_1 \nabla_{\mathbf{r}_1} (r_{12}^2) \int d\mathbf{r}_3 s(1, 3) \beta \mathbf{F}_{32}^c \\ &= -\frac{1}{2} \int d\mathbf{r}_1 \nabla_{\mathbf{r}_2} (r_{12}^2) \int d\mathbf{r}_3 s(1, 3) \beta \mathbf{F}_{32}^c \\ &= \frac{1}{2} \int d\mathbf{r}_1 r_{12}^2 \int d\mathbf{r}_3 s(1, 3) \beta \nabla_{\mathbf{r}_2} \mathbf{F}_{32}^c \\ &= \frac{1}{2} \int d\mathbf{r}_1 r_{12}^2 s(1, 2) 4\pi e^2 \beta, \end{aligned} \quad (10)$$

where we used the property that $\nabla_{\mathbf{r}_2} \mathbf{F}_{32}^c = 4\pi e^2 \delta(3, 2)$. And finally we find for the second moment sum-rule

$$I_2 = \int d\mathbf{r}_2 r_{12}^2 s(1, 2) = \frac{3}{2\pi\rho\beta e^2} = \frac{6}{k_D^2}, \quad (11)$$

where $\lambda_D = k_D^{-1} = (4\pi\rho\beta e^2)^{-1/2}$ is the Debye-Hückel screening length.

4. Derivation of the fourth moment sum-rule

Starting from Eq. (6) we multiply by $r_{12}^2 \mathbf{r}_{12}$ and integrate over \mathbf{r}_1 to get

$$\begin{aligned} \int d\mathbf{r}_1 r_{12}^2 \mathbf{r}_{12} \cdot \nabla_{\mathbf{r}_2} u_2(1, 2) &= \int d\mathbf{r}_1 r_{12}^2 \mathbf{r}_{12} \left\{ \beta \mathbf{F}_{12} \right. \\ &+ \rho \int d\mathbf{r}_3 \{ u_2(1, 3) + [\delta(1, 3) + \delta(1, 2)] u_2(2, 3) / \rho \\ &+ u_3(1, 2, 3) \} \beta \mathbf{F}_{32} \left. \right\} \\ &= \int d\mathbf{r}_1 r_{12}^2 \mathbf{r}_{12} \left\{ \int d\mathbf{r}_3 [\rho u_2(1, 3) + \delta(1, 3)] \beta \mathbf{F}_{32} \right. \\ &+ \rho \int d\mathbf{r}_3 c_3(1|2, 3) \beta \mathbf{F}_{32} \left. \right\} \\ &= \int d\mathbf{r}_1 r_{12}^2 \mathbf{r}_{12} \int d\mathbf{r}_3 s(1, 3) \beta \mathbf{F}_{32} \\ &+ \rho \int d\mathbf{r}_3 \beta \mathbf{F}_{32} \int d\mathbf{r}_1 r_{12}^2 \mathbf{r}_{12} c_3(1|2, 3). \end{aligned} \quad (12)$$

Note that splitting again into a short-range term and the Coulomb one we find for the first term on the right hand side of Eq. (12)

Author's personal copy

R Fantoni

$$\begin{aligned} & \int d\mathbf{r}_3 \beta \mathbf{F}_{32}^{sr} \int d\mathbf{r}_1 r_{12}^2 \mathbf{r}_{12} s(1,3) \\ &= - \int d\mathbf{r}_3 \beta v^{sr}(3,2) \int d\mathbf{r}_{12} \mathbf{V}_{\mathbf{r}_{12}} [r_{12}^2 \mathbf{r}_{12} s(1,3)], \quad (13) \\ &= \int d\mathbf{r}_{32} \beta v^{sr}(3,2) \int d\mathbf{S}_{12} r_{12}^2 \mathbf{r}_{12} s(1,3) = 0. \end{aligned}$$

Since $s(1,3) = s(|\mathbf{r}_{32} + \mathbf{r}_{21}|)$ decays exponentially fast as r_{12} tends to infinity and the surface integral is over a sphere centered on $r_{12} = 0$ and with an infinite radius. The same holds for the second term on the right hand side of Eq. (12).

This proves that the result we will find is independent from the addition of a short-range part to the Coulomb pair-potential.

Now we observe that

$$\int d\mathbf{r}_1 r_{12}^2 \mathbf{r}_{12} \int d\mathbf{r}_3 s(1,3) \beta \mathbf{F}_{32}^c \quad (14)$$

$$= \frac{1}{4} \int d\mathbf{r}_1 \mathbf{V}_{\mathbf{r}_1}(r_{12}^4) \int d\mathbf{r}_3 s(1,3) \beta \mathbf{F}_{32}^c$$

$$= -\frac{1}{4} \int d\mathbf{r}_1 \mathbf{V}_{\mathbf{r}_2}(r_{12}^4) \int d\mathbf{r}_3 s(1,3) \beta \mathbf{F}_{32}^c \quad (15)$$

$$= \frac{1}{4} \int d\mathbf{r}_1 r_{12}^4 \int d\mathbf{r}_3 s(1,3) \beta \mathbf{V}_{\mathbf{r}_2} \mathbf{F}_{32}^c \quad (16)$$

$$= \frac{1}{4} \int d\mathbf{r}_1 r_{12}^4 s(1,2) 4\pi e^2 \beta. \quad (17)$$

And also using integration by parts

$$\int d\mathbf{r}_1 r_{12}^2 \mathbf{r}_{12} \cdot \mathbf{V}_{\mathbf{r}_2} u_2(1,2) \quad (18)$$

$$= \int d\mathbf{r}_1 \mathbf{V}_{\mathbf{r}_{12}}(r_{12}^2 \mathbf{r}_{12}) u_2(1,2)$$

$$= 5 \int d\mathbf{r}_1 r_{12}^2 u_2(1,2) \quad (19)$$

$$= -\frac{15}{2\pi\rho^2\beta e^2}, \quad (20)$$

where in the last equation we used the main result of previous section for the second moment condition (11).

In this case $\int d\mathbf{r}_1 d\mathbf{r}_3 \beta \mathbf{F}_{32} r_{12}^2 \mathbf{r}_{12} c_3(1|2,3) \neq 0$ and we may recognize in such a term the one giving rise to the isothermal compressibility in Eq. (21).

Putting together Eqs. (12), (13), (14), (18), and (22) we should reach the following fourth moment result

$$I_4 = \int d\mathbf{r}_2 r_{12}^4 s_2(1,2) = \frac{15}{2\pi^2\rho^2\beta^2 e^4} \frac{\chi_T^0}{\chi_T} = \frac{120}{k_D^4} \frac{\chi_T^0}{\chi_T}, \quad (21)$$

where $\frac{1}{\chi_T^0} = \frac{\partial \rho}{\partial \rho}|_T$ is the isothermal compressibility and $\chi_T^0 = \beta/\rho$ the one of the ideal gas. As already stressed this result is independent from the addition of a short-range term to the Coulomb pair-potential.

Then we should be able to prove that

$$\begin{aligned} 1 - \frac{\chi_T^0}{\chi_T} &= \frac{\rho \int d\mathbf{r}_3 \beta \mathbf{F}_{32}^c \int d\mathbf{r}_1 r_{12}^2 \mathbf{r}_{12} c_3(1|2,3)}{\int d\mathbf{r}_1 r_{12}^2 \mathbf{r}_{12} \cdot \mathbf{V}_{\mathbf{r}_2} u_2(1,2)} \\ &= \frac{\rho \int d\mathbf{r}_3 \beta \mathbf{F}_{32}^c \int d\mathbf{r}_1 r_{12}^2 \mathbf{r}_{12} c_3(1|2,3)}{5 \int d\mathbf{r}_1 r_{12}^2 u_2(1,2)} \\ &= -\frac{2\pi\rho^3\beta^2 e^2}{15} \int d\mathbf{r}_{32} d\mathbf{r}_{12} c_3(1|2,3) r_{12}^2 \mathbf{r}_{12} \cdot \mathbf{V}_{\mathbf{r}_{32}} v^c(3,2) \\ &= -\frac{2\pi\rho^3\beta^2 e^2}{9} \int d\mathbf{r}_{32} d\mathbf{r}_{12} c_3(1|2,3) r_{12}^2 \mathbf{r}_{32} \cdot \mathbf{V}_{\mathbf{r}_{32}} v^c(3,2), \quad (22) \end{aligned}$$

where in the last equality we used $\mathbf{r}_{12} = \mathbf{r}_{13} + \mathbf{r}_{32}$, $\mathbf{V}_{\mathbf{r}}(r^2\mathbf{r}) = 5r^2$, $r^2\mathbf{V}_{\mathbf{r}}(\mathbf{r}) = 3r^2$, and integration by parts. This will be done in the next section.

5. Compressibility sum-rule

From the virial theorem follows that the pressure estimator can be written as follows [10],

$$\beta P = \rho - \frac{\beta\rho^2}{6} \int d\mathbf{r} u_2(r) \mathbf{r} \cdot \mathbf{V}_{\mathbf{r}} v^c(r). \quad (23)$$

So that

$$1 - \frac{\chi_T^0}{\chi_T} = 1 - \beta \frac{\partial P}{\partial \rho}|_T = \frac{\beta}{6} \int d\mathbf{r} \frac{\partial \rho^2 u_2(r)}{\partial \rho} \mathbf{r} \cdot \mathbf{V}_{\mathbf{r}} v^c(r), \quad (24)$$

We then see that Eq. (22) can be obtained using an analysis similar to the one of Vieillefosse et al. [16], thus finding

$$\frac{\partial \rho^2 u_2(r_{32})}{\partial \rho} = -\frac{4\pi\rho^3\beta e^2}{3} \int d\mathbf{r}_{12} r_{12}^2 c_3(1|2,3). \quad (25)$$

We then see how χ_T is the isothermal compressibility of a plasma with a Coulomb interaction pair-potential among the particles.

6. Conclusions

We determined the first three (even) structure factor moment sum-rules (4), (11), (21) for a three-dimensional Jellium with the particles interacting with a pair-potential that is the sum of the Coulomb potential e^2/r and a short-range term with either a finite range or decaying exponentially fast at large r . We found that they are all invariant in form respect to the addition of the short-range term. Moreover our derivations of the sum-rules are different and simpler than the ones already found in the literature (as described in the review of Ph. Martin [1]). This strategy carry us to the determination of a compressibility sum-rule (24) and (25) in agreement with the one of Vieillefosse [16].

Author's personal copy

Form invariance of the moment sum-rules\dots

When studying common matter, whose constituents are made of charged particles, the Coulomb interaction plays a special role, ruling the fundamental correlation sum-rules. What really matter is the long-range nature of the Coulomb interaction and the short-range details do not have an influence on the statistical behaviors of the many-body correlations. This allows to use different models for the charges behavior at short-range where we may have some sort of indeterminacy in the description of the point-wise constituents particles microscopic character. All these models will have the same macroscopic behavior.

We could for example apply our general setting to the particular case of charged hard-spheres, when the short-range term is just a hard-core repulsion of a certain diameter. This is just one of the commonly used short-range regularization employed in a two-component-plasma (TCP) with particles of opposite charges [13, 17, 18] that would otherwise collapse one over the other. Moreover the hard-core model has been historically the favorite playground in statistical mechanics as it represents the simplest model of many-body systems of interacting particles.

In a recent work Das, Kim, and Fisher [11, 12] found out, through finely discretized grand canonical Monte Carlo simulations, that in the Restricted Primitive Model (RPM) of an electrolyte [17, 18], the second- and fourth-moment charge-charge sum-rules, typical for ionic fluids, are violated at criticality. For a 1:1 equisized charge-symmetric hard-sphere electrolyte their grand canonical simulations, with a new finite-size scaling device, confirm the Stillinger-Lovett second-moment sum-rule except, contrary to current theory [19], for its failure at the critical point (T_c, ρ_c) . Furthermore, the k^4 term in the charge-charge correlation or structure factor $S_{ZZ}(k)$ expansion is found to diverge like the compressibility when $T \rightarrow T_c$ at ρ_c . These findings are in evident disagreement with available theory for *charge-symmetric* models and, although their results are qualitatively similar to behavior expected for *charge-asymmetric* systems [19], even a semi-quantitative understanding has eluded them. Our present study could be a first step towards an explanation of such puzzling behavior. Even if, as pointed out in Ref. [14], from the work of Santos and Piasecki [15] follows that the Ursell functions of any order are likely to have a long-range behavior on a critical point, thus violating our exponential clustering working-hypothesis.

The zeroth-, second-, and fourth-moment sum-rules are rigorously derived starting from the Born-Green-Yvon equations and the exponential clustering hypothesis by Suttrop and van Wonderen [20–22] for a thermodynamically stable ionic mixture made of point-wise particles of charges all of the same sign immersed in a neutralizing background, the Jellium-mixture. Our results show that the

addition of a hard-core, or more generally any finite-range or exponentially decaying contribution to the pair-potential, to the particles, which would be necessary in order to make thermodynamically stable the system of Suttrop and van Wonderen for mixtures with particles of opposite charges, does not change the form of the first two three moments of the structure factor of the one-component Jellium.

It is still an open problem the extension of our study to the more general case of a mixture. A semi-heuristic derivation has recently been carried out [13, 14] showing that the addition of the short-range term should not play any role at the level of the first three (even) structure factor moments for a neutral TCP without the background. Strictly speaking, in these derivations we had to use results that are only rigorously valid in the Debye regime, like the local neutrality of the homogeneous system. Our present rigorous result confirms this scenario, at least in the weak coupling limit. Another interesting project is to generalize these sum-rule results to the case of Jellium living in curved surfaces [23–26]. In these cases the system can be mapped in an equivalent flat Jellium interacting with an external potential generated by the curvature of the surface in which the particles live. Another interesting extension of our work consists in studying the case in which the short-range pair-potential decays at large distances as an inverse power s of the distance, in which case the decay of correlations is also always algebraic, with the only exception of $s = \nu - 2$ with ν the space dimension [9]. In this case we must drop the exponential clustering hypothesis and our present derivation is not valid anymore.

References

- [1] P. A. Martin *Rev. Mod. Phys.* **60**, 1075 (1988).
- [2] P. Debye and E. Hückel *Phys. Z.* **9**, 185 (1923).
- [3] F. H. S. Jr. and R. Lovett *J. Chem. Phys.* **49**, 1991 (1968)
- [4] P. A. Martin and C. Gruber *J. Stat. Phys.* **31**, 691 (1983)
- [5] P. Vieillefosse *J. Stat. Phys.* **41**, 1015 (1985)
- [6] D. Pines and P. Nozières, *The Theory of Quantum Liquids* (Benjamin, New York, 1966) p. 219
- [7] P. Vieillefosse and J. P. Hansen *Phys. Rev.* **A12**, 1106 (1975)
- [8] M. Baus *J. Phys.* **A11**, 2451 (1978)
- [9] A. Alastuey and P. A. Martin *J. Stat. Phys.* **39**, 405 (1985)
- [10] J. -P. Hansen and I. R. McDonald, *Theory of Simple Liquids*, 2nd ed. (Academic Press, London, 1986)
- [11] [S. K. Das, Y. C. Kim, and M. E. Fisher *Phys. Rev. Lett.* **107**, 215701 (2011)
- [12] [S. K. Das, Y. C. Kim, and M. E. Fisher *J. Chem. Phys.* **137**, 074902 (2012)
- [13] A. Alastuey and R. Fantoni, *J. Stat. Phys.* **163**, 887 (2016)
- [14] R. Fantoni *Physica A* **477C**, 187 (2017)
- [15] A. Santos and J. Piasecki *Mol. Phys.* **113**, 2855 (2015)
- [16] P. Vieillefosse and M. Brajon *J. Stat. Phys.* **55**, 1169 (1989)

Author's personal copy

R Fantoni

-
- [17] R. Fantoni and G. Pastore *Europhys. Lett.* **101**, 46003 (2013a) <https://doi.org/10.1209/0295-5075/101/46003>
- [18] R. Fantoni and G. Pastore *Phys. Rev. E* **87**, 052303 (2013b) <https://doi.org/10.1103/PhysRevE.87.052303>
- [19] G. Stell *J. Stat. Phys.* **78**, 197 (1995)
- [20] L. G. Suttorp and A. J. van Wonderen *Physica A* **145**, 533 (1987)
- [21] A. J. van Wonderen and L. G. Suttorp *Physica A* **145**, 557 (1987)
- [22] L. G. Suttorp *J. Phys. A: Math. Theor.* **41**, 495001 (2008)
- [23] R. Fantoni, B. Jancovici and G. Téllez *J. Stat. Phys.* **112**, 27 (2003) <https://doi.org/10.1023/A:1023671419021>
- [24] R. Fantoni and G. Téllez *J. Stat. Phys.* **133**, 449 (2008) <https://doi.org/10.1007/s10955-008-9616-x>
- [25] R. Fantoni *J. Stat. Mech.*, P04015 (2012a) <https://doi.org/10.1088/1742-5468/2012/04/P04015>
- [26] R. Fantoni *J. Stat. Mech.*, P10024 (2012b) <https://doi.org/10.1088/1742-5468/2012/10/P10024>
- Publisher's Note** Springer Nature remains neutral with regard to jurisdictional claims in published maps and institutional affiliations.
-

Chapter 63

How should we choose the boundary conditions in a simulation which could detect anyons in one and two dimensions?

Fantoni R., J. Low Temp. Phys. **202**, 247 (2021)

Title: “How should we choose the boundary conditions in a simulation which could detect anyons in one and two dimensions?” *Abstract:* We discuss the problem of anyonic statistics in one and two spatial dimensions from the point of view of statistical physics. In particular we want to understand how the choice of the Born-von Karman or the twisted periodic boundary conditions necessary in a Monte Carlo simulation to mimic the thermodynamic limit of the many body system influences the statistical nature of the particles. The particles can either be just bosons, when the configuration space is simply connected as for example for particles on a line. They can be bosons and fermions, when the configuration space is doubly connected as for example for particles in the tridimensional space or in a Riemannian surface of genus greater or equal to one (on the torus, etc ...). They can be scalar anyons with arbitrary statistics, when the configuration space is infinitely connected as for particles on the plane or in the circle. They can be scalar anyons with fractional statistics, when the configuration space is the one of particles on a sphere. One can further have multi components anyons with fractional statistics when the configuration space is doubly connected as for particles on a Riemannian surface of genus greater or equal to one. We determine an expression for the canonical partition function of hard core particles (including anyons) on various geometries. We then show how the choice of boundary condition (periodic or open) in one and two dimensions determines which particles can exist on the considered surface.

Author's personal copy

Journal of Low Temperature Physics (2021) 202:247–262
https://doi.org/10.1007/s10909-020-02532-0

TECHNICAL NOTE



How Should We Choose the Boundary Conditions in a Simulation Which Could Detect Anyons in One and Two Dimensions?

Riccardo Fantoni¹

Received: 18 February 2020 / Accepted: 13 September 2020 / Published online: 1 October 2020
© Springer Science+Business Media, LLC, part of Springer Nature 2020

Abstract

We discuss the problem of anyonic statistics in one and two spatial dimensions from the point of view of statistical physics. In particular, we want to understand how the choice of the Born–von Karman or the twisted periodic boundary conditions necessary in a Monte Carlo simulation to mimic the thermodynamic limit of the many body system influences the statistical nature of the particles. The particles can either be just bosons, when the configuration space is simply connected as for example for particles on a line. They can be bosons and fermions, when the configuration space is doubly connected as for example for particles in the tridimensional space or in a Riemannian surface of genus greater or equal to one (on the torus, etc.). They can be scalar anyons with arbitrary statistics, when the configuration space is infinitely connected as for particles on the plane or in the circle. They can be scalar anyons with fractional statistics, when the configuration space is the one of particles on a sphere. One can further have multi-components anyons with fractional statistics when the configuration space is doubly connected as for particles on a Riemannian surface of genus greater or equal to one. We determine an expression for the canonical partition function of hard core particles (including anyons) on various geometries. We then show how the choice of boundary condition (periodic or open) in one and two dimensions determines which particles can exist on the considered surface.

Keywords Statistical physics · Fractional statistics · Anyons · Computer simulation · Periodic boundary conditions · Twisted boundary conditions

✉ Riccardo Fantoni
riccardo.fantoni@posta.istruzione.it

¹ Dipartimento di Fisica, Università di Trieste, strada Costiera 11, 34151 Grignano, Trieste, Italy

1 Introduction

For the statistical mechanics of a systems of many anyons, very partial results can be obtained, because the exact solution of a gas of anyons is not known. In fact, in contrast to the bosonic or fermionic case where the statistics is implemented by hand on the many body Hilbert space by constructing completely symmetric or antisymmetric products of single particle wave functions, for anyons the complicated boundary conditions for the interchange of any two particles require the knowledge of the complete many-body configurations. Only the two-body problem is exactly soluble for anyons, and hence only the two-body partition function can be computed exactly. Since the thermodynamic limit cannot be performed, one has to resort to approximate or alternative methods to study the statistical mechanics of anyons [1, 2]. For example, if the thermodynamic functions are analytic in the particle density, it is well-known that the low density, or equivalently the high temperature limit, of a (free) gas can be investigated using the virial expansion.

Anyons have had important physical applications, and it would be wrong to convey the idea that they are just mathematical fantasies. For example, physical objects which can be described as anyons are the quasi-particle and quasi-hole excitations of planar systems of electrons exhibiting the fractional quantum Hall effect (QHE) (for a review see for instance [3]). Most of the great interest that anyonic theories have attracted in the past few years derives precisely from their relevance to a better understanding of the fractional QHE [4], in conjunction with several claims that anyons can provide also a non-standard explanation of the mechanism of high temperature superconductivity [5]. Even if recent experiments have cast some shadow on the relevance of fractional statistics to the observed high temperature superconductivity [6–8].

In this work, we focus on the important problem of how the boundary conditions on the simulation box influence the statistics of the anyonic (see chapter 2 of Ref. [9]) particles. We will consider various cases: the infinite line, the circle, the infinite plane, the torus, and the sphere. In each case, we will determine the nature of the statistics of the many anyons system. This is important because in a simulation of a real material one usually chooses periodic boundary conditions in order to approach the thermodynamic limit.

Another interesting problem is the determination of a spinor for an anyon with a given rational or even irrational (either algebraic or even transcendental) statistics. If the spin-statistics theorem [10] which states that, as a consequence of Lorentz invariance and of locality, half integer spin particles must obey to Fermi statistics and integer spin particles must obey to Bose statistics, there is nothing similar for anyonic statistics [11]. Citing Wilczek [12] we can say that “The basic difficulty, which makes this problem much more difficult for generic anyons than for bosons or fermions, is that for generic anyons the many-body Hilbert space is in no sense the tensor product of the one-particle Hilbert space. This circumstance can be understood in various ways. Its root is that in the general case the weighting supplied by anyon statistics depends not only on the initial and final

states, but also on a (topological) property of the trajectory connecting them. This means that in the general case it is impossible to summarize the effect of quantum statistics by projection on the appropriate weighted states, as we do for bosons and fermions—where, of course, we project, respectively, on symmetric and antisymmetric states.” We will consider this problem in a future work.

The work is organized as follows: in Sect. 2, we describe the statistical physics anyons problem in two dimensions; in Sect. 3, we prove for a two particle case that the periodic boundary conditions of the Born–von-Karman type needed in a simulation of a real material play a relevant role in the anyons problem and we review, accordingly, various cases: For scalar, many body wave functions on the segment or the infinite line one can have only bosons, on the circle one can only have anyons with arbitrary statistics, on the square or the infinite plane one can also have only anyons with arbitrary statistics, and on the torus which has two periodicities only bosons and fermions are allowed as on the infinite three-dimensional Euclidean space. We gave an original proof of these different behaviors for just a system of two, body with scalar wave functions; Sect. 4 is for our final remarks and conclusions.

2 The Statistical Physics Anyon Problem in Two Dimensions

The statistical mechanical properties of a quantum system of N hard core particles in a volume V in d spatial dimensions occupying positions $q \in (\mathbb{R}^d)^N$ and described by an Hamiltonian $\hat{\mathcal{H}}$ in thermal equilibrium at the inverse temperature $\beta = 1/k_B T$, with k_B the Boltzmann constant and T the absolute temperature, are obtainable from the thermal density matrix operator [13],

$$\hat{\rho} = \exp(-\beta\hat{\mathcal{H}}). \tag{1}$$

In the configurations space representation, the thermal density matrix can be written using the following path integral notation,

$$\rho(q', q; \beta) = \sum_{\alpha \in \pi_1(M_N^d)} \chi(\alpha) \iint_{q_\alpha(0)=q}^{q_\alpha(\hbar\beta)=q'} e^{-\frac{1}{\hbar} \int_0^{\hbar\beta} d\tau \mathcal{H}(q_\alpha(\tau), \dot{q}_\alpha(\tau))} \mathcal{D}q_\alpha, \tag{2}$$

where $\mathcal{H}(q, \dot{q})$ is the classical Hamiltonian of the N hard core, identical particles. The meaning of $\pi_1(M_N^d)$ and of the phases χ will be shown in the next two sections.

The canonical partition function can then be found from the trace of the density matrix,

$$Z(N, V, T) = \int \rho(q, q; \beta) dq. \tag{3}$$

2.1 M_N^d and Its Fundamental Group

Consider a system of N identical hard core particles moving in the Euclidean d -dimensional space, \mathbf{R}^d . A configuration of such a system is clearly specified by the N coordinates of the particles, i.e., by an element of $(\mathbf{R}^d)^N$. However, because of the hard core assumption, any two particles cannot occupy the same position. So from $(\mathbf{R}^d)^N$ we have to remove the diagonal,

$$\Delta = \{(\mathbf{r}_1, \dots, \mathbf{r}_N) \in (\mathbf{R}^d)^N : \mathbf{r}_i = \mathbf{r}_j \text{ for some } i \neq j\}. \tag{4}$$

Furthermore, our particles are identical and indistinguishable, so we should identify configurations which differ only in the ordering of the particles. In other words, we should divide by the permutation group S_N . Therefore, we conclude that the configuration space for our system is

$$M_N^d = \frac{(\mathbf{R}^d)^N - \Delta}{S_N}. \tag{5}$$

To find the fundamental group of such space is a standard problem in algebraic topology, which was solved in the early 60's [14–16]. It turns out that the fundamental group of M_N^d is given by

$$\pi_1(M_N^d) = \begin{cases} S_N & \text{if } d \geq 3 \\ B_N & \text{if } d = 2 \end{cases} \tag{6}$$

where B_N is Artin's braid group of N objects which has the permutation group S_N as a homomorphic image [17, 18].

Even from this formal point of view, we see that there is a crucial difference between two and three or more dimensions. To have a more explicit understanding of (6), let us consider a two particle example in light of what we have just observed. Let us start with the case of two dimensions. Instead of assigning the position vectors \mathbf{r}_1 and \mathbf{r}_2 for the two particles, is more convenient to introduce the center of mass coordinate,

$$\mathbf{R} = \frac{1}{2}(\mathbf{r}_1 + \mathbf{r}_2) \in \mathbf{R}^2, \tag{7}$$

and the relative coordinate,

$$\mathbf{r} = \mathbf{r}_1 - \mathbf{r}_2 \in \mathbf{R}^2 - \{0\}. \tag{8}$$

We have removed the origin because of the hard core requirement. Since \mathbf{R} is invariant under the permutations of S_2 , we can write,

$$M_2^2 = r_2^2 \times \mathbf{R}^2, \tag{9}$$

where r_2^2 is some space describing the two degrees of freedom of the relative motion. We now argue that r_2^2 has the topology of a cone. Since two configurations which differ only in the ordering of the particle indexes are indistinguishable, \mathbf{r} and $-\mathbf{r}$

Fig. 1 Schematic representation of r_2^2 with the topology of a cone without the tip. It is an infinitely connected space (Color figure online)

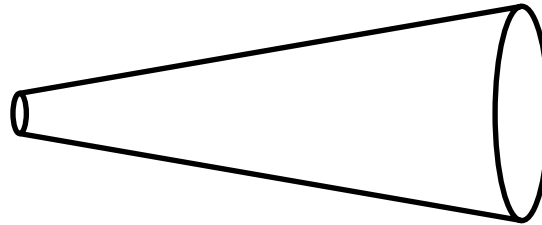
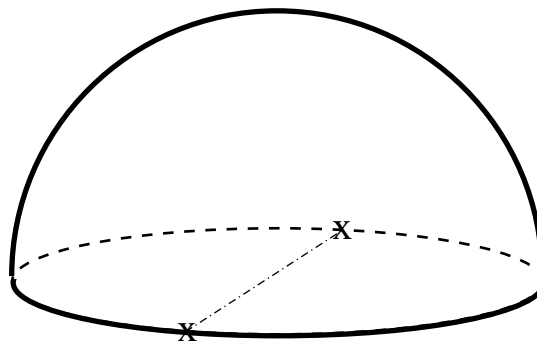


Fig. 2 Schematic representation of \mathcal{P}_2 as the northern hemisphere with opposite points on the equator being identified. It is a doubly connected space (Color figure online)



must be identified. The space r_2^2 is then the upper half plane without the origin and with the positive x -axis identified with the negative one, i.e., is a cone without the tip (see Fig. 1).

According to the decomposition (9), any loop in M_2^2 can be classified by the number of times it winds around the cone r_2^2 . Two loops q and q' with different winding numbers are homotopically inequivalent: it is not possible to deform one into the other since the vertex of the cone has been removed. Thus, the space r_2^2 and $r_2^2 \times R^2$ are infinitely connected, and,

$$\pi_1(M_2^2) = \pi_1(r_2^2 \times R^2) = \mathbb{Z} = B_2. \tag{10}$$

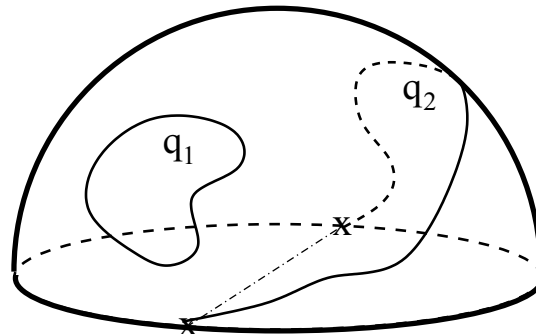
It is important to realize that if the vertex of the cone was included (i.e., allowing particles to occupy the same position in space), the configuration space would be simply connected. Any loop, even when winding around the cone, would be contracted to a point by deforming and unwinding it through the tip. Thus, if we do not impose the hard core constraint on the particles, we can describe only bosonic statistics.

Let us now turn to the case of two particles in three dimensions. After introducing the center of mass coordinate $\mathbf{R} \in R^3$, we can decompose the configurations space as,

$$M_2^3 = r_2^3 \times R^3, \tag{11}$$

where the space r_2^3 describes the three degrees of freedom of the relative motion. These are the length and the two angles of the relative coordinate \mathbf{r} . As before, \mathbf{r} and $-\mathbf{r}$ are identified. It is easy to realize that r_2^3 is just the product of the semi-infinite

Fig. 3 Schematic representation of a typical contractible loop q_1 and a typical non-contractible loop q_2 on M_2^3 which is a doubly connected space. The two points marked with an X are the same point. The path q_1 cannot be deformed continuously into the path q_2 (Color figure online)



line describing $|\mathbf{r}|$ and the projective space \mathcal{P}_2 describing the orientation of $\pm\mathbf{r}/|\mathbf{r}|$. In turn, \mathcal{P}_2 can be described as the northern hemisphere with opposite points on the equator being identified (see Fig. 2).

The space \mathcal{P}_2 is doubly connected and admits two classes of loops: those which can be shrunk to a point by a continuous transformation and those which cannot. In Fig. 3, we exhibit a typical contractible loop q_1 and a typical non-contractible loop q_2 .

Therefore, from the decomposition (11) and the topology of r_2^3 , we deduce that,

$$\pi_1(M_2^3) = \pi_1(r_2^3 \times R^3) = \mathbb{Z}_2 = S_2. \tag{12}$$

Thus, only bosons and fermions can exist, the former corresponding to contractible loops and the latter to non-contractible loops.

We have seen that at the heart of the anyonic statistics, there is the braid group B_N in place of the permutation group S_N which is responsible for ordinary statistics. There are only two one-dimensional unitary representations of S_N , namely the identical one, $\chi(\text{even and odd permutations}) = +1$ (bosonic statistics) and the alternating one, $\chi(\text{even permutations}) = +1, \chi(\text{odd permutations}) = -1$ (fermionic statistics). Whereas the braid group admits a whole variety of one-dimensional¹ unitary representations whose labeling parameter will be identified with the parameter ν also called the *statistics*.

2.2 Statistical Mechanics Problem

One is usually interested in calculating the partition function of the system which is given by the trace of the density matrix. So we choose $q = q'$, or loops in M_N^d . Two loops are considered equivalent (or homotopic) if one can be obtained from the other by a continuous deformation. All homotopic loops are grouped into one class and the set of all such classes is called the *fundamental group* and is denoted by π_1 .²

¹ When dealing with non-scalar quantum mechanics, i.e., when the wave functions are multiplets instead of one component objects as assumed in the discussion, appropriate higher-dimensional representations of $\pi_1(M_N^d)$ would be necessary.

² In the set π_1 one can define a product \cdot in a very simple and natural way: if α_1 and α_2 are two classes with representatives path q_1 and q_2 , then $\alpha_1 \cdot \alpha_2$ is the class whose representative is the path $q_1 q_2$ (that is the path q_1 followed by the path q_2). It can be shown that this product furnishes π_1 with a group structure.

Thus, an element of $\pi_1(M_N^d)$ is simply the set of all loops in M_N^d which can be continuously deformed into each other. On the other hand, loops belonging to two different elements of $\pi_1(M_N^d)$ cannot be connected by a continuous transformation. Naturally, $\rho(q', q; \beta)$ has to be a real positive probability function.

In order for (2) to make sense as a probability amplitude, the complex weights $\chi(\alpha)$ cannot be arbitrary. In fact, since we want to maintain the usual rule for combining probabilities,

$$\rho(q', q; \beta) = \int_{M_N^d} dq_o \rho(q', q_o; t_o/\hbar) \rho(q_o, q; \beta - t_o/\hbar), \tag{13}$$

the weights $\chi(\alpha)$ must satisfy,

$$\chi(\alpha_1) \chi^*(\alpha_2) = \chi(\alpha_1 \cdot \alpha_2), \tag{14}$$

for any α_1 and α_2 . Equation (14) can also be read as the statement that $\chi(\alpha)$ must be a one-dimensional unitary ($|\chi|^2 = 1$) representation of the fundamental group $\pi_1(M_N^d)$ [19]. To see which representations are possible, we have to specify better what is M_N^d and its fundamental group.

This means that we have to look for one-dimensional unitary representations $\chi(\alpha)$ of the fundamental group, i.e.,

$$\chi(\alpha) = e^{-i\nu n_\alpha \pi}, \quad n_\alpha \text{ integer}, \tag{15}$$

or in the notation used by Wilczek [12], $n = 4\omega$ and $\nu = \theta/2\pi$ where ω is the winding number and ν the relative angular momentum in units of \hbar quantized in units of $\nu + \text{integer}$ in each sector α .

In $d \geq 3$, there are only 2 possible representations of the permutation group: the one corresponding to the bosonic statistics ($\nu = 0 \pmod 2$) and the one corresponding to the fermionic statistics ($\nu = 1 \pmod 2$). In $d = 2$, one has to choose representations of the braid group (see chapter 2 of Ref. [9]) and the statistical parameter ν can be arbitrary at least in principle.³ Particles with this property are called *anyons*. In $d = 2$, it is not enough to specify the initial and final configurations to completely characterize the system; it is also necessary to specify how the different trajectories wind or *braid* around each other. In other words, the time evolution of the particles is important and cannot be neglected in $d = 2$. This fact implies that in order to classify and characterize anyons, and the representations of the permutation group must be replaced by those of the more complicated *braid group*.

The following is always true (here t and t' are two different imaginary times at which particles are found at the same spatial positions),

³ There are restrictions on ν coming from the topology of the two-dimensional space. For example for particles moving on a torus (or a 2D box with periodic boundary conditions), ν can only be a rational number (see Sect. 3.4).

$$\sum_{i < j} [\theta_{ij}(t') - \theta_{ij}(t)] = n\pi, \tag{16}$$

where the symbol θ_{ij} denotes the azimuthal angle of particle j with respect to particle i and n is an integer. This can be interpreted by saying that to complete a loop in configuration space an integer number of exchanges is always necessary. And one can write (see chapter 2 of Ref. [9])

$$\theta_{ij} = \tan^{-1} \left(\frac{x_j^2 - x_i^2}{x_j^1 - x_i^1} \right), \tag{17}$$

($x_i^1 - x_i^2$) being the Cartesian coordinates of the i th particle.

So, we can formally express

$$\chi(\alpha) = \exp \left[-i\nu \sum_{i,j} \int_0^{\hbar\beta} d\tau \frac{d}{d\tau} \theta_{ij}^{(\alpha)}(\tau) \right]. \tag{18}$$

Notice that the functions $\theta_{ij}^{(\alpha)}(\tau)$, where α represents an arbitrary braiding (see chapter 2 of Ref. [9]) are in general very complicated and can be specified only when the dynamics of the particles is fully taken into account. However, the formal definition (18) may come useful when inserted into the density matrix expression (19). So that the expression for the diagonal of the density matrix gets the suggestive form,

$$\begin{aligned} \rho(q, q; \beta) &= \sum_{\alpha \in \pi_1(M_N^2)} \chi(\alpha) \rho_\alpha(q, q; \beta) \\ &= \sum_{\alpha \in \pi_1(M_N^2)} \iint_{q_\alpha(0)=q}^{q_\alpha(\hbar\beta)=q} e^{-\frac{1}{\hbar} \int_0^{\hbar\beta} d\tau \left[\mathcal{H}(q_\alpha(\tau), q_\alpha(\tau)) + i\hbar\nu \sum_{i,j} \frac{d\theta_{ij}^{(\alpha)}(\tau)}{d\tau} \right]} \mathcal{D}q_\alpha. \end{aligned} \tag{19}$$

Expression (2) tells us that instead of dealing with anyons governed with the Hamiltonian \mathcal{H} , we can work with bosons whose dynamics is dictated by the new Hamiltonian $\mathcal{H}' = \mathcal{H} + i\hbar\nu \sum_{i,j} d\theta_{ij}^{(\alpha)}(\tau)/d\tau$. In particular, we could treat fermions governed by an Hamiltonian \mathcal{H} as bosons with a “fictitious” Hamiltonian $\mathcal{H}' = \mathcal{H} + i\hbar \sum_{i,j} d\theta_{ij}^{(\alpha)}(\tau)/d\tau$. Notice that this statistical interaction is very peculiar and intrinsically topological in nature (it is actually a total derivative). Its addition to the Hamiltonian \mathcal{H} does not change the equations of motion, which are a reflection of the local structure of the configuration space, but does change the statistical properties of the particles, which are instead related to the global topological structure of the configuration space (it can be locally realized as a gauge theory with a Chern–Simons kinetic term).

Now, since $\rho(q, q; \beta)$ has to be a real positive function as well as all the $\rho_\alpha(q, q; \beta)$ one has to add the constraints

$$\sum_{\alpha \in \pi_1(M_N^2)} \sin(vn_\alpha \pi) \rho_\alpha(q, q; \beta) = 0, \quad (20)$$

$$\sum_{\alpha \in \pi_1(M_N^2)} \cos(vn_\alpha \pi) \rho_\alpha(q, q; \beta) > 0. \quad (21)$$

3 Periodic Boundary Conditions

The configuration space M of identical hard core two-dimensional particles has a non-trivial topology.

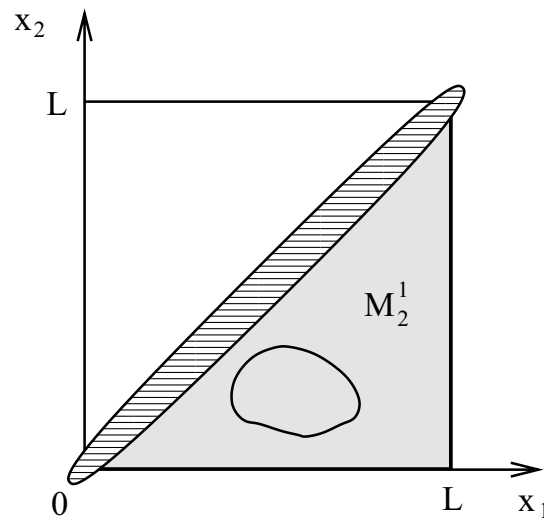
- If the particles are free to move in R^2 or in a finite $L \times L$ box, then the configuration space is infinitely connected (see Fig. 1). Its fundamental group is the braid group whose representations are labeled by an arbitrary parameter v . This unusual statistics can be implemented on ordinary particles (for instance bosons) by the addition of a topological statistical interaction as we saw in Eq. (19).
- If the particles are free to move in a finite box with periodic boundary conditions, a torus, a compact Riemannian surface of genus 1, then only bosons and fermions are possible [9] if the multi-particle wavefunctions carry a one-dimensional (appropriate for scalar wave functions) unitary representation of the braid group. However, anyons are possible even on a torus provided that wave functions with many components are considered, as for example for spin one-half electrons. In this case, one has to look at higher-dimensional representations of the braid group which lead to the concepts of *generalized fractional statistics and generalized anyons* [20–23]. Now, only fractional statistics are possible and $v = p/q$ can only be a rational number, with p and q coprime integers and $N = qn$ where n is a nonnegative integer. This is essentially due to the requirement to have nonzero winding numbers along the two periods (the two handles) of the torus: one periodicity winding acts on a wave function with k components by multiplying all components by the same phase factor, while the other periodicity winding mix among themselves the components of the wave function (at the end of chapter 2 of Ref. [9] the general case of a Riemannian surface of a generic genus is also made).

In order to avoid periodic boundary conditions, one could work on the surface of a sphere, in this case scalar anyons with fractional statistics will emerge [9].

So, this poses the following conceptual problem. If one is to simulate, for example through the Monte Carlo technique, a system of identical hard core particles living in two dimensions, he should use, for the many body wave function of the system contained in a two-dimensional box of sides L_1 and L_2 , either the Born–von Karman periodic boundary conditions

Author's personal copy

Fig. 4 In the plane (x_1, x_2) , the uniformly shaded region M_2^1 of Eq. (24) is simply connected. The slashed shaded region is the forbidden one (Color figure online)



$$\psi(\mathbf{r}_1, \dots, \mathbf{r}_j + \mathbf{L}, \dots) = e^{i\Theta/2} \psi(\mathbf{r}_1, \dots, \mathbf{r}_j, \dots), \quad \forall j = 1, \dots, N \quad (22)$$

with $\Theta = 0$ and $\mathbf{L} = (L_1, L_2)$ or the twisted boundary conditions [24], with $\Theta \neq 0$, to mimic the thermodynamic limit. Then, the fractional statistics or the anyonic nature of the particles is necessarily changed by the topological change of the configurational space. Moreover, as we will discuss in the conclusions the twisted boundary conditions, even if they do not alter the qualitative picture respect to the Born–von Karman boundary conditions, regarding the topological properties of the underlying configurational space, they become essential in the description of anyons or the fractional QHE (see [9] chapter 4). We can in fact say that in the interchange of two particles each one of the two changes identity when winding across the boundary (22) as follows,

$$\psi(\mathbf{r}_1, \dots, \mathbf{r}_j, \dots, \mathbf{r}_k, \dots) = e^{i\Theta} \psi(\mathbf{r}_1, \dots, \mathbf{r}_k, \dots, \mathbf{r}_j, \dots). \quad (23)$$

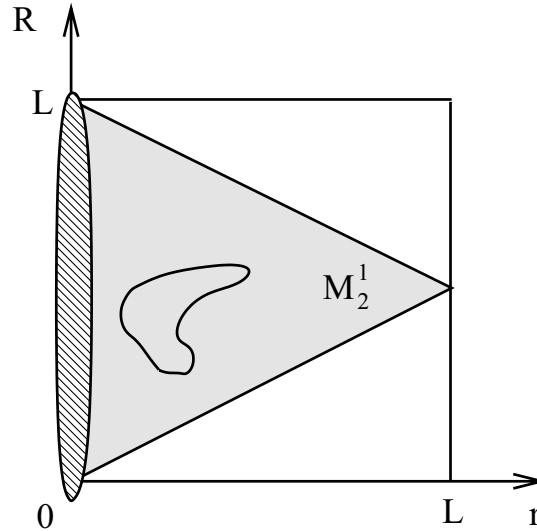
Since the discovery of the twisted boundary conditions by Chang Lin et al. in 2001 to optimize the approach to the thermodynamic limit of a generic Monte Carlo simulation of a many-body system, we are unaware of their use in computer experiment for anyons as in Eq. (23).

Let us now reduce ourselves to the $N = 2$ case. We have seen that when the particles are free to move on all \mathbf{R}^d , then the center of mass coordinate splits off in a trivial way. Let us see what we can easily say about the configuration spaces of particles confined in a box (B) or in a periodic box (PB). We start with a one-dimensional space and then, study the two-dimensional one.

3.1 For a Box in $d = 1$ [1d-B]

Call $x_1 \in [0, L]$ and $x_2 \in [0, L]$ the particles coordinates. In this case (see Fig. 4),

Fig. 5 Another view of M_2^1 of Eq. (24), now in the plane (r, R) with R the center of mass coordinate and r the relative coordinate r . Again, the slashed region is the forbidden one (Color figure online)



$$M_2^1 = \{(x_1, x_2) : x_2 \in [0, L], x_2 < x_1 \leq L\}, \tag{24}$$

which is simply connected. So, only boson statistics is allowed.

We could, as well, have introduced the center of mass coordinate $R = (x_1 + x_2)/2 \in]0, L[$ and the relative coordinate $r = x_1 - x_2$. Using this coordinates, $M_2^1 = r_2^1 \times]0, L[$ (see Fig. 5).

As expected again, M_2^1 is simply connected.

3.2 For a Box with Periodic Boundary Conditions in $d = 1$ [1d-PB]

We now consider the case of particles on a circle of length L . Using the center of mass coordinate $R = (x_1 + x_2)/2$ and the relative coordinate $r = x_1 - x_2$, one sees by inspection that,

$$\begin{aligned} M_2^1 = \{ & (r, R) : R \in [0, L/2], 2R - L \leq r \leq 2R, \\ & (2R, R) = (2R - L, R), (-r, 0) = (r, L/2) \} \\ & - \{(0, R) \forall R, (-L, 0), (0, L/2)\}, \end{aligned} \tag{25}$$

which is infinitely connected (as shown in Fig. 6 two loops with different winding around the missing point $(-L, 0) = (L, L/2)$ are homotopically inequivalent). So, anyons with arbitrary statistics ν is allowed.

The same thing can be seen introducing the center of mass angle ϕ and the relative angle θ (see Fig. 7). The rectangle in the (ϕ, θ) plane defined by $0 \leq \phi \leq \pi$ and $0 \leq \theta \leq 2\pi$ includes all possible configurations, except for the left and right edges where $(0, \theta)$ and $(\pi, 2\pi - \theta)$ both represent the same configuration. Because of this identification, the rectangle becomes a Möbius band which is still infinitely connected. In this case, though even with a multi-component wave function the statistics

Author's personal copy

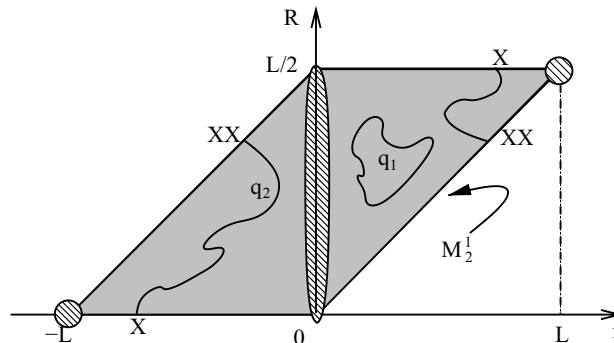


Fig. 6 In the plane (r, R) with R the center of mass coordinate and r the relative coordinate r , we show the uniformly shaded region M_2^1 of Eq. (25) which is infinitely connected. The points labeled X are the same point. The points labeled XX are the same point. The slashed shaded regions are the forbidden ones. The path q_1 cannot be deformed continuously into the path q_2 (Color figure online)

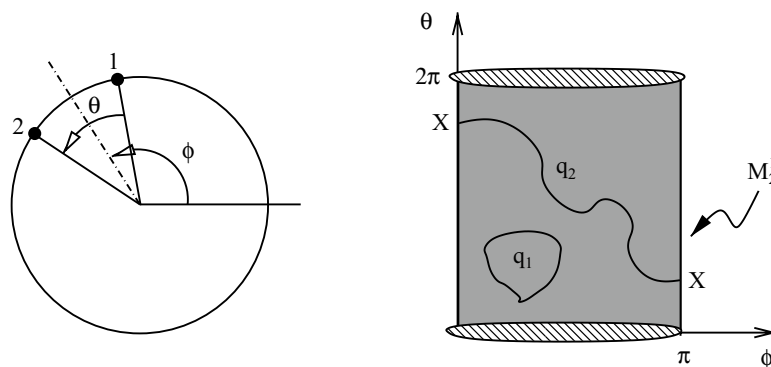


Fig. 7 On the right, we show the meaning of the angles θ , between the two particles 1 and 2 on the circle, and ϕ , the polar angle to the line joining the center of the circle to the center of mass of the two particles. The uniformly shaded region M_2^1 of Eq. (25) is infinitely connected. The points labeled X are coincident. The slashed shaded regions are the forbidden ones. The path q_1 cannot be deformed continuously into the path q_2 (Color figure online)

must remain arbitrary and not fractionary as in the two-dimensional one since we have only one periodicity.

3.3 For a Box in $d = 2$ [2d-B]

Using the same argument used for the [1d-B], we can say that $M_2^2 = r_2^2 \times [0, L]^2$ where r_2^2 is a space with the same topology as the cone without the tip introduced in the case of particles without boundaries. The only difference being that the cone now does not extend to infinity but is finite and its height depends on L . So once again, since r_2^2 is infinitely connected, also M_2^2 is. And anyon statistics is allowed with arbitrary ν .

3.4 For a Box with Periodic Boundary Conditions in $d = 2$ [2d-PB]

In this case, we can say that something similar was happening from going from the 2d plane (M infinitely connected) to the 3d space (M doubly connected). Now, in [1d-PB] M is infinitely connected and in [2d-PB] M is doubly connected. We split again M_2^2 into the product of the center of mass configuration space and of the two impenetrable particles relative coordinates one, r_2^2 . It turns out that now, due to the periodic boundary conditions, r_2^2 is a cone without the tip, of finite height, as in Fig. 1, and with the end points of a diameter of the base identified. This is a doubly connected space. All this is only true if we consider scalar wave functions, i.e., one-dimensional representations of the fundamental group of the configuration space. For wave functions with many components, the generators of the representations of the fundamental group of the configuration space are such that [9] $\nu = p/q$ a rational number, with p and q coprime numbers and a restriction on the total number of particles, $N = qn$, where n is a nonnegative integer. For an extensive discussion of anyons on compact surfaces and on the torus in particular, we refer the reader to the review by Lengo and Lechner [25].

4 Conclusions

Twisted boundary conditions play a relevant role in the anyons problem where the topology of the underlying configuration space determines the statistics of the particles. We review various cases. For scalar, many body wave functions on the segment or the infinite line one can have only bosons, on the circle one can only have anyons with arbitrary statistics, on the square or the infinite plane one can also have only anyons with arbitrary statistics, and on the torus which has two periodicities only bosons and fermions are allowed as on the infinite three-dimensional Euclidean space. In Sect. 3, we gave an original proof of these different behaviors for just a two-body system. This is enough to determine the anyonic symmetry of the many-body wave function as we discussed in Sect. 2.2, but one cannot exclude other kinds of three and higher body symmetries where it is necessary to substitute θ_{ij} of Eq. (17) with a different $\theta_{ijk\dots}$. We gave proofs of these circumstances based on the geometrical topological properties of the configurational space in each case, which we regard as the simplest way to proceed.

If we allow for a many components wave function on the torus, we may have anyons *but* with only *fractional statistics* which proved to give an interpretation for the fractional QHE. In this case, a series of new states of matter emerge as incompressible quantum liquids [26, 27] around which the low-energy excitations are localized quasi-particles with unusual fractional quantum numbers, i.e., anyons. The Laughlin variational ground-state wave functions requires the statistics, ν , to be an odd integer m , whereas the excited states require it to be rational. Laughlin chooses the trial ground-state wave function of the Bijl–Dingle–Jastrow product form

Author's personal copy

$$\psi_m = \mathcal{N}_m \prod_{i < j} (z_i - z_j)^m e^{-\frac{1}{4\ell_0^2} \sum_i |z_i|^2}, \quad (26)$$

where $\ell_0 = \sqrt{\hbar c/eB}$ is the magnetic length, B the magnetic field orthogonal to the metallic plate, z_i is the complex coordinate of the i -th electron and \mathcal{N}_m is a normalization factor. Since m is an odd integer, ψ is totally antisymmetric, and so it describes ordinary fermions. The prefactor $(z_i - z_j)^m$ is also of the Jastrow type: it has a zero of order m at coincident points ($z_i = z_j$), showing that electrons tend very strongly to repel each other in a way that is appropriate to minimize the Coulomb interaction. If z_i goes around z_j by an angle $\Delta\theta$, the wave function acquires a phase $e^{im\Delta\theta}$, as if each particle carried m units of flux. This allows Laughlin to use the fact that the $|\psi_m|^2$ can be interpreted as the Boltzmann factor $e^{-\beta\phi}$ of a One Component Plasma of classical particles of charge $Q = m$ living in two dimensions where the neutralizing background has a surface charge density $\sigma = m/2\pi\ell_0^2$ at an inverse temperature $\beta = 2/m$. The coupling constant of the plasma is $\Gamma = \beta Q^2 = 2m^2$, and its properties are available exactly analytically at the special value of the coupling constant $\Gamma = 2$ [28–30] when the two-dimensional electron gas corresponds to a full Landau level $m = 1$ (see Ref. [9] chapter 8).

A word of caution when thinking at the physical implications of all this is nonetheless necessary. From a purely conceptual point of view, the fact that in order to have a fractional statistics one has to impose twisted periodic boundary conditions that are an artificial means to approach the thermodynamic limit and have no physical meaning sheds some doubts on the relevance of the anyonic theory on the interpretation of the fractional QHE. From the point of view of the numerical experiment, the presence of a magnetic field implies that the ground state wave function will, in general, be complex valued and in order to deal with the symmetry given by the anyonic statistics one should use methods similar to the ones used in Ref. [31, 32]. Also, we proposed to combine these methods with the twisted boundary conditions first employed in 2001 by Chang Lin et al. [24] for a generic many-body system. It would be desirable to perform the simulation on a sphere with a Dirac magnetic monopole at the center [33] in order to be able to simulate scalar anyons with fractional statistics, without the necessity of implementing any sort of boundary conditions.

Another issue in disfavor of the description of the physically observed QHE is the fact that in a laboratory the electrons will surely not be exactly living in a two-dimensional world, but one deals rather with a quasi-two-dimensional, very very thin, metallic layer [34] at the interface between two different semiconductors or between a semiconductor and an insulator even if the low temperature and/or the strong magnetic field freezes the motion along the direction perpendicular to the layer (something similar as explained in the satirical novella by the English schoolmaster Edwin Abbott: “Flatland: A Romance of Many Dimensions” first published in 1884 by Seeley & Co. of London). This of course would modify also the Coulomb potential of interaction between the electrons from one $\propto -\log(r/L)$ to one $\propto 1/r$, with r the separation between electrons, which are in any case

both divergent at $r = 0$. Naturally, the Coulomb repulsion is essential to give the incompressibility condition avoiding two particles to overlap.

The real experiment is too complicated to describe in its completeness so one has to resort to approximations and the approximation of considering the electrons as “living” in a two-dimensional world with periodic twisted boundary conditions seems to be an effective one. There are many experiments in the field. A mostly interesting one is described in Ref. [35] where it is shown that the sign of the Hall effect in the transport properties of doped lanthanum manganites films for small polaron [36, 37] hopping can be “anomalous.” A small polaron based on an electron can be deflected in a magnetic field as if it was positively charged and, conversely, a hole-based polaron can be deflected in the sense of a free electron. Measurements of the high-temperature Hall coefficient of manganite samples reveal that it exhibits Arrhenius behavior and a sign anomaly relative to both the nominal doping and the thermoelectric power. The results are discussed in terms of an extension of the Emin–Holstein theory of the Hall mobility in the adiabatic limit.

There are now several proposed experiments aimed at identifying the existence of non-Abelian statistics in nature. Non-Abelian phases are gapped phases of matter in which the adiabatic transport of one excitation around another implies a unitary transformation within a subspace of degenerate wavefunctions which differ from each other only globally [38].

Another more recent experimental interest in anyons is for topological quantum computation [39, 40]: Systems exhibiting non-Abelian statistics can store topologically protected qubits [41].

Acknowledgements I would like to acknowledge fruitful discussions with Rob Leigh, Eduardo Fradkin, Michael Stone, and last but not least Myron Salamon who showed me the physics of calorimeters, way back in 2000 in Urbana.

References

1. S. Ouvry, Séminaire Poincaré **11**, 77 (2007)
2. A. Stern, Ann. Phys. **323**, 204 (2008)
3. R. Prange, S. Girvin, in *The Quantum Hall Effect*, ed. by R. Prange, S. Girvin (Springer, Berlin, 1990)
4. B. Halperin, Phys. Rev. Lett. **52**, 1583 (1984)
5. Y.-H. Chen, F. Wilczek, E. Witten, B. Halperin, Int. J. Mod. Phys. B **3**, 1001 (1989)
6. K. Lyons, J. Kwo, J. Dillon Jr., G. Espinosa, M. McGlashan-Powell, A. Ramirez, L. Schneemeyers, Phys. Rev. Lett. **64**, 2949 (1990)
7. R. Kiefl, J. Brewer, I. Affieck, J. Carolan, W.H.P. Dosanjh, T. Hsu, R. Kadono, J. Kempton, S. Kretitzman, A.O.Q. Li, T. Riseman, P. Schleger, P. Stamp, H. Zhou, G.L.L.P. Le, B. Sternlieb, Y. Venmra, H. Hart, K. Lay, Phys. Rev. Lett. **64**, 2082 (1990)
8. S. Spielman, K. Fesler, C. Eom, T. Geballe, M. Fejer, A. Kapitulnik, Phys. Rev. Lett. **65**, 123 (1990)
9. A. Lerda, *Anyons. Quantum Mechanics of Particles with Fractional Statistics, Lecture Notes in Physics* (Springer, Berlin, 1992)
10. W. Pauli, Phys. Rev. **58**, 716 (1940)
11. R. Oeckl, J. Geom. Phys. **39**, 233 (2001)
12. F. Wilczek, *Fractional Statistics and Anyon Superconductivity* (World Scientific, Singapore, 1990)
13. Y.S. Wu, Phys. Rev. Lett. **53**, 111 (1984)
14. E. Fadell, L. Neuwirth, Math. Scand. **10**, 111 (1962)

15. R. Fox, L. Neuwirth, *Math. Scand.* **10**, 119 (1962)
16. E. Fadell, J.V. Buskirk, *Duke Math. J.* **29**, 243 (1962)
17. E. Artin, *Abh. Math. Sem. Hamburg.* **4**, 47 (1926)
18. E. Artin, *Ann. Math.* **48**, 101 (1947)
19. M.G.G. Laidlaw, M.D. Witt, *Phys. Rev. D* **3**, 1375 (1971)
20. T. Einarsson, *Phys. Rev. Lett.* **64**, 1995 (1990)
21. T. Einarsson, *Mod. Phys. Lett. B* **5**, 675 (1991)
22. T. Imbo, J. March-Russell, *Phys. Lett.* **252B**, 84 (1990)
23. X.-G. Wen, *Phys. Rev. Lett.* **64**, 2206 (1990)
24. C. Lin, F.H. Zong, D.M. Ceperley, *Phys. Rev. E.* **64**, 016702 (2001)
25. R. Jengo, K. Lechner, *Phys. Rep.* **213**, 179 (1992)
26. R. Laughlin, *Phys. Rev. Lett.* **50**, 1395 (1983)
27. R. Laughlin, *Phys. Rev. B.* **B23**, 3383 (1983)
28. B. Jancovici, *Phys. Rev. Lett.* **46**, 386 (1981)
29. R. Fantoni, B. Jancovici, G. Téllez, *J. Stat. Phys.* **112**, 27 (2003)
30. R. Fantoni, G. Telléz, *J. Stat. Phys.* **133**, 449 (2008)
31. L. Zhang, G. Canright, T. Barnes, in *Computer Simulation Studies*, in *Condensed-Matter Physics VI, Springer Proceedings in Physics*, vol. 76, ed. by D.P. Landau, K.K. Mon, H.-B. Schüttler (Springer, Heidelberg, 1993), pp. 199–203
32. M.D. Jones, G. Ortiz, D.M. Ceperley, *Phys. Rev. E.* **55**, 6202 (1997)
33. V. Melik-Alaverdian, G. Ortiz, N.E. Bonesteel, *J. Stat. Phys.* **104**, 449 (2001)
34. R. Fantoni, *Regole di somma in un gas di elettroni stratificato*, edited by R. Fantoni (Gruppo Editoriale l'Espresso S.p.A., Roma, *Laurea thesis at "Scuola Normale Superiore" in Pisa (1995)* (M. P. Tosi, Advisor, 2012). ISBN 978-889-101-539-6
35. M. Jaime, H.T. Hardner, M.B. Salamon, M. Rubinstein, P. Dorsey, D. Emin, *Phys. Rev. Lett.* **78**, 951 (1997)
36. R. Fantoni, *Phys. Rev. B.* **86**, 144304 (2012)
37. R. Fantoni, *Physica B* **412**, 112 (2013)
38. N. Read, G. Moore, *Prog. Theor. Phys. Suppl.* **107**, 157 (1992)
39. A. Stern, *Nature* **464**, 187 (2010)
40. C.W. von Keyserlingk, S.H. Simon, B. Rosenow, *Phys. Rev. Lett.* **115**, 126807 (2015)
41. S.D. Sarma, M. Freedman, C. Nayak, *Phys. Rev. Lett.* **94**, 166802 (2005)

Publisher's Note Springer Nature remains neutral with regard to jurisdictional claims in published maps and institutional affiliations.

Chapter 64

Jellium at finite temperature using the restricted worm algorithm

Fantoni R., Eur. Phys. J. B **94**, 63 (2021)

Title: “Jellium at finite temperature using the restricted worm algorithm”

Abstract: We study the Jellium model of Wigner at finite, non zero, temperature through a computer simulation using the canonical path integral worm algorithm where we successfully implemented the fixed node free particles restriction necessary to circumvent the fermion sign problem. Our results show good agreement with the recent simulation data of Brown et al. and of other similar computer experiments on the Jellium model at high density and low temperature. Our algorithm can be used to treat any quantum fluid model of fermions at finite, non zero, temperature and has never been used before in literature.



Jellium at finite temperature using the restricted worm algorithm

Riccardo Fantoni^a

Dipartimento di Fisica, Università di Trieste, Strada Costiera 11, Grignano, Trieste 34151, Italy

Received 15 December 2020 / Accepted 6 March 2021

© The Author(s), under exclusive licence to EDP Sciences, SIF and Springer-Verlag GmbH Germany, part of Springer Nature 2021

Abstract. We study the Jellium model of Wigner at finite, non-zero, temperature through a computer simulation using the canonical path integral worm algorithm where we successfully implemented the fixed-node free particle restriction necessary to circumvent the fermion sign problem. Our results show good agreement with the recent simulation data of Brown et al. and of other similar computer experiments on the Jellium model at high density and low temperature. Our algorithm can be used to treat any quantum fluid model of fermions at finite, non-zero, temperature and has never been used before in the literature.

1 Introduction

The free electron gas or the *Jellium* model of Wigner [1] is the simplest physical model for the valence electrons in a metal [2] (more generally it is an essential ingredient for the study of ionic liquids (see Ref. [3] Chapters 10 and 11): molten-salts, liquid-metals, and ionic-solutions) or the plasma in the interior of a white dwarf [4]. It can be imagined as a system of pointwise electrons of charge e made thermodynamically stable by the presence of a uniform, inert, neutralizing background of opposite charge density inside which they move. In this work, we will only be interested in Jellium in three-dimensional Euclidean space even if some progress has been made to study this system in curved surfaces, too [5–9].

The zero-temperature, ground-state, properties of the statistical mechanical Jellium model thus depend just on the electronic density n , or the Wigner–Seitz radius $r_s = (3/4\pi n)^{1/3}/a_0$ where a_0 is Bohr radius, or the Coulomb coupling parameter $\Gamma = e^2/(a_0 r_s)$. Free electrons in metallic elements [2] has $2 \lesssim r_s \lesssim 4$, whereas in the interior of a white dwarf [4] $r_s \simeq 0.01$. This model has been intensively studied in the second half of last century.

The finite, non-zero, temperature model depends additionally on a parameter $\Theta = T/T_F$ where T is the absolute temperature and T_F the Fermi temperature. This model has received much attention more recently.

The past 2 decades have witnessed an impressive progress in experiments and also in quantum Monte Carlo simulations, which have provided the field with the most accurate thermodynamic data available. The

simulations started with the pioneering work by Ceperley and co-workers later developed by Filinov and co-workers. These have been carried on for the pure Jellium model [10–19], for hydrogen, hydrogen–helium mixtures, and electron–hole plasmas. Also, we recently applied our newly developed simulation methods to the one-component system of charged bosons and fermions, both in the three-dimensional Euclidean space and on the surface of a sphere, and to the binary fermion–boson plasma mixture at finite temperature [9, 20]. In the latter study, we discussed the thermodynamic stability, from the simulation point of view, of the two-component mixture where the two species are both bosons, both fermions, and one boson and one fermion. Shortly after our results were published, other groups reported [21] about computer experiments using methods partly similar to ours.

Today we are able to simulate on a computer the structural and thermodynamic properties of Jellium at finite, non-zero, temperature. This allows us to predict thermodynamic states that would be rather difficult to obtain in nature or in the laboratory, such as Jellium under extreme conditions, partially polarized Jellium. In this work, we will carry on some of these path integral simulations which make use of the Monte Carlo technique. Monte Carlo is the best known method to compute a path integral [22]. The computer experiment is alternative to theoretical analytic approximations like the Random-Phase-Approximation [23–30].

As will be made clear in Sect. 3, until recently, we were unable to obtain exact numerical results even through computer experiments since one had to face the so called *fermions sign problem* which had not been solved before the advent of recent simulation techniques [15, 16]. When it was demonstrated that the fermions sign problem can be partly avoided and nearly

^a e-mail: riccardo.fantoni@posta.istruzione.it (corresponding author)

exact results for the thermodynamic functions can be obtained with an error below 1%. In other words, we were not able to extract exact results not even numerically from a simulation for fermions, unlike for bosons or boltzmannons. Therefore, to circumvent the fermion sign problem, we will here resort to the most widely used approximation in quantum Monte Carlo that is the restricted path integral fixed-node method [31,32]. But unlike previous studies, we will implement this method upon the worm algorithm [33,34] in the canonical ensemble. Recently, we carried on [35] simulations in the grand canonical ensemble; in the present study, we will instead worry about a precise comparison with the data of Brown et al. [10] who worked in the canonical ensemble. The worm algorithm is preferable over the usual path integral Monte Carlo methods [22] since it is able to build the sum over the permutation through a menu of moves on open paths—the worms—instead of sampling the permutation sum explicitly.

The work is organized as follows: in Sect. 2, we describe the Jellium model from a statistical physics point of view; in Sect. 3, we describe the simulation method; in Sect. 4, we outline the problem we want to solve on the computer; in Sect. 5, we present our new algorithm in detail; Sect. 6 is for our numerical results; in Sect. 7, we summarize our concluding remarks.

2 The model

The Jellium model of Wigner [36–39] is an assembly of N_+ spin up pointwise electrons and N_- spin down pointwise electrons of charge e moving in a positive, inert background that ensures charge neutrality. The total number of electrons is $N = N_+ + N_-$ and the average particle number density is $n = N/\Omega$, where Ω is the volume of the electron fluid. In the volume $\Omega = L^3$, there is a uniform, neutralizing background with a charge density $\rho_b = -en$. So that the total charge of the system is zero. The fluid polarization is then $\xi = |N_+ - N_-|/N$: $\xi = 0$ in the unpolarized (paramagnetic) case and $\xi = 1$ in the fully polarized (ferromagnetic) case.

Setting lengths in units of $a = (4\pi n/3)^{-1/3}$ and energies in Rydberg's units, $Ry = \hbar^2/2ma_0^2$, where m is the electron mass and $a_0 = \hbar^2/me^2$ is the Bohr radius, the Hamiltonian of Jellium is

$$\mathcal{H} = -\frac{1}{r_s^2} \sum_{i=1}^N \nabla_{\mathbf{r}_i}^2 + V(R), \tag{2.1}$$

$$V = \frac{1}{r_s} \left(2 \sum_{i < j} \frac{1}{|\mathbf{r}_i - \mathbf{r}_j|} + \sum_{i=1}^N r_i^2 + v_0 \right), \tag{2.2}$$

where $R = \{\mathbf{r}_1, \mathbf{r}_2, \dots, \mathbf{r}_N\}$ with \mathbf{r}_i the coordinate of the i th electron, $r_s = a/a_0$, and v_0 a constant containing the self energy of the background. Note that the presence

of the neutralizing background produces the harmonic confinement shown in Eq. (2.1).

The kinetic energy scales as $1/r_s^2$ and the potential energy (particle–particle, particle–background, and background–background interaction) scales as $1/r_s$, so for small r_s (high electronic densities), the kinetic energy dominates and the electrons behave like an ideal gas. In the limit of large r_s , the potential energy dominates and the electrons crystallize into a Wigner crystal [40]. No liquid phase is realizable within this model since the pair-potential has no attractive parts, even though a superconducting state [41] may still be possible (see chapter 8.9 of Refs. [42] and [43]).

The Jellium in its ground state has been solved either by integral equation theories [27] or by computer experiments [44] in the second half of last century but more recently it has been studied at finite, non-zero, temperatures by several research groups [10–12,14–18].

Following Brown et al. [10], it is convenient to introduce the electron degeneracy parameter $\Theta = T/T_F$ for the Jellium at finite temperature, where T_F is the Fermi temperature of either the unpolarized ($\xi = 0$) or polarized ($\xi = 1$) system

$$T_F = T_D \frac{(2\pi)^2}{2[(2 - \xi)\alpha_3]^{2/3}}, \tag{2.3}$$

ξ is the polarization of the fluid, $\alpha_3 = 4\pi/3$ is the volume of the unit sphere, and

$$T_D = \frac{n^{2/3}\hbar^2}{mk_B} = \frac{\hbar^2}{mk_B\alpha_3^{2/3}(a_0r_s)^2} \tag{2.4}$$

is the degeneracy temperature [22], i.e. the temperature at which the de Broglie thermal wavelength becomes comparable to the mean separation between the particles ($\propto n^{-1/3}$). For temperatures higher than T_D quantum effects are less relevant.

The state of the fluid will also depend upon the Coulomb coupling parameter, $\Gamma = e^2/(a_0r_s)k_B T$ [10], so that

$$\Theta = \frac{r_s}{\Gamma} \left[\frac{2(2 - \xi)^{2/3}\alpha_3^{4/3}}{(2\pi)^2} \right]. \tag{2.5}$$

The behavior of the internal energy of Jellium in its ground state ($\Theta = 0$) has been determined through Diffusion Monte Carlo (DMC) by Ceperley and Alder [44]. Three phases of the fluid appeared: for $r_s < 75$, the stable phase is the one of the unpolarized Jellium, for $75 < r_s < 100$, the one of the polarized fluid, and for $r_s > 100$, the one of the Wigner crystal. They used systems from $N = 38$ to $N = 246$ electrons.

It was shown in Ref. [13] that the data of Brown et al. [10,11], for the finite, non-zero temperature case, are inaccurate at high densities, $r_s \lesssim 1$. This appears to be a systematic error, of up to 10%, of the restricted path integral fixed node method. Thus,

it would be interesting to know whether this problem may be solved with our present method, which seems a promising route to access higher densities. They provide results for the thermodynamic properties of Jellium with 33 fully polarized, $\xi = 1$ electrons and 66 unpolarized, $\xi = 0$ electrons, in the warm-dense regime: $r_s = 1, 2, 4, 6, 8, 10, 40$ and $\Theta = 0.0625, 0.125, 0.25, 0.5, 1, 2, 4, 8$.

3 The simulation

The density matrix of a system of many fermions at temperature $k_B T = \beta^{-1}$ can be written as an integral over all paths $\{R_t | 0 \leq t \leq \beta\}$

$$\begin{aligned} \rho_F(R_\beta, R_0; \beta) &= \frac{1}{N!} \sum_{\mathcal{P}} (-1)^{\mathcal{P}} \int_{\mathcal{P}R_0 \rightarrow R_\beta} dR_t \exp(-S[R_t]), \end{aligned} \tag{3.1}$$

where $R_t = \{\mathbf{r}_1(t), \dots, \mathbf{r}_N(t)\}$ represents the positions of all the particles at *imaginary time* t . The path begins at $\mathcal{P}R_0$ and ends at R_β ; \mathcal{P} is a permutation of particles labels. For non-relativistic particles interacting with a potential $V(R)$, the action of the path, $S[R_t]$, is given by

$$S[R_t] = \int_0^\beta dt \left[\frac{r_s^2}{4} \left| \frac{dR_t}{dt} \right|^2 + V(R_t) \right]. \tag{3.2}$$

Thermodynamic properties, such as the energy, are related to the diagonal part of the density matrix, so that the path returns to its starting place or to its permutation \mathcal{P} after a time β .

To perform Monte Carlo calculations of the integrand, one makes the imaginary time discrete with a time step τ , so that one has a finite (and hopefully small) number of time slices and thus an isomorphic classical system of N particles in $M = \beta/\tau$ time slices; an equivalent NM particle classical system of “polymers” [22].

Note that in addition to sampling the path, the permutation is also sampled. This is equivalent to allowing the ring polymers to connect in different ways. This macroscopic “percolation” of the polymers is directly related to superfluidity, as Feynman [45–47] first showed for bosons. Any permutation can be broken into cycles. Superfluid behavior can occur at low temperature when the probability of exchange cycles on the order of the system size is non-negligible. The superfluid fraction can be computed in a path integral Monte Carlo (PIMC) calculation as described in Ref. [43]. The same method could be used to calculate the superconducting fraction in Jellium at low temperature. However, the straightforward application of those techniques to Fermi systems means that odd permutations must be subtracted from the integrand. This is

the “fermions sign problem” [31] first noted by Feynman [48] who after describing the path integral theory for boson superfluid ^4He , pointed out: “The [path integral] expression for Fermi particles, such as ^3He , is also easily written down. However in the case of liquid ^3He , the effect of the potential is very hard to evaluate quantitatively in an accurate manner. The reason for this is that the contribution of a cycle to the sum over permutations is either positive or negative depending whether the cycle has an odd or an even number of atoms in its length [...]. At very low temperature [...], it is very difficult to sum an alternating series of large terms which are decreasing slowly in magnitude when a precise analytic formula for each term is not available.”

Thermodynamic properties are averages over the thermal, N -fermions density matrix which is defined as a thermal occupation of the exact eigenstates $\phi_i(R)$

$$\rho_F(R, R'; \beta) = \sum_i \phi_i^*(R) e^{-\beta E_i} \phi_i(R'). \tag{3.3}$$

The partition function is the trace of the density matrix

$$Z(\beta) = e^{-\beta F} = \int dR \rho_F(R, R; \beta) = \sum_i e^{-\beta E_i}. \tag{3.4}$$

Other thermodynamic averages are obtained as

$$\langle \mathcal{O} \rangle = Z(\beta)^{-1} \int dR dR' \langle R | \mathcal{O} | R' \rangle \rho_F(R', R; \beta). \tag{3.5}$$

Note that for any density matrix the diagonal part is always positive

$$\rho_F(R, R; \beta) \geq 0, \tag{3.6}$$

so that $Z^{-1} \rho_F(R, R; \beta)$ is a proper probability distribution. It is the diagonal part which we need for many observables, so that probabilistic ways of calculating those observables are, in principle, possible.

Path integrals are constructed using the product property of density matrices

$$\begin{aligned} \rho_F(R_2, R_0; \beta_1 + \beta_2) &= \int dR_1 \rho_F(R_2, R_1; \beta_2) \rho_F(R_1, R_0; \beta_1), \end{aligned} \tag{3.7}$$

which holds for any sort of density matrix. If the product property is used M times we can relate the density matrix at a temperature β^{-1} to the density matrix at a temperature $M\beta^{-1}$. The sequence of intermediate points $\{R_1, R_2, \dots, R_{M-1}\}$ is the path, and the time step is $\tau = \beta/M$. As the time step gets sufficiently small the Trotter theorem tells us that we can assume that the kinetic \mathcal{T} and potential \mathcal{V} operator commute so that: $e^{-\tau \mathcal{H}} = e^{-\tau \mathcal{T}} e^{-\tau \mathcal{V}}$ and the primitive approximation for the fermions density matrix is found [22]. The Feynman–Kac formula for the fermions density matrix results from taking the limit $M \rightarrow \infty$. The price we

have to pay for having an explicit expression for the density matrix is additional integrations; all together $3N(M - 1)$. Without techniques for multidimensional integration, nothing would have been gained by expanding the density matrix into a path. Fortunately, simulation methods can accurately treat such integrands. It is feasible to make M rather large, say in the hundreds or thousands, and thereby systematically reduce the time-step error.

One can then measure [22] the internal energy (kinetic plus potential energy) per particle using the thermodynamic estimator, the pressure using the virial theorem estimator, the static structure (the radial distribution function), and the superconducting fraction of Jellium.

One solution to Feynman’s task of rearranging terms to keep only positive contributing paths for diagonal expectation values is the restricted or fixed-nodes path integral identity. Suppose ρ_F is the density matrix corresponding to some set of quantum numbers which is obtained using the antisymmetrization operator \mathcal{A} acting on the same spin groups of particles on the distinguishable particle density matrix. Then the following Restricted Path Integral identity holds [31,32].

$$\rho_F(R_\beta, R_0; \beta) = \int dR' \rho_F(R', R_0; 0) \oint_{R' \rightarrow R_\beta \in \gamma(R_0)} dR_t e^{-S[R_t]}, \tag{3.8}$$

where the subscript means that we restrict the path integration to paths starting at R' , ending at R_β and node-avoiding (those for which $\rho_F(R_t, R_0; t) \neq 0$ for all $0 < t \leq \beta$), i.e. paths staying inside the reach of the reference point R_0 , [32] $\gamma(R_0)$ or the nodal cell [31]. The weight of the walk is $\rho_F(R', R_0; 0) = (N!)^{-1} \sum_{\mathcal{P}} (-)^{\mathcal{P}} \delta(R' - \mathcal{P}R_0)$. It is clear that the contribution of all the paths for a single element of the density matrix will be of the same sign, thus solving the sign problem; positive if $\rho_F(R', R_0; 0) > 0$, negative otherwise. On the diagonal the density matrix is positive and on the path restriction we can always choose $\rho_F(R_t, R_0; t) > 0$ for $0 < t \leq \beta$, then only even permutations are allowed since $\rho_F(R_0, \mathcal{P}R_0; \beta) = (-)^{\mathcal{P}} \rho_F(R_0, R_0; \beta)$. It is then possible to use a bosons calculation to get the fermions case once the restriction has been correctly implemented.

The problem we now face is that the unknown density matrix appears both on the left-hand side and on the right-hand side of Eq. (3.8) since it is used to define the criterion of node-avoiding paths. To apply the formula directly, we would somehow have to self-consistently determine the density matrix. In practice what we need to do is make an ansatz, which we call ρ_T , for the nodes of the density matrix needed for the restriction. The trial density matrix, ρ_T , is used to define the trial reach: $\gamma_T(R_0)$.

Then if we know the reach of the fermion density matrix we can use the Monte Carlo method to solve the fermion problem, restricting the path integral (RPIMC)

to the space-time domain where the density matrix has a definite sign (this can be done, for example, using a trial density matrix whose nodes approximate well the ones of the true density matrix). Furthermore, we use the antisymmetrization operator to extend it to the whole configuration space (using the tiling [31] property of the reach), $\bigcup_{\mathcal{P}_e} \gamma_T(\mathcal{P}_e R_0)$, where only even permutations \mathcal{P}_e are needed. This will require the complicated task of sampling the permutation space of the N -particles [22]. Recently, an intelligent method has been devised to perform this sampling through a new algorithm called the worm algorithm [33,34]. To sample the path in coordinate space, one generally uses various generalizations of the Metropolis rejection algorithm [49] and the bisection method [22] to accomplish multistep moves which becomes necessary as τ decreases.

The pair-product approximation for the action [22] was used by Brown et al. [10] to write the many-body density matrix as a product of high-temperature, two-body density matrices [22]. The pair Coulomb density matrix was determined using the results of Pollock [50], even if these could be improved using the results of Vieillefosse [51,52]. This procedure comes with an error that scales as $\sim \tau^3/r_s^2$ where $\tau = \beta/M$ is the time step, with M the number of imaginary time discretizations. A more dominant form of time step error originates from paths which cross the nodal constraint in a time less than τ . To help alleviate this effect, Brown et al. [10] use an image action to discourage paths from getting too close to nodes. Additional sources of error are the finite size one and the sampling error of the Monte Carlo procedure itself. In their analysis, for the highest density points, statistical errors are an order of magnitude higher than time step errors.

In our calculation, for simplicity, we will use the primitive approximation [22] for the action. This procedure comes with an error that scales as $\sim \tau^2/r_s^2$. And we will have the additional sources of error due to the finite size and the sampling of the Monte Carlo procedure itself, as usual. For the highest density points, statistical errors are of order 10^{-3} , in the potential energy or in the pressure, whereas $\tau^2/r_s^2 \approx 10^{-6}$.

4 The problem

Like Brown et al. [10] we adopted as trial density matrix for the path integral nodal restriction a free fermion density matrix. This allowed us to implement the restriction in the path integral calculation from the worm algorithm [34,53] to the reach of the reference point in the moves ending in the Z sector: remove, close, wiggle, and displace. The worm algorithm is a particular path integral algorithm where the permutations need not to be sampled as they are generated with the simulation evolution. Instead of the pair-product action used by Brown et al. [10], we used the primitive approximation for the action [22] and modified the original worm algorithm so that it would work in the presence of the nodal restriction and in a canonical ensemble calcu-

lation at fixed number of particles N , volume $\Omega = N\alpha_3$, and temperature T . We should mention that, due to the choice of approximation for the action, our results will suffer of some additional systematic error respect to the data of Brown et al., although small.

The restriction implementation is rather simple: we just reject the move whenever the proposed path is such that the ideal fermion density matrix calculated between the reference point and any of the time slices subject to newly generated particles positions has a negative value. Our algorithm is described in detail in the following section.

The trial density matrix used to perform the restriction of the fixed-nodes path integral is chosen as the one of ideal fermions which is given by

$$\rho_0(R, R'; t) \propto \mathcal{A} \left[e^{-\frac{(\mathbf{r}_i - \mathbf{r}'_j)^2}{4\lambda t}} \right] \equiv \det \left[\exp \left(-\frac{r_s^2(\mathbf{r}_i - \mathbf{r}'_j)^2}{4t} \right) \right], \quad (4.1)$$

where $\lambda = \hbar^2/2m$, t is the imaginary time, and \mathcal{A} is the antisymmetrization operator acting on the same spin groups of particles, which for polarized electrons reduces to a single determinant, and the distances $\sqrt{(\mathbf{r}_i - \mathbf{r}'_j)^2}$ are calculated taking care, as usual, of the wrapping due to the periodic boundary conditions. We expect this approximation to be best at high temperatures (high Θ) and high densities (low r_s) when the quantum and correlation effects are weak. Clearly in a simulation of the ideal gas ($V = 0$) this restriction returns the exact result for fermions.

The Coulomb potential is treated through the method of Fraser et al. [54] which is alternative to the Ewald summation of Natoli and Ceperley [55], to cure its long-range nature.

5 Our algorithms

Our algorithm, that we will call algorithm A, briefly presented in the previous section is based on the worm algorithm of Boninsegni et al. [34, 53, 56–58]. The algorithm of Boninsegni et al. solves the path integral in the grand canonical ensemble and uses a menu of 9 moves. Three are self-complementary: swap, displace, and wiggle, and the other six are 3-couples of complementary moves: insert–remove, open–close, and advance–recede. These moves act on “worms” with an head Ira and a tail Masha in the β -periodic imaginary thermal time, which can swap a portion of their bodies (swap move), can move forward and backward (advance–recede moves), can be subdivided in two or joined into a bigger one (open–close moves), and can be born or die (insert–remove moves) since we are working in the grand-canonical ensemble. The configuration space of the worms is called the G sector. When the worms recombine to form a closed path (“world line”) we enter the

so called Z sector and the path can translate in space (displace move) and can propagate in space through the bisection algorithm (wiggle move), carefully explained in Ref. [22]. To reduce the grand canonical algorithm to a canonical calculation it is sufficient to choose the chemical potential equal to zero everywhere in the algorithm and to reject all the moves attempting to change the number of particles N in the Z sector. Of course it is necessary to initialize the calculation from a path containing the given number N of particles.

To get the restricted path integral we choose the trial density matrix as the one of the non-interacting fermions (4.1) and restrict the Z to Z and the G to Z moves, that is: displace, wiggle, close, and remove. To implement the restriction we reject the move whenever the proposed path is such that the ideal fermions density matrix of Eq. (4.1) calculated between the reference point R_0 and any of the time slices subject to newly generated particles positions, R_t with $0 < t \leq \beta$, changes sign. That is, whenever the path ends up in a region not belonging to the trial reach of the reference point. So, we implemented the rejection every time we encounter $\rho_0(R_t, R_0; t)\rho_0(R_\tau, R_0; \tau) < 0$ for all $\tau < t \leq \beta$. We generally run our simulations with an acceptance ratio for the occupation of the Z sector close to 1/2. When calculating diagonal properties we consider the density matrix averaged over the entire path and not only at the reference point. For each move we can decide the frequency of the move and the maximum number of time slices it operates on, apart from the displace move where instead of the maximum number of time slices we can decide the maximum extent of the spatial translation displacement.

We noticed that doing like so, at low temperature, the simulation with all the moves activated would enter the G sector without being able to get out of it (To exit the G sector the temporal distance between Ira and Masha must be close to 0 or β and the spatial distance close to 0. The temporal distance is a stochastic variable which change of an amount β in a number of moves of the order of M^2 . So at larger M the change of sector becomes rarer). So at first we switched off the advance–recede and swap moves and more generally the access to the G sector (by properly adjusting the dimensionless parameter C [34, 53] which controls the relative statistics of Z and G -sectors) in our simulations. This is equivalent to restrict the configuration space to only the primal nodal cell $\gamma_T(R_0)$ neglecting the other tiles obtained applying even permutations to the reference point R_0 according to the tiling property [31].

To include correctly the permutations and the transition through the G sector of the worm algorithm, in our low-temperature simulations, we had to use a different algorithm that we will call algorithm B. Instead of using a generic G sector, we work in a restricted one where we impose equal imaginary times for Ira and Masha and a spatial distance between Ira and Masha equal to ϵL with $\epsilon < 1$ (here it is important not to take ϵ too small otherwise the acceptance ratios of the various moves ending in the G sector will go to zero). That is, rather than using the sector of the numerator

Table 1 Thermodynamic results in our simulations with $\xi = 1$ and $N = 33$ electrons interacting through the pair-potential $\phi(r) = v(r) - ND/(N - 1)$ of Eqs. (6.1)–(6.2), at a density fixed by r_s , temperature fixed by Θ (at a Coulomb coupling constant Γ), and with M time slices: e_0 (Ry) is the internal energy per particle of the ideal gas, P_0 (Ry/ $r_s^3 a_0^3$) is the pressure of the ideal gas, e_k (Ry) is the kinetic energy per particle in our simulation, e_k^{Brown} (Ry) is the kinetic energy per particle in Brown et al. [10] simulation, e_p (Ry) is the potential energy per particle in our simulation, e_p^{Brown} (Ry) is the potential energy per particle in Brown et al. [10] simulation, e_t (Ry) = $e_k + e_p$ is the total energy per particle in our simulation, and P (Ry/ $r_s^3 a_0^3$) is the pressure in our simulation. In these simulations, we used algorithm A with the advance–recede and swap moves switched off

M	r_s	Θ	Γ	e_0	P_0	e_k^{Brown}	e_p^{Brown}	e_k	e_p	e_t	P
244	1	1	0.342	9.920268	1.578860	9.72(2)	− 0.938(1)	9.67(5)	− 0.970(3)	8.70(5)	2.670(7)
489	1	0.5	0.684	5.973201	0.950664	5.72(2)	− 1.088(1)	5.67(8)	− 1.133(3)	4.53(8)	2.02(1)
977	1	0.25	1.368	4.307310	0.685530	4.12(4)	− 1.171(1)	4.9(1)	− 1.233(2)	3.7(1)	1.89(2)
1000	1	0.125	2.737	3.727579	0.593263	3.64(1)	− 1.1961(5)	4.73(6)	− 1.276(1)	3.46(6)	1.861(9)
253	2	1	0.684	2.480067	0.394715	2.419(5)	− 0.5280(4)	2.39(1)	− 0.542(1)	1.85(1)	0.941(2)
507	2	0.5	1.368	1.493300	0.237666	1.435(5)	− 0.5917(2)	1.46(2)	− 0.612(1)	0.85(2)	0.788(3)
1000	2	0.25	2.737	1.076827	0.171382	1.050(7)	− 0.6219(2)	1.24(3)	− 0.6484(9)	0.59(3)	0.750(4)
1000	2	0.125	5.473	0.931895	0.148316	0.906(4)	− 0.6302(1)	1.22(2)	− 0.663(1)	0.55(2)	0.745(4)
128	4	1	1.368	0.620017	0.098679	0.597(1)	− 0.2885(3)*	0.593(1)	− 0.3026(1)	0.290(1)	0.3725(2)
256	4	0.5	2.737	0.373325	0.059416	0.367(1)	− 0.3206(1)	0.361(2)	− 0.3282(2)	0.033(2)	0.3335(3)
512	4	0.25	5.473	0.269207	0.042846	0.269(1)	− 0.3302(1)	0.303(2)	− 0.3396(1)	− 0.036(2)	0.3234(3)
1000	4	0.125	10.946	0.232974	0.037079	0.237(1)	− 0.3318(1)	0.30(1)	− 0.3444(6)	− 0.05(1)	0.322(2)

of the whole Green’s function, one works with the sector of the single-particle density matrix at a distance less than ϵL . We accomplished this by constructing the following set of three, Z to G , G to Z , and G to G , moves obtained by combining the elementary moves of the usual worm algorithm [34, 53]: open–advance (removes a random number m of time slices and advances Ira of m time slices), recede–close (recedes Ira by a random number m of time slices and closes the worm), advance–recede (advances Ira by a random number m of time slices and advances Masha by the same number of time slices). Moreover we just killed the usual insert and remove moves which would have to use a number of time slices equal to M and would thus have very low acceptance ratios. Each of these three combined moves produces a configuration with an Ira and a Masha at the same imaginary time. We did not change all the other moves: swap, wiggle, and displace. This amounts to simulate a G sector for the one-body density matrix (which can be obtained from the histogram of the spatial distance between Ira and Masha). We note that this algorithm is inherently a canonical ensemble one. Moreover we rejected those moves which would bring to have a spatial distance between Ira and Masha larger than ϵL . We then introduced the nodal restriction also on this set of three moves: open–advance, recede–close, advance–recede, choosing as the reference point the one immediately next to Ira in imaginary time.

We used this other algorithm to simulate just two of the low-temperature cases among the twelve cases considered in the next section and observed a relevant improvement in the numerical results as compared with the existing literature data. This fact validated our algorithms.

It is well known that Monte Carlo algorithms works better as long as we have a richer moves’ menu, unless

of course one violates detailed balance. So our modified worm algorithm is very efficient in exploring all the electrons path configurations with all the necessary permutation exchanges, even if in our restricted version, the winding numbers will reflect the restriction. We will not be able to determine the superfluid fraction in our simulations. This is a shortcoming of applying the restricted path integral method where the winding numbers are biased by the restriction.

6 Results

We simulated the Jellium at high density and low temperature. Given the bare Coulomb potential $v(r) = 2 \text{ Ry}/r_s r$, according to Fraser et al. [54], it is possible to use in the simulation the following pair-potential ϕ ,

$$\phi(r) = v(r) - \frac{N}{N - 1} D, \tag{6.1}$$

$$D = \frac{1}{\Omega} \int_{\text{cell}} v(r) \text{ dr}. \tag{6.2}$$

This method is equivalent to the Ewald summation technique or to its developments like the one carried on by Natoli and Ceperley [55] and gives smaller finite-size effects. The method is much more simple to implement than the more common Ewald sums but of course it has discontinuities when jumping from one side of the simulation cell to the other. The additive constant D is chosen to make sure that the average value of the interaction is zero and the self energy of the electrons is taken as zero.

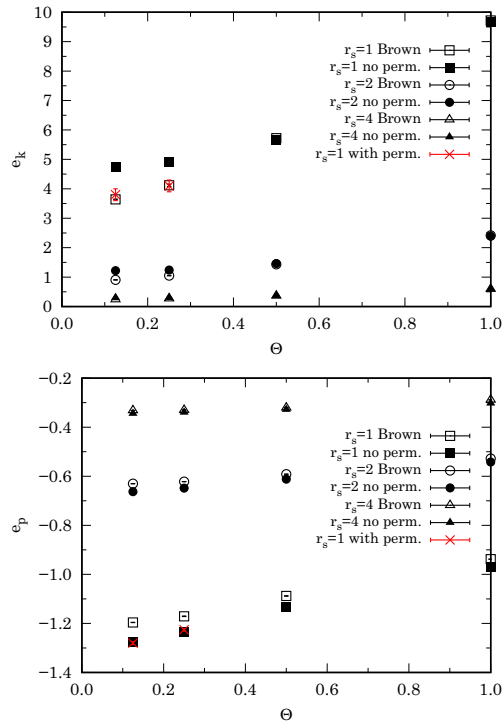


Fig. 1 We show a comparison of our results at the three different values of density ($r_s = 1, 2, 4$), with (with perm.) and without (no perm.) permutations, for the kinetic energy per particle (top panel) and the potential energy per particle (bottom panel) with the results of Brown et al. [10] (Brown) as they are reported in Tables 1 (no perm.) and 2 (with perm.)

In Table 1, we present our results for various thermodynamic quantities in the fully polarized $\xi = 1$ case with $N = 33$ particles. The statistical errors in the various measured quantities were determined, as usual, through the estimate of the correlation time of the given observable \mathcal{O} , $\tau_{\mathcal{O}}$, as error $= \sqrt{\tau_{\mathcal{O}} \sigma_{\mathcal{O}}^2} / N$, where $\sigma_{\mathcal{O}}^2$ is the variance of \mathcal{O} and N is the number of MC steps. Our results can be directly compared with the ones of Brown et al. [10]. Benchmark data correcting systematic errors [59] up to a 10% in the high-density $r_s \lesssim 1$ and low-temperature cases of Brown et al., can be found in Refs. [13, 15, 16, 60, 61]. The time steps τ chosen in the simulations are like the ones chosen by Brown et al. [10] as a function of r_s at all temperatures: $\tau = 0.0007$ for $r_s = 1$, $\tau = 0.0027$ for $r_s = 2$, and $\tau = 0.0214$ for $r_s = 4$ but in any case with M not bigger than 10^3 . From the table, we can see how our results agree well with the ones of Brown et al. [10]: The kinetic energy, in the highest density case, is within a 0.5% at high temperatures (in the correct direction given by the later results of

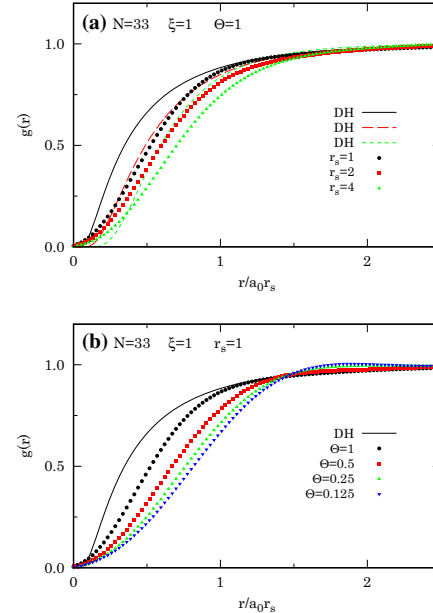


Fig. 2 The radial distribution function for Jellium in selected states of Table 1, from algorithm A, at fixed temperature in the upper panel (a) and at fixed density in the lower panel (b). Also shown is the Debye–Hückel (DH) result [39] for the high temperature and low density limit, $g_{\text{DH}}(r) = \exp\left[-\frac{\Gamma}{r} \exp(-\sqrt{3\Gamma}r)\right]$

Refs. [13, 61]) and up to a 35% in the lower temperature case. This discrepancy increase is due to the fact that in these simulations we had the advance–recede and swap moves switched off, so we were not sampling the whole fermions configuration space but only the primal nodal cell (the one connected directly to the reference point itself), as explained in the previous section. This clearly becomes more and more important at low temperature when the quantum effects are more relevant.

The data denoted with an asterisk in the table have been considerably corrected by the later work of Groth et al. [61], who give $e_p = -0.305012(33)$, which is much closer to our result.

In Fig. 1, we show a comparison of our results for the kinetic energy per particle (top panel) and the potential energy per particle (bottom panel) with the results of Brown et al. [10]. From the figure, we see clearly how our results with no permutations reproduce well the results of Brown et al., at sufficiently high temperatures and low densities. And our results with the permutations switched on corrects the discrepancy observed at low temperatures (small Θ) and high densities (small r_s).

Table 2 Same as Table 1 but using our algorithm B in the high-density low-temperature simulations

M	r_s	Θ	Γ	e_0	P_0	e_k^{Brown}	e_p^{Brown}	e_k	e_p	e_t	P
977	1	0.25	1.368	4.307310	0.685530	4.12(4)	- 1.171(1)	4.1(2)	- 1.226(5)	2.9(2)	1.76(4)
1000	1	0.125	2.737	3.727579	0.593263	3.64(1)	- 1.1961(5)	3.8(2)	- 1.280(6)	2.5(2)	1.73(2)

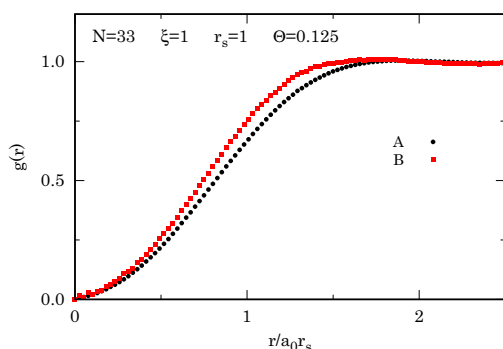


Fig. 3 The radial distribution function for Jellium in the $\xi = 1, r_s = 1, \Theta = 0.125$ state as obtained from our two algorithms A and B: The one without G sector and the one with G sector, respectively

In Fig. 2, we show our results for the radial distribution function [62], $g(r)$, for selected states of Table 1 at fixed temperature and at fixed density, respectively.

As outlined in the previous section we repeated the calculation for the low temperature cases $\xi = 1, r_s = 1, \Theta = 0.25$ and $\Theta = 0.125$ with our modified algorithm B, with $\epsilon = 1/2$, able to sample the whole fermions configuration space including the necessary permutations. The result in these cases were encouraging and are shown in Table 2. They were much closer to the corresponding result of Brown et al. [10] than the results obtained with the previous algorithm A: The kinetic energy, in the highest density case, is within a 5% at low temperatures. We also checked that the two algorithms, A and B, coincide at high temperature. This validates our algorithms A and B.

In Fig. 3, we show our results for the radial distribution function for the $\xi = 1, r_s = 1, \Theta = 0.125$ state obtained with the algorithm with the G sector switched off (A) and with the algorithm with the G sector switched on (B).

From the figure, we see how the Fermi hole diminishes by the introduction of the permutations in the calculation.

7 Conclusions

We have successfully implemented the ideal fermion density matrix restriction on the path integral worm algorithm which is able to generate the necessary

RPIMC moves during the simulation evolution thereby circumventing the otherwise inevitable sign problem. This allowed us to reach the finite, non-zero, temperature properties of a given fluid model of Fermi particles interacting through a given pair-potential. We worked in the canonical ensemble and applied our method to the Jellium fluid of Wigner. We explicitly compared our results with the previous canonical calculation of Brown et al. [10] in the high density and low temperature regime where their algorithm had problems in sampling the path [59]. Our results complement the ones of Brown et al., with the treatment of the high density $r_s \leq 4$ and low temperature cases which were found to be inaccurate by Bonitz et al. [13, 16, 61] who suggested an alternative algorithm to circumvent the systematic errors in Brown calculations [59].

The relevance of our study relies in the fact that our simulation method is different from both the method of Ceperley et al. [10, 11] who uses the fixed-nodes approximation in the canonical ensemble of a regular, and not worm, PIMC [22], and from the one of Bonitz et al. [12, 14–16] who combine configuration- and permutation-blocking PIMC. Our method is also different from other quantum Monte Carlo methods like the one of Malone et al. [17] that agrees well with the one of Bonitz et al. at high densities and the direct PIMC one of Filinov et al. [18] that agrees well with Brown et al., at low density and moderate temperature. So our new algorithms add to the ones already used in the quest for an optimal way to calculate the properties of the fascinating Wigner’s Jellium model at finite, non zero, temperatures. We devised two different algorithms, A and B. In algorithm A, we used a restricted, fixed-nodes, worm algorithm which never passes through the G sector. In algorithm B we used a restricted, fixed-nodes, worm algorithm with a G sector which has Masha and Ira always at the same imaginary time and at a given small spatial distance. In both cases, the restriction of the fixed-nodes path integral is the one from a trial density matrix equal to the one of ideal fermions.

We obtained results for both the static structure (the radial distribution function) and various thermodynamic quantities (energy and pressure) for the Jellium model with $N = 33$ fully polarized ($\xi = 1$) electrons at high density and low temperature. Our results compare favorably with the ones of Brown et al. [10] with a discrepancy on the kinetic energy, in the highest density case, up to a 0.5% at high temperatures (with our algorithm A) and up to 5% at low temperatures (with our algorithm B). Our results can also be compared with the later ones of Refs. [13, 61] with which the agreement increases even further. This validates our

algorithms which are alternative to the ones that have already been used in the literature.

We expect in the near future to explicitly determine the dependence of the Jellium properties (structural and thermodynamic) on the polarization ξ . We would also like to carry out a more comprehensive comparison with the results in the literature and to predict other results yet to be determined through quantum Monte Carlo methods, like the static structure function. Regarding improvements to the algorithm we would like to implement the use of better approximations for the action in the path integral and a search for better trial density matrices to guide the fixed nodes at low temperatures or the implementation of the released-nodes recipe.

Another important problem to solve is the one of calculating the superfluid fraction for fermions or superconducting fraction for electrons. The winding numbers that one is computing in RPIMC are not sufficient to determine the superfluid fraction since there is the restriction on the paths.

We would like to thank Saverio Moroni for several relevant discussions at S.I.S.S.A. of Trieste, Boris Svistunov for useful e-mail and Skype suggestions on how to implement our algorithm B, and David Ceperley for many e-mail exchanges which have been determinant for the completion of the work.

Data Availability Statement This manuscript has no associated data or the data will not be deposited. [Authors' comment: All data generated or analyzed during this study are included in this published article.]

References

- R. Fantoni, Eur. Phys. J. B **86**, 286 (2013)
- N.W. Ashcroft, N.D. Mermin, *Solid State Physics* (Harcourt Inc., San Diego, 1976)
- J.P. Hansen, I.R. McDonald, *Theory of Simple Liquids* (Academic Press, London, 1986)
- S.L. Shapiro, S.A. Teukolsky, *Black Holes, White Dwarfs, and Neutron Stars. The Physics of Compact Objects* (Wiley, Germany, 1983)
- R. Fantoni, B. Jancovici, G. Téllez, J. Stat. Phys. **112**, 27 (2003)
- R. Fantoni, G. Téllez, J. Stat. Phys. **133**, 449 (2008)
- R. Fantoni, J. Stat. Mech. **P04015**, 4 (2012a)
- R. Fantoni, J. Stat. Mech. **P10024**, 5 (2012b)
- R. Fantoni, International Journal of Modern Physics C **29**, 1850028 (2018a)
- E.W. Brown, B.K. Clark, J.L. DuBois, D.M. Ceperley, Phys. Rev. Lett. **110**, 146405 (2013)
- E. Brown, M.A. Morales, C. Pierleoni, D.M. Ceperley, in *Frontiers and Challenges in Warm Dense Matter*, ed by F. Graziani et al. (Springer, Berlin, 2014) pp. 123–149
- T. Schoof, M. Bonitz, A. Filinov, D. Hochstul, J.W. Dufty, Contrib. Plasma. Phys. **51**, 687 (2011)
- T. Schoof, S. Groth, J. Vorberger, M. Bonitz, Phys. Rev. Lett. **115**, 130402 (2015)
- T. Dornheim, S. Groth, A. Filinov, M. Bonitz, New J. Phys. **17**, 073017 (2015)
- T. Dornheim, S. Groth, T. Sjöstrom, F.D. Malone, W.M.C. Foulkes, M. Bonitz, Phys. Rev. Lett. **117**, 156403 (2016a)
- S. Groth, T. Dornheim, T. Sjöstrom, F.D. Malone, W.M.C. Foulkes, M. Bonitz, Phys. Rev. Lett. **119**, 135001 (2017)
- F.D. Malone, N.S. Blunt, E.W. Brown, D.K.K. Lee, J.S. Spencer, W.M.C. Foulkes, J.J. Shepherd, Phys. Rev. Lett. **117**, 115701 (2016)
- V.S. Filinov, V.E. Fortov, M. Bonitz, Z. Moldabekov, Phys. Rev. E **91**, 033108 (2015)
- R. Fantoni, G. Pastore, Phys. Rev. E **87**, 052303 (2013)
- R. Fantoni, Int. J. Modern Phys. C **29**, 1850064 (2018)
- T. Dornheim, S. Groth, M. Bonitz, Phys. Rep. **744**, 1 (2018)
- D.M. Ceperley, Rev. Mod. Phys. **67**, 279 (1995)
- J.P. Hansen, Phys. Rev. A **8**, 3096 (1973)
- J.P. Hansen, P. Vieillefosse, Phys. Lett. **53A**, 187 (1975)
- U. Gupta, A.K. Rajagopal, Phys. Rev. A **22**, 2792 (1980)
- F. Perrot, M.W.C. Dharma-wardana, Phys. Rev. A **30**, 2619 (1984)
- K.S. Singwi, M.P. Tosi, R.H. Land, A. Sjölander, Phys. Rev. **176**, 589 (1968)
- S. Tanaka, S. Ichimaru, J. Phys. Soc. Jpn. **55**, 2278 (1986)
- F.M.C. Perrot, M.W.C. Dharma-wardana, Phys. Rev. B **62**, 16536 (2000)
- M.W.C. Dharma-wardana, F. Perrot, Phys. Rev. Lett. **84**, 959 (2000)
- D.M. Ceperley, J. Stat. Phys. **63**, 1237 (1991)
- D.M. Ceperley, In *Monte Carlo and Molecular Dynamics of Condensed Matter Systems*, ed by K. Binder, G. Ciccotti (Editrice Compositori, Bologna, 1996)
- N.V. Prokof'ev, B.V. Svistunov, I.S. Tupitsyn, J. Exp. Theor. Phys. **87**, 310 (1998)
- M. Boninsegni, N. Prokof'ev, B. Svistunov, Phys. Rev. Lett. **96**, 070601 (2006a)
- R. Fantoni, Int. J. Modern Phys. B (2020) (note under review)
- N.H. March, M.P. Tsi, *Coulomb Liquids* (Academic Press, London, 1984)
- K.S. Singwi, M.P. Tosi, Sol. State Phys. **36**, 177 (1981)
- S. Ichimaru, Rev. Mod. Phys. **54**, 1017 (1982)
- P.A. Martin, Rev. Mod. Phys. **60**, 1075 (1988)
- E. Wigner, Phys. Rev. **46**, 1002 (1934)
- A.J. Leggett, Rev. Mod. Phys. **47**, 331 (1975)
- G.F. Giuliani, G. Vignale, *Quantum Theory of the Electron Liquid* (Cambridge University Press, Cambridge, 2005)
- E.L. Pollock, D.M. Ceperley, Phys. Rev. B **36**, 8343 (1987)
- D.M. Ceperley, B.J. Alder, Phys. Rev. Lett. **45**, 566 (1980)
- R.P. Feynman, Phys. Rev. **90**, 1116 (1953a)
- R.P. Feynman, Phys. Rev. **91**, 1291 (1953b)
- R.P. Feynman, Phys. Rev. **90**, 1301 (1953c)
- R.P. Feynman, A.R. Hibbs, *Quantum Mechanics and Path Integrals* (McGraw-Hill Publishing Company, New York, 1965), pp. 292–293

49. N. Metropolis, A.W. Rosenbluth, M.N. Rosenbluth, A.M. Teller, E. Teller, *J. Chem. Phys.* **1087**, 21 (1953)
50. E.L. Pollock, *Comput. Phys. Commun.* **52**, 49 (1988)
51. P. Vieillefosse, *J. Stat. Phys.* **74**, 1195 (1994)
52. P. Vieillefosse, *J. Stat. Phys.* **80**, 461 (1995)
53. M. Boninsegni, N.V. Prokof'ev, B.V. Svistunov, *Phys. Rev. E* **74**, 036701 (2006b)
54. L.M. Fraser, W.M.C. Foulkes, G. Rajagopal, R.J. Needs, S.D. Kenny, A.J. Williamson, *Phys. Rev. B* **53**, 1814 (1996)
55. V.D. Natoli, D.M. Ceperley, *J. Comput. Phys.* **117**, 171 (1995)
56. R. Fantoni, S. Moroni, *J. Chem. Phys.* **141**, 114110 (2014)
57. R. Fantoni, *Phys. Rev. E* **92**, 012133 (2015)
58. R. Fantoni, *Eur. Phys. J. B* **89**, 1 (2016)
59. D.M. Ceperley, *Phys. Rev. Lett.* **69**, 331 (1992)
60. T. Dornheim, S. Groth, T. Schoof, C. Hann, M. Bonitz, *Phys. Rev. B* **93**, 205134 (2016b)
61. S. Groth, T. Schoof, T. Dornheim, M. Bonitz, *Phys. Rev. B* **93**, 085102 (2016)
62. M.P. Allen, D.J. Tildesley, *Computer Simulation of Liquids* (Clarendon Press, Oxford, 1987)

Chapter 65

Affine quantization of $(\varphi^4)_4$ succeeds while canonical quantization fails

Fantoni R. and Klauder J. R., Phys. Rev. D **103**, 076013 (2021)

Title: “Affine quantization of $(\varphi^4)_4$ succeeds while canonical quantization fails”

Abstract: Covariant scalar field quantization, nicknamed $(\varphi^r)_n$, where r denotes the power of the interaction term and $n = s + 1$ where s is the spatial dimension and 1 adds time. Models such that $r < 2n/(n - 2)$ can be treated by canonical quantization, while models such that $r > 2n/(n - 2)$ are nonrenormalizable, leading to perturbative infinities, or, if treated as a unit, emerge as ‘free theories’. Models such as $r = 2n/(n - 2)$, e.g., $r = n = 4$, again using canonical quantization also become ‘free theories’, which must be considered quantum failures. However, there exists a different approach called affine quantization that promotes a different set of classical variables to become the basic quantum operators and it offers different results, such as models for which $r > 2n/(n - 2)$, which has recently correctly quantized $(\varphi^{12})_3$. In the present paper we show, with the aid of a Monte Carlo analysis, that one of the special cases where $r = 2n/(n - 2)$, specifically the case $r = n = 4$, can be acceptably quantized using affine quantization.

Affine quantization of $(\varphi^4)_4$ succeeds while canonical quantization fails

Riccardo Fantoni^{1,*} and John R. Klauder^{2,†}

¹Università di Trieste, Dipartimento di Fisica, Strada Costiera 11, 34151 Grignano (Trieste), Italy

²Department of Physics and Department of Mathematics University of Florida, Gainesville, Florida 32611-8440, USA

 (Received 15 December 2020; accepted 25 March 2021; published 22 April 2021)

Covariant scalar field quantization, nicknamed $(\varphi^r)_n$, where r denotes the power of the interaction term and $n = s + 1$ where s is the spatial dimension and 1 adds time. Models such that $r < 2n/(n - 2)$ can be treated by canonical quantization, while models such that $r > 2n/(n - 2)$ are nonrenormalizable, leading to perturbative infinities, or, if treated as a unit, emerge as ‘free theories’. Models such as $r = 2n/(n - 2)$, e.g., $r = n = 4$, again using canonical quantization also become ‘free theories’, which must be considered quantum failures. However, there exists a different approach called affine quantization that promotes a different set of classical variables to become the basic quantum operators and it offers different results, such as models for which $r > 2n/(n - 2)$, which has recently correctly quantized $(\varphi^{12})_3$. In the present paper we show, with the aid of a Monte Carlo analysis, that one of the special cases where $r = 2n/(n - 2)$, specifically the case $r = n = 4$, can be acceptably quantized using affine quantization.

DOI: 10.1103/PhysRevD.103.076013

I. INTRODUCTION

The family of covariant scalar field theories under consideration have classical Hamiltonians given by

$$H(\pi, \varphi) = \int \left\{ \frac{1}{2} [\pi(x)^2 + (\vec{\nabla}\varphi)(x)^2 + m^2\varphi(x)^2] + g\varphi(x)^r \right\} d^s x, \tag{1}$$

where the mass $m > 0$, the coupling constant $g \geq 0$, r is the power of the interaction term, and s is the number of spatial dimensions. As classical elements they lead to suitable equations of motion and these solutions automatically guarantee that, for $T > 0$, all such solutions obey the rule that $\int_0^T \int H(\pi(x, t), \varphi(x, t)) d^s x dt < \infty$.

However, acceptable classical solutions do not tell the whole story. The domain of the example in (1) includes the complete set of *arbitrary continuous paths*, $\pi(x, t)$ and $\varphi(x, t)$, that determine the domain

$$\mathcal{D}(\pi, \varphi) = \left\{ \int_0^T \int H(\pi(x, t), \varphi(x, t)) d^s x dt < \infty \right\}. \tag{2}$$

*riccardo.fantoni@posta.istruzione.it
†klauder@phys.ufl.edu

Published by the American Physical Society under the terms of the Creative Commons Attribution 4.0 International license. Further distribution of this work must maintain attribution to the author(s) and the published article's title, journal citation, and DOI. Funded by SCOAP³.

This expression for the domain is unchanged if the interaction term is excluded, while, on the other hand, the given domain will be dramatically reduced from the true free theory domain if the interaction term is sufficiently strong and has been introduced. These questions can be answered if we show the domains may be studied.

A. Review of principal domains

The term $\pi(x, t)^2$ is equal to $\dot{\varphi}(x, t)^2$, and if we include t as just another spatial variable the classical Hamiltonian becomes

$$H(\varphi) = \int \left\{ \frac{1}{2} [(\vec{\nabla}\varphi)(x)^2 + m^2\varphi(x)^2] + g\varphi(x)^r \right\} d^s x, \tag{3}$$

where now $x = (x_0, x_1, x_2, \dots, x_s)$, where $x_0 = ct$ and $n = s + 1$. The contribution of the separate terms can be captured if we observe that the three following cases must be treated separately and constitute unitarily inequivalent quantizations,

$$\left\{ \int \varphi(x)^r d^n x \right\}^{2/r} < \text{or} = \text{or} > \int \left\{ (\vec{\nabla}\varphi)(x)^2 + m^2\varphi(x)^2 \right\} d^n x. \tag{4}$$

The domain of this expression consists of all $\{\phi(x)\}$ for which $H(\phi) < \infty$. For a given finite spacetime dimension n and power r , it is of considerable interest to learn if the domain changes when the interaction coupling constant changes from $g = 0$ to $g > 0$. The study of that issue for all

$\{\phi(x)\}$ involves an explicit expression in which t becomes an additional “spatial variable”

$$\left\{ \int \phi(x)^r d^n x \right\}^{2/r} = C \int [(\vec{\nabla}\phi)^2 + m^2\phi^2] d^n x. \quad (5)$$

If C is bounded above for all ϕ , then the domain of H is the same with $g = 0$ or $g > 0$. If $C = \infty$ then the domain of H is larger when $g = 0$ than it is when $g > 0$. It follows [1,2] that the domain does not change provided that $r < 2n/(n - 2)$. If, on the other hand, $r > 2n/(n - 2)$, then the domain of H drops as soon as $g > 0$, and thus when one seeks the domain in the limit that $g \rightarrow 0$, continuity forces the resultant domain to be the smaller domain.

The focus hereafter, in this paper, is on the case $r = 2n/(n - 2)$, and more explicitly, we choose $r = n = 4$.¹ This model has been studied by applying canonical quantization, and the universally accepted result [3–5] is that this model becomes a “free model” despite the presence of the interaction and $g > 0$. Such a result may be considered as a quantum failure. Additional efforts has been made in Ref. [6] to quantize $(\phi^4)_4$ models using alternative procedures that, regrettably, have also led only to a “free theory.”

Affine quantization can account for certain classical models that experience two different classical domains, one (free) without an interaction term, $g = 0$, and one (nonfree) with the interaction term, $g > 0$. If necessary, such models automatically choose the smaller domain as $g \rightarrow 0$ by simple continuity.² This feature can imply either that the quantization leads only to the free theory, or the quantization leads to the form of a nonfree theory. As an example, canonical quantization of $(\varphi^4)_4$ leads only to a free theory [3–5], which, incidentally, may lead to unexpected difficulties in the Standard Model (SM). Our quantization of $(\varphi^4)_4$ by affine quantization is a procedure that is just like canonical quantization, after choosing a different pair of classical variables to promote to operators, and can fit well with other quantization procedures, as is implicit in our study.

Affine quantization [8] has offered positive results for several models, one of which includes the nonrenormalizable model $(\varphi^{12})_3$ [9]. In this paper we seek to find out whether affine quantization will lead to a positive quantization of the model $(\varphi^4)_4$, or, if not positive, what behavior is actually found.

II. CANONICAL AND AFFINE QUANTIZATION OF THE SCALAR EUCLIDEAN FIELD THEORY

Canonical quantization has been the go to method of quantization for many decades. Clearly, the reason for this loyalty is because its use has been so successful. The simple

examples from quantum mechanics have led to similar procedures when dealing with field quantization. The formulations of continuous fields can also lead to unwanted divergences. This behavior invites the use of a formal analysis, which addresses selected equations as beacons that regularization of the procedure enables preliminary analysis to occur. This section is devoted to a formal analysis of both canonical and affine quantization of fields initially guided by elementary examples.

For a single classical degree of freedom, the favored variables $-\infty < p, q < \infty$ and a Poisson bracket $\{q, p\} = 1$ lead to the basic quantum operators P, Q , which obey $[Q, P] = i\hbar 1$. A similar story for classical scalar fields $-\infty < \pi(x), \varphi(x) < \infty$ has a Poisson bracket $\{\varphi(x), \pi(y)\} = \delta^s(x - y)$ which points toward basic quantum operators $\hat{\pi}(x), \hat{\phi}(x)$, that obeys $[\hat{\phi}(x), \hat{\pi}(y)] = i\hbar\delta^s(x - y)$. Ideally, the semiclassical action functional for a field theory model is given by

$$S^{(c)}[\varphi] = \int \left\{ \frac{1}{2} [(\vec{\nabla}\varphi)^2 + m^2\varphi^2] + g\varphi(x)^r \right\} d^n x. \quad (6)$$

The affine story introduces an important new structure. To see that feature, we return to a single degree of freedom, with p, q . Our analysis instead focuses on the case where $q > 0$. This case implies that the operator $P \neq P^\dagger$. We then seek an operator that can be self adjoint. The new classical variables are $p q, \ln(q)$, which, with $q > 0$, permits each variable to be self adjoint. However, we also need to admit $q < 0$, which can be done when we select unusual classical variables, namely, $p q, q$ which permits $-\infty < q \neq 0 < \infty$, and joins together the cases where $q > 0$ and $q < 0$. Affine quantization then involves $p q \rightarrow (P^\dagger Q + Q P)/2 \equiv D = D^\dagger$ and $q \rightarrow Q = Q^\dagger$, which obeys $[Q, D] = i\hbar Q$, and already offers a Lie algebra for the “affine group.” Thus, we are led to the dilation operator $-\infty < D < \infty$ and the position operator $-\infty < Q \neq 0 < \infty$. This analysis will implicitly be used in discussing the affine quantization of scalar fields.

For an affine field story we need $\pi(x)\varphi(x) \equiv \kappa(x)$ and $\varphi(x)$, for which $-\infty < \varphi(x) \neq 0 < \infty$, and, as basic operators, $[\hat{\phi}(x), \hat{\kappa}(y)] = i\hbar\delta^s(x - y)\hat{\phi}(x)$. Just like the single degrees of freedom, we also have the classical relation that $\pi(x)^2 = \kappa(x)^2/\varphi(x)^2$ as well. However, such a relation does not hold when quantized. In particular, for a single degree of freedom $DQ^{-2}D = P^2 + (3/4)\hbar^2Q^{-2}$. For the scalar field, the analogous story leads to the relation that $\hat{\kappa}(x)\varphi(x)^{-2}\hat{\kappa}(x) = \hat{\pi}(x)^2 + (3/4)\hbar^2\delta^{2s}(0)\hat{\phi}(x)^{-2}$.

The new term involves a Dirac delta function, $\delta(0) = \infty$, raised to the power $2s$. This new formal expression follows the similarly formal expression $\pi(x)^2 = -\hbar^2[\delta^2/\delta\varphi(x)^2]$, wherein such formal terms require regularization, a procedure that we will introduce very soon. The latest relation is featured as an all important semi-classical relation in the following affine action

¹The only other similar model is $r = 6, n = 3$.

²The paper [7] using ultralocal field models clearly illustrates how the smaller domain wins.

$$S^{(a)}[\varphi] = \int \left\{ \frac{1}{2} [(\vec{\nabla}\varphi(x))^2 + m^2\varphi(x)^2] + g\varphi(x)^r + \frac{3}{8}\hbar^2 \frac{\delta^{2s}(0)}{\varphi(x)^2 + \epsilon} \right\} d^n x, \quad (7)$$

where ϵ is a regularization parameter.

A. Lattice formulation of the field theory

We used a lattice formulation of the field theory. The theory considers a real scalar field φ taking the value $\varphi(x)$ on each site of a periodic, hypercubic, n -dimensional lattice of lattice spacing a and periodicity Na . The affine action for the field, Eq. (7), is then approximated by

$$S^{(a)}[\varphi]/a^n \approx \frac{1}{2} \left[\sum_{x,\mu} a^{-2} (\varphi(x) - \varphi(x + e_\mu))^2 + m^2 \sum_x \varphi(x)^2 \right] + \sum_x g\varphi(x)^r + \frac{3}{8} \sum_x \hbar^2 \frac{a^{-2s}}{\varphi(x)^2 + \epsilon}, \quad (8)$$

where e_μ is a vector of length a in the $+\mu$ direction.

In this paper we are interested in reaching the continuum limit by taking Na fixed and letting $N \rightarrow \infty$.

III. MONTE CARLO SIMULATION

Our Monte Carlo (MC) simulations use the Metropolis algorithm [10,11] to calculate the vacuum expectation of a functional observable $\mathcal{O}[\varphi]$

$$\langle \mathcal{O} \rangle \approx \frac{\int \mathcal{O}[\varphi] \exp(-S[\varphi]) \prod_x d\varphi(x)}{\int \exp(-S[\varphi]) \prod_x d\varphi(x)}, \quad (9)$$

where $S = \int Hd x_0$ is the action. This is a N^n multidimensional integral. The simulation is started from the initial condition $\varphi = 0$. One MC step consisted in a random displacement of each one of the N^n components of φ as $\varphi \rightarrow \varphi + (\eta - 1/2)\delta$ where η is a uniform pseudo random number in $[0, 1]$ and δ is the amplitude of the displacement. Each one of these N^n moves is accepted if $\exp(-\Delta S) > \eta$ where ΔS is the change in the action due to the move (it can be efficiently calculated considering how the kinetic part and the potential part change by the displacement of a single component of φ) and rejected otherwise. The amplitude δ is chosen in such a way to have acceptance ratios as close as possible to $1/2$ and is kept constant during the evolution of the simulation. One simulation consisted of $M = 10^6$ steps. The statistical error on the average $\langle \mathcal{O} \rangle$ will then depend on the correlation time necessary to decorrelate the property \mathcal{O} , $\tau_{\mathcal{O}}$, and will be determined as $\sqrt{\tau_{\mathcal{O}}\sigma_{\mathcal{O}}^2/(MN^n)}$, where $\sigma_{\mathcal{O}}^2$ is the intrinsic variance for \mathcal{O} .

From the real field $\varphi(x)$ we extract the Fourier transform

$$\tilde{\varphi}(p) = \int d^n x e^{ip \cdot x} \varphi(x), \quad (10)$$

with $\tilde{\varphi}^*(p) = \tilde{\varphi}(-p)$. We then find the ensemble averages $\langle \tilde{\varphi}(0)^2 \rangle$ and $\langle \tilde{\varphi}(0)^4 \rangle$ and construct the following observable (a renormalized unitless coupling constant at zero momentum),

$$g_R = \frac{3\langle \tilde{\varphi}(0)^2 \rangle^2 - \langle \tilde{\varphi}(0)^4 \rangle}{\langle \tilde{\varphi}(0)^2 \rangle^2}, \quad (11)$$

so that clearly, using path integrals in the Fourier transform of the field, we immediately find for the canonical version of the theory,

$$g_R \xrightarrow{g \rightarrow 0} 0. \quad (12)$$

This remains true even for the calculation on a discrete lattice.

We then choose the momentum p with one component equal to $2\pi/Na$ and all other components zero and calculate the ensemble average $\langle |\tilde{\varphi}(p)|^2 \rangle$. We then construct the renormalized mass

$$m_R^2 = \frac{p^2 \langle |\tilde{\varphi}(p)|^2 \rangle}{\langle \tilde{\varphi}(0)^2 \rangle - \langle |\tilde{\varphi}(p)|^2 \rangle}. \quad (13)$$

When $g = 0$ the canonical version of the theory can be solved exactly yielding

$$m_R \xrightarrow{g \rightarrow 0} [\pi/N \sin(\pi/N)]m. \quad (14)$$

Following Freedman *et al.* [3] we will call g_R a dimensionless renormalized coupling constant and we will use it to test the “freedomness” of our field theories in the continuum limit. Note that the sum rules of Eqs. (12) and (14) do not hold for the affine version (7) of the field theory due to the additional $(3/8)\hbar^2\delta^{2s}(0)/[\varphi(x)^2 + \epsilon]$ interaction term.

A. MC results

In our MC simulation, following Freedman *et al.* [3], for each N and g , we adjusted the bare mass m in such a way to maintain the renormalized mass approximately constant $m_R \approx 3$ to within a few percent (in all cases less than 15%), and we measured the renormalized coupling constant g_R of Eq. (11) for various values of the bare coupling constant g at a given small value of the lattice spacing $a = 1/N$. In order to keep the renormalized mass constant at large g , it was necessary to choose a negative m^2 giving rise to a double well interaction density. So that, with Na and m_R fixed, as a was made smaller, whatever change we found in $g_R m_R^4$ as a function of g could only be due to the change in

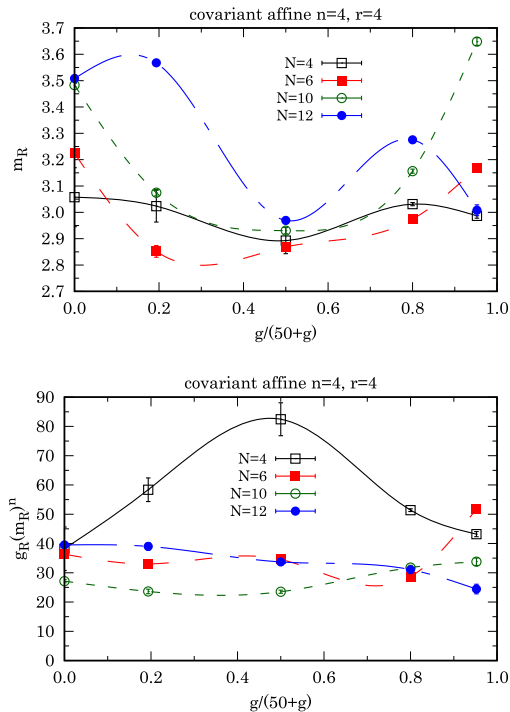


FIG. 1. We show the renormalized mass m_R of Eq. (13) (top panel) and the renormalized coupling constant $g_R m_R^n$ of Eq. (11) (bottom panel) as calculated from Eq. (10) for $m_R \approx 3$ and various values of the bare coupling constant g at decreasing values of the lattice spacing $a = 1/N$ ($N \rightarrow \infty$ continuum limit) for the affine $(\varphi^4)_4$ Euclidean scalar field theory described by the action in Eq. (7). The lines connecting the simulation points are just a guide for the eye.

a. We generally found that a depression in m_R produced an elevation in the corresponding value of g_R and viceversa. The results are shown in Fig. 1 for the affine version with $\hbar = 1$ and $\epsilon = 10^{-10}$, where, following Freedman *et al.* [3] we decided to compress the range of g for display, by choosing the horizontal axis to be $g/(50 + g)$. As we can see from the top panel of the figure the renormalized mass was made to stay around the chosen value of 3, even if this constraint was not easy to implement since for each N and g we had to run the simulation several (5–10) times with different values of the bare mass m .

These results should be compared with the results of Fig. 1 of Freedman *et al.* [3] where the same calculation was done for the canonical version of the field theory. As we can see from Fig. 1, contrary to the figure of Freedman, the renormalized coupling constant of the affine version remains far from zero in the continuum limit ($Na = 1$ and

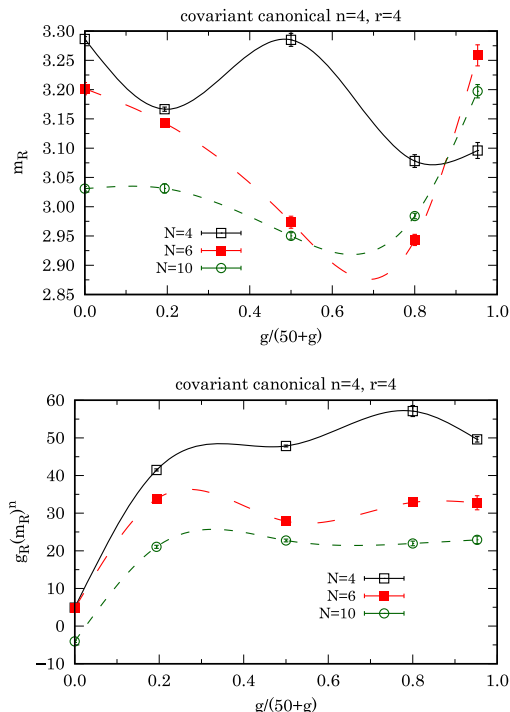


FIG. 2. We show the renormalized mass m_R of Eq. (13) (top panel) and the renormalized coupling constant $g_R m_R^n$ of Eq. (11) (bottom panel) as calculated from Eq. (10) for $m_R \approx 3$ and various values of the bare coupling constant g at decreasing values of the lattice spacing $a = 1/N$ ($N \rightarrow \infty$ continuum limit) for the canonical $(\varphi^4)_4$ Euclidean scalar field theory described by the action in Eq. (6). The lines connecting the simulation points are just a guide for the eye.

$N \rightarrow \infty$) for all values of the bare coupling constant. Here, unlike in the canonical version used by Freedman, the diminishing space between higher N curves is a pointer toward a nonfree ultimate behavior as $N \rightarrow \infty$. Moreover going from $N = 10$ to $N = 12$ we actually observe a growth in the renormalized coupling constant.

In order to test our calculations we repeated the Freedman calculation for the canonical version of the $(\varphi^4)_4$ theory, by keeping as before $m_R \approx 3$ (to within a 10%) for all cases. Our results, shown in Fig. 2, compare favorably with the ones of Freedman Fig. 1.

IV. CONCLUSIONS

The model on which this paper has focused is $(\varphi^4)_4$ and normally uses canonical quantization that was the only procedure, or other procedures designed to get equivalent results. For our model, canonical quantization leads to a

free theory, as if the interaction term was missing. Affine quantization is a newer procedure that is qualitatively different than canonical quantization. The difference is such that favored Cartesian classical variables [12] choose the basic quantum operators, while for affine quantization, the favored classical variables arise from a constant negative curvature. This is different from the constant zero curvature, i.e., a flat surface suitable for canonical quantization. Indeed, it leads to affine quantization becoming a *partner procedure* and not a substitute for canonical quantization, with each procedure appropriate for distinct

sets of problems for them to treat. This distinction of procedures offered by affine quantization has already clarified the analysis of half-harmonic oscillators [13], a favorable quantization of the nonrenormalizable model $(\varphi^{12})_3$ [9], and now the strongest test yet for affine quantization, specifically, quantizing the $(\varphi^4)_4$ model.

It is expected that additional quantum examples may lead to problems when canonical quantization is used. Such examples deserve to consider affine quantization, which might be the answer to those problems.

-
- [1] O. A. Ladyzenskaja, V. Solonnikov, and N. N. Ural'ceva, *Linear and Quasi-Linear Equations of Parabolic Type* (American Mathematical Society, Providence, 1968).
 - [2] J. R. Klauder, *Beyond Conventional Quantization* (Cambridge University Press, Cambridge, England, 2000), Chap. 5.
 - [3] B. Freedman, P. Smolensky, and D. Weingarten, Monte Carlo evaluation of the continuum limit of ϕ_4^4 and ϕ_3^4 , *Phys. Lett.* **113B**, 481 (1982).
 - [4] M. Aizenman, Proof of the Triviality of ϕ_d^4 Field Theory and Some Mean-Field Features of Ising Models for $d > 4$, *Phys. Rev. Lett.* **47**, 886(E) (1981).
 - [5] J. Fröhlich, On the triviality of $\lambda\phi_d^4$ theories and the approach to the critical point in $d \geq 4$ dimensions, *Nucl. Phys.* **B200**, 281 (1982).
 - [6] J. Siefert and U. Wolff, Triviality of φ^4 theory in a finite volume scheme adapted to the broken phase, *Phys. Lett. B* **733**, 11 (2014).
 - [7] J. R. Klauder, An ultralocal classical and quantum gravity theory, *J. High Energy Phys., Gravitation Cosmol.* **06** (2020) 656.
 - [8] J. R. Klauder, The benefits of affine quantization, *J. High Energy Phys., Gravitation Cosmol.* **06** (2020) 175.
 - [9] R. Fantoni, Monte Carlo evaluation of the continuum limit of $(\phi^{12})_3$, [arXiv:2011.09862](https://arxiv.org/abs/2011.09862).
 - [10] M. H. Kalos and P. A. Whitlock, *Monte Carlo Methods* (Wiley-Vch Verlag GmbH & Co., Germany, 2008).
 - [11] N. Metropolis, A. W. Rosenbluth, M. N. Rosenbluth, A. M. Teller, and E. Teller, Equation of state calculations by fast computing machines, *J. Chem. Phys.* **21**, 1087 (1953).
 - [12] P. A. M. Dirac, *The Principles of Quantum Mechanics* (Clarendon Press, Oxford, 1958) in a footnote on page 114.
 - [13] L. Gouba, Affine quantization on the half line, *J. High Energy Phys., Gravitation Cosmol.* **07** (2021) 352.

Chapter 66

Monte Carlo evaluation of the continuum limit of $(\phi^{12})_3$

Fantoni R., J. Stat. Mech. 083102 (2021)

Title: “Monte Carlo evaluation of the continuum limit of $(\phi^{12})_3$ ”

Abstract: We study canonical and affine versions of non-renormalizable euclidean classical scalar field-theory with twelfth-order power-law interactions on three dimensional lattices through the Monte Carlo method. We show that while the canonical version of the model turns out to approach a “free-theory” in the continuum limit, the affine version is perfectly well defined as an interaction model.

PAPER: Quantum statistical physics, condensed matter, integrable systems

Monte Carlo evaluation of the continuum limit of $(\phi^{12})_3$

Riccardo Fantoni*

Università di Trieste, Dipartimento di Fisica, strada Costiera 11, 34151
Grignano (Trieste), Italy
E-mail: riccardo.fantoni@posta.istruzione.it

Received 16 May 2021

Accepted for publication 10 June 2021

Published 2 August 2021

Online at stacks.iop.org/JSTAT/2021/083102
<https://doi.org/10.1088/1742-5468/ac0f69>



CrossMark

Abstract. We study canonical and affine versions of non-renormalizable Euclidean classical scalar field-theory with twelfth-order power-law interactions on three dimensional lattices through the Monte Carlo method. We show that while the canonical version of the model turns out to approach a ‘free-theory’ in the continuum limit, the affine version is perfectly well defined as an interaction model.

Keywords: integrable quantum field theory

Contents

1. Introduction	2
2. Affine version of the field-theory	3
3. The lattice formulation of the field-theory model	3
4. Simulation details and relevant observables	4
5. Simulation results	5
6. Conclusions	7
Acknowledgments	8

*Author to whom any correspondence should be addressed.

Appendix A. The origin of the ‘3/4’ extra term **8**
Appendix B. Error analysis in the simulation **9**
References **10**

1. Introduction

Classical versions of all covariant scalar field-theory models with positive interactions admit acceptable solutions, but some models will lead to divergences when trying to solve them when using canonical quantum versions [1].

Although classical covariant models, such as $(\phi^{12})_3$, lead to acceptable solutions, canonical quantization leads only to free solutions, as if the interaction term was not present. There are simple classical models, e.g. a half-harmonic oscillator that is limited to $0 < q < \infty$, which also fails using canonical quantization. A newer procedure, called affine quantization [2–5], differs from canonical quantization only because it promotes different canonical variables to quantum operators. It has been shown that affine quantization can successfully quantize the oscillator example, and the purpose of this paper is to demonstrate that affine quantization, in effect, just adds one additional term, which is proportional to \hbar^2 , to the Hamiltonian. Which extra term to add is guided by affine quantization, and the result leads to a valid quantization of $(\phi^{12})_3$ ¹.

The problem treated in this work deals with covariant scalar fields with power-law interactions. For the $(\phi^r)_d$ theory, the Euclidean time version of the action functional is then given by,

$$S[\phi] = \int \left\{ \frac{1}{2} \left[\sum_{\mu=0}^s \left(\frac{\partial \phi(x)}{\partial x_\mu} \right)^2 + m^2 \phi^2(x) \right] + g \phi^r(x) \right\} d^d x, \tag{1.1}$$

with $x = (x_0, x_1, \dots, x_s)$ for s spatial dimensions, x_0 being time, and $d = s + 1$ for the number of space-time dimensions, m is the bare mass, $g > 0$ is the interaction term coupling constant and $r = 4, 6, 8, 10 \dots$ is the power of the interaction term.

Monte Carlo (MC) [6–8] studies in 1982 [9] showed that these models were correct for $r = 4$ and $d = 3$ but when $r = 4$ and $d = 4$ they led only to free models, with a vanishing renormalized coupling constant in the continuum limit, and this was later confirmed by analytic studies and that even became simply free models when $r = 4$ and $d > 4$, which includes non-renormalizable models as well.

All of the above stories used canonical procedures, which then failed when $r \geq 2d/(d - 2)$ [2–4]. It is believed that affine quantization procedures will solve those problems.

In this work, we chose the $(\phi^{12})_3$ theory. Classically, this is a straightforward problem that in the $g \rightarrow 0$ limit reduces to a free-theory. But in its canonical version it is non-renormalizable, which means that the domain of the free model, $\mathcal{D}_{g=0}$, is larger than

¹The example $(\phi^{12})_3$ has been deliberately chosen to be highly nonrenormalizable, while requiring the least amount of computer time.

Monte Carlo evaluation of the continuum limit of $(\phi^{12})_3$

that of the interacting model $\mathcal{D}_{g>0}$ (integrating ϕ^{12} will be finite for less ϕ than in the free model). In the continuum limit, the domains disagree and by continuity the new domain for the ‘free’ version (we can call it a ‘pseudofree’ situation) is the domain $\mathcal{D}_{g>0}$, not $\mathcal{D}_{g=0}$. That is the source of having free models using canonical quantization, such as $(\phi^r)_d$ with $r > 2d/(d - 2)^2$. On the other hand, affine quantization will lead to a non-free model to begin with and so it is appropriate when $g \rightarrow 0$. In parallel to the covariant theory, one can also define an ultralocal theory that is obtained by neglecting the kinetic part of the action (the term $\sum_{\mu=1}^s (\partial\phi(x)/\partial x_\mu)^2$) [3]. It turns out that such a theory will have a divergent perturbation series already for $r > 2$ for any $d \geq 2$. In these cases, the field theory will lead to a free-theory, non-renormalizable. So, with $r = 12$ there should be an even greater difference between the canonical and affine versions.

Various efforts have been tried in literature [10] to get a good result for the $(\phi^4)_4$ models, only to find that every effort came to the same conclusion that the result was a ‘free-theory’. Hence, the affine approach is the first to find an acceptable result [11].

2. Affine version of the field-theory

Our model has a standard classical Hamiltonian given by,

$$H[\pi, \phi] = \int \left\{ \frac{1}{2} \left[\pi^2(x) + \sum_{\mu=1}^s \left(\frac{\partial\phi(x)}{\partial x_\mu} \right)^2 + m^2\phi^2(x) \right] + g\phi^r(x) \right\} d^s x, \quad (2.1)$$

where s denotes the number of spatial coordinates and x_0 is the time. The momentum field $\pi(x) = \partial\phi(x)/\partial x_0$ and the canonical action $S = \int H dx_0$ is the one of equation (1.1).

Next, we introduce the affine field $\kappa(x) \equiv \pi(x)\phi(x)$, with $\phi(x) \neq 0$ and modify the classical Hamiltonian to become [2–4],

$$H'[\kappa, \phi] = \int \left\{ \frac{1}{2} \left[\kappa(x)\phi^{-2}(x)\kappa(x) + \sum_{\mu=1}^s \left(\frac{\partial\phi(x)}{\partial x_\mu} \right)^2 + m^2\phi^2(x) \right] + g\phi^r(x) \right\} d^s x. \quad (2.2)$$

In an affine quantization, the operator term $\widehat{\kappa}(x)\phi^{-2}(x)\widehat{\kappa}(x) = \widehat{\pi}^2(x) + \hbar^2(3/4)\delta^{2s}(0)\phi^{-2}(x)$, which leads to an extra ‘3/4’ potential [12] term (see appendix A), so that the new affine action will formally read,

$$S'[\phi] = \int \left\{ \frac{1}{2} \left[\sum_{\mu=0}^s \left(\frac{\partial\phi(x)}{\partial x_\mu} \right)^2 + m^2\phi^2(x) \right] + g\phi^r(x) + \frac{3}{8}\hbar^2 \frac{\delta^{2s}(0)}{\phi^2(x) + \epsilon} \right\} d^d x, \quad (2.3)$$

where $\epsilon > 0$ is a parameter used to regularize the ‘3/4’ extra term. In the $g \rightarrow 0$ limit, this model remains different from a free-theory, exactly due to the new $(3/8)\hbar^2\delta^{2s}(0)/[\phi^2(x) + \epsilon]$ interaction term.

²One requires that $\int d^d x |\nabla\phi(x)|^2 < [\int d^d x \phi^r(x)]^{2/r}$.

3. The lattice formulation of the field-theory model

We used a lattice formulation of the field theory. The theory considers a real scalar field ϕ taking the value $\phi(x)$ on each site of a periodic, hypercubic, d -dimensional lattice of lattice spacing a and periodicity na . The canonical action for the field, equation (1.1), is then approximated by

$$S[\phi] \approx \left\{ \frac{1}{2} \left[\sum_{x,\mu} a^{-2} (\phi(x) - \phi(x + e_\mu))^2 + m^2 \sum_x \phi^2(x) \right] + g \sum_x \phi^r(x) \right\} a^d, \tag{3.1}$$

where e_μ is a vector of length a in the $+\mu$ direction. The vacuum expectation of a functional observable $F[\phi]$ is

$$\langle F \rangle \approx \frac{\int F[\phi] \exp(-S[\phi]) \prod_x d\phi(x)}{\int \exp(-S[\phi]) \prod_x d\phi(x)}. \tag{3.2}$$

We will approach the continuum limit by choosing $na = 1$ fixed and increasing the number of discretizations n of each component of the space-time, so that the lattice spacing $a = 1/n \rightarrow 0^3$.

4. Simulation details and relevant observables

From each real field $\phi(x)$, we extract the Fourier transform

$$\tilde{\phi}(p) = \int d^d x e^{ip \cdot x} \phi(x), \tag{4.1}$$

with $\tilde{\phi}^*(p) = \tilde{\phi}(-p)$, so that the action of equation (1.1) becomes

$$S[\tilde{\phi}] = \int \frac{1}{2} [p^2 + m^2] |\tilde{\phi}(p)|^2 \frac{d^d p}{(2\pi)^d} + g I_r[\tilde{\phi}], \tag{4.2}$$

where we denote with I_r the power-law interaction functional.

We then find the ensemble averages $\langle \tilde{\phi}^2(0) \rangle$ and $\langle \tilde{\phi}^4(0) \rangle$ and construct the following observable (a renormalized unitless coupling constant at zero momentum),

$$g_R = \frac{3 \langle \tilde{\phi}^2(0) \rangle^2 - \langle \tilde{\phi}^4(0) \rangle}{\langle \tilde{\phi}^2(0) \rangle^2}, \tag{4.3}$$

so that clearly, using path integrals in the Fourier transform of the field, we immediately find for the canonical version of the theory,

$$g_R \xrightarrow{g \rightarrow 0} 0. \tag{4.4}$$

³Note that one could change the field $\phi \rightarrow \phi' a^{1-d/2}$ so that for example the kinetic term of the action goes to simply $\sum_{x,\mu} [\phi'(x) - \phi'(x + e_\mu)]^2 / 2$.

This remains true even for the calculation on a discrete lattice.

We then choose the momentum p with one component equal to $2\pi/na$ and all other components zero and calculate the ensemble average $\langle |\tilde{\phi}(p)|^2 \rangle$. We then construct the renormalized mass

$$m_R^2 = \frac{p^2 \langle |\tilde{\phi}(p)|^2 \rangle}{\langle \tilde{\phi}^2(0) \rangle - \langle |\tilde{\phi}(p)|^2 \rangle}. \tag{4.5}$$

When $g = 0$ the canonical version of the theory can be solved, exactly yielding

$$m_R \xrightarrow{g \rightarrow 0} [\pi/n \sin(\pi/n)]m. \tag{4.6}$$

Following Freedman *et al* [9], we will call g_R a dimensionless renormalized coupling constant and we will use it to test the ‘freedomness’ of our field theories in the continuum limit. Note that the sum-rules of equations (4.4) and (4.6) do not hold for the affine version (2.3) of the field theory due to the additional $(3/8)\hbar^2\delta^{2s}(0)/[\phi^2(x) + \epsilon]$ interaction term.

Our MC simulations use the Metropolis algorithm [6, 8] to calculate the discretized version of equation (3.2), which is a n^d multidimensional integral. The simulation is started from the initial condition $\phi = 0$. One MC step consisted in a random displacement of each one of the n^d components of ϕ as follows

$$\phi \rightarrow \phi + (\eta - 1/2)\delta, \tag{4.7}$$

where η is a uniform pseudo random number in $[0, 1]$ and δ is the amplitude of the displacement. Each one of these n^d moves is accepted if $\exp(-\Delta S) > \eta$, where ΔS is the change in the action due to the move (it can be efficiently calculated considering how the kinetic part and the potential part change by the displacement of a single component of ϕ) and rejected otherwise. The amplitude δ is chosen in such a way to have acceptance ratios as close as possible to 1/2 and is kept constant during the evolution of the simulation. One simulation consisted of $N = 10^6$ steps. The statistical error on the average $\langle F \rangle$ will then depend on the correlation time necessary to decorrelate the property F , τ_F , and will be determined as $\sqrt{\tau_F \sigma_F^2 / (N n^d)}$, where σ_F^2 is the intrinsic variance for F , as shown in appendix B.

5. Simulation results

We first chose the Euclidean covariant scalar interaction model with $d = 3$ and $r = 12$. In its canonical version (see the action of equation (1.1)), this is a non-renormalizable model and, following a perturbation expansion of g , there is an infinite number of different, divergent terms; or, if treated as a whole, such a model collapses to a ‘free-theory’ with a vanishing interaction term [13, 14]. This is even more true for the ultralocal version of the theory.

Following Freedman *et al* [9], in our MC simulation, for each n and g , we adjusted the bare mass m in such a way to maintain the renormalized mass approximately constant $m_R \approx 3$ (for large g it was necessary to take a complex bare mass so that m^2

J. Stat. Mech. (2021) 083102

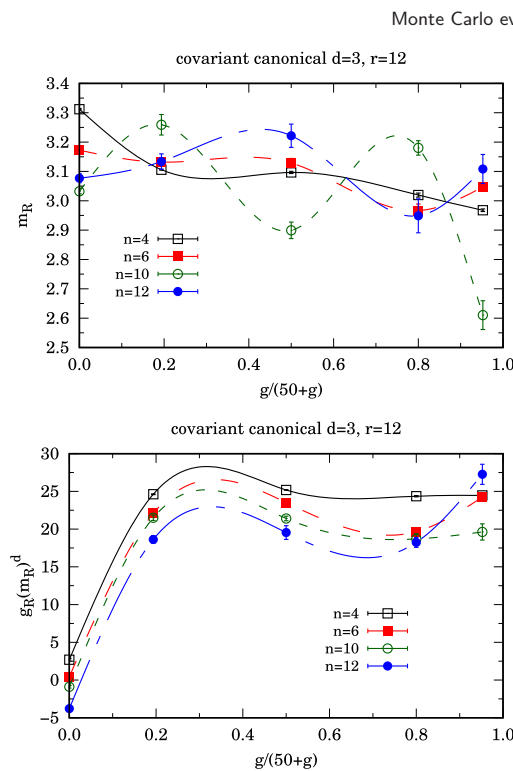


Figure 1. We show the renormalized mass m_R of equation (4.5) (top) and the renormalized coupling constant $g_R m_R^d$ of equation (4.3) (bottom) as calculated from equation (3.2) for $m_R \approx 3$ and various values of the bare coupling constant g at decreasing values of the lattice spacing $a = 1/n$ ($n \rightarrow \infty$ continuum limit) for the canonical $(\phi^{12})_3$ Euclidean scalar field theory described by the action in equation (1.1). The lines connecting the simulation points are just a guide for the eye.

was negative), to within a few percent (in all cases less than 15%), and we measured the renormalized coupling constant g_R of equation (4.3) for various values of the bare coupling constant g at a given small value of the lattice spacing $a = 1/n$. Thus, with na and m_R fixed, as a was made smaller, whatever change we found in $g_R m_R^d$ as a function of g could only be due to the change in a . We generally found that a depression in m_R produced an elevation in the corresponding value of g_R and vice-versa. The results are shown in figure 1 for the covariant version, where, following Freedman *et al* [9], we decided to compress the range of g for display by choosing the horizontal axis to be $g/(50 + g)$. As we can see from the figure the renormalized mass was made to stay around a value of 3, even if this constraint was not easy to implement, since for each n and g we had to run the simulation several (5–10) times with different values of the bare mass m .

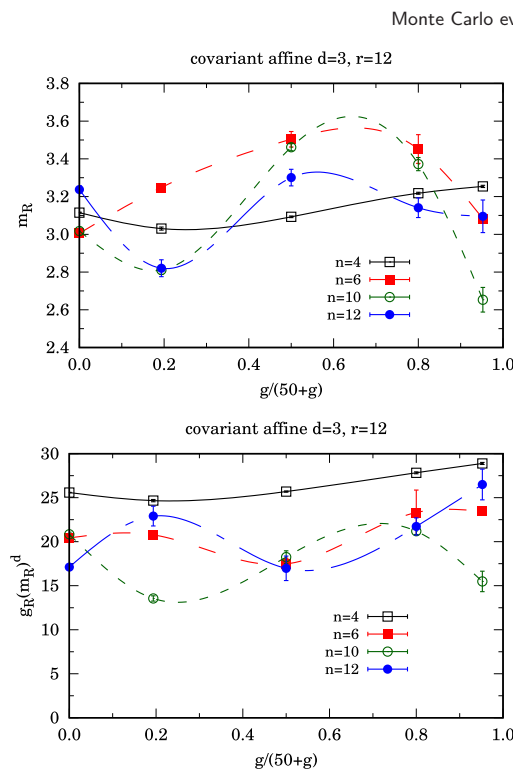


Figure 2. We show the renormalized mass m_R of equation (4.5) (top) and the renormalized coupling constant $g_R m_R^d$ of equation (4.3) (bottom) as calculated from equation (3.2) for $m_R \approx 3$ and various values of the bare coupling constant g at decreasing values of the lattice spacing $a = 1/n$ ($n \rightarrow \infty$ continuum limit) for the affine $(\phi^{12})_3$ Euclidean scalar field theory described by the action in equation (1.1). The lines connecting the simulation points are just a guide for the eye.

In figure 2, we show the same calculation but for the regularized affine field-theory (see the action of equation (2.3)), where we take $\hbar = 1$ and $\epsilon = 10^{-10}$.

From figure 1, we can see how at all finite values for the bare coupling constants g the renormalized coupling at zero momentum $g_R m_R^d$ appears to move to zero uniformly as the lattice spacing gets small, for $n \rightarrow \infty$. This numerically suggests that the canonical theory becomes asymptotically a free-theory in the continuum limit of large n , which is in agreement with the well known theoretical results [2–4]. This does not happen for the affine theory as shown in figure 2, where the renormalized coupling of the theory stays far from zero in the continuum limit for all values of the bare coupling constant.

6. Conclusions

Using MC simulations, we determined the dimensionless renormalized coupling constant of a Euclidean classical scalar field-theory with twelfth-order power-law interactions on a three-dimensional lattice. Our results for the canonical version of the theory are consistent with a noninteracting continuum limit. The renormalized coupling constant tends to zero at each finite value of the bare coupling constant as the lattice spacing gets small.

We then formulated an affine version of the same field-theory with the ‘3/4’ interaction term and observed that the MC results for the renormalized coupling constant stays far from zero for all values of the bare coupling constant as the lattice spacing diminishes. This means that the affine model remains a well-defined interacting model in the continuum limit.

A classical model, such as $(\phi^{12})_3$ with a positive coupling constant, has a natural behavior, while it becomes a free-theory with a positive coupling constant using canonical quantization. Canonical quantization also fails for a half-harmonic oscillator, e.g. $0 < q < \infty$ as well. Affine quantization solves both of these problems. There is a genuinely new procedure that permits various problem models to achieve a proper quantization. Affine quantization just selects different classical variables to promote to operators, and then it proceeds just like canonical quantization thereafter.

The present paper shows that the model $(\phi^{12})_3$ also generates a nontrivial behavior with an affine quantization. It is designed to feature a region where canonical quantization fails and there is a new procedure that can help. The classical limit of this quantized model leads back to a classical model with a positive coupling constant. That does not happen for canonical quantization. This implies that while canonical quantization is good for some models, affine quantization is needed for other models.

There are many other models that canonical quantization cannot solve, or struggle to quantize, that may be possible to quantize using affine quantization. Some of those models may be useful to specific problems in present-day high energy physics.

Acknowledgments

I would like to thank John R Klauder who proposed the problem, for the lively discussion exchanges. I would also like to acknowledge the constant support of my wife Laure Gouba who introduced me to the method of affine quantization.

Appendix A. The origin of the ‘3/4’ extra term

The operator corresponding to the affine field κ will be the dilation operator $\hat{\kappa} = (\hat{\pi}\hat{\phi} + \hat{\phi}\hat{\pi})/2$, where the regularized basic quantum Schrödinger operators are given by $\hat{\phi}(x) = \phi(x)$ and $\hat{\pi}(x) = -i\hbar\delta_{\phi(x)} = -i\hbar\delta/\delta\phi(x)$ so that the commutator $[\hat{\phi}(x), \hat{\pi}(y)] = i\hbar\delta^s(x-y)$, where $\delta^s(x)$ is a s -dimensional Dirac delta function since $\delta_{\phi(x)}\phi(y) = \delta^s(x-y)$. Multiplying this by $\hat{\phi}$, we find $[\hat{\phi}, \hat{\phi}\hat{\pi}] = [\hat{\phi}, \hat{\pi}\hat{\phi}] = [\hat{\phi}, \hat{\kappa}] = i\hbar\delta^s\hat{\phi}$,

Monte Carlo evaluation of the continuum limit of $(\phi^{12})_3$

which is only valid for $\phi \neq 0$. Then $\widehat{\kappa} = -i\hbar\{\delta_{\phi(x)}[\phi(x)] + \phi(x)\delta_{\phi(x)}\}/2 = -i\hbar\{\delta^s(0)/2 + \phi(x)\delta_{\phi(x)}\}$. Now, for $\phi(x) \neq 0$, we will have that affine quantization sends $\widehat{\pi}^2(x)$ to

$$\begin{aligned} \widehat{\kappa}(x)\phi^{-2}(x)\widehat{\kappa}(x) &= -\hbar^2\{\delta^s(0)/2 + \phi(x)\delta_{\phi(x)}\}\phi^{-2}(x)\{\delta^s(0)/2 + \phi(x)\delta_{\phi(x)}\} \\ &= -\hbar^2\{\delta^{2s}(0)\phi^{-2}(x)/4 + \delta^s(0)\phi(x)\delta_{\phi(x)}[\phi^{-2}(x)]/2 \\ &\quad + \delta^s(0)\phi^{-1}(x)\delta_{\phi(x)}/2 \\ &\quad + \delta^s(0)\phi^{-1}(x)\delta_{\phi(x)}/2 - \delta^s(0)\phi^{-1}(x)\delta_{\phi(x)} + \delta_{\phi(x)}^2\} \\ &= -\hbar^2\{\delta^{2s}(0)\phi^{-2}(x)/4 - 2\delta^{2s}(0)\phi^{-2}(x)/2 + \delta_{\phi(x)}^2\} \\ &= \hbar^2(3/4)\delta^{2s}(0)\phi^{-2}(x) - \hbar^2\delta_{\phi(x)}^2 \\ &= \hbar^2(3/4)\delta^{2s}(0)\phi^{-2}(x) + \widehat{\pi}^2(x). \end{aligned} \tag{A1}$$

We then see the appearance of an extra ‘3/4’ potential term. The lattice version of such a term will then be

$$\hbar^2(3/4)a^{-2s}\phi^{-2}(x) \tag{A2}$$

where a is the lattice spacing.

Appendix B. Error analysis in the simulation

Let F be a given property and let its value at step k of the random walk be F_k . Let the mean and intrinsic variance of F be denoted by

$$\bar{F} = \langle F_k \rangle = \frac{1}{P} \sum_{k=1}^P F_k \tag{B1}$$

and

$$\sigma_F^2 = \langle (F_k - \bar{F})^2 \rangle. \tag{B2}$$

These quantities depend only on the distribution $e^{-S}/\int e^{-S}$, not on the MC procedure. We can show that the standard error of the estimate of the average, \bar{F} , over a Markov chain with P steps, is

$$\text{error}[\bar{F}] = \sqrt{\left\langle \left(\frac{1}{P} \sum_{k=1}^P F_k - \frac{1}{P} \sum_{k=1}^P \bar{F} \right)^2 \right\rangle} = \sqrt{\frac{\sigma_F^2 \tau_F}{P}}, \tag{B3}$$

where τ_F is the correlation time that can be estimated as follows:

$$\tau_F \approx 1 + 2 \sum_{k=1}^P \frac{\langle (F_0 - \bar{F})(F_k - \bar{F}) \rangle}{\sigma_F^2}, \tag{B4}$$

Monte Carlo evaluation of the continuum limit of $(\phi^{12})_3$

and it gives the average number of steps to decorrelate the property F . The correlation time will depend crucially on the transition rule and has a minimum value of 1 if one can move so far in the configuration space that successive values are uncorrelated. In general, the number of independent steps that contribute to reducing the error bar from equation (B3) is not P but P/τ .

Hence, to determine the true statistical error in a random walk, one needs to estimate the correlation time. To do this, it is very important that the total length of the random walk be much greater than τ_F . Otherwise, the result and the error will be unreliable. Runs in which the number of steps is $P \gg \tau_F$ are called well-converged. In general, there is no mathematically rigorous procedure to determine τ . Usually one must determine it from the random walk. It is a good practice occasionally to run very long runs to test that the results are well-converged.

References

- [1] Klauder J R 2010 *A Modern Approach to Functional Integration* (Berlin: Springer)
- [2] Klauder J R 2020 Using affine quantization to analyze non-renormalizable scalar fields and the quantization of Einstein's gravity *J. High Energy Phys. Gravit. Cosmol.* **06** 802
- [3] Klauder J R 2020 An ultralocal classical and quantum gravity theory *J. High Energy Phys. Gravit. Cosmol.* **06** 656
- [4] Klauder J R 2020 The benefits of affine quantization *J. High Energy Phys. Gravit. Cosmol.* **06** 175
- [5] Fantoni R and Klauder J R 2021 Monte Carlo evaluation of the continuum limit of the two-point function of the Euclidean free real scalar field subject to affine quantization (arXiv:2103.06746)
- [6] Kalos M H and Whitlock P A 2008 *Monte Carlo Methods* (New York: Wiley)
- [7] Allen M P and Tildesley D J 1987 *Computer Simulation of Liquids* (Oxford: Clarendon)
- [8] Metropolis N, Rosenbluth A W, Rosenbluth M N, Teller A M and Teller E 1953 Equation of state calculations by fast computing machines *J. Chem. Phys.* **1087** 21
- [9] Freedman B, Smolensky P and Weingarten D 1982 Monte Carlo evaluation of the continuum limit of ϕ_4^4 and ϕ_3^4 *Phys. Lett. B* **113** 481
- [10] Siefert J and Wolff U 2014 Triviality of φ^4 theory in a finite volume scheme adapted to the broken phase (arXiv:1403.2570)
- [11] Fantoni R and Klauder J R 2021 Affine quantization of $(\varphi^4)_4$ succeeds while canonical quantization fails *Phys. Rev. D* **103** 076013
- [12] Gouba L 2021 Affine quantization on the half line *J. High Energy Phys. Gravit. Cosmol.* **07** 352
- [13] Aizenman M 1981 Proof of the triviality of ϕ_d^4 field theory and some mean-field features of Ising models for $d > 4$ *Phys. Rev. Lett.* **47** 886
- [14] Fröhlich J 1982 On the triviality of $\lambda\phi_d^4$ theories and the approach to the critical point in $d \geq 4$ dimensions *Nucl. Phys. B* **200** 281

Chapter 67

Monte Carlo evaluation of the continuum limit of the two-point function of the Euclidean free real scalar field subject to affine quantization

Fantoni R. and Klauder J. R., J. Stat. Phys. **184**, 28 (2021)

Title: “Monte Carlo evaluation of the continuum limit of the two-point function of the Euclidean free real scalar field subject to affine quantization”

Abstract: We study canonical and affine versions of the quantized covariant Euclidean free real scalar field-theory on four dimensional lattices through the Monte Carlo method. We calculate the two-point function at small values of the bare coupling constant and near the continuum limit at finite volume.



Monte Carlo Evaluation of the Continuum Limit of the Two-Point Function of the Euclidean Free Real Scalar Field Subject to Affine Quantization

Riccardo Fantoni¹ · John R. Klauder²

Received: 10 June 2021 / Accepted: 25 August 2021

© The Author(s), under exclusive licence to Springer Science+Business Media, LLC, part of Springer Nature 2021

Abstract

We study canonical and affine versions of the quantized covariant Euclidean free real scalar field-theory on four dimensional lattices through the Monte Carlo method. We calculate the two-point function near the continuum limit at finite volume. Our investigation shows that affine quantization is able to give meaningful results for the two-point function for which is not available an exact analytic result and therefore numerical methods are necessary.

Keywords Monte Carlo method · Euclidean free real scalar field-theory · Canonical quantization · Affine quantization · Two-point function · Continuum limit

Mathematics Subject Classification 03.50.-z · 11.10.-z · 11.10.Gh · 11.10.Kk · 02.70.Ss · 02.70.Uu · 05.10.Ln

1 Introduction

The aim of this work is to find out what affine quantization does to a classical field-theory. The simplest such theory is a free real scalar field of mass m . In that case, the spectrum of physical states obtained with canonical quantization is known: states containing many indistinguishable particles with momenta $\mathbf{p}_1, \mathbf{p}_2, \dots$ and energies $\sqrt{|\mathbf{p}_i|^2 + m^2}$ (here $c = 1$) obeying Bose statistics. The simplest question to ask now is: what becomes of this if the free real scalar field is subject to affine quantization [1,2] rather than canonical quantization [3]? Does the system describe particles in this case as well? If so, do they interact with one

Communicated by Luca Peliti.

Riccardo Fantoni
riccardo.fantoni@posta.istruzione.it

John R. Klauder
klauder@phys.ufl.edu

¹ Dipartimento di Fisica, Università di Trieste, strada Costiera 11, 34151 Trieste, Grignano, Italy

² Department of Physics and Department of Mathematics, University of Florida, Gainesville, FL 32611-8440, USA

another? Working out the two-point function of the free field in that framework should be of use to answer these questions.

The free real scalar field is well understood by canonical quantization. The standard set of problems that can be resolved by canonical quantization is distinct from the standard set of problems that can be resolved by affine quantization, and one can therefore expect that an affine quantization of the classical free real scalar differs from that of canonical quantization. The purpose of this paper is to try to understand in what ways an affine quantization is similar as well as dissimilar from a canonical quantization. We add that some non-free real scalar fields have already been observed and that canonical quantization fails for several non-renormalizable fields, such as $(\phi^{12})_3$ [4] and $(\phi^4)_4$ [5]. The key to that result is the introduction of a highly unusual, additional, non-quadratic, term that is dictated by affine quantization. While affine quantization employs an additional term, that particular term formally disappears when $\hbar \rightarrow 0$, which makes it a plausible modification of the quadratic terms of traditional free real scalar fields in order to extend acceptable quantization of traditional non-renormalizable models.

The Euclidean action in canonical quantization [3], in units where $\hbar = 1$, is

$$S^{(c)}[\phi] = \int \left\{ \frac{1}{2} \sum_{\mu=0}^s \left[\frac{\partial \phi(x)}{\partial x_\mu} \right]^2 + V(\phi(x)) \right\} d^n x, \tag{1.1}$$

with $x = (x_0, x_1, \dots, x_s) = (x_0, \mathbf{x})$ for s spatial dimensions and $n = s + 1$ for the number of space-time dimensions with $x_0 = ct$. We will work at $s = 3$. And V is the self-interaction potential density for which we will choose $V(\phi) = (1/2)m^2\phi^2$ corresponding to a free-theory with a bare mass m .

The Euclidean action in affine quantization [1,2] is

$$S^{(a)}[\phi] = \int \left\{ \frac{1}{2} \sum_{\mu=0}^s \left[\frac{\partial \phi(x)}{\partial x_\mu} \right]^2 + \frac{3}{8} \frac{\delta^{2s}(0)}{\phi^2(x) + \epsilon} + V(\phi(x)) \right\} d^n x, \tag{1.2}$$

where $\epsilon > 0$ is a parameter used to regularize the “3/8” extra term (see Appendix A in [4]) and δ is a Dirac delta function. In this case the Hamiltonian density contains a divergent term, in the total potential density $\mathcal{V}(\phi) = \frac{1}{2}m^2\phi^2 + \frac{3}{8}\delta^s(0)/(\phi^2 + \epsilon)$, in the continuum, but the field theory can be treated on a lattice, and the approach toward the continuum will be taken under exam in this work. In fact, the path integral needs this feature since we have examples such as $\int \phi^2(x) e^{-S^{(a)}[\phi]} \mathcal{D}\phi / \int e^{-S^{(a)}[\phi]} \mathcal{D}\phi$ which is a creation of $\langle \psi | \hat{\phi}^2(x) | \psi \rangle$, namely it creates a quantum version of the classical $\phi^2(x)$. The quantum operator $\hat{\phi}^2(x) \sim \delta^s(0)$ and must be passed through the functional integral which deals with terms within $S^{(a)}[\phi]$ leading to the fact that the term $\phi^2(x)$ needs to be $\sim \delta^s(0)$ (at the minima of \mathcal{V}) to handle the integration and that factor being “passed” to the quantum operator term $\hat{\phi}^2(x)$. In the $V \rightarrow 0$ limit, this model remains different from a massless free-theory due to exactly the new $(3/8)\delta^{2s}(0)/[\phi^2(x) + \epsilon]$ interaction term (we have a “pseudofree” situation).

In our previous works we studied the non-renormalizable canonical cases with $V(\phi) = (1/2)m^2\phi^2 + g\phi^4$ [5] in $s = 3$ and $(1/2)m^2\phi^2 + g\phi^{12}$ in $s = 2$ [4], where g is the bare coupling constant. And we showed that the corresponding affine cases are indeed renormalizable.

Monte Carlo (MC) [6,7] is the numerical method of choice to treat multidimensional integrals of high D dimensions (it supercedes the traditional integration methods, like the trapezoidal rule, the Simpson rule, . . . , based on the knowledge of the α^{th} derivative of the integrating function already for $D > 2\alpha$) therefore is especially useful to compute path

integrals. We will use it to study the two-point function of the Euclidean action of a real scalar field in affine quantization. Our estimate of the path integrals will be generally subject to three sources of numerical uncertainties: The one due to the statistical errors, the one due to the space-time discretization, and the one due to the finite-size effects. Of these the statistical errors scale like $M^{-1/2}$ where M is the computer time, the discretization of space-time is responsible for the distance from the continuum limit (which corresponds to a lattice spacing $a \rightarrow 0$), and the finite-size effects stems from the necessity to approximate the infinite space-time system with one in a periodic box of volume L^n with $L = Na$ being the box side, subject to N discretization points.

The work is organized as follows: In Sect. 2 we derive the lattice formulation of the field theory needed in the treatment on the computer, in Sect. 3 we describe our computer experiment and introduce the observables that will be measured during our simulations, in Sect. 4 we present our results, and section 5 is for final remarks.

2 The Lattice Formulation of the Field-Theory Model

We used a lattice formulation of the field theory. The theory considers a real scalar field ϕ taking the value $\phi(x)$ on each site of a periodic, hypercubic, n -dimensional lattice of lattice spacing a and periodicity $L = Na$. The canonical action for the field, Eq. (1.1), is then approximated by

$$S^{(c)}[\phi] \approx \left\{ \frac{1}{2} \sum_{x,\mu} a^{-2} [\phi(x) - \phi(x + e_\mu)]^2 + \sum_x V(\phi(x)) \right\} a^n, \tag{2.1}$$

where e_μ is a vector of length a in the $+\mu$ direction and we are at a temperature $T = 1/Na$, in units where Boltzmann constant $k_B = 1$. An analogous expression holds for the affine action of Eq. (1.2) where the Dirac delta function is replaced by $\delta^{2s}(0) \rightarrow a^{-2s}$.

We will use this ‘‘primitive approximation’’ for the action even if it can be improved in several ways [8] in order to reduce the error due to the space-time discretization. In reaching to the expression (2.1) we neglected the term $\propto a^{2n}$ due to the commutator of the kinetic and potential parts of the Hamiltonian, in the Baker–Campbell–Hausdorff formula. In reaching to the path integral expression this is justified by the Trotter formula.

The affine regularization of the previous paragraphs, leading to $\mathbf{x} \rightarrow \mathbf{k}a$, where $a > 0$ is the tiny lattice spacing, is helpful in our analysis but needs not be the final regularization. In particular, the new term $\phi(x_0, \mathbf{x})^{-2} \rightarrow \phi_{\mathbf{k}}^{-2}$ leads to a divergence when, at a fixed value of \mathbf{k} , the integral over the region $|\phi_{\mathbf{k}}| < 1$, of $\int (\phi_{\mathbf{k}})^{-2} d\phi_{\mathbf{k}} = \infty$. This behavior can be overcome in an additional form of regularization.¹ Instead of just $\phi_{\mathbf{k}}$ we choose $2s$ additional terms that are nearest neighbors to \mathbf{k} . These additional terms enter in the form $\phi_{\mathbf{k}}^{-2} \rightarrow [\sum_{\mathbf{l}} J_{\mathbf{k},\mathbf{l}} \phi_{\mathbf{l}}^2]^{-1}$, where $J_{\mathbf{k},\mathbf{l}} = (2s + 1)^{-1}$ for $\mathbf{l} = \mathbf{k}$ plus \mathbf{l} is each of the $2s$ nearest neighbors of \mathbf{k} . This averaging of $\phi_{\mathbf{k}}$ also leads to a finite integration where, with all $|\phi_{\mathbf{l}}| < 1$, we have

$$\int \cdots \int \left[\sum_{\mathbf{l}} J_{\mathbf{k},\mathbf{l}} \phi_{\mathbf{l}}^2 \right]^{-1} \prod_{\mathbf{l}} d\phi_{\mathbf{l}} < \infty, \tag{2.2}$$

which is finite as determined by choosing $\phi_{\mathbf{l}} = r u_{\mathbf{l}}$ such that $\sum_{\mathbf{l}} u_{\mathbf{l}}^2 < \infty$ leading to the integral $U \int r^{-2} r^{2s} dr < \infty$, for all $s > 0$, where $U < \infty$ accounts for the remaining finite integrations.

¹ The additional regularization is essentially taken from Eq. (14) in [9].

Clearly, this procedure of averaging the expression $\phi_{\mathbf{k}}^{-2}$ offers a smoother regulation, and we shall also adopt that procedure for our MC studies. We will refer to this affine regularization as term B and the one discussed earlier, obtained by choosing $J_{\mathbf{k},1} = \delta_{\mathbf{k},1}$, as term A.

The vacuum expectation of a functional observable $\mathcal{O}[\phi]$ is

$$\langle \mathcal{O} \rangle \approx \frac{\int \mathcal{O}[\phi] \exp(-S[\phi]) \prod_x d\phi(x)}{\int \exp(-S[\phi]) \prod_x d\phi(x)}, \tag{2.3}$$

for a given action S .

We will approach the continuum limit by choosing a fixed L and increasing the number of discretizations N of each component of the space-time. So that the lattice spacing $a = L/N \rightarrow 0$. To make contact with the continuum limit, two conditions must be met $a \ll 1/m \ll L$ where $1/m$ is the Compton wavelength.

3 Simulation Details and Relevant Observables

We want to determine the two-point function

$$K(x, y) = \langle [\phi(x) - \langle \phi(x) \rangle][\phi(y) - \langle \phi(y) \rangle] \rangle = \langle \phi(x)\phi(y) \rangle - \langle \phi(x) \rangle^2, \tag{3.1}$$

replacing x by $x + k$ with $k = aw_n$ with $w_n = (n_0, n_1, \dots, n_s)$ and $n_\mu \in \mathbb{Z}$ amounts to a mere relabeling of the lattice points. Hence, due to translational invariance, $K(x, y)$ can only depend on the difference between the coordinates of the two points and we can define,

$$D(z) = \frac{1}{L^n} \sum_x K(x, x + z)a^n, \tag{3.2}$$

For the massless free-theory with $V \rightarrow 0$ in canonical quantization, we find that in non periodic space-time (at zero temperature)

$$D'(z) = \int \frac{e^{-ip \cdot z}}{p^2} \frac{d^n p}{(2\pi)^n} = \begin{cases} -|z|/2 & n = 1 \\ -(\ln |z|/l)/2\pi & n = 2 \\ 1/|z|4\pi & n = 3 \\ 1/|z|^2 4\pi^2 & n = 4 \end{cases}, \tag{3.3}$$

where $|z| = \sqrt{z_0^2 + z_1^2 + \dots + z_s^2}$ and l is a length. This shows how the massless field generates long range interactions.

For a massive free-theory with $V(\phi(x)) = \frac{1}{2}m^2\phi^2(x)$ in canonical quantization, we find that in non periodic space-time (at zero temperature) with $n = 4$

$$D'(z) = \int \frac{e^{-ip \cdot z}}{p^2 + m^2} \frac{d^n p}{(2\pi)^n} = mK_1(m|z|)/|z|4\pi^2, \tag{3.4}$$

where m is the mass and K_1 is a modified Bessel function.

In periodic space-time (at a temperature $T = 1/Na$)

$$D(z) = \sum_{w_n} D'(z + Lw_n), \tag{3.5}$$

where the sum can be restricted by an infrared cutoff irc such that $-irc \leq n_\mu \leq irc$ (without any physical significance) in order to reach a given numerical accuracy. If we remove the cutoff the function diverges for the massless case.

Our MC simulations use the Metropolis algorithm [6,7] to calculate the ensemble average of Eq. (2.3) which is a N^n multidimensional integral. The simulation is started from the initial condition $\phi = 0$. One MC step consisted in a random displacement of each one of the N^n $\phi(x)$ as follows

$$\phi \rightarrow \phi + (2\eta - 1)\delta, \tag{3.6}$$

where η is a uniform pseudo random number in $[0, 1]$ and δ is the amplitude of the displacement. Each one of these N^n moves is accepted if $\exp(-\Delta S) > \eta$ where ΔS is the change in the action due to the move (it can be efficiently calculated considering how the kinetic part and the potential part change by the displacement of a single $\phi(x)$) and rejected otherwise. The amplitude δ is chosen in such a way to have acceptance ratios as close as possible to $1/2$ and is kept constant during the evolution of the simulation. One simulation consisted of M MC steps. The statistical error on the average $\langle \mathcal{O} \rangle$ will then depend on the correlation time necessary to decorrelate the property \mathcal{O} , $\tau_{\mathcal{O}}$, and will be determined as $\sqrt{\tau_{\mathcal{O}} \sigma_{\mathcal{O}}^2 / (MN^n)}$, where $\sigma_{\mathcal{O}}^2$ is the intrinsic variance for \mathcal{O} .

4 Simulation Results

We worked in units where $c = \hbar = k_B = 1$. We chose the regularization parameter of the affine quantization A term to be $\epsilon = 10^{-10}$.²

For a massive free-theory, $V(\phi) = \frac{1}{2}m^2\phi^2$, in canonical quantization (1.1) with $m = 1$, $N = 15$, $L = 3$, $a = L/N = 0.2$ we obtained the result shown in Fig. 1 where we compare the MC results with the exact expression of Eq. (3.5) with an infrared cutoff of $irc = 2$ which is sufficient for an accuracy of 10^{-3} . The run was $M = 10^6$ MC steps long. The figure shows good agreement between the MC and the exact expression except at the origin due to the space-time discretization.

For a free massive theory $V(\phi) = \frac{1}{2}m^2\phi^2$ in affine quantization (1.2) using term A, the self-interaction is a double well with a spike barrier at $\phi = 0$. We tuned the width of the displacement, δ in Eq. (3.6), so that the random walk in the $\phi(x)$ will sample the probability distribution $\exp(-S[\phi])$ most efficiently, with short equilibration times. In Fig. 2 we show the result for a free real scalar field subject to affine quantization with a total self-interaction of the form $\mathcal{V}(\phi) = \frac{1}{2}m^2\phi^2 + \frac{3}{8}a^{-2s}/(\phi^2 + \epsilon)$ with $m = 1$, $N = 15$, $L = 3$, $a = L/N = 0.2$, and $\epsilon = 10^{-10}$ after cutting the first equilibration MC steps of a run made of $M = 2.5 \times 10^6$ steps. During the simulations we also calculated the renormalized mass m_R and the renormalized coupling constant g_R [4]. As we can see from the figure the symmetry $z \rightarrow L - z$ of the two-point function is preserved within the errorbars. The minima of the classical \mathcal{V} is at $\phi = \pm\Phi$ with $\Phi^2 = -\epsilon + \sqrt{3}/(2a^3m)$ which diverges in the continuum limit $a \rightarrow 0$ (this of course does not happen in the harmonic oscillator case [10] which is independent of the lattice spacing). Moreover the minimum of the action $L^{s+1}m(\sqrt{3} - m\epsilon a^s)/2a^s$ also diverges, both in the continuum limit at finite volume ($ma \rightarrow 0$) and in the infinite volume limit at fixed lattice spacing ($mL \rightarrow \infty$) (this also happen for the affine harmonic oscillator [10] which has a well defined zero temperature limit). The corresponding contribution to the vacuum expectation only occurs together with the normalization constant in front of the path integral and drops out in quantities of physical interest (as long as the system is not placed in

² Note that we could as well choose a regularization putting hard walls at $\phi = \pm\epsilon$ therefore rejecting MC moves whenever $\phi \in [-\epsilon, \epsilon]$

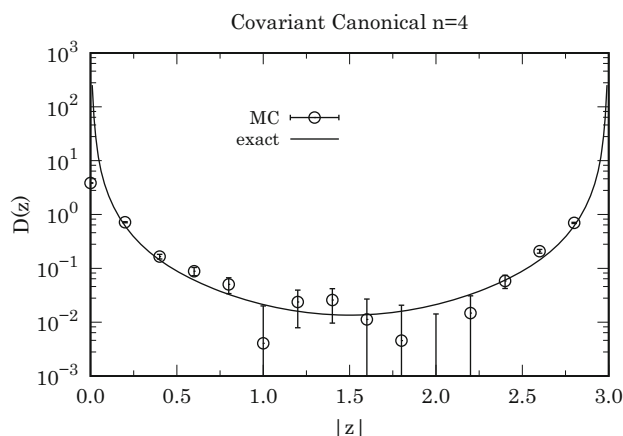


Fig. 1 Two-point function $D(z)$ of Eq. (3.2), for a free real scalar field subject to canonical quantization with a self-interaction potential density of the form $V(\phi) = \frac{1}{2}m^2\phi^2$ in Eq. (1.1) with $m = 1, N = 15, L = 3, a = L/N = 0.2$. We compare with the analytic exact expression of Eq. (3.5) with an infrared cutoff of $irc = 2$. A logarithmic scale is used on the y-axis

a curved geometry, i.e. in a gravitational field - there, the cosmological constant does have physical significance)

The symmetry $\phi \rightarrow -\phi$ is broken in the simulations (see Appendix 1) and as a result $\langle \phi(x) \rangle$ is different from zero. The action $S = \bar{K} + \bar{V}$ where \bar{K} is the kinetic term and \bar{V} the total potential term. Imagine now that we are in a configuration where all the N^n components, $\phi(x)$, are around $+\Phi$. In order to start migrating one single x' component, $\phi(x')$, around the other minimum at $-\Phi$ will have no cost in the potential, $\Delta \bar{V} \approx 0$, but it will have a big cost in the kinetic term between “neighboring” x , resulting in a big $\Delta \bar{K}$ (as long as the distance between the two minima, 2Φ , which diverges in the continuum limit, is large). As a consequence $\exp(-\Delta S)$ will be very small and the move will be almost surely rejected according to the Metropolis rule. Moreover, once the system reaches the phase with all $\phi(x)$ in one of the minima, it is very unlikely that a single $\phi(x')$ will move to the other minimum but it cannot be excluded, in principle. If this happens one has a situation where the field is around $+\Phi$ at all x except at x' where it is around $-\Phi$. But we can easily see that now it would be statistically favorable for the single field on the left to rejoin the fields on the right other than all the fields on the right join the field on the left. Exactly the same holds for affine quantization (1.2) using term B, since due to the kinetic energy term in the action the fields at neighboring points tend to assume similar values. On the other hand this would not hold for an *ultralocal* [11] theory where we could have the field visiting both wells at $\pm\Phi$ but only at not “neighboring” times, resulting in a vanishing $\langle \phi(x) \rangle$. Apart from this the shape of the two-point function is qualitatively similar to the one of the *covariant* case of Eq. (1.2). In addition in a covariant *complex* field one could go “slowly” “around” the “mountain” at $\phi = 0$ with no need of “jumps”.

For our choice of the parameters we have $\Phi \approx 10.404$ with $\Phi^2 \approx 108.253$. The results in Fig. 2 indicate that the quantization increases this number by about 10%. The minimum of $D(z)$ is reached around $|z| = L/2$. The two-point function is qualitatively similar to the one of the free field. This is supported by recent results on a one dimensional harmonic oscillator treated with affine quantization [10] where it is shown that the eigenvalues are still equally spaced. A non-linear fit of the MC data (removing the first point at $|z| = 0$) with the function

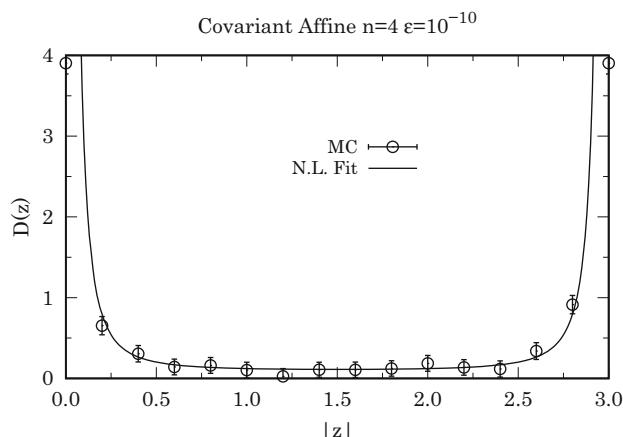


Fig. 2 Two-point function $D(z)$ of Eq. (3.2), for a free real scalar field subject to affine quantization with term A and a self-interaction potential density of the form $V(\phi) = \frac{1}{2}m^2\phi^2$ in Eq. (1.2) with $m = 1$, $N = 15$, $L = 3$, $a = L/N = 0.2$, and $\epsilon = 10^{-10}$. Also shown is the result of a non-linear fit of the data (except the first point at $|z| = 0$) with the function $D_{m_D}(z)$ where D_{m_D} is the two-point function of a free field of mass m_D of Eq. (3.5) with an $irc = 2$, taking m_D as the only fit parameter

$D_{m_D}(z)$ where D_{m_D} is the two-point function of a free field of mass m_D of Eq. (3.5) with an $irc = 2$, taking m_D as the only fit parameter, gives $m_D \approx 0.9$. The result of the fit is also shown in Fig. 2.

For a free real scalar field subject to affine quantization with term A, in $n = 4$ space-time dimensions in a volume 3^4 with a regularization parameter $\epsilon = 10^{-10}$, we studied the continuum limit, $N \rightarrow \infty$, (by choosing values lower of 15) and the dependence on the bare mass m , of the five quantities m_R , g_R , $\langle\phi(x)\rangle^2$, m_D , and $D(0)$. The results are shown in Table 1. From the table we see how moving towards the continuum limit $m_D \approx m$ but m_R becomes small due to the fact that when the field picks up an expectation value, the Fourier transform of the field $\tilde{\phi}(0)$ picks up a contribution proportional to the volume of the box. Moreover, for the same reason, $g_R \approx 2$. The Table also shows the value of Φ^2 and of $\langle\phi(x)\rangle^2$ to be compared. We see that the second is always larger than the first one by a percentage increasing with increasing m and with increasing a . The value of $D(0)$ is increasing with a decrease of the lattice spacing a , signaling a divergence in the continuum limit.

Summarizing, the two-point function for $\phi - \langle\phi\rangle$ looks similar to the two-point function of a free field with mass m_D . In other words, the correlation length of the affine quantum field theory is m/m_D times the Compton wavelength of the canonical quantum theory of the free scalar field. Our results seem to suggest that, going towards the continuum, the affine model is approaching a free field with the same bare mass.

The value of m_D is not easy to understand, however. If the action is treated at the classical level, small deviations from the minimum are determined by the curvature of the total potential, $m_c^2 = d^2\mathcal{V}/d\phi^2$ at $\phi = \Phi$. The mass term contributes m^2 and the “3/8” term yields a contribution that is 3 times larger. For $\epsilon = 0$, the mass relevant for the relation between frequency of the waves and wavelength is: $m_c = 2m$ independently of a .

In Fig. 3 we show $D(z)$ as obtained for $m = 1$ ($L = 3$, $\epsilon = 10^{-10}$) and three choices of N , in the long simulations of the Table 1. One can then see the approach to the continuum of the two-point function of the affine model.

Table 1 We determined, for a free real scalar field subject to affine quantization with term A, in $n = 4$ space-time dimensions, the dependence of m_R , g_R , m_D , and $D(0)$ on the number of one dimensional discretization points N and the bare mass m at $L = 3$ with a regularization parameter $\epsilon = 10^{-10}$

N	m	m_R	g_R	Φ^2	$\langle \phi(x) \rangle^2$	m_D	$D(0)$
15	1	0.0122(3)	1.9979(1)	108.2	120.6(1)	0.934	3.69(6)
	2	0.00646(4)	1.99983(3)	54.13	65.7(1)	1.785	3.32(6)
	3	0.0186(6)	1.99925(8)	36.08	45.85(7)	3.009	2.97(6)
12	1	0.01053(5)	1.99958(5)	55.43	63.25(8)	0.302	2.38(5)
	2	0.00967(9)	1.99992(2)	27.71	34.54(5)	2.467	2.00(5)
	3	0.0095(1)	1.99905(8)	18.47	24.00(4)	5.483	1.66(5)
10	1	0.01417(4)	1.999464(4)	32.07	37.46(5)	0.587	1.58(3)
	2	0.0124(1)	1.99995(1)	16.04	20.43(3)	3.789	1.29(3)
	3	0.0119(2)	1.99996(1)	10.69	14.03(2)	5.647	1.02(3)

The runs were $M = 5 \times 10^6$ MC steps long. The value of Φ^2 and of $\langle \phi(x) \rangle^2$ are also shown for comparison

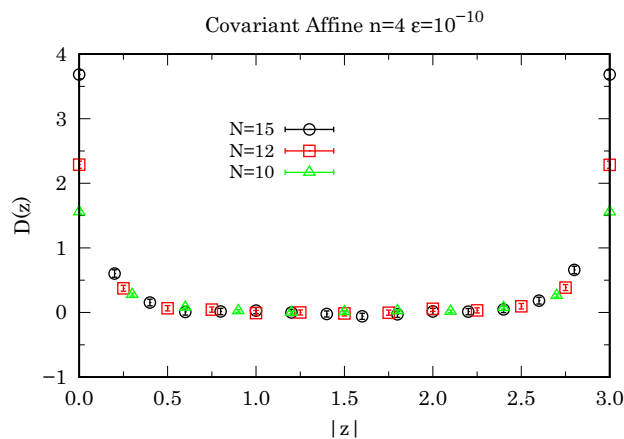


Fig. 3 (color online) Two-point function $D(z)$ of Eq. (3.2) for a free real scalar field subject to affine quantization with term A and a self-interaction potential density of the form $V(\phi) = \frac{1}{2}m^2\phi^2$ in Eq. (1.2) with $m = 1$, $L = 3$, $\epsilon = 10^{-10}$ and increasing $N = 10, 12, 15$

5 Conclusions

In a recent work [5] we studied the case of a non-renormalizable $(\phi^4)_4$ canonical theory (where the self-interaction potential is $V(\phi) = g\phi^4$) in four space-time dimensions and proved through MC that the theory becomes renormalizable if one treats the field through affine quantization.

In the present work we observed that for $g = 0$ the simplest question to ask was: Does the affine system describe particles as for the canonical one? If so, do they interact with one another?

We tried to answer these question by looking at the two-point function. What we proved through our MC analysis was that the affine case with $g = 0$ has to be considered like a “sort” of free-theory of “quasiparticles” (in the sense of Lev Landau in his theory for Fermi liquids) where the “3/8” term just offers itself like a sort of “collective excitation” term. In this case

the $\phi \rightarrow -\phi$ symmetry is broken and the field acquires a non-zero vacuum expectation. The two-point function nonetheless has all the same features as those of a free scalar field of similar mass, in the continuum limit.

One shortcoming of the affine formulation of the field theory is the divergence (in the continuum) of the vacuum expectation value of the field which generates the disconnected contribution to the Green's functions. The path integral is fully determined by the local properties of the field that enter through the action. The expectation value of the field does not represent a local property of the field. We cannot imagine how one could possibly get rid of it. In the Standard Model, however, one of the crucial properties of the Higgs fields is that they pick up a vacuum expectation value v . The masses of the W- and Z-bosons as well as those of the leptons and quarks are proportional to v . In order to remedy to this drawback one should perform the following scaling $\phi \rightarrow a^{-s/2}\phi$ (together with $g \rightarrow a^s g$ in a possible interaction term of the form $g\phi^4$) which would bring about an additional factor a^{-s} multiplying the action. This scaling proved successful in our forthcoming work on the affine quantization of a Higgs complex scalar field [12].

The present paper is wanted to confirm that both canonical and affine procedures lead to desired and expected behavior for quadratic potential terms. A later paper [12] will be designed to deal with quartic potential terms with canonical and affine procedures.

Acknowledgements Many thanks to Heinrich Leutwyler for his suggestions, comments, and someone who proposed the canonical and affine programs with regard to the required features including what to examine and what to expect, which has influenced our program and its results, and led to many positive results and highlighted the expected canonical and affine differentiation.

Appendix: Field Configurations in the Vicinity of the Two Degenerate Minima in the Affine Version

Classically, the affine version of the free Hamiltonian has two degenerate minima, $\phi = \pm\Phi$. If the path integral is dominated by those field configurations that are located in the vicinity of one of these everywhere on the entire lattice or in the vicinity of the other, then it consists of two equal pieces

$$\begin{aligned}
 Z &= \int \mathcal{D}\phi \exp(-S[\phi]), \\
 Z_+ &= \int \mathcal{D}\phi \exp(-S[\phi]), \quad \text{integral only over } \phi(x) \approx \Phi, \\
 Z_- &= \int \mathcal{D}\phi \exp(-S[\phi]), \quad \text{integral only over } \phi(x) \approx -\Phi,
 \end{aligned}$$

and $Z_+ = Z_-$. Under a broken symmetry $\phi \rightarrow -\phi$ one would get either $Z \approx Z_+$ or $Z \approx Z_-$. This has to be expected in the present case of a real field since in order to move the field $\phi(x)$ at a single x from around Φ to around $-\Phi$ in the MC path integral one has to overcome a large kinetic cost. This is not true for a complex field where one can go “slowly” “around” the “mountain” at $\phi = 0$.

The expectation value of the field

$$\begin{aligned}
 \langle \phi(x) \rangle &= \int \mathcal{D}\phi \phi(x) \exp(-S[\phi]) / Z, \\
 \langle \phi(x) \rangle_+ &= \int \mathcal{D}\phi \phi(x) \exp(-S[\phi]) / Z_+, \quad \text{over } \phi(x) \approx \Phi
 \end{aligned}$$

$$\langle \phi(x) \rangle_- = \int \mathcal{D}\phi \phi(x) \exp(-S[\phi])/Z_-, \text{ over } \phi(x) \approx -\Phi,$$

with $\langle \phi(x) \rangle_+ \approx \Phi$, $\langle \phi(x) \rangle_- \approx -\Phi$, and under the broken symmetry, $\langle \phi(x) \rangle \approx \langle \phi(x) \rangle_{\pm} \approx \pm\Phi$ where the simulation, starting from $\phi = 0$, will choose among the two different cases just after the first equilibration steps.

For the two-point function

$$D_+(x-y) = \int \mathcal{D}\phi \phi(x)\phi(y) \exp(-S[\phi])/Z_+ - \langle \phi(x) \rangle_+^2, \text{ over } \phi(x) \approx \Phi,$$

$$D_-(x-y) = \int \mathcal{D}\phi \phi(x)\phi(y) \exp(-S[\phi])/Z_+ - \langle \phi(x) \rangle_-^2, \text{ over } \phi(x) \approx -\Phi,$$

so that $D_+(z) \approx 0$, $D_-(z) \approx 0$, and $D(z) \approx D_{\pm}(z) \approx 0$.

Moreover one can see how in the broken symmetry configuration in which $\phi^2(x) \approx \Phi^2 \sim a^{-3}$, the “3/8” term in the Hamiltonian density is also of the same order in the continuum limit $a \rightarrow 0$. This will lead to a convergent two-point function for $\phi - \langle \phi \rangle$ in the continuum limit.

References

1. Klauder, J.R.: The benefits of affine quantization. *J. High Energy Phys. Gravit. Cosmol.* **6**, 175 (2020)
2. Klauder, J.R.: *Beyond Conventional Quantization*. Cambridge University Press, Cambridge (2000)
3. Dirac, P.A.M.: *The Principles of Quantum Mechanics*. Clarendon Press, Oxford (1958)
4. Fantoni, R.: Monte Carlo evaluation of the continuum limit of $(\phi^{12})_3$. *J. Stat. Mech.* 083102 (2021)
5. Fantoni, R., Klauder, J.R.: Affine Quantization of $(\varphi^4)_4$ Succeeds While Canonical Quantization Fails. *Phys. Rev. D* **103**, 076013 (2021)
6. Kalos, M.H., Whitlock, P.A.: *Monte Carlo Methods*. Wiley, Hoboken (2008)
7. Metropolis, N., Rosenbluth, A.W., Rosenbluth, M.N., Teller, A.M., Teller, E.: Equation of state calculations by fast computing machines. *J. Chem. Phys.* **1087**, 21 (1953)
8. Ceperley, D.M.: Path integrals in the theory of condensed helium. *Rev. Mod. Phys.* **67**, 279 (1995)
9. Klauder, J.R.: Using affine quantization to analyze non-renormalizable scalar fields and the quantization of Einstein’s gravity. *J. High Energy Phys. Gravit. Cosmol.* **6**, 802 (2020)
10. Gouba, L.: Affine quantization on the half line. *J. High Energy Phys. Gravit. Cosmol.* **7**, 352 (2021)
11. Klauder, J.R.: An ultralocal classical and quantum gravity theory. *J. High Energy Phys. Gravit. Cosmol.* **6**, 656 (2020)
12. Fantoni, R., Klauder, J. R.: Monte Carlo evaluation of the continuum limit of the two-point function of two Euclidean Higgs real scalar fields subject to affine quantization. *Phys. Rev. D* (2021) [arXiv:2107.08601](https://arxiv.org/abs/2107.08601)

Publisher’s Note Springer Nature remains neutral with regard to jurisdictional claims in published maps and institutional affiliations.

Chapter 68

Monte Carlo evaluation of the continuum limit of the two-point function of two Euclidean Higgs real scalar fields subject to affine quantization

Fantoni R. and Klauder J. R., Phys. Rev. D **104**, 054514 (2021)

Title: “Monte Carlo evaluation of the continuum limit of the two-point function of two Euclidean Higgs real scalar fields subject to affine quantization”

Abstract: We study canonical and affine versions of the quantized covariant Euclidean Higgs scalar field theory for two real fields on four dimensional lattices through the Monte Carlo method. We calculate the two-point function near the continuum limit at finite volume.

Monte Carlo evaluation of the continuum limit of the two-point function of two Euclidean Higgs real scalar fields subject to affine quantization

Riccardo Fantoni^{1,*} and John R. Klauder^{2,†}

¹Università di Trieste, Dipartimento di Fisica, strada Costiera 11, 34151 Grignano (Trieste), Italy

²Department of Physics and Department of Mathematics University of Florida, Gainesville, Florida 32611-8440, USA

(Received 23 July 2021; accepted 13 September 2021; published 29 September 2021)

We study canonical and affine versions of the quantized covariant Euclidean Higgs scalar field-theory for two real fields on four dimensional lattices through the Monte Carlo method. We calculate the two-point function near the continuum limit at finite volume.

DOI: 10.1103/PhysRevD.104.054514

I. INTRODUCTION

The aim of this work is to find out what affine quantization [1,2] does to a classical field-theory for two real scalar fields, or equivalently a complex scalar field, of mass m subject to the Mexican-hat, Higgs potential, rather than canonical quantization [3]. To this aim we will compare the two-point function of the two fields in the two frameworks.

In particular in this paper we try to understand in what ways an affine quantization is similar as well as dissimilar from a canonical quantization. We add that some nonfree real scalar fields have already been observed and that canonical quantization fails for several nonrenormalizable fields, such as $(\phi^{12})_3$ [4] and $(\phi^4)_4$ [5]. The key to that result is the introduction of a highly unusual, additional, nonquadratic, term that is dictated by affine quantization. While affine quantization employs an additional term, that particular term formally disappears when the Planck constant $\hbar \rightarrow 0$, which makes it a plausible modification of the quadratic terms of traditional free real scalar fields in order to extend acceptable quantization of traditional nonrenormalizable models. [6–10]

This work should be considered as a follow up of our previous work [11] where the two-point function of a single Euclidean free real scalar field subject to affine quantization was found through Monte Carlo (MC) methods. In particular in that work we found that the vacuum expectation value of the field diverges in the continuum limit. This

shortcoming is expected to disappear in the present case of a complex field $\varphi = \phi_1 + i\phi_2$. In fact, in this case, one can go “slowly” “around” the peak at $\varphi = 0$ with no need of “jumps” [11].

The covariant Euclidean action in canonical quantization [3] is¹

$$S^{(c)}[\phi_1, \phi_2] = \int \left\{ \frac{1}{2} \sum_{\mu=0}^s \left[\left(\frac{\partial \phi_1(x)}{\partial x_\mu} \right)^2 + \left(\frac{\partial \phi_2(x)}{\partial x_\mu} \right)^2 \right] + V(\phi_1(x), \phi_2(x)) \right\} d^n x, \quad (1.1)$$

$$V(\phi_1, \phi_2) = \frac{1}{2} m^2 (\phi_1^2 + \phi_2^2) + g [(\phi_1^2 + \phi_2^2) - \Phi]^2, \quad (1.2)$$

with $x = (x_0, x_1, \dots, x_s) = (x_0, \vec{x})$ for s spatial dimensions and $n = s + 1$ for the number of space-time dimensions with $x_0 = ct$, where c is the speed of light constant and t extends from zero to $\hbar\beta$ with $\beta = 1/k_B T$, k_B being the Boltzmann constant and T the absolute temperature. We will work at $s = 3$. And V is the self-interaction potential density corresponding to an interacting Higgs theory with a bare mass m and a bare coupling g .

The covariant Euclidean action in affine quantization [1,2] is

$$S^{(a)}[\phi_1, \phi_2] = \int \left\{ \frac{1}{2} \sum_{\mu=0}^s \left[\left(\frac{\partial \phi_1(x)}{\partial x_\mu} \right)^2 + \left(\frac{\partial \phi_2(x)}{\partial x_\mu} \right)^2 \right] + \frac{3}{8} \frac{\delta^{2s}(0) \hbar^2}{\phi_1^2(x) + \phi_2^2(x) + \epsilon} + V(\phi_1(x), \phi_2(x)) \right\} d^n x, \quad (1.3)$$

¹Note however that Eq. (1.3) can be simplified to $V = g[(\phi_1^2 + \phi_2^2) - A^2]^2 + \text{constant}$, where A involves a combination of Φ and m : $A^2 = \Phi^2 - m^2/4g$.

*riccardo.fantoni@posta.istruzione.it
†klauder@ufl.edu

Published by the American Physical Society under the terms of the Creative Commons Attribution 4.0 International license. Further distribution of this work must maintain attribution to the author(s) and the published article's title, journal citation, and DOI. Funded by SCOAP³.

where $\epsilon > 0$ is a parameter used to regularize the “3/8” extra term stemming from considering the complex field $\varphi(x) = \phi_1(x) + i\phi_2(x)$ and the momentum field $\pi(x) = -i\hbar\partial/\partial\varphi(x)$ as the two conjugate canonical variables (see Appendix A in [4]) and δ is a Dirac delta function. In this case the Hamiltonian density formally contains a divergent term,² in the total potential density $\mathcal{V}(\phi) = \frac{3}{8}\delta^{2s}(0)\hbar^2/(\phi_1^2 + \phi_2^2 + \epsilon) + V(\phi)$, in the continuum, but the field theory can be regularized and treated on a lattice, and the *approach* toward the continuum will be taken under exam in this work. In the following we will use natural units with $c = \hbar = k_B = 1$.

In our previous works we studied the single real scalar field nonrenormalizable canonical cases with $V(\phi) = \frac{1}{2}m^2\phi^2 + g\phi^4$ [5] in $s = 3$ and $\frac{1}{2}m^2\phi^2 + g\phi^{12}$ in $s = 2$ [4], where g is the bare coupling constant. And we showed that the corresponding affine cases are indeed renormalizable.

MC [12,13] is the numerical method of choice to treat multidimensional integrals of high dimensions and, therefore, is especially useful to compute path integrals. We will use it to study the two-point function of the Euclidean action of two real scalar field in affine quantization. Our estimate of the path integrals will be generally subject to three sources of numerical uncertainties: The one due to the statistical errors, the one due to the space-time discretization, and the one due to the finite-size effects. Of these, the statistical errors scale like $M^{-1/2}$ where M is the computer time, the discretization of space-time is responsible for the distance from the *continuum limit* (which corresponds to a lattice spacing $a \rightarrow 0$), and the finite-size effects stems from the necessity to approximate the infinite space system with one in a periodic box of volume L^s with $L = Na$ being the box side, subject to N discretization points. The finite-size effects are due to the distance from the *thermodynamic limit* (which corresponds to $N \rightarrow \infty$). [14]

The work is organized as follows: In Sec. II we derive the lattice formulation of the field theory needed in the treatment on the computer; in Sec. III we describe our computer experiment and introduce the observables that will be measured during our simulations; in Sec. IV we present our partial results obtained by working with the two scalar fields ϕ_1 and ϕ_2 where we encounter ergodicity problems for the affine case; in Sec. V we are able to overcome the ergodicity breakdown observed in the previous section and we present our final results for the affine case obtained by working with the two scalar fields $\rho = \sqrt{\phi_1^2 + \phi_2^2}$ and $\theta = \arctan(\phi_2/\phi_1)$ such that $d\phi_1 d\phi_2 = \rho d\theta d\rho$. Section VI is for final remarks.

²The divergent integral $\int_{-N}^N d\phi/\phi^2$, can be made finite simply by a regularized integral such as $\int \sum_{n=-N}^N (1/3r^2)[(n+1)^2\cos^2(k) + n^2\sin^2(k)\cos^2(k') + (n-1)^2\sin^2(k)\sin^2(k')]^{-1} dr^3 dk dk'$ where the prime over the sum indicates that we are considering a periodic closure $-N, N$ for the three terms in square brackets.

II. THE LATTICE FORMULATION OF THE FIELD-THEORY MODEL

We used a lattice formulation of the field theory. The theory considers a complex scalar field $\varphi = \phi_1 + i\phi_2$ taking the value $\varphi(x)$ on each site of a periodic, hypercubic, n -dimensional lattice of lattice spacing a and periodicity $L = Na$. The canonical covariant action for the field, Eq. (1.1), is then approximated by

$$\frac{S^{(c)}[\phi_1, \phi_2]}{a^n} \approx \frac{1}{2a^2} \sum_{x,\mu} \{ [\phi_1(x) - \phi_1(x + e_\mu)]^2 + [\phi_2(x) - \phi_2(x + e_\mu)]^2 \} + \sum_x V(\phi_1(x), \phi_2(x)), \quad (2.1)$$

where e_μ is a vector of length a in the $+\mu$ direction and we are at a temperature $T = 1/Na$, in units where Boltzmann constant $k_B = 1$.

Note that in our model the continuous symmetry $\varphi \rightarrow e^{i\alpha}\varphi$ breaks down spontaneously and the mass spectrum contains a Goldstone boson. The accepted signal of a system being in the symmetry broken phase in a finite volume, in the absence of a small symmetry breaking term, is not a nonzero order parameter, but rather the fact that a product of order parameters, at points x, y , tends to a nonzero limit with increasing $|x - y|$. To understand the properties of the system at finite volume, it is convenient to add a small symmetry breaking term and to work with the potential

$$V = g(\phi_1^2 + \phi_2^2 - A^2)^2 + (\epsilon^2/2)\phi_2^2 + \text{constant}, \quad (2.2)$$

The term proportional to ϵ^2 ensures that the classical action has a proper minimum at the point $\phi_1 = A, \phi_2 = 0$. The expansion of the potential in powers of $\psi = \phi_1 - A$, and ϕ_2 starts with

$$V = (M^2/2)\psi^2 + (\epsilon^2/2)\phi_2^2 + \dots, \quad (2.3)$$

$$M = A\sqrt{8g}. \quad (2.4)$$

The first term represents a free particle of mass M , the second a free particle of mass ϵ . The situation is the same as in the case of the free real scalar field: the perturbative expansion of the two-point function starts with

$$\langle \phi_1(x)\phi_1(y) \rangle = A^2 + D(x - y, M, L), \quad (2.5)$$

$$\langle \phi_2(x)\phi_2(y) \rangle = D(x - y, \epsilon, L), \quad (2.6)$$

$$\langle \phi_1(x)\phi_2(y) \rangle = 0, \quad (2.7)$$

where $\langle \dots \rangle$ is the vacuum expectation value [defined in Eq. (2.11)] and $D(z, m, L)$ is the propagator of a free particle

of mass m on a hypercubic Euclidean box of size L^n . For $\epsilon = 0$, the term $D(z, \epsilon, L)$ reduces to a sum of free massless propagators:

$$D(z, 0, L) = (1/4\pi^2) \sum_{n_0, n_1, n_2, n_3} 1/[(z_0 + n_0 L)^2 + \dots + (z_3 + n_3 L)^2], \quad (2.8)$$

where $z = (z_0, z_1, \dots, z_s)$ and $n_\mu \in \mathbb{Z}$ for $\mu = 0, 1, \dots, s$, but this expression does not make sense because the sum

diverges. As long as ϵ is different from zero, the limit $L \rightarrow \infty$ ensures that a single term in the sum survives, the one with $n_0 = \dots = n_3 = 0$, which describes the contribution from the Goldstone boson.

Expression (2.1) needs to be modified for the affine action of Eq. (1.3). In this case the Dirac delta function is replaced by $\delta^{2s}(0) \rightarrow a^{-2s}$. Moreover it is convenient the following scaling: $\phi_i = a^{-s/2} \bar{\phi}_i$, $\Phi_i = a^{-s/2} \bar{\Phi}_i$, $g = a^s \bar{g}$, and $\epsilon = a^{-s} \bar{\epsilon}$ which gives the following discretized approximation for the affine action

$$\begin{aligned} \frac{S^{(a)}[\bar{\phi}_1, \bar{\phi}_2]}{a^{-s} a^n} &\approx \frac{1}{2a^2} \sum_{x, \mu} \{ [\bar{\phi}_1(x) - \bar{\phi}_1(x + e_\mu)]^2 + [\bar{\phi}_2(x) - \bar{\phi}_2(x + e_\mu)]^2 \} \\ &+ \sum_x \frac{3}{8} \frac{1}{\bar{\phi}_1^2(x) + \bar{\phi}_2^2(x) + \bar{\epsilon}} \\ &+ \sum_x \left\{ \frac{1}{2} m^2 (\bar{\phi}_1^2(x) + \bar{\phi}_2^2(x)) + \bar{g} [(\bar{\phi}_1^2(x) + \bar{\phi}_2^2(x)) - \bar{\Phi}^2] \right\}. \end{aligned} \quad (2.9)$$

Note that if g is taken different from zero, the relation $g = a^s \bar{g}$ shows that \bar{g} carries a dimension. Setting $\bar{g} = M^s$, M is of dimension mass (we are using natural units $c = \hbar = 1$). If M as well as m are kept fixed when the cutoff is removed, the model contains the two dimensional parameters m and M . The lattice spacing a must be small compared to $1/m$ as well as compared to $1/M$ and the box must be large compared to $1/M$. Since $\bar{\phi}$ is of dimension $\text{mass}^{-1/2}$, the two-point function of $\bar{\phi}$ is of the form

$$\langle \bar{\phi}_i(x) \bar{\phi}_j(y) \rangle = f_{ij} \{ M(x-y), m/M, aM, LM \} / M. \quad (2.10)$$

To approach the continuum limit, the last two argument must be in the range: $aM \ll 1$, $LM \ll 1$. The only relevant parameter, apart from the number of lattice points, used to regularize the system should be the ratio m/M .

We will use the so called ‘‘primitive approximation’’ for the action [see Eqs. (2.1) or (2.9)] even if it can be improved in several ways [15] in order to reduce the error due to the space-time discretization. In reaching to the expression (2.1) or (2.9) we neglected the term $\propto a^{2n}$ due to the commutator of the kinetic and potential parts of the Hamiltonian, in the BakerCampbellHausdorff formula. In reaching to the path integral expression this is justified by the Trotter formula.

The vacuum expectation of a functional observable $\mathcal{O}[\phi_1, \phi_2]$ is

$$\langle \mathcal{O} \rangle \approx \frac{\int \mathcal{O}[\phi_1, \phi_2] \exp(-S[\phi_1, \phi_2]) \prod_x d\phi_1(x) d\phi_2(x)}{\int \exp(-S[\phi_1, \phi_2]) \prod_x d\phi_1(x) d\phi_2(x)}, \quad (2.11)$$

for a given action S .

We will approach the continuum limit by choosing a fixed L and increasing the number of discretizations N of each component of the space-time. So that the lattice spacing $a = L/N \rightarrow 0$. To make contact with the continuum limit, two conditions must be met $a \ll 1/m \ll L$ where $1/m$ is the Compton wavelength.

III. SIMULATION DETAILS AND RELEVANT OBSERVABLES

We want to determine the two-point function

$$K_{ij}(x, y) = \langle \phi_i(x) \phi_j(y) \rangle, \quad (3.1)$$

where in the affine case we need to replace the fields ϕ_i by the scaled fields $\bar{\phi}_i$. Replacing x by $x + k$ with $k = a w_n$ with $w_n = (n_0, n_1, \dots, n_s)$ and $n_\mu \in \mathbb{Z}$ amounts to a mere relabeling of the lattice points. Hence, due to translational invariance, $K(x, y)$ can only depend on the difference between the coordinates of the two points and we can define,

$$D_{ij}(z) = \frac{1}{L^n} \sum_x K_{ij}(x, x+z) a^n. \quad (3.2)$$

Moreover due to the symmetry $1 \leftrightarrow 2$ we will have $D_{11} = D_{22} \equiv D_{\text{like}}$ and $D_{12} = D_{21} \equiv D_{\text{unlike}}$. In our simulations we

work in periodic space-time (at a temperature $T = 1/Na$) so that $\phi_i(x_\mu + N) = \phi_i(x_\mu)$ for any $x, \mu = 0, 1, \dots, s$, and $i = 1, 2$.

Our MC simulations use the Metropolis algorithm [12,13] to calculate the ensemble average of Eq. (2.11) which is a $2N^n$ multidimensional integral. The simulation is started from the initial condition $\phi_i = 0$ for $i = 1, 2$. One MC step consisted in a random displacement of each one of the $2N^n$ variables $\phi_i(x)$ for $i = 1, 2$, as follows

$$\phi_i \rightarrow \phi_i + (2\eta - 1)\delta, \quad (3.3)$$

where η is a uniform pseudo random number in $[0, 1]$ and δ is the amplitude of the displacement. The fields $\phi_i \in (-\infty, \infty)$ for $i = 1, 2$ and $x_\mu \in [0, L]$ for $\mu = 0, 1, \dots, s$. Each one of these $2N^n$ moves is accepted if $\exp(-\Delta S) > \eta$ where ΔS is the change in the action due to the move (it can be efficiently calculated considering how the kinetic part and the potential part change by the displacement of a single $\phi_i(x)$) and rejected otherwise. The amplitude δ is chosen in such a way to have acceptance ratios as close as possible to 1/2 and is kept constant during the evolution of the simulation. One simulation consisted of M MC steps each of which consisted in a sweep of $2N^n$ displacement moves of all the fields variables. The statistical error on the average $\langle \mathcal{O} \rangle$ will then depend on the correlation time necessary to decorrelate the property \mathcal{O} , $\tau_{\mathcal{O}}$, and will be determined as $\sqrt{\tau_{\mathcal{O}}\sigma_{\mathcal{O}}^2/(M2N^n)}$, where $\sigma_{\mathcal{O}}^2$ is the intrinsic variance for \mathcal{O} .

IV. SIMULATION RESULTS

We worked in units where $c = \hbar = k_B = 1$. We chose the regularization parameter of the affine quantization term to be $\epsilon = 10^{-10.3}$.

In Fig. 1 we show $D_{\text{like}}(z)$ and $D_{\text{unlike}}(z)$ as obtained for $m = 1, g = 1, \Phi = 1, L = 3$ and three choices of N , in the canonical scenario. One can then see the approach to the continuum of the two-point functions of the canonical model. From the figure we can see that the unlike two-point function is zero over the whole space-time volume. This can be explained observing that during the random-walk the field will be localized around the minima of the potential density so that $\phi_1^2 + \phi_2^2 \approx \Pi_c^2$ with Π_c the radius of the minima ring, the circle of vacua, around the origin $\varphi = 0$, which is a function of m, g , and Φ :

$$\Pi_c^2 = \frac{4g\Phi^2 - m^2}{4g}. \quad (4.1)$$

So that the Higgs potential density in the action does not actually contribute to correlate the two fields ϕ_i for $i = 1, 2$.

³Note that we could as well choose a regularization putting hard walls at $\phi_i = \pm\epsilon$ therefore rejecting MC moves whenever $\phi_i \in [-\epsilon, \epsilon]$, for $i = 1, 2$.

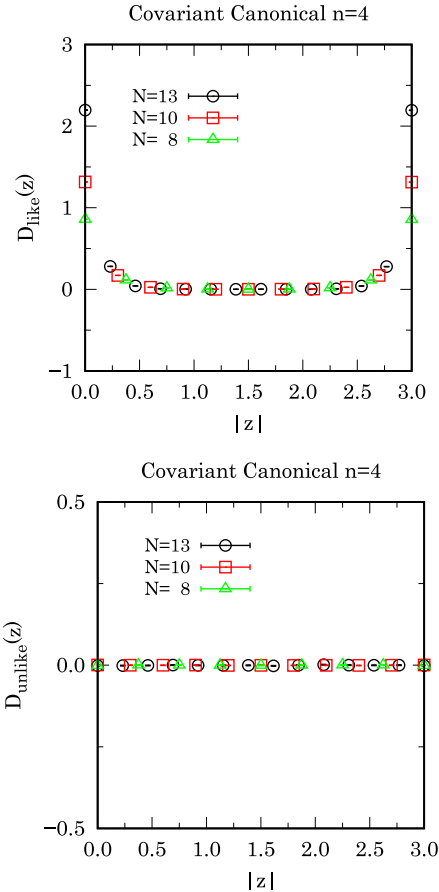


FIG. 1. Two-point functions, $D_{\text{like}}(z)$ (top panel) and $D_{\text{unlike}}(z)$ (bottom panel), of Eq. (3.2) for the complex scalar Higgs field $\varphi = \phi_1 + i\phi_2$ subject to canonical quantization with a self-interaction potential density of the form $V = \frac{1}{2}m^2(\phi_1^2 + \phi_2^2) + g(\phi_1^2 + \phi_2^2 - \Phi^2)^2$ in Eq. (1.3) with $m = 1, g = 1, \Phi = 1, L = 3$ ($\Pi_c^2 = 3/4$) and increasing $N = 8, 10, 13$. On the abscissa axis we have $|z| = \sqrt{z_0^2 + z_1^2 + \dots + z_s^2}$ which is a length.

Moreover, the expectation values $\langle \phi_i \rangle = 0$ for $i = 1, 2$ because the complex field φ tends to rotate around the origin on the minima ring. The approach to the continuum is manifested through increasing values of $D_{\text{like}}(0)$ with increasing N . For our choice of the parameters $m^2 < 4g\Phi^2$ and we must have symmetry breaking [8–10], with the circle of vacua having a radius different from zero. The renormalized coupling constant [5] was found to be: $g_R = -0.0069(6)$ for $N = 8, g_R = -0.0006(4)$ for $N = 10, g_R = +0.0000(5)$ for $N = 13$. Since g_R must be non-negative, by

Lebowitz inequality, our results signal a free trivial system in the continuum limit.

For the affine quantization case the circle of vacua has a radius $\bar{\Pi}_a$, which is now a function of m , \bar{g} , and $\bar{\Phi}$:

$$\bar{\Pi}_a^2 = \frac{4\bar{g}\bar{\Phi}^2 - m^2}{12\bar{g}} + \frac{(4\bar{g}\bar{\Phi}^2 - m^2)^2}{12\bar{g}[162\bar{g}^2 + \Xi + 18\bar{g}^{2/3}(81\bar{g}^2 + \Xi)^{1/3}]} + \frac{162\bar{g}^2 + \Xi + 18\bar{g}^{2/3}[81\bar{g}^2 + \Xi]^{1/3}}{12\bar{g}}, \quad (4.2)$$

$$\Xi = -m^6 + 12\bar{g}m^4\bar{\Phi}^2 - 48\bar{g}^2m^2\bar{\Phi}^4 + 64\bar{g}^3\bar{\Phi}^6, \quad (4.3)$$

where without loss of generality we assumed $\epsilon = 0$. It is different from zero irrespectively from the values of the parameters, so symmetry is always broken. In Fig. 2 we show $D_{\text{like}}(z)$ and $D_{\text{unlike}}(z)$ as obtained for $m = 1, \bar{g} = 1, \bar{\Phi} = 1, L = 3$ (so that $m/M = 1$), $\epsilon = 10^{-10}$ (the simulation results are not affected by ϵ as long as it is chosen sufficiently small), and three choices of N , in the affine scenario, for the $\bar{\phi}_i$ fields introduced in Eq. (2.9). One can then see the approach to the continuum of the two-point functions of the affine model. Note, however, that now the region around $\bar{\phi}_i = 0$ for $i = 1, 2$ is forbidden due to the affine $3/8$ diverging term in the potential density [see Eq. (2.9)], therefore the complex field in its “winding” around the origin, in proximity of the potential minima ring, cannot take a “shortcut” through the “mountain” at the origin (the forbidden region) and this, in turn, is responsible for a loss of ergodicity and the appearance of systematic errors in addition to the usual statistical ones. It is then necessary an extremely long simulation (much longer than the average time for a “round trip” of the field), much longer than in the canonical case. Notice, moreover, that the action is penalized by the additional a^{-5} factor which grows as we approach the continuum $a \rightarrow 0$. A possible solution would be to choose the field displacement δ larger than the diameter of the potential minima ring $2\bar{\Pi}_a$. But unfortunately this will not work because the kinetic energy term in the action doesn’t allow the field to undergo big “jumps.” In addition this would generate low acceptance ratios thereby slowing down the simulation. An alternative solution will be given in the next section. In our simulations, that were $M = 10^7$ MC steps long, the expectation value of the field $\langle \bar{\phi}_1 \rangle = \langle \bar{\phi}_2 \rangle$ was equal to $-0.23(4)$ for $N = 8$, to $-0.24(4)$ for $N = 10$, and to $-0.784(9)$ for $N = 13$. A nonzero value for the vacuum expectation of the field is due to the systematic errors described above and will eventually disappear in an extremely long simulation. From the figure we see how the two-point like function seems to be increasing with N , while the unlike one has a constant behavior fluctuating around the expected zero value. These results are still affected by the ergodicity systematic errors

stemming from the “winding” random walk. In order to show this behavior, we calculated the histograms of the values for $\langle \bar{\phi}_1 \rangle$ obtained by averaging over blocks of 100 MC steps during the simulation, that we call $H\bar{\phi}$, of $D_{\text{like}}(0)$ that we call HD_{like} , and of $D_{\text{unlike}}(0)$, that we call HD_{unlike} . The behavior of these histograms is shown in Figs. 3–5 respectively. From the histogram of Fig. 3 we see how for $N = 13$ the field did not have the chance of rotating around the origin and this explains the lack of the first peak in the histogram of Fig. 4. We then conclude that

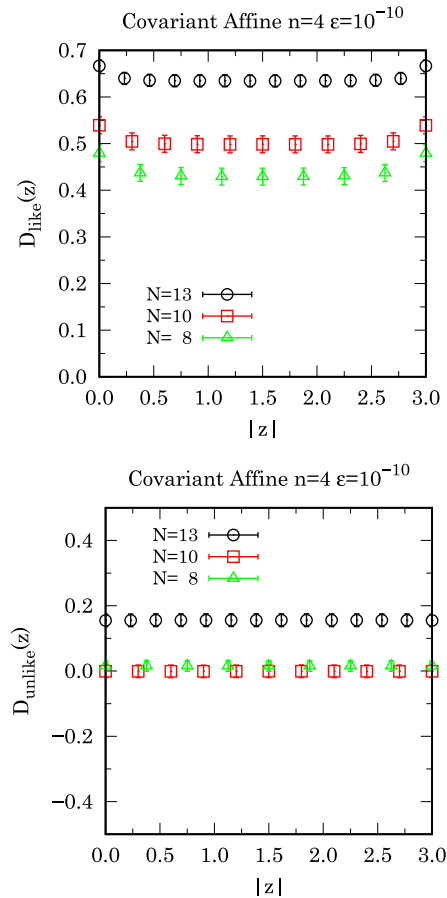


FIG. 2. Two-point functions, $D_{\text{like}}(z)$ (top panel) and $D_{\text{unlike}}(z)$ (bottom panel), of Eq. (3.2) for the complex scalar Higgs field $\bar{\phi} = \bar{\phi}_1 + i\bar{\phi}_2$ subject to affine quantization with a self-interaction potential density of the form $V = \frac{1}{2}m^2(\phi_1^2 + \phi_2^2) + g(\phi_1^2 + \phi_2^2 - \Phi^2)^2$ in Eq. (1.3) with $m = 1, \bar{g} = 1, \bar{\Phi} = 1, L = 3, \epsilon = 10^{-10}$ ($\bar{\Pi}_a^2 \approx 0.955410$) in Eq. (2.9) and increasing $N = 8, 10, 13$. The simulation used $M = 10^7$ MC steps. On the abscissa axis we have $|z| = \sqrt{z_0^2 + z_1^2 + \dots + z_s^2}$ which is a length.

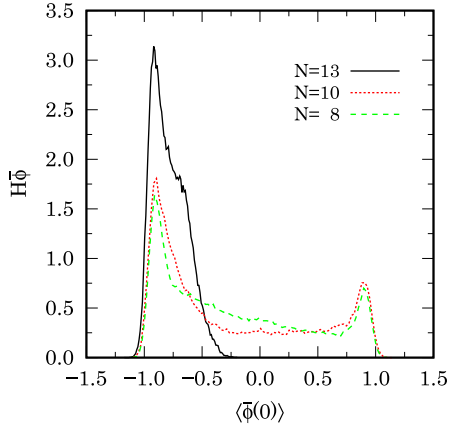


FIG. 3. Histogram of $\langle \bar{\phi}_1 \rangle$ block values during the simulation shown in Fig. 2. The figure shows the “rotation” of the field around the origin in proximity of the potential minima ring of radius $\bar{\Pi}_a \approx 0.977451$, for $N = 8$ and 10 , but not for $N = 13$. Even for $N = 8$ and 10 the rotation was not symmetric (this would only be obtained in an extremely long simulation), which explains the not exactly zero value of the expectation value of field.

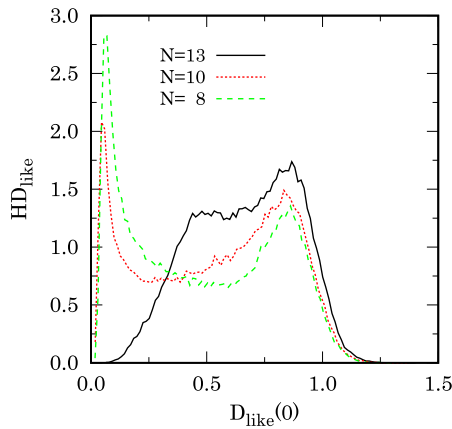


FIG. 4. Histogram of $D_{\text{like}}(0)$ block values during the simulation shown in Fig. 2. The missing first peak in the $N = 13$ data is due to the fact that the field did not perform a full rotation around the origin as is shown by Fig. 3.

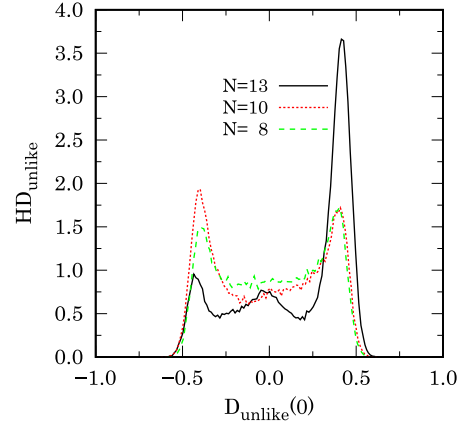


FIG. 5. Histogram of $D_{\text{unlike}}(0)$ block values during the simulation shown in Fig. 2. The $N = 13$ data presents a high asymmetry during the evolution of the simulation, which again signals that the simulation was not long enough.

the simulation for $N = 13$ was not long enough. And this is responsible for the high value of the two-point like function observed for $N = 13$, as shown in Fig. 2. In order to obtain a fully symmetric rotation of the field random walk around the origin we would clearly need an extremely long simulation. Nonetheless from the partial results of our long simulation we can gather a flavor of the convergence of the two-point functions in the affine case in the continuum limit at finite volume.

These results, albeit partial in their nature, give to affine quantization a role as a method producing meaningful quantum field theories even when, as we have already seen in our previous works [4,5,11], the more common canonical quantization fails. Moreover with the scaling used in Eq. (2.9) the field theory does not suffer from the unpleasant feature of a diverging vacuum expectation value of the field in the continuum limit, which was observed in Ref. [11].

V. EXPONENTIAL REPRESENTATION OF THE COMPLEX FIELD

In order to solve the ergodicity breakdown problem encountered in the previous section for the affine case we decided to rewrite our path integral in terms of the fields $\rho(x)$ and $\theta(x)$ such that $\bar{\varphi}(x) = \rho(x) \exp[i\theta(x)]$. Equation (2.9) may be rewritten as follows

$$\begin{aligned} \frac{S^{(a)}[\rho, \theta]}{a^{-s} a^n} \approx & \frac{1}{2a^2} \sum_{x, \mu} \{ [\rho(x) - \rho(x + e_\mu)]^2 + \rho^2(x) [\theta(x) - \theta(x + e_\mu)]^2 \} \\ & + \sum_x \left\{ \frac{3}{8} \frac{1}{\rho^2(x) + \bar{\epsilon}} + \frac{1}{2} m^2 \rho^2(x) + \bar{g} [\rho^2(x) - \bar{\Phi}^2]^2 \right\}, \end{aligned} \quad (5.1)$$

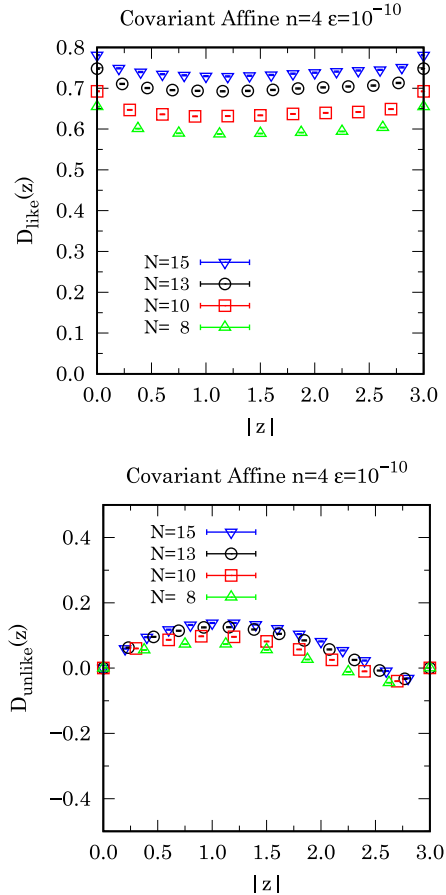


FIG. 6. Two-point functions, $D_{\text{like}}(z)$ (top panel) and $D_{\text{unlike}}(z)$ (bottom panel), of Eq. (3.2) for the complex scalar Higgs field $\tilde{\varphi} = \tilde{\phi}_1 + i\tilde{\phi}_2 = \rho \exp(i\theta)$ subject to affine quantization with a self-interaction potential density of the form $V = \frac{1}{2}m^2\rho^2 + g(\rho^2 - \Phi^2)^2$ in Eq. (1.3) with $m = 1, \bar{g} = 1, \bar{\Phi} = 1, L = 3, \epsilon = 10^{-10}$ in Eq. (5.1) and increasing $N = 8, 10, 13, 15$. The simulation used $M = 10^6$ MC steps. On the abscissa axis we have $|z| = \sqrt{z_0^2 + z_1^2 + \dots + z_s^2}$ which is a length.

and the path integral over $\rho \in [0, \infty]$ and $\theta \in [-\infty, \infty]$ will not suffer anymore from the ergodicity problem. In the Metropolis algorithm we will now have acceptance when $\exp[-(S' - S)] \prod_x \rho'(x)/\rho(x) > \eta$ where the primed quantities are the newly generated ones and as usual η is a pseudo random number in $[0, 1]$. The modulus displacement move, $\rho \rightarrow \rho' = \rho + (2\eta - 1)\delta_\rho$, is rejected whenever $\rho' < 0$. And the argument displacement move is chosen purposely asymmetric, $\theta \rightarrow \theta' = \theta + \eta\delta_\theta$, in order to allow for the required rotation and break the symmetry. This

transition rule for the argument will not violate the detailed balance, required by the Metropolis algorithm, as long as the maximum displacement is chosen $\delta_\theta \geq 2\pi$ so that the probability to go from an angle θ_A to θ_B will be equal to the one to return to θ_A from θ_B always using counterclockwise rotations.

In Fig. 6 we show $D_{\text{like}}(z)$ and $D_{\text{unlike}}(z)$ as obtained for $m = 1, \bar{g} = 1, \bar{\Phi} = 1, L = 3, \epsilon = 10^{-10}$, and four choices of increasing N , in the affine scenario, for the fields $\tilde{\phi}_1 = \rho \cos \theta$ and $\tilde{\phi}_2 = \rho \sin \theta$. The simulations, an order of magnitude shorter than the one of Fig. 2, rapidly converged and we had vanishing $\langle \tilde{\phi}_i \rangle$ as required. From the figure we can see how the symmetry $z \rightarrow L - z$ appears to be broken in both two-point functions. In particular the unlike one appears to be oscillating close to the value of zero. This can be seen as an artifact due to the chosen asymmetric expression for the kinetic part of the primitive approximation. The two-point functions, that are now well converged, seem to have a well defined continuum limit $N \rightarrow \infty$. In fact the difference between $D_{\text{like}}(|z| = L/2)$ from $N = 10$ and $N = 8$ is 0.043 but the one from $N = 15$ and $N = 13$ is 0.036. This supports the conclusion that affine quantization leads to a well-defined field theory. This is also supported by looking at the renormalized mass and coupling constant [5]: $m_R = 0.101748(8), \bar{g}_R = 1.50000(1)$ for $N = 8$, $m_R = 0.097307(8), \bar{g}_R = 1.50000(2)$ for $N = 10$, $m_R = 0.08949(4), \bar{g}_R = 1.50000(3)$ for $N = 13$, $m_R = 0.08398(6), \bar{g}_R = 1.49997(4)$ for $N = 15$. We can see how the renormalized coupling constant remains constant upon the increase of N .

VI. CONCLUSIONS

Summarizing, in this work we studied, through Monte Carlo simulations, the two-point function of a classical Euclidean covariant complex scalar field of mass m subject to the Higgs Mexican-hat potential in four space-time dimensions, treated either with canonical quantization and with affine quantization. And we analyzed the continuum limit at finite fixed volume. The finite volume constraint rules out the formation of the massless Goldstone boson due to the spontaneous symmetry breaking of the continuous phase symmetry $\varphi(x) \rightarrow e^{i\theta(x)}\varphi(x)$ that we continue to observe in the simulations even if only as a smooth transition (free energies in finite volume systems are always analytic).

We first studied the path integral in the two real fields ϕ_1 and ϕ_2 with $\varphi = \phi_1 + i\phi_2$ through standard Metropolis [13] simulations. In the canonical case we found rapidly converging simulations: the unlike two-point function is zero everywhere and the like one shows the approach to the continuum through a diverging value at the origin. It is periodic of periodicity L and satisfies the symmetry $z \rightarrow L - z$ as it should. It has a minimum at half simulation box $|z| = L/2$ close to zero, indicating that the scalar field

theory is in the unbroken phase under canonical quantization, at the chosen couplings and dimension.

In the affine case we found that due to the appearance of the forbidden region around the origin $\varphi \approx 0$, the ergodicity of the random walk is broken. Once the field spontaneously breaks the symmetry falling in the circle of vacua, it can only rotate around the peak in the potential at the origin. Therefore very long simulations are necessary in order to find reliable results for the expectation values—more so approaching the continuum. This suggested to change variables from ϕ_1 and ϕ_2 to the modulus ρ and the argument θ of the complex field, with $\varphi = \rho \exp(i\theta)$ and choose an asymmetric transition rule for the argument move in the Metropolis algorithm in order to allow only for counterclockwise rotations around the origin. This proved an effective way to overcome the ergodicity problem encountered previously, and the simulations converged quickly.

The approach to the continuum appears to be well behaved also for the affine case where the unlike two-point function continues to be everywhere close to zero and the like one develops a minimum at half simulation box higher than the one observed in the canonical case indicating that the system under affine quantization is in the broken phase. Therefore we can say that affine quantization produces a meaningful quantum field theory. It would be interesting to carry on a detailed and systematic study of the approach to the continuum of the renormalized coupling constant in order to understand whether the affine approach is able to produce a nontrivial [6,8–10,16] interacting field theory in the continuum limit also for the present case of a scalar complex field subject to the Higgs potential, as was done in our previous works for scalar real fields [4,5]. This would solve the problem of the believed triviality of the canonical Higgs particle in four space-time dimensions.

-
- [1] J. R. Klauder, The benefits of affine quantization, *J. High Energy Phys. Gravit. Cosmol.* **6**, 175 (2020).
 - [2] J. R. Klauder, *Beyond Conventional Quantization* (Cambridge University Press, Cambridge, England, 2000), Chap. 5.
 - [3] P. A. M. Dirac, *The Principles of Quantum Mechanics* (Clarendon Press, Oxford, 1958), in a footnote on page 114.
 - [4] R. Fantoni, Monte Carlo evaluation of the continuum limit of $(\phi^{12})_3$, *J. Stat. Mech.* (2021) 083102.
 - [5] R. Fantoni and J. R. Klauder, Affine quantization of $(\varphi^4)_4$ succeeds while canonical quantization fails, *Phys. Rev. D* **103**, 076013 (2021).
 - [6] J. Fröhlich, On the triviality of $\lambda\phi_d^4$ theories and the approach to the critical point in $d \geq 4$ dimensions, *Nucl. Phys.* **B200**, 281 (1982).
 - [7] M. Aizenman, Proof of the Triviality of ϕ_d^4 Field Theory and Some Mean-Field Features of Ising Models for $d > 4$, *Phys. Rev. Lett.* **47**, 886(E) (1981).
 - [8] M. Lüscher and P. Weisz, Scaling laws and triviality bounds in the lattice ϕ^4 theory: (I). One-component model in the symmetric phase, *Nucl. Phys.* **B290**, 25 (1987).
 - [9] M. Lüscher and P. Weisz, Scaling laws and triviality bounds in the lattice ϕ^4 theory: (II). One-component model in the phase with spontaneous symmetry breaking, *Nucl. Phys.* **B295**, 65 (1988).
 - [10] M. Lüscher and P. Weisz, Scaling laws and triviality bounds in the lattice ϕ^4 theory: (III). n -component model, *Nucl. Phys.* **B318**, 705 (1989).
 - [11] R. Fantoni and J. R. Klauder, Monte Carlo evaluation of the continuum limit of the two-point function of the Euclidean free real scalar field subject to affine quantization, *J. Stat. Phys.* **184**, 28 (2021).
 - [12] M. H. Kalos and P. A. Whitlock, *Monte Carlo Methods* (Wiley-Vch Verlag GmbH & Co., Germany, 2008).
 - [13] N. Metropolis, A. W. Rosenbluth, M. N. Rosenbluth, A. M. Teller, and E. Teller, Equation of state calculations by fast computing machines, *J. Chem. Phys.* **21**, 1087 (1953).
 - [14] U. Wolff, Triviality of four dimensional ϕ^4 theory on the lattice, *Scholarpedia* **9**, 7367 (2014).
 - [15] D. M. Ceperley, Path integrals in the theory of condensed helium, *Rev. Mod. Phys.* **67**, 279 (1995).
 - [16] K. G. Wilson and J. Kogut, The renormalization group and the ϵ expansion, *Phys. Rep.* **12**, 75 (1974).

Chapter 69

Finite-size effects and thermodynamic limit in one-dimensional Janus fluids

Fantoni R., Maestre M. A. G., and Santos A., J. Stat. Mech. 103210 (2021)

Title: “Finite-size effects and thermodynamic limit in one-dimensional Janus fluids”

Abstract: The equilibrium properties of a Janus fluid made of two-face particles confined to a one-dimensional channel are revisited. The exact Gibbs free energy for a finite number of particles N is exactly derived for both quenched and annealed realizations. It is proved that the results for both classes of systems tend in the thermodynamic limit ($N \rightarrow \infty$) to a common expression recently derived (Maestre M A G and Santos A 2020 J Stat Mech 063217). The theoretical finite-size results are particularized to the Kern-Frenkel model and confirmed by Monte Carlo simulations for quenched and (both biased and unbiased) annealed systems.

PAPER: Classical statistical mechanics, equilibrium and non-equilibrium

Finite-size effects and thermodynamic limit in one-dimensional Janus fluids

R Fantoni¹, M A G Maestre² and A Santos^{2,3,*}

¹ Dipartimento di Fisica, Università di Trieste, Strada Costiera 11,
34151 Grignano (Trieste), Italy

² Departamento de Física, Universidad de Extremadura, E-06006 Badajoz,
Spain

³ Instituto de Computación Científica Avanzada (ICCAEx),
Universidad de Extremadura, E-06006 Badajoz, Spain

E-mail: riccardo.fantoni@posta.istruzione.it, maestre@unex.es and
andres@unex.es

Received 29 July 2021

Accepted for publication 18 September 2021

Published 26 October 2021



CrossMark

Online at stacks.iop.org/JSTAT/2021/103210
<https://doi.org/10.1088/1742-5468/ac2897>

Abstract. The equilibrium properties of a Janus fluid made of two-face particles confined to a one-dimensional channel are revisited. The exact Gibbs free energy for a finite number of particles N is exactly derived for both quenched and annealed realizations. It is proved that the results for both classes of systems tend in the thermodynamic limit ($N \rightarrow \infty$) to a common expression recently derived (Maestre and Santos 2020 *J. Stat. Mech.* 063217). The theoretical finite-size results are particularized to the Kern–Frenkel model and confirmed by Monte Carlo simulations for quenched and (both biased and unbiased) annealed systems.

Keywords: exact results, classical Monte Carlo simulations, colloids, bio-colloids and nano-colloids

*Author to whom any correspondence should be addressed.

Contents

1. Introduction	2
2. Finite-N Gibbs free energy of a quenched binary mixture of Janus rods	4
2.1. The system	4
2.2. Isothermal–isobaric partition function	4
2.3. Gibbs free energy, internal energy, and equation of state	7
2.4. Limit $N \rightarrow \infty$	8
2.5. Equimolar mixture	9
3. Finite-N Gibbs free energy of annealed Janus fluids	10
4. Particularization to the Kern–Frenkel model	11
5. Monte Carlo simulations	12
5.1. Equimolar quenched and unbiased annealed systems	12
5.2. Biased annealed systems	14
6. Conclusions	16
Acknowledgments	19
Appendix A. Function $\Phi_{N_1 N_2}$ for large N	19
Appendix B. Proof of equation (2.27)	20
Appendix C. Function χ_N for large N	21
Appendix D. Technical details of the MC simulations	21
Appendix E. A heuristic approximation for the dependence of $\langle x \rangle$ on q for biased annealed systems	23
References	24

J. Stat. Mech. (2021) 103210

1. Introduction

New materials chemical technology allows for the synthesis of colloidal-size particles with patches exhibiting an interaction pattern different from that of the rest of the surface [1–3]. When the patch occupies a hemisphere, we are in the presence of so-called Janus particles [3–8].

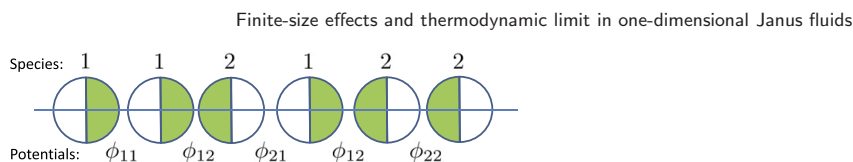


Figure 1. Sketch of a binary mixture of one-dimensional Janus particles. Particles of species 1 (2) have a white (green) left face and a green (white) right face. In general, four types of interactions are possible: green–white (ϕ_{11}), green–green (ϕ_{12}), white–white (ϕ_{21}), and white–green (ϕ_{22}). However, in most of this paper we will assume $\phi_{11} = \phi_{22} = \phi_{21}$. In this particular example, $x_1 = x_2 = \frac{1}{2}$ and $N = 6$.

One-dimensional fluids play an important role in statistical mechanics because they often offer integrable systems [9–34]. In a recent paper [35], two of us derived the exact equilibrium thermodynamic and structural properties of one-dimensional Janus fluids in the thermodynamic limit (TL). The system consisted in a binary mixture of two-face $N_i = x_i N$ particles of species $i = 1, 2$, where x_i is the mole fraction of species i and N is the total number of particles. See figure 1 for a sketch of the system. In this type of systems (henceforth referred to as *quenched*), the number of particles (N_1 and N_2) with each face orientation is kept fixed but of course one needs to average over all possible microscopic configurations to obtain macroscopic quantities. Interestingly, the theoretical predictions for quenched systems agreed excellently well with Monte Carlo (MC) simulations for *annealed* systems (where at each MC attempt a particle is assigned the face orientation 1 or 2 with probabilities q_1 and $q_2 = 1 - q_1$, respectively) with $N = 500$.

The investigation of [35] stimulates a few questions: (i) can the exact derivation of the Gibbs free energy in the TL ($N \rightarrow \infty$) be extended to quenched and/or annealed finite- N systems? (ii) Does the quenched \leftrightarrow annealed equivalence break down at finite N ? (iii) Can those theoretical predictions be validated by MC simulations? (iv) Is the dependence of the average mole fraction $\langle x_1 \rangle$ on the probability q_1 robust with respect to N in annealed MC simulations for biased situations ($q_1 \neq \frac{1}{2}$)? The main aim of this paper is to address those questions. As will be seen, the answers are affirmative in all the cases.

The remainder of this paper is organized as follows. Section 2 presents the derivation of the configuration integral, and hence of the Gibbs free energy G , for a finite-size quenched binary mixture in the isothermal–isobaric ensemble. Those results are then used in section 3 to derive G for an annealed fluid. Since the exact results in sections 2 and 3 apply to any choice of the two nearest-neighbor interaction potentials $\phi_{11} = \phi_{22} = \phi_{21}$ and ϕ_{12} (see figure 1), the expressions are particularized in section 4 to the Kern–Frenkel model [36], where ϕ_{11} and ϕ_{12} are the hard-rod and square-well potentials, respectively. The theoretical results are validated and confirmed by MC simulations in section 5, where also the case of biased annealed systems is addressed. Finally, the main results of the work are summarized in section 6. The most technical parts of the paper are relegated to five appendices.

J. Stat. Mech. (2021) 103210

2. Finite- N Gibbs free energy of a quenched binary mixture of Janus rods

2.1. The system

Let us consider a one-dimensional binary fluid mixture made of N_1 particles of species 1 (right ‘spin’) and $N_2 = N - N_1$ particles of species 2 (left ‘spin’) on a line of length L (see figure 1). Henceforth, we will use Latin and Greek indices for species and particles, respectively. A particular spatial configuration will be denoted as $\mathbf{x} \equiv \{x_\alpha; \alpha = 1, 2, \dots, N\}$. Analogously, a particular spin (or species) configuration will be denoted as $\mathbf{s} \equiv \{s_\alpha; \alpha = 1, 2, \dots, N\}$, where $s_\alpha = 1, 2$ represents the spin of particle α . Since we are considering a quenched mixture, the number of possible spin configurations are restricted by the constraint

$$\sum_{\alpha=1}^N \delta_{s_\alpha, 1} = N_1. \tag{2.1}$$

The total number of allowed spin configurations is $\binom{N}{N_1}$.

We assume that the rods are impenetrable and that their interaction is restricted to nearest neighbors. Given \mathbf{s} and \mathbf{x} , the total potential energy can be written as

$$\Phi_N(\mathbf{s}, \mathbf{x}) = \sum_{\alpha=1}^{N-1} \phi_{s_\alpha, s_{\alpha+1}}(x_{\alpha+1} - x_\alpha) + \omega \phi_{s_N, s_1}(x_1 + L - x_N), \tag{2.2}$$

where, without loss of generality, we assume that particles $1, 2, \dots, N$ are ordered from left to right. In equation (2.2), $\omega = 1$ if periodic boundary conditions are applied and $\omega = 0$ otherwise (open systems).

2.2. Isothermal–isobaric partition function

In the isothermal–isobaric ensemble, the partition function is [32, 37]

$$\mathcal{Z}_{N_1, N_2}(\beta, \gamma) = \mathcal{Z}_{N_1, N_2}^{\text{id}}(\beta, \gamma) \mathcal{Q}_{N_1, N_2}(\beta, \gamma), \tag{2.3}$$

where

$$\mathcal{Z}_{N_1, N_2}^{\text{id}}(\beta, \gamma) = \frac{C_{N_1, N_2}}{L_{\text{ref}} [\Lambda_1(\beta)]^{N_1} [\Lambda_2(\beta)]^{N_2}}, \quad C_{N_1, N_2}(\gamma) \equiv \binom{N}{N_1} \gamma^{-(N+1)}, \tag{2.4}$$

is the ideal-gas partition function and

$$\mathcal{Q}_{N_1, N_2}(\beta, \gamma) = \frac{1}{C_{N_1, N_2}(\gamma)} \sum_{\mathbf{s}} \int_0^\infty dL e^{-\gamma L} \int_{0 < x_1 < \dots < x_N < L} d^N \mathbf{x} e^{-\beta \Phi_N(\mathbf{s}, \mathbf{x})} \tag{2.5}$$

is the configuration integral. Here, $\beta \equiv 1/k_B T$ (k_B and T being the Boltzmann constant and the absolute temperature, respectively) and $\gamma \equiv \beta p$ (p being the pressure).

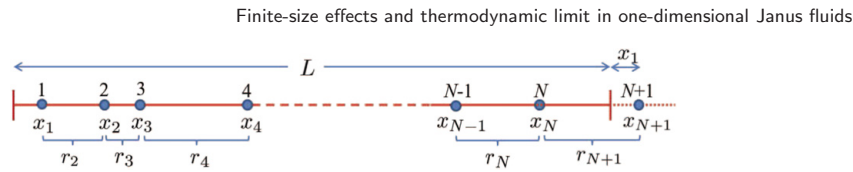


Figure 2. Illustration of the change of variables (2.7).

In equation (2.4), L_{ref} is a reference length (introduced to make Z_N^{id} dimensionless) and $\Lambda_i(\beta) \equiv h\sqrt{\beta/2\pi m_i}$ is the thermal de Broglie wavelength (h being the Planck constant and m_i being the mass of a particle of species i). In equation (2.5), the prime in the summation denotes the constraint (2.1). Note that, by construction, $\mathcal{Q}_{N_1, N_2} = 1$ if $\Phi_N = 0$.

Let us make \mathcal{Q}_{N_1, N_2} more explicit. First,

$$\begin{aligned} \mathcal{Q}_{N_1, N_2} &= \frac{1}{C_{N_1, N_2}} \sum_s \int_0^\infty dL e^{-\gamma L} \int_0^L dx_1 \int_{x_1}^L dx_2 \dots \int_{x_{N-1}}^L dx_N e^{-\beta \Phi_N(s, \mathbf{x})} \\ &= \frac{1}{C_{N_1, N_2}} \sum_s \int_0^\infty dx_1 \int_{x_1}^\infty dx_2 \dots \int_{x_{N-1}}^\infty dx_N \int_{x_N}^\infty dL e^{-\gamma L - \beta \Phi_N(s, \mathbf{x})}, \end{aligned} \quad (2.6)$$

where in the second step we have changed the order of integration. Next, we perform the change of variables $\{x_1, x_2, \dots, x_N, L\} \rightarrow \{x_1, r_2, \dots, r_N, r_{N+1}\}$, where (see figure 2)

$$r_i \equiv x_i - x_{i-1} \quad (i = 2, \dots, N), \quad r_{N+1} \equiv x_1 + L - x_N. \quad (2.7)$$

Note that $L = \sum_{\alpha=2}^{N+1} r_\alpha$. With this change of variables, equation (2.6) becomes

$$\begin{aligned} \mathcal{Q}_{N_1, N_2} &= \frac{1}{C_{N_1, N_2}} \sum_s \left[\prod_{\alpha=2}^N \int_0^\infty dr_\alpha e^{-\gamma r_\alpha - \beta \phi_{s_{\alpha-1}, s_\alpha}(r_\alpha)} \right] \\ &\quad \times \int_0^\infty dx_1 \int_{x_1}^\infty dr_{N+1} e^{-\gamma r_{N+1} - \beta \omega \phi_{s_N, s_1}(r_{N+1})} \\ &= \frac{1}{C_{N_1, N_2}} \sum_s \left[\prod_{\alpha=2}^N \Omega_{s_{\alpha-1}, s_\alpha}(\beta, \gamma) \right] \left[-\frac{\partial \Omega_{s_N, s_1}(\beta \omega, \gamma)}{\partial \gamma} \right], \end{aligned} \quad (2.8)$$

where

$$\Omega_{ij}(\beta, \gamma) \equiv \int_0^\infty dr e^{-\gamma r - \beta \phi_{ij}(r)}. \quad (2.9)$$

Finite-size effects and thermodynamic limit in one-dimensional Janus fluids

Table 1. Spin configurations \mathbf{s} for $N_1 = 4$ and $N_2 = 2$, organized according to the number (n_{ij}) of pairs ij . The number of spin configurations sharing the same values of n_{ij} is given by $w(\{n_{ij}\})$; analogously, $w_{12}(n_{12})$ is the number of spin configurations sharing the same n_{12} , regardless of the values of n_{11} , n_{22} , and n_{21} .

n_{11}	n_{22}	n_{12}	n_{21}	\mathbf{s}	w	w_{12}
3	1	0	1	{221111}	1	1
3	1	1	0	{111122}	1	8
3	0	1	1	{211112}	1	
2	1	1	1	{111221}, {112211}, {122111}	3	
2	0	1	2	{211121}, {211211}, {212111}	3	6
2	0	2	1	{111212}, {112112}, {121112}	3	
1	0	2	2	{112121}, {121121}, {121211}	3	

Henceforth, we particularize to open systems ($\omega = 0$), so that

$$\mathcal{Q}_{N_1, N_2} = \frac{\gamma^{-2}}{C_{N_1, N_2}} \sum_{\mathbf{s}} \prod_{\alpha=2}^N \Omega_{s_{\alpha-1}, s_{\alpha}}. \tag{2.10}$$

Given a spin configuration \mathbf{s} , let us call $n_{ij}(\mathbf{s})$ the number of pairs ij . Thus,

$$\prod_{\alpha=2}^N \Omega_{s_{\alpha-1}, s_{\alpha}} = \Omega_{11}^{n_{11}(\mathbf{s})} \Omega_{22}^{n_{22}(\mathbf{s})} \Omega_{12}^{n_{12}(\mathbf{s})} \Omega_{21}^{n_{21}(\mathbf{s})}. \tag{2.11}$$

Obviously, $n_{11} + n_{22} + n_{12} + n_{21} = N - 1$. If we call $w(n_{11}, n_{22}, n_{12}, n_{21})$ the number of spin configurations with n_{ij} pairs ij , equation (2.10) can be rewritten as

$$\mathcal{Q}_{N_1, N_2} = \frac{\gamma^{-2}}{C_{N_1, N_2}} \sum_{n_{11}, n_{22}, n_{12}, n_{21}} w(n_{11}, n_{22}, n_{12}, n_{21}) \Omega_{11}^{n_{11}} \Omega_{22}^{n_{22}} \Omega_{12}^{n_{12}} \Omega_{21}^{n_{21}}. \tag{2.12}$$

Table 1 shows the possible values of n_{ij} and w for the simple example of $N_1 = 4$ and $N_2 = 2$.

In general, the evaluation of the number of combinations $w(\{n_{ij}\})$ is quite hard. On the other hand, since in the end we will apply the results to the Kern–Frenkel Janus model [36], we can particularize to the case where $\phi_{11}(r) = \phi_{22}(r) = \phi_{21}(r)$, what implies $\Omega_{11} = \Omega_{22} = \Omega_{21}$, so that equation (2.12) reduces to

$$\mathcal{Q}_{N_1, N_2} = \frac{\gamma^{N-1}}{\binom{N}{N_1}} \sum_{n_{12}=0}^{\min\{N_1, N_2\}} w_{12}(n_{12}) \Omega_{11}^{N-1-n_{12}} \Omega_{12}^{n_{12}}, \tag{2.13}$$

where $w_{12}(n_{12})$ stands for the number of spin configurations with n_{12} pairs 12.

To determine $w_{12}(n_{12})$, imagine that we enumerate particles of each species $i = 1$ and 2 from left to right as $\alpha_i = 1, \dots, N_i$. Then, each pair of type 12 can be identified

Finite-size effects and thermodynamic limit in one-dimensional Janus fluids

with a label (α_1, α_2) . Thus, given a number n_{12} , each compatible spin configuration \mathbf{s} is characterized by n_{12} pairs of the form (α_1, α_2) . For example, if $N_1 = 4$ and $N_2 = 2$ (table 1), the spin configuration $\mathbf{s} = \{112121\}$ has $n_{12} = 2$ pairs: $(\alpha_1, \alpha_2) = (2, 1)$ and $(3, 2)$, while the spin configuration $\mathbf{s} = \{211121\}$ has a single n_{12} pair: $(\alpha_1, \alpha_2) = (3, 2)$. There is a one-to-one correspondence between the n_{12} pairs of the form (α_1, α_2) and the associated spin configuration \mathbf{s} . As a consequence, the number of spin configurations $w_{12}(n_{12})$ with n_{12} pairs of type 12 is given by the number of ways of choosing the n_{12} labels α_1 out of N_1 possible values and the n_{12} labels α_2 out of N_2 possible values. Therefore,

$$w_{12}(n_{12}) = \binom{N_1}{n_{12}} \binom{N_2}{n_{12}}. \tag{2.14}$$

As a test of consistency, note that the total number of spin configurations is recovered as $\sum_{n_{12}=0}^{\min\{N_1, N_2\}} w_{12}(n_{12}) = \binom{N}{N_1}$. Finally, the configuration integral is

$$\mathcal{Q}_{N_1, N_2} = \frac{(\gamma \Omega_{11})^{N-1}}{\binom{N}{N_1}} \Xi_{N_1, N_2}, \quad \Xi_{N_1, N_2} \equiv \sum_{n=0}^{\min\{N_1, N_2\}} \xi_{N_1, N_2}(n), \tag{2.15}$$

where

$$\xi_{N_1, N_2}(n) \equiv \binom{N_1}{n} \binom{N_2}{n} (1 - R)^{-n}, \quad R \equiv 1 - \frac{\Omega_{11}}{\Omega_{12}}. \tag{2.16}$$

Interestingly, Ξ_{N_1, N_2} can be formally rewritten in terms of the hypergeometric function:

$$\Xi_{N_1, N_2} = {}_2F_1 \left(-N_1, -N_2; 1, \frac{1}{1 - R} \right). \tag{2.17}$$

2.3. Gibbs free energy, internal energy, and equation of state

The finite-size Gibbs free energy $G_N(T, p, x_1)$ is related to the partition function $\mathcal{Z}_{N_1, N_2}(\beta, \gamma)$ as $G_N = -k_B T \ln \mathcal{Z}_{N_1, N_2}$ [32, 37]. According to equations (2.3), (2.4) and (2.15), the finite-size Gibbs free energy per particle $g_N = G_N/N$ can be decomposed as $g_N = g_N^{\text{id}} + g_N^{\text{ex}}$, with

$$\beta g_N^{\text{id}} = x_1 \ln(\gamma \Lambda_1) + x_2 \ln(\gamma \Lambda_2) - N^{-1} \ln \binom{N}{N_1} + N^{-1} \ln(\gamma L_{\text{ref}}), \tag{2.18a}$$

$$\beta g_N^{\text{ex}} = -(1 - N^{-1}) \ln(\gamma \Omega_{11}) - N^{-1} \ln \frac{\Xi_{N_1, N_2}}{\binom{N}{N_1}}. \tag{2.18b}$$

By viewing g_N as a function of β and γ (instead of as a function of T and p), it is easy to obtain the average volume (length) per particle (v_N) and the excess energy per particle (u_N) at finite N as

$$v_N = \left(\frac{\partial \beta g_N}{\partial \gamma} \right)_\beta = v_N^{\text{id}} + v_N^{\text{ex}}, \quad u_N = \left(\frac{\partial \beta g_N}{\partial \beta} \right)_\gamma = u_N^{\text{id}} + u_N^{\text{ex}}. \tag{2.19}$$

From equations (2.18a) and (2.18b), one has

$$v_N^{\text{id}} = \frac{1 + N^{-1}}{\gamma}, \quad u^{\text{id}} = \frac{1}{2\beta}, \quad (2.20a)$$

$$v_N^{\text{ex}} = - (1 - N^{-1}) \left(\frac{\partial \ln(\gamma \Omega_{11})}{\partial \gamma} \right)_\beta - N^{-1} \frac{\partial \ln \Xi_{N_1, N_2}}{\partial R} \left(\frac{\partial R}{\partial \gamma} \right)_\beta, \quad (2.20b)$$

$$u_N^{\text{ex}} = - (1 - N^{-1}) \left(\frac{\partial \ln \Omega_{11}}{\partial \beta} \right)_\gamma - N^{-1} \frac{\partial \ln \Xi_{N_1, N_2}}{\partial R} \left(\frac{\partial R}{\partial \beta} \right)_\gamma, \quad (2.20c)$$

where, in view of equation (2.17),

$$\frac{\partial \Xi_{N_1, N_2}}{\partial R} = \frac{N_1 N_2}{(1 - R)^2} {}_2F_1 \left(-N_1 + 1, -N_2 + 1; 2, \frac{1}{1 - R} \right). \quad (2.21)$$

2.4. Limit $N \rightarrow \infty$

Equations (2.18b), (2.20b) and (2.20c) provide the excess quantities for any finite N . It is important to take the limit $N \rightarrow \infty$ to obtain the TL expressions and their first finite- N corrections.

In appendix A, it is proved that, for large N at fixed mole fractions,

$$\Xi_{N_1, N_2} \approx \frac{e^{N\bar{\psi}_0}}{\sqrt{2\pi N y_0 (2 - y_0/x_1 x_2)}}, \quad (2.22)$$

where

$$\bar{\psi}_0 = -x_1 \ln \left(1 - \frac{y_0}{x_1} \right) - x_2 \ln \left(1 - \frac{y_0}{x_2} \right), \quad y_0 = \frac{1 - \sqrt{1 - 4x_1 x_2 R}}{2R}. \quad (2.23)$$

As a consistency test, note that in the case of equal interactions ($R \rightarrow 0$), one has $y_0 \rightarrow x_1 x_2$ and $\bar{\psi}_0 \rightarrow -x_1 \ln x_1 - x_2 \ln x_2$, so that $\Xi_{N_1, N_2} \rightarrow (x_1^{N_1} x_2^{N_2} \sqrt{2\pi N x_1 x_2})^{-1}$. The latter expression is not but the Stirling approximation of $\binom{N}{N_1}$, as it should be.

Thus, from equation (2.18b) we obtain

$$\beta g_N^{\text{ex}} \approx \beta g_{\text{TL}}^{\text{ex}} + N^{-1} \ln \left[\gamma \Omega_{11} \sqrt{(2 - y_0/x_1 x_2) y_0/x_1 x_2} \right], \quad (2.24)$$

where

$$\beta g_{\text{TL}}^{\text{ex}} = -\ln(\gamma \Omega_{11}) - \bar{\psi}_0 - x_1 \ln x_1 - x_2 \ln x_2 \quad (2.25)$$

and we have taken into account that $N^{-1} \ln \binom{N}{N_1} \approx -x_1 \ln x_1 - x_2 \ln x_2 - N^{-1} \ln \sqrt{2\pi N x_1 x_2}$. Obviously, $g_{\text{TL}}^{\text{ex}}$ is the excess Gibbs free energy per particle in the TL. That quantity was evaluated by a completely independent route in [35] with the result

Finite-size effects and thermodynamic limit in one-dimensional Janus fluids

$$\beta g_{\text{TL}}^{\text{ex}} = -\ln(\gamma\Omega_{11}) - \ln \frac{1 + \sqrt{1 - 4x_1x_2\bar{R}}}{2\sqrt{1 - \bar{R}}} + |x_1 - x_2| \ln \frac{|x_1 - x_2| + \sqrt{1 - 4x_1x_2\bar{R}}}{(|x_1 - x_2| + 1)\sqrt{1 - \bar{R}}}. \quad (2.26)$$

Taking into account the identity (see appendix B for a proof)

$$\begin{aligned} \bar{\psi}_0 &= -x_1 \ln x_1 - x_2 \ln x_2 + \ln \frac{1 + \sqrt{1 - 4x_1x_2\bar{R}}}{2\sqrt{1 - \bar{R}}} \\ &\quad - |x_1 - x_2| \ln \frac{|x_1 - x_2| + \sqrt{1 - 4x_1x_2\bar{R}}}{(|x_1 - x_2| + 1)\sqrt{1 - \bar{R}}}, \end{aligned} \quad (2.27)$$

it is obvious that equations (2.25) and (2.26) are equivalent. Note, however, that equation (2.25) is more compact than equation (2.26).

As for the average volume and internal energy per particle, application of equation (2.19) yields

$$v_{\text{TL}}^{\text{ex}} = -\left(\frac{\partial \ln(\gamma\Omega_{11})}{\partial \gamma}\right)_{\beta} - \frac{y_0^3/x_1x_2}{(1 - y_0/x_1)(1 - y_0/x_2)} \left(\frac{\partial R}{\partial \gamma}\right)_{\beta}, \quad (2.28a)$$

$$u_{\text{TL}}^{\text{ex}} = -\left(\frac{\partial \ln \Omega_{11}}{\partial \beta}\right)_{\gamma} - \frac{y_0^3/x_1x_2}{(1 - y_0/x_1)(1 - y_0/x_2)} \left(\frac{\partial R}{\partial \beta}\right)_{\gamma}, \quad (2.28b)$$

$$v_N^{\text{ex}} - v_{\text{TL}}^{\text{ex}} \approx N^{-1} \left(\frac{\partial \ln(\gamma\Omega_{11})}{\partial \gamma}\right)_{\beta} + \frac{N^{-1}(1 - y_0/x_1x_2)y_0^2/2x_1x_2}{2(1 - y_0/2x_1x_2)^2} \left(\frac{\partial R}{\partial \gamma}\right)_{\beta}, \quad (2.28c)$$

$$u_N^{\text{ex}} - u_{\text{TL}}^{\text{ex}} \approx N^{-1} \left(\frac{\partial \ln \Omega_{11}}{\partial \beta}\right)_{\gamma} + \frac{N^{-1}(1 - y_0/x_1x_2)y_0^2/2x_1x_2}{2(1 - y_0/2x_1x_2)^2} \left(\frac{\partial R}{\partial \beta}\right)_{\gamma}. \quad (2.28d)$$

Note that, while u^{id} has no finite- N contribution, this is not so for v_N^{id} . According to equation (2.20a), $v_N^{\text{id}} = v_{\text{TL}}^{\text{id}} + (\gamma N)^{-1}$, with $v_{\text{TL}}^{\text{id}} = \gamma^{-1}$.

2.5. Equimolar mixture

In the special case of an equimolar binary mixture ($x_1 = x_2 = \frac{1}{2}$), equations (2.25), (2.28a) and (2.28b) become

$$\beta g_{\text{TL}}^{\text{ex}} = -\ln \left[\frac{\gamma\Omega_{11}}{2} \left(1 + \frac{1}{\sqrt{1 - \bar{R}}} \right) \right], \quad (2.29a)$$

$$v_{\text{TL}}^{\text{ex}} = -\left(\frac{\partial \ln(\gamma\Omega_{11})}{\partial \gamma}\right)_{\beta} - \frac{1 - \sqrt{1 - \bar{R}}}{2R(1 - R)} \left(\frac{\partial R}{\partial \gamma}\right)_{\beta}, \quad (2.29b)$$

$$u_{\text{TL}}^{\text{ex}} = -\left(\frac{\partial \ln \Omega_{11}}{\partial \beta}\right)_{\gamma} - \frac{1 - \sqrt{1 - \bar{R}}}{2R(1 - R)} \left(\frac{\partial R}{\partial \beta}\right)_{\gamma}. \quad (2.29c)$$

Finite-size effects and thermodynamic limit in one-dimensional Janus fluids

Analogously, equations (2.24), (2.28c) and (2.28d) simplify to

$$g_N^{\text{ex}} - g_{\text{TL}}^{\text{ex}} \approx N^{-1} \ln \left[2\gamma\Omega_{11} \frac{(1 - \sqrt{1-R})(1-R)^{1/4}}{R} \right], \quad (2.30a)$$

$$v_N^{\text{ex}} - v_{\text{TL}}^{\text{ex}} \approx N^{-1} \left(\frac{\partial \ln(\gamma\Omega_{11})}{\partial \gamma} \right)_\beta - N^{-1} \frac{(1 - \sqrt{1-R})^2}{4R(1-R)} \left(\frac{\partial R}{\partial \gamma} \right)_\beta, \quad (2.30b)$$

$$u_N^{\text{ex}} - u_{\text{TL}}^{\text{ex}} \approx N^{-1} \left(\frac{\partial \ln \Omega_{11}}{\partial \beta} \right)_\gamma - N^{-1} \frac{(1 - \sqrt{1-R})^2}{4R(1-R)} \left(\frac{\partial R}{\partial \beta} \right)_\gamma. \quad (2.30c)$$

3. Finite- N Gibbs free energy of annealed Janus fluids

In the case of (unbiased) annealed systems, the total number of particles (N) is fixed but the number of particles (N_1 or N_2) with either spin orientation species is allowed to take any value between 0 and N . Thus, the associated configuration integral is

$$\mathcal{Q}_N(\beta, \gamma) = \frac{1}{C_N(\gamma)} \sum_{N_1=0}^N \sum_s^l \int_0^\infty dL e^{-\gamma L} \int_{0 < x_1 < \dots < x_N < L} d^N x e^{-\beta \Phi_N(s, \mathbf{x})}, \quad (3.1)$$

where now $C_N(\gamma) = \sum_{N_1=0}^N C_{N_1, N_2} = 2^N \gamma^{-(N+1)}$ to guarantee that $\mathcal{Q}_N = 1$ if $\Phi_N = 0$.

By following the same steps as those followed to arrive to equation (2.15), we now get

$$\mathcal{Q}_N = \frac{(\gamma\Omega_{11})^{N-1}}{2^N} \Xi_N, \quad \Xi_N \equiv \sum_{N_1=0}^N \Xi_{N_1, N_2}. \quad (3.2)$$

Consequently,

$$\beta g_N^{\text{ex}} = -(1 - N^{-1}) \ln(\gamma\Omega_{11}) + \ln 2 - N^{-1} \ln \Xi_N, \quad (3.3a)$$

$$v_N^{\text{ex}} = -(1 - N^{-1}) \left(\frac{\partial \ln(\gamma\Omega_{11})}{\partial \gamma} \right)_\beta - N^{-1} \frac{\partial \ln \Xi_N}{\partial R} \left(\frac{\partial R}{\partial \gamma} \right)_\beta, \quad (3.3b)$$

$$u_N^{\text{ex}} = -(1 - N^{-1}) \left(\frac{\partial \ln \Omega_{11}}{\partial \beta} \right)_\gamma - N^{-1} \frac{\partial \ln \Xi_N}{\partial R} \left(\frac{\partial R}{\partial \beta} \right)_\gamma, \quad (3.3c)$$

where we recall that the quantity R is defined by the second equality in equation (2.16).

In the limit of large N it is proved in appendix C that

$$\Xi_N \approx \left(1 + \frac{1}{\sqrt{1-R}} \right)^N \frac{1 + \sqrt{1-R}}{2}. \quad (3.4)$$

Therefore,

$$\beta g_N^{\text{ex}} - \beta g_{\text{TL}}^{\text{ex}} \approx N^{-1} \ln \frac{2\gamma\Omega_{11}}{1 + \sqrt{1-R}}, \tag{3.5a}$$

$$v_N^{\text{ex}} - v_{\text{TL}}^{\text{ex}} \approx N^{-1} \left(\frac{\partial \ln(\gamma\Omega_{11})}{\partial \gamma} \right)_\beta + N^{-1} \frac{1 - \sqrt{1-R}}{2R\sqrt{1-R}} \left(\frac{\partial R}{\partial \gamma} \right)_\beta, \tag{3.5b}$$

$$u_N^{\text{ex}} - u_{\text{TL}}^{\text{ex}} \approx N^{-1} \left(\frac{\partial \ln \Omega_{11}}{\partial \beta} \right)_\gamma + N^{-1} \frac{1 - \sqrt{1-R}}{2R\sqrt{1-R}} \left(\frac{\partial R}{\partial \beta} \right)_\gamma, \tag{3.5c}$$

where the TL quantities are given by equations (2.29a)–(2.29c).

Comparison between equations (2.30a)–(2.30c) and equations (3.5a)–(3.5c) shows that, although the quenched and annealed systems are equivalent in the TL, they differ in their respective finite-size corrections.

4. Particularization to the Kern–Frenkel model

Thus far, except for the constraint to nearest neighbors, the interaction potentials $\phi_{11}(r)$ and $\phi_{12}(r)$ are arbitrary. In the special case of *isotropic* interactions, one has $\phi_{11}(r) = \phi_{12}(r)$, so that $R = 0$. In that case,

$$\Xi_{N_1, N_2} = \binom{N_1}{N_2}, \quad \Xi_N = 2^N, \quad \mathcal{Q}_{N_1, N_2} = \mathcal{Q}_N = (\gamma\Omega_{11})^{N-1}, \tag{4.1a}$$

$$\beta g_N^{\text{ex}} = -(1 - N^{-1}) \ln(\gamma\Omega_{11}), \tag{4.1b}$$

$$v_N^{\text{ex}} = -(1 - N^{-1}) \left(\frac{\partial \ln(\gamma\Omega_{11})}{\partial \gamma} \right)_\beta, \quad u_N^{\text{ex}} = -(1 - N^{-1}) \left(\frac{\partial \ln \Omega_{11}}{\partial \beta} \right)_\gamma. \tag{4.1c}$$

Thus, the finite-size effects become almost trivial if the interactions are isotropic and, of course, no distinction between quenched and annealed systems remains.

The situation becomes much more interesting in the genuine Janus case $\phi_{11}(r) \neq \phi_{12}(r)$. We take now the well-known Kern–Frenkel model [7, 36, 38–41], in which case $\phi_{11}(r)$ and $\phi_{12}(r)$ correspond to the hard-rod and square-well potentials, respectively, i.e.

$$\phi_{11}(r) = \begin{cases} \infty, & r < \sigma, \\ 0, & r > \sigma, \end{cases} \quad \phi_{12}(r) = \begin{cases} \infty, & r < \sigma, \\ -\epsilon, & \sigma < r < \lambda\sigma, \\ 0, & r > \lambda\sigma, \end{cases} \tag{4.2}$$

Finite-size effects and thermodynamic limit in one-dimensional Janus fluids

Table 2. Values of the average volume (length) per particle, v_N , in equimolar quenched mixtures and in annealed systems for $N = 4, 10, 20$, and 100 . In all cases, $\lambda = 1.2$ and $p = 0.6$. The TL values are $v_{TL} = 2.6000$ and 1.2265 at $T = 1$ and 0.2 , respectively.

N	T = 1				T = 0.2			
	Quenched		Annealed		Quenched		Annealed	
	Exact	MC	Exact	MC	Exact	MC	Exact	MC
4	2.7658	2.77(2)	2.7819	2.80(2)	1.0502	1.050(3)	1.0547	1.063(4)
10	2.6664	2.68(1)	2.6728	2.69(1)	1.1540	1.150(4)	1.1591	1.152(4)
20	2.6332	2.646(5)	2.6364	2.647(5)	1.1903	1.189(3)	1.1936	1.193(3)
100	2.6067	2.612(8)	2.6073	2.623(8)	1.2194	1.218(2)	1.2200	1.219(1)

where $\lambda \leq 2$. Henceforth, we take $\sigma = 1$, $\epsilon = 1$, and $\epsilon/k_B = 1$ as units of length, energy, and temperature, respectively. Therefore,

$$\Omega_{11} = \frac{e^{-\gamma}}{\gamma}, \quad \Omega_{12} = e^\beta \frac{e^{-\gamma}}{\gamma} - (e^\beta - 1) \frac{e^{-\lambda\gamma}}{\gamma}, \quad R = \left\{ 1 + \frac{1}{(e^\beta - 1) [1 - e^{-(\lambda-1)\gamma}]} \right\}^{-1}, \tag{4.3a}$$

$$\left(\frac{\partial \ln(\gamma \Omega_{11})}{\partial \gamma} \right)_\beta = -1, \quad \left(\frac{\partial \ln \Omega_{11}}{\partial \beta} \right)_\gamma = 0, \tag{4.3b}$$

$$\left(\frac{\partial R}{\partial \gamma} \right)_\beta = (1 - R)^2 (e^\beta - 1) (\lambda - 1) e^{-(\lambda-1)\gamma}, \quad \left(\frac{\partial R}{\partial \beta} \right)_\gamma = (1 - R)^2 e^\beta [1 - e^{-(\lambda-1)\gamma}]. \tag{4.3c}$$

5. Monte Carlo simulations

5.1. Equimolar quenched and unbiased annealed systems

In order to confirm the theoretical results provided by equations (2.20b) and (2.20c) for quenched systems and by equations (3.3b) and (3.3c) for (unbiased) annealed systems, we have performed isothermal–isobaric MC simulations. To make contact between the annealed and quenched results in the TL, we have considered equimolar mixtures ($x_1 = \frac{1}{2}$) in the latter case. Moreover, the Kern–Frenkel model (4.2) with $\lambda = 1.2$ is chosen. Some technical details about the simulation method are given in appendix D.

Tables 2 and 3 give the MC results of v_N and $-u_N^{\text{ex}}$, respectively, for $p = 0.6$, $T = 1$ and 0.2 , and $N = 4, 10, 20$, and 100 . Tables 2 and 3 also include the exact theoretical values given by equations (2.20b) and (3.3b) for v_N and by equations (2.20c) and (3.3c) for $-u_N^{\text{ex}}$. The deviations from the TL values are displayed in figures 3 and 4, which also include the asymptotic behaviors obtained from equations (2.30b) and (2.30c)

Finite-size effects and thermodynamic limit in one-dimensional Janus fluids

Table 3. Absolute values of the excess energy per particle, $-u_N^{\text{ex}}$, in equimolar quenched mixtures and in annealed systems for $N = 4, 10, 20,$ and 100 . In all the cases, $\lambda = 1.2$ and $p = 0.6$. The TL values are $-u_{\text{TL}}^{\text{ex}} = 0.06720$ and 0.4421 at $T = 1$ and 0.2 , respectively.

N	T = 1				T = 0.2			
	Quenched		Annealed		Quenched		Annealed	
	Exact	MC	Exact	MC	Exact	MC	Exact	MC
4	0.06815	0.0690(8)	0.05183	0.0510(6)	0.4820	0.481(2)	0.4635	0.461(2)
10	0.06752	0.0677(4)	0.06105	0.0610(4)	0.4664	0.468(3)	0.4453	0.447(2)
20	0.06735	0.0676(3)	0.06412	0.0645(3)	0.4539	0.453(2)	0.4402	0.442(2)
100	0.06723	0.0674(3)	0.06658	0.0668(3)	0.4441	0.444(2)	0.4416	0.439(2)

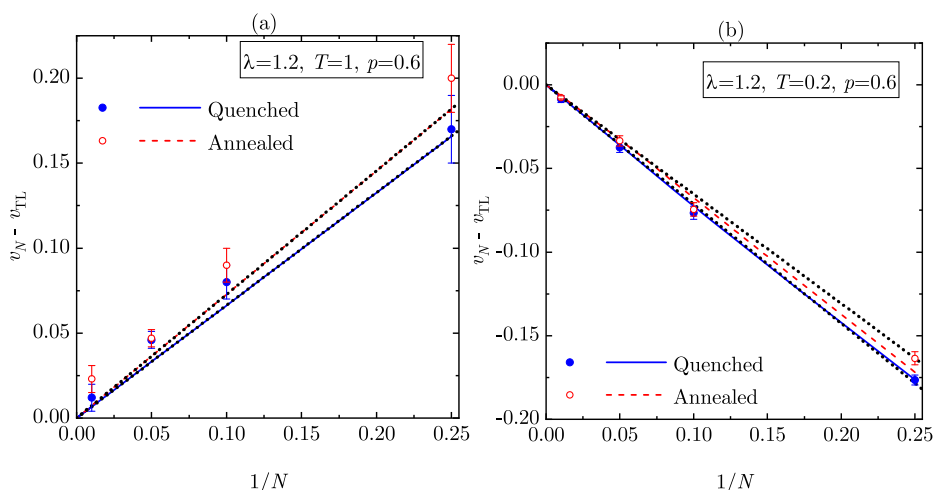


Figure 3. Plot of the finite- N correction $v_N - v_{\text{TL}}$ vs $1/N$ for $\lambda = 1.2, p = 0.6$, and (a) $T = 1$ and (b) $T = 0.2$. The filled circles and solid lines correspond to MC simulations and exact theoretical results, respectively, for an equimolar ($x_1 = x_2 = \frac{1}{2}$) quenched mixture, while the open circles and dashed lines correspond to MC simulations and exact theoretical results, respectively, for an annealed system. The dotted lines represent the exact asymptotic behaviors. Note that the asymptotic and full lines for the quenched and annealed systems are practically indistinguishable in (a).

for (equimolar) quenched systems and from equations (3.5b) and (3.5c) for (unbiased) annealed systems.

We can observe from tables 2 and 3 and figures 3 and 4 that the simulations nicely confirm our theoretical results. The differences between quenched and annealed finite-size corrections are much more important for the energy than for the volume. In the latter case, there is a change of the sign of $v_N - v_{\text{TL}}$ when decreasing temperature from

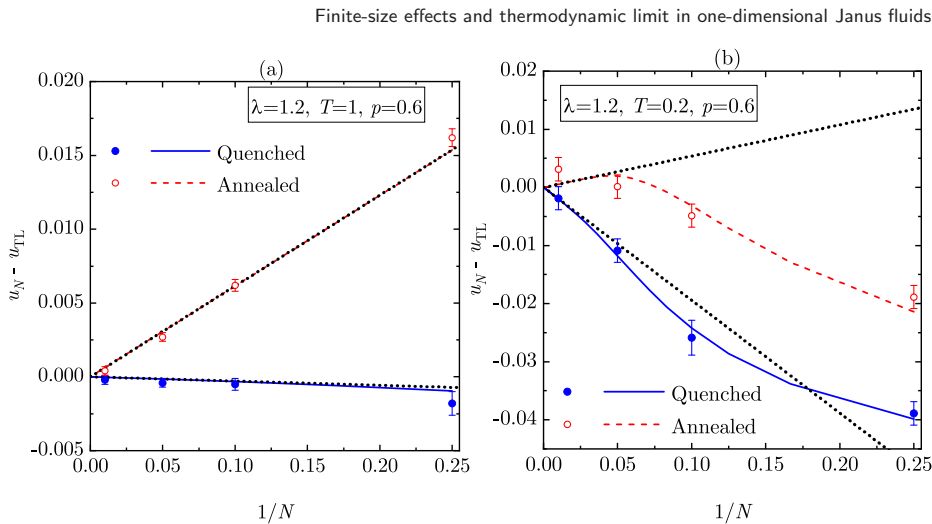


Figure 4. Plot of the finite- N correction $u_N - u_{TL}$ vs $1/N$ for $\lambda = 1.2$, $p = 0.6$, and (a) $T = 1$ and (b) $T = 0.2$. The filled circles and solid lines correspond to MC simulations and exact theoretical results, respectively, for an equimolar ($x_1 = x_2 = \frac{1}{2}$) quenched mixture, while the open circles and dashed lines correspond to MC simulations and exact theoretical results, respectively, for an annealed system. The dotted lines represent the exact asymptotic behaviors. Note that the asymptotic and full lines for the annealed system are practically indistinguishable in (a).

$T = 1$ to $T = 0.2$. Interestingly, except for the energy at low temperature ($T = 0.2$), the asymptotic behaviors given by equations (2.30b), (2.30c), (3.5b) and (3.5c) apply very well for any N , including $N = 4$.

5.2. Biased annealed systems

The MC simulations for annealed systems presented above are *unbiased* in the sense that, even though the identities of the particles are not fixed and thus the mole fraction x_1 is a fluctuating quantity, no preference to either spin orientation is imposed, so that $\langle x_1 \rangle = \frac{1}{2}$. As a consequence, the unbiased annealed results become equivalent to the equimolar quenched ones in the TL.

On the other hand, it is possible to carry out *biased* annealed simulations by introducing a parameter $q \neq \frac{1}{2}$ which favors one of the two possible spin orientations (see appendix D). As observed in [35], the average value $\langle x_1 \rangle \equiv \langle x \rangle$ does not coincide with q , but a natural question arises as to whether or not the inequality $\langle x \rangle \neq q$ is a finite-size artifact.

To address that question, we have performed MC simulations for biased annealed systems with $q = 0.55, 0.65, 0.75, 0.85$, and 0.95 . As before, we have fixed $\lambda = 1.2$,

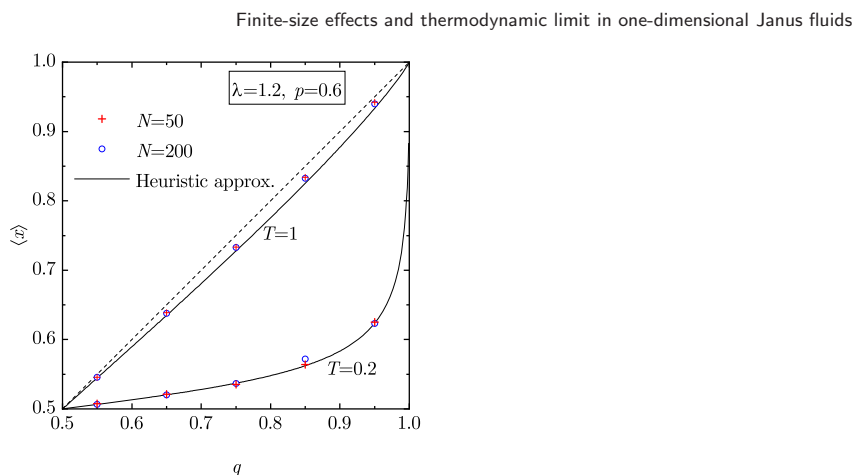


Figure 5. Plot of the average mole fraction $\langle x \rangle$ vs q for biased annealed systems, as obtained from MC simulations with $N = 50$ and 200 for $\lambda = 1.2$, $p = 0.6$, and $T = 1$ and 0.2 . The size of the symbols is larger than the error bars. The solid lines represent the simple heuristic approximation given by the solution to equation (E.7) with $a = 10$, while the straight dashed line is the reference $\langle x \rangle = q$.

$p = 0.6$, and temperatures $T = 1$ and 0.2 . As for the number of particles, the values $N = 50$ and 200 have been chosen. The results are displayed in figure 5, which shows that the data with $N = 50$ and 200 practically coincide. Therefore, the property $\langle x \rangle \neq q$ (actually, $\frac{1}{2} \leq \langle x \rangle \leq q$ or $q \leq \langle x \rangle \leq \frac{1}{2}$) and the dependence $\langle x \rangle(q)$ are robust with respect to N and must hold in the TL. While the derivation of the exact function $\langle x \rangle(q)$ seems to be rather involved and lies outside of the scope of this work, we have constructed a simple heuristic approximation in appendix E. Figure 5 shows that equation (E.7) with $a = 10$ displays an excellent agreement with the MC data.

In the MC simulations for biased annealed systems we have also evaluated the specific volume (v) and the excess internal energy per particle (u^{ex}). Once the robustness of the relationship $\langle x \rangle(q)$ has been checked, one can take q as a parameter and plot v and u^{ex} as functions of the mole fraction $\langle x \rangle$. This is done in figure 6. While in the case $T = 1$ the mapped range is $0.55 \lesssim \langle x \rangle \lesssim 0.94$, the range shrinks to $0.51 \lesssim \langle x \rangle \lesssim 0.63$ if $T = 0.2$. Again, a very weak influence of N is observed. As a matter of fact, comparison with the exact theoretical results for non-equimolar mixtures in the TL (see equations (2.28a) and (2.28b)) presents a very good agreement. It is worth mentioning that v exhibits a rather weak dependence on the mole fraction, with a local minimum at $\langle x \rangle = \frac{1}{2}$. On the other hand, the excess energy u^{ex} is much more sensitive to $\langle x \rangle$, vanishing at $\langle x \rangle = 0$ and $\langle x \rangle = 1$, as expected.

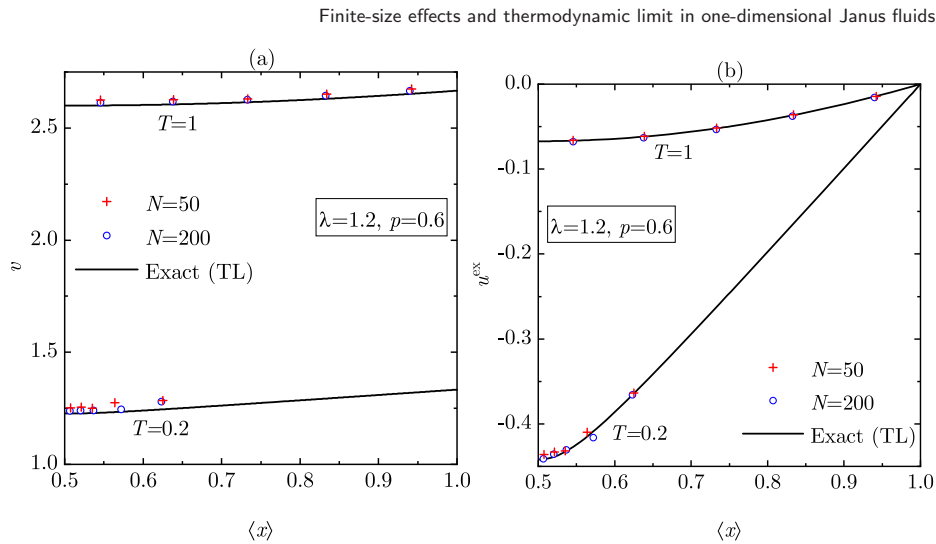


Figure 6. Plot of (a) the volume v and (b) the excess internal energy u^{ex} vs the average mole fraction $\langle x \rangle$ for biased annealed systems, as obtained from MC simulations with $N = 50$ and 200 for $\lambda = 1.2$, $p = 0.6$, and $T = 1$ and 0.2 . The size of the symbols is larger than the error bars. The lines represent the exact theoretical results in the TL.

6. Conclusions

This paper has focused on the study of finite-size effects on the thermodynamic quantities of Janus fluids confined to one-dimensional configurations. Two classes of systems (quenched and annealed) have been considered. In the quenched case, the fraction x_i of particles with a particular face (or spin) orientation is kept fixed. On the other hand, particles can flip their orientations in annealed systems, so that the mole fraction x_i fluctuates around a value $\langle x_i \rangle = \frac{1}{2}$ (unbiased case, $q_i = \frac{1}{2}$) or $\langle x_i \rangle \neq \frac{1}{2}$ (biased case, $q_i \neq \frac{1}{2}$).

Our study allows us to answer affirmatively the four questions initially posed in section 1:

(i) Can the exact derivation of the Gibbs free energy in the TL ($N \rightarrow \infty$) be extended to quenched and/or annealed finite- N systems?

By working on the isothermal–isobaric ensemble with open boundary conditions, we have been able to derive exactly the configuration integral (and hence the Gibbs free energy, the specific volume, and the internal energy) for quenched systems with arbitrary values of number of particles N , mole fraction x_1 , temperature T , pressure p , and nearest-neighbor interactions ϕ_{11} and ϕ_{12} . The results are summarized by equations (2.15)–(2.20c).

The exact results for quenched systems are next exploited to get the finite-size quantities for unbiased annealed systems, as given by equations (3.2)–(3.3c).

(ii) Does the quenched \leftrightarrow annealed equivalence break down at finite N ?

The exact results referred to in the previous point apply to any finite N . An interesting problem consists in taking the limit $N \rightarrow \infty$ in order to obtain well-defined expressions for the thermodynamic quantities in the TL, as well as the first N^{-1} -correction. This is done in appendices A and C, the correction results being given by equations (2.24), (2.28c) and (2.28d) for the quenched case and by equations (3.5a)–(3.5c) for the unbiased annealed case.

The quenched quantities in the TL are provided by equations (2.25), (2.28a) and (2.28b). As proved in appendix B, equation (2.25) is equivalent to (but more compact than) the Gibbs free energy derived in [35] from a completely different method. While in [35] the thermodynamic results were derived directly in the TL from the structural correlation functions, here they have been derived by carefully taking the limit $N \rightarrow \infty$ from the configuration integral. The equivalence between both routes reinforces the exact character of the results.

The results for equimolar quenched systems and those for unbiased annealed systems agree in the TL (equations (2.29a)–(2.29c)), but they differ in the first N^{-1} -correction (compare equations (2.30a)–(2.30c) with equations (3.5a)–(3.5c)). Therefore, the quenched \leftrightarrow annealed equivalence does break down at finite N .

(iii) Can those theoretical predictions be validated by MC simulations?

The conclusions summarized by the two preceding points apply to any choice of the interaction potentials ϕ_{11} and ϕ_{12} . In order to validate them by simulations, we have specialized to the Kern–Frenkel model [36], as defined by equation (4.2). MC results have been measured for a well range $\lambda = 1.2$, a common pressure $p = 0.6$, two temperatures ($T = 1$ and 0.2), and four values of the number of particles ($N = 4, 10, 20$, and 100). As shown by figures 3 and 4, the agreement is very good. Interestingly, except for the case of the internal energy at $T = 0.2$, the deviations from the TL values closely follow the N^{-1} rule even for system sizes as small as $N = 4$.

(iv) Is the dependence of the average mole fraction $\langle x \rangle$ on the probability q robust with respect to N in annealed MC simulations for biased situations ($q \neq \frac{1}{2}$)?

The finite-size corrections mentioned above for annealed systems apply to unbiased situations. In particular, in each MC step an attempt to assign the orientation identity $i = 1$ to a given particle is carried out with a probability $q = \frac{1}{2}$, what results in an average mole fraction $\langle x \rangle = \frac{1}{2}$. The procedure can be extended in a straightforward way to a biased choice $q \neq \frac{1}{2}$, which gives rise to $\langle x \rangle \neq \frac{1}{2}$. The naive expectation would be $\langle x \rangle = q$, but preliminary results in [35] showed that either $\frac{1}{2} < \langle x \rangle < q$ or $\frac{1}{2} > \langle x \rangle > q$, depending on whether $q > \frac{1}{2}$ or $q < \frac{1}{2}$, respectively. One might reasonably wonder whether the property $\langle x \rangle \neq q$ is a finite-size effect that would disappear in the TL.

However, our MC results provide strong evidence about the robustness of the inequality $\langle x \rangle \neq q$ and the dependence of $\langle x \rangle$ on q (see figure 5). This can be qualitatively explained as follows. In the quenched case, the configuration integral presents a peaked local maximum at $N_1 = N/2$, i.e. $x = \frac{1}{2}$, as can be seen from equations (2.15), (2.22) and (E.1). For annealed systems, this competes against a weight function $w_N(x)$ exhibiting a peaked local maximum at $x = q$. The annealed probability density $P_N(x)$ is proportional to the product of both functions and then it has a peaked maximum at an

intermediate value $x = \langle x \rangle$. Based on these arguments, a heuristic approach has been put forward in appendix E. Its theoretical predictions (with a single fitting parameter $a = 10$ independent of T and q) agree excellently well with MC simulations, as figure 5 shows.

As a bonus of the biased annealed simulations, and given the weak influence of N observed in figure 5, we have compared the measured MC values of volume and energy with the theoretical exact results in the TL as functions of the mole fraction. The results displayed by figure 6 show again an excellent agreement.

To put our findings in a proper context, some of their limitations should be remarked. First, the theoretical results have been obtained for open boundary conditions ($\omega = 0$ in equation (2.2)). As shown by equation (2.8), application of periodic boundary conditions ($\omega = 1$) significantly hampers the quest for an exact treatment at finite N . While the choice of the boundary conditions (open or periodic) becomes irrelevant in the TL, finite-size effects are affected by such a choice.

A second limitation arises from the use of the isothermal–isobaric ensemble rather than the standard canonical ensemble. Of course, the partition function and its associated configuration integral can be formally written in the canonical ensemble [consider equation (2.5) with the integration over L removed], but then it is much more difficult to reduce the problem to a purely combinatorial one at finite N , as happens, however, with equations (2.10)–(2.13). One might believe that it would be possible to get the finite-size Helmholtz free energy from the finite-size Gibbs free energy derived here by means of the conventional Legendre transformation. However, this transformation is justified in the TL only and washes out finite-size effects, as we have checked by comparison with canonical MC simulations (not shown).

Third, we have not addressed in the present paper the problem of deriving the exact relationship between $\langle x \rangle$ and q in biased annealed systems, even in the TL. The theoretical approach in appendix E is heuristic and depends upon a parameter a whose value must be obtained by a fitting procedure. It would be very interesting to analyze in detail the random walk represented by the annealed MC simulations and derive the dependence $\langle x \rangle(q)$, at least in the TL. However, this goal is outside of the scope of the present work.

The last limitation refers to the choice of the one-dimensional geometry itself. Of course, two- and three-dimensional systems are much more realistic, but the one-dimensional setting, apart from being applicable to single-file confinement situations, has the enormous advantage of allowing for the derivation of nontrivial exact results. For instance, we have explicitly shown in a clean way that the first corrections to the TL values are of order N^{-1} , as usually assumed in the literature to get rid of finite-size effects and extrapolate the simulation data to the TL. Moreover, exact results are utterly important to test simulation methods and/or theoretical approaches that can then be extended to scenarios where exact solutions are absent.

Acknowledgments

A S acknowledges financial support from Grant PID2020-112936GB-I00 funded by MCIN/AEI/10.13039/501100011033, and from Grants IB20079 and GR18079 funded by Junta de Extremadura (Spain) and by ERDF: A way of making Europe.

Appendix A. Function Ξ_{N_1, N_2} for large N

In this appendix, we prove that the function Ξ_{N_1, N_2} defined in equations (2.15) and (2.16) reduces to equation (2.22) in the limit $N \rightarrow \infty$.

First, application of the Stirling approximation $x! \approx \sqrt{2\pi x}(x/e)^x$ yields

$$\xi_{N_1, N_2}(n = Ny) \approx \exp [N\psi(y)], \quad \psi(y) = \psi_0(y) + N^{-1}\psi_1(y), \tag{A.1}$$

where

$$\psi_0(y) = -x_1 \ln \left(1 - \frac{y}{x_1}\right) - x_2 \ln \left(1 - \frac{y}{x_2}\right) + y \ln \frac{(x_1 - y)(x_2 - y)}{y^2(1 - R)}, \tag{A.2}$$

$$\psi_1(y) = -\ln \left[2\pi Ny \sqrt{\left(1 - \frac{y}{x_1}\right) \left(1 - \frac{y}{x_2}\right)}\right]. \tag{A.3}$$

Equating to zero the first derivative of $\psi(y)$ with respect to y , one can find that the maximum value of $\psi(y)$ corresponds to

$$y_{\max} \approx y_0 + N^{-1}y_1, \tag{A.4}$$

where

$$y_0 = \frac{1 - \sqrt{1 - 4x_1x_2R}}{2R}, \quad y_1 = -\frac{1 + (4y_0 - 3)y_0/2x_1x_2}{2 - y_0/x_1x_2}. \tag{A.5}$$

Note that $\psi'_0(y_0) = 0$ and $y_1 = -\psi'_1(y_0)/\psi''_0(y_0)$, where the second derivative of the $\psi_0(y)$ is

$$\psi''_0(y) = -\frac{2 - y/x_1x_2}{y(1 - y/x_1)(1 - y/x_2)}. \tag{A.6}$$

Note also that the last term on the right-hand side of equation (A.2) vanishes at $y = y_0$, so that $\bar{\psi}_0 \equiv \psi_0(y_0)$ is given by equation (2.23).

As a second step, let us expand $\psi(y)$ around $y = y_{\max}$ to get

$$\psi(y) \approx \psi(y_{\max}) + \frac{\psi''(y_{\max})}{2}(y - y_{\max})^2. \tag{A.7}$$

Next, we replace the sum in Ξ_{N_1, N_2} by an integral:

J. Stat. Mech. (2021) 103210

Finite-size effects and thermodynamic limit in one-dimensional Janus fluids

$$\begin{aligned} \Xi_{N_1, N_2} &\approx N \int_{-\infty}^{\infty} dy \xi_{N_1, N_2}(Ny) \\ &\approx Ne^{N\psi(y_{\max})} \int_{-\infty}^{\infty} dy e^{\frac{N\psi''(y_{\max})}{2}(y-y_{\max})^2} \\ &= Ne^{N\psi(y_{\max})} \sqrt{\frac{2\pi}{-N\psi''(y_{\max})}}, \end{aligned} \tag{A.8}$$

where in the second step use has been made of equation (A.7). Finally, taking into account that $\psi(y_{\max}) \approx \psi_0(y_0) + N^{-1}\psi_1(y_0)$ and $\psi''(y_{\max}) \approx \psi''_0(y_0)$, equation (A.8) becomes

$$\Xi_{N_1, N_2} \approx Ne^{N\psi_0(y_0) + \psi_1(y_0)} \sqrt{\frac{2\pi}{-N\psi''_0(y_0)}}. \tag{A.9}$$

Insertion of equations (A.3) and (A.6) into equation (A.9) yields equation (2.22).

Appendix B. Proof of equation (2.27)

While $\bar{\psi}_0$ is expressed in terms of y_0 (see equation (2.23)), the right-hand side of equation (2.27) is expressed in terms of R . The latter quantity is related to y_0 by the identities

$$R = \frac{y_0 - x_1x_2}{y_0^2}, \quad \sqrt{1 - 4x_1x_2R} = \frac{2x_1x_2}{y_0} - 1, \quad \sqrt{1 - R} = \frac{\sqrt{(x_1 - y_0)(x_2 - y_0)}}{y_0}, \tag{B.1}$$

$$\frac{1 + \sqrt{1 - 4x_1x_2R}}{2\sqrt{1 - R}} = \frac{x_1x_2}{\sqrt{(x_1 - y_0)(x_2 - y_0)}}, \tag{B.2}$$

$$\frac{|x_1 - x_2| + \sqrt{1 - 4x_1x_2R}}{(|x_1 - x_2| + 1)\sqrt{1 - R}} = \frac{x_2}{x_1} \sqrt{\frac{x_1 - y_0}{x_2 - y_0}}, \tag{B.3}$$

where, without loss of generality, we have assumed $x_1 \geq x_2$ in equation (B.3).

The right-hand side of equation (2.27) can be rewritten as

$$\begin{aligned} \text{r.h.s.} &= -x_1 \ln \left[x_1 \frac{2\sqrt{1 - R}}{1 + \sqrt{1 - 4x_1x_2R}} \frac{x_1 - x_2 + \sqrt{1 - 4x_1x_2R}}{(x_1 - x_2 + 1)\sqrt{1 - R}} \right] \\ &\quad - x_2 \ln \left[x_2 \frac{2\sqrt{1 - R}}{1 + \sqrt{1 - 4x_1x_2R}} \frac{(x_1 - x_2 + 1)\sqrt{1 - R}}{x_1 - x_2 + \sqrt{1 - 4x_1x_2R}} \right] \\ &= -x_1 \ln \left(1 - \frac{y_0}{x_1} \right) - x_2 \ln \left(1 - \frac{y_0}{x_2} \right), \end{aligned} \tag{B.4}$$

where we have made use of equations (B.2) and (B.3). Comparison with equation (2.23) closes the proof of equation (2.27).

Appendix C. Function Ξ_N for large N

The method is analogous to the one followed in appendix A. The quantities $\bar{\psi}_0$ and y_0 defined in equation (2.23) are functions of the mole fraction x_1 . It can be checked that $\bar{\psi}_0$ presents a maximum at $x_1 = \frac{1}{2}$. Expanding in powers of $x_1 - \frac{1}{2}$,

$$\bar{\psi}_0 \approx \ln \left(1 + \frac{1}{\sqrt{1-R}} \right) - \frac{2}{\sqrt{1-R}} \left(x_1 - \frac{1}{2} \right)^2. \tag{C.1}$$

Combination of equations (2.22) and (C.1) yields

$$\Xi_{N_1, N_2} \approx \left(1 + \frac{1}{\sqrt{1-R}} \right)^N \frac{1 + \sqrt{1-R}}{\sqrt{2\pi N \sqrt{1-R}}} e^{-2N(x_1 - \frac{1}{2})^2 / \sqrt{1-R}}. \tag{C.2}$$

As a second step, for large N the summation of Ξ_{N_1, N_2} over N_1 can be approximated by an integral over x_1 :

$$\sum_{N_1=0}^N \Xi_{N_1, N_2} \approx \left(1 + \frac{1}{\sqrt{1-R}} \right)^N \frac{1 + \sqrt{1-R}}{\sqrt{2\pi N \sqrt{1-R}}} N \int_{-\infty}^{\infty} dx_1 e^{-2N(x_1 - \frac{1}{2})^2 / \sqrt{1-R}}. \tag{C.3}$$

This finally gives equation (3.4).

Appendix D. Technical details of the MC simulations

Since our exact finite-size results are found in the isothermal–isobaric ensemble and the Legendre transform ‘washes out’ the finite-size effects, we found it necessary to perform our numerical experiments also in the isothermal–isobaric ensemble [42]. Moreover, in order to find agreement with our theoretical exact results, open boundary conditions were used. Of course, only in the TL open and periodic boundary conditions become equivalent.

We performed two kinds of MC experiments, which we label as MCa and MCq for annealed and quenched systems, respectively.

The MCa transition rule consists of single particle MC moves (one MC step), which are the combination of a particle position displacement $x_\alpha \rightarrow x_\alpha + (2\eta - 1)\delta$, where η is a pseudo-random number in $[0, 1]$ and $\delta < \sigma$ is the maximum displacement (to be kept fixed during the whole simulation to preserve detailed balance) and a particle assignment to species $i = 1, 2$ with probability q_i (where $q_1 = q$ and $q_2 = 1 - q$). Open boundary conditions were enforced by generating a new position until it falls inside the segment $x_\alpha \in [-L/2, L/2]$. According to the Metropolis algorithm [43, 44] the move is accepted with probability $e^{-\beta\Delta\Phi_N}$, $\Delta\Phi_N$ being the change in potential energy due

J. Stat. Mech. (2021) 103210

to the combined move. This would be enough in the canonical ensemble, while in the isothermal–isobaric ensemble we also need to perform a volume move. The latter is computationally the most expensive one, since it requires a full energy calculation at each attempt and therefore should be used with a low frequency during the run. We chose 30% for the frequency of the volume move in all our simulations. For the transition and acceptance probability for this volume move, see for example [42].

In contrast to the MCa case, in the MCq simulations the particles are assigned an identity $i = 1, 2$ with probability $x_i = q_i$ from the start and the species assignment is never changed afterwards. The MCq transition rule consists of single particle MC moves that amount to a particle position displacement with $\delta > \sigma$ (note that this condition may be relieved in dimensions higher than one), which is accepted with probability $e^{-\beta\Delta\Phi_N}$, $\Delta\Phi_N$ being the change in potential energy due to the displacement. Again, in the isothermal–isobaric ensemble we also have the volume move [42].

Notice that we can obtain the same result for quenched systems by using a third simulation strategy that we will call MCaq. The MCaq transition rule consists of single particle MC moves that are the combination of a particle position displacement (with $\delta > \sigma$), which is accepted with probability $e^{-\beta\Delta\Phi_N}$ (where $\Delta\Phi_N$ is the change in potential energy due to the displacement only), followed by a particle assignment to species $i = 1, 2$ with probability q_i , which is always accepted and therefore completely disentangled from the displacement move. As before, we also have the volume move [42] in the isothermal–isobaric ensemble.

In all cases we chose δ so to have acceptance ratios as close as possible to $\frac{1}{2}$. The equilibration time for MCa was much longer than for MCq.

Given an observable \mathcal{O} , its statistical-mechanical average $\langle \mathcal{O} \rangle$ was evaluated by averaging \mathcal{O} over a sufficiently large number of MC configurations after a sufficiently long equilibration time. The measured observables were the mole fraction $x = N^{-1} \sum_{\alpha=1}^N \delta_{s_\alpha, 1}$, the specific volume (or reciprocal density) $v = L/N$, and the excess internal energy per particle $u^{\text{ex}} = \Phi_N/N$.

The statistical error on $\langle \mathcal{O} \rangle$ is as usual given by $\sigma_{\langle \mathcal{O} \rangle} = \sqrt{\sigma_{\mathcal{O}}^2 \tau_{\mathcal{O}} / M}$, where M is the number of MC steps, $\sigma_{\mathcal{O}}^2$ is the intrinsic variance of \mathcal{O} , and $\tau_{\mathcal{O}}$ is the correlation time for the observable \mathcal{O} [44]. The latter quantity depends crucially on the transition rule and has a minimum value equal to 1 if one can move so far in configuration space that successive values become uncorrelated. In general, the number of independent steps which contribute to reducing the error bar is not M but $M/\tau_{\mathcal{O}}$. Hence, to determine the true statistical error in the random walk, one needs to estimate the correlation time. To do this, it is very important that the total length of the random walk be much greater than $\tau_{\mathcal{O}}$. Otherwise, the result and its error bar will not be reliable. In general, there is no mathematically rigorous procedure to determine $\tau_{\mathcal{O}}$, so that usually one must determine it from the random walk itself. It is a good practice occasionally to carry out very long runs to test that the results are well converged. In order to equilibrate the random walk, we generally found it necessary to use 10^6 MC steps at high temperature ($T = 1$) and 2×10^7 MC steps at low temperature ($T = 0.2$), and collect averages over $M = 10^5$ MC steps.

Appendix E. A heuristic approximation for the dependence of $\langle x \rangle$ on q for biased annealed systems

From equations (C.2) and (3.4), we have that, for large N , the probability that the mole fraction x_1 lies between x and $x + dx$ in the unbiased annealed system is

$$P_N(x)dx = \frac{1}{\Xi_N} \sum_{N_1=Nx}^{N(x+dx)} \Xi_{N_1, N_2} \approx \frac{N \Xi_{Nx, N(1-x)}}{\Xi_N} dx \approx \frac{e^{-2N(x-\frac{1}{2})^2/\sqrt{1-R}}}{\sqrt{\pi\sqrt{1-R}/2N}} dx. \quad (E.1)$$

Obviously, $\langle x \rangle = \frac{1}{2}$.

Imagine now a *biased* annealed system where each value of $x = N_1/N$ is weighed with a certain function $w_N(x)$ centered around a value $x = q \neq \frac{1}{2}$. In that case,

$$P_N(x) \propto w_N(x) \Xi_{Nx, N(1-x)}, \quad (E.2)$$

which, for large N , would be extremely peaked around a value (comprised between $\frac{1}{2}$ and q) that coincides with the average $\langle x \rangle = \int_0^1 dx x P_N(x)$. Thus, the value $\langle x \rangle$ can be determined as the solution to the equation

$$\begin{aligned} 0 &= \frac{\partial}{\partial x} \lim_{N \rightarrow \infty} N^{-1} [\ln w_N(x) + \ln \Xi_{Nx, N(1-x)}] \\ &= \frac{\partial}{\partial x} \lim_{N \rightarrow \infty} N^{-1} \ln w_N(x) + \frac{\partial \bar{\psi}_0}{\partial x}, \end{aligned} \quad (E.3)$$

where in the second step we have made use of equation (2.22). Note that here, in contrast to equation (E.1), we need to take into account the full dependence of $\bar{\psi}_0$ on x because the solution to equation (E.3) is not, in general, close to $\frac{1}{2}$. According to equation (2.23),

$$\frac{\partial \bar{\psi}_0}{\partial x} = -\ln \left[1 - \frac{1 - \sqrt{1 - 4x(1-x)R}}{2xR} \right] + \ln \left[1 - \frac{1 - \sqrt{1 - 4x(1-x)R}}{2(1-x)R} \right]. \quad (E.4)$$

The simplest choice for the weight function $w_N(x)$ is the binomial distribution $w_N(x) = \binom{N_{\text{eff}}}{N_{\text{eff}}x} q^{N_{\text{eff}}x} (1-q)^{N_{\text{eff}}(1-x)}$, where $N_{\text{eff}} \equiv Nb$, b being an *effective* factor accounting for the expected dependence of $w_N(x)$ on the thermodynamic state (T and p). In that case,

$$\lim_{N \rightarrow \infty} N^{-1} \ln w_N(x) = b \left[x \ln \frac{q}{x} + (1-x) \ln \frac{1-q}{1-x} \right], \quad (E.5)$$

$$\frac{\partial}{\partial x} \lim_{N \rightarrow \infty} N^{-1} \ln w_N(x) = b \ln \frac{q(1-x)}{x(1-q)}. \quad (E.6)$$

Finite-size effects and thermodynamic limit in one-dimensional Janus fluids

Therefore, equation (E.3) becomes

$$0 = -\ln \left[1 - \frac{1 - \sqrt{1 - 4x(1-x)R}}{2xR} \right] + \ln \left[1 - \frac{1 - \sqrt{1 - 4x(1-x)R}}{2(1-x)R} \right] + a\sqrt{1-R} \ln \frac{q(1-x)}{x(1-q)}, \quad (\text{E.7})$$

where we have taken $b = a\sqrt{1-R}$, a being a constant to be empirically determined. A simple and yet optimal value is $a = 10$.

References

- [1] Roh K-H, Martin D C and Lahann J 2005 Biphasic Janus particles with nanoscale anisotropy *Nat. Mater.* **4** 759–63
- [2] Wang B, Li B, Zhao B and Li C Y 2008 Amphiphilic Janus gold nanoparticles via combining ‘solid-state grafting-to’ and ‘grafting-from methods’ *J. Am. Chem. Soc.* **130** 11594–5
- [3] Walther A and Müller A H E 2013 Janus particles: synthesis, self-assembly, physical properties, and applications *Chem. Rev.* **113** 5194–261
- [4] Binks B P and Fletcher P D I 2001 Particles adsorbed at the oil–water interface: a theoretical comparison between spheres of uniform wettability and ‘Janus’ particles *Langmuir* **17** 4708–10
- [5] Sciortino F, Giacometti A and Pastore G 2009 Phase diagram of Janus particles *Phys. Rev. Lett.* **103** 237801
- [6] Yuet K P, Hwang D K, Haghgooe R and Doyle P S 2010 Multifunctional superparamagnetic Janus particles *Langmuir* **26** 4281–7
- [7] Fantoni R 2013 *The Janus Fluid: A Theoretical Perspective* vol 923 (New York: Springer)
- [8] Onishi S, Tokuda M, Suzuki T and Minami H 2015 Preparation of Janus particles with different stabilizers and formation of one-dimensional particle arrays *Langmuir* **31** 674–8
- [9] Herzfeld K F and Goepfert-Mayer M 1934 On the states of aggregation *J. Chem. Phys.* **2** 38–45
- [10] Tonks L 1936 The complete equation of state of one, two and three-dimensional gases of hard elastic spheres *Phys. Rev.* **50** 955–63
- [11] Nagamiya T 1940 Statistical mechanics of one-dimensional substances I *Proc. Phys.-Math. Soc. Japan* **22** 705–20
- [12] Nagamiya T 1940 Statistical mechanics of one-dimensional substances II *Proc. Phys.-Math. Soc. Japan* **22** 1034–47
- [13] Takahasi H 1942 Eine einfache methode zur behandlung der statistischen mechanik eindimensionaler substanzen *Proc. Phys.-Math. Soc. Japan* **24** 60–2
- [14] van Hove L 1950 Sur l’intégrale de configuration pour les systèmes de particules à une dimension *Physica* **16** 137–43
- [15] Salsburg Z W, Zwanzig R W and Kirkwood J G 1953 Molecular distribution functions in a one-dimensional fluid *J. Chem. Phys.* **21** 1098–107
- [16] Kikuchi R 1955 Theory of one-dimensional fluid binary mixtures *J. Chem. Phys.* **23** 2327–32
- [17] Lebowitz J L, Percus J K and Zucker I J 1962 Radial distribution functions in crystals and fluids *Bull. Am. Phys. Soc.* **7** 415
- [18] Katsura S and Tago Y 1968 Radial distribution function and the direct correlation function for one-dimensional gas with square-well potential *J. Chem. Phys.* **48** 4246–51
- [19] Lebowitz J L and Zomick D 1971 Mixtures of hard spheres with nonadditive diameters: some exact results and solution of PY equation *J. Chem. Phys.* **54** 3335–46
- [20] Percus J K 1976 Equilibrium state of a classical fluid of hard rods in an external field *J. Stat. Phys.* **15** 505–11
- [21] Percus J K 1982 One-dimensional classical fluid with nearest-neighbor interaction in arbitrary external field *J. Stat. Phys.* **28** 67–81
- [22] Borzi C, Ord G and Percus J K 1987 The direct correlation function of a one-dimensional Ising model *J. Stat. Phys.* **46** 51–66
- [23] Korteweg D T 1891 On van Der Waals’s isothermal equation *Nature* **45** 152–4
- [24] Rayleigh L 1891 On the virial of a system of hard colliding bodies *Nature* **45** 80–2

Finite-size effects and thermodynamic limit in one-dimensional Janus fluids

- [25] Heying M and Corti D S 2004 The one-dimensional fully non-additive binary hard rod mixture: exact thermophysical properties *Fluid Phase Equilib.* **220** 85–103
- [26] Santos A 2007 Exact bulk correlation functions in one-dimensional nonadditive hard-core mixtures *Phys. Rev. E* **76** 062201
- [27] Santos A, Fantoni R and Giacometti A 2008 Penetrable square-well fluids: exact results in one dimension *Phys. Rev. E* **77** 051206
- [28] Ben-Naim A and Santos A 2009 Local and global properties of mixtures in one-dimensional systems. II. Exact results for the Kirkwood–Buff integrals *J. Chem. Phys.* **131** 164512
- [29] Fantoni R, Giacometti A, Malijevský A and Santos A 2010 A numerical test of a high-penetrability approximation for the one-dimensional penetrable-square-well model *J. Chem. Phys.* **133** 024101
- [30] Fantoni R 2010 Non-existence of a phase transition for penetrable square wells in one dimension *J. Stat. Mech.* **P07030**
- [31] Santos A 2014 Playing with marbles: structural and thermodynamic properties of hard-sphere systems *5th Warsaw School of Statistical Physics* ed B Cichocki, M Napiórkowski and J Piasecki (Warsaw: Warsaw University Press)
- [32] Santos A 2016 *A Concise Course on the Theory of Classical Liquids Basics and Selected Topics (Lecture Notes in Physics vol 923)* (New York: Springer)
- [33] Fantoni R and Santos A 2017 One-dimensional fluids with second nearest-neighbor interactions *J. Stat. Phys.* **169** 1171–201
- [34] Montero A M and Santos A 2019 Triangle-well and ramp interactions in one-dimensional fluids: a fully analytic exact solution *J. Stat. Phys.* **175** 269–88
- [35] Maestre M A G and Santos A 2020 One-dimensional Janus fluids. Exact solution and mapping from the quenched to the annealed system *J. Stat. Mech.* **063217**
- [36] Kern N and Frenkel D 2003 Fluid–fluid coexistence in colloidal systems with short-ranged strongly directional attraction *J. Chem. Phys.* **118** 9882–9
- [37] Hansen J P and McDonald I R 2013 *Theory of Simple Liquids* 4th edn (New York: Academic)
- [38] Fantoni R, Giacometti A, Sciortino F and Pastore G 2011 Cluster theory of Janus particles *Soft Matter* **7** 2419–27
- [39] Fantoni R 2012 A cluster theory for a Janus fluid *Eur. Phys. J. B* **85** 108
- [40] Maestre M A G, Fantoni R, Giacometti A and Santos A 2013 Janus fluid with fixed patch orientations: theory and simulations *J. Chem. Phys.* **138** 094904
- [41] Fantoni R, Giacometti A, Maestre M A G and Santos A 2013 Phase diagrams of Janus fluids with up-down constrained orientations *J. Chem. Phys.* **139** 174902
- [42] Frenkel D and Smit B 2002 *Understanding Molecular Simulation: From Algorithms to Applications* 2nd edn (New York: Academic)
- [43] Metropolis N, Rosenbluth A W, Rosenbluth M N, Teller A H and Teller E 1953 Equation of state calculations by fast computing machines *J. Chem. Phys.* **21** 1087–92
- [44] Kalos M H and Whitlock P A 2008 *Monte Carlo Methods* (New York: Wiley)

J. Stat. Mech. (2021) 103210

Chapter 70

Jellium at finite temperature

Fantoni R., Mol. Phys. **120**, 4 (2021)

Title: “Jellium at finite temperature”

Abstract: We adopt the fixed node restricted path integral Monte Carlo method within the “Worm algorithm” to simulate Wigner’s Jellium model at finite, non zero, temperatures using free-particle nodes of the density matrix. The new element is that we incorporate the Worm algorithm paradigm of Prokof’ev and Svistunov in order to more efficiently handle the fermionic exchanges. We present results for the structure and thermodynamic properties of the ideal Fermi gas and three points for the interacting electron gas. We treat explicitly the case of the partially polarized electron gas.

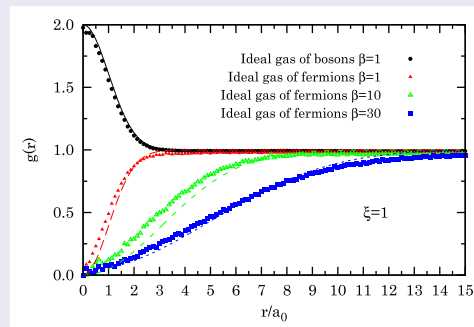
Jellium at finite temperature

Riccardo Fantoni 

Dipartimento di Fisica, Università di Trieste, Grignano (Trieste), Italy

ABSTRACT

We adopt the fixed node restricted path integral Monte Carlo method within the 'Worm algorithm' to simulate Wigner's Jellium model at finite, non zero, temperatures using free-particle nodes of the density matrix. The new element is that we incorporate the Worm algorithm paradigm of Prokof'ev and Svistunov in the grand canonical ensemble in order to more efficiently handle the fermionic exchanges. We present results for the structure and thermodynamic properties of the ideal Fermi gas and three points for the interacting electron gas. We treat explicitly the case of the partially polarized electron gas.



ARTICLE HISTORY

Received 25 August 2021
Accepted 14 October 2021

KEYWORDS

Jellium; path integral Monte Carlo simulation; worm algorithm; restricted path integral; fermions sign problem

1. Introduction

The free electron gas or the Jellium model of Wigner [1,2] is the simplest physical model for the valence electrons in a metal [3] (more generally it is an essential ingredient for the study of ionic liquids (see Ref. [4] Chapter 10 and 11): molten-salts, liquid-metals, and ionic-solutions) or the plasma in the interior of a white dwarf [5]. It can be imagined as a system of pointwise electrons of charge e made thermodynamically stable by the presence of a uniform inert neutralising background of opposite charge density inside which they move. In this work we will only be interested in the jellium in the three dimensional Euclidean space, leaving its study in a curved surface [6–9] to later studies.

The zero temperature, ground-state, properties of the statistical mechanical system thus depends just on the

electronic density n , or the Wigner-Seitz radius $r_s = (3/4\pi n)^{1/3}/a_0$ where a_0 is Bohr radius, or the Coulomb coupling parameter $\Gamma = e^2/(a_0 r_s)$. Free electrons in metallic elements [3] has $2 \lesssim r_s \lesssim 4$ whereas in the interior of a white dwarf [5] $r_s \simeq 0.01$.

The recent two decades have witnessed an impressive progress in experiments and also in quantum Monte Carlo simulations which have provided the field with the most accurate thermodynamic data available. These simulations started with the work by Ceperley and co-workers and Filinov and co-workers for jellium [10–18], hydrogen, hydrogen-helium mixtures and electron-hole plasmas in the 1990s and have been improved dramatically. We recently also applied our newly developed method to the binary fermion-boson plasma mixture at finite temperature [19], where we discussed the

2  R. FANTONI

thermodynamic stability of the two component mixture where the two species are both bosons, both fermions, and one boson and one fermion.

According to the Lindhard theory of static screening, March and Tosi [20] suppose we switch on an appropriately screened test charge potential δV in a free electron gas. The Hartree potential $\delta V(\mathbf{r})$ created at a distance r from a static point charge of magnitude e at the origin, should be evaluated self-consistently from the Poisson equation,

$$\nabla^2 \delta V(\mathbf{r}) = -4\pi e^2 [\delta(\mathbf{r}) + \delta n(\mathbf{r})], \quad (1)$$

where $\delta n(\mathbf{r})$ is the change in electronic density induced by the test charge. The electron density $n(\mathbf{r})$ may be written as

$$n(\mathbf{r}) = 2 \sum_{\mathbf{k}} |\psi_{\mathbf{k}}(\mathbf{r})|^2, \quad (2)$$

where $\psi_{\mathbf{k}}(\mathbf{r})$ are single-electron orbitals, the sum over \mathbf{k} is restricted to occupied orbitals ($|\mathbf{k}| \leq k_F$, where k_F is the Fermi wave vector) and the factor 2 comes from the sum over spin orientations. We must now calculate how the orbitals in the presence of the test charge, differ from plane waves $\exp(i\mathbf{k} \cdot \mathbf{r})$. We use for this purpose the Schrödinger equation,

$$\nabla^2 \psi_{\mathbf{k}}(\mathbf{r}) + \left[k^2 - \frac{2m}{\hbar^2} \delta V(r) \right] \psi_{\mathbf{k}}(\mathbf{r}) = 0, \quad (3)$$

having imposed that the orbitals reduce to plane waves with energy $\hbar^2 k^2 / (2m)$ at large distance.¹

With the aforementioned boundary condition the Schrödinger equation may be converted into an integral equation,

$$\psi_{\mathbf{k}}(\mathbf{r}) = \frac{1}{\sqrt{\Omega}} e^{i\mathbf{k} \cdot \mathbf{r}} + \frac{2m}{\hbar^2} \int G_{\mathbf{k}}(\mathbf{r} - \mathbf{r}') \delta V(\mathbf{r}') \psi_{\mathbf{k}}(\mathbf{r}') d\mathbf{r}', \quad (4)$$

with $G_{\mathbf{k}}(\mathbf{r}) = -\exp(i\mathbf{k} \cdot \mathbf{r}) / (4\pi r)$ and Ω the volume of the system.

Within linear response theory we can replace $\psi_{\mathbf{k}}(\mathbf{r})$ by $\Omega^{-1/2} \exp(i\mathbf{k} \cdot \mathbf{r})$ inside the integral. This yields

$$\delta n(\mathbf{r}) = -\frac{mk_F^2}{2\pi^3 \hbar^2} \int j_1(2k_F |\mathbf{r} - \mathbf{r}'|) \frac{\delta V(\mathbf{r}')}{|\mathbf{r} - \mathbf{r}'|^2} d\mathbf{r}', \quad (5)$$

with $j_1(x)$ being the first-order spherical Bessel function $[\sin(x) - x \cos(x)]/x^2$. Using this result in the Poisson equation we get

$$\begin{aligned} \nabla^2 \delta V(r) &= -4\pi e^2 \delta(\mathbf{r}) \\ &+ \frac{2mk_F^2 e^2}{\pi^2 \hbar^2} \int j_1(2k_F |\mathbf{r} - \mathbf{r}'|) \frac{\delta V(\mathbf{r}')}{|\mathbf{r} - \mathbf{r}'|^2} d\mathbf{r}', \end{aligned} \quad (6)$$

which is easily soluble in Fourier transform. Writing $\delta V(k) = 4\pi e^2 / [k^2 \varepsilon(k)]$ we find,

$$\varepsilon(k) = 1 + \frac{2mk_F e^2}{\pi k^2 \hbar^2} \left[1 + \frac{k_F}{k} \left(\frac{k^2}{4k_F^2} - 1 \right) \ln \left| \frac{k - 2k_F}{k + 2k_F} \right| \right], \quad (7)$$

which is the static dielectric function in RPA.

For $k \rightarrow 0$ this expression gives $\varepsilon(k) \rightarrow 1 + k_{TF}^2/k^2$ with $k_{TF} = 3\omega_p^2/\nu_F^2$ (ω_p being the plasma frequency and ν_F the Fermi velocity) i.e. the result of the Thomas-Fermi theory. However $\varepsilon(k)$ has a singularity at $k = \pm 2k_F$, where its derivative diverges logarithmically.² This singularity in $\delta V(k)$ determines, after Fourier transform, the behaviour of $\delta V(r)$ at large r . $\delta V(r)$ turns out to be an oscillating function [21] rather than a monotonically decreasing function as in the Thomas-Fermi theory. Indeed,

$$\delta V(r) = \int \frac{d\mathbf{k}}{(2\pi)^3} \frac{4\pi e^2}{k^2 \varepsilon(k)} e^{i\mathbf{k} \cdot \mathbf{r}} = \frac{e^2}{i\pi r} \int_{-\infty}^{\infty} dk \frac{e^{ikr}}{k \varepsilon(k)}, \quad (8)$$

and the integrand has non-analytic behaviour at $q = \pm 2k_F$,

$$\begin{aligned} \left[\frac{1}{k \varepsilon(k)} \right]_{k \rightarrow \pm 2k_F} \\ = -A(k - (\pm)2k_F) \ln |k - (\pm)2k_F| + \text{regular terms}, \end{aligned} \quad (9)$$

with $A = (k_{TF}^2/4k_F^2)/(k_{TF}^2 + 8k_F^2)$. Hence,

$$\begin{aligned} \delta V(r)|_{r \rightarrow \infty} &= -\frac{Ae^2}{i\pi r} \int_{-\infty}^{\infty} dk e^{ikr} \left[(k - 2k_F) \ln |k - 2k_F| \right. \\ &\quad \left. + (k + 2k_F) \ln |k + 2k_F| \right] \\ &= -2Ae^2 \frac{\cos(2k_F r)}{r^3}. \end{aligned} \quad (10)$$

This result is based on a theorem on Fourier transforms, Lighthill [22] stating that the asymptotic behaviour of $\delta V(r)$ is determined by the low- k behaviour as well as the singularities of $\delta V(k)$. Obviously, in the present case the asymptotic contribution from the singularities is dominant over the exponential decay of Thomas-Fermi type. The result implies that the screened ion-ion interaction in a metal has oscillatory character and ranges over several shells of neighbours.

Today we are able to simulate on a computer the structural and thermodynamic properties of Jellium at finite, non zero, temperature. This allows us to predict thermodynamic states that would be rather difficult to obtain in nature or in the laboratory. Such as Jellium under extreme conditions, partially polarised Jellium, etc. In this work we will carry on some of these path

integral simulations which make use of the Monte Carlo technique, which is the best known method to compute a path integral [23]. The computer experiment is alternative to the theoretical analytical approximations like RPA that has been developed, during the years, with various degrees of accuracies in different thermodynamic conditions. Such theoretical approximations generally fall into two categories: those which extend down from the classical regime and those which assume some interpolation between the $T = 0$ and high- T regimes. From the former group we recall the Debye-Hückel (DH) theory which solves for the Poisson-Boltzmann equations for the classical one-component plasma and the quantum corrections of Hansen *et al.* [24,25] of the Coulomb system both with Wigner-Kirkwood corrections (H+WK) and without (H). Clearly these methods do not perform well in the quantum regime below the Fermi temperature since they lack quantum exchange. The Random Phase Approximation (RPA) [26,27] is a reasonable approximation in the low-density, high-temperature limit (where it reduces to DH) and the low-temperature, high-density limit, since these are both weakly interacting regimes. Its failure, however, is most apparent in its estimation of the equilibrium, radial distribution function $g(r)$ which becomes negative for stronger coupling. Extensions of the RPA into intermediate densities and temperatures have largely focused on constructing local-field corrections (LFC) through interpolation since diagrammatic resummation techniques often become intractable in strongly coupled regimes. Singwi *et al.* [28] introduced one such strategy. Tanaka and Ichimaru [29] (TI) extended this method to finite temperatures and provided the parameterisation of the Jellium correlation energy. This method appears to perform marginally better than the RPA at all temperatures, though it still fails to produce a positive-definite $g(r)$ at values of $r_s > 2$. A third, more recent approach introduced by Perrot and Dharma-wardana (PDW) [30] relies on a classical mapping where the distribution functions of a classical system at temperature T_{cf} , solved for through the hypernetted-chain equation, reproduce those for the quantum system at temperature T . In a previous work, PDW showed such a temperature T_q existed for the classical system to reproduce the correlation energy of the quantum system at $T = 0$. Dharma-wardana and Perrot [31] To extend this work to finite temperature quantum systems, they use the simple interpolation formula $T_{cf} = \sqrt{T^2 + T_q^2}$. This interpolation is clearly valid in the low- T limit where Fermi liquid theory gives the quadratic dependence of the energy on T . Further in the high- T regime, T dominates over T_q as the system becomes increasingly classical. The PDW results match well with the simulation results in these two limits.

It is not surprising, however, that in the intermediate temperature regime, where correlation effects are greatest, the quadratic interpolation fails. A contemporary, but similar approach by Dutta and Dufty [32] uses the same classical mapping as PDW which relies on matching the $T = 0$ pair correlation function instead of the correlation energy. While we expect this to give more accurate results near $T = 0$, we would still expect a breakdown of the assumed Fermi liquid behaviour near the Fermi temperature. Strict benchmarks have only recently been presented in Ref. [33]. Future Jellium work will include creating a new parameterisation of the exchange-correlation energy which uses the simulation data directly [16,34,35]. In doing so, simulations at higher densities and both lower and higher temperatures may be necessary in order to complete the interpolation between the ground-state and classical limits.

As will be made clear in Section 4, till recently, not even through computer experiments we were able to obtain exact numerical results, since one had to face the so called fermions sign problem which had not been solved before the advent of recent simulation [15,16] when it was demonstrated that the fermion sign problem can be completely avoided and exact results (with an error below 1%) for the thermodynamic functions can be obtained. In other words we were not able to extract exact results not even numerically from a simulation for fermions, unlike for bosons or boltzmannons. Therefore, in order to circumvent the fermion sign problem, we will here resort to the most widely used approximation in quantum Monte Carlo that is the restricted path integral fixed nodes method [36,37]. But unlike previous studies we will implement this method upon the worm algorithm [38,39] in the grand canonical ensemble. This complements our previous study [2] carried out in the canonical ensemble. In this work we will be just interested in proving the validity of our new numerical scheme but not its accuracy. We will then not worry about the finite size corrections, the imaginary thermal time discretization error, and about a stringent comparison with previous canonical ensemble studies available in literature since this program has been already carried on in Ref. [2].

The work is organised as follows: in Section 2 we describe the Jellium model from a physical point of view, in Section 3 we introduce the parameter space necessary for the description of Jellium at finite temperature, in Section 4 we describe the simulation method, in Section 5 we outline the problem we want to solve on a computer, in Section 6 we presents some details of our new algorithm, Section 7 is for our numerical results, and in Section 8 we summarise our concluding remarks.

4  R. FANTONI

2. The model

The Jellium model of Wigner [20,40–42] is an assembly of N_+ spin up pointwise electrons and N_- spin down pointwise electrons of charge e moving in a positive inert background that ensures charge neutrality. The total number of electrons is $N = N_+ + N_-$ and the average particle number density is $n = N/\Omega$, where Ω is the volume of the electron fluid. In the volume $\Omega = L^3$ there is a uniform neutralising background with a charge density $\rho_b = -en$. So that the total charge of the system is zero. The fluid polarisation is then $\xi = |N_+ - N_-|/N$: $\xi = 0$ in the unpolarised (paramagnetic) case and $\xi = 1$ in the fully polarised (ferromagnetic) case.

Setting lengths in units of $a = (4\pi n/3)^{-1/3}$ and energies in Rydberg's units, $\text{Ry} = \hbar^2/2ma_0^2$, where m is the electron mass and $a_0 = \hbar^2/me^2$ is the Bohr radius, the Hamiltonian of Jellium is

$$\mathcal{H} = -\frac{1}{r_s^2} \sum_{i=1}^N \nabla_{\mathbf{r}_i}^2 + V(R), \quad (11)$$

$$V = \frac{1}{r_s} \left(2 \sum_{i<j} \frac{1}{|\mathbf{r}_i - \mathbf{r}_j|} + \sum_{i=1}^N r_i^2 + v_0 \right), \quad (12)$$

where $R = (\mathbf{r}_1, \mathbf{r}_2, \dots, \mathbf{r}_N)$ with \mathbf{r}_i the coordinate of the i th electron, $r_s = a/a_0$, and v_0 a constant containing the self energy of the background. Note that the presence of the neutralising background produces the harmonic confinement shown in Equation (12).

The kinetic energy scales as $1/r_s^2$ and the potential energy (particle-particle, particle-background, and background-background interaction) scales as $1/r_s$, so for small r_s (high electronic densities), the kinetic energy dominates and the electrons behave like an ideal gas. In the limit of large r_s , the potential energy dominates and the electrons crystallize into a Wigner crystal. Wigner [43] No liquid phase is realisable within this model since the pair-potential has no attractive parts even though a superconducting state [44] may still be possible (see chapter 8.9 of Refs. [45,46]).

The Jellium has been solved either by integral equation theories in its ground-state [28] or by computer experiments in its ground-state [47] in the second half of last century but more recently it has been studied at finite, non zero, temperatures by several research groups [10–12,14–18].

It was shown in Ref. [13] that the data of Brown *et al.* [10,11] are inaccurate at $r_s = 1$. This appears to be a systematic error of the fixed node method so it would be interesting to know whether this problem may be solved with the present method which seems a promising route

to access higher densities which was not possible in the paper by Brown *et al.*

3. Jellium at finite temperature

For the Jellium at finite temperature it is convenient to introduce the electron degeneracy parameter $\Theta = T/T_F$, where T_F is the Fermi temperature

$$T_F = T_D \frac{(2\pi)^2}{2[(2-\xi)\alpha_3]^{2/3}}, \quad (13)$$

here ξ is the polarisation of the fluid that can be either $\xi = 0$, for the unpolarised case, and $\xi = 1$, for the fully polarised case, $\alpha_3 = 4\pi/3$, and

$$T_D = \frac{n^{2/3}\hbar^2}{mk_B} = \frac{\hbar^2}{mk_B\alpha_3^{2/3}(a_0r_s)^2}, \quad (14)$$

is the degeneracy temperature, [23] for temperatures higher than T_D quantum effects are less relevant.

The state of the fluid will then depend also upon the Coulomb coupling parameter, $\Gamma = e^2/(a_0r_s)k_B T$ [10]. So that

$$\Theta = \frac{r_s}{\Gamma} \left[\frac{2(2-\xi)^{2/3}\alpha_3^{4/3}}{(2\pi)^2} \right]. \quad (15)$$

The behaviour of the internal energy of the Jellium in its ground-state ($\Theta = 0$) has been determined through Diffusion Monte Carlo (DMC) by Ceperley and Alder [47]. Three phases of the fluid appeared, for $r_s < 75$ the stable phase is the one of the unpolarised Jellium, for $75 < r_s < 100$ the one of the polarised fluid, and for $r_s > 100$ the one of the Wigner crystal. They used systems from $N = 38$ to $N = 246$ electrons.

4. The simulation

The density matrix of a system of many fermions at temperature $k_B T = \beta^{-1}$ can be written as an integral over all paths $\{R_t\}$

$$\begin{aligned} \rho_F(R_\beta, R_0; \beta) \\ = \frac{1}{N!} \sum_{\mathcal{P}} (-1)^{\mathcal{P}} \oint_{\mathcal{P}R_0 \rightarrow R_\beta} dR_t \exp(-S[R_t]), \end{aligned} \quad (16)$$

the path R_t begins at $\mathcal{P}R_0$ and ends at R_β and \mathcal{P} is a permutation of particles labels. For nonrelativistic particles interacting with a potential $V(R)$ the action of the path, $S[R_t]$, is given by (see Appendix 1)

$$S[R_t] = \int_0^\beta dt \left[\frac{r_s^2}{4} \left| \frac{dR_t}{dt} \right|^2 + V(R_t) \right]. \quad (17)$$

Thermodynamic properties, such as the energy, are related to the diagonal part of the density matrix, so that

the path returns to its starting place or to a permutation \mathcal{P} after a time β .

To perform Monte Carlo calculations of the integrand, one makes imaginary time discrete with a time step τ , so that one has a finite (and hopefully small) number of time slices and thus a classical system of N particles in $M = \beta/\tau$ time slices; an equivalent NM particle classical system of ‘polymers’ [23].

Note that in addition to sampling the path, the permutation is also sampled. This is equivalent to allowing the ring polymers to connect in different ways. This macroscopic ‘percolation’ of the polymers is directly related to superfluidity as Feynman [48–50] first showed. Any permutation can be broken into cycles. Superfluid behaviour can occur at low temperature when the probability of exchange cycles on the order of the system size is non-negligible. The superfluid fraction can be computed in a path integral Monte Carlo calculation as described in Ref. [46]. The same method could be used to calculate the superconducting fraction in Jellium at low temperature. However, the straightforward application of those techniques to Fermi systems means that odd permutations subtract from the integrand. This is the ‘fermions sign problem’ [36] first noted by Feynman [51] who after describing the path integral theory for boson superfluid ^4He , pointed out:

The [path integral] expression for Fermi particles, such as ^3He , is also easily written down. However in the case of liquid ^3He , the effect of the potential is very hard to evaluate quantitatively in an accurate manner. The reason for this is that the contribution of a cycle to the sum over permutations is either positive or negative depending whether the cycle has an odd or an even number of atoms in its length L .

Thermodynamic properties are averages over the thermal N -fermions density matrix which is defined as a thermal occupation of the exact eigenstates $\phi_i(R)$

$$\rho_F(R, R'; \beta) = \sum_i \phi_i^*(R) e^{-\beta E_i} \phi_i(R'). \quad (18)$$

The partition function is the trace of the density matrix

$$Z(\beta) = e^{-\beta F} = \int dR \rho_F(R, R; \beta) = \sum_i e^{-\beta E_i}. \quad (19)$$

Other thermodynamic averages are obtained as

$$\langle \mathcal{O} \rangle = Z(\beta)^{-1} \int dR dR' \langle R | \mathcal{O} | R' \rangle \rho_F(R', R; \beta). \quad (20)$$

Note that for any density matrix the diagonal part is always positive

$$\rho_F(R, R; \beta) \geq 0, \quad (21)$$

so that $Z^{-1} \rho_F(R, R; \beta)$ is a proper probability distribution. It is the diagonal part which we need for many

observables, so that probabilistic ways of calculating those observables are, in principle, possible.

Path integrals are constructed using the product property of density matrices

$$\begin{aligned} & \rho_F(R_2, R_0; \beta_1 + \beta_2) \\ &= \int dR_1 \rho_F(R_2, R_1; \beta_2) \rho_F(R_1, R_0; \beta_1), \end{aligned} \quad (22)$$

which holds for any sort of density matrix. If the product property is used M times we can relate the density matrix at a temperature β^{-1} to the density matrix at a temperature $M\beta^{-1}$. The sequence of intermediate points $\{R_1, R_2, \dots, R_{M-1}\}$ is the path, and the time step is $\tau = \beta/M$. As the time step gets sufficiently small the Trotter theorem tells us that we can assume that the kinetic \mathcal{T} and potential \mathcal{V} operator commute so that: $e^{-\tau \mathcal{H}} = e^{-\tau \mathcal{T}} e^{-\tau \mathcal{V}}$ and the primitive approximation for the fermions density matrix is found [23]. The Feynman-Kac formula for the fermions density matrix results from taking the limit $M \rightarrow \infty$. The price we have to pay for having an explicit expression for the density matrix is additional integrations; all together $3N(M-1)$. Without techniques for multidimensional integration, nothing would have been gained by expanding the density matrix into a path. Fortunately, simulation methods can accurately treat such integrands. It is feasible to make M rather large, say in the hundreds or thousands, and thereby systematically reduce the time-step error.

In addition to the internal energy and the static structure of the Jellium one could also measure its dynamic structure, the ‘superconducting fraction’, the specific heat, and the pressure [23].

4.1. Restricted path integral Monte Carlo

In this section we give a brief review of the restricted path integral Monte Carlo (RPIMC) method fully described in Refs. [36,37]. The fermion density matrix is defined by the Bloch equation which describes its evolution in imaginary time

$$\frac{\partial}{\partial \beta} \rho_F(R, R_0; \beta) = -\mathcal{H} \rho_F(R, R_0; \beta), \quad (23)$$

$$\rho_F(R, R_0; 0) = \mathcal{A} \delta(R - R_0), \quad (24)$$

where $\beta = 1/k_B T$ with T the absolute temperature and \mathcal{A} is the operator of antisymmetrisation. The reach of R_0 , $\gamma(R_0, t)$, is the set of points $\{R_i\}$ for which

$$\rho_F(R_i, R_0; t') > 0 \quad 0 \leq t' \leq t, \quad (25)$$

where $\hbar t$ is the imaginary thermal time, and is illustrated in Figure 1.

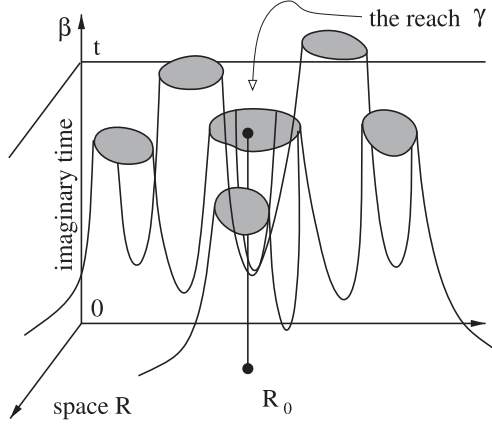
6  R. FANTONI


Figure 1. Illustration of the reach $\gamma(R_0, t)$ of the fermion density matrix.

Note that

$$\rho_F(R_0, R_0; t) > 0, \quad (26)$$

and clearly

$$\rho_F(R, R_0; t)|_{R \in \partial\gamma(R_0, t)} = 0. \quad (27)$$

We want to show that (27) uniquely determines the solution. Suppose $\delta(R, t)$ satisfies the Bloch equation

$$\left(\mathcal{H} + \frac{\partial}{\partial t} \right) \delta(R, t) = 0, \quad (28)$$

in a space-time domain $\alpha = \{t_1 \leq t \leq t_2, R \in \Omega_t\}$ where Ω_t is the space domain at fixed imaginary thermal time. And the two conditions

$$\delta(R, t_1) = 0, \quad (29)$$

$$\delta(R, t)|_{R \in \partial\Omega_t} = 0 \quad t_1 \leq t \leq t_2, \quad (30)$$

are also satisfied. Consider

$$\int_{t_1}^{t_2} dt \int_{\Omega_t} dR e^{2V_0 t} \delta(R, t) \left(\mathcal{H} + \frac{\partial}{\partial t} \right) \delta(R, t) = 0, \quad (31)$$

where V_0 is a lower bound for $V(R)$.

We have

$$\begin{aligned} & \frac{\partial}{\partial t} [e^{2V_0 t} \delta^2(R, t)] \\ &= 2V_0 e^{2V_0 t} \delta^2(R, t) + 2e^{2V_0 t} \delta(R, t) \frac{\partial}{\partial t} \delta(R, t). \end{aligned} \quad (32)$$

Since

$$\begin{aligned} & \int_{t_1}^{t_2} dt \int_{\Omega_t} dR \frac{\partial}{\partial t} \left(\frac{e^{2V_0 t}}{2} \delta^2(R, t) \right) \\ &= \int_{t_1}^{t_2} dt \frac{\partial}{\partial t} \left(\frac{e^{2V_0 t}}{2} \int_{\Omega_t} dR \delta^2(R, t) \right) \\ &= \frac{e^{2V_0 t_2}}{2} \int_{\Omega_{t_2}} dR \delta^2(R, t_2), \end{aligned} \quad (33)$$

where in the last equality we used Equation (29). Then from Equation (31) follows

$$\begin{aligned} & \frac{e^{2V_0 t_2}}{2} \int_{\Omega_{t_2}} dR \delta^2(R, t_2) \\ & - \int_{t_1}^{t_2} dt e^{2V_0 t} \int_{\Omega_t} dR \\ & \times [V_0 \delta^2(R, t) - \delta(R, t) \mathcal{H} \delta(R, t)] = 0. \end{aligned} \quad (34)$$

Then using Equation (30) we find

$$\begin{aligned} & \frac{e^{2V_0 t_2}}{2} \int_{\Omega_{t_2}} dR \delta^2(R, t_2) \\ & + \int_{t_1}^{t_2} dt e^{2V_0 t} \int_{\Omega_t} dR \\ & \times [(V(R) - V_0) \delta^2(R, t) + \lambda (\nabla \delta(R, t))^2] = 0. \end{aligned} \quad (35)$$

With $\lambda = \hbar^2/2m$. Each term in Equation (35) is non-negative so it must be

$$\delta(R, t) = 0 \quad \text{in } \alpha. \quad (36)$$

Let ρ_1 and ρ_2 be two solutions of the restricted path problem and let $\delta = \rho_1 - \rho_2$. Then $\delta(R, t)|_{R \in \partial\gamma(R_0, t)} = 0$ for $t_1 \leq t \leq t_2$. By taking t_2 to infinity and t_1 to zero we conclude that the fermion density matrix is the unique solution.

Equation (35) also shows that the reach γ has the tiling property [36]. Suppose it did not. Then there would exist a space-time domain with the density matrix non-zero inside and from which it is only possible to reach R_0 or any of its images $\mathcal{P}R_0$, with \mathcal{P} any permutation of the particles, crossing the nodes of the density matrix. But such a domain cannot extend to $t = 0$ because in the classical limit there are no nodes. Then this density matrix satisfies for some $t_1 > 0$ the boundary conditions (29) and (30) and as a consequence it must vanish completely inside the domain contradicting the initial hypothesis.

We now derive the restricted path identity. Suppose ρ_F is the density matrix corresponding to some set of quantum numbers which is obtained by using the projection operator \mathcal{A} on the distinguishable particle density matrix. Then it is a solution to the Bloch equation (23)

with boundary condition (24). Thus we have proved the Restricted Path Integral identity

$$\begin{aligned} \rho_F(R_\beta, R_0; \beta) &= \int dR' \rho_F(R', R_0; 0) \oint_{R' \rightarrow R_\beta \in \gamma(R_0)} dR_t e^{-S[R_t]}, \end{aligned} \quad (37)$$

where the subscript means that we restrict the path integration to paths starting at R' , ending at R_β and node-avoiding. The weight of the walk is $\rho_F(R', R_0; 0) = (N!)^{-1} \sum_{\mathcal{P}} (-)^{\mathcal{P}} \delta(R' - \mathcal{P}R_0)$. It is clear that the contribution of all the paths for a single element of the density matrix will be of the same sign, thus solving the sign problem; positive if $\rho_F(R', R_0; 0) > 0$, negative otherwise. On the diagonal the density matrix is positive and on the path restriction $\rho_F(R, R_0; \beta) > 0$ then only even permutations are allowed since $\rho_F(R, \mathcal{P}R; \beta) = (-)^{\mathcal{P}} \rho_F(R, R; \beta)$. It is then possible to use a bosons calculation to get the fermions case.

Important in this argument is that the random walk is a continuous process so we can say definitely that if sign of the density matrix changed, it had to have crossed the nodes at some point.

The restricted path identity is one solution to Feynman's task of rearranging terms to keep only positive contributing paths for diagonal expectation values.

The problem we now face is that the unknown density matrix appears both on the left-hand side and on the right-hand side of Equation (37) since it is used to define the criterion of node-avoiding paths. To apply the formula directly, we would somehow have to self-consistently determine the density matrix. In practice what we need to do is make an ansatz, which we call ρ_T , for the nodes of the density matrix needed for the restriction. The trial density matrix, ρ_T , is used to define trial nodal cells: $\gamma_T(R_0)$.

Then if we know the reach of the fermion density matrix we can use the Monte Carlo method to solve the fermion problem restricting the path integral (RPIMC) to the space-time domain where the density matrix has a definite sign (this can be done, for example, using a trial density matrix whose nodes approximate well the ones of the true density matrix) and then using the antisymmetrisation operator to extend it to the whole configuration space. This will require the complicated task of sampling the permutation space of the N -particles [23]. Recently it has been devised an intelligent method to perform this sampling through a new algorithm called the worm algorithm [38,39]. In order to sample the path in coordinate space one generally uses various generalisations of the Metropolis rejection algorithm [52] and the

bisection method [23] in order to accomplish multislice moves which becomes necessary as τ decreases.

The pair-product approximation was used by Brown *et al.* [10] (see Appendix 2) to write the many-body density matrix as a product of high-temperature two-body density matrices [23]. The pair Coulomb density matrix was determined using the results of Pollock [53] even if these could be improved using the results of Vieillefosse [54,55]. This procedure comes with an error that scales as $\sim \tau^3/r_s^2$ where $\tau = \beta/M$ is the time step, with M the number of imaginary time discretizations. A more dominant form of time step error originates from paths which cross the nodal constraint in a time less than τ . To help alleviate this effect, Brown *et al.* [10] use an image action to discourage paths from getting too close to nodes. Additional sources of error are the finite size one and the sampling error of the Monte Carlo algorithm itself. For the highest density points, statistical errors are an order of magnitude higher than time step errors.

The results at a given temperature T where obtained starting from the density matrix in the classical limit, at small thermal times, and using repetitively the squaring method

$$\rho_F(R_1, R_2; \beta) = \int dR' \rho_F(R_1, R'; \beta/2) \rho_F(R', R_2; \beta/2). \quad (38)$$

Time doubling is an improvement also because if we have accurate nodes down to a temperature T , we can do accurate simulations down to $T/2$. Equation (38) is clearly symmetric in R_1 and R_2 . The time doubling cannot be repeated without reintroducing the sign problem.

Brown *et al.* [10] use $N = 33$ electrons for the fully spin polarised system and $N = 66$ electrons for the unpolarised system.

5. The problem

We need to adopt a free fermion density matrix restriction [10] for the path integral calculation from the worm algorithm [39,56] to the reach of the reference point in the moves ending in the Z sector: remove, close, wiggle, and displace. The worm algorithm is a particular path integral algorithm where the permutations need not to be sampled as they are generated with the simulation evolution. We will use the primitive approximation of Equations (A8)–(A10), randomise the reference point time slice, restrict also the G sector, in particular the advance and swap moves, choose the probability of being in the G sector, C_0 defined in Ref. [39], as small as possible, in order not to let the worm algorithm get stuck in the G sector when we have many time slices. Usually choosing a smaller time step allows to use a larger C_0 since the path is smoother and the restriction gives less problems

in the transition from the G to the Z sector. Or equivalently increasing the number of time slices at fixed C_0 gives a larger permanence in the Z sector. The algorithm chooses autonomously the optimal τ to be used.

The restriction implementation is rather simple: we just reject the move whenever the proposed path is such that the ideal fermion density matrix calculated between the reference point and any of the time slices subject to newly generated particles positions has a negative value. Our algorithm is described in detail in the following section.

The trial density matrix used to perform the restriction of the fixed nodes path integral is chosen as the one of ideal fermions which is given by

$$\rho_0(R, R'; t) \propto \mathcal{A} \left[e^{-\frac{(r_i - r'_i)^2}{4\lambda t}} \right], \quad (39)$$

where $\lambda = \hbar^2/2m$ and \mathcal{A} is the antisymmetrisation operator acting on the same spin groups of particles. We expect this approximation to be best at high temperatures and low densities when the correlation effects are weak. Clearly in a simulation of the ideal gas ($V = 0$) this restriction returns the exact result for fermions.

We will use the primitive approximation in a grand canonical ensemble calculation at fixed chemical potential μ , volume Ω , and temperature T . Decreasing the chemical potential the average number of particles diminishes. Decreasing C_0 the simulation spends more time in the Z sector.

So, we will take the Bohr radius a_0 as units of length and energies in Rydberg's units. In particular in the grand canonical simulation the path integral time step τ (Ry^{-1}) will be independent from r_s , unlike the simulations of Brown *et al.* [10]

The Coulomb potential is treated through the method of Natoli and Ceperley [57] which cures its long range nature (see Appendix 3). Even if the comparison with the direct method by Fraser *et al.* [58] gives already reasonable results.

We will explicitly determine the dependence of the Jellium properties (structural and thermodynamic) on the polarisation ξ .

6. Our algorithm

Our algorithm briefly presented in the previous section is based on the worm algorithm of Boninsegni *et al.* [39,56,59–61]. This algorithm uses a menu of nine moves. Three self-complementary: swap, displace, and wiggle, and the other six are three couples of complementary moves: insert-remove, open-close, and advance-recede. These moves act on 'worms' with a head I and a tail

Masha in the β -periodic imaginary thermal time, which can swap a portion of their bodies (swap move), can move forward and backward (advance-recede moves), can be subdivided in two or joined into a bigger one (open-close moves), and can be born or die (insert-remove moves) since we are working in the grand-canonical ensemble. The configuration space of the worms is called the G sector. When the worms recombine to form a closed path we enter the so called Z sector and the path can translate in space (displace move) and can propagate in space through the bisection algorithm (wiggle move) carefully explained in Ref. [23].

In order to reach a restricted path integral we restrict the moves that end in the Z sector, that is: displace, wiggle, close, and remove. This is pictorially shown in Figure 2 for the first three moves. It is important to stress the fact that we choose the reference point time slice randomly (i.e. we choose an integer random number between 1 and M , say m , and the reference point will then be $R_0 = R_{m\tau}$), before each move, to increase the acceptances in the restrictions. This is allowed because we are free to perform a translation in the β -periodic imaginary thermal time. The reaches of different reference points will in general be different. In the figure the reach is schematically represented as a double cone.

In order to increase the acceptances in the restrictions we also restricted some moves in the G sector: swap and advance.

In order to implement the restriction we reject the move whenever the proposed path is such that the ideal fermion density matrix of Equation (39) calculated between the reference point and any of the time slices subject to newly generated particles positions has a negative value. That is, whenever the path ends up in a region not belonging to the reach of the reference point as shown in Figure 2. The restriction of the G sector moves acts in the same way but on worms rather than on closed paths. When calculating diagonal properties we consider only the density matrix at the reference point.

Since the averages are only taken during the permanence in the Z sector it is fundamental to restrict the moves that end in the Z sector. Since these are the ones that have an influence on the measures of the various estimators during the run. If we enter the Z sector in such a way that we are out of the reach of the reference point the algorithm will continue wandering in the G sector till a door to the Z sector opens up. The code without restrictions gives the bosonic calculation so we are free to restrict also the G sector in order to increase the acceptances of the Z sector.

For each move we can decide the frequency of the move and the maximum number of time slices it operates on, apart from the displace move where instead of

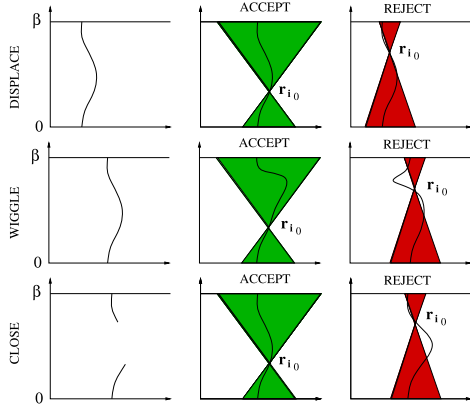


Figure 2. (Color online) Illustration of the rejection algorithm within the worm algorithm. The bold line represents schematically the closed path or the open worm, of a single electron. In the most general case these will wind through the beta periodic imaginary thermal time circle, but this is not shown in the illustration. The reference point is r_{i_0} and the microscopic reach is represented schematically as the shaded doubly cylindrical region. In general the reach will be a complicated region of space-time as pointed out in Figure 1 for the macroscopic reach. Only the three moves: displace ($Z \rightarrow Z$), wiggle ($Z \rightarrow Z$), and close ($G \rightarrow Z$) are shown. On the left we have the starting configuration and on the right we show two different actions of each move, one accepted and one rejected.

the maximum number of time slices we can decide the maximum extent of the spatial translation displacement. It is well known that Monte Carlo algorithms works better as long as we have a longer moves menu, unless of course one violates detailed balance. So the worm algorithm is very efficient in exploring all the electrons path configuration with all the necessary exchanges.

7. Results

In order to test the validity of the restriction procedure we first simulated a system of free ($V = 0$) particles without the restriction (bosons) and with the restriction (fermions). The result for the radial distribution function is shown in Figure 3. The small discrepancy with the analytic result of Bosse *et al.* [62] is due to the finite size effect. The average number of particles in the simulation for the bosons being around 107 and for the fermions 46 for $\beta = 1 \text{ Ry}^{-1}$, 27 for $\beta = 10 \text{ Ry}^{-1}$, and 21 for $\beta = 30 \text{ Ry}^{-1}$. For the free particles we do not have any source of error coming from the imaginary time discretization. Since we were not interested in a quantitative accurate analysis we chose the simulations at smaller temperatures shorter.

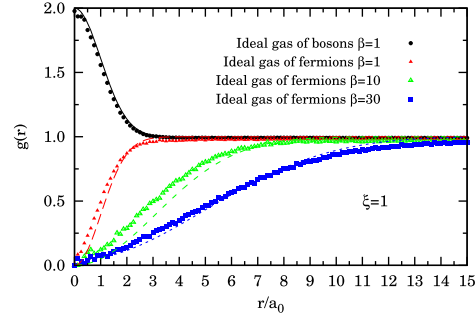


Figure 3. (Color online) The radial distribution function for an ideal gas of bosons at one inverse temperature ($\beta = 1 \text{ Ry}^{-1}$) and an ideal gas of fermions at three inverse temperatures ($\beta = 1 \text{ Ry}^{-1}, 10 \text{ Ry}^{-1}, 30 \text{ Ry}^{-1}$). We simulate fully polarised ($\xi = 1$) particles. The exact analytical results are shown as guiding lines and were derived from the work of Bosse *et al.* [62]

The volume was kept fixed at $\Omega = 1.25 \times 10^5 a_0^3$ corresponding to a half box side of $L/2 = 25a_0$. We used 20 time slices for the boson case and 80 for the fermion cases.

In these simulations we find good agreement with the exact analytic results also for the internal energy per particle (kinetic and potential) and for the pressure.

Then we simulated the Jellium using for the potential energy, V , the image potential, V_I , of Equation (A33) where we chose the short and long range splitting, necessary for the bare Coulomb potential $v(r) = 2 \text{ Ry}/r$, using the optimised method of Natoli and Ceperley [57] with an eight-order polynomial for the radial interpolation. In the long range part we keep up to 128 Fourier components.

In Table 1 we present our results for various thermodynamic quantities. Our results cannot be directly compared with the ones of Brown *et al.* [10] since we are running at fixed chemical potential but we believe that we are able to extend their results at higher density $r_s < 1$. Benchmark data can be found in Refs. [63,64]. We leave a careful comparison in a subsequent work.

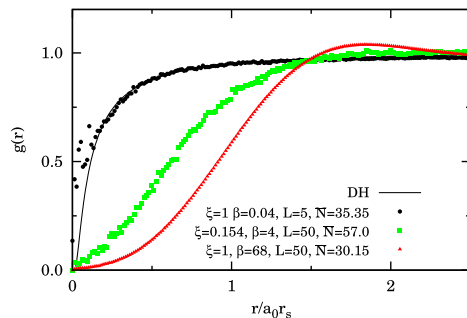
In Figure 4 we show our results for the radial distribution function for the states of Table 1.

8. Conclusions

We have successfully implemented the ideal fermion density matrix restriction on the path integral worm algorithm which is able to generate the necessary permutations during the simulation evolution without the need of their explicit sampling. This allowed us to reach the fermionic finite temperature properties of a given fluid of particles interacting through a pair potential. We worked

10  R. FANTONI**Table 1.** Thermodynamic results in our simulations: β (Ry^{-1}) inverse temperature, e_k (Ry) kinetic energy per particle, e_p (Ry) potential energy per particle, P (Ry/a_0^3) pressure.

M	ξ	\bar{N}	L	β	r_s	Θ	Γ	e_k	e_p	P
60	1	35.35(4)	5	0.04	0.945	3.819	0.085	31.5(5)	-0.736(3)	5.7(1)
80	0.154	57.0(2)	50	4	8.060	4.180	0.993	0.365(8)	-0.0921(4)	$5.2(2) \times 10^{-5}$
680	1	30.15(3)	50	68	9.966	0.250	13.647	0.016(1)	-0.12198(5)	≈ 0

**Figure 4.** (Color online) The radial distribution function for Jellium in the states of Table 1. Also shown is the DH result for the highest temperature state, $g_{DH}(r) = \exp[-\frac{1}{r}] \exp(-\sqrt{3}\Gamma r)$.

in the grand canonical ensemble and applied our method to the Jellium fluid of Wigner. Even if our results cannot be directly compared with the previous canonical calculation of Brown *et al.* [10] (this program was already carried out in our previous work [2]) we believe that they complement them with the access to the high density regime and with the treatment of the general polarisation case. In this preliminary paper we just address the validity of our method, its accuracy will be treated in a forthcoming work.

The relevance of our study relies in the fact that our simulation method is different from both the method of Ceperley *et al.* [10,11] who uses the fixed nodes approximation in the canonical ensemble and explicitly samples the necessary permutations, and from the one of Bonitz *et al.* [12,14–16] who combine configuration path integral Monte Carlo and permutation blocking path integral Monte Carlo. Our method is also different from others quantum Monte Carlo methods like the one of Malone *et al.* [17] that agrees well with the one of Bonitz at high densities and the direct path integral Monte Carlo one of Filinov *et al.* [18] that agrees well with Brown at low density and moderate temperature. So our new algorithm adds to the ones already used in the quest for an optimal way to calculate the properties of the fascinating Wigner's Jellium model at finite temperatures.

We obtained results for both the structure, the radial distribution function, and various thermodynamic quantities.

We intend to adopt this method to simulate Jellium in a curved surface [6–9] in the near future. For example the Jellium on the surface of a sphere with a Dirac magnetic monopole at the centre could be used to study the quantum Hall effect [65]. We already successfully applied the present method to Jellium on the surface of a sphere [66] and to two component boson-fermion plasma on a plane [19].

Notes

1. This approach (which leads to the Random Phase Approximation, RPA) is approximate insofar as the potential entering the Schrödinger equation has been taken as the Hartree potential, thus neglecting exchange and correlation between an incoming electron and the electronic screening cloud.
2. The discontinuity in the momentum distribution across the Fermi surface introduces a singularity in elastic scattering processes with momentum transfer equal to $2k_F$.

Acknowledgements

We would like to thank Saverio Moroni for several relevant discussions at S.I.S.S.A. of Trieste and David Ceperley for many e-mail exchanges which has been determinant for the realisation of the new algorithm.

Disclosure statement

No potential conflict of interest was reported by the author(s).

ORCID

Riccardo Fantoni  <http://orcid.org/0000-0002-5950-8648>

References

- [1] R. Fantoni, *J. Stat. Mech.*, 04015 (2012).
- [2] R. Fantoni, *Eur. Phys. J. B* **94**, 63 (2021). doi:10.1140/epjb/s10051-021-00078-y
- [3] N.W. Ashcroft and N.D. Mermin, *Solid State Physics* (Harcourt Inc., Forth Worth, 1976).
- [4] J.P. Hansen and I.R. McDonald, *Theory of Simple Liquids*, 2nd ed. (Academic Press, London, 1986).
- [5] S.L. Shapiro and S.A. Teukolsky, *Black Holes, White Dwarfs, and Neutron Stars. The Physics of Compact Objects* (John Wiley & Sons Inc., Germany, 1983).
- [6] R. Fantoni, B. Jancovici and G. Téllez, *J. Stat. Phys.* **112**, 27 (2003). doi:10.1023/A:1023671419021
- [7] R. Fantoni and G. Téllez, *J. Stat. Phys.* **133**, 449 (2008). doi:10.1007/s10955-008-9616-x

- [8] R. Fantoni, *J. Stat. Mech.* **04015**, P04015 (2012). doi:10.1088/1742-5468/2012/04/P04015
- [9] R. Fantoni, *J. Stat. Mech.* **10024**, P10024 (2012). doi:10.1088/1742-5468/2012/10/P10024
- [10] E.W. Brown, B.K. Clark, J.L. DuBois and D.M. Ceperley, *Phys. Rev. Lett.* **110**, 146405 (2013). doi:10.1103/PhysRevLett.110.146405
- [11] E. Brown, M.A. Morales, C. Pierleoni and D.M. Ceperley, in *Frontiers and Challenges in Warm Dense Matter*, edited by F. Graziani et al. (Springer, 2014), pp. 123–149.
- [12] T. Schoof, M. Bonitz, A. Filinov, D. Hochstul and J.W. Dufty, *Contrib. Plasma Phys.* **51**, 687 (2011). doi:10.1002/ctpp.v51.8
- [13] T. Schoof, S. Groth, J. Vorberger and M. Bonitz, *Phys. Rev. Lett.* **115**, 130402 (2015). doi:10.1103/PhysRevLett.115.130402
- [14] T. Dornheim, S. Groth, A. Filinov and M. Bonitz, *New J. Phys.* **17**, 073017 (2015). doi:10.1088/1367-2630/17/7/073017
- [15] T. Dornheim, S. Groth, T. Sjostrom, F.D. Malone, W.M.C. Foulkes and M. Bonitz, *Phys. Rev. Lett.* **117**, 156403 (2016). doi:10.1103/PhysRevLett.117.156403
- [16] S. Groth, T. Dornheim, T. Sjostrom, F.D. Malone, W.M.C. Foulkes and M. Bonitz, *Phys. Rev. Lett.* **119**, 135001 (2017). doi:10.1103/PhysRevLett.119.135001
- [17] F.D. Malone, N.S. Blunt, E.W. Brown, D.K.K. Lee, J.S. Spencer, W.M.C. Foulkes and J.J. Shepherd, *Phys. Rev. Lett.* **117**, 115701 (2016). doi:10.1103/PhysRevLett.117.115701
- [18] V.S. Filinov, V.E. Fortov, M. Bonitz and Z. Moldabekov, *Phys. Rev. E* **91**, 033108 (2015). doi:10.1103/PhysRevE.91.033108
- [19] R. Fantoni, *Int. J. Mod. Phys. C* **29**, 1850028 (2018). doi:10.1142/S0129183118500286
- [20] N.H. March and M.P. Tosi, *Coulomb Liquids* (Academic Press, London, 1984).
- [21] J. Friedel, *N. Cimen. Suppl.* **7**, 287 (1958). doi:10.1007/BF02751483
- [22] M.J. Lighthill, *Introduction to Fourier Analysis and Generalized Functions* (Cambridge University Press, London/Great Britain, 1959).
- [23] D.M. Ceperley, *Rev. Mod. Phys.* **67**, 279 (1995). doi:10.1103/RevModPhys.67.279
- [24] J.P. Hansen, *Phys. Rev. A* **8**, 3096 (1973). doi:10.1103/PhysRevA.8.3096
- [25] J.P. Hansen and P. Vieillefosse, *Phys. Lett.* **53A**, 187 (1975). doi:10.1016/0375-9601(75)90523-X
- [26] U. Gupta and A.K. Rajagopal, *Phys. Rev. A* **22**, 2792 (1980). doi:10.1103/PhysRevA.22.2792
- [27] F. Perrot and M.W.C. Dharma-wardana, *Phys. Rev. A* **30**, 2619 (1984). doi:10.1103/PhysRevA.30.2619
- [28] K.S. Singwi, M.P. Tosi, R.H. Land and A. Sjölander, *Phys. Rev.* **176**, 589 (1968). doi:10.1103/PhysRev.176.589
- [29] S. Tanaka and S. Ichimaru, *J. Phys. Soc. Japan* **55**, 2278 (1986). doi:10.1143/JPSJ.55.2278
- [30] F.M.C. Perrot and M.W.C. Dharma-wardana, *Phys. Rev. B* **62**, 16536 (2000). doi:10.1103/PhysRevB.62.16536
- [31] M.W.C. Dharma-wardana and F. Perrot, *Phys. Rev. Lett.* **84**, 959 (2000). doi:10.1103/PhysRevLett.84.959
- [32] S. Dutta and J. Dufty, *Phys. Rev. E* **87**, 032102 (2013). doi:10.1103/PhysRevE.87.032102
- [33] S. Groth, T. Dornheim and M. Bonitz, *Contrib. Plasma Phys.* **57**, 137 (2017). doi:10.1002/ctpp.2017.57.issue-3
- [34] V.V. Karasiev, T. Sjostrom, J. Dufty and S. Trickey, *Phys. Rev. Lett.* **112**, 076403 (2014). doi:10.1103/PhysRevLett.112.076403
- [35] V.V. Karasiev, S.B. Trickey and J.W. Dufty, *Phys. Rev. B* **99**, 195134 (2019). doi:10.1103/PhysRevB.99.195134
- [36] D.M. Ceperley, *J. Stat. Phys.* **63**, 1237 (1991). doi:10.1007/BF01030009
- [37] D.M. Ceperley, in *Monte Carlo and Molecular Dynamics of Condensed Matter Systems*, edited by K. Binder and G. Ciccotti (Editrice Compositori, Bologna, Italy, 1996).
- [38] N.V. Prokof'ev, B.V. Svistunov and I.S. Tupitsyn, *J. Exp. Theor. Phys.* **87**, 310 (1998). doi:10.1134/1.558661
- [39] M. Boninsegni, N. Prokof'ev and B. Svistunov, *Phys. Rev. Lett.* **96**, 070601 (2006). doi:10.1103/PhysRevLett.96.070601
- [40] K.S. Singwi and M.P. Tosi, *Sol. State Phys.* **36**, 177 (1981). doi:10.1016/S0081-1947(08)60116-2
- [41] S. Ichimaru, *Rev. Mod. Phys.* **54**, 1017 (1982). doi:10.1103/RevModPhys.54.1017
- [42] P.A. Martin, *Rev. Mod. Phys.* **60**, 1075 (1988). doi:10.1103/RevModPhys.60.1075
- [43] E. Wigner, *Phys. Rev.* **46**, 1002 (1934). doi:10.1103/PhysRev.46.1002
- [44] A.J. Leggett, *Rev. Mod. Phys.* **47**, 331 (1975). doi:10.1103/RevModPhys.47.331
- [45] G.F. Giuliani and G. Vignale, *Quantum Theory of the Electron Liquid* (Cambridge University Press, Cambridge, 2005).
- [46] E.L. Pollock and D.M. Ceperley, *Phys. Rev. B* **36**, 8343 (1987). doi:10.1103/PhysRevB.36.8343
- [47] D.M. Ceperley and B.J. Alder, *Phys. Rev. Lett.* **45**, 566 (1980). doi:10.1103/PhysRevLett.45.566
- [48] R.P. Feynman, *Phys. Rev.* **90**, 1116 (1953). doi:10.1103/PhysRev.90.1116.2
- [49] R.P. Feynman, *Phys. Rev.* **91**, 1291 (1953). doi:10.1103/PhysRev.91.1291
- [50] R.P. Feynman, *Phys. Rev.* **90**, 1301 (1953). doi:10.1103/PhysRev.90.1301
- [51] R.P. Feynman and A.R. Hibbs, *Quantum Mechanics and Path Integrals* (McGraw-Hill Publishing Company, New York, 1965), pp. 292–293.
- [52] N. Metropolis, A.W. Rosenbluth, M.N. Rosenbluth, A.M. Teller and E. Teller, *J. Chem. Phys.* **1087**, 21 (1953). doi:10.1063/1.1699114[Q9]
- [53] E.L. Pollock, *Comput. Phys. Commun.* **52**, 49 (1988). doi:10.1016/0010-4655(88)90171-3
- [54] P. Vieillefosse, *J. Stat. Phys.* **74**, 1195 (1994). doi:10.1007/BF02188223
- [55] P. Vieillefosse, *J. Stat. Phys.* **80**, 461 (1995). doi:10.1007/BF02178368
- [56] M. Boninsegni, N.V. Prokof'ev and B.V. Svistunov, *Phys. Rev. E* **74**, 036701 (2006). doi:10.1103/PhysRevE.74.036701
- [57] V.D. Natoli and D.M. Ceperley, *J. Comput. Phys.* **117**, 171 (1995). doi:10.1006/jcph.1995.1054
- [58] L.M. Fraser, W.M.C. Foulkes, G. Rajagopal, R.J. Needs, S.D. Kenney and A.J. Williamson, *Phys. Rev. B* **53**, 1814 (1996). doi:10.1103/PhysRevB.53.1814

12  R. FANTONI

- [59] R. Fantoni and S. Moroni, *J. Chem. Phys.* **141**, 114110 (2014). doi:10.1063/1.4895974
- [60] R. Fantoni, *Phys. Rev. E* **92**, 012133 (2015). doi:10.1103/PhysRevE.92.012133
- [61] R. Fantoni, *Eur. Phys. J. B* **89**, 1 (2016). doi:10.1140/epjb/e2016-60917-9
- [62] J. Bosse, K.N. Pathak and G.S. Singh, *Phys. Rev. E* **84**, 042101 (2011). doi:10.1103/PhysRevE.84.042101
- [63] T. Dornheim, S. Groth, T. Schoof, C. Hann and M. Bonitz, *Phys. Rev. B* **93**, 205134 (2016). doi:10.1103/PhysRevB.93.205134
- [64] S. Groth, T. Schoof, T. Dornheim and M. Bonitz, *Phys. Rev. B* **93**, 085102 (2016). doi:10.1103/PhysRevB.93.085102
- [65] V. Melik-Alaverdian, G. Ortiz and N.E. Bonesteel, *J. Stat. Phys.* **104**, 449 (2001). doi:10.1023/A:1010326231389
- [66] R. Fantoni, *Int. J. Mod. Phys. C* **29**, 1850064 (2018). doi:10.1142/S012918311850064X
- [67] H.F. Trotter, *Proc. Am. Math. Soc.* **10**, 545 (1959). doi:10.1090/S0002-9939-1959-0108732-6
- [68] B. Simon, *Functional Integration and Quantum Physics* (Academic, New York, 1979).
- [69] M. Abramowitz and I.A. Stegun, *Handbook of Mathematical Functions* (Dover, New York, 1970).
- [70] J.A. Barker, *J. Chem. Phys.* **70**, 2914 (1979). doi:10.1063/1.437829

Appendices

Appendix 1. The primitive action

In this appendix we give a brief review of the derivation of the primitive approximation given in Ref. [23]. Suppose the Hamiltonian is split into two pieces $\mathcal{H} = \mathcal{T} + \mathcal{V}$, where \mathcal{T} and \mathcal{V} are the kinetic and potential operators. Recall the exact Baker-Campbell-Hausdorff formula to expand $\exp(-\tau\mathcal{H})$ into the product $\exp(-\tau\mathcal{T})\exp(-\tau\mathcal{V})$. As $\tau \rightarrow 0$ the commutator terms which are of order higher than τ^2 become smaller than the other terms and thus can be neglected. This is known as the primitive approximation

$$e^{-\tau(\mathcal{T}+\mathcal{V})} \approx e^{-\tau\mathcal{T}} e^{-\tau\mathcal{V}}. \quad (\text{A1})$$

hence we can approximate the exact density matrix by product of the density matrices for \mathcal{T} and \mathcal{V} alone. One might worry that this would lead to an error as $M \rightarrow \infty$, with small errors building up to a finite error. According to the Trotter [67] formula, one does not have to worry

$$e^{-\beta(\mathcal{T}+\mathcal{V})} = \lim_{M \rightarrow \infty} \left[e^{-\tau\mathcal{T}} e^{-\tau\mathcal{V}} \right]^M. \quad (\text{A2})$$

The Trotter formula holds if the three operators \mathcal{T} , \mathcal{V} , and $\mathcal{T} + \mathcal{V}$ are self-adjoint and make sense separately, for example, if their spectrum is bounded below [68]. This is the case for the Hamiltonian describing Jellium.

Let us now write the primitive approximation in position space

$$\rho(R_0, R_2; \tau) \approx \int dR_1 \langle R_0 | e^{-\tau\mathcal{T}} | R_1 \rangle \langle R_1 | e^{-\tau\mathcal{V}} | R_2 \rangle, \quad (\text{A3})$$

and evaluate the kinetic and potential density matrices. Since the potential operator is diagonal in the position representation, its matrix elements are trivial

$$\langle R_1 | e^{-\tau\mathcal{V}} | R_2 \rangle = e^{-\tau V(R_1)} \delta(R_2 - R_1). \quad (\text{A4})$$

The kinetic matrix can be evaluated using the eigenfunction expansion of \mathcal{T} . Consider, for example, the case of distinguishable particles in a cube of side L with periodic boundary conditions. Then the exact eigenfunctions and eigenvalues of \mathcal{T} are $L^{-3N/2} e^{iK_n R}$ and λK_n^2 , with $K_n = 2\pi \mathbf{n}/L$ and \mathbf{n} a $3N$ -dimensional integer vector. We are using here dimensional units. Then

$$\langle R_0 | e^{-\tau\mathcal{T}} | R_1 \rangle = \sum_{\mathbf{n}} L^{-3N} e^{-\tau\lambda K_n^2} e^{-iK_n(R_0 - R_1)} \quad (\text{A5})$$

$$= (4\pi\lambda\tau)^{-3N/2} \exp\left[-\frac{(R_0 - R_1)^2}{4\lambda\tau}\right], \quad (\text{A6})$$

where $\lambda = \hbar^2/2m$. Equation (A6) is obtained by approximating the sum by an integral. This is appropriate only if the thermal wavelength of one step is much less than the size of the box, $\lambda\tau \ll L^2$. In some special situations this condition could be violated, in which case one should use Equation (A5) or add periodic 'images' to Equation (A6). The exact kinetic density matrix in periodic boundary conditions is a theta function, $\prod_{i=1}^{3N} \theta_3(z_i, q)$, where $z_i = \pi(R_0^i - R_1^i)/L$, R^i is the i th component of the $3N$ dimensional vector R , and $q = e^{-\lambda\tau(2\pi/L)^2}$ (see chapter 16 of Ref. [69]). Errors from ignoring the boundary conditions are $O(q)$, exponentially small at large M .

A link m is a pair of time slices (R_{m-1}, R_m) separated by a time step $\tau = \beta/M$. The action S^m of a link is defined as minus the logarithm of the exact density matrix. Then the exact path-integral expression becomes

$$\rho(R_0, R_M; \beta) = \int dR_1 \dots dR_{M-1} \exp\left[-\sum_{m=1}^M S^m\right]. \quad (\text{A7})$$

It is convenient to separate out the kinetic action from the rest of the action. The exact kinetic action for link m will be denoted K^m

$$K^m = \frac{3N}{2} \ln(4\pi\lambda\tau) + \frac{(R_{m-1} - R_m)^2}{4\lambda\tau}. \quad (\text{A8})$$

The inter-action is then defined as what is left

$$U^m = U(R_{m-1}, R_m; \tau) = S^m - K^m. \quad (\text{A9})$$

In the primitive approximation the inter-action is

$$U_1^m = \frac{\tau}{2} [V(R_{m-1}) + V(R_m)], \quad (\text{A10})$$

where we have symmetrised U_1^m with respect to R_{m-1} and R_m , since one knows that the exact density matrix is symmetric and thus the symmetrised form is more accurate.

A capital letter U refers to the total link inter-action. One should not think of the exact U as being strictly the potential action. That is true for the primitive action but, in general, is only correct in the small- τ limit. The exact U also contains kinetic contributions of higher order in τ . If a subscript is present on the inter-action, it indicates the order of approximation; the primitive approximation is only correct to order τ . No subscript implies the exact inter-action.

The residual energy of an approximate density matrix is defined as

$$E_A(R, R'; t) = \frac{1}{\rho_A(R, R'; t)} \left[\mathcal{H} + \frac{\partial}{\partial t} \right] \rho_A(R, R'; t). \quad (\text{A11})$$

The residual energy for an exact density matrix vanishes; it is a local measure of the error of an approximate density matrix. The Hamiltonian \mathcal{H} is a function of R ; thus the residual energy is not symmetric in R and R' .

It is useful to write the residual energy as a function of the inter-action. We find

$$E_A(R, R'; t) = V(R) - \frac{\partial U_A}{\partial t} - \frac{(R - R') \cdot \nabla U_A}{t} + \lambda \nabla^2 U_A - \lambda (\nabla U_A)^2. \quad (\text{A12})$$

The terms on the right hand side are ordered in powers of τ , keeping in mind that $U(R)$ is of order τ , and $|R - R'|$ is of order $\tau^{1/2}$. One obtains the primitive action by setting the residual energy to zero and dropping the last three terms on the right hand side.

The residual energy of the primitive approximation is

$$E_1(R, R'; t) = \frac{1}{2} [V(R) - V(R')] - \frac{1}{2} (R - R') \cdot \nabla V + \frac{\lambda t}{2} \nabla^2 V - \frac{\lambda t^2}{4} (\nabla V)^2. \quad (\text{A13})$$

With a leading error of $\sim \lambda \tau^2$.

Appendix 2. The pair-product action

An often useful method to determine the many-body action is to use the exact action for two electrons [70]. To justify this approach, first assume that the potential energy can be broken into a pairwise sum of terms

$$V(R) = \sum_{i < j} v(|\mathbf{r}_i - \mathbf{r}_j|), \quad (\text{A14})$$

with $|\mathbf{r}_i - \mathbf{r}_j| = r_{ij}$. Next, apply the Feynman-Kac formula for the inter-action

$$e^{-U(R_0, R_F; \tau)} = \left\langle \exp \left[- \int_0^\tau dt V(R(t)) \right] \right\rangle_{\text{RW}}, \quad (\text{A15})$$

where the notation $\langle \dots \rangle_{\text{RW}}$ means the average over all Gaussian random walks from R_0 to R_F in a 'time' τ . So that

$$e^{-U(R_0, R_F; \tau)} = \left\langle \exp \left[- \int_0^\tau dt \sum_{i < j} v(r_{ij}(t)) \right] \right\rangle_{\text{RW}} \quad (\text{A16})$$

$$= \left\langle \prod_{i < j} \exp \left[- \int_0^\tau dt v(r_{ij}(t)) \right] \right\rangle_{\text{RW}} \quad (\text{A17})$$

$$\approx \prod_{i < j} \left\langle \exp \left[- \int_0^\tau dt v(r_{ij}(t)) \right] \right\rangle_{\text{RW}} \quad (\text{A18})$$

$$= \prod_{i < j} \exp \left[-u_2(r_{ij}, r'_{ij}; \tau) \right] \quad (\text{A19})$$

$$= \exp \left[- \sum_{i < j} u_2(r_{ij}, r'_{ij}; \tau) \right] = e^{-U_2(R_0, R_F; \tau)}, \quad (\text{A20})$$

where U_2 is the pair-product action and u_2 is the exact action for a pair of electrons. At low temperatures the pair action approaches the solution of the two particle wave equation. The result is the pair-product or Jastrow ground-state wave function, which is the ubiquitous choice for a correlated wave function because it does such a good job of describing most ground-state correlations.

The residual energy (see Equation (A11)) for the pair-product action is less singular than for other forms. We have that

$$u_2(r_{ij}, r'_{ij}; \tau) = - \ln \left\langle \exp \left(- \int_0^\tau dt v(r_{ij}(t)) \right) \right\rangle_{\text{RW}}, \quad (\text{A21})$$

is of order τ^2 since the two body problem can be factorised into a centre-of-mass term and a term that is a function of the relative coordinates. Moreover we must have

$$\frac{\partial u_2}{\partial \tau} = v(r_{ij}(\tau)), \quad (\text{A22})$$

so that

$$\frac{\partial U_2}{\partial \tau} = V(R(\tau)), \quad (\text{A23})$$

which tells that only the last three terms on the right hand side of Equation (A12) contribute to the residual energy. We also have

$$\nabla U_2 = \sum_i \sum_{i \neq j} \nabla_i u_2(r_{ij}, r'_{ij}; \tau), \quad (\text{A24})$$

where the indices run over the particles. So the leading error of the pair-product action is $\sim \lambda \tau^3$.

Appendix 3. Long-range potentials with the Ewald image technique

Suppose the bare potential in infinite d dimensional space is $v(r)$. Let us define the Fourier transform by

$$\tilde{v}_{\mathbf{k}} = \int_{-\infty}^{\infty} d^d \mathbf{r} e^{-i\mathbf{k} \cdot \mathbf{r}} v(r). \quad (\text{A25})$$

Then its inverse is

$$v(r) = \int_{-\infty}^{\infty} \frac{d^d \mathbf{k}}{(2\pi)^d} e^{i\mathbf{k} \cdot \mathbf{r}} \tilde{v}_{\mathbf{k}}. \quad (\text{A26})$$

Now let us find the energy of a single particle interacting with an infinite rectangular lattice of another particle a distance \mathbf{r} away. To make it converge we also add a uniform background of the same density ($\Omega = \text{volume}$) of opposite charge. Thus the 'image pair-potential' is equal to

$$v_I(r) = \sum_{\mathbf{L}} v(\mathbf{r} + \mathbf{L}) - \tilde{v}_0 / \Omega. \quad (\text{A27})$$

The \mathbf{L} sum is over the Bravais lattice of the simulation cell $\mathbf{L} = (m_x L_x, m_y L_y, \dots)$ where m_x, m_y, \dots range over all positive and negative integers. Converting this to k -space and using the Poisson sum formula we get

$$v_I(r) = \frac{1}{\Omega} \sum'_{\mathbf{k}} \tilde{v}_{\mathbf{k}} e^{i\mathbf{k} \cdot \mathbf{r}}, \quad (\text{A28})$$

where the prime indicates that we omit the $\mathbf{k} = 0$ term; it cancels out with the background. The \mathbf{k} -sum is over reciprocal lattice vectors of the simulation box $\mathbf{k} = (2\pi n_x / L_x, 2\pi n_y / L_y, \dots)$.

14  R. FANTONI

Because both sums are so poorly convergent, we make the division into k -space and r -space; taking the long-range part into k -space. We write

$$v(r) = v_s(r) + v_l(r), \tag{A29}$$

where the optimal splitting is discussed in the work by Natoli and Ceperley [57]. Since Fourier transform is linear, we can also write

$$\tilde{v}_k = \tilde{v}_{sk} + \tilde{v}_{lk}. \tag{A30}$$

Then the image pair-potential is written as

$$v_I(r) = \sum_{\mathbf{L}} v_s(|\mathbf{r} + \mathbf{L}|) + \frac{1}{\Omega} \sum_{\mathbf{k}} \tilde{v}_{lk} e^{i\mathbf{k}\cdot\mathbf{r}} - \frac{1}{\Omega} \tilde{v}_0. \tag{A31}$$

Now let us work with N particles of charge q_i in a periodic box and let us compute the total potential energy of the unit cell. Particles i and j are assumed to interact with a pair-potential $q_i q_j v(r_{ij})$. The image potential energy for the N -particle system is

$$V_I = \sum_{i<j} q_i q_j v_I(r_{ij}) + \sum_i q_i^2 v_M, \tag{A32}$$

where v_M is the interaction of a particle with its own images; it is a Madelung constant for particle i interacting with the perfect lattice of the simulation cell. If this term were not present, particle i would only see $N-1$ particles in the surrounding cells instead of N . We can find its value by considering the limit as two particles get close together with the image pair-potential. Hence

$$v_M = \frac{1}{2} \lim_{r \rightarrow 0} [v_I(r) - v(r)]. \tag{A33}$$

Now we substitute the split up image pair-potential and collect all the terms together

$$\begin{aligned} V_I &= \sum_{i<j} \sum_{\mathbf{L}} q_i q_j v_s(|\mathbf{r}_{ij} + \mathbf{L}|) + \frac{1}{\Omega} \sum_{\mathbf{k}} \tilde{v}_{lk} \sum_{i<j} q_i q_j e^{i\mathbf{k}\cdot\mathbf{r}_{ij}} \\ &\quad - \frac{1}{\Omega} \sum_{i<j} \tilde{v}_{s0} q_i q_j + \sum_i q_i^2 v_M. \end{aligned} \tag{A34}$$

Part XXI

2022

Chapter 71

Eliminating Nonrenormalizability Helps Prove Scaled Affine Quantization of φ_4^4 is Nontrivial

Fantoni R. and Klauder J. R., Int. J. Mod. Phys. A **37**, 2250029 (2022)

Title: “Eliminating Nonrenormalizability Helps Prove Scaled Affine Quantization of φ_4^4 is Nontrivial”

Abstract: Following a modest comparison between canonical and affine quantization, which points to positive features in the affine procedures. We prove through Monte Carlo analysis that the covariant euclidean scalar field theory, φ_n^r , where r denotes the power of the interaction term and $n = s + 1$ where s is the spatial dimension and 1 adds imaginary time, such that $r = n = 4$ can be acceptably quantized using scaled affine quantization and the resulting theory is nontrivial, unlike what happens using canonical quantization.

International Journal of Modern Physics A
Vol. 37, No. 6 (2022) 2250029 (6 pages)
© World Scientific Publishing Company
DOI: 10.1142/S0217751X22500294



Eliminating nonrenormalizability helps prove
scaled affine quantization of φ_4^4 is nontrivial

Riccardo Fantoni*

*Università di Trieste, Dipartimento di Fisica,
Strada Costiera 11, 34151 Grignano (Trieste), Italy
riccardo.fantoni@posta.istruzione.it*

John R. Klauder

*Department of Physics and Department of Mathematics,
University of Florida, Gainesville, FL 32611-8440, USA
klauder@ufl.edu*

Received 16 December 2021

Accepted 20 January 2022

Published 25 February 2022

Following a modest comparison between canonical and affine quantization, which points to positive features in the affine procedures. We prove through Monte Carlo analysis that the covariant Euclidean scalar field theory, φ_n^r , where r denotes the power of the interaction term and $n = s + 1$ where s is the spatial dimension and 1 adds imaginary time, such that $r = n = 4$ can be acceptably quantized using scaled affine quantization and the resulting theory is nontrivial, unlike what happens using canonical quantization.

Keywords: Covariant Euclidean scalar field theory; affine quantization; path integral Monte Carlo; renormalization.

PACS numbers: 03.65.-w, 11.10.Cd, 11.10.Ef, 11.10.Gh, 11.10.Lm

1. Introduction

Covariant Euclidean scalar field quantization, henceforth denoted φ_n^r , where r is the power of the interaction term and $n = s + 1$ where s is the spatial dimension and 1 adds imaginary time, such that $r < 2n/(n - 2)$ can be treated by canonical quantization (CQ), while models such that $r > 2n/(n - 2)$ are trivial.¹⁻⁵ Models such as $r = 2n/(n - 2)$, e.g. $r = n = 4$, also are nonrenormalizable using

*Corresponding author.

R. Fantoni & J. R. Klauder

canonical quantization.¹ However, there exists a different approach called affine quantization (AQ)^{6,7} that promotes a different set of classical variables to become the basic quantum operators and it offers different results, such as models for which $r > 2n/(n - 2)$, which has been recently correctly quantized φ_3^{12} .⁸ In this work, we show, with the aid of a Monte Carlo (MC) analysis, that one of the special cases where $r = 2n/(n - 2)$, specifically the case $r = n = 4$, can be acceptably quantized using affine quantization.⁹⁻¹¹

This program was already carried on with partial success in Refs. 9 and 10, where, however, a diverging value of the vacuum expectation value of the field was found. We show here that using a simple rescaling of the affine quantized theory allows to solve this shortcoming keeping the field theory nontrivial.

2. A Comparison Between Canonical Quantization and Affine Quantization for Fields

2.1. Canonical quantization of scalar fields

Let us begin with the classical Hamiltonian for a single field $\varphi(x)$

$$H(\pi, \varphi) = \int \left\{ \frac{1}{2} [\pi(x)^2 + (\nabla\varphi(x))^2 + m^2\varphi(x)^2] + g\varphi(x)^r \right\} d^s x, \quad (1)$$

where $n = s + 1$ is the number of space-time variables, and r is a positive, even, integer. When g is zero, the remaining expression involves a domain in which a full set of variables, i.e. $\pi(x)$ and $\varphi(x)$, leads to a finite Hamiltonian value. If $g = 0 \rightarrow g > 0$, there are two possible results. If $r < 2n/(n - 2)$, then the domain remains the same. However, if $r \geq 2n/(n - 2)$, then there is a new domain that is smaller than the original domain because the interaction term $\int \varphi(x)^r d^s x = \infty$ leads to a reduction of certain fields. The fields that cause that divergence are not $\varphi(x) = \infty$, because that would have eliminated the original domain when $g = 0$. The only way for $\int \varphi(x)^r d^s x = \infty$ is, for example, given by $\varphi(x) = 1/[(x - c)^2]^k$ where k is small enough so that the gradient term will diverge sooner than the mass term, while $r > 2$ is big enough so that $\int \varphi(x)^r d^s x = \infty$. Such behavior leads to immediate results in perturbation infinities in a power series of g , leading to a nonrenormalizable process, for which quantum efforts, using canonical quantization, collapse to “free” results, despite that $g > 0$, as all that is continuously connected to the original free theory where $g = 0$.

This analysis is confirmed with several efforts. As examples, we note that MC and analytical methods have confirmed that the model φ_4^4 leads only to “free” results,¹⁻⁴ as well as the model φ_3^{12} also leads to “free” results.⁸ Having seen what CQ can show us what it can do, now let us turn to AQ.

Eliminating nonrenormalizability helps prove scaled affine quantization

2.2. Affine quantization of scalar fields

The classical affine variables are $\kappa(x) \equiv \pi(x)\varphi(x)$ and $\varphi(x) \neq 0$. The reason we insist that $\varphi(x) \neq 0$ is because if $\varphi(x) = 0$ then $\kappa(x) = 0$ and $\pi(x)$ cannot help.

We next introduce the same classical Hamiltonian we chose before now expressed in affine variables. This leads us to

$$H'(\kappa, \varphi) = \int \left\{ \frac{1}{2} [\kappa(x)^2 \varphi(x)^{-2} + (\nabla\varphi(x))^2 + m^2 \varphi(x)^2] + g\varphi(x)^r \right\} d^s x, \quad (2)$$

in which $\varphi(x) \neq 0$ is an important fact. With these variables we do not let $\varphi(x) = \infty$ for the reasons made in the CQ story, but now we must forbid $\varphi(x) = 0$ which would admit $\varphi(x)^{-2} = \infty$. The fact that $0 < \varphi(x)^{-2} < \infty$, it follows that, using these variables, $0 < \varphi(x)^r < \infty$, with any $2 < r < \infty$. This essential result leads to the fact that these AQ bounds on $\varphi(x)$ forbid any nonrenormalizability, a “disease” which plagues the CQ analysis. With AQ, this new insight implies that every model φ_n^r does not become a “free” result, but leads to an appropriate “nonfree” result. Specifically, this assertion should lead to “nonfree” results for φ_3^{12} and φ_4^4 , as MC results, have already shown.⁸⁻¹¹

What follows in the coming sections is additional MC studies using AQ procedures. As the former story promises, that study will definitely succeed.

3. Lattice Formulation of the Field Theory

We used a lattice formulation of the AQ field theory studied in Eq. (8) of Ref. 9 using the scaling $\varphi \rightarrow a^{-s/2}\varphi$, $g \rightarrow a^s g$, $\epsilon \rightarrow a^{-s}\epsilon$ where ϵ is the regularization parameter. The theory considers a real scalar field φ taking the value $\varphi(x)$ on each site of a periodic, hypercubic, n -dimensional lattice of lattice spacing a , our ultraviolet cutoff and periodicity $L = Na$. The affine action for the field, $S' = \int H' dx_0$ (with $x_0 = ct$ where c is the speed of light constant and t is imaginary time), is then approximated by

$$\begin{aligned} \frac{S'[\varphi]}{a^{n-s}} \approx & \frac{1}{2} \left\{ \sum_{x,\mu} a^{-2} [\varphi(x) - \varphi(x + e_\mu)]^2 + m^2 \sum_x \varphi(x)^2 \right\} \\ & + \sum_x g \varphi(x)^r + \frac{3}{8} \sum_x \hbar^2 \frac{1}{\varphi(x)^2 + \epsilon}, \end{aligned} \quad (3)$$

where e_μ is a vector of length a in the $+\mu$ direction.

In this work, we are interested in reaching the continuum limit by taking Na fixed and seeking $N \rightarrow \infty$ at fixed volume L^s and absolute temperature $T = 1/k_B L$ with k_B the Boltzmann’s constant.

3.1. MC results

We repeated the path integral MC¹²⁻¹⁵ calculation for the AQ field theory previously done in Ref. 9 for the case $r = n = 4$ using now the scaling $\varphi \rightarrow a^{-s/2}\varphi$,

R. Fantoni & J. R. Klauder

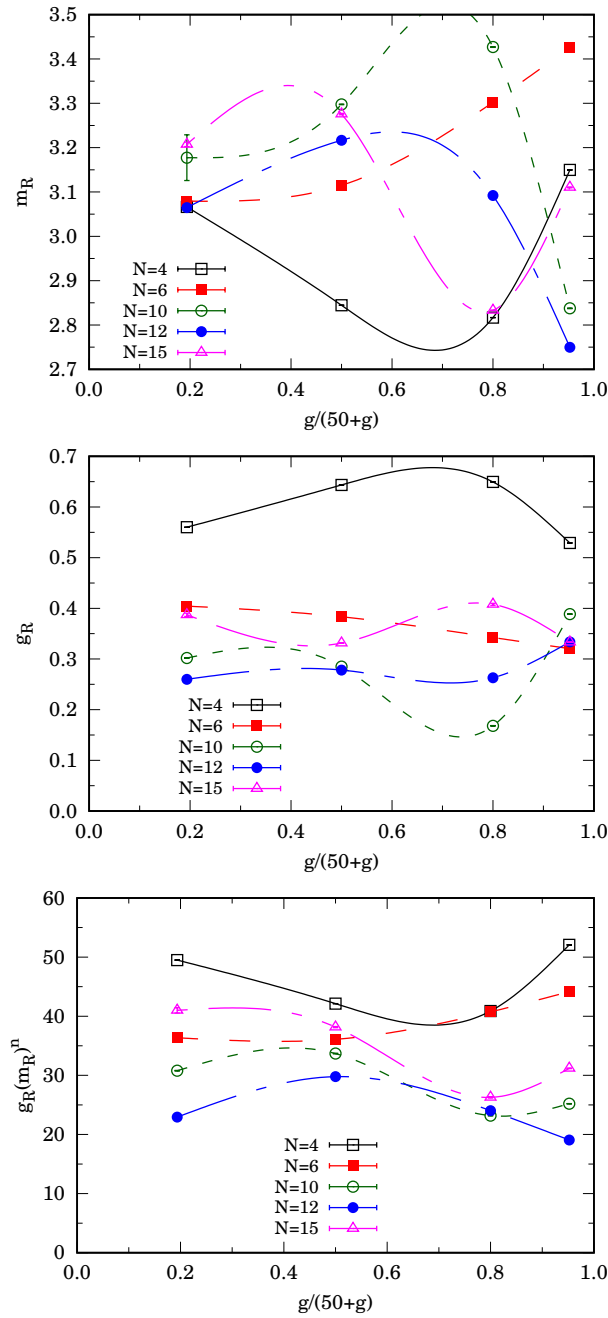


Fig. 1. The renormalized mass $m_R \approx 3$ (top panel), the renormalized coupling constants g_R (central panel), and $g_R m_R^n$ (bottom panel) for various values of the bare coupling constant g at decreasing values of the lattice spacing $a = 1/N$ ($N \rightarrow \infty$ idealized limit) for the scaled *affine* φ_4^4 covariant Euclidean scalar field theory described by the action in Eq. (3) for $r = n = 4$. The lines connecting the simulation points are just a guide for the eye.

Eliminating nonrenormalizability helps prove scaled affine quantization

$g \rightarrow a^s g$, $\epsilon \rightarrow a^{-s} \epsilon$, which brings to using the lattice formulation for the action of Eq. (3). In particular, we calculated the renormalized coupling constant g_R and mass m_R defined in Eqs. (11) and (13) of Ref. 9, respectively.

Following Freedman *et al.*,¹ for each N and g , we adjusted the bare mass m in such a way to maintain the renormalized mass approximately constant $m_R \approx 3$,^a to within a few percent (in all cases less than 10%), and we measured the renormalized coupling constant g_R defined in Refs. 8 and 9 for various values of the bare coupling constant g at a given small value of the lattice spacing $a = 1/N$ (this corresponds to choosing an absolute temperature $k_B T = 1$ and a fixed volume $L^3 = 1$). With Na and m_R fixed, as a was made smaller, whatever change we found in $g_R m_R^2$ as a function of g could only be due to the change in a . We generally found that a depression in m_R produced an elevation in the corresponding value of g_R and vice versa. The results are shown in Fig. 1 for the scaled affine action (3) in natural units $c = \hbar = k_B = 1$ and $\epsilon = 10^{-10}$ (the results are independent from the regularization parameter as long as this is chosen sufficiently small), where, following Freedman *et al.*,¹ we decided to compress the range of g for display, by choosing the horizontal axis to be $g/(50 + g)$. The constraint $m_R \approx 3$ was not easy to implement since for each N and g we had to run the simulation several times with different values of the bare mass m in order to determine the value which would satisfy the constraint $m_R \approx 3$.

These results should be compared with the results of Fig. 1 of Freedman *et al.*¹ where the same calculation was done for the canonical version of the field theory. As we can see from our figure, contrary to the figure of Freedman, the renormalized coupling constant of the affine version remains far from zero in the continuum limit when the ultraviolet cutoff is removed ($Na = 1$ and $N \rightarrow \infty$) for all values of the bare coupling constant. Here, unlike in the canonical version used by Freedman, the diminishing space between higher N curves is a pointer toward a nonfree ultimate behavior as $N \rightarrow \infty$ at fixed volume. Moreover as one can see the $N = 15$ results for the renormalized coupling fall above the ones for $N = 12$.

During our simulations we kept under control also the vacuum expectation value of the field which in all cases was found to vanish in agreement with the fact that the symmetry $\varphi \rightarrow -\varphi$ is preserved.

4. Conclusions

In conclusion, we performed a path integral Monte Carlo study of the properties (mass and coupling constant) of the renormalized covariant Euclidean scalar field theory φ_4^4 quantized through scaled affine quantization. As shown in Ref. 11 the vacuum expectation values for the field and the two-point function are well defined. We show here that, unlike what happens for the theory quantized through canonical

^aDifferently from our previous study⁹ with the unscaled version of the affine field theory we did not need to choose complex m in order to fulfill this constraint. Moreover, the needed m was only very slightly depending on g .

R. Fantoni & J. R. Klauder

quantization, the renormalized coupling constant g_R does not tend to vanish in the continuum limit, where we remove the ultraviolet cutoff at fixed volume. This success of affine quantization to produce a well defined, renormalizable, nontrivial, “nonfree” quantum field theory is one of its merits and benefits.

References

1. B. Freedman, P. Smolensky and D. Weingarten, *Phys. Lett. B* **113**, 481 (1982).
2. M. Aizenman, *Phys. Rev. Lett.* **47**, 886 (1981) [Erratum].
3. J. Fröhlich, *Nucl. Phys. B* **200**, 281 (1982).
4. J. Siefert and U. Wolff, *Phys. Lett. B* **733**, 11 (2014).
5. M. Aizenman and H. Duminil-Copin, *Ann. Math.* **194**, 163 (2021).
6. J. R. Klauder, *Beyond Conventional Quantization* (Cambridge University Press, 2000), Chap. 5.
7. J. R. Klauder, *J. High Energy Phys.* **6**, 175 (2020).
8. R. Fantoni, *J. Stat. Mech.* 083102 (2021).
9. R. Fantoni and J. R. Klauder, *Phys. Rev. D* **103**, 076013 (2021).
10. R. Fantoni and J. R. Klauder, *J. Stat. Phys.* **184**, 28 (2021).
11. R. Fantoni and J. R. Klauder, *Phys. Rev. D* **104**, 054514 (2021).
12. R. Fantoni, *Phys. Rev. B* **86**, 144304 (2012).
13. N. Metropolis, A. W. Rosenbluth, M. N. Rosenbluth, A. M. Teller and E. Teller, *J. Chem. Phys.* **1087**, 21 (1953).
14. M. H. Kalos and P. A. Whitlock, *Monte Carlo Methods* (Wiley-VCH Verlag GmbH & Co., 2008).
15. D. M. Ceperley, *Rev. Mod. Phys.* **67**, 279 (1995).

Chapter 72

Kinetic Factors in Affine Quantization and Their Role in Field Theory Monte Carlo

Fantoni R. and Klauder J. R., Int. J. Mod. Phys. A **37**, 2250094 (2022)

Title: “Kinetic Factors in Affine Quantization and Their Role in Field Theory Monte Carlo”

Abstract: Affine quantization, which is a parallel procedure with canonical quantization, needs to use its principal quantum operators, most simply $D = (PQ + QP)/2$ and $Q \neq 0$, to represent appropriate kinetic factors, normally P^2 , which involve only one canonical quantum operator. The need for this requirement stems from the quantization of selected problems that require affine quantization to achieve valid Monte Carlo results. This task is resolved for introductory examples as well as examples that involve scalar quantum field theories.

International Journal of Modern Physics A
Vol. 37, No. 14 (2022) 2250094 (10 pages)
© World Scientific Publishing Company
DOI: 10.1142/S0217751X22500944



**Kinetic factors in affine quantization and their role
in field theory Monte Carlo**

Riccardo Fantoni*

*Università di Trieste, Dipartimento di Fisica,
Strada Costiera 11, 34151 Grignano (Trieste), Italy
riccardo.fantoni@posta.istruzione.it*

John R. Klauder

*Department of Physics and Department of Mathematics
University of Florida, Gainesville, FL 32611-8440, US
klauder@ufl.edu*

Received 4 April 2022

Accepted 5 May 2022

Published 15 June 2022

Affine quantization, which is a parallel procedure with canonical quantization, needs to use its principal quantum operators, most simply $D = (PQ + QP)/2$ and $Q \neq 0$, to represent appropriate kinetic factors, normally P^2 , which involve only one canonical quantum operator. The need for this requirement stems from the quantization of selected problems that require affine quantization to achieve valid Monte Carlo results. This task is resolved for introductory examples as well as examples that involve scalar quantum field theories.

Keywords: Kinetic factors; covariant Euclidean scalar field theory; affine quantization; path integral Monte Carlo; renormalization.

PACS numbers: 03.65.-w, 11.10.Cd, 11.10.Ef, 11.10.Gh, 11.10.Lm

1. Introduction

In our previous papers, where some suitable Monte Carlo (MC) calculations have been reported, it was established that the quantum procedure called affine quantization (AQ) finds “nonfree” results for the model $\varphi_4^{4,1,2}$ while identical studies, which used canonical quantization (CQ), have only found “free” results, as if the coupling constant had been zero.³⁻⁷ After a careful comparison between the procedures of both CQ and AQ, a detailed MC study of the model $(\varphi^2 - \Phi^2)_4^2$ is

*Corresponding author.

R. Fantoni & J. R. Klauder

presented. While the differences between AQ and CQ for the first model are significant, the differences between AQ and CQ for the second model are much smaller, and a detailed study has found the reason why that could happen. Even if the AQ and CQ results for the second model are rather close, only one of those results can be physically correct.

A general effort to transform a variety of affine expressions opens up a variety of problems regarding their interaction terms and our present work was designed to do just that.

MC studies are greatly simplified by transforming affine variables back into canonical variables, so the π^2 can join $(\sum_j d\varphi/dx_j)^2$ and imaginary time, to ensure a vast simplification of the MC work. Such a transformation from affine to equivalent canonical variables being required to achieve nontrivial results.

2. Some Relations Involving the Quantum Operators P , Q , and D

We need $[Q, P] = i\hbar\mathbb{1}$, $F = F(Q) \neq 0$, and we define $D = [PF + FP]/2$, so that $P^\dagger F = PF$.^a Then we examine

$$\begin{aligned} 2[F, D] &= F(PF + FP) - (PF + FP)F \\ &= FPF + FFP - PFF - FPF = FFP - PFF = [F^2, P]. \end{aligned} \quad (1)$$

This leads to $[F, D] = [F^2, P]/2 = i\hbar(F^2)'/2$, where the prime denotes a derivative with respect to Q . As a familiar example, choose $F(Q) = Q$, then $[Q, D] = [Q^2, P]/2 = i\hbar(Q^2)'/2 = i\hbar Q$, analogues to the Lie algebra of the affine group,⁸ and from which AQ got its name.

3. The Kinetic Factor in Hamiltonians

In simple problems, the most commonly chosen classical kinetic factor is p^2 . In that realm, we can choose $f(q) = 1/g(q) \neq 0$ ($g(q) \neq 0$ is added because $1/f(q)$ is very often used). Now we define $d = pf(q)$ and we then recover p^2 from $d^2g^2 = d^2/f^2 = p^2$. Admittedly, this is utterly trivial. However, when we quantize these variables to P , $D = (PF + FP)/2$, $F = F(Q) \neq 0$ and $G = G(Q) = 1/F(Q) \neq 0$, difficulties can arise.

The quantum kinetic term (with $\hbar = 1$) in affine variables is DG^2D . This expression, helped by $FP - PF = iF'$ and $GP - PG = iG'$, leads to

$$\begin{aligned} 4DG^2D &= (PF + FP)GG(PF + FP) \\ &= PP + FPGGPF + FPGP + PGPF \\ &= PP + (PF + iF')GG(FP - iF') + (PF + iF')GP + PG(FP - iF') \end{aligned}$$

^aAs AQ permits, the dilation operator, D , may take different forms, namely, $D = [PF(Q) + F(Q)P]/2$, for a variety of $F(Q) \neq 0$ functions — chosen such that $P^\dagger F(Q) = PF(Q)$ — and which are of assistance in solving various problems.

Kinetic factors in AQ and their role in field theory MC

$$\begin{aligned}
 &= 4PP + 2i(F'GP - PGF') + F'GGF' \\
 &= 4PP - 2(F'G)' + (F')^2G^2.
 \end{aligned} \tag{2}$$

Restoring \hbar , it follows that

$$DG^2D = P^2 + (1/4)\hbar^2[(F')^2G^2 - 2(F'G)']. \tag{3}$$

As a check on this expression, the example in which $F(Q) = Q$ and thus $G(Q) = 1/Q$, leads to $P^2 + (3/4)\hbar^2/Q^2$, which is the result previously found when $F(Q) = Q$. There is every reason to accept this latter equation as the proper kinematical operator for the half-harmonic oscillator.⁹⁻¹¹

4. Application to Some Field Theory Examples

4.1. A straightforward example for φ_n^p

Regarding our field theory examples, our procedures will naturally encounter $\delta(0)$ divergences. A scaling procedure that eliminates such divergences will be introduced as well as illustrated. As our first example, we choose the classical canonical kinematic field $\pi(x)^2$, for which we choose the dilation field $\kappa(x) = \pi(x)\varphi(x)$, with $\varphi(x) \neq 0$. The classical Hamiltonian in affine variables is

$$H_1 = \int \left\{ \frac{1}{2}[\kappa(x)^2/\varphi(x)^2 + (\nabla\varphi(x))^2 + m^2\varphi(x)^2] + g\varphi(x)^p \right\} d^s x, \tag{4}$$

where $p = 4, 6, 8, \dots$ is the interaction power and $n = s + 1$ is the number of space-time dimensions. The advantage of this pair of variables is that $0 < \varphi(x)^{-2} < \infty$ which implies that $0 < \varphi(x)^p < \infty$, for all p , and thus the Hamiltonian does not experience any non-renormalizability.

Adopting the message from the half-harmonic oscillator, the affine quantum Hamiltonian for this model is

$$\mathcal{H}_1 = \int \left\{ \frac{1}{2}[\hat{\kappa}(x)(\hat{\varphi}(x))^{-2}\hat{\kappa}(x) + (\nabla\hat{\varphi}(x))^2 + m^2\hat{\varphi}(x)^2] + g\hat{\varphi}(x)^p \right\} d^s x, \tag{5}$$

where

$$\hat{\kappa}(x)(\hat{\varphi}(x))^{-2}\hat{\kappa}(x) = \hat{\pi}(x)^2 + (3/4)\hbar^2\delta(0)^{2s}/\varphi(x)^2. \tag{6}$$

The origin of $\delta^s(0) = \infty$ is simply the fact that $[\hat{\varphi}(x), \hat{\pi}(x)] = i\hbar\delta^s(0)\mathbb{1}$.

In a sense, this result is strange. For example, for a single classical variable $(pq)^2 < \infty$ and $|QP - PQ|^2 = \hbar^2\mathbb{1}$. However, for a classical field $(\pi(x)\varphi(x))^2 < \infty$ while $|\hat{\varphi}(x)\hat{\pi}(x) - \hat{\pi}(x)\hat{\varphi}(x)|^2 = \infty\hbar^2\mathbb{1}$. When approximated, as for an integration, then $\hat{\varphi}(x) \rightarrow \hat{\varphi}_k$ and $\hat{\pi}(x) \rightarrow \hat{\pi}_k$, where instead of the continuum that x represents, k identifies different points on a discrete lattice. This leads to $[\hat{\varphi}_k, \hat{\pi}_k] = i\hbar a^{-s}\mathbb{1}$, where a is a tiny spatial distance between neighboring lattice points. In preparation for our integration, just as every integral involves a continuum limit of an appropriate summation, these expressions are used in MC calculations which involve proper sums for their “integrals”. All of these are designed to provide a path integral

R. Fantoni & J. R. Klauder

quantization, and, when necessary, their sums need to be regularized. In our case, the regularized version becomes appropriately “scaled”: specifically $\varphi_k \rightarrow a^{-s/2}\varphi_k$, $\pi_k \rightarrow a^{-s/2}\pi_k$, $\kappa_k \rightarrow a^{-s}\kappa_k$, $g \rightarrow a^{s(p-2)/2}g$, and the regularized $d^s x \rightarrow a^s$ may also be scaled as $a^s \rightarrow a^{2s}$.

Using such scaling, in an AQ formulation with MC, has led to a “nonfree” result for the scalar field φ_4 .¹ However, a CQ formulation with MC, along with analytic studies, has led to a “free” result.^{1,3-7}

4.2. A less common example using CQ and AQ

With first using CQ for the next example, our next classical Hamiltonian is given by

$$H_2 = \int \left\{ \frac{1}{2} [\pi(x)^2 + (\nabla\varphi(x))^2 + m^2\varphi(x)^2] + g(\varphi(x)^2 - \Phi^2)^r \right\} d^s x, \quad (7)$$

where the interaction power has been changed to $r = 2, 4, 6, \dots$, and $n = s + 1$ is the same as before. This unusual interaction term deserves a new dilation variable,^b and in this section we choose $\kappa(x) = \pi(x)(\varphi(x)^2 - \Phi^2)$, where $(\varphi(x)^2 - \Phi^2) \neq 0$. In this case, the classical Hamiltonian in affine variables becomes

$$H_3 = \int \left\{ \frac{1}{2} [\kappa(x)^2 / (\varphi(x)^2 - \Phi^2)^2 + (\nabla\varphi(x))^2 + m^2\varphi(x)^2] + g(\varphi(x)^2 - \Phi^2)^r \right\} d^s x. \quad (8)$$

In these variables, $0 < (\varphi(x)^2 - \Phi^2)^{-2} < \infty$, which implies that $0 < (\varphi(x)^2 - \Phi^2)^r < \infty$, for all r , thereby eliminating any non-renormalizability.

Next we find that the quantum Hamiltonian, using affine variables and Schrödinger’s representation, is given by

$$\mathcal{H}_3 = \int \left\{ \frac{1}{2} [\hat{\kappa}(x)(\varphi(x)^2 - \Phi^2)^{-2}\hat{\kappa}(x) + (\nabla\varphi(x))^2 + m^2\varphi(x)^2] + g(\varphi(x)^2 - \Phi^2)^r \right\} d^s x, \quad (9)$$

and this expression will become more useful after the kinetic term is fully analyzed. In order to obtain a valid quantum Hamiltonian for this model, we are first drawn back to Eq. (3) in Sec. 2, which reads $DG^2D = P^2 + (1/4)\hbar^2[(F')^2G^2 - 2(F'G)']$. In the present case, temporally ignoring (x) and still using Schrödinger’s representation, $F = (\varphi^2 - \Phi^2)$ and $G = 1/F$. It follows, that $F' = 2\varphi$ and $G' = -2\varphi/(\varphi^2 - \Phi^2)^2$. We also need $(F')^2G^2 = 4\varphi^2/(\varphi^2 - \Phi^2)^2$ and $-2(F'G)' = -4/(\varphi^2 - \Phi^2) + 8\varphi^2/(\varphi^2 - \Phi^2)^2 = 4(\varphi^2 + \Phi^2)/(\varphi^2 - \Phi^2)^2$. Hence, for this model, the kinematic factor is

$$\begin{aligned} & \hat{\kappa}(x)(\varphi(x)^2 - \Phi^2)^{-2}\hat{\kappa}(x) \\ & = \hat{\pi}(x)^2 + \hbar^2\delta^{2s}(0)(2\varphi(x)^2 + \Phi^2)/(\varphi(x)^2 - \Phi^2)^2. \end{aligned} \quad (10)$$

^bBeing able to change the dilation variable is an important feature of AQ.

As was the case in Sec. 3.1, scaling can eliminate the $\delta^{2s}(0)$ factor by including the additional scaling factor $\Phi^2 \rightarrow a^{-s}\Phi^2$, and changing the scaling of g to $g \rightarrow a^{s(r-1)}g$.

5. Lattice Formulation of the Field Theory

We used a lattice formulation of the AQ field theory stemming from the Hamiltonian of Eq. (9) for $r = 2$ and $s = 3$ using the scaling $\varphi \rightarrow a^{-s/2}\varphi, \Phi \rightarrow a^{-s/2}\Phi, g \rightarrow a^s g$ already employed in Refs. 2, 12, 13. The theory considers a real scalar field φ taking the value φ_k on each site of a periodic, hypercubic, n -dimensional lattice of lattice spacing a , our ultraviolet cutoff, and periodicity $L = Na$. Using the usual classical expression $\pi = d\varphi/dt$, where t is imaginary time, for the momentum field, the affine action, $S = \int \mathcal{H}_3 dx_0$, with $x_0 = ct$ where c is the speed of light constant, is then approximated on the lattice by

$$S[\varphi]/a^{n-s} \approx \frac{1}{2} \left\{ \sum_{k,\mu} a^{-2} (\varphi_k - \varphi_{k+e_\mu})^2 + m^2 \sum_k \varphi_k^2 \right\} + \sum_k g (\varphi_k^2 - \Phi^2)^2 + \frac{1}{2} \sum_k \hbar^2 \frac{2\varphi_k^2 + \Phi^2}{(\varphi_k^2 - \Phi^2)^2}, \tag{11}$$

where e_μ is 1 in the $+\mu$ direction and 0 else. This is known as the *primitive approximation* for the action and could be improved in various ways.¹⁴ For the CQ field theory, the last term in (11), proportional to \hbar^2 should be dropped.

In this work, we are interested in reaching the continuum limit by taking Na fixed and letting $N \rightarrow \infty$ at fixed volume L^s and absolute temperature $T = 1/k_B L$ with k_B the Boltzmann’s constant. We will always work in natural units $c = \hbar = k_B = 1$.

6. PIMC Results

We performed path integral MC¹⁴⁻¹⁷ calculation for the AQ field theory described by Eq. (11) for $n = 3 + 1$ and $\Phi = 1$, and compared it with the corresponding CQ field theory. In particular, we calculated the renormalized coupling constant g_R (which must be non-negative due to Lebowitz inequality) and mass m_R defined in Eqs. (4.3) and (4.5) of,¹⁸ respectively. This will allow us to explore the behavior of the renormalized system, for a given set of parameters m, g , as a function of N at fixed volume and temperature.

Following Freedman *et al.*,³ for each N and g , we adjusted the bare mass m in such a way to maintain the renormalized mass approximately constant $m_R \approx 3$ to within a few percent (in all cases less than 25%). Differently from our previous study¹ with the unscaled version of the affine field theory we did not need to choose complex m in order to fulfill this constraint, as shown in Table 1. In fact, our present CQ model can be obtained from the φ_4^4 model studied in Ref. 1 by changing $m^2 \rightarrow m^2 - 4g\Phi^2 \equiv M^2$ which will become negative for g big enough. From the

R. Fantoni & J. R. Klauder

Table 1. Choice of the bare mass m in the simulations for CQ and AQ cases. Also shown is $M^2 = m^2 - 4g\Phi^2$ and $m^2/4g\Phi^2$.

N	g	CQ			AQ		
		m	M^2	$m^2/4g\Phi^2$	m	M^2	$m^2/4g\Phi^2$
4	12	7.00	1.000	1.021	6.65	-3.777	0.921
	50	13.70	-12.31	0.938	13.55	-16.397	0.918
	200	27.20	-60.16	0.925	27.10	-65.590	0.918
	1000	61.25	-248.438	0.938	61.20	-254.56	0.936
6	12	7.20	3.840	1.080	6.80	-1.76	0.963
	50	14.00	-4.000	0.980	13.75	-10.937	0.945
	200	27.50	-43.750	0.945	27.40	-49.240	0.938
	1000	61.57	-209.135	0.948	61.53	-214.059	0.946
10	12	7.40	6.760	1.141	7.00	1.000	1.021
	50	14.20	1.640	1.008	14.00	-4.000	0.980
	200	27.80	-27.160	0.960	27.80	-27.160	0.960
	1000	62.10	-143.590	0.964	62.00	-156.000	0.961
12	12	7.40	6.760	1.141	7.30	5.29	1.110
	50	14.20	1.640	1.008	14.20	1.640	1.008
	200	27.90	-21.590	0.973	27.90	-21.590	0.973
	1000	62.20	-131.160	0.936	62.20	-131.160	0.936
15	12	7.40	6.760	1.141	7.40	6.760	1.141
	50	14.40	7.36	1.037	14.20	1.640	1.008
	200	28.10	-10.390	0.987	27.90	-21.590	0.973
	1000	62.40	-106.240	0.973	62.40	-106.240	0.973

table, we can see how for the chosen cases $m^2/4g \sim \Phi^2$, meaning that the minima $\varphi_{\pm} = \pm\sqrt{-M^2/4g}$ of the potential profile $\mathcal{V}[\phi] = m^2\varphi^2/2 + g(\varphi^2 - \Phi^2)^2$ are far from $\pm\Phi$, where the effective potential term, $(2\varphi^2 + \Phi^2)/2(\varphi^2 - \Phi^2)^2$, stemming from the kinetic part of the action (the last term in Eq. (11) proportional to \hbar^2) diverges. As a consequence, CQ will be very similar to AQ, which means that the required bare masses to reach a given renormalized mass in the two cases are very close. Then we measured the renormalized coupling constant g_R defined in Refs. 1, 18 for various values of the bare coupling constant g at a given small value of the lattice spacing $a = 1/N$ (this corresponds to choosing a fixed absolute temperature $k_B T = 1$ and a fixed volume $L^3 = 1$) as already explained for example in Refs. 1, 18. With Na and m_R fixed, as a was made smaller, whatever change we found in $g_R m_R^2$ as a function of g could only be due to the change in a . We generally found that a depression in m_R produced an elevation in the corresponding value of g_R and vice-versa. The results are shown in Fig. 1 for the scaled affine action (AQ case) (11), where, following Freedman *et al.*³ we decided to compress the range of g for display, by choosing the horizontal axis to be $g/(50 + g)$. For comparison we also show in Fig. 2 the results for canonical quantized action (CQ case) which is given by Eq. (11) without the last term proportional to \hbar^2 . The constraint $m_R \approx 3$ was not easy to implement since for each N and g we had to run the simulation several (5–10) times with different values of the bare mass m in order to determine

Kinetic factors in AQ and their role in field theory MC

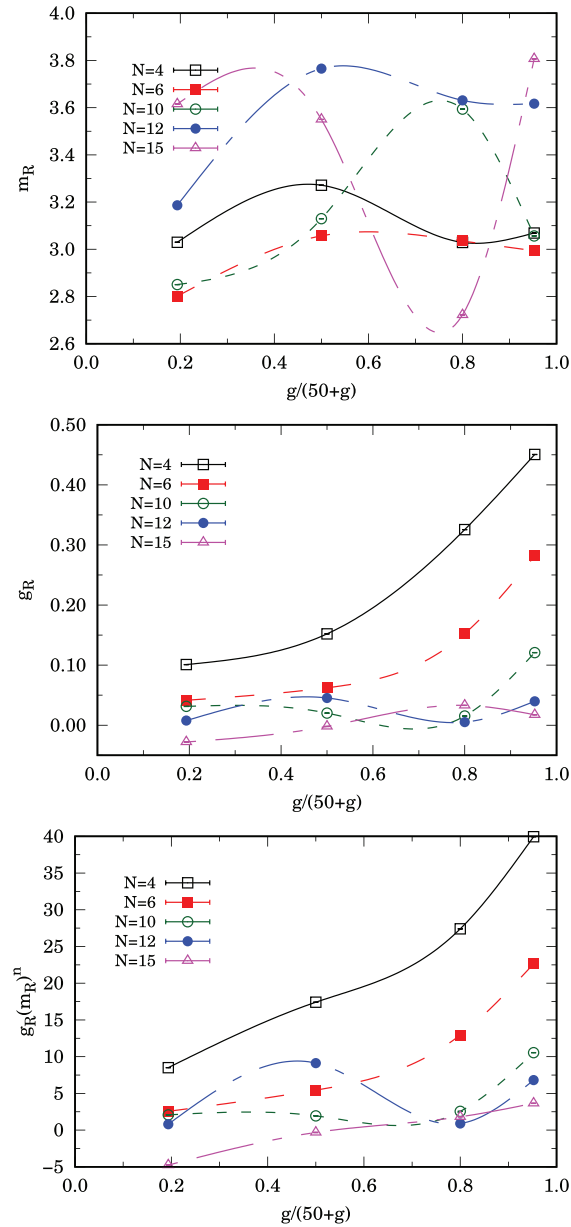


Fig. 1. AQ case. We show the renormalized mass $m_R \approx 3$ (top panel), the renormalized coupling constants g_R (central panel), and $g_R m_R^n$ (bottom panel) for various values of the bare coupling constant g at decreasing values of the lattice spacing $a = 1/N$ ($N \rightarrow \infty$ continuum limit) for the *scaled affine covariant* Euclidean scalar field theory described by the lattice action of Eq. (11) for $n = 3 + 1$ and $\Phi = 1$. The lines connecting the simulation points are just a guide for the eye. The lack of error bars in the data presented is justified by the fact that the errors are dominated not from the statistical ones but rather from the ones due to the adjustments in the bare mass required by the trial and error procedure suggested by Freedman *et al.*³ This error is very hard to be estimated.

R. Fantoni & J. R. Klauder

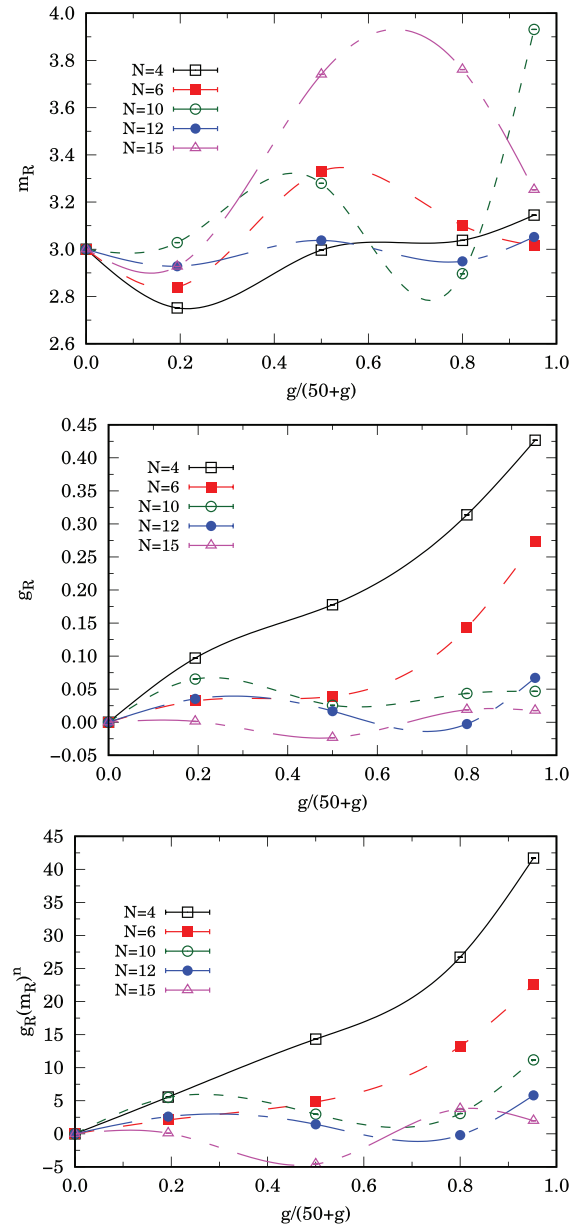


Fig. 2. CQ case. We show the renormalized mass $m_R \approx 3$ (top panel), the renormalized coupling constants g_R (central panel), and $g_R m_R^n$ (bottom panel) for various values of the bare coupling constant g at decreasing values of the lattice spacing $a = 1/N$ ($N \rightarrow \infty$ continuum limit) for the canonical covariant Euclidean scalar field theory described by the lattice action of Eq. (11) without the last term proportional to \hbar^2 , for $n = 3 + 1$ and $\Phi = 1$. The lines connecting the simulation points are just a guide for the eye. The lack of error bars in the data presented is justified by the fact that the errors are dominated not from the statistical ones but rather from the ones due to the adjustments in the bare mass required by the trial and error procedure suggested by Freedman *et al.*³ This error is very hard to be estimated.

the value which would satisfy the constraint $m_R \approx 3$. In our simulations we always used 3×10^7 MC sweeps (where one sweep moves all the N^n field points which took about one week of computer time for the $N = 15$ case). We estimated that it took roughly 10% of each run in order to reach equilibrium from the arbitrarily chosen initial field configuration, for each set of parameters.

As we can see from our figures, the renormalized coupling constant $g_R(m_R)^4$ of the scaled affine version (AQ of Fig. 1) behaves very similarly to the one of the canonical version (CQ of Fig. 2) going toward the continuum limit, taken at fixed volume and temperature, when the ultraviolet cutoff is gradually removed ($Na = 1$ and $N \rightarrow \infty$). The only difference is at $g = 50 - 100$ where in the AQ case the $N = 12$ results for the renormalized coupling fall above the ones for $N = 10$, unlike what happens in the CQ case. Note that for the CQ case the results at $N = 12, 15$ are new, since Freedman *et al.*³ and ourselves¹ only previously studied up to $N = 10$ discretization points.

During our simulations, we kept under control also the vacuum expectation value of the field which is not diverging going toward the continuum limit, like what was happening in Ref. 12 but not in Ref. 19. Choosing the initial configuration with $\varphi = 0$ at all lattice points, when M^2 is not too negative the symmetry $\varphi \rightarrow -\varphi$ is not broken and we find $\langle \varphi \rangle \sim 0$.

We also studied the behavior of the AQ case when choosing a much lower renormalized mass $m_R \sim 1/10$. In this case, the necessary bare mass is such that $m^2/4g \ll \Phi^2$, at all studied values of the bare coupling $g = 12, 50, 200, 1000$. In particular, the potential profile \mathcal{V} becomes a symmetric double well with the two minima, at φ_{\pm} , near the two repulsive spikes localized at $\varphi = \pm\Phi$ and forbidding paths to access the minima of the double well.^c In this case, we found that the paths tend to be very localized just outside of the forbidden region due to the repulsive spikes. As a consequence, we found $g_R \sim 2$ for all N . So in this case, AQ is very different from CQ and the bare masses necessary to reach the same renormalized mass are very different. Note that when $M^2 > 0$ the two repulsive spikes do not forbid the path from sitting at the minimum of the potential profile at $\varphi = 0$ and as a consequence AQ and CQ are very similar. Note also that in the limit $\Phi \rightarrow 0$ the situation is inverted and for m^2 positive, AQ is very different from CQ, whereas for m^2 negative, AQ is very similar to CQ.

7. Conclusions

We studied through path integral MC a plausible kinetic factor in AQ of a scalar covariant Euclidean field theory of mass m subject to a potential energy of the form $g(\varphi^2 - \Phi^2)^2$ in $3 + 1$ space-time dimensions, which is known to suffer from asymptotic freedom in the continuum limit when it is quantized through CQ. This

^cThe case when the classical minima of the potential and the extra spikes in the potential of the affine Hamiltonian are close together has been already studied in several of our previously published papers.^{1, 2, 13, 18, 20}

R. Fantoni & J. R. Klauder

kinetic factor reduces to the usual one previously introduced in Refs. 1, 2, 12, 13, 18, 19 in the limit $\Phi \rightarrow 0$, apart from the multiplicative coefficient. Moreover, its behavior is similar to the one found in the $\Phi \rightarrow 0$ limit in the sense that it gives rise to an additive effective potential term which diverges in a neighborhood of the minima in the potential therefore producing a forbidden region for the field paths exactly where it would naturally sit in a CQ framework. This exclusion of the field path from the minima of the potential renders the AQ version of the field theory asymptotically non-free in the continuum limit.

Our numerical results clearly show how the two field theories obtained through CQ and AQ behave very differently whenever $m^2/4g \ll \Phi^2$. Otherwise they are very similar.

References

1. R. Fantoni and J. R. Klauder, *Phys. Rev. D* **103**, 076013 (2021).
2. R. Fantoni and J. R. Klauder, *Int. J. Mod. Phys. A* **37**, 2250029 (2022).
3. B. Freedman, P. Smolensky and D. Weingarten, *Phys. Lett. B* **113**, 481 (1982).
4. M. Aizenman, *Phys. Rev. Lett.* **47**, 886(E) (1981).
5. J. Fröhlich, *Nucl. Phys. B* **200**, 281 (1982).
6. J. Siefert and U. Wolff, *Phys. Lett. B* **733**, 11 (2014).
7. M. Aizenman and H. Duminil-Copin, *Ann. Math.* **194**, 163 (2021).
8. https://en.wikipedia.org/wiki/Affine_group.
9. J. R. Klauder, *J. High Energy Phys.* **6**, 90 (2020).
10. L. Gouba, *J. High Energy Phys.* **7**, 352 (2021).
11. C. Handy and J. R. Klauder, arXiv:2108.00289.
12. R. Fantoni and J. R. Klauder, *Phys. Rev. D* **104**, 054514.
13. R. Fantoni, *J. Stat. Mech. (submitted)* (2021).
14. D. M. Ceperley, *Rev. Mod. Phys.* **67**, 279 (1995).
15. N. Metropolis, A. W. Rosenbluth, M. N. Rosenbluth, A. M. Teller and E. Teller, *J. Chem. Phys.* **1087**, 21 (1953).
16. M. H. Kalos and P. A. Whitlock, *Monte Carlo Methods* (Wiley-Vch Verlag GmbH & Co., Germany, 2008).
17. R. Fantoni, *Phys. Rev. B* **86**, 144304 (2012), doi:10.1103/PhysRevB.86.144304.
18. R. Fantoni, *J. Stat. Mech.* 083102 (2021).
19. R. Fantoni and J. R. Klauder, *J. Stat. Phys.* **184**, 28 (2021).
20. R. Fantoni and J. R. Klauder, *Phys. Rev. D (submitted)* (2022), arXiv:2203.05988.

Chapter 73

Scaled Affine Quantization of φ_4^4 in the Low Temperature Limit

Fantoni R. and Klauder J. R., Eur. Phys. J. C **82**, 843 (2022)

Title: “Scaled Affine Quantization of φ_4^4 in the Low Temperature Limit”

Abstract: We prove through Monte Carlo analysis that the covariant euclidean scalar field theory, φ_n^r where r denotes the power of the interaction term and $n = s+1$ where s is the spatial dimension and 1 adds imaginary time, such that $r = n = 4$ can be acceptably quantized using scaled affine quantization and the resulting theory is nontrivial and renormalizable even at low temperatures in the highly quantum regime.

Scaled affine quantization of φ_4^4 in the low temperature limitRiccardo Fantoni^{1,a} , John R. Klauder^{2,b}¹ Dipartimento di Fisica, Università di Trieste, Strada Costiera 11, Grignano, 34151 Trieste, Italy² Department of Physics and Department of Mathematics, University of Florida, Gainesville, FL 32611-8440, USAReceived: 18 May 2022 / Accepted: 14 September 2022
© The Author(s) 2022

Abstract We prove through Monte Carlo analysis that the covariant Euclidean scalar field theory, φ_n^r , where r denotes the power of the interaction term and $n = s + 1$ where s is the spatial dimension and 1 adds imaginary time, such that $r = n = 4$ can be acceptably quantized using scaled affine quantization and the resulting theory is nontrivial and renormalizable even at low temperatures in the highly quantum regime.

1 Introduction

The classical limit only imposes a constraint on the quantum theory of a given system so there is no reason why the classical limit should determine the quantum theory uniquely. Accordingly, it is worthwhile to look for alternative quantization recipes, such as affine quantization. We recently showed [1–4] that a covariant Euclidean scalar field quantization, henceforth denoted φ_n^r , where r is the power of the interaction term and $n = s + 1$, where s is the spatial dimension and 1 adds imaginary time, such that $r = 2n/(n - 2)$, e.g., $r = n = 4$, can be acceptably quantized using scaled *affine quantization* (AQ) [5, 6] and the resulting theory is nontrivial, unlike what happens using the usual canonical quantization (CQ) [7–10].¹ In such studies the temperature was kept constant throughout the whole analysis. It is therefore important

¹ In a CQ covariant model the interaction term $g \int \phi(x)^r d^n x$ has a power r/n per integration. This should be compared with the kinetic term $\int [\nabla\phi(x)]^2 d^n x$ which has a power $2/(n - 2)$ per integration. Now, since we work in a finite volume region, if $r/n > 2/(n - 2)$ then the domain where the CQ action is finite $\mathcal{D}_{g>0} \subset \mathcal{D}_{g=0}$ and the domains change because of reducing g back to zero will only retain the smallest version of the domain by continuity, and that will not be the theory you started out with so that the CQ model is trivial. Models for which $r > 2n/(n - 2)$ have been also recently correctly quantized, as for example φ_3^2 [11, 12].

^a e-mail: riccardo.fantoni@posta.istruzione.it (corresponding author)

^b e-mail: klauder@ufl.edu

to study the behavior of the system as we allow temperature to become lower and lower thereby approaching the extreme quantum regime.

The present study will show, through a path integral Monte Carlo (MC) analysis, that as the temperature is lowered the renormalized mass is almost unaffected but the renormalized coupling constant diminishes. Nonetheless at any given temperature, even in the low temperature, strongly quantum, regime, the scaled AQ model appears to be renormalizable showing a non-free behavior in the continuum limit. This success of scaled AQ suggests that for the φ_4^4 field theory the more common CQ should be replaced by the less known AQ.

2 Affine quantization field theory

For a single scalar field, with spacial degrees of freedom $x = (x_1, x_2, \dots, x_s)$, $\varphi(x)$ with canonical momentum $\pi(x)$, the classical affine variables are $\kappa(x) \equiv \pi(x)\varphi(x)$ and $\varphi(x) \neq 0$. The reason we insist that $\varphi(x) \neq 0$ is because if $\varphi(x) = 0$ then $\kappa(x) = 0$ and $\pi(x)$ can not help.

We next introduce the classical Hamiltonian expressed in affine variables. This leads us to

$$\mathcal{H}(\kappa, \varphi) = \int \left\{ \frac{1}{2} [\kappa(x)^2 \varphi(x)^{-2} + (\nabla\varphi(x))^2 + m^2 \varphi(x)^2] + g \varphi(x)^r \right\} d^s x, \quad (1)$$

where r is a positive, even, integer and $g \geq 0$ is the bare coupling constant such that for $g \rightarrow 0$ we fall into the free field theory. With these variables we do not let $\varphi(x) = \infty$ otherwise $\varphi(x)^{-2} = 0$ which is not fair to $\kappa(x)$ and, as we already observed, we must forbid also $\varphi(x) = 0$ which would admit $\varphi(x)^{-2} = \infty$ giving again an undetermined kinetic term. Therefore the AQ bounds $0 < |\varphi(x)| < \infty$ *forbid any nonrenormalizability* which is otherwise possible for CQ [7–10].

The quantum affine operators are the scalar field $\hat{\varphi}(x) = \varphi(x)$ and the dilation operator $\hat{k}(x) = [\hat{\varphi}(x)\hat{\pi}(x) + \hat{\pi}(x)\hat{\varphi}(x)]/2$ where the momentum operator is $\hat{\pi}(x) = -i\hbar\delta/\delta\varphi(x)$. Accordingly for the self adjoint kinetic term $\hat{k}(x)\hat{\varphi}(x)^{-2}\hat{k}(x) = \hat{\pi}(x)^2 + (3/4)\hbar\delta(0)^{2s}\varphi(x)^{-2}$ and one finds for the quantum Hamiltonian operator

$$\hat{H}(\hat{k}, \hat{\varphi}) = \int \left\{ \frac{1}{2}[\hat{\pi}(x)^2 + (\nabla\varphi(x))^2 + m^2\varphi(x)^2] + g\varphi(x)^r + \frac{3}{8}\hbar^2\frac{\delta(0)^{2s}}{\varphi(x)^2} \right\} d^s x. \tag{2}$$

The affine action is found adding time, $x_0 = ct$, where c is the speed of light constant and t is imaginary time, so that $S = \int_0^\beta H dx_0$, with H the semi-classical Hamiltonian corresponding to the one of Eq. (2), will then read

$$S[\varphi] = \int_0^\beta dx_0 \int_{L^s} d^s x \left\{ \frac{1}{2} \left[\sum_{\mu=0}^s \left(\frac{\partial\varphi(x)}{\partial x_\mu} \right)^2 + m^2\varphi(x)^2 \right] + g\varphi(x)^r + \frac{3}{8}\hbar\frac{\delta(0)^{2s}}{\varphi(x)^2} \right\}, \tag{3}$$

where with an abuse of notation we here use x for $(x_0, x_1, x_2, \dots, x_s)$ and $\beta = 1/k_B T$, with k_B the Boltzmann's constant, is the inverse temperature. At low temperatures the quantum effects become more relevant and this is the regime we are interested in this work.

The vacuum expectation value of an observable $\mathcal{O}[\varphi]$ will then be given by the following expression

$$\langle \mathcal{O} \rangle = \frac{\int \mathcal{O}[\varphi] \exp(-S[\varphi]) \mathcal{D}\varphi(x)}{\int \exp(-S[\varphi]) \mathcal{D}\varphi(x)}, \tag{4}$$

where the functional integrals will be calculated on a lattice using the path integral Monte Carlo method as explained further on.

3 Lattice formulation of the field theory

The theory considers a real scalar field φ taking the value $\varphi(x)$ on each site of a periodic n -dimensional lattice, with $n = s + 1$ space-time dimensions, of lattice spacing a , the ultraviolet cutoff, and spacial periodicity $L = Na$ and temporal periodicity $\beta = N_0 a$. The field path is a closed loop on an n -dimensional surface of an $(n + 1)$ -dimensional β -cylinder. We used a lattice formulation of the AQ field theory of Eq. (3) (also studied in Eq. (8) of [1]) using the scaling $\varphi \rightarrow a^{-s/2}\varphi$ and $g \rightarrow a^{s(r-2)/2}g$ which is necessary² to

² Note that from a physical point of view one never has to worry about the mathematical divergence since the lattice spacing will necessarily have a lower bound. For example at an atomic level one will have $a \gtrsim 1\text{\AA}$. In other words the continuum limit will never be a mathematical one.

eliminate the Dirac delta factor $\delta(0) = a^{-1}$ divergent in the continuum limit $a \rightarrow 0$. The affine action for the field (in the primitive approximation [13]) has then the following valid discretization

$$S[\varphi]/a = \frac{1}{2} \left\{ \sum_{x,\mu} a^{-2} [\varphi(x) - \varphi(x + e_\mu)]^2 + m^2 \sum_x \varphi(x)^2 \right\} + \sum_x g \varphi(x)^r + \frac{3}{8} \sum_x \frac{\hbar^2}{\varphi(x)^2}, \tag{5}$$

where e_μ is a vector of length a in the $+\mu$ direction with $\mu = 0, 1, 2, \dots, s$. We will have $S \approx \mathcal{S}$.

In this work we are interested in reaching the continuum limit by taking Na fixed and letting $N \rightarrow \infty$ at fixed volume L^s . The absolute temperature $T = 1/k_B\beta$ is allowed to vary so that the number of discretization points for the imaginary time interval $[0, \beta]$ will be $N_0 = \beta/a$. We are here interested in the $N_0 \gg N$ (or $\beta \gg L$) regime.

3.1 Monte Carlo results

We performed a path integral MC [13–16] calculation for the AQ field theory described by the action of Eq. (5). We calculated the renormalized coupling constant g_R and mass m_R defined in Eqs. (11) and (13) of [1] respectively, measuring them in the path integral MC through vacuum expectation values like in Eq. (4). In particular

$$m_R^2 = \frac{p_0^2 \langle |\tilde{\varphi}(p_0)|^2 \rangle}{\langle \tilde{\varphi}(0)^2 \rangle - \langle |\tilde{\varphi}(p_0)|^2 \rangle}, \tag{6}$$

and at zero momentum

$$g_R = \frac{3\langle \tilde{\varphi}(0)^2 \rangle^2 - \langle \tilde{\varphi}(0)^4 \rangle}{\langle \tilde{\varphi}(0)^2 \rangle^2}, \tag{7}$$

where $\tilde{\varphi}(p) = \int d^n x e^{ip \cdot x} \varphi(x)$ is the Fourier transform of the field and we choose the 4-momentum p_0 with one spacial component equal to $2\pi/Na$ and all other components equal to zero.

In our previous studies [1, 4] we set $L = \beta = 1$. Here we will consider $L = 1$ and $\beta \gg L$ instead. As usual we will impose periodic boundary conditions both in space and in imaginary time. We will use natural units $c = \hbar = k_B = 1$ throughout the whole analysis.

Following Freedman et al. [7], we fix (within 10%) the renormalized mass $m_R \approx 3$, tuning appropriately the bare mass m by trial and error, and we measure the renormalized coupling constant g_R at various values of the bare coupling g . We found that the renormalized mass is almost independent on β . So we chose the same values of m for all the temperatures studied. But the renormalized coupling g_R diminishes as β and/or m increase. It is then convenient to define a

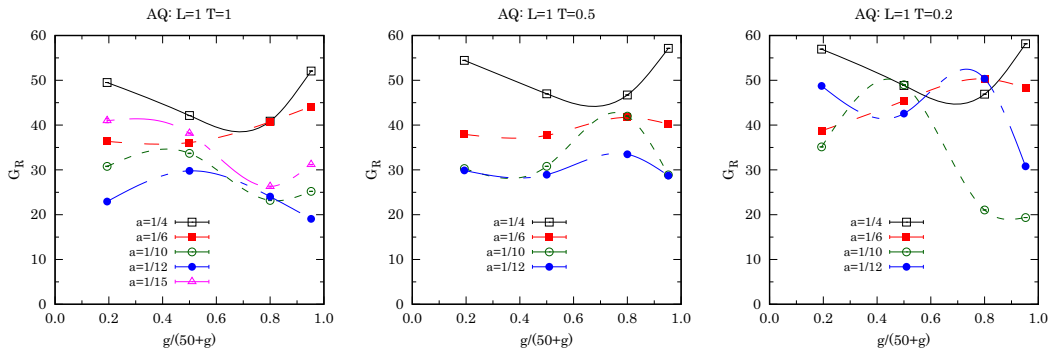


Fig. 1 The left panel is for AQ with $L = 1$ and $T = 1$, The central panel is for AQ with $L = 1$ and $T = 0.5$, and the right panel is for AQ with $L = 1$ and $T = 0.2$. We show the renormalized coupling constant G_R , defined in the text, as a function of $g/(50 + g)$ for decreasing values of the lattice spacing a . The renormalized mass was kept fixed to $m_R \approx 3$ (within 10%) in all cases. The statistical errors

in the Monte Carlo were in all cases smaller than the symbols used. The main source of uncertainty is nonetheless the indirect one stemming from the unavoidable difficulty of keeping the renormalized mass constant throughout all cases. The lines connecting the points are just a guide for the eye

second renormalized coupling constant which is less dependent on β, L , and m . Following Freedman et al. [7] we set $G_R = g_{RM}^n L^3 \beta$.

We chose two low temperatures (the case $T = 1$ had already been studied in Ref. [4]), namely an intermediate one $T = 0.5$ and an extreme one $T = 0.2$. In each case we study the continuum limit by choosing decreasing values of a , namely $a = 1/4, 1/6, 1/10, 1/12$ and $1/15$ corresponding respectively to $N_0 = 1/Ta = 8, 12, 20, 24, 30$ for $T = 0.5$ and to $N_0 = 20, 30, 50, 60, 75$ for $T = 0.2$. In each run we used 3×10^7 MC steps, where one step consists in $N^s N_0$ Metropolis [14] configuration moves of each field component, reaching equilibrium after 10% of the largest a run to 50% of the smallest a run. In our simulations we used block averages and estimated the statistical errors using the jakknife method (described in Section 3.6 of [17]) to take into account of the correlation time. It took roughly 25 days of computer time for the $T = 0.2, a = 1/12$ run to complete. In Fig. 1 we show the numerical results.

From the figure we can see how at all temperatures and all bare coupling constants G_R tends to stay far from zero as we approach the continuum limit $a \rightarrow 0$. Moreover, with respect to the case $T = 1$, already studied in Ref. [4], where the value for G_R tends to revert its trend to decrease for a decrease of the lattice spacing only for an ultraviolet cutoff as small as $a = 1/15$, now we find that at $T = 0.5$ this inversion happens already for $a = 1/10$ at least at intermediate bare coupling and at $T = 0.2$ already for $a = 1/6$. This had to be expected on general grounds because it is impossible to distinguish time from the other spacial components just by looking at the action expression (5) and the $T = 1, a = 1/15$ case has a total of $15^4 = 50625$ lattice points which is very close to

the total lattice points of the case $T = 0.2, a = 1/10$ which are $10^3 \cdot 50 = 50000$. We are just choosing an hyperrectangle instead of an hypercube periodic lattice. Nonetheless there is a strong indication that our scaled AQ model is indeed non-free in the continuum thus resulting renormalizable, unlike the corresponding CQ model.³ And the more so at lower temperatures. We can therefore infer that the same should continue to hold also in the $T \rightarrow 0$, ground state, limit.

4 Conclusions

In conclusion we studied the renormalizability property of one real scalar covariant Euclidean field quantized through scaled affine quantization (AQ) with the path integral Monte Carlo method on a lattice permeating the whole spacetime. We therefore used periodic spacial boundary conditions at finite unit volume to simulate an infinite volume system and in measuring the renormalized mass and coupling constant of the model we also enforced periodic temporal boundary conditions which are necessary in order to determine the required vacuum expectation values. The periodicity on the imaginary time, i.e. the inverse temperature $\beta = 1/T$, was chosen at increasing values equal to 1, 2, 5. Keeping fixed the renormalized mass, our numerical results for the renor-

³ For a comparison with the corresponding scaled CQ results see Ref. [18] and for the unscaled CQ ones see Ref. [1].

malized coupling constant showed how this has a non monotonically decreasing behavior with respect to a decreasing lattice spacing. This remains true even at low temperature thus proving the renormalizability of the model even when the temperature is lowered in the extreme quantum regime. We therefore suspect that the non triviality still holds for the ground state.

On general grounds we should accept affine quantization as a way to remove infinities, which are mathematical but not physical, from the field theory. In fact just by looking at the kinetic term in Eq. (1) we can say that if φ is allowed to become infinity (or zero) then κ cannot help. If κ becomes infinite then φ cannot help. $\kappa = 0$ is allowed so that $\pi = 0$. When π and φ were alone, as in the canonical quantization picture, they could allow mathematical infinities. In a physical (or Monte Carlo) measure of an observable there is no space for mathematical infinities.

For the Higgs sector of the Standard Model, the low energy properties are very specific and, so far, observation confirms that they are well described by canonical φ^4 . It is certainly true that canonical quantization (CQ) of φ^4 does not reach down to distances of the order of the Planck length – in that realm, anyway, gravity cannot be dealt with classically – so affine quantization (AQ) may be used to solve this problem.

Data Availability Statement This manuscript has no associated data or the data will not be deposited. [Authors' comment: No data will be deposited because it can be extracted directly from our Figures.]

Open Access This article is licensed under a Creative Commons Attribution 4.0 International License, which permits use, sharing, adaptation, distribution and reproduction in any medium or format, as long as you give appropriate credit to the original author(s) and the source, provide a link to the Creative Commons licence, and indicate if changes were made. The images or other third party material in this article are included in the article's Creative Commons licence, unless indicated otherwise in a credit line to the material. If material is not included in the article's Creative Commons licence and your intended use is not permitted by statutory regulation or exceeds the permitted use, you will need to obtain permission directly from the copyright holder. To view a copy of this licence, visit <http://creativecommons.org/licenses/by/4.0/>.

Funded by SCOAP³. SCOAP³ supports the goals of the International Year of Basic Sciences for Sustainable Development.

References

1. R. Fantoni, J.R. Klauder, Affine quantization of $(\varphi^4)_4$ succeeds while canonical quantization fails. *Phys. Rev. D* **103**, 076013 (2021)
2. R. Fantoni, J.R. Klauder, Monte Carlo evaluation of the continuum limit of the two-point function of the Euclidean free real scalar field subject to affine quantization. *J. Stat. Phys.* **184**, 28 (2021)
3. R. Fantoni, J.R. Klauder, Monte Carlo evaluation of the continuum limit of the two-point function of two Euclidean Higgs real scalar field subject to affine quantization. *Phys. Rev. D* **104**, 054514 (2021)
4. R. Fantoni, J. R. Klauder, Eliminating nonrenormalizability helps prove scaled affine quantization of φ_4^4 is nontrivial. *Int. J. Mod. Phys. A* **37**, 2250029 (2022)
5. J.R. Klauder, *Beyond Conventional Quantization*, chap. 5 (Cambridge University Press, Cambridge, 2000)
6. J.R. Klauder, The benefits of affine quantization. *J. High Energy Phys. Gravit. Cosmol.* **6**, 175 (2020)
7. B. Freedman, P. Smolensky, D. Weingarten, Monte Carlo evaluation of the continuum limit of ϕ_4^4 and ϕ_3^4 . *Phys. Lett.* **113B**, 481 (1982)
8. M. Aizenman, Proof of the triviality of ϕ_d^4 field theory and some mean-field features of Ising models for $d > 4$. *Phys. Rev. Lett.* **47**, 886(E) (1981)
9. J. Fröhlich, On the triviality of $\lambda\phi_d^4$ theories and the approach to the critical point in $d \geq 4$ dimensions. *Nucl. Phys. B* **200**, 281 (1982)
10. J. Siefert, U. Wolff, Triviality of φ^4 theory in a finite volume scheme adapted to the broken phase. *Phys. Lett. B* **733**, 11 (2014)
11. R. Fantoni, Monte Carlo evaluation of the continuum limit of $(\phi^{12})_3$. *J. Stat. Mech.* 083102 (2021)
12. R. Fantoni, Scaled affine quantization of φ_3^{12} is nontrivial. *Int. J. Mod. Phys. A* (submitted) (2022)
13. D.M. Ceperley, *Rev. Mod. Phys.* **67**, 279 (1995)
14. N. Metropolis, A.W. Rosenbluth, M.N. Rosenbluth, A.M. Teller, E. Teller, Equation of state calculations by fast computing machines. *J. Chem. Phys.* **1087**, 21 (1953)
15. M.H. Kalos, P.A. Whitlock, *Monte Carlo Methods* (Wiley-VCH Verlag GmbH & Co., Weinheim, 2008)
16. R. Fantoni, Localization of acoustic polarons at low temperatures: a path integral Monte Carlo approach. *Phys. Rev. B* **86**, 144304 (2012). <https://doi.org/10.1103/PhysRevB.86.144304>
17. W. Janke, Statistical analysis of simulations: data correlations and error estimation, in *Quantum Simulations of Complex Many-Body Systems: From Theory to Algorithms*, NIC Series, vol. 10, ed. by J. Grotendorst, D. Marx, A. Muramatsu (John von Neumann Institute for Computing, Jülich, 2002), pp. 423–445. ISBN:3-00-009057-6
18. R. Fantoni, J. R. Klauder, Kinetic factors in affine quantization and their role in field theory Monte Carlo. *Int. J. Mod. Phys. A* **37**, 2250094 (2022)

Chapter 74

Scaled Affine Quantization of Ultralocal φ_2^4 a comparative Path Integral Monte Carlo study with scaled Canonical Quantization

Fantoni R. and Klauder J. R., Phys. Rev. D **106**, 114508 (2022)

Title: “Scaled Affine Quantization of Ultralocal φ_2^4 a comparative Path Integral Monte Carlo study with scaled Canonical Quantization”

Abstract: After the success of affine quantization in proving through Monte Carlo analysis that the covariant euclidean scalar field theory, φ_n^r , where r denotes the power of the interaction term and $n = s + 1$ with s the spatial dimension and 1 adds imaginary time, such that $r \geq 2n/(n - 2)$ can be acceptably quantized and the resulting theory is nontrivial, unlike what happens using canonical quantization, we show here that the same has to be expected for $r > 2$ and any n even for the ultralocal field theory. In particular we consider the ultralocal φ_2^4 model and study its renormalized properties for both the scaled canonical quantization version and the scaled affine quantization version through path integral Monte Carlo.

Scaled affine quantization of ultralocal φ_2^4 a comparative path integral Monte Carlo study with scaled canonical quantization

Riccardo Fantoni^{1,*} and John R. Klauder^{2,†}

¹*Dipartimento di Fisica, Università di Trieste, strada Costiera 11, 34151 Grignano (Trieste), Italy*

²*Department of Physics and Department of Mathematics, University of Florida, Gainesville, Florida 32611-8440, USA*

 (Received 30 November 2022; accepted 6 December 2022; published 23 December 2022)

After the success of affine quantization in proving through Monte Carlo analysis that the covariant euclidean scalar field theory, φ_n^r , where r denotes the power of the interaction term and $n = s + 1$ with s the spatial dimension and 1 adds imaginary time, such that $r \geq 2n/(n - 2)$ can be acceptably quantized and the resulting theory is nontrivial, unlike what happens using canonical quantization, we show here that the same has to be expected for $r > 2$ and any n even for the ultralocal field theory. In particular we consider the ultralocal φ_2^4 model and study its renormalized properties for both the scaled canonical quantization version and the scaled affine quantization version through path integral Monte Carlo.

DOI: 10.1103/PhysRevD.106.114508

I. INTRODUCTION

Ultralocal euclidean scalar field quantization, henceforth denoted φ_n^r , where r is the power of the interaction term and $n = s + 1$ where s is the spatial dimension and 1 adds imaginary time, such that $r < 2$ can be treated by canonical quantization (CQ), while models such that $r > 2$ and any $n \geq 2$ are trivial [1–5]. However, there exists a different approach called *affine quantization* (AQ) [1,6,7] that promotes a different set of classical variables to become the basic quantum operators and it offers different results, such as models for which $r > 2$. In particular one can show that while the Fubini-Study metric for the canonical coherent states that evaluates the distance-squared between two infinitesimally close ray vectors (minimized over any simple phase) leads to a *flat space* that already involves Cartesian coordinates, in the affine case the Fubini-Study metric describes a *Poincaré half plane* [7,8], has a constant negative curvature [9], and is geodesically complete. Unlike a flat plane, or a constant positive curvature surface (which holds the metric of three-dimensional spin coherent states), a space of constant negative curvature can not be visualized in a three-dimensional flat space. At every point in this space the negative curvature appears like a saddle having an

“up curve” in the direction of the rider’s chest and a “down curve” in the direction of the rider’s legs.¹

In the present work we show, with the aid of a path integral Monte Carlo (PIMC) analysis, that $r = 4$ and $n = 2$ can be acceptably quantized using scaled affine quantization which had been previously successfully used for the covariant case [12–19]

Being the current study in a lower, therefore unphysical, spacial dimension it nonetheless allowed us to get closer to the continuum limit than it was feasible for the physically relevant four-dimensional case on the computer due to the rapid increase of necessary lattice points as dimensionality is increased. Therefore, this work can indirectly give us a better understanding of the physically relevant case which had been already preliminarily studied by us in its covariant version [13]. Interestingly, the triviality of the scaling limits of the canonical Ising and covariant self-interacting scalar field models in four dimensions has been rigorously demonstrated recently [20].

II. A COMPARISON BETWEEN CANONICAL QUANTIZATION AND AFFINE QUANTIZATION FOR ULTRALOCAL FIELDS

A. Canonical quantization of scalar fields

Let us begin with the classical Hamiltonian for a single ultralocal field $\varphi(x)$

$$H(\pi, \varphi) = \int \left\{ \frac{1}{2} [\pi(x)^2 + m^2 \varphi(x)^2] + g |\varphi(x)|^r \right\} d^s x, \quad (1)$$

¹Of course other types of more complex quantizations may still be possible which involve nonconstant curvature surfaces [10,11].

*riccardo.fantoni@posta.istruzione.it
†klauder@ufl.edu

Published by the American Physical Society under the terms of the Creative Commons Attribution 4.0 International license. Further distribution of this work must maintain attribution to the author(s) and the published article’s title, journal citation, and DOI. Funded by SCOAP³.

RICCARDO FANTONI and JOHN R. KLAUDER

PHYS. REV. D **106**, 114508 (2022)

where $n = s + 1$ is the number of spacetime variables, and r is any real number. When g is zero, the remaining expression involves a domain in which a full set of variables, i.e., $\pi(x)$ and $\varphi(x)$, lead to a finite Hamiltonian value. If $g = 0 \rightarrow g > 0$, there are two possible results. If $r < 2$, then the domain remains the same. However, if $r > 2$, then there is a new domain that is smaller than the original domain because the interaction term $\int |\varphi(x)|^r d^s x = \infty$ leads to a reduction of certain fields. Since we work in a finite volume region, the fields that cause that divergence are not $\varphi(x) = \infty$, because that would have eliminated the original domain when $g = 0$. The only way for $\int |\varphi(x)|^r d^s x = \infty$ is, for example, given by $\varphi(x) = 1/|x - c|^k$ where k is small enough so that $\int \varphi(x)^2 d^s x < \infty$, while $r > 2$ is big enough so that $\int |\varphi(x)|^r d^s x = \infty$ for example for $r = 5/2$. Such behavior leads to immediate results in perturbation infinities in a power series of g , leading to a nonrenormalizable process, for which quantum efforts, using canonical quantization, collapse to “free” results, despite that $g > 0$, as all that is continuously connected to the original free theory where $g = 0$. Here we should be more precise since the relevant quantity to look at is the action rather than the Hamiltonian, so we should really compare the interaction term $\int |\varphi(x)|^r d^n x$ and the kinetic term $\int [\partial\varphi(x)/\partial x_0]^2 d^n x$ or the mass term $\int \varphi(x)^2 d^n x$. If we consider stationary fields as particular cases then the relevant integral is the mass term and we immediately see that we may have triviality for $r > 2$. But the same remains true also for space independent fields.² As we will see in Sec. IV, our numerical results give evidence for a “free” behavior of the CQ theory in this case.

Having seen what CQ can show us, now let us turn to AQ.

B. Affine quantization of scalar fields

The classical affine variables are the *dilation* $\kappa(x) \equiv \pi(x)\varphi(x)$ and the field $\varphi(x) \neq 0$. The reason we insist that $\varphi(x) \neq 0$ is because if $\varphi(x) = 0$ and $\kappa(x) = 0$ then $\pi(x)$ is not well-defined.

²If we consider $\varphi(x) = 1/|x_0 - c|^k$ then in order to have $\mathcal{D}_{g>0} \subset \mathcal{D}_{g=0}$, where \mathcal{D}_g is the domain of those $\varphi(x)$, in the ultralocal theory, where the action is not divergent, we require a divergent interaction term but a convergent kinetic term or $rk > 1 > 2(k+1)$ that is possible if $r > -2$. Additionally, since we always want a convergent mass term we must also have $0 < k < 1/2$ which again requires $r > 2$ for triviality. This means that for $r > 2$ the domains change because of reducing g back to zero will only retain the smallest version of the domain by continuity, and that will not be the theory you started out with. For space independent fields the ultralocal theory is the same as the covariant theory which is trivial for $r > 2n/(n-2) > 2$. This is due to the fact that $\mathcal{D}_g^{\text{covariant}} \neq \mathcal{D}_g^{\text{ultralocal}}$.

We next introduce the same classical Hamiltonian we chose before now expressed in affine variables. This leads us to

$$H'(k, \varphi) = \int \left\{ \frac{1}{2} [k(x)^2 \varphi(x)^{-2} + m^2 \varphi(x)^2] + g |\varphi(x)|^r \right\} d^s x, \quad (2)$$

in which $\varphi(x) \neq 0$ is an important fact. With these variables we see that $\pi = k/\varphi$ so we should not let neither $\varphi = 0$ nor $\varphi = \pm\infty$ otherwise in either cases we could find a form of indecision ($0/0$ or ∞/∞) for the dilation k which would then be not well defined. The essential result $0 < |\varphi(x)| < \infty$, leads to the fact that these AQ bounds on $\varphi(x)$ forbid any nonrenormalizability, a ‘disease’ which plagues the CQ analysis. With AQ, this new insight implies that any model φ_n^r does not become a “free” result, but leads to an appropriate “nonfree” result.

What follows in the coming sections is additional PIMC studies using AQ and CQ procedures.

III. LATTICE FORMULATION OF THE FIELD THEORY

The quantum affine operators are the scalar field $\hat{\varphi}(x) = \varphi(x)$ and the *dilation* operator³ $\hat{\kappa}(x) = [\hat{\varphi}(x)\hat{\pi}(x) + \hat{\pi}(x)\hat{\varphi}(x)]/2$ where the momentum operator is $\hat{\pi}(x) = -i\hbar\delta/\delta\varphi(x)$. Accordingly for the self-adjoint kinetic term $\hat{\kappa}(x)\hat{\varphi}(x)^{-2}\hat{\kappa}(x) = \hat{\pi}(x)^2 + (3/4)\hbar\delta(0)^{2s}\varphi(x)^{-2}$ and one finds for the quantum Hamiltonian operator

$$\hat{H}'(\hat{\kappa}, \hat{\varphi}) = \int \left\{ \frac{1}{2} [\hat{\pi}(x)^2 + m^2 \varphi(x)^2] + g |\varphi(x)|^r + \frac{3}{8} \hbar^2 \frac{\delta(0)^{2s}}{\varphi(x)^2} \right\} d^s x. \quad (3)$$

As in previous works [16,17,19] we use the scaling $\pi \rightarrow a^{-s/2}\pi, \varphi \rightarrow a^{-s/2}\varphi, g \rightarrow a^{s(r-2)/2}g$, which is necessary⁴ to eliminate the Dirac delta factor $\delta(0) = a^{-1}$ divergent in the continuum limit $a \rightarrow 0$. Of course for $r > 2$ the rescaled coupling constant, g , vanishes in the continuum limit since $a \rightarrow 0$, therefore we expect no difference between the interacting and the free model in such a limit. The theory considers a real scalar field φ taking the value $\varphi(x)$ on each site of a periodic, hypercubic, n -dimensional

³Since $\varphi(x) \neq 0$, that means $\pi^\dagger \neq \pi$ so, to make that clear we should say that $\hat{\kappa}(x) \equiv [\hat{\varphi}(x)\hat{\pi}(x) + \hat{\pi}^\dagger(x)\hat{\varphi}(x)]/2$ to make sure that $\hat{\kappa}^\dagger = \hat{\kappa}$. But $\hat{\pi}^\dagger\hat{\varphi} = \hat{\pi}\hat{\varphi}$ because in that case $\hat{\pi}^\dagger$ acts like $\hat{\pi}$ thanks to having $\hat{\pi}$ acting on $\hat{\varphi}$.

⁴Note that from a physical point of view one never has to worry about the mathematical divergence since the lattice spacing will necessarily have a lower bound. For example at an atomic level one will have $a \gtrsim 1 \text{ \AA}$. In other words the continuum limit will never be a mathematical one.

lattice of lattice spacing a , our ultraviolet cutoff, and periodicity $L = Na$. The affine action for the field, $S' = \int \overline{H} dx_0$ (with $x_0 = ct$ where c is the speed of light constant and t is imaginary time), with \overline{H} the semiclassical Hamiltonian corresponding to the one of Eq. (3), is then approximated by

$$S'[\varphi]/a \approx \frac{1}{2} \left\{ \sum_x a^{-2} [\varphi(x) - \varphi(x + e_0)]^2 + m^2 \sum_x \varphi(x)^2 \right\} + \sum_x g |\varphi(x)|^r + \frac{3}{8} \sum_x \hbar^2 \frac{1}{\varphi(x)^2}, \quad (4)$$

where e_μ is a vector of length a in the $+\mu$ direction. Respect to the previously considered covariant case [12–19], being now absent derivatives with respect to space, the field is allowed to be discontinuous in space (but will still be continuous in time).

The corresponding canonical action, $S = \int \tilde{H} dx_0$, is then approximated by

$$S[\varphi]/a \approx \frac{1}{2} \left\{ \sum_x a^{-2} [\varphi(x) - \varphi(x + e_0)]^2 + m^2 \sum_x \varphi(x)^2 \right\} + \sum_x g |\varphi(x)|^r. \quad (5)$$

In this work we are interested in reaching the continuum limit by taking Na fixed and letting $N \rightarrow \infty$ at fixed volume L^s and absolute temperature $T = 1/k_B L$ with k_B the Boltzmann's constant.

The vacuum expectation value of an observable $\mathcal{O}[\varphi]$ will then be given by the following expression

$$\langle \mathcal{O} \rangle = \frac{\int \mathcal{O}[\varphi] \exp(-S[\varphi]) \mathcal{D}\varphi(x)}{\int \exp(-S[\varphi]) \mathcal{D}\varphi(x)}, \quad (6)$$

where the functional integrals will be calculated on a lattice using the path integral Monte Carlo method as explained further on.

IV. PATH INTEGRAL MONTE CARLO SIMULATION

We performed PIMC [21–24] for the action of Eq. (4) with $r = 4$ and $n = 2$. In particular we calculated the renormalized coupling constant g_R and mass m_R defined in Eqs. (11) and (13) of [13] respectively, measuring them in the path integral MC through vacuum expectation values like in Eq. (6). In particular $m_R^2 = p_0^2 \langle |\tilde{\varphi}(p_0)|^2 \rangle / \langle \tilde{\varphi}(0)^2 \rangle - \langle |\tilde{\varphi}(p_0)|^2 \rangle$ and at zero momentum $g_R = [3 \langle \tilde{\varphi}(0)^2 \rangle^2 - \langle \tilde{\varphi}(0)^4 \rangle] / \langle \tilde{\varphi}(0)^2 \rangle^2$, where $\tilde{\varphi}(p) = \int d^n x e^{ip \cdot x} \varphi(x)$ is the Fourier transform of the field and we choose the 2-momentum p_0 with the zero component equal to $2\pi/Na$ and the other component equal to zero. Since the integration variables in Eq. (6) are N^n , being able to choose

$n = 2$ allowed us to greatly speed up the calculations compared to our previous covariant studies for $n > 2$ [12–19] and this made possible to push ourselves closer to the continuum limit, to bigger N .

Following Freedman *et al.* [2], for each N and g , we adjusted the bare mass m in such a way to maintain the renormalized mass approximately constant, $m_R \approx 3$, to within a few percent (in all cases less than 20%), and we measured the renormalized coupling constant g_R for various values of the bare coupling constant g at a given small value of the lattice spacing $a = 1/N$ (this corresponds to choosing an absolute temperature $k_B T = 1$ and a fixed length $L = 1$). Note that in the CQ case it was necessary to choose imaginary bare masses for $g > 0$. With Na and m_R fixed, as a was made smaller, whatever change we found in $g_R m_R^n$ as a function of g could only be due to the change in a . We generally found that a depression in m_R produced an elevation in the corresponding value of g_R and viceversa; for this reason it is convenient to define an alternative renormalized coupling constant less sensitive to small variations of m_R , namely $g_R(m_R)^n$ (see Ref. [2]). The results are shown in Fig. 1 for the scaled canonical action (5) and the scaled affine action (4) in natural units $c = \hbar = k_B = 1$, where, following Freedman *et al.* [2] we decided to compress the range of g for display, by choosing the horizontal axis to be $g/(50 + g)$. The constraint $m_R \approx 3$ was not easy to implement since for each N and g we had to run the simulation several times with different values of the bare mass m in order to determine the value which would satisfy the constraint $m_R \approx 3$. This was the main source of uncontrolled uncertainty in the data.

In our simulations we used 10^8 MC steps where in each step we attempt to move once all the N^n fields variables of integration through the Metropolis algorithm [21]. We used block averages and estimated the statistical errors using the jackknife method (described in Sec. 3.6 of [25]) to take into account of the correlation time of the simulations. We always adjusted the field displacement in the random walk so to keep the acceptance ratios as close as possible to 1/2.

Comparing the results for the scaled canonical and affine action we can see how the renormalized coupling constant of the two approaches behaves very similarly at $g \neq 0$,⁵ but in a neighborhood of $g = 0$ the affine version remains far from zero in the continuum limit when the ultraviolet cutoff is removed ($Na = 1$ and $N \rightarrow \infty$). The decrease of the renormalized coupling g_R for increasing N has to be expected, both for the CQ and the AQ cases, due to the use we made of the scaling $g \rightarrow a^{s(r-2)/2} g$ which makes the model a “free” one in the continuum limit, $a \rightarrow 0$, when $r > 2$. Of course the scaling we used has just a mathematical

⁵Comparing with the previous covariant studies [12–19] we can now say that removing the gradient term leads to a wilder behavior of the paths which could complicate finding any difference between CQ and AQ.

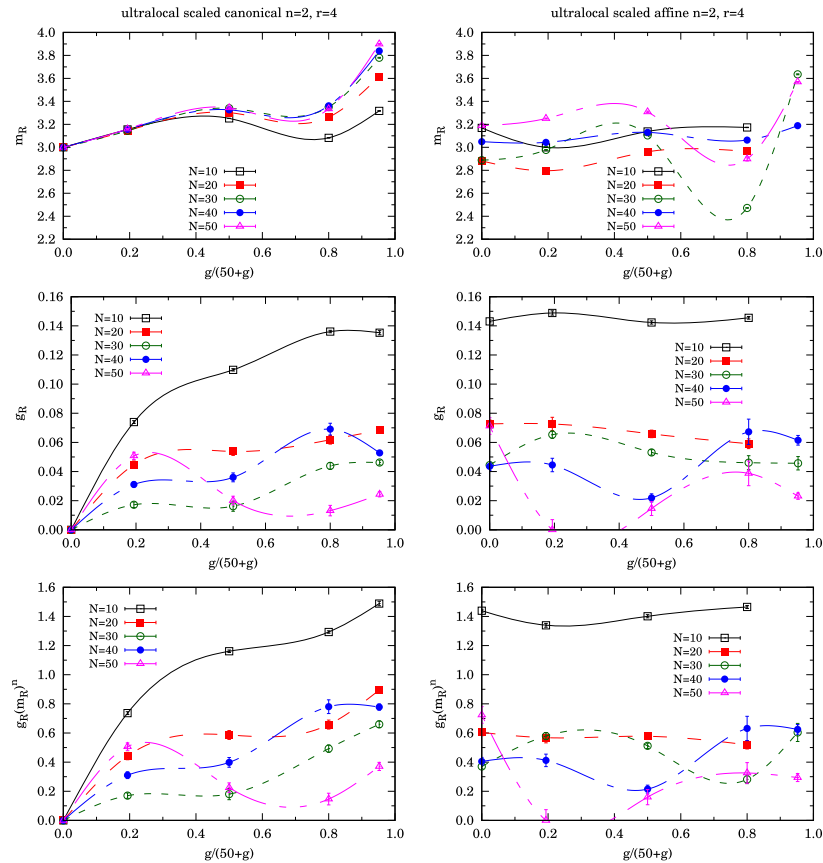


FIG. 1. For the scaled *canonical* (left panels) and scaled *affine* (right panels) φ_2^4 ultralocal euclidean scalar field theory, we show the renormalized mass m_R (top panels), the renormalized coupling constants g_R (central panels), and $g_R m_R^n$ (bottom panels) for various values of the bare coupling constant g at decreasing values of the lattice spacing $a = 1/N$ ($N \rightarrow \infty$ continuum limit). The statistical errors in the Monte Carlo were smaller than the symbols used. The main source of uncertainty is nonetheless the indirect one stemming from the unavoidable difficulty of keeping the renormalized mass constant throughout all cases. The lines connecting the simulation points are just a guide for the eye.

and not a physical justification (see footnote 4). In particular the scaling permits to have nondiverging field expectation values in the AQ approach. Therefore, as already observed in several previous covariant studies [12–15,18], we expect that also in this ultralocal case the AQ approach gives rise to a “nonfree” field theory contrary to what happens for the CQ approach for $r > 2$. This success of affine quantization to produce a well-defined, renormalizable, nontrivial, “non-free” quantum field theory is one of its merits and benefits.

During our simulations we kept under control also the vacuum expectation value of the field which in all cases was found to vanish in agreement with the fact that the symmetry $\varphi \rightarrow -\varphi$ of the scaled canonical action is

preserved in the scaled affine case. The random walk in the field is always able to tunnel through the barrier at $\varphi = 0$ due to the affine effective term, $\frac{3}{8}(\hbar/\varphi)^2$, in the interaction. This is a consequence of working at finite N and we expect the symmetry to be spontaneously broken in the continuum $N \rightarrow \infty$ limit⁶ when the point at $\varphi = 0$ is excluded. Our results also show how the sum rules $g_R \rightarrow 0$ and $m_R \rightarrow m$ for $g \rightarrow 0$ are satisfied for CQ as it should for any gaussian weighting factor $\exp(-S[\varphi])$ for any N .

⁶Once again this is only possible in a mathematical world but not in the physical (see footnote 4).

V. CONCLUSIONS

In conclusion we performed a path integral Monte Carlo study of the properties (mass and coupling constant) of the renormalized ultralocal euclidean scalar field theory φ_2^4 quantized through scaled affine and canonical quantization. Our results confirm the theoretical expectation for a “free” theory in the continuum limit. This is merely a consequence of the chosen scaling. As in previous works on covariant theories we expect that also in this ultralocal case the un-scaled AQ approach gives rise to a “nonfree”

field theory contrary to what happens for the unscaled CQ approach for $r > 2$. Indeed already for the scaled version in the AQ theory the renormalized coupling does not seem to go towards zero at least when the bare coupling is zero when one approaches the continuum limit, as stems from our path integral Monte Carlo results. This means that a “free” scaled AQ theory is profoundly different from a “free” scaled CQ one; the former is therefore nontrivial and renormalizable and the latter is trivial and nonrenormalizable.

- [1] J. R. Klauder, An ultralocal classical and quantum gravity theory, *J. High Energy Phys., Gravitat. Cosmol.* **06**, 656 (2020).
- [2] B. Freedman, P. Smolensky, and D. Weingarten, Monte carlo evaluation of the continuum limit of ϕ_4^4 and ϕ_3^4 , *Phys. Lett.* **113B**, 481 (1982).
- [3] M. Aizenman, Proof of the Triviality of ϕ_d^4 Field Theory and Some Mean-Field Features of Ising Models for $d > 4$, *Phys. Rev. Lett.* **47**, 886 (1981).
- [4] J. Fröhlich, On the triviality of $\lambda\phi_d^4$ theories and the approach to the critical point in $d \geq 4$ dimensions, *Nucl. Phys.* **B200**, 281 (1982).
- [5] J. Siefert and U. Wolff, Triviality of φ^4 theory in a finite volume scheme adapted to the broken phase, *Phys. Lett. B* **733**, 11 (2014).
- [6] J. R. Klauder, *Beyond Conventional Quantization* (Cambridge University Press, Cambridge, England, 2000), Chap. 5.
- [7] J. R. Klauder, The benefits of affine quantization, *J. High Energy Phys., Gravit. Cosmol.* **06**, 175 (2020).
- [8] J. R. Klauder, Quantum gravity made easy, *J. High Energy Phys., Gravitat. Cosmol.* **06**, 90 (2020).
- [9] R. Fantoni, B. Jancovici, and G. Téllez, Pressures for a one-component plasma on a pseudosphere, *J. Stat. Phys.* **112**, 27 (2003).
- [10] R. Fantoni and G. Téllez, Two dimensional one-component plasma on a Flamm’s paraboloid, *J. Stat. Phys.* **133**, 449 (2008).
- [11] R. Fantoni, Plasma living in a curved surface at some special temperature, *Physica (Amsterdam)* **177A**, 524 (2019).
- [12] R. Fantoni, Monte Carlo evaluation of the continuum limit of $(\phi^{12})_3$, *J. Stat. Mech.* (2021) 083102.
- [13] R. Fantoni and J. R. Klauder, Affine quantization of $(\varphi^4)_4$ succeeds while canonical quantization fails, *Phys. Rev. D* **103**, 076013 (2021).
- [14] R. Fantoni and J. R. Klauder, Monte Carlo evaluation of the continuum limit of the two-point function of the Euclidean free real scalar field subject to affine quantization, *J. Stat. Phys.* **184**, 28 (2021).
- [15] R. Fantoni and J. R. Klauder, Monte Carlo evaluation of the continuum limit of the two-point function of two Euclidean Higgs real scalar field subject to affine quantization, *Phys. Rev. D* **104**, 054514 (2021).
- [16] R. Fantoni and J. R. Klauder, Eliminating nonrenormalizability helps prove scaled affine quantization of φ_4^4 is nontrivial, *Int. J. Mod. Phys. A* **37**, 2250029 (2022).
- [17] R. Fantoni, Scaled affine quantization of φ_3^{12} is nontrivial (to be published).
- [18] R. Fantoni and J. R. Klauder, Kinetic factors in affine quantization and their role in field theory Monte Carlo, *Int. J. Mod. Phys. A* **37**, 2250094 (2022).
- [19] R. Fantoni and J. R. Klauder, Scaled affine quantization of φ_4^4 in the low temperature limit, *Eur. Phys. J. C* **82**, 843 (2022).
- [20] M. Aizenman and H. Duminil-Copin, Marginal triviality of the scaling limits of critical 4D Ising and ϕ_4^4 models, *Ann. Math.* **194**, 163 (2021).
- [21] N. Metropolis, A. W. Rosenbluth, M. N. Rosenbluth, A. M. Teller, and E. Teller, Equation of state calculations by fast computing machines, *J. Chem. Phys.* **1087**, 21 (1953).
- [22] M. H. Kalos and P. A. Whitlock, *Monte Carlo Methods* (Wiley-Vch Verlag GmbH & Co., Germany, 2008).
- [23] D. M. Ceperley, Path integrals in the theory of condensed helium, *Rev. Mod. Phys.* **67**, 279 (1995).
- [24] R. Fantoni, Localization of acoustic polarons at low temperatures: A path integral Monte Carlo approach, *Phys. Rev. B* **86**, 144304 (2012).
- [25] W. Janke, Statistical Analysis of Simulations: Data Correlations and Error Estimation, in *Quantum Simulations of Complex Many-Body Systems: From Theory to Algorithms*, NIC Series Vol. 10, edited by J. Grotendorst, D. Marx, and A. Muramatsu (John von Neumann Institute for Computing, Jülich, 2002), pp. 423–445, ISBN: 3-00-009057-6.

Chapter 75

One-component fermion plasma on a sphere at finite temperature: the anisotropy of the path conformations

Fantoni R., J. Stat. Mech. 083103 (2023)

Title: “One-component fermion plasma on a sphere at finite temperature: the anisotropy of the path conformations”

Abstract: In our previous work (Fantoni 2018 Int. J. Mod. Phys. C 29 1850064) we studied, through a computer experiment, a one-component fermion plasma on a sphere at finite, non-zero temperature. We extracted thermodynamic properties, such as the kinetic and internal energy per particle, and structural properties, such as the radial distribution function, and produced some snapshots of the paths to study their shapes. Here, we revisit this study, giving more theoretical details explaining the path shape anisotropic conformation due to the inhomogeneity in the polar angle of the variance of the random walk diffusion from the kinetic action.

PAPER: Quantum statistical physics, condensed matter, integrable systems

One-component fermion plasma on a sphere at finite temperature: the anisotropy of the path conformations

Riccardo Fantoni*

Dipartimento di Fisica, Università di Trieste, strada Costiera 11, 34151
Grignano Trieste, Italy
E-mail: riccardo.fantoni@posta.istruzione.it

Received 27 March 2023
Accepted for publication 18 July 2023
Published 16 August 2023

Online at stacks.iop.org/JSTAT/2023/083103
<https://doi.org/10.1088/1742-5468/aceb54>



Abstract. In our previous work (Fantoni 2018 *Int. J. Mod. Phys. C* **29** 1850064) we studied, through a computer experiment, a one-component fermion plasma on a sphere at finite, non-zero temperature. We extracted thermodynamic properties, such as the kinetic and internal energy per particle, and structural properties, such as the radial distribution function, and produced some snapshots of the paths to study their shapes. Here, we revisit this study, giving more theoretical details explaining the path shape anisotropic conformation due to the inhomogeneity in the polar angle of the variance of the random walk diffusion from the kinetic action.

Keywords: one-component plasma, Monte Carlo simulation, finite temperature, restricted path integral, fermion sign problem, observables, path shape conformation

*Author to whom any correspondence should be addressed.

Contents

1. Introduction 2
2. The problem 3
3. Theoretical study 7
4. Conclusions 10
References 11

1. Introduction

In our work in [1] we studied, through restricted path integral Monte Carlo, a one-component fermion plasma on a sphere of radius a at finite, non-zero, absolute temperature T . We extracted thermodynamic properties like the kinetic and internal energy per particle and structural properties like the radial distribution function, and produced some snapshots of the paths to study their shapes.

Our results extend to the quantum regime the previous non-quantum results obtained for the analytically exactly solvable plasma on curved surfaces [2–7] and for its numerical Monte Carlo experiment [8]. In particular, we show how the configuration space (see figure 1 of [1]) appears much more complicated than in the classical case (see figures 5 and 6 of [8]). The first notable phenomenon is the fact that whereas the particle distribution is certainly isotropic, the path conformation is not. Some paths tend to wind around the sphere running along the parallels in proximity to the poles, while others run along the meridians in proximity to the equator. This is a direct consequence of the coordinate dependence of the variance of the diffusion. At high temperatures, the paths tend to be localized, whereas at low temperatures, they tend to be delocalized and distributed over a larger part of the surface with long links between the beads.

The plasma is an ensemble of point-wise electrons that interact through the Coulomb potential, assuming that the electric field lines can permeate the three-dimensional space where the sphere is embedded. The system of particles is thermodynamically stable even if the pair-potential is purely repulsive because the particles are confined to the compact surface of the sphere, and we do not need to add a uniform neutralizing background as in the Wigner Jellium model [9–13]. Therefore, our spherical plasma made of N spinless indistinguishable electrons of charge $-e$ and mass m will carry a total negative charge $-Ne$, a total mass Nm , and will have a radius a .

In this work, we conduct a thought computer experiment such as the one carried out in [1] in order to extract some theoretical conclusions on the path shape and conformation and try to explain the results found in [1].

Our study can be used to predict the properties of a metallic spherical shell, such as a spherical shell of graphene. Today, we assisted to a rapid development of the laboratory

J. Stat. Mech. (2023) 083103

One-component fermion plasma on a sphere at finite temperature: the anisotropy of the path conformations

realization of graphene hollow spheres [14, 15] with many technological interests. These are used as electrodes for supercapacitors and batteries, as superparamagnetic materials, as electrocatalysts for oxygen reduction, in drug delivery, and as a conductive catalyst for photovoltaic applications [16–24]. Of course, with simulation we can access the more various and extreme conditions otherwise not accessible in a laboratory.

A possible further study would be the simulation of the neutral sphere, where we model the plasma of electrons embedded in a spherical shell that is uniformly positively charged in such a way that the system is globally neutrally charged. This could easily be done by changing the Coulomb pair-potential into $e^2/r \rightarrow e^2(1/r - 1)$. In the $a \rightarrow \infty$ limit, this would reduce to the Wigner Jellium model that has received much attention lately, from the point of view of a path integral Monte Carlo simulation [1, 25–33]. Alternatively, we could study the two-component plasma on the sphere, as has recently been done in the tridimensional Euclidean space [33]. Another possible extension of our work is the realization of the simulation of the full anyonic plasma on the sphere, taking appropriate care of the fractional statistics and the phase factors to append to each disconnected region of the path integral expression for the partition function [1]. This could become important in a study of the quantum Hall effect by placing a magnetic Dirac monopole at the center of the sphere [34, 35]. In addition, the adaptation of our simulation to a fully relativistic Hamiltonian could be of some interest in the study of graphinos.

The paper is organized as follows: in section 2 we describe the thought system and the method used for its study, in section 3 we present our theoretical study and predictions, and section 4 contains the concluding discussion.

2. The problem

A point \mathbf{q} on the sphere of radius a , the surface of constant positive curvature, is given by

$$\mathbf{r}/a = \sin\theta \cos\varphi \hat{\mathbf{x}} + \sin\theta \sin\varphi \hat{\mathbf{y}} + \cos\theta \hat{\mathbf{z}}, \tag{2.1}$$

where θ is the polar angle and φ is the azimuthal angle. The N particle positions are at $\mathbf{R} = (\mathbf{r}_1, \mathbf{r}_2, \dots, \mathbf{r}_N)$. The surface density of the plasma will then be $\sigma = N/4\pi a^2$. On the sphere we have the following metric:

$$ds^2 = g_{\mu\nu} dq^\mu dq^\nu = a^2 [d\theta^2 + \sin^2\theta d\varphi^2], \tag{2.2}$$

where Einstein summation convention on repeated indices is assumed. We will use Greek indices for either the surface components or the surface components of each particle coordinate and Roman indices for either the particle index or the time-slice index, $q^1 = \theta \in [0, \pi)$, $q^2 = \varphi \in [-\pi, \pi)$, and the positive definite and symmetric metric tensor is given by

$$g_{\mu\nu} = \begin{pmatrix} a^2 & 0 \\ 0 & a^2 \sin^2\theta \end{pmatrix}. \tag{2.3}$$

One-component fermion plasma on a sphere at finite temperature: the anisotropy of the path conformations

We have periodic boundary conditions in $\theta + \pi = \theta$ and in $\varphi + 2\pi = \varphi$. We will also define $\mathbf{Q} = (\mathbf{q}_1, \mathbf{q}_2, \dots, \mathbf{q}_N)$. The geodesic distance between two infinitesimally close points \mathbf{Q} and \mathbf{Q}' is $ds^2(\mathbf{Q}, \mathbf{Q}') = \sum_{i=1}^N ds^2(\mathbf{q}_i, \mathbf{q}'_i)$, where the geodesic distance between the points \mathbf{q} and \mathbf{q}' on the sphere is

$$s(\mathbf{q}, \mathbf{q}') = a \arccos \left[\cos(q^1) \cos(q'^1) + \sin(q^1) \sin(q'^1) \cos(q^2 - q'^2) \right]. \quad (2.4)$$

The Hamiltonian of the N non-relativistic indistinguishable particles of the one-component spinless fermion plasma is given by

$$\mathcal{H} = \mathcal{T} + \mathcal{V} = -\lambda \sum_{i=1}^N \Delta_i + \sum_{i < j} v_{ij}, \quad (2.5)$$

with $\lambda = \hbar^2/2m$, where m is the electron mass, and $\Delta_i = g_i^{-1/2} \partial(g_i^{1/2} g_i^{\mu\nu} \partial/\partial q_i^\nu) / \partial q_i^\mu$ the Laplace–Beltrami operator for the i th particle on the sphere of radius a in local coordinates, where $g_{\mu\alpha} g^{\alpha\nu} = \delta_\mu^\nu$ and $g_i = \det ||g_{\mu\nu}(\mathbf{q}_i)||$. We have assumed that \mathcal{H} in curved space has the same form as in flat space. For the pair-potential, v , we will choose

$$v_{ij} = e^2/r_{ij}, \quad (2.6)$$

where e is the electron charge and r_{ij} is the Euclidean distance between two particles at \mathbf{q}_i and \mathbf{q}_j , which is given by

$$r_{ij} = a \sqrt{2 - 2\hat{\mathbf{r}}_i \cdot \hat{\mathbf{r}}_j} = 2a \sin[\arccos(\hat{\mathbf{r}}_i \cdot \hat{\mathbf{r}}_j)/2], \quad (2.7)$$

where $\hat{\mathbf{r}}_i = \mathbf{r}_i/a$ is the versor that from the center of the sphere points toward the center of the i th particle. So, the electrons *move on* a spherical shell with the electric field lines permeating the surrounding three-dimensional space, but they do not *live in* the shell.

Given the antisymmetrization operator $\mathcal{A} = \sum_P / N!$, where the sum runs over all particle permutations P , and the inverse temperature $\beta = 1/k_B T$, where k_B is Boltzmann’s constant, the one-component fermion plasma density matrix, $\rho_F = \mathcal{A} e^{-\beta \mathcal{H}}$, in the coordinate representation, on a generic Riemannian manifold of metric g [5, 36], is

$$\rho_F(\mathbf{Q}', \mathbf{Q}; \beta) = \int \rho_F(\mathbf{Q}', \mathbf{Q}((M-1)\tau); \tau) \cdots \rho_F(\mathbf{Q}(\tau), \mathbf{Q}; \tau) \prod_{j=1}^{M-1} \sqrt{\tilde{g}_{(j)}} \prod_{i=1}^N dq_i^1(j\tau) \wedge dq_i^2(j\tau), \quad (2.8)$$

where as usual we discretize the *imaginary thermal time* in bits $\tau = \hbar\beta/M$. We will often use the following shorthand notation for the *path integral* measure: $\prod_{j=1}^{M-1} \sqrt{\tilde{g}_{(j)}} \prod_{i=1}^N dq_i^1(j\tau) \wedge dq_i^2(j\tau) \rightarrow \mathcal{D}\mathbf{Q}$ as $M \rightarrow \infty$. The path of the i th particle is given by $\{\mathbf{q}_i(t) | t \in [0, \hbar\beta]\}$ with t the imaginary thermal time. Each $\mathbf{q}_i(j\tau)$ with $i = 1, \dots, N$ and $j = 1, \dots, M$ represents the various *beads* forming the discretized path. The N particle path

J. Stat. Mech. (2023) 083103

One-component fermion plasma on a sphere at finite temperature: the anisotropy of the path conformations is given by $\{\mathbf{Q}(t)|t \in [0, \hbar\beta]\}$. Moreover,

$$\tilde{g}_{(j)} = \det \|\tilde{g}_{\mu\nu}(\mathbf{Q}(j\tau))\|, \quad j = 1, 2, \dots, M - 1, \tag{2.9}$$

$$\tilde{g}_{\mu\nu}(\mathbf{Q}) = g_{\alpha_1\beta_1}(\mathbf{q}_1) \otimes \dots \otimes g_{\alpha_N\beta_N}(\mathbf{q}_N), \tag{2.10}$$

In the small τ limit, we have

$$\rho_F(\mathbf{Q}(2\tau), \mathbf{Q}(\tau); \tau) \propto \mathcal{A} \left[\tilde{g}_{(2)}^{-1/4} \sqrt{D(\mathbf{Q}(2\tau), \mathbf{Q}(\tau); \tau)} \tilde{g}_{(1)}^{-1/4} e^{\lambda\tau R(\mathbf{Q}(\tau))/6\hbar} e^{-\frac{1}{\hbar}S(\mathbf{Q}(2\tau), \mathbf{Q}(\tau); \tau)} \right], \tag{2.11}$$

where \mathcal{A} can act on the first, the second, or on both *time slices*. $R(\mathbf{Q})$ is the scalar curvature of the curved manifold, S is the action and D is van Vleck's determinant

$$D_{\mu\nu} = \frac{\partial^2 S(\mathbf{Q}(2\tau), \mathbf{Q}(\tau); \tau)}{\partial Q^\mu(2\tau) \partial Q^\nu(\tau)}, \tag{2.12}$$

$$\det \|D_{\mu\nu}\| = D(\mathbf{Q}(2\tau), \mathbf{Q}(\tau); \tau), \tag{2.13}$$

where here the Greek index denotes the two components of each particle coordinate.

For the *action* and the *kinetic action*, we have

$$S(\mathbf{Q}', \mathbf{Q}) = K(\mathbf{Q}', \mathbf{Q}) + U(\mathbf{Q}', \mathbf{Q}), \tag{2.14}$$

$$K(\mathbf{Q}', \mathbf{Q}) = N\hbar \ln(4\pi\lambda\tau/\hbar) + \frac{\hbar^2 s^2(\mathbf{Q}', \mathbf{Q})}{4\lambda\tau}, \tag{2.15}$$

where in the *primitive approximation* [37] we find the following expression for the *interaction*,

$$U(\mathbf{Q}', \mathbf{Q}) = \frac{\tau}{2} [V(\mathbf{Q}') + V(\mathbf{Q})], \tag{2.16}$$

$$V(\mathbf{Q}) = \sum_{i < j} v_{ij}. \tag{2.17}$$

In particular, the kinetic action is responsible for the diffusion of the random walk with a variance of $2\lambda\tau g^{\mu\nu}/\hbar$.

On the sphere, we have $R = N\mathcal{R}$ with $\mathcal{R} = 2/a^2$, the scalar curvature of the sphere of radius a , and in the $M \rightarrow \infty$ limit $s^2(\mathbf{Q}', \mathbf{Q}) \rightarrow ds^2(\mathbf{Q}', \mathbf{Q})$ and $\tilde{g}_{(2)}^{-1/4} \sqrt{D(\mathbf{Q}(2\tau), \mathbf{Q}(\tau); \tau)} \tilde{g}_{(1)}^{-1/4} \rightarrow (\hbar^2/2\lambda\tau)^N$ [38]. We recover the Feynman–Kac path integral formula on the sphere in the $\tau \rightarrow 0$ limit. We will then have to deal with $2NM$ multidimensional integrals for which Monte Carlo [39] is a suitable computational method. For example, to measure an observable \mathcal{O} we need to calculate the following quantity:

$$\langle \mathcal{O} \rangle = \frac{\int \mathcal{O}(\mathbf{Q}, \mathbf{Q}') \rho_F(\mathbf{Q}', \mathbf{Q}; \beta) d\mathbf{Q} d\mathbf{Q}'}{\int \rho_F(\mathbf{Q}, \mathbf{Q}; \beta) d\mathbf{Q}}, \tag{2.18}$$

One-component fermion plasma on a sphere at finite temperature: the anisotropy of the path conformations

where $\sqrt{g} \prod_{i=1}^N dq_i^1 \wedge dq_i^2 \equiv d\mathbf{Q}$. Notice that most of the properties that we will measure are diagonal in coordinate representation, requiring then just the diagonal density matrix, $\rho_F(\mathbf{Q}, \mathbf{Q}; \beta)$.

For example, for the density $\rho(\mathbf{q}) = \langle \mathcal{O} \rangle$ with

$$O(\mathbf{Q}; \mathbf{q}) = \sum_{i=1}^N \delta^{(2)}(\mathbf{q} - \mathbf{q}_i), \tag{2.19}$$

where $\delta^{(2)}(\mathbf{q}) = \delta(q^1)\delta(q^2)$ and δ is the Dirac delta function. Clearly $\int \sigma(\mathbf{q}) \sqrt{g(\mathbf{q})} d\mathbf{q} = N$ and a uniform distribution of electrons is signaled by a constant density throughout the surface of the sphere.

Fermion properties cannot be calculated exactly with the path integral Monte Carlo because of the fermion sign problem [40, 41]. We then have to resort to an approximated calculation. The one we chose in [1] was the restricted path integral approximation [40, 41] with a ‘free fermion restriction’. The trial density matrix used in the restriction is chosen as the one reducing to the ideal density matrix in the limit of $t \ll 1$, and is given by

$$\rho_0(\mathbf{Q}', \mathbf{Q}; t) \propto \mathcal{A} \left\| e^{-\frac{\hbar s^2(q'_i, q_j)}{4\lambda t}} \right\|. \tag{2.20}$$

The *restricted path integral identity* that can be used [40, 41] is as follows: mathindent0pt

$$\rho_F(\mathbf{Q}', \mathbf{Q}; \beta) \propto \int \sqrt{g''} d\mathbf{Q}'' \rho_F(\mathbf{Q}'', \mathbf{Q}; 0) \oint_{\mathbf{Q}'' \rightarrow \mathbf{Q}' \in \gamma_0(\mathbf{Q})} \mathcal{D}\mathbf{Q}''' e^{-S[\mathbf{Q}''']/\hbar}, \tag{2.21}$$

where S is the Feynman–Kac action

$$S[\mathbf{Q}] = \int_0^{\hbar\beta} dt \left[\frac{\hbar^2}{4\lambda} \dot{\mathbf{Q}}_\mu \dot{\mathbf{Q}}^\mu + V(\mathbf{Q}) \right], \tag{2.22}$$

where the dot indicates a total derivative with respect to the imaginary thermal time, and the subscript in the path integral of equation (2.21) means that we restrict the path integration to paths starting at \mathbf{Q}'' , ending at \mathbf{Q}' and avoiding the nodes of ρ_0 , that is to the *reach* of \mathbf{Q} , γ_0 . The nodes are on the reach boundary $\partial\gamma_0$. The weight of the walk is $\rho_F(\mathbf{Q}'', \mathbf{Q}; 0) = \mathcal{A} \delta(\mathbf{Q}'' - \mathbf{Q}) = (N!)^{-1} \sum_{\mathcal{P}} (-)^{\mathcal{P}} \delta^{(2N)}(\mathbf{Q}'' - \mathcal{P}\mathbf{Q})$, where the sum is over all the permutations \mathcal{P} of the N fermions, $(-)^{\mathcal{P}}$ is the permutation sign, positive for an even permutation and negative for an odd permutation, and δ is a Dirac delta function. It is clear that the contribution of all the paths for a single element of the density matrix will be of the same sign, thus solving the sign problem; it is positive if $\rho_F(\mathbf{Q}'', \mathbf{Q}; 0) > 0$, and negative otherwise. On the diagonal, the density matrix is positive and on the path restriction $\rho_F(\mathbf{Q}', \mathbf{Q}; \beta) > 0$ then only even permutations are allowed since $\rho_F(\mathbf{Q}, \mathcal{P}\mathbf{Q}; \beta) = (-)^{\mathcal{P}} \rho_F(\mathbf{Q}, \mathbf{Q}; \beta)$. It is then possible to use a boson calculation to get the fermion case. Clearly, the restricted path integral identity with the free fermion restriction becomes exact if we simulate free fermions, but otherwise is

One-component fermion plasma on a sphere at finite temperature: the anisotropy of the path conformations

just an approximation. The approximation is expected to improve at low density and high temperature, i.e. when correlation effects are weak. The implementation of the restricted, fixed-node, path integral identity within the worm algorithm was also the subject of our previous study on the three-dimensional Euclidean Jellium [11].

In [1] we worked in the grand canonical ensemble with fixed chemical potential μ , surface area $A = 4\pi a^2$, and absolute temperature T . At a higher value of the chemical potential we will have a higher number of particles on the surface and a higher density. On the other hand, increasing the radius of the sphere at constant chemical potential will produce a plasma with lower surface density. The *Coulomb coupling constant* is $\Gamma = \beta e^2/a_0 r_s$ with $a_0 = \hbar^2/me^2$ the Bohr radius and $r_s = (4\pi\sigma)^{-1/2}/a_0$. At weak coupling, $\Gamma \ll 1$, the plasma becomes weakly correlated and approaches the ideal gas limit. This will occur at high temperatures and/or low densities. The *electron degeneracy parameter* is $\Theta = T/T_D$, where the degeneracy temperature $T_D = \sigma\hbar^2/mk_B$. For temperatures higher than T_D , $\Theta \gg 1$, the quantum effects are less relevant.

3. Theoretical study

In order to understand the anisotropic conformation of the path snapshots and their dependence on the azimuthal angle φ and polar angle θ , we observe that in the primitive approximation we have in the path integral a weight factor $\propto \exp(-\hbar ds^2/4\lambda\tau)$ stemming from the kinetic part of the action, where ds^2 is given by equation (2.2). In particular, we see that if we are near the poles, $\theta \approx 0$ or π , then $ds^2 \approx a^2 d\theta^2$ and we see that it costs nothing to change the azimuthal angle. This explains the paths winding along the parallels in proximity to the poles. On the other hand, near the equator, at $\theta \approx \pi/2$, we find $ds^2 \approx a^2(d\theta^2 + d\varphi^2)$ so that the paths will tend to wander around the equator in no particular direction.

The same can be seen when studying the behavior of the finite geodesic distance of equation (2.5). In figure 1 we show a three-dimensional plot for $\theta' = 0.2$ and $\varphi' = 0$. Again, we see that around the pole at $\theta \approx 0$ it costs nothing to change φ , that is, to go along a parallel, while a path traveling along a meridian will be unfavored since we need to increase θ . In figure 2 we show a three-dimensional plot for $\theta' = \pi/2$ and $\varphi' = 0$. We now see that around the equator at $\theta \approx \pi/2$ a path wandering around the initial position is favored, with no preferred direction along the parallels or the meridians.

Clearly, if we rotate the sphere, the path shape will simply rotate following the rotation of its poles. This anisotropy of the path conformations is rather counter-intuitive since the sphere is notoriously isotropic, but it reflects the inhomogeneity of the metric with respect to the polar angle.

It is important to distinguish the effect that we just described due to the weight factor $\propto \exp(-\hbar ds^2/4\lambda\tau)$ stemming from the kinetic part of the primitive action from the measure factor $\prod_{j=1}^M \sqrt{\tilde{g}(j)}$ also entering the path integral. This last factor, being also independent of the azimuthal angles, will produce the same local density $\rho(\mathbf{q})$ under a rotation of the sphere around its axis through the poles. As a result, by isotropy, we conclude that the density must be a constant under any rotation, which means that the plasma must be uniform [5].

One-component fermion plasma on a sphere at finite temperature: the anisotropy of the path conformations

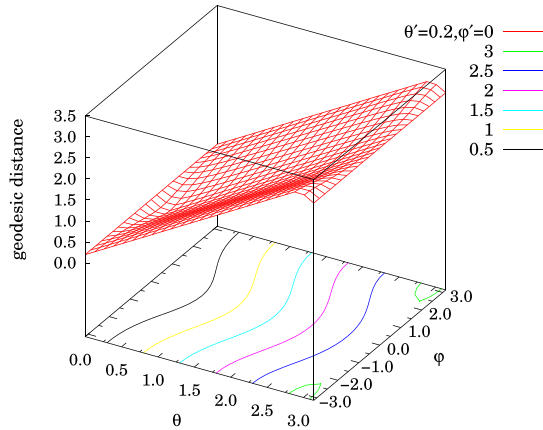


Figure 1. Three-dimensional plot of the geodesic distance of equation (2.5) for $\theta' = 0.2$ and $\varphi' = 0$. From the surface graph we see how in the proximity of the poles the geodesic distance between points moving along parallels is small, while it increases rapidly if one moves along the meridians.

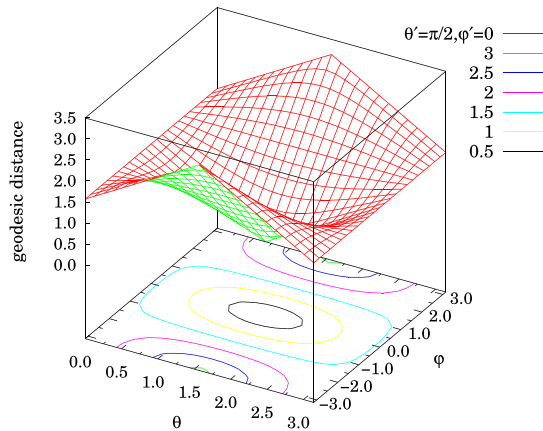


Figure 2. Three-dimensional plot of the geodesic distance of equation (2.5) for $\theta' = \pi/2$ and $\varphi' = 0$. From the surface graph we see how in the proximity of the equator the geodesic distance between points moving in circles in the (θ, φ) plane is small, while it increases rapidly if one moves along the parallels.

The temperature dependence can also be easily explained. At high temperature, β is small, $\Theta \gg 1$, and the path extending from $t = 0$ to $t = \hbar\beta$ will be localized, of a small size, and quantum effects will be less relevant. Meanwhile, at low temperature, β is large, $\Theta \ll 1$, and the path will be delocalized, increased in size, it diffuses more

One-component fermion plasma on a sphere at finite temperature: the anisotropy of the path conformations

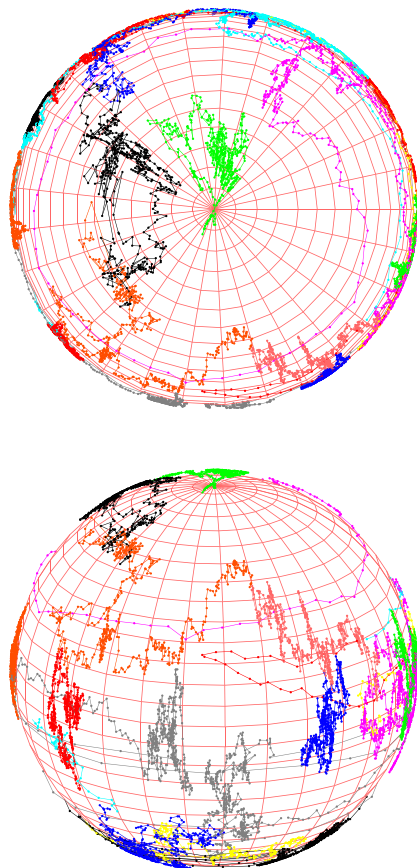


Figure 3. Snapshot of the macroscopic path during a simulation. The different paths have different colors. The simulation parameters specifying the thermodynamic conditions are as follows: $a = 5, \lambda = 1, \beta = 5, \mu = 8$.

on the surface, and quantum effects are more relevant. Usually, we are interested in measuring observables that are diagonal so that when dealing with the diagonal density matrix $\rho_F(\mathbf{Q}, \mathbf{Q}; \beta)$ we will observe *ring* paths, such that $\mathbf{Q}(0) = \mathbf{Q}(\hbar\beta)$. Moreover, at high temperature, the diagonal density matrix will involve almost straight localized ring paths closing themselves on the identity permutation. At low temperatures, the delocalized paths will eventually wind through the $\hbar\beta$ periodicity by means of several different permutations \mathcal{P} , so that $\mathbf{Q}(0) = \mathcal{P}\mathbf{Q}(\hbar\beta)$ and so on. Any permutation can be broken into a product of cyclic permutations. Each cycle corresponds to several paths ‘cross-linking’ and forming a larger ring path. Quantum mechanically, the plasma does

J. Stat. Mech. (2023) 083103

One-component fermion plasma on a sphere at finite temperature: the anisotropy of the path conformations

this to lower its kinetic energy. According to Feynman's 1953 theory [37], the superconductor transition is represented by the formation of macroscopic paths, i.e. those stretching across the whole sphere and involving on the order of N electrons. In other words, the ring paths percolate through the periodic boundary conditions $\theta = \theta + \pi$ and $\varphi = \varphi + 2\pi$ by means of permutations.

In figure 3 we show a snapshot of the macroscopic path during a simulation of [1].

4. Conclusions

In this work we revised our restricted path integral Monte Carlo simulation [1] of a one-component spinless fermion plasma at finite, non-zero temperature on the surface of a sphere. The Coulomb interaction is e^2/r with r the Euclidean distance between two electrons of elementary charge e (we could also have chosen instead of r the geodesic distance, s , within the sphere). This gives us an approximated numerical solution of the many-body problem. The exact solution cannot be accessed due to the fermion sign catastrophe. Impenetrable indistinguishable particles on the surface of a sphere admit, in general, anyonic statistics [42]. Here, we just project the larger braid group onto the permutation group and choose the fermion sector for our study.

The path integral Monte Carlo method chosen in [1] used the primitive approximation for the action, which can be improved, for example, by the use of the pair-product action [37]. The restriction was carried out choosing as guiding trial density matrix the one of ideal free fermions. This choice would of course return an exact solution for the simulation of ideal fermions, but it furnishes just an approximation for the interacting coulombic plasma.

In this work we showed how the conformation anisotropy of the paths observed in the simulations of [1] can be explained through the inhomogeneous nature of the metric in the polar angle, or equivalently, from the inhomogeneous nature of the geodesic distance on the surface of the sphere. This is ultimately due to the fact that the metric enters with the negative sign in the exponent of the primitive approximation of the density matrix. We should not confuse the anisotropy in the path conformation with the fact that the plasma will always be homogeneous (with a constant local density ρ) on the sphere. In the degenerate regime (low T) the observed strong anisotropy in the path conformation near the poles or the equator of the sphere should also be due to a peculiar behavior in the properties of the N -particle off-diagonal density matrix. This, as is well known, is directly related to a number of physical properties, such as the quasi-particle excitation spectrum and the momentum distribution. Therefore, the system properties can deviate significantly from just a pure homogeneous 2D system, and the inhomogeneous nature of the space metric is of particular importance.

We also suggest the possibility to observe a superconducting plasma at low temperature when we observe ring paths percolating through the periodic boundary conditions $\theta = \theta + \pi$ and $\varphi = \varphi + 2\pi$ by means of permutations, even if some care has to be addressed to take into account the peculiar asymptotic behavior of the one-particle density matrix.

One-component fermion plasma on a sphere at finite temperature: the anisotropy of the path conformations

References

- [1] Fantoni R 2018 One-component fermion plasma on a sphere at finite temperature *Int. J. Mod. Phys. C* **29** 1850064
- [2] Fantoni R, Jancovici B and Téllez G 2003 Pressures for a one-component plasma on a pseudosphere *J. Stat. Phys.* **112** 27
- [3] Fantoni R and Téllez G 2008 Two dimensional one-component plasma on a Flamm's paraboloid *J. Stat. Phys.* **133** 449
- [4] Fantoni R 2012 Two component plasma in a Flamm's paraboloid *J. Stat. Mech.* **2012** 04015
- [5] Fantoni R 2012 The density of a fluid on a curved surface *J. Stat. Mech.* **2012** 10024
- [6] Fantoni R 2016 Exact results for one dimensional fluids through functional integration *J. Stat. Phys.* **163** 1247
- [7] Fantoni R 2017 The moment sum-rules for ionic liquids at criticality *Physica A* **477C** 187
- [8] Fantoni R, Salari J W O and Klumperman B 2012 The structure of colloidosomes with tunable particle density: simulation vs experiment *Phys. Rev. E* **85** 061404
- [9] Fantoni R and Tosi M P 1995 Coordinate space form of interacting reference response function of d -dimensional jellium *Il Nuovo Cimento D* **17D** 1165
- [10] Fantoni R 2013 Radial distribution function in a diffusion monte carlo simulation of a fermion fluid between the ideal gas and the jellium model *Eur. Phys. J. B* **86** 286
- [11] Fantoni R 2021 Jellium at finite temperature using the restricted worm algorithm *Eur. Phys. J. B* **94** 63
- [12] Fantoni R 2021 Form invariance of the moment sum-rules for jellium with the addition of short-range terms in the pair-potential *Indian J. Phys.* **95** 1027
- [13] Fantoni R 2021 Jellium at finite temperature *Mol. Phys.* **120** 4
- [14] Rashid A and Yusoff M (eds) 2015 *Graphene-Based Energy Devices* (Wiley)
- [15] Tiwari A and Syväjärvi M (eds) 2015 *Graphene Materials: Fundamentals and Emerging Applications* (Scrivener Publishing)
- [16] Guo P, Song H and Chena X 2010 Hollow graphene oxide spheres self-assembled by W/O emulsion *J. Mater. Chem.* **20** 4867
- [17] Cao J, Wang Y, Xiao P, Chen Y, Zhou Y, Ouyang J-H and Jia D 2013 Hollow graphene spheres self-assembled from graphene oxide sheets by a one-step hydrothermal process *Carbon* **56** 389
- [18] Wu L, Feng H, Liu M, Zhang K and Li J 2013 Graphene-based hollow spheres as efficient electrocatalysts for oxygen reduction *Nanoscale* **5** 10839
- [19] Shao Q, Tang J, Lin Y, Zhang F, Yuan J, Zhang H, Shinyaa N and Qinc L-C 2013 Synthesis and characterization of graphene hollow spheres for application in supercapacitors *J. Mater. Chem. A* **1** 15423
- [20] Zhao Y, Chen M and Wu L 2016 Recent progress in hollow sphere-based electrodes for high-performance supercapacitors *Nanotechnology* **27** 342001
- [21] Cho J S, Lee J-K and Y C Yong 2016 Graphitic carbon-coated FeSe₂ hollow nanosphere-decorated reduced graphene oxide hybrid nanofibers as an efficient anode material for sodium ion batteries *Sci. Rep.* **6** 23699
- [22] Hao D, Xuefen C, Liangdong Q and Xiaohui Z 2016 Fabrication, characterization and properties of superparamagnetic reduced graphene oxide/Fe₃O₄ hollow sphere nanocomposites *Rare Met. Mater. Eng.* **45** 1669
- [23] Huang W, Ding S, Chen Y, Hao W, Lai X, Peng J, Tu J, Cao Y and Li X 2017 3D NiO hollow sphere/reduced graphene oxide composite for high-performance glucose biosensor *Sci. Rep.* **7** 5220
- [24] Bi E, Chen H, Yang X, Ye F, Yin M and Han L 2017 Fullerene-structured MoSe₂ hollow spheres anchored on highly nitrogen-doped graphene as a conductive catalyst for photovoltaic applications *Sci. Rep.* **5** 5220
- [25] Brown E W, Clark B K, DuBois J L and Ceperley D M 2013 Path-integral Monte Carlo simulation of the warm dense homogeneous electron gas *Phys. Rev. Lett.* **110** 146405
- [26] Brown E, Morales M A, Pierleoni C and Ceperley D M *et al* 2014 Quantum Monte Carlo techniques and applications for warm dense matter *Frontiers and Challenges in Warm Dense Matter* ed F Graziani (Springer) pp 123–49
- [27] Dornheim T, Groth S, Sjoström T, Malone F D, Foulkes W M C and Bonitz M 2016 *Ab initio* quantum Monte Carlo simulation of the warm dense electron gas in the thermodynamic limit *Phys. Rev. Lett.* **117** 156403
- [28] Dornheim T, Groth S, Schoof T, Hann C and Bonitz M 2016 *Ab initio* quantum Monte Carlo simulations of the uniform electron gas without fixed nodes: the unpolarized case *Phys. Rev. B* **93** 205134
- [29] Groth S, Schoof T, Dornheim T and Bonitz M 2016 *Ab initio* quantum Monte Carlo simulations of the uniform electron gas without fixed nodes *Phys. Rev. B* **93** 085102

J. Stat. Mech. (2023) 083103

One-component fermion plasma on a sphere at finite temperature: the anisotropy of the path conformations

- [30] Groth S, Dornheim T, Sjostrom T, Malone F D, Foulkes W M C and Bonitz M 2017 *Ab initio* exchange-correlation free energy of the uniform electron gas at warm dense matter conditions *Phys. Rev. Lett.* **119** 135001
- [31] Malone F D, Blunt N S, Brown E W, Lee D K K, Spencer J S, Foulkes W M C and Shepherd J J 2016 Accurate exchange-correlation energies for the warm dense electron gas *Phys. Rev. Lett.* **117** 115701
- [32] Filinov V S, Fortov V E, Bonitz M and Moldabekov Z 2015 Fermionic path-integral Monte Carlo results for the uniform electron gas at finite temperature *Phys. Rev. E* **91** 033108
- [33] Fantoni R 2018 Two component boson–fermion plasma at finite temperature *Int. J. Mod. Phys. C* **29** 1850028
- [34] Melik-Alaverdian V, Bonesteel N E and Ortiz G 1997 Fixed-phase diffusion Monte Carlo study of the quantum-hall effect on the haldane sphere *Phys. Rev. Lett.* **79** 5286
- [35] Melik-Alaverdian V, Ortiz G and Bonesteel N E 2001 Quantum projector method on curved manifolds *J. Stat. Phys.* **104** 449
- [36] Schulman L S 1981 *Techniques and Applications of Path Integrals* (Wiley) ch 24
- [37] Ceperley D M 1995 Path integrals in the theory of condensed helium *Rev. Mod. Phys.* **67** 279
- [38] For a space of constant curvature there is clearly no effect, as the term due to the curvature just leads to a constant multiplicative factor that has no influence on the measure of the various observables. One might have hoped that certain constrained coordinates, perhaps a relative coordinate in a molecule, would effectively live in a space of variable curvature. Perhaps gravitation will give us the system on which the effect of curvature can be seen, but at present the effect is purely in the realm of theory
- [39] Kalos M H and Whitlock P A 2008 *Monte Carlo Methods* (Wiley)
- [40] Ceperley D M 1991 Fermion nodes *J. Stat. Phys.* **63** 1237
- [41] Ceperley D M 1996 Path integral Monte Carlo methods for fermions *Monte Carlo and Molecular Dynamics of Condensed Matter Systems* ed K Binder and G Ciccotti (Editrice Compositori)
- [42] Fantoni R 2021 How should we choose the boundary conditions in a simulation which could detect anyons in one and two dimensions? *J. Low Temp. Phys.* **202** 247

J. Stat. Mech. (2023) 083103

Chapter 76

The Magnificent Realm of Affine Quantization: Valid Results for Particles, Fields, and Gravity

Klauder J. R. and **Fantoni R.**, *Axioms* **12**, 911 (2023)

Title: “The Magnificent Realm of Affine Quantization: Valid Results for Particles, Fields, and Gravity”

Abstract: Affine quantization is a relatively new procedure, and it can solve many new problems. This essay reviews this new, and novel, procedure for particle problems, as well as those of fields and gravity. New quantization tools, which are extremely close to, and even constructed from, the tools of canonical quantization, are able to fully solve selected problems that using the standard canonical quantization would fail. In particular, improvements can even be found with an affine quantization of fields, as well as gravity.



Review

The Magnificent Realm of Affine Quantization: Valid Results for Particles, Fields, and Gravity

John R. Klauder ^{1,2} and Riccardo Fantoni ^{3,*}

¹ Department of Physics, University of Florida, Gainesville, FL 32610, USA; klauder@ufl.edu

² Department of Mathematics, University of Florida, Gainesville, FL 32610, USA

³ Department of Theoretical Physics, University of Trieste, 34151 Grignano, Italy

* Correspondence: riccardo.fantoni@posta.istruzione.it or rfantoni3@gmail.com

Abstract: Affine quantization is a relatively new procedure, and it can solve many new problems. This essay reviews this new, and novel, procedure for particle problems, as well as those of fields and gravity. New quantization tools, which are extremely close to, and even constructed from, the tools of canonical quantization, are able to fully solve selected problems that using the standard canonical quantization would fail. In particular, improvements can even be found with an affine quantization of fields, as well as gravity.

Keywords: affine quantization; field theory; quantum gravity

MSC: 11K45; 65C05; 81S40; 81T10; 81T16; 81T20; 81T25; 81T27; 82M31; 83C45; 83C47; 91G60



Citation: Klauder, J.R.; Fantoni, R. The Magnificent Realm of Affine Quantization: Valid Results for Particles, Fields, and Gravity. *Axioms* **2023**, *12*, 911. <https://doi.org/10.3390/axioms12100911>

Academic Editor: Jan Śladkowski

Received: 27 August 2023

Revised: 15 September 2023

Accepted: 19 September 2023

Published: 25 September 2023



Copyright: © 2023 by the authors. Licensee MDPI, Basel, Switzerland. This article is an open access article distributed under the terms and conditions of the Creative Commons Attribution (CC BY) license (<https://creativecommons.org/licenses/by/4.0/>).

1. A Preface

The scope of quantum physics has expanded remarkably, as will be clear in this presentation. Many problems have new and novel results.

The basic rules of quantization were largely set around mid-(1920), and have changed very little thereafter. There are many problems that using those rules can lead to acceptable results, but there are many more problems that those rules are inadequate. As an example, the traditional harmonic oscillator, which is set on the whole real line, can be fully solved with the original rules. However, if the harmonic oscillator is set only on the positive real line, it can not be solved with the old quantization rules despite the fact that it can be solved classically. Many problems that can be solved classically cannot be solved with old rules known as canonical quantization (CQ). Those procedures fail on non-renormalizable examples which include certain relativistic scalar fields and Einstein's gravity.

A new quantization procedure, called affine quantization (AQ), has now been added to the old rules. This procedure is now about 30 years old. AQ is not well known and it deserves to be as strongly known as CQ. While CQ chooses the momentum, e.g., p , and the coordinate, e.g., q , to promote to quantum operators, AQ chooses what we call the dilation, namely $d = pq$.

We start slowly with simple models to appreciate what AQ is able to accomplish. Already, using Monte Carlo methods, several non-renormalizable relativistic scalar models have confirmed what AQ can do for them. Einstein's gravity is more complicated, but the rules of AQ offer considerably positive results.

A brief example of the affine procedures, and a brief integration interval, $H = \int_{-1}^1 [\pi(x)^2 + |\varphi(x)|^p] dx < \infty$, with $p = 1, 2, 3, \dots$, then H can be finite if the integrand reaches infinity, e.g., $\pi(x)^2 = A/|x|^{1/4}$. This is proper mathematics, but the fields of nature should never reach infinity. Our solution introduces a new field, $\kappa(x) = \pi(x) \varphi(x)$. Now, $H = \int H(x) dx = \int [\kappa(x)^2 / \varphi(x)^2 + |\varphi(x)|^p] dx < \infty$. To represent $\pi(x)$, then $0 < |\varphi(x)| < \infty$, $0 \leq |\kappa(x)| < \infty$, and $H(x) < \infty$. While $\varphi(x) \neq 0$, $\hat{\pi}(x)^\dagger \neq \hat{\pi}(x)$, then

$\hat{\kappa}(x) = [\hat{\pi}(x)^\dagger \hat{\phi}(x) + \hat{\phi}(x) \hat{\pi}(x)]/2$, and after scaling, then $\mathcal{H} = \int [\hat{\pi}(x)^2 + 2\hbar^2/\hat{\phi}(x)^2 + |\hat{\phi}(x)|^p] dx < \infty$. Note that $|\hat{\phi}(x)|^p < \infty$ for all x , and all p , $0 < p < \infty$, due to $0 < |\hat{\phi}(x)| < \infty$ as well as $0 \leq |\hat{\pi}(x)| < \infty$!

2. An Introduction to the Variables

Quantum operators are promoted from classical variables that can play an important role and need to be presented here because it is poorly covered. Our story involves three sets of classical variables that will, later, find their importance when they are promoted to basic quantum variables.

2.1. A Survey of Principal Topics

The common examination of quantum topics starts with a classical review, and we shall do the same. Our focus features three different classical versions. These three have some similar features as well as their differences, but they all play a role in the quantum story.

The three versions of quantum theory, which develop from the three classical versions, have important and distinct roles to play. After studying the procedures, we will apply them to specific problems. It follows that the various procedures fit specific sets of problems, and fail when the wrong procedures are applied to any wrong set of problems. In particular, problems that are non-renormalizable quantum problems, and which have been unsolved for decades, can, in fact, be properly solved by using the correct quantum procedures instead of the wrong procedures. While they may have been favored, they also may have been the incorrect procedure for decades! In later chapters, we will solve non-renormalizable covariant scalar fields as well as Einstein’s gravity.

2.2. A Familiar Example of Classical Variables

The everyday behavior of most objects consists of its position, abbreviated by q , and its momentum, namely its mass multiplied by its velocity, like $p = mv$. These objects also change place and/or motion, which is represented by $q(t)$ and $p(t)$, with t serving as time. In an ideal universe, there would be no friction to slow motion down, while instead energy is typically considered to be a constant. The important Hamilton expression, $H(p, q)$, and the equations of motion are given by

$$\dot{q}(t) = \partial H(p, q) / \partial p(t), \quad \dot{p}(t) = -\partial H(p, q) / \partial q(t). \tag{1}$$

A common example is the harmonic oscillator, for which, like all systems, the energy is contained in the Hamiltonian,

$$H(p, q) = [p(t)^2/m + \omega^2 m q(t)^2]/2. \tag{2}$$

This leads to the equations of motion given by $\dot{q}(t) = p(t)/m$, while $\dot{p}(t) = -\omega^2 m q(t)$. These equations lead to $\ddot{q}(t) = -\omega^2 q(t)$ and $\ddot{p}(t) = -\omega^2 p(t)$, with solutions given by

$$q(t) = A \cos(\omega t) + B \sin(\omega t) \tag{3}$$

$$p(t) = Bm\omega \cos(\omega t) - Am\omega \sin(\omega t) \tag{4}$$

2.3. Selected Canonical Topics

The action functional is an important expression that also leads to the same equations that we dealt with in the section above, e.g.,

$$A = \int_0^T [p(t) \dot{q}(t) - H(p(t), q(t))] dt, \tag{5}$$

and which leads to tiny variations in the variables, $\delta q(t)$ and $\delta p(t)$, and now $\delta q(T) = \delta q(0) = 0$ as well as $\delta p(T) = \delta p(0) = 0$. The variations lead to

$$\delta A = 0 = \int_0^T \{ [\dot{q}(t) - \delta H(p(t), q(t)) / \delta p(t)] \delta p(t) + [-\dot{p}(t) - \delta H(p(t), q(t)) / \delta q(t)] \delta q(t) \} dt \tag{6}$$

which leads to the correct equations of motion being recovered when arbitrary variations are implied.

3. Phase Space, Poisson Brackets, and Constant Curvature Spaces

Phase space consists of a collection of general, continuous, functions $p(t)$ and $q(t)$. These functions can be turned into different functions, such as $\bar{f}(t) = \bar{F}(f(t))$; a simple example is $\bar{f}(t) = f(t)^3$. The family of functions is chosen to observe the integral

$$\int \bar{F}(\bar{p}(t), \bar{q}(t)) d\bar{p}(t) d\bar{q}(t) = \int F(p(t), q(t)) dp(t) dq(t). \tag{7}$$

The Poisson brackets for these variables is given by

$$\{g(p, q), f(p, q)\} = \frac{\partial g(p, q)}{\partial q} \frac{\partial f(p, q)}{\partial p} - \frac{\partial g(p, q)}{\partial p} \frac{\partial f(p, q)}{\partial q}. \tag{8}$$

Poisson brackets play a reducing lever putting multiple expressions into fixed sets. For example, $\{q, p\} = 1$ and $\{q^3/3, p/q^2\} = 1$, and also as $\{q, pq\} = q$.

The pair of functions, $p(t)$ & $q(t)$, also has a geometric role to play. Let us assume we choose to create a flat, two-dimensional surface, by using the following expression,

$$d\sigma^2 = \omega^{-1} dp(t)^2 + \omega dq(t)^2, \tag{9}$$

where ω is a positive constant that does not depend on $p(t)$ or $q(t)$ in any way. A common name for this case is ‘Cartesian variables’. It is noteworthy that this two-dimensional surface is completely identical if you move to any other location. That property may be called a ‘constant zero curvature’.

Moreover, such a mathematical plane is infinitely big, meaning that $-\infty < p \text{ \& } q < \infty$.

Observe that this property of p & q is *complete*, which means *every* point in \mathbb{R}^2 is included. There is no case where $q = 17$, for example, is excluded from the rest of $-\infty < q < \infty$.

3.1. A Brief Review of Spin Quantization

The operators in this story are S_i with $i = 1, 2, 3$, and which – here $i = \sqrt{-1}$, as well – satisfy $[S_i, S_j] = i\hbar \epsilon_{ijk} S_k$. These operators obey $\sum_{l=1}^3 S_l^2 = \hbar^2 s(s+1) \mathbb{1}_{2s+1}$, where $2s+1 = 2, 3, 4, \dots$ is the dimension of the spin matrices. The normalized eigenvectors of S_3 are $S_3 |s, m\rangle = m\hbar |s, m\rangle$, where $m \in \{-s, \dots, s-1, s\}$.

3.1.1. Spin Coherent States

The spin coherent states are defined by

$$|\theta, \varphi\rangle \equiv e^{-i\varphi S_3/\hbar} e^{-i\theta S_2/\hbar} |s, s\rangle, \tag{10}$$

where $-\pi < \varphi \leq \pi$, and $-\pi/2 \leq \theta \leq \pi/2$. It follows that

$$d\sigma(\theta, \varphi)^2 \equiv 2\hbar [\|d|\theta, \varphi\rangle\|^2 - |\langle\theta, \varphi|d|\theta, \varphi\rangle|^2] = (s\hbar)[d\theta^2 + \cos(\theta)^2 d\varphi^2]. \tag{11}$$

We can also introduce $q = (s\hbar)^{1/2} \varphi$ and $p = (s\hbar)^{1/2} \sin(\theta)$, with $|p, q\rangle = |p(\theta, \varphi), q(\theta, \varphi)\rangle$, which leads to

$$d\sigma(p, q)^2 \equiv 2\hbar [\|d|p, q\rangle\|^2 - |\langle p, q|d|p, q\rangle|^2] = (1 - p^2/s\hbar)^{-1} dp^2 + (1 - p^2/s\hbar) dq^2. \tag{12}$$

Equation (11) makes it clear that we are dealing with a spherical surface with a radius of $(s\hbar)^{1/2}$; this space is also known as a ‘constant positive curvature’ surface, and it has been created!

These classical variables can not lead to a physically correct canonical quantization. Instead, they offer a distinct quantization procedure that applies to different problems.

However, Equation (12) makes it clear that if $s \rightarrow \infty$, in which case both p and q span the real line, we are led to ‘Cartesian coordinates’, a basic property of canonical quantization.

3.1.2. A Brief Review of Affine Quantization

Consider a classical system for which $-\infty < p < \infty$, but $0 < q < \infty$, that does not lead to a self-adjointed quantum operator P , i.e., $P^\dagger \neq P$. Perhaps we can do better if we change classical variables. For example, $0 < q < \infty$ – or it may arise instead that $-\infty < q < 0$. To capture these possibilities for q – and thus also for $Q (=Q^\dagger)$ – we are led to $d = pq \Rightarrow D = (P^\dagger Q + QP)/2 (=D^\dagger)$, which leads to $[Q, D] = i\hbar Q$. This expression happens to be like the Lie algebra of the “affine group” [1], and, incidentally, that name has been adopted by “affine quantization”. Again, it is useful to choose dimensions such that q & Q are dimensionless while d & D have the dimensions of \hbar .

3.1.3. Affine Coherent States

The affine coherent states involve the quantum operators D and Q , where now $Q > 0$. We use the classical variables p and $\ln(q)$, with $q > 0$. Specifically, we choose

$$|p; q\rangle \equiv e^{ipQ/\hbar} e^{-i\ln(q)D/\hbar} |\beta\rangle, \tag{13}$$

where the fiducial vector $|\beta\rangle$ fulfills the condition $[(Q - \mathbb{1}) + iD/\beta\hbar]|\beta\rangle = 0$, which implies that $\langle\beta|Q|\beta\rangle = 1$ and $\langle\beta|D|\beta\rangle = 0$ (the semicolon in $|p; q\rangle$ distinguishes the affine ket from the canonical ket $|p, q\rangle$). If $-\infty < q < 0$, change $\ln(q)$ to $\ln(|q|)$, but keep $q \rightarrow Q < 0$ so that $|q|Q = q|Q\rangle$. This expression leads to

$$H'(pq, q) = \langle p; q|\mathcal{H}'(D, Q)|p; q\rangle = \langle\beta|\mathcal{H}'(D + pqQ, qQ)|\beta\rangle = \mathcal{H}'(pq, q) + \mathcal{O}'(\hbar; pq, q), \tag{14}$$

and, as $\hbar \rightarrow 0$, and $\mathcal{O}'(\hbar; pq, q) = 0$, $H'(d, q) = \mathcal{H}'(d, q)$, a relation very similar to $H(p, q) = \mathcal{H}(p, q)$ when using CQ.

It follows that the Fubini–Study metric, for $q > 0$, becomes

$$d\sigma(p; q)^2 \equiv 2\hbar [\|d|p; q\rangle\|^2 - |\langle p; q|d|p; q\rangle|^2] = (\beta\hbar)^{-1} q^2 dp^2 + (\beta\hbar) q^{-2} dq^2. \tag{15}$$

This expression leads to a surface that has a ‘constant negative curvature’ [2] of magnitude $-2/\beta\hbar$, which, like the other curvatures, has been ‘created’ (as noted, while constant zero and positive curvatures can be seen in our three spatial dimensions, a visualization of a complete constant negative curvature is not possible. A glance of one would be a single point on a saddle, namely the highest point from the rider’s feet direction, and the lowest point from the horse’s head direction). The set of classical variables can not lead to a physically correct canonical quantization. Instead, they offer a distinct quantization procedure that applies to different problems. Any use of classical variables that do not form a ‘constant negative curvature’ subject to an affine quantization is very likely not a physically correct quantization.

The inner product of two affine coherent state vectors is given by

$$\langle p'; q' | p; q \rangle = \left[\frac{(q'/q)^{1/2} + (q/q')^{1/2}}{2} + i(q'q)^{1/2} (p' - p)/2\beta\hbar \right]^{-2\beta}, \tag{16}$$

while $\iint |p; q\rangle \langle p; q| (1 - 1/2\beta) dp dq / 2\pi\hbar = \mathbb{1}$, provided that $\beta > 1/2$. While the variable change for all $p, q \rightarrow cp, q/c$ leaves a Cartesian metric still Cartesian, it can be seen that there is no change whatsoever in (15), illustrating the significance of the affine Fubini–Study metric.

The rule that $0 < q < \infty$ is limited and we can easily consider $0 < q + k < \infty$, where $k > 0$. This changes the coherent states from $\ln(q)$ to $\ln(q + k)$, which then changes the Fubini–Study metric to $(\beta\hbar)^{-1}(q + k)^2 dp^2 + (\beta\hbar)(q + k)^{-2} dq^2$. If we choose to let $k \rightarrow \infty$, and at the same time let $\beta\hbar \rightarrow (\beta\hbar + \omega k^2)$, we are led to $\omega^{-1} dp^2 + \omega dq^2$, now with $q \in \mathbb{R}$, which, once again, applies to canonical quantization. Briefly stated, we can arrange that AQ \rightarrow CQ!

3.2. Summarizing Constant Curvatures and Coherent States

These three stories complete our family of ‘constant curvature’ spaces, specifically, constant positive, zero, and negative curvatures. Additionally, the various coherent states can be used to build “bridges” in each case that enable one to pass from the classical realm to the quantum realm or pass in the other direction [3].

4. Learning to Quantize Selected Problems

We begin with two different quantization procedures, and two simple, but distinct, problems, one of which is successful and the other one is a failure in trying to use both of the quantization procedures on each example.

This exercise serves as a prelude to a valid and straightforward clarification of the fact that affine quantization and canonical quantization solve completely different sets of problems. This fact will help us when we turn to the quantization of field theories and of gravity in later chapters.

4.1. Choosing a Canonical Quantization

The classical variables, p & q , which are elements of a constant zero curvature, better known as Cartesian variables, such as those featured by Dirac [4], are promoted to self-adjointed quantum operators $P(=P^\dagger)$ and $Q(=Q^\dagger)$, ranged so that $-\infty < P \text{ \& } Q < \infty$, and scaled so that $[Q, P] = i\hbar\mathbb{1}$ (in particular, in [4], the mid-page of 114, Dirac wrote “However, if the system does have a classical analogue, its connexion with classical mechanics is specially close and one can usually assume that the Hamiltonian is the same function of the canonical coordinates and momenta in the quantum theory as in the classical theory † Footnote †: This assumption is found in practice to be successful only when applied with the dynamical coordinates and momenta referring to a Cartesian system of axes and not to more general curvilinear coordinates”).

4.1.1. First Canonical Example

Our example is just the familiar harmonic oscillator, for which $-\infty < p \text{ \& } q < \infty$ and a Poisson bracket $\{q, p\} = 1$, also a classical Hamiltonian, with the common factors $m = \omega = 1$, given by $H(p, q) = (p^2 + q^2)/2$. The quantum Hamiltonian is $\mathcal{H}(P, Q) = (P^2 + Q^2)/2$, and Schrödinger’s representation is given by $P = -i\hbar(\partial/\partial x)$ and $Q = x$, for $-\infty < x < \infty$. Finally, for our example, Schrödinger’s equation is given by

$$i\hbar(\partial\psi(x, t)/\partial t) = (-\hbar^2\partial^2/\partial x^2 + x^2)/2 \psi(x, t). \tag{17}$$

Solutions to Equation (7) for our example are well known. In particular, for the harmonic oscillator, the eigenvalues are given by $E_n = \hbar(n + 1/2)$ for $n = 0, 1, 2, \dots$, and

the eigenfunctions (with $\hbar = 1$) are given by $\psi_n(x) = N_n H_n(x) e^{-x^2/2}$ with $n = 0, 1, 2, \dots$. Here, N_n serves to enforce normalization, and the remainder is

$$H_n(x) e^{-x^2/2} = e^{x^2/2} (-d/dx)^n e^{-x^2}. \tag{18}$$

This model is one of the most well understood of all examples.

4.1.2. Second Canonical Example

For our next example, we keep the same classical Hamiltonian, and we retain $-\infty < p < \infty$, but now we restrict $0 < q < \infty$. This new model is called the ‘half-harmonic oscillator’. It follows that the operator $P^\dagger \neq P$, which leads to a different behavior to that when P is self adjointed, i.e., $P^\dagger = P$. In particular, this can lead to infinitely many different self-adjointed Hamiltonians each of which passes to the same classical Hamiltonian that would be $(p^2 + q^2)/2$ in this case. Just two of the different quantum Hamiltonians could be $\mathcal{H}_0(P, Q) = (PP^\dagger + Q^2)/2$, while the other is $\mathcal{H}_1(P, Q) = (P^\dagger P + Q^2)/2$. Clearly, both of these quantum Hamiltonians lead to the same classical Hamiltonian, namely $(p^2 + q^2)/2$, when $\hbar \rightarrow 0$ (here is one example of infinitely many quantum Hamiltonians for the half-harmonic oscillator, when $P^\dagger \neq P$, would be $[(P^\dagger)^{n+4}/P^{n+2} + P^{n+4}/P^{\dagger n+2}]/2 + Q^2/2$, for all $n = 0, 1, 2, \dots$).

This judgement renders the canonical quantization of the half-harmonic oscillator to be an invalid quantization.

We interrupt our present story to bring the reader an important message.

A Simple Truth

Consider $A \times B = C$, as well as $A = B/C$

If $B = C = 0$, what is A ?

If $B = C = \infty$, what is A ?

To ensure getting A one must require $0 < |B| \ \& \ |C| < \infty$.

This is good mathematics, but physics has an opinion as well.

Consider $mv = p$. If the velocity $v = 0$, then the momentum $p = 0$, which makes good sense. However, if the mass $m = 0$ and the velocity $v = 9$, then the momentum, $p = 0$, makes bad physics. However, if any of them are infinite, that is certainly bad math as well as bad physics.

We will especially use this topic for the dilation variable $d = pq$, where q is the coordinate of a position and p denotes its time derivative (times its mass too). The position $q(t)$ is continuous, while $p(t)$ is traditionally continuous, but it can change sign, like bouncing a ball off a wall.

We may point to an ABC-item to remind the reader of its relevance.

This important notification is finished.

4.1.3. First Affine Example

The traditional classical affine variables are $d \equiv pq$ and $q > 0$ (ABC), and they have a Poisson bracket given by $\{q, d\} = q$. In addition, we can choose a different dilation variable, $d = p(q + b)$, for which $-b < q < \infty$, generally, with $b > 0$. For very large b we can approximate a full-line harmonic oscillator and even see what happens if we choose $b \rightarrow \infty$ to mimic the full-line story.

The classical affine variables now are $-\infty < d \equiv p(q + b) < \infty$ and $0 < (q + b) < \infty$, while the classical harmonic oscillator Hamiltonian is given by $H'(d, q) = [d^2/(q + b)^2 + q^2]/2$, an expression that obeys $H(p, q) = (p^2 + q^2)/2$ albeit that $-b < q < \infty$.

Now, we consider basic quantum operators, namely $D = [P^\dagger(Q + b) + (Q + b)P]/2$ and $Q + b$, which lead to $[Q + b, D] = i\hbar(Q + b)$, along with $Q + b > 0$. The quantum ‘partial-harmonic oscillator’ is now given by

$$H'(D, Q) = [D(Q + b)^{-2}D + Q^2]/2 = [P^2 + (3/4)\hbar^2/(Q + b)^2 + Q^2]/2, \quad (19)$$

while, in a proper limit, an affine quantization becomes a canonical quantization when the partial real line ($-b < q$ & $Q < \infty$) is stretched to its full length, ($-\infty < q$ & $Q < \infty$).

Evidently, an affine quantization fails to quantize a full harmonic oscillator.

4.1.4. Second Affine Example

The common canonical operator expression, $[Q, P] = i\hbar\mathbb{1}$, directly implies $[Q, (P^\dagger Q + QP)/2] = i\hbar Q$, which are the basic affine operators.

To confirm this affine expression, let us multiply $i\hbar\mathbb{1} = [Q, P]$ by Q , which gives $i\hbar Q = (Q^2P - QPQ + QPQ - PQ^2)/2$, i.e., $i\hbar Q = [Q, (QP + PQ)/2]$, which is the basic affine expression, $[Q, D] = i\hbar Q$, where $D \equiv (PQ + QP)/2 \equiv (P^\dagger Q + QP)/2$. This derivation assumes that $Q > 0$ or $Q < 0$. Canonical quantization implies affine quantization, but adds a limitation, for classical as well as quantum, on the coordinates.

Regarding our problem, now $b = 0$, and so the classical affine variables are $d \equiv pq$ and $q > 0$, which lead to the half-harmonic oscillator $H'(d, q) = (d^2/q^2 + q^2)/2$. The basic affine quantum operators are D and Q , where $D (= D^\dagger)$ and $Q > 0 (= Q^\dagger > 0)$. These quantum variables lead to $[Q, D] = i\hbar Q$. The half-harmonic oscillator quantum Hamiltonian is given by $\mathcal{H}'(D, Q) = (DQ^{-2}D + Q^2)/2$, and Schrödinger’s representation is given by $Q \rightarrow x > 0$ and

$$D = -i\hbar[x(\partial/\partial x) + (\partial/\partial x)x]/2 = -i\hbar[x(\partial/\partial x) + 1/2]. \quad (20)$$

Finally, Schrödinger’s equation is given by

$$\begin{aligned} i\hbar(\partial\psi(x, t)/\partial t) &= \\ &= [-\hbar^2(x(\partial/\partial x) + 1/2)x^{-2}(x(\partial/\partial x) + 1/2) + x^2]/2 \psi(x, t) \\ &= [-\hbar^2(\partial^2/\partial x^2) + (3/4)\hbar^2/x^2 + x^2]/2 \psi(x, t). \end{aligned} \quad (21)$$

We note that kinetic factors, such as P and D , can annihilate separate features. Adopting Schrödinger’s representation, it follows that $P1 = 0$ while $Dx^{-1/2} = 0$. We will exploit this simple fact in later chapters.

Solutions of (21) have been provided by L. Gouba [5]. Her solutions for the half-harmonic oscillator contain eigenvalues that are equally spaced as are the eigenvalues of the full-harmonic oscillator, although the spacing itself differs in the two cases. The relevant differential equation in (21) is known as a ‘spiked harmonic oscillator’, and its solutions are based on confluent hypergeometric functions. It is noteworthy that every eigenfunction, $\psi_n(x) \propto x^{3/2}(\text{polynomial}_n)e^{-x^2/2\hbar}$, which applies for all $n = 0, 1, 2, \dots$. The leading factor of the eigenfunctions, i.e., $x^{3/2}$, provides a continuous result after the first derivative, but the second derivative could lead to an $x^{-1/2}$ behavior, except that $[-d^2/dx^2 + (3/4)/x^2]x^{3/2} = 0$. This zero ensures that after two derivatives, the wave function is still finite, continuous, and belongs in a Hilbert space (there are examples in which a/x^2 , with $a > 0$, such potentials are studied, but some are negative, i.e., $-a/x^2$, with $a > 0$, which has a completely different behavior).

It is interesting to consider an increase in the coordinate space by choosing $x + b > 0$. This leads to a related Schrödinger’s equation, given by

$$[-\hbar^2(\partial^2/\partial x^2) + (3/4)\hbar^2/(x + b)^2 + x^2]/2 \psi(x, t) = E_b \psi(x), \quad (22)$$

which has been shown to also have equally spaced eigenvalues that become narrower as b becomes larger. Moreover, if $b \rightarrow \infty$, then the \hbar -term disappears and the full-harmonic

oscillator, with its canonical quantization features, is fully recovered [6]. In this fashion, we observe that AQ can pass to CQ, but the reverse is, apparently, impossible.

Finally, we can assert that an affine quantization of the half-harmonic oscillator can be considered to be a correctly solved problem.

4.1.5. A Canonical Version of the Half-Harmonic Oscillator

We start again with the classical Hamiltonian for the half-harmonic oscillator which is still $H = (p^2 + q^2)/2$ and $q > 0$, but this time we will use different coordinates. To let our new coordinate variables span the whole real line, which makes them ‘Ashtekar-like’ [7], we choose $q = s^2$, where $-\infty < s < \infty$. Thus, s is the new coordinate. For the new momentum, r , we choose $p = r/2s$. We choose it because the Poisson bracket $\{s, r\} = \{\sqrt{q}, 2p\sqrt{q}\} = 1$ (it may be noticed that while $q > 0$, and now $q = s^2$, this would imply that $s \neq 0$. However, we will skip over this “unimportant point” until later). The classical Hamiltonian now becomes $H = (p^2 + q^2)/2 = (r^2/4s^2 + s^4)/2$.

4.1.6. A CQ Attempt to Solve the Half-Harmonic Oscillator

For quantization, the new variables use canonical quantum operators, $r \rightarrow R$ and $s \rightarrow S$, with $[S, R] = i\hbar\mathbb{1}$. Following the CQ rules, this leads to $\mathcal{H}_{CQ} = [RS^{-2}R/4 + S^4]/2 \leq \infty$. This quantum operator, using canonical operators where $[S, R] = i\hbar\mathbb{1}$, is quite different from the affine expression $\mathcal{H}_{AQ} = [DQ^{-2}D + Q^2]/2 < \infty$; rearranged into canonical operators with $[Q, P] = i\hbar\mathbb{1}$, that leads to $\mathcal{H}_{AQ} = [P^2 + (3/4)\hbar^2/Q^2 + Q^2]/2 < \infty$.

It is self-evident that these two canonical quantum Hamiltonian operators, \mathcal{H}_{AQ} and \mathcal{H}_{CQ} , have different eigenfunctions and eigenvalues. Does it matter that $\mathcal{H}_{AQ} < \infty$ while $\mathcal{H}_{CQ} \leq \infty$, due to $S = 0$ while $R \neq 0$? It is clear that answer to this question is “No”. Trying to quantize the half-harmonic oscillator, using CQ variables, has led to physically incorrect results.

Now, we examine a very different model using both CQ and AQ.

5. Using CQ and AQ to Examine ‘The Particle in a Box’

5.1. An Example That Needs More Analysis

This model has often been used in teaching and it is introduced early in the process as an easy example to solve. The classical Hamiltonian for this model is simply $H = p^2$, allowing, for simplicity, that $2m = 1$. Now, the coordinate space is $-b < q < b$, where $0 < b < \infty$ (which also may be chosen as $0 < q < 2b \equiv L < \infty$). To accommodate the CQ operators, we assume that outside the box there are infinite potentials that force any wave functions to be zero in the entire outside region where $|x| \geq b$. Inside the box, we have the quantum equation

$$-\hbar^2(d^2 \phi_n(x)/dx^2) = E_n \phi_n(x) . \tag{23}$$

Evidently, cos and sin are relevant. In particular, $\phi(-b) = \phi(b) = 0$ is necessary to continuously join the squashed wave functions, $\phi(|x| \geq b) = 0$. This leads to eigenfunctions which are $\cos(n\pi x/2b)$ for $n = 1, 3, 5, \dots$ and $\sin(n\pi x/2b)$ for $n = 2, 4, 6, \dots$. That leads to the eigenvalues $n^2\pi^2/4b^2$, now for $n = 1, 2, 3, 4, \dots$.

5.1.1. Failure of the Canonical Quantization of the Particle in a Box

While the statements in the last section seem to be correct, there is a problem. Let us focus on the ground state, $\cos(\pi x/2b)$. We need to consider two derivatives of this function, so let us start with $\cos'(\pi x/2b) = -(\pi/2b) \sin(\pi x/2b)$ which leads to $\cos'(\pm\pi/2) = \mp\pi/2b$, i.e., the first derivative is *not* a continuous function with the squashed portion. This forces the second derivative to contain two factors proportional to $\delta(|x| = b)$, the Dirac delta function $\delta(x)$, which vanishes everywhere but $x = 0$ where $\delta(0) = \infty$, such that $\int_{-a}^{a(>0)} \delta(x) dx = 1$. It now follows that $\int \delta(x)^2 dx = \infty$, which then excludes such a function, which is supposed to be finite, e.g., $\int |\phi(x)|^2 dx < \infty$, to join any Hilbert space.

It was remarked in Wikipedia’s discussion of the particle in a box [8] that the first derivative was not continuous as it should have been, but it was effectively ignored afterwards.

In summary, we conclude that by using CQ, the standard treatment and results for the particle in a box are incorrect.

The reduced coordinate space now requires a newly named dilation variable, $d' = p(b + q)(b - q) = p(b^2 - q^2)$, along with accepting only $-b < q < b$. Using affine variables, the classical Hamiltonian now becomes $H' = d'^2 / (b^2 - q^2)^2$. Following the affine quantization rules means that the $D' = [P^\dagger(b^2 - Q^2) + (b^2 - Q^2)P] / 2$, and the quantum Hamiltonian is

$$\mathcal{H}' = D'(b^2 - Q^2)^{-2}D' = P^2 + \hbar^2[2Q^2 + b^2] / [b^2 - Q^2]^2. \tag{24}$$

The new \hbar -expression is unravelled later in the Appendix A to Section 5.

When comparing the different \hbar -terms, we find, with using $Q \rightarrow x$, that if $x \simeq \pm b$, then $[2x^2 + b^2] / (b^2 - x^2)^2 \simeq 3b^2 / (b \mp x)^2 4b^2$, which mimics the (3/4)-factor for the half-harmonic oscillator. This implies that the x term in eigenfunctions, extremely close to either $\pm b$, should be like $\psi(x) \simeq (b^2 - x^2)^{3/2}$ (remainder).

For a moment, we take an about face.

A very different use of (24) is to accept the outside space, $|x| > b$, and reject $|x| < b$, which then becomes an ‘anti-box’.

Note that this system has a similarity to a toy ‘black hole’. It could happen that particles would pile up close to an ‘end of space’, while having been attracted there by a simple, “gravity-like”, pull of a potential, such as $V(x) = W^2 x^4$. If you choose AQ, then the barracked, \hbar -like term, in (24), would prevent the particles from falling ‘out of space’, while the shores exhibit light from the fires of trapped trash.

5.1.2. Removing a Single Point

Assuming that we still have chosen the outside, $|x| > b$, coordinates, it is noteworthy that if we focus on the region where $b \rightarrow 0$, while insisting that $|x| > 0$. In this case, the \hbar -term becomes $2\hbar^2 / x^2$. However, the previous eigenfunction behavior of $(x^2 - b^2)^{3/2}$, now with $x^2 > b^2$, implies that any eigenstates (again, having potentials, like $V(x) = |x|^r$, for $r \geq 2$, that reach infinity) must start like $\psi_n(x) \simeq x^3$ (remainder_n). This offers effective continuity for the eigenfunction and its first two derivatives, even though $x \neq 0$ can permit a more different behavior on either side of $x = 0$. This, then, is the ‘cost’ to remove a single point in the usual coordinate space, e.g., in this case, removing just the single point at $q = 0$.

This result has been made possible using AQ and not using CQ, which requires including all x , i.e., $-\infty < x < \infty$.

A Vector Version: The point we now wish to remove is $\vec{q} = 0$; stated, we want to retain all the variables that obey $\vec{q}^2 > 0$ and all those of $\vec{p}^2 \geq 0$. In addition, we introduce $\vec{P}^2 = \sum_{j=1}^s P_j^2$ and $\vec{Q}^2 = \sum_{j=1}^s Q_j^2 > 0$.

Using these variables, we are led to $d^* = |\vec{P}|(\vec{q}^2 - b^2)$, which leads to $\vec{p}^2 = d^{*2} / (\vec{q}^2 - b^2)^2$. Quantizing, we have $D^* = [|\vec{P}|(\vec{Q}^2 - b^2) + (\vec{Q}^2 - b^2)|\vec{P}|] / 2$ ($= D^{*+}$). Adopting the kinetic factor, $D^*(\vec{Q}^2 - b^2)^{-2}D^*$, that equation also unfolds, in a fashion similar to that shown in the Appendix A to Section 5, below, and leads to the quantum Hamiltonian

$$\mathcal{H} = \frac{1}{2} [\vec{P}^2 + \hbar^2(2\vec{Q}^2 + b^2) / (\vec{Q}^2 - b^2)^2] + V(\vec{Q}^2). \tag{25}$$

Just by sending $b^2 \rightarrow 0$, we achieve the situation where only the single point, i.e., $\vec{q}^2 = 0 \rightarrow \vec{Q}^2 = 0$ is removed from our s -dimensional space. The quantum Hamiltonian in this case is

$$\mathcal{H}_s = \frac{1}{2} [\vec{P}^2 + 2\hbar^2 / \vec{Q}^2] + V(\vec{Q}^2). \tag{26}$$

To offer a justification that this relation holds for all \vec{Q} including just the case where $s = 1$, i.e., just Q^2 . To do so, let us introduce the wave function $\psi(x) = U(x) W_B(Bx_j)$, by introducing a partial expectation of the Hamiltonian given by

$$\begin{aligned} & \int W_B(Bx_j)^* [\vec{P}^2 - 2V(x^2)] W_B(Bx_j) d^{s-1}x \\ & = \int W_B(Bx_j)^* 2\hbar^2 [2/(x^2 + \sum_{j=2}^s x_j^2)] W_B(Bx_j) d^{s-1}x \end{aligned} \tag{27}$$

in which we have integrated all x_j except $x = x_1$. Now, for all, but x_1 , we let $x_j \rightarrow x_j/B$, which changes the previous equation to become

$$\begin{aligned} & \int W_C(x_j)^* [\vec{P}^2 - 2V(x^2 + B^{-2}\sum_j x_j^2)] W_C(x_j) d^{s-1}x \\ & = \int W_C(x_j)^* 2\hbar^2 [2/(x^2 + B^{-2}\sum_j x_j^2)] W_C(x_j) d^{s-1}x . \end{aligned} \tag{28}$$

The purpose of this exercise is to show that the original quantum Hamiltonian (26) for s many dimensions holds the equation for a final quantum Hamiltonian (28) as $B \rightarrow \infty$ for a single dimension.

Briefly stated, an $(s - 1)$ -dimensional reduction may be arranged that can force all of those coordinates to become zero. This leaves behind just one of the coordinates, which is part of a proper equation, and is already waiting to fulfill its duty (additional x_j factors may be made active by simply removing their B factor from the beginning).

5.2. Lessons from Canonical and Affine Quantization Procedures

An important lesson from the foregoing set of examples is that canonical quantization requires special classical variables, i.e., $-\infty < p \ \& \ q < \infty$, that create a flat surface, to be promoted to valid quantum operators that satisfy $-\infty < P \ \& \ Q < \infty$. However, an affine quantization requires different classical variables, e.g., $-\infty < d_b = p(b + q) < \infty$ and $-b < q < \infty$, chosen so that $0 < b < \infty$, to be promoted to valid affine quantum operators, which satisfy $-\infty < D < \infty$ and $-b < Q < \infty$, provided that the classical variables arise from a constant negative curvature.

The essential information from this exercise is that affine quantization variables are created from canonical quantization variables and they permit classical and quantum alike in having a limited behavior where $-b < q \ \& \ Q < \infty$, b is finite, and $-\infty < d \ \& \ D < \infty$.

6. Ultralocal Field Models

6.1. Introduction

In some ways, our first example of a field theory is the hardest to deal with its quantization. An ultralocal form of any classical field theory eliminates all spatial (but *not* temporal) derivatives in its action functional, and specifically, in its classical Hamiltonian such as $H = \int \{ \frac{1}{2}[\pi(x)^2 + m^2\phi(x)^2] + g\phi(x)^p \} d^s x$, where $p = 4, 6, 8, \dots$ and $s = 1, 2, 3, \dots$

If we can handle this model, we should be able to handle more relevant relativistic field models that restore spatial derivatives.

6.2. What Is the Meaning of Ultralocal

The phrase ‘ultralocal’ implies there are no spatial derivatives of the fields only a separate time derivative. Previously, one of the authors has quantized ultralocal scalar fields by affine quantization to show that these non-renormalizable theories can be correctly quantized by affine quantizations; the story of such scalar models is introduced in this chapter. The present chapter will also show that ultralocal gravity can be successfully quantized by affine quantization.

The purpose of this study is to show that a successful affine quantization of any ultralocal field problem would imply that, with properly restored spacial derivatives, the classical theory can, in principle, be guaranteed a successful quantization result using either a canonical quantization in some cases or an affine quantization in different cases.

In particular, Einstein’s gravity requires an affine quantization, and it will be successful, as we will find out in a following chapter.

6.3. Classical and Quantum Scalar Field Theories

The purpose of this section is to review a modest summary of the results of canonical quantization when it has been used to study a variety of covariant scalar field models.

We interrupt our present story to upgrade ‘A Simple Truth’ to prepare the reader for its use with fields:

Another Simple Truth

Consider $A(x) \times B(x) = C(x)$ as well as $A(x) = C(x)/B(x)$

If $B(x) = C(x) = 0$ what is $A(x)$?

If $B(x) = C(x) = \infty$ what is $A(x)$?

To ensure getting $A(x)$ one must require $0 < |B(x)| \ \& \ |C(x)| < \infty$.

This is good mathematics, but physics has an opinion as well.

Consider $k(x) = \pi(x)\varphi(x)$, where $\varphi(x)$ is a chosen physical field, $\pi(x)$ is its momentum field, and their product is $\kappa(x)$, which we will call the dilation field. Since $\pi(x)$ serves as the time derivative of $\varphi(x)$, it can vanish along with $\kappa(x)$. However, requiring that both plus and minus sides of $\varphi(x) \neq 0$ are acceptable, since the derivative term ensures it will still seem to come from a continuous function. Moreover, if $\varphi(x) = 0$ it could be confused with any other field, e.g., $\alpha(x) = 0$ (if you think dimensions can distinguish two such fields, we can eliminate dimensional features by first introducing $\varphi(y) \neq 0$ and $\alpha(z) \neq 0$. Now, dimensionless factors lead to $\varphi(x)/\varphi(y) = 0 = \alpha(x)/\alpha(z)$. Thus, omitting points, or streams of them, where $\varphi(x) = 0$, do not violate any physics. In fact, it may seem logical to say that $\varphi(x) = 0$ never even belonged in physics. It fact, since numbers were used to count physical things, in very early times, zero = 0, was banned for 1500 years; see [9]).

It is good math for finite integrations if there are examples where the fields may reach infinity, e.g., $\int_{-1}^1 \varphi^{-2/3} d\varphi < \infty$. However, such cases are very likely to be bad physics because no item of nature reaches infinity. Accepting $\kappa(x)$ ($= \pi(x)\varphi(x)$) and $\varphi(x) \neq 0$, instead of $\pi(x)$ and $\varphi(x)$, as the basic variables, will have profound consequences.

For example, the classical Hamiltonian expressed as

$$H = \int \{ \frac{1}{2} [\kappa(x)^2 / \varphi(x)^2 + m^2 \varphi(x)^2] + g \varphi(x)^p \} d^s x, \tag{29}$$

in which $0 \leq |\kappa(x)| < \infty$ and $0 < |\varphi(x)| < \infty$, to well represent $\pi(x)$, fulfills the remarkable property that $H(x) < \infty$, where $H = \int H(x) d^s x$, as nature requires! This fact shows that $\kappa(x)$ and $\varphi(x) \neq 0$ should be the new variables!

We now point to our new ABC-items to remind the reader of their relevance.

This important notification is finished.

6.4. Canonical Ultralocal Scalar Fields

These models have a classical (labelled by c) Hamiltonian given by

$$H_c = \int \{ \frac{1}{2} [\pi(x)^2 + m^2 \varphi(x)^2] + g \varphi(x)^p \} d^s x, \tag{30}$$

with $p = 4, 6, 8, \dots$ and $s = 1, 2, 3, \dots$. With $n = s + 1$ spacetime dimensions, and first using canonical quantization, we examine these models. In preparation for a possible path

integration, the domain of H_c consists of all, momentum functions $\pi(x)$ and scalar fields $\varphi(x)$, for which $0 \leq H_c < \infty$.

Since all derivatives have now been removed, even stronger issues can be expected by path integrations being swamped by integrable infinities of the field, or by vast numbers of almost integrable infinities. However, effectively, that strong behavior fails to contribute to the path integration results, e.g., for $p \geq 4$, while the middle range contributions have the most influence on the final result.

To confirm that view, Monte Carlo computations have shown an effectively free-like behavior for analogous CQ models.

6.5. An Affine Ultralocal Scalar Field

Affine classical variables are given by $\kappa(x) \equiv \pi(x) \varphi(x)$ and $\varphi(x)$, with the restriction that $\varphi(x) \neq 0$ (ABC), and the Poisson bracket is given by $\{\varphi(x), \kappa(x')\} = \delta(x - x')^s \varphi(x)$. The ultralocal classical Hamiltonian, expressed in affine variables, is given by

$$H_u = \int \left\{ \frac{1}{2} [\kappa(x)^2 / \varphi(x)^2 + m^2 \varphi(x)^2] + g \varphi(x)^p \right\} d^s x. \tag{31}$$

The term $\kappa(x)^2 / \varphi(x)^2$ requires that $0 < |\varphi(x)| < \infty$ to be fair to $\kappa(x)$, while $\kappa(x)$ is limited only by $|\kappa(x)| < \infty$ to be fair to $\varphi(x)$ (ABC). Observe that $0 < |\varphi(x)| < \infty$ now implies that $0 < |\varphi(x)|^p < \infty$ for all $0 < p < \infty$ and for all $s = 1, 2, 3, \dots$

The basic quantum operators are $\hat{\varphi}(x) \neq 0$ and $\hat{\kappa}(x)$, and their commutator is given by $[\hat{\varphi}(x), \hat{\kappa}(x')] = i\hbar \delta^s(x - x') \hat{\varphi}(x)$. The quantum, ultralocal, affine Hamiltonian, is now given by

$$\mathcal{H} = \int \left\{ \frac{1}{2} [\hat{\kappa}(x) \hat{\varphi}(x)^{-2} \hat{\kappa}(x) + m^2 \hat{\varphi}(x)^2] + g \hat{\varphi}(x)^p \right\} d^s x, \tag{32}$$

with $\hat{\kappa}(x) = -\frac{1}{2} i\hbar [\varphi(x) (\delta / \delta \varphi(x)) + (\delta / \delta \varphi(x)) \varphi(x)]$.

Clearly, this is a formal equation for the Hamiltonian operator, etc. Such expressions deserve a regularization and rescaling of these equations.

The kinetic term in (32) is $\mathcal{K}(\hat{\pi}, \hat{\varphi}) = \hat{\kappa}(x) \hat{\varphi}(x)^{-2} \hat{\kappa}(x) = \hat{\pi}(x)^2 + 2\hbar^2 W / \hat{\varphi}(x)^2$, where $W = \delta(0)^{2s} = \infty$, and $\delta(x)$ is a special function of Dirac. Now, a kinetic scaling can be taken simply by first letting that $Z = (a^2 W)^{1/4}$ and then $\mathcal{K}(\hat{\pi}, \hat{\varphi})_{new} = Z^{-2} \mathcal{K}(Z\hat{\pi}, Z\hat{\varphi}) = \hat{\pi}(x)^2 + 2\hbar^2 / a^2 \hat{\varphi}(x)^2$, and since $0 < a < \infty$, any factor is allowed.

It is noteworthy that Monte Carlo computations have shown a reasonable active behavior for analogous AQ models [10].

7. An Ultralocal Gravity Model

An affine formulation would use the classical metric $g_{ab}(x)$, which, as before, has a positivity requirement, while the momentum field will be replaced by the dilation field, $\pi_b^a(x) [\equiv \pi^{ac}(x) g_{bc}(x)]$, summed by c. These basic affine variables are promoted to quantum operators, both of which can be self-adjointed, while the metric operator is also positive as required.

The principle of using ultralocal rules, as before, is that spacial derivatives must be eliminated. To satisfy that rule, we drop the factor ${}^{(3)}R(x)$, the Ricci scalar field composed of the metric field and its spacial derivatives, and replace it with a new function, $\Lambda(x)$, which will be called a ‘Cosmological Function’ to imitate the standard constant factor, Λ , known as the ‘Cosmological Constant’. This new function is independent of the dilation and metric functions, and is simply used as a continuous function that obeys $0 < \Lambda(x) < \infty$, or otherwise.

With this substitution, the ultralocal classical Hamiltonian is now given by

$$H_u = \int \left\{ g(x)^{-1/2} [\pi_b^a(x) \pi_a^b(x) - \frac{1}{2} \pi_a^a(x) \pi_b^b(x)] + g(x)^{1/2} \Lambda(x) \right\} d^3 x. \tag{33}$$

Since there are no spatial derivatives, we are given another example that every spatial point x labels a pair of distinct variables, namely $\pi_b^a(x)$ and $g_{cd}(x)$. Once again, we find a

quantum wave function, using the Schrödinger representation for the metric field $g_{ab}(x)$, that is a product of independent spacial values of the form $\Psi(\{g\}) = \Pi_x W(x)$, where $\{g\}$ denotes $g_{ab}(\cdot)$ for all x .

When this Hamiltonian is quantized, the only variables that are promoted to quantum operators are the metric field, $g_{ab}(x)$, and the dilation (sometimes known as ‘momentric’ to include *momentum* and *metric*) field, $\pi_b^a(x) = \pi^{ac}(x) g_{bc}(x)$, and the field $\Lambda(x)$ is **fixed** and **not** made into any operator.

7.1. An Affine Quantization of Ultralocal Gravity

The quantum operators are $\hat{g}_{ab}(x)$ and $\hat{\pi}_d^c(x)$, and their Schrödinger representations are given by $\hat{g}_{ab}(x) = g_{ab}(x)$ and $\hat{\pi}_b^a(x) = -i\frac{1}{2}\hbar[g_{bc}(x)(\delta/\delta g_{ac}(x)) + (\delta/\delta g_{ac}(x))g_{bc}(x)]$. The Schrödinger equation for the ultralocal Hamiltonian is then given by

$$i\hbar \partial \psi(\{g\}, t) / \partial t = \int \{ \hat{\pi}_b^a(x) g(x)^{-1/2} \hat{\pi}_a^b(x) - \frac{1}{2} \hat{\pi}_a^a(x) g(x)^{-1/2} \hat{\pi}_b^b(x) + g(x)^{1/2} \Lambda(x) \} d^3x \psi(\{g\}, t), \tag{34}$$

where, as noted, the symbol $\{g\}$ denotes the full metric matrix. Solutions of (34) are governed by the Central Limit Theorem.

7.2. A Regularized Affine Ultralocal Quantum Gravity

Much like the regularization of the ultralocal scalar fields, we introduce a discrete version of the underlying space such as $x \rightarrow \mathbf{k}a$, where $\mathbf{k} \in \{\dots, -1, 0, 1, 2, 3, \dots\}^3$ and $a > 0$ is the spacing between rungs in which, for the Schrödinger representation, $g_{ab}(x) \rightarrow g_{ab\mathbf{k}}$ and $\hat{\pi}_d^c(x) \rightarrow \hat{\pi}_{d\mathbf{k}}^c$. It can be helpful by assuming that the metric has been diagonalized so that $g_{ab\mathbf{k}} \rightarrow \{g_{11\mathbf{k}}, g_{22\mathbf{k}}, g_{33\mathbf{k}}\}$, as it becomes

$$\hat{\pi}_{d\mathbf{k}}^c = -i\frac{1}{2}\hbar[g_{de\mathbf{k}}(\partial/\partial g_{ce\mathbf{k}}) + (\partial/\partial g_{ce\mathbf{k}})g_{de\mathbf{k}}] a^{-s} = -i\hbar[g_{de\mathbf{k}}(\partial/\partial g_{ce\mathbf{k}}) + \delta_d^c/2] a^{-s}. \tag{35}$$

Take note that $\hat{\pi}_{b\mathbf{k}}^a g_{\mathbf{k}}^{-1/2} = 0$, where $g_{\mathbf{k}} = \det(g_{ab\mathbf{k}})$. We will exploit such an expression one more time.

The regularized Schrödinger equation is now given by

$$i\hbar \partial \psi(g, t) / \partial t = \sum_{\mathbf{k}} \{ \hat{\pi}_{b\mathbf{k}}^a g_{\mathbf{k}}^{-1/2} \hat{\pi}_{a\mathbf{k}}^b - \frac{1}{2} \hat{\pi}_{a\mathbf{k}}^a g_{\mathbf{k}}^{-1/2} \hat{\pi}_{b\mathbf{k}}^b + g_{\mathbf{k}}^{1/2} \Lambda_{\mathbf{k}} \} a^s \psi(g, t). \tag{36}$$

Observe that $g_{\mathbf{k}} = \det(g_{ab\mathbf{k}})$ is now the only representative of the metric $g_{ab\mathbf{k}}$.

A normalized, stationary solution to this equation may be given by some $Y(g_{\mathbf{k}})$, which obeys $\Pi_{\mathbf{k}} \int |Y(g_{\mathbf{k}})|^2 (ba^3) / g_{\mathbf{k}}^{(1-ba^3)} dg_{\mathbf{k}} = 1$, which offers a unit normalization for

$$\Psi_Y(g) = \Pi_{\mathbf{k}} Y(g_{\mathbf{k}}) (ba^3)^{1/2} g_{\mathbf{k}}^{-(1-ba^3)/2}. \tag{37}$$

The Characteristic Function for such expressions is given by

$$C_Y(f) = \lim_{a \rightarrow 0} \Pi_{\mathbf{k}} \int e^{if_{\mathbf{k}}g_{\mathbf{k}}} |Y(g_{\mathbf{k}})|^2 (ba^3) g_{\mathbf{k}}^{-(1-ba^3)} dg_{\mathbf{k}} = \lim_{a \rightarrow 0} \Pi_{\mathbf{k}} \{ 1 - (ba^3) \int [1 - e^{if_{\mathbf{k}}g_{\mathbf{k}}}] |Y(g_{\mathbf{k}})|^2 g_{\mathbf{k}}^{-(1-ba^3)} dg_{\mathbf{k}} \} = \exp\{-b \int d^3x \int [1 - e^{if(x)g(x)}] |Y(g(x))|^2 dg(x)/g(x)\}, \tag{38}$$

where the scalar $g_{\mathbf{k}} \rightarrow g(x) > 0$ and Y accommodates any change due to $a \rightarrow 0$. The final result is a (generalized) Poisson distribution, which obeys the Central Limit Theorem.

The formulation of Characteristic Functions for gravity establishes the suitability of an affine quantization as claimed. Although this analysis was only for an ultralocal

model, it nevertheless points to the existence of proper quantum solutions for Einstein’s general relativity.

7.3. The Main Lesson from Ultralocal Gravity

Just like the success of quantizing ultralocal scalar models, we have also showed that ultralocal gravity can be quantized using affine quantization. The purpose of solving ultralocal scalar models was to ensure that non-renormalizable covariant fields can be solved using affine quantization. Likewise, the purpose of quantizing an ultralocal version of Einstein’s gravity shows that we should, in principle, and using affine quantization, be able to quantize the genuine version of Einstein’s gravity using affine quantization.

The analysis of certain gravity models with significant symmetry may provide examples that can be completely solved using the tools of affine quantization.

8. How to Quantize Relativistic Fields

If the reader thinks that canonical quantization is the best way to quantize relativistic field theories, the reader should read this chapter carefully.

8.1. Reexamining the Classical Territory

We now turn from ultralocal models to those that are relativistic. These are models that really can represent nature, and they are clearly the most important examples. The principal example of a covariant scalar field theory is the usual one that we focus on, namely

$$H = \int H(x) d^s x = \int \left\{ \frac{1}{2} [\pi(x)^2 + (\vec{\nabla} \varphi(x))^2 + m^2 \varphi(x)^2] + g \varphi(x)^p \right\} d^s x. \tag{39}$$

This example is meant to deal with fields that obey the rule that $|\pi(x)| + |\varphi(x)| < \infty$ to ensure that $H(x) < \infty$. That is a very reasonable restriction; however, a path integration can violate that rule. We have in mind integrable infinities, such as $\pi(x)^2 = 1/|x|^{2s/3}$, where s is the number of spatial coordinates, i.e., $|x|^2 = x_1^2 + x_2^2 + \dots + x_s^2$, which from a classical viewpoint seem unlikely, but from a path integration point of view seem very likely. Such integrable infinities encountered here in the classical analysis lead to non-renormalizable behavior in which the domain of the variables for a free model, i.e., $g = 0$, becomes reduced then, when $g > 0$, and $p \geq 2n/(n - 2)$, with $n = s + 1$. Since the domain of the classical variables becomes reduced, it remains that way when the coupling constant is reduced to zero using $g \rightarrow 0$. With such behavior for the classical analysis, there is every reason to expect considerable difficulties in using canonical quantization.

To make that statement clear, it is a fact that Monte Carlo calculations for the scalar fields φ_3^2 and φ_4^2 apparently led to *free results*, using CQ, as if the coupling constant $g = 0$ when that was not the case, but offered reasonable results using AQ. Clearly, integrable infinities are *not* welcome!

This section will draw on Section 5 to a large extent, although it has been somewhat changed by the introduction of the gradient term. That may lead to some repeats of certain topics.

8.1.1. A Simple Way to Avoid Integrable-Infinities

Let us, again, introduce a new field, $\kappa(x) \equiv \pi(x) \varphi(x)$, as a featured variable rather than $\pi(x)$, to accompany $\varphi(x) \neq 0$ (ABC). We do not really ‘change any variable’, but just give the usual ones ‘a new role’.

Some care is needed in choosing $\kappa(x)$ and $\varphi(x)$ as the new pair of variables, and physics can be a good guide.

Let us recall the simple analog, namely $p = mv$. If the velocity $v = 0$, then physics agrees that the momentum $p = 0$. However, if the mass $m = 0$ and $v = 6$, then having $p = 0$, along with any term being infinity, is very bad physics. Instead, physics requires that $0 \leq |v|$ & $|p| < \infty$ and $0 < m < \infty$ makes good physics. This story can apply to other variables, and as has often been noted, we point to such items as (ABC).

In our case, we assume $\varphi(x)$ is a physical field, $\pi(x)$ is its time derivative, and $\kappa(x) \equiv \pi(x) \varphi(x)$, their product, which will be called the ‘dilation field’, serves as a kind of momentum. Now, using a similar argument as above, we accept the assertion that $0 \leq |\kappa(x)|$ & $|\pi(x)| < \infty$ and $0 < |\varphi(x)| < \infty$, which makes good physics.

The reader may still worry about requiring $\varphi(x) \neq 0$. Surely, integrations like $\int \varphi(x)^r d^s x$, $r > 0$, are not affected. However, there is a good reason to accept it. Such an equation lends itself to $\varphi(x) = 0 = \zeta(x)$ if two different fields might find this fact. If you worry about dimensions, or different charges (denoted here by $*$), you can use $\varphi(y) \neq 0$ and $\zeta(z) \neq 0$ or $\zeta^*(z) \neq 0$, which then leads to $\varphi(x)/\varphi(y) = 0 = \zeta(x)/\zeta(z)$ or $\varphi(x)/\varphi(y) = 0 = \zeta(x)^*/\zeta(z)^*$ which equates two fully dimensionless terms. Adopting $\varphi(x) \neq 0$ still leads to continuity thanks to the presence of the gradient term, $(\vec{\nabla} \varphi(x))^2$, which enforces a necessarily continuous field behavior.

8.1.2. The Absence of Infinities by Using Affine Field Variables

Now, let us use $\kappa(x)$ and $\varphi(x) \neq 0$ as the new variables to be used in the classical Hamiltonian (39), which then becomes

$$H = \int \left\{ \frac{1}{2} [\kappa(x)^2 / \varphi(x)^2 + (\vec{\nabla} \varphi(x))^2 + m^2 \varphi(x)^2] + g \varphi(x)^p \right\} d^s x. \tag{40}$$

Now, things are different. To represent $\pi(x)$, then $\kappa(x)$ and $\varphi(x)$, must serve their role. Hence we require that $0 < |\varphi(x)| < \infty$, which implies that $0 < |\varphi(x)|^p < \infty$ for all $0 < p < \infty$ and all s . In addition, we require that $|\kappa(x)| < \infty$ for a similar reason. The gradient term, which arises in the spacial derivative $(\vec{\nabla} \kappa(x)) = (\vec{\nabla} \pi(x)) \varphi(x) + \pi(x) (\vec{\nabla} \varphi(x))$, creates another kind of (ABC) issue that leads to $|\vec{\nabla} \varphi(x)| < \infty$. The Hamiltonian density, $H(x)$, is now *finite everywhere!* It follows that the Hamiltonian, $H = \int H(x) d^s x$, will be finite if it is confined to any finite spacial region, or if the field values taper off sufficiently, as is customary.

Although we have pointed out some difficulties that might arise in a canonical quantization, we follow a careful road to see how far we can get.

The usual continuum limit of the canonical quantum Hamiltonian leads to

$$\mathcal{H} = \int \left\{ \frac{1}{2} [\hat{\pi}(x)^2 + (\vec{\nabla} \hat{\varphi}(x))^2 + m^2 \hat{\varphi}^2(x)] + g \hat{\varphi}(x)^p \right\} d^s x, \tag{41}$$

but now there is some confusion.

The confusion arises in comparing $[Q_k, P_l] = i\hbar \delta_{kl} \mathbb{1}$ with $[\hat{\varphi}(x), \hat{\pi}(y)] = i\hbar \delta(x - y) \mathbb{1}$. As with the ultralocal case, it seems that we have a big difference in scale when $p \geq 2n/(n - 2)$ and the domain reduction appears when the interaction term is active compared with if it is not active. The same issue applied to the ultralocal case, which the p -value happened even earlier due to the absence of the gradient term, which, then is $p > 2$. From a path integration viewpoint, fields like $|\varphi(x)| \gg 1$ are less likely to help their contribution. That can also apply to $|\varphi(x)| \ll 1$ about the fields. Indeed, having both $\pi(x)$ and $\varphi(x)$ fields in ‘the middle’ tends to make them more prominent features in a path integration.

8.2. Affine Quantization of Relativistic Field Models

8.2.1. Affine Classical Variables for Selected Field Theories

We first reexamine the features of a classical Hamiltonian once again, now with the affine variables $\kappa(x)$ and $\varphi(x) \neq 0$, which becomes

$$H = \int \left\{ \frac{1}{2} [\kappa(x)^2 / \varphi(x)^2 + (\vec{\nabla} \varphi(x))^2 + m^2 \varphi(x)^2] + g \varphi(x)^p \right\} d^s x. \tag{42}$$

In this case, we need $0 < |\varphi(x)| < \infty$, and $|\vec{\nabla} \varphi(x)|$ & $|\kappa(x)| < \infty$ (ABC). This requirement leads to the Hamiltonian *density*, $H(x)$, which will entirely be $0 \leq H(x) < \infty$, for all x , signaling that integrable infinities may be excluded. That is true, and it must be

obeyed, also in a path integration. This rule, regarding quantization, already distinguishes AQ from CQ.

If new variables can calm down the classical Hamiltonian, is it possible that they might also calm down the quantum Hamiltonian? Let us see how we can do just that!

8.2.2. An Affine Quantization of Relativistic Fields

We first focus on the several field factors, which obey $\pi(x)^2 = \kappa(x)^2/\varphi(x)^2$. Using Schrödinger’s representation, the quantization of these fields leads to $\pi(x)^2 \Rightarrow \hat{\kappa}(x)(\varphi(x))^{-2}\hat{\kappa}(x)$, where $\hat{\kappa}(x) = [\hat{\pi}(x)^\dagger\varphi(x) + \varphi(x)\hat{\pi}(x)]/2$. In a similar case, in an earlier chapter, we found that $p^2 = d^2/q^2 \rightarrow DQ^{-2}D = P^2 + 2\hbar^2/Q^2$, with $D = (P^\dagger Q + QP)/2$. Now, we follow the same path, more or less.

Still using Schrödinger’s representation, then

$$\begin{aligned} \pi(x)^2 &= \kappa(x)^2/\varphi(x)^2 \Rightarrow \hat{\kappa}(x)(\varphi(x))^{-2}\hat{\kappa}(x) \\ &= \hat{\pi}(x)^2 + 2\hbar^2\delta(0)^{2s}/\varphi(x)^2, \end{aligned} \tag{43}$$

which involves the Dirac delta function much like $[\hat{\varphi}(x), \hat{\pi}(x)] = i\hbar\delta(0)^s\mathbb{1}$ does as well.

Now is the time to introduce some scaling. Such a feature can adopt $\pi_\kappa \rightarrow a^{-s/2}P_\kappa$ and $\varphi_\kappa \rightarrow a^{-s/2}Q_\kappa$, with $\hat{\kappa}_\kappa = (\hat{\pi}_\kappa^\dagger\hat{\varphi}_\kappa + \hat{\varphi}_\kappa\hat{\pi}_\kappa)/2 = a^{-s}[P_\kappa^\dagger Q_\kappa + Q_\kappa P_\kappa]/2$. Now, we re-examine the kinetic factor for which $\hat{\kappa}_\kappa(\hat{\varphi}_\kappa^{-2})\hat{\kappa}_\kappa = a^{-s}P_\kappa^2 + 2a^{-2s}\hbar^2/a^{-s}Q_\kappa^2$. This regularization now leads to a regularized quantum Hamiltonian

$$\mathcal{H} = \Sigma_\kappa a^{-s} \{ \frac{1}{2}[P_\kappa^2 + 2\hbar^2/Q_\kappa^2 + m^2Q_\kappa^2] + gQ_\kappa^p \} a^s, \tag{44}$$

provided that $g a^{-s(p-2)/2} \rightarrow g a^{-s}$ by properly changing g .

8.2.3. Schrödinger’s Representation and Equation

We are now in position to suggest the important affine quantization of standard classical models such as

$$H = \int \{ \frac{1}{2}[\kappa(x)^2/\varphi(x)^2 + (\vec{\nabla}\varphi(x))^2 + m^2\varphi(x)^2] + g\varphi(x)^p \} d^s x, \tag{45}$$

followed by the usual rules leading to

$$\begin{aligned} &\int \{ \frac{1}{2}[\hat{\kappa}(x)(\varphi(x))^{-2}\hat{\kappa}(x) \\ &\quad + (\vec{\nabla}\varphi(x))^2 + m^2\varphi(x)^2] + g\varphi(x)^p \} d^s x \Psi(\varphi) = E \Psi(\varphi). \end{aligned} \tag{46}$$

As like other Characteristic Functions, such as were used for the ultralocal models, we note that for any normalized wave function, such as $\Pi_x W(\varphi(x))/\varphi(x)^{1/2}$ in the Hilbert space, a Fourier transformation leads to

$$C_W(f) = \exp\{-b \int d^s x \int [1 - e^{if(x)\varphi(x)}] |W(\varphi(x))|^2 d\varphi(x)/|\varphi(x)|\}. \tag{47}$$

9. How to Quantize Einstein’s Gravity

If the reader thinks that canonical quantization is the best way to quantize Einstein’s gravity, the reader should read this chapter carefully.

9.1. Gravity and AQ, Using Basic Operators

In order to quantize gravity it is important to render a valid quantization of the Arnowitt, Deser, and Misner classical Hamiltonian [11]. We first choose our new classical variables which include what we also call the dilation field $\pi_b^a(x) \equiv \pi^{ac}(x) g_{bc}(x)$ (summed on c) along with the metric field $g_{ab}(x)$. We do not need to impose any restriction on the metric field because physics already requires that $ds(x)^2 = g_{ab}(x) dx^a dx^b > 0$ provided that $\Sigma_{a=1}^3 (dx^a)^2 > 0$. The metric can also be diagonalized by non-physical, orthogonal matrices, and then it includes only $g_{11}(x)$, $g_{22}(x)$, & $g_{33}(x)$, each of which must be

strictly positive as required by physics (the reader should compare the three diagonalized positive metric variables with $q > 0$, which then requires an affine quantization for the half-harmonic oscillator, and also then appreciate the need for such a quantization that lead to positive results).

Next we present the ADM classical Hamiltonian in our chosen affine variables, which, introducing $g(x) \equiv \det[g_{ab}(x)] > 0$, leads to

$$H(\pi, g) = \int \{ g(x)^{-1/2} [\pi_b^a(x) \pi_a^b(x) - \frac{1}{2} \pi_a^a(x) \pi_b^b(x)] + g(x)^{1/2} {}^3R(x) \} d^3x, \tag{48}$$

where ${}^3R(x)$ is the Ricci scalar for three spatial coordinates and which contains all of the derivatives of the metric field. Already, this version of the classical Hamiltonian contains reasons that restrict $g(x)$ to $0 < g(x) < \infty$, $0 \leq |\pi_b^a(x)| < \infty$, and $0 \leq |{}^3R(x)| < \infty$, which, like the previous field theory examples, and lead to no integral-infinities for the gravity story.

Finally, we introduce the dilation gravity operator $\hat{\pi}_b^a(x) = [\hat{\pi}^{ac}(x)^\dagger \hat{g}_{bc}(x) + \hat{g}_{bc}(x) \hat{\pi}^{ac}(x)]/2$ along with $\hat{g}_{ab}(x) > 0$, and adopting Schrödinger's representation and equation, we are led to

$$\mathcal{H}'(\hat{\pi}, g) = \int \{ [\hat{\pi}_b^a(x) g(x)^{-1/2} \hat{\pi}_a^b(x) - \frac{1}{2} \hat{\pi}_a^a(x) g(x)^{-1/2} \hat{\pi}_b^b(x)] + g(x)^{1/2} {}^3R(x) \} d^3x. \tag{49}$$

And now, as before, we close with Schrödinger's equation

$$i\hbar \partial \Psi(g, t) / \partial t = \mathcal{H}'(\hat{\pi}, g) \Psi(g, t), \tag{50}$$

which offers the necessary ingredients for the foundation of a valid quantization of the classical Hamiltonian, which is an important part of the full story.

As before, it may be necessary to introduce some version of regularization for these equations, but these same equations point the way to proceed. In that effort, note that although $\hat{\pi}^{ac}(x)^\dagger \neq \hat{\pi}^{ac}(x)$ it can be helpful to know that $\hat{\pi}^{ac}(x)^\dagger g_{bc}(x) = \hat{\pi}^{ac}(x) g_{bc}(x)$.

A full quantization of gravity must deal with first and likely second order constraints, which are designed to reduce the overall Hilbert space to secure a final quantization. This project is not the proper place to finalize a quantization of gravity, but several of the author's articles have been designed to go further toward the final steps [12].

Additional Aspects of Quantum Gravity

This section is relevant to follow sections which lead toward a path integration. These topics involve constraints required in the ADM approach. The present story, told just above, follows in the pattern of establishing a Schrödinger equation using his representation, has been the rule in discussing prior examples, e.g., the half-harmonic oscillator, quantum field theories over multiple powers of the interaction term, ultralocal examples of fields and gravity, and covariant field theories.

Now, in the forthcoming section, we offer a careful treatment of constraints and their analysis, which is prominent in gravity and needs its own analysis.

9.2. Gravity and AQ, Using Path Integration

We first recall the Arnowitt, Deser, and Misner version of the classical Hamiltonian, seen in [11], as originally expressed in the standard classical variables, namely the momentum, $\pi^{ab}(x)$, the metric, $g_{cd}(x)$, the metric determinant, $g(x) = \det[g_{ab}(x)]$, and ${}^3R(x)$,

which is the Ricci scalar for three spatial variables. Now, the ADM classical Hamiltonian is essentially given by

$$H(\pi, g) = \int \{g(x)^{-1/2} [\pi^{ac}(x)g_{bc}(x)\pi^{bd}(x)g_{ad}(x) - \frac{1}{2} \pi^{ac}(x)g_{ac}(x)\pi^{bd}(x)g_{bd}(x)] + g(x)^{1/2} {}^{(3)}R(x)\} d^3x, \tag{51}$$

9.2.1. Introducing the Favored Classical Variables

The ingredients in providing a path integration of gravity include proper coherent states, the Fubini–Study metric which turns out to be affine in nature, and affine-like Wiener measures are used for the quantizing of the classical Hamiltonian. While that effort is only part of the story, it is an important portion to ensure that the quantum Hamiltonian is a bonafide self-adjointed operator.

According to the ADM classical Hamiltonian, it can also be expressed in affine-like variables, as we did in the previous chapter, namely by introducing, in some papers of this author, the ‘momentric’ (a name that is the combination of *momentum* and *metric*) and, instead, this item is now called the ‘dilation variable’ becoming $\pi_b^a(x) (\equiv \pi^{ac}(x)g_{bc}(x))$, along with the metric $g_{ab}(x)$. The essential physical requirement is that $g_{ab}(x) > 0$, which means that $ds(x)^2 = g_{ab}(x) dx^a dx^b > 0$, provided that $\Sigma_a(dx^a)^2 > 0$.

Now, the classical Hamiltonian, expressed in affine classical variables, is again given by

$$H \equiv \int H(x) d^3x = \int \{g(x)^{-1/2} [\pi_b^a(x)\pi_a^b(x) - \frac{1}{2} \pi_a^a(x)\pi_b^b(x)] + g(x)^{1/2} {}^{(3)}R(x)\} d^3x. \tag{52}$$

9.2.2. The Gravity Coherent States

The principal operators $\hat{\pi}_b^a(x) = [\hat{\pi}^{ac}(x)\hat{g}_{bc}(x) + \hat{g}_{bc}(x)\hat{\pi}^{ac}(x)]/2 (\equiv \hat{\pi}_b^a(x)^\dagger)$ and $\hat{g}_{ab}(x) = \hat{g}_{ab}(x)^\dagger > 0$ offer a closed set of commutation relations given by

$$\begin{aligned} [\hat{\pi}_b^a(x), \hat{\pi}_d^c(y)] &= i\frac{1}{2} \hbar \delta^3(x, y) [\delta_d^a \hat{\pi}_b^c(x) - \delta_b^c \hat{\pi}_d^a(x)], \\ [\hat{g}_{ab}(x), \hat{\pi}_d^c(y)] &= i\frac{1}{2} \hbar \delta^3(x, y) [\delta_a^c \hat{g}_{bd}(x) + \delta_b^c \hat{g}_{ad}(x)], \\ [\hat{g}_{ab}(x), \hat{g}_{cd}(y)] &= 0. \end{aligned} \tag{53}$$

We now choose the basic affine operators to build our coherent states for gravity, specifically

$$|\pi; \eta\rangle = e^{(i/\hbar) \int \pi^{ab}(x) \hat{g}_{ab}(x) d^3x} e^{-(i/\hbar) \int \eta_b^a(x) \hat{\pi}_a^b(x) d^3x} |\beta\rangle [= |\pi; g\rangle]. \tag{54}$$

Note: The last item in this equation is the new name of these vectors hereafter.

A new fiducial vector, also named $|\beta\rangle$ but now different, has been chosen now in connection with the relation $[e^{\eta(x)}]_{ab} \equiv g_{ab}(x) > 0$, while $-\infty < \{\eta(x)\} < \infty$, and which enters the coherent states as shown, using $|\beta\rangle$ as the new fiducial vector that is affine-like, and obeys $[(\hat{g}_{ab}(x) - \delta_{ab} \mathbb{1}) + i\hat{\pi}_d^c(x)/\beta(x)\hbar]|\beta\rangle = 0$. It follows that $\langle \beta | \hat{g}_{cd}(x) | \beta \rangle = \delta_{cd}$ and $\langle \beta | \hat{\pi}_d^c(x) | \beta \rangle = 0$, which leads to the form given by

$$\begin{aligned} \langle \pi; g | \hat{g}_{ab}(x) | \pi; g \rangle &= [e^{\eta(x)/2}]_a^c \langle \beta | \hat{g}_{cd}(x) | \beta \rangle [e^{\eta(x)/2}]_b^d \\ &= [e^{\eta(x)}]_{ab} = g_{ab}(x) > 0. \end{aligned} \tag{55}$$

In addition, we introduce the inner product of two gravity coherent states, which is given by

$$\begin{aligned} \langle \pi''; g'' | \pi'; g' \rangle &= \exp \left\{ -2 \int \beta(x) d^3x \right. \\ &\times \ln \left\{ \frac{\det [g''^{ab}(x) + g'^{ab}(x)] + i/(2\beta(x)\hbar) [\pi''^{ab}(x) - \pi'^{ab}(x)]}{\det [g''^{ab}(x)]^{1/2} \det [g'^{ab}(x)]^{1/2}} \right\} \left. \right\}. \end{aligned} \tag{56}$$

Finally, for some C , we find the Fubini–Study gravity metric to be

$$d\sigma_g^2 = C\hbar[\|d|\pi;g\rangle\|^2 - |\langle\pi;g|d|\pi;g\rangle|^2] = \int[\beta(x)\hbar^{-1}(g_{ab}(x)d\pi^{ab}(x))^2 + (\beta(x)\hbar)(g^{ab}(x)dg_{ab}(x))^2]d^3x, \tag{57}$$

which is seen to imitate an affine metric, leading to a constant negative curvature, as well, and that will provide a genuine Wiener-like measure for a path integration. In no way could we transform this metric into a proper Cartesian form, as was carried out for the half-harmonic oscillator. That is because there is no physically proper Cartesian metric for the variables $\pi^{ab}(x)$ and $g_{cd}(x)$.

9.2.3. A Special Measure for the Lagrange Multipliers

To ensure a proper treatment of the operator constraints, we choose a special measure of the Lagrange multipliers, $R(N_a, N)$, guided by the following procedures.

The first step is to unite the several classical constraints by using

$$\begin{aligned} \int \int e^{i(y^a H_a(x) + y H(x))} W(u, y^a, y, g^{ab}(x)) \Pi_a dy^a dy \\ = e^{-iu[H_a(x)g^{ab}(x)H_b(x) + H(x)^2]} \\ \equiv e^{-iuH_v(x)^2} \end{aligned} \tag{58}$$

with a suitable measure W .

An elementary Fourier transformation (in mathematics, the following function being Fourier transformed is known as (a version of) $\text{rect}(u) = 1$ for $|u| \leq 1$, and 0 for $|u| > 1$) is given by $M \int_{-\delta^2}^{\delta^2} e^{i\epsilon\tau uy} dy / 2 = \sin(u\epsilon\tau\delta^2) / u$, using a suitable M , which then ensures that the inverse Fourier transformation, where ϵ represents a tiny spatial interval and τ represents a tiny time interval, as part of a fully regularized integration in space and time, and u is another part of the Lagrange multipliers, $N_a(n\epsilon)$ and $N(n\epsilon)$, which leads to

$$\begin{aligned} \lim_{\zeta \rightarrow 0^+} \lim_{L \rightarrow \infty} \int_{-L}^L e^{-iu\epsilon\tau\mathcal{H}_v^2(x)} \sin(u\epsilon\tau(\delta^2 + \zeta)) / u \pi du \\ = \mathbb{E}(\epsilon\tau\mathcal{H}_v(x)^2 \leq \epsilon\tau\delta^2) \\ = \mathbb{E}(\mathcal{H}_v(x)^2 \leq \delta^2). \end{aligned} \tag{59}$$

This expression covers all self-adjointed operators, and leads to a self-adjointed $\mathcal{H}_v = \int \mathcal{H}_v(x) d^3x$.

Bringing together our present tools lets us first offer a path integral for the gravity overlap of two coherent states, as given by

$$\begin{aligned} \langle\pi'';g''|\pi';g'\rangle &= \lim_{\nu \rightarrow \infty} \mathcal{N}_\nu \int \exp[-(i/\hbar)\int_0^T \int [(g_{ab}\pi^{ab}) d^3x dt] \\ &\times \exp\{-(1/2\nu\hbar)\int_0^T \int [(\beta(x)\hbar)^{-1}(g_{ab}\pi^{ab})^2 + (\beta(x)\hbar)(g^{ab}\dot{g}_{ab})^2] d^3x dt\} \\ &\times \Pi_{x,t} \Pi_{a,b} d\pi^{ab}(x,t) dg_{ab}(x,t) \\ &= \exp\left\{-2 \int \beta(x) d^3x \right. \\ &\left. \times \ln \left\{ \frac{[g''^{ab}(x) + g'^{ab}(x)] + i/(2\beta(x)\hbar)[\pi''^{ab}(x) - \pi'^{ab}(x)]}{\det[g''^{ab}(x)]^{1/2} \det[g'^{ab}(x)]^{1/2}} \right\} \right\}, \end{aligned} \tag{60}$$

where the second equation indicates what such a path integration has been designed to achieve for its goal.

9.3. The Affine Gravity Path Integration

By adding all the necessary tools, and implicitly having examined a regularized integration version in order to effectively deal with suitable constraint projection terms, we have chosen $\mathbf{E} \equiv \mathbf{E}(\mathcal{H}_v^2 \leq \delta(\hbar)^2)$ for simplicity here, all of which leads us to

$$\begin{aligned} \langle \pi''; g'' : T | \mathbf{E} | \pi'; g' : 0 \rangle &= \langle \pi''; g'' | \mathbf{E} e^{-(i/\hbar)\mathbf{E}T} \mathbf{E} | \pi'; g' \rangle \\ &= \lim_{v \rightarrow \infty} \mathcal{N}'_v \int \exp\left\{-(i/\hbar) \int_0^T [g_{ab} \dot{\pi}^{ab} + N^a H_a + NH] d^3x dt\right\} \\ &\times \exp\left\{-(1/2v\hbar) \int_0^T [(\beta(x)\hbar)^{-1} (g_{ab} \dot{\pi}^{ab})^2 + (\beta(x)\hbar) (g^{ab} \dot{g}_{ab})^2] d^3x dt\right\} \\ &\times [\prod_{x,t} \Pi_{a,b} d\pi^{ab}(x,t) dg_{ab}(x,t) \mathcal{D}R(N^a, N)]. \end{aligned} \tag{61}$$

The role of the measure $R(N^a, N)$ is defined so that the operators, $\mathcal{H}_a \mathcal{H}$, only support a sample of non-zero eigenvalues, e.g., $\mathbf{E}(\mathcal{H}_v^2 \leq \delta(\hbar)^2)$, where, e.g., $\delta(\hbar)^2 \sim c\hbar^2$, or some other tiny value that vanishes if $\hbar \rightarrow 0$ if $\mathcal{H}_v^2 \leq \delta(\hbar)^2$ consists only of a continuous spectrum; see [12].

We let the reader choose their own regularization of the last equation to ensure that the ϵ terms are proper, and that the ϵ^2 terms —And higher ϵ^K , $K > 2$, terms as well —Lead to a proper continuum limit. In so doing, the overlap of two gravity coherent states, as above in (60), could be particularly useful.

Several papers by the author offer additional information regarding topics, and additional procedures to use, has been discussed in [Kla-2].

10. Summary, and Outlook

Each Field Problem Needs AQ or CQ, Otherwise, There Can Be Incorrect Results

Could it be the time now to pass from CQ to AQ to solve difficult problems? Perhaps new procedures can help. The passing of years can often lead to the introduction of improved procedures. For example, though history, people first took around the mail on horses, then trains, then cars, then switched to the internet, etc. Likewise, first there was CQ, now AQ, which is added to become CQ & AQ = EQ, known as 'Enhanced Quantization'. It has introduced a huge jump that greatly extends quantization procedures, along with a noteworthy proof that, essentially, AQ \rightarrow CQ.

In an artistic sense, CQ represents the beautiful surface of a brick made of pure gold, while AQ represents the wonderful interior of the same gold brick. Hence, moving around within an inside path, AQ points can reach a point on the CQ surface!

While the half-harmonic oscillator using AQ was shown to be valid, the validity of AQ for field theories or for gravity are not as yet proved to be true, and there are opportunities for others to test their out coming. While every attempt to maintain correctness has been made, something may still have been overlooked. The improvement of every step is open to consideration and further recommendation.

Author Contributions: Conceptualization, J.R.K.; methodology, J.R.K.; software, R.F.; validation, R.F. and J.R.K.; formal analysis, J.R.K. and R.F.; investigation, J.R.K. and R.F.; resources, J.R.K. and R.F.; data curation, J.R.K. and R.F.; writing—original draft preparation, J.R.K.; writing—review and editing, R.F.; visualization, J.R.K. and R.F.; supervision, J.R.K.; project administration, J.R.K. All authors have read and agreed to the published version of the manuscript.

Funding: This research received no external funding.

Data Availability Statement: No data associated in the manuscript.

Conflicts of Interest: The authors declare no conflict of interest.

Appendix A. Appendix to Section 5

Any tired reader may skip to the last paragraph.

Our analysis of general dilation variables is given as follows. The quantum kinetic term (now, with $\hbar = 1$) in affine variables is $DF^{-2}D$. This expression, is helped by $F = F(Q), G =$

$G(Q) \equiv 1/F(Q), F(Q)P - PF(Q) = iF'(Q)$. and $G(Q)P - PG(Q) = iG'(Q)$ leads to $4DG^2D = (PF + FP)GG(PF + FP) = PP + FPGGPF + FPGP + PGPF = PP + (PF + iF')GG(FP - iF') + (PF + iF')GP + PG(FP - iF') = 4PP + 2i(F'GP - PGF') + F'GGF' = 4PP - 2(F'G)' + (F')^2G^2$. Restoring \hbar , we have $DG^2D = P^2 + (1/4)\hbar^2[(F')^2G^2 - 2(F'G)']$. Keeping \hbar , and here, using $D = [P^\dagger F(Q) + F(Q)P]/2$, then $DF^{-2}D = P^2 + (1/4)\hbar^2[(\ln(F)')^2 - 2(\ln(F))'']$, where, symbolically, $F'(Q) = dF(Q)/dQ$. For $F(Q) = (Q^2 - b^2)$, we now find the \hbar -term to be $\hbar^2(2Q^2 + b^2)/(b^2 - Q^2)^2$.

References

1. Wikipedia: "Fubini–Study Metric". Available online: https://en.wikipedia.org/wiki/Fubini%E2%80%93Study_metric (accessed on 14 September 2023).
2. Wikipedia: "Pseudosphere". Available online: <https://en.wikipedia.org/wiki/Pseudosphere> (accessed on 14 September 2023).
3. Klauder, J.R. The Benefits of Affine Quantization. *J. High Energy Phys. Gravity Cosmol.* **2020**, *6*, 175. [CrossRef]
4. Dirac, P.A.M. *The Principles of Quantum Mechanics*; Clarendon Press: Oxford, UK, 1958; p. 114.
5. Gouba, L. Affine Quantization on the Half Line. *J. High Energy Phys. Grav. Cosmol.* **2021**, *7*, 352. [CrossRef]
6. Handy, C. Affine Quantization of the Harmonic Oscillator on the Semi-bounded Domain $(-b, \infty)$ for $b : 0 \rightarrow \infty$. *arXiv* **2021**, arXiv:2111.10700.
7. Ashtekar, A. New Variables for Classical and Quantum Gravity. *Phys. Rev. Lett.* **1986**, *57*, 2244. [CrossRef] [PubMed]
8. Wikipedia: "The Particle in a Box". Available online: https://en.wikipedia.org/wiki/Particle_in_a_box (accessed on 14 September 2023).
9. Watch: "Why the Number 0 Was Banned for 1500 Years". Available online: <https://www.youtube.com/watch?v=ndmwB8F2kxA> (accessed on 14 September 2023).
10. Fantoni, R.; Klauder, J.R. Scaled Affine Quantization of Ultralocal ϕ_2^4 a comparative Path Integral Monte Carlo study with Scaled Canonical Quantization. *Phys. Rev. D* **2022**, *106*, 114508. [CrossRef]
11. Arnowitt, R.; Deser, S.; Misner, C. *Gravitation: An Introduction to Current Research*; Witten, L., Ed.; Wiley & Sons: New York, NY, USA, 1962; p. 227.
12. Klauder, J.R. Quantization of Constrained Systems. *Lect. Notes Phys.* **2001**, *572*, 143–182.

Disclaimer/Publisher's Note: The statements, opinions and data contained in all publications are solely those of the individual author(s) and contributor(s) and not of MDPI and/or the editor(s). MDPI and/or the editor(s) disclaim responsibility for any injury to people or property resulting from any ideas, methods, instructions or products referred to in the content.

Chapter 77

Monte Carlo simulation of hard-, square-well, and square-shoulder disks in narrow channels

Fantoni R., Eur. Phys. J. B **96**, 155 (2023)

Title: “Monte Carlo simulation of hard-, square-well, and square-shoulder disks in narrow channels”

Abstract: We perform Monte Carlo simulation of the thermodynamic and structural properties of hard-, square-well, and square-shoulder disks in narrow channels. For the thermodynamics, we study the internal energy per particle and the longitudinal and transverse compressibility factor. For the structure, we study the transverse density and density of pairs profiles, the radial distribution function and longitudinal distribution function, and the (static) longitudinal structure factor. We compare our results with a recent exact semi-analytic solution found by Montero and Santos for the single file formation and first nearest neighbor fluid, and explore how their solution performs when these conditions are not fulfilled making it just an approximation.



Monte Carlo simulation of hard-, square-well, and square-shoulder disks in narrow channels

Riccardo Fantoni^a

Dipartimento di Fisica, Università di Trieste, strada, Costiera 11, Grignano, 34151 Trieste, Italy

Received 5 October 2023 / Accepted 17 November 2023
 © The Author(s), under exclusive licence to EDP Sciences, SIF and Springer-Verlag GmbH Germany, part of Springer Nature 2023

Abstract. We perform Monte Carlo simulation of the thermodynamic and structural properties of hard-, square-well, and square-shoulder disks in narrow channels. For the thermodynamics, we study the internal energy per particle and the longitudinal and transverse compressibility factor. For the structure, we study the transverse density and density of pairs profiles, the radial distribution function and longitudinal distribution function, and the (static) longitudinal structure factor. We compare our results with a recent exact semi-analytic solution found by Montero and Santos for the single file formation and first nearest neighbor fluid, and explore how their solution performs when these conditions are not fulfilled making it just an approximation.

1 Introduction

Confined fluids are an important field of study due to the wide range of applications and situations where they can be found [1]. Interesting systems in physics, chemistry, or biology involve dealing with confined particles. Examples are carbon nanotubes [2, 3] or biological ion channels [4]. In many of these systems, the geometry is so restrictive that one or more spatial dimensions become negligible. One can, therefore, often describe these systems as living in a one (1D) or two (2D) dimensional space to simplify the mathematical model and its subsequent study. Yet, in some cases, it is necessary a more realistic description which can be obtained by modeling the geometrical restriction without recurring to a dimensionality reduction. So, for particles living in three dimensions, we will talk about *quasi* two-dimensional (quasi 2D) or *quasi* one-dimensional (quasi 1D) fluids. In this work, we will study particles living in 2D which are quasi 1D.

Despite its clear importance, systems whose structural properties are amenable to exact analytic solutions are very scarce, and usually limited to 1D fluids [5–14] with only nearest neighbor interactions [15–17]. Even if for restricted values of the thermodynamic parameters, even 2D fluids may offer an exact analytic classical equilibrium statistical mechanics solution [18–21]. Otherwise, one must resort to approximations, numerical methods, or simulations.

Recently, Montero and Santos [22, 23] developed an exact semi-analytic formalism able to solve the *longi-*

tudinal structure and thermodynamics of a quasi 1D problem of *single file* formation and *first nearest neighbor* fluids of *hard-core* particles in *narrow channels*.

In particular, the single file confinement constraint [24, 25] implies that particles are inside a *pore* that is not wide enough to allow particles to bypass each other, therefore confining them into a single file formation.

Whereas, the first nearest neighbor constraint implies that the particles are not allowed to interact with their second (or beyond) nearest neighbors [14].

The pore is a 2D narrow channel or band with *periodic boundary conditions* along the longitudinal direction and *open boundary conditions* along the transverse direction where the particles are assumed to be confined by *hard walls*.

The nearest neighbor constraint allows the use of the exact solution that is available for 1D fluids subject to such constraint [15–17]. In fact, Montero and Santos study their quasi 1D fluids of particles interacting through a *pairwise* potential $\varphi_{2D}(r)$ with a mapping to a 1D *non-additive* mixture [26] of equal chemical potentials species, where the species index i denotes those particles with the ordinate equal to a fixed value within the channel and the interaction potential becomes $\varphi_{ij}(x) = \varphi_{2D}(\sqrt{x^2 + (y_i - y_j)^2})$. They further assume the mixture to be *polydisperse* [27–29], so that the molar fraction x_i of the i th species can be rewritten as $F(y)dy$ which represents the fraction of particles with the ordinate lying in the interval $[y, y + dy]$. What they find [30] is that working in the isothermal isobaric ensemble, the average of a function of y can be expressed as $\langle f(y) \rangle = \int dy F(y)f(y)$, where $F(y) = \phi^2(y)$. Here $\phi(y)$ is the eigenfunction of the

^a e-mail: riccardo.fantoni@posta.istruzione.it (corresponding author)

maximum eigenvalue of a certain operator $K(y_1, y_2) = \exp\{-\beta P_L \sigma(y_1, y_2) - \frac{1}{2} \beta [\Phi_{ext}(y_1) + \Phi_{ext}(y_2)]\}$, where $\beta = 1/k_B T$ with k_B Boltzmann constant and T the absolute temperature, P_L is the longitudinal pressure, $\sigma(y_1, y_2)$ is the distance of closest approach of particles 1 and 2, which are nearest neighbors, and $\Phi_{ext}(y)$ is the external potential which acts only in the dimension of the y coordinates and confines the particles within the channel.

In this work, we will perform Monte Carlo (MC) simulations [31, 32], in the *canonical ensemble* (for results using molecular dynamics see Ref. [33]), to study the thermodynamic and structural properties of Hard (HD), Square-Well (SW), and Square-Shoulder (SS) disks in narrow channels. For the thermodynamics, we will study the internal energy and the compressibility factor. For the structure, we will study the Transverse Density Profile (TDP), the Transverse Density of Pairs Profile (TDPP), the Radial Distribution Function (RDF) and Longitudinal Distribution Function (LDF), and the (static) Longitudinal Structure Factor (LSF).

Of course with our MC simulations, we are not bound to fulfill the single file and nearest neighbor constraints. We will, therefore, also study the performance of the solution of Montero and Santos outside the nearest neighbor regime where it is expected to be just an approximation.

The work is organized as follows: In Sect. 2, we will describe the mathematical model of the physical fluid of interest, the MC estimators for the quantities we want to measure in our computer experiments, and some MC results for the thermodynamics. In Sect. 3, we present our MC results for the structure. Section 4 is for concluding remarks.

2 Model and simulation details

Consider a 2D system of N particles interacting via a *pairwise potential* $\varphi_{2D}(r)$. The particles are confined in a very long channel of width $w = 1 + \epsilon$ and length $L \gg w$, in such a way that they are in *single file* formation and only *first nearest neighbor* interactions take place. The *channel surface density* of the fluid will be $\sigma = N/Lw = \lambda/w$ with λ the *longitudinal density*. The total potential energy of the fluid will be

$$\Phi(\mathbf{Q}) = \frac{1}{2} \sum_{i,j \neq i} \varphi_{2D}(q_{ij}) + \Phi_{ext}, \quad (2.1)$$

where $\mathbf{Q} = (\mathbf{q}_1, \mathbf{q}_2, \dots, \mathbf{q}_N)$ are the positions of the particles in the channel and $\mathbf{q} = (x, y)$ with $x \in [-L/2, L/2]$ and $y \in [-\epsilon/2, \epsilon/2]$. We have *periodic boundary conditions* (PBC) along x so that $x_i \rightarrow x_i - \text{nint}(x_i/L)L$ where 'nint' is the nearest integer and enforce the usual minimum image convention so that $x_i - x_j \rightarrow x_i - x_j - \text{nint}[(x_i - x_j)/L]L$. Along y , instead, we have *open boundary conditions* (OPC) where in particular we assume to have an infinitely repulsive exter-

nal potential Φ_{ext} for $y > \epsilon/2$ and $y < -\epsilon/2$ and we do not employ the minimum image convention. We will denote with $q_{ij} = \sqrt{(x_i - x_j)^2 + (y_i - y_j)^2}$ the distance between particles at \mathbf{q}_i and at \mathbf{q}_j .

For Hard Disks (HD), we have

$$\varphi_{2D}(r) = \begin{cases} \infty & \text{if } r < 1 \\ 0 & \text{else} \end{cases}. \quad (2.2)$$

If the transverse separation between two disks at contact is s , their longitudinal separation is

$$a(s) = \sqrt{1 - s^2}. \quad (2.3)$$

The single file constraint in this case requires clearly $\epsilon < \epsilon_{sf} = 1$. In this case, we have a close packing limit longitudinal density given by $\lambda_{cp} = 1/a(\epsilon)$. To enforce also the first nearest neighbor constraint we require $\epsilon < \epsilon_{nn-HD} = \sqrt{3}/2$. For $\epsilon = \sqrt{3}/2$, the close packing longitudinal density is $\lambda_{cp} = 2$ and the surface density is $\sigma_{cp} = 2/(1 + \sqrt{3}/2) = 1.071 \dots$

For Square-Wells (SW) or Square-Shoulders (SS), we have

$$\varphi_{2D}(r) = \begin{cases} \infty & \text{if } r < 1 \\ -\varphi_0 & \text{if } 1 < r < r_0 \\ 0 & \text{else} \end{cases}, \quad (2.4)$$

with $\varphi_0 > 0$ for SW and $\varphi_0 < 0$ for SS.

In this case, to enforce the first nearest neighbor constraint, we require $\epsilon < \epsilon_{nn} = \sqrt{1 - (r_0/2)^2}$. Since $r_0 > 1$, we will have $\epsilon_{nn} < \epsilon_{nn-HD}$.

In our computer experiment, we measured various thermodynamic and structural properties of these fluids. We could than compare our numerical *meta data* with analytic or semi-analytic theoretical data available in the literature. To *measure* an observable \mathcal{O} , we need to calculate [34] the following quantity

$$\langle \mathcal{O} \rangle = \frac{\int \mathcal{O}(\mathbf{Q}) \exp[-\beta \Phi(\mathbf{Q})] d\mathbf{Q}}{\int \exp[-\beta \Phi(\mathbf{Q})] d\mathbf{Q}}, \quad (2.5)$$

where $\beta = 1/k_B T$ with k_B Boltzmann constant and T absolute temperature. In our canonical (at fixed number of particles, surface area, and temperature) Monte Carlo (MC) simulation, we employed the usual M(RT)² algorithm [34] to sample the probability distribution $\propto \exp[-\beta \Phi(\mathbf{Q})]$.

We generally found it sufficient to use $N = 100$ with runs up to 10^9 MC single particle moves long. The spatial extent of the uniform particle displacement move was tuned so to have acceptance ratios around 1/2 and kept constant during the run, even if this was not always possible at high densities.

2.1 Structure

For the Radial Distribution Function (RDF) [35,36], $g(r) = \langle O \rangle$, we have the following histogram estimator

$$O(\mathbf{Q}; r) = \sum_{i,j \neq i} \frac{1_{[r-\Delta/2, r+\Delta/2]}(q_{ij})}{N n_{id}(r)}, \tag{2.6}$$

where Δ is the histogram bin, $1_{[a,b]}(t) = 1$ if $t \in [a, b]$ and 0 otherwise, and $n_{id}(r)$ is the average number of particles on the interception of the circular crown $[r - \Delta/2, r + \Delta/2]$ with the part of the channel accessible to the particles centers, for the uniform gas at the same longitudinal density λ , which for a narrow channel can be approximated to

$$n_{id} = 2\lambda\Delta, \tag{2.7}$$

independent of r . We have that $g(r)$ gives the probability density that sitting on a particle at \mathbf{q} one has to find another particle at \mathbf{q}' , where $r = \sqrt{(x-x')^2 + (y-y')^2}$.

Instead of counting how many disks are separated a 2D distance r we can count how many are separated a 1D longitudinal distance $|x|$. So, doing the same calculation described above, but, in the end, keeping track only of the relative abscissas, $r = \sqrt{(x-x')^2} = |x-x'|$, of the particles, we find the quasi 1D or Longitudinal Distribution Function (LDF) $g(|x|)$.

The Fourier transform of the radial distribution function is the (static) structure factor $S(k)$ which for an isotropic system is given by

$$S(k) = 1 + \frac{\lambda}{\epsilon} \int [g(r) - 1] \exp(-i\mathbf{k} \cdot \mathbf{r}) \mathbf{dr} + \frac{\lambda}{\epsilon} (2\pi)^2 \delta(\mathbf{k}), \tag{2.8}$$

where usually the Dirac delta function is neglected. Note also that from the definition (2.6) we find the following sum rule

$$\frac{\lambda}{\epsilon} \int [g(r) - 1] \mathbf{dr} = -1, \tag{2.9}$$

and from the definition (2.8) follows $\lim_{k \rightarrow 0} S(k) = 0$. Moreover if $\lim_{r \rightarrow 0} g(r) = 0$ then $\lim_{k \rightarrow \infty} S(k) = 1$. Now for our quasi 1D geometry of the narrow channel, the isotropy is clearly lost and when we count just the longitudinal distances between the particles, for the LDF $g(|x|)$, we may still find $\lim_{k_x \rightarrow 0} S(k_x) \neq 0$ since the sum rule becomes $\frac{\lambda}{\epsilon} \int [g(|x|) - 1] dx = -\frac{1}{\epsilon} < -1$. In the following, we will always refer to this Longitudinal Structure Factor (LSF) $S(k_x)$ and for brevity, we will simply rewrite $k_x \rightarrow k$.

Another structural property to study is the Transverse Density Profile (TDP) $F(y)$ such that $F(y)dy$ gives the fraction of particles with the ordinate in the interval $[y, y + dy]$. By symmetry, we clearly must have for F an even function. A related function is $F_2(y)$,

the fraction of pairs of different particles 1 and 2 such that their transverse distance $|y_2 - y_1| \in [y, y + dy]$. We will call this the Transverse Density of Pairs Profile (TDPP).

2.2 Internal energy

For the internal energy per particle of the fluid [35,36], we have $u = \langle \mathcal{O} \rangle$ with the following internal energy per particle estimator

$$O(\mathbf{Q}) = \Phi(\mathbf{Q})/N. \tag{2.10}$$

For SW/SS with $|\beta\varphi_0| = 1$, we found the results of Table 1.

2.3 Compressibility factor

For the compressibility factor $Z = \beta P/(\lambda/\epsilon)$ of the confined 2D fluid, we have, from the virial theorem [37]

$$Z = 1 - \beta \frac{\lambda}{\epsilon} \frac{1}{4} \iint_{\substack{x_1, x_2 \in [-L/2, L/2] \\ y_1, y_2 \in [-\epsilon/2, \epsilon/2]}} r \varphi'_{2D}(r) g(\mathbf{r}) \mathbf{dr} \approx 1 + \frac{\lambda}{2} \int_0^\infty \frac{d \exp[-\beta\varphi_{2D}(r)]}{dr} r y(r) \mathbf{dr} = 1 + \frac{\lambda}{2} [g(1^+) + (1 - e^{\beta\varphi_0}) r_0 g(r_0^+)], \tag{2.11}$$

where in the first line $\mathbf{dr} = d(x_1 - x_2)d(y_1 - y_2)$, $g(\mathbf{r}) = g(|x_1 - x_2|; y_1, y_2)$, and we used polar coordinates so that $\mathbf{dr} = r d\theta dr$. In the second line, we approximated $\int_{\text{channel}} r d\theta \approx 2\epsilon$ for the narrow channel, we then introduced the continuous indirect correlation function $y(r) = g(r) \exp[-\beta\varphi_{2D}(r)]$, where $g(r)$ is the 2D RDF of Eq. (2.6), and used the fact that for the SW/SS pair potential of Eq. (2.4), we have

$$\frac{d \exp[-\beta\varphi_{2D}(r)]}{dr} = e^{\beta\varphi_0} \delta(r - 1) + (1 - e^{\beta\varphi_0}) \delta(r - r_0). \tag{2.12}$$

The total thermodynamic pressure $P = (P_L + P_T)/2$, where P_L and P_T are the longitudinal and transverse 2D pressures, respectively. In Table 1, we present some results for SW/SS.

Let us now specialize to the HD case so that $\varphi_0 = 0$. We will also introduce $p = P_L \epsilon$. From the Table I of Ref. [22], we find that $Z_L^{\text{exact}} = \beta p / \lambda = 12.774$ when $\epsilon = 0.4$ and $\beta p = 12$. From these data, we extract $\lambda = \beta p / Z_L^{\text{exact}} = 0.671w$ and, at this longitudinal density, our canonical simulation gives $\beta P = 15.85(2)$ for $\Delta = 10^{-2}$ and $\beta P = 16.53(1)$ for $\Delta = 10^{-3}$. Since the exact longitudinal pressure is $\beta P_L^{\text{exact}} = \beta p / \epsilon = 30$, we estimate a transverse pressure of $\beta P_T \approx 2(16.53) - 30 = 3.06$. For the case when $\epsilon = 0.8$ and $\beta p = 12$, we find $\beta P = 14.46(1)$ (these measures tend to slightly increase even further at lower Δ). See Table 2 for these Z measurement. Exact results from the Montero and Santos

Table 1 Internal energy per particle (2.10) and total pressure (2.11) for $N = 100$ SW/SS with $|\beta\varphi_0| = 1$. The results were determined from runs made of 5×10^7 single particle moves

ϵ	r_0	λ_{cp}	λ	σ	u		βP	
					SW	SS	SW	SS
4/5	6/5	1.66667	1.080	0.6	-0.9303(4)	+0.7673(7)	7.351(1)	9.965(3)
4/5	6/5	1.66667	1.260	0.7	-0.9797(4)	+0.9176(8)	14.653(4)	16.45(1)
$\sqrt{7}/4$	3/2	1.33333	0.997	0.6	-0.99837(2)	+0.9895(2)	9.865(2)	10.160(2)
$\sqrt{7}/4$	3/2	1.33333	1.163	0.7	-0.9999989(6)	+0.99998(1)	23.856(7)	23.12(2)

Table 2 Results for $N = 100$ HD from Eqs. (2.11) and (2.13a) and comparison with the exact values of Table I of Ref. [22]. Z_L^{Mon} are the MC values of Ref. [31]. The two low-density cases were determined from runs made of 5×10^7 single particle moves, $\Delta = 10^{-5}$ for Z_L , and $\Delta = 10^{-3}$ for Z

ϵ	p	Z_L^{exact}	Z_L^{Mon}	λ	λ/ϵ	λ_{cp}	$2 + a(\epsilon)p$	Z	Z_L	Z_L^{exact}/Z_L	$\lambda(I_0 - I_0^{asy})$	$\lambda^2(I_1 - I_1^{asy})$
0.4	12	12.774	12.774	0.939408	2.34852	1.09109	12.998	7.04(1)	12.8094(3)	0.997	2.1	2.3
0.4	120	112.04	112.03	1.07105	2.67762	1.09109	111.98	-	?	?	$+3.6 \times 10^{-4}$	$+3.5 \times 10^{-4}$
0.8	12	9.6547	9.6548	1.24292	1.55365	1.66667	9.2000	9.31(1)	9.780(4)	0.987	-2.4×10^{-2}	-2.5×10^{-2}
0.8	120	74.017	74.016	1.62125	2.02656	1.66667	74.000	-	?	?	$< 10^{-15}$	-4.9×10^{-6}

analysis [38] give $\beta P = 16.722$ for $\epsilon = 0.4, \beta p = 12$ and $\beta P = 14.8551$ for $\epsilon = 0.8, \beta p = 12$. Alternatively, one can use the canonical ensemble exact expression found by Pergamenschchik [39].

Alternatively, one can use the quasi 1D scenario and the LDF $g(|x|)$ to find the longitudinal compressibility factor $Z_L = \beta P_L / (\lambda/\epsilon)$. To do this, we need to calculate (see Appendix A [40])

$$Z_L = \frac{1 - \lambda I_0}{1 - \lambda + \lambda^2(I_0 - I_1)}, \tag{2.13a}$$

$$I_n = \int_{a(\epsilon)}^1 x^n g(x) dx. \tag{2.13b}$$

We computed the integrals I_n for $n = 0, 1$ numerically with a discretization Δ on the abscissa $x^i = \Delta i$ with $i = 0, 1, 2, 3, \dots$. In Table 2, we show our results compared with the ones of Ref. [22]. Note that for the two high-density cases, this way of estimating numerically Z_L is not useful since for $\lambda \rightarrow \lambda_{cp}$ we find

$$\lambda I_0 \rightarrow 1 - 8 \exp\{-\beta p[1 - a(\epsilon)]\} = \lambda I_0^{asy},$$

$$\lambda^2 I_1 \rightarrow 1 - \frac{1}{2}\{1 + [2 - a(\epsilon)]\lambda\}(1 - \lambda I_0^{asy}) \tag{2.14a}$$

$$= \lambda^2 I_1^{asy}, \tag{2.14b}$$

and both numerator and denominator in Eq. (2.13a) vanish. In this case, one can use the analytic expression (see Appendix C of Ref. [22])

$$Z_L \rightarrow 2 + a(\epsilon)p = \frac{2}{1 - \lambda/\lambda_{cp}}, \tag{2.15}$$

valid asymptotically for λ near to its close packing limit λ_{cp} .

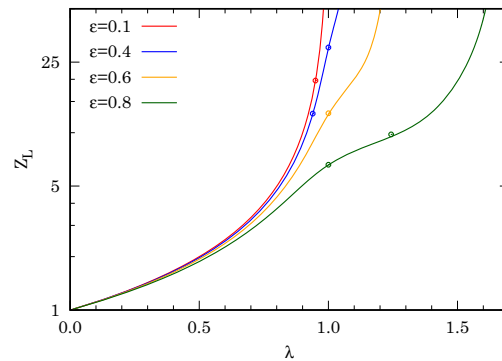


Fig. 1 Comparison between our MC (points) and the exact results (lines) of Ref. [22] for the longitudinal compressibility factor. The statistical error in the MC points is smaller than the point symbol. The MC simulations were up to 10^9 single particle moves long

Additional points are presented in Fig. 1, where we compare with the exact results of Ref. [22] (results shared privately and not all previously published). We found that at the same value of λ , it takes longer to equilibrate the large ϵ cases. For example, the MC points at $\epsilon = 0.1$ required just 10^7 single particle moves; whereas, the ones at $\epsilon = 0.8$ required up to 10^9 moves (Figs. 2, 3).

Note that a drawback of this way of estimating the longitudinal pressure is that it is hard to tell if the statistical error is more or less important than the systematic error due to the choice of the discretization Δ . In this respect, instead of working in the canonical $N\lambda T$ ensemble, it would be desirable to work in the isother-

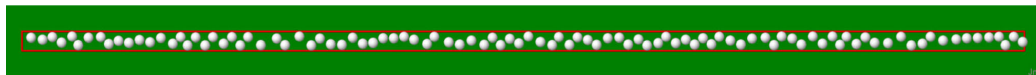


Fig. 2 Snapshot of the simulation box for $N = 100$ HD of radius $r_0 = 1$ with $\epsilon = \sqrt{3}/2$ and $\lambda = 1$



Fig. 3 Snapshot of the simulation box for $N = 100$ SW with $\beta\varphi_0 = 1$ and radius $r_0 = 6/5$ with $\epsilon = 4/5$ and $\sigma = 7/10$

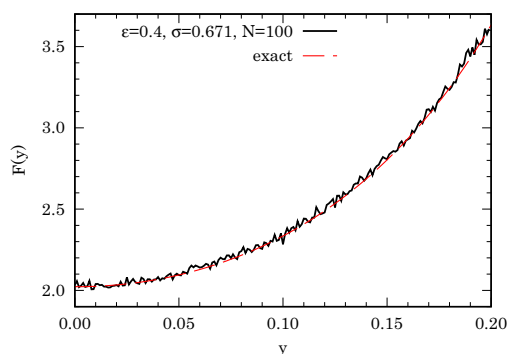


Fig. 4 TDP for $N = 100$ HD with $\epsilon = 0.4$ and $\lambda = 0.671w$. The exact result, shared privately by A. Montero and not published before, fits our MC results very well. In particular from Fig. 4 of Ref. [22], we see how the particles tend to escape from the center of the channel preferring to stay in contact with the walls as density approaches the packing density

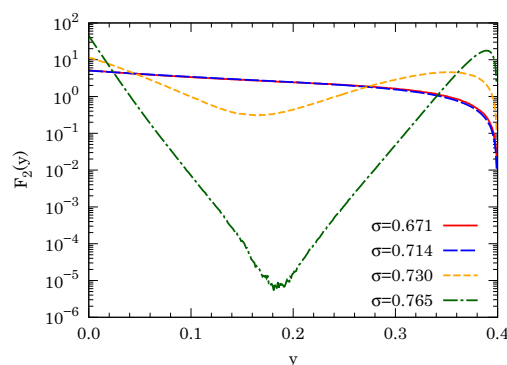


Fig. 5 TDPP for $N = 100$ HD with $\epsilon = 0.4$ and $\sigma = 0.671, 0.714, 0.730, 0.765$ corresponding to $\lambda = 0.939, 1.000, 1.022, 1.071$, respectively. We can see how this density function starts changing only really near to the close packing density $\lambda_{cp} = 1.091$, when the TDP becomes very small at $y \approx 0$

mal isobaric NpT ensemble with a volume change move where one only varies the length of the channel L .

For the HD case, with $\epsilon = 0.4$ and $\lambda = 0.671w$, we find the TDP $F(y)$ shown in Fig. 4. As you can see the exact result of Ref. [22] fits our MC data very well. For the same case the TDPP, $F_2(y)$, is shown in Fig. 5. From this figure, we can see how the TDPP changes drastically only getting really near to the close packing density $\lambda_{cp} = 1.091$.

3 Results for the structure

In this section, we present our MC results for the structural properties of the confined quasi 1D fluids of our interest.

3.1 Ideal gas (id)

We first tried to switch off the pair potential between the particles taking $\varphi_{2D}(r) = 0$ but keeping the confining infinitely repulsive external potential Φ_{ext} switched on. For the case $\lambda = \sigma w = 1$ and $\epsilon = \sqrt{3}/2$ we found the results for the LDF and RDF shown in Figs. 6 and 7, respectively. As you can clearly see from the MC results,

the LDF, and as a consequence the LSF, is uniform but the RDF is not.

Note that this is just an effect of the geometry of the confinement in fact using periodic boundary conditions also along the transverse, y , direction one gets both a uniform LDF and RDF as expected. Moreover, the TDP turns out to be uniform $F(y) = 1/\epsilon$ irrespective of using open or periodic boundary conditions along the transverse direction.

For the case of our interest, with periodic boundary conditions along x and open boundary conditions along y , the RDF can be calculated exactly analytically as follows (see Appendix B [40])

$$g_{id}(r) = \frac{2r}{\epsilon} \begin{cases} \pi/2 - r/\epsilon & r < \epsilon \\ \sqrt{(r/\epsilon)^2 - 1} - r/\epsilon + \arctan[1/\sqrt{(r/\epsilon)^2 - 1}] & \text{else} \end{cases} \quad (3.1)$$

3.2 Hard disks (HD)

We tried to reproduce the case $\epsilon = \sqrt{3}/2, \lambda = \sigma w = 1$ of Fig. 5(a) of Ref. [23]. Our results for the LDF, LSF,

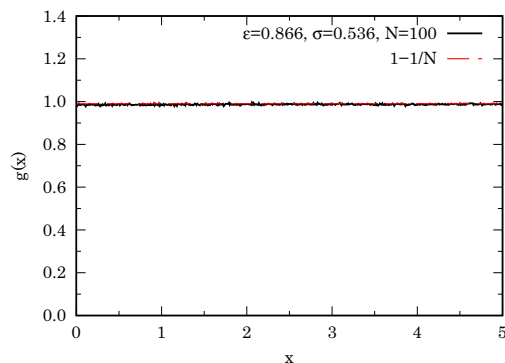


Fig. 6 LDF for the ideal gas with $\lambda = 1$ and $\epsilon = \sqrt{3}/2$. The MC data are fitted very well by the exact result of $g_{id}(x) = 1 - 1/N$

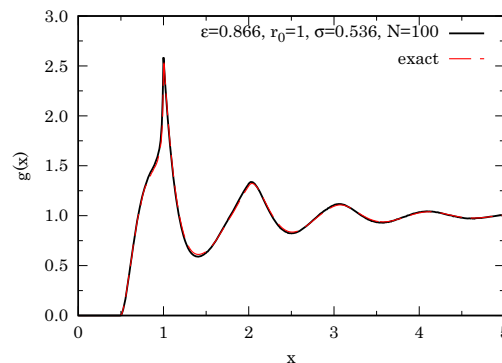


Fig. 8 LDF for $N = 100$ HD of radius $r_0 = 1$ with $\epsilon = \sqrt{3}/2$ and $\lambda = 1$. Our MC data are fitted very well by the exact result of Ref. [23] which is in the thermodynamic limit

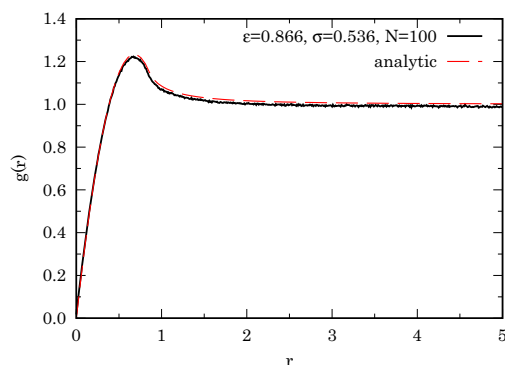


Fig. 7 RDF for the ideal gas with $\lambda = 1$ and $\epsilon = \sqrt{3}/2$. Here, the $g(r)$ is calculated from Eq. (2.6) using for $n_{id}(r)$ its asymptotic value $2\lambda\Delta$ everywhere. The analytic result is the one in the thermodynamic limit of Eq. (3.1). The slight discrepancy is the expected finite size effect. Remember that $\lim_{r \rightarrow \infty} g_{id}(r) = 1 - 1/N$

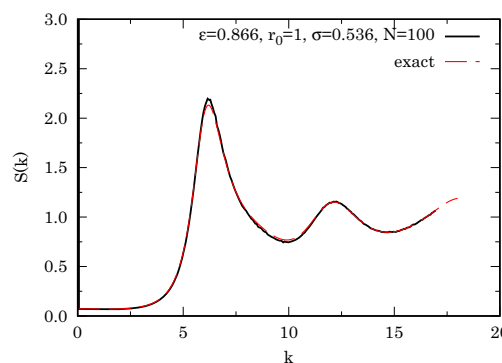


Fig. 9 LSF for $N = 100$ HD of radius $r_0 = 1$ with $\epsilon = \sqrt{3}/2$ and $\lambda = 1$. We used $2n_{max} + 1$ wave numbers with $n_{max} = 270$. The exact result in the thermodynamic limit, shared privately by A. Montero and not published before, fits our MC results very well

and RDF are shown in Figs. 8, 9, and 10, respectively. In Fig. 2, we show a snapshot of the simulation box.

We also run simulations for the cases considered in Fig. 10 of Ref. [23]. The results are shown in Fig. 10. Comparison with the work of Montero and Santos [23] shows that our RDF is different from what they define as g_{2D} [40].

It is interesting to study how the solution of Montero and Santos [23] performs outside of the nearest neighbor regime where it is expected to be not exact anymore. Such a study was carried out at the level of the compressibility factor in Fig. 7 of Ref. [22]. We want here to repeat it for the structure. In Fig. 11 we show the comparison for the LDF between our exact MC simulations and the approximate solution of Montero and Santos for HD at $\lambda = 1.2$ and $\epsilon = 0.9, 1.0, 1.118$. From

the comparison, we see that the solution of Montero & Santos, which is exact for $\epsilon \leq \epsilon_{nn-HD}$, is a rather good approximation for $\epsilon_{nn-HD} < \epsilon < \epsilon_{sf}$, but it becomes a poor approximation for $\epsilon \geq \epsilon_{sf}$. The breakdown of their solution at $\epsilon > 1$ manifests itself through an LDF that does not follow the exact result from the MC simulation. This confirms the findings of Kofke and Post [30].

It is interesting to note that Hu and Charbonneau [41] have shown how the envelope of the LDF $g(x) - 1$ has an exponential decay at large distances.

3.3 Square-wells (SW) and square-shoulders (SS)

For SW/SS, we explored the following two limiting nearest neighbor cases considered in Table 1, namely:

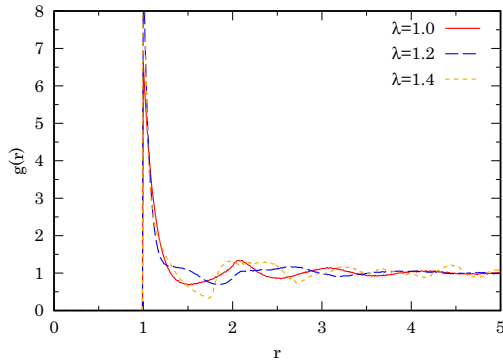


Fig. 10 RDF for $N = 100$ HD of radius $r_0 = 1$ with $\epsilon = \sqrt{3}/2$ and $\lambda = 1.0, 1.2, 1.4$. The contact value for the $\lambda = 1.2, 1.4$ cases is not shown. To be compared with Fig. 10 of Ref. [23]

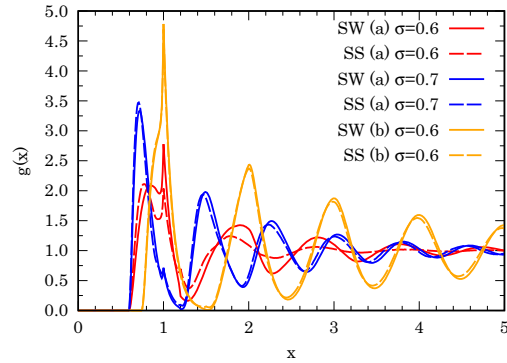


Fig. 12 LDF for $N = 100$ SW/SS cases **a** with $\sigma = 6/10, 7/10$ and **b** with $\sigma = 6/10$

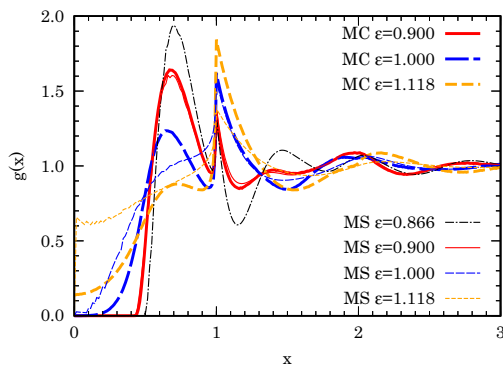


Fig. 11 LDF for $N = 100$ HD of radius $r_0 = 1$ with $\lambda = 1.2$ and $\epsilon = 0.9, 1.0, 1.118$. Comparison between our exact MC simulation (thick lines) and the theoretical approximate solution of Montero and Santos (MS) of Refs. [22, 23] (thin lines). For the MS data, we also show the exact result at $\epsilon = \sqrt{3}/2$ already published in Fig. 5(a) of Ref. [23]. The remaining theoretical MS data were shared privately by A. Montero and was not published before

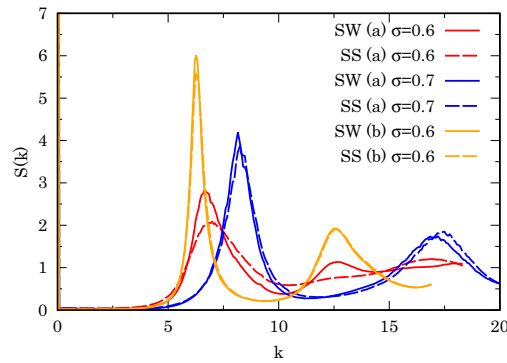


Fig. 13 LSF for $N = 100$ SW/SS cases **a** with $\sigma = 6/10, 7/10$ and **b** with $\sigma = 6/10$. We used $2n_{\max} + 1$ wave numbers with $n_{\max} = 270$

(a) $\epsilon = 4/5$, $r_0 = 6/5$ and (b) $\epsilon = \sqrt{7}/4$, $r_0 = 3/2$, with $|\beta\varphi_0| = 1$, and a surface density $\sigma = 6/10, 7/10$. Our results for the LDF, LSF, and RDF are shown in Figs. 12, 13, and 14, respectively. In Fig. 3, we show a snapshot of the simulation box for SW case (a) with $\sigma = 7/10$.

Our results show how the two cases SW and SS have very similar structures in the confined geometry under the nearest neighbor condition near close packing. The difference in structure between the two cases can be better seen at the level of the RDF where the SW produce a negative jump at $r = r_0$; whereas, the SS produce a positive jump as expected.

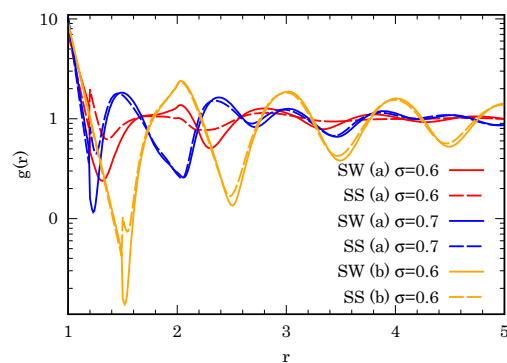


Fig. 14 RDF for $N = 100$ SW/SS cases **a** with $\sigma = 6/10, 7/10$ and **b** with $\sigma = 6/10$. Clearly $g(r) = 0$ for $r < 1$. Note the logarithmic scale on the ordinates

It would be an interesting project to explore how the *sticky limit* is approached in this constrained geometry [27–29, 42–46].

4 Conclusions

In this work, we performed Monte Carlo computer experiments to extract meta data for the thermodynamic and structural properties of hard-, square-well, and square-shoulder disks in narrow channels. We worked in the canonical ensemble. Our data are subject only to the statistical (we never used more than 10^9 single particle moves) and finite size errors (we used always 100 particles).

The novelty respect to previous studies relies in the use of the canonical ensemble instead of the isothermal isobaric one and in the study of both the radial and the linear distribution functions and of both the longitudinal and transverse pressures.

We compare our exact results for hard-disks with the semi-analytic ones of Montero and Santos [22, 23] which are also exact in the nearest neighbor regime. We further compare our results with the results of the same authors but when the nearest neighbor condition is not met, making their solution just an approximation. In particular, we see how such theoretical solution ceases to be a good approximation as soon as the single file condition is violated.

Regarding the comparison with the works of Montero and Santos, it is important to point out that the “exact” approach of those authors is based on a mapping to a pure 1D system, while our simulations deal with a true (confined) 2D system. Thus, our results reinforce the exact character of their method.

We are aware that Montero and Santos are currently working at extending their theoretical framework to include the description of particles with a potential tail which would make possible the comparison with our Monte Carlo simulations of the square-Well and square-shoulder particles.

Acknowledgements. I am grateful to Ana M. Montero and Andrés Santos for proposing the project, stimulating its publication, and for the very many fruitful discussions and profound insights. I am grateful to Ana M. Montero for providing me with her results used in Figs. 1, 4, 8, 9, 11 some of which had not been published before.

Data availability This manuscript has no associated data or the data will not be deposited. [Authors’ comment: The data that support the findings of this study are available from the corresponding author upon reasonable request.]

Declarations

Conflict of interest The author has no conflicts to disclose.

Appendix A: On the longitudinal pressure of HD from the LDF

Using the notation of Refs. [22, 23], we have for the Equation Of State (EOS)

$$Z_L = \frac{\beta p}{\lambda} = 1 + A^2 \sum_{i,j} \phi_i \phi_j a_{ij} e^{-\beta p a_{ij}}, \quad (A1)$$

where A^2 and ϕ_i are the solutions to

$$\sum_j e^{-\beta p a_{ij}} \phi_j = \frac{\beta p}{A^2} \phi_i. \quad (A2)$$

The LDF in the range $a(\epsilon) < x < 2a(\epsilon)$ is

$$g(x) = \frac{A^2}{\lambda} \sum_{i,j} \phi_i \phi_j a_{ij} e^{-\beta p x} \Theta(x - a_{ij}). \quad (A3)$$

Our aim is to express the EOS in terms of the integrals

$$I_n = \int_{a(\epsilon)}^1 dx x^n g(x), \quad n = 0, 1 \quad (A4)$$

Inserting Eq. (A3) into Eq. (A4)

$$I_0 = \frac{A^2}{\beta p \lambda} \sum_{i,j} \phi_i \phi_j (e^{-\beta p a_{ij}} - e^{-\beta p}), \quad (A5a)$$

$$I_1 = \frac{A^2}{(\beta p)^2 \lambda} \sum_{i,j} \phi_i \phi_j [e^{-\beta p a_{ij}} (1 + \beta p a_{ij}) - e^{-\beta p} (1 + \beta p)]. \quad (A5b)$$

From Eq. (A2), we have $\sum_{i,j} \phi_i \phi_j e^{-\beta p a_{ij}} = \beta p / A^2$. Therefore,

$$\lambda I_0 = 1 - \frac{A^2}{\beta p} e^{-\beta p} \sum_{i,j} \phi_i \phi_j, \quad (A6a)$$

$$\beta p \lambda I_1 = 1 + A^2 \left[\sum_{i,j} \phi_i \phi_j a_{ij} e^{-\beta p a_{ij}} - e^{-\beta p} \left(1 + \frac{1}{\beta p} \right) \sum_{i,j} \phi_i \phi_j \right]. \quad (A6b)$$

Comparison with Eq. (A1) yields

$$\beta p \lambda I_1 = Z_L - (1 + \beta p)(1 - \lambda I_0). \quad (A7)$$

This is a linear equation in Z_L which is solved by Eq. (2.13a) in the main text. From which immediately follows that for the pure 1D (Hard Rods) case, we find $Z_L = 1/(1 - \lambda)$, since $\epsilon \rightarrow 0$ and $a(\epsilon) \rightarrow 1$ so that $I_n = 0$, as it should be [16].

Note also that from Appendix C of Ref. [23] follows that in the $p \rightarrow \infty$ limit or equivalently in the $\lambda \rightarrow \lambda_{cp}$ limit one finds $\lim_{\lambda \rightarrow \lambda_{cp}} \lambda I_0 = \lim_{\lambda \rightarrow \lambda_{cp}} \lambda^2 I_1 = 1$. In the continuum limit, one has from Eq. (A6a)

$$\lambda I_0 = 1 - \frac{e^{-\beta p}}{\ell} J^2, \quad (A8a)$$

$$J = \int_{-\epsilon/2}^{\epsilon/2} \phi(y) dy. \quad (A8b)$$

In the high-pressure regime

$$\phi(y) \rightarrow \frac{1}{\sqrt{N}}[\phi_+(y) + \phi_-(y)], \tag{A9a}$$

$$\phi_{\pm}(y) = e^{-a(y \pm \epsilon/2)\beta p}, \tag{A9b}$$

$$N \rightarrow \frac{a(\epsilon)}{\epsilon\beta p} e^{-2a(\epsilon)\beta p}, \tag{A9c}$$

$$\ell \rightarrow \frac{a(\epsilon)}{2\epsilon\beta p} e^{-a(\epsilon)\beta p}. \tag{A9d}$$

Thus,

$$J = \frac{2}{\sqrt{N}} \int_{-\epsilon/2}^{\epsilon/2} \phi_+(y) dy. \tag{A10}$$

By expanding $a(y + \epsilon/2)$ around $y = \epsilon/2$

$$a(y + \epsilon/2) \rightarrow a(\epsilon) + \frac{\epsilon}{a(\epsilon)}(\epsilon/2 - y) + \dots \tag{A11}$$

Therefore,

$$\begin{aligned} J &\rightarrow \frac{2}{\sqrt{N}} e^{-a(\epsilon)\beta p} \int_{-\epsilon/2}^{\epsilon/2} e^{-\frac{\epsilon\beta p}{a(\epsilon)}(\epsilon/2 - y)} dy \\ &\rightarrow \frac{2}{\sqrt{N}} e^{-a(\epsilon)\beta p} \frac{a(\epsilon)}{\epsilon\beta p} = 2\sqrt{\frac{a(\epsilon)}{\epsilon\beta p}}. \end{aligned} \tag{A12}$$

Consequently

$$\lambda M_0 \rightarrow 1 - 8e^{-\beta p[1 - a(\epsilon)]}. \tag{A13}$$

Consistency between this result and Eq. (2.15) gives Eqs. (2.14a)–(2.14b) in the main text.

Appendix B: RDF of the ideal gas in a narrow channel

We arrive at the analytically exact Eq. (3.1) for the RDF of the ideal gas confined in the narrow channel with the following steps

$$\begin{aligned} g_{id}(r) &= \frac{\lambda}{2N} \int_0^L dx_1 \int_0^L dx_2 \int_{-\epsilon/2}^{\epsilon/2} dy_1 \frac{1}{\epsilon} \int_{-\epsilon/2}^{\epsilon/2} dy_2 \frac{1}{\epsilon} \\ &\quad \times \delta(r - \sqrt{(x_2 - x_1)^2 + (y_2 - y_1)^2}). \end{aligned} \tag{B1}$$

Since the integrand depends only on $x = |x_2 - x_1|$, we have $\int_0^L dx_1 \int_0^L dx_2 \dots = 2 \int_0^L dx (L - x) \dots$. Moreover,

$$\delta(r - \sqrt{x^2 + s^2}) = \frac{r}{x} \delta(x - \sqrt{r^2 - s^2}). \tag{B2}$$

Therefore,

$$\begin{aligned} g_{id}(r) &= \frac{\lambda}{N\epsilon^2} r \int_{-\epsilon/2}^{\epsilon/2} dy_1 \int_{-\epsilon/2}^{\epsilon/2} dy_2 \left(\frac{L}{\sqrt{r^2 - (y_2 - y_1)^2}} - 1 \right) \\ &= \frac{2}{\epsilon^2} r \int_0^{\min(\epsilon, r)} ds (\epsilon - s) \left(\frac{1}{\sqrt{r^2 - s^2}} - \frac{1}{L} \right) \\ &\approx \frac{2}{\epsilon^2} r \int_0^{\min(\epsilon, r)} ds \frac{\epsilon - s}{\sqrt{r^2 - s^2}}. \end{aligned} \tag{B3}$$

Where in the first step, we have assumed that $\sqrt{r^2 - (y_2 - y_1)^2} < L$ and in the third step we have taken the limit $L \rightarrow \infty$. In the limit $r \gg 1$, $\sqrt{r^2 - s^2} \approx r$, so that $g_{id}(r) \approx 1$ as expected.

The integral in Eq. (B3) can be analytically performed and the result is given by Eq. (3.1) in the main text.

References

- R. Fantoni, A. Santos, Multicomponent fluid of nonadditive hard spheres near a wall. *Phys. Rev. E* **87**, 042102 (2013). <https://doi.org/10.1103/PhysRevE.87.042102>
- H. Kyakuno, K. Matsuda, H. Yahiro, Y. Inami, T. Fukuoka, Y. Miyata, K. Yanagi, Y. Maniwa, H. Kataura, T. Saito, M. Yumura, S. Iijima, Confined water inside single-walled carbon nanotubes: global phase diagram and effect of finite length. *J. Chem. Phys.* **134**, 244501 (2011)
- M. Majumder, N. Chopra, B.J. Hinds, Mass transport through carbon nanotube membranes in three different regimes: ionic diffusion and gas and liquid flow. *ACS Nano* **5**, 3867 (2011)
- D. Boda, W. Nonner, D. Henderson, B. Eisenberg, D. Gillespie, Volume exclusion in calcium selective channels. *Biophys. J.* **94**, 3486 (2008)
- R. Fantoni, Exact results for one dimensional fluids through functional integration. *J. Stat. Phys.* **163**, 1247 (2016). <https://doi.org/10.1007/s10955-016-1510-3>
- R. Fantoni, One-dimensional fluids with positive potentials. *J. Stat. Phys.* **166**, 1334 (2017). <https://doi.org/10.1007/s10955-016-1707-5>
- R. Fantoni, How should we choose the boundary conditions in a simulation which could detect anyons in one and two dimensions? *J. Low Temp. Phys.* **202**, 247 (2021). <https://doi.org/10.1007/s10909-020-02532-0>
- A. Santos, R. Fantoni, A. Giacometti, Penetrable square-well fluids: exact results in one dimension. *Phys. Rev. E* **77**, 051206 (2008). <https://doi.org/10.1103/PhysRevE.77.051206>
- R. Fantoni, A. Giacometti, A. Malijevský, A. Santos, A numerical test of a high-penetrability approximation for the one-dimensional penetrable-square-well model. *J. Chem. Phys.* **133**, 024101 (2010). <https://doi.org/10.1063/1.3455330>
- R. Fantoni, Non existence of a phase transition for the penetrable square well model in one dimension. *J. Stat. Mech.* (2010). <https://doi.org/10.1088/1742-5468/2010/07/P07030>
- M.A.G. Maestre, R. Fantoni, A. Giacometti, A. Santos, Janus fluid with fixed patch orientations: theory and simulations. *J. Chem. Phys.* **138**, 094904 (2013). <https://doi.org/10.1063/1.4793626>
- R. Fantoni, A. Giacometti, M.A.G. Maestre, A. Santos, Phase diagrams of janus fluids with up-down constrained orientations. *J. Chem. Phys.* **139**, 174902 (2013). <https://doi.org/10.1063/1.4827861>
- R. Fantoni, M.A.G. Maestre, A. Santos, Finite-size effects and thermodynamic limit in one-dimensional janus fluids. *J. Stat. Mech.* (2021). <https://doi.org/10.1088/1742-5468/ac2897>
- R. Fantoni, A. Santos, One-dimensional fluids with second nearest-neighbor interactions. *J. Stat.*

- Phys. **169**, 1171 (2017). <https://doi.org/10.1007/s10955-017-1908-6>
15. A. Santos, *A Concise Course on the Theory of Classical Liquids. Basics and Selected Topics*, Lecture Notes in Physics, Vol. 923 (Springer, New York, 2016)
 16. L. Tonks, The complete equation of state of one, two and three-dimensional gases of hard elastic spheres. *Phys. Rev.* **50**, 955 (1936)
 17. Z.W. Salsburg, R.W. Zwanzig, J.G. Kirkwood, Molecular distribution functions in a one-dimensional fluid. *J. Chem. Phys.* **21** (1953)
 18. R. Fantoni, B. Jancovici, G. Téllez, Pressures for a one-component plasma on a pseudosphere. *J. Stat. Phys.* **112**, 27 (2003). <https://doi.org/10.1023/A:1023671419021>
 19. R. Fantoni, G. Téllez, Two dimensional one-component plasma on a flamm's paraboloid. *J. Stat. Phys.* **133**, 449 (2008). <https://doi.org/10.1007/s10955-008-9616-x>
 20. R. Fantoni, Two component plasma in a flamm's paraboloid. *J. Stat. Mech.* (2012). <https://doi.org/10.1088/1742-5468/2012/04/P04015>
 21. R. Fantoni, Jellium at finite temperature. *Mol. Phys.* **120**, 4 (2021). <https://doi.org/10.1080/00268976.2021.1996648>
 22. A.M. Montero, A. Santos, Equation of state of hard-disk fluids under single-file confinement. *J. Chem. Phys.* **158**, 154501 (2023)
 23. A.M. Montero, A. Santos, Structural properties of hard-disk fluids under single-file confinement. *J. Chem. Phys.* **159**, 034503 (2023)
 24. A. Poncet, A. Grabsch, P. Illien, O. Bénichou, Generalized correlation profiles in single-file systems. *Phys. Rev. Lett.* **127**, 220601 (2021)
 25. A. Horner, P. Pohl, Single-file transport of water through membrane channels. *Faraday Discuss.* **209**, 9 (2018)
 26. R. Fantoni, A. Santos, Nonadditive hard-sphere fluid mixtures. A simple analytical theory. *Phys. Rev. E* **84**, 041201 (2011). <https://doi.org/10.1103/PhysRevE.84.041201>
 27. R. Fantoni, D. Gazzillo, A. Giacometti, Stability boundaries, percolation threshold, and two phase coexistence for polydisperse fluids of adhesive colloidal particles. *J. Chem. Phys.* **122**, 034901 (2005). <https://doi.org/10.1063/1.1831275>
 28. D. Gazzillo, R. Fantoni, A. Giacometti, Phase behavior of polydisperse sticky hard spheres: analytical solutions and perturbation theory. *Mol. Phys.* **104**, 3451 (2006). <https://doi.org/10.1080/00268970601050892>
 29. R. Fantoni, D. Gazzillo, A. Giacometti, P. Sollich, Phase behavior of weakly polydisperse sticky hard spheres: perturbation theory for the percus-yevick solution. *J. Chem. Phys.* **125**, 164504 (2006). <https://doi.org/10.1063/1.2358136>
 30. D.A. Kofke, A.J. Post, Hard particles in narrow pores. Transfer-matrix solution and the periodic narrow box. *J. Chem. Phys.* **98**, 4853 (1993)
 31. K.K. Mon, Analytical evaluation of third and fourth virial coefficients for hard disk fluids in narrow channels and equation of state. *Phys. A* **556**, 124833 (2020)
 32. S. Varga, G. Balló, P. Gurin, Structural properties of hard disks in a narrow tube. *J. Stat. Mech.* (2011)
 33. A. Huerta, T. Bryk, V.M. Pergamenschik, A. Trokhymchuk, Collective dynamics in quasi-one-dimensional hard disk system. *Front. Phys.* **9**, 636052 (2021)
 34. M.H. Kalos, P.A. Whitlock, *Monte Carlo Methods* (Wiley, New York, 1986)
 35. M.P. Allen, D.J. Tildesley, *Computer Simulation of Liquids* (Oxford University Press, Oxford, 1987). (Section 6.2)
 36. D. Frenkel, B. Smit, *Understanding Molecular Simulation* (Academic Press, San Diego, 1996)
 37. J.-P. Hansen, I.R. McDonald, *Theory of Simple Liquids*, 2nd edn. (Academic Press, San Diego, 1986). (Section 2.5)
 38. A.M. Montero, private communication (2023)
 39. V.M. Pergamenschik, Analytical canonical partition function of a quasi-one-dimensional system of hard disks. *J. Chem. Phys.* **153**, 144111 (2020)
 40. A. Santos, private communication (2023)
 41. Y. Hu, P. Charbonneau, Kosterlitz-thouless-type caging-uncaging transition in a quasi-one-dimensional hard disk system. *Phys. Rev. Res.* **3**, 038001 (2021)
 42. R. Fantoni, D. Gazzillo, A. Giacometti, The thermodynamic instabilities of a binary mixture of sticky hard spheres. *Phys. Rev. E* **72**, 011503 (2005). <https://doi.org/10.1103/PhysRevE.72.011503>
 43. D. Gazzillo, A. Giacometti, R. Fantoni, P. Sollich, Multicomponent adhesive hard sphere models and short-ranged attractive interactions in colloidal or micellar solutions. *Phys. Rev. E* **74**, 051407 (2006). <https://doi.org/10.1103/PhysRevE.74.051407>
 44. R. Fantoni, D. Gazzillo, A. Giacometti, M.A. Miller, G. Pastore, Patchy sticky hard spheres: analytical study and Monte Carlo simulations. *J. Chem. Phys.* **127**, 234507 (2007). <https://doi.org/10.1063/1.2805066>
 45. R. Fantoni, Andersen-weeks-chandler perturbation theory and one-component sticky-hard-spheres. *J. Stat. Phys.* **168**, 652 (2017). <https://doi.org/10.1007/s10955-017-1810-2>
 46. R. Fantoni, Effect of quantum dispersion on the radial distribution function of a one-component sticky-hard-sphere fluid. *J. Stat. Mech.* (2018). <https://doi.org/10.1088/1742-5468/aab690>
- Springer Nature or its licensor (e.g. a society or other partner) holds exclusive rights to this article under a publishing agreement with the author(s) or other rightsholder(s); author self-archiving of the accepted manuscript version of this article is solely governed by the terms of such publishing agreement and applicable law.

Chapter 78

Scaled Affine Quantization of φ_3^{12} is Nontrivial

Fantoni R., J. Stat. Phys. submitted (2023)

Title: “Scaled Affine Quantization of φ_3^{12} is Nontrivial”

Abstract: We prove through Monte Carlo analysis that the covariant euclidean scalar field theory, φ_n^r , where r denotes the power of the interaction term and $n = s + 1$ where s is the spatial dimension and 1 adds imaginary time, such that $r = 12, n = 3$ can be acceptably quantized using scaled affine quantization and the resulting theory is nontrivial, unlike what happens using canonical quantization.

Chapter 79

Glossary

1. *fluid*: in statistical physics a fluid is a system of particles interacting through a particular potential energy.
2. *mixture*: In chemistry, a mixture is a material system made up by two or more different substances which are mixed but are not combined chemically. Mixture refers to the physical combination of two or more substances the identities of which are retained and are mixed in the form of alloys, solutions, suspensions, and colloids.
3. *polydispersity*: in physical and organic chemistry, the dispersity is a measure of the heterogeneity of sizes of molecules or particles in a mixture. A collection of objects is called monodisperse if the objects have the same size, shape, or mass. A sample of objects that have an inconsistent size, shape and mass distribution is called polydisperse. The objects can be in any form of chemical dispersion, such as particles in a colloid, droplets in a cloud, crystals in a rock, or polymer molecules in a solvent.
4. *plasma*: a plasma is a classical fluid of charged particles. A one component plasma is made of one species of charges moving in a uniform neutralizing background.
5. *jellium fluid*: a quantum one component plasma.
6. *sticky hard spheres fluid*: a fluid made of hard spheres which have surface adhesion as in the model of R. Baxter.
7. *penetrable square well fluid*: a fluid made of square well particles with a certain degree of penetrability.
8. *non additive hard spheres fluid*: a binary mixture of hard spheres where the diameter of closest approach between two different species is not equal to the average of the diameters of the two particles species. The Widom-Rowlinson fluid is a special case.
9. *Janus fluid*: a fluid made of Janus particles, hard spheres with the hemispheres of different functionalities.
10. *polymer*: a polymer is a large molecule (macromolecule) composed of repeating structural units. These sub-units are typically connected by covalent chemical bonds. Although the term polymer is sometimes taken to refer to plastics, it actually encompasses a large class of compounds comprising both natural and synthetic materials with a wide variety of properties.

11. *patch*: a portion of the surface of a spherical particle.
 12. *cluster*: a stable structure that may occur in particular fluids made of an ensemble of particles.
 13. *percolation*: a transition that may occur in particular fluids where there is the formation of a thermodynamically relevant number of clusters of particles spanning the whole volume of the fluid.
 14. *binodal or coexistence curve*: the curve in the phase diagram delimiting the coexistence region of two phases of matter (as the vapor and the liquid one).
 15. *Monte Carlo simulation*: Monte Carlo methods (or Monte Carlo experiments) are a class of computational algorithms that rely on repeated random sampling to compute their results. Monte Carlo methods are often used in computer simulations of physical and mathematical systems. These methods are most suited to calculation by a computer and tend to be used when it is infeasible to compute an exact result with a deterministic algorithm. This method is also used to complement theoretical derivations.
 16. *integral equation theory*: integral equations are commonly found in the study of the statistical theory of fluids as approximate theories used to determine the structure and the thermodynamics of the fluid. Most known integral equations are the Percus-Yevick, the hypernetted chain, and the mean spherical approximation. It is usual practice to compare the approximate results stemming from an integral equation theory with the exact Monte Carlo results.
 17. *correlation function*: A correlation function is the correlation between random variables at two different points in space or time, usually as a function of the spatial or temporal distance between the points.
 18. *radial distribution function or pair correlation function*: the two body correlation function. Measures the probability that if one sits on a particle has to find another particle at a distance r .
 19. *structure factor*: the Fourier transform of the two body correlation function. This quantity can be measured through experiments of diffraction on the fluid sample.
 20. *density*: the density of a fluid is the number of particles divided by the volume occupied by the fluid.
 21. *Chemical potential*: In thermodynamics, Chemical potential, symbolized by μ , is a measure of the potential that a substance has to produce in order to alter a system. In broadest terms, it is an analogue to electric potential or gravitational potential, utilizing the same idea of force fields as being the cause of things moving, be they charges, masses, or, in this case, chemicals. Chemical potential was first described by the American engineer, chemist and mathematical physicist Josiah Willard Gibbs. He defined it as follows: "if to any homogeneous mass in a state of hydrostatic stress we suppose an infinitesimal quantity of any substance to be added, the mass remaining homogeneous and its entropy and volume remaining unchanged, the increase of the
-

energy of the mass divided by the quantity of the substance added is the potential for that substance in the mass considered.”

22. *pressure*: the pressure is the force per unit area applied in a direction perpendicular to the surface of an object.
 23. *isothermal compressibility*: in thermodynamics and fluid mechanics, compressibility is a measure of the relative volume change of a fluid or solid as a response to a pressure (or mean stress) change. The above statement is incomplete, because for any object or system the magnitude of the compressibility depends strongly on whether the process is adiabatic or isothermal.
-